SPRINGER NATURE
Reference

George Z. Voyiadjis
Editor

Handbook of Damage Mechanics

Nano to Macro Scale for Materials and Structures

Second Edition

Springer

Handbook of Damage Mechanics

George Z. Voyiadjis
Editor

Handbook of Damage Mechanics

Nano to Macro Scale for Materials and Structures

Second Edition

With 582 Figures and 89 Tables

Springer

Editor
George Z. Voyiadjis
Department of Civil and Environmental Engineering
Louisiana State University
Baton Rouge, LA, USA

ISBN 978-3-030-60241-3 ISBN 978-3-030-60242-0 (eBook)
ISBN 978-3-030-60243-7 (print and electronic bundle)
https://doi.org/10.1007/978-3-030-60242-0

1st edition: © Springer Science+Business Media New York 2014
2nd edition: © Springer Nature Switzerland AG 2022
This work is subject to copyright. All rights are reserved by the Publisher, whether the whole or part of the material is concerned, specifically the rights of translation, reprinting, reuse of illustrations, recitation, broadcasting, reproduction on microfilms or in any other physical way, and transmission or information storage and retrieval, electronic adaptation, computer software, or by similar or dissimilar methodology now known or hereafter developed.
The use of general descriptive names, registered names, trademarks, service marks, etc. in this publication does not imply, even in the absence of a specific statement, that such names are exempt from the relevant protective laws and regulations and therefore free for general use.
The publisher, the authors, and the editors are safe to assume that the advice and information in this book are believed to be true and accurate at the date of publication. Neither the publisher nor the authors or the editors give a warranty, expressed or implied, with respect to the material contained herein or for any errors or omissions that may have been made. The publisher remains neutral with regard to jurisdictional claims in published maps and institutional affiliations.

This Springer imprint is published by the registered company Springer Nature Switzerland AG.
The registered company address is: Gewerbestrasse 11, 6330 Cham, Switzerland.

Preface to the Second Edition

In the 7 years since the first edition of the *Handbook of Damage Mechanics* appeared, many advances have been made in this field. A need arises now for a second edition of the Handbook. Damage characterization and mechanics is a broad and highly interdisciplinary field that has been continuously evolving in the last half century.

It is hoped that a wide spectrum of topics of damage mechanics can be covered in a single book like this handbook in order to reach a wide audience of readers. The handbook is directed toward both students and active researchers in academia and industry. This was a monumental challenge for the authors involved to overcome. A very select group of internationally recognized authors in damage mechanics from both academia and industry coming from three continents to write 47 chapters on this topic and its various branches. Tremendous developments have taken place within the research topic of continuum damage mechanics in the past 70 years. There are currently one dedicated journal to this topic, a handful of books, and thousands of research papers. In the framework of continuum damage mechanics, the collection of micro-defects (like micro-cracks, micro-voids, etc.) is treated as a continuous region within which the laws of continuum mechanics are assumed to apply. This is in contrast to what is done in fracture mechanics where individual defects are treated separately and discontinuities are allowed.

Our goal was to assimilate the existing damage mechanics knowledge of academic interest into one consistent, self-contained volume accessible to engineers in practice, researchers in this field, and interested people in academia. Another objective was to motivate nonspecialists with a strong desire to learn damage mechanics. Such a task was beyond the scope of each of the collected research papers, which by nature focus on narrow topics using very specialized terminology. Our intent was to provide a detailed presentation of those areas of damage mechanics which we have found to be of great practical utility in our industrial experience, while maintaining a sufficiently formal approach both to be suitable as a trustworthy reference for those whose primary interest is further research and to provide a solid foundation for students and others first learning the subject. Each chapter was written to provide a self-contained treatment of one major topic. Collectively, however, the chapters have been designed and carefully integrated to be entirely complementary with respect to definitions, terminology, and notation.

Furthermore, there is essentially no duplication of material across chapters. The *Handbook of Damage Mechanics* comprises 8 distinct parts including 47 chapters covering the basics of damage mechanics as well as recent research.

The topics covered include the fundamentals of continuum damage mechanics, composite damage mechanics, rock damage mechanics, micromechanical damage and healing for concrete, damage and failure of ductile metals, damage in brittle materials, damage for disordered materials, and damage in crystalline metals and alloys. One of the major features of the handbook is coverage of the latest research in the new topic of healing mechanics of materials. The second edition includes four chapters on this emerging subject. The fundamentals of continuum damage mechanics are presented in nine selected chapters in a part of their own.

The handbook integrated knowledge from the theoretical, numerical, and experimental areas of damage mechanics. This book mainly targets graduate students of damage mechanics, researchers in academia and industry who are active or intend to become active in this field, and practicing engineers and scientists who work in this topic and would like to solve problems utilizing the tools offered by damage mechanics. This handbook should serve as an excellent text for a series of graduate courses in mechanical engineering, civil engineering, materials science, engineering mechanics, aerospace engineering, applied mathematics, applied physics, and applied chemistry. The second edition of the handbook is basically intended as a textbook for university courses as well as a reference for researchers in this field. It will serve as a timely addition to the literature on damage mechanics and as an invaluable resource to members of the international scientific and industrial communities.

We hope that the reader will find this handbook a useful resource as he/she progresses in their study and research in damage mechanics. We would also like to wish the readers much success and welcome their suggestions for future improvement of the handbook. Each of the individual parts of this handbook could be considered a compact, self-contained mini-book right under its own title. However, these topics are presented in relation to the basic principles of damage mechanics. What is finally presented in the handbook is the work contributed by celebrated international experts for their best knowledge and practices on specific and related topics in damage characterization and mechanics.

The editor would like to thank all the contributors who wrote chapters for this handbook. Finally, the editor would like to acknowledge the help and support of his family members and the editors at Springer who made this handbook possible.

Baton Rouge, Louisiana, USA George Z. Voyiadjis
February 2022

Preface to the First Edition

Damage characterization and mechanics is a broad and highly interdisciplinary field that has been continuously evolving in the last half century. This handbook is an attempt to cover the wide spectrum of topics of damage mechanics in a single book in order to reach a wide audience of readers ranging from students to active researchers in both academia and industry. This was a monumental challenge for the authors involved to overcome. An enormous group of internationally recognized authors from both academia and industry assembled from three continents to write 47 chapters on this topic and its various branches.

Tremendous developments have taken place within the research topic of continuum damage mechanics in the past 50 years. There are currently one dedicated journal to this topic as well as numerous books and thousands of research papers. In the framework of continuum damage mechanics, the collection of micro-defects (like micro-cracks, micro-voids, etc.) are treated as a continuous region within which the laws of continuum mechanics are assumed to apply. This is in contrast to what is done in fracture mechanics where individual defects are treated separately and discontinuities are allowed.

Our goal was to assimilate the existing damage mechanics knowledge of academic interest into one consistent, self-contained volume accessible to engineers in practice, researchers in this field, and interested people in academia and to motivate nonspecialists with a strong desire to learn damage mechanics. Such at ask was beyond the scope of each of the collected research papers, which by nature focus on narrow topics using very specialized terminology. Our intent was to provide a detailed presentation of those areas of damage mechanics which we have found to be of great practical utility in our industrial experience, while maintaining a sufficiently formal approach both to be suitable as a trustworthy reference for those whose primary interest is further research and to provide a solid foundation for students and others first learning the subject.

Each chapter was written to provide a self-contained treatment of one major topic. Collectively, however, the chapters have been designed and carefully integrated to be entirely complementary with respect to definitions, terminology, and notation. Furthermore, there is essentially no duplication of material across chapters.

The *Handbook of Damage Mechanics* comprises 12 distinct sections including 47 chapters covering the basics of damage mechanics as well as recent research. The

topics covered include the fundamentals of continuum damage mechanics, damage in disordered media, damage in crystalline metals and alloys, damage in structures, damage in electronic packaging, damage in metal forming, micromechanics of damage in composite materials, coupled elastoplastic damage and healing mechanics in granular materials, damage under dynamic loading, experimental characterization of damage, micromechanics of damage in laminated composites, nuclear damage characterization, and recent trends in damage and healing mechanics.

One of the major features of the *Handbook of Damage Mechanics* is coverage of the latest research in the new topic of healing mechanics of materials. The handbook includes four chapters on this emerging subject. In addition, it includes three chapters on the experimental characterization of damage in materials. The fundamentals of continuum damage mechanics are presented in four chapters of the very first section.

The handbook integrated knowledge from the theoretical, numerical, and experimental areas of damage mechanics. This book mainly targets graduate students of damage mechanics, researchers in academia and industry who are active or intend to become active in this field, and practicing engineers and scientists who work in this topic and would like to solve problems utilizing the tools offered by damage mechanics. This handbook should serve as an excellent text for a series of graduate courses in mechanical engineering, civil engineering, materials science, engineering mechanics, aerospace engineering, applied mathematics, applied physics, and applied chemistry.

The handbook is basically intended as a textbook for university courses as well as a reference for researchers in this field. It will serve as a timely addition to the literature on damage mechanics and as an invaluable resource to members of the international scientific and industrial communities.

We hope that the reader will find this handbook a useful resource as he/she progresses in their study and research in damage mechanics. We would also like to wish the readers much success and welcome their suggestions for future improvement of the handbook.

Each of the individual sections of this handbook could be considered a compact, self-contained mini-book right under its own title. However, these topics are presented in relation to the basic principles of damage mechanics.

What is finally presented in the handbook is the work contributed by celebrated international experts for their best knowledge and practices on specific and related topics in damage characterization and mechanics.

The editor would like to thank all the contributors who wrote chapters for this handbook. Finally, the editor would like to acknowledge the help and support of his family members and the editors at Springer who made this handbook possible.

Baton Rouge, LA, USA George Z. Voyiadjis
March 2014

Contents

Volume 1

Part I Fundamentals in Damage 1

1 The True Nature of the Decomposition of the Damage Variable 3
George Z. Voyiadjis and Peter I. Kattan

2 Damageability and Integrity of Materials: New Concepts of the Damage and Healing Fields 23
George Z. Voyiadjis, Peter I. Kattan, and Juyoung Jeong

3 Damageability and Integrity of Materials: Unrecoverable Damage and Generalized Healing Model 61
George Z. Voyiadjis, Peter I. Kattan, and Juyoung Jeong

4 Partial Damage Mechanics: Introduction 83
George Z. Voyiadjis and Peter I. Kattan

5 Mechanics of Self-Regenerating Materials 101
George Z. Voyiadjis and Peter I. Kattan

6 Damage and Nonlinear Super Healing with Application to the Design of New Strengthening Theory 119
George Z. Voyiadjis, Chahmi Oucif, Peter I. Kattan, and Timon Rabczuk

7 Vibration Analysis of Cracked Microbeams by Using Finite Element Method 155
Şeref Doğuşcan Akbaş, Mustafa ÖzgürYaylı, Babür Deliktaş, and Büşra Uzun

8 Size Effect on Damage Response of Triangular Flexural Test Method 167
Babür Deliktaş, Hakan Tacettin Türker, Faiz Agh Shareef, and Ferhun Cem Caner

9 **Predicting Damage Behavior of Self-Healing Sandwich Panels: Computational Modeling** 197
Murat Yazici, Harun Güçlü, and Babür Deliktaş

Part II Damage and Failure of the Ductile Metals **213**

10 **Problems of Deformation and Damage Studies of Additively Manufactured Regular Cellular Structures** 215
Paweł Płatek, Paweł Baranowski, Jacek Janiszewski, and Michał Kucewicz

11 **Thermo-mechanics of Polymers at Extreme and Failure Conditions: Influence of Strain Rate and Temperature** 249
Daniel Garcia-Gonzalez, Sara Garzon-Hernandez, Daniel Barba, and Angel Arias

12 **Failure Behavior of Aluminum Alloys Under Different Stress States** 277
M. Rodríguez-Millán, Daniel Garcia-Gonzalez, and Angel Arias

13 **Modeling of Failure Resulting from High-Velocity Ballistic Impact** 303
T. Fras

14 **Ductile Crack Growth Using Cohesive GTN Model** 333
Mamadou Méïté, Noé Brice Nkoumbou Kaptchouang, Yann Monerie, Frédéric Perales, and Pierre-Guy Vincent

15 **Auxetic Damping Systems for Blast Vulnerable Structures** 353
Hasan Al-Rifaie and Wojciech Sumelka

Part III Damage in Brittle Materials **377**

16 **Dynamic Deformation, Damage, and Fracture in Geomaterials** . . . 379
Qian-Bing Zhang, Kai Liu, Gonglinan Wu, and Jian Zhao

17 **High-Speed Real-Time X-Ray Visualization of Impact Damage Inside Geomaterials** 423
Junyu Wang, Niranjan Parab, and Wayne Chen

18 **Tensile Damage Mechanisms of Concrete Using X-Ray: In Situ Experiments and Mesoscopic Modeling** 453
Olga Stamati, Emmanuel Roubin, Edward Andò, and Yann Malecot

19 **Damage Model Strategies to Forecast Concrete Structure Behaviors Under Static and Dynamic Loadings** 489
Jacky Mazars and Stephane Grange

20 Discrete Element Approach to Model Advanced Damage in Concrete Structures Under Impact 517
Laurent Daudeville, Andria Antoniou, Philippe Marin, Pascal Forquin, and Serguei Potapov

21 Damage in Concrete Subjected to Impact Loading 551
Pascal Forquin

22 Failure Mechanisms of Ceramics Under Quasi-static and Dynamic Loads: Overview 579
Salil Bavdekar and Ghatu Subhash

23 Damage in Armor Ceramics Subjected to High-Strain-Rate Dynamic Loadings: The Spherical Expansion Shock Wave Pyrotechnic Test 609
Antonio Cosculluela and Pascal Forquin

24 Damage in Armor Ceramics Subjected to High-Strain-Rate Dynamic Loadings: The Edge-On Impact Test 639
Pascal Forquin and Antonio Cosculluela

Volume 2

Part IV Composite Damage Mechanics **663**

25 Effective Modeling of Interlaminar Damage in Multilayered Composite Structures Using Zigzag Kinematic Approximations 665
Roberta Massabò

Part V Rock Damage Mechanics **699**

26 Numerical Analysis of Damage by Phase-Field Method 701
Z. Yu, J. F. Shao, and Q. Z. Zhu

27 Micromechanics-Based Models for Induced Damage in Rock-Like Materials 725
Q. Z. Zhu, J. F. Shao, and L. Y. Zhao

28 Application of Continuum Damage Mechanics in Hydraulic Fracturing Simulations 751
Amir Shojaei and Jianfu Shao

29 Damage and Fracture in Brittle Materials with Enriched Finite Element Method: Numerical Study 769
Yue Sun, Emmanuel Roubin, Jean-Baptiste Colliat, and Jianfu Shao

30 Damage and Failure of Hard Rocks Under True Triaxial Compression 801
Rui Kong, Yaohui Gao, and Yan Zhang

31 Plastic Deformation and Damage in Rocks Under Coupled Thermo-hydromechanical Conditions: Numerical Study 819
Dashnor Hoxha and Duc Phi Do

32 Frictional Contact Between a Blunt Tool and Quasi-brittle Rock with Damage: Numerical Modeling 853
George Z. Voyiadjis and Yaneng Zhou

Part VI Micromechanical Damage and Healing for Concrete 893

33 Stochastic Micromechanics-Based Probabilistic Damage and Repair Models for Cementitious Composites 895
Q. Chen, Jiann-Wen Woody Ju, H. H. Zhu, and Z. G. Yan

34 Class of Damage-Healing Models for Cementitious Composites at Multi-scales 933
S. Zhou, Jiann-Wen Woody Ju, H. H. Zhu, and Z. G. Yan

35 Influences of Imperfect Interfaces on Effective Elastoplastic Responses of Particulate Composites 959
K. Yanase and Jiann-Wen Woody Ju

36 New Chemo-Mechanical Theory of Corrosion Damage in Concrete Under Sulfate Attack 997
Jiankang Chen and Zhuping Huang

37 Strain Energy-Based Thermo-elastoviscoplastic Two-Parameter Damage Self-Healing Formulations for Bituminous Composite Materials 1021
Seongwon Hong and Jiann-Wen Woody Ju

38 Computational Algorithms for Strain Energy-Based Thermo-elastoviscoplastic Two-Parameter Damage Self-Healing Models for Bituminous Composites 1045
Seongwon Hong and Jiann-Wen Woody Ju

Part VII Damage for Disordered Materials 1075

39 Failure Mechanics of Geomaterials 1077
Florent Prunier, François Nicot, Richard Wan, Jérôme Duriez, and Félix Darve

40 Fractals and Mechanics of Fracture 1111
Michael P. Wnuk

41 Lattice and Particle Modeling of Damage Phenomena 1143
Sohan Kale and Martin Ostoja-Starzewski

42 Toughening and Instability Phenomena in Quantized Fracture Process: Euclidean and Fractal Cracks 1181
Michael P. Wnuk

43 Two-Dimensional Discrete Damage Models: Lattice and Rational Models 1215
Antonio Rinaldi and Sreten Mastilovic

Part VIII Damage in Crystalline Metals and Alloys **1249**

44 From Single Crystal to Polycrystal Plasticity: Overview of Main Approaches 1251
Esteban P. Busso

45 Micromechanics for Heterogeneous Material Property Estimation 1277
Muneo Hori

46 Microstructural Behavior and Fracture in Crystalline Materials: Overview 1301
Pratheek Shanthraj and Mohammed A. Zikry

47 Molecular Dynamics Simulations of Plastic Damage in Metals . . . 1335
Shijing Lu, Dong Li, and Donald W. Brenner

Index 1371

About the Editor

George Z. Voyiadjis is the Boyd Professor at the Louisiana State University in the Department of Civil and Environmental Engineering. This is the highest professorial rank awarded by the Louisiana State University System. He is also the holder of the Freeport-McMoRan Endowed Chair in Engineering. He joined the Faculty of Louisiana State University in 1980. He is currently the Chair of the Department of Civil and Environmental Engineering. He holds this position since February of 2001. He currently also serves, since 2012, as the Director of the Louisiana State University Center for Geo Informatics (LSUC4G; http://c4g.lsu.edu/).

Voyiadjis is a Foreign Member of both the Academia Europaea – Physics & Engineering Sciences – and the European Academy of Sciences. He is a Foreign Member of both the Polish Academy of Sciences, Division IV (Technical Sciences), and the National Academy of Engineering of Korea. He is the recipient of the 2008 Nathan M. Newmark Medal of the American Society of Civil Engineers and the 2012 Khan International Medal for outstanding lifelong contribution to the field of plasticity. He was also the recipient of the Medal for his significant contribution to continuum damage mechanics, presented to him during the Second International Conference on Damage Mechanics (ICDM2), Troyes, France, July 2015. This is sponsored by the *International Journal of Damage Mechanics* and is held every 3 years. However, due to COVID-19 May 2022 the Fourth International Conference on Damage Mechanics (ICDM4) will be held after 4 years in Louisiana State University, Baton Rouge, Louisiana.

Voyiadjis was honored in April 2012 by the International Symposium on "Modeling Material Behavior at Multiple Scales" sponsored by Hanyang University, Seoul, South Korea, chaired by T. Park and X. Chen (with a dedicated special issue in the *Journal of Engineering Materials and Technology* of the ASME). He was also honored by an International Mini-Symposium on "Multiscale and Mechanism Oriented Models: Computations and Experiments" sponsored by the International Symposium on Plasticity and Its Current Applications, chaired by V. Tomar and X. Chen, in January 2013.

He is a Distinguished Member of the American Society of Civil Engineers; Fellow of the American Society of Mechanical Engineers, the Society of Engineering Science, the American Academy of Mechanics, and the Engineering Mechanics Institute of ASCE; and Associate Fellow of the American Institute of Aeronautics and Astronautics. He was on the Board of Governors of the Engineering Mechanics Institute of the American Society of Civil Engineers and Past President of the Board of Directors of the Society of Engineering Science. He was also the Chair of the Executive Committee of the Materials Division (MD) of the American Society of Mechanical Engineers. Dr. Voyiadjis is the Founding Chief Editor of the *Journal of Nanomechanics and Micromechanics* of the ASCE and is on the editorial board of numerous engineering journals. He was also selected by Korea Science and Engineering Foundation (KOSEF) as one of the only two world-class university foreign scholars in the area of civil and architectural engineering to work on nanofusion in civil engineering. This is a multimillion research grant.

Voyiadjis' primary research interest is in plasticity and damage mechanics of metals, metal matrix composites, polymers, and ceramics with emphasis on the theoretical modeling, numerical simulation of material behavior, and experimental correlation. Research activities of particular interest encompass macro-mechanical and micro-mechanical constitutive modeling, experimental procedures for quantification of crack densities, inelastic behavior, thermal effects, interfaces, damage, failure, fracture, impact, and numerical modeling.

Dr. Voyiadjis' research has been performed on developing numerical models that aim at simulating the

damage and dynamic failure response of advanced engineering materials and structures under high-speed impact loading conditions. This work will guide the development of design criteria and fabrication processes of high-performance materials and structures under severe loading conditions. Emphasis is placed on survivability area that aims to develop and field a contingency armor that is thin and lightweight, but with a very high level of an overpressure protection system that provides low penetration depths. The formation of cracks and voids in the adiabatic shear bands, which are the precursors to fracture, is mainly investigated.

He has 2 patents, over 364 refereed journal articles, and 22 books (12 as editor) to his credit. He has given over 420 presentations as plenary, keynote, and invited speaker as well as other talks. Over 68 graduate students (39 Ph.D.) completed their degrees under his direction. He has also supervised numerous postdoctoral associates. Voyiadjis has been extremely successful in securing more than $30 million in research funds as a principal investigator/investigator from the National Science Foundation, the Department of Defense, the Air Force Office of Scientific Research, the Louisiana Department of Transportation and Development, the Federal Highway Administration, the National Oceanic and Atmospheric Administration (NOAA), and major companies such as IBM and Martin Marietta.

He has been invited to give plenary presentations and keynote lectures in many countries around the world. He has also been invited as guest editor in numerous volumes of the *Journal of Computer Methods in Applied Mechanics and Engineering*, *International Journal of Plasticity, Journal of Engineering Mechanics of the ASCE*, and *Journal of Mechanics of Materials*. These special issues focus in the areas of damage mechanics, structures, fracture mechanics, localization, and bridging of length scales.

He has extensive international collaborations with universities in France, the Republic of Korea, and Poland.

Section Editors

J. F. Shao
University of Lille, CNRS, EC Lille, LaMcube
Lille, France

Peter I. Kattan
Independent Researcher
Petra Books
Amman, Jordan

Alexis Rusinek
Laboratory of Microstructure Studies and
Mechanics of Materials
Lorraine University
Metz Cedex, France

Jiann-Wen Woody Ju
Department of Civil and Environmental Engineering
University of California
Los Angeles, CA, USA

G. Kardomateas
School of Aerospace Engineering
Georgia Institute of Technology
Atlanta, GA, USA

Pascal Forquin
Laboratory of Soils, Solids, Structures and Risks (3SR)
Saint-Martin d'Hères, France

Contributors

Hasan Al-Rifaie Institute of Structural Analysis, Poznan University of Technology, Poznan, Poland

Edward Andò 3SR Lab, Université Grenoble Alpes, Grenoble, France

Andria Antoniou Université Grenoble Alpes, CNRS, Grenoble, France

Angel Arias Department of Continuum Mechanics and Structural Analysis, University Carlos III of Madrid, Madrid, Spain

Paweł Baranowski Faculty of Mechanical Engineering, Military University of Technology, Warsaw, Poland

Daniel Barba Escuela Técnica Superior de Ingeniería Aeronáutica y del Espacio, Universidad Politécnica de Madrid, Madrid, Spain

Salil Bavdekar Department of Mechanical and Aerospace Engineering, University of Florida, Gainesville, FL, USA

Donald W. Brenner Department of Materials Science and Engineering, North Carolina State University, Raleigh, NC, USA

Esteban P. Busso Materials and Structures Branch, ONERA, Chemin de la Huniere, Palaiseau, Cedex, France

Ferhun Cem Caner Institute of Energy Technologies, School of Industrial Engineering, Universitat Politècnica de Catalunya, Barcelona, Spain

Department of Materials Science and Metallurgical Engineering, Universitat Politècnica de Catalunya, Barcelona, Spain

Jiankang Chen School of Mechanical Engineering and Mechanics, Ningbo University, Ningbo, China

Q. Chen Key Laboratory of Advanced Civil Engineering Materials, Ministry of Education, Tongji University, Shanghai, China

School of Materials Science and Engineering, Tongji University, Shanghai, China

Wayne Chen Purdue University, West Lafayette, IN, USA

Jean-Baptiste Colliat University Lille, CNRS, Centrale Lille, LaMcube – Laboratoire de Mécanique, Multiphysique, Multi-échelle, Lille, France

Antonio Cosculluela CEA-CESTA, Le Barp, France

Félix Darve Grenoble INP, UJF, CNRS, Grenoble, France

Laurent Daudeville Université Grenoble Alpes, CNRS, Grenoble, France

Babür Deliktaş Department of Civil Engineering, Faculty of Engineering-Architecture, Uludag University, Bursa, Turkey

Duc Phi Do Univ Orléans, Univ Tours, INSA CVL, Orléans, France

Civil Engineering, University of Orléans, Laboratory of Mechanics Gabriel Lamé, Orléans, France

Şeref Doğuşcan Akbaş Department of Civil Engineering, Bursa Technical University, Bursa, Turkey

Jérôme Duriez Grenoble INP, UJF, CNRS, Grenoble, France

Pascal Forquin Laboratoire 3SR, Université Grenoble Alpes, Grenople INP, CNRS, Grenoble, France

T. Fras French-German Research Institute of Saint-Louis (ISL), Saint-Louis, France

Yaohui Gao Institute of Rock and Soil Mechanics, Chinese Academy of Sciences, Wuhan, China

Daniel Garcia-Gonzalez Department of Continuum Mechanics and Structural Analysis, University Carlos III of Madrid, Madrid, Spain

Sara Garzon-Hernandez Department of Continuum Mechanics and Structural Analysis, University Carlos III of Madrid, Madrid, Spain

Stephane Grange Universite Lyon, INSA-Lyon, GEOMAS, Villeurbanne cedex, France

Harun Güçlü Department of Automotive Engineering, Bursa Uludag Universitesi, Bursa, Turkey

Seongwon Hong Department of Safety Engineering, Korea National University of Transportation, Chungju-si, Chungbuk, Republic of Korea

Muneo Hori Earthquake Research Institute, The University of Tokyo, Tokyo, Japan

Dashnor Hoxha Univ Orléans, Univ Tours, INSA CVL, Orléans, France

Civil Engineering, University of Orléans, Laboratory of Mechanics Gabriel Lamé, Orléans, France

Zhuping Huang Department of Mechanics and Engineering Science, College of Engineering, Peking University, Beijing, China

Jacek Janiszewski Faculty of Mechatronics and Aviation, Military University of Technology, Warsaw, Poland

Juyoung Jeong Department of Civil and Environmental Engineering, Louisiana State University, Baton Rouge, LA, USA

Jiann-Wen Woody Ju Department of Civil and Environmental Engineering, University of California, Los Angeles, CA, USA

State Key Laboratory for Disaster Reduction in Civil Engineering, Tongji University, Shanghai, China

Sohan Kale Department of Mechanical Science and Engineering, also Institute for Condensed Matter Theory and Beckman Institute, University of Illinois at Urbana-Champaign, Urbana, IL, USA

Noé Brice Nkoumbou Kaptchouang Institut de Radioprotection et de Sûreté Nucléaire, Saint-Paul-lez-Durance, France

MIST Laboratory, IRSN-CNRS-UM, Montpellier, France

Peter I. Kattan Department of Civil and Environmental Engineering, Louisiana State University, Baton Rouge, LA, USA

Rui Kong Key Laboratory of Ministry of Education on Safe Mining of Deep Metal Mines, Northeastern University, Shenyang, China

Michał Kucewicz Faculty of Mechanical Engineering, Military University of Technology, Warsaw, Poland

Dong Li Department of Materials Science and Engineering, North Carolina State University, Raleigh, NC, USA

Kai Liu Department of Civil Engineering, Monash University, Melbourne, VIC, Australia

Shijing Lu Department of Materials Science and Engineering, North Carolina State University, Raleigh, NC, USA

Yann Malecot 3SR Lab, Université Grenoble Alpes, Grenoble, France

Philippe Marin Université Grenoble Alpes, CNRS, Grenoble, France

Roberta Massabò Department of Civil, Chemical and Environmental Engineering, Università di Genova, Genova, Italy

Sreten Mastilovic Faculty of Construction Management, Union–Nikola Tesla University, Belgrade, Serbia

Jacky Mazars Institute of Engineering Univ. Grenoble-Alpes, CNRS, 3SR, Grenoble, France

Mamadou Méïté Institut de Radioprotection et de Sûreté Nucléaire, Saint-Paul-lez-Durance, France

MIST Laboratory, IRSN-CNRS-UM, Montpellier, France

Yann Monerie MIST Laboratory, IRSN-CNRS-UM, Montpellier, France

LMGC, University of Montpellier, CNRS, Montpellier, France

François Nicot IRSTEA, Geomechanics Group, ETNA, Grenoble, France

Martin Ostoja-Starzewski Department of Mechanical Science and Engineering, also Institute for Condensed Matter Theory and Beckman Institute, University of Illinois at Urbana-Champaign, Urbana, IL, USA

Chahmi Oucif Institute of Structural Mechanics (ISM), Bauhaus-Universität Weimar, Weimar, Germany

Mustafa ÖzgürYaylı Department of Civil Engineering, Bursa Uludag University, Bursa, Turkey

Niranjan Parab Purdue University, West Lafayette, IN, USA

Frédéric Perales Institut de Radioprotection et de Sûreté Nucléaire, Saint-Paul-lez-Durance, France

MIST Laboratory, IRSN-CNRS-UM, Montpellier, France

Paweł Płatek Faculty of Mechatronics and Aviation, Military University of Technology, Warsaw, Poland

Serguei Potapov IMSIA UMR 9219, EDF-CNRS-CEA-ENSTA, Palaiseau, France

Florent Prunier INSA de Lyon, LGCIE, Villeurbanne, France

Timon Rabczuk College of Civil Engineering, Department of Geotechnical Engineering, Tongji University, Shanghai, China

Antonio Rinaldi Materials Technical Unit, ENEA, C.R. Casaccia, Rome, Italy

Center for Mathematics and Mechanics of Complex System (MEMOCS), University of L'Aquila, L'Aquila, Italy

M. Rodríguez-Millán Department of Mechanical Engineering, University Carlos III of Madrid, Madrid, Spain

Emmanuel Roubin 3SR Lab, Université Grenoble Alpes, Grenoble, France

Pratheek Shanthraj Department of Mechanical and Aerospace Engineering, North Carolina State University, Raleigh, NC, USA

Department of Microstructure–Physics and Alloy Design, Max Planck Institut ür Eisenforschung, Düsseldorf, Germany

J. F. Shao Laboratory of Multiscale and Multiphysics Mechanics, University of Lille, CNRS, EC Lille, LaMcube, Lille, France

Jianfu Shao Laboratory of Mechanics of Lille, Villeneuve d'Ascq, France

University Lille, CNRS, Centrale Lille, LaMcube – Laboratoire de Mécanique, Multiphysique, Multi-échelle, Lille, France

Faiz Agh Shareef Department Faculty of Engineering, Department of Civil Engineering, Bursa Uludag Universitesi, Bursa, Turkey

Amir Shojaei Varian Medical Systems, Palo Alto, CA, USA

Olga Stamati 3SR Lab, Université Grenoble Alpes, Grenoble, France

Ghatu Subhash Department of Mechanical and Aerospace Engineering, University of Florida, Gainesville, FL, USA

Wojciech Sumelka Institute of Structural Analysis, Poznan University of Technology, Poznan, Poland

Yue Sun University Lille, CNRS, Centrale Lille, LaMcube – Laboratoire de Mécanique, Multiphysique, Multi-échelle, Lille, France

Hakan Tacettin Türker Department Faculty of Engineering, Department of Civil Engineering, Bursa Uludag Universitesi, Bursa, Turkey

Büşra Uzun Department of Civil Engineering, Bursa Uludag University, Bursa, Turkey

Pierre-Guy Vincent Institut de Radioprotection et de Sûreté Nucléaire, Saint-Paul-lez-Durance, France

MIST Laboratory, IRSN-CNRS-UM, Montpellier, France

George Z. Voyiadjis Center for GeoInformatics C4G and Computational Solid Mechanics Laboratory, Department of Civil and Environmental Engineering, Louisiana State University, Baton Rouge, LA, USA

Richard Wan Department of Civil Engineering, University of Calgary, Calgary, AB, Canada

Junyu Wang Purdue University, West Lafayette, IN, USA

Michael P. Wnuk Department of Civil Engineering and Mechanics, College of Engineering and Applied Science, University of Wisconsin, Milwaukee, WI, USA

Gonglinan Wu Department of Civil Engineering, Monash University, Melbourne, VIC, Australia

Z. G. Yan Department of Geotechnical Engineering, State Key Laboratory for Disaster Reduction in Civil Engineering, Tongji University, Shanghai, China

K. Yanase Department of Mechanical Engineering, Institute of Materials Science and Technology, Fukuoka University, Fukuoka, Japan

Murat Yazici Department of Automotive Engineering, Bursa Uludag Universitesi, Bursa, Turkey

Z. Yu University of Lille, CNRS, EC Lille, LaMcube, Lille, France

Yan Zhang Key Laboratory of Ministry of Education on Safe Mining of Deep Metal Mines, Northeastern University, Shenyang, China

Qian-Bing Zhang Department of Civil Engineering, Monash University, Melbourne, VIC, Australia

Jian Zhao Department of Civil Engineering, Monash University, Melbourne, VIC, Australia

L. Y. Zhao College of Civil and Transportation Engineering, Hohai University, Nanjing, China

S. Zhou College of Materials Science and Engineering, Chongqing University, Chongqing, China

Yaneng Zhou Center for GeoInformatics C4G and Computational Solid Mechanics Laboratory, Department of Civil and Environmental Engineering, Louisiana State University, Baton Rouge, LA, USA

H. H. Zhu Department of Geotechnical Engineering, State Key Laboratory for Disaster Reduction in Civil Engineering, Tongji University, Shanghai, China

Q. Z. Zhu College of Civil and Transportation Engineering, Hohai University, Nanjing, China

Mohammed A. Zikry Department of Mechanical and Aerospace Engineering, North Carolina State University, Raleigh, NC, USA

Part I

Fundamentals in Damage

The True Nature of the Decomposition of the Damage Variable

1

George Z. Voyiadjis and Peter I. Kattan

Contents

Introduction 4
Decomposition for the Scalar Case 5
How the Damage Variable Is Decomposed in One Dimension 6
Decomposition of Two Defects Only 6
Decomposition Due to Three Types of Defects 9
Decomposition for the Tensor Case 10
Decomposition Due to Two Defect Types Only 12
Decomposition Due to Three Defect Types 13
The Case of Plane Stress 13
Conclusion 20
References 20

Abstract

The true nature of the decomposition of the damage variable in light of continuum damage mechanics. Damage consists of cracks and voids in a solid body. In this regard, the usual decomposition of damage into a part due to cracks and a part due to voids is reviewed. This is further extended into general cases consisting of three types of defects: cracks, voids, and a third unknown defect. The formulation is presented first using scalars for simple types of deformation and damage. This is later extended to general states of deformation and damage using tensors. Finally, an example of the problem of plane stress is illustrated for this specific decomposition scheme.

G. Z. Voyiadjis (✉)
Center for GeoInformatics C4G and Computational Solid Mechanics Laboratory, Department of Civil and Environmental Engineering, Louisiana State University, Baton Rouge, LA, USA
e-mail: voyiadjis@eng.lsu.edu

P. I. Kattan
Department of Civil and Environmental Engineering, Louisiana State University, Baton Rouge, LA, USA
e-mail: info@PetraBooks.com; pkattan@PetraBooks.com

© Springer Nature Switzerland AG 2022

G. Z. Voyiadjis (ed.), *Handbook of Damage Mechanics*,
https://doi.org/10.1007/978-3-030-60242-0_82

Keywords

Damage mechanics · Damage variable · Decomposition · Elastic · Elasticity · Damage

Introduction

Initial work on continuum damage mechanics was performed by Kachanov (1958) and continued later by Lee et al. (1985), Voyiadjis and Kattan (1992, 2005, 2006a, 2009), Sidoroff (1981), Krajcinovic (1996), and Kattan and Voyiadjis (1993, 2001a, b).

Kachanov (1958) introduced the idea of effective stress in light of continuum damage mechanics. This initial research was elaborated on by Rabotnov (1969) and by others later (Kattan and Voyiadjis 2001a, b; Ladeveze and Lemaitre 1984; Voyiadjis and Kattan 2005, 2006a, 2009, 2012a). Furthermore, damage mechanisms in series and in parallel were examined by the authors (Voyiadjis and Kattan 2012b). In light of continuum damage mechanics, a scalar damage variable ϕ is used that has values between 0 and 1. Therefore, the value of the damage variable ranges from 0 for the undamaged material to 1 for complete failure. The authors also examined and elaborated in detail on basic topics of continuum damage mechanics (Voyiadjis and Kattan 2017a) and used damage mechanics to study damage in graphene (2017b).

Tremendous progress has been made in the past few years into the topic of damage mechanics (Celentano et al. 2004; Doghri 2000; Hansen and Schreyer 1994; Kattan and Voyiadjis 1990, 1993; Ladeveze et al. 1982; Lubineau 2010; Lubineau and Ladeveze 2008; Lee et al. 1985; Luccioni and Oller 2003; Rice 1971; Sidoroff 1981; Voyiadjis 1988; Voyiadjis and Kattan 1990, 1992; Lemaitre 1984; Chow and Wang 1987). Furthermore, Voyiadjis and Kattan (2006b, c) derived a relationship between fabric tensors and damage variables. Recently, Voyiadjis and Kattan (2017c) introduced various templates for damage mechanics in order to accurately characterize damage in materials using a consistent and systematic approach.

Also progress was made in the study of damage mechanics in composite materials (Chaboche 1981, 1986, 1988a, b; Lemaitre 1985, 1986, 1992; Lemaitre and Chaboche 1985; Lemaitre and Dufailly 1987).

Kattan and Voyiadjis (2001a) derived a decomposition of the damage tensor into two distinct parts: one part was due to cracks and the other part was due to voids. Thus, the damaged solid material was assumed to consist of cracks and voids. The current work extends this decomposition and generalizes it in a very special way.

An analysis of the classical decomposition of the damage variable is carried out in section "Decomposition for the Scalar Case." This is further elaborated upon by deriving an exponential decomposition of the damage variable. This exponential decomposition is very general and the classical decomposition can be obtained from it as a special case. The two aspects of damage, namely, cracks and voids, are examined in light of the new exponential decomposition.

The generalization of the scalar exponential decomposition is made in section "Decomposition for the Tensor Case" using tensors. This general case applies to general states of deformation and damage. The tensors are represented by matrices in this work for ease of use. Again, cracks and voids are examined in light of the new tensorial exponential decomposition.

Finally in section "The Case of Plane Stress" is solved. This is performed twice: once in terms of the classical decomposition and again in terms of the exponential decomposition. It is illustrated how the general tensorial equations can be reduced to those of the plane stress case.

Decomposition for the Scalar Case

In this section, one uses scalars to account for the damage processes. Using scalars implies the assumption of isotropic damage. Consider Fig. 1 where two configurations of the body are shown. The first configuration is the actual deformed and damaged configuration while the second configuration is the fictitious undamaged configuration. These are the two classical configurations of damage mechanics. Considering the equation for the tension T in each cylinder. From this equation, one concludes the following equation for the effective stress:

$$\overline{\sigma} = \frac{A}{\overline{A}}\sigma \tag{1}$$

where σ and $\overline{\sigma}$ are the stress and effective stress, respectively, while A and $\overline{A}$ are the cross-sectional area and effective cross-sectional area, respectively. The next step involves the use of the definition of the damage variable as follows:

$$\phi = \frac{A - \overline{A}}{A} \tag{2}$$

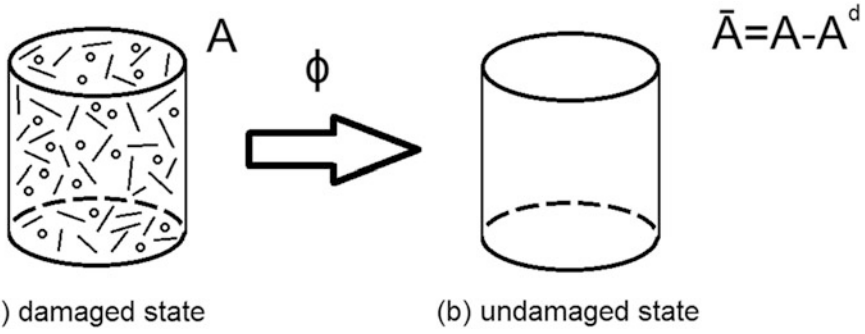

Fig. 1 Damaged and undamaged configurations of the cylinder

Next one substitutes for the ratio of the areas from Eq. (2) into Eq. (1) to obtain:

$$\overline{\sigma} = \frac{\sigma}{1-\phi} \tag{3}$$

How the Damage Variable Is Decomposed in One Dimension

In this section, one assumes the presence of isotropic damage – thus the use of scalars. It is also assumed that damage occurs in the form of cracks and voids only. Thus, two types of damages are considered here. The total cross-sectional area is thus written as follows:

$$A = \overline{A} + A^v + A^c \tag{4}$$

where A^v is the total area of voids in the cross-section and A^c is the total area of cracks in the cross-section (The superscripts "v" and "c" denote voids and cracks, respectively.). In addition to the total damage variable ϕ, two more damage variables ϕ^v and ϕ^c are presented to account for the damage in voids and cracks, respectively.

The following is the classical decomposition formula that was derived by Kattan and Voyiadjis (2001a):

$$1-\phi = (1-\phi^v)(1-\phi^c) \tag{5}$$

Expanding Eq. (5) and simplifying it, one obtains:

$$\phi = \phi^v + \phi^c - \phi^v\phi^c \tag{6}$$

Decomposition of Two Defects Only

It is concluded from Eq. (6) that the decomposition of the damage variable is symmetrical with respect to the two defects of cracks and voids. In order to derive an unsymmetrical decomposition, one adds the term $-\phi^{c^2}$ to the right-hand-side as follows:

$$\phi = \phi^v + \phi^c - \phi^v\phi^c - \phi^{c^2} \tag{7}$$

Alternatively one can add the term $-\phi^{v^2}$ to the right-hand-side to obtain another unsymmetrical decomposition:

$$\phi = \phi^v + \phi^c - \phi^v\phi^c - \phi^{v^2} \tag{8}$$

Thus, the expressions in Eqs. (7) and (8) present two unsymmetrical modifications of the original symmetrical decomposition of Eq. (6). One can modify Eq. (6)

further by adding both terms $-\phi^{c^2}$ and $-\phi^{v^2}$ simultaneously to obtain the following symmetrical decomposition:

$$\phi = \phi^v + \phi^c - \phi^v \phi^c - \phi^{c^2} - \phi^{v^2} \tag{9}$$

One can explore this further by including a coefficient ½ for each one of the two added terms as follows:

$$\phi = \phi^v + \phi^c - \phi^v \phi^c - \frac{1}{2}\phi^{c^2} - \frac{1}{2}\phi^{v^2} \tag{10}$$

One can re-write Eq. (10) as follows:

$$\phi = \phi^v + \phi^c - \frac{1}{2}\left(\phi^{c^2} + 2\phi^v \phi^c + \phi^{v^2}\right) \tag{11}$$

One can further rewrite Eq. (11) as follows:

$$\phi = \phi^v + \phi^c - \frac{1}{2}(\phi^c + \phi^v)^2 \tag{12}$$

Examining the expression of Eq. (12), one can generalize it by adding higher-order terms as follows:

$$\phi = (\phi^v + \phi^c) - \frac{1}{2!}(\phi^c + \phi^v)^2 + \frac{1}{3!}(\phi^c + \phi^v)^3 - \frac{1}{4!}(\phi^c + \phi^v)^4 + \ldots\ldots\ldots \tag{13}$$

One next compares Eq. (13) with the following Taylor series expansion of the exponential function:

$$e^{-x} = 1 - x + \frac{1}{2!}x^2 - \frac{1}{3!}x^3 + \frac{1}{4!}x^4 - \ldots\ldots\ldots\ldots\ldots\ldots \tag{14}$$

Therefore, the following simplified equations can be derived directly from Eq. (13):

$$\phi = 1 - e^{-(\phi^c + \phi^v)} \tag{15}$$

It should be noted that the decomposition of Eq. (15) is the most general one and it is clearly exponential. The classical polynomial decomposition can be obtained as a special case of the general exponential decomposition.

Other generalized decompositions of the damage variable can be obtained using the following general form:

$$\phi = f(\phi^c + \phi^v) \tag{16}$$

where the function f is unknown. For example, in Eq. (15), the function f is given by $f(x, y) = 1 - e^{-(x+y)}$.

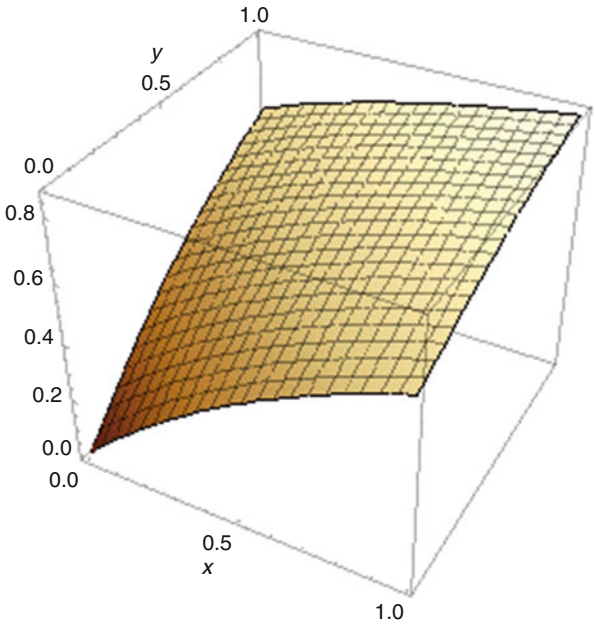

Fig. 2 A Plot of the Exponential Decomposition

A 3D graph of the exponential decomposition is shown in Fig. 2. (Figure 2 was generated using Wolfram Alpha online at http://www.wolframalpha.com). It is noted that for small damage, i.e., when the value of the expression $\phi^c + \phi^v$ is small, the expression of Eq. (15) becomes:

$$\phi = 1 - e^{-(\phi^c + \phi^v)} \approx 1 - [1 - (\phi^c + \phi^v) + \ldots.] \approx \phi^c + \phi^v \tag{17}$$

Therefore, an additive decomposition of the damage variable is obtained for small values of damage, i.e., $\phi \approx \phi^c + \phi^v$. Therefore, f of Eq. (16) is given by $f(x, y) = x + y$.

Next one assumes that the two damages of the two types of defects (cracks and voids) are equal, i.e., assuming $\phi^c = \phi^v = \phi_0$, Eq. (15) becomes:

$$\phi = 1 - e^{-2\phi_0} \tag{18}$$

Thus using Eq. (18), when the maximum value of ϕ_0 reaches 1, the maximum value of ϕ reaches 0.87 only (ϕ never reaches 1). Suppose there are multiple defects present (more than two). If one assumes there exist n different types of defects each with equal damage of ϕ_0, then Eq. (15) can be re-written as follows:

$$\phi = 1 - e^{-n\phi_0} \tag{19}$$

The case when $n = 2$ (cracks and voids) is considered above. Other cases with other values of n, along with the corresponding maximum value of ϕ as computed using Eq. (19), are shown in Table 1.

Table 1 Maximum values of the damage variable for different numbers of defect types

n	$1 - e^{-n}$	Maximum value of ϕ
1	$1 - e^{-1}$	0.632
2	$1 - e^{-2}$	0.865
3	$1 - e^{-3}$	0.950
4	$1 - e^{-4}$	0.982
5	$1 - e^{-5}$	0.993

Decomposition Due to Three Types of Defects

In this section, one considers three different types of defects present in the damaged solid material. In this case, the classical decomposition is given by the following expression where w is the third unspecified defect:

$$1 - \phi = (1 - \phi^v)(1 - \phi^c)(1 - \phi^w) \tag{20}$$

Expanding Eq. (20) and simplifying the result, one obtains the following:

$$\phi = \phi^v + \phi^c + \phi^w - \phi^v\phi^c - \phi^v\phi^w - \phi^c\phi^w + \phi^v\phi^c\phi^w \tag{21}$$

In this case, the generalized exponential decomposition becomes:

$$\phi = 1 - e^{-(\phi^c + \phi^v + \phi^w)} \tag{22}$$

Expanding the exponential decomposition of Eq. (22) using a Taylor series results in the following expression:

$$\phi = 1 - \left[1 - (\phi^v + \phi^c + \phi^w) + \frac{1}{2!}(\phi^v + \phi^c + \phi^w)^2 - \ldots\ldots\ldots\right] \tag{23}$$

Upon expanding Eq. (23) and simplifying the resulting expression, one obtains;

$$\phi = \phi^v + \phi^c + \phi^w - \phi^v\phi^c - \phi^v\phi^w - \phi^c\phi^w + \phi^v\phi^c\phi^w - \frac{1}{2}\phi^{v^2} - \frac{1}{2}\phi^{c^2} - \frac{1}{2}\phi^{w^2} \tag{24}$$

One then compares the two decompositions of Eqs. (21) and (24) to see the similarities between them. Therefore, the exponential decomposition of Eq. (22) is a general formulation of the usual decomposition of Eq. (20).

One next compares the exponential decomposition with the classical decomposition as follows. Different numbers of defect types are used in this comparison. The comparison is shown schematically in Table 2 and on the subsequent four figures (Figs. 3, 4, 5, and 6).

Table 2 Comparison between the classical decomposition and the exponential decomposition for different numbers of defect types

Equation of classical decomposition (Based on Eq. (20))	Equation of exponential decomposition (Based on Eq. (22))	Figure number for graphical comparison
$\phi_2 = \phi_0$	$\phi_1 = 1 - e^{-\phi_0}$	Figure 3
$\phi_2 = 2\phi_0 - \phi_0^2$	$\phi_1 = 1 - e^{-2\phi_0}$	Figure 4
$\phi_2 = 3\phi_0 - 3\phi_0^2 + \phi_0^3$	$\phi = 1 - e^{-3\phi_0}$	Figure 5
$\phi_2 = 4\phi_0 - 6\phi_0^2 + 4\phi_0^3 - \phi_0^4$	$\phi_1 = 1 - e^{-4\phi_0}$	Figure 6

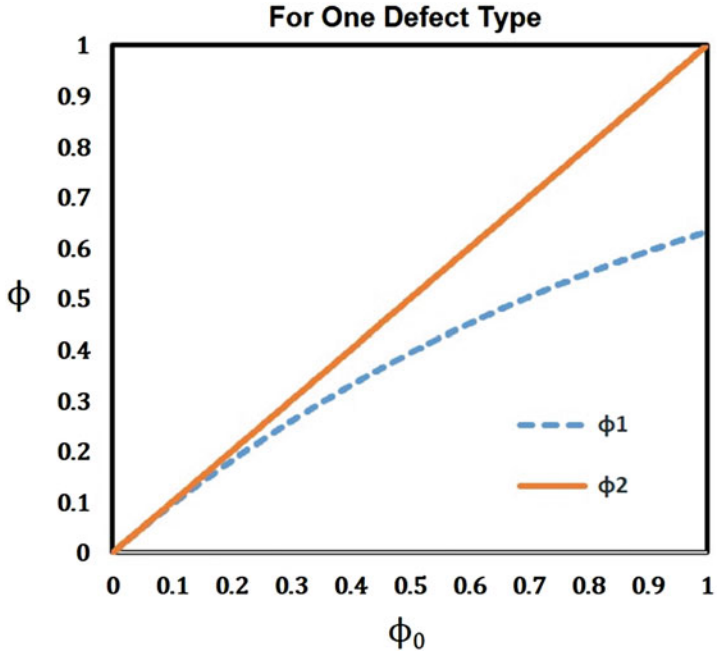

Fig. 3 Comparison between the two decompositions for one defect type

Decomposition for the Tensor Case

The scalar equation of the effective stress is generalized as follows using tensors (Sidoroff 1981; Voyiadjis and Kattan 1992, 2005, 2006a):

$$\{\overline{\sigma}\} = [M]\{\sigma\} \tag{25}$$

where tensors are represented by vectors and matrices. In Eq. (23), the vectors $\{\sigma\}$ and $\{\overline{\sigma}\}$ represent the stress tensor and its effective counterpart, respectively, while the matrix $[M]$ represents the fourth-rank damage effect tensor. For more details

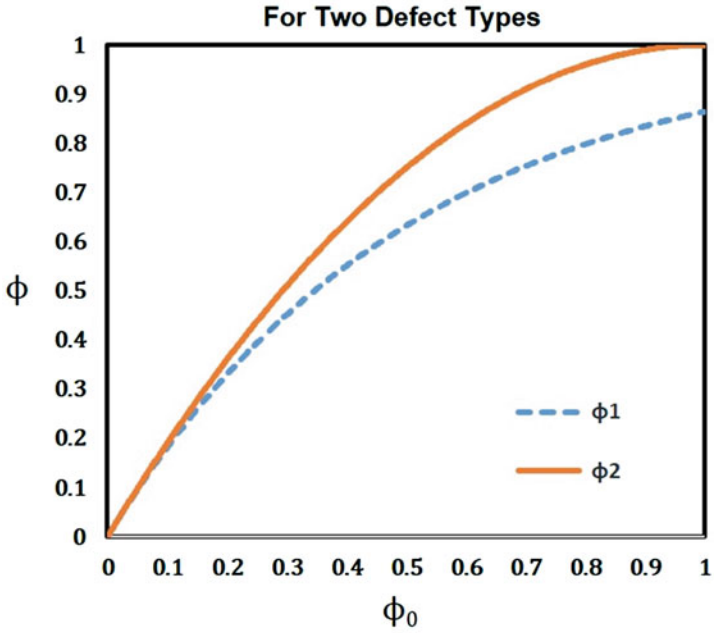

Fig. 4 Comparison between the two decompositions for two defect types

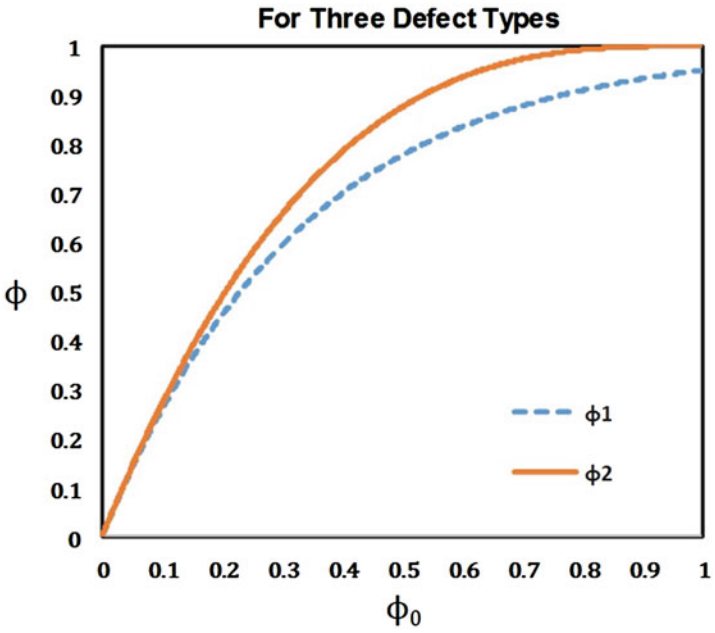

Fig. 5 Comparison between the two decompositions for three defect types

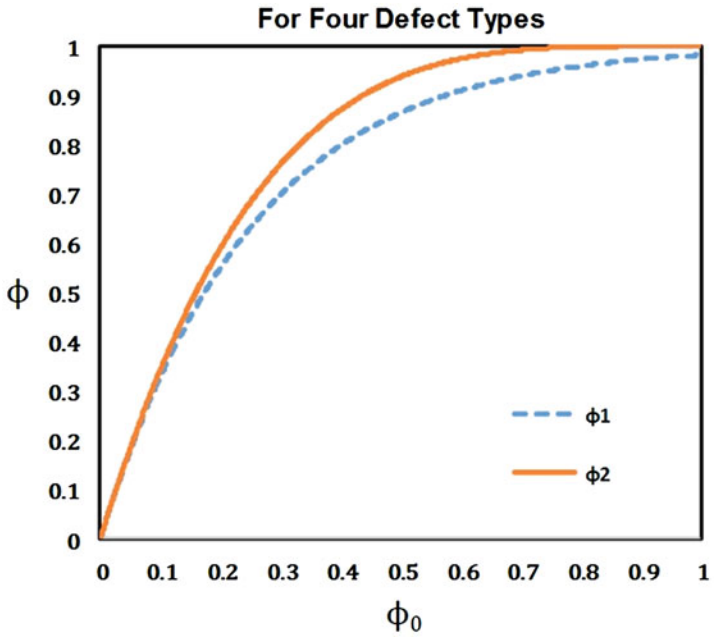

Fig. 6 Comparison between the two decompositions for four defect types

about the fourth-rank damage effect tensor, see the references by the authors where extensive research is conducted in this regard (Voyiadjis and Kattan 1992, 2005, 2006a).

Decomposition Due to Two Defect Types Only

When two defect types are used only for, for example, voids and cracks, the authors (Kattan and Voyiadjis 2001a) have shown that the scalar decomposition Eq. (5) can be re-written in a general form using tensors and matrices as follows:

$$[M] = [M^c]\,[M^v] \tag{26}$$

$$[M] = [M^v]\,[M^c] \tag{27}$$

One notes that Eqs. (26) and (27) give the same result because one can show that the multiplication of the matrices is commutative (Kattan and Voyiadjis 2001a).

Next, the exponential decomposition of Eq. (15) can be generalized using tensors as follows:

$$[M] = \left[e^{\left([M^c]^{-1}+[M^v]^{-1}-2\,[I]\right)}\right]^{-1} \tag{28}$$

where $[I]$ is the matrix representation of the fourth-rank identity tensor. Equation (28) can be re-written in the following form if certain conditions are met:

$$[M] = e^{-\left([M^c]^{-1}+[M^v]^{-1}-2[I]\right)} \tag{29}$$

Evaluating the matrix exponential of Eqs. (28) and (29) usually involves expanding it into its Taylor series, written as follows for a general matrix $[A]$:

$$e^{[A]} = [I] + [A] + \frac{1}{2!}[A]^2 + \frac{1}{3!}[A]^3 + \frac{1}{4!}[A]^4 + \ldots\ldots \tag{30}$$

Decomposition Due to Three Defect Types

For the case of three defect types (cracks, voids, and a third unspecified defect), the tensorial equation for the decomposition of two defect types can be generalized as follows where w is the third defect type:

$$[M] = [M^c]\,[M^v]\,[M^w] \tag{31}$$

One notes that the multiplication of the matrices is commutative (Kattan and Voyiadjis 2001a).

The exponential decomposition of Eq. (22) can be generalized as follows based on matric and tensor conventions:

$$[M] = \left[e^{\left([M^c]^{-1}+[M^v]^{-1}+[M^w]^{-1}-3[I]\right)}\right]^{-1} \tag{32}$$

where $[I]$ is the matrix representation of the fourth-rank identity tensor. Equation (32) can be re-phrased using the following expression which is simpler than before.

$$[M] = e^{-\left([M^c]^{-1}+[M^v]^{-1}+[M^w]^{-1}-3[I]\right)} \tag{33}$$

The Case of Plane Stress

Next, one solves the case of plane stress. For this case, the fourth-rank damage effect tensor $[M]$ of Eq. (25) can be represented by the following 3×3 matrix (Voyiadjis and Kattan 2006a):

$$[M] = \frac{1}{\Delta}\begin{bmatrix} 1-\phi_{22} & 0 & \phi_{12} \\ 0 & 1-\phi_{11} & \phi_{12} \\ \frac{1}{2}\phi_{12} & \frac{1}{2}\phi_{12} & \frac{1}{2}[(1-\phi_{11})+(1-\phi_{22})] \end{bmatrix} \tag{34}$$

where Δ is given by:

$$\Delta = (1-\phi_{11})(1-\phi_{22}) - \phi_{12}^2 \tag{35}$$

In Eqs. (34) and (35), ϕ_{11}, ϕ_{22}, and ϕ_{12} are the nonzero components of the second-rank damage tensor ϕ_{ij}, where $i, j = 1, 2, 3$. Similarly, the two fourth-rank damage effect tensors $[M^c]$ and $[M^v]$ for the cracks and voids, respectively, can be represented by the following two 3×3 matrices:

$$[M^c] = \frac{1}{\Delta^c}\begin{bmatrix} 1-\phi_{22}^c & 0 & \phi_{12}^c \\ 0 & 1-\phi_{11}^c & \phi_{12}^c \\ \frac{1}{2}\phi_{12}^c & \frac{1}{2}\phi_{12}^c & \frac{1}{2}\left[(1-\phi_{11}^c)+(1-\phi_{22}^c)\right] \end{bmatrix} \tag{36}$$

$$[M^v] = \frac{1}{\Delta^v}\begin{bmatrix} 1-\phi_{22}^v & 0 & \phi_{12}^v \\ 0 & 1-\phi_{11}^v & \phi_{12}^v \\ \frac{1}{2}\phi_{12}^v & \frac{1}{2}\phi_{12}^v & \frac{1}{2}\left[(1-\phi_{11}^v)+(1-\phi_{22}^v)\right] \end{bmatrix} \tag{37}$$

where Δ^c and Δ^v are given by:

$$\Delta^c = \left(1-\phi_{11}^c\right)\left(1-\phi_{22}^c\right) - \left(\phi_{12}^c\right)^2 \tag{38}$$

$$\Delta^v = \left(1-\phi_{11}^v\right)\left(1-\phi_{22}^v\right) - \left(\phi_{12}^v\right)^2 \tag{39}$$

In Eqs. (36–39), ϕ_{11}^c, ϕ_{22}^c, and ϕ_{33}^c are the nonzero components of the second-rank "crack" damage tensor ϕ_{ij}^c, where $i, j = 1, 2, 3$,while ϕ_{11}^v, ϕ_{22}^v, and ϕ_{33}^v are the nonzero components of the second-rank "void" damage tensor ϕ_{ij}^v, where $i, j = 1, 2, 3$.

Substituting Eqs. (34–39) into Eq. (26), one obtains the following system of nine algebraic equations (the matrix multiplication was performed using Wolfram Alpha online at http://www.wolframalpha.com):

$$\frac{1-\phi_{22}}{\Delta} = \frac{\left(1-\phi_{22}^c\right)\left(1-\phi_{22}^v\right) + \frac{1}{2}\phi_{12}^c\phi_{12}^v}{\Delta^c\,\Delta^v} \tag{40}$$

$$\frac{1-\phi_{11}}{\Delta} = \frac{\left(1-\phi_{11}^c\right)\left(1-\phi_{11}^v\right) + \frac{1}{2}\phi_{12}^c\phi_{12}^v}{\Delta^c\,\Delta^v} \tag{41}$$

$$\frac{(1-\phi_{11})+(1-\phi_{22})}{2\Delta} = \frac{\frac{1}{4}\left[\left(1-\phi_{11}^c\right)+\left(1-\phi_{22}^c\right)\right]\left[\left(1-\phi_{11}^v\right)+\left(1-\phi_{22}^v\right)\right] + \phi_{12}^c\phi_{12}^v}{\Delta^c\,\Delta^v} \tag{42}$$

$$0 = \frac{\frac{1}{2}\phi_{12}^{c}\phi_{12}^{v}}{\Delta^{c}\Delta^{v}} \tag{43}$$

$$\frac{\phi_{12}}{\Delta} = \frac{\left(1-\phi_{22}^{c}\right)\phi_{12}^{c} + \frac{1}{2}\left[\left(1-\phi_{11}^{v}\right) + \left(1-\phi_{22}^{v}\right)\right]\phi_{12}^{v}}{\Delta^{c}\Delta^{v}} \tag{44}$$

$$0 = \frac{\frac{1}{2}\phi_{12}^{c}\phi_{12}^{v}}{\Delta^{c}\Delta^{v}} \tag{45}$$

$$\frac{\phi_{12}}{\Delta} = \frac{\left(1-\phi_{11}^{c}\right)\phi_{12}^{v} + \frac{1}{2}\left[\left(1-\phi_{11}^{v}\right) + \left(1-\phi_{22}^{v}\right)\right]\phi_{12}^{c}}{\Delta^{c}\Delta^{v}} \tag{46}$$

$$\frac{\frac{1}{2}\phi_{12}}{\Delta} = \frac{\frac{1}{2}\left(1-\phi_{22}^{v}\right)\phi_{12}^{c} + \frac{1}{4}\left[\left(1-\phi_{11}^{c}\right) + \left(1-\phi_{22}^{c}\right)\right]\phi_{12}^{v}}{\Delta^{c}\Delta^{v}} \tag{47}$$

$$\frac{\frac{1}{2}\phi_{12}}{\Delta} = \frac{\frac{1}{2}\left(1-\phi_{11}^{v}\right)\phi_{12}^{c} + \frac{1}{4}\left[\left(1-\phi_{11}^{c}\right) + \left(1-\phi_{22}^{c}\right)\right]\phi_{12}^{v}}{\Delta^{c}\Delta^{v}} \tag{48}$$

Next, one delves into the process if simplifying the above equations trying to find a reasonable conclusion.

It is noted that the above equations show that $\phi_{12}^{c} = \phi_{12}^{v} = 0$. In addition, one can immediately show that $\phi_{12} = 0$. Substituting these results into Eqs. (40) and (41), and simplifying, one obtains the following relationships:

$$1-\phi_{11} = \left(1-\varphi_{11}^{c}\right)\left(1-\phi_{11}^{v}\right) \tag{49}$$

$$1-\phi_{22} = \left(1-\varphi_{22}^{c}\right)\left(1-\phi_{22}^{v}\right) \tag{50}$$

The decompositions in Eqs. (49) and (50) look eerily similar to the scalar decomposition of Eq. (5). In order to obtain the third equation which is the coupling equation between the various damage tensor components, one substitutes $\phi_{12}^{c} = \phi_{12}^{v} = 0$ into Eq. (42) and simplifies the result to obtain:

$$\begin{aligned}&\left(1-\varphi_{11}^{c}\right)\left(1-\phi_{11}^{v}\right) + \left(1-\varphi_{22}^{c}\right)\left(1-\phi_{22}^{v}\right)\\ &\quad = \left(1-\varphi_{11}^{c}\right)\left(1-\phi_{22}^{v}\right) + \left(1-\varphi_{22}^{c}\right)\left(1-\phi_{11}^{v}\right)\end{aligned} \tag{51}$$

It is clear that the relationship in Eq. (51) is a coupling expression between the four parts of the damage tensor. ϕ_{11}^{c}, ϕ_{22}^{c}, ϕ_{11}^{v}, and ϕ_{22}^{v}, i.e., this is a coupling expression between the void damage and crack damage for this special case of plane stress. The coupling expression (51) can be simplified as follows:

$$\phi_{11}^{c}\,\phi_{11}^{v}+\phi_{22}^{c}\,\phi_{22}^{v}=\phi_{11}^{c}\,\phi_{22}^{v}+\phi_{22}^{c}\,\phi_{11}^{v} \tag{52}$$

One solves the plane stress example next for the generalized exponential decomposition Eq. (29). Substituting the matrices of Eqs. (36–39) into Eq. (29) produces a complex expression looks like the following:

$$[M]=e^{[A]} \tag{53}$$

where the components of the exponent matrix $[A]$ are given next (the results were obtained using Wolfram Alpha online at http://www.wolframalpha.com):

$$A_{11}=2-\frac{1}{\Psi}\begin{bmatrix}
2\left(1-\phi_{11}^{v}\right)\left(\phi_{12}^{c}\right)^{2}\left(\phi_{12}^{v}\right)^{2}\Delta^{c}+2\left(1-\phi_{11}^{c}\right)\left(\phi_{12}^{c}\right)^{2}\left(\phi_{12}^{v}\right)^{2}\Delta^{v}\\
-2\left[\left(1-\phi_{11}^{v}\right)+\left(1-\phi_{22}^{v}\right)\right]\left(1-\phi_{22}^{c}\right)\left(1-\phi_{11}^{v}\right)\left(\phi_{12}^{c}\right)^{2}\Delta^{v}+2\left(1-\phi_{11}^{c}\right)\left(\phi_{12}^{c}\right)^{2}\left(\phi_{12}^{v}\right)^{2}\Delta^{v}\\
-2\left[\left(1-\phi_{11}^{v}\right)+\left(1-\phi_{22}^{v}\right)\right]\left(1-\phi_{11}^{c}\right)\left(1-\phi_{11}^{v}\right)\left(\phi_{12}^{c}\right)^{2}\Delta^{v}+2\left(1-\phi_{22}^{v}\right)\left(\phi_{12}^{c}\right)^{2}\left(\phi_{12}^{v}\right)^{2}\Delta^{c}\\
-2\left[\left(1-\phi_{11}^{v}\right)+\left(1-\phi_{22}^{v}\right)\right]\left(1-\phi_{11}^{v}\right)\left(1-\phi_{22}^{v}\right)\left(\phi_{12}^{c}\right)^{2}\Delta^{c}\\
-2\left[\left(1-\phi_{11}^{c}\right)+\left(1-\phi_{22}^{c}\right)\right]\left(1-\phi_{11}^{c}\right)\left(1-\phi_{11}^{v}\right)\left(\phi_{12}^{v}\right)^{2}\Delta^{c}\\
-2\left[\left(1-\phi_{11}^{c}\right)+\left(1-\phi_{22}^{c}\right)\right]\left(1-\phi_{11}^{c}\right)\left(1-\phi_{22}^{c}\right)\left(\phi_{12}^{c}\right)^{2}\Delta^{v}\\
+2\left[\left(1-\phi_{11}^{c}\right)+\left(1-\phi_{22}^{c}\right)\right]\left[\left(1-\phi_{11}^{v}\right)+\left(1-\phi_{22}^{v}\right)\right]\left(1-\phi_{11}^{c}\right)\left(1-\phi_{22}^{c}\right)\left(1-\phi_{11}^{v}\right)\Delta^{v}\\
-2\left[\left(1-\phi_{11}^{c}\right)+\left(1-\phi_{22}^{c}\right)\right]\left(1-\phi_{11}^{c}\right)\left(1-\phi_{22}^{v}\right)\left(\phi_{12}^{v}\right)^{2}\Delta^{c}\\
+2\left[\left(1-\phi_{11}^{c}\right)+\left(1-\phi_{22}^{c}\right)\right]\left[\left(1-\phi_{11}^{v}\right)+\left(1-\phi_{22}^{v}\right)\right]\left(1-\phi_{11}^{c}\right)\left(1-\phi_{11}^{v}\right)\left(1-\phi_{22}^{v}\right)\Delta^{c}
\end{bmatrix} \tag{54}$$

$$A_{22}=2-\frac{1}{\Psi}\begin{bmatrix}
2\left(1-\phi_{11}^{v}\right)\left(\phi_{12}^{c}\right)^{2}\left(\phi_{12}^{v}\right)^{2}\Delta^{c}+2\left(1-\phi_{11}^{c}\right)\left(\phi_{12}^{c}\right)^{2}\left(\phi_{12}^{v}\right)^{2}\Delta^{v}\\
-2\left[\left(1-\phi_{11}^{v}\right)+\left(1-\phi_{22}^{v}\right)\right]\left(1-\phi_{11}^{c}\right)\left(1-\phi_{22}^{v}\right)\left(\phi_{12}^{c}\right)^{2}\Delta^{v}+2\left(1-\phi_{11}^{c}\right)\left(\phi_{12}^{c}\right)^{2}\left(\phi_{12}^{v}\right)^{2}\Delta^{v}\\
-2\left[\left(1-\phi_{11}^{c}\right)+\left(1-\phi_{22}^{c}\right)\right]\left(1-\phi_{11}^{c}\right)\left(1-\phi_{22}^{c}\right)\left(\phi_{12}^{v}\right)^{2}\Delta^{v}+2\left(1-\phi_{22}^{v}\right)\left(\phi_{12}^{c}\right)^{2}\left(\phi_{12}^{v}\right)^{2}\Delta^{c}\\
-2\left[\left(1-\phi_{11}^{v}\right)+\left(1-\phi_{22}^{v}\right)\right]\left(1-\phi_{11}^{v}\right)\left(1-\phi_{22}^{v}\right)\left(\phi_{12}^{c}\right)^{2}\Delta^{c}\\
-2\left[\left(1-\phi_{11}^{c}\right)+\left(1-\phi_{22}^{c}\right)\right]\left(1-\phi_{22}^{c}\right)\left(1-\phi_{22}^{v}\right)\left(\phi_{12}^{v}\right)^{2}\Delta^{c}\\
-2\left[\left(1-\phi_{11}^{v}\right)+\left(1-\phi_{22}^{v}\right)\right]\left(1-\phi_{22}^{c}\right)\left(1-\phi_{22}^{v}\right)\left(\phi_{12}^{c}\right)^{2}\Delta^{v}\\
+2\left[\left(1-\phi_{11}^{c}\right)+\left(1-\phi_{22}^{c}\right)\right]\left[\left(1-\phi_{11}^{v}\right)+\left(1-\phi_{22}^{v}\right)\right]\left(1-\phi_{22}^{c}\right)\left(1-\phi_{11}^{v}\right)\left(1-\phi_{22}^{v}\right)\Delta^{c}\\
-2\left[\left(1-\phi_{11}^{c}\right)+\left(1-\phi_{22}^{c}\right)\right]\left(1-\phi_{22}^{c}\right)\left(1-\phi_{11}^{v}\right)\left(\phi_{12}^{v}\right)^{2}\Delta^{c}\\
+2\left[\left(1-\phi_{11}^{c}\right)+\left(1-\phi_{22}^{c}\right)\right]\left[\left(1-\phi_{11}^{v}\right)+\left(1-\phi_{22}^{v}\right)\right]\left(1-\phi_{11}^{c}\right)\left(1-\phi_{22}^{c}\right)\left(1-\phi_{22}^{v}\right)\Delta^{v}
\end{bmatrix} \tag{55}$$

$$A_{33}=2-\frac{1}{\Psi}\begin{bmatrix}
-2\left(1-\phi_{11}^{c}\right)\left(1-\phi_{22}^{c}\right)\left(1-\phi_{11}^{v}\right)\left(\phi_{12}^{c}\right)^{2}\Delta^{v}+2\left(1-\phi_{11}^{c}\right)\left(1-\phi_{11}^{v}\right)\left(1-\phi_{22}^{v}\right)\left(\phi_{12}^{c}\right)^{2}\Delta^{v}\\
-2\left(1-\phi_{11}^{c}\right)\left(1-\phi_{22}^{c}\right)\left(1-\phi_{11}^{v}\right)\left(\phi_{12}^{v}\right)^{2}\Delta^{c}-2\left(1-\phi_{11}^{c}\right)\left(1-\phi_{22}^{c}\right)\left(1-\phi_{22}^{v}\right)\left(\phi_{12}^{v}\right)^{2}\Delta^{c}\\
+2\left[\left(1-\phi_{11}^{c}\right)+\left(1-\phi_{22}^{c}\right)\right]\left(1-\phi_{11}^{c}\right)\left(1-\phi_{22}^{c}\right)\left(1-\phi_{11}^{v}\right)\left(1-\phi_{22}^{v}\right)\Delta^{v}\\
+2\left[\left(1-\phi_{11}^{v}\right)+\left(1-\phi_{22}^{v}\right)\right]\left(1-\phi_{11}^{c}\right)\left(1-\phi_{22}^{c}\right)\left(1-\phi_{11}^{v}\right)\left(1-\phi_{22}^{v}\right)\Delta^{c}
\end{bmatrix} \tag{56}$$

$$A_{12}=\frac{1}{\Psi}\begin{bmatrix}2\left(1-\phi_{11}^{v}\right)\left(\phi_{12}^{c}\right)^{2}\left(\phi_{12}^{v}\right)^{2}\Delta^{c}+2\left(1-\phi_{22}^{c}\right)\left(\phi_{12}^{c}\right)^{2}\left(\phi_{12}^{v}\right)^{2}\Delta^{v}+2\left(1-\phi_{11}^{c}\right)\left(\phi_{12}^{c}\right)^{2}\left(\phi_{12}^{v}\right)^{2}\Delta^{v}\\ +2\left(1-\phi_{22}^{v}\right)\left(\phi_{12}^{c}\right)^{2}\left(\phi_{12}^{v}\right)^{2}\Delta^{c}-2\left[\left(1-\phi_{11}^{v}\right)+\left(1-\phi_{22}^{v}\right)\right]\left(1-\phi_{11}^{v}\right)\left(1-\phi_{22}^{v}\right)\left(\phi_{12}^{c}\right)^{2}\Delta^{c}\\ -2\left[\left(1-\phi_{11}^{c}\right)+\left(1-\phi_{22}^{c}\right)\right]\left(1-\phi_{11}^{c}\right)\left(1-\phi_{22}^{c}\right)\left(\phi_{12}^{v}\right)^{2}\Delta^{v}\end{bmatrix} \tag{57}$$

$$A_{13}=\frac{2}{\Psi}\begin{bmatrix}-2\left(1-\phi_{11}^{v}\right)\left(1-\phi_{22}^{c}\right)\left(\phi_{12}^{c}\right)^{2}\phi_{12}^{v}\Delta^{v}-2\left(1-\phi_{11}^{c}\right)\left(1-\phi_{11}^{v}\right)\left(\phi_{12}^{c}\right)^{2}\phi_{12}^{v}\Delta^{v}\\ -2\left(1-\phi_{11}^{c}\right)\left(1-\phi_{11}^{v}\right)\phi_{12}^{c}\left(\phi_{12}^{v}\right)^{2}\Delta^{c}-2\left(1-\phi_{11}^{c}\right)\left(1-\phi_{22}^{v}\right)\phi_{12}^{c}\left(\phi_{12}^{v}\right)^{2}\Delta^{c}\\ +2\left[\left(1-\phi_{11}^{c}\right)+\left(1-\phi_{22}^{c}\right)\right]\left[\left(1-\phi_{11}^{v}\right)+\left(1-\phi_{22}^{v}\right)\right]\left(1-\phi_{11}^{c}\right)\left(1-\phi_{11}^{v}\right)\left(1-\phi_{22}^{v}\right)\phi_{12}^{c}\Delta^{c}\\ +2\left[\left(1-\phi_{11}^{c}\right)+\left(1-\phi_{22}^{c}\right)\right]\left(1-\phi_{11}^{c}\right)\left(1-\phi_{22}^{c}\right)\left(1-\phi_{11}^{v}\right)\phi_{12}^{v}\Delta^{v}\end{bmatrix} \tag{58}$$

$$A_{23}=\frac{2}{\Psi}\begin{bmatrix}-2\left(1-\phi_{22}^{c}\right)\left(1-\phi_{22}^{v}\right)\left(\phi_{12}^{c}\right)^{2}\phi_{12}^{v}\Delta^{v}-2\left(1-\phi_{11}^{c}\right)\left(1-\phi_{22}^{v}\right)\left(\phi_{12}^{c}\right)^{2}\phi_{12}^{v}\Delta^{v}\\ -2\left(1-\phi_{22}^{c}\right)\left(1-\phi_{11}^{v}\right)\phi_{12}^{c}\left(\phi_{12}^{v}\right)^{2}\Delta^{c}-2\left(1-\phi_{22}^{c}\right)\left(1-\phi_{22}^{v}\right)\phi_{12}^{c}\left(\phi_{12}^{v}\right)^{2}\Delta^{c}\\ +2\left[\left(1-\phi_{11}^{c}\right)+\left(1-\phi_{22}^{c}\right)\right]\left[\left(1-\phi_{11}^{v}\right)+\left(1-\phi_{22}^{v}\right)\right]\left(1-\phi_{22}^{c}\right)\left(1-\phi_{22}^{v}\right)\phi_{12}^{c}\Delta^{c}\\ -2\left[\left(1-\phi_{11}^{c}\right)+\left(1-\phi_{22}^{c}\right)\right]\left(1-\phi_{11}^{c}\right)\left(1-\phi_{22}^{c}\right)\left(1-\phi_{11}^{v}\right)\phi_{12}^{v}\Delta^{v}\end{bmatrix} \tag{59}$$

$$A_{12}=A_{12} \tag{60}$$

$$A_{31}=\frac{1}{2}A_{13} \tag{61}$$

$$A_{32}=\frac{1}{2}A_{23} \tag{62}$$

where

$$\Psi=2\left[\left(1-\phi_{11}^{c}\right)+\left(1-\phi_{22}^{c}\right)\right]\left[\left(1-\phi_{11}^{v}\right)+\left(1-\phi_{22}^{v}\right)\right]\Delta^{c}\,\Delta^{v} \tag{63}$$

When examining Eqs. (54–63) and substituting the conditions $\phi_{12}^{c}=\phi_{12}^{v}=0$, one obtains the following simplified form of the equations:

$$A_{11}=2-\frac{1}{\Psi}\begin{bmatrix}2\left[\left(1-\phi_{11}^{c}\right)+\left(1-\phi_{22}^{c}\right)\right]\left[\left(1-\phi_{11}^{v}\right)+\left(1-\phi_{22}^{v}\right)\right]\left(1-\phi_{11}^{c}\right)\left(1-\phi_{22}^{c}\right)\left(1-\phi_{11}^{v}\right)\Delta^{v}\\ +2\left[\left(1-\phi_{11}^{c}\right)+\left(1-\phi_{22}^{c}\right)\right]\left[\left(1-\phi_{11}^{v}\right)+\left(1-\phi_{22}^{v}\right)\right]\left(1-\phi_{11}^{c}\right)\left(1-\phi_{11}^{v}\right)\left(1-\phi_{22}^{v}\right)\Delta^{c}\end{bmatrix} \tag{64}$$

$$A_{22} = 2 - \frac{1}{\Psi}\begin{bmatrix} 2\left[\left(1-\phi_{11}^{c}\right)+\left(1-\phi_{22}^{c}\right)\right]\left[\left(1-\phi_{11}^{v}\right)+\left(1-\phi_{22}^{v}\right)\right]\left(1-\phi_{22}^{c}\right)\left(1-\phi_{11}^{v}\right)\left(1-\phi_{22}^{v}\right)\Delta^{c} \\ +2\left[\left(1-\phi_{11}^{c}\right)+\left(1-\phi_{22}^{c}\right)\right]\left[\left(1-\phi_{11}^{v}\right)+\left(1-\phi_{22}^{v}\right)\right]\left(1-\phi_{11}^{c}\right)\left(1-\phi_{22}^{c}\right)\left(1-\phi_{22}^{v}\right)\Delta^{v} \end{bmatrix} \tag{65}$$

$$A_{33} = 2 - \frac{1}{\Psi}\begin{bmatrix} 2\left[\left(1-\phi_{11}^{c}\right)+\left(1-\phi_{22}^{c}\right)\right]\left(1-\phi_{11}^{c}\right)\left(1-\phi_{22}^{c}\right)\left(1-\phi_{11}^{v}\right)\left(1-\phi_{22}^{v}\right)\Delta^{v} \\ +2\left[\left(1-\phi_{11}^{v}\right)+\left(1-\phi_{22}^{v}\right)\right]\left(1-\phi_{11}^{c}\right)\left(1-\phi_{22}^{c}\right)\left(1-\phi_{11}^{v}\right)\left(1-\phi_{22}^{v}\right)\Delta^{c} \end{bmatrix} \tag{66}$$

$$A_{12} = 0 \tag{67}$$

$$A_{13} = 0 \tag{68}$$

$$A_{23} = 0 \tag{69}$$

$$A_{21} = 0 \tag{70}$$

$$A_{31} = 0 \tag{71}$$

$$A_{32} = 0 \tag{72}$$

and

$$\Psi = 2\left[\left(1-\phi_{11}^{c}\right)+\left(1-\phi_{22}^{c}\right)\right]\left[\left(1-\phi_{11}^{v}\right)+\left(1-\phi_{22}^{v}\right)\right]\left(1-\phi_{11}^{c}\right)\left(1-\phi_{22}^{c}\right)\left(1-\phi_{11}^{v}\right)\left(1-\phi_{22}^{v}\right) \tag{73}$$

$$\Delta^{c} = \left(1-\phi_{11}^{c}\right)\left(1-\phi_{22}^{c}\right) \tag{74}$$

$$\Delta^{v} = \left(1-\phi_{11}^{v}\right)\left(1-\phi_{22}^{v}\right) \tag{75}$$

It is noted that only three equations remain. All the other have vanished. This is similar to what happened in the previous case. One next simplifies the three equations that are left. This simplification is accomplished by substituting Eqs. (73), (74), and (75) into Eqs. (64), (65), and (66). Finally, the following simple expressions are obtained:

$$A_{11} = -\left(\phi_{11}^{c} + \phi_{11}^{v}\right) \tag{76}$$

$$A_{22} = -\left(\phi_{22}^{c} + \phi_{22}^{v}\right) \tag{77}$$

$$\begin{aligned} A_{33} = 2 &- \left(1-\phi_{11}^{v}\right)\left(1-\phi_{22}^{v}\right)\left[\left(1-\phi_{11}^{v}\right)+\left(1-\phi_{22}^{v}\right)\right] \\ &- \left(1-\phi_{11}^{C}\right)\left(1-\phi_{22}^{c}\right)\left[\left(1-\phi_{11}^{c}\right)+\left(1-\phi_{22}^{c}\right)\right] \end{aligned} \tag{78}$$

The exponential decomposition Eq. (53) takes the following form:

$$[M] = e^{\begin{bmatrix} A_{11} & 0 & 0 \\ 0 & A_{22} & 0 \\ 0 & 0 & A_{33} \end{bmatrix}} = \begin{bmatrix} e^{A_{11}} & 0 & 0 \\ 0 & e^{A_{22}} & 0 \\ 0 & 0 & e^{A_{33}} \end{bmatrix} \tag{79}$$

Substituting Eqs. (34) and (35) into Eq. (79), one obtains:

$$\frac{1}{\Delta}\begin{bmatrix} 1-\phi_{22} & 0 & \phi_{12} \\ 0 & 1-\phi_{11} & \phi_{12} \\ \frac{1}{2}\phi_{12} & \frac{1}{2}\phi_{12} & \frac{1}{2}\left[\left(1-\phi_{11}\right)+\left(1-\phi_{22}\right)\right] \end{bmatrix} = \begin{bmatrix} e^{A_{11}} & 0 & 0 \\ 0 & e^{A_{22}} & 0 \\ 0 & 0 & e^{A_{33}} \end{bmatrix} \tag{80}$$

where, in this special case, Δ is given by (see Eq. (35) and also see Eqs. (74) and (75)):

$$\Delta = \left(1-\phi_{11}\right)\left(1-\phi_{22}\right) \tag{81}$$

Substituting Eqs. (76–78) into Eq. (80), and simplifying the result, one obtains the following system of three algebraic equations

$$\frac{1}{1-\phi_{11}} = e^{-\left(\phi_{11}^{c}+\phi_{11}^{v}\right)} \tag{82}$$

$$\frac{1}{1-\phi_{22}} = e^{-\left(\phi_{22}^{c}+\phi_{22}^{v}\right)} \tag{83}$$

$$\begin{aligned} &\frac{\left(1-\phi_{11}\right)+\left(1-\phi_{22}\right)}{2\left(1-\phi_{11}\right)\left(1-\phi_{22}\right)} \\ &= e^{\left\{2-\left(1-\phi_{11}^{v}\right)\left(1-\phi_{22}^{v}\right)\left[\left(1-\phi_{11}^{v}\right)+\left(1-\phi_{22}^{v}\right)\right]-\left(1-\phi_{11}^{C}\right)\left(1-\phi_{22}^{c}\right)\left[\left(1-\phi_{11}^{c}\right)+\left(1-\phi_{22}^{c}\right)\right]\right\}} \end{aligned} \tag{84}$$

Equations (82) and (83) are two explicit and simple decomposition equations for the damage tensor components ϕ_{11} and ϕ_{22}, respectively. One next uses the Taylor series of the left hand side, i.e., using $\frac{1}{1-x} \approx 1 + x$, then both Eqs. (82) and (83) take the following form:

$$\phi_{11} \approx 1 - e^{-\left(\phi_{11}^{c}+\phi_{11}^{v}\right)} \tag{85}$$

$$\phi_{22} \approx 1 - e^{-\left(\phi_{22}^{c}+\phi_{22}^{v}\right)} \tag{86}$$

The third exponential Eq. (84) is the coupling expression that relates the various "crack" and "void" damage tensor components. The exponential coupling Eq. (84) may be simplified by approximating it using the appropriate Taylor series expansions. Therefore, the following approximate simplified coupling equation is obtained from Eq. (84):

$$\begin{aligned}&\frac{5}{2}\phi_{11}^{v}+\frac{5}{2}\phi_{22}^{v}+\frac{5}{2}\phi_{11}^{c}+\frac{5}{2}\phi_{22}^{c}-4\phi_{11}^{v}\phi_{22}^{v}-4\phi_{11}^{c}\phi_{22}^{c}-\left(\phi_{11}^{v}\right)^{2}-\left(\phi_{22}^{v}\right)^{2}-\left(\phi_{11}^{c}\right)^{2}-\left(\phi_{22}^{v}\right)^{2}\\&\quad+\left(\phi_{11}^{v}\right)^{2}\phi_{22}^{v}+\phi_{11}^{v}\left(\phi_{22}^{v}\right)^{2}+\left(\phi_{11}^{c}\right)^{2}\phi_{22}^{c}+\phi_{11}^{c}\left(\phi_{22}^{c}\right)^{2} \;=\; 2\end{aligned} \tag{87}$$

Equation (87) represents an implicit generalized coupling equation for plane stress obtained through the exponential decomposition.

Conclusion

A mathematical study is presented to investigate in detail the true nature of the decomposition of the damage variable in continuum damage mechanics. For this purpose, the classical scalar and tensorial decompositions are reviewed first. Then these are generalized using an exponential function type of decomposition. It is shown that the exponential decomposition is more general than the classical decomposition. It is also shown that the classical decomposition can be obtained as a special case of the exponential decomposition.

Two defect types, mainly cracks and voids, are used first in the analysis. This is followed by three defect types consisting of cracks, voids, and a third unspecified defect type. The mathematical formulation proves to be systematic and elegant. Finally, the case of plane stress is solved in which three equations are ultimately derived: two equations represent explicit and simple decomposition formulas, while the third equation is a coupling relation between the various damage tensor components.

References

D.J. Celentano, P.E. Tapia, J.-L. Chaboche, Experimental and numerical characterization of damage evolution in steels, in *Mecanica Computacional*, ed. by G. Buscaglia, E. Dari, O. Zamonsky, vol. XXIII, (ONERA, Bariloche, 2004)

J.L. Chaboche, Continuum damage mechanics: A tool to describe phenomena before crack initiation. Nucl. Eng. Design **64**, 233–247 (1981)

J.L. Chaboche, *Continuum Damage Mechanics: Present State and Future Trends*, International Seminar on Modern Local Approach of Fracture, Moret-sur-Loing, France (1986)
J.L. Chaboche, Continuum damage mechanics: Part I: General concepts. J. Appl. Mech. ASME **55**, 59–64 (1988a)
J.L. Chaboche, Continuum damage mechanics: Part II: Damage growth, crack initiation, and crack growth. J. Appl. Mech. ASME **55**, 65–72 (1988b)
C. Chow, J. Wang, An anisotropic theory of elasticity for continuum damage mechanics. Int. J. Fract. **33**, 3–16 (1987)
I. Doghri, *Mechanics of Deformable Solids: Linear and Nonlinear, Analytical and Computational Aspects* (Springer, Berlin, 2000)
N.R. Hansen, H.L. Schreyer, A thermodynamically consistent framework for theories of elastoplasticity coupled with damage. Int. J. Solids Struct. **31**(3), 359–389 (1994)
L. Kachanov, On the creep fracture time. Izv Akad Nauk USSR Otd Tech. **8**, 26–31 (1958). (in Russian)
P.I. Kattan, G.Z. Voyiadjis, A coupled theory of damage mechanics and finite strain Elasto-plasticity – Part I: Damage and elastic deformations. Int. J. Eng. Sci. **28**(5), 421–435 (1990)
P.I. Kattan, G.Z. Voyiadjis, A plasticity-damage theory for large deformation of solids – Part II: Applications to finite simple shear. Int. J. Eng. Sci. **31**(1), 183–199 (1993)
P.I. Kattan, G.Z. Voyiadjis, Decomposition of damage tensor in continuum damage mechanics. J. Eng. Mech. ASCE **127**(9), 940–944 (2001a)
P.I. Kattan, G.Z. Voyiadjis, *Damage Mechanics with Finite Elements: Practical Applications with Computer Tools* (Springer, Berlin, 2001b)
D. Krajcinovic, *Damage Mechanics* (North Holland, 1996)., 776 p
P. Ladeveze, J. Lemaitre, *Damage Effective Stress in Quasi-Unilateral Conditions*, The 16th International Cogress of Theoretical and Applied Mechanics, Lyngby (1984)
P. Ladeveze, M. Poss, L. Proslier, Damage and fracture of Tridirectional composites. Progr. Sci. Eng. Compos. **1**, 649–658 (1982)
H. Lee, K. Peng, J. Wang, An anisotropic damage criterion for deformation instability and its application to forming limit analysis of metal plates. Eng. Fract. Mech. **21**, 1031–1054 (1985)
J. Lemaitre, How to use damage mechanics. Nucl. Eng. Des. **80**, 233–245 (1984)
J. Lemaitre, A continuous damage mechanics model for ductile fracture. J. Eng. Mater. Technol. **107**, 83–89 (1985)
J. Lemaitre, Local approach of fracture. Eng. Fract. Mech. **25**(5/6), 523–537 (1986)
J. Lemaitre, *A Course on Damage Mechanics* (Springer, New York, 1992)
J. Lemaitre, J.L. Chaboche, *Mecanique de Materiaux Solides* (Dunod, Paris, 1985)
J. Lemaitre, J. Dufailly, Damage measurements. Eng. Fract. Mech. **28**(5/6), 643–661 (1987)
G. Lubineau, A pyramidal modeling scheme for laminates – Identification of transverse cracking. Int. J. Damage Mech. **19**(4), 499–518 (2010)
G. Lubineau, P. Ladeveze, Construction of a micromechanics-based intralaminar mesomodel, and illustrations in ABAQUS/standard. Comput. Mater. Sci. **43**(1), 137–145 (2008)
B. Luccioni, S. Oller, A directional damage model. Comput. Methods Appl. Mech. Eng. **192**, 1119–1145 (2003)
Y. Rabotnov, Creep rupture, in *Proceedings, Twelfth International Congress of Applied Mechanics*, ed. by M. Hetenyi, W. G. Vincenti, (Springer, Berlin, 1969), pp. 342–349
J.R. Rice, Inelastic constitutive relations for solids: An internal variable theory and its application to metal plasticity. J. Mech. Phys. Solids **19**, 433–455 (1971)
F. Sidoroff, Description of anisotropic damage application in elasticity, in *IUTAM Colloqium on Physical Nonlinearities in Structural Analysis*, (Springer, Berlin, 1981), pp. 237–244
G.Z. Voyiadjis, Degradation of elastic modulus in elastoplastic coupling with finite strains. Int. J. Plast. **4**, 335–353 (1988)
G.Z. Voyiadjis, P.I. Kattan, A coupled theory of damage mechanics and finite strain elasto-plasticity – Part II: Damage and finite strain plasticity. Int. J. Eng. Sci. **28**(6), 505–524 (1990)
G.Z. Voyiadjis, P.I. Kattan, A plasticity-damage theory for large deformation of solids – Part I: Theoretical formulation. Int. J. Eng. Sci. **30**(9), 1089–1108 (1992)

G.Z. Voyiadjis, P.I. Kattan, *Damage Mechanics* (Taylor and Francis/CRC Press, 2005)
G.Z. Voyiadjis, P.I. Kattan, *Advances in Damage Mechanics: Metals and Metal Matrix Composites with an Introduction to Fabric Tensors*, 2nd edn. (Elsevier, 2006a)
G.Z. Voyiadjis, P.I. Kattan, A new fabric-based damage tensor. J. Mech. Behav. Mater. **17**(1), 31–56 (2006b)
G.Z. Voyiadjis, P.I. Kattan, Damage mechanics with fabric tensors. Mech. Adv. Mater. Struct. **13**(4), 285–301 (2006c)
G.Z. Voyiadjis, P.I. Kattan, A comparative study of damage variables in continuum damage mechanics. Int. J. Damage Mech. **18**(4), 315–340 (2009)
G.Z. Voyiadjis, P.I. Kattan, A new class of damage variables in continuum damage mechanics. ASME J. Mater. Technol. **134**(2), 021016 (2012a). 10 p
G.Z. Voyiadjis, P.I. Kattan, Mechanics of damage processes in series and in parallel: A conceptual framework. Acta Mech. **223**(9), 1863–1878 (2012b)
G.Z. Voyiadjis, P.I. Kattan, Mechanics of damage, healing, damageability, and integrity of materials: A conceptual framework. Int. J. Damage Mech. **26**(1), 50–103 (2017a). accepted for publication, 55 p
G.Z. Voyiadjis, P.I. Kattan, Elasticity of damaged graphene: A damage mechanics approach. Int. J. Damage Mech. **25**(8), 1184 (2017b). accepted for publication, 50 p
G.Z. Voyiadjis, P.I. Kattan, Introducing damage mechanics templates for the systematic and consistent formulation of holistic material damage models. Acta Mech. Published Online, 40 manuscript pages (2017c)

Damageability and Integrity of Materials: New Concepts of the Damage and Healing Fields

2

George Z. Voyiadjis, Peter I. Kattan, and Juyoung Jeong

Contents

Introduction 24
A New Damage Variable 25
Scalar Formulation 25
Tensorial Formulation 29
Additional Damage Variables 30
Another New Damage Variable 32
Integrity and Damageability of Materials 34
Scalar Formulation 34
Damageability Variable 38
Integrity Versus Damageability 40
The Integrity Field 42
Scalar Formulation 42
Illustrative Example 47
Approximation of the Integrity Field 50
The Healing Field 51
Summary/Conclusions 53
Appendix 55
Appendix I: Are There Any Limits to the Damage Variable 55
Appendix II: How to Compose Damage Variables 56
References 58

G. Z. Voyiadjis (✉)
Center for GeoInformatics C4G and Computational Solid Mechanics Laboratory, Department of Civil and Environmental Engineering, Louisiana State University, Baton Rouge, LA, USA
e-mail: voyiadjis@eng.lsu.edu

P. I. Kattan · J. Jeong
Department of Civil and Environmental Engineering, Louisiana State University, Baton Rouge, LA, USA
e-mail: pkattan@petrabooks.com; jjeong7@lsu.edu

© Springer Nature Switzerland AG 2022

G. Z. Voyiadjis (ed.), *Handbook of Damage Mechanics*,
https://doi.org/10.1007/978-3-030-60242-0_83

Abstract

Within the framework of continuum damage mechanics, several novel and basic notions are proposed in this chapter. These ideas focus on the nature of the two damage and healing processes, as well as providing a consistent and systematic description for the concepts of damageability and material integrity. To that goal, the following four sections are presented: The logarithmic and exponential damage variables are introduced in section "A New Damage Variable" along with comparisons to the classical damage variable. Section "Integrity and Damageability of Materials" introduces a novel damage mechanics formulation that includes the two aspects of damage-integrity and healing-damageability. The damage and integrity variables can all be derived from the damage-integrity angle, while the healing variable and damageability variable can be calculated from the healing-damageability angle. Section "The Integrity Field" introduces the new integrity field concept, whereas section "The Healing Field" introduces the new healing field concept. These two domains are offered as a broadening of the traditional damage and integrity ideas.

Keywords

New damage variable · Integrity field · Damageability of materials · Healing field

Introduction

Kachanov (1958) was the first to establish the concept of effective stress and the concept of continuum damage mechanics. Rabotnov (1969) and others afterward followed in his footsteps (Kattan and Voyiadjis 2001a, b; Ladeveze and Lemaitre 1984; Voyiadjis and Kattan 2005, 2006, 2009, 2012). A scalar damage variable ϕ is introduced in the context of continuum damage mechanics, with values ranging $0 \leq \phi \leq 1$. As a result, when the virgin material is undamaged, the value of the damage variable is zero, whereas when the material is completely ruptured, the value approaches one. However, without breaking the concept of a continuum, the damage value cannot surpass 0.3–0.4.

Damage mechanics research has accelerated dramatically in recent years (Celentano et al. 2004; Doghri 2000; Hansen and Schreyer 1994; Kattan and Voyiadjis 1990; Kattan and Voyiadjis 1993; Ladeveze et al. 1982; Lubineau 2010; Lubineau and Ladeveze 2008; Lee et al. 1985; Luccioni and Oller 2003; Rice 1971; Sidoroff 1981; Voyiadjis 1988; Voyiadjis and Kattan 1990; Voyiadjis and Kattan 1992). There have also been some important scientific attempts in the related field of healing mechanics (Voyiadjis et al. 2011, 2012a, b). Some of the most recent research efforts have taken the form of mixed damage/healing models for various materials. Instead of using the harm potential surface as a damage measure, another method of damage characterization is to employ an entropy generation rate (Basaran and Yan 1998; Basaran and Tang 2002; Basaran et al. 2003, 2004; Basaran and Nie 2004; Gunel and Basaran 2011a, b). This work is divided into four sections, each of which covers a different aspect of damage and healing mechanisms. In addition, new

concepts such as damageability, integrity, unhealable damage, the integrity field, and the healing field are introduced.

Section "A New Damage Variable" is separated into four primary subsections, one of which contains a novel damage mechanics formulation. The fundamental ideas of a logarithmic damage variable are described in the first section. The logarithmic damage variable is computed systematically, and numerous comparisons with the traditional damage variable utilized in the literature are made. Although the first half of the chapter gives a scalar formulation of the logarithmic damage variable, the second portion goes through its tensorial generalization. The third and fourth parts introduce additional related damage variables, including a consistently generated exponential damage variable.

Section "Integrity and Damageability of Materials" introduces the two new ideas of material damageability and integrity. Two new angular metrics are introduced for this purpose. The damage-integrity angle is the first, while the healing-damageability angle is the second. These two angles are given precise mathematical definitions from which all four variables of damage, healing, damageability, and integrity can be calculated. The final part discusses some important links between material integrity and damageability.

Section "The Integrity Field" introduces a new notion called the integrity field, which is demonstrated with an example. The integrity field is proven to be a stress-like quantity with stress units. It is further demonstrated that the integrity field is limitless in the virgin, undamaged condition, but becomes finite after damage occurs. An example is given to illustrate the theoretical formulation and an approximation for the integrity field is offered.

The healing field is similarly presented in section "The Healing Field" to the way the integrity field is described in section "The Integrity Field." Both the integrity field and the healing field equations are proposed in the expectation that they may be beneficial in future research of the damage and healing mechanics and applications. It should be emphasized that this presentation is solely about theoretical formulations.

Finally, there are two appendices: one that has a mathematical derivation of the limits of classical damage variables, and the other that contains a new idea of damage variable composition that can be used to build new, more rigorous, and intricate damage variables. The new composition approach can be used to create new damage variables that meet the analyst's needs for a certain damage process.

A New Damage Variable

In this section, the equations of a new damage variable are derived. The new damage variable is logarithmic and is termed the logarithmic damage variable. It is derived based on sound mathematical principles. Both scalars and tensors are used in the derivation. Additional damage variables, including an exponential damage variable, are also proposed.

Scalar Formulation

In terms of cross-sectional areas, the traditional damage variable ϕ is defined as follows (Kachanov 1958; Rabotnov 1969):

$$\phi = \frac{A - \overline{A}}{A} \tag{1}$$

where A is the cross-sectional area of the material in its damaged configuration and $\overline{A}$ is the cross-sectional area of the material in its hypothetical effective (undamaged) configuration. The damage variable has values ranging from 0 (for a virgin, undamaged state) to 1 (for complete rupture). These limits are derived from the expression of Eq. (1) based on the physics of the situation, but Appendix I provides a coherent mathematical derivation.

The classical formula for the effective stress $\overline{\sigma}$ in terms of the stress σ and the damage variable ϕ may be obtained using Eq. (1) and the equilibrium relation $\sigma A = \overline{\sigma}\overline{A}$:

$$\overline{\sigma} = \frac{\sigma}{1 - \phi} \tag{2}$$

When the natural logarithms of both sides of Eq. (2) are added together, the result is:

$$\ln \overline{\sigma} = \ln \sigma - \ln (1 - \phi) \tag{3}$$

The equation $\ln(1 - \phi)$ is then expanded using the Taylor series expansion around $\phi = 0$ to obtain:

$$\ln (1 - \phi) = -\phi + \ldots\ldots \tag{4}$$

To emphasize the approximate character of this derivation, take the first term of the series in Eq. (5) and substitute it into Eq. (3), using the variable L rather than ϕ to show the approximate aspect of this derivation:

$$L = \ln \overline{\sigma} - \ln \sigma \tag{5}$$

The following is a rewriting of the above equation:

$$\overline{\sigma} = \sigma e^{L} \tag{6}$$

The effective stress $\overline{\sigma}$ is expressed in terms of the stress σ and the logarithmic damage variable L in the above equation. In this case, unlike the standard damage variable ϕ, the logarithmic variable L can have values greater than one. It should be emphasized that Eq. (6) should be compared to Eq. (2). The logarithmic damage variable had previously been discussed in the literature (Basaran and Yan 1998; Krajcinovic 1996; Carol et al. 2002), but not thoroughly and consistently.

A different definition of the logarithmic damage variable is derived next. This is done using the cross-sectional area as an independent variable. The following explicit expression for L can be obtained using Eq. (6) and the equilibrium relation $\sigma A = \overline{\sigma}\overline{A}$.

$$L = -\ln\left(\frac{\overline{A}}{A}\right) \tag{7}$$

The logarithmic damage variable L has a formal definition in Eq. (7). Equation (7) should be compared to Eq. (1). Table 1 summarizes the outcomes achieved thus far.

Figure 1 shows the effective stress ratio $\overline{\sigma}/\sigma$ against the damage variable for each event. The value of the effective stress for the undamaged virgin material is the same in both circumstances, as shown in the figure (when $\phi = L = 0$). Both curves begin to increase in value as damage increases, but the increase is slower with the logarithmic damage variable than with the classical damage variable.

The decrease of the elastic modulus in both instances is then investigated. The hypothesis of elastic energy equivalence is used for this purpose. This takes the following form:

$$\frac{1}{2}\overline{\sigma}\,\overline{\varepsilon} = \frac{1}{2}\sigma\varepsilon \tag{8}$$

The aforementioned relationship is used twice: first with the classical damage variable and again with the logarithmic damage variable. As a result of inserting Eq. (2) into Eq. (8), simplifying, and solving for $\overline{\varepsilon}$, one gets:

$$\overline{\varepsilon} = \varepsilon(1-\phi) \tag{9}$$

Table 1 A comparison table between the different damage variables

	Classical damage formulation	Logarithmic damage formulation
Damage variable	$\phi = \frac{A-\overline{A}}{A}, \quad 0 < \phi < 1$	$L = -\ln\left(\frac{\overline{A}}{A}\right), \quad L > 0$
Effective stress	$\overline{\sigma} = \frac{\sigma}{1-\phi}$	$\overline{\sigma} = \sigma e^{L}$

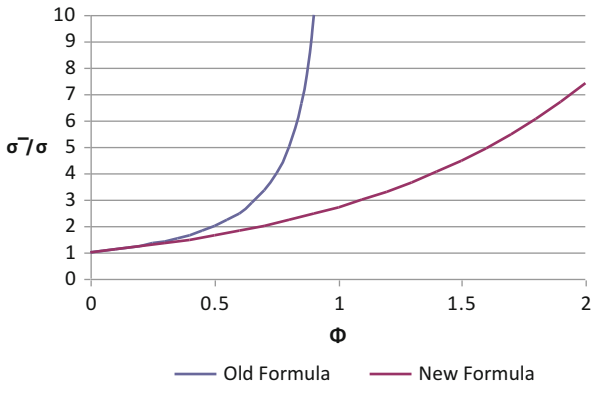

Fig. 1 The different damage variables compared

By replacing Eq. (6) into Eq. (8), simplifying, and solving for the logarithmic damage variable, the following result is obtained:

$$\overline{\varepsilon} = \varepsilon e^{-L} \tag{10}$$

Next, one follows with the elastic constitutive equations as follows:

$$\sigma = E\varepsilon \tag{11}$$

$$\overline{\sigma} = \overline{E}\overline{\varepsilon} \tag{12}$$

Using the conventional damage variable, one derives the following transformation equation for the elastic modulus by replacing Eqs. (2) and (9) into Eq. (12), simplifying, and comparing the result with Eq. (11).

$$E = \overline{E}(1-\phi)^2 \tag{13}$$

While using the logarithmic damage variable, one substitutes Eqs. (6) and (10) into Eq. (12), simplifies the result, and compares it to Eq. (11), yielding the following transformation equation for the elastic modulus:

$$E = \overline{E}e^{-2L} \tag{14}$$

The degradation relations for the elastic modulus in the instances of the classical damage variable and the logarithmic damage variable are represented by Eqs. (13) and (14) respectively. Table 2 summarizes the outcomes achieved here so far.

Table 2 The two damage variables compared

	Classical damage formulation	Logarithmic damage formulation
Effective strain	$\overline{\varepsilon} = \varepsilon(1-\phi)$	$\overline{\varepsilon} = \varepsilon e^{-L}$
Elastic modulus	$E = \overline{E}(1-\phi)^2$	$E = \overline{E}e^{-2L}$

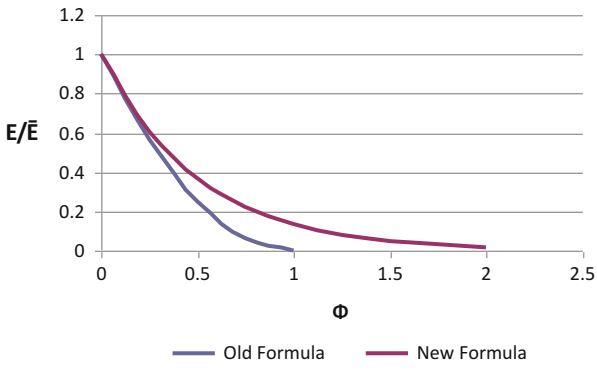

Fig. 2 The effect of the damage variables on the elastic stiffness

Equations (13) and (14) are plotted in Fig. 2 to analyze the elastic stiffness degradation. The elastic stiffness diminishes more rapidly in the classical situation than in the logarithmic case. Furthermore, while both situations begin with the ratio $E/\overline{E}$ equal to 1, the classical case quickly approaches the value 0 at $\phi = 1$, whereas the logarithmic case progressively degrades to the value 0 (at $L = 2$ and higher).

Tensorial Formulation

The next step is to generalize Eq. (6) to the case of deformation and damage in general. Tensors must be used instead of scalars for this purpose. Tensors are represented using the following vector and matrix notation. The stress tensor and the effective stress tensor are represented by the vectors $\{\sigma\}$ and $\{\overline{\sigma}\}$, respectively. As a result, the following expression can be used to tensorial Eq. (6):

$$\{\overline{\sigma}\} = \left[e^{[L]}\right]\{\sigma\} \tag{15}$$

where $[L]$ is the logarithmic damage tensor's matrix representation. The tensorial generalization of Eq. (2)'s effective stress is stated in terms of the fourth-rank damage effect tensor $[M]$ which is equivalent here to $[e^{[L]}]$ as follows:

$$\{\overline{\sigma}\} = [M]\{\sigma\} \tag{16}$$

It is time to look into the fourth-rank exponential matrix form $[e^{[L]}]$. The Taylor series expansion of the matrix $[e^{[L]}]$ is written as follows:

$$\left[e^{[L]}\right] = [I] + [L] + \frac{1}{2}[L]^2 + \ldots\ldots\ldots \tag{17}$$

where both $[I]$ and $[L]$ are matrix representations of fourth-rank tensors. The following formula for the generalization of the effective stress tensor is obtained by taking the first two terms of the series expansion of Eq. (17):

$$\{\overline{\sigma}\} = ([I] + [L])\{\sigma\} \tag{18}$$

The following equation can be written in indicial notation:

$$\overline{\sigma}_{ij} = (\delta_{ik} + L_{ik})\,\sigma_{kj} \tag{19}$$

Alternatively, one can obtain the following formula for the generalization of the effective stress tensor by taking the first three terms of the series expansion of Eq. (17):

$$\{\overline{\sigma}\} = \left([I] + [L] + \frac{1}{2}[L]^2\right)\{\sigma\} \tag{20}$$

The following equation can be written in indicial notation:

$$\overline{\sigma}_{ij} = \left(\delta_{ik} + L_{ik} + \frac{1}{2}L_{im}L_{mk}\right)\sigma_{kj} \tag{21}$$

Equations (18) and (20) are two different approaches to generalizing the scalar formulation of the equation's effective stress (6).

Additional Damage Variables

The exact link between the classical and logarithmic damage variables is then determined. On starting with Eq. (7) and replacing for $\overline{A}/A$ from Eq. (1), then simplifying, the following result is obtained:

$$L = \ln\left(\frac{1}{1-\phi}\right) \tag{22}$$

The precise connection between the two damage variables is represented by the expression in Eq. (22). This term had already been mentioned in the literature (Basaran and Yan 1998; Krajcinovic 1996; Carol et al. 2002) but without more explanation. Figure 3 shows how to compare the behavior of both variables by plotting both ϕ and L versus $\frac{A-\overline{A}}{A}$. The figure clearly shows that, whereas ϕ is linear, L is exponential. With the logarithmic damage variable, more damage results in a dramatic increase in the value of the damage variable. Furthermore, when $\frac{A-\overline{A}}{A}$ reaches the number of 0.632, L achieves the value of 1.

Finally, the relationship denoted by Eq. (22) can be rewritten with respect to ϕ as follows:

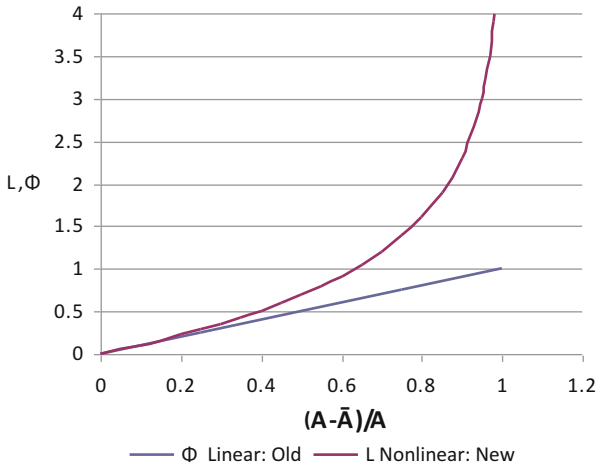

Fig. 3 The two damage variables compared

$$\phi = 1 - e^{-L} \tag{23}$$

It should be mentioned that the above remark emerged in the literature without more explanation (Basaran and Yan 1998; Krajcinovic 1996; Carol et al. 2002). Several different but equivalent definitions of the damage variable are discussed toward the end of this subsection. Assume the following expression is used to define a damage variable ϕ_2:

$$\phi_2 = \frac{\ln(1+A) - \ln\left(1+\overline{A}\right)}{\ln(1+A)} \tag{24}$$

Using the Taylor series expansion, expand each natural logarithm in the following formula as follows:

$$\ln(1+x) = x - \frac{1}{2}x^2 + \ldots\ldots \tag{25}$$

by removing the first term of the series, inserting it into Eq. (24), and simplifying, the conventional damage variable of Eq. (1) is obtained as follows:

$$\phi_2 \approx \frac{A - \overline{A}}{A} \tag{26}$$

As a result, the proposed definition in Eq. (24) and the classical definition are equivalent for small quantities of damage. The following is another useful formulation for defining the damage variable that requires further investigation:

$$\phi_3 = \frac{e^{A-1} - e^{\overline{A}-1}}{e^{A-1}} \tag{27}$$

Using a Taylor series expansion, expand each exponential term in the above expression as follows:

$$e^x = 1 + x + \frac{1}{2}x^2 + \ldots\ldots \tag{28}$$

The classical damage variable of Eq. (1) is obtained by taking only the first two terms of the series, inserting them into Eq. (27), and simplifying:

$$\phi_3 \approx \frac{A - \overline{A}}{A} \tag{29}$$

As a result, the proposed definition in Eq. (27) and the classical definition is equivalent for small quantities of damage. It is worth noting that the expression in Eq. (27) can be rewritten in the following way:

$$\phi_3 = \frac{e^{A} - e^{\overline{A}}}{e^{A}} \tag{30}$$

As a result, both the logarithmic and exponential definitions of the damage variable are identical to the classical definition of the damage variable if the amount of damage is minimal.

Another New Damage Variable

A simple derivation is offered in this section to create a new exponential damage variable. As will be seen later, this new damage variable has both advantages and drawbacks. One begins by rewriting the definition of the conventional damage variable in Eq. (1) as follows:

$$\phi = 1 - \frac{\overline{A}}{A} \tag{31}$$

Taking the square root of Eq. (31) yields the following:

$$\phi^{\frac{1}{2}} = \sqrt{\phi} = \sqrt{1 - \frac{\overline{A}}{A}} \approx 1 - \frac{1}{2}\frac{\overline{A}}{A} \tag{32}$$

where the series expansion $\sqrt{1+x} \approx 1 + \frac{1}{2}x + \ldots$ is employed for small x. The square root of the expression of Eq. (32) is obtained in the next step:

$$\phi^{\frac{1}{4}} = \sqrt{\sqrt{\phi}} = \sqrt{1 - \frac{1}{2}\frac{\overline{A}}{A}} \approx 1 - \frac{1}{2}\cdot\frac{1}{2}\frac{\overline{A}}{A} \tag{33}$$

Taking the square root of the expression of Eq. (33), one gets the following:

$$\phi^{\frac{1}{8}} = \sqrt{\sqrt{\sqrt{\phi}}} = \sqrt{1 - \frac{1}{2}\cdot\frac{1}{2}\frac{\overline{A}}{A}} \approx 1 - \frac{1}{2}\cdot\frac{1}{2}\cdot\frac{1}{2}\frac{\overline{A}}{A} \tag{34}$$

Proceed in this manner until it arrives at the following general statement, where n = 0, 1, 2, 3,..., infinite.

$$\phi^{\frac{1}{2^n}} \approx 1 - \frac{1}{2^n}\frac{\overline{A}}{A} \tag{35}$$

It is worth noting that when n = 0, the expression in Eq. (35) reduces to the conventional expression of Eq. (31). The next step is to use the equilibrium equation $\overline{\sigma}\overline{A} = \sigma A$ and plug it into Eq. (35) above to get:

$$\overline{\sigma} = \frac{\sigma}{2^n\left(1 - \phi^{\frac{1}{2^n}}\right)} \tag{36}$$

It is worth noting that for n = 0, the above formulation of Eq. (36) reduces to the classical expression of Eq. (2). The next step is to look into what occurs as n approaches infinity. As a result, the following results:

$$\overline{\sigma} = \lim_{n\to\infty} \frac{\sigma}{2^n\left(1-\phi^{\frac{1}{2^n}}\right)} = -\frac{\sigma}{\ln\phi} \tag{37}$$

As a result, the following new equation for effective stress is obtained:

$$\overline{\sigma} = -\frac{\sigma}{\ln\phi} \tag{38}$$

When the equilibrium equation $\overline{\sigma}\overline{A} = \sigma A$ is substituted into the expression of Eq. (38) above, the expression of what is known as the exponential damage variable is obtained:

$$\phi = e^{-\frac{\overline{A}}{A}} \tag{39}$$

The new exponential damage variable's values begin with $1/e = 0.368$ for the virgin (undamaged) material and increase to 1 for full rupture. This unique property of the new damage variable could be beneficial in identifying specific sorts of materials or describing specific types of damage processes. The following step is to compare the three scalar damage variables described in this section. Figure 4a plots the expressions of the classical damage variable in Eq. (1), the logarithmic damage variable in Eq. (7), and the exponential damage variables in Eq. (39). It can be seen in this figure that the classical and exponential damage variables have comparable behavior, which differs from the logarithmic damage variable's behavior, especially in the virgin (undamaged) stage.

Another comparison is show in Fig. 4b. It can be seen in this graph that the classical and logarithmic damage variables behave similarly in the virgin (undamaged) state but diverge significantly in the state of rupture. On the other hand, the figure shows that the classical and exponential damage variables differ significantly in the virgin (undamaged) state but appear similar in the ruptured state.

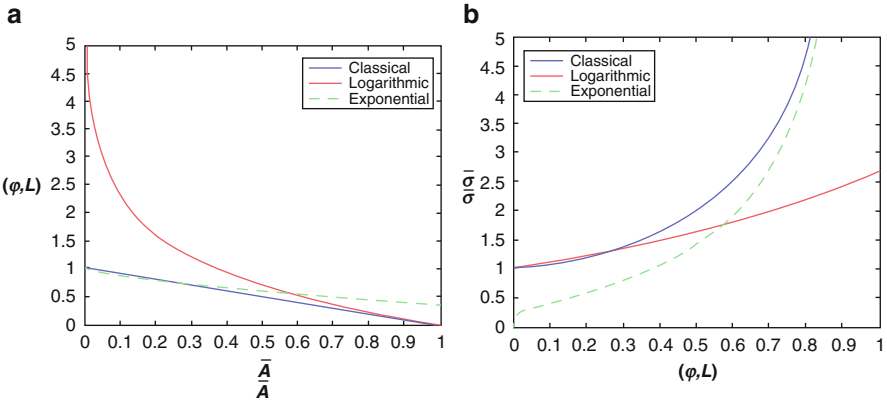

Fig. 4 Comparison between the three damage variables: (**a**) comparison among the three scalar damage variables based on Eqs. (1), (7), and (39) (**b**) comparison of the effective stress ratio for the three damage variables based on Eqs. (2), (6), and (38)

A method of leveraging the composition of existing damage variables can be used to build more novel, sophisticated, and rigorous damage variables. Appendix II describes a new way of generating damage variables. This method can be used to create new damage variables that are tailored to the analyst's needs for a particular material or damage process.

Finally, tensors can be used to generalize the new exponential damage variable to other states of deformation and damage. Using tensors, we can generalize the scalar expression of Eq. (38) to:

$$\{\overline{\sigma}\} = -\left[\ln\left([I] - [M]^{-1}\right)\right]^{-1}\{\sigma\} \tag{40}$$

where vectors and matrices represent tensors. When the following changes are made, the generalized tensorial Eq. (40) simplifies to the scalar Eq. (38): $[M] \equiv \frac{1}{1-\phi}$ and $[I] \equiv 1$. It is worth noting that $[M]$ and $[I]$ represent fourth-rank tensors.

Integrity and Damageability of Materials

New notions of material integrity and damageability are presented in this section. Damageability has not been mathematically defined or even utilized descriptively in materials science or damage mechanics, according to the literature. On the other hand, some researchers (Carol et al. 2002) have employed the concept of integrity as a mathematical statement, although only in a primitive and inconsistent manner. Both the integrity and damageability variables are specified uniformly in this section, and their mathematical expressions are determined from the damage and healing variables, respectively. In terms of notation, the symbol (h y) denotes the integrity variable, whereas the symbol (ϕ y) denotes the damageability variable.

Scalar Formulation

Webster's New Collegiate Dictionary defines integrity as "an undamaged condition or the quality or state of being complete or undivided." The damage-integrity angle must be introduced first to construct a consistent mathematical equation for the integrity variable (DIA). The sine of DIA is used to define the traditional damage variable ϕ:

$$\sin(DIA) = \phi \tag{41}$$

Figure 5 is a schematic diagram depicting how damage grows as DIA (shown θ in the figure) increases, starting with the virgin (undamaged) condition at $DIA = 0$ and ending with full rupture at $DIA = \pi/2$. Following the description above, the integrity variable is defined as the cosine of DIA:

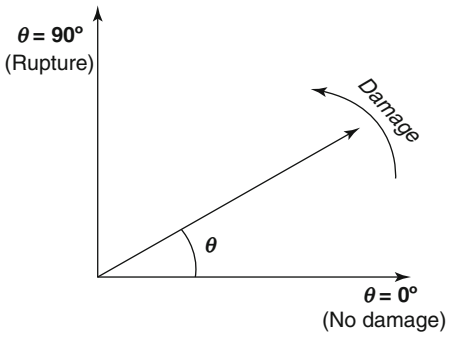

Fig. 5 Damage-integrity angle

$$\cos(DIA) = (hy) \tag{42}$$

The sine and cosine functions, on the other hand, satisfy the trigonometric identity:

$$\sin^2(DIA) + \cos^2(DIA) = 1 \tag{43}$$

Equations (41) and (42) are substituted into Eq. (43), yielding the following expression for the integrity variable ($h\ y$):

$$(hy) = \sqrt{1 - \phi^2} \tag{44}$$

The angle DIA, as can be seen from the equations above, provides a coherent explanation of material damage and integrity. The following expression for the integrity variable is used in the literature (Carol et al. 2002), but it lacks a valid definition or a coherent mathematical formulation:

$$(hy)^* = 1 - \phi \tag{45}$$

Both integrity variables have a value of 1 for the virgin (undamaged) condition and a value of 0 for the state of full rupture, as shown in Fig. 6. A new damage-integrity angle (DIA^*) can be associated with the integrity variable $(h\ y)^*$, as follows:

$$\cos(DIA^*) = (hy)^* = 1 - \phi \tag{46}$$

As a result of the above, a new damage variable ϕ^* connected with the integrity variable $(h\ y)^*$ that may be obtained from the angle DIA^* can be defined as follows:

$$\sin(DIA^*) = \phi^* \tag{47}$$

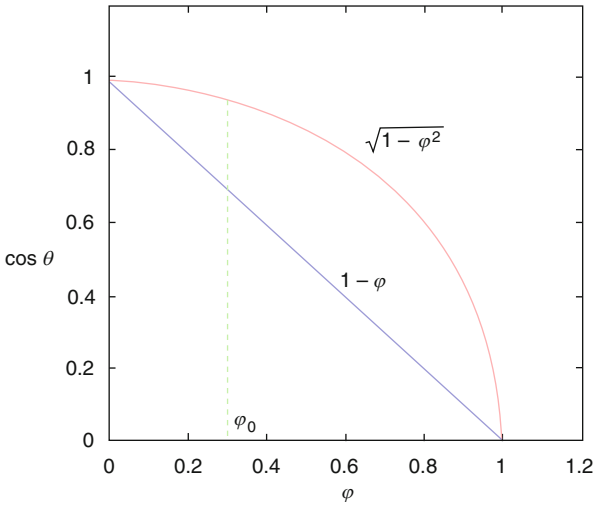

Fig. 6 The integrity variables compared

The following expression for the new damage variable ϕ^* is obtained by applying the trigonometric identity of Eq. (43) to the angle DIA^* instead of DIA and substituting Eq. (46):

$$\phi^* = \sqrt{2\phi - \phi^2} \tag{48}$$

A comparison of the two damage variables ϕ and ϕ^* is shown in Fig. 7:

Figure 7 shows that both damage variables fulfill the same boundary condition, but the new damage variable ϕ^* is nonlinear, whereas the old damage variable ϕ is linear. Table 3 contains a summary of these equations.

On the complex plane, the damage and integrity variables form a unit circle, as shown in the next diagram (as shown in Fig. 8). Consider the following Euler's identity expression:

$$e^{DIA} = \cos(DIA) + i \sin(DIA) \tag{49}$$

Equations (41) and (44) are substituted into Eq. (49), yielding:

$$e^{DIA} = \sqrt{1 - \phi^2} + i\phi \tag{50}$$

The magnitude of the above complex expression is then computed as follows:

$$\left|e^{DIA}\right| = \sqrt{\left(\sqrt{1 - \phi^2}\right)^2 + \phi^2} = 1 \tag{51}$$

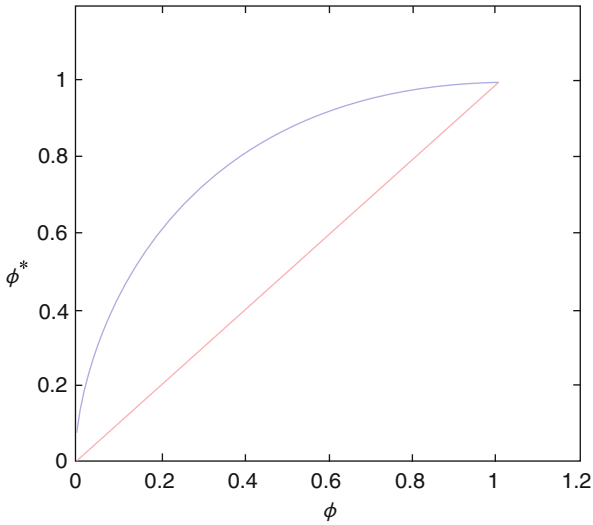

Fig. 7 The damage variables compared

Table 3 Some of the results summarized

	Damage variable	Integrity variable
Classical	ϕ (linear damage)	$\sqrt{1-\phi^2}$ (nonlinear integrity)
New	$\sqrt{2\phi-\phi^2}$ (nonlinear damage)	$1-\phi$ (linear integrity)

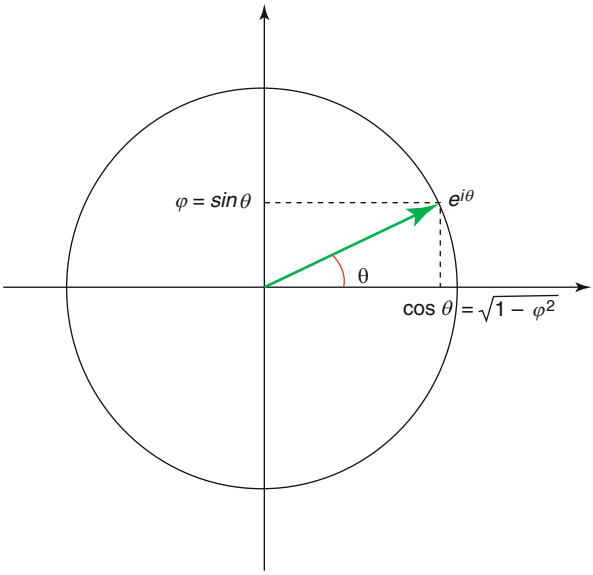

Fig. 8 Damage and integrity on the unit circle

As a result, the magnitude of the complex expression is 1. On the complex plane, the damage and integrity variables form a unit circle. When the angle is substituted for the angle, the same result is achieved. Figure 8 clearly shows that the x-axis represents integrity, whereas the y-axis represents damage.

The damage variable's ratio to the integrity variable is then calculated. This ratio turns out to be the tangent of the angle DIA. In this situation, the proportion is:

$$\frac{\text{damage}}{\text{integrity}} = \tan(DIA) = \frac{\phi}{\sqrt{1-\phi^2}} \tag{52}$$

If the new nonlinear damage variable is used, the ratio becomes:

$$\frac{\text{damage}}{\text{integrity}} = \tan(DIA^*) = \frac{\sqrt{2\phi-\phi^2}}{1-\phi} \tag{53}$$

At this moment, the authors do not believe there is a physical interpretation for this ratio.

Damageability Variable

An effective damage variable ϕ_{eff} is derived as follows in damage and healing mechanics (Voyiadjis et al. 2012a, b, 2011; Darabi et al. 2012):

$$\phi_{eff} = \phi(1-h) \tag{54}$$

where ϕ is the conventional damage variable and h is the conventional healing variable. The integrity variable is linked to the damage variable in the previous subsection. The damageability variable is, nevertheless, related to the healing variable in this part.

Webster's New Collegiate Dictionary defines damageability as "susceptibility to damage or the quality or state of being susceptible to damage." The healing-damageability angle must be introduced first to develop a consistent mathematical equation for the damageability variable (HDA). The sine of HDA is used to define the classical healing variable:

$$\sin(HDA) = h \tag{55}$$

The integrity damageability variable ($\phi\ y$) is defined as the cosine of HDA in light of the previous definition:

$$\cos(HDA) = (\phi y) \tag{56}$$

However, because the sine and cosine functions are trigonometrically equivalent:

$$\sin^2(HDA) + \cos^2(HDA) = 1 \tag{57}$$

Equations (55) and (56) are substituted into Eq. (57), yielding the following expression for the integrity variable ($\phi\ y$):

$$(\phi y) = \sqrt{1 - h^2} \tag{58}$$

As can be seen from the equations above, the angle HDA gives a unified account of material healing and damageability.

For the damageability variable, on the other hand, and as the treatment of the integrity variable in the preceding subsection, the following expression can be used:

$$(\phi y)^* = 1 - h \tag{59}$$

It is important to note that the damgeability variable $(\phi\ y)^*$ has the same boundary constraints as the integrity variable ($\phi\ y$) discussed here. It should be observed that the second damageability variable is linear, whereas the first is nonlinear, and both are consistently obtained from the healing-damageability angle (HDA). Both damageability variables have a value of 0 for the virgin (undamaged) state and a value of 1 for the state of total rupture, it should be highlighted.

A new healing-damageability angle (HDA^*) can be associated with the damageability variable $(\phi\ y)^*$, such that:

$$\cos(HDA^*) = (\phi y)^* = 1 - h \tag{60}$$

As a result of the preceding, a new healing variable h^* connected with the damageability variable $(\phi\ y)^*$ that may be obtained from the angle HDA^* can be defined as follows:

$$\sin(HDA^*) = h^* \tag{61}$$

The following expression for the new healing variable h^* is obtained by applying the trigonometric identity of Eq. (57) to the angle HDA^* instead of HDA and substituting Eq. (60):

$$h^* = \sqrt{2h - h^2} \tag{62}$$

Both healing variables h and h^* meet the same boundary condition; however, the new healing variable h^* is nonlinear, whereas the old healing variable h is linear. Table 4 presents a summary of the findings.

The healing variable's ratio to the damageability variable is then calculated. This ratio turns out to be the tangent of the angle HDA. In this situation, the proportion is:

$$\frac{healing}{damageability} = \tan(HDA) = \frac{h}{\sqrt{1 - h^2}} \tag{63}$$

Table 4 Some of the results summarized

	Healing variable	Damageability variable
Classical	h (linear healing)	$\sqrt{1-h^2}$ (nonlinear damageability)
New	$\sqrt{2h-h^2}$ (nonlinear healing)	$1-h$ (linear damageability)

If the new nonlinear healing variable is used, the ratio becomes:

$$\frac{healing}{damageability} = \tan\left(HDA^*\right) = \frac{\sqrt{2h-h^2}}{1-h} \tag{64}$$

At this moment, the authors do not believe there is a physical interpretation for this ratio. It should be noted that schematic diagrams comparing healing and damageability variables are comparable to the figures comparing damage and integrity variables in the previous paragraph and are not included here.

Integrity Versus Damageability

The goal of this section is to find a mathematical formula for the effective integrity variable $(h\ y)_{eff}$ in terms of the integrity and damageability variables that look like this:

$$(hy)_{eff} = f\left((hy),(\phi y)\right) \tag{65}$$

where f is a function that needs to be determined. The effective integrity variable $(h\ y)_{eff}$ is specified in the imaginary effective (undamaged) configuration of the material in the above equation. The exact correlations between the four variables of damage, healing, integrity, and damageability are shown in Fig. 9.

Starting with the initial expression for the integrity variable in Eq. (44), the effective integrity variable is assumed to be connected to the effective damage variable using the following expression:

$$(hy)_{eff} = \sqrt{1-\phi_{eff}^2} \tag{66}$$

Equation (66) is obtained by substituting for ϕ_{eff} from Eq. (54) and squaring both sides:

$$(hy)_{eff}^2 = 1-\phi^2(1-h)^2 \tag{67}$$

Equation (67) is obtained by solving Eqs. (44) for $(h\ y)$and (58) for $(\phi\ y)$ and then substituting the answers in Eq. (67) as follows:

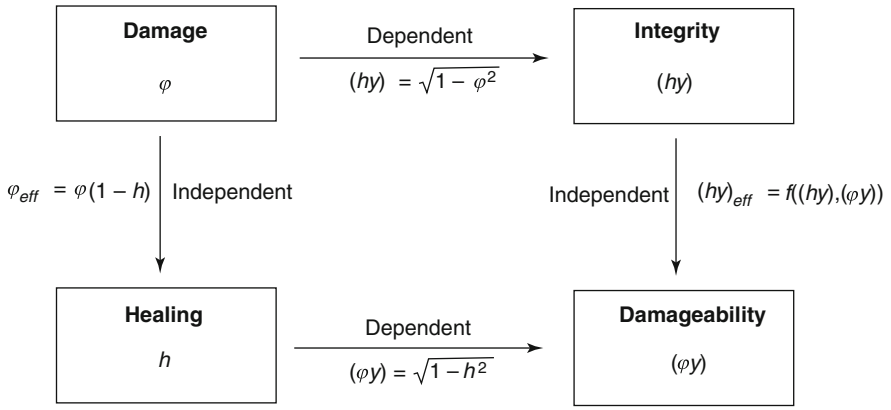

Fig. 9 The four different variables shown schematically

$$(hy)_{eff}^2 = 1 - \left[1 - (hy)^2\right]\left[1 - 2\sqrt{1 - (\phi y)^2} + 1 - (\phi y)^2\right] \tag{68}$$

The final expression can be written as follows after expanding and simplifying Eq. (68):

$$(hy)_{eff} = \sqrt{1 + \left[1 - (hy)^2\right]\left[(\phi y)^2 - 2 + 2\sqrt{1 - (\phi y)^2}\right]^2} \tag{69}$$

Equation (69) expresses the effective integrity variable in terms of the integrity and damageability variables explicitly. The first form of integrity, as given by the equation, is used to obtain this expression (44). When the damageability variable ($\phi\ y$) is set to zero, the integrity variable ($h\ y$) reduces to the value of 1 signifying total integrity when damageability is absent, as shown in Eq. (69). Equation (69) also reveals another boundary condition: when the damageability variable is set to 1, Eq. (69) becomes identically zero. As a result, both mathematically and physically, Eq. (69) is correct. Then, using the second expression of integrity given by Eq. (46), one derives a second expression for the effective integrity variable $(h\ y)_{eff}$.

Starting with the second expression for the integrity variable in Eq. (46), the effective integrity variable is assumed to be connected to the effective damage variable using the following expression:

$$(hy)_{eff} = 1 - \phi_{eff} \tag{70}$$

Equation (70) is obtained by substituting for ϕ_{eff} from Eq. (54):

$$(hy) = 1 - \phi(1 - h) \tag{71}$$

Equation (71) is obtained by solving Eqs. (44) for ($h\ y$) and (58) for ($\phi\ y$) and substituting the answers in Eq. (71) as follows:

$$(hy) = 1 + \sqrt{1 - (hy)^2}\left(\sqrt{\left[1 - (\phi y)^2\right]} - 1\right) \tag{72}$$

The Integrity Field

An example of an integrity field is provided to demonstrate the idea. The integrity field is demonstrated to be a stress-like quantity with stress units. It is further demonstrated that the integrity field is unlimited in the virgin, undamaged condition, but becomes finite after damage occurs. An example is given to illustrate the theoretical concept.

Scalar Formulation

The notion of the integrity field is introduced in this subsection. Fundamental concepts in material mechanics are employed for this aim. In this case, the stress σ is generally expressed in the following way:

$$\sigma = \frac{F}{A} \tag{73}$$

where F is the applied force and A is the cross-sectional area in the deformed and damaged shape. Consider a fictional effective (undamaged) configuration of the material that has no damage using continuum damage mechanics concepts (see Fig. 10). The cross-sectional area in this arrangement is given by $\overline{A}$ where $\overline{A} = A - A^d$ represents the damaged area A^d in the original form. As a result, the scalar damage variable is defined as:

$$\phi = \frac{A^d}{A} = \frac{A - \overline{A}}{A} \tag{74}$$

In contrast to Eq. (73) in which the applied force is divided by the whole area, what happens if the total force is divided by the damaged area A^d is now considered. As an example, consider the following new variable g:

$$g = \frac{F}{A^d} \tag{75}$$

It is important to realize that in Eq. (75), the variable has an infinite value for virgin (undamaged) material with no defects, that is, $A^d = 0$. When damage occurs $A^d > 0$, however, the value of the new variable started to decrease until it reaches a finite value σ_{ult} when the maximum value of A^d is achieved upon total rupture.

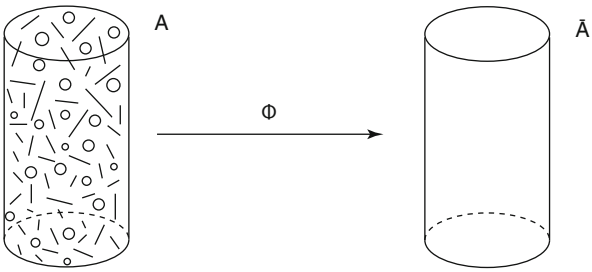

Fig. 10 The two states of damage and undamage compared schematically

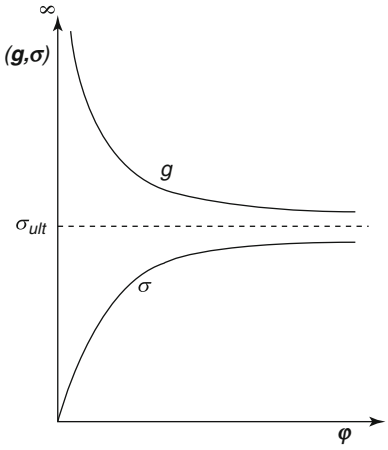

Fig. 11 The integrity field illustrated schematically

Figure 11 shows a graphic representation of this observation. The integrity field is the term given to this quantity g. For pristine, undamaged materials, the integrity field is limitless, as shown above. When the integrity field reaches a finite value, damage begins.

By substituting $F = \sigma A$ into Eq. (75) and using the definition of the damage variable from Eq. (74), the damage field $g$is given the following final expression:

$$g = \frac{F}{A^d} = \frac{\sigma A}{A - \overline{A}} = \frac{\sigma}{\phi} \tag{76}$$

The applied force is divided by the area of defects, which is simply an empty region, in Eq. (75). As a result, the resulting quantity, that is, the integrity field, appears to be fictitious stress. To continue along this line of reasoning, imagine complex stress s with the real component σ being the stress and the imaginary part g being the stress-like quantity:

$$s = \sigma + i\,g = \sigma + i\,\frac{\sigma}{\phi} \tag{77}$$

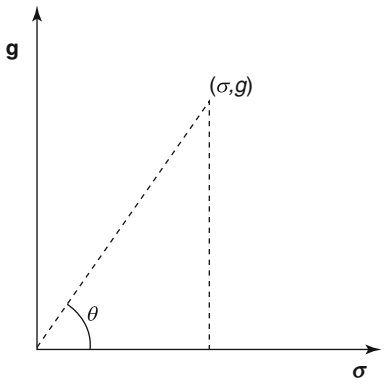

Fig. 12 The stress and integrity field on the complex plane

As seen in Fig. 12, the complex stress is represented as a point on the complex plane. From the origin to the point s, the magnitude and angle of the complex stress vector are as follows (see Fig. 12):

$$|s| = \sqrt{\sigma^2 + g^2} = \frac{\sigma}{\phi}\sqrt{\phi^2 + 1} = g\sqrt{\phi^2 + 1} \tag{78}$$

$$\theta = \tan^{-1}\left(\frac{g}{\sigma}\right) = \tan^{-1}\left(\frac{1}{\phi}\right) \tag{79}$$

Equation (79) shows that $\theta = \pi/2$ represents virgin, undamaged material (where $\phi = 0$), while $\theta = \pi/4$ represents complete rupture (when $\phi = 1$). As a result, the angle of the complex stress (which determines the relationship between actual and imaginary stress) ranges from 45^o to 90^o. With increased damage, the value of this angle decreases. The value of this angle is 45^o at the point of full rupture, and both the actual and imaginary stress is equal to the ultimate stress, that is, $\sigma = g = \sigma_{ult}$. It is apparent that the actual stress and the imagined stress only meet at the point of rupture. It is worth noting that the quantity g is referred to as both the imaginary stress and the integrity field.

Kinematic variables (i.e., strain) will be explored in connection to actual and imaginary stress in the next section of this subsection. Consider the following linear elastic material that obeys Hooke's law:

$$\sigma = E\,\varepsilon \tag{80}$$

where E is the elastic stiffness and ε is the strain. Equation (80) is substituted for Eq. (76), yielding:

$$g = \frac{E\,\varepsilon}{\phi} = E\,\frac{\varepsilon}{\phi} \tag{81}$$

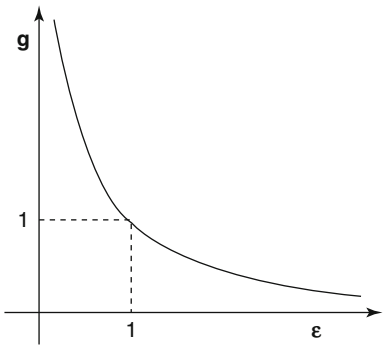

Fig. 13 Relationship between strain and integrity field

where ε/ϕ is the integrity field g that is a kinematic strain-like variable (see Fig. 13). The symbol represents this variable e. As a result, based on Eq. (81):

$$e = \frac{\varepsilon}{\phi} \tag{82}$$

$$g = E\,e \tag{83}$$

Equation (83) denotes a new elastic constitutive relationship between the stress-like variable $g$and the strain-like variable$e$. This relationship is linear, as shown by Eq. (83). The nature of the new strain-like variable e is then investigated. At rupture (at $\phi = 1$), the value of e reduces from infinity for the virgin (undamaged) state to a minimum nonzero value — see Fig. 13. The minimal value is calculated as follows (using Eq. (82)):

$$e_{\min} = \frac{\varepsilon_{\max}}{1} = \varepsilon_{\max} > 0 \tag{84}$$

As a result, the integrity field's minimum value may be written as follows:

$$g_{\min} = E\,e_{\min} = E\,\varepsilon_{\max} \tag{85}$$

For a linear elastic material, the strain energy function U is given by the following expression:

$$U = \int \sigma \; d\varepsilon = \frac{1}{2}\sigma\,\varepsilon \tag{86}$$

The strain energy function is then calculated in relation to the integrity field. The following is the definition of the strain energy U^* based on the integrity field and its related kinematic strain-like variable:

$$U^* = \int g\,de \tag{87}$$

Equation (87) is obtained by substituting for g from Eq. (83) and integrating:

$$U^* = \frac{1}{2} E e^2 = \frac{1}{2} g e \tag{88}$$

The strain energy function U^* is hence linear, as shown by Eq. (88). To determine the connection between the two strain energy functions U and U^*, put g and e from Eqs. (81) and (82), respectively, into Eq. (88), simplify the resultant expression, and compare to Eq. (86), to obtain:

$$U^* = \frac{U}{\phi^2} \tag{89}$$

Using tensors, the scalar formulation above may readily be expanded to three-dimensional states of deformation and damage. The scalar integrity field g of Eq. (76) is thus generalized to the integrity field tensor $\{g\}$ as follows (all tensors are represented by vectors and matrices in this work):

$$\{g\} = \left([I] - [M]^{-1}\right)^{-1} \{\sigma\} \tag{90}$$

where $[M]$ is the damage effect tensor of the fourth rank, $[I]$ is the fourth-rank identity tensor, and $\{\sigma\}$ is the stress tensor. When the following replacements are used for the one-dimensional case, the tensorial Eq. (90) simplifies to the scalar Eq. (76): $[M] \equiv \frac{1}{1-\phi}$ and $[I] \equiv 1$. The expression for the generic integrity field tensor is given by Eq. (90).

In the same way, the kinematic strain-like variable is generalized to create the strain-like tensor $\{e\}$ as follows:

$$[e] = \left([I] - [M]^{-1}\right)^{-1} \{\varepsilon\} \tag{91}$$

Using the generalized form of the elastic constitutive relation in Eq. (80) as follows:

$$\{\sigma\} = [E]\{\varepsilon\} \tag{92}$$

where $\{\varepsilon\}$ is the strain tensor and $[E]$ is the fourth-rank elasticity tensor. Equation (90) is obtained by substituting Eqs. (92) and (91) into it:

$$\{g\} = \left([I] - [M]^{-1}\right)^{-1} [E] \left([I] - [M]^{-1}\right) \{e\} \tag{93}$$

The elastic constitutive relation between the stress-like tensor $\{g\}$ and the strain-like tensor $\{e\}$ is represented by Eq. (93), which is a general tensorial expression. The following is a rewritten formulation of Eq. (93):

$$\{g\} = [E^*]\{e\} \tag{94}$$

where the modified elasticity tensor of the fourth rank $[E^*]$ is provided by:

$$[E^*] = \left([I] - [M]^{-1}\right)^{-1}[E]\left([I] - [M]^{-1}\right) \tag{95}$$

which represents the generalized tensorial form of the transformed fourth-rank elasticity tensor. When the following replacements are applied for the one-dimensional situation, the tensorial Eqs. (94) and (95) reduce to the scalar Eq. (83): $[M] \equiv \frac{1}{1-\phi}$ and $[I] \equiv 1$.

Illustrative Example

The example of damage evolution given by part (Voyiadjis and Kattan 2005, 2006) is used to demonstrate the idea proposed in the preceding. This example was established in accordance with basic thermodynamic principles (Voyiadjis and Kattan 2005, 2006). The following scalar relation was determined between the strain and the damage variable:

$$\frac{\phi}{(1-\phi)^3} = \frac{\overline{E}^3}{3\,(\partial L/\partial \ell)}\varepsilon^6 \tag{96}$$

One next assumes the following approximation:

$$\frac{1}{(1-x)^3} = 1 + 3x + \ldots\ldots\ldots \tag{97}$$

Equation (96) becomes for small values of the damage variable ϕ and using the series expansion of Eq. (97) as follows:

$$3\phi^2 + \phi - \frac{\overline{E}^3}{3\,(\partial L/\partial \ell)}\varepsilon^6 = 0 \tag{98}$$

Because the expression of Eq. (98) is a quadratic equation inϕ, it can be solved using the quadratic formula to get:

$$\phi = -\frac{1}{6} \pm \frac{1}{6}\sqrt{1 + 4\frac{\overline{E}^3}{\partial L/\partial \ell}\varepsilon^6} \tag{99}$$

The above phi expression does not yet show a clear relationship between the strain and the damage variable. The following Taylor series expansion may then be used to further reduce the aforementioned expression:

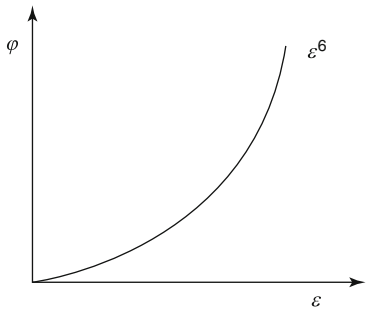

Fig. 14 Result of the example illustrated

$$\sqrt{1+x} = 1 + \frac{1}{2}x + \ldots\ldots\ldots \tag{100}$$

The following explicit link between the strain and the damage variable is obtained by extending the square root expression of Eq. (99) using Eq. (100) (which is valid for modest levels of strain):

$$\phi \approx \frac{\overline{E}^3}{3\left(\partial L/\partial \ell\right)}\varepsilon^6 \tag{101}$$

For tiny amounts of strain and small values of the damage variable, the Eq. (101) connection is true. It is worth noting that the second negative sign in Eq. (99) is removed since it produces a pointless result. Figure 14 depicts the plot of this connection. The connection between damage and strain is linearly increased, as seen in this figure.

When one solves Eq. (101) for εin terms ofϕ, one gets:

$$\varepsilon = \left(\frac{3\left(\partial L/\partial \ell\right)}{\overline{E}^3}\right)^{1/6}\phi^{1/6} \tag{102}$$

As a result of Eq. (102), it is obvious that $\varepsilon = f(\phi^{1/6})$. Figure 15 shows the plot of the aforesaid connection. The connection between strain and damage is monotonically rising, as can be seen in this graph. The following explicit expression between the stress and the damage variable is obtained by substituting Eq. (102) into Eq. (80):

$$\sigma = E\left(\frac{3\left(\partial L/\partial \ell\right)}{\overline{E}^3}\right)^{1/6}\phi^{1/6} \tag{103}$$

As a result of Eq. (103), it is obvious that $\sigma = f(\phi^{1/6})$. Figure 16 depicts the relationship depicted in Eq. (103) on a graph. The connection between stress and damage is monotonically increasing. Finally, by inserting Eq. (103) into Eq. (76), the integrity field $g$is obtained:

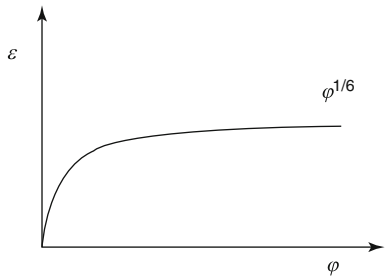

Fig. 15 Strain vs. damage for the illustrative example

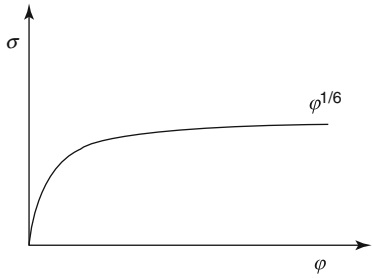

Fig. 16 Stress vs. Damage for the Illustrative Example

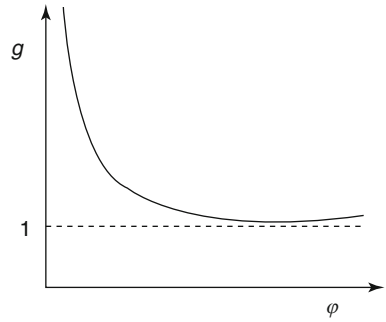

Fig. 17 Damage field vs. damage for the illustrative example

$$g = E\left(\frac{3\,(\partial L/\partial \ell)}{\overline{E}^3}\right)^{1/6} \phi^{-5/6} \tag{104}$$

As a result, Eq. (104) clearly shows that the integrity field (a stress-like variable) is a function of $\phi^{-5/6}$. As seen in Fig. 17, this connection is displayed.

The integrity field declines from infinity for the virgin (undamaged) state to a minimum finite nonzero value during rupture, as seen in Fig. 17. It should be noticed that Eqs. (101), (102), (103), and (104) all contain nonlinear relations. Finally, the

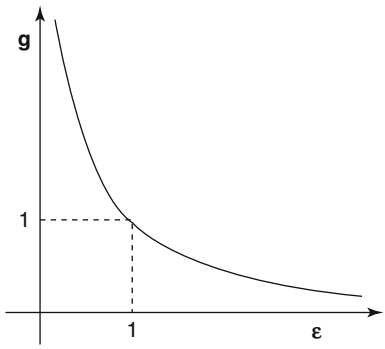

Fig. 18 Damage field vs. strain for the illustrative example

following relation is found between the strain and the integrity field. Equation (101) is substituted into Eq. (104) to achieve the required relationship:

$$g = \frac{3\left(\partial L/\partial \ell\right)}{\overline{E}^3} E\,\varepsilon^{-5} \tag{105}$$

The integrity field is thus a function of ε^{-5}, as shown by Eq. (105). Fig. 18 depicts the relationship of Eq. (105). This connection is nonlinear, as stated previously.

Approximation of the Integrity Field

Approximate expressions for the integrity field are derived in this section. One begins with the fundamental formulation of the integrity field of equations for this purpose (76). The following Taylor series expansion around $x = 0$ can be used for small values of the damage variable as follows:

$$\frac{1}{x} = 3 - 3x + x^2 - \ldots\ldots \tag{106}$$

After applying the first three terms of the series expansion of Eq. (106) to the integrity field in Eq. (76), the expression becomes:

$$g \approx \sigma\left(\phi^2 - 3\phi + 3\right) \tag{107}$$

For values of the damage variable close to zero, the integrity field expression above is valid. However, a generalized expansion of the integrity field may be written around any value $\phi = \phi_o$ as follows:

$$g \approx \sigma\left[\frac{1}{\phi_o} - \frac{(\phi - \phi_o)}{\phi_o^2} + \frac{(\phi - \phi_o)^2}{\phi_o^3}\right] \tag{108}$$

The given formula is a general approximation of the equation's fundamental integrity field expression (76).

The Healing Field

The notion of a healing field is introduced in this section in the same way that the concept of the integrity field was introduced in the previous section. The healing field k is defined by dividing the applied force F by the healed area A^h like Eq. (75) as follows:

$$k = \frac{F}{A^h} \tag{109}$$

Equation (76) yields the following explicit equation for the healing field in terms of stress, damage, and healing variables when the effective damage variable of Eq. (54) is substituted for ϕ:

$$k = \frac{\sigma}{\phi(1-h)} \tag{110}$$

Equation (110) for the healing field is compared to the formula for the integrity field in Eq. (76). The following explicit connection between the integrity field $g$and the healing field $k$may be obtained by dividing Eq. (110) by Eq. (76) and rearranging the components.

$$k = \frac{g}{1-h} \tag{111}$$

The healing variable h is connected to the integrity field and the healing field, as shown by the relationship in Eq. (111). It is important to note that the healing variable's values are within a certain range $0 < h < 1$ for normal healing. In the case of super healing, however, Voyiadjis and Kattan (2014) show that the healing variable h can reach values greater than 1.

In Fig. 19, the expression of the healing field from Eq. (110) is shown. Several healing field curves are shown in the upper part of the figure for values of the healing variable in the range $0 < h < 1$, as indicated in the figure. It is interesting to note that the curve produced in the case of $h = 0$ is similar to that acquired in the preceding section's integrity field. It is noticed that the healing field curves drop from infinity in the virgin (undamaged) state to a finite value at rupture for each healing field curve. This is comparable to the integrity field's behavior. Figure 19 additionally shows that numerous healing field curves are displayed in the lower half of the figure for the situation of super healing (when $h > 1$).

The next parts seek to apply the definition of the healing field in Eq. (110) to the general state of deformation, damage, and healing. As a result, the statement in Eq.

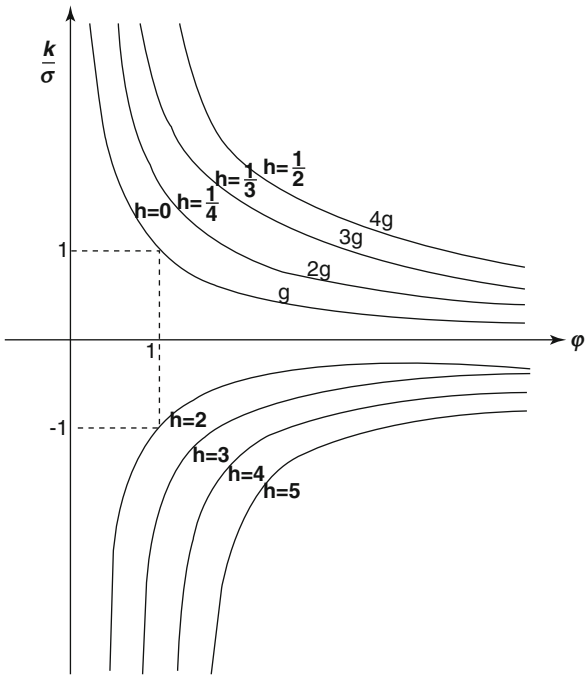

Fig. 19 The healing field illustrated with the damage variables

(110) can be generalized using a tensor simply utilizing one of the two alternative equations below:

$$\{k\} = \left([I] - [M]^{-1}\right)^{-1}\left([I] - [H]^{-1}\right)^{-1}\{\sigma\} \tag{112}$$

$$\{k\} = \left([I] - [H]^{-1}\right)^{-1}\left([I] - [M]^{-1}\right)^{-1}\{\sigma\} \tag{113}$$

Where $\{k\}$ is a vector that represents the healing field tensor, $[M]$is a matrix that represents the fourth-rank damage tensor, $[H]$is a matrix that represents the fourth-rank healing tensor, and $[I]$ is a matrix that represents the fourth-rank identity tensor. When the following substitutes are applied for the one-dimensional case, both tensorial Eqs. (112) and (113) resolve to the scalar Eq. (110): $[M] \equiv \frac{1}{1-\phi}$, $[H] \equiv \frac{1}{h}$, and$[I] \equiv 1$. The generalized formulations for the healing field tensor are Eqs. (112) and (113).

When the integrity field is defined in section "The Integrity Field" and the logarithmic damage variable is defined in section "A New Damage Variable," the logarithmic damage variable L can be proposed as a better definition of the integrity field than the classical damage variable ϕ. When Eq. (74) is substituted for Eq. (7), the following expression for the damaged area in terms of the logarithmic damage variable is obtained:

$$\frac{A^d}{A} = 1 - e^{-L} \tag{114}$$

When Eq. (114) is substituted for Eq. (76), the integrity field has the following expression:

$$g = \frac{\sigma}{1 - e^{-L}} \tag{115}$$

One can compare the two expressions of the integrity field g found in Eqs. (76) and (115) (using the conventional damage variable) (using the logarithmic damage variable). Figure 20 depicts the comparison using both equations. The new integrity field does not dissolve as quickly as the previous integrity field as damage progresses. This is significant because damage increases as the integrity field dissipates (starting from infinity and falling to a nonzero finite value). As a result, the new integrity field differs from the old integrity field in terms of characterization of damage and integrity.

Equation (114) is substituted for Eq. (110), yielding the following new expression for the healing field k:

$$k = \frac{\sigma}{(1 - e^{-L})(1 - h)} \tag{116}$$

Figure 21 depicts the expression of the healing field from Eq. (116). Several healing field curves are displayed in the upper portion of the figure for values of the healing variable in the range $0 < h < 1$. It is important to note that the curve obtained when $h = 0$ is similar to the integrity field from the previous section. It is noted that the healing field curves drop from infinity in the virgin (undamaged) state to a finite value at rupture for each healing field curve. This is analogous to the integrity field's behavior. Figure 21 further shows that various healing field curves are drawn in the lower portion of the figure for the instance of super healing (where $h > 1$).

Summary/Conclusions

Within the context of continuum damage mechanics, new fundamental topics are considered. In addition, new ideas relating to material damageability and integrity are introduced. Damage and healing are investigated in depth using novel mathematical relations that are reliably derived. In addition, using rigorous mathematical calculations, the new concepts of damage field, integrity field, damageability variable, and integrity variable are introduced. Furthermore, two new "angles" are provided from which all four variables of damage, integrity, damageability, and healing can be calculated. The logarithmic and exponential damage variables are among the new damage variables introduced.

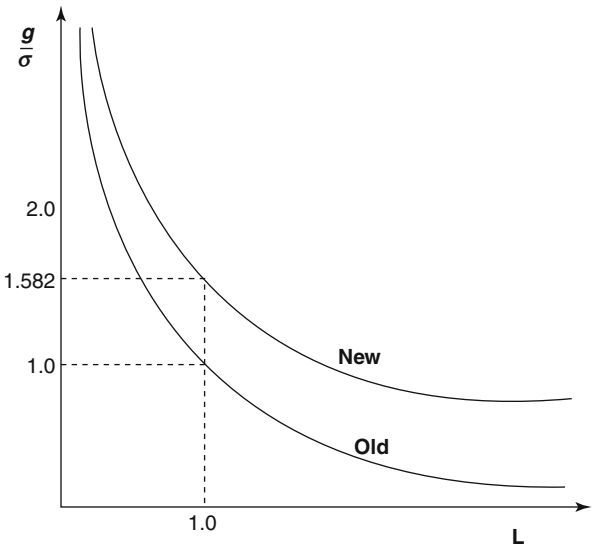

Fig. 20 The integrity field illustrated with the damage variables

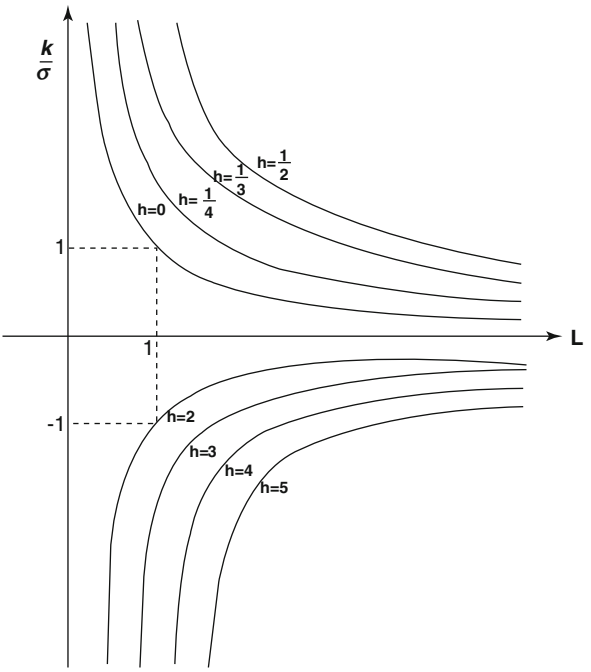

Fig. 21 The healing field illustrated with the damage variables

The following are the main points raised in this chapter:

1. At the virgin (undamaged) state of the material, the logarithmic damage variable resembles the classical damage variable. When they are entirely ruptured, however, they are completely different. The logarithmic damage variable approaches infinity at rupture, whereas the classical damage variable reaches a value of 1 at rupture.
2. At the virgin (undamaged) condition of the material, the exponential damage variable differs from the classical damage variable. They do, however, coincide at the point of full rupture, when the value of 1 is reached.
3. The cosine of the damage-integrity angle (DIA) is used to define the integrity variable. The sine of DIA can be used to calculate the typical damage variable in this case.
4. The cosine of the healing-damageability angle is used to define the damageability variable (HDA). In this case, the sine of HDA can be used to generate the classical healing variable.
5. A stress-like quantity with stress units is the integrity field. When a material is a virgin (undamaged), the integrity field is boundless, but when damage occurs, it becomes finite.
6. The healing field is identical to the integrity field, except instead of the damage variable, it is linked to the healing variable.

For various reasons, the majority of this work's presentation is offered in terms of scalars: (1) to explain the fundamental principles and (2) to keep the presentation basic and easy to understand by the reader. In some parts of this study, however, the tensorial generalization of the scalar equations has been possible to present. To account for generalized states of deformation, damage, and healing, tensors must be used. The work given is mathematical formalism and theoretical, and it is hoped that other academics will be able to use and build on these equations to develop more advanced damage and healing mechanics models. The current work is also provided for it to be used in the future to tackle numerical difficulties and practical applications. In addition, new and holistic research routes in damage and healing mechanics of materials open up.

Appendix

Appendix I: Are There Any Limits to the Damage Variable

The restrictions on the values of the damage classical damage variable are derived in this Appendix using a mathematical formulation that is completely consistent. The derivation is dependent on mathematical manipulations rather than the obvious physical components of the problem.

Consider the Eq. (48) as the form of an alternate damage variable ϕ^*. In this example, the effective stress can be expressed as follows:

$$\overline{\sigma} = \frac{\sigma}{1-\phi^*} = \frac{\sigma}{1-\sqrt{2\phi-\phi^2}} \tag{117}$$

When the numerator and denominator of Eq. (117) are multiplied by the quantity $1+\sqrt{2\phi-\phi^2}$ and the result is simplified, one gets:

$$\overline{\sigma} = \frac{\sigma\left(1+\sqrt{2\phi-\phi^2}\right)}{(1-\phi)^2} \tag{118}$$

When one compares Eq. (118) for alternative damage variables to Eq. (2) for classical damage variables, equating these two equations, canceling the stress, and simplifying, one gets the quadratic equation in ϕ:

$$2\phi^2 - 2\phi = 0 \tag{119}$$

Appendix II: How to Compose Damage Variables

Damage variable composition is provided as a new way for creating more complex and adaptable damage variables. This method is based on the calculus concept of function composition. Consider the following two functions $f(x)$ and $g(x)$, where x is an independent variable. The function $(f \circ g)(x) = f(g(x))$ is described as the combination of the functions $f \circ g$.

Damage variables will be defined using the preceding definition of function composition. Consider the following two damage variables: $\phi_1\left(\frac{\overline{A}}{A}\right)$ and $\phi_2\left(\frac{\overline{A}}{A}\right)$, with $x \equiv \frac{\overline{A}}{A}$ as the independent variable. When considering composition $\phi_1 \circ \phi_2$, one will notice that it does not create a consistent damage variable. However, further research reveals that the triple composition $\phi_1 \circ \phi_2 \circ \phi_1$ will generate a new and consistent damage variable. One also discovers that the other triple composition $\phi_2 \circ \phi_1 \circ \phi_2$ may be used to generate a valid damage variable. A variety of basic examples are provided here to demonstrate these observations. Consider the classical damage variable ϕ in Eq. (1) and the exponential damage variable ψ in Eq. (39). The composition will then create a new damage variable as follows:

$$\phi \circ \psi \circ \phi \equiv \phi(\psi(\phi)) = \phi\left(\psi\left(1-\frac{\overline{A}}{A}\right)\right) = \phi\left(e^{-\left(1-\frac{\overline{A}}{A}\right)}\right) = 1 - e^{\frac{\overline{A}}{A}-1} \tag{120}$$

The new damage variable $\phi \circ \psi \circ \phi$ starts at 0 for virgin (undamaged) material (at $\frac{\overline{A}}{A} = 1$) and develops monotonically to its maximum value of $1 - 1/e = 0.632$ upon rupture (at $\frac{\overline{A}}{A} = 0$), as shown in Eq. (120). This new damage variable would be

beneficial in cases where the maximum amount of damage is constrained and cannot exceed 1, causing the effective stress to burst at infinity (like the classical damage variable).

The next step is to explore a different combination of the two damage factors, ϕ and ψ. As follows, the composition $\psi \circ \phi \circ \psi$ will create a new damage variable as follows:

$$\psi \circ \phi \circ \psi \equiv \psi(\phi(\psi)) = \psi\left(\phi\left(e^{-\frac{\overline{A}}{A}}\right)\right) = \psi\left(1 - e^{-\frac{\overline{A}}{A}}\right) = e^{-\left(1-e^{-\frac{\overline{A}}{A}}\right)}$$
$$= e^{\left(e^{-\frac{\overline{A}}{A}}-1\right)} \tag{121}$$

The new damage variable $\psi \circ \phi \circ \psi$ starts at the value $e^{\frac{1}{e}-1} = 0.531$ for virgin (undamaged) material (at $\frac{\overline{A}}{A} = 1$) and grows monotonically to its maximum value of 1 at rupture (at $\frac{\overline{A}}{A} = 0$), as shown in Eq. (121) above. This additional damage variable would be beneficial in instances when the minimum damage value is nonzero and may be increased to 1. This differs from the conventional damage variable, which starts at 0. The classical damage variable ϕ of Eq. (1) and the logarithmic damage variable L of Eq. (7) will be used to show two more damage variable compositions. The composition $\phi \circ L \circ \phi$ will then create a new damage variable as follows:

$$\phi \circ L \circ \phi \equiv \phi(L(\phi)) = \phi\left(L\left(1 - \frac{\overline{A}}{A}\right)\right) = \phi\left(-\ln\left(1 - \frac{\overline{A}}{A}\right)\right)$$
$$= 1 + \ln\left(1 - \frac{\overline{A}}{A}\right) \tag{122}$$

The new damage variable $\phi \circ L \circ \phi$ starts at negative infinity for virgin (undamaged) material (at $\frac{\overline{A}}{A} = 1$) and grows linearly to its maximum value of 1 at rupture, as shown in Eq. (122) above (at $\frac{\overline{A}}{A} = 0$). This new damage variable would be beneficial in instances when the damage variable should have a nonzero initial value.

The next step is to explore a different combination of the two damage variables ϕ and L. As follows, the composition $L \circ \phi \circ L$ will create a new damage variable:

$$L \circ \phi \circ L \equiv L(\phi(L)) = L\left(\phi\left(-\ln\frac{\overline{A}}{A}\right)\right) = \psi\left(1 + \ln\frac{\overline{A}}{A}\right)$$
$$= -\ln\left(1 + \ln\frac{\overline{A}}{A}\right) \tag{123}$$

The new damage variable $L \circ \phi \circ L$ starts at 0 for virgin (undamaged) material (at $\frac{\overline{A}}{A} = 1$) and grows linearly to infinity at rupture (at $\frac{\overline{A}}{A} = 0$), as seen in Eq. (123) above. The logarithmic damage variable ψ and this new damage variable are quite comparable.

Other compositions are conceivable, but the four examples above will suffice for this work. Compositions such as $\psi \circ L \circ \psi$, $L \circ \psi \circ L$, $\phi \circ \psi \circ L$, $\psi \circ \phi \circ L$, $L \circ \phi \circ \psi$, $L \circ \psi \circ \phi$, and others may be of interest to the reader. One can develop (or construct) a customized damage variable that meets his or her demands using the defined process of damage variable composition as provided below. For a damage variable to be legitimate, the following requirements must be met:

1. For the given range of acceptable $\frac{\overline{A}}{A}$ values, the damage variable must have positive values.
2. The damage variables must increase in a monotonic manner.
3. The third criterion is optional, although it is desired. The values of the damage variables must be in the range of 0–1. This is not required because certain damage variables fall outside of this range. The logarithmic damage variable, for example, can reach infinity.

Each damage variable created via the process of damage variable composition must meet the first two requirements stated above.

References

C. Basaran, S. Nie, An irreversible thermodynamic theory for damage mechanics of solids. Int. J. Damag. Mech. **13**(3), 205–224 (2004)

C. Basaran, H. Tang, Implementation of a thermodynamic framework for damage mechanics of solder interconnects in microelectronic packaging. Int. J. Damag. Mech. **11**(1), 87–108 (2002)

C. Basaran, C.Y. Yan, A thermodynamic framework for damage mechanics of solder joints. Trans. ASME J. Electron. Packag. **120**, 379–384 (1998)

C. Basaran, M. Lin, H. Ye, A thermodynamic model for electrical current induced damage. Int. J. Solids Struct. **40**(26), 7315–7327 (2003)

C. Basaran, H. Tang, S. Nie, Experimental damage mechanics of microelectronics solder joints under fatigue loading. Mech. Mater. **36**, 1111–1121 (2004)

I. Carol, E. Rizzi, K. William, *An 'Extended' Volumetric/Deviatoric Formulation of Anisotropic Damage Based on a Pseudo-Log Rate*. Technical Report No. GT-023, ETSECCPB-UPC, E-08034. (Barcelona, 2002)

D.J. Celentano, P.E. Tapia, J.-L. Chaboche, Experimental and numerical characterization of damage evolution in steels, in *Mecanica Computacional*, ed. by G. Buscaglia, E. Dari, O. Zamonsky, vol. XXIII, (Bariloche, 2004)

M.K. Darabi, R.K. Abu Al-Rub, D.N. Little, A continuum damage mechanics framework for modeling micro-damage healing. Int. J. Solids Struct. **49**, 492–513 (2012)

I. Doghri, *Mechanics of Deformable Solids: Linear and Nonlinear, Analytical and Computational Aspects* (Springer-Verlag, Berlin, 2000)

E.M. Gunel, C. Basaran, Damage characterization in non-isothermal stretching of acrylics: Part I theory. Mech. Mater. **43**(12), 979–991 (2011a)

E.M. Gunel, C. Basaran, Damage characterization in non-isothermal stretching of acrylics: Part II experimental validation. Mech. Mater. **43**(12), 992–1012 (2011b)

N.R. Hansen, H.L. Schreyer, A thermodynamically consistent framework for theories of elastoplasticity coupled with damage. Int. J. Solids Struct. **31**(3), 359–389 (1994)

L. Kachanov, On the creep fracture time. Izv Akad, Nauk USSR Otd Tech **8**, 26–31 (1958) (in Russian)

P.I. Kattan, G.Z. Voyiadjis, A coupled theory of damage mechanics and finite strain Elasto-plasticity – Part I: damage and elastic deformations. Int. J. Eng. Sci. **28**(5), 421–435 (1990)
P.I. Kattan, G.Z. Voyiadjis, A plasticity-damage theory for large deformation of solids – Part II: Applications to finite simple shear. Int. J. Eng. Sci. **31**(1), 183–199 (1993)
P.I. Kattan, G.Z. Voyiadjis, Decomposition of damage tensor in continuum damage mechanics. J. Eng. Mech. ASCE **127**(9), 940–944 (2001a)
P.I. Kattan, G.Z. Voyiadjis, *Damage Mechanics with Finite Elements: Practical Applications with Computer Tools* (Springer-Verlag, Berlin, 2001b)
D. Krajcinovic, *Damage Mechanics* (North Holland, 1996, 776 page)
P. Ladeveze, J. Lemaitre, Damage effective stress in quasi-unilateral conditions, in *The 16th International Congress of Theoretical and Applied Mechanics*, (Lyngby, Denmark, 1984)
P. Ladeveze, M. Poss, L. Proslier, Damage and fracture of tridirectional composites, in *Progress in Science and Engineering of Composites. Proceedings of the Fourth International Conference on Composite Materials, Japan Society for Composite Materials*, vol. 1, (1982), pp. 649–658
H. Lee, K. Peng, J. Wang, An anisotropic damage criterion for deformation instability and its application to forming limit analysis of metal plates. Eng. Fract. Mech. **21**, 1031–1054 (1985)
G. Lubineau, A pyramidal Modeling scheme for laminates – Identification of transverse cracking. Int. J. Damag. Mech. **19**(4), 499–518 (2010)
G. Lubineau, P. Ladeveze, Construction of a micromechanics-based intralaminar mesomodel, and illustrations in ABAQUS/standard. Comput. Mater. Sci. **43**(1), 137–145 (2008)
B. Luccioni, S. Oller, A directional damage model. Comput. Methods Appl. Mech. Eng. **192**, 1119–1145 (2003)
Y. Rabotnov, Creep rupture, in *Proceedings, Twelfth International Congress of Applied Mechanics, Stanford, 1968*, ed. by M. Hetenyi, W. G. Vincenti, (Springer-Verlag, Berlin, 1969), pp. 342–349
J.R. Rice, Inelastic constitutive relations for solids: An internal variable theory and its application to metal plasticity. J. Mech. Phys. Solids **19**, 433–455 (1971)
F. Sidoroff, Description of anisotropic damage application in elasticity, in *IUTAM Colloqium on Physical Nonlinearities in Structural Analysis*, (Springer-Verlag, Berlin, 1981), pp. 237–244
G.Z. Voyiadjis, Degradation of elastic modulus in elastoplastic coupling with finite strains. Int. J. Plast. **4**, 335–353 (1988)
G.Z. Voyiadjis, P.I. Kattan, A coupled theory of damage mechanics and finite strain elasto-plasticity – Part II: Damage and finite strain plasticity. Int. J. Eng. Sci. **28**(6), 505–524 (1990)
G.Z. Voyiadjis, P.I. Kattan, A plasticity-damage theory for large deformation of solids – Part I: Theoretical formulation. Int. J. Eng. Sci. **30**(9), 1089–1108 (1992)
G.Z. Voyiadjis, P.I. Kattan, *Damage Mechanics* (Taylor and Francis (CRC Press), 2005)
G.Z. Voyiadjis, P.I. Kattan, *Advances in damage mechanics: Metals and metal matrix composites with an introduction to fabric tensors*, 2nd edn. (Elsevier, 2006)
G.Z. Voyiadjis, P.I. Kattan, A comparative study of damage variables in continuum damage mechanics. Int. J. Damag. Mech. **18**(4), 315–340 (2009)
G.Z. Voyiadjis, P.I. Kattan, Mechanics of damage processes in series and in parallel: A conceptual framework. Acta Mech. **223**(9), 1863–1878 (2012)
G.Z. Voyiadjis, P.I. Kattan, Healing and super healing in continuum damage mechanics. Int. J. Damag. Mech. **23**(2), 245–260 (2014)
G.Z. Voyiadjis, A. Shojaei, G. Li, A thermodynamic consistent damage and healing model for self-healing materials. Int. J. Plast. **27**(7), 1025–1044 (2011)
G.Z. Voyiadjis, A. Shojaei, G. Li, P.I. Kattan, A theory of anisotropic healing and damage mechanics of materials. Proc. R. Soc. A Math. Phys. Eng. Sci. **468**(2137), 163–183 (2012a)
G.Z. Voyiadjis, A. Shojaei, G. Li, P.I. Kattan, Continuum damage-healing mechanics with introduction to new healing variables. Int. J. Damag. Mech. **21**, 391–414 (2012b)

Damageability and Integrity of Materials: Unrecoverable Damage and Generalized Healing Model

3

George Z. Voyiadjis, Peter I. Kattan, and Juyoung Jeong

Contents

Introduction 62
Unhealable Damage and Nondamageable Integrity 62
Generalized Nonlinear Healing 66
Scalar Formulation 66
Quadratic Healing 69
Tensorial Formulation 70
Concept of Unhealable Damage 71
Damage and Healing Models Compared 71
The Healing Process Dissected 75
Summary/Conclusions 79
References 80

Abstract

Some fundamental and new concepts are proposed within the framework of continuum damage mechanics. In this work, one delves deeply into the nature of damage and healing as two fundamental processes in damage and healing mechanics. One introduces the new concept of unhealable damage or unrecoverable damage in section "Unhealable Damage and Nondamageable Integrity." Also, the new concept of nondamageable integrity or permanent integrity is also introduced in this section. The section "Generalized Nonlinear Healing" discusses generalized healing, with a clear difference between linear and nonlinear healing. The equations of quadratic healing are obtained as an example of nonlinear healing. Finally, section

G. Z. Voyiadjis (✉)
Center for GeoInformatics C4G and Computational Solid Mechanics Laboratory, Department of Civil and Environmental Engineering, Louisiana State University, Baton Rouge, LA, USA
e-mail: voyiadjis@eng.lsu.edu

P. I. Kattan · J. Jeong
Department of Civil and Environmental Engineering, Louisiana State University, Baton Rouge, LA, USA
e-mail: pkattan@petrabooks.com; jjeong7@lsu.edu

© Springer Nature Switzerland AG 2022

G. Z. Voyiadjis (ed.), *Handbook of Damage Mechanics*,
https://doi.org/10.1007/978-3-030-60242-0_96

"The Healing Process Dissected" discusses the healing process in detail in a logical/mathematical manner. These novel and basic ideas are intended to open the way for new, consistent, and comprehensive paths in damage mechanics and material characterization research.

Keywords

Unhealable damage · Nondamageable integrity · Generalized nonlinear healing

Introduction

The two novel notions of unhealable damage and nondamageable integrity are introduced in section "Unhealable Damage and Nondamageable Integrity." Unhealable damage is described as the damage that cannot be cured utilizing current healing mechanics theories. A numerical derivation is presented in an attempt to calculate the percentage of damage that cannot be healed. Nondamageable integrity, on the other hand, is defined as the component of integrity that cannot be damaged. A numerical calculation of the proportion of nondamageable integrity is attempted once again.

Section "Generalized Nonlinear Healing" presents a generalized nonlinear healing model. The governing equations of this model are compared to those of a traditional linear healing model that has been established. Quadratic healing is a particular version of the nonlinear healing model that is developed. The scalar and tensorial formulations of the extended nonlinear healing model are provided. A comparison of the different healing models in this section is given in the latter portion of this section.

The work concludes with a systematic and quantitative investigation of the healing process in section "The Healing Process Dissected." The healing process is proven to have multiple stages, including primary healing, secondary healing, tertiary healing, and so on. To demonstrate these many healing stages, a numerical example is provided.

Unhealable Damage and Nondamageable Integrity

The notions of integrity and damage are investigated further in this section. There is also the idea of irreversible damage. Take a look at the equations' damage and integrity variables using the sine and cosine functions such as (1), (41), (44), (46), (48), and (54) in ▶ Chap. 2, "Damageability and Integrity of Materials: New Concepts of the Damage and Healing Fields." The equations are renumbered to prevent duplicate numbering of equations: (1*), (41*), (44*), (46*), (48*), and (54*). Consider also an incremental increase of damage $\Delta\phi = \phi_2 - \phi_1 > 0$ where $\phi_2 > \phi_1$. Now it is time to look into the resulting decrease in integrity as a result of the increased damage. It is important to note that the damage increase is presumed to be linear and small.

The following expression, using the Eq. (44*), gives the corresponding decrease in integrity:

$$\Delta(hy) = \sqrt{1-\phi_2^2} - \sqrt{1-\phi_1^2} \tag{1}$$

The Taylor series expansion of the square root function $\sqrt{1+x} \approx 1 + \frac{1}{2}x$ is then used to expand the preceding statement for small values of damage. As a result, one gets:

$$\Delta(hy) \approx \left(1 - \frac{1}{2}\phi_2^2\right) - \left(1 - \frac{1}{2}\phi_1^2\right) \tag{2}$$

Equation (2) may be simplified as follows:

$$\Delta(hy) \approx \frac{1}{2}(\phi_1 + \phi_2)(\phi_1 - \phi_2) \tag{3}$$

ϕ_m where $\phi_m = \frac{1}{2}(\phi_1 + \phi_2)$ denotes the mean value of the damage variable between ϕ_1 and ϕ_2, resulting in the statement in Eq. (3):

$$\Delta(hy) \approx -\phi_m \cdot \Delta\phi \tag{4}$$

As a result, it is apparent from Eq. (4) that the change in the integrity variable is negative. This change in the integrity variable is equal to the mean value of the damage variable in the chosen interval multiplied by the change in the damage variable. After that, one investigates the damage and integrity factors in greater depth. The amount H is defined as the sum of the damage and integrity variables as follows (where H = damage + integrity):

$$H(\phi) = \phi + \sqrt{1-\phi^2} \tag{5}$$

The function $H(\phi)$ has nothing to do with the fourth-rank healing tensor represented by the matrix $[H]$, which is utilized below in this chapter. The quantity H, as described in Eq. (5), is intriguing, as evidenced by the following findings. At the two damage regime boundary points, the function $H(\phi)$ is precisely equal to 1, that is, at $\phi = 0$ and $\phi = 1$. Equation (5) is displayed in Fig. 1 to study the behavior of the function $H(\phi)$ between these two locations.

Figure 1 shows that the values of $H(\phi)$ increase slowly from 1 (at virgin material, when $\phi = 0$) to a maximum value, then return to 1 (at full rupture, when $\phi = 1$). This is unusual behavior because one would anticipate $H(\phi)$ values to remain constant throughout the damaging process (this is because the damage and integrity values may cancel each other out). According to Eq. (5) and the accompanying Fig. 1, however, this is not the case.

The next step is to determine the maximum value of the function $H(\phi)$, as well as the damage value at which this maximum is reached. This is significant because it is

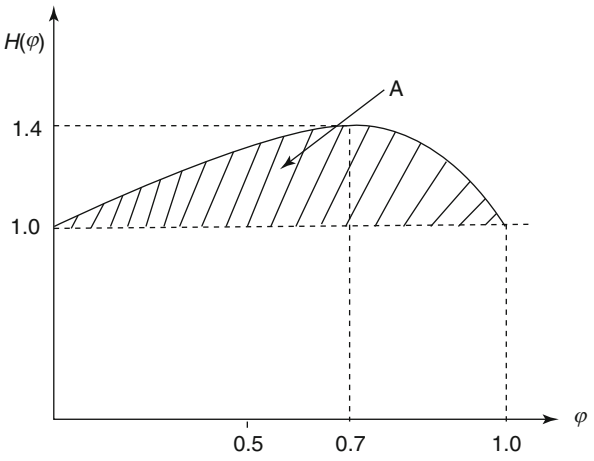

Fig. 1 Shaded area represents unhealable damage and nondamageable integrity

necessary to know how much the values of this function vary from 1. As will be demonstrated later, this deviation has significant consequences for both damage and integrity. Set the derivative of the function $H(\phi)$ to zero to obtain the maximum value of the function. As a result of calculating the derivative of Eq. (5) for ϕ, one gets:

$$\frac{dH(\phi)}{d\phi} = 1 - \frac{\phi}{\sqrt{1-\phi^2}} \tag{6}$$

The function $H(\phi)$ is always positive between 0 and 1, as seen in Fig. 1. The fact that the second derivative of $H(\phi)$ is always negative emphasizes this point. When the derivative of Eq. (6) is applied to ϕ, the following results are obtained:

$$\frac{dH^2(\phi)}{d\phi^2} = -\frac{1}{\left(1-\phi^2\right)^{3/2}} < 0 \tag{7}$$

Since the second derivative of $H(\phi)$ for ϕ is always negative, the function $H(\phi)$ is always positive, as demonstrated by Eq. (7). After that, one solves the resultant equation for ϕ by setting the first derivative of Eq. (6) equal to zero. As a result, $\phi = \frac{1}{\sqrt{2}} \approx 0.707$ is obtained. As a result, at the value of $\phi = \frac{1}{\sqrt{2}} \approx 0.707$, the function $H(\phi)$ reaches its maximum value. When this value ϕ is substituted into Eq. (5), the result is $H_{\max} = \sqrt{2} \approx 1.414$. As a result, the maximum value of the function $H(\phi)$ occurs around $\phi = 0.7$, not around the midpoint of the damage regime $\phi = 0.5$. Figure 1 schematically depicts this fact.

The shaded area in Fig. 1 is then examined. This is an essential region that may be connected to damage buildup in such a way. This shaded area's physical significance is hypothesized below. The value of the shaded region in the figure is first calculated as follows:

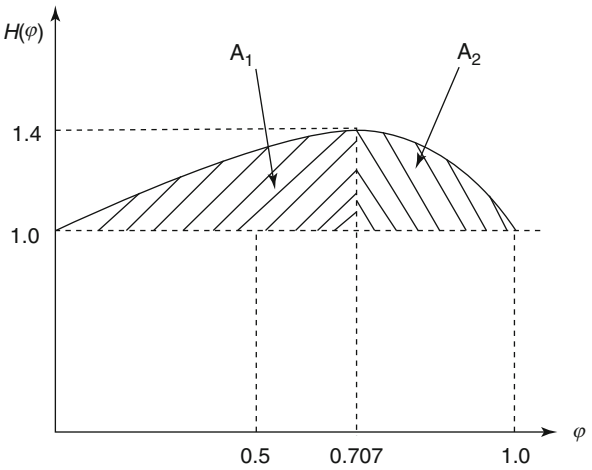

Fig. 2 The first shaded region represents unhealable damage while the second shaded region represents nondamageable integrity

$$A = \int_0^1 [H(\phi) - 1]\, d\phi = \int_0^1 \left(\phi + \sqrt{1 - \phi^2} - 1\right) d\phi = \frac{\pi}{4} - \frac{1}{2} \approx 0.285 \quad (8)$$

As a result, the shaded area is roughly 0.285. This region is shown to reflect lost cumulative damage, or damage that is unrecoverable or unhealable. It could also mean "permanent integrity" or "nondamageable integrity," which means "integrity that cannot be compromised by damage." It should be noted that the grey region represents the deviation from 1 that Hg usually achieves in the damage range of 0 to 1. If damage and integrity cancel each other out, this deviation should not occur, yet it does not.

Subdividing the shaded region A as two shaded sub-regions A_1 and A_2, as indicated in Fig. 2 such that $A = A_1 + A_2$, one can examine the nature of the shaded area in Fig. 1. The next step is to compute the area of each shaded sub-region independently and try to predict the physical importance of each sub-region.

The following two integrals are used to calculate the two shaded sub-areas A_1 and A_2, as illustrated below:

$$A_1 = \int_0^{0.707} [H(\phi) - 1]\, d\phi = \int_0^{0.707} \left(\phi + \sqrt{1 - \phi^2} - 1\right) d\phi \approx 0.185 \quad (9)$$

$$A_2 = \int_{0.707}^1 [H(\phi) - 1]\, d\phi = \int_{0.707}^1 \left(\phi + \sqrt{1 - \phi^2} - 1\right) d\phi \approx 0.100 \quad (10)$$

When the two shaded sub-areas of Fig. 2 are analyzed, it only notices that as the function Hg increases from 1 to 1.414 along with the first shaded sub-area A1, the material exhibits greater and irreversible (or unhealable) damage. As a result, the first shaded sub-area A_1 indicates cumulative unhealable damage and has a value of 0.185, indicating that this type of damage accounts for about 18.5% of overall

accumulated damage and integrity. Furthermore, the material experiences some sort of nondamageable or permanent integrity when the function $H(\phi)$ drops from 1.414 to 1 along the second shaded sub-area A_2. As a result, the second shaded sub-area A_2 reflects cumulative nondamageable integrity and has a value of 0.1, indicating that this type of integrity accounts for roughly 10% of overall accumulated damage and integrity. Finally, it is noted that alternative interpretations of the shaded regions may exist in addition to those described in the preceding discussion. The aforementioned interpretation of the two shaded sub-areas might be only one approach to determining the physical significance of the deviation from 1.

The foregoing analysis of the function $H(\phi)$ of Eq. (5), as well as the damage increases and decreases in the integrity of Eq. (4), is based on the traditional formulation of the damage variable and its related integrity variable, as provided in Eqs. (1*) and (44*). The previous analysis and discussion may be performed with another formulation of the function $H(\phi)$ in the form $H(\phi) = \sqrt{2\phi - \phi^2} + (1 - \phi)$, which is based on the alternative damage variable of the Eq. (48*) and the related integrity variable of the Eq. (46*). This interpretation, on the other hand, is clear and is left to the reader's discretion. Furthermore, by utilizing the alternate definitions of damage and integrity found in Eqs. (46*) and (48*), one finds that increasing damage $\Delta\phi$ causes a reduction in $(1 - \phi_m)\,\Delta\phi$ integrity, as opposed to the conclusion obtained in Eq. (4).

Generalized Nonlinear Healing

In the literature (Voyiadjis et al. 2011, 2012; Darabi et al. 2012), a damage-healing model is derived, which is characterized by the effective stress equation:

$$\overline{\sigma} = \frac{\sigma}{1 - \phi_{eff}} = \frac{\sigma}{1 - \phi(1 - h)} \tag{11}$$

Since the formula for the damage variable (effective) ϕ_{eff} of the Eq. (54*) is linear in the healing variable h, where ϕ is the usual damage variable, the above healing model is referred to as a linear healing model in this chapter. In this section, a nonlinear alternative healing model is developed and compared to the linear healing model discussed previously.

Scalar Formulation

Next, one develops a generalized nonlinear healing model. This generalized nonlinear healing model is then compared with the linear healing model of the literature. It is expected that the generalized nonlinear healing model will be able to model generalized states of healing and provide a more rigorous description of material healing. In addition, it will be demonstrated in this section that the literature's

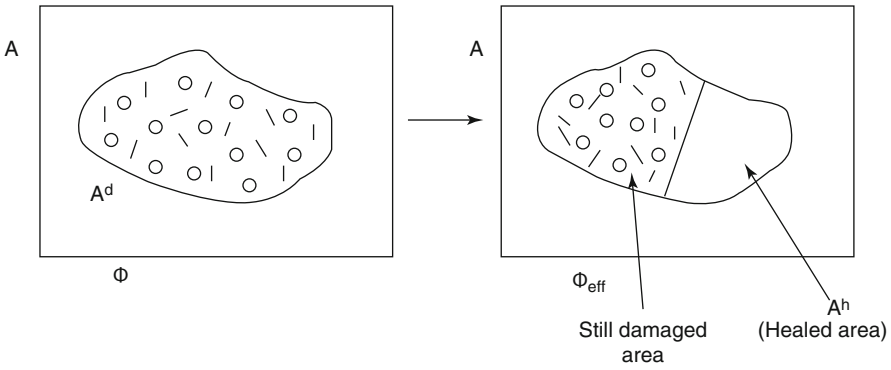

Fig. 3 Schematic diagram for healed and damaged areas

conventional linear healing model may be derived as a special instance of the generalized nonlinear healing model for small healing cases.

Figure 3 depicts the basic concept behind the development of the generalized nonlinear healing model. It should be emphasized that cross-sectional areas of damage will not be considered in the new healing model's mathematical derivation. Instead, users will be created from the damage variables, which will be sufficient to generate the required equations.

The damage state is given by the traditional scalar damage variable ϕ in Fig. 3, which shows a deformed and damaged region A^d in the left portion of the figure. A healed region A^h is represented in the right part of the figure, where healing is provided from the left to the right part of the figure.

The classical damage variables are then decomposed (Kattan and Voyiadjis 2001; Voyiadjis and Kattan 2012):

$$\phi = \phi_1 + \phi_2 - \phi_1 \phi_2 \tag{12}$$

For two damage processes working in series, that is, acting sequentially after each other, the above decomposition is the common damage variable decomposition used in damage mechanics (Kattan and Voyiadjis 2001; Voyiadjis and Kattan 2012). The decomposition of Eq. (12) was originally determined using the relevant cross-sectional areas (Kattan and Voyiadjis 2001; Voyiadjis and Kattan 2012), so damage and healing cross-sectional areas are employed indirectly in the derivation below.

The next step is to introduce a healing variable h that satisfies $0 < h < 1$ and meets the following two criteria:

$$\phi_1 = h\phi \tag{13}$$

$$\phi_2 = \phi_{eff} \tag{14}$$

The healed damage stage (first stage) is represented by the first condition, whereas the effective damage stage is represented by the second condition (second

stage). ϕ_1 is the part of ϕ that has been healed. Eqs. (13) and (14) are thus substituted into Eq. (12), yielding:

$$\phi = h\phi + \phi_{eff} - h\phi\phi_{eff} \tag{15}$$

When one solves Eq. (15) for ϕ_{eff}, one gets:

$$\phi_{eff} = \frac{\phi(1-h)}{1-h\phi} \tag{16}$$

The above expression is a generalization of the Eq. (54*)'s linear healing model. It should be emphasized that Eq. (16) is a nonlinear generalized healing model since ϕ_{eff} is a nonlinear function of h, as demonstrated in Eq. (16). Additionally, Eq. (16) meets both of the boundary conditions: (1) when $h = 0$, $\phi_{eff} = \phi$ (no healing) and (2) when $h = 1$, $\phi_{eff} = 0$ (complete healing). When the healing is small, the linear healing expression is a specific instance of the nonlinear healing expression, as shown below.

The effective stress $\overline{\sigma}$ can be stated as follows using Eq. (16):

$$\overline{\sigma} = \frac{\sigma}{1-\phi_{eff}} = \frac{\sigma(1-h\phi)}{1-\phi} \tag{17}$$

The conventional effective stress in Eq. (11) is generalized in Eq. (17). The current results are shown in Table 1. A comparable equation to (17) has recently been published in the literature (Hong et al. 2015a, b), but with a different form and derivation.

The linear healing model, as a specific case of the nonlinear healing model, is next demonstrated. To begin, consider the Taylor series expansion around the point $h\ \phi = 0$:

$$\frac{1}{1-h\phi} = 1 + h\phi + h^2\phi^2 + h^3\phi^3 + \ldots\ldots\ldots \tag{18}$$

When the first two terms of the series on the right-hand side of Eq. (18) are substituted for the effective damage variable in Eq. (16), the following results are obtained:

$$\phi_{eff} = \frac{\phi(1-h)}{1-h\phi} \approx \phi(1-h)(1+h\phi) \tag{19}$$

Table 1 Some of the results summarized

Effective damage	$\phi_{eff} = \phi\ (1-h)$, linear	$\phi_{eff} = \frac{\phi(1-h)}{1-h\phi}$
Effective stress	$\overline{\sigma} = \frac{\sigma}{1-\phi(1-h)}$, nonlinear	$\overline{\sigma} = \frac{\sigma(1-h\phi)}{1-\phi}$

If one simplifies Eq. (19) above, one gets:

$$\phi_{eff} \approx \phi(1-h) + \phi^2 h(1-h) \tag{20}$$

When looking at Eq. (20) thoroughly and noticing that for small damage and healing, the quadratic term in ϕ on the right-hand side may be disregarded (because h is likewise quadratic in the second term), one gets:

$$\phi_{eff} \approx \phi(1-h) \tag{21}$$

The above approximate expression for effective stress is identical to the one used in the linear healing model literature. For circumstances of small healing and small damage, the linear healing model is a specific example of the generalized nonlinear healing model.

Quadratic Healing

A special instance of the generalized nonlinear healing model is investigated in depth in this subsection. Quadratic healing is an example of this. As demonstrated below, this instance is obtained consistently from the generalized healing model.

To begin, evaluate the linear healing expression of the Eq. (54*) and rewrite it as follows:

$$\phi_{eff} = \phi - h\phi \tag{22}$$

As stated above, the term $h\ \phi$ stands for the healed damage component, which is removed from ϕ. The unhealed damage, also known as effective damage, is represented by Eq. (22). The expression of generalized nonlinear healing in Eq. (16) is then rewritten as follows using the Taylor series expansion:

$$\phi_{eff} = \phi(1-h)\left(1 + \phi h + \phi^2 h^2 + \phi^3 h^3 + \ldots\ldots\right) \tag{23}$$

When only the first two components of the series expansion are considered, and higher-order terms of the series expansion are ignored (valid for small values), Eq. (23) can be rewritten as follows:

$$\phi_{eff} \approx \phi(1-h)(1+\phi h) \tag{24}$$

The expression of Eq. (24) is then expanded and rewritten as follows:

$$\phi_{eff} \approx (\phi - h\phi) + \left(h\phi^2 - h^2\phi^2\right) \tag{25}$$

Because the effective damage variable ϕ_{eff} is a quadratic function of the healing variable h, the expression of Eq. (25) is known as quadratic healing. The effective

damage is made up of two parts that are added together, as shown in Eq. (25): (1) the first component is $\phi - h\,\phi$, which represents unhealed linear damage, and (2) the second part is $\phi^2 h - \phi^2 h^2$, which represents unhealed quadratic damage. In the second term, it is noticed that $\phi^2 h^2 = h\ (\phi^2 h)$ reflects the part of $\phi^2 h$ that has been healed (and thus is subtracted from $\phi^2 h$). The effective stress in the instance of quadratic healing is stated as follows:

$$\overline{\sigma} = \frac{\sigma}{1 - \phi_{eff}} = \frac{\sigma}{1 - (\phi - h\phi) - \left(h\phi^2 - h^2\phi^2\right)} \tag{26}$$

Tensorial Formulation

Then, for the general circumstance of deformation and damage, one tries to generalize the Eq. (54*). Tensors must be used instead of scalars for this purpose. Tensors are represented using the following vector and matrix notation. The stress tensor and the effective stress tensor are represented by the vectors $\{\sigma\}$ and $\{\overline{\sigma}\}$, respectively. As a result, the linear healing model's Eq. (54*) can be tensorially generalized as follows:

$$\{\overline{\sigma}\} = \left([M]^{-1} + \left([I] - [M]^{-1}\right)[H]^{-1}\right)^{-1}\{\sigma\} \tag{27}$$

where $[M]$ is the fourth-rank damage effect tensor, $[H]$ is the fourth-rank healing tensor, and $[I]$ is the fourth-rank identity tensor (Doghri 2000; Hansen and Schreyer 1994; Kattan and Voyiadjis 1990; Kattan and Voyiadjis 1993; Ladeveze et al. 1982; Lubineau 2010; Lubineau and Ladeveze 2008; Lee et al. 1985; Luccioni and Oller 2003; Rice 1971; Sidoroff 1981; Voyiadjis 1988; Voyiadjis and Kattan 1990, 1992). It should be noticed that when the substitutions $[M] \equiv \frac{1}{1-\phi}$, $[H] = \frac{1}{h}$, and $[I] = 1$ are made, the tensorial Eq. (27) reduces to the scalar Eq. (54*).

The generalized nonlinear healing model's Eq. (17) can be tensorially generalized using one of two alternative expressions:

$$\{\overline{\sigma}\} = [M]^{-1}\left([I] - \left([I] - [M]^{-1}\right)[H]^{-1}\right)\{\sigma\} \tag{28}$$

$$\{\overline{\sigma}\} = \left([I] - \left([I] - [M]^{-1}\right)[H]^{-1}\right)[M]^{-1}\{\sigma\} \tag{29}$$

When the substitutions $[M] \equiv \frac{1}{1-\phi}$, $[H] = \frac{1}{h}$, and $[I] = 1$ are made, both of the foregoing formulas reduce to the scalar Eq. (17).

The quadratic healing model's Eq. (26) can be tensorially generalized using the following expression:

$$\begin{aligned}\{\bar{\sigma}\} = \Big[[M]^{-1} + \left([I] - [M]^{-1}\right)[H]^{-1} - \left([I] - [M]^{-1}\right)\left([I] - [M]^{-1}\right)[H]^{-1} \\ + \left([I] - [M]^{-1}\right)\left([I] - [M]^{-1}\right)[H]^{-1}[H]^{-1}\Big]^{-1}\{\sigma\}\end{aligned} \tag{30}$$

When the substitutions $[M] \equiv \frac{1}{1-\phi}$, $[H] = \frac{1}{h}$, and $[I] = 1$ are made, the preceding expression reduces to the scalar Eq. (26) once more.

Concept of Unhealable Damage

The linear healing model of Eq. (54*) and the modified nonlinear healing model of Eq. (54*) have a significant difference (16). For the virgin undamaged condition (when $\phi = 0$), both models create zero effective stress ($\phi_{eff} = 0$). In the case of a rupture, however, things are different (when $\phi = 1$). The linear healing model yields $\phi_{eff} = 1 - h$ in this situation, and therefore complete healing is achieved when $h = 1$. The generalized healing model, on the other hand, yields $\phi_{eff} = 1$ regardless of the value of the healing variable h, suggesting that some sort of damage persists in the ruptured state. Unhealable damage is the term for residual damage. Unhealable damage is a key characteristic of the generalized nonlinear healing model, which is not present in the conventional linear healing model.

Thus, for complete healing and full recovery of damage, the healing process must be completed before the stage of rupture, that is, before $\phi = 1$ for general nonlinear healing. As a result, it is hypothesized that complete healing happens for this model at a certain value of the damage $\phi = \phi_o < 1$.

To accommodate for unhealable damage, the linear healing model's classical Eq. (54*) can be significantly adjusted. As a result, the linear healing Eq. (54*) is modified as follows:

$$\phi_{eff} = \phi(1 - h + \alpha h) \tag{31}$$

where α is called the unhealable damage parameter. Equation (31) simplifies to the classical Eq. (54*) without any unhealable damage characteristics when α is zero. When $\alpha \neq 0$ is present, however, the modified linear healing model of Eq. (31) can be used to account for unhealable damage. Finally, this section's idea of unhealable damage may or may not be connected to section "Unhealable Damage and Non-damageable Integrity" concept of unhealable damage. This problem has yet to be researched.

Damage and Healing Models Compared

When comparing the three healing models described in the preceding paragraph, the ratio AB for all three models is calculated as shown in Table 2.

Several curves are shown on a graph using the formulas in Table 2, as illustrated in Fig. 4. Both the nonlinear and quadratic healing models generate larger values of the effective damage ratio, implying less healing in these two situations, as seen in the figure. The curves in Fig. 4 are then explored in further depth. The first derivative of the difference function will be used to calculate the greatest differences between the curves (and hence the healing models). This is quantitatively depicted below. The

Table 2 Healing models compared

Healing mode	Abbreviation	Equation
Linear healing	(LH)	$\frac{\phi_{eff}}{\phi} = 1 - h$
Generalized nonlinear healing	(NH,ϕ)	$\frac{\phi_{eff}}{\phi} = \frac{1-h}{1-\phi h}$
Quadratic healing	(QH,ϕ)	$\frac{\phi_{eff}}{\phi} = 1 - h + \phi h - \phi h^2$

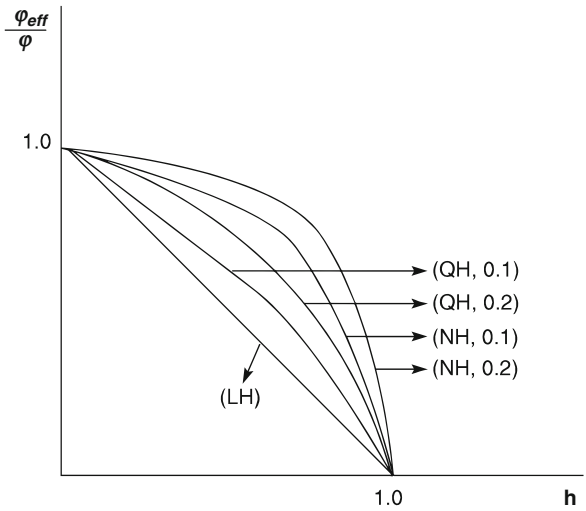

Fig. 4 Comparison between the three healing models

distinction between linear and nonlinear healing models is discussed first. Using Eqs. (54*) and (16), the difference function is constructed as follows:

$$f_1(h) = \frac{\phi(1-h)}{1-\phi h} - \phi(1-h) \tag{32}$$

The following final form is obtained by simplifying the statement of Eq. (32):

$$f_1(h) = \frac{\phi^2 h(1-h)}{1-\phi h} \tag{33}$$

Take the first derivative of the expression of Eq. (33) for h (i.e., df_1/dh) and set it to zero to obtain the maximum value of the difference function $f_1(h)$. As a result, one obtains:

$$\phi h^2 - 2h + 1 = 0 \tag{34}$$

In h, the expression above is a quadratic equation. When one solves for h, one gets two roots: $h = \frac{1 \pm \sqrt{1-\phi}}{\phi}$. Because it yields values higher than 1, the root with the "+"

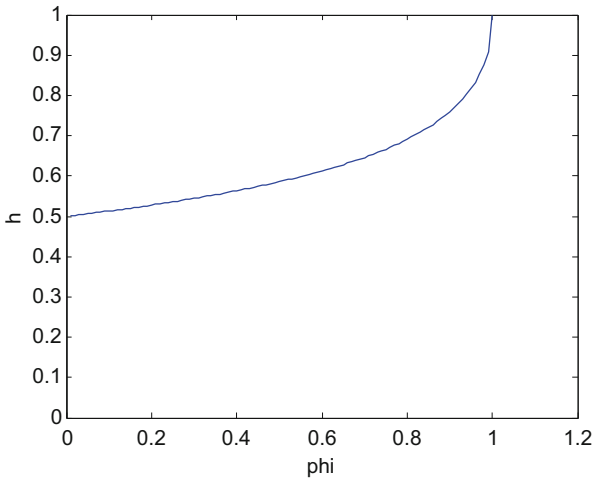

Fig. 5 Relationship between healing and damage based on Eq. (35)

sign may be omitted (but see the explanation below, which follows Eq. (38)). As a result, the value of the healing variable at which the greatest change occurs is:

$$h = \frac{1 - \sqrt{1 - \phi}}{\phi} \tag{35}$$

The precise value of the healing variable h is dependent on the value of the damage variable ϕ, as shown above. Figure 5 depicts a visualization of the expression provided in Eq. 35. The small value of ϕ is about 0.5. So, for all values of the damage variable in the range $0 < \phi < 0.5$, one assumes that $h \approx 0.5$. The healing variable has values in the range $0.5 < h < 1$ for higher values of ϕ. $h = 0.585$ is obtained when $\phi = 0.5$.

The equation may be used to get an approximate value for h (35). When the expression of Eq. (35) is expanded using a Taylor series (valid for small values of ϕ), the following results are obtained:

$$h \approx \frac{1 - \left(1 - \frac{1}{2}\phi + \ldots.\right)}{\phi} = \frac{1}{2} \tag{36}$$

For the range $0 < \phi < 0.5$, the above approximation is acceptable. The greatest difference between the linear and nonlinear healing models is then calculated. This is done by inserting $h = 0.5$ in Eq. (33)'s difference function $f_1(h)$ to get:

$$f_1\left(\frac{1}{2}\right) = \frac{\phi^2}{2(2 - \phi)} \tag{37}$$

The above expression reaches its maximum value at $\phi = 1$, resulting in $(f_1)_{\max} = 0.5$. As a result, the linear and nonlinear healing models have a maximum

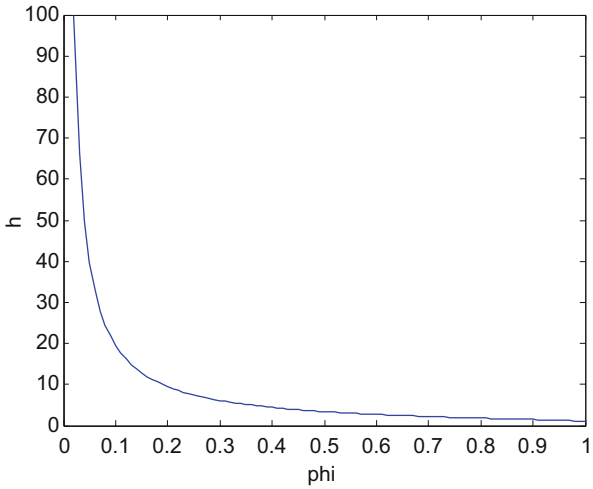

Fig. 6 Relationship between healing and damage based on Eq. (38)

difference of 0.5. The second value of h is then examined using the "+" symbol, which is expressed as follows:

$$h = \frac{1 + \sqrt{1 - \phi}}{\phi} \tag{38}$$

The precise value of the healing variable h1 is dependent on the value of the damage variable phi1, as shown above. Figure 6 depicts a visualization of the expression provided in Eq. (38). The values of the healing variable h are larger than 1 as seen in the figure. If the healing variable values are assumed to be in the range $0 < h < 1$, then this expression of h must be ignored. However, given the authors' hypothesis of super healing in their study (Voyiadjis and Kattan 2014), values of $h > 1$ imply super healing. As a result, this case may be allowed. As illustrated in Fig. 6, the values of the healing variable h decrease from infinity to a finite value of $h = 1$ for the damage variable normal range $0 < \phi < 1$.

The difference between linear and quadratic healing models is next examined. Using Eqs. (54*) and (25) as a reference, the difference function $f_2\ (h)$ is constructed as follows:

$$f_2(h) = \left(\phi - \phi h + \phi^2 h - \phi^2 h^2\right) - \phi(1 - h) \tag{39}$$

The following final form is obtained by simplifying the statement of Eq. (40):

$$f_2(h) = \phi^2 h(1 - h) \tag{40}$$

Take the first derivative of the expression of Eq. (40) for h (i.e., df_2/dh) and set it to zero to obtain the maximum value of the difference function $f_2(h)$. As a result, one obtains:

$$\phi^2(1-2h)=0 \tag{41}$$

Clearly, $h = 0.5$ is the answer to the preceding quadratic equation in h. The discrepancy between the linear and quadratic healing models reaches its greatest point at this precise value. It should also be noted that when comparing the linear and nonlinear healing models, this is the same value achieved. Finally, by replacing the value $h = 0.5$ into the difference function $f_2(h)$ of Eq. (40), the greatest difference between linear and quadratic healing is obtained:

$$f_2\left(\frac{1}{2}\right)=\frac{1}{4}\phi^2 \tag{42}$$

The highest value occurs at $\phi = 1$ as can be seen from the preceding formula. As a result, the greatest difference between the linear and quadratic healing models is $(f_2)_{\max} = 0.25$.

Finally, for typical tiny values of the damage variable, such as $\phi = 0.1$, the two maximum difference functions $f_1(h)$ and $f_2(h)$ are compared. As a result, one gets:

$$f_1(0.1)=0.00263 \tag{43}$$

$$f_2(0.1)=0.00250 \tag{44}$$

The differences between the two healing models are tiny and insignificant for extremely small values of the damage variable, as seen by the above numbers.

The Healing Process Dissected

The healing process is mathematically examined in this section using a geometric series. The goal of this dissection is to break down each stage of the healing process. The dissection procedure is carried out twice: once for linear healing expression and again for nonlinear healing expression. With linear healing, one begins with the expression of effective stress. For dissection, this expression is rewritten as in the following:

$$\overline{\sigma}=\frac{\sigma}{1-\phi(1-h)}=\frac{\sigma}{(1-\phi)+\phi h} \tag{45}$$

The Taylor series expansion around $x = 0$ can be expressed as follows: The above expression is in the form $\frac{1}{a+bx}$, which can be represented as follows:

$$\frac{1}{a+bx}=\frac{1}{a}-\frac{bx}{a^2}+\frac{b^2x^2}{a^3}-\frac{b^3x^3}{a^4}+\frac{b^4x^4}{a^5}-\ldots\ldots\ldots \tag{46}$$

As a result, using the Taylor series expansion around $h = 0$ (utilizing $a \equiv 1 - \phi$, $b \equiv \phi$, and$x \equiv h$), Eq. (45) can be expressed as follows:

Table 3 Stages of linear healing for $\phi = 0.7$ and $h = 0.5$

Linear healing model	Value of $\frac{\overline{\sigma}}{\sigma}$
No healing	+3.33333
Primary healing	-3.88889
Secondary healing	+4.53704
Tertiary healing	-5.29321
Quaternary healing	+6.17431
Quinary healing	-7.204647
Senary healing	-8.404260

$$\overline{\sigma} = \sigma \left[\frac{1}{1-\phi} - \frac{\phi h}{(1-\phi)^2} + \frac{\phi^2 h^2}{(1-\phi)^3} - \frac{\phi^3 h^3}{(1-\phi)^4} + \frac{\phi^4 h^4}{(1-\phi)^5} - \ldots\ldots\ldots \right] \tag{47}$$

The above healing dissection is presented as an alternating geometric sequence. The unhealed stage is assigned as the first term of the series $\frac{1}{1-\phi}$, the primary healing stage is marked as the second term of the series $\frac{\phi h}{(1-\phi)^2}$, the secondary healing stage is classified as the third term of the series $\frac{\phi^2 h^2}{(1-\phi)^3}$, and the tertiary healing stage is designated as the fourth term of the series $\frac{\phi^3 h_3}{(1-\phi)^4}$, etc. The given statement distinguishes between the linear healing model's sequential healing stages.

It is also obvious that the term $-\frac{\phi h}{1-\phi}$ gives the ratio between two healing stages. In the following numerical example, this ratio is used to depict the stages of healing. The value of $\frac{\overline{\sigma}}{\sigma}$ is calculated using Eq. (47) and the parameters $\phi = 0.7$ and $h = 0.5$. The values of the sequential healing stages are obtained as given in Table 3.

The aforementioned data in the table are then plotted as illustrated in Fig. 7. The effective stress in each succeeding healing stage grows in an oscillatory fashion, as seen in the graph. This is the linear healing process' inferred behavior. This behavior will be contrasted to the nonlinear healing model in the following section.

The aforementioned formulation is then repeated for the nonlinear healing model. To do this, one should begin by expressing effective stress through nonlinear healing. For dissection, the statement is rewritten as follows:

$$\overline{\sigma} = \frac{\sigma}{1 - \frac{\phi(1-h)}{1-\phi h}} = \frac{\sigma(1-\phi h)}{1-\phi} \tag{48}$$

The following Taylor series expansion around $x = 0$ can be used to represent the above equation in the form $\frac{1}{1-x}$:

$$\frac{1}{1-x} = 1 + x + x^2 + x^3 + x^4 + \ldots\ldots\ldots \tag{49}$$

As a result, using the Taylor series expansion around $\phi = 0$ (using $x \equiv \phi$), Eq. (48) may be expressed as follows:

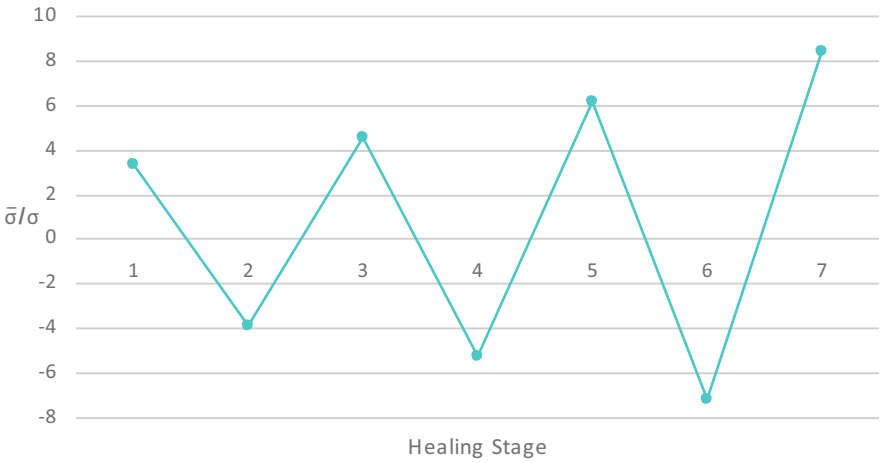

Fig. 7 Nonlinear healing model stages expanded around h = 0

$$\overline{\sigma} = \sigma(1 - \phi h)\left[1 + \phi + \phi^2 + \phi^3 + \phi^4 + \ldots\ldots\right] \tag{50}$$

The above equation can be simplified and expanded to produce the following more suitable form:

$$\overline{\sigma} = \sigma\left[1 + \phi(1 - h) + \phi^2(1 - h) + \phi^3(1 - h) + \phi^4(1 - h) + \ldots\ldots\right] \tag{51}$$

The above healing dissection is presented as a geometric series. The unhealed stage is designated as the first term of the series (does not include any healing), the primary healing stage is assigned as the second term of the series $\phi\ (1 - h)$, the secondary healing stage is marked as the third term of the series $\phi^2\ h^2$, the tertiary healing stage is classified as the fourth term of the series $\phi^3(1 - h)$, etc. The above statement distinguishes between the nonlinear healing model's various healing stages.

It is also obvious that the formula phi1 gives the ratio between two healing phases. In the following numerical example, this ratio is used to depict the processes of healing.

Using the parameters $\phi = 0.7$ and $h = 0.5$, the value of $\frac{\overline{\sigma}}{\sigma}$ is calculated using Eq. (51). The values of the different healing phases are obtained as given in Table 4.

Both series expansions should be made at the same point to compare the healing stages for the two examples of linear and nonlinear healing. As a result, the above two tables cannot be compared since the expansion in Table 3 is produced around $h = 0$ for linear healing, while the expansion in Table 4 is made around $\phi = 0$ for nonlinear healing. So the healing model will be expanded around $\phi = 0$ to compare the healing stages. As a result, the following Taylor series expansion is obtained using Eq. (45) (utilizing$a \equiv 1$, $b \equiv\ -(1 - h)$, and $x \equiv \phi$):

Table 4 Stages of nonlinear healing for $\phi = 0.7$ and $h = 0.5$

Nonlinear healing model	Value of $\frac{\overline{\sigma}}{\sigma}$
No healing	1.00000
Primary healing	0.35000
Secondary healing	0.24500
Tertiary healing	0.17150
Quaternary healing	0.12005
Quinary healing	0.084035

Table 5 Stages of linear healing for $\phi = 0.7$ and $h = 0.5$

Nonlinear healing model	Value of $\frac{\overline{\sigma}}{\sigma}$
No healing	1.00000
Primary healing	0.35000
Secondary healing	0.12250
Tertiary healing	0.042875
Quaternary healing	0.015006
Quinary healing	0.00525

$$\overline{\sigma} = \sigma\left[1 + \phi(1-h) + \phi^2(1-h)^2 + \phi^3(1-h)^3 + \phi^4(1-h)^4 + \ldots\ldots\right] \quad (52)$$

The above healing dissection is presented as a geometric series. The unhealed stage is assigned as the first term of the series (does not include any healing), the primary healing stage is marked as the second term of the series $\phi\ (1-h)$, the secondary healing stage is marked as the third term of the series $\phi^2(1-h)^2$, the tertiary healing stage is designated as the fourth term of the series $\phi^3(1-h)^3$, etc. The above statement distinguishes between the linear healing model's consecutive healing stages.

It is also obvious that the term $\phi(1-h)$ gives the ratio between two healing phases. In the following numerical example, this ratio is used to depict the phases of healing. Using the parameters $\phi = 0.7$ and $h = 0.5$, the value of $\frac{\overline{\sigma}}{\sigma}$ is calculated using Eq. (52). The values of the different healing phases are obtained as given in Table 5.

It is reasonable to compare the expansion in Eq. (51) to the expansion in Eq. (52). Figure 8 depicts the contrast. The two curves in this image indicate that both models provide the same values for the main healing stage, but that the discrepancies begin with the secondary healing stage. As predicted, the quantity of healing reduces with each subsequent healing stage. However, compared to the linear healing model, the nonlinear healing model displays a somewhat lower decline in healing with each succeeding healing stage. This finding might imply that the nonlinear healing model is more reliable and allows for more material healing. This study presents a more simple and reliable model of healing represented by the newly generated nonlinear healing model, which is the one utilized in the literature on damage and healing mechanics.

Finally, Table 6 summarizes the key findings of this section. Because the expression of the effective stress in h is linear in the case of nonlinear healing (see Eq. (51)),

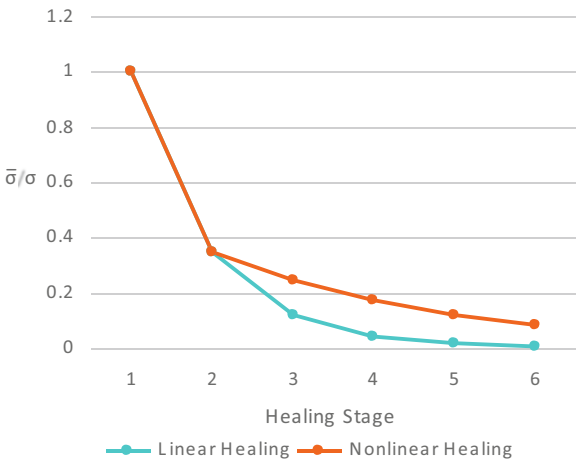

Fig. 8 Linear and nonlinear healing model stages expanded about $\phi = 0$

Table 6 Summary of results for section "The Healing Process Dissected"

The expressions shown are the terms of the expansion of the effective stress ratio $\bar{\sigma}/\sigma$	Linear healing expanded about $\phi = 0$	Nonlinear healing expanded about $\phi = 0$	Linear healing expanded about $h = 0$	Nonlinear healing expanded about $h = 0$
No healing	1	1	$+\frac{1}{1-\phi}$	$+\frac{1}{1-\phi}$
Primary stage	$\phi\ (1-h)$	$\phi\ (1-h)$	$-\frac{\phi h}{(1-\phi)^2}$	$-\frac{\phi h}{1-\phi}$
Secondary stage	$\phi^2(1-h)^2$	$\phi^2\ (1-h)$	$+\frac{\phi^2 h^2}{(1-\phi)^3}$	Not applicable
Tertiary stage	$\phi^3(1-h)^3$	$\phi^3\ (1-h)$	$-\frac{\phi^3 h^3}{(1-\phi)^4}$	Not applicable
Quaternary stage	$\phi^4(1-h)^4$	$\phi^4\ (1-h)$	$+\frac{\phi^4 h^4}{(1-\phi)^5}$	Not applicable

the fifth column of the table does not include an expansion around $h = 0$. Figures 7 and 8 also show that the series expansion around $\phi = 0$ produces good and reasonable results, but the series expansion around $h = 0$ produces oscillatory behavior and should be avoided.

Summary/Conclusions

New basic themes are explored in the framework of continuum damage mechanics. In addition, new material damageability and integrity concepts are introduced. Damage and healing are thoroughly studied utilizing unique mathematical relations that may be relied on.

In addition, nonlinear healing mathematical equations are provided and compared to existing linear healing literature. The difficulty of quadratic healing is illustrated as an example. Unhealable damage and nondamageable integrity are two additional new concepts presented. A numerical calculation of the percentage of unhealable damage and nondamageable integrity concerning total cumulative damage has been attempted. Finally, the healing process is examined and the various stages of healing are quantitatively deduced.

The key points raised in this study are as follows:

1. It has been mathematically proven that only a tiny portion of the total damage can be restored. Unhealable damage is the proportion of damage that cannot be healed. The evidence is theoretical and has not been investigated in terms of its applicability to practical applications.
2. It has been mathematically proven that only a small portion of the total integrity may be compromised. Nondamageable integrity refers to the amount of integrity that has not been damaged. The evidence is theoretical and has not been investigated in terms of its applicability to real-world situations.
3. The conventional linear healing model is contrasted with a novel generalized nonlinear healing model. The benefits and drawbacks of the nonlinear healing model are discussed.
4. The quadratic healing model is generated as a specific interpretation of the generalized nonlinear healing model. The classical linear healing model is compared to this unique type of healing.
5. A geometric series is used to examine the healing process quantitatively. Several healing stages are depicted both conceptually and quantitatively in this dissection procedure.

References

M.K. Darabi, R.K. Abu Al-Rub, D.N. Little, A continuum damage mechanics framework for modeling micro-damage healing. Int. J. Solids Struct. **49**, 492–513 (2012)

I. Doghri, *Mechanics of Deformable Solids: Linear and Nonlinear, Analytical and Computational Aspects* (Springer-Verlag, Berlin, 2000)

N.R. Hansen, H.L. Schreyer, A thermodynamically consistent framework for theories of elastoplasticity coupled with damage. Int. J. Solids Struct. **31**(3), 359–389 (1994)

S. Hong, K.Y. Yuan, J.W. Ju, New strain energy-based thermo-elastoviscoplastic isotropic damage-self-healing for bitumimous composites – Part I: Formulations. Int. J. Damag. Mech. (2015a). https://doi.org/10.1177/1056789515610706

S. Hong, K.Y. Yuan, J.W. Ju, New strain energy-based thermo-elastoviscoplastic isotropic damage-self-healing for bitumimous composites – Part II: Computational aspects. Int. J. Damag. Mech. (2015b). https://doi.org/10.1177/1056789515610707

P.I. Kattan, G.Z. Voyiadjis, A coupled theory of damage mechanics and finite strain elasto-plasticity – Part I: Damage and elastic deformations. Int. J. Eng. Sci. **28**(5), 421–435 (1990)

P.I. Kattan, G.Z. Voyiadjis, A plasticity-damage theory for large deformation of solids – Part II: Applications to finite simple shear. Int. J. Eng. Sci. **31**(1), 183–199 (1993)

P.I. Kattan, G.Z. Voyiadjis, Decomposition of damage tensor in continuum damage mechanics. J. Eng. Mech, ASCE **127**(9), 940–944 (2001)

P. Ladeveze, M. Poss, L. Proslier, Damage and fracture of tridirectional composites, in *Progress in Science and Engineering of Composites. Proceedings of the Fourth International Conference on Composite Materials, Japan Society for Composite Materials*, vol. 1, (1982), pp. 649–658

H. Lee, K. Peng, J. Wang, An anisotropic damage criterion for deformation instability and its application to forming limit analysis of metal plates. Eng. Fract. Mech. **21**, 1031–1054 (1985)

G. Lubineau, A pyramidal modeling scheme for laminates – Identification of transverse cracking. Int. J. Damag. Mech. **19**(4), 499–518 (2010)

G. Lubineau, P. Ladeveze, Construction of a micromechanics-based intralaminar mesomodel, and illustrations in ABAQUS/Standard. Comput. Mater. Sci. **43**(1), 137–145 (2008)

B. Luccioni, S. Oller, A directional damage model. Comput. Methods Appl. Mech. Eng. **192**, 1119–1145 (2003)

J.R. Rice, Inelastic constitutive relations for solids: An internal variable theory and its application to metal plasticity. J. Mech. Phys. Solids **19**, 433–455 (1971)

F. Sidoroff, Description of anisotropic damage application in elasticity, in *IUTAM Colloqium on Physical Nonlinearities in Structural Analysis*, (Springer-Verlag, Berlin, 1981), pp. 237–244

G.Z. Voyiadjis, Degradation of elastic modulus in elastoplastic coupling with finite strains. Int. J. Plast. **4**, 335–353 (1988)

G.Z. Voyiadjis, P.I. Kattan, A coupled theory of damage mechanics and finite strain elasto-plasticity – Part II: Damage and finite strain plasticity. Int. J. Eng. Sci. **28**(6), 505–524 (1990)

G.Z. Voyiadjis, P.I. Kattan, A plasticity-damage theory for large deformation of solids – Part I: Theoretical formulation. Int. J. Eng. Sci. **30**(9), 1089–1108 (1992)

G.Z. Voyiadjis, P.I. Kattan, Mechanics of damage processes in series and in parallel: A conceptual framework. Acta Mech. **223**(9), 1863–1878 (2012)

G.Z. Voyiadjis, P.I. Kattan, Healing and super healing in continuum damage mechanics. Int. J. Damag. Mech. **23**(2), 245–260 (2014)

G.Z. Voyiadjis, A. Shojaei, G. Li, A thermodynamic consistent damage and healing model for self-healing materials. Int. J. Plast. **27**(7), 1025–1044 (2011)

G.Z. Voyiadjis, A. Shojaei, G. Li, P.I. Kattan, Continuum damage-healing mechanics with introduction to new healing variables. Int. J. Damag. Mech. **21**, 391–414 (2012)

Partial Damage Mechanics: Introduction

4

George Z. Voyiadjis and Peter I. Kattan

Contents

Introduction 84
Review of Continuum Damage Mechanics 85
Introduction to Partial Damage Mechanics 86
Conclusion 96
References 98

Abstract

In this work, advanced models for material damage in metals are presented. The models are based on new concepts in continuum damage mechanics, namely, the concept of partial damage modeling. This new concept is illustrated both mathematically and graphically. The classical equations of damage mechanics are obtained as special cases of the equations of partial damage mechanics. It is hoped that this work lays the groundwork for new avenues of research in damage mechanics and materials science.

In this work advanced models for material damage in metals are presented. The models are based on new concepts in continuum damage mechanics, namely, the concept of partial damage modeling. This new concept is illustrated both mathematically and graphically. The classical equations of damage mechanics are obtained as special cases of the equations of partial damage mechanics. It is hoped that this work lays the groundwork for new avenues of research in damage mechanics and materials science.

G. Z. Voyiadjis
Center for GeoInformatics C4G and Computational Solid Mechanics Laboratory, Department of Civil and Environmental Engineering, Louisiana State University, Baton Rouge, LA, USA
e-mail: voyiadjis@eng.lsu.edu

P. I. Kattan (✉)
Department of Civil and Environmental Engineering, Louisiana State University, Baton Rouge, LA, USA
e-mail: pkattan@PetraBooks.com; info@PetraBooks.com

© Springer Nature Switzerland AG 2022

G. Z. Voyiadjis (ed.), *Handbook of Damage Mechanics*,
https://doi.org/10.1007/978-3-030-60242-0_85

Keywords

Damage mechanics · Damage · Partial damage · Partial damage mechanics · Scalar formulation · Tensorial formulation

Introduction

The beginnings of damage mechanics were set initially by Kachanov (1958) and then elaborated on by Lee et al. (1985), Voyiadjis and Kattan (1992, 2005, 2006, 2009), Sidoroff (1981), Krajcinovic (1996), and Kattan and Voyiadjis (1993, 2001a, b).

The initial development of damage mechanics was based on the effective stress concept as developed by Kachanov (1958). Rabotnov (1969) continued with these developments along with others later (Kattan and Voyiadjis 2001a, b; Ladeveze and Lemaitre 1984; Voyiadjis and Kattan 2005, 2006, 2009, 2012). In this context, one utilized a scalar damage variable to characterize damage in the material where the values of the damage variable range from 0 to 1. The smallest value of 0 applies to the case of undamaged material, while the maximum value of 1 applies to the case of complete failure. This ultimate value is not usually reached in practical applications.

New developments in damage mechanics appeared quickly in the past few decades (Celentano et al. 2004; Doghri 2000; Hansen and Schreyer 1994; Kattan and Voyiadjis 1990, 1993; Ladeveze et al. 1982; Lubineau 2010; Lubineau and Ladeveze 2008; Lee et al. 1985; Rice 1971; Sidoroff 1981; Voyiadjis and Kattan 1990, 1992). Healing mechanics which is closely related to damage mechanics also progressed in those years (Voyiadjis et al. 2011, 2012a, b; Darabi et al. 2012). Other avenues of research in damage mechanics include the use of entropy generation (Basaran and Yan 1998; Basaran and Nie 2004). Additional research work in damage mechanics has been conducted recently by Voyiadjis and Kattan (2017a, b, c).

The new subject of partial damage mechanics is based on the use of a partial damage variable in the formulation. This new subject is introduced in this work based on sound mathematical principles. This is summarized in two sections as follows.

A review and summary of the principles of damage mechanics are presented in section "Review of Continuum Damage Mechanics." The review is based on the introduction of a scalar damage variable. The use of this damage variable is paramount to the success of the formulation. The damage variable is based on the cross-sectional area of the material. Other definitions of the damage variable are not used in this work because they are not useful in the definition of the partial damage variable.

In section "Introduction to Partial Damage Mechanics" the principles of partial damage mechanics are described. This is based on the assumption that a fraction of the damage in the material is considered. The equations of partial damage mechanics are developed based on sound mathematical principles. Finally it is seen that the classical equations of damage mechanics are obtained as a special case of the equations of partial damage mechanics. Thus, the new

subject of partial damage mechanics is more general and is considered as generalized damage mechanics.

Review of Continuum Damage Mechanics

The classical damage variable is described in this section briefly. It is based on the cross-sectional area of the material. It should be noted that there is another damage variable used that is based on the reduction of elastic stiffness of the material (Voyiadjis and Kattan 2009). However, this other damage variable is not used in this work because it is not relevant to the subject of partial damage mechanics.

One considers two configurations of the material body: one is the initial undamaged and undeformed state of the material while the other one is the damaged and deformed state of the material (see Fig. 1). The next step is to consider a new third state that is called fictitious where all the damage is removed from the damaged state (see Fig. 1). It should be noted that the classical damage variable exists in the damaged state but vanishes in the fictitious undamaged state.

The classical damage variable ϕ is described and defined as in the following expression:

$$\phi = \frac{A - \overline{A}}{A} \tag{1}$$

where A is the cross-sectional area in the damaged state, while $\overline{A}$ is the cross-sectional area in the fictitious undamaged state with $A > \overline{A}$. It is clear that when a body is undamaged, i.e., when $A = \overline{A}$, then $\phi = 0$.

The stress in the fictitious undamaged state is labelled the effective stress and is denoted by $\overline{\sigma}$. The generation of the effective stress $\overline{\sigma}$ may be developed utilizing the equilibrium equation $\overline{\sigma}A = \sigma A$ where σ is the stress in the damaged state. Therefore, using this equilibrium equation along with the definition in Eq. (1), one reaches the following expression:

$$\overline{\sigma} = \frac{\sigma}{1 - \phi} \tag{2}$$

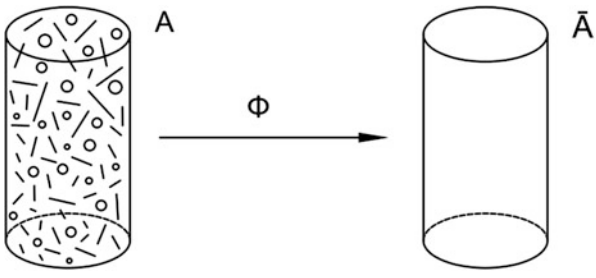

Fig. 1 Damaged and fictitious undamaged configurations

Table 1 Equation (3) as a generalization of the hypotheses of equivalence

n	Equation	Hypothesis title
$n = 0$	$\overline{\sigma} = \sigma$	Hypothesis of stress equivalence
$n = 1$	$\frac{1}{2}\overline{\sigma}\overline{\varepsilon} = \frac{1}{2}\sigma\varepsilon$	Hypothesis of elastic energy equivalence
$n = 2$	$\frac{1}{2}\overline{\sigma}\overline{\varepsilon}^2 = \frac{1}{2}\sigma\varepsilon^2$	Hypothesis of elastic energy equivalence of order 2
...	...	...
...	...	...
$n \to \infty$	$\overline{\varepsilon} = \varepsilon$	Hypothesis of elastic strain equivalence

One next develops the generalized hypothesis of elastic strain energy equivalence of order n. This new generalized hypothesis of equivalence is a generalization of all the existing hypotheses of equivalence in the literature:

$$\frac{1}{2}\overline{\sigma}\overline{\varepsilon}^n = \frac{1}{2}\sigma\varepsilon^n \tag{3}$$

where $n = 0, 1, 2, \ldots$. The classical hypothesis of elastic energy equivalence is obtained as a special case of Eq. (3) when $n = 1$. Next one investigates what happens to Eq. (3) when $n \to \infty$. To investigate this extreme and hypothetical case, one raises both sides of Eq. (3) to the power $\frac{1}{n}$ to obtain:

$$\frac{1}{2}\overline{\sigma}^{\frac{1}{n}}\overline{\varepsilon} = \frac{1}{2}\sigma^{\frac{1}{n}}\varepsilon \tag{4}$$

Substituting $n \to \infty$ into Eq. (4) and noting that $\overline{\sigma}^{\frac{1}{\infty}} \to 1$ and $\sigma^{\frac{1}{\infty}} \to 1$, Eq. (4) reduces to:

$$\overline{\varepsilon} = \varepsilon \tag{5}$$

It is noted that the expression given in Eq. (5) represents exactly the hypothesis of elastic strain equivalence that is used frequently in the literature. The simple derivation in Eqs. (3), (4), and (5) establishes the *missing link* in damage mechanics and shows that the hypothesis of elastic strain equivalence is a special case of the hypothesis of elastic energy equivalence of order n. These results are summarized in Table 1.

Introduction to Partial Damage Mechanics

In this section, the concept of partial damage is introduced through simple equations and schematic diagrams. The fundamentals of partial damage mechanics are introduced in this section for metals only. Future work is expected to apply this new concept to metal matrix composites. Both the scalar and tensorial formulations are presented.

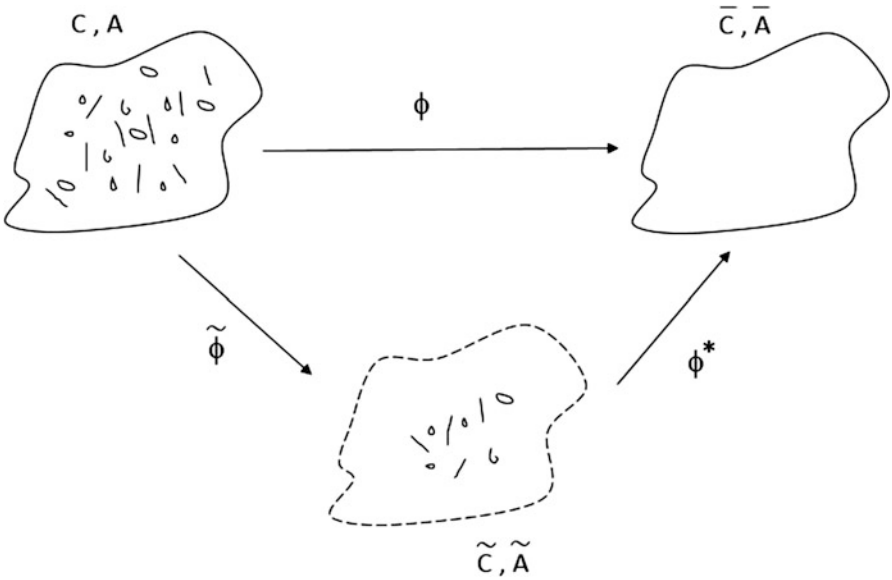

Fig. 2 Schematic diagram of the partial damage concept

Consider a body in the initial undeformed and undamaged configuration. Consider also the configuration of the body that is both deformed and damaged after a set of external agencies act on it (this is the configuration C in Fig. 2). Next, consider a fictitious configuration of the body obtained from the damaged configuration C by removing all the damage that the body has undergone, i.e., this is the state of the body after it had only deformed without damage (this is the configuration $\overline{C}$ in Fig. 2). Therefore, in defining a damage variable ϕ, its value must vanish in the fictitious configuration. Next, consider an intermediate fictitious configuration that is partially damaged, i.e., obtained from the damaged configuration C by removing only a fraction of the damage that the body has undergone, i.e., this is the state of the body after it had deformed with only partial damage (this is the configuration $\widetilde{C}$ in Fig. 2). In this respect, the partial damage variable is denoted by $\widetilde{\phi}$, while the total damage variable is denoted by the symbol ϕ (see Fig. 2). Both damage variables ϕ and $\widetilde{\phi}$ are scalar.

Consider next a third scalar damage variable ϕ^* which accounts for the remaining damage in the partially damaged configuration $\widetilde{C}$, i.e., the damage variable ϕ^* accounts for the damage that is removed from the intermediate fictitious configuration $\widetilde{C}$ in order to obtain the fictitious configuration $\overline{C}$.

One can write the relation between the partial damage variable $\widetilde{\phi}$ and the total damage variable ϕ as follows:

$$\widetilde{\phi} = \alpha \phi \tag{6}$$

where α is called the partial damage fraction and has values in the range $0 \leq \alpha \leq 1$. Physically, α accounts for the fraction of the damage that is not removed between the configurations C and $\widetilde{C}$.

Based on the schematic diagram shown in Fig. 2, one can utilize the following decomposition of the total scalar damage variable ϕ (the general derivation of this decomposition is given by Kattan and Voyiadjis (2001a) and Voyiadjis and Kattan (2012)):

$$\phi = \widetilde{\phi} + \phi^* - \widetilde{\phi}\phi^* \tag{7}$$

The decomposition of Eq. (7) applies for two processes of damage that occur in series, i.e., the two damages occur following each other, or consecutively (Voyiadjis and Kattan 2012).

Substituting Eq. (6) into Eq. (7), one obtains:

$$\phi = \alpha\phi + \phi^* - \alpha\phi\phi^* \tag{8}$$

Solving Eq. (8) for ϕ^*, one obtains the sought expression as follows:

$$\phi^* = \frac{(1-\alpha)\phi}{1-\alpha\phi} \tag{9}$$

The above relation shows how to obtain the damage variable ϕ^* from the total damage variable ϕ using the partial damage fraction α. The relationship of Eq. (9) between ϕ^* and ϕ is plotted in Fig. 3 for several values of α. It is shown in the figure that both ϕ^* and ϕ have values in the range from 0 to 1. It is clear also that when $\alpha = 0$ (this is the case when there is no partial damage), then $\phi^* = \phi$. This observation can be also deduced directly from the schematic diagram in Fig. 2. In general, and as observed in Fig. 3, ϕ^* is a monotonically increasing function of ϕ. In addition, the curves of Fig. 3 imply that the relationship of Eq. (9) can be approximated by a polynomial. In order to do this, one expands the expression of Eq. (9) using a Taylor series with respect to ϕ around $\phi = 0$. Thus, Eq. (9) can be expanded in the following form (this is valid for small values of ϕ):

$$\phi^* \approx ((1-\alpha)\phi)(1+\alpha\phi) = (1-\alpha)\phi + \alpha(1-\alpha)\phi^2 \tag{10}$$

Thus it is seen that the relationship between ϕ^* and ϕ can be approximated by a quadratic equation, i.e., a parabola. This is further confirmed by the curves appearing in Fig. 3.

Next, one investigates what happens to the effective stress of Eq. (2) in the case of partial damage. In this respect, one can write the following expression based on Eq. (2):

$$\widetilde{\sigma} = \frac{\sigma}{1-\widetilde{\phi}} \tag{11}$$

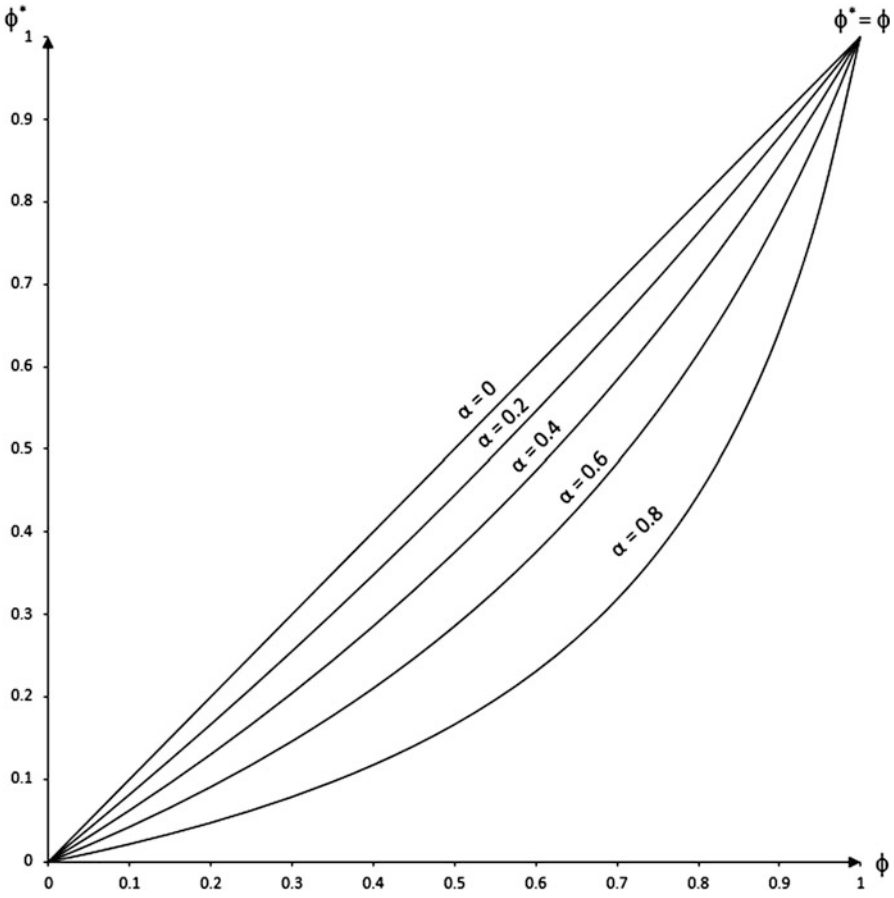

Fig. 3 Relationship between the partial damage variable and the total damage variable based on Eq. (9)

where $\widetilde{\sigma}$ is the effective stress with respect to the partially damaged fictitious configuration. Similarly, one can write the following expression:

$$\overline{\sigma} = \frac{\widetilde{\sigma}}{1 - \phi^*} \tag{12}$$

Substituting Eq. (11) into Eq. (12), then substituting Eqs. (6) and (9) into the resulting equation, one obtains:

$$\overline{\sigma} = \frac{\frac{\sigma}{1-\alpha\,\phi}}{1 - \frac{(1-\alpha)\,\phi}{1-\alpha\,\phi}} \tag{13}$$

Simplifying the expression of Eq. (13), one recovers the classic expression of the effective stress of Eq. (2).

Next, one tries to generalize the concept of partial damage of Eqs. (6) and (7) along with the associated schematic diagram of Fig. 3. For this purpose, instead of considering only one partially damaged fictitious configuration $\widetilde{C}$, one now considers a sequence of a number of partially damaged fictitious configurations $\overline{C}_1, \overline{C}_2, \overline{C}_3, \ldots, \overline{C}_n$ where n is the number of these intermediate configurations, as shown in Fig. 4. In terms of the amount of damage present in each intermediate configuration, it is assumed that the sequence of partially damaged fictitious configurations satisfy the relationship:

$$C \supset \overline{C}_1 \supset \overline{C}_2 \supset \overline{C}_3 \supset \ldots \supset \overline{C} \tag{14}$$

which signifies that each intermediate configuration is a subset of the preceding intermediate configuration. The amount of partial damage in each intermediate configuration is seen to reduce monotonically until the damage completely vanishes in the final fictitious configuration $\overline{C}$.

Consider next a sequence of scalar partial damage variables $\phi_1, \phi_2, \phi_3, \ldots, \phi_n$ defined as follows (see Fig. 4):

$$\phi_1 = \alpha_1 \phi, \quad 0 \leq \alpha_1 \leq 1 \tag{15}$$

$$\phi_2 = \alpha_2 \phi, \quad 0 \leq \alpha_2 \leq 1 \tag{16}$$

$$\begin{aligned} \phi_3 &= \alpha_3 \phi, \quad 0 \leq \alpha_3 \leq 1 \\ &\ldots \qquad\qquad \ldots \end{aligned} \tag{17}$$

$$\phi_n = \alpha_n \phi, \quad 0 \leq \alpha_n \leq 1 \tag{18}$$

where $\alpha_1, \alpha_2, \alpha_3, \ldots, \alpha_n$ are the partial damage fractions in the configurations $\overline{C}_1$, $\overline{C}_2$, $\overline{C}_3$, …, $\overline{C}_n$, respectively. In this case, the decomposition of Eq. (7) is generalized as follows (Voyiadjis and Kattan 2012) based on the schematic diagram of Fig. 4:

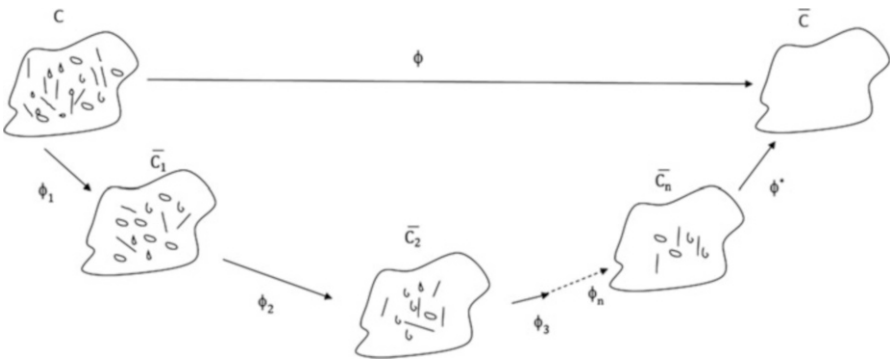

Fig. 4 Schematic diagram of the generalized partial damage concept

$$1-\phi=(1-\phi_1)(1-\phi_2)(1-\phi_3)\ldots(1-\phi_n)(1-\phi^*) \tag{19}$$

Substituting Eqs. (15), (16), (17), and (18) into Eq. (19), one obtains:

$$1-\phi=(1-\alpha_1\phi)(1-\alpha_2\phi)(1-\alpha_3\phi)\ldots(1-\alpha_n\phi)(1-\phi^*) \tag{20}$$

In order to proceed further, one needs to make a simplifying assumption. It is assumed that *uniform partial damage* exists, i.e., partial damage fractions α_1, α_2, α_3, . . ., α_n are equal to each other, i.e.:

$$\alpha_1=\alpha_2=\alpha_3=\ldots=\alpha_n=\alpha \tag{21}$$

In general, there is no reason why the partial damage fraction are equal to each other in Eq. (21). It can be a special case for example, but not true in general. Substituting Eq. (21) into Eq. (20), one obtains:

$$1-\phi=(1-\alpha\phi)^n(1-\phi^*) \tag{22}$$

Solving Eq. (22) for ϕ^*, one obtains the following expression:

$$\phi^*=1-\frac{1-\phi}{(1-\alpha\phi)^n} \tag{23}$$

It is noted that when the value of the exponent n is equal to 1, then the expression of the generalized partial damage mechanics model of Eq. (22) reduces to the simple expression of partial damage mechanics of Eq. (9).

In Eq. (23), one can assume that the value of the uniform partial damage fraction α is equal to $1/n$. Substituting this value into Eq. (23) results in the following expression:

$$\phi^*=1-\frac{1-\phi}{\left(1-\frac{\phi}{n}\right)^n} \tag{24}$$

There is no physical justification or meaning to require that the value of the uniform partial damage fraction α equal to $1/n$. This is only a simplified mathematical exercise without any physical foundation, or any relevance to the micromechanics of material damage processes. Finally, when one considers *continuous uniform partial damage*, i.e., when the value of the exponent n approaches infinity, one obtains:

$$\phi^*=\lim_{n\to\infty}\left[1-\frac{1-\phi}{\left(1-\frac{\phi}{n}\right)^n}\right]=1-(1-\phi)e^{\phi} \tag{25}$$

The exponential expression appearing in Eq. (25) applies when one considers an infinite number of intermediate partial damage fictitious configurations, i.e., when partial damage occurs continuously. The expression of Eq. (25) is plotted on a graph

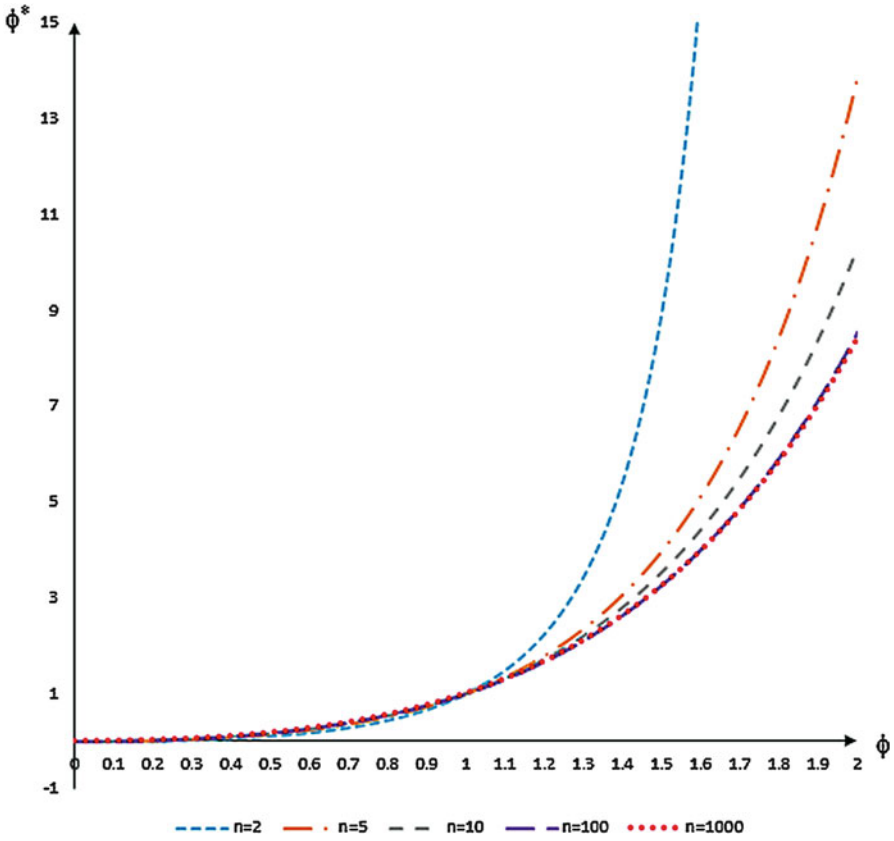

Fig. 5 Relationship between the two damage variables for various values of n

as shown in Fig. 5. In this figure, the exponential nature of continuous uniform partial damage is clearly evident (Fig. 6).

The exponential expression for the damage variable ϕ^* satisfies the boundary conditions, i.e., it satisfies $0 \leq \phi^* \leq 1$. For the special case of small damage, one can use the Taylor series expansion of the exponential function $e^{\phi} = 1 + \phi + \phi^2/2 + \phi^3/6 + \ldots$. For this purpose and taking the first two terms of the series expansion, Eq. (25) can be simplified for this special case as follows (Fig. 7):

$$\phi^* \approx 1 - (1 - \phi)(1 + \phi) = 1 - \left(1 - \phi^2\right) = \phi^2 \tag{26}$$

It is assumed that small damage would be less than 10% of material damage. This means that for small values of the damage variable, the damage variable ϕ^* is equal in value to the square of the value of the classical damage variable. It is interesting to investigate what happens to the partial damage variable $\widetilde{\phi}$ in this case. Utilizing the decomposition of Eq. (8) and substituting $\phi^* = \phi^2$, one obtains:

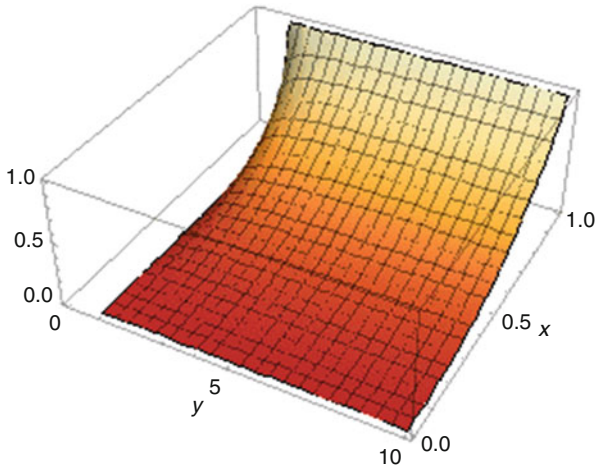

Fig. 6 Relationship between the two damage variables as a 3D graph where x represents ϕ, y represents n, and z represents ϕ^*

$$\phi = \widetilde{\phi} + \phi^2 - \widetilde{\phi}\phi^2 \tag{27}$$

Solving the above equation for $\widetilde{\phi}$, one obtains:

$$\widetilde{\phi} \approx \frac{\phi}{1+\phi} \tag{28}$$

Investigating the above expression for the partial damage variable $\widetilde{\phi}$, one concludes the following:

1. For this special case of small damage, one can take the approximate expression of Eq. (28) further. Utilizing the Taylor series expansion $\frac{1}{1+\phi} \approx 1 - \phi + \ldots$, Eq. (28) is simplified further to become:

$$\widetilde{\phi} \approx \phi(1-\phi) = \phi - \phi^2 \tag{29}$$

2. It is clearly seen that for this special case of small damage, the decomposition of Eq. (27) becomes additive, i.e., the third term (the coupling term) can be neglected. Thus, in this special case, the decomposition of Eq. (27) reduces to the following equation:

$$\phi \approx \left(\phi - \phi^2\right) + \phi^2 \tag{30}$$

3. Comparing Eqs. (23) and (28) for the partial damage variable $\widetilde{\phi}$, one concludes that the partial damage fraction α can be taken to be equal to $\frac{1}{1+\phi} \approx 1 - \phi$, or effectively, equal to 1. This means that partial damage is equal to total damage for the special case of small damage. Thus, performing partial damage mechanics

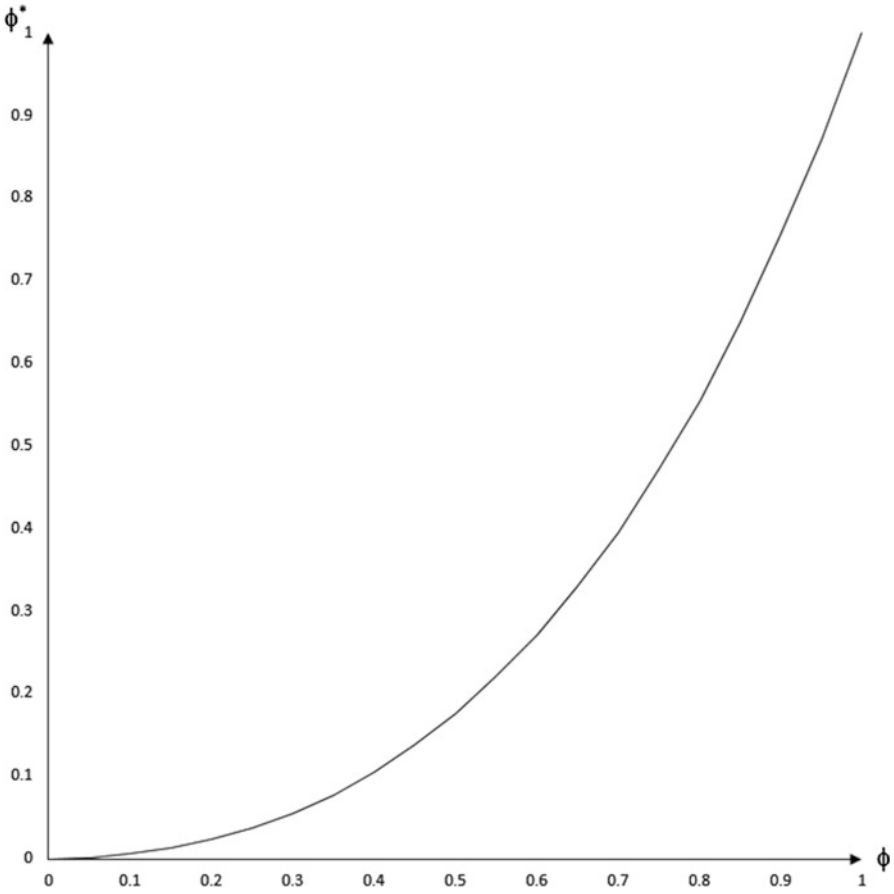

Fig. 7 Relationship between the partial damage variable ϕ^* and the total damage variable ϕ based on continuous uniform partial damage

does not produce any significant or additional advantages if the damage variable has small values.

The authors do not provide any examples or analysis or physical development of general damage (i.e., not small damage) in this work, other than the discussion of small damage provided earlier.

Next, one tries to generalize the scalar equations of partial damage of this section to general states of deformation and damage. For this purpose, one needs to use tensors instead of scalars. In this work, tensors are represented vectors and matrices, depending on the rank of the tensor.

The classical Eq. (2) for the effective stress is usually generalized as follows in the literature of continuum damage mechanics (Sidoroff 1981; Voyiadjis and Kattan 2005, 2006):

$$\{\overline{\sigma}\} = [M]\{\sigma\} \tag{31}$$

where the two vectors $\{\sigma\}$ and $\{\overline{\sigma}\}$ represent the stress tensor with six components and its effective counterpart, respectively, while the matrix $[M]$ is a 6×6 matrix that represents the fourth-rank damage effect tensor. It is noted that the tensorial Eq. (31) reduces to the scalar Eq. (2) when the substitutions $\sigma_{11} \equiv \sigma$, $\overline{\sigma}_{11} \equiv \overline{\sigma}$, and $M_{1111} \equiv \frac{1}{1-\phi}$ are made.

In order to derive the equations of partial damage mechanics using tensors, one introduces the fourth-rank partial damage effect tensor $\left[\widetilde{M}\right]$ that corresponds to the scalar partial damage variable $\widetilde{\phi}$ in the sense that $\widetilde{M}_{1111} \equiv \frac{1}{1-\alpha\phi}$.

One can derive the following relation between the fourth-rank damage effect tensor $[M]$ and the fourth-rank partial damage effect tensor $\left[\widetilde{M}\right]$:

$$\left[\widetilde{M}\right] = \left(\alpha[I_4] + (1-\alpha)[M]\right)^{-1}[M] \tag{32}$$

where $[I_4]$ is the matrix representation of the fourth-rank identity tensor such that $(I_4)_{1111} \equiv 1$. It can be easily shown that the above tensorial relation reduces to the scalar equation provided that $M_{1111} \equiv \frac{1}{1-\phi}$ and $\widetilde{M}_{1111} \equiv \frac{1}{1-\alpha\phi}$.

Next, one introduces the fourth-rank damage effect tensor $[M^*]$ that corresponds to the scalar damage variable ϕ^* such that $M^*_{1111} \equiv \frac{1}{1-\phi^*}$. Based on this definition, one can show that the tensorial generalization of the scalar equation can be made using any one of the following two alternative tensorial equations:

$$[M^*] = \alpha[I_4] + (1-\alpha)[M] \tag{33}$$

$$[M^*] = [M]^{-1}\left(\alpha[I_4] + (1-\alpha)[M]\right)[M] \tag{34}$$

It can be shown that both tensorial Eqs. (33) and (34) reduce to the scalar Eq. (9) when one uses the substitutions $M_{1111} \equiv \frac{1}{1-\phi}$, $M^*_{1111} \equiv \frac{1}{1-\phi^*}$, and $(I_4)_{1111} \equiv 1$. The above tensorial generalizations of the scalar Eq. (9) may not be the only ones. Other tensorial generalizations may be possible that also reduce to Eq. (9).

It should be noted that the derivation of the tensorial Eqs. (33) and (34) was based on the tensorial decomposition of the fourth-rank damage tensor $[M]$ given by the following expression (Kattan and Voyiadjis 2001a)

$$[M] = \left[\widetilde{M}\right][M^*] = [M^*]\left[\widetilde{M}\right] \tag{35}$$

The general tensorial decomposition of Eq. (35) above reduce to the scalar decomposition of Eq. (7) when one uses the substitutions $M_{1111} \equiv \frac{1}{1-\phi}$, $M^*_{1111} \equiv \frac{1}{1-\phi^*}$, and $\widetilde{M}_{1111} \equiv \frac{1}{1-\widetilde{\phi}}$.

Next, one writes the tensorial equations for the generalized partial damage mechanics model. The scalar Eq. (23) of generalized partial damage mechanics can be re-written as either one of the two forms using tensors:

$$[M^*] = \left((1-\alpha)[I_4] + \alpha[M]^{-1}\right)^n [M] \tag{36}$$

$$[M^*] = [M]\left((1-\alpha)[I_4] + \alpha[M]^{-1}\right)^n \tag{37}$$

It should be noted that both tensorial Eqs. (36) and (37) reduce to the scalar Eq. (23) when one uses the substitutions $M_{1111} \equiv \frac{1}{1-\phi}$, $M^*_{1111} \equiv \frac{1}{1-\phi^*}$, and $(I_4)_{1111} \equiv 1$.

Finally, one tries to generalize the exponential form of continuous partial damage mechanics of Eq. (25). The tensorial generalization can be written using either one of the following two alternative forms:

$$[M^*] = \left(e^{[I_4]-[M]^{-1}}\right)^{-1} [M] \tag{38}$$

$$[M^*] = [M]\left(e^{\left([I_4]-[M]^{-1}\right)}\right)^{-1} \tag{39}$$

Both tensorial Eqs. (38) and (39) reduce to the scalar Eq. (25) for continuous partial damage when one uses the substitutions $M_{1111} \equiv \frac{1}{1-\phi}$, $M^*_{1111} \equiv \frac{1}{1-\phi^*}$, and $(I_4)_{1111} \equiv 1$.

It should be noted that the discussions of the tensorial damage tensor provided earlier are given without any rigorous physical foundation or microstructural meaning for material damage mechanics. It is hoped that in the future some physical foundation for this work will be established.

Conclusion

The equations of partial damage mechanics are postulated in this work. They apply when a partially damaged configuration of the body is considered. These equations have been illustrated both mathematically and graphically. It should be noted that the classical equations of damage mechanics are obtained as special cases of the equations of partial damage mechanics. This fact has been proved in the above presentation. It should be noted that partial damage may also represent damage in composites where the components of damage represent damage in the fiber, matrix, debonding, etc.

The framework projected here for the partial damage may be incorporated in material models and used for the analysis of fiber-reinforced metal matrix composite materials and composites in general. These partial damage micromechanical based composite models may be used in such a way that separate the local

constitutive damage relations which are used for each of the matrix and fiber. This is coupled with the interfacial damage between the matrix and fiber exclusively. The damage relations are linked to the overall response through a certain homogenization procedure. Individual damage tensors may be used for the individual constituents (matrix, fibers, lamina, etc.) of the composite system. The matrix damage effect tensor in itself may also be expressed in terms of partial damage to reflect all types of damages that the matrix material undergoes such as nucleation and coalescence of voids and microcracks. The fiber damage effect tensor is considered to reflect all types of fiber damage such as fracture of fibers. An additional tensor may be incorporated in the overall formulation that represents interfacial damage between the matrix and fiber. An overall damage effect tensor, accounts for all these separate damage tensors.

The authors have presented the mathematical and theoretical foundation of what they call partial damage mechanics. The presentation has been kept to a mere mathematical exercise hoping that in the future researchers can build on it. It is hoped that future researchers can provide physical (micromechanical and microstructural) foundation or evidence and offer new physical insight into continuum or micromechanical damage mechanics. This is hoped for the purpose of offering tangible benefits or advantages to damage mechanics. It is hoped that future researchers also will provide practical or numerical applications to the physics-based modeling of damage mechanics, provide experimental or material validation, and offer scientific merits or innovation.

Nomenclature

A	Cross-sectional area
$\overline{A}$	Effective cross-sectional area
ϕ	Total damage variable
σ	Cauchy stress
$\overline{\sigma}$	Effective Cauchy stress
ε	Strain
$\overline{\varepsilon}$	Effective strain
n	Exponent
$\widetilde{\phi}$	Partial damage variable
α	Partial damage fraction
ϕ^*	Damage variable associated with partial damage
$\widetilde{\sigma}$	Effective Cauchy stress associated with partial damage
e	Exponential function
$\{\sigma\}$	Stress vector
$\{\overline{\sigma}\}$	Effective stress vector
$[M]$	Fourth-rank damage effect tensor
$\left[\widetilde{M}\right]$	Fourth-rank partial damage effect tensor
$[M^*]$	Fourth-rank damage effect tensor associated with partial damage
$[I_4]$	Fourth-rank identity tensor

References

C. Basaran, S. Nie, An irreversible thermodynamic theory for damage mechanics of solids. Int. J. Damage Mech. **13**(3), 205–224 (2004)

C. Basaran, C.Y. Yan, A thermodynamic framework for damage mechanics of solder joints. Trans. ASME J. Electron. Packag. **120**, 379–384 (1998)

D.J. Celentano, P.E. Tapia, J.-L. Chaboche, Experimental and numerical characterization of damage evolution in steels, in *Mecanica Computacional*, vol. XXIII, ed. by G. Buscaglia, E. Dari, O. Zamonsky (Bariloche, 2004)

M.K. Darabi, R.K. Abu Al-Rub, D.N. Little, A continuum damage mechanics framework for modeling micro-damage healing. Int. J. Solids Struct. **49**, 492–513 (2012)

I. Doghri, *Mechanics of Deformable Solids: Linear and Nonlinear, Analytical and Computational Aspects* (Springer, 2000)

N.R. Hansen, H.L. Schreyer, A thermodynamically consistent framework for theories of elastoplasticity coupled with damage. Int. J. Solids Struct **31**(3), 359–389 (1994)

L. Kachanov, On the creep fracture time. Izv. Akad. Nauk USSR Otd. Tech. **8**, 26–31 (1958) (in Russian)

P.I. Kattan, G.Z. Voyiadjis, A coupled theory of damage mechanics and finite strain elasto-plasticity – part I: damage and elastic deformations. Int. J. Eng. Sci. **28**(5), 421–435 (1990)

P.I. Kattan, G.Z. Voyiadjis, A plasticity-damage theory for large deformation of solids – part II: applications to finite simple shear. Int. J. Eng. Sci. **31**(1), 183–199 (1993)

P.I. Kattan, G.Z. Voyiadjis, Decomposition of damage tensor in continuum damage mechanics. J. Eng. Mech. ASCE **127**(9), 940–944 (2001a)

P.I. Kattan, G.Z. Voyiadjis, *Damage Mechanics with Finite Elements: Practical Applications with Computer Tools* (Springer, 2001b)

D. Krajcinovic, *Damage Mechanics* (North Holland, 1996), 776 page

P. Ladeveze, J. Lemaitre, Damage effective stress in quasi-unilateral conditions, in *The 16th International Congress of Theoretical and Applied Mechanics, Lyngby* (1984)

P. Ladeveze, M. Poss, L. Proslier, Damage and fracture of tridirectional composites, in *Progress in Science and Engineering of Composites. Proceedings of the Fourth International Conference on Composite Materials*, vol. 1 (Japan Society for Composite Materials, 1982), pp. 649–658

H. Lee, K. Peng, J. Wang, An anisotropic damage criterion for deformation instability and its application to forming limit analysis of metal plates. Eng. Fract. Mech. **21**, 1031–1054 (1985)

G. Lubineau, A pyramidal modeling scheme for laminates – identification of transverse cracking. Int. J. Damage Mech. **19**(4), 499–518 (2010)

G. Lubineau, P. Ladeveze, Construction of a micromechanics-based intralaminar mesomodel, and illustrations in ABAQUS/standard. Comput. Mater. Sci. **43**(1), 137–145 (2008)

Y. Rabotnov, Creep rupture, in *Proceedings, Twelfth International Congress of Applied Mechanics, Stanford, 1968*, ed. by M. Hetenyi, W. G. Vincenti (Springer, Berlin, 1969), pp. 342–349

J.R. Rice, Inelastic constitutive relations for solids: an internal variable theory and its application to metal plasticity. J. Mech. Phys. Solids **19**, 433–455 (1971)

F. Sidoroff, Description of anisotropic damage application in elasticity, in *IUTAM Colloqium on Physical Nonlinearities in Structural Analysis* (Springer, Berlin, 1981), pp. 237–244

G.Z. Voyiadjis, P.I. Kattan, A coupled theory of damage mechanics and finite strain elasto-plasticity – part II: damage and finite strain plasticity. Int. J. Eng. Sci. **28**(6), 505–524 (1990)

G.Z. Voyiadjis, P.I. Kattan, A plasticity-damage theory for large deformation of solids – part I: theoretical formulation. Int. J. Eng. Sci. **30**(9), 1089–1108 (1992)

G.Z. Voyiadjis, P.I. Kattan, *Damage Mechanics* (Taylor and Francis (CRC Press), 2005)

G.Z. Voyiadjis, P.I. Kattan, *Advances in Damage Mechanics: Metals and Metal Matrix Composites with an Introduction to Fabric Tensors*, 2nd edn. (Elsevier, 2006)

G.Z. Voyiadjis, P.I. Kattan, A comparative study of damage variables in continuum damage mechanics. Int. J. Damage Mech. **18**(4), 315–340 (2009)

G.Z. Voyiadjis, P.I. Kattan, Mechanics of damage processes in series and in parallel: a conceptual framework. Acta Mech. **223**(9), 1863–1878 (2012)

G.Z. Voyiadjis, P.I. Kattan, Mechanics of damage, healing, damageability, and integrity of materials: a conceptual framework. Int. J. Damage Mech. **26**(1), 50–103 (2017a). https://doi.org/10.1177/1056789516635730

G.Z. Voyiadjis, P.I. Kattan, Decomposition of elastic stiffness degradation in continuum damage mechanics. J. Eng. Mater. Technol. ASME **139**(2), 021005-1–021005-15 (2017b). https://doi.org/10.1115/1.4035292

G.Z. Voyiadjis, P.I. Kattan, Introducing damage mechanics templates for the consistent and systematic formulation of holistic material damage models. Acta Mech. **228**(3), 951–990 (2017c). https://doi.org/10.1007/s00707-016-1747-6

G.Z. Voyiadjis, A. Shojaei, G. Li, A thermodynamic consistent damage and healing model for self-healing materials. Int. J. Plast. **27**(7), 1025–1044 (2011)

G.Z. Voyiadjis, A. Shojaei, G. Li, P.I. Kattan, A theory of anisotropic healing and damage mechanics of materials. Proc. R. Soc. A Math. Phys. Eng. Sci. **468**(2137), 163–183 (2012a)

G.Z. Voyiadjis, A. Shojaei, G. Li, P.I. Kattan, Continuum damage-healing mechanics with introduction to new healing variables. Int. J. Damage Mech. **21**, 391–414 (2012b)

Mechanics of Self-Regenerating Materials

5

George Z. Voyiadjis and Peter I. Kattan

Contents

Introduction 102
Basics of Continuum Damage Mechanics 103
The Scalar Theory 105
The Elastic Stiffness 107
The Concept of a Magical Material 108
The Tensor Theory 110
The Case of Plane Stress 112
Conclusion and Discussion 116
References 117

Abstract

A new kind of material is introduced within the framework of continuum damage mechanics. A robust mathematical formulation is presented. One of the main characteristics of self-regenerating materials is that they are subject to a process of reintegration when the load is increased. When the load reaches a specific value the damage is reversed and full recovery of the material is achieved. This is accompanied by an increase in the elastic modulus value until the original undamaged material is recovered. The self-regenerating material as proposed here does not exist in reality at the present time but its mathematical foundations are given. It is anticipated that advances in the materials industry will allow such materials to exist in the near future.

G. Z. Voyiadjis
Center for GeoInformatics C4G and Computational Solid Mechanics Laboratory, Department of Civil and Environmental Engineering, Louisiana State University, Baton Rouge, LA, USA
e-mail: voyiadjis@eng.lsu.edu; cegzv1@lsu.edu

P. I. Kattan (✉)
Department of Civil and Environmental Engineering, Louisiana State University, Baton Rouge, LA, USA
e-mail: info@PetraBooks.com; pkattan@PetraBooks.com

© Springer Nature Switzerland AG 2022

G. Z. Voyiadjis (ed.), *Handbook of Damage Mechanics*,
https://doi.org/10.1007/978-3-030-60242-0_86

Keywords

Damage mechanics · Damage · Elastic · Recovery · Self-regenerating material · Stiffness

Introduction

Continuum Damage Mechanics was pioneered by Kachanov (1958) and more fully later by Lee et al. (1985), Voyiadjis and Kattan (1992, 2005, 2006a, 2009), Sidoroff (1981), and Kattan and Voyiadjis (1993, 2001a, b).

In 1958, Kachanov (1958) pioneered the concept of effective stress and introduced the topic of continuum damage mechanics. This pioneering work was followed by Rabotnov (1969) and by others later (Kattan and Voyiadjis 2001a, b; Ladeveze and Lemaitre 1984; Voyiadjis and Kattan 2005, 2006a, 2009, 2012a; Voyiadjis et al. 2012). In the framework of continuum damage mechanics, a scalar damage variable φ is introduced that has values in the range $0 \leq \varphi \leq 1$. The value of the damage variable is zero when the virgin material is undamaged while the value approaches 1 upon complete rupture. However, practically the damage value cannot exceed 0.3 to 0.4 without violating the concept of a continuum mechanics.

Research on damage mechanics has appeared by several researchers in the past few years (Celentano et al. 2004; Doghri 2000; Hansen and Schreyer 1994; Kattan and Voyiadjis 1990, 1993; Ladeveze et al. 1982; Lubineau 2010; Lubineau and Ladeveze 2008; Lee et al. 1985; Luccioni and Oller 2003; Rice 1971; Sidoroff 1981; Voyiadjis 1988; Voyiadjis and Kattan 1990, 1992). This work consists of seven main sections.

Recently, damage mechanics has been extended to characterize damage in microelectronic components and electronic packaging using entropy and entropy generation rate (Basaran and Yan 1998; Basaran and Tang 2002; Basaran et al. 2003; Basaran and Nie 2004, 2007). Furthermore, Sosnovskiy and Sherbakov (2016) developed a new theory called "mechanothermodynamics" that provides for a unification of mechanics and thermodynamics. As a result, self-healing or self-generating materials can be easily accounted for just like in any biological system.

This section is the Introduction. Section "Basics of Continuum Damage Mechanics" elaborates on and discusses the theory of continuum damage mechanics. It is noted that a new scalar damage variable is introduced in this section for the purpose of deriving the mechanics of self-regenerating materials in later sections.

In section "The Scalar Theory," the theory of self-regenerating materials is presented. In this respect, the new scalar damage variable that was introduced in section "Basics of Continuum Damage Mechanics" is utilized in this section for this purpose.

The self-regenerating material undergoes a complete recovery of the elastic stiffness. This issue is illustrated in section "The Elastic Stiffness." The illustration is presented in mathematical and graphical terms. In addition, the hypothesis of elastic strain equivalence is used alongside the hypothesis of elastic energy equivalence.

A general integer exponent is introduced in section "The Concept of a Magical Material" laying the groundwork for what are called magical materials. This concept of magical materials is an extension of the concept of self-regenerating materials as the integer exponent goes to infinity. It is as infinity is approached, the material undergoes strange and unexplained behavior that can only be described as magical.

Section "The Concept of a Magical Material" introduces the theory of magical materials using scalars for the one-dimensional case. This is extended in section "The Tensor Theory" using tensors for general states of deformation and damage. Finally, an example problem is solved in section "The Case of Plane Stress" based on plane stress to illustrate the applications of self-regenerating materials.

Basics of Continuum Damage Mechanics

In this section, the basics of continuum damage mechanics are presented briefly. This is achieved using two different formulations. The first formulation uses the scalar damage variable based on the cross-sectional area while the second formulation uses a scalar damage variable that is different mathematically from the one in the first formulation (Voyiadjis and Kattan 2017a).

Consider a body cast in the initial, undeformed, and undamaged state. Consider also the state of the body that is both deformed and damaged after a number of external forces act on it (see Fig. 1). Next, consider a fictitious state of the body obtained from the damaged state by removing all the damage that the body has undergone, i.e., this is the state of the body after it had only deformed without damage (see Fig. 1). Therefore, in defining a damage variable, ϕ, its value must be zero in the fictitious state.

The first damage variable ϕ is defined as follows in terms of cross-sectional areas:

$$\varphi = \frac{A - \overline{A}}{A} \tag{1}$$

where A is the cross-sectional area in the damaged state while $\overline{A}$ is the cross-sectional area in the fictitious state with $A > \overline{A}$. It is clear that when a body is undamaged, i.e., when $A = \overline{A}$, then $\varphi = 0$.

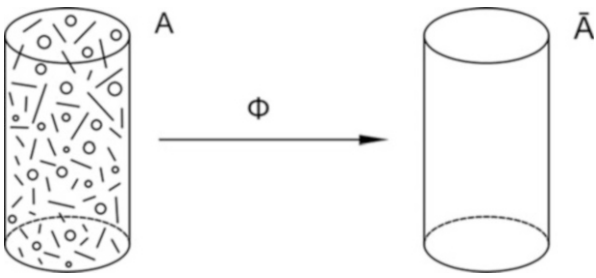

Fig. 1 Damaged and fictitious undamaged configurations

The stress in the fictitious state is called the effective stress and is denoted by $\overline{\sigma}$. The value of the effective stress $\overline{\sigma}$ may be obtained using the equilibrium relation $\overline{\sigma}\overline{A} = \sigma A$ where σ is the stress in the damaged state. Using this relation along with the definition in Eq. (1), one obtains:

$$\overline{\sigma} = \frac{\sigma}{1-\varphi} \tag{2}$$

Next, a hypothesis needs to be used. For this purpose, one introduces the generalized hypothesis of elastic strain equivalence of order n. The expression for the generalized hypothesis was introduced recently by the authors within the context of the theory of undamageable materials (Voyiadjis and Kattan 2012b, c, 2013, 2014). It will be shown that all the equivalence hypotheses of damage mechanics can be obtained as special cases of this generalized hypothesis:

$$\frac{1}{2}\overline{\sigma}\overline{\varepsilon}^{n} = \frac{1}{2}\sigma\varepsilon^{n} \tag{3}$$

where $n = 0, 1, 2, \ldots$. The classical hypothesis of elastic energy equivalence is obtained as a special case of Eq. (3) when substituting $n = 1$. Investigating what happens to Eq. (3) when $n \to \infty$ leads to a surprise result. In order to study this ultimate case deeply, one raises both sides of Eq. (3) to the power $\frac{1}{n}$ to obtain:

$$\frac{1}{2}\overline{\sigma}^{\frac{1}{n}}\overline{\varepsilon} = \frac{1}{2}\sigma^{\frac{1}{n}}\varepsilon \tag{4}$$

Substituting $n \to \infty$ into Eq. (4) and knowing that $\overline{\sigma}^{\frac{1}{\infty}} \to 1$ and $\sigma^{\frac{1}{\infty}} \to 1$, Eq. (4) becomes:

$$\overline{\varepsilon} = \varepsilon \tag{5}$$

Expression (5) above is what is known in the literature as the hypothesis of elastic strain equivalence. It is shown above that this hypothesis is a special case of the general hypothesis of elastic energy equivalence. These results are now summarized in Table 1.

Table 1 Different hypotheses of equivalence in the literature of damage mechanics shown as special cases of Eq. (3)

n	Equation	Hypothesis title
$n = 0$	$\overline{\sigma} = \sigma$	Hypothesis of stress equivalence
$n = 1$	$\frac{1}{2}\overline{\sigma}\overline{\varepsilon} = \frac{1}{2}\sigma\varepsilon$	Hypothesis of elastic energy equivalence
$n = 2$	$\frac{1}{2}\overline{\sigma}\overline{\varepsilon}^{2} = \frac{1}{2}\sigma\varepsilon^{2}$	Hypothesis of elastic energy equivalence of order 2
...	...	...
...	...	...
$n \to \infty$	$\overline{\varepsilon} = \varepsilon$	Hypothesis of elastic strain equivalence

The Scalar Theory

Using the recent work of the authors (Voyiadjis and Kattan 2017a), one uses a new scalar bur nonlinear damage variable φ^* defined as follows:

$$\varphi^* = \sqrt{2\varphi - \varphi^2} \tag{6}$$

The new form of the damage variable introduced in Eq. (6) above was derived by the authors recently (Voyiadjis and Kattan 2017a). A graphical comparison between the classical damage variable and the new damage variable is presented in Fig. 2.

Based on the graph shown in Fig. 2, it is concluded that the new damage variable is nonlinear. This is in contrast to the classical damage variable which is clearly shown to be linear.

One next derived the following expression for the effective stress of Eq. (2) based on the new damage variable:

$$\overline{\sigma} = \frac{\sigma}{1 - \varphi^*} = \frac{\sigma}{1 - \sqrt{2\varphi - \varphi^2}} \tag{7}$$

Based on the expression of Eq. (7) above, one concludes that the values of the effective stress are complex numbers everywhere except in the small range of the

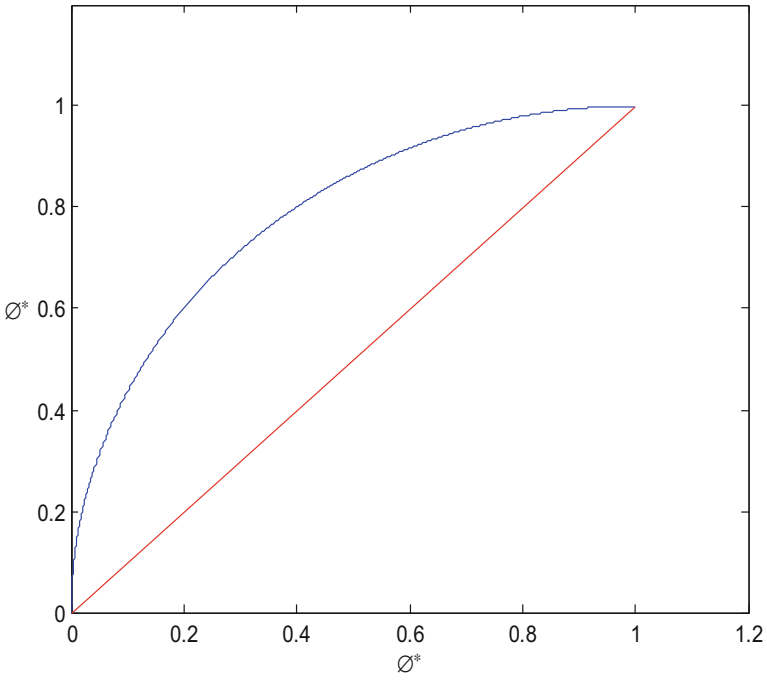

Fig. 2 Comparison between the linear and nonlinear damage variables

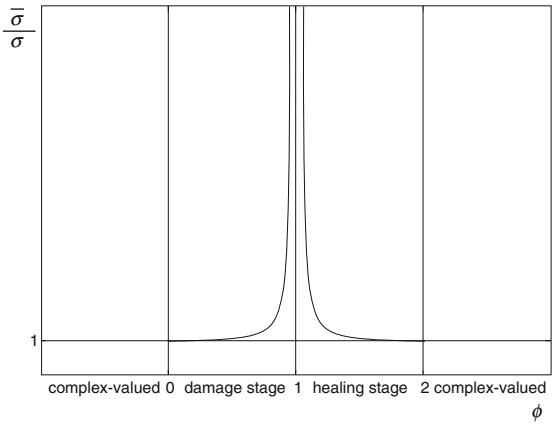

Fig. 3 Effective stress behavior for self-regenerating materials

damage variable values between 0 and 2. A plot of the expression of the effective stress of Eq. (7) is shown in Fig. 3 for the range of values $0 < \varphi < 2$.

Next, one writes the following notes based on Fig. 3 and Eq. (7):

1. There are two clear distinct stages of behavior as shown in Fig. 3. The first stage is a damage stage that is followed by the second stage which is a healing stage.
2. The damage state as shown in Fig. 3 resembles that of soft materials and biological tissue.
3. Both Fig. 3 and Eq. (7) lay the groundwork for a new type of material behavior. This new material is called here a self-regenerating material. This material is currently hypothetical and mathematical in nature. It is hoped that the manufacturing technology will advance to such a stage such that this material may be realized in the future.
4. In section "The Elastic Stiffness," one develops fully the constitutive equations of self-regenerating materials. This is achieved through the use of the elastic stiffness as the prime factor in the formulation.
5. The virgin undamaged material undergoes damage in the classical sense in the range of values of the damage variable between 0 and 1. In this respect, this behavior in the damage stage is totally consistent with the classical theory of damage mechanics.
6. When the loading is increased beyond the value of the damage variable of 1, something totally bizarre happens. The material undergoes a healing stage in which the elastic stiffness is recovered. In addition, by the time the damage variable reaches its maximum value of 2, a complete recovery of the elastic stiffness is achieved.
7. The material behavior is symmetrical about the value of the damage variable of 1. The two boundary conditions are exactly the same at 0 and 2 with the exact value of the elastic stiffness.

The Elastic Stiffness

In this section, one delves deeply into the behavior of self-regenerating material – specifically the elastic stiffness is studied in detail. This is performed twice for the two different hypotheses of damage mechanics. In a previous paper, the authors investigated the degradation of the elastic stiffness using a consistent and systematic mathematical formulation (Voyiadjis and Kattan 2017b).

Using the elastic constitutive equations $\varepsilon = \sigma/E$ and $\overline{\varepsilon} = \overline{\sigma}/\overline{E}$ for the case of the hypothesis of elastic strain equivalence, along with using Eq. (7) into (5), and simplifying, the following equation is derived for the transformation of the elastic stiffness:

$$E = \overline{E}\left(1 - \sqrt{2\varphi - \varphi^2}\right) \tag{8}$$

Performing the same operations this time using the hypothesis of elastic energy equivalence (while assuming $n = 1$), the following equation is derived for the transformation of the elastic strain:

$$\overline{\varepsilon} = \varepsilon\left(1 - \sqrt{2\varphi - \varphi^2}\right) \tag{9}$$

Using the elastic constitutive relations $\varepsilon = \sigma/E$ and $\overline{\varepsilon} = \overline{\sigma}/\overline{E}$ along with Eq. (9), while utilizing Eq. (7), the following equation is derived for the transformation of the elastic stiffness:

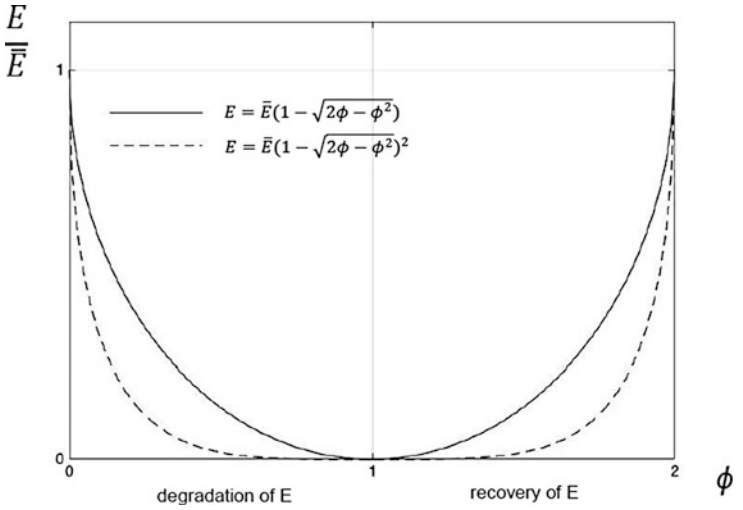

Fig. 4 Elastic stiffness degradation and recovery for the two hypotheses of damage mechanics

Table 2 Degradation of the elastic stiffness and its recovery for the scalar theory

	Equation	Type of behavior
Hypothesis of elastic strain equivalence	$\bar{\varepsilon} = \varepsilon\left(1 - \sqrt{2\varphi - \varphi^2}\right)$	Linear
Hypothesis of elastic energy equivalence	$E = \overline{E}\left(1 - \sqrt{2\varphi - \varphi^2}\right)^2$	Nonlinear – Quadratic
Generalized hypothesis of elastic energy equivalence of order n	$E = \overline{E}\left(1 - \sqrt{2\varphi - \varphi^2}\right)^n$	Nonlinear – General

$$E = \overline{E}\left(1 - \sqrt{2\varphi - \varphi^2}\right)^2 \tag{10}$$

Next a comparison is made between the two transformation equations for the elastic stiffness. Figure 4 is the result of this comparison. Only the real part of $E/\overline{E}$ is shown as the two expressions have complex values except in the range $0 < \varphi < 2$. Table 2 shows a summary of this comparison.

The Concept of a Magical Material

In this section, the concept of a magical material is introduced. This is obtained from the equations of self-regenerating materials as the value of the exponent n approaches infinity. One investigates what happens to the elastic stiffness for the two stages of damage and healing. This investigation is illustrated below through a series of figures and equations.

The expression below is a generalization of the elastic stiffness equations of the previous section for any integer n:

$$E = \overline{E}\left(1 - \sqrt{2\varphi - \varphi^2}\right)^n \tag{11}$$

where n is an integer exponent with $n = 1, 2, 3, 4, \ldots$. The material that follows Eq. (11) above is termed here a self-regenerating material of order n.

Figures 5 and 6 illustrate the material behavior depicted in Eq. (11) for the general case. Figure 5 shows the behavior for several values of the integer exponent n while Fig. 6 shows the behavior when n goes to infinity. It should be noted that the curve obtained in Fig. 6 is the limiting case for the sequence of curves of Fig. 5. Again, Fig. 5 shows the behavior of the self-regenerating material of order n while Fig. 6 shows the behavior of the magical material. It is clear that the magical material is the limit of the self-regenerating material of order n as n goes to infinity.

Next one discusses the behavior of the limit magical material of Fig. 6. It is seen that the elastic stiffness is zero everywhere except at the two end points. Upon loading, the elastic stiffness suddenly vanishes and it suddenly reappears at the end of loading fully and completely. This bizarre behavior is like magic and is characteristic of the limit material. This is why the limit material is called a

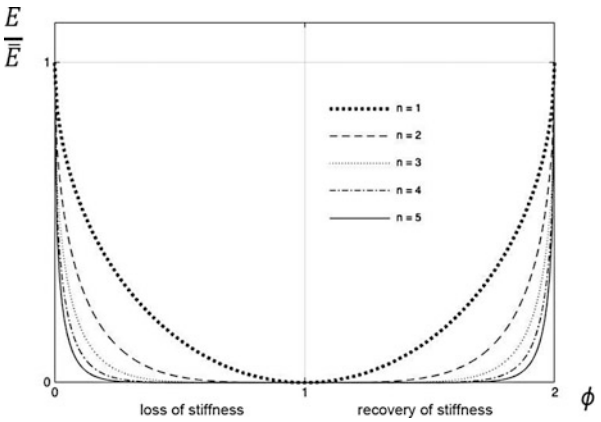

Fig. 5 Elastic stiffness degradation and recovery for different values of the integer exponent n

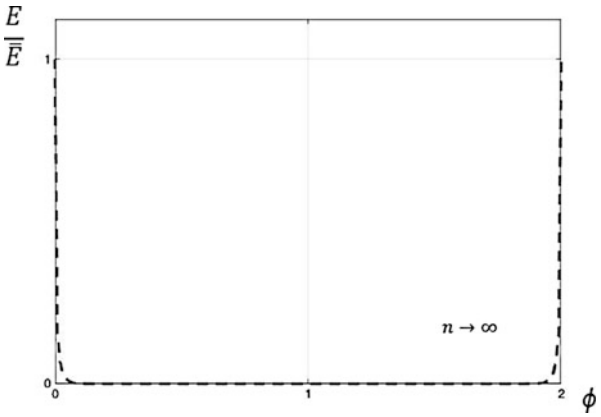

Fig. 6 Elastic stiffness behavior as n approaches infinity

magical material. It should be noted that this magical material does not currently exist in reality. It is hoped that some sort of self-regenerating material with a reasonable integer exponent can be realized by the manufacturing technology of the future.

Based on the information in Fig. 6 and Eq. (11), one can write the following features of the magical material:

1. The elastic stiffness suddenly vanishes at the start of loading.
2. The magical material keeps a value of zero for the elastic stiffness throughout the deformation process.
3. The elastic stiffness is recovered suddenly, totally, and completely at the end point of loading.
4. The magical material is the limit of the self-regenerating material of order n as $n \rightarrow \infty$.

The Tensor Theory

In this section, the scalar theory of the previous sections is generalized using tensors to three-dimensional general states of deformation and damage. The tensors are represented by matrices.

The general three-dimensional equation for the effective stress tensor is given by the equation (Sidoroff 1981; Voyiadjis and Kattan 1992, 2006a):

$$\{\overline{\sigma}\} = [M]\{\sigma\} \tag{12}$$

where the stress tensor and its effective counterpart are given by the vectors g and $\{\overline{\sigma}\}$, respectively, and the fourth-rank damage tensor is given by the matrix $[M]$. For details about the nature of the tensor $[M]$ and its components, the interested reader is referred to the work of Sidoroff (1981) and Voyiadjis and Kattan (1992, 2006a).

The fourth-rank damage effect tensor given by the damage matrix $[M]$ in the three-dimensional case can be written in terms of the scalar damage variable φ of Eq. (1). However, for the nonlinear scalar damage variable of the previous sections, one introduces a new fourth-rank damage effect tensor represented by the damage matrix $[M^*]$. In view of the scalar Eq. (6), one can similarly write a tensor equation for $[M^*]$:

$$[M^*]^{-1} = [I_4] - \left[2\left([I_4] - [M]^{-1}\right) - \left[[I_4] - [M]^{-1}\right]^2\right]^{1/2} \tag{13}$$

The tensor Eq. (13) can be rewritten in the following form:

$$[M^*]^{-1} = [I_4] - \left[[I_4] - \left([M]^{-1}\right)^2\right]^{1/2} \tag{14}$$

The expression given in Eq. (14) stands for the matrix representation of the fourth-rank damage effect tensor M^*_{ijkl} of self-regenerating materials.

For the hypothesis of elastic strain equivalence, Eq. (8) for the elastic stiffness becomes generalized as follows:

$$[E] = \left([I_4] - \left[[I_4] - \left([M]^{-1}\right)^2\right]^{1/2}\right)[\overline{E}] \tag{15}$$

On the other hand, for the hypothesis of elastic energy equivalence, the equation of transformation of elastic stiffness is generalized as follows:

$$[E] = \left([I_4] - \left[[I_4] - \left([M]^{-1}\right)^2\right]^{1/2}\right)[\overline{E}]\left([I_4] - \left[[I_4] - \left([M]^{-1}\right)^2\right]^{1/2}\right)^Y \tag{16}$$

Equations (15) and (16) can be written using general values of the integer exponent n as follows:

$$[E] = \left([I_4] - \left[[I_4] - \left([M]^{-1}\right)^2\right]^{1/2}\right)^{1/n} [\overline{E}] \left([I_4] - \left[[I_4] - \left([M]^{-1}\right)^2\right]^{1/2}\right)^{1/nT} \tag{17}$$

Table 3 summarized these results using tensors.

One next uses the Taylor series expansion shown below in order to be able to perform computations based on the previous equations:

$$\sqrt{1-x} \cong 1 - \frac{1}{2}x + \ldots\ldots \tag{18}$$

One can then write the following approximation valid for small values of damage:

$$[I_4] - \left\{[I_4] - \left([M]^{-1}\right)^2\right\}^{1/2} \cong [I_4] - \left\{[I_4] - \frac{1}{2}\left([M]^{-1}\right)^2\right\} = \frac{1}{2}\left([M]^{-1}\right)^2 \tag{19}$$

One next substitutes the approximate expression above into Eqs. (14), (15), and (16), to obtain the following simplified expressions:

$$[M^*]^{-1} = \frac{1}{2}\left([M]^{-1}\right)^2 \tag{20}$$

$$[E] = \frac{1}{2}\left([M]^{-1}\right)^2 [\overline{E}] \tag{21}$$

Table 3 Degradation of the elastic stiffness and its recovery using tensors

	Equation
Hypothesis of elastic strain equivalence	$[E] = \left([I_4] - \left[[I_4] - \left([M]^{-1}\right)^2\right]\right)[\overline{E}]$
Hypothesis of elastic energy equivalence	$[E] = \left([I_4] - \left[[I_4] - \left([M]^{-1}\right)^2\right]^{1/2}\right)[\overline{E}]\left([I_4] - \left[[I_4] - \left([M]^{-1}\right)^2\right]^{1/2}\right)^{Y}$
Generalized hypothesis of elastic energy equivalence of order n	$[E] = \left([I_4] - \left[[I_4] - \left([M]^{-1}\right)^2\right]^{1/2}\right)^{1/n}[\overline{E}]\left([I_4] - \left[[I_4] - \left([M]^{-1}\right)^2\right]^{1/2}\right)^{1/nT}$

$$[E] = \frac{1}{4}\left([M]^{-1}\right)^2 [\overline{E}] \left([M]^{-1}\right)^2 \tag{22}$$

It should be noted that the hypothesis of elastic strain equivalence is used in expression (21) while the hypothesis of elastic energy equivalence is used in expression (22). These simplified expressions are used in the next section to solve the problem of plane stress for self-regenerating materials.

The Case of Plane Stress

Based on the tensor equations of section "The Tensor Theory," the simple case of plane stress is solved now for self-regenerating materials. This is a simple example showing how to apply the generalized equations to solve practical problems.

The general fourth-rank damage effect tensor $[M]$ is written for the case of plane stress as a 3×3 matrix as follows (see the previous work of Voyiadjis and Kattan 2006a for its full derivation):

$$[M] = \frac{1}{\Delta}\begin{bmatrix} \psi_{22} & 0 & \varphi_{12} \\ 0 & \psi_{11} & \varphi_{12} \\ \frac{\varphi_{12}}{2} & \frac{\varphi_{12}}{2} & \frac{\psi_{11}+\psi_{22}}{2} \end{bmatrix} \tag{23}$$

$$\psi_{11} = 1 - \varphi_{11} \tag{24}$$

$$\psi_{22} = 1 - \varphi_{22} \tag{25}$$

$$\Delta = \psi_{11}\psi_{22} - \varphi_{12}^2 \tag{26}$$

and φ_{11}, φ_{22}, and φ_{12} are the nonzero components of the damage tensor for the case of plane stress.

The elasticity tensor $[E]$ and the effective elasticity tensor $[\overline{E}]$ are represented by the following 3×3 matrices for the case of plane stress (Bower 2009; Doghri 2000): These are classical expressions from the solid mechanics literature.

$$[E] = \frac{E}{1-\upsilon^2}\begin{bmatrix} 1 & \upsilon & 0 \\ \upsilon & 1 & 0 \\ 0 & 0 & \frac{1-\upsilon}{2} \end{bmatrix} \tag{27}$$

$$[\overline{E}] = \frac{\overline{E}}{1-\overline{\upsilon}^2}\begin{bmatrix} 1 & \overline{\upsilon} & 0 \\ \overline{\upsilon} & 1 & 0 \\ 0 & 0 & \frac{1-\overline{\upsilon}}{2} \end{bmatrix} \tag{28}$$

where E and υ are Young's modulus and Poisson's ratio, respectively, in the actual damaged state, while $\overline{E}$ and $\overline{\upsilon}$ are the effective Young's modulus and Poisson's ratio, respectively, in undamaged state.

Substituting Eqs. (24), (25), (26), and (27) into Eq. (20), one obtains the following results (by using Wolfram Alpha online at www.wolframalpha.com):

$$\left([M^*]^{-1}\right)_{11} = \frac{1}{2}\Delta^2\left[\frac{\varphi_{12}^4}{4\alpha^2} + \frac{\psi_{11}^2\varphi_{12}^2}{2\alpha^2} + \frac{\left[\psi_{11}(\psi_{11}+\psi_{22}) - \varphi_{12}^2\right]^2}{4\alpha^2}\right] \tag{29}$$

$$\left([M^*]^{-1}\right)_{22} = \frac{1}{2}\Delta^2\left[\frac{\varphi_{12}^4}{4\alpha^2} + \frac{\psi_{22}^2\varphi_{12}^2}{2\alpha^2} + \frac{\left[\psi_{22}(\psi_{11}+\psi_{22}) - \varphi_{12}^2\right]^2}{4\alpha^2}\right] \tag{30}$$

$$\left([M^*]^{-1}\right)_{33} = \frac{1}{2}\Delta^2\left[\frac{\psi_{11}^2\psi_{22}^2}{\alpha^2} + \frac{\psi_{11}^2\varphi_{12}^2}{2\alpha^2} + \frac{\psi_{22}^2\varphi_{12}^2}{2\alpha^2}\right] \tag{31}$$

$$\left([M^*]^{-1}\right)_{12} = \frac{1}{2}\Delta^2\left[\frac{\psi_{11}\psi_{22}\varphi_{12}^2}{2\alpha^2} + \frac{\left[\psi_{11}(\psi_{11}+\psi_{22}) - \varphi_{12}^2\right]\varphi_{12}^2}{4\alpha^2} + \frac{\left[\psi_{22}(\psi_{11}+\psi_{22}) - \varphi_{12}^2\right]\varphi_{12}^2}{4\alpha^2}\right] \tag{32}$$

$$\left([M^*]^{-1}\right)_{13} = \frac{1}{2}\Delta^2\left[-\frac{\psi_{22}\varphi_{12}^3}{2\alpha^2} - \frac{\psi_{11}^2\psi_{22}\varphi_{12}}{\alpha^2} - \frac{\psi_{11}\left[\psi_{11}(\psi_{11}+\psi_{22}) - \varphi_{12}^2\right]\varphi_{12}}{2\alpha^2}\right] \tag{33}$$

$$\left([M^*]^{-1}\right)_{23} = \frac{1}{2}\Delta^2\left[-\frac{\psi_{11}\varphi_{12}^3}{2\alpha^2} - \frac{\psi_{11}\psi_{22}^2\varphi_{12}}{\alpha^2} - \frac{\psi_{22}\left[\psi_{22}(\psi_{11}+\psi_{22}) - \varphi_{12}^2\right]\varphi_{12}}{2\alpha^2}\right] \tag{34}$$

$$\left([M^*]^{-1}\right)_{21} = \left([M^*]^{-1}\right)_{12} \tag{35}$$

$$\left([M^*]^{-1}\right)_{31} = \frac{1}{2}\left([M^*]^{-1}\right)_{13} \tag{36}$$

$$\left([M^*]^{-1}\right)_{32} = \frac{1}{2}\left([M^*]^{-1}\right)_{23} \tag{37}$$

where

$$\alpha = -\frac{\psi_{11}\varphi_{12}^2}{2} - \frac{\psi_{22}\varphi_{12}^2}{2} + \frac{\psi_{11}\psi_{22}(\psi_{11}+\psi_{22})}{2} \tag{38}$$

Next, one uses the hypothesis of elastic strain equivalence. For this purpose, one substitutes Eqs. (24), (25), (26), (27), (28), (29), and (30), into Eq. (21) to obtain the following system of nine simultaneous algebraic equations (by using Wolfram Alpha online at www.wolframalpha.com):

$$\frac{E}{1-\upsilon^2}=\frac{1}{2}\left(\frac{\bar{E}}{1-\overline{\upsilon}^2}\right)\Delta^2\left[\begin{array}{l}\dfrac{\varphi_{12}^4}{4\alpha^2}+\dfrac{\psi_{11}^2\varphi_{12}^2}{2\alpha^2}+\dfrac{\left[\psi_{11}(\psi_{11}+\psi_{22})-\varphi_{12}^2\right]^2}{4\alpha^2}\\ \quad+\left\{\dfrac{\psi_{11}\psi_{22}\varphi_{12}^2}{2\alpha^2}+\dfrac{\left[\psi_{11}(\psi_{11}+\psi_{22})-\varphi_{12}^2\right]\varphi_{12}^2}{4\alpha^2}+\dfrac{\left[\psi_{22}(\psi_{11}+\psi_{22})-\varphi_{12}^2\right]\varphi_{12}^2}{4\alpha^2}\right\}\overline{\upsilon}\end{array}\right] \tag{39}$$

$$\frac{E}{1-\upsilon^2}=\frac{1}{2}\left[\frac{\bar{E}}{1-\overline{\upsilon}^2}\right]\Delta^2\left[\begin{array}{l}\dfrac{\varphi_{12}^4}{4\alpha^2}+\dfrac{\psi_{22}^2\varphi_{12}^2}{2\alpha^2}+\dfrac{\left[\psi_{22}(\psi_{11}+\psi_{22})-\varphi_{12}^2\right]^2}{4\alpha^2}\\ \quad+\left\{\dfrac{\psi_{11}\psi_{22}\varphi_{12}^2}{2\alpha^2}+\dfrac{\left[\psi_{11}(\psi_{11}+\psi_{22})-\varphi_{12}^2\right]\varphi_{12}^2}{4\alpha^2}+\dfrac{\left[\psi_{22}(\psi_{11}+\psi_{22})-\varphi_{12}^2\right]\varphi_{12}^2}{4\alpha^2}\right\}\overline{\upsilon}\end{array}\right] \tag{40}$$

$$\left(\frac{E}{1-\upsilon^2}\right)\left(\frac{1-\upsilon}{2}\right)=\frac{1}{2}\left(\frac{\overline{E}}{1-\overline{\upsilon}^2}\right)\Delta^2\left[\frac{\psi_{11}^2\psi_{22}^2}{\alpha^2}+\frac{\psi_{11}^2\varphi_{12}^2}{2\alpha^2}+\frac{\psi_{22}^2\varphi_{12}^2}{2\alpha^2}\right]\left(\frac{1-\overline{\upsilon}}{2}\right) \tag{41}$$

$$\frac{E\upsilon}{1-\upsilon^2}=\frac{1}{2}\left(\frac{\bar{E}}{1-\overline{\upsilon}^2}\right)\Delta^2\left[\begin{array}{l}\dfrac{\psi_{11}\psi_{22}\varphi_{12}^2}{2\alpha^2}+\dfrac{\left[\psi_{11}(\psi_{11}+\psi_{22})-\varphi_{12}^2\right]\varphi_{12}^2}{4\alpha^2}+\dfrac{\left[\psi_{22}(\psi_{11}+\psi_{22})-\varphi_{12}^2\right]\varphi_{12}^2}{4\alpha^2}\\ \quad+\left\{\dfrac{\varphi_{12}^4}{4\alpha^2}+\dfrac{\psi_{11}^2\varphi_{12}^2}{2\alpha^2}+\dfrac{\left[\psi_{11}(\psi_{11}+\psi_{22})-\varphi_{12}^2\right]\varphi_{12}^2}{2\alpha^2}\right\}\overline{\upsilon}\end{array}\right] \tag{42}$$

$$0=\frac{1}{2}\left(\frac{\bar{E}}{1-\overline{\upsilon}^2}\right)\Delta^2\left[-\frac{\psi_{22}\varphi_{12}^3}{2\alpha^2}-\frac{\psi_{11}^2\psi_{22}\varphi_{12}}{\alpha^2}-\frac{\psi_{11}\left[\psi_{11}(\psi_{11}+\psi_{22})-\varphi_{12}^2\right]\varphi_{12}}{\alpha^2}\right]\frac{1-\overline{\upsilon}}{2} \tag{43}$$

$$0=\frac{1}{2}\left(\frac{\bar{E}}{1-\overline{\upsilon}^2}\right)\Delta^2\left[-\frac{\psi_{11}\varphi_{12}^3}{2\alpha^2}-\frac{\psi_{11}\psi_{22}^2\varphi_{12}}{\alpha^2}-\frac{\psi_{22}\left[\psi_{22}(\psi_{11}+\psi_{22})-\varphi_{12}^2\right]\varphi_{12}}{\alpha^2}\right]\frac{1-\overline{\upsilon}}{2} \tag{44}$$

$$\frac{E\upsilon}{1-\upsilon^2}=\frac{1}{2}\left(\frac{\bar{E}}{1-\overline{\upsilon}^2}\right)\Delta^2\left[\begin{array}{l}\dfrac{\psi_{11}\psi_{22}\varphi_{12}^2}{2\alpha^2}+\dfrac{\left[\psi_{11}(\psi_{11}+\psi_{22})-\varphi_{12}^2\right]\varphi_{12}^2}{4\alpha^2}+\dfrac{\left[\psi_{22}(\psi_{11}+\psi_{22})-\varphi_{12}^2\right]\varphi_{12}^2}{4\alpha^2}\\ \quad+\left\{\dfrac{\varphi_{12}^4}{4\alpha^2}+\dfrac{\psi_{22}^2\varphi_{12}^2}{2\alpha^2}+\dfrac{\left[\psi_{22}(\psi_{11}+\psi_{22})-\varphi_{12}^2\right]\varphi_{12}^2}{2\alpha^2}\right\}\overline{\upsilon}\end{array}\right] \tag{45}$$

$$0=\frac{1}{2}\left(\frac{\overline{E}}{1-\overline{\upsilon}^2}\right)\Delta^2\left[\begin{array}{l}-\dfrac{\psi_{22}\varphi_{12}^3}{4\alpha^2}-\dfrac{\psi_{11}^2\psi_{22}\varphi_{12}}{2\alpha^2}-\dfrac{\psi_{11}\left[\psi_{11}(\psi_{11}+\psi_{22})-\varphi_{12}^2\right]\varphi_{12}}{4\alpha^2}\\ \quad+\left\{-\dfrac{\psi_{11}\varphi_{12}^3}{4\alpha^2}-\dfrac{\psi_{11}\psi_{22}^2\varphi_{12}}{2\alpha^2}-\dfrac{\psi_{22}\left[\psi_{22}(\psi_{11}+\psi_{22})-\varphi_{12}^2\right]\varphi_{12}}{4\alpha^2}\right\}\overline{\upsilon}\end{array}\right] \tag{46}$$

$$0=\frac{1}{2}\left(\frac{\bar{E}}{1-\overline{\upsilon}^2}\right)\Delta^2\left[\begin{array}{l}-\dfrac{\psi_{11}\varphi_{12}^3}{4\alpha^2}-\dfrac{\psi_{11}\psi_{22}^2\varphi_{12}}{2\alpha^2}-\dfrac{\psi_{22}\left[\psi_{22}(\psi_{11}+\psi_{22})-\varphi_{12}^2\right]\varphi_{12}}{4\alpha^2}\\ \quad+\left\{-\dfrac{\psi_{22}\varphi_{12}^3}{4\alpha^2}-\dfrac{\psi_{11}^2\psi_{22}\varphi_{12}}{2\alpha^2}-\dfrac{\psi_{11}\left[\psi_{11}(\psi_{11}+\psi_{22})-\varphi_{12}^2\right]\varphi_{12}}{4\alpha^2}\right\}\overline{\upsilon}\end{array}\right] \tag{47}$$

One now considers a special case when $\varphi_{12} = 0$. This is the case of *plane stress and plane damage*. Substituting the condition, $\varphi_{12} = 0$, into Eqs. (29), (30), (31), (32), (33), (34), (35), (36), (37), and (38), one obtains the following set of nine simplified equations:

$$\left([M^*]^{-1}\right)_{11} = \frac{1}{2}\psi_{11}^2 \tag{48}$$

$$\left([M^*]^{-1}\right)_{22} = \frac{1}{2}\psi_{22}^2 \tag{49}$$

$$\left([M^*]^{-1}\right)_{33} = \frac{2\psi_{11}^2\psi_{22}^2}{(\psi_{11}+\psi_{22})^2} \tag{50}$$

$$\left([M^*]^{-1}\right)_{12} = 0 \tag{51}$$

$$\left([M^*]^{-1}\right)_{13} = 0 \tag{52}$$

$$\left([M^*]^{-1}\right)_{23} = 0 \tag{53}$$

$$\left([M^*]^{-1}\right)_{21} = 0 \tag{54}$$

$$\left([M^*]^{-1}\right)_{31} = 0 \tag{55}$$

$$\left([M^*]^{-1}\right)_{32} = 0 \tag{56}$$

It is clear from the above equations that one obtains a diagonal matrix for [*M**]. This diagonal matrix is written explicitly as follows:

$$[M^*]^{-1} \equiv \begin{bmatrix} \frac{1}{2}\psi_{11}^2 & 0 & 0 \\ 0 & \frac{1}{2}\psi_{22}^2 & 0 \\ 0 & 0 & \frac{2\psi_{11}^2\psi_{22}^2}{(\psi_{11}+\psi_{22})^2} \end{bmatrix} \tag{57}$$

Next one substitutes $\phi_{12} = 0$ into Eqs. (39), (40), (41), (42), (43), (44), (45), (46), and (47) to obtain the following set of nine simplified simultaneous algebraic equations:

$$\frac{E}{1-\upsilon^2} = \frac{1}{2}\left(\frac{\overline{E}}{1-\overline{\upsilon}^2}\right)\psi_{11}^2 \tag{58}$$

$$\frac{E}{1-\upsilon^2} = \frac{1}{2}\left[\frac{\overline{E}}{1-\overline{\upsilon}^2}\right]\psi_{22}^2 \tag{59}$$

$$\frac{E}{1+\upsilon} = \frac{\overline{E}(1-\overline{\upsilon})}{1+\overline{\upsilon}}\,\frac{8\psi_{11}^2\psi_{22}^2}{(\psi_{11}+\psi_{22})^2} \tag{60}$$

$$\frac{E\upsilon}{1-\upsilon^2} = 0 \tag{61}$$

$$0 = 0 \tag{62}$$

$$0 = 0 \tag{63}$$

$$\frac{E\upsilon}{1-\upsilon^2} = 0 \tag{64}$$

$$0 = 0 \tag{65}$$

$$0 = 0 \tag{66}$$

If one assumes that Poisson's ratio does not undergo any damage in this case, i.e., assuming that $\overline{\upsilon} = \upsilon$, one may conclude from Eqs. (58) and (59) that $E = \overline{E}\psi_{11}^2/2 = \overline{E}\psi_{22}^2/2$.

The corresponding equations for the hypothesis of elastic energy equivalence are not derived here. This is because they may turn out to be complicated and do not form closed-form expressions as shown above. Thus, this other hypothesis is left to the reader as an exercise.

Conclusion and Discussion

A theory of the mechanics of self-regenerating materials is developed using the definition of a new scalar damage variable. A consistent mathematical and graphical analysis of the situation is presented in this work. The behavior of the self-regenerating materials consists of a damage stage followed by a healing stage. In the damage state, there is a clear and noticeable loss in the elastic stiffness while the opposite is shown to occur in the healing stage where a clear gain in the elastic stiffness is detected.

The concept of a magical material is also discussed. This new material type is the limit of the self-regenerating material as the integer exponent n goes to infinity. This new material is characterized by a sudden drop in the elastic stiffness to zero upon loading then a sudden recovery of the total elastic stiffness at the end of loading. During loading, the material maintains a zero elastic stiffness throughout.

There is an existing material whose behavior is very close to that of self-regenerating materials. Self-healing polymers composed of microencapsulated healing agents exhibit remarkable mechanical performance and regenerative ability (Toohey et al. 2007). In these types of materials, self-healing is triggered by

crack-induced rupture of the embedded capsules; thus, once a localized region is depleted of healing agent, further repair is precluded. Toohey et al. (2007) report a self-healing system capable of autonomously repairing repeated damage events.

The authors believe that this work is still in its infancy stage. In this work, the authors presented the mathematical aspects but without the physical and metallurgical ones. However, it is not clear to the authors what these issues are at the present time and how they can be approached. The authors reiterate their viewpoint that this mathematical formulation lays a possible groundwork for any future development in this regard. The authors are still hopeful that some form of strengthened material may be achieved in the industry in the near future. The use of the fabric tensor is the approach to link the mathematics with the material characterization. The authors have extensively published on this subject including several chapters in their last book (Voyiadjis and Kattan 2006a, b, c).

References

C. Basaran, S. Nie, An irreversible thermodynamic theory for damage mechanics of solids. Int. J. Damage Mech. **13**(3), 205–224 (2004)

C. Basaran, S. Nie, A thermodynamic based damage mechanics model for particulate composites. Int. J. Solids Struct. **44**, 1099–1114 (2007)

C. Basaran, H. Tang, Implementation of a thermodynamic framework for damage mechanics of solder interconnects in microelectronic packaging. Int. J. Damage Mech. **11**(1), 87–108 (2002)

C. Basaran, C.Y. Yan, A thermodynamic framework for damage mechanics of solder joints. Trans. ASME J. Electron. Packag. **120**, 379–384 (1998)

C. Basaran, M. Lin, H. Ye, A thermodynamic model for electrical current induced damage. Int. J. Solids Struct. **40**(26), 7315–7327 (2003)

A.F. Bower, *Applied Mechanics of Solids* (CRC Press, Boca Raton, 2009)

D.J. Celentano, P.E. Tapia, J.-L. Chaboche, Experimental and numerical characterization of damage evolution in steels, in *Mecanica Computacional*, ed. by G. Buscaglia, E. Dari, O. Zamonsky, vol. XXIII (Bariloche, 2004)

I. Doghri, *Mechanics of Deformable Solids: Linear and Nonlinear, Analytical and Computational Aspects* (Springer, Berlin, 2000)

N.R. Hansen, H.L. Schreyer, A thermodynamically consistent framework for theories of elastoplasticity coupled with damage. Int. J. Solids Struct. **31**(3), 359–389 (1994)

L. Kachanov, On the creep fracture time. Izv Akad, Nauk USSR Otd Tech. **8**, 26–31 (1958). (in Russian)

P.I. Kattan, G.Z. Voyiadjis, A coupled theory of damage mechanics and finite strain elasto-plasticity – part I: damage and elastic deformations. Int. J. Eng. Sci. **28**(5), 421–435 (1990)

P.I. Kattan, G.Z. Voyiadjis, A plasticity-damage theory for large deformation of solids – part II: applications to finite simple shear. Int. J. Eng. Sci. **31**(1), 183–199 (1993)

P.I. Kattan, G.Z. Voyiadjis, Decomposition of damage tensor in continuum damage mechanics. J. Eng. Mech. ASCE **127**(9), 940–944 (2001a)

P.I. Kattan, G.Z. Voyiadjis, *Damage Mechanics with Finite Elements: Practical Applications with Computer Tools* (Springer, Berlin, 2001b)

P. Ladeveze, J. Lemaitre, Damage effective stress in quasi-unilateral conditions, in *The 16th International Cogress of Theoretical and Applied Mechanics*, Lyngby (1984)

P. Ladeveze, M. Poss, L. Proslier, Damage and fracture of tridirectional composites, in *Progress in Science and Engineering of Composites. Proceedings of the Fourth International Conference on Composite Materials*, vol. 1 (Japan Society for Composite Materials, Tokyo, 1982), pp. 649–658

H. Lee, K. Peng, J. Wang, An anisotropic damage criterion for deformation instability and its application to forming limit analysis of metal plates. Eng. Fract. Mech. **21**, 1031–1054 (1985)
G. Lubineau, A pyramidal modeling scheme for laminates – identification of transverse cracking. Int. J. Damage Mech. **19**(4), 499–518 (2010)
G. Lubineau, P. Ladeveze, Construction of a micromechanics-based intralaminar mesomodel, and illustrations in ABAQUS/standard. Comput. Mater. Sci. **43**(1), 137–145 (2008)
B. Luccioni, S. Oller, A directional damage model. Comput. Methods Appl. Mech. Eng. **192**, 1119–1145 (2003)
Y. Rabotnov, Creep rupture, in *Proceedings, Twelfth International Congress of Applied Mechanics*, Stanford, 1968, ed. by M.Hetenyi, W.G. Vincenti (Springer, Berlin, 1969), pp. 342–349
J.R. Rice, Inelastic constitutive relations for solids: an internal variable theory and its application to metal plasticity. J. Mech. Phys. Solids **19**, 433–455 (1971)
F. Sidoroff, Description of anisotropic damage application in elasticity, in *IUTAM Colloqium on Physical Nonlinearities in Structural Analysis* (Springer, Berlin, 1981), pp. 237–244
L.A. Sosnovskiy, S. Sherbakov, Mechanothermodynamic entropy and analysis of damage state of complex systems. Entropy **18**, 268 (2016). https://doi.org/10.3390/e18070268
K.S. Toohey, N.R. Sottos, J.A. Lewis, J.S. Moore, S.R. White, Self-healing materials with microvascular networks. Nat. Mater. **6**, 581–585 (2007)
G.Z. Voyiadjis, Degradation of elastic modulus in elastoplastic coupling with finite strains. Int. J. Plast. **4**, 335–353 (1988)
G.Z. Voyiadjis, P.I. Kattan, A coupled theory of damage mechanics and finite strain elasto-plasticity – part II: damage and finite strain plasticity. Int. J. Eng. Sci. **28**(6), 505–524 (1990)
G.Z. Voyiadjis, P.I. Kattan, A plasticity-damage theory for large deformation of solids – part I: theoretical formulation. Int. J. Eng. Sci. **30**(9), 1089–1108 (1992)
G.Z. Voyiadjis, P.I. Kattan, *Damage Mechanics* (Taylor and Francis (CRC Press), Boca Raton, 2005)
G.Z. Voyiadjis, P.I. Kattan, *Advances in Damage Mechanics: Metals and Metal Matrix Composites with an Introduction to Fabric Tensors*, 2nd edn. The Netherlands (Elsevier, The Netherlands, 2006a)
G.Z. Voyiadjis, P.I. Kattan, A new fabric-based damage tensor. J. Mech. Behav. Mater. **17**(1), 31–56 (2006b)
G.Z. Voyiadjis, P.I. Kattan, Damage mechanics with fabric tensors. Mech. Adv. Mater. Struct. **13**(4), 285–301 (2006c)
G.Z. Voyiadjis, P.I. Kattan, A comparative study of damage variables in continuum damage mechanics. Int. J. Damage Mech. **18**(4), 315–340 (2009)
G.Z. Voyiadjis, P.I. Kattan, Mechanics of damage processes in series and in parallel: a conceptual framework. Acta Mech. **223**(9), 1863–1878 (2012a)
G.Z. Voyiadjis, P.I. Kattan, Introduction to the mechanics and design of undamageable materials. Int. J. Damage Mech. (2012b). https://doi.org/10.1177/1056789512446518. (13 manuscript pages)
G.Z. Voyiadjis, P.I. Kattan, A new class of damage variables in continuum damage mechanics. ASME J. Eng. Mater. Technol. **134**(2), 021016, 1–10 (2012c)
G.Z. Voyiadjis, P.I. Kattan, On the theory of elastic undamageable materials. ASME J. Eng. Mater. Technol. (2013). Accepted for publication J. Eng. Mater. Technol. 135(2): 021002 (6 pages)
G.Z. Voyiadjis, P.I. Kattan, Healing and super healing in continuum damage mechanis. Int. J Damage Mech. **23**(2), 245–260 (2014)
G.Z. Voyiadjis, P.I. Kattan, Mechanics of damage, healing, damageability, and integrity of materials: a conceptual framework. Int. J. Damage. Mech. **50**(26), 1 (2017a). Accepted for Publication
G.Z. Voyiadjis, P.I. Kattan, Decomposition of elastic stiffness degradation in continuum damage mechanics. ASME J. Eng. Mater. Technol. **139**(2), 021005 (15 pages) (2017b). Submitted for Publication, 55 pages
G.Z. Voyiadjis, M.A. Yousef, P.I. Kattan, New tensors for anisotropic damage in continuum damage mechanics. ASME J. Eng. Mater. Technol. **134**(2), 021015, 1–10 (2012)

Damage and Nonlinear Super Healing with Application to the Design of New Strengthening Theory

6

George Z. Voyiadjis, Chahmi Oucif, Peter I. Kattan, and Timon Rabczuk

Contents

Introduction 120
Damage Healing and Super Healing Mechanics 122
Healing and Super Healing in Anisotropic Formulation 125
Linear Refined Super Theory 126
Anisotropic Formulation of Linear Super Healing Mechanics 128
Plane Stress Example of the Refined Super Healing 129
One-Dimensional Example 132
Generalized Nonlinear Super Healing 134
Quadratic Super Healing 137
Anisotropic Formulation of Nonlinear Super Healing 138
Plane Stress Example of the Generalized Nonlinear Super Healing Theory 138
Plane Stress Example of the Quadratic Super Healing Theory 140
Non-super-Healed Damage Concept 141
Comparative Analysis of Super Healing Models 141
Super Healing Efficiency 146

G. Z. Voyiadjis (✉)
Center for GeoInformatics C4G and Computational Solid Mechanics Laboratory, Department of Civil and Environmental Engineering, Louisiana State University, Baton Rouge, LA, USA
e-mail: voyiadjis@eng.lsu.edu

C. Oucif
Institute of Structural Mechanics (ISM), Bauhaus-Universität Weimar, Weimar, Germany
e-mail: chahmi.oucif@uni-weimar.de

P. I. Kattan
Department of Civil and Environmental Engineering, Louisiana State University, Baton Rouge, LA, USA
e-mail: info@PetraBooks.com; pkattan@PetraBooks.com

T. Rabczuk
College of Civil Engineering, Department of Geotechnical Engineering, Tongji University, Shanghai, China
e-mail: timon.rabczuk@uni-weimar.de

© Springer Nature Switzerland AG 2022

G. Z. Voyiadjis (ed.), *Handbook of Damage Mechanics*,
https://doi.org/10.1007/978-3-030-60242-0_87

Theory of Undamageable Materials 148
Conclusions 151
References 151

Abstract

The use of self-healing materials has recently received much attention due to the efficacy of these materials to repair cracks and rehabilitate structures. Recent investigations revealed that self-healing concept can be extended and used in the strengthening of materials. This theory was termed super healing. The idea is that further healing takes place as a strengthening mechanism after the material stiffness is recovered. This chapter presents a refined theory of super healing using continuum damage-healing mechanics. An extension of the proposed theory from linear to nonlinear super healing theory will be presented. The present chapter reviews first the continuum damage-healing mechanics framework. Afterward, we introduce mathematically and mechanically the concepts of self-healing and super healing using isotropic and anisotropic presentations. Following that, we introduce the nonlinear formulation of the proposed theory along with its anisotropic presentation. In addition, the proposed theory will be linked to the theory of undamageable materials. One-dimensional and plane stress examples are applied on the proposed theory. In the present chapter, the authors aim to provide guidance and contribution to the concept of super healing that can be applied in the industry in the future. The authors believe that this theory will pave a way for new researches in materials science.

Keywords

Damage · Healing · Super healing · Continuum mechanics · Elasticity · Anisotropy · Undamageable materials

Introduction

The use of self-healing materials has recently received much attention due to the efficacy of these materials to repair cracks and rehabilitate structures (Oucif et al. 2018a, b, 2019; Oucif and Mauludin 2018). The aim of self-healing is the recovery of material stiffness. The material completely healed should exhibit similar behavior to the undamaged (initial) material. Many researchers have focused on self-healing materials (Joseph et al. 2009; Breugel 2012). The self-healing concept was first discovered by the French Academy of Science in 1936, which revealed that calcium carbonate is resulted from calcium hydroxide when exposed to the atmosphere. Two categories of self-healing are given: autonomous (Patel et al. 2010; Gardner et al. 2014; Joseph et al. 2007) and autogenous healing mechanisms (Hilloulin et al. 2014; Yang et al. 2009). White et al. (2001) were the first who proposed the autonomous healing mechanism which can also be called extrinsic healing. This mechanism is based on embedding some capsules or hollow fibers containing healing agents inside

the material (Brown et al. 2006; Wang et al. 2014; Mauludin and Oucif 2018, 2019). The second mechanism can also be called intrinsic healing and is based on ongoing hydration of clinker mineral or formation of $(Ca(OH)_2)$ (Giannaros et al. 2016). Some researchers have revealed that the second mechanism is limited to small cracks and is only controlled by water. Autonomous and autogenous healing mechanisms can be divided into active mode (Dry 1994) which need human intervention and passive mode in which no human intervention is needed (Dry and Sottos 1993; Lia et al. 1998).

Numerical modeling of self-healing materials is still in its infancy. Few researchers have conducted numerical investigations of self-healing concrete, while many experimental studies were carried out (e.g., Brown et al. 2002, 2004, 2005; Joseph et al. 2010; Granger et al. 2007; Tittelboom et al. 2011). An effort is needed to complete these investigations in order to describe the behavior of self-healing materials. The aim of self-healing is to reduce and eliminate damage in the material. Based on this idea, several investigations were conducted using continuum damage mechanics (CDM). Kachanov (1958) was the first who proposed CDM. Later on, many researchers investigated the same framework (Voyiadjis 1988; Voyiadjis and Kattan 1992; Rabczuk et al. 2005; Thai et al. 2017; Areias et al. 2016). CDM has been used to also study damage in microelectronic components using the concepts of entropy generation rate (Basaran and Yan 1998; Basaran and Nie 2004; Gunel and Basaran 2011a, b; Yao and Basaran 2013). A mechanothermodynamics theory was developed by Sosnovskiy and Sherbakov (2016) who revealed that self-healing materials can be simulated in a biological system.

The CDM was extended to continuum damage-healing mechanisms by Barbero et al. (2005). The authors introduced in their work the healing variable into the constitutive equations and proposed a thermodynamic framework of self-healing materials. Following the CDHM, many investigations were conducted. Many theoretical aspects of self-healing materials were studied by Voyiadjis et al. (2011a, b, 2012, 2013, 2015, 2016).

In (Voyiadjis et al. 2011a), the authors proposed a damage-healing process coupled to inelasticity. Isotropic hardening effect was taken into consideration using new yield surfaces for damage and healing. This work was further expended in (Voyiadjis et al. 2011b) in which the behavior of self-healing polymers was described. The authors presented two anisotropic damage-healing variables in the application of multiaxial anisotropic damage and healing cases. In (Voyiadjis et al. 2012), the authors studied the self-healing behavior using two new healing variables based on elastic stiffness and cross-sectional area and proposed the coupled damage-healing mechanism.

The super healing theory was first proposed in (Voyiadjis and Kattan 2013). The authors defined the material that is subjected to super healing as super material. The role of super healing starts after the material is fully healed (100% of healing). It should be noted that the unhealed material is represented by the healing variable $h = 0$, while the fully healed material is represented by $h = 1$. In the case of super healing, the healing variable takes the value greater than 1 ($h > 1$). Super healing

gives the material the ability to strengthen its stiffness which should be greater than the original (initial) one. In (Voyiadjis and Kattan 2013, 2015), the damage was decomposed mathematically into damage due to voids and damage due to cracks. New concept of damageability and integrity of materials was presented. Linear and nonlinear damage-healing models were introduced by Voyiadjis and Kattan (2015). The authors showed that the self-healing mechanism can be appropriately described by the nonlinear healing variable comparing to the linear healing variable. They also showed that the linear healing model can be presented as special case of nonlinear healing model. Darabi et al. (2012) proposed a continuum micro-damage-healing framework using different hypothesis equivalences. A hydro-chemo-mechanical model was proposed by Hilloulin et al. (2014) in order to simulate the behavior of autogenous healing in ultrahigh performance concrete. A micromechanical damage-healing model was proposed by Zhu et al. (2014) in order to simulate the physical behavior of microcapsule-based self-healing concrete along with the consideration of different parameters (fracture toughness of healing agent, damage degree, volume fraction of microcapsules). In the case of isotropic materials, the damage variable was defined as scalar (Brencich and Gambarotta 2001), while in the case of anisotropic materials, the damage variable was defined as tensor (Voyiadjis et al. 2011b).

In the present chapter, the authors present a refined theory of super healing materials based on CDHM. The role of this theory starts after complete healing of the material and complete recovery of the material stiffness. The authors assume in this theory that the healing and super healing processes are activated using the same material. Therefore, the value of the healing variable can increase beyond the necessary limit for the recovery of the original material stiffness. In this work, the authors review first the self-healing and super healing mechanics and theory anisotropic presentations. Afterward, the refined super healing theory is defined. They also introduce the nonlinear super healing theory and the anisotropic formulation. In order to elucidate the applicability of the proposed theory, the authors solve two examples, namely, a special case of stress and a one-dimensional self-healing model. A link between the super healing theory with the undamageable theory is also outlined in the last section. The characteristics of the proposed theory in terms of CDHM are also given. The authors would like to note that the material used in the present theory is not characterized in the present work. They only point the way of the theory and its possible exploitation in industry. It is hoped that the possible production of this material will be available in the future.

Damage Healing and Super Healing Mechanics

The authors review in this section the damage, healing, and super healing variables within the framework of CDHM. Only scalar formulation is given in the present section. Figure 1 illustrates the initial, damaged, and effective material states defined by S_0, S_φ, and $\overline{S}$ as the initial cross-section and damaged cross-section and effective

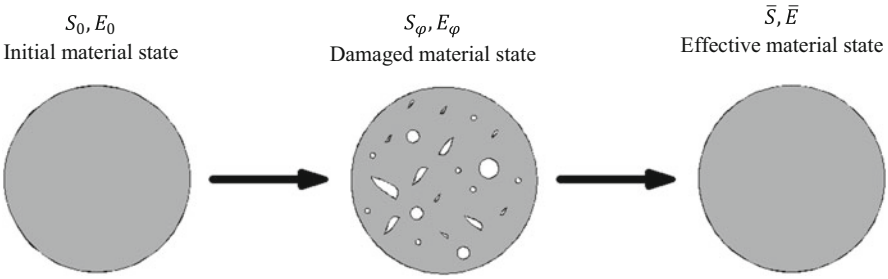

Fig. 1 Initial, damaged, and effective material states

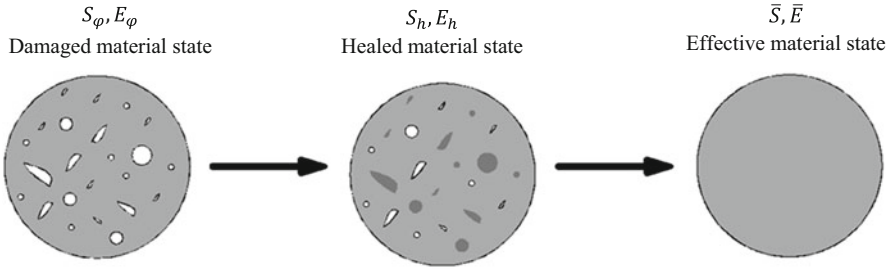

Fig. 2 Damaged, partially healed, and effective material states

cross-section, respectively. They can also be represented, respectively, by E_0, $E_{\varphi,}$ and $\overline{E}$ as the initial, damage, and effective elastic moduli. In this section, the authors limit the definition of variables in terms of cross-section reduction. The damage variable is defined as:

$$\varphi = \frac{S_\varphi}{S_0} \text{ with } 0 \leq \varphi \leq 1 \tag{1}$$

The damage in the material is represented by $\varphi = 0$ as undamaged material state, $0 < \varphi < 1$ as partially damaged material state, and $\varphi = 1$ as fully damaged material state, respectively. If damage is removed from the second material state, the relation between the nominal stress σ and effective stress $\overline{\sigma}$ can be given as (Kachanov 1958; Voyiadjis and Kattan 1999):

$$\overline{\sigma} = \frac{\sigma}{1 - \varphi} \tag{2}$$

Damaged sections are affected by the healing mechanism, and the cracks and voids are filled. Figure 2 illustrates the damaged, partially healed, and effective material states. Equation (2) is defined according to CDHM as follows (Voyiadjis et al. 2012; Voyiadjis and Kattan 2013; Darabi et al. 2012):

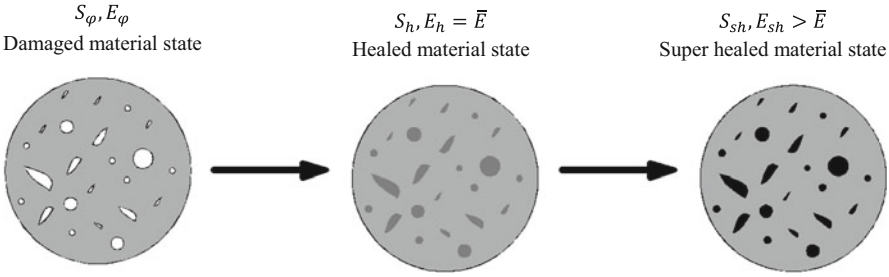

Fig. 3 Damaged, healed, and super healed material states

$$\overline{\sigma} = \frac{\sigma}{1 - \varphi(1 - h)} \tag{3}$$

where the healing variable is represented by h. It should be noted that the unhealed, partially healed, and fully healed material states are defined, respectively, by $h = 0$, $0 < h < 1$, and $h = 1$. After the material is completely healed, it recovers its original stiffness, and similarity of the effective stress with the nominal stress resulted. The healed material state can also be defined by the healed elastic modulus E_h which becomes equal to damaged elastic modulus E_φ in the case of damaged material state and to the effective elastic modulus $\overline{E}$. In Eq. (3), the damage variable of Eq. (2) is replaced by the $\varphi(1 - h)$. In the present work, we call this variable the eliminated damage variable which reflects the elimination of damage from the total cross-section under self-healing effect.

Voyiadjis and Kattan (2013) proposed the concept of super healing materials. Using super healing concept, the material becomes able not only to heal itself but to also strengthen itself. From Eq. (3), the material shows complete recovery when the healing variable h takes the value of 1. In the case of super healing theory, the variable h takes values greater than 1 after complete recovery of material stiffness. In this phase, strengthening process will take place instead of healing process. Figure 3 illustrates the super healing material state which is represented by its high elastic modulus E_{sh} comparing to the effective elastic modulus ($E_{sh} > \overline{E}$).

In Fig. 4, the evolution of elastic modulus in different material states is shown as a chart. The elastic modulus E_0 represents the stiffness of the undamaged material. External loading and energy increase result in damage of the material which is measured by the variable φ and represented by the elastic modulus E_φ. The effect of self-healing results in damage elimination and stiffness recovery, and the material can either be partially healed (E_{ph}) or fully healed (E_{fh}). The effect of super healing results in the enhancement and strengthening of the material stiffness. In this phase, the super healed elastic modulus becomes greater than the original and effective elastic moduli.

Voyiadjis and Kattan (2013) presented a formulation in which the healing variable starts from 1 and increases to the values 2, 3, 4, . . ., n + 1. In this case, Eq. (3) was defined as:

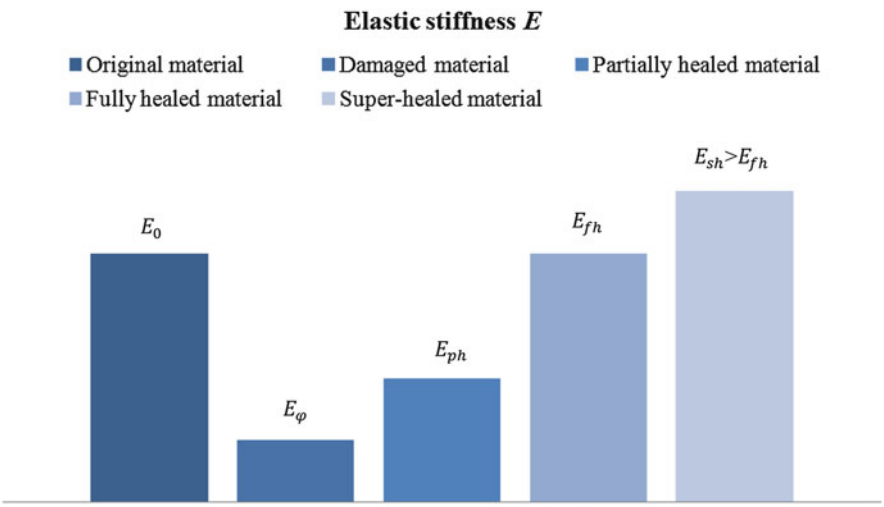

Fig. 4 Evolution of material stiffness from initial to super healing states

$$\overline{\sigma} = \frac{\sigma}{1 + n\varphi} \tag{4}$$

One can observe from Eq. (4) that the effective stress value approaches zero when the value of n approaches infinity. In addition, Eq. (4) is restricted to the healing value of 1 only. For healing values of 2 and n, respectively, Eqs. (5) and (6) were proposed.

$$\overline{\sigma} = \frac{\sigma}{1 + 2n\varphi} \tag{5}$$

$$\overline{\sigma} = \frac{\sigma}{1 + n^2\varphi} \tag{6}$$

The proposition of the super healing theory presented in Eqs. (4) and (5) is limited due to the assumption that the super healing concept is represented only by an integer, and the super healing variable can only take the values of 1 and 2. On the other hand, only multiple super healing mechanisms were considered and represented by the parameter n. Unlike this definition, the authors will show in the present work that both single and multiple super healing mechanisms can be defined using the parameter n.

Healing and Super Healing in Anisotropic Formulation

In this section, the anisotropic formulation of damage, healing, and super healing mechanics is reviewed (Voyiadjis and Kattan 2013). In this case, capital letters are used as tensors instead of scalar variables. In the following, the fourth-rank damage

tensor of CDM and the fourth-rank healing tensor of CDHM are denoted by M and H, respectively. If more details are needed, the reader can refer to (Voyiadjis and Kattan 1999; Voyiadjis et al. 2011b; Voyiadjis et al. 2012). The anisotropic definition of Eqs. (3) and (4) is given, respectively, as:

$$\overline{\sigma}_{ij} = \left[M^{-1}_{ijkl} + \left(I_{ijmn} - M^{-1}_{ijmn}\right) : H^{-1}_{mnkl}\right]^{-1} \sigma_{kl} \tag{7}$$

$$\overline{\sigma}_{ij} = \left[n\left(I_{ijkl} - M^{-1}_{ijkl}\right) + I_{ijkl}\right]^{-1} \sigma_{kl} \tag{8}$$

where I_{ijmn} is the fourth-rank identity tensor and σ_{kl} and $\overline{\sigma}_{ij}$ are second-rank stress tensors. From Eq. (7), $\left(I_{ijmn} - M^{-1}_{ijmn}\right)\left(I_{mnkl} - H^{-1}_{mnkl}\right)$ represents the anisotropic definition of the eliminated damage variable $\varphi(1 - h)$. In addition, these equations are defined based on the assumption that the components of M and H correspond to $1/(1 - \varphi)$ $1/h$, respectively.

Linear Refined Super Theory

In this section, the authors introduce the linear (classical) refined super healing theory following the standard definition of self-healing which was defined above by Eq. (3).

According to CDHM framework, damage is eliminated in the material, and original stiffness is recovered due to self-healing effect. The fully damaged material state is defined by the maximum damage variable $\varphi = 1$. The fully healed material state is also defined by the maximum healing variable $h = 1$. In contract, $\varphi = 0$ and $h = 0$ represent, respectively, the unhealed and undamaged material states. Reloading of material should be applied in order to describe the healing efficiency and stiffness recovery. After reloading is applied, the healed material stiffness E_h and the original material stiffness E_0 should be compared. Complete healing ($h = 1$) of the material is reflected by the similarity between the healed material stiffness E_h and original material stiffness E_0. On the other hand, zero healing ($h = 0$) of the material is reflected by the similarity of the healed material stiffness E_h with the damaged material stiffness E_φ. One should note that the effective and initial material states ($\varphi = 0$) are similar. Then, one concludes that the fully healed and effective material states are similar (see above Fig. 4).

In this proposed theory, the authors propose that the healing continues beyond the maximum value $h = 1$ after the original stiffness was recovered. In this phase, large values such as 2, 3, 4,. . . ., x are reached by the healing variable. In addition, the strengthening effect and enhancement of material stiffness will take place instead of healing. In this case, the maximum value of the super healing is represented by x. We denote h_s the super healing variable. This variable is used to differentiate between self-healing and super healing phases.

In this theory, the authors propose two mechanisms of super healing. The first concept concerns the single super healing mechanism in which the variable h_s is defined by single large value, and the super healing acts at single point of the material. This mechanism can be found, for instance, when microcapsule-based self-healing concrete is applied (White et al. 2001; Wang et al. 2014; Dong et al. 2016). In this case, when single crack in the material is healed, strengthening of the this material will take place which is reflected by one single large value of h_s. The second mechanism concerns the super healing of a material that is damaged with multiple cracks. In this case, the super healing variable takes small values ($h_s \geq 1$). This mechanism can be found, for instance, when multiple cracks appear in concrete. This mechanism is known by the dependency of the value of h_s with the number of cracks that are subjected to healing. Therefore, we denote n the number of super healing variables. It should be noted that only one constant value of the super healing is considered at every point (crack) in the material.

The single and multiple super healing mechanisms are formulated in the present work. The authors will show that the super healing variable h_s can take non-integer values. It is in the proposed theory assumed that same material used for self-healing is used for super healing. The present work does not intend to characterize the material of super healing but rather to highlight the concept and possible exploitation of the proposed theory. It is hoped that this material will find place in the industry in the future.

The multiple super healing mechanisms are proposed such that the super healing variable h_s is active at the same time in different points, and it takes the same values of 1, 2, 3, . . ., x which increases through $x + 1$. In this case, small values of the super healing parameter h_s are considered, while large values are considered for single super healing mechanism with the assumption that $n = 0$. To describe these mechanisms, the following expression is proposed:

$$\overline{\sigma} = \frac{\sigma}{1 + [h_s(n+1) - 1]\varphi} \tag{9}$$

The super healing material is characterized by the variable h_s ($h_s \geq 1$). n represents the number of the super healing variables that are active in the material at the same time. From Eq. (9), one can observe that the effective stress approaches zero when the number of the super healing parameters n approaches infinity, which is irrespective of the damage and super healing variables. This reflects the behavior of the material which enhances mechanical properties due to strengthening application. This first characteristic of the proposed theory is in accordance with the strengthening theory applied on materials (Choi 2014).

From Eq. (2), it is seen that the effective stress goes to infinity indicating material failure when the damage variable $\varphi = 1$. In contrast, using Eq. (9), the effective stress retains a finite value. This can be explained by the fact the effect of super healing voids rupture in the material even though damage is high. This is due to the enhancement of material stiffness.

According to the proposed multiple super healing concepts, the healing variable h in Eq. (3) is replaced with a resultant super healing variable h_r. h_r represents the sum of multiple super healing variables as follows:

$$h_r = h_1 + h_2 + h_3 + \ldots + h_{n+1} \tag{10}$$

Using Eqs. (10) and (3) becomes:

$$\overline{\sigma} = \frac{\sigma}{1 - \varphi(1 - h_1 - h_2 - h_3 - \cdots - h_{n+1})} \tag{11}$$

One should note that the single super healing mechanisms can be described by Eq. (11) with setting $n = 0$. In the case of this mechanism, the super healing is represented by single large values of h_r. One should also note that not only the values of 1 and 2 can be considered rather any value. It is supposed that the multiple super healing mechanisms are active at the same time with the same value of 1. If the value of 1 is substituted into Eq. (11) for each super healing variable, Eq. (9) of the super healing will be obtained.

Anisotropic Formulation of Linear Super Healing Mechanics

In this section, anisotropic generalization of the refined super healing theory is presented. Damage is presented by tensors as capital letters in the form of matrices in the case of anisotropic formulation.

We denote Hs the fourth-rank super healing tensor which represent the anisotropic generalization of the super healing variable h_r. The same notation of the fourth-rank damage tensor is used as presented above. According to the proposed theory, the norm of the fourth-rank super healing tensor exceeds the limit of complete healing which becomes greater than the norm of the fourth-rank identity tensor I ($\|Hs\| \geq \|I\|$). I represents the state of compete healing ($\|Hs\| = \|I\|$) which is 1 in the case of isotropic materials Eq. (3). Following Eq. (10) and similarly to the isotropic formulation, the components of the multiple fourth-rank healing tensors increase through $(n + 1)I_{ijkl}$ ($Hs1_{ijkl}$, $Hs2_{ijkl}$, $Hs3_{ijkl}$, $(n + 1)Hs_{ijkl}$) and evolve at the same time. On set $n = 0$, the case of single super healing mechanism and large values of the fourth-rank super healing tensor Hs are considered. The following expression is considered in the case of anisotropic generalization of Eq. (9):

$$\overline{\sigma}_{ij} = \left[M^{-1}_{ijkl} + (n+1)Hs^{-1}_{ijmn} : \left(I_{mnkl} - M^{-1}_{mnkl}\right)\right]^{-1} \sigma_{kl} \tag{12}$$

From Eq. (12), one can see that the effective stress approaches zero when the number of healing variables n or Hs goes to infinity. One should note that in reality, this assumption is not reached, but large values of n and Hs can be supposed which

minimize the effective stress due to the strengthening of the material comparing to initial material.

Plane Stress Example of the Refined Super Healing

In this section, an example of plane stress is applied on the proposed refined theory of super healing based on CDHM. Plane stress considers x and y directions, and the stress components σ_{13}, σ_{23}, and σ_{33} vanish ($\sigma_{13} = \sigma_{23} = \sigma_{33} = 0$). Therefore, the matrix presentation of the tensor in Eq. (12) is defined as follows (Voyiadjis and Kattan 1999):

$$\{\sigma\} = \begin{Bmatrix} \sigma_{11} \\ \sigma_{22} \\ \sigma_{12} \end{Bmatrix} \tag{13}$$

$$\{\overline{\sigma}\} = \begin{Bmatrix} \overline{\sigma}_{11} \\ \overline{\sigma}_{22} \\ \overline{\sigma}_{12} \end{Bmatrix} \tag{14}$$

$$I = \begin{bmatrix} 1 & 0 & 0 \\ 0 & 1 & 0 \\ 0 & 0 & 1 \end{bmatrix} \tag{15}$$

$$M = \frac{1}{\Delta} \begin{bmatrix} \psi_{22} & 0 & \varphi_{12} \\ 0 & \psi_{11} & \varphi_{12} \\ \frac{\varphi_{12}}{2} & \frac{\varphi_{12}}{2} & \frac{\psi_{11} + \psi_{22}}{2} \end{bmatrix} \tag{16}$$

where $\psi_{11} = 1 - \varphi_{11}$ and $\psi_{22} = 1 - \varphi_{22}$. Voyiadjis and Kattan (1999) defined the denominator Δ as:

$$\Delta = \psi_{11}\psi_{22} - \varphi_{12}^2 \tag{17}$$

Next, we define the super healing matrix of Eq. (9) using plane stress example. One should note that the same definition of self-healing matrix is followed to define the super healing matrix. On the other hand, the components of the healing matrix are lower than the components of the super healing matrix. Equation (7) can be expressed as Voyiadjis et al. (2011b):

$$\overline{\sigma}_{ij} = Q_{ijkl}\sigma_{kl} \tag{18}$$

Q_{ijkl} represents the fourth-rank damage-healing transformation tensor. After comparison of Eq. (7) with Eq. (8), one obtains:

$$Q_{ijkl} = \left(M_{ijkl}^{-1} + \left(I_{ijmn} - M_{ijmn}^{-1}\right)H_{mnkl}^{-1}\right)^{-1} \tag{19}$$

Equating the real and effective material states using the hypothesis of elastic energy equivalence leads to the following expression:

$$Q_{ijuw}Q_{klpq} = \left(h_{mnij}E_{klmn}^{d} + E_{klij}^{d}\right)\overline{E}_{uwpq}^{-1} \tag{20}$$

h_{ijkl}, E_{ijkl}^{d}, and $\overline{E}_{ijkl}$ represent, respectively, the fourth-rank healing variable tensor, damaged elastic modulus, and the effective elastic modulus. M_{ijkl} and H_{ijkl} are defined as (Voyiadjis et al. 2011b):

$$M_{ijkl} = \left[\left(I_{ij} - \varphi_{ij}\right)\left(I_{kl} - \varphi_{kl}\right)\right]^{-1/2} \quad \text{and} \quad H_{ijkl} = \left[h_{ij}h_{kl}\right]^{-1/2} \tag{21}$$

From Eq. (9), one substitutes Q_{ijkl} in Eq. (20) and finds:

$$\begin{aligned}&\left(M_{ijuw}^{-1} + \left(I_{ijmn} - M_{ijmn}^{-1}\right)H_{mnuw}^{-1}\right)^{-1}\left(M_{klpq}^{-1} + \left(I_{klmn} - M_{klmn}^{-1}\right)H_{mnpq}^{-1}\right)^{-1}\\ &= \left(h_{mnij}E_{klmn}^{d} + E_{klij}^{d}\right)\overline{E}_{uwpq}^{-1}\end{aligned} \tag{22}$$

Next, one obtains the following expression of the effective elastic modulus (Voyiadjis and Kattan 1992):

$$\overline{E}_{uwpq} = M_{ijuw}^{-1}E_{ijkl}^{d}M_{klpq}^{-T} \tag{23}$$

$-T$ represents the transpose of the inverse of the tensor. The relationship between the second- rank damage and healing variable tensors, φ_{ij} and h_{ij}, and the fourth-rank damage and healing tensors, φ_{ijkl} and $h_{ijkl,}$ is obtained by substituting M_{ijkl} and H_{ijkl} from Eq. (21) into Eq. (22). One set of the damage-healing variable is obtained by knowing the other set of Eq. (22). The super healing matrix of plane stress example is obtained as:

$$Hs^{-1} = \begin{bmatrix} hs_{11} & 0 & hs_{12} \\ 0 & hs_{22} & hs_{12} \\ hs_{12} & hs_{12} & \dfrac{hs_{11} + hs_{22}}{2} \end{bmatrix} \tag{24}$$

One should note that the same form of the inverse super healing and damage matrices is used in Eqs. (24) and (16), respectively. The relation of the effective stress is obtained by substituting Eqs. (13) to (24) into Eq. (12) as follows:

$$\{\sigma\} = [A]\{\overline{\sigma}\} \tag{25}$$

After simplification, the fourth-rank tensor $[A]$ is obtained using MATLAB Symbolic Math Toolbox as follows:

$$A_{11} = \big(3\varphi_{11} + \varphi_{22} - \varphi_{11}\varphi_{22} - \varphi_{11}^2 + \varphi_{12}^2 - \varphi_{12}^2 hs_{11}(n+1) + \varphi_{11} hs_{11}(n+1) (\varphi_{11} + \varphi_{22} - 2) + \varphi_{12} hs_{12}(\varphi_{11} + 1)(n+1) - 2)/(\varphi_{11} + \varphi_{22} - 2) \tag{26a}$$

$$A_{12} = (\varphi_{12}(\varphi_{12} hs_{11} - hs_{12} - \varphi_{12} + \varphi_{12} hs_{12} - nhs_{12} + n\varphi_{12} hs_{11} + n\varphi_{22} hs_{12}))/ (\varphi_{11} + \varphi_{22} - 2) \tag{26b}$$

$$A_{13} = (2\varphi_{12} hs_{11}(\varphi_{11} - 1)(n+1)(\varphi_{11} + \varphi_{22} - 2) - (n+1) hs_{12}(\varphi_{11} + \varphi_{22} - 2\varphi_{11}\varphi_{22}) - 2\varphi_{12}(\varphi_{11} - 1))/(\varphi_{11} + \varphi_{22} - 2) \tag{26c}$$

$$A_{21} = (\varphi_{12}(\varphi_{11} hs_{12} - hs_{12} - \varphi_{12} + \varphi_{12} hs_{22} - nhs_{12} + n\varphi_{11} hs_{12} + n\varphi_{12} hs_{22}))/ (\varphi_{11} + \varphi_{22} - 2) \tag{26d}$$

$$A_{22} = \big(\varphi_{11} + 3\varphi_{22} - \varphi_{11}\varphi_{22} + \varphi_{22}^2 - \varphi_{12}^2 - \varphi_{12}^2 hs_{22}(n+1) + \varphi_{22} hs_{22}(n+1) (\varphi_{11} + \varphi_{22} - 2) + \varphi_{12} hs_{12}(\varphi_{22} - 1)(n+1) - 2)/(\varphi_{11} + \varphi_{22} - 2) \tag{26e}$$

$$A_{23} = (2(n+1)\varphi_{12} hs_{22}(\varphi_{22} - 1) - (n+1) hs_{12}(\varphi_{11} + \varphi_{22} - 2\varphi_{11}\varphi_{22} - 2\varphi_{12}(\varphi_{22} - 1))/ (\varphi_{11} + \varphi_{22} - 2) \tag{26f}$$

$$A_{31} = (n+1)\varphi_{11} hs_{12} + (\varphi_{12}(\varphi_{11} - 1)(hs_{11} + hs_{22} + nhs_{11} + nhs_{22} - 2))/ (2(\varphi_{11} + \varphi_{22} - 2)) \tag{26g}$$

$$A_{32} = (n+1)\varphi_{22} hs_{12} + (\varphi_{12}(\varphi_{22} - 1)(hs_{11} + hs_{22} + nhs_{11} + nhs_{22} - 2))/ (2(\varphi_{11} + \varphi_{22} - 2)) \tag{26h}$$

$$A_{33} = -(4(2\varphi_{11} - 1)(\varphi_{22} - 1) - 4\varphi_{12} hs_{12}(\varphi_{11} - 1)(n+1) - 4\varphi_{12} hs_{12}(\varphi_{22} - 1)(n+1) + ((hs_{11} + hs_{22})(n+1)(\varphi_{11} + \varphi_{22} - 2)(\varphi_{11} + \varphi_{22} - 2\varphi_{11}\varphi_{22}))/2)/ (2(\varphi_{11} + \varphi_{22} - 2)) \tag{26i}$$

Next, Equation (26) is simplified, and the principal components $\varphi_{12} = \varphi_{21} = 0$ and $hs_{12}\, hs_{21} = 0$ are considered. Then, the simplified equations are substituted into Eq. (25), and the following expressions are obtained after simplification:

$$\overline{\sigma}_{11} = \frac{\sigma_{11}}{1 + [hs_{11}(n+1) - 1]\varphi_{11}} \tag{27}$$

$$\overline{\sigma}_{22} = \frac{\sigma_{22}}{1 + [hs_{22}(n+1) - 1]\varphi_{22}} \tag{28}$$

$$\overline{\sigma}_{12} = \frac{\sigma_{12}}{\frac{-4(\varphi_{11}-1)(\varphi_{22}-1)-(hs_{11}+hs_{22})(n+1)(\varphi_{11}+\varphi_{22}-2\varphi_{11}\varphi_{22})}{2(\varphi_{11}+\varphi_{22}-2)}} \tag{29}$$

From Eqs. (27) and (28), one can see that damage and super healing equations reduce to the scalar formulation Eq. (9) using plane stress example. Consequently, the applicability of plane stress example on the proposed super healing theory is confirmed. Next, the authors consider a special case of similarity of damage and super healing in x and y directions. In this case, it is assumed that $\varphi_{11} = \varphi_{22}$ and $hs_{11} = hs_{22}$ in Eq. (29). One obtains the following expression after algebraic manipulations:

$$\overline{\sigma}_{22} = \frac{\sigma_{22}}{1 + [hs_{22}(n+1) - 1]\varphi_{22}} \tag{30}$$

From Eq. (29), one can see that it becomes similar to Eq. (28) when damage and super healing are similar in both directions. It is concluded that the super healing theory is applicable in the case of plane stress.

One-Dimensional Example

In this section, the authors will apply the proposed super healing theory on one-dimensional example based on CDHM. In Fig. 5, the strain history applied on the 1-D example is shown. Loading is first applied on the element until 0.005 of strain. It is followed by unloading until zero strain and reloaded again. Damage appears during loading phase until failure and becomes constant during unloading. The healing is introduced during the unloading phase when damage is deactivated ($\dot{\varphi} = 0$). After the end of the healing process, the element is reloaded, and the healing efficiency is analyzed. The behavior of the fully healed material should be similar to the behavior of the original, and similarity between the healed elastic modulus and effective elastic modulus is obtained ($E_{fh} = E_0$). On the other hand, similarity between the healed elastic modulus and damaged elastic modulus is obtained when the material is not healed ($E_h = E_\varphi$).

Recovery of material stiffness is reached when the material is subjected to self-healing process. In Fig. 6, the authors present the healing efficiency with the an assumption of healing variables $h = 0.5$ and $h = 0.99$. This figure illustrates the

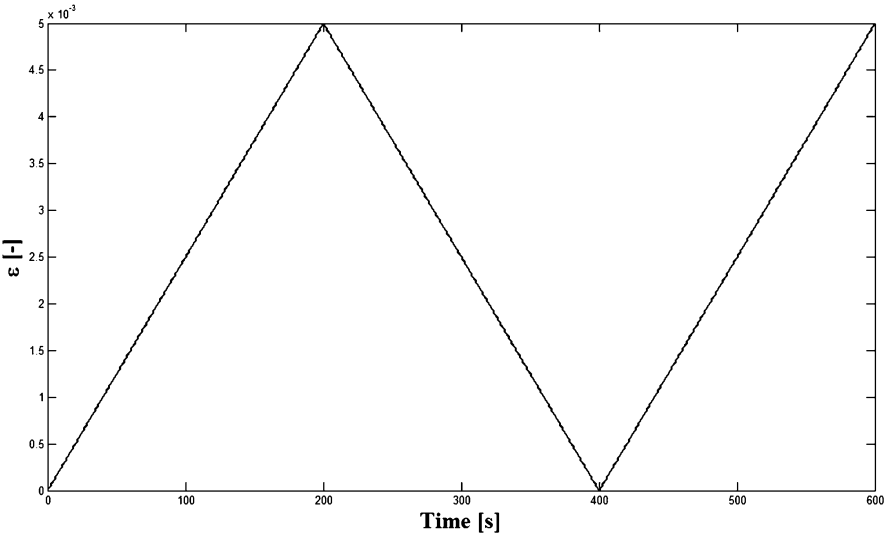

Fig. 5 Strain history

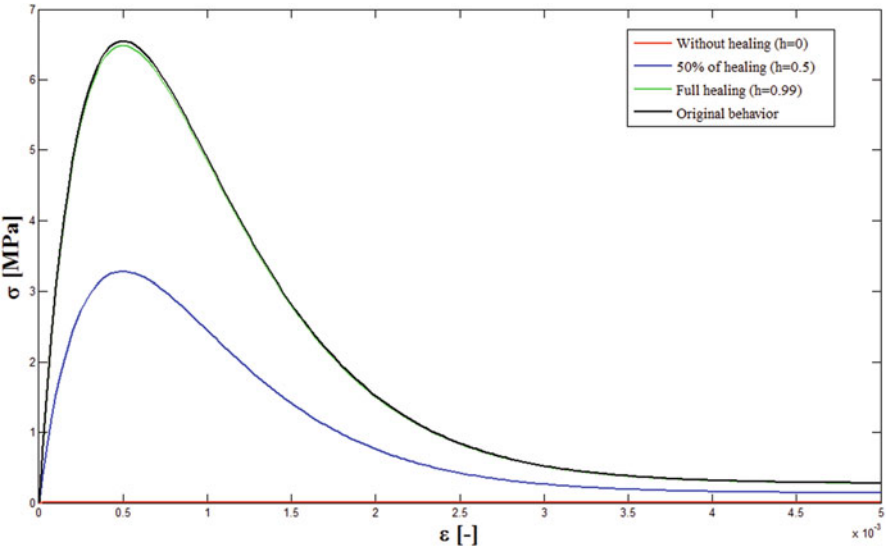

Fig. 6 Effect of self-healing mechanism

behavior of the unhealed material ($h = 0$) in red curve. The introduction of the healing with $h = 0.5$ results in the recovery of material stiffness (blue curve), and with $h = 0.99$ results in complete recovery of the material stiffness (green curve), while the original behavior of the material is represented with the black curve.

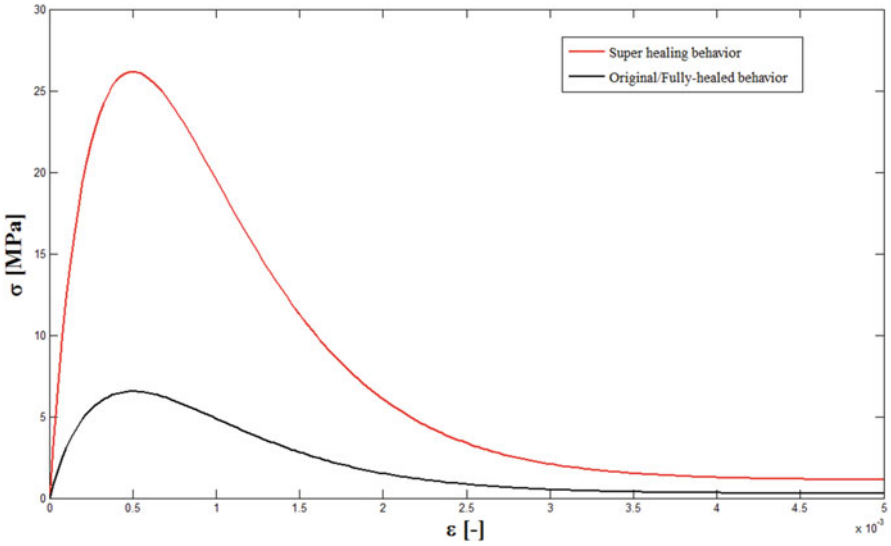

Fig. 7 Effect of refined super healing mechanism

In Fig. 7, the super healing behavior is shown according to Eq. (9). The authors assume as an example of multiple super healing mechanisms that the super healing variable $h_s = 1$ and the number of super healing parameters $n = 3$. From this figure, it is seen that the material enhances its stiffness due to the super healing effect. The authors should note that this example only highlights theoretically the proposed framework. A realistic example can be applied using microcapsule-based super healing concrete with choosing an appropriate healing agent. When the microcapsules are broken by damage evolution, the healing agent releases from the microcapsule and reacts with the catalyst. Afterward, the cracks are filled, and the healing agent is solidified in the crack area. In the present work, it is supposed that the same healing agent when it reacts with appropriate chemical components forms the super healing material and becomes a strengthening material. This process will result in high material stiffness comparing to the stiffness of the healed and original materials. It is hoped that the present investigation will be exploited in the future along the lines of the proposed super healing theory.

Generalized Nonlinear Super Healing

Voyiadjis and Kattan (2016) were the first who introduced the nonlinear self-healing theory. The classical (linear) self-healing theory is presented in Eq. (9). The present section introduces the nonlinear generalized super healing model and compares it with the linear refined super healing model. φ_{sd} of Eq. (9) is denoted the combined super healing damage variable which can be expressed as:

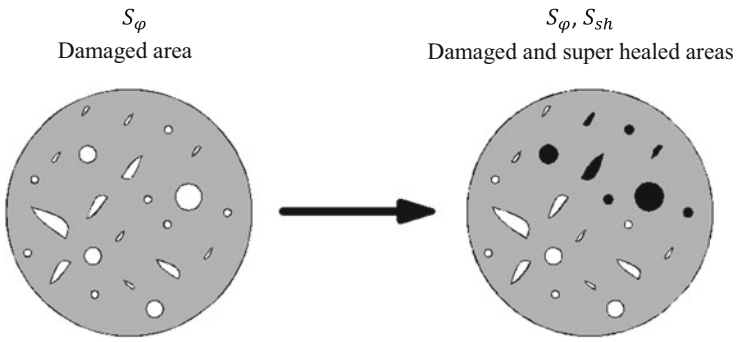

Fig. 8 Nonlinear super healing representation

$$\varphi_{sd} = [1 - h_s(n+1)]\varphi \tag{31}$$

Then, one can rewrite Eq. (9) as:

$$\overline{\sigma} = \frac{\sigma}{1 - \varphi_{sd}} = \frac{\sigma}{1 - [1 - h_s(n+1)]\varphi} \tag{32}$$

One should note that Eq. (32) describes the linear super healing model due to the linearity of the combined super healing/damage variable φ_{sd} in h_s. Voyiadjis and Kattan (2016) demonstrated in their work that the nonlinear healing model is robust in terms self-healing characterization. Thus, the same result is expected in the case of generalized nonlinear super healing model. It is also revealed that the linear generalized healing model represents a special case of the nonlinear generalized healing model when damage variable is small.

In Fig. 8, the geometric representation of the nonlinear super healing model is illustrated. In the left part of the figure, damaged material state is presented with its classical damage variable φ, while in the right part, the super healed material state is shown with less super healed area S_{sh} comparing to the damaged area S_φ. In accordance with the nonlinear healing theory, only a partial region of the damaged area is considered for healing and super healing processes.

The following derivation of the nonlinear super healing theory follows the derivation presented in (Voyiadjis and Kattan 2016). The following expression of the decomposed damage variable is proposed (Voyiadjis and Kattan 2012b):

$$\varphi = \varphi_1 + \varphi_2 - \varphi_1\varphi_2 \tag{33}$$

where φ_1 and φ_2 represent the damage variables of two damage processes acting in series following each other. For more details, the reader can refer to (Voyiadjis and Kattan 2012a).

Next, one introduces the super healing variable $h_s(n + 1)$ following the conditions:

$$\varphi_1 = h_s(n+1)\varphi \tag{34}$$

$$\varphi_2 = \varphi_{sd} \tag{35}$$

where first and second stages of super healing are represented, respectively, in Eqs. (34) and (35). Equations (34) and (35) are substituted into Eq. (33), and the following expression is obtained:

$$\varphi = h_s(n+1)\varphi + \varphi_{sd} - h_s(n+1)\varphi\varphi_{sd} \tag{36}$$

The expression of the combined super healing/damage variable can be extracted from Eq. (36) as:

$$\varphi_{sd} = \frac{\varphi[1 - h_s(n+1)]}{1 - h_s(n+1)\varphi} \tag{37}$$

Comparing Eqs. (31) and (37), the later represents nonlinear super healing model due to the nonlinearity of φ_{sd} in $h_s(n+1)$. The boundary conditions of Eq. (37) are presented in Table 1.

Now, the authors will show that the super healing model represents a special case of the nonlinear super healing model. Equation (37) is used to define the nonlinear expression of the effective stress as follows:

$$\overline{\sigma} = \frac{\sigma[1 - h_s(n+1)\varphi]}{1 - \varphi} \tag{38}$$

Next, the Taylor series expansion around the point $h_s(n+1)\varphi = 0$ is calculated:

$$\frac{1}{1 - h_s(n+1)\varphi} = 1 + h_s(n+1)\varphi + h_s^2(n+1)^2\varphi^2 + h_s^3(n+1)^3\varphi^3 + \ldots. \tag{39}$$

Then, one takes only the first two terms of the right-hand side series from Eq. (39) and substitutes them into Eq. (37). The following expressions are obtained:

$$\varphi_{sd} = \varphi(1 - h_s(n+1))(1 + h_s(n+1)\varphi) \tag{40}$$

After simplification of Eq. (40), one obtains:

$$\varphi_{sd} = \varphi(1 - h_s(n+1)) + \varphi^2 h_s(n+1)(1 - h_s(n+1)) \tag{41}$$

Table 1 Boundary conditions of Eq. (37)

	Zero healing	Complete healing	Super healing
φ	>0	0	0
h_s	0	1	>1
n	0	0	>1
φ_{sd}	φ	0	$>\varphi$

If the quadratic term in φ is ignored from the right-hand side of Eq. (41), one obtains:

$$\varphi_{sd} = \varphi[1 - h_s(n+1)] \tag{42}$$

One can clearly see that Eq. (42) is similar to the expression of the combined super healing/damage variable defined in Eq. (31). One can conclude that when damage is small, the linear super healing theory represents a special case of the nonlinear super healing theory.

Quadratic Super Healing

In this section, the authors investigate the quadratic super healing theory as a special case of the generalized nonlinear super healing. One can rewrite Eq. (31) as follows:

$$\varphi_{sd} = \varphi - h_s(n+1)\varphi \tag{43}$$

One should note that the super healed damage part subtracted from φ is represented by $h_s(n+1)\varphi$. Equation (37) is rewritten using the Taylor series expansion as follows:

$$\begin{aligned}\varphi_{sd} &= \varphi(1 - h_s(n+1)) \\ &\times \left(1 + \varphi h_s(n+1) + \varphi^2 h_s^2(n+1)^2 + \varphi^3 h_s^3(n+1)^3 + \ldots.\right)\end{aligned} \tag{44}$$

Again, the only first two terms of the right-hand side are considered. Therefore, Eq. (44) becomes:

$$\varphi_{sd} = (\varphi - h_s(n+1)\varphi)(1 + \varphi h_s(n+1)) \tag{45}$$

Equation (45) can be expanded and rewritten as follows:

$$\varphi_{sd} = (\varphi - h_s(n+1)\varphi) + \left(h_s(n+1)\varphi^2 - h_s^2(n+1)^2\varphi^2\right) \tag{46}$$

The quadratic super healing theory is represented in Eq. (46). It is clear that the combined super healing/damage variable φ_{sd} is a quadratic function of the parameter $h_s(n+1)$. φ_{sd} consists of two parts. The first part represents the linear damage part with zero super healing ($(\varphi - h_s(n+1)\varphi)$), while the second part represents the quadratic damage with zero super healing $\left(\left(h_s(n+1)\varphi^2 - h_s^2(n+1)^2\varphi^2\right)\right)$. Using Eq. (45), one write the effective stress expression of the quadratic super healing theory as follows:

$$\overline{\sigma} = \frac{\sigma}{1 - (\varphi - h_s(n+1)\varphi)(1 + \varphi h_s(n+1))} \tag{47}$$

Anisotropic Formulation of Nonlinear Super Healing

In this section, the anisotropic formulation is generalized using Eq. (38). Therefore, tensors are used instead of scalars following the same notations used above. The anisotropic formulation of Eq. (38) is expressed as follows:

$$\{\overline{\sigma}\} = [M]\Big([I] - (n+1)\Big([I] - [M]^{-1}\Big)[Hs]^{-1}\Big)\{\sigma\} \tag{48}$$

where $\{\overline{\sigma}\}$ and $\{\sigma\}$ are the effective and nominal stress tensors, respectively. One should note that the same assumption of the self-healing is considered for super healing such that $[M] = \frac{1}{1-\varphi}$, $[Hs] = \frac{1}{hs}$ and $[I] = 1$.

Equation (47) of the quadratic super healing is written in anisotropic form as follows:

$$\{\overline{\sigma}\} = \Big[[I] - \Big([I] - [M]^{-1}\Big)\Big([I] - (n+1)[Hs]^{-1}\Big)\Big([I] + (n+1)\Big([I] - [M]^{-1}\Big)[Hs]^{-1}\Big]^{-1}\{\sigma\} \tag{49}$$

Plane Stress Example of the Generalized Nonlinear Super Healing Theory

In this section, the authors apply the plane stress case on the generalized nonlinear super healing theory. The same conditions of plane stress case applied on the linear refined super healing theory are considered in this section ($\sigma_{13} = \sigma_{23} = \sigma_{33} = 0$). In addition, the vectors and matrices used in this section are similar to the ones used in Eq. (13) and (24). These equations are substituted into Eq. (48), and the following expression is found:

$$\{\overline{\sigma}\} = [B]\{\sigma\} \tag{50}$$

The components of the fourth-rank tensor $[B]$ are obtained using MATLAB Symbolic Math Toolbox as follows:

$$B_{11} = (\varphi_{22} + hs_{11} - \varphi_{22}hs_{11} + nhs_{11} + \varphi_{12}(hs_{12} + nhs_{12}) - n\varphi_{22}hs_{11} + (n+1)hs_{11} \big(\varphi_{12}^2 + \varphi_{22} - \varphi_{11}(\varphi_{22} - 1) - 1\big) - 1\big)/\big(\varphi_{12}^2 + \varphi_{22} - \varphi_{11}(\varphi_{22} - 1) - 1\big) \tag{51a}$$

$$B_{12} = ((n+1)\varphi_{12}hs_{12})/\big(\varphi_{12}^2 + \varphi_{11} - \varphi_{22}(\varphi_{11} - 1) - 1\big) \tag{51b}$$

$$B_{13} = (n+1)hs_{12} + (hs_{12} + \varphi_{12}(hs_{11}/2 + hs_{22}/2 + nhs_{11}/2 + nhs_{22}/2 - 1) - \varphi_{22}hs_{12} + nhs_{12} - n\varphi_{22}hs_{12})/\big(\varphi_{12}^2 + \varphi_{22} - \varphi_{11}(\varphi_{22} - 1) - 1\big) \tag{51c}$$

$$B_{21} = ((n+1)\varphi_{12}hs_{12})/\left(\varphi_{12}^2 + \varphi_{11} - \varphi_{22}(\varphi_{11}-1) - 1\right) \tag{51d}$$

$$\begin{aligned} B_{22} =& (\varphi_{11} + hs_{22} - \varphi_{11}hs_{22} + nhs_{22} + \varphi_{12}(hs_{12} + nhs_{12}) - n\varphi_{11}hs_{22} + (n+1)hs_{22} \\ & \left(\varphi_{12}^2 + \varphi_{11} - \varphi_{22}(\varphi_{11}-1) - 1\right) - 1\big)/\left(\varphi_{12}^2 + \varphi_{11} - \varphi_{22}(\varphi_{11}-1) - 1\right) \end{aligned} \tag{51e}$$

$$\begin{aligned} B_{23} =& (n+1)hs_{12} + (hs_{12} + \varphi_{12}(hs_{11}/2 + hs_{22}/2 + nhs_{11}/2 + nhs_{22}/2 - 1) \\ & -\varphi_{11}hs_{12} + nhs_{12} - n\varphi_{11}hs_{12})/\left(\varphi_{12}^2 + \varphi_{11} - \varphi_{22}(\varphi_{11}-1) - 1\right) \end{aligned} \tag{51f}$$

$$\begin{aligned} B_{31} =& (n+1)hs_{12} - (\varphi_{12}/2 - hs_{12} + (\varphi_{11}hs_{12})/2 - (\varphi_{12}hs_{11})/2 \\ & +(\varphi_{22}hs_{12})/2 - nhs_{12} + (n\varphi_{11}hs_{12})/2 - (n\varphi_{12}hs_{11})/2 \\ & +(\varphi_{22}hs_{12})/2)/\left(\varphi_{12}^2 + \varphi_{11} + \varphi_{22} - \varphi_{11}\varphi_{22} - 1\right) \end{aligned} \tag{51g}$$

$$\begin{aligned} B_{32} =& (n+1)hs_{12} - ((\varphi_{11}hs_{12})/2 - \varphi_{12}(hs_{12}/2 + (nhs_{22})/2 - 1/2) \\ & -hs_{12} + (\varphi_{22}hs_{12})/2 - nhs_{12} + (n\varphi_{11}hs_{12})/2 \\ & +(n\varphi_{22}hs_{12})/2)/\left(\varphi_{12}^2 + \varphi_{11} + \varphi_{22} - \varphi_{11}\varphi_{22} - 1\right) \end{aligned} \tag{51h}$$

$$\begin{aligned} B_{33} =& ((hs_{11} + hs_{22})(n+1))/2 - \big((\varphi_{11}hs_{11}/4 - \varphi_{22}/2 - hs_{11}/2 - hs_{22}/2 - \varphi_{11}/2 \\ & + (\varphi_{11}hs_{22})/4 + (\varphi_{22}hs_{11})/4 + + (\varphi_{22}hs_{22})/4 - (nhs_{11})/2 - (nhs_{22})/2 \\ & - \varphi_{12}(hs_{12} + nhs_{12}) + (n\varphi_{11}hs_{11})/4 + (n\varphi_{11}hs_{22})/4 + (n\varphi_{22}hs_{11})/4 \\ & +(n\varphi_{22}hs_{22})/4 + 1)/\left(\varphi_{12}^2 + \varphi_{11} + \varphi_{22} - \varphi_{11}\varphi_{22} - 1\right) \end{aligned} \tag{51i}$$

Next, the special case of principal components is considered. The authors set $\varphi_{12} = \varphi_{21} = 0$ and $hs_{12} = hs_{21} = 0$. After substituting Eq. (51) into Eq. (50) with algebraic manipulation, the following expressions are obtained:

$$\overline{\sigma}_{11} = \frac{\sigma_{11}[1 - hs_{11}(n+1)\varphi_{11}]}{1 - \varphi_{11}} \tag{52}$$

$$\overline{\sigma}_{22} = \frac{\sigma_{22}[1 - hs_{22}(n+1)\varphi_{22}]}{1 - \varphi_{22}} \tag{53}$$

$$\begin{aligned} \bar{\sigma}_{12} =& \sigma_{12}\big[(hs_{11}/4 + hs_{22}/4 + (nhs_{11})/4 + (nhs_{22})/4 - 1/2)/\big((\varphi_{11} - 1) \\ & - (hs_{11} + hs_{22} - 2\varphi_{22}hs_{11} - 2\varphi_{22}hs_{22} + nhs_{11} + nhs_{22} + 2n\varphi_{22}hs_{11} \\ & -2n\varphi_{22}hs_{22} + 2)/(4(\varphi_{22} - 1))\big] \end{aligned} \tag{54}$$

One can see that Eqs. (52) and (53) reduce to the expression of scalar formulation in Eq. (38). This confirms the applicability of the generalized nonlinear super healing theory in plane stress.

Next, a special case of similarity of damage and super healing in x and y directions is considered ($\varphi_{11} = \varphi_{22}$ and $hs_{11} = hs_{22}$). The following expression is obtained after algebraic manipulation:

$$\overline{\sigma}_{22} = \frac{\sigma_{22}[1 - hs_{22}(n+1)\varphi_{22}]}{1 - \varphi_{22}} \tag{55}$$

It is found that Eqs. (54) and (53) become similar when similarity of damage and super healing variables is considered. This confirms again the applicability of the nonlinear super healing theory in plane stress case.

Plane Stress Example of the Quadratic Super Healing Theory

In this section, the application of the quadratic super healing theory in plane stress case is presented. One should note that a brief presentation of the results is given in this section due to the long expressions of the analytical solutions. One can rewrite Eq. (47) as:

$$\sigma = [1 - (\varphi - h_s(n+1)\varphi)(1 + \varphi h_s(n+1))]\overline{\sigma} \tag{56}$$

Equations (13) to (24) are substituted into Eq. (49), and the following expression is obtained:

$$\{\overline{\sigma}\} = [C]\{\sigma\} \tag{57}$$

Following the same special case considered in the case of generalized nonlinear super healing theory ($\varphi_{12} = \varphi_{21} = 0$ and $hs_{12} = hs_{21} = 0$), and substituting the components of fourth-rank tensor $[C]$ into Eq. (56) along with algebraic manipulation, one finds:

$$\sigma_{11} = [1 - (\varphi_{11} - hs_{11}(n+1)\varphi_{11})(1 + \varphi_{11}hs_{11}(n+1))]\overline{\sigma}_{11} \tag{58}$$

$$\sigma_{22} = [1 - (\varphi_{22} - hs_{22}(n+1)\varphi_{22})(1 + \varphi_{22}hs_{22}(n+1))]\overline{\sigma}_{22} \tag{59}$$

$$\sigma_{12} = \Big[\Big(\Big(\Big(\Big(2\,(\varphi_{22}-1)^2/(\,\varphi_{11}+\varphi_{22}-2)+1\Big)(n+1)(hs_{11}/2+hs_{22}/2)+1\Big)(\,2\varphi_{22}^2 - 3\varphi_{22}+\varphi_{11})((n+1)\,hs_{11}+(n+1)\varphi_{22}\;\;-2))/(2\varphi_{11}+\varphi_{22}-2)) + 1\Big]\bar{\sigma}_{12} \tag{60}$$

It is seen that Eqs. (58) and (59) become similar to the scalar formulation in Eq. (47). This confirms the applicability of the quadratic super healing theory in plane stress case.

Next, the special case of $\varphi_{11} = \varphi_{22}$ and $hs_{11} = hs_{22}$ is also considered in this section. After simplification, the following expression is obtained:

$$\sigma_{22} = [1 - (\varphi_{22} - hs_{22}(n+1)\varphi_{22})(1 + \varphi_{22}hs_{22}(n+1))]\overline{\sigma}_{22} \tag{61}$$

It is found that Eqs. (61) and (59) are similar. This confirms again the applicability of the quadratic super healing theory in plane stress case.

Non-super-Healed Damage Concept

In this section, the authors will show that there is a difference between the linear generalized super healing and nonlinear generalized super healing theories. It can be seen from Eqs. (31) and (37) that the combined super healing/damage variable φ_{sd} becomes equal to zero when the material is undamaged. On the other hand, it becomes equal to $1 - h_s(n + 1)$ when the material is totally damaged in the case of linear super healing theory Eq. (31). However, in the case of generalized super healing theory, it becomes equal to 1 irrespective to the super healing parameter. This is explained by the fact that a part of damaged region is neither healed nor super healed remains in the material, which represents the main feature of the nonlinear super healing theory. Before complete failure of the material, the process of super healing needs to be completed. Therefore, an assumption is adopted so that the complete super healing should occur before failure of material ($\varphi < 1$). Therefore, the authors modify Eq. (31) so that damage is not subjected to super healing. This modification is applied on nonlinear super healing theory and expressed as:

$$\varphi_{sd} = [1 - h_s(n+1) + \alpha h_s(n+1)]\varphi \tag{62}$$

where α is the non-super-healed damage parameter. Equations (62) and (31) become similar when α is equal to zero. However, the material contains non-super-healed damage areas when $\alpha \neq 0$.

Comparative Analysis of Super Healing Models

Comparison of linear (LSH), generalized nonlinear (NSH), and quadratic (QSH) super healing equations is summarized in Table 2. The ratios $\frac{\varphi_{sd}}{\varphi}$ and $\frac{\overline{\sigma}}{\sigma}$ are used to show the comparison.

The ratios $\overline{\sigma}/\sigma$ are plotted for each super healing model in Fig. 9. Both self-healing and super healing domains are illustrated, respectively, in Figs. 9a, b. In order to plot the ratios for comparison, the authors use an example of damage variable $\varphi = 0.5$ and super healing variable $h_s = 1$ with $n = 3$. From Fig. 9a, one can see that the ratio $\overline{\sigma}/\sigma = 2$ when the material is unhealed ($h_s(n + 1) = 0$). This phase represents the damaged state of the material in which the effective stress is greater than the nominal stress. The upper limits of self-healing and super healing parameters are, respectively, 1 and 4. It is also observed that the nonlinear healing models overestimate the ratio $\overline{\sigma}/\sigma$ comparing to the linear healing model. In addition, the generalized nonlinear healing model overestimated the ratio $\overline{\sigma}/\sigma$

Table 2 Comparison between super healing models

Super healing model	$\frac{\varphi_{sd}}{\varphi}$	$\frac{\overline{\sigma}}{\sigma}$
LSH	$\frac{\varphi_{sd}}{\varphi} = 1 - h_s(n+1)$	$\frac{\overline{\sigma}}{\sigma} = \frac{1}{1-[1-h_s(n+1)]\varphi}$
NSH	$\frac{\varphi_{sd}}{\varphi} = \frac{1-h_s(n+1)}{1-\varphi h_s(n+1)}$	$\frac{\overline{\sigma}}{\sigma} = \frac{1-h_s(n+1)\varphi}{1-\varphi}$
QSH	$\frac{\varphi_{sd}}{\varphi} = 1 - h_s(n+1) + \varphi h_s(n+1) - \varphi h_s^2(n+1)^2$	$\frac{\overline{\sigma}}{\sigma} = \frac{1}{1-\left[1-h_s(n+1)+\varphi h_s(n+1)-\varphi h_s^2(n+1)^2\right]\varphi}$

comparing to the quadratic healing model. On the other hand, it is found that all the models meet at one point in the case of complete healing ($h_s(n + 1) = 1$). At this point, the effective and nominal stresses become equal ($h_s(n + 1) = 1$). One can conclude that the healing concept can be described appropriately by all the three models with which the healing variable varies from 0 to 1 and is represented by ($h_s(n + 1) = 1$) with setting $n = 0$.

Figure 9b illustrates the comparison of linear, generalized nonlinear, and quadratic super healing models. Similar to the previous example, the super healing variables take values from 1 to 4. From Fig. 9b, one can see that the results of the ratio $\overline{\sigma}/\sigma$ in linear and quadratic super healing models are, respectively, 0.4 and 0.18 corresponding to the values $\varphi = 0.5$ and $h_s(n + 1) = 4$. One can observe that the quadratic super healing model underestimates the ratio $\overline{\sigma}/\sigma$ comparing to the linear super healing model. One can say that the quadratic super healing model overestimates the healing efficiency. From the same figure, the ratio $\overline{\sigma}/\sigma$ approaches zero in the case of generalized nonlinear super healing model when the value of the super healing parameter is low. It is found that the ratio $\overline{\sigma}/\sigma$ vanishes with $h_s(n + 1) = 2$. It also observed that the ratio $\overline{\sigma}/\sigma$ approaches zero in a different value of super healing variable.

From Fig. 9b, it is also observed that the minimum ratios of linear and quadratic super healing models are reached by the generalized nonlinear super healing model with, respectively, the super healing variables 1.6 and 1.82. It is concluded that the healing efficiency is overestimated by the generalized nonlinear super healing model comparing to the linear and quadratic models with, respectively, a difference of 25% and 9.9%. One should note that Eqs. (9) and (38) are used to plot the curves of linear and nonlinear healing and super healing models, respectively. The nonlinear models are shown as straight lines because of the assumption that of the decomposition of damage variable to nominal damage and combined super-healing-damage variables Eqs. (33), (34), and (35). This is clearly shown in Table 2 in which the ratio φ_{sd}/φ is linear in the case of linear super healing model and nonlinear in the case of nonlinear super healing model.

In the following, the authors will investigate the maximum difference between the super healing models using the first derivative and difference function. The ratio φ_{sd}/φ will be used to calculate the difference.

R is denoted the super healing parameter ($R = h_s(n + 1)$), and $f_1(R)$ is denoted the difference function between the linear and generalized nonlinear super healing models. $f_1(R)$ is written as:

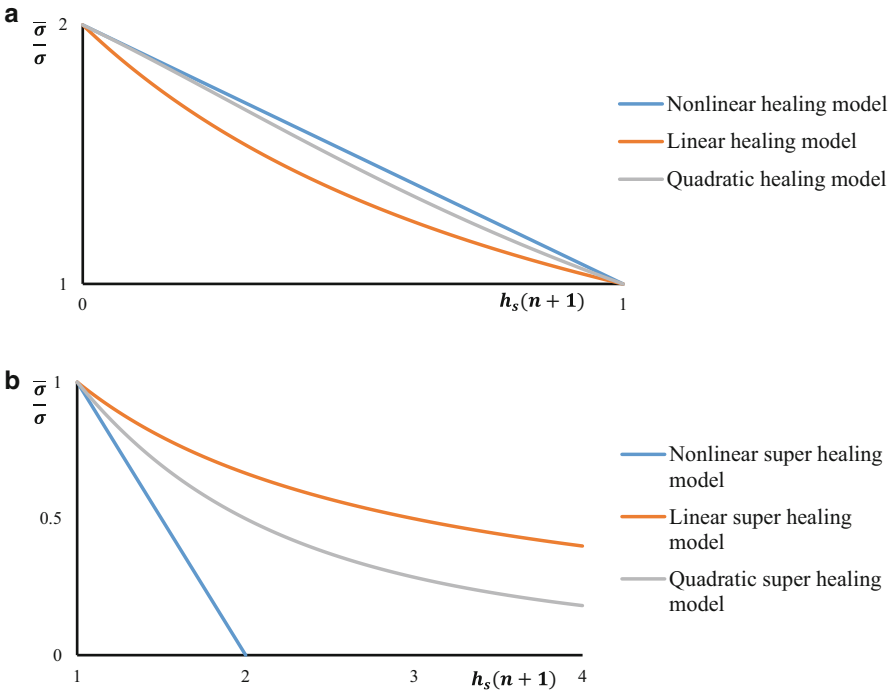

Fig. 9 Comparison between (a) self-healing models and (b) super healing models

$$f_1(R) = \frac{\varphi(1-R)}{1-\varphi R} - \varphi(1-R) \tag{63}$$

Simplifying Eq. (63), one obtains:

$$f_1(R) = \frac{\varphi^2 R(1-R)}{1-\varphi R} \tag{64}$$

Next, one calculates the first derivative of Eq. (64) with respect to R for the calculation of the maximum value of the difference function. The derivative is set to be equal to zero as follows:

$$\varphi R^2 - 2R + 1 = 0 \tag{65}$$

The solution of Eq. (65) gives one positive expression appropriate for super healing which is:

$$R = h_s(n+1) = \frac{1+\sqrt{1-\varphi}}{\varphi} \tag{66}$$

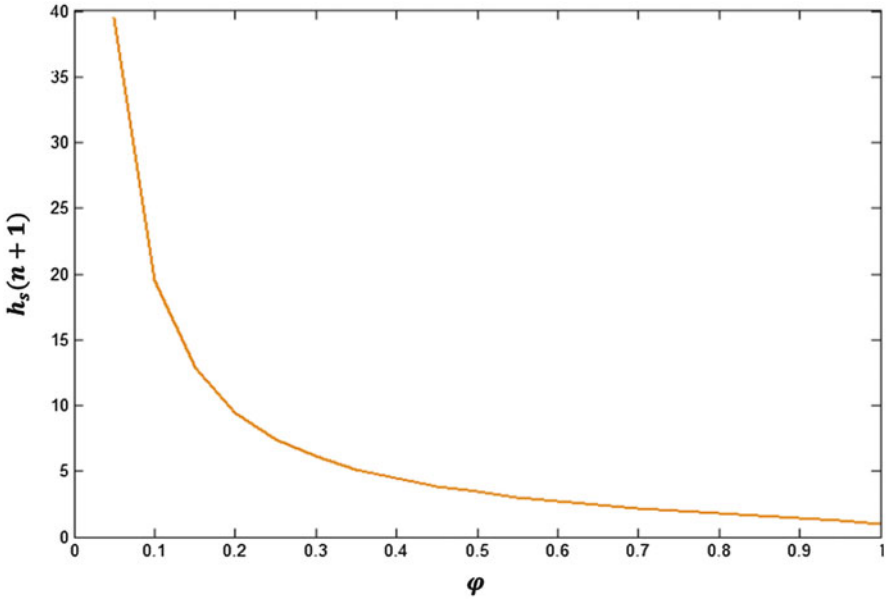

Fig. 10 Evolution of Eq. (66) as function of damage variable

From Eq. (66), one can see that the result of super healing variable is a function of the damage variable. This result is plotted in Fig. 10. One can clearly see that the results reflect the super healing behavior in which the super healing variable is greater than 1. In addition, the values of R drop from infinity to a finite value of 1 between the interval of damage $\varphi \in [0, 1]$.

One can observe that the super healing variable R is equals to 40 corresponding to the damage variable $\varphi = 0.05$. One should note that the super healing variable can describe the multiple super healing mechanisms with different numbers of healing parameter n and values of super healing parameter h_s (e.g., $h_s = 2$ and $n = 19$). The value of $R = 40$ is substituted into Eq. (46) which results in:

$$f_1(40) = \frac{-1560\varphi^2}{1 - 40\varphi} \tag{67}$$

If it is supposed that at $\varphi = 0.05$, the maximum value of Eq. (67) occurs, one finds $f_1(40) = 3.9$. Consequently, this result represents the maximum difference between the linear and generalized nonlinear super healing models.

Now, the difference between the linear and quadratic super healing models denoted as $f_2(R)$ is examined. It is expressed as:

$$f_2(R) = \varphi\left(1 - R + \varphi R - \varphi R^2\right) - \varphi(1 - R) \tag{68}$$

Simplifying Eq. (68), one obtains:

$$f_2(R) = \varphi^2 R(1-R) \tag{69}$$

The first derivative of Eq. (69) is applied with respect to R with setting it to be equal to zero:

$$\varphi^2(1-2R) = 0 \tag{70}$$

From Eq. (70), one finds that the solution is $R = 0.5$ which represents the healing concept. One can say that the solution of Eq. (70) describes the healing behavior. Therefore, the authors discard this solution in the case of super healing theory.

Next, the difference between the generalized nonlinear and quadratic super healing models is calculated and denoted as $f_3(R)$. It is expressed as follows:

$$f_3(R) = \frac{\varphi(1-R)}{1-\varphi R} - \varphi\left(1 - R + \varphi R - \varphi R^2\right) \tag{71}$$

After simplification of Eq. (71), one obtains:

$$f_3(R) = \frac{\varphi^3 R^2(1-R)}{1-\varphi R} \tag{72}$$

Next, the first derivative is applied on Eq. (72) in order to find the maximum value of $f_3(R)$ with respect to R. The following expression is obtained after simplification:

$$2\varphi R^2 - (3+\varphi)R + 2 = 0 \tag{73}$$

The solution of Eq. (73) obtained is expressed as:

$$R = \frac{3+\varphi \pm \sqrt{\varphi^2 - 10\varphi + 9}}{4\varphi} \tag{74}$$

One can see that the parameter R depends on the damage variable φ. The authors discard the negative solution of Eq. (74) as shown in Fig. 11. It is shown in this figure that negative solution represents healing behavior. Consequently, this solution is not appropriate to describe the nonlinear super healing behavior.

The second solution which is positive is considered which takes the following expression:

$$R = \frac{3+\varphi + \sqrt{\varphi^2 - 10\varphi + 9}}{4\varphi} \tag{75}$$

Equation (75) is plotted in Fig. 12. From this figure, one can see that curve represents the super healing behavior with $h_s(n+1)$ greater than 1. The parameter R drops from infinity to a finite value of 1 in the interval of damage $\varphi \in [0, 1]$. In addition, when damage variable $\varphi = 0.05$, the value of super healing parameter R becomes equal to 30. This value can represent the multiple super healing

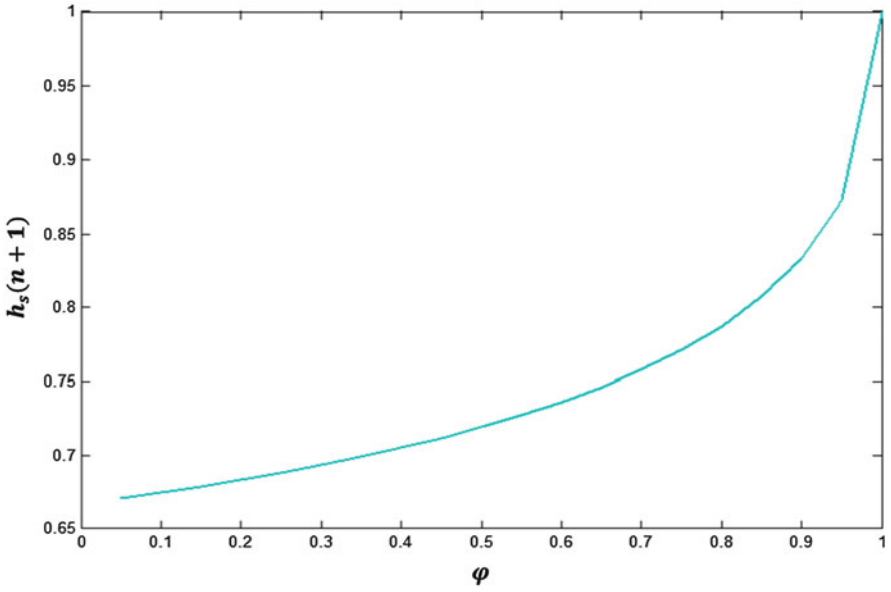

Fig. 11 Evolution of Eq. (74) as function of damage variable

mechanisms with setting $h_s = 2$ and $n = 14$. The value $R = 30$ is substituted into Eq. (71), and the following result is obtained:

$$f_3(30) = \frac{-26100\varphi^3}{1 - 30\varphi} \tag{76}$$

If it is supposed that the maximum value of $f_3(30)$ occurs at $\varphi = 0.05$, one finds $f_3(30) = 6.52$ which represents the maximum difference between the linear and generalized nonlinear super healing models. Comparison of Figs. 10 and 12 shows the same evolution of $h_s(n + 1)$ as function of the damage variable φ. However, $h_s(n + 1)$ takes the values of 40 and 30, respectively, in Figs. 10 and 12 at the damage variable $\varphi = 0.05$. It is concluded that the maximum super healing variable given by $f_1(R)$ is greater than the maximum super healing variable given by $f_3(R)$.

Super Healing Efficiency

In this section, the authors examine the super healing efficiency of the three models and demonstrate the most appropriate one to describe the super healing mechanism. In the previous section, it was found that $f_1(R) = 40$ and $f_3(R) = 30$ at damage variable $\varphi = 0.05$. The difference function $f_2(R)$ was discarded due to the results of the super healing parameter R which is less than 1. It was also found that the

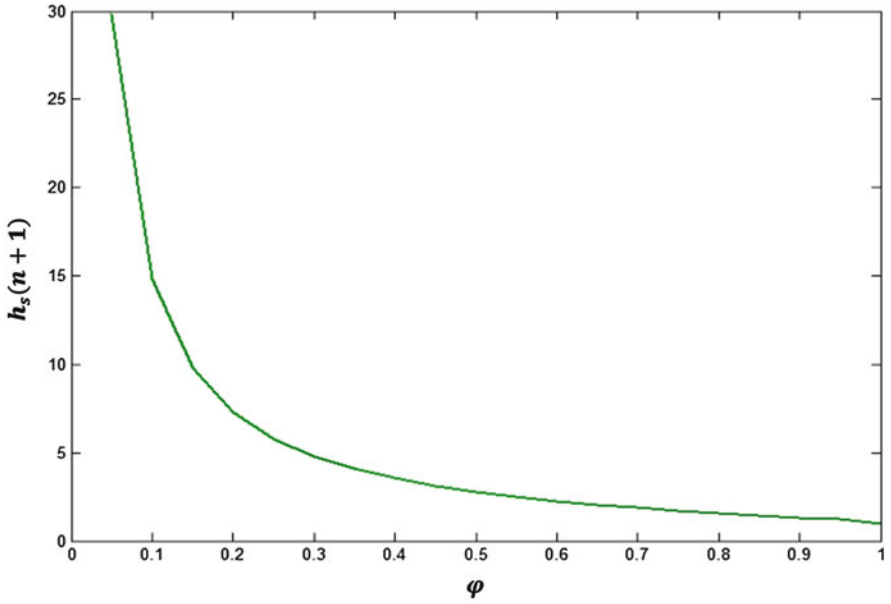

Fig. 12 Evolution of Eq. (75) as function of damage variable

difference functions $f_3(R)$ and $f_1(R)$ take, respectively, the values of 6.52 and 3.9 at damage variable $\varphi = 0.05$. It can be concluded that the difference function $f_1(R)$ overestimates the super healing variable.

Next, the authors examine the difference functions $f_1(R)$ and $f_3(R)$ in the damage interval $\varphi \in [0, 1]$. The same super healing variables already used in Figs. 10 and 12 will be used in this section. The super healing variables in the intervals $h_s(n + 1) \in [0, 40]$ and $h_s(n + 1) \in [0, 30]$ are extracted, respectively, from Figs. 10 and 12 and substituted, respectively, into Eqs. (64) and (73). Figure 13 illustrates the variation of the difference functions.

From Fig. 13, the difference functions $f_1(R)$ and $f_3(R)$ take, respectively, the values of 1.49 and 1.76 at damage variable $\varphi = 0.95$. However, they take, respectively, the values of 3.9 and 6.52 when $\varphi = 0.05$. The figure shows a decrease in the difference functions with the increase of the damage variable with large difference at damage variable $\varphi = 0.05$ ($f_1(R) = 40$ and $f_3(R) = 30$). At this point, the difference function $f_3(R)$ is diverging from $f_1(R)$. One can conclude that the difference function $f_1(R)$ is more reasonable due to the obtained small difference. This confirms that the nonlinear super healing behavior is more appropriately described by the generalized nonlinear super healing model.

The expression $(\varphi^3 R(1 - R))/(1 - \varphi R)$ is extracted from Eq. (64) and substituted into Eq. (71), and the following relationship between $f_1(R)$ and $f_3(R)$ is found:

$$f_3(R) = \varphi R f_1(R) \tag{77}$$

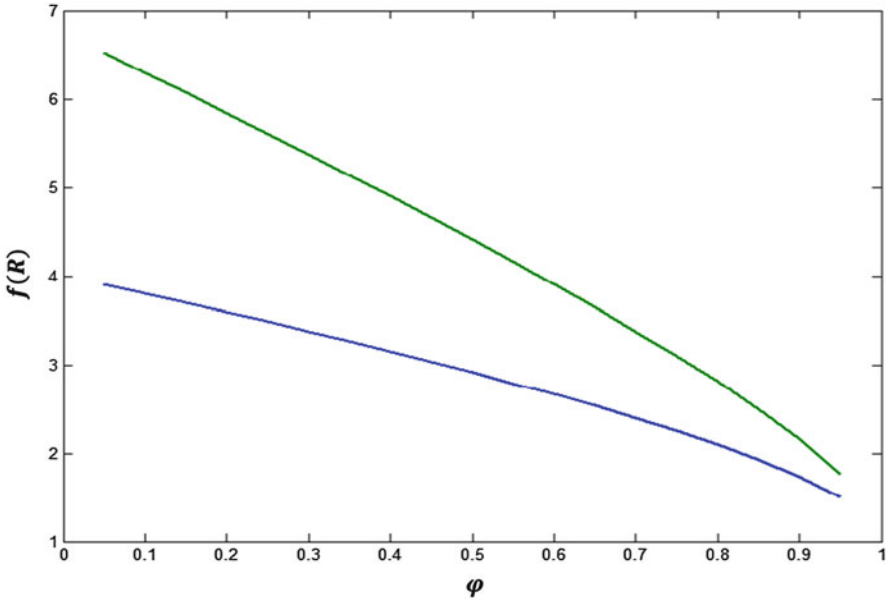

Fig. 13 Evolution of $f_1(R)$ and $f_3(R)$ as function of damage

One should note that the $R\varphi$ represents the damaged part that is subjected to super healing. The evolution of the super healing parameter R is shown after extracting it from Eq. (77) which becomes:

$$R = \frac{f_3(R)}{\varphi\, f_1(R)} \tag{78}$$

The evolution of R a function of the difference function $f_1(R)$ is illustrated in Fig. 14. The figure shows a decrease of the difference function $f_1(R)$ with the increase of the super healing variable R.

Theory of Undamageable Materials

Voyiadjis and Kattan (2012b, c, d, 2014) defined the theory of undamageable materials. According to this theory, it is assumed that the material can undergo deformation, while no damage is maintained. In this section, the authors give a combination of the proposed super healing theory with the theory of undamageable materials and show the characteristics of each theory. This combination is defined using the following proposed expression:

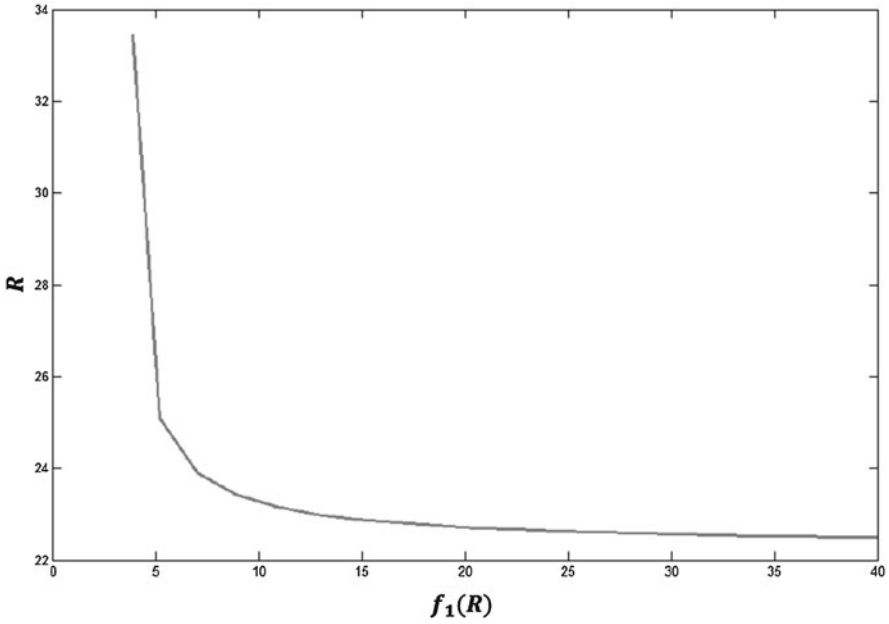

Fig. 14 Evolution of R as function of $f_1(R)$

$$\overline{\sigma} = \frac{\sigma}{1 + [h_s(n+1) - 1]\varphi^{1/k}} \tag{79}$$

k represents an integer value that goes from 1 to infinity. The following expression of the parameter $1/k$ is proposed:

$$\frac{1}{k} = h_s(n+1) + 1 \tag{80}$$

One should note that this proposition satisfies both the theory of undamageable materials and the proposed super healing theory which both results in a strengthened material with zero damage. The authors call the parameter $\varphi^{1/k}$ the combined super-healed/zero damage variable. Equation (80) is substituted into Eq. (79), and the expression of the effective stress using the combined super healing/undamageable is obtained as follows:

$$\overline{\sigma} = \frac{\sigma}{1 + [h_s(n+1) - 1]\varphi^{(h_s(n+1)+1)}} \tag{81}$$

According to CDHM and the super healing theory, three states of the material are developed as shown in Table 3.

Table 3 History of material states

Phases	Material state	φ	h	h_s	$\overline{\sigma}$
1	Material failure	1	0	0	$\overline{\sigma} \to \infty$
2	Totally healed material	0	1	0	$\overline{\sigma} = \sigma$
3	Super healed material	0	1	>1	$\overline{\sigma} < \sigma$

Next, it will be shown that the three material states given in Table 3 can be described by the proposed Eq. (81). When the material is totally damaged ($\varphi = 1$) with no healing, the effective stress will explode and approach infinity. However, in the case of complete healing ($h_s = 1$ and $n = 0$), the effective stress becomes equivalent to the nominal stress. On the other hand, when the material is super healed ($h_s \geq 1$ and $n \geq 0$), two cases are obtained. An example is given to explain these two cases. It is assumed that in the case of multiple super healing mechanisms with $h_s = 1$ and $n = 5$, Eq. (80) becomes:

$$\overline{\sigma} = \frac{\sigma}{1 + 5\varphi^7} \tag{82}$$

From Eq. (82), one can observe that the exact solution of Eq. (9) is obtained if the totally damaged material is defined by $\varphi = 1$ using the super healing theory. This confirms the equality of the combined super healing/undamageable material theories. On the other hand, the maximum damage variable $\varphi < 1$ represents the totally damaged material; the super healed/zero damage variable φ^7 is minimized by the parameter $1/k$. Therefore, the effective and nominal stresses become equal when $1/k$ approaches infinity. In addition, when k approaches infinity, the exact solution of Eq. (9) is obtained, and this is irrespective of the damage variable ($\varphi \leq 1$).

From the combination of both theories, one can conclude that the super healing theory is satisfied when totally damaged material is represented by $\varphi = 1$, while the theory of undamageable material is satisfied when the totally damaged material is represented by $\varphi < 1$. Based on these results, the following characteristics of the proposed super healing theory can be extracted:

- Due to the dependency of material degradation on many parameters, the maximum damage with value of 1 is not always reached. It can be reached, for instance, with $\varphi = 0.9$. In this case of material fully healed and further super healed, the healing variable takes a value greater than the maximum damage variable. Thus, one can conclude that the super healing theory is irrespective of the damaged material state.
- Two super healing mechanisms can be described by the proposed Eq. (9), namely, single and multiple super healing mechanisms.
- According to Eq. (9), three cases were found in which the effective stress approaches zero, namely, when h_s approaches infinity, when n approaches infinity, and when both of them approach infinity.

- It was found that the effective stress retains a finite value when damage variable $\varphi = 1$.
- It was found that when $\varphi < 1$ and $1/k$ approaches infinity, the proposed super healing theory and the theory of undamageable materials become equal.
- The super healing variable h_s is not limited only to integer values, but, can also take non-integer values.
- The generalized nonlinear super healing theory was found to be the most appropriate model for the description of the nonlinear super healing mechanism.
- The plane stress is applicable using the generalized nonlinear super healing model.
- The healing mechanism can be described by all healing models provided that $n = 0$ and $h_s(n + 1) \in [0, 1]$.

Conclusions

In the present work, the authors proposed a refined theory of super healing materials based on CDHM in isotropic and anisotropic forms. After the material stiffness is recovered, the healing continues beyond its limit and acts a strengthening material. In the present framework, the authors assume that the same material used for self-healing can be used for super healing. Two examples were applied using the super healing theory, namely, plane stress example and one-dimensional example. In the first example, it was shown that the anisotropic formulation reduces to the isotropic formulation. In the second example, the behavior of super healing material was described. An extension of the linear super healing theory to the nonlinear super healing theory was given, and comparative study was conducted. The results revealed that the generalized nonlinear super healing model is more appropriated for the description of the super healing mechanism. The authors also examined in this work the link between super healing theory and the theory of undamageable materials. The results revealed that both theories result in a material that contains no damage during the deformation process.

The present work was theoretically presented to develop the super healing materials along with a nonlinear formulation. It is believed that this theory will find place in the future to be exploited as a strengthening technique of material construction. The authors hope that further physical investigations will be conducted in the future to design the appropriate material along the lines of the assumptions given in the present work.

Acknowledgments The second author would like to acknowledge the Deutscher Akademischer Austauschdienst (DAAD) for the financial support of this work.

References

P. Areias, M.A. Msekh, T. Rabczuk, Damage and fracture algorithm using the screened Poisson equation and local remeshing. Eng. Fract. Mech. **158**, 116–143 (2016)

E.J. Barbero, F. Greco, P. Lonetti, Continuum damage-healing mechanics with application to self healing composites. Int J Damage Mech. **14**, 51–81 (2005)

C. Basaran, S. Nie, An irreversible thermodynamic theory for damage mechanics of solids. Int J Damage Mechanics. **13**(3), 205–224 (2004)
C. Basaran, C.Y. Yan, A thermodynamic framework for damage mechanics of solder joints. Trans. of ASME, J Electron Packag **120**, 379–384 (1998)
A. Brencich, L. Gambarotta, Isotropic damage model with different tensile-compressive response for brittle materials. Int. J. Solids Struct. **38**(34–35), 5865–5892 (2001)
K.V. Breugel, Self-healing material concepts as solution for aging infrastructure. 37th Conference on Our World in Concrete & Structures, 2012
E.N. Brown, N.R. Sottos, S.R. White, Fracture testing of a self-healing polymer composite. Exp. Mech. **42**(4), 372–379 (2002)
E.N. Brown, S.R. White, N.R. Sottos, Microcapsule induced toughening in a self-healing polymer composite. J. Mater. Sci. **39**(5), 1703–1710 (2004)
E.N. Brown, S.R. White, N.R. Sottos, Retardation and repair of fatigue cracks in a microcapsule toughened epoxy composite-Part II: In situ self-healing. Compos. Sci. Technol. **65**(15–16), 2474–2480 (2005)
E.N. Brown, S.R. White, N.R. Sottos, Fatigue crack propagation in microcapsule-toughened epoxy. J. Mater. Sci. **41**(19), 6266–6273 (2006)
J. Choi, Comparative study of effective stresses of concrete beams strengthened using carbon-fibre-reinforced polymer and external prestressing tendons. Struct Infrastruct E. **10**(6), 753–766 (2014)
M.K. Darabi, R.K. Abu Al-Rub, D.N. Little, A continuum damage mechanics framework for modeling micro-damage healing. Int. J. Solids Struct. **49**(3-4), 492–513 (2012)
B. Dong, G. Fang, Y. Wang, Y. Liu, S. Hong, J. Zhang, S. Lin, Y. Liu, F. Xing, Performance recovery concerning the permeability of concrete by means of a microcapsule based self-healing system. Cement Concrete Comp. **78**, 84–96 (2016)
C. Dry, Matrix cracking repair and filling using active and passive modes for smart timed release of chemicals from fibers into cement matrices. Smart Mater. Struct. **3**(2), 118–123 (1994)
C.M. Dry, N.R. Sottos, Passive smart self-repair in polymer matrix composite materials. Smart Mater. Struct. **438**, 1–7 (1993)
D. Gardner, A. Jefferson, A. Hoffman, R. Lark, Simulation of the capillary flow of an autonomic healing agent in discrete cracks in cementitious materials. Cement Concrete Res. **58**, 34–44 (2014)
P. Giannaros, A. Kanellopoulos, A. Al-Tabbaa, Sealing of cracks in cement using micro-encapsulated sodium silicate. Smart Mater. Struct. **25**, 1–13 (2016)
S. Granger, A. Loukili, G. Pijaudier-Cabot, G. Chanvillard, Experimental characterization of the self-healing of cracks in an ultra high performance cementitious material: Mechanical tests and acoustic emission analysis. Cement Concrete Res **37**(4), 519–527 (2007)
E.M. Gunel, C. Basaran, Damage characterization in non-isothermal stretching of acrylics: Part I theory. Mech. Mater. **43**(12), 979–991 (2011a)
E.M. Gunel, C. Basaran, Damage characterization in non-isothermal stretching of acrylics: Part II experimental validation. Mech. Mater. **43**(12), 992–1012 (2011b)
B. Hilloulin, F. Grondin, M. Matallah, A. Loukili, Modelling of autogenous healing in ultra high performance concrete. Cement Concrete Res. **61-61**, 64–70 (2014)
C. Joseph, A.D. Jefferson, M.B. Cantoni, Issues relating to the autonomic healing of cementitious materials, in *Proceedings of the First International Conference on Self-Healing Materials*, (Noordwijk aan Zee, The Netherlands, 2007), pp. 1–8
C. Joseph, R. Lark, T. Jefferson, D. Gardner, Potential application of self-healing materials in the construction industry, in *A Report for the Institution of Civil Engineers*, vol. 59, (Cardif University, 2009)
C. Joseph, A.D. Jefferson, B. Isaacs, R. Lark, D. Gardner, Experimental investigation of adhesive-based self-healing of cementitious materials. Mag Concrete Res **62**(11), 831–843 (2010)
L. Kachanov, On the creep fracture time. Izv Akad, Nauk USSR Otd Tech. **8**, 26–31 (1958)

V.C. Lia, Y.M. Limb, Y.W. Chanc, Feasibility study of a passive smart self-healing cementitious composite. Compos Part B-Eng. **29**(6), 819–827 (1998)
L.M. Mauludin, C. Oucif, Interaction between matrix crack and circular capsule under uniaxial tension in encapsulation-based self-healing concrete. Underground Space **3**(3), 181–189 (2018)
L.M. Mauludin, C. Oucif, The effects of interfacial strength on fractured microcapsule. Front. Struct. Civ. Eng. **13**(2), 353–363 (2019)
C. Oucif, L.M. Mauludin, Continuum damage-healing and super healing mechanics in brittle materials: A state-of-the-art review. Appl. Sci. **8**(12), 2350 (2018)
C. Oucif, G.Z. Voyiadjis, T. Rabczuk, Modeling of damage-healing and nonlinear self-healing concrete behavior: Application to coupled and uncoupled self-healing mechanisms. Theor. Appl. Fract. Mech. **96**, 216–230 (2018a)
C. Oucif, G.Z. Voyiadjis, P.I. Kattan, T. Rabczuk, Nonlinear superhealing and contribution to the design of a new strengthening theory. J. Eng. Mech. **144**(7), 04018055 (2018b)
C. Oucif, G.Z. Voyiadjis, P.I. Kattan, T. Rabczuk, Investigation of the super healing theory in continuum damage and healing mechanics. Int J Damag Mech **28**(6), 896–917 (2019)
A.J. Patel, N.R. Sottos, E.D. Wetzel, S.R. White, Autonomic healing of low velocity impact damage in fiber-reinforced composites. Compos Part A-Appl S. **41**(3), 360–368 (2010)
T. Rabczuk, J. Akkermann, J. Eibl, A numerical model for reinforced concrete structures. Int. J. Solids Struct. **42**(5–6), 1327–1354 (2005)
L.A. Sosnovskiy, S.S. Sherbakov, Mechanothermodynamic entropy and analysis of damage state of complex systems. Entropy **18**, 268 (2016). https://doi.org/10.3390/e18070268
T.Q. Thai, T. Rabczuk, Y. Bazilevs, G. Meschke, A higher-order stress-based gradient-enhanced damage model based on isogeometric analysis. Comput Method Appl M. **304**, 584–604 (2017)
K.V. Tittelboom, N.D. Belie, D.V. Loo, P. Jacobs, Self-healing efficiency of cementitious materials containing tubular capsules filled with healing agent. Cement Concrete Comp. **33**(4), 497–505 (2011)
G.Z. Voyiadjis, Degradation of elastic modulus in elastoplastic coupling with finite strains. Int J Plasticity. **4**(4), 335–353 (1988)
G.Z. Voyiadjis, P.I. Kattan, A plasticity-damage theory for large deformation of solids-I. theoretical formulation. Int. J. Eng. Sci. **30**(6), 1089–1108 (1992)
G.Z. Voyiadjis, P.I. Kattan, *Advances in Damage Mechanics: Metals and Metal Matrix Composites* (Elsevier, 1999)
G.Z. Voyiadjis, P.I. Kattan, Mechanics of damage processes in series and in parallel: A conceptual framework. Acta Mech. **223**(9), 1863–1878 (2012a)
G.Z. Voyiadjis, P.I. Kattan, Introduction to the mechanics and design of undamageable materials. Int J Damage Mech. **22**, 323–335 (2012b)
G.Z. Voyiadjis, P.I. Kattan, A new class of damage variables in continuum damage mechanics. J Eng Mater-T ASME. **134**(2), 1–10 (2012c)
G.Z. Voyiadjis, P.I. Kattan, On the theory of elastic undamageable materials. J Eng Mater-T ASME. **135**(2), 1–7 (2012d)
G.Z. Voyiadjis, P.I. Kattan, Healing and super healing in continuum damage mechanics. Int J Damage Mech. **24**, 245–260 (2013)
G.Z. Voyiadjis, P.I. Kattan, Governing differential equations for the mechanics of undamageable materials. Eng. Trans. **62**(6), 241–267 (2014)
G.Z. Voyiadjis, P.I. Kattan, Investigation of the damage variable basic issues in continuum damage and healing mechanics. Mech. Res. Commun. **68**, 89–94 (2015)
G.Z. Voyiadjis, P.I. Kattan, Mechanics of damage, healing, damageability, and integrity of materials: A conceptual framework. Int J Damage Mech. **26**(1), 1–54 (2016)
G.Z. Voyiadjis, A. Shojaei, G. Li, A thermodynamic consistent damage and healing model for self-healing materials. Int J Plasticity. **27**(7), 1025–1044 (2011a)
G.Z. Voyiadjis, A. Shojaei, G. Li, P.I. Kattan, A theory of anisotropic healing and damage mechanics of materials. Proc. R. Soc. A. **468**(2137), 1–23 (2011b)

G.Z. Voyiadjis, A. Shojaei, P.I. Kattan, Continuum damage-healing mechanics with introduction to new healing variables. Int J Damage Mech. **21**, 1–24 (2012)

J.Y. Wang, H. Soens, W. Verstraete, N. DeBelie, Self-healing concrete by use of microencapsulated bacterial spores. Cement Concrete Res. **56**, 139–152 (2014)

S.R. White, N.R. Sottos, P.H. Geubelle, J.S. Moore, M.R. Kessler, S.R. Sriram, E.N. Brown, S. Viswanathan, Autonomic healing of polymer composite. Nature **409**, 794–797 (2001)

Y. Yang, M.D. Lepech, E.H. Yang, V.C. Li, Autogenous healing of engineered cementitious composites under wet–dry cycles. Cement Concrete Res. **39**(5), 382–390 (2009)

W. Yao, C. Basaran, Electromigration damage mechanics of lead-free solder joints under pulsed DC loading: A computational model. Comput. Mater. Sci. **71**, 76–88 (2013)

H. Zhu, S. Zhou, Z. Yan, J.W. Ju, Q. Chen, A two-dimensional micromechanical damage-healing model on microcrack-induced damage for microcapsule-enabled self-healing cementitious composites under tensile loading. Int J Damage Mech. **24**(1), 95–115 (2014)

Vibration Analysis of Cracked Microbeams by Using Finite Element Method

7

Şeref Doğuşcan Akbaş, Mustafa ÖzgürYaylı, Babür Deliktaş, and Büşra Uzun

Contents

Introduction 156
Modified Couple Stress Theory 157
Finite Element Formulation 159
Numerical Results 162
Summary/Conclusions 163
References 164

Abstract

A finite element method procedure applicable for calculating the free vibration of cracked microbeams is presented in this study. The basic mathematical theory and the background of the cracked microbeam is shown, which included the kinematic energy and the total potential energy of the cracked microbeam. Euler–Lagrange equation and the kinematic boundary conditions are obtained with the help of first variation of cracked microbeam. The accuracy, efficiency, and generality of the proposed approach are fully verified and demonstrated through numerical examples involving different values of the crack location.

Ş. D. Akbaş (✉)
Department of Civil Engineering, Bursa Technical University, Bursa, Turkey
e-mail: seref.akbas@btu.edu.tr

M. ÖzgürYaylı · B. Uzun
Department of Civil Engineering, Bursa Uludag University, Bursa, Turkey
e-mail: ozguryayli@uludag.edu.tr; buzun@uludag.edu.tr

B. Deliktaş
Department of Civil Engineering, Faculty of Engineering-Architecture, Uludag University, Bursa, Turkey
e-mail: bdeliktas@uludag.edu.tr

© Springer Nature Switzerland AG 2022

G. Z. Voyiadjis (ed.), *Handbook of Damage Mechanics*,
https://doi.org/10.1007/978-3-030-60242-0_88

Keywords

Microbeam · Crack · Modified couple stress theory · Vibration · Finite element method

Introduction

The rapid advancements in nanotechnology and microtechnology are accomplished by numerous theoretical and computational studies carried out on understanding the mechanical behaviors of microscale and nanoscale structures. In these theoretical studies, size-dependent higher-order theories (Mindlin 1963, 1965; Mindlin and Tiersten 1962; Toupin 1962; Eringen 1972, 1983; Lam et al. 2003; Yang et al. 2002) are used developed by taking into account the size effect which has an important role in the behaviors of these very small-scale structures. A major part of the theoretical studies developed for microscale structures like microbeam, microplate, microbar, etc. are based on the modified couple stress theory (MCST) since the classical continuum theories fail to account for the size effect noticeable at small scales. The modified couple stress theory introduced by Yang et al. (2002) overcomes the size effect with a material length scale parameter included in their eqs. A size-dependent FG piezoelectric microplate model was proposed via the MCST and sinusoidal plate theory by Li and Pan (2015). Rahaeifard et al. (2015) examined the natural frequencies of electrostatically actuated microbridges in conjunction with the MCST. Akgoz and Civalek (2013) developed the analytical solution for static bending, buckling, and free vibration analyses of microscaled plates embedded in Winkler elastic foundation on the basis of MCST. Akbaş (2016a) presented the static bending behavior of a rectangular nanoplate subjected to uniform distributed load based on MCST by using generalized differential quadrature (GDQ) method. Farokhi et al. (2013) studied the nonlinear dynamics of a geometrically imperfect microbeam based on the modified couple stress theory. Ghadiri and Safarpour (2016) investigated the free vibration of magneto-electro-elastic (MEE) nanoshell embedded in elastic medium based on the modified couple stress and the first-order shear deformation theories. Yayli (2018) presented torsional vibration response of carbon nanotubes with torsional restraints on the basis of MCST. Akbaş (2020) investigated modal analysis of viscoelastic nanorods analytically.

The finite element method, which is used as the solution method in this section, has recently attracted the attention of many researchers interested in micromechanics and nanomechanics. It has recently been observed that finite element formulation is frequently utilized by many researchers (Hemmatnezhad and Ansari 2013; Demir and Civalek 2017; Uzun and Civalek 2019; Phadikar and Pradhan 2010; Shi and Voyiadjis 2011; Ansari et al. 2018; Yayli 2011; Zargaripoor et al. 2018; Mahmoud et al. 2012; Civalek et al. 2020; Uzun and Yayli 2020) to investigate a number of behaviors (buckling, bending, vibration, etc.) of the small-scale structures based on size-dependent higher-order theories. Akbaş (2016b) presented forced vibration of naobeams resting on elastic foundation by using MCST and finite element method.

In addition, finite element method based on modified couple stress theory has also been reported by researchers in some articles. Akbaş (2017a) derived the finite

element formulation of nanobeams and investigated the static, buckling, and vibration responses via Euler Bernoulli beam theory and MCST. Also, Akbaş (2018a) presented the forced vibration responses of cracked functionally graded (FG) microbeams based on Timoshenko beam theory and MCST using finite element method. Kazemi et al. (2017) proposed the vibration of microplates with piezoelectric layers in conjunction with modified couple stress theory and finite element method.

In the micro- or nanostructures, crack problems are very important topic. In the literature, some of the studies about crack problems in the micro−/nanostructures are as follows: Liu et al. (2013) examined vibration of a cracked microbeam subjected to electrostatic excitation; Roostai and Haghpanahi (2014) presented free vibration of nanobeams with crack for different boundary conditions; Akbaş (2017b) investigated free vibration of cracked microbeams made of functionally graded material-based MCST by using finite element method; Akbaş (2018b) analyzed forced vibration nanobeams with crack by using finite element method within MCST; Loya et al. (2009) analyzed free vibration of cracked nanobeams analytically with nonlocal elasticity theory; Kim et al. (2006) investigated detection of damage on the beam structures with vibration-based damage evaluation method; Akbaş (2016c) presented analytical static solution of cracked microbeams with different boundary conditions based on MCST; Tadi Beni et al. (2015) investigated vibration of cracked nanobeams by using MCST; Torabi and Nafar Dastgerdi (2012) investigated free vibration of nanobeams with cracks analytically within Timoshenko beam theory and nonlocal elasticity theory; Wang and Wang (2015) presented free vibration of cracked Timoshenko nanobeams with surface energy; Yayli and Çerçevik (2015) and Yayli et al. (2019) investigated vibration of cracked nanorods and carbon nanotubes; Park et al. (2004) and Lee et al. (2003) investigated vibration analysis of delaminated beam; Peng et al. (2015) analyzed deflections of the cracked nanosbeams; and finally Hasheminejad et al. (2011) presented free vibration of cracked nanobeams with surface effects.

The main objective of this chapter is to examine free vibration solution of cracked microbeam on the basis of modified couple stress theory. The finite element formulation is derived for vibration problem of cracked microbeam in the framework MCST. The influences of locations of crack, geometry parameters, and flexibility of crack on the natural frequencies of the cracked microbeam are presented for both classical beam thery (CBT) and MCST.

Modified Couple Stress Theory

In Fig. 1, a cantilever circular microbeam with the edge crack is shown, where L is length and D is diameter, a indicates the crack depth, and L_1 indicates the crack location from the left end.

Based on modified couple stress theory (MCST), the strain energy is presented as follows (Yang et al. 2002):

$$U = \int_V (\boldsymbol{\sigma} : \boldsymbol{\varepsilon} + \boldsymbol{m} : \boldsymbol{\chi}) dV \tag{1}$$

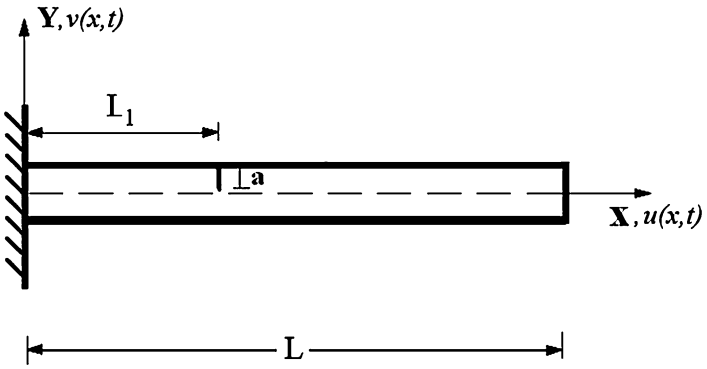

Fig. 1 A cantilever microbeam with the edge crack

where σ, m, χ, and ε, indicate stress, couple stress, curvature, and strain tensors, respectively,

$$\boldsymbol{\sigma} = \frac{E\nu}{(1+\nu)(1-2\nu)} tr(\boldsymbol{\varepsilon}) I + 2\frac{E}{2(1+\nu)}\boldsymbol{\varepsilon} \tag{2a}$$

$$\boldsymbol{\varepsilon} = \frac{1}{2}\left[\nabla \boldsymbol{u} + (\nabla \boldsymbol{u})^T\right] \tag{2b}$$

$$\boldsymbol{m} = 2l^2 \mu \boldsymbol{\chi} \tag{2c}$$

$$\boldsymbol{\chi} = \frac{1}{2}\left[\nabla \boldsymbol{\theta} + (\nabla \boldsymbol{\theta})^T\right] \tag{2d}$$

where l indicates the length scale parameter that characterizes the couple stress influences. ν is the Poisson's ratio. $\boldsymbol{\theta}$ and u indicate rotation and displacement vectors, respectively, expressed as follows:

$$\boldsymbol{\theta} = \frac{1}{2}\text{curl } \boldsymbol{u} \tag{3}$$

According to the Euler–Bernoulli beam theory, strain and curvature tensor expressions are presented in any time t as follows:

$$\varepsilon_{xx} = \frac{\partial u}{\partial X} = \frac{\partial u_0(X,t)}{\partial X} - Y\frac{\partial^2 v_0(X,t)}{\partial X^2} \tag{4a}$$

$$\begin{aligned} \chi_{xz} &= \frac{1}{2}\frac{\partial^2 v_0(X,t)}{\partial X^2} \\ \chi_{xx} &= \chi_{xy} = \chi_{yy} = \chi_{yz} = \chi_{zz} = 0 \end{aligned} \tag{4b}$$

where u_0 and v_0 are the componenets of displacement. Ø indicates the rotation.

The constitutive relation of the problem is given with using the Kelvin–Voigt viscoelastic model as follows:

$$\sigma_{xx} = E\varepsilon_{xx} = E\left[\frac{\partial u_0(X,t)}{\partial X} - Y\frac{\partial^2 v_0(X,t)}{\partial X^2}\right] \tag{5a}$$

$$\begin{aligned} m_{xz} &= l^2\mu\frac{1}{2}\frac{\partial^2 v_0(X,t)}{\partial X^2}, \\ m_{xx} &= m_{xy} = m_{yy} = m_{yz} = m_{zz} = 0 \end{aligned} \tag{5b}$$

The elastic strain energy (U_i) and the kinetic energy (T) of the beam are presented as follows:

$$U_i = \frac{1}{2}\int_0^L \left[EA\left(\frac{\partial u_0(X,t)}{\partial X}\right)^2 + EI\left(\frac{\partial^2 v(X,t)}{\partial X^2}\right)^2 + \frac{1}{4}l^2\mu A\left(\frac{\partial^2 v(X,t)}{\partial X^2}\right)^2\right]dX \tag{6}$$

$$T = \frac{1}{2}\int_0^L \left[\rho A\left(\frac{\partial u_0}{\partial t}\right)^2 + \rho A\left(\frac{\partial v_0}{\partial t}\right)^2 + \rho I\left(\frac{\partial^2 v_0}{\partial X\,\partial t}\right)^2\right]dX \tag{7}$$

where A is the area of the cross section and I is the moment of inertia.

Finite Element Formulation

The nodal displacements q for a two-node beam element contain three degrees of freedom at each node, as shown in Fig. 2, namely,

$$\{q(t)\}_e = \left[u_i^{(e)}(t), v_i^{(e)}(t), \theta_i^{(e)}(t), u_j^{(e)}(t), v_j^{(e)}(t), \theta_j^{(e)}(t)\right]^T \tag{8}$$

The displacement field of the finite element is expressed in terms of the nodal displacements as follows:

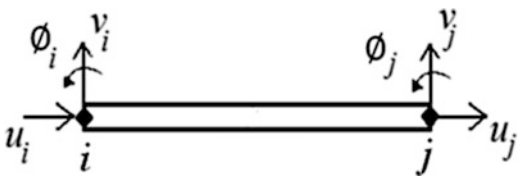

Fig. 2 Two-node finite element

$$u^{(\mathrm{e})}(X,\mathrm{t}) = \varphi_1^{(U)}(X)u_\mathrm{i}(t) + \varphi_2^{(U)}(X)u_\mathrm{j}(t) = \left[\varphi^{(U)}\right]\left\{\begin{array}{c} u_\mathrm{i} \\ u_\mathrm{j} \end{array}\right\} = \left[\varphi^{(U)}\right]\{\mathrm{q}\}_U \tag{9a}$$

$$v^{(\mathrm{e})}(X,\mathrm{t}) = \varphi_1^{(V)}(X)v_\mathrm{i}(t) + \varphi_2^{(V)}(X)\theta_\mathrm{i}(t) + \varphi_3^{(V)}(X)v_\mathrm{j}(t) + \varphi_4^{(V)}(X)\theta_\mathrm{j}(t) \tag{9b}$$

$$\left[\varphi^{(V)}\right]\left\{\begin{array}{c} v_\mathrm{i} \\ \theta_\mathrm{i} \\ v_\mathrm{j} \\ \theta_\mathrm{j} \end{array}\right\} = \left[\varphi^{(V)}\right]\{q\}_V \tag{9c}$$

where u_i, v_i, and θ_i are the axial displacements, transverse displacements, and slopes at the two end nodes of the beam element, respectively, and $\varphi^{(U)}$ and $\varphi^{(V)}$ are the Hermite shape functions for the axial and transverse displacements, respectively. The interpolation functions for the axial displacement are

$$\varphi^{(U)}(\mathrm{X}) = \left[\varphi_1^{(U)}(\mathrm{X})\ \varphi_2^{(U)}(\mathrm{X})\right]^T \tag{10}$$

where

$$\varphi_1^{(U)}(\mathrm{X}) = \left(-\frac{X}{L_\mathrm{e}} + 1\right) \tag{11a}$$

$$\varphi_2^{(U)}(\mathrm{X}) = \left(\frac{X}{L_\mathrm{e}}\right) \tag{11b}$$

The interpolation functions for the transverse displacement are

$$\varphi^{(V)}(\mathrm{X}) = \left[\varphi_1^{(V)}(\mathrm{X})\varphi_2^{(V)}(\mathrm{X})\varphi_3^{(V)}(\mathrm{X})\varphi_4^{(V)}(\mathrm{X})\right]^T \tag{12}$$

where

$$\varphi_1^{(V)}(\mathrm{X}) = \left(1 - \frac{3X^2}{L_\mathrm{e}^2} + \frac{2X^3}{L_\mathrm{e}^3}\right) \tag{13a}$$

$$\varphi_2^{(V)}(\mathrm{X}) = \left(-X + \frac{2X^2}{L_\mathrm{e}} - \frac{X^3}{L_\mathrm{e}^2}\right) \tag{13b}$$

$$\varphi_3^{(V)}(\mathrm{X}) = \left(\frac{3X^2}{L_\mathrm{e}^2} - \frac{2X^3}{L_\mathrm{e}^3}\right) \tag{13c}$$

$$\varphi_4^{(V)}(\mathrm{X}) = \left(\frac{X^2}{L_\mathrm{e}} - \frac{X^3}{L_\mathrm{e}^2}\right) \tag{13d}$$

with L_e indicating the length of the beam element. By using The Lagrange's procedure, the finite element equation of the free vibration problem is presented as follows:

$$\left([K] - \omega^2[M]\right)\{\widehat{q}\} = 0 \tag{14}$$

where ω is the natural frequency, $\{\widehat{q}\}$ is a vector of displacement amplitudes of the vibration, and $[M]$ is the mass matrix. The stiffness matrix [K] and mass matrix [M] can be given as:

$$[K] = \begin{bmatrix} & 0 & 0 & & 0 & 0 \\ \frac{\mathrm{EA}}{\mathrm{L}_e} & \frac{12(\mathrm{EI}+0.25l^2\mu A)}{\mathrm{L}_e{}^3} & \frac{-6(\mathrm{EI}+0.25l^2\mu A)}{\mathrm{L}_e{}^2} & -\frac{\mathrm{EA}}{\mathrm{L}_e} & \frac{-12(\mathrm{EI}+0.25l^2\mu A)}{\mathrm{L}_e{}^3} & \frac{-6(\mathrm{EI}+0.25l^2\mu A)}{\mathrm{L}_e{}^2} \\ 0 & \frac{-6(\mathrm{EI}+0.25l^2\mu A)}{\mathrm{L}_e{}^2} & \frac{4(\mathrm{EI}+0.25l^2\mu A)}{\mathrm{L}_e} & 0 & \frac{6(\mathrm{EI}+0.25l^2\mu A)}{\mathrm{L}_e{}^2} & \frac{2(\mathrm{EI}+0.25l^2\mu A)}{\mathrm{L}_e} \\ 0 & & & & & \\ -\frac{\mathrm{EA}}{\mathrm{L}_e} & 0 & 0 & \frac{\mathrm{EA}}{\mathrm{L}_e} & 0 & 0 \\ 0 & \frac{-12(\mathrm{EI}+0.25l^2\mu A)}{\mathrm{L}_e{}^3} & \frac{6(\mathrm{EI}+0.25l^2\mu A)}{\mathrm{L}_e{}^2} & 0 & \frac{12(\mathrm{EI}+0.25l^2\mu A)}{\mathrm{L}_e{}^3} & \frac{6(\mathrm{EI}+0.25l^2\mu A)}{\mathrm{L}_e{}^2} \\ 0 & \frac{-6(\mathrm{EI}+0.25l^2\mu A)}{\mathrm{L}_e{}^2} & \frac{2(\mathrm{EI}+0.25l^2\mu A)}{\mathrm{L}_e} & 0 & \frac{6(\mathrm{EI}+0.25l^2\mu A)}{\mathrm{L}_e{}^2} & \frac{4(\mathrm{EI}+0.25l^2\mu A)}{\mathrm{L}_e} \end{bmatrix} \tag{15a}$$

$$[M] = \begin{bmatrix} & 0 & 0 & & 0 & 0 \\ \frac{\rho \mathrm{AL}_e}{3} & \left(\frac{13\rho \mathrm{AL}_e}{35} + \frac{6\rho I}{5\mathrm{L}_e}\right) & \left(\frac{-11\rho \mathrm{AL}_e{}^2}{210} - \frac{\rho I}{10}\right) & \frac{\rho \mathrm{AL}_e}{6} & \left(\frac{9\rho \mathrm{AL}_e}{70} - \frac{6\rho I}{5\mathrm{L}_e}\right) & \left(\frac{13\rho \mathrm{AL}_e{}^2}{420} - \frac{\rho I}{10}\right) \\ 0 & \left(\frac{-11\rho \mathrm{AL}_e{}^2}{210} - \frac{\rho I}{10}\right) & \left(\frac{\rho \mathrm{AL}_e{}^3}{105} + \frac{2\rho I \mathrm{L}_e}{15}\right) & 0 & \left(\frac{-13\rho \mathrm{AL}_e{}^2}{420} + \frac{\rho I}{10}\right) & \frac{-\rho \mathrm{AL}_e{}^3}{140} - \frac{\rho I \mathrm{L}_e}{30} \\ 0 & & & & & \\ \frac{\rho \mathrm{AL}_e}{6} & 0 & 0 & \frac{\rho \mathrm{AL}_e}{3} & 0 & 0 \\ 0 & \left(\frac{9\rho \mathrm{AL}_e}{70} - \frac{6\rho I}{5\mathrm{L}_e}\right) & \left(\frac{-13\rho \mathrm{AL}_e{}^2}{420} + \frac{\rho I}{10}\right) & 0 & \left(\frac{13\rho \mathrm{AL}_e}{35} + \frac{6\rho I}{5\mathrm{L}_e}\right) & \left(\frac{11\rho \mathrm{AL}_e{}^2}{210} + \frac{\rho I}{10}\right) \\ 0 & \left(\frac{13\rho \mathrm{AL}_e{}^2}{420} - \frac{\rho I}{10}\right) & \left(\frac{-\rho \mathrm{AL}_e{}^3}{140} - \frac{\rho I \mathrm{L}_e}{30}\right) & 0 & \left(\frac{11\rho \mathrm{AL}_e{}^2}{210} + \frac{\rho I}{10}\right) & \left(\frac{\rho \mathrm{AL}_e{}^3}{105} + \frac{2\rho I \mathrm{L}_e}{15}\right) \end{bmatrix} \tag{15b}$$

In the crack model, an elastic rotational spring which connects the right and left subelements is used at the cracked cross-section, as shown Fig. 3.

According to elastic rotational spring model, compatibility conditions of the cracked location are.

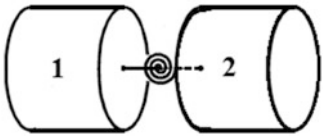

Fig. 3 Rotational spring model in cracked section

$$u_1 = u, v_1 = v_2, \Delta\varnothing = (\varnothing_1 - \varnothing_2) = \frac{1}{C_M}\frac{\partial^2 v}{\partial X^2}\, X = L_1 \tag{16}$$

where k_M and $\Delta\text{Ø}$ are the flexibility constant and the slope increment respectively, at the cracked section. Ø_1 and Ø_2 indicate the angles on the two sides of the crack. The stiffness matrix and the displacement vector of the cracked section for the spring model is given as follows:

$$[K]_{(Cr)} = \begin{bmatrix} 1/C_M & -1/C_M \\ -1/C_M & 1/C_M \end{bmatrix}, \{q\}_{(Cr)} = \{\varnothing_1, \varnothing_2\}^T \tag{17}$$

Substituting Eq. (17) into Eq. (14), the equation of motion with crack is expressed as follows:

$$\left(\left([K] + [K]_{(Cr)}\right) - \omega^2[M]\right)\{\widehat{q}\} = 0 \tag{18}$$

$$\eta = \frac{L_1}{L} \tag{19}$$

where η is the crack location ratio.

Numerical Results

In the numerical results, effects of locations of crack, geometry parameters, and flexibility of crack on the natural frequencies of the cracked microbeam are presented and discussed in both modified couple stress theory (MCST) and classical theory (CT). The microbeam is taken to be made of epoxy ($E = 1{,}44$ *GPa*, $\nu = 0.38$, $l = 17.6$ *μm*, $\rho = 1600$ *kg/m*^{3}). In the numerical calculations, the number of finite elements is taken as 100. The dimension of the microbeam is selected as $D = 10$ *μm*, whereas the length L is selected as the L/D ratio.

In Fig. 4, effects of flexibility of crack on the natural frequencies of the cracked microbeam are presented for different values of L/D for the crack location ratio $\eta = 0.1$ in both modified couple stress theory (MCST) and classical theory (CT).

In Fig. 5, effects of crack location ratio (η) on the natural frequencies of the cracked microbeam are presented for different values of L/D for the crack location

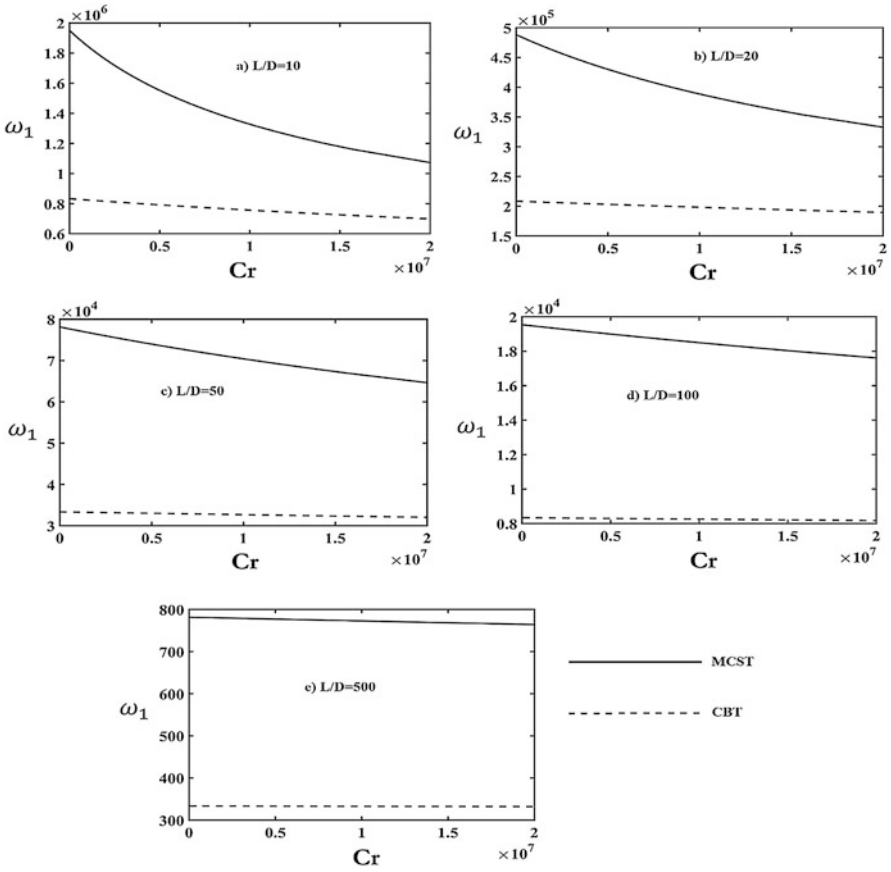

Fig. 4 Effects of flexibility of crack on the natural frequencies of the cracked microbeam for MCST and for (**a**) L/D = 10, (**b**) L/D = 20, (**c**) L/D = 50, (**d**) L/D = 100, and (**e**) L/D = 500

ratio $Cr = 3.5 \times 10^6$ in both modified couple stress theory (MCST) and classical theory (CT).

Summary/Conclusions

Free vibration of cracked microbeam is investigated based on modified couple stress theory using finite element solution. The finite element formulation is derived for free vibration of cracked microbeam on the basis of modified couple stress theory. The effects of some parameters such as locations of crack, geometry parameters, and flexibility of crack on the natural frequencies of the microbeam are investigated. It is

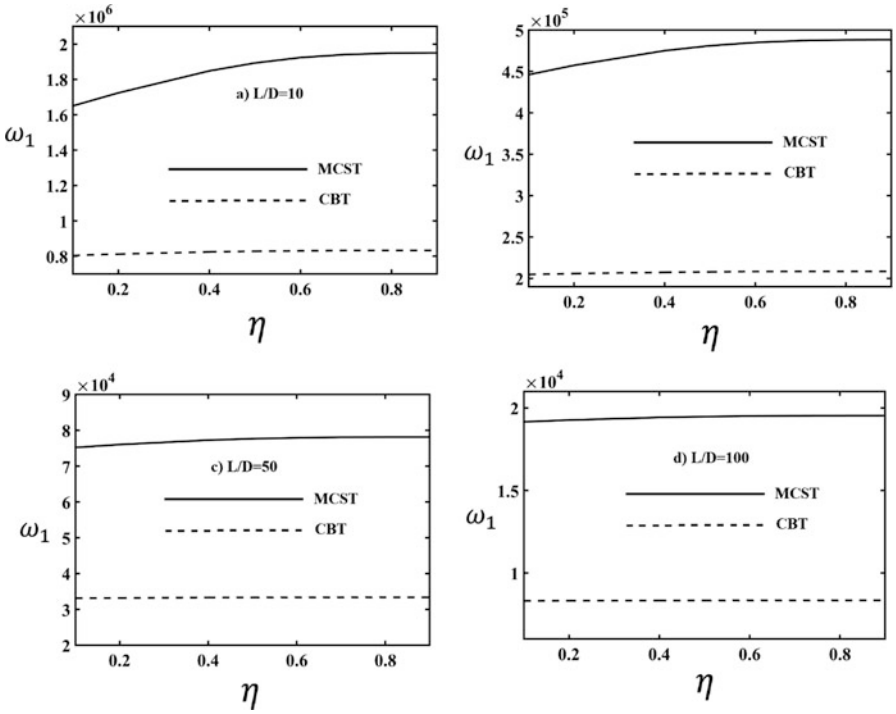

Fig. 5 Effects of crack location ratio (η) on the natural frequencies of the cracked microbeam for MCST and CT for (**a**) L/D = 10, (**b**) L/D = 20, (**c**) L/D = 50, and (**d**) L/D = 100

concluded from the investigations that the obtained frequency values based on MCST are higher than the frequency values based on CBT. An increment of the flexibility of crack causes a decrease in the frequencies of microbeam. Similarly, as L/D ratio increases, values of frequency decrease. In addition, when the crack location ratio increases, frequency values of microbeam increase.

References

Ş.D. Akbaş, Static analysis of a nano plate by using generalized differential quadrature method. Int. J. Eng. Appl. Sci. **8**(2), 30–39 (2016a)

Ş.D. Akbaş, Forced vibration analysis of viscoelastic nanobeams embedded in an elastic medium. Smart Struct. Syst. **18**, 1125–1143 (2016b)

Ş.D. Akbaş, Analytical solutions for static bending of edge cracked micro beams. Struct. Eng. Mech. **59**, 579–599 (2016c)

Ş.D. Akbaş, Static, vibration, and buckling analysis of Nanobeams. Nano **123** (2017a)

Ş.D. Akbaş, Free vibration of edge cracked functionally graded microscale beams based on the modified couple stress theory. Int. J. Struct. Stab. Dyn. **17**, 1750033 (2017b)

Ş.D. Akbaş, Forced vibration analysis of cracked functionally graded microbeams. Advances in Nano Research **6**(1), 39 (2018a)

Ş.D. Akbaş, Forced vibration analysis of cracked nanobeams. J. Braz. Soc. Mech. Sci. Eng. **40**(8), 392 (2018b)
Ş.D. Akbaş, Modal analysis of viscoelastic nanorods under an axially harmonic load. Adv. Nano Res. **8**(4), 277 (2020)
B. Akgoz, O. Civalek, Modeling and analysis of micro-sized plates resting on elastic medium using the modified couple stress theory. Meccanica **48**(4), 863–873 (2013)
R. Ansari, J. Torabi, A. Norouzzadeh, Bending analysis of embedded nanoplates based on the integral formulation of Eringen's nonlocal theory using the finite element method. Phys. B Condens. Matter **534**, 90–97 (2018)
O. Civalek, B. Uzun, M.O. Yayli, B. Akgoz, Size-dependent transverse and longitudinal vibrations of embedded carbon and silica carbide nanotubes by nonlocal finite element method. The Eur. Phys. J. Plus **135**(4), 381 (2020)
C. Demir, O. Civalek, A new nonlocal FEM via Hermitian cubic shape functions for thermal vibration of nano beams surrounded by an elastic matrix. Compos. Struct. **168**, 872–884 (2017)
A.C. Eringen, Nonlocal polar elastic continua. Int. J. Eng. Sci. **10**(1), 1–16 (1972)
A.C. Eringen, On differential equations of nonlocal elasticity and solutions of screw dislocation and surface waves. J. Appl. Phys. **54**(9), 4703–4710 (1983)
H. Farokhi, M.H. Ghayesh, M. Amabili, Nonlinear dynamics of a geometrically imperfect microbeam based on the modified couple stress theory. Int. J. Eng. Sci. **68**, 11–23 (2013)
M. Ghadiri, H. Safarpour, Free vibration analysis of embedded magneto-electro-thermo-elastic cylindrical nanoshell based on the modified couple stress theory. Appl. Phys. A **122**(9), 833 (2016)
B.S.M. Hasheminejad, B. Gheshlaghi, Y. Mirzaei, S. Abbasion, Free transverse vibrations of cracked nanobeams with surface effects. Thin Solid Films **519**, 2477–2482 (2011)
M. Hemmatnezhad, R. Ansari, Finite element formulation for the free vibration analysis of embedded double-walled carbon nanotubes based on nonlocal Timoshenko beam theory. J. Theor. Appl. Phys. **7**(1), 6 (2013)
A. Kazemi, R. Vatankhah, M. Farid, Natural frequency of size-dependent microplates with piezoelectric layers, in *2017 7th International Conference on Modeling, Simulation, and Applied Optimization (ICMSAO)*, (IEEE, 2017, April), pp. 1–5
B.H. Kim, T. Park, G.Z. Voyiadjis, Damage estimation on beam-like structures using the multi-resolution analysis. Int. J. Solids Struct. **43**(14–15), 4238–4257 (2006)
D.C.C. Lam, F. Yang, A.C.M. Chong, J. Wang, P. Tong, Experiments and theory in strain gradient elasticity. J. Mech. Phys. Solids **51**(8), 1477–1508 (2003)
G. Lee, T. Park, G.Z. Voyiadjis, Vibration analysis of multi-delaminated beams. Compos. Part B **34**, 647–659 (2003)
Y. Li, E.S. Pan, Static bending and free vibration of a functionally graded piezoelectric microplate based on the modified couple-stress theory. Int. J. Eng. Sci. **97**, 40–59 (2015)
S.J. Liu, S.H. Qi, W.M. Zhang, Vibration behavior of a cracked micro-cantilever beam under electrostatic excitation. *ZhendongyuChongji/*J. Vib. Shock **32**, 41–45 (2013)
J. Loya, J. López-Puente, R. Zaera, J. Fernández-Sáez, Free transverse vibrations of cracked nanobeams using a nonlocal elasticity model. J. Appl. Phys. **105**, 044309 (2009)
F.F. Mahmoud, M.A. Eltaher, A.E. Alshorbagy, E.I. Meletis, Static analysis of nanobeams including surface effects by nonlocal finite element. J. Mech. Sci. Technol. **26**(11), 3555–3563 (2012)
R.D. Mindlin, Influence of couple-stresses on stress concentrations. Exp. Mech. **3**, 1–7 (1963)
R.D. Mindlin, Second gradient of strain and surface-tension in linear elasticity. Int. J. Solids Struct. **1**(4), 417–438 (1965)
R.D. Mindlin, H.F. Tiersten, Effects of couple-stresses in linear elasticity. Arch. Ration. Mech. Anal. **11**, 415–448 (1962)
T. Park, S. Lee, G.Z. Voyiadjis, Recurrent single delaminated beam model for vibration analysis of multi-delaminated beams. J. Eng. Mech., ASCE **130**(9), 1072–1082 (2004)
X.-L. Peng, X.-F. Li, G.-J. Tang, Z.-B. Shen, Effect of scale parameter on the deflection of a nonlocal beam and application to energy release rate of a crack. ZAMM – J. Appl. Math. Mech. **95**, 1428–1438 (2015)

J.K. Phadikar, S.C. Pradhan, Variational formulation and finite element analysis for nonlocal elastic nanobeams and nanoplates. Comput. Mater. Sci. **49**(3), 492–499 (2010)
M. Rahaeifard, M. Ahmadian, K. Firoozbakhsh, Vibration analysis of electrostatically actuated nonlinear microbridges based on the modified couple stress theory. Appl. Math. Model. **39**(21), 6694–6704 (2015)
H. Roostai, M. Haghpanahi, Vibration of nanobeams of different boundary conditions with multiple cracks based on nonlocal elasticity theory. Appl. Math. Model. **38**, 1159–1169 (2014)
G. Shi, G.Z. Voyiadjis, A sixth-order theory of shear deformable beams With variational consistent boundary conditions. J. Appl. Mech., ASME. **78**(2), 11 pages (2011). https://doi.org/10.1115/1.4031896
Y. Tadi Beni, A. Jafari, H. Razavi, Size effect on free transverse vibration of cracked Nano-beams using couple stress theory. Int. J. Eng. **28**, 296–304 (2015)
K. Torabi, J. Nafar Dastgerdi, An analytical method for free vibration analysis of Timoshenko beam theory applied to cracked nanobeams using a nonlocal elasticity model. Thin Solid Films **520**, 6595–6602 (2012)
R.A. Toupin, Elastic materials with couple-stresses. Arch. Ration. Mech. Anal. **11**(1), 385–414 (1962)
B. Uzun, O. Civalek, Free vibration analysis Silicon nanowires surrounded by elastic matrix by nonlocal finite element method. Adv. Nano Res. **7**(2), 99 (2019)
B. Uzun, M.O. Yayli, Nonlocal vibration analysis of Ti-6Al-4V/ZrO_2 functionally graded nano-beam on elastic matrix. Arab. J. Geosci. **13**(4), 1–10 (2020)
K. Wang, B. Wang, Timoshenko beam model for the vibration analysis of a cracked nanobeam with surface energy. J. Vib. Control. **21**(12), 2452–2464 (2015)
F.A.C.M. Yang, A.C.M. Chong, D.C.C. Lam, P. Tong, Couple stress based strain gradient theory for elasticity. Int. J. Solids Struct. **39**(10), 2731–2743 (2002)
M.Ö. Yayli, Weak formulation of finite element method for nonlocal beams using additional boundary conditions. J. Comput. Theor. Nanosci. **8**(11), 2173–2180 (2011)
M.O. Yayli, Torsional vibrations of restrained nanotubes using modified couple stress theory. Microsyst. Technol. **24**(8), 3425–3435 (2018)
M.Ö. Yayli, A.E. Çerçevik, Axial vibration analysis of cracked nanorods with arbitrary boundary conditions. J. Vibroeng. **17**(6), 2907–2921 (2015)
M.Ö. Yayli, S.Y. Kandemir, A.E. Çerçevik, Torsional vibration of cracked carbon nanotubes with torsional restraints using Eringen's nonlocal differential model. J. Low Freq. Noise, Vib. Active Control **38**(1), 70–87 (2019)
A. Zargaripoor, A. Daneshmehr, I. Isaac Hosseini, A. Rajabpoor, Free vibration analysis of nanoplates made of functionally graded materials based on nonlocal elasticity theory using finite element method. J. Comput. Appl. Mech. **49**(1), 86–101 (2018)

Size Effect on Damage Response of Triangular Flexural Test Method

8

Babür Deliktaş, Hakan Tacettin Türker, Faiz Agh Shareef, and Ferhun Cem Caner

Contents

Introduction 168
Experimental Program 171
Experimental Setup 171
Experimental Results 173
Determining Size Effect on Biaxial Tensile Strength 174
Biaxial Tensile Strength 174
Regression Analysis to Determine Size Effect Parameters 174
Numerical Analysis of the Triangular Plate Test (TPT) Specimens 177
Microplane Model (M7) 178
Validation of the Numerical Procedure 180
Finite Element Model for the Triangular Plate Test 183
Summary/Conclusions 192
References 194

B. Deliktaş (✉)
Department of Civil Engineering, Faculty of Engineering-Architecture, Uludag Universitesi, Bursa, Turkey
e-mail: bdeliktas@uludag.edu.tr

H. T. Türker · F. A. Shareef
Department Faculty of Engineering, Department of Civil Engineering, Bursa Uludag Universitesi, Bursa, Turkey
e-mail: hakantturker@uludag.edu.tr

F. C. Caner
Institute of Energy Technologies, School of Industrial Engineering, Universitat Politècnica de Catalunya, Barcelona, Spain

Department of Materials Science and Metallurgical Engineering, Universitat Politècnica de Catalunya, Barcelona, Spain
e-mail: ferhun.caner@upc.edu

© Springer Nature Switzerland AG 2022

G. Z. Voyiadjis (ed.), *Handbook of Damage Mechanics*,
https://doi.org/10.1007/978-3-030-60242-0_89

Abstract

The size effect is an important application of concrete fracture mechanics. Many studies have been done on the size effect in recent years. Most of studies carried out by using specimens under uniaxial tensile stress. In this study, the size effect on the tensile strength of mortar mixtures was investigated. The triangular plate method was used to find size effect on the tensile strength of the mortar mixtures. In the study, the mortar mixtures specimens having two different water-cement ratios and various sizes in the absence and presence of steel fibers were prepared. For this purpose, two classes of mortar having water-cement ratios of 0.42 without steel fiber and containing 1% steel fibers were designed. By adding 1%, steel fiber by a total of 30 triangular plate specimens with five different sizes was prepared. The size effect analyses were made on the data obtained from the experiments and size effect curves were established. Classical Type I size effect analyses of peak loads obtained from these tests are performed. The Microplane Model M7 is used to predict the peak loads and fracture patterns, size effect, and the load-deflection curves of both the geometrically similar triangular test specimens. As a result of this study, it is concluded that the triangular plates testing method can be used as an alternative test to determine the size effect on the tensile strength and fracture behavior of the mortar mixture in both presence and absence of steel fibers.

Keywords

Size Effect · Biaxial Strength of Concrete · Triangular Biaxial Testing · Biaxial Flexure Test · Finite Element Analysis

Introduction

Concrete is undoubtedly the most important and widely used construction material of the late twentieth century. Conventionally, concrete is usually utilized for its compressive strength in the structure and its tensile strength is neglected due to the fact that it is approximately 8–12% of their compressive strength (Chen et al. 2013, 2014). However, in most of the cases in practice, concrete members are subjected to a wide range of complex states of stress where both concrete compressive strength and tensile strength are critical mechanical properties, therefore the tensile strength of concrete members cannot be avoided in structure design (Lemnitzer et al. 2008). Especially, in many unreinforced concrete structures, such as road pavements, airplane runways, dams, and nuclear containments, concrete members are subjected to biaxial tension that needs to be known for the analysis of concrete elastic and inelastic deformational behavior. Because concrete is a nonhomogeneous material it collapses usually in brittle manner where a sudden reduction in the load occurs after the load carrying capacity is reached. One of the reasons of this sudden load reduction which negatively affects behavior and safety is the size effect (Bazant and Kazemi 1991).

Size effects in the tensile behavior of concrete have been explained in great detail by Bazant and Kazemi (1991) and Tang et al. (1996). Although extensive experimental and numerical studies have been performed to determine the size effect on the tensile strength of concrete (Zheng et al. 2001; Dabbagh 2016), two types of testing methodologies such direct and indirect have been widely used to determine the 63 tensile strength of concrete. However, the direct tensile test method is hard to perform on plain concrete because the gripping and alignment of a specimen during placement of the testing specimen in the testing machine is not very easy (Li et al. 1996; Naaman and Reinhardt 1996; Gettu and Bryan E. Barragán et al. 2003). On the contrary, in the indirect test methods such as the splitting (or Brazilian) test and the three- or four-point bending tests the testing procedure and the specimen preparation are simple (Carmona 2009).

Therefore, an indirect testing method such as biaxial flexure test (BFT) that was suggested by Kupfer et al. (1969); Muzyka (2002); Zi et al. (2008) has been used to determine the biaxial tensile strength of concrete. They used disc specimens where a circular ring was placed throughout its perimeter for supporting, and a small circular ring was used for loading at its center.

Kim et al. (2011) have performed a number of BFTs to investigate the size effect on the biaxial strength of concrete specimens having three different sizes. They compared their results obtained for the biaxial strength with the tensile strength obtained from the uniaxial flexural test. They showed that the tensile strength obtained from the biaxial test was 19% greater than the tensile strength measured in the classical modulus of rupture test. The detailed experimental procedure and the results for the determining the size effects on the biaxial tensile strength of concrete were reported in the paper by Zi et al. (2014a, b), where they have tested three different sized unreinforced circular plates. They reported that the size effect on the equi-biaxial tensile strength was stronger than it was on the uniaxial tensile strength. Type of the size effect was found to be the characteristics of the deterministic Type I size effect. Kim et al. (2013) and Zi et al. (2014a, b) performed the biaxial flexure tests on the various sizes of specimens under axisymmetric loading. They showed that although the stress state in these tests was axisymmetric, the fracture patterns were not. Kirane et al. (2014) performed three-dimensional stochastic finite-element analysis where they predicted the size effect type and investigated the fracture behavior of biaxially loaded concrete members. They implemented the microplane constitutive Model M7 in to the finite element code. Verification and calibration of the model were made by fitting the measured load-deflections curves and fracture patterns of discs with various thicknesses of 30, 48, and 75 mm, similar in three dimensions, and on flexure tests on four-point loaded beams. They showed that deformability of the supports and the type of interaction types of supports in term of their lifting and sliding have a large effect on the fracture pattern, the strength, and Young's modulus of concrete.

As reported from previous studies the strength measured by BFT was influenced by several factors. Therefore, a new test method for the biaxial tensile strength of concrete was proposed by Türker (2015). In the proposed test setup, specimens prepared in a triangular plate was supported on its bottom face by three small

spherical silver balls and loaded externally on the top face by a small spherical silver ball from the center of gravity of specimen. He derived a simple equation for biaxial flexural tensile strength of concrete by using yield line theory (YLT), which is a kinematic method of plastic analysis. Based on the results of three-point flexural tests and FE analyses it was concluded that the proposed method and the derived closed-form equation were robust and reliable in determining the biaxial tensile strength of concrete. Experimental results also exhibited that biaxial tensile strength measured by proposed method was about 22% lower than that of the flexural strength obtained from three-point flexural test. The more detailed experimental studies on the triangular plate test have been performed by Mirkheel (2018) to investigate the size effect on tensile strength of two different water-cement ratio concretes material considering both cases of plain concrete and fiber reinforced concrete.

Supports play crucial roles in the test setup of this type testing due to the friction that exists between the supports and the specimen. The interaction between the support and the specimen can be treated properly by the finite element method in order to provide better understanding of the stress state in the specimen as well as the interaction between the specimen and the supports. However, the finite element method requires a good description of the actual material behavior under different load combinations in order to yield accurate and realistic results.

This study encompasses a numerical investigation on the fracture behavior of concrete under biaxial loading conditions, with particular emphasis on both the size effect and a constitutive modeling. In order to enable numerical prediction of such a behavior through the finite element method a number of numerical studies were carried out on the geometrically similar triangle plate series. The size effect on the fracture parameters of test specimens were investigated by using peak loads obtained from the finite element analyses with M7 model, which is the last series microplane model developed by Bazant group as a constitutive model for concrete. To this end, a total of 30 triangular plate test specimens in five different sizes, including three samples in each of the two different water cement ratio, have been analyzed to determine their peak loads.

The scopes of the numerical study are as follows: To investigate the size effect on biaxial tensile strength of concrete considering both cases of plain concrete and fiber reinforced concrete; to produce reliable test data of strength concrete by designing an appropriate test setup for biaxial testing; to determine biaxial the strength and to predict the load-deformation behavior of concrete under biaxial loading conditions; to identify the different failure modes and crack patterns caused by the biaxial loading; to determine the effect of the support condition, the geometry, and the size on failure modes and crack patterns on the test specimens; and to calibrate and implement the constitutive model for concrete, namely microplane model M7f, suitable for the finite element analysis of concrete. The detailed numerical procedures and the results of the analyses are reported in this chapter.

The robust homogeneous stress and displacement distributions throughout top face of the specimens have been observed from the results of the finite element simulation. However, a distinct continuous crack develops only after the peak load

and leads to a deterministic Type I size effect. The results of the numerical simulation verified that triangular test method can be used to determine the biaxial tensile strength of concrete.

Experimental Program

Experimental procedures of triangle plate method (TPM) are explained in detail and a comprehensive group of test results obtained from the performed tests are presented in this section.

Experimental Setup

In this new testing method, the samples are prepared in the form of equilateral triangular plates where the load is applied to the center of gravity of the sample and the supports are placed at one-third of the median of the triangle (Fig. 1).

In this new testing method, the samples are prepared in the form of equilateral triangular plates where the load is applied to the center of gravity of the sample. The supports are placed at one-third of the median of the triangle to kept them away from the edges of the sample in order to prevent formation of crushing fractures at the edges due to the supports. In order to measure the displacement in the plates, a precision of one-thousandth of an LVDT plates was placed at the point where the triangular intersection of the triangles at the lower surface of the sample. The loading is carried out by means of steel balls at the point where the triangular side of the triangle intersects at the upper surface of the sample. The bearing and loading balls are secured using hex nuts and thus free supports are formed (Fig. 2).

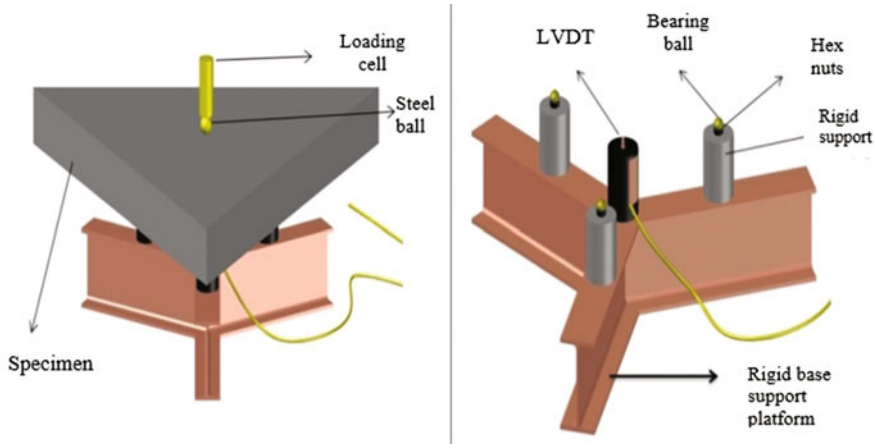

Fig. 1 Demonstration of bearing platform and sample loading in the TPM

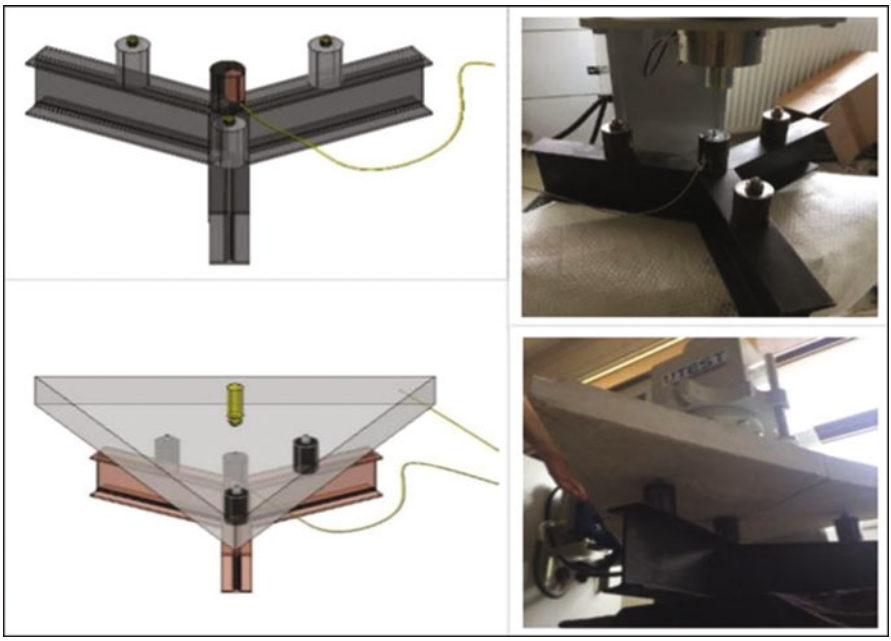

Fig. 2 Display of triangle plate loading and support platforms

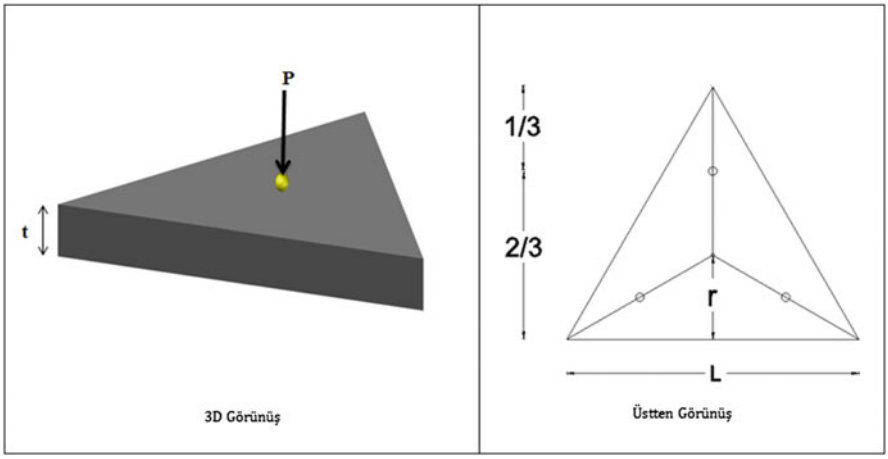

Fig. 3 Test setup of triangle plate samples

In order to examine the size effect on tensile strengths of the triangular plate samples, the thickness of the plates, t, was considered to be characteristic dimension and five different samples of R1, R2, R3, R6, and R7 having constant, t/r ratios were prepared (Fig. 3).

Table 1 Details of supporting and loading of TP samples

Sample	Number	L (mm)	t (mm)	r (mm)	t/r
R1	3	1050	75	303.10	0.25
R2	3	875	62.50	252.60	0.25
R3	3	700	50	202.10	0.25
R6	3	420	30	121.20	0.25
R7	3	350	25	101.00	0.25

Table 2 Details of mix proportion for concrete mix design

Mix Proportions for Concrete Mix Design		
		Unit weight: Kg/m^3
Water/cement ratio	Materials	(gr)
0.42	Water	210
	Cement	500
	Aggregate	1375
	Admixture	1.5
	Steel fiber	68.78
Total		2155.28

The details about the values of geometrical dimensions of the triangular plates are given in Table 1.

A total of 30 triangular plate test specimens of both plain and fibrous concrete in five different sizes having three samples in each of size with the water cement ratio of 0.42 were using mix proportions given in Table 2.

Concrete types are named as 042PC for the plain concrete and 042FC for the fibrous concrete. The peak load of each test specimen was measured to determine the size effect on the biaxial tensile strength of the both plain and fibrous concrete.

Experimental Results

The test results for the collapse loads obtained from the seven different triangle test specimens having different sizes, including three samples in each of the two different types of plain concrete and fibrous concretes, are given in Table 3.

In Table 3 the measured peak loads at the collapse are presented for plain concrete specimens and for the fibrous reinforced concrete specimens with the water-cement ratio, 0.42. As one can see in the table that for some samples there are no values presented for their measured peak loads since these samples were either damaged during transportation or not proper casting into forms tensile strength of concrete, the peak loads results obtained from the triangle plate test method is used in the simple formula, derived by Turker using the Yield Line Method (YLM) Kennedy and Goodchild (2004) was used by Türker (2015), which is given as

$$\sigma_N = \frac{2P_u}{t^2\sqrt{3}} \tag{1}$$

Table 3 Collapse loads of triangular plate samples

Samples		Dimensions		Collapse loads for various types of concrete specimens	
				042 PC	042 FC
		L (mm)	t (mm)	Pu (kN)	Pu (kN)
R1	R11	1050	75	16.987	30.711
	R12	1050	75	18.746	33.877
	R13	1050	75	19.561	35.287
R2	R21	875	62.5	12.113	23.481
	R22	875	62.5	10.953	24.163
	R23	875	62.5	10.926	23.265
R3	R31	700	50	9.294	14.039
	R32	700	50	8.357	13.278
	R33	700	50	9.56	16.595
R6	R61	420	30	3.462	5.688
	R62	420	30	3.796	6.261
	R63	420	30	3.693	6.461
R7	R71	350	25	3.375	4.412
	R72	350	25	3.172	3.906
	R73	350	25	3.051	5.51

Determining Size Effect on Biaxial Tensile Strength

Biaxial Tensile Strength

In Eq. 1 Reference source not found., σ_N is calculated tensile strength, t is the thickness of TP, and P_u is the peak load of the plate at the time of collapse. The biaxial tensile strength of the concrete calculated based on the developed tensile strength formula in Eq. (1) is presented in the Tables 4 and 5

Regression Analysis to Determine Size Effect Parameters

For the size effect analysis of the triangular plates, Type I size effect relation given by Bazant was used. Type I size effect relation applies to the non-notched elements or elements having no preexisting crack where the maximum load occurs as soon as the fracture process zone is fully developed and its expression is given as Korol and Tejhman (2012).

$$\sigma_N = f_r^{\infty}\left[1 + \frac{rD_b}{D}\right]^{\frac{1}{r}} \tag{2}$$

In Eq. (2), D is characteristic structure size which is represented here by thickness of the triangular plate test elements chosen as the characteristic dimension. f_r^{∞}, D_b,

Table 4 The average collapse loads and stresses in **042PC**

Samples		Dimensions		Peak Load Pu (kN)	Stress (MPa)	Average Stress (MPa)
		L (mm)	t (mm)			
R1	R11	1050	75	16.987	3.487	3.784
	R12	1050	75	18.746	3.848	
	R13	1050	75	19.561	4.015	
R2	R21	875	62.5	12.113	3.581	3.349
	R22	875	62.5	10.953	3.238	
	R23	875	62.5	10.926	3.23	
R3	R31	700	50	9.294	4.293	4.189
	R32	700	50	8.357	3.86	
	R33	700	50	9.56	4.416	
R6	R61	420	30	3.462	4.441	4.684
	R62	420	30	3.796	4.871	
	R63	420	30	3.693	4.738	
R7	R71	350	25	3.375	6.235	5.911
	R72	350	25	3.172	5.86	
	R73	350	25	3.051	5.636	

Table 5 The average collapse loads and stresses in **042FC**

Samples		Dimensions		Peak Load Pu (kN)	Stress (MPa)	Average Stress (MPa)
		L (mm)	t (mm)			
R1	R11	1050	75	30.711	6.304	6.834
	R12	1050	75	33.877	6.954	
	R13	1050	75	35.287	7.244	
R2	R21	8750	62.5	23.481	6.941	6.987
	R22	8750	62.5	24.163	7.143	
	R23	8750	62.5	23.265	6.877	
R3	R31	700	50	14.039	6.484	6.761
	R32	700	50	13.278	6.133	
	R33	700	50	16.595	7.665	
R6	R61	420	30	5.688	7.298	7.873
	R62	420	30	6.261	8.033	
	R63	420	30	6.461	8.289	
R7	R71	350	25	4.412	8.151	8.516
	R72	350	25	3.906	7.216	
	R73	350	25	5.51	10.18	

r are positive unknown empirical constants need to be determined from experiments. f_r^{∞} represents the solution elastic brittle strength reached as the nominal strength for large structure. r controls the curvature and shape of the curve. The values $r = 1$ or 2 have been used for concrete. D_b is the deterministic characteristic length having the meaning of the thickness of the cracked layer. Linear regression analysis performed using experimental data along with Eq. (2) to determine unknown empirical

constants, f_r^{∞} and D_b. The empirical constant, r in Eq. 2, was taken to be equal to 1. Type I size effect relation given by Eq. (2) can be linearized in the form of $Y = C + A\,X$ by introducing the following relations, $Y = \sigma_N$,, $C = f_{r^{\infty}}$, $A = C\,D_b$, and $X = 1/D$. After linearizing relation of Type I size effect law, the unknown empirical constants, f_r^{∞} and D_b, for each set of testing group are determined using linear regression analyses. The linear regression analysis is first performed for the plain concrete having the water-cement ratios of 0.42 using test data given in Table 1 to obtain the empirical constants, f_r^{∞} and D_b, which are presented in Table 6.

As one can see from Table 6 the values obtained from linear regression analysis for empirical constants C and A are found to be statistically meaningful ($p < 0.000$). The relation between σ_N and 1/D can be given using determined empirical constants in the following expression

$$\sigma_N = 3.616 + 34.761/D \tag{3}$$

The line obtained from this equation and experimental data between σ_N and 1/D is presented in (Fig.4).

Figure 5 shows that there is a clear size effect observed on the tensile strength of the plain triangular plate specimens. The regression analysis is also performed for the fibrous concrete having water-cement ratios of 0.42 using test data given in Table 5 to obtain the empirical constants, f_r^{∞} and D_b, which are presented in (Table 7).

As one can see from Table 7 the values obtained from linear regression analysis for empirical constants ($f_{r^{\infty}} = C$) and A are found to be statistically meaningful

Table 6 Linear regression constants for **042PC**

Model	Unstandardized Coefficients		Standardized Coefficients	t-test	Statistical significance
	B	Std. Error	Beta		
Constant	3.616	0.147		24.549	0
X	34.761	5.531	0.867	6.284	0

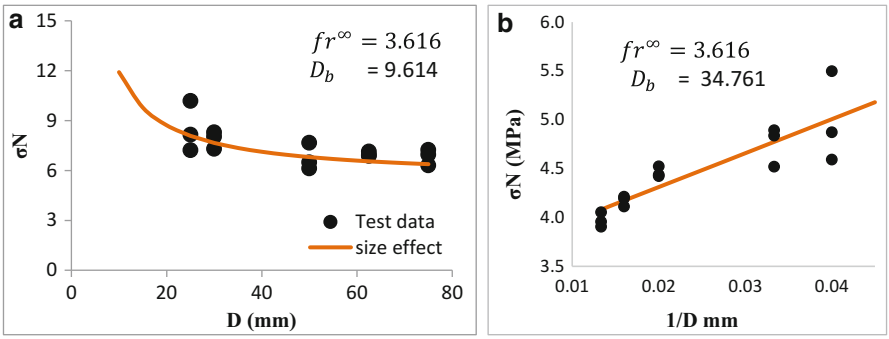

Fig. 4 (**a**) Size effect in 042PC, (**b**) linearized results for 042PC

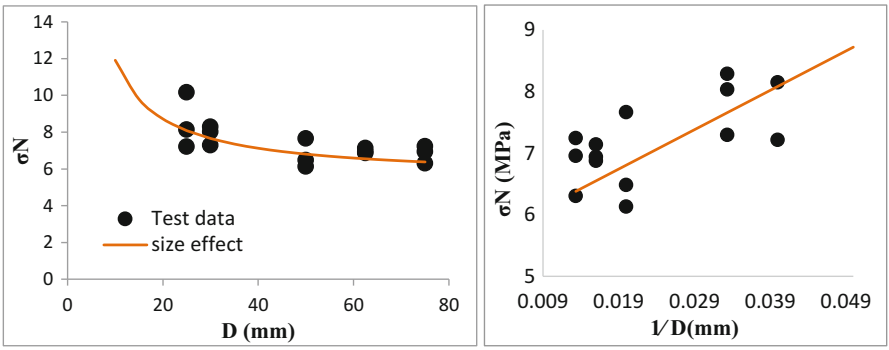

Fig. 5 **(a)** Size effect in 042PC, **(b)** Linearized results for 042FC

Table 7 Linear regression constants for **042FC**

Model	Unstandardized Coefficients		Standardized Coefficients	t-test	Statistical significance
	B	Std. Error	Beta		
Constant	5.828	0.504	0	11.574	0
X	63.84	18.911	0.683	3.376	0.005

($p < 0.005$). The relation between σ_N and 1/D can be given using determined empirical constants in the following expression

$$\sigma_N = 5,828 + 63,84/D \tag{4}$$

As a result of this size effect analysis, it can be concluded that there is size effect on the tensile strength of the fiber reinforced concrete. For our interest of investigating the effects of fibrous content on the size effect, it is found that fibrous concrete specimens show more strong size effect than the plain concrete specimens (Fig.6)

Numerical Analysis of the Triangular Plate Test (TPT) Specimens

In this section a number of finite element simulations have been performed to predict the biaxial flexural strength of concrete and to gain some insight into failure mechanisms of two different centrally loaded concrete panel such as round panel test (ASTM C 1150) and the recently proposed biaxial triangular flexure test (BTFT). These simulations provide acceptable numerical procedures for validation of experimentally determined tensile strength of cement-based materials.

To achieve these objectives three-dimensional nonlinear finite-element models were developed using the commercial software Abacus/CAE along with the use of the microplane models as material constitutive law. The microplane model, developed by Bazant et al. 2000; Caner and Bazant 2000 for quasi-brittle materials predicts has been proven capable of accurately capturing the damage, fracture

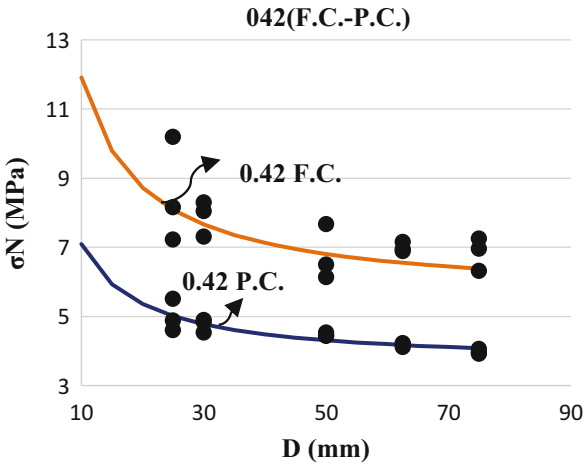

Fig. 6 Comparison of size effects in 042FC and 042PC specimens

behavior, and size effect in various quasi-brittle materials, which exhibit post peak softening damage because of distributed cracking.

The finite element models can reproduce many useful results such as the fracture patterns observed on the test specimens failure loads, the size effects, and the load-deflection curves of both the disc and triangular plates.

Microplane Model (M7)

In this study, latest version of the microplane model, M7f, which was developed primarily for concrete (Bazant and Oh 1985), is used. There are many other microplane models that have been developed for clays, soils, rocks, rigid foams, clays, shape memory alloys, annulus fibrous, and composites (prepreg laminates and braided) (Bazant et al. 2000; Caner and Bazant 2012; Cusatis and Figini 2008; Caner et al. 2011).

The basic idea of the microplane model is that the constitutive law is expressed in terms of vectors of stresses and strains rather than their tensor forms. Figure 7 shows the vectors of stress and strain acting on a generic plane of any orientation in the material microstructure, which is called the microplane.

The Model M7f consists of constitutive laws which are prescribed on various planes in material mesostructure called the "microplane" that relates to stress and strain vectors on these planes. The homogenization of the macroscopic stress tensor is achieved by integration of stress vectors expressed as functions of strain vectors acting on these planes. The strain tensor, called as "kinematic constraint," is projected onto microplanes of different orientations given by the unit normal vector $\vec{n}$.:

$$\epsilon_N = \epsilon_{ij} n_i n_j = \epsilon_{ij} N_{ij} \tag{5}$$

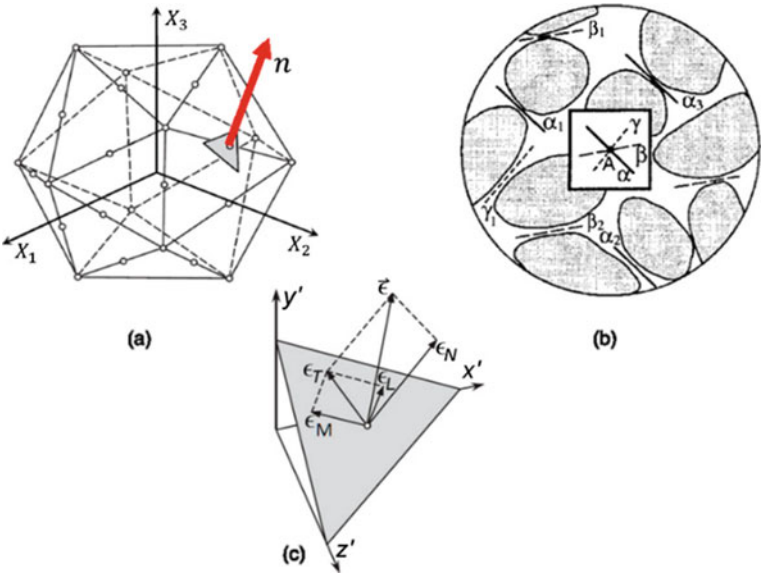

Fig. 7 Schematic representation of microplane model

where there are summation on the repeated indices ranging from 1 to 3. The projected shear strains then are given by

$$\epsilon_L = \epsilon_{ij}\frac{1}{2}\left(n_i l_j + l_i n_j\right) = \epsilon_{ij} L_{ij} \tag{6}$$

And

$$\epsilon_M = \epsilon_{ij}\frac{1}{2}\left(n_i m_j + m_i n_j\right) = \epsilon_{ij} M_{ij} \tag{7}$$

The corresponding normal and shear stress vector can be obtained by using the projected strains on a microplane given by Eqs. (6) and (7), into the prescribed microplane constitutive laws generically given by

$$\begin{aligned}
\sigma_N &= f_N(\epsilon_N, \sigma_v) \quad for\ {\sigma_N}^e > 0 \\
\sigma_N &= f_N(\epsilon_N, \sigma_v) \\
\sigma_v^- &= f_v(\epsilon_v, \epsilon_I, \epsilon_{III}) \\
\sigma_N &= {\sigma_v}^- + \sigma_D^- \quad for\ {\sigma_N}^e < 0 \\
\tau_L &= F_\tau(\sigma_N)\, cos\,(\alpha) \\
\tau_M &= F_\tau(\sigma_N)\, sin\,(\alpha)
\end{aligned} \tag{8}$$

where the functions $\mathcal{F}_N$, $\mathcal{F}_V$, $\mathcal{F}_D$ and $\mathcal{F}_\tau$ represent the microplane normal, volumetric, deviatoric, and shear constitutive laws, respectively. σ_N^e is the elastic microplane

normal stress, ϵ_v is the volumetric strain, σ_v is the volumetric stress, ϵ_I is the maximum principal strain, and ϵ_{III} is the minimum principal strain (for details see Caner and Bažant (2012)). In Eq. (8) the arguments to the microplane constitutive functions include not only the corresponding microplane strains but also other microplane stress variables. Caner and Bažant (2000) identified the set of model parameters through extensive data fitting involving numerous data sets on different concretes. The macroscopic stress tensor without introducing any spurious anisotropy can be calculated by integrating the microplane normal and shear stresses given in Eq. (8) over the surface of a unit hemisphere using the principle of virtual work

$$\sigma_{ij} = \frac{3}{2\pi}\int_S \left(\sigma_N N_{ij} + \tau_l L_{ij} + \tau_M M_{ij}\right) ds \tag{9}$$

The integral in Eq. (9) is evaluated numerically using the Gaussian quadrature for best efficiency and accuracy. Although as low as 21 points can be used to get an approximately isotropic response, in the post-peak region of the stress-strain response the error in isotropy may become too large (Bažant et al. 2000). Thus, a 37-point Gaussian quadrature is employed in the calculations, which allows the complete stress-strain response to be approximately isotropic (Caner and Bažant 2000). Most of the foregoing equations are common to the Model M7 and its many predecessors (models called M1 Bažant and Oh 1985; through M6f Caner and Bažant 2000). However, the Model M7 performs better than its predecessors by (1) predicting correctly the tensile and compressive behavior of concrete under loading and unloading cycles *in addition to* predicting correctly other concrete multiaxial behavior, and (2) predicting correctly the lateral contraction in uniaxial tension.

To accomplish the correct predictions of concrete behavior under such load cycles as well as the correct prediction of lateral contraction under uniaxial tension, the Model M7 uses the so-called volumetric-deviatoric split in microplane normal stress and strain in the inelastic range of response in compression as shown in Eq. (5) but the normal stress and strain without split in both elastic and inelastic ranges of tensile response. Moreover, the model M7 features about the same number of fixed and free parameters as its more recent predecessors (e.g., the Model M4 Bažant et al. 2000; Caner and Bažant 2000).

Validation of the Numerical Procedure

In this section, in order to ensure the accuracy of the proposed numerical modeling, the Centrally Loaded Circular Plate Test, ASTM C1550 (Fig. 10) is simulated to regenerate similar results provided by Kirane et al. (2014). For this purpose, a finite element model for the Circular Plate of ASTM C1550 is established using the geometrical properties given in Table 8.

The circular disc plate is meshed by four-nodded 80,927 tetrahedral elements (C3D4) having average size, wc = 13 mm as shown in Fig. 8. Microplane model is

Table 8 Dimension of the large disc plate

Dimension (mm)	Large disc
Thickness	75
Radius	328.5
Radius of support ring	312.5

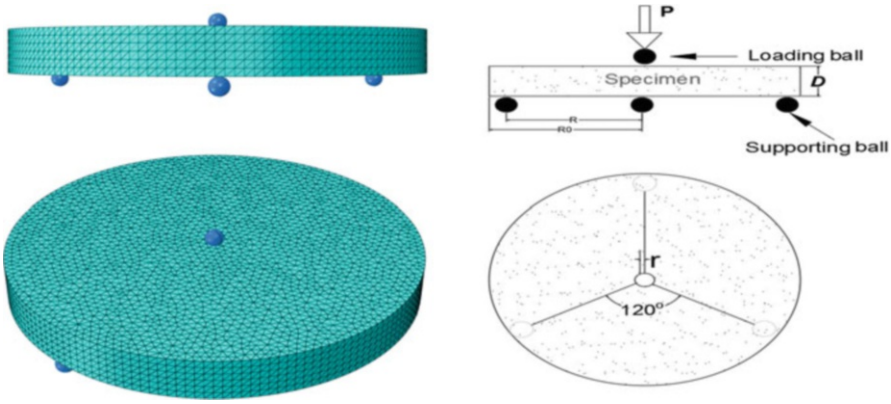

Fig. 8 Finite element model of Centrally Loaded Circular Plate Test, ASTM C1550

Table 9 Elastic material constants of the microplane model (M7) (Kirane et al. 2014)

Material parameter (unit)	Value
Young's modulus E (MPa) (mean)	27,264
Poisson's ratio	0.22
Compressive strength f_c (28 days) (MPa)	33
Density (kg = m^3)	2800
Radial scaling parameter k_1	1.05E-4
k2	80
k3	9.66
k4	10
k5	1
k6	1 × 10e-4
k7	1.8
C4	18.677

incorporated into ABAQUS as user defined material model where all the adjustable M7 free parameters are taken from the paper by (Kirane et al. 2014) Table 9.

In Fig. 9, the dotted lines represent the test data whereas the solid lines represent the prediction obtained from the model. One can see that the force-displacement curve predicted by model is in good match with those ones obtained from experiments in the paper by Kirane et al. (2014). The peak load calculated from the finite element simulation is found as 25 kN which is only 7% lower than the experimental one.

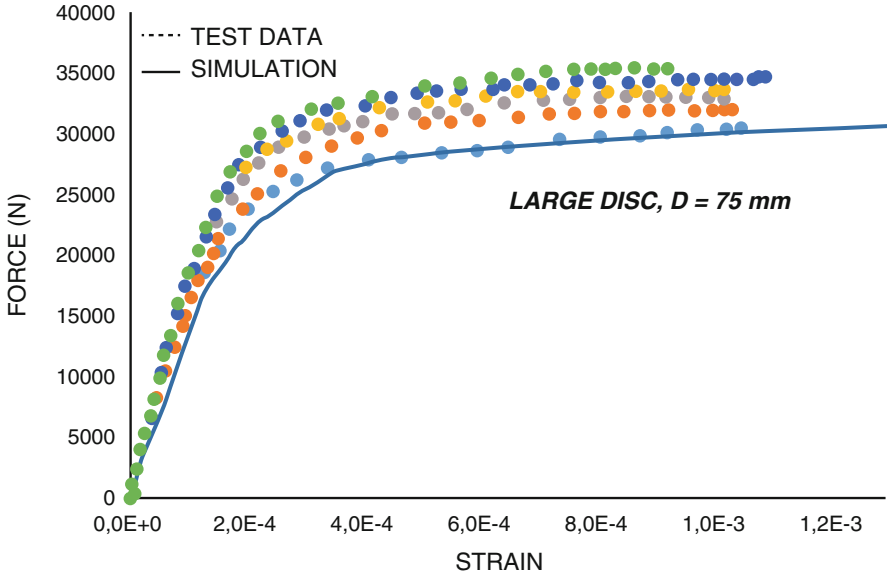

Fig. 9 The force-strain curves obtained from both the simulation and experiments of the circular disc plate

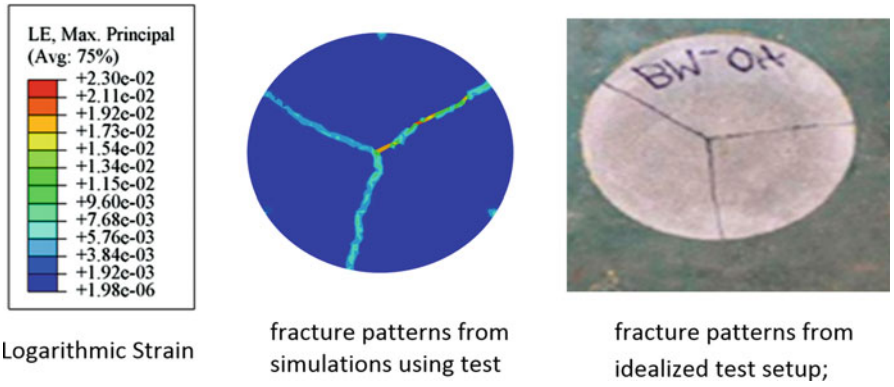

Fig. 10 Counter plot of the maximum principal strain distribution on the circular disc plate. (**a**) Logarithmic strain, (**b**) fracture patterns from simulations using test, (**c**)fracture patterns from idealized test setup

The contour plots of maximum principal strain distribution on the circular plate specimen (Fig. 10) in order to check whether the fracture patterns given in the paper by Zi et al. (2013) and Kim et al. (2014) in their biaxial flexure tests are matched with the fracture pattern obtained from numerical simulation.

As one can see from Fig. 10 that in the centrally loaded circular plate test, ASTM C1550, cracks are developed in the area between the supporting pivots and the center

of the test plate due to the triply axisymmetric stress distribution where the plate broken into three pieces. This type of breaking in the test specimens has been observed and captured by performed finite element simulation (Fig. 10). The presented results indicate that the established finite element model is accurate enough to generate the similar results as those in the experiments provided in the paper by Kirane et al. (2014).

Finite Element Model for the Triangular Plate Test

Having shown the correctness of numerical model in predicting flexural response of the Centrally Loaded Circular Plate Test, a finite element model for the Triangular Plate Test specimen using the geometrical properties given in Table 10 is established in order to predict numerically the biaxial tensile strength of concrete.

In the finite element model, the triangular plate test specimens are meshed by four-nodded 80,927 tetrahedral elements (C3D4) having average size, wc = 13 mm as shown in (Fig. 11). All the adjustable M7 free parameters, similar to those used in the analysis of the centrally loaded circular plate test (Table 9), are also used in the finite element model.

The force-strain curves obtained from both the model prediction and the experimental data are presented in Fig. 12.

The dotted lines represent the test data whereas the solid lines represent the prediction using the model. As one can see that the prediction of the force-strain curve by the simulation of the triangular plate is agree with the results of the test data and the simulation of circular plate. If the peak load estimated by finite element simulation as 27 kN is used in analytical Eq. (1) to calculate biaxial tensile strength, one can find its value as 5.54 MPa, which is quite closer to the one obtained from circular plates test simulation as 5.5 MPa.

Numerical Analysis of the Triangular Plate Test

The experimental test setups presented in section (Table 1) are simulated in this section in order to reach the following objectives of this study: (i) examine the failure modes and crack patterns for different specimen sizes, (ii) determine the effect of the support condition, the geometry, and the size on failure modes and crack patterns on the test specimens, and (ii)adopt a constitutive model suitable for the finite element analysis of concrete and to calibrate it using the experimental test results. To achieve these objectives the M7 free parameters were first calibrated by using the triangular plate tests data provided by Mirkheel (2018).

Table 10 The details of the large discs of triangle plate

Dimension (mm)	Large disc
Thickness	75
Length	657
Length of support ring	312.5

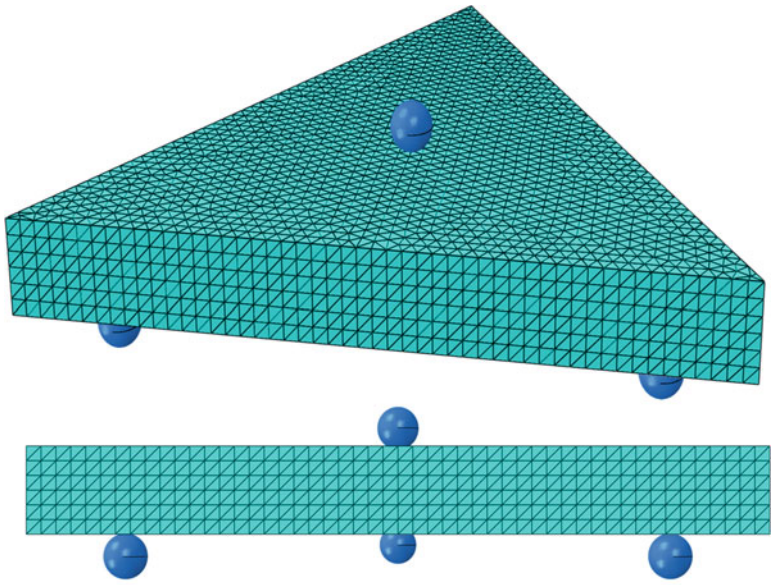

Fig. 11 Finite element Model for the centrally loaded triangle testing

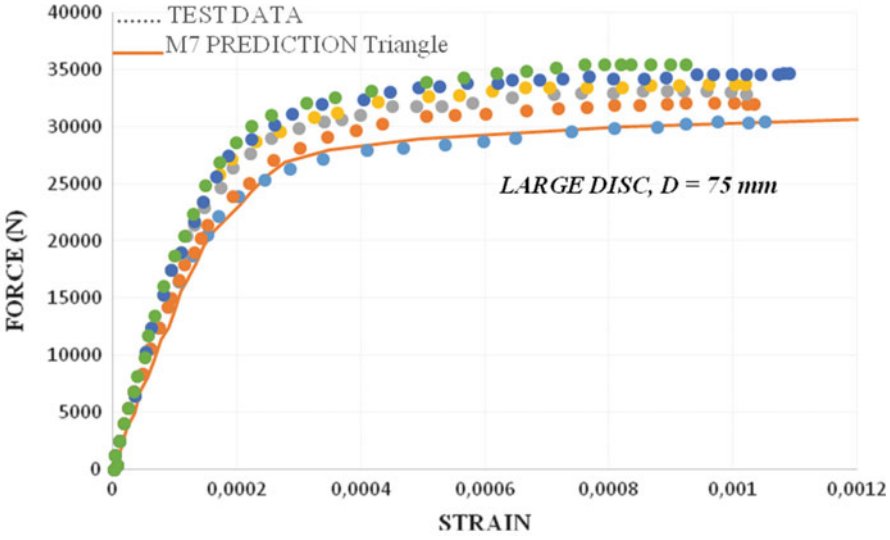

Fig. 12 The force-strain curves of the centrally loaded triangle test

The M7 free parameters are given in Table 11. Enable the model to perform the best fitting of the force-displacement curve to the experimental data as depicted in Fig. 13.

Table 11 Microplane model parameters

Material parameter (unit)	Value
Young's modulus E (MPa) (mean)	18,000
Poisson's ratio	0.12
Compressive strength f_c (28 days)	30
Density (kg = m^3)	2400
Radial scaling parameter $k1_1$	30 E-6
k2	110
k3	9.66
k4	100
k5	1
k6	1 × 10e-4
k7	1.8
C4	80
d1	1.1

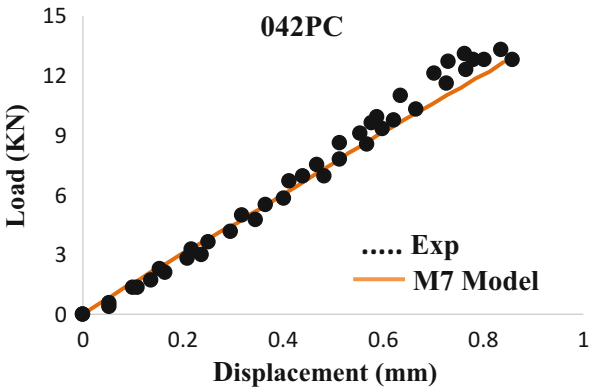

Fig. 13 The model fitting the force-displacement curve to experimental data

Having calibrated M7 free parameters, several finite element simulations are performed on the geometrically scaled triangular plate specimens of various sizes to predict size effect on the tensile strength of concrete. Geometrical properties and their corresponding number of element and nodes generated by the finite element model are presented in Table 12.

The biaxial strength for each of specimen in five different sizes is calculated by using the peak loads predicted by the microplane model into (Eq.1). The measured and predicted peak loads and the biaxial strength calculated using both peak load in to equation are presented in Table 13.

The predicted biaxial strength of each of testing specimens in five different sizes specimens as listed in Table 5.3 are plotted against size D and compared with the test results as shown in Fig. 14 in order to determine experimentally observed size effect on the biaxial tensile strength of the material (Fig. 17).

Table 12 Geometrical dimensions and their corresponding number of elements and nodes in finite-element models for each of five different test specimens

Specimens	Dimensions		Number of Elements	Number of Nods
	L	T		
R1	1050	75	18,448	4176
R2	875	62.5	8381	2023
R3	700	50	11,003	2620
R6	420	30	6213	1544
R7	350	25	5750	1441

Table 13 Biaxial tensile strength for the each of 042 PC in five different sizes

Specimens	Dimensions		Experimental Results		Numerical Predictions	
	L	t	Load Pu (kN)	Strength (MPa)	Load Pu (kN)	Strength (MPa)
R1	1050	75	18.431	3.784	17.78	3.65
R2	875	62.5	11.331	3.349	11.45	3.385
R3	700	50	9.071	4.189	9.14	4.222
R6	420	30	3.65	4.684	3.86	4.952
R7	350	25	3.199	5.911	3.1	5.727

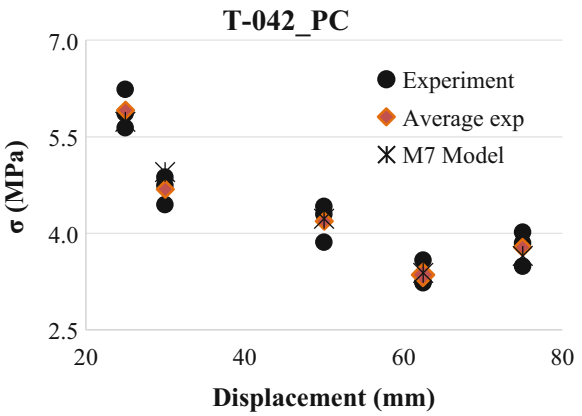

Fig. 14 Variation of the biaxial tensile strength with respect to characteristic size, D of the testing specimen

In Fig. 14 the strength values from individual tests are shown by crosses, and their mean is shown by solid dots. The predicted uniaxial strength values are in good agreement with the mean strength values from the test. These results indicate numerical predictions and verify the experimentally observed size effect on the tensile strength.

Fracture Pattern of the Triangular Plate Tests

In order to examine the failure modes and crack patterns of each specimen in five different specimen sizes of the plain triangular plates, the contour plots of the maximum principal strain distribution on the bottom surface of the biaxial triangular flexure test panels obtained by finite element model and the fracture pattern observed in the performed tests are presented in Fig. 15.

In all testing specimens, no matter of their sizes, the maximum principal strain occurred in the center of the tensile surface of the panels where the cracks were expected to initiate. The strain field of the triangular panel showed threefold symmetry in strain distribution caused by the three supports. These results suggested that cracks in the triangular plates were initiated in the area of higher stress and developed between the support pivots and the center of the test panel. These crack eventually caused the specimen to break into three pieces upon failure, which is coincided with the experimental observations.

Numerical Analysis of the Fibrous Triangular Plate Tests

Embedding fibrous materials into the concrete mixture improves the post-cracking behavior of the concrete and increases the energy absorption capacity of the concrete specimen. For example, enrichment of the concrete mixture with the steel fibers that hold the concrete matrix induces a passive confinement in the out-of-plane direction for the concrete under loading (Marti 1989). The confinement effects of steel fiber on the fibrous concrete specimen under biaxial compression is similar to plain concrete under triaxial loading (Hoover and Bazant 2013; Ince 2013; Mallat and Alliche 2011; Neville 2011). Therefore, due to confinement effect of the steel fiber, the fibrous concrete has biaxial strength generally greater than the biaxial strength of plain concrete.

The increase in biaxial strength of the steel fiber reinforced concrete (SFRC) can be associated to several factors such as fiber volume fraction, fiber aspect ratio, fiber bond strength, and concrete strength (Murugappan et al. 1993). For example, Ince (2013) showed that orientation of fibers due to the direction of casting also affect the biaxial strength of the specimens. Chen et al. suggested that the biaxial compressive strength depends on both the concrete uniaxial compressive strength and the fracture toughness (Ince 2012a, b; Mallat and Alliche 2011). The increase of volume fraction of the steel fiber and the aspect ratio can improve biaxial compressive strength and failure (Muzyka 2002;Hoover and Bazant 2013). Yin et al. and Foltz et al. concluded that the addition of fibers in concrete reinforces the concrete specimen and prevents propagation of tensile cracks, which change the failure mode from splitting tensile failure type to shear failure type (). This indicates that the inclusion of fiber can transform the concrete specimens form brittle to ductile behavior.

Concrete under biaxial tension behaves similar to uniaxial tension and the biaxial strength does not depends on the stress ratio (Kupfer 1989; Kankov 2007; Yazici 2010). However, according to Hussein and Marzouk (2000), the biaxial tensile strength of concrete increases when the biaxial tensile stress ratio is equal to 1, which is different from other researchers mentioned above. They concluded that

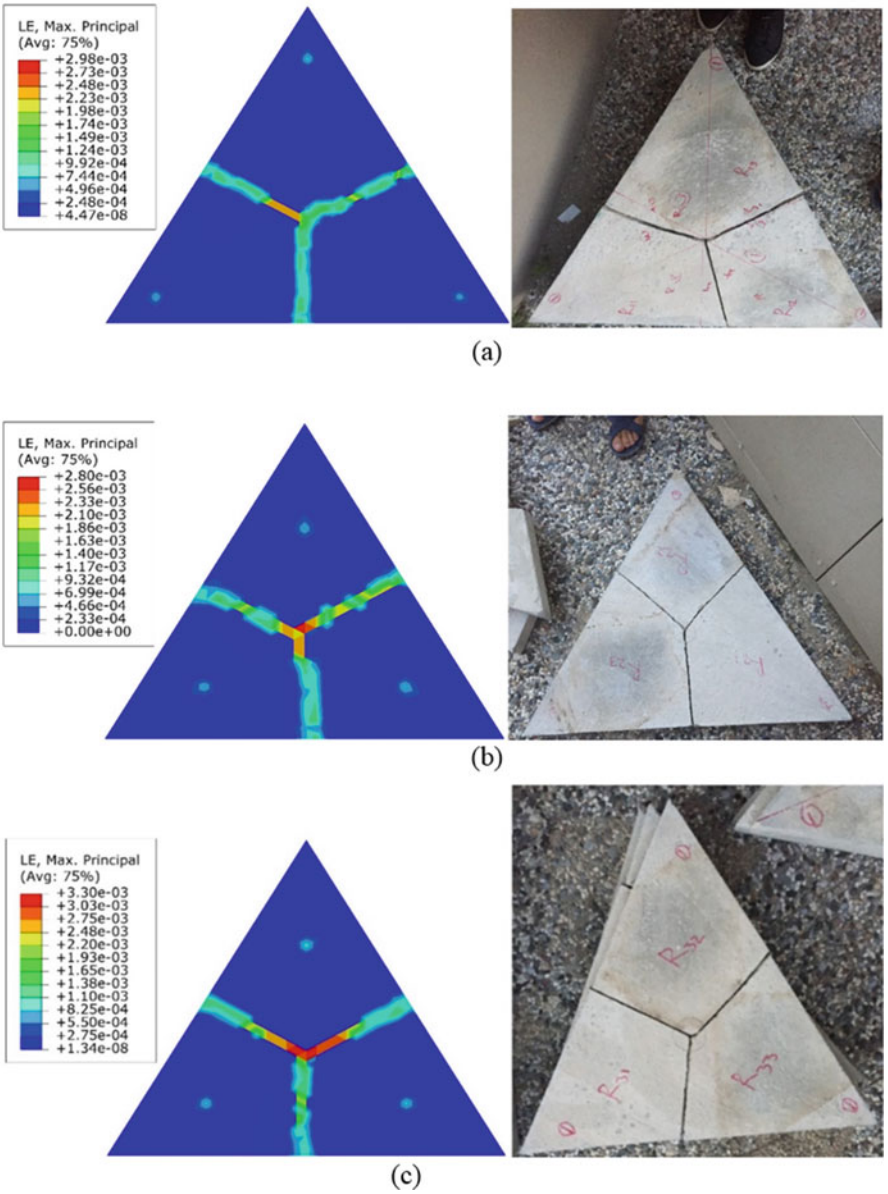

Fig. 15 (continued)

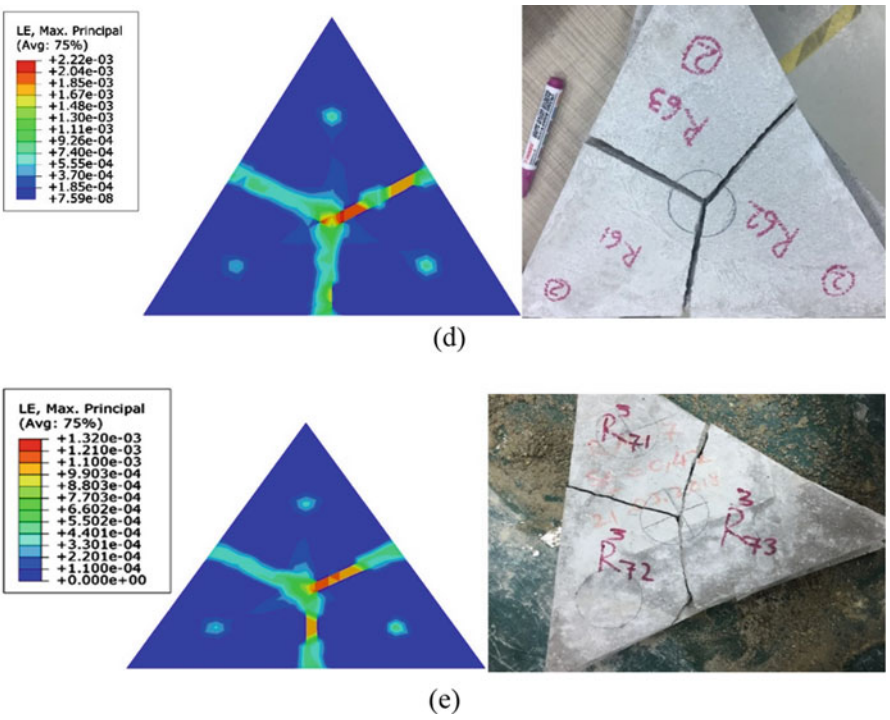

Fig. 15 Fracture patterns of each specimen in five different sizes, starting from larger

since the variation of ultimate tensile strain is insignificant under different stress ratio. The biaxial tensile behavior of concrete is independent on stress ratio.

For SFRC, there is limited data and information about the size effect on the biaxial tensile strength of SFRC. Therefore, in this study a numerical study performed on the fibrous triangular plate test specimens by using of microplane model (M7f) in order to determine the size effect on the biaxial strength of SFRC. To this end, the M7f free parameters were calibrated by using the fibrous triangular plate tests data provided by Mirkheel (2018). The calibrated M7f free parameters set, given in Table 14, enable the model to perform the best fitting of the force-displacement curve to the experimental data as depicted in Fig. 16.

From Fig. 17 one can see that the peak loads predicted by the microplane model and measured by experiments are in good agreement. However, one can see in Fig. 13 that there is some deviations between the finite element simulation and the experimental data about the stiffness and post peak behavior of SFRC. The difference between the test results and the simulation can be attributable to either model parameter calibrations that require more robust and reliable fitting procedure such as using optimization tool rather than manual trial error or finite element modeling issues on defining interactions between the specimens and the support as well as the

Table 14 Microplane Model M7f parameters

Material parameter (unit)	Value
Young's modulus E (MPa) (mean)	18,000
Poisson's ratio	0.18
Compressive strength f_c (28 days)	30
Density (kg = m^3)	2400
Radial scaling parameter k_1	50 E-6
k2	110
k3	5
k4	100
k5	1
k6	1 × 10e-4
k7	1.8
C4	78,6769
d1	1.1
Vf	0.01

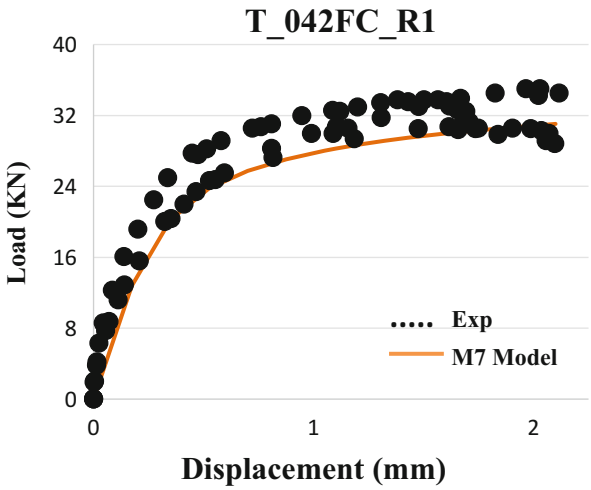

Fig. 16 The model fitting the force-displacement curve to experimental data

loading balls. The biaxial strength for each of the specimen in five different sizes is then calculated by using the peak loads in Eq. (1) and presented in Table 15.

The predicted biaxial strengths of each of testing specimens in five different sizes as listed in Table 15 are plotted against size D and compared with the test results as shown in Fig. 18 in order to determine experimentally observed size effect on the biaxial tensile strength of the material.

Fracture Pattern of the Fibrous Triangular Plate Tests

The contour plots of the maximum principal strain distribution on the bottom surface of the fibrous triangular plate test specimens obtained by finite element

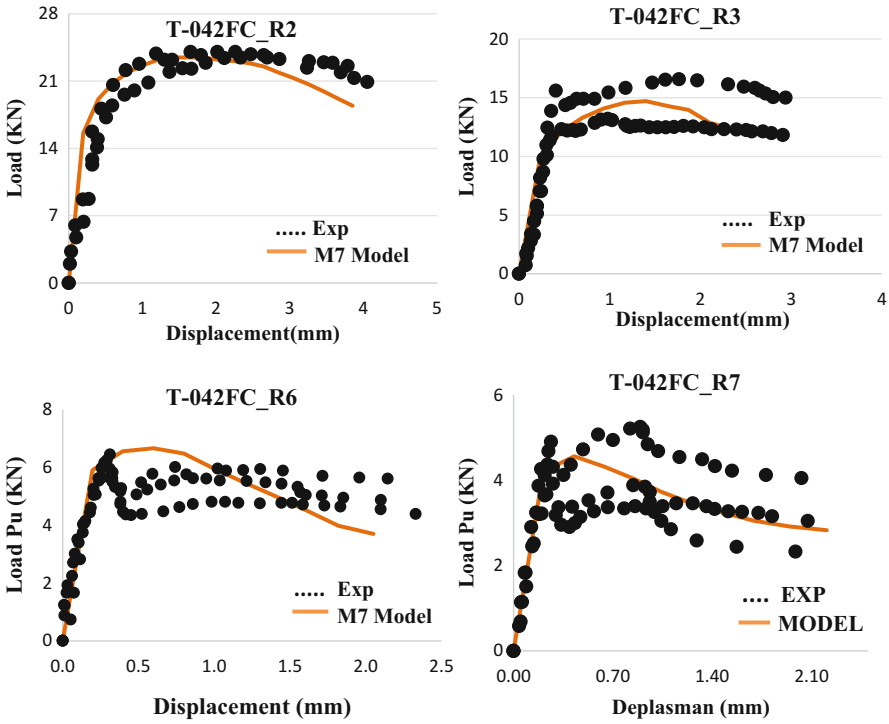

Fig. 17 The force-displacement curves of the test fibrous specimens R2-R7

Table 15 Geometrical dimensions and the biaxial tensile strength for the each of **042FC** in five different sizes

	Dimensions		Experiment		Numerical	
			Load	Stress	Load	Stress
Samples	L	T	(KN)	(MPa)	(KN)	(MPa)
R1	1050	75	33.292	6.834	33.364	6.849
R2	875	62.5	23.636	6.987	23.457	6.934
R3	700	50	14.637	6.761	14.708	6.793
R6	420	30	6.137	7.873	6.666	8.553
R7	350	25	4.609	8.516	4.562	8.428

model and the fracture pattern observed in the performed tests are presented in Fig. 19.

Fracture patterns of both panels were similar and the fracture initiated from the maximum tensile surface of the panels. The strain field of the triangular panel showed threefold symmetric strain distribution caused by three support pivots. These results

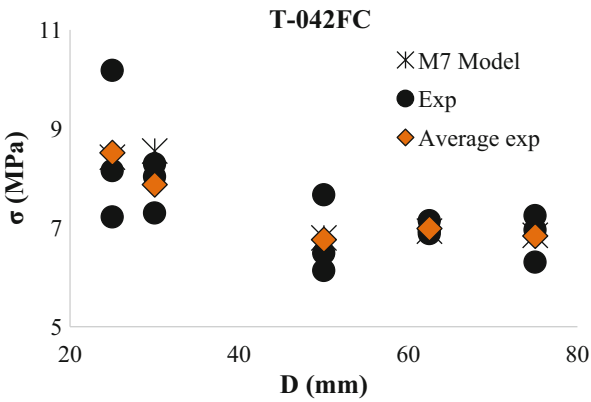

Fig. 18 Variation of the biaxial tensile strength with respect to the characteristic size, D

suggested that cracks in the triangular plates would be prone to form in the area of higher stress, between the support pivots and the center of the test panel, causing the specimen to break into three pieces upon failure, which coincides with the experimental observations.

Summary/Conclusions

The size effect on the biaxial flexural strength of a concrete panel was studied numerically by simulating triangular plate tests using microplane model. The finite-element analysis showed that

- The fracture is initiated at the maximum tensile surface on the center of the bottom surface of both panels.
- The fracture patterns of panels are similar in all test specimens and the fracture is initiated at the locations where the maximum principal strain occurs.
- The cracks develop generally between the support pivots and the center of the test panel, causing the specimen to break into three pieces upon failure that coincided with the experimental result.
- Size effect on the biaxial tensile strength is predicted for both test panels; however, fibrous concrete specimens show more strong size effect than the plain concrete specimens.

The M7 predictions obtained from the both test panel simulations match quite well with the mean values of the test data and fracture behavior observed experiments. The results indicate that microplane model is an appropriate theoretical constitutive model suitable for the finite element analysis of concrete to obtain realistic predictions of the constitutive and fracture behavior of the tested specimens.

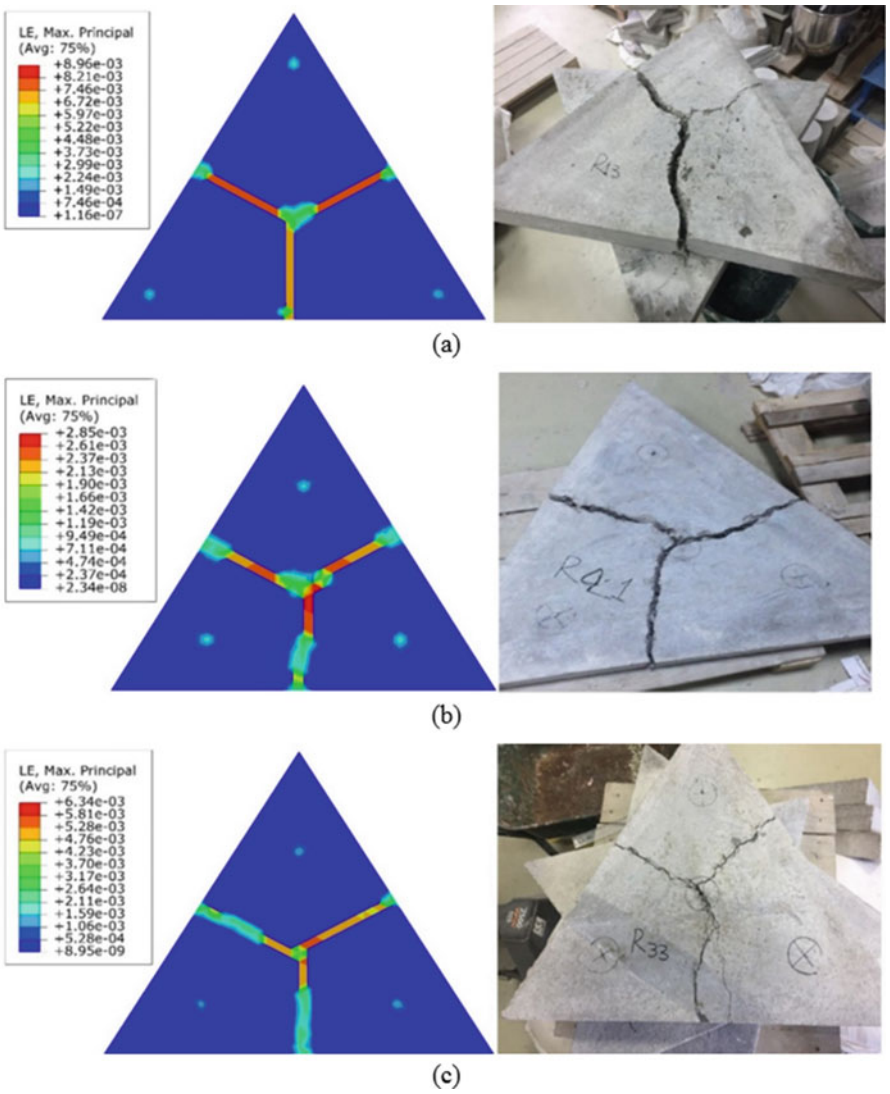

Fig. 19 (continued)

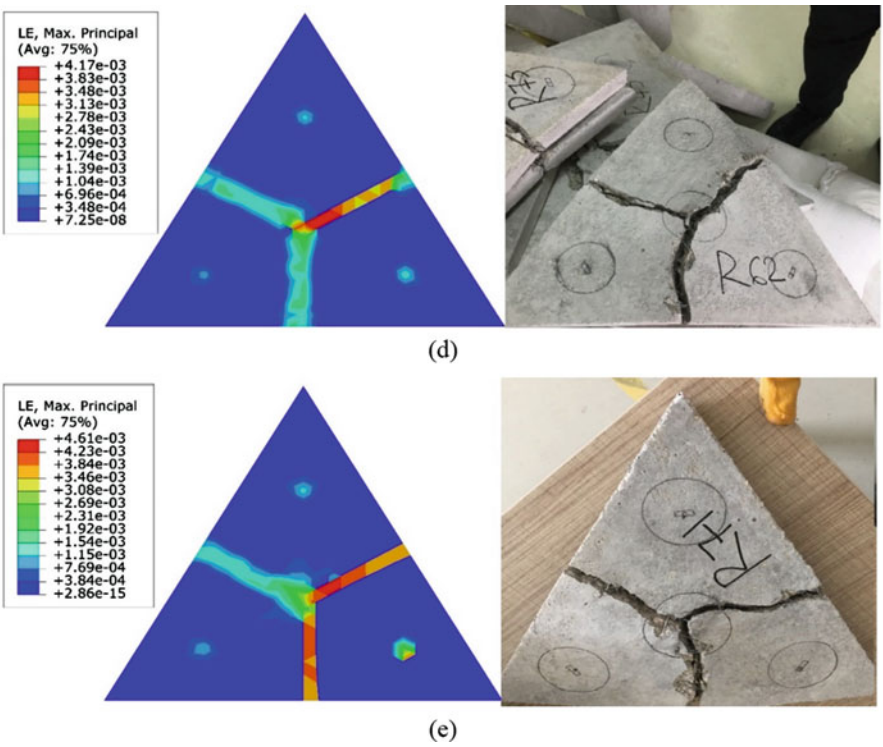

Fig. 19 Fracture patterns of each specimen in five different sizes starting from larger size to smaller size

References

B. E. Barragán, R. Gettu, M.A. Martín, R. L. Zerbino, Uniaxial tension test for steel fibre reinforced concrete–a parametric study. Cem. Concr. Compos. **25**(7) (2003)

Z.P. Bazant, F.C. Caner, I. Carol, M.D. Adley, S.A. Akers, Microplane model M4 for concrete I: Formulation with work-conjugate deviatoric stress. J. Eng. Mech. **126**(9), 944–953 (2000)

Z.P. Bažant, B.H. Oh, Microplane model for progressive fracture of concrete and rock. J. Eng. Mech. ASCE. **111**, 559–582 (1985)

Z.P. Bažant, M.T. Kazemi, Size dependence of concrete fracture energy determined by RILEM work-of-fracture method. Int. J. Fract. **51**, 121–138 (1991)

F.C. Caner, Z.P. Bažant, C.G. Hoover, A.M. Waas, K.W. Shahwan, Microplane model for fracturing damage of triaxially braided fiber-polymer composites. J. Eng. Mater. Technol. Trans. ASME. **133**(2), 021024–12 (2011)

F.C. Caner, Z.P. ve Bazant, Microplane model M7 for plain concrete. I: formulation. J. Eng. Mech. **139**(12), 1714–1723 (2012)

F. C. Caner, Z. P. Bazant, Mıcroplane model M4 for concrete. II: algorıthm and calıbratıon. **126**(12), 954–961 (2000)

S. Carmona, Efecto del tamaño de la probeta y condiciones de carga en el ensayo de tracción indirecta. Mater. Constr. **59**(294), 7–18 (2009)

G. Cusatis, A.M. Figni, Lattice Discrete Particle Model (LDPM) for fracture dynamics and rate effect in concrete, in *Proceedings of 18th Analysis and Computation Speciality Conference – Structures Congress*, 2008

X. Chen, S. Wu, J. Zhou, Analysis of mechanical properties of concrete cores using statistical approach. Mag. Concr. Res. **65**, 1463–1471 (2013)

X. Chen, S. Wu, J. Zhou, Strength values of cementitious materials in bending and in tension test methods. J. Mater. Civil Eng. **26**, 484–490 (2014)

R. Danzer, W. Harrer, P. Supancic, T. lubea, Z. Wang, A. Borger, The ball on three balls test strength And failure analysis of different materials. J. Eur. Ceram. Soc. **27**(2–3), 1481–1485 (2007)

H. Dabbagh, S. Akbarpour, K. Amoorezaei, Effect of geometric characteristics of steel fiber on the mechanical properties of structural lightweight aggregate concrete, in *9th National Congress on Civil Engineering* (Ferdowsi University of Mashhad, Iran, 2016)

M.E. Eren, Betonun küp yarmada çekme dayanımuı üzerine malzeme ve boyut etkisi. *Yüksek Lisans Tezi*, Fırat Üniversitesi Fen Bilimleri Enstitüsü, İnşaat Mühendisliği Anabilim Dalı, Elâzığ, 07115101 (2015)

Ö.F. Eser, *Betonun kırılma parametrelerinin değişik yöntemlere belirlenmesi* (Doktora Lisans Tezi, İTÜ, Fen Bilimleri Enstitüsü, İnşaat Mühendisliği Anabilim Dalı, İstanbul, 2002)

A. Hussein, H. Marzouk, Behavior of high-strength concrete under biaxial stresses. ACI Mater. J. **97**(1), 27–36 (2000)

C.G. Hoover, Z.P. Bazant, Comprehensive concrete fracture tests: Size effects of types 1 & 2, crack length effect and post peak. Eng. Fract. Mech. **110**, 281–289 (2013)

R. Ince, S. Yilmaz, M. Gör, Size effect in splitting diagonal cubes. International Balkans Conferance on Challenges of Civil Engineering, BCCCE, 23–25 May 2013 (EPOKA University, 2013)

R. Ince, Determination of concrete fracture parameters based on peak-load method with diagonal split-tension cubes. Eng. Fract. Mech. **80**, 100–114 (2012a)

R. Ince, Determination of the fracture parameters of the double-k model using weigth functions of split-tension specimens. Eng. Fract. Mech. **96**, 416–432 (2012b)

V. Kankov, Çelik Kılıflı Beton Kolonlarda Boyut Etkisi. Yüksek Lisans Tezi, Gazi Üni Fen Bilimleri Enstitüsü, İnşaat Mühendisliği Anabilim Dalı, Ankara (2007)

G. Kennedy, C.H. Goodchild, *Practical Yield Line Design* (Concrete Centre, Surrey, 2004)

J. Kim, C. Thanh, Zi, G., *The Characteristics of the Biaxial Flexure Test for Concrete* (Korea Concrete Institute, Seoul, 2010), pp. 5–7

J. Kim, Y. Kwak, G. Zi, The experimental comparison of the uniaxial and biaxial flexural tensile strengths according to the size of specimens. Procedia Eng. **14**, 662–666 (2011)

J. Kim, D.J. Kim, G. Zi, Improvement of the biaxial flexure test method for concrete. Cem. Concr. Compos. **37**, 154–160 (2013)

J. Kim, C. Yi, G. Zi, Biaxial flexural strength of concrete by two different methods. Mag. Conr. Res. **64**(12), 1057–1065 (2012)

K. Kirane, P.Z. Bazant, G. Zi, Fracture and size effect on strength of plain concrete disks under biaxial flexure analyzed by microplane model M7. J. Eng. Mech. **140**, 604–613 (2014)

H. Kupfer, K.H. Hubert, R. Hubert, Behavior of concrete under biaxial stresses. ACI J. **66**(8), 656–666 (1969)

L. Lemnitzer, L. Eckfeldt, A. Lindorf, M. Curbach, Biaxial tensile strength of concrete – answers from statistics, in *Proceedings of the International fib Symposium Tailor Made Concrete Structures*, New Solutions for Our Society, Amsterdam (CRC Press/Balkema, UK, 2008), pp. 1101–1102

A. Mallat, A. Alliche, A modified tensile test to study the behaviour of cementitious materials. Strain: An Int. J. Exp. Mech. **47**, 499–504 (2011)

P. Marti, Size effect in double-punch test on concrete sylinders. ACI Mater. J. **86**, 597–601 (1989)

H. Mirkheel, Lifli Betonlardaki Boyut Etkisinin Deneysel Ve Anal İtik Yöntemler İle Belirlenmesi, Yüksek Lisans Tezi, Bursa uludağ üniversitesi, İnşaat Mühendisliği Bölümü, Bursa (2018)

K. Murugappan, P. Paramasivam, K. Tan, Failure envelope for steel-fiber concrete under biaxial compression. J. Mater. Civil Eng. **5**, 436–446 (1993)

N.R. Muzyka, Equipment for testing sheet structural materials under biaxial loading. Part 2. Testing by biaxial loading in the plane of the sheet. Str. Mat. **34**, 206–212 (2002)
A.E. Naaman, H.W. Reinhardt, High performance fiber reinforced cement composites: HPFRCC 2, RILEM, No. 31, E. & FN Spon, London, 1996
A.M. Neville, *Properties of Concrete*, 5th edn. (Pearson Education Limited, England, 2011), pp. 169–174
K.S. Prebhakumari, P. Jayakumar, High strength concrete by size effect method. Int. J. Sci. Eng. Res. **4**(5), 2229–5518 (2013)
T. Tang, Z.P. Bažant, S. Yang, D. Zollinger, Variablenotch one-size test method for fracture energy and process zone length. Eng. Fract. Mech. **5503**, 383–404 (1996)
H.T. Türker, Çimento Esaslı Malzemelerin Çekme Dayanımlarını Bulabilmek İçin Yeni Bir Yöntem Önerisi ÜÇGEN PLAKA YÖNTEMI. Gazi Üniversitesi Müh. Mim. Fakültesi Dergisi **30**, 693–699 (2015)
Z.F. Türkmenoğlu, O. Varol, *Lifli Beton T–rleri ve Kullanım Alanları* (International Mediterranean Science and Engineering Congress Center, Adana, 2014), pp. 3792–3795
H. Yazici, Özel Betonlar. *Dokuz Eylül Üniversitesi* İnşaat Mühendisliği Bölümü Ders notları (2010)
S. Yin, R. Tuladhar, M. Sheehan, M. Combe, T. Collister, A life cycle assessment of recycled polypropylene fibre in concrete footpaths. J. Clean. Prod. **112**(Part 4), 2231–2242 (2016)
G. Zi, H. Oh, S.K. Park, A novel indirect tensile test method to measure the biaxial tensile strength of concretes and other Quasibrittle materials. Cem. Concr. Res. **38**, 751–756 (2008)
G. Zi, J. Kim, P.Z. Bazant, Size effect on biaxial flexural strength of Concrete. ACI Mater. J. **111**, 319–326 (2014a)
G. Zi, J. Kim, Z.P. Bažant, Size effect on biaxial flexural strength of concrete. ACI Mater. J. **111**(3), 319–326 (2014b)
X.X. Zhang, G. Ruiz, R.C. Yu, Experimental study of combined size and strain rate effects on the fracture of reinforced concrete. J. Mater. Civil Eng. **20**(8), 544–551 (2008)
G. Zi, J. Kim, Z.P. Bazant, Size effect on biaxial flexural strength of concrete. ACI Mater. J. **111**, 3 (2014)

Predicting Damage Behavior of Self-Healing Sandwich Panels: Computational Modeling

9

Murat Yazici, Harun Güçlü, and Babür Deliktaş

Contents

Introduction 198
Self-Healing Mechanisms and Syntactic Foams 199
Self-Healing Syntactic Foam-Filled Sandwich Structures 200
Finite Element Modeling for Self-Healing Materials 205
Summary/Conclusions 209
References 210

Abstract

Sandwich materials have a lightweight core and two face sheets combined with increasing the materials' bending rigidity with low density. Sandwich materials can be designed according to structural requirements. Nowadays, airplanes, ships, space vehicles, satellites, or wind turbines require lightweight structures with easy repairing. Self-healing materials present a good opportunity for these kinds of designs to increase the systems' life span. Damages can occur in these kinds of structures due to impact or blast, or any other unexpected reason; the structural repairing of these kinds of devices is too expensive due to difficulties in handling. Self-healing sandwich structures combine self-healing material properties with light-weighting and high bending rigidity of sandwich structures. Self-healable sandwiches give this kind of device an advantage to extend their structural life span at a low cost. This chapter presents four main topics: self-healing sandwich panels, blast phenomena and their effects on systems, finite element modeling of

M. Yazici (✉) · H. Güçlü
Department of Automotive Engineering, Bursa Uludag Universitesi, Bursa, Turkey
e-mail: myazici@uludag.edu.tr; harunguclu@uludag.edu.tr

B. Deliktaş (✉)
Department of Civil Engineering, Faculty of Engineering-Architecture, Uludag University, Bursa, Turkey
e-mail: bdeliktas@uludag.edu.tr

© Springer Nature Switzerland AG 2022

G. Z. Voyiadjis (ed.), *Handbook of Damage Mechanics*,
https://doi.org/10.1007/978-3-030-60242-0_90

sandwich panels under blast loading, and finite element modeling of damaged sandwich panels with self-healing.

Keywords

Self-healing · Sandwich structures · Blast · Damage behavior · Finite element analysis

Introduction

Sandwich materials have been widely used for blast and impact mitigation, including their high specific strength and specific stiffness. A traditional sandwich material has one lightweight core and two stiff face sheets. The face sheets carry almost all the bending and in-plane loads, and the core helps to stabilize face sheets and define flexural stiffness, out-of-plane shear, and compressive behavior (Reddy and Madhu 2017). The choice of the core is critical to the performance of the sandwich, as the core properties control the energy absorption and magnitude of the force transfer through the structure. The classical sandwich theory suggests that the primary function of the sandwich core is to transmit shear stress to the thin face sheets, thereby rendering high bending stiffness and strength from a panel with a minimum weight penalty (Hoo Fatt et al. 2018). The core materials are generally preferred from cellular materials, depending on the designed structure, composite materials, and metals can be as face sheets materials (Yazici et al. 2014b). Commonly used cores are made up of metallic and nonmetallic honeycombs, cellular foams, balsa wood, truss, and lattice structures. The cellular materials can undergo extensive plastic deformation under constant stress and thus can absorb large amounts of kinetic energy before densification, which is the critical feature of cellular foams to mitigate a blast or shock loads. The behavior of the sandwich structures under dynamic conditions is very complex due to many factors such as the strain rate sensitivity of polymer resins, the architecture of face sheets, core geometry and properties, and complex loading conditions. However, understanding the behavior of the sandwich materials under dynamic conditions is very important to design structures for armor applications. Common dynamic loading methods are velocity impact loading, drop-weight impact tests, shock wave loading using shock tubes, and explosive testing.

Many studies have been performed for developing metallic sandwich cores; the most common topologies are corrugated core (Yazici et al. 2014b, 2015), honeycomb, folded, and lattice truss shapes. Under these main topologies, many configurations can form the core of the sandwich panels to provide adequate stiffness and strength for structural load support(Ahmed and Galal 2019). A new trend toward increasing metallic foam core impact and shock mitigation ability is filling core cells with foams (Karen et al. 2016; Fahr et al. 2018), with gels (Devrim and Yazici 2020), and with fluids (Wang et al. 2020). In all cases, the material filling improved the impact and shock wave mitigation (Fig. 1).

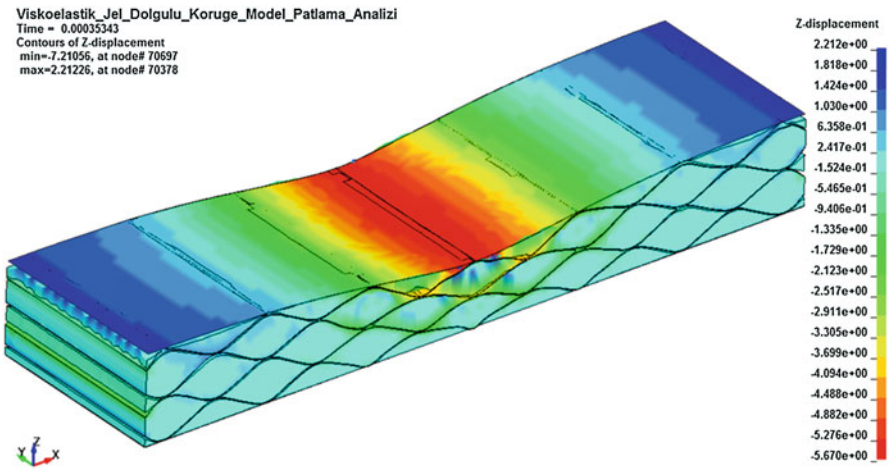

Fig. 1 Gel-filled corrugated core sandwich panel under shock loading. (Devrim and Yazici 2020)

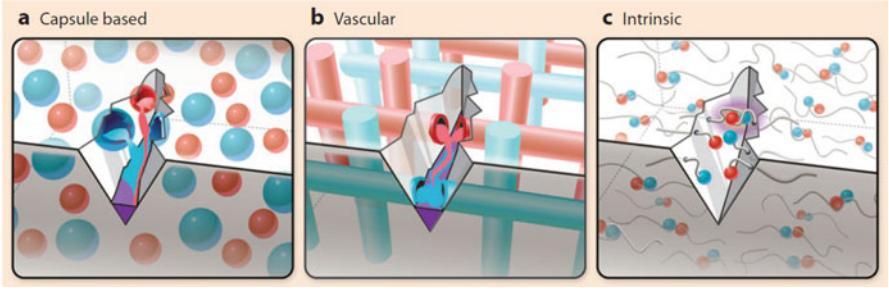

Fig. 2 Schematic illustration of the self-healing concepts: (**a**) embedded microcapsules; (**b**) vascular; (**c**) intrinsic. (Blaiszik et al. 2010)

Self-Healing Mechanisms and Syntactic Foams

Self-healing materials can restore their structural integrity during or after failure, e.g., self-healing abilities of natural creatures (Wang et al. 2015; Kanu et al. 2019). Self-healing materials can be achieved through extrinsic (Fig. 2a, b) and intrinsic self-healing mechanisms (Fig. 2c) (Cao et al. 2020). Inherent self-healing is activated by the repairing resin under external stimuli, including various thermo-mechanical/chemical activators. Extrinsic self-healing can be achieved through releasing the prefilled healing agents within either vascular or capsular containers when damage occurs. The capsular-based self-healing process is inspired by innate cells that self-healing agents carry inside the cell. Therefore, the healing process occurs at a cellular level. The capsular system has three approaches, i.e., capsules-catalysts system, mono-capsules system, and dual capsule system. The healing effect

can be achieved when the released resin and hardener are mixed at damage locations (Cao et al. 2020). Due to the dual capsule system, the capsules contain resin and hardener in the same capsule by dual capsulation, it is the most efficient capsule approach for self-healing. Capsular self-healing systems are suitable for industrial-scale production with the advantages of easy fabrication, low cost, and versatility. The vascular self-healing systems emulate, on a macro level, healing by the vascular and circulation systems in animals. With a circulation system, the healing agent can be refilled, providing the potential for continuous healing agent delivery and flow control (Wang et al. 2015).

Figure 2a presents a schematic illustration of the capsular healing mechanism, stored healing agent stored in the capsules until they are ruptured by damage or dissolved. Figure 2b shows the vascular system principal, the healing agents, and activator stored in hollow channels or fibers until damage ruptures the vasculature and releases the carried fluids (Blaiszik et al. 2010).

Self-Healing Syntactic Foam-Filled Sandwich Structures

Syntactic foams are a class of closed-cell foam manufactured by filling a matrix with hollow spheres called microballoons. They can be produced with any type of polymer matrix and have been widely employed in engineering applications. They were first developed as buoyancy materials for submarines, thermal insulation materials for buildings, trains, aircraft, cushion materials for packing, etc.(Li and John 2008). Figure 3 shows a high-temperature-resistive syntactic foam SEM picture (Yazici et al. 2014a). These foam materials can be developed according to structural, physical, or environmental requirements (Yazici et al. 2014b; Yazici 2016). One of the most functional applications is to use syntactic foams as a core material for developing sandwich structures or filler in metallic sandwich panels (Li and John

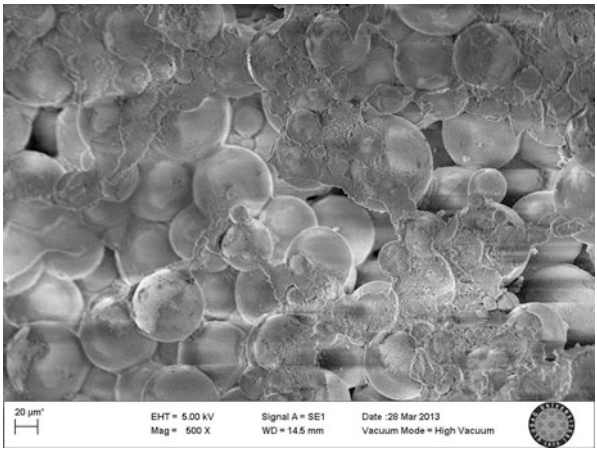

Fig. 3 High-temperature-resistive syntactic foam SEM pictures after 500°C heat treatment. (Yazici et al. 2014a)

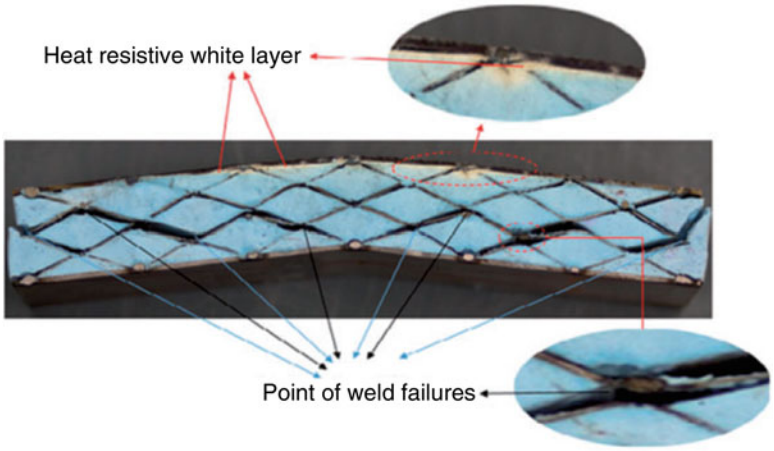

Fig. 4 High-temperature-heat-resistive syntactic foam-filled sandwich panel after shock loading and 330°C temperature performed on the sandwich's front face. (Fahr et al. 2018)

2008; John and Li 2010; Fahr et al. 2018). Figure 4 demonstrates high-temperature-resistive syntactic foam-filled corrugated core sandwich panels.

Sandwich structures are mostly preferred for their lightweight and load-bearing capability. Failure mechanisms in sandwich structures due to loading typically occur through core crushing, shear cracking of the core, debonding of the face sheets-core interface, and fracture of the face sheets (Chen et al. 2013). A couple of studies have been performed on the self-healing of sandwich structures as including healing mechanisms to the face sheets-core interfaces and foam cores (Williams et al. 2007, 2008; Li and John 2008; John and Li 2010; Patrick et al. 2012; Chen et al. 2013). Self-healing mechanisms can be imported from the metallic core sandwich panels. Self-healing macrocapsules are developed in AMAMRG Lab (Bursa Uludag University/Turkey) by Yazici and his group to provide self-healing properties to the metallic core sandwich panels. The capsules are two types, which are monomer and activation agents. These macrocapsules are filled into the aluminum honeycomb cells to obtain self-healable metallic core sandwich panels. In Fig. 5a and b, the macrocapsules and aluminum honeycomb core filling are shown, respectively.

In Fig. 6, compression experiment results of self-healing microcapsule-filled aluminum honeycomb sandwich panels are presented. Apparently, the healing agents ensured the healing effect on the sandwich panels' mechanical performance. In this example, the healing capsules filled directly into the metallic sandwich foam cells. In the case of micro- or nanohealing capsules, the foam cells can be filled by the syntactic foams to hold healing agent-filled spheres together.

Another most preferred approach for rigid foam core sandwich structures is the vascular system. The vascular networks for self-healing are incorporated into the interfacial layer or inside the foam core for hard foam cores. In Fig. 7, avascular

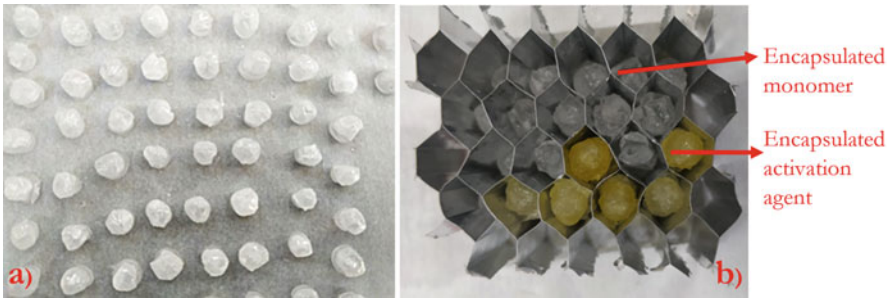

Fig. 5 (**a**) Self-healing macrocapsules. (**b**) Self-healing macrocapsule-filled aluminum honeycomb sandwich core section

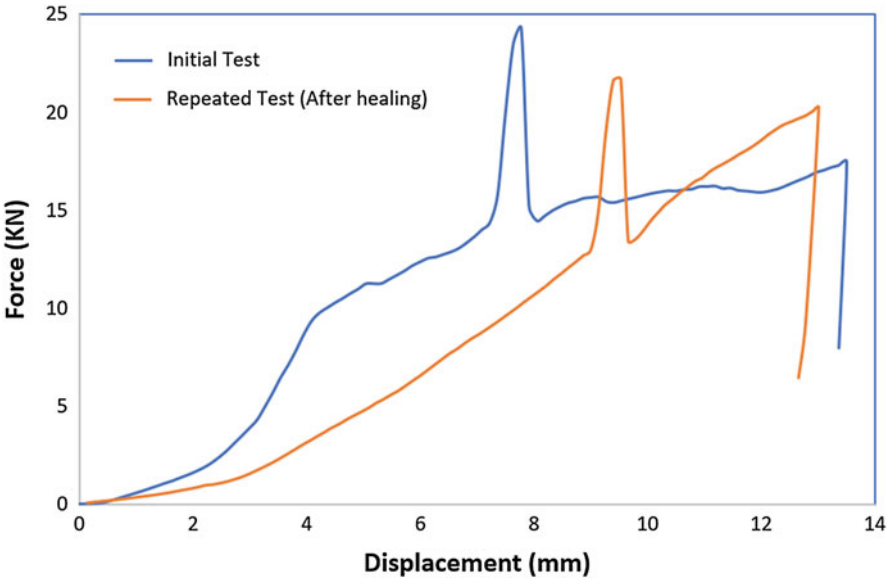

Fig. 6 (**a**) Self-healing macrocapsules. (**b**) Self-healing microcapsule-filled aluminum honeycomb sandwich core section

self-healing application foam core and healing behavior are presented. In Patrick et al. (2012)'s study, two microvascular channels were placed inside the polyurethane foam shaped as a single-edge-notched three-point bending (SENB) specimen, and a healing agent was pumped inside them, initially. Once the filling process was complete, the virgin self-healing SENB specimen was loaded at 3 mm displacement to propagate the initial crack and fracture through both channels. The loading sequence then paused, and one-half of the desired amount of both healing agents was delivered to the crack plane over a time of 1 min. The sample was then unloaded faster, while the remaining half of the healing agents was concurrently provided to the fracture plane. The fractured specimen was then stayed on the support fixture

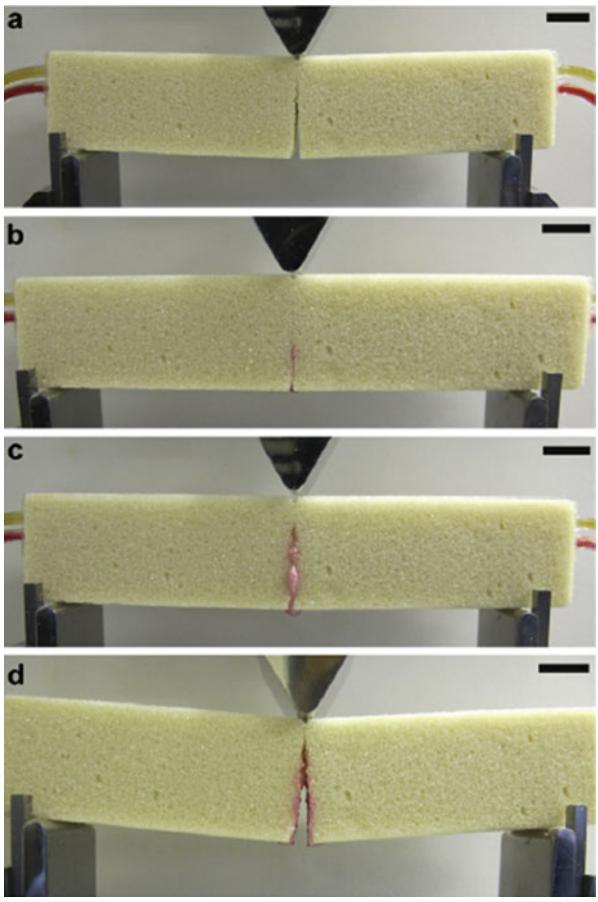

Fig. 7 Vascular system application in PIR (Polyisocyanurate) foam core and measurement of the self-healing performance with single-edge-notch beam three-point-bending experiment. (**a**) Fracturing first prefilled channels containing liquid healing agents. (**b**) The sample is unloaded, and healing agents are delivered to the fracture plane. (**c**) The sample is healing at room temperature. (**d**) The "healed" sample reloading. (Patrick et al. 2012)

freely for 30 min while healing (foaming) reaction. After that, foamed material was removed from the outer surfaces, and the original precrack using the same razor blade. The healed specimen was made the same as a virgin specimen to ensure equivalent precrack length to the original precrack. The results of these experiments are shown in Fig. 8. The representative healing curve shows a considerable recovery of mechanical integrity in terms of stiffness and peak load, which was used to determine fracture toughness.

For microcapsule-based self-healing (see Fig. 9a) characterization of syntactic foam core sandwich materials, TDCB (tapered double-cantilever beam) experiments are more preferred to obtain material modeling due to easy applicable and direct measuring fracture behavior of the material. The TDCB experiments provide a crack length-independent measure of fracture toughness (Fig. 10). Based on the observations, a metric for quantifying healing efficiencies was presented (Brown et al. 2002).

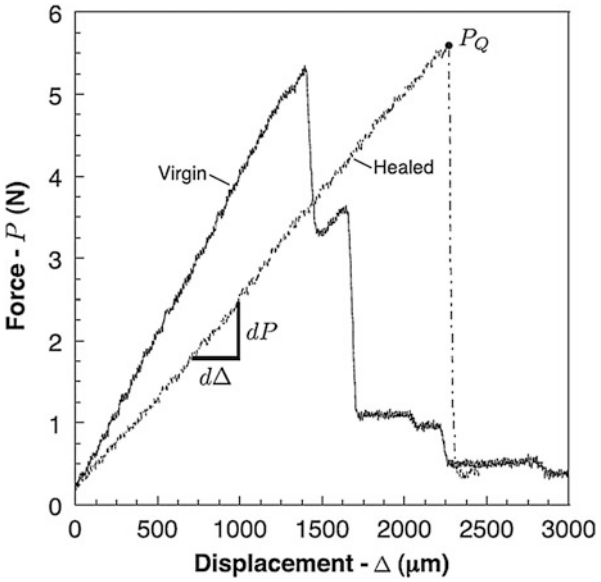

Fig. 8 Virgin and healed foam's SENB specimen load-midspan displacement curves. (Patrick et al. 2012)

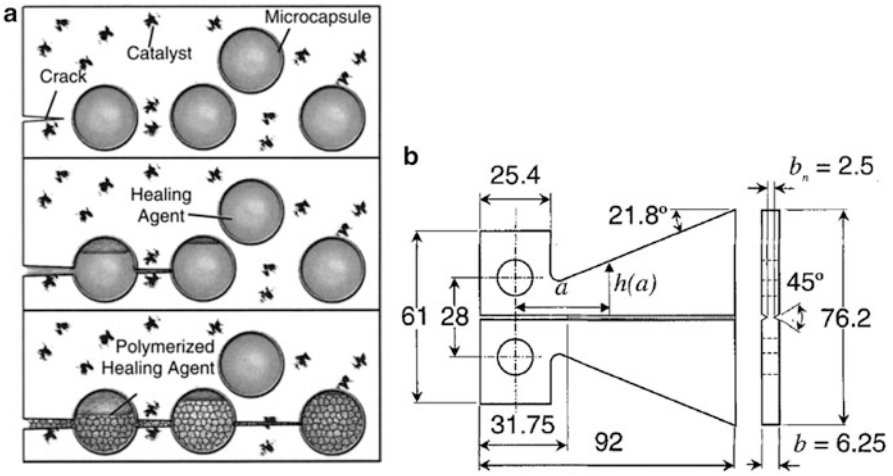

Fig. 9 (**a**) Microcapsule-based healing mechanism. (**b**) TDCB experiment specimen geometry. (Brown et al. 2002)

$$K_{IC} = 2P_C \frac{\sqrt{m}}{\beta} \tag{1}$$

$\mathbf{P_C}$ is the critical load at fracture, and **m** and $\boldsymbol{\beta}$. The value of the $\boldsymbol{\beta}$ depends on the specimen and crack widths b and b_n, respectively. The value of **m** is defined by the theoretical relation,

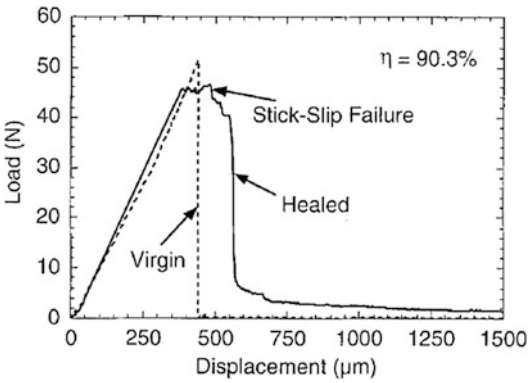

Fig. 10 Examples of TDCB specimens for healable material produced by epoxy polymer include healing microcapsules. (Brown et al. 2002)

$$m = \frac{3a^2}{h(a)^3} + \frac{1}{h(a)} \tag{2}$$

or determined experimentally by the Irwiin-Kiess method,

$$m = \frac{E.b}{8}\frac{dC}{da} \tag{3}$$

Young's modulus is given by **E**, **C** is the compliance, **a** crack length from the line of loading, and h(a) is the specimen height profile, demonstrated in Fig. 9b. For this particular geometry,

$$\beta = b^{0.61}.b_n^{0.39} \tag{4}$$

For the TDCB sample geometry, the self-healing efficiency can be written as

$$\eta = \frac{K_{IC}^{Healed}}{K_{IC}^{Virgin}} \tag{5}$$

or the more simple equation is obtained

$$\eta = \frac{P_C^{Healed}}{P_C^{Virgin}} \tag{6}$$

Finite Element Modeling for Self-Healing Materials

The tapered double cantilever beam (TDCB) application to characterize the self-healing materials is explained in the previous heading. This experiment presents an opportunity for the calculation of the materials' Mode I fracture toughness. In this section, a two-dimensional TDCB specimen is modeled in the ABAQUS

commercial finite element analysis (FEM) software using the extended finite element method (XFEM) approach. In this analysis, a quasi-static crack propagation simulates by helping virgin and self-healed material properties. Used material properties are used as given in Table 1.

The geometrical model was built according to the given dimensions in Fig. 9b. The created geometrical model in Abaqus software is presented in Fig. 11.

In Abaqus software, to calculate crack propagation and fracture analysis, some special modeling tools exist. The crack propagation can be simulated using two different damage models, the cohesive damage (XFEM-COHE), or the virtual crack closure technique (VCCT). In the presented simulations, the VCCT technique is preferred due to mesh dependency which is lower than XFEM-COHE.

A precrack can be described with a one-dimensional wire geometry in Fig. 12; XFEM modeling a two-dimensional geometry and three-dimensional geometry in Abaqus software with an existing precrack is illustrated (Fig. 13).

The created one-dimensional wire geometry was assembled into the TDCB specimen model as a precrack. It is demonstrated in Fig. 14.

Table 1 The properties of the TDCB specimen material (Gómez et al. 2015)

	Epoxy resin (EPON 828 with a diethylenetriamine curing agent)
Young modulus (E)	3400 MPa
Poisson's ratio (v)	0.38
Yield strength (σ_y)	39 MPa
Ultimate strength (σ_{UT})	39 MPa
Fracture toughness (K_{IC})	0.55 MPa.m$^{1/2}$
Fracture energy (G_{IC})	76 N/m
Density (ρ)	1160 kg/m^3
The radius of the plastic zone(Γ_ρ)	32 μm

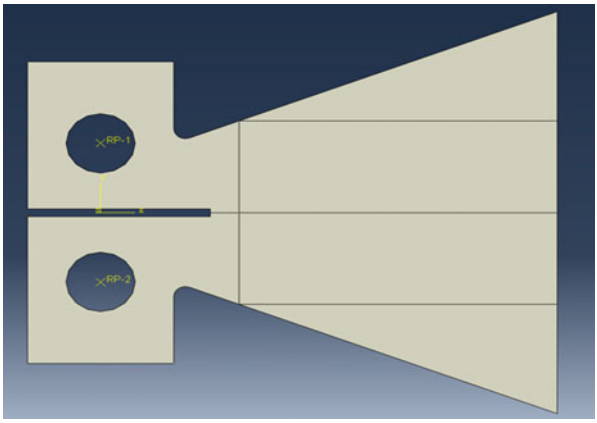

Fig. 11 TDCB specimen geometrical model

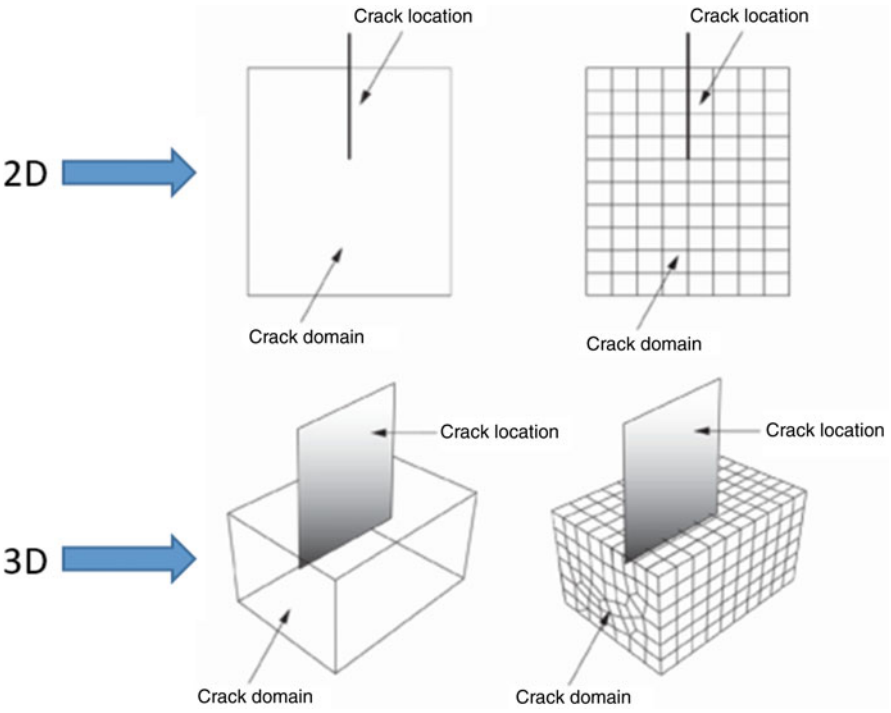

Fig. 12 XFEM modeling of two-dimensional and three-dimensional parts with a precrack in Abaqus software

The contacts are described as a fracture criterion in this stage, and Mode I and Mode II fracture toughness values are inserted. The 0.5-mm vertical displacements are subjected to the center points of the hole to the boundaries using MPC (multi-point constraints).

The TDCB geometry was divided into parts to obtain a better mesh structure, and then, 5796 nodes and 5543 linear quadrilateral plane stress elements (CPS4R element; a 4-node-bilinear plane stress quadrilateral, reduced integration, and hour-glass control) were generated. Obtained results can be seen in Figs. 15 and 16. In Fig. 15, crack propagations are presented according to the step-time. Equivalent Von-Mises stress distribution is shown in Fig. 16 when the crack reaches the specimen's end.

The healing efficiency can be found by simulating both virgin and self-healing TDCB experiments using XFEM analysis. The healing efficiency can be calculated easily using Eq. 6. In Fig. 17, an example result from XFEM simulation of the TDCB specimen is presented. The representative load-displacement curve's behavior is similar to the experimental virgin and healed TDCB specimen results, as shown in Fig. 10. The continuum approaches are extremely successful within their limits in accurately modeling self-healing behavior of the material.

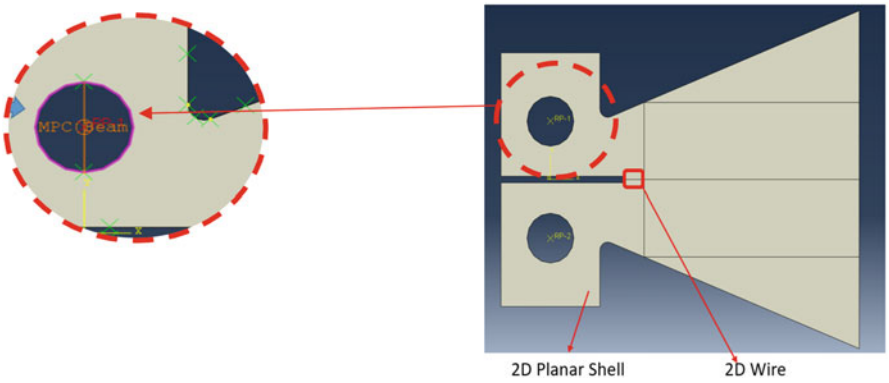

Fig. 13 XFEM model with a precrack and displacement loading points of TDCB specimen

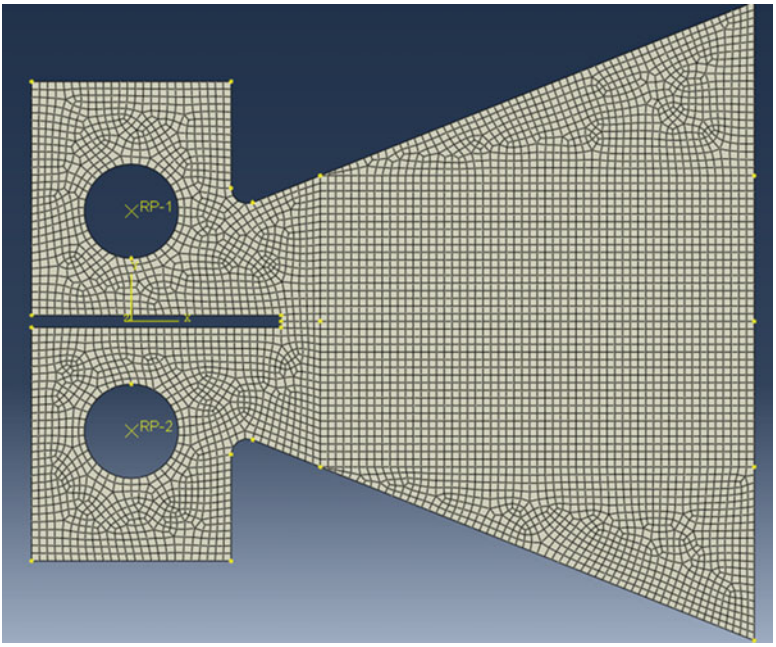

Fig. 14 The finite element mesh model of the TDCB specimen

However, they require empirical constitutive models that describe healing usually by a phenomenological approach (Miao et al. 1995) or thermodynamically based damage and healing models (Barbero et al. 2005). Recently, Voyiadjis and Kattan (2014, 2017, 2018) proposed new concepts in damage mechanics by introducing a new type of healing/strengthening process in materials called superhealing.

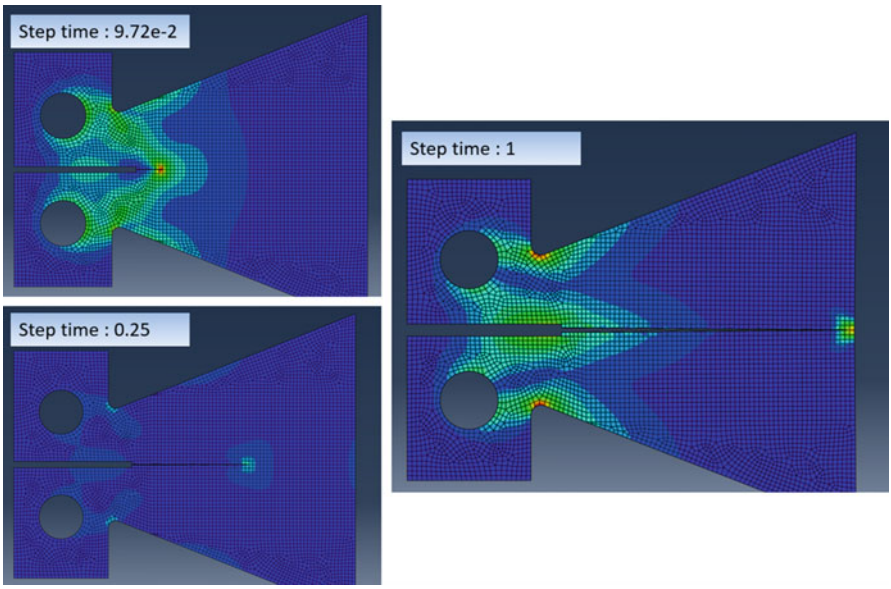

Fig. 15 Crack propagation in the TDCB specimen according to step-time

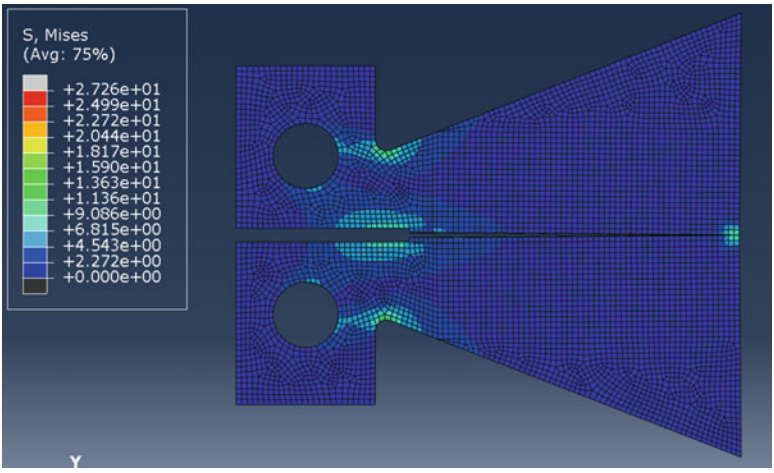

Fig. 16 Von-Mises equivalent stress distribution when the crack arrives at the end of the specimen

Summary/Conclusions

In this chapter, first, a literature review is presented about the self-healing mechanisms. Then, measurement of the self-healing efficiency approach is discussed based on fracture toughness variation using TDCB experimental results. Finally, an

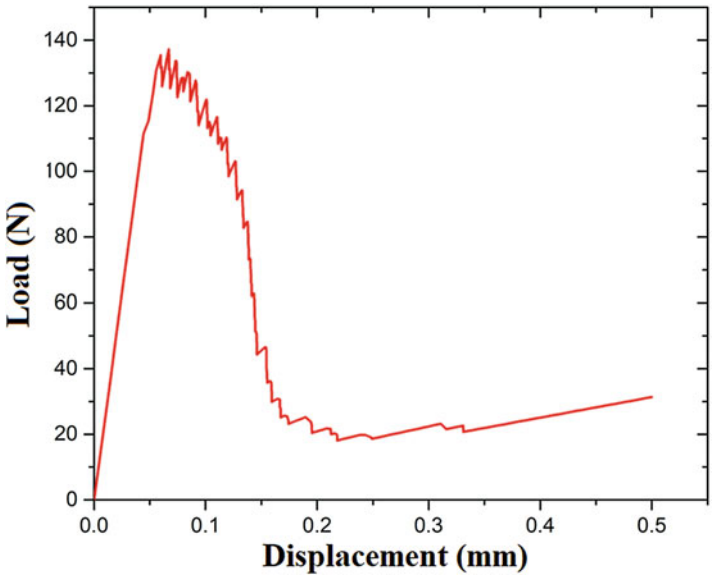

Fig. 17 An example of a load-displacement curve for TDCB specimen obtained from XFEM simulation

example of computational modeling of self-healing materials with XFEM method is applied to the TDCB test specimen, and the obtained load-displacement curve is compared to the experimental results. The function of the curves for both ways is in good agreement. If the virgin self-healable material and self-healed material properties are obtained experimentally, the data can be evaluated in the XFEM simulations. The healing efficiency can be measured with computational simulations for complex parts as well.

References

S. Ahmed, K. Galal, Response of metallic Sandwich panels to blast loads. J. Struct. Eng. (United States) **145**, 1–21 (2019). https://doi.org/10.1061/(ASCE)ST.1943-541X.0002397

E.J. Barbero, F. Greco, P. Lonetti, Continuum damage-healing mechanics with application to self-healing composites. Int. J. Dam. Mech. **14**, 51–81 (2005)

B.J. Blaiszik, S.L.B. Kramer, S.C. Olugebefola, et al., Self-healing polymers and composites. Annu. Rev. Mater. Res. **40**, 179–211 (2010). https://doi.org/10.1146/annurev-matsci-070909-104532

E.N. Brown, N.R. Sottos, S.R. White, Fracture testing of a self-healing polymer composite. Exp. Mech. **42**, 372–379 (2002). https://doi.org/10.1007/bf02412141

S. Cao, W. Zhu, T. Liu, Bio-inspired self-healing polymer foams with bilayered capsule systems. Compos. Sci. Technol. **195**, 108189 (2020). https://doi.org/10.1016/j.compscitech.2020.108189

C. Chen, K. Peters, Y. Li, Self-healing sandwich structures incorporating an interfacial layer with vascular network. Smart Mater. Struct. **22** (2013). https://doi.org/10.1088/0964-1726/22/2/025031

S. Devrim, M. Yazici, *Finite element analysis of viscoelastic gel filled corrugated core sandwich panels subjected to explosive blast loading* (Un Publ Work, 2020)

P. Fahr, M. Yazici, A. Shukla, Shock response of filled corrugated sandwich structures under extreme temperatures. J. Sandw. Struct. Mater. **20**, 130–149 (2018). https://doi.org/10.1177/1099636216650987

G.D. Gómez, F.A. Gilabert, E. Tsangouri, et al., In-depth numerical analysis of the TDCB specimen for characterization of self-healing polymers. Int. J. Solids Struct. **64**, 145–154 (2015). https://doi.org/10.1016/j.ijsolstr.2015.03.020

M.S. Hoo Fatt, M. Alkhtany, D. Sirivolu, Blast mitigation effects of foam-Core, composite Sandwich structures, in *Blast Mitigation Strategies in Marine Composite and Sandwich Structures*, ed. by S. R. Y. Gopalakrishnan, (Springer, Singapore, 2018), pp. 265–280

M. John, G. Li, Self-healing of sandwich structures with a grid stiffened shape memory polymer syntactic foam core. Smart Mater. Struct., 19 (2010). https://doi.org/10.1088/0964-1726/19/7/075013

N.J. Kanu, E. Gupta, U.K. Vates, G.K. Singh, Self-healing composites: A state-of-the-art review. Compos. Part A Appl. Sci. Manuf. **121**, 474–486 (2019). https://doi.org/10.1016/j.compositesa.2019.04.012

I. Karen, M. Yazici, A. Shukla, Designing foam filled sandwich panels for blast mitigation using a hybrid evolutionary optimization algorithm. Compos. Struct. **158**, 72–82 (2016). https://doi.org/10.1016/j.compstruct.2016.07.081

G. Li, M. John, A self-healing smart syntactic foam under multiple impacts. Compos. Sci. Technol. **68**, 3337–3343 (2008). https://doi.org/10.1016/j.compscitech.2008.09.009

S. Miao, M.L. Wang, H.L. Schreyer, Constitutive models for healing of materials with application to compaction of crushed rock salt. ASCE, J. Eng. Mech. **121**, 1122–11129 (1995)

J.F. Patrick, N.R. Sottos, S.R. White, Microvascular based self-healing polymeric foam. Polymer (Guildf) **53**, 4231–4240 (2012). https://doi.org/10.1016/j.polymer.2012.07.021

C.J. Reddy, V. Madhu, Dynamic behaviour of foams and Sandwich panels under shock wave loading. Procedia. Eng. **173**, 1627–1634 (2017). https://doi.org/10.1016/j.proeng.2016.12.260

G.Z. Voyiadjis, P.I. Kattan, Healing and super healing in continuum damage mechanics. Int. J. Dam. Mech. **23**(2), 245–260 (2014)

G.Z. Voyiadjis, P.I. Kattan, Mechanics of damage, healing, damageability, and integrity of materials: A conceptual framework. Int. J. Dam. Mech. **26**(1), 50–103 (2017). https://doi.org/10.1177/1056789516635730

G.Z. Voyiadjis, P.I. Kattan, Decomposition of healing tensor in continuum damage and healing mechanics. Int. J. Dam. Mech. **27**(7), 1020–1057 (2018). https://doi.org/10.1177/1056789517720969

Y. Wang, D.T. Pham, C. Ji, Self-healing composites: a review. Cogent. Eng. **2**, 1–28 (2015). https://doi.org/10.1080/23311916.2015.1075686

X. Wang, R.P. Yu, Q.C. Zhang, et al., Dynamic response of clamped sandwich beams with fluid-filled corrugated cores. Int. J. Impact. Eng. **139**, 103533 (2020). https://doi.org/10.1016/j.ijimpeng.2020.103533

H.R. Williams, R.S. Trask, I.P. Bond, Self-healing composite sandwich structures. Smart Mater. Struct. **16**, 1198–1207 (2007). https://doi.org/10.1088/0964-1726/16/4/031

H.R. Williams, R.S. Trask, I.P. Bond, Self-healing sandwich panels: restoration of compressive strength after impact. Compos. Sci. Technol. **68**, 3171–3177 (2008). https://doi.org/10.1016/j.compscitech.2008.07.016

M. Yazici, A novel high strain rate sensitive rigid polyurethane resin based syntactic foam. Acta Phys. Pol. A **129**, 613–616 (2016). https://doi.org/10.12693/APhysPolA.129.613

M. Yazici, P. Fahr, A. Shukla, et al., Development of a polymer based syntactic foam for high temperature applications. Acta Phys. Pol. A, 125 (2014a). https://doi.org/10.12693/APhysPolA.125.526

M. Yazici, J. Wright, D. Bertin, A. Shukla, Experimental and numerical study of foam filled corrugated core steel sandwich structures subjected to blast loading. Compos. Struct. **110**, 98–109 (2014b). https://doi.org/10.1016/j.compstruct.2013.11.016

M. Yazici, J. Wright, D. Bertin, A. Shukla, Preferentially filled foam core corrugated steel sandwich structures for improved blast performance. J. Appl. Mech. Trans. ASME **82**, 1–13 (2015). https://doi.org/10.1115/1.4030292

Part II

Damage and Failure of the Ductile Metals

Problems of Deformation and Damage Studies of Additively Manufactured Regular Cellular Structures

10

Paweł Płatek, Paweł Baranowski, Jacek Janiszewski, and Michał Kucewicz

Contents

Introduction 216
Experimental Investigations of the Mechanical Response of Regular Cellular Materials 221
Quasi-Static Strength Tests 223
Medium Strain Rate Tests 226
High Strain Rate Tests 229
Numerical Investigations of the Mechanical Response of Regular Cellular Structural Materials 234
Numerical Erosion 235
Constitutive Modelling 236
Special Numerical Techniques 239
Summary 241
References 243

Abstract

Regular cellular materials manufactured additively attract the attention of many scientists due to specific mechanical properties including low mass and high strength. They pose a new very prospective proposal as an engineering material for the demanding branches of industry, bio-engineering and civil engineering. In addition to high geometrical stiffness, they are characterized with high capacity of energy absorption, ability to deformation in a programmable way based on adopted unit cell topology, and special mechanical properties of the applied original material. The main aim of this chapter is related to the problem of investigating the mechanical behavior of additively manufactured regular cellular structures under dynamic loading conditions, particularly during compression

P. Płatek (✉) · J. Janiszewski
Faculty of Mechatronics and Aviation, Military University of Technology, Warsaw, Poland
e-mail: pawel.platek@wat.edu.pl; jacek.janiszewski@wat.edu.pl

P. Baranowski · M. Kucewicz
Faculty of Mechanical Engineering, Military University of Technology, Warsaw, Poland
e-mail: pawel.baranowski@wat.edu.pl; michal.kucewicz@wat.edu.pl

© Springer Nature Switzerland AG 2022

G. Z. Voyiadjis (ed.), *Handbook of Damage Mechanics*,
https://doi.org/10.1007/978-3-030-60242-0_65

tests. Two available approaches, experimental and numerical, were discussed in details. The main experimental methods of investigations were described based on results of state-of-the-art as well as the authors' own experience. Additionally, the problem of structure damage mechanisms arriving during compression was discussed. Referring to the numerical approach, available techniques validated successfully by the authors were also presented. Furthermore, the key issues related to the definition of numerical models, undertaken initial-boundary conditions, as well as material constitutive relations were taken into account.

Keywords

Additive manufacturing · Compression tests · Dynamic loading · Damage mechanisms · Honeycomb · Lattice structures · Ls-Dyna · Numerical investigations · Regular cellular structures

Introduction

Development of new, cutting-edge products from various branches of industry demands to search for new, alternatively engineering materials, method of their synthesis, as well as elaboration of more effective techniques of manufacturing (Meyers et al. 2008). Although a wide range of studies in the field of material engineering are permanently undertaken, it could be noticed that typical engineering materials that are commonly used have reached a certain limit of their application that is not easy to exceed (Jia et al. 2019). Analyzing current state of the art in the field of material engineering, growing interests in regular cellular structural materials are observed (Banhart 2001; Restrepo et al. 2016a; du Plessis et al. 2019). This group of materials consists of periodic elementary unit cells with a specific shape. Contrary to stochastic foams, they indicate a homogenous structure that results in better mechanical properties (Crupi et al. 2013). One of the commonly known representatives of regular cellular topology is honeycomb structure with several modifications. Some selected topologies based on the honeycomb unit cell geometry are presented in Fig. 1. It is worth noticing that some geometrical features of the elementary unit cell often are bio-inspired (Zhang et al. 2015).

Nowadays, dynamic progress in the field of additive manufacturing attracts attention of many researchers studying the discussed issue (Gao et al. 2015;

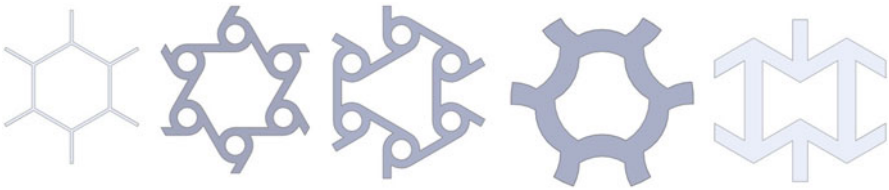

Fig. 1 The honeycomb unit cell topology and its modifications

Buchanan and Gardner 2019). The "layer by layer" additive techniques of object fabrication connected with a wide spectrum of available materials (polymers, metal powders, resins, etc.) additionally increase the range of studies that have been undertaken in the area of cellular materials (Bandyopadhyay and Heer 2018; Ngo et al. 2018). They are produced with the use of various groups of materials and manufacturing methods (Yang et al. 2014; Kucewicz et al. 2018; Mohsenizadeh et al. 2018; Abe and Sasahara 2019; Antolak-Dudka et al. 2019). Depending on applied techniques, they are produced as a 2D or 3D structures (Figs. 2 and 3).

Taking into account manufacturability, the 3D variants are more difficult in fabrication due to the necessity of applying the powder bed fusion techniques (Harun et al. 2018). The 2D variants can be produced with the use of all AM systems. However, there are certain limits resulting from the size of the elementary unit cell and the value of the wall thickness. Low mass resulting from the low value of a relative density and high geometrical stiffness make regular cellular materials very promising as a solution to optimize newly developed products (Tang et al. 2015; Mazloomi et al. 2018). Nevertheless, the group of 3D structures, sometimes called lattice structures, indicates a significantly lower value of the relative density compared to the typical 3D topologies.

Over the last few decades, a range of regular cellular materials applications has been increased. Generally, they are used as engineering materials due to low mass and high geometrical stiffness. Additionally, their high ability to controlled deformation resulted in their use in energy absorption applications. Moreover, they are used as thermal and vibro-insulators. Analyzing from the mechanical point of view, aspect of their application as a typical engineering material is possible to state that it depends on the load direction scenario, i.e., "out-of-plane" and "in-plane." It is especially important in the case of the 2D structure specimens, e.g., honeycombs (Fig. 4), its modification, as well as gradient topologies.

The first one is related to situations where high geometrical stiffness and low mass are key issues. This solution allows for optimization of mass of structure, taking into construction the high mechanical strength. The second group of structural material applications refers to their high ability to energy absorption under quasi-static and dynamic loading conditions. This feature is used in the development of new, advanced shields, protective panels used in automotive, and civilian as well as military implementations (Zhao et al. 2018). Both of the mentioned examples are presented in Fig. 5. The key feature which is used in energy absorption applications is the high ability of structural materials to densification during the deformation process. This phenomenon is generally determined by two variables. The first one is conditioned by mechanical properties of applied material like high ductility, high strength, and manufacturability. The second one refers to unit cell topology. Depending on the applied shape of the elementary unit cell, a different characteristic of deformation can be obtained. It is determined by the geometrical stiffness of the unit cell. The proper connection of the both mentioned features allows for programming mechanical response of regular cellular structural material. This feature is crucial in reference for developing new cutting-edge products, and it also allows to exceed the current limitation of traditional commonly used engineering materials.

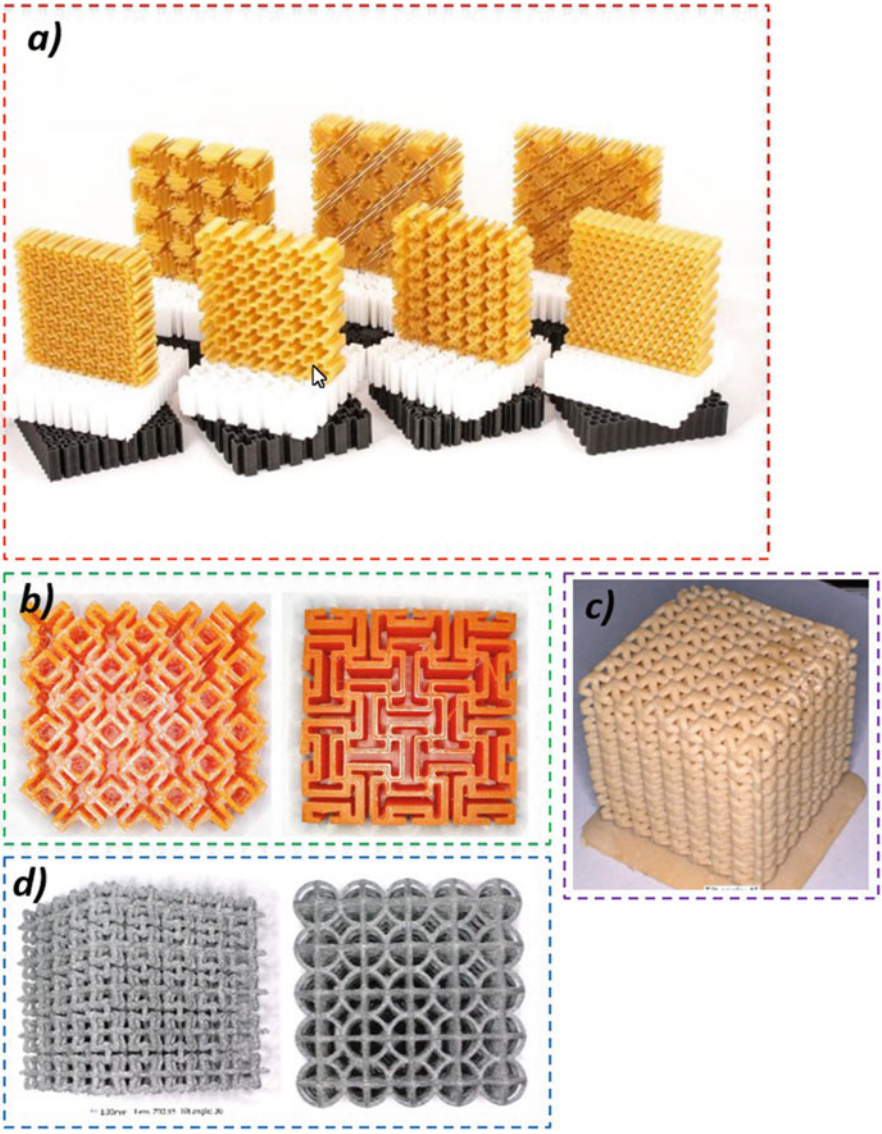

Fig. 2 Examples of the polymer regular cellular structure materials manufactured additively: (**a**) made from polymers with the use of FDM technique, (**b**) made from thermoplastic polyurethane with the use of FFF technique, (**c**) made from resin with the use of DLP technique, (**d**) made from polymer powder with the use of SLS technique (authors' work)

Achievement of the high range of deformation during regular cellular structure materials loading demands studies concern to material damage mechanisms. Based on the data presented in the literature and based on the authors' experience, it could be stated that the mechanical response of this group of materials consists of three

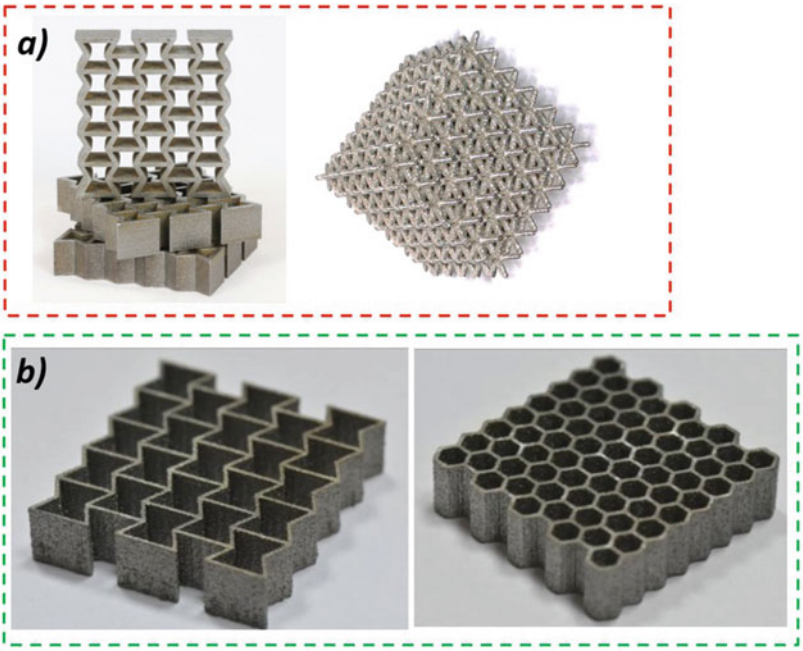

Fig. 3 Examples of the metallic regular cellular structure materials manufactured additively: (**a**) made from metal powder with the use of SLM technique, (**b**) made from Ti6Al4V titanium alloy powder with the use of LENS technique (authors' work)

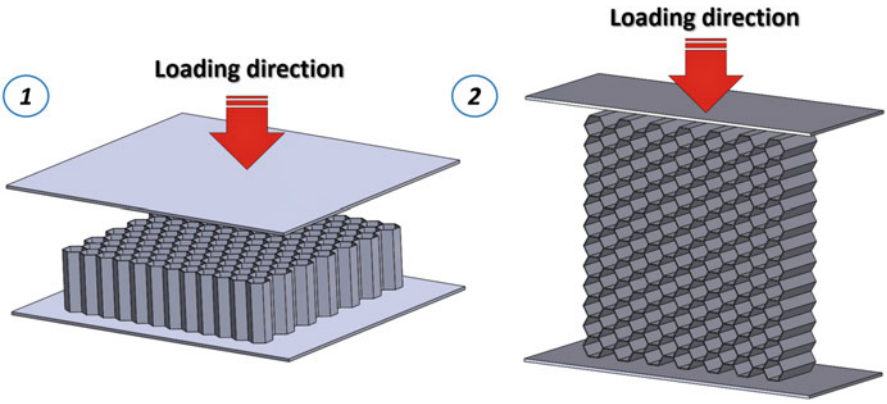

Fig. 4 Orientation-directed application of the regular cellular structure material: (1) out-of-plane, (2) in-plane

main stages, which are presented in Fig. 6. The first one is linear elastic deformation, followed by a plateau, and finally increase of the loading force caused by the densification. The first stage generally depends on geometrical stiffness of a structure

Fig. 5 Selected examples of the honeycomb structure material applications: (1) run-flat honeycomb tire (www.motor1.com/news/12355/honeycomb-tire-of-the-future), (2) side crashworthiness panel of car body frame (www.motortrend.com/news/touring-the-innovative-bmw-i3-assembly-plant-359439), (3) inserts in UAV wings (www.designboom.com/technology/aurora-flight-sciences-stratasys-3d-printed-jet-powered-drone-11-11-2015), (4) advanced solution of new gas piston (www.wardsauto.com/engines/iav-sees-huge-potential-3d-printed-pistons), (5) modern light and a resistant military helmet (www.soldiersystems.net/tag/team-wendy/page/5)

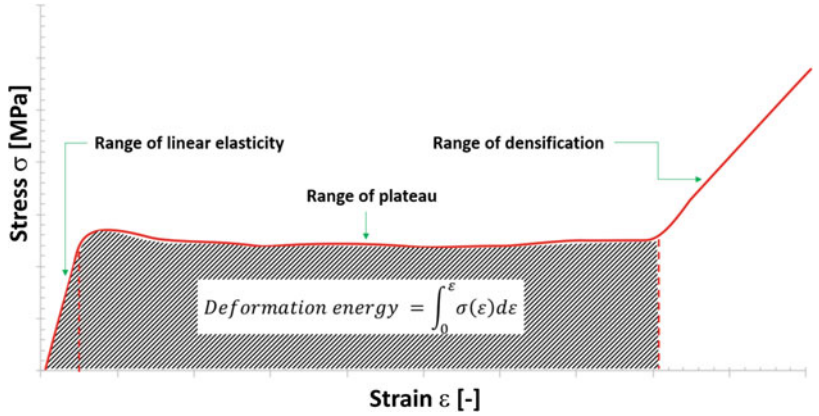

Fig. 6 The main stages of regular cellular structure material deformation process

and material's elastic properties. Afterward, when a material yield is reached, damage mechanisms including bending and cracking occur. These two mechanisms define the plateau deformation range; however, the cracking is more destructive because it results in collapsing of elementary cells and finally may cause disintegration of the structure. Significant increase of the loading force during the last stage is related to the densification of structure.

The key issue that should be considered during the development of regular cellular structure is programing a deformation process in a way where cracking mechanism appears only in the final stage of the structure deformation process. This solution allows extending the range of deformation and finally increases a structure's energy absorption capacity. This challenge demands to conduct extended studies on regular cellular materials damage mechanisms, which is possible to achieve based on the results from experimental and numerical investigations.

The main goal of this handbook chapter is to present the fundamental issues that should be considered during development and studies of new regular cellular structural materials dedicated to energy absorption application. The chapter consists of two parts. The first one presents the experimental approach that can be used to determine the mechanical response of regular cellular materials subjected to quasi-static and dynamic loading. The second refers to numerical modelling methods that can be applied to predict the behavior of cellular structural materials.

Experimental Investigations of the Mechanical Response of Regular Cellular Materials

Experimental investigations are one of the most popular methods used to predict the mechanical response of material and structures in engineering. It is no different in the case of the regular cellular materials subjected to mechanical loading. They enable analyzing the cellular material deformation process in detail, understanding the main mechanisms responsible for their structure damage. Furthermore, experimental studies allow to consider many additional aspects, like geometrical deviation of the elementary unit cell, material imperfections, and heat distribution which results from the additive nature of manufacturing process. Due to complexity of the mentioned phenomena, they are usually simplified in analytical and numerical studies. Based on the results of conducted literature review, it can be stated that experimental studies of cellular materials manufactured additively are commonly carried out, and a considerable number of available research papers are related to this approach (Ozdemir et al. 2016; Novak et al. 2018; Sun and Li 2018; Antolak-Dudka et al. 2019). One of the basic tests used to determine the mechanical response of additively manufactured regular cellular structure materials is uniaxial compression test under quasi-static and dynamic loading conditions. The obtained deformation force versus displacement or stress versus strain characteristics allow for estimation of energy absorption capacity of the tested structures. Generally, these investigations can be divided into two groups (Fig. 7). The first one is conditioned by the anisotropic behavior of cellular materials subjected to mechanical loading. The second one results from strain rate effects. Referring to the first criterion, two main "out-of-plane" and "in-plane" orientations of specimens subjected to loading can be identified. Generally, the orientation depends on the kind of cellular material application (high stiffness and low mass or high energy absorption capacity and low mass). Furthermore, it is also conditioned by applied additive manufacturing technique, mechanical properties of used material, assumed size of the elementary unit

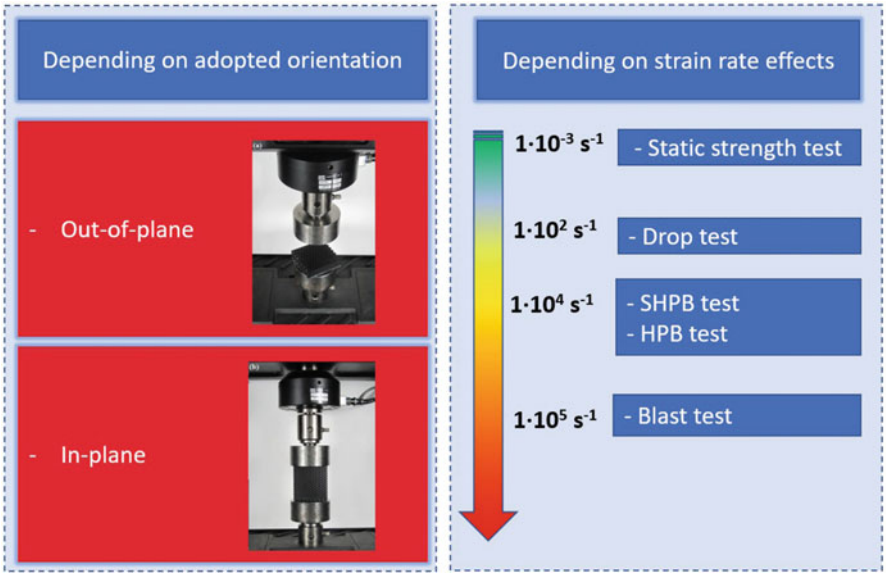

Fig. 7 Typical experimental techniques in compression applied in cellular materials studies

cell, and wall-thickness. The out-of-plane orientation refers to specimens made from ductile and strength materials. The typical representatives of cellular materials with a low density and high strength are honeycomb structures. Their mechanical behavior under out-of-plane loading orientated conditions is well-known, and nowadays they are produced as ready-to-use prefabricated panels with specified geometrical features. Nevertheless, in the past, regular cellular materials with simple geometrical shapes of the elementary unit cell were generally used because of reduced manufacturability. Nowadays, undertaken research works refer to new composite modifications (Tao et al. 2015; Wang et al. 2017) where additional filling of the material structure is used. Dynamic progress in the field of additive manufacturing caused a growing interest in cellular materials. New fabrication methods allowed for the definition and manufacturing of elementary unit cells with sophisticated shapes that have not been possible so far (Ozdemir et al. 2016). The problem of the influence of adopted unit cell shape on the mechanical behavior of cellular materials attracted the attention of many scientists. Based on adopted geometrical features, it enables programming the mechanical response of materials (Bates et al. 2016; Habib et al. 2018). Furthermore, many researchers focused their attention on the in-plane direction of structure loading. The orientation aspect gives a higher range of material deformation and results in a higher capacity of energy absorption. Furthermore, the in-plane loading direction is also preferred due to the technological limitations of currently available additive manufacturing techniques, problems with fabrication, and flawless structures with thin-wall (below 0.5 mm).

The second criterion concerning experimental studies on the mechanical behavior of cellular materials refers to strain rate effects. Results of investigations presented in

papers focused on the discussed problem generally are related to "in-plane" uniaxial compression tests conducted under quasi-static loading conditions.

Similar investigations on cellular structures are also carried out under dynamic loading conditions; however, the available research techniques are more sophisticated and complex. Materials testing at higher strain rates has to consider inertia effects, wave propagation effects, and shock wave effects. Furthermore, thermal effects and difficulties with accurate strain measurements are additional factors in dynamic tests. Referring to the cellular materials subjected to dynamic loading conditions, consideration of two main dynamic effects, i.e., the inertia effects of the structure and the strain rate effects of original material, is required (Sun and Li 2018; Tancogne-Dejean and Mohr 2018; Zhang et al. 2018; Baranowski et al. 2019b).

Quasi-Static Strength Tests

The first commonly used method of cellular materials experimental studies is related to compression tests under quasi-static loading conditions. Its main advantage is the possibility to identify the main mechanisms causing cellular material damage due to the controllable and programmable experiment conditions. This group of methods enables conducting studies in detail concerned on the definition between adopted regular cellular structure topology and its influence on the energy absorption capacity (Fig. 8a). Furthermore, it is commonly used to determine the mechanical properties of the original material used in manufacturing process (tensile tests – Fig. 8b).

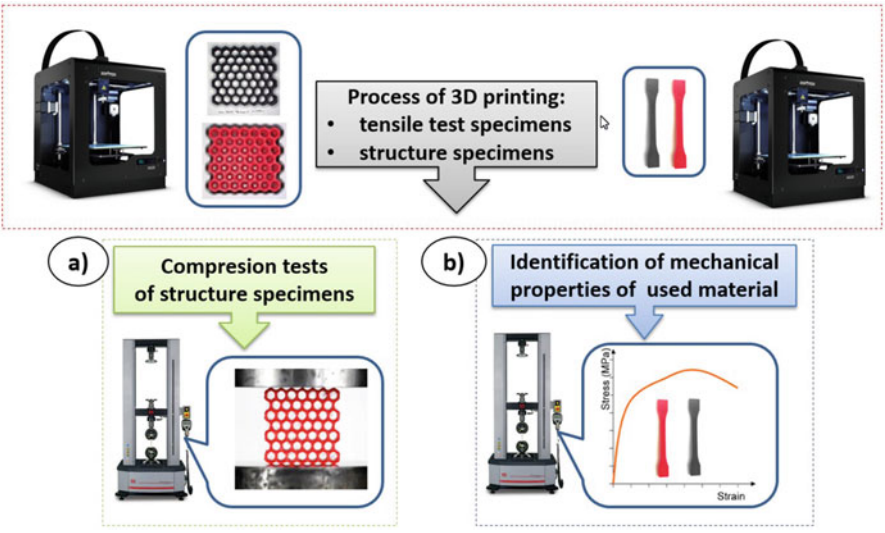

Fig. 8 The scheme illustration of application of quasi-static tests in studies of regular cellular materials: (**a**) strength tests of structure, (**b**) strength test of original material

Results obtained in quasi-static tests are a good benchmark for validation of numerical models describing the mechanical behavior of cellular materials. Taking into account the anisotropic properties of additively manufactured materials, it is necessary to fabricate structure samples and typical dog-bone specimens used in uniaxial tensile tests. Results from both tests enable conducting additional numerical studies, significantly reducing the time and the cost of investigations. Additionally, they are the first step for optimization studies.

One of the most typical research problems that is undertaken during quasi-static uniaxial compression tests is the evaluation of the adopted structure topology influence on its mechanical response defined by the loading force history. Exemplary results of the authors' works related to this problem are presented in Fig. 9, where a typical honeycomb topology and its modifications were evaluated. Specimens used in the mentioned tests were made from thermoplastic polymers and fabricated via 3D printing with the use of selective laser sintering (SLS) and fused filament fabrication (FFF) techniques. Based on conducted studies, the relationship between specimens' relative density and their capacity to energy absorption was determined. The relative density parameter *RD* (Gibson and Ashby 1997) directly refers to specimens topology. It indicates the proportion of solid content in the cell structure, and it is expressed as

$$RD = \frac{\rho}{\rho_s} \tag{1}$$

where ρ is the bulk density and ρ_s is the density of the base material.

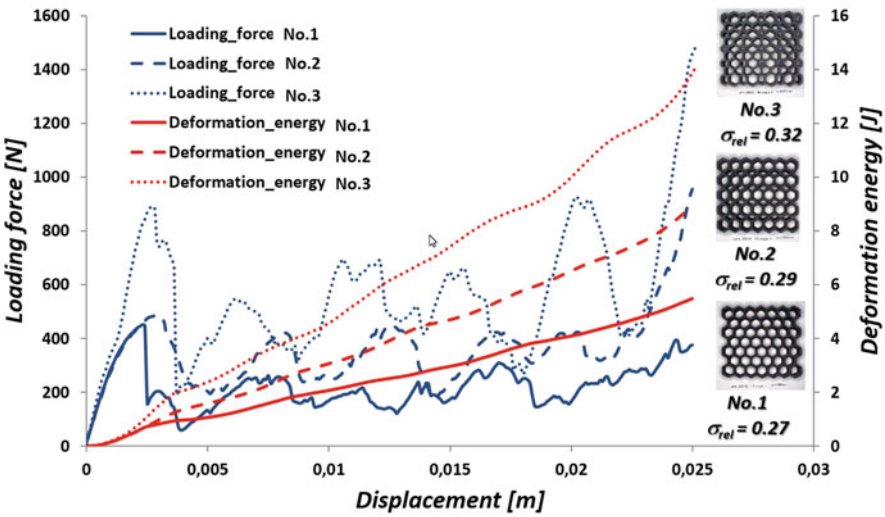

Fig. 9 Exemplary results of quasi-static compression tests of regular cellular structures manufactured additively from polyamide material

Presented results of the loading force versus displacement (Fig. 9) enabled assessment of the influence of adopted topology on the mechanical response of cellular material subjected to compression. Analyzing these data, three main stages of the deformation and damage process can be highlighted – linear elastic, long plateau, and densification. Additionally, the impact of the adopted unit cell shape on the structure deformation history plots can be observed. The damage mechanism that can be identified in the first stage of this process for all cases was the buckling. Further increase of the compression load value resulted in structure walls' instability and caused the bending mechanism. The next stage of deformation was related to material yielding, afterward the shearing, and finally, cracking mechanism occurred. Comparing results obtained for the specimen (No. 5) with higher geometrical stiffness to the standard honeycomb (higher value of the relative density), a longer range of linear-elastic deformation process can be observed. Nevertheless, high geometrical stiffness caused a rapid damage mechanism which resulted in considerable fluctuations of loading force during further stages of deformation.

A high influence of adopted topology on specimen deformation process can be observed in the case of structures that demonstrate auxetic effects. It is a group of structural materials which, based on specific geometrical features of the elementary unit cell, the structures during deformation indicate a negative Poisson's ratio (NPR). It means that they become thicker in one or more perpendicular directions during tension and become thinner during compression. Figure 10 presents results obtained for typical honeycomb and re-entrant honeycomb which demonstrate an auxetic behavior. Both structure specimens were made from 316 L stainless steel with the

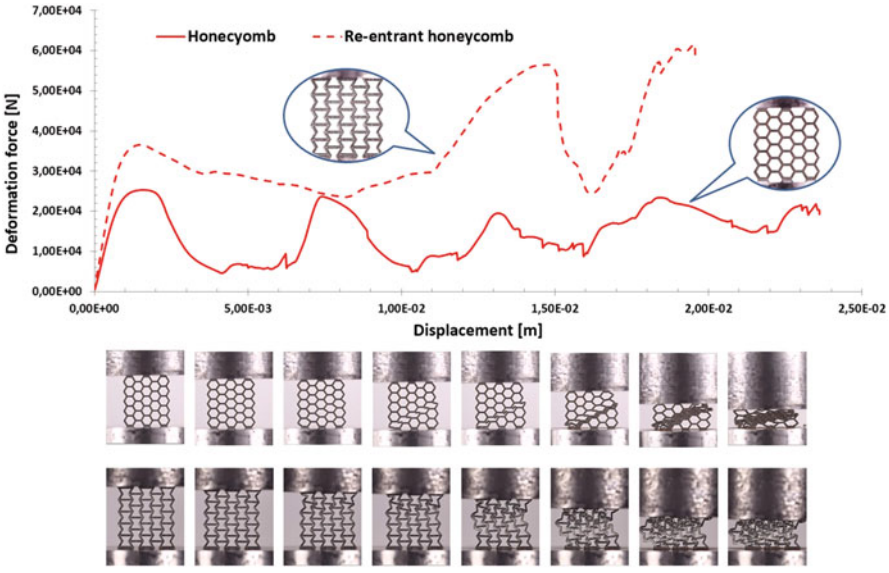

Fig. 10 Results of compression tests of honeycomb and re-entrant honeycomb under quasi-static uniaxial compression tests

use of selective laser melting (SLM) AM techniques. The relative density of both specimens subjected to tests was similar. Based on obtained results, it can be observed the influence of the adopted shape of elementary unit cell on the deformation history plots. Referring to honeycomb structure, the range of buckling deformation is very short, and very quickly bending mechanisms were observed. Instability of structure's walls and progressive deformation caused that shearing and cracking mechanisms have been initiated in connection points localized on the diagonal line of structure. Further deformation caused progressive cracking which resulted in collapsing of successive arrays of elementary unit cells. This process has been repeated itself until all arrays defining structure were collapsed, and the final densification was observed. Referring to the auxetic re-entrant honeycomb specimen, this process proceeds in a different way. Based on the history plot presented in Fig. 10, it can be seen that initially buckling and then bending deformation processes proceed longer. Adopted geometrical shape of the elementary unit cell indicates a high tendency to bending and resulted in walls folding during the deformation process. Comparing both deformation history plots, it can be observed that force-displacement curve for re-entrant honeycomb is smoother, and visible increase of the force value can be observed during the plateau stage. It is due to the instability of the structure wall thickness.

Medium Strain Rate Tests

One of the commonly used methods of investigating the mechanical response of additively manufactured regular cellular structures under medium strain rate loading conditions is a drop impact test. The universal column impact machine (drop-weight impact apparatus) is used to perform these tests. Based on conducted experiments, the history of deformation force and displacement of impactor are obtained. The value of the deformation force is registered continuously by the additional acquisition system, whereas the displacement of the impactor is measured by various non-contact, optoelectronic systems (e.g., high-speed camera). Initial loading test conditions are defined by the mass of the impactor and its initial velocity. This method of investigation was used in the past, where a standard honeycomb crashworthiness efficiency was evaluated (Yamashita and Gotoh 2006). Nevertheless, versatility of this testing method is currently used in studies related to cellular materials manufactured additively. Authors of work (Yang et al. 2017) used it to predict the crashing behavior of a thin-wall circular tube with internal gradient grooves. Specimens subjected to impact tests were made from a 316 L stainless steel with the use of the SLM technique. Adopted by the Authors' internal grooves enable them controlling the crashing process. Drop tests were also used in research work published by Antolak-Dudka et al. (2019). This method was used to determine the mechanical response of honeycomb structures with different sizes of the elementary unit cell during in-plane uniaxial compression tests. Tested specimens were made form Ti6Al4V titanium alloy and fabricated via the Laser Engineering Net Shaping system (LENS). Exemplary results of authors' research work related to drop impact compression tests of honeycomb specimens are presented in Fig. 11. In order

to illustrate the main difference between quasi-static and drop impact test results, three variants of honeycomb specimens were used. Presented results were obtained based on the methodology described in the paper published by Antolak-Dudka et al. (2019). The main difference between tested honeycomb specimens was the size of the elementary unit cell. The value of the inscribed circle diameter in the hexagon was appropriately: No. 1, 3 mm; No. 2, 4 mm.; and No. 3, 6 mm. The main dimension of fabricated specimens was approximately 40 × 40 × 10 mm, and the wall thickness was assumed as a 0.7 ± 0.1 mm. The values of relative densities resulted from adopted geometrical assumptions are presented in Table 1.

Tests were carried out with the use of universal tensile machine MTS Criterion C45 and universal column impact machine Instron Dynatup 9250 HV. The strain rate for quasi-static tests was 0.001 s^{-1}, whereas in the case of impact tests, the averaged value of strain rate was in the range of 10^2 s^{-1}. Results obtained from both tests are presented in Fig. 11, which contains a comparison of deformation energy plots under quasi-static and drop impact compression tests with consideration of the influence of the specimen relative density. The maximum values of achieved deformation energy at a specified range of deformation are presented in Table 2. Referring to the

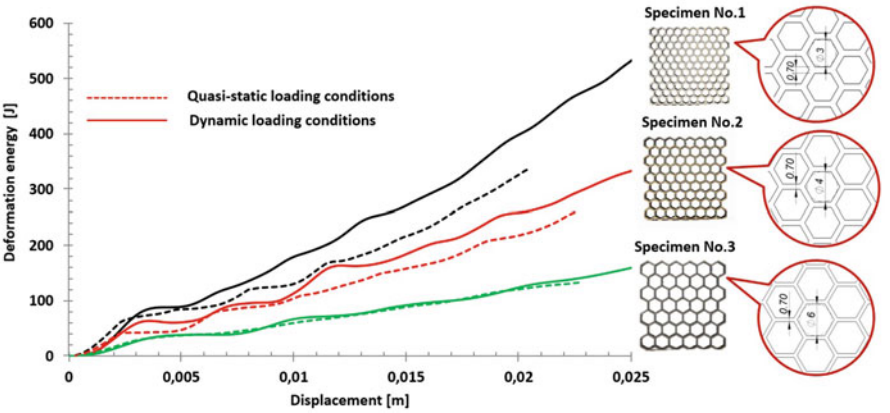

Fig. 11 The comparison of the quasi-static and drop impact compression tests of the honeycomb specimens

Table 1 Relationship between unit cell size and the value of relative density

Specimen	No. 1	No. 2	No. 3
Unit cell size [mm]	3	4	6
Relative density [−]	0.36	0.31	0.23

Table 2 The comparison of maximum values of deformation energy referring to honeycomb structure specimens

	No. 1	No. 2	No. 3
Relative density [−]	0.36	0.31	0.23
Max. Value of absorbed energy in drop impact test [J]	532	332	160
Max. Value of absorbed energy in quasi-static test [J]	336	259	132

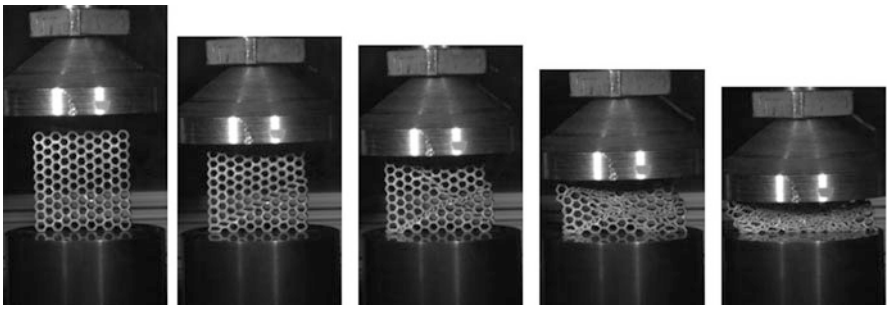

Fig. 12 The main steps of honeycomb No. 1 deformation in drop-weight test

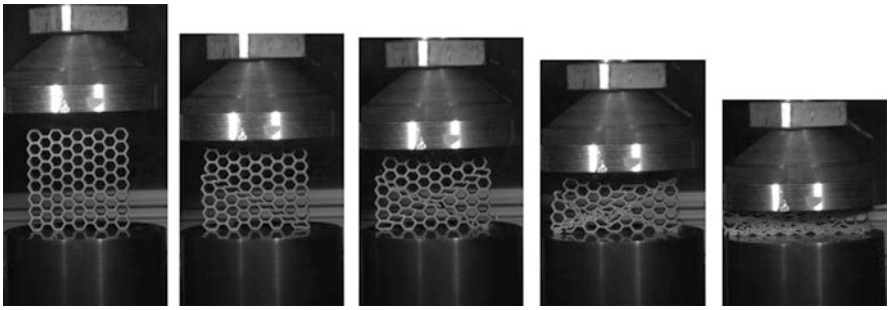

Fig. 13 The main steps of honeycomb No. 2 deformation in drop-weight test

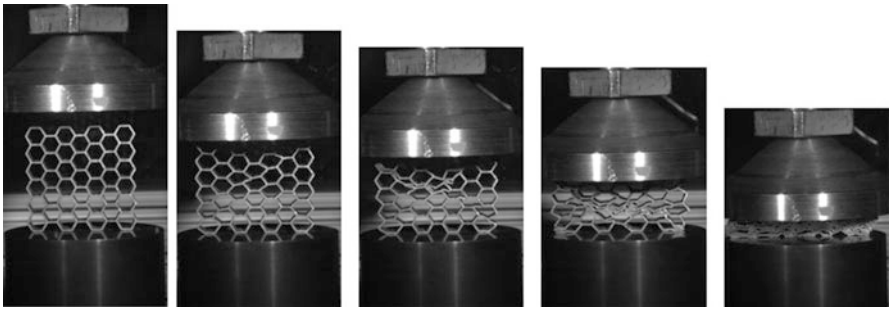

Fig. 14 The main steps of honeycomb No. 3 deformation in drop-weight test

presented data, a strain rate sensitivity of honeycomb structures can be observed. Results obtained for Specimen No. 1 under drop impact compression test significantly differ compared to quasi-static outcomes. This is due to a higher value of the specimen relative density resulting in stiffer response and larger inertia effects. In Figs. 12, 13, and 14, selected moments of time of honeycomb structure deformation

are presented. Despite a different relative density, a similar structure damage mechanisms can be observed.

High Strain Rate Tests

Further method of experimental investigations of regular cellular structures with consideration of high strain rate effects requires application of the split-Hopkinson pressure bar (SHPB) technique. The principle of operation of the SHPB has been described in detail in many papers and books (Chen and Song 2011). The SHPB set-up usually consists of a striker bar and two long bars, called an input bar and an output bar, with the same diameter and material, typically steel, aluminum; however, polyamide and polycric bars can be also used (Fig. 15).

The SHPB apparatus is generally used to identify the mechanical properties of materials under high strain rates. The experimental test procedure is as follows: the material specimen is placed between the bars, and it is loaded by a stress impulse generated by the striker impact in the front surface of the input bar. This generates a trapezoidal stress impulse (incident wave - ε_i) which travels through the impacted bar. When the elastic wave reaches the specimen, due to the mismatch of mechanical impedances between the bar and the specimen material, part of the incident wave is reflected back (reflected wave - ε_r), and the rest of the incident wave is transmitted through the specimen. It compresses the specimen with high rates, and the rest of the wave travels to the output bar as a transmitted wave - ε_t. The wave propagation is measured by the strain gauges placed at the half-length of input and output bar. The stress, strain, and strain rate in the specimen can be determined according to one-dimension wave propagation using the well-known equation (Chen and Song 2011).

Comparing to the drop tests, the SHPB tests allow increasing the range of strain rate from 10^2 s^{-1} to 10^4 s^{-1}. The SHPB technique had been widely used in studies concerned with strain rate effects of metallic foams (Sun and Li 2018). The versatility of investigation methodology caused that it has been started to be used also in the case of regular cellular materials. Based on data presented in the papers (Ozdemir et al. 2016; Xiao and Song 2017; Sun and Li 2018; Zhang et al. 2018; Fíla et al. 2019; Jin et al. 2019), several configurations of SHPB laboratory set-ups can be used to carry out studies referring to dynamic response of cellular materials. All of them are illustrated in schemes presented in Fig. 16. The first one – standard configuration – assumes that specimen subjected to dynamic loading is placed between input and

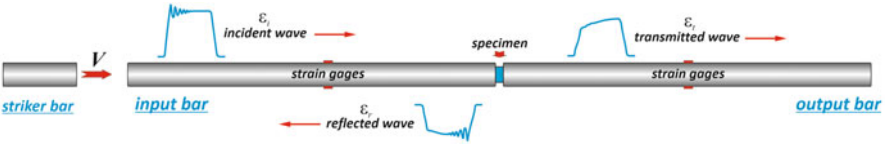

Fig. 15 The schematic representation of the SHPB set-up

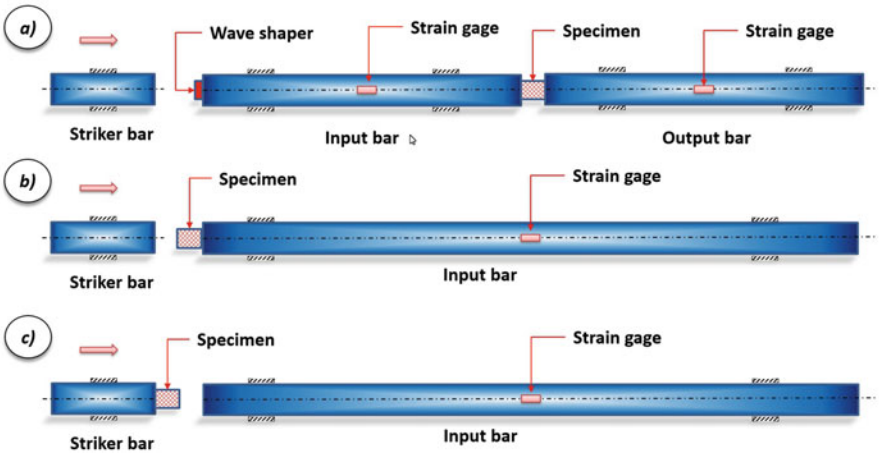

Fig. 16 Three commonly used configuration of SHPB and HPB during investigations of dynamic response of the cellular materials: (**a**) standard SHPB, (**b**) forward direction, (**c**) reverse direction

output bars (Fig. 16a). This kind of experimental study with the obtained results are described in detail in (Tao et al. 2015; Jin et al. 2019). Its main drawback is a limited range of structure deformation. This type of test enables taking into account only the first stage of the linear deformation and partially plateau range, where damage mechanisms have been initiated (without densification of the structure). The other mentioned SHPB test configurations, in turn, are described in the following papers (Ozdemir et al. 2016; Zhang et al. 2018). The main difference with the other configurations of the laboratory set-up is the position of the tested specimen. It is located on the impact surface of the input bar in forward direction (Fig. 16b) or on the impact surface of the striker bar in reverse direction (Fig. 16c). Mentioned configurations allow for direct impact of the striker into the specimens. It affects higher strain rate effects and more destructive impact on structure mechanical behavior (considering structure densification). Based on conducted SHPB tests, regardless of applied configuration, the loading force versus displacement history is obtained as one of the results. The value of loading force is calculated based on the strain gauge signal, whereas a specimen deformation history is defined with the use of non-contact optoelectronic measuring systems (e.g., high-speed camera).

The main advantage resulted from the application of the mentioned dynamic investigation technique is the possibility of obtaining loading conditions similar to the blast loading scenario. In (Ozdemir et al. 2016), the adopted initial conditions of the test (velocity and mass of the striker bar) enabled for obtaining conditions similar to effects caused by the blast of 10 kg TNT at the distance of 1.5 and 2.5 m.

Generally, regular cellular materials are tested mainly in compression than in tensile or shearing. The process of identifying the mechanical behavior of cellular materials is similar like in the case of testing solid materials. However, it needs a special approach which is conditioned by proper size of specimen defined by the

number of elementary unit cells. Based on the data presented in (Liebenstein et al. 2018), it is suggested that specimens size effect can be neglected when minimal number of the elementary unit cell in a single row is larger than 7. The application of the larger size of the unit cell results in a significant increase in specimen dimensions. Conducting high strain rate investigations with the use of large-scale specimens causes a serious technical challenge. In this case, a special large-scale SHPB set-up (total length exceeds even 10 m) is strongly recommended to perform this type of tests.

The other issue that has to be solved in the case of testing regular cellular specimens is the problem of the low amplitude of transmitted wave. The cellular materials are classified as low mechanical impedance materials. Representatives of this group of material are polymers, elastomers, wood, etc. High difference in strength and mechanical impedance between cellular material specimen and SHP bars results in a low value of the transmitted wave amplitude and causes serious problems with the data signal registration. Based on the data presented in the literature, few approaches to solve this problem can be used. The first one suggests the application of piezoelectric gauge instead of strain gauge (Chen et al. 2000). Another approach involves using SHPB bars made of low mechanical impedance materials, e.g., plexiglass of polyamide (Zhao et al. 1997; Casem et al. 2003; Baranowski et al. 2017). In this case, the issue of dispersion of waves propagating in low impedance bars should be considered, and additional complex procedure of numerical correction and reconstruction of wave signals registered by the strain gauge measurement system has to be implemented. The last and the simplest method of improving incident signal quality is replacing bars with light alloy hollow tube bars (Chen et al. 1999).

The key issues related to the problem of studies concerned on regular cellular specimens with consideration of high strain rate effects are presented based on the authors' experiences. Figure 17 contains the main view of the exemplary lattice specimens made additively from 316 L stainless steel with the use of the SLM technique. They were designed as cuboids with similar global dimensions (approximately equal 24 × 24 × 24 mm) and elementary unit size dimension equal to 3 mm. Applied various values of the lattice strut diameter caused that different values of the relative density were obtained.

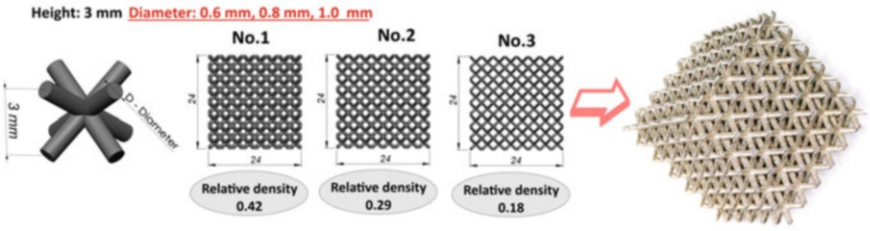

Fig. 17 Lattice structures manufactured additively from 316 stainless steel with the use of SLM technique

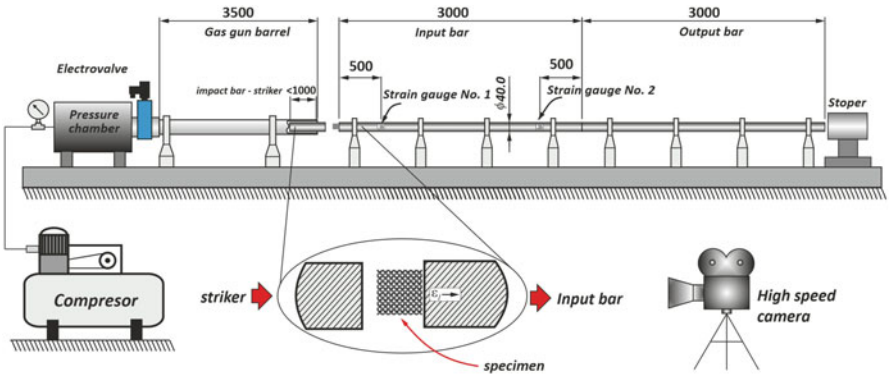

Fig. 18 The scheme of split Hopkinson pressure bar laboratory set-up used in dynamic investigations of lattice structures

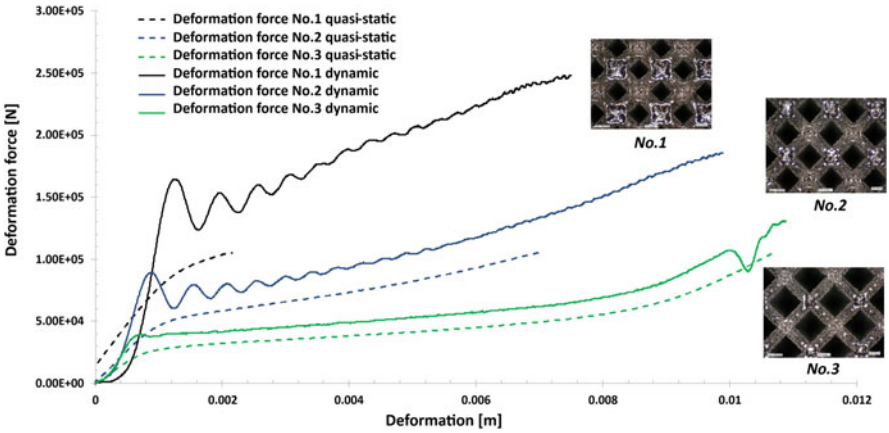

Fig. 19 Deformation process of the lattice specimens made from 316 L stainless steel during compression tests with the use of SHPB laboratory set-up

Specimens presented in Fig. 17 were subjected to quasi-static and high strain rate compression tests to identify the mechanical response depending on the applied kind of loading conditions. The main features of applied SHPB laboratory stand are presented in Fig. 18.

Exemplary results of conducted compression tests with the use of SHPB laboratory set-up are presented in Figs. 19 and 20. Based on registered footage by high-speed camera, it can be stated that investigated specimen topology in combination with 316 L stainless steel mechanical properties resulted in a high range of structure deformation process. The achieved force histories are similar to the reference plot illustrated in Fig. 6.

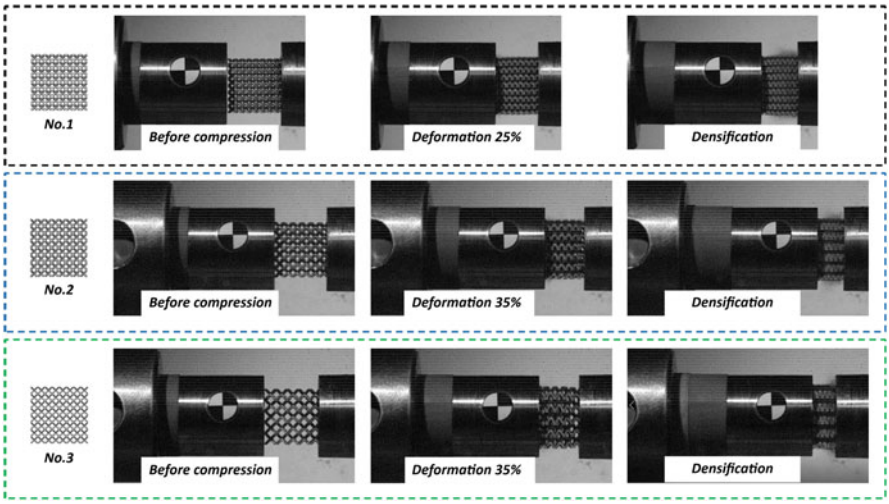

Fig. 20 The results of dynamic compression tests of lattice specimens with different values of the relative density

The mechanisms causing structure damage arrived in the final stage of deformation where densification occurred. Referring to the data presented in Fig. 20, a visible difference between quasi-static and SHPB results can be observed. It is worth noticing that similar results were reported by the other researchers (Xiao and Song 2017; Sun and Li 2018). These differences proved a high strain rate sensitivity of cellular materials. Furthermore, the inertia effects which existed in the case of specimen with the higher value of relative density caused higher differences between obtained results.

The other aspect that has to be considered during dynamic investigations of regular cellular materials is the necessity of identification of the mechanical properties of original material used during manufacturing process with consideration to strain rate effects. This process requires conducting both quasi-static and dynamic compression tests under various strain rate loading conditions. Based on obtained results, one of the well-known constitutive relations can be adopted to describe the mechanical properties of material with consideration to additional effects such as strain hardening, viscosity, and thermal softening. These data are essential in terms of additional numerical studies. Based on the literature study, some of the commonly known constitutive models that can be used are Johnson-Cook (Johnson and Cook 1983) and Rusinek-Klepaczko (Rusinek et al. 2009; Simon et al. 2018). However, different material models can be also implemented, which are discussed in further section of the chapter. Additionally, accurate representation of the dynamic response of regular cellular material with the use of numerical approach requires detailed knowledge regarding material damage mechanisms. This problem was discussed in detail in the following papers (Voyiadjis and Kattan 2006; Voyiadjis et al. 2014).

Numerical Investigations of the Mechanical Response of Regular Cellular Structural Materials

The experimental or laboratory tests can be very accurate; however, they are time-consuming and expensive. On the other hand, the crashworthiness of cellular structures can be studied using other approaches, e.g., analytical methodologies can be effectively used but only for investigating simple cellular geometries or benchmark models (Tantikom and Aizawa 2005; Babaee et al. 2012; Yan et al. 2012; Campanelli et al. 2014). The equations are based on a momentum law and are in good agreement with simple geometries such as honeycomb (Hyun and Torquato 2000; Hu and Yu 2013; Fu et al. 2017), rhombic (Babaee et al. 2012; Golaszewski et al. 2018; Barchiesi et al. 2019), or lattice (Yan et al. 2012; Du et al. 2016) structures. Nevertheless, when it comes to more sophisticated models or complex failure mechanisms, analytical approach is not enough. The numerical methods are a remedy for the abovementioned problems (Campanelli et al. 2014; Karamooz Ravari et al. 2014; Zhang et al. 2014; Dziewit et al. 2017; Ozdemir et al. 2017) (Roberts and Garboczi 2002; Tantikom and Aizawa 2005; Bauer et al. 2014; Restrepo et al. 2016b). For effective and correct analyses, a precise numerical model of the structure must be developed. The final form and properties of the finite element (FE) model are affected by many factors, and knowledge of the properties of the material is crucial for obtaining reliable results with good correspondence to the real-world structure (Świerczewski et al. 2012; Rozylo et al. 2017; Mayer et al. 2017).

Despite the modelled problem, all numerical investigations should correctly describe several processes responsible for the deformation of the structure, from which the most important is a fracture. Proper numerical representation of this phenomena significantly influences the simulation result quality and their correlation with the actual tests. The question is how to include such phenomena and simulate it using available numerical solutions? In LS-DYNA code, the material damage, failure, and fracture can be modelled and simulated using:

- Special constitutive models
- Erosion criteria
- Special numerical techniques
- Methods of structure representation

Damage and fracture of a material can be simulated using several constitutive models, which can be found in LS-DYNA hydrocode. To introduce the material failure, which is considered as deletion (erosion) of FEs from a model, a simple plastic strain criterion can be implemented, i.e., simplified Johnson-Cook, plastic kinematic, or piecewise linear plasticity material models. Additionally, damage or softening is also available in several constitutive models, e.g., plasticity with damage, Johnson-Cook, etc. Furthermore, for most constitutive models Add Erosion card can be added, where more complicated models such as Gurson or Gissmo are implemented (Zhang and Thaulow 2000; Hallquist 2019; Gurson 1977), can be

defined. Erosion is a numerical option that improves the stability of solution by removing the highly deformed elements from a FE model. This causes a decrease in the model total mass that is crucial in strongly dynamic problems. To prevent this Schwer (Schwer 2010) identified an application of weight functions that can be applied for FEs independently of their size. Moreover, meshless methods can be also used for preventing the mentioned problem, i.e., ALE (arbitrary Lagrangian-Eulerian method) and SPH (smooth particle hydrodynamics), which are more numerically stable in large deformation simulations compared to a typical FE modelling (Schwer 2009). One of the relatively new approaches is to implement adhesion, usually adopted for composite-like materials (Meo and Thieulot 2005), which in some cases can be replaced with a tiebreak contact with properly calibrated parameters (Dogan et al. 2012). Eventually, SPH particles can replace the removed elements based on defined criterion (Brad et al. 2018).

During the undertaken investigations related to energy-absorption cellular structures, the authors have tested most of the abovementioned solutions and numerical techniques. Nevertheless, the meshless methods were not included in the presented study. The applicability of the selected solution can be presented based on honeycomb topology subjected to external load. In the following section, the discussion is based on the authors' previous studies regarding the crashworthiness properties of different cellular topologies fabricated by the FDM and LENS additive technologies. Despite a significant difference in materials used (ABSplus in FDM and Ti-6Al-4 V in LENS), a similar structure behavior was observed. In all carried out simulations, the initial-boundary conditions were nearly identical. The honeycomb structures were inserted between two rigid surfaces representing heads of the universal strength machine. To simulate an interaction between parts of the model, a penalty-based contact with the Coulomb friction formulation was used (Hallquist 2019). Moreover, eight-node brick elements with a single interaction point were adopted for developing the FE models of the structures. The LS-DYNA code was used for all numerical simulations.

Numerical Erosion

In implicit computations, the implementation of the erosion (deleting of elements) results in the formation of a large number of additional degrees of freedom at each time step, which is very problematic and time-consuming due to the need to compute and invert the stiffness matrix after each element is deleted. On the other hand, the problem can be simulated under a fully dynamic regime with direct integration in the time domain with a relatively easy implementation of the erosion criterion based on, i.e., effective strain. In order to analyze the influence of the numerical erosion consideration on the results, both implicit and explicit approaches were applied in the numerical studies of the deformation process of the honeycomb cellular structure manufactured using FDM technology (Kucewicz et al. 2018). To avoid unnecessary dynamics in explicit simulations, one of the rigid walls compressing the structure had the following prescribed velocity (Hanssen et al. 2002; Baranowski et al. 2015):

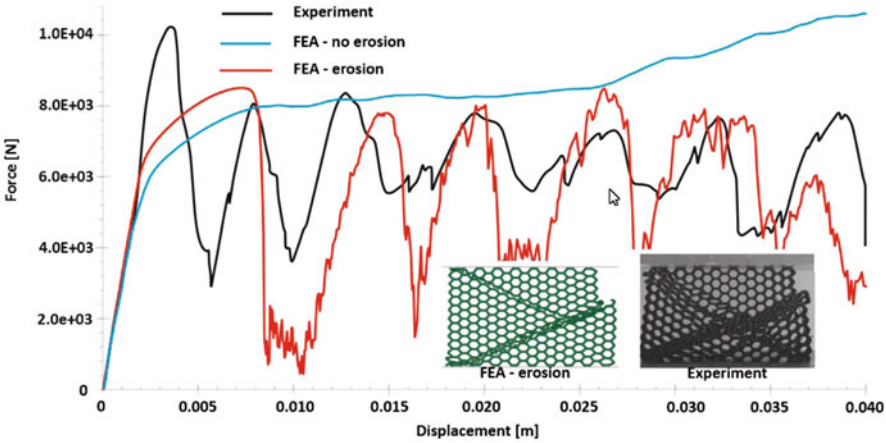

Fig. 21 Comparison of (**a**) force vs. displacement and (**b**) deformation of the honeycomb structure, from the experimental test and simulations (Kucewicz et al. 2019)

$$v(t) = \frac{\pi}{\pi - 2} \frac{s_{max}}{T\left[1 - cos\left(\frac{\pi}{2T}t\right)\right]} \tag{2}$$

where T is the total duration of loading and S_{max} is the final displacement.

From the conducted experimental tests and numerical simulations, the relationships between force and displacement were compared (Fig. 21). Results from the FE models with and without erosion are also included. Visible differences between both approaches can be noticed. The first force peak equals 10 kN was not obtained in explicit and implicit numerical simulations. However, the force oscillations that resulted from cell failure are similar in the case of explicit FEA and actual tests. Without considering the numerical erosion, it was not possible to effectively simulate the structure behavior. The differences between force histories are reflected in the values of absorbed energies: 234.7 J and 303.5 J for the model with erosion and without erosion, respectively. It is worth noticing that the actual honeycomb structure absorbed energy equals to 260.0 J. Deformation of the honeycomb structure at the selected stages of test presented in Fig. 21b confirms the effectiveness of the erosion inclusion in FEA.

Constitutive Modelling

The damage and failure of material can be also simulated using special material models, which incorporate parameters responsible for softening, strain rate influence, and/or erosion. One of the relatively simple models, which enables to omit a sudden loss of material continuity due to numerical erosion, is *Mat_Plasticity_With_Damage – MPD* available in LS-DYNA package. It is an elasto-visco-plastic material model that uses two curves: effective stress (ES) vs. effective plastic strain

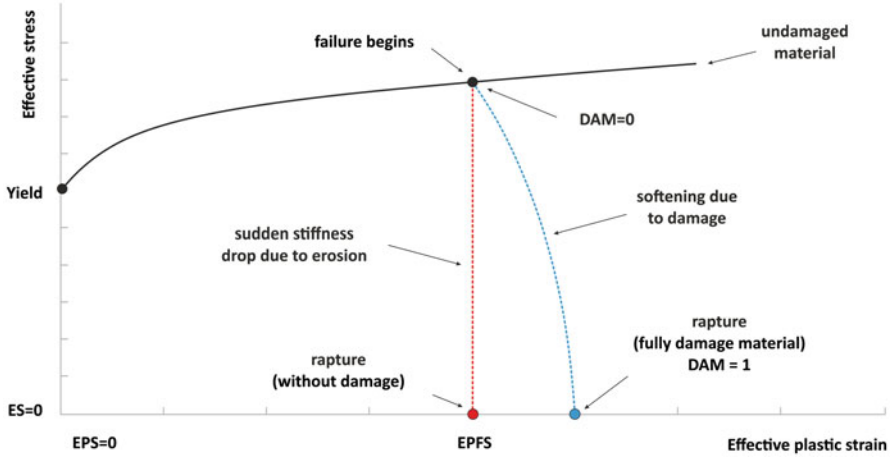

Fig. 22 Stress strain curve with damage in MPD model (Hallquist 2019; Baranowski et al. 2019b)

(EPS) and damage (DAM) vs. EPS. Implementation of the second characteristic allows elements to remain in the FE model much longer compared to the same model including constitutive model without softening curve. However, the point of the curve should be carefully added so as not to drastically change the stiffness of material.

The MPD model with damage curve was successfully used for simulating the deformation process of honeycomb structure made of ABSplus and Ti-4Al-6 V materials (Baranowski et al. 2019a, b). The FEA were based on experimental tests conducted using a universal strength machine with a loading velocity of 1 mm/s (Fig. 22).

In Fig. 23 force vs. displacement is presented for actual test and numerical simulations using two different constitutive models: the abovementioned MPD model with the damage curve and the Mat Piecewise Linear Plasticity (MPL), which is a typical elasto-plastic model. In both cases, the erosion criterion was used; however, different values of effective failure strain (EFPS) were implemented. In the MPL model, the value of EFPS (20%) was taken from the uniaxial tensile tests carried out using dog-bone specimens. For the MPD model with damage curve, the element could be deleted when reaching the 400% of EPS. The force vs. displacement curve obtained from the FEA with MPL model matched well the experimental characteristic only in the initial stages of the deformation. A similar stiffness can be observed compared to actual tests; however, the first peak value is slightly underestimated. Subsequent stages of structures deformation show significantly smaller values of force, which is a result of FEs erosion. On the other hand, the MPD provided excellent similarity between numerical and experimental results. Thanks to the possibility for maintaining material continuity, the force oscillations, resulted from fracture of the cells walls, were also obtained.

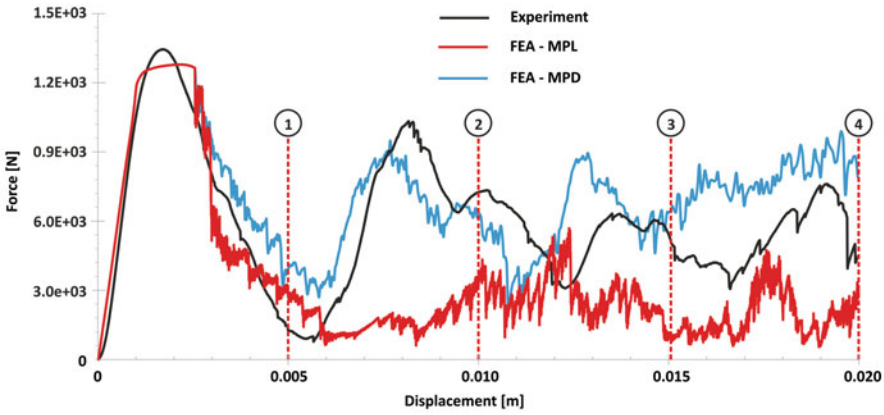

Fig. 23 Force characteristics obtained from FEA using two constitutive models and experiment (Baranowski et al. 2019b)

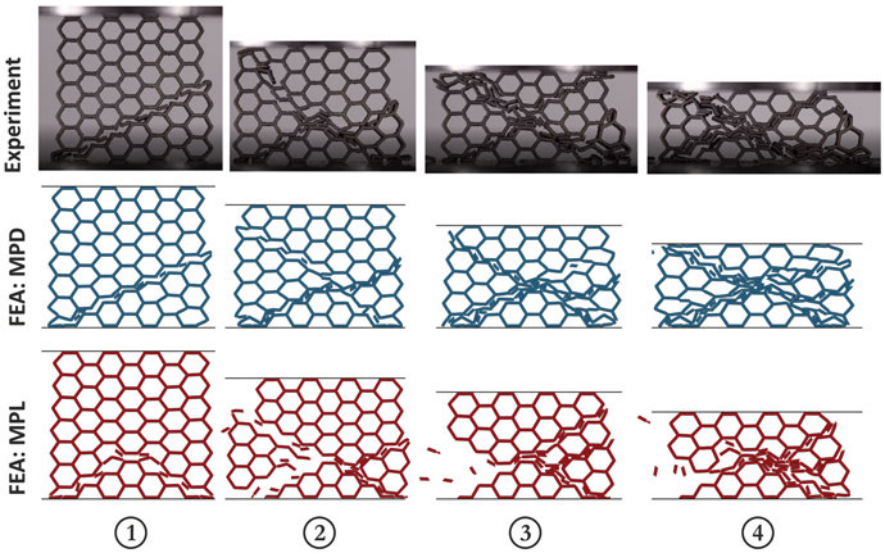

Fig. 24 Selected time frames of compression process of the honeycomb structure: comparison between the FEA using two constitutive models and the experiment (Baranowski et al. 2019b)

In Fig. 24, the actual and simulated honeycomb structure deformation is presented in the selected stages of the compression test. Due to FE deletion from the model, it is not possible to effectively reproduce the behavior of structure with the MPL model. However, an excellent reproduction of the structure deformation and fracture characteristics can be observed for the FE model with the MPD model. Nevertheless, the major drawback of the proposed methodology is nonphysical behavior of elements, in which the damage accumulates. Moreover, despite the

very large value of EFPS, the erosion of elements was not omitted. Therefore, mass loss could not be avoided (Dziewit et al. 2017).

Special Numerical Techniques

Except the techniques mentioned previously, the failure of material can be modelled with numerical treatment of interaction between elements instead of the constitutive modelling of material. The proposed approach (denoted as MTC) for failure consideration based on tiebreak contact algorithm was used for modelling the honeycomb cellular structure manufactured using FDM technology. This method reproduces the model integrity with implementation of the contact algorithm. The main condition behind the proposed method is modelling of each zone of sample as a separate body that do not share common nodes with other parts of the same structure. To enable the interaction between them, tied contact is defined between faces simulating the continuity of the material. The main disadvantage of this approach is related to definition of each segment separately, which is time-consuming. There are a few implementations of contact algorithm in many hydrocodes that allow for constraint of two bodies together, and the main difference between them is related to the manner how the interaction and distance between tied segments are calculated. However, additional parameter describing the tensile and shear forces after which contact is released has to be supported by the algorithm. The main advantage of this method compared to the previous ones is the progressive evolution of rupture. When the finite element erodes, a part of internal energy absorbed in the remained structure is immediately released, and unphysical acceleration on nodes which remain on the free surface occurs. On the described method, when the contact failure conditions are exceeded, the elements are not deleted, but a plastic part of deformation remains. This causes that only a small elastic part of internal energy changes into acceleration, so the integrity of structure is preserved.

In order to assess failure parameters of tiebreak contact, a parametric study was conducted based on standard material tests. The first, uniaxial tension, provides an information about the strength of material. The second, shearing test, provides an information about shearing forces that results in rupture of material. Both conditions are combined and implemented as a function limiting the maximum forces for which contact remains active (Eq. 3). After crossing the value of 1.0, the penalty function that ties nodes to segments is deactivated, and the separation of elements is possible. However, the interaction of elements resulting from compression is still active even for faces tied at the beginning.

$$\left(\frac{|\sigma_n|}{NFLS}\right)^2 + \left(\frac{|\sigma_s|}{SFLS}\right)^2 \geq 1 \tag{3}$$

where σ_n is the stress in the normal direction, *NFLS* maximum tensile stress in the normal direction, σ_s stress in the transverse direction, and *SFLS* maximum shear

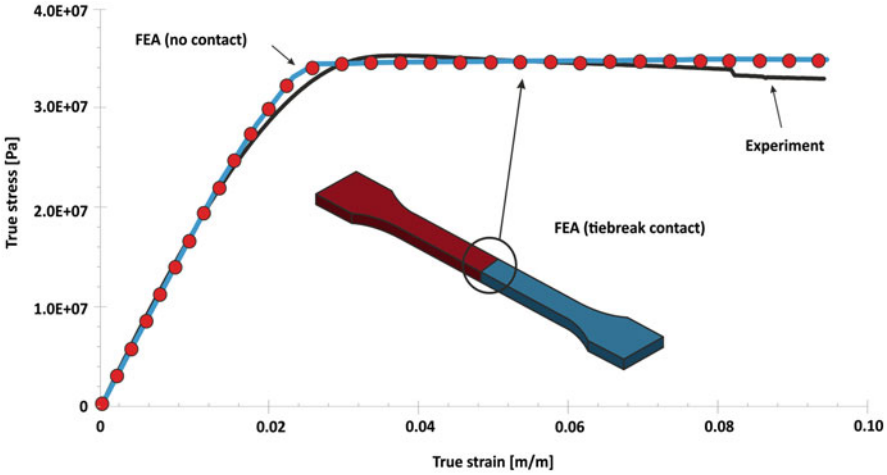

Fig. 25 Comparison of true stress vs. true strain curves obtained from experimental tests and FEA using standard modelling method and tiebreak contact (Kucewicz et al. 2019)

stress. When the criterion exceeds the value of 1, failure occurs. This option is applied to two-way contact types only. For one-way tiebreak contacts, stress is replaced by force. The first one was implemented for the simulations.

The method was correlated based on uniaxial tensile test (Fig. 25). For this method a dog-bone specimen was modelled to calibrate the contact failure properties. The model was cut in half so that two identical parts with two free surfaces were obtained. A tiebreak contact representing the material continuity was defined between them. It can be seen that the true stress characteristics for the actual tests and FEA with the standard and contact-based model of specimen are in good agreement, which proves the correctness of this approach.

Using the contact segments, plastic joints of the honeycomb structure were connected with cell walls with the correlated contact parameters from the previous step. Subsequently, uniaxial compression of the structure was simulated using the MTC methods and using the two abovementioned constitutive models: elastic-plastic and elastic-plastic with damage denoted as MPL and MPD, respectively. The comparison of force-displacement curve and structure behavior is presented in Fig. 26. As described previously, a material-based method is characterized by the immediate drop in stiffness of structure after deformation, while the contact-based method faithfully reproduces the gradual decrease of strength, and the structure integrity is preserved. The satisfactory reproduction of force vs. displacement curve for the MTC method is confirmed in an excellent reproduction of the honeycomb behavior, compared to the other two methods of modelling.

In Fig. 8, the single cell deformation obtained from FEA using all three approaches is compared with experimental test. As mentioned before, the cells' walls deform progressively due to rotation relative to the plastic joint, and a fracture propagates from the tensile section of each wall until the cell collapse. In the first

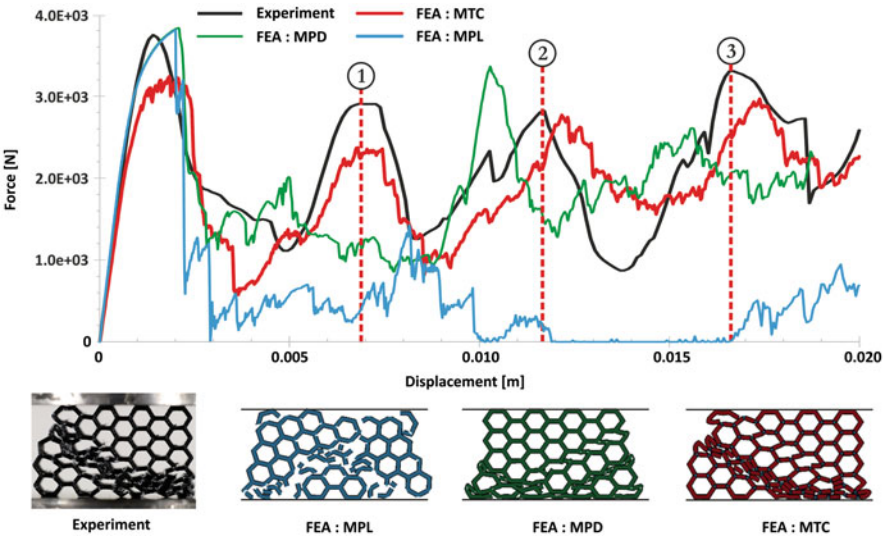

Fig. 26 Comparison of force vs. displacement and deformation of the honeycomb structure, from the experimental test and simulations

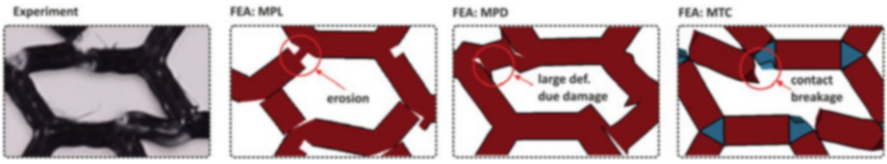

Fig. 27 Deformation of a single cell: comparison between the experiment and the FEA for three different modelling methods (Kucewicz et al. 2019)

case with applied erosion, most of plastic joints broke earlier. In the MPD model, the elements creating cross-section struts near the plastic joints eroded, whereas the FE that remained in the model resulted in a relatively correct structure behavior. The last of the proposed method, with an application of the tiebreak contact, was able to reproduce the deformation in a best manner (Fig. 27).

Summary

Regular cellular materials manufactured additively indicate a specific mechanical response which is not available for typical engineering materials. It results from adopted geometrical features of the elementary unit cell and mechanical properties of original material applied in fabrication process. Nowadays progress in the field of additive manufacturing and increasing spectrum of available materials allow defining their mechanical behavior depending on their applications. Nevertheless, during

such investigations it is necessary to consider several aspects, which are not included in testing and studying of typical materials and solid structures. In the presented paper the following were discussed:

1. Experimental testing of the regular cellular structures under quasi-static and dynamic loading. Due to anisotropic properties of the cellular specimens, it is necessary to conduct tests in two directions of the loading. Thus, two main orientations of tested topologies can be distinguished: "out-of-plane" and "in-plane." The choice of the loading direction should be dependent on the application of the structure. In the case of high stiffness and low mass, the first orientation should be used. On the other hand, for high-energy absorption properties with simultaneous low mass, the in-plane configuration is advisable.
2. The outcomes obtained from the quasi-static tests are mainly used for validation of numerical models describing the mechanical behavior of cellular materials. However, in order to obtain satisfactory outcomes from numerical simulations and to take into account the anisotropic properties of additively manufactured materials, it is necessary to fabricate structure samples and dog-bone specimens at the same time for uniaxial tensile tests. Results from both tests enable conducting additional numerical studies, which significantly reduce the time and the cost of investigations. Quasi-static tests provide a deep analysis of the influence of adopted topology on the mechanical response of material. Based on the deformation behavior a thorough study of damage and fracture mechanism is possible.
3. Testing the structures within higher strain rates provides an opportunity to analyze the influence of loading velocity on the topology behavior and material response. In the case of drop-weight impact test, the methodology of testing is relatively simple. However, when it comes to SHPB testing, several aspects with a major importance should be considered. Firstly, a proper size of the specimen with a minimum number of seven elementary cells in a single row of the structure is advisable. Moreover, due to low mechanical impedance of cellular structures, it is necessary to use piezoelectric gauges or different materials for the bars (plexiglass, polyamide, or hollow tube). Additional correction of wave signals is crucial due to dispersion effects.
4. Quite effective experimental tests can be coupled with numerical modelling, where a precise numerical model of the structure must be developed in order to consider the outcomes reliable and close to the actual. Nevertheless, a proper representation of the damage and fracture in cellular structure requires the adoption of sophisticated constitutive models with softening and/or erosion criteria or special numerical techniques such as tie-break contact implementation. Moreover, meshless methods can be also adopted for preventing the numerical erosion, which is a major drawback of typical FEA.

The main intention of the chapter was to present some selected aspects of experimental testing and numerical studies regarding cellular structures. Selected key aspects were discussed based on the authors' experience and literature data. The presented data with discussed outcomes are parts of a wider study aimed at

optimizing the crashworthiness behavior of regular cellular structures. Different materials as well as numerous topologies are tested and analyzed. In the case of numerical modelling, meshless methods and optimization procedures are implemented for a more thorough study of mechanical behavior and energy-absorption response of the cellular structures. The presented study can be a basis for scientists dealing with a similar topic.

References

T. Abe, H. Sasahara, Layer geometry control for the fabrication of lattice structures by wire and arc additive manufacturing. Addit. Manuf. **28**, 639–648 (2019). https://doi.org/10.1016/j.addma.2019.06.010

A. Antolak-Dudka, P. Płatek, T. Durejko, et al., Static and dynamic loading behavior of Ti6Al4V honeycomb structures manufactured by laser engineered net shaping (LENSTM) technology. Materials (Basel) **12** (2019). https://doi.org/10.3390/ma12081225

S. Babaee, B.H. Jahromi, A. Ajdari, et al., Mechanical properties of open-cell rhombic dodecahedron cellular structures. Acta Mater. **60**, 2873–2885 (2012). https://doi.org/10.1016/j.actamat.2012.01.052

A. Bandyopadhyay, B. Heer, Additive manufacturing of multi-material structures. Mater. Sci. Eng. R Rep. **129**, 1–16 (2018). https://doi.org/10.1016/j.mser.2018.04.001

J. Banhart, Manufacture, characterisation and application of cellular metals and metal foams. Prog. Mater. Sci. **46**, 559–632 (2001). https://doi.org/10.1016/S0079-6425(00)00002-5

P. Baranowski, K. Damaziak, J. Malachowski, et al., A child seat numerical model validation in the static and dynamic work conditions. Arch. Civ. Mech. Eng. **15**, 361–375 (2015). https://doi.org/10.1016/j.acme.2014.07.001

P. Baranowski, J. Janiszewski, J. Małachowski, Tire rubber testing procedure over a wide range of strain rates. J. Theor. Appl. Mech. **55**, 727–739 (2017). https://doi.org/10.15632/jtam-pl.55.2.727

P. Baranowski, J. Małachowski, P. Płatek, A. Szafrańska, LENS Ti-6Al-4V alloy material properties determination for LS-Dyna package. 020058 (2019a). https://doi.org/10.1063/1.5092061

P. Baranowski, P. Płatek, A. Antolak-Dudka, et al., Deformation of honeycomb cellular structures manufactured with laser engineered net shaping (LENS) technology under quasi-static loading: Experimental testing and simulation. Addit. Manuf. **25**, 307–316 (2019b). https://doi.org/10.1016/j.addma.2018.11.018

E. Barchiesi, M. Spagnuolo, L. Placidi, Mechanical metamaterials: A state of the art. Math Mech Solids **24**, 212–234 (2019). https://doi.org/10.1177/1081286517735695

S.R.G. Bates, I.R. Farrow, R.S. Trask, 3D printed polyurethane honeycombs for repeated tailored energy absorption. Mater. Des. **112**, 172–183 (2016). https://doi.org/10.1016/j.matdes.2016.08.062

J. Bauer, S. Hengsbach, I. Tesari, et al., High-strength cellular ceramic composites with 3D microarchitecture. Proc. Natl. Acad. Sci. U. S. A. **111**, 2453–2458 (2014). https://doi.org/10.1073/pnas.1315147111

D. Brad, O. Michael, M. Joseph, Modeling Reinforced Concrete Protective Construction for Impact Scenarios (Port Hueneme, 2018).

C. Buchanan, L. Gardner, Metal 3D printing in construction: A review of methods, research, applications, opportunities and challenges. Eng. Struct. **180**, 332–348 (2019). https://doi.org/10.1016/j.engstruct.2018.11.045

S.L. Campanelli, N. Contuzzi, A.D. Ludovico, et al., Manufacturing and characterization of Ti6Al4V lattice components manufactured by selective laser melting. Materials (Basel) **7**, 4803–4822 (2014). https://doi.org/10.3390/ma7064803

D.T. Casem, W.L. Fourney, P. Chang, A polymeric split Hopkinson pressure bar instrumented with velocity gages. Exp. Mech. **43**, 420–427 (2003). https://doi.org/10.1177/0014485103434007

W.W. Chen, B. Song, *Split Hopkinson (Kolsky) Bar Design, Testing and Applications* (Springer, New York/Dordrecht/Heidelberg/London, 2011). https://doi.org/10.1007/978-1-4419-7982-7 ISBN 9781441979810

W. Chen, B. Zhang, M.J. Forrestal, A split Hopkinson bar technique for low-impedance materials. Exp. Mech. **39**, 81–85 (1999). https://doi.org/10.1007/BF02331109

W. Chen, F. Lu, B. Zhou, A quartz-crystal-embedded split Hopkinson pressure bar for soft materials. Exp. Mech. **40**, 1–6 (2000). https://doi.org/10.1007/BF02327540

V. Crupi, G. Epasto, E. Guglielmino, Comparison of aluminium sandwiches for lightweight ship structures: Honeycomb vs. foam. Mar. Struct. **30**, 74–96 (2013). https://doi.org/10.1016/j.marstruc.2012.11.002

F. Dogan, H. Hadavinia, T. Donchev, B. Prasannakumar, Delamination of impacted composite structures by cohesive zone interface elements and tiebreak contact. Cent. Eur. J. Eng. **2**, 612–626 (2012). https://doi.org/10.2478/s13531-012-0018-0

A. du Plessis, C. Broeckhoven, I. Yadroitsava, et al., Beautiful and functional: A review of biomimetic design in additive manufacturing. Addit. Manuf. **27**, 408–427 (2019). https://doi.org/10.1016/j.addma.2019.03.033

Y. Du, H. Li, Z. Luo, Q. Tian, Topological design optimization of lattice structures to maximize shear stiffness. Adv. Eng. Softw. **112**, 211–221 (2016). https://doi.org/10.1016/j.advengsoft.2017.04.011

T. Fíla, P. Koudelka, P. Zlámal, et al., Strain dependency of Poisson's ratio of SLS printed auxetic lattices subjected to quasi-static and dynamic compressive loading. Adv. Eng. Mater. **1900204**, 1–12 (2019). https://doi.org/10.1002/adem.201900204

M.H. Fu, Y. Chen, L.L. Hu, A novel auxetic honeycomb with enhanced in-plane stiffness and buckling strength. Compos. Struct. **160**, 574–585 (2017). https://doi.org/10.1016/j.compstruct.2016.10.090

W. Gao, Y. Zhang, D. Ramanujan, et al., The status, challenges, and future of additive manufacturing in engineering. Comput. Des. **69**, 65–89 (2015). https://doi.org/10.1016/j.cad.2015.04.001

L.J. Gibson, M.F. Ashby, *Cellular Solids* (Cambridge University Press, Cambridge, 1997)

M. Golaszewski, R. Grygoruk, I. Giorgio, et al., Metamaterials with relative displacements in their microstructure: Technological challenges in 3D printing, experiments and numerical predictions. Contin. Mech. Thermodyn., 1–20 (2018). https://doi.org/10.1007/s00161-018-0692-0

A.L. Gurson, Continuum theory of ductile rupture by void nucleation and growth: Part I—Yield Criteria and Flow Rules for Porous Ductile Media. ASME. J. Eng. Mater. Technol. **99**(1), 2–15 (1977)

F.N. Habib, P. Iovenitti, S.H. Masood, M. Nikzad, Cell geometry effect on in-plane energy absorption of periodic honeycomb structures. Int. J. Adv. Manuf. Technol. **94**, 2369–2380 (2018). https://doi.org/10.1007/s00170-017-1037-z

J.O. Hallquist, LS-DYNA Theory Manual, Livermore Software Technology Corporation (LSTC), 2019, Livermore

A.G. Hanssen, O.S. Hopperstad, M. Langseth, H. Ilstad, Validation of constitutive models applicable to aluminium foams. Int. J. Mech. Sci. **44**, 359–406 (2002). https://doi.org/10.1016/S0020-7403(01)00091-1

W.S.W. Harun, M.S.I.N. Kamariah, N. Muhamad, et al., A review of powder additive manufacturing processes for metallic biomaterials. Powder Technol. **327**, 128–151 (2018). https://doi.org/10.1016/j.powtec.2017.12.058

L.L. Hu, T.X. Yu, Mechanical behavior of hexagonal honeycombs under low-velocity impact – Theory and simulations. Int. J. Solids Struct. (2013). https://doi.org/10.1016/j.ijsolstr.2013.05.017

S. Hyun, S. Torquato, Effective elastic and transport properties of regular honeycombs for all densities. J. Mater. Res. **15**, 1985–1993 (2000). https://doi.org/10.1557/JMR.2000.0285

Z. Jia, Y. Yu, L. Wang, Learning from nature: Use material architecture to break the performance tradeoffs. Mater. Des. **168**, 107650 (2019). https://doi.org/10.1016/j.matdes.2019.107650

N. Jin, F. Wang, Y. Wang, et al., Failure and energy absorption characteristics of four lattice structures under dynamic loading. Mater. Des. **169**, 107655 (2019). https://doi.org/10.1016/j.matdes.2019.107655

G.R. Johnson, W.H. Cook, A constitutive model and data for metals subjected to large strains, high strain rates, and high temperatures, in *Proceedings 7th International Symposium on Ballistics* (The Hague, 1983), pp. 541–547

M.R. Karamooz Ravari, M. Kadkhodaei, M. Badrossamay, R. Rezaei, Numerical investigation on mechanical properties of cellular lattice structures fabricated by fused deposition modeling. Int. J. Mech. Sci. **88**, 154–161 (2014). https://doi.org/10.1016/j.ijmecsci.2014.08.009

M. Kucewicz, P. Baranowski, J. Małachowski, et al., Modelling, and characterization of 3D printed cellular structures. Mater. Des. **142** (2018). https://doi.org/10.1016/j.matdes.2018.01.028

M. Kucewicz, P. Baranowski, J. Małachowski, A method of failure modeling for 3D printed cellular structures. Mater. Des. **174** (2019). https://doi.org/10.1016/j.matdes.2019.107802

S. Liebenstein, S. Sandfeld, M. Zaiser, Size and disorder effects in elasticity of cellular structures: From discrete models to continuum representations. Int. J. Solids Struct., 1–20 (2018). https://doi.org/10.1016/j.ijsolstr.2018.03.023

P. Mayer, D. Pyka, K. Jamroziak, et al., Experimental and numerical studies on ballistic laminates on the polyethylene and polypropylene matrix. J. Mech., 1–11 (2017). https://doi.org/10.1017/jmech.2017.103

M.S. Mazloomi, M. Ranjbar, L. Boldrin, et al., Vibroacoustics of 2D gradient auxetic hexagonal honeycomb sandwich panels. Compos. Struct. **187**, 593–603 (2018). https://doi.org/10.1016/j.compstruct.2017.10.077

M. Meo, E. Thieulot, Delamination modelling in a double cantilever beam. Compos. Struct. **71**, 429–434 (2005). https://doi.org/10.1016/j.compstruct.2005.09.026

M.A. Meyers, P.Y. Chen, A.Y.M. Lin, Y. Seki, Biological materials: Structure and mechanical properties. Prog. Mater. Sci. **53**, 1–206 (2008). https://doi.org/10.1016/j.pmatsci.2007.05.002

M. Mohsenizadeh, F. Gasbarri, M. Munther, et al., Additively-manufactured lightweight metamaterials for energy absorption. Mater. Des. **139**, 521–530 (2018). https://doi.org/10.1016/j.matdes.2017.11.037

T.D. Ngo, A. Kashani, G. Imbalzano, et al., Additive manufacturing (3D printing): A review of materials, methods, applications and challenges. Compos. Part B **143**, 172–196 (2018). https://doi.org/10.1016/j.compositesb.2018.02.012

N. Novak, M. Vesenjak, L. Krstulović-Opara, Z. Ren, Mechanical characterisation of auxetic cellular structures built from inverted tetrapods. Compos. Struct. **196**, 96–107 (2018). https://doi.org/10.1016/j.compstruct.2018.05.024

Z. Ozdemir, E. Hernandez-Nava, A. Tyas, et al., Energy absorption in lattice structures in dynamics: Experiments. Int. J. Impact Eng. **89**, 49–61 (2016). https://doi.org/10.1016/j.ijimpeng.2015.10.007

Z. Ozdemir, A. Tyas, R. Goodall, H. Askes, Energy absorption in lattice structures in dynamics: Nonlinear FE simulations. Int. J. Impact Eng. **102**, 1–15 (2017). https://doi.org/10.1016/j.ijimpeng.2016.11.016

P. Platek, J. Janiszewski, J. Małachowski, P. Dziewit, M. Grązka, R. Paszkowski, M. Sarzynski, Mechanical response of additive manufactured regular cellular sctructures in quasi-static loading conditions-part II: Numerical investigations, in *Progress in Mechanics and Materials in Design*, 2017, pp. 1075–1090

D. Restrepo, N.D. Mankame, P.D. Zavattieri, Programmable materials based on periodic cellular solids. Part I: Experiments. Int. J. Solids Struct. **100–101**, 485–504 (2016a). https://doi.org/10.1016/j.ijsolstr.2016.09.022

D. Restrepo, N.D. Mankame, P.D. Zavattieri, Programmable materials based on periodic cellular solids. Part I: Experiments. Int. J. Solids Struct. **100–101**, 485–504 (2016b). https://doi.org/10.1016/j.ijsolstr.2016.09.021

A.P. Roberts, E.J. Garboczi, Elastic properties of model random three-dimensional open-cell solid. J. Mech. Phys. Solids **50**, 33–55 (2002). https://doi.org/10.1016/S0022-5096(01)00056-4

P. Rozylo, H. Debski, T. Kubiak, A model of low-velocity impact damage of composite plates subjected to compression-after-impact (CAI) testing. Compos. Struct. **181**, 158–170 (2017). https://doi.org/10.1016/j.compstruct.2017.08.097

A. Rusinek, J.R. Klepaczko, J.A. Rodríguez-Martínez, A. Arias, Advanced constitutive relations for steel alloys: Strain hardening and phase transformation effects, 1285–1289 (2009). https://doi.org/10.1051/dymat/2009181

L.E. Schwer, Aluminum plate perforation: a comparative case study using lagrange with erosion, multi-material ale, and smooth particle hydrodynamics, in 7th European LS-DYNA Conference ALUMINUM, Salzburg (2009).

L.E. Schwer, A brief look at * MAT _ NONLOCAL: A possible cure for erosion illness? in 11th International LS-DYNA® Users Conference, Detroit (2010), pp. 19–36.

P. Simon, Y. Demarty, A. Rusinek, G. Voyiadjis, Material behavior description for a large range of strain rates from low to high temperatures: Application to high strength steel. Metals (Basel) **8**, 795 (2018). https://doi.org/10.3390/met8100795

Y. Sun, Q.M. Li, Dynamic compressive behaviour of cellular materials: A review of phenomenon, mechanism and modelling. Int. J. Impact Eng. **112**, 74–115 (2018). https://doi.org/10.1016/j.ijimpeng.2017.10.006

M. Świerczewski, M. Klasztorny, P. Dziewulski, P. Gotowicki, Numerical modelling, simulation and validation of the SPS and PS systems under 6 kg TNT blast shock wave. Acta Mech. Automat. **6**, 77–87 (2012)

T. Tancogne-Dejean, D. Mohr, Stiffness and specific energy absorption of additively-manufactured metallic BCC metamaterials composed of tapered beams. Int. J. Mech. Sci. (2018). https://doi.org/10.1016/j.ijmecsci.2018.03.027

Y. Tang, A. Kurtz, Y.F. Zhao, Bidirectional evolutionary structural optimization (BESO) based design method for lattice structure to be fabricated by additive manufacturing. Comput. Aided Des. **69**, 91–101 (2015). https://doi.org/10.1016/j.cad.2015.06.001

K. Tantikom, T. Aizawa, Compressive deformation simulation of regularly cell-structured materials with various column connectivity. Mater. Trans. **46**, 1154–1160 (2005). https://doi.org/10.2320/matertrans.46.1154

Y. Tao, M. Chen, H. Chen, et al., Strain rate effect on the out-of-plane dynamic compressive behavior of metallic honeycombs: Experiment and theory. Compos. Struct. **132**, 644–651 (2015). https://doi.org/10.1016/j.compstruct.2015.06.015

G. Voyiadjis, P. Kattan, Advances in damage mechanics: metals and metal matrix composites (Second Edition), 2006. Elsevier Science Ltd, ISBN 9780080446882

G.Z. Voyiadjis, P.I. Kattan, M.A. Yousef, Some basic issues of isotropic and anisotropic continuum damage mechanics, in Voyiadjis G (eds) *Handbook of Damage Mechanics* (Springer, New York, NY, 2014) https://doi.org/10.1007/978-1-4614-8968-9_1-1

Z. Wang, J. Liu, Z. Lu, D. Hui, Mechanical behavior of composited structure filled with tandem honeycombs. Compos. Part B Eng. **114**, 128–138 (2017). https://doi.org/10.1016/j.compositesb.2017.01.018

L. Xiao, W. Song, Additively-manufactured functionally graded Ti-6Al-4V lattice structures with high strength under static and dynamic loading: Experiments. Int. J. Impact Eng. **111**, 255–272 (2017). https://doi.org/10.1016/j.ijimpeng.2017.09.018

M. Yamashita, M. Gotoh, Impact behavior of honeycomb structures with various cell specifications – numerical simulation and experiment. Int. J. Impact Eng. **32**, 618–630 (2006). https://doi.org/10.1016/j.ijimpeng.2004.09.001

C. Yan, L. Hao, A. Hussein, D. Raymont, Evaluations of cellular lattice structures manufactured using selective laser melting. Int. J. Mach. Tools Manuf. **62**, 32–38 (2012). https://doi.org/10.1016/j.ijmachtools.2012.06.002

L. Yang, O. Harrysson, H. West, D. Cormier, Mechanical properties of 3D re-entrant honeycomb auxetic structures realized via additive manufacturing. Int. J. Solids Struct. **69–70**, 475–490 (2014). https://doi.org/10.1016/j.ijsolstr.2015.05.005

Z. Yang, Y. Yu, Y. Wei, C. Huang, Crushing behavior of a thin-walled circular tube with internal gradient grooves fabricated by SLM 3D printing. Thin-Walled Struct. **111**, 1–8 (2017). https://doi.org/10.1016/j.tws.2016.11.004

Z.L. Zhang, C. Thaulow, A complete Gurson model approach for ductile fracture. Eng Fract Mech **67**, 155–168 (2000)

X. Zhang, L. An, H. Ding, Dynamic crushing behavior and energy absorption of honeycombs with density gradient. J. Sandw. Struct. Mater. **16**, 125–147 (2014). https://doi.org/10.1177/1099636213509099

Q. Zhang, X. Yang, P. Li, et al., Bioinspired engineering of honeycomb structure – using nature to inspire human innovation. Prog. Mater. Sci. (2015). https://doi.org/10.1016/j.pmatsci.2015.05.001

Y. Zhang, T. Liu, H. Ren, et al., Dynamic compressive response of additively manufactured AlSi10Mg alloy hierarchical honeycomb structures. Compos. Struct. **195**, 45–59 (2018). https://doi.org/10.1016/j.compstruct.2018.04.021

H. Zhao, G. Gary, J.R. Klepaczko, On the use of a viscoelastic split Hopkinson pressure bar. Int. J. Impact Eng. **19**, 319–330 (1997). https://doi.org/10.1016/S0734-743X(96)00038-3

L. Zhao, X. Qian, Y. Sun, et al., Ballistic behaviors of injection-molded honeycomb composite. J. Mater. Sci. **53**, 14287–14298 (2018). https://doi.org/10.1007/s10853-018-2611-y

Thermo-mechanics of Polymers at Extreme and Failure Conditions: Influence of Strain Rate and Temperature

11

Daniel Garcia-Gonzalez, Sara Garzon-Hernandez, Daniel Barba, and Angel Arias

Contents

Current State of Polymers and Future Perspectives 250
Mechanical Deformation of Polymers and Material Dependences 251
Deformation Mechanisms of Thermoplastic Polymers 252
Temperature and Strain Rate Dependences on Polymeric Deformation 254
Mechanical Behavior of 3D Printed Polymers by FDM 258
Constitutive Modelling of Mechanical Deformation in Polymers 260
Damage and Failure Behavior of Polymers 262
Failure Mechanisms of Thermoplastic Polymers 263
Temperature and Strain Rate Dependences of Polymeric Failure 265
Failure Behavior of 3D Printed Polymers by FDM 268
Constitutive Modelling of Damage and Failure in Polymers 269
Summary/Conclusions 273
References 274

Abstract

Polymeric materials are increasingly receiving scientific and industrial interest due to the new advances in 3D printing techniques and the possibility to introduce smart responses under external stimuli. Among the industrial sectors, we find interesting applications for biomedical devices, aeronautical components, or smart structures for soft robotics. Regarding the mechanical behavior of these materials, this is rather complex combining nonlinear large deformations, strain rate and temperature dependences, and viscoelastic and viscoplastic responses.

D. Garcia-Gonzalez (✉) · S. Garzon-Hernandez · A. Arias
Department of Continuum Mechanics and Structural Analysis, University Carlos III of Madrid, Madrid, Spain
e-mail: danigarc@ing.uc3m.es; sgarzon@ing.uc3m.es; aariash@ing.uc3m.es

D. Barba
Escuela Técnica Superior de Ingeniería Aeronáutica y del Espacio, Universidad Politécnica de Madrid, Madrid, Spain
e-mail: daniel.barba@upm.es

© Springer Nature Switzerland AG 2022

G. Z. Voyiadjis (ed.), *Handbook of Damage Mechanics*,
https://doi.org/10.1007/978-3-030-60242-0_67

When these materials are manufactured by 3D printing techniques or when they include stimuli-responsive particles embedded, their mechanical response becomes even more complex presenting anisotropy and physically coupled effects. All these dependences together make the modelling of their mechanical deformation and failure extremely difficult. This chapter aims at providing the background on the main mechanical features of thermoplastic polymers and the current state of the art in their constitutive modelling. To this end, we first introduce an overview of the deformation mechanisms of thermoplastic polymers and their principal mechanical dependences. Then, the main failure mechanisms presented by these polymers are discussed along with material dependences on brittle-to-ductile transitions. Finally, an extensive review of the state of the art in the modelling of thermoplastic polymers is provided.

Keywords

Polymers · Mechanical behavior · Strain rate · Temperature · Viscoelastic · Viscoplastic · 3D printing · Constitutive modelling · Brittle-to-ductile transition · PEEK · FDM · Semi-crystalline polymers · Amorphous polymers · Inelastic dissipation · Hyperelasticity · Failure mechanisms · Glass transition temperature

Current State of Polymers and Future Perspectives

Polymers are increasingly receiving the attention of several industrial areas due to their rapid processing, good mechanical properties, and low manufacturing cost (Garcia-Gonzalez et al. 2015a, 2018). Among these polymers, it is worth to highlight some of them such as polyether-ether-ketone (PEEK), ultra-high-molecular-weight polyethylene (UHMWPE), and acrylonitrile butadiene styrene (ABS) because of their extensive use in different industrial applications. In this regard, PEEK is a semi-crystalline thermoplastic polymer that is being proposed as replacement for metallic components exposed at high-temperature conditions in oil gas, aerospace, automotive, and space applications (Voyiadjis et al. 2017; Yang et al. 2017). In addition, PEEK and PEEK reinforced with a wide variety of fillers are currently used in the biomedical industry (Garcia-Gonzalez et al. 2015a, 2017a; Lovald and Kurtz 2012). Some of these applications provide structural functions such as cranial implants and acetabular and dental prostheses (Garcia-Gonzalez et al. 2017a; Lovald and Kurtz 2012). Moreover, UHMWPE is also used for different biomedical components such as hip and knee prostheses (Garcia-Gonzalez et al. 2018). Regarding ABS, this polymer (as well as PEEK) has drawn the attention of the scientific community due to the great opportunities offered by additive manufacturing (Ngo et al. 2018).

An important characteristic of thermoplastic polymers to be accounted for during the design of structural components subjected to extreme conditions is the presence of thermal transitions. In this regard, these polymers can present different micro-structural transitions associated with relaxation responses that result in significant changes of their mechanical response (Nasraoui et al. 2012). The most important

transitions in thermoplastic polymers are glass transition and beta transition, which are related to a ductile-to-brittle change in the material behavior (Garcia-Gonzalez et al. 2015b). During these transitions, the polymer experiences a gradual and reversible transition from a brittle glassy state into a rubbery state characterized by a much higher ductility.

Although thermoplastic polymers and their composites have been extensively used, they are due to experience a growing prominence in several applications due to the new possibilities arising from the incipient additive manufacturing techniques (Wang et al. 2017). Among additive manufacturing techniques, fused deposition modelling (FDM) is one of the most widely used for rapid prototyping and composites components design due to its simplicity, high speed, and low cost (Ngo et al. 2018). Both PEEK and ABS have positioned as preferred solutions for FDM components providing customizability not only of the geometry but also of mechanical properties by controlling the porosity and anisotropic responses. However, there is still a big gap of knowledge in the understanding of the mechanical behavior of 3D printed polymers and their relationship with the printing process. In this regard, the thermo-mechanics of traditional thermoplastics must be first fully understood and then extended to these novel materials. Moreover, polymers are currently used as matrix material for stimuli-responsive or smart structures. In this regard, polymers can be filled with different particles that react under an external stimulus such as thermal or magnetic. By this way, their mechanical deformation can be controlled remotely by the environmental temperature or external magnetic field (Kong et al. 2019; Kim et al. 2018; Garcia-Gonzalez 2019; Garcia-Gonzalez and Landis 2020). Other examples of stimuli-responsive materials are electroactive polymers, whose mechanical deformation can be activated by an external electrical current and vice versa (Zurlo et al. 2018). These novel polymeric materials have opened new possibilities such as for soft robotics, biomedical applications, or automobile dampers and are currently in the spotlight.

This chapter introduces the background on the main mechanical features of thermoplastic polymers and the current state of the art in their constitutive modelling. In the first section of this chapter, an overview of the deformation mechanisms of thermoplastic polymers and their principal mechanical dependences is presented. Then, the main failure mechanisms shown by these polymers are discussed along with material dependences on brittle-to-ductile transitions. Along the different sections, a special focus is taken on additive manufactured (3D printed) polymers as well as on the current state of the art in the modelling of the mechanical behavior of thermoplastic polymers.

Mechanical Deformation of Polymers and Material Dependences

This section introduces the main characteristics of the mechanical behavior of polymers and the principal deformation mechanisms. In addition, mechanical dependences on temperature and strain rate are presented along with some implications on

viscoelastic response. Finally, a review on the mechanical behavior of 3D printed polymers is presented along with original results.

Deformation Mechanisms of Thermoplastic Polymers

In this section, the main mechanisms that govern the deformation process in polymers are introduced. These deformation mechanisms strongly depend on the arrangement of the molecular chains and their nature by means of chemistry, molecular weight, molecular shape, and molecular structure. Attending to the molecular structure of the polymer, we can identify four principal groups: linear, branched, crosslinked, and network polymers (Callister 2006); see Fig. 1. *Linear polymers* are composed of repeat units that are joined together along single chains. These chains are rather flexible and are connected between them by van der Waals and hydrogen bonding. *Branched polymers* represent a main polymeric branch to which smaller ones are joined. These branches can be considered as part of the main chain, reducing the packing efficiency and resulting in lower polymer densities. *Crosslinked polymers* are formed by molecular chains strongly joined by covalent bonds. Finally, *network polymers* consist of three-dimensional networks formed by three or more active covalent bonds. The mechanical response of the polymer and, especially, its dependence on temperature are directly related to its dominant molecular structure. In this regard, we can classify polymers into thermoplastics and thermosets. This chapter is focused on thermoplastic polymers that, in turn, can be classified into amorphous and semi-crystalline polymers.

The main difference between thermoplastics is the arrangement of their molecular chains and their influence on the polymeric thermal behavior. In this regard, semi-crystalline polymers present organized and tightly packed molecular chains. They can be understood as a two-phase microstructure composed of amorphous regions

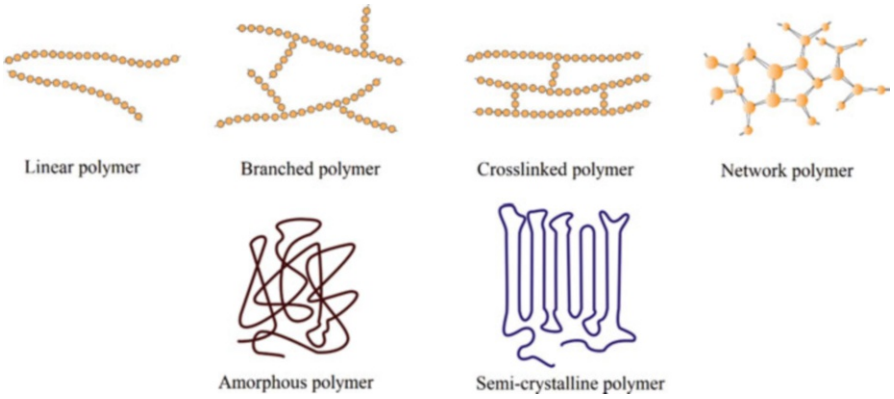

Fig. 1 Classification of polymers according to their molecular structure. (Adapted from Callister (2006))

connecting crystallized regions (called spherulites). This internal organization leads to the appearance of a defined melting point. These semi-crystalline polymers have good strength and wear properties as well as good chemical resistance. Moreover, amorphous polymers present a more disorganized structure and they do not include crystalline phases. The mechanical behavior of amorphous polymers significantly depends on temperature showing a marked transition at the glass transition temperature. The glass transition is a temperature region (specific for each thermoplastic) where there is a transition from a hard and glassy material to a soft and rubbery material. This transition corresponds to a strong dumping effect of the material followed by a fast decrease of the storage modulus. Regarding the properties of amorphous thermoplastics, they usually have better impact resistance but poor fatigue resistance and are prone to stress cracking.

The macroscopic deformation of the polymer is determined by the mobility of the molecular chains. In this regard, many authors have pointed out the concept of free volume. Free volume is the space present inside the polymer that is not occupied by the molecular chains. Therefore, the higher the free volume, the higher mobility of the molecular chains. This variable is strongly influenced by temperature and determines the deformation mode of the polymer: at temperatures below glass transition, the polymer free volume is reduced, the mobility of the polymer chains decreases, and, consequently, a hard and brittle response occurs; for temperature above glass transition, the free volume increases resulting in higher molecular chains mobility and, therefore, softer and more ductile behavior (Barba et al. 2020).

Regarding semi-crystalline polymers, their macroscopic deformation commonly shows upper and lower yield points followed by a plateau region. In a previous work, Garcia-Gonzalez and coauthors (Barba et al. 2020) provide a microstructurally based interpretation of the deformation process of PEEK under tensile loading; see Fig. 2. Semi-crystalline polymer can be understood as a combination of two phases: crystalline and amorphous. The crystalline regions, composed of crystallites or lamellae, govern the early stages of the material behavior. Moreover, the amorphous regions, composed of amorphous polymer chains or fibrils, govern the latter deformation stages. During the deformation of semi-crystalline polymers, different stages can be identified. First, there is an elongation of amorphous tie chains and a reversible increase of lamellar crystallite thickness, describing the viscoelastic deformation stage (Jabbari-Farouji et al. 2015). Then, crystalline block segments are separated and lamellar chain folds are tiled resulting in yielding. The stress induced leads to material softening due to split of the larger crystalline domains and the release of amorphous chains (Chang et al. 2018; Jabbari-Farouji et al. 2015). In the final stage, there is a reorientation of the amorphous regions and crystalline block segments along the loading direction, which results in a continuous entropic hardening (Garcia-Gonzalez et al. 2017b, 2018). Furthermore, temperature and rate of deformation play a strong role in the activation and relevance of these different mechanisms. Regarding the thermal effects, these become critical when comparing the material behavior below and above glass transition.

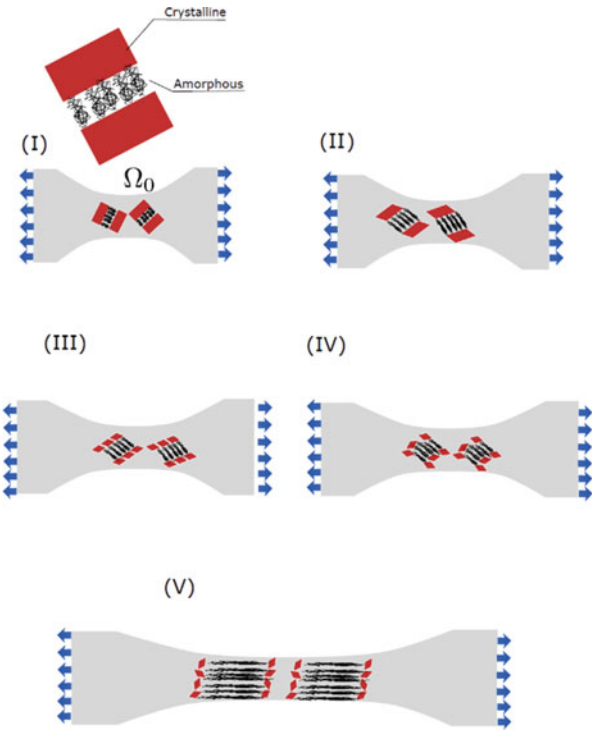

Fig. 2 Relationship between the deformation stages of PEEK under tensile loading and the deformation mechanisms involved. (Adapted from Barba et al. (2020))

Temperature and Strain Rate Dependences on Polymeric Deformation

As inferred in the previous section, temperature and the rate of deformation are going to introduce significant dependences in the mechanical behavior of thermoplastic polymers. This section summarizes some of these main dependences.

In the very first deformation stage, the mechanical response of the polymer can be linearized and thus defined by its Young's modulus. This Young's modulus describes the polymer stiffness and is highly dependent on temperature. Although for rubber-like materials the Young's modulus increases with temperature, thermoplastic polymers present an inverse relation between this variable and temperature. In addition, the influence of temperature is not linear, and there is a sharp change of material properties when the polymer goes through its glass transition (see Fig. 3a). As shown in Fig. 3a, we can observe different behavioral regions: (i) glassy region; (ii) leathery or glass transition region; (iii) rubbery region; (iv) rubbery flow; (v) viscous flow. These regions are a priori defined by the magnitude of the Young's modulus but are usually divided into three main groups with respect to the transition regions: glassy below glass transition temperature; leathery within the glass transition; and rubbery between glass transition and melting temperatures. In the glassy region at the lowest

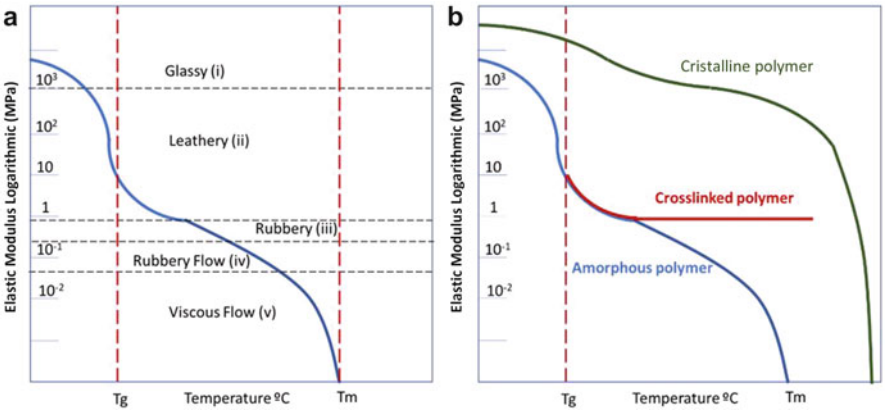

Fig. 3 Mechanical response transitions in polymers with temperature (**a**) and differences between different types of polymer (**b**). (Adapted from Callister (2006))

temperatures, the material is rigid and brittle. As the temperature is increased, the polymer specimen becomes leathery; that is, deformation will be time dependent and not fully recoverable. Within the rubbery plateau temperature region, the material deforms in a rubbery manner; here, both elastic and viscous components are present, and deformation is easy to produce because the elastic modulus is relatively low. During the rubbery and viscous flows, the material experiences a gradual transition to a soft rubbery state and finally to a viscous liquid. From a molecular view, chain motion intensifies leading to independent vibration and rotational motion between chain segments resulting in an entirely viscous deformation.

Moreover, these transitions in the polymer mechanical response with temperature depend on its molecular structure; see Fig. 3b for different examples. In this figure, the characteristic response of an amorphous polymer (blue curve) is compared with the corresponding response of a crystalline polymer (green curve) and a crosslinked polymer (red curve).

From the previous analysis by means of temperature, a clear dependence on strain rate can be intuited. In this regard, the polymer behaves like a glass at low temperatures, like a rubbery solid at intermediate temperatures, and like a viscous liquid as higher temperatures. Therefore, when the polymer is subjected to higher temperatures, the material presents relevant viscoelastic deformation mechanisms. These mechanisms imply a combined response to deformation based on an instantaneous resistance that is relaxed with time toward a constant value. Note that these effects are, therefore, both time and temperature dependent and are related to molecular relaxation processes (sometimes related to free volume).

These dependences on temperature and strain rate are not only present in the elastic response but also in the yielding and post-yielding processes. These variables have a critical influence on the polymer behavior. Greater mobility of polymer chains is observed at the microscale for higher temperatures. From a macroscopic view, this increase in chains' mobility leads to thermal softening in terms of elastic modulus

and yield/flow stress (Rae et al. 2007). Oppositely, hardening and a loss of ductility by means of elastic modulus and yield/flow stress are observed for higher strain rates (Rae et al. 2007). In addition, there is an intrinsic coupling of these variables at medium and high deformation rates. At these conditions, there is a competition where strain rate sensitivity results in hardening effects and temperature sensitivity results in softening effects (Chang et al. 2018; Garcia-Gonzalez et al. 2017b, 2018).

All these dependences can be observed for tensile testing of semi-crystalline thermoplastics in Fig. 4 (for PEEK) and Fig. 5 (for polyethylene materials). Attending to Fig. 4, some remarks can be stated. (i) Glassy region: Typically, a linear elastic response is initially observed prior to polymer yielding. Then, the apparent macroscopic stress presents a smooth drop. This drop is explained by a continuous thermal softening due to adiabatic heating. In the final deformation stage, an abrupt material rupture is observed. This rupture occurs at a critical strain that decreases with strain rate. In addition, as the strain rate is increased, higher local softening develops as a consequence of heating from plastic dissipation within the deformed regions. This local increase in temperature translates into material softening and, consequently, into further concentration of plastic deformation at the necking region, finally producing the local rupture at lower macroscopic strains. This process does not happen at lower strain rates due to the homogenization of the plastic deformation along the gauge length. Therefore, lower strain rates result in larger macroscopic strains at failure. This is because, below the glass transition temperature, there is a reduction of polymer free volume decreasing the mobility of the polymer chains and, consequently, leading to a hard and brittle response. This low free volume also explains the higher resistance to creep within the glassy regime. (ii) Glass transition: A completely different behavior with respect to glassy region. The first loading phase is described by an initial elastic response which depends on the strain rate. This initial region develops until reaching the yield point. For most polymers, the yield stress also depends on strain rate, increasing with higher strain rates. After

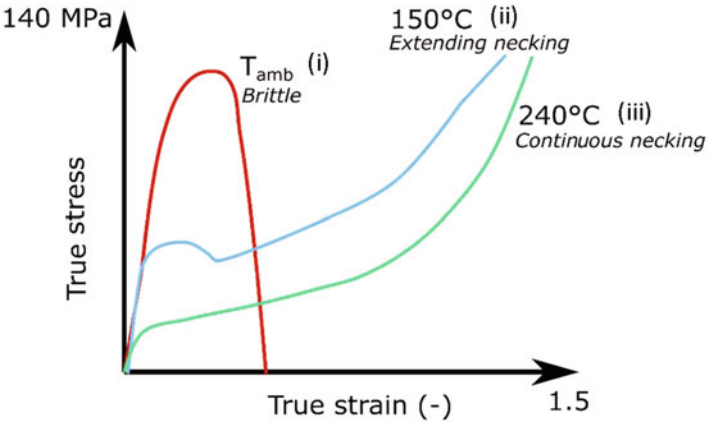

Fig. 4 Constitutive modelling of semi-crystalline polymer PEEK at different testing temperatures. (Adapted from Barba et al. (2020))

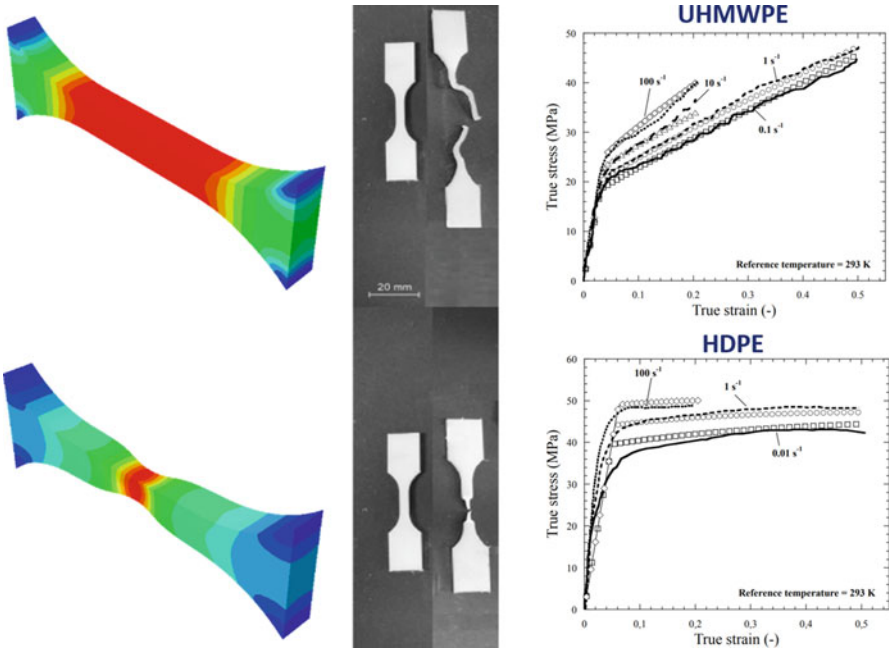

Fig. 5 Computational and experimental tests on the tensile deformation behavior of polyethylene polymers: (*above*) UHMWPE; (*below*) HDPE. (Adapted from Garcia-Gonzalez et al. (2018) and Mohagheghian et al. (2015))

yielding, the polymer exhibits a softening phase by means of the macroscopic stress. At the final deformation stage, there is a material hardening until rupture. (iii) Rubbery region: at high temperature (above glass transition), there is no yield drop, and two differentiated loading regions can be identified with a smooth transition: initial strain rate-dependent elastic region and a hardening region. The strain rate dependence within this region is much lower than in the other two ones. Moreover, at higher temperatures, larger segments can reorient due to higher mobility of polymer chains. Higher mobility leads to an increase in free volume that, in turn, results in relevant creep mechanisms and higher sensitivity to strain rate within the initial viscoelastic response. In addition, higher temperatures favor the orientation of polymer chains leading to a governing role of the entropic resistance associated with the amorphous phase over plastic mechanisms associated with the crystalline phase. Therefore, a more homogeneous deformation is observed within the specimen due to higher orientation degree of the polymer chains, thus hindering the necking formation.

Regarding Fig. 5, a clear influence of both temperature and strain rate is observed related to the yield stress, increasing with strain rate and decreasing with temperature. In addition, other dependences can be observed from the comparison of UHMWPE and HDPE. In this regard, although both materials present same tendencies with strain rate and temperature, they present a very different response after

yielding (observations from both experimental and modelling tests). A higher importance of the viscoelastic resistance is observed in UHMWPE, whereas its role in the HDPE behavior is much less relevant. The mechanical response of these polymers can be interpreted as a competition between softening due to thermal effects and plastic deformation hardening along with hardening due to strain rate effects. This interplay becomes even more complex at high strain rates. During these conditions, the polymer experiences a considerable hardening due to strain rate sensitivity, but, in turn, a higher thermal softening occurs due to a strong thermo-mechanical coupling under such conditions. Regarding the deformation mode of UHMWPE and HDPE, the former presents a uniform deformation along the gauge length, whereas the latter presents a pronounced necking at a localized deformation region. This can be explained by the higher hardening after yielding and higher viscosity of UHMWPE with respect to HDPE. These hardening effects play a stabilizing role in necking formation. Moreover, thermal softening can be interpreted as a negative hardening. Therefore, heterogeneous temperature distribution due to local inelastic dissipation favors the necking formation leading to instabilities within higher temperature zones.

Mechanical Behavior of 3D Printed Polymers by FDM

Among the different additive manufacturing processes, FDM remains as one of the most widely used to manufacture thermoplastic components. FDM was conceived for quick prototyping. However, the incorporation of high-performance thermoplastics and composite materials, together with the development of new robust 3D printers, has led to FDM being suitable for most sectors of industrial production.

The temperature and strain rate dependences presented in the previous section are also observed in 3D printed thermoplastics (Rodríguez et al. 2001). Moreover, due to the manufacturing process, these materials present extra dependences with printing parameters, which not only affect the appearance of the final component but also its mechanical response. In this regard, FDM is based on the extrusion of a thermoplastic filament through a nozzle, where the polymer is heated to a semiliquid state and deposited as a thread (filament or raster) on the 3D printed platform. Once the filament is deposited, its temperature decreases from the extrusion temperature to environmental temperature, while bonding with its adjacent filament occurs. However, this bonding process is not perfect, leading to the formation of voids between filaments. In addition, due to the manufacturing layer-by-layer, the microstructure inside each layer is different from that at the boundaries between layers (Ngo et al. 2018). These characteristics are responsible for the inferior mechanical properties and the anisotropic behavior of 3D printed thermoplastics. Therefore, the understanding of the influence of the printing parameters and processing conditions is essential to have control over the flaw sensitivity and anisotropic behavior. In this regard, the influence of layer height, air gap, infill raster orientation, or extrusion and ambient temperature on the tensile mechanical behavior of FDM thermoplastics has been widely studied in the literature.

Layer height, air gap, and processing temperatures have a direct influence on the mesostructure and, therefore, on the void density. A decrease in the void density is observed as layer height decreases (Fig. 6) resulting in an improvement in terms of elastic modulus and yield stress. Air gap controls the distance between two adjacent filaments. While a zero air gap results in a distance between filaments' centers equal to the printing parameter width line, the use of negative air gap results in an overlay between filaments that tends to lower void density (Ahn et al. 2002).

Extrusion and environment temperatures affect the cooling process that takes place during the printing and, therefore, the level of filament fusion and interlayer adhesion (Aliheidari et al. 2017). As the extrusion temperature increases, the viscosity of the material decreases resulting in an easier flow. On the other hand, the environment temperature affects the cooling process and, thus, the bonding process. In addition, although both temperatures have a great influence on the degree of crystallinity reached in semi-crystalline thermoplastics, higher crystallinity is achieved as the environment temperature increases (Yang et al. 2017). Environment temperatures above glass transition cause an isothermal crystallization process, in which the amorphous polymer chains have enough energy to transform and crystallize. Likewise, an increase in the final mechanical properties (tensile strength and elastic modulus) is obtained as environment temperature increases.

Regarding the anisotropic behavior of 3D printed thermoplastics, the raster orientation defines the direction of voids and, therefore, the axis of anisotropy. This has a direct influence on the stress-strain tensile response of 3D printed thermoplastic components. In this regard, different studies have shown that a longitudinal or 0° raster orientation, understanding that as deposition sequence where all the filaments follow a direction parallel to the loading, provides the highest tensile performance (Rodríguez et al. 2001; Ziemian et al. 2012). On the contrary, the lowest tensile performance is achieved with a transverse or 90° raster orientation, understanding that as deposition sequence where all the filaments follow a perpendicular direction to the loading. In addition, different deformation mechanisms are observed as a function of this parameter; see Fig. 7. These differences are explained

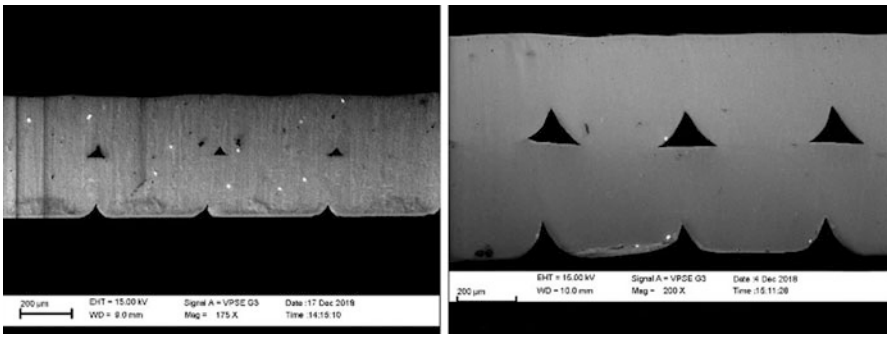

Fig. 6 Cross-sectional area of specimens for a layer height of 0.2 and 0.3 mm (Garzon-Hernandez et al. 2020)

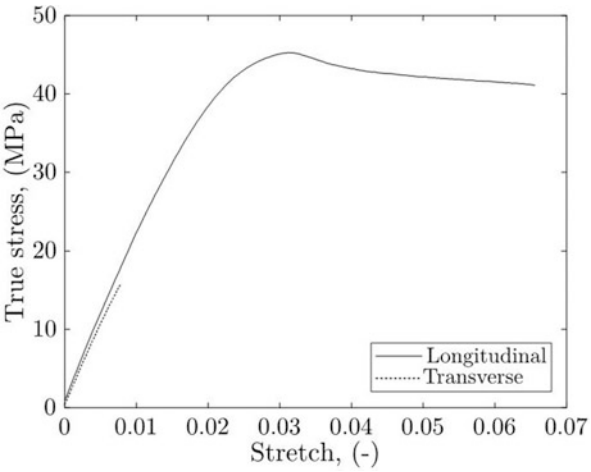

Fig. 7 Comparison of stress-strain response of FDM ABS with different raster orientations. (Original data)

by the fact that for a transverse raster orientation, the load is taken by the bond between filaments instead of by the filaments themselves as for the longitudinal case.

Printing parameters have a great influence on the mechanical behavior of 3D printed polymers. Moreover, when a FDM printer is used, it is necessary to know some practical recommendations. In this regard, while the printing time decreases when a higher layer height is used, the use of a lower layer height improves the surface roughness and geometrical accuracy. Moreover, although components with all the layers in a longitudinal direction present the highest mechanical response, in practice, it is recommended to use a pattern altering layers 90° to improve the residual stress distribution ensuring the adherences of the 3D printed component (Zhang et al. 2017).

Constitutive Modelling of Mechanical Deformation in Polymers

Computational models represent extremely useful tools to help at designing and optimizing structural components. In addition, they provide alternatives to experimental testing to (i) complement the experimental analysis allowing for the evaluation of strain and stress distribution as well as other mechanical variables and (ii) reduce the number of experimental tests, thus reducing associated costs. Although powerful tools, constitutive models for polymers are specially challenging due to their complex mechanical behavior. In this regard, thermoplastic polymers present nonlinear behavior, strain rate and temperature dependences, viscoelastic and viscoplastic responses, microstructural transitions, as well as a complex strong coupling between rate effects and temperature at high deformation rates. This subject has been addressed by several authors in the literature, and, according to their

conception nature, these models can be divided into two main approaches: phenomenological and physically motivated.

Regarding the phenomenological approaches, Popelar et al. (2004) developed a model for semi-crystalline polymers to describe the mechanical behavior of these polymers by a nonlinear viscoelastic theory. These viscoelastic approaches were later extended to viscoplastic models to introduce yielding (Zaïri et al. 2008). These phenomenological approaches are widely applied to simulate technological problems such as the study of cranial implants. Other phenomenological models are based on previous approaches for metals to describe the viscoplastic behavior of thermoplastic polymers (Louche et al. 2009; Garcia-Gonzalez et al. 2015a).

Moreover, physically motivated approaches introduce microstructural characteristics in the mathematical formulation of the constitutive models. One of these first approaches was the one-dimensional model proposed by Haward and Thackray (1968) that incorporated both yielding and strain hardening. Later, other authors developed three-dimensional descriptions inspired by the latter (Arruda and Boyce 1993). Recent efforts have been made to model the thermo-mechanical coupling during polymeric deformation. In this regard, Garcia-Gonzalez and coauthors (Garcia-Gonzalez et al. 2017b, 2018, 2020b; Barba et al. 2020) developed a series of thermodynamically consistent models for thermoplastic materials taking into account strain rate, temperature and stress state dependences, temperature evolution due to inelastic dissipation, as well as thermal transitions in the response of the material.

Although many constitutive models have been developed to reproduce the mechanical behavior of thermoplastics, components manufactured by 3D printing present extra dependences with the printing parameters. In addition, due to the manufacturing process, 3D printed thermoplastics are porous material with anisotropic behavior. In this regard, FDM thermoplastics are usually modelled as a composite material, where each lamina is composed of bonded filaments. Following this approach, few authors have modelled the elastic response of FDM polymers using the Hooke's law for orthotropic materials (Zou et al. 2016; Alaimo et al. 2017). In addition, both Tsai-Hill and Tsai-Wu failure criteria as well as Hill yield criterion have been used to predict the tensile strength of different materials (Ahn et al. 2003; Alaimo et al. 2017; Song et al. 2017). However, although these models capture the elastic behavior of FDM materials for different raster orientations, they are limited to a specific set of printing parameters and are not able to capture the full mechanical response, including plastic and viscous dependences of FDM thermoplastics. More recent efforts are made to develop general models to describe the full mechanical response of 3D printed polymers. In this regard, a recent work by the authors proposes a thermodynamically consistent model for 3D printed polymers accounting for nonlinear response; anisotropic hyperelasticity related to a transversely isotropic distribution of porous; strain rate dependence and softening related to 3D printing processing (Garzon-Hernandez et al. 2020).

From most of the models presented, a general framework to develop thermodynamically consistent formulations can be provided. This framework is based on the choice of different rheological elements combined in different branches, each one

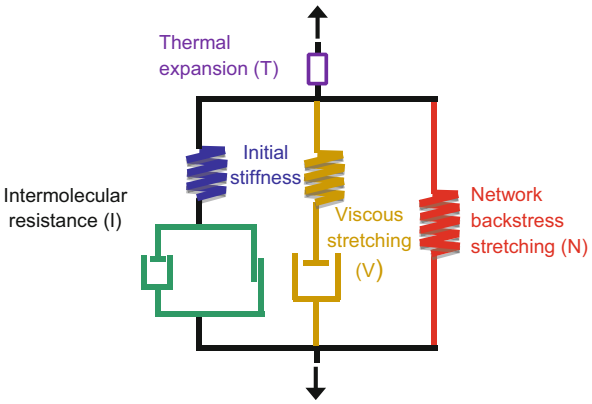

Fig. 8 Example of rheological scheme for a polymeric model (Garcia-Gonzalez et al. 2018)

related to a specific response of the material (see Fig. 8 for an example). These rheological elements are representative of an elastic resistance to deformation (springs) or to an inelastic deformation mechanism (dashpot). In addition, these schemes can include thermal elements related to thermal expansion mechanisms or friction elements to define yield functions. The formulation of the constitutive model is based on the definition of stress equations for the springs and flow rules for the dashpots. Then, the summation of the stress responses gives the total stress experienced by the polymer, and the definition of the flow rules describes the evolution of inelastic deformation mechanisms. These constitutive equations for finite deformations are consistently derived from energetic potentials $\psi(\boldsymbol{F}, \mathcal{Z}_i)$ (also called Helmholtz free energy), where $\boldsymbol{F}$ is the deformation gradient and $\mathcal{Z}_i$ are state variables. The expressions that relate these energetic potentials can be obtained from the combination of thermodynamics principles, and for the purely elastic case read:

$$\boldsymbol{P} = \frac{\delta \psi}{\delta \boldsymbol{F}} \tag{1}$$

$$\boldsymbol{\sigma} = \frac{2}{J} \boldsymbol{F} \frac{\delta \psi}{\delta \boldsymbol{C}} \boldsymbol{F}^{\boldsymbol{T}} \tag{2}$$

where $\boldsymbol{P}$ and $\boldsymbol{\sigma}$ are the first Piola-Kirchhoff stress tensor and the Cauchy stress tensor, respectively; $J =$ det $(\boldsymbol{F})$ the total Jacobian; and $\boldsymbol{C} = \boldsymbol{F}^{\boldsymbol{T}}\boldsymbol{F}$ is the right Cauchy-Green deformation tensor.

Damage and Failure Behavior of Polymers

The understanding of material failure is essential when designing industrial components to ensure their structural integrity under service conditions. Failure in polymers is extremely difficult as different mechanisms can govern the fracture process and,

depending on which ones do, the macroscopic response changes drastically. This section summarizes the main features of polymer fracture and the current approaches to model this problem.

Failure Mechanisms of Thermoplastic Polymers

In this section, the main deformation and failure mechanisms are introduced and discussed by means of macroscopic fracture. The fracture in polymers can be directly related to their chain molecular nature and the different interaction levels of their molecule segments. The grade of polymeric chains orientation also plays an important role on the fracture type, with low orientation grades leading to more brittle responses (Argon 2013). In this regard, the higher the orientation grade, the more important the role of chain scission in the fracture process, while for unoriented polymers, the role played by chain scission is negligible.

Under loading conditions, the polymer deforms and can show shear banding along directions aligned with principal shear stress; see Fig. 9. This is the primary mechanisms in amorphous polymers within the glassy region and is observed both under tension and compression conditions. These shear bands can accumulate in local regions leading to necks during yielding. Usually, when the polymer experiences this deformation mechanism, the continued application of the load results in a ductile fracture. In this process, if a crack is formed, the stresses are strongly altered in the plastic region and lose their singularity, thus leading to strain concentrations. In such situations, the polymeric behavior after yielding (i.e., plastic softening, plastic hardening) governs the eventual forms and growth mechanisms of the crack and the final fracture.

Crazing is another phenomenon associated with crack advance in flexible-chain glassy polymers. This mechanism leads to microvoid formation in a plane perpendicular to the maximum principal tensile stress. Then, these microvoids grow and coalesce leading to the formation of cracks. Contrary to shear banding, crazing takes

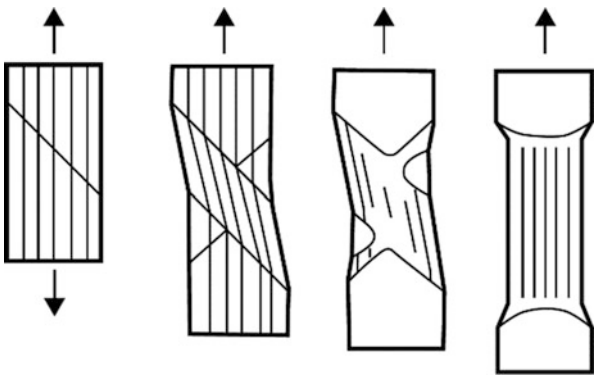

Fig. 9 Shear banding in polymers

place only under tension conditions. This phenomenon occurs in regions of high hydrostatic stress state, or in regions of very localized yielding. When thermoplastics are stressed, stress-whitening zones can be observed being a sign of crazing in some cases. While shear banding is more prevalent in semi-crystalline polymers, crazing is typical in amorphous and glassy polymers. A representative scheme of crazing development is shown in Fig. 10.

The cavitation phenomenon can also be observed in many semi-crystalline polymers deformed at temperatures above glass transition (Pawlak et al. 2014). Moreover, this phenomenon is observed in rubbers and crosslinked and glassy polymers. As crazing, cavitation is produced under tension conditions but does not form in compression or shear. This mechanism is activated by reaching a cavitation strength (stress threshold, also called de-cohesion strength) and can be estimated by the universal binding-energy relation.

Moreover, both amorphous and semi-crystalline thermoplastics have a ductile-to-brittle transition temperature whereby at temperatures below it, a brittle failure is expected (Laiarinandrasana et al. 2009); see Fig. 11. This transition from brittle to ductile can be explained by the nature of fracture and deformation mechanisms. The brittle fracture is usually defined by a given brittle strength (stress threshold) that is associated with extrinsic imperfections, being relatively independent of temperature and strain rate. However, the yield stress (also stress threshold) is strongly dependent on both temperature and strain rate, increasing with strain rate and decreasing with temperature. Therefore, a polymer that behaves in a brittle manner at low temperature can become tough and more ductile at higher temperatures. This is explained by the reduction in yield stress with temperature resulting in plastic deformation before reaching the brittle strength and, therefore, leading to a ductile failure. In a similar fashion, a polymer that behaves ductile at a given temperature and low strain rates can present a brittle fracture for higher strain rates as a consequence of a yield stress increase above the brittle strength.

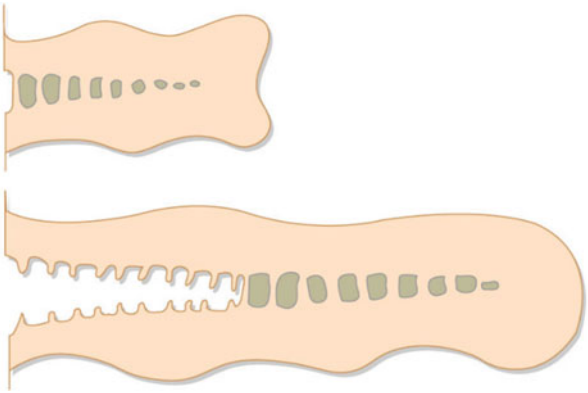

Fig. 10 Crazing mechanism in polymers

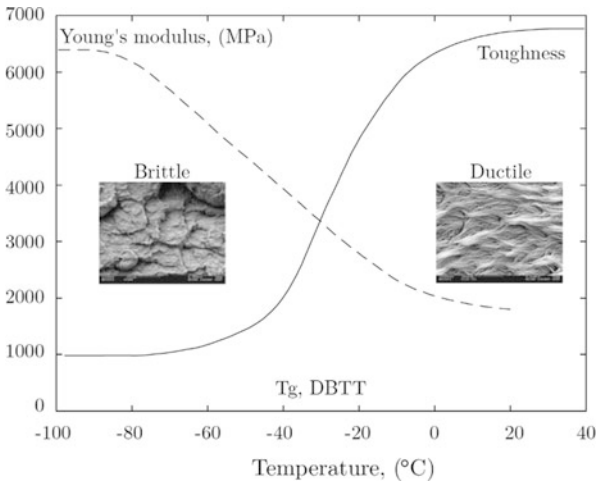

Fig. 11 Evolution of Young's modulus and toughness versus temperature for glassy polymers (Laiarinandrasana et al. 2009)

Temperature and Strain Rate Dependences of Polymeric Failure

As inferred in the previous section, the predominant failure mechanism in polymers is strongly dependent on temperature and strain rate changes. This dependence has been the focus of several studies in the literature (Aranda-Ruiz et al. 2020; Fan and Wang 2018; Ohara and Kodama 2019; Barba et al. 2020; Garcia-Gonzalez et al. 2020a). There are three important physical phenomena governing the temperature and strain dependence of the polymeric failure: the ductile-to-brittle transition, the adiabatic heating, and the glass transition temperature (directly related to chain mobility). These aspects are detailed next.

Fan and Wang (2018) performed a complete study on the different micro-mechanisms governing the brittle or ductile nature of polymer composite materials. They identified different active mechanisms depending on the type of fracture. The different mechanisms found are presented in Fig. 12. In brittle fractures, they found facelet type surfaces, sharp cracks, and planar features. Void formation and the development of wrinkle structures were associated with a more ductile fracture. In this study, they found dependence of these failure mechanisms on the strain rate changing from ductile to brittle for higher strain rate tests (from 10^{-4} to 10^{3} s^{-1}).

The **ductile-to-brittle transition (DBT)** is a critical phenomenon in fracture mechanics of materials (including metals and polymers). For the case of polymers, several authors have focused on the change of regime with strain rate and temperature (Aranda-Ruiz et al. 2020; Fan and Wang 2018; Ohara and Kodama 2019; Barba et al. 2020). The extended fracture theory of polymers states that the material presents a ductile behavior if the yield stress σ_y is below the critical brittle stress σ_b required to produce and propagate micromechanical Griffith flaw (Ohara and Kodama 2019). This is presented in Fig. 13. In principle, neglecting adiabatic effects, the yield stress

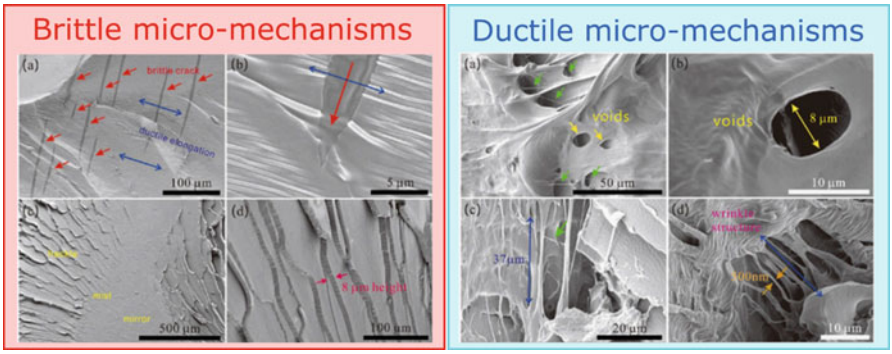

Fig. 12 Different mechanisms for brittle and ductile failures in polymers including facelet cracks, ductile void formation, and wrinkle structures. (Adapted from Fan and Wang (2018))

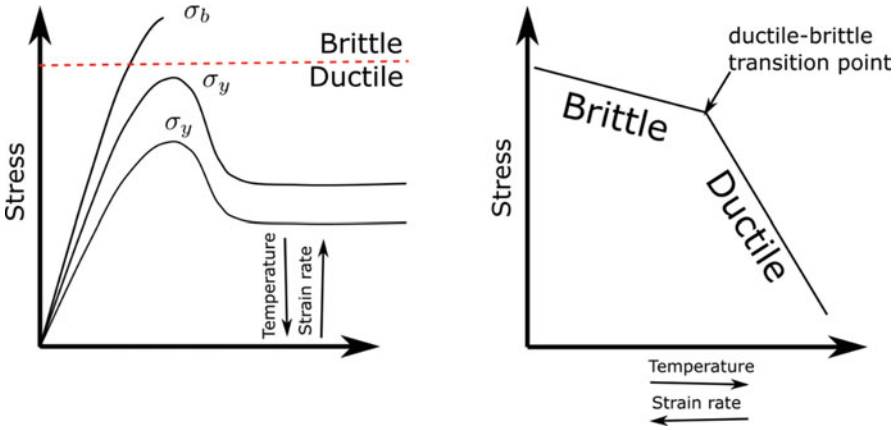

Fig. 13 Ductile-brittle transition behavior for glassy polymers. (Adapted from Ohara and Kodama (2019).) In the left figure, the arrows indicate the tendency of yield stress (σ_y) with temperature and strain rate. In the right figure, the arrows show the transition in the fracture mode with temperature and strain rate

of the polymer increases with higher strain rates and lower temperatures. This explains the DBT transition not only on the temperature but also on the strain rate (Ohara and Kodama 2019; Barba et al. 2020).

Barba et al. (2020) have spotted this transition in semi-crystalline polymer PEEK. The fracture mechanism changes abruptly from a more brittle fracture (ε_R= 15%) at room temperature to super-ductile fracture above 150 °C (ε_R> 125%), as stated in Fig. 4. The extension of the deformation or necking area to the whole gauge length allows to extend the plastic deformation at fracture by almost ten times. This is explained in terms of changes in the plastic behavior controlled by the glass transition temperature T_g detailed next.

Most of these studies point to the **glass transition temperature** as the critical material parameter controlling the change in failure from brittle to ductile. This

phase transformation plays an important role in controlling plastic flow of the polymeric chains, limiting their reorientation with the stress state depending on the temperature and thus affecting the amount of strain before failure and the nature of the fracture mechanism (chain extension or premature failure). The effects of this microstructural transition have been studied by the authors (Barba et al. 2020; Garcia-Gonzalez et al. 2020a). Barba et al. (2020) showed an abrupt increase of ductility above the glass transition temperature in PEEK. This enhancement of the plastic flow producing a ductile fracture is shown in Fig. 14.

These effects have also been observed at high strain rates under impact loading. In this regard, Garcia-Gonzalez et al. (2020a) studied the mechanical response of PMMA to impact conditions at different testing temperatures; see Fig. 15. This polymer behaves in a brittle manner with crack propagation inducing debris at low

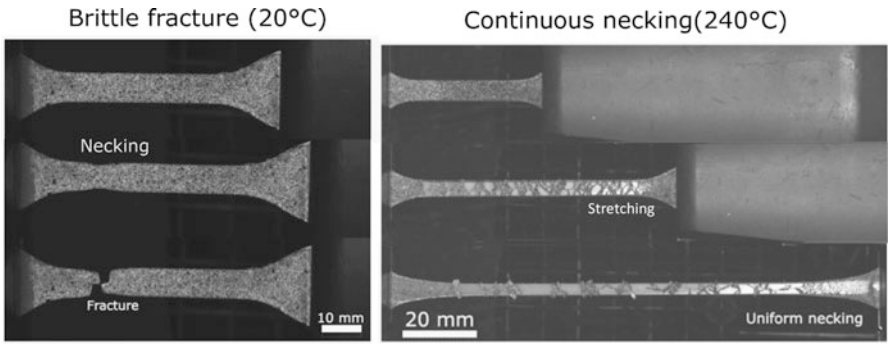

Fig. 14 DIC images of PEEK tested samples at room temperature and 240 °C showing the change in failure mechanism below and above the T_g of the polymer (T_g = 150 °C). (Adapted from Barba et al. (2020))

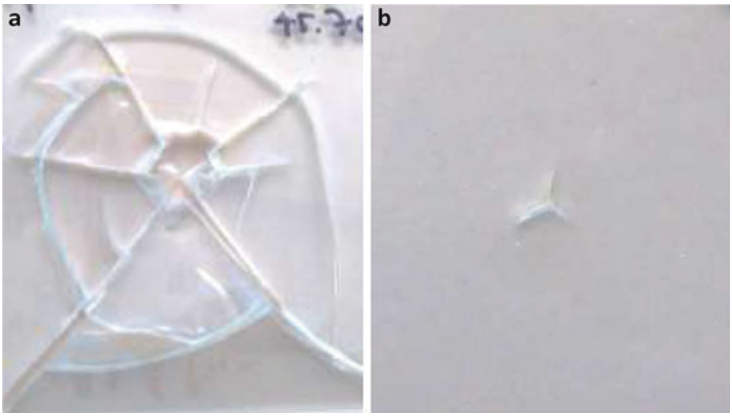

Fig. 15 Failure mode of PMMA under impact loading at different temperatures: (**a**) Room temperature; (**b**) 105 °C. (Adapted from Garcia-Gonzalez et al. (2020a))

temperatures. However, a clear transition to ductile fracture was observed at temperatures above its glass transition, where perforation induces a hole enlargement without showing cracks and, after complete perforation, there is a spring back mechanism resulting in the hole reclosing.

Finally, another important point in determining the fracture type dependence of the polymer on temperature and strain rate is the adiabatic heating effect. This phenomenon is important at high strain rates and lower temperatures. This effect consists in a localized increase of temperature (within the plastic deformation regions) which can reduce the severity of the embrittlement at higher strain rates and lower temperature. Thus, there is a local change of deformation conditions which can lead to material softening at higher strain rates, thus balancing the embrittlement due to the previous statements (higher strain rates leading to brittle failure). This produces a brittle-to-ductile transition (BDT) at higher strain rates caused by the local plastic flow enhanced by the temperature increase. This effect has been studied by Aranda-Ruiz et al. (2020) in polycarbonate polymer (PC) as a function of the sample thickness and strain rate. They found a BDT at lower strain rates around $1.5 \cdot 10^4$ s^{-1} produced by a change in deformation mechanism and a second BDT at around $5.0 \cdot 10^4$ s^{-1} in which the ductility of the polymer is recovered as the adiabatic effects are quick in producing local softening. The threshold values for these transitions are found to depend on the sample thickness.

Failure Behavior of 3D Printed Polymers by FDM

Among the different printing parameters that control the final mechanical response of 3D printed polymers, the raster orientation has a high influence on the failure and deformation mechanisms. The influence of this parameter on the fracture phenomenon of FDM ABS under tensile conditions has been widely studied (Rodríguez et al. 2001; Ziemian et al. 2012). As during the mechanical deformation, an anisotropic failure is observed where a ductile fracture takes place under longitudinal loading and brittle interface fracture under transverse loading; see Fig. 16. In this

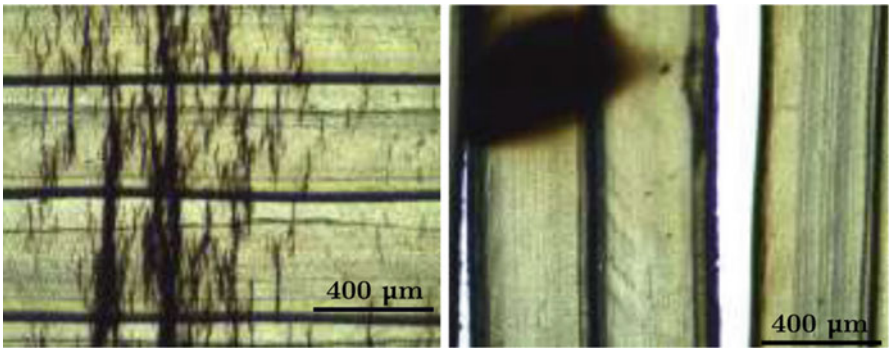

Fig. 16 Failure mechanisms on longitudinal and transverse specimens. (Original data)

regard, during the deformation process of longitudinal specimens, shear banding governs the process. Shear banding appears on each filament and propagates obliquely before yielding. Then, it continues propagating along the whole gauge length after yielding. In addition, crazes are formed along whitened areas due to this phenomenon, resulting in a crack normal to loading direction; see Fig. 17. This phenomenon is also observed in the monolithic ABS material. On the other hand, for specimens with 90° or 45° raster orientations, the failure occurs along filament-to-filament interface, which is the weakest path.

Moreover, the influence of the nozzle temperature on the tensile failure of 3D printed PEEK has been analyzed for specimens manufactured with a [−45/45] filling path (Ding et al. 2019). In this regard, at extrusion temperatures below 380 °C, a clear stratification is observed due to the low bonding force between layers. At extrusion temperatures above, the PEEK exhibits an oblique and ductile fracture.

Constitutive Modelling of Damage and Failure in Polymers

Computational models represent essential tools to evaluate the structural integrity of different components. As shown in the previous section, numerous approaches have been done to predict the deformation behavior of polymeric materials. However, the prediction of polymer fracture through numerical models is not that well-established yet. In this regard, failure of polymers has been tackled by different approaches. Among them, a division between two main approaches by fracture nature can be done: brittle fracture and ductile fracture. Often, most of the polymeric materials show both brittle and ductile failure depending on the material temperature and loading and boundary conditions. In this section, different approaches to simulate polymer failure are presented, highlighting their advantages and some reference works.

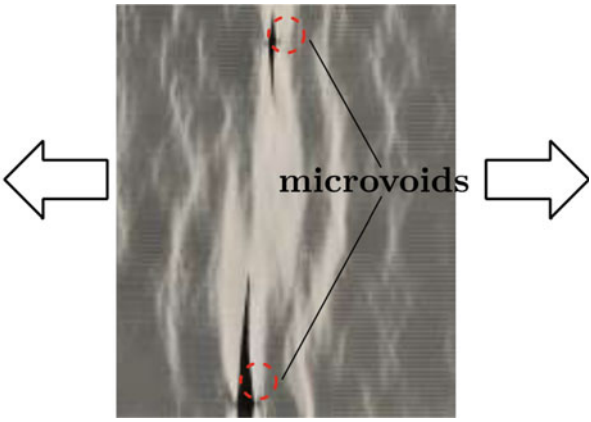

Fig. 17 Shear bands and crazing on longitudinal specimen. (Original data)

Critical Mechanical Thresholds The simplest solution used to simulate polymer failure in the literature is based on the definition of a mechanical threshold related to an equivalent strain, an equivalent stress, or a specific principal component (Aranda-Ruiz et al. 2020). This approach usually considers that the polymeric material first behaves in an elastic regime until reaching yielding and, then, plastic deformation starts and develops until reaching a maximum strain or stress resulting in the sudden fracture of the material. Other approaches include dependences of these mechanical thresholds on temperature and strain rate (Garcia-Gonzalez et al. 2015a). In addition, some works complement these criteria with element deletion allowing for the visualization of the complete fracture of the component (Garcia-Gonzalez et al. 2015a; Aranda-Ruiz et al. 2020). This last approach must be used with extreme care to avoid fictitious numerical effects due to mass balance issues. Overall, this type of criterion is the most widely used due to the ease in implementing it in a finite element solver and the low computational cost with respect to other alternatives. However, these criteria are usually merely phenomenological approaches and, although they allow for reproducing the failure process, they cannot be employed to further understand the specific mechanisms involved in the polymer fracture.

Representative Volume Element (RVE)-Based Approaches An alternative to direct mechanical thresholds approaches is the development of RVE to simulate the fracture problem at the microscale. These models allow for the analysis of the main failure mechanisms and, then, to propose homogenized models that can be translated to macroscale simulations. Therefore, the overall view of these approaches is to simulate the micromechanics of the polymer to identify mechanical thresholds for the onset of damage and the catastrophic failure, as well as the evolution of the material degradation. Among these approaches, van Melick et al. (2003) studied the effect of the intrinsic properties on the macroscopic deformation behavior of polymers. By this manner, they were able to obtain failure criteria related to the onset of craze nucleation and the subsequent macroscopic brittle fracture (see Fig. 18 for an example).

Ductile-to-Brittle Transition Modelling in Polymers Particularly difficult is the modelling of ductile-to-brittle transitions in the fracture mode of polymers. This

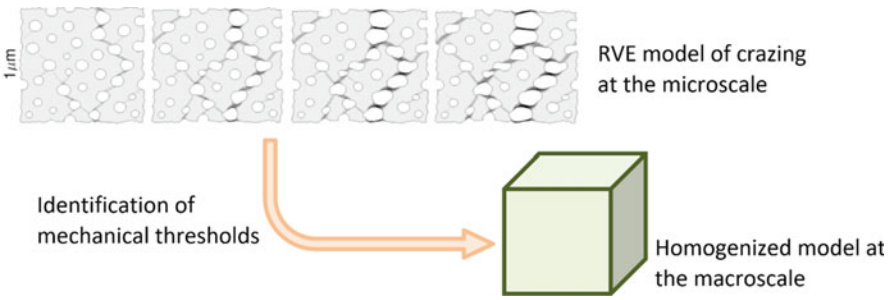

Fig. 18 Scheme of RVE-based fracture models for polymers. Part of the figure has been adapted from van Melick et al. (2003)

transition corresponds to a change in the microstructure of the polymer, and this is of great relevance for shape memory polymers. In this regard, a recent paper by Foyouzat et al. (2020) proposed an extended finite element method (XFEM) formulation coupling thermo-mechanics to simulate stationary and propagating cracks in shape memory polymers. In a more general context, the failure of polymers can be understood as the competition between shear yielding and crazing. Damage models that include brittle and ductile fractures describe different activation mechanisms that depend on temperature (and sometimes strain rate). For the brittle criterion, Gearing and Anand (2004) developed a continuum mechanics approach for craze initiation, widening, and breakdown. This model was recently extended by Jiang et al. (2017) to incorporate strain rate dependence on the craze initiation criterion. To this end, a critical stress value for craze initiation, σ_{cr}, is defined depending on material parameters c_i, the hydrostatic stress σ_m, and the strain rate. Then, if the hydrostatic stress is positive (required condition for crazing), the maximum principal stress component σ_1 is compared to σ_{cr} to activate the damage process:

$$\sigma_1 \geq \sigma_{cr} = c_1 + \frac{c_2}{\sigma_m} + c_3 \, ln\left(\|\boldsymbol{D}\|\right) > 0 \qquad \text{and} \qquad \sigma_m > 0 \tag{3}$$

where $\boldsymbol{D}$ is the deformation rate tensor.

Non-Local Phase Field Approaches Finally, we can find more sophisticated models that deal with the polymer fracture and the propagation of cracks by non-local approaches. These models do not only evaluate the damage in the finite element but also account for damage within the surrounding by spatial gradients (see Fig. 19).

Non-local approaches allow for overcoming modelling issues related to sharp crack discontinuities when we deal with complex crack topologies. To this end, a crack phase field is introduced based on diffusive mechanisms providing a consistent framework for continuum phase field modelling of crack propagation (Miehe et al. 2010; Borden et al. 2014). The basis for these formulations relies on the introduction of a crack surface density function $\gamma_l(d, \nabla d)$ depending on a local damage variable d that indicates the degradation state of the polymer (going from 0 for non-degradation to 1 for fully damaged), the spatial gradient of this damage variable ∇d, and a characteristic length scale l. This density function must be particularized for the specific material and, together with the length scale, defines a spatially regularized total crack surface in reference configuration Ω_o as:

$$\Gamma_l(d) = \int_{\Omega_o} \gamma_l(d, \nabla d) dV \tag{4}$$

To make the finite element implementation easier, surface integrals on the crack surface (Eq. 4) can be approximated by volume integrals leading to a critical fracture energy as:

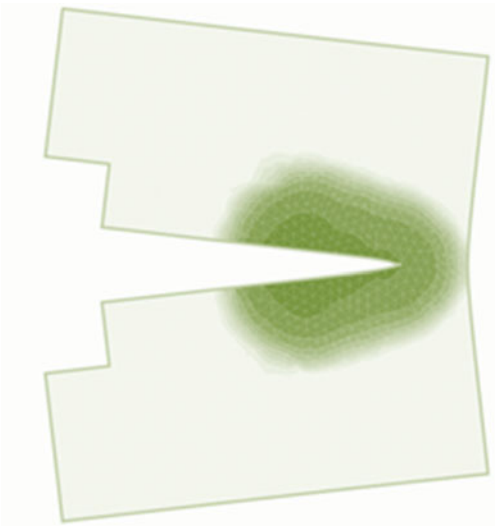

Fig. 19 Damage evaluation in a non-local formulation. The damage variable is not computed as purely local but accounts for the surrounding elements' damage, thus leading to a continuous damage distribution. (Adapted from Saloustros et al. (2018))

$$\int_{\Gamma} g_c dA = \int_{\Omega_o} g_c \gamma_l dV \tag{5}$$

with g_c being the Griffith's critical energy release and $g_c\gamma_l$ being the critical fracture energy per unit reference volume.

Apart from the definition of the crack surface density function γ_l, to complete this framework, the local evolution of the damage d must be consistently defined. To this end, the time derivative of d is usually computed as a function of the critical fracture energy $g_c\gamma_l$ and the elastic free energy that describes the material behavior $\psi(\boldsymbol{F}, d)$, with $\boldsymbol{F}$ being the deformation gradient. As an example, Miehe et al. (2010) proposed the local evolution of the phase field as a non-smooth equation:

$$\dot{d} = \frac{1}{\eta} \left\langle -\frac{\delta(\psi + g_c\gamma_l)}{\delta d} \right\rangle \tag{6}$$

where η is a viscosity-like parameter for the crack evolution.

The previous ideas were generalized by Miehe et al. (2015a) providing a brittle fracture framework for multi-physics problems at large strains. To this end, these authors proposed a geometric approach to the diffusive crack modelling which is motivated on a regularized crack surface balance and solved by phase field modelling. In a second paper, Miehe et al. (2015b) extended this phase field framework to combined brittle-ductile fracture within a thermo-plasticity gradient formulation. To this end, these authors introduced state variables associated with the different deformation mechanisms and driven by elastic and plastic work densities. In addition, barrier functions were included to define critical values activating fracture

modes. A final application was provided to simulate crazing-induced fracture in glassy polymers under quasi-static conditions.

Fracture Modelling for 3D Polymers Different studies have shown that polymers printed by additive manufacturing techniques present higher porosity and, thus, a more brittle response. This failure is usually addressed by critical mechanical thresholds and assumed linear elastic response until fracture. However, more sophisticated approaches are recently proposed in the literature. In this regard, Ghandriz et al. (2019) implemented a XFEM model within an anisotropic cohesive zone model. This approach is motivated on the nature of such 3D printed polymers, which can be understood as a combination of filaments bounded by a sintered interphase. In this work, the combination of the XFEM coupled to the anisotropic cohesive zone model allowed for the modelling of fracture between filaments (brittle fracture), fracture through filaments (ductile fracture), and kinked fracture behaviors. In addition, both crack propagation between filaments and penetration through filaments are included by the definition of two crack initiation and evaluation criteria. Future advances in this field may couple these fracture models to more complex constitutive models to, at the end, link printing parameters with the failure response of 3D printed components, allowing their evaluation by means of structural integrity.

Summary/Conclusions

This chapter introduces the background on the main mechanical features of thermoplastic polymers and the current state of the art in their constitutive modelling. In this regard, it is highlighted the importance of analyzing polymeric materials from the microstructural to the macrostructural level. It is shown the great relevance of the molecular structure of the polymer and how these characteristics will determine the macrostructural response. In this regard, the deformation and fracture mechanisms of polymers can be inferred from the molecular chains' mobility and arrangement, both of which present strong coupling with time- and temperature-dependent processes.

A wide collection of results from the available literature and original data are presented in order to illustrate the different polymeric fundamentals. In addition, we review the different approaches in the current literature to model the mechanical behavior, both deformation and fracture, of polymers. Moreover, an especial remark on polymers manufactured by 3D printing technologies is done along the different sections of the chapter.

Acknowledgments The authors acknowledge support from Programa de Apoyo a la Realización de Proyectos Interdisciplinares de I+D para Jóvenes Investigadores de la Universidad Carlos III de Madrid and Comunidad de Madrid (project: BIOMASKIN_CM-UC3M), and from Ministerio de Ciencia, Innovación y Universidades, Agencia Estatal de Investigación y Fondo Europeo de Desarrollo Regional (RTI2018-094318-B-I00). D. Garcia-Gonzalez acknowledges support from the Talent Attraction grant (CM 2018 - 2018-T2/IND-9992) from the Comunidad de Madrid.

References

S. Ahn, M. Montero, D. Odell, S. Roundy, P.K. Wright, Anisotropic material properties of fused deposition modeling ABS. Rapid Prototyp. J. **8**(4), 248–257 (2002)

S.-H. Ahn, C. Baek, S. Lee, I. Ahn, Anisotropic tensile failure model of rapid prototyping parts – fused deposition modeling (fdm). IJMPB **17**, 1510–1516 (2003)

G. Alaimo, S. Marconi, L. Costato, F. Auricchio, Influence of meso-structure and chemical composition on fdm 3d-printed parts. Compos. Part B-Eng. **113**, 371–380 (2017)

N. Aliheidari, R. Tripuraneni, A. Ameli, S. Nadimpalli, Fracture resistance measurement of fused deposition modeling 3D printed polymers. Polym. Test. **60**, 94–101 (2017)

J. Aranda-Ruiz, K. Ravi-Chandar, J.A. Loya, On the double transition in the failure mode of polycarbonate. Mech. Mater. **140**, 103242 (2020)

A.S. Argon, *The Physics of Deformation and Fracture of Polymers* (Cambridge University Press, Cambridge, 2013)

E.M. Arruda, M.C. Boyce, A three-dimensional constitutive model for the large stretch behavior of rubber elastic materials. J. Mech. Phys. Solids **41**, 389–412 (1993)

D. Barba, A. Arias, D. Garcia-Gonzalez, Temperature and strain rate dependences on hardening and softening behaviours in semi-crystalline polymers: application to PEEK. Int. J. Solids Struct. **182–183**, 205–217 (2020)

M.J. Borden, T.J.R. Hughes, C.M. Landis, C.V. Verhoosel, A higher-order phase-field model for brittle fracture: formulation and analysis within the isogeometric analysis framework. Comput. Methods Appl. Mech. Eng. **273**, 100–118 (2014)

W.D. Callister, *Materials Science and Engineering: An Introduction* (Wiley, New York, 2006)

B. Chang, X. Wang, Z. Long, Z. Li, J. Gu, S. Ruan, C. Shen, Constitutive modeling for the accurate characterization of the tension behavior of PEEK under small strain. Polym. Testing **69**, 514–521 (2018)

S. Ding, B. Zou, P. Wang, H. Ding, Effects of nozzle temperature and building orientation on mechanical properties and microstructure of PEEK and PEI printed by 3D-FDM. Polym. Test. **78**, 105948 (2019)

J. Fan, C. Wang, Dynamic compressive response of a developed polymer composite at different strain rates. Compos. Part B **152**, 96–101 (2018)

A. Foyouzat, H. Bayesteh, S. Mohammadi, A brittle to ductile phase transition fracture analysis of shape memory polymers. Eng. Fract. Mech. **224**, 106751 (2020)

D. Garcia-Gonzalez, Magneto-visco-hyperelasticity for hard-magnetic soft materials: theory and numerical applications. Smart Mater. Struct. **28**, 085020 (2019)

D. Garcia-Gonzalez, C.M. Landis, Magneto-diffusion-viscohyperelasticity for magneto-active hydrogels: rate dependences across time scales. J. Mech. Phys. Solids **139**, 103934 (2020)

D. Garcia-Gonzalez, A. Rusinek, T. Jankowiak, A. Arias, Mechanical impact behavior of polyether-ether-ketone (PEEK). Compos. Struct. **124**, 88–99 (2015a)

D. Garcia-Gonzalez, M. Rodriguez-Millan, A. Rusinek, A. Arias, Low temperature effect on impact energy absorption capability of PEEK composites. Compos. Struct. **134**, 440–449 (2015b)

D. Garcia-Gonzalez, J. Jayamohan, S.N. Sotiropoulos, S.H. Yoon, J. Cook, C.R. Siviour, A. Arias, A. Jérusalem, On the mechanical behaviour of PEEK and HA cranial implants under impact loading. J. Mech. Behav. Biomed. Mater. **69**, 342–354 (2017a)

D. Garcia-Gonzalez, R. Zaera, A. Arias, A hyperelastic-thermoviscoplastic constitutive model for semi-crystalline polymers: application to PEEK under dynamic loading conditions. Int. J. Plast. **88**, 27–52 (2017b)

D. Garcia-Gonzalez, S. Garzon-Hernandez, A. Arias, A new constitutive model for polymeric matrices: application to biomedical materials. Compos. Part B **139**, 117–129 (2018)

D. Garcia-Gonzalez, A. Rusinek, A. Bendarma, R. Bernier, M. Klosak, S. Bahi, Material and structural behaviour of PMMA from low temperatures to over the glass transition: Quasi-static and dynamic loading. Polym. Test. **81**, 106263 (2020a)

D. Garcia-Gonzalez, S. Garzon-Hernandez, A. Rusinek, R. Bernier, A. Arias, Low temperature mechanical behaviour of PVDF: cryogenic pre-treatment, quasi-static, cyclic and dynamic experimental testing and modelling. Mech. Mater. **147**, 103436 (2020b)

S. Garzon-Hernandez, A. Arias, D. Garcia-Gonzalez. A continuum constitutive model for FDM 3D printed thermoplastics. Composites Part B: Engineering, 108373 (2020). https://doi.org/10.1016/j.compositesb.2020.108373

S. Garzon-Hernandez, D. Garcia-Gonzalez, A. Jerusalem, A. Arias, Design of FDM 3D printed polymers: an experimental-modelling methodology for mechanical properties prediction. Mater. Des. **188**, 108414 (2020)

B. Gearing, L. Anand, On modeling the deformation and fracture response of glassy polymers due to shear-yielding and crazing. Int. J. Solids Struct. **41**, 3125–3150 (2004)

R. Ghandriz, K. Hart, J. Li, Extended finite element method (XFEM) modeling of fracture in additively manufactured polymers. Addit. Manuf. (2019). https://doi.org/10.1016/j.addma.2019.100945

R.N. Haward, G. Thackray, The use of a mathematical model to describe isothermal stress-strain curves in glassy thermoplastics. Proc. R. Soc. Lond. Ser. A, Math.Phys. Sci. **302**, 453–472 (1968)

S. Jabbari-Farouji, J. Rottler, O. Lame, A. Makke, M. Perez, J.L. Barrat, Plastic deformation mechanisms of semicrystalline and amorphous polymers. ACS Macro Lett **4**(2), 147–150 (2015)

H. Jiang, J. Zhang, Z. Yang, C. Jiang, G. Kang, Modeling of competition between shear yielding and crazing in amorphous polymers' scratch. Int. J. Solids Struct. **124**, 215–228 (2017)

Y. Kim, H. Yuk, R. Zhao, S.A. Chester, X. Zhao, Printing ferromagnetic domains for untethered fast-transforming soft materials. Nature **558**, 274–279 (2018)

D. Kong, J. Li, A. Guo, X. Zhang, X. Xiao, Self-healing high temperature shape memory polymer. Eur. Polym. J. **120**, 109279 (2019)

L. Laiarinandrasana, M. Lafarge, G. Hochstetter, Accounting for porosity, time and temperature dependency in fracture mechanics concepts on polyvinylidene fluoride material. Eng. Fract. Mech. **76**(18), 2766–2779 (2009)

H. Louche, F. Piette-Coudol, R. Arrieux, J. Issartel, An experimental and modeling study of the thermomechanical behavior of an ABS polymer structural component during an impact test. Int. J. Impact Eng. **36**, 847–861 (2009)

S. Lovald, S.M. Kurtz, *Applications of Polyetheretherketone in Trauma, Arthroscopy, and Cranial Defect Repair* (Elsevier, Amsterdam, 2012)

C. Miehe, F. Welschinger, M. Hofacker, Thermodynamically consistent phase-field models of fracture: variational principles and multi-field FE implementations. Int. J. Numer. Methods Eng. **83**, 1273–1311 (2010)

C. Miehe, L.M. Schanzel, H. Ulmer, Phase field modeling of fracture in multi-physics problems. Part I. Balance of crack surface and failure criteria for brittle crack propagation in thermo-elastic solids. Comput. Methods Appl. Mech. Eng. **294**, 449–485 (2015a)

C. Miehe, M. Hofacker, L.M. Schanzel, F. Aldakheel, Phase field modeling of fracture in multi-physics problems. Part II. Coupled brittle-to-ductile failure criteria and crack propagation in thermo-elastic–plastic solids. Comput. Methods Appl. Mech. Eng. **294**, 486–522 (2015b)

I. Mohagheghian, G.J. McShane, W.J. Stronge, Impact perforation of monolithic polyethylene plates: projectile nose shape dependence. Int. J. Impact Eng. **80**, 162–176 (2015)

M. Nasraoui, P. Forquin, L. Siad, A. Rusinek, Influence of strain rate, temperature and adiabatic heating on the mechanical behaviour of poly-methylmethacrylate: experimental and modelling analyses. Mater. Des. **37**, 500–509 (2012)

T.D. Ngo, A. Kashani, G. Imbalzano, K.T.Q. Nguyen, D. Hui, Additive manufacturing (3D printing): a review of materials, methods, applications and challenges. Compos. Part B Eng. **143**, 172–196 (2018)

A. Ohara, H. Kodama, Correlation between enthalpy relaxation and mechanical response on physical aging of polycarbonate in relation to the effect of molecular weight on ductile-brittle transition. Polymer **181**, 121720 (2019)

A. Pawlak, A. Galeski, A. Rozanski, Cavitation during deformation of semicrystalline polymers. Prog. Polym. Sci. **39**(5), 921–958 (2014)
C.F. Popelar, C.H. Popelar, V.H. Kenner, Viscoelastic material characterization and modelling of polyethylene. Polym. Eng. Sci. **30**, 577–586 (2004)
P.J. Rae, E.N. Brown, E.B. Orler, The mechanical properties of poly(ether-ether-ketone) (PEEK) with emphasis on the large compressive strain response. Polymer **48**(2), 598–615 (2007)
J.F. Rodríguez, J.P. Thomas, J.E. Renaud, Mechanical behavior of acrylonitrile butadiene styrene (abs) fused deposition materials. Experimental investigation. Rapid Prototyp. J. **7**(3), 148–158 (2001)
S. Saloustros, M. Cervera, L. Pela, Challenges, tools and applications of tracking algorithms in the numerical modelling of cracks in concrete and masonry structures. Arch. Comput. Method E. **26**, 961–1005 (2018)
Y. Song, Y. Li, W. Song, K. Yee, K.-Y. Lee, V. Tagarielli, Measurements of the mechanical response of unidirectional 3d-printed pla. Mater. Design. **123**, 154–164 (2017)
H.G.H. van Melick, L.E. Govaert, H.E.H. Meijer, Prediction of brittle-to-ductile transitions in polystyrene. Polymer **44**, 457–465 (2003)
G.Z. Voyiadjis, A. Samadi-Dooki, L. Malekmotiei, Nanoindentation of high performance semi-crystalline polymers: a case study on PEEK. Polym. Testing **61**, 57–64 (2017)
X. Wang, M. Jiang, Z. Zhou, J. Gou, D. Hui, 3D printing of polymer matrix composites: a review and prospective. Compos. Part B **110**, 442–458 (2017)
C. Yang, X. Tian, D. Li, Y. Cao, F. Zhao, C. Shi, Influence of thermal processing conditions in 3D printing on the crystallinity and mechanical properties of PEEK material. J. Mater. Process. Technol. **248**, 1–7 (2017)
F. Zaïri, M. Naït-Abdelaziz, J.M. Gloaguen, J.M. Lefebvre, Modelling of the elasto-viscoplastic damage behaviour of glassy polymers. Int. J. Plast. **24**, 945–965 (2008)
W. Zhang, A.S. Wu, J. Sun, Z. Quan, B. Gu, B. Sun, C. Cotton, D. Heider, T.-W. Chou, Characterization of residual stress and deformation in additively manufactured ABS polymer and composite specimens. Compos. Sci. Technol. **150**, 102–110 (2017)
C. Ziemian, M. Sharma, S. Ziemian, Anisotropic mechanical properties of ABS parts fabricated by fused deposition modelling, in *Mechanical Engineering*, ed. by M. Gokcek, (IntechOpen, London, 2012) 2002
R. Zou, Y. Xia, S. Liu, P. Hu, W. Hou, Q. Hu, C. Shan, Isotropic and anisotropic elasticity and yielding of 3d printed material. Compos. Part B-Eng. **99**, 506–513 (2016)
G. Zurlo, M. Destrade, T. Lu, Fine tuning the electro-mechanical response of dielectric elastomers. Appl. Phys. Lett. **113**, 162902 (2018)

Failure Behavior of Aluminum Alloys Under Different Stress States

12

M. Rodríguez-Millán, Daniel Garcia-Gonzalez, and Angel Arias

Contents

Introduction 278
Damage Models 281
Experimental and Numerical Analysis of Ductile Failure 285
Summary/Conclusions 297
References 298

Abstract

This chapter analyzes the current state of the art on ductile damage in aluminum alloys. To this end, the main experimental methodologies developed to date for this purpose are identified and introduced. The analysis of failure in this type of materials is rather complex and requires the consideration of two parameters dependent on the stress state: triaxiality and Lode parameter. Different values of triaxiality and Lode parameter can be obtained by properly defining the testing load and the specimen geometry. These results are especially interesting to feed constitutive and failure models such as the Johnson-Cook model or the Bai-Wierzbicki model. This chapter focuses on different stress states associated to different Lode parameter and triaxialities: tension, compression, shear, and combined tension-torsion. To this end, a wide variety of testing specimens are introduced describing their relation to these parameters. Thus, this content aims at providing guidance for characterization testing of ductile fracture of metals and further calibration of failure models.

M. Rodríguez-Millán (✉)
Department of Mechanical Engineering, University Carlos III of Madrid, Madrid, Spain
e-mail: mrmillan@ing.uc3m.es

D. Garcia-Gonzalez · A. Arias
Department of Continuum Mechanics and Structural Analysis, University Carlos III of Madrid, Madrid, Spain
e-mail: danigarc@ing.uc3m.es; aariash@ing.uc3m.es

© Springer Nature Switzerland AG 2022

G. Z. Voyiadjis (ed.), *Handbook of Damage Mechanics*,
https://doi.org/10.1007/978-3-030-60242-0_68

The chapter first introduces fundamental concepts, then a brief description of failure models, and, finally, a detailed methodological description on the characterization of metals at different triaxialities and Lode parameters.

Keywords

Triaxiality · Lode parameter · Johnson and Cook · Ductile failure criterion · Tension stress · Bridgman · Grooved flat specimen · Dog-bone specimen · Uniaxial compression · Shear specimens · Arcan specimens · Equi-biaxial test · Butterfly specimen · Punch test · Hasek tests · Modified shear specimen · Double notched tube specimen · 5754-H111 · 6082-T6;2024-T3 · Modified Lindholm specimen

Introduction

In the last 60 years, ductile failure in metallic materials has been studied due to its importance in the design of mechanical and structural components. When plastic strain reaches a certain limit value, there is a loss of the capacity to support loads giving rise to the phenomenon of ductile failure. In this regard, large plastic deformations around crystalline defects lead to instabilities resulting into the failure phenomenon. The ductile fracture in metals is based on voids distributed within the material and nucleated during deformation that grow together (*coalescence*) to form a continuous path to fracture (Garrison Jr and Moody 1987). The stages at which the fracture phenomenon occurs can be divided into:

- *Vacuum Initiation*. It occurs by separation of the particle-matrix interface and by fracture of the particle. The deformation to which the nucleation of voids occurs is very dependent on the stress state (Garrison Jr and Moody 1987).
- *Growth of Voids*. After nucleation, the voids expand with a certain volume and shape. The development of this process is governed by plastic deformation. Microvacuum growth models include McClintock's work (McClintock et al. 1966; McClintock 1968) in which the importance of high triaxialities in void growth is highlighted.
- *Vacuum Coalescence*. The voids are joined in such a way that material fracture occurs.

In this regard, the stages involved in failure deformation are highly dependent on the stress state according to various studies (Brigdman 1935; Hancock and MacKenzie 1975; Bao 2005; Barsoum and Faleskog 2007a; Rice and Tracery 1969). One mechanical variable to define the stress state is the hydrostatic pressure, defined by:

$$p = -\sigma_m = -\frac{1}{3}I_1 = -\frac{1}{3}\sigma_{ij} = -\frac{1}{3}(\sigma_1 + \sigma_2 + \sigma_3) \quad (1)$$

where σ_{ij} are the stress tensor components; σ_1, σ_2 and σ_3 are the principal stress components; and I_1 is the first invariant of the stress tensor. The hydrostatic stress is insufficient to characterize the stress state, so it is necessary to introduce the deviatoric stress components. Thus, denoting σ'_{ij} as the deviatoric stress and σ'_1, σ'_2 and σ'_3 as its principal components, then

$$\sigma'_{ij} = \sigma_{ij} - \sigma_m \, \delta_{ij} \tag{2}$$

where δ_{ij} is the unit matrix. The invariants of the deviatoric stress tensor can be expressed as:

$$\begin{gathered} J_1 = 0 \\ J_2 = \frac{1}{2}\sigma'_{ij}\sigma'_{ji} = -\left(\sigma'_1\sigma'_2 + \sigma'_2\sigma'_3 + \sigma'_3\sigma'_1\right) = \frac{1}{6}\left[(\sigma_1 - \sigma_2)^2 + (\sigma_2 - \sigma_3)^2 + (\sigma_3 - \sigma_1)^2\right] \\ J_3 = \det\left(\sigma'_{ij}\right) = \frac{1}{3}\sigma'_{ij}\sigma'_{jk}\sigma'_{ki} = \sigma'_1\sigma'_2\sigma'_3 \end{gathered} \tag{3}$$

and the effective or equivalent stress is defined as:

$$\overline{\sigma} = \sqrt{3\,J_2} \tag{4}$$

The state of principal stresses can be geometrically represented as a vector in a three-dimensional space, where principal stresses are taken as Cartesian coordinates (Fig. 1a). The vector $\overrightarrow{OP}$ is the principal stress vector which represents the stress state (σ_1, σ_2, σ_3). This vector can be broken down into two components: the vector $\overrightarrow{ON}$, which corresponds to the state of hydrostatic stress, and the vector $\overrightarrow{NP}$, which represents the deviatoric term (Eq. 5):

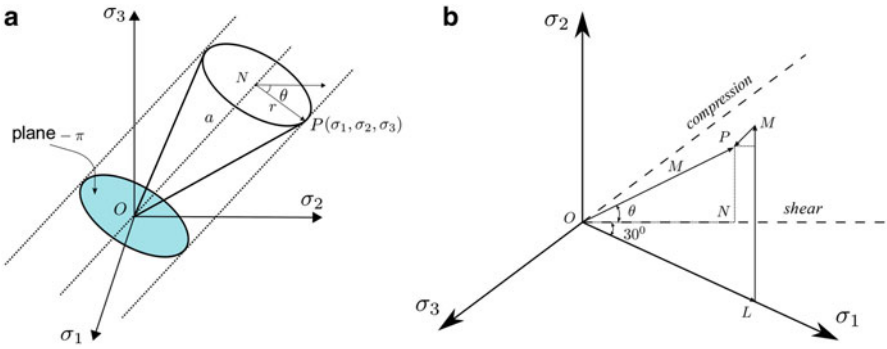

Fig. 1 (**a**) Stress states with the same triaxiality, (**b**) deviatoric stress tensor vector and its components along the projected axes

$$\begin{aligned}\overrightarrow{ON} &= a = \sqrt{3}\sigma_m \\ \overrightarrow{NP} &= r = \sqrt{\frac{2}{3}}\,\overline{\sigma}\end{aligned} \tag{5}$$

To distinguish different stress states having the same hydrostatic stress ratio, the location in the plane π of the projection point P is considered (Fig. 1b). Since each tension axis is inclined relative to the deviatoric plane at an angle of 120° at origin, each projection along the axes is $\sqrt{\frac{2}{3}}$ times the actual length. So, the vector lengths in the deviatoric plane are: $\overrightarrow{OL} = \sqrt{\frac{2}{3}}\,\sigma_1$, $\overrightarrow{LM} = \sqrt{\frac{2}{3}}\,\sigma_2$, and $\overrightarrow{MP} = \sqrt{\frac{2}{3}}\,\sigma_3$. Considering $\sigma_1 > \sigma_2 > \sigma_3$, the vector $\overrightarrow{OP}$ can be divided with respect to the horizontal and vertical components as:

$$\begin{aligned}\overrightarrow{ON} &= \overrightarrow{OL}\cdot\cos 30 - \overrightarrow{MP}\cdot\cos 30 = \sqrt{\frac{2}{3}}\sigma_1\cdot\sqrt{\frac{3}{2}} - \sqrt{\frac{2}{3}}\sigma_3\cdot\sqrt{\frac{3}{2}} = \frac{\sigma_1-\sigma_2}{\sqrt{2}} = r\cos\theta \\ \overrightarrow{PN} &= \overrightarrow{LM} - \overrightarrow{MP}\cdot\sin 30 - \overrightarrow{OL}\cdot\sin 30 = \sqrt{\frac{2}{3}}\sigma_2 - \sqrt{\frac{2}{3}}\sigma_1\cdot\frac{1}{2} - \sqrt{\frac{2}{3}}\sigma_3\cdot\frac{1}{2} \\ &= \frac{2\sigma_2-\sigma_1-\sigma_3}{\sqrt{2}} = r\sin\theta\end{aligned} \tag{6}$$

Consequently, **triaxiality** is defined as the ratio between hydrostatic stress and equivalent stress as reflected in Eq. 7.

$$\eta = \frac{\sigma_m}{\overline{\sigma}} = \frac{\frac{1}{3}I_3}{\sqrt{3J_2}} = \frac{\sqrt{2}}{3}\frac{a}{r} \tag{7}$$

Triaxiality has often been used in ductile fracture as a measure of material ductility and has been directly correlated with failure deformation by numerous researchers (McClintock et al. 1966; Rice and Tracery 1969; Johnson and Cook 1985; Bao and Wierzbicki 2004a).

Bao and Wierzbicki (Bao and Wierzbicki 2004a, b; Bao 2003), as well as Barsoum and Faleskog (2007a), concluded that triaxiality alone was not sufficient to properly describe the behavior of the material at failure. Therefore, they introduced a second parameter, stress state indicator, **Lode's parameter**, which is defined as:

$$\frac{2\sigma_2-\sigma_1-\sigma_3}{\sigma_1-\sigma_3} = \sqrt{3}\tan\theta \qquad \sigma_1 > \sigma_2 > \sigma_3 \tag{8}$$

where θ is Lode's angle. Lode's parameter, μ, was first raised by Walter Lode in 1925 who subjected pipes of various materials (iron, copper, and nickel) to various stress states by means of internal pressure (Lode 1925). Thus, the Lode's parameter, μ, can

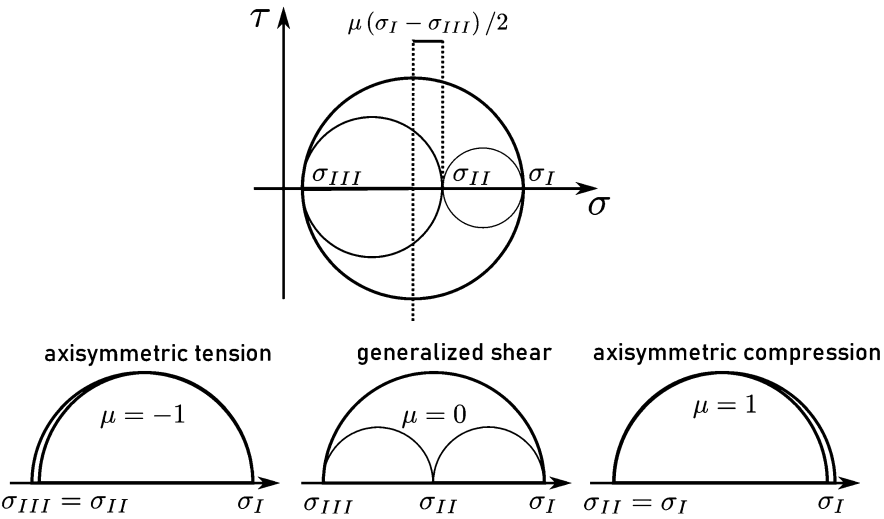

Fig. 2 Representation of the Lode parameter, μ for three cases: tension (μ = − 1); shear (μ = 0); and compression (μ = 1)

be illustrated by Mohr's circle, as shown in Fig. 2, where three cases are founded: tensile (μ = − 1); shear (μ = 0); and compression (μ = 1).

The Lode's angle can be easily related to the third invariant, giving rise to the dimensionless Lode's angle parameter, ξ, as:

$$\xi = \cos\ 3\theta = \frac{27}{2}\frac{J_3}{\bar{\sigma}^3} = \frac{3\sqrt{3}}{2}\frac{J_3}{J_2^{3/2}} \tag{9}$$

The Lode's angle θ can be normalized according to the results of Bai et al. (Bai and Wierzbicki 2008) as:

$$\bar{\theta} = 1 - \frac{6\theta}{\pi} = 1 - \frac{2}{\pi}\ \arccos\ \xi \tag{10}$$

The range of the Lode's parameter, μ, in Eq. 8, and the normalized Lode's angle $\bar{\theta}$, Eq. 10, is $-1 \leq (\mu \text{ or } \bar{\theta}) \leq 1$. It is important to note that triaxiality is a function of the invariants I_1 and J_2, while Lode's angle is related to the invariants J_2 and J_3.

Damage Models

Generally, the study of the ductile fracture phenomenon has been divided into two types of models: coupled damage models and decoupled damage models.

- *Coupled Damage Model*

The constitutive model and the failure criterion are coupled. They are known as models based on Continuum Damage Mechanics (CDM) which were first developed by Kachanov (1986) and later studied by numerous researchers (Chaboche 1988; Alves and Jones 1999). They describe the degradation of the material with an internal state variable, D (Rice 1971). Thus, failure occurs when the accumulated damage reaches a critical value. A detailed summary of these models can be found at Refs. (Khan and Liu 2012; Brünig 2003; Badreddine et al. 2010).

Some models introduce damage within the plasticity criterion, as in the Gurson model (Gurson 1977) for porous materials. An alternative is to introduce the damage into the hardening law, inducing a progressive weakening (Xue 2007a, b). A realistic physical foundation is presented in these models; however, the calibration of the model parameters is rather complex. For example, the Gurson model requires the identification of nine parameters (Teng 2008).

- *Decoupled Failure Models*

The failure is considered an unforeseen event when the stress and deformational state reach a critical level. The criteria developed by McClintock in 1968 (McClintock 1968) demonstrated that failure strain was related to stress state and void geometry. Rice and Tracey in 1969 (Rice and Tracery 1969) proposed a vacuum growth model to show how the stress state affected void growth (Eq. 11):

$$\overline{\varepsilon}_f^p = \overline{\varepsilon}_f^p(\eta) = C_1 e^{-C_2\,\eta} \tag{11}$$

where C_1 and C_2 are material constants; and η is a parameter that considers the stress state, called *triaxiality*, defined as the ratio between the hydrostatic pressure and the von Mises effective stress.

Initially, numerous studies have shown that failure deformation decreases as triaxiality increases (Hancock and MacKenzie 1975; Johnson and Cook 1985; Le Roy et al. 1981). Following up this research field, Johnson and Cook proposed a failure criterion which is widely used nowadays. To this end, they postulated that equivalent plastic strain to failure $\overline{\varepsilon}_f^p$ is a function of triaxiality η. The damage variable *D* in the Johnson-Cook criterion is an integral weighting with respect to equivalent plastic strain (Johnson and Cook 1985), as shown in Eq. 12:

$$D = \int_0^{\overline{\varepsilon}_c} \frac{d\overline{\varepsilon}^p}{\overline{\varepsilon}_f\left(\eta, \dot{\overline{\varepsilon}}^p, T\right)} \tag{12}$$

where $\overline{\varepsilon_c}$ is the equivalent critical plastic strain failure value for an applied load. Failure strain in criterion JC is defined by triaxiality, η; plastic strain rate, $\dot{\overline{\varepsilon}}^p$; temperature, T; and five material constants $D_1 - D_5$ as described in Eq. 13:

$$\bar{\varepsilon}_f = \left[D_1 + D_2\, e^{(D_3\,\eta)}\right] \cdot \left[1 + D_4\, \log \frac{\dot{\bar{\varepsilon}}^p}{\dot{\varepsilon}_o}\right] \cdot \left[1 + D_5\, \frac{T - T_0}{T_{melt} - T_0}\right] \tag{13}$$

where T_0 is the ambient or reference temperature and T_{melt} is the melting temperature. In Eq. 13, the effects of pressure (or triaxiality), strain rate, and temperature are expressed as an independent three-component product.

Generally, it is not possible to analyze the effect of the stress state on the effective plastic strain of failure from experimental results in a straightforward manner. This is why numerical-experimental methodologies are needed (Bao 2005; Bao and Wierzbicki 2004a, b, 2003a; Bai et al. 2006; Mohr and Henn 2007). Traditionally, the uniaxial tensile tests are used to obtain failure strains. These tests can be carried out in axisymmetric or in flat specimens, as Brigdman developed in 1952. The research group of Wierzbicki (Bai and Wierzbicki 2008; Wierzbicki et al. 2005; Wierzbicki 2006), Mohr and Henn (Mohr and Henn 2007; Mohr and Ebnoether 2009), Kim et al. (Kim et al. 2003, 2004, 2007), and Gao et al. (Gao et al. 2005, 2009a; Gao and Kim 2006) developed experimental campaigns using different geometries and loading conditions to obtain failure deformation.

In 2004, Bao and Wierzbicki (2004a, b, 2003a) studied the effective plastic deformation at failure in a wide range of triaxialities $\left(-\frac{1}{3} \le \eta < 2\right)$, as shown in Fig. 3, and proposed a criterion that is reflected in Eq. 14:

$$\bar{\varepsilon}_f = \begin{cases} \dfrac{D_1}{1 + 3\eta} + D_2 & \text{if } -1/3 < \eta \le 0 \\ D_3\eta^2 + D_4\eta + D_5 & \text{if } 0 < \eta \le \eta_T \\ D_6 + D_7 e^{-D_6\eta} & \text{if } \eta_T < \eta \end{cases} \tag{14}$$

where η_T is the transition triaxiality.

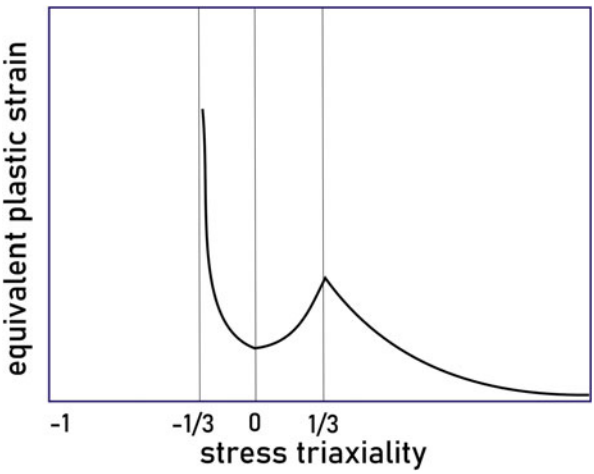

Fig. 3 Dependence of equivalent plastic strain with triaxiality

Bao et al. deduced that, as shown in Fig. 3, the equivalent deformation at failure was not represented by monotonous decreasing function in triaxiality.

Furthermore, these researchers, together with studies by Barsoum and Faleskog in 2007 (Barsoum and Faleskog 2007a), showed that triaxiality was insufficient to adequately describe the behavior of the material under failure conditions. In order to improve the accuracy of the failure prediction criteria and to be able to describe in a more complete way the stress state, the Lode's parameter was introduced. In this regard, Xue et al. (Xue 2007a, b) found that there was a great dependence of the Lode's parameter on ductile failure in metals. Thus, they developed a 3D and symmetrical failure criterion in the space of triaxiality and the third normalized invariant ξ as expressed in Eq. 15. The envelope is shown in Fig. 4b. In addition, the difference between the JC criterion and the Xue-Wierzbicki criterion is shown in Fig. 4, where the dependence of the deformation at failure with the Lode's parameter is clearly observed:

$$\overline{\varepsilon}_f(\eta,\xi) = D_1\, e^{-D_2\,\eta} - \left(D_1\, e^{-D_2\,\eta} - D_3\, e^{-D_4\,\eta}\right)\left(1-\xi^{1/n}\right) \tag{15}$$

where D_1, D_2, D_3, and D_4 are parameters that must be calibrated and n is the hardening coefficient.

However, the symmetric consideration of the failure criterion may be too restrictive, as it is not based on experimental evidence.

Subsequently, Bai (Bai and Wierzbicki 2008) in 2008 simplified the criterion proposed by Xue, assuming that the behavior of the material followed a Mohr-Coulomb failure criterion. A geometric representation of the 3D failure criterion proposed by Bai and Wierzbicki is shown in Fig. 5.

Therefore, the interest of numerous researchers to study the influence of the stress state (*triaxiality and Lode parameter*) on the equivalent plastic deformation at failure is evident. On the one hand, it has been demonstrated that the equivalent plastic deformation at failure (at high values of triaxiality and considering that the material has a great dependence both on the hydrostatic pressure and the Lode's parameter)

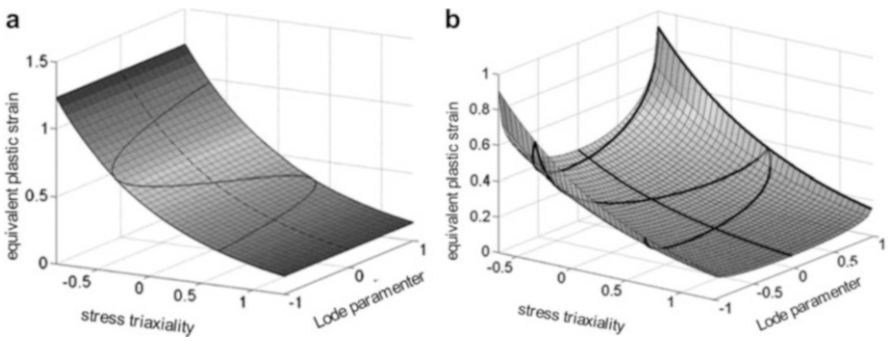

Fig. 4 (**a**) Independent failure criterion of ξ postulated by Johnson and Cook (1985), (**b**) symmetrical 3D failure criterion taking into account ξ postulated by Xue and Wierzbicki (Xue 2007a). (Adapted figure)

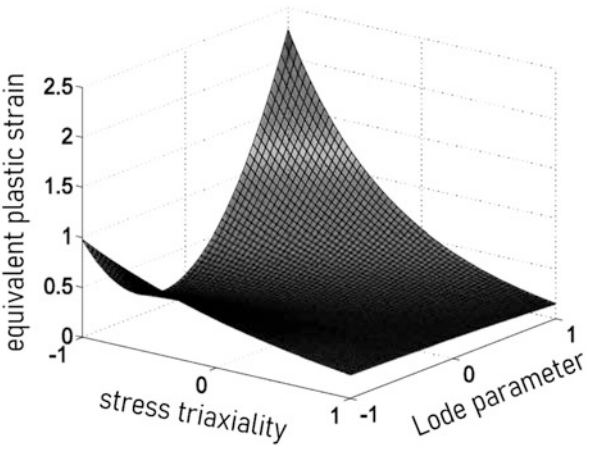

Fig. 5 Failure strain versus triaxiality and Lode parameter proposed by Bai and Wierzbicki (2008) in AA 2024-T351. (Adapted figure)

decreases when the triaxiality value is increased. This can be explained by the major role played by spherical void growth mechanisms during the damage process (Bao and Wierzbicki 2004a). However, at low triaxiality values, the equivalent plastic strain at failure increases with triaxiality, because void elongation becomes the predominant mechanism (Bao and Wierzbicki 2004a). Nevertheless, Bai et al. (Bai 2008) and Gao et al. (Gao et al. 2009a) found that for materials with a weak dependence on hydrostatic pressure and Lode's parameter, e.g., 1045 steel or 5083-H116 aluminum alloy, the equivalent plastic strain at failure decreased with increasing triaxiality. In particular, for the aluminum alloy AA 5082-H116, Gao et al. (Gao et al. 2009a, 2011a; Graham et al. 2012; Zhao and Holmedal 2012) concluded that triaxiality has a relatively small effect on plasticity but a relevant effect on ductile failure deformation. On the other hand, the effect of Lode's parameter on ductile failure is negligible, while in plasticity its effect is important.

Experimental and Numerical Analysis of Ductile Failure

In general, the calibration of a ductile failure criterion in a wide range of triaxiality and Lode's parameter values requires a large campaign of experimental tests using different specimen geometries and loading conditions (Gao et al. 2009a; Mirone and Corallo 2010; Sun et al. 2009). Seidt (Seidt 2010) used 12.7 mm thick plates to calibrate the ductile failure criteria and performed tensile tests on axisymmetric specimens and plastic plane strain specimens, along with experimental tests of tensile-torsion and pure shear. The triaxiality range obtained by Seidt was from -0.157 to 0.855, and the range of the Lode's parameter was from -0.420 to 1. Studies performed by Gao et al. (2009a, 2011b), using axisymmetric specimens and plastic plane strain specimens, predicted that triaxiality depended not only on the geometry of the specimen but also on the plastic behavior of the material.

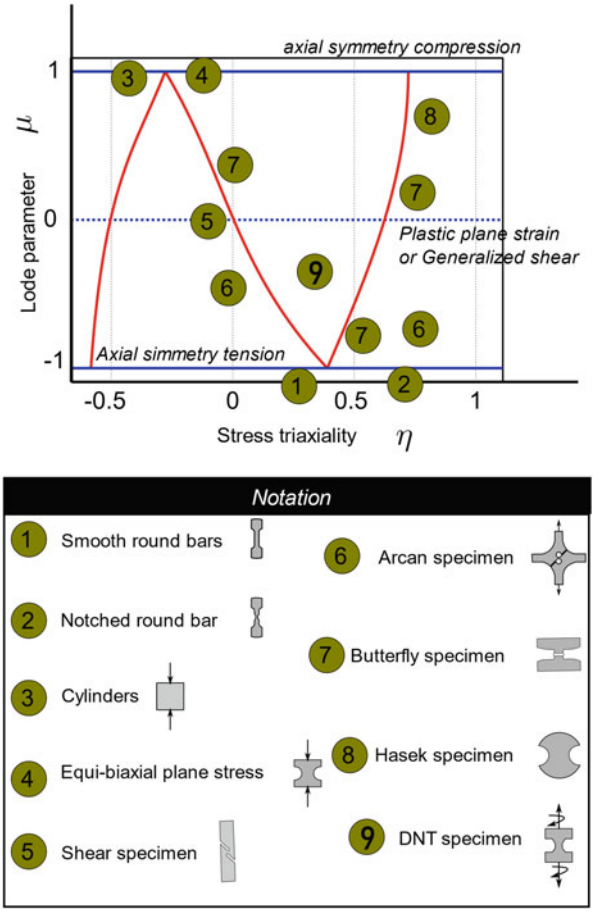

Fig. 6 Conceptual representation of the stress states on the plane of stress triaxiality and Lode parameter

The following is a description of the most commonly used specimens in the literature in the calibration of ductile failure criteria. Bai and Wierzbicki (2008) summarized the specimens used in plasticity and fracture that can only be defined by the set of parameters (η, μ). Figure 6 shows the evolution of η and $\bar{\theta}$ where the common essays are shown.

- *Specimens Subjected to Tension Stresses*

  The most commonly used specimens for the calibration of failure criteria under tension stress conditions in literature are presented next:

  – *Cylindrical Axial Symmetry Specimens*

    Tensile tests on bars with different notches are commonly used to investigate the effect of triaxiality on failure deformation (Johnson and Cook 1985; Mackenzie et al. 1977). Bridgman (1935) was the first to analyze the

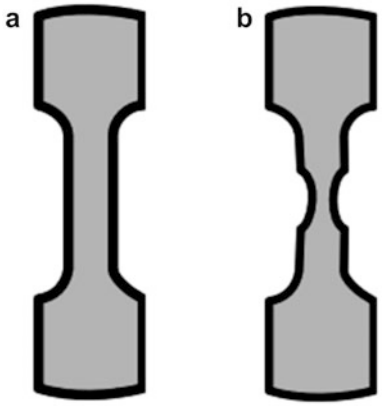

Fig. 7 (**a**) Smooth round bars and (**b**) notched round bar

distribution of stresses in solid bars with different notches and resulted in the expression of triaxiality for the specimen geometry from Fig. 7.

In the center section of the notch, where the fracture begins, Bridgman's expression is:

$$\eta = \frac{1}{3} + \ln\left(1 + \frac{a}{2R}\right) \tag{16}$$

where η is the triaxiality, a is the neck section radius, and R is the neck curvature radius.

The equivalent failure strain for notched axial symmetric bars can be approximated using Eq. 17:

$$\overline{\varepsilon}_f = 2 \ln\left(\frac{a_o}{a_f}\right) \tag{17}$$

The Bridgman's formula and the failure formula are frequently used to calibrate the parameters of the failure criterion (Rice and Tracery 1969; Johnson and Cook 1985; Børvik et al. 2002). However, the lack of consideration of Lode's parameter introduces several difficulties when using this calibration on smooth or notched bars. In this regard, the range of stress state parameters in smooth or notched specimens is $\eta \geq 1/3$ and $\overline{\theta} = 1$ ($\mu = -1$).

– *Grooved Flat Specimens*

Grooved flat specimen is a geometry developed to obtain plastic plane strain states, which corresponds to a Lode's parameter of $\mu = 0$, where the main strain component in the width direction is very small compared to the other two main deformation components. By changing the radius of the notch, different triaxiality values can be obtained for a constant Lode's parameter $\mu = 0$.

To ensure plane strain conditions, the specimens must be properly dimensioned, since the thickness t, width w, and the minimum thickness of the center of the notch t_m (Fig. 8) have a remarkable influence on the stress state. Bai and Wierzbicki used ratios of $w/t_m = 33.25$ and $t/t_m = 3.125$; Benzerga used ratios of $w/t_m = 16.6$ and $t/t_m = 3.0$; and Basaran (2011) performed a numerical study in which they observed that the ratio w/t_m has a significant influence on the evolution of Lode's parameter with plastic strain and that for values greater than $w/t_m = 12.5$, plane strain conditions are obtained. Thus, ratios of $w/t_m = 12.5$ and t/t_m = 2.5 were used.

The analytical expression, Eq. 18, shows that for plane strain plates with or without slots, the loading conditions are $\eta \geq \frac{1}{\sqrt{3}}$ and $\overline{\theta} = 0$ due to the plane strain condition. Comparing notched and smooth bars, the triaxiality range is the same as in slotted plates but with a different $\overline{\theta}$ value. So, Bai and Wierzbicki postulated the expression in Eq. 18 for slotted plates in flat deformation:

$$\eta = \frac{\sqrt{3}}{3}\left[1 + 2\ \ln\left(1 + \frac{a}{2R}\right)\right] = \frac{\sqrt{3}}{3}\left[1 + 2\ \ln\left(1 + \frac{t}{4R}\right)\right] \tag{18}$$

where t is the thickness on the plate. This equation implies that triaxiality is $\eta \geq 1/\sqrt{3}$. In addition, it can be shown that Lode's parameter is zero. The equivalent failure strain in the neck section for a slotted plate like the one in Fig. 19 is defined as:

$$\overline{\varepsilon_f} = \frac{2}{\sqrt{3}} \ln\left(\frac{t_0}{t_f}\right) \tag{19}$$

where t_0 is the initial thickness of the slot and t_f is the fracture thickness.

– *Dog-Bone Specimen*

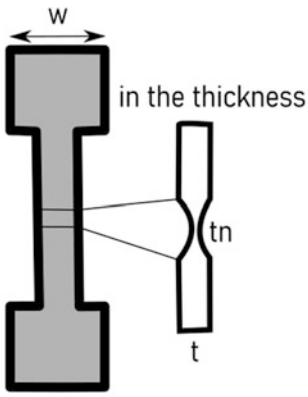

Fig. 8 Grooved flat specimen

The tests with dog-bone specimen (Fig. 9) provide failure strains for high triaxiality values. Triaxiality is a function of the radius of the notch (Eq. 20). For large notch radii, the stress state in the center of the test tube (where strictness occurs) corresponds to uniaxial tension, while the plane strain condition (along the direction of width) is achieved for very small notch radii. In the case of isotropic materials, the variation of the stress state corresponds to a range of triaxial values from 0.33 to 0.58:

$$\eta = \frac{1 + 2\Lambda}{3\sqrt{\Lambda^2 + \Lambda + 1}} \tag{20}$$

where $\Lambda = \left(1 + \frac{t}{4R}\right)$, with R being the radius of the notch and t the thickness of the plate.

- *Specimens Subjected to Compression Stress*

  The most commonly used specimens for the calibration of failure criteria under compression stress conditions in literature are the conventional cylindrical specimen, the notched cylindrical specimen, and the flat specimen whose characteristics are listed below:

  – *Cylinders Compression Test*

    One of the most frequent tests to study fracture is the uniaxial compression test of small cylinders (Fig. 10) using two perfectly horizontal plates. Due to friction between the specimen and the two plates, the barrelling effect occurs during the test about half of the specimen. The test of these specimens provides failure strains for a negative triaxiality range. Depending on the ratio between diameter and cylinder height, different triaxial values are obtained. Bao and Wierzbicki (2003a) used different specimen dimensions and obtained triaxiality values from -0.278 to -0.2235 and Lode parameter from 0.625 to 0.821.

    Friction plays an important role in the *barrelling effect* and in the fracture, which entails a certain difficulty in the realization of numerical simulations.

  – *Notched Cylinders*

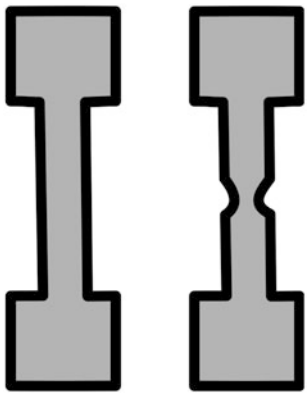

Fig. 9 Dog-bone specimen

Fig. 10 Cylinders

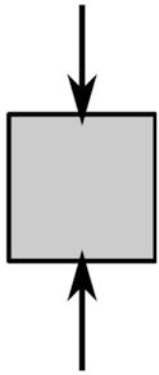

Fig. 11 Notched cylinder

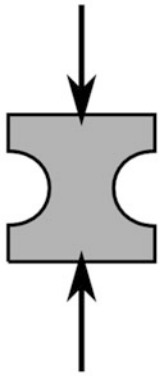

The specimen has a cylindrical geometry with a circular notch in the middle of the height, which causes the deformation to be very localized (Fig. 11). It also avoids the undesirable friction effect that originated in conventional compression specimens.

– *Plane Stress*

Recently, Beese and Mohr (Experimental Investigation 2011) developed a device capable of performing compression tests on flat specimens (Fig. 12). The main problem when performing compression tests on flat specimens is the buckling of the specimen axis. Based on previous studies, these authors developed a device capable of avoiding this phenomenon. They also modified the initial geometry of the specimen and proposed a procedure to correct the effects of friction. This procedure was validated with conventional compression specimens (*for more details see (*Experimental Investigation 2011*)*). This specimen geometry has been used for plasticization, although it is foreseeable that it has a great utility to obtain values of triaxiality – *in a negative regime* – and Lode parameter.

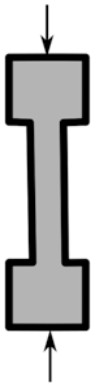

Fig. 12 Plane stress specimens

Fig. 13 Shear specimen

- *Specimens Subjected to Shear*

  The main specimens subjected to shear are the notched one at 45º and the Arcan specimen whose characteristics are listed below:

  – *Shear Specimens*

    Shear specimens tested under tension allow to obtain pure shear states in the central zone associated with triaxiality values close to zero. The geometry is shown in Fig. 13.

    To obtain information on the dependence of triaxiality on the behavior of the material for low triaxiality values, shear specimens are developed with a notch out of the plane between the two central holes.

  – *Arcan Specimens*

    The specimen was modified by Driemeier et al. (2010) is used to obtain information on the material behavior depending on triaxiality. Details of the geometry are shown in Fig. 14. This geometry allows for deformations at low, $\eta \approx 0$, *similar to shear specimens*, and high, $\eta > 0.4$, *similar to notched*

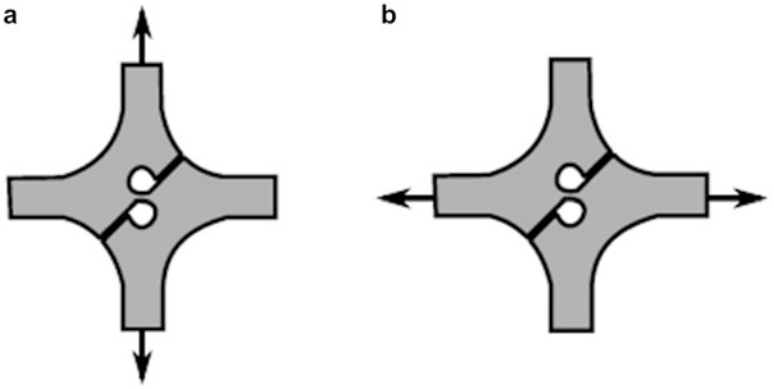

Fig. 14 Arcan specimen. (**a**) Low triaxiality, shear; (**b**) high triaxiality, tension

specimens, triaxiality values depending on the loading direction (Fig. 14). The specimen thickness must be large enough to prevent instabilities due to torsional buckling during the test – Driemeier et al. considered using a specimen thickness of 6.35 mm.

Experimental tests with this specimen geometry can be used to analyze the effect of hydrostatic pressure on the material behavior. However, the effect of the Lode's parameter in the case of plane stress cannot be studied because it depends on triaxiality and is not an independent variable.

- *Equibiaxial Test: Butterfly Specimen*

  Wierzbicki et al. (2005) developed a specimen in the form of a *butterfly* (Fig. 15), which is tested by combining tension and shear to investigate failure at low triaxiality values. This specimen is designed in such a way that the highest strains are located in its central zone, locally increasing the probability of fracture. The length for the calculation section in the central zone is the smallest, as it increases towards the free edges of the specimen. The range of triaxial values and Lode's parameter that can be achieved is $-0.191 \leq 1.01$ and $-0.858 \leq 0.503$; however, it requires a complex experimental device and the manufacture of a complicated specimen to perform the tests. The clamping of the test piece is shown in Fig. 15. The tests performed with this specimen are suitable only for validation, not for calibrating failure criteria (Beese et al. 2010).
- *Punch Tests*

  Punch test or Hasek tests (1978) are normally used to evaluate deformation under biaxial conditions in metal sheets. In this test, a circular flat specimen is embedded in its contour and subjected to the impact of a rigid penetrator by means of a drop tower device (Fig. 16). A lubricant is usually used between the impactor and the sheet metal to avoid possible friction effects. By changing the geometry of the sheet metal, a range of tension state can be covered between uniaxial tension $\left(\eta = \frac{1}{3}, \mu = -1\right)$ and equibiaxial tension ($\eta = 2/3, \quad \mu = \ -\ 1$) (Walters 2009).

Fig. 15 Butterfly specimen

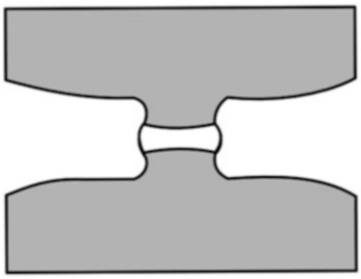

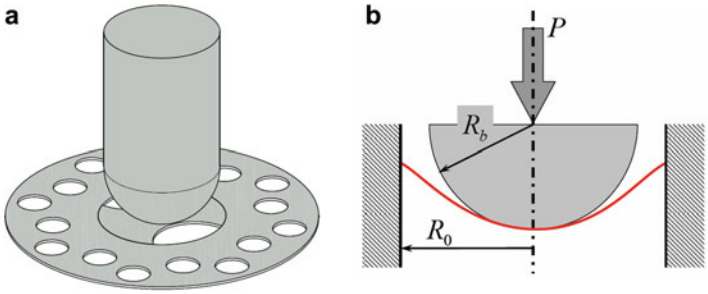

Fig. 16 Punch test

The modification of the specimen's geometry in this type of test allows to obtain different stress states (Fig. 17). Thus, an increase in the circular notch radius, R_n, means a decrease in triaxiality and an increase in the Lode parameter.

- *Test with Modified Shear Specimen*

  By changing the shape of the notch section of the pure shear specimen in such a way that it induces a stress state of combined tension-shear, Fig. 18. With this geometry a triaxiality interval from 0 to 0.4 is achieved (Bao and Wierzbicki 2004a).

- *Combined Tensile-Torsion Tests*

  This type of test consists of subjecting the specimen to combined tension-torsion states in a simultaneous manner. It is worth mentioning the double-notch tubular specimen and the Lindholm tubular specimen, whose characteristics are defined below:

  – *Double-Notch Tubular Specimen*

    Barsoum and Faleskog (Barsoum and Faleskog 2007b; Barsoum et al. 2012) developed the double-notched tube specimen (Fig. 19) to carry out tests in a range from low to medium triaxiality. This type of specimens is loaded with combined tension and torsion maintaining a constant that regulates triaxiality. With this specimen geometry, you can obtain variations in triaxiality in a range of ($0 \leq \eta \leq 1.1$) and of the Lode parameter in an interval

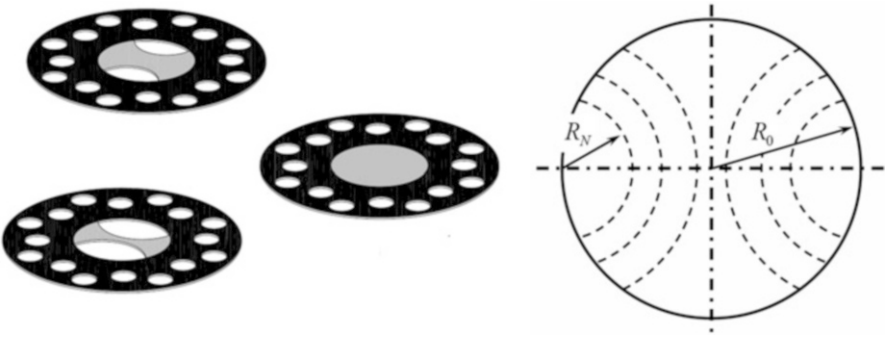

Fig. 17 Types of specimens for dynamic punch tests. Modification of the radius R_n of circular notch allows to obtain different values of the triaxiality and the Lode parameter

Fig. 18 Modified shear specimen

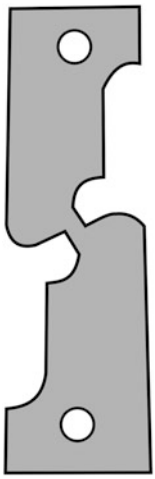

of $(-1 \leq \mu \leq 0)$ using the same specimen geometry. Both the evolution of triaxiality and the Lode parameter are calculated at the center of the notch during the loading process using numerical simulations.

Recently, three different aluminum alloys (5754-H111, 6082-T6, and 2024-T3) have been studied to analyze the influence of the stress triaxiality and Lode parameter on the failure strain (Rodríguez-Millán et al. 2015, 2018a) (Fig. 20). Rodríguez-Millán et al. (2015, 2018a) concluded that the failure strain was not monotonic with decreasing triaxiality in all cases. In fact, in the case of AA 2024, a maximum peak is reached for a triaxiality threshold of $\mu \sim 0.68$ and then decreases again. A similar behavior is found in AA 5754-H111, with a peak value of 0.8. According to several researchers, this behavior can be explained by means of the Lode parameter (Bao and Wierzbicki 2003b).

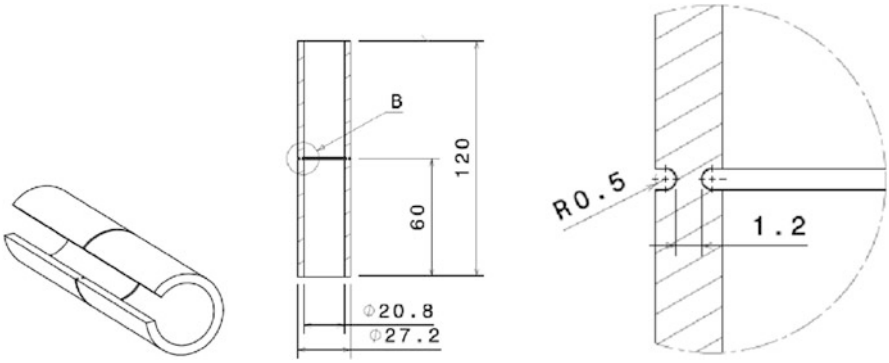

Fig. 19 Double-notch tubular specimen

Void growth and coalescence are the dominant failure mechanisms at high triaxialities, while at low triaxialities shearing between voids becomes the main failure mechanism. These behaviors do not occur in all materials. In this regard, there are examples in the literature where certain metals have a low dependence on the third invariant (Lode parameter), such as 5083-H116 aluminum alloy (Gao et al. 2009b) or DH36 steel (Gao et al. 2010).

Among the three aluminum alloys studied by Rodriguez-Millan and collaborators, AA 5754-H111 showed the highest failure strain, while 6082-T6 presented the lowest values. The maximum values of failure strain for AA 2024-T3 and 5754-H111 were identified to be tensile failure mechanisms, while for AA 6082-T6, the maximum values were determined to be shearing mechanisms. The low influence of the Lode parameter on AA 6082-T6 is similar to that shown by Zhou and collaborators (2012).

The experimental tests conducted by Rodriguez-Millan and co-authors (2014, 2018b) revealed relevant insights into the mechanical performance of three different aluminums (in terms of strength and hardening): AA 2024 shows the highest values for both terms, while AA5754 has a low strength and moderate hardening; AA 6082 presents intermediate values of strength and hardening. As Barsoum et al. (2012) demonstrated, the influence of the Lode parameter increases with the yield stress accompanied by a decrease in hardening.

– *Modified Lindholm Specimen*

Gao et al. (2011b) developed an alternative design to the double-notch tubular specimen used by Faleskog et al. The specimen is a modification to the specimen used by Lindholm et al. (Lindholm 1980) for experimental torsion tests at high strain rate. The dimensions of the specimen are shown in Fig. 21. The main differences with the geometry developed by Lindholm are that the length is longer and the ends are cylindrical rather than hexagonal.

The modified Lindholm specimen is quite similar to the double-notch tubular specimen; they are the same size, but the sections are significantly

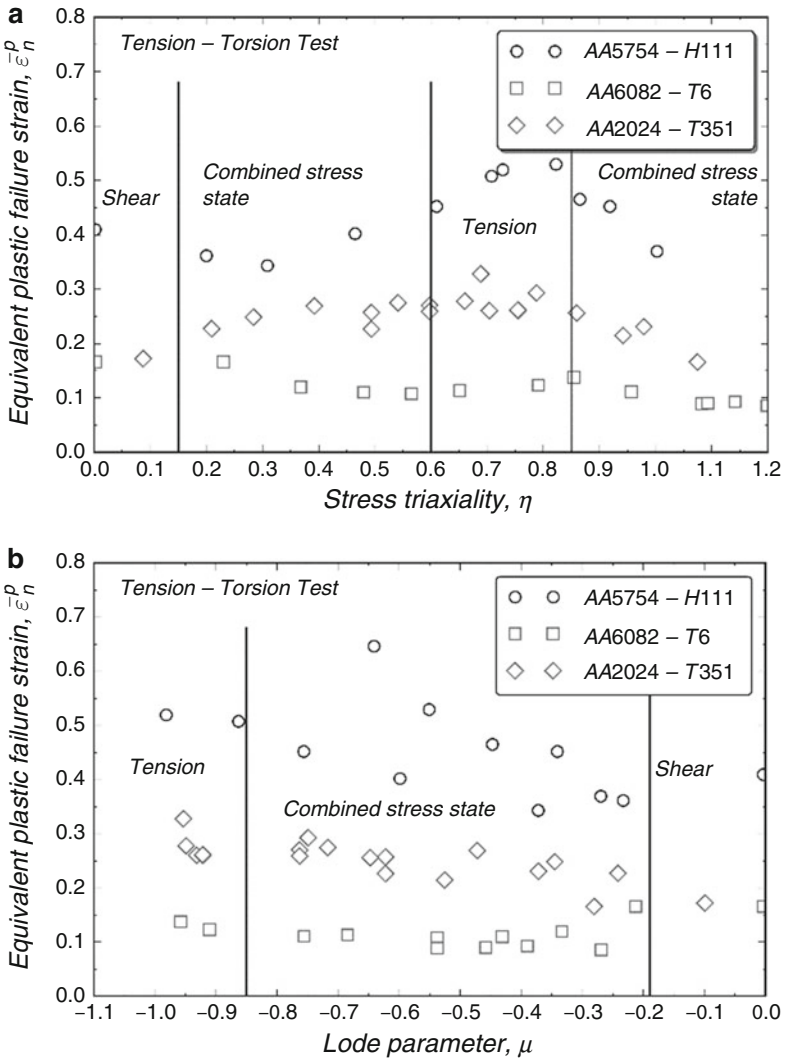

Fig. 20 Failure locus on the space of equivalent plastic strain versus: (**a**) stress triaxiality; (**b**) Lode parameter

different. The specimen developed by Barsoum has both internal and external circular notches, while the modified Lindholm specimen has a single notch on the outside with a trapezoidal groove profile. The height of the notch in the modified Lindholm specimen is 2.54 mm, while in the double-notch specimen, it is circular radius 0.5 mm. The notch width in the double-notch specimen is 1.2 mm at the narrowest point, which is approximately twice the thickness of the notch in the Lindholm specimen (~0.74 mm).

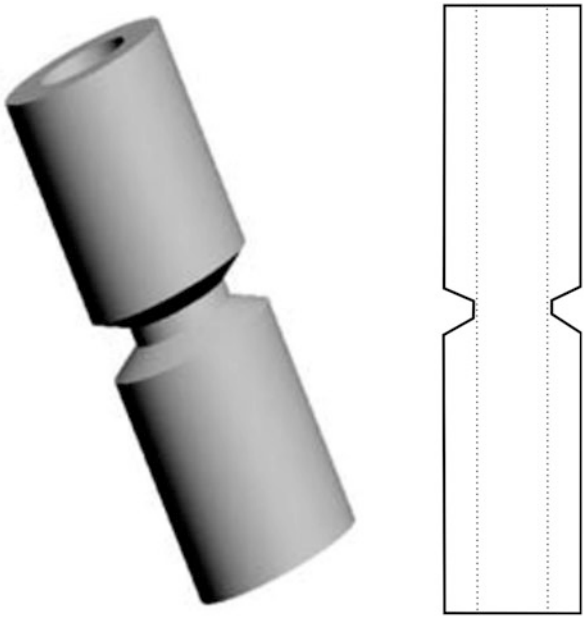

Fig. 21 Modified Lindholm specimen and its transversal area

As the geometry of both specimens is different, the same values of triaxiality and Lode's parameter cannot be achieved with the same state of tensile and torsional loads. As shown in Fig. 22, different ranges of triaxiality and Lode's parameter values are obtained depending on the geometry of the specimen for the same material. Thus, the behavior of the Lindholm specimen covers an interval of $\eta = 0$ and $\mu = 0$, in pure torsion, passing through a state close to that obtained in tension in flat specimens ($\eta = 0.33$ and $\mu = -1$), until obtaining a biaxial state of tension ($\sigma_1 = 2\sigma_2$ and $\sigma_3 = 0$) where $\eta = 0.58$ and $\mu = 0$.

Summary/Conclusions

An analysis of the most common specimens used for characterization of the influence of the stress state on the ductile fracture of metals has been described in this chapter. To this end, the relation between different specimens' geometry and stress states has been presented to obtain tensile, compressive, shear, and mixed states. The wide variety of geometries and their influence on the determination of failure deformation has been proven. These dependences are of critical relevance to determine the fracture process of different components and need to be accounted for modelling tools tackling this problem. In this regard, the stress state dependence on failure deformation is still an open problem where further efforts must be done to incorporate temperature and deformation rate dependences.

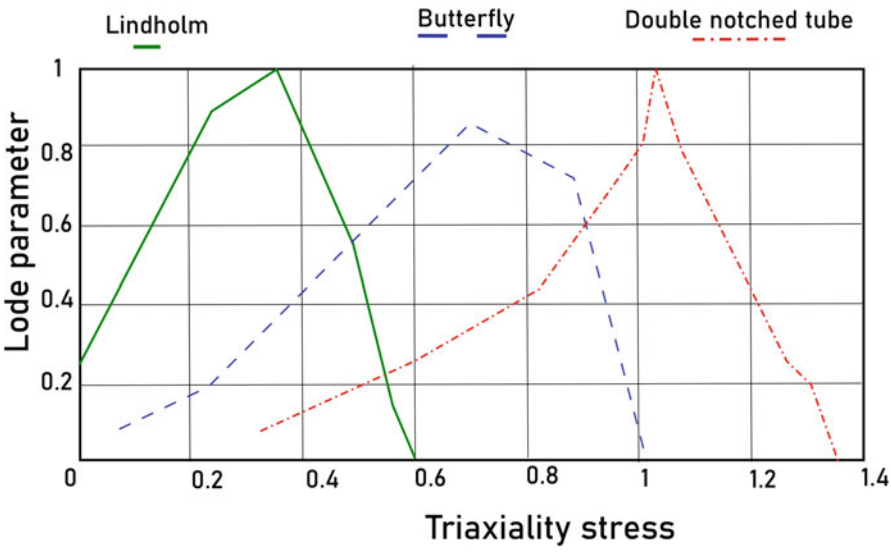

Fig. 22 Comparison of the values of triaxiality and Lode parameter for the modified Lindholm specimens, the butterfly specimen, and double-notch tubular specimen

References

M. Alves, N. Jones, Influence of hydrostatic stress on failure of axisymmetric notched specimens. J. Mech. Phys. Solids **47**, 643–667 (1999)

H. Badreddine, K. Saanouni, A. Dogui, On non-associative anisotropic finite plasticity fully coupled with isotropic ductile damage for metal forming. Int. J. Plast. **26**, 1541–1575 (2010). https://doi.org/10.1016/j.ijplas.2010.01.008

Y. Bai, *Effect of Loading History on Necking and Fracture* (Massachusetts Institute of Technology, 2008)

Y. Bai, T. Wierzbicki, a new model of metal plasticity and fracture with pressure and Lode dependence. Int. J. Plast. **24**, 1071–1096 (2008). https://doi.org/10.1016/j.ijplas.2007.09.004

Y. Bai, Y. Bao, T. Wierzbicki, Fracture of prismatic aluminum tubes under reverse straining. Int. J. Impact Eng. **32**, 671–701 (2006). https://doi.org/10.1016/j.ijimpeng.2005.05.002

Y. Bao, *Prediction of Ductile Crack Formation in Uncracked Bodies* (2003)

Y. Bao, Dependence of ductile crack formation in tensile tests on stress triaxiality, stress and strain ratios. Eng. Fract. Mech. **72**, 505–522 (2005). https://doi.org/10.1016/j.engfracmech.2004.04.012

Y. Bao, T. Wierzbicki, *Prediction of Ductile Crack Formation in Uncracked Bodies* (Massachusetts Institute of Technology, 2003a)

Y. Bao, T. Wierzbicki, *Prediction of Ductile Crack Formation in Uncracked Bodies* (Massachusetts Institute of Technology, 2003b).

Y. Bao, T.A. Wierzbicki, Comparative study on various ductile crack formation criteria. J. Eng. Mater. Technol. **126**, 314 (2004a). https://doi.org/10.1115/1.1755244

Y. Bao, T. Wierzbicki, On fracture locus in the equivalent strain and stress triaxiality space. Int. J. Mech. Sci. **46**, 81–98 (2004b). https://doi.org/10.1016/j.ijmecsci.2004.02.006

I. Barsoum, J. Faleskog, Rupture mechanisms in combined tension and shear – experiments. Int. J. Solids Struct. **44**, 1768–1786 (2007a). https://doi.org/10.1016/j.ijsolstr.2006.09.031

I. Barsoum, J. Faleskog, Rupture mechanisms in combined tension and shear – experiments. Int. J. Solids Struct. **44**, 1768–1786 (2007b). https://doi.org/10.1016/j.ijsolstr.2006.09.031

I. Barsoum, J. Faleskog, S. Pingle, The effect of stress state on ductility in the moderate stress triaxiality regime of medium and high strength steels. Int. J. Mech. Sci., 1–10 (2012). https://doi.org/10.1016/j.ijmecsci.2012.10.003

M. Basaran, *Stress State Dependent Damage Modeling with a Focus on the Lode Angel Influence* (2011)

A.M. Beese, M. Luo, Y. Li, Y. Bai, T. Wierzbicki, Partially coupled anisotropic fracture model for aluminum sheets. Eng. Fract. Mech. **77**, 1128–1152 (2010). https://doi.org/10.1016/j.engfracmech.2010.02.024

T. Børvik, M. Langseth, O.S.S. Hopperstad, K.A. Malo, T. Berstad, Perforation of 12 mm thick steel plates by 20 mm diameter projectiles with flat, hemispherical and conical noses part II: numerical simulations. Int J Impact Eng **27**, 37–64 (2002)

P.W. Brigdman, Theoretically interesting aspects of high pressure phenomena. Rev. Mod. Phys. **7**, 1–33 (1935)

M. Brünig, An anisotropic ductile damage model based on irreversible thermodynamics. Int. J. Plast. **19**, 1679–1713 (2003). https://doi.org/10.1016/S0749-6419(02)00114-6

J. Chaboche, Continuum damage mechanics: part I-general concepts. J. Appl. Mech. **55**, 59–64 (1988)

L. Driemeier, M. Brünig, G. Micheli, M. Alves, Experiments on stress-triaxiality dependence of material behavior of aluminum alloys. Mech. Mater. **42**, 207–217 (2010). https://doi.org/10.1016/j.mechmat.2009.11.012

A.M. Beese, Experimental investigation and constitutive modeling of the large deformation behavior of anisotropic steel sheets undergoing strain-induced phase. Transformation (2011)

X. Gao, J. Kim, Modeling of ductile fracture: significance of void coalescence. Int. J. Solids Struct. **43**, 6277–6293 (2006). https://doi.org/10.1016/j.ijsolstr.2005.08.008

X. Gao, T. Wang, J. Kim, On ductile fracture initiation toughness: effects of void volume fraction, void shape and void distribution. Int J Solids Struct **42**, 5097–5117 (2005). https://doi.org/10.1016/j.ijsolstr.2005.02.028

X. Gao, T. Zhang, M. Hayden, C. Roe, Effects of the stress state on plasticity and ductile failure of an aluminum 5083 alloy. Int. J. Plast. **25**, 2366–2382 (2009a). https://doi.org/10.1016/j.ijpla1s.2009.03.006

X. Gao, T. Zhang, M. Hayden, C. Roe, Effects of the stress state on plasticity and ductile failure of an aluminum 5083 alloy. Int. J. Plast. **25**, 2366–2382 (2009b). https://doi.org/10.1016/j.ijplas.2009.03.006

X. Gao, G. Zhang, C. Roe, A study on the effect of the stress state on ductile fracture. Int J Damage Mech **19**, 75–94 (2010). https://doi.org/10.1177/1056789509101917

X. Gao, T. Zhang, J. Zhou, S.M. Graham, M. Hayden, C. Roe, On stress-state dependent plasticity modeling: significance of the hydrostatic stress, the third invariant of stress deviator and the non-associated flow rule. Int. J. Plast. **27**, 217–231 (2011a). https://doi.org/10.1016/j.ijplas.2010.05.004

X. Gao, T. Zhang, J. Zhou, S.M. Graham, M. Hayden, C. Roe, On stress-state dependent plasticity modeling: significance of the hydrostatic stress, the third invariant of stress deviator and the non-associated flow rule. Int. J. Plast. **27**, 217–231 (2011b). https://doi.org/10.1016/j.ijplas.2010.05.004

W.M. Garrison Jr., N.R. Moody, Ductile Fracture. J. Phys. Chem. Solids **48**, 1035–1074 (1987)

S.M. Graham, T. Zhang, X. Gao, M. Hayden, Development of a combined tension–torsion experiment for calibration of ductile fracture models under conditions of low triaxiality. Int. J. Mech. Sci. **54**, 172–181 (2012). https://doi.org/10.1016/j.ijmecsci.2011.10.007

A.L. Gurson, Continuum theory of ductile rupture by void nucleation and growth: part I – yield criteria and flow rules for porous ductile media. J. Eng. Mater. Technol. **99**, 2–15 (1977). https://doi.org/10.1115/1.3443401

J. Hancock, A. MacKenzie, On the mechanism of ductile failure in high-strength steels subjected to multi-axial stress-states. J. Mech. Phys. Solids **24**, 147–169 (1975)

G.R. Johnson, W.H. Cook, Fracture characteristics of three metals subjected to various strains, strain rates, temperatures and pressures. Eng. Fract. Mech. **21**, 31–48 (1985)

L. Kachanov, On creep stresses in a Bridgman notched bar. Mech. Mater. **5**, 229–234 (1986). https://doi.org/10.1016/0167-6636(86)90020-7

A.S. Khan, H. Liu, Strain rate and temperature dependent fracture criteria for isotropic and anisotropic metals. Int. J. Plast. **37**, 1–15 (2012). https://doi.org/10.1016/j.ijplas.2012.01.012

J. Kim, X. Gao, T.S. Srivatsan, Modeling of crack growth in ductile solids: a three-dimensional analysis. Int. J. Solids Struct. **40**, 7357–7374 (2003). https://doi.org/10.1016/j.ijsolstr.2003.08.022

J. Kim, X. Gao, T.S. Srivatsan, Modeling of void growth in ductile solids: effects of stress triaxiality and initial porosity. Eng. Fract. Mech. **71**, 379–400 (2004). https://doi.org/10.1016/S0013-7944(03)00114-0

J. Kim, G. Zhang, X. Gao, Modeling of ductile fracture: application of the mechanism-based concepts. Int. J. Solids Struct. **44**, 1844–1862 (2007). https://doi.org/10.1016/j.ijsolstr.2006.08.028

G. Le Roy, J.D. Embury, G. Edward, Ashby MF. A model of ductile fracture based on the nucleation and growth of voids. Acta Metall. **29**, 1509–1522 (1981)

A. Lindholm, Large strain high strain rate testing of copper. J. Eng. Mater. Technol. **102**, 376–381 (1980)

V.W. Lode, Versuche uber den einflub der mittleren hauptspannug auf die fliebgrenze. Zeitschrift Fur Angew Math Und Mech **5**, 142–144 (1925)

A.C. Mackenzie, J.W. Hancock, D.K. Brown, On the influence of state of stress on ductile failure initiation in high strength steels. Eng. Fract. Mech. **9**, 167–188 (1977). https://doi.org/10.1016/0013-7944(77)90062-5

F.A.A. McClintock, Criterion for ductile fracture by the growth of holes. J. Appl. Mech. **32**, 363–372 (1968)

F.A. McClintock, S.M. Kaplan, C.A. Berg, Ductile fracture by hole growth in shear bands. Int. J. Fract. Mech. **2**, 614–644 (1966)

G. Mirone, D. Corallo, A local viewpoint for evaluating the influence of stress triaxiality and Lode angle on ductile failure and hardening. Int. J. Plast. **26**, 348–371 (2010). https://doi.org/10.1016/j.ijplas.2009.07.006

D. Mohr, F. Ebnoether, Plasticity and fracture of martensitic boron steel under plane stress conditions. Int. J. Solids Struct. **46**, 3535–3547 (2009). https://doi.org/10.1016/j.ijsolstr.2009.05.011

D. Mohr, S. Henn, Calibration of stress-triaxiality dependent crack formation criteria: a new hybrid Experimental–numerical method. Exp. Mech. **47**, 805–820 (2007). https://doi.org/10.1007/s11340-007-9039-7

J.R. Rice, Inelastic constitutive relations for solids: an internal-variable theory and its application to metal plasticity. J. Mech. Phys. Solids **19**, 433–455 (1971). https://doi.org/10.1016/0022-5096(71)90010-X

J.R. Rice, D.M. Tracery, On the ductile enlargement of voids in triaxial stress fields. J. Mech. Phys. Solids **17**, 201–217 (1969)

M. Rodríguez-Millán, A. Vaz-Romero, A. Rusinek, J.A. Rodríguez-Martínez, A. Arias, Experimental study on the perforation process of 5754-H111 and 6082-T6 Aluminium plates subjected to Normal impact by conical, hemispherical and blunt projectiles. Exp. Mech. **54**, 729–742 (2014). https://doi.org/10.1007/s11340-013-9829-z

M. Rodríguez-Millán, Á. Vaz-Romero, Á. Arias, Failure behavior of 2024-T3 aluminum under tension-torsion conditions. J. Mech. Sci. Technol. **29**, 4657–4663 (2015). https://doi.org/10.1007/s12206-015-1011-3

M. Rodriguez-Millan, D. Garcia-Gonzalez, A. Rusinek, A. Arias, Influence of stress state on the mechanical impact and deformation behaviors of aluminum alloys. Metals (Basel) **8**, 520 (2018a). https://doi.org/10.3390/met8070520

M. Rodriguez-Millan, D. Garcia-Gonzalez, A. Rusinek, F. Abed, A. Arias, Perforation mechanics of 2024 aluminium protective plates subjected to impact by different nose shapes of projectiles. Thin-Walled Struct. **123**, 1–10 (2018b). https://doi.org/10.1016/j.tws.2017.11.004

J.D. Seidt, *Plastic Deformation and Ductile Fracture of 2024-T351 Aluminum under Various Loading Conditions* (The Ohio State University, 2010)

X. Sun, K.S. Choi, A. Soulami, W.N. Liu, M.A. Khaleel, On key factors influencing ductile fractures of dual phase (DP) steels. Mater. Sci. Eng. A **526**, 140–149 (2009). https://doi.org/10.1016/j.msea.2009.08.010

X. Teng, Numerical prediction of slant fracture with continuum damage mechanics. Eng. Fract. Mech. **75**, 2020–2041 (2008). https://doi.org/10.1016/j.engfracmech.2007.11.001

C.L. Walters, *Development of a Punching Technique for Ductile Fracture Testing Over a Wide Range of Stress States and Strain Rates* (Massachusetts Institute of Technology, 2009)

T. Wierzbicki, *Fracture of Advance High Strength Steels (AHSS)* (2006:48)

T. Wierzbicki, Y. Bao, Y.-W. Lee, Y. Bai, Calibration and evaluation of seven fracture models. Int. J. Mech. Sci. **47**, 719–743 (2005). https://doi.org/10.1016/j.ijmecsci.2005.03.003

L. Xue, Damage accumulation and fracture initiation in uncracked ductile solids subject to triaxial loading. Int. J. Solids Struct. **44**, 5163–5181 (2007a). https://doi.org/10.1016/j.ijsolstr.2006.12.026

L. Xue, *Ductile fracture modeling - theory, Experimental Investigation and numerical verification* (Massachusetts Institute of Technology, 2007b)

Q. Zhao, B. Holmedal, The effect of silicon on the strengthening and work hardening of aluminum at room temperature. Mater. Sci. Eng. A (2012). https://doi.org/10.1016/j.msea.2012.11.062

J. Zhou, M. Hayden, X. Gao, An investigation of the strain rate and temperature effects on the plastic flow stress and ductile failure strain of aluminum alloys 5083-H116, 6082-T6 and a 5183 weld metal. Proc Inst Mech Eng part C. J. Mech. Eng. Sci. (2012). https://doi.org/10.1177/0954406212450962

Modeling of Failure Resulting from High-Velocity Ballistic Impact

13

T. Fras

Contents

Introduction 304
Ballistic Impact Experiment 308
Ballistic Impact Testing: Measurement and Observation Techniques 309
Common Kinetic Threats 311
Failure Modes in Metallic Targets 313
Example: Failure Modes in Thick AA7020-T651 Plates 315
Ballistic Limit Curve: The Recht-Ipson and Lambert Approaches 316
Failure Modes Transition 319
Microscopic Observations 320
Modeling Approach to Analyze the Observed Failure Mechanism 322
The Johnson–Cook Flow and Fracture Model 322
Material Characterization 324
Numerical Visualization of the Failure Modes Observed Experimentally 326
Conclusions 328
References 330

Abstract

This chapter presents an example of a high-velocity impact due to which the interacting bodies undergo severe deformation and damage. Based on literature sources fundamental for the topic, types of failure modes characteristic for thick metallic targets perforated by kinetic threats with high impact energy are shown and explained. A concept of the ballistic limit curve is introduced as a feature characterizing an impact configuration. The experimental example shows a range of phenomena occurring during an impact test and a research method aimed for their analysis. On its basis, a visualization of impact-induced changes in the aluminum target microstructure is presented. Furthermore, a finite element method (FEM) numerical analysis of threat–target interactions is performed

T. Fras (✉)
French-German Research Institute of Saint-Louis (ISL), Saint-Louis, France
e-mail: teresa.fras@isl.eu

© Springer Nature Switzerland AG 2022

G. Z. Voyiadjis (ed.), *Handbook of Damage Mechanics*,
https://doi.org/10.1007/978-3-030-60242-0_69

employing a characterization of flow and fracture properties of the materials involved in the impact event. The modeling approach accounts for the strain rate and temperature sensitivity providing an insight into conditions leading to the deformation and failure of the colliding bodies. The given discussion will allow the reader to become familiar with processes modeled in experimental and numerical investigations encountered in the ballistic protection.

Keywords

Terminal ballistics · Penetration and perforation processes · Aluminium · Fragment-simulating projectiles · Strain-rate senisitivity · Impact-induced failure modes · Johnson-Cook models · FEM · Numerical modelling of impacts

Introduction

A variety of complex physical phenomena occurs during a ballistic impact. An impact loading induces in both colliding bodies, a range of phenomena, which severely affects their structures, i.e., elastic-plastic and shockwave propagation, hydrodynamic flow, large strains, heating or frictional effects, strain rate and temperature-affected deformation leading to initiation and propagation of a fracture and the final target perforation (Jonas and Zukas 1978). The target is penetrated by the fast-moving projectile and it may be perforated. The target fails in dependence to the geometric characteristics of the interacting bodies (plate thickness, projectile diameter, and its nose shape), their material properties, and the impact velocity. A generalized effect of an impact in a target may be then presented as a function of the impact velocity, Table 1. To stop the threat and to minimize its effects on the protective shield, armor designers must understand the character of impact-imposed structural deformation of the target and the resulted failure.

During a ballistic impact, strain rates of deformation often exceed 10^5 s^{-1} (Jonas and Zukas 1978). If the material is strain rate sensitive, its structural properties

Table 1 The response of materials to impacts based on Jonas and Zukas (1978)

v_0 [m/ s]	$\dot{\varepsilon}$ [/s]	Launching device	Generalized effect
>3000	$>10^6$	Double-stage gas guns, explosive acceleration	Hydrodynamics
1000–3000	10^5–10^6	Powder guns, double-stage gas guns	Fluid behavior in materials; pressures approach or exceed of material strength; density a dominant parameter
50–1000	10^3–10^5	Mainly powder guns	Strain-rate and temperature-dependent deformation, material strength still important
50–500	10^1–10^2	Single-stage gas guns	Primary plastic
<50	~10^0	Mechanical devices, compressed air gun	Primary elastic, some local plasticity

change considerably with an increase of the strain rate. Knowing that a deformation also involves a local rise in temperature, materials may soften affected by temperature changes and then, undergo severe structural transformation. Upon impacts, most of the structures not only deform but are also damaged. Then, with the advancing strain rate and temperature, the material's failure mechanism also changes.

Deformation and fracture of armor components should be also understood as a process preventing the threat from entering the protected structure. Minimizing the energy transferred from the projectile to the target takes advantage of all mechanisms leading to absorption of the threat energy in the armor by making it do work on the subsequent armor layers by their deformation and breaking (Cooper and Gotts 2005). To stop a threat with high impact energy, armors would have to be thick and then heavy. The ratio of protective efficiency to armor weight is an important factor in the design of modern armored systems, in which light-weight solutions are valued. Therefore, another adequate protection mechanism is often incorporated in armored vehicles, which is a reduction of the projectile lethality by its disruption, fragmentation, shattering, or deflection before it reaches the main armor. This concept is the basis of add-on prearmors and passive/reactive armors against small- and large-caliber kinetic threats.

Because of a complex character of structures interactions during a high-velocity impact, researches in a domain of the ballistic protection are experimental in their nature. However, modern, robust numerical software may be a useful tool helping to obtain an insight into a dynamic event and then, to understand better its physics and effects. Among other computational techniques, the finite-element method (FEM) is popularly used to model a variety of engineering topics. In the explicit schemes to advance the solution in time, FE codes are applicable to calculate wave propagation and material failure resulted from ballistic impacts. There are two general approaches to address impacts scenarios, the Eulerian and Lagrangian FEM formulations. To simulate penetration at impact velocity up to 1000 m/s, the Lagrangian approach is applicable, Table 1. Its advantage is intuitive modeling of an experimental configuration since the computational grid is embedded in the material and deforms with it (Saleh et al. 2016). The Lagrangian codes also have a large number of implemented material models, different functions to describe a contact, libraries of elements with various formulations, and finally, many examples illustrating the successful applications (e.g., Zukas 2004). While modeling penetration and perforation, a significant mesh distortion may cause numerical difficulties in the Lagrangian calculations. To eliminate distorted elements, erosion threshold conditions are applied (there are also other techniques, like a "pilot hole" or node-splitting (Schwer and Windsor 2009)). Element erosion is considered as a numerical technique due to which distorted elements are removed from the mesh according to a specific erosion criterion. As there are many possible criteria to force element deletion, the method is criticized for its arbitrariness. Smoothed particle hydrodynamics (SPH) is a meshless Lagrangian method adequate to model high-velocity impacts as initially, the SPH method was applied to astrophysical problems (Liu and Liu 2010). Currently, the SPH method is often used in the dynamics of fluids and metals and considered as

comparative to the classical FEM (Zukas 2004). The modeled configuration is discretized by nodes, which represent particles with assigned material characteristics. In comparison to the Lagrange formulation, a major advantage of SPH is a material deformation without severe mesh distortion – no algorithm of element erosion is then required. Some authors however reported problems of improper material failure modeling; and SPH may be computationally less efficient comparing to FEM (Schwer and Windsor 2009; Swaddiwudhipong et al. 2010; Fras et al. 2015). Besides SPH, to model impacts at velocities above 1 km/h, the Eulerian or arbitrary Lagrangian-Eulerian (ALE) techniques may also be suitable (Zukas 2004). On the contrary to the Lagrangian approach in which no material flow is allowed across the discretized elements, the Eulerian description is based upon fixed grid points in the spatial domain which positions and volume are invariant in time – thus allowing the material to flow across element boundaries. The Euler and ALE formulations are often used in blast simulations, hypervelocity impact, and to model fluid-structure interactions (Zukas 2004; Saleh et al. 2016).

Next to the choice of the model geometry and a way of its discretization, a numerical code requires a mathematical description of the behavior of the modeled structures. Among several aspects of the mechanics of continuum, which must be involved in the calculations, the attention of the computational code user focuses on a model of the material flow and fracture. Knowing that the penetration and perforation processes involve fast deformation and failure of the interacting materials, the material, mechanical, and thermal properties of the penetrators and targets should be implemented in the computational model. Many constitutive models describe the thermo-mechanical behavior of steels and metals. They are divided generally into three groups: physically based, empirical (phenomenological), and semi-empirical. Physically based constitutive models are grounded in the material microstructure and the micromechanics of defects growth. To represent differences in structures' deformation, the micro-mechanical constitutive relations describe cases of metals with different crystal structures (face-cantered cubic (FCC) and body-cantered cubic (BCC) materials) for static and dynamic applications separately. The flow stress is defined by functions accounting for the thermal activation energy, dislocations interactions mechanisms, and the dislocations dynamics in crystals. The most known examples of the physically based approach are the Zerilli and Armstrong model (Zerilli and Armstrong 1990), the Voyiadjis and Abed model (Voyiadjis and Abed 2005), and the Rusinek-Klepaczko model (Rusinek and Klepaczko 2001). However, an exact determination of physical model parameters may cause problems, and their inaccuracy may lead to a deviation from the macroscopic response of structures (Abed 2010; Abed et al. 2014). Empirical models based on observations of the material response to various loading states are prevalent. Parameters of such models are obtained due to a characterization of the material behavior – a testing procedure should cover maximum possible loading cases to provide an optimal description of the material deformation and failure to different strain states, various strain rates, and temperatures. The Johnson–Cook (JC) flow model is probably the most widely used phenomenological model (Johnson and Cook 1983, 1985). The individual expressions in three sets of brackets represent the

strain hardening, strain rate hardening, and thermal softening and can be calibrated separately using experimental data presented as stress–strain curves at different strain rates and temperatures. A flow model based on the JC approach combined with a Swift–Voce strain hardening function and a nonassociated anisotropic flow rule was recently proposed by Roth and Mohr (2014), who obtained correct results for different advanced high strength steels as well as for titanium alloys (Pack and Roth 2016). Despite their efficiency and simplicity, the JC-based models may fail to present all materials' behavior, since the models' parameters can be not physically justifiable (Rusinek and Klepaczko 2001; Voyiadjis and Abed 2005; Abed 2010). A report on the JC model limitations may be also found in Saleh et al. (2016).

To model a ductile fracture in metal materials, several approaches have been proposed for years. A first porous plasticity model by Gurson (1977) incorporates the effect of a void volume fraction on the plastic flow accounting for void growth and also for the effects of void shearing (Gurson 1977; Tvergaard and Needleman 1984; Nahshon and Hutchinson 2008). Micromechanical fracture models are rarely used in the terminal ballistics – a high cost of material characterization and a localized nature of material responses limits their application potential (Saleh et al. 2016). In engineering, the most popular approaches are based on a damage indicator approach. The plastic material response does not change in these models and when the fracture occurs, a scalar damage indicator reaches a critical value. Stress-state dependent weighting functions derived from the theoretical analyses of McClintock (1968) and Rice and Tracey (1969) are used in phenomenological fracture models (e.g., Johnson and Cook (1985) or Bai and Wierzbicki (2010)). In the fracture model proposed by Johnson and Cook (1985), it is assumed that the increasing hydrostatic pressure leads to increasing nucleation of voids, which is proportional to a decrease in ductility, and then causes a reduction of the fracture strain (Saleh et al. 2016). Based on the phenomenological observations on steel/metal damage processes, the model is dependent on the stress triaxiality, and it also accounts for effects of temperature, strain rate, and strain path in the fracture function. Another empirical approach popularly used in the terminal ballistics calculations was proposed (Cockcroft and Latham 1968). The CL damage criterion does not state the role of the stress triaxiality in the fracture explicitly. Still, it is involved through a limitation of the applicable stresses, i.e., only tensile stresses cause failure (Saleh et al. 2016). The model does not account directly for temperature or strain-rate effects but remains accurate in describing the general processes in damaged metallic structures, i.e., an increase in ductility and reduction in strength with increasing temperature and strain rate. In a series of work (Mohr et al. 2010; Mohr and Marcadet 2015; Roth and Mohr 2014, 2016), the strain rate dependent Hosford–Coulomb model was introduced which incorporates the effects of the stress state and the strain rate on ductile fracture in dependence to the stress triaxiality and the Lode angle parameter. The model treats the temperature as an internal variable and thereby, accounts approximately for the effect of thermal softening without solving the thermal field equations. The effect of the Lode angle parameter on fracture modeling has been discussed. For example, conventional fracture models cannot explain an experimentally observed drop in ductility for

biaxial tension stress states ($0.33 < \eta < 0.667$), which is demonstrated correctly by the Lode angle-dependent theories (Fras et al. 2018, 2019, 2020).

The presented theoretical background is completed by an example of the ballistic impact test, showing ballistic performance of an aluminum alloy AA7020-T651 against fragment-simulating projectiles (FSPs) shot at impact velocities ranging between 900 and 1500 m/s. The exemplary ballistic impact test provides a basis for a discussion on the typical failure modes that may occur in semithick metallic plates. As one of the features describing a threat/target configuration, a concept of the ballistic limit curve is introduced which visualizes a dependence between the initial and residual projectile velocities. With the increasing impact velocities, the failure modes in the perforated 40 mm thick aluminum target plates change from plugging to disking, showing a transition between two failure modes characteristic for metal targets. An analysis of the material deformation and changes in its microstructure shows an interrelation between mechanisms leading to the plate perforation. The stress state proceeding the failure is then modeled numerically by a FEM Lagrangian approach with the use of the phenomenological strain rate and temperature-dependent Johnson–Cook flow and fracture model. Numerical modeling based on a material characterization is often considered as a useful tool contributing to an analysis of an impact event. The provided hereby discussion reveals the complexity and the multidisciplinary character of phenomena which must be addressed in terminal ballistics investigations.

Ballistic Impact Experiment

The ballistic impact is a high-velocity impact, during which in a short time and at high-strain rates the colliding bodies – a threat launched against a protective structure – undergo an extensive deformation and failure. The science which describes effects occurring when a projectile ends its flight hitting a target is known as the **terminal ballistics** (Rosenberg and Dekel 2012). The terminal ballistics is one of four subdomains of the ballistics, which may be concerned as the science or art of designing and accelerating projectiles so that in each phase, they achieve the desired performance (Ballistics 2020). It is the science of mechanics that deals with all stages which concern a shot projectile, its launching, flight, and effects when it reaches a target. Besides the terminal ballistics, the ballistics is divided into the **internal ballistics** (studies on projectiles acceleration), the **transition/intermediate ballistics** (analyses projectile's behavior from the time it leaves the muzzle until the pressure behind it is equalized), and the **external ballistics** (concerns the projectile behavior during its flight).

In particular, the terminal ballistics is the research on:

- Interactions between an object (projectile) which had kinetic energy and lost it due to the contact with a target
- Effects of a threat when it hits and transfers its energy to a target

- Behavior of a target under an impact loading
- Understanding of processes responsible for absorption of the impact energy

It employs experimental, analytical, and numerical investigations to analyze various threat/target configurations aiming to understand their interactions, which in perspective leads to an optimized, lighter, more efficient armor system. Each threat affects differently an impacted armor, therefore, understanding of defeating mechanisms observed in the specific threat/target configuration is crucial to propose new, improved armor designs.

Ballistic Impact Testing: Measurement and Observation Techniques

During years, sets of test methods and procedures have been collected to specify the ballistic testing. Properly performed ballistic impact test requires a laboratory equipped with appropriate devices – a typical impact experiment lasts only some microseconds. The laboratory environment models and simplifies conditions that may occur on battlefields. The ballistic testing laboratory must provide test conditions that are reproducible, reportable, and auditable since the final objective of the testing procedures is a verification of a product designed to protect lives (Crouch 2016).

Ballistic tests are often performed according to a specific standard describing strictly requirements that testing procedures must fulfill (e.g., standards of the NATO Standardization Agreement (STANAG), National Institute of Justice (NIJ), or Association of test laboratories for bullet-resistant materials and constructions (VPAM)). Almost all ballistic test standards specify a protection level to an exact projectile that must be used. In the procedures of protection systems evaluation standards, a threat type and initial conditions of a shot are described (impact velocity, impact angle, the distance where a launcher is positioned, number of shots and their location, applied backing material, etc.). To accelerate a threat, launchers may use the compression or expansion of gases. Pneumatic and light-gas guns use compressed gases, while most other guns and firearms utilize expanding gases liberated by sudden chemical reactions. Rail-guns take advantage of electromagnetic fields to provide a constant acceleration along the entire length of the device, greatly increasing the muzzle velocity. Some projectiles provide propulsion during the flight using a rocket engine or jet engine.

Launchers which accelerate a threat may be different but the most typical one, a powder gun, requires professionally trained pyrotechnical staff. Guns can launch projectiles up to velocities of 2.0 km/s with gun powder, and to 10 km/s when two-stage light gas guns are used, Fig. 1.

An exemplary schema of the ballistic test with a so-called fragment-simulating projectile (FSP) is presented in Fig. 2. The FPSs, embedded in sabots before the launch, are accelerated up to 1100 m/s utilizing a powder gun. Projectiles are packaged in plastic (or aluminum) sabots to stabilize their flight and prevent a metallic contact with the inside of the barrel. Sabots are often made of several

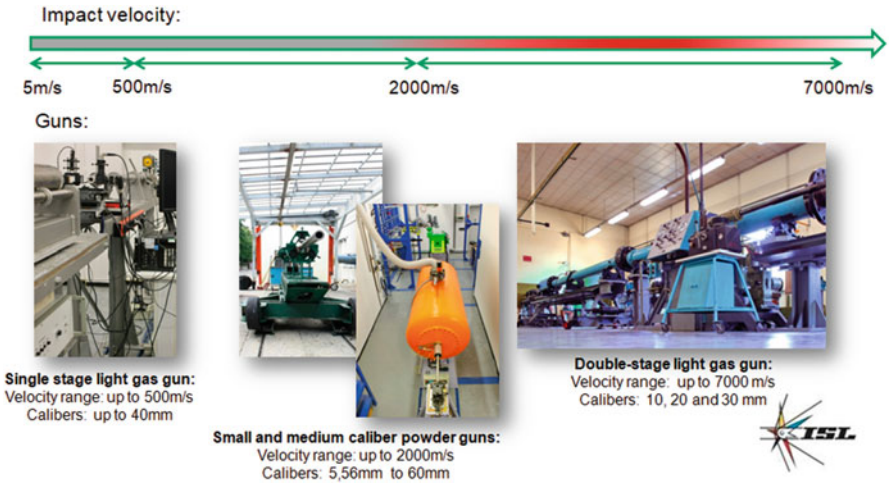

Fig. 1 Exemplary threat launchers available in a ballistic laboratory

parts which separate after leaving the gun barrel. That they do not disturb measurements or the target, a shield stops them before they reach a so-called catch-box. It is a specially designed instrumented target chamber, inside which the target is placed and which contains ports for high-speed photography, pulsed X-ray shadowgraphy, velocity interferometry, or other diagnostic devices. During a ballistic test, it is essential to measure the initial impact velocity of a threat. Knowing this value and the striker mass, an amount of the kinetic energy transferred to a target may be calculated. Most of the laboratories are equipped with devices which allow observations of the threat and target behavior. Typically, high-speed cameras capable of capturing moving images with exposures of less than 1/1000 s or frame rates over 250 frames per second (Balch 1999) or flash X-ray radiography are applied (Citizendium 2020). The impact velocity of the FSP projectile presented in Fig. 2 is measured using a pair of light-barriers; the impact yaw angle and the residual velocity after perforation are obtained with a triple-exposure flash X-ray device (300-kV). A flash X-ray image record a shot, in which a target plate is perforated by a projectile having an initial velocity of 1100 m/s. In this case, a characteristic failure for ductile materials perforated by blunt-nosed projectiles – a so-called plugging, is observed. The image contains three time frames taken before and after the plate perforation. After an impact, all found debris and fragments from the target and projectile are recovered for further analysis. If the target is perforated, the residual velocity of the projectile (or its fragments) is calculated – in the given example, based on a flash X-ray image (as the distance between the registered objects and a time delay is known). "Post-mortem" examination of the target/threat deformation and damage is attainted and may become a basis for a numerical simulation leading to a detailed analysis of phenomena occurred during the penetration and perforation phases.

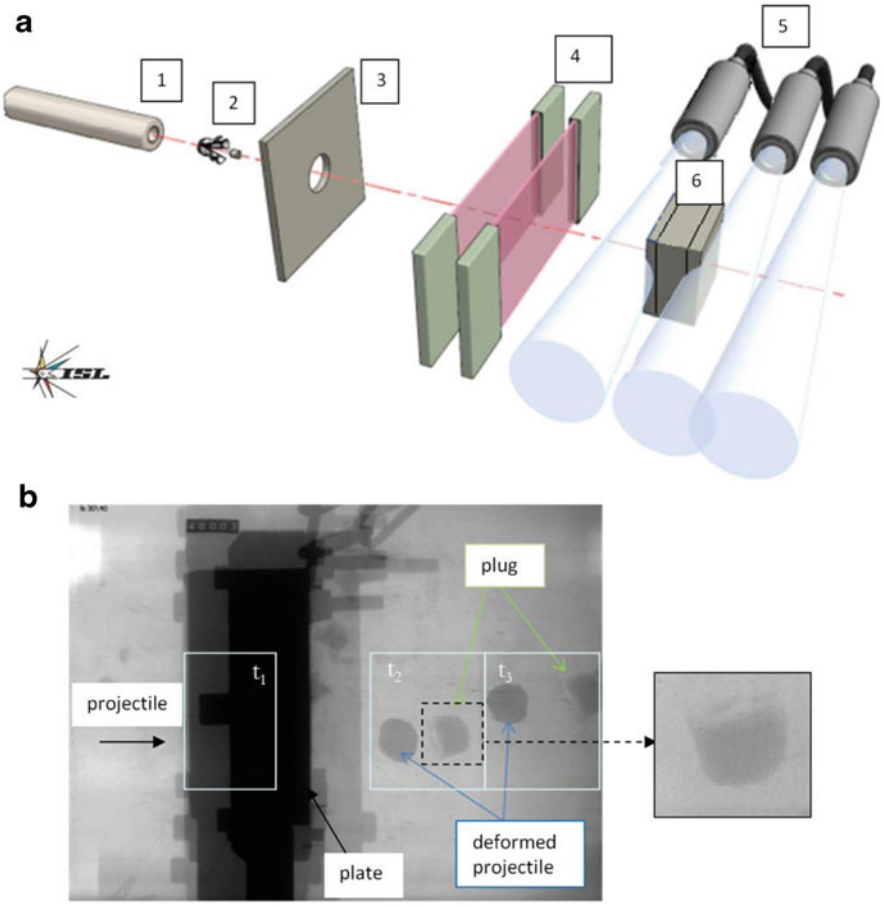

Fig. 2 (**a**) Schematic view of the experimental set-up: (1) barrel, (2) projectile with its sabot, (3) shield against the debris of sabots, (4) optical barriers to measure the impact velocity, (5) flash X-ray tubes, (6) target. (**b**) Flash X-ray image made before (t_1) and after the impact (two time steps: t_2 and t_3) of the fragment simulating projectile with impact velocity close to 1100 m/s (next to it: a magnified ejected material debris: so-called plug)

Common Kinetic Threats

A projectile is any object propelled through the space by an exertion of a force that ceases after launch (Crosby 2002). In general, kinetic threats may be classified in subsequent general groups (Rosenberg and Dekel 2012): **(1)** projectile simulants and surrogates, **(2)** small-arms projectiles, **(3)** fragment simulating projectiles (FSP), **(4)** high-energy projectiles (e.g., kinetic-energy penetrators, shaped charge jets, explosively formed projectiles (EFPs), etc.).

An example of strikers simulating an impact in purely laboratory conditions are presented in Fig. 3a. Since the 1970s, this type of projectiles is popularly used to

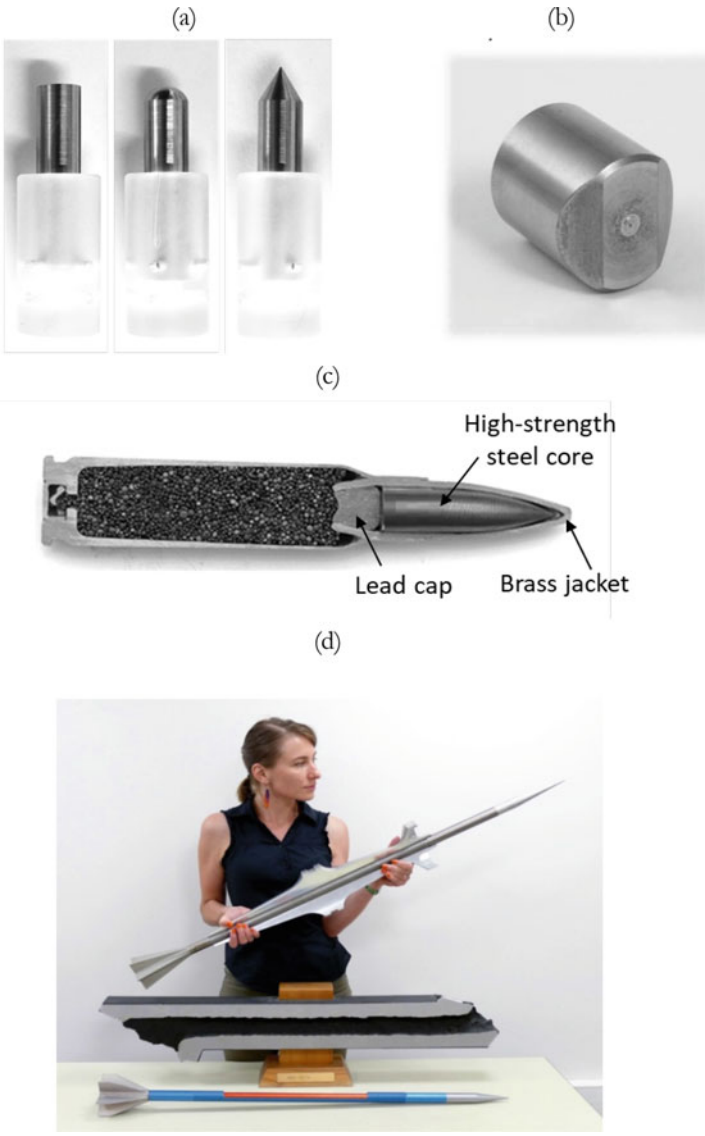

Fig. 3 (**a**) Projectile simulants with different noses (blunt, hemispherical, conical) with diameter 8 mm (**c**) 7.61 × 52 AP P80 projectile in a cartridge case filled with propellant, (**b**) 20 mm fragment-simulating projectile, (**d**) kinetic-energy penetrator. Presented threats are not in a comparable scale

evaluate effects of the projectile's shape on the energy-absorption properties of thin targets and the resulted failure modes. They are accelerated to impact velocities lower than 500 m/s by a pneumatic or light-gas gun. Small- and medium-caliber projectiles (an example of a cal. 7.61 armor-piercing projectile is given in Fig. 3c), which are shot from rifles, machine guns, or powder guns, have either soft (usually

lead) or hard cores made of steel or tungsten carbide. Their diameters vary between 5 and 15 mm and their muzzle velocities are in the range of 600–1000 m/s. Armor-piercing (AP) projectiles have a high hardness core (around 60RC), which is high enough to penetrate and serious damage thicker targets.

Fragment simulating projectiles (FSPs) are the reference penetrators used to simulate artillery shell fragments. Fragment simulators are steel cylinders with an aspect ratio of about 1.0, having diameters in the range of 5–20 mm and hardness of about 30RC. They are usually used for testing new armor concepts which are supposed to stop these fragments at impact velocities of about 1.0 km/s.

An example of a high-energy kinetic projectile is given in Fig. 3b – it is a kinetic-energy penetrator. It a long and thin high-density jet (made with a tungsten alloy or depleted uranium) with the length to diameter aspect ratio ranging between 20 and 30. Accelerated up to 2000 m/s, it transfers large kinetic energy to a narrow target area. In consequence, they can penetrate armor steel targets as thick as their length, so that they are considered as one of the most lethal warheads by which armored vehicles are endangered.

Failure Modes in Metallic Targets

The major factors which influence the impact-resulted failure modes of the target are the material properties of the penetrator and target, the impact configuration geometry, and the projectile velocity. The process of a target penetration is frequently divided into two fundamental phases (Hazell 2015): subhydrodynamic, where the strength of the material is of great importance, and hydrodynamic, where the material strength takes a lower role. During penetration of the target structure, a complex state of stress is introduced by a moving projectile. The target fails according to one of the general mechanisms, which are dependent on its material properties. **Brittle failure** occurs in materials of low fracture toughness, such as a ceramic or glass. Most of the projectile energy is transferred to the target, resulting in its fragmentation. **Gross cracking** is a failure that occurs in hard and resistant materials, such as metals. Cracks propagate at the velocity that is close to the speed of sound in the material, and therefore, the cracking process happens very quickly (Hazell 2015). **Shear plug failure** is characteristic for materials susceptible to (adiabatic) shear processes. The energy required to generate shear bands in metals is quite low and depends on several material properties including the material's propensity to thermally soften and low work-hardening coefficients. This is particularly important as ballistic penetration events are completed in a very short time. Thus, the heat generated through plastic deformation processes does not have time to dissipate and therefore, it can lead to the separation of a shear plug. **Lamination failure (disking, spalling)** occurs when the material is subjected to stress wave reflections, which ultimately results in exceeding the tensile strength of the impacted material. Spalling is a unique failure phenomenon, which takes place under dynamic conditions when shock waves reflecting from the back target surfaces as release waves, which induces high tensions inside the target. If the amplitude of these tensile

waves is high enough, the material fails and spall delamination is created between the target internal layer, no parts of the target are ejected out. General types of failure modes to which thick and semi-thick metallic targets may be subjected have been described in early thematic publications (e.g., Wingrove 1973; Backman and Goldsmith 1978; Woodward 1978, 1984), and also in reviews of the terminal ballistics (e.g., Rosenberg and Dekel 2012; Crouch 2016).

Targets in terminal ballistics are classified according to their thickness as semi-infinite, intermediate, and thin (Rosenberg and Dekel 2012). A semi-infinite target is large enough so that its back surface does not influence the penetration process. The measurements performed with semi-infinite targets are usually postmortem determinations of the final penetration depth, crater dimensions, and characteristics of the residual projectile fragment left at the crater bottom. Experiments with semi-infinite targets focus on the physics of the penetration process rather than simulating actual armor designs. The thickness of intermediate/semi-thick and thick targets is enough to stop the projectile but it is not large enough to prevent damage at its back surface. Interactions with such targets may represent a real projectile/armor encounter. An impact to a thick target may result in a more complicated penetration process since it involves various failure mechanisms which can take place during the interaction. When thin target plates are perforated, they tend to stretch and bend around the impact area, absorbing a significant part of the projectile's kinetic energy through. Less work is required to bend the target forward than to push the material to the side. First published results of impact analysis which aimed to describe typical types of failure modes were performed with samples of the thickness 20–30 mm. Such targets than can be considered as semi-thick compared to the impactor diameter, $2R_{projectile} = H_{plate}$ (Laible 2012).

Assuming no brittle fracture and a rigid striker, the types of failure modes characteristic for metallic targets caused by a pointed-nose and a blunt projectile are presented in Fig. 4. Pointed projectiles push the target material to the sides, causing radial flow or ductile hole formation, Fig. 4a, whereas for flat-ended projectiles, the target material is geometrically constrained to move ahead of the projectile and a shear fracture is necessary to remove a plug in this ductile failure mode, Fig. 4d. The disking fracture, Fig. 4f, occurs along planes which appear to be bands of intense delamination between internal structure layers and which are also intersected by sets of intense shears cracks.

The study by Wingrove (1973) is one of the earliest studies in which nose-shape effects on perforation efficiency was investigated. It was reported that blunt projectiles are the most efficient penetrators (followed by hemispherical and ogive-nosed projectiles) if the target thickness to projectile diameter ratio is less than 1. In Ipson and Recht (1977), it was found that blunt projectiles penetrated the target more efficiently than conical ones when the thickness of the target was moderate. For thin and thick steel targets, however, an opposite trend was observed. An increase of the projectiles nose-radius changes the penetration and perforations mechanisms from ductile hole enlargement to tensile stretching resulting in plate thinning and shearing leading to a plug separation.

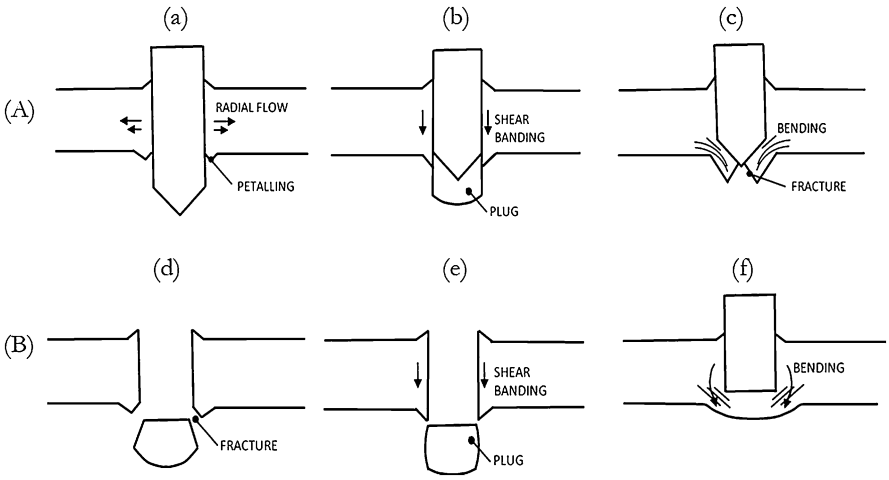

Fig. 4 General types of failure modes for: (**A**) pointed projectile: (a) ductile hole formation, (b) adiabatic shear plugging, and (c) disking; (**B**) blunt projectile: (d) ductile plugging, (e) adiabatic shear plugging, and (f) disking (Woodward 1984)

Example: Failure Modes in Thick AA7020-T651 Plates

The aluminum alloy AA7020-T651 belongs to a group of Aluminum Zinc Magnesium ternary alloys (Al-Zn-Mg alloys) of 7xxx series aluminum. The major alloying element in 7xxx series is Zinc, Magnesium, and a reduced percentage of other elements are added to obtain a higher strength (Embury and Nicholson 1965). The 7xxx series alloys are used in airframe structures, mobile equipment, and other highly stressed parts. The investigated aluminum alloy was delivered as 40 mm thick rolled plates, tempered, and aged in T651 conditions (defined in European Standard NF EN 515), which are cold drawing and artificially aging to the peak strength. In Table 2, some physical properties of the discussed Al alloy are collected (Cobden and Banbury 1994).

To check the ballistic properties of AA7020-T651, the samples are impacted by the fragment-simulating projectiles (FSP) of 20 mm diameter and weight of 53.8 grams represents a 155 mm artillery shell fragment, Fig. 3b. It has a flat, chiseled nose possessing a chiseled angle of 35°. Projectiles consist of AISI 4340-H steel alloy, heat-treated to the hardness of HRC 30 $\pm$ 1, Table 2. The ballistic impact test, in which these projectiles are used, is mandatory for the evaluation of protection levels 4 and 5 in the component acceptance tests (Stanag AEP55). By altering the velocities, after a number of shots an estimation of the ballistic limit can be obtained, which is the speed up to which the material defeats the fragment.

Table 2 Some physical properties of AA7020-T651 (the target material) and 4340-H steel (the projectile material)

	AA7020-T651	Steel 4340-H
ρ [kg/m^3]	2770	7850
G [GPa]	25	80
E [GPa]	71	205
v [−]	0.3	0.3
C_p [J/kg.K)]	910	475
Hardness	138 HV ± 2	30 HRC ± 1

Ballistic Limit Curve: The Recht-Ipson and Lambert Approaches

Based on the conservation of the energy and momentum, in Recht and Ipson (1963), an analytical equation Eq. (1) to model dependence between the initial and residual velocities of the projectile after the target perforation was proposed. Further assumption concerned a striker, which must remain undeformed. The ballistic limit curve is determined for a specific target-projectile configuration.

$$v_R = \begin{cases} 0 & 0 \le \mathrm{v}_0 \le v_{bl.\,\mathrm{exp}} \\ a\left(v_0^p - v_{bl.\,\mathrm{exp}}^p\right)^{\frac{1}{p}} & \mathrm{v}_0 > v_{bl.\,\mathrm{exp}} \end{cases} \tag{1}$$

where v_0 and v_R are the initial and residual velocities, a and p are constants, $v_{bl.\mathrm{exp}}$ is the ballistic limit velocity. The ballistic limit velocity is then the greatest impact velocity the target can withstand without being perforated; its value is obtained by tests. The parameter a is related to the mass of the projectile and the plug. The parameter p in the Recht–Ipson model equals 2.0.

$$a = \frac{m_{\mathrm{projectile}}}{m_{\mathrm{projectile}} - m_{\mathrm{plug}}} \tag{2}$$

The parameters a and $v_{bl.\mathrm{exp}}$ are determined from a nonlinear regression fit of the data, with a constrain that a must be lower than 1. To obtain a unique set of the parameters, the minimum of two residual perforation velocities is required. The Recht–Ipson model provides also a visualization representing the dependence between the initial and residual projectile velocities.

In Recht and Ipson (1963), it was observed that a perforation process may be described as an inelastic impact which occurs in two steps. Firstly, a primary deceleration of the fragment inside the target which causes an acceleration of the pushed plug mass – the projectile and the plate plug attain similar velocities. Impact interface pressures arising from the acceleration-deceleration process are extremely high and are responsible for deformation of the fragment and plate material. The impact interface cannot move through a distance greater than $(\mathrm{v}_0/\mathrm{v}_C)^T$ during the first step (v_0 – initial impact velocity, v_C – sonic velocity, T – plate thickness) unless wave-propagation velocities exceed the sonic velocity in the material. Therefore, at the usual ballistic impact velocities, the first step is completed early in the perforation. A contribution to the interface pressure (relatively small) is supplied by the

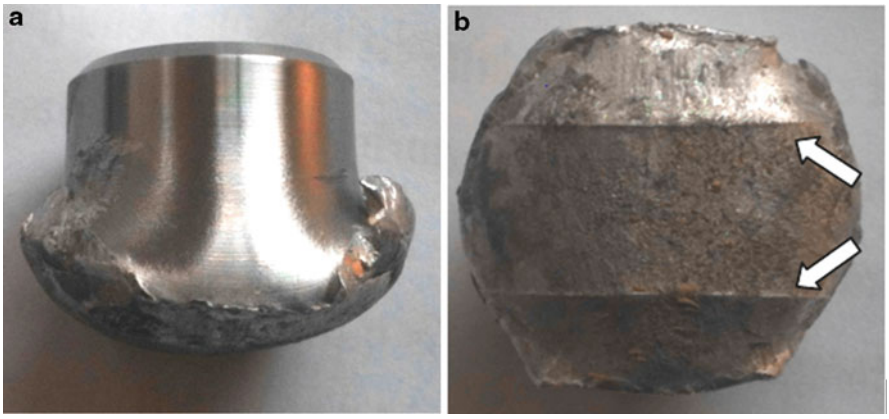

Fig. 5 20 mm FSP projectile after the impact with an initial velocity of 1100 m/s: (**a**) the side view and (**b**) the bottom view

resistance to shear at the plate plug periphery. In the second perforation phase, the plug is sheared from the plate. The kinetic energy of the fragment-plug mass provides the necessary energy to overcome this shear resistance. The Eq. (1) presented for predicting residual velocities of penetrating projectiles, also pointed-nose armor-piercing rounds, is valid at impact velocities near the minimum perforation velocity. As the velocity increases, the shear strength of the material becomes less important than the lateral inertia pressure. Thus, the residual-velocity equation becomes inadequate.

The Recht–Ipson analytical model is valid only if the plastic deformation of the projectile during impact is negligible. If this condition is not fulfilled, the Lambert formulation is used to describe ballistic curves resulted from impacts of deforming projectiles (e.g., Børvik et al. 1999). In that case, the p parameter differs from 2.0.

In the analyzed impact configuration, the FSPs are deformed after perforation of 40 mm thick aluminum plates. The length of the FSP decreases and its "nose" diameter increases with the impact velocity – projectiles are mushrooming, Fig. 5. The mass of the residual projectiles has been only slightly reduced – its average values vary between 52 and 53 g.

In Fig. 6a, the ballistic limit curve for the 40 mm thick plates made of AA7020-T651 impacted by 20 mm FSPs is shown, as a relation between the initial (v_0) and residual (v_R) projectile velocities. In the discussed impact test, the ballistic limit velocity is close to $v_{bl.\exp} \approx$ 890 m/s. The experimental data are fitted to a model proposed to Eq. (1). Due to a curve fitting by using the method of least squares with the assumption that the ballistic limit velocity is taken directly from the experimental data, the model constants, a and p, are estimated as $a = 0.85$ and $p = 1.23$.

In Fig. 6b, an amount of the initial kinetic energy converted into work carried out by the system target/projectile is plotted. For each shot, the work is calculated, which results in one point of the graph, presented as a function of the initial kinetic energy. Each point corresponds to the adequate residual velocity also presented versus the

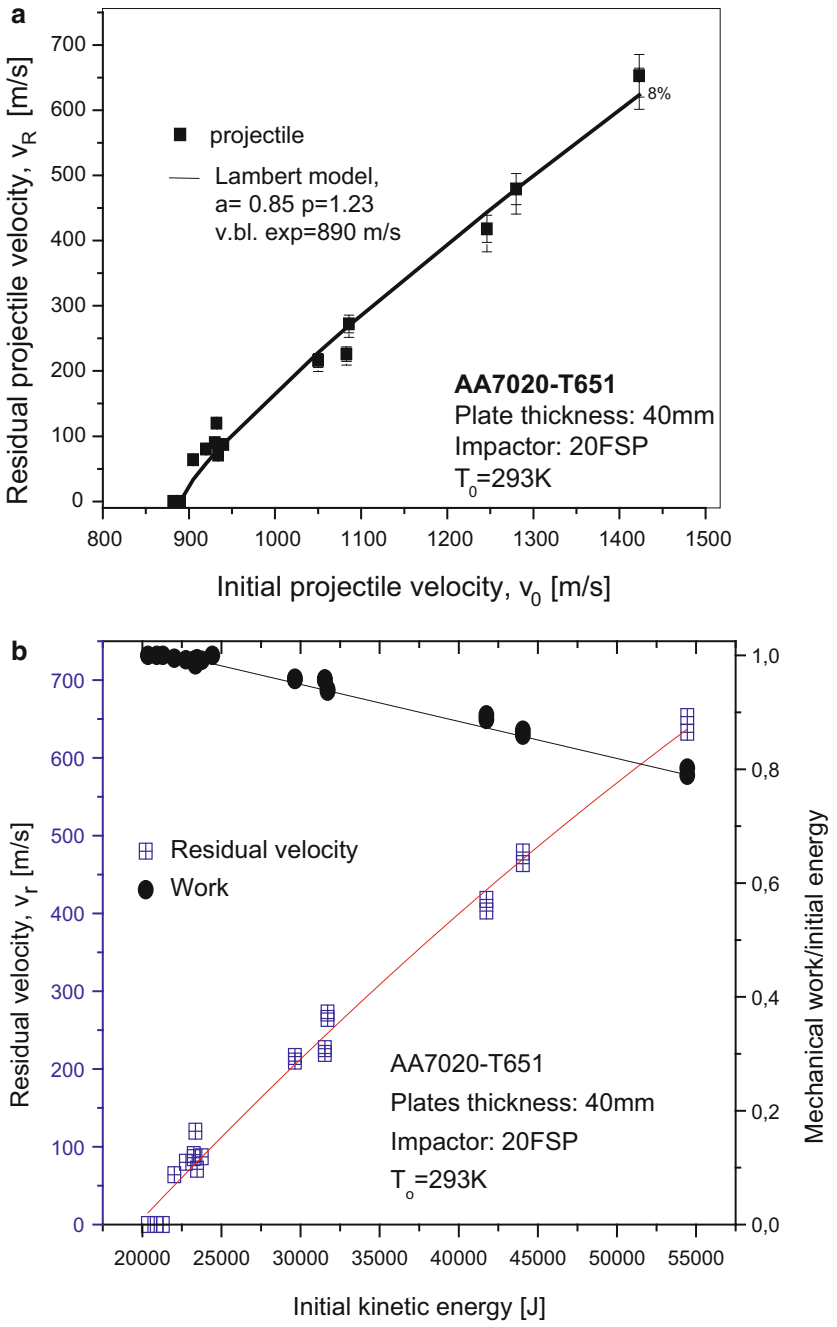

Fig. 6 (**a**) Ballistic curve for 40 mm thick plates of AA7020-T651 impacted by 20 mm FSPs and (**b**) energy dissipation presented for the corresponding values of residual velocity

initial kinetic energy. The energy absorbed by the system is calculated using the principle of energy conservation with the assumption that the residual mass of the projectile is unchanged. It is observed that with the increasing impact velocity, the mechanical work carried out by the target – projectile system decreases. In cases when projectiles stuck in the plates, the work is calculated as equal to 1. For the highest value of impact velocity, it is noticed that almost 80% of the energy is lost due to the processes related to the perforation of the plate (i.e., heat, fracture, acoustic wave, plastic deformation of plate and projectiles, etc.). For the target plates, made of a similar Al alloy (AA7075-T651), which are much thinner (12 mm), the dissipation of energy is not higher than 50% of the projectile initial kinetic energy. It is estimated that 10–15% of the total energy dissipates in a projectile plastic deformation (Pedersen et al. 2011).

Failure Modes Transition

Due to the performed series of impact with the increasing impact velocities, it is observed that the global deformation mode of the targets changes from a ductile hole enlargement, through a mechanism of highly localized shear around the projectile nose leading to plugging and then with an increase of impact velocity, disking, dominated by bending stresses, Fig. 7. **The plug** is a part of a metallic material which is sheared out from a target plate by a projectile – it is characteristic for ductile materials stroke by blunt projectiles (e.g., Wilkins 1978; Woodward 1984, 1990). **The disking** leads to a material separation within horizontal planes, parts of such planes are ejected from a target, it is determined by the local inhomogeneities or anisotropies resulting from the rolling texture of a material.

Disking fracture is observed on rear layers of the targets which were shot at impact velocities higher than 1200 m/s. A remained plate thickness, below the projectile, is stretched and bent forward. A series of thin internal material layers (resulted from the subsequent processes of rolling during the material

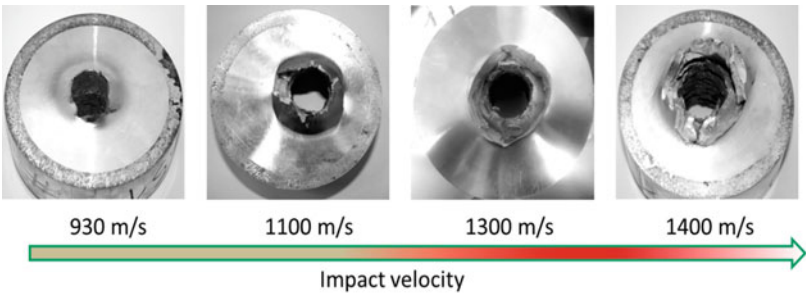

Fig. 7 The transition of the failure modes from plugging to disking with the increasing impact velocity

manufacturing) is stretched and cracks occur laterally between their interfaces. From the rear side of the target plate, fragmented ring-shaped pieces are ejected out. The failure of the target plates due to plugging is observed when impact velocities are lower than 1200 m/s. In the initial stage of the deformation, the target material is pushed to the sides and compressed in front of the projectile forming a bulge on the rear plate surface. Large shear strains develop in the target on the periphery of the projectile which pushes the target structure directly in front of its deforming nose. When highly localized shear bands occur, the process changes to a plug formation, where the final step is a plug ejection. Shear zones are present in a material when a rate of work softening due to the heat generated in plastic flow is greater than a rate of work hardening (Woodward 1984).

In the tested AA7020-T651 plates, the main stress state leading to the plate failure changes from the shear- to tensile-dominating state. An interrelation and transition between failure modes depend on the impact velocity and microstructural influences, which was also noted by Woodward (1984). According to Woodward (1984), the bending deformation occurs with a compensating shear in the plane of the impacted plate. The bending failure takes place more readily over a series of thin layers characteristic for the rolling material texture and affects them one after another rather than affecting a larger part of the structure at once. In the plugging failure, shear bands nucleate independently toward the rear surface of the target and at the same time propagate to join up circumferentially. Once a shear band reaches the rear surface, slip along this band occurs very easily. The impacts at lower velocities result in a localized deformation with high shear rates, which reduces the energy of deformation and in consequence, favors a plug formation. An amount of energy consumption during homogenous and adiabatic shearing is smaller, thus the impacts with lower velocities cause plugging failure mode. Disking occurs at higher impact velocities, since larger amounts of energy are necessary to break through a series of internal material layers.

Microscopic Observations

Figure 8 shows microstructural details of the zone close to the penetration channel in the plate affected by plugging. The plug is already formed but not fully ejected. Undeformed grains with the size 10–20 μm have elongated shapes typical for the rolled texture.

Inside the penetration channel, the image (*) depicts cracks being are a kind of "delamination" between internal layers of the aluminum structure. The orientation of these cracks is common with the material structure. Due to extensive stretching of \lower material parts by the moving projectiles, voids between material layers occur (the detail B). Continuing tensile deformation leads to a coalescence of voids and the growing cracks separate the horizontal parts (i.e., internal layers resulting from the rolling processes) of the material. Tensile stresses lead to the interlayer crack development, which in case of the faster impacts results in a separation of disking rings from the bottom part of the plates.

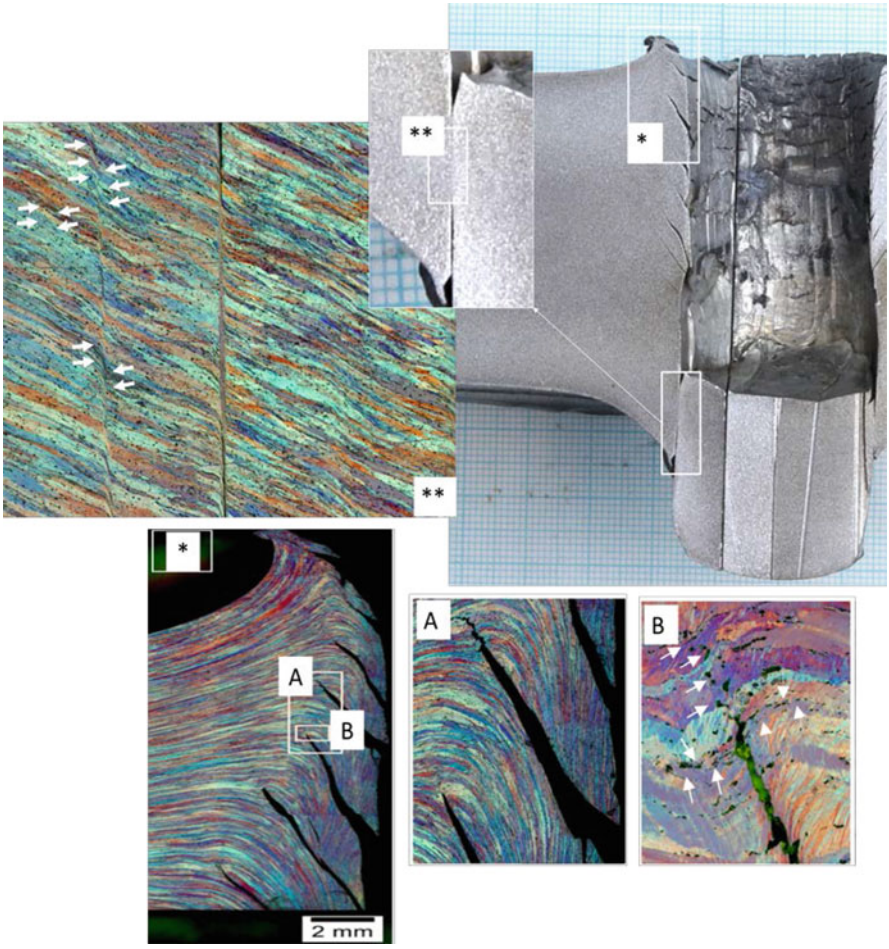

Fig. 8 LEM image of the plate perforated at the velocity of 900 m/s – plug formation

The crack visible on the image (**) results from an intensive, localized shear band. A narrow fracture follows a whitish etching trace, which is a sign of a localized adiabatic shear band (presence of an adiabatic shear band may be additionally proven by micro-hardness measurements; locally in the band the hardness increases). An adiabatic shear band is a thermo-mechanical instability predominantly determined by a thermal softening of the metallic material and by a preceding work hardening (Dodd 1992). Adiabatic shear bands result in a narrower localization of the deformation than the homogenous shearing (Pintat 1988). Adiabatic shearing is proceeded by a homogenous shearing, Fig. 9. And this phase is also visible on the micrograph (indicated by arrows). In Fig. 9, the first part of the curve represents an increase in the energy consumption caused by higher shear rates. The slope of the

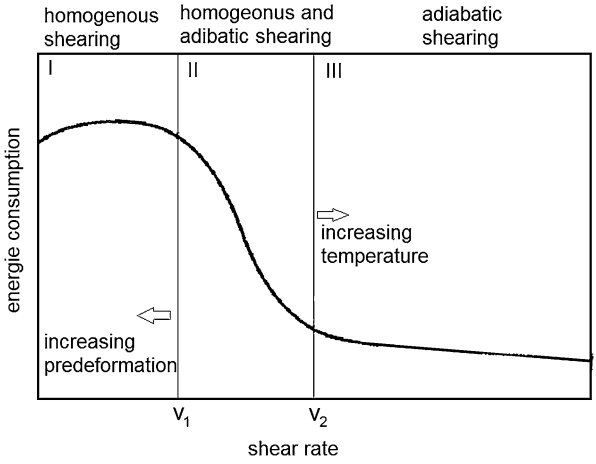

Fig. 9 Shear development with an increasing strain rate based on Pintat (1988)

curve caused by the adiabatic shearing is shifted to higher shear rates by locally increasing temperature, while a predeformation shifts the slope to lower shear rates.

To obtain a more detailed analysis of penetration and perforation processes observed during impact loadings, numerical simulations of the performed experiment may be a useful method, under the assumption that the implemented models are correctly chosen and their parameters are identified and validated based on a detailed material characterization.

Modeling Approach to Analyze the Observed Failure Mechanism

In Fras et al. (2015), a description of microstructural, mechanical, and thermal properties of the AA7020-T651 aluminum alloy identified due to a quasi-static and dynamic material testing is presented. Based on the results, a thermo-viscoplastic constitutive model and a fracture criterion are determined by using the Johnson–Cook models (Johnson and Cook 1983, 1985) is calibrated. This material model is implemented in numerous FE codes, including the explicit software LS-Dyna dedicated to analyze the material behavior under dynamic loadings.

The Johnson–Cook Flow and Fracture Model

To describe a ballistic impact numerically, the material model implemented into calculations should account for the material responses to deformation at large strains ε, increasing strain rates $\dot{\bar{\varepsilon}}_p$, and temperatures T; as well as for an accumulation of damage causing the structural failure. The numerical analysis is carried out basing on the material model of visco-plasticity and ductile damage being a modified

formulation of the classical Johnson–Cook model developed for impacts, wave propagation, and penetration/perforation problems. It is the flow function coupled with the fracture model – as shown in Eq. (3). The detailed theoretical considerations describing the model background are presented in Berstad et al. (1994) and Børvik et al. (2001). The model formulation is implemented in Ls-Dyna as *MAT_MODIFIED_JOHNSON_COOK (*MAT_107) (Ls Dyna Manual). The model is developed for isotropic materials and includes the linear thermo-elasticity, visco-plasticity, and ductile damage. The elastic and visco-plastic properties of the material depend on the temperature generated by adiabatic heating under high strain-rate loading conditions without any thermo-mechanical coupling with the surroundings.

$$\sigma\left(\varepsilon, \dot{\bar{\varepsilon}}_p, T\right) = (1-D)(A + B\varepsilon^n)\left(1 + \frac{\dot{\bar{\varepsilon}}_p}{\dot{\varepsilon}_0}\right)^C \left[1 - \left(\frac{T - T_0}{T_m - T_0}\right)^m\right] \tag{3}$$

where D is the damage variable, A, B, C, m, n are material constants, $\dot{\varepsilon}_0$ is a user-defined reference strain rate, and T_0, T_m are the reference and melting temperatures.

The parameter $D = 0$ for an element in an initial state of loading and for an element which failed $D = 1$. The evolution of damage is related to irreversible strains; therefore, it may be taken as a function of the accumulated plastic strain. The function of damage evolution is based on the Johnson and Cook fracture strain model and the extended version of the Johnson–Cook damage evolution is given by Eq. (4). The model is coupled with a damage evolution rule and with an element-kill algorithm, which enables a crack growth during the penetration process. As the damage variable D reaches its critical value D_C, a damaged element is removed from the mesh.

$$\dot{D} = \begin{cases} 0 & \text{when } \varepsilon < p_d \\ \dfrac{D_C}{\varepsilon_f - p_d}\dot{\bar{\varepsilon}}_p & \text{when } \varepsilon \geq p_d \end{cases} \tag{4}$$

where D_C is the critical damage, p_d is the damage threshold, and ε_f is the fracture strain.

The fracture strain ε_f in the Johnson and Cook model is a function dependent on the stress triaxiality η defined as a ratio between the hydrostatic stress σ_m and the effective stress σ_{eq}, strain rate $\dot{\bar{\varepsilon}}_p$, and temperature T. The modified expression of the Johnson–Cook fracture strain is given in Eq. (3).

$$\varepsilon_f\left(\eta, \dot{\bar{\varepsilon}}_p, T\right) = \left[D_1 + D_2 \exp\left(D_3\eta\right)\right]\left[1 + \frac{\dot{\bar{\varepsilon}}_p}{\dot{\varepsilon}_0}\right]^{D_4}\left[1 + D_5\frac{T - T_0}{T_m - T_0}\right] \tag{5}$$

where ε_f is the equivalent plastic fracture strain, $D_1 - D_5$ are fracture model constants.

As it is shown by Eqs. (3), (4), and (5), the JC model includes the effects of the strain path, strain rate, temperature, and the stress triaxiality in the flow stress and

fracture strain. Consequently, the degradation of a material and its damage contribute to the localization of plastic deformation in the penetration process. The damage evolution is fully coupled with the constitutive equation, which is an advantage of the proposed approach.

Material Characterization

To investigate the behavior of the AA7020-T651 alloy, several tests were performed under various loading conditions in a quasi-static and dynamic range of strain rates. The tests of dynamic compression are obtained using the technique of the split-Hopkinson pressure bar. Additionally, the data are completed by the results of the Taylor impact test, Fig. 10a. The results of the Taylor impact test characterize the behavior of AA7020-T651 for strain rates greater than 10^4 s^{-1}. Low strain rates have a minor influence on the flow stress of the tested alloy, thus the stress is a linear function of strain rates. After the point of transition, which occurs for a strain rate close to 1500 s^{-1}, the strain-rate sensitivity increases rapidly and the slope becomes more pronounced. An increase in temperature leads to a decrease in stress values when the loading is quasi-static, Fig. 10b. This effect is stronger at higher temperatures. A reduction in the flow stress is more distinct when the temperature increases from 373 K to 473 K; while, for lower temperatures, the flow stress decrease is less significant.

The stress triaxiality is defined as a ratio $\eta = \frac{\sigma_m}{\sigma_{eq}}$ (σ_m – hydrostatic stress and σ_{eq} – effective stress) and is used to describe material deformation (Rice and Tracey 1969). The triaxiality shows the influences of an amount of plastic strain which a material may undergo before a ductile failure occurs. The experimental data are collected from the quasi-static tensile tests of AA7020-T651 notched specimens. A notch in the geometry of a standard tensile specimen increases the stress level and reduces the strain to fracture (Bridgman 1952). The induced stress triaxiality increases with the decreasing notch radius, which reduced ductility of tested specimens and leads to a localized fracture. Figure 10c presents the average fracture strain as a function of the initial stress triaxiality at room temperature. The fracture strain depends considerably on the stress triaxiality, which is governed by the notch geometry – the fracture strain is reduced for the increasing stress triaxiality. At the high-stress triaxiality, the final rupture is caused by the internal void nucleation mechanism (Bao and Wierzbicki 2004). The high plastic strain level promotes nucleation of voids, inclusions by particle cracking, or interface decohesion. If the specimen is subjected to a shear dominated stress state then the failure mode is characterized by shallow small elongated shear dimples, which are oriented along the shear direction. This rupture mode involves internal shearing between voids and is favored at the lower stress triaxiality values. Due to the dominating shear stress state, the voids will undergo substantial shearing, which is characteristic for the low-stress triaxiality which impedes the growth of the formed voids (Bao and Wierzbicki 2004).

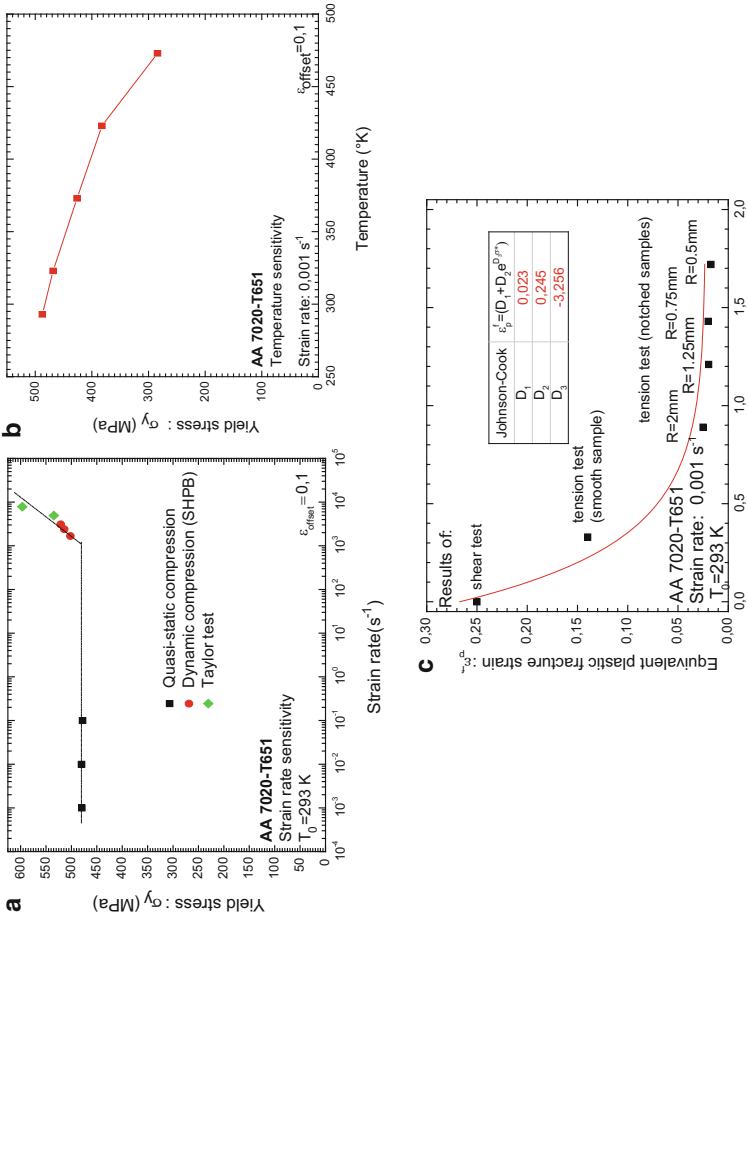

Fig. 10 AA7020-T651 material characterization: (**a**) strain-rate sensitivity, (**b**) temperature sensitivity, (**c**) average fracture strain versus stress triaxiality

Numerical Visualization of the Failure Modes Observed Experimentally

Numerical modeling is applied to find out why and how things work and which processes occur during a modeled loading. Simulations may also predict possible failure and finally, they may be used to prototype new structures. According to a specified goal, a simulation accounts for a different level of complexity and accuracy in a representation of an analyzed configuration. Whether the objective is to model a large-scale armored vehicle or a structural impact, a keen understanding of the physics and mechanics, as well as an appropriate choice of a computational tool to model and to evaluate received results are required. To obtain valuable results, a simulation should represent well a discretized domain, the boundary, and initial conditions and finally, a mathematical model of the materials' behavior, which accounts for main features of their deformation and failure. Impact calculations induce demands for high strain rate materials data and accurate descriptions of materials dynamic properties and their failure at high loading rates.

Basing on the results of material testing summarized in Eqs. (3) and (5), the parameters *MAT_ 107 – the modified Johnson–Cook model are calibrated and validated (see Fras et al. 2015a, b), Table 3. This model formulation is often applied to simulate various impact scenarios (e.g., Børvik et al. 1999, 2002a, b). The physical constants of material AA7020-T651 are given in Table 2. Since the parameters D_4 and D_5 of Eq. (5) have not been obtained experimentally their values are taken from (Brar et al. 2009), which describes another alloy of the series 7xxx, AA7075-T651 (set 1).

The simulation represents the discussed in the previous paragraphs impact configuration. The model parts are meshed by 350,000 elements (8-node constant-stress solid elements with one integration point and stiffness-based hourglass control). The contact between the target and projectile is modeled using an *Eroding_surface_to_surface algorithm, which allows for element deletion. Friction between parts is not accounted for.

Figure 11a shows a comparison between the numerically obtained representation of the plate which failed due to the impact with the initial velocity 1300 m/s and its experimental equivalent. The computational result does not repeat regular cracks inside the penetration channel but their initiation takes place. On the front face of the plate, the crater is created with a flanged edge. The parts of the target structure close to the rear face are torn away in a way, which resembles closely the disking failure

Table 3 Parameters of the Johnson–Cook models for AA7020-T651

AA7020-T651	A [MPa]	B [MPa]	n	C	m	T_m [K]	Reference strain rate [s^{-1}]
	295	260	1.65	0.000889	1.26	880	0.0001
	D_1	**D_2**	**D_3**	**D_4**	**D_5**	**D_c**	**P_d**
Set 1	0.011	0.42	−3.26	0.016	1.1	1.0	0
Set 2				0.15	16.8		

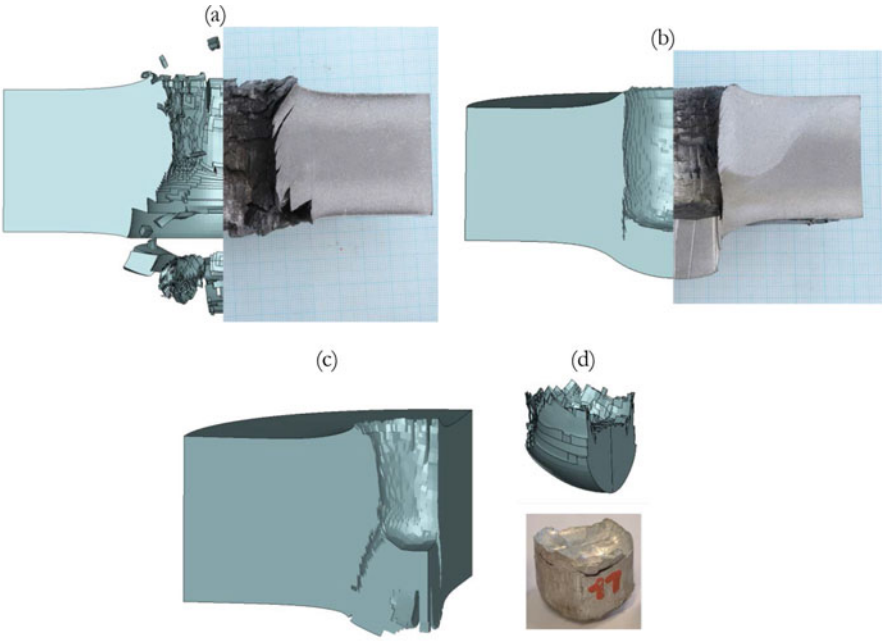

Fig. 11 Modeling of: (**a**) disking failure, $v_0 = 1300$ m/s (**set 1**), (**b**) plugging failure $v_0 = 1100$ m/s (**set 2**), (**c**) plugging failure $v_0 = 1100$ m/s (**set 1**); (**d**) comparison between the plugs obtained experimentally and numerically (half of the simulated plug geometry, **set 1**)

mode obtained experimentally. Although the disking failure mode is simulated with an acceptable accuracy by the model with the set 1 of the fracture parameters, it does not model correctly the plugging failure mode for a lower impact velocity. The numerical visualization of an impact at 1100 m/s is depicted in Fig. 11c. A plug-like debris is formed and separated from the target but it has a shape differing much from the experimental result, Fig. 11d.

In consequence, another simulation is performed with the conditions identical as in the first approach but this time, the D_4 and D_5 parameters of the fracture strain are taken based on the analysis of Clausen et al. (2004) and collected in Table 3 as the set 2. By using the fracture model, in which the D_4 and D_5 are 10 times higher ($D_4 = 0.15$ and $D_4 = 16.8$) than in the previous example, it is possible to obtain a plug of the shape close to the experimental ones, Fig. 11b and d. In the case of this second set of D parameters, despite a properly modeled plugging, a disking failure mode at higher impact velocities is unachievable. The numerical calculation does not model cracks inside the channel, either.

Two different failure modes are obtained by varying the function of the fracture strain, Eq. (5). The parameter D_4, which describes the influence of strain rate on the strain at fracture, affects the initiation of the crack. In the first case, when $D_4 = 0.016$, the disking failure mode is obtained; in the second case, when $D_4 = 0.15$, the complete plug separation is observed. The calculations showed that in the analyzed

case, the failure mode is insensitive to changes applied to the parameter D_5 (the temperature influence). In the case of AA7020-T651, the temperature does not affect the material failure in such an extent as the strain rate, which can be proven also by the analysis of the function describing the fracture strain (Fras et al. 2015a, b). The effective fracture strain Eq. (5) is presented as the function of the stress triaxiality and the D_4 parameter, where the temperature and the strain rate are constant and equal to 293 K and 1000 s^{-1}, respectively. Such defined functions of the strain at fracture are presented in Fig. 12a. The parameter D_4 is considered a function variable, which values vary between −0.4 and 0.4. In Fig. 12b, values of ε_f are determined for the triaxiality equal to 0, i.e., corresponding to the shear process (D_4 is a variable). It is observed that an increase of strain at fracture has an exponential character with the increasing values of D_4. In the case of the values of D_4 used in the calculation, i.e., 0.016 and 0.15, the calculated ε_f increased almost three times, which must affect the sensitivity of the model to the loading and the crack onset.

In the case of the aluminum alloy AA7020-T651, the parameter D_4 has a large influence on the calculated fracture strain. Changes in the D_4 parameter result in distinctly different values of fracture strain. Consequently, a way of the damage accumulation differs (via direct dependency between D_C and ε_f, Eq. (4)), which leads to changes in the resulted failure mode. Strain evolution leading to the final failure of a target plate depends on many factors (like geometry, strain accumulation, mesh erosion, etc.). A change of one parameter influences the whole system of calculations. The above analysis shows the importance of a proper material characterization in a description and understanding of ballistic impacts, and in particular in their numerical analysis.

Conclusions

The discussion presented in the preceding paragraphs shows the complexity of phenomena analyzed in terminal ballistic laboratories. Ballistic impacts concern various projectile/target combinations with complicated geometries, multimaterial components and a variety of mechanisms during penetration and perforation. Understanding the character of the projectile–target interactions and the resulted deformation and damage is crucial to propose improved protection. Comprehension of the physical phenomena may be gained basing on a precisely performed impact test supported by modern measurement and observation techniques. An experimental result is often complemented by its numerical simulation, characterization of material and dynamic properties of the colliding bodies and an analysis of changes in the damaged microstructure. Recent years of development of computational techniques prove that a numerical simulation may add credibility to the experimental outcome. It should be remembered, however, that as each tool, numerical modeling has its limitations and should be used with consideration.

The presented example of a ballistic impact study completes the given theoretical background. It concerns an impact test of thick aluminum plates shot by projectiles with initial velocities higher than 1000 m/s. The experimental case exemplifies

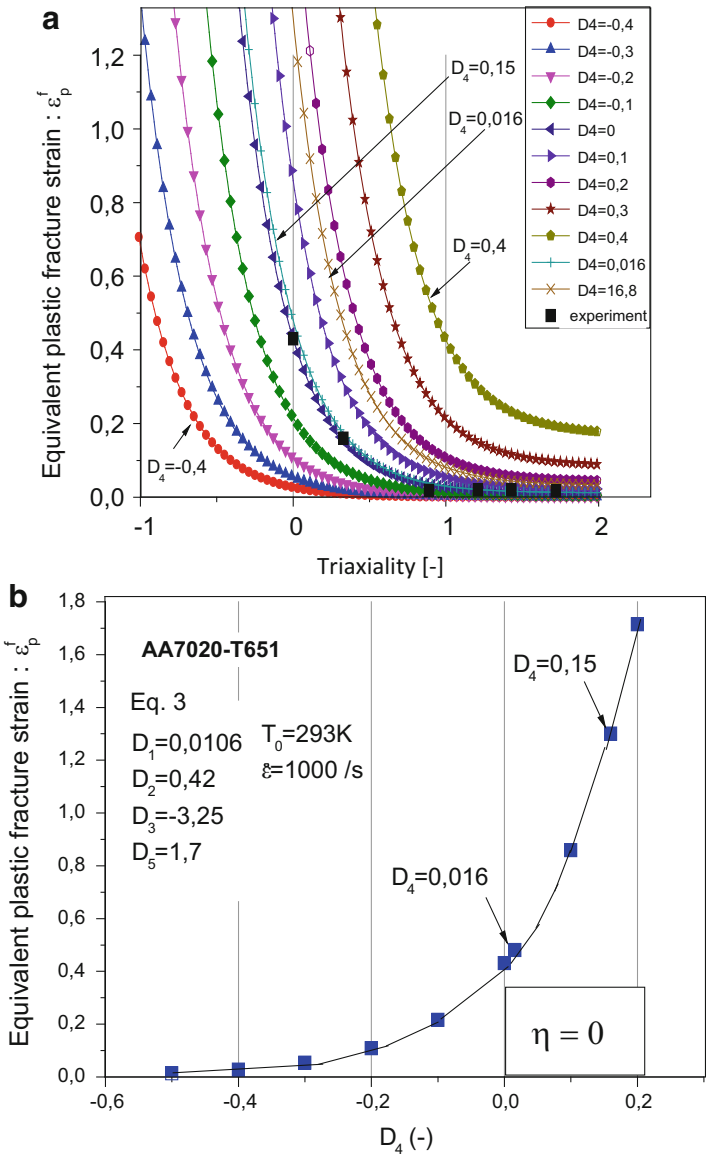

Fig. 12 (**a**) Fracture loci for AA7020-T651 depending on different values of the D_4 parameter and (**b**) dependence between the fracture strain and D_4 for the stress triaxiality η equal to 0

processes that occur during an impact proving a complexity of ballistic investigations and shows a research method of their analysis. Based on the discussed impact configuration, the ballistic limit curve is determined. The failure modes observed during the experimental investigation depend on the impact velocity and change

from plugging to disking, as a result of interrelation between shearing and bending stresses in the targets characterized by the rolling structure. The numerical simulation analyses conditions leading to the occurrence of the target failure, which complements the experimental study. Based on the material characterization, the phenomenological constitutive relation and the fracture criterion – the Johnson–Cook coupled models are identified and applied in the simulation. The models, often used in ballistic impact investigations, describe the flow and fracture material behavior as a function of the strain rate and temperature and account for the damage accumulation. An element-killing algorithm linked with the fracture strain function is sensitive to a variation of the function parameters, which affects the final modeled failure. Thus, a careful analysis should proceed with a choice of the fracture description and the calibration of the fracture model parameters.

Computations method, ballistic testing, dynamic materials characterization cannot separately lead to a better understanding of the mechanisms which govern the behavior of materials and structures subjected to intense impulsive loading. However, a combination of these research methods contributes to advances in the understanding of short-time response phenomena, which results in optimized, light-weight designs capable of withstanding high-velocity impacts.

References

F.H. Abed, Constitutive modelling of the mechanical behaviour of high strength ferritic steels for static and dynamic applications. Mech. Time-Depend. Mater. **14**(4), 329–335 (2010)

F.H. Abed, S.I. Ranganathan, M.A. Serry, Constitutive modelling of nitrogen-alloyed austenitic stainless steel at low and high strain rates and temperatures. Mech. Mater. **77**, 142–157 (2014)

M.E. Backman, W. Goldsmith, The mechanics of penetration of projectiles into targets. Int. J. Eng. Sci. **16**, 1–99 (1978)

Y. Bai, T. Wierzbicki, Application of extended Mohr-Coulomb criterion to ductile fracture. Int. J. Fract. **161**(1), 1–20 (2010)

K. Balch, *High Frame Rate Electronic Imaging*. Motion Video Products (1999). https://web.archive.org/web/20160304000301/http://www.motionvideoproducts.com/MVP%20papers/HSV%20White%20Paper.pdf. Accessed 05 July 2020

Ballistics (2020), https://en.wikipedia.org/wiki/Ballistics. Accessed 05 July 2020

Y. Bao, T. Wierzbicki, On fracture locus in the equivalent strain and stress triaxiality space. Int. J. Mech. Sci. **46**(1), 81–98 (2004)

T. Berstad, O.S. Hopperstad, M. Langseth, Elasto-viscoplastic constitutive models in the explicit finite element code LS-DYNA 3D, in: *Proceedings of the Second International LS-DYNA 3D Conference*, San Francisco, USA, 20–21 September 1994

T. Børvik, M. Langseth, O.S. Hopperstad, K.A. Malo, Ballistic penetration of steel plates. Int. J. Impact Eng **22**(9), 855–886 (1999)

T. Børvik, O.S. Hopperstad, T. Berstad, M. Langseth, A computational model of viscoplasticity and ductile damage for impact and penetration. Eur. J. Mech. A/Solids. **20**(5), 685–712 (2001)

T. Børvik, M. Langseth, O.S. Hopperstad, K.A. Malo, Perforation of 12 mm thick steel plates by 20 mm diameter projectiles with flat, hemispherical and conical noses: part I: experimental study. Int. J. Impact Eng **27**(1), 19–35 (2002a)

T. Børvik, M. Langseth, O.S. Hopperstad, K.A. Malo, Perforation of 12 mm thick steel plates by 20 mm diameter projectiles with flat, hemispherical and conical noses: part II: numerical simulations. Int. J. Impact Eng **27**(1), 37–64 (2002b)

N.S. Brar, V.S. Joshi, B.W. Harris, Constitutive model constants for Al7075-T651 and Al7075-T6. AIP Conf. Proc. **1195**(1), 945–948 (2009)
P.W. Bridgman, *Studies in Large Plastic Flow and Fracture with Special Emphasis on the Effects of Hydrostatic Pressure*, 1st edn. (McGraw-Hill, New York, 1952)
Citizendium, Flash radiography (2020), https://en.citizendium.org/wiki/Flash_radiography. Accessed 05 July 2020
A.H. Clausen, T. Børvik, O.S. Hopperstad, A. Benallal, Flow and fracture characteristics of aluminium alloy AA5083-H116 as function of strain rate, temperature and triaxiality. Mater. Sci. Eng. A **364**(1), 260–272 (2004)
R. Cobden, A. Banbury, Aluminium: physical properties, characteristics and alloys, Talat lectures, 19–26 (1994)
M.G. Cockcroft, D.J. Latham, Ductility and the workability of metals. J. Inst. Metals. **96**(1), 33–39 (1968)
G. Cooper, P. Gotts, Ballistic protection, in *Ballistic Trauma* (Springer, London, 2005), pp. 67–90
A. Crosby, *Throwing Fire: Projectile Technology Through History* (Cambridge University Press, Cambrdige 2002)
I. Crouch (ed.), *The Science of Armour Materials* (Woodhead Publishing, Duxford 2016)
B. Dodd, *Adiabatic Shear Localization: Occurrence, Theories, and Applications* (Pergamon Press, Oxford 1992)
J.D. Embury, R.B. Nicholson, The nucleation of precipitates: the system Al-Zn-Mg. Acta Metall. **13**(4), 403–417 (1965)
T. Fras, L. Colard, E. Lach, A. Rusinek, B. Reck, Thick AA7020-T651 plates under ballistic impact of fragment-simulating projectiles. Int. J. Impact Eng **86**, 336–353 (2015a)
T. Fras, L. Colar, P. Pawlowski, Perforation of aluminum plates by fragment simulating projectiles. Int. J. Multiphysics **9**(3), 267–286 (2015b)
T. Fras, C.C. Roth, D. Mohr, Fracture of high-strength armour steel under impact loading. Int. J. Impact Eng **111**, 147–164 (2018)
T. Fras, C.C. Roth, D. Mohr, Dynamic perforation of ultra-hard high-strength armor steel: impact experiments and modeling. Int. J. Impact Eng **131**, 256–271 (2019)
T. Fras, C.C. Roth, D. Mohr, Two models of fracture applied to impact simulations. Bull. Pol. Acad. Sci-Tech. **68**(2), 1–16 (2020)
A.L. Gurson, Continuum theory of ductile rupture by void nucleation and growth: part I-yield criteria and flow rules for porous ductile media. J. Eng. Mater. Technol. **99**(1), 2–15 (1977)
P.J. Hazell, *Armour: Materials, Theory, and Design* (CRC Press, Boca Raton 2015)
T.W. Ipson, R.F. Recht, *Perforation by Fragments of Arbitrary Shape*, NWC TP 5927 Denver Research Institute, Naval Weapons Centre, China Lake (1977)
G.R. Johnson, W.H. Cook, A constitutive model and data for metals subjected to large strains, high strain rates and high temperatures, in *7th Int. Symp. on Ballistics* 1983
G.R. Johnson, W.H. Cook, Fracture characteristics of three metals subjected to various strains, strain rates, temperatures and pressures. Eng. Fract. Mech. **21**(1), 31–48 (1985)
G.H. Jonas, J.A. Zukas, Mechanics of penetration: analysis and experiment. Int. J. Eng. Sci. **16**(11), 879–903 (1978)
R. Laible (ed.), *Ballistic Materials and Penetration Mechanics*, vol 5 (Elsevier, Amsterdam 2012)
M.B. Liu, G.R. Liu, Smoothed particle hydrodynamics (SPH): an overview and recent developments. Arch. Comp. Met. Eng. **17**(1), 25–76 (2010)
Ls Dyna Manual. http://www.dynasupport.com/news/ls-dyna-971-manual-pdf. Accessed 05 July 2020
F. McClintock, A criterion of ductile fracture by the growth of holes. J. Appl. Mech. **35**(2), 363–371 (1968)
D. Mohr, S.J. Marcadet, Micromechanically-motivated phenomenological Hosford-Coulomb model for predicting ductile fracture initiation at low stress triaxialites. Int. J. Solids Struct. **67**(68), 40–55 (2015)
D. Mohr, M. Dunand, K.H. Kim, Evaluation of associated and non-associated quadratic plasticity models for advanced high strength steel sheets under multi-axial loading. Int. J. Plast. **26**(7), 939–956 (2010)

K. Nahshon, J.W. Hutchinson, Modification of the Gurson model for shear failure. Eur. J. Mech. A-Solid. **27**(1), 1–17 (2008)
K. Pack, C.C. Roth, The second Sandia Fracture Challenge: blind prediction of dynamic shear localization and full fracture characterization. Int. J. Fract. **198**(1–2), 197–220 (2016)
K.O. Pedersen, T. Børvik, O.S. Hopperstad, Fracture mechanisms of aluminum alloy AA7075-T651 under various loading conditions. Mater. Design. **32**(1), 97–107 (2011)
T. Pintat, Measurements of the work of deformation under shearing at high strain rates, in *Impact Loading and Dynamic Behavior of Materials* (Verlag, Dortmund 1988)
R.F. Recht, T.W. Ipson, Ballistic perforation dynamics. J. Appl. Mech. **30**(3), 384–390 (1963). https://doi.org/10.1115/1.3636566
J.R. Rice, D.M. Tracey, On the ductile enlargement of voids in triaxial stress fields. J. Mech. Phys. Solids **17**, 201–217 (1969)
Z. Rosenberg, E. Dekel, *Terminal Ballistics* (Springer, Berlin, 2012)
C.C. Roth, D. Mohr, Effect of strain rate on ductile fracture initiation in advanced high strength steel sheets: experiments and modelling. Int. J. Plast. **56**, 19–44 (2014)
C.C. Roth, D. Mohr, Ductile fracture experiments with locally proportional loading histories. Int. J. Plast. **79**, 328–354 (2016)
A. Rusinek, J.R. Klepaczko, Shear testing of a sheet steel at wide range of strain rates and a constitutive relation with strain-rate and temperature dependence of the flow stress. Int. J. Plast. **17**(1), 87–115 (2001)
M. Saleh, L. Edwards, I.G. Crouch, Numerical modelling and computer simulations, in *The Science of Armour Materials*, (Woodhead Publishing, Duxford 2016), pp. 483–579
L.E. Schwer, C.A. Windsor, Aluminum plate perforation: a comparative case study using lagrange with erosion, multi-material ALE, and smooth particle hydrodynamics, in *7th European LS-DYNA Conference*, 2009
Stanag AEP55, Procedures for evaluating the protection level of logistic and light armored vehicles, Nato 1 AEP-55, 2005
S.M. Swaddiwudhipong, J. Islamb, Z.S. Liu, High velocity penetration/perforation using coupled smooth particle hydrodynamics-finite element method. Int. J. Protective Struct. **1**(4), 489–506 (2010)
V. Tvergaard, A. Needleman, Analysis of the cup-cone fracture in a round tensile bar. Acta Metall. **32**(1), 157–169 (1984)
G.Z. Voyiadjis, F.H. Abed, Microstructural based models for BCC and FCC metals with temperature and strain rate dependency. Mech. Mater. **37**(2), 355–378 (2005)
M.L. Wilkins, Mechanics of penetration and perforation. Int. J. Eng. Sci. **16**, 793–807 (1978)
A.L. Wingrove, The influence of projectile geometry on adiabatic shear and target failure. Metall. Trans. A. **4**, 1829–1833 (1973)
R.L. Woodward, The penetration of metal targets which fail by adiabatic shear plugging. Int. J. Mech. Sci. **20**(9), 599–607 (1978)
R.L. Woodward, The interrelation of failure modes observed in the penetration of metallic targets. Int. J. Impact Eng **2**(2), 121–129 (1984)
R.L. Woodward, Material failure at high strain rates, in *High Velocity Impact Dynamics*, ed. by J.A. Zukas (Wiley, New York, 1990), pp. 65–126
F.J. Zerilli, R.W. Armstrong, Dislocation-mechanics-based constitutive relations for material dynamics calculations. J. Appl. Phys. **61**(5), 1816–1825 (1990)
J. Zukas, *Introduction to Hydrocodes*, vol 49 (Elsevier, Amsterdam 2004)

Ductile Crack Growth Using Cohesive GTN Model

14

Mamadou Méïté, Noé Brice Nkoumbou Kaptchouang, Yann Monerie, Frédéric Perales, and Pierre-Guy Vincent

Contents

Introduction 334
Cohesive Zone Model for Ductile Failure 336
Cohesive Interface Model 336
GTN Model 337
Cohesive GTN Traction-Separation Law 338
Estimate of the In-Plane Strain 339
Unloading Rule and Initial Stiffness 340
Implementation into XPER Computer Code 340
Application: 3D Numerical Simulation of a Compact Tension Fracture Specimen 341
Modeling 341
Results 343
Conclusion 349
References 350

Abstract

This chapter presents a three-dimensional simulation of ductile crack growth using a recent Gurson-Tvergaard-Needleman (GTN) cohesive approach. A cohesive-volumetric finite element approach is adopted. The behavior of the material is characterized by a hardening bulk constitutive law inside the finite elements together with a softening traction-separation law at the interfaces

M. Méïté · N. B. N. Kaptchouang · F. Perales · P.-G. Vincent
Institut de Radioprotection et de Sûreté Nucléaire, Saint-Paul-lez-Durance, France

MIST Laboratory, IRSN-CNRS-UM, Montpellier, France
e-mail: mamadou.meite@irsn.fr; noe-brice.nkoumboukaptchouang@irsn.fr; frederic.perales@irsn.fr; pierre-guy.vincent@irsn.fr

Y. Monerie (✉)
MIST Laboratory, IRSN-CNRS-UM, Montpellier, France

LMGC, University of Montpellier, CNRS, Montpellier, France
e-mail: yann.monerie@umontpellier.fr

© Springer Nature Switzerland AG 2022

G. Z. Voyiadjis (ed.), *Handbook of Damage Mechanics*,
https://doi.org/10.1007/978-3-030-60242-0_70

between elements. The traction-separation law recently proposed by (Nkoumbou Kaptchouang et al. Eng Fract Mech 242:107437, 2021) rests on the micro-mechanical Gurson-Tvergaard-Needleman model for ductile damage and fracture, and the reduced kinematics of a surface. It takes into account the effect of local I1 and J2 stress invariants via a dependence of the cohesive model to the surrounding bulk stress. The efficiency of this cohesive-GTN model is underlined through the 3D numerical simulation of a compact tension test. The results show a strong tunneling in the crack front shape. The crack propagates faster at the midsection than at the side-surface. Large gradients of local stress and strain through the specimen thickness during crack growth are observed. Especially, the stress triaxiality is higher at the midsection than at the side-surface, leading to more damage in the cohesive zone due to cavity growth.

Keywords

Ductile failure · GTN · Cohesive zone model · Stress triaxiality

Introduction

One way to simulate crack initiation and propagation involves finite elements with cohesive zones. In this approach, the micromechanisms of material degradation that take place in the fracture process zone ahead of the crack tip is modeled by a cohesive function termed as traction-separation law (TSL). It is expressed as a relationship $R = \mathcal{R}([u])$ between the stress vector R and the displacement jump $[u]$ across the two surfaces of the crack. The peak value of such a cohesive function defines the cohesive strength, R_0. The area under this curve refers to the separation energy, Γ_0, giving the work spent in the cohesive zone for the creation of a unit crack area. Although several authors (Roy and Dodds 2001; Roychowdhury et al. 2002; Scheider and Brocks 2006; Scheider et al. 2006) have successively simulated several crack growth experiments with one set of cohesive parameters (R_0, Γ_0), it is now admitted that in the course of ductile fracture, these parameters are not material constants and therefore are not directly transferable from one experiment to another. In other works such as those of (Chen et al. 2005), different cohesive parameters depending on the position through the thickness of the specimen have been introduced in order to simulate crack growth experiments on steels with good accuracy. Moreover, the values of the cohesive parameters for a single material also depend on the shape of the TSL used in the simulations (Scheider and Brocks 2003; Schwalbe et al. 2012). One drawback of phenomenological cohesive functions is that they don't explicitly take into account the physics of micromechanical phenomenon leading to fracture such as the void nucleation, growth, and coalescence in ductile failure of metals. Furthermore, cohesive zone model capabilities are also limited by their surface reduced kinematics, which only contain relevant quantities such as the crack normal opening and the crack sliding displacement, but nothing to describe the effect of crack plane stretching due to in-plane strain as in a volumetric 3D element

(Remmers et al. 2013). This limitation makes it difficult to use a single set of cohesive parameters to model crack growth under different constraint conditions. Contrastingly, the framework of continuum micromechanics, with a physical modeling of the kinematics of voids nucleation, growth, and coalescence inside a matrix material have led to a set of poroplasticity models that can properly describe damage process in ductile metals under different constraints conditions. Within this approach, the Gurson-Tvergaard-Needleman (GTN) model (Gurson 1977; Tvergaard 1981; Tvergaard and Needleman 1984; Koplik and Needleman 1988) is surely the most widespread model to characterize ductile fracture. A physically based TSL that captures the mechanism of the ductile failure process of metals can be derived from a micromechanical modeling of a voided unit cell. This idea has been introduced by (Tvergaard and Hutchinson 1992) who computed a TSL as a response of a GTN unit cell under uniaxial straining conditions. A step to improve the cohesive zone models for a wider range of local constraints has been undertaken by introducing a dependency of the shape of the traction separation law and the magnitudes of cohesive parameters to some variables characterizing the local stress and strain states such as the accumulated plastic strain $\varepsilon_{\text{eq}}^{\text{p}}$ (Tvergaard and Hutchinson 1996; Tvergaard 1997), the stress triaxiality η_{Σ} (Siegmund and Brocks 1999, 2000a, b; Scheider 2009; Banerjee and Manivasagam 2009), and the equivalent strain rate $\dot{\varepsilon}_{\text{eq}}^{\text{p}}$ (Anvari et al. 2006, 2007). In these works, the cohesive strength R_0 and the cohesive energy Γ_0 are updated during the simulation according to the local stress and strain states through some specific functions ($R_0 = R_0(\varepsilon_{\text{eq}}^{\text{p}}, \dot{\varepsilon}_{\text{eq}}^{\text{p}}, \eta_{\Sigma}, \ldots)$, $\Gamma_0 = \Gamma_0(\varepsilon_{\text{eq}}^{\text{p}}, \dot{\varepsilon}_{\text{eq}}^{\text{p}}, \eta_{\Sigma}, \ldots)$) where the variables ($\varepsilon_{\text{eq}}^{\text{p}}$, $\dot{\varepsilon}_{\text{eq}}$, η_{Σ}) are computed in the nearest continuum element to the cohesive zone. The dependency of the cohesive parameters to stress triaxiality and strain rate was obtained through a range of unit cell simulations under different biaxial loadings with a GTN model in (Siegmund and Brocks 1999, 2000a, b; Scheider 2009) and a rate-dependent GTN model in (Anvari et al. 2006, 2007). Some authors also characterize the cohesive parameters for simulation of the tearing of large ductile plate by using a combination of GTN simulations and experiments. The peak stress and dissipated energy are identified throughout a detailed analysis of the process of necking localization and shear failure performed with GTN-like models (Nielsen and Hutchinson 2012; Woelke et al. 2015; Andersen et al. 2018, 2019). Another straightforward approach to develop physically based TSL consists in modeling the cohesive zone as a virtual thin layer representing a discontinuity band in the material with the corresponding regularized discontinuity kinematics (Michel et al. 1994; Oliver et al. 1999; Kulkarni et al. 2010). The jumps of displacements fields across the discontinuity band naturally induce a projection of the stress-strain constitutive model into a traction stress-displacement jumps law as discussed in Oliver (2000). This formalism enables the use of bulk constitutive relations embedding more details on the damage micromechanisms and crack initiation than a pure phenomenological TSL. The cohesive response is given by the traction stress and the displacement jump across the band. It can be used with a conventional zero thickness cohesive element, and in this case, the band thickness introduced to derive the cohesive model remains a parameter.

Nonetheless, the surface (or thin layer) kinematics does not give rise to in-plane strains. As a consequence, the capability of cohesive band models to properly handle high triaxiality effects remains limited. One way to overcome this limitation is discussed in (Remmers et al. 2013), where the cohesive band strain tensor is enhanced with in-plane components, which are evaluated as the average of the in-plane strains from the nearest volumetric elements on each side of the cohesive zone.

Following these ideas, (Nkoumbou Kaptchouang et al. 2021) recently derived a TSL from the original GTN model and applied it to simulate crack growth in a compact tension specimen made with a standard ferritic steel (2D plane strain computations). The TSL results from a projection of the GTN porous plasticity model into a finite thickness discontinuity band kinematics. A single variable has been added to enhance the kinematics and to take into account the high triaxiality effects. Here, a 3D finite element computation is presented to investigate the capability of this new TSL to simulate ductile crack growth. This chapter is organized as follows. First, the equations of the GTN traction-separation law of (Nkoumbou Kaptchouang et al. 2021) are recalled. Second, an analysis of a 3D finite element simulation of crack growth in a steel compact tension specimen is performed. Particular attention is paid to the crack front shape and to the heterogeneity of the stress and strain fields along the thickness of the specimen. In particular, the local traction-separation evolution is not a priori given. Its spatial evolution near the crack tip when going from the specimen midsection to the side-surface is investigated.

Cohesive Zone Model for Ductile Failure

A GTN-like cohesive zone model has been developed in (Nkoumbou Kaptchouang et al. 2021) by a projection of the so-called volumetric GTN damage model onto a cohesive kinematics. The TSL reproduces the behavior of a single bulk element made of a GTN material. This cohesive model is briefly described below.

Cohesive Interface Model

The cohesive zone is seen as a thin layer interface inside a bulk material, and the strain tensor is approximated by a function of the displacement jump $[u]$ across the interface with the help of a scaling rule (Michel et al. 1994; Oliver et al. 1999; Suquet 1988)

$$\varepsilon \approx \frac{[u]\bigotimes_s n}{h} = \begin{bmatrix} \varepsilon_{\mathrm{nn}} & \varepsilon_{\mathrm{nt}} & \varepsilon_{\mathrm{ns}} \\ \varepsilon_{\mathrm{nt}} & 0 & 0 \\ \varepsilon_{\mathrm{ns}} & 0 & 0 \end{bmatrix} \text{ with } \varepsilon_{\mathrm{nn}} = \frac{[u_n]}{h}, \varepsilon_{\mathrm{nt}} = \frac{[u_{\mathrm{t}}]}{2h}, \varepsilon_{\mathrm{ns}} = \frac{[u_{\mathrm{s}}]}{2h} \qquad (1)$$

where (n, t, s) is the local basis, n being a unit normal vector to the interface and t, s the two unit vectors defining the tangent plane. The h parameter is a length scale of the cohesive model and $(u \bigotimes_s v)_{ij} = (u_i v_j + u_j v_i)/2$. The kinematics (Eq. 1) is extended by introducing an additional in-plane parameter p in order to enhance the range of strain triaxiality affordable by the cohesive model

$$\varepsilon = \begin{bmatrix} \varepsilon_{\mathrm{nn}} & \varepsilon_{\mathrm{nt}} & \varepsilon_{\mathrm{ns}} \\ \varepsilon_{\mathrm{nt}} & p & 0 \\ \varepsilon_{\mathrm{ns}} & 0 & p \end{bmatrix} \tag{2}$$

GTN Model

The GTN yield surface writes (Gurson 1977; Tvergaard 1981; Tvergaard and Needleman 1984; Koplik and Needleman 1988)

$$\frac{\sum_{eq}^2}{\sigma_y^2} + 2q_1 f^* \cosh\left(\frac{3}{2} q_2 \frac{\sum m}{\sigma_y}\right) - 1 - q_3 f^* 2 = 0 \tag{3}$$

where Σ is the stress q tensor, $\Sigma \mathrm{m} = (1/3)\ \mathrm{tr}\ \Sigma$ is the hydrostatic stress, $\sum_{\mathrm{eq}} = \sqrt{(3/2)\sum^{\mathrm{d}} : \sum^{\mathrm{d}}}$ is the on Mises equivalent stress, $\sum^{\mathrm{d}} = \sum - \sum_{\mathrm{m}} i$ is the deviatoric part of Σ, and i is the second-order identity tensor. Coefficients $\left(q_1, q_2, q_3 = q_1^2\right)$ are constants. The flow strength of the homogeneous and incompressible plastic matrix surrounding the voids is denoted by σ_y. The porosity is denoted by f and an effective porosity f^* related to void coalescence is introduced

$$f^* \equiv \begin{cases} f & \text{for } 0 \le f \le f_c \\ f_c + \dfrac{f_u^* - f_c}{f_f - f_c}(f - f_c) & \text{for } f_c < f \end{cases} \tag{4}$$

where f_c is the porosity at onset of void coalescence, and f_f is the fracture porosity, $f^*(f_f) = f_u^* = 1/q_1$. Isotropic hardening is introduced by the expression of $\sigma_y(\bar{\varepsilon})$, where the scalar variable $\bar{\varepsilon}$ is interpreted as an average plastic strain of the matrix material surrounding the voids. The evolution of $\bar{\varepsilon}$ is governed by an equivalent plastic work expression

$$\sum : \dot{\varepsilon} = (1 - f)\sigma_y \dot{\bar{\varepsilon}} \tag{5}$$

The evolution of the porosity is governed by a void growth rate and a strain controlled void nucleation rate (Chu and Needleman 1980)

$$\dot{f} = (1-f)\mathrm{tr}\dot{\varepsilon} + A\dot{\overline{\varepsilon}} \text{ with } \mathrm{A}(\overline{\varepsilon}) = \frac{f_N}{s_N\sqrt{2\pi}} \exp\left(-\frac{1}{2}\left(\frac{\overline{\varepsilon}-\varepsilon_N}{S_N}\right)^2\right) \tag{6}$$

where f_N is the volume fraction of void nucleating particles, ε_N is an average nucleation strain parameter, and s_N is a standard deviation.

Cohesive GTN Traction-Separation Law

The time integration of the model derived in (Nkoumbou Kaptchouang et al. 2021) is briefly summarized below. Let us denote ε, f, and $\overline{\varepsilon}$ the cohesive strain, porosity, and average plastic strain at time t. At the previous time step, their values are denoted by $\varepsilon^{(t-\delta t)}$, $f^{(t-\delta t)}$, and $\overline{\varepsilon}^{(t-\delta t)}$. The increment between two time steps of the cohesive strain $\delta\varepsilon$ writes

$$\delta\varepsilon = \begin{bmatrix} \delta\varepsilon_{\mathrm{nn}} & \delta\varepsilon_{\mathrm{nt}} & \delta\varepsilon_{\mathrm{ns}} \\ \delta\varepsilon_{\mathrm{nt}} & \delta p & 0 \\ \delta\varepsilon_{\mathrm{ns}} & 0 & \delta p \end{bmatrix} \tag{7}$$

Giving quantities at time t, and average strain at time $t - \delta t$, the porosity and the average strain are updated

$$f = f^{(t-\delta t)} + \left(1 - f^{(t-\delta t)}\right)(\delta\varepsilon_{\mathrm{nn}} + 2\delta p) + A\left(\overline{\varepsilon}^{(t-\delta t)}\right)\delta\overline{\varepsilon} \tag{8}$$

$$\overline{\varepsilon} = \overline{\varepsilon}^{(t-\delta t)} + \delta\overline{\varepsilon} \tag{9}$$

with

$$\delta\overline{\varepsilon} = \frac{T_{\mathrm{nn}}\delta\varepsilon_{\mathrm{nn}} + 2T_{\mathrm{nt}}\delta\varepsilon_{\mathrm{nt}} + 2T_{\mathrm{ns}}\delta\varepsilon_{\mathrm{ns}} + T_{\mathrm{tt}}\delta p + T_{\mathrm{ss}}\delta p}{1 - f(t-\delta t)} \tag{10}$$

and

$$\begin{cases} T_{\mathrm{nn}} = \dfrac{1}{q_2}H\left(\chi^{(t-\delta t)}\right) + \dfrac{4}{9}D\left(\chi^{(t-\delta t)}\right)\dfrac{\delta\varepsilon_{\mathrm{nn}} - \delta p}{(\delta\varepsilon)_{\mathrm{eq}}} \\ T_{\mathrm{nt}} = \dfrac{2}{3}D\left(\chi^{(t-\delta t)}\right)\dfrac{\delta\varepsilon_{\mathrm{nt}}}{(\delta\varepsilon)_{\mathrm{eq}}} \\ T_{\mathrm{ns}} = \dfrac{2}{3}D\left(\chi^{(t-\delta t)}\right)\dfrac{\delta\varepsilon_{\mathrm{ns}}}{(\delta\varepsilon)_{\mathrm{eq}}} \\ T_{\mathrm{tt}} = T_{\mathrm{ss}}\dfrac{1}{q_2}H\left(\chi^{(t-\delta t)}\right) - \dfrac{2}{9}D\left(\chi^{(t-\delta t)}\right)\dfrac{\delta\varepsilon_{\mathrm{nn}} - \delta p}{(\delta\varepsilon)_{\mathrm{eq}}} \\ \eta_{\dot{\varepsilon}} = \dfrac{(\delta\varepsilon)\mathrm{m}}{(\delta\varepsilon)\mathrm{eq}} \end{cases} \tag{11}$$

where $\chi^{(t-\delta t)}$ stands for $\left\{\eta_{\dot{\varepsilon}}, q_1 f^*\left(f^{(f-\delta t)}\right)\right\}$ and H and D are two general functions

$$H(\eta_{\dot{\varepsilon}}, f) = \frac{2}{3}\left(\operatorname{arcsinh}\left(\frac{2\eta_{\dot{\varepsilon}}}{f}\right) - \operatorname{arcsinh}(2\eta_{\dot{\varepsilon}})\right) \tag{12}$$

$$D(\eta_{\dot{\varepsilon}}, f) = \sqrt{(2\eta_{\dot{\varepsilon}})^2 + 1} - \sqrt{(2\eta_{\dot{\varepsilon}})^2 + f^2} \tag{13}$$

Then, the components of the cohesive stress $R = \mathrm{S}_n$ are straightforwardly evaluated at time t

$$\begin{cases} R_{\mathrm{n}} = \sigma_y(\bar{\varepsilon})\left(\dfrac{1}{q_2}H(\chi) + \dfrac{4}{9}D(\chi)\dfrac{\delta\varepsilon_{\mathrm{nn}} - \delta p}{(\delta\varepsilon)_{\mathrm{eq}}}\right) \\ R_{\mathrm{t}} = \sigma_y(\bar{\varepsilon})\dfrac{2}{3}D(\chi)\dfrac{\delta\varepsilon_{\mathrm{nt}}}{(\delta\varepsilon)_{\mathrm{eq}}} \\ R_s = \sigma_y(\bar{\varepsilon})\dfrac{2}{3}D(\chi)\dfrac{\delta\varepsilon_{\mathrm{ns}}}{(\delta\varepsilon)_{\mathrm{eq}}} \end{cases} \tag{14}$$

where χ stands for $\{\eta_{\dot{\varepsilon}}, q_1 f^*(f)\}$.

Estimate of the In-Plane Strain

The in-plane strain p is estimated by considering information coming from a volumetric element adjacent to the cohesive zone. A strain rate triaxiality $\eta_{\dot{\varepsilon}}^{\mathrm{vol}}$ is computed using both the stress state Σ^{vol} in a volumetric element adjacent to the cohesive zone and the normality rule of the GTN model

$$\eta_{\dot{\varepsilon}}^{\mathrm{vol}} = \frac{q_1 q_2 f^* \sinh\left(\frac{3}{2}q_2\frac{\sum_{\mathrm{m}}^{\mathrm{vol}}}{\sigma_y}\right)}{2\frac{\sum_{\mathrm{eq}}^{\mathrm{vol}}}{\sigma_y}} \tag{15}$$

The in-plane strain increment δp is estimated such that the strain rate triaxiality inside the cohesive zone is equal to $\eta_{\dot{\varepsilon}}^{\mathrm{vol}}$. As outlined in (Nkoumbou Kaptchouang et al. 2021), it was observed that the resulting triaxiality $\eta_{\dot{\varepsilon}}^{\mathrm{vol}}$ decreases when increasing damage in the cohesive zone during a C(T) test simulation. This can lead to an artificial delay of crack growth because the standard GTN model does not predict any damage at low stress triaxiality. Therefore, (Nkoumbou Kaptchouang et al. 2021) propose to transfer the volumetric stress Σ^{vol} to the cohesive zone up to the onset of coalescence (when f reaches f_c). For the post-coalescence stage, Σ^{vol} is kept constant.

Unloading Rule and Initial Stiffness

An unloading rule and an initial finite stiffness are then added to the TSL by modifying the cohesive stress as below (Nkoumbou Kaptchouang et al. 2021)

$$R^{(\mathrm{int})} = \begin{cases} R_{\mathrm{n}} \dfrac{[u_{\mathrm{n}}]}{[u_{\mathrm{n}}]_{\max}} \left(1 - \exp\left(-\alpha_{\mathrm{n}} \dfrac{[u_{\mathrm{n}}]\max}{h}\right)\right) \\ R_{\mathrm{t}} \dfrac{[u_{\mathrm{t}}]}{[u_{\mathrm{t}}]_{\max}} \left(1 - \exp\left(-\alpha_{\mathrm{t}} \dfrac{[u_{\mathrm{t}}]\max}{h}\right)\right) \\ R_{\mathrm{s}} \dfrac{[u_{\mathrm{s}}]}{[u_{\mathrm{s}}]_{\max}} \left(1 - \exp\left(-\alpha_{\mathrm{s}} \dfrac{[u_{\mathrm{s}}]\max}{h}\right)\right) \end{cases} \tag{16}$$

where $[u_{\mathrm{n}}]_{\max}$, $[u_{\mathrm{t}}]_{\max}$, $[u_{\mathrm{s}}]_{\max}$ are the maximum values of separation in each direction occurred so far during the loading process. The terms $[u_i]/[u_i]_{\max}$ with $i = \{n, t, s\}$ in (Eq. 16) describe an elastic linear unloading up to the origin. The exponential part allows to introduce an initial stiffness to the TSL when $[u]$ vanishes. The initial slope in various directions is calibrated by setting the parameters α_{n}, α_{t}, and α_{s} accordingly. The unloading behavior is completed by assuming the irreversibility of damage and hardening during loading process. From a practical point of view, two additional tests are performed in the integration scheme

$$\text{if } f < f^{(t-\delta t)} \text{ then } f = f^{(t-\delta t)} \tag{17}$$

and

$$\text{if } \overline{\varepsilon} < \overline{\varepsilon}^{(t-\delta t)} \text{ then } \overline{\varepsilon} = \overline{\varepsilon}^{(t-\delta t)} \tag{18}$$

Implementation into XPER Computer Code

The GTN cohesive zone model has been implemented in the XPER computer code dedicated to the simulation of fracture dynamics of heterogeneous materials (Perales et al. 2008, 2010). Each mesh element or group of mesh elements is treated as an independent body. Frictional cohesive zone models are introduced at interface between bodies by a modification of Signorini-Coulomb conditions (Jean et al. 2001; Acary and Monerie 2006). The bulk behavior inside each element is governed by a hardening behavior without any damage. The cohesive model has been implemented under the assumption of proportional loading and the cohesive stress given by (Eq. 14) is estimated using the total cohesive strain ε instead of the strain increment tensor $\delta\varepsilon$. Under this assumption, the strain rate triaxiality in the cohesive zone is equal to the strain triaxiality defined in (Eq. 15). The transfer of information from the volume element to the cohesive zone, which is a key point of the model, is schematically illustrated in Fig. 1. The general equations used for the numerical

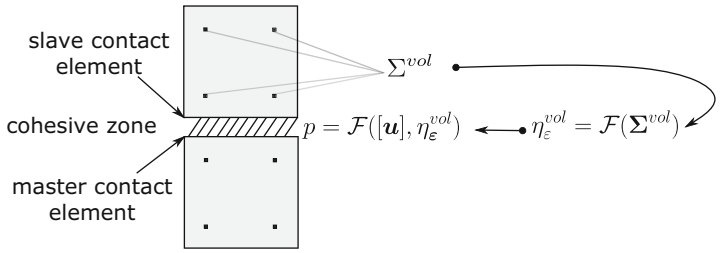

Fig. 1 The average stress in the slave element adjacent to the cohesive zone is used to evaluate an imposed strain triaxiality $\eta_{\varepsilon}^{\mathrm{vol}}$ in the cohesive zone. The in-plane strain p in the cohesive zone is a function of $\eta_{\varepsilon}^{\mathrm{vol}}$ e and $[u]$

implementation of the cohesive model are summarized in Appendix C of (Nkoumbou Kaptchouang et al. 2021) and the reader is referred to this for an exhaustive and detailed description.

Application: 3D Numerical Simulation of a Compact Tension Fracture Specimen

Modeling

A finite element analysis is performed on a deeply cracked compact tension C(T) fracture specimen with smooth side-surfaces. Remind that the primary motivation to use deeply cracked specimens is to guarantee conditions leading to high crack-tip constraint (i.e., high triaxiality of stress) with limited-scale plasticity (Cravero and Ruggieri 2005). Moreover, this type of specimen displays the highest triaxiality compared to any type of standard fracture specimen (Roy and Dodds 2001; Chen et al. 2005; Cravero and Ruggieri 2005; Brocks et al. 2002; Brocks and Steglich 2006; Silva et al. 2006; Zhu 2017). Here, a_0 denotes the initial crack depth and is set to 19.92 mm, while $W = 40$ mm is the specimen width (ratio $a_0/W \approx 0.5$). The specimen thickness is set to $B = 20$ mm. The details of the specimen dimensions and the finite element mesh are displayed in Fig. 2. The axes of the global coordinate system (x, y, z) are along the crack extension direction, the loading direction, and the thickness direction, respectively. The plane $z = 0$ defines the midsection of the specimen, and $z = 10$ mm defines the side-surface (see Fig. 2). Symmetry conditions enable analyses using a quarter of C(T)-specimen. But since it is not possible to apply symmetry conditions on the cohesive elements in the crack plane in XPER code, one-half of the specimen is modeled with appropriate constraints ($Uz = 0$) at the midsection ($z = 0$). The mesh is refined over a surface $10 \times 7 \times 10$ mm^3 in front of the crack tip. The mesh size for the elements in this central zone is $0.2 \times 0.2 \times 0.5$ mm^3 along the (x, y, z), respectively, while a coarser mesh is used outside this zone. The half-symmetric, 3D model for this specimen has a total number of 82,803 nodes and 74,560 hexahedra solid elements with eight-nodes.

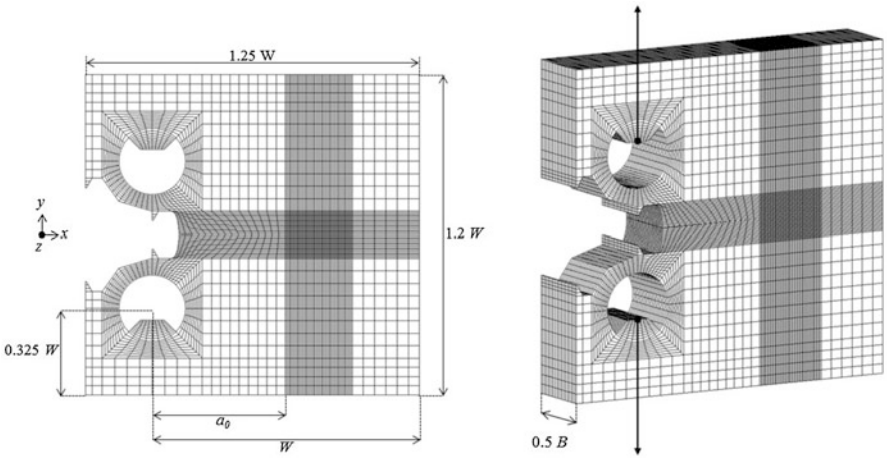

Fig. 2 C(T) specimen: Details of the geometry and half-symmetric three-dimensional finite element mesh. Mesh size in the crack propagation region is $0.2 \times 0.2 \times 0.5$ mm^3 in (x, y, z)-axis, respectively

Since the crack path is known, cohesive zones are only put on the crack plane in front of the crack tip, assuming pure mode I crack propagation. Four contact nodes per cohesive zone are introduced. The material surrounding the cohesive zones is an isotropic elastic-plastic solid with incremental J2 plasticity constitutive model. The Young modulus and Poisson's ratio are, respectively, denoted by E and ν. The GTN cohesive model described in the previous section is used for the cohesive zones. The hardening (for both solid elements and cohesive zones) is described by

$$\sigma_y(\bar{\varepsilon}) \;=\; \sigma_0(1 + K\bar{\varepsilon})^{1/n} \tag{19}$$

where σ_0, K, and n are three coefficients. The material parameters are reported in Table 1 for a specific ferritic steel (15NiCuMoNb5, German designation WB36). The initial porosity is denoted by f_0. Computation is performed under the small strain assumption. The length scale parameter controlling the localization is set to $h = 0.4$ mm, which is in the order of magnitude for ductile fracture in ferritic steels. The numerical parameters controlling the initial slope of the cohesive stress are set to $\alpha_n = 2.3\ 10^4\ \alpha_t = \alpha_s = 1.8\ 10^5$ Those values lead to an initial stiffness of the cohesive stress of the order of 10^{17} *Pa/m* in both normal and tangential directions. An estimate of those parameters as a function of the GTN material properties is given in appendix B in (Nkoumbou Kaptchouang et al. 2021).

Two vertical displacement increments, U_y and $-U_y$, are simultaneously applied at the two upper and lower pin holes, respectively. Both pin holes are partially filled with a purely elastic material having the same elastic properties than the specimen material. A tie constraint is used on the nodes at the interface between the load pin and the specimen. Computation is made using an explicit finite element solver with an implicit contact resolution within a dynamical formulation (Perales et al. 2010). A

time step $\delta t = 1.610^{-8}\ s$ is used. Since all the involved constitutive laws are time-independent, a high velocity $\left(\dot{U}_y = 0.2m.s^{-1}\right)$ is prescribed in order to run the simulation in a reasonable time. The mass density is set to 7.8103 kg/m^3 as a standard value for most of steels. It is worth mentioning that this implicit-explicit coupled cohesivevolumetric computation was approximately performed in 60 days with 10 GB of RAM memory and 40 cores.

Results

Figure 3 shows the load (Force F_y) vs Crack Opening Displacement (COD approximated here by $2U_y$) curve obtained from the simulation. The simulation reproduces the drop of the load typically observed in C(T) tests. Furthermore, Figs. 4 and 5 illustrate the high level of heterogeneity of the local fields in terms of von Mises stress and accumulated plastic strain. Two specific surfaces of the specimen are shown, namely, the mid-thickness surface (at $z = 0$, symmetry plane) and the side-surface (at $z = 10$ mm, free-edge surface). It is seen that large plasticity develops in the crack-front vicinity promoting stable crack propagation. Note that the zone with high level of accumulated plastic strain in the crack front vicinity is different for the two surfaces. It appears to have a more rounded shape on the mid-section surface than on the side-surface. Note also that this plastic zone is larger at the free surface near the rear of the specimen in the case of the mid-section surface compared to the

Table 1 Material parameters of the study

Elasticity	E (GPa)	ν						
	205	0.3						
Hardening	$\sigma_0(MPa)$	K	n					
	376	900	7.2					
GTN	f_0	f_c	f_f	ε_N	S_N	f_N	q_1	q_2
	0.001	0.05	0.2	0.3	0.05	0.2	1.25	1

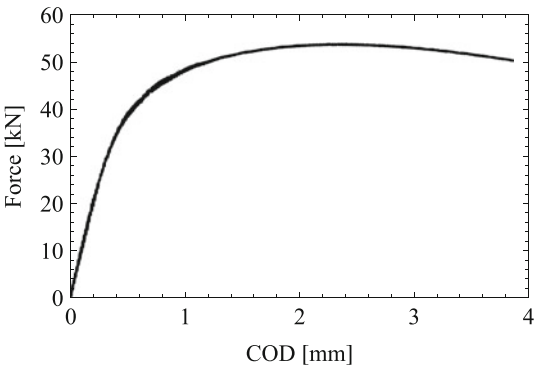

Fig. 3 Load (Force Fy) vs. Crack Opening Displacement (COD approximated by 2Uy) curve obtained from the 3D numerical simulation of a compact tension fracture specimen

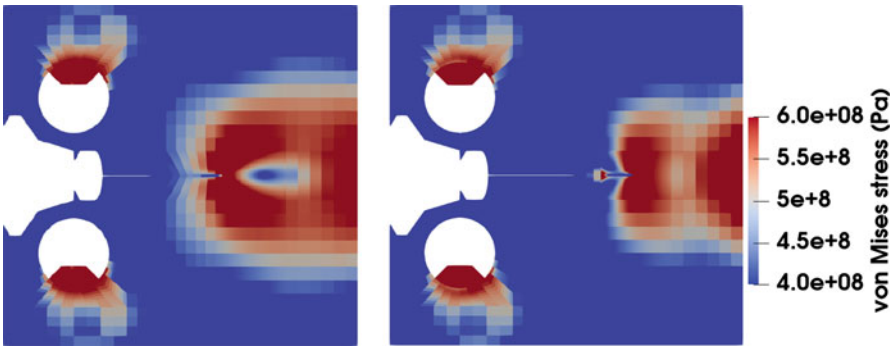

Fig. 4 Half-symmetric, 3D FE simulation of the C(T) specimen with smooth side-surfaces. Von Mises stress field on the smooth side-surface (left) and at the midsection-surface corresponding to the symmetry plane (right). Initial configuration. Uy = 1:9244 mm

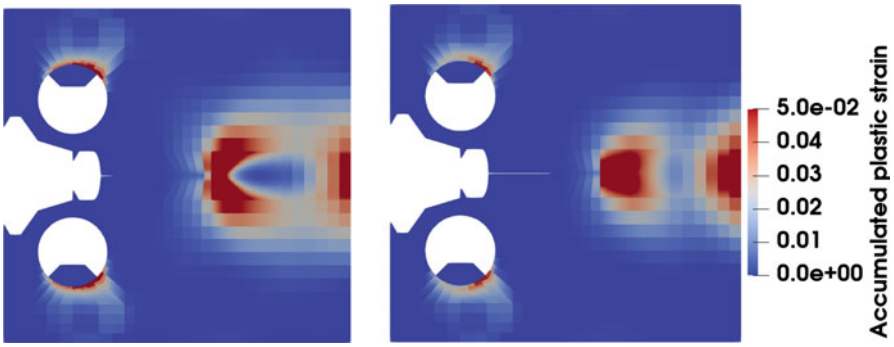

Fig. 5 Half-symmetric, 3D FE simulation of the C(T) specimen with smooth side-surfaces. Accumulated plastic strain field on the smooth side-surface (left) and at the midsection-surface (right). Initial configuration. $U_y = 1.9244$ mm

side-surface. Figure 6 shows the deformed mesh of the specimen geometry model with the separation of its crack lips (crack mouth) and von Mises stress distribution in the uncracked ligament. Figure 7 shows the shape of the crack front for some COD values. According to the plot, the crack-front, initially straight and uniform through the thickness, propagates faster in the specimen midsection than near the side-surfaces. For a given value of the crack opening displacement, the crack extension Δa has the highest value at the midsection and sharply decreases when going from the midsection to the side-surfaces. This kind of crack profile exhibiting a tunneling effect through specimen thickness has been observed both numerically and experimentally for specimen geometries with smooth side-surfaces (Chen et al. 2003, 2005; Gao et al. 1998; Chen and Kolednik 2005; Paredes et al. 2016). From a microscopic point of view, the gradient of local constraint through the thickness leads to a damage mainly governed by void growth at the center of the specimen and

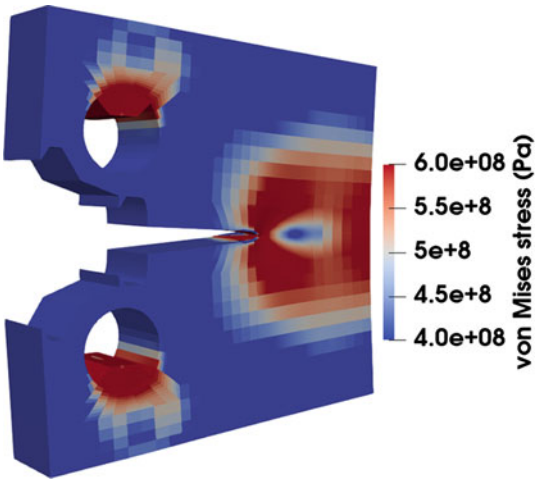

Fig. 6 Half-symmetric, 3D FE simulation of the C (T) specimen. Deformed mesh: opening of crack lips and von Mises stress localization during ductile crack propagation. $U_y = 1.9244$ mm

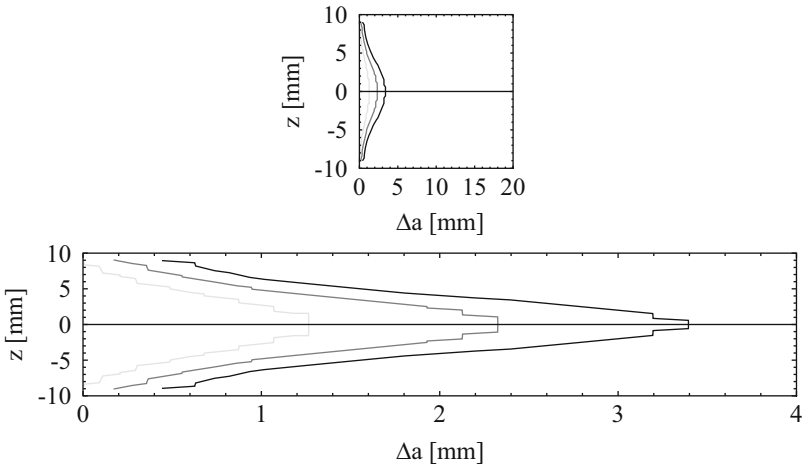

Fig. 7 Evolution of the crack front. COD ≃1.67 mm, (light gray line), COD ≃2.08 mm (gray line), COD ≃2.5 mm (dark line). Top: crack in real dimensions. Bottom: figure is stretched in the crack extension direction for a better visualization. COD approximated by $2U_y$

shear dominated conditions at the side-surface, the latter often leading to shear-lip formation (Paredes et al. 2016). Note that the crack growth due to shear dominated conditions at edges is limited in the current simulation since the cohesive model is based on the GTN model, which predicts low damage at low triaxiality. Nevertheless, the simulation can still predict crack growth through the entire thickness of the specimen. Figure 8 shows the evolution of the stress triaxiality during loading. It is plotted at the initial crack tip (at a_0) for different points through the thickness (different z values). This figure illustrates the strong heterogeneity of the stress

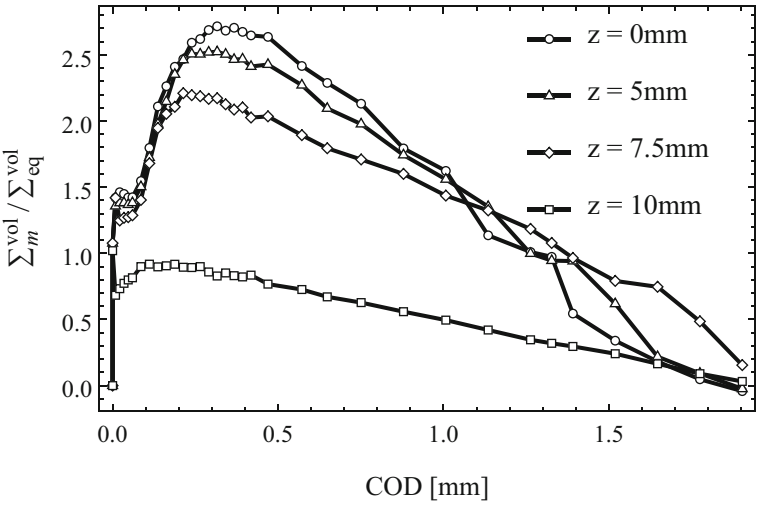

Fig. 8 Evolution of stress triaxiality with respect to Crack Opening Displacement (COD approximated by $2U_y$). Stress triaxiality is reported at the initial crack tip (at a_0) for four distinct points through the thickness (four distinct z values)

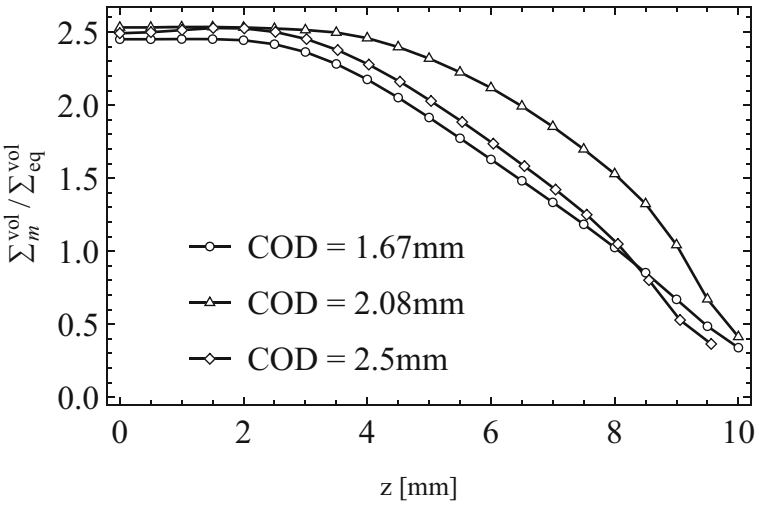

Fig. 9 Evolution of the stress triaxiality through the thickness for different COD values (approximated by $2U_y$). Stress triaxiality is reported at the maximum current crack tip (at $a(t, z = 0)$)

triaxiality through the thickness and also its complex evolution during loading. It appears that the stress triaxiality is higher at the midsection ($z = 0$) than at the side-surface ($z = 10$ mm). Figure 9 shows the stress triaxiality with respect to the position through the thickness for different COD values. Here, it is plotted at the maximum current crack tip (at $a(t, z = 0)$). It appears that the stress triaxiality is relatively high

at the midsection and sharply decreases at the side-surface. The observation that the crack advances faster in the midsection than at the side-surfaces is related to a higher stress triaxiality at midsection than at the side-surfaces. Let us recall that, in the cohesive model, damage is related to cavity growth. This cavity growth is controlled by the trace of the plastic strain rate. The high values of the stress triaxiality observed here should induce high values of the triaxiality of the strain rate in the cohesive model (the strain rate triaxiality in the cohesive model depends on the local stress around the cohesive zone through Eq. (15)), which should favor cavity growth and damage. This is verified in Fig. 10, which displays the strain triaxiality $\eta_{\dot{\varepsilon}}^{\mathrm{vol}}$ at the crack front (remind that under the assumption of proportional loading, the strain rate triaxiality in the cohesive zone is equal to the strain triaxiality, see paragraph related to the implementation of the cohesive zone model into XPER). It is seen that the peak of the strain rate triaxiality is reached faster in the midsection than on the side-surface.

The spatial and temporal heterogeneity of the stress and strain triaxiality fields lead to various traction-separation responses along the crack-front as it is depicted in Fig. 11. From this figure, it can be observed that a higher peak cohesive stress is obtained at midsection (points with label "A") than at the side-surface (points with

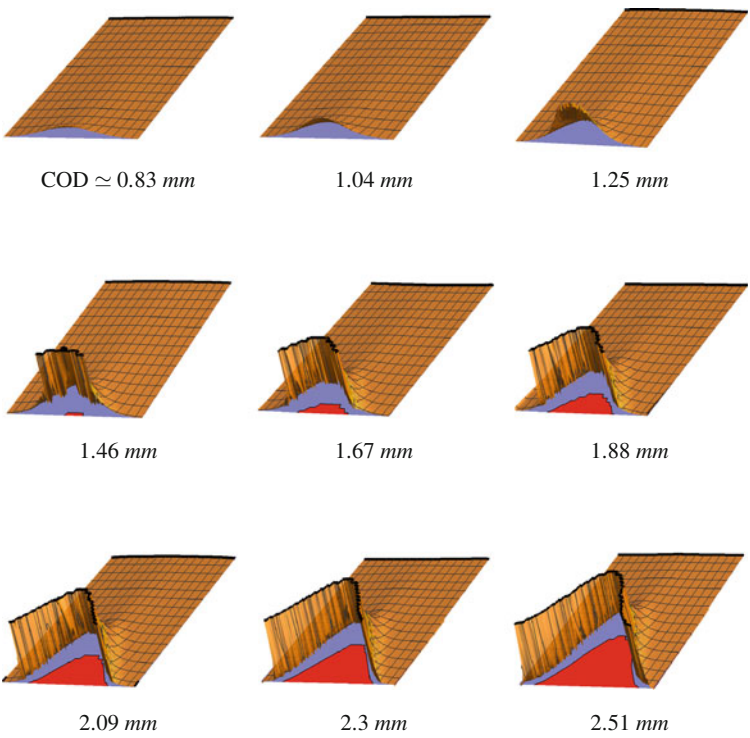

Fig. 10 Strain triaxiality field $\eta_{\dot{\varepsilon}}^{\mathrm{vol}}$ (yellow) and crack surface (red) for different COD values (approximated by $2U_y$). The triaxiality field is clipped above the value of 0.2

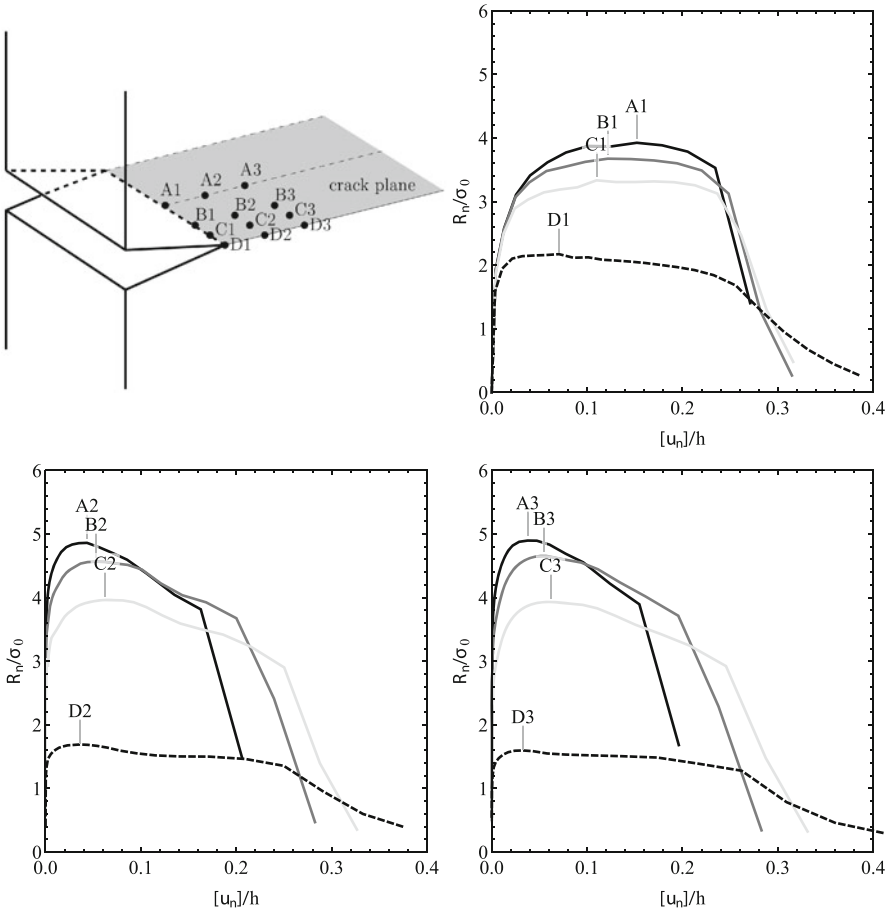

Fig. 11 Local cohesive responses at distinct points: normal cohesive stress with respect to normal displacement jump (normalized values)

label "D"). Moreover, at midsection, the peak cohesive stress increases between the positions "1" and "2" and then seems to stabilize between the positions "2" to "3." An opposite trend is obtained at the side surface where the peak cohesive stress decreases between the positions "1" and "2" and then seems to stabilize between the positions "2" and "3." As pointed out in (Nkoumbou Kaptchouang et al. 2021), a significant feature of the cohesive model is that the shape of the local cohesive response is not a priori given but directly arises from the loading and the micro-mechanical model. In a close way, at midsection the shape of the cohesive response goes from a door-like model to a triangular model during crack propagation. At side-surface, the overall shape does not vary significantly but the curve seems more flattened and spread out. From this figure, the surface cohesive energy (estimated as the area under the curve) is computed and reported in Fig. 12. The surface cohesive

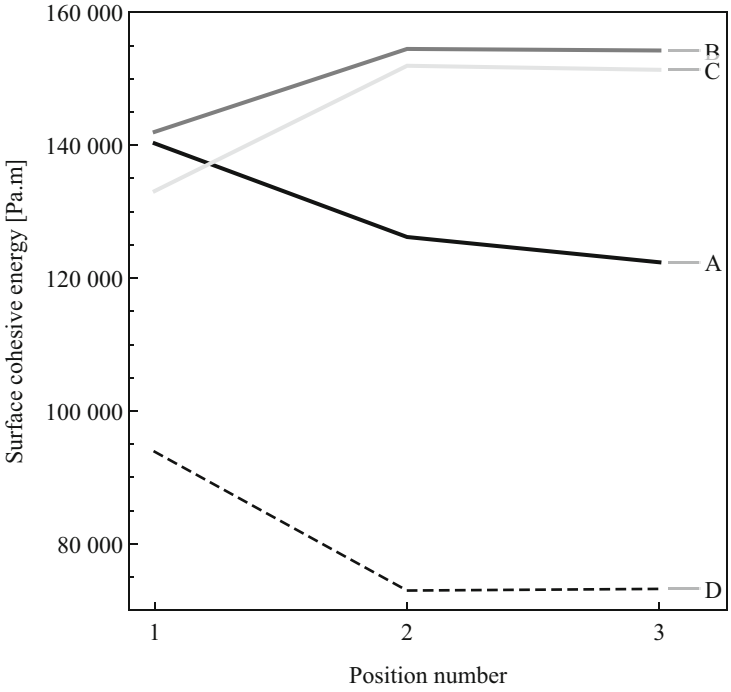

Fig. 12 Local surface cohesive energy at distinct points

energy is higher at midsection than at the side surface. At midsection and side surface, it decreases between the positions "1" and "2" and then seems to stabilize between the positions "2" and "3." At intermediate points (points with labels "B" and "C"), it increases between the positions "1" and "2" and then seems to stabilize between the positions "2" and "3." After a phase of crack propagation initiation, it appears that the crack propagation is done at a steady state

Conclusion

This chapter presented a 3D numerical simulation of ductile crack growth in a 20 mm thick compact tension C(T) fracture specimen with smooth side-surfaces made of a ferritic steel by employing a cohesive model. This cohesive model was developed in (Nkoumbou Kaptchouang et al. 2021) by incorporating the concepts of micromechanics based upon the GTN poroplasticity model within a cohesive zone model. The traction-separation law of the cohesive model derives from the projection of the volumetric GTN damage model onto a cohesive kinematics. It takes into account the effect of local I1 and J2 stress invariants via a dependence of the cohesive model to the surrounding bulk stress. The simulation showed a high level of heterogeneity of von Mises stress and accumulated plastic strain fields in the

specimen. Moreover, the simulation showed that the crack growth profile through the thickness exhibits a relatively strong tunneling effect. During the simulation, it appears that the crack-front, initially straight and uniform through the thickness, propagates faster in the specimen midsection than near the side-surfaces. It is shown that this crack-front extension is related to a higher stress triaxiality at midsection than at the side-surfaces. It is also shown that the peak of the strain triaxiality is reached faster in the midsection than on the side-surfaces, which favors damage by cavity growth. After a phase of crack propagation initiation, the local cohesive response stabilizes leading to a steady state propagation of the crack. All the findings provided from the present simulation are consistent with the literature observations. Hence, this triaxiality-dependent cohesive GTN model seems relevant to deal with problems of ductile fracture in thick-specimen made of ferritic steel and also in thick components. The model efficiency could be tested in the case of crack initiation and propagation in other types of fracture specimens in order to estimate the feasibility of transfer of ductile tearing properties from specimens to components, which remains a challenging task. This is the scope of next coming works

Acknowledgments The project ATLAS+ (Advanced Structural Integrity Assessment Tools for Safe Long Term Operation) has received funding from the Euratom research and training program 2014–2018 under the grant agreement No.: 754589. The project is jointly funded by the EU and individual partners. M. M. and F. P. thank the EU and all the ATLAS+ contributors for their support and contributions.

References

V. Acary, Y. Monerie, *Nonsmooth Fracture Dynamics Using a Cohesive Zone Approach, Research Report* (INRIA, 2006)
R.G. Andersen, P.B. Woelke, K.L. Nielsen, Eur. J. Mech. A Solids **71**, 199 (2018)
R.G. Andersen, C.L. Felter, K.L. Nielsen, Int. J. Solids Struct. **160**, 265 (2019)
M. Anvari, I. Scheider, C. Thaulow, Eng. Fract. Mech. **73**(15), 2210 (2006). https://doi.org/10.1016/j.engfracmech.2006.03.016
M. Anvari, J. Liu, C. Thaulow, Int. J. Fract. **143**(4), 317 (2007). https://doi.org/10.1007/s10704-007-9062-9
A. Banerjee, R. Manivasagam, Eng. Fract. Mech. **76**(12), 1761 (2009). https://doi.org/10.1016/j.engfracmech.2009.03.009
W. Brocks, D. Steglich, *Hybrid Methods, Chapter 11-07. Doc, Comprehensive Structural Integrity – 11 Mechanical Characterization of Materials. Technical Report* (GKSS Research Center, 2006). Technical Note GKSS/WMS/02/05
W. Brocks, A. Cornec, I. Scheider, *Computational Aspects of Nonlinear Fracture Mechanics. Technical Report* (Institute of Materials Research GKSS Research Centre Geesthacht, 2002). Technical Note GKSS/WMS/02/05
C. Chen, O. Kolednik, Int. J. Fract. **132**, 135 (2005)
C. Chen, O. Kolednik, I. Siegmund, A. Tatschl, F. Fischer, Int. J. Fract. **120**, 517536 (2003)
C. Chen, O. Kolednik, J. Heerens, F. Fischer, Eng. Fract. Mech. **72**, 2072 (2005)
C.C. Chu, A. Needleman, J. Eng. Mater. Technol. **102**(3), 249 (1980)
S. Cravero, C. Ruggieri, Eng. Fract. Mech. **72**(1), 1344 (2005)
X. Gao, J. Faleskog, C. Shih, Int. J. Fract. **89**, 375 (1998)
A.L. Gurson, J. Eng. Mater. Technol. **99**(1), 2 (1977). https://doi.org/10.1115/1.3443401

M. Jean, V. Acary, Y. Monerie, Philos. Trans. R. Soc. A Math. Phys. Eng. Sci. **359**(1789), 2497 (2001)
J. Koplik, A. Needleman, Int. J. Solids Struct. **24**(8), 835 (1988). https://doi.org/10.1016/0020-7683(88)90051-0
M.G. Kulkarni, K. Matouš, P.H. Geubelle, Int. J. Numer. Methods Eng. **84**(8), 916 (2010). https://doi.org/10.1002/nme.2923
J.C. Michel, P. Suquet, F. Thébaud, Rev. Eur. Élém. Finis **3**(4), 573 (1994). https://doi.org/10.1080/12506559.1994.10511149
K.L. Nielsen, J.W. Hutchinson, Int. J. Impact Eng. **48**, 15 (2012)
N.B. Nkoumbou Kaptchouang, Y. Monerie, F. Perales, P.G. Vincent, Eng. Fract. Mech. **242**, 107437 (2021)
J. Oliver, Int. J. Solids Struct. **37**(48), 7207 (2000). https://doi.org/10.1016/S0020-7683(00)00196-7
J. Oliver, M. Cervera, O. Manzoli, Int. J. Plast. **15**(3), 319 (1999). https://doi.org/10.1016/S0749-6419(98)00073-4
M. Paredes, T. Wierzbicki, P. Zelenak, Eng. Fract. Mech. **168**, 92111 (2016)
F. Perales, S. Bourgeois, A. Chrysochoos, Y. Monerie, Eng. Fract. Mech. **75**(11), 3378 (2008). Local Approach to Fracture (1986–2006): Selected papers from the 9th European Mechanics of Materials Conference
F. Perales, F. Dubois, Y. Monerie, B. Piar, L. Stainier, Eur. J. Comput. Mech. **19**(4), 389 (2010)
J.J.C. Remmers, R. de Borst, C.V. Verhoosel, A. Needleman, Int. J. Fract. **181**(2), 177 (2013). https://doi.org/10.1007/s10704-013-9834-3
Y.A. Roy, R.H. Dodds Jr., Int. J. Fract. **110**, 21 (2001)
S. Roychowdhury, Y.D. Arun Roy, R.H. Dodds, Eng. Fract. Mech. **69**(8), 983 (2002). https://doi.org/10.1016/S0013-7944(01)00113-8
I. Scheider, Eng. Fract. Mech. **76**(10), 1450 (2009). https://doi.org/10.1016/j.engfracmech.2008.12.006
I. Scheider, W. Brocks, Key Eng. Mat. **251**, 313 (2003). https://doi.org/10.4028/www.scientific.net/KEM.251-252.313
I. Scheider, W. Brocks, Comput. Mater. Sci. **37**(1), 101 (2006). https://doi.org/10.1016/j.commatsci.2005.12.042
I. Scheider, M. Schödel, W. Brocks, W. Schönfeld, Eng. Fract. Mech. **73**(2), 252 (2006). https://doi.org/10.1016/j.engfracmech.2005.04.005
K.H. Schwalbe, I. Scheider, A. Cornec, *Guidelines for Applying Cohesive Models to the Damage Behaviour of Engineering Materials and Structures* (Springer Science & Business Media, 2012)
T. Siegmund, W. Brocks, Int. J. Fract. **99**(1–2), 97 (1999)
T. Siegmund, W. Brocks, (2000a). https://doi.org/10.1520/STP13400S
T. Siegmund, W. Brocks, Eng. Fract. Mech. **67**(2), 139 (2000b). https://doi.org/10.1016/S0013-7944(00)00054-0
L.A. Silva, S. Cravero, C. Ruggieri, Eng. Fract. Mech. **73**, 2123 (2006)
P.M. Suquet, *Nonsmooth Mechanics and Applications, International Centre for Mechanical Sciences* (Springer, Vienna, 1988), pp. 279–340
V. Tvergaard, Int. J. Fract. **17**(4), 389 (1981). https://doi.org/10.1007/BF00036191
V. Tvergaard, *IUTAM Symposium on Nonlinear Analysis of Fracture, Solid Mechanics and Its Applications* (Springer, Dordrecht, 1997), pp. 93–104
V. Tvergaard, J.W. Hutchinson, J. Mech. Phys. Solids **40**(6), 1377 (1992). https://doi.org/10.1016/0022-5096(92)90020-3
V. Tvergaard, J.W. Hutchinson, Int. J. Solids Struct. **33**(20), 3297 (1996). https://doi.org/10.1016/0020-7683(95)00261-8
V. Tvergaard, A. Needleman, Acta Metall. **32**(1), 157 (1984). https://doi.org/10.1016/0001-6160(84)90213-X
P.B. Woelke, M.D. Shields, J.W. Hutchinson, Eng. Fract. Mech. **147**, 293 (2015)
X. Zhu, Int. J. Press. Vessel. Pip. **156**, 40 (2017)

Auxetic Damping Systems for Blast Vulnerable Structures

15

Hasan Al-Rifaie and Wojciech Sumelka

Contents

Introduction 354
Blast-Induced Reaction Forces 355
Uniaxial Graded Auxetic Damper (UGAD) 357
Blast-Vulnerable Steel Gate 357
Designing a Reinforced Concrete Supporting Structure 365
Conclusions 373
References 374

Abstract

Blast-resistant gates are necessary for critical infrastructure, such as embassies, ministries, or parliaments. Lightweight doors/gates equipped with "energy absorbers" have more desirable operational performance than the traditional costly and bulky options. Auxetic damping systems have not yet been used in the supporting structure of blast-resistant gates. Consequently, this chapter tries to propose a complete system consisting of a steel gate, auxetic dampers, and RC supporting structure. The system is supposed to withstand high-intensity blast pressure of 6.6 MPa. Blast behavior of a steel gate was assessed, with and without the proposed uniaxial graded auxetic damper (UGAD), using Abaqus/Explicit solver. Results revealed that the attachment of the proposed UGAD to the gate led to a dramatic drop in permanent deformations (a critical factor for gate operability after a blast event). Hence, a lighter, more economical gate (with 50% reduction of mass) was required to satisfy the operability condition. Moreover, 49% of peak reaction forces were diminished that had a direct impact on the concrete supporting frame. Additional plastic dissipation energy was gained from those sacrificial lightweight auxetics, which justifies the significant reduction in

H. Al-Rifaie (✉) · W. Sumelka
Institute of Structural Analysis, Poznan University of Technology, Poznan, Poland
e-mail: hasan.al-rifaie@put.poznan.pl; wojciech.sumelka@put.poznan.pl

© Springer Nature Switzerland AG 2022

G. Z. Voyiadjis (ed.), *Handbook of Damage Mechanics*,
https://doi.org/10.1007/978-3-030-60242-0_71

permanent deformations, mass of the gate, and reaction forces. Finally, the impact of the blast pressure and the auxetic dampers on the reinforced concrete supporting structure was thoroughly covered using CDP and J-C material models. Results of the designed structure showed that the reinforcement stays in the elastic range. In terms of the concrete, no damage in compression was observed with very limited tension cracks that can be neglected. The complete gate system proposed here can be considered as a novel robust solution for blast vulnerable structures.

Keywords

Blast gate · Steel door · Shock · Impact · Auxetic material · Damping systems · Reaction forces · ConWep · Abaqus

Introduction

Accidental or intentional explosions have become an important global security problem. Civil protection is a priority which includes predicting and mitigating losses arising from these events. Most nations are vulnerable and take serious measures to such man-made disasters. A building explosion nearby can damage structural and non-structural buildings catastrophically. Loss of life or death occurs as a result of explosion, building failure, effects of debris, fire, or smoke (Ngo et al. 2007). A reinforced concrete perimeter wall is the first defense line for sensitive infrastructure, such as embassies, ministries, or parliaments. This perimeter wall requires robust door/gate that can withstand blasts of high intensity.

The identification of the weakest components in the structure is key to successful implementation of a protection system. A research at the US Air Force Research Laboratory points out that doors/gates in many structures have always been one of the weakest points (Anderson and Dover 2003). The traditionally solid and heavy design of the doors also resulted in increased production costs and poor operating performance (Chen and Hao 2014). Gates must therefore be lightweight and can mitigate the effect of extreme loading. The "innovative conception of a gate" and its "supporting frame" can achieve this goal. In literature the first is well covered, but the second is often overlooked (Anderson and Dover 2003).

Researchers have investigated several techniques of energy absorption in terms of the door/gate itself. A US Air Force Research Laboratory study recommends that Accordion-Flex Door be used (Anderson and Dover 2003). The proposed door is an accordion panel that is allowed to deform significantly when exposed to blast pressure. Chen and Hao (2012) present a new blast door configuration consisting of a double layered panel with a multi-arched-surface structural form. Numerically, FE code was used to evaluate blast resistance and energy absorption capacities. The research has shown that multi-arched panels can bear higher explosive charges. The use of innovative materials instead of changing structural form was of interest to Yun et al. (2014). The study suggests the use of aluminum alloy foam to increase the

mitigation of blast pressure. Significant reduction in permanent deformation with high-density foam was observed (Yun et al. 2014). These techniques aim to absorb the energy from the blast by the door structure and decrease the amount of forces transferred to the supporting frame.

In blast events, support frames of blastproof gates play an important role. In literature, the frames of blast-resistant doors, and according to the author's survey, are usually considered as rigid or firm enough to hold the gate, and the failure is either found in the door itself or in the hinges between the door and the supporting frame. This is possible if the door itself can absorb dynamic energy. However, the supporting frame can also be designed to dynamically absorb the impact by incorporating passive damping systems for improved performance. One of the very few studies that implement a damping system is the one done by Fang et al. (2008). The study mentions that "the resistance of the blast doors can be increased obviously by the springs and the dampers, and the shorter the duration of the loads, the more effective the increasing of the resistance."

One of the preferred options is to use cellular materials such as metal foams, honeycomb, and auxetic materials to absorb energy by plastic deformation (Imbalzano et al. 2016). A research by Hou et al. (2016) reveals that re-entrant topology, where the auxetic effect of negative Poisson's ratio appears, sustained larger impact strength than hexagon honeycomb of the same size and material. In the supporting frame of blast-resistant gates, auxetic materials were not yet used as potential damping systems. This chapter therefore seeks to propose a complete system consisting of a steel gate, auxetic dampers, and RC supporting structure. The system is supposed to withstand high-intensity blast pressure of 6.6 MPa. The impact of the blast pressure and the auxetic dampers on the reinforced concrete supporting structure is thoroughly investigated.

Blast-Induced Reaction Forces

As mentioned earlier, blast-resistant gates must be lightweight and capable of mitigating extreme loading effects. This energy absorption can be acquired by innovative design of the gate and its supporting structure. The design of the supporting structure relies mostly on boundary conditions and corresponding reaction forces. The detailed results of this section was published by the authors the as an article titled "Numerical analysis of reaction forces in blast resistant gates" (Al-Rifaie and Sumelka 2017a). Flat steel plate was used as a simplified door structure, as the focus was on reaction forces instead of gate behavior itself. The analyses cover both static and dynamic cases using empirical and numerical methods to illustrate the difference between the two approaches and include some practical tips for engineers as well. The systematic analysis of reaction forces included four distinct boundary conditions (BC) and three aspect ratios (AR). In addition, it also covered the effect of explosive charge and stand-off distance on reaction forces. The objectives were:

- Finding the reaction forces of plates subjected to static uniform pressure (as an equivalent static approximation of a far-field explosion) using numerical simulation (Abaqus/Standard) and then validating the results with analytical solution at specific points.
- Finding the reaction forces of plates subjected to dynamic loading using numerical method (Abaqus/Explicit) and comparing the results with the static outcomes. Then, selecting the optimum BC case for possible implementation of passive damping systems.
- Examining the influence of changing explosive mass or its position on reaction forces.

The following conclusions summarize the results:

- Static analyses revealed that the numerical results were of high similarity to the analytical outcomes. In addition, shear and moment factors for the SFSF and CFCF cases were less affected by the aspect ratio (AR) as the other edges are already not supported. The moment factor of CCCC case has increased significantly with the increase of AR ratio unlike the SSSS case which had slight increase in shear factors due to AR change.
- For dynamic loading, distributed reaction forces on the edges of the plates had different values than the static one. The average increase or decrease in the reaction for each supporting edge of a case was examined. For CFCF and SFSF cases, changing AR had no effect on values of dynamic/static ratio (D/S)avg. as the horizontal edges are already not supported. For SSSS and CCCC cases, changing AR had slight influence. The second point is that less constrained BC cases, such as SSSS and SFSF, revealed lower (D/S)avg. than more constrained cases, CCCC and CFCF. In other words, simply supported cases showed better blast mitigation effects since the motion of the plates are greater than that of the clamped cases, thus reducing the transmitted impulse and, as a consequence, the effects of the blast. Therefore, SFSF or SSSS cases are more favored upon CCCC and CFCF cases due to their potential blast mitigation. Moreover, the distribution of reaction forces in simply supported cases allows efficient implementation of shock absorbers at the supports. The research, therefore, selects SFSF case as optimum option.
- The effect of changing the explosive mass or position on reaction forces was then examined. Results revealed that the percentage of increase in reaction forces due to mass change was approximately linear. On the other hand, the increase in stand-off distance from 5 m to 15 m led to a sharp drop of up to 80% in the reaction forces. Then, more flat curve was observed. Changing the position of the centroid of the explosive material in a plane parallel to the plate under consideration had negligible effect on reaction forces. This was true for far-field explosion scenarios, when the stand-off distance was more than the longest plate side. The results were compared with literature and showed high similarity.

The conclusions made have been used for the design of a "blast-absorbing supporting frame," which will increase the absorbing properties of the gate. This, in return, may lead to lighter and more operational blast-resistant gates.

Uniaxial Graded Auxetic Damper (UGAD)

Auxetic structures are cellular structures that by plastic deformation can absorb impact/blast energy to protect the target (Al-Rifaie et al. 2018). Because of its negative Poison's ratio, they are promising sacrificial systems with high specific strength, lightweight, good energy dissipation, and high specific toughness. The aim of this section is to describe a new uniaxial graded auxetic damper (UGAD) that can function as a shock absorber for variant applications. For more details on the numerical modeling, parametric study and detailed properties of the UGAD refer to (Al-Rifaie and Sumelka 2019a). Figure 1 shows the components of the UGAD, with the cross section and 3D view of one auxetic core.

The parametric study, conducted by the authors (Al-Rifaie and Sumelka 2019a), focused on six parameters that were optimized for efficient response of the uniaxial graded auxetic damper (UGAD). The chosen parameters were loading direction, auxetic cell dimension, aluminum grade, cell angle θ, and the effective number of layers (as summarized in Fig. 2). The last important parameter was cell wall thickness t. The optimum parameters were selected based on plastic dissipation energy (PDE) and the ratio of reaction force to applied load (RFd/P). The achieved mechanical and geometrical properties of the three auxetic cores are listed in Table 1. They have identical L, θ, material grade, size and hence, overall volume. Results showed that the three auxetic cores had a wider strength range of (1–10 MPa) and plateau region (80% of the total crushing strain) that can justify the superior performance of the UGAD under distinct blast levels.

Blast-Vulnerable Steel Gate

The gate is assumed to secure a critical structure's main entrance, such as an embassy, ministry, or hospital, that requires the highest level of protection (Buildings levels of protection (Dusenberry 2010)). Evacuation is not required, and only superficial damage is expected. A reinforced concrete structure, of 4 m height, supports the gate that serves as the main entrance to the facility. In terms of the gate itself, the blast performance of gate assembly supposed to be in Category II of ASTM F2247–03, where the gate stays operable with small permanent deformation. UFC mentions that a door can be still be considered as "operable," when the rotation of the door edge does not exceed 2°. In addition, the following assumptions were made here; the gate is not within the explosion fireball; the blast occurs at sea level; and the charge was uncased without extra loading from fragmentations. The steel gate, UGADs, and conceptual supporting concrete structure are shown in Fig. 3. It presents where those sacrificial auxetic dampers are located. According to Fig. 3, the gate requires twenty UGADs uniformly distributed (10 at the top and 10 at the bottom) to mitigate potential blast energy.

The entrance/gate system is supposed to have a clear height of 2600 mm with a clear width of 4100 mm. These dimensions are suitable for entry of small to medium-sized vehicles, in addition to a pedestrian lane on either side (Fig. 4). Hence, the sliding steel door dimensions are 3000 mm high and 4500 mm wide (providing a

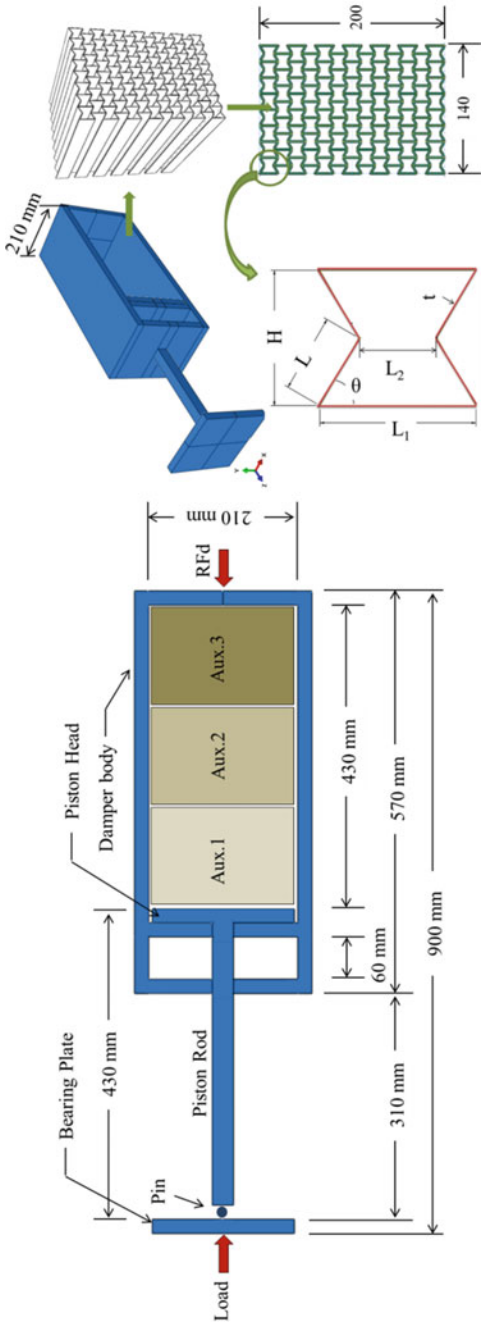

Fig. 1 Components of the UGAD and its auxetic core

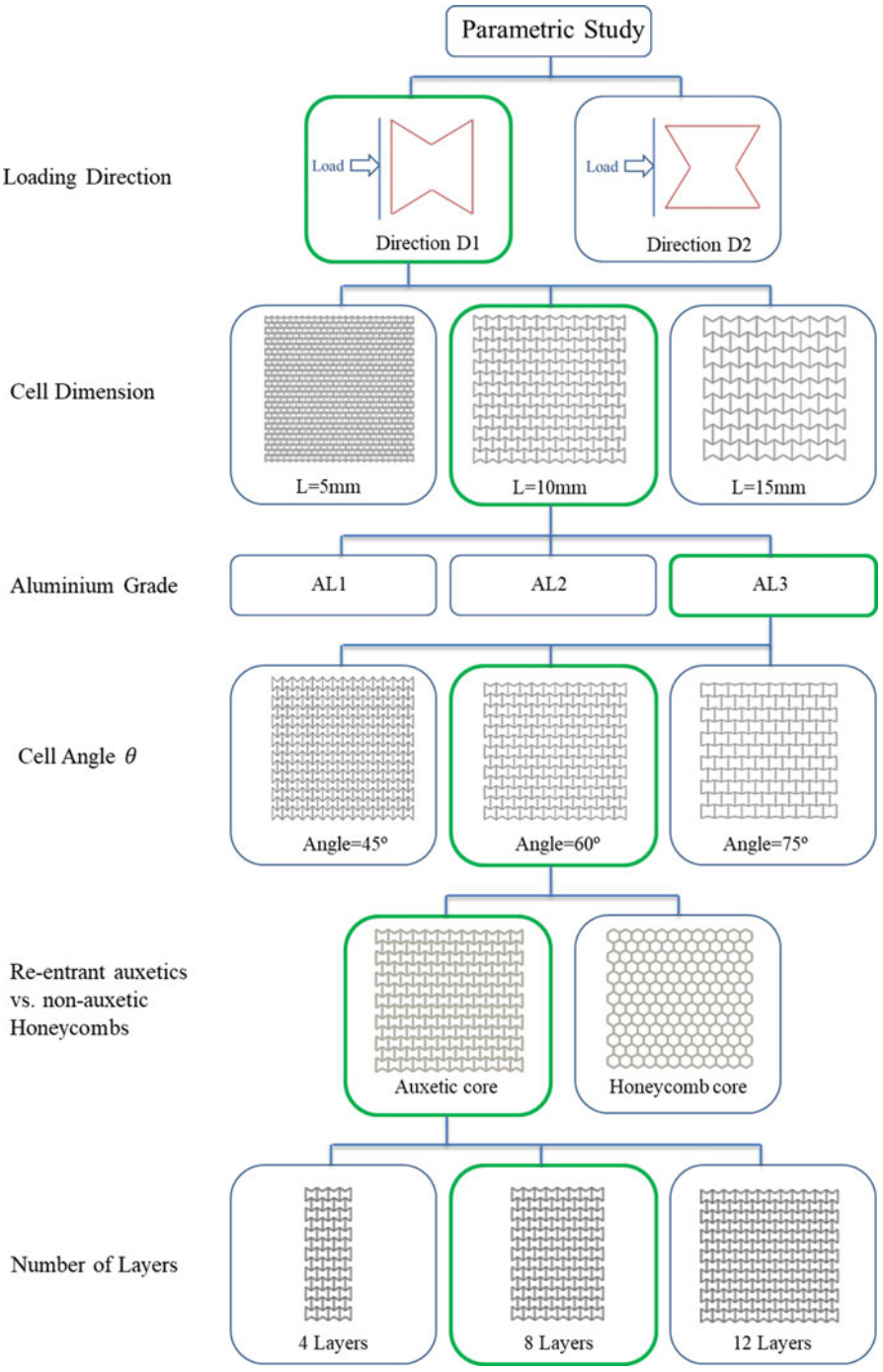

Fig. 2 Tree diagram of the auxetic core parametric study and the selected parameters (highlighted in green)

Table 1 The three auxetic cores of the UGAD, with their geometrical and mechanical characteristics

	Auxetic core 1	Auxetic core 2	Auxetic core 3
Shape	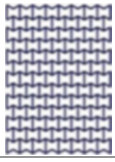	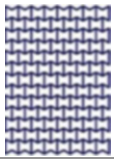	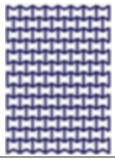
Similar parameters	$L = 10$ mm, cell angle $\theta = 60°$, Grade AL3 ($\rho_s = 2.703^* 10^{-9}$ t/mm^3), Size $= 140 \times 200 \times 200$ mm, volume of one core $V = 5.6 \times 10^6$ mm^3		
t (mm)	1.4	1.8	2.2
t/L	0.14	0.18	0.22
Mass in (ton)	0.00338	0.00434	0.00530
Mass in (kg)	3.38	4.34	5.30
Density ρ in (t/mm^3)	6.036×10^{-10}	7.75×10^{-10}	9.46×10^{-10}
Relative density $\rho^* = \rho/\rho_s$	0.223	0.287	0.35
Void ratio %	77.7	71.3	65

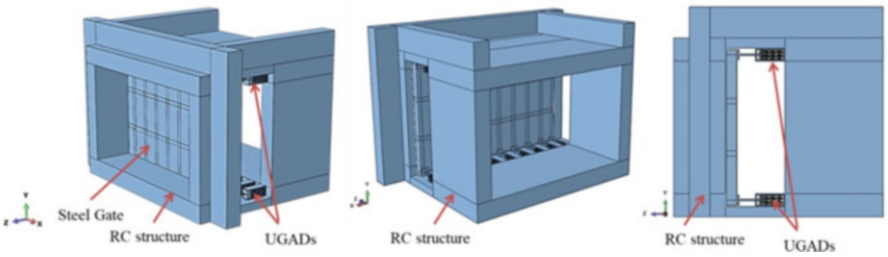

Fig. 3 The 3D and side views of the gate system, showing the steel gate, the 20 UGADs, and the RC supporting structure

bearing surface of 200 mm on the supports and fulfilling the previously mentioned clear opening requirement). The simply supported free SFSF case was selected as the optimum boundary conditions based on the conclusions of Al-Rifaie and Sumelka (2017a). Therefore, the door was presumed to slide between two gutters here, i.e., the longest horizontal sides are simply supported and the vertical sides are free.

The gate/door structure consists of a steel frame welded to steel plates on both the front and the back. The frame consists of 10 vertical and 4 horizontal, rectangular, 180 × 100 mm hollow sections, each with 500 mm and 1000 mm c/c spacing. Front, top, side, and 3D views of the gate are shown in Fig. 5. The front and back plate are assumed to have the same thickness t as the rectangular hollow sections. The dimensions of the gate are constant, while the thickness t varies. Four different t-values, 2.5, 5, 7.5, and 10 mm, for four different gates, are, respectively, abbreviated as G2.5, G5, G7.5, and G10.

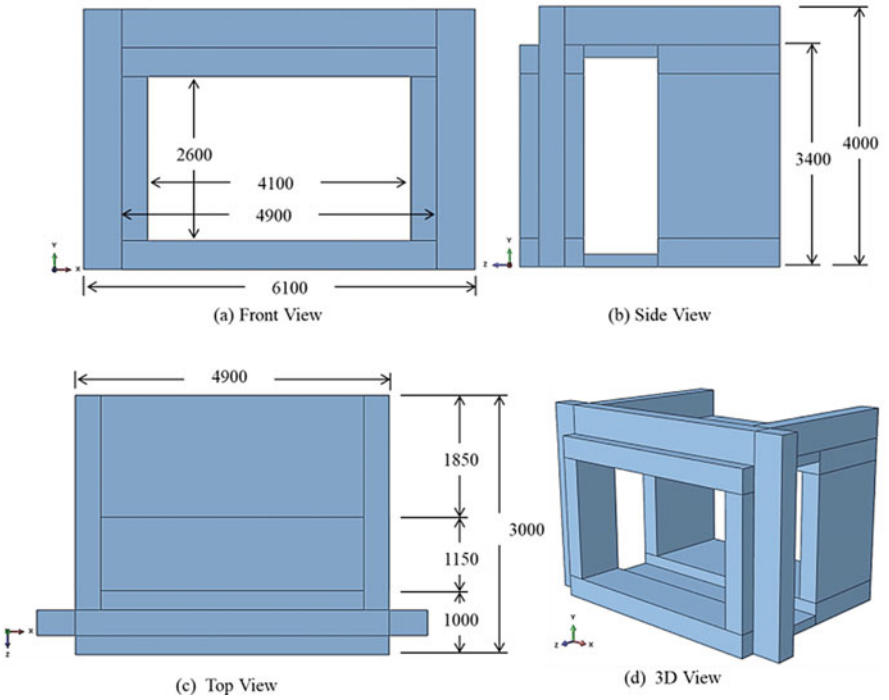

Fig. 4 Front, side, top, and 3D view of the proposed concrete frame with its dimensions

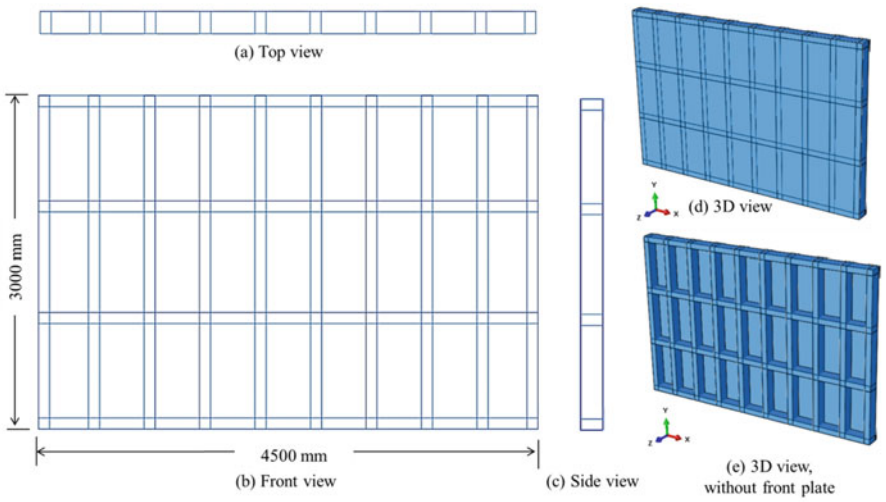

Fig. 5 Top (**a**), front (**b**), side (**c**), and 3D views of the steel gate (**d**, **e**)

Weldox 460 E steel material was used for both the plates and the hollow sections. Weldox is a class of thermomechanically rolled ferritic structural steels that offer both ductility and high strength (Børvik et al. 2001). Børvik et al. (2001) give material parameters for the Weldox 460 E steel as shown in Table 2. Such a choice was based on previous outcomes of (Sumelka and Łodygowski 2011; Łodygowski et al. 2012; Sielicki et al. 2017; Szymczyk et al. 2018). In the present research, Johnson-Cook model (known also as Litonski model (Litonski 1977)) was used for plasticity and damage description.

Johnson-Cook material model is one of the semi-empirical constitutive models that can describe the material's plastic behavior at "high" strains, strain rates, and temperatures. The model (in Eq. (1)) describes the evolution of yield stress σ_y and takes into account the strain rate hardening and thermal softening effects (Johnson and Cook 1983, 1985; Grazka and Janiszewski 2012; Shrot and Bäker 2012).

Table 2 Material parameters for Weldox 460 E Steel

Category	Constant	Description	Unit	Value
Elastic constants	E	Modulus of elasticity	MPa	$200*10^3$
	ν	Poisson's ratio	–	0.33
Density	ρ	Mass density	t/mm^3	$7.85*10^{-9}$
Yield stress and strain hardening	A	Yield strength	MPa	490
	B	Ultimate strength	MPa	807
	n	Work-hardening exponent	–	0.73
Strain-rate hardening	$\dot{\varepsilon}_0$	Reference strain rate	S^{-1}	$5*10^{-4}$
	C	Strain rate factor	–	0.0114
Damage evolution	D_c	Critical damage	–	0.3
	p_d	Damage threshold	–	0
Adiabatic heating and temperature softening	C_p	Specific heat	$mm^2/S^2 K$	$452*10^6$
	χ	Taylor-Quinney empirical constant/inelastic heat fraction	–	0.9
	α	Coefficient of thermal expansion	K^{-1}	$1.1*10^{-5}$
	T_m	Melting temperature	K	1800
	T_0	Room temperature	K	293
	m	Thermal-softening exponent	–	0.94
	K	–	–	0.74
Fracture strain constants	d_1	–	–	0.0705
	d_2	–	–	1.732
	d_3	–	–	−0.54
	d_4	–	–	−0.015
	d_5	–	–	0

Adopted from (Børvik et al. 2001)

The dimensionless temperature parameter $\widehat{\mathrm{T}}$ is defined in Eq. (2), and it was assumed that adiabatic regime holds, therefore temperature rise came from plastic work only.

$$\sigma_y = (A + B\,\varepsilon^n)\left[1 + C\,\ln\left(\frac{\dot{\varepsilon}}{\dot{\varepsilon_0}}\right)\right]\left[1 - \left(\widehat{T}\right)^m\right], \tag{1}$$

$$\begin{cases} \widehat{T} = 0 \text{ for } T < T_0 \\ \widehat{T} = \dfrac{T - T_0}{T_m - T_0} \text{ for } T_0 < T < T_m \\ \widehat{T} = 1 \text{ for } T > T_m \end{cases} \tag{2}$$

where ε is the plastic strain, $\dot{\varepsilon_0}$ is the reference plastic strain rate, $\dot{\varepsilon}$ is the plastic strain rate, T is the current material temperature, T_0 is transition or room temperature, and T_m is the melting threshold of a material. It is assumed that at or below room temperature, the yield stress has no temperature dependence. The material parameters covered at or below T_0 are A, B, C, m, and n, where A is the yield stress, B is the pre-exponential factor, C is the strain rate factor, m is the thermal-softening exponent, and n is the work-hardening exponent.

Moreover, the Johnson-Cook dynamic failure model is provided by Abaqus/Explicit (Dassault Systèmes 2016). The failure is supposed to start when damage parameter ω is more than 1. Damage parameter is:

$$\omega = \sum\left(\frac{\Delta\varepsilon}{\varepsilon_f}\right), \tag{3}$$

where ε_f is the plastic strain at failure, $\Delta\varepsilon$ is an increment of plastic strain, and the summation is done for all increments within an analysis. The pressure to HMH stress ratio $\frac{p}{q}$, nondimensional plastic strain rate $\frac{\dot{\varepsilon}}{\dot{\varepsilon_0}}$, and the dimensionless temperature parameter $\widehat{T}$ are the main factors that plastic strain at failure ε_f is dependent on. Hence, strain at failure ε_f can be written as follows:

$$\varepsilon_f = \left[d_1 + d_2 \exp\left(d_3\,\frac{p}{q}\right)\right]\left[1 + d_4\,\ln\left(\frac{\dot{\varepsilon}}{\dot{\varepsilon_0}}\right)\right]\left(1 + d_5\,\widehat{T}\right), \tag{4}$$

where $d_1 - d_5$ are the failure parameters.

According to literature review of current blast-resistant doors in Al-Rifaie and Sumelka (2017b) and Al-Rifaie (2019), it was perceived that the design of a relatively lightweight, 3000 × 4500 mm, gate that could sustain 6.6 MPa of pressure is a challenging target. Therefore, the 6.6 MPa is set as the criteria required to be met (not necessarily a specific mass or stand-off distance). However, to demonstrate the 6.6 MPa, a combination of 100 kg of TNT at 5 m was selected here as ConWep input parameters. This blast pressure can also be achieved from other M-R combinations, such as 45 kg luggage at 3.8 m, 200 kg car at 6.2 m or 2000 kg van at 13.5 m. It is important to mention that all the M-R combinations above have the same scaled

distance of =1.07 m/kg$^{1/3}$, which is greater than the scaled distance 0.4 m/kg$^{1/3}$ (limit to avoid close-range detonations).

The gates, G2.5, G5, G7.5, and G10, are tested for 4 levels of blast pressures, 1.65 MPa, 3.3 MPa, 4.95 MPa, and the maximum 6.6 MPa, received from 25 kg, 50 kg, 75 kg, and 100 kg of TNT at $R = 5$ m, respectively. The levels are useful to assess the corresponding difference in reaction forces and hence, the response of UGAD dampers for each specific level. The overpressure and positive impulse time histories of the four levels is shown in Fig. 6, based on ConWep loading on the gate frontal plate.

Permanent deformation and operability of the gates are shown in Table 3 with the proposed auxetic damper, subjected to 6.6 MPa blast pressure from 100 kg TNT at $R = 5$ m. Both G7.5 and G5 have passed the operability requirement with $d_{\text{frame}} < D_{\text{limit}}$ (26.2 mm). The frame permanent deformation of G7.5 dropped from 28.4 to 4 mm with the addition of the UGADs. Furthermore, the frame permanent deformation of G5 decreased from 40.5 to 22 mm with the addition of the UGADs, making G5 as the lightest-operable gate that can withstand the blast pressure target of 6.6 MPa.

Results showed that up to 3.3 MPa blast pressure, the first auxetic core (Aux.1) was the only deformed one with maximum deformation of 92 mm. In other words, only Aux.1 has to be changed after such a blast event. Blast pressures between 3.3 and 6.6 MPa induce a plastic deformation in both Aux.1 and Aux.2 cores, i.e., both of them should be replaced after such a high blast event. Permanent deformation of Gate G5 and the UGAD are shown in Fig. 7, for 6.6 MPa blast pressure. Although Aux.3 was designed to absorb the 6.6 MPa blast pressure, the first two cores were

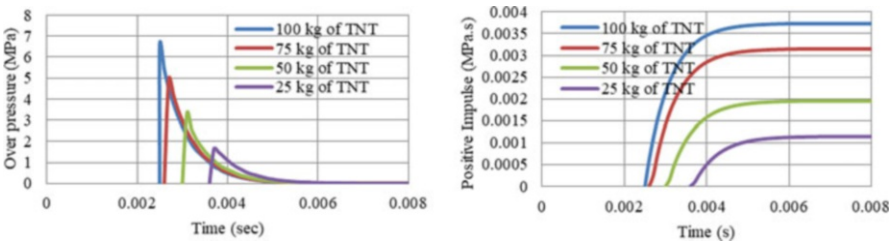

Fig. 6 Overpressure and positive impulse time histories of the four blast levels (25 kg, 50 kg, 75 kg, and 100 kg, $R = 5$ m)

Table 3 Permanent deformation and operability of the gates without and with the proposed auxetic damper, when subjected to 6.6 MPa blast pressure from 100kgTNT at $R = 5$ m

		Without UGADs		With UGADs	
Gate	t (mm)	Frame	Operable (Yes/No)	Frame	Operable (Yes/No)
G2.5	2.5	551.0	No	676	No
G5	5	40.5	No	22	Yes
G7.5	7.5	28.4	No	4	Yes
G10	10	4.4	Yes		

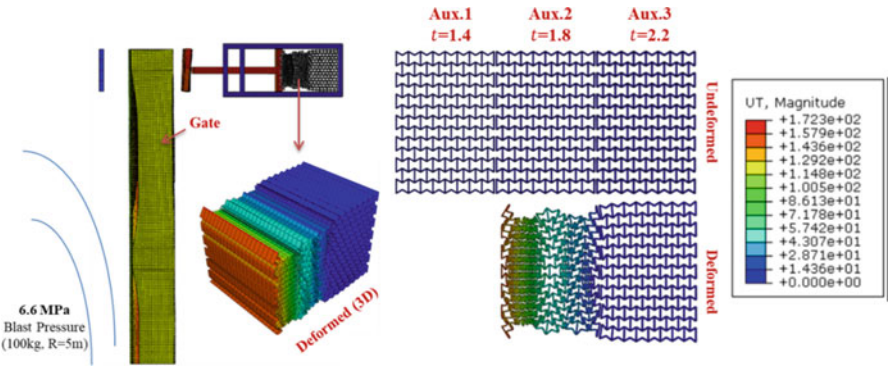

Fig. 7 Displacement of Gate G5 and the auxetic damper after a blast pressure of 6.6 MPa from 100 kg TNT at $R = 5$ m

able to absorb the impact up to their capacity without affecting the third core (Aux.3). Hence Aux.3 hereafter would function as a factor of safety for unexpected higher blast loads or multiple explosions in a short period of time.

In addition, 49% reduction in peak reaction forces was achieved that can reduce the required cross section and strength of the concrete supports. Results also revealed that internal energy in the whole model composed mainly of plastic dissipation, small frictional dissipation, and no dissipation due to damage. Moreover, 56% of the total plastic dissipation energy in the system was achieved from the UGADs, while 44% from the gate. Based on that significant energy dissipation, the kinetic energy was mitigated. The additional plastic dissipation energy achieved from those sacrificial lightweight auxetic cores justifies the noticeable drop in permanent deformations and reaction forces. For more details on the numerical modeling and results, refer to Al-Rifaie and Sumelka (2020).

Designing a Reinforced Concrete Supporting Structure

The final stage was to propose a reinforced concrete frame that would support the gate and the UGADs. This concrete frame supposed to stay in elastic range within the 6.6 MPa blast level under consideration. It is subjected to a direct blast from the explosion in addition to loads from the UGADs (distributed on small surfaces). The reinforced concrete structure consists of a slab, beams, columns, and a base. The total size of the structure has a length of 6100 mm (in x-axis), height of 4000 mm (in y-axis), and depth of 3000 mm (in z-axis). Figure 4 provides the dimensions, where the front (a), side (b), top (c), and 3D view (d) are shown.

In terms of reinforcement, Fig. 8 shows their distribution in the concrete frame. The main reinforcement of the beams and columns were ∅25 mm distributed evenly @150 mm c/c, while the stirrups were ∅12 mm@150 mm c/c. Each of the slab and the base had two grids of ∅12 mm@150 mm c/c in both directions. B490 was the

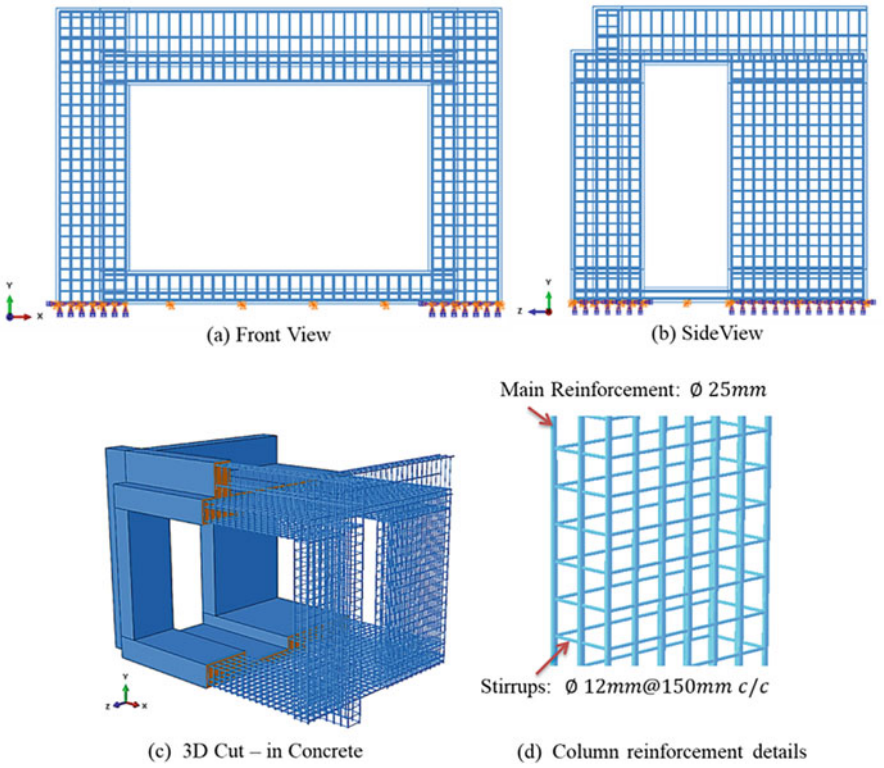

Fig. 8 Reinforcement and boundary conditions of the concrete frame

chosen grade for steel reinforcement with yield strength of 490 MPa. Reinforcement material parameters were the same provided in Table 2 leading to a comprehensive material model that covers elastic, plastic, strain hardening, and damage stages. Generally, reinforcing steel grades, with ~500 MPa characteristic strength, has replaced Grade 250 and Grade 460 throughout Europe, as they satisfy the three recommended ductility classes in BS 1992-1-1:2004 (Eurocode 2). The steel bars were modeled using two-node linear beam element (B31) with mesh size of 100 mm. The interaction between the steel bars and the concrete were added using the "embedded elements" feature provided by Abaqus, as recommended in literature.

In terms of boundary conditions, the concrete frame is assumed to be fixed at bottom surface of its base, in addition to fixing the end nodes of the main columns' steel bars (as shown in Fig. 8a, b). The simulation of the substructure (foundation and soil) was out of the scope of this chapter as it required detailed geotechnical modelling with soil-structure interaction.

The concrete was modelled using explicit 8-node linear brick element (C3D8R) with reduced integration and hourglass control. Mesh size was 50 mm, which proved to be accurate for the scale of the problem under investigation. The ultra-high-performance fiber-reinforced concrete (UHP-FRC) was used due to its superior

mechanical properties, of quasi-static compression and tension of up to 200 MPa and 15 MPa, respectively (Hassan et al. 2012; Solhmirzaei and Kodur 2017; Al-Rifaie and Sumelka 2019b).

The material behavior of concrete has been specified using the concrete damage plasticity (CDP) model. CDP model provides a general capability of modelling concrete or any quasi-brittle materials under static, dynamic, or cyclic loading. The model was first introduced by Lubliner et al. (1989) for monotonic loading, and later was extended, by Lee and Fenves (1998), for dynamic and cyclic loading. The CDP is selected here as it allows the definition of plastic range together with strain rate hardening and damage, both in tension and compression, using a set of adjustable parameters measured experimentally for any type of concrete (Othman 2016).

The typical uniaxial compression and tensile stress-strain curves, specified by CDP model, are shown in Fig. 9. The compression response starts with an elastic phase till reaching initial yield (σ_{c0}). Then, it is followed by plastic hardening phase up to an ultimate stress (σ_{cu}). The final phase is the stress-softening response. In uniaxial tension, the response follows a linear elastic phase up to a failure stress (σ_{t0}), beyond which, the formation of micro-cracks is presented by a softening/cracking phase, inducing strain localization in the concrete (Dassault Systèmes 2016).

In ABAQUS built-in CDP model, the non-linear response of concrete is defined as tabular input of stress-inelastic strain. From experimental stress-strain curves, the inelastic/cracking strain can be calculated as

$$\begin{aligned} \varepsilon_c^{\text{in}} &= \varepsilon_c - \frac{\sigma_c}{E_0}, \\ \varepsilon_t^{\text{in}} &= \varepsilon_t - \frac{\sigma_t}{E_0}, \end{aligned} \tag{5}$$

where the subscripts c and t refer to the compression and tension, respectively; ε_c^{in} and ε_t^{in} are the inelastic strains; ε_c and ε_t are the total strains; σ_c and σ_t are the stresses; and E_0 is the initial (undamaged) elastic modulus.

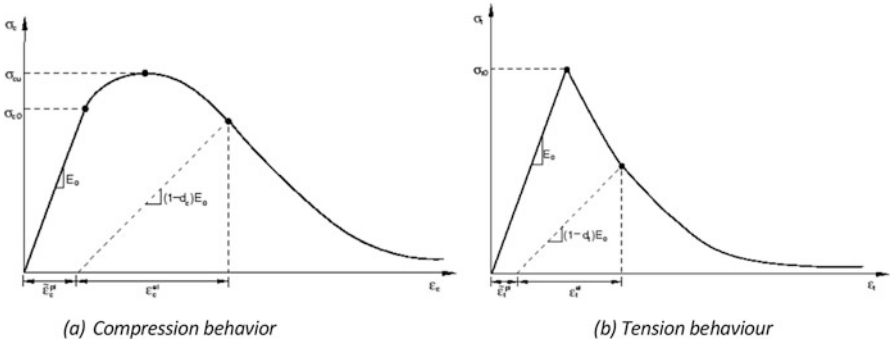

Fig. 9 The typical uniaxial compression and tensile stress-strain constitutive relations in the CDP model (Dassault Systèmes 2016)

The stiffness degradation is considered by defining two scalar variables: compressive damage parameter (d_c) and tensile damage parameter (d_t). They are assumed to be functions of plastic strains and can take values from zero (representing the undamaged material), to one (representing the complete damage) (Dassault Systèmes 2016). Damage parameters can be calculated as follows:

$$\begin{aligned} d_c &= 1 - \frac{\sigma_c E_0^{-1}}{\sigma_c E_0^{-1} + \varepsilon_c^{in}\,(1 - b_c)}, \\ d_t &= 1 - \frac{\sigma_t E_0^{-1}}{\sigma_t E_0^{-1} + \varepsilon_t^{in}\,(1 - b_t)}, \end{aligned} \tag{6}$$

where the proportional factors, b_c and b_t, range between 0 and 1 and can be determined experimentally based on curve-fitting of cyclic uniaxial compressive and tension tests. The inelastic strains (ε_c^{in} and ε_t^{in}) and damage parameters (d_c and d_t) are automatically converted by ABAQUS to plastic strains (ε_c^{pl} and ε_t^{pl}) using

$$\begin{aligned} \varepsilon_c^{\mathrm{pl}} &= \varepsilon_c^{\mathrm{in}} - \frac{d_c}{(1 - d_c)}\,\frac{\sigma_c}{E_0}, \\ \varepsilon_t^{\mathrm{pl}} &= \varepsilon_t^{\mathrm{in}} - \frac{d_t}{(1 - d_t)}\,\frac{\sigma_t}{E_0}. \end{aligned} \tag{7}$$

Stiffness recovery factors for compression (ω_c) and tension (ω_t) can be specified for reverse loading. The compressive stiffness can be assumed as recoverable after crack closure, when the load changes from tension to compression, i.e., $\omega_c = 1$. However, tensile stiffness is not recoverable, as crushing micro-cracks have already developed at that stage, i.e., $\omega_t = 0$ (Dassault Systèmes 2016; Othman 2016). The later values are the default stiffness recovery factors defined in ABAQUS, which give the load cycle presented in Fig. 10.

It is critical here to model the increase of concrete strength at high strain rates, for both compression and tensile behavior. The dynamic increase factor (DIF) for normal strength of concrete is well-documented in the literature (Malvar and Crawford 1998; Malvar and Ross 1998; Li and Meng 2003). Figure 11 shows the strain rate-DIF relationship based on different studies (Guner and Vecchio 2012). Millard et al. (2010) state that those DIF can be used in a conservative design of UHP-FRC structures. Based on Fig. 11, Table 4 was prepared, for the range of strain rates expected in the model.

As an input values for the ABAQUS concrete damage plasticity (CDP) model, the material parameters of the UHP-FRC are adopted from Solhmirzaei and Kodur (2017) and listed in Table 5. The quasi-static tension and compression stress-strain relationships for the UHP-FRC applied in the modelling are based on the experimental tests, presented by Yang et al. (2012). Then, they were increased, for different strain rates, based on the dynamic increase factor listed in Table 4. Using the CDP analytical model (mentioned earlier) and damage parameters (presented in Fig. 12), the plastic strains were computed and then plotted versus compressive and tensile

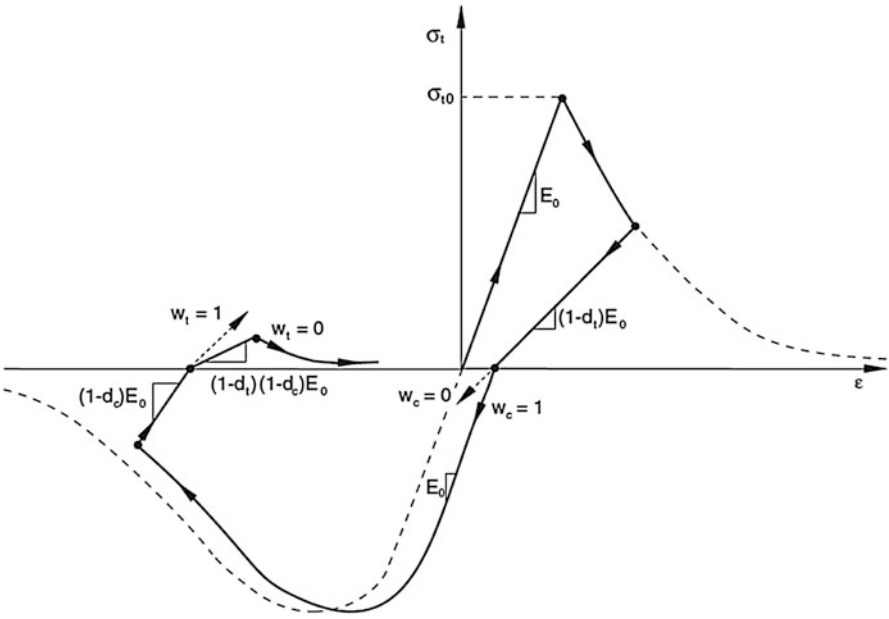

Fig. 10 The uniaxial load cycle of CDP model with default stiffness recovery factors (Dassault Systèmes 2016)

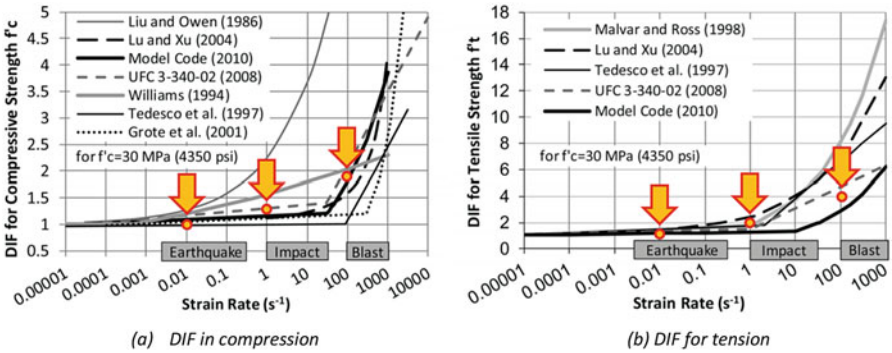

Fig. 11 (**a**) DIF in compression. (**b**) DIF for tension. Strain rate-DIF relationship for compression and tension. (Adopted from Guner and Vecchio (2012))

Table 4 Dynamic increase factors (DIF)

	Dynamic increase factors (DIF)	
Strain rate	Compression	Tension
0.01	1	1
1	1.2	2
100	1.8	4

Highlighted in Fig. 11

Table 5 UHP-FRC material parameters

Description	Value	Description	Value
Modulus of elasticity	43,970 MPa	Eccentricity	0.1
Poisson's ratio	0.2	K_c	0.666
Mass density	2.565* 10^{-9} t/mm^3	σ_{b0}/σ_{c0}	1.16
Dilation angle	39°	Viscosity parameter	0.0001

Adopted from (Solhmirzaei and Kodur 2017)

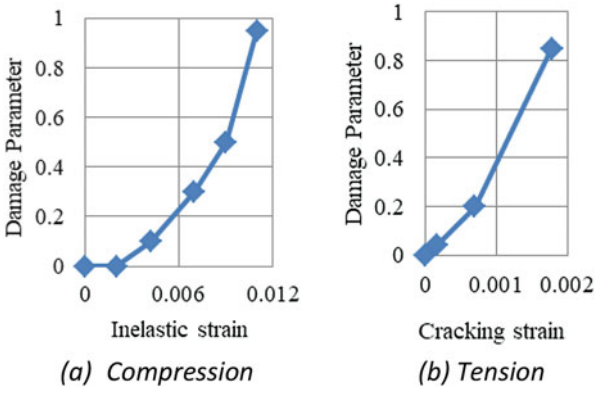

Fig. 12 (**a**) Compression. (**b**) Tension. Damage parameters with respect to uniaxial compression and tension, respectively, adopted in the CDP material model of the UHP-FRC

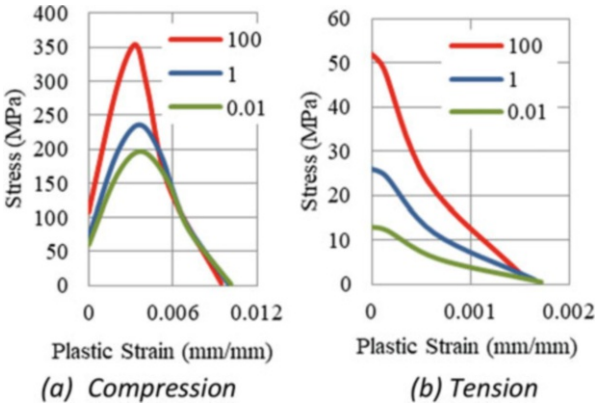

Fig. 13 (**a**) Compression. (**b**) Tension. Plastic strain with respect to compressive and tensile stresses, for different strain rates, used in the CDP material model of the UHP-FRC

stresses (as shown in Fig. 13). It is clear that peak quasi-static compressive strength is 196.7 MPa, while the tension strength is 13 MPa (for strain rate ~ 0.01 s-1), which reflects the high strength and ductility of this type of concrete.

The discussed constitutive parameters for concrete were then applied to check supporting structure validity for the $M = 100$ kg, $R = 5$ m explosion. It is important to mention that the standoff distance $R = 5$ m is counted from the centroid of the explosive mass to the steel gate. While the concrete frame was 1 m closer to the detonation source, therefore, the blast peak overpressure on concrete frame was 8 MPa; more than the 6.6 MPa limit specified earlier. Under the recently mentioned intense blast pressure, the reinforcement was successful in keeping the integrity of the concrete frame, gate, and UGADs in place. However, although UHP-FRC with sufficient reinforcement was used, the concrete frame experienced tension damage in the form of multiple cracks. This can be linked to the fact that the concrete frame (with longest exposed dimension = 6100 mm > $R = 4$ m) is within the "close-range" concentrated blast pressure. To prevent such tension cracks in the concrete for $M = 100$ kg, the stand-off distance have to be increased through vehicle barriers/bullroads. Therefore, in the next stage, the closest allowable stand-off distance was investigated. It was found that the stand-off distance should be doubled to $R = 10$ m ($R = 9$ m to the concrete frontal face).

Thus, for the $M = 100$ kg at $R = 10$ m, results revealed that the reinforcement stays in the elastic range (as shown in Fig. 14). In terms of the concrete, no damage in compression was observed with very limited tension cracks that can be neglected. Figure 15 shows the tension and compression damage in the concrete material.

The deformations of the concrete frame were also checked, as excessive elastic deflections may indirectly influence the performance of the UGADs and hence the operability of the gate. Figure 16 shows peak elastic deflections in the concrete frame and its reinforcement, for $M = 100$ kg TNT, $R = 10$ m. The deflections are increasing gradually from 0 (near the base) to only 1 mm (in the area supporting upper UGADs). The influence of such a drift of (1/3000) = 0.03% is very small and can be neglected. The maximum deflections can be seen at upper inverted beams with

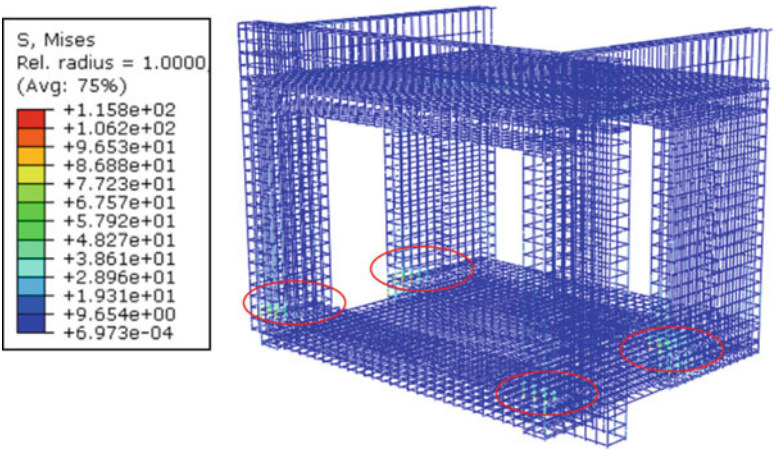

Fig. 14 Distribution of peak HMH stresses in the steel reinforcement, for $M = 100$ kg TNT, $R = 10$ m

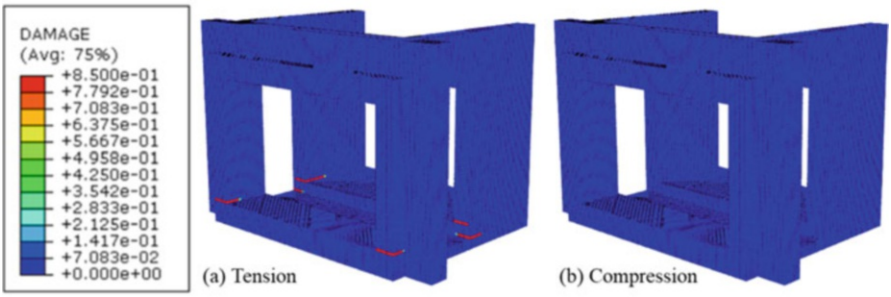

Fig. 15 Tension and compression damage in the concrete material, for $M = 100$ kg TNT, $R = 10$ m

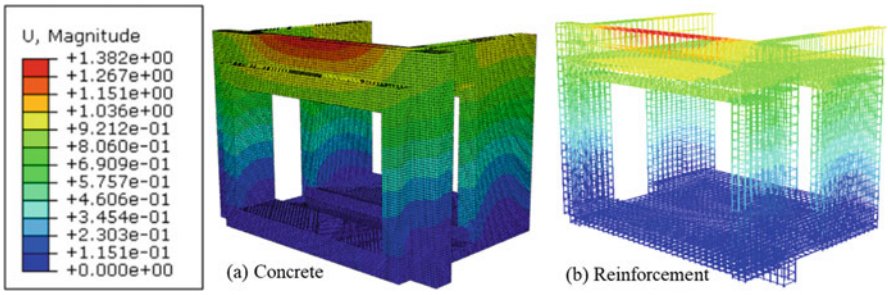

Fig. 16 Peak deflections (mm) in the concrete fame and reinforcement, for $M = 100$ kg TNT, $R = 10$ m

peak value of only 1.38 mm. In short, the concrete structure proposed in this section showed to be effective in supporting the gate and the UGADs. It was demonstrated that, for $M = 100$ kg and $R = 10$ m, the performance of the steel reinforcement was in the elastic range, with minimal damage in UHP-FRC that can be accepted. Further re-designing of the concrete frame, for $M = 100$ kg and $R = 5$ m, is the author's interest as a future task.

The final numerical model (gate, UGADs, and the reinforced concrete support) consists of 2,976,364 elements, from which 387,776 are linear hexahedral elements of type C3D8R, 2,560,560 are linear quadrilateral elements of type S4R, and 28,028 are linear line elements of type B31. The computational time of running the model with the explicit solver, on 8 cores processor, was approximately 25 hrs. The final step was to look at the energy components, to check the accuracy of the whole numerical model (gate, UGADs, and the reinforced concrete support). According to Fig. 17, the internal energy was mainly composed of plastic and frictional energy dissipations. About 93% of the kinetic energy was dropped sharply in only 0.01 s, showing the superior influence of the UGADs to eliminate the movement of the gate. Finally, the artificial strain energy was so small, fluctuating near zero, which reflects the accuracy of the whole numerical model.

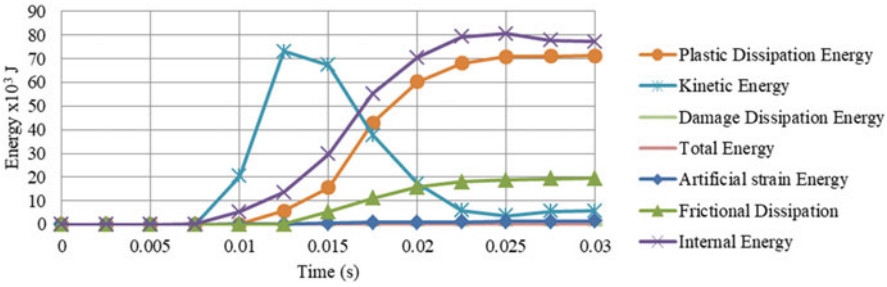

Fig. 17 Energy components in the whole numerical model (gate, UGADs, and the reinforced concrete support), subjected to a blast pressure from 100 kg of TNT, $R = 10$ m

Conclusions

The aim of the chapter was to propose a new system that consists of auxetic passive dampers, a relatively lightweight steel gate, and RC supporting frame. The system is supposed to resist multiple high intensity blast pressure, of up to 6.6 MPa.

The proposed UGAD is composed of four main parts, which are the bearing plate, piston, damper body, and three auxetic cores, for three different blast levels. The parametric study looked at six parameters that had to be optimized for more desirable performance of the UGAD. The chosen parameters were loading direction D1, cell dimension B (L = 10 mm), aluminum grade AL3 (6063-T4), and cell angle $\theta = 60°$, auxetic rather than honeycomb, and 8–12 layers was the range for effective number of layers. Regarding cell wall thickness t of the auxetic cores, the lightest-most effective three auxetic cores that were fitted in the UGAD, namely, Aux.1, Aux.2, and Aux.3, had cell wall thickness t of 1.4, 1.8, and 2.2 mm, respectively.

The case and threat possibilities were highlighted including geometrical and material properties of the gate. The design of the gate was conducted for four levels of blast pressures, 1.65 MPa, 3.3 MPa, 4.95 MPa, and the maximum 6.6 MPa, achieved from 25 kg, 50 kg, 75 kg, and 100 kg of TNT at $R = 5$ m, respectively. The structural behavior of four gates, G2.5, G5, G7.5, and G10, was assessed numerically using ABAQUS/Explicit solver. With the UGADs, the frame permanent deformation of G5 decreased from 40.5 to 22 mm, making G5 as the lightest-operable gate that can withstand the blast pressure target of 6.6 MPa. In addition, 49% reduction in peak reaction forces was recorded. The plastic energy dissipation gained from those sacrificial lightweight auxetic cores justifies the significant reduction in the gate's permanent deformations and reaction forces.

Finally, a reinforced concrete supporting frame was proposed. Material parameters for both concrete and reinforcement were defined using CDP and J-C material models, respectively. Under the 6.6 MPa intense blast pressure, the reinforcement was successful in keeping the integrity of the concrete frame, gate, and UGADs in place. However, although UHP-FRC with sufficient reinforcement was used, the concrete frame experienced tension damage in the form of multiple cracks. The

concrete frame (with longest exposed dimension = 6100 mm > R = 4 m) is within the "close-range" concentrated blast pressure. To prevent such tension cracks in the concrete for M = 100 kg, the stand-off distance have to be increased to R = 10 m. Then, for the M = 100 kg at R = 10 m, results showed that the reinforcement stays in the elastic range. In terms of the concrete, no damage in compression was observed with very limited tension cracks that can be neglected.

The complete system proposed can be designed to withstand other blast pressures, based on changing the cell wall thickness of the UGAD auxetic cores. For future research, the author recommends testing the same UGAD for other applications, trying different auxetic topologies/materials, where additive manufacturing techniques play an important role.

References

H. Al-Rifaie, in *Application of Passive Damping Systems in Blast Resistant*, ed. by I. Gates (Wydawnictwo Politechniki Poznańskiej, Poznan, 2019)

H. Al-Rifaie, W. Sumelka, Numerical analysis of reaction forces in blast resistant gates. Struct. Eng. Mech. **63**(3), 347–359 (2017a)

H. Al-Rifaie, W. Sumelka, Numerical assessment of a blast-protective steel gate with a new damping system. 22nd International Conference on Computer Methods in Mechanics, Lublin, Poland, 2017b, pp. MS11 (15–16). Lublin University of Technology

H. Al-Rifaie, W. Sumelka, The developement of a new shock absorbing uniaxial graded Auxetic damper (UGAD). Materials **12**(16), 2573 (2019a). https://doi.org/10.3390/ma12162573

H. Al-Rifaie, W. Sumelka, Numerical analysis of a reinforced concrete supporting structure for blast resistant gates. Paper presented at the 4th Polish Congress of Mechanics and 23rd International Conference on Computer Methods in Mechanics (PCM-CMM), (2019b) Krakow, Poland

H. Al-Rifaie, W. Sumelka, Improving the blast resistance of large steel Gates-numerical study. Materials **13**(9), 2121 (2020). https://doi.org/10.3390/ma13092121

H. Al-Rifaie, W. Sumelka, P. Sielicki, Parametric Design of Re-Entrant Auxetics for Efficient Blast Energy Absorption. Paper presented at the 5th International Conference on Protective Structures (ICPS5), Poznan, Poland, 2018

M. Anderson, D. Dover, Lightweight, blast-resistant doors for retrofit protection against the terrorist threat. 2nd International Conference on Innovation in Architecture, Engineering and Construction (AEC), Loughborough University, 2003. Applied Research Associate

T. Børvik, O. Hopperstad, T. Berstad, M. Langseth, A computational model of viscoplasticity and ductile damage for impact and penetration. Eur J Mech-A/Solids **20**(5), 685–712 (2001)

W. Chen, H. Hao, Numerical study of a new multi-arch double-layered blast-resistance door panel. Int J Impac Eng **43**, 16–28 (2012)

W. Chen, H. Hao, Experimental investigations and numerical simulations of multi-arch double-layered panels under uniform impulsive loadings. Int J Impac Eng **63**, 140–157 (2014)

Dassault Systèmes, Abaqus documentation. Dassault Systemes Simulia Corporation, USA, 2016

D. Dusenberry, *Handbook for Blast Resistant Design of Buildings* (Wiley, 2010)

Q. Fang, L. Chen, M. Du, Theoretical and numerical investigations in effects of end-supported springs and dampers on increasing resistance of blast doors. Eng Mech **3**, 035 (2008)

M. Grazka, J. Janiszewski, Identification of Johnson-Cook equation constants using finite element method. Eng. Trans. **60**(3), 215–223 (2012)

S. Guner, F.J. Vecchio, Simplified method for nonlinear dynamic analysis of shear-critical frames. ACI Struct. J. **109**(5), 727 (2012)

A. Hassan, S. Jones, G. Mahmud, Experimental test methods to determine the uniaxial tensile and compressive behaviour of ultra high performance fibre reinforced concrete (UHPFRC). Constr. Build. Mater. **37**, 874–882 (2012)
X. Hou, Z. Deng, K. Zhang, Dynamic crushing strength analysis of Auxetic honeycombs. Acta Mech Solida Sin **29**(5), 490–501 (2016)
G. Imbalzano, P. Tran, T.D. Ngo, P.V. Lee, A numerical study of auxetic composite panels under blast loadings. Compos. Struct. **135**, 339–352 (2016)
G.R. Johnson, W.H. Cook, A constitutive model and data for metals subjected to large strains, high strain rates and high temperatures. Proceedings of the 7th International Symposium on Ballistics, vol. 1 (The Netherlands, 1983), pp. 541–547
G.R. Johnson, W.H. Cook, Fracture characteristics of three metals subjected to various strains, strain rates, temperatures and pressures. Eng. Fract. Mech. **21**(1), 31–48 (1985)
J. Lee, G.L. Fenves, Plastic-damage model for cyclic loading of concrete structures. J. Eng. Mech. **124**(8), 892–900 (1998)
Q. Li, H. Meng, About the dynamic strength enhancement of concrete-like materials in a split Hopkinson pressure bar test. Int. J. Solids Struct. **40**(2), 343–360 (2003)
J. Litonski, Plastic Flow of a Tube Under Adiabatic Torsion. (1977)
T. Łodygowski, A. Rusinek, T. Jankowiak, W. Sumelka, Selected topics of high speed machining analysis. Eng. Trans. **60**(1), 69–96 (2012)
J. Lubliner, J. Oliver, S. Oller, E. Onate, A plastic-damage model for concrete. Int. J. Solids Struct. **25**(3), 299–326 (1989)
L.J. Malvar, J.E. Crawford, Dynamic increase factors for concrete. Naval Facilities Engineering Service Center Port hueneme CA, 1998
L.J. Malvar, C.A. Ross, Review of strain rate effects for concrete in tension. Mater J **95**(6), 735–739 (1998)
S. Millard, T. Molyneaux, S. Barnett, X. Gao, Dynamic enhancement of blast-resistant ultra high performance fibre-reinforced concrete under flexural and shear loading. Int J Impac Eng **37**(4), 405–413 (2010)
T. Ngo, P. Mendis, A. Gupta, J. Ramsay, Blast loading and blast effects on structures–an overview. Electron. J. Struct. Eng. **7**, 76–91 (2007)
H. Othman, *Performance of Ultra-High Performance Fibre Reinforced Concrete Plates under Impact Loads* (Ryerson University, 2016)
A. Shrot, M. Bäker, Determination of Johnson–Cook parameters from machining simulations. Comput. Mater. Sci. **52**(1), 298–304 (2012)
P. Sielicki, T. Łodygowski, H. Al-Rifaie, W. Sumelka, Designing of blast resistant lightweight elevation system-numerical study. Procedia Eng **172**, 991–998 (2017)
R. Solhmirzaei, V. Kodur, Modeling the response of ultra high performance fiber reinforced concrete beams. Procedia Eng **210**, 211–219 (2017)
W. Sumelka, T. Łodygowski, The influence of the initial microdamage anisotropy on macrodamage mode during extremely fast thermomechanical processes. Arch. Appl. Mech. **81**(12), 1973–1992 (2011)
M. Szymczyk, W. Sumelka, T. Łodygowski, Numerical investigation on ballistic resistance of aluminium multi-layered panels impacted by improvised projectiles. Arch. Appl. Mech. **88**, 51–63 (2018). https://doi.org/10.1007/s00419-017-1247-8
I. Yang, C. Joh, B. Kim, Flexural response predictions for ultra-high-performance fibre-reinforced concrete beams. Mag. Concr. Res. **64**(2), 113–127 (2012)
N. Yun, D. Shin, S. Ji, C. Shim, Experiments on blast protective systems using aluminum foam panels. KSCE J. Civ. Eng. **18**(7), 2153–2161 (2014)

Part III

Damage in Brittle Materials

Dynamic Deformation, Damage, and Fracture in Geomaterials

16

Qian-Bing Zhang, Kai Liu, Gonglinan Wu, and Jian Zhao

Contents

Introduction 380
Dynamic Loading Techniques 383
Split Hopkinson Bar System 385
Traditional Triaxial Hopkinson Bar 387
Triaxial Hopkinson Bar System 389
Dynamic Testing Methods 392
Uniaxial Compression Tests 392
Multiaxial Compression Tests 392
Dynamic Indirect Tension and Shear Tests under Confinement 394
Dynamic Indentation Tests 397
Multiple Impact Tests 397
Optical Measurement Techniques 398
High-Speed Photography 399
Digital Image Correlation (DIC) 399
X-Ray Imaging and Computed Tomography (CT) 401
Dynamic Deformation, Damage, and Fracture Behaviors 404
Full-Field Deformation Fields and Stress-Strain Curves 405
Dynamic Damage and Fracture 408
Modeling Damage Ratio with Typical Experimental Results 413
Summary 417
References 418

Abstract

Dynamic events with high-pressure magnitude and high strain rate can originate from nature and human-generated sources, such as meteorite, earthquake, and resource extraction activities. Understanding of dynamic geomaterial behaviors relies heavily on laboratory-scale experiments that can replicate complex in situ

Q.-B. Zhang (✉) · K. Liu · G. Wu · J. Zhao
Department of Civil Engineering, Monash University, Melbourne, VIC, Australia
e-mail: qianbing.zhang@monash.edu; kai.liu@monash.edu; gonglinan.wu@monash.edu; jian.zhao@monash.edu

© Springer Nature Switzerland AG 2022

G. Z. Voyiadjis (ed.), *Handbook of Damage Mechanics*,
https://doi.org/10.1007/978-3-030-60242-0_73

stresses and dynamic sources, while appropriate measurement methods will provide necessary information for further understanding. Experimental methods for geomaterials are described for materials subjected to dynamic loading under complex in situ stress conditions by using a Triaxial Hopkinson bar (Tri-HB) system. The basics of dynamic testing methods are described, including the determination of uniaxial and multiaxial compressive, tensile, and shear strength, and indentation. Optical measurement techniques in the forms of two-dimensional (2D) and three-dimensional (3D) digital image correlation (DIC) and X-ray imaging techniques are briefly described in conjunction with experimental methods, and the full-field deformation measurement and ejection velocity of geomaterials are examined using the 3D-DIC technique. Stress-strain relationships obtained through experiments are combined with the DIC measured strain fields for analysis of dynamic damage and fracture processes. Microscopic examinations such as scanning electron microscope (SEM) and X-ray computed tomography (CT) are utilized for damage mechanism and microstructural effect studies of geomaterial. Lastly, numerical modeling using a 3D continuum-discrete coupled method is introduced. By calibrating models with existing experimental data measured and microscopic damage understanding, numerical modeling is becoming a powerful tool for studying geomaterial damage behavior.

Keywords

Rock dynamics · Split Hopkinson bar · Triaxial Hopkinson bar · Digital image correlation · Dynamic fracture

Introduction

Geomaterials are defined as "processed or unprocessed soils, rocks or minerals used in the construction of buildings or structures, including man-made construction materials manufactured from soils, rocks or minerals" (Fookes 1991). Geomaterials are frequently exposed to extreme environments in terms of high pressure and strain rate loading conditions (Asay and Shahinpoor 1993; Clayton 2010; Forquin 2017; Hild et al. 2003; Mazars and Millard 2009; Ramesh et al. 2015; Subhash et al. 2008; Zhang and Zhao 2014b). Dynamic events with such pressure magnitude and strain rate may originate from numerous sources. Natural phenomenon such as meteorite impact (Kenkmann et al. 2014), earthquake rupture (Braunagel and Griffith 2019; Doan and Gary 2009), landslides (Davies and McSaveney 2009), and explosive volcanic activity (Cassidy et al. 2018) can generate enormous energy and pressure in an instant. As shown in Fig. 1a, two natural (left column) (Aben et al. 2016; Kenkmann et al. 2014) and two human-induced scenarios (middle column) at the surface (top row) (Relph 2018) and underground (bottom row) (Flores-Gonzalez 2019) environments highlight the significance of stress conditions and dynamic loading rate for geomaterials. In nature, rocks deform at the strain rate of 10^{-1}–10^{2} s^{-1} in super-

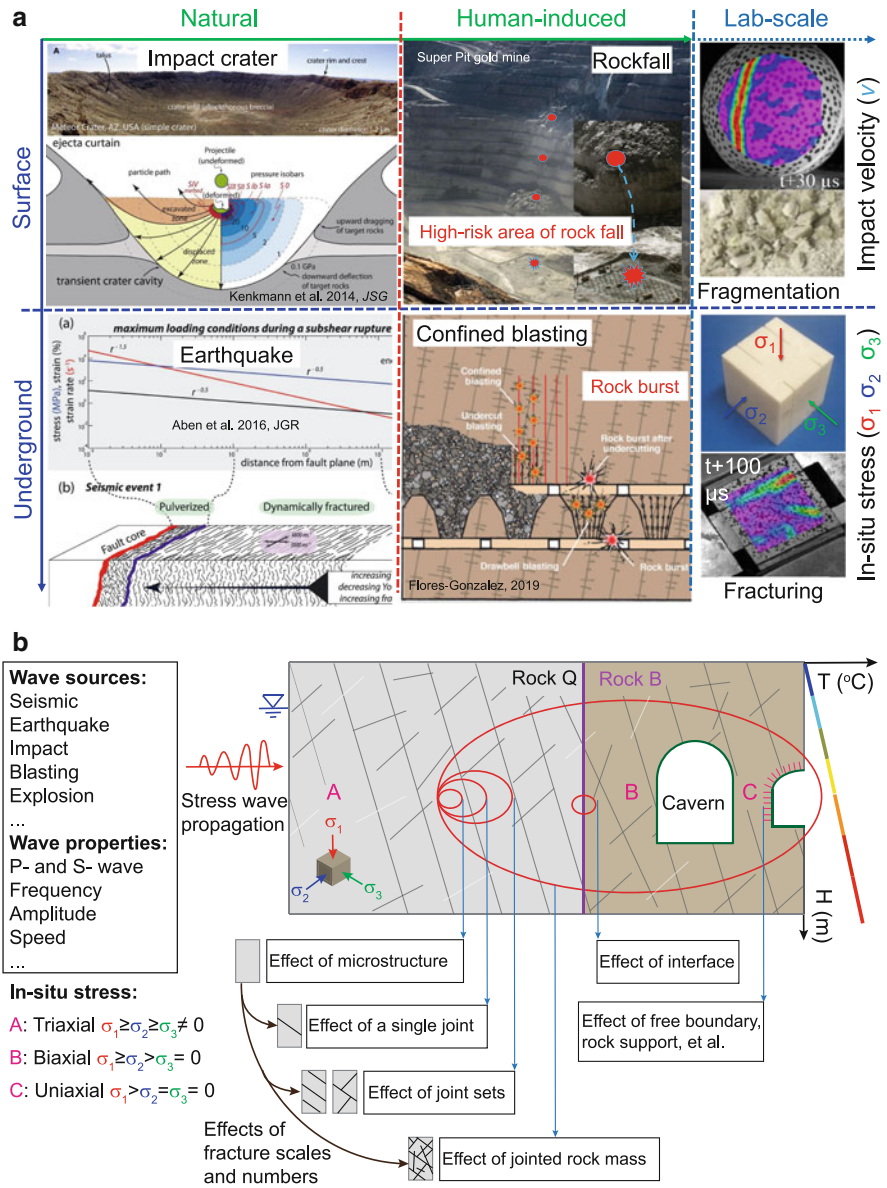

Fig. 1 (**a**) Natural and human-induced hazards under confinement and impact velocity, (**b**) overview of rock dynamics problems and influencing factors in underground engineering design

shear earthquake activities and can even reach ultra-high strain rates over 10^4 s^{-1} during impact crater process. Human-induced events such as ballistic impact (Forquin 2017; Hazell 2015; Subhash et al. 2008; Xing et al. 2020), rockfall (Chau et al. 2000; Giacomini et al. 2009), fragmentation (Paluszny et al. 2016; Shockey et al. 1974),

percussive drilling (Fourmeau et al. 2017; Saadati et al. 2014; Saksala 2013), confined blasting and rock bursts (Flores-Gonzalez 2019) can also generate high pressure at a fast loading rate. Furthermore, although these are smaller-scale events compare to natural occurrences, they are equally as dangerous. These events produce geomaterials that are strongly fractured, brecciated, and even pulverized due to the pressure and loading rate magnitudes. The mechanical properties and fracture behavior of geomaterials are also altered under high loading rates and may deviate significantly from the static counterparts (Clayton 2010; Forquin 2017; Ramesh et al. 2015; Subhash et al. 2008; Zhang and Zhao 2014b). At the lab scale, dynamic fragmentation is investigated by performing dynamic experiments under similar conditions as real-world problems, such as sphere impact, dynamic compression, and shearing shown in Fig. 1a (right column). Geomaterials in underground environments also experience existing ground stresses (Li et al. 2017; Liu et al. 2019, 2020a), that is, uniaxial, biaxial, and triaxial stress, as illustrated in Fig. 1b. Moreover, Liu et al. (2020a) summarized several rock ejection phenomena in underground engineering, including damage mechanisms, overburden, stress conditions, and ejection velocities (refer to Table 1 in Liu et al. (2020a) for detailed parameters). These dynamic fracturing phenomena, such as confined blasting and rockbursts, are most likely to be triggered when the stresses induced by dynamic events exceed the strength of rock. The mechanical behavior of rock under coupled static-dynamic loads is different from those under individual static or dynamic loads, which results in further complexity for damage and failure behavior. In this regard, the knowledge regarding dynamic behavior of rock/rock mass under different prestresses and dynamic loadings is critical for the engineering of geomaterials, such as earthquakes, rockfall, rock bursts, confined blasting, and explosions.

Given the importance of understanding the dynamic behaviors of geomaterials in engineering, it is crucial that systematic studies on those behaviors are in place. Laboratory scale experiments have become essential for obtaining such knowledge. By taking geomaterials from large scale natural and engineered environments and reduce its size to laboratory scale, experiments can be precisely controlled and repeated for accurate measurement of strength and other properties. Many testing devices and systems have been developed to replicate the stress condition and loading history of dynamic events in geomaterials. Zhang and Zhao (2014b) critically discussed the development and the state-of-the-art in dynamic experimental techniques and their applications to rock testing since the pioneering work in the 1960s. Despite all the major advances in dynamic geomaterial experiments, there are some shortcomings in replicating in situ stress conditions. In many engineering cases, particularly in the underground, geomaterials are subjected to existing biaxial and triaxial stress conditions. The dynamic strength, fracture, and fragmentation behaviors of geomaterials under triaxial conditions are significantly different from the uniaxial condition, which makes it challenging to study using traditional dynamic loading facilities. Traditional measurement using electrical resistance strain gages and mechanical extensometers have limitations in terms of measuring range and frequency response, which is also

insufficient for dynamic experiments under complex stress conditions. Therefore, more advanced high-frequency and full-filed 3D measurement techniques are necessary to extend the knowledge of dynamic geomaterial properties and behaviors. In terms of microscale damage mechanics, the interaction between crack front and material heterogeneities, as well as the resultant fracture surface morphology, is not fully understood. It remains unclear whether a simple continuum limit exists, or a crucial ingredient in the understanding of fracture lies within the discreteness of underlying atoms. It is necessary to quantify the multiscale physical properties of materials, which are controlling scale-dependent materials behavior. Thus, the development and calibration of constitutive models for numerical simulations require experimental data to reflect the various stress and confinement, strain paths, and strain or loading rates.

This chapter concerns mainly on the experimental techniques for high strain rate testing and dynamic behavior of geomaterials. These dynamic loading techniques include the split Hopkinson pressure bar (SHPB) and confined Hopkinson bar, as well as the recently developed Triaxial Hopkinson bar. The dynamic measurement methods utilized for experiments are introduced alongside the loading techniques. Dynamic optical measurement techniques, including high-speed photography, digital image correlation (DIC), and X-ray computed tomography (CT), are used for measuring the real-time fracture and postfailure behaviors of geomaterials. Based on novel dynamic loading and measurement techniques, dynamic deformation, damage, and fracture behaviors of geomaterials are presented over a wide range of strain rates. Finally, the microscopic examination on postfailure specimens and improved numerical modeling are presented to explore the damage mechanics and potential theoretical development of dynamic damage mechanics in geomaterials.

Dynamic Loading Techniques

For an overview of loading rate in natural and human-made events, loading techniques and mechanical state classifications for geomaterials over a wide range of strain rates are shown in Fig. 2. The duration of loading decreases with increasing strain rate and stress magnitude, while the damage and fracture also change accordingly, from fracture to fragmentation and eventually pulverized (Fig. 2a). It can be seen from the classification that the creep in tectonic plates has a strain rate from 10^{-8} to 10^{-5} s^{-1} (Brantut et al. 2013; Scholz 2019), which can be replicated using specialized hydraulic machine. Construction and rock engineering are often within the region of quasi-static with a loading rate from 10^{-5} to 10^{-3} s^{-1}, and servo-hydraulic machines are often used for laboratory study at this region. Intermediate strain rate from 10^{-1} to 10^{1} s^{-1} is often associated with mechanical excavation and earthquake events. Devices such as pneumatic-hydraulic machines and drop weight apparatus are frequently used to produce such rates in the laboratory environment (Liang et al. 2016). Loading

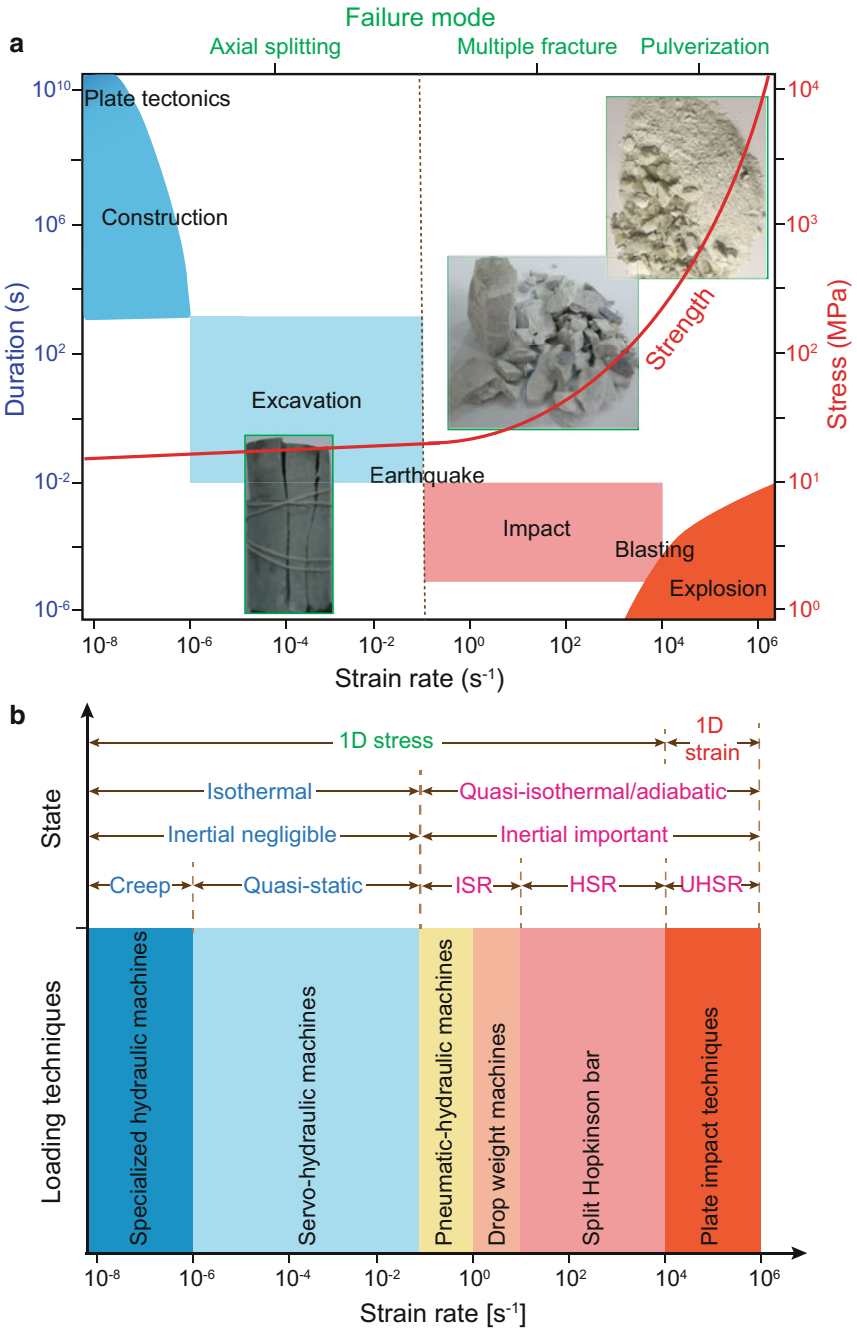

Fig. 2 (**a**) The strength and failure modes rock materials under varied conditions, and (**b**) classification of loading techniques over a wide range of strain rates (To clearly demonstrate the classifications, the overlapped zones of strain rates are not drawn. ISR: Intermediate strain rate; HSR: high strain rate; UHSR: ultra-high strain rate)

rate beyond 10^1 s^{-1} is classified as high strain rate and particularly within the strain rate of 10^1–10^4 s^{-1}, which corresponds to most mechanical impact events. The Hopkinson bar technique has been widely utilized for this region. Zhang and Zhao (2014b) reviewed a detailed description of the pneumatic-hydraulic, drop-weight, and the split Hopkinson bar tests. A fundamental difference between quasi-static and dynamic tests is that inertia and wave propagation effects become more pronounced at higher strain rates. Strain rate of 10^4 s^{-1} or higher is generally referred to as the ultra-high strain rate regime, and plate impact techniques have been successfully employed for 1D strain condition (Asay and Shahinpoor 1993; Bourne 2013; Field et al. 2004; Zhang et al. 2017). Shock-wave events are mostly found in meteorite impact phenomenon and center of blasting (Kenkmann et al. 2014). The Springer Book Series on *Shock Wave and High Pressure Phenomena* contains comprehensive references within this field (Asay and Shahinpoor 1993), and thus the contents are not covered in this chapter.

Split Hopkinson Bar System

The split Hopkinson bar (Hopkinson 1914) or the Kolsky bar (Kolsky 1949) has been widely used for material tests at high strain rate. Readers interested in the theory, history, extensive modifications, and recent advances in the Hopkinson bar are referred to the ASM handbook (Gray III 2000), recent books (Bourne 2013; Chen and Song 2010; Othman 2018), and critical reviews (Field et al. 2004; Gama et al. 2004; Jiang and Vecchio 2009; Pierron et al. 2014; Ramesh 2008; Zhang and Zhao 2014b). The principle of the split Hopkinson bar is briefly presented. It is mainly composed of a gas gun unit, a striker bar, an incident bar, and a transmission bar, as shown in Fig. 3. A specimen is sandwiched between the incident and transmission bars, and the dynamic load is generated when the striker bar impacts the incident bar. Strain gages are mounted on the incident and transmission bars to record the generated pulses. Several basic requirements must be satisfied during a SHPB test: (a) the specimen is under a uniaxial stress condition, (b) the specimen is in stress equilibrium, and (c) the specimen deforms uniformly, that means there is no friction and no inertia effect. Prior to interpreting the experimental data, the dimensions (A is the cross-sectional area, D is the diameter, and L is the length) and properties (ρ is the density, C is the longitudinal wave speed, E is Young's modulus) of the specimen and the bars should be well measured. The subscripts "S" and "B" correspond to the specimen and the bar, respectively. The duration of the incident wave ($t_{\text{In.}}$) equals to a round-trip travel time of the longitudinal wave in the striker, which can be expressed by the length (L_{str}) and wave speed (C_B) of the striker, $t_{\text{In.}} = 2L_{\text{str}}/C_B$ (e.g., $L_{\text{str}} = 500$ mm, $C_{\text{B}} = 5000$ m/s, and thus $t_{\text{In.}} = 200$ μs). The strain rate ($\dot{\varepsilon}$) of the tested specimen can be derived from (Gray III 2000),

$$\dot{\varepsilon} = \frac{(\dot{u}_1 - \dot{u}_2)}{L_{\text{S}}} \tag{1}$$

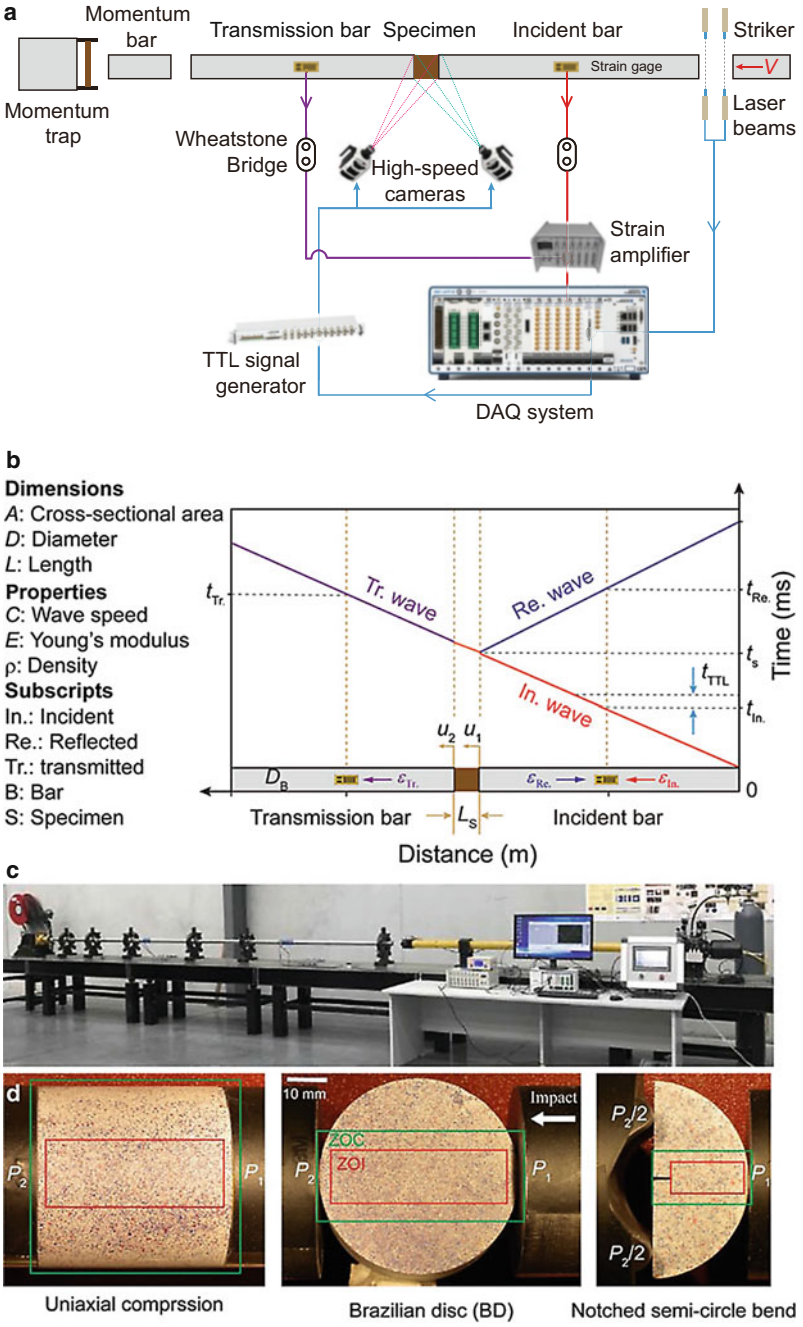

Fig. 3 (**a**) Schematic of a SHPB system, (**b**) displacement-time diagram of stress wave propagation of the SHPB, (**c**) photo of the SHPB system at Monash University, and (**d**) dynamic uniaxial compression, Brazilian disc, and notched semi-circle bend tests (ZOC: Zone of Camera; ZOI: Zone of Interest)

where $\dot{u}_1$ and $\dot{u}_2$ are the velocities at the interfaces of incident bar-specimen and specimen-transmission bar, respectively.

From the one-dimensional wave-propagation theory, the strain rate is

$$\dot{\varepsilon} = \frac{C_B}{L_s}(\varepsilon_{In.} - \varepsilon_{Re.} - \varepsilon_{Tr.}) \tag{2}$$

The forces at interfaces of bar-specimen are defined as

$$P_1 = A_B E_B(\varepsilon_{In.} + \varepsilon_{Re.}), P_2 = A_B E_B \varepsilon_{Tr.} \tag{3}$$

where ε is the strain measured by strain gages on the bars. The subscripts In., Re., and Tr. correspond to the incident pulse, reflected pulse, and transmitted pulse, respectively.

The engineering stress, strain rate, and the strain in the specimen are obtained under the state of stress equilibrium (i.e., $P_1 \approx P_2$):

$$\sigma(t) = \frac{A_B E_B}{A_S}\varepsilon_{Tr.}(t), \dot{\varepsilon}(t) = -\frac{2C_B}{L_S}\varepsilon_{Re.}(t), \varepsilon(t) = \int_0^t \dot{\varepsilon}(t)\mathrm{d}t \tag{4}$$

Zhang and Zhao (2013a, b) presented the detailed experimental procedures for the determination of mechanical properties and full-field deformation by using the SHPB and high-speed DIC technique, as shown in Fig. 3d. Moreover, a critical review of the split Hopkinson bar systems and their applications to rocks in the range of 1960–2014 is given by Zhang and Zhao (2014b); therefore, only the latest topics will be covered in this chapter.

Traditional Triaxial Hopkinson Bar

To study dynamic behavior of geomaterials under confinement conditions, the modified SHPB, in which specimens are confined before dynamic impact, has also developed since the 1970s. Commonly, there are two different techniques to achieve confinement prior to impact, that is, by pressure and displacement boundary conditions, corresponding to active and passive methods, respectively, as shown in Fig. 4a–b. Active confinement is typically realized by using the high-pressure hydrostatic fluid (e.g., oil and water) or gas to apply radial confining pressure on the sealed cylindrical specimen in the transverse direction, and the axial preload is provided by the hydraulic actuator at the far end of the transmission bar. Their original designs (Christensen et al. 1972; Lindholm et al. 1974) were further improved by other researchers (Du et al. 2020; Frew et al. 2010; Gong et al. 2019; Li et al. 2008; Malvern and Jenkens 1990; Nemat-Nasser et al. 2000; Wu et al. 2016) to study the strain rate and confinement dependencies of geomaterials. For the passive confinement method, displacement boundary condition is typically achieved by using a shrink-fit metal sleeve/passive thick vessel (Bailly et al. 2011; Chen and Ravichandran 2000; Forquin et al. 2008, 2010; Gong and Malvern 1990; Yuan et al. 2011) or planar confinement (Paliwal et al. 2008). In general, the confining pressure depends on the

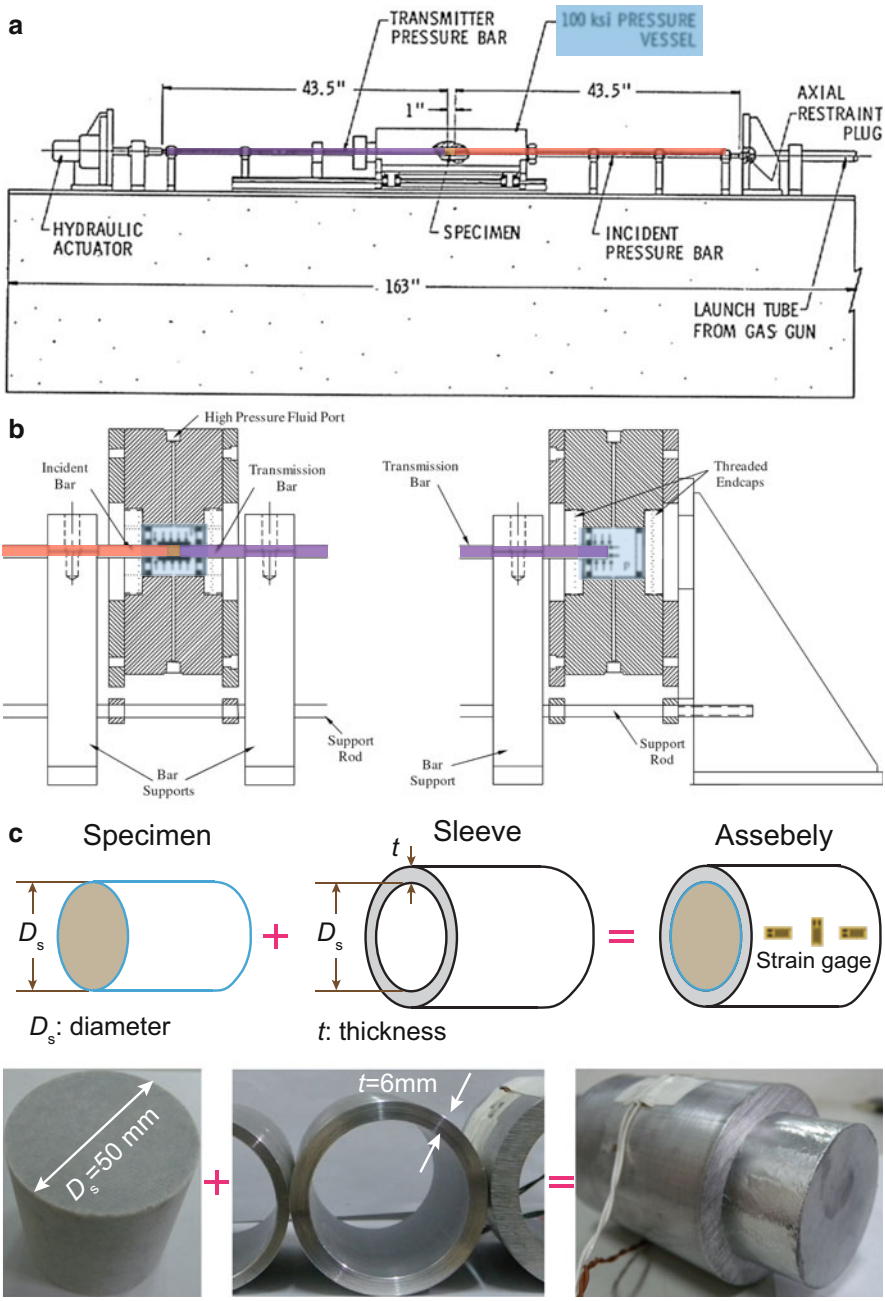

Fig. 4 Traditional confined Hopkinson bar: (**a**) Southwest Research Institute apparatus with a diameter of 12.7 mm (Lindholm et al. 1974), (**b**) radial and axial confining vessel details at US Army Engineer Research and Development Center, with a diameter of 12.7 mm (Frew et al. 2010), and (**c**) passive thick vessel and specimen assembly

thickness and material type of the sleeve, and the impact velocity, as shown in Fig. 4c. Strain gages are mounted on the sleeve surface to record the stress state of the specimen with time. Once the confinement setup is chosen, the dynamically axial load is applied by firing the gas gun. The confined SHPB device is capable of testing geomaterials subjected to coupled static and dynamic loads. Studies on dynamic behaviors of geomaterials under high strain rate loading and high confining stress condition are summarized in Table 2 of (Liu et al. 2020b). However, these triaxial Hopkinson bar systems account for traditional triaxial stress state ($\sigma_1 > \sigma_2 = \sigma_3 \neq 0$) rather than true triaxial stress state ($\sigma_1 \geq \sigma_2 \geq \sigma_3 \neq 0$). When impacted axially, the testing specimen dilates in the radial direction due to the Poisson effect, which results in the change of confinement. It should be noted that for the active confinement method using high-pressure hydrostatic fluid or gas, it is challenging for the direct measurement of the variation of confinement induced by the impact in the chamber. Besides, when using shrink-fit metal sleeve or passive thick vessel for passive confinements, the value of initial prestress cannot be accurately controlled before the impact.

Triaxial Hopkinson Bar System

The Triaxial Hopkinson bar (Tri-HB) system developed originally to conduct dynamic tests under different in situ static stress conditions, including the uniaxial ($\sigma_1 > \sigma_2 = \sigma_3 = 0$), biaxial ($\sigma_1 > \sigma_2 > \sigma_3 = 0$), and triaxial ($\sigma_1 > \sigma_2 > \sigma_3 \neq 0$) stresses. The Tri-HB system consisted of three independent pairs of high-strength steel square bars (the incident and transmission bars, and two pairs of output bars, with the cross-section area of 50×50 mm^2), a hydraulic servo system, gas gun, an energy absorption unit, a high-frequency data acquisition system, six pieces of steel reaction frames, and a strong supporting platform, as shown in Fig. 5a–b. A cubic specimen is enclosed within three pairs of square bars in X, Y, and Z directions. Hydraulic cylinders installed at the ends of bars to achieve multiaxial confining pressures, and the striker is launched by a gas gun to generate the dynamic load towards the X direction. During a test, the specimen is preloaded to a static stress condition and then impacted by the striker from one direction. The bars and striker are made of high-strength steel (42CrMo), and the physico-mechanical properties include $\sigma_B = 7850$ kg/m^3, $E_B = 210$ GPa, $C_B = 5200$ m/s, yield strength $\sigma_y = 930$ MPa. Six sets of strain gages are mounted on the incident bar (2.5 m), transmission bar (2 m), and four output bars (2 m), to record the signals at the frequency of 1 MHz during the test. The details of design, operation, and calibration can be found in Liu et al. (2019). During a dynamic test, the specimen sandwiched between 2/4/6 bars (Fig. 5c) is initially subjected to a desired multiaxial stress condition, and then dynamic load is generated by the striker bar which is similar to the SHPB system. A typical loading path of the testing specimen subjected to triaxial static dynamic loading is illustrated in Fig. 5b, in which dynamic loading can be applied on either direction rather than only along σ_1 once the desired static stress is achieved. Besides, one can apply uniaxial, biaxial, or

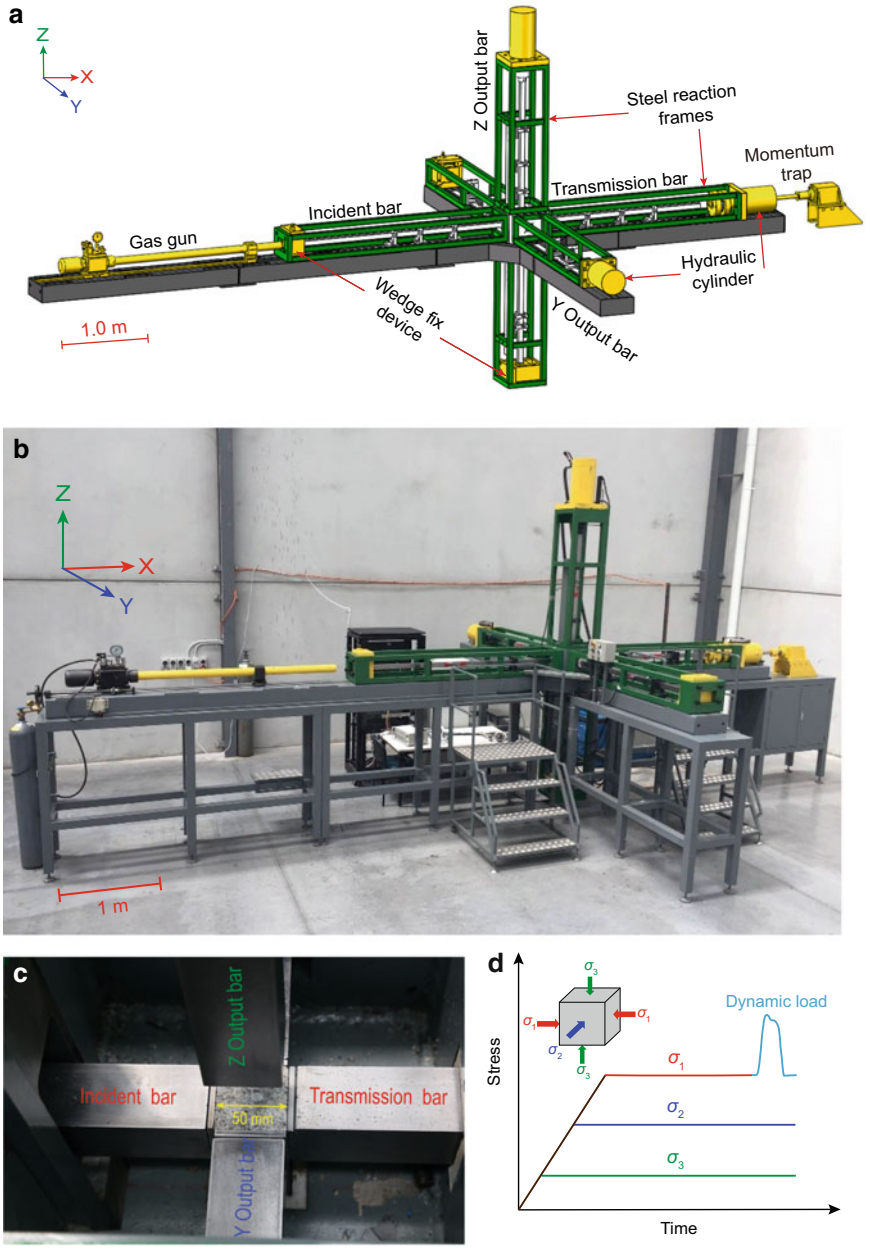

Fig. 5 Schematic (**a**) and photo (**b**) of the Triaxial Hopkinson bar (X-axis refers to impact direction), (**c**) cubic specimen placed between bars in the loading cell, and (**d**) a typical loading path (Liu et al. 2019)

triaxial prestress by independently controlling the hydraulic cylinders prior to impact, thus achieving multiaxial loading on the specimen.

During the Tri-HB test, the specimen is initially subjected to a desired multiaxial prestress condition, and then, dynamic loading is achieved by varying the impact velocity of the striker bar. The generated incident pulse propagates along with the incident bar and impacts on the testing specimen until failure, leading to the reflected wave and transmission wave as well as output waves in Y/Z directions. Under the state of stress equilibrium, the average stress $\sigma_x(t)$, strain rate $\dot{\varepsilon}_x(t)$, and strain $\varepsilon_x(t)$ of the specimen can be calculated as:

$$\sigma_x(t) = \frac{E_B A_B}{2A_S}\left[\varepsilon_{In.}(t) + \varepsilon_{Re.}(t) + \varepsilon_{Tr.}(t)\right] = \frac{E_B A_B}{A_S}\varepsilon_{Tr.}(t) \tag{5}$$

$$\dot{\varepsilon}_x(t) = \frac{C_B}{L_S}\left[\varepsilon_{In.}(t) - \varepsilon_{Re.}(t) - \varepsilon_{Tr.}(t)\right] = -\frac{2C_B}{L_S}\varepsilon_{Re.}(t) \tag{6}$$

$$\varepsilon_x(t) = \int_0^T \dot{\varepsilon}_x(t)dt = -\frac{2C_B}{L_S}\int_0^T \varepsilon_{Re.}(t)dt \tag{7}$$

where E_B is Young's modulus of bars; A_B and A_S are the cross-sectional area of bars and specimen, respectively; L_S is the length of the specimen; $\varepsilon_{In.}(t)$, $\varepsilon_{Re.}(t)$, and $\varepsilon_{Tr.}(t)$ are the incident, reflected, and transmitted strains, respectively.

The respective dynamic stress (without prestress component) and strain of the specimen in the Y and Z directions can be calculated as (Cadoni and Albertini 2011; Liu et al. 2019),

$$\sigma_y(t) = \frac{E_B A_B}{2A_S}\left[\varepsilon_{y1}(t) + \varepsilon_{y2}(t)\right] \tag{8}$$

$$\varepsilon_y(t) = \frac{C_B}{L_S}\int_0^t \left[\varepsilon_{y1}(t) + \varepsilon_{y2}(t)\right]dt \tag{9}$$

$$\sigma_z(t) = \frac{E_B A_B}{2A_S}\left[\varepsilon_{z1}(t) + \varepsilon_{z2}(t)\right] \tag{10}$$

$$\varepsilon_z(t) = \frac{C_B}{L_S}\int_0^t \left[\varepsilon_{z1}(t) + \varepsilon_{z2}(t)\right]dt \tag{11}$$

where $\sigma_y(t)$ and $\sigma_z(t)$, $\varepsilon_y(t)$, and $\varepsilon_z(t)$ are the dynamic stress and strain of specimen along the Y and Z directions, respectively. $\sigma_{y1}(t)$ and $\sigma_{y2}(t)$ are strain waves in two output bars along the Y direction, while $\sigma_{z1}(t)$ and $\sigma_{z2}(t)$ are strain waves in two output bars along the Z direction. With these equations, the total principal stress (including prestress-component), dynamic volume stress and volume strain, dynamic deviant stress and deviant strain during static-dynamic loading are also obtained (Liu and Zhang 2019). Thus, the dynamic responses of the tested material in three directions can be quantitatively determined.

Dynamic Testing Methods

Uniaxial Compression Tests

International Society for Rock Mechanics (ISRM) and American Society for Testing and Materials (ASTM) published a series of Suggested Methods and Technical Standards for determining mechanical properties of rock materials under quasi-static loading. Dynamic testing methods are mainly modified from the corresponding quasi-static ones, as summarized in "Table 3" of Zhang and Zhao (2014b). There are three groups of testing methods according to loading types, including compression, tension, and bending methods. ISRM suggested three methods, that is, uniaxial compression, Brazilian disc (BD), and notched semi-circular bend (NSCB), for determining dynamic uniaxial compressive strength, tensile strength, and Mode-I fracture toughness of rocks, respectively (Zhou et al. 2012). Zhang and Zhao (2013a) presented detailed procedures for determining mechanical properties and DIC full-field deformation, as shown in Fig. 3d. Zhang and Zhao (2014b) summarized dynamic mechanical properties as a function of loading/strain rate, and there is a definite increase in strength under dynamic loads which is generally called as the dynamic increase factor (DIF). For example, Fig. 6 shows the normalized uniaxial compressive strength and tensile strength of geomaterials.

Geomaterials are often present in the in-situ condition and these stress conditions can be uniaxial, biaxial, or triaxial depending on the location, as shown in Fig. 1. Geomaterials in underground mines and tunnels are common examples of such a scenario. Since dynamic sources such as earthquakes, mechanical impact, blasting, and explosion are frequently presented in the underground with geomaterials in place, it is crucial that detailed dynamic strength and behavior studies are conducted with replicated stress conditions. The compressive strength is the most commonly measured parameter of geomaterials, since it provides a good reference on the damage and fracture behaviors. Other properties, such as tensile and shear strength, and deformation under concentrated loadings are also essential for the study of the dynamic behavior of geomaterials and their applications. The dynamic testing methods for compressive strength, indirect tensile strength, shear strength, and response to concentrated loading under multiaxial prestress conditions are presented in the following, along with their stress-strain relationships and measured strength over a range of strain rates.

Multiaxial Compression Tests

By controlling the servo-hydraulic system, the specified loading path and stress states can be achieved easily in the Tri-HB system. Once the desired prestress is reached, the dynamic load is applied by releasing the compressed gas to drive the impact of the striker bar on the incident bar. The prestress is recorded by the hydraulic confinement control system, while dynamic signals are measured by the strain gage attached to the bars, and by using Eqs. (5–11) the dynamic stress, strain, strain rate, and dissipated energy are quantitatively determined in three

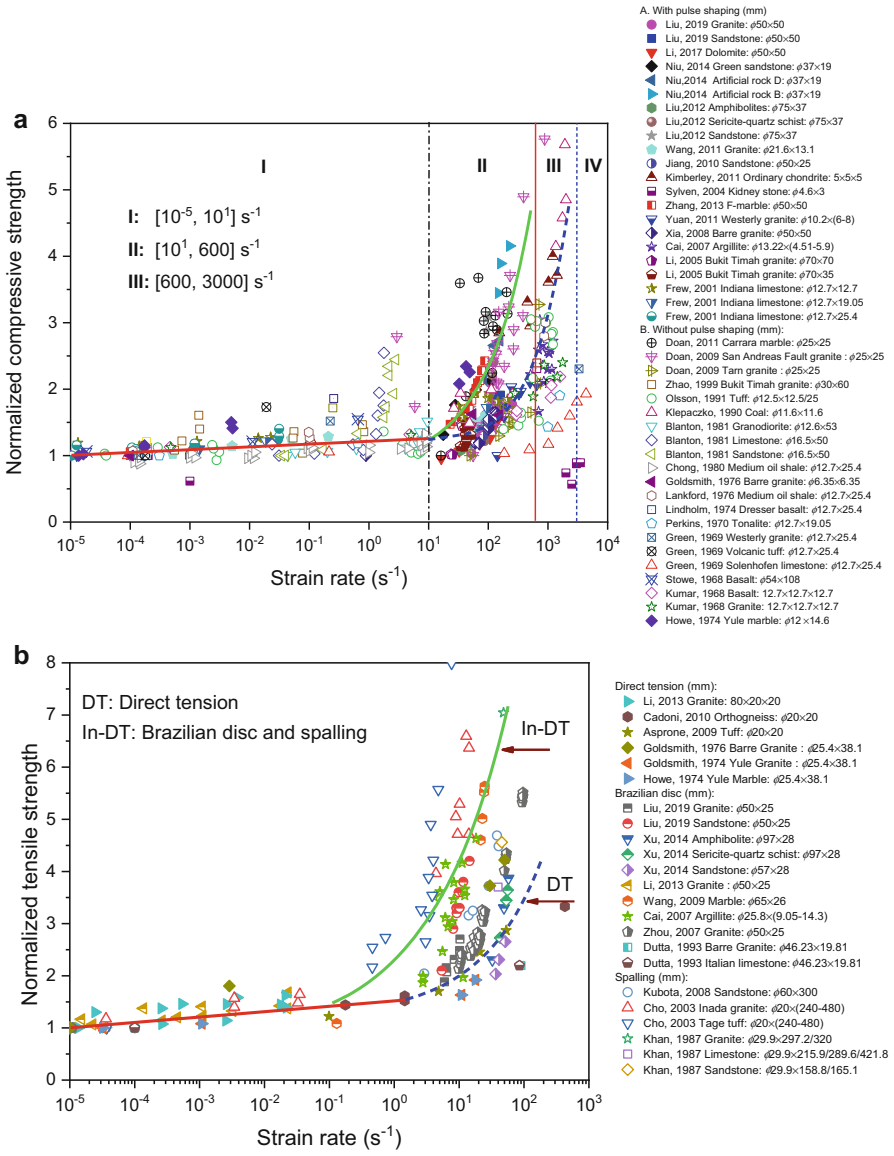

Fig. 6 Dynamic normalized (**a**) uniaxial compressive strength, and (**b**) tensile strength of rocks as function of strain rate

directions. The details of data interpretation can be referred to Liu et al. (2019). Typical experimental data of sandstone under prestress conditions (30, 20, 10) MPa at the impact velocity of 20 m/s are shown in Fig. 7.

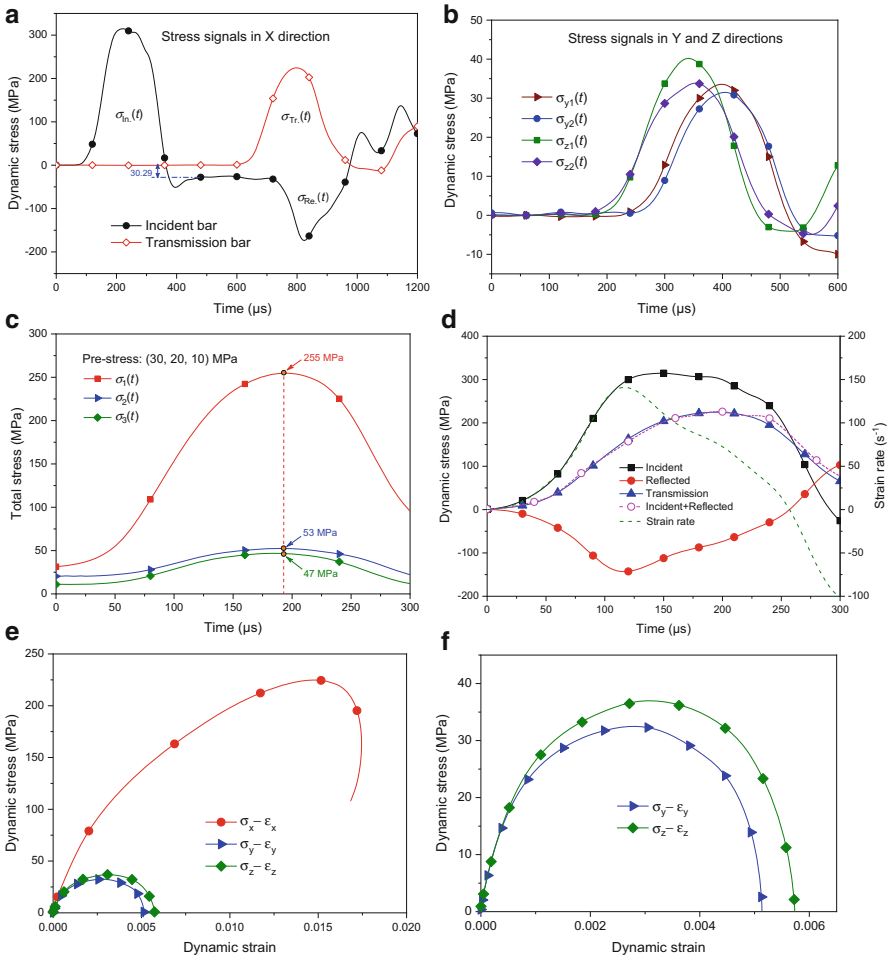

Fig. 7 Typical experimental data of sandstone under prestress conditions (30, 20, 10) MPa at the impact velocity of 20 m/s: (**a**) stress waves in impact direction, (**b**) stress waves in Y/Z direction, (**c**) total stress (with prestress component) evolution applied on the specimen, (**d**) dynamic stress (without prestress component) equilibrium check, (**e**) dynamic stress and strain history in three directions, and (**f**) dynamic stress and strain history in Y/Z directions

Dynamic Indirect Tension and Shear Tests under Confinement

Understanding the dynamic shear behavior of rock under high loading rate and confining stress is important to reveal the generation mechanism of rock faults and earthquake activities. Additionally, dynamic shear strength is an essential parameter in material failure models to describe the dynamic failure behavior of solid materials under high rate loading. Three different experimental configurations for dynamic shear are shown in Fig. 8a, b, c, that is, direct shear, double-edge notched,

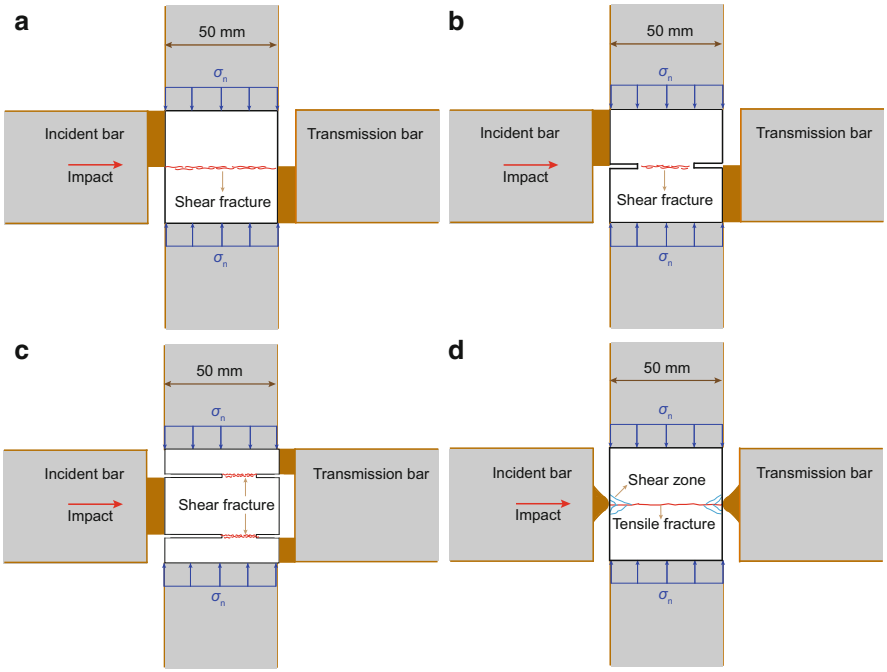

Fig. 8 Dynamic shear tests using (**a**) direct-shear, (**b**) double-edge notched, and (**c**) modified punch-through-shear specimens, and (**d**) dynamic tensile test with the cubic specimen

and modified punch-through shear. Pieces of rectangular steel blocks are inserted into the front and back interfaces between incident bar, specimen, and transmission bar for the generation of shear stress conditions. The steel blocks have a thickness of 5 mm, and the same mechanical properties with bars and steel blocks are precisely aligned with the specimen to achieve shear stress in the intact portion. The specimen is initially subjected to a desired biaxial prestress condition, and then dynamic loading is applied. The definition and calculation method of shear stress, the normal stress, the shear strain, and the normal strain are provided in the reference (Liu 2020). Furthermore, a new experimental setup, that is, dynamic indirect tension with the cubic specimen, is used to investigate the dynamic tensile behavior of rocks. As shown in Fig. 8d, two loading heads are inserted between the cubic specimen and bars to apply loads. The size of the cubic specimen $50 \times 50 \times 50$ mm^3 is the same as that of compression and shearing tests. The setup can investigate the dynamic tensile behavior of geomaterials under confinements at high strain rates. During the impact, the dynamic stress equilibrium is well achieved within the specimen. Signals are measured by strain gages on the bars and further processed to obtain the dynamic tensile strength, strain/loading rate, and the time to fracture.

As shown in Fig. 9, the generated incident pulse propagates along with the incident bar and impacts on the testing specimen until failure, leading to the reflected

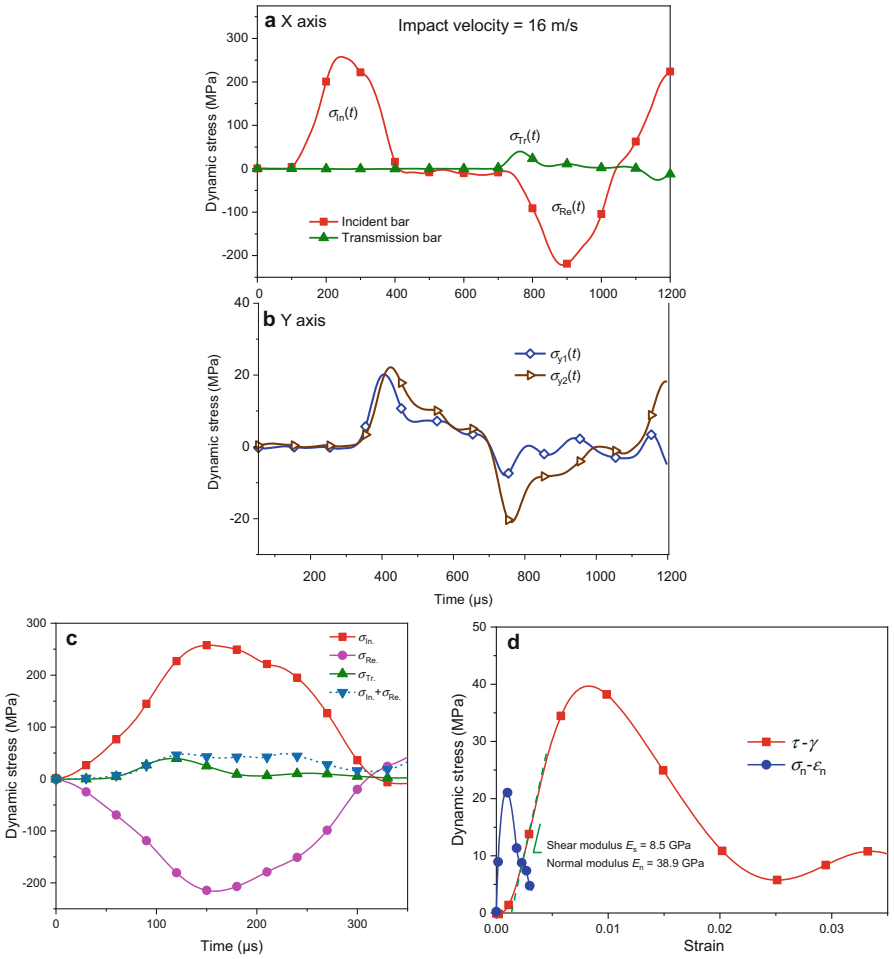

Fig. 9 (**a**–**b**) Typical signals measured on bars, (**c**) dynamic stress equilibrium, and (**d**) shear stress-strain curve in dynamic direct shear test at the impact velocity of 16 m/s

wave and transmission wave as well as output waves in Y direction. The dynamic stress equilibrium can be well achieved during shearing, as presented in Fig. 9c (Liu 2020; Wu et al. 2019). Thus, the dynamic shear strength of rock under different impact velocities and normal prestresses is determined. The single and double notched cubic specimens are also used to determine the Mode II fracture toughness (K_{II}) and dynamic shear crack initiation and propagation behaviors. The length of the notch is 10 mm from the free surfaces of the specimen. Crack initiates at the tip of the crack and then propagate across the whole specimen, generating shear fractures. Strain gage signals are used to obtain the shear strength and shear stress-strain (Fig. 9d) of materials, while the free face of specimens can be recorded by optical measurements.

Dynamic Indentation Tests

Dynamic indentation has been widely utilized for material testing and strength determinations (Subhash 2000). Comparing with traditional laboratory methods that measure the compressive, tensile, and shear strength, the indentation of geomaterials is more complicated yet essential for understanding dynamic damage and failure. In fact, the deformation and damage caused by indentation is a closer representation of real-world impact contacts than traditional dynamic testing methods. Percussive drilling is one of the typical applications of dynamic indentation in geomaterials. During the drilling process, stress waves propagate from a hammer to the drill bits, which deform and fracture materials that are being drilled. Several research groups have utilized dynamic indentation techniques, which include edge-on impact (Forquin and Ando 2017; Hild et al. 2003), percussive drilling (Saadati et al. 2014; Saksala 2013), indentation (Subhash et al. 2008), and drill bit drop (Fourmeau et al. 2017) tests to study the strength and fragmentation characteristics of rock and other brittle materials. During indentation events, the material beneath the indenters undergoes intense compression and shear deformation, while tensile cracks originate from the crater boundary and propagate outwards. Essentially, indentation damage is a combination of compression, shear, and tensile failures. As shown in Fig. 10a–b, the dynamic indentation of geomaterials under multiaxial confinement stress is performed using the Tri-HB system. Single or multiple indenters made of tungsten carbide are installed onto the incident bar, while bi-directional prestresses are applied in the Y and Z-axis of the apparatus. The striker will then deliver stress waves that drive indenters into the specimen. Strain gages are utilized to capture the stress wave (Fig. 10c) propagation during the indentation, which subsequently produces the force-displacement of dynamic rock indentation tests, as shown in Fig. 10d.

Multiple Impact Tests

Both of natural and engineering rocks commonly have experienced numerous dynamic loadings, and they are the production of long-term damage accumulation (Aben et al. 2016; Doan and Gary 2009; Rempe et al. 2013), progressively accumulated deformation under successive episodes of dynamic loads should be considered in excavation design. Therefore, it is unreasonable to compare the field data or observation directly with single-impact loading experiments. Studies are required to investigate the mechanical behavior of rocks subjected to multiple impacts. At high strain rates, the progressive damage and failure of rocks subjected to repeated impact loading were investigated using SHPB, and the results show that the dynamic stress-strain, elastic modulus, microcrack evolution, and cumulative damage are highly related to impact energy and numbers (Aben et al. 2016; Braunagel and Griffith 2019; Li et al. 2004; Wu et al. 2016). The effect of confining pressure on the dynamic weakening behavior of rock under repetitive impacts was studied using a modified SHPB. With the Tri-HB system, experiments are also conducted to investigate the

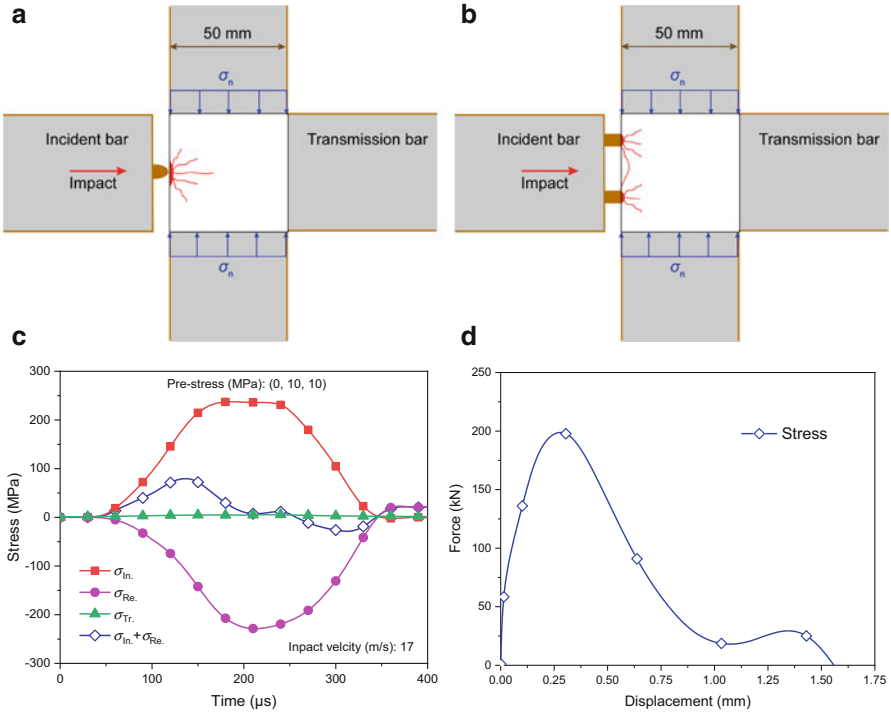

Fig. 10 Dynamic rock indentation using (**a**) a single indenter and (**b**) multiple indenters on granite, (**c**) typical stress times histories and (**d**) dynamic force-displacement curve of one indenter (with the diameter of 13 mm and length of 8 mm) under the confining pressure (0, 10, 10) MPa at the impact velocity of 17 m/s

progressive damage mechanism of rocks subjected to different static prestresses (i.e., uniaxial, biaxial, and triaxial) and repetitive dynamic loadings.

Optical Measurement Techniques

Some common noncontact full-field optical measurement techniques are presented in Table 1. The dynamic stress, strain, and temperature measuring applications of these techniques in geomaterial experiments are summarized (Field et al. 2004; Xing et al. 2017). These techniques can be classified into two categories, which are interferometric and noninterferometric. Photoelasticity, Moiré interferometry (MI), caustic and holographic interferometry are interferometry methods, which require a coherent light source and can be very susceptible to disturbances like vibrations. The interferometric data often require further fringe processing and phase analysis techniques to obtain kinematic information. Particle image velocimetry (PIV) and geometric Moiré are noninterferometric techniques; for example, PIV is widely utilized in fluid mechanics. Noninterferometric techniques do not require coherent

Table 1 Summary of digital optical measurement techniques (Field et al. 2004; Xing et al. 2017)

Method	Measured parameter	Sensitivity	Accuracy	Light source
Photoelasticity	σ_1–σ_2	Variable	Variable	Incoherent
Geometric Moiré	u_x or u_y	Grating pitch $p \approx 5$–1000 μm	$\sim p/10$	Incoherent
Moiré interferometry	u_x or u_y	Grating pitch $p \approx \lambda$	$\sim p/10$	Coherent
Caustics	$\partial u_z/\partial x$, $\partial u_z/\partial y$	Variable	Variable	Incoherent
Holographic interferometry	u_x, u_y and u_z	$\lambda/2$	$\sim\lambda/50$	Coherent
Particle image velocimetry	u_x, u_y and u_z	~1 pixel of digital image	~1/10 pixel of digital image	Incoherent
Digital image correlation	u_x, u_y and u_z	~1/100,000 of the field of view	~1/100 pixel of digital image	Incoherent
Thermal imaging	*Temperature*		~1% of reading	Self-lighting

lighting. These techniques generally have less strict experimental requirements and determine the deformation by comparing light intensity changes from the specimen surface before and after deformation. For the scope of this chapter, a brief introduction of high-speed photography is given for dynamic experiment purposes. An introduction of DIC techniques in 2D and 3D configurations is provided, including their applications on dynamic geomaterials experiments and basic setup for Tri-HB experiments.

High-Speed Photography

The performance of CCD- and CMOS-based digital cameras are shown in Fig. 11. The frame rates (i.e., frames per second) of CCD-based cameras can exceed 100 million fps with high resolution, yet normally capture less than 100 images. Although the CMOS-based cameras have a relatively low frame rate and small resolution, their frame rates can easily exceed 50,000 fps. The resolution of CMOS-based cameras decreases with increasing frame rate, but that of CCD-based cameras is independent on frame rate. A detailed review of the applications of high-speed cameras and their related digital optical measurement techniques to geomaterials was presented in Xing et al. (2017).

Digital Image Correlation (DIC)

The strain gage is commonly used to measure the strain of solid objects, but only provide strain at a single location and direction. DIC is a noncontacting measuring method that acquires digital images and obtains full-field deformation and motion by

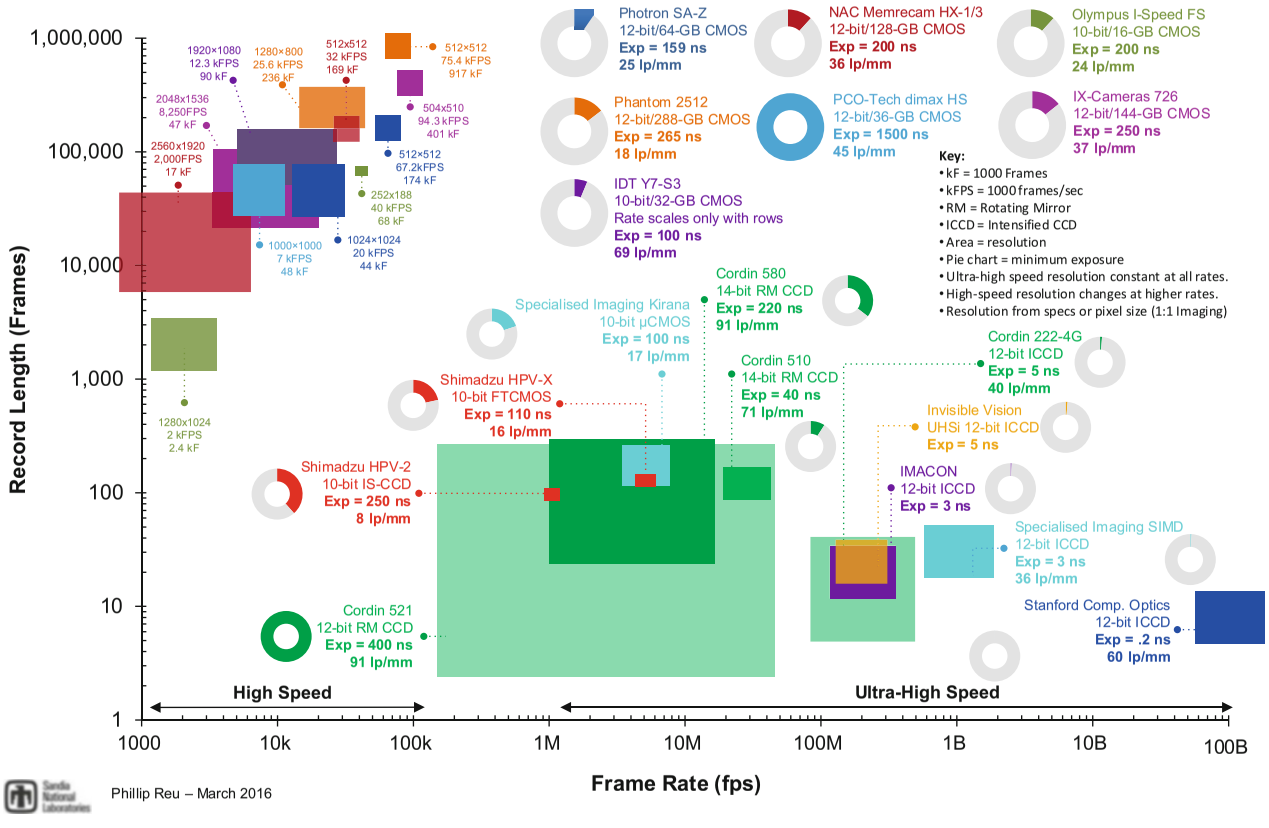

Fig. 11 Technical status of CCD- and CMOS-based high-speed cameras (The maximum resolution is proportional to the rectangle area of each camera). (Courtesy of Dr. Phillip L. Reu (Reu and Miller 2008))

image analysis (Sutton et al. 2009). DIC techniques include 2D-DIC for in-plane deformation, 3D-DIC for surface 3D changes, and digital volume correlation (DVC) for material internal deformation. For the 2D-DIC method, as schematically illustrated in Fig. 12a, the matching of the same subset from two images is conducted to determine the desired displacement. For example, to quantify the changes of a point $P(x, y)$, a square subset centered at this point is selected as a reference. Then, the DIC algorithms search its corresponding subset in the deformed image as the target subset centered at the point $P(x', y')$. Sufficient contrast of the surface is also required, which can be achieved by either material texture, or random speckle patterns for cases like sandstone and other geomaterials, as shown in Fig. 12. Different definitions of the correlation criteria are developed for evaluating the degree of similarity between the reference and target subset, which can be categorized into the cross-correlation and the sum of squared difference criteria. Once the displacement of the center point is determined, the deformed subset can be determined by the first-order shape function from the pixel (x_i, y_i) in the reference subset. However, it should be mentioned that when there is apparent nonhomogeneous deformation, the second-order shape function has the capability to depict more complex deformation and further provide higher accuracy. 3D-DIC was developed based on the binocular stereovision principle (Sutton et al. 2009). Two cameras are necessary to establish the stereovision by calibrating the space coordinates to reconstruct the 3D position from transformation matrices. Once calibration is done, "x" and "y" coordinates are determined from two synchronized cameras first (2D-DIC process). The 3D shape is then established by the "z" coordinate which is determined by binocular stereovision of two deformed images. Pairs of neighboring 3D shapes are used to obtain displacement. Differentiation on displacement field provides strain field, and another differentiation on strain field provides the strain rate field. An illustration of 3D-DIC process is shown in Fig. 12b. With the application of the Tri-HB system, a series of dynamic biaxial compression and shearing tests is performed to explore the behavior and failure mechanism of specimens, especially under the superimposed stress field of static stress and dynamic impact. Dynamic strength, strain, rock fracture, and ejection characteristics are presented, and the fracture behavior of rocks under the combined static and dynamic biaxial compression is investigated.

X-Ray Imaging and Computed Tomography (CT)

There has been a great interest in combining dynamic loading experiments such as SHPB and gas gun tests with X-ray imaging techniques. Development of Synchrotron X-ray has allowed in-situ, high photon flux, and high-temporal and spatial-resolution measurement during dynamic loading experiments. The utilization of the synchrotron source significantly improves both the scanning speed and image quality. With an additional scintillator that converts X-ray radiation into visible light, commercially available optical cameras can capture the dynamic experiment process. In high-speed X-ray imaging of a dynamic test, the X-ray light source is generated in the Synchrotron and passed through shutters and slit before it is directed onto the test subject. The

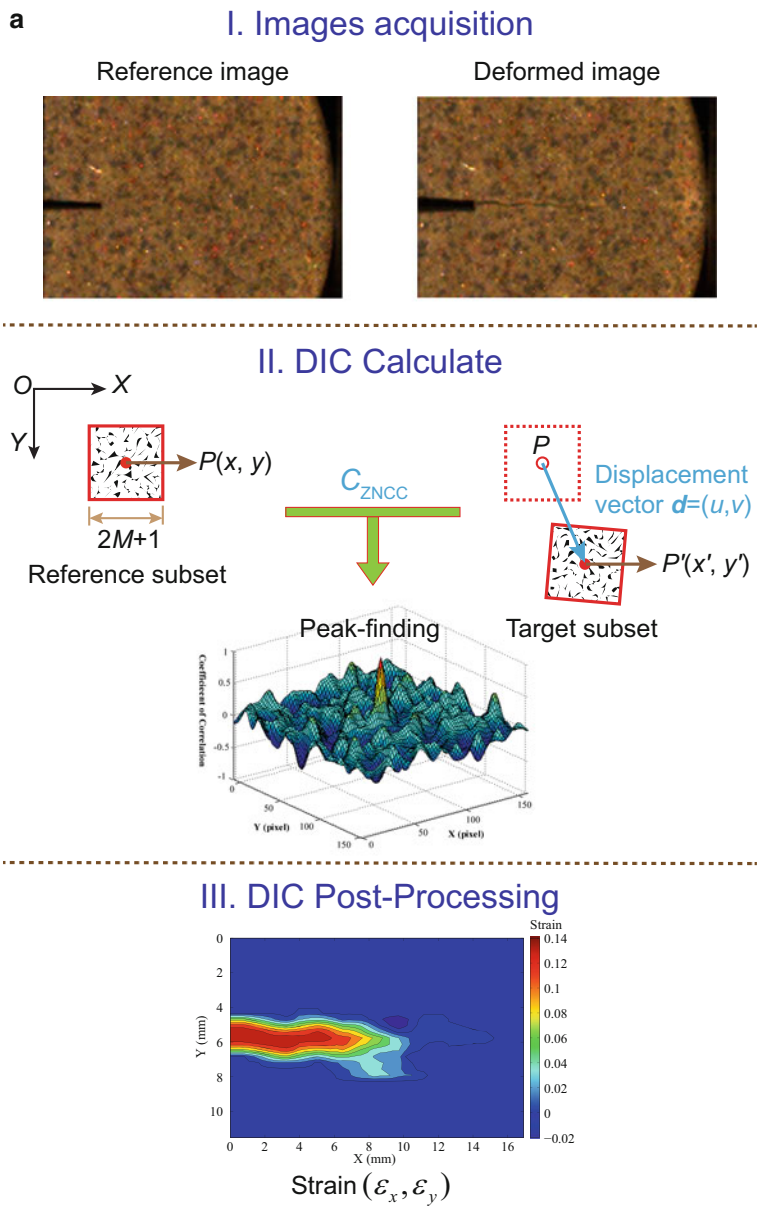

Fig. 12 (continued)

X-ray then passes through the specimen and arrives at the scintillator, which converts X-ray into visible light. This visible light is reflected by a mirror and captured using cameras. As for the X-ray imaging technique, phase contrast imaging is the most likely

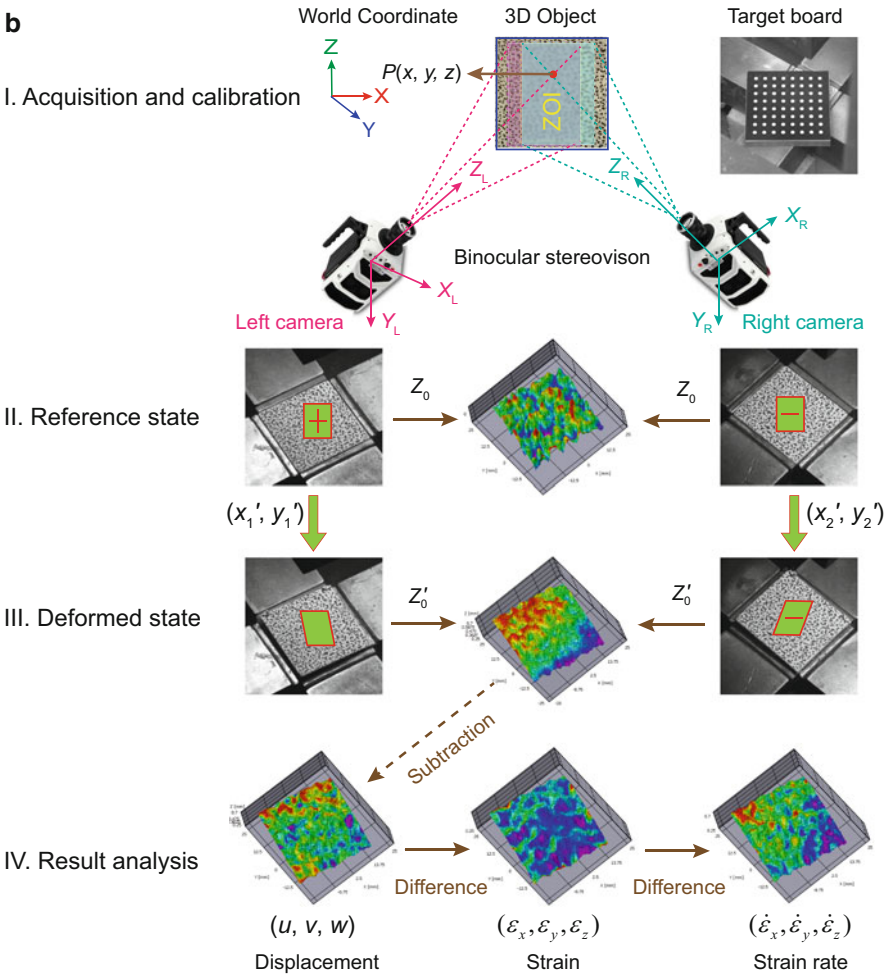

Fig. 12 (**a**) Schematic of 2D-DIC with a reference subset before deformation and a target subset after deformation, and (**b**) schematic of 3D-DIC with binocular stereovision calibration and analysis

choice for studying structural changes such as fracture, due to its ability for edge enhancement, and the orientation of X-ray beam is often perpendicular to the direction of dynamic loading, while diffraction techniques require the camera to be capturing at an angle to the loading direction. It is noteworthy that careful consideration and planning are required for achieving good imaging quality. Several studies have adopted in situ X-ray imaging to examine failure behavior of solid materials (e.g., rock, concrete, ceramic, glass, and Ti-6Al-4 V) and performed quantitative analysis for dynamic experiments. High-speed X-ray imaging is a powerful tool in achieving

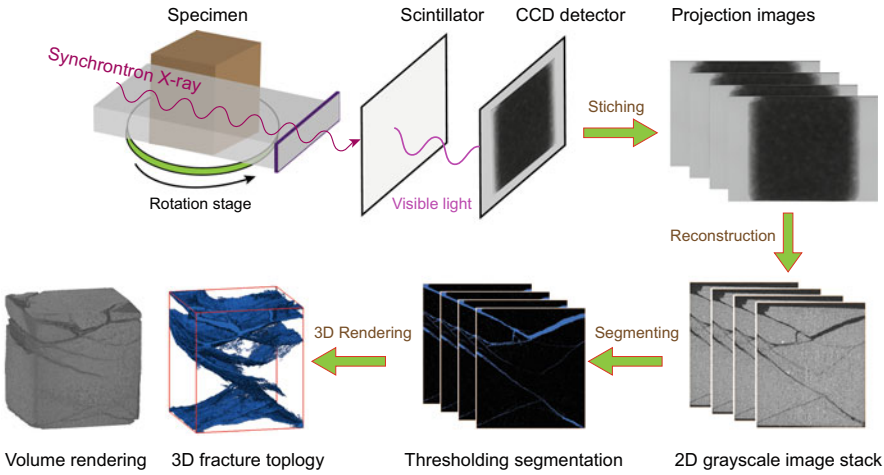

Fig. 13 The workflow of Synchrotron μ-CT imaging and digital rock analysis (Liu et al. 2020a)

quantitative relationships among crack network evolutions, impact velocities, and loading directions of geomaterials under coupled loading conditions (Chen et al. 2014). The capability of internal measurements for crackfront dynamics within specimens can provide useful insights on damage and fracture mechanics of geomaterials. One major setback of dynamic X-ray imaging is the size and material constraints of the specimen since the specimen needs to be small and has relatively low atomic numbers, which limits the testing methods that can be performed while using this imaging technique.

Postfailure X-ray CT study is selected for quantification of dynamic geomaterial deformation, damage, and fracture. The basic procedure is shown in Fig. 13. The damaged specimen after dynamic biaxial compression was scanned using a monochromatic beam available at Australian Synchrotron's Imaging and Medical beamline (IMBL), which provides nondestructive 3D imaging of fracture networks induced by the impact. The principle of X-ray CT is based on the variations in X-ray absorption and attenuation coefficient with different materials. Dense minerals, such as barite appear brighter, and less dense components, such as clay, appear dull in CT images. The crack network, generated surface area, and volume of fractures of impacted rock are determined by synchrotron-based CT.

Dynamic Deformation, Damage, and Fracture Behaviors

The understanding of dynamic damage and fracture behaviors of geomaterials relies heavily on measurements and analysis of dynamic experiments. By quantifying different strengths and deformation parameters, major developments can be made for theoretical researches and numerical verifications. The typical results of each

testing technique, including stress-strain relationships of various testing configurations, 2D and 3D full-field deformation fields under different stress and loading conditions, crack development patterns, and microscopic fracture characteristics are presented. By using the loading techniques and optical measurement methods mentioned above, the dynamic deformation, damage, and fracture behaviors of geomaterials can be quantitatively examined in laboratory conditions. Major discoveries made using the Tri-HB and high-speed DIC method are also presented, and their contributions to dynamic damage mechanics of geomaterials are also discussed based on the findings.

Full-Field Deformation Fields and Stress-Strain Curves

The macroscopic deformation and fracture behavior of rock materials are associated with microcracks initiation, propagation, and coalescence under external loading. The full-field measurement and fracture characterizations of cylindrical sandstone specimen under dynamic uniaxial compression are presented in Fig. 14a. Stress thresholds and corresponding strain fields of sandstone at the strain rate of 120 s^{-1} are determined using the high-speed 3D-DIC method, and the evolution of crack strain and volume strain indicates the different deformation and fracture stages of the cylindrical specimen (Xing et al. 2018a, b). During the dynamic biaxial compression or shearing test using the Tri-HB system, the high-speed 3D-DIC technique is applied for the measurement of the full-field deformation and ejection velocity of the specimen free-surface, as shown in Fig. 14b. The time sequences of the stress-strain curves obtained from the strain-gages signals are synchronized with the full-field strain field. Fig. 14c–d shows the dynamic failure of sandstone under biaxial compression (20, 20, 0) MPa at the impact velocity of 26 m/s, and the deformation and ejection velocities from the free surfaces captured by the 3D-DIC technique (Liu et al. 2020a).

Dynamic behaviors (e.g., dynamic strength, strain, and failure modes) of rock exhibit confinement dependence at high strain rates. Fig. 15 presents the dynamic stress-strain curves of under uniaxial, biaxial, and triaxial prestress states sandstone at the impact velocity of 20 m/s (average strain rate of 110 s^{-1}) (Liu et al. 2019). The dynamic stress (without prestress component) and strain are obtained by the Eqs. (5–11). The enhancement of dynamic strength depends on confinement conditions under the constant impact velocity. The dynamic compressive strength of sandstone falls into three levels (i.e., 50–100, 100–150, and 180–250 MPa), corresponding to under uniaxial, biaxial, and triaxial confinements. Dynamic stress-strain curve of rock consists of compaction, elastic deformation, nonlinear deformation to peak strength, and postpeak failure stages under dynamic uniaxial compression. However, when subjected to confinement, the stress-strain curve presents no compaction stage due to the close of microcracks and voids prior to impact. Dynamic compressive strength is sensitive to three principal stresses under biaxial and triaxial precompression. Generally, dynamic compressive strength decreases with increasing prestress σ_1, while it increases with the increase of the

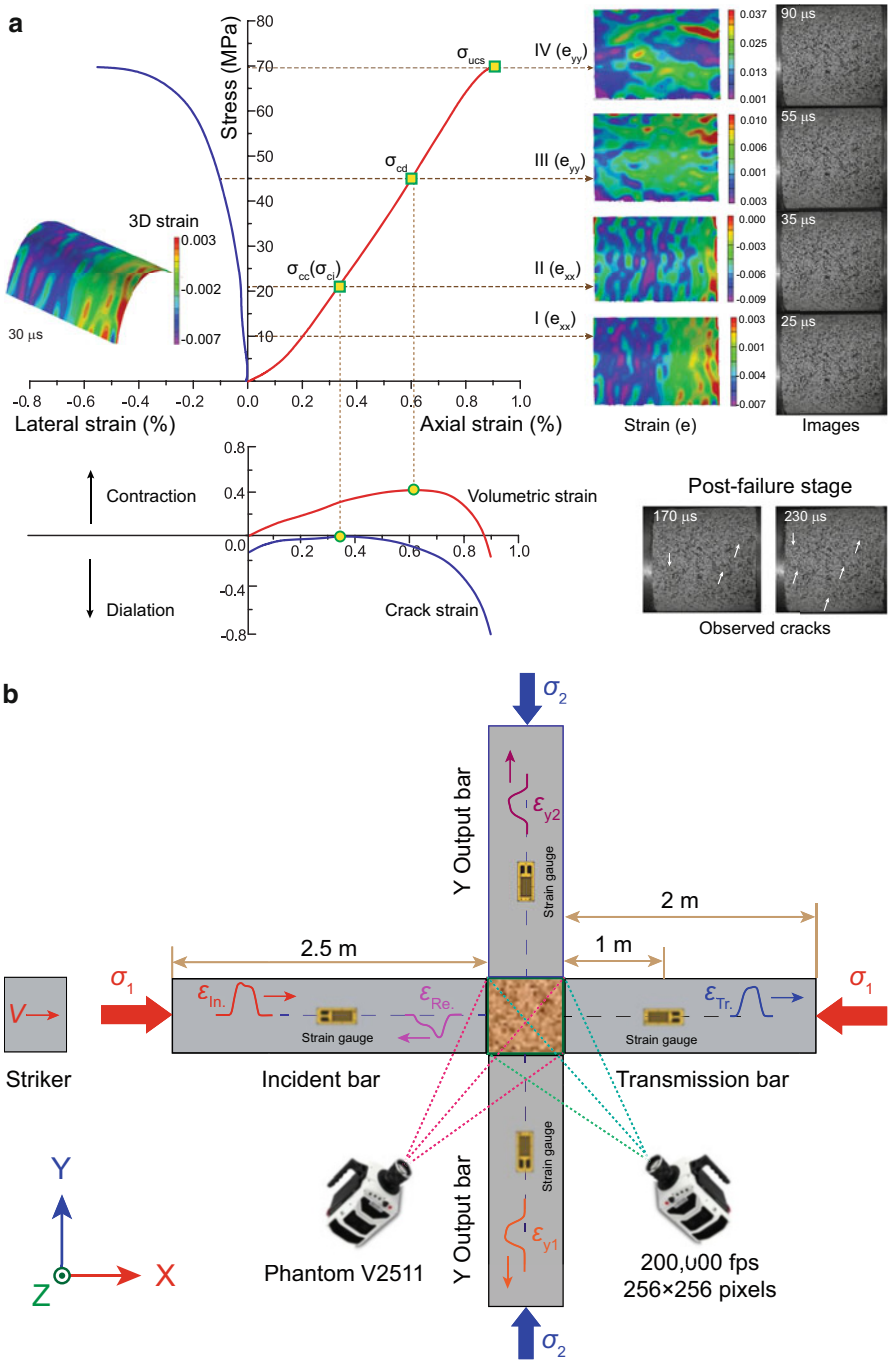

Fig. 14 (continued)

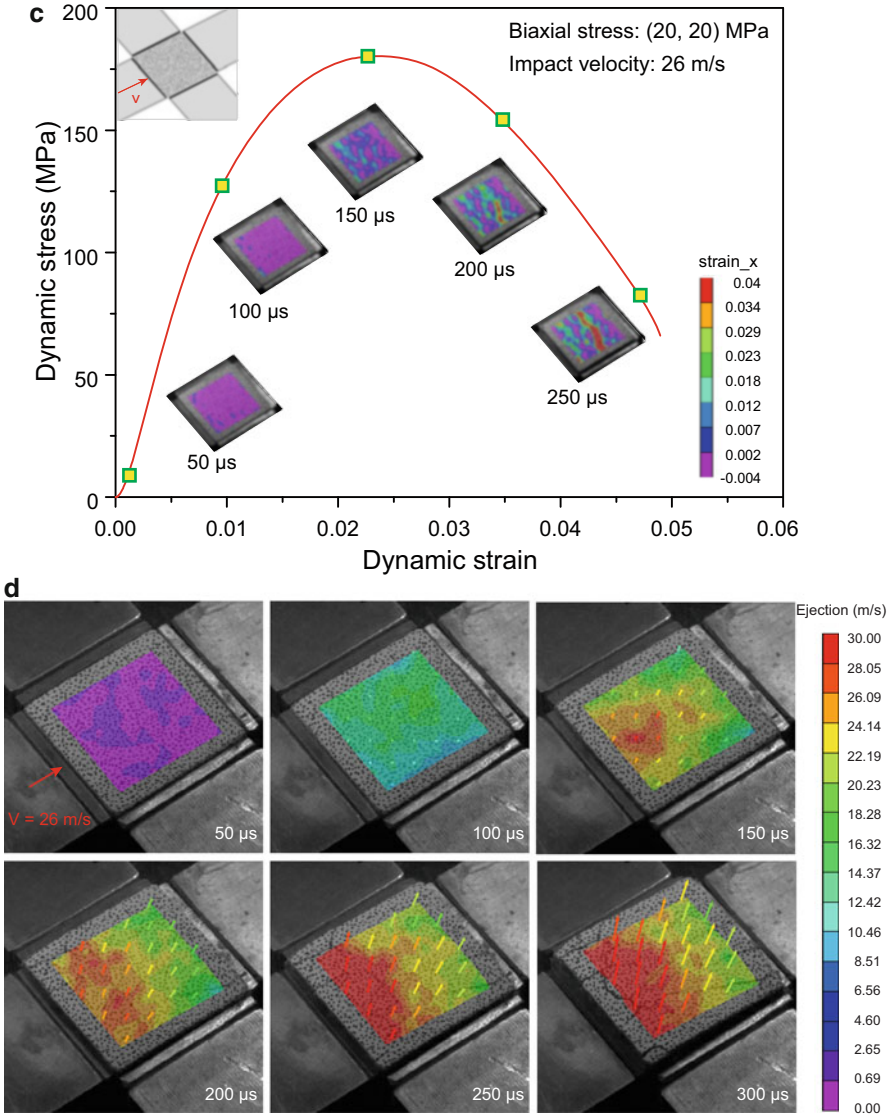

Fig. 14 (**a**) Stress thresholds and corresponding strain fields of cylindrical sandstone specimen at the strain rate of 120 s^{-1} (Xing et al. 2018a), (**b**) real-time stereo imaging set up (not to scale, top view from vertical Z direction), (**c**) dynamic stress-strain curve, and (**d**) dynamic ejection failure of sandstone under biaxial compression (20, 20, 0) MPa at the impact velocity of 26 m/s (Liu et al. 2020a)

lateral prestresses σ_2 and σ_3. Besides, the dynamic elastic modulus also presents an increasing trend with varying prestress from uniaxial, biaxial to triaxial compression.

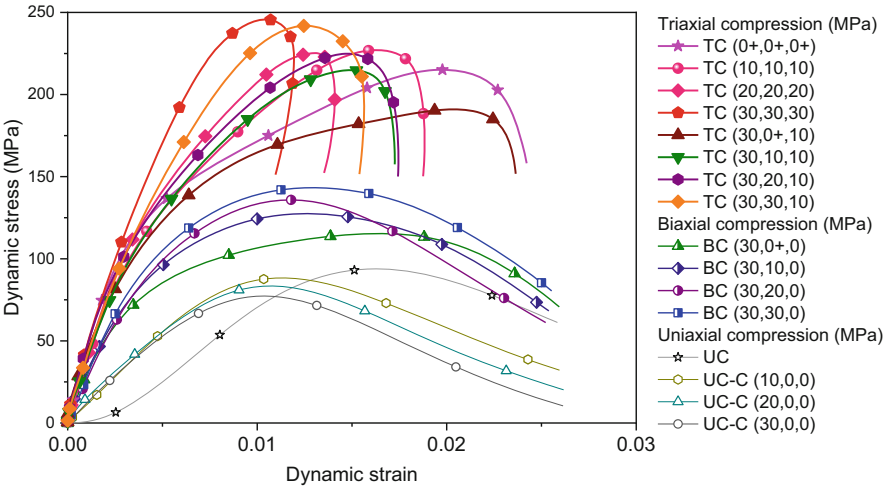

Fig. 15 Dynamic compressive stress-strain curves of sandstone under multiaxial prestresses (UC: uniaxial compression; UC-C: confined UC; BC: biaxial compression; TC: triaxial compression) at the impact velocity of 20 m/s (Liu et al. 2019)

Dynamic Damage and Fracture

Dynamic damage and fracture of geomaterials under different loading conditions and test configurations are presented. Both damage and fracture behaviors are important knowledge for a deeper understanding of geomaterials behaviors under complex prestress conditions and dynamic loadings. The influence of loading rates and prestress conditions on the resulting material damage are discussed, while fracture characteristics of different geomaterials are examined at the surface and internal levels using SEM and X-ray CT, respectively.

Dynamic failure modes of rock under multiaxial loading exhibit obvious confinement dependency. Sandstone is broken into small fragments and fine powders due to severe damage under uniaxial compression (Fig. 16a). With the aid of X-ray CT techniques, the inside fractures after impact can be clearly visualized. The failure mode becomes more distinct under biaxial compression test, as shown in Fig. 16b. Several dominant fractures are observed linking the corners to the center and intersect with each other. As a result, sandstone is divided by fracture planes into approximately two symmetrical V-shaped damage zones at the top and bottom and a relatively intact concaved block in the middle. When all lateral confinements are applied in the triaxial compression test, the damage degree is significantly reduced, and only several visible fractures along the edge and surface can be observed (Fig. 16c). In the dynamic shearing test, a shear fracture generated in the middle of sandstone under prestress condition of (0, 0+, 0) MPa and impact velocity of 9 m/s, as shown in Fig. 16d. Tensile crack also created after shearing due to the tensile stress wave reflected from the free surface.

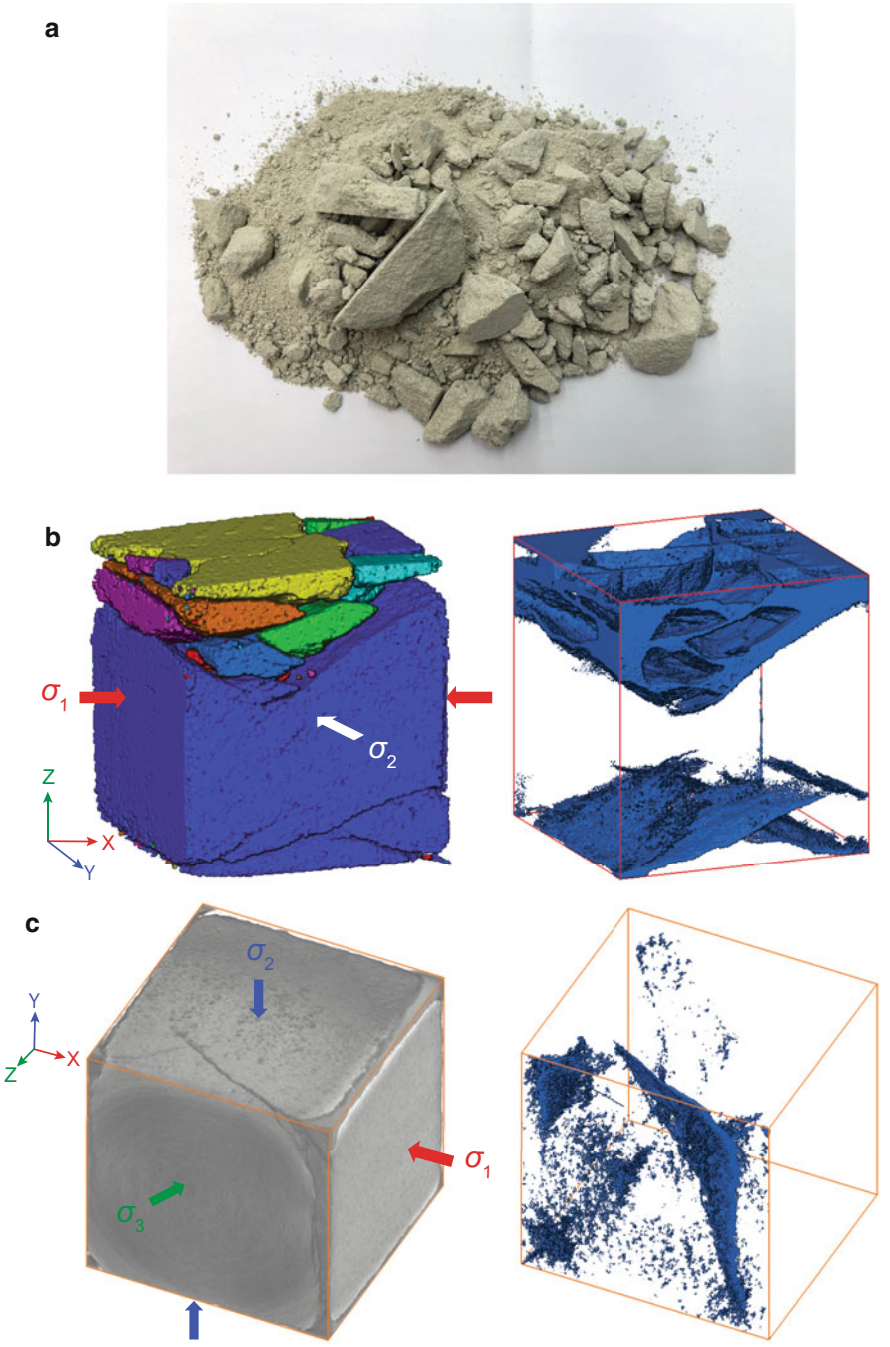

Fig. 16 (continued)

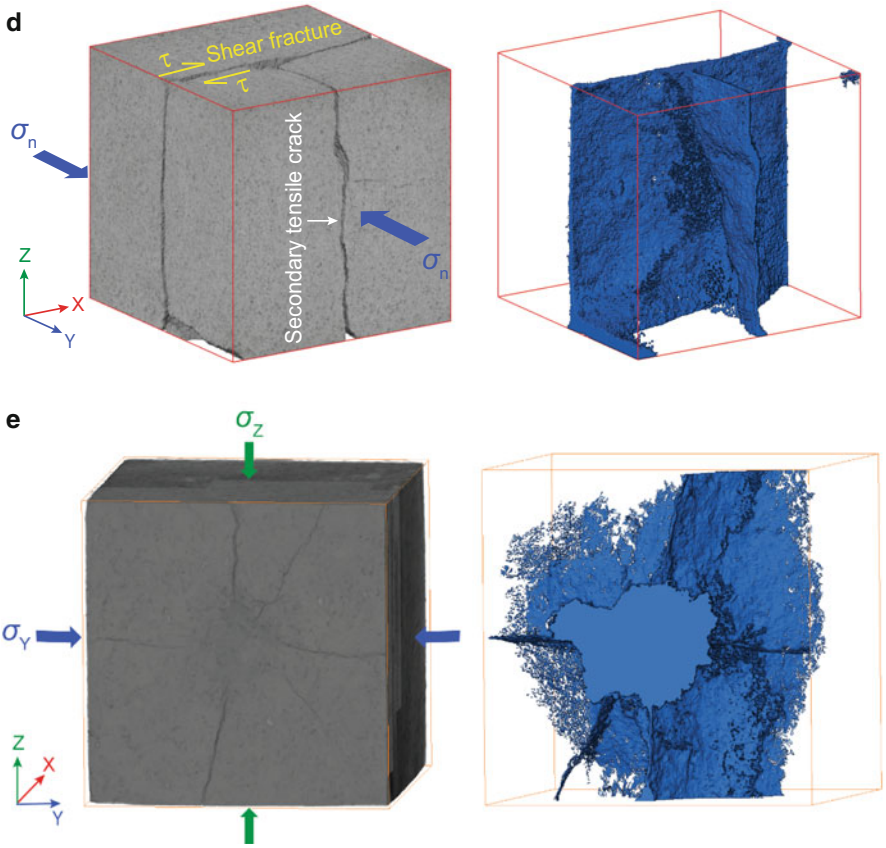

Fig. 16 Failure modes of specimens under (**a**) uniaxial (10, 0, 0) MPa, (**b**) biaxial (30, 10, 0) MPa, and (**c**) triaxial (30, 20, 10) MPa compression on sandstone at the impact velocity of 20 m/s (Refer to Fig. 19 for numerical modeling.), and (**d**) dynamic shearing and shear fracture of sandstone at the impact velocity of 9 m/s, and (**e**) dynamic indentation of granite (one indenter with the diameter of 13 mm and length of 8 mm) under the confining pressure (0, 10, 10) MPa at the impact velocity of 17 m/s

The damage and failure of geomaterials under dynamic indentation can be separated into a number of stages. Initially, the indenter is in contact with the specimen with no loading force applied. As the loading increases, the region beneath indenter loading undergoes compressive and shear damage. Once the loading exceeds the dynamic compressive and shear strength of the material, cracks coalesce and generate intense fracturing. This damage is not seen in the postfailure specimen since the damaged materials are heavily fragmented and crushed as the loading increases. As loading approaches maximum, the penetration depth of indenter reaches its maximum, while tensile cracks begin developing in radial and median directions. The crater is formed at

this stage and crushed materials are compacted in a powder form inside the crater. The unloading of indenter will extent the tensile cracks, resulting in extended crack network surrounding the crater. Chipping may also occur on surfaces near the crater, depending on the material properties and loading conditions. A typical test specimen is shown in Fig. 16e, with crater and visible cracks. In addition to loading rate, prestress conditions also influence the propagation of radial cracks. Tensile cracks will extend parallel to the direction of maximum prestress. Post-tested granite specimens are subjected to X-ray CT scan to obtain the 3D features, such as damage and fractures induced by dynamic indentation. Geometrical measurements such as the crater depth and diameter and more advanced analysis such as volume and area of indentation induced damage are obtained. These quantitative measurements can be utilized to quantify the relationship between loading input energy and prestress conditions of indentation, and the resultant damage in rock specimens using parameters such as specific energy and energy efficiency. The material within the crushed zone can also help provide knowledge regarding the energy consumed during crushing and compaction of fragments during concentrated loading.

Zhang and Zhao (2014a) conducted a comprehensive microscopic analysis on quasi-static and dynamic fracture behavior of marble, gabbro, and sandstone. Under quasi-static loading, as shown in Fig. 17a, intergranular (IG) microcracks were predominant with some contribution of transgranular (TG) microcracks in the fine-grained marble. However, under dynamic loads, as shown in Fig. 17b, there were cleavage and noticeably rugged surfaces with a substantially high number of TG microcracks. In gabbro, as shown in Fig. 17c–d, although TG microcracks were the dominant cracking forms on both quasi-statically and dynamically fractured surfaces, TG microcracks more frequently occurred and even there were few/no IG cracks with increasing strain rate. The dynamically fractured surfaces were smooth at the low magnification, while more curved steps were observed on the rugged surface at the higher magnification (see Fig. 17d). The dynamic shear fracture of granite and marble under similar loading conditions were shown in Fig. 17e, f, respectively. The SEM images showed the fracture of different minerals under dynamic shearing. Granite specimen consisted mainly of feldspar, quartz and mica minerals, while marble was 99% calcite grains. The shear fracture of granite produced breakage of feldspar and quartz grains that were parallel to the fracture surface. However, the mica mineral could be seen in vertical or oblique orientations to the fractured feldspar grains. This was due to the plasticity of mica minerals, as feldspar and quartz generally fractured in a brittle manner, while mica minerals could deform plastically without fracture occurring. This resulted in a fracture surface that had many irregularities due to the remaining mica minerals. The fracture of calcite in dynamic shear of marble produced TG fractures that were parallel to the shear surface. This indicated that during shear fracture, the grain boundary and grain orientation has little influence on the fracture. The final surface was smooth as nearly all fractures were on the same plane.

With the Tri-HB system, dynamic multiple impact experiments are also conducted to investigate the progressive damage mechanism of rocks subjected to different static prestresses and repetitive impact loadings. Figure 18 shows dynamic stress-strain curves and fracture networks identified by X-ray CT scanning under the

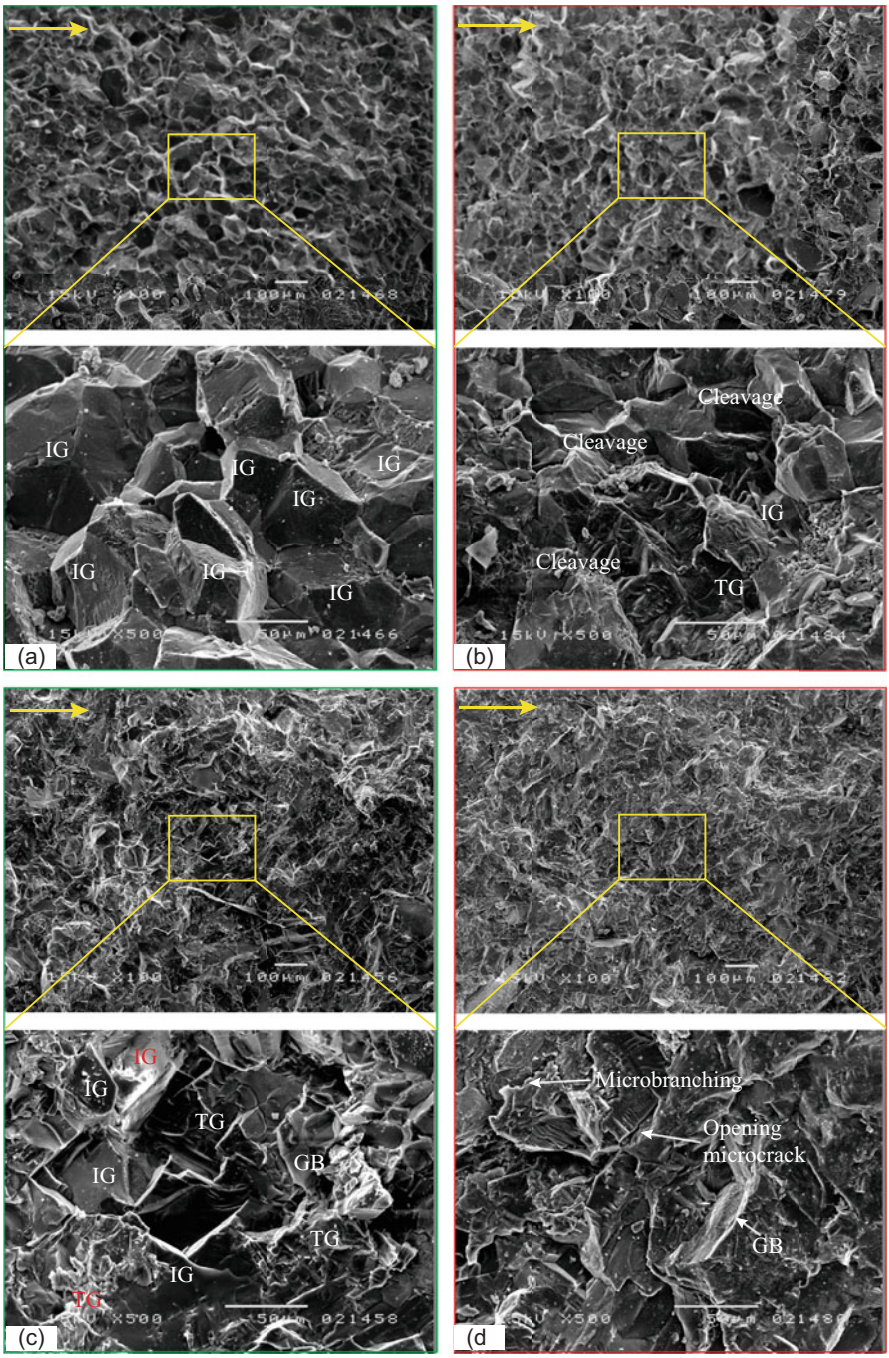

Fig. 17 (continued)

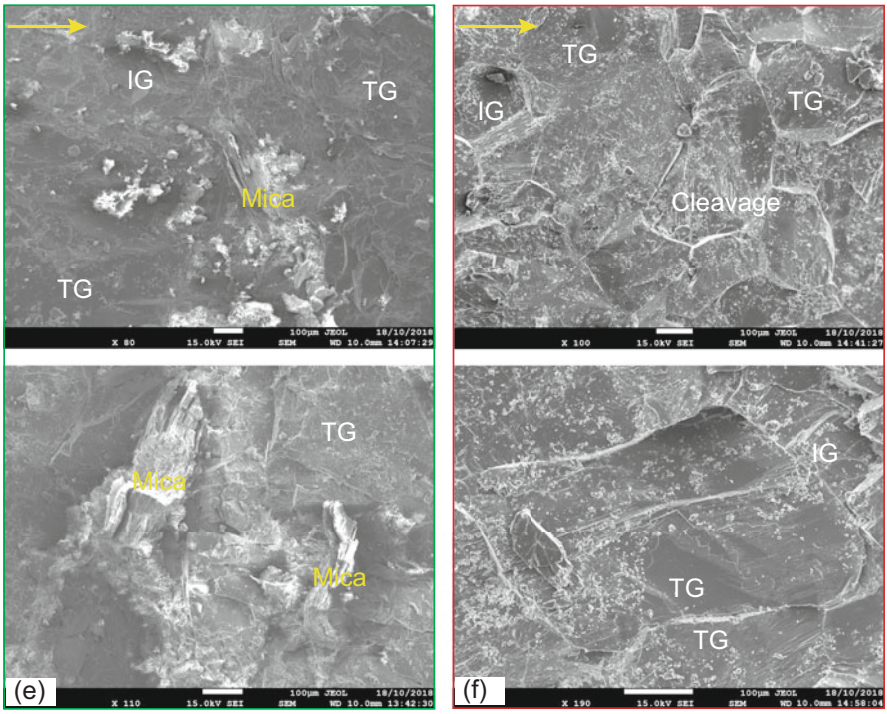

Fig. 17 SEM micrographs at the increasing magnification of (**a**) quasi-static and (**b**) dynamic fractures of fine-grained marble, (**c**) quasi-static and (**d**) dynamic fractures of gabbro (Zhang and Zhao 2014a), and shear-induced microcracks on (**e**) granite and (**f**) marble (The arrow indicates the direction of crack propagation)

triaxial prestress state of (30, 20, 10) MPa at the impact velocity of 27 m/s (Liu 2020). Dynamic triaxial compressive strength of rock decrease with increasing impact times due to the accumulated damage inside the specimen. The microcrack initiation, propagation, and coalescence are observed digitally with the increase of impact times.

Modeling Damage Ratio with Typical Experimental Results

Numerical simulation has been extensively utilized as an important research tool to not only evaluate the SHPB test performance but also clarify the dynamic failure process and associated mechanism (Fukuda et al. 2020; Gui et al. 2016; Li et al. 2018a, b; Zhao et al. 2011, 2014; Zhu et al. 2012, 2018). Dynamic damage and fracture of geomaterials are complex processes, while measurement techniques can provide only partial information during and after the experiments. Therefore, numerical simulation often serves as verification and validation tools. As the modeling

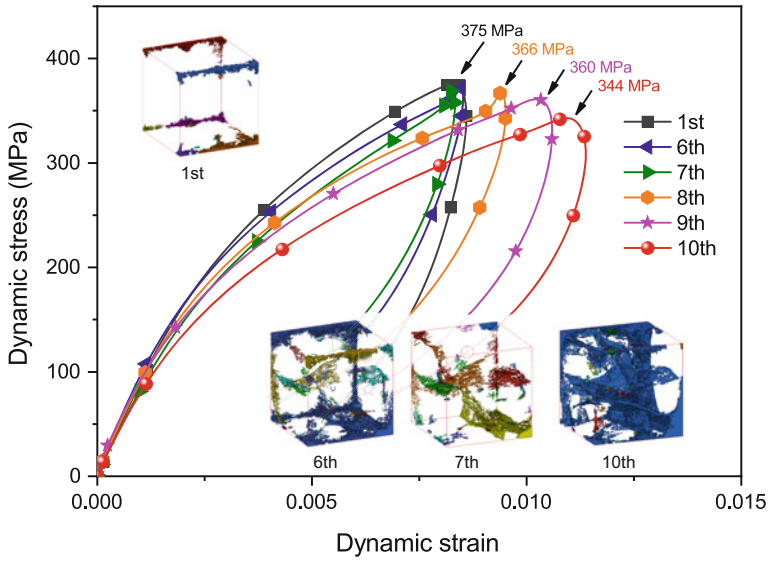

Fig. 18 Deformation and damage evolution of impacted granite under confining pressure (30, 20, 10) MPa and multiple impacts with the same impact velocity of 27 m/s

accuracy and efficiency increase in recent years, more and more numerical research is not only aiming for validation, but also exploring new dynamic geomaterial behavior knowledge. Among all numerical simulation methods, discontinnum-based methods have been extensively utilized for geomaterials. The discrete element method (DEM) is believed to be an efficient technique for simulating dynamic failure process of brittle material since it has advantages of reproducing progressive damage as microcracks form and coalesce into macroscopic fractures without incorporation of complex damage constitutive relationships (Potyondy and Cundall 2004). 2D grain-based modeling (GBM) approach was adopted to perform SHPB uniaxial compression (Li et al. 2018b) and Brazilian disc (Li et al. 2018a) tests. The numerical modeling for the newly developed Tri-HB is still insufficient; thus, a feasible hybrid model capable of simulating dynamic damage and fracturing of brittle materials under multiaxial loading with excellent computational performance is necessary. There are three key issues to be considered: (1) full-scale modeling of the entire Tri-HB system including six bars and rock specimen; (2) material representation considering 3D microstructural effects; (3) true triaxial confining pressure condition under combined static and dynamic loads. A coupled continuum-discrete method is adopted to establish the numerical model of Tri-HB system for improving computational efficiency, simulating real boundary conditions, and explicitly capturing rock breakage (Hu et al. 2020). This model consists of six steel bars and one cubic specimen, which is represented by continuous zones and bonded-particle material, respectively, as schematically shown in Fig. 19a. In the DEM modeling, rock can be represented by rigid grains bonded by deformable and breakable cement

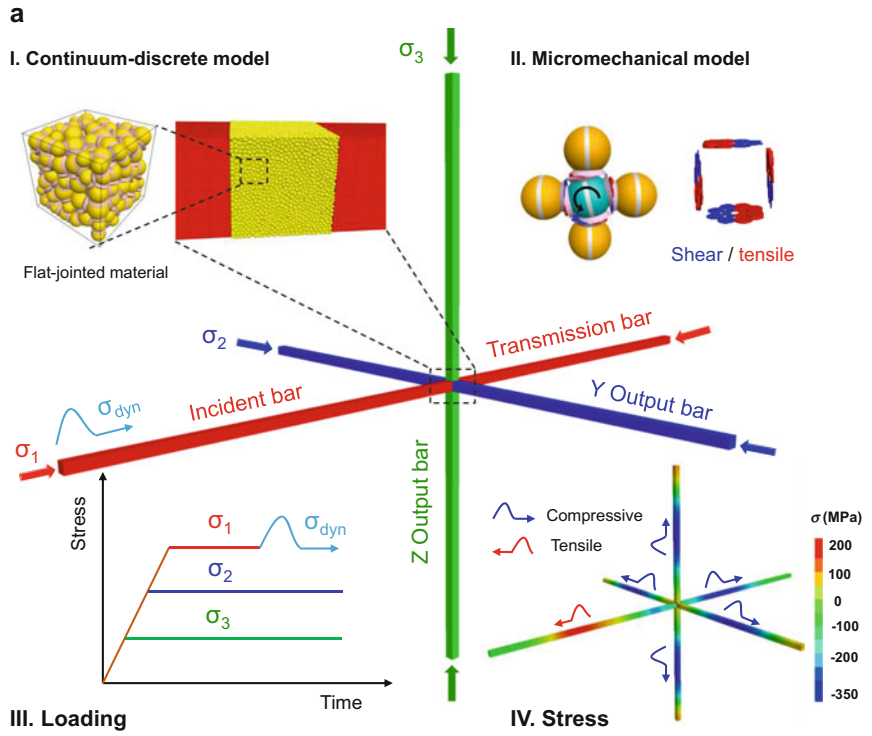

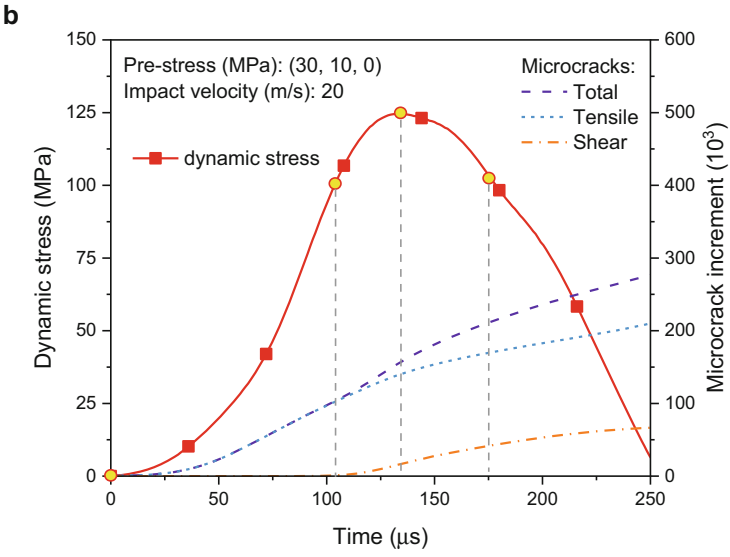

Fig. 19 (continued)

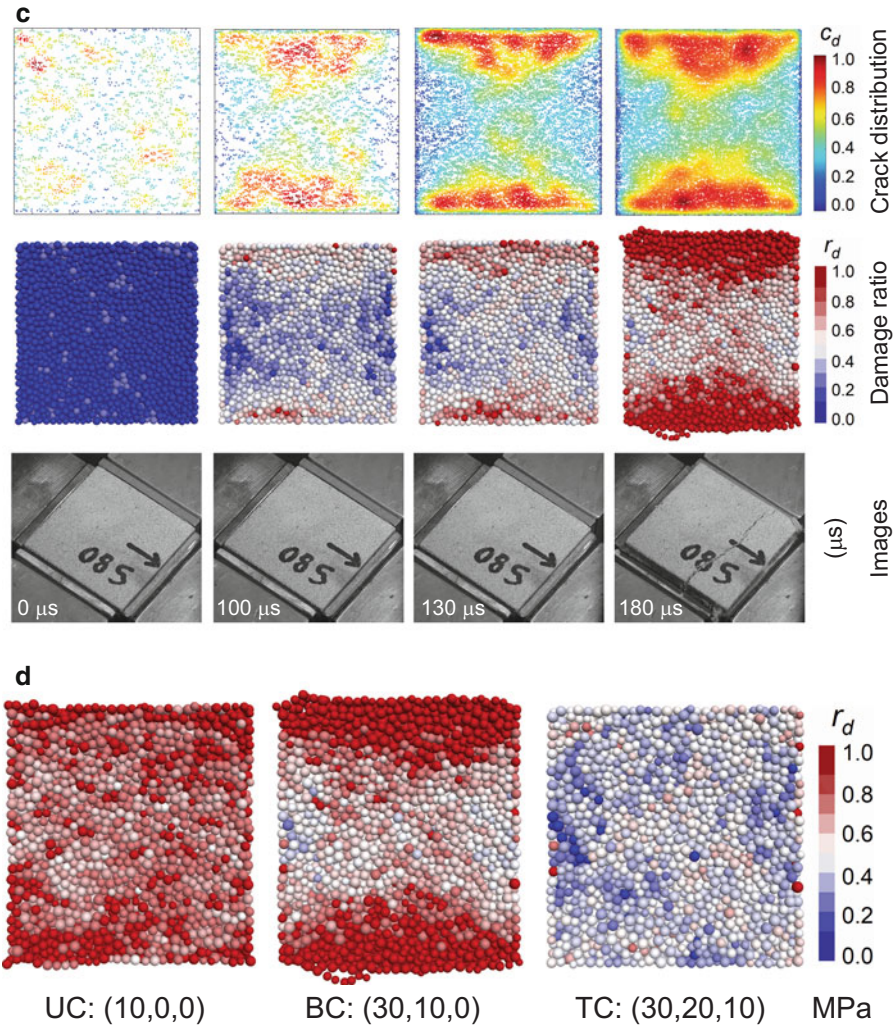

Fig. 19 (**a**) A framework of 3D continuum-discrete coupled model simulating the Tri-HB system, (**b**) typical stress times histories and microcrack increments of a biaxial compression test at (30, 10, 0) MPa and the impact velocity of 20 m/s, (**c**) the corresponding damage and failure process, and (**d**) failure modes of specimens under uniaxial (10, 0, 0) MPa, biaxial (30, 10, 0) MPa and triaxial (30, 20, 10) MPa compression tests at the impact velocity of 20 m/s (Refer to Figs. 14 and 16 for experimental results.) (Hu et al. 2020)

at grain-grain contacts with the bonded-particle model (BPM), in which the flat-joint model (FJM) is adopted owing to its clear microstructural physics without complex constitutive models and efficient computational performance in both 2D and 3D. The movements of particles follow Newton's second law and the contact force is

determined by the relative motion of adjacent particles. When the contact force exceeds the tensile or shear strength of the bond, corresponding bond breakage occurs, and tensile or shear cracks will be generated. The specimen assembly consists of 20,127 particles that satisfy a uniform size distribution specified by the minimum diameter $D_{\min} = 1.6$ mm and the ratio of the maximum to the minimum diameter $D_{\max}/D_{\min} = 1.5$. The sample width is approximately 25 times the average particle diameter, which satisfies the requirement of sample resolution. Numerical modeling can reproduce not only stress-strain curves, but also the damage evolution process (Fig. 19b). Sandstone is broken into small fragments and fine powders due to severe damage under uniaxial compression test (Fig. 19d). A damage ratio r_d ranging from 0 to 1 is defined as the ratio of number of broken bonds to initial bonds of a particle, which evaluates the damage degree of the particle occupied space. A part of particles may experience state from no damage ($r_d = 0$) to full damage ($r_d = 1$) as loading increases. A central slice with a thickness of 10 mm parallel to the X-Z plane is selected to plot the microcracks, while a normalized relative crack density index c_d ranging from 0 to 1 is calculated to show concentration degree of crack distribution. The failure mode becomes more distinct under biaxial compression test as shown in Fig. 19c. Several dominant fractures are observed linking the corners to the center and intersect with each other, dividing sandstone into approximately two symmetrical V-shaped damage zones at the top and bottom by fracture planes with a relatively intact concaved block at the middle. In triaxial compression tests, the damage degree is significantly reduced and only several visible fractures along the edge and surface can be observed.

Summary

Dynamic deformation, damage, and fracture of geomaterial play a vital role in solving civil and mining engineering problems. This chapter concerns firstly on the experimental techniques for both intermediate and high strain rate testing, with the basics of traditional SHPB and Triaxial Hopkinson bar (Tri-HB) briefly introduced. The Tri-HB has demonstrated the capabilities of dynamic loading under complex prestress conditions, and the validation of Tri-HB provides experimental data that better replicates in deep underground and high loading rate scenarios.

Testing configurations for compressive, tensile, shear, indentation, and multiple impact experiments under multiaxial prestress conditions have been achieved, and the corresponding stress-strain relationships and failure modes have been determined. This knowledge is crucial for numerical and theoretical developments regarding dynamic damage and fracture behaviors. High frame rate, 3D-DIC measuring method has been successfully implemented for dynamic geomaterial experiments, especially in conjunction with experiments performed using the Tri-HB system. Full-field strain measurements are combined with stress-strain relationships to expand the knowledge of damage and failure processes during dynamic loading. The effect of heterogeneities on dynamic damage and failure processes are also captured and identified using optical measurement and DIC techniques. Real-time

measurement using Synchrotron X-ray and SHPB has also been achieved, although the specimen size is strictly constrained by experimental setup, which limits the testing capacity. For specimens that require larger sizes, X-ray CT that measures and analyzes the internal failure of geomaterials is a better option. The importance of developing testing systems and experimental techniques that simulate the loading and stress conditions of the real-world problem is shown, that's why the Tri-HB system is a crucial milestone in dynamic experiments of geomaterials. Microscopic examinations are also crucial for unlocking damage and fracture mechanics of geomaterials. Surfaces of dynamic fracture specimens are examined using SEM to study fracture characteristics at the grain level. There are some more advanced microscopies that can be incorporated into the postfailure analysis of dynamically deformed geomaterials, to unveil the subgrain and atomic level damage and failure of geomaterials. Advanced numerical modeling is irreplaceable for dynamic deformation and damage research. To bridge the gap between experimental results and theoretical models, numerical modeling capable of more than validation is required. The coupled numerical modeling method has shown its ability to efficiently and accurately simulate dynamic geomaterial behaviors, including the validation of Tri-HB and replicating experiments in a virtual environment. By incorporating insights made from experimental and microscopic results, numerical modeling can unlock new knowledge in the dynamic behavior of geomaterials.

Acknowledgments This work was supported by the Australian Research Council (LE150100058, IH150100006, DP160100119, DE200101293), Monash Centre for Electron Microscopy, and Imaging and Medical beamline (IMBL) at Australian Synchrotron (M13469, M14047 and M14428). We would also like to thank our colleagues and students, including Wanrui Hu, Xiaofeng Li and Haozhe Xing for their gracious support and input.

References

F.M. Aben, M.-L. Doan, T.M. Mitchell, R. Toussaint, T. Reuschlé, M. Fondriest, J.-P. Gratier, F. Renard, Dynamic fracturing by successive coseismic loadings leads to pulverization in active fault zones. J. Geophys. Res. **121**, 2338–2360 (2016)

J.R. Asay, M. Shahinpoor, High-pressure shock compression of solids, in *Shock Wave and High Pressure Phenomena*, ed. by G. Ben-Dor, F. K. Lu, N. Thadhani, L. Davison, Y. Horie, (Springer Science & Business Media, 1993)

P. Bailly, F. Delvare, J. Vial, J.L. Hanus, M. Biessy, D. Picart, Dynamic behavior of an aggregate material at simultaneous high pressure and strain rate: SHPB triaxial tests. Int. J. Impact Eng. **38**, 73–84 (2011)

N. Bourne, *Materials in Mechanical Extremes: Fundamentals and Applications* (Cambridge University Press, 2013)

N. Brantut, M.J. Heap, P.G. Meredith, P. Baud, Time-dependent cracking and brittle creep in crustal rocks: A review. J. Struct. Geol. **52**, 17–43 (2013)

M.J. Braunagel, W.A. Griffith, The effect of dynamic stress cycling on the compressive strength of rocks. Geophys. Res. Lett. **46**, 6479–6486 (2019)

E. Cadoni, C. Albertini, Modified Hopkinson bar technologies applied to the high strain rate rock tests, in *Advances in Rock Dynamics and Applications*, ed. by J. Zhao, Y. Zhou, (CRC Press, USA, 2011), pp. 79–104

M. Cassidy, M. Manga, K. Cashman, O. Bachmann, Controls on explosive-effusive volcanic eruption styles. Nat. Commun. **9**, 2839 (2018)
K.T. Chau, X.X. Wei, R.H.C. Wong, T.X. Yu, Fragmentation of brittle spheres under static and dynamic compressions: Experiments and analyses. Mech. Mater. **32**, 543–554 (2000)
W. Chen, G. Ravichandran, Failure mode transition in ceramics under dynamic multiaxial compression. Int. J. Fract. **101**, 141–159 (2000)
W.W. Chen, B. Song, *Split Hopkinson (Kolsky) Bar: Design, Testing and Applications* (Springer Science & Business Media, 2010)
W.W. Chen, M.C. Hudspeth, B. Claus, N.D. Parab, J.T. Black, K. Fezzaa, S.N. Luo, In situ damage assessment using synchrotron X-rays in materials loaded by a Hopkinson bar. Phil. Trans. R. Soc. A **372**, 20130191 (2014)
R.J. Christensen, S.R. Swanson, W.S. Brown, Split-hopkinson-bar tests on rock under confining pressure. Exp. Mech. **12**, 508–513 (1972)
J.D. Clayton, Deformation, fracture, and fragmentation in brittle geologic solids. Int. J. Fract. **163**, 151–172 (2010)
T.R. Davies, M.J. McSaveney, The role of rock fragmentation in the motion of large landslides. Eng. Geol. **109**, 67–79 (2009)
M.-L. Doan, G. Gary, Rock pulverization at high strain rate near the San Andreas fault. Nat. Geosci. **2**, 709–712 (2009)
H.-B. Du, F. Dai, Y. Xu, Z. Yan, M.-D. Wei, Mechanical responses and failure mechanism of hydrostatically pressurized rocks under combined compression-shear impacting. Int. J. Mech. Sci. **165**, 105219 (2020)
J.E. Field, S.M. Walley, W.G. Proud, H.T. Goldrein, C.R. Siviour, Review of experimental techniques for high rate deformation and shock studies. Int. J. Impact Eng. **30**, 725–775 (2004)
G. Flores-Gonzalez, *Major hazards associated with cave mining: are they manageable? Proceedings of the First International Conference on Mining Geomechanical Risk* (Australian Centre for Geomechanics, 2019), pp. 31–46
P.G. Fookes, Geomaterials. Q. J. Eng. Geol. Hydroge. **24**, 3–15 (1991)
P. Forquin, Brittle materials at high-loading rates: An open area of research. Phil. Trans. R. Soc. A **375**, 20160436 (2017)
P. Forquin, E. Ando, Application of microtomography and image analysis to the quantification of fragmentation in ceramics after impact loading. Philos Trans A Math Phys Eng Sci **375** (2017)
P. Forquin, G. Gary, F. Gatuingt, A testing technique for concrete under confinement at high rates of strain. Int. J. Impact Eng. **35**, 425–446 (2008)
P. Forquin, K. Safa, G. Gary, Influence of free water on the quasi-static and dynamic strength of concrete in confined compression tests. Cem. Concr. Res. **40**, 321–333 (2010)
M. Fourmeau, A. Kane, M. Hokka, Experimental and numerical study of drill bit drop tests on Kuru granite. Phil. Trans. R. Soc. A **375**, 20160176 (2017)
D.J. Frew, S.A. Akers, W. Chen, M.L. Green, Development of a dynamic triaxial Kolsky bar. Meas. Sci. Technol. **21**, 105704 (2010)
D. Fukuda, M. Mohammadnejad, H. Liu, Q. Zhang, J. Zhao, S. Dehkhoda, A. Chan, J.-I. Kodama, Y. Fujii, Development of a 3D hybrid finite-discrete element simulator based on GPGPU-parallelized computation for modelling rock fracturing under quasi-static and dynamic loading conditions. Rock Mech. Rock. Eng. **53**, 1079–1112 (2020)
B.A. Gama, S.L. Lopatnikov, J.W. Gillespie, Hopkinson bar experimental technique: A critical review. Appl. Mech. Rev. **57**, 223 (2004)
A. Giacomini, O. Buzzi, B. Renard, G.P. Giani, Experimental studies on fragmentation of rock falls on impact with rock surfaces. Int. J. Rock Mech. Min. Sci. **46**, 708–715 (2009)
J.C. Gong, L.E. Malvern, Passively confined tests of axial dynamic compressive strength of concrete. Exp. Mech. **30**, 55–59 (1990)
F.-Q. Gong, X.-F. Si, X.-B. Li, S.-Y. Wang, Dynamic triaxial compression tests on sandstone at high strain rates and low confining pressures with split Hopkinson pressure bar. Int. J. Rock Mech. Min. Sci. **113**, 211–219 (2019)

G.T. Gray III, Classic Split-Hopkinson pressure Bar testing, in *Mechanical Testing and Evaluation*, ed. by H. Kuhn, D. Medlin, (ASM International, 2000), pp. 462–476

Y.-L. Gui, H.H. Bui, J. Kodikara, Q.-B. Zhang, J. Zhao, T. Rabczuk, Modelling the dynamic failure of brittle rocks using a hybrid continuum-discrete element method with a mixed-mode cohesive fracture model. Int. J. Impact Eng. **87**, 146–155 (2016)

P.J. Hazell, *Armour: Materials, Theory, and Design* (CRC press, 2015)

F. Hild, P. Forquin, A. Cordeiro da Silva, Single and multiple fragmentation of brittle geomaterial. Eur. J. Environ. Civ. Eng. **7**, 973–1002 (2003)

B. Hopkinson, A method of measuring the pressure produced in the detonation of high, explosives or by the impact of bullets. Phil. Trans. R. Soc. Lond. A **213**, 437–456 (1914)

W.R. Hu, K. Liu, D.O. Potyondy, Q.B. Zhang, 3D continuum-discrete coupled modelling of triaxial Hopkinson bar tests on rock under multiaxial static-dynamic loads. Int. J. Rock Mech. Min. Sci. **134**, 104448 (2020)

F. Jiang, K.S. Vecchio, Hopkinson Bar loaded fracture experimental technique: A critical review of dynamic fracture toughness tests. Appl. Mech. Rev. **62** (2009)

T. Kenkmann, M.H. Poelchau, G. Wulf, Structural geology of impact craters. J. Struct. Geol. **62**, 156–182 (2014)

H. Kolsky, An investigation of the mechanical properties of materials at very high rates of loading. Proc. Phys. Soc. Lond. B **62**, 676–700 (1949)

X.B. Li, T.S. Lok, J. Zhao, Dynamic characteristics of granite subjected to intermediate loading rate. Rock Mech. Rock. Eng. **38**, 21–39 (2004)

X. Li, Z. Zhou, T.-S. Lok, L. Hong, T. Yin, Innovative testing technique of rock subjected to coupled static and dynamic loads. Int. J. Rock Mech. Min. Sci. **45**, 739–748 (2008)

X. Li, F. Gong, M. Tao, L. Dong, K. Du, C. Ma, Z. Zhou, T. Yin, Failure mechanism and coupled static-dynamic loading theory in deep hard rock mining: A review. J. Rock Mech. Geotech. Eng. **9**, 767–782 (2017)

X.F. Li, X. Li, H.B. Li, Q.B. Zhang, J. Zhao, Dynamic tensile behaviours of heterogeneous rocks: The grain scale fracturing characteristics on strength and fragmentation. Int. J. Impact Eng. **118**, 98–118 (2018a)

X.F. Li, Q.B. Zhang, H.B. Li, J. Zhao, Grain-based discrete element method (GB-DEM) modelling of multi-scale fracturing in rocks under dynamic loading. Rock Mech. Rock. Eng **51**, 3785 (2018b)

C.Y. Liang, Q.B. Zhang, X. Li, P. Xin, The effect of specimen shape and strain rate on uniaxial compressive behavior of rock material. Bull. Eng. Geol. Environ. **75**, 1669–1681 (2016)

U.S. Lindholm, L.M. Yeakley, A. Nagy, The dynamic strength and fracture properties of dresser basalt. Int. J. Rock Mech. Min. Sci. Geomech. Abstr. **11**, 181–191 (1974)

K. Liu, *Dynamic Behaviours of Rock Materials under Coupled Multi-Axial Confinement and Dynamic Loading* (Monash University, 2020)

K. Liu, Q. Zhang, *Dynamic Behaviors of Sandstone under True Triaxial Confinements: Triaxial Hopkinson Bar Tests, 53rd US Rock Mechanics/Geomechanics Symposium* (American Rock Mechanics Association, 2019)

K. Liu, Q.B. Zhang, G. Wu, J.C. Li, J. Zhao, Dynamic mechanical and fracture behaviour of sandstone under multiaxial loads using a triaxial Hopkinson bar. Rock Mech. Rock. Eng. **52**, 2175–2195 (2019)

K. Liu, J. Zhao, G. Wu, A. Maksimenko, A. Haque, Q.B. Zhang, Dynamic strength and failure modes of sandstone under biaxial compression. Int. J. Rock Mech. Min. Sci. **128**, 104260 (2020a)

P. Liu, K. Liu, Q.-B. Zhang, Experimental characterisation of mechanical behaviour of concrete-like materials under multiaxial confinement and high strain rate. Constr. Build. Mater. **258**, 119638 (2020b)

L.E. Malvern, D.A. Jenkens, *Dynamic Testing of Laterally Confined Concrete* (Air Force Engineering & Services Center, Tyndall Air Force Base, 1990), p. 84

J. Mazars, A. Millard, *Dynamic Behavior of Concrete and Seismic Engineering* (ISTE Ltd, London, 2009)
Nemat-Nasser, S., Isaacs, J., Rome, J., 2000. Triaxial hopkinson techniques, in: Kuhn, H., Medlin, D. (Eds.), Mechanical Testing and Evaluation. ASM International, pp. 516–518
R. Othman, *The Kolsky-Hopkinson Bar Machine: Selected Topics* (Springer, 2018)
B. Paliwal, K.T. Ramesh, J.W. McCauley, M. Chen, Dynamic compressive failure of AlON under controlled planar confinement. J. Am. Ceram. Soc. **91**, 3619–3629 (2008)
A. Paluszny, X. Tang, M. Nejati, R.W. Zimmerman, A direct fragmentation method with Weibull function distribution of sizes based on finite- and discrete element simulations. Int. J. Solids Struct. **80**, 38–51 (2016)
F. Pierron, H. Zhu, C. Siviour, Beyond Hopkinson's bar. Phil. Trans. R. Soc. A **372**, 20130195 (2014)
D.O. Potyondy, P.A. Cundall, A bonded-particle model for rock. Int. J. Rock Mech. Min. Sci. **41**, 1329–1364 (2004)
K.T. Ramesh, High rates and impact experiments, in *Springer Handbook of Experimental Solid Mechanics*, ed. by W. N. Sharpe, (Springer, Boston, 2008), pp. 929–960
K.T. Ramesh, J.D. Hogan, J. Kimberley, A. Stickle, A review of mechanisms and models for dynamic failure, strength, and fragmentation. Planet. Space Sci. **107**, 10–23 (2015)
Z. Relph, *What does a mega Kalgoorlie Super Pit rock slide look like?, What does a mega Kalgoorlie Super Pit rock slide look like?* (Kalgoorlie Miner, 2018)
M. Rempe, T. Mitchell, J. Renner, S. Nippress, Y. Ben-Zion, T. Rockwell, Damage and seismic velocity structure of pulverized rocks near the San Andreas fault. J. Geophys. Res. **118**, 2813–2831 (2013)
P.L. Reu, T.J. Miller, The application of high-speed digital image correlation. J. Strain Anal. Eng. Des. **43**, 673–688 (2008)
M. Saadati, P. Forquin, K. Weddfelt, P.L. Larsson, F. Hild, Granite rock fragmentation at percussive drilling – Experimental and numerical investigation. Int. J. Numer. Anal. Methods Geomech. **38**, 828–843 (2014)
T. Saksala, 3D numerical modelling of bit–rock fracture mechanisms in percussive drilling with a multiple-button bit. Int. J. Numer. Anal. Methods Geomech. **37**, 309–324 (2013)
C.H. Scholz, *The Mechanics of Earthquakes and Faulting*, 3rd edn. (Cambridge University Press, Cambridge, 2019)
D.A. Shockey, D.R. Curran, L. Seaman, J.T. Rosenberg, C.F. Petersen, Fragmentation of rock under dynamic loads. Int. J. Rock Mech. Min. Sci. Geomech. Abstr. **11**, 303–317 (1974)
Subhash, G., 2000. Dynamic indentation testing, in: Kuhn, H., Medlin, D. (Eds.), Mechanical Testing and Evaluation. ASM International, p. 0
G. Subhash, S. Maiti, P.H. Geubelle, D. Ghosh, Recent advances in dynamic indentation fracture, impact damage and fragmentation of ceramics. J. Am. Ceram. Soc. **91**, 2777–2791 (2008)
M.A. Sutton, J.J. Orteu, H. Schreier, *Image Correlation for Shape, Motion and Deformation Measurements: Basic Concepts, Theory and Applications* (Springer Science & Business Media, 2009)
B. Wu, W. Yao, K. Xia, An experimental study of dynamic tensile failure of rocks subjected to hydrostatic confinement. Rock Mech. Rock. Eng. **49**, 3855–3864 (2016)
G. Wu, H.Z. Xing, Q.B. Zhang, S. Dehkhoda, *Dynamic Shear Fracture and SEM Study of Granite and Marble, 53rd US Rock Mechanics/Geomechanics Symposium* (American Rock Mechanics Association, 2019)
H.Z. Xing, Q.B. Zhang, C.H. Braithwaite, B. Pan, J. Zhao, High-speed photography and digital optical measurement techniques for geomaterials: Fundamentals and applications. Rock Mech. Rock. Eng. **50**, 1611–1659 (2017)
H.Z. Xing, Q.B. Zhang, D. Ruan, S. Dehkhoda, G.X. Lu, J. Zhao, Full-field measurement and fracture characterisations of rocks under dynamic loads using high-speed three-dimensional digital image correlation. Int. J. Impact Eng. **113**, 61–72 (2018a)

H.Z. Xing, Q.B. Zhang, J. Zhao, Stress thresholds of crack development and Poisson's ratio of rock material at high strain rate. Rock Mech. Rock. Eng. **51**, 945–951 (2018b)
H.Z. Xing, J. Zhao, G. Wu, D. Ruan, S. Dehkhoda, G.X. Lu, Q.B. Zhang, Perforation model of thin rock slab subjected to rigid projectile impact at an intermediate velocity. Int. J. Impact Eng **139**, 103536 (2020)
F. Yuan, V. Prakash, T. Tullis, Origin of pulverized rocks during earthquake fault rupture. J. Geophys. Res. **116** (2011)
Q.B. Zhang, J. Zhao, Determination of mechanical properties and full-field strain measurements of rock material under dynamic loads. Int. J. Rock Mech. Min. Sci. **60**, 423–439 (2013a)
Q.B. Zhang, J. Zhao, Effect of loading rate on fracture toughness and failure micromechanisms in marble. Eng. Fract. Mech. **102**, 288–309 (2013b)
Q.B. Zhang, J. Zhao, Quasi-static and dynamic fracture behaviour of rock materials: Phenomena and mechanisms. Int. J. Fract. **189**, 1–32 (2014a)
Q.B. Zhang, J. Zhao, A review of dynamic experimental techniques and mechanical behaviour of rock materials. Rock Mech. Rock. Eng. **47**, 1411–1478 (2014b)
Q.B. Zhang, C.H. Braithwaite, J. Zhao, Hugoniot equation of state of rock materials under shock compression. Phil. Trans. R. Soc. A **375**, 20160169 (2017)
G.F. Zhao, J. Fang, J. Zhao, A 3D distinct lattice spring model for elasticity and dynamic failure. Int. J. Numer. Anal. Methods Geomech. **35**, 859–885 (2011)
G.-F. Zhao, A.R. Russell, X. Zhao, N. Khalili, Strain rate dependency of uniaxial tensile strength in Gosford sandstone by the distinct lattice spring model with X-ray micro CT. Int. J. Solids Struct. **51**, 1587–1600 (2014)
Y.X. Zhou, K. Xia, X.B. Li, H.B. Li, G.W. Ma, J. Zhao, Z.L. Zhou, F. Dai, Suggested methods for determining the dynamic strength parameters and mode-I fracture toughness of rock materials. Int. J. Rock Mech. Min. Sci. **49**, 105–112 (2012)
W.C. Zhu, Y. Bai, X.B. Li, L.L. Niu, Numerical simulation on rock failure under combined static and dynamic loading during SHPB tests. Int. J. Impact Eng. **49**, 142–157 (2012)
J.B. Zhu, T. Zhou, Z.Y. Liao, L. Sun, X.B. Li, R. Chen, Replication of internal defects and investigation of mechanical and fracture behaviour of rock using 3D printing and 3D numerical methods in combination with X-ray computerized tomography. Int. J. Rock Mech. Min. Sci. **106**, 198–212 (2018)

High-Speed Real-Time X-Ray Visualization of Impact Damage Inside Geomaterials

17

Junyu Wang, Niranjan Parab, and Wayne Chen

Contents

Introduction 424
Materials Investigated 425
Experimental Method 426
Kolsky (Split-Hopkinson) Bar Setup 426
High-Speed Synchrotron X-Ray PCI 426
Particle Arrangement 429
Damage Mechanisms Under Boundary-Particle Contact Condition 430
Soda Lime Glass 430
Polycrystalline Silica 432
Polycrystalline Silicon 434
Damage Mechanisms Under Particle-Particle Contact Condition 437
Soda Lime Glass 437
Polycrystalline Silica 441
Polycrystalline Silicon 443
Yttria-Stabilized Zirconia (YSZ) 445
Ottawa Sand 446
Ohio Gold Sand 448
Q-Rock Sand 448
Summary of the Visualized Damage Mechanisms 449
Conclusions and Prospective 451
References 452

Abstract

High-speed X-ray phase contrast imaging enables in situ visualization of damage in optically opaque materials under high-rate loading conditions. This technique fits well in studying the impact damage mechanisms in geomaterials at the particle or meso-scale with observation window size in the order of millimeters. This chapter presents a series of experiments visualizing the impact damage

J. Wang · N. Parab · W. Chen (✉)
Purdue University, West Lafayette, IN, USA
e-mail: wang4123@purdue.edu; nparab@purdue.edu; wchen@purdue.edu

© Springer Nature Switzerland AG 2022

G. Z. Voyiadjis (ed.), *Handbook of Damage Mechanics*,
https://doi.org/10.1007/978-3-030-60242-0_74

process of various geomaterial particles. These experiments were performed with a synchronized system consisting of high-speed camera, full-field X-ray phase contrast imaging, and Kolsky compression bars. In these experiments, both single- and multiparticle configurations were examined. The X-ray phase contract images clearly demonstrated the evolution of damage within the particles, which were discussed for each configuration, revealing fundamental failure mechanisms in a particulate system under impact.

Keywords

High-speed X-ray PCI · Particle impact · Failure upon impact · Hertzian contact

Introduction

Understanding the damage mechanisms of geomaterials under impact loading conditions is important in particle size reduction or granulation, and other industrial applications for optimizing energy efficiency and minimizing damage caused by high-speed powder flow. When a particulate geomaterial system is loaded, the force transmission through the system is through a series of force chains. Breakage of particles will change the chain distribution and affect the load-bearing capacity. Thus, it is important to understand how particles break under loading. Research efforts on the damage mechanisms in geomaterials have mainly been invested on two aspects. One is studying the damage mode in an aggregated geomaterial system, which represents the geomaterial system that is encountered in engineering processes. The other aspect is studying the damage behavior of individual geomaterial particles, where detailed failure modes and critical parameters may be identified and quantified. The study shown in this chapter falls in the second aspect. With improved understanding of how individual particles fail, more accurate models can be developed to simulate the damage evolution of a particulate system.

The damage mechanisms in geomaterials under impact loading can be complicated due to possible evolvement of multiple failure modes dictated by various factors such as strain rate, microstructure, and contact conditions. For example, most of these materials are optically opaque. Although techniques such as arrested dynamic experiments or sarcophagus impact experiments can be used to study the damage mechanics of geomaterial particles, the in situ damage inside the materials cannot be visualized by optical high-speed imaging. Such a challenge can be addressed by an experimental technique that integrates high-speed X-ray phase contrast imaging (PCI) and Kolsky bars (Hudspeth et al. 2013; Chen et al. 2014). Utilizing the continuous high-intensity X-ray available at the Advance Photon Source (APS) of Argonne National Laboratory (ANL) in the United States for high-speed PCI, this technique enabled in situ visualization of the deformation and damage evolution inside an opaque sample under high-rate loading. This chapter mainly summarizes the findings of a series of studies on impact damage inside geomaterials using the aforementioned novel experimental technique

(Parab et al. 2014a, b; Parab 2017). In these studies, the damage inside particles was visualized for eight types of geomaterial particles of various sizes with different contacting conditions. In particular, the initiation and evolution of damage were carefully investigated for both boundary-particle and particle-particle contact conditions.

In this chapter, the materials investigated are first introduced, followed by the descriptions of the experimental setup and procedures. The visualization of the damage processes within the particles along with digested discussion is then provided, divided into two sections based on contact conditions. The force-displacement relationship during the impact process is also presented for each condition studied, along with comparison to the Hertzian contact theory if the contact is well defined. Within each section, each type of material is separately discussed, focusing on explaining the damage evolution and potential factors that dictate the processes.

Materials Investigated

The list of the materials investigated in this chapter is given in Table 1. Eight different materials were studied, including five manufactured particles materials and three types of naturally occurring sand particles. Most of the manufactured particle materials have a broader range of sizes with a nominally spherical shape. These particles such as glass and silicon, though apart from the classification of geomaterials, are also important to study in this chapter because their regular shapes and microstructure guarantee well-defined contact conditions and consistency in damage process such that their damage process can be more easily quantified. These materials can serve as a good starting point in studying the impact damage behavior at discrete particle scale. The three types of naturally occurring sand materials were quarried from different locations across the United States and have more confined size ranges and irregular shapes. Their failure process is more qualitatively discussed as quantitative conclusions are difficult to draw at the current stage.

Table 1 Details of particles used in the study

Material	Diameters (μm)
Manufactured particles	
Soda lime glass	1000–1180
	1700–2000
Polycrystalline silicon	1000–1180
	1700–2000
Polycrystalline silica	1700–2000
Yttria stabilized zirconia (YSZ)	710–850
	1350–1550
Naturally occurring sand particles	
Ohio gold sand	850–1000
Q-rock	1000–1180
Ottawa sand	600–760

Since the X-ray window size is 2.5 mm × 1.6 mm, most of the particles were studied within two diameter ranges: 850–1100 μm and 1700–2000 μm. For particles smaller than 850 μm, it becomes challenging to clearly visualize the damage process. Some of the soda lime glass between 1000 and 1180 μm were annealed to study the effect of residual stresses on damage mechanisms. Although glass is transparent, damage-induced new surfaces scatter light, which make optical observation infeasible. The glass particles were first heated to 540°C, then cooled to room temperature. Although glass particles are optically transparent, the fracture surfaces are highly reflective when damage occurs, which makes the effort to identify the damage details very challenging. X-ray PCI is employed instead to investigate the dynamic damage evolution effectively.

Experimental Method

A modified Kolsky bar was used for controlled impact loading, which was integrated with a high-speed synchrotron X-ray phase contrast imaging (PCI) system to record the in situ damage process inside the particles. The high-intensity X-ray was available at beamline 32-ID at the APS at Argonne National Laboratory, USA. This experimental setup has been widely used and can be applied to many other materials ranging from ductile to brittle (Parab 2017).

Kolsky (Split-Hopkinson) Bar Setup

A miniature Kolsky compression bar was used to perform the particle impact experiments. A schematic of the experimental setup is presented in Fig. 1. The bar was composed of a high-strength steel striker and a high-strength steel incident bar, with the transmission bar replaced by a heavy aluminum backstop, on which a load cell was mounted. A fast-response solenoid valve was used for firing, which was remotely controlled by a DC current. In general, pulse shaping is needed to ensure dynamic equilibrium and constant strain rate. In this study, the focus was on the damaging process under constant motion of loading platens; rather than stress-strain response of the sample materials, pulse shapers were not used. Force transmitting through the failing samples was measured directly by a force transducer.

High-Speed Synchrotron X-Ray PCI

The X-ray radiation in a synchrotron source is emitted from the electron bunches stored in a circular storage ring. In the experiments reported here, the storage ring had 24 electron bunches moving at relativistic speed, with 153 ns separation between each electron bunch. Using an undulator with the gap between the magnetic poles set to be 11 mm, the fundamental energy of the X-ray beam was peaked at 25.4 KeV. The size of the X-ray beam on the sample was 2560 × 1600 μm^2. The X-ray

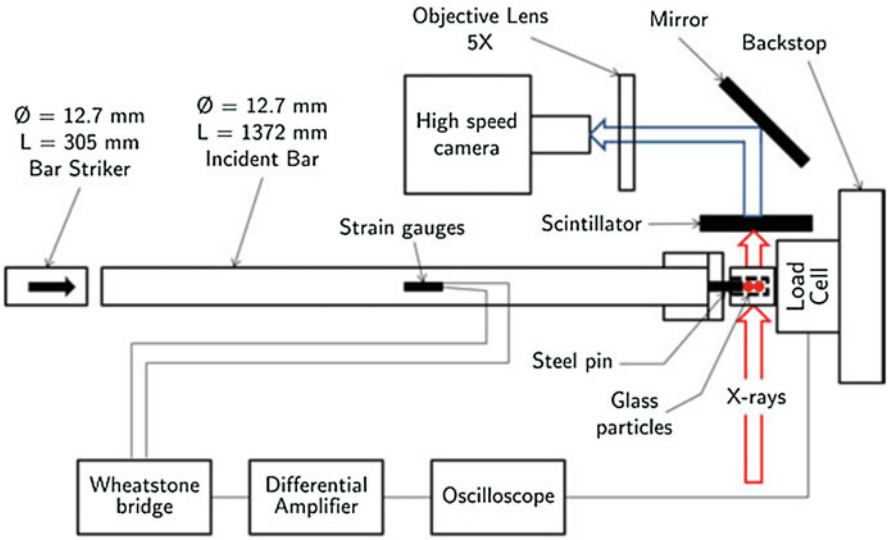

Fig. 1 Schematic of Kolsky bar setup synchronized with high-speed X-ray PCI

intensity on the sample was 1.4×10^{16} photons/s/mm^2/0.1% Bandwidth. The distance between the X-ray source and the sample was approximately 37 m.

When the X-ray passes through materials with different refractive indices, the interference between adjacent X-rays with change in phase can be seen from the contrast in the images. We used in-line holographic technique to obtain the phase contrast. Furthermore, edge enhancement was achieved by adjusting the distance from the sample to the detector. This is critical for detecting the early onset of cracking in the particles. A single crystal scintillator (dimensions: 10 mm $\times$ 10 mm $\times$ 100 μm) was used to convert the X-ray signal to visible light, which was recorded by high-speed cameras. The scintillator is made of $Lu_3Al_5O_{12}$, has a decay time around 70 ns, and has the emission spectrum peak at 530 nm. Over the time of conducting the reported experiments, four different high-speed cameras were used: Photron SA1.1 (Photron, Tokyo, Japan), Photron SA-Z (Photron, Tokyo, Japan), Shimadzu HPV-X (Shimadzu, Kyoto, Japan), and Shimadzu HPV-X2 (Shimadzu, Kyoto, Japan). The specifications of these cameras are provided in Table 2. The exposure time is not perfectly synchronized with the X-ray pulse frequency, resulting in different number of impinged X-ray pulses onto one frame. At higher frame rates, some frames are taken when there is no impinged X-ray pulse on the sample, but these frames are not completely dark because of the decay from the scintillator. Therefore, the brightness is uneven across frames. The images were postprocessed to correct the variation in brightness and contrast due to this mismatch between exposure time of the frames and separation between X-ray pulses.

To prevent the X-ray beam from damaging the sample and the scintillator, two water-cooled copper blocks were used as a shuttering system, which has an approximately 50-ms opening and shutting delay, requiring synchronization of X-ray

Table 2 Details of the high-speed cameras used

Camera	Photron SA1.1	Photron SA-Z	Shimadzu HPV-X	Shimadzu HPV-X2
Max. frame rate: A (million fps)	0.675	2.1	10	10
Frame size @A ($pixel^2$)	64 × 16	128 × 8	400 × 250	400 × 250
Commonly used frame rate: B (fps)	45,000	120,000	2,000,000	2,000,000
Frame size @B ($pixel^2$)	320 × 320	416 × 256	400 × 250	400 × 250
Exposure time @B (ns)	1000	35	200	200
Inherent pixel size (μm)	20	20	32	32
Pixel size in the experiments (μm)	5	5	6.4	6.4

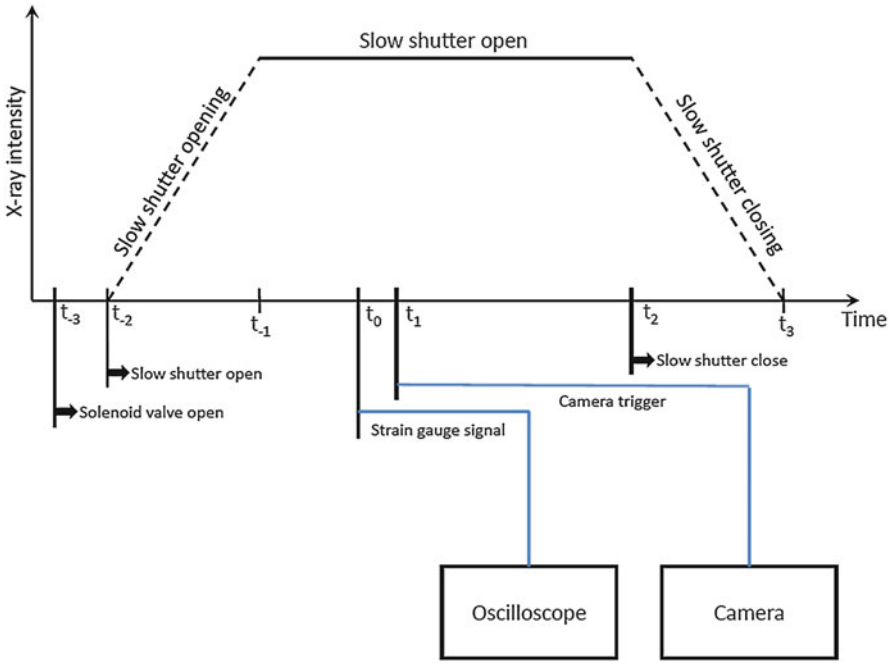

Fig. 2 Synchronization scheme of the experimental system

shuttering system, firing of Kolsky bar, the loading event, and image recording. The synchronization was fulfilled by using delay generators. The time scheme is shown in Fig. 2. The dynamic measurement was defined within time window between t_1 and t_2.

Particle Arrangement

For the experiments with particle-boundary contact conditions, a single particle is constrained in an aluminum holder and compressed between two steel pins. Three configurations were used for the experiments with particle-particle contact condition. Two-particle configuration was used for all the materials investigated, while three-particle and five-particle configurations were only used for soda lime glass. Schematics of sample arrangements are presented in Fig. 3. For two-particle configuration, the two particles were constrained in the same aluminum holder as those used for single particle experiments, with a steel pin compressing the two particles against each other and against the holder. The inside diameter of the aluminum holder is larger than particle size, allowing free lateral deformation of the particles. Aluminum holder was used since it was nearly transparent to X-ray. For three-particle and five-particle configurations, the particles were placed between two 1.0-mm thick polymethyl methacrylate (PMMA) plates, separated by a 1.1-mm-thick steel plate. The steel plate was machined to have a channel to fit the particles, which were compressed by a steel pin against the steel plate. In the experiments, the steel pin was mounted on the end of the compression bar, and the aluminum holder was mounted between the bar and the load cell.

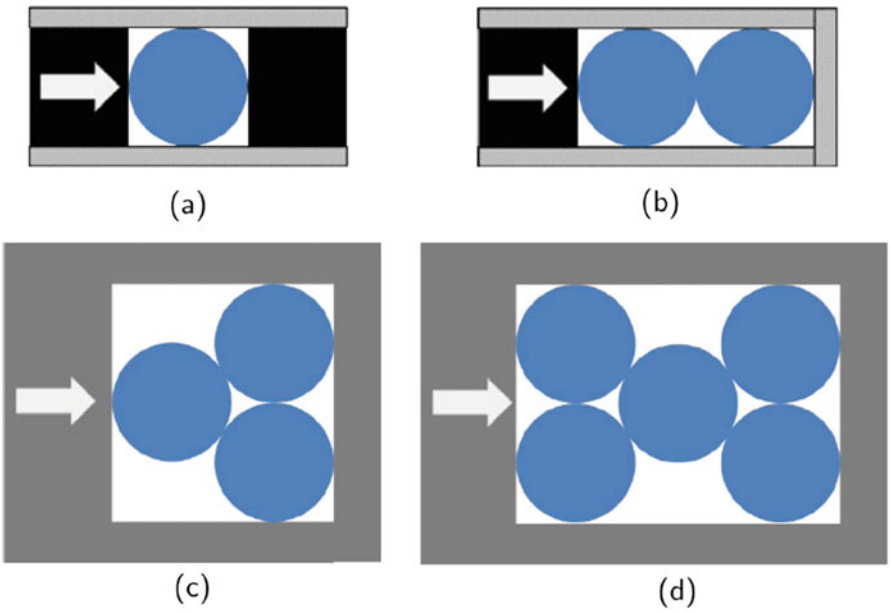

Fig. 3 Schematic of the particle arrangements. (**a**) single particle, (**b**) two contacting particles, (**c**) three contacting particles, and (**d**) five contacting particles

Damage Mechanisms Under Boundary-Particle Contact Condition

Soda Lime Glass

The impact damage of both sizes (~1 mm and ~ 2 mm) of heat-treated and untreated soda lime glass particles was investigated, with experiments on each type repeated three times. In each experiment, a single particle was compressed between two steel pins. The steel pin that was attached to the incident bar started compressing the particle when the stress wave reached the end of the bar. The X-ray images, along with the force-displacement histories, of smaller (1.00–1.18 mm) annealed particles under impact, are presented in Fig. 4. Smaller untreated particles are presented in Fig. 5, larger ones (1.7–2.0 mm) annealed in Fig. 6, and larger untreated ones in

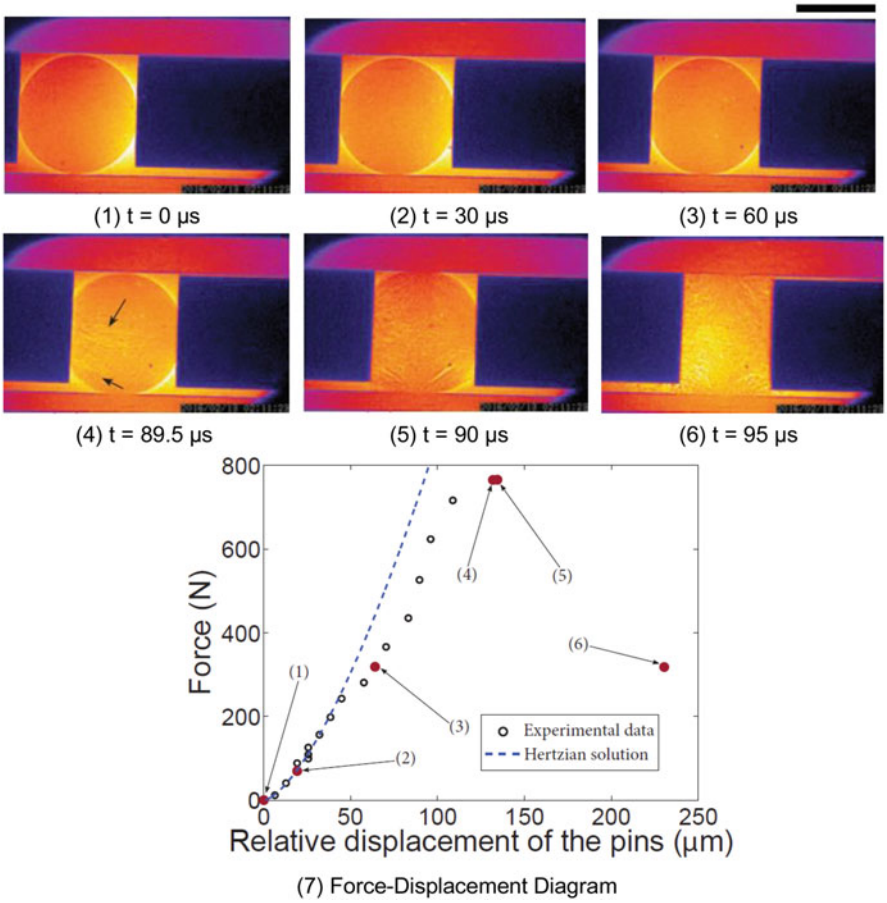

Fig. 4 X-ray images of a single particle experiment for smaller (1.00–1.18 mm) untreated soda lime glass. The scale bar represents 500 μm. The black arrows in (4) indicate the meriodinal cracks

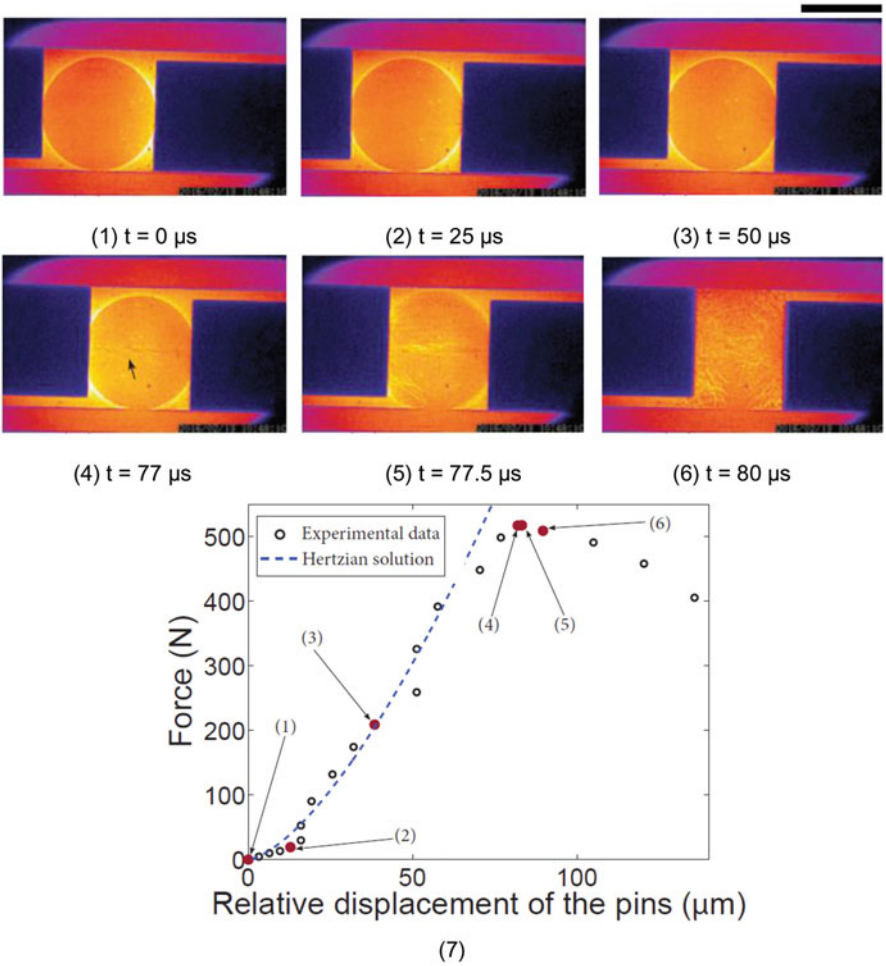

Fig. 5 X-ray images of a single particle experiment for smaller (1.00–1.18 mm) annealed soda lime glass. The scale bar represents 500 μm. The black arrow in (4) indicates the meridional crack

Fig. 7. Each figure presents the damage process at various time instants that are also marked in the force-displacement diagram. For the untreated particles, it was observed that the particle was elastically compressed at first until a critical compressive load was reached, which was measured by the load cell. At this point, multiple meridional cracks were initiated near either one of the particle-pin contacts (Frame 4 in Fig. 4). As the particle was further compressed, these meridional cracks propagated toward the other particle-pin contact, during which they bifurcated, then caused the particle to pulverize (Frames 5, 6). As seen in the force-displacement diagrams, the load dropped rapidly during the last stage. The same damage mechanisms were observed for both sizes of both annealed and untreated particles. For

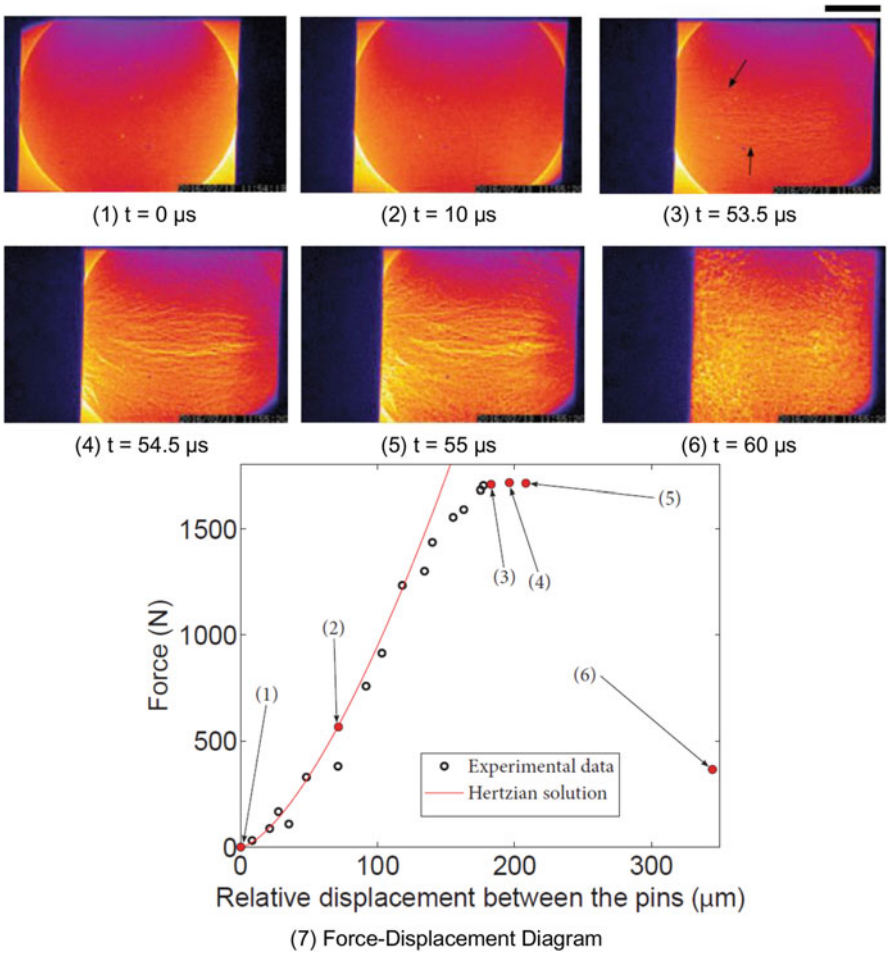

Fig. 6 X-ray images of a single particle experiment for larger (1.7–2.0 mm) untreated soda lime glass. The scale bar represents 500 μm. The black arrows in (3) indicate the meridional cracks

larger soda lime glass particles, multiple meridional cracks were observed to form and bifurcate through the particle, which then lead to explosive fragmentation of the particles (Frames 4–6 in Fig. 6). Similar behavior was observed in all the repeated experiments. Overall, the force-displacement relationship agrees with Hertzian contact theory up to the point where cracks start to form.

Polycrystalline Silica

The X-ray images along with the force-displacement relationship of a single silica particle under impact are shown in Fig. 8. A meridional crack was initiated near the

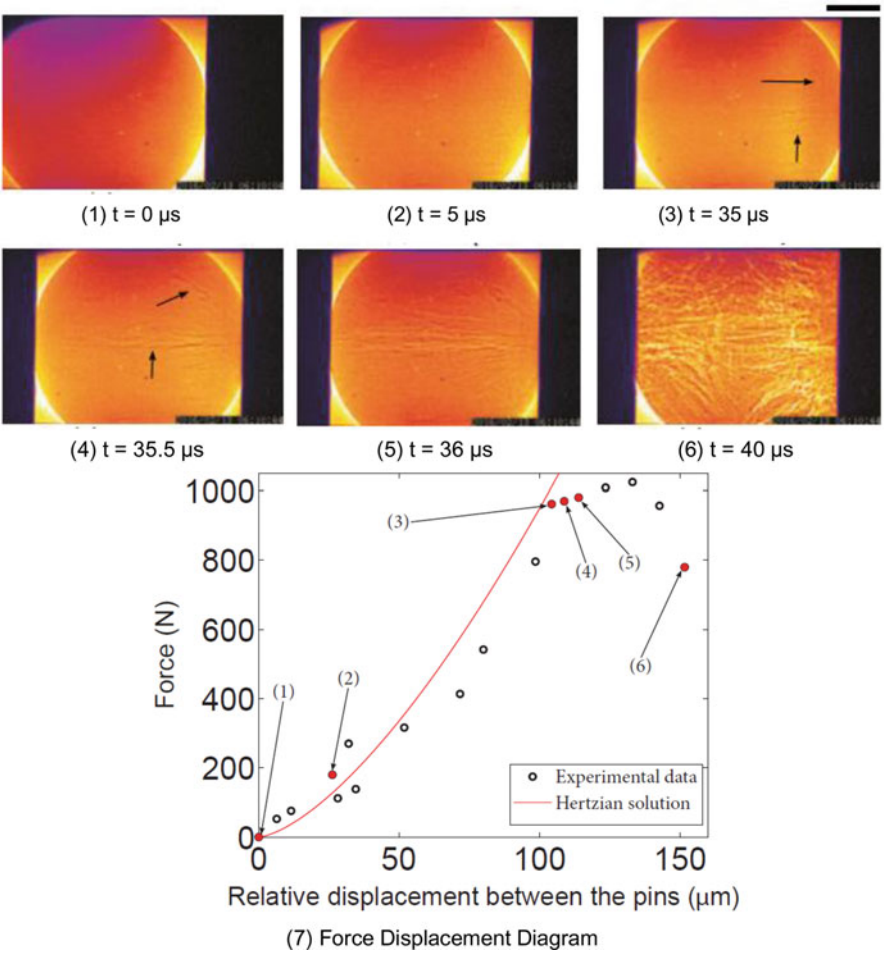

Fig. 7 X-ray images of a single particle experiment for larger (1.7–2.0 mm) annealed soda lime glass. The scale bar represents 500 μm. The black arrows in (3) and (4) indicate the onset and propagation of the meridional crack and subcracks, respectively

center of the particle and quickly propagated toward the contacts, splitting the particle into two roughly hemispherical parts (3–5). Upon being further compressed, bending-induced cracks were observed near the spherical surfaces (5). These bending-induced cracks and the major meridional crack eventually fractured the particle into a large number of small fragments (6). The force exhibits a small plateau region while the cracks form, before rapidly dropping upon separation of the particle. For this material, even though the contact is well defined, Hertzian contract theory can only predict the force at initial small portion of the displacement and underpredict at larger displacements.

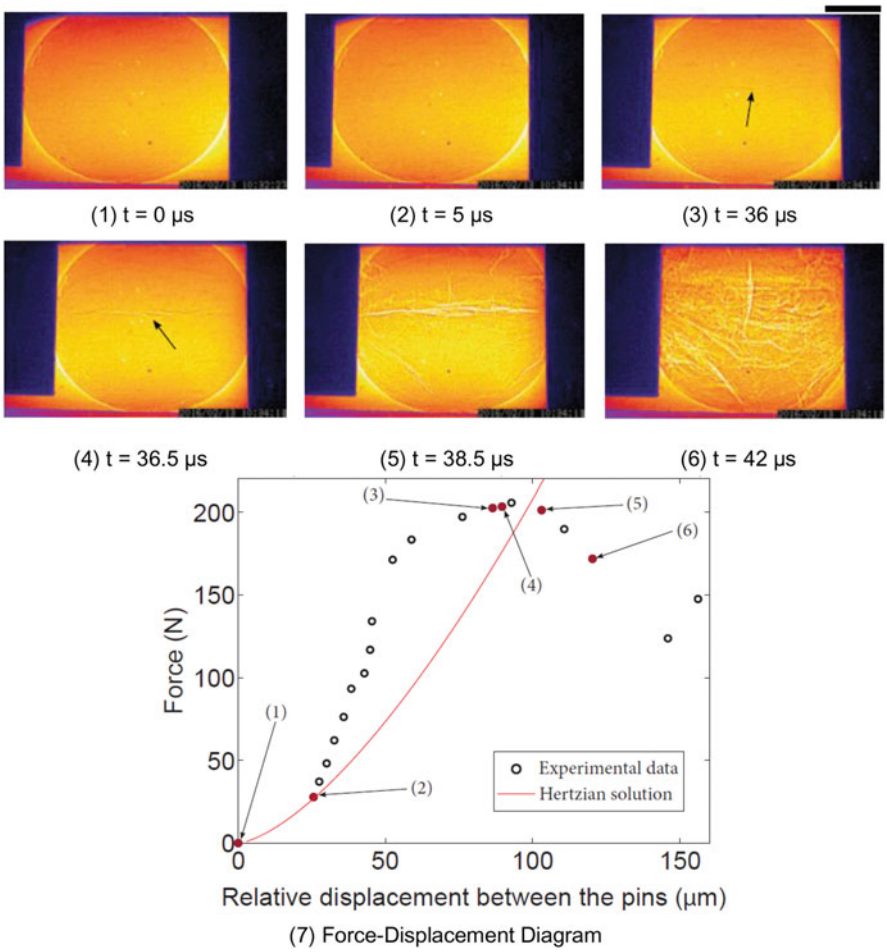

Fig. 8 X-ray images of a single particle experiment for polycrystalline silica. The scale bar represents 500 μm. The black arrow in (3) indicates the onset of the meridional crack. The black arrow in (4) indicates the propagating meridional crack

Polycrystalline Silicon

The X-ray images and force-displacement relationships of representative impact experiments on smaller (1.00–1.18 mm) silicon particles are given in Fig. 9. As the particle was compressed, its irregular shape caused that particle to rotate (2). Such rotation was not observed in all the experiments because it was shape related. When the load reaches a critical level, a meridional crack was initiated near the center of the particle, which propagated toward the two contacts (3). Simultaneously, several angular cracks formed at the contacts (3–4), and several minor cracks developed in the meridional direction and eventually fractured the particle in several

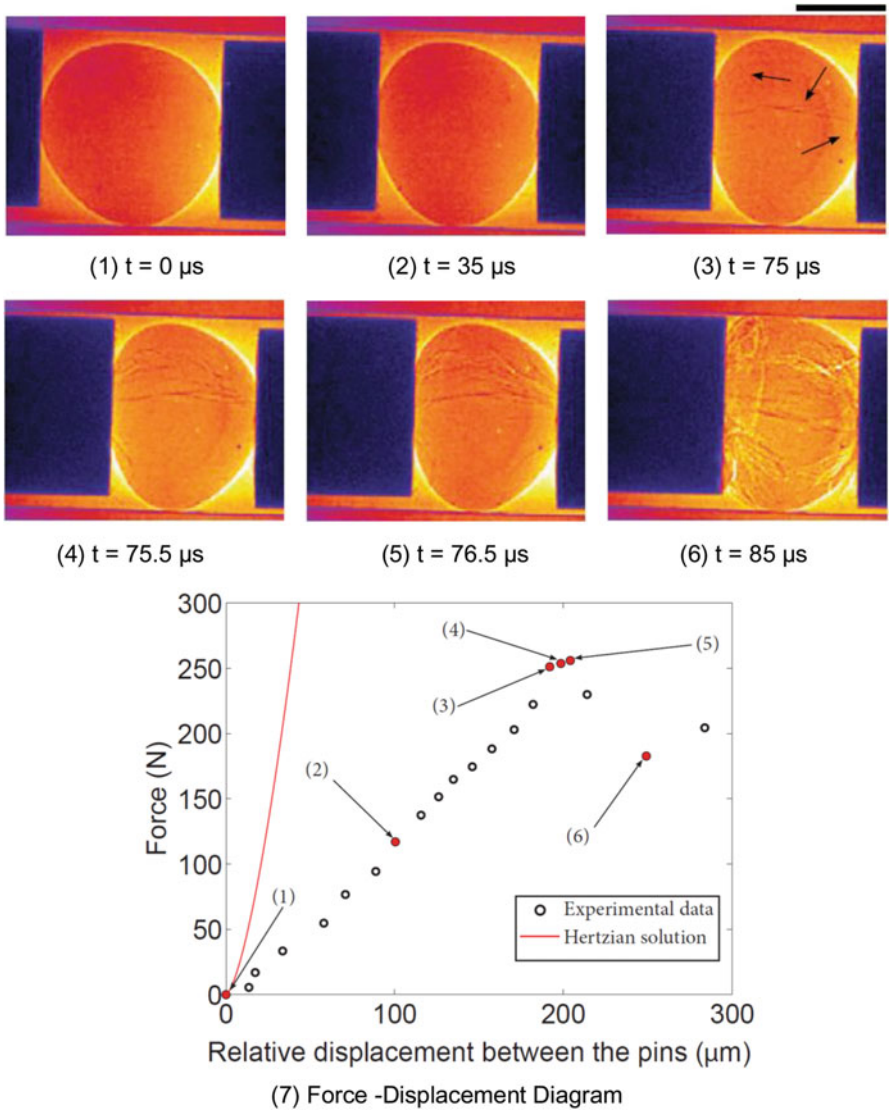

Fig. 9 X-ray images of a single particle experiment for smaller (1.00–1.18 mm) polycrystalline silicon. The scale bar represents 500 μm. The black arrows in (3) indicate the onset of the meridional crack and angular cracks

fragments, which were retained between the pins and compressed to further fracture (4–6). The load in the experiment shown does not agree well with Hertzian contact theory. This can be due to the rotation caused by the irregular contact condition.

The X-ray images and force-displacement relationships of representative impact experiments on larger particles (1.7–2.0 mm) are given in Fig. 10. Although no

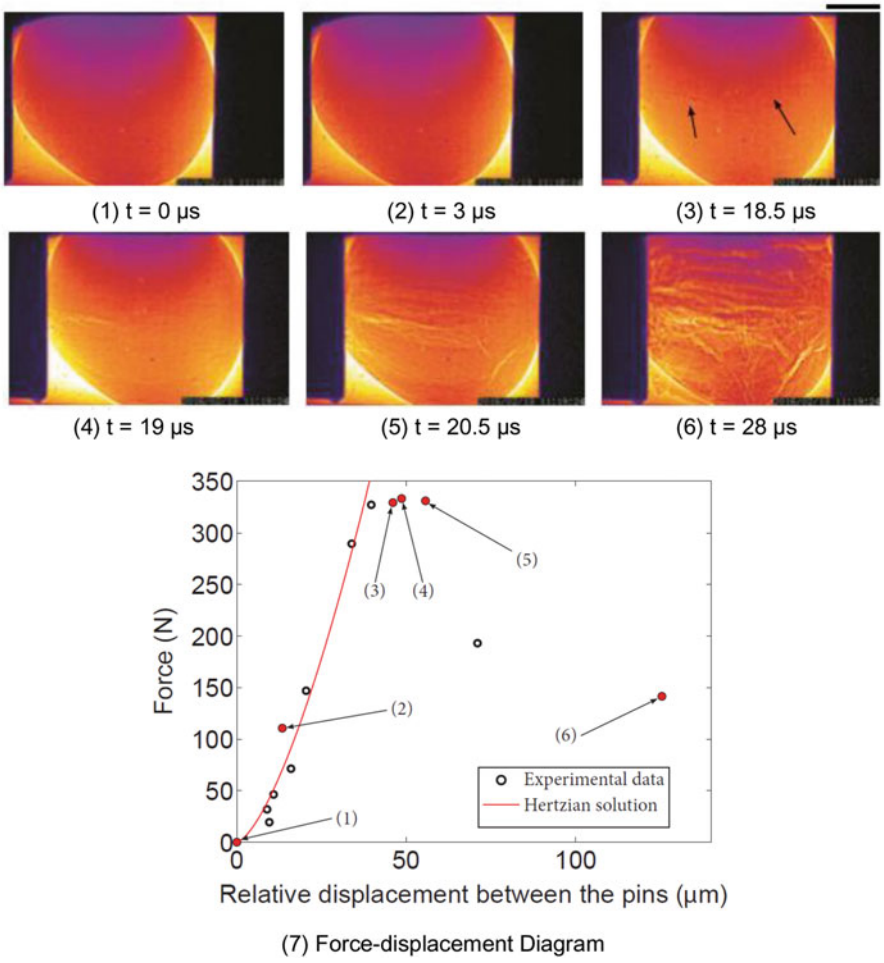

Fig. 10 X-ray images of a single particle experiment for larger (1.7–2.0 mm) polycrystalline silicon. The scale bar represents 500 μm. The black arrows in (3) indicate the onset of the meridional crack

obvious rotation was observed, the failure mechanism was very similar to the smaller ones. A meridional crack was initiated near the center of the particle and propagated toward the contacts (3–5). As the major meridional crack formed, several subcracks also developed in the meridional direction, fracturing the particle in several fragments (5–6). These fragments were retained between the pins even after significant cracking was observed. Hertzian contact theory predicts well the force-displacement history until the cracks start to form. The larger size and therefore larger contact can contribute to this agreement.

Damage Mechanisms Under Particle-Particle Contact Condition

Soda Lime Glass

Four types of soda lime glass were investigated: smaller (1.00–1.18 mm) untreated particles, smaller heat-treated, larger (1.7–2.0 mm) untreated particles, and large annealed particles. Three types of particle arrangement were used: two particles, three particles, and five particles.

The X-ray images along with the force-displacement relationships of representative experiments on smaller untreated and annealed particles with two-particle configuration are presented in Figs. 11 and 12, respectively. As the untreated particles were compressed, their positions were first rearranged such that firm contacts between each other and between the pins were formed. Once good contacts were formed, the particles started deforming elastically. As the particles were compressed, the contact area gradually increased, until the stresses at the area near the particle-particle contact reached a critical value and an angular crack of approximately 65° initiated at that point. A fragment was observed to separate from the particle due to this crack (Frames 2–3 in Fig. 11). After the fragment was separated, the particle was further compressed until multiple cracks initiated near the particle-particle contact where the angular crack formed (4). These cracks rapidly propagated and bifurcated away from the contacting area, then explosively fractured the particle into many small fragments (5–6).

It should be noted that although significant fracturing happened to one of the particles, only minor damage was observed in the other particle. Although the two contacting particles were nearly identical initially, damage to the two particles was uneven. The particle which suffered slightly more damage became less rigid, and further deformation led to more severe damage. On the other hand, the less-damaged particle retained its rigidity and endured less further damage. As the deformation continued, one particle was eventually pulverized, whereas the other survived nearly intact. This can be due to that, upon one particle pulverizing, the force chain suddenly breaks, and therefore no further load was transferred onto the other particle. This mechanism arrests the damage of the entire system as each particle fails progressively and requires significant movement of the projectile to rebuild the force chains after each particle is pulverized.

The damage mechanisms of the smaller annealed particles were very similar to the untreated ones. The results were observed to be consistent in 15 repeated untreated experiments and 3 annealed experiments. It is worth noting that the sequence of the particles relative to the direction in which the stress wave approaches does not affect which particle receives more damage upon impact. Whether the left or the right particle breaks first is completely random across the 15 repeated experiments. For these smaller glass particles, Hertzian contact theory once again predicts the force-displacement trend until cracks form.

The X-ray images and the force-displacement relationships of representative experiments on larger untreated and annealed particles with two-particle configuration are presented in Figs. 13 and 14, respectively. For the untreated particles,

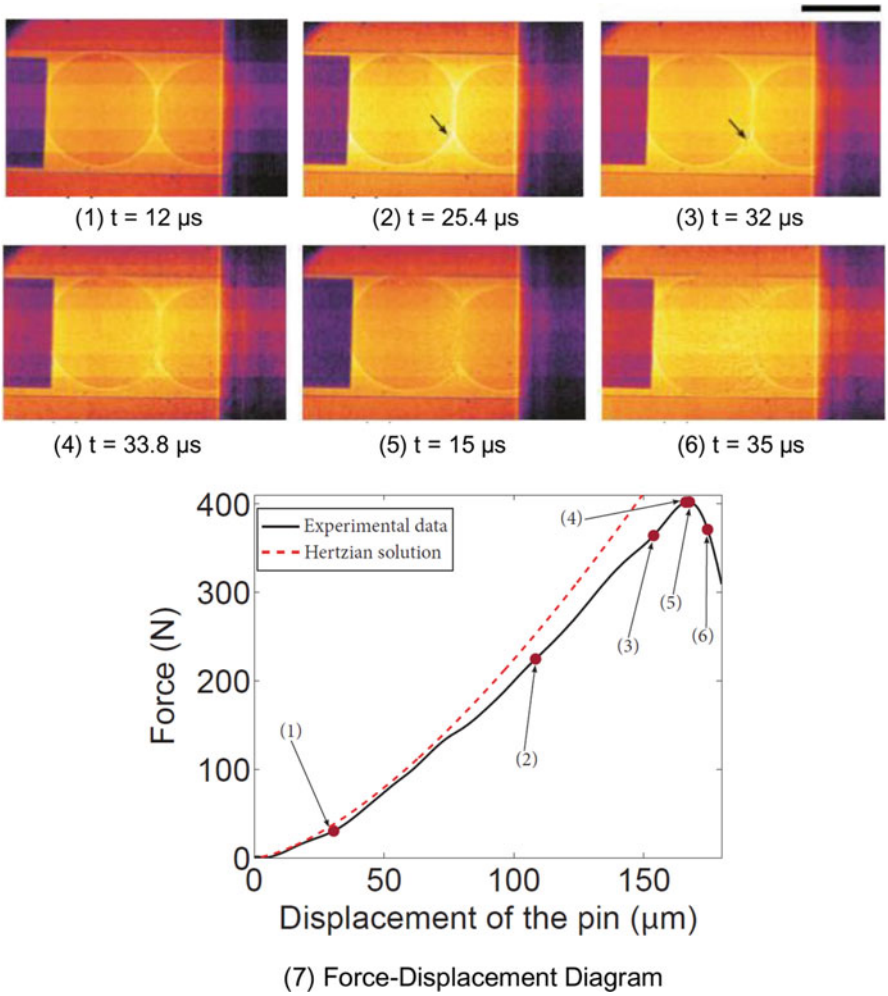

Fig. 11 The X-ray images of a two-particle experiment on smaller (1.00–1.18 mm) untreated soda lime glass. The scale bar represents 500 μm. The black arrows in (2) and (3) indicate the onset of angular cracks

similarly, an angular crack formed near the particle-particle contact area inside one of the particles, which only chipped a small fragment off the particle, without causing significant fracturing (Frames 2–3 in Fig. 13). As the particles were further compressed, multiple cracks initiated near the contact area where the angular crack formed. These cracks quickly bifurcated and pulverized that particle (4–6). No significant damage was observed in the other particle. Unlike the single particle case, Hertzian contact theory underpredicts the load as the displacement progresses.

The X-ray images of a representative experiment on soda lime glass with three-particle arrangement are presented in Fig. 15. The force-displacement relationship

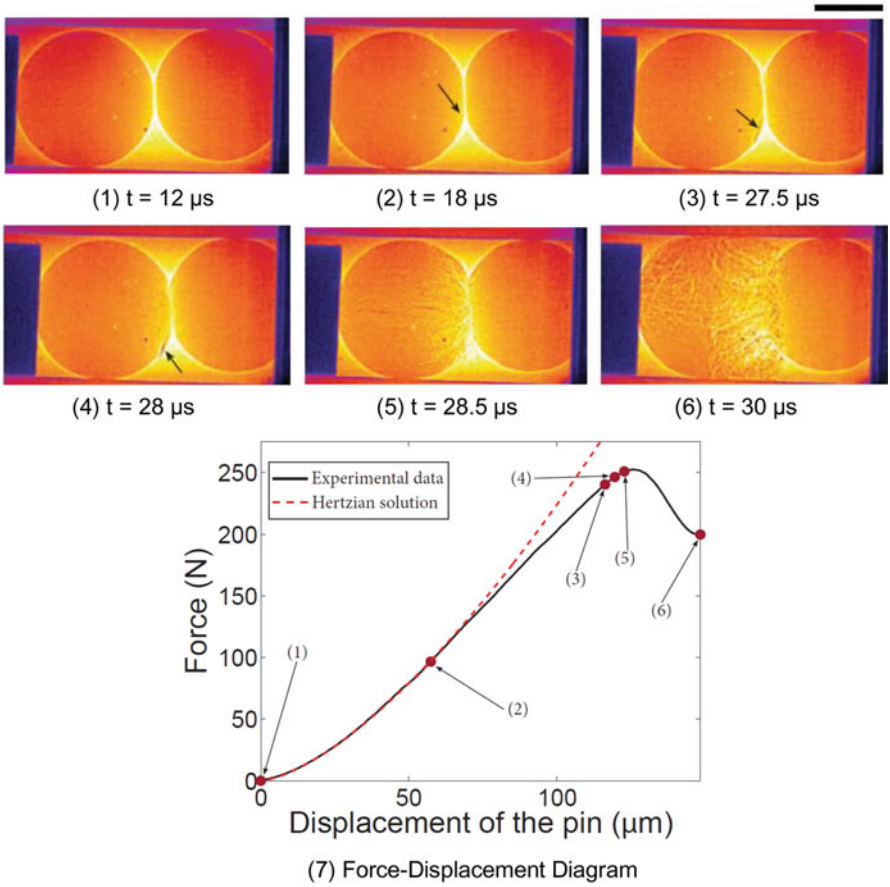

Fig. 12 The X-ray images of a two-particle experiment on smaller (1.00–1.18 mm) annealed soda lime glass. The scale bar represents 500 μm. The black arrows in (2) and (3) indicate the angular cracks. The black arrow in (4) indicates the separation of a fragment by the angular crack

was not obtained due to the physical inability to fit the load cell to the fixture with this setup. For this arrangement, only smaller untreated particles were used. As the particles were compressed, small fragments were separated from one of the particles near the particle-particle contact (2–3). A major set of cracks followed by subcracks then developed near the particle-particle contact inside the damaged particle and propagated in the direction that spanned the contacts (4–5). These cracks eventually pulverized that particle (6). In some of the experiments, the same damage mechanisms were observed on one of the other two particles after the first particle was pulverized.

The X-ray images of a representative experiment on soda lime glass with five-particle arrangement are presented in Fig. 16. Only smaller untreated particles were tested for this arrangement. Fragment separation was observed at two of the four

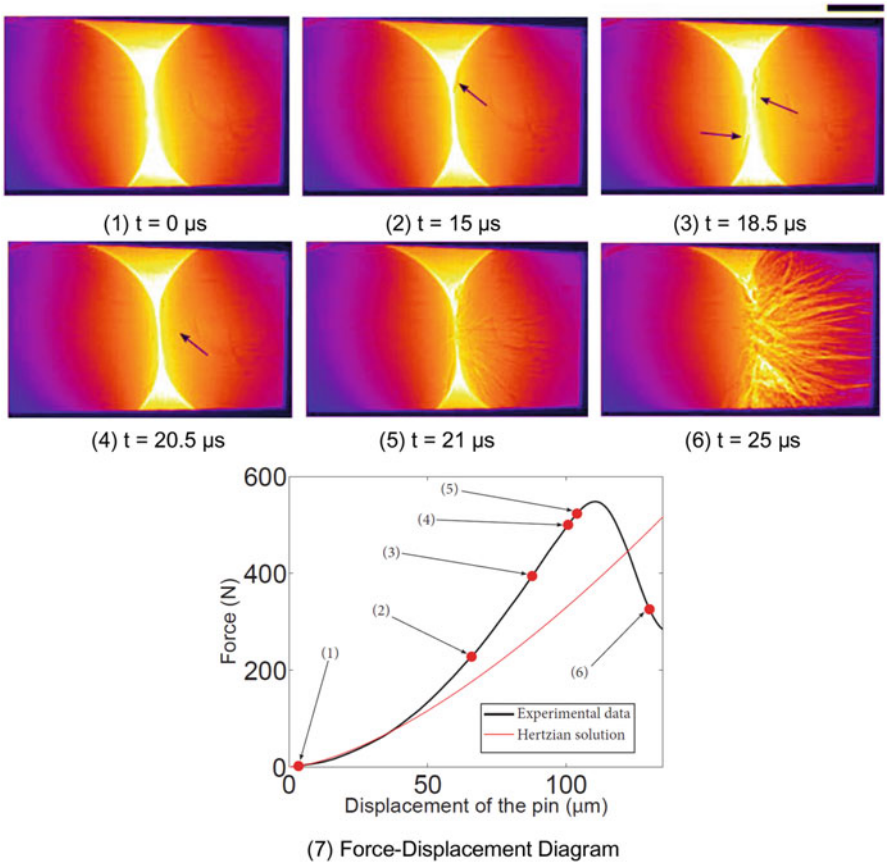

Fig. 13 The X-ray images of a two-particle experiment on larger (1.7–2.0 mm) untreated soda lime glass. The scale bar represents 500 μm. The black arrows in (2) and (3) indicate the angular cracks. The black arrow in (4) indicates the onset of final fracture

particle-particle contacts inside the central particle (3). A meridional crack then initiated near the center of the central particle and propagated toward two particle-particle contacts that aligned diametrically (3). Along with the meridional crack, two other cracks formed in the directions that spanned other particle-particle contacts and had approximately 45° to the meridional crack (3–4). Subcracks rapidly formed along with these major cracks and eventually pulverized the central particle (4–6). The damage mechanisms were similar for the repeated experiments. Note that there are areas of the particles that appear to be penetrated near the contacts from (2) to (4). These are due to nonperfect alignment of the particles within the same vertical plane. The contact is not perfectly normal to the X-ray direction, and part of one particle is in front of or behind another particle.

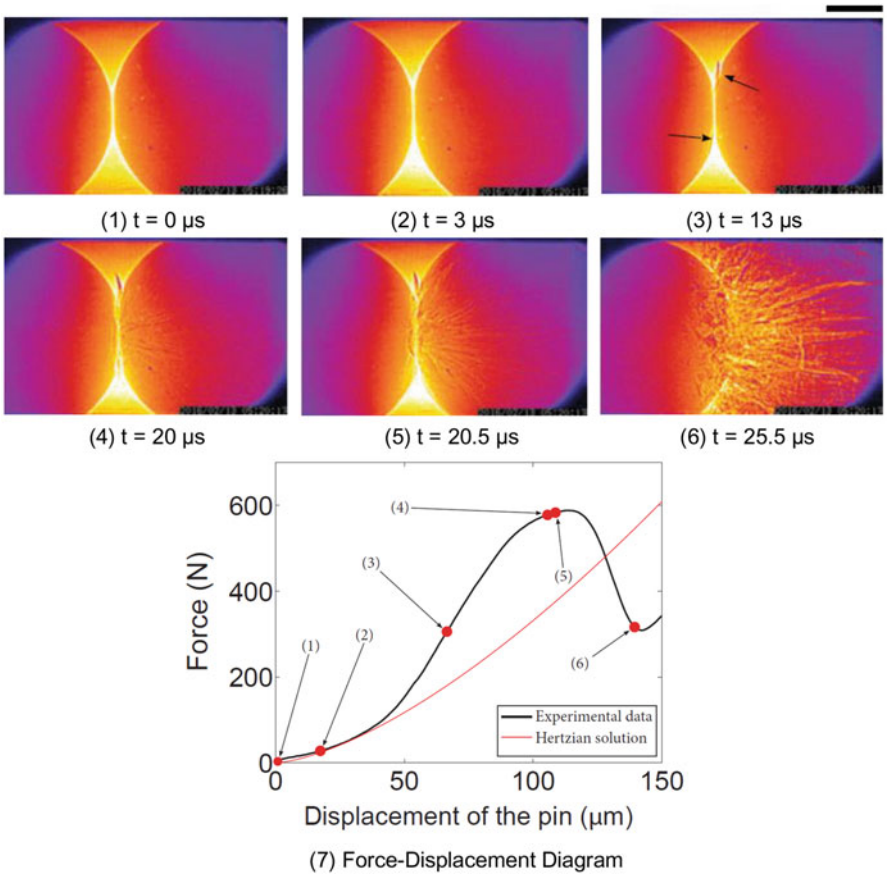

Fig. 14 The X-ray images of a two-particle experiment on larger (1.7–2.0 mm) annealed soda lime glass. The scale bar represents 500 μm. The black arrows in (3) indicate the angular cracks that separated fragments

Polycrystalline Silica

The X-ray images along with the force-displacement relationships of a representative experiment on silica particles under particle-particle contact condition are presented in Fig. 17. As the particles were compressed, the contact area increased until angular cracks initiated near the particle-particle contact area in both particles. Unlike the soda lime glass, the angular cracks did not propagate to the surface of the sphere and cause fragmentation (2). The crack that caused the ultimate failure was initiated near the center of one of the particles, and in this specific case, the particle, on the left side, then propagated toward the contacts (3–4). Subcracks further developed within the particle as the deformation continued, and the initial angular crack opened up, causing the particle to fracture into many small fragments (4–6). No major damage was observed in the other particle. It is worth noting that, unlike the consistent angles

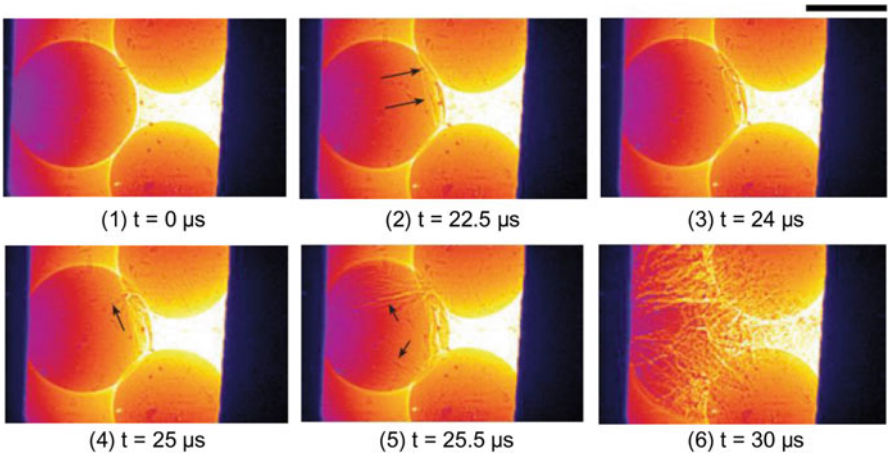

Fig. 15 The X-ray images of a three-particle experiment on larger (1.00–1.18 mm) untreated soda lime glass. The scale bar represents 500 μm. The black arrows in (2) indicate the angular cracks that separated fragments from the damaged particle. The black arrows in (3) indicate the set of cracks that caused the ultimate failure

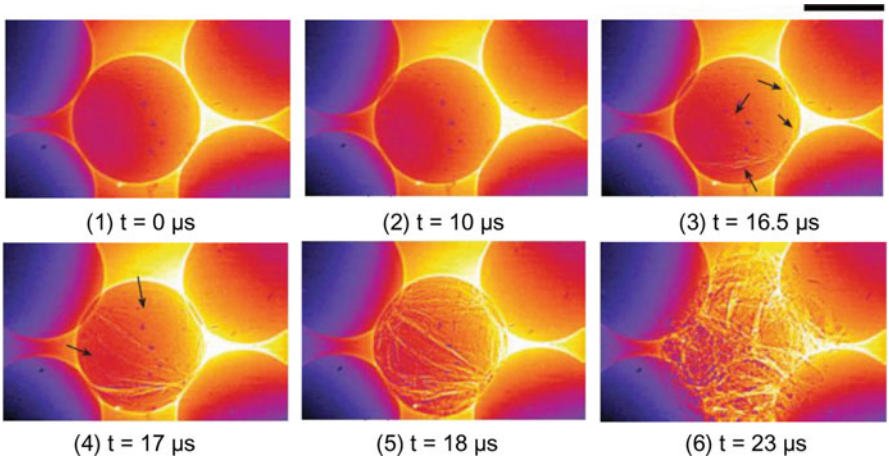

Fig. 16 The X-ray images of a five-particle experiment on larger (1.00–1.18 mm) untreated soda lime glass. The scale bar represents 500 μm. The black arrows in (3) indicate the angular cracks that separated fragments from the damaged particle, as well as the meridional crack and the crack that spanned other contacts. The black arrows in (4) indicate the subcracks following the meridional crack and another crack that spanned other particle-particle contacts

of the angular cracks observed in the soda lime glass, the angles of the initial cracks ranged between 43° and 64°, which might be resulted from the nonperfect spherical shapes. Similar to the single particle case, Hertzian contact underpredicts the contact force for this case.

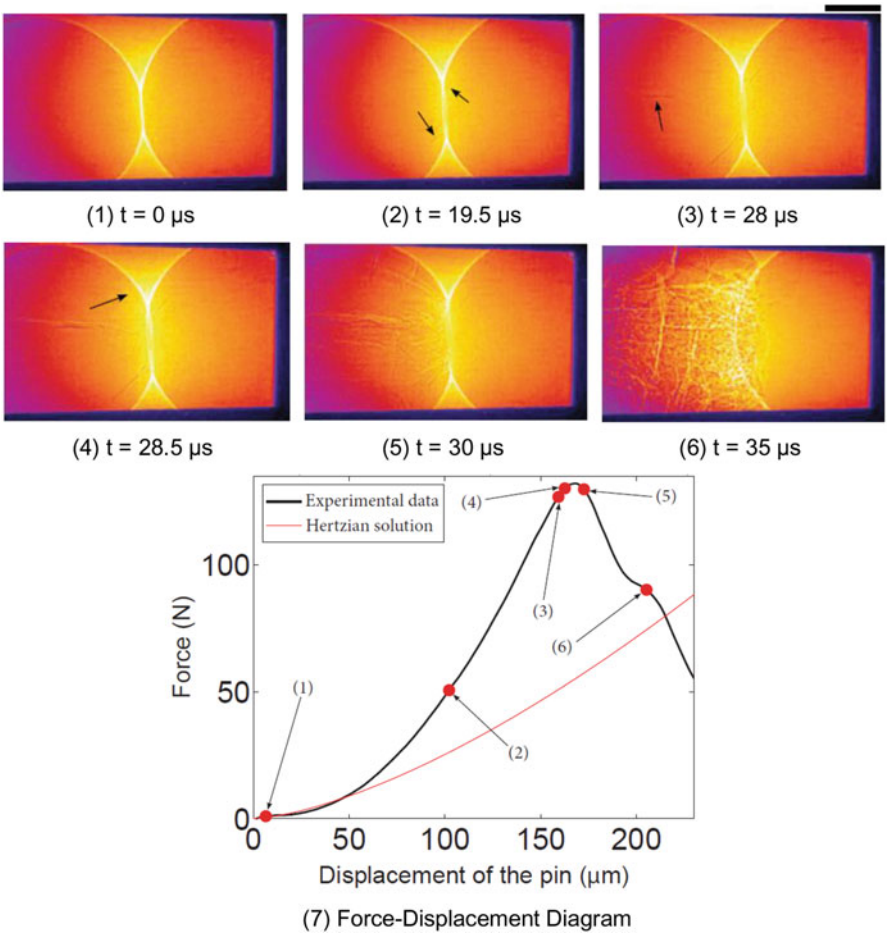

Fig. 17 The X-ray images of a two-particle experiment on polycrystalline silica. The scale bar represents 500 μm. The black arrows in (2) indicate the angular cracks. The black arrow in (3) indicates the onset of the meridional crack. The arrow in (4) indicates the further propagation of an initial angular crack

Polycrystalline Silicon

The X-ray images along with the force-displacement relationships of representative experiments on smaller (1.00–1.18 mm) and larger (1.7–2 mm) silicon particles are presented in Figs. 18 and 19, respectively. Angular contact cracks were first observed as the particles were compressed. The subsequent damage behavior varied for the repeated experiments. The angle of the initial cracks ranged between 32° and 55°. The angular contact cracks caused fragmentation only in some of the experiments and were retained inside the particles in most of the experiments (Frames 2–3 in

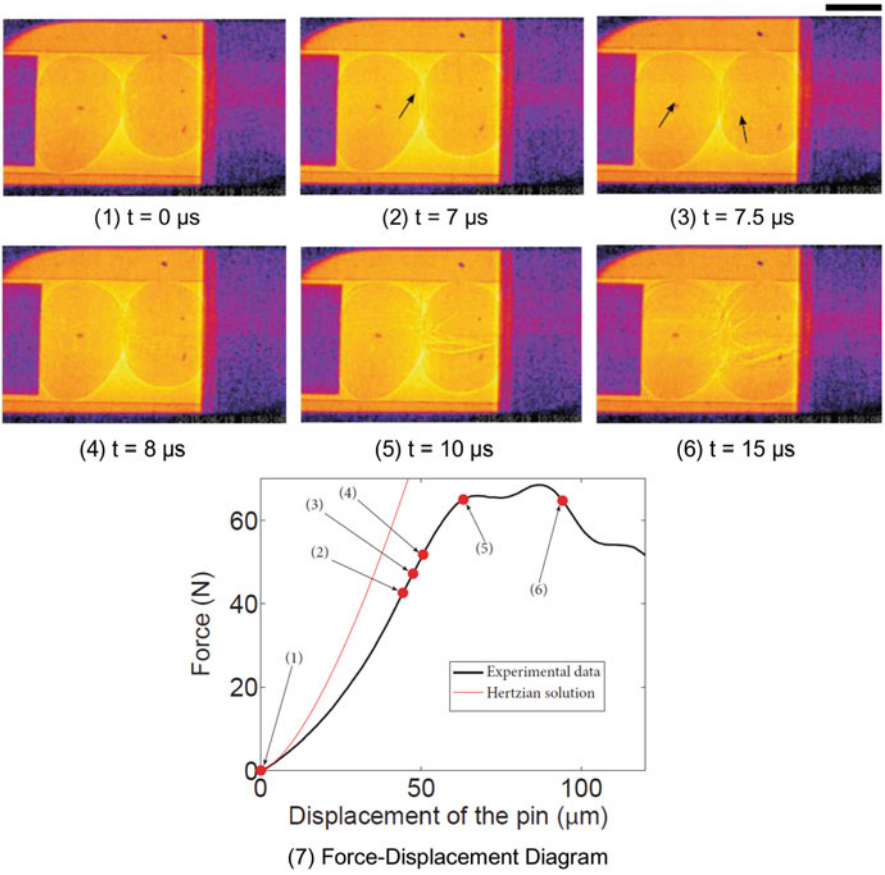

Fig. 18 The X-ray images of a two-particle experiment on smaller (1.00–1.18 mm) polycrystalline silicon. The scale bar represents 500 μm. The black arrow in (2) indicates the angular cracks. The black arrows in (3) indicate the onset of the meridional cracks

Fig. 18). After the angular cracks formed, several cracks were initiated near the particle-particle contact area and propagated through the particle (3–4). These meridional cracks ultimately fractured that particle into several fragments (5–6). These fragments were retained between the loading pin and back support after failure. In some experiments, the meridional cracks also propagated toward the angular crack, causing the ultimate fragmentation along with the angular cracks. Similar damage mechanisms were observed for the larger particles. None of the particles fragmented as extensively as those observed from glass particles. The Hertzian contact theory overpredicts the force-displacement trend just like the single-particle case. Both rotation and irregular contact can contribute to such discrepancy.

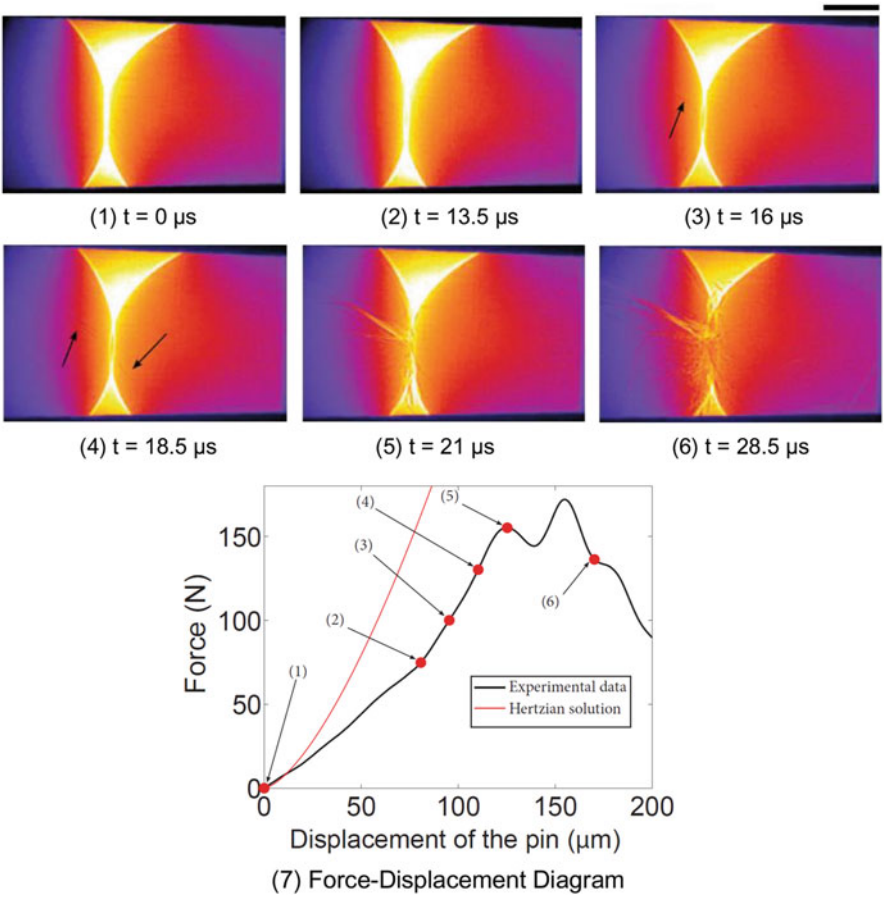

Fig. 19 The X-ray images of a two-particle experiment on larger (1.7–2.0 mm) polycrystalline silicon. The scale bar represents 500 μm. The black arrow in (3) and (4) indicates the angular cracks

Yttria-Stabilized Zirconia (YSZ)

The X-ray images along with the force-displacement relationships of a representative experiment on two YSZ particles are presented in Fig. 20. Due to the high-level of X-ray absorption of the sample material, the images obtained appear darker. Note that although the particles seem darker, the internal features can still be identified. For example, if a crack initiates inside the particle, it is still possible to identify the phase change. From this lower resolution, darker images, we could observe that, as the particles were compressed, a single meridional crack initiated in one of the particles and propagated through the particle (2). The particle then broke into two almost hemispherical fragments (3–4). These fragments then slid away from the pins. The other particle remained intact. No smaller subsequent cracks or initial

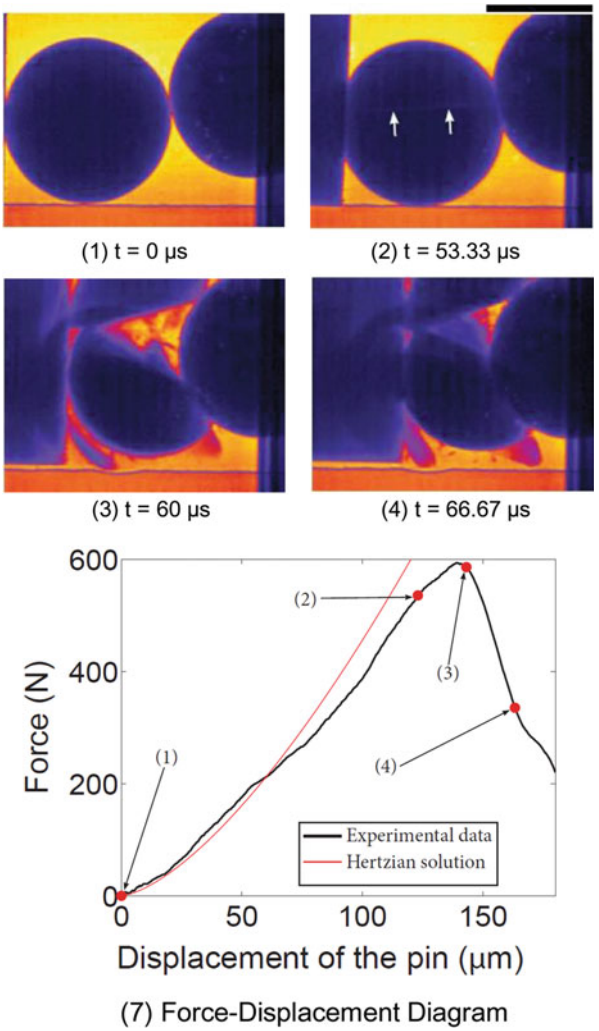

Fig. 20 The X-ray images of a two-particle experiment on YSZ (0.71–0.85 mm). The scale bar represents 500 μm. The white arrows in (2) indicate the propagating meridional crack

angled contact cracks was observed. Hertzian contact theory predicts well with the force-displacement trend until the major crack forms.

Ottawa Sand

In addition to the manufactured geomaterials, some naturally occurring geomaterials were also investigated for the particle-particle contact condition. The X-ray images along with the force-displacement relationships of a representative experiment on two Ottawa sand particles are shown in Fig. 21. The

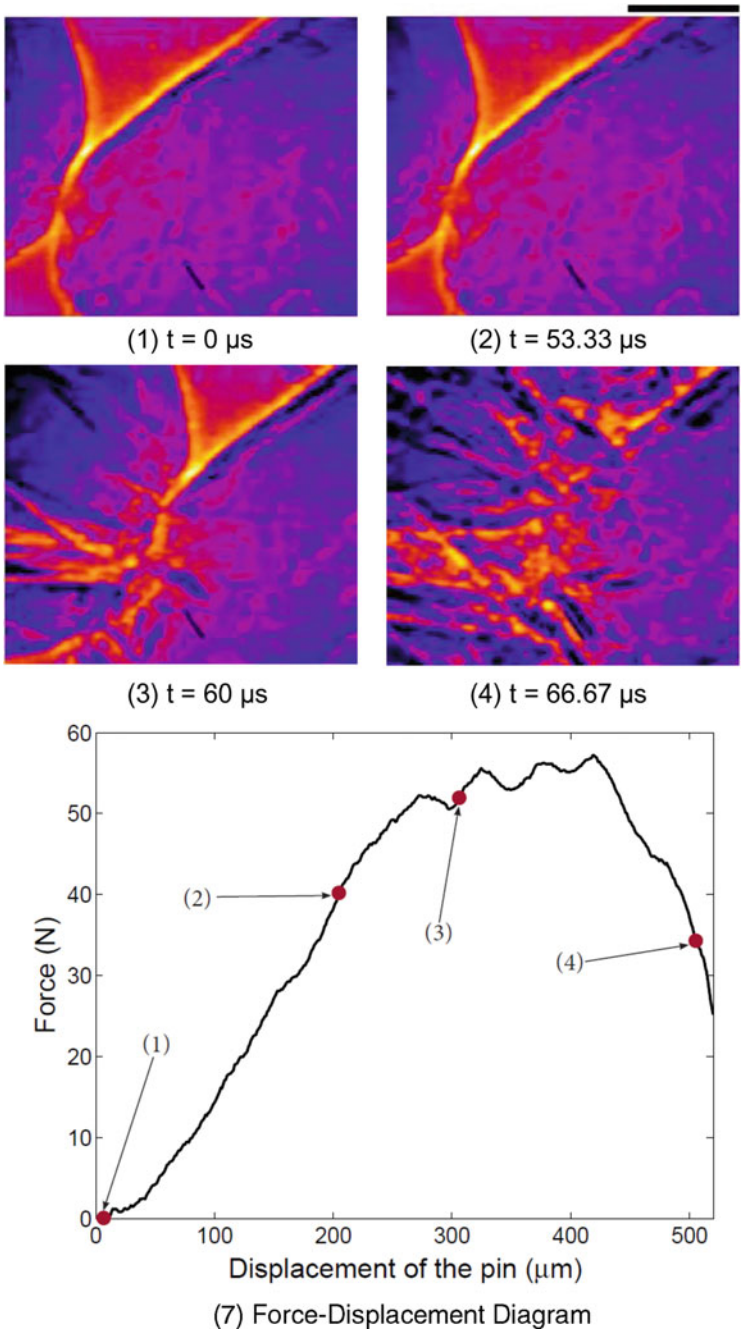

Fig. 21 The X-ray images of a two-particle experiment on Ottawa Sand (0.60–0.71 mm). The scale bar represents 500 μm

Hertzian contact trend is not applied to the natural sand particles due to highly irregular contacts. As the particles were compressed, it was observed that extensive cracks were initiated in one of the particles near the contact. These cracks rapidly bifurcated and pulverized that particle. During this process, the other particle remained still and kept compressing on the damaged particle until it was fully fractured. The force-displacement relationship exhibits similar trend with the manufactured particles. During the fracturing process, subsequent rises in the force are seen as the fractured portion keeps carrying load until further fracture.

Ohio Gold Sand

The X-ray images along with the force-displacement relationships of a representative experiment on Ohio gold sand particles under particle-particle contact condition are presented in Fig. 22. The images are of less resolution because they were taken in the earlier years with a less advanced high-speed camera. As the particle was compressed, several cracks were observed at both particle-particle and particle-pin contacts in both particles (2–3). The first particle (the one that is compressed first) was fractured into fragments by several meridional cracks (3–4). The fragments remained still and were further compressed against the second particle, causing meridional cracks to initiate in the second particle (4–5). Eventually, the first particle fractured into large number of small fragments, and the second particle fractured into several large fragments (6). The force and displacement exhibit similar trend with other particles. However, these sand particles withstand more load steadily even after major cracks have formed and the particles separate into pieces.

Q-Rock Sand

The X-ray images along with the force-displacement relationships of a representative experiment on the Q-rock sand particles under particle-particle contact condition are given in Figure 23. The Q-rock particles exhibited significantly different damage mechanisms. As the particles were compressed, the preexisting flaws near the contact areas opened up, separating fragments from the particles (2–3). As the rest of the particles continued to be compressed, meridional cracks developed in one of the particles and further separated fragments from the particle but did not cause catastrophic failure (3–4). The fragments remained in place and transferred load to the other particle, causing fracturing in that particle (5–6). Eventually, both particles pulverized as they were further compressed. The overall force-displacement trend agrees with other tested particles. It is interesting that these sand particles keep baring loads all the way until the catastrophic failure despite any partial fracture of the particles (4).

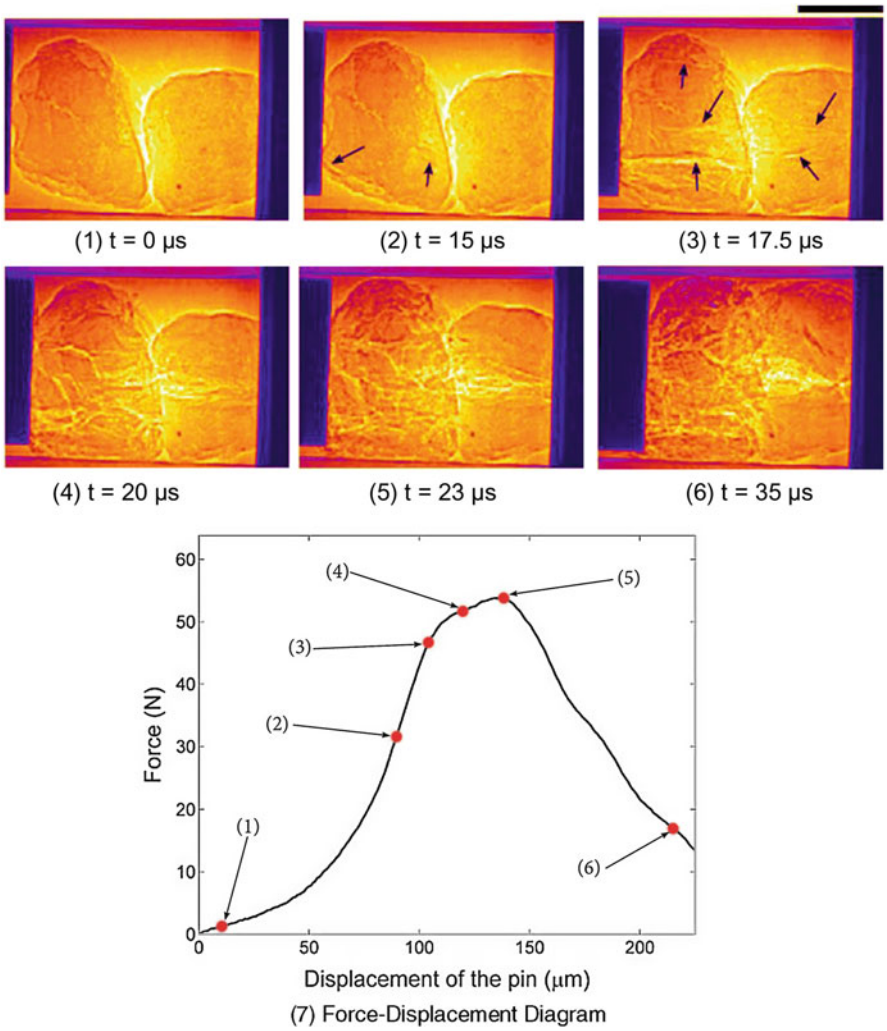

Fig. 22 The X-ray images of a two-particle experiment on Ohio Gold Sand (0.71–0.85 mm). The scale bar represents 500 μm. The black arrows in (2) indicate the contact cracks. The black arrows in (3) indicate the propagation of contact cracks and major meridional cracks

Summary of the Visualized Damage Mechanisms

From the visualization of the damage mechanisms of the investigated geomaterials with various configurations, it was revealed that most of the investigated materials, with the exception of the YSZ particles, showed evolution of multiple damage mechanisms during the impact process corresponding to different levels of stress states. The YSZ particles showed only one type of damage mechanisms. The types

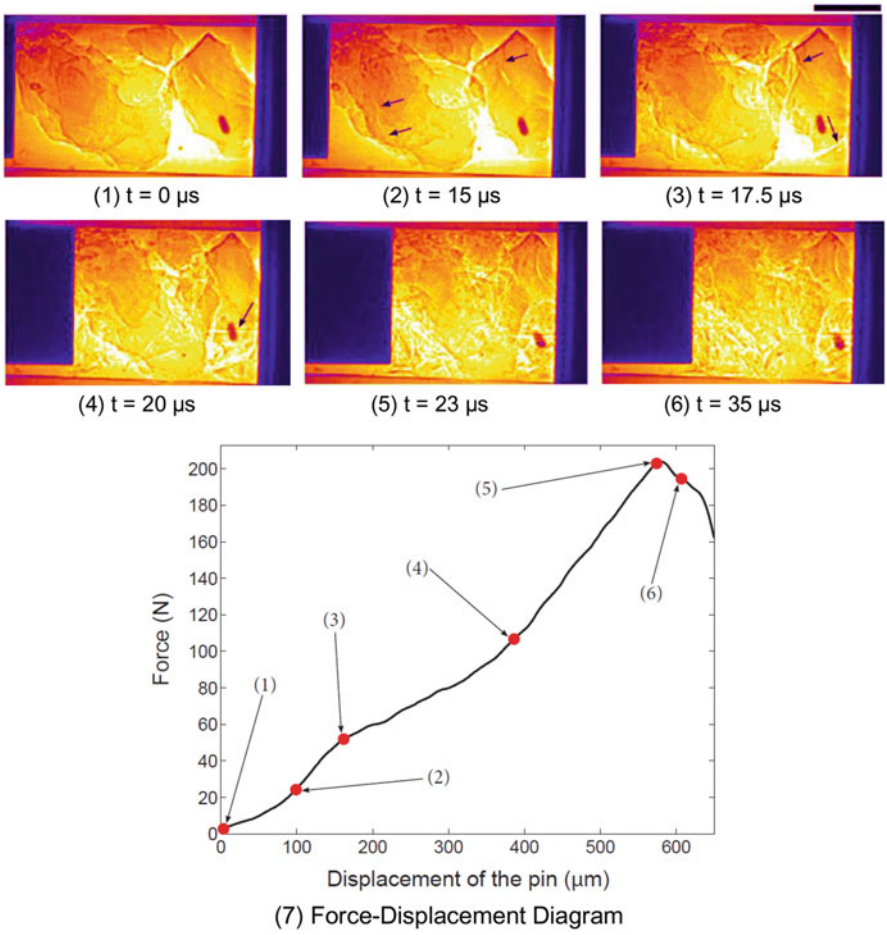

Fig. 23 The X-ray images of a two-particle experiment on Q-Rock Sand (0.71–0.85 mm). The scale bar represents 500 μm. The black arrows in (2) indicate the opening of preexisting flaws. The black arrows in (3) indicate those cracks separating fragments. The black arrow in (4) indicates development of a meridional crack

of damage mechanisms observed include angular cracks, angular-crack-induced fragmentation, meridional cracks from central cracking, meridional cracks from contact cracking, crack bifurcation, whole-particle fragmentation, and pulverization. Angular cracking tends to occur at the earliest stage of the failure process and rarely evolves into catastrophic failure. It tends to cause fragmentation of small pieces near the contact area. Contact cracks and center meridional cracks usually signal the onset of catastrophic failure. These cracks, if bifurcated, are likely to cause whole-particle fragmentation or pulverization. The fragments may also remain in place after fracture is caused by meridional cracks, such as the case for YSZ particles.

The exact damage mechanisms of a particle depend heavily on the geometry. This tendency is apparent for cracks that initiated near the contacts. For silicon particles, the angular cracks showed a broader range than those of soda lime glass, which had more regular shapes. The size also affects the damage mechanisms. The exact location where the cracks initiate and the angles of the cracks tend to be more inconsistent for larger particles, possibly due to more internal flaws.

The ultimate failure of the particles appears to be intrinsic to the material. The ultimate failure mode can be characterized as pulverization (Soda Lime glass, Q-rock sand), major crack fracturing that leaves a few large fragments (silicon, YSZ), and multiple-crack fracturing that fractures the particles into large number of fragments (silica, Ohio gold sand, and Ottawa sand). It leaves a very interesting question: What specific material property governs the ultimate failure mode? For particle-particle contact condition, the ultimate failure mechanism in one particle affects the failure mechanism of the two-particle system. For materials that fail by pulverization, no major damage was observed in the unpulverized particle throughout the process. However, for materials that showed large fragmentation, the other particle often exhibited more significant damage or continued to be damaged even after the first particle failed. This can be because pulverization rapidly breaks the force chain so that the other particle is not compressed further, while during and after large fragmentation, the fragments can be retained between the contacts and further damage the next particle.

There is an apparent trend that the force it takes to fracture the particles with particle-particle contacts is lower than that with only particle-platen contacts. The fracture force is almost half for the particle-particle contacts. This is because the sphere-sphere contact induces four times of tensile stress inside the sphere compared to that of sphere-plate contact. This, combined with the modulus mismatch between the materials of the particles and the platen, results in tensile stress inside the sphere around twice as that with only particle-plate contact. This may explain the difference in the fracture force ratios (fracture force for single and multiple particles) across different materials.

It is also important to note that, depending on the contact conditions, particle arrangement, or material properties, the Hertzian contact theory may significantly under- or overpredict the force-displacement relationship for particles upon impact. Corrections are advised if Hertzian-contact-theory-based model is to be used in a simulation of particulate systems under impact.

Conclusions and Prospective

The work presented showcased what can be accomplished with the high-speed X-ray PCI at the APS in studying damage mechanisms of geomaterials. An in situ, through-volume visualization of the impact process can be very helpful in understanding the damage process of geomaterials especially at the particle scale. The synchronization of visualization and measurement enables quantified fracture analysis for each corresponding stage of the damage process. Furthermore, the

multiparticle experiments involved systems with 1-D and 2-D force chains. Further study on multiple contacting particles under impact could potentially bridge the gap between the damage mechanisms of geomaterials at bulk scale and particle scale. Study on particles upon impact similar to the study presented in this chapter would greatly help calibrating the discrete-based models of particulate systems with load histories with correspondence to each stage of the failure process.

However, challenges also exist for future researchers to overcome. The current setup can only measure 1-D compressive load and cannot contribute in acquiring stress state in the system for multiple contact particles. Also, quantitative analysis at particle scale can be performed only on manufactured geomaterials with regular shapes. The irregular shapes and internal flaw distribution of the naturally occurring geomaterials introduce too many variables quantitative analysis can currently handle.

References

W. Chen, M. Hudspeth, B. Claus, N. Parab, J. Black, K. Fezzaa, S. Luo, In situ damage assessment using synchrotron X-rays in materials loaded by a Hopkinson bar. Philos. Trans. A. Math. Phys. Eng. Sci. **372**(2015), 1–15 (2014)

M. Hudspeth, B. Claus, S. Dubelman, J. Black, A. Mondal, N. Parab, C. Funnell, F. Hai, M.L. Qi, K. Fezzaa, S.N. Luo, W. Chen, High speed synchrotron x-ray phase contrast imaging of dynamic material response to split Hopkinson bar loading. Rev. Sci. Instrum. **84**(2), 025102 (2013)

N. Parab, *Fracture of spherical particles under compression* (Purdue University. Aeronautics Astronautics. Degree Granting Institution, West Lafayette, 2017)

N. Parab, J. Black, B. Claus, M. Hudspeth, J. Sun, K. Fezzaa, W. Chen, Observation of crack propagation in glass using X-ray phase contrast imaging. Int. J. Appl. Glas. Sci. **5**(4), 363–373 (2014a)

N. Parab, B. Claus, M. Hudspeth, J. Black, A. Mondal, J. Sun, K. Fezzaa, X. Xiao, S.N. Luo, W. Chen, Experimental assessment of fracture of individual sand particles at different loading rates. Int. J. Impact Eng. **68**(C), 8–14 (2014b)

Tensile Damage Mechanisms of Concrete Using X-Ray: In Situ Experiments and Mesoscopic Modeling

18

Olga Stamati, Emmanuel Roubin, Edward Andò, and Yann Malecot

Contents

Introduction 454
Studied Material: Characteristic Scales and Composition 456
Characteristic Sizes of the Specimens 456
Specimens Preparation 457
Phase Segmentation Procedure of Concrete from X-Ray Tomographic Images 458
Scanning of the Specimen 458
Segmentation Procedure 459
Validation with Neutron Tomography 465
FE Meso-model Description 469
Local Kinematics Enhancement 470
Phenomenology and Resolution Scheme 473
In Situ Tensile Test 474
In Situ Experimental Setup 474
Experimental Stress-Strain Curve and Macrocrack Identification 476
Following the Microstructural Evolution 478
Numerical Simulations of Tensile Tests 479
Identification of Numerical Parameters 479
Numerical Prediction 483
Conclusions and Perspectives 483
References 486

Abstract

This work concerns the study of concrete at meso-scale where the local failure mechanisms are known to drive the macroscopic behavior of the material. In order to highlight the impact of the mechanical and morphological properties of each phase (aggregates, macropores, and mortar matrix), microconcrete specimens are prepared with rather small dimensions compared to the size of the heterogeneities.

O. Stamati · E. Roubin · E. Andò · Y. Malecot (✉)
3SR Lab, Université Grenoble Alpes, Grenoble, France
e-mail: yann.malecot@univ-grenoble-alpes.fr

© Springer Nature Switzerland AG 2022

G. Z. Voyiadjis (ed.), *Handbook of Damage Mechanics*,
https://doi.org/10.1007/978-3-030-60242-0_75

X-ray tomography is used to obtain 3D images of the morphology of the meso-structure, from which trinary 3D images are obtained, where each phase of the material's meso-structure is separated. A validation of the segmentation method is made by comparing the grain size distribution curves computed from images of the same set of aggregates coming from x-rays and neutron scans.

The three-phase segmented 3D morphology of the sample is then given as an input to a 3D FE meso-model with enhanced discontinuities. To validate the numerical model, a uniaxial tensile test of the same microconcrete specimen is performed inside the x-ray scanner, and the in situ evolution of the microstructure is followed. After identification of the numerical parameters, comparison of experimental and numerical results reveals the capability of the meso-model to reproduce the actual material response.

Keywords

Meso-scale FE modeling · Cementitious materials · Concrete · Aggregates · Porosity · Phase segmentation · Macroscopic response · Local failure mechanisms · Morphological description · X-ray tomography · Neutron tomography · Image analysis tools · In situ evolution · DVC

Introduction

Being a manufacturing material widely used in the world, the mechanical behavior of concrete has been investigated over decades. However, its failure mechanisms are complex phenomena and still constitute a very active area of research. The quasi-brittle behavior observed at the macroscale is strongly influenced by the morphology and the properties of the material constituents and their mutual interactions over a large range of scales: from nano- to meso-scale, referring to nm (hydrated cement scale) and cm (largest aggregates scale), respectively, both under in static (Lulu et al. 2005; Piotrowska et al. 2014; Zingg et al. 2016; Malecot et al. 2019), or dynamic loading (Piotrowska et al. 2016).

At the meso-scale, concrete can be viewed as a three-phase geomaterial, constituted of aggregates and macropores embedded within a mortar matrix (mix of cement paste and fine sand). Macroporosity refers to the pores being much larger than the capillary voids (50 nm). It corresponds to both the entrained air voids (usually ranging from 50 to 500 μm) and the entrapped air voids (almost as large as the largest aggregates, depending on the concrete workability). The capillary porosity, referred to as micropores, plays an important part in desiccation, shrinkage, and creep, whereas macropores are more influential in determining the strength and permeability of the material (Mehta 1986).

The presence of both aggregates and macropores in the concrete mix, with various sizes and shapes, results in an heterogeneous stress field at meso-scale, even under a uniform loading, leading to stress concentrations and initial micro-cracking around the weakest regions (usually the interfaces). With the increase of the

loading, these microcracks growth and coalescence leads to a critical macrocrack resulting in the failure of the material.

Consequently, the meso-scale is a scale of interest to study the local failure mechanisms of concrete, and therefore, in recent years, many numerical meso-models have been developed. These models, by explicitly representing the meso-structure (particularly in 3D), could be an effective and practical alternative to experimental studies. They can be used to reveal the influence of the meso-scale heterogeneities on the global response by easily changing global descriptors, such as phase volume fractions, aggregates and macropores size distributions, aggregates shape, and phase or mechanical properties of each phase. A multiscale approach could also be achieved by using the meso-model as a constitutive law at the macroscale.

These numerical approaches can fit within the context of continuum finite element models (FEM) (Gitman et al. 2008; Tejchman et al. 2010; Kim and Abu Al-Rub 2011; Shahbeyk et al. 2011), discrete element models (DEM) (Lilliu and van Mier 2003; Dupray et al. 2009; Suchorzewski et al. 2017), or finite element models enhanced with discontinuities (Benkemoun et al. 2010; Roubin et al. 2015a), which is the approach followed in this work. No matter the selected approach, two main aspects have to be considered in these models: the morphological description of the meso-structure and how to account for the quasi-brittle behavior of the material.

Concerning the former, the most common method is the use of morphological models, such as sphere packing (Lilliu and van Mier 2003; Wriggers and Moftah 2006; Dupray et al. 2009) or excursions of correlated Random Fields (Roubin et al. 2015b). However, these methods have limitations regarding both the representativeness of the generated morphology and the possibility of a quantitative validation of the models with experimental results. To overcome this, in recent years, real meso-morphologies are obtained by taking advantage of recent advances in nondestructive 3D imaging combined with image analysis. This is the approach, in particular the use of x-ray tomography (Poinard et al. 2012a; b; Ren et al. 2015; Nitka and Tejchman 2018), followed in this work.

Once the meso-structure morphology is reliably obtained, the question that follows is how to account for its complex heterogeneous aspects (explicit representation of aggregates and macropores) and how to represent the quasi-brittle behavior of the material. In the context of the E-FEM (embedded finite element method), adopted in this study, two sets of local discontinuities are introduced inside each element: in the strain field (accounting for the difference in the material properties between the phases), on the one hand, and in the displacement field (accounting for microcracking), on the other hand.

Having introduced the basic characteristics of the meso-model, the question that then arises is the validation and the predictive ability of the adopted numerical approach. Therefore, in this work, the development of a suitable experimental setup and the direct comparison of the numerical outcomes with the experimental results are done.

In short, advanced numerical and experimental techniques are used in this chapter to get a better understanding of the local failure mechanisms of concrete at

meso-scale. The main originality comes from conducting in situ direct tensile tests on microconcrete specimens of realistic composition (including cement, sand, aggregates, and water). The evolution of the fracture processes as the load progresses is followed, by mapping the relative deformations between consecutive x-ray 3D images. The construction of a three-phase 3D meso-model based on the morphology obtained from the initial x-ray scan and the direct experiment–modeling comparison, at meso-scale, during the loading are also rare in literature (Huang et al. 2015; Nitka and Tejchman 2018; Yu et al. 2018; Stamati et al. 2019).

The detailed outline of the chapter is the following: First, microconcrete specimens are prepared with rather small dimensions compared to the size of the heterogeneities (section "Studied Material: Characteristic Scales and Composition"). X-ray tomography is used to obtain grey scale 3D images of the concrete meso-structure. The concrete images segmentation to identify a trinary morphology (aggregates, macropores, and mortar matrix) is based on an image analysis procedure that is then presented (section "Phase Segmentation Procedure of Concrete from X-Ray Tomographic Images"). This automatic extraction of aggregates is validated both from scans of aggregates before casting, as well as neutron tomography images. The resulted segmented x-ray 3D image is then used as an input to a 3D FE meso-model, and a uniaxial tensile test is simulated (section "FE Meso-model Description"). For validating the numerical model, a suitable experimental setup, compatible with the x-ray apparatus, is developed (section "In Situ Tensile Test"). Thus, by following the in situ microstructural evolution, both a direct validation of the numerical model and an insight of the 3D fracture mechanisms during loading and up to failure are achieved. After parameter identification, comparison of experimental and numerical results shows that the meso-model is capable to reproduce both the material response and the cracking patterns (section "Numerical Simulations of Tensile Tests"). For a further validation of the 3D meso-model, another microconcrete specimen with a new morphology is tested, and the model is used to predict its macroscopic behavior without new identification.

Studied Material: Characteristic Scales and Composition

Characteristic Sizes of the Specimens

To investigate the local failure mechanisms in concrete at the meso-scale, specimens are required with significant heterogeneities which will give insights into the impact of both the mechanical and the morphological properties of each phase (aggregates, macropores, and mortar matrix) along with their respective interfaces on the macroscopic response of the material.

A number of factors affect the choice of the specimen size:

- The specimen must be of a sufficient size with respect to the largest heterogeneities so that it has some mechanical resistance and some relevance to real concrete.

- The use of x-ray tomography, to obtain an image of the microstructure representation, implies a trade-off between field-of-view (i.e., specimen size) and spatial resolution (i.e., the smallest heterogeneity that can be identified). In this case, the smallest heterogeneities are the smallest macropores (size of about 100 μm). This encourages a pixel size of at least 20 μm/px in order to be able to describe these pores coarsely thus limiting the field of view to around 30 mm.
- The specimens are mechanically loaded in situ in the x-ray scanner, meaning that their dimensions and failure force must be in agreement with the limitations of the mechanical loading system. The current limitation of the loading system used herein is 500 N in tension (and 10 kN in compression) for 20 mm in diameter.
- The FE mesh that explicitly represents the heterogeneities of the material imposes additional constrains to the specimen size, due to computational limitations. Particularly, the characteristic element size in the FE mesh should be as small as the smallest heterogeneities.
- Another characteristic scale to be chosen is the size of the largest heterogeneities (i.e., size of largest aggregates). These aggregates have to be large enough compared to the size of the specimen to give some direct effect on the macroscopic behavior so as to easily test the predictive ability of the meso-model.
- The points above point toward a small specimen size, meaning that a microconcrete is automatically selected. In preliminary tests performed, it was not possible to core a specimen smaller than 10 mm.

Making a trade-off between the difference constraints, cylindrical specimens are chosen of 11 mm in diameter and 23 mm height. Such a size, considering the tensile concrete strength (about 3.5 MPa), means a tensile failure load that should not exceed 350 N which is compatible with the system mentioned above. The largest aggregates are chosen with a characteristic size of 3.8 mm (about the quarter of the specimen diameter) which is both quite large to have some discrepancy between different specimens but also small enough to have a behavior that is still representative of concrete.

Specimens Preparation

A regular concrete mix is prepared, using ordinary Portland cement, aggregates, fine sand (D = 1800 μm), and water. The mix proportion is 1:3:3.8:0.6, by weight of cement: sand: aggregates: water. The aggregates used are rolled and siliceous (chemical composition: $SiO_2 > 97.3\%$) coming from Mios (France), with a maximum size of 3.8 mm. The material is mixed with a benchtop rotary mixer, casted into blocs of about 10 cm^3 in volume, and cured in wet conditions for 7 days. The cylindrical specimens are extracted from the material bloc using a 11-mm inside diameter diamond coring bit. The extracted cylindrical core is then cut to a nominal 24-mm length with a diamond wire, and both surfaces are rectified, resulting to the specimen to be tested.

Phase Segmentation Procedure of Concrete from X-Ray Tomographic Images

Isolating phases from an x-ray image is challenging when phases have similar x-ray attenuation coefficients. This unfortunately happens to be the case of concrete's meso-structure (aggregates embedded into mortar matrix) adding considerable difficulty in the identification procedure. Some authors use a series of manual operations (see Yang et al. 2017), which are extremely time-consuming and certainly not reproducible. The technical challenge of rendering this operation more objective is the principal issue addressed in this section which presents an image analysis procedure to obtain the morphology from x-ray tomography images of concrete. The segmentation of matrix and aggregates, that have very close mean gray levels, is based on a region-based segmentation technique, which uses the information of the local variance, as has already been used in the medical field (Scholkmann et al. 2010; Li et al. 2011; Zhan et al. 2013). This automatic extraction of aggregates will be validated both from scans of aggregates before casting as well as from neutron tomography images.

Scanning of the Specimen

X-ray tomography is a method of reconstructing a 3D field of x-ray attenuation coefficients within an object by assembling 2D radiographic images (projections) taken at different angles. These attenuation coefficients vary according to the atomic number (closely related to density) of the individual materials that compose the investigated object. It is exactly this variation (in attenuation) that makes x-rays so suitable for studying the internal structure of multiphase heterogeneous materials, such as concrete in meso-scale.

A tomographic scan of a microconcrete specimen is performed in the x-ray scanner in Laboratoire 3SR (Université Grenoble Alpes). The voltage and current of the x-ray source are set to 125 kV and 80 μA, respectively, and the generated x-ray beam is polychromatic of a conical shape. With this scanning apparatus, the voxel size is 13 μm achieving a spatial resolution that captures efficiently the smallest considered heterogeneities of the specimen (about 0.1 mm). Projections are acquired in 1120 different angular positions between 0° and 360°, as the specimen is rotated around a vertical axis and six images of each angle are averaged in order to reduce the noise. By assembling the 2D radiographs using a filtered back projection algorithm (Feldkamp et al. 1984) available in the XAct software provided by RX-Solutions (Annecy, France), the reconstructed 3D image of the scanned specimen is obtained, representing a field of x-ray attenuation coefficients, as shown in Fig. 1a. Figure 2a shows an horizontal slice of it on which macropores appear black, while coarse aggregates and mortar matrix (mix of finer aggregates and sand) share shades of gray. Note that the porosity observed on this scale refers only to the entrapped air porosity formed during the mixing of concrete (macroporosity). This image contains a certain amount of random noise, which is typically modeled as Gaussian, as well as a number of well-known artifacts such as *beam hardening* (due to the polychromatic source) and rings. As explained in detail in the following

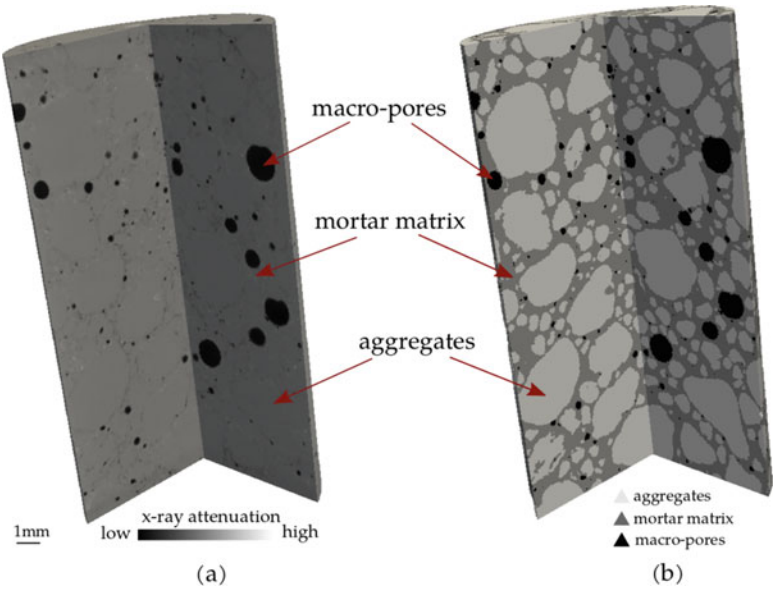

Fig. 1 Reconstructed 3D image coming from the x-ray scan of the microconcrete specimen in the initial configuration: (**a**): gray scale image; (**b**): segmented image

section, some postreconstruction image analysis operations are essential for reducing the noise level and correcting the artificially nonuniform spatial distribution of gray values due to beam hardening.

Although the three phases are easily distinguishable by eye, the 3D image is not easy to trinarize as shown in Fig. 1b., since the contrast between aggregates and the mortar matrix is well below the noise, resulting in a combined peak in the histogram of Fig. 2b. Even assuming there is no noise or artifacts, considering the fact that the 3D image is composed of discrete voxels of 13 μm size, a range of gray values will still exist, since an intermediate value of two phases is unavoidably measured in their interfaces (known as partial volume effect). The separation between the solid and void phases can be achieved with relative ease, due to their obvious density contrast, directly visible on the reconstructed 3D image (see Fig. 2). The next section will focus on the proposed procedure of separating the aggregates from mortar matrix by taking into account the *homogeneity* of the x-ray attenuation distribution inside these materials. From an image analysis point of view, this difference (in *homogeneity*) can be revealed by a spatial variance filter (see also Stamati et al. 2018).

Segmentation Procedure

As a first step of the segmentation procedure, a series of postreconstruction steps are necessary to get the best possible quality of the reconstructed 3D image. First of all, beam hardening is corrected. The unequal repartition of the gray values in the

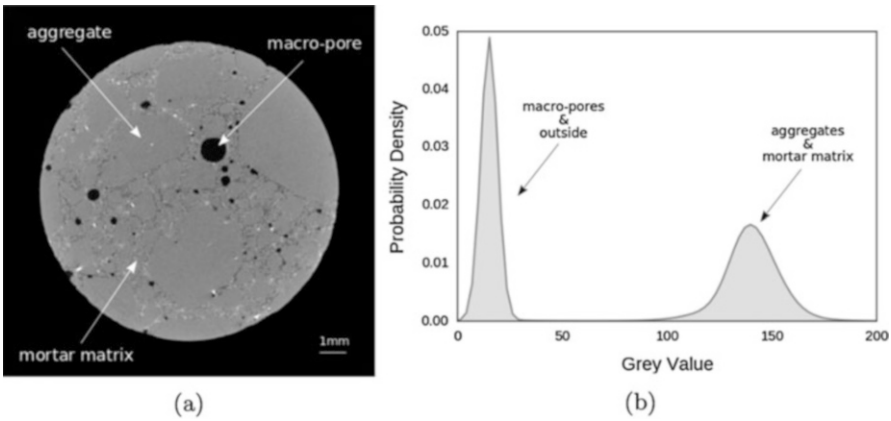

Fig. 2 (**a**): Characteristic horizontal slice of a reconstructed 3D image coming from a micro-concrete sample x-ray scan, (**b**): The histogram of its gray values (where the y axis is normalized frequency so that $\int = 1$)

cylindrical specimen studied – with an artificially darkening of the inside – is corrected radially before proceeding into a phase segmentation.

An algorithm is implemented, by collecting gray values of a representative number of randomly distributed macropores (lowest gray values) and aggregates (highest gray values) and fitting them, separately for each material, with respect to their radial position (see Fig. 3a). Each voxels gray value is then corrected as a function of the specimens radius, based on the following equation: $GV^{new}(r) = \frac{GV(r)-GV^{p}(r)}{GV^{a}(r)-GV^{p}(r)}$, where $GV^{new}(r)$ is the corrected gray value for each voxel, r is the distance (in pixels) of every voxel to the center of the specimen, $GV(r)$ is the initial gray value of each voxel, and $GV^{a}(r)$ and $GV^{p}(r)$ are the fitted initial gray values of the macropores and aggregates at a distance r, respectively.

As a further step, for decreasing the noise level, an anisotropic diffusion filter is applied (Perona and Malik 1990). A low value (three) is set for the constant conductance parameter in the basic anisotropic diffusion equation, in order to preserve better the image features, mainly the edges of the objects. In Fig. 3b, the corrected slice is depicted together with the vertical profiles of gray values crossing the specimen's center before and after the quality-improving operations. The artificially lower gray values in the center due to beam hardening are corrected, and the high frequency content (random noise) is reduced.

After having improved the quality of the image, the macropores segmentation follows (see Fig. 4a). As shown in the histogram of Fig. 2b, a peak on the left represents the void phase and the outside of the specimen, having lower x-ray attenuation. Macropores are defined by implementing an algorithm for thresholding the corrected image, while directly marking and excluding the outside of the specimen from the operation. In the presented case, the threshold is arbitrarily selected as the minimum between the two peaks in the corrected histogram

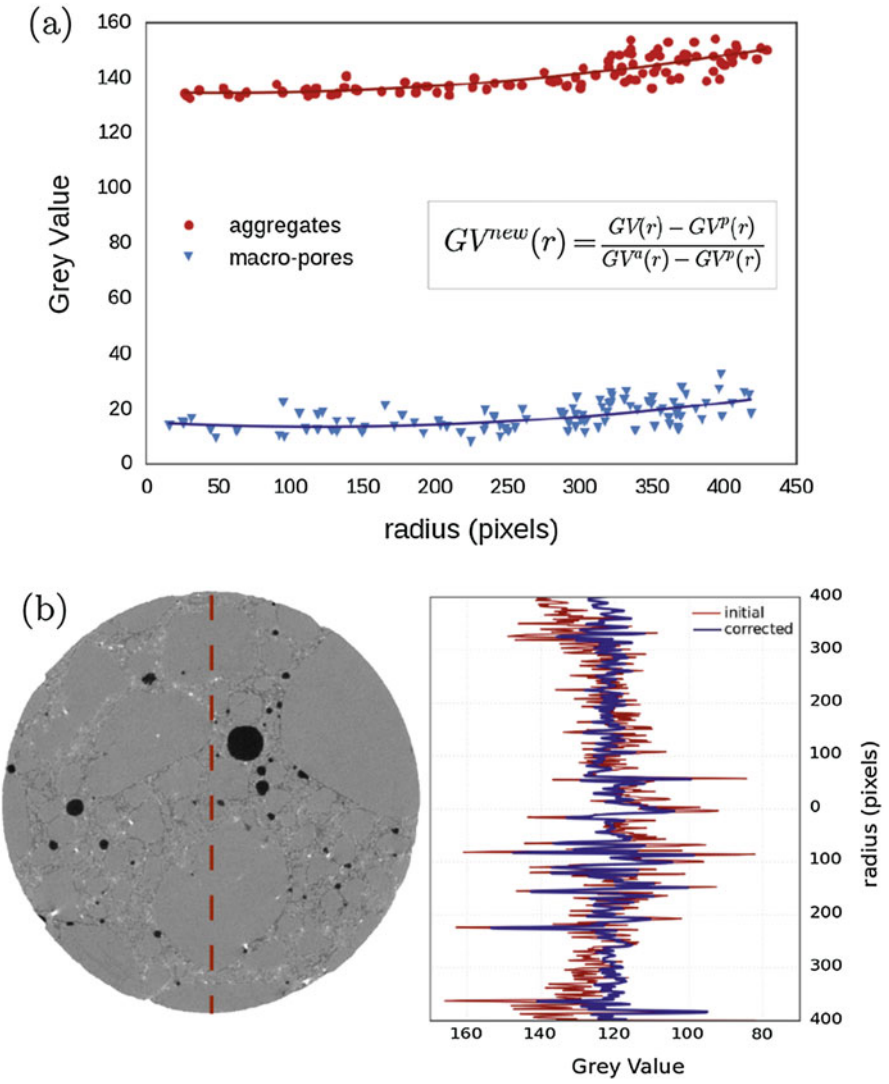

Fig. 3 Quality improving operations: (**a**): *beam hardening* artifact correction by a new repartition of the gray values; (**b**): horizontal slice after correcting the *beam hardening* artifact and application of denoising filter, presented with a vertical profile of gray values (crossing the center of the slice) before and after the corrections

(see Fig. 4b). In cases where the volume fraction of air in the fresh concrete has been measured with an aerometer, the chosen threshold value should lead to a macropore volume fraction close to the latter, if the imaging resolution is good enough (voxel size $<<$ 50 μm). Indeed, aerometers measure the volume fraction of air in the fresh concrete which after hardening will become porosity due to entrained air (during

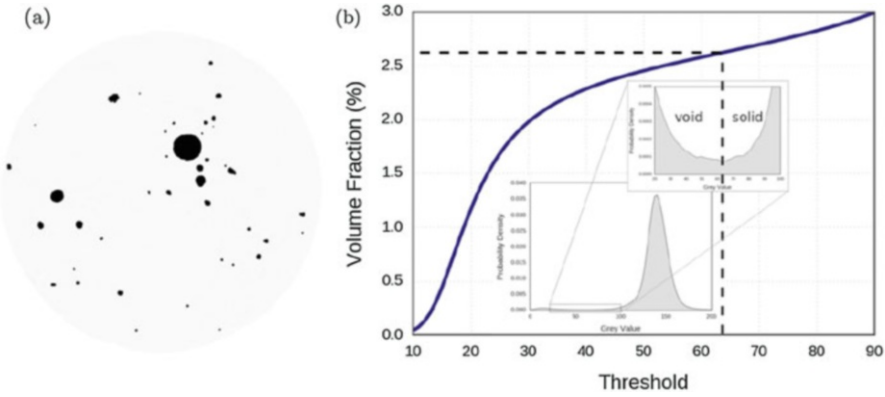

Fig. 4 Segmentation of macropores based on a thresholding operation: (**a**): binary slice of the macropores; (**b**): relation between the selected threshold and the resulted macroporosity. The optimal threshold value is chosen to be the minimum value between the two peaks of the histogram

mixing) and entrapped air (during pouring). Then the size of this porosity ranges from about 50 μm to about the size of largest aggregates.

Concerning the separation of coarse aggregates from the mortar matrix, the key lies in another distinguishing characteristic between these two materials, as already introduced in the previous section. Since mortar matrix is by nature a more heterogeneous material compared to aggregates, the *variation* of gray values inside this material should be more irregular. Thus, instead of separating the solid phase based on the *absolute* gray values (density of the material), a separation based on the *variation* of the gray values (homogeneity of the material) is the approach followed and proposed in this work. This is achieved by applying a sequence of morphological operations and filters using structuring elements (A structuring element is a binary matrix that selects a local neighborhood around a voxel of interest and is defined by its shape and its size (Efford 2000). As *size,* we define the length of the edge of the cube that contains the structuring element (for example, for a cubical structuring element, the total number of voxels is size^3).), as explained in detail below.

An algorithm for calculating the variance map of a 3D image based on a structuring element, which size and shape can vary according to each specific case, is developed. The variance can be given by the formula: $\mathrm{VAR}[X] = \mathrm{E}[X^2] - \mathrm{E}[X]^2$, where $E[X]$ is the averaged gray scale image over the structuring element. As a general rule, depending on the quality and the spatial resolution of the scan, the structuring element size should be just large enough to separate low and high variance areas, while remaining sufficiently small to detect the smallest aggregates to be segmented. Moreover, structuring element sizes should be minimized to preserve details of the aggregate's shapes.

To evaluate this shape deterioration, the segmentation procedure was applied to already segmented images for several sizes and shapes of structuring elements. The percentage of voxels affected by a change of material during the process was then

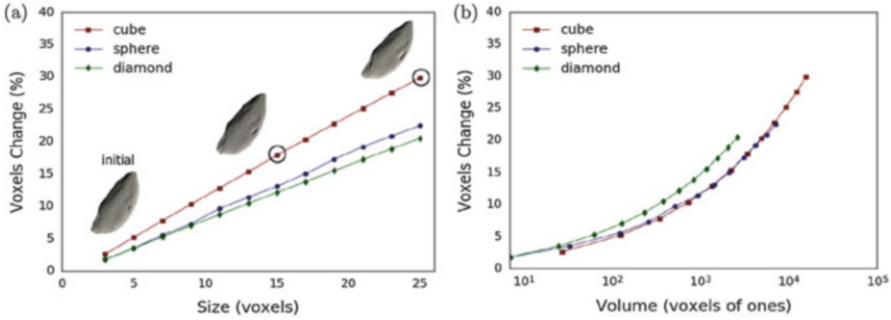

Fig. 5 Deterioration of the aggregates shape during the segmentation process after the application of the variance filter versus (**a**): the size (length of the edge of the cube that contains the structuring element) of the structuring element. Illustrative example of an aggregate's morphological evolution between the initial state and after the application of a variance filter with a cubical structuring element of 15 and 25 voxels size; and (**b**): the volume (number of ones containing in the binary matrix) of the structuring element

evaluated. Figure 5a shows the evolution of this percentage versus the size of the structuring element for several structuring element shapes (cube, sphere, and diamond) of the variance filter. An illustrative example of an aggregate's morphological evolution between the initial state (no filter) and after the application of a variance filter with a cubic structuring element of 15 and 25 voxels size is also shown. Concerning the optimal choice of the structuring element, the parameter that most affects the final result is the volume of the structuring element (number of ones contained in the binary matrix), as shown in Fig. 5b, while the shape is a second order parameter. However, in our opinion, a spherical structuring element should be generally preferred, since it does not have any preference in orientation and should preserve the details of aggregates shape slightly better, as illustrated in Fig. 5.

An estimation of the lower limit of the structuring element can be made by assuming that gray levels inside aggregates follow a normal distribution $\mathcal{N}(\mu, \sigma^2)$ with mean μ, and standard deviation σ. After the application of an average filter with the selected structuring element, the standard deviation of the aggregates gray values will be reduced monotonically with the size of the structuring element. A first approximation of the minimal value of the structuring element size can then be given by setting the ratio σ'/μ lower than 3%, where σ' is the new value of the standard deviation of the gray levels inside the aggregates after the application of the average filter.

In the presented example (see Fig. 6a), a spherical structuring element of nine voxels size is selected, and the variance map of the image is calculated. Considering that the spatial resolution in the 3D reconstructed image is 13 μm/voxel, the smallest object that can be captured is 0.1 mm. Note that the smallest aggregate size used during the casting of the examined microconcrete specimen was 0.5 mm. Here, it should be mentioned that in lower quality scans (in terms of noise levels) with lower spatial resolutions (around 50 μm/voxel), presented in the following section, a

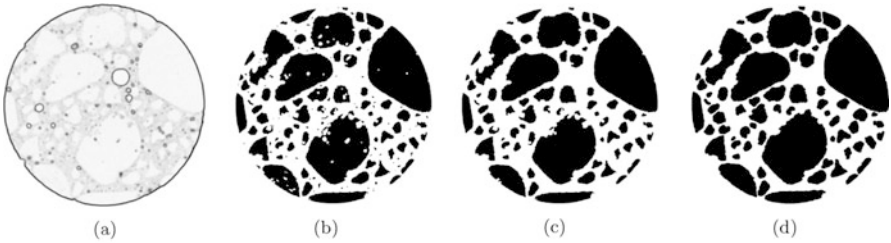

Fig. 6 Developed procedure for extracting the aggregates from a 3D image coming from a concrete x-ray scan: (**a**): calculation of the variance map based on a specific structuring element; (**b**): thresholding the variance image and keeping only the aggregates; (**c**): filling holes and discarding the small size objects; and (**d**): morphological dilation to retrieve the original size and shape of the objects

cubical structuring element of 25 voxels has been selected, meaning that aggregates smaller than 1.3 mm cannot be captured.

By keeping the lower variance areas (aggregates and macro-pores) and discarding the already segmented macropores, a binary 3D image containing the aggregates is obtained (see Fig. 6b). A sequence of morphological filters based on structuring elements is then applied on the aggregate binary image to retrieve their original size and shape. An opening morphological operation (for removing the morphological noise) and a filling-holes operation (for closing the artificially created holes inside the aggregates) are applied, followed by a sieving operation (for discarding small size objects). In the presented example, based on the aggregate size distribution used for the casting of the microconcrete sample, any extracted object smaller than 0.5 mm is considered part of the mortar matrix and thus discarded. The results of these filters are shown in Fig. 6c. As a last step, a morphological dilation is applied, so as to retrieve the original size of the aggregates, using a structuring element of the same shape and half the size of the one selected for the variance filter (see Fig. 6d).

By combining the two 3D binary images (one for macropores and one for aggregates), the final trinary 3D image is obtained, where each phase is represented strictly by a unique value, as shown in Fig. 7. A quantitative analysis for each phase is now possible, by calculating, for example, the aggregate and macropore size distribution curves (see Fig. 8a). By combining the trinary image with the initial one, the distribution of gray levels inside the aggregates and the mortar matrix are obtained individually for each material (see Fig. 8b). The mean values of the two phases are very close: 137 and 134, while the difference in variance is obvious: 5.24 and 15.4, for aggregates and mortar matrix, respectively. Note that after an application of an average filter with the selected structuring element, the standard deviation inside the aggregates is reduced to $\sigma' = 3.3$, leading to a ratio $\sigma'/\mu = 2.5\%$. From the probability density functions of Fig. 8b, it is obvious that a separation based on a single (mean threshold) value would have been impossible. On the contrary, the difference in variation is rather clear, revealing that the proposed segmentation procedure, based on a variance filter, is a simple, efficient, and quite a suitable tool.

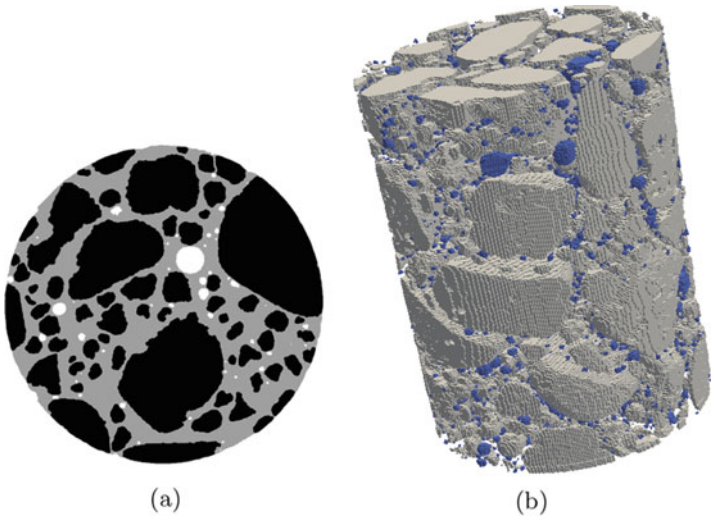

Fig. 7 Result of the proposed segmentation procedure: (**a**): representative horizontal slice as a trinary image where each phase is strictly composed of a set of pixels sharing a unique predecided value; (**b**): the obtained 3D trinary image of the scanned concrete sample; blue: macropores, light gray: aggregates and the rest of the volume are occupied by the mortar matrix

Validation with Neutron Tomography

For the reliability of the segmentation procedure presented in the previous section, a representative set of aggregates, used for an ordinary concrete mix (largest aggregate size of about 1 cm), is embedded into a gel (to limit contacts between aggregates) and scanned with x-rays (see Fig. 9a). The aim of this scan is to obtain a binary 3D image of the aggregates surrounded by a low-density medium, making them easy to identify, without the need to perform any image analysis operations that may have affected any of their morphological characteristics. Indeed, this time, due to the obvious density contrast between gel and aggregates, the set of aggregates in the reconstructed 3D image is directly extracted through a simple thresholding operation.

A mixture and casting of a *real concrete* sample followed, using the exact same set of aggregates, and a new x-ray scan is performed, obtaining a spatial resolution of 50 μm/voxel. The procedure presented in the previous section is applied, using a cubical structuring element of 25 voxels size, and a second binary 3D image representing the same set of aggregates is obtained (see Fig. 9b).

As a further validation step, a neutron tomography scan is performed on the same concrete sample. In this case, due to the physics of neutron interaction with matter, in the reconstructed 3D image, aggregates and mortar matrix do not share the same range of gray values (see Fig. 9c). Thus, by applying a thresholding operation based on the absolute (mean) gray values, a third binary 3D image representing the same set of aggregates is obtained, this time coming from a neutron scan.

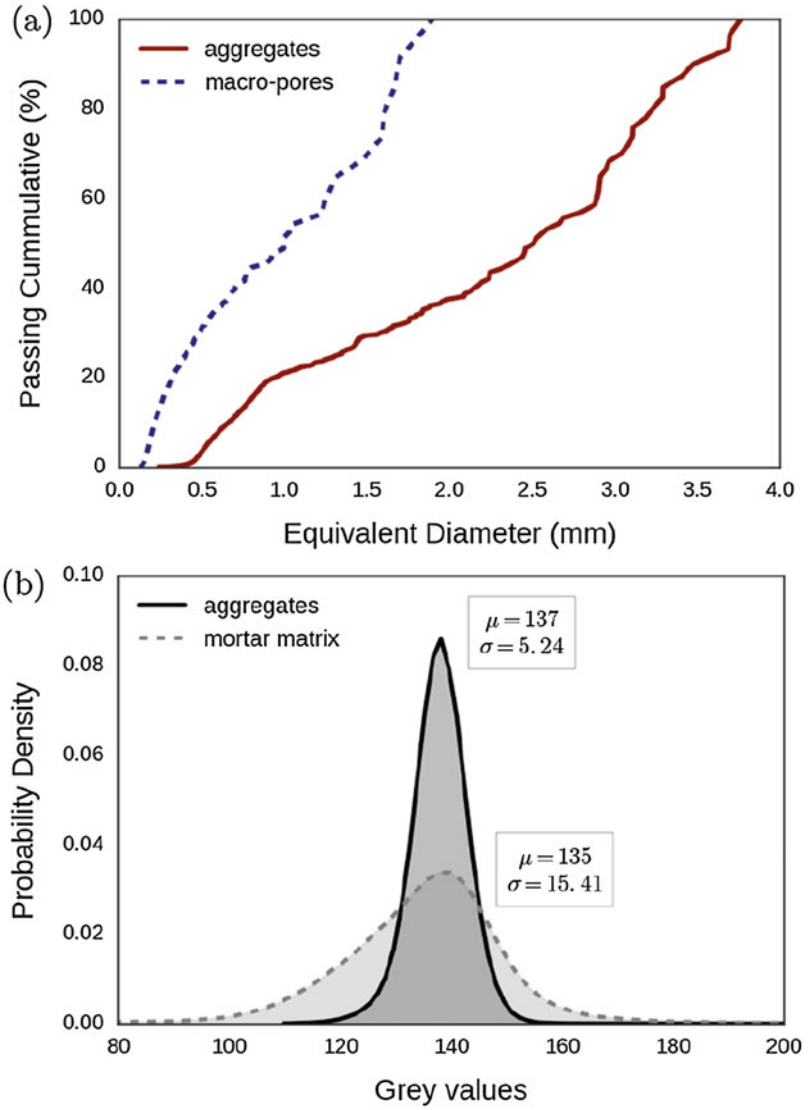

Fig. 8 (**a**): Aggregate and macropore size distribution curves. (**b**): Distribution of gray values inside the aggregates and mortar matrix in the original gray scale image. The resulting mean value and standard deviation are respectively equal to 137 and 5.24 for aggregates, while 135 and 15.41 for mortar matrix.

In the obtained binary 3D images of the extracted aggregates, each individual particle is identified, and the three extracted sets of aggregates are compared by plotting the particle size distribution curves (see Fig. 10). Note that, concerning the x-ray concrete scan, due to the size of the selected structuring element for the

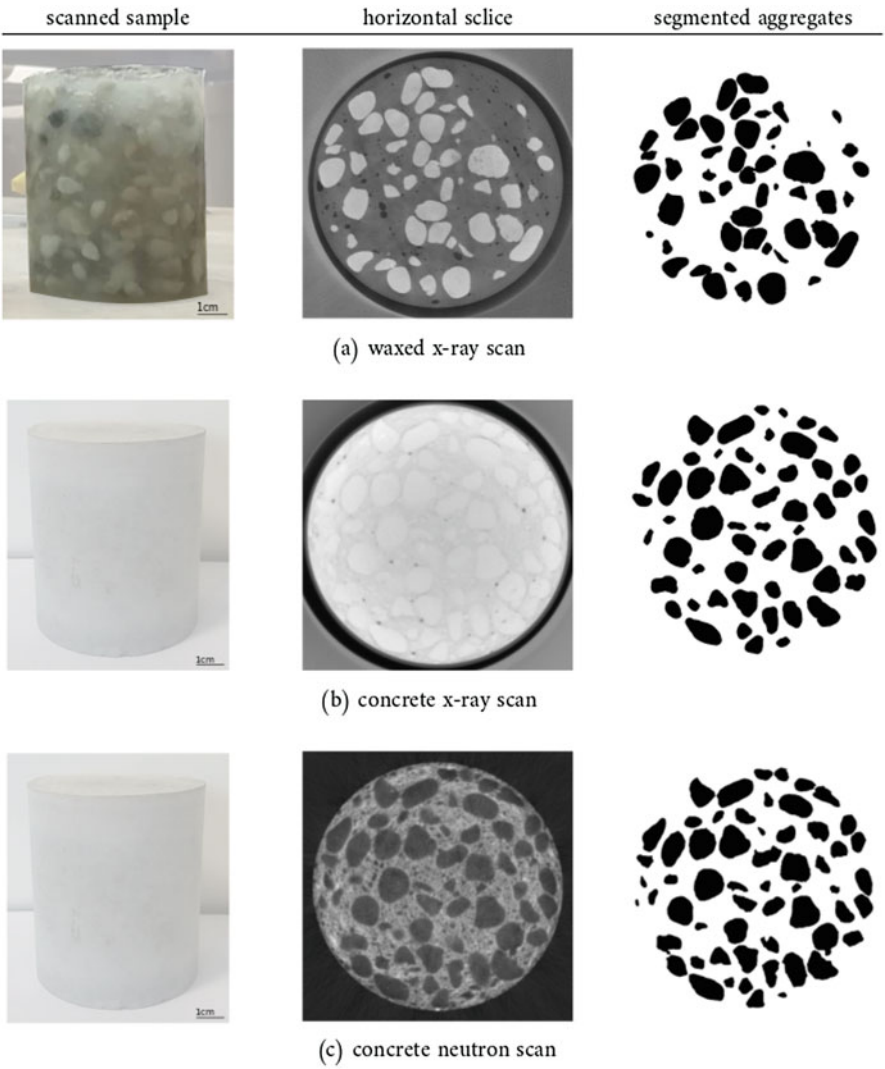

Fig. 9 Validation of the aggregates segmentation procedure. A representative set of coarse aggregates is scanned three times and extracted as 3D binary images: (**a**): embedded in gel; (**b**): casted as regular concrete and scanned with x-rays; and (**c**): same concrete sample scanned with neutrons

variance filter (cube of 25 voxels size), only aggregates bigger than 1.3 mm are captured. The comparison of the three curves coming from three different scans is satisfactory, but not enough to prove that the extraction from the concrete x-ray scan is necessarily successful.

Since the same concrete sample has been imaged by two different modalities (x-rays and neutrons), segmented images can be locally compared. As an illustration,

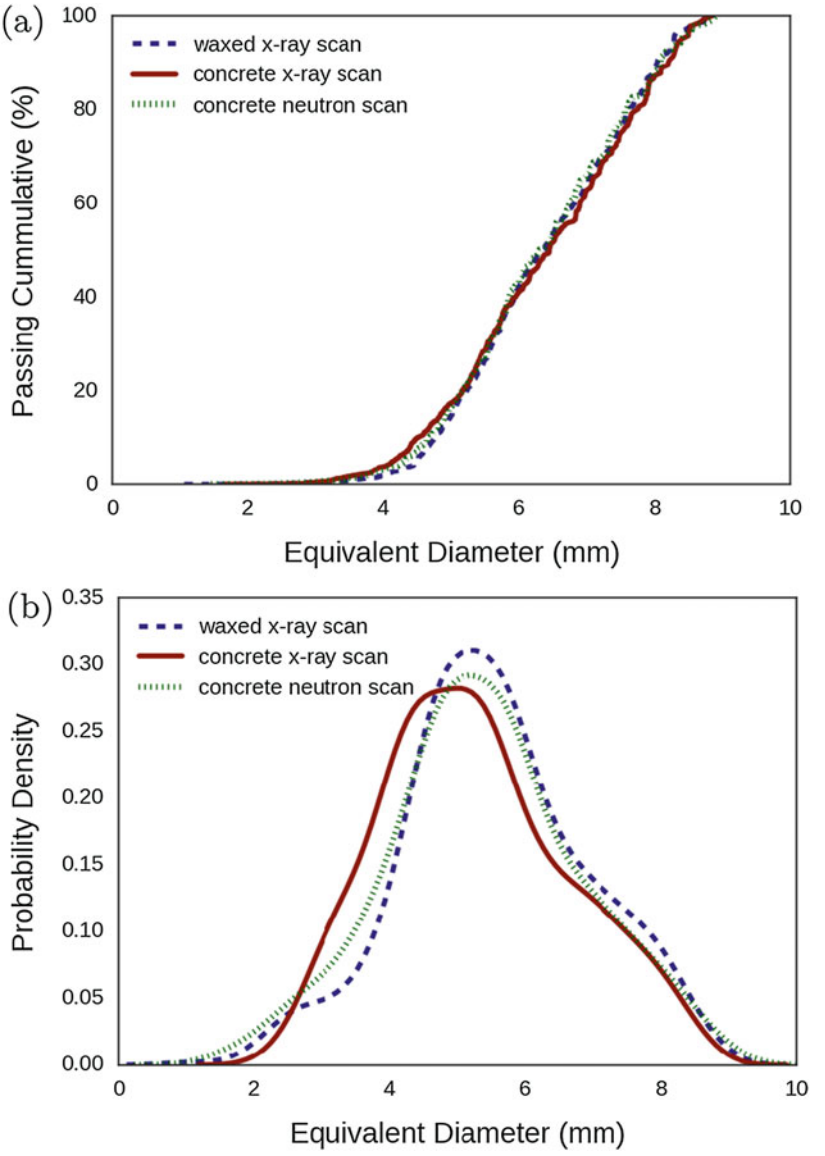

Fig. 10 Comparison of the aggregate size distributions coming from the three different scans: (**a**): cumulative distribution function; (**b**): density function (where the y axis is normalized frequency so that $\int = 1$)

the same horizontal 2D slice as captured first from the x-ray and later from the neutron scan is presented on Fig. 9b and c, respectively. To give a more quantitative evidence, the two 3D binary images of segmented aggregates are registered and then

Fig. 11 Characteristic slice of the difference between the two binarized 3D images (neutron and x-ray scan)

subtracted from one another. The difference of the characteristic 2D slices of Fig. 9b and c is represented in Fig. 11, which shows a good agreement in shape and sizes of the extracted aggregates. The number of voxels that do not coincide between the two segmented 3D images is equal to 4% of the total volume. Assuming that the segmented image obtained from neutron tomography is the reference, this value gives a quantitative order of magnitude of the error of the x-rays scan segmentation procedure. Note that this error would probably be even lower with the images of the microconcrete sample, presented in Sections "Studied Material: Characteristic Scales and Composition" and "Phase Segmentation Procedure of Concrete from X-Ray Tomographic Images," for which unfortunately no neutron scan was performed. According to this validation, the developed and presented procedure leads to a reliable separation of the three phases and consequently to a useful characterization of concrete's meso-structure. The obtained repartition of phases can now be used as the input morphology of a FE meso-model, as described in detail in the following section.

FE Meso-model Description

From a numerical point of view, the main challenges to model the quasi-brittle behavior of materials such as concrete at the meso-scale are as follows:

- Explicitly take the morphology into account.
- Model the local discrete failure mechanisms.

In this study, an FE model that tackles both issues within a framework of embedded kinematics enhancement is used. Only the main ingredients of the model are presented here; for a detailed description see Roubin et al. (2015a).

Local Kinematics Enhancement

Accounting for the Morphology

A first challenge for a meso-model consists in taking into account the morphology of the meso-structure. The most commonly used method to address this issue, referred to as *adapted mesh method,* roughly consists in: first, a surface meshing of the interfaces and then a volumetric meshing of each phase. This results in very accurate representation of the morphology, requiring, though, complex and time-costly algorithms (see Sonon et al. 2015). Furthermore, particular attention has to be paid on the interface modeling (zero thickness elements or cohesive bands, for example).

A lighter framework, referred to as *nonadapted mesh method* (Moës et al. 2003), is used here. First of all, an FE mesh (made of 4-noded tetrahedra) is generated regardless of any morphology (i.e., with randomly and evenly distributed nodes in space) (12b). Then the morphology resulting from the segmentation above (12a) is *projected* onto this mesh. This consists in inspecting each element and identifying what phase of the morphology each node falls into. Based on this identification, two kinds of elements can emerge: elements where all the nodes belong to the same phase and elements where nodes belong to two different phases.

The first kind are classical FE where the material properties of the phase are defined. Thus, for each of the three phases (aggregates, mortar matrix, and macro-pores) a maximum of two elastic and two failure parameters could be required: the Young's modulus E and the Poisson ratio ν, and the yield stress (σ_y) and the fracture energy $\left(\mathcal{G}_f\right)$, respectively. For physical reasons and also to simplify the problem, in the present case, aggregates are considered elastic, i.e., no crack initiation and propagation allowed inside these elements. Regarding the macropores, the physically required negligible (zero) stiffness, would potentially cause numerical problems and further mechanical influences, due to the high contrast in material properties among the phases. Therefore, elements, which after the projection are identified as macropores, have been removed from the final FE mesh, creating some cavities in the mesh. On the inside of these cavities, a free surface boundary condition is applied; consequently, these nodes cannot carry any load which does not attract any spurious stress concentrations. In the case where nodes are both in a macropore and a solid phase, the choice has been made to consider the full element as part of the solid phase. A sensibility analysis (not presented here) has been made showing a negligible effect of this choice over considering weak discontinuities with a very soft material that would represent macropores.

The second kind needs to account for two phases and the interface between them. In this work, this is handled by a kinematics enhancement, called *weak discontinuity.*

This kinematic enhancement accounts for the material discontinuity by introducing a jump in the strain field (Sukumar et al. 2001), accounting for the interface. See Roubin et al. (2015a) for more details.

In the examined case, the two kinds of elements resulting from the morphological projection are those that have all their nodes within the same phase (macropores, aggregates, or mortar matrix) and those that have nodes in two different phases.

It is the later ones that are enhanced by a weak discontinuity to account for the differences in the material properties of the two phases. This can be written for an element as:

$$\varepsilon = \boldsymbol{Bd} + \boldsymbol{G}_{\mathrm{w}}[|\varepsilon|] \tag{1}$$

where the first term is the classical FE strain field (derivative of the shape functions $\boldsymbol{B}$ and nodal displacements $\boldsymbol{d}$), and the second term corresponds to the weak discontinuity. $[|\varepsilon|]$ is a vector of new unknowns, i.e., the weak discontinuities, and $\boldsymbol{G}_{\mathrm{w}}$ an operator that represents the interface geometry. This geometry accounts for the volume fraction of each phase along with the orientation of their respective interface, both being computed during the projection, regardless of any mechanical state (details here Roubin et al. 2015a).

As shown in Fig. 12, the projection leads to five sets of FE, three with no weak discontinuities (inside aggregates, mortar matrix, or macropores) and two with weak discontinuities accounting for aggregates/mortar and pores/mortar along with their respective interfaces. Regarding these elements with shared material properties (enhanced with a weak discontinuity), no specific parameters are required in the elastic regime, whereas specific failure parameters are defined. Equal failure

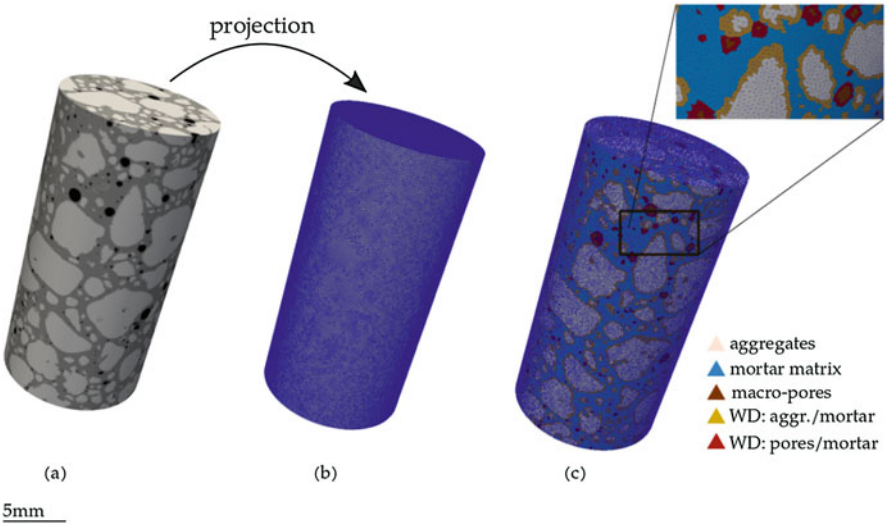

Fig. 12 Nonadapted mesh method: (**a**): the heterogeneous morphology (segmented 3D image) is (**b**): projected into a FE mesh (**c**): leading to five sets of FE

properties with the mortar matrix are assigned to these elements, still leading to a weaker behavior of the interface, since the difference of the elastic properties between the phases results to a higher stress concentration at the interfaces.

Accounting for the Local Failure Mechanisms

The local failure mechanism considered is microcracking, being the key phenomenon, with the coalescence and bridging of these microcracks resulting to the macroscopic failure of the specimen. In order to account for it, another set of local discontinuities is introduced. Similarly, with the weak discontinuities, the FE kinematics are enhanced, this time, by a jump within the displacement field, thus representing the discontinuous aspect of a crack. This new discontinuity is referred to as *strong discontinuity* and can be written for one element as:

$$\varepsilon = \boldsymbol{Bd} + \boldsymbol{G}_{\mathrm{s}}[|\boldsymbol{u}|] \tag{2}$$

where the first term is still the classical FE strain, and the second one corresponds to the strong discontinuity. $[|\boldsymbol{u}|]$ is directly the crack opening, a vector of new unknowns, and G_s an operator that represents the position and the orientation of the crack.

Double Kinematics Enhancement

The two enhancements presented above can be combined together leading to a formulation within an element written as:

$$\varepsilon = \boldsymbol{Bd} + \underbrace{\boldsymbol{G}_{\mathrm{w}}[|\varepsilon|]}_{\text{weak disc.}} + \underbrace{\boldsymbol{G}_{\mathrm{s}}[|\boldsymbol{u}|]}_{\text{strong disc.}} \tag{3}$$

This permits a material interface (weak discontinuity) to fail (strong discontinuity), thus modeling debonding. Figure 13 shows the three kinds of discontinuity settings that can occur inside an element.

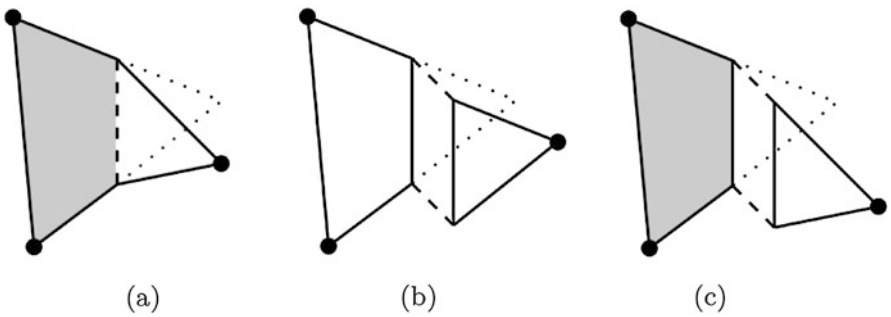

Fig. 13 Element with: (**a**) one weak discontinuity; (**b**) one strong discontinuity; and (**c**) both weak and strong discontinuity. (Adapted from Jirsek 2000)

It is assumed here that if both discontinuities are present inside an element, the strong discontinuity orientation is taken to be the same as the weak one, thus making the crack open following the material geometry.

Phenomenology and Resolution Scheme

The double kinematics enhancement brings two additional sets of unknowns in the mechanical problem, one being the weak discontinuity vectors $[|\boldsymbol{\varepsilon}|]$ and the other the crack-openings $[|\boldsymbol{u}|]$. Thus, the behavior law can be written as a function of them. It is assumed here that the relationship between stress and strain remains elastic (no damage within the material), leading to the following behavior law:

$$\boldsymbol{\sigma}(\boldsymbol{d}, [|\varepsilon|], [|\boldsymbol{u}|]) = \boldsymbol{\mathcal{C}}\varepsilon = \boldsymbol{\mathcal{C}}\left(\boldsymbol{B}\boldsymbol{d} + \boldsymbol{G}_{\mathrm{w}}[|\varepsilon|] + \boldsymbol{G}_{\mathrm{s}}[|\boldsymbol{u}|]\right. \tag{4}$$

where $\boldsymbol{\mathcal{C}}$ contains the elastic material properties of each phases.

It is important to note here that the stress softening does not come from material degradation (through modification of $\boldsymbol{\mathcal{C}}$), but through kinematics considerations, i.e., a crack opening (modification of $[|\boldsymbol{u}|]$). The energy is thus dissipated through the discontinuity which plays the role of softening regularization.

The phenomenology of the failure mechanism follows the Discrete Strong Discontinuity Approach (Oliver 2000), which links the crack opening with the stress state through a traction-separation law. This discrete approach is activated when a certain stress state within an element is reached, the tensile strength σ_y. This is expressed by the following localization criterion:

$$\Phi_l = \boldsymbol{T} \cdot \boldsymbol{n} - \sigma_y \tag{5}$$

where $\boldsymbol{n}$ is the discontinuity orientation and $\boldsymbol{T} = \boldsymbol{\sigma} \cdot \boldsymbol{n}$ is the traction vector at the discontinuity surface. As mentioned above, in case of weak discontinuities, $\boldsymbol{n}$ is considered to be the geometrical orientation (material interface). In case of no weak discontinuities, $\boldsymbol{n}$ is considered to be the direction of the largest principal stress. In opposition to rotating crack models, here, when the localization occurs ($\Phi_l = 0$), the orientation is recorded and remains fixed.

Then, the following criterion drives the opening:

$$\Phi_o = \boldsymbol{T} \cdot \boldsymbol{n} - \sigma_y \exp\left(-\frac{\sigma_y}{\mathcal{G}_f}[u]\right) \tag{6}$$

where $\mathcal{G}_f$ is the fracture energy of the phase and $[u] = ||[|\boldsymbol{u}|]||$ is the norm of the crack opening vector, which leads to a local brittle behavior. Since this law provides information only on the norm $[u]$ of the crack vector $[|\boldsymbol{u}|]$, it is assumed that the orientation of this vector is the same as $\boldsymbol{n}$, thus corresponding to a mode I opening.

Following the Embedded FE formulation (Oliver 1996; Wells and Sluys 2001; Roubin et al. 2015a), the equations added by the presence of these enhanced parts of

the strain field are solved at the element level, by performing a local resolution. Then a static condensation (Wilson 1974) allows the system to keep the same size as without enhancements (i.e., there are no additional global unknowns). This specific feature of the embedded formulation allows for constant systems sizes no matter the number of cracks or the complexity of the geometry.

The presented framework is implemented in the FE code FEAP (Taylor 1987), and the implemented quasi-Newton BFGS resolution scheme coupled with an iterative solver (Conjugate Gradient) is used to solve the nonlinear set of equations of the global system. Now that the basic characteristics of the model have been introduced, the free software GMSH (Geuzaine and Remacle 2009), based on a 3D Delaunay triangulation of randomly positioned nodes, is used to create the FE mesh. In the studied case, this is a cylinder of the dimensions of the microconcrete specimen consisting of 4-node tetrahedra elements. In order to model the morphological information of the smallest heterogeneities of the 3D segmented image, the edge length of each tetrahedron is chosen to be 0.1 mm generating a mesh of 6.3×10^6 4-node tetrahedra elements and 3.4×10^6 degrees of freedom, as shown in Fig. 12b. Taken from bibliography, the first assigned material properties are $E_a = 70$ GPa, $E_m = 12$ GPa, $\nu_a = \nu_m = 0.2$, and $\sigma_{y_m} = 6$ MPa, $\mathcal{G}_{f_m} = 0.1\ Jm^{-2}$.

In Situ Tensile Test

Using x-ray tomography on both intact (before loading) and damaged (after unloading) materials is quite valuable for obtaining the internal microstructure before and after failure. However, scanning the internal microstructure during loading can reveal important information about the actual evolution of the fracturing process (De Wolski et al. 2014; Yang et al. 2017; Nitka and Tejchman 2018). Specific experimental facilities are required for these in situ studies, though, making them less commonly used. In this work, a suitable experimental setup compatible with the x-ray scanner of Laboratoire 3SR is developed, allowing the microconcrete specimen to be scanned while it is under load. This permits both a direct validation of the 3D E-FE meso-model presented in previous section and an insight into the 3D fracture mechanisms while the load increases.

In Situ Experimental Setup

Figure 14a shows a sketch of the loading cell, along with its key features, and Fig. 14b shows a photo of the loading cell inside the in situ x-ray facility. The load frame is built into a low x-ray absorption plexiglass cell designed for triaxial testing of rocks with 7 MPa confining pressure. The two surfaces of the specimen are glued in two specifically designed aluminum caps with a high strength epoxy. The shape of the caps is designed (see Fig. 14a) to ensure good centering and to avoid any stress concentration or failure on the axial faces of the specimen. In order to ensure that the

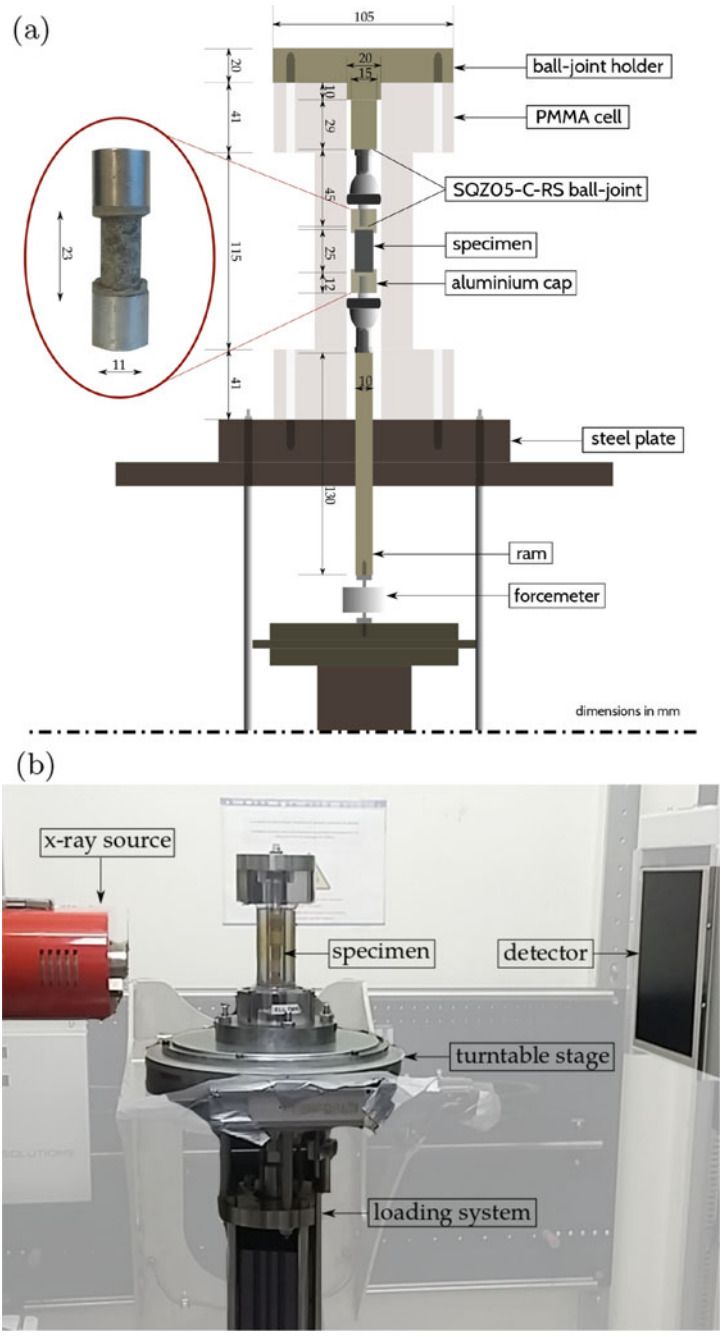

Fig. 14 In situ tensile test. (**a**): Sketch of the designed load frame. (**b**): In *situ* x-ray facility at Laboratoire 3SR

applied load remains purely axial, each aluminum cap is screwed into a ball joint, allowing free rotation in the two planes normal to the loading direction and eliminating any bending moment due to potential defects in parallelism. The bottom ball joint is screwed into a ram, while the top one remains fixed into a ball-joint holder as shown in the sketch. Once the specimen is mounted into the loading cell, a uniaxial tensile load can be applied to its bottom surface through the ram, while an LVDT sensor is used to measure the displacement. Since the shape of the x-ray beam is conical, a displacement of the loading cell, closer to the source, makes the specimen enlarged on the detector (due to geometric magnification), and the desired spatial resolution (13 μm) can be achieved. The voxel size of 13 μm yields a magnification factor of 9.5, resulting to a field of view to 25.5 × 20.5 mm. Once the setup is ready, the in situ experiment can be conducted.

Experimental Stress-Strain Curve and Macrocrack Identification

The first tomographic scan is performed prior to any load application, once the specimen is mounted in the loading cell and positioned at the desired distance from the source that is kept fixed during the whole test. The meso-structure obtained from this scan (see Fig. 1) is the one used in the FE model presented in section "Phase Segmentation Procedure of Concrete from X-Ray Tomographic Images." After the first scan is completed, a tensile load is applied by moving the ram downward with a fixed displacement rate till a load value of 150 N is reached. At this stage, the displacement is stopped and a second scan is performed. The specimen is then loaded, with the same strain rate, up to 250 N when a third scan is carried out. The initial objective is to have at least: a scan in the initial configuration, two others at two intermediate load values before the peak, and a fourth one after failure. Since the exact tensile strength of the specimen is not known a priori, these loading steps were chosen approximately by using information concerning the concrete composition, the dimensions of the specimen, and previous mechanical tests done on similar microconcrete specimens.

Figure 15 shows the experimental macroscopic stress-strain curve, after subtracting the strain corresponding to the elastic stiffness of the loading cell and assuming a level of zero stress in the specimen after the material failure. Note that due to the use of a polycarbonate cell, the loading system is not stiff enough to capture the postpeak. The loading points where the tomographic scans were carried out are indicated along with the reconstructed 3D images of the specimen. No obvious microstructural change is visible in the 3D images between the initial and the two following scans, whereas a clear macrocrack, normal to the direction of loading, appears in the one after failure. While the specimen size is admittedly small compared to its heterogeneities, the measured tensile strength is 3.2 MPa and the macroscopic Young's modulus is 32 GPa, values that are very close to the ordinary concrete from which the microconcrete composition is derived.

Conducting a postpeak scan gives valuable information about the damaged internal microstructure. By isolating the voids and keeping the largest connecting

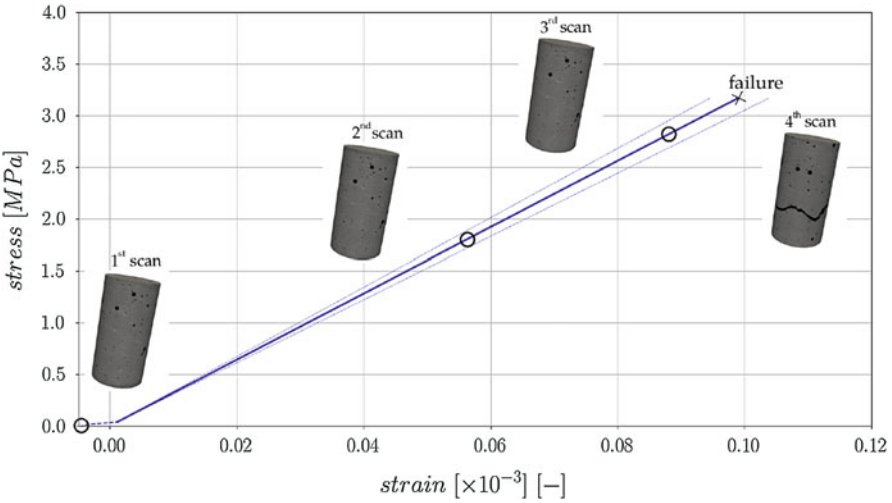

Fig. 15 Macroscopic response of in situ tensile test. The loading points where the scans were conducted are indicated, along with the reconstructed 3D image of the microconcrete specimen

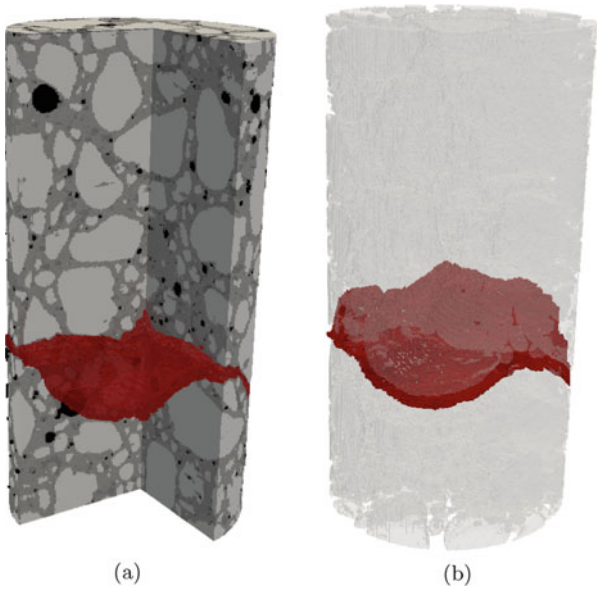

Fig. 16 Postpeak x-ray scan: (**a**): segmented 3D image with the macrocrack; (**b**): skeletonized extracted macrocrack of 1 pixel width

component in the postpeak 3D image, the experimental macrocrack can be extracted and is shown in Fig. 16. A typical macrocrack for fracture mode I is formed, crossing the cylindrical specimen. It is clear that the shape and location of both aggregates and macropores form its morphology. The crack is formed around the aggregates,

sometimes propagating through macropores and rarely only through a single aggregate. Note that, at the scale observed, in the postpeak scan, only the failure macrocrack can be extracted. However, microcracks of too small thickness to be identified from a single scan and zones with localized deformation surely exist in the specimen before the failure. To identify these, it is necessary to proceed to DVC measurements as explained in detail in the following subsection.

Following the Microstructural Evolution

In addition to the presented macroscopic measures, having performed multiple successive scans under progressive loading is ideally suited for following the microstructural evolution while the microconcrete specimen deforms. Digital volume correlation (DVC) is, in particular, a suitable technique for obtaining the full 3D displacement field between a reference and a deformed state of the specimen from which the 3D strain field can then be calculated (Hild and Roux 2006). Moreover, cracks with widths less than the voxel size (too narrow to be visible on the x-ray 3D images) can also be detected by DVC, giving valuable insight into the initiation and propagation of microcracks.

In this work, a software called SPAM (the authors are core developers) is used for the DVC analysis of the examined microconcrete specimen. The level of uncertainty in the DVC procedure was estimated through a so-called "double tap" scan. Two scans of the same microconcrete sample were performed with some rigid-body motion between the two acquisitions, but without any mechanical loading. The correlation of this double tap scan showed that there is a clear trade-off between the spatial resolution of the measurement and the level of the measurement uncertainty. For the selected window size, any measured displacement smaller than 0.05 pixel falls below the uncertainty level. No mechanical regularization of the DVC was made. A local DVC approach was used on a regularly spaced grid of contiguous correlation windows (see below). As a postprocess step, the displacements of the grid points that did not correlate successfully were replaced by the mean-weighted displacement values (based on the distance) of the 12 closest successfully correlated points. Also, before proceeding into strains calculation, the displacement field was smoothed by applying a 3D median filter of a 1 voxel radius. The choice of the 1 voxel radius reduces the risk of oversmoothing the field and thus losing mechanical information.

In the "local" DVC approach used, the region of interest in the reference configuration is subdivided into a set of independent subvolumes (zones of interest). Correlation between the two configurations (two pairs of 3D images) is done by calculating a linear transformation operator that gradually deforms each reference subvolume so as to best match the 3D volume of the deformed configuration. Here, a fine 3D regular grid with a node spacing of 20 voxels (i.e., 0.26 mm) in each direction is created to capture the small microstructural changes. This grid imposes subvolumes that are far too small to capture features within large aggregates, and so, subvolumes that fall completely inside aggregates are not successfully correlated.

However, aggregates are identified using the procedure in (Stamati et al. (2018) (which are recognized due to their low variance, i.e., lack of features), and large aggregates are correlated using the "Discrete DIC" option in SPAM (in the style of Hall et al. 2010; Ando et al. 2012), meaning that a single linear transformation operator is measured for each aggregate. The displacement of each point of the grid (center of each subvolume) that has successfully correlated (i.e., mainly points that fall in the mortar matrix and partially between the phases) is independently calculated resulting to a 3D displacement field. By combining this field with the displacements calculated separately for each large aggregate, the final 3D displacement field is obtained. The strain field is then calculated using TomoWarp2 (Tudisco et al. 2017) following the large strains hypothesis, with the displacements of the large aggregates being excluded from the calculation.

It should be noted here, that the transformation operator is a linear operator, unable to capture large strains linked to the total fracture of the material. In other words, a correlation between any 3D image and the final (postpeak) one is not possible. Figure 17 presents the central vertical slices of the reconstructed 3D images of the first three scans along with the central vertical slices of the calculated displacement and strain fields in the axial direction. Note that between the first two scans, there is a big displacement step (rigid body motion of the specimen) in the range of 300 μm, while the range of the relative displacements corresponding to the microstructural evolution of the material is only 4 μm. From the computed 3D fields, it is shown that the response of the material is not purely elastic-brittle. Even for the first correlated pair of 3D images (at a load 50% of the maximum failure load), a heterogeneous displacement field appears, pointing out strain localizations and crack initiations, an observation that justifies that performing an in situ tensile test gave indeed valuable information about the evolution of the fracture processes of the material.

Numerical Simulations of Tensile Tests

Identification of Numerical Parameters

Since the actual material response is known, the numerical parameters used in the mesomodel can be identified to better fit the numerical response to the experimental results. Examining the 3D image coming from the postpeak x-ray scan, it seems that some of the aggregates did break. This means that crack initiation and propagation should be allowed inside these elements but with much higher failure parameters compared to the mortar matrix. A parametric analysis is performed by assuming the same value of Poisson ratio $\nu_a = \nu_m = 0.2$ and keeping a constant ratio between: $E_a : E_m, \sigma_{y_a} : \sigma_{y_m}$ and $\mathcal{G}_{f_a} : \mathcal{G}_{f_m}$. The calibrated material properties are summarized in Table 1. The comparison of the experimental and numerical stress-strain curves is shown in Fig. 18 with a good agreement both in terms of macroscopic strength and in terms of Young's modulus.

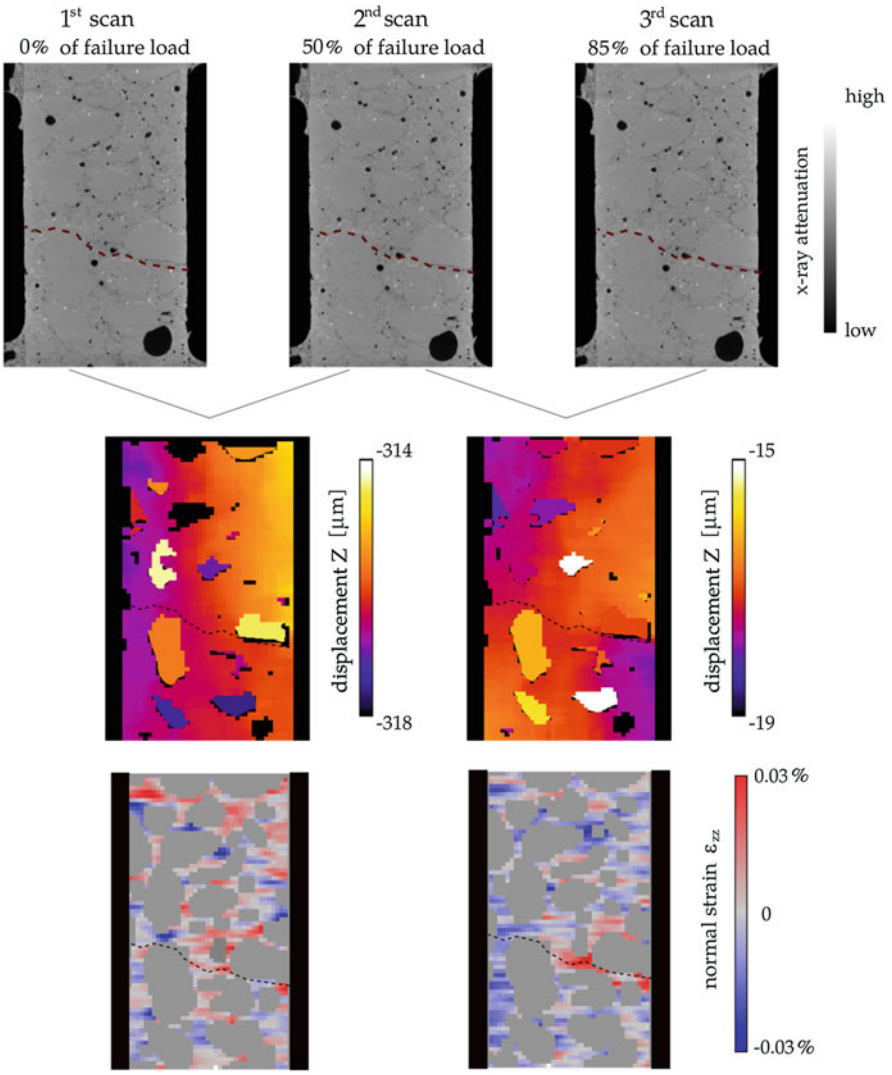

Fig. 17 Central vertical slice of the incremental displacement and incremental strain fields in the axial direction computed with DVC. A combination of a "local" (for matrix and small aggregates) and a "Discrete" (for large aggregates) DVC approach is followed for the calculation of incremental displacements. The strain field derives from the displacement field with the displacements of large aggregates being excluded from the calculation (gray color in the strain field corresponds to the position of the large aggregates). The dashed line represents the macrocrack that appears after failure

Figure 19 illustrates the evolution of the displacement fields in the direction of loading during the computation. At the beginning of the loading, the displacement field is rather homogeneous, while at the end, the discontinuity in the displacement

Table 1 Calibrated parameters of each phase and their interfaces

Phase	E [GPa]	ν	σ_y [MPa]	$\mathcal{G}_f$ $[Jm^{-2}]$
Aggr.	70	0.2	45	0.5
Mortar	14	0.2	9	0.1
Pores	–	–	–	–
Aggr./mortar	–	–	9	0.1

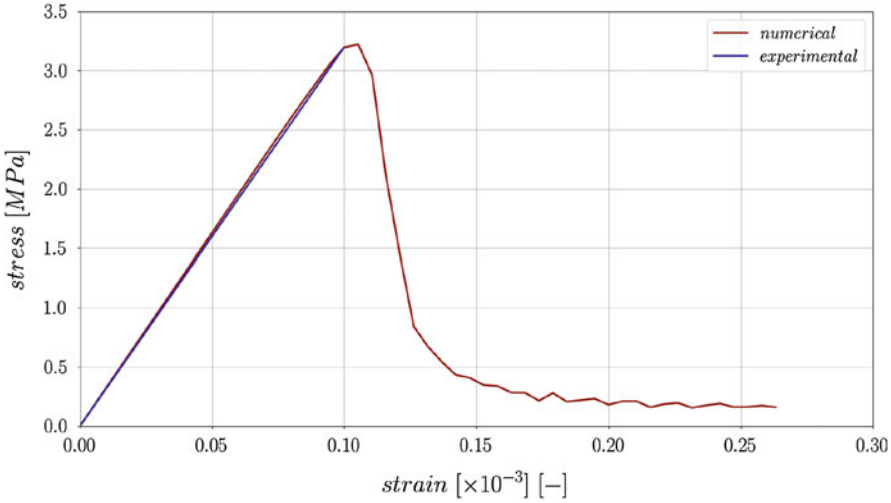

Fig. 18 Comparison of experimental-numerical macroscopic stress-strain curves

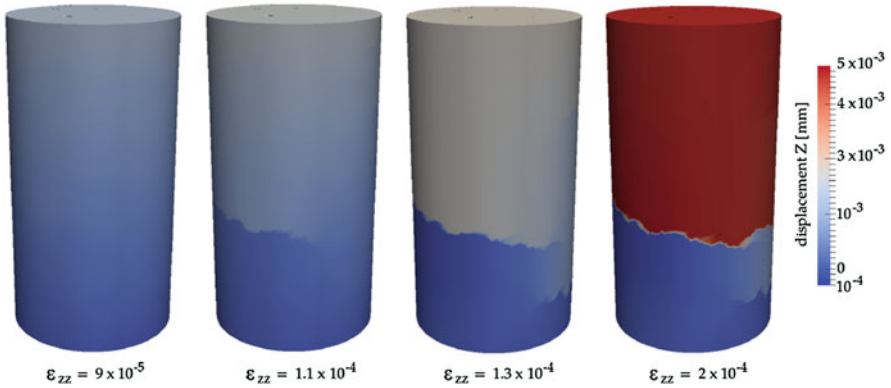

Fig. 19 Evolution of displacement fields in the axial direction during the numerical simulation

field in a roughly horizontal plane (perpendicular to the loading direction) indicates the presence of a single macrocrack. Figure 20 shows the elements for which a strong discontinuity has been activated, which could be associated to a visualization of the crack patterns predicted by the numerical model. Its evolution with the loading gives

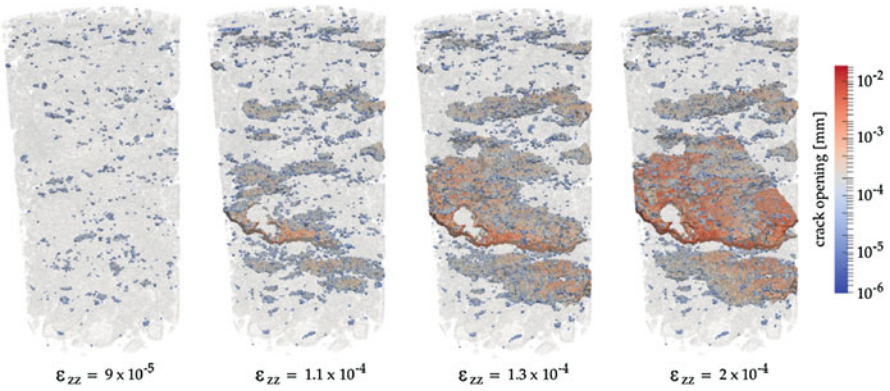

Fig. 20 Evolution of crack patterns during the numerical simulation

an idea about the failure process during the numerical computation. Note that the magnitude of the jump in the displacement field directly corresponds to the crack opening. At the beginning of the loading, due to the difference in elastic moduli between the phases, a stress concentration around the weakest points (around aggregates and macropores) appears, which leads to cracks initiation at these points that will propagate in perpendicular direction (mode I). One element being locally under failure, certainly, does not correspond to any specific macroscopic feature. However, when a large number of them appears, then it can be said that a macroscopic response does emerge. This is exactly what is shown in Fig. 20, where, due to the quasi-brittle behavior of the material, these microcracks quickly bridge into a final critical macrocrack that leads finally to the macroscopic failure of the material.

A qualitative comparison of the crack patterns in the end of the loading obtained experimentally and numerically (see Fig. 21) shows a very good agreement between the two responses. The ability of the numerical meso-model to predict the macrocrack location highlights the influence of the heterogeneities on the failure process of concrete. The shape and location of aggregates and macropores are two of the key parameters that form the geometry of the macrocrack which propagates by bridging the interfacial microcracks. It should be noted here, that at the observed scale, one single critical macrocrack has been extracted from the postpeak 3D image, whereas in the numerical model there are several regions with localized deformation outside the macrocrack. This difference between the experiment and the modeling is due to limitations of both the model and the experiment. The model is not able to simulate cracks closure when the stress level decreases in the sample. This means that all the microcracks that were open during the loading still appear as open at the end of the loading even if the stress level is equal to zero. Concerning the experiment, we have the opposite situation. The intermediate scans were not close enough from the failure to catch these microcracks (and perhaps these microcracks were also too small to be caught) while at failure all these microcracks were probably almost fully closed due to the decrease of the tensile stress in the sample.

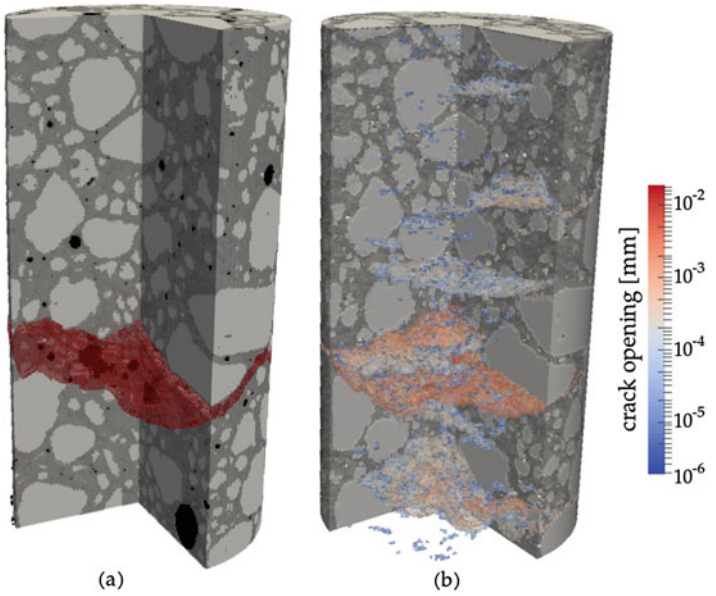

Fig. 21 Comparison between: (**a**): experimental macrocrack (coming from the segmented 3D image of the postpeak x-ray scan) and (**b**): numerical crack patterns (at the end of simulation)

Numerical Prediction

The explicit representation of the meso-scale heterogeneities seems to be the key feature of the presented meso-model that allows a realistic prediction of the material's macroscopic response. For strengthening this assumption and further challenging the numerical model, an x-ray scan of another microconcrete specimen is performed and a new heterogeneous morphology is introduced to the meso-model. This time, the numerical response of the second specimen is computed without any new identification, only based on the material parameters that were calibrated from the first test. Similarly, with the first specimen, an in situ tensile test is conducted.

Figure 22 shows the comparison between the experimental and the numerical macroscopic stress-strain curves for the second microconcrete specimen. A very good agreement both in terms of macroscopic strength and in terms of Young's modulus is observed. A good qualitative comparison of the crack patterns at the end of the loading is also observed again highlighting the impact of the meso-scale heterogeneities on the formation of the cracks.

Conclusions and Perspectives

In this work, a combination of numerical and experimental techniques revealed the impact of the meso-scale heterogeneities on small specimens of concrete on their local failure mechanisms under uniaxial tension. The use of x-ray tomography

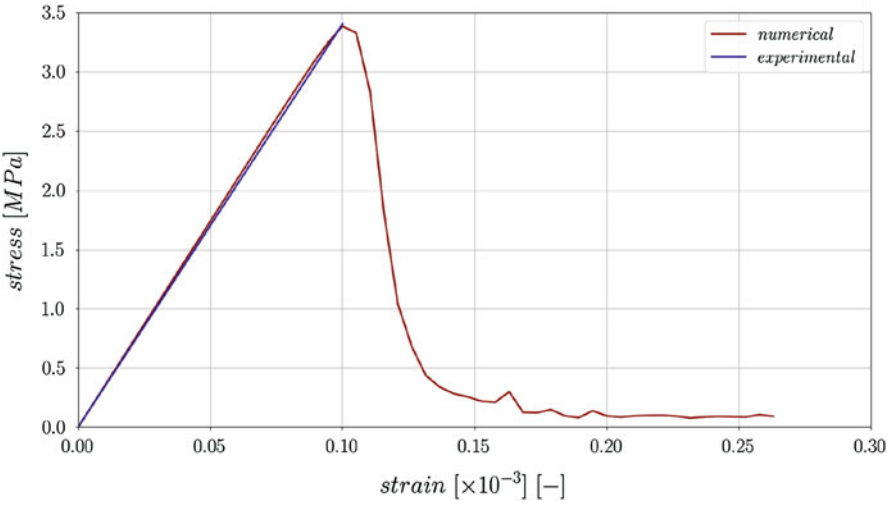

Fig. 22 Comparison of experimental-numerical macroscopic stress-strain curves for the second microconcrete specimen

combined with a mechanical loading system imposed certain size constrains on the examined specimens. Small, cylindrical, microconcrete specimens (11 mm diameter and 23 mm height) compared to the size of the largest heterogeneities (macropores reaching 2 mm and aggregates reaching 3.8 mm) were prepared. These morphologies directly give valuable insight into the impact of the mechanical and morphological properties of each phase (aggregates, macropores, and mortar matrix), along with their respective interfaces, on the macroscopic response of the material.

An x-ray scan of the initial undamaged specimen was conducted to reliably extract the morphology of the meso-structure. It was shown how a 3D gray scale image coming from a concrete x-ray scan can be treated to finally obtain a trinary 3D image, where each phase of concrete's meso-structure is separated.

The principal technical challenge of separating the solid phase into aggregates and mortar matrix was successfully achieved, having as a key the segmentation based on the *variation* of gray values inside each material (homogeneity of the material), instead of the *absolute* gray values (density of the material). From an image analysis point of view, the variance map of the gray scale image needed to be computed, according to a selected structuring element. The size and the shape of the latter can vary according to each case, depending strongly on the noise level and the spatial resolution of the image, setting as a maximum size limit, the minimum aggregate size wanted to be extracted. The distribution of gray levels, in the original gray scale image, individually computed for each phase (after their segmentation), revealed that a segmentation based on a single mean (threshold) value was rather impossible, whereas the implementation of a variance filter was a simple, efficient, and very suitable tool for coarse aggregates segmentation.

The proposed procedure has been successfully validated by extracting and comparing the particle size distributions of the same set of aggregates coming from three

different scans: aggregates embedded into gel, casting a concrete sample using the exact same set of aggregates and scanned first with x-rays and later with neutrons. As a general remark, the proposed procedure has been based on simple reproducible functions, and an open-source release is planned. The reliably obtained representation of concrete's meso-scale morphology can provide a basis for direct physical simulations, as well as data to improve morphological models.

This morphology was then given as an input to a 3D meso-model with enhanced discontinuities, and a uniaxial tensile test was simulated. Meanwhile, a uniaxial tensile test was conducted by progressively loading the specimen until failure while scanning, allowing a direct validation of the numerical response. After identification of the numerical parameters, comparison of experimental and numerical results revealed the capability of the meso-model to reproduce the actual material response (in terms of macroscopic strength, Young's modulus and fracture pattern), with the explicit representation of the meso-scale heterogeneities being its key feature.

While the specimen size was admittedly small compared to its heterogeneities, the measured tensile strength and macroscopic Young's modulus were very close to those of the ordinary concrete from which the microconcrete composition was derived. A similar critical macrocrack to the experimental one was predicted with the numerical model, and it is thus clear that the shape and location of both aggregates and macropores drove its geometry. Meanwhile, with the DVC technique, the relative deformations between consecutive x-ray 3D images were mapped. Zones of localized deformations, corresponding to the macrocrack location, were revealed at only 50% of the maximum failure load. These zones are not identifiable by examining each x-ray 3D image separately, thus justifying the use of x-ray scanning during the tensile test.

The meso-model was further challenged by introducing a new heterogeneous morphology obtained by scanning another microconcrete specimen and computing its numerical response without any new identification. Starting from an x-ray scan of a microconcrete specimen, it was shown that the model was able to predict both the macroscopic response of the specimen and the location of the macrocrack after failure.

The numerical results presented in this chapter, directly compared to corresponding experiments, suggest interesting future potential applications of the meso-model. Through a parametric analysis of different morphologies and material properties, information about the quantitative and qualitative influence of each phase on the global response of the material can be obtained. Moreover, the fact that the proposed approach may accurately model the characteristic features of the quasi-brittle behavior, of concrete under tensile loading, allows the future consideration of other types of loading with more complex failure patterns (compressive or bending loading, for instance).

Acknowledgments This research was financially supported by CEA Gramat. The authors would also like to thank Dr. Alessandro Tengattini for performing the neutron scan on the NeXT instrument on D50 at the Institut Laue-Langevin (ILL) in Grenoble.

Disclosure This manuscript is partly based on the following papers by the authors: Stamati et al. (2018, 2019).

Conflict of Interest The authors declare that they have no conflict of interest.

References

E. Ando, S.A. Hall, G. Viggiani, J. Desrues, P. Besuelle, Experimental micromechanics: Grain-scale observation of sand deformation. Geotech. Lett. **2**(3), 107–112 (2012)

N. Benkemoun, H. Martin, J.-B. Colliat, A. Ibrahimbegovic, Failure of heterogeneous materials: 3D meso-scale FE models with embedded discontinuities. Int. J. Numer. Methods Eng. **82**(13), 1671–1688 (2010)

S.C. De Wolski, J.E. Bolander, E.N. Landis, An in-situ x-ray microtomography study of split cylinder fracture in cement-based materials. Exp. Mech. **54**(7), 1227–1235 (2014)

F. Dupray, Y. Malecot, L. Daudeville, E. Buzaud, A mesoscopic model for the behaviour of concrete under high confinement. Int. J. Numer. Anal. Methods Geomech. **33**(11), 1407–1423 (2009)

N. Efford, *Digital Image Processing: A Practical Introduction Using Java (with CD-ROM)* (Addison-Wesley Longman Publishing Co., Inc., 2000), (352 p.)

L.A. Feldkamp, L.C. Davis, J.W. Kress, Practical cone-beam algorithm. J. Opt. Soc. Am. A **1**(6), 612–619 (1984)

C. Geuzaine, J.-F. Remacle, GMSH: A 3-D finite element mesh generator with built-in pre-and post-processing facilities. Int. J. Numer. Methods Eng. **79**(11), 1309–1331 (2009)

I.M. Gitman, H. Askes, L.J. Sluys, Coupled-volume multi-scale modelling of quasibrittle material. Eur. J. Mech. A Solids **27**(3), 302–327 (2008)

S.A. Hall, M. Bornert, J. Desrues, Y. Pannier, N. Lenoir, G. Viggiani, P. Besuelle, Discrete and continuum experimental study of localised deformation in hostun sand under triaxial compression using x-ray CT and 3D digital image correlation. Geotechnique **60**(5), 315–322 (2010)

F. Hild, S. Roux, Digital image correlation: From displacement measurement to identification of elastic properties-a review. Strain **42**(2), 69–80 (2006)

Y. Huang, Z. Yang, W. Ren, G. Liu, C. Zhang, 3d meso-scale fracture modelling and validation of concrete based on in-situ x-ray computed tomography images using damage plasticity model. Int. J. Solids Struct. **67**, 340–352 (2015)

M. Jirsek, Comparative study on finite elements with embedded discontinuities. Comput. Methods Appl. Mech. Eng. **188**(1), 307–330 (2000)

S.-M. Kim, R.K. Abu Al-Rub, Meso-scale computational modeling of the plastic-damage response of cementitious composites. Cem. Concr. Res. **41**(3), 339–358 (2011)

C. Li, R. Huang, Z. Ding, J.C. Gatenby, D.N. Metaxas, J.C. Gore, A level set method for image segmentation in the presence of intensity inhomogeneities with application to MRI. IEEE Trans. Image Process. **20**(7), 2007–2016 (2011)

G. Lilliu, J.G.M. van Mier, 3d lattice type fracture model for concrete. Eng. Fract. Mech. **70**(7), 927–941 (2003)

B. Lulu, P.A.M. Basheer, A.E. Long, Influence of coarse aggregate on the permeation, durability and the microstructure characteristics of ordinary Portland cement concrete. Constr. Build. Mater. **19**(9), 682–690 (2005)

Y. Malecot, L. Zingg, M. Briffaut, J. Baroth, Influence of free water on concrete triaxial behavior: The effect of porosity. Cem. Concr. Res. **120**, 207–216 (2019)

P.K. Mehta, *Concrete. Structure, Properties and Materials* (Prentice-Hall, Englewood Cliffs, 1986)

N. Moës, M. Cloirec, P. Cartraud, J.-F. Remacle, A computational approach to handle complex microstructure geometries. Comput. Methods Appl. Mech. Eng. **192**(28), 3163–3177 (2003) Multiscale computational mechanics for materials and structures

M. Nitka, J. Tejchman, A three-dimensional meso-scale approach to concrete fracture based on combined dem with x-ray μct images. Cem. Concr. Res. **107**, 11–29 (2018)

J. Oliver, Modelling strong discontinuities in solid mechanics via strain softening constitutive equations. Int. J. Numer. Methods Eng. **39**, 3575–3600 (1996)
J. Oliver, On the discrete constitutive models induced by strong discontinuity kinematics and continuum constitutive equations. Int. J. Solids Struct. **37**(48), 7207–7229 (2000)
P. Perona, J. Malik, Scale-space and edge detection using anisotropic diffusion. IEEE Trans. Pattern Anal. Mach. Intell. **12**(7), 629–639 (1990)
E. Piotrowska, Y. Malecot, Y. Ke, Experimental investigation of the effect of coarse aggregate shape and composition on concrete triaxial behavior. Mech. Mater. **79**, 45–57 (2014)
E. Piotrowska, F. Forquin, Y. Malecot, Experimental study of static and dynamic behavior of concrete under high confinement: Effect of coarse aggregate strength. Mech. Mater. **92**, 164–167 (2016)
C. Poinard, E. Piotrowska, Y. Malecot, L. Daudeville, E.N. Landis, Compression triaxial behavior of concrete: The role of the mesostructure by analysis of X-ray tomographic images. Eur. J. Environ. Civ. Eng. **16**(sup1), s115–s136 (2012a)
C. Poinard, E. Piotrowska, Y. Malecot, L. Daudeville, E.N. Landis, Compression triaxial behavior of concrete: The role of the mesostructure by analysis of x-ray tomographic images. Eur. J. Environ. Civ. Eng. **16**(sup1), s115–s136 (2012b)
W. Ren, Z. Yang, S. Rajneesh, C.H. Zhang, P.J. Withers, Two-dimensional x-ray ct image based meso-scale fracture modelling of concrete. Eng. Fract. Mech. **133**, 24–39 (2015)
E. Roubin, A. Vallade, N. Benkemoun, J.-B. Colliat, Multi-scale failure of heterogeneous materials: A double kinematics enhancement for embedded finite element method. Int. J. Solids Struct. **52**, 180–196 (2015a)
E. Roubin, J.-B. Colliat, N. Benkemoun, Meso-scale modeling of concrete: A morphological description based on excursion sets of random fields. Comput. Mater. Sci. **102**(Supplement C), 183–195 (2015b)
F. Scholkmann, S. Spichtig, T. Muehlemann, M. Wolf, How to detect and reduce movement artifacts in near-infrared imaging using moving standard deviation and spline interpolation. Physiol. Meas. **31**(5), 649 (2010)
S. Shahbeyk, M. Hosseini, M. Yaghoobi, Mesoscale finite element prediction of concrete failure. Comput. Mater. Sci. **50**(7), 1973–1990 (2011)
B. Sonon, B. Francois, T.J. Massart, An advanced approach for the generation of complex cellular material representative volume elements using distance fields and level sets. Comput. Mech. **56**(2), 221–242 (Aug 2015)
O. Stamati, E. Roubin, E. Ando, Y. Malecot, Phase segmentation of concrete x-ray tomographic images at meso-scale: Validation with neutron tomography. Cem. Concr. Compos. **88**, 8–16 (2018)
O. Stamati, E. Roubin, E. Ando, Y. Malecot, Tensile failure of micro-concrete: From mechanical tests to fe meso-model with the help of x-ray tomography. Meccanica **54**(4-5 SI), 707–722 (2019)
J. Suchorzewski, J. Tejchman, M. Nitka, Discrete element method simulations of fracture in concrete under uniaxial compression based on its real internal structure. Inter. J. Damage Mech. **1056789517690915** (2017)
N. Sukumar, D.L. Chopp, N. Moes, T. Belytshko, Modelling holes and inclusions by level sets in the extended finite element method. Comput. Methods Appl. Mech. Eng. **190**(46–47), 6183–6200 (2001)
R.L. Taylor. FEAP-ein finite element analysis program. Ing.-Gemeinschaft Klee & Wrigges, 1987
J. Tejchman et al., Calculations of fracture process zones on meso-scale in notched concrete beams subjected to three-point bending. Eur. J. Mech. A Solids **29**(4), 746–760 (2010)
E. Tudisco, E. Ando, R. Cailletaud, S.A. Hall, Tomowarp2: A local digital volume correlation code. SoftwareX **6**, 267–270 (2017)
G.N. Wells, L.J. Sluys, Three-dimensional embedded discontinuity model for brittle fracture. Int. J. Solids Struct. **38**(5), 897–913 (2001)
E.L. Wilson, The static condensation algorithm. Int. J. Numer. Methods Eng. **8**(1), 198–203 (1974)
P. Wriggers, S.O. Moftah, Mesoscale models for concrete: Homogenisation and damage behaviour. Finite Elem. Anal. Des. **42**(7), 623–636 (2006)

Z. Yang, W. Ren, R. Sharma, S. McDonald, M. Mostafavi, Y. Vertyagina, T.J. Marrow, In-situ x-ray computed tomography characterisation of 3d fracture evolution and image-based numerical homogenisation of concrete. Cem. Concr. Compos. **75**, 74–83 (2017)

Q. Yu, H. Liu, T. Yang, H. Liu, 3d numerical study on fracture process of concrete with different ITZ properties using x-ray computerized tomography. Int. J. Solids Struct. **147**, 204–222 (2018)

T. Zhan, J. Zhang, X. Liang, Y. Chen, Z. Wei, An improved variational level set method for mr image segmentation and bias field correction. Magn. Reson. Imaging **31**(3), 439–447 (2013)

L. Zingg, M. Briffaut, J. Baroth, Y. Malecot, Influence of cement matrix porosity on the triaxial behaviour of concrete. Cem. Concr. Res. **80**, 52–59 (2016)

Damage Model Strategies to Forecast Concrete Structure Behaviors Under Static and Dynamic Loadings

19

Jacky Mazars and Stephane Grange

Contents

Introduction 490
Modelling Aspects 492
Constitutive Equations 492
Damage Evolutions 492
Model Responses 493
1D Version of the Model 494
Strain Rate Effects (Mazars and Grange 2017) 495
2D FE Description for Structural Applications 498
Experimental Program on a Beam Under Cyclic Loading 498
Finite Element Description 499
Simplified Modelling for Structural Applications 501
Cyclic Behavior 503
Results Obtained with These Enhancements 506
Low- and Medium-Velocity Loading on Reinforced Concrete Structures 506
Impact on a RC Beam (Mazars and Grange 2017) 507
2D-1D Coupling for RC Beam-Column Substructure 509
Summary/Conclusions 514
References 515

Abstract

Cementitious matrix damage conditions the behavior of concrete and concrete structures under static and dynamic loading. For this purpose, we present here a strategy to deal with the problem in real structures, which requires a combination of an efficient behavior model, the μ damage model, and a description of the

J. Mazars (✉)
Institute of Engineering Univ. Grenoble-Alpes, CNRS, 3SR, Grenoble, France
e-mail: jacky.mazars@3sr-grenoble.fr

S. Grange
Universite Lyon, INSA-Lyon, GEOMAS, Villeurbanne cedex, France
e-mail: stephane.grange@insa-lyon.fr

© Springer Nature Switzerland AG 2022

G. Z. Voyiadjis (ed.), *Handbook of Damage Mechanics*,
https://doi.org/10.1007/978-3-030-60242-0_77

structures based on a simplified finite element modeling using multifiber beams enhanced to take into account non secondary effects (hysterical effects, strain rate effects, steel–concrete sliding in reinforced concrete). Applications show that such a strategy leads to an efficient tool to simulate the response of slender structures under static and dynamic loadings. It is also shown that the problem of describing assembly nodes between slender elements in space frame structures can be addressed by coupling complete description (2D-3D) for nodes and simplified descriptions (1D) for elements.

Keywords

Concrete · Damage models · Cyclic loading · Dynamic loading · Simplified modelling · Reinforced concrete · Cracking indicators

Introduction

Concrete is considered as brittle in tension and more ductile under compressive loading. As opposed to uniaxial tension, under which just a single crack propagates, compression caused by the presence of heterogeneities (aggregates surrounded by a cement matrix) produces transverse tensile strains that generate mesoscopic cracks nucleating perpendicularly to the direction of extension. These mesoscopic cracks then coalesce until reaching the point of complete rupture. A pure mode I (extension) is thus considered for the purpose of describing behavior in both tension (cracking) and compression (crushing). This situation can be extended to multiaxial loading at low and moderate confinement that allows for extension in at least one direction. When the material is highly confined, hydrostatic pressure serves to compact the porous cement matrix and shear favors mode II (Gabet et al. 2008). Within this framework, it has been shown (Mazars 1986; Mazars et al. 2015) that two distinct damage modes essentially need to be considered: (i) the extension allowed (EA) domain: uni-, bi-, or triaxial situations allowing for extension ($\varepsilon > 0$) in at least one direction and, accordingly, for a local cracking (mode I) and (ii) the no extension allowed (NEA) domain: a triaxial situation at high confinement generating both the collapse of the cement porous matrix, as a result of the spherical part of the stress tensor, and shear cracking (mode II) due to the deviatoric part.

In the framework of continuum media, to simulate concrete behavior, either plasticity (Ottosen 1979), fracture-based approaches (Carpinteri et al. 1997), damage models (Mazars 1986, 2015; La Borderie et al. 1992; Jirásek 2004), or plastic-damage models (Lee and Fenves 1998; Lubliner et al. 1989; Forquin and Hild 2010; Forquin et al. 2015) are used. Depending on the specific case, one or the other approach may be suitable for certain situations (whether classical or not) found in common structures for conventional loads.

But concrete is rarely used alone and reinforced concrete (RC) is the main component of civil engineering structures, and for complete RC structures, structural

analyses generate large complex numerical problems. The discretization technique proves to be a key step in controlling the size of such problems; moreover, damage remains a major component of concrete behavior.

The μ damage model (Mazars et al. 2015), designed on the basis of previous work (Mazars 1986) (Pontiroli et al. 2010), offers a simple and as complete as possible configuration to deal with major phenomena associated with the nonlinear behavior of concrete. It is based on the following set of main assumptions:

- Concrete behavior is considered as the combination of elasticity and damage
- The damage description is assumed to be isotropic and directly affects the stiffness evolution of the material. Indeed, while it is accepted that the damage evolves anisotropically within the concrete, it has been shown that the isotropic description gives relevant results for most loading situations encountered in concrete structures (Fichant et al. 1999). Let $\mathbf{\Lambda}$ be the stiffness matrix of the original material, then the stress tensor $\underline{\underline{\sigma}}$ – strain tensor $\underline{\underline{\varepsilon}}$ relationship for the damaged material is governed by:

$$\underline{\underline{\sigma}} = \underline{\underline{\underline{\underline{\Lambda}}}}(1-d):\underline{\underline{\varepsilon}} \tag{1}$$

- As opposed to classical damage models, d denotes the effective damage. Classically speaking, damage is a variable that describes the micro-cracking state of the material. Moreover, d indicates the effect of damage on the stiffness activated by loading ($d > 0$ if cracks are opened, $d = 0$ if not). Then, in a cracked structure, d must serve to describe the effects of crack opening and crack closure (unilateral effect).
- Two principal damage modes are considered (cracking and crushing) and subsequently associated with two thermodynamic variables Y_t and Y_c, which characterize the extreme loading state reached respectively in the tensile and compressive parts of the strain space.

The relevance of this model has been shown in the context of classical finite element (FE) description (2D or 3D) for either monotonous or cyclic loadings. However, in order to reduce the size of nonlinear problems for engineering purposes on real structures, a simplified FE description is considered, based on the use of multifiber elements for both, beams and columns. In addition, enhancements are introduced to limit the dependence on mesh size during damage evolution as well as to take specific phenomena into account, such as strain rate effects, hysteretic loops, and permanent strains due to friction between crack lips and initial stresses or else steel–concrete debonding. These concepts yield a tool as good as the conventional finite element calculation for accessing results, including at the local level (e.g., strain on rebar, average crack width), yet with better control over convergence problems and significant computational time savings.

However, the multifiber description remains limited to structures for which the areas of degradation are mainly limited within the slender elements themselves.

When it is the connections between elements that are the critical areas, appropriate modeling becomes necessary. It is shown here that a 2D (or 3D) coupling for node description and 1D (Timoshenko multifiber beams) for beam and/or column description is a good solution.

Modelling Aspects

Constitutive Equations

A summary of the μ damage model is proposed below. For a more detailed presentation, see Mazars et al. (2015). Like for a previous model (Mazars 1986), let us consider the *equivalent strain* concept.

Below, we define ε_t and ε_c as the equivalent strain for cracking and crushing, respectively (ν is the Poisson ratio):

$$\varepsilon_t = \frac{I_\varepsilon}{2(1-2\nu)} + \frac{\sqrt{J_\varepsilon}}{2(1+\nu)} \tag{2}$$

$$\varepsilon_c = \frac{I_\varepsilon}{5(1-2\nu)} + \frac{6\sqrt{J_\varepsilon}}{5(1+\nu)} \tag{3}$$

$$I_\varepsilon = \varepsilon_1 + \varepsilon_2 + \varepsilon_3 \quad J_\varepsilon = 0.5\left[(\varepsilon_1-\varepsilon_2)^2 + (\varepsilon_2-\varepsilon_3)^2 + (\varepsilon_3-\varepsilon_1)^2\right] \tag{4}$$

Two independent loading surfaces are now associated:

$$f_t = \varepsilon_t - Y_t \text{ and } f_c = \varepsilon_c - Y_c \tag{5}$$

such that during gradual $Y_{t(c)}$ evolution, the identity $f_{t(c)} = 0$ holds, else $f_{t(c)} < 0$.

Y_t and Y_c define the maximum equivalent strain values reached on the loading path:

$$Y_t = Sup[\varepsilon_{0t}, \max \varepsilon_t] \text{ and } Y_c = Sup[\varepsilon_{0c}, \max \varepsilon_c] \tag{6}$$

ε_{0t} and ε_{0c} are the initial damage threshold values of ε_t and ε_c, respectively.

Damage Evolutions

The effective damage d is directly correlated with the thermodynamic variables Y_t and Y_c through the driving variable Y, i.e.:

$$Y = rY_t + (1-r)Y_c, \text{ with } r = \frac{\sum <\overline{\sigma}_i>_+}{\sum|\overline{\sigma}_i|} \tag{7}$$

r is the triaxiality factor (Lee and Fenves 1998), which evolves within the stress space from 0, for the compressive stress zone, to 1 for the tensile stress zone; $<x>_+$ and $|x|$ denote the positive part and absolute value of x, respectively; $\overline{\underline{\underline{\sigma}}} = \frac{\underline{\underline{\sigma}}}{(1-d)} = \underline{\underline{\underline{\underline{\Lambda}}}} : \underline{\underline{\varepsilon}}$ is the "effective stress."Therefore, r is damage independent and can be determined at each calculation step without iteration. As was the case with the Mazars' model (1986), the damage evolution law is defined by:

$$d = 1 - \frac{(1-A)Y_0}{Y} - A\exp\left(-B(Y - Y_0)\right), \quad \text{where } Y_0 = r\varepsilon_{0t} + (1-r)\varepsilon_{0c} \tag{8}$$

Y_0 is the initial threshold for Y. Variables A and B determine the shape of the effective damage evolution laws and subsequent behavioral laws. $[A, B]$ evolves from $[A_t, B_t]$ for the "cracking" curves to $[A_c, B_c]$ for the "crushing" curves. A_t, B_t, A_c, and B_c are all material parameters directly identified from uniaxial experiments (tensile or flexural tests and uniaxial compression tests).

The proposal for A and B is as follows:

$$\begin{aligned} A &= A_t\left(2r^2(1-2k) - r(1-4k)\right) + A_c\left(2r^2 - 3r + 1\right) \\ B &= r^{\left(r^2-2r+2\right)}B_t + \left(1 - r^{\left(r^2-2r+2\right)}\right)B_c \end{aligned} \tag{9}$$

When $r = 0$ (i.e., compressive stress domain), $A = A_c$ and $B{=}B_c$; conversely, when $r = 1$ (i.e., tensile stress domain), $A = A_t$ and $B{=}B_t$. k is introduced to calibrate the asymptotic stress value at large displacements in shear (useful to describe concrete-rebar friction): $k = A_{r\,=\,0.5}/A_t$; a standard value for k is 0.7 (see Fig. 2).

It is straightforward to demonstrate that when r is a constant (i.e., radial path), compliance with thermodynamic principles (Lemaitre and Chaboche 1990) is ensured. When r is a variable, however, it has been shown that these principles are still being respected, even for complex loading situations.

Model Responses

In the $\sigma_3 = 0$ plane, Fig. 1 displays the plots of both the damage initiation surface ($d = 0$) and the failure surface. The resulting plot corresponds to the maximum stress envelope (normalized by the compressive strength f_c), as obtained from curves at the prescribed σ_1/σ_2 ratios: three specific curves are shown in Fig. 1, uniaxial tension ($\sigma_2 = 0$), unconfined shear ($\sigma_2 = -\sigma_1$), and uniaxial compression ($\sigma_1 = 0$). This figure also plots experimental data used for the failure surface and derived from several biaxial tests along various loading paths on an ordinary concrete specimen (Kupfer and Gerstle 1973). This model offers very good results, with just a few differences observed near the bisector in the bi-compression area.

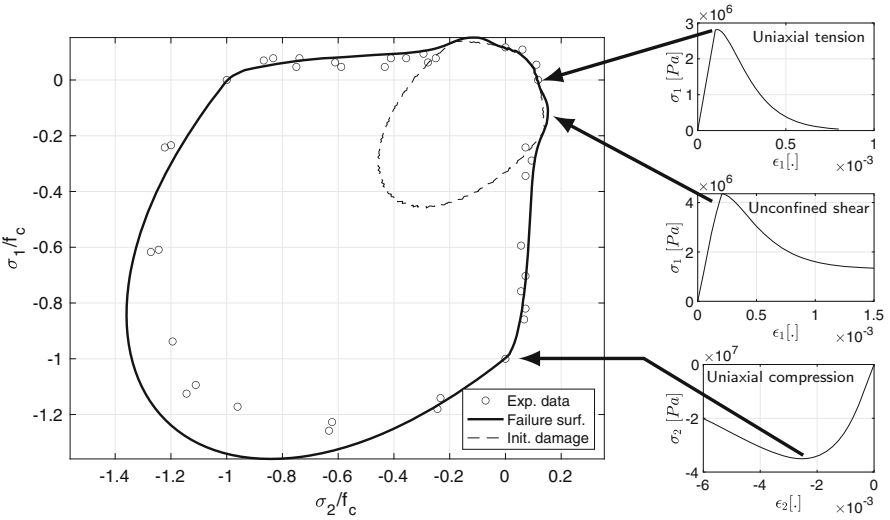

Fig. 1 Plane $\sigma_3 = 0$: plots of both, the damage initiation surface (dashed line) and the failure surface (strength envelop from different loading paths) compared to the experimental results provided by Kupfer and Gerstle (1973)

1D Version of the Model

It was observed in the previous section that the driven variable for d is Y. From Eq. (7) and for a uniaxial situation, it is derived that: $Y{=}Y_t$ for tension ($r = 1$), and $Y{=}Y_c$ for compression ($r = 0$).

From Eqs. (1) and (8) therefore, two expressions are found to describe uniaxial behavior.

- For tension:

$$\sigma = E(1 - d_t)\varepsilon \text{ with } d_t = 1 - \frac{(1 - A_t)Y_0}{Y_t} - A_t \exp\left(-B_t(Y_t - Y_0)\right) \tag{10}$$

where $Y_t = Sup[\varepsilon_{0t}, \max\varepsilon_t]$ and $Y_0 = \varepsilon_{0t} = \sigma_{0t}/E$; for 1D calculations, it can be useful to use σ_{0t} as tension damage threshold.

- For compression:

$$\sigma = E(1 - d_c)\varepsilon \text{ with } d_c = 1 - \frac{(1 - A_c)Y_0}{Y_c} - A_c \exp\left(-B_c(Y_c - Y_0)\right) \tag{11}$$

where $Y_c = Sup[\varepsilon_{0c}, \max\varepsilon_c]$ and $Y_0 = \varepsilon_{oc} = -\sigma_{0c}/E$; for 1D calculations, it can be useful to use σ_{0c} as compression damage threshold.

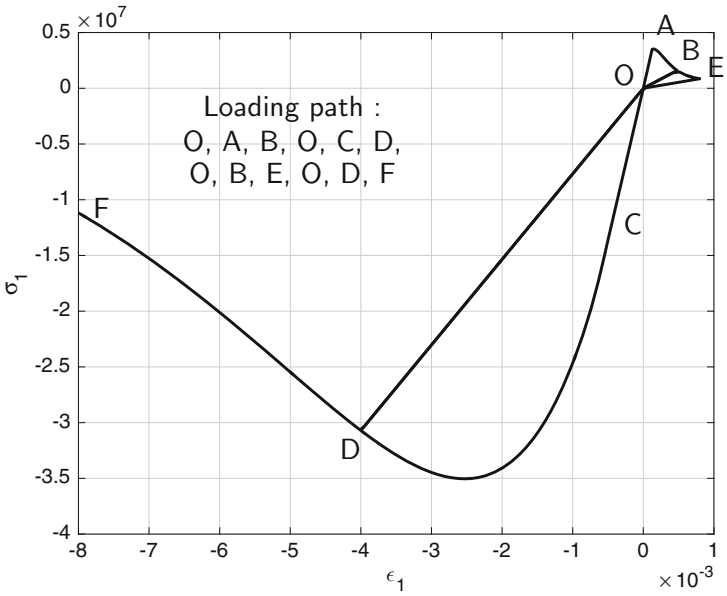

Fig. 2 Tension-compression loading path exhibiting the unilateral effect

Figure 2 shows the corresponding uniaxial response with a specific loading path, from OAB in tension to OCD in compression while highlighting the range of evolution in stiffness due to crack opening and closure (i.e., the unilateral effect).

We will demonstrate in the next section the relevance of this model in describing the behavior of reinforced concrete structural elements. On the basis of the same experiments on cyclic RC beams, two approaches, namely, a 2D classical FE and a multifiber (MF) beam description, will be used and compared. From this comparison, enhancements will be proposed to improve the MF description in including an enhanced version of the 1D model starting below with the introduction of strain rate effects in order to be able to address medium or fast dynamics issues.

Strain Rate Effects (Mazars and Grange 2017)

The dependence of concrete strength on strain rate is well known, particularly under tension whereby inertia effects cannot explain the phenomenon (Fig. 3a).

An experimental campaign has been conducted at the LEM3 Laboratory in Metz – France (Erzar and Forquin 2011, 2014); it has focused on quasi-static tests and dynamic tests performed on both dry and wet concrete specimens. A high-speed hydraulic press was used for the medium strain rates and an experimental Hopkinson bar device, based on the spalling technique, was used for the higher strain rates. From these tests, identification techniques could be developed in order to deduce the tensile strength of the material. For an ordinary concrete, the results are given Fig. 3a.

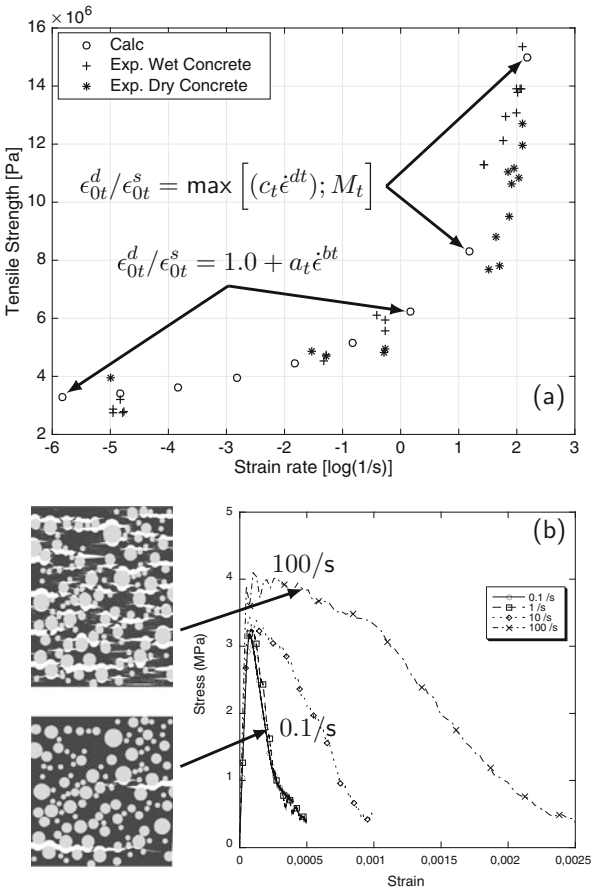

Fig. 3 (**a**) Concrete tensile strength vs. strain rate: experiments (Erzar and Forquin 2011) and retarded damage concept to fit evolutions. (**b**) Mesoscopic model: effect of strain rate on the cracking process and related tensile behavior (Gatuingt et al. 2013)

As presented in Pontiroli et al. (2010), this effect is taken into account using the so-called *retarded damage concept*.

A dynamic threshold (${\varepsilon_{0t}}^d$) is used instead of a static one (${\varepsilon_{0t}}^s$) through an increase factor dependent on the strain rate $\dot{\varepsilon}$ ($=d\varepsilon/dt$):

$$R_t = \varepsilon^d_{0t}/\varepsilon^s_{0t} = \min\left[\max\left(1.0 + a_t\dot{\varepsilon}^{bt}, c_t\dot{\varepsilon}^{dt}\right),\ Mt\right] \tag{12}$$

a_t, b_t, c_t, d_t, and M_t are material coefficients defined by the user, derived from experimental results.

From Eqs. (10) and (12), the dynamic tensile strength, $f_t^d = f(\dot{\varepsilon})$, can be deduced. These results are implemented in the μ model and have been plotted in Fig. 3a, thus confirming that the calculations provide excellent results. It is a simple step to extend such a calculation to 3D situations by introducing ${\varepsilon_{ot}}^d$ into Eqs. (6) and (8), in order to define the initial threshold of the 3D driving variable of damage, Y. The modelling

of strain rate effects is greatly related to the scale of description. From a mesoscopic scale modelling (Gatuingt et al. 2013), Fig. 3b shows that the failure at a macroscopic scale changes from a mono-cracking to a multi-cracking with the strain rate intensity. This leads to a double effect, visible on the overall curves: (i) the increase of the tensile strength and (ii) the increase of the energy consumed to break the element. In a description on a macroscopic scale, as is the case here, the second point must be treated by increasing the fracture energy with the velocity.

On this basis, the proposal for the peak (Eq. 12) is complemented by acting on the evolution of the cracking energy with the introduction, at the peak, of a plateau which increases the area under the curve and, therefore, increases G_f. In the absence of experimental data on the subject, the problem was solved using inverse method from spalling tests (Mazars and Grange 2017).

In this context, we propose as a first approach:

- At low and medium velocities: $\varepsilon_{0t}^{d}/\varepsilon_{0t}^{s} = 1.0 + a_t \dot{\varepsilon}^{bt}$; the evolution beyond the threshold is always given by the classical damage Eq. (9).
- At high velocities: $\varepsilon_{0t}^{d}/\varepsilon_{0t}^{s} = \min\left[\left(c_t \dot{\varepsilon}^{dt}\right),\ Mt\right]$; the evolution beyond the threshold of the $\sigma-\varepsilon$ curve comprises a plateau followed by a linear post peak evolution.

The threshold between the two domains is about $\dot{\varepsilon}$=10/s. Figure 4 shows the resulting results for the various $\sigma-\varepsilon$ uniaxial tension curves.

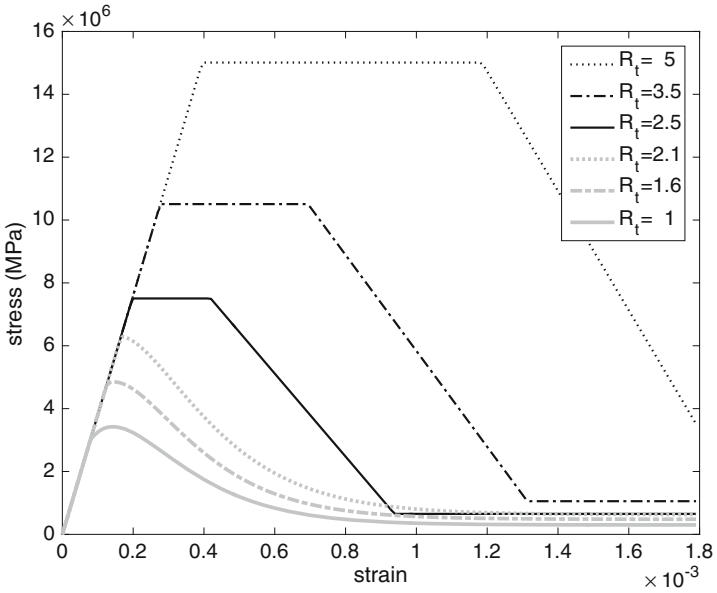

Fig. 4 Tensile behavior for various velocities: $Rt = \varepsilon_{0t}{}^{d}/\varepsilon_{0t}{}^{s}$ is the increase factor for the damage threshold (gray curves: $Rt < 2.5$, low and medium velocities; black curves: $Rt > 2.5$, high velocities)

In compression, the phenomenon is less pronounced. For example, at $\dot{\varepsilon}$#1/s, the increase for the tensile strength is about 100%, while it is only 30% for compression. To represent this evolution, we use the same kind of law as for tension at low and medium velocities: $\varepsilon_{0c}^{d}/\varepsilon_{0c}^{s} = 1.0 + a_c \dot{\varepsilon}^{bc}$.

2D FE Description for Structural Applications

The applications available using the μ model are primarily severe loadings on concrete structures. Among these applications, earthquakes are a key focus since they generate nonlinear cyclic loadings on structural elements. The strain rate is small enough to be neglected as an issue, unlike the case with blasts and shocks which we will then discuss. The LMT Laboratory at ENS Paris-Saclay (France) conducted an experimental campaign on reinforced concrete (RC) beams in order to study the phenomena that play a major role in RC structural responses during an earthquake (Crambuer et al. 2013). The phenomena of damage evolution during increased loading, unilateral effects and energy dissipation due to cyclic loads have all been analyzed. These results will serve for the subsequent applications.

Experimental Program on a Beam Under Cyclic Loading

This entire campaign entailed various longitudinal reinforcement steel ratios, though this chapter only considers the specimens reinforced with four 12 mm rebar (Fig. 5a). The concrete tested was a regular C30/37, whose characteristics and model parameters are listed in Table 1.

The RC beams were designed for testing with a simple three-point bending set-up in a two-way vertical direction. A custom hinge device ensured a free-rotation condition at the end of the support beams. The specimens measured 1.5 m long (between supports), by 0.22 m high, by 0.15 m wide. The loading path was

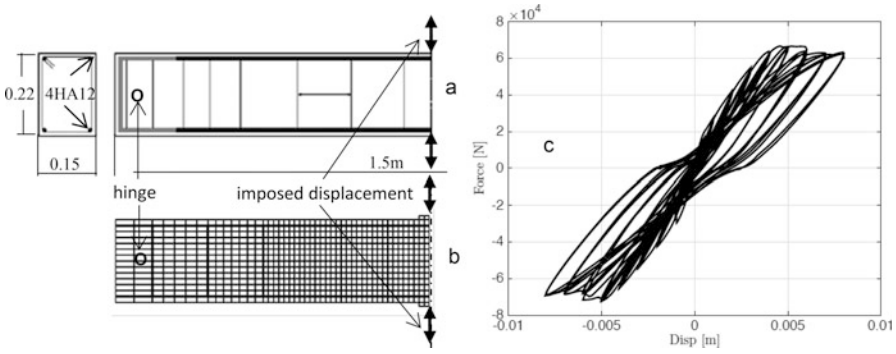

Fig. 5 Three-point bending tests: (**a**) specimen geometry and boundary conditions, (**b**) FE mesh used for calculations, and (**c**) experimental results for the entire loading path

Table 1 RC bending tests: experimental data and material specifications for the FE calculations

Experimental data				Concrete parameters (μ model)								
Steel		Concrete										
E GPa	f_e MPa	E GPa	f_c MPa	E GPa	ν	ε_{0t}	ε_{0c}	A_t	B_t	A_c	B_c	G_f N/m
205	500	28	35	28	0.2	1e-4	3.6e-4	0.8	7000	1.25	395	30

displacement-controlled and included sets of three cycles with gradually increasing intensity (from ±0.5 mm to ±8 mm). Figure 5c shows the force-displacement response of the beam for the full loading path; more specifically, it indicates: (i) a gradual decrease in stiffness due to concrete damage during the first series of cycles and (ii) the appearance of rebar plasticity after the ±4 mm cycles and a continued predominance beyond this stage.

Finite Element Description

The test specimen was modeled *using Q4* (four nodes) elements under a plane stress assumption and bar elements for the rebar. The symmetry of the problem was introduced, and the mesh for the half-beam (711 nodes, 776 elements) was uniform over the central part of the beam; moreover, boundary conditions were defined so as to correctly represent the experimental test (Fig. 5b). The imposed displacement U_y was applied on both the upper and lower parts within the central section of the beam.

To avoid mesh sensitivity, the crack band approach based on the fracture energy concept was introduced into this application (Bazant and Oh 1983). The definition of G_f was derived according to Planas et al. (1992), meaning that in the central part of the beam (i.e., where damage and plasticity are concentrated), element size is consistent with the crack band width h:

$$h = \frac{2G_f}{f_t^2}\left(\frac{1}{E} - \frac{1}{E_t}\right)^{-1} \tag{13}$$

E_t is the post-peak tangent stiffness for an equivalent triangular shape of the $\sigma-\varepsilon$ curve drawn in accordance with the respect of G_f. The model parameter values used were selected in accordance with the data provided in Table 1.

Regarding the rebar, bar elements have been used, in compliance with a simple elasto-perfectly plastic model, whose parameter values are also given Table 1.

Results at the Global Level

A number of situations have been modeled herein. For example, Fig. 6a compares, for the total loading path, the load-displacement calculation curve, performed without any cycle, with the envelope for the entire set of experimental curves. Figure 6b then compares the curve resulting from the simulations with experimental points for the

same loading path up to ±2 mm. These comparisons indicate a very good level of agreement.

From these results, it can be concluded that stiffness recovery, as depicted by the μ model, accurately reproduces the experimental results. Let us also point out, however, that introducing hysteretic loops and permanent strains in the concrete behavior could improve the result.

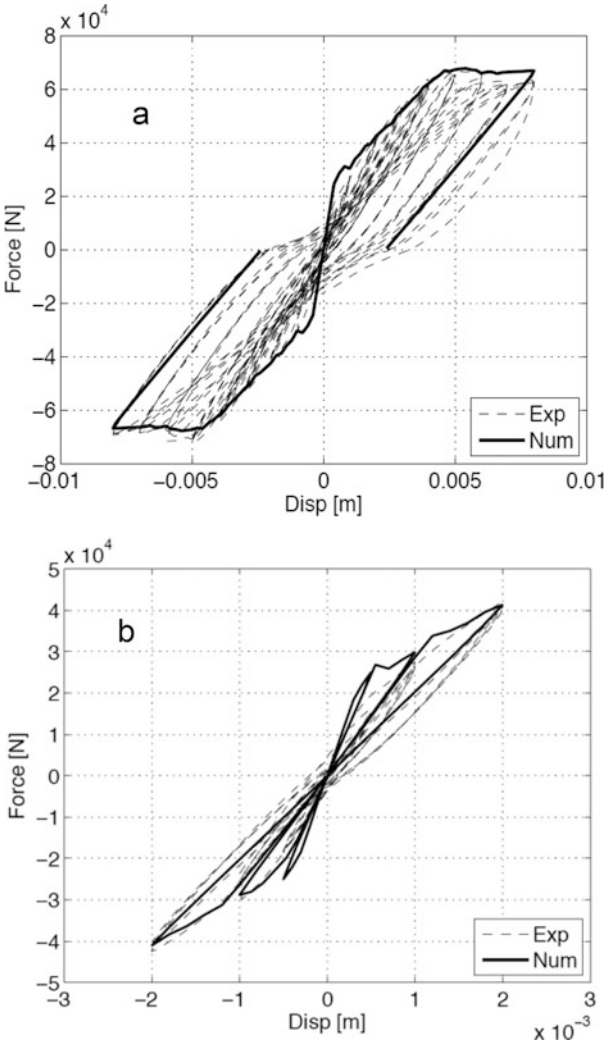

Fig. 6 Bending test on RC beams, experiment-calculation comparisons: (**a**) comparison of the envelope of the total experimental response with a calculation driven without any cycle; and (**b**) comparison for the total path up to ±2 mm

Local Results

Such a modeling approach serves to access the local information that indicates what is taking place inside the damaged areas in both the concrete and rebar. Figure 7 shows, at a given stage of the loading (−3 mm), the damage field on the lateral beam surface predicted by calculation after a series of cycles extending to ±3 mm (the colored marks indicate where $0.9 < d < 1$).

Simplified Modelling for Structural Applications

To decrease the number of degrees of freedom, 3*D* Timoshenko multifiber beam elements have been used to treat the same kind of problem (Kotronis and Mazars 2005).

Based on a 1D model, nonlinear fibers were associated with the μ damage model for concrete as well as with an elastic-perfectly plastic model for rebar. This beam description generates kinematic constraints to ensure respecting both the continuity of displacement between two elements and all plane sections. The concrete section of the multifiber beam is a matrix containing 5 × 7 fibers.

Beams of the same size (the same as in figure 5) are used in the different calculations presented in Table 2, with various boundary conditions (Mazars and Grange 2015).

More generally speaking, a multifiber beam description contains localization if the behavior of the beam element displays softening. Localization is thus present for:

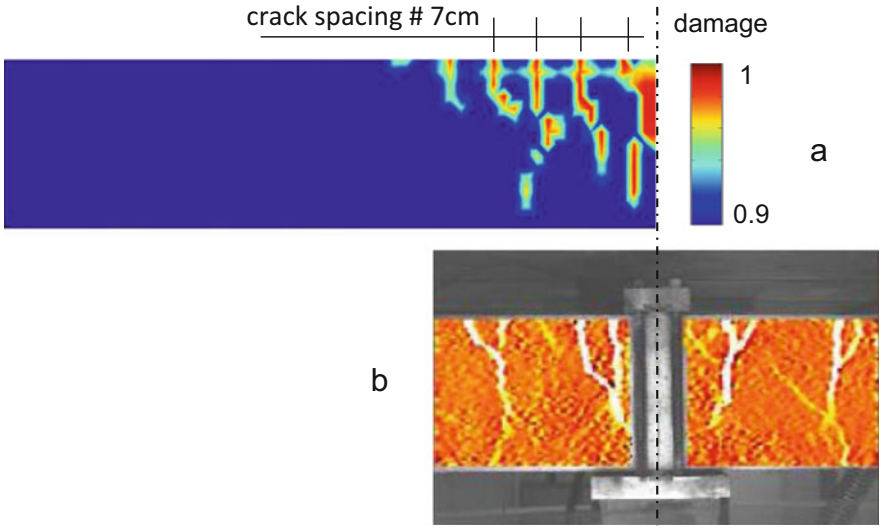

Fig. 7 RC beam, cracks at ±3 mm: (**a**) effective damage used as a crack opening indicator (d > 0.9) after a deflection of −3 mm and (**b**) corresponding cracks observed through digital image correlation

Table 2 Multifiber description: various types of loadings applied on the same RC element and the corresponding damage fields, therefore proving that localization is not always systematic. (Copyright © 2015 Techno-Press, Ltd.)

Type of loading	Overall behavior (load-displacement)	Damage contour (at a given loading)	Type of response
Tensile loading (tie) 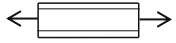	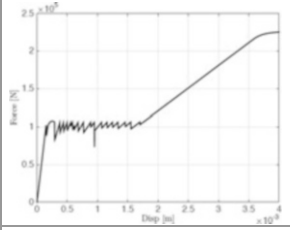	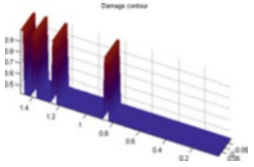	Strain is localized
Four-point bending 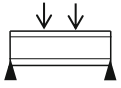	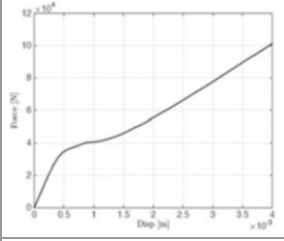	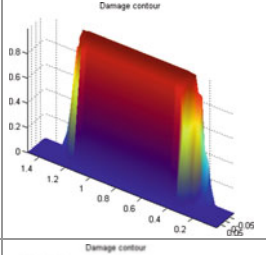	Strain is distributed
Three-point bending 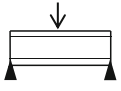	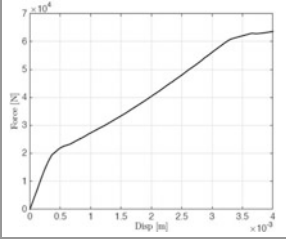	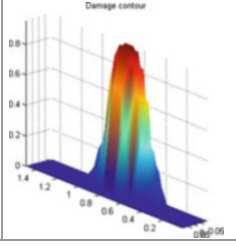	Strain is distributed

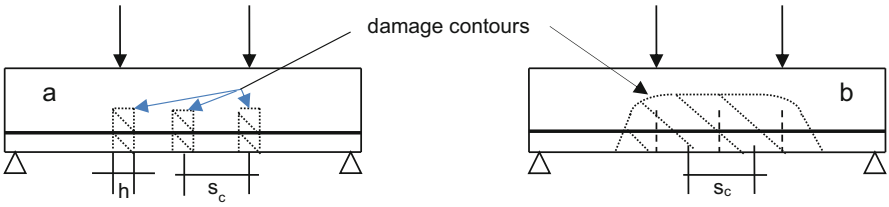

Fig. 8 Localization processes on RC beams: (**a**) 2D finite element description: damage is localized on bands of elements (size h) and (**b**) 1D multifiber beam description: damage is distributed along the cracking zone (s_c is the crack spacing)

- A plain concrete element, regardless of its loading (tension or bending)
- A RC element if the loading is uniaxial and tensile (localization appears once the concrete has failed)
- A RC element in bending when the reinforcement ratio is less than a minimum value, referred to as the fragility ratio (see Eurocode 2 2004)

For other reinforcement ratio values, if bending is dominant (should bending and tension be combined), no localization is present.

Hillerborg et al. (1976) stipulated that the energy dissipated at failure in a unit concrete volume must be equal to the fracture energy. In the presence of localization, the control of result objectivity would then be the same as for classical 2D-3D FE calculations. Localization takes place within a band of elements, and the material parameters must be calibrated with the size h of these elements (Fig. 8a).

In the absence of localization, the damage-cracking processes for one crack are distributed on both sides of the crack over a volume defined by the distance s_c between two cracks (Fig. 8b). Therefore, the concept of crack band cannot be applied here. The calculation must be calibrated so that the fracture energy is consumed in a s_c wide area, leading us to write (see Mazars and Grange 2015, for details):

$$G_f = s_c \int \sigma d\varepsilon \tag{14}$$

$$\text{with :} \quad s_c \int_{MF} \sigma d\varepsilon = h \int_{FE} \sigma d\varepsilon \tag{15}$$

The material parameters must then be calibrated in relation to this distance (s_c). The value used here is $s_c = 7$ cm, and it comes from the results of the finite element simulation (cf. Figure 7).

Cyclic Behavior

In a Timoshenko multifiber beam, the behavior of each fiber is uniaxial. To improve replication of the concrete cyclic behavior, we have upgraded the 1D version of the μ

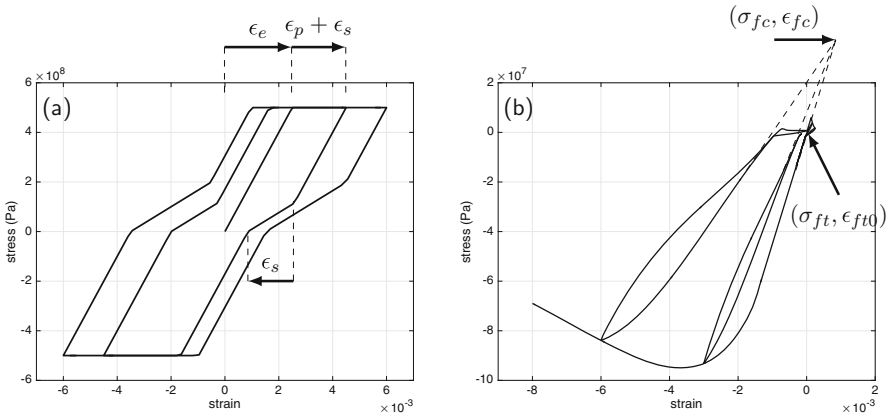

Fig. 9 Enhanced MF beam: (**a**) rebar-concrete bond curve obtained by introducing a sliding stage into the global steel fiber behavior and (**b**) concrete curve with hysteretic loops and permanent strain

model presented before, by introducing a hysteretic loop as well as the permanent strain generated from friction between the crack lips and the release of initial stresses (Fig. 9).

Hysteretic Loop

During unloading or reloading, the hysteretic loop is described using a specific partition of the total strain, i.e.: $\sigma_t = \sigma + \sigma_d$, where $\sigma = E(1-d_i)\varepsilon$ and, as shown in Pontiroli et al. (2010), the damping stress (σ_d) is given by:

$$\sigma_d = (\beta_1 + \beta_2 d_i)E(1-d_i)\varepsilon . f_i(\varepsilon) . sign(\dot{\varepsilon}) \quad (i = t, c) \tag{16}$$

β_2 and β_1 are related to damping with and without damage, respectively. The sign is – for unloading ($\dot{\varepsilon} < 0$) and + for reloading ($\dot{\varepsilon} > 0$); d_i is used to distinguish the damage value in tension (d_t) from that in compression (d_c); moreover, $f_i(\varepsilon)$ is associated with d_i and its driven variable Y_i, and it provides both the shape and size of the loop:

$$f_i(\varepsilon) = 4\frac{\varepsilon^2}{Y_i^2}(\varepsilon - Y_i) \quad (i = t, c) \tag{17}$$

Permanent Strain

This principle consists of considering a shift (ε_{ft}, σ_{ft}) in the $\sigma - \varepsilon$ axis, such that:

$$\left(\sigma - \sigma_{ft}\right) = E(1-d_i)\left(\varepsilon - \varepsilon_{ft}\right) \tag{18}$$

Assuming the same concurrent point (ε_{fc}, σ_{fc}) for elastic unloading in compression, we obtain:

Table 3 Concrete material parameters for enhanced MF calculations

E GPa	σ_{0t} MPa	G_f N/m	A_t	B_t	σ_{0c} MPa	A_c	B_c	ε_{ft0}	ε_{fc}	β_1	β_2
28	2.8	30	1	8000	−10	1.25	395	−0.35e-4	4e-4	0.05	0.20

$$\sigma_{ft} = E(1 - d_c)\left(\varepsilon_{ft} - \varepsilon_{fc}\right) + \sigma_{fc} \tag{19}$$

ε_{ft} depends on the damage value in compression; it equals ε_{ft0} if $d_c = 0$. Assuming a constant value regardless of d_c for the stress at crack-closure ($\sigma_{ft} = E\varepsilon_{ft0}$), from Eq. (19) it can be deduced that:

$$\varepsilon_{ft} = \frac{\varepsilon_{ft0} - \varepsilon_{fc} d_c}{1 - d_c} \tag{20}$$

where ε_{ft0} and ε_{fc} are material parameters.

The resulting $\sigma - \varepsilon$ curve is shown in Fig. 9b, and the corresponding material parameters are listed in Table 3. The curve improvements only modify the unloading and reloading responses. For a monotonic loading in tension or compression, the $\sigma - \varepsilon$ curve remains exactly the same as before. Let us note (Fig. 9b) that permanent strain is created whenever damage evolves in tension but vanishes during unloading. Conversely, the permanent strain created in compression is definitive.

Multifiber Beams and the Steel–Concrete Bond

It is widely acknowledged that debonding between concrete and rebar occurs at large deformations. This phenomenon is especially sensitive whenever cracks open and steel yields. In a fiber beam description, given that no interaction is taking place between the fibers except at their ends and that the damage-fracture processes are distributed, debonding cannot be reproduced. This point leads to overestimating the plastic strain (Mazars and Grange 2015).

As proposed by various authors (Richard et al. 2011), one way to introduce bond degradation and the relative sliding of rebar over concrete in a multifiber beam description is to split the total strain in the steel fiber into two parts: the first part associated with the proper strain of the steel ($\varepsilon_e + \varepsilon_p$) and the second part related to the sliding strain (ε_s) occurring at the steel/concrete interface:

$$\varepsilon = \varepsilon_e + \varepsilon_p + \varepsilon_s \tag{21}$$

ε_e, ε_p, and ε_s are elastic strain ($\varepsilon_e = \sigma/E$), plastic strain, and sliding strain, respectively. Plastic strain depends on the selected elastoplastic model. For a perfectly plastic model, the tensile response is:

$$\sigma = \varepsilon_e E \text{ if } \varepsilon_p = 0, \text{and } \sigma = f_e \text{ if } \varepsilon_p > 0 \tag{22}$$

In Braga et al. (2012), it is proposed that a modified steel bar model to account for bond slips in considering a nonlinear monotonic relationship for sliding. In order to

minimize computational effort, the present proposal is based on the following assumptions:

- Sliding strain evolves from a threshold and, assuming that the main sliding evolution occurs when plasticity is activated, this threshold is assumed to be the plastic threshold.
- A linear link exists between plastic strain and sliding deformation.

From these assumptions, the proposed sliding strain is:

$$\varepsilon_s = \kappa \varepsilon_p \text{ if } \varepsilon_p > 0, \text{and } \varepsilon_s = 0 \text{ otherwise} \tag{23}$$

For a cyclic loading, as the tensile load decreases (unloading), two stages appear: (1) a partial recovery of ε_e and (2) from a given stage to zero stress, ε_s gradually vanishes and both ε_e and ε_s reach 0 when the strain rate sign changes. Then in continuing loading, as the load moves to compression, assuming that no sliding is possible when cracks are closed, $\varepsilon_s = 0$ and (as shown in Fig. 9a) the sliding strain gradually reappears upon reloading in tension up to its previous value and then increases with ε_p.

Results Obtained with These Enhancements

With this new behavior, the material parameters given in Table 3 and the use of the Hillerborg method respecting Eq. (14), the response of the beam presented in Fig. 5 can be calculated.

Presented Fig. 10, the results include comparison experiment-calculation for different loading paths:

- A cyclic path during the cracking stage to up ±2 mm (Fig. 10a)
- A cyclic path of two cycles at ±5 mm for which steel plasticity and rebar-concrete debonding are activated (Fig. 10b)
- The total path up to ±8 mm (Fig. 10c experiment, Fig. 10d calculation)

A very accurate description of the experimental response can indeed be observed.

Low- and Medium-Velocity Loading on Reinforced Concrete Structures

The applications proposed here aims to show that a modelling strategy combining a refined model and a simplified finite element description, as presented in previous sections, can provide satisfactory solutions at low cost for a reinforced concrete structure under severe loading. Two types of applications are thus proposed: firstly, the modelling of the effects of an impact at the center of a reinforced concrete beam,

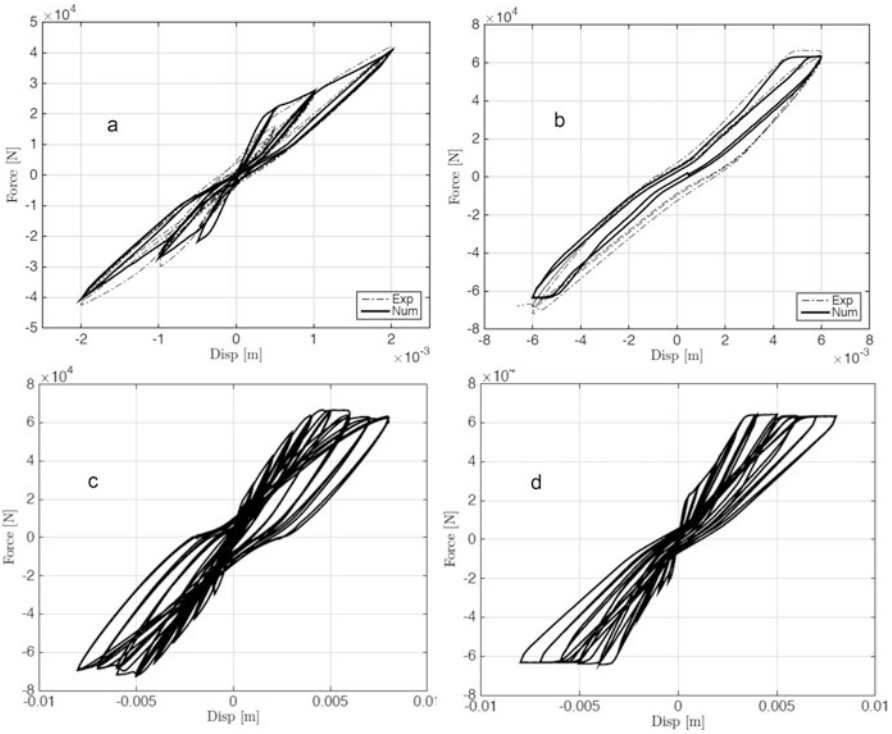

Fig. 10 Enhanced MF beam cyclic response: (**a**) experiment-calculation comparison up to ±2 mm, (**b**) comparison for a set of three cycles at ±6 mm and a total cyclic loading path, (**c**) is experiment, and (**d**) is calculation

and secondly, the simulation of the effects of a loss of load-bearing capacity of a beam by a sudden collapse of a column in a reinforced concrete frame.

Impact on a RC Beam (Mazars and Grange 2017)

An impact experiment on reinforced concrete beams was carried out at FOI laboratory (Sweden). Five beams were tested each with dimensions according to Fig. 11 (Ågårdh et al. 1999). The impact consisted of a heavy drop weight striking each beam at mid-span. The striker, with a mass of 718 kg, was dropped from a height of 2.68 m. Its head struck a steel pad (50x30mm) positioned on the beam with a velocity of about 6.7 m/s. The supports had a spacing of 4 m and were considered rigid.

In order to avoid upward displacements of the beam-ends during impact, restraints were used at the supports as illustrated in Fig. 11. Two accelerometers were positioned on the beam. For the last beam tested, an accelerometer was also positioned on the striker head. In addition, two strain gauges were positioned on the

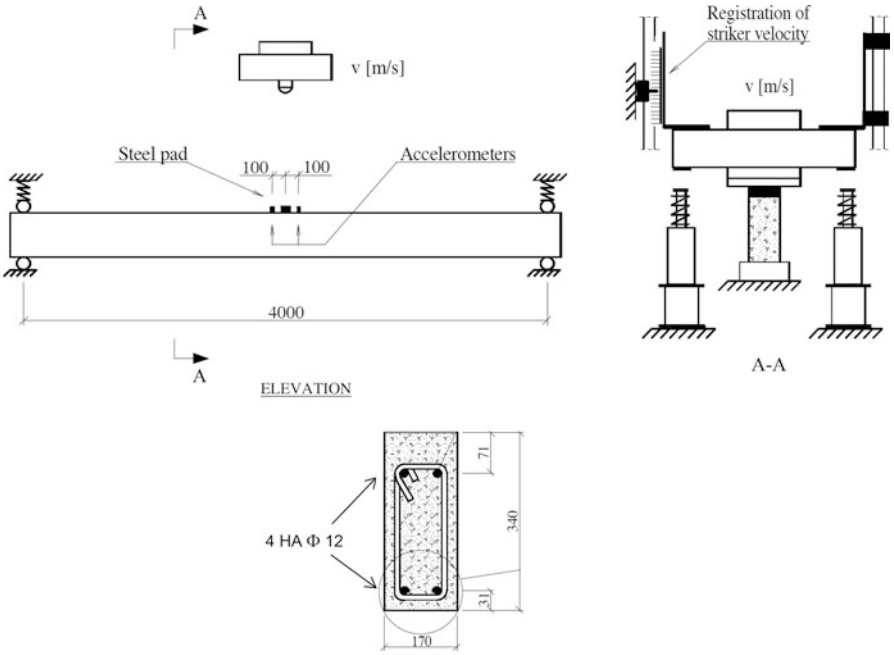

Fig. 11 Experimental set-up for the impact test on a RC beam and detail of the rebar scheme (from Ågårdh et al. 1999)

concrete surface on both sides of the beam at the same level as the middle gauge on the rebar, and four strain gauges were used on the rebar. Furthermore, the striker velocity was registered with a pulse transducer which was also used for the beam velocity in the last of the five experiments. Therefore, it is this last experience that is considered in the following.

The modelling principles used are as follows:

- Concrete mesh includes 30 Timoshenko beam elements in length (4 m between supports); the multifiber section includes 10 fibers high and, the problem being plan, only two fibers thick.
- Reinforcement mesh includes bars reinforcement elements located in the section with respect to the scheme Fig. 11 (stirrups are not considered).
- The μ uniaxial damage model is used for concrete including strain rate effects, and a perfect elastoplastic model is used for steel.
- The Hillerborg method is used (Eq. 15), assuming that the crack spacing s_c is the same whatever is the G_f value which changes with the strain velocity.

Table 4 gives the materials parameters used for this calculation. As indicated below, the beam velocity was measured on the central part of the beam for the last experiment. This signal was used as velocity load in the central part of the beam

Table 4 Experimental data and material parameters used for the RC beam under impact

Experimental data													
Steel		Concrete											
E (GPa)	f_e (MPa)	f_c (MPa)				E (GPa)			σ_{0t} MPa		σ_{0c} MPa		G_f N/m
200	500	95				45			5		−10		60
Concrete material parameters (enhanced μ model)													
A_t	B_t	ε_{ft0}	σ_{0c} (MPa)	A_c	B_c	ε_{fc}	β_1	β_2	a_t	b_t	d_t	c_t	M_t
0.9	2 e+4	−0.33e-4	−10	1.35	300	5e-4	0.05	0.10	1	0.176	1.39	0.255	5

(Fig. 12a), the corresponding acceleration and displacement histories are given in Fig. 12b and c, respectively; they show the good computed response of the beam.

Due to the shock, the beam exhibits a multimodal response which justify the specific damage contour observed (Fig. 12e), including three main strong damage zones:

- In the central portion of the beam, a strong tensile damage area on the lower part (widely extended to the ends)
- A longitudinal compressive damage area on the upper part (at impact location); however, the local crushing due to the impact cannot be simulated by the fibers orthogonal to the direction of the fall. This is the price to pay for using a simplified description by multifiber elements
- At about 1 m from each end of the beam, a tensile damage zone, on the upper part of the beam, more or less connected with the previous one at the end of the test.

These results are consistent with the cracking pattern observed after the test (Fig. 12f). Furthermore, the permanent displacements are correctly reproduced by calculation (Fig. 12g).

In conclusion, we can say that the model reproduces the response of the beam under impact and correctly describes the resulting degradations.

2D-1D Coupling for RC Beam-Column Substructure

The results given in the previous sections shows the interest of a 1D description to address the behavior of slender structural elements. The question that remains to be asked to simulate the behavior of complete structures is the treatment of column girder connection nodes that cannot always be satisfied with a 1D description due to the particularity of the reinforcement layout in these areas and the multiaxiality of local stress fields.

In this situation, the solution is to mix the use of a 1D description for beams and columns and a 2D or 3D description for connections. To this end, we propose here an application on a structure representative of a part of a double span, multistory gantry

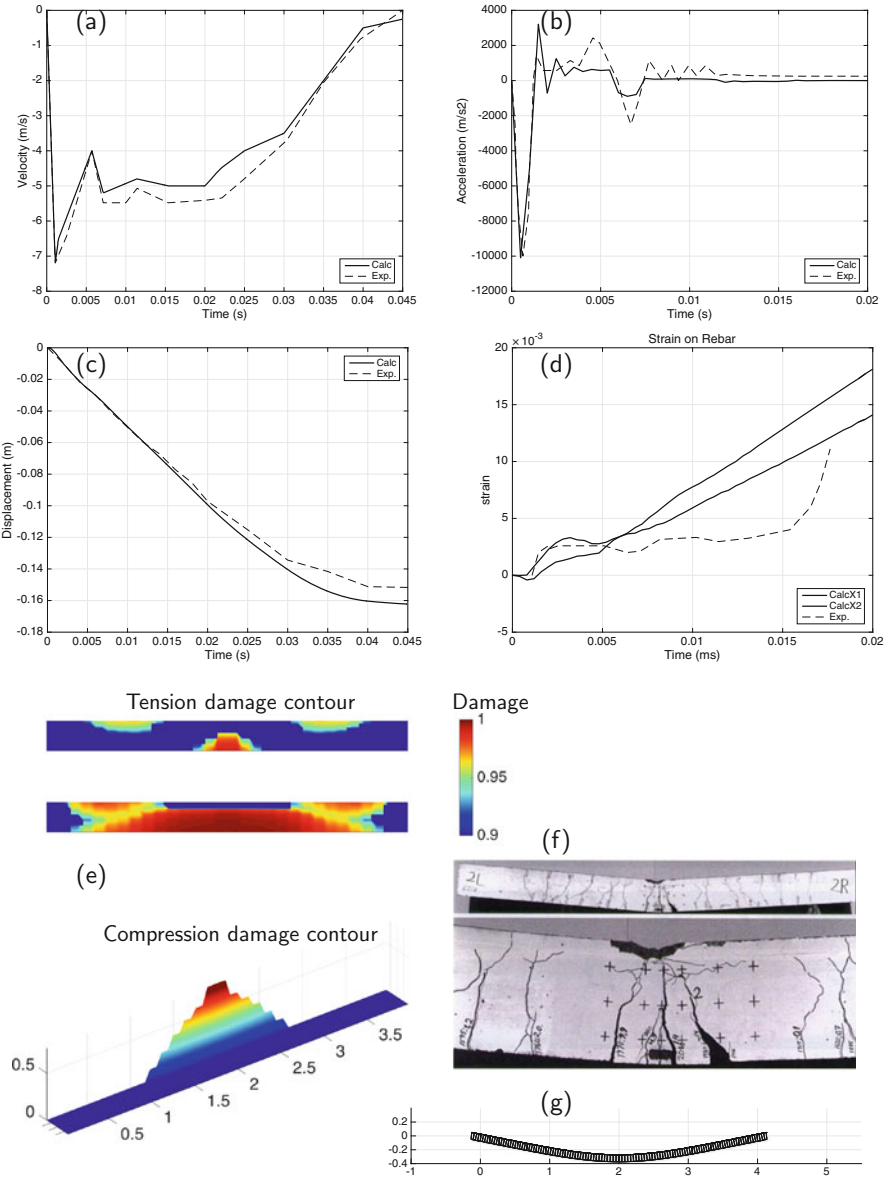

Fig. 12 Impact on a reinforced concrete beam: (**a**) velocity signal used for loading, (**b** and **c**) acceleration response and displacement history of the beam at the impact location, (**d**) strain evolution on rebar close to the location of a strain gage (200 mm from the middle section), (**e**) damage contours at 2 10^{-3} s and at the end of the test (tension) and at the end of the test (compression), (**f**) cracking pattern (from Ågårdh et al. 1999), and (**g**) computed displacement state at the end of the test

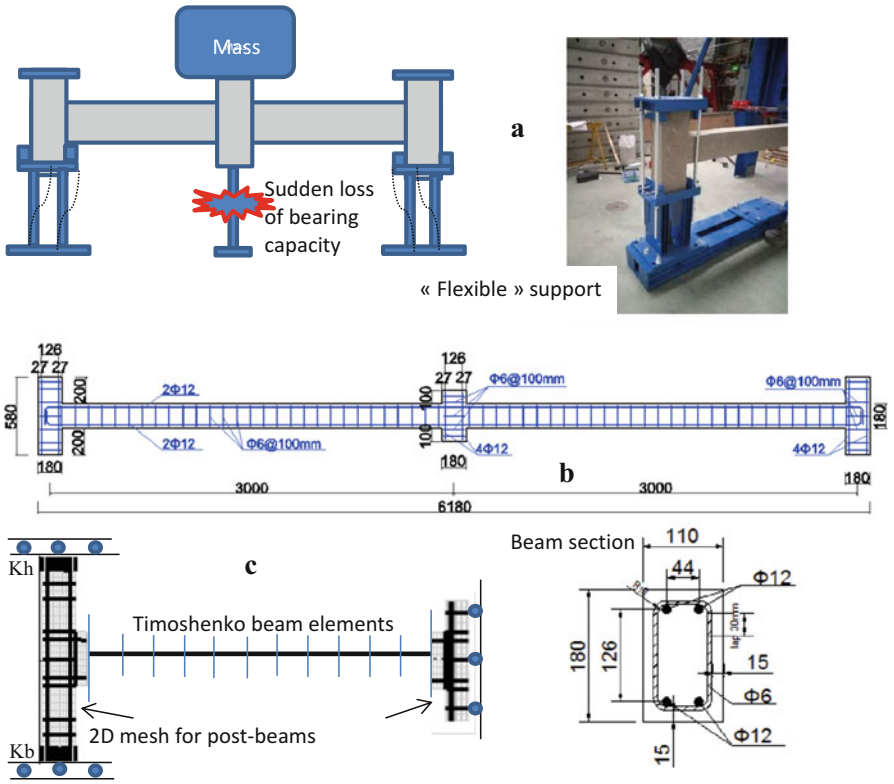

Fig. 13 Loss of bearing capacity test on a 2-span beam; (**a**) detail of the supports and the loading system; (**b**) beam characteristics; and (c) mesh and boundary conditions used (K_h and K_b are the stiffness of semirigid connections)

structure for which, following an accident (impact, explosion), a loss of bearing capacity of the central column appears. The tested element represents a beam of this structure. The primers of the three support posts are integrated, the load is applied at the central post, and the experimental system reproduces the boundary conditions associated with the presence of the edge posts. For this purpose, deformable supports were designed to allow horizontal translation but limiting the rotation of the edge posts (see Fig. 13a). The details of the reinforcement are given in Fig. 13b.

The problem is considered plane and symmetrical. Consequently, the discretization of the left node and the central half node are 2D and the beam is represented as a Timoshenko multifiber element (see Fig. 13c).

Discretization, 2D-1D Coupling

The 2D discretization represents the node itself and a beam primer. The Timoshenko multifiber description induces the fact that the sections of the beam remain plane.

Thus, the coupling with the 2D node must be done on a plane. These kinematic constraints were imposed by an elimination method already proposed by Webb (1990) in the case of static problems and generalized here for dynamic problems. This method consists in finding a projection matrix B of the linked degrees of freedom of the 2D domain in order to condense them on the end node of the Timoshenko beam. If U is the displacement and if M, C, K, are the mass, damping, and stiffness matrix, respectively, then, the equation of motion is written:

$$ {}^{t}BMB\ddot{U} + {}^{t}BCB\dot{U} + {}^{t}BKBU = {}^{t}BF \tag{24} $$

This method is equivalent of the use of Lagrange multiplier but has the advantage to reduce the size of the system, instead of increasing it (see Grange 2017 for details).

Figure 13c gives details of this assembly:

- For the beam, multifiber elements are 10 cm long and the cross section includes 8×2 fibers
- For the nodes, Quad4 elements of 1.5 cm side
- For the reinforcement, bar elements
- To represent the boundary conditions at the end node, a horizontal degree of freedom and flexibility at the interface with the horizontal supports are introduced through two stiffness values, K_b, K_h (Fig. 13c), the values of which (calibrated from preliminary static tests) are given in Table 5.

Test Results

This experimental program involved many beams and loading situations that can be found in (Zhao 2019). As an example, we present here the modeling of one of these tests, which consisted in loading the beam in its center with a mass generating a load lower than the collapse load, thus the sudden release of the central support caused a nonlinear dynamic response of the whole system.

Table 5 gives the different values of the parameters and characteristics used for the calculation presented. It should be noted that the concrete Young modulus has been reduced to take into account initial damage related, in particular, to the formwork and conservation conditions of the structure which generated shrinkage cracking leading to an apparent reduction in stiffness (Chen and Forquin 2019). Also note that the cracking characteristics are not the same for the two types of discretization (FE and MF): the fracture energy G_f to be considered is the same,

Table 5 Material parameters and characteristics used for the 2D-1D coupling

	E GPa	σ_{0t} MPa	G_f/x N/m^2	x m	A_t	B_t	σ_{0c} MPa	A_c	B_c	K_b MN/m	K_h MN/m
FE calc.	16	2.2	400	1.5 e-2	0.9	3000	−18	1	395	400	40
MF calc.	16	2.2	2000	7.5 e-2	0.9	14,500	−18	1	215		

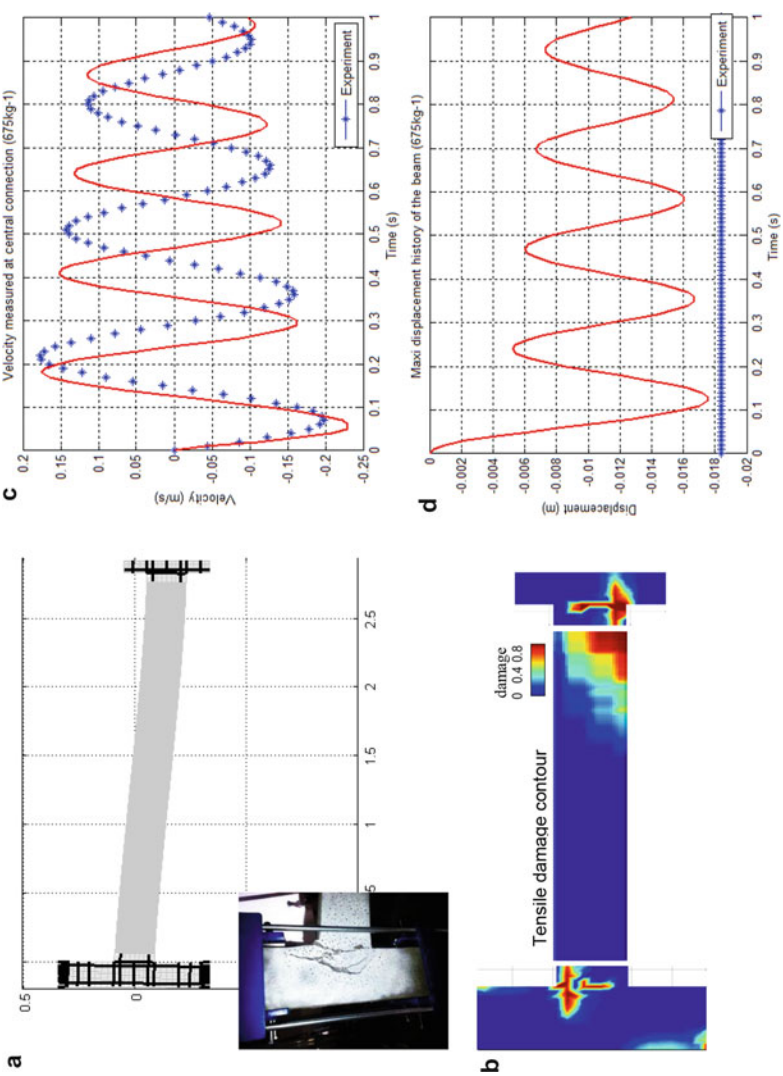

Fig. 14 Loss of bearing capacity test on a 2-span beam; (**a**) deformed mesh after loading with a mass of 675 kg; (**b**) damage contour and crack pattern in the left node; (**c**) time history of the velocity in the central node (red curve is calculation); and (**d**) time history of the displacement of the central node (blue lines gives the maximum value measured during experiment)

but due to localization or not, the size x on which this energy dissipates is different ($x = h$ for the FE calculation and $x = s_c$ for the MF calculation as seen Eq. 15). Moreover, in the absence of dedicated experiments, the parameters related to strain rate effects are identical to those presented in Table 4.

Loading is done in sequence. The following are applied in order: (i) the effects of the dead weight and (ii) the sudden release of the central vertical boundary condition generating an inertial load created by a mass of 675 kg (Fig. 13a).

As this load is lower than the one generating the collapse (>1600 kg), the beam vibrates and it can be seen that the calculation leads to a good reproduction of the time history of the velocities peak and the maximum deformation achieved. The few frequency deviations (#20%) are related to the difficulty to apprehend the real boundary conditions with only the stiffness coefficients K_b and K_h. Additional parameters in rotation could advantageously complete the description.

At the local level, damage is created in the vicinity of the beam node interface generating the opening of a crack and a strong localization of deformations on the longitudinal reinforcement ($\varepsilon > 1.5\ 10^{-3}$) and consequently damage around the corresponding bar. This cracking continues, but in a diffuse manner, on the Timoshenko beam. All these results are consistent with the experimental observations.

Summary/Conclusions

Based on previous work, the μ damage model has been designed to activate the various damage effects correlated with monotonic and cyclic loading, including unilateral effects. Assumptions are formulated to simplify constitutive relationships while still allowing for a correct description of the main nonlinear effects. The chapter presents a simplified FE description based on the use of Timoshenko multifiber beam elements and enhancements are introduced to limit the dependence on mesh size during damage evolution as well as to take specific phenomena into account, such as strain rate effects, steel–concrete debonding, hysteretic loop, and permanent strains due to friction between crack lips and initial stresses.

In a first application, such a strategy based on a simplified but enhanced description shows that it makes possible to forecast the effects of an impact at about 6.7 m/s on the central part of a RC beam.

To account for the damage that can occur in the connections between beams and columns, it is proposed a discretization coupling a complete description (2D-3D) of the node and a simplified description of the elements (1D). The proposed application on the effects of the loss of bearing capacity of a pole in a frame shows the relevance of the approach to reach global and local effects.

In addition, this type of modeling, based on 1D nonlinearity descriptions, leads to a highly stable, low-cost calculation on the ATL4S software platform (Grange 2017), which is a critical issue for engineering purposes.

References

L. Ågårdh, J. Magnusson, H. Hansson, *High Strength Concrete Beams Subjected to Impact Loading. An Experimental Study*, FOA-R-99-01187-311-SE (Defence Research Establish, Stockholm, 1999)

Z.P. Bazant, B.H. Oh, Crack band theory for fracture of concrete. Mater. Struct. **16**(3), 155–177 (1983)

F. Braga, R. Gigliotti, M. Laterza, M. D'Amato, S. Kunnath, Modified steel bar model incorporating bondslip for seismic assessment of concrete structures. J. Struct. Eng. **138**(11), 1342–1350 (2012)

A. Carpinteri, B. Chiaia, K.M. Nemati, Complex fracture energy dissipation in concrete under different loading conditions. Mech. Mater. **26**, 93–108 (1997)

W. Chen, P. Forquin, Experimental and numerical study of the damage process in RC beam-column sub-assemblages during a progressive collapse scenario. Int. J. Numer. Anal Methods Geomech **43**(9), 1704–1723 (2019)

R.B. Crambuer, B. Richard, F. Ile, F. Ragueneau, Experimental characterization and modeling of energy dissipation in reinforced concrete beams subjected to cyclic loading. Eng. Struct. **56**, 919–934 (2013)

EN1992-2, Eurocode 2, Design of concrete structures (2004)

B. Erzar, P. Forquin, Experiments and mesoscopic modelling of dynamic testing of concrete. Mech. Mater. **43**, 505–527 (2011)

B. Erzar, P. Forquin, Analysis and modelling of the cohesion strength of concrete at high strain-rates. Int. J. Solids Struct. **51**(14), 2559–2574 (2014)

S. Fichant, C. La Borderie, G. Pijaudier-Cabot, Isotropic and anisotropic descriptions of damage in concrete structures. Mech Cohesive-Frictional Mater **4**(4), 339–359 (1999)

P. Forquin, F. Hild, A probabilistic damage model of the dynamic fragmentation process in Brittle materials. Adv. Appl. Mech. **44**, 1–72 (2010)

P. Forquin, L. Sallier, C. Pontiroli, A numerical study on the influence of free water content on the ballistic performances of plain concrete targets. Mech. Mater. **89**, 176–189 (2015)

T. Gabet, Y. Malecot, L. Daudeville, Triaxial behaviour of concrete under high stresses: Influence of the loading path on compaction and limit states. Cem. Concr. Res. **38**, 403–412 (2008)

F. Gatuingt, L. Snozzi, J.F. Molinari, Numerical determination of the tensile response and the dissipated fracture energy of concrete: role of the mesostructure and influence of the loading rate. Int. J. Numer. Anal. Methods Geomech. **37**, 3112–3130 (2013)

S. Grange, *ATL4S – A Tool and Language for Simplified Structural Solution Strategy – Internal Report* (Geomas Lab., INSA Lyon – France, 2017)

A. Hillerborg, M. Modeer, P.E. Peterssonn, Analysis of crack formation and growth in concrete by means of fracture mechanics and finite elements. Cem. Concr. Res. **6**, 773–782 (1976)

M. Jirásek, Non-local damage mechanics with application to concrete. French J. Civ. Eng. **8**, 683–707 (2004)

P. Kotronis, J. Mazars, Simplified modelling strategies to simulate the dynamic behavior of R/C walls. J. Earthq. Eng. **9**(2), 285–306 (2005)

H.B. Kupfer, K.H. Gerstle, Behavior of concrete under biaxial stresses. J .Eng. Mech. Div. **99**(4), 853–866 (1973)

C. La Borderie, J. Mazars, G. Pijaudier-Cabot, Response of plain and reinforced concrete structures under cyclic loadings, A.C.I special publication, SP-134, ed. by W. Gerstle, Z.P. Bazant (1992), pp. 147–172

J. Lee, G.L. Fenves, Plastic-damage model for cyclic loading of concrete structures. J. Eng. Mech. **124**, 892 (1998)

J. Lemaitre, J.L. Chaboche, *Mechanics of Solid Materials* (Cambridge University Press, Cambridge (UK), 1990)

J. Lubliner, J. Oliver, S. Oller, E. Onate, A plastic-damage model for concrete. Int. J. Solids Struct. **25**(3), 299–326 (1989)

J. Mazars, A description of micro and macroscale damage of concrete structure. Eng. Fract. Mech. **25**, 729–737 (1986)
J. Mazars, S. Grange, Simplified modeling of reinforced concrete structures for engineering issues. Comput. Concr. **16**(5), 683–701 (2015)
J. Mazars, S. Grange, Simplified strategies based on damage mechanics for concrete under dynamic loading. Phil. Trans. R. Soc. A **375**, 20160170 (2017). https://doi.org/10.1098/rsta.2016.0170
J. Mazars, F. Hamon, S. Grange, A new 3D damage model for concrete under monotonic, cyclic and dynamic loading. Mater. Struct. **48**, 3779–3793 (2015)
N.S. Ottosen, Constitutive model for short time loading of concrete. J. Eng. Mech. **105**, 127–141 (1979)
J. Planas, M. Elices, G.V. Guinea, Measurement of the fracture energy using three-point bend tests: Part 2, influence of bulk energy dissipation. Mater. Struct. **25**, 305–316 (1992)
C. Pontiroli, A. Rouquand, J. Mazars, Predicting concrete behaviour from quasi-static loading to hypervelocity impact. Eur. J. Environ. Civ. Eng. **14**(6–7), 703–727 (2010)
B. Richard, F. Ragueneau, A. Lucas, C. Crémona, A multifiber approach for modelling corroded reinforced concrete structures. Eur. J. Appl. Mech. A/Solids **30**, 950–961 (2011)
J.P. Webb, Imposing linear constraints in finite-element analysis. Commun. Appl. Numer. Methods **6**(6), 471–475 (1990). https://doi.org/10.1002/cnm.1630060607
G. Zhao, Experimental and numerical investigation of the progressive collapse resistance of reinforced concrete beam-column sub-assemblages (Ph.D. report, Grenoble-Alpes University, 2019)

Discrete Element Approach to Model Advanced Damage in Concrete Structures Under Impact

20

Laurent Daudeville, Andria Antoniou, Philippe Marin, Pascal Forquin, and Serguei Potapov

Contents

Introduction 518
Discrete Element Model 521
Definition of Interactions 521
Linar Elastic Constitutive Behavior 522
Moment Transfer Law 523
Failure Criterion 524
Nonlinear Elastic with Damage Tensile Constitutive Behavior 524
Constitutive Behavior in Compression – Compaction 525
Strain Rate Dependency 525
Identification of Constitutive Parameters of the Discrete Element Model for Concrete 528
Discrete Element Modeling of Samples 528
Identification of Constitutive Parameters by Means of Simulations of Quasi-Static Tests 529
Identification of Constitutive Parameters by Means of Simulations of Spalling Tests Using a Hopkinson Bar 531
Validation of the Model by the Simulation of Hard Impact Tests 533
Edge-On Impact Tests 533
Perforation and Penetration Tests Performed by the CEA-Gramat (CEG) 535
Simulation of a Drop-Weight Impact on a Reinforced Concrete (RC) Beam 541
Conclusions 545
References 548

L. Daudeville (✉) · A. Antoniou · P. Marin
Université Grenoble Alpes, CNRS, Grenoble, France
e-mail: laurent.daudeville@univ-grenoble-alpes.fr

P. Forquin
Laboratoire 3SR, Université Grenoble Alpes, Grenople INP, CNRS, Grenoble, France

S. Potapov
IMSIA UMR 9219, EDF-CNRS-CEA-ENSTA, Palaiseau, France

© Springer Nature Switzerland AG 2022

G. Z. Voyiadjis (ed.), *Handbook of Damage Mechanics*,
https://doi.org/10.1007/978-3-030-60242-0_78

Abstract

Concrete structures are used as shielding barriers to protect sensitive infrastructures under severe loadings such as impacts. When subjected to extreme loading conditions, concrete material undergoes complex dissipative phenomena characterized by intense fragmentation, irreversible compaction, and high rate of loading. The discrete element method (DEM) allows easily handling the occurrence of discontinuities and dealing with large deformation; it was implemented in Europlexus, a finite element software dedicated to the analysis of fast transient phenomena. This chapter presents the constitutive discrete element (DE) models developed for concrete with a focus on compaction under high confinement and on strain rate dependency of tensile strength and fracture energy. DE does not represent aggregates, the proposed interaction laws between DE are inspired by observations at the macroscopic scale. The identification of constitutive parameters uses results of laboratory tests under quasi-static tension and compression, confined compression. Parameters characterizing the strain rate dependency are identified with results of spalling tests performed with an Hopkinson bar apparatus. This chapter first presents the constitutive model and its calibration. In the second part, the whole DEM approach is validated thanks to simulations of hard impact tests performed on concrete structures.

Keywords

Discrete element model · Concrete · Compaction · Strain-rate effect · Hard impact test · Edge-on-impact test · Perforation

Introduction

Natural or man-made hazards such as rock falls or missile impacts against protective concrete structures may lead to advanced damage (cracking, perforation, compaction. . .) and thus require the development of valid design methods able to describe these phenomena.

Present design methods of concrete protection walls of nuclear power plants are mainly based on full-scale experiments and empirical formulae, such as the Riera method (Riera 1968) for soft impacts and, for hard impacts, the Petry formula for the prediction of the penetration depth (Kennedy 1976) or the perforation limit formula (Berriaud et al. 1978). Experiments on structures are very expensive and empirical formulae are only valid within the range of parameters for which they were validated. The demand for realistic vulnerability predictions of concrete protection structures leads to the development of advanced numerical tools. However, the relevance of numerical predictions is significantly dependent on the accuracy of the constitutive model employed to describe the behavior of the material.

Bischoff and Perry (1991) evaluated the strain rate involved in concrete when subjected to various loading conditions (Fig. 1); it may reach hundreds of s^{-1} in case of hard impact.

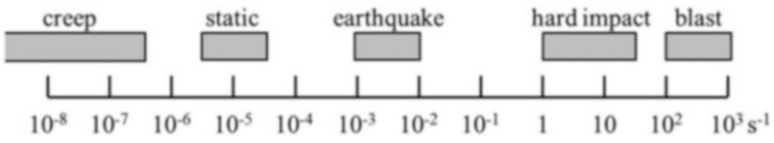

Fig. 1 Magnitude of strain rates expected for different loading cases from Bischoff and Perry (1991)

When a concrete structure is subjected to an impact, the material in the vicinity of the impact zone undergoes high levels of stress leading to irreversible compaction, whereas farther from this location, compression with a moderate triaxial stress level occurs (Daudeville and Malecot 2011; Gran and Frew 1979; Shiu et al. 2008a). In addition, a tensile stress state may occur close to free boundaries leading to scabbing and spalling.

Under tensile loading, concrete exhibits a constitutive behavior that strongly depends on the strain rate (Malvar and Ross 1998); concrete strength and fracture energy increase with the increase of strain rate. Under unconfined compression, the observed strain rate effect is much lower. Cusatis (2011) has shown that for unconfined compression tests and for strain rates higher than 10^{-1} s^{-1}, the inertia forces cannot be neglected and provide a significant contribution to the strength enhancement recorded during experiment.

Piotrowska et al. (2016) have compared the dynamic and the quasi-static behaviors of concrete under confined compression; the dynamic strength of concrete is slightly greater than the quasi-static strength. Thus, in a first approximation, the dynamic and the quasi-static behaviors of concrete under confined and unconfined compression are considered as identical. From these experimental results and their analysis, the authors consider that the prediction of the response of concrete structures under impact requires, in addition to the usual compressive strength at 28 days, the correct knowledge of both the behavior of concrete under tensile loading on a large range of strain rates and the behavior of concrete under confined compression in quasi-static conditions.

Many authors (Schmidt et al. 2009; Sfer et al. 2002; Warren et al. 2004) observed higher concrete resistance and transition from brittle to ductile behavior with high triaxial stresses.

A research program has been conducted in 3SR laboratory of Univ. Grenoble Alpes aiming at characterizing concrete triaxial behavior under high confinement pressure in quasi-static conditions. Several studies have been performed on samples issued from the same reference concrete called R30A7 where its compressive strength is equal to 30 MPa at 28-days (Vu et al. 2009a). The maximum aggregate size (8 mm) has been chosen with respect to specimen diameter (70 mm). The experimental campaign has deeply investigated the influence of the water/cement ratio (Vu et al. 2009b), the saturation degree (Vu et al. 2009c), and the effect of coarse aggregate shape (Vu et al. 2011) on the concrete behavior under high confinement.

The Finite element method (FEM) is widely spread for nonlinear analysis of structures but it can hardly describe cracking or fragmentation phenomena that commonly occur in impact problems without using erosion techniques that are not

based on physical criteria. Gingold and Monaghan (1977) and Lucy (1977) developed a mesh-free method suitable in problems with very large deformations; the smoothed-particle hydrodynamics (SPH) method. SPH has the advantage of solving continuum mechanics equation adjusting easily to the appearance of discontinuities without mesh adaption. Nevertheless, it requires high computational cost to obtain accurate results and it can hardly deal with contact problems between solids.

DEM is suitable to simulate advanced damage states due to its discontinuous nature. DEM is a powerful alternative to FEM because it allows naturally obtaining realistic macro-cracks. This method was established by Cundall and Strack (1979) to model granular media. A drawback of initial DEM was its difficulty to model the cohesive behavior of solids. Afterward, DEM was improved with cohesive bond models, which made possible to simulate cohesive materials such as concrete. Hentz et al. (2004) used a spring-like model with cohesive interactions for two particles that are not necessarily in contact. This cohesive interaction is created by assuming an interaction range around each particle and it is treated with micro–macro constitutive laws.

Cusatis et al. (2003) presented a hybrid lattice-particle method where a 3D lattice connects the centroids of aggregates particles. The particle distribution of their model is determined by the mix design of concrete. An influence zone of particles is also defined by the authors for each particle; the forces are transmitted through the lattice struts. In conclusion, the two methods are very similar; Cusatis et al. (2003) approach has the advantage to describe precisely the microstructure of a concrete specimen. However, it is quite time consuming since the assembly requires a large number of particles. Hentz et al. (2004) method aims at developing constitutive laws at the macroscopic scale for structural engineering applications, so the particles of the assembly do not represent the mesoscale constituents of concrete mixture. As a result, one has the possibility to create a packing with a reasonable amount of spheres and lower computational cost, the authors identify the model parameters thanks to simulations of quasi-static laboratory tests.

In this chapter, the previously DEM model for concrete proposed by Hentz et al. (2004) is extended to deal with impact loading leading to high mean stress and high strain rate into concrete material. Many authors such as Frangin et al. (2006), Shiu et al. (2008b), Rousseau et al. (2008, 2009), and Potapov et al. (2016) contributed to improvements of the model that can now be considered as completed. A compaction constitutive law is presented; it was implemented to properly describe porosity closure under high confinement. Strain rate sensitivity of concrete tensile strength and fracture energy are identified. The local constitutive law for the strain rate dependency of concrete strength derives from the formula proposed by the Euro-international committee (CEB 1988), it is bilinear. The first regime follows the modified CEB formula by Malvar and Crawford (1998) while the second one is identified thanks to dynamic spalling experiments performed in the 3SR laboratory (Antoniou 2018).

The fundamentals of the DEM model are given briefly in section "Discrete Element Model." Section "Identification of Constitutive Parameters of the Discrete Element Model for Concrete" presents the calibration of the DEM parameters thanks

to results of tests performed on plain ordinary concrete R30A7 (quasi-static tension tests, unconfined and confined compression tests, and dynamic spalling tests). The numerical results are compared with the experimental data and are discussed. Section "Validation of the Model by the Simulation of Hard Impact Tests" presents the validation of the model with simulation of hard impact experiments performed on concrete structures. All the developments were made in Europlexus, a finite element (FE) software for the simulation of fast dynamics phenomena co-ownership of CEA and European Commission (Joint Research Center).

Discrete Element Model

The DEM used for this study is a macroscopic approach based on the initial developments of Cundall and Strack (1979) to model granular materials with the use of rigid elements. Donze et al. (1999) and Hentz et al. (2004) have extended the original method to cohesive materials such as concrete, by adding cohesive interactions. Concrete is represented by a polydisperse assembly of rigid and spherical elements with different sizes and masses. The specimen's packing is obtained using a geometric algorithm described in Jerier et al. (2009); it is based on a tetrahedral FE mesh originated from the technique developed by Cui and O'Sullivan (2003). This algorithm is implemented in SpherePadder++ free software, which is introduced in the open-source SALOME platform.

It is noteworthy to mention that the DE do not represent concrete mesoscale constituents (aggregates, cement paste, voids, etc.). The current model is of higher scale and seeks to reproduce the macroscopic experimental behavior of concrete in both linear and nonlinear regimes. For that reason, the proposed constitutive behavior of links between DE is inspired by observations at the macroscale. The behavior of undamaged plain concrete is assumed to be linear, elastic, isotropic, and homogeneous. Thus the DE assembly is necessary to be isotropic such as to reproduce the isotropic property of undamaged concrete and prevent the development of nonphysical cleavage, which may appear when concrete behavior becomes nonlinear with aligned elements and a non-polydisperse distribution of elements sizes (Herrmann et al. 1989).

Definition of Interactions

Two types of interactions are considered; contact and cohesive. Once a cohesive interaction is broken then a new contact interaction might be created between the two DE if they come in contact. Spherical DE are selected due to the simplicity to handle with interactions between them. The cohesive interaction was introduced by Hentz et al. (2004) to model the cohesive nature of geomaterials such as concrete; it is defined between two spheres a and b of radii R_a and $R_{b,}$ respectively, inside an interaction range, which is determined by an interaction range coefficient λ (Fig. 2).

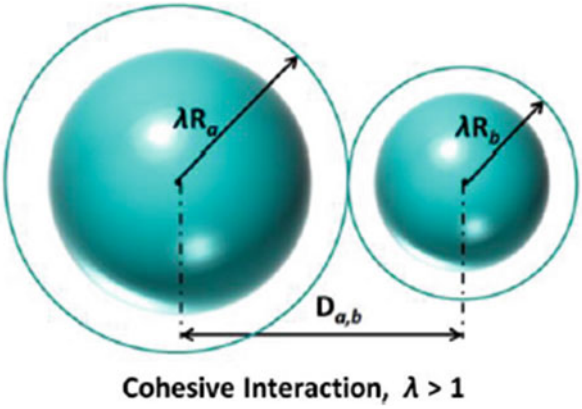

Fig. 2 Cohesive interactions

Additionally, it allows defining an adequate number of interactions per DE to guaranty the macroscopic isotropic feature of the DE assembly. The interaction range is defined in Eq. 1, where $D_{a,b}$ stands for the distance between the centroids of the elements a and b, with $\lambda > 1$.

$$\lambda \left(R_a + R_b\right) \geq D_{a,b} \tag{1}$$

Linar Elastic Constitutive Behavior

The elastic behavior between DE is characterized by spring-like interactions which are defined through normal K_N and tangential K_S stiffnesses. Micro–macro relations defined by Donzé et al. (1999) link K_N and K_S to the macroscopic elastic parameters on Young's modulus E and Poisson's ratio ν (Eqs. 2 and 3). $D_{a,b}^{\text{init}}$ represents the initial distance between the two elements a and b, with radii R_a and R_b. An interaction surface is defined as $S_{\text{int}} = \pi \min\left(R_a^2, R_b^2\right)$. Young's modulus E and Poisson's ratio ν are the input values, whereas α, β, and γ are the set of parameters considered as specific to the packing algorithm. All details about the identification of the elastic parameters (i.e., general procedure, order of identification, choice of the form, and size of the samples, etc.) can be found in Rousseau et al. (2008).

$$K_N = \frac{E\, S_{\text{int}}}{D_{a,b}^{\text{init}}} \frac{1+\alpha}{\beta(1+\nu)+\gamma\,(1-\alpha\nu)} \tag{2}$$

$$K_S = K_N \frac{1-\alpha\nu}{1+\nu} \tag{3}$$

Moment Transfer Law

The modeling of the cohesive interaction between DE without any rolling resistance leads to a too brittle behavior of the DE assembly. A rolling resistance has to be introduced between DE to account for the complex geometry of concrete constituents (cement paste, aggregates) that prevent local rotations.

Furthermore, Chareyre and Villard (2005) showed that the shear capacity of the medium is underestimated when rolling between the particles is allowed without restriction. For this reason, a Moment Transfer Law (MTL), was implemented into the model by Omar et al. (2013) in order to get a rolling resistance and then to increase the shear capacity of the assembly. Iwashita and Oda (1998) developed the original idea to model two-dimensional circular elements and to simulate the shear band zone of biaxial tests.

The MTL is chosen elastic perfectly plastic as shown in Fig. 3, a rolling stiffness K_r and a plastic limit M_{plas} are defined. The rolling resistance in the elastic domain is here to help getting a bulk behavior, where the plastic part is here for a material effect reason.

A cylindrical beam of radius $r = \min(R_a, R_b)$ is considered between the DE a and b. The rolling stiffness K_r is thus proportional to EI/D_{ab} where I is the bending inertia; a factor β_r is introduced to control the rolling resistance (Eq. 4). The plastic limit of a cylindrical beam depends on the factor $\frac{TI}{r}$, where T is the local tensile strength (Fig. 4). Similarly, a factor η is added to control the plastic limit (Eq. 5).

$$K_r = \beta_r \frac{EI}{D_{ab}} \tag{4}$$

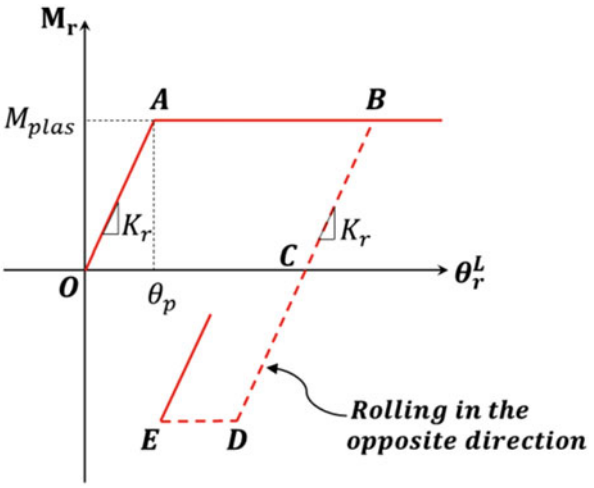

Fig. 3 Elasto-plastic model for the rolling resistance by Omar et al. (2013)

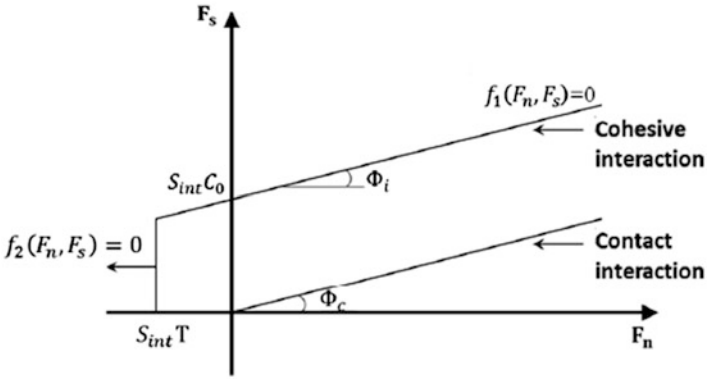

Fig. 4 Modified Mohr-Coulomb model

$$M_{\text{plas}} = \eta \frac{TI}{r} \tag{5}$$

Failure Criterion

Cohesive links follow a modified Mohr-Coulomb model, with a tension cut off criterion describing failure into the material. Sawamoto et al. (1998) proposed this modified model with a shear sliding function f_1 and a tensile damage function f_2 (Fig. 4). The characteristic parameters of the cohesive interactions modified Mohr-Coulomb model are the friction angle Φ_i, the cohesion stress C_0, and the local tensile cut off stress T. The shear function f_1 limits the tangential force; the function f_2 activates the tensile damage of the link.

When the cohesive interaction is broken, the two spheres may be in interaction if they come in contact. Then a new contact interaction is created that follows a standard Mohr-Coulomb criterion with a contact angle Φ_c. This interaction cannot exert tensile forces and acts in compression only.

Nonlinear Elastic with Damage Tensile Constitutive Behavior

The tensile constitutive behavior is assumed brittle without plastic deformations at the link scale (left side of Fig. 5). The softening behavior is characterized by the softening factor ξ and it is activated once the normal force between the two DE exceeds the local tensile strength. The cohesive interaction is considered as broken when the distance between DE reaches D_{max}.

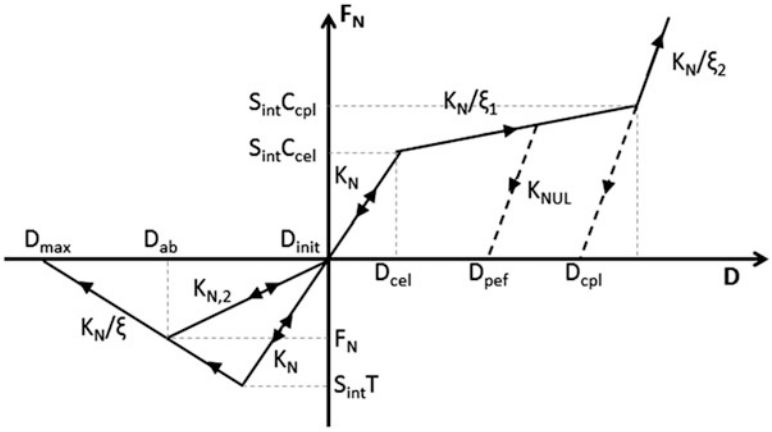

Fig. 5 Normal interaction: force-displacement constitutive model (left: tensile elastic with damage behavior, right: compaction law)

Constitutive Behavior in Compression – Compaction

Under high mean stress, concrete behavior is governed by the compaction phenomenon due to the porosity closure (Gabet et al. 2008). Under confined compression and increasing mean stress levels, concrete first follows a linear behavior, and then its tangent stiffness decreases due to the cement matrix damage, which leads to porosity closure. During the porosity closure, the stiffness of the material increases and tends to the elastic stiffness of the fully consolidated material Malecot et al. (2010). This behavior at the macroscopic scale can be reproduced through simple interaction laws between DE.

Shiu et al. (2008b) proposed a tri-linear with elasto-plastic-hardening behavior to adequately describe the experimental behavior concrete under high mean stresses (right side of Fig. 5). The elastic domain is described by the initial stiffness of concrete K_N and the compressive elastic limit ($F_{Cel} = S_{int}C_{cel}$). In the compaction zone, hardening is characterized by the hardening coefficient ξ_1 and a continuous increase of the elastic stiffness. Finally, the consolidated material zone is reached when the compressive force reaches F_{Cpl}; concrete material is then fully compacted, the stiffness is raised thanks to the hardening coefficient ξ_2.

Strain Rate Dependency

Bischoff and Perry (1991) explored in a wide range the strain rate dependency of concrete compressive strength evaluating experimental data from the literature. Besides, Malvar and Ross (1998) and Malvar and Crawford (1998) collected

experimental data by different authors to observe the strain rate sensitivity of concrete in tensile loading. Tensile and compressive strengths of concrete increase with strain rate, especially for strain rates greater than a transition strain rate, around 10^0 s^{-1}. Erzar and Forquin (2014) have shown that the strength increase is particularly important in tension. The strain rate effect in both tension and compression for moderate rates depends on the moisture content of concrete.

However, the strain rate enhancement of the unconfined compressive strength in concrete-like materials is largely caused by the introduction of radial confinement in split Hopkinson pressure bar (SHPB) tests (Li and Meng (2003), Zhang et al. (2009), Li et al. (2009), Zhou and Hao (2008)), which cannot be simply interpreted as material behavior. Brace and Jones (1971) first explained that the unconfined compressive strength increase could be due to the change of stress state from uniaxial stress to uniaxial strain under increasing radial confinement.

In addition, Cusatis (2011) demonstrates that for strain rates higher than 10^{-1} s^{-1} the inertia forces cannot be neglected and provide a significant contribution to the strength enhancement recorded during experiments. He also shows that taking into account inertia forces, thanks to a 3D transient dynamics model, allows describing most of the strain rate effect observed in uniaxial compression. Moreover, it is necessary to include a strain rate dependency in the microscopic model in order to describe correctly the observed strain rate effect in uniaxial tension.

Hence, in the present DEM approach, the strain rate sensitivity is implemented in tension at the scale of DE (that is not the macroscale) only thanks to a dynamic increase factor (DIF) that is the ratio of dynamic to quasi-static strengths (T_{dyn}/T_{st}). The DIF evolution into two regimes is inspired by the CEB formula (1993) and is given in Eq. 6.

$$\mathrm{DIF} = \frac{T_{\mathrm{dyn}}}{T_{\mathrm{st}}} = \begin{cases} 1 & \text{if } \dot{\varepsilon} \le \dot{\varepsilon}_{\mathrm{st}} \\ \left(\frac{\dot{\varepsilon}}{\dot{\varepsilon}_{\mathrm{st}}}\right)^{\delta 1} & \text{if } \dot{\varepsilon}_{\mathrm{st}} < \dot{\varepsilon} \le \dot{\varepsilon}_m \\ \theta\left(\frac{\dot{\varepsilon}}{\dot{\varepsilon}_{\mathrm{st}}}\right)^{\delta 2} & \text{if } \dot{\varepsilon} > \dot{\varepsilon}_m \end{cases} \quad \text{with } \delta_1 = \frac{1}{1 + 8\frac{\sigma_C}{\sigma_{C0}}} \text{ and } \theta = \left(\frac{\dot{\varepsilon}_m}{\dot{\varepsilon}_{\mathrm{st}}}\right)^{(\delta 1 - \delta 2)} \tag{6}$$

where $\dot{\varepsilon}_{st}$ and $\dot{\varepsilon}_m$ are the quasi-static and moderate strain rates, respectively, δ_1 and δ_2 are the first and second regime slopes, σ_C is the quasi-static compressive strength, σ_{C0}= 10 MPa.

The first regime of DIF evolution follows the modified CEB formula by Malvar and Crawford (1998), it depends on the quasi-static compressive strength of concrete, thus the tensile strength increase is higher for concretes with lower strengths.

Fracture energy is another significant property of concrete. Zhang et al. (2009) reported its sensitivity to loading rates by conducting three-point bending tests on notched beams over a wide loading range from 10^{-4} to 10^3 mm/s. They showed that under low strain rates there is only a slight effect on the fracture energy. Weerheijm

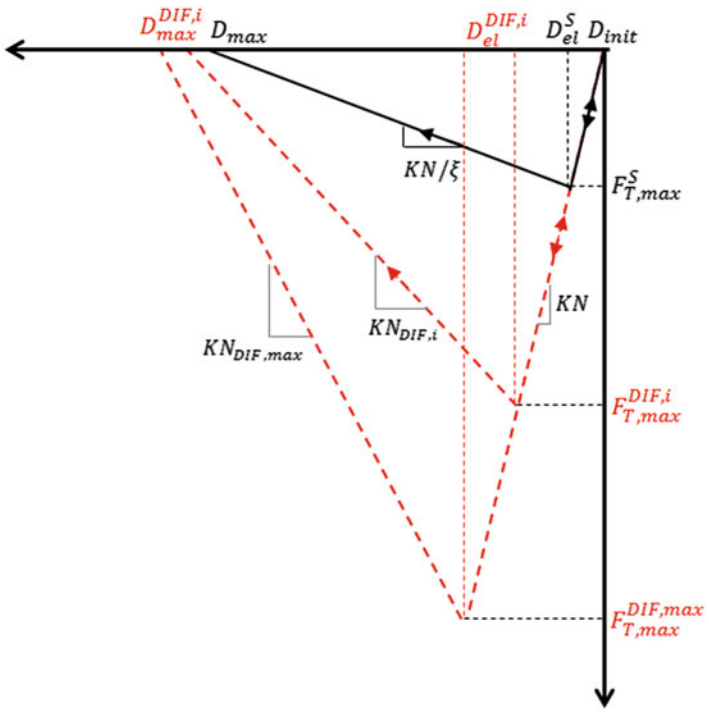

Fig. 6 Strain rate effect in tension

(1992) obtained a slight influence on the fracture energy for loading rates less than 1000 GPa/s and a rate-dependent softening curve that becomes more brittle with the rate increase.

Figure 6 illustrates the strain rate effect in tension corresponding to Eqs. 7–9. This pragmatic choice of DIF evolution allows a simple identification of the DIF through an inverse analysis based on the numerical simulation of spalling Hopkinson bar tests.

Note that the dynamic increase factor may decrease in case a medium-low strain rate occurs after a high strain-rate state Nevertheless, authors did not notice any numerical instabilities in simulations presented further despite the possible variation of tensile strength and the no introduction of artificial damping.

$$\mathrm{KN}_{\mathrm{DIF},i} = \mathrm{KN}_{\mathrm{DIF},1} + \left(\mathrm{KN}_{\mathrm{DIF},max} - \mathrm{KN}_{\mathrm{DIF},1}\right)\left(\frac{\mathrm{DIF}-1}{\mathrm{DIF}_{\mathrm{MAX}}-1}\right) \tag{7}$$

$$\frac{1}{\xi_{\mathrm{DIF},i}} = \frac{1}{\xi} + \left(\frac{1}{\xi_{\mathrm{MAX}}} - \frac{1}{\xi}\right)\left(\frac{\mathrm{DIF}-1}{\mathrm{DIF}_{\mathrm{MAX}}-1}\right) \tag{8}$$

$$\frac{D_{\max}^{\mathrm{DIF},i}}{D_{\max}} = \frac{\mathrm{DIF}\ \left(1+\xi_{\mathrm{DIF},i}\right)}{1+\xi} \tag{9}$$

Furthermore, Erzar and Forquin (2014) have shown that the shear response of concrete is also strain rate dependent. This dependency is significantly lower than in tension, the corresponding DIF is arbitrary limited to value of 2, the Mohr-Coulomb criterion (Fig. 4) allows then deducing the maximum dynamic increase factor $\mathrm{DIF}_{\max}$ with Eq. 10.

$$\mathrm{DIF}_{\max} = \frac{2.0\ C_0}{\tan\left(\varphi_i\right) T_{\mathrm{st}}} \tag{10}$$

Identification of Constitutive Parameters of the Discrete Element Model for Concrete

The constitutive parameters are calibrated to reproduce the macroscopic behavior of an ordinary fully saturated concrete R30A7. High quality cement is used for a good reproducibility of tests with a quite high water/cement ratio for a moderate strength. It contains rolled siliceous aggregates with a maximum size of 8 mm. Table 1 gives the composition and the mechanical properties of R30A7. The compressive strength of R30A7 is about 34 MPa after 28 days of aging and the tensile strength is assumed the tenth of the compressive strength due to the lack of experimental data.

Discrete Element Modeling of Samples

The current DEM approach requires the use of the same packing technique to avoid the possible dependency of model parameters on discretization. Potapov et al. (2016)

Table 1 Composition and mechanical properties of R30A7 ordinary concrete (Vu et al. 2009a)

Composition		Mechanical Properties	
Cement CEM I 52.5 N [Kg/m^3]	263	Compressive strength [MPa]	34
Sand D_{max} 1.8 mm [kg/m^3]	838	Porosity accessible to water [%]	12
Gravel 0.5–8 mm [kg/m^3]	1008	Slump [cm]	7
Water [kg/m^3]	169	Density [kg/m^3]	2278
W/C ratio	0.64	Young's modulus [GPa]	25
		Poisson's ratio	0.16

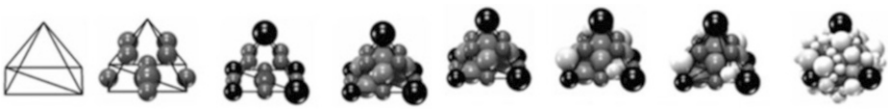

Fig. 7 DE assembly technique

have shown that for a given set of geometrical parameters (ratio of the DE radius Rmax/Rmin, ratio of the mean tetrahedral FE size over the mean DE radius, and a random distribution of DE sizes) the geometric algorithm described in Jerier et al. (2009), and illustrated in Fig. 7, can generate a homogeneous assembly with nondependency of constitutive parameters on discretization.

For each DE, the number of links with its neighbors varies with the value of λ (Eq. 1). The desired number of interactions can be set by adjusting the interaction coefficient λ. Rousseau et al. (2008) selected an average number of 12 links per DE (coordination number = 12). This arbitrary choice and the proper packing technique guarantee an isotropic assembly.

Identification of Constitutive Parameters by Means of Simulations of Quasi-Static Tests

Simulation of Quasi-Static Uniaxial Tests

The identification procedure of the linear elastic parameters α, β, and γ (Eqs. 2–3) has been proposed by Hentz et al. (2004); it is detailed in Antoniou et al. (2018) and Antoniou (2018). The parameters $\alpha = 3.9$, $\beta = 3.75$, and $\gamma = 5$ are seen to be the best fit to satisfy the macroscopic linear elastic behavior.

The MTL (Eqs. 4–5) is governed by the pair of parameters (β_r, η). These parameters have quasi no influence on the linear elastic behavior, they are calibrated by adjusting the smoothness of the peak stress and the post-peak ductility to the experimental results (Omar et al. 2013). This calibration process allowed identifying $\beta_r = 5$ and $\eta = 5$.

The higher the tensile cut off stress T the higher the macroscopic peak stress in both tension and compression. The softening factor ξ has almost no effect on the ductility of the stress-strain curve in compression; however it increases the ultimate tensile strain. The cohesion stress C_0, the friction angles Φ_i and Φ_c do not influence the tensile behavior of concrete. C_0 affects the compressive peak stress and the two angles slightly influence the post-peak regime.

After studying the influence of each parameter on the macroscopic behavior in uniaxial tension and compression, the constitutive parameters acting on the non-linear behavior were identified for R30A7 concrete: $T = 2.5$ MPa, $\xi = 3$, $C_0 = 4.5$ MPa, $\Phi_i = \Phi_c = 20°$

Simulation of Quasi-Static Triaxial Confined Compression Tests

The constitutive parameters of the compaction law (Fig. 5) are defined through inverse modeling of hydrostatic and oedometric tests at high confinement performed with the high capacity triaxial press Giga (Fig. 8, Vu et al. 2009a). A hydrostatic test consists in the application of isotropic pressure around the entire specimen that increases linearly with time. An oedometric test restricts all the radial deformations while the specimen is compressed axially (Fig. 9).

For the simulation of hydrostatic and oedometric tests, the DE packing is assembled using the same discretization parameters (Potapov et al. 2016) as for the

Fig. 8 Giga press

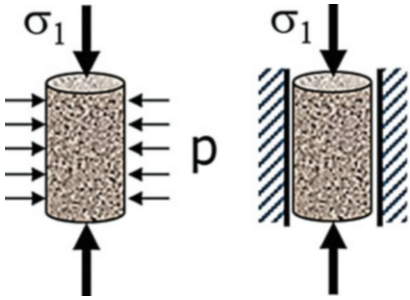

Fig. 9 Hydrostatic ($\sigma_1 = p$) and oedometric compression tests

simulation of uniaxial tests. For sake of simplicity in the appliance of the radial pressure, numerical samples are $0.1 \times 0.1 \times 0.1$ m^3 cubes (Fig. 10) while experimental specimens are cylindrical. This choice has no influence since the experimental stress state is homogeneous because of frictionless boundary conditions (Vu et al. 2009a).

The polydisperse assembly consist in 4427 DE with a 5.5 mm maximum radius, a 1.8 mm minimum radius, and a 0.59 compactness. The loading is applied by means of rigid elements on each side (Fig. 10).

The best comparison with experimental results (Fig. 11) is obtained with $C_{\text{cel}} = 50$ MPa, $C_{\text{cpl}} = 300$ MPa, $\xi_1 = 1.5$, and $\xi_2 = 0.3$.

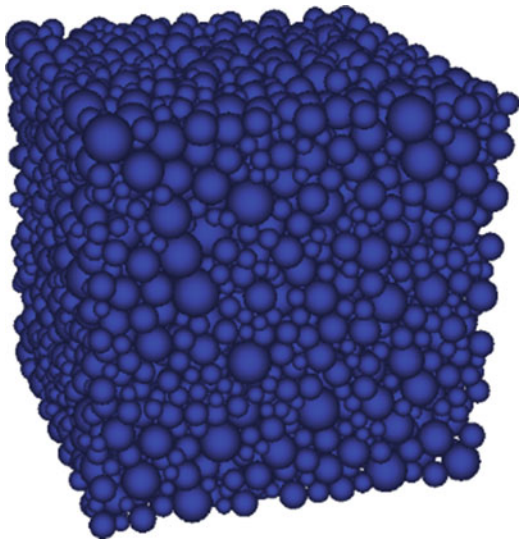

Fig. 10 Numerical cubic specimen

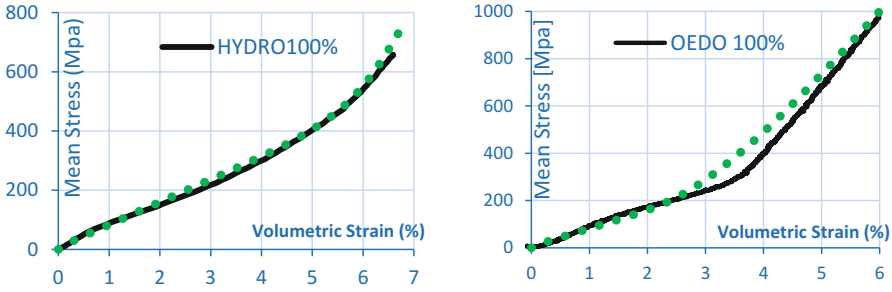

Fig. 11 Experimental and numerical stress-strain curves in hydrostatic (left) and oedometric (right) tests

Identification of Constitutive Parameters by Means of Simulations of Spalling Tests Using a Hopkinson Bar

The aim is the identification of strain rate effect parameters of the DE model (Eqs. 6–9). It is recalled that only the tensile behavior of concrete is assumed to be concerned with the material strain rate effect. In addition, the first regime of the strain rate effect (Fig. 6) is modeled thanks to the modified CEB formula by Malvar and Crawford (1998). The second high strain rate regime is identified by means of simulations of spalling tests using a Hopkinson bar (Fig. 12) performed on two fully saturated R30A7 specimens at strain rates 30 s^{-1} and 50 s^{-1} by Antoniou (2018). The specimen is submitted to a compression wave that is reflected as a tensile pulse. When the reflected pulse exceeds the transmitted one in amplitude a dynamic tensile loading develops in the core of the

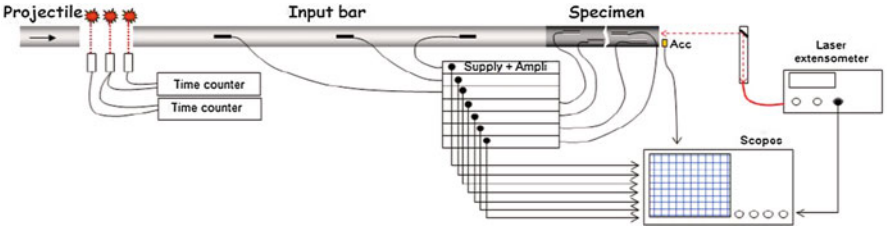

Fig. 12 Spalling Hopkinson bar experimental setup (Forquin and Erzar 2010)

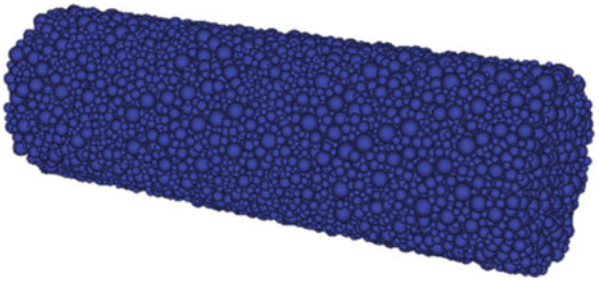

Fig. 13 Discrete element assembly of the spalling Hopkinson bar test specimen

specimen leading to its possible fragmentation. The difference between the maximum value and the rebound of particle velocity observed on the rear face called pullback velocity is proportional to the dynamic tensile strength of the concrete specimen (Novikov et al. 1966). Thus, the correct prediction of the pullback velocity is a good indicator to validate the identification of the dynamic tensile behavior of the tested material.

The same procedure as before is used for the creation of the DE assembly for the dynamic spalling test modeling. The specimen is cylindrical with a 46 mm diameter and a 142 mm length. It consists of 18,376 DE with a 2.1 mm maximum radius, a 0.7 mm minimum radius, and a 0.59 compactness (Fig. 13). The transmitted compressive pulse is applied on the front face of the sample and the rear face velocity is recorded to identify the dynamic increase factor law parameters.

According to Malvar and Crawford (1998) the quasi-static strain rate of the first strain effect regime (Fig. 6) is $\dot{\varepsilon}_{st} = 10^{-6}\ s^{-1}$ and the slope of this regime is $\delta_1 = 0.0355$ for $\sigma_C = 34$ MPa (Eq. 6).

The transition point from moderate to intense strain rates $\dot{\varepsilon}_m$ and the slope coefficient of the second regime δ_2 were identified thanks to the simulation of the two spalling tests at $30s^{-1}$ and $50s^{-1}$. Those two parameters were selected to capture properly the peak and rebound velocity recorded on the rear face velocity of the two spalling tests. The tests were thoroughly reproduced with the parameters $\dot{\varepsilon}_m = 1\ s^{-1}$ and $\delta_2 = 0.333$. Figure 14 compares the experimental data with the numerical simulations.

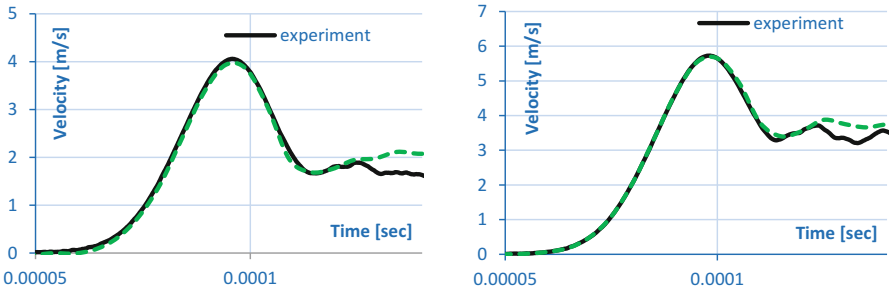

Fig. 14 Experimental and numerical pull back velocity of the spalling test at $30s^{-1}$ (left) and $50s^{-1}$ (right)

However, it is necessary to validate the identified DE model on a wider range of strain rates. Erzar and Forquin (2011) used the spalling technique to investigate the response of wet R30A7 concrete in a broad range of strain rates. Figure 15 presents the spalling test from Erzar and Forquin (2011) with dots while the dashed line gives DEM numerical results. The modeling of the tensile strength enhancement with the proposed DIF law is in good agreement with the experimental data.

Validation of the Model by the Simulation of Hard Impact Tests

This sub-chapter presents three different types of hard impact tests performed on ordinary concrete that are simulated for the validation of the DE model for concrete. All these blind simulations were carried out with the FE code Europlexus in which the DE model was implemented and with the constitutive parameters identified in section E, i.e., with approximately the same coordination number (12) and the same compactness (0.60).

Edge-On Impact Tests

The edge-on impact (EOI) test was initially developed by Hornemann et al. (1984) to study the fragmentation of brittle materials like glass at high strain rates. This experiment is particularly adapted to analyze the dynamic fragmentation since the thin material tile is not confined so damage is mainly due to tensile stresses. This test is thus relevant to validate the DE damage model for high strain rates.

Forquin and Erzar (2010) performed EOI tests on fully saturated concrete R30A7. A cylindrical ogive-nose steel projectile with a 1.99 cm diameter hits a thin concrete tile of dimension $20 \times 12 \times 1.5$ cm^3. Two rigid plates constrain the vertical displacements of the top and bottom specimen faces, whereas a flexible vertical plate limits the horizontal displacement of the tile's rear face. Figure 16 shows a schematic of the experimental setup. Two EOI tests were performed with a short

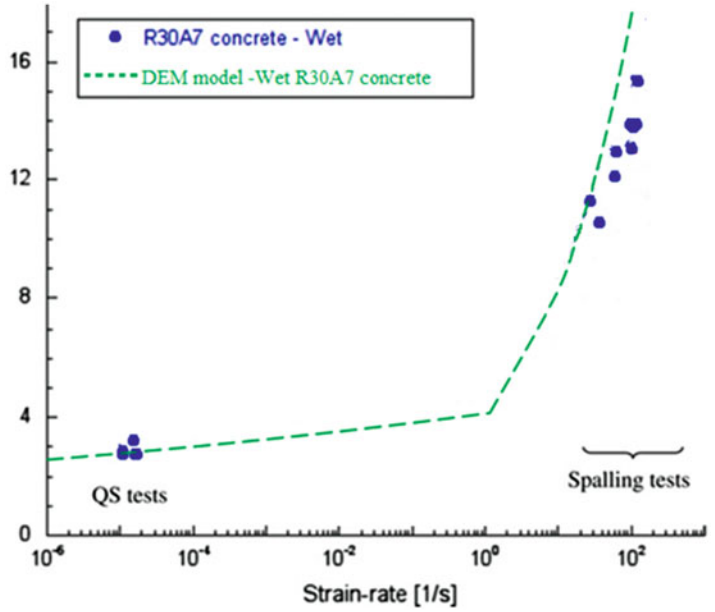

Fig. 15 Experimental results on wet R30A7 concrete (Erzar and Forquin 2011) and DE model

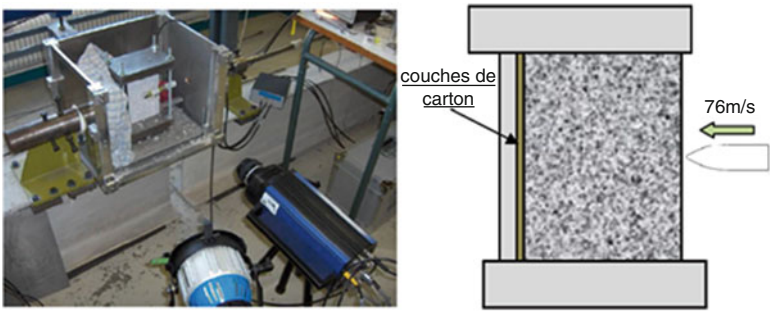

Fig. 16 Edge-on impact setup

projectile (62.15 mm, 130.4 g) and with a long projectile (122.15 mm, 273.9 g) launched at 76 ms^{-1} and 56 ms^{-1}, respectively.

The concrete tile is modeled with DE whereas tetrahedral FE are used for the projectiles and hexahedral FE for the three rigid plates. A linear elastic behavior is assumed for the steel projectile and supports. The concrete DE assembly is composed of 118,209 DE with a 1.4 mm maximum radius, a 0.47 mm minimum radius, and a 0.61 compactness. Figure 17 presents the EOI test model with the FE short projectile and the DE concrete tile surrounded by the three FE plates.

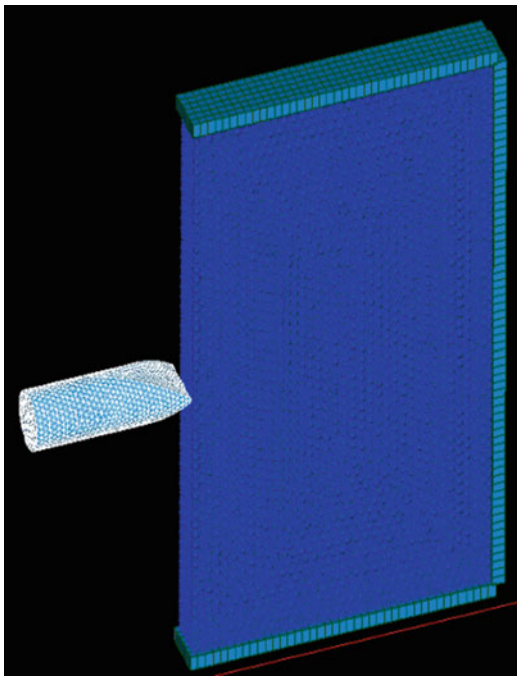

Fig. 17 Edge-on impact DE/FE model

Figure 18 illustrates the final damage stage of the first test (EOI-short). For a given DE, the damage d is defined as the ratio of the number of broken links to the number of initial links ($d = 1$ in red, $d = 0$ in blue). The numerical simulation (Fig. 19) is consistent with the experiment; the cratering damage mode is perfectly described. The calculated projectile's penetration depth corresponds exactly to the measured crater length as can be seen on Fig. 20.

Likewise, Figs. 21, 22, and 23 present the perfect match between the experimental observations and the numerical results for the second test (EOI-long).

In conclusion of these EOI tests simulations, the DE model of tensile damage and of its strain rate effect is validated.

Perforation and Penetration Tests Performed by the CEA-Gramat (CEG)

Perforation and penetration tests allow validating the DE model for both the tensile damage including rate effects (Fig. 6) and the compaction law (Fig. 5) because high mean stresses occur during such tests.

CEG performed a series of hard impact tests (Pontiroli et al. 2014; Bian et al. 2016) using a gas launcher and ogive-nosed steel projectiles with a nose radius to diameter ratio of 5.77, a 52.06 mm shank diameter, a 299.43 mm length, and a

Fig. 18 EOI-short: Final damage state

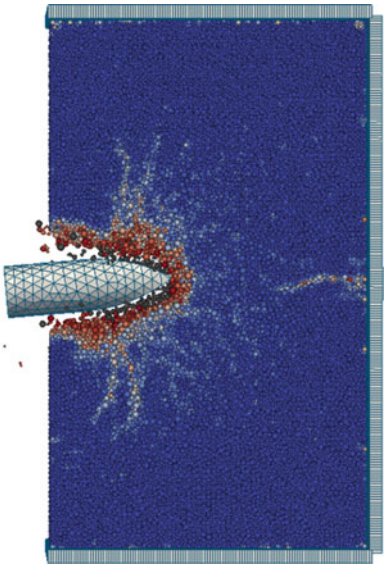

Fig. 19 EOI-short: Calculated final damage state

2.442 kg mass (Fig. 24). An acceleration recorder system was embedded into the steel projectile to measure axial deceleration during the experiment. Targets were made of fully saturated plain R30A7 concrete confined with a 15 mm thick steel jacket. Three tests are simulated; the targets diameter is 800 mm, while the thickness

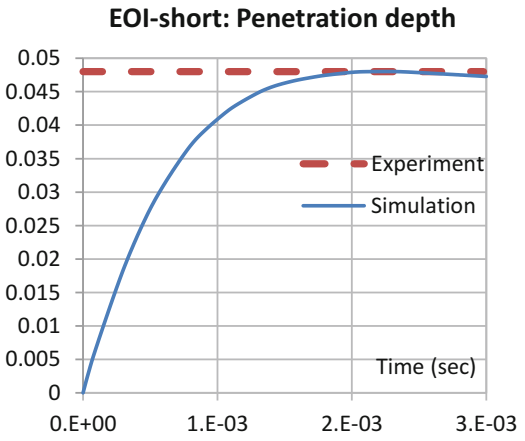

Fig. 20 EOI-short projectile's penetration depth

Fig. 21 EOI-long: Final damage state

is 300 mm for the perforation test at 333 ms^{-1} and 800 mm for the two penetration tests at high velocity (HV, 347.4 ms^{-1}) and low velocity (LV, 227 ms^{-1}) (Fig. 25). After the test, the crater dimension and the penetration depth were measured thanks to a topographic laser system.

The concrete target is modeled with DE while tetrahedral FE are used for the steel confining jacket and the steel projectile (Fig. 26). A linear elastic behavior is assumed for the steel elements. Table 2 presents the number of DEs, the maximum radius, the minimum radius, and the compactness of the DE packing for the perforation and penetration tests.

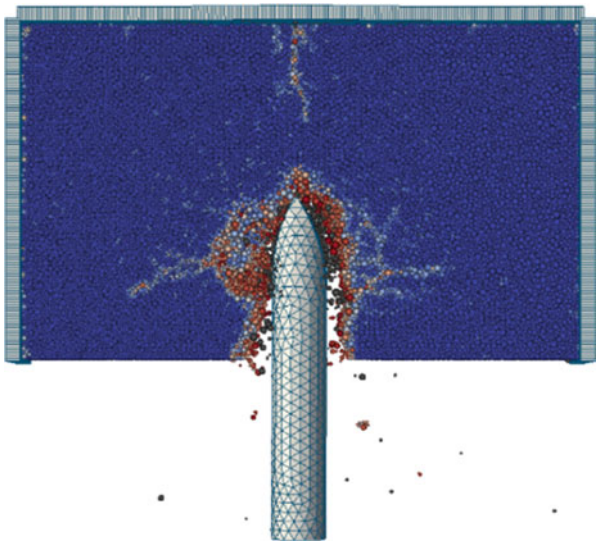

Fig. 22 EOI-long: Calculated final damage state

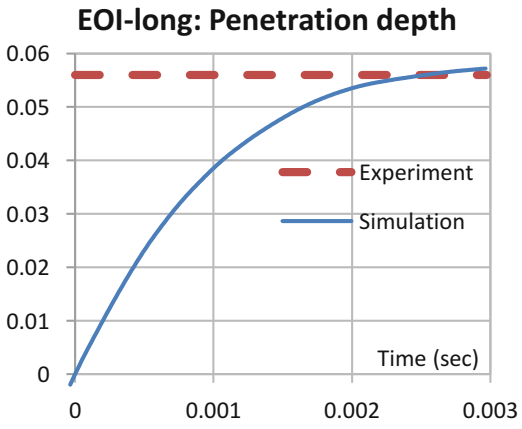

Fig. 23 EOI-long projectile's penetration depth

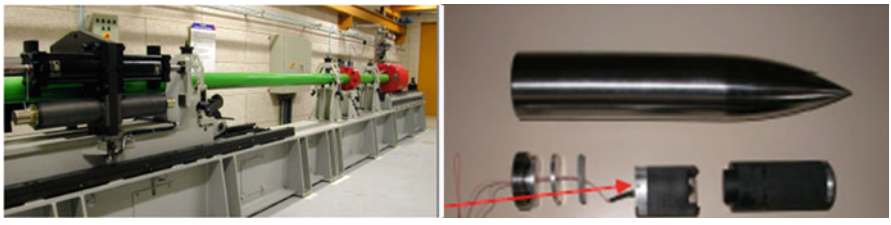

Fig. 24 Gas launcher and projectile with its accelerometer

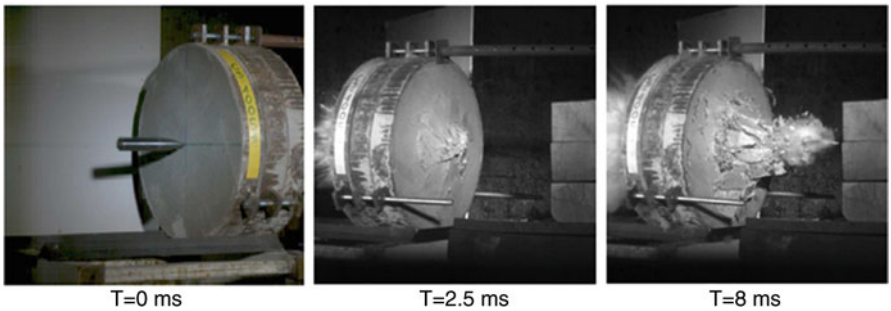

Fig. 25 Snapshots of the perforation test on front and rear face

Fig. 26 DE/FE model

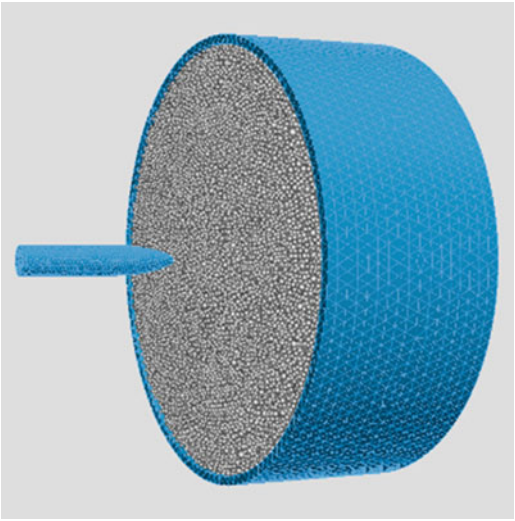

Table 2 DE packing characteristics

	Number of DE	R_{max} [mm]	R_{min} [mm]	Compactness
Perforation	141,765	9	3	0.61
Penetration	336,467	9.38	3.13	0.61

Numerical simulation results (projectile axial displacement and velocity) of the perforation test perfectly match with experimental data (Fig. 27).

Figure 28 presents the damage pattern observed after the perforation test (right side) and the damage state obtained from the numerical simulation (left side). The phenomena observed experimentally, such as spalling on the front face and scabbing on the rear face, are successfully described by the perforation test simulation.

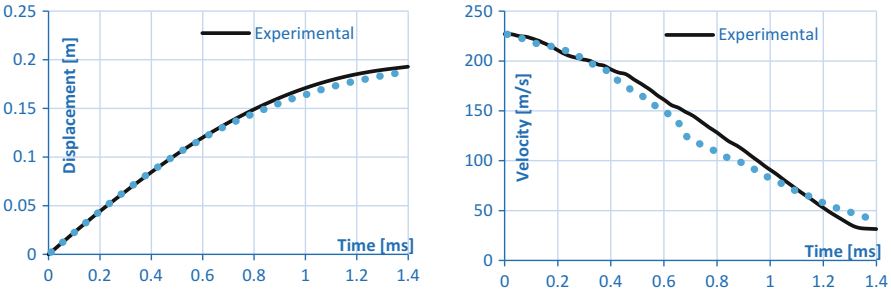

Fig. 27 Perforation test: Projectile axial displacement (left), velocity (right)

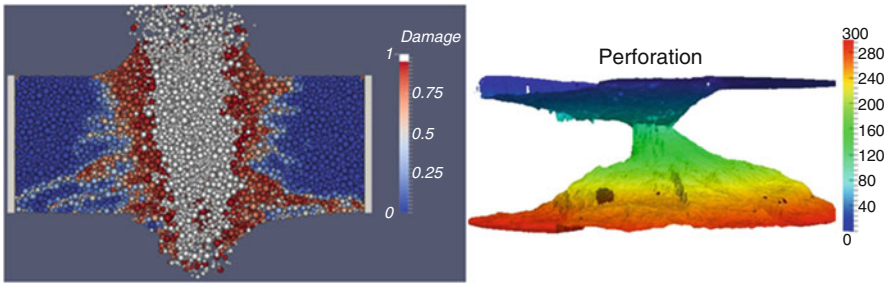

Fig. 28 Damage pattern of perforation test, simulation (left) and experiment (right)

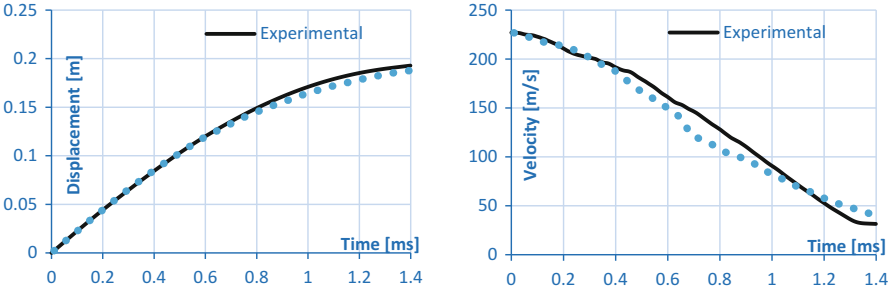

Fig. 29 LV penetration test: Projectile axial displacement (left), velocity (right)

Figure 29 plots the axial displacement and the axial velocity of the projectile during the LV penetration test and Fig. 30 shows the damage pattern after the penetration. Note that experimental results were available on [0., 1.4 ms] only, results are shown on that duration.

Numerical results predict well the experimental observations. For the penetration test, the target is thicker than for the perforation test thus the projectile does not perforate the specimen. The simulation produces well all the impact effects into concrete with spalling and cratering on the front face by conical cracks and the

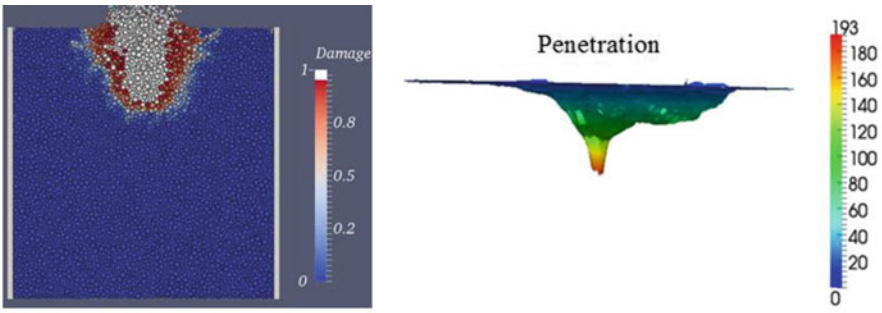

Fig. 30 Damage pattern of LV penetration test, simulation (left) and experiment (right)

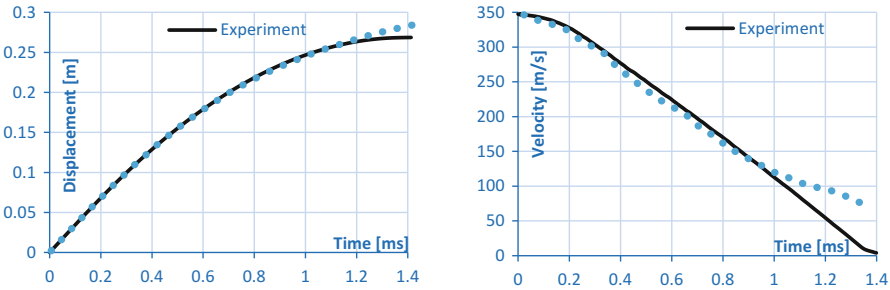

Fig. 31 HV penetration test: Projectile axial displacement (left), velocity (right)

penetration of the projectile creates a cylindrical hole with diameter very close to the projectile's diameter.

Similarly, Fig. 31 shows the axial displacement and velocity of the projectile during the HV penetration test; a slight difference is observed at the end of the HV penetration test. Figure 32 shows the crack pattern after the HV penetration simulation (right side) and the experiment (left side).

In conclusion of these simulations of perforation and penetration tests, the DE model of compaction, of tensile damage and of its strain rate effect is validated.

Simulation of a Drop-Weight Impact on a Reinforced Concrete (RC) Beam

Test Description

In order to show the capability of the DEM approach to represent advanced damaged states of RC structures under severe dynamic loading, a drop-weight test performed at the University of Toronto is modeled (SS0b test, Saatci 2007). Figure 33 gives the dimensions of the RC beam.

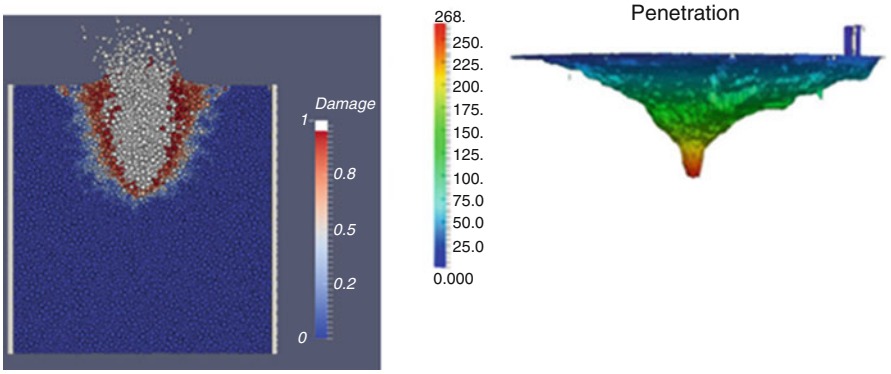

Fig. 32 Damage pattern of HV penetration test, simulation (left) experiment (right)

Fig. 33 Specimen dimensions

The SS0b beam was reinforced with four 30 mm diameter longitudinal bars. The steel rebars (density 5.3 kg/m) were placed symmetrically along the height in order to have the same resistance properties of the beam in positive and negative bending and they spanned the entire length of the beam. In the considered SS0b test no transverse reinforcement was used that maximized damage. The beam was simply supported as shown in Fig. 33. However, to prevent uplift of the beam from the supports during the impact, four rebars were used holding the beam down. At the bottom end these vertical bars were fitted to spherical bearings to enable free rotation, whereas at the top they were fixed to a structural steel section with a hinge allowing the beam to rotate freely at the supports.

The concrete used for the beam was an ordinary concrete with 10 mm aggregate size (density 2437 kg/m^3). During the casting of the beams several standard cylinder samples (150 mm in diameter and 300 mm in height) were created to determine the compressive strength of the concrete. The age of the beam specimens and the cylinder samples was more than 1 year at the time of impact testing. The compressive peak stress measured on the cylinders was 50.1 MPa and the strain at peak stress was 0.23%. Standard prisms (152 × 153 × 508 mm) were tested to determine the tensile coupon strength of the concrete. The direct tensile strength for 1-year dried specimen was estimated at 3.2 MPa. Standard tensile tests were carried out to determine the properties of the steel reinforcement (Table 3).

A heavy drop-weight of 600 kg was used for the testing. It was manufactured by filling a 300 mm square HSS (hollow structural steel) section with concrete and

Table 3 Steel coupon test results

Yield Strain ($\times 10^{-3}$)	Yield Stress	Ultimate Strength	Modulus of Elasticity
2.38	464 MPa	630 MPa	195 GPa

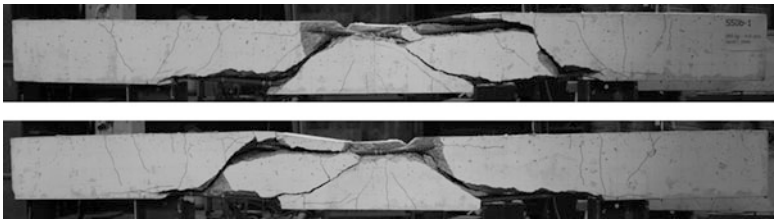

Fig. 34 Photographs of front and back faces after the drop-weight test

adding thick steel plates welded to the HSS section. The weight was hung on the crane by a nylon rope that was cut resulting in the fall of the weight on the specimen. Two I-shaped steel column were used to guide the weight and ensure hitting the right point on the beam. A 30 mm clearance between the weight and the flanges of the columns excluded any friction during the fall. To obtain a well-distributed impact force, a 50 mm thick 300 mm square steel plate was placed on the beam in the impact point. The weight was dropped from the clear height of 3.26 m above the specimen resulting in an impact velocity of 8 ms^{-1}.

The drop-weight punched through and caused massive concrete spalling both at the top and the bottom of the beam (Fig. 34).

The longitudinal rebars were exposed and severely bent. There were also signs of bond failure of the rebars at the supports. One distinctive result was the formation of a shear plug with major diagonal cracks starting at the top from the impact point and propagating downward with an angle of approximately 45°. Because SS0b test had no stirrups, the middle segment punched through with almost no visible bending deformations. In addition, several diagonal cracks parallel to the major shear-plug cracks also developed as well as some bending cracks at the mid-span and at the supports. Another diagonal crack developed alongside the shear plug starting from the supports and becoming horizontal close to the top before reaching the impact zone.

DE/FE Modeling of the Drop-Weight Test

The present chapter aims at describing a DE model for concrete thus only a brief presentation of the steel reinforcement model is given.

Common beam-like FE is used to represent the steel reinforcement allowing to easily model complex grids of rebars in real-scale RC structures. A special concrete-steel bond model was developed by Potapov et al. (2016) to represent interactions between the concrete spherical DE and the steel FE. This model describes interaction between a given rebar and a group of neighboring DE by using two nonlinear

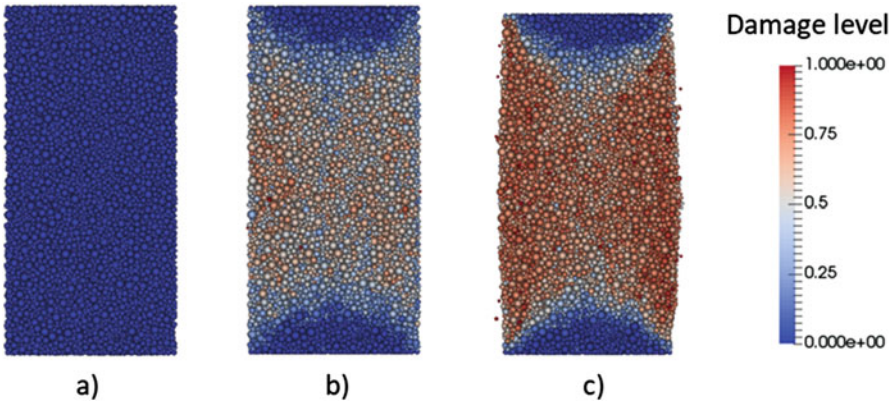

Fig. 35 Damage state of the cylinder (**a**) initial state, (**b**) $\varepsilon = 0.2\%$, (**c**) $\varepsilon = 0.6\%$

springs, one normal and one tangential to the direction of the rebar. The behavior of the normal spring is elasto-plastic in compression and brittle in tension, whereas the tangential one relies on the response of the concrete-steel link observed in pull-out tests.

The set of constitutive parameters identified for the R30A7 concrete must be modified in order to take into account the compressive strength of concrete used in the SS0b test (50.1 MPa). Only the coordination number (12) and the compactness (0.60) are the same. Figure 35 shows the damage state of the cylinder for different strain levels. The stress-strain curve obtained in this simulation is shown in Fig. 36. It is assumed that the tensile strain rate effect and the compaction behavior of SS0b concrete is the same as ones of R30A7 concrete.

A detailed numerical model of the experimental set-up was built (top of Fig. 37). Standard FEM is used to model the longitudinal steel reinforcement, the upper and lower support plates, the anti-uplift bars, the weight, and a square steel plate inserted under the drop weight. The DE model used for concrete relies on the same packing technique described earlier. The concrete DE assembly is composed of 60,488 DE with a 17.8 mm maximum radius, a 5.95 mm minimum radius, and a 0.60 compactness. Unilateral contact conditions are prescribed everywhere between the DE and FE parts of the model. Steel-concrete bond laws presented in Potapov et al. (2016) are applied to describe the interaction between the concrete and the steel reinforcement. The friction coefficient of 0.5 is used for steel-concrete contact, and 0.3 for steel-steel contact. Gravity is taken into account for the whole DE/FE model.

Figure 37 shows the evolution of damage of the RC beam for five consecutive moments.

It should be noted that damage is defined as a ratio of remaining cohesive links of the considered DE to the initial number of its cohesive links. Thus, this kind of damage indicator allows detecting zones of material degradation but cannot attest definitively the presence of macro-cracks. For the considered case the real material discontinuities can be seen when plotting the vertical displacement field (Fig. 38).

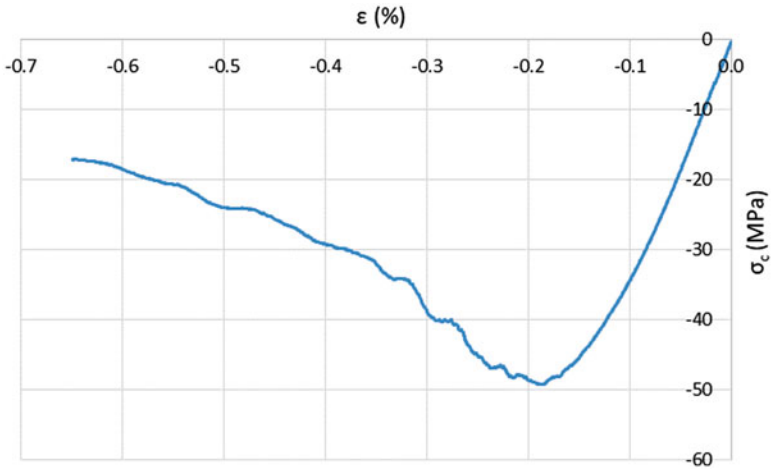

Fig. 36 DE model stress-strain curve of SS0b concrete

The basic color changes reveal the presence of at least three oblique macro-cracks delimiting different material fragments. These are in good agreement with the macro-cracks observed in the experiment (Figs. 34 and 39).

Analysis of the results obtained in the simulation of SS0b impact test shows that the main physical phenomena observed in the experiment are correctly represented by the mixed DE/FE model.

Conclusions

The discrete element model presented in this chapter aims at simulating concrete and reinforced concrete structures under impact. The identification of the model was first presented for the fully saturated R30A7 ordinary concrete. The identification of constitutive parameters relies on simulations of quasi-static uniaxial tensile and compressive tests, quasi-static triaxial confined compression tests, and dynamic tensile tests to account for strain rate effects. The discrete element model was extensively validated in the second part of the present chapter by blind simulations of hard impact tests. Three series of experiments were analyzed. Firstly, two edge-on-impact tests were simulated to validate the tensile damage model including strain rate effects. Secondly, three penetration and perforation tests on thick confined specimens were simulated to validate the compaction model as well as the tensile damage one. These two latter series of impact tests were performed on fully saturated R30A7 concrete targets. Thirdly, a drop weight impact test performed on a reinforced concrete beam was simulated to validate the ability of the discrete element model to describe advanced damage in reinforced concrete structures under complex dynamic loading.

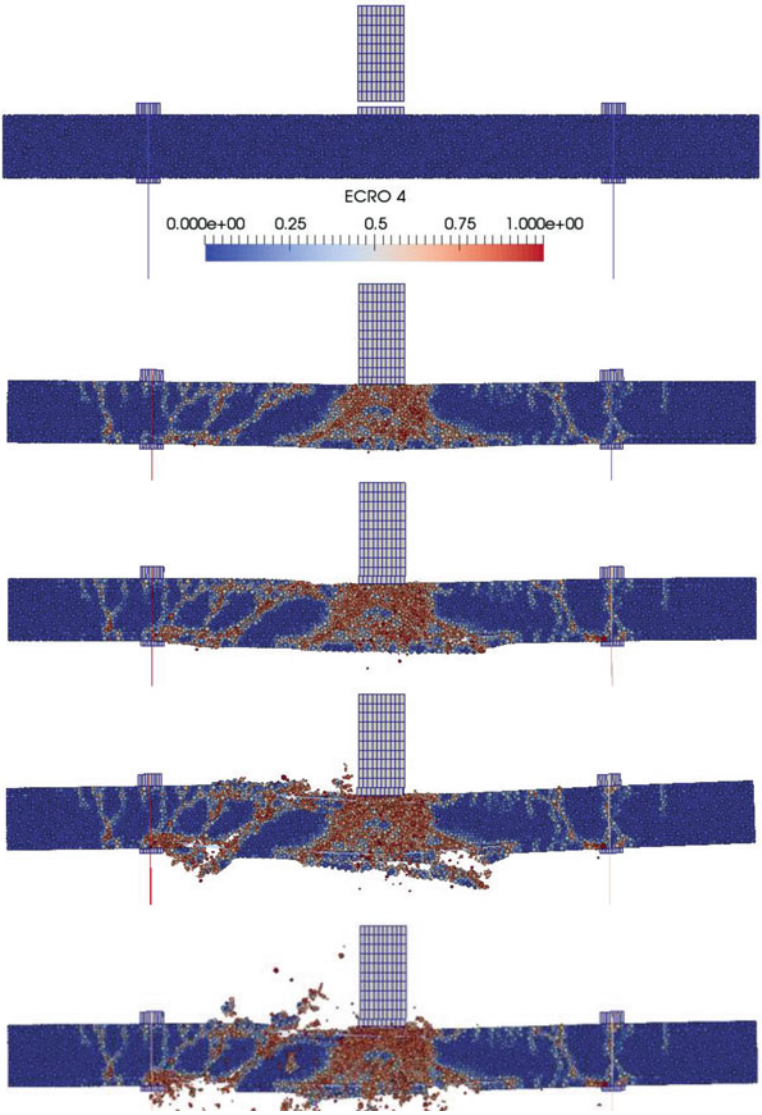

Fig. 37 Damage state of concrete at t = 0, 10 ms, 20 ms, 50 ms, and 200 ms (from top to bottom)

The discrete element numerical simulations are in good accordance with the experimental results and the model reproduces thoroughly the damage modes observed under impact loading. The cratering damage was successfully produced for the edge-on impact simulations and the penetration depth of the projectile was precisely captured. The numerical axial displacement and velocity of the perforation test were perfectly matched with the recorded ones. Similarly, the simulation of the

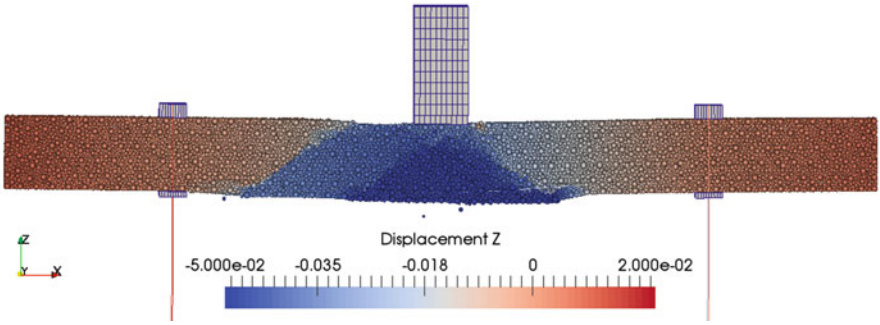

Fig. 38 Vertical displacement U_Z at 17 ms

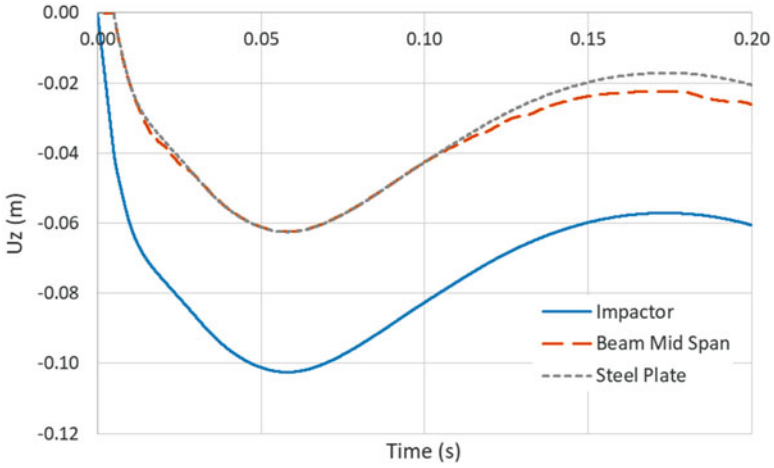

Fig. 39 Vertical displacements versus time in simulation

low velocity penetration test reproduced the experiment quite well. However, a slight difference was observed on the curves of the high velocity penetration test. For all experiments, damage seems to be quite accurately represented by the discrete element model. The phenomena observed experimentally, such as spalling on the front face with an injection of fragments, tunneling and scabbing on the rear face were generated successfully through all the simulations. In addition, diagonal cracking was well described into the perforation test specimen as well as in the beam submitted to the drop-weight impact.

After several years of development, these results show that the presented discrete element model is a powerful computational tool now capable to perform realistic simulations of concrete and reinforced concrete protection structures subjected to extreme loading in an industrial context.

References

A. Antoniou, Discrete element modelling of concrete structures under impact. PhD thesis. Université Grenoble Alpes (2018)

A. Antoniou, L. Daudeville, P. Marin, A. Omar, S. Potapov, Discrete element modelling of concrete structures under hard impact by ogive-nose steel projectiles. Eur. Phys. J. Spec. Top. **227**(1–2), 143–154 (2018)

C. Berriaud, A. Sokolovsky, R. Gueraud, J. Dulac, R. Labrot, Comportement local des enceintes en beton sous l'impact d'un projectile rigide: Local behaviour of reinforced concrete walls under missile impact. Nucl. Eng. Design **45**(2), 457–469 (1978)

H. Bian, Y. Jia, J. Shao, C. Pontiroli, Numerical study of a concrete target under the penetration of rigid projectile using an elastoplastic damage model. Eng. Struct. **111**, 525–537 (2016)

P.H. Bischoff, S.H. Perry, Compressive behaviour of concrete at high strain rates. Mater. Struct. **24**(6), 425–450 (1991)

W.F. Brace, A.H. Jones, Comparison of uniaxial deformation in shock and static loading of three rocks. J. Geophys. Res. **76**(20), 4913–4921 (1971)

CEB. Concrete structures under impact and impulsive loading. Comité Euro-International du Béton, Synthesis report, Lausanne, Switzerland (1988)

CEB-FIP model code 1990, in Comité Euro-international du Béton, ed. by Thomas Telford (1993)

B. Chareyre, P. Villard, Dynamic spar elements and discrete element methods in two dimensions for the modeling of soil-inclusion problems. J. Eng. Mech. **131**(7), 689–698 (2005)

L. Cui, C. O'Sullivan, Analysis of a triangulation based approach for specimen generation for discrete element simulations. Granul. Matter **5**(3), 135–145 (2003)

P.A. Cundall, O.D. Strack, A discrete numerical model for granular assemblies. Geotechnique **29**(1), 47–65 (1979)

G. Cusatis, Strain-rate effects on concrete behavior. Int. J. Impact Eng. **38**(4), 162–170 (2011)

G. Cusatis, Z.P. Bažant, L. Cedolin, Confinement-shear lattice model for concrete damage in tension and compression: I. Theory. J. Eng. Mech. **129**(12), 1439–1448 (2003)

L. Daudeville, Y. Malecot, Concrete structures under impact. Eur. J. Environ. Civ. Eng. **15**(1), 101–140 (2011)

F.V. Donze, S.A. Magnier, L. Daudeville, C. Mariotti, L. Davenne, Numerical study of compressive behavior of concrete at high strain rates. J. Eng. Mech. **125**(10), 1154–1163 (1999)

B. Erzar, P. Forquin, Experiments and mesoscopic modelling of dynamic testing of concrete. Mech. Mater. **43**(9), 505–527 (2011)

B. Erzar, P. Forquin, Analysis and modelling of the cohesion strength of concrete at high strain-rates. Int. J. Solids Struct. **51**(14), 2559–2574 (2014)

P. Forquin, B. Erzar, Dynamic fragmentation process in concrete under impact and spalling tests. Int. J. Fract. **163**(1–2), 193–215 (2010)

E. Frangin, P. Marin, L. Daudeville, On the use of combined finite/discrete element method for impacted concrete structures. J Phys IV (Proc.) **134**, 461–466, EDP sciences (2006)

T. Gabet, Y. Malécot, L. Daudeville, Triaxial behaviour of concrete under high stresses: Influence of the loading path on compaction and limit states. Cem. Concr. Res. **38**(3), 403–412 (2008)

R.A. Gingold, J.J. Monaghan, Smoothed particle hydrodynamics: Theory and application to non-spherical stars. Mon. Not. R. Astron. Soc. **181**(3), 375–389 (1977)

J.K. Gran, D.J. Frew, In-target radial stress measurements from penetration experiments into concrete by ogive-nose steel projects. Int. J. Impact Eng. **19**, 715–726 (1979)

S. Hentz, L. Daudeville, F.V. Donzé, Identification and validation of a discrete element model for concrete. J. Eng. Mech. **130**(6), 709–719 (2004)

H.J. Herrmann, A. Hansen, S. Roux, Fracture of disordered, elastic lattices in two dimensions. Phys. Rev. B **39**, 637–647 (1989)

U. Hornemann, J.F. Kalthoff, H. Rothenhaüsler, H. Senf, S. Winkler, Experimental investigation of wave and fracture propagation in glass—slabs loaded by steel cylinders at high impact velocities. EMI Report E4 (1984)

K. Iwashita, M. Oda, Rolling resistance at contacts in simulation of shear band development by DEM. J. Eng. Mech. **124**(3), 285–292 (1998)
J.F. Jerier, D. Imbault, F.V. Donze, P. Doremus, A geometric algorithm based on tetrahedral meshes to generate a dense polydisperse sphere packing. Granul. Matter **11**(1), 43–52 (2009)
R.P. Kennedy, A review of procedures for the analysis and design of concrete structures to resist missile impact effects. Nucl. Eng. Design **37**(2), 183–203 (1976)
Q.M. Li, H. Meng, About the dynamic strength enhancement of concrete-like materials in a split Hopkinson pressure bar test. Int. J. Solids Struct. **40**(2), 343–360 (2003)
Q.M. Li, Y.B. Lu, H. Meng, Further investigation on the dynamic compressive strength enhancement of concrete-like materials based on split Hopkinson pressure bar tests. Part II: Numerical simulations. Int. J. Impact Eng. **36**(12), 1335–1345 (2009)
L.B. Lucy, A numerical approach to the testing of the fission hypothesis. Astron. J. **82**, 1013–1024 (1977)
Y. Malecot, L. Daudeville, F. Dupray, C. Poinard, E. Buzaud, Strength and damage of concrete under high triaxial loading. Eur. J. Environ. Civ. Eng. **14**(6–7), 777–803 (2010)
L.J. Malvar, J.E. Crawford, Dynamic increase factors for concrete. Naval Facilities Engineering Service Center Port hueneme CA (1998)
L.J. Malvar, C.A. Ross, Review of strain rate effects for concrete in tension. ACI Mater. J. **95**(6), 735–739 (1998)
S.A. Novikov, I.I. Divnov, A.G. Ivanov, The study of fracture of steel, aluminium and copper under explosive loading. Fiz. Met. Metalloved. **21**(4), 608–615 (1966)
A. Omar, P. Marin, S. Potapov, L. Daudeville, 3D discrete element modeling of concrete: Study of the rolling resistance effects on the macroscopic constitutive behavior, in *Computational Plasticity XII: Fundamentals And Applications, Proceedings of the 12th International Conference on Computational Plasticity (COMPLAS)*, ed. by E. Onate, D. R. J. Owen, D. Peric, B. Suarez, (2013), pp. 575–586
E. Piotrowska, P. Forquin, Y. Malecot, Experimental study of static and dynamic behavior of concrete under high confinement: Effect of coarse aggregate strength. Mech. Mater. **92**, 164–174 (2016)
C. Pontiroli, B. Erzar, E. Buzaud, Concrete behaviour under ballistic impacts: Effects of materials parameters to penetration resistance and modeling with PRM model, in *Computational Modelling of Concrete Structures: Proceedings of the EURO-C*, vol. 2, (2014), pp. 685–693
S. Potapov, A. Masurel, P. Marin, L. Daudeville, Mixed DEM/FEM modeling of advanced damage in reinforced concrete structures. J. Eng. Mech. **143**(2), 04016110 (2016)
J.D. Riera, On the stress analysis of structures subjected to aircraft impact forces. Nucl. Eng. Design **8**(4), 415–426 (1968)
J. Rousseau, E. Frangin, P. Marin, L. Daudeville, Damage prediction in the vicinity of an impact on a concrete structure: A combined FEM/DEM approach. Comput. Concr. **5**(4), 343–358 (2008)
J. Rousseau, E. Frangin, P. Marin, L. Daudeville, Multidomain finite and discrete elements method for impact analysis of a concrete structure. Eng. Struct. **31**(11), 2735–2743 (2009)
S. Saatci, Behaviour and modelling of reinforced concrete structures subjected to impact loads, Ph. D. Thesis, University of Toronto (2007)
SALOME, Computer software, http://www.salome-platform.org
Y. Sawamoto, H. Tsubota, Y. Kasai, N. Koshika, H. Morikawa, Analytical studies on local damage to reinforced concrete structures under impact loading by discrete element method. Nucl. Eng. Design **179**(2), 157–177 (1998)
M.J. Schmidt, O. Cazacu, M.L. Green, Experimental and theoretical investigation of the high-pressure behavior of concrete. Int. J. Numer. Anal. Methods Geomech. **33**(1), 1–23 (2009)
D. Sfer, I. Carol, R. Gettu, G. Etse, Study of the behavior of concrete under triaxial compression. J. Eng. Mech. **128**(2), 156–163 (2002)
W. Shiu, F.V. Donzé, L. Daudeville, Penetration prediction of missiles with different nose shapes by the discrete element numerical approach. Comput. Struct. **86**(21–22), 2079–2086 (2008a)

W. Shiu, F.V. Donzé, L. Daudeville, Compaction process in concrete during missile impact: A DEM analysis. Comput. Concr. **5**(4), 329–342 (2008b)

SpherePadder++, Computer software, http://subversion.assembla.com/svn/spherepadder

X.H. Vu, Y. Malecot, L. Daudeville, Strain measurements on porous concrete samples for triaxial compression and extension tests under very high confinement. J. Strain Anal. Eng. Design **44**(8), 633–657 (2009a)

X.H. Vu, Y. Malecot, L. Daudeville, E. Buzaud, Effect of the water/cement ratio on concrete behaviour under extreme loading. Int. J. Numer. Anal. Methods Geomech. **33**, 1867–1888 (2009b)

X.H. Vu, Y. Malecot, L. Daudeville, E. Buzaud, Experimental analysis of concrete behavior under high confinement: Effect of the saturation ratio. Int. J. Solids Struct. **46**, 1105–1120 (2009c)

X.H. Vu, L. Daudeville, Y. Malecot, Effect of coarse aggregate size and cement paste volume on concrete behavior under high triaxial compression loading. Constr. Build. Mater. **25**(10), 3941–3949 (2011)

T.L. Warren, A.F. Fossum, D.J. Frew, Penetration into low-strength (23 MPa) concrete: Target characterization and simulations. Int. J. Impact Eng. **30**(5), 477–503 (2004)

J. Weerheijm, Concrete under impact tensile loading and lateral compression. Doctoral dissertation, Delft University of Technology (1992)

M. Zhang, H.J. Wu, Q.M. Li, F.L. Huang, Further investigation on the dynamic compressive strength enhancement of concrete-like materials based on split Hopkinson pressure bar tests. Part I: Experiments. Int. J. Impact Eng. **36**(12), 1327–1334 (2009)

X.Q. Zhou, H. Hao, Modelling of compressive behaviour of concrete-like materials at high strain rate. Int. J. Solids Struct. **45**(17), 4648–4661 (2008)

Damage in Concrete Subjected to Impact Loading

21

Pascal Forquin

Contents

Why Damage Modes in Concrete Targets Subjected to Impact Loading Need to be Investigated? 552
Examples of Damage Processes Involved in Concrete Targets Subjected to Small Caliber Projectile 557
Investigation of Damage Processes in Concrete Under Edge-On Impact Test 561
Presentation of the EOI Testing Technique Applied to Concrete 561
EOI Test Applied to Ductal® UHPC Concrete 563
EOI Test Applied to Dry and Wet MB50 Microconcrete and R30A7 Common Concrete 565
Summary of Damage Modes Expected in Concrete Under Various Loading Conditions 567
Numerical Simulation of a Ballistic Impact Against a Concrete Target 570
Presentation of the KST-DFH Coupled Plasticity-Anisotropic Damage Model 570
Numerical Simulation of the Impact of a Striker Against a Common Concrete Slab 572
Conclusion 573
References 575

Abstract

This chapter aims to illustrate the damage modes observed in concrete structures subjected to high-strain-rate and impact loadings. During the impact of soft or hard projectile against a concrete target complex high-stresses and strain-rates-transient dynamic loading develops leading to various damage modes such as cratering on the front face, crushing and shearing in the projectile-target contact area, radial fracturing in the whole target, and, in case of the perforation, spalling on the rear face. In order to improve the constitutive models and numerical tools used to describe projectile-target interaction, these damage modes need to be

P. Forquin (✉)
Laboratoire 3SR, Université Grenoble Alpes, Grenople INP, CNRS, Grenoble, France
e-mail: pascal.forquin@3sr-grenoble.fr

© Springer Nature Switzerland AG 2022

G. Z. Voyiadjis (ed.), *Handbook of Damage Mechanics*,
https://doi.org/10.1007/978-3-030-60242-0_79

studied and better understood. The present chapter first illustrates various observations of fracturing processes in concrete targets reported in different experimental works. Next, "laboratory impact experiments" in which the damage modes were carefully analyzed are presented. In addition, various experimental techniques that are used to analyze the strength and damage of concrete under high-strain-rates are illustrated. The expected damage modes induced under impact loading depending on the level of confinement and strain-rates are summarized. Finally, based on the experimental data of spalling tests and quasi-oedometric compression tests, a coupled plasticity-damage model is fitted and numerical calculations are used to predict the ballistic performances of a common concrete.

Keywords

Concrete · Dynamic impact · Damage model · Numerical simulation

Why Damage Modes in Concrete Targets Subjected to Impact Loading Need to be Investigated?

The problem of better predicting the strength of concrete structures under hard projectile impact loading is relatively old since it was already present during the Second World War during which the Tallboy bombs (mass: 5.5 t including 2.3 Torpex, total length: 6.4 m) and Grand Slam (mass: 10 t including 4.3 Torpex, total length: 7.7 m) capable of perforating concrete bunkers about, respectively, 5 and 7 m in thickness were used by the Royal Air Force (RAF) with the aim of destroying the bases that hosted the German submarines or the operational command centers (Buzaud 2002). This problem accelerated during the 1990s with the use during the First Gulf War of a 1.8 t kinetic penetrator (BLU-113) capable of perforating 4.6 m of reinforced concrete. Conventional kinetic penetrators consist of a steel body containing the explosive charge. With a mass of between 250 and 800 kg, they impact their target at a speed of around 300 m/s. In order to reduce their mass or increase their penetrating capacity, they can be associated with a shaped charge that is triggered near the impact point, which creates a tunnel of smaller diameter than the diameter of the kinetic penetrator but sufficient to guide the latter in the target (Hewish 1998). In 1990s, in order to investigate the impact behavior of concrete, ogive-nosed projectiles of reduced dimensions compared to real kinetic penetrators were developed to perform ballistic impacts in laboratory.

In the example of Fig. 1, a penetration test was conducted in the CEA-Gramat research center with a 2.4 kg ogive-nosed steel penetrator, 52 mm in diameter and 300 mm in length (CRH = 5.77). The cylindrical target, 800 mm in thickness and 800 mm in diameter, is made of unreinforced concrete. The concrete is considered as water-saturated since the time needed for drying such concrete slab at its center may exceed several decades. The hard-steel projectile was instrumented with an embedded acceleration recording system to measure the axial deceleration during the tests.

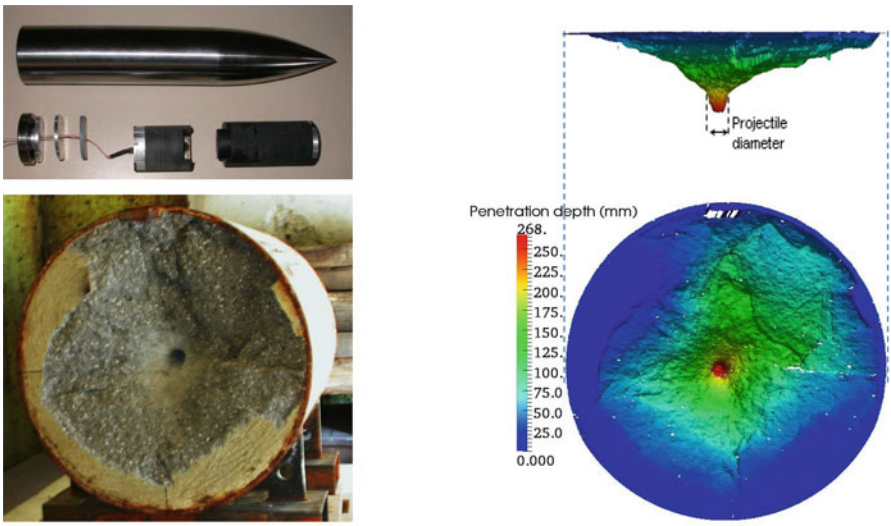

Fig. 1 (**a**) Rigid projectile with its acceleration recording system, (**b**) front face of target after shot ($V_{impact} = 347$ m/s) (Forquin et al. 2015)

Table 1 Concrete strength and kinetic penetrator considered in several studies reporting impact experiments conducted with reduced scale ogive-nosed projectiles

Reference:	(Forrestal et al. 1996)	(Frew et al. 1998)	(Gomez and Shukla 2001)	(Buzaud 1998)	(Forquin et al. 2015)
Diameter D (mm)	12.92, 20.3, 30.5	20.3, 30.5	6.35	25	52
Ratio L/D	6.9, 10	10–15, 10	10	6.0	5.8
CRH (R_{ogive}/D)	3.0–4.25	3.0	3.0	3.0	3.0
Mass (Kg)	0.064, 0.48, 1.6	0.48, 1.6	0.015	0.5	2.4
f_c^{28} (MPa)	13.5–62.8	58.4	38.15	38, 200, 600	30
Striking velocity (m/s)	370–1430	400–1200	200–600	200–600	225–425

After the test, a topographic laser system was employed to measure the dimensions of the crater and the tunnel (Fig. 1) showing a penetration depth about 5 times larger than the projectile diameter.

Ballistic impacts in laboratory tests make it possible to study the influence of impact parameters (impact speed, impact angle, attack angle, L/D ratio, R_{ogive}/D ratio, projectile mass) as well as the influence of the concrete strength (under uniaxial compression) on the crater dimensions and on the depth of penetration at reduced cost compared to real impact performed on concrete block of several cubic meters (Table 1).

Based on these reduced-scale experiments, several closed-form solutions were proposed for predicting the penetration depth of ogive-noise projectile as proposed by Luk and Forrestal (1987). The model proposed by Forrestal et al. (1994) is derived from a spherical cavity expansion theory in which the radial stress is related the square of the applied speed to the cavity. The ogive-shape of the projectile noise is taken into account by means of the variable N (Eq. 2) assuming a rigid projectile. The contact force F applied by the projectile during the tunneling process is given approximately by:

$$F = \pi a^2 \left(S f_c{}' + N \rho V^2 \right) \quad \text{when z} > 4\text{a}, \tag{1}$$

where ($a = D/2$) corresponds to the radius of the projectile, S to an adimensional parameter which depends on the concrete strength, $f_{c'}$ to the concrete uniaxial compressive strength at 28 days, ρ being the density of the concrete, and N is defined as a function of the ogive radius (R_{ogive}) by the function (Gomez and Shukla 2001):

$$N = \frac{8CRH - 1}{24(CRH)^2}, \tag{2}$$

where *CRH,* the caliber radius head ratio, is defined as the ratio of the radius of curvature of the noise to the projectile diameter. The penetration depth P is taken equal to the sum of the depth associated to the "crater" region assumed to be equal to two projectile diameters and that corresponding to the "tunnel" region:

$$P = P_c \ln \left(1 + \left(\frac{V_t}{V_c} \right)^2 \right) + 4a, \tag{3}$$

where V_t corresponds to the speed of the projectile when entering into the tunnel ($V_t \approx V_{\text{impact}}$), P_c and V_c are parameters defined by

$$P_c = \frac{m}{2\pi a^2 \rho N}, \tag{4}$$

$$V_c = \left(\frac{S f_c{}'}{N \rho} \right)^{\frac{1}{2}}, \tag{5}$$

where m is the projectile mass and S is a parameter expressed as a function of the uniaxial compressive strength that was identified on concretes with uniaxial compression strength ($f_{c'}$) ranging from 13.5 to 97 MPa (Frew et al. 1998) based on impact experimental results:

$$S = 82,6 \ (f_c{}')^{-0,544}. \tag{6}$$

During the two last decades, several experimental and analytical works have been developed to improve the predictive capabilities of such closed-form solutions

(Forrestal et al. 1994, 2003; Warren et al. 2004; Wen and Yang 2014) and a literature review was proposed by Li et al. (2005). More recently, by considering the same spherical cavity-expansion approach, Warren and Forquin (2016) proposed to replace the parameter S, which needs depth of penetration data, with a description of concrete behavior assuming a linear pressure–volumetric strain relation that takes into account the irreversible compaction and a pressure-dependent shear strength plasticity envelope along with a tensile cutoff. After obtaining the parameters from laboratory scale material tests from quasi-oedometric compression tests and spalling tests, the analytical model was able to predict the projectile deceleration and the final depth of penetration of a kinetic penetrator impacting a target made of saturated common concrete with a striking velocity of 347 m/s.

However, despite their many advantages (predictive capabilities, zero calculation cost, and possibility to perform parametric studies...), these approaches present several limitations and drawbacks. Among them, one may note the simplistic description of concrete behavior, the lack of information regarding the growth of damage, final damage state and residual strength of concrete target, or their weak predictive capabilities in the case of impact against thin targets (target thickness less than a few projectile diameters).

Another way to predict the response of concrete structures and their damage modes under projectile impact is to use the numerical modeling. Among the most used numerical tools to describe the interaction between a projectile and a concrete target stands out the Finite element method (FEM) in which each solid is discretized into a finite number of parts (elements) and can be used in conjunction with an explicit dynamic scheme. The mechanical behavior of each material needs to be implemented through a constitutive model connecting the displacement increment to the stress tensor in relation with internal variables (for instance, damage variables).

For the last decades, continuum damage models have been developed with the aim to describe the physics of damage processes in concrete and more generally in brittle materials. For instance, the isotropic damage model proposed by Lu and Xu (2004) is based on the use of continuum fracture mechanics applied to preexisting microcracks for predicting the processes of crack nucleation, growth, and coalescence. Another example of micromechanics-based model that relies on a description of the physical phenomena involved in brittle materials under high-strain-rates loading is the Denoual, Forquin, and Hild (DFH) model. This anisotropic damage model is based on the concepts of obscuration probability (Denoual and Hild 2000) and local weakest-link hypothesis (Forquin and Hild 2010). Microstructural parameters are introduced through an explicit law of critical defects and through parameters related to crack propagation. The model provided a prediction of strength and cracking density as function of the applied strain-rate and material parameters related to the triggering of critical defects and the growth of obscuration zones around unstable cracks.

This model was extensively used in the last two decades to predict the fragmentation properties of ceramics (Denoual and Hild 2000; Forquin et al. 2018), concretes (Forquin and Hild 2008; Forquin and Erzar 2010), and rocks [Grange et al. 2008; Saadati et al. 2015, 2017). The development of such micromechanics-based models

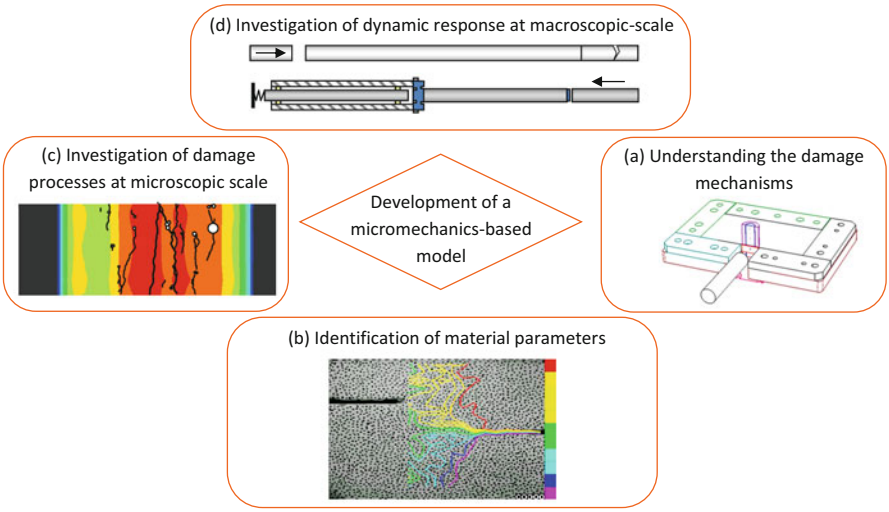

Fig. 2 Use of different testing methods for the development of a micromechanics-based model. (**a**) Techniques to characterize the damage mechanisms in brittle materials; among them the edge-on impact testing technique with ultra-high speed imaging and postmortem observation. (**b**) Techniques to identify model parameters; among them the rocking spalling test to characterize the crack speed in concrete (Forquin 2012). (**c**) Techniques to validate the constitutive model based on comparison a microscopic scale; the spalling technique can be used for this purpose. (**d**) Techniques used to characterize the dynamic response at the macroscopic scale; among them the Hopkinson pressure bar apparatus (Figure derived from Forquin (2017))

needs first a careful identification of damage processes at a microscale that can be supported by in situ observations (ultra-high speed imaging, full field measurements) and postmortem studies (measurements of cracking densities, microtomography analysis) (Fig. 2a), parameters adjustment (Fig. 2b), validation steps through a comparison between numerical predictions, and experimental observations at a microscopic scale (Fig. 2c) and at a macroscopic scale (Fig. 2d). It is the reason why the damage processes need to be experimentally and numerically investigated.

Many other types of numerical methods have been developed to describe the behavior of concrete structures under impact. Among them one may mention the mesh-free methods such as the smoothed-particle hydrodynamics method (SPH) or the discrete element method (DEM) (Antoniou et al. 2018), which are well suited in problems involving very large deformations and weak (strain) or strong (displacement) discontinuities. Another approach is the lattice discrete particle method (LDPM) as proposed by Cusatis et al. (2011) that is a mesoscale model in which the behavior of concrete is formulated at the length scales of coarse aggregate particles by postulating the interaction laws of a system of discrete polyhedral cells. The LDPM method allows capturing the transition from single localized cracks to complete material fragmentation and comminution (Cusatis et al. 2017).

Whatever the applied numerical method, it needs a careful validation based on an accurate comparison between the numerical predictions and several experimental

observations at the microscopic and macroscopic scales. For this purpose, the damage processes involved in concrete subjected to high loading-rates still need to be addressed.

Examples of Damage Processes Involved in Concrete Targets Subjected to Small Caliber Projectile

In the present subsection, several examples of damage processes induced in concrete structures under impact loadings are presented. Several ballistic experiments were conducted with a mortar reinforced (M2M) or not (M2) with ceramic particles and with an ultra-high performance concrete called Ductal®. The small size of aggregates (0.5 mm in M2 and Ductal® concretes and 6 mm in M2M concrete) facilitates the post-mortem observations of the fracturing pattern. The composition, the uniaxial compression strength, and the flexural strength (3-point bending tests) of each tested concrete are listed in Table 2.

In the first example (Fig. 3), two mortars reinforced or not with ceramic particles where subjected to ballistic impact experiments. The first target called M2 is a mortar without particle and composed of fine sand (maximum size ≈ 500 μm), cement (Lafarge PEMS 52.5), silica fumes, water, and additive silica fume. The second target called M2M has the same composition as M2 – fine sand, cement, silica fumes, water, additive – with an addition of the alumina particles (41.1% by mass, around 30% vol.) of size 3–6 mm (Table 2). The silica fume and admixture allow to reduce the amount of water so the water to cement + binder ratio is around 0.41 in both materials. The two impact tests were conducted with perfectly cylindrical steel projectiles, 5.3 mm in diameter, 8 mm in length, of mass 1.2 g and of high hardness (65 HRC) (Forquin et al. 2006; Arias et al. 2009). Fired at a speed about 750 m/s, their velocity was measured with two optical barriers. The targets of dimensions $70 \times 70 \times 50$ mm^3·were placed in an aluminum casing to restrict any movement of debris during the impact within the damaged block. In addition, to prevent erosion on the front face of the block, a ply-wood strip was placed side by side to the block surface inside the sarcophagus. Tests performed without this strip showed that it did not change the depth of penetration. After the impact, each block was infiltrated with a hyper-fluid colored resin. The block was then cut, reinfiltrated, and polished for inspection.

Two post-mortem fracturing patterns are shown in Fig. 3. Whereas the penetrated depth in M2 block is 14.9 mm, the penetrated depth in M2M is much less (about 7.0 mm) and the projectile is tilted. This result demonstrates the beneficial effect of large aggregate compared to projectile diameter also reported in Werner et al. (2013).

Different kinds of damage mechanisms can be observed in M2 target. In the first 5–10 mm around the tunnel, an intense microcracking is observed and the large pores, which are observed beyond this zone, seem to have disappeared. It is supposed that microcracking and pore collapse occurred in this area due to dynamic shearing and high confining pressure. In addition, numerous long cracks radiating from this first zone are observed. There cracks should result from tensile hoop

Table 2 Composition and main mechanical properties of five concretes

Composition	M2	M2M	Ductal®	MB50	Wet R30A7
Reference	(Forquin et al. 2006, 2008a, b)		(Forquin 2003)	(Bernier and Dalle 1998)	(Erzar and Forquin 2011)
Aggregates (kg/m^3)	0	1084	0	0	1008
Sand (kg/m^3)	1332	941	885	1783	838
Crushed quartz (kg/m^3)	0	0	220	0	0
Silica fume (kg/m^3)	55.5	39.2	235	0	0
Cement (kg/m^3)	555	392	730	400	263
Water (kg/m^3)	253	179	160	200	169
Admixture (kg/m^3)	4.6	3.3	10	12	0
Water/(cement + SF)	0.415	0.415	0.166	0.50	0.64
Max. aggregate size (mm)	0.5	6	0.5	5	8
Steel fibers (vol. %)	0	0	2	0	0
Compressive strength (MPa)	70.8	66.8	220	70	29
Flexural strength (MPa) Loaded volume (mm^3) (Lxhxw)	8.9 (100 × 20 × 15)	9.24 (100 × 20 × 15)	21.9 (130 × 11 × 10)	5.29 (120 × 40 × 40)	6.1 (120 × 40 × 20)

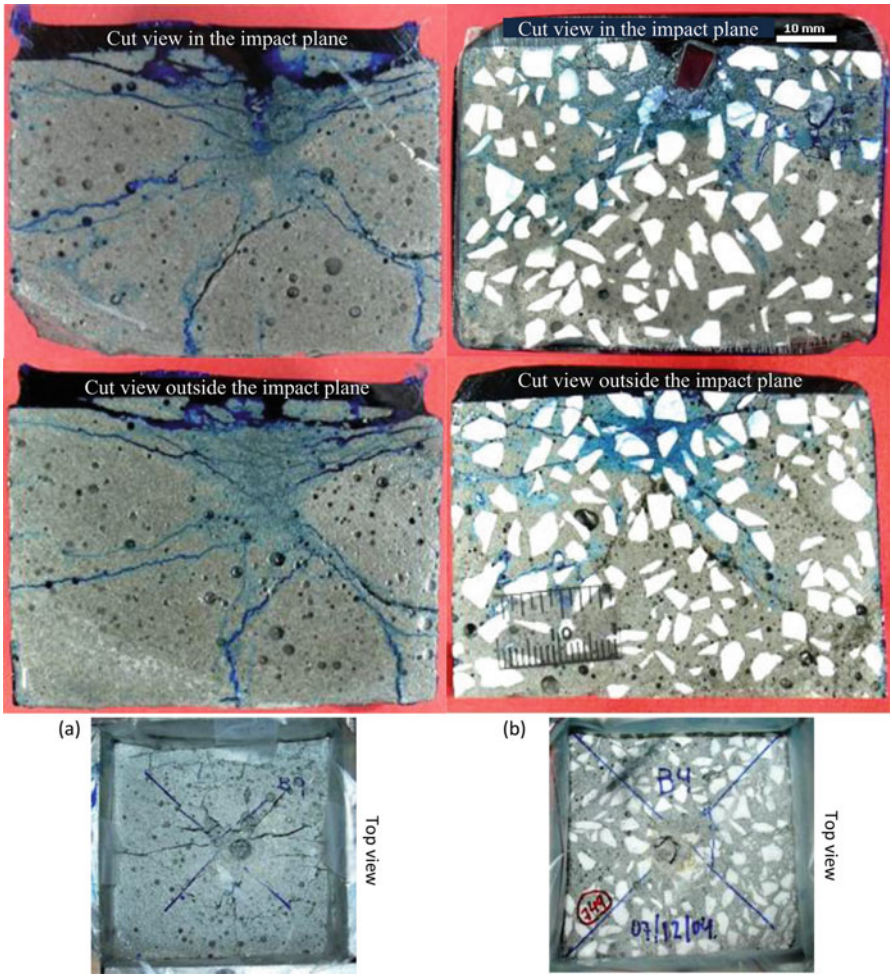

Fig. 3 Ballistic impact of small bullet (**a**) Mortar M2 (impact velocity: 762 m/s, depth of penetration: 14.9 mm), (**b**) Mortar M2M (Impact velocity: 749 m/s, depth of penetration: 7 mm) (Forquin et al. 2006; Arias et al. 2009)

stresses that spread out the target during the penetration process. In addition saucer-shaped cracks develop parallel to the impact surface before emerging on the top surface. This mode II cracking mode results from dynamic shearing leading to the target cratering.

In the second example (Fig. 4), ballistic impact tests were carried out on a multilayer targets made of two tiles of Ductal® concrete (of thickness: 2 × 30 mm) backed with an aluminum alloy plate (10 mm in thickness). The Ductal® concrete is reinforced with steel fibers (Fig. 4a) or not (Fig. 4b). The projectile is an armor-piercing projectile (AP7.62 mm P80) with a mass of 9.8 g

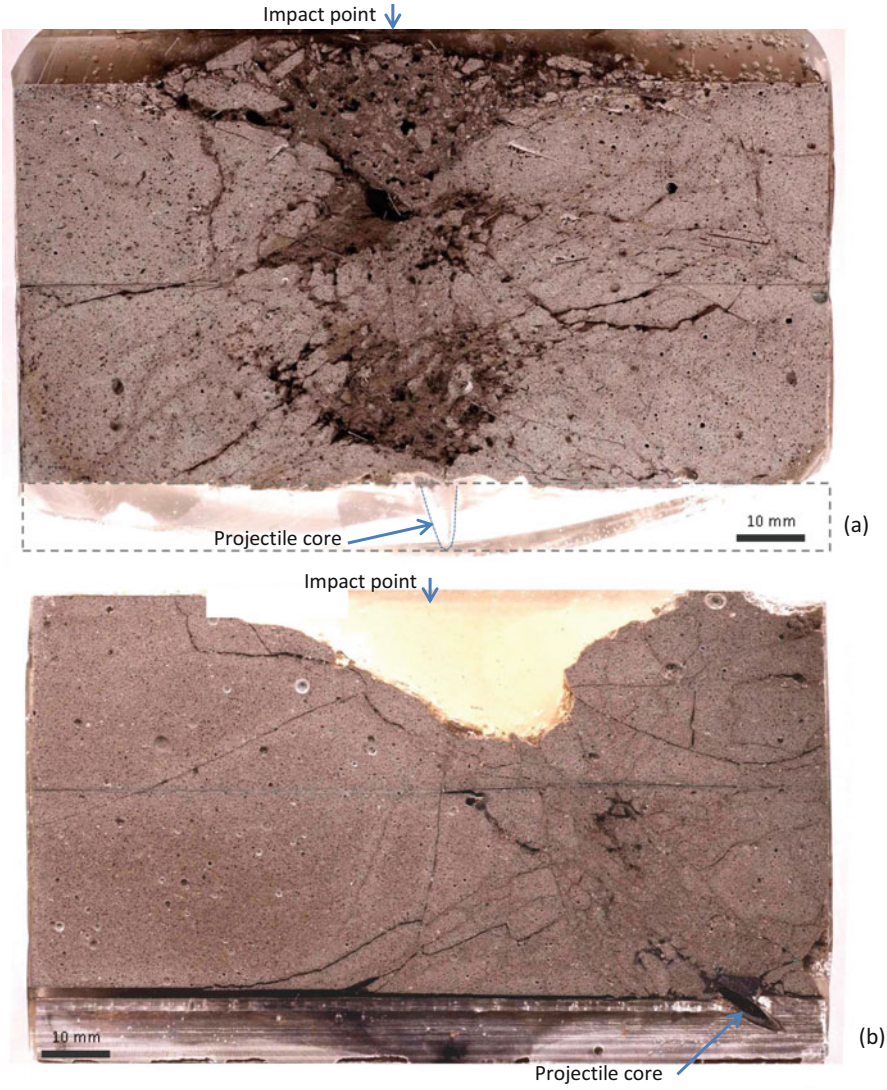

Fig. 4 Ballistic impacts of P80 AP Armor-Piercing projectile (850 m/s) against targets made of two UHPC concrete plates 30 mm thick backed with an aluminum alloy plate 10 mm (Forquin 2003; Forquin and Hild 2010). (**a**) Fiber-reinforced UHPC (the dotted rectangle represents the backing), (**b**) nonfibered UHPC

impacting the target with a nominal speed of 840 m/s. A complex fracturing pattern is observed. First, an important erosion of the target is observed all around the impact point. The cratering process on the front face is only slightly reduced in the fiber-reinforced target. Second, numerous radial cracks originating from the impact zone are noted. Furthermore, scabbing developed on the rear face. In addition, a complex

cracking network appears all around the tunnel region. The damage processes that result from the transient dynamic confined, shear, and tensile loadings induced at the time of impact and during the penetration stage is supposed to influence the penetration resistance of the target and need to be investigated.

For this purpose, different testing methods were applied to ultra-high performance concrete (UHPC) with and without fibers. The confined behavior of Ductal® concrete was explored through quasi-oedometric compression (QOC) tests and confined shear experiments in Forquin and Lukic (2016). In the QOC test, the concrete sample was inserted in a confining vessel and axially compressed. Hydrostatic pressures as high as 800 MPa were obtained and the hydrostatic and deviatoric behavior was deduced. The shear strength of concrete was characterized by means of Punch-Trough-Shear (PTS) tests, under lateral pressure ranging from 30 to 80 MPa in the sheared zone (Lukić and Forquin 2016). The PTS experiments conducted with a modified Hopkinson pressure bar apparatus revealed a more pronounced influence of confining pressure than of the loading-rate. Finally, it was concluded that the influence of fibers is weak under confined loading. Furthermore, the tensile behavior of UHPC was investigated through spalling tests in Forquin et al. (2017) considering four sets of samples. Samples of UHPC without fibers, with randomly oriented fibers, badly oriented fibers and well-oriented fibers were subjected to spalling tests, which demonstrated a small influence of fibers and fiber orientation on the peak stress along with a strong influence of fibers and fibers orientation on the postpeak (softening) behavior of UHPC. This conclusion was also supported by mesoscopic numerical simulations in which steel fibers were introduced within a concrete matrix that was modeled with an anisotropic damage model.

Finally, as considered in Liu et al. (2009), Kong et al. (2016), Forquin et al. (2015), a constitutive modeling able to describe both, the hydrostatic and deviatoric confined behavior and the tensile response and strain-rate sensitivity of concrete, is necessary in order to correctly simulate numerically the ballistic performance of concrete.

Investigation of Damage Processes in Concrete Under Edge-On Impact Test

Presentation of the EOI Testing Technique Applied to Concrete

The experimental configuration drawn in Fig. 5 was developed to perform edge-on impact on tests on geomaterials. This experimental configuration consists in the impact of a cylindrical projectile against one of the edges of the tested concrete or rock tile. The projectile diameter (Table 3) is usually larger than the target thickness and much smaller than the target length. It results in an impulsive loading characterized by a very short rising time (less than a few μs). The loading, of triaxial shape in the vicinity of the contact area, turns into a bi-dimensional (plane stress) divergent wave propagating in the whole target. It is the reason why the stress amplitude is expected to decline more slowly (in $1/\sqrt{r}$) compared to a spherical expansion for

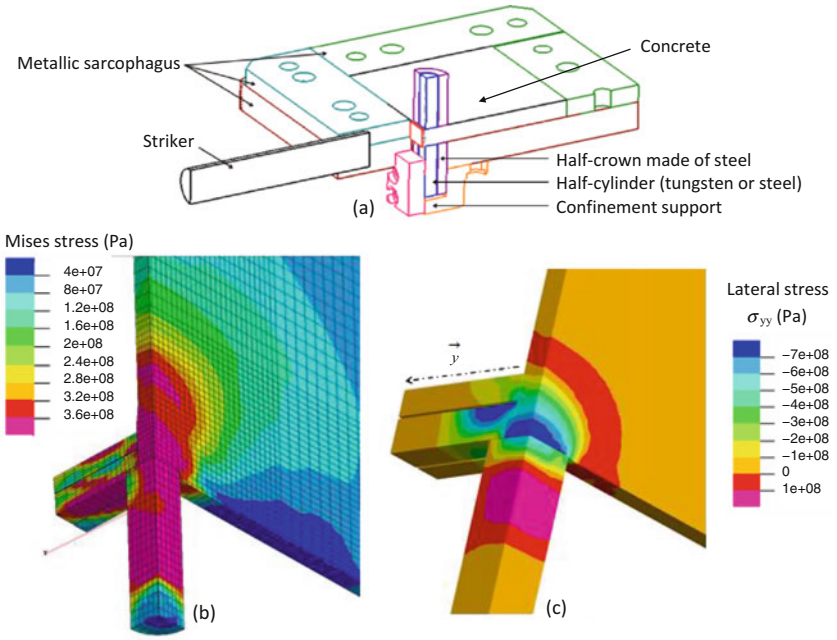

Fig. 5 Edge-on impact experiments conducted with Ductal® concrete in Forquin (2003). (**a**) Experimental configuration used to perform the test. The dynamic confinement system is placed in contact with the concrete plate near the impact point. (**b**) and (**c**) Numerical simulation of EOI test performed with a finite-element code. (**b**) Mises stress in the target. (**c**) Lateral stress in the target and in the confinement parts

Table 3 Material properties and dimensions of solids involved in EOI test in Forquin (2003)

Solids	Material	Dimension (mm)	ρ (kg/m^3)	$C_0 = (E/\rho)^{0,5}$ (m/s)	Yield strength (MPa)
Tile	Ductal®	300 × 150 × 10	2400	4800	–
Projectile	Steel	ϕ 20, H 50	7890	5100	>800
Projectile	Aluminum	ϕ 20, H 50	2840	4900	350
Confinement	Tungsten	ϕ 13, H 30	17,600	4500	>800
Confinement	Steel	ϕ_{int} 14, ϕ_{ext} 24, H 30	7890	5100	>600

which a decrease in $(1/r)$ is expected. In addition, contrary to the testing configuration used with ceramics (Riou et al. 1998; Forquin et al. 2003), a dynamic confinement system is employed for testing geomaterials. This confinement system consists in two half-cylinders made of tungsten and two half-crowns made of steel (or only two cylinders made of steel) that are put in contact with the lateral faces of the concrete tile near the impact point (Fig. 5a) (Forquin and Hild 2008). It ensures a plane-strain compression loading in front of the projectile. The increase of hydrostatic pressure in this area reduces the tensile damage and the spalling of the target. In

this way, the compressive wave is able to spread out the whole tile. The radial displacement of the matter induced by the passage of the incident pulse generates dynamic tensile stresses in the hoop direction that result in intense fragmentation composed of radial cracks.

EOI Test Applied to Ductal® UHPC Concrete

This testing configuration applied to Ductal® UHPC was numerically simulated with a finite-element code (Pamshock explicit FE code) considering an elastoplastic model for the concrete plate with a yield strength (400 MPa) that corresponds to the maximum deviatoric strength measured in oedometric (1D-strain) loading conditions (Forquin 2003). Two configurations were developed based on these calculations. In the first one, an aluminum alloy striker (yield strength: 350 MPa) impacting the target with an impact speed of 80 m/s allows to prevent any compressive damage beneath and beyond the confinement system. In the second one, a striker made of steel (yield strength: 800 MPa) impacts the target with an impact speed of 130 m/s. As illustrated in Fig. 5b, in this configuration, the concrete yield strength is reached beneath and beyond the confinement system leading to plastic deformation. The field of lateral stresses is illustrated in Fig. 5c. Beneath the confinement system, lateral stresses ranging from 200 to 700 MPa are noted which illustrates the beneficial effect of this system. However, the level of confinement is maintained during a time interval restricted to about one round-trip in the confinement parts. For this reason, the system is called "dynamic confinement."

A metallic casing called sarcophagus was developed to keep fragments close to their original position. After the test, a colored hyperfluid resin is injected to highlight the damage pattern. This testing configuration was first applied to Ductal® concrete with and without fibers (Forquin 2003; Forquin and Hild 2008), to limestone (Grange et al. 2008), MB50 microconcrete (Forquin and Erzar 2010), R30A7 common concrete (Erzar and Forquin 2011), and more recently to granite (Saadati et al. 2015). The main experimental results and conclusions obtained with Ductal® UHPC, MB50 microconcrete, and R30A7 common concrete are briefly reported below.

EOI experiments reported in Forquin (2003); Forquin and Hild (2008) were conducted with fibered and nonfibered Ductal® concrete considering two types of striker (aluminum alloy and steel) and striking velocities ranging from 70 to 140 m/s (Table 3). In the example of Fig. 6, fiber-reinforced Ductal® concrete tiles are subjected to EOI test with a steel projectile and a striking velocity about 130 m/s. The first EOI test (Fig. 6a) was conducted in open configuration in which an ultra-high speed camera is used to visualize the development of the fragmentation process. A compressive damage composed of involute (curved) cracks develops in less than 20 μs after impact. Then, the damage zone darkens due to the tilt of the visualized surface. Furthermore, 44 μs after impact, multiple straight radial cracks appear due to tensile hoop stresses. Spall cracks, oriented perpendicularly to the projectile axis, are observed 44 μs after impact 70 mm from the impact point. The distance between

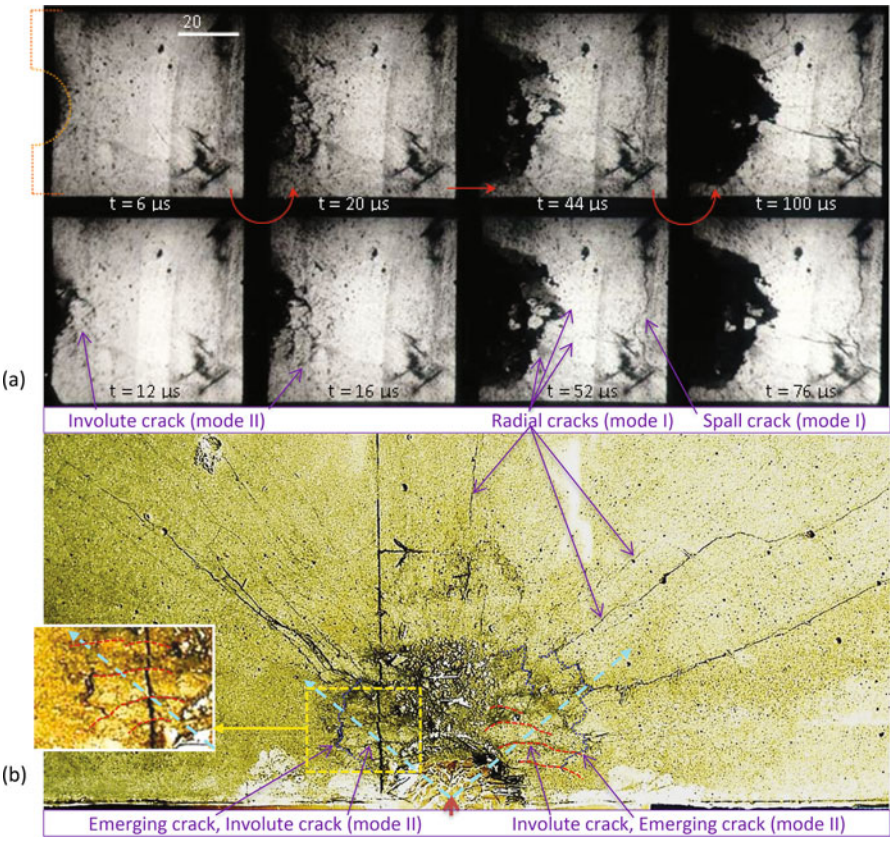

Fig. 6 EOI test conducted with steel projectile and dynamic confinement system with fiber reinforced Ductal® concrete. (**a**) Open configuration, striking velocity: 132 m/s. (**b**) Sarcophagus configuration, striking velocity: 130 m/s

spall cracks and the rear edge (60 mm) corresponds approximately to the projectile length (50 mm). The time to initiation is consistent with a wave velocity close to 5000 m/s (38 µs are required to travel 190 mm).

The final damage pattern more easily analyzed with the sarcophagus configuration (Fig. 6b) and several damage modes are observed as a function of the distance from the impact point:

- Close to the impact point the confined zone is totally damaged and reduced in debris despite the fibers that reinforce the target.
- Beyond the confined area, involute cracks (also called snail cracks) are observed. It can be noted that these cracks are more or less oriented at 45° with respect to the radial and hoop directions and correspond to crack in mode II with rubbing lips.
- Moreover, circular-front cracks centered on the impact point. These cracks are thought to emerge to the surface leading to the dark areas observed on pictures

given by the ultra-high speed camera between 16 μs and 44 μs after impact. These "emerging crack" or "shell cracks" are supposed to result from unconfined compression beyond the confined area.
- This confined damage does not prevent an intense fragmentation of the tile at a distance of 40 mm to 130 mm from the impact point. This fragmentation is composed of numerous radial cracks, which are few centimeters long.
- In addition, spall cracks (not visible in Fig. 6b) are observed at a distance of 50 mm from the rear edge which corresponds to the projectile length.

EOI experiments conducted with Ductal® concrete without fiber subjected to the impact of a steel projectile at a striking velocity led to similar observations. In the target tested in open configuration (Fig. 7a), the Imacon 790 ultra-high speed camera shows involute cracks and emerging cracks that develop in a dozen of microseconds. In addition, numerous radial cracks are generated in less than 44 μs in addition to the spall cracks oriented parallel to the rear edge. Fig. 7b illustrates a target tested in sarcophagus configuration. The confined area appears as completely eroded. Beyond the confinement, several cut views show the shell cracks that are inclined with respect to the radial and normal directions to the tile. These cracks are supposed to propagate in (shearing) mode II. In addition, a little further from the confined area, chimney (or balcony) cracks are also observed. These (half-) cylindrical (or slightly conical) cracks initiate from the spherical pores (near the equator) and propagate along the compression axis forming a chimney-shaped (or balcony-shaped) fracture surface. This type of fracturing mode was previously numerically described in Forquin (2003) by simulating the cracking process around a spherical pore within a volume subjected to a uniaxial compression loading (Fig. 8a). It was also experimentally observed on the fracturing pattern of a cylindrical sample of M2 mortar subjected to a uniaxial compression (Forquin et al. 2007; Arias et al. 2008) (Fig. 8b) and is supposed to result from low-confinement compression loading. However, in the detailed view of Fig. 7b, it seems to contribute to the start of pore-collapse process in a pore located close to confinement area where much higher compression stresses operate.

EOI Test Applied to Dry and Wet MB50 Microconcrete and R30A7 Common Concrete

The EOI testing technique with dynamic confinement system was applied to MB50 microconcrete plates ($200 \times 120 \times 15$ mm^3) in Forquin and Erzar (2010) by using cylindrical projectile 22.5 mm in diameter and 100 mm in length made of high-strength aluminum alloy. The projectile is projected onto the edge of the target at a speed of 50 m/s. In these experiments, half-cylinders made of steel are used as dynamic confinement. The specimens were infiltrated postmortem and polished to reveal the damage pattern. The results obtained on dry and wet specimens are reported in Fig. 9a. It is remarked that the cracking density is much higher in dry specimen compared to wet sample. Moreover, the cracks induced in the wet target

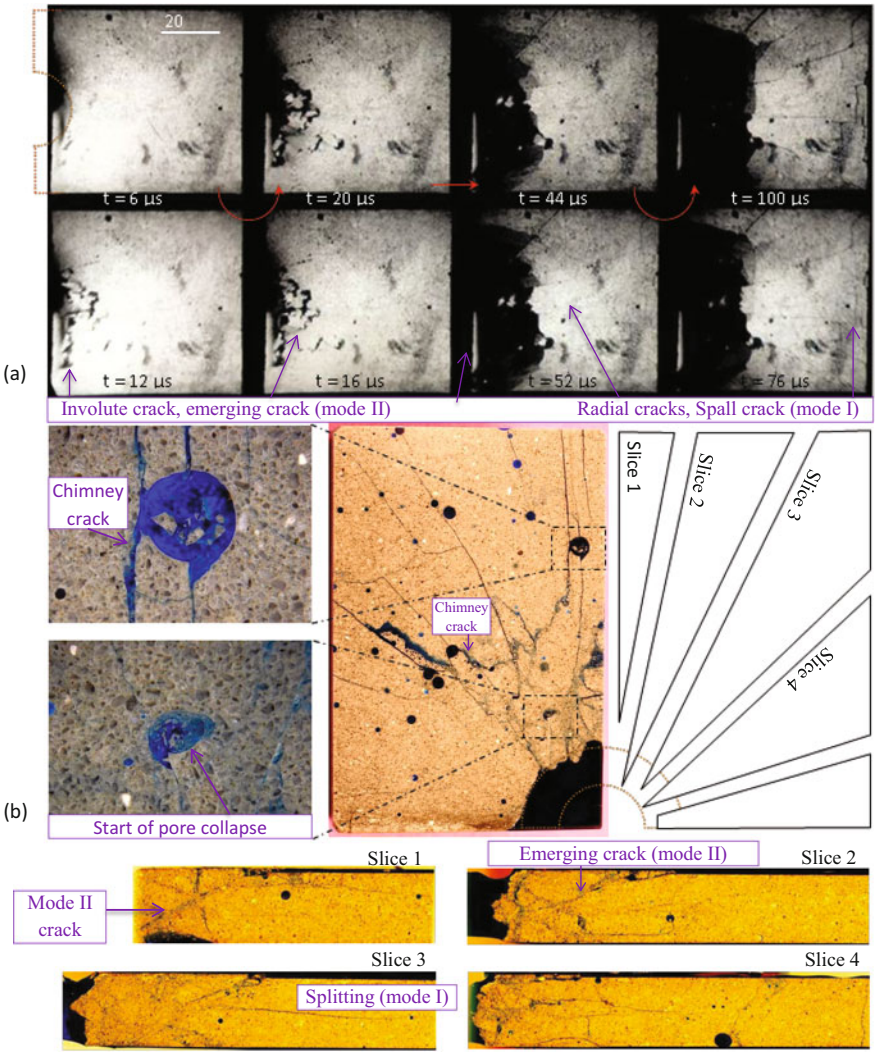

Fig. 7 EOI test conducted with steel projectile and dynamic confinement system with Ductal® concrete without fiber. (**a**) Open configuration, striking velocity: 130 m/s. (**b**) Sarcophagus configuration, striking velocity: 130 m/s

seem to be much thinner. Finally, free water in the microconcrete is seen to play a major role on the damage pattern. This result is consistent with spalling tests which show a lower tensile strength in dry MB50 microconcrete compared to wet MB50 microconcrete over the whole range of explored strain rates (30–150 s^{-1}) (Forquin and Erzar 2010). Edge-on impact experiments as well as spalling tests were also conducted on R30A7 concrete (max. aggregate size: 8 mm) to determine the influence of aggregate size (Erzar and Forquin 2011). The damage patterns presented

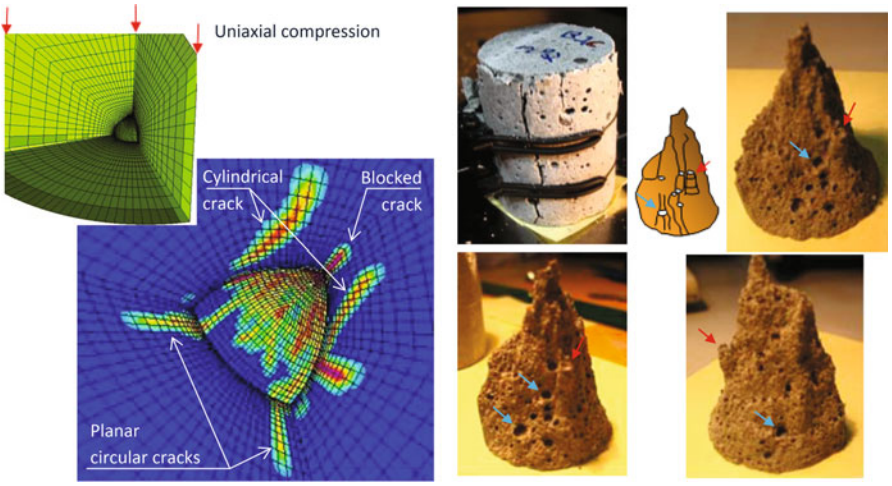

Fig. 8 Damage process induced under uniaxial compression loading. (**a**) Numerical prediction considering a spherical pore into a cylindrical volume (Forquin 2003). (**b**) Post-test failure pattern of M2 mortar cylindrical sample subjected to a uniaxial compression test (Forquin et al. 2007). Stress to failure is 67 MPa. Red arrows indicate chimney-shaped fracture surface. Blue arrows indicate balcony-shaped fracture surfaces

in Fig. 9b confirm the previous observations: Damage is much more pronounced in the dry tile compared to the wet specimen. In the same way as the dry MB50 microconcrete, an intense cracking developed near the impacted area. Farther, many long radial cracks are observed in the dry R30A7 plate. Oppositely, the cracking network is less developed in the wet tile: Several cracks are presented but their opening is limited. Besides, one can see that few aggregates are broken: Cracks have circumvented the inclusions during their propagation. Again, this result is seen to be consistent with spalling experiments which exhibited a much higher strength with wet samples than with dry samples (Erzar and Forquin 2011). It is the reason why the water content needs to be taken into account in a numerical modeling to be used for numerically simulated the ballistic impact against a concrete target.

Summary of Damage Modes Expected in Concrete Under Various Loading Conditions

A summary of damage modes observed in concrete samples subjected to different kinds of quasi-static and dynamic tests are depicted on the drawing of Fig. 10. The loading paths are represented in a plot in which the horizontal axis corresponds to the hydrostatic pressure defined as function of the principles stresses (σ_I, σ_{II}, σ_{III}):

$$P = -\frac{\sigma_I + \sigma_{II} + \sigma_{III}}{3}, \tag{7}$$

and the vertical axis corresponds to the Huber-Mises equivalent stress (Eq. (8)).

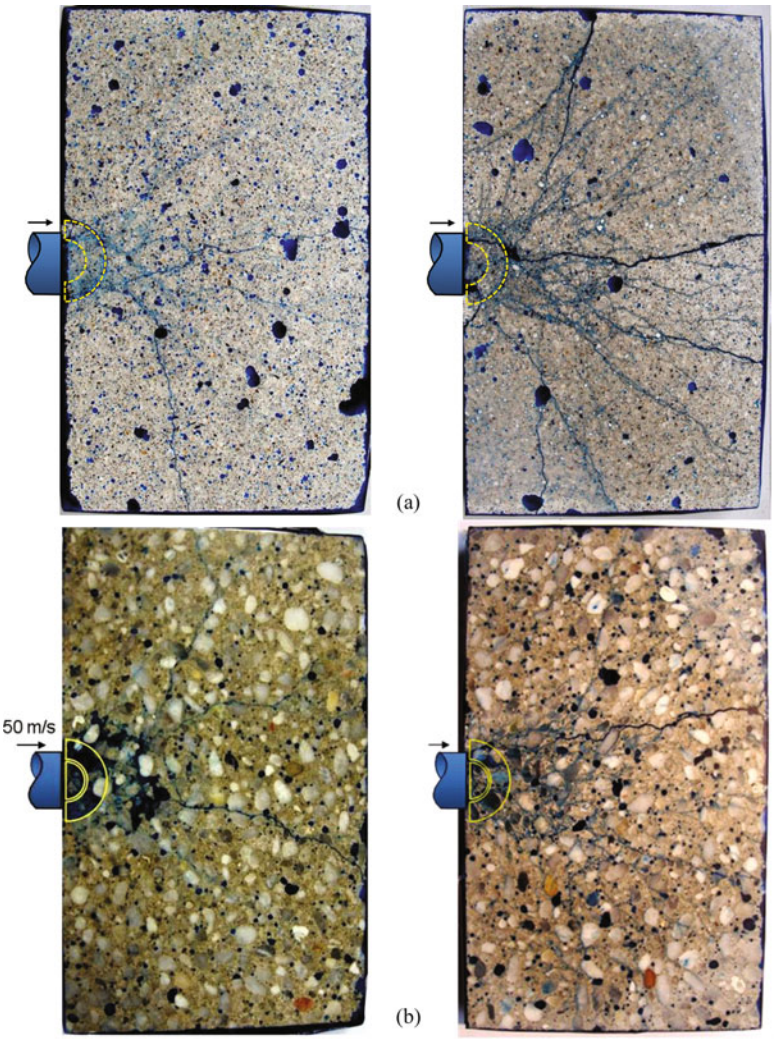

Fig. 9 EOI test conducted with dynamic confinement in sarcophagus configuration at striking velocity: 50 m/s. (**a**) MB50 microconcrete (Forquin and Erzar 2010), (**b**) R30A7 concrete (Erzar and Forquin 2011) tested in wet condition (left) and dry condition (right)

$$q = \sqrt{\frac{1}{2}\left[(\sigma_I - \sigma_{II})^2 + (\sigma_{II} - \sigma_{III})^2 + (\sigma_{III} - \sigma_I)^2\right]} \tag{8}$$

In this representation, the uniaxial compression test corresponds to a straight line starting from the origin of slope equal to 3. The oedometric path that corresponds to a

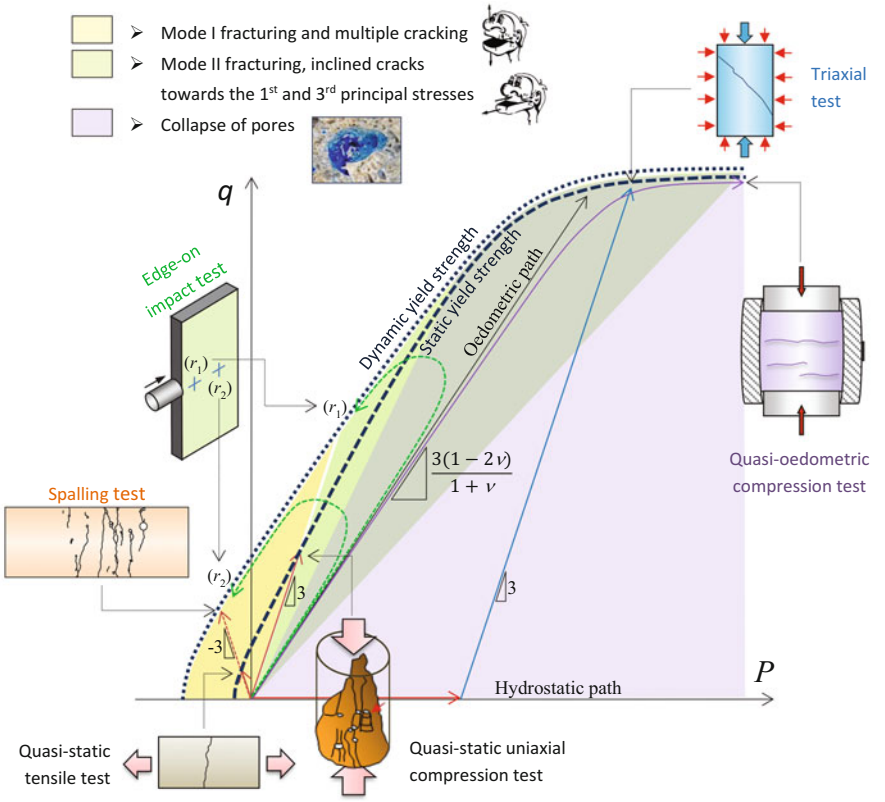

Fig. 10 Representation of the loading paths involved in various quasi-static and dynamic experiments applied to concrete. The areas in which mode I fracturing, mode II fracturing (inclined cracks towards the 1st and 3rd principal stresses), and pore collapse are expected are depicted with different colors

compression in uniaxial strain ($\varepsilon_I = \varepsilon_{II} = 0, \varepsilon_{III} < 0$) is a straight line starting from the origin with a slope equal to:

$$\frac{q}{P} = \frac{3(1-2\nu)}{1+\nu}. \tag{9}$$

In a dynamic spalling test conducted with a Hopkinson bar apparatus, radial and hoop stresses are supposed to be small compared to the axial stress and the slope in a (P, q) diagram would be equal to -3 (uniaxial tensile loading). Figure 10 illustrates the expected damage modes as function of the applied loading. Mode I multiple-fracturing is observed in spalling tests as well as in edge-on impact tests far from the impact point (radius r_2). Mode II fracturing was observed in EOI tests in the vicinity of the dynamic confinement system (radius r_1). Pore collapse is anticipated under high confining pressures (in triaxial test, quasi-oedometric compression test, or

within the confined area of EOI test). Furthermore, the plot of Fig. 10 illustrates the strong increase of yield strength with pressure in concretes and their higher strain-rate sensitivity under tensile loading compared to confined compression loading. It is the reason why a constitutive model able to describe at the same time the anisotropic damage due to mode I multiple fracturing in dynamic tensile loading, the pressure-dependent plastic yielding under high confining pressure, and the plastic volumetric response due to irreversible collapse of pores is needed to numerically simulate the behavior of a concrete structure subjected to hard-projectile impact. In the further section, a coupled plasticity-anisotropic damage model is presented to model the behavior of concrete under dynamic tensile loading and confined compression.

Numerical Simulation of a Ballistic Impact Against a Concrete Target

Presentation of the KST-DFH Coupled Plasticity-Anisotropic Damage Model

The KST-DFH model is a coupled plasticity-anisotropic damage model that was developed to numerically simulate the behavior of concrete and rock under impact loading. The Krieg, Swenson, and Taylor model (Krieg 1978; Swenson and Taylor 1983) provides a description of both the hydrostatic and the deviatoric behavior of concrete under high confinement. It includes an equation of state linking the volumetric strain to the hydrostatic pressure which is a piecewise linear curve entered point by point. Furthermore, the model accounts for the increase of the yield strength (Y) (in the sense of Huber-Mises criterion) of concrete with confining pressure (P) according to the following equation:

$$Y = \min_{P} \left(Y_{\max}, \sqrt{a_0 + a_1 P + a_2 (P)^2} \right), \tag{10}$$

where $Y_{\max}$, a_0, a_1, a_2 are parameters to be identified from quasi-oedometric compression tests or triaxial tests. In particular $Y_{\max}$ is used to describe the limitation of strength observed in water saturated concrete under high hydrostatic pressure (Forquin et al. 2010; Vu et al. 2009). The KST model parameters of wet R30A7 concrete are reported in Table 4 according to the data from Erzar and Forquin (2011).

The Denoual-Forquin-Hild (DFH) model (Denoual and Hild 2000; Forquin and Hild 2010) is an anisotropic damage model in which three independent damage variables (D_i) associated to each orthogonal principal direction (d_i) are calculated. The strain components (ε_i) are related to the macroscopic stress components (Σ_i) and to the microscopic stress components (σ_i) according to:

Table 4 Parameters of KST-DFH plasticity-damage model for wet (water saturated) R30A7 concrete

Density, elasticity	Wet R30A7	KST parameter	Wet R30A7	DFH parameter	Wet R30A7
ρ [kg/m^3]	2390	a_0 [MPa^2]	$1.61.10^{15}$	ε_0 [s^{-1}]	10^{-5}
ν	0.2	a_1 [MPa]	$9.8.10^7$	n_{QS}	0.05
E [GPa]	42	a_2	0.54	$\sigma_0{}^d$ [MPa]	11
		Y_{max} [MPa]	210	$\varepsilon_0{}^d$	4.10^{-3}
		K_{final}[Pa]	$2.3.10^{10}$	n^d	1
		$\{\varepsilon_v, P_i$ [MPa]$\}$	(−0.0017,30)	$\sigma_0{}^w$ [MPa]	4
			(−0.025, 100)	$\varepsilon_0{}^w$	1.10^{-3}
			(−0.045, 195)	n^w	1
			(−0.055, 300)	$\sigma_w{}^{QS}$ [MPa]	6.1
			(−0.065, 500)	Z_{eff} [mm^3]	284
			(−0.073, 700)	m	12
			(−0.080, 900)	S	3.74
				k	0.32

$$\begin{pmatrix}\varepsilon_1\\ \varepsilon_2\\ \varepsilon_3\end{pmatrix} = \frac{1}{E}\begin{bmatrix}\frac{1}{1-D_1} & -\nu & -\nu\\ -\nu & \frac{1}{1-D_2} & -\nu\\ -\nu & -\nu & \frac{1}{1-D_3}\end{bmatrix}\begin{pmatrix}\Sigma_1\\ \Sigma_2\\ \Sigma_3\end{pmatrix} = \frac{1}{E}\begin{bmatrix}1 & -\nu & -\nu\\ -\nu & 1 & -\nu\\ -\nu & -\nu & 1\end{bmatrix}\begin{pmatrix}\sigma_1\\ \sigma_2\\ \sigma_3\end{pmatrix} \tag{11}$$

where E is the Young's modulus and ν is the Poisson's ratio of the undamaged material. The damage variable D_1 being associated to the maximum principle stress σ_1 (such as $\sigma_1 \geq \sigma_2 \geq \sigma_3$), it is the reason why D_1 isocontours are plotted in the next figure.

In addition, cohesion strength in obscured zones was introduced in Erzar and Forquin (2014) for better describing the post-peak tensile behavior of concrete. Accordingly each macroscopic stress variable (Σ_i) is related to the corresponding obscuration probability (P_{oi}):

$$\Sigma_i = (1 - P_{oi})\sigma_i + (P_{oi})^{\alpha_D}\sigma_i^{\text{coh}} = (1 - D_i)\sigma_i \tag{12}$$

where P_{oi} denotes the obscuration probability in each cracking directions (d_i) calculated according to equation:$\frac{d^2}{dt^2}\left(\frac{1}{1-P_{oi}}\frac{dP_{oi}}{dt}\right) = \lambda_t[\sigma_i(t)]\, n!S(kC)^3$ when $\frac{d\sigma_i}{dt} > 0$ and $\sigma_i > 0$, (13)where S is a shape parameter ($S = 3.74$), C is 1D wave speed

($C = \sqrt{E/\rho}$), and k is a constant ($k = 0.32$) identified in Forquin (2012). The density of critical defect is given by Hild et al. (2003):

$$\lambda_t[\sigma_i(t)] = \begin{cases} 0 & if \quad \sigma_i(t) \leq \sigma_k \\ \lambda_0 \left(\dfrac{\sigma_i(t)}{\sigma_0} \right)^m & \text{otherwise} \end{cases} \tag{14}$$

where σ_k is stress generated randomly for each finite element k according to the inverted Weibull law of Eq. (6)

$$\sigma_k = \sigma_w \left(\frac{Z_{eff}}{Z_{FE}} \ln \left(\frac{1}{1 - p_k} \right) \right)^{\frac{1}{m}} \tag{15}$$

p_k being obtained by drawing lot numbers varying between 0 and 1, Z_{FE} being the volume of the finite element k and m, σ_w and Z_{eff} being, respectively, the Weibull modulus, the average tensile strength, and effective volume identified in quasi-static bending tests. The cohesion strength σ_i^{coh} considered in obscured zones is defined as:

$$\sigma_i^{\text{coh}} = \sigma_0^d \text{Exp}\left(-\left(\frac{\varepsilon_i}{\varepsilon_0^d} \right)^{n_d} \right) + \sigma_0^w \text{Exp}\left(-\left(\frac{\varepsilon_i}{\varepsilon_0^w} \right)^{n_w} \right) \tag{16}$$

First part of Eq. (16) provides the cohesion strength of the dry concrete, whereas the second part describes the additional strength provided by the free water. The parameters of the cohesion strength $\sigma_0^d, \sigma_0^w, n_d, n_w, \varepsilon_0^d, \varepsilon_0^w$ can be identified based on the experimental data of spalling tests by comparing the velocity profiles measured on the rear face of spalling samples to the predictions of numerical modeling. The parameters of wet R30A7 concrete are reported in Table 3. The whole identification procedure is explained in Erzar and Forquin (2011, 2014). The coupled KST-DFH model was implemented as a VUMAT routine used in Abaqus-explicit finite-element software.

Numerical Simulation of the Impact of a Striker Against a Common Concrete Slab

The numerical predictions in terms of projectile deceleration and velocity are compared to experimental results in Fig. 11a considering the configuration presented in Fig. 1 (thickness: 800 mm, impact velocity: 347 m/s) and the parameters of the wet R30A7 concrete (Table 4). A good compliance between the simulation results and the experimental data is observed. In addition the final penetration depth predicted by the numerical simulation (0.3 m) is quite close to the experimental value (0.27 m). The damage pattern predicted by the numerical simulation at 500 μs and 1100 μs is shown in Fig. 11b and c. The cratering process due to near-top surface is seen to develop within the first 500 μs. At this moment, the tunneling process

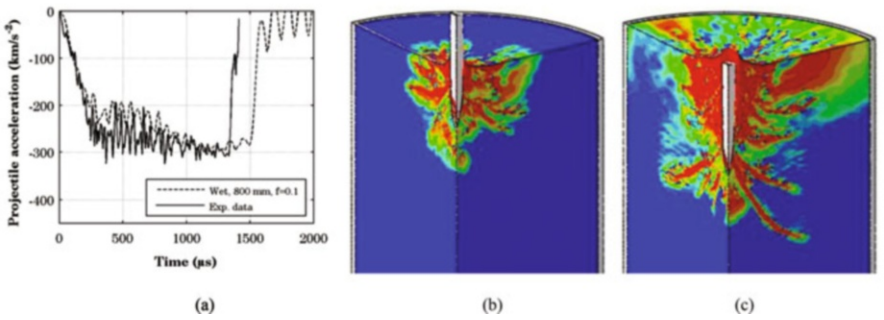

Fig. 11 Numerical simulation of the impact of a striker at $V_{impact} = 347$ m/s against a concrete slab made of wet R30A7 of thickness 800 mm (Forquin et al. 2015). (**a**) Comparison between experimental and numerical acceleration profiles. Predicted damage with KST-DFH model (**b**) at 500 μs, (**c**) at 1100 μs

begun and the projectile deceleration is close to being constant. During the whole penetration process, very high pressures (about 300 MPa) are noted in front of the projectile. However, it was demonstrated that penetration process was influenced both by the plastic yielding and hydrostatic response of concrete as well as its tensile strength. Indeed, even after the first 500 μs others tensile fractures propagate through the target. The projectile suddenly stops at 1500 μs (1400 μs in the test).

The influence of free water content in the concrete was investigated in Forquin et al. (2015) by considering successively parameters of wet and dry concrete in the KST (confined behavior) and DFH (tensile strength) models. It was demonstrated that the water-saturation ratio is of major importance as dry concrete was better resisting than wet concrete at the beginning of the impact loading, whereas wet concrete provides higher deceleration amplitude than dry concrete in the second part of the impact loading. Finally, as claimed in Kong et al. (2016), it is concluded that a modeling able to describe both, the confined behavior and the tensile strength and fracture energy of concrete, is of utmost necessity in order to correctly simulate numerically the damage processes such as scabbing and cratering phenomenon and the ballistic performance of concrete structures.

Conclusion

In the present chapter, experimental data and numerical simulations are presented to elucidate the loading conditions and the resulting damage modes in concrete structures when subjected to high-strain-rate and impact loadings. First, post-mortem analyses of impacted targets illustrate the deformation and failure modes involved in concrete targets under ballistic impact of small projectiles. It is observed that in the tunnel region, an intense microcracking due to dynamic shearing and high confining pressure is observed and the large pores, which are observed beyond this zone, are collapsed. In addition, numerous oriented cracks are noted which results from tensile

hoop stresses that spread out the target during the penetration process. Moreover, cratering (saucer-shaped cracks) fracture develops parallel to the impacted surface before emerging on the front surface. Scabbing is observed near the rear face in case of perforation of the target.

To investigate the damage modes induced under dynamic tensile loading and confined compression, the edge-on impact experiments with dynamic confinement system are considered. These experiments performed in open configuration (with a visualization of the lateral surface with an ultra-high speed camera) and in sarcophagus configuration shed a new light on the damage processes involved in concrete targets under impact loading. Depending on striker velocity, the nature of projectile and the distance from the impact point several damage modes can be observed. Thus, with steel projectile impacting the target at about 130 m/s, "involute" cracks (also called "snail" cracks) with rubbing lips (mode II) were seen to develop in UHPC target due to dynamic shearing. In addition, close to the impact point, start of pore collapse was observed. "Emerging" cracks (also called "shell" cracks) that result from unconfined compression beyond the confined area were also noted. These high-confinement and low-confinement damage modes do not prevent a multiple cracking composed of numerous radial cracks that result from tensile hoop stresses neither a spall fracture that develops parallel to the rear edge. Conversely, another configuration, in which a projectile made of aluminum alloy impacts the target with a striking velocity about 50 m/s, prevents these compression damage modes. This configuration applied to dry and wet MB50 microconcrete and R30A7 common concrete reveals an intense fragmentation process composed of radially oriented cracks. However, consistent to spalling tests, the cracking network is less more pronounced in dry specimen than in the wet target in which the crack opening is limited. As conclusion, the water content appears as a key parameter to take into account in a numerical modeling of ballistic impact against a concrete target.

In the third part of the present chapter, a coupled plasticity-anisotropic damage model is proposed in view of simulating the impact of hard projectile against concrete targets. The Krieg-Swenson-Taylor (KST) plasticity model accounts for the increase of yield strength with pressure and irreversible compaction under high confining pressure. The Denoual-Forquin-Hild (DFH) anisotropic damage model provides a description of the fragmentation process, in terms of crack-inception, crack propagation, and cohesion strength in the so-called obscured zones, that takes place in concrete under dynamic tensile loading. The DFH-KST model being implemented in a numerical code it is used to simulate a case of impact against a wet R30A7 concrete slab. This numerical simulation shows a good compliance with the experimental data in terms of penetration depth and acceleration profile and highlights the chronology of damage processes involved in the impacted concrete target.

In conclusion, this chapter illustrates the variety and complexity of loadings and resulting damage modes induced in concrete target subjected to hard-projectile impact. Indeed, different kinds of transient dynamic loadings are generated in the concrete volume corresponding to short pulses (a few μs, for instance, in the case of tensile fracturing) or much longer continuous loadings (for instance, about 1 ms for

the whole penetration process). Therefore, the behavior of concrete needs to be identified over a wide range of strain-rates (typically 10 s^{-1} to 1E4 s^{-1}) and considering distinct loading paths (spalling test, triaxial test, shear test, quasi-oedometric compression test). The development of more predictive models (such as micromechanics based model) and numerical approaches able to better describe these damage modes and the role of concrete microstructure (aggregates, cement matrix, free water content, fibers reinforcement...) at the microscopic and macroscopic scales still remains a strong prospect for further works.

References

A. Antoniou, L. Daudeville, P. Marin, A. Omar, S. Potapov, Discrete element modelling of concrete structures under hard impact by ogive-nose steel projectiles. Eur. Phys. J. Spec. Top. EDP Sci. **227**(1–2), 143–154 (2018)

A. Arias, P. Forquin, R. Zaera, C. Navarro, Relationship between bending and compressive behaviour of particle-reinforced cement composites. Compos. Part B **39**, 1205–1215 (2008)

A. Arias, P. Forquin, R. Zaera, Impact damage in concrete targets subjected to perforation of high velocity metallic fragment. DYMAT 2009 **2009**(2), 1215–1221 (2009). https://doi.org/10.1051/dymat/2009171

G. Bernier, J.-M. Dalle, Rapport d'essai de caractérisation des mortiers. Science Pratique S.A. (1998)

E. Buzaud, Performances mécaniques et balistiques du microbéton MB50. DGA/Centre d'Etudes de Gramat. Report (1998)

E. Buzaud, Les têtes explosives. Charges à éclats et à effets de souffle. SAE. Rapport (2002)

G. Cusatis, A. Mencarelli, D. Pelessone, J. Baylot, Lattice Discrete Particle Model (LDPM) for failure behavior of concrete. II: calibration and validation. Cem. Concr. Compos. **33**(9), 891–905 (2011)

G. Cusatis, R. Rezakhani, E.A. Schauert, Discontinuous cell method (DCM) for the simulation of cohesive fracture and fragmentation of continuous media. Eng. Fract. Mech. **170**, 1–22 (2017). https://doi.org/10.1016/j.engfracmech.2016.11.026

C. Denoual, F. Hild, A damage model for dynamic fragmentation of brittle solids. Comput. Methods Appl. Mech. Eng. **183**, 247–258 (2000)

B. Erzar, P. Forquin, Experiments and mesoscopic modelling of dynamic testing of concrete. Mech. Mater. **43**(9), 505–527 (2011)

B. Erzar, P. Forquin, Analysis and modelling of the cohesion strength of concrete at high strain-rates. Int. J. Solids Struct. **51**(14), 2559–2574 (2014). https://doi.org/10.1016/j.ijsolstr.2014.01.023

P. Forquin, Endommagement et fissuration de matériaux fragiles sous impact balistique, rôle de la microstructure. Ph.D. dissertation, Ecole Normale Supérieure de Cachan, France (2003)

P. Forquin, An optical correlation technique for characterizing the crack velocity in concrete. Eur. Phys. J. Spec. Top. **206**(1), 86–95 (2012)

P. Forquin, Brittle materials at high-loading rates: an open area of research. Phil. Trans. R. Soc. A **375**(2085), 20160436 (2017). https://doi.org/10.1098/rsta.2016.0436

P. Forquin, B. Erzar, Dynamic fragmentation process in concrete under impact and spalling tests. Int. J. Fract. **163**, 193–215 (2010)

P. Forquin, F. Hild, Dynamic fragmentation of an ultra-high strength concrete during edge-on impact tests. J. Eng. Mech. **134**(4), 302–315 (2008)

P. Forquin, F. Hild, A probabilistic damage model of the dynamic fragmentation process in brittle materials, in *Advances in Applied Mechanics*, ed. by Giessen, Aref, vol. 44, (Academic, San Diego, 2010), pp. 1–72

P. Forquin, B. Lukic, Experimental techniques to characterize the mechanical behaviour of ultra-high-strength-concrete under extreme loading conditions, in *Dynamic Behavior of Materials*, ed. by B. Song, L. Lamberson, D. Casem, J. Kimberley, vol. 1, (2016), pp. 229–237. https://doi.org/10.1007/978-3-319-22452-7_32

P. Forquin, L. Tran, P.-F. Louvigné, L. Rota, F. Hild, Effect of aluminum reinforcement on the dynamic fragmentation of SiC ceramics. Int. J. Impact Eng. **28**, 1061–1076 (2003)

P. Forquin, A. Arias, R. Zaera, An experimental method of measuring the confined compression strength of high-performance concretes to analyse their ballistic behaviour. J. Phys. IV **134**, 629–634 (2006). https://doi.org/10.1051/jp4:2006134097

P. Forquin, A. Arias, R. Zaera, Role of porosity in controlling the mechanical and impact behaviours of cement-based materials. Int. J. Impact Eng. **35**(3), 133–146 (2008a)

P. Forquin, A. Arias, R. Zaera, Relationship between mesostructure, mechanical behaviour and damage of cement composites under high-pressure confinement. Exp. Mech. **49**, 613–625 (2008b)

P. Forquin, K. Safa, G. Gary, Influence of free water on the quasi-static and dynamic strength of concrete in confined compression tests. Cement Concrete Res. **40**(2), 321–333 (2010)

P. Forquin, L. Sallier, C. Pontiroli, A numerical study on the influence of free water content on the ballistic performances of plain concrete targets. Mech. Mater. **89**, 176–189 (2015)

P. Forquin, J.L. Zinszner, B. Lukic, Mesoscopic modelling of ultra-high performance fiber reinforced concrete under dynamic loading, in *Dynamic Behavior of Materials*, ed. by D. Casem, L. Lamberson, J. Kimberley, vol. 1, (2017), pp. 123–129. https://doi.org/10.1007/978-3-319-41132-3_17

P. Forquin, J.-L. Zinszner, G. Rossiquet, B. Erzar, Microstructure influence on the fragmentation properties of dense silicon carbides under impact. Mech. Mater. **123**, 59–76 (2018)

M.J. Forrestal, B.S. Altman, J.D. Cargile, S.J. Hanchak, An empirical equation for penetration depth of ogive-nose projectiles into concrete targets. Int. J. Impact Eng. **15**(4), 395–405 (1994)

M.J. Forrestal, D.J. Frew, S.J. Hanchak, N.S. Brar, Penetration of grout and concrete targets with ogive-nose steel projectiles. Int. J. Impact Eng. **18**(5), 465–476 (1996)

M.J. Forrestal, D.J. Frew, J.P. Hickerson, T.A. Rohwer, Penetration of concrete targets with deceleration-time measurements. Int. J. Impact Eng. **28**, 479–497 (2003)

D.J. Frew, S.J. Hanchak, M.L. Green, M.J. Forrestal, Penetration of concrete targets with ogive-nose steel rods. Int. J. Impact Eng. **21**(6), 489–497 (1998)

J.T. Gomez, A. Shukla, Multiple impact penetration of semi-infinite concrete. Int. J. Impact Eng. **25**, 965–979 (2001)

S. Grange, P. Forquin, S. Mencacci, F. Hild, On the dynamic fragmentation of two limestones using edge-on impact tests. Int. J. Impact Eng. **35**, 977–991 (2008)

M. Hewish, Adding new punch to cruise missiles. Jane's Int. Def. Rev., **31**(1), 40–45 (1998)

F. Hild, C. Denoual, P. Forquin, X. Brajer, On the probabilistic-deterministic transition involved in a fragmentation process of brittle materials. Comput. Struct. **81**(12), 1241–1254 (2003)

X. Kong, Q. Fang, H. Wu, Y. Peng, Numerical predictions of cratering and scabbing in concrete slabs subjected to projectile impact using a modified version of HJC material model. Int. J. Impact Eng. **95**, 61–71 (2016)

R.D. Krieg, A simple constitutive description for soils and crushable foams. Sandia National Laboratory, Report SC-DR-7260883 (1978)

Q.M. Li, S.R. Reid, H.M. Wen, A.R. Telford, Local impact effects of hard missiles on concrete targets. Int. J. Impact Eng. **32**, 224–284 (2005)

Y. Liu, A. Ma, F.L. Huang, Numerical simulations of oblique-angle penetration by deformable projectiles into concrete targets. Int. J. Impact Eng. **36**(3), 438–446 (2009)

Y. Lu, K. Xu, Modelling modelling of dynamic behaviour of concrete materials under blast loading. Int. J. Solids Struct. **41**, 131–143 (2004)

V.K. Luk, M.J. Forrestal, Penetration into semi-infinite reinforced concrete targets with spherical and ogival nose projectiles. Int. J. Impact Eng. **6**, 291–301 (1987)

B. Lukić, P. Forquin, Experimental characterization of the punch through shear strength of an ultra-high performance concrete. Int. J. Impact Eng. **91**, 34–45 (2016). https://doi.org/10.1016/j.ijimpeng.2015.12.009

P. Riou, C. Denoual, C.E. Cottenot, Visualization of the damage evolution in impacted silicon carbide ceramics. Int. J. Impact Eng. **21**(4), 225–235 (1998)

M. Saadati, P. Forquin, K. Weddfelt, P.L. Larsson, F. Hild, A numerical study of the influence of pre-existing cracks on granite rock fragmentation at percussive drilling. Int. J. Numer. Anal. Methods Geomechan. **39**(5), 558–570 (2015)

M. Saadati, P. Forquin, K. Weddfelt, P.L. Larsson, F. Hild, On the mechanical behavior of granite material with particular emphasis on the influence from pre-existing cracks and defects. J. Test. Eval. **46**(1), 20160072 (2017). https://doi.org/10.1520/JTE20160072

D.V. Swenson, L.M. Taylor, A finite element model for the analysis of tailored pulse stimulation of boreholes. Int. J. Numer. Anal. Methods Geomechan. **7**, 469–484 (1983)

X.H. Vu, Y. Malécot, L. Daudeville, E. Buzaud, Experimental analysis of concrete behavior under high confinement: effect of the saturation ratio. Int. J. Solids Struct. **46**, 1105–1120 (2009)

T. Warren, P. Forquin, Penetration of common ordinary strength water saturated concrete targets by rigid ogive-nosed steel projectiles. Int. J. Impact Eng. **90**, 37–45 (2016)

T.L. Warren, A.F. Fossum, D.J. Frew, Penetration into low-strength (23MPa) concrete: Target characterization and simulations. Int. J. Impact Eng. **30**, 477–503 (2004)

H.M. Wen, Y. Yang, A note on the deep penetration of projectiles into concrete. Int. J. Impact Eng. **66**, 1–4 (2014)

S. Werner, K.-C. Thienel, A. Kustermann, Study of fractured surfaces of concrete caused by projectile impact. Int. J. Impact Eng. **52**, 23–27 (2013)

Failure Mechanisms of Ceramics Under Quasi-static and Dynamic Loads: Overview

22

Salil Bavdekar and Ghatu Subhash

Contents

Main Body Text 580
Introduction 580
Failure Mechanisms Based on Microstructural Defects 582
Failure Mechanisms Under Dynamic Loads 588
Constitutive Models and Damage Formulations 595
Summary 604
References 605

Abstract

In the last few decades, a variety of brittle materials (ceramics and glasses) have found new applications in the armor, nuclear and semiconductor, and energy storage industries. However, the constitutive behavior of these materials is drastically different from that of commonly used materials like metals and polymers. As these materials possess limited dislocation-based inelastic deformation mechanisms, intrinsic defects and inhomogeneities are the primary microstructural features that control their failure behavior. This chapter provides an overview of the deformation mechanisms that dominate the failure of ceramics and discusses the effect of strain rate and lateral confinement on their failure strength. As their high impact resistance is the primary driver of the research effort into the mechanical properties of these ceramics, additional deformation mechanics pertaining to their dynamic response to ballistic impact and penetration – such as fragmentation, spallation, cavity expansion, phase change, and amorphization – are also summarized. The latter part of the chapter deals with a survey of commonly used constitutive models under a wide range of applied pressures and strain rates. A

S. Bavdekar (✉) · G. Subhash (✉)
Department of Mechanical and Aerospace Engineering, University of Florida, Gainesville FL, USA
e-mail: salil.bavdekar@ufl.edu; subhash@ufl.edu

© Springer Nature Switzerland AG 2022

G. Z. Voyiadjis (ed.), *Handbook of Damage Mechanics*,
https://doi.org/10.1007/978-3-030-60242-0_80

number of these models are described and compared, with an aim to provide the reader an overview of their applicability.

Keywords

Strain rate · Confinement · Constitutive model · Fracture

Main Body Text

Introduction

Ceramics are nonmetallic, inorganic solids with ionic and covalent bonds; most of which are compounds of metallic elements with light elements such as B (borides), C (carbides), N (nitrides), or O (oxides). Among oxides, the most commonly used structural ceramics are alumina (Al_2O_3), zirconia (ZrO_2), urania (UO_2), ceria (CeO_2), etc. Silica (SiO_2), the most abundant material on earth (sand), is also the basis for glass, an amorphous brittle solid. In addition to oxides, some other commonly used structural ceramics are borides of zirconium (ZrB_2); carbides of tungsten (WC), boron (B_4C),and silicon (SiC); and nitrides of aluminum (AlN) and boron (BN).

A characteristic feature of ceramics is that their Peierls barrier (Nabarro 1947; Peierls 1940) to dislocation motion is high and anisotropic (Mitchell et al. 1985). Hence, under low confinement and at ambient temperatures, they tend deform elastically at low loads and undergo brittle fracture with little or no plastic strain when the applied stress exceeds their strength. Compared to metals, ceramics typically exhibit superior properties (see Table 1) such as high elastic modulus, hardness, compressive strength, and melting point and possess excellent thermal, chemical, and wear resistance. These properties result in ceramics being the leading

Table 1 Material properties for selected brittle materials – popular structural ceramics, a ceramic composite, a glass, and a rock – along with a few common metals for comparison (Bavdekar et al. 2017; Bourne 2008, 2012; Grady 1995; Holmquist and Johnson 2002; Johnson and Cook 1985; Meyers 1994)

	ρ (kg/m^3)	E (GPa)	ν	σ_{comp} (GPa)	σ_{ten} (GPa)	HEL (GPa)	P_{HEL} (GPa)	σ_{HEL} (GPa)
Al_2O_3	3890	373	0.23	0.26	2.6	6.7	3.97	5.4
AlN	3226	315	0.25	1.0	3.0	9.0	5.0	6.0
SiC	3215	449	0.17	0.75	5.2	11.7	5.13	9.86
B_4C	2510	462	0.17	0.26	3.1	19.0	8.71	15.54
TiB_2	4480	521	0.11	0.40	3.0	15.0	6.0	13.5
ZrB_2-SiC	6090	517	0.13	0.2	2.3	11.63	5.4	9.1
Float glass	2530	86	0.18	0.15	2.3	5.95	2.92	4.54
Granite	2670	67	0.30	0.15	0.5	4.5	2.73	2.66
OFHC Cu	8960	124	0.34	0.15		0.6	0.41	0.49
2024 Al	2770	73	0.33	0.32		0.6	0.40	0.31
4340 Steel	7830	200	0.29	0.89		2.4	1.46	1.41

candidates for several applications including bearings, machine tools, high temperature furnaces, abrasives, and armor. However, they also exhibit poor ductility, tensile strength, and fracture toughness. In fact, their compressive strength is often an order of magnitude higher than their tensile strength, which is why they are often utilized in applications where large compressive stresses are encountered.

However, the mechanical behavior of ceramics is highly sensitive to internal defects and inhomogeneities in the microstructure, which may result in premature failure of the material below its expected failure strength (Griffith 1921). Hence, probabilistic approaches, based on distribution of defects, are often utilized to predict their behavior and study their reliability for a given application. Such approaches, often based on Weibull distribution, have been well studied for estimation of quasi-static strength of ceramics. To obtain the quasi-static mechanical response of a ceramic, the load is applied slowly, over several seconds to hours, resulting in a strain rate (rate of deformation) of 10^{-5} s^{-1} to 10^{-2} s^{-1} (ASTM 2014). However, ceramic materials are extensively used in applications where the loading conditions are dynamic (e.g., bearings, high-speed cutting and grinding tools, performance brakes, ballistic armor plates), i.e., the loading duration is on the order of microseconds, resulting in a strain rate greater than 10^{2} s^{-1}. Hence, along with studying their quasi-static mechanical response, investigating the dynamic deformation mechanisms such dynamic fracture, fragmentation,` and spall is vital for a comprehensive understanding of these materials. In this case as well, a Weibull distribution of defects can be considered to model the dynamic fragmentation process. However, multiple fragmentation leads to a deterministic strength and to a sudden increase of strength with strain-rate above a transition loading-rate (Denoual and Hild 2000; Forquin et al. 2018; Forquin and Hild 2010).

In many dynamic applications discussed above, the load on the ceramic structure is localized. For example, in ballistic applications, the load is concentrated around the area of impact resulting in large compressive stresses in the longitudinal and lateral directions. However, tensile stresses are also present due to the thin configuration of the ceramic target and wave reflections from the boundaries. As the tensile strength of the ceramic is much lower than its compressive strength, fracture often initiates due to the tensile stresses, leading to cracking and fragmentation, even under high local compressive loading. However, the region beneath the applied load is surrounded by undeformed material, resulting in a large lateral confining pressure. Different modes of deformation (crack growth, crack closure, microplasticity, etc.) are activated at different levels of confinement pressures, thus influencing the failure behavior of the ceramic (Chen and Ravichandran 2000; Grady 1998; Heard and Cline 1980). Hence, examining the influence of pressure and strain rate on the strength and deformation behavior of these materials is crucial to predicting their mechanical response under the applied load.

In this chapter, the influence of microstructural inhomogeneities, strain rate and confining pressure, on the mechanical response of brittle materials is discussed. The various regimes of deformation based on strain rate and pressure, and the dominant failure modes corresponding to each regime are described. Some additional failure mechanisms, unique to certain advanced structural ceramics and/or loading

conditions, are also presented. Finally, constitutive models to capture the response of brittle materials in these regimes and formulations to quantify the damage in the material are reviewed.

Failure Mechanisms Based on Microstructural Defects

Brittle fracture occurs when the elastic deformation progresses to the extreme limit (i.e., the material can no longer support the load), resulting in the cleavage of interatomic bonds. The theoretical fracture strength (σ_f) of a brittle material under tensile load, defined as the maximum stress required to separate or cleave the atomic planes of a solid material, can be calculated as

$$\sigma_f = \sqrt{\frac{\gamma_s E}{a_0}} \tag{1}$$

where E is the elastic modulus, γ_s is the surface energy and a_0 is the equilibrium (virgin) interplanar spacing (at zero applied stress). In reality, the fracture strength of most ceramics, determined experimentally, is about 2 orders of magnitude lower than that predicted by Eq. (1). This lower strength is due to the preexisting structural defects and growing microcracks, which act as initiation sites for crack growth leading to catastrophic failure (Hild and Marquis 1992; Jayatilaka and Trustrum 1977). These structural imperfections are thus responsible for the experimental fracture strength of a brittle material being much lower than its theoretical fracture strength. This result is similar to the case of ductile materials, whose experimental shear strength is observed to be orders of magnitude lower than their theoretical shear strength due to lattice dislocations. Griffith (1921), often revered as the father of fracture mechanics, postulated that the microcracks in the material act as stress concentrators, causing the local stresses to grow high enough to initiate crack growth into macrocracks, eventually leading to brittle fracture. The energy available for crack propagation is the difference between the energy required to form a new fracture surface and the strain energy released due to the increase in crack length. Following the first law of thermodynamics, the criterion for spontaneous crack growth is that the total energy associated with the process must decrease (i.e., net energy is released) or stay the same. The cracks can be assumed to be elliptical in shape. Under uniaxial tensile loading, those oriented with their semi-major axis perpendicular to the direction of the applied load possess the highest stress concentration at the crack tip, resulting in the local stress to approach or surpass the theoretical strength predicted in Eq. (1). Fracture occurs when this critical crack, shown in Fig. 1a, starts to grow. Under these conditions, fracture strength, or the critical far-field tensile stress required to initiate crack growth can be expressed as

$$\sigma_f = \sqrt{\frac{2\gamma_s E}{\pi a}} \tag{2}$$

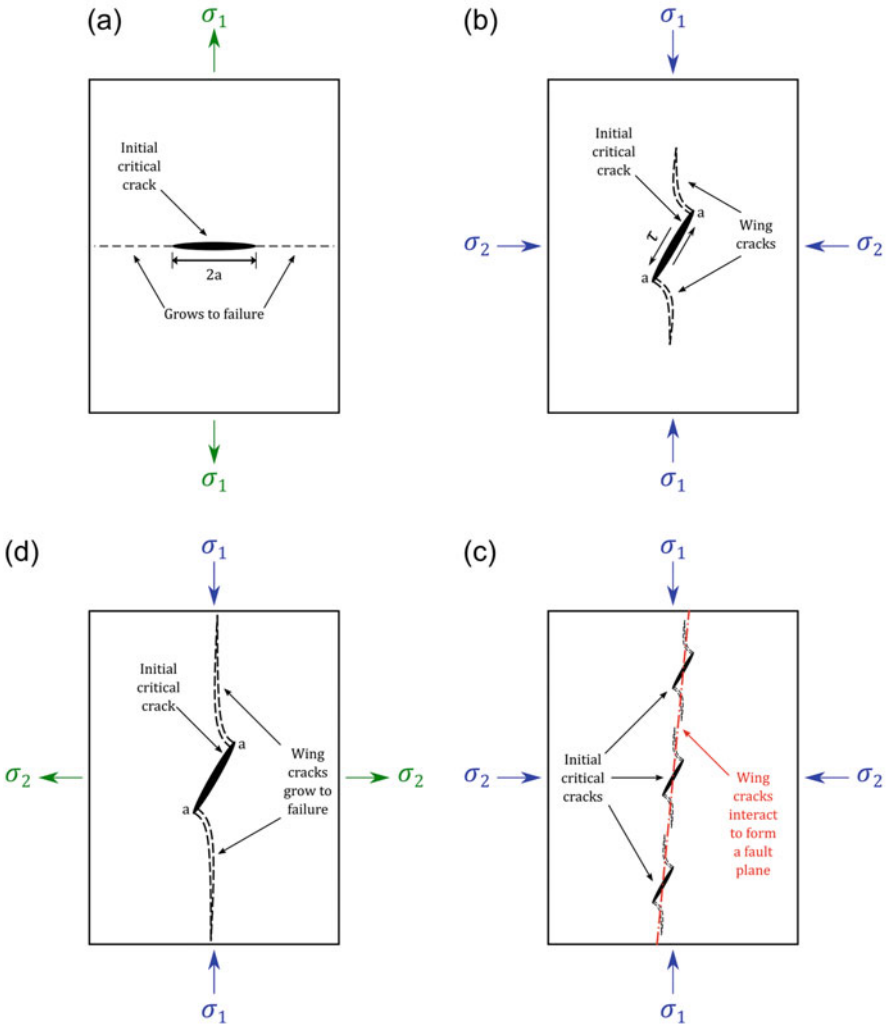

Fig. 1 Brittle crack growth under (**a**) uniaxial tension, where the critical crack is oriented perpendicular to σ_1 and grows to macroscopic failure in the same direction; and (**b**–**d**) axial compression ($\sigma_1 > \sigma_2$), where the critical crack is oriented at about 30° to σ_1 and branches off into wing cracks that grow in a curved path toward σ_1. (**b**) Under lateral compression, the wing cracks cease to grow once they are parallel to σ_1 and (**c**) multiple suitably oriented cracks interact to form a macroscopic fault plane (shown in red). (**d**) Under lateral tension, wing cracks from a single critical crack grow until macroscopic failure via axial splitting

where $2a$ is the length of the preexisting crack as shown in Fig. 1a. Eqs. (1) and (2) have a similar form, the primary difference being the scalar parameter ($\sqrt{2/\pi}$). The theoretical fracture strength in Eq. (1) is based on interplanar spacing (on the order of angstroms, 10^{-10} m) while the Griffith criterion in Eq. (2) is based on the size of

microcracks (on the order of microns, 10^{-6} m). This corelates with the two orders of magnitude ($\sqrt{10^4}$) difference between the theoretical and experimentally observed fracture strengths. The crack continues to propagate perpendicular to the loading direction. As the orientation of the crack does not change, the local stress at the crack tip continuously increases as the crack grows, until it reaches a free surface, or its progress is blocked. Hence, σ_f as calculated from Eq. (2), is approximately equal to the tensile strength of the brittle material. It must be noted that Eq. (2) is valid for a through-thickness crack in a thin plate (plane stress). For penny-shaped cracks in thick plates (plane strain), the equation is of the same form, differing only in the value of the constants (Griffith 1921), given by

$$\sigma_f = \sqrt{\frac{2\gamma_s E}{\pi a(1-\nu^2)}} \tag{3}$$

where ν is the Poisson's ratio of the material.

While the critical crack is perpendicular to the direction of loading under uniaxial tension, Brace and Bombolakis (1963) found that, under compression, the critical crack is inclined at about 30° to the loading direction, as shown in Fig. 1b. The maximum tensile stress on the crack surface is in the sector between the semi-major axis and the direction of maximum far-field compression. The initial crack propagates by branching off into "wing cracks" at both ends, which follow a curved path until they are parallel to the uniaxial loading direction. At this point, the wing crack growth ceases due to a decrease in the stress concentration at the crack-tips. Hence, under tension, the crack continues to grow until a free surface of obstruction; while under compression, it curves toward the loading direction and stabilizes after a few crack lengths (Fig. 1). As a result, a macroscopic crack can develop from a single preexisting crack under uniaxial tensile loading but not under compressive loading. The applied compressive stress must be further increased to continue crack growth and achieve macroscopic failure. Hence, the critical stress required to initiate crack growth under compression, based on the Griffith criterion, is lower than that required to cause ultimate compressive failure in the material. In fact, Lankford et al. (1998) observed that the stress level required for crack nucleation from preexisting defects in a ceramic is approximately half its ultimate failure strength.

Studies by Horii and Nemat-Nasser (1985, 1986) and Ashby and Hallam (1986) determined that along with the size and orientation of the initial crack, the critical stress to initiate crack growth was also dependent on the fracture toughness, coefficient of friction, cohesive strength, and shear strength of the material. In addition to the tensile stress at the crack tip discussed above, the shear stress induced on the inclined crack surfaces causes them to slide and wedge open. However, this sliding motion is opposed by the frictional stress between the surfaces, which increases with the applied confinement level (compressive stress, σ_2). The stress intensity at the tip of the preexisting crack (no wing cracks formed yet) is determined by the shear stress on its surface. As the wing crack grows to approximately the size of the initial crack, the stress intensity is dominated by the sliding of the initial crack surfaces, wedging the wing crack open, as shown in Fig. 1b. With increasing stress, the number and

length of wedged cracks increase, causing the material to expand laterally, even though the stress state is compressive. This inelastic expansion (i.e., beyond the Poisson effect) is termed as dilatancy or bulking (Brace et al. 1966; Mead 1925). As the wing cracks grow longer, their growth is primarily affected by the presence of lateral stress on the material which is discussed below.

Effect of Lateral Confinement

Any amount of the lateral tensile stress causes the crack to become unstable since the large wing cracks are perpendicular to the direction of the tensile load and would grow until macroscopic failure, resulting in axial splitting of the specimen, as shown in Fig. 1d. However, if the lateral stress is compressive, crack growth tends to be stable as the lateral confinement opposes the opening of the crack and limits the rate of growth as well as the final crack length (Horii and Nemat-Nasser 1985).

How then does a brittle material fail under compressive loading? Brittle materials contain a distribution of several grain-sized microcracks, often nucleating from defects such as pores, inclusions, grain boundary intersections, triple points, and secondary phase boundaries. Initially, the growth of the wing cracks is dominated by the stress field around the flaw from which it grows. As the crack grows, the stress intensity on the crack tips is severely magnified due to the presence of other cracks and defects in the vicinity. If the lateral confinement is low, the wing cracks interact and, if suitably oriented, form a narrow region of high crack density, as shown in Fig. 1c. When the axial stress is close to the ultimate strength of the material, these (mostly axial) cracks grow in an unstable manner and coalesce to create a macroscopic fault plane, eventually leading to ultimate failure via shear (Horii and Nemat-Nasser 1985). The maximum length of the wing cracks decreases with increasing lateral confinement, thus suppressing the faulting process. Additionally, crack surfaces slide against each other and the friction resistance between the crack surface increases with lateral confinement, which tends to close the crack. Both these features impede brittle fracture and result in an increase in the failure strength of the material. As the stress intensity rises, numerous cracks grow slowly, leading to a pseudo-ductile behavior which resembles plastic flow at the macroscopic level; however, failure still occurs via brittle mechanisms such as distributed microcracking and crack sliding (Horii and Nemat-Nasser 1986). With further increase in confinement, crack growth and interaction is severely inhibited, and the stress rises well beyond the fracture strength of the material, initiating other deformation mechanisms, such as ductile flow through dislocation motion/plasticity (Cagnoux and Cosculluela 1991; Horii and Nemat-Nasser 1986). Hence, the material loses its "brittleness" and undergoes a brittle-to-ductile transition.

The dominant plastic deformation mechanisms in most ceramics is intracrystalline slip (Heard and Cline 1980), with twinning prevalent in some materials such as alumina (Hockey 1971). However, the high Peierls barrier in ceramics results in limited slip systems and prevents the activation of conventional thermally activated plastic deformation modes such as cross-slip and dislocation climb (under ambient conditions), thus causing dislocation pile-up along grain boundaries. As the pileup continues, the stress concentration continues and the

generated dislocations either block the source of the dislocation or nucleate transgranular microcracks once the stress exceeds the local fracture strength. The critical resolved shear stress on a slip plane to nucleate a crack is inversely proportional to the length of the dislocation pileup (Lankford et al. 1998). Larger grains favor large pileups, and hence favor the nucleation of microcracks whereas the back stress from the noncritical pile-ups in smaller grains "toughen" the grain boundaries, blocking the dislocation source and inhibiting microfracture.

Effect of Strain Rate

Microcrack nucleation and growth as well as localized plasticity are both strain rate-dependent phenomena and the fracture strength of ceramics under dynamic compression is higher than its fracture strength under quasi-static compression, sometimes by an order of magnitude (Grady and Kipp 1979). The effect of strain rate on the compressive strength of a brittle material is summarized in Fig. 2.

At low strain rates ($\dot{\varepsilon} < 10^2 \ \ s^{-1}$), the theoretical uniaxial compressive quasi-static yield strength of an isotropic ceramic, defined as the stress level required for macroscopic plastic flow in the absence of defects, is approximately given as

$$\sigma_s = H/3 \tag{4}$$

where H is the material's indentation hardness (Hill 1950; Tabor 1951). This implies that only one-third of the stress beneath the indenter is the shear stress, which induces plastic flow, with the balance being hydrostatic pressure. Lankford et al. (1998) found that materials with a high purity, negligible porosity, and small grains, resulting in "toughened" grain boundaries that inhibit microcrack nucleation, can indeed reach this value. However, most brittle materials contain larger grains and inhomogeneities in the form of porosity, secondary phases (due to sintering additives), and low-toughness glassy grain boundaries. These features cause microcracks to nucleate at stress levels below that required to activate plastic deformation mechanisms, leading to a lower fracture strength (Griffith 1921). Hence, the growth

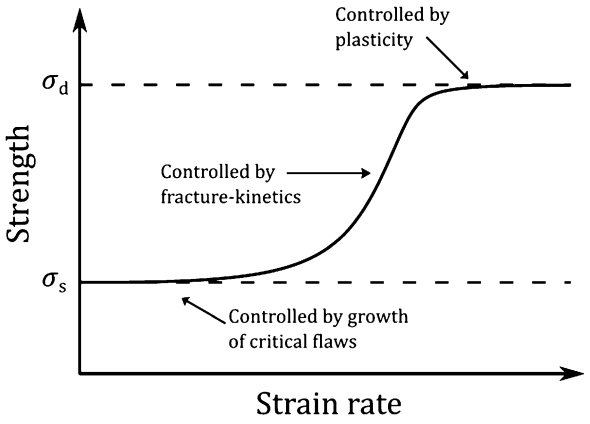

Fig. 2 Dynamic failure in brittle solids based on fracture-kinetics and mechanism-transition model (Grady 1998). Strain rate sensitivity is only observed at intermediate strain rates (10^2–10^5 s^{-1})

of critical flaws (i.e., the largest flaws in the preferred orientation) dominates the fracture response of the material within this quasi-static regime (Horii and Nemat-Nasser 1985; Nemat-Nasser and Horii 1982). This process is independent of strain rate, as shown in Fig. 2.

At higher strain rates, ($10^2 < \dot{\varepsilon} < 10^5$), the material response is highly strain rate sensitive, especially under low lateral confinement, where the dominant failure mechanisms are crack initiation, propagation, and interaction. However, due to material inertia (i.e., the limited propagating speed of cracks), these processes are delayed as the stress rises more rapidly than the ability of the crack to open and grow, leading to an increased failure strength (Denoual and Hild 2000; Forquin and Hild 2010). The higher stress simultaneously activates multiple cracks of different sizes and the material fractures through the growth of these cracks, independent of crack shape and orientation, leading to a dramatic decrease in the average fragment size relative to those under quasi-static failure (Forquin et al. 2018). In addition, dislocation-induced crack nucleation is suppressed with increased strain rate, leading to a commensurate rise in strength (Lankford et al. 1998).

At extremely high strain rates ($\dot{\varepsilon} > 10^5$), plastic flow becomes the dominant deformation mechanism and within this regime, the flow stress is strain rate-independent (Grady 1998; Grady et al. 1977). Macroplastic flow is observed at stress levels above the Hugoniot elastic limit (HEL), which is defined as the uniaxial yield strength of the material under a dynamic plane strain configuration (i.e., the material transitions from an elastic state to an elastic-plastic state). The HEL can be obtained through plate impact experiments that induce shock loading in the material and the theoretical uniaxial compressive dynamic yield strength of the ceramic is given by

$$\sigma_d = \frac{(1-2\nu)^2}{1-\nu}\mathrm{HEL} \tag{5}$$

where ν is the Poisson's ratio of the material (Rosenberg 1993).

Hence, the compressive strength of brittle materials transitions from strain rate-dependent behavior at low pressures and intermediate strain rates to pressure-dependent behavior at higher pressures and higher strain rates, i.e., from the crack inertia-dominated mechanism to crack shutdown mechanism. In the pre-HEL regime, microcracking is the dominant mechanism and plasticity can be sporadic. At higher pressures, the lateral confinement suppresses crack growth and hence, dislocations nucleate at sufficiently high stresses. These dislocations activate inelastic deformation mechanisms (e.g., plasticity, phase transformations, etc.) in the immediate post-HEL regime. However, as ceramics do not have well-defined slip systems, dislocation slide does not occur with continued plastic deformation. Thus, the activation of dislocations contributes its own population of microcracks apart from those intrinsic to the ceramic and, with increasing pressure and strain rate, the failure mechanism transitions from crack growth to dislocation-assisted crack nucleation. Hence, plasticity can be considered to be the limiting factor for a ceramic's ultimate attainable strength, through inertial or external confinement (Lankford et al. 1998).

Failure Mechanisms Under Dynamic Loads

While fracture due to inherent microstructural defects is the primary mode of failure in brittle materials, dynamic impact loading also promotes other fracture modes. However, most of these mechanisms are activated due to the pressure associated with dynamic impact and are not limited to high strain rates.

Fragmentation and Spall

Fragmentation in ceramics results from nucleation of cracks from volume or surface microstructural defects, their growth, interaction, and coalescence (Forquin and Hild 2010). Under quasi-static loads, a few critical cracks dominate the failure process and the resulting fragments are larger and fewer in number. Under dynamic loads, numerous cracks are nucleated from several preexisting defects and because of their proximity, they quickly coalesce, resulting in an increase in the number of fragments and a decrease in the fragment sizes with increasing strain rate (Forquin et al. 2018). Under impact conditions, two fragmentation mechanisms are observed. One mechanism is active at nominally lower strain rates in regions farther away from the impact site (Hogan et al. 2017). The far field stress from impact activates large defects such as inclusions in these regions and cracks originating from these defects are controlled by the spacing between the inclusions. Large fragments are created due to the coalescence of these cracks and thus, structural deformation in the material is the dominant factor in this mechanism. The second mechanism is activated at high stresses and strain rates close to the impact site, with fragments forming by the coalescence of microcracks originating from all the defects in the localized region. These fragments are smaller, and this mechanism is microstructurally controlled by the distribution of defect sizes and the spacing between the defects (Hogan et al. 2016). Hence, controlling the spacing between the defects is critical in controlling the size of the fragments. Reducing the number of defects would increase the fragment size which, in turn, would improves the ballistic performance of the ceramic as larger fragments increase projectile erosion during penetration (Krell and Strassburger 2014).

Spallation is a special fragmentation mechanism, typically observed as material separation on the rear side of a dynamically impacted target. It results from the dynamic nucleation, growth, and coalescence of voids or cracks under a macroscopically hydrostatic tensile state (Meyers 1994). The spall strength of a material, defined as the maximum hydrostatic tensile stress it can withstand, is considered to be a material property (like fracture toughness).

Projectile and target geometries play a major role in the location of the spall, as the tensile stress state is generally created by the interaction of release waves from the rear end of the projectile and target. These release waves, which are the reflection of the compressive shock wave, bring an internal material plane rapidly into tension. The simplest and most studied case is that of planar spall (Grady 1980), arising from the flat impact of plates of projectile and target material, as shown in Fig. 3. At the time of impact ($t = 0$), a compressive shock wave is emitted into the projectile and the target, starting from the impact location ($x = 0$). These waves are reflected as tensile waves from the rear free surface of the projectile and target. If the projectile

and target are of the same material, the material plane at a distance of one projectile width from the rear surface of the target is the first region to experience a tensile stress state, and the location for the spall nucleation. For a defect-free material, a spall nucleates if the sum of the tensile stresses from the release wave from the rear of the projectile and that from the rear/side of the target ceramic is greater than the tensile strength of the ceramic (Grady 1988). The spall creates an internal free surface, reflecting the tensile release waves back toward the rear surface of the target as compressive waves, thereby reducing the intensity of the tensile stress in the spall region (Murray et al. 1998).

Hence, the spall strength can be theoretically expressed as the tensile strength of the material in a plane strain configuration (Rosenberg 1993)

$$\sigma_{spall} = \frac{(1-2\nu)^2}{(1-\nu)} \frac{\mathrm{HEL}}{8} = \frac{\sigma_d}{8} \tag{6}$$

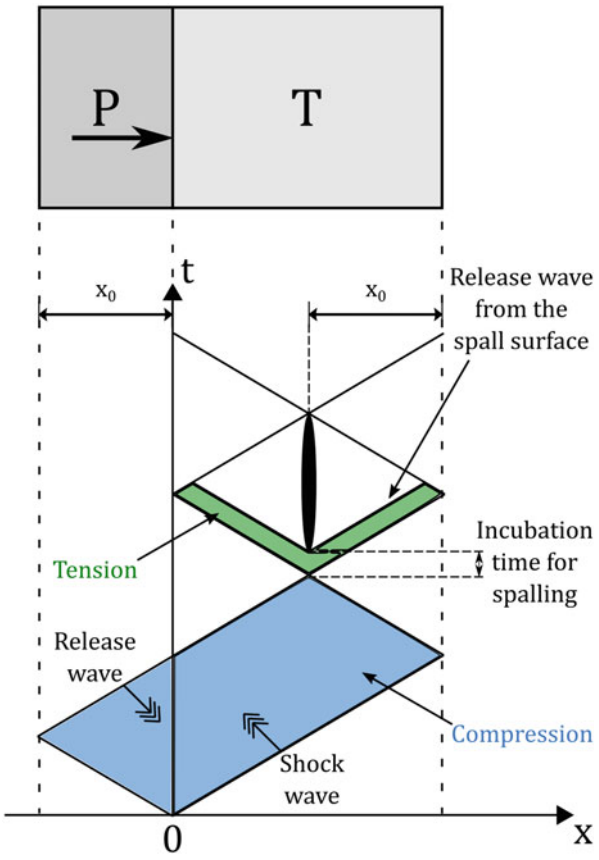

Fig. 3 Distance-time plot showing the propagation of the shock and release waves in the projectile (P) and target (T) after impact

However, the presence of microstructural flaws (microcracks, inclusions, sintering defects, etc.) reduces the strength of a ceramic. As discussed earlier, (Fig. 1a), a state of homogeneous tensile stress is intrinsically unstable – these flaws grow and coalesce into macroscopic faults and initiate the spalling process. For other dynamic loading conditions (other than planar impact), such as ball impact (LaSalvia et al. 2005) and edge-on impact (Forquin et al. 2018), the wavefront is spherical and release waves may be created from lateral surfaces of the target as well, resulting in a spherical spall. It must be noted that if the initial shock wave completely pulverizes the material such that it can no longer support a tensile (or shear) load, there will be no release wave and hence, no spall.

Cavity Expansion

Cavity expansion is not an independent microscopic failure mechanism but instead a macroscopic representation of the loading history induced under the impact of penetrator (projectile, punch, etc.). Understanding the growth of a spherical or cylindrical cavity from zero radius to its maximum size is important in the determination of ballistic efficiency of a target ceramic (Bishop et al. 1945). The cavity expansion process in a semi-infinite medium (i.e., the material is large enough such that boundary effects are absent) is mostly a function of material properties.

The response of a brittle material to impact and penetration is a complex process involving macroscale cracking and comminution along with elastic and plastic deformation. If the cavity is assumed to be spherical, the material surrounding the cavity is under a compressive radial stress and a tensile hoop stress. This complex stress state further complicates the material response because, in a ceramic, the tensile strength is often much lower than its compressive strength. Also, in a dynamic event, the material close to the surface of the cavity may be highly damaged, but it is surrounded by the material that is still intact, leading to a lateral confinement, which (as discussed before) tends to increase the strength of the material and change its deformation mechanism from crack growth and coalescence at low pressures to inelastic flow at higher pressures. Concurrently, an increase in cracking and fragmentation reduces the strength, resulting in a competing mechanism affecting the strength of the material. Numerous cavity expansion theories for metals and ceramics have been proposed in literature to capture these complex interactions. The most widely used model for ceramics (Bavdekar et al. 2017; Satapathy 2001; Satapathy and Bless 2000), is described below.

When a projectile impacts the surface of a brittle material, it exerts a high magnitude of localized pressure on the material beneath the impact site. This pressure results in high shear stresses in the material, with the maximum shear stress at a depth of about one projectile radius beneath the surface, resulting in extensive cracking and fragmentation within the material in this region. This region was defined as the “Mescall zone” by Shockey et al. (1990) after John Mescall, a scientist at the US Army Materials and Mechanics Research Center who first deduced the existence of this region through computational simulations (Mescall and Tracy 1986; Mescall and Weiss 1983). When this damage zone grows and reaches the surface, a spherical cavity opens. The damage extends beyond the cavity, with the severity of

damage decreasing with radial distance from the cavity surface. These damage zones appear as nested regions of comminuted, cracked, and elastic continuum surrounded by undeformed material, as shown in Fig. 4. The material in the region farthest away from the cavity is undamaged and its behavior is considered "elastic-brittle." The radial and hoop stresses in this region are elastic and increase in magnitude with decreasing radial distance to the cavity. As the tensile strength is lower than the compressive strength, radial cracks originate when the hoop stress exceeds the tensile strength of the material, leading to the cracked region. These cracks are generally transgranular (but can be intergranular in some types of alumina) and radially oriented. Hence, the material in this region can be thought of to be in the shape of thin columns or needles, unable to support any macroscopic hoop stress. Hence, only a compressive radial stress is present in this region, increasing in magnitude closer to the cavity. When this compressive radial stress exceeds the uniaxial compressive strength of the material, the thin columns are pulverized and the material is fully comminuted. This comminuted region experiences the greatest damage and contains a high amount of randomly oriented and interconnected intergranular cracks, leading to the material within this region being highly fragmented and granular in form. This material in the cracked and comminuted regions is held in place due to the pressure from the projectile and the lateral confinement due to the surrounding elastic/undeformed material.

It is important to note that due to the impact being a dynamic event, the cavity is expanding and hence, these nested regions are also growing within the target material throughout the duration of the penetration event. The cavity continues to expand as long as the projectile has enough kinetic energy to accelerate the ceramic fragments out of its path and deform the material around the cavity. However, the projectile is continuously losing kinetic energy due to its deceleration and erosion at the cavity surface. Various models have been developed to capture all the relevant

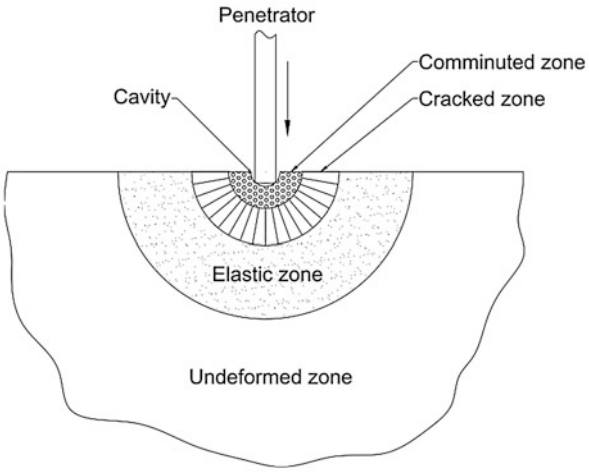

Fig. 4 Schematic of deformation regions in the target ceramic during an impact event. (Bavdekar et al. 2017; Satapathy 2001; Satapathy and Bless 2000)

mechanisms during the penetration of the projectile into a target ceramic. Insights from experiments and numerical simulations are used to formulate the velocity fields in the target and projectile and cavity expansion solutions, along with a suitable constitutive model, are used to capture the stress fields in the target. The Eulerian conservation of momentum equation is then integrated along the axis of the projectile and target to provide the equation of motion. Thus, the models can provide estimations for the rate of erosion of the projectile and its depth of penetration into the target from their material properties. For details, the readers are referred to the articles by Walker and Anderson (1995) and Bavdekar et al. (2019).

Phase Transformation

Under shock pressures well beyond their HEL, some ceramics, such as AlN and SiC, undergo a phase transformation into new crystal structures. This phenomenon is often accompanied with a volume change in the material, resulting in cracking along the phase boundaries.

At shock pressures on the order of 17 GPa, AlN undergoes a first-order phase transformation from a wurtzite (hexagonal) structure to a rock salt (cubic) structure, which has a ~20% higher density (Kondo et al. 1982). The large change in volume and the lattice mismatch between the two crystal structures create tensile stresses at the interface which leads to crack nucleation. The shock wave-front splits into an elastic compression wave-front and a slower phase transformation wave-front (representing the wurtzite–rock salt interface) that nucleates rock salt grains in the material and is a favorable spot for stress concentration and defect generation (Kipp and Grady 1994). When the tensile wave-front, generated by the reflection of the compression wave-front from the rear free surface, reaches the phase transformation wave-front, the stresses due to the lattice mismatch cleave the bonds and nucleate nanoscale voids in the wurtzite–rock salt interfacial region. The tension in this region triggers Mode I crack growth from these nanovoids into the wurtzite crystal. Additionally, dislocations and kink bands (i.e., crystalline regions with a different crystallographic orientation from the surrounding) also nucleate at the phase transformation wave-front and extend into the wurtzite crystal (Branicio et al. 2006). Dislocations on one side of the kink band align to form a superdislocation and a high-angle tilt boundary that glides to the edge of the grain (Romanov 2003; Romanov and Vladimirov 1992). Cracks are nucleated along the superdislocation boundary of the kink bands, and propagate mainly in mode II, releasing the shear stress due to localized expansion. Hence, the phase transformation in AlN at high pressures give rise to new deformation mechanisms in the form of nanocavities leading to mode I cracking, and kink band formation leading to mode II cracking.

SiC is another high strength ceramic that exhibits phase transformation under shock loading (Yoshida et al. 1993). This complex ceramic, known for its numerous polytypic structures (over 250 at ambient conditions), is often found in cubic, hexagonal, or rhombohedral forms depending on the stacking sequence (Shaffer 1969). Among these, the most well-studied and/or naturally occurring structures are α-SiC (umbrella term for the hexagonal wurtzite and rhombohedral structures) and β-SiC (zinc-blende cubic structure). Under shock loading, both α-SiC and β-SiC

undergo varying degrees of phase transformations between the numerous polytypes, depending on the pressure and temperature range (Daviau and Lee 2018). The shear stresses from the passing shock wave-front lead to a reduction in particle size and a change in the stacking sequence of the Si-C layers. As a result, rhombohedral structures are more commonly found at higher pressures and temperatures. However, at pressures above 100 GPa, the most dominant phase transformation is from the cubic zinc-blende structure to the cubic rock salt structure (Sekine and Kobayashi 1997). This phase transformation is reversible with a large hysteresis; the reverse transition occurs around 35 GPa upon unloading. Similar to AlN, this phase transformation to the rock salt structure in SiC is accompanied by a 15–20% increase in density, and likely exhibits deformation mechanisms such as nanovoid formation and crack nucleation.

Amorphization

Boron carbide (B_4C) is another structural ceramic with one of the lowest densities (2510 kg/m^3) and the highest HEL (18–20 GPa) among all structural ceramics. These features, coupled with its high hardness (>30 GPa) and compressive strength (>3 GPa), should make it an optimal candidate for various structural applications as the dynamic shear strength of most brittle materials scales with their HEL (see Fig. 5). However, the dynamic shear strength of B_4C is much lower than expected, given its high HEL. This result is attributed to a deleterious deformation behavior, called "amorphization" (Domnich et al. 2002), which results in the formation of a noncrystalline phase or complete bond breakage within the material's rhombohedral crystal structure. The macroscopic effect of this mechanism is a loss of shear strength above its HEL.

This anomalous behavior was first observed in plate impact experiments by Grady (Grady 1994), as a catastrophic loss of strength or post-yield softening above the HEL with a near-fluid-like response during subsequent deformation in the shock load and release cycle. The features in the shock wave profiles were interpreted to represent a heterogeneous deformation in boron carbide in contrast to homogeneous deformation in other ceramics such as silicon carbide. The material was hypothesized to undergo an anomalous volume compression and a phase-change-like volume collapse. Domnich et al. (2002) performed nanoindentation experiments followed by Raman spectroscopy on single crystal B_4C. Several new broad bands (at ~1330, ~1520, and ~1810 cm^{-1}) were seen to appear in the Raman spectrum in the region beneath the indent. The high stress during the contact loading results in the formation of a new material, due to a pressure-induced solid-state phase transformation, reflected as new bands in the Raman spectrum, thereby confirming one of the hypotheses proposed by Grady (1994). Chen et al. (Chen et al. 2003) measured the amount of ejected fragments following ballistic impact experiments on B_4C and observed a marked increase in the mass of fine fragments above a critical impact velocity. This observation coincided with precipitous loss of target resistance above this critical impact velocity. These results were taken as further evidence to a change in fracture mechanism and a drop in overall shear strength of the ceramic at high pressures. Electron micrographs of the fragments revealed the presence of

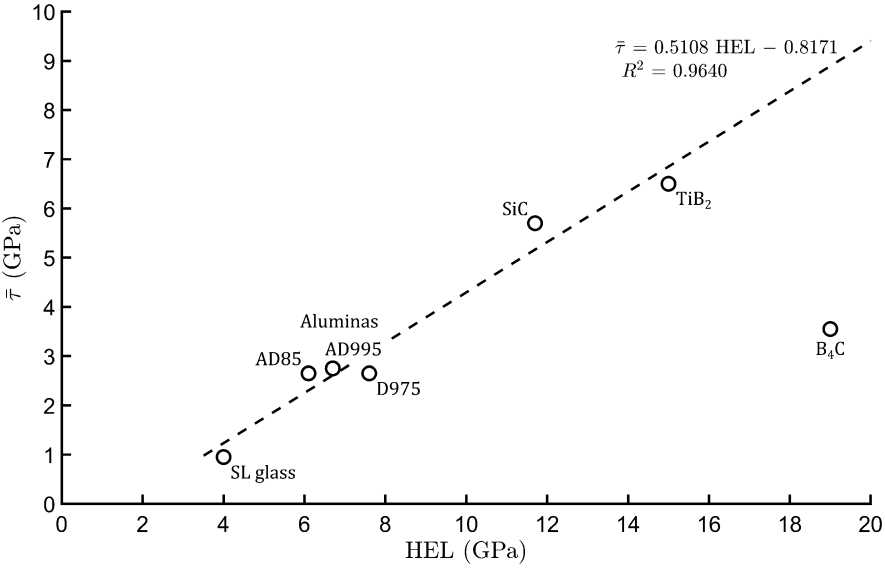

Fig. 5 The relationship between dynamic shear strength of comminuted ceramics and their HEL (Bavdekar et al. 2017). B_4C has a much lower shear strength than expected

localized phase transformation in the form of nanoscale intragranular amorphous bands along specific crystallographic planes and contiguous long bands with apparent cleaved fracture surfaces. Further indentation studies (Subhash et al. 2016) discovered that amorphization manifests on two distinct length scales: nanometer-sized islands dispersed close to the tip of the indentation profile and micron-length slender bands that spread far from the tip (see Fig. 6).

Recent molecular dynamic (MD) studies (DeVries et al. 2020) have revealed a thermodynamic component to the amorphization process. Under the high pressure encountered during indentation and shock loading, the temperature in localized regions of high stress concentration rises to near or above the melting point of the material. This high temperature leads to bond breakage and, due to the sudden nature of the unloading, the subsequent reduction in temperature and solidification does not restore the bonds. The free atoms are locked in their amorphous state, surrounded by the crystalline matrix, giving rise to the amorphous bands. This theory explains the near-fluid-like response and heterogeneous deformation observed by Grady (1994). The MD simulations also revealed that, upon amorphization (i.e., loss of structural order), the interatomic distance doubles (DeVries et al. 2020). Due to this volume change, the amorphous regions induce stresses in the surrounding crystalline matrix. These stresses generate dislocations that cause shear displacements, lattice rotations, and stacking faults in the regions surrounding the amorphous regions, as shown in Fig. 6, and may also act as nucleation sites for intergranular cracks (Subhash et al. 2016). Hence, even though the amorphized volume is only a small fraction of the

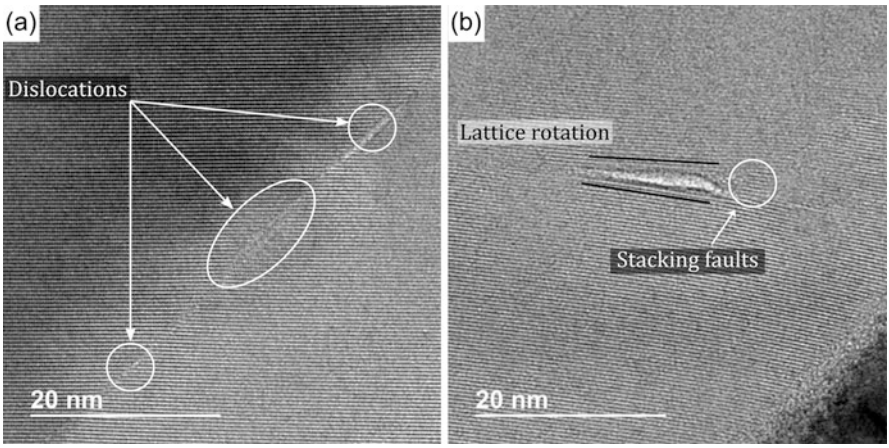

Fig. 6 Transmission electron micrographs revealing (**a**) dislocations around an amorphous band and (**b**) lattice rotations and stacking faults around an amorphous island

material, they are favorable spots for defect generation and crack nucleation, leading to the premature failure of the material.

Density functional theory simulations of hydrostatic compression on a B_4C unit cell (Awasthi and Subhash 2019) have found that the bands in the Raman spectra of the undeformed material shift to the new positions observed experimentally in the deformation of B_4C (Parsard et al. 2018). These results suggest that the new bands observed in the Raman spectra of amorphized B_4C are from the compressed crystalline matrix surrounding the amorphous regions, and not the amorphous material itself. This narrative attests to the fact that amorphous regions cannot produce a Raman spectrum as these atoms are not bonded and hence, have no vibrational modes.

Constitutive Models and Damage Formulations

Micromechanical Models

Micromechanical models are useful in describing the physics of the damage mechanisms, and a number of these models have been proposed to capture the growth, sliding, interaction, and coalescence of wing-cracks at quasi-static and dynamic strain rates. Deng and Nemat-Nasser (1992, 1994) investigated the rate-dependent damage evolution in brittle solids by modeling an interactive array of growing wing cracks while Ravichandran and Subhash (1995) studied the strain rate dependence of fracture strength by considering noninteracting sliding cracks. Huang and Subhash (2003) investigated the pressure dependence of fracture strength through a dynamic damage growth model. Paliwal and Ramesh (2008) considered interacting microcracks and assumed a power law form for the growth rate of the wing cracks. Their analysis showed that, along with strain rate and confinement level, the strength of the

material is dependent on the flaw size, with a narrow distribution resulting in a higher strength. They also uncovered that a material with a lower flaw density had a higher strain rate sensitivity. Lastly, they observed that higher strain rates result in not only a higher failure stress, but also a larger plastic strain. A recent micromechanical model by the same group (Hu et al. 2015) captures the inelastic behavior at high confinement as well. Their model showed that at low confining stresses, the wing-cracking mechanism dominates, leading to the degradation of the modulus and peak strength of the material, whereas at high enough confining stresses, the cracking mechanism is completely shut down and dislocation mechanisms become dominant.

Thus, these micromechanical models have provided valuable insight into the behavior of brittle materials and the failure mechanisms. Additionally, such models are more suitable to capture the physics of material-specific deformation mechanisms such as phase transformation and amorphization. For example, an integrative multi-mechanism model was recently proposed by Zeng, Tonge, and Ramesh (2019a, b) to capture the amorphization behavior of B_4C along with microcracking and granular flow.

Phenomenological Models

Compared to the micromechanical models, phenomenological models are often more convenient and more efficient to use, especially in computational codes, as they have an easier formulation. Since ceramics are primarily used under compressive loads, the stresses are taken to be positive in compression. One of the most primitive constitutive models for brittle materials is the Mohr–Coulomb model (Coulomb 1776; Mohr 1900). The pressure (P)-dependent shear strength, τ, of a ceramic is denoted by a discontinuous bilinear function

$$\tau = \begin{cases} \tau_0 + \alpha P, & P < \overline{P} \\ \overline{\tau}, & P \geq \overline{P} \end{cases} \tag{7}$$

where τ_0 is the cohesive strength of the material (i.e., the shear strength at $P = 0$), α is a constant representing the sliding friction between crack surfaces, $\overline{\tau}$ is the maximal shear strength, and $\overline{P} = (\overline{\tau} - \tau_0)/\alpha$.

A similar bilinear model for the flow stress, σ (instead of shear strength, τ), was proposed by Drucker and Prager (1952) and is given by

$$\sigma = \begin{cases} \sigma_0 + \beta P, & P < \overline{P} \\ \overline{\sigma}, & P \geq \overline{P} \end{cases} \tag{8}$$

where β is a material constant, similar to α, $\overline{\sigma}$ is the maximal flow stress, and $\overline{P} = (\overline{\sigma} - \sigma_0)/\beta$.

Both models are equivalent to each other when any two principal stresses are equal, e.g., $\sigma_2 = \sigma_3$ (e.g., bar impact and plate impact experiments, spherical cavity expansion, etc.) as, under such cases, $\sigma = 2\tau$. As this condition is often satisfied in most of the typical loading conditions, all the properties of the Mohr–Coulomb

model discussed here also apply to the Drucker–Prager model. Due to their bilinear formulation, these models are the easiest to implement into analytical and numerical codes and can be found in most commercial FEA software packages. However, they are unable to capture the nonlinear behavior of ceramics resulting from inelasticity at stress levels near and above HEL. Therefore, these two models are only applicable in applications with low confinement pressures.

In recent times, some of the most widely used constitutive models in numerical analyses for brittle materials are those proposed by Johnson and Holmquist (1992, 1994) and Johnson et al. (2003), which model the response of the brittle material as a nonlinear function of not only pressure but also strain rate. The JH-1 (Johnson and Holmquist 1992) model uses three or more linear segments (as opposed to the two segments in the previous models) to capture the nonlinear pressure-dependent strength of the material. The final segment is generally a pressure-independent strength regime where, similar to the high-pressure regime of the Drucker–Prager model, $\sigma = \overline{\sigma}$. The JH-2 model (Johnson and Holmquist 1994), on the other hand, is continuous, and the strength is defined as an analytical function of pressure and strain rate. All quantities in the model are normalized by the strength and pressure components of the HEL and hence, the variables and constants in the model are dimensionless. This allows for easier comparison between different materials and estimation of constants. The normalized strength of the intact ceramic is given by

$$\sigma^* = A(P^* + T^*)^N \tag{9}$$

where A and N are model constants and the superscript (*) denotes normalized quantities with their corresponding HEL components, i.e., $\sigma^* = \sigma/\sigma_{\mathrm{HEL}}$ and $P^* = P/P_{\mathrm{HEL}}$. $T^* = T/P_{\mathrm{HEL}}$ is the normalized hydrostatic tensile strength of the material. P_{HEL} and σ_{HEL} are the hydrostatic and deviatoric components of the stress state at HEL, obtained through plate impact experiments, and are available in literature for several commonly used ceramics and glasses (see Table 1). For other materials for which this plate impact data is not readily available, the values of these parameters can also be approximated from other material properties as follows (Westerling et al. 2001):

$$P_{HEL} = \frac{(1+\nu)}{3(1-\nu)}\mathrm{HEL} \tag{10a}$$

$$\sigma_{HEL} = \frac{(1-2\nu)}{(1-\nu)}\mathrm{HEL} \tag{10b}$$

The JHB model (Johnson et al. 2003) is an extension of these two models – its primary feature is the capability to include a phase change, as required for materials like AlN. This model also uses two segments to capture the pressure-dependent strength of the material. The first segment (low pressures) is similar to the Drucker–Prager model and is linear from $\sigma = 0$ at $P = -T$ up to $\sigma = \sigma_1$ at $P = P_1$. At higher pressures, the strength is given by the following equation:

$$\sigma = \sigma_1 + (\overline{\sigma} - \sigma_1)\left(1 - e^{-\alpha(P - P_1)}\right) \tag{11}$$

To provide a continuous slope at P_1,

$$\alpha = \frac{\sigma_1}{(\overline{\sigma} - \sigma_1)(P_1 + T)} \tag{12}$$

In all the JH models, the strain-rate dependence of strength is given by

$$\sigma = \sigma_0(1 + C \ln \dot{\varepsilon}) \tag{13}$$

where σ_0 is the strength at $\dot{\varepsilon} = 1\ \mathrm{s}^{-1}$ and C is a material constant.

The JH models have been implemented in computational codes and have been reasonably successful in modeling ceramic behavior. However, they too have some drawbacks. For example, determining model constants for each material through multiaxial compression and plate impact experiments is nontrivial and non-economical, especially for new promising materials being developed through computational simulations. In some cases, the strength curves are also forced into unusual and nonphysical shapes, due to the requirement to pass through HEL and *T*. Additionally, none of these models are a one-stop-shop for simulating ceramic behavior as they all possess features that are better at capturing certain phenomena but fail at capturing others (for example, the JH-2 model cannot capture the strength saturation post-HEL). A schematic of the models discussed above is shown in Fig. 7a, b and a brief review of the features and drawbacks of all these models is provided in Table 2 to assist the reader in selecting the appropriate model for specific applications. A detailed comparison between the models discussed in this chapter can be found in (Bavdekar and Subhash 2018).

To mitigate these drawbacks, Shafiq and Subhash (2016) proposed an extended Mohr–Coulomb (SS-EMC) model, which is applicable over the entire range of confinement pressure. This model has an exponential form given by

$$\tau^* = a + b\mathrm{e}^{-kP^*} \tag{14}$$

where $\tau^* = \tau/\tau_{\mathrm{HEL}}$ and $\tau_{\mathrm{HEL}} = \sigma_{\mathrm{HEL}}/2$. By fitting the curve to experimental data on numerous ceramics, glasses, and rocks over a wide range of strain rates and confinement pressures, the model constants were determined to be $a = 1.15$, $b = -1.06$, and $k = 1.78$. As these constants were determined from a dataset encompassing a variety of materials and loading states, they can be treated as universal constants. Thus, a single "master-curve" can capture the normalized pressure-dependent strength of several brittle materials without a strain rate-dependence. It was found that the universal constants could be used to capture the response of most brittle materials; except in the post-HEL regime for some anomalous materials which undergo phase changes at high pressures, e.g., B_4C (Bavdekar and Subhash 2018). This unique feature of the model improves its predictive capability and reduces the need for expensive experimental data to simulate the performance of new materials.

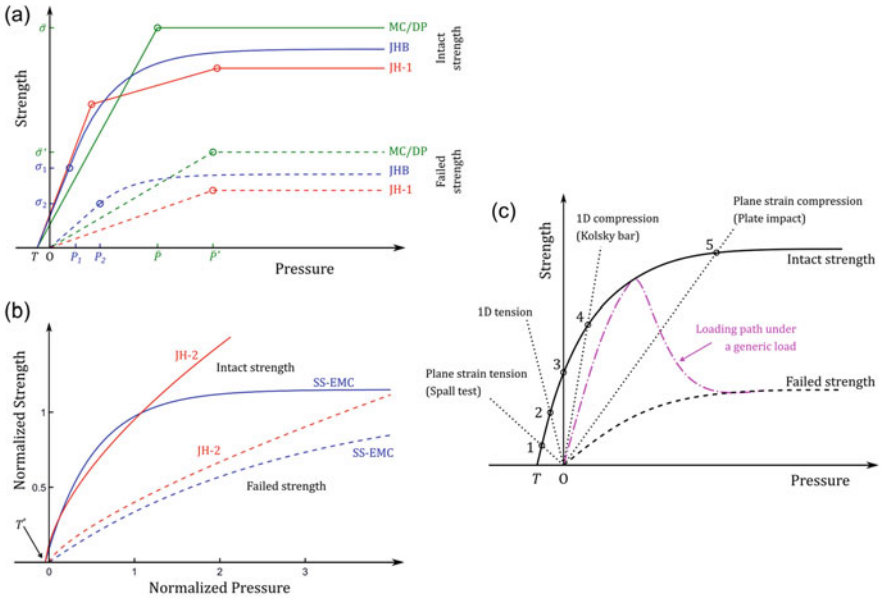

Fig. 7 Schematic of the phenomenological ceramic strength models. (**a**) Piecewise absolute strength models. (**b**) Continuous normalized strength models. The intact strength is represented by solid lines and the failed strength by dashed lines. (**c**) Qualitative description of the two-curve behavior of brittle materials (Satapathy and Bless 2000). The dotted lines represent the paths followed by the material for various experimental loading conditions and the points, 1–5, represent the failure stress under each condition. These points are connected to form the intact strength curve. A general path followed by a material is represented by the dash-dotted magenta curve

Table 2 Comparison of phenomenological constitutive models

	MC/DP	JH-1	JH-2	JHB	SS-EMC
Mathematical formulation	Bilinear	Linear segments	Nonlinear (power law)	Linear and exponential	Nonlinear (exponential)
Piecewise	Yes	Yes	No	Yes	No
Continuous	No	No	Yes	Yes	Yes
Normalized variables	No	No	Yes	No	Yes
Strength cap	Yes	Yes	No	Yes	Yes
Linear at low pressures	Yes	Yes	No	Yes	Yes
Strain rate dependence	No	Yes	Yes	Yes	No
Universal constants	No	No	No	No	Yes
Valid at					
Low pressures	Yes	Yes	Yes	Yes	Yes
Int. pressures	No	Approx.	Up to HEL	Yes	Yes
High pressures	Yes	Yes	No	Yes	Yes

In Eq. (14), the term $e^{-kP^*} \to 0$ as P^* increases beyond HEL and hence $\tau^* = a$ when $P^* \gg 1$. This implies that the parameter "a" signifies the normalized maximal shear strength of the material as follows:

$$\overline{\tau} = a\tau_{\text{HEL}} \tag{15a}$$

And, as $\sigma = 2\tau$,

$$\overline{\sigma} = a\sigma_{\text{HEL}} \tag{15b}$$

Additionally, at $P = 0$, Eq. (14) reduces to $\tau^*|_{P=0} = \tau_0^* = a + b$. Therefore, the parameters 'a' and 'b' together control the cohesive strength (τ_0) of the material, given by

$$\tau_0 = (a + b)\tau_{\text{HEL}} = 0.09 \times \tau_{\text{HEL}} \tag{16a}$$

And, by extension,

$$\sigma_0 = 0.09 \times \sigma_{\text{HEL}} \tag{16b}$$

Another important feature of this model is that it reduces to the linear form of the Mohr–Coulomb model at low pressures. A Taylor series expansion of Eq. (14) results in

$$\tau^* = (a + b) + (-bk)P^* = \tau_0^* + \alpha^* P^* \tag{17}$$

To make a comparison to this linear model, Eq. (17) can be written as

$$\frac{\tau}{\tau_{\text{HEL}}} = \frac{\tau_0}{\tau_{\text{HEL}}} + \frac{(-bk)P}{P_{\text{HEL}}} \tag{18}$$

or

$$\tau = \tau_0 + \frac{(-bk)\tau_{\text{HEL}}}{P_{\text{HEL}}} P = \tau_0 + \alpha P \tag{19}$$

Hence, from Eqs. (17) and (19),

$$\alpha = -\frac{bk\tau_{\text{HEL}}}{P_{\text{HEL}}} = -\frac{bk\sigma_{\text{HEL}}}{2P_{\text{HEL}}} = \beta \tag{20}$$

Thus, if the HEL of the material is known, the maximal shear strength ($\overline{\tau}$), cohesive strength (τ_0), and the pressure-shear slope (α) of any material that follows the "master-curve" (i.e., most brittle materials) can be easily determined using Eqs. (15), (16), and (20) and the universal constants of the SS-EMC model. This constitutive model has been utilized to predict the material properties of ceramics (Shafiq and Subhash 2016), and capture their response to impact so as to evaluate their ballistic performance (Bavdekar et al. 2017, 2019).

Damage Formulations

If the material is held under a constant pressure and subjected to increasing shearing deformation at a constant strain rate, the equivalent/shear stress continues to increase until it reaches the material's intact strength at that pressure. Beyond this, the material begins to flow plastically as damage begins to accumulate, causing it to weaken until it completely fails. Hence, constitutive models must be able to include the strength of the damaged and failed ceramics as well as their intact forms. The failed material has suffered from extensive cracking and comminution and is highly fragmented. This granular material cannot support any shear load in the absence of a confining pressure, and hence possesses no cohesive or tensile strength. The failed strength curve passed through the origin and hence, $T = 0$. Past this, however, there is a large amount of uncertainty regarding their behavior due to the difficulty in conducting experiments on failed ceramics with different levels of damage. Hence, the form of the failed strength model is either assumed to be linear or similar to that of the intact material.

For the bilinear models, obtaining the failed strength is trivial; the y-intercept is set to zero, leading to the following equations (Johnson and Holmquist 1992; Satapathy and Bless 2000).

Mohr–Coulomb:

$$\tau = \begin{cases} \alpha' P, & P < \overline{P}' \\ \overline{\tau}', & P \geq \overline{P}' \end{cases} \tag{21}$$

Drucker–Prager:

$$\sigma = \begin{cases} \beta' P, & P < \overline{P}' \\ \overline{\sigma}', & P \geq \overline{P}' \end{cases} \tag{22}$$

In the JH models, the formulation for the failed strength is assumed to be the same as that of the intact counterparts, with the tensile strength (T) set to zero. The JH-1 model generally contains only two segments for the strength of the failed material and is practically equivalent to the Drucker–Prager model given by Eq. (22).

For the JH-2 model, the strength of the failed material is given by

$$\sigma^* = B(P^*)^M \tag{23}$$

If $M = 1$, Eq. (23) reduces to the DP model (Eq. 22).

The JHB model for the failed material contains two segments, with the first being linear from $\sigma = 0$ at $P = 0$ up to $\sigma = \sigma_2$ at $P = P_2$. At pressures greater than P_2,

$$\sigma = \sigma_2 + (\overline{\sigma}' - \sigma_2)\left(1 - e^{-\alpha'(P - P_2)}\right) \tag{24}$$

where

$$\alpha' = \frac{\sigma_2}{P_2(\overline{\sigma}' - \sigma_2)} \tag{25}$$

The effect of strain rate is still given by Eq. (13).

The SS-EMC model is also modified to give the strength of failed materials by forcing the exponential curve to pass through the origin. This reduces the constitutive model to a two-parameter equation, given by

$$\tau^* = a'\left(1 - e^{-k'P^*}\right) \tag{26}$$

It has been shown that, similar to the corresponding intact strength model, the constants are universal and can be applied to most brittle materials, with $a_1 = 1.11$ and $k_1 = 0.36$ (Bavdekar et al. 2017).

It is important to note that while the parameters in all the failed strength models (i.e., α', β', B, M, P_2, a', k', etc.) have the same physical meaning as their respective parameters in the intact strength models, their values are different. As there is often insufficient data to calculate the values of these model parameters due to the difficulty associated with testing the failed material, they are often chosen by fitting simulation results to experimental data.

Hence, the strength of brittle materials can be represented by two separate pressure-strength curves – an upper curve describes the strength of the intact material and the lower curve describes the strength of the failed material (Satapathy and Bless 2000). This two-curve pressure-shear behavior is graphically illustrated in Fig. 7c. Multiple experimental techniques, summarized in Table 3, can be used to obtain distinct data points along the upper curve. The loading path of these tests is represented by the dotted lines in Fig. 7c and the failure point for each test is represented by the points 1–5. The upper curve is then constructed by the interpolation or regression of these points. Additional points can be obtained through multiaxial confinement tests by superposing external lateral confinement on the test sample in the Kolsky bar. As discussed above, constructing the lower curve is much more difficult and assumptions are made regarding its form.

It is important to note that these curves do not describe the path that a material follows under a given load, but rather prescribes the limiting strength of the material at a given pressure. The upper curve provides the failure criterion and

Table 3 Experimental techniques used to obtain data points on the intact strength curve as shown in Fig. 7(c). σ_1 is the maximum principal stress, i.e., the axial stress along the loading direction

	Configuration	Experiment	Pressure (P)	Shear Strength (τ)
1	Plain strain	Spall	$-\frac{\sigma_1}{3}\frac{(1+\nu)}{(1-\nu)}$	$\frac{\sigma_1}{2}\frac{(1-2\nu)}{(1-\nu)}$
2	1D stress	Uniaxial Tension	$-\frac{\sigma_1}{3}$	$\frac{\sigma_1}{2}$
3	Simple shear		0	τ_0
4	1D stress	Kolsky bar	$\frac{\sigma_1}{3}$	$\frac{\sigma_1}{2}$
5	Plane strain	Plate impact	$\frac{\sigma_1}{3}\frac{(1+\nu)}{(1-\nu)}$	$\frac{\sigma_1}{2}\frac{(1-2\nu)}{(1-\nu)}$

the lower curve is akin to a flow curve. Depending on the type of load, the actual path followed by the material under increasing load lies between these two curves with the failure point lying on the upper curve, as shown by the dash-dotted magenta line in Fig. 7c. Macroscopic failure occurs when the material stress state reaches the upper curve. Beyond this, damage accumulates, and the material follows a path toward the lower curve. In analytical and numerical models, the damage can be tracked by a unitless parameter D such that $0 \leq D \leq 1$. Once the material completely fails and drops to the lower curve ($D = 1$), it stays on that curve. In most models (JH-2, JHB, and SS-EMC), the material weakens gradually with increasing damage accumulation and the deteriorated strength of the damaged material is described as

$$\Sigma = \Sigma_i - D\left(\Sigma_i - \Sigma_f\right) \tag{27}$$

where Σ_i is the intact strength and Σ_f is the failed strength of the material. Σ may refer to the (normalized or absolute) flow stress (σ) or shear strength (τ) of the material, depending on the constitutive model being used. On the other hand, the JH-1 model is unique in the sense that the material does not weaken until $D = 1$, after which its strength drops instantaneously from σ_i to σ_f. This response is better at modeling some special cases such as projectile dwell and interface defeat. However, interchanging the weakening mechanism in any of the models discussed here is trivial and can be easily accomplished based on the simulation requirement.

The damage formulation often used in numerical studies is based on the incremental plastic strain accumulated in the material as it is loaded (Johnson and Cook 1985; Johnson and Holmquist 1992). The material weakening is theorized to be related to the material transitioning from a larger fragment size to a smaller fragment size under increased plastic strain. This formulation is given by

$$D = \int \frac{\mathrm{d}\varepsilon^P}{\varepsilon_f^P} \tag{28}$$

where $\mathrm{d}\varepsilon^P$ is the incremental plastic strain during a cycle of integration and ε_f^P is the plastic strain required to fracture at a pressure P. ε_f^P is also pressure-dependent and is given by

$$\varepsilon_f^P = D_1(P + T)^{D_2} \tag{29}$$

where D_1 and D_2 are constants P and T may be normalized depending on the formulation of the strength model (Johnson and Holmquist 1994). This formulation provides for increased ductility at higher pressures to account for plasticity becoming the dominant deformation mechanism at these pressures (Grady 1998; Heard and Cline 1980; Horii and Nemat-Nasser 1986). Tensile hydrostatic pressure loads greater than T would cause instantaneous failure ($D = 1$). This damage formulation is widely used in computational studies, especially in the simulation of long rod

penetration and plate impact experiments (Anderson and Holmquist 2013; Holmquist et al. 2016).

However, another formulation for damage has been proposed by Partom (2012) based on the overstress principle. According to this principle, the stress state point can go above failure curve. Whenever this happens, damage is accumulated at a rate that is proportional to the magnitude of overstress in the target. This rate of damage accumulation is given by

$$\dot{\mathrm{D}} = \phi(S - \Sigma) \tag{30}$$

where S is the equivalent stress or shear stress in the material, depending on the constitutive model being used and ϕ is an increasing function used to characterize the damage accumulation. ϕ is often assumed to be a linear function and can be replaced with a suitable constant damage increment coefficient. This type of formulation has been more successful in capturing certain phenomena such as interface defeat and dwell of a projectile on the surface of a target ceramic prior to penetration.

As damage accumulates in a material, increased microcracking results in a bulk expansion of the material. In the comminuted material, grains which were previously interlocked have the freedom to move due to shearing strains. This phenomenon, termed as dilatancy or bulking (Brace et al. 1966; Mead 1925), is countered by the compaction of the material due to the applied pressure. Studies have shown that, to the first order, the effects of compaction and bulking cancel each other out as long as a compressive load is present (Bavdekar et al. 2017; Curran et al. 1993). However, the effect of bulking can be included in the damage model through an incremental pressure ΔP, such that the pressure is given by

$$P = K_1\mu + K_2\mu^2 + K_3\mu^3 + \Delta P \tag{31}$$

where K_1, K_2, and K_3 are material constants (K_1 is the bulk modulus) and $\mu = \rho/\rho_0 - 1$ is the volumetric strain for current density ρ and initial density ρ_0. ΔP varies from zero to $\Delta P_{\max}$ as damage increases and is determined from energy considerations. The reduction in strength with increased damage represents a loss in the elastic internal energy of the deviatoric and shear stresses, which is converted to potential hydrostatic internal energy by the addition of ΔP (Johnson and Holmquist 1992).

Summary

This chapter provides a short summary of the dominant failure mechanisms in ceramics and describes the effect of strain rate and confinement on their failure strength. Lateral confinement has a larger influence than strain rate, with the strength of the material increasing with confinement pressure due to the suppression of crack growth. At high levels of confinement (i.e., above HEL), plasticity is the dominant deformation mechanism and material strength saturates. The strength of ceramics shows the highest strain rate-dependence at low pressures and intermediate strain

rates. Additional failure mechanisms relevant to the dynamic impact response of ceramics are also discussed to provide for a deeper understanding of the utility of these materials in resisting ballistic impact. A few important phenomenological models that describe the pressure-dependent material strength are surveyed and a thorough comparison is made to assist the reader in selecting the appropriate formulation for their needs. However, there remain areas within ceramic science where the understanding of material response and failure is limited. Recent advances in additive manufacturing have resulted in 3D printed ceramics that are being used in numerous scientific and commercial applications. The microstructure of ceramics fabricated via these processes are different from that of ceramics fabricated via traditional techniques such as hot pressing, resulting in a different constitutive response and failure mode (DeVries et al. 2018). Further studies are needed to characterize these materials and validate or modify the current models to capture their failure behavior.

References

C.E. Anderson, T.J. Holmquist, Int. J. Impact Eng. **56**, 2 (2013)
ASTM, *ASTM D7012-14e1, Standard Test Methods for Compressive Strength and Elastic Moduli of Intact Rock Core Specimens under Varying States of Stress and Temperatures* (ASTM International, West Conshohocken, 2014)
A.P. Awasthi, G. Subhash, J. Appl. Phys. **125**, 215901 (2019)
S. Bavdekar, G. Subhash, Int. J. Impact Eng. **118**, 60 (2018)
S. Bavdekar, G. Parsard, G. Subhash, S. Satapathy, Int. J. Solids Struct. **125**, 77 (2017)
S. Bavdekar, G. Subhash, S. Satapathy, Int. J. Impact Eng. **131**, 304 (2019)
R.F. Bishop, R. Hill, N.F. Mott, Proc. Phys. Soc. **57**, 147 (1945)
N.K. Bourne, Int. J. Impact Eng. **35**, 674 (2008)
N.K. Bourne, Exp. Mech. **52**, 153 (2012)
W.F. Brace, E.G. Bombolakis, J. Geophys. Res. **68**, 3709 (1963)
W.F. Brace, B.W. Paulding, C. Scholz, J. Geophys. Res. **71**, 3939 (1966)
P.S. Branicio, R.K. Kalia, A. Nakano, P. Vashishta, Phys. Rev. Lett. **96**, 065502 (2006)
J. Cagnoux, A. Cosculluela, in *Dyn. Fail. Mater.* (Springer Netherlands, Dordrecht, 1991), pp. 73–84
W. Chen, G. Ravichandran, Int. J. Fract. **101**, 141 (2000)
M. Chen, J.W. McCauley, K.J. Hemker, Science **299**(80), 1563 (2003)
C.A. Coulomb, Mem. Acad. Roy. Div. Sav **7**, 343 (1776)
D.R. Curran, L. Seaman, T. Cooper, D.A. Shockey, Int. J. Impact Eng. **13**, 53 (1993)
K. Daviau, K. Lee, Crystals **8**, 217 (2018)
H. Deng, S. Nemat-Nasser, Mech. Mater. **14**, 83 (1992)
H. Deng, S. Nemat-Nasser, Int. J. Damage Mech. **3**, 3 (1994)
C. Denoual, F. Hild, Comput. Methods Appl. Mech. Eng. **183**, 247 (2000)
M. DeVries, G. Subhash, A. Mcghee, P. Ifju, T. Jones, J. Zheng, V. Halls, J. Eur. Ceram. Soc. **38**, 3305 (2018)
M. DeVries, G. Subhash, A. Awasthi, Phys. Rev. B **101**, 144107 (2020)
V. Domnich, Y. Gogotsi, M. Trenary, T. Tanaka, Appl. Phys. Lett. **81**, 3783 (2002)
D.C. Drucker, W. Prager, Q. Appl. Math. **10**, 157 (1952)
P. Forquin, F. Hild, Adv. Appl. Mech. **44**, 1 (2010)
P. Forquin, G. Rossiquet, J.-L. Zinszner, B. Erzar, Mech. Mater. **123**, 59 (2018)
D.E. Grady, J. Geophys. Res. **85**, 913 (1980)

D.E. Grady, J. Mech. Phys. Solids **36**, 353 (1988)
D.E. Grady, Le J. Phys. IV **04**, C8 (1994)
D.E. Grady, *Dynamic Properties of Ceramic Materials* (Sandia National Laboratories, Albuquerque/Livermore, 1995)
D.E. Grady, Mech. Mater. **29**, 181 (1998)
D.E. Grady, M.E. Kipp, Int. J. Rock Mech. Min. Sci. Geomech. Abstr. **16**, 293 (1979)
D.E. Grady, R.E. Hollenbach, K.W. Schuler, J.F. Callender, J. Geophys. Res. **82**, 1325 (1977)
A.A. Griffith, Philos. Trans. R. Soc. A Math. Phys. Eng. Sci. **221**, 163 (1921)
H.C. Heard, C.F. Cline, J. Mater. Sci. **15**, 1889 (1980)
F. Hild, D. Marquis, Eur. J. Mech. – A/Solids **11**, 753 (1992)
R. Hill, *The Mathematical Theory of Plasticity* (Clarendon Press, Oxford, 1950)
B.J. Hockey, J. Am. Ceram. Soc. **54**, 223 (1971)
J.D. Hogan, L. Farbaniec, N. Daphalapurkar, K.T. Ramesh, J. Am. Ceram. Soc. **99**, 2159 (2016)
J.D. Hogan, L. Farbaniec, D. Mallick, V. Domnich, K. Kuwelkar, T. Sano, J.W. McCauley, K.T. Ramesh, Int. J. Impact Eng. **102**, 47 (2017)
T.J. Holmquist, G.R. Johnson, J. Appl. Phys. **91**, 5858 (2002)
T.J. Holmquist, G.R. Johnson, C.A. Gerlach, Philos. Trans. R. Soc. A Math. Eng. Sci. **375** (2016)
H. Horii, S. Nemat-Nasser, J. Geophys. Res. **90**, 3105 (1985)
H. Horii, S. Nemat-Nasser, Philos. Trans. R. Soc. A Math. Phys. Eng. Sci. **319**, 337 (1986)
G. Hu, J. Liu, L. Graham-Brady, K.T. Ramesh, J. Mech. Phys. Solids **78**, 269 (2015)
C. Huang, G. Subhash, J. Mech. Phys. Solids **51**, 1089 (2003)
A.D.S. Jayatilaka, K. Trustrum, J. Mater. Sci. **12**, 1426 (1977)
G.R. Johnson, W.H. Cook, Eng. Fract. Mech. **21**, 31 (1985)
G.R. Johnson, T.J. Holmquist, Shock Wave High-Strain-Rate Phenom. Mater., 1075 (1992)
G.R. Johnson, T.J. Holmquist, *AIP Conf. Proc.* (AIP, New York, 1994), pp. 981–984
G.R. Johnson, T.J. Holmquist, S.R. Beissel, J. Appl. Phys. **94**, 1639 (2003)
M.E. Kipp, D.E. Grady, Le J. Phys. IV **04**, 249 (1994)
K. Kondo, A. Sawaoka, K. Sato, M. Ando, *AIP Conf. Proceeding*, vol 78 (AIP, New York, 1982), pp. 325–329
A. Krell, E. Strassburger, Mater. Sci. Eng. A **597**, 422 (2014)
J. Lankford, W.W. Predebon, J.M. Staehler, G. Subhash, B.J. Pletka, C.E. Anderson, Mech. Mater. **29**, 205 (1998)
J.C. LaSalvia, M.J. Normandia, H.T. Miller, D.E. MacKenzie, Adv. Ceram. Armor **183** (2005)
M.F. Ashby, S.D. Hallam (Née Cooksley), Acta Metall. **34**, 497 (1986)
W.J. Mead, J. Geol. **33**, 685 (1925)
J. Mescall, C. Tracy, *Proc. 1986 Army Sci. Conf.* (U.S. Military Academy, West Point, 1986)
J. Mescall, V. Weiss, *Material Behavior Under High Stress and Ultrahigh Loading Rates* (Springer US, Boston, 1983)
M.A. Meyers, *Dynamic Behavior of Materials* (John Wiley & Sons, Inc., Hoboken, 1994)
T.E. Mitchell, K.P.D. Lagerlöf, A.H. Heuer, Mater. Sci. Technol. **1**, 944 (1985)
O. Mohr, Zeitschrift Des Vereins Dtsch. Ingenieure Band **44**, 1524 (1900)
N.H. Murray, N.K. Bourne, Z. Rosenberg, J.E. Field, J. Appl. Phys. **84**, 734 (1998)
F.R.N. Nabarro, Proc. Phys. Soc. **59**, 256 (1947)
S. Nemat-Nasser, H. Horii, J. Geophys. Res. **87**, 6805 (1982)
B. Paliwal, K.T. Ramesh, J. Mech. Phys. Solids **56**, 896 (2008)
G. Parsard, G. Subhash, P. Jannotti, J. Am. Ceram. Soc. **101**, 2606 (2018)
Y. Partom, *AIP Conf. Proc.*, 76–79 (2012)
R. Peierls, Proc. Phys. Soc. **52**, 34 (1940)
G. Ravichandran, G. Subhash, Int. J. Solids Struct. **32**, 2627 (1995)
A.E. Romanov, Eur. J. Mech. – A/Solids **22**, 727 (2003)
A.E. Romanov, V.I. Vladimirov, in *Dislocations in Solids: Dislocations and Disclinations*, ed. by F. R. N. Nabarro, (North-Holland, Amsterdam, 1992), p. 191
Z. Rosenberg, J. Appl. Phys. **74**, 752 (1993)

S. Satapathy, Int. J. Solids Struct. **38**, 5833 (2001)
S. Satapathy, S.J. Bless, J. Appl. Phys. **88**, 4004 (2000)
T. Sekine, T. Kobayashi, Phys. Rev. B **55**, 8034 (1997)
P.T.B. Shaffer, Acta Crystallogr. Sect. B Struct. Crystallogr. Cryst. Chem. **25**, 477 (1969)
M. Shafiq, G. Subhash, J. Am. Ceram. Soc. **99**, 627 (2016)
D.A. Shockey, A.H. Marchand, S.R. Skaggs, G.E. Cort, M.W. Burkett, R. Parker, Int. J. Impact Eng. **9**, 263 (1990)
G. Subhash, A.P. Awasthi, C. Kunka, P. Jannotti, M. DeVries, Scr. Mater. **123**, 158 (2016)
D. Tabor, *The Hardness of Metals* (Oxford University Press, New York, 1951)
J.D. Walker, C.E. Anderson, Int. J. Impact Eng. **16**, 19 (1995)
L. Westerling, P. Lundberg, B. Lundberg, Int. J. Impact Eng. **25**, 703 (2001)
M. Yoshida, A. Onodera, M. Ueno, K. Takemura, O. Shimomura, Phys. Rev. B **48**, 10587 (1993)
Q. Zeng, A.L. Tonge, K.T. Ramesh, J. Mech. Phys. Solids **130**, 370 (2019a)
Q. Zeng, A.L. Tonge, K.T. Ramesh, J. Mech. Phys. Solids **131**, 20 (2019b)

Damage in Armor Ceramics Subjected to High-Strain-Rate Dynamic Loadings: The Spherical Expansion Shock Wave Pyrotechnic Test

23

Antonio Cosculluela and Pascal Forquin

Contents

Introduction 610
Description of the Problem 611
State of the Art and Position of the Problem for the Divergent Spherical Wave Test 614
Numerical Investigation of the Loading History 615
Elastic Behavior Hypothesis 615
Elastic Perfectly Plastic Behavior Hypothesis 617
Experiments Performed on Two Alumina Ceramics 618
Presentation of the Two Alumina Ceramics 618
Experimental Setup and Instrumentation 619
Experimental Results Obtained with Coarse-Grained Alumina AL23 621
Experimental Results Obtained with Fine-Grained Alumina T299 622
Discussion on the Experimental Results 624
Postmortem Macroscopic Observations After Recovery Tests 625
Macroscopic Observations for Coarse-Grained Alumina 625
Macroscopic Observations for Fine-Grained Alumina 626
Postmortem Analysis with SEM Microscopy 626
SEM Observations for Coarse-Grained Alumina 627
SEM Observations for Fine-Grained Alumina 629
Postmortem Analysis with TEM Microscopy 629
TEM Observations for Coarse-Grained Alumina 630
TEM Observations for Fine-Grained Alumina 631

A. Cosculluela (✉)
CEA-CESTA, Le Barp, France
e-mail: antonio.cosculluela@cea.fr

P. Forquin
Laboratoire 3SR, Université Grenoble Alpes, Grenople INP, CNRS, Grenoble, France
e-mail: pascal.forquin@3sr-grenoble.fr

© Springer Nature Switzerland AG 2022

G. Z. Voyiadjis (ed.), *Handbook of Damage Mechanics*,
https://doi.org/10.1007/978-3-030-60242-0_81

Discussion About the Physical Phenomena 632
Analysis of Microscopic Observations 632
Influence of Microstructural Parameters 634
Conclusion 636
References 637

Abstract

For shielding type or armor applications, it is important to know the state of the material well after the passage of the divergent spherical wave which comes off in front of the impactor projectile.

The objective of this chapter is to present an experimental technique which make it possible to load materials in a large range of dynamic strain and stress: the spherical expansion shock wave pyrotechnic test.

The paths of loading, the observed microphysical phenomena and the associated behaviors of two brittle materials (two ceramics) are described. A particular focus is made on the influence of the microstructure and the nature of the ceramic on their dynamic behavior. Numerical simulations are presented. Some of them give the history of the states of strain and stress as well as contribute to the understanding of the physical phenomenology; the others report on the experimental mechanical behavior of these ceramics.

This chapter show that is important to consider the state of the material after being submitted to an initial divergent spherical wave before modelling the mechanical response of the material in a shielding type structure.

These analyses allow to better consider physical phenomena in the mechanical behavior modelling and so the improvement of the mechanical strength/density ratio of the constituent materials of these kind of structures.

Keywords

Alumina · Divergent spherical wave · Dynamic behavior · High-strain-rate · Microplasticity · Microcracks · Spherical expansion shock wave pyrotechnic test

Introduction

In the context of armor system design, the main goal of material selection whatever their type (plastics, glasses, composites, ceramics. . .) often boils down to a double technical challenge: mass reduction and increase of performances, especially in the manufacturing of mobile structures (space shuttle, aircraft, armor tanks, helicopters, automotive industry) and personal armor systems. This results in a permanent search to improve the mechanical strength/density ratio of the constituent materials of these structures.

In the case of shielding used against light to heavy caliber armor-piercing (AP) projectile, polycrystalline ceramics are of particular interest because they combine qualities of lightness and high mechanical performances in compression. During an impact, in the first moments of the interaction between a projectile and a ceramic

shield, a divergent precursor spherical wave originates and propagates in the ceramic structure. In some cases of very light armor built with a ceramic front plate of small thickness, the mass and velocity of the projectile generate a too low energy and stress level. In this case, the study can rather focus on the structural response of the shield backing.

Conversely, in the other cases, the stresses increment induced by the precursor wave can alter the ceramic due to microplasticity and tensile damage mechanisms and change the subsequent structural response of the shield. It is therefore essential to first investigate all the physical changes induced by this wave.

The objective of the present chapter is a contribution to the phenomenological study of the damage modes induced in ceramic materials by a divergent spherical wave (explosive test). In particular, the influences of the stress field, the stress rate, and the microstructural parameters are studied. A special focus to the influence of material parameters (flaws, grain size) is given. The description and understanding of the physical phenomena aim to provide the basis of mechanical models that may constitute the purpose of a future study. The outline of the present chapter is dictated to the use of spherical expansion pyrotechnic tests. The structural response of the shield is outside of the scope of this chapter.

This chapter contributes to the identification of macro- and micro-phenomena observed in two types of alumina during a divergent spherical wave loading. This chapter exhibits some microscopic results too. SEM and TEM observations illustrate the physical phenomena that are involved in the response of these materials loading by a divergent spherical wave. The two studied ceramic grades are 99.7% pure alumina with coarse-grained and fine-grained microstructures. The grain size is observed to be an essential microstructural parameter in the mechanism of cracking and ruin of alumina under divergent spherical wave loading.

Description of the Problem

The framework of this chapter is the investigation of the damage processes that precede the subsonic penetration of an armor-piercing projectile impacting a heavy armor ceramic. If ones consider the interaction between a high-intensity aggression (AP projectile, medium-caliber projectile, arrow projectile, hollow charge) and a heavy ceramic shield, in the first moments of the interaction, a divergent precursor spherical wave originates at the point of impact and propagates in the ceramic structure. In the particular case of arrow projectiles or hollow charges, the typical impact velocities are respectively 1500 $m.s^{-1}$ and 9000 $m.s^{-1}$ and the kinetic energies are of the order of 5 MJ; the stresses conveyed by the diverging precursor spherical wave go up to a few tens of GPa. The penetration rates reach from 500 $m.s^{-1}$ (arrow projectiles) to 3000 $m.s^{-1}$ (shaped charge; https://fr.qaz.wiki/wiki/Shaped_charge). Given the propagation speed of the precursor wave of the order of 10,000 $m.s^{-1}$, it means that the stress wave have enough time to modify the ceramic before the

penetrator interacts with the ceramic. In addition, the stress values are such that they can cause microstructural modifications of the ceramic.

In the cases of light- and medium-caliber armor-piercing (AP) projectile, the physical phenomenon is the same but the energy and the stresses level are lower. The different states of stress experienced by an isolated volume element of a ceramic shielding plate are illustrated in the Fig. 1. At time t_1, the precursor spherical wave has detached itself in front of the projectile but has not yet reached the considered volume element. At time t_2, the wave interacts with this volume element which then undergoes a triaxial compression state corresponding to a uniaxial strain loading-path. Then, when the wave front moves away, the material relaxes and the stress state becomes uniaxial compression (time t_3) before reaching a state of compression biaxial tensile state (t_4). Given the brittle nature of ceramics, this state of biaxial tensile state generates a tensile damage in the material. It is therefore scientifically legitimate to be interested in the modifications (such as plasticity, damage, and cracking mechanisms) made by the precursor wave to the material in order to predict the state of the latter before it interacts with the projectile. In this perspective, this work consists in studying the mechanical behavior of ceramics loading by a divergent spherical wave can be studied.

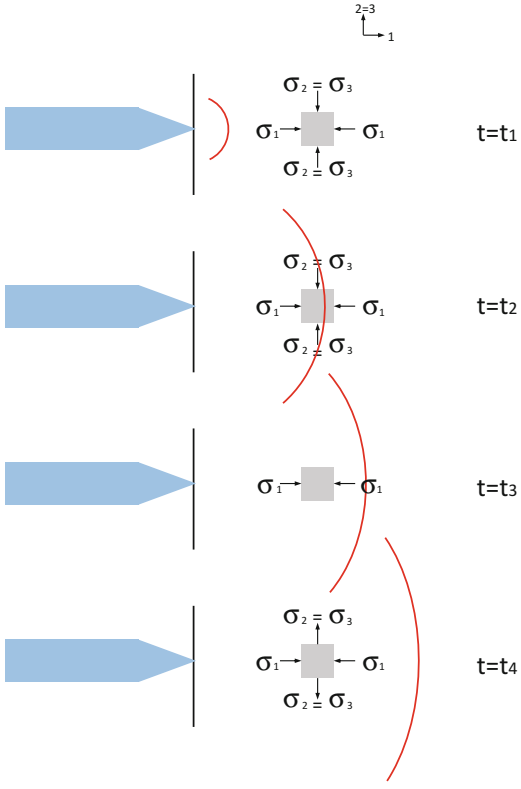

Fig. 1 States of stresses imposed on an element of volume by a divergent spherical wave

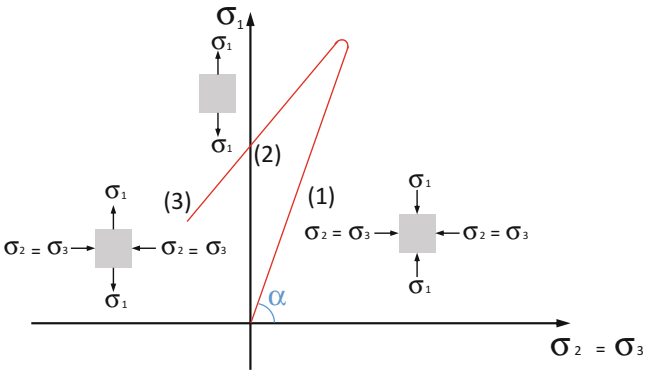

Fig. 2 Loading path imposed by a divergent spherical wave to an elastic material

Figure 2 shows the loading path, in the stress space, imposed on an elastic material by a divergent spherical longitudinal wave. The compression is taken as positive. This loading is complex insofar as it involves a sequence of states of different stresses. If the state of the material changes during the loading (plasticity, damage, for example), then, at a given moment, the response of the material depends on the state of stresses but also on the history of the previous states of stresses.

It is therefore necessary to identify the behavior of materials at various stages to reconstruct the history of its response; so, it is possible to integrate for a given stage the modifications of the materials of the previous stage.

To better understand the interest in carrying out divergent spherical wave loading tests (Cosculluela 1992) or edge-on impact tests (Forquin et al. 2003), it is necessary to more explain the Fig. 2. This figure, established from numerical simulations presented below in section "Numerical Investigation of the Loading History," shows the loading path imposed by a divergent spherical longitudinal wave to a material whose behavior remains elastic in this example.

Let us detail the different phases of this complex loading:

- The compression phase takes place in a state of uniaxial strain (1). The strain rates involved in the stage are of the order of 10^5 s^{-1}.
- A relaxation phase passes through the axis of uniaxial compression (2) (Cosculluela et al. 1991a, 1991b), and then the material undergoes compression-bitension (3). The strain rates involved are of the order of 10^3 s^{-1} to 10^4 s^{-1}.

In order to investigate the damage and deformation modes of the component material in situ, experiments allowing the identification of the response material for different states of stress must be carried out. Experiments developed to recreate this stress-state using an explosive (Cosculluela 1992) or using edge-on-impact tests (Forquin et al. 2003; Riou et al. 1998) can be performed.

State of the Art and Position of the Problem for the Divergent Spherical Wave Test

The interaction of a spherical divergent wave and a brittle material has been studied for a long time (Blake 1952; Ghosh 1969); some studies focused on ceramics (Bless et al. 1990; Evans and Fu 1984; Satapathy 2001) and rare studies focused on microstructural aspects (Louro and Meyers 1989; Howitt and Kelsey 1988; Cosculluela 1992).

The purpose of this subsection is to exhibit the response of two sintered aluminas loaded by a divergent spherical wave and to show the influence of the grain size on the induced mechanisms and their mechanical behavior.

Figure 3 shows the loading path imposed on an elastic material by a spherical longitudinal divergent wave. Compared to classical uniaxial compressive strain and uniaxial compressive stress test, this kind of experimental procedure explores a new domain in the space of stresses, located between the axis of uniaxial strain and the axis of uniaxial tensile stress. So, if new phenomena appear, they would be then attributed to the new stress states. The divergent character of the spherical wave makes it possible to impose on different sub-volumes of the same sample, a different history of stresses (Fig. 3).

In this chapter, the phenomenology of the behavior is associated with the history of radial stress. To do so, post-test analyses are carried out. Fragments collected at

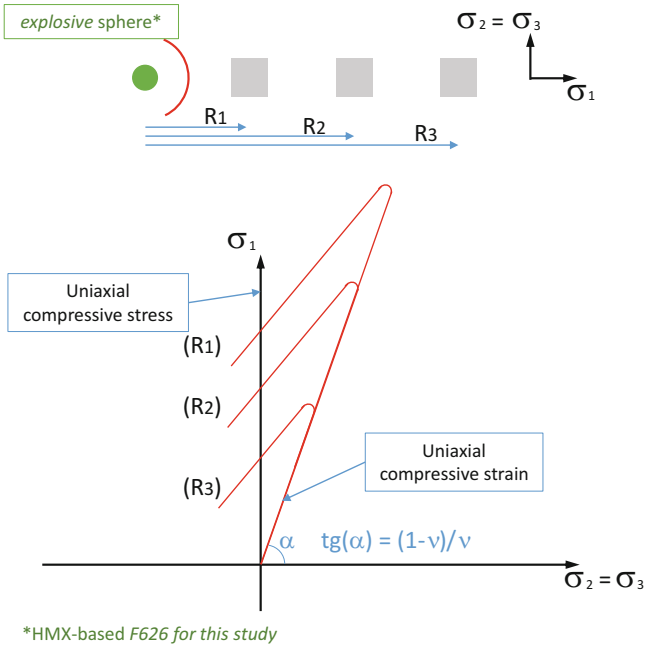

Fig. 3 Loading path applied to a material loading at three different abscissas

different abscissas, after the passage of the wave, are observed at macro- and microscopic levels. Next, these observations are connected to the measurements made at the same abscissa. Before that and to facilitate the interpretation of the measurement results, some numerical simulations of the experiments are carried out.

This subsection is therefore structured as follows: in a first time, the results of numerical simulations are presented. Next, in a second step, the measurements are provided. Finally, the observations made on each alumina at the end of the recovery tests are commented. Finally, the last part is devoted to discussion.

Numerical Investigation of the Loading History

A Lagrangian one-dimensional explicit code (EPIC) is used to simulate the divergent spherical wave test. This code is based on a finite difference scheme and therefore specially designed for wave propagation problems. The explosive, the alumina sample, and a PMMA window are meshed using mesh made of 500 1D finite-elements. The behavior of alumina is elastic in a first simulation, then perfectly plastic elastic in a second simulation.

Assumptions for numerical simulations are that the geometry is 1D, the pressure is not measured in contact with the explosive, so the stress level is chosen with theoretical calculations on F626 explosive. Regarding the material constitutive behavior, two cases are considered: in the first calculation, the material behavior remains elastic, whereas in the second calculation, a yield stress equal to 3.5 GPa with a perfect plastic behavior is used. The density of the material is 3.92 and the Young modulus is 380 GPa.

Elastic Behavior Hypothesis

In the case of elastic behavior, the waves are elastic waves, not shock waves because shock waves occur when a material is stressed far beyond its elastic limit by a pressure disturbance. All the particle velocity profiles have the same shape, with a steep rise, a maximum and a decrease.

The decrease of the maxima is of type $1/r$ in accordance with the closed-form solution proposed by Rinehart (1975). Furthermore, the same author also specifies that, on the rising edge, the radial stress is proportional to the radial particle velocity u_r, the mass density ρ, and the longitudinal wave celerity C_L:

$$\sigma_r = \rho\, C_L\, u_r \tag{1}$$

After the maxima and during stress relaxation, the particle velocity $u_r(r, t)$ depends on the radial stress $\sigma_r(t)$, the radius r (abscissa of the Fig. 3), and the longitudinal wave velocity C_L:

$$u_r(r,t) = \frac{\sigma_r(t)}{4G}\left[\left(\frac{a}{r^2}\right) - \sqrt{\frac{3}{2}\frac{a}{r^2}e^{-\omega t/\sqrt{2}}}\sin\left(\omega t + \tan^{-1}\sqrt{2}\right) + \sqrt{2}\frac{a}{r}e^{-\omega t/\sqrt{2}}\sin\omega t\right], \tag{2}$$

where

$$\omega = 2\sqrt{2}\,C_L/3a \tag{3}$$

For elastic behavior, some relationships exist between the elastic parameters of a material and the wave velocities, and between its different elastic parameters:

$$C_L = \sqrt{\frac{K + 4/3G}{\rho}} \tag{4}$$

$$C_s = \sqrt{\frac{G}{\rho}} \tag{5}$$

$$C_0 = \sqrt{\frac{K}{\rho}} \tag{6}$$

$$C_b = \sqrt{\frac{E}{\rho}} \tag{7}$$

$$E = 2\mu(1+\nu) = 3K(1-2\nu) = \frac{\mu(3\lambda+2\mu)}{\lambda+\mu} = \frac{9\mu K}{3K+\mu} \tag{8}$$

$$G = \mu = \frac{E}{2(1+\nu)} = \frac{3K(1-2\nu)}{2(1+\nu)} = \frac{3EK}{9K+E} \tag{9}$$

$$K = \frac{E\mu}{9\mu - 3E} = \frac{E}{3(1-2\nu)} = \frac{3\mu(1+\nu)}{3(1-2\nu)} = \frac{2\mu}{3} + \lambda \tag{10}$$

$$\nu = \frac{\lambda}{2!\lambda+\mu)} = \frac{3K-E}{6K} = \frac{3K-2\mu}{2(3K+\mu)} = \frac{E}{2\mu} - 1 \tag{11}$$

$$\lambda = \frac{(E-2\mu)\mu}{3\mu - E} = \frac{E\nu}{(1+\nu)(1-2\nu)} = \frac{3K(3K-E)}{9K-E} = \frac{2\mu\nu}{1-2\nu} = K - \frac{2\mu}{3} = \frac{3K\nu}{1+\nu}, \tag{12}$$

where E is the Young's modulus, G the Shear modulus, K the Bulk modulus, ν the Poisson's ratio, λ and d μ the Lamé's parameters ($G = \mu$), C_L is the longitudinal wave velocity, C_s the shear wave velocity, C_0 the bulk wave velocity, and C_b the rod wave velocity.

The divergent spherical expansion is simulated considering, first, a purely elastic behavior for the ceramic material. Fig. 4 shows the profile of radial stress as function

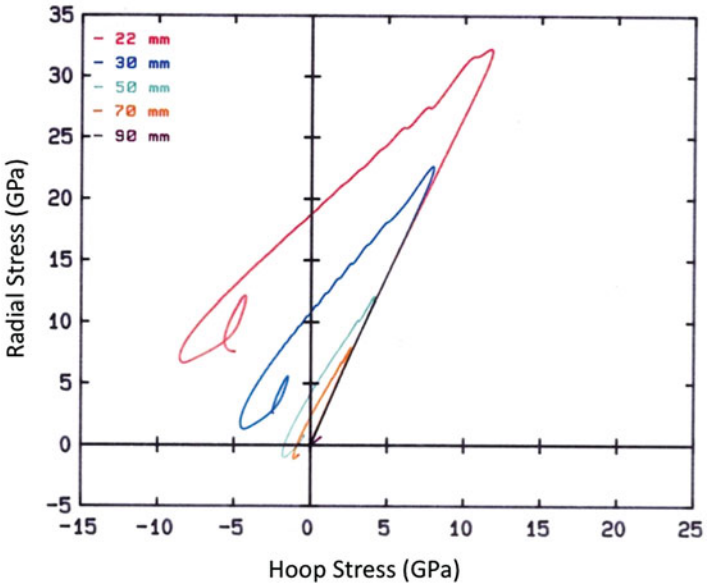

Fig. 4 Numerical simulation of the loading path imposed by a divergent spherical wave to an elastic material

of the orthoradial (hoop) stress for different abscissas. The maximum radial stresses reached for abscissa 22 mm, 30 mm, 50 mm, and 70 mm are respectively 35, 32, 23, 12, and 8 Mpa. An elastic perfectly plastic behavior is considered for the ceramic material in the next subsection.

Elastic Perfectly Plastic Behavior Hypothesis

Figure 5a, b show the profiles of particle velocities and radial stresses for different radii. The history of stresses is presented in the main stresses space (Fig. 5c). The abscissa considered is the same than in the previous subsection. The maximum radial particle velocities are respectively: 850 m/s, 552 m/s, 240 m/s, and 111 m/s.

All these profiles exhibit a detachment of an elastic precursor. The greater the distance of propagation the more marked this detachment. Level of this precursor also decreases with the propagation distance. So, it cannot be considered as an intrinsic parameter of the material, yet it is significant of the alumina behavior change. Fig. 5c raises this paradox. Indeed, this figure shows that the change in slope of the elastic precursor corresponds to the moment when the loading path leaves the uniaxial strain axis (Andriyash et al. 2019). The arrival of this route on the plasticity criterion (von Mises cylinder) induced on the material

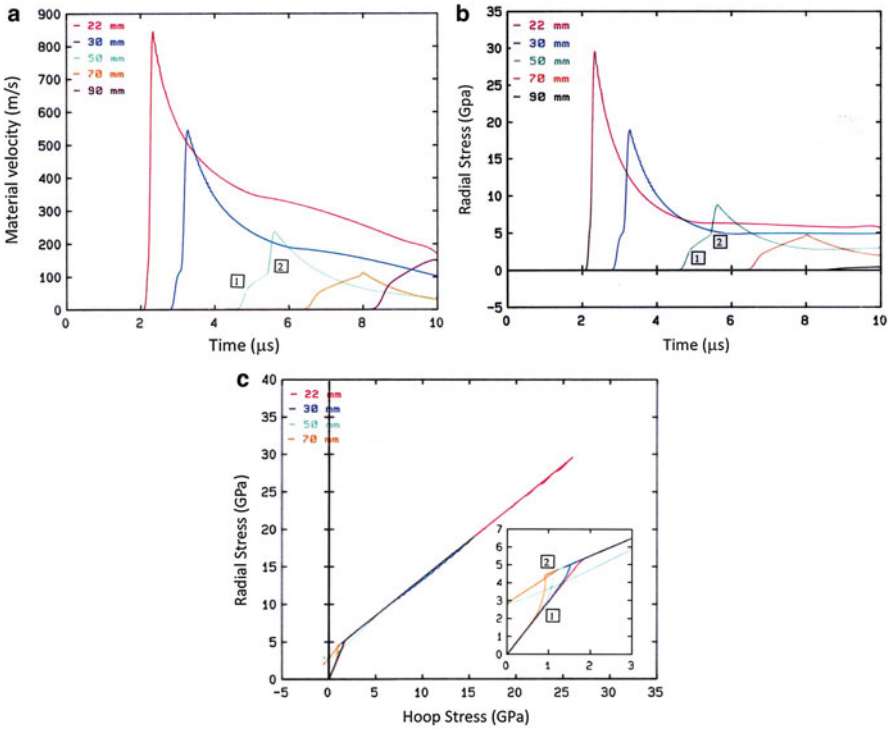

Fig. 5 Numerical simulation of a divergent spherical wave considering an elastoplastic behavior for the ceramic material. (**a**) Radial particle velocity versus time, (**b**) radial stress versus time, and (**c**) radial stress versus hoop stress

velocity profile a second wave front (Blake 1952). The elastic precursor level slightly decreases with the increase of the distance from the center of the explosive radius.

Experiments Performed on Two Alumina Ceramics

The numerical simulations presented in the previous paragraph can help us to exploit and interpret the experimental results. Before that, the studied materials are introduced hereafter.

Presentation of the Two Alumina Ceramics

The processes for making sintered alumina are diverse. For making the two studied alumina, the main following steps are completed:

- Choice of one or more alumina powders
- Production of a manipulable mixture
- Pouring, spinning, or pressing the mixture so as to obtain the raw
- Machining, if necessary, of the raw material according to the type of part manufactured
- Raw cooking: sintering cycle with or without pre-sintering cycle
- Machining of the cooked parts according to the tolerances required on the final product

The main production parameters of each studied alumina are described hereafter.

The alumina AL23 is manufactured by the company DEGUSSA France. The applied uniaxial stress is around 100 MPa. The slip is dried, pressed, and then cooked. The parts are then sintered without additions. The sintering temperature is 1780 °C. The maximum temperature level is 2 h. The density is about 3.92. The grain size distribution is between 10 and 50 microns.

The alumina T299 is manufactured by the company ALCOA France. This alumina is obtained by cold isostatic pressing at a pressure of 150 MPa. Initial powder contains 2% acrylic binder. The role of the binder acrylic is to give cohesion to the grains during the atomization process. This process consists of granulating the powder. The parts are then sintered without additions. The sintering temperature is 1600 °C. The density is about 3.86 and the grain size distribution is between 1 and 20 microns.

Table 1 provides some acoustic and mechanical properties of the two studied alumina.

Experimental Setup and Instrumentation

For each material described above, several cylindrical blocks are machined with a good surface finish to bond window material; the particle velocity measurements are carried out using a DOPPLER-LASER interferometry chain (IDL). This means makes possible to measure the particle velocity on a free surface or at an interface (with a PMMA window material) with an accuracy of the order of 1% and a temporal

Table 1 Physical properties of materials used in this experimental study (uncertainties: 7%)

Physical property	Alumina AL23	Alumina T299	Polymethyl methacrylate PMMA
Longitudinal wave speed (m/s)	10,800	10,300	–
Shear wave speed (m/s)	6200	6100	–
Density (–)	3.86	3.85	1.19
Young modulus (GPa)	380	353	13
Poisson ratio (–)	0.26	0.23	–
Mean grain size (μm)	40	5	–
Purity (%)	99.7	99.6	–

resolution of the order of 10 ns. Its operating principle is the same than that of VISAR (velocity interferometer system for any reflector). Fig. 6 describes the experimental setup.

Alumina blocks are finely machined. A hemispherical cavity is machined at the center of each block. This cavity is used to place the explosive (HMX-based F626). The explosive is machined into a hemispherical shape and is initiated in the middle of the flat part; thus a divergent spherical wave is generated. The window material is made of PMMA because it has a refractive index roughly constant as function of the applied pressure. The window is polished and metallized with gold. Its center is located thanks to four bands made on the metallization.

This window is centered and glued with a slow araldite on the rear face of the alumina block. The whole setup rests on a PVC (polyvinyl chloride) ring. The laser beam is in turn centered thanks to a ferrule oriented by two micrometric screws. This centering operation is very important because it conditions the validity of the measurement.

Fig. 6 Experimental setup dedicated to the material velocity measurements at the rear face of the material loaded by a divergent spherical wave

Experimental Results Obtained with Coarse-Grained Alumina AL23

Figures 7 shows the measured velocity profiles at the alumina-PMMA interface. The distance between the center of the explosive and the measuring points depends on the size of the block of alumina. The recorded profiles present a similar shape compared to the material velocity profiles obtained from numerical simulations (Fig. 5a). However, an improvement of the constitutive law is recommended.

The presence of an elastic precursor is noted. The slope discontinuity [A] corresponds to the moment when the material ceases to be in a state of uniaxial strain. The decrease in velocity peaks [B] is a function in 1/r (r = radial distance to the explosive center). However, the plastic wave detachment is not clearly observed. This is related to the viscous nature of plastic strain (Cosculluela 1992). So, in the case of alumina, as in uniaxial strain loading (plate impact), detachment of the plastic wave does not appear as a divergent spherical wave.

With regard to the mitigation of the material velocity profiles (Fig. 7), they are composed of an exponential decrease ([B] to [C]), followed by an almost straight part ([C] to [D]). The shape of the unloading can be compared to the shape of the velocity profiles obtained by numerical simulation in the perfectly plastic elastic case (Fig. 5a). It is supposed that this mitigation is related to plastic phenomena although,

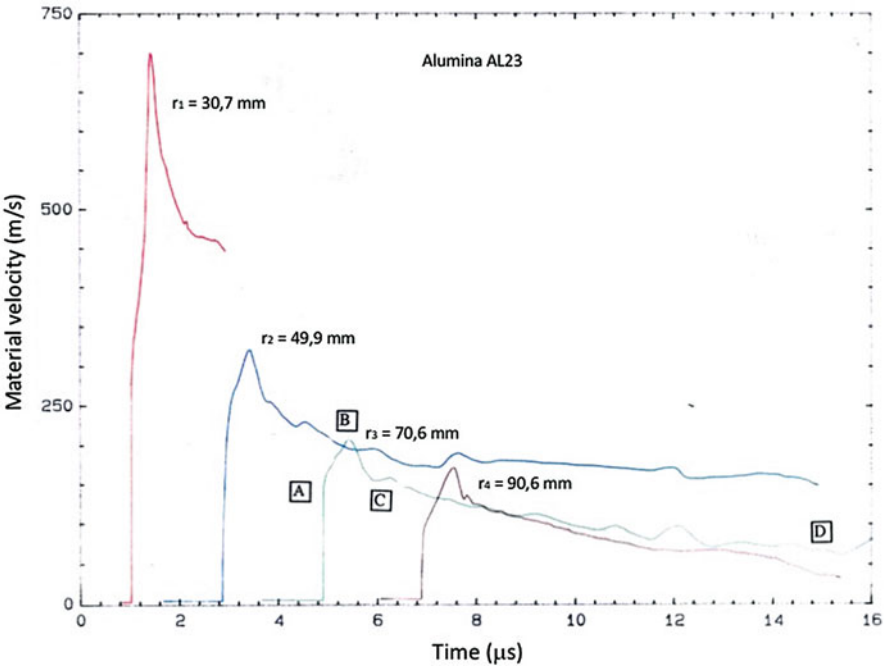

Fig. 7 Velocity profile at the AL23 alumina-PMMA interface for different distances from the center of the detonation

on the other hand, only the almost straight part ([C] to [D]) would account for the multiple-cracking of the blocks. Indeed, this cracking phenomenon seems to have damping effect on the release.

It is difficult to properly exploit these velocity profiles to identify the state of stresses as it could be done in the case of plate impact tests or in the case of the impact against a long bar.

Experimental Results Obtained with Fine-Grained Alumina T299

The stacking of T299 alumina discs allowed performing IDL measurements at different radii as in the case of alumina AL23. On the other hand, in addition to these material velocity measurements, stress and strain measurements are performed by using gauges glued between the discs. The glue used is a slow araldite. Here again, several abscissas are instrumented. These measurements are made using of manganin/constantan gauges. When this gauge inserted in between the discs is pressured by a divergent spherical longitudinal stress wave, the reaction of the manganin frame causes an increase in its resistance due to the piezo resistivity of the manganin. This frame also undergoes elongation from the unevenness of the shock wave. It is the sum of these two effects which is measured by recording the change of resistance of the manganin frame during the passage of the stress wave. As the constantan frame is bounded to the manganin, the levels of stress and elongation is the same. Unlike manganin, constantan is little piezo resistive, so its reaction is mainly provided by the elongation of its frame. This double measurement ("DOPPLER-LASER interferometry chain" and manganin/constantan gauges) allows us to control the validity of gauge measurements from IDL measurements (Cosculluela 1992).

Figure 8 shows the velocity profiles at the alumina-PMMA interface. Again, the distance between the explosive center to the measuring point depends on the size of the block of alumina. The obtained profiles have a similar appearance to those derived from numerical simulations (Fig. 5a).

Nevertheless, some differences are noted with the ones obtained with coarse-grained alumina. The rise times of elastic precursors are higher. The decrease in particle velocity peaks is less regular. These profiles do not show a clear plastic wave detachment. So, the compression behavior is supposed to differ to that of coarse-grained alumina. On the other hand, the appearance of the detents shows a different behavior between both aluminas.

The authors draw attention on the following remark: apart from the measurement made near the explosive, these other velocity profiles come from a stack of discs. Special care has been taken for the centering of the measurement location. The plates are glued. However, some studies show some issues experienced when divergent spherical wave is encountering an interface, even of identical material. These problems have been raised theoretically by Rinehart (1975) and experimentally by Heuze et al. (1991). Their results suggest that, during the compression phase, the particle velocity profiles can be used with confidence, but for the expansion phase,

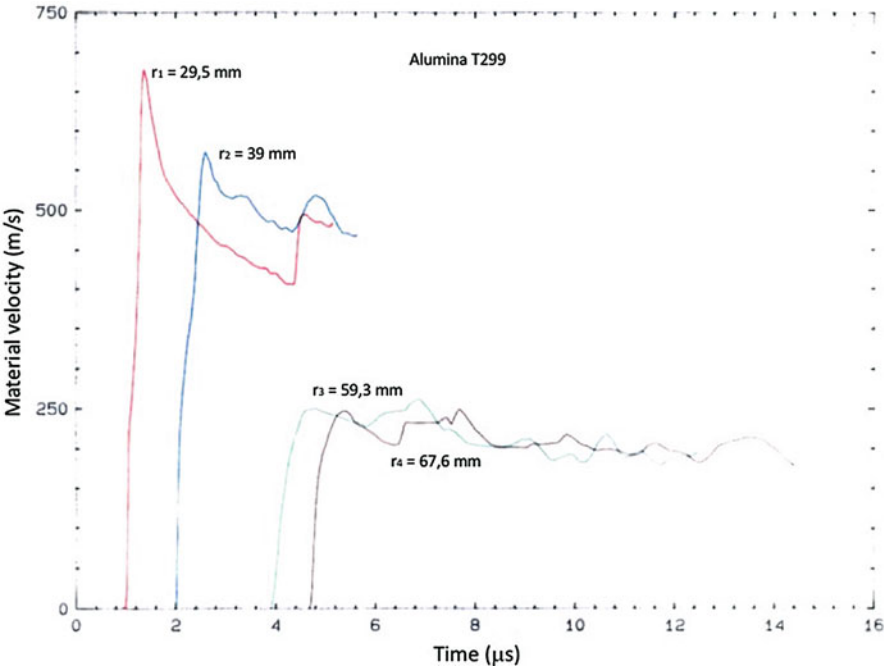

Fig. 8 Profile of the T299 alumina-PMMA interface velocity for different distances from the center of the detonation

the profiles must be used with caution; the ideal is to model each experiment as properly as possible.

For fine-grained and coarse-grained aluminas, the estimated maximum values of radial stress are calculated from Eq. (1) in which the particle velocity takes into account the difference of acoustic impedance between the PMMA and the alumina ceramic (Table 2). These values can then be compared to those obtained by using manganin-constantan gauges (Fig. 9).

As previously explained, the gauges measurements allow us to know the history of the radial stress and the hoop (orthoradial) strain (Fig. 9). All signals are shifted in time to be compared. During the compression phase, hoop strains remain nil. This is consistent with the fact that this compression phase corresponds to a uniaxial-strain loading. It can also be noted that characteristic signals of small hoop strains are disturbed. That said, they could be used as part of a Lagrangian analysis. The maximum values of radial stress given by the manganin frame are slightly different from those calculated from the interface particle velocity profiles. This difference increases when the measurement abscissa is far from the explosive. The material velocity measured at r = 59.3 mm and r = 67.6 mm seems to be underestimated because the stress wave crosses several alumina interfaces before reaching the measuring point.

Table 2 Maximal values of alumina-PMMA interface velocity and estimated associated stresses (uncertainties:15%)

Material	Measurement abscissa (mm)	Maximum material velocity (m/s)	Estimated maximum stress (GPa)
AL23	30,7	700	15
AL23	49,9	320	7
AL23	70,6	205	4,4
AL23	90,6	185	3,5
T299	29,5	680	15
T299	39	570	12,5
T299	59,3	260	5,7
T299	67,6	248	5,4

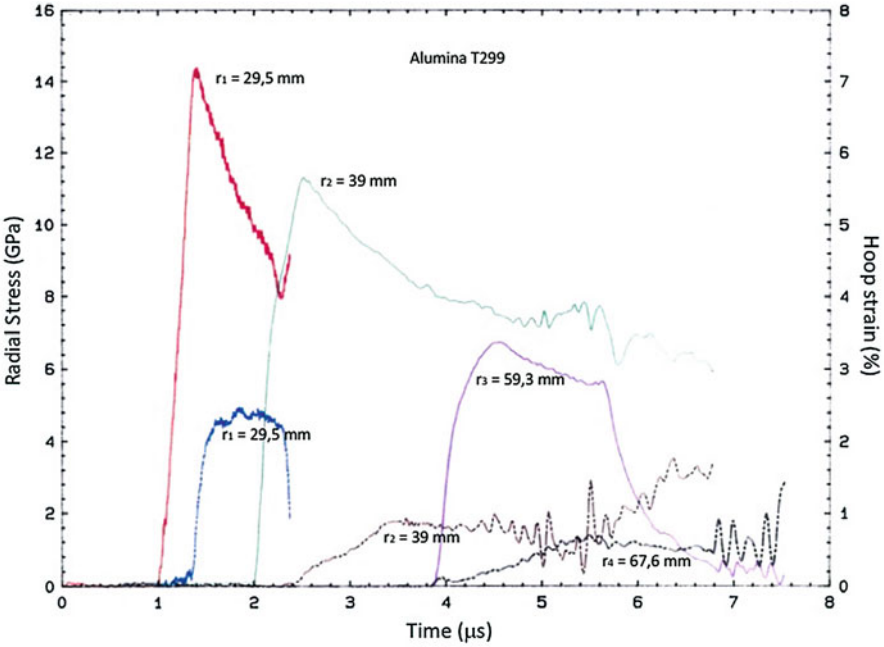

Fig. 9 Profile of the radial stress for different distances from the center of the detonation

Discussion on the Experimental Results

Material velocity measurements are carried out with DOPPLER-LASER interferometry to deduce the radial stress and hoop strain, so the maximum value achieved in each measurement is deduced. This study demonstrates the feasibility of such measurements and the interest they can represent. However, it is observed that the interfaces may degrade, even slightly, the measurements. Also, some recommendations for future tests are made:

- For hardware speed measurements, it is better to use a single block. The window material must be well known and the correction impedance that needs to be considered should be as small as possible. Indeed, this correction is well established in the case of purely uniaxial-strain loading but is not so-well known in spherical expansion.
- Regarding manganin/constantan gauges, it is preferable to use only one block on either side of the gauge and to avoid a stack of discs. This therefore implies that only one measurement is made per test. In addition, it is essential to properly center the gauge frame. These recommendations being made, the recovery tests and the postmortem observations performed can be now presented. Indeed, the objective is to relate the maximum value of the radial stress to the observations resulting from fragments collected at the same abscissa as the abscissa of measurements.

Postmortem Macroscopic Observations After Recovery Tests

In order to perform postmortem observation of the samples with a scanning electron microscope, next to a single divergent spherical longitudinal wave test, different kinds of recovery tests are conducted: configurations are developed with the explosive in contact with a steel frame containing the alumina, whereas in other configurations the explosive is placed in contact with alumina.

The first objective of these tests is to ensure that the material could be recovered in an observable state. These tests allowed the observation of several planes perpendicular to the direction of wave propagation.

The second objective of these tests is to recover a sample only loaded by the divergent spherical compressive wave. For that, it is necessary to eliminate any interfaces in the target that could induce parasitic effects. Some steel plates are put around the target to trap the reflected tensile waves. The steel-alumina interface is removed by machining a hemispherical cavity in alumina to receive the explosive. The reflection of tensile waves in alumina is also avoided by choosing sufficiently large samples. Their dimensions are designed by numerical simulation.

These tests provide post-test observations of the damage mechanisms involved in each alumina when subjected to a divergent spherical wave. This kind of stress wave imposes to the material a one- dimensional motion in a spherical frame. This property makes easier the location and positioning of the recovered samples so the observations can be easily connected to the experimental measurements.

Macroscopic Observations for Coarse-Grained Alumina

For coarse-grained alumina, apart from the disc located near the explosive (too fragmented, powdery appearance), each disc alumina is recovered in one block. Radial cracking of these discs is visible to the naked eye (Fig. 10). The central area of the discs has a fragmented appearance.

Fig. 10 Coarse-grained alumina disc recovered after a preliminary spherical expansion shock wave pyrotechnic test

Macroscopic Observations for Fine-Grained Alumina

For fine-grained alumina, the central area that is closest to the explosive is neither fragmented nor cracked. Its color is darker than that of the material in the initial state (Fig. 11). As it is well-known that a very porous alumina is white and its color tends towards dark ivory when the porosity tends to zero, it can be supposed that, in this zone close to the explosive, the divergent spherical wave has densified the fine-grained alumina. This alumina seems to densify without microcracking in an area very close to the explosive

Postmortem Analysis with SEM Microscopy

For each material, the observations are made in areas close to those where the measurements are performed. The objective pursued is to relate the observed microphysical phenomena to the stress levels reached within the material.

First, traces of plasticity phenomena (Fig. 12) are exhibited. Such observations are particularly unusual in quasi-static mechanical loading, but in the context of high strain-rate dynamic loadings and in triaxial stress states, they are more common (Hockey 1971; Lankford 1977). However, the observation of microplasticity mechanisms needs TEM analysis.

Examination of the failure surface pattern by means of SEM microscopy shows that the cracking is completely intergranular. Some intergranular microcracks are shown. No particular site of crack nucleation can be identified. Some twins can be observed in the coarser grains (see arrows in Fig. 12).

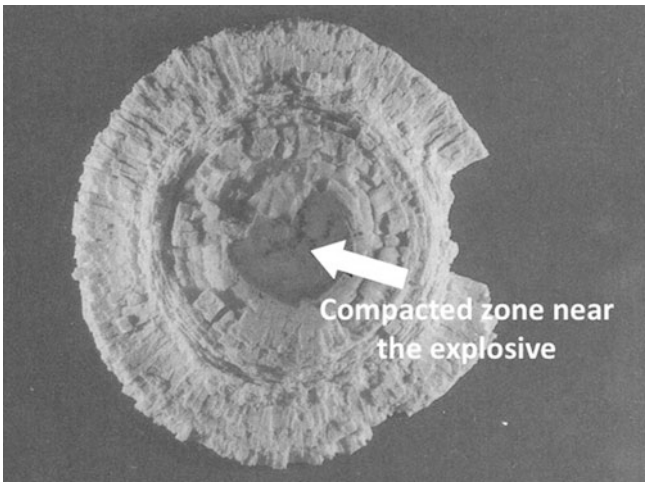

Fig. 11 Fine-grained alumina disc recovered after a preliminary spherical expansion shock wave pyrotechnic test

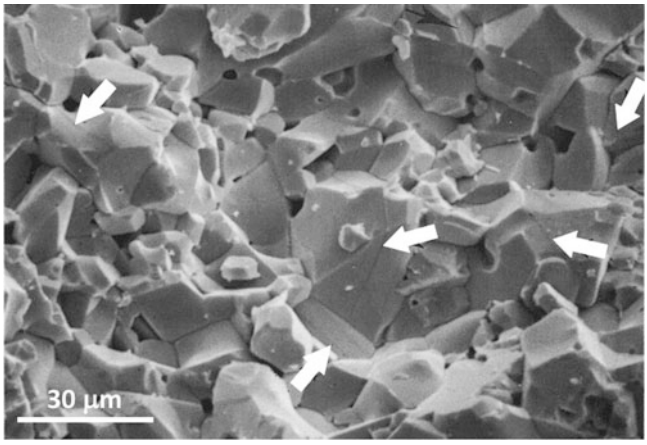

Fig. 12 SEM observations showing twinning (black arrows) in a coarse-grained alumina recovered after a divergent spherical wave test, r ~ 25 mm

SEM Observations for Coarse-Grained Alumina

The results of SEM observations are presented, considering five different abscissas where the abscissa r represents the distance between the observation locations to the center of the explosive.

- r = 20 mm (Fig. 13a): This observation area is the closest to the explosive that is observed. The cracking pattern is completely intergranular. All the grains are separated from each other. It is possible to see traces of glassy phase (black arrows) on the faces of some grains. No transgranular microcracks are visible.
- r = 30 mm (Fig. 13b): The cracking pattern is intergranular. Some grains are lost. The black arrows mark the remaining glassy phase. Some intergranular microcracks can be noted.

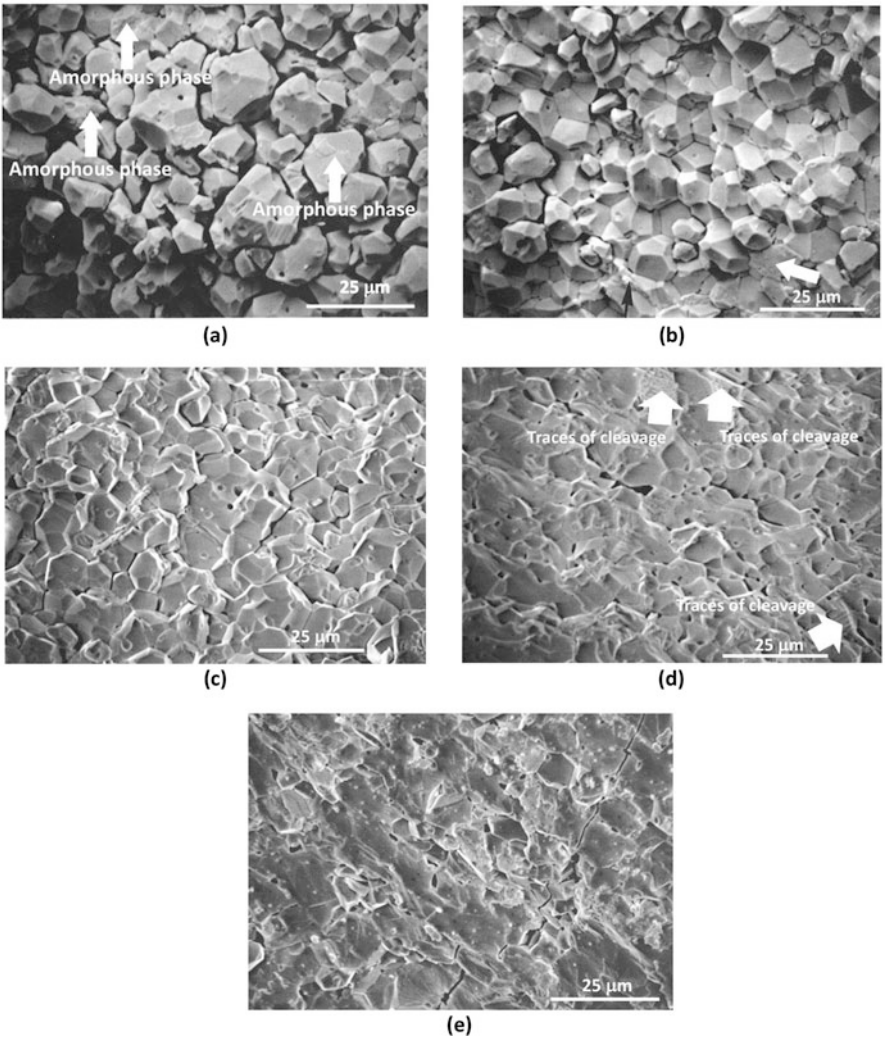

Fig. 13 SEM fractography showing intergranular failure pattern in a coarse-grained alumina recovered after a divergent spherical wave test. (**a**) r = 20 mm, (**b**) r = 30 mm, (**c**) r = 35 mm, (**d**) r = 50 mm, and (**e**) r = 60 mm

- r = 35 mm (Fig. 13c): The cracking pattern is mainly intergranular. All the grains are linked to each other. The microcracks are mainly intergranular. Microcracks of size smaller to the grain size are intergranular whereas cracks of size of the order of several grains are transgranular.
- r = 50 mm (Fig. 13d): A mixed intergranular–transgranular cracking pattern is observed. One can note the presence of cleavage marks. Cracking is mainly intergranular.
- r = 60 mm (Fig. 13e): The cracking pattern is clearly transgranular. The same observations are made for abscissa much further from the explosive. These cracks are induced by the tensile hoop stresses.

SEM Observations for Fine-Grained Alumina

Like what has been presented for coarse grain alumina, the results of observations made in the case of fine-grained alumina for five abscissas exhibit very different phenomena (Fig. 14). Each of them is representative of different radius r (r is the distance between the observation location to the center of the explosive).

- r = 20 mm (Fig. 14a): The failure pattern shows intergranular cracking. Many grains are separated. In the center, that the material seems to be compacted and transgranular cracks are exhibited. The pattern is much less homogeneous than in the case of alumina AL23.
- r = 25 mm (Fig. 14b): The failure pattern is intergranular. This fractography shows some microcracks and intergranular cracks. Few grains are separated. The black arrow indicates a grain that looks twinned. Transmission electron microscope observations should provide more specific answers.
- r = 40 mm (Fig. 14c): The failure pattern is completely intergranular. This fractography shows the presence of some cracks intergranular. These cracks seem to be more open at the places where the heterogeneity of grain size is more marked.
- r = 50 mm (Fig. 14d): The previous remark is even better illustrated by this fractography. Here the pattern has become mainly transgranular. Some intergranular cracks remain visible (black arrows).
- r = 70 mm (Fig. 14e): The pattern is fully transgranular. Note the presence of cleavage marks and intergranular cracks. These cracks are preferentially located around the large pores and the smaller grains.

Postmortem Analysis with TEM Microscopy

The aim of this analysis is to answer qualitatively to the following questions: Do microplastic phenomena really exist in the alumina loaded under such high pressure and high strain rates? Where these mechanisms take place and what it the nature or these mechanisms? To answer to these questions, several observations are performed considering small abscissas.

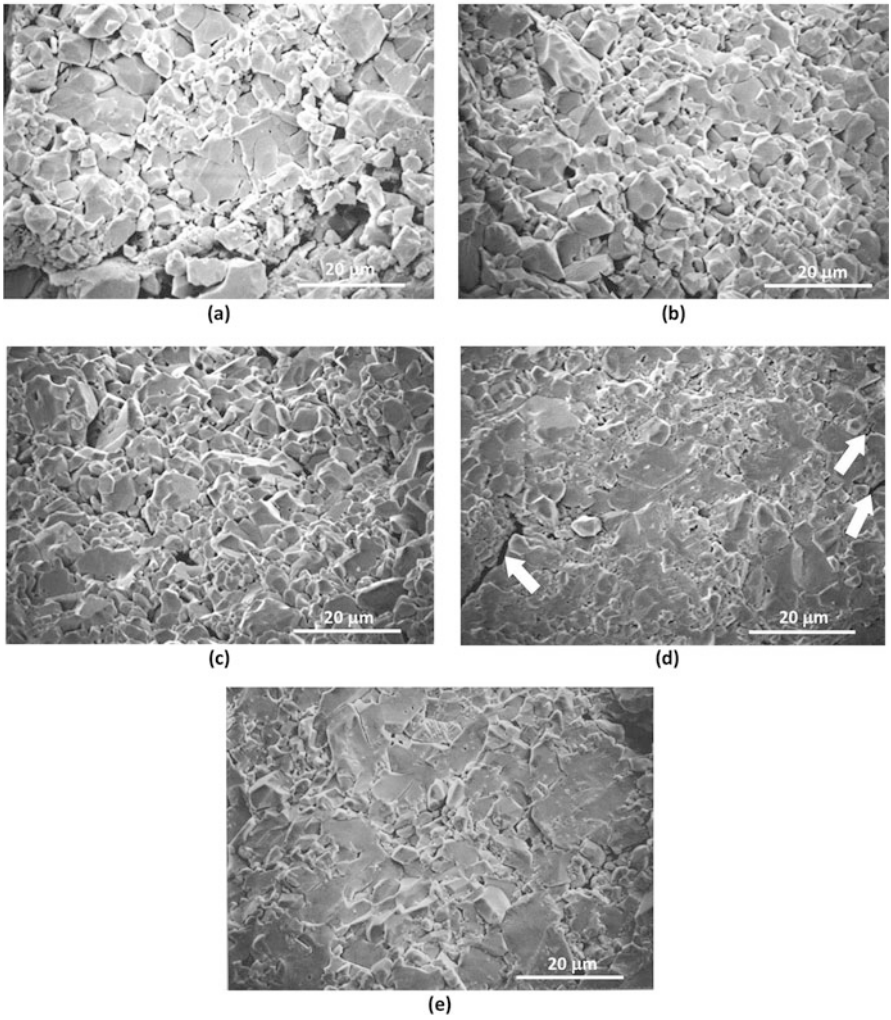

Fig. 14 SEM fractography showing the failure pattern in a fine-grained alumina recovered after a divergent spherical wave test. (**a**) r = 20 mm, (**b**) r = 25 mm, (**c**) r = 40 mm, (**d**) r = 50 mm, and (**e**) r = 70 mm

TEM Observations for Coarse-Grained Alumina

Given the observations made by SEM microscopy, the number of observations by TEM microscopy is reduced to only three abscissas (Fig. 15).

- r = 25 mm (Fig. 15a): Very close to the explosive, microplastic phenomena are very numerous (twins, dislocations). The picture also shows a network of intergranular microcracks. The micrographs show at the grain boundaries,

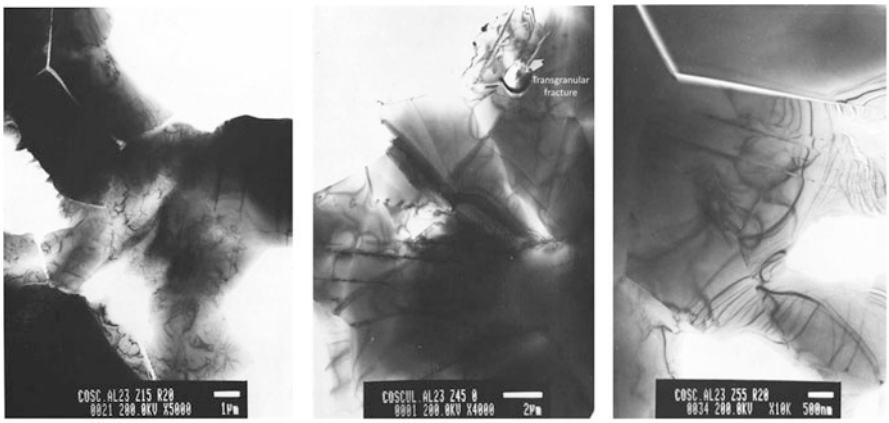

Fig. 15 TEM observations of coarse-grained alumina recovered after a divergent spherical wave behavior test. (**a**) $r = 25$ mm, (**b**) $r = 45$ mm, the arrow shows a transgranular microcrack from a pore and not connected with the grain seal, and (**c**) $r = 58$ mm

residues of glassy phase. Otherwise, it seems that the microcracks appear preferentially near the most microplasticized grains.

- r = 45 mm (Fig. 15b): Microplastic activity is much less important. It is reduced to a few dislocation movements observed on part of the grains (approximately 50%). The picture shows a presence of a transgranular microcracks. But this phenomenon is not representative of all the observations performed (Cosculluela 1992). Some rare intergranular microcracks are observed.
- r = 58 mm (Fig. 15c): Microplastic activity is relatively a little less to what has been observed for the abscissa previous. The micrograph exhibits an intergranular microcrack. The black curves represent fringes of shapes.

TEM Observations for Fine-Grained Alumina

Like coarse-grained alumina, the aim is not to perform a TEM study proper on fine-grained alumina. The results of the observations are only intended to help us describe physical phenomena in a way that understand mechanical behavior.

Based on the results obtained at the SEM, only three abscissas are selected for TEM observations:

- r = 20 mm (Fig. 16a): Near the explosive, the microplasticity activity is very important. Most of grains exhibit dislocations and twins. Micrographs show (white lines) an important network of intergranular microcracks. Additional observations made it possible to find that this network is dense and not oriented. The density of microcracks is not more prominent in the most microplasticized areas. These microcracks seem to be wider when they are next to the larger grains.

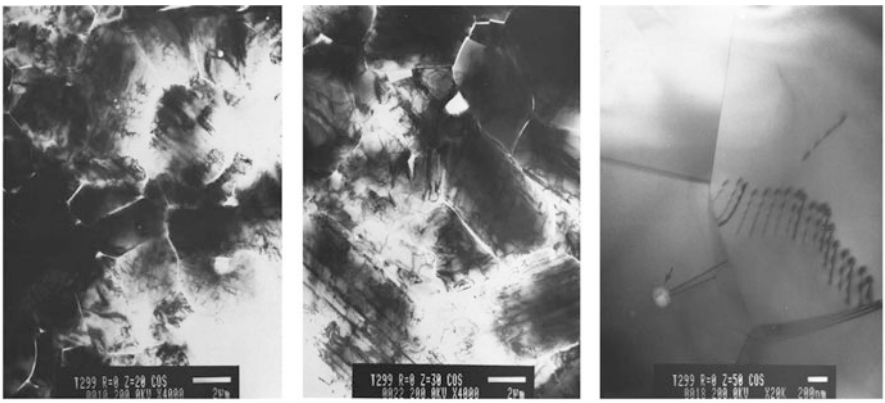

Fig. 16 TEM observations of fine-grained alumina recovered after a divergent spherical wave test. (**a**) $r = 20$ mm, (**b**) $r = 30$ mm, and (**c**) $r = 50$ mm, the arrow indicates an intragranular pore

- r = 30 mm (Fig. 16b): Microplasticity activity is still very important. Alumina is the seat of the same physical phenomena than at the previous abscissa with a decrease in the densities of microcracks and twins. However, the relationship between microplasticity and microcracking remains difficult to establish.
- r = 50 mm (Fig. 16c): The observations made at this abscissa show the absence of intergranular microcracks. Microplasticity activity has almost disappeared even if few dislocations stacks are still observed.

Discussion About the Physical Phenomena

Analysis of Microscopic Observations

The purpose of the recovery tests is to conduct a postmortem analysis of a material which is only subjected to a divergent spherical wave loading. All parasitic effects must be eliminated to make the observations valid. The experimental setup that is best suited to this problem is the test with one bloc alumina. In the case of the fine-grained alumina, the steel confinement of the preliminary tests allowed the observation of a compacted area without microcracking network.

A single divergent spherical expansion test allows observing several very different phenomena. This is related to the divergent nature of the spherical wave. Many observations are common to the two alumina: diffuse damage – transition from an intergranular failure pattern to a transgranular failure pattern further away from the explosive – radial cracking network, oriented fragmentation, and the increase of the fragments size far from the explosive (tensile damage).

The important difference between the two alumina lies in the nature of the area fragmented close to the explosive:

- In the case of coarse-grained alumina, all of the grains are separated from each other, so the fragments take on the appearance of a powder.
- In the case of fine-grained alumina, this phenomenon also appears but is much less pronounced.

To synthesize the results obtained by the measurement tests and recovery tests, for each characteristic abscissa, the maximum stress measured is related to the observations performed using SEM and TEM techniques (Figs. 17 and 18).

Several comments can be made regarding these divergent spherical expansion tests: The values of the stresses provided are more precise in the case of the fine-grained alumina (T299). Indeed, the stresses are derived from measurements by stress gauges. In the case of coarse-grained alumina (AL23), the stresses are calculated from the IDL velocity signals. For this, it is assumed that the level of maximum compression takes place according to a uniaxial strain path. The numerical simulations show that this is not entirely true. In the Figs. 17 and 18, the positions of the boundaries separating two physical phenomena does not represent a significant

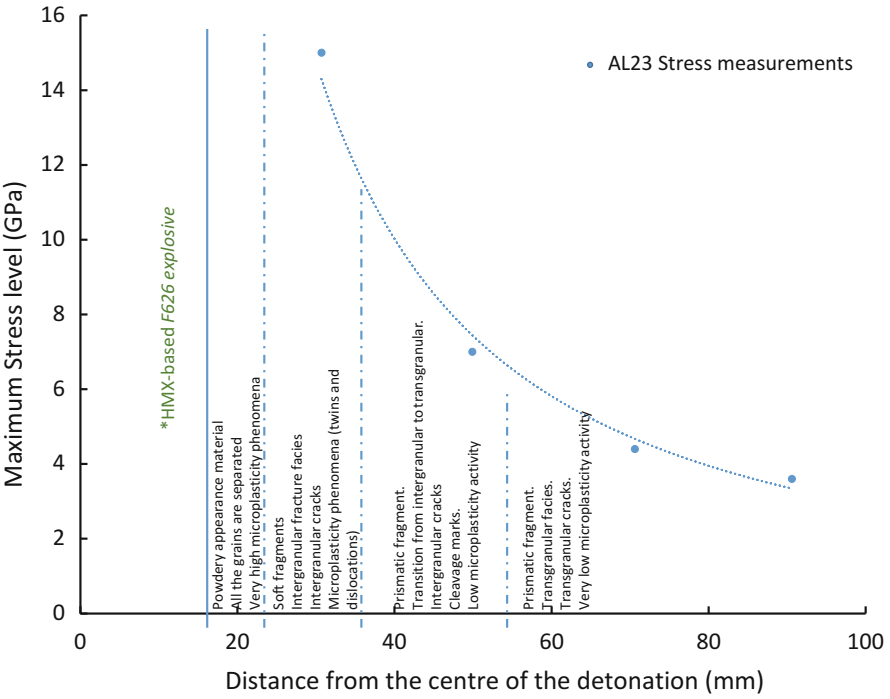

Fig. 17 Synthesis of the physical phenomena observed from a recovered coarse-grained alumina loaded by a divergent spherical wave

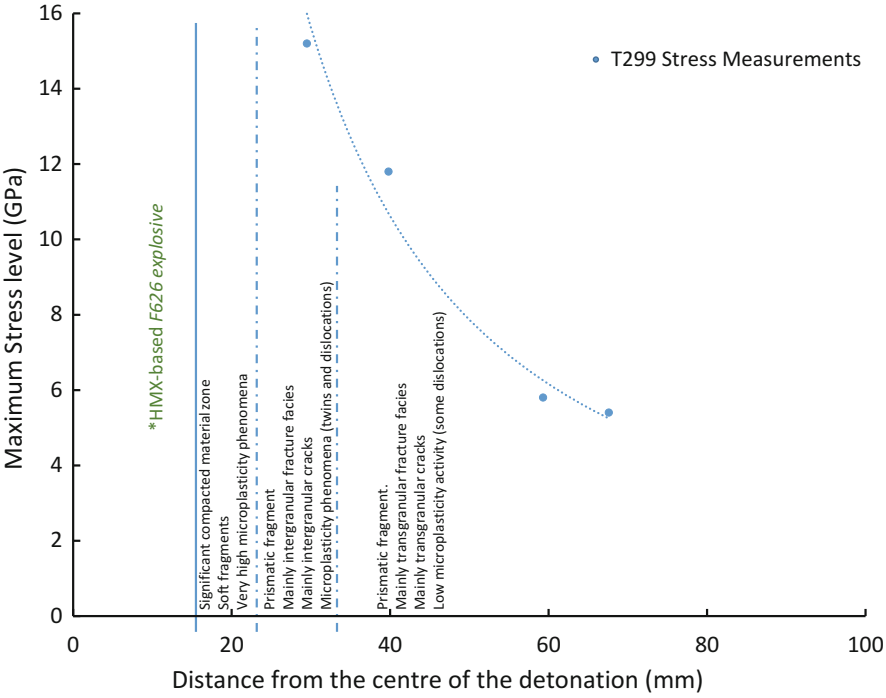

Fig. 18 Synthesis of the physical phenomena observed from a recovered fine-grained alumina loaded by a divergent spherical wave

discontinuity according the above observations. For AL23 alumina, there is a rapid decrease in damage with the abscissa due to a fast decrease of maximum level of stress. For T299 alumina, this same phenomenon appears. But, in this case, the transition between both mechanisms is much closer to the center of the explosive. In addition, there is no area where all the grains are completely separated. Therefore, to cause equivalent damage, the necessary stress level would be much greater in the case of fine-grained alumina.

Influence of Microstructural Parameters

The three microstructural parameters which mainly influence the dynamic behavior of alumina are the glassy phase, the porosity and the grain size.

Throughout the stresses space, the role of the *glassy phase* is the same. Indeed, it is always linked to cracking phenomena (Moya et al. 1981). When the percentage of this amorphous phase is low (6%), it hardly changes the elastic characteristics of the alumina.

As regards to the plastic behavior in uniaxial-strain compression, the results obtained by Longy (1992) on a 94% pure alumina, show that the Hugoniot elastic

limit (HEL) is not affected by the presence of the *glassy phase*. On the other hand, this intergranular phase is at the origin of the appearance of intergranular cracks in alumina in triaxial compression (Yeshurun et al. 1989; Longy 1992).

P*orosity* plays a major role in the domain of the stresses between the uniaxial compressive strain axis and the uniaxial compressive stress axis (Fig. 3). The measurements and observations made in several works (Knudsen 1962; Wachtman 1969; Cosculluela 1992) show that the increase in *porosity* reduces the elastic moduli and the tensile strength of the alumina. Intergranular pores are generally the sites of cracks nucleation.

In triaxial compressive state, the low *porosity* does not modify the microplasticity activity of pure alumina. Plastic deformation of the grains induces a compaction of the porous structure. This compaction is accompanied by damage which begins for levels of stresses that do not dependent on the initial porosity of the material. In this case, the elastic limit of Hugoniot (HEL) corresponds to the coupling between the pores collapse and the microplasticity activity. A reduction of the porosity induces an increase of the elastic moduli and of the elastic limit (HEL) of the alumina.

So, the HEL depends on the initial *porosity* of alumina (Gust and Royce 1971) according to a relation:

$$\sigma_{HEL} = \sigma_0 e^{-bp} \tag{13}$$

where p is the initial porosity and σ_0, b are material parameters.

To accommodate the excessive strain that is imposed to the material loaded in divergent spherical wave test, the material (even ceramics) must develop plasticity or microcracking to dissipate the excessive energy. The results obtained from the plate impact tests and divergent spherical expansion tests show that *small grain alumina plasticizes without microcracking* up to 12 GPa. This mode of energy dissipation seems to be related to the small grain size. Therefore, energy dissipation by microcracking in fine-grained alumina takes place for higher pressure levels with shear deformation mode.

In the case of small grain alumina (A 16-2), fracturing corresponds to a tensile transgranular cracking far from the explosive. In the case of large grain alumina (AL23) the orientation of the cracks depends on the triaxiality level of stresses: whereas, the fracturing is transgranular far from the explosive (tensile damage); it is intergranular closer to the explosive (compression damage). Far from explosive, the orientation of the cracks remains parallel to the radial direction.

Finally, the *influence of the grain size is stronger* in the zone where the intergranular cracking occurs. In both aluminas, the tensile fracturing is transgranular. The cracks propagate perpendicularly to the direction of maximum traction (hoop direction).

Closer to the explosive compression stresses are supposed to initiate damage which comes from the existence of local shear stresses due to the heterogeneities in the materials (difference between the grain size, grain orientation and porosities). These cracks then propagate parallel to the direction of compression.

For fine-grained alumina, transgranular fracturing is restricted to uniaxial compression stress state. A weak triaxiality state of the stresses seem to inhibit this kind of damage. The compaction phase is due to microplastic deformation of the grains. Microcracks only appear for very high stress levels in uniaxial contraction (>12 GPa).

Compared to this behavior, the enlargement of the grains has two consequences:

- The formation of intergranular cracks near the explosive, where the triaxiality state of the stresses is high. Intergranular damage can be due to a weakening of the grain boundaries due to a relatively greater thickness of the secondary phase in coarse grain alumina and a more marked anisotropy of the deformation in the case of coarse-grained alumina, therefore *higher local shear stresses*.
- A reduction in the microplasticity threshold and compaction of alumina. Indeed, the Hugoniot elastic limit depends on the size of the grains according to the Petch's law (1953). A micromechanical justification is given by the dislocation theory applied to polycrystalline solids.

Conclusion

The aim of this chapter is to understand to what extent the microstructural parameters are responsible for cracking and microplasticity mechanisms in the aluminas during a loading by a divergent spherical wave. The studied stress history is representative of the first moments of the interaction between a projectile and an alumina armor shield. The role of each microstructural parameter (glassy phase, porosity, and grain size) during this short time phase can be identified. Different microstructural phenomena are highlighted. During the triaxial compression phase, for very dense ceramics, the two microstructural parameters which conditioned the microcracking of the aluminas are the vitreous phase and the grain size. Too large glass phase percentage (>1%) leads to a microcracking of this phase. An increase in grain size lowers the nucleation threshold of microcracks. The latter are generated at the grain boundaries by local shear stresses proportional to the grain size. In addition, for an equal percentage of vitreous phase, the thickness of this glassy phase at the grain boundaries is greater in coarse grain alumina, which weakens the grain boundary.

A similarity exists between the increase of the grains size on the one hand and the increase of percentage of glassy phase on the other hand.

During the relaxation phase, microcracks nucleated in triaxial compression loading stage then become potential defects in the same way as the pores. The activation of these defects takes place only when the state of compression ceases to be triaxial.

This study made it possible to highlight and understand the phenomena involved in aluminas when they are stressed by a divergent spherical wave. According to the observations made in the present study it can be concluded that, for armor application, it would be better using pure ceramic (purity>99.5%), with high density (for alumina $\rho > 3.8$ g.cm^{-3}) and fine-grained polycrystalline alumina (d < 5 μm).

The pyrotechnic divergent spherical wave experimental technique can be applied to any kinds of brittle materials in general. The influence of microstructural parameters can be transposed to other polycrystalline ceramics.

References

A.V. Andriyash et al., Long-term evolution of spherical shell with boron carbide layer after explosive compression. J. Appl. Phys. **126**, 085903 (2019)

F.G. Blake Jr., Spherical wave propagation in solid media. J. Acoust. Am. Soc. **24**, 211–215 (1952)

S.J. Bless, N.S. Brar, Z. Rosenberg, Failure of ceramic and glass rods under dynamic compression, in *Proceedings of the American Physical Society Topical Conference, Shock Compression of Condensed Matter, Albuquerque 1989*, ed. by S.C. Schmidt, J.N. Johnson, (L.W. Davison, North Holland, 1990), pp. 939–942

J. Cagnoux, A. Cosculluela, Influence of grain-size on triaxial dynamic behavior of alumina, in *Proceedings of the International Seminar on Dynamic Failure of Materials: Theory, Experiments and Numerics*, ed. by H.P. Rossmanith, A.J. Rosakis, (Technische Universität Wien, Vienna, 1991), pp. 73–84

A. Cosculluela, *Plasticité, endommagements et ruptures des alumines sous sollicitations dynamiques triaxiales: influence de la taille des grains (Ph.D. dissertation)* (University of Bordeaux, Bordeaux, 1992)

A. Cosculluela, J. Cagnoux, F. Collombet, Uniaxial compression of alumina: structure, microstructure and strain rate, in *Proceedings of 3rd DYMAT Conference*, (Les Editions de Physique, Strasbourg, 1991a), pp. 109–116

A. Cosculluela, J. Cagnoux, F. Collombet, Two types of experiments for studying uniaxial dynamic compression of alumina, in *Proceedings of the American Physical Society Topical Conference* (Williamsburg, 1991b)

A.G. Evans, Y. Fu, The mechanical behavior of alumina: a model anisotropic brittle solid, in *Fracture in Ceramics Materials*, ed. by N. Evans. (Noyes Publications, Park Ridge, 1984)

P. Forquin, L. Tran, P.-F. Louvigné, L. Rota, F. Hild, Effect of aluminum reinforcement on the dynamic fragmentation of SiC ceramics. Int. J. Impact Eng. 28, 1061–1076 (2003)

M.L. Ghosh, On the propagation of spherical waves due to large underground explosions. Pure Appl. Geophys. **72**, 22–34 (1969)

W.H. Gust, E.B. Royce, Dynamic yield Of B4C, BeO and Al2O3 ceramics, J. Appl. Phys. **42**(1), pp. 276 (1971)

F.E. Heuze et al., Explosion phenomenology in jointed rocks, in *Explosion Source Phenomenology, Geophysical Monograph* 65, ed. by S.R. Taylor, H.J. Patton, P.G. Richards. (American Geophysical Union, Washington, DC, 1991), pp 253–260

B.J. Hockey, Plastic deformation of aluminum oxide by indentation and abrasion. J. Am. Ceram. Soc. **54**, 223–231 (1971). https://doi.org/10.1111/j.1151-2916.1971.tb12277.x

D.G. Howitt, P.V. Kelsey, Dislocation microstructure of shock-loaded alumina, in *Proceeding of the International Conference on Impact Loading and Dynamic Behavior of Materials, Bremen, FRG*, ed. by b. C.Y. Chiem, H.D. Kunze, L.W. Meyer, DGM Informationsgesellshaft MbH, (FRG, Oberursels, 1988), pp. 249–256

F.P. Knudsen, Effect of porosity on young modulus of alumina. J. Am. Ceram. Soc. **45**(2), 94–95 (1962)

J. Lankford, Compressive strength and microplasticity in polycrystalline alumina. J. Mater. Sci. **12**, 791–796 (1977). https://doi.org/10.1007/BF00548172

F. Longy, Déformation et endommagement de céramiques soumises à un choc intense : aspects macro et micromécaniques, Ph.D. dissertation, University of Limoges, Bordeaux, 1992

L.H. Louro, M.A. Meyers, Effect of stress state and microstructural parameters on impact damage of alumina-based ceramics. J. Mater. Sci. **24**, 2516–2532 (1989)

J.S. Moya, W.H. Kriven, J.A. Pask, Influence of grain boundary silica impurity on alumina thoughness, in *Proceedings of the 17th Conference on Ceramics* (1981), pp. 317–322

N.J. Petch, J. Iron Steel Inst. Lond. **174**, 25–28 (1953)

J.S. Rinehart, *Stress Transients in Solids* (Hyper Dynamics, Santa Fe, 1975)

P. Riou, C. Denoual, C.E. Cottenot, Visualization of the damage evolution in impacted silicon carbide ceramics. Int. J. Impact Eng. **21**(4), 225–235 (1998)

S. Satapathy, Dynamic spherical cavity expansion in brittle ceramics. Int. J. Solids Struct. **38**, 5833–5845 (2001)

S.M. Wiederhorn, Fracture of ceramics, in *Proceedings of the Symposium Mechanical and Thermal Properties of Ceramics, Gaithersburg, April 1–2, 1968*, ed. by J.B. Wachtman Jr. (Forgotten Books, London, 2018)

Y. Yeshurun et al., The dynamic shear strength of shock-loaded two-phase ceramics, in *Proceedings of the Fourth International Conference on the Mechanical Properties of Materials*, High Rates of Strain, Oxford, March 19–22, ed. by J. Harding. (Inst. Physics Pub. Div., Bristol, 1989)

Damage in Armor Ceramics Subjected to High-Strain-Rate Dynamic Loadings: The Edge-On Impact Test

24

Pascal Forquin and Antonio Cosculluela

Contents

Introduction: Why Tensile Damage in Armor Ceramics Needs to Be Investigated? 640
The Edge-On Impact Testing Technique: A Short Review 641
Numerical Investigation of an Edge-On Impact Test 646
Experiments Conducted on Four Silicon Carbide Ceramics 647
Presentation of the SiC Ceramics 647
Experimental Setup and Instrumentation 648
Experimental Results Obtained in Open Configuration 650
Experimental Results Obtained in Sarcophagus Configuration 650
Tomographic Analysis of Fragments 652
Discussion: Role of the Flaws Population on the Fragmentation Process in Ceramics 653
Conclusions 658
References 660

Abstract

The objective of this chapter devoted to "Damage in Armor Ceramics Subjected to High-Strain-Rate Dynamic Loadings" is dedicated to the edge-on impact (EOI) testing technique. This experimental method is commonly used to investigate the high-strain-rate tensile damage induced in armor ceramics when subjected to impact loading. The principle of EOI test is the following: a metallic cylindrical projectile hits the edge of a rectangular tile which thickness is generally smaller than the projectile diameter. The compressive strength of ceramics is much higher than their tensile strength; tensile damage occurs without inducing any compressive damage near the impact point. This anisotropic damage, called multiple

P. Forquin (✉)
Laboratoire 3SR, Université Grenoble Alpes, Grenople INP, CNRS, Grenoble, France
e-mail: pascal.forquin@3sr-grenoble.fr

A. Cosculluela
CEA-CESTA, Le Barp, France
e-mail: antonio.cosculluela@cea.fr; Antonio.COSCULLUELA@cea.fr

© Springer Nature Switzerland AG 2022

G. Z. Voyiadjis (ed.), *Handbook of Damage Mechanics*,
https://doi.org/10.1007/978-3-030-60242-0_94

fragmentation process, is composed of a large number of oriented cracks. Two testing configurations are generally considered. In the so-called open configuration, an ultra-high-speed camera is used to visualize the fragmentation process as function of time. In the sarcophagus configuration, a metallic or polymeric casing is used to keep the fragments in place so the damage pattern can be analyzed further by microscopy or X-ray micro-tomography analysis. Next the damage pattern can be compared to numerical predictions. In this chapter, a short review of experimental works proposed in the literature based on the use of EOI tests is presented. A numerical study is introduced to assess the loading history and loading rate involved in such test. Next, experimental results conducted with four silicon carbide ceramics are presented. Finally, these experiments are numerically simulated in a FE code with the DFH (Denoual-Forquin-Hild) anisotropic damage model, and the final damage patterns are compared to post-mortem observations in terms of cracking density. Lastly, the strengths, weaknesses and drawbacks of EOI tests are discussed.

Keywords

Impact tests · Multiple fragmentation · Ceramics · Tensile damage · Cracking density · Armor · Dynamic behavior

Introduction: Why Tensile Damage in Armor Ceramics Needs to Be Investigated?

During a ballistic impact, complex successive loadings develop leading to extensive damage modes within the ceramic plate (den Reijer 1991; Cosculluela 1992; Forquin 2003; Normandia et al. 2004; Chen et al. 2007; Zinszner 2014). In the first microseconds, high pressures are supposed to induce microplasticity and micro-damage mechanisms into the ceramic (Cagnoux and Cosculluela 1991) and also the fracture of the projectile's core. However, during the second step, tensile stresses develop in the whole ceramic plate leading to an intense fragmentation process in the material composed of a high density of oriented cracks triggered on pre-existing flaws (Forquin et al. 2003). Finally, in the third and last steps, the (broken) projectile penetrates into the comminuted ceramic target. In that stage, the behavior of the fragmented ceramic may have a strong influence on the penetration resistance of the protective armor system. According to Krell and Strassburger, the top priority factor driving armour ballistic performance is the ceramic fragmentation (2014). It is the reason why this tensile damage needs to be investigated and numerically simulated. For instance, the tensile damage induced under normal impact was investigated by (Riou 1996) considering a bilayer target, composed of a front plate 20 mm thick made of silicon carbide and a steel rear plate, which is subjected to the ballistic impact of a cylindrical projectile (11 mm in diameter, 100C6 steel) considering an impact velocity of 250 m/s (Fig. 1). In this configuration, the compression stresses generated in the ceramic tile are not high enough to induce any compression damage

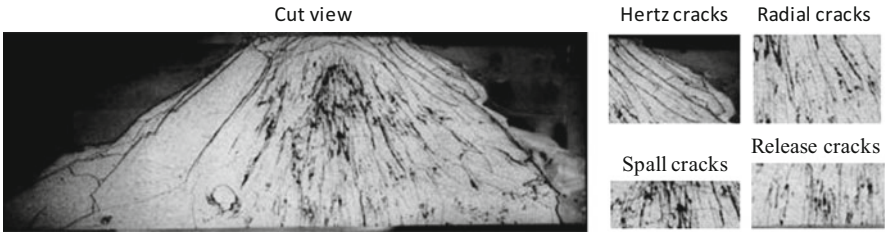

Fig. 1 Cut view of a SiC ceramic plate impacted with a steel cylindrical projectile at an impact speed of 250 m/s (Riou 1996)

and plastic deformation. However, in the wake of the longitudinal incident wave, tensile stresses develop at high-strain rates leading to an intense fragmentation process within the target. The ceramic plate is infiltrated with a hyperfluid resin, and a cut view of the target is shown in Fig. 1. A tensile damage that consists of cracks of millimeter size spaced from about 200 to 500 μm is observed. The damage pattern is composed of "Hertz cracks" initiated near the front surface and "radial cracks" within the bulk of the plate. In addition, "release cracks" are initiated on the rear face of the ceramic tile due to the reflection of the waves at the ceramic-backing interface. Furthermore, "spall cracks" parallel to the front and rear faces are detected resulting, a priori, from the crossing of release waves in the bulk of ceramic plate. This tensile damage is difficult to observe in the case of the ballistic impact of an armor-piercing projectile due to the penetration process and the ejection of debris. However, thanks to EOI experiments instrumented with ultra-high-speed photography, it is known that tensile damage develops in a few microseconds and precedes the penetration stage. Therefore, tensile damage in armor ceramics needs to be investigated, and the role or microstructure needs to be understood. In particular, the distribution of the critical flaws from which cracks are triggered has to be determined and implemented in an analytical or numerical modeling of the fragmentation process, which needs to be validated (Forquin et al. 2021). To do so, the EOI testing method may constitute a convenient and easy experimental method. A short review of existing experimental works is presented in the next subsection. Next, a numerical study of an EOI tests is introduced. Experimental results obtained with four grades of SiC are presented in the last subsection of this chapter.

The Edge-On Impact Testing Technique: A Short Review

The edge-on impact testing technique constitutes one of the most efficient and easiest experimental methods to investigate and to visualize the growth of tensile damage induced in brittle solids when subjected to high-strain rates. This method was pioneered, almost simultaneously, by Strassburger and coworkers in EMI (Ernst-Mach-Institut) (Strassburger and Senf 1995; Senf et al. 1994) and by Riou and coworkers in CTA (Centre Technique d'Arcueil, DGA) (Riou 1996; Riou et al.

1998a; Denoual and Hild 2000; Forquin et al. 2003). It consists in the impact of a cylindrical projectile against one of the edges of the tested ceramic tile. The projectile is usually larger in diameter than the target thickness and much smaller than the target height. It results in an impulsive loading characterized by a very short rising time (less than 1 μs). The loading, of triaxial shape in the vicinity of the contact area, turns into a bidimensional (plane stress) divergent wave propagating in the whole target. It is the reason why the stress amplitude is expected to decline more slowly (in $1/\sqrt{r}$) compared to a spherical expansion for which a decrease in $(1/r)$ is observed. Accordingly, damage develops much further in distance which facilitates the observations with high-speed imaging system. Thus, in the so-called open configuration, the lateral face of the target is visualized, thanks to ultra-high-speed photography equipment used at frame rates usually set from 2 μs down to 0.1 μs. In this configuration, the camera is installed along the axis of the light reflection of the incident light provided by a flash unit or continuous light unit. The visualized surface is usually polished to increase the amount of light captured by the camera but also to improve the observation of cracks by contrast.

This experimental method provides several advantages compared to other testing techniques. For instance, Brazilian tests performed with Split-Hopkinson pressure bar apparatus are limited to much lower strain rates (about a few tens of s^{-1}) when applied to ceramics. The limited loading rate results from long rising time of loading (above 20 μs) that needs to be applied to the sample to ensure a correct mechanical balance. For instance, typical stress rates ranging from 3 to 6 MPa.μs^{-1} are obtained in Brazilian tests applied to alumina samples in (Galvez et al. 1997; Chen et al. 2014) and in Scapin et al. (2017) leading to a single fracture in each tested specimen. On the other hand, in edge-on impact experiments, typical strain rates ranging from few thousands of s^{-1} to a few tens of thousands of s^{-1} are generated (Forquin et al. 2018), leading to an intense multiple fragmentation process in the target.

In contrast, the spalling testing method by shockless plate impact (Dargaud and Forquin, 2021) or by pulsed-power technology provides the advantage of a direct measurement of the spall strength (Zinszner et al. 2015a, 2017) and provides much higher strain rates (mostly above 10^4 s^{-1}). However, the spall fracture is hidden in the bulk of the sample and cannot be visualized by high-speed photography. In addition, the fracture pattern remains difficult to analyze through post-mortem observations. The edge-on impact testing technique requires also much less costly gas gun facility compared to those used for plate-impact tests, which operates with a larger caliber and under vacuum, or compared to pulsed-power generator facilities.

Different dimensions of projectiles, impacted plates, and impacting velocities have been considered in the literature. For instance, ceramic plates 100 × 100 × 10 mm^3 were impacted with steel cylinders of 30 mm in diameter and 23 mm in length with impact velocities ranging from 50 to 1000 m/s in (Senf et al. 1994) (Strassburger and Senf 1995). The damage formation was visualized by means of high-speed Cranz-Schardin film camera during the first 12 μs after projectile impact. Experiments performed with glass and SiC ceramics (Brajer et al. 2003; Strassburger 2004) and more recently with boron carbide (B4C) ceramic (Strassburger et al. 2013) were used to characterize the so-called damage velocity (velocity of the damage

front), the cone crack velocity, and the secondary crack velocity (cracks initiated by the shear wave travelling along the impacted edge of the specimen) as function of the impact velocity.

In the experiments performed by Riou (1996) and by Riou et al. (1998a, b), a hard-steel cylinder projectile (D11H20) impacts the edge of a dense natural-sintered α silicon carbide at an impact velocity ranging from 100 to 300 m/s. The ceramic tile is backed or not with a steel confinement beam. The beam dimensions are 100 mm × 10 mm × T with a thickness T equal to 15 or 20 mm. A schematic of the test configuration is given in Fig. 2a. Two pictures taken 2.9 μs after impact with an Imacon 790 high-speed camera are shown in Fig. 2b and c. In the first picture (Fig. 2b) a SiC beam sample is subjected to the impact of a projectile at an impact speed of 250 m/s. In the second test (Fig. 2c), the SiC target is constrained on its back with a steel beam and is impacted roughly at the same impact speed (260 m/s). A damage pattern composed of a large number of oriented short cracks is observed in less than 3 μs. It is concluded by the authors that the back steel confinement seems to not interfere with initial damage shape generated in the first 3 μs, whereas the presence of the confinement seems to limit the initiation of transverse cracks in the next 2 μs.

The fragmentation process induced in a porous SiC ceramic filled or not with an aluminum alloy though its open porosity was investigated in Forquin et al. (2003) by means of EOI tests in open configuration (use of a high-speed camera) and in sarcophagus configuration. This last configuration is depicted on Fig. 3a. It is composed of a metallic casing made of aluminum alloy that surrounds the ceramic tile with the aim to keep the fragments in place. However, small paper wedges are placed in between the ceramic tile and the aluminum casing to ensure an impedance discontinuity. It is the reason why the same number of cracks is expected for both (open and sarcophagus) configurations. After impact, the fragmented ceramic tiles were infiltrated in the sarcophagus with a hyperfluid resin (epoxy, Struers) and then polished for optical observations as shown in Fig. 3b, c, and d. The tests conducted at

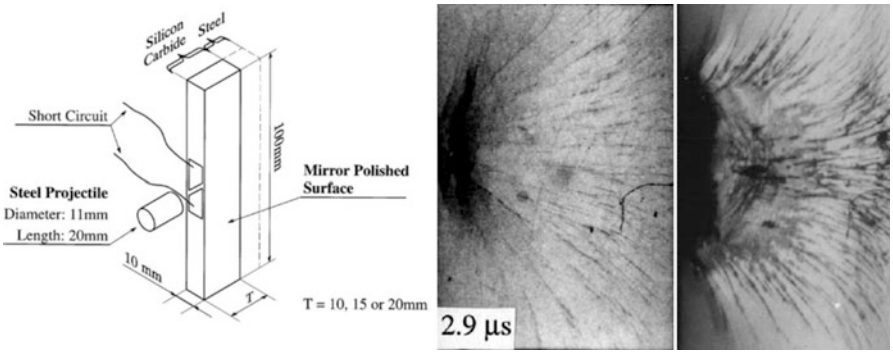

Fig. 2 Edge-on impact experiments performed by Riou et al. (1998a). (**a**) Experimental setup, (**b**) and (**c**) damage at 2.9 μs, (**b**) unconfined 15-mm-thick SiC target impacted at 250 m/s, and (**c**) back steel-confined 15-mm-thick SiC target impacted at 260 m/s

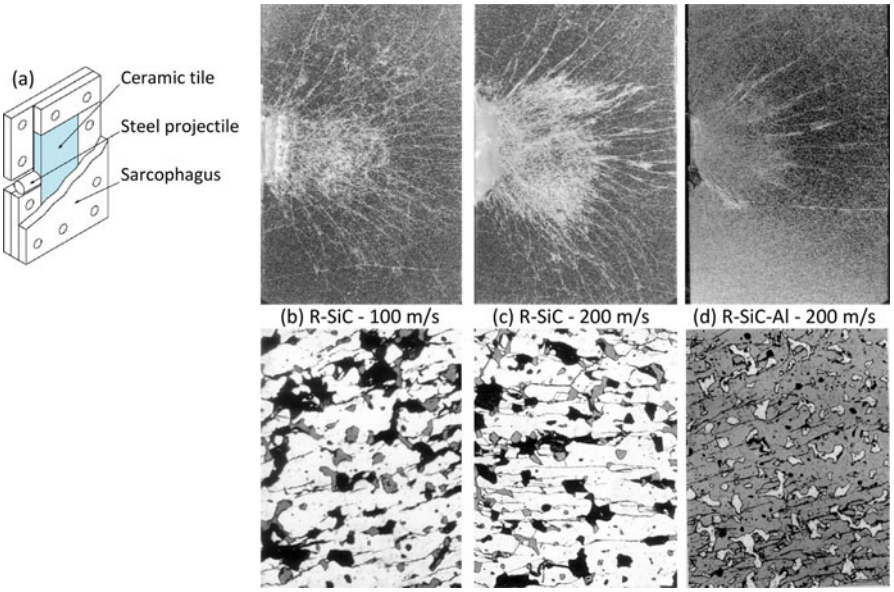

Fig. 3 Edge-on impact experiments performed in Forquin et al. (2003). (**a**) Sarcophagus configuration, (**b**) R-SiC target impacted at 100 m/s, (**c**) R-SiC target impacted at 200 m/s, and (**d**) R-SiC-Al target impacted at 200 m/s

100 m/s and 200 m/s revealed an increase of the cracking density in R-SiC ceramic with the increase of loading rate. The test performed at an impact speed of 200 m/s with the infiltrated ceramic showed a decrease of the intensity of fragmentation compared to the non-infiltrated ceramic and a very good residual strength. The fragmentation process was simulated with a finite-element code considering the DFH (Denoual-Forquin-Hild) anisotropic damage model considering the Weibull parameters identified from bending tests as input parameters. The experimental and numerical results demonstrated that the aluminum alloy infiltrated through the open porosity of the ceramic results in two beneficial effects: on the one hand, it increases the crack inception stresses lowering the cracking density. On the other hand, it creates a bridging effect leading to a much higher residual strength of the fragmented targets. Both effects are seen to be beneficial regarding a multi-hit loading scenario.

In the work developed in Riedel et al. (2010), the elastic stress histories involved in an EOI test were numerically investigated and compared to those involved in a depth-of-penetration (DOP) test configuration and planar plate-impact (PPI) experiments. In addition, the fracture processes in the target was numerically simulated with a mesh-free SPH code. It is concluded that an anisotropic damage representation along with tensile stress failure criteria is requested to represent the damage propagation produced by diverging shock waves.

In the work conducted in Leavy et al. (2013), the EOI technique was used as benchmark to validate ceramic constitutive models implemented in a dynamic simulation code. To do so, a Weibull distribution is introduced in a hydrostatic

tension criterion for describing the variability of material strength, and the numerical predictions in terms of damage velocity versus impact velocity were compared to experimental observations provided by high-speed photography.

More recently, the edge-on impact techniques were extended to the investigation of the fracturing process in transparent armor ceramics such as single crystal (sapphire) and AlON (spinel) polycrystalline ceramics (McCauley et al. 2013). The kinetics of damage and fracturing features in transparent ZnS ceramic and in sapphire single crystal was more recently analyzed in Forquin (2016) and in Forquin and Zinszner (2017). In the experiments reported in Fig. 4, monocrystalline sapphire ceramic targets of size $60 \times 60 \times 4$ mm^3 are impacted on the edge with a cylindrical projectile 10 mm in diameter at an impact speed about 230 m/s. As illustrated by the pictures of Kirana ultra-high-speed camera, the fragmentation process develops in a ten of microseconds. It is observed that cracks propagate following specific orientations in relation to the C axis direction.

The intergranular and transgranular fracturing observed in polycrystalline AlON transparent ceramics subjected to EOI tests in McCauley et al. (2013) was numerically simulated by Zhang et al. (2018) considering a peridynamic numerical method. For this purpose, a model in which individual grains are represented was built. This numerical approach allows describing the primary failure front that grows at intersonic (supershear) propagation speed as well as the localized cracks which develop at sub-Rayleigh propagation speed.

The EOI experiments conducted on AlON in Strassburger (2004) and Strassburger et al. (2005, 2006) were analyzed and modeled in (Tonge and Ramesh 2016) by considering a micromechanic-based model in order to describe the damage growth, the deviatoric and volumetric granular flow, and pore compaction mechanisms that develop preferentially in the interior of the plate rather than on the surface due to inertial confinement. Again, the flaw distribution is observed to be

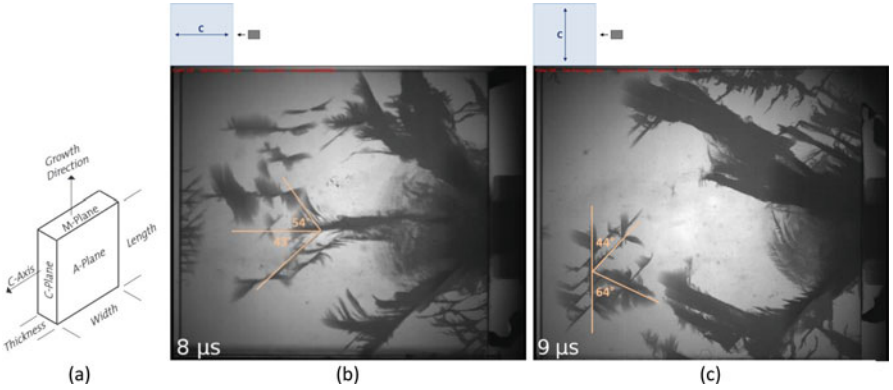

Fig. 4 Edge-on impact experiments performed against sapphire single crystal at an impact speed around 230 m/s (Forquin and Zinszner 2017). (**a**) Sapphire single crystal orientation (Saint-Gobain doc.). (**b**) Impact direction parallel to the C axis (horizontal axis). (**c**) Impact direction orthogonal to the C axis (vertical axis)

an important parameter to account for the role of microstructure on the damage process.

In conclusion, the edge-on impact testing configuration has been used extensively for the last three decades to explore the fragmentation process in different kinds of ceramic armors. The high-speed photography has revealed several features of the fragmentation process generated in these materials under impact loading. In particular, it is observed that the fragmentation process is composed of a high number of cracks oriented perpendicularly to the positive principle stress. A numerical investigation of the loading history is presented thereafter. Next, a comparison of the fragmentation properties of four SiC ceramics is proposed.

Numerical Investigation of an Edge-On Impact Test

The mechanical loading involved in an edge-on impact experiment was investigated in Forquin et al. (2018) by means of numerical simulations conducted with the commercial Abaqus-Explicit finite-element code. The considered target is a silicon carbide plate 60 × 30 × 8 mm^3 impacted with a cylindrical projectile (D10 × H15) at a striking velocity of 175 m/s. These numerical simulations aim to estimate the level of loading rate leading to the ceramic fragmentation. For this purpose, an isotropic elastic behavior is considered for the ceramic with Young's modulus $E = 410$ GPa and Poisson's ratio $v = 0.14$. A mesh made of "C3D8R" eight-node solid brick elements with reduced integration is considered for the projectile and target with a mesh size of approximately 1 mm. An elastic-perfectly plastic model is used for the projectile with a yield stress of $Y = 1300$ MPa. Two symmetry planes are considered so a quarter of the projectile-target configuration is meshed. The field of hoop stresses at 1, 2, and 3 μs after impact is depicted in Fig. 5 with a cylindrical coordinate system ($\vec{e}_r$, $\vec{e}_\theta$, $\vec{e}_z$) centered at the initial point of impact. Tensile stresses

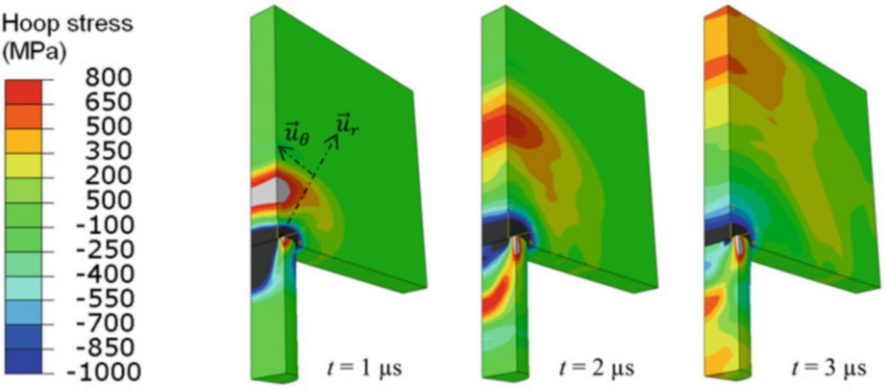

Fig. 5 Numerical simulation of edge-on impact experiments with a striking velocity of 175 m/s using an elastic model for the ceramic target

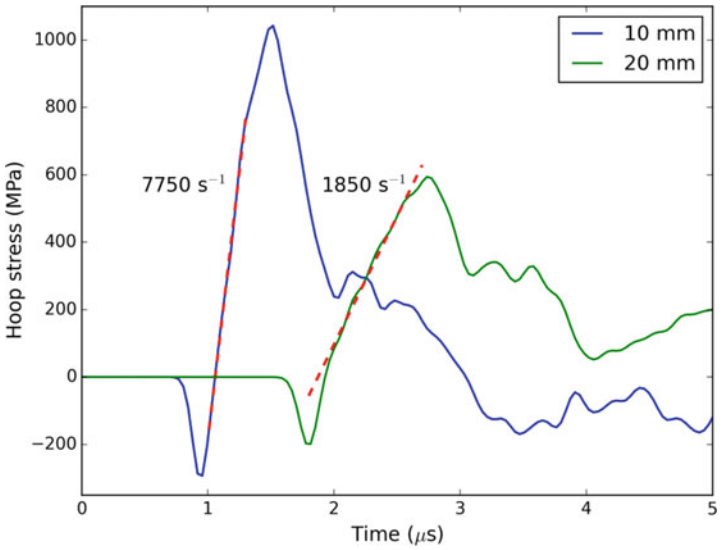

Fig. 6 Profile of the hoop stress as a function of time in edge-on impact experiments at 10 and 20 mm toward the initial impact point and an estimation of the strain rate

are observed at 7 mm ($t = 1$ µs) and 15 mm ($t = 2$ µs) from the initial point of impact and at $t = 3$ µs near the target rear edge. The strain rate level in finite elements located along the impact axis at a distance of 10 and 20 mm from the initial impact point was estimated. It is about 7750 s^{-1} and 1850 s^{-1}, respectively, at 10 and 20 mm (Fig. 6).

Experiments Conducted on Four Silicon Carbide Ceramics

Presentation of the SiC Ceramics

The edge-on impact testing method was applied to four SiC ceramics of different microstructures in (Rossiquet 2012; Zinszner 2014; Forquin et al. 2018). The first grade, referred to as "PS-S" (pressure-less sintered in solid state) corresponds to a commercial product of Saint-Gobain also named Hexoloy SA®. It is performed in pressure-less solid state sintering at 2150 °C. Its density corresponds to 98% of the theoretical density, and its microstructure is characterized by fine and equiaxed grains about 4 to 10 µm (Fig. 7a). The SPS (spark plasma sintered in solid state) SiC ceramic is produced in solid-state sintering at 2000 °C for 5 min under a 40 MPa compaction pressure and is called "SPS-S." The resulting microstructure for this grade shows elongated grains, 100 µm in length, distributed among smaller and more equiaxed grains (Fig. 7b). Its density reaches around 99% of the theoretical one. The third grade referred to as "PS-L" is sintered in pressure-less condition and in liquid phase state at 1875 °C for 30 min under argon. Its microstructure exhibits equiaxed

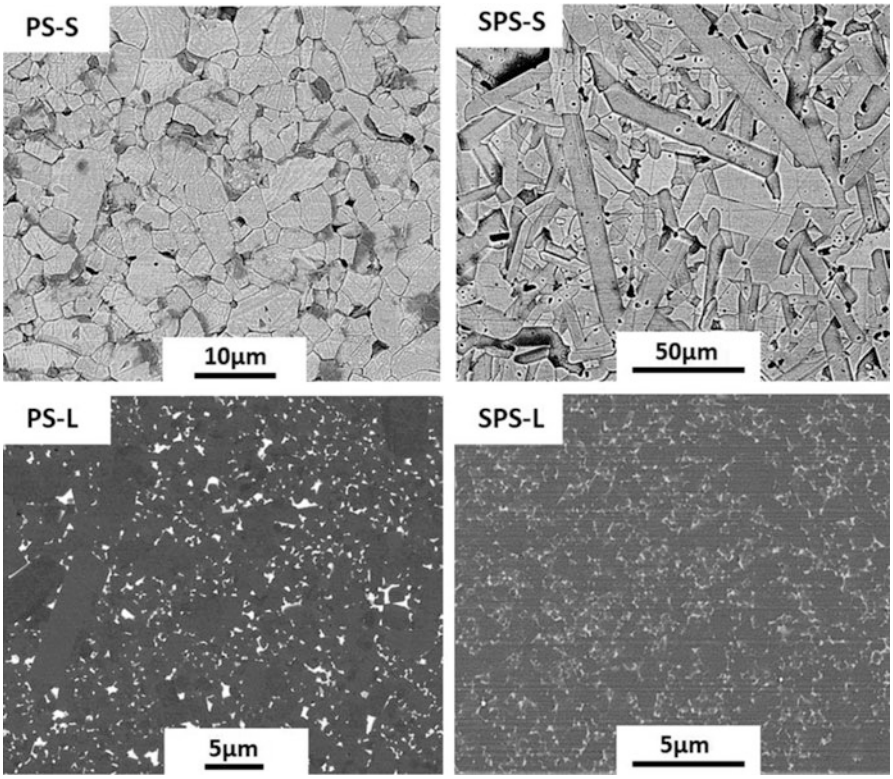

Fig. 7 SEM images of microstructures from grades (**a**) PS-S, (**b**) SPS-S, (**c**) PS-L, and (**d**) SPS-L after mirror polishing (Rossiquet 2012). Samples (**a**) and (**b**) have been chemically etched in order to reveal microstructures. Samples (**c**) and (**d**) have not been etched since the contrast between SiC grains and secondary phases allows an easy observation of the microstructures

grains of average grain size around 3 µm surrounded by a secondary phase which is mainly composed of YAG ($Y_3Al_5O_{12}$) (Fig. 7c). Its density corresponds to 98% of the theoretical density. The last SiC grade called "SPS-L" (spark plasma sintering in liquid state) is sintered in liquid-phase state by SPS at 2050 °C for 15 min under a 40 MPa. Its microstructure is characterized by a equiaxed submicron grains of average size about 500 nm bounded by an amorphous secondary phase made of Al and Y as shown in Fig. 7d. The measured density reaches 98.5% of the theoretical density. Several basic properties of each ceramic are listed in Table 1. The experimental results obtained with each SiC grade are reported in the next subsection.

Experimental Setup and Instrumentation

Edge-on impact tests are performed in "open configuration" and in a "sarcophagus configuration" with cylindrical projectile 10 mm in diameter and

Table 1 Main sintering and mechanical properties of the four SiC grades (Rossiquet 2012; Zinszner 2014)

SiC grade	Sintering process	Sintering phase state	Sintering additives	Average grain size (μm)	Hardness H_{V1} (GPa)	Density (kg/m^3)	Toughness (MPa√m)
PS-S	Pressure-less	Solid	$B_4C + C$	6	24.3	3150	3.0
SPS-S	SPS	Solid	$B_4C + C$	/	27.0	3170	2.5
PS-L	Pressure-less	Liquid	YAG	3	22.2	3260	5.2
SPS-L	SPS	Liquid	YAG	0.5	23.9	3210	3.8

15 mm in length made of high strength steel (elastic limit, 1300 MPa). The specimen is 60 mm in length and 8 mm thick, and the visualized side is 60 × 30 mm^2. The impact velocity is approximately 170 ± 5 m/s. In the open configuration, the ceramic tile is free with no casing. An aluminum casing is used in the sarcophagus configuration to keep most of the fragments in place. In addition, small paper wedges are inserted in between the ceramic plate and the metallic casing to ensure an impedance discontinuity, so the expected number of cracks in both (open and sarcophagus) configurations is the same.

Experimental Results Obtained in Open Configuration

In open configuration EOI experiments are performed with an ultra-high-speed camera (Shimadzu HPV-1) with an inter-frame time set to 1 μs in order to visualize the growth of the fragmentation during impact. A velocity interferometer pointed out to the ceramic rear edge is used to trig the camera. The fragmentation pattern of each ceramic tile is depicted in Fig. 8 at 4 and 7 μs after impact. In the first 4 μs, "radial cracks" initiates and develops within the whole target, and "release cracks" are triggered at the rear edge of the target. At t = 7 μs, cracks initiate perpendicularly to the radial cracks, so the target is completely damaged. The cracking density appears to be clearly smaller in PS-L and SPS-L ceramic grades compared to the PS-S and the SPS-S grades, which confirms the influence of microstructure on the fragmentation process.

Experimental Results Obtained in Sarcophagus Configuration

Edge-on impact experiments in sarcophagus configuration were conducted with the four SiC ceramics as detailed in Forquin et al. (2018). The impacted targets were infiltrated post-test with a hyperfluid epoxy resin before polishing for optical observations. A different set of cracks are observed in Fig. 9. Numerous radial cracks are observed as already noted in the high-speed camera images. So-called conical cracks initiate on the impacted edge of the target. Cracks initiate at the rear edge of the target due to release waves. Last, a few cracks propagate perpendicularly to the radial cracks in the center of the target. The crack density (λ_{cracks}) is estimated at about 10 mm from the initial impact point for each grade by considering the mean distance (d_{cracks}) between parallel cracks according to the formula: $\lambda_{cracks} = 1/(d_{cracks})^3$ (Forquin et al. 2018). In PS-S grade, the mean distance between cracks 0.21 mm corresponds to a crack density of 1.0×10^{11} cracks/m^3. In SPS-S grade, the estimated crack density at 10 mm from the initial impact point is about 7.3×10^{10} cracks/m^3. In PS-L and SPS-L grades, the crack density is significantly about 7.6×10^9 cracks/m^3 and 4.2×10^9 cracks/m^3, respectively, in the PS-L and SPS-L grades.

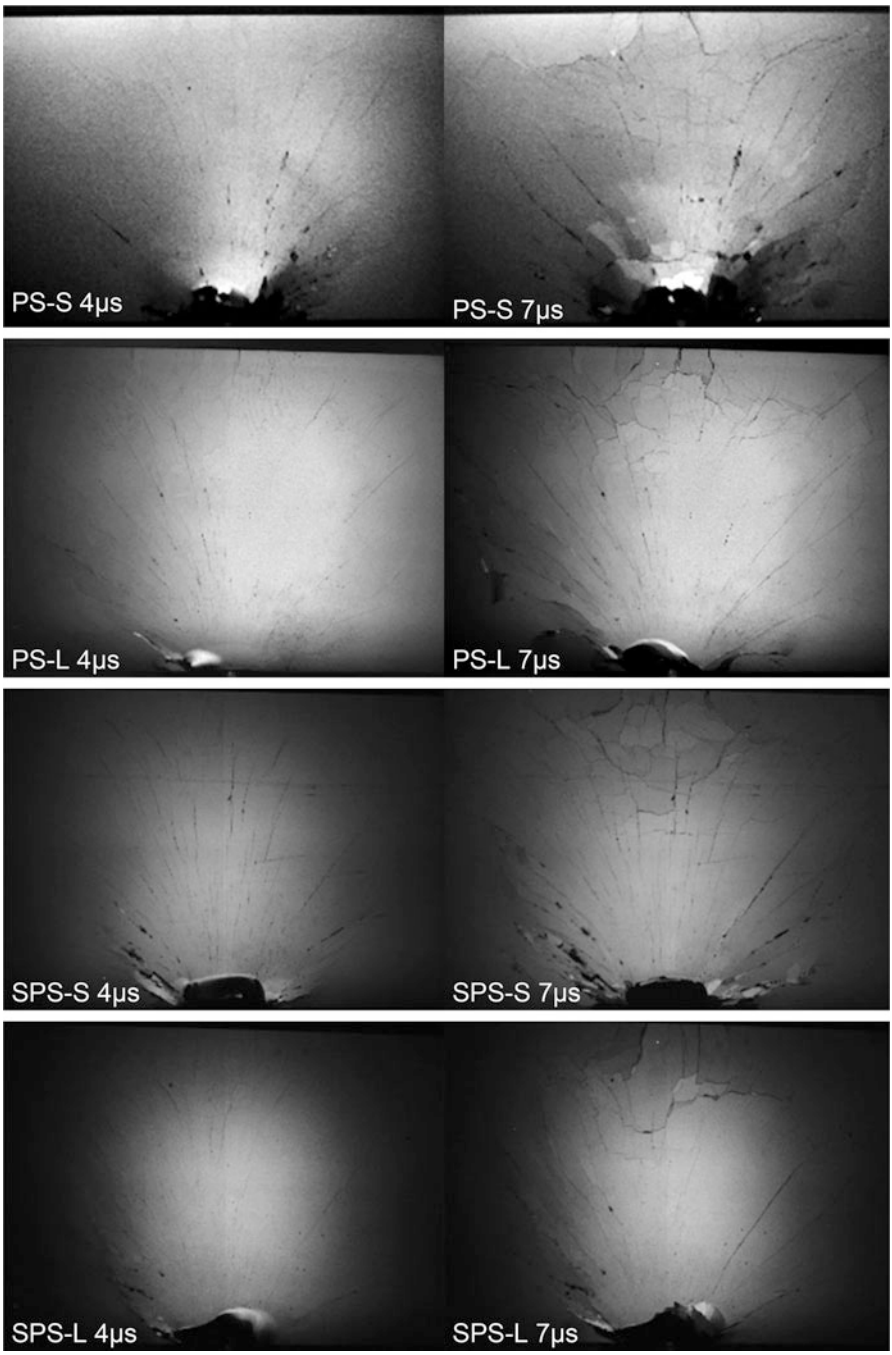

Fig. 8 Images at t = 4 and 7 μs of EOI tests performed with four SiC ceramics. The striking velocity is 181, 169, 170, and 172 m/s for PS-S, PS-L, SPS-S, and SPS-L targets, respectively (Forquin et al. 2018)

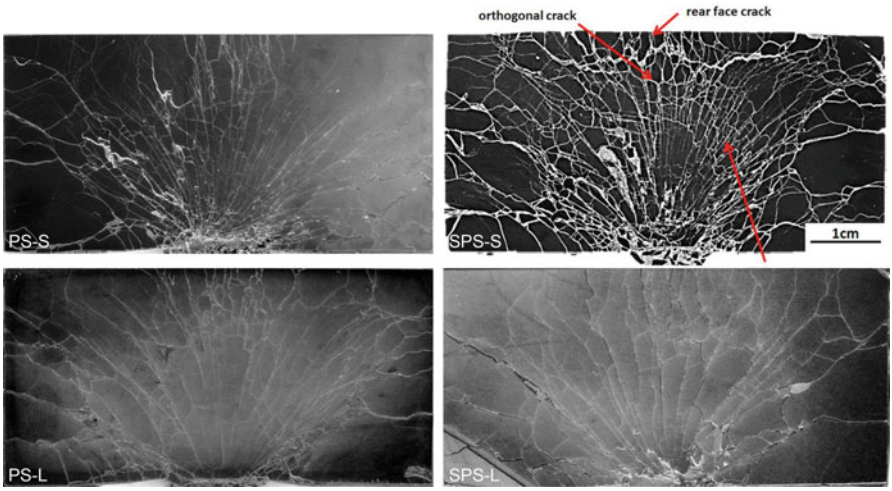

Fig. 9 Post-mortem damage patterns for four impacted SiC tiles in the sarcophagus configuration. The striking velocity is 166, 175, 165, and 174 m/s for PS-S, PS-L, SPS-S, and SPS-L targets, respectively (Forquin et al. 2018)

Tomographic Analysis of Fragments

The infiltrated targets of two SiC grades (SPS-L and SPS-S) were scanned using the micro-x-ray tomography machine in 3SR Laboratory. In this setup, a micro-focus x-ray beam generates a polychromatic cone beam (generated with a 150 kV and 200 μA electron beam against a Tungsten target) which is detected by a flat panel detector with 1536 × 1920 pixels each measuring 0.127 × 0.127 mm. The distance between the source and the detector is 767 mm.

The sample is placed on a rotation stage so the sample is X-rayed by considering 1440 angles spread out equally over 360°. At each angle, eight radiographs are acquired and averaged together to reduce noise. Between each angle a small dithering motion is applied to the detector to avoid ring artifacts. The impacted target is set in between the source and the screen at a position resulting in a pixel size of 40 μm/px.

In the work proposed by Forquin and Ando (2017), a processing of images was developed to analyze the fragment size distribution. For this purpose, cracks in the matrix are first identified. If crack opening exceeds 40 μm, the grayscale value inside the crack is constant and corresponds to the value of the resin. However, when crack opening is smaller than 40 μm, the traces on the grey levels are faint, and the cracks are detected from a local measurement of gradient. To do so, 3D Sobel operator (gradient filter typically used for edge detection) is used. After thresholding, a 3D binary image is obtained providing a good identification of cracks opened of less than or equal to one pixel. Next, the binary image is separated into individual particles by calculating the Euclidean distance map of the solid phase, whose maxima are used as seed points in a marker-based watershed on the Euclidean distance map (Jeon et al. 2004). This analysis was applied to two scanned samples (SPS-L and SPS-S SiC grades). The

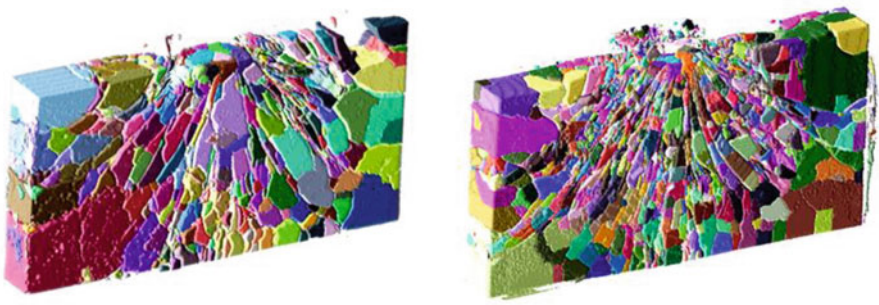

Fig. 10 Particle 3D rending provided by the fragment labeling procedure developed in Forquin and Ando (2017). Left, SPS-L; right, SPS-S

3D-rendered labeled images and crack networks are depicted in Fig. 10. Starting from the final labeled images, the volume in voxels of each individual particle is measured and converted into a physical volume (in μm^3) given the volume of one voxel, $40 \times 40 \times 40\ \mu m^3$.

Finally, the fragment size distribution is compared to results from physical sieving on similar specimens. The obtained particle size distributions and those obtained from post-mortem sieves of the fragments of other tests on the same materials (SPS-L and SPS-S) (Rossiquet 2012) are shown in Fig. 10; the results obtained with both techniques appear to match quite well. In addition, the Weibull and Rosin-Rammler distribution model $y = 1 - \exp\left(-\left(\frac{x}{x_0}\right)^m\right)$ was considered to identify a size distribution function. The corresponding values of m that describes the spread of the distribution are reported on Fig. 11. In conclusion, the X-ray tomography analyses developed in Forquin and Ando (2017) confirm that, depending on the initial microstructure of SiC ceramics, strong differences can be observed regarding their final fragmentation properties and final damage pattern when subjected to the same impact loading.

This conclusion was recently extended to dense and nacre-like alumina ceramics which fragmentation pattern was analyzed through tomographic analysis after a normal impact test (Duplan and Forquin 2021). In addition, their post-fragmentation behavior was investigated by means of tandem impact experiments which consist to perform a penetrating impact against the fragmented ceramic backed with an aluminum plate. These experiments illustrated the effect of fragment size, orientation, and anisotropy on the penetrating resistance of the fragmented ceramics.

Discussion: Role of the Flaws Population on the Fragmentation Process in Ceramics

The edge-on impact experiments were numerically simulated considering the Denoual-Forquin-Hild anisotropic damage model (Denoual and Hild 2000; Forquin and Hild 2010). As observed in EOI tests, at high strain rates, a large number of

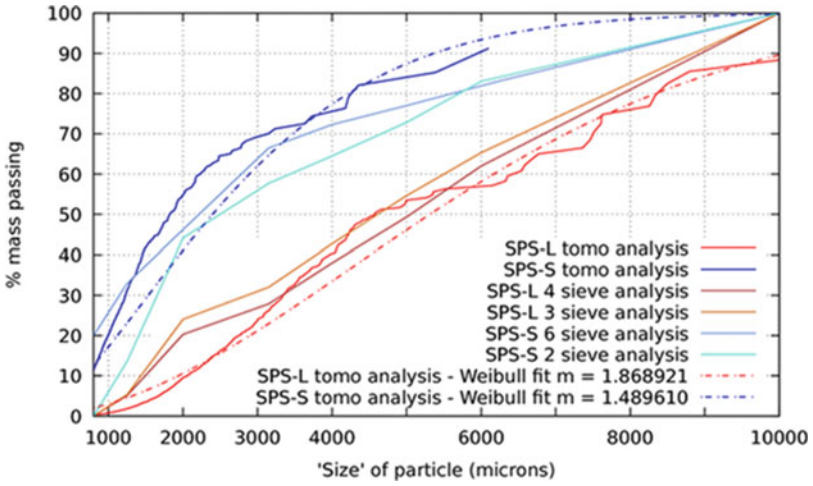

Fig. 11 Particle size distributions of post-mortem fragment sizes from sieving (SPS-L 4, SPS-L 3, SPS-S 6, SPS-S 2) (Rossiquet 2012) and tomography analysis (Forquin and Ando 2017). Comparison with Weibull and Rosin-Rammler distribution model fits

cracks initiate and propagate from existing defects resulting in a multiple fragmentation. The phenomenology of the fragmentation process can be explained in the following way: as the tensile stress increases at a specific loading rate, first cracks initiate from critical (activated) defects. Their propagation through the loaded volume prevents the triggering of other critical defects in their vicinity. However, the stress level continues to increase far from these growing "obscuration zones." The fragmentation process is analogous to a "competition" between stress increase in non-obscured zone and a sudden drop of loading in obscured zones. The concept of obscuration probability P_o (Denoual and Hild 2000; Forquin and Hild 2010) provides a representation of the part of the volume that is currently obscured by cracks already initiated on critical defects. The obscuration probability related to a multiple fragmentation process P_o reads:

$$P_o^{(i)}(T) = 1 - \exp\left(\int \frac{d\lambda_t(\sigma_i)}{\mathrm{dt}} Z_o(T-t)\mathrm{dt}\right), \tag{1}$$

where λ_t is the density of critical defects related to the local principal stress component σ_i and Z_o $(T-t)$ is the obscured zone at the current time T due to a crack triggered at time t. By considering an obscuration zone growing in a self-similar way and assuming a constant crack speed ($V_{crack}k.\mathrm{C}$ with k a dimensionless parameter and C the 1D wave speed), the obscuration volume can be expressed as

$$Z_o(T-t) = S[\mathrm{k.C}(T-t)]^n, \tag{2}$$

where S being a shape parameter ($4\pi/3$ if spherical obscuration volumes would be assumed) and n being the dimension of the space considered ($n = 3$ in 3D). Considering a Weibull density of critical defects, λ_t is expressed as a power law function of the positive principal stress:

$$\lambda_t(\sigma_i) = \lambda_0 \left(\frac{\langle \sigma_i \rangle}{S_0} \right)^m, \tag{3}$$

where m is the Weibull modulus and $\lambda_0 (S_0)^{-m}$ is the scale Weibull parameter deduced by averaging the tensile strength measured in quasi-static bending experiments according to

$$\sigma_w = S_0 (V_{\text{eff}} \lambda_0)^{-\frac{1}{m}} \Gamma\left(\frac{m+1}{m} \right), \tag{4}$$

where Γ is the Eulerian integral of the second kind (gamma function) defined as

$$\Gamma(1+x) = \int_0^\infty t^x \exp(-t) dt, \tag{5}$$

and V_{eff} is the effective volume of bending tests provided by Davies (1973):

$$V_{\text{eff}} = \int_\Omega \left(\frac{\langle \sigma_I(\underline{x}) \rangle}{\sigma_m} \right)^m dv, \tag{6}$$

with $\langle \sigma_I(\underline{x}) \rangle$ the positive part of the first principle stress at a given point of coordinates $(\underline{x})$ and σ_m its maximum value in the loaded volume. The obscuration probability can be expressed in differential form and implemented in an FE code according to

$$\frac{d^{n-1}}{dt^{n-1}} \left(\frac{1}{1 - P_o^{(i)}} \frac{dP_o^{(i)}}{dt} \right) = n! S (k.\mathrm{C})^n{}_t (\sigma_i) \text{ when } \frac{d\sigma_i}{dt} > 0 \ \ \& \ \ \sigma_i > 0. \tag{7}$$

Three macroscopic principle stress components Σ_i are computed as function of each obscuration probability variable $P_o^{(i)}$ and the microscopic strain components ε_i (Denoual and Hild 2000; Forquin and Hild 2010):

$$\overline{\Sigma} = \overline{\overline{\mathrm{K}}} \left(\mathrm{E}, \nu, P_o^{(i)} \right) \overline{\varepsilon} \text{ with } \overline{\varepsilon} = \begin{bmatrix} \varepsilon_1 \\ \varepsilon_2 \\ \varepsilon_3 \end{bmatrix}, \overline{\Sigma} = \begin{bmatrix} \Sigma_1 \\ \Sigma_2 \\ \Sigma_3 \end{bmatrix} \text{ and } \overline{\overline{\mathrm{K}}}^{-1} = \frac{1}{E} \begin{bmatrix} \frac{1}{1 - P_o^{(1)}} & -\nu & -\nu \\ -\nu & \frac{1}{1 - P_o^{(2)}} & -\nu \\ -\nu & -\nu & \frac{1}{1 - P_o^{(3)}} \end{bmatrix} \tag{8}$$

where E and ν being Young's modulus and Poisson's ratio of the undamaged ceramic. If ones consider that the only critical defects located in non-obscured

zones can be triggered, the crack density associated to each principal stress can be calculated by integrating the following differential equation:

$$\frac{d\lambda_{\text{cracks}}^{(i)}}{\text{dt}} = P_o^{(i)} \frac{d\lambda_t(\sigma_i)}{\text{dt}}. \tag{9}$$

Therefore, the cracking density at any time T can be calculated as an output variable of the numerical simulation by integrating Eq. (9).

A series of calculations are conducted with Abaqus-Explicit finite-element code. The ceramic sample and the steel projectile are meshed with C3D8R elements (reduced integration), and the yield strength of the steel projectile is set to 1350 MPa. The striking velocity of the projectile is set to 170 m/s. The DFH anisotropic damage model is considered to model the ceramic target. The parameters considered in DFH model are reported in Table 2. The Weibull parameters (Weibull modulus and scale Weibull parameter) were obtained from four-point bending tests. In the case of PS-S samples, the dimensions of the tested specimens were $3 \times 4 \times 45$ mm^3 (height x width x length) and the support and loading spans were 40 and 20 mm, whereas in the case of PS-L, SPS-S, and SPS-L ceramics, the tested samples were $3 \times 5 \times 24$ mm^3 (height x width x length) and the support and loading spans were 20.8 and 10 mm. The field of final cracking density (T = 7 μs) is illustrated in Fig. 12 for each SiC ceramic and is compared to the post-mortem cracking pattern (Fig. 9). The numerical simulation enables to explain the strong differences in cracking density visualized in the fragmented targets. Indeed, thanks to their lower Weibull modulus and higher average tensile strength, SPS-L and PS-L ceramics generate a lower number of cracks and larger fragments than the PS-S and SPS-S grades.

Table 2 Parameters of DFH model considered in the numerical simulation for the PS-S, SPS-S, PS-L, and SPS-L SiC ceramics. Weibull parameters of SPS-S, PS-L and SPS-L SiC grades are provided from quasi-static 4-point bending tests detailed in (Rossiquet 2012). Weibull parameters for PS-S grade are deduced from data of 160 4-point bending tests provided by Saint-Gobain Research North America (NRDC) (Dargaud 2021)

Parameters	PS-S	SPS-S	PS-L	SPS-L
Samples size (height × width × length) (mm^3)	$3 \times 4 \times 45$		$3 \times 5 \times 24$	
Support and loading spans (mm)	40, 20		20.8, 10	
Weibull modulus, m	14.0	13.3	5.1	7.9
Effective volume, V_{eff} (mm^3)	8.5	5.6	14.5	9.5
Mean tensile failure stress, $\sigma_w(V_{eff})$ (MPa)	406	388	306	440
Mean tensile failure stress for $V_{eff} = 1$ mm^3 (MPa)	473	442	517	585
k	0.38			
Shape parameter, S	3.74			
1D wave speed, C_0 (m/s)	11,535			
Young's modulus (GPa)	410			
Poisson's ratio	0.14			
Density (kg/m^3)	3180			

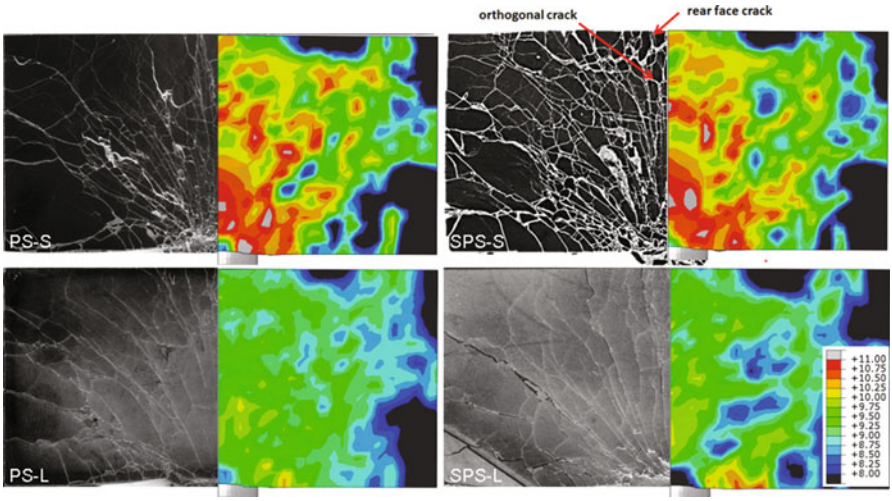

Fig. 12 Numerical simulation of the fragmentation process in PS-S, SPS-S, PS-L, and SPS-L SiC ceramics subjected to EOI test (170 m/s) with DFH damage model. Isocontours of the final cracking density in log scale (m^{-3}): for instance, $\lambda = 9$ would correspond to 10^9 cracks per m^3 or 1 crack per mm^3

In addition, if ones assume a constant stress rate $\dot{\sigma}$, the final crack density (i.e., when the whole volume is obscured) is given by the following analytic expression which illustrates the influence of the Weibull parameters (first term), the loading rate (second term), and the parameters related to the size of obscuration volume (third term) (Denoual and Hild 2000; Forquin and Hild 2010):

$$\lambda_{\text{cracks}}^{T\to\infty} = \underbrace{\left(S_0{\lambda_0}^{-1/m}\right)^{\frac{-mn}{m+n}}}_{\text{Crack inception}} \underbrace{(\dot{\sigma})^{\frac{mn}{m+n}}}_{\text{Loading rate}} \underbrace{\left(S^{1/n}k.C\right)^{\frac{-mn}{m+n}}}_{\text{Crack propagation}} \left(\frac{(m+n)!}{m!n!}\right)^{\frac{m}{m+n}} \Gamma\left(\frac{2m+n}{m+n}\right), \quad (10)$$

Now, if ones consider the same parameters (S, k, and C) for each SiC microstructure and considering the strain rate estimated in edge-on impact experiments at 10 mm from the impact point (7750 s^{-1} according to Fig. 6), the quasi-static mean failure stress (Y-axis) associated with a given crack density and an effective volume of 1 mm^3 can be calculated as function of the Weibull modulus (X-axis) by combining Eqs. (4) and (10):

$$\sigma_w = \frac{\dot{\sigma}}{kC.(S)^{\frac{1}{n}}.(V_{\text{eff}})^{\frac{1}{m}}.\left(\lambda_{\text{cracks}}^{T\to\infty}\right)^{\frac{m+n}{mn}}} \Gamma\left(\frac{m+1}{m}\right)\Gamma\left(\frac{2m+n}{m+n}\right)^{\frac{m+n}{mn}}\left(\frac{(m+n)!}{m!n!}\right)^{1/n}. \quad (11)$$

As illustrated in the graph of Fig. 13, the higher the quasi-static mean failure stress, the lower the final crack density. Conversely, the higher the Weibull modulus, the higher the final crack density. Finally, whereas the SPS-S and PS-S grades suffer

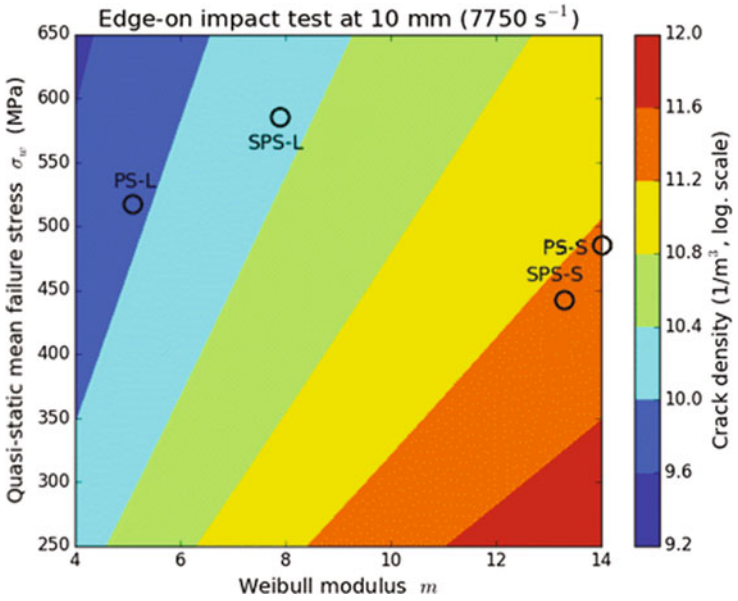

Fig. 13 Predictions of crack density with Eq. 10 as function of the quasi-static failure stress ($V_{\text{eff}} = 1$ mm^3) and the Weibull modulus considering a strain rate of 7750/s and parameters in Table 2. The quasi-static failure stress (with $V_{eff} = 1$ mm^3) and the Weibull modulus for each SiC grade are also reported

from higher Weibull modulus and lower quasi-static tensile strength compared to others, the PS-L and SPS-L grades benefit from their low Weibull modulus and higher quasi-static tensile strength compared to SPS-S and PS-S grades. So, these predictions are consistent with the previous experimental findings (Figs. 8, 9, 10, and 11) and with the numerical results illustrated in Fig. 12.

Conclusions

During the last three decades, the edge-on impact testing technique has been widely used to explore the fragmentation properties of different types of transparent and non-transparent ceramic grades. This technique presents strong advantages but also some limitations and drawbacks compared to other experimental techniques. Among the advantages, one may note that typical strain rates ranging from few thousands of s^{-1} to a few tens of thousands of s^{-1} are generated leading to an intense multiple fragmentation process in the target. On the other hand, dynamic experiments conducted with Split Hopkinson pressure bar apparatus are limited to much lower strain rates (about a few tens to few hundreds of s^{-1}) when applied to ceramics, which leads to a single fracture in the tested specimen. In addition, in the so-called open configuration, the edge-on impact testing method provides the

possibility to visualize the growth of fragmentation "in real time" by using high-speed photography with inter-frame time set in between 2 μs down to 0.1 μs. In addition; the fracture pattern can be analyzed with the so-called sarcophagus configuration by infiltrating the fragmented ceramic tile or by using a transparent sarcophagus to the visual light or to X-ray. These two types of analysis remain difficult to perform in the case of the spalling testing by plate impact or by pulsed-power technology. Furthermore, the edge-on impact testing technique requires also much less costly equipment compared to pulsed-power generator facilities or to the gas gun facilities that are used for plate-impact tests, which generally operate with a larger caliber and under vacuum. As the main limitation, it can be observed that the edge-on impact testing configuration does not provide any direct strength measurement. The visualization of damage is usually restricted to the lateral surface in the case of non-transparent ceramic. In addition, the field of stress and stress rate is nonuniformed, so a numerical analysis can be required to complement the experimental analysis.

In the present chapter, the properties of fragmentation process generated in four SiC ceramic grades with different microstructures under impact are compared. The edge-on impact tests conducted in the "open configuration" and "sarcophagus configuration" confirm that depending on the microstructures of SiC ceramics, very different crack densities during and after impact are observed. The fragmentation pattern is also analyzed with X-ray micro-tomography CT scan analysis applied to two of the four grades, which confirm the strong differences in terms of cracking density and fragment size distribution.

Numerical simulations conducted with the DFH anisotropic damage model that is based on a description of the fragmentation process (i.e., initiation of cracks on non-obscured critical defects and obscuration of other critical defects due to release waves in the vicinity of propagating cracks) provide an explanation of the experimental result. Indeed, consistently with the experiments, much higher cracking densities are numerically predicted with the PS-S and SPS-S SiC ceramics compared to PS-L and SPS-L SiC grades when subjected to roughly the same impact loading conditions. The single difference being the Weibull parameters considered as input of the DFH model, it is concluded that the fragmentation process is mainly driven by the population of flaws from which cracks are triggered in the tested ceramic specimens. A quantitative comparison between the cracking patterns deduced from X-ray micro-tomography to the cracking density predictions provided by numerical modeling constitutes a prospect of this analysis.

Acknowledgments This research was conducted in the framework of the Brittle's CODEX chair, supported by the UGA (Univ. Grenoble Alpes) Foundation and sponsored by the Saint-Gobain and Lafarge-Holcim companies. These sponsors are gratefully acknowledged.

Disclosure This manuscript is partly based on the following papers by the authors.

P. Forquin, J.-L. Zinszner, G. Rossiquet, B. Erzar, Microstructure influence on the fragmentation properties of dense silicon carbides under impact. Mech. Mater. **123**, 59–76 (2018)

P. Forquin, E. Ando, Application of micro-tomography and image analysis to the quantification of fragmentation in ceramics after impact loading. Phil. Trans. R. Soc. A, 20160166 (2017)

P. Forquin, J.L. Zinszner, Experimental study of the dynamic fragmentation in transparent ceramic subjected to projectile impact, in *Dynamic Behavior of Materials*, ed. by D. Casem, L. Lamberson, J. Kimberley, vol. 1 (2017), pp. 165–170

References

X. Brajer, P. Forquin, R. Gy, F. Hild, The role of surface and volume defects in the fracture of glass under quasi-static and dynamic loadings. J. Non-Crystalline Solids **316**, 42–53 (2003)

J. Cagnoux, J.A. Cosculluela, Influence of grain-size on triaxial dynamic behavior of alumina, in *Proceedings of the International Seminar on Dynamic Failure of materials: Theory, experiments and numerics*, (Technische Universität Wien, 1991), pp. 73–84, 2–4 Jan., Ed. By H.P. Rossmanith and A.J. Rosakis

W.W. Chen, A.M. Rajendran, B. Song, X. Nie, Dynamic fracture of ceramics in armor applications. J. Am. Ceram. Soc. **90**(4), 1005–1018 (2007)

J.J. Chen, B.Q. Guo, H.B. Liu, H. Liu, P.W. Chen, Dynamic brazilian test of brittle materials using the split hopkinson pressure bar and digital image correlation. Strain **50**, 563–570 (2014)

A. Cosculluela, Plasticité, endommagements et ruptures des alumines sous sollicitations dynamiques triaxiales: Influence de la taille des grains (Ph.D. dissertation), University of Bordeaux, France (1992)

D.G.S. Davies, The statistical approach to engineering Design in Ceramics. Proc. Brit. Ceram. Soc. **22**, 429–452 (1973)

P.C. den Reijer, Impact on Ceramic Faced Armour (Ph.D. dissertation), Delft University of Technology, Netherlands, 1991

M. Dargaud, Experimental and numerical analysis of the failure modes induced in ceramic materials under dynamic loading. (Ph.D. dissertation), Université Grenoble Alpes, France (2021)

C. Denoual, F. Hild, A damage model for the dynamic fragmentation of brittle solids. Comput. Methods Appl. Mech. Eng. **183**, 247–258 (2000)

Y. Duplan, P. Forquin. Investigation of the multiple-fragmentation process and post-fragmentation behaviour of dense and nacre-like alumina ceramics by means of tandem impact experiments and tomographic analysis. Int. J. Impact Eng., 155, 103891 (2021). https://doi.org/10.1016/j.ijimpeng.2021.103891

P. Forquin, Endommagement et fissuration de matériaux fragiles sous impact balistique, rôle de la microstructure, (Ph.D. dissertation), Ecole Normale Supérieure de Cachan, France, 2003

P. Forquin, Experimental investigation of the dynamic fragmentation process in a transparent ceramic under impact loading, in *Dynamic Behavior of Materials*, ed. by B. Song, L. Lamberson, D. Casem, J. Kimberley, vol. 1, (2016), pp. 5–11. https://doi.org/10.1007/978-3-319-22452-7_2. Book series: Proceedings of the Society for Experimental Mechanics Series. Springer

P. Forquin, E. Ando, Application of micro-tomography and image analysis to the quantification of fragmentation in ceramics after impact loading. Phil. Trans. R. Soc. A, 20160166 (2017). https://doi.org/10.1098/rsta.2016.0166

P. Forquin, M. Blasone, D. Georges, M. Dargaud. Continuous and discrete methods based on X-ray computed-tomography to model the fragmentation process in brittle solids over a wide range of strain-rates - application to three brittle materials. J. Mech. Physics Solids, **152**, 104412 (2021). https://doi.org/10.1016/j.jmps.2021.104412

P. Forquin, F. Hild, A probabilistic damage model of the dynamic fragmentation process in brittle materials. Adv. Appl. Mech. **44**, 1–72 (2010)

P. Forquin, J.L. Zinszner, Experimental study of the dynamic fragmentation in transparent ceramic subjected to projectile impact, in *Dynamic Behavior of Materials*, ed. by D. Casem, L. Lamberson, J. Kimberley, vol. 1, (2017), pp. 165–170. https://doi.org/10.1007/978-3-319-41132-3_23. Book series: Proceedings of the Society for Experimental Mechanics Series. Springer

P. Forquin, L. Tran, P.-F. Louvigné, L. Rota, F. Hild, Effect of aluminum reinforcement on the dynamic fragmentation of SiC ceramics. Int. J. Impact Eng. **28**, 1061–1076 (2003)

P. Forquin, J.-L. Zinszner, G. Rossiquet, B. Erzar, Microstructure influence on the fragmentation properties of dense silicon carbides under impact. Mech. Mater. **123**, 59–76 (2018)
F. Galvez, J. Rodriguez, V. Sanchez, Tensile Strength Measurements of Ceramic Materials at High Rates of Strain. J. Physique IV **7**(C3), 151–156 (1997)
B.-K. Jeon, J.-H. Jang, K.-S. Hong, Robust region segmentation based on a pseudo-distance map. J. Electron. Imaging **13**(3), 602–612 (2004)
A. Krell, E. Strassburger, Order of influences on the ballistic resistance of armor ceramics and single crystals. Materials Science and Engineering: A. **597**, 422–430 (2014)
R.B. Leavy, J.D. Clayton, O.E. Strack, R.M. Brannon, E. Strassburger, Edge on impact simulations and experiments. Procedia Eng. **58**, 445–452 (2013)
J.W. McCauley, E. Strassburger, P. Patel, B. Paliwal, K.T. Ramesh, Experimental observations on dynamic response of selected transparent armor materials. Exp. Mech. **53**(1), 3–29 (2013)
M. Normandia, J. Lasalvia, W. Gooch, J.W. Rajendran, A.M. Rajendran, *Protecting the Future Force: Ceramics Research Leads to Improved Armor Performance* (AMMTIAC, New York, 2004)
W. Riedel, S. Hiermaier, K. Thoma, Transient stress and failure analysis of impact experiments with ceramics. Mater. Sci. Eng. B **173**, 139–147 (2010)
P. Riou, Contribution à l'étude de l'endommagement du Carbure de Silicium lors d'un impact de basse énergie: Application aux blindages, (Ph.D. dissertation), Ecole Nationale Supérieure des Mines de Paris, 1996
P. Riou, C. Denoual, C.E. Cottenot, Visualization of the damage evolution in impacted silicon carbide ceramics. Int. J. Impact Eng. **21**(4), 225–235 (1998a)
P. Riou, C.E. Cottenot, M. Boussuge, Anisotropic damage model for impacted ceramic material; application to silicon carbide. Int. J. Impact Eng. **21**(8), 683–693 (1998b)
G. Rossiquet, Carbure de silicium pour application blindage: élaboration et étude du comportement à l'impact, (Ph.D. dissertation), Université de Bourgogne, France, 2012
M. Scapin, L. Peroni, M. Avalle, Dynamic Brazilian test for mechanical characterization of ceramic ballistic protection. Hindawi Shock Vib. **2017**, Article ID 7485856 (2017)
H. Senf, E. Strassburger, H. Rothenhäusler, Stress wave induced damage and fracture in impacted glasses. J. Phys. IV France **04**, C8-741-C8-746 (1994). https://doi.org/10.1051/jp4:19948114
E. Strassburger, Visualization of impact damage in ceramics using the edge-on impact technique. Int. J. Appl. Ceram. Technol. **1**(3), 235–242 (2004)
E. Strassburger, H. Senf, *Experimental Investigations of Wave and Fracture Phenomena in Impacted Ceramics and Glasses* (ARL-CR-214, Army Research Laboratory, 1995)
E. Strassburger, P. Patel, J.-W. McCauley, D.W. Templeton, W. Douglas, Visualization of wave propagation and impact damage in a polycrystalline transparent ceramic–ALON, In: 22nd International Symposium on Ballistics, 2005
E. Strassburger, P. Patel, J.-W. McCauley, D.W. Templeton, High speed photographic study of wave propagation and impact damage in fused silica and ALON using the edge-on impact EOI method. AIP Conf. Proc. **845**(II), 892–895 (2006)
E. Strassburger, M. Hunzinger, P. Patel, J.W. McCauley, Analysis of the fragmentation of AlON and spinel under ballistic impact. J. Appl. Mech. **80**, 031807 (2013)
A.L. Tonge, K.T. Ramesh, Multi-scale defect interactions in high-rate brittle material failure. Part I: Model formulation and application to ALON. J. Mech. Physics Solids **86**, 117–149 (2016)
G. Zhang, G.A. Gazonas, F. Bobaru, Supershear damage propagation and sub-Rayleigh crack growth from edge-on impact: A peridynamic analysis. Int. J. Impact Eng. **113**, 73–87 (2018)
J.-L. Zinszner, Identification des paramètres matériau gouvernant les performances de céramiques à blindage, (Ph.D. dissertation), Université de Lorraine, France, 2014
J.-L. Zinszner, B. Erzar, P. Forquin, E. Buzaud, Dynamic fragmentation of an alumina ceramic subjected to shockless spalling: An experimental and numerical study. J. Mech. Phys. Solids **85**, 112–127 (2015a)
J.-L. Zinszner, P. Forquin, G. Rossiquet, Experimental and numerical analysis of the dynamic fragmentation in a SiC ceramic under impact. Int. J. Impac Eng. **76**, 9–19 (2015b)
J.-L. Zinszner, B. Erzar, P. Forquin, Strain-rate sensitivity of the tensile strength of two silicon carbides: Experimental evidence and micromechanical modelling. Phil. Trans. R. Soc. A, 20160167 (2017). https://doi.org/10.1098/rsta.2016.0167

Part IV

Composite Damage Mechanics

Effective Modeling of Interlaminar Damage in Multilayered Composite Structures Using Zigzag Kinematic Approximations

25

Roberta Massabò

Contents

Introduction 666
Zigzag Theories for Structures with Perfect Bonding Between Adjacent Layers 671
Original Zigzag Theories 671
Refined Zigzag Theories 675
Zigzag Theories for Structures with Continuous Interfacial Imperfections, Damaged Layers, and Stationary Delaminations 677
Theories Using the Compliant Layer Concept 678
Theories Using Imperfect Interfaces and the Spring Layer Model 679
Theories Using the Sublaminate Approach or Additional Degrees of Freedom 685
Zigzag Theories for Effective Modeling of Progressive Delamination Damage 685
The Cohesive Crack Model, Cohesive Interfaces, and Brittle Fracture 687
Zigzag Theories Using Compliant Layers and Continuum Damage Mechanics 688
Zigzag Theories Using Cohesive Interfaces and Fracture Mechanics 690
Conclusions 693
References 694

Abstract

The chapter gives an overview of the main approaches formulated to model interlaminar damage and imperfections in layered structures using zigzag kinematic approximations and concentrates on the models which have been extended to analyze delamination damage progression. The zigzag theories are structural theories which assume different kinematic fields in the layers, to account for zigzag effects associated to their elastic mismatch, and use a fixed number of variables that is independent of the number of layers. Interfacial imperfections, interlayer damage, and delaminations are included using the compliant layer concept, imperfect interfaces, or by adding additional variables. Delamination

R. Massabò (✉)
Department of Civil, Chemical and Environmental Engineering, Università di Genova, Genova, Italy
e-mail: roberta.massabo@unige.it

© Springer Nature Switzerland AG 2022

G. Z. Voyiadjis (ed.), *Handbook of Damage Mechanics*,
https://doi.org/10.1007/978-3-030-60242-0_91

damage progression is studied using continuum mechanics and fracture mechanics techniques. The focus of the presentation is on the theoretical aspects and uses simple examples and applications to discuss and compare the different formulations and show relevant behaviors.

Keywords

Multilayered composites · Structural theories · Zigzag theories · Delamination fracture · Interfaces · Cohesive zone model

Introduction

Multilayer systems are used for structural applications in many engineering fields, e.g., aerospace, aeronautical, automotive, naval, civil, and wind energy, and include laminated and sandwich composites, laminated glass, steel-concrete and FRP-concrete systems, and layered wood. Often these structures are thick, formed by many layers, with highly anisotropic layups and a large mismatch of the elastic constants of the layers. They may be subjected to static, dynamic, and repeated loadings and impacts and often operate in extreme environmental conditions.

Layered structures suffer damage at several scales through various interlayer and intralayer failure mechanisms. Damage may be present as a consequence of manufacturing errors or arise in service. In laminated composites, damage includes delamination of the layers at or near their interfaces and matrix cracks and fiber failures within the layers. In sandwich composites, damage includes delamination within the face sheets, debond fracture at the face–core interfaces, and other local failures, such as face wrinkling, indentation/core crushing, and core fracture.

Other forms of interfacial imperfections, which generate relative displacements at the layer interfaces similar to those produced by delaminations, are due to the presence of resin-rich layers or thin soft interlayers, such as adhesives in sandwich composites, polymeric layers in laminated glass, and interleaving layers in laminates. Relative displacements at the layer interfaces also arise in layered wood and steel-concrete systems, where the mechanical fasteners used to join the layers (nails, dowels, and screws) allow partial relative motion.

The response of multilayer structures in the elastic and postelastic regimes is accurately studied using three-dimensional finite element models which use continuum damage mechanics and fracture mechanics techniques to model intra- and interlayer damage evolution. These approaches however are cumbersome and computationally expensive. One- and two-dimensional models are computationally more efficient and for simple structural systems offer the advantage of providing insightful closed-form solutions.

The equivalent single-layer theories, ESL, for layered beams, plates, and shell structures, accurately describe global displacement fields and force and moment resultants in the elastic regime, for most layered systems but for some sandwich composites with extreme elastic mismatch. They use a limited number of

displacement variables, which coincide with those of the structural theories for homogeneous materials and are effective in the solution of complex structures. However, the ESL theories, even when accounting for high-order terms and transverse normal and shear deformations, assume a continuous and smooth through-thickness displacement field and are unable to capture the zigzag displacement patterns or accurately define the local stress fields which control the onset and propagation of damage; neither they can capture the interfacial jumps due to delaminations or interfacial imperfections, or accurately predict stress concentrations. Figure 1 shows displacement and stress fields in a thick layered plate with a highly anisotropic layup and perfect bonding of the layers. Figure 2 highlights the effects of interfacial imperfections and delaminations between the layers.

In structures with perfectly bonded layers, the limitations of ESL theories are overcome by theories based on a layerwise approximation of the displacement field which, at the expenses of an increased number of variables depending on the number of layers, have an accuracy comparable to 3D models. The theories assume independent kinematic descriptions in the layers and enforce certain physical continuity

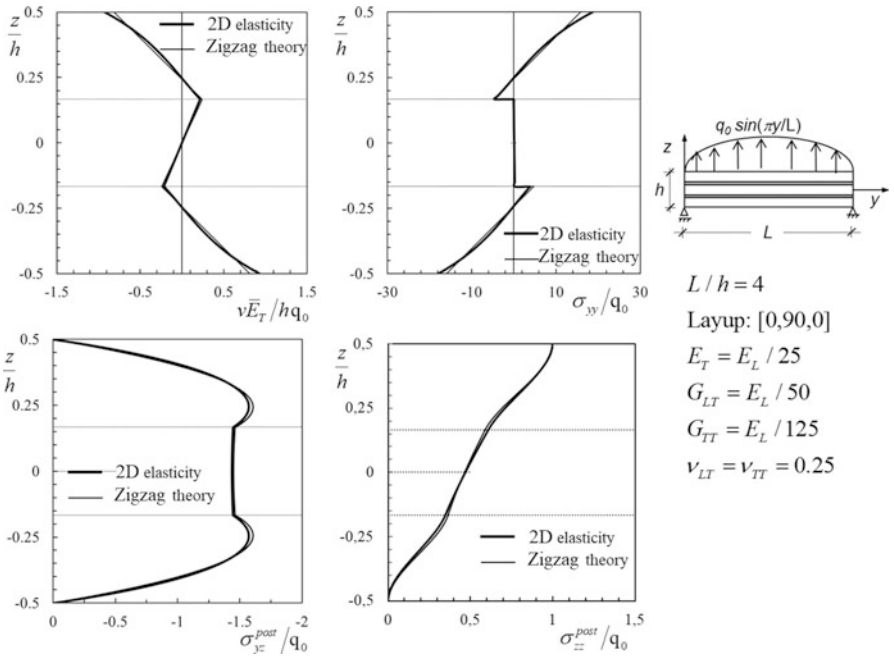

Fig. 1 Local fields in a simply supported wide plate with three symmetrically oriented orthotropic layers subjected to transverse loading (cylindrical bending). Two-dimensional elasticity results (Pagano 1969) and zigzag theory in Eq. 1. (**a**) In-plane displacements at $y = 0$, (**b**) bending stresses at $y = L/2$, (**c**) transverse shear stresses at $y = L$, and (**d**) transverse normal stresses at $y = L/2$, shown through thickness. Zigzag transverse stresses are calculated a posteriori through local equilibrium; geometry and elastic constants are given in the figure, with $\bar{E}_T = E_T/(1 - \nu_{LT}\nu_{TL})$. (Adapted after (Massabò and Campi 2015))

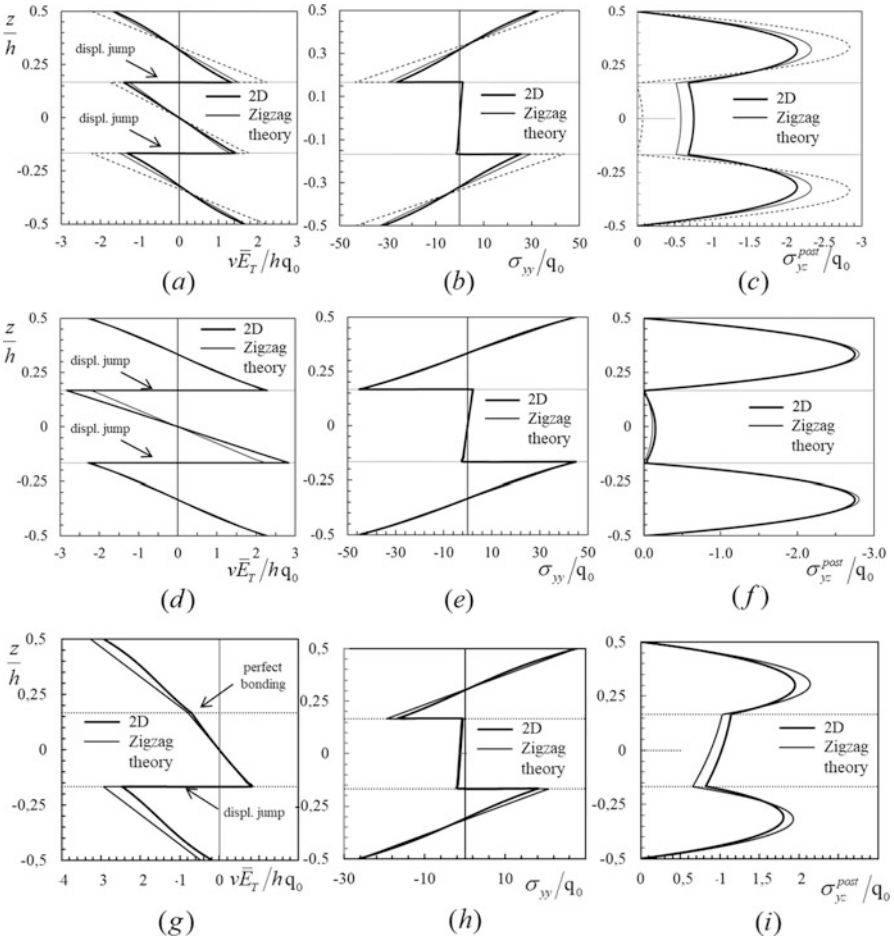

Fig. 2 (**a**–**f**) Effects of imperfect bonding between adjacent layers, assuming interfacial stiffnesses $K_{yy}h/\overline{E}_T = 0.25$ and $1/K_{zz} = 0$ in Eq. (10) (**a**–**c**) and traction-free sliding delaminations (**d**–**f**), on the fields presented in Fig. 1 (2D elasticity solutions in Massabò and Campi (2015) and zigzag theory in Eq. 11). Dashed lines: early, energetically inconsistent zigzag models. (**g**–**i**) Modifications of the local fields in Fig. 1 when only the lower interface is imperfect. (Adapted after (Massabò and Campi 2014))

requirements at the layer interfaces. Several literature surveys have been published on these models, e.g., (Carrera 2002, 2003), with the most recent in Abrate and Di Sciuva (2018).

The zigzag theories, as the layerwise theories, capture the zigzag effects and predict the local fields in the layers with good accuracy; however they use a number of variables that is independent of the number of layers. In structures with perfectly bonded layers this is obtained by enriching a global displacement field, for instance that of an ESL theory (first order or higher order), with piecewise linear in-plane

displacement functions (zigzag functions). Continuity conditions on interface displacements and tractions are then enforced to eliminate the additional degrees of freedom. In this sense the zigzag theories belong to the multiscale approaches and the governing equations account for effects occurring at different length scales. Schematics of the in-plane displacements assumed by different zigzag theories are shown in Figs. 3 and 4.

The presence of adhesives, thin interlayers or mechanical fasteners, is modeled using the compliant layer concept, imperfect interfaces (or the spring-layer model), and the sublaminate approach. In the three approaches, stationary delaminations are described by introducing fictitious very compliant layers, zero-stiffness interfaces, or treating the jumps as additional displacement variables. The introduction of compliant layers and imperfect interfaces within zigzag formulations present some challenges which will be discussed in this chapter.

The cohesive zone model, linear elastic fracture mechanics, and continuum damage mechanics are used within discrete layer models to predict and simulate

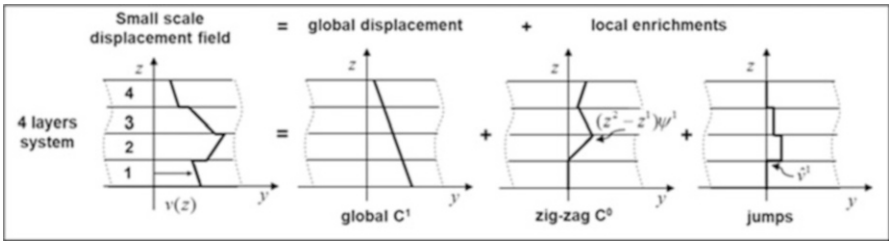

Fig. 3 Zigzag kinematics in Di Sciuva original theory (Di Sciuva 1986) modified to account for the presence of imperfect interfaces as in Massabò and Campi (2015). The global in-plane displacements in a layered plate are enriched by a local piecewise linear field (zigzag functions), Eq. (1), and by a discontinuous field (interfacial jumps), Eq. (11); the interfacial jumps are not present if the layers are perfectly bonded

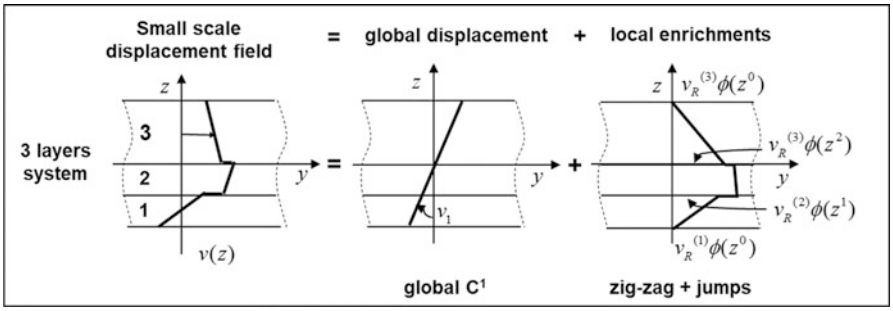

Fig. 4 Zigzag kinematics in the refined zigzag theory in Tessler et al. (2009) modified to account for the presence of imperfect interfaces as in Darban and Massabò (2018). The global displacement field of a layered beam is enriched by zigzag functions and interfacial jumps, Eq. (5). When the layers are perfectly bonded the enrichment functions of adjacent layers coincide at the interface

onset and propagation of damage and delaminations (Alfano and Crisfield 2001; Allix et al. 1995; Allix and Ladevèze 1992; Andrews and Massabò 2006; Bruno and Greco 2001; Carpinteri et al. 1999; Massabò and Cavicchi 2012; Mi et al. 1998; Monetto 2015; Turon et al. 2010; Williams and Addessio 1997). Modeling is complicated by the presence of multiple delaminations and multiple damage mechanisms, which develop and interact and profoundly affect the global response. Figure 5 shows experimental results often used as a benchmark where snap-back and snap-through instabilities are generated in the response diagram of a laminated beam by the interaction of two propagating delaminations.

Continuum damage and fracture mechanics frameworks have been formulated for zigzag theories only recently (Eijo et al. 2013, 2014; Groh et al. 2015; Massabò and Darban 2019). Other finite element strategies to describe progressive delamination fracture use higher-order beam, plate and shell, or solid-like shell elements with enhanced kinematics, which are able to capture 3D transverse fields and integrate cohesive interfaces or damaged layers, e.g., (Gruttmann and Knust 2019; Larsson 2004; Remmers et al. 2003).

In this chapter we present some of the zigzag theories used to analyze structures with continuous interfacial imperfections and their recent extensions to study progressive delamination damage, focusing on the theoretical aspects more than on the finite element implementations. We discuss the approaches, their strengths, and weaknesses and highlight some open issues which need to be solved for an efficient numerical implementation of these techniques.

The chapter is organized as follows. The zigzag theories that have been formulated for structures with perfect bonding of the layers and have been later used to analyze damage progression are briefly described in section "Zigzag Theories for Structures with Perfect Bonding Between Adjacent Layers." The extensions of the theories to model structures with interfacial imperfections, damaged layers, and

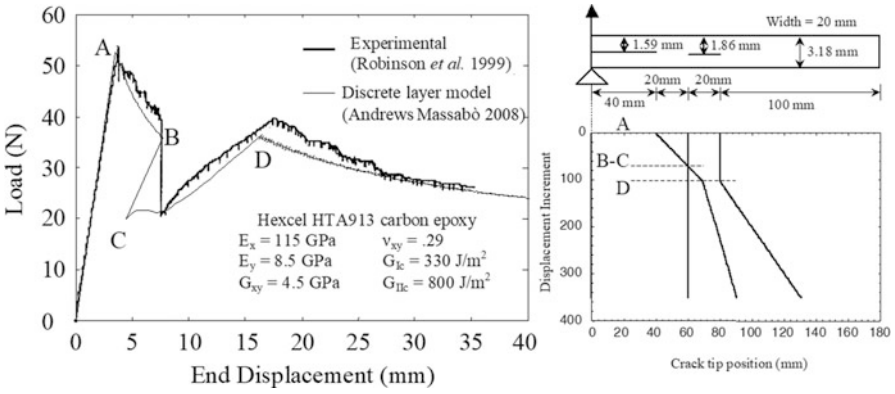

Fig. 5 Local snap-back and snap-through instabilities generated by the interaction of two delaminations propagating in a double cantilever beam specimen; material properties given in the figure. Experimental results in Robinson et al. (2000); theoretical prediction using a discrete layer cohesive crack model with elastic spring contact. (Adapted after (Andrews and Massabò 2008))

stationary delaminations are presented in section "Zigzag Theories for Structures with Continuous Interfacial Imperfections, Damaged Layers and Stationary Delaminations." In section "Zigzag Theories for Effective Modeling of Progressive Delamination Damage" the recent developments of the zigzag theories for the analysis of delamination damage progression using continuum and fracture mechanics frameworks are presented and discussed. Section "Conclusions" presents some conclusions.

Zigzag Theories for Structures with Perfect Bonding Between Adjacent Layers

This section introduces the zigzag theories for structures with perfect bonding between adjacent layers and focuses on the displacement-based theories which have been later extended in order to model progressive delamination damage. A recent literature survey on all zigzag formulations is presented in Abrate and Di Sciuva (2018).

Original Zigzag Theories

The axiomatic zigzag theories are based on two main approaches which date back to the work by Murakami (1986) and Di Sciuva (1986). Both approaches introduce piecewise linear zigzag functions to enrich a global displacement field and describe the zigzag effects. Murakami zigzag functions depend on the thickness of the layers and are independent of layup and material properties; they can be easily used to enrich all ESL models, are effective for periodic layups but do not allow to fulfill the continuity of the transverse stresses at the interfaces, and are inaccurate for arbitrary nonperiodic layups (Gherlone 2013). Di Sciuva zigzag functions depend on geometrical and material properties and ensure the continuity of the transverse stresses without increasing the number of displacement variables.

In the original zigzag formulation in Di Sciuva (1986) and using the terminology in Abrate and Di Sciuva (2018), the displacement components along the coordinate directions, x, y, z, in an arbitrary layer k of a layered plate are given by:

$$\begin{aligned} {}^{(k)}u &= u_0 + zu_1 + \sum_{i=1}^{k-1} \left(z - z^i\right)\varphi^i H^i \\ {}^{(k)}v &= v_0 + zv_1 + \sum_{i=1}^{k-1} \left(z - z^i\right)\psi^i H^i \\ {}^{(k)}w &= w_0 \end{aligned} \tag{1}$$

where z^k is the position of the layer k relative to the bottom surface, u_0, v_0, w_0 are the displacements at the bottom surface, u_1, v_1 are the rotations of the normal in the

bottom layer, H^i are Heaviside unit functions, and φ^i, ψ^i are zigzag functions, which define $2(n-1)$ additional local variables. Transverse inextensibility is assumed and the transverse displacements are constant in the layers. A schematic of the displacement field is presented in Fig. 3.

Stresses and strains in the layers are defined using the assumed displacement field and compatibility and constitutive equations. Enforcing continuity of the transverse shear tractions at the layer interfaces, which implies ${}^{(k)}\sigma_{xz}(z^k) = {}^{(k+1)}\sigma_{xz}(z^k)$ and ${}^{(k)}\sigma_{yz}(z^k) = {}^{(k+1)}\sigma_{yz}(z^k)$ at each interface, then defines the zigzag functions in terms of the global, or primary, variables, u_0, v_0, w_0, u_1, v_1, as $\varphi^i = a^i(u_1 + w_{0,x})$ and $\psi^i = b^i(v_1 + w_{0,y})$, with a^i, b^i constants depending on the thickness and layup of the layers and their relative transverse shear stiffness. The theory then depends on only five global displacement variables (three in a plane beam). For homogeneous cross sections, e.g., a unidirectionally reinforced laminate, the zigzag functions vanish $\varphi^i = \psi^i = 0$ and the model describes first-order shear deformation theory.

The total potential energy and the work of the inertial forces, in the absence of body forces, are given by:

$$\begin{aligned}\Pi &= \frac{1}{2}\int_{\mathcal{V}} \sigma_{ij}\varepsilon_{ij} dV - \int_{\mathcal{S}} \left(q_x u + q_y v + q_z w\right) dS, \qquad K \\ &= \frac{1}{2}\sum_{k=1}^{n} \int_{{}^{(k)}V} {}^{(k)}\rho(\ddot{u} + \ddot{v} + \ddot{w}) dV \end{aligned} \tag{2}$$

where σ_{ij} and ε_{ij} for $i, j = x, y, z$ are stress and strain components in the layers, q_x, q_y, q_z are external surface tractions, and ${}^{(k)}\rho$ is the mass density in layer k (the σ_{zz} are neglected in this original formulation and in most of later developments). Equilibrium equations and boundary conditions are obtained using variational analysis and the theorem of minimum potential energy, for statics, or Hamilton principle, for dynamics.

The base formulation in Eq. (1) defines a {1, 0}-order theory, with a first-order in-plane and zero-order out-of-plane global displacement field. Transverse shear stresses derived through compatibility, ${}^{(k)}\sigma_{xz}$, ${}^{(k)}\sigma_{yz}$, are constant through the thickness and do not fulfill boundary conditions at the upper and lower surfaces. On the other hand, accurate predictions of the shear stresses, ${}^{(k)}\sigma_{xz}^{post}$, ${}^{(k)}\sigma_{yz}^{post}$, are obtained a posteriori by integrating the local equilibrium equations; local equilibrium also yields a posteriori predictions of the transverse normal stresses ${}^{(k)}\sigma_{zz}^{post}$. The accuracy of the a posteriori predictions in beams, also for extreme layups in sandwich systems, has been verified in Tessler et al. (2009) showing that some inaccuracies occur only in sandwich systems with very stiff inner cores. Local fields predicted in a thick highly inhomogeneous plate subjected to transverse loadings are shown in Fig. 1.

The original zigzag theories based on the formulation in Di Sciuva (1986) are poorly suited for finite element implementation due to the C^1 continuity requirement on the transverse deflections. This limitation, along with some inconsistensies related to the shear forces and difficulties in simulating clamped boundaries noted

in Tessler et al. (2009) have substantially limited their use and widespread application in numerical codes and favored the development of other formulations.

However, recent applications of the original theory in Massabò (2014), Massabò and Campi (2015) show that most of the inconsistencies observed in Tessler et al. (2009) are resolved by noting that the variationally consistent equilibrium equations obtained using Eq. (2) do not relate the "classical" internal force and moment resultants, which would lead to inconsistencies. For instance, in a layered beam with thickness h and unit width, aligned along the y axis and subjected to static transverse forces q_z, the variationally consistent equilibrium equations are:

$$\begin{aligned} N_{y,\,y} &= 0 \\ M_{y,\,y} &= Q_{yg} \\ Q_{yg,\,y} &= q_z \end{aligned} \tag{3}$$

where M_y and N_y are the classical bending moment and axial force per unit width while Q_{yg} is a generalized shear force per unit width, which differs from the resultant of the internal shear stresses obtained through compatibility and depends on all internal stresses and zigzag enrichments; it is easily proven that Q_{yg} is also the gross resultant of the internal shear stresses calculated a posteriori by enforcing local equilibrium, ${}^{(k)}\sigma_{yy,\,y} + {}^{(k)}\sigma^{post}_{yz,\,z} = 0$:

$$Q_{yg} = \sum\nolimits_{k=1}^{n} \int_{k_h} {}^{(k)}\sigma^{post}_{yz}\, dz \tag{4}$$

The constant shear stresses, ${}^{(k)}\sigma_{yz} = \sigma_{yz}$, obtained from the displacement field in Eq. (1) using compatibility and the constitutive equations of the layers and their resultant $Q_y = \sigma_{yz} h$ are not variationally consistent, and variationally consistent quantities are the generalized force Q_{yg} and the generalized average stresses $\sigma_{yzg} = Q_{yg}/h$. In homogeneous cross sections, $Q_{yg} = Q_y$ due to the vanishing of the zigzag functions and Eq. (3) becomes the classical equilibrium equation of first-order shear deformation theory.

The above observations are clarified using a simple example. In a layered clamped beam subjected to an applied transverse force F at the beam end, equilibrium and the solution of the equilibrium equations in term of displacements show that the generalized shear force equates the applied force at all positions, $Q_{yg} = F$. The "classical" shear force Q_y differs due to the geometric boundary condition, $v_1 + w_{0,y} = 0$ which implies $\sigma_{yz} = Q_y = 0$ at the clamped support, and to the elastic mismatch of the layers, which implies $Q_y \neq F$ along the beam length. When the elastic mismatch of the layers becomes negligible, the resultant of the shear stresses calculated from compatibility equates the generalized shear force and the applied force at all positions, $Q_y = Q_{yg} = F$, but shows a sudden transition to zero at the clamped boundary where it must satisfy the boundary conditions. This phenomenon is similar to that occurring in the boundary layer of a fluid flowing over a surface and is due to a singularity in the model that will be explained using perturbation theory in section "Original Zigzag Theory with Imperfect and Smooth Interfaces" (Pelassa and Massabò 2015).

The formulation of the original zigzag theory in Di Sciuva (1986) does not include shear correction factors based on the observation that the enrichment with the zigzag functions yields accurate predictions of the local fields. However, the shear strains obtained through compatibility from the displacement field in Eq. (1) are constant in the thickness, as in first-order shear deformation theory; in addition, shear correction factors are required for a homogeneous cross section, when the theory coincides with first-order shear deformation theory, and the constitutive equation for the transverse shear force in a beam is accurately described by $Q_y = kG_{yz}h(v_1 + w_{0,y})$, with k, G_{yz} shear correction factor and shear modulus. Applications of the theory to dynamic and static problems in Darban and Massabò (2018), Massabò (2017a, b) shows that including shear correction factors obtained for homogeneous cross sections in the constitutive equations relating the generalized shear force Q_{yg} to $(v_1 + w_{0,y})$ improve predictions for all layups in thick structures and ensure a smooth transition of the theory to first-order shear deformation theory for vanishing elastic mismatch of the layers. Using a dynamic shear correction factor equal to $k = \pi^2/12$, which is the classical value derived for the first-order shear deformation theory by Mindlin (1951), yields predictions of the cutoff frequency of the second lowest flexural mode of vibration in a highly inhomogeneous bilayer which virtually coincide with exact predictions, as shown in Fig. 6. Using the same shear correction factor, the theory accurately predicts the frequencies of the lowest modes of vibration in sandwich beams with a highly deformable core in the long wavelengths regime, substantially improving solutions using first order shear deformation theory, as shown in Fig. 7. The use of higher-order global displacement fields in Eq. (1) the need of introducing shear correction factors (Di Sciuva 1992).

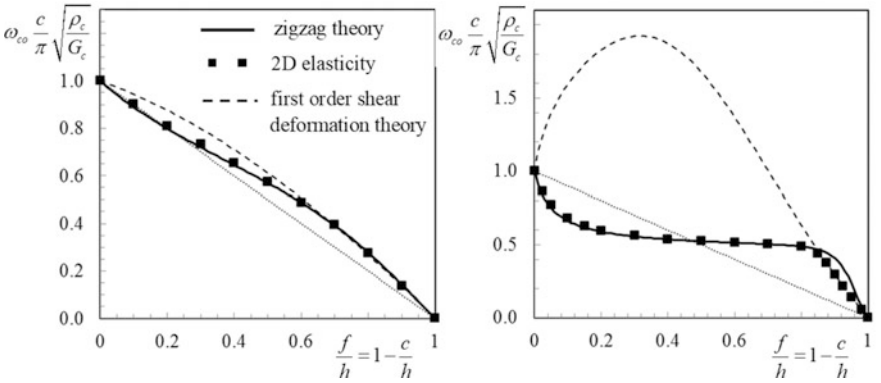

Fig. 6 Cutoff frequency of the second lowest flexural mode in a bilayer with f and c the thicknesses of the layers, $h = f + c$, and G_f, ρ_f and G_c, ρ_c the corresponding shear moduli and mass density (propagation of plane strain harmonic waves). The results of the zigzag theory in Eq. (1) and first-order shear deformation theory obtained assuming a shear correction factor equal to $\pi^2/12$ are compared with exact results in Jones (1964), Yang et al. (1966). (**a**) $G_c = G_f/2$ and $\rho_c = \rho_f$ (e.g., cross-ply laminate); (**b**) $G_c = 0.02G_f$ and $\rho_c = 0.15\rho_f$ (e.g., composite sandwich with foam core). (Adapted after (Massabò 2017b))

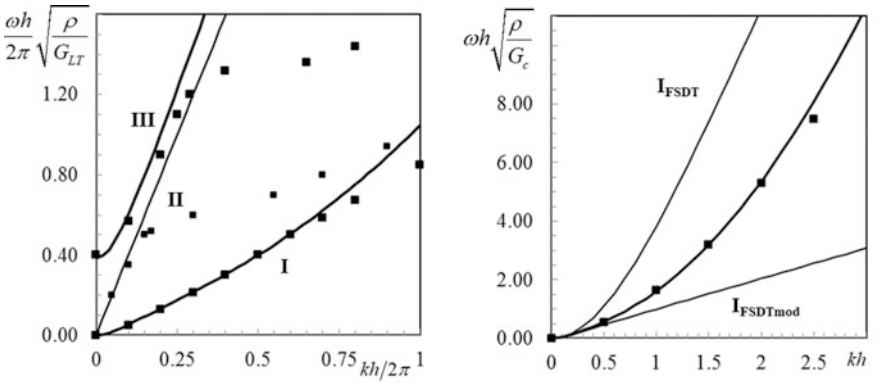

Fig. 7 Dispersion curves relating wave propagation frequencies (I, II, III) and wave number. The results of the zigzag theory in Eq. (1) with shear correction factor $\pi^2/12$ (solid lines) are compared with 2D results (boxes) in Datta et al. (1988) and Whitney and Sun (1973b): (**a**) a plate with three orthotropic layers of thickness $h/3$, density ρ, stacking sequence (0,90,0), and elastic moduli $G_{LT} = \overline{E}_L/22.9$, $G_{TT} = \overline{E}_L/46.28$, $\overline{E}_T = \overline{E}_L/11.64$. (the lines indicate plane strain moduli), lowest antisymmetric (I and III) and symmetric modes (II). (**b**) three-layer sandwich plate with equal thickness and equal density isotropic layers and $G_f/G_c = 100$, $\nu_f = 0.25$, $\nu_c = 0.3$. I_{FSDT} are results obtained using first-order shear deformation theory with correction factor $k = \pi^2/12$; $I_{FSDTmod}$ has correction factor defined by matching the lowest cutoff frequency of 2D elasticity, $k = 0.0158$. (Adapted after (Massabò 2017b))

Several formulations have been proposed for structures with perfect bonding of the layers by extending the basic approach in Eq. (1) in order to improve description of different problems, for instance by assuming {1, 1}-, {3, 0}-, {3, 2}-order global displacement fields, removing the C^1continuity requirement, or extending the formulation to account for geometric nonlinearities (Abrate and Di Sciuva 2018; Averill 1994; Cho and Parmerter 1993; Di Sciuva 1993, 1997). The refined zigzag theories are among these extensions.

Refined Zigzag Theories

The refined zigzag theory formulated by Tessler and coworkers in Tessler et al. (2007, 2009) for a n-layer plane beam with material axes parallel to the geometrical axes and global thickness h, assumes the following kinematics in the arbitrary layer k:

$$\begin{aligned} {}^{(k)}v &= v_0 + zv_1 + {}^{(k)}\phi(z)v_R \\ {}^{(k)}w &= w_0 \end{aligned} \tag{5}$$

where the longitudinal axis of the beam has been assumed along the midplane y axis, the three global variables, v_0, v_1, w_0, define the kinematic field of first-order shear

deformation theory. The fourth global variable, v_R, defines the variation along y of a local piecewise linear enrichment function,

$$^{(k)}\phi(z) = {}^{(k)}\beta\left(z - z^{k-1}\right) + {}^{(k)}\phi\left(z^{k-1}\right) \text{ with } {}^{(1)}\phi\left(z^0\right) = {}^{(n)}\phi(z^n) = 0, \tag{6}$$

which is introduced to account for the inhomogeneous material structure and is assumed to vanish at the upper and lower surfaces of the beam at z^0 and z^n. A schematic of the displacement field is shown in Fig. 4, where the case of perfect bonding between adjacent layers studied here is obtained by enforcing $^{(k)}\phi(z^k) = {}^{(k+1)}\phi(z^k)$.

The displacement field is similar to that of the original zigzag theory in Eq. (1) which would be obtained by imposing the kinematic constraint $v_R = v_1 + w_{0,y}$. In the absence of this constraint, the refined zigzag theory has an additional global variable, for a total of four in a beam (seven in a plate). The slope of the zigzag function in the layer k, $^{(k)}\beta$, is obtained by imposing partial continuity of the shear stresses at the layer interfaces. Continuity is imposed only on the stresses associated to the constraint above (Di Sciuva shear stresses) and implies:

$$^{(k)}\beta = \frac{G}{{}^{(k)}G_{yz}} - 1 \text{ with } G = \frac{h}{\sum_{i=1}^{n} \frac{{}^{(i)}h}{{}^{(i)}G_{yz}}} \tag{7}$$

where G is a homogenized shear rigidity and $^{(k)}G_{zy}$, $^{(k)}h$ are transverse shear modulus and thickness of layer k. The partial continuity implies that the shear stresses calculated through compatibility are piecewise constant in the cross section. In beams with homogeneous cross sections $G = G_{yz}$, $^{(k)}\beta = 0$ and the zigzag functions vanish so that first-order shear deformation theory is recovered. Equilibrium equations and boundary conditions are obtained using variational analysis and Eq. (2).

The refined zigzag theory overcomes some limitations of the original theory. The resultant of the shear stresses calculated from compatibility and constitutive equations directly satisfies the equilibrium equations, $M_{y,y} = Q_y$ with $Q_y = \sum_{k=1}^{n} \int_h {}^{(k)}\sigma_{yz} dz$, and the solution does not present the boundary layer occurring with the original theory. On the other hand, accurate prediction of the transverse shear stresses within the layers still requires a posteriori calculations through local equilibrium. The theory has predictive capabilities which are similar to those of three-dimensional models in the solution of static, dynamic, and buckling problems (Iurlaro et al. 2013). Recent applications in Flores et al. (2018) show for instance that the theory captures the changes in transverse shear stress distribution in sandwich composites with very soft cores when warping is prevented at the clamped supports or free to occur along the beam length.

In addition to its accuracy, the success of the refined zigzag theory in the community is because it relies on C^0-continuous kinematics for finite element modeling (Gherlone et al. 2011; Oñate et al. 2012). A posteriori stress recovery for the accurate derivation of the transverse stresses can be avoided if the theory is

extended using a mixed variational approach (Groh and Weaver 2015; Iurlaro et al. 2015b; Tessler 2015). Literature surveys on the developments of the refined zigzag theory, its extensions to plate and shell structures and to the solution of nonlinear problems, the formulation of C^0 finite elements and higher-order formulations are given in Abrate and Di Sciuva (2018), Gherlone (2013).

On the other hand, the partial relaxation of the continuity conditions on the shear stresses and the presence of the additional global variable are responsible for an important shortcoming of the theory when used for structures with in-plane discontinuities, due for instance to the use of different materials (Darban and Massabò 2018). If the elastic mismatch between the materials is large, the homogenized shear rigidities in different regions of the structure in Eq. (7) substantially differ and the global displacements predicted imposing variationally consistent continuity conditions on internal forces and global displacements are incorrect. This problem will be further discussed in sections "Theories Using the Compliant Layer Concept" and "Original Zigzag Theory with Imperfect and Smooth Interfaces," since similar effects are produced, and have been first observed, in the presence of damaged regions.

The first-order refined zigzag theory in Tessler et al. 2009 does not use a shear correction factor as most of its applications/extensions (Gherlone 2013). Indeed when dealing with problems where the force and moment resultants can be calculated enforcing global equilibrium, the local fields will not be modified by the use of a shear correction factor and predictions are very accurate. Shear correction factors however appear to be necessary to improve predictions of the flexural response, e.g., transverse displacements, in shear deformable plates, such as thick plates and beams (Darban and Massabò 2018; Flores et al. 2018; Iurlaro et al. 2015b; Oñate et al. 2012). Results in Darban and Massabò (2018) show that including shear correction factors obtained for homogeneous structures yield very good predictions of the transverse displacements also in very thick plates and ensures a smooth transition to the limiting cases of vanishing elastic mismatch and fully debonded layers (see discussion in section "Zigzag Theories for Structures with Continuous Interfacial Imperfections, Damaged Layers and Stationary Delaminations"). Shear correction factors are not required when using the higher-order refined zigzag theory (Iurlaro et al. 2015a) or other techniques (Tessler et al. 2011).

Zigzag Theories for Structures with Continuous Interfacial Imperfections, Damaged Layers, and Stationary Delaminations

The presence of interfacial imperfections, damaged layers, and stationary delaminations has important effects on global and local responses. Main effects are: a reduction of the global stiffness; modification of natural vibration modes and frequencies and wave propagation and dispersion; changes in buckling loads and mode shapes; localized jumps in in-plane and transverse displacements; and changes in the through-thickness distribution of in-plane and transverse stresses. The main

effects on local stress and displacement fields in thick and highly inhomogeneous plates have been presented in Fig. 2.

The presence of such imperfections has been included in models which use the zigzag kinematic approximations following three main approaches. The first approach is based on the compliant layer concept, where regular layers of the stack have reduced elastic constants to simulate continuous intralayer damage, or fictitious, very thin, and compliant layers are introduced to represent interfacial imperfections and stationary delaminations. The second approach uses imperfect interfaces (or the spring layer model), which allows partial interaction between adjacent layers with relative displacements controlled by the stiffness of the interfaces (springs). The third approach couples layerwise and zigzag theories: the zigzag kinematic approximation is used to describe the layered structure or within sublaminates separated by imperfect interfaces or delaminations and the displacement jumps are kept as unknowns of the problem.

All approaches are able to capture the effects of the presence of interfacial imperfections and stationary delaminations. The third approach provides more accurate results at the expense of an increased computational cost, since the number of displacement variables depends on the number of sublaminates and delaminations. In the first two approaches, the unknowns coincide with those of the base zigzag theory.

Theories Using the Compliant Layer Concept

The zigzag theories which use the compliant layer concept to describe interfacial imperfections and delaminations introduce thin and compliant layers between the main layers of the structure. The fictitious layers are then treated as regular layers of the stack so that no additional unknowns are added to the problem and the governing equations are the same derived for perfectly bonded structures. The displacement fields of the original and refined theories, for instance, are still described by Eqs. (1) and (5) where the total number of layers now include also the fictitious layers and plate thickness and zigzag functions, φ^i, ψ^i, ${}^{(i)}\phi$, modify accordingly.

The first application to describe beams with continuous and finite size stationary delaminations is due to Averill (1994) and is limited to problems where transverse normal effects due to the presence of the imperfections can be neglected (sliding imperfections/delaminations). The first-order theory generalizes the original theory in Eq. (1) (Di Sciuva 1986) and introduces thin compliant layers. The zigzag model correctly reproduces the tangential jumps and the effects on local stress fields and static and dynamic global behavior.

The effects of the presence of the compliant layers are easily understood by referring to the first-order refined zigzag theory in Eq. (5). If $(n-1)$ thin and compliant fictitious layers of thickness $\overline{h}$ and shear modulus ${}^{(j)}\overline{G}_{yz}$ are added between the n layers of the beam, the homogenized shear rigidity which defines the slope of the zigzag functions in Eq. (6) modifies as:

$$\overline{G} = \frac{h + (n-1)\overline{h}}{\sum_{i=1}^{n} \frac{{}^{(i)}h}{{}^{(i)}G_{yz}} + \sum_{j=1}^{n-1} \frac{\overline{h}}{{}^{(j)}\overline{G}_{yz}}} \tag{8}$$

The compliant interlayers therefore reduce the homogenized modulus and make it vanish, so that ${}^{(k)}\beta = -1$, when the shear modulus of at least one of the interlayers is zero, in order to describe a sliding delamination. Section "Refined Zigzag Theory with Imperfect and Smooth Interfaces" will show that for $\overline{h} \to 0$ the description of interfacial imperfections and delaminations using compliant layers or imperfect interfaces yields the same governing equations.

The compliant layer concept has been applied within higher-order models (Averill and Yip 1996a) and various zigzag theories (Averill and Yip 1996b; Darban and Massabò 2018; Flores et al. 2018; Groh et al. 2015; Groh and Tessler 2017). Most applications neglect transverse normal strains and jumps.

When the compliant layer model is used to describe damage areas or delaminations of finite size, which do not extend over the whole structure, the accuracy of the results depend on the assumptions of the zigzag theory and the continuity conditions imposed between the delaminated and intact regions. Static and dynamic global response and local fields have been successfully reproduced by many theories, e.g., (Averill 1994; Darban and Massabò 2018). On the other hand, predictions of the global displacements are incorrect for certain geometries when using the refined zigzag theory. This has been shown in Flores et al. (2018) for a layered clamped beam and in Darban and Massabò (2018) for a simply supported beam with an edge delamination and is a consequence of the application of the variationally consistent continuity conditions. This problem will be discussed in section "Original Zigzag Theory with Imperfect and Smooth Interfaces."

Theories Using Imperfect Interfaces and the Spring Layer Model

Interfaces and the Spring Layer Model

A second approach to model interfacial imperfections and delaminations is through interfaces, which are mathematical surfaces connecting two layers where interfacial tractions are continuous while material properties and displacements may change discontinuously. A *perfect interface* (or *rigid*) implies continuous displacements and tractions across the interface, an *imperfect interface* (or *nonrigid*) allows controlled relative displacements of the adjacent layers, and *a fully debonded interface* (or *smooth*) allows free relative displacements and is used to approximate traction-free delaminations. Imperfect interfaces have been used to describe thin resin-rich layers, interlayers, adhesives, or the effects of uniformly distributed mechanical fasteners within discrete layer and zigzag models (see survey in Abrate and Di Sciuva (2018))

The simplest interface model, also called linear spring layer model, assumes that the jumps in normal and tangential displacements are proportional to the interfacial tractions. The jumps at the interface position z^k between layer k and $k+1$ are defined as:

$$\begin{aligned} \widehat{u}^k &= {}^{(k+1)}u\left(z^k\right) - {}^{(k)}u\left(z^k\right), \qquad \widehat{v}^k = {}^{(k+1)}v\left(z^k\right) - {}^{(k)}v\left(z^k\right), \\ \widehat{w}^k &= {}^{(k+1)}w\left(z^k\right) - {}^{(k)}w\left(z^k\right) \end{aligned} \tag{9}$$

and the interfacial tractions are:

$$\begin{aligned} \widehat{\sigma}_x^k &= K_{xx}^k \widehat{u}^k + K_{xy}^k \widehat{v}^k \\ \widehat{\sigma}_y^k &= K_{yx}^k \widehat{u}^k + K_{yy}^k \widehat{v}^k \\ \widehat{\sigma}_z^k &= K_{zz}^k \widehat{w}^k \end{aligned} \tag{10}$$

where $K_{xx}^k, K_{xy}^k, K_{yx}^k, K_{yy}^k, K_{zz}^k$ are stiffness coefficients. All stiffness coefficients are infinity and $\widehat{u}^k = \widehat{v}^k = \widehat{w}^k = 0$ in a rigid interface; they are zero in a fully debonded interface where $\widehat{\sigma}_x^k = \widehat{\sigma}_y^k = \widehat{\sigma}_z^k = 0$. General interfaces allow relative sliding and opening displacements between adjacent layers. Most models in the literature assume interfaces which allow only in-plane jumps, namely sliding or slip interfaces, where K_{zz}^k is infinity and $\widehat{w}^k = 0$.

Original Zigzag Theory with Imperfect and Smooth Interfaces

Imperfect interfaces have been included in formulations of first- and higher-order zigzag theories both as sliding interfaces or general interfaces. Sliding interfaces were first introduced in the works by Schmidt and Librescu (1996), Cheng et al. (1996), and Di Sciuva (1997); general interfaces by Librescu and Schmidt (2001).

Referring to the displacement field of the original Di Sciuva theory in Eq. (1), the inclusion of imperfect sliding interfaces yields:

$$\begin{aligned} {}^{(k)}u &= u_0 + zu_1 + \sum_{i=1}^{k-1} \left(z - z^i\right)\varphi^i H^i + \sum_{i=1}^{k-1} \widehat{u}^i H^i \\ {}^{(k)}v &= v_0 + zv_1 + \sum_{i=1}^{k-1} \left(z - z^i\right)\psi^i H^i + \sum_{i=1}^{k-1} \widehat{v}^i H^i \\ {}^{(k)}w &= w_0 \end{aligned} \tag{11}$$

where $\widehat{u}^i, \widehat{v}^i$ are in-plane jumps at the interface at z^i. The field is shown in Fig. 3 and is defined by five global variables and $4(n-1)$ local variables. Enforcing equilibrium, $\widehat{\sigma}_j^i = {}^{(i)}\sigma_{jz}(z^i) = -{}^{(i+1)}\sigma_{jz}(z^i)$ (for $j = x, y$), and the traction laws in Eq. (10) at each interface yields $\widehat{u}^i = c^i(u_1 + w_{0,x})$ and $\widehat{v}^i = d^i\left(v_1 + w_{0,y}\right)$, with c^i, d^i constants depending on interfacial stiffness coefficients, thickness, and layup of the layers and their relative transverse shear stiffness; the zigzag functions are still given by $\varphi^i = a^i(u_1 + w_{0,x})$ and $\psi^i = b^i(v_1 + w_{0,y})$ as for layers with perfect bonding in Eq. (1). The model maintains the five displacement variables of the original theory and for homogeneous cross sections and rigid interfaces returns the displacement field of first-order shear deformation theory.

The third equation in the displacement field in (Eq. 11) is modified in order to add general interfaces and account for normal jumps:

$$^{(k)}w = w_0 + zw_1 + \sum_{i=1}^{k-1} \left(z - z^i\right)\Omega^i H^i + \sum_{i=1}^{k-1} \widehat{w}^i H^i \tag{12}$$

where Ω^i is an additional zigzag function, $\widehat{w}^i$ are interfacial normal jumps, and w_1 is an additional global variable that describes a constant transverse strain in the layers. Adding w_1 and Ω^i is necessary in order to describe opening and elastic contact along the interfaces. The $2(n-1)$ additional local variables are derived as functions of the global variables by imposing continuity of the transverse normal stresses and the interfacial traction laws (Librescu and Schmidt 2001; Massabò and Campi 2015). The model is described by six global displacement variables and for homogeneous cross section and rigid interfaces corresponds to first-order shear and normal deformation theory (Whitney and Sun 1973a); in the case of rigid interfaces and inhomogeneous cross section, with $\widehat{w}^i = 0$ and w_1, $\Omega^i \neq 0$ at all interfaces, the theory improves the base theory in Eq. (1) and better describe materials with transverse compressibility, e.g., sandwich composites.

The governing equations of the problem are obtained using variational analysis. The presence of imperfect interfaces requires a modification to the total potential energy in Eq. (2):

$$\begin{aligned}\Pi = \frac{1}{2}\int_{\mathcal{V}} \sigma_{ij}\varepsilon_{ij} dV + \sum_{k=1}^{n-1} \int_{^{(k)}\mathcal{S}^+} \left(\widehat{\sigma}_x^k \widehat{u}^k + \widehat{\sigma}_y^k \widehat{v}^k + \widehat{\sigma}_z^k \widehat{w}^k\right) dS^k \\ - \int_{\mathcal{S}} \left(q_x u + q_y v + q_z w\right) dS\end{aligned} \tag{13}$$

where an additional term describes the internal energy of the imperfect interfaces. This energy is zero only for the limiting configurations of fully bonded layers, where $\widehat{u}^k = \widehat{v}^k = \widehat{w}^k = 0$ at all interfaces, and fully delaminated layers, where $\widehat{\sigma}_x^k = \widehat{\sigma}_y^k = \widehat{\sigma}_z^k = 0$ at all interfaces (Mau 1973; Shu and Soldatos 2001; Massabò and Campi 2015).

The additional term in Eq. (13) was disregarded in the original zigzag formulations in Cheng et al. (1996), Librescu and Schmidt (2001), Schmidt and Librescu (1996), Di Sciuva (1997) as well as in several formulations that followed (see list in Massabò and Campi (2015)), where the total potential energy in Eq. (2) was instead used, also in the presence of imperfect interfaces. This led to the prediction of "unexpected patterns" (Cheng et al. 1996), unusual "slip-locking phenomena" (Tessler et al. 2009), and "inaccuracies when bonding imperfections are present" (Chen et al. 2003), and to the conclusion that the zigzag approach was valid only for slightly imperfect interfaces. The technique was then essentially abandoned by the

authors in favor of other zigzag formulations, such as the refined zigzag theory and the sublaminate approach.

Using the total potential energy in Eq. (13), Massabò and Campi (2015) added corrections to the original theories (Cheng et al. 1996; Librescu and Schmidt 2001; Di Sciuva 1997) and solved all anomalies. Predictions of local fields in thick layered plates with imperfect and smooth interfaces are shown in Fig. 2, where also incorrect results obtained using the total potential energy in Eq. (2) are presented. The authors also obtained novel governing equations for plates with general interfaces, using the displacement field in Eq. (12), and generalized the interfacial tractions laws in (Eq. 10) in order to simulate more complex piecewise linear laws.

Closed-form solutions for layered beams with sliding-only interfaces and subjected to thermomechanical loadings are given in Massabò and Campi (2014), Pelassa and Massabò (2015) using the kinematics in Eq. (11). Governing equations and solutions in the asymptotic limits of rigid interfaces and fully debonded interfaces are derived using perturbation analysis, so overcoming the issues associated with numerical calculations. These solutions help understanding the effects of the kinematic assumptions. The global displacements of a plane beam with a homogeneous cross section and fully debonded interfaces, for instance, are governed by the equations of an Euler Bernoulli beam with flexural stiffness equivalent to that of the stack of layers free to slide along their surfaces. The equilibrium equations neglect in this limit the contribution of the shear deformability, as a consenquence of the imposition of continuity conditions on the transverse shear tractions at fully debonded interfaces. This is a limitation of the model that tipically has negligible effect on the predictions in statically determinate structures but could be relevant in shear deformable structures.

The derivation in Pelassa and Massabò (2015) also shows that the governing equations have different orders when $1/K_{yy} = 0$, (order IV, first-order shear deformation theory), and when $1/K_{yy} << 1$ (order VI). This indicates a singularity in the model and that singular phenomena may be expected in the solutions. Similar conclusions are drawn on the parameter b^i which describes the elastic mismatch of the layers in Eq. (11), and the order of the equations changes between inhomogeneous beams with $b^i << 1$, and homogeneous beams, $b^i = 0$. These results explain the anomalous effects which arise at clamped edges and are similar to those observed in the boundary layer of a fluid flowing over a surface. These effects however are concentrated in a small boundary region near the edges and do not affect global displacements and the variationally consistent force and moment resultants.

As for the model discussed in section "Original Zigzag Theories" for beams with perfect bonding between adjacent layers, the variationally consistent equilibrium equations in beams with imperfect interfaces involve a generalized transverse shear force, Q_{yg}, which now depends also on the relative jumps, is the variationally consistent internal shear force. This force differs from the resultant of the shear stresses calculated using compatibility, Q_y. The equilibrium equations (3) for layered beams subjected to transverse loadings are still correct.

Small regions where the theory does not accurately predicts the local fields occur at the cross sections separating delaminated and intact regions, since local continuity

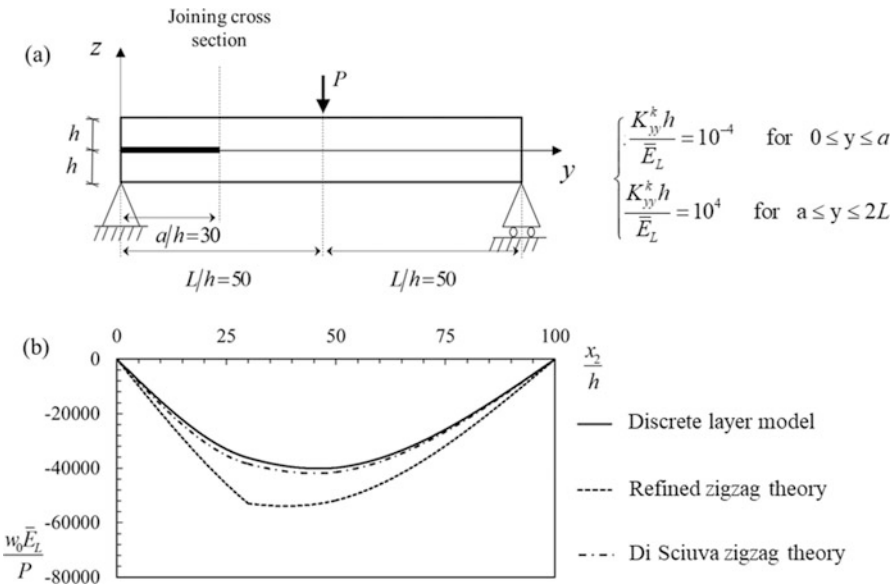

Fig. 8 Three-point bending beam with homogeneous cross section and a mid-thickness delamination. The beam is studied introducing an imperfect interface with different stiffnesses in the delaminated, $K_{yy}h/\bar{E}_L = 10^{-4}$, and intact region, $K_{yy}h/\bar{E}_L = 10^4$ using (i) the Di Sciuva zigzag theory with imperfect interfaces, Eq. (11), (ii) the refined zigzag theory with imperfect interfaces/compliant layers, Eqs. (5) and (14), (iii) the discrete layer model in Andrews and Massabò (2008). Using $K_{yy}h/E = 0$ in the delaminated region (not shown) would still provide good agreement between (i) and (iii) but generate unrealistically large linear displacements in the two parts of the beam separated by the crack tip in (ii). (Adapted after (Darban and Massabò 2018))

is not satisfied due to the imposition of the continuity conditions on the global quantities. However these inaccuracies do not affect the global displacements or force and moment resultants which are accurately predicted. Figure 8 shows the transverse displacements in a three-point bending beam calculated using the kinematic approximation in Eq. (11) with a linear interface law to describe the effects of a mid-thickness delamination. The displacements are accurately predicted and the small discrepancies compared to the solution of a discrete layer model are due to the missing contribution of the shear deformations in the delaminated region.

Refined Zigzag Theory with Imperfect and Smooth Interfaces

A framework to introduce sliding interfaces in the refined zigzag theory for layered beams by Tessler et al. (2009) has been formulated by Darban and Massabò (2018). The formulation uses the displacement field in Eq. (5), and defines the slope of the zigzag functions in Eq. (6) and the jumps at the interfaces, using the analogy between the compliant layer, discussed in section "Theories Using the Compliant Layer Concept," and the interface approach, discussed in section "Original Zigzag Theory with Imperfect and Smooth Interfaces." An interlayer j of thickness $\bar{h}$ and shear

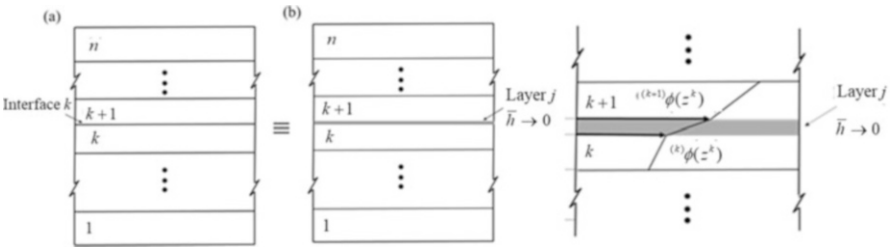

Fig. 9 Analogy between a very thin compliant layer and an imperfect sliding interface. (Modified after (Darban and Massabò 2018))

modulus ${}^{(j)}\overline{G}_{yz}$ placed at z^k can be treated in the limit for $\overline{h} \to 0$, as a sliding interface of stiffness $K_{yy}^k = {}^{(j)}\overline{G}_{yz}/\overline{h}$ which produces an interfacial jump $\widehat{v}^k = {}^{(j)}v\left(z^k + \overline{h}\right) - {}^{(j)}v\left(z^k\right)$. The schematic in Fig. 9 illustrates the analogy. The homogenized shear rigidity of a beam with $(n-1)$ interfaces is then obtained as the limit $G_{int} = \lim_{\overline{h}\to 0} \overline{G}$ of the shear rigidity of the beam with $(n-1)$ compliant interlayers given in Eq. (8), which yields:

$$G_{int} = \frac{h}{\sum_{i=1}^{n} \frac{{}^{(i)}h}{{}^{(i)}G_{zy}} + \sum_{i=1}^{n-1} \frac{1}{K_{yy}^i}} \tag{14}$$

The homogenized rigidity has two relevant limits: the perfect bonding case, when G_{int} is given by Eq. (7), and the delaminated case, when at least one of the imperfect interfaces is a delamination, and $G_{int} = 0$.

To understand the limiting solution of fully delaminated beams, it is useful to consider beams with homogeneous cross sections. The equilibrium equations derived using the refined zigzag theory with compliant layers or imperfect interfaces coincide in this limit with the first-order shear deformation theory equations of a beam with flexural stiffness equivalent to that of the stack of delaminated layers; an additional equation depending on the additional global variables define all local zigzag effects. The necessity of introducing a shear correction factor in the first-order refined zigzag theory is then confirmed for beams with delaminations (Darban and Massabò 2018). This problem is not solved using zigzag theories with higher-order description of the global displacement field (Averill and Yip 1996b; Darban and Massabò 2018; Flores et al. 2018), which would also require a shear correction factor.

The variationally consistent formulation of the refined zigzag theory with imperfect interfaces or compliant layers is unable to describe structures with abrupt in-plane changes of the properties, which could be due to changes in material or to the presence of finite size delaminations or interfacial imperfections. In this latter case, the homogenized shear modulus in Eqs. (8) and (14) approaches zero when the interface stiffness of at least one interface or the shear modulus of at least one

compliant layer vanishes, $K^k_{yy} \to 0$ or $\overline{G}_{yz} \to 0$. The variationally consistent continuity conditions on the transverse shear force then implies a discontinuity in the transverse displacement gradient which directly depends on the difference between the two homogenized shear rigidities and generates incorrect displacements. Figure 8 shows this behavior in a simply supported two-layer beam with a finite size delamination which is described using an imperfect interface with a very small stiffness. The transverse displacements are incorrect and the inaccuracy would increase and the model predicts unrealistic linear deflections in the two regions of the specimen separated by the crack tip for $K^k_{yy} = 0$. Similar conclusions have been obtained by the numerical analyses conducted in Flores et al. (2018) on clamped partially delaminated beams, where different numerical techniques have been used to try and overcome the limitations of the theory. On the other hand, accurate displacements have been obtained through the numerical implementation of the mixed refined zigzag theory in Groh and Tessler (2017) to a layered clamped beam with a short midspan delamination, where only some inaccuracies in the local field were observed probably due to the limited length of the delamination.

Theories Using the Sublaminate Approach or Additional Degrees of Freedom

The models that use the sublaminate approach to represent imperfect interfaces and delaminations in layered structures follow the original layerwise model with zigzag sublaminate approximation formulated by Averill and Yip (1996b) for structures with perfect bonding. The structure is divided into sublaminates which are joined by the imperfect or fully debonded interfaces and the zigzag kinematic approximation is used within each sublaminate while a discrete layer approach is used to model the stack of sublaminates enforcing certain continuity conditions on interfacial tractions and displacements at the layer interfaces. This approach has been applied in Gherlone and Di Sciuva (2007) to plates with continuous delaminations.

Theories have been developed that assume kinematic approximations similar to Eqs. (11) and (12), with a first- or higher-order global displacement field and local zigzag functions, and where the jumps at the layer interfaces describe delaminations and are kept among the unknowns of the problem. Continuity conditions are enforced on the transverse stresses to reduce the number of local variables. In these theories the number of variables is independent on the number of layers but depend on the number of delaminations, e.g., (Kim et al. 2003) (Cho and Kim 2001).

Zigzag Theories for Effective Modeling of Progressive Delamination Damage

Brittle and cohesive delamination fracture in layered beams, plates, and shells is accurately modeled using discrete layer approaches (see references in the Introduction). However, these models are controlled by a number of unknowns which depend

on the number of layers and delaminations; they are computationally expensive and closed-form solutions are limited to simple problems. Using a zigzag kinematic approximation could reduce computational costs and extend the number of problems for which closed-form solutions can be obtained. Figure 10a shows a layered beam with multiple delaminations. Using a classical discrete layer model, the beam is discretized in the thickness direction (the z axis), subdividing it into layers joined by cohesive interfaces, and along the longitudinal direction (the y axis), subdividing it into regions or finite elements (the subdivision into regions separated by the cross sections where the properties change is typically applied for analytical solutions). A zigzag theory requires only the in-plane discretization, as shown by the homogenized zigzag description in Fig. 10b.

The application of the zigzag theories to analyze progressive delamination damage has been investigated only recently and in a limited number of studies. The results presented in the literature, while promising, highlight some issues which need to be resolved for an efficient application of the models. The models build up on the three zigzag approaches formulated to study structures with interfacial imperfections and make use of the compliant layer concept, the imperfect interface model and the sublaminate approach. They apply continuum damage mechanics and cohesive/brittle fracture mechanics concepts and techniques to define criteria for damage/fracture initiation and evolution. The application of the cohesive crack model in combination with the sublaminate technique is straightforward, directly follows what is done within discrete layer models and the number of variables depend on the number of delaminations. This approach will not be presented here.

Section "The Cohesive Crack Model, Cohesive Interfaces, and Brittle Fracture" presents some fundamental concepts on the cohesive crack model, the cohesive

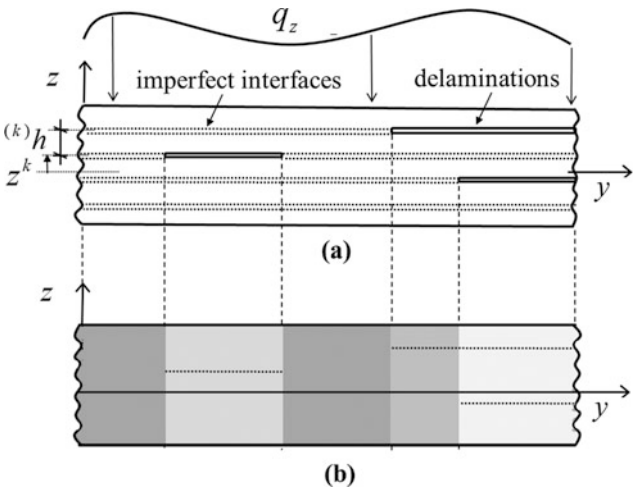

Fig. 10 (**a**) Layered beam with imperfect interfaces and multiple delaminations and homogenized zigzag description requiring only in-plane discretization

interfaces, and their use to analyze cohesive and brittle fracture, focusing on sliding interfaces and Mode II fracture. Sections "Zigzag Theories Using Compliant Layers and Continuum Damage Mechanics" and "Zigzag Theories Using Cohesive Interfaces and Fracture Mechanics" then present the zigzag theories formulated to analyze delamination damage progression using compliant layers and cohesive interfaces.

The Cohesive Crack Model, Cohesive Interfaces, and Brittle Fracture

The cohesive crack model, also known as cohesive zone model, was formulated by Barenblatt (1959) and Dugdale (1960) to study fracture in brittle and elasto-plastic materials, respectively. The model replaces the process zone ahead of a real traction-free crack, where the nonlinear mechanisms associated to the propagation of the crack take place, by a fictitious crack and cohesive tractions which oppose the relative crack displacements. The tractions are related to the relative crack displacements by cohesive tractions laws, which are generally nonlinear and can be defined through micro- or macromechanics models and experiments. In addition to the formation of new free surfaces, associated to the extension of the crack, the nonlinear mechanisms can be due to microcracks formation and coalescence or bridging mechanisms produced by crossover fibers or a through-thickness reinforcement, such as z-pins or stitching (Lundsgaard-Larsen et al. 2012; Massabò 2013). In a mode II crack, the cohesive traction law relates the tangential cohesive tractions to the relative sliding displacement and the area beneath the curve defines the mode II fracture energy or fracture toughness of the material, $\mathcal{G}_{IIC}$. Similar considerations apply to mode I and mode III cracks, characterized, respectively, by relative opening displacement and out-of-plane sliding of the fracture surfaces. Figure 11a shows the bilinear traction law which is often used in the numerical simulations using interface cohesive elements and Fig. 11b shows a piecewise linear cohesive traction law that could be used to approximate arbitrary nonlinear cohesive laws.

In the cohesive crack model the crack tip stress field is finite (nonsingular) and the evolution of the crack is directly controlled by the cohesive tractions. This is straightforward in the presence of pure mode loading, while for mixed-mode loading

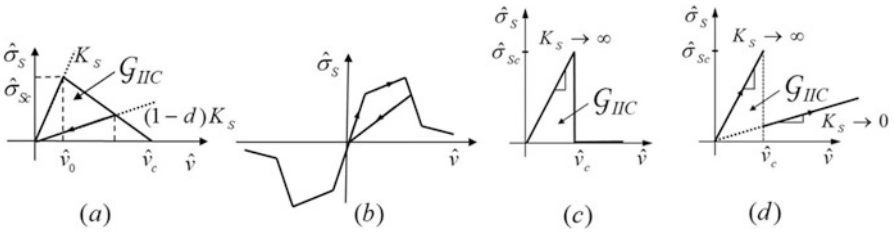

Fig. 11 (**a**) Bilinear cohesive law used for mode II fracture. (**b**) Piecewise linear cohesive traction law used for mode II fracture. (**c**) Piecewise linear cohesive law used to describe brittle mode II fracture. (**d**) Two-branch law used to approximate the law in (**c**) within the zigzag formulation

different strategies are used to account for the coupling of the cohesive responses and define mixed-mode criteria for initiation and propagation (see (Abrate et al. 2015) for a recent review).

The interfacial traction laws that are used within the zigzag formulations presented in section "Theories Using Imperfect Interfaces and the Spring Layer Model" and are based on the linear spring model in Eq. (10) must be modified in order to reproduce the cohesive laws presented in Fig. 11 or other nonlinear laws used within discrete layer models, e.g., (Campi and Monetto 2013; Monetto and Campi 2017), and use them to propagate delaminations. This can be done by describing each branch, *i,* of the law in Fig. 11b as a linear nonproportional (affine) law, $\widehat{\sigma}_s = K_s^i \widehat{v} + \widehat{t}^i$, with $\widehat{t}^i$ the intercept with the vertical axis for $\widehat{v} = 0$ and K_S^i the slope of the branch (which can be negative). An extended formulation of the zigzag theory based on Di Sciuva zigzag functions that accounts for interfaces characterized by affine laws has been presented in Massabò and Campi (2014, 2015).

For perfectly brittle fracture, the size of the process zone is very small and remains constant during propagation so that the shape of the law does not affect the response; this is also known as the small scale yielding limit where linear elastic fracture mechanics applies. The cohesive law in Fig. 11c is conveniently used, with a very stiff branch up to a critical value of the displacement, $\widehat{v}_c$, beyond which the cohesive tractions are assumed to vanish; the area under the law defines the mode II fracture energy, $\mathcal{G}_{IIC} = 1/2 K_S \widehat{v}_c^{\,2}$ (Alfano and Crisfield 2001; Andrews et al. 2006; Andrews and Massabò 2008). Similar laws can be defined for the other modes of fracture.

Purely brittle fracture occurs when the energy release rate, which is the total potential energy released due to a unit crack extension, equates a critical value that corresponds to the fracture energy. For collinear mode II crack propagation this implies:

$$\mathcal{G}_{II} = \mathcal{G}_{IIC} = 1/2 K_S \widehat{v}_c^{\,2} \tag{15}$$

with $\mathcal{G}_{II}$ the mode II component of the energy release rate. Similar equations describes mode I and mode II fracture, while for mixed-mode loading the critical value of the energy release rate will depend on the mode ratios. Equation (15) offers an effective methodology useful to analyze damage evolution within zigzag theories: the energy release rate is a global quantity which can be calculated using global variables, so avoiding any inaccuracies in the prediction of the cohesive tractions at the crack tips.

Zigzag Theories Using Compliant Layers and Continuum Damage Mechanics

The first models formulated to analyze delamination damage progression in layered structures using the zigzag kinematic approximation apply the compliant layer

concept and continuum damage mechanics. The models assume the delaminations to propagate under mode II conditions.

Eijo et al. (2013) developed a damage framework to model interlaminar damage evolution in layered beams using the two-noded beam finite element constructed in Oñate et al. (2012) and based on the refined zigzag theory described in section "Refined Zigzag Theories" (Tessler et al. 2009, 2010). Thin interlayers are inserted at the location where the delaminations are expected to develop and the properties of the layer are controlled by an isotropic damage model governed by a single internal damage variable. The model defines an initiation stress–based criterion and an exponential evolution law depending on fracture energy and tensile strength of the layer. An extension to plate-shell structures is presented in Eijo et al. (2014) with applications to a plate with a central hole subjected to bending. The results do not show the inconsistencies highlighted by the analytical solutions in Darban and Massabò (2018), the numerical solutions in Flores et al. (2018), and recalled in sections "Zigzag Theories for Structures with Perfect Bonding Between Adjacent Layers" and "Zigzag Theories for Structures with Continuous Interfacial Imperfections, Damaged Layers and Stationary Delaminations" when the refined zigzag theory is used to describe structures with in-plane discontinuities. The progressive transition of the level of damage (between 0 and 1) occuring over a large area of the plate analyzed in Eijo et al. (2014) could explain why the chosen geometry does not highlight the problem.

A different damage framework has been developed for the refined zigzag theory by Groh et al. (2015) in order to enable tracking of mode II delamination propagation in laminated beams. Thin interlayers are inserted at all locations where delaminations are expected to develop and the problem is solved using a finite element implementation of the refined zigzag theory presented in sections "Refined Zigzag Theories" and "Theories Using the Compliant Layer Concept." Damage in the thin layers is analyzed using the continuum damage mechanics model formulated by Fan et al. (2008). The damage evolution law is formulated using the bilinear cohesive traction law in Fig. 11a so that the damage variable, d, and the isotropic degradation of the elastic constants in the thin layers is directly related to the mode II interface fracture energy.

Damage initiation is defined through a multiaxial stress–based criterion which uses the interlayer stresses calculated from the refined zigzag theory equations (transverse shear and normal stresses are calculated a posteriori enforcing local equilibrium); the transverse shear stress at damage initiation is $\sigma_{yz}^{\max}$. The parameters of the bilinear cohesive traction law are defined so that the stiffness of the first branch is related to shear modulus and thickness of the interlayer, $K_S = \overline{G}_{yz}/\overline{h}$, and the critical stress is set $\widehat{\sigma}_{Sc} = \sigma_{yz}^{\max}$; the area beneath the law defines the mode II fracture energy and the critical sliding displacement beyond which the cohesive tractions vanish is $\widehat{v}_c = 2\mathcal{G}_{IIC}/\sigma_{yz}^{\max}$. The damage variable is defined in terms of the parameters of the cohesive law by imposing that the degrading stiffness of the cohesive law for $\widehat{v}_0 \le \widehat{v} \le \widehat{v}_c$ is $(1-d)K_S$, with $d = 0, 1$ for $\widehat{v} = \widehat{v}_0, \widehat{v}_c$, as shown in Fig. 11a.

The model has been used to simulate experimental three-point bending tests on a unidirectionally reinforced laminate with a 90-degree ply inserted at different thickness-wise locations. Experimental and numerical load–displacement curves are similar and show that a catastrophic crack propagation occurs at the critical load when a delamination forms at the mid-span and suddenly grows over a long distance, approaching the supports in almost all cases. The fact that the thin interlayer has uniform or almost uniform elastic properties both in the initial phase, before crack initiation, and in the unloading phase, after crack propagation, could explain why the numerical solution does not suffer from the problems observed in Fig. 10 where the refined zigzag theory was applied to model a similar problem but with a strong in-plane discontinuity of the elastic properties.

While the numerical applications of the refined zigzag theory to analyze delamination damage progression do not seem to suffer from the inconsistensies noted in Flores et al. (2018) and Darban and Massabò (2018) a deeper investigation appears to be necessary.

Zigzag Theories Using Cohesive Interfaces and Fracture Mechanics

The second approach to analyze interlaminar damage progression combines the use of the zigzag kinematic approximation and the cohesive crack model. A model based on the zigzag formulation for imperfect interfaces in Eqs. (11) and (13) has been formulated to study mode II dominant fracture in layered beams by Massabò and Darban (2019) will be summarized in the following. Mode II dominant defines shear dominated mixed-mode states where delamination growth is driven by mode II loadings. This typically occurs for phase angles, ψ, greater than 75°, with $\psi = 90°$, 0° for pure Mode II, I loading. Mode II dominant conditions occurs when the relative opening displacements are prevented, for instance by a through-thickness reinforcement or because the delamination surfaces are in contact.

An effective strategy to implement the cohesive traction law for purely brittle fracture shown in Fig. 11c within the zigzag theory and describe mode II crack propagation along the y axis in layered beams, modifies the interfacial traction law of a generic interface at z^k in Eq. (10) as follows:

$$\widehat{\sigma}_y^k\left(z^k\right) = \begin{cases} K_{yy}^k \widehat{v}^k & \text{for } \widehat{v}^k \le \widehat{v}_c \quad \text{with } 1/K_{yy}^k \to 0 \\ K_{yy}^k \widehat{v}^k & \text{for } \widehat{v}^k \ge \widehat{v}_c \quad \text{with } K_{yy}^k \to 0 \end{cases} \tag{16}$$

The new law is depicted in the schematic in Fig. 11d, with $\widehat{\sigma}_y^k\left(z^k\right) = \widehat{\sigma}_s$, $K_{yy}^k = K_S$ and $\widehat{v}^k = \widehat{v}$. Pre-existing delaminations will be characterized by $\widehat{\sigma}_y^k\left(z^k\right) = 0$, while the status of the interfaces in the originally intact regions of the beam may change during loading from the first to the second equations in (Eq. 16).

Crack propagation in a layered beam with arbitrary delaminations can be solved in closed form using an in-plane discretization of the structure, as shown in Fig. 10,

which is divided into regions where zigzag functions and displacement field in Eq. (11) differs due to the presence of a different number of traction-free delaminations. The global variables are obtained by solving the equilibrium equations with variationally consistent continuity and boundary conditions; local fields and jumps are derived following the standard procedure.

The propagation of pre-existing delaminations can be studied using different fracture mechanics techniques. The simplest approach uses the energy fracture criterion in Eq.(15) where the energy release rate is easily calculated from the total potential energy or using the compliance method (for beams subjected to single point forces, P):

$$\mathcal{G}_{II} = -\frac{d\Pi}{bda} \quad \text{or} \quad \mathcal{G}_{II} = \frac{P^2}{2b}\frac{dC}{da} \tag{17}$$

where Π is the total potential energy calculated using Eq. (13), a is the length of the propagating delamination, $C = w_0(P)/P$ is the load point displacement due to a unit point load, and b is the beam width. Some interesting results, which highlight the strengths of the zigzag approach, are presented in Figs. 12, 13, and 14.

Figure 12 shows predictions of the critical load for crack propagation versus load point displacement in End Notched Flexure and End-Loaded Split specimens. The specimens are made of a graphite-epoxy unidirectionally reinforced laminate, tested in Madhukar and Drzal (1992), and of a cross-ply carbon-epoxy laminate, analyzed using a 2D finite element model in Massabò and Monetto (2020). Predictions using the zigzag theories have been obtained in closed form. The zigzag model is able to capture, with just three displacement variables, the onset of propagation and the

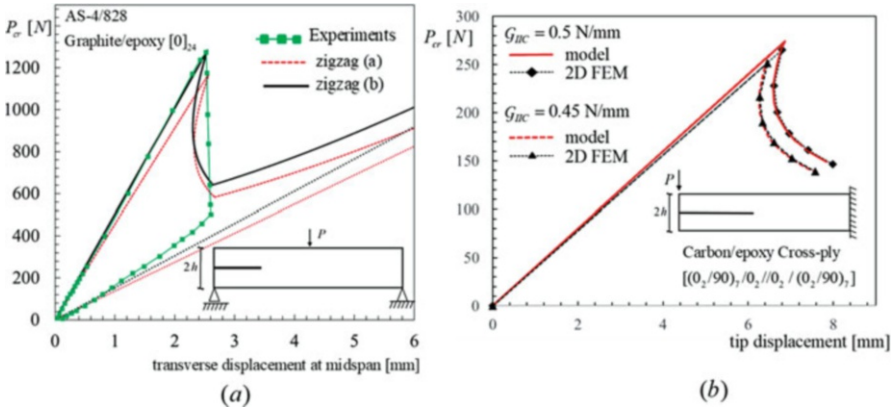

Fig. 12 (**a**) Critical load for crack propagation versus load point displacement in a ENF specimen (Modified after (Massabò and Darban 2019)). Geometry and materials given in Massabò and Darban (2019); zigzag (**a**) and (**b**) are results obtained using the zigzag theory and average/max/min experimental values of the material properties. (**b**) Critical load for crack propagation versus load point displacement in a ELS specimen. Geometry and properties given in Massabò and Monetto (2020)

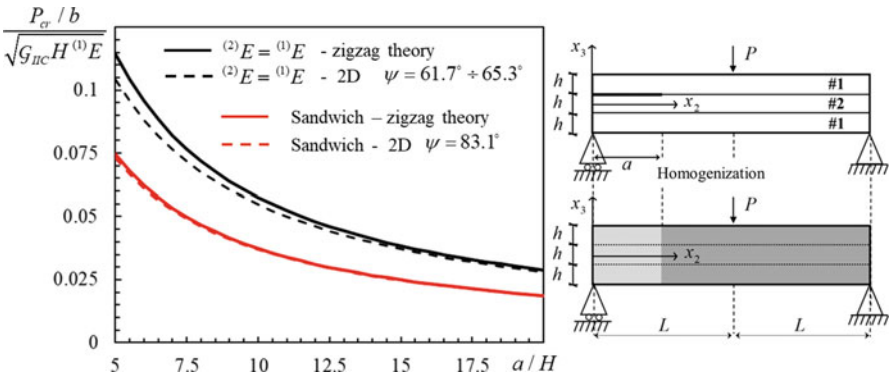

Fig. 13 Dimensionless diagram of critical load for crack propagation versus crack length in three-point bend sandwich beams with isotropic layers, $H = 3\,h$. Black curves: homogeneous beam with asymmetric delamination, $^{(2)}E/^{(1)}E = 1$; red curves: sandwich beam, $^{(2)}E/^{(1)}E = 1/4$. Two-dimensional results in Barbieri et al. 2018. (Adapted after (Massabo and Darban 2019))

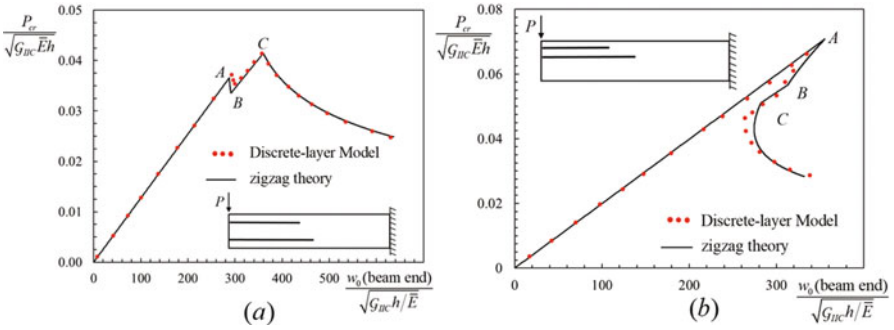

Fig. 14 Critical load for crack propagation versus load point displacement in the homogeneous and isotropic cantilever beams with multiple delaminations shown in the insets (results of zigzag theory in Massabò and Darban (2019) and discrete layer model in Andrews et al. (2006)): (**a**) symmetrically positioned cracks; (**b**) asymmetrically positioned cracks. In (**a**) upper delamination propagates in A, approaches tip of other crack in B where a local shielding of the crack tip field arrests propagation (hyper-strength and snap-through instability); propagation continues on increasing applied load up to C when both cracks start to propagate simultaneously. In (**b**) upper crack starts to propagate catastrophically in A (snap-back instability), approaches tip of other crack in B where an amplification of the local fields generates a sudden decrease of critical load up to C, where upper crack continue to propagate unstably

unstable postcritical response which is characterized by a snap-back instability when the load suddenly drops in the displacement-controlled experimental tests. The zigzag model and the finite element model, with an efficient crack length control technique, follow the evolution of the crack along the virtual snap-back branch and the subsequent stable propagation.

Figure 13 shows predictions of the critical load for crack propagation for on varying the length of an asymmetric delamination in a sandwich specimen. Results

are compared with accurate 2D solutions from the literature (Barbieri et al. 2018). As expected, predictions are less accurate when the crack is not under mode II dominant conditions. In this case, the results of the zigzag approach coincides with results of a discrete layer model using the constrained-contact assumption, which limits accuracy.

Figure 14 highlights the capability of the zigzag model to accurately capture the interaction effects of multiple propagating delaminations. The interaction effects are due to amplification and/or shielding of the local crack tip fields of a propagating delamination when it approaches other delaminations. These effects produce local instabilities in the response diagram and have been observed in the experimental tests presented in Fig. 5. In the structures analyzed in Fig. 14 different effects are generated by the different locations of two delaminations in an isotropic clamped beam; inhomogeneous layups would generate similar behaviors. The zigzag model is able to reproduce, with just three displacement variables, the onset and propagation of the delaminations, the unstable response, snap-back and snap-through instabilities generated by the interactions between delaminations, the hyper-strength phenomena due to a local shielding of the crack tip field, as well as the simultaneous propagation of the delaminations Fig. 14a. An efficient crack length control allows to follow the evolution of the cracks.

Conclusions

The main focus of this chapter has been on the presentation of zigzag theories formulated and applied to analyze the mechanical response of layered structures with interfacial imperfections and interlaminar damage and to investigate progressive delamination damage. The zigzag theories are part of the discrete layer structural theories, which assume different kinematic fields in the layers of the structure in order to describe the zigzag effects due to their elastic mismatch and the effects of imperfections and delaminations on global behavior and local fields. The zigzag theories apply certain continuity conditions at the layer interfaces in order to reduce the number of displacement variables. A zigzag theory therefore describes a layered structure with imperfections and delaminations using the same number of variables of an equivalent single-layer theory, with advantages in term of computational cost and, more importantly, allowing the closed-form solution of problems that would otherwise require a numerical solution.

In this chapter, zigzag theories based on the kinematic approximations of the displacement field originally proposed by Di Sciuva (1986) and Tessler et al. (2009) for structures where the layers are perfectly bonded have been presented; their strengths and weaknesses have been critically discussed, using simple examples and applications.

The main strength of all theories presented in the chapter is the ability to predict local fields in highly inhomogeneous structures and in the presence of continuous delaminations and imperfections with an accuracy comparable to that of discrete layer models or even three-dimensional models. The recent formulation of

continuum damage mechanics and fracture mechanics frameworks allow the use of the zigzag kinematics in the analysis of delamination damage progression. In particular, the combined use of the cohesive crack model and the zigzag kinematics enables the effective analysis of single and multiple delamination crack propagation in laminates and sandwich systems (currently only for mode II dominant problems). Applications to various problems have been presented that show that the zigzag theories are able to reproduce local effects, such as snap-back and snap-through instabilities, hyper-strength phenomena, crack arrest, and the simultaneous propagation of systems of cracks, with an accuracy comparable to discrete layer models.

The presentation show that some of the weaknesses of the theories based on the original formulation by Di Sciuva can be resolved by introducing unconventional internal forces and using perturbation theory to explain boundary layer effects which occur at the clamped edges and do not affect global variables or the solutions outside the boundary regions. On the other hand, some weaknesses in the theories based on the refined zigzag kinematics, when dealing with problems with in-plane discontinuities, which have been noted in the literature only recently, have been highlighted and explained.

The main weaknesses of the zigzag approaches, when applied to analyze delamination damage progression, are due to the imposition of the variationally consistent continuity conditions in terms of global quantities. This implies that continuity of the local quantities, such as bending and shear stresses and relative crack displacements, are not satisfied at the delamination crack tips and it is only at a certain (small) distance from the crack tips that the expected distributions are recovered. It also implies that the near-tip deformations (root rotations), which are important for short and intermediate crack lengths, are only partially accounted for through the zigzag functions.

Current formulations of zigzag theories for the analysis of delamination damage progression, both using continuum damage or fracture mechanics frameworks, are limited to mode II delamination cracks. Results presented in the chapter show that this implies that accurate solutions can be obtained only for mode II dominant problems, where the mode mixity is not too far from pure mode II conditions. The extension of the theories to account for mixed-mode crack tip conditions is therefore a necessary step if the theories have to be applied to layered systems under arbitrarily loading and boundary conditions.

References

S. Abrate, M. Di Sciuva, Multilayer models for composite and sandwich structures, in *Comprehensive Composite Materials II*, ed. by C. H. Zweben, P. W. R. Beaumont, (Elsevier, Amsterdam, 2018), pp. 399–425

S. Abrate, J.F. Ferrero, P. Navarro, Cohesive zone models and impact damage predictions for composite structures. Meccanica **50**, 2587–2620 (2015). https://doi.org/10.1007/s11012-015-0221-1

G. Alfano, M.A. Crisfield, Finite element interface models for the delamination analysis of laminated composites: Mechanical and computational issues. Int. J. Numer. Methods Eng. (2001). https://doi.org/10.1002/nme.93

O. Allix, P. Ladevèze, Interlaminar interface modelling for the prediction of delamination. Compos. Struct. (1992). https://doi.org/10.1016/0263-8223(92)90060-P
O. Allix, P. Ladevéze, A. Corigliano, Damage analysis of interlaminar fracture specimens. Compos. Struct. (1995). https://doi.org/10.1016/0263-8223(95)00002-X
M.G. Andrews, R. Massabò, Delamination in flat sheet geometries with material imperfections and thickness variations. Compos. Part B Eng. **39**, 139–150 (2008). https://doi.org/10.1016/j.compositesb.2007.02.017
M.G. Andrews, R. Massabò, B.N. Cox, Elastic interaction of multiple delaminations in plates subject to cylindrical bending. Int. J. Solids Struct. **43**, 855–886 (2006). https://doi.org/10.1016/j.ijsolstr.2005.04.025
R.C. Averill, Static and dynamic response of moderately thick laminated beams with damage. Compos. Eng. **4**(4), 381–395 (1994). https://doi.org/10.1016/S0961-9526(09)80013-0
R.C. Averill, Y.C. Yip, Development of simple, robust finite elements based on refined theories for thick laminated beams. Comput. Struct. (1996a). https://doi.org/10.1016/0045-7949(95)00269-3
R.C. Averill, Y.C. Yip, Thick beam theory and finite element model with zig-zag sublaminate approximations. AIAA J **34**, 1627–1632 (1996b). https://doi.org/10.2514/3.13281
L. Barbieri, R. Massabò, C. Berggreen, The effects of shear and near tip deformations on interface fracture of symmetric sandwich beams. Eng. Fract. Mech. **201**, 298–321 (2018). https://doi.org/10.1016/j.engfracmech.2018.06.039
G.I. Barenblatt, The formation of equilibrium cracks during brittle fracture. General ideas and hypotheses. Axially-symmetric cracks. J. Appl. Math. Mech. **23**, 622–636 (1959). https://doi.org/10.1016/0021-8928(59)90157-1
D. Bruno, F. Greco, Mixed mode delamination in plates: A refined approach. Int. J. Solids Struct. (2001). https://doi.org/10.1016/S0020-7683(01)00179-2
F. Campi, I. Monetto, Analytical solutions of two-layer beams with interlayer slip and bi-linear interface law. Int. J. Solids Struct. (2013). https://doi.org/10.1016/j.ijsolstr.2012.10.032
A. Carpinteri, R. Massabò, A. Brencich, Comparisons and conclusions, book chapter, in *Nonlinear Crack Models for Nonmetallic Materials*, ed. by A. Carpinteri, (Kluwer, Dordrecht, 1999), pp. 285–310
E. Carrera, Theories and finite elements for multilayered, anisotropic, composite plates and shells. J. Arch. Comput. Methods Eng. **9**, 87–140 (2002)
E. Carrera, Historical review of Zig-Zag theories for multilayered plates and shells. Appl. Mech. Rev. (2003). https://doi.org/10.1115/1.1557614
W.Q. Chen, J.B. Cai, G.R. Ye, Exact solutions of cross-ply laminates with bonding imperfections. AIAA J. (2003). https://doi.org/10.2514/2.6817
Z.Q. Cheng, A.K. Jemah, F.W. Williams, Theory for multilayered anisotropic plates with weakened interfaces. J. Appl. Mech. Trans. ASME. **63**, 1019–1026 (1996). https://doi.org/10.1115/1.2787221
M. Cho, J.-S. Kim, Higher-order zig-zag theory for laminated composites with multiple delaminations. J. Appl. Mech. Trans. ASME. **68**, 869–877 (2001). https://doi.org/10.1115/1.1406959
M. Cho, R.R. Parmerter, Efficient higher order composite plate theory for general lamination configurations. AIAA J. **31**, 1299–1306 (1993). https://doi.org/10.2514/3.11767
H. Darban, R. Massabò, A homogenized structural model for shear deformable composites with compliant interlayers. Multiscale Multidiscip. Model. Exp. Des. **1**, 269–290 (2018). https://doi.org/10.1007/s41939-018-0032-x
S.K. Datta, R.L. Bratton, T. Chakraborty, A.H. Shah, Wave propagation in laminated composite plates. J. Acoust. Soc. Am. **83**, 2020–2026 (1988). https://doi.org/10.1121/1.396382
M. Di Sciuva, Bending, vibration and buckling of simply supported thick multilayered orthotropic plates: An evaluation of a new displacement model. J. Sound Vib. **105**(3), 425–442 (1986). https://doi.org/10.1016/0022-460X(86)90169-0
M. Di Sciuva, Multilayered anisotropic plate models with continuous interlaminar stresses. Compos. Struct. **22**, 149–167 (1992). https://doi.org/10.1016/0263-8223(92)90003-U

M. Di Sciuva, A general quadrilateral multilayered plate element with continuous interlaminar stresses. Comput. Struct. (1993). https://doi.org/10.1016/0045-7949(93)90282-I

M. Di Sciuva, Geometrically nonlinear theory of multilayered plates with interlayer slips. AIAA J. **35**(11), 1753–1759 (1997). https://doi.org/10.2514/2.23

D.S. Dugdale, Yielding of steel sheets containing slits. J. Mech. Phys. Solids **8**, 100–103 (1960). https://doi.org/10.1016/0022-5096(60)90013-2

A. Eijo, E. Oñate, S. Oller, A numerical model of delamination in composite laminated beams using the LRZ beam element based on the refined zigzag theory. Compos. Struct. **104**, 270–280 (2013). https://doi.org/10.1016/j.compstruct.2013.04.035

A. Eijo, E. Oñate, S. Oller, Delamination in laminated plates using the 4-noded quadrilateral QLRZ plate element based on the refined zigzag theory. Compos. Struct. **108**, 456–471 (2014). https://doi.org/10.1016/j.compstruct.2013.09.052

C. Fan, P.Y.B. Jar, J.J.R. Cheng, Cohesive zone with continuum damage properties for simulation of delamination development in fibre composites and failure of adhesive joints. Eng. Fract. Mech. **75**, 3866–3880 (2008). https://doi.org/10.1016/j.engfracmech.2008.02.010

F.G. Flores, S. Oller, L.G. Nallim, On the analysis of non-homogeneous laminates using the refined zigzag theory. Compos. Struct. **204**, 791–802 (2018). https://doi.org/10.1016/j.compstruct.2018.08.018

M. Gherlone, On the use of zigzag functions in equivalent single layer theories for laminated composite and sandwich beams: A comparative study and some observations on external weak layers. J. Appl. Mech. Trans. ASME. **80**, 061004 (2013). https://doi.org/10.1115/1.4023690

M. Gherlone, M. Di Sciuva, Thermo-mechanics of undamaged and damaged multilayered composite plates: A sub-laminates finite element approach. Compos. Struct. **81**, 137–155 (2007). https://doi.org/10.1016/j.compstruct.2006.08.004

M. Gherlone, A. Tessler, M. Sciuva Di, C0 beam elements based on the refined zigzag theory for multilayered composite and sandwich laminates. Compos. Struct. (2011). https://doi.org/10.1016/j.compstruct.2011.05.015

R.M.J. Groh, A. Tessler, Computationally efficient beam elements for accurate stresses in sandwich laminates and laminated composites with delaminations. Comput. Methods Appl. Mech. Eng. **320**, 369–395 (2017). https://doi.org/10.1016/j.cma.2017.03.035

R.M.J. Groh, P.M. Weaver, On displacement-based and mixed-variational equivalent single layer theories for modelling highly heterogeneous laminated beams. Int. J. Solids Struct. **59**, 147–170 (2015). https://doi.org/10.1016/j.ijsolstr.2015.01.020

R.M.J. Groh, P.M. Weaver, A. Tessler, Application of the refined zigzag theory to the modeling of delaminations in laminated composites. AIAA J **53**, 3788–3804 (2015)

F. Gruttmann, G. Knust, A shell element for the prediction of residual load-carrying capacities due to delamination. Int. J. Numer. Methods Eng. **118**, 132–158 (2019). https://doi.org/10.1002/nme.6010

L. Iurlaro, M. Gherlone, M. Di Sciuva, A. Tessler, Assessment of the refined zigzag theory for bending, vibration, and buckling of sandwich plates: A comparative study of different theories. Compos. Struct. **106**, 777–792 (2013). https://doi.org/10.1016/j.compstruct.2013.07.019

L. Iurlaro, M. Gherlone, M. Di Sciuva, The (3, 2)-mixed refined zigzag theory for generally laminated beams: Theoretical development and C0 finite element formulation. Int. J. Solids Struct. **73–74**, 1–19 (2015a). https://doi.org/10.1016/j.ijsolstr.2015.07.028

L. Iurlaro, M. Gherlone, M. Di Sciuva, A. Tessler, Refined zigzag theory for laminated composite and sandwich plates derived from Reissner's mixed variational theorem. Compos. Struct. **133**, 809–817 (2015b). https://doi.org/10.1016/j.compstruct.2015.08.004

J.P. Jones, Wave propagation in a two-layered medium. J. Appl. Mech. Trans. ASME. **31**, 213–222 (1964). https://doi.org/10.1115/1.3629589

H.S. Kim, A. Chattopadhyay, A. Ghoshal, Characterization of delamination effect on composite laminates using a new generalized layerwise approach. Comput. Struct. **81**(5), 1555–1566 (2003). https://doi.org/10.1016/S0045-7949(03)00150-0

R. Larsson, A discontinuous shell-interface element for delamination analysis of laminated composite structures. Comput. Methods Appl. Mech. Eng. **30–32**, 3173–3194 (2004). https://doi.org/10.1016/j.cma.2003.08.009

L. Librescu, R. Schmidt, A general linear theory of laminated composite shells featuring interlaminar bonding imperfections. Int. J. Solids Struct. (2001). https://doi.org/10.1016/S0020-7683(00)00263-8

C. Lundsgaard-Larsen, R. Massabò, B.N. Cox, On acquiring data for large-scale crack bridging at high strain rates. J. Compos. Mater. **46**, 949–971 (2012). https://doi.org/10.1177/0021998311413622

M.S. Madhukar, L.T. Drzal, Fiber-matrix adhesion and its effect on composite mechanical properties: IV. mode I and mode II fracture toughness of graphite/epoxy composites. J. Compos. Mater. **26**, 936–968 (1992). https://doi.org/10.1177/002199839202600701

R. Massabò, Bridged and cohesive crack models for fracture in composite materials, in *Mechanics Down Under – Proceedings of the 22nd International Congress of Theoretical and Applied Mechanics, ICTAM 2008* (2013)

R. Massabò, Influence of boundary conditions on the response of multilayered plates with cohesive interfaces and delaminations using a homogenized approach. Frat. Integrita Strutt. **8**, 230–240 (2014). https://doi.org/10.3221/IGF-ESIS.29.20

R. Massabò, Cut-off frequencies and correction factors of equivalent single layer theories. Proc. Eng. **199**, 1466–1471 (2017a)

R. Massabò, Propagation of Rayleigh-Lamb waves in multilayered plates through a multiscale structural model. Int. J. Solids Struct. **124**, 108–124 (2017b). https://doi.org/10.1016/j.ijsolstr.2017.06.020

R. Massabò, F. Campi, An efficient approach for multilayered beams and wide plates with imperfect interfaces and delaminations. Compos. Struct. **116**, 311–324 (2014). https://doi.org/10.1016/j.compstruct.2014.04.009

R. Massabò, F. Campi, Assessment and correction of theories for multilayered plates with imperfect interfaces. Meccanica **50**, 1045–1071 (2015). https://doi.org/10.1007/s11012-014-9994-x

R. Massabò, A. Cavicchi, Interaction effects of multiple damage mechanisms in composite sandwich beams subject to time dependent loading. Int. J. Solids Struct. **49**, 720–738 (2012). https://doi.org/10.1016/j.ijsolstr.2011.11.012

R. Massabo, H. Darban, Mode II dominant fracture of layered composite beams and wide-plates: A homogenized structural approach. Eng. Fract. Mech. **213**, 280–301 (2019). https://doi.org/10.1016/j.engfracmech.2019.03.002

R. Massabò, I. Monetto, Local zigzag effects and brittle delamination fracture of n-layered beams using a structural theory with three displacement variables. Frat. Integrita Strutt. **14**, 275–287 (2020). https://doi.org/10.3221/IGF-ESIS.51.22

S.T. Mau, A refined laminated plate theory. J. Appl. Mech. Trans. ASME. **40**, 606–607 (1973). https://doi.org/10.1115/1.3423032

Y. Mi, M.A. Crisfield, G.A.O. Davies, H.B. Hellweg, Progressive delamination using interface elements. J. Compos. Mater. (1998). https://doi.org/10.1177/002199839803201401

R.D. Mindlin, Thickness-shear and flexural vibrations of crystal plates. J. Appl. Phys. **22**, 316 (1951). https://doi.org/10.1063/1.1699948

I. Monetto, Analytical solutions of three-layer beams with interlayer slip and step-wise linear interface law. Compos. Struct. **120**, 543–551 (2015). https://doi.org/10.1016/j.compstruct.2014.09.003

I. Monetto, F. Campi, Numerical analysis of two-layer beams with interlayer slip and step-wise linear interface law. Eng. Struct. **144**, 201–209 (2017). https://doi.org/10.1016/j.engstruct.2017.04.010

H. Murakami, Laminated composite plate theory with improved in-plane responses. J. Appl. Mech. Trans. ASME. **53**(3), 661–666 (1986). https://doi.org/10.1115/1.3171828

E. Oñate, A. Eijo, S. Oller, Simple and accurate two-noded beam element for composite laminated beams using a refined zigzag theory. Comput. Methods Appl. Mech. Eng. **213–216**, 362–382 (2012). https://doi.org/10.1016/j.cma.2011.11.023

N.J. Pagano, Exact solutions for composite laminates in cylindrical bending. J. Compos. Mater. (1969). https://doi.org/10.1177/002199836900300304

M. Pelassa, R. Massabò, Explicit solutions for multi-layered wide plates and beams with perfect and imperfect bonding and delaminations under thermo-mechanical loading. Meccanica **50**, 2497–2524 (2015). https://doi.org/10.1007/s11012-015-0147-7

J.J.C. Remmers, G.N. Wells, R. de Borst, A solid-like shell element allowing for arbitrary delaminations. Int. J. Numer. Methods Eng. **58**, 2013–2040 (2003). https://doi.org/10.1002/nme.907

P. Robinson, T. Besant, D. Hitchings, Delamination growth prediction using a finite element approach. Eur. Struct. Integr. Soc. **27**, 135–147 (2000). https://doi.org/10.1016/S1566-1369(00)80014-X

R. Schmidt, L. Librescu, Geometrically nonlinear theory of laminated anisotropic composite plates featuring interlayer slips. N J Math Game Theory Algebr. **5**, 131–137 (1996)

X. Shu, K.P. Soldatos, An accurate stress analysis model for angle-ply laminates with weakly bonded layers. Acta Mech. **150**(3–4), 161–178 (2001). https://doi.org/10.1007/BF01181809

A. Tessler, Refined zigzag theory for homogeneous, laminated composite, and sandwich beams derived from Reissner's mixed variational principle. Meccanica **50**, 2621–2648 (2015). https://doi.org/10.1007/s11012-015-0222-0

A. Tessler, M. Di Sciuva, M. Gherlone, Refinement of Timoshenko Beam Theory for Composite and Sandwich Beams Using Zigzag Kinematics. Natl. Aeronaut. Sp. Adm. NASA/TP-2007-215086. (2007)

A. Tessler, M. Di Sciuva, M. Gherlone, A refined zigzag beam theory for composite and sandwich beams. J. Compos. Mater. **43**(9), 1051–1081 (2009). https://doi.org/10.1177/0021998308097730

A. Tessler, M. Di Sciuva, M. Gherlone, A consistent refinement of first-order shear deformation theory for laminated composite and sandwich plates using improved zigzag kinematics. J. Mech. Mater. Struct. (2010). https://doi.org/10.2140/jomms.2010.5.341

A. Tessler, M. Di Sciuva, M. Gherlone, A homogeneous limit methodology and refinements of computationally efficient zigzag theory for homogeneous, laminated composite, and sandwich plates, in *Numerical Methods for Partial Differential Equations* (2011), pp. 208–229

A. Turon, P.P. Camanho, J. Costa, J. Renart, Accurate simulation of delamination growth under mixed-mode loading using cohesive elements: Definition of interlaminar strengths and elastic stiffness. Compos. Struct. (2010). https://doi.org/10.1016/j.compstruct.2010.01.012

J.M. Whitney, C.T. Sun, A higher order theory for extensional motion of laminated composites. J. Sound Vib. **30**, 85–97 (1973a). https://doi.org/10.1016/S0022-460X(73)80052-5

J.M. Whitney, C.T. Sun, A higher order theory for extensional motion of laminated composites. J. Sound Vib. (1973b). https://doi.org/10.1016/S0022-460X(73)80052-5

T.O. Williams, F.L. Addessio, A general theory for laminated plates with delaminations. Int. J. Solids Struct. **34**(16), 2003–2024 (1997). https://doi.org/10.1016/s0020-7683(96)00131

P.C. Yang, C.H. Norris, Y. Stavsky, Elastic wave propagation in heterogeneous plates. Int. J. Solids Struct. (1966). https://doi.org/10.1016/0020-7683(66)90045-X

Part V

Rock Damage Mechanics

Numerical Analysis of Damage by Phase-Field Method

26

Z. Yu, J. F. Shao, and Q. Z. Zhu

Contents

Introduction 702
Presentation of a Double-Phase-Field Method 703
Regularized Crack Density Distribution 703
Free Energy of Cracked Materials 704
Initially Isotropic Materials 705
Initially Anisotropic Materials 706
Evolution of Damage Fields 707
Numerical Implementation in Finite Element Method 709
Numerical Assessment 711
Tension Test of a Single-Edge Notched Plate 711
Shear Test of a Single-Edge Notched Plate 713
Analysis of Laboratory Tests 716
Sandstone 716
Jinping Marble 721
Conclusion 722
References 723

Abstract

In this chapter, a phase-field method is discussed for modeling damage and cracking in rock-like materials. Two phase fields are introduced in order to describe both tensile and shear cracks. The evolutions of two phase fields are

Z. Yu
University of Lille, CNRS, EC Lille, LaMcube, Lille, France
e-mail: zhan.yu.etu@univ-lille.Fr

J. F. Shao (✉)
Laboratory of Multiscale and Multiphysics Mechanics, University of Lille, CNRS, EC Lille, LaMcube, Lille, France
e-mail: jian-fu.shao@polytech-lille.fr

Q. Z. Zhu
College of Civil and Transportation Engineering, Hohai University, Nanjing, China
e-mail: qzhu@hhu.edu.cn

© Springer Nature Switzerland AG 2022

G. Z. Voyiadjis (ed.), *Handbook of Damage Mechanics*,
https://doi.org/10.1007/978-3-030-60242-0_57

determined within the thermodynamic framework, and they are coupled with that of the displacement field. The related boundary value problems are solved with the finite element method. The efficiency of the phase-field method is illustrated through numerical examples and comparisons with laboratory tests.

Keywords

Damage · Tensile crack · Shear crack · Phase-field · Rocks · Concrete

Introduction

Failure or fracture of rock-like materials is generally due to the transition from diffuse damage to localized cracking. Based on mathematical representations of damage by scalar and tensorial internal variables, phenomenological models have been first formulated and applied to the analysis of materials and structures. Such models do not provide direct links between microscopic cracks and macroscopic properties. As an alternative approach, different kinds of micro-mechanics-based models have been developed by using either fracture mechanics-based approaches or homogenization techniques. Some advanced models account for coupling between friction and growth of micro-cracks (Zhao et al. 2018). On the other hand, the description of onset and propagation of localized macroscopic cracks has attracted much attention during the last decades and still remain a challenging issue. Remaining in the framework of continuum mechanics, nonlocal damage models have first been proposed for modeling damage localization and post-localization behavior (Pijaudier-Cabot and Bazant 1987). Further, isotropic and anisotrpoic nonlocal damage models were combined with phase-field method (Voyiadjis and Mozaffari 2013; Mozaffari and Voyiadjis 2015). On the other hand, gradient damage models have been developed for fracture modeling of ductile materials and alloys (Mozaffari and Voyiadjis 2016; Bahrami et al. 2019). In the framework of finite element method, enriched finite elements (EFEM) have been introduced to capture the onset of cracks by introducing elementary-enriched shape functions (Oliver 1996). By using global-enriched degrees of freedom, extended finite element methods (XFEM) have been developed and widely used (Moes et al. 1999). However, in these methods, it is not easy to consider the transition from diffuse damage to localized cracking. More recently, phase-field methods have attracted more and more attention to deal with this crucial issue. In the case of brittle materials, inspired by the variational principle for fracture mechanics (Francfort and Marigo 1998) and optimal approximation methods of functionals with jumps (Ambrosio and Tortorelli 1990; Mumford and Shah 1989; Bourdin et al. 2000), the sharp crack morphology is approximated by a regularized field of crack density or damage. Unlike integral nonlocal damage models, the phase field is solved as a boundary value problem. Different kinds of phase-field methods have been proposed in various studies (Miehe et al. 2010a; Borden et al. 2012; Ambati et al. 2015). Recently, the phase-field method has been applied to geological materials incorporating tension-compression asymmetry and extended to anisotropic damage process (You et al. 2020; Wu et al. 2020).

In this chapter, a new phase-field method is presented for modeling the transition from diffuse damage to the onset of localized macroscopic cracks. In most previous studies, only a single phase field is considered and generally driven by tensile strains. However, when rock-like materials are submitted to compressive stresses, both tensile and shear cracks are initiated. Therefore, two phase fields are here introduced to describe this kind of mixed cracking process in rock-like materials.

Presentation of a Double-Phase-Field Method

Regularized Crack Density Distribution

Cracks are here seen as localized damage bands. Therefore, sharp cracks are approximated by regularized crack density fields with the help of auxiliary damage variables. In rock-like materials subjected to compression-dominated stresses, both tensile and shear cracks can initiate and propagate. Tensile cracks are generally induced by tensile stress, while shear cracks are rather related to deviatoric stress. In order to take into account these two kinds of cracks, two phase fields are here introduced. The tensile damage is described by the phase field d^t (**x**) and the shear damage by $d^{sh}(x)$. The schematic presentation of regularized crack density fields is shown in Fig. 1.

It is shown that the solution for each phase field is defined by the following boundary value problem (Miehe et al. 2010a), with $\alpha = t, sh$:

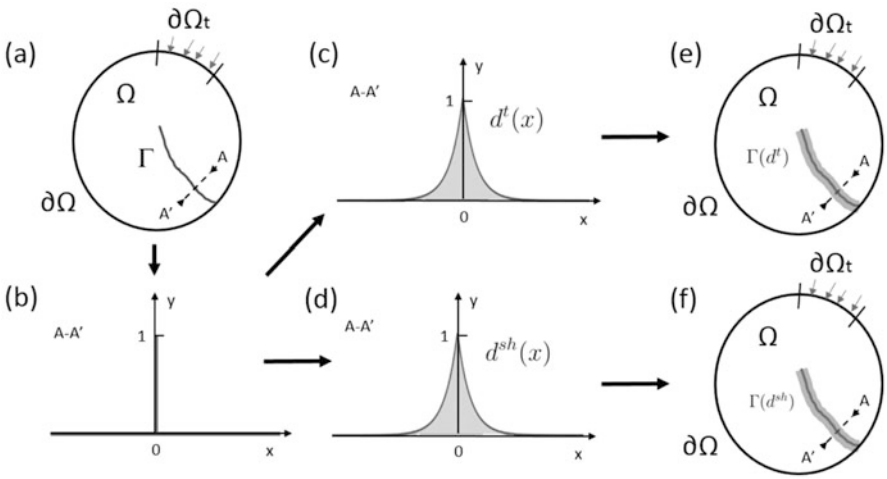

Fig. 1 (**a**) The sharp crack Γ in the solid Ω, (**b**) the sharp crack topology along the 1D line A-A', (**c**) and (**d**) the regularized tensile and shear crack density fields along the 1D line A-A', (**e**) and (**f**) the regularized tensile and shear crack surfaces $\Gamma(d^t)$ and $\Gamma(d^{sh})$

$$\begin{cases} d^{\alpha} - l_d^2 \Delta d^{\alpha} = 0 \quad \text{in } \Omega \\ d^{\alpha}(\mathbf{x}) = 1 \quad \text{on } \Gamma^{\alpha} \\ \nabla d^{\alpha}(\mathbf{x}).\mathbf{n} = 0 \quad \text{on } \partial\Omega \end{cases} \tag{1}$$

where l_d is a length scale parameter controlling the width of regularized cracks. According to Miehe et al. (2010a), the boundary value problem (1) is equivalent to the following variational problem:

$$d^{\alpha}(\mathbf{x}) = Arg\left\{ \inf_{d \in S_{d^{\alpha}}} \Gamma_{l_d}^{\alpha}(d^{\alpha}) \right\} \tag{2}$$

with $S_{d^{\alpha}} = \{d^{\alpha} | d^{\alpha}(\mathbf{x}) = 1 \text{ at } \mathbf{x} \in \Gamma^{\alpha}\}$. $\Gamma_{l_d}^{\alpha}(d^{\alpha})$ denotes the total density (surface) of tensile and shear crack, defined by

$$\Gamma_{l_d}^{\alpha}(d^{\alpha}) = \int_{\Omega} \gamma^{\alpha}(d^{\alpha}, \nabla d^{\alpha}) d\Omega; \alpha = t, sh \tag{3}$$

$\gamma_{\alpha}(d^{\alpha},\nabla d^{\alpha})$ denotes the tensile or shear crack density (surface) per unit volume, defined by

$$\gamma^{\alpha}(d^{\alpha}, \nabla d^{\alpha}) = \frac{1}{2}\left\{ \frac{1}{l_d}(d^{\alpha})^2 + l_d \nabla d^{\alpha}.\nabla d^{\alpha} \right\} \tag{4}$$

Free Energy of Cracked Materials

In the framework of variational approach to fracture mechanics for elastic brittle materials proposed by (Francfort and Marigo 1998), an energy functional was introduced and composed of the elastic strain energy and the energy requested to create the crack. With the regularized damage fields, the energy requested to create the sharp crack is replaced by that for the creation of regularized crack surfaces. Thus, the extended form of the total energy functional is given by

$$\begin{aligned} E\left(\mathbf{u}, d^{t}, d^{sh}\right) &= E_u\left(\mathbf{u}, d^{t}, d^{sh}\right) + E_s\left(d^{t}, d^{sh}\right) \\ E_u\left(\mathbf{u}, d^{t}, d^{sh}\right) &= \int_{\Omega} W_e\left(\varepsilon(\mathbf{u}), d^{t}, d^{sh}\right) d\Omega \\ E_s\left(d^{t}, d^{sh}\right) &= g_c^{t} \int_{\Omega} \gamma^{t}(d^{t}, \nabla d^{t}) d\Omega + g_c^{sh} \int_{\Omega} \gamma^{sh}\left(d^{sh}, \nabla d^{sh}\right) d\Omega \end{aligned} \tag{5}$$

W_e is the elastic strain energy density of cracked material. $\mathbf{u}(\mathbf{x})$ denotes the displacement field. The parameters g_c^{t} and g_c^{sh} are the material toughness, respectively, for the tensile and shear cracks. Note that the total functional E can also be rewritten in the following form:

$$E(\mathbf{u}, d^t, d^{sh}) = \int_{\Omega} W(\mathbf{u}, d^t, d^{sh}) d\Omega \tag{6}$$

with

$$W(\mathbf{u}, d^t, d^{sh}) = W_e(\varepsilon(\mathbf{u}), d^t, d^{sh}) + g_c^t \gamma^t(d^t, \nabla d^t) + g_c^{sh} \gamma^{sh}(d^{sh}, \nabla d^{sh}) \tag{7}$$

$W(\mathbf{u}, d^t, d^{sh})$ can be identified as the equivalent free energy of cracked material.

The elastic properties of materials are affected by the growth of damage fields, while the evolutions of damage fields are controlled by those of stress and strain fields. In order to describe this elastic damage coupling process, appropriate free energy functions should be defined. In this chapter, both isotropic and anisotropic materials are considered.

Initially Isotropic Materials

In order to suitably consider the tensile and shear cracks, the elastic strain energy function of the undamaged material is decomposed into a tensile part and compressive part:

$$W_e^0(\varepsilon) = W_{e+}^0(\varepsilon) + W_{e-}^0(\varepsilon) \tag{8}$$

By introducing the decomposition of strain tensor into a tensile tensor and compressive one, the elastic strain energy can be further written as

$$W_{e\pm}^0(\varepsilon) = \frac{\lambda}{2} \left(\langle Tr(\varepsilon) \rangle_{\pm} \right)^2 + \mu Tr\left\{ \left(\varepsilon^{\pm} \right)^2 \right\} \tag{9}$$

with

$$\varepsilon^{\pm} = \sum_{i=1}^{3} \langle \varepsilon^i \rangle \pm \mathbf{n}^i \bigotimes \mathbf{n}^i \tag{10}$$

λ and μ are Lamé constants of the undamaged material. The operator $\langle x \rangle_{\pm}$ denotes $\langle x \rangle_+ = (x + |x|)/2$) and $\langle x \rangle_- = (x - |x|)/2$).

There are different possibilities to define the degradation of elastic properties of materials by induced damage. Two typical cases are here considered. In the first case (denoted as isotropic model 1), it is assumed that only the tensile part of the elastic strain energy is affected by the induced damage. Thus, the elastic strain energy of cracked material is written as

$$W_e(\varepsilon, d^t, d^{sh}) = h_1(d^t) \frac{\lambda}{2} \left(\langle Tr(\varepsilon) \rangle_{+} \right)^2 + h_3(d^{sh}) \mu Tr\left\{ \left(\varepsilon^{+} \right)^2 \right\} + W_{e-}^0(\varepsilon) \tag{11}$$

Two functions $h_1(d^t)$ and $h_3(d^{sh})$ are introduced to describe the degradation of elastic properties. As an example, the following functions are proposed:

$$\begin{cases} h_1(d^t) = (1 - \beta_1 d^t)^2 \\ h_3(d^{sh}) = (1 - \beta_3 d^{sh})^2 \end{cases} \tag{12}$$

$\beta_1 \leq 1$ and $\beta_3 \leq 1$ are two model's parameters used to control the degradation kinetics of elastic properties. Note that with this choice of elastic energy function, the elastic coefficient λ is affected by the tensile damage, while the shear modulus μ by the shear damage.

In the second case (denoted as isotropic model 2), both parts of the elastic strain energy are assumed to be affected by the induced damage as follows:

$$W_e(\varepsilon, d^t, d^{sh}) = h_1(d^t) W^0_{e+}(\varepsilon) + \frac{\lambda}{2}\left(\langle Tr(\varepsilon)\rangle_-\right)^2 + h_3(d^{sh})\mu Tr\left\{(\varepsilon^-)^2\right\} \tag{13}$$

In this situation, the elastic coefficient λ is still affected by the tensile damage, while the shear modulus μ is deteriorated by both the tensile and shear damages.

Initially Anisotropic Materials

In order to suitably describe the elastic damage coupling in initially anisotropic materials, the elastic strain energy of the undamaged material is decomposed into a spherical part and a deviatoric part as follows (Amor et al. 2009):

$$W^0_e(\varepsilon) = W^0_{sph}(\varepsilon) + W^0_{dev}(\varepsilon) = \frac{1}{2}\varepsilon : \mathbb{C}_{sph} : \varepsilon + \frac{1}{2}\varepsilon : \mathbb{C}_{dev} : \varepsilon \tag{14}$$

The spherical and deviatoric elastic stiffness tensors $\mathbb{C}^0_{sph}$ and $\mathbb{C}^0_{dev}$ are given by

$$\begin{cases} \mathbb{C}_{sph} = k^0_{reuss} 1 \bigotimes 1; \\ \mathbb{C}_{dev} = \mathbb{C}^0 - \mathbb{C}_{sph} \end{cases} \tag{15}$$

$\mathbb{C}^0$ denotes the initial elastic stiffness tensor of undamaged material and k^0_{reuss} is the so-called Reuss bulk modulus.

In order to distinguish the different effects of open and closed cracks on the elastic behavior, the following crack state coefficients $r^{\pm}_e$ are introduced:

$$\begin{cases} \text{if } Tr(\varepsilon) > 0 : r^+ = 1, r^- = 0 \\ \text{if } Tr(\varepsilon) \leq 0 : r^+ = 0, r^- = 1 \end{cases} \tag{16}$$

Three different possibilities are here considered to express the elastic strain energy function of cracked materials with two damage variables d^t and d^{sh}. In case

1 (called anisotropic model 1), the spherical part is affected by the tensile damage, while the deviatoric part by the shear damage. The elastic energy is expressed by

$$W_e\left(\varepsilon, d^t, d^{sh}\right) = \left(h_1(d^t)r^+ + r^-\right)W^0_{sph} + h_3\left(d^{sh}\right)W^0_{dev} \tag{17}$$

According to typical experimental data on rock-like materials, the elastic shear modulus can also be affected by tensile damage. Therefore, in case 2 (called anisotropic model 2), the deviatoric part of energy is simultaneously affected by the tensile and shear damages, while the spherical part by the tensile damage only:

$$W_e\left(\varepsilon, d^t, d^{sh}\right) = \left(h_1(d^t)r^+ + r^-\right)W^0_{sph} + h_2(d^t)h_3\left(d^{sh}\right)W^0_{dev} \tag{18}$$

The additional function $h_2(d^t) = (1 - \beta_2 d^t)^2$ is introduced to define the effect of tensile damage on the deviatoric part of elastic strain energy. In the last case (called anisotropic model 3), the different effects of open and closed cracks on the deviatoric part of strain energy are even distinguished with the help of crack state indicator $r^{\pm}$, and the elastic energy is defined as follows:

$$\begin{aligned} W_e\left(\varepsilon, d^t, d^{sh}\right) = &\left[h_1(d^t)r^+ + r^-\right]W^0_{sph} \\ &+ \left[h_2(d^t)h_3\left(d^{sh}\right)r^+ + h_3\left(d^{sh}\right)r^-\right]W^0_{dev}(\varepsilon) \end{aligned} \tag{19}$$

The different effects of open and closed cracks on the spherical and deviatoric parts of strain energy function are illustrated in Table 1.

Evolution of Damage Fields

With the assumption of isothermal condition, the reduced Clausius-Duhem inequality relative to the evolutions of damage fields is written by

$$\mathcal{A}^\alpha \dot{d}^\alpha \geqslant 0 \tag{20}$$

$\mathcal{A}^\alpha = -\frac{\partial W}{\partial d^\alpha}$ is the thermodynamic force associated with the damage field $d^\alpha (\alpha = t, sh)$. Further, the damage evolution is determined by the threshold function $F^\alpha(\mathcal{A}^\alpha)$ which can be expressed in the following general form:

$$F^\alpha(\mathcal{A}^\alpha) = \mathcal{A}^\alpha \leq 0 \tag{21}$$

Considering that the damage growth is an irreversible process and the damage threshold function verifies the consistency condition such as for $\dot{d}^\alpha > 0$, $\dot{F}^\alpha = 0$. One gets

$$F^\alpha = -\left\{\frac{\partial W_e}{\partial d^\alpha} + g_c^\alpha \delta\gamma^\alpha(d^\alpha)\right\} \leq 0 \tag{22}$$

Table 1 Different effects of open and closed crack on spherical and deviatone parts of strain energy

Spherical/deviatoric	Open/closed	Mode	Degradation
Spherical energy	Open crack		$h_1(d^t)$
	Closed crack		–
Deviatoric energy	Open crack		$h_2(d^t)h_3(d^{sh})$
	Closed crack		$h_3(d^{sh})$

where $\delta\gamma^{\alpha}(d^{\alpha})$ is the variational derivative of the crack density function (Miehe et al. 2010b). By using the expressions of free energy function given above, the damage criteria can be obtained as follows:

$$\begin{cases} -r_e^+ h_1' W_{sph}^0 - r_e^+ h_2' h_3 W_{dev}^0 - g_c^t \left(\dfrac{1}{l_d} d^t - l_d^2 \Delta d^t \right) \leq 0 \\ -h_3' \left(r_e^+ h_2 W_{dev}^0 + r_e^- W_{dev}^0 \right) - g_c^{sh} \left(\dfrac{1}{l_d} d^{sh} - l_d^2 \Delta d^{sh} \right) \leq 0 \end{cases} \tag{23}$$

In order to consider general loading paths with unloading and reloading cycles and considering that the crack growth is an irreversible process, the energy history functionals are introduced in Miehe et al. (2010b). Inspired by that, three energy history functionals are defined as follows:

$$\begin{cases} \mathcal{H}_{sph} = \max \left[r_e^+ W_{sph}^0 \right] \\ \mathcal{H}_{dev}^t = \max \left[h_3 r_e^+ W_{dev}^0 \right] \\ \mathcal{H}_{dev}^{sh} = \max \left[r_e^+ h_2 W_{dev}^0 + r_e^- W_{dev}^0 \right] \end{cases} \tag{24}$$

With these energy history functionals at hand, the evolutions of two damage fields are controlled by the following criteria:

$$\begin{cases} -h_1' \mathcal{H}_{sph} - h_2' \mathcal{H}_{dev}^t - g_c^t \left(\dfrac{1}{l_d} d^t - l_d^2 \Delta d^t \right) = 0 \\ -h_3' \mathcal{H}_{dev}^{sh} - g_c^{sh} \left(\dfrac{1}{l_d} d^{sh} - l_d^2 \Delta d^{sh} \right) = 0 \end{cases} \tag{25}$$

Numerical Implementation in Finite Element Method

The boundary value problems governing the damage and displacement fields are here solved by using the standard framework of finite element method. Two damage fields are considered in the solid body Ω, which is subjected to the body force $\mathbf{f}_b$ in Ω, the surface force $\mathbf{t}_N$ on its external boundary $\partial\Omega_f$, and the prescribed displacement $\overline{\mathbf{u}}$ on its boundary $\partial\Omega_u$, as shown in Fig. 1. The total potential energy can be written as

$$\Pi = E\left(\mathbf{u}, d^t, d^{sh}\right) - \int_\Omega \mathbf{f}_b \cdot \mathbf{u} d\Omega - \int_{\partial\Omega_f} \mathbf{t}_N \cdot \mathbf{u} dA \tag{26}$$

The stationarity condition of the potential energy $\delta\Pi = 0$ leads to three coupled boundary value problems, respectively, for the displacement field, the tensile damage field, and the shear damage field.

The local equilibrium equations for the displacement field are given by

$$\begin{cases} \nabla \cdot \sigma + \mathbf{f}_b = 0 & \text{in } \Omega \\ \sigma \cdot \mathbf{n} = \mathbf{t}_N & \text{on } \partial\Omega_t \end{cases} \tag{27}$$

With the help of shape functions and their derivatives in elements, the discrete weak form for the displacement field for the current loading step can be established as follows:

$$\begin{cases} \mathbf{K}_u \Delta\mathbf{U} = \Delta\mathbf{F} \\ \mathbf{K}_u = \int_\Omega \mathbf{B}_u^T \mathbb{C} \mathbf{B}_u d\Omega \\ \Delta\mathbf{F} = \int_\Omega \mathbf{N}_u^T \Delta\mathbf{f}_b d\Omega + \int_{\partial\Omega_f} \mathbf{N}_u^T \Delta\mathbf{t}_N dA \end{cases} \tag{28}$$

N_u and B_u are, respectively, the matrix of shape functions and their derivatives for the displacement components. $\mathbf{K}_u$ is the global stiffness matrix. $\Delta\mathbf{U}$ and $\Delta\mathbf{F}$, respectively, denote the column matrix of increment nodal displacements and forces. The current elastic stiffness matrix of cracked material is given by

$$\mathbb{C}\left(d^t, d^{sh}\right) = \left[r_e^+ h_1 + r_e^-\right] \mathbb{C}_{sph}^0 + \left[r_e^+ h_2 h_3 + r_e^- h_3\right] \mathbb{C}_{dev}^0 \tag{29}$$

For the tensile damage field, one has the following local equations:

$$\begin{cases} h_1' \mathcal{H}_{\text{sph}} + h_2' \mathcal{H}^t_{\text{dev}} + g_c^t \left(\dfrac{1}{l_d} d^t - l_d^2 \Delta d^t \right) = 0 \quad \text{in } \Omega \\ \dot{d}^t \geq 0 \quad \text{in } \Omega \\ d^t = 1 \quad \text{on } \Gamma^t \\ \nabla d^t \cdot \mathbf{n} = 0 \quad \text{on } \partial\Omega \end{cases} \tag{30}$$

And for the shear damage field, one gets

$$\begin{cases} h_3' \mathcal{H}^{sh}_{dev} + g_c^{sh} \left(\dfrac{1}{l_d} d^{sh} - l_d^2 \Delta d^{sh} \right) = 0 \quad \text{in } \Omega \\ \dot{d}^{sh} \geq 0 \quad \text{in } \Omega \\ d^{sh} = 1 \quad \text{on } \Gamma^{sh} \\ \nabla d^{sh} \cdot \mathbf{n} = 0 \quad \text{on } \partial\Omega \end{cases} \tag{31}$$

Similar to the displacement field, the two damage fields and their gradients inside each element are also approximated by the nodal values by using appropriate shape functions. With such approximations, the weak forms and discrete systems of equations are established for each damage field. Namely, for the tensile damage field, one gets

$$\begin{cases} \mathbf{K}_{d^t} \mathbf{d}^t = \mathbf{F}_{d^t} \\ \mathbf{K}_{d^t} = \int_\Omega \left\{ \left(g_c^t \, l_d + 2\beta_1^2 \mathcal{H}_{sph} + 2\beta_2^2 \mathcal{H}^t_{dev} \right) \mathbf{N}_d^T \mathbf{N}_d + g_c^t l_d \mathbf{B}_d^T \mathbf{B}_d \right\} d\Omega \\ \mathbf{F}_{d^t} = \int_\Omega 2 \left(\beta_1 \mathcal{H}_{sph} + \beta_2 \mathcal{H}^t_{sph} \right) \mathbf{N}_d^T d\Omega \end{cases} \tag{32}$$

and for the shear damage field

$$\begin{cases} \mathbf{K}_{d^{sh}} \mathbf{d}^{sh} = \mathbf{F}_{d^{sh}} \\ \mathbf{K}_{d^{sh}} = \int_\Omega \left\{ g_c^t \, l_d + 2\beta_3^2 \mathcal{H}^{sh}_{dev} \right) \mathbf{N}_d^T \mathbf{N}_d + g_c^t l_d \mathbf{B}_d^T \mathbf{B}_d \} d\Omega \\ \mathbf{F}_{d^{sh}} = \int_\Omega 2\beta_3 \mathcal{H}^{sh}_{dev} \mathbf{N}_d^T d\Omega \end{cases} \tag{33}$$

$\mathbf{N}_d$ and $\mathbf{B}_d$ are the shape functions and their derivatives for the two damage fields.

It is obvious that three fields are coupled. The calculation of displacement field is influenced by the phase fields due to the fact that the elastic stiffness matrix $\mathbb{C}(\mathbf{x})$ is a function of $d^t(\mathbf{x})$ and $d^{sh}(\mathbf{x})$. On the other hand, the evolutions of damage fields are controlled by the energy history functionals which are functions of displacement variations.

Numerical Assessment

In this section, the numerical assessment of the phase-field method is presented through two typical examples. These examples are taken from benchmarks widely investigated in literature: the tension and shearing of a single-edge notched plate. In order to show the specificity of the double-phase-field method, comparisons with three existing phase-field models are presented. In the total energy phase-field model (Miehe et al. 2010b) (called as Miehe model 1), the entire elastic strain energy is used as the driving force of induced damage evolution. In the tensile energy model (Miehe et al. 2010b) (named as Miehe model 2), the elastic energy is decomposed into a tensile and compressive part, and only the tensile part is used for the damage evolution. In the model proposed in Amor et al. (2009) (called as the Amor model), the elastic energy is decomposed into a spherical and deviatoric part as in the present study, but only a single damage field was considered.

Tension Test of a Single-Edge Notched Plate

In this example, a square plate (1×1 imn) is studied. A straight horizontal notch (0.5 imn) is placed at the mid-height of the left edge. The sizes and boundary conditions are shown in Fig. 2a. The top outer surface is subjected to the prescribed displacement $u(t)$.

For the purpose of comparison with the results found in the previous studies (Miehe et al. 2010a; Amor et al. 2009), the same values of parameters are used such as $\lambda = 121.15 kN/mm^2$, $\mu = 80.77 kN/mm^2$, $l_d = 5.0 \times 10^{-3} mm$, and $g_c^t = g_c^{sh} = 2.7 \times 10^{-3} kN/mm$. The finite element mesh is composed of 11,790 elements and 3998 nodes. The prescribed displacement increment is $\Delta u = 1 \times 10^{-5} mm$.

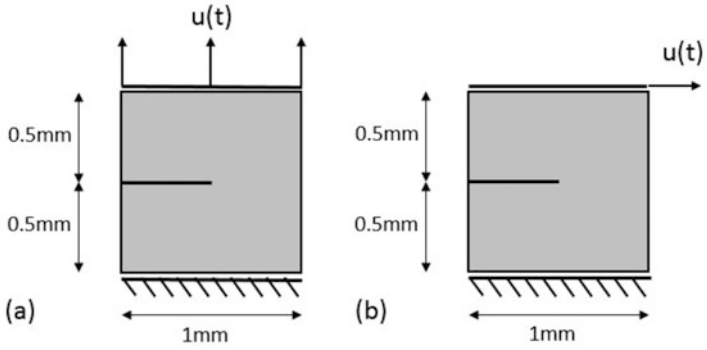

Fig. 2 Geometry and boundary conditions of single-edge notched plate under tension

The distributions of damage and cracking patterns at different levels of prescribed displacement, obtained, respectively, with the three versions of the double-phase-field method (used here for an isotropic material), are, respectively, presented in Figs. 3, 4, and 5. For the three cases, the localized damage bands or cracks are formed along the direction of the initial notch (or crack). As a clear difference, in cases 1 and 3, the tensile damage is dominating with respect to the shear one, while in case 2, the shear damage field is as important as the tensile one.

The comparisons of global force-displacement curves between the Miehe's models, Amor's model and the double field model 3 are given in Fig. 6. It is found

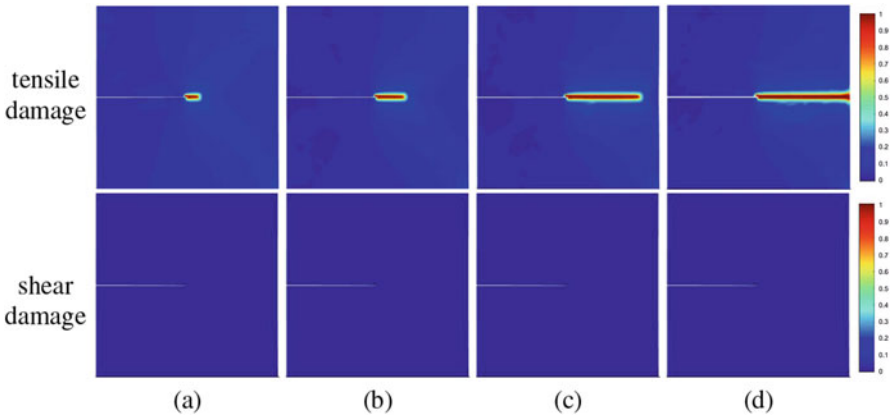

Fig. 3 Tensile and shear damage distribution obtained by double field model 1 for different values of tensile displacement: (**a**) $u = 5.3 \times 10^{-3}\ mm$, (**b**) $u = 5.5 \times 10^{-3}\ mm$, and (**c**) $u = 6 \times 10^{-3}\ mm$; (**d**) $u = 6.2 \times 10^{-3}\ mm$

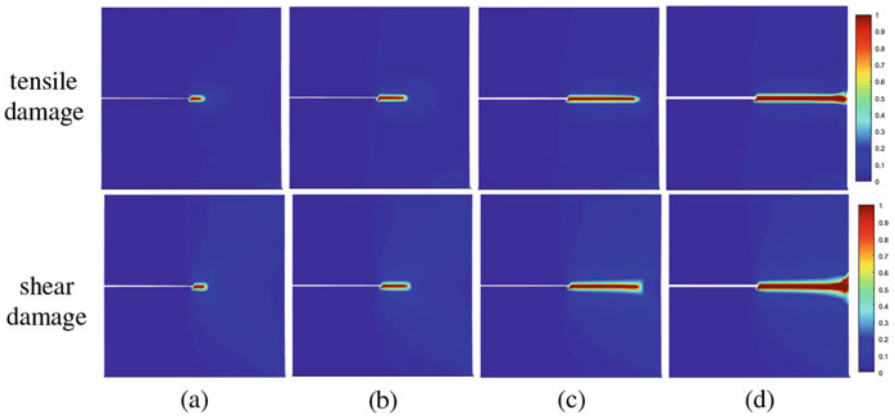

Fig. 4 Tensile and shear damage distribution obtained by double field model 2 for different values of tensile displacement: (**a**) $u = 5.3 \times 10^{-3}\ mm$, (**b**) $u = 5.5 \times 10^{-3}\ mm$, and (**c**) $u = 6 \times 10^{-3}\ mm$; (**d**) $u = 6.2 \times 10^{-3}\ mm$

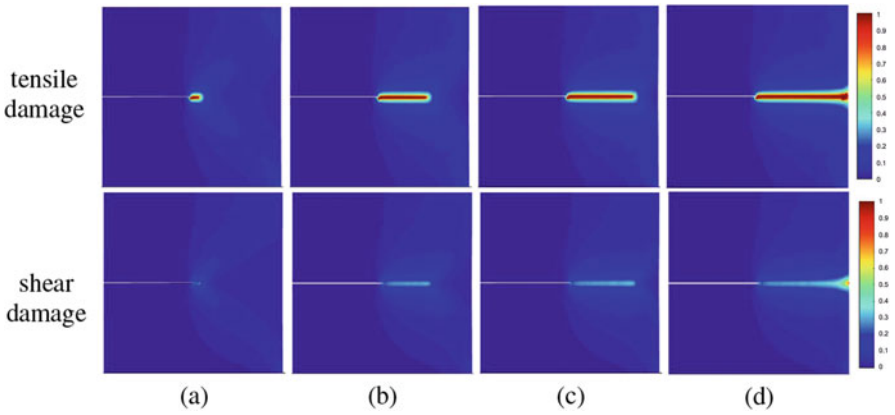

Fig. 5 Tensile and shear damage distribution obtained by double field model 3 for different values of tensile displacement: (**a**) $u = 5.3 \times 10^{-3}\ mm$, (**b**) $u = 5.5 \times 10^{-3}\ mm$, and (**c**) $u = 6 \times 10^{-3}\ mm$; (**d**) $u = 6.2 \times 10^{-3}\ mm$

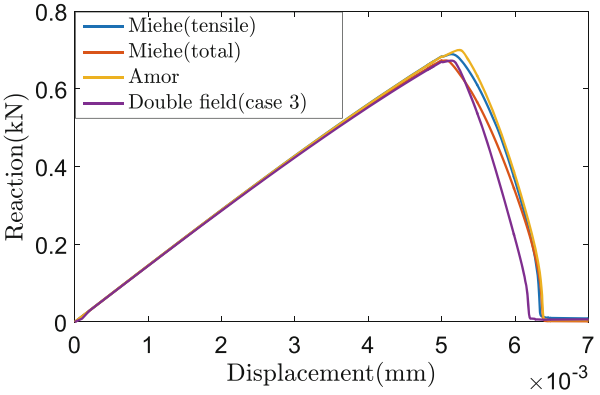

Fig. 6 Comparisons of global force-displacement curves between different models

that the global responses of the plate are quite similar, mainly due to the fact that the damage localization patterns are nearly the same for all the models.

Shear Test of a Single-Edge Notched Plate

The single-edge notched plate is now subjected to shear test. The boundary conditions are presented in Fig. 2b. The mesh contains 22,500 elements and 22,876 nodes. The increment of prescribed displacement is set as $\Delta u = 1 \times 10^{-5}\ mm$.

The damage distributions and localized cracking patterns, respectively, obtained with the three cases of the double-field method, are shown in Figs. 7, 8, and 9. Unlike the results obtained with the isotropic total energy model in Miehe et al. (2010b) showing two symmetrical tensile cracks, only one tensile crack is here obtained, and it propagates toward to the lower-right angle of the plate. It seems that the cracking

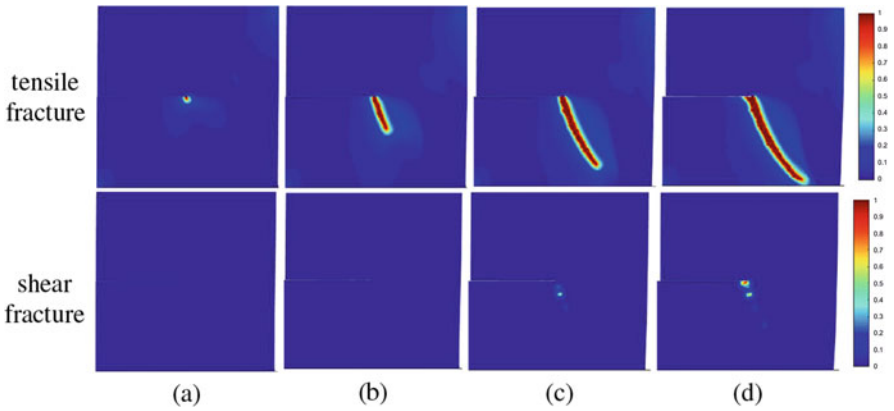

Fig. 7 Tensile and shear damage distributions obtained by the double field model 1 for different values of shear displacement: (**a**) $u = 1 \times 10^{-2}\ mm$. (**b**) $u = 1.5 \times 10^{-2}\ mm$, (**c**) $u = 2 \times 10^{-2}\ mm$, and (**d**) $u = 2.5 \times 10^{-2}\ mm$.

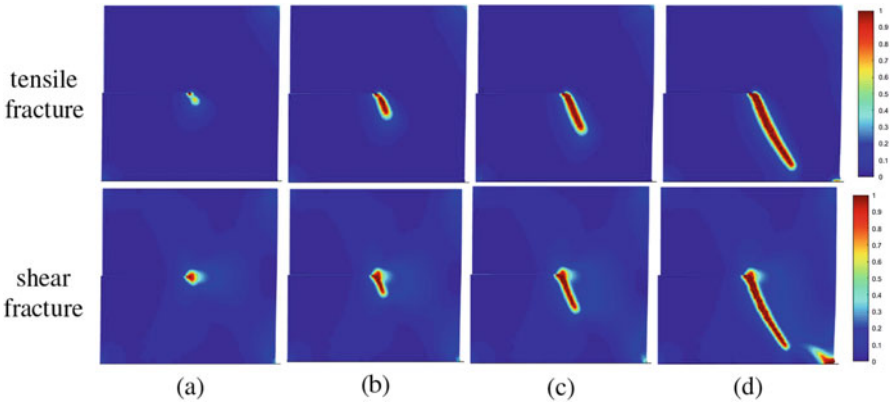

Fig. 8 Tensile and shear damage distributions obtained by double field model 2 for different values of shear displacement: (**a**) $u = 1 \times 10^{-2}\ mm$, (**b**) $u = 1.5 \times 10^{-2}\ mm$, (**c**) $u = 2 \times 10^{-2}\ mm$, and (**d**) $u = 2.5 \times 10^{-2}\ mm$

pattern given by the double-field model is in good agreement with the experimental result reported in Bourdin et al. (2000), reporting that the principal crack is deviated from the initial crack with an angle of $\beta = 61°$.

There are also some significant differences between the three cases of the double-phase-field model. In case 1 (see Fig. 7), the tensile damage growth and localization are the principal process. Indeed, even under the shear loading, important tensile strains are induced in the right-lower zone starting from the end of the initial crack. In case 2 (see Fig. 8), it is seen that there is the growth and localization of both tensile and shear cracks. This is due to the fact that the deviatoric part of elastic energy becomes the driving force of shear damage. In case 3 (see Fig. 9), also both the

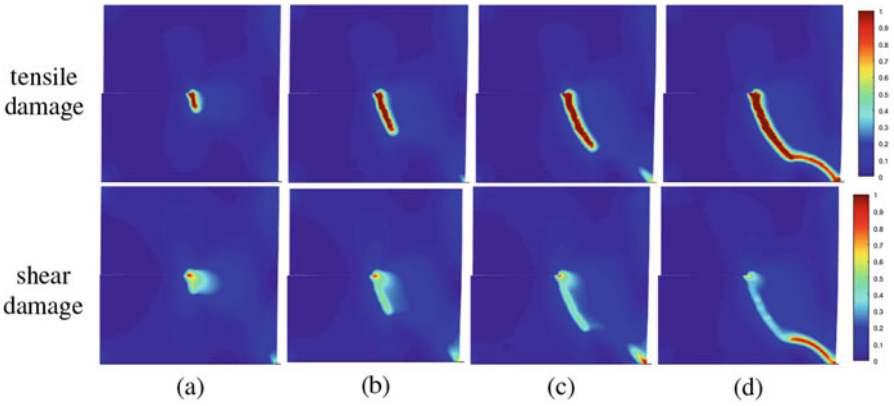

Fig. 9 Tensile and shear damage distributions obtained by double field model 3 for different values of shear displacement: (**a**) $u = 1 \times 10^{-2}\ mm$, (**b**) $u = 1.5 \times 10^{-2}\ mm$, (**c**) $u = 2 \times 10^{-2}\ mm$, and (**d**) $u = 2.5 \times 10^{-2}\ mm$

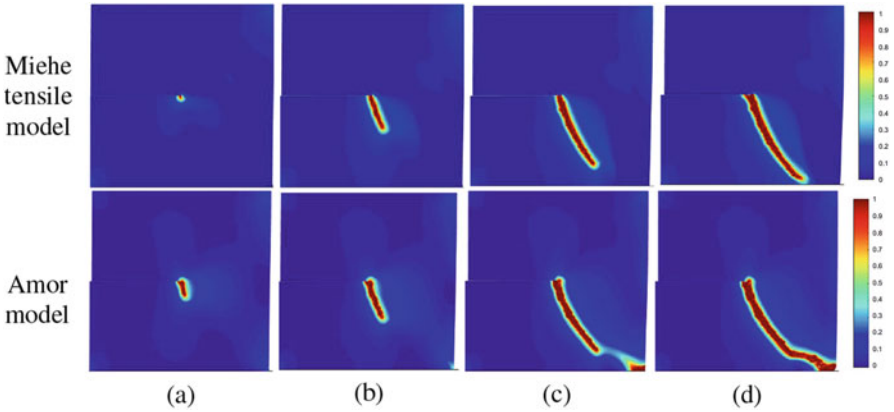

Fig. 10 Damage distributions obtained by the Miehe tensile energy model and Amor model for different values of shear displacement: (**a**) $u = 1 \times 10^{-2}\ mm$, (**b**) $u = 1.5 \times 10^{-2}\ mm$, (**c**) $u = 2 \times 10^{-2}\ mm$, and (**d**) $u = 2.5 \times 10^{-2}\ mm$

tensile and shear damages evolve and localize. Nevertheless, the localization band of tensile damage has a curved shape, appearing more realistic than that of case 2. But it seems that an important edge effect is observed for the localization of shear damage.

The damage distributions and cracking patterns obtained by the Miehe tensile energy model and Amor model are also presented in Fig. 10. The general trends of damage localization obtained by these two models are quite similar to those of the tensile damage evolution provided by the double-field model. It seems that in the Amor model, a second damage localization band appears from the right-lower edge, like cases 2 and 3 of the double-field model. However, it is possible that this is

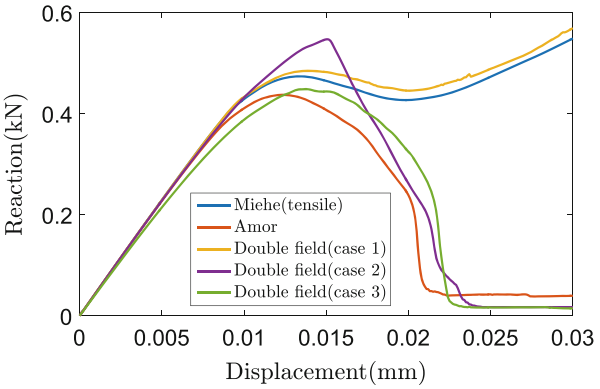

Fig. 11 Comparisons of global force-displacement curves between different models

related to some edge effects due to the small size of plate with respect to the length of initial crack.

In Fig. 11, the global curves of shear displacement versus generated shear force are presented. The curve given by case 1 of double-phase model is quite similar to that by the Miehe p-f model. There is an increase of shear force in the post-peak region. This increase of force is due to the fact there is the recovering (or increase) of some components of the stiffness matrix during the transition from the tensile damage state to the compressive one. This issue is overcome in case 2 of double-phase model. The peak shear force of case 2 is slightly higher than those of the other models, due to the difference of values taken, respectively, for g_c^t and g_c^{sh}. Indeed, in the previous models, only the single value of g_c^t was employed. However, the curve of case 2 has the same trend as that obtained with Amor's model.

Analysis of Laboratory Tests

In this section, the double-field model (case 3) is applied to study the mechanical response of two typical rocks in triaxial compression tests.

Sandstone

Triaxial compression tests were performed on cylindrical sandstone samples. The size of samples is 37 mm in diameter and 74 mm in height. Four different values of confining pressure were used such as 5, 20, 40, and 60 MPa. From the experimental results obtained, it is found that the global elastic modulus varies from 15 to 18 GPa when the confining pressure increases from 5 to 60 MPa. The value of Poisson's ratio is nearly constant and equal to 0.25.

The sandstone is considered as an isotropic elastic material exhibiting damage due to onset and growth of cracks. Each sample is no longer seen as a single material

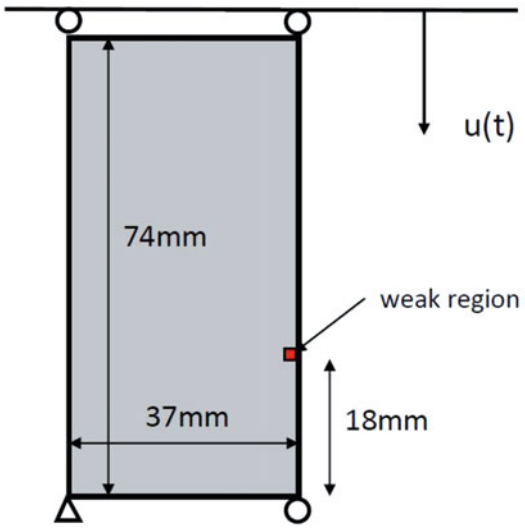

Fig. 12 Size and boundary conditions on sandstone samples in compression tests

point but considered as a small structure subjected to the prescribed radial stress (confining pressure) and axial displacement as shown in Fig. 12. The stress, strain, and damage fields inside the sample are determined by solving the boundary value problems with the double-phase-field method. However, an important simplification is here introduced. Laboratory tests were actually performed under three-dimensional conditions on cylindrical samples. In this study, for the sake of simplicity, only two-dimensional simulations are realized with plane strain conditions. Therefore, the numerical results should be compared with experimental data for the purpose of verifying the capacity of the double-phase-field model in reproducing the progressive cracking process. The mesh contains 20,000 elements and 20,301 nodes. The increment of prescribed axial displacement is $\Delta u = 1 \times 10^{-3}\ mm$. The length scale of damage localization band is taken as $l_d = 0.37\ mm$ which equals to the size of the smallest element.

On the other hand, the crack energy of most rocks generally increases with confining pressure. Therefore, the values of g_c^t and g_c^{sh} are here taken varying from 0.01kN/mm to 0.055kN/mm when the confining pressure increases from 5 to 60 MPa. Further, the onset of damage localization generally occurs in weak zones which are related to material heterogeneities such as mineralogy and porosity. However, for the sake of simplicity and as a first approximation, a weak element is selected in the mesh as shown in Fig. 12. In this weak element, the values of g_c^t and g_c^{sh} are reduced by 1%.

The global stress-strain curves obtained from numerical simulations are presented and compared with experimental data in Fig. 13. A good agreement is obtained for all of four tests. In particular, the dependency of mechanical response on confining pressure is well reproduced. Under a low confining pressure, one observes a sharp material softening in the post-peak regime due to the onset of

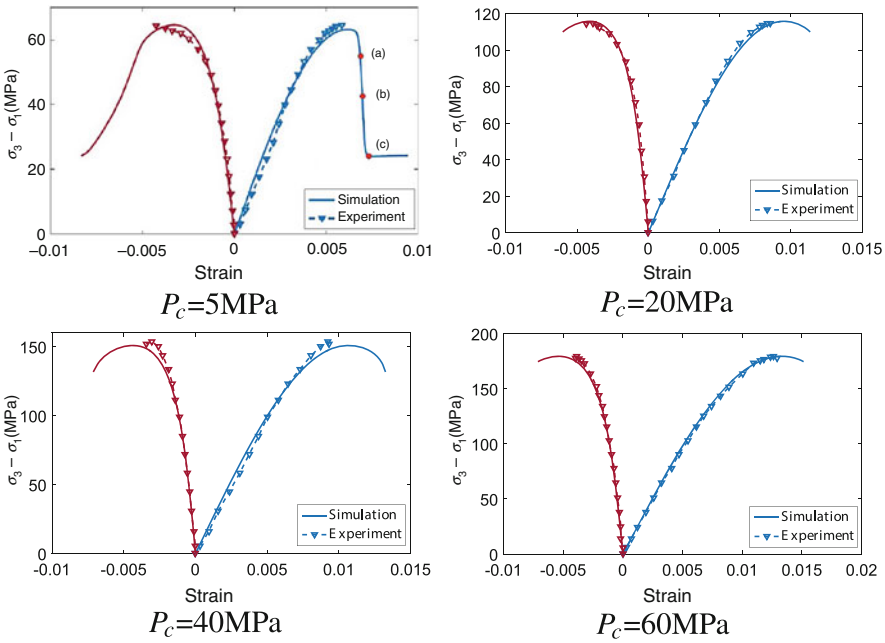

Fig. 13 Axial (blue) and lateral (red) strains versus differential stress in conventional compression tests with different confining pressures P_c = 5, 20, 40, 60 MPa: comparison between numerical results (continuous lines) and experiment data (dotted line)

macroscopic cracks. Under a high confining pressure, the sample failure occurs progressively like in perfect plastic materials. The phase-field model reproduces correctly the transition from brittle to ductile behavior widely observed in rock-like materials.

The distributions of tensile and shear damage as well as their localization patterns are shown in Fig. 14 for the test under 5 MPa confining pressure and for three values of axial displacement. It is found that the shear damage initiates and localizes earlier than the tensile one. The localization of both tensile and shear damages starts from the weak element. Two localized bands (cracks) are observed. The localized shear damage remains much larger than the tensile one during the loading process. Therefore, the shear damage is the principal process in this triaxial compression test.

In Fig. 15, one shows the damage distribution when the weak element is located at the middle point of right side of the sample. The general trends are similar to those obtained in the previous calculation.

It is known that in classical continuum mechanics modeling, the mechanical behavior in the post-localization regime suffers mesh dependency. In order to look at this issue, another calculation is performed by using a coarse mesh with 5000 elements against the fine mesh (20,000 elements) used in the previous calculations.

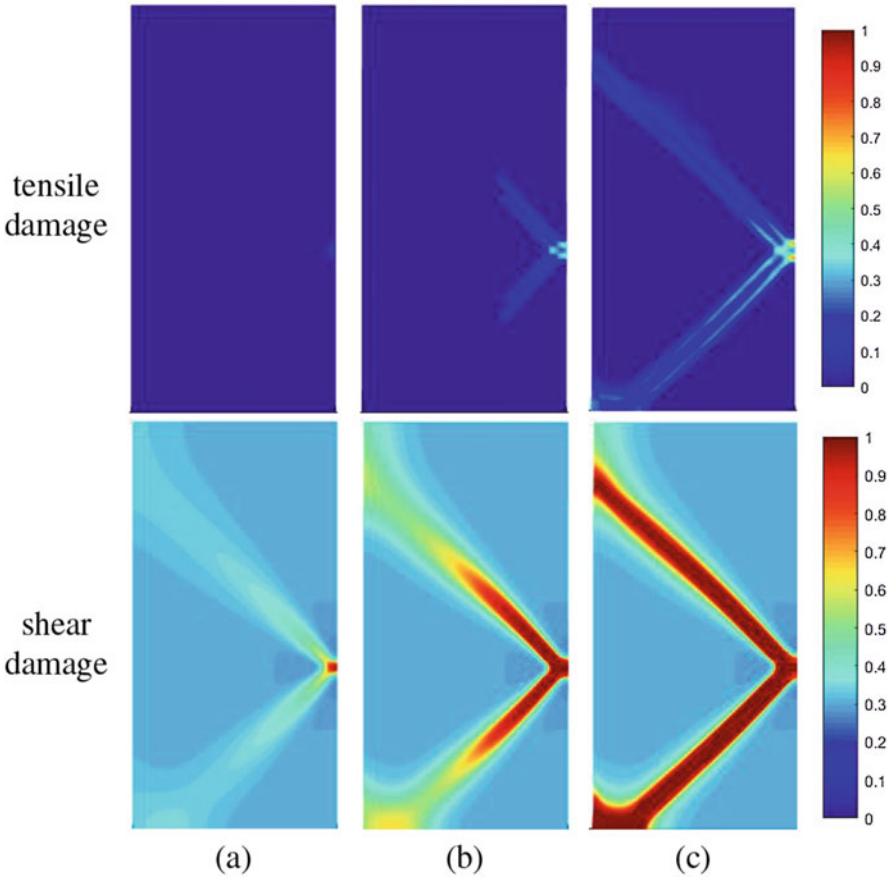

Fig. 14 Distribution and localization of tensile and shear damage inside sandstone sample during triaxial compression test under 5 MPa confining pressure, for different values of axial displacement: (**a**) $u = 0.51$ mm, (**b**) $u = 0.516$ mm, and (**c**) $u = 0.52$ mm

The comparisons between two calculations are presented in Fig. 16. It is found that the difference is quite small. It means that due to the regularization of damage fields in the phase-field method, the mesh dependency is significantly reduced.

Due to the growth and localization of damage, numerical results can also be dependent on load increment size. For this purpose, two comparative calculations are made with large increment sizes of axial displacement Δu than that used in the previous calculations. The comparisons are given in Fig. 17. One can see that the numerical results are indeed dependent on the displacement increment size. However, when the increment becomes small enough, a good stabilization is obtained. For example, the differences between the calculations with $\Delta u = 2 \times 10^{-3}$ mm and $\Delta u = 1 \times 10^{-3}$ mm are very small.

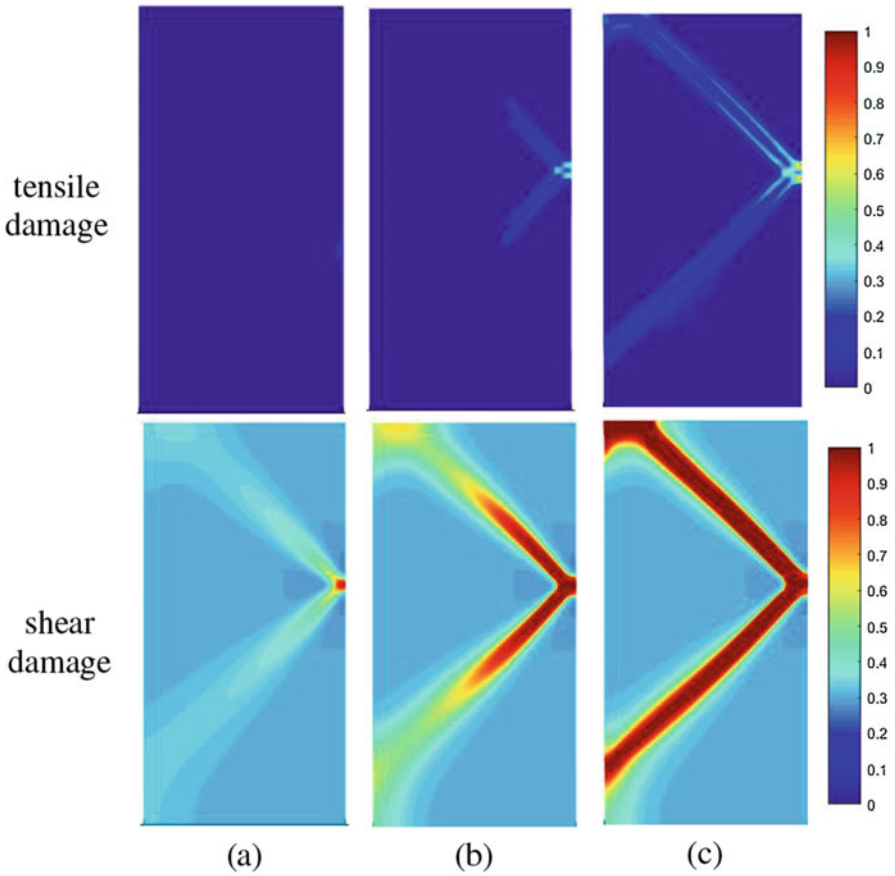

Fig. 15 Distribution and localization of tensile and shear damage inside sandstone sample during triaxial compression test under 5 MPa confining pressure for different values of axial displacement (weak element located at the middle point of right side): (**a**) $u = 0.51\ mm$, (**b**) $u = 0.516\ mm$, and (**c**) $u = 0.52\ mm$

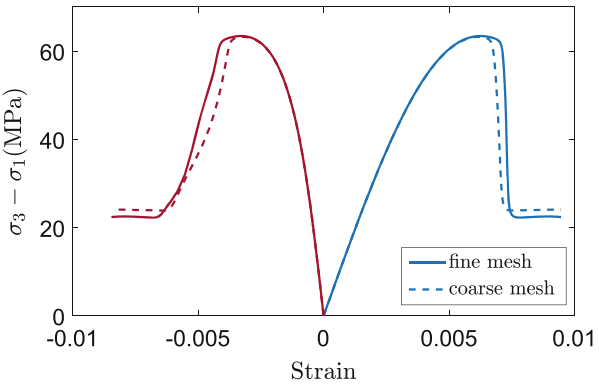

Fig. 16 Axial (blue) and lateral (red) strains versus differential stress in triaxial compression test with 5 MPa confining test: comparison between coarse mesh (dotted line) and fine mesh (continuous lines)

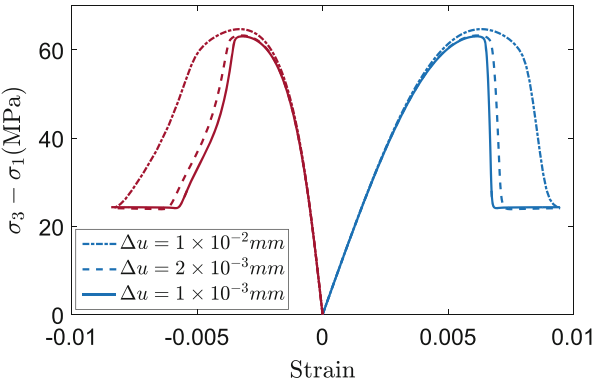

Fig. 17 Axial (blue) and lateral (red) strains versus differential stress in triaxial compression test with 5 MPa confining pressure: comparison between different axial displacement increments: $\Delta u = 1 \times 10^{-2}$ *mm* (dash-dotted line), $\Delta u = 2 \times 10^{-3}$ *mm* (dotted line), and Au $= 1 \times 10^{-3}$ mm (continuous lines)

Jinping Marble

In this example, the mechanical behavior of Jinping marble in triaxial compression tests is studied. Fortunately, stress-strain curves in the post-peak regime were obtained in four tests with confining pressures of $P_c = 4$, 10, 20, *30 MPa* (Liu and Shao 2017). The size of samples is the same as the sandstone (74 mm $\times$ 37 mm; see Fig. 12). The elastic modulus and Poisson's ratio are 30 GPa and 0.15. The same mesh as that for the sandstone is used. The incremental of axial displacement is $\Delta u = 1 \times 10^{-3}$ mm. The length scale of localization band is $l_d = 0.37$ mm.

The global stress-strain curves are presented in Fig. 18. However, it is found that in order to better reproduce the post-peak behavior of this rock, the parameter β_2 of the degradation function of shear damage $h_3(d^{sh})$ should vary with confining pressure. Therefore, its value is taken varying from 0.88 to 0.65 when the confining pressure increases from 4 to 30 MPa. Further, the post-peak response is characterized by two distinct stages. In this first stage, the differential stress drops quickly due to the formation of localized cracks. During the second stage, one obtains a nearly stable residual value of differential stress, which is related to the frictional strength of localized cracks. Further, the drop of differential stress is less pronounced when the confining pressure is higher. Thus, the phase-field model again reproduces the transition from brittle to ductile behavior with the increase of confining pressure.

The distributions of tensile and shear damage fields are presented in Fig. 19 for four values of confining pressure at the end of loading. Like in sandstone, the shear damage is the dominant process, and the sample failure is due to two localized shear damage bands (cracks). Further, one observes that the shear damage field is almost independent on confining pressure, while the tensile damage field is strongly influenced. Under a high confining pressure, the tensile damage even becomes negligible, and only the shear damage evolves.

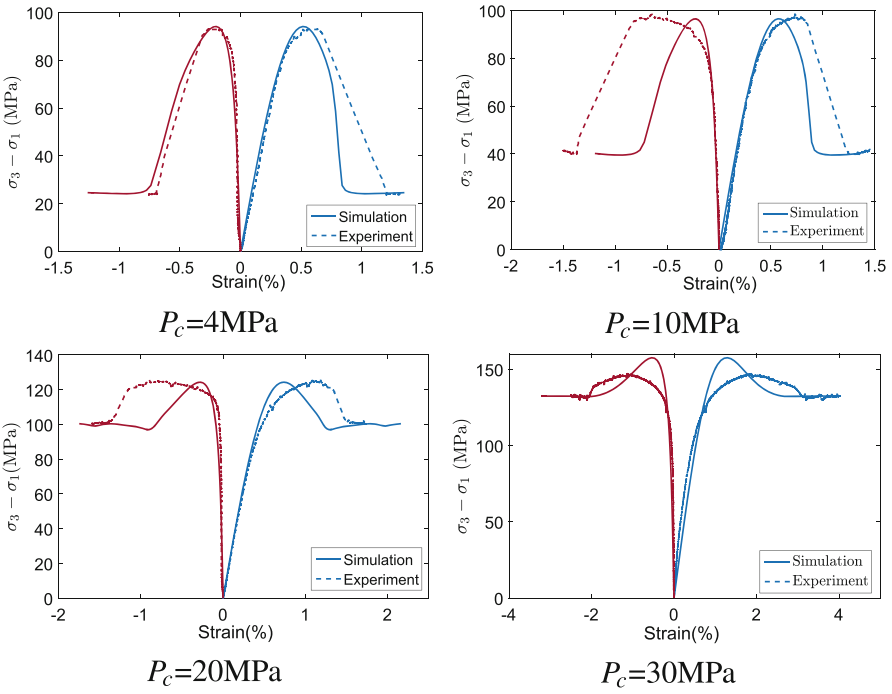

Fig. 18 Axial (blue) and lateral (red) strains versus differential stress in triaxial compression tests with different values of confining pressure $P_c = 4$, 10, 20, 30 MPa: comparison between numerical results (continuous lines) and experiment data (Liu and Shao 2017) (dotted line)

Conclusion

In this chapter, a double-phase-field method is presented for modeling onset and localization of induced damage in rock-like materials. Both tensile and shear damage processes are taken into account. Macroscopic cracks are seen as thin localized damage bands by using a regularized topology. The width of localized bands is controlled by a length scale parameter. As a consequence, the phase-field method is suitable for modeling the transition from diffuse damage to localized cracking with the continuum mechanic framework.

The double-phase-field model is applied to some benchmark examples. Its advantage in capturing separately the tensile and shear damages is highlighted. The model is also used for studying the mechanical behavior of two typical rocks, sandstone and marble, in triaxial compression tests. Both the global stress-strain responses and damage fields as well as their localization patterns are provided and compared with experimental data. It is found that the mechanical behaviors of two rocks in the pre- and post-peak regimes are well reproduced. In particular, the double-phase-field model is able to describe the transition from brittle to ductile behavior with increase of confining pressure.

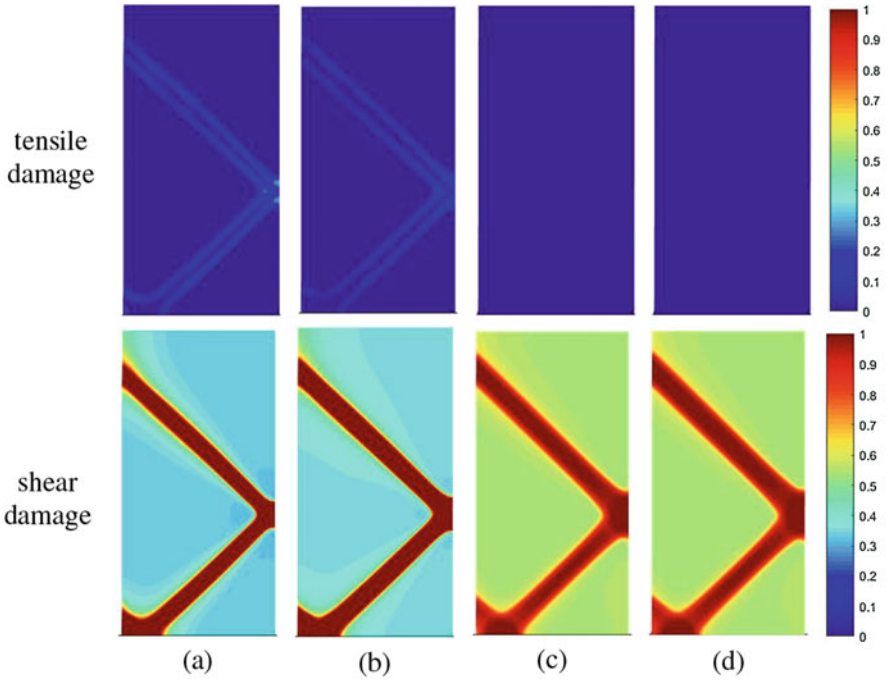

Fig. 19 Tensile and shear damage field and localization in triaxial compression tests on Jinping marble under different values of confining pressure: (**a**) $P_c = 4$ MPa, (**b**) $P_c = 10$ MPa, (**c**) $P_c = 20$ MPa, and (**d**) $P_c = 30$ MPa

The phase-field method can be easily extended to quasi-brittle materials by considering plastic deformation and to thermal hydro-mechanical coupling in porous materials.

References

M. Ambati, T. Gerasimov, L. De-Lorenzis, A review on phase-field models of brittle fracture and a new fast hybrid formulation. Comput. Mech. **55**(2), 383–405 (2015)

L. Ambrosio, V.M. Tortorelli, Approximation of functional depending on jumps by elliptic functional via t-convergence. Commun. Pure Appl. Math. **43**(8), 999–1036 (1990)

H. Amor, J.-J. Marigo, C. Maurini, Regularized formulation of the variational brittle fracture with unilateral contact: Numerical experiments. J. Mech. Phys. Solids **57**(8), 1209–1229 (2009)

H. Bahrami, S.H. Hoseini, G.Z. Voyiadjis, Fracture analysis of shape memory alloys in martensite and austenite phase based on the voids behavior. Mech. Mater. **137** (2019). https://doi.org/10.1016/j.mechmat.2019.103119

M.J. Borden, C.V. Verhoosel, M.A. Scott, T.J.R. Hughes, C.M. Landis, A phase-field description of dynamic brittle fracture. Comput. Methods Appl. Mech. Eng. **217**, 77–95 (2012)

B. Bourdin, G.A. Francfort, J.J. Marigo, Numerical experiments in revisited brittle fracture. J. Mech. Phys. Solids **48**(4), 797–826 (2000)

G.A. Francfort, J.J. Marigo, Revisiting brittle fracture as an energy minimization problem. J. Mech. Phys. Solids **46**(8), 1319–1342 (1998)
Z.B. Liu, J.F. Shao, Strength behavior, creep failure and permeability change of a tight marble under triaxial compression. Rock Mech. Rock. Eng. **50**(3), 529–541 (2017)
C. Miehe, M. Hofacker, F. Welschinger, A phase field model for rate-independent crack propagation: Robust algorithmic implementation based on operator splits. Comput. Methods Appl. Mech. Eng. **199**(45–48), 2765–2778 (2010a)
C. Miehe, F. Welschinger, M. Hofacker, Thermodynamically consistent phase-field models of fracture: Variational principles and multi-field FE implementations. Int. J. Numer. Methods Eng. **83**(10), 1273–1311 (2010b)
N. Moes, J. Dolbow, T. Belytschko, A finite element method for crack growth without remeshing. Int. J. Numer. Methods Eng. **46**, 131–150 (1999)
N. Mozaffari, G.Z. Voyiadjis, Phase field based nonlocal anisotropic damage mechanics model. Physica D **308**, 11–25 (2015)
N. Mozaffari, G.Z. Voyiadjis, The coupled gradient damage-viscoplasticity model for ductile materials: Phase field approach. Int. J. Plast. **83**, 55–73 (2016)
D. Mumford, J. Shah, Optimal approximations by piecewise smooth functions and associated variational problems. Commun. Pure Appl. Math. **42**(5), 577–685 (1989)
J. Oliver, Modelling strong discontinuities in solid mechanics via strain softening constitutive equations, part 1: Fundamentales. Int. J. Numer. Methods Eng. **39**, 3575–3600 (1996)
G. Pijaudier-Cabot, Z.P. Bazant, Nonlocal damage theory. J. Eng. Mech. ASCE **113**, 1512–1533 (1987)
G.Z. Voyiadjis, N. Mozaffari, Nonlocal damage model using the phase field method: Theory and applications. Int. J. Solids Struct. **50**, 3136–3151 (2013)
J.Y. Wu, V.P. Nguyen, H. Zhou, Y. Huang, A variationally consistent phase-field anisotropic damage model for fracture. Comput. Methods Appl. Mech. Eng. **358** (2020). https://doi.org/10.1016/j.cma.2019.112629
T. You, Q.Z. Zhu, P.F. Li, J.F. Shao, Incorporation of tension-compression asymmetry into plastic damage phase-field modeling of quasi brittle geomaterials. Int. J. Plast. **124**, 71–95 (2020)
L.Y. Zhao, Q.Z. Zhu, J.F. Shao, A micromechanics-based plastic damage model for quasi brittle materials under a large range of compressive stress. Int. J. Plast. **100**, 156–176 (2018)

Micromechanics-Based Models for Induced Damage in Rock-Like Materials

27

Q. Z. Zhu, J. F. Shao, and L. Y. Zhao

Contents

Introduction 726
Fundamentals of Upscaling Analyses by Homogenization 727
Description of the Representative Volume Element 727
Principle of the Linear Homogenization Method 728
Comparison in the Case of Randomly Distributed Microcracks 734
Damage-Friction Coupling Under Compression-Dominated Loading 737
Strain Problem Decomposition 737
Auxiliary Problem Decomposition 739
Full Determination of the System Free Energy 740
State Equations 740
Friction Criterion and Plastic Flow 741
Damage Criterion and Damage Evolution 741
Consistency Conditions and Stress–Strain Relation in Rate Form 742
Analytical Solution to the Constitutive Equations 743
Case of Conventional Triaxial Compression 743
Case of Triaxial Proportional Compression 745
Basic Features of the Damage Resistance Function $R(d)$ 745
Illustration of the Model's Predictions 746
Extension to Take into Account Cracking-Induced Material Anisotropies 746
Summary/Conclusions 749
References 749

Q. Z. Zhu (✉) · L. Y. Zhao
College of Civil and Transportation Engineering, Hohai University, Nanjing, China
e-mail: qzhu@hhu.edu.cn

J. F. Shao
Laboratory of Multiscale and Multiphysics Mechanics, University of Lille, CNRS, EC Lille, LaMcube, Lille, France
e-mail: jian-fu.shao@polytech-lille.fr

© Springer Nature Switzerland AG 2022

G. Z. Voyiadjis (ed.), *Handbook of Damage Mechanics*,
https://doi.org/10.1007/978-3-030-60242-0_58

Abstract

Rocks are typical cohesive-frictional heterogeneous geomaterials. The existence and growth of cracks plays a predominant role in their nonlinear mechanical behavior. When rocks are subjected to external loads or suffer unloading process from their initial stress state, there may involve two main dissipation processes: material damage induced by crack growth as well as inelastic deformation caused by frictional sliding along closed cracks. The main difficulty in constitutive modelling is to consider the inherent coupling between these two competing processes. This chapter presents in a unified homogenization-thermodynamics framework some micromechanical formulations for modelling induced damage in rock-like materials. Rocks weakened by microcracks are viewed as a matrix-cracks heterogeneous system where microcracks are considered as inclusions embedded in the matrix phase. The linear homogenization method and problem decomposition technique are applied to derive the effective properties and the system free energy particularly with the Mori-Tanaka scheme. Under the isotropic simplifications for both damage and plastic strains, the damage-friction coupling analyses are performed and the analytical solution to the constitutive equations are achieved under the conventional triaxial compression loading conditions. As an illustration, the analytical stress–strain relations are applied to simulate a typical quasi-brittle rock. In addition, further extension of the present formulation to take into account induced anisotropies and unilateral effects is finally addressed.

Keywords

Damage · Friction · Homogenization · Unilateral effects · Irreversible thermodynamics · Analytical solutions · Quasi-brittle solids

Introduction

Quasi-brittle rocks, no matter in their natural state or undergoing external loads, are susceptible to be weakened by various defects like pores, cracks, dislocations, etc. (Kranz 1983). Constitutive modeling of the degradation of material properties is most popularly performed using continuum damage theory and within the framework of irreversible thermodynamics, the latter providing standard model formulations under thermodynamic constraints. Since the pioneering works of M. Kachanov and then Y. Rabotnov that introduced the concept of damage variable and of the damage-based effective stress, damage mechanics has been continuously developing and is now largely applied to rock-like materials for describing inelastic deformation and material deterioration with strain softening.

In the early stage, continuum damage models were commonly formulated phenomenologically by making use of scalar or tensorial damage variables. The phenomenological approaches provide an efficient tool for modelling progressive failure of geomaterials (Murakami 2012). However, some concepts involved therein such as the effective stress concept and the use of high order variables to describe induced

anisotropy are not physically justified. Up to now, it is still difficult for these models to take some important theoretical issues into account properly, such as induced anisotropy, unilateral effects, volumetric dilatancy, strong coupling between damage and frictional sliding.

Micromechanical approaches have gained a strong impetus owing to the dramatically increasing interest in relating the macroscopic (global) behaviors of material to its microstructure characteristics and local (phase) properties (Mura 1987; Nemat-Nasser and Hori 1998). This chapter summarizes the application of the linear homogenization method to microcracked solids and micromechanics-based constitutive modelling of nonlinear mechanical behavior of quasi-brittle rocks with particular focus on unilateral effects due to crack's closure, damage-friction coupling, failure criterion, and analytical solutions.

Fundamentals of Upscaling Analyses by Homogenization

Description of the Representative Volume Element

Rocks are by nature heterogeneous materials containing diverse microdefects (microcracks, microvoids, etc.). The homogenization method initiated for studying composite materials is thus applicable. For that, an elementary volume which is representative for the material under investigation is mandatory for theoretical derivations. For microcracked rocks, the representative volume element (RVE), geometrically denoted by Ω with external boundary $\partial\Omega$, consists of a solid matrix phase and a large number of randomly oriented and distributed microcracks, the latter embedded in and weakening the former. To proceed mathematical formulations, the following two aspects are generally taken into account:

(i) Geometrically, all microcracks are simplified to be penny-shaped and self-similarly propagating during loading, with the aim to make direct use of the Eshelby's solution to the well-known ellipsoidal inclusion problem for achieving some analytical results. As shown in Fig. 1, one crack family is the set of all microcracks with the same normal $\boldsymbol{n}$, which can be sufficiently described by its mean radius a, half-opening c, and its density in space N (crack number in per unit volume).

The volume fraction of microcracks in a family is given as:

$$\varphi = \frac{4}{3}\pi a^2 cN = \frac{4}{3}\pi\varsigma d \tag{1}$$

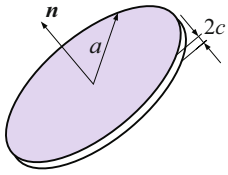

Fig. 1 Illustration of a penny-shaped crack

where $\varsigma = c/a$ denotes the aspect ratio and the dimensionless crack density parameter $d = Na^3$ initially defined by Budiansky and O'Connell (1976) is widely used as internal damage variable in micromechanics-based analyses.

(ii) Mechanically, the matrix phase is most often assumed to be isotropic and linearly elastic with elasticity tensor $\mathbb{C}^0 = 2\mu_0\mathbb{K} + 3k_0\mathbb{J}$ where μ_0 and k_0 are the shear modulus and bulk modulus of the matrix, respectively. By introducing the second-order identity tensor δ_{ij} and the fourth-order identity tensor $I_{ijkl} = (\delta_{ik}\delta_{jl} + \delta_{il}\delta_{jk})/2$, the fourth-order hydrostatic and deviatoric operators $\mathbb{J}$ and $\mathbb{K}$ are given as $J_{ijkl} = \delta_{ij}\delta_{kl}/3$ and $K_{ijkl} = I_{ijkl} - J_{ijkl}$, respectively.

Principle of the Linear Homogenization Method

The homogenization method aims first at determining the effective properties of heterogeneous materials by involving the information on local constitutive equations, material microstructure, as well as its evolution (Nemat-Nasser and Hori 1998). For that, one has to set up some relationships between the local variables such as the strain $\boldsymbol{\varepsilon}(\boldsymbol{x})$ and the stress $\boldsymbol{\sigma}(\boldsymbol{x})$ and their counterparts on macroscopic level $\overline{\boldsymbol{\varepsilon}}$ and $\overline{\boldsymbol{\sigma}}$. We can consider the following two types of uniform boundary conditions (Zaoui 2002; Dormieux et al. 2006).

Strain Boundary Condition

Now consider a macroscopic uniform strain applied onto $\partial\Omega$, which is equivalent to impose the displacement field at $\partial\Omega$ (see Fig. 2):

$$\boldsymbol{u}^0 = \overline{\boldsymbol{\varepsilon}} \cdot \boldsymbol{x}, \quad \forall \boldsymbol{x} \in \partial\Omega \tag{2}$$

Under the assumption of small deformations,

$$\begin{aligned} \int_\Omega \varepsilon_{ij} \mathrm{d}V = \frac{1}{2}\int_\Omega \left(u_{i,j} + u_{j,i}\right)\mathrm{d}V = \frac{1}{2}\int_{\partial\Omega}\left(u_i^0 n_j + u_j^0 n_i\right)\mathrm{d}S \\ = \frac{1}{2}\left(\overline{\varepsilon}_{ik}\int_{\partial\Omega} x_k n_j \mathrm{d}S + \overline{\varepsilon}_{jk}\int_{\partial\Omega} x_k n_i \mathrm{d}S\right) = \frac{V}{2}\left(\overline{\varepsilon}_{ik}\delta_{kj} + \overline{\varepsilon}_{jk}\delta_{ki}\right) = V\overline{\varepsilon}_{ij} \end{aligned} \tag{3}$$

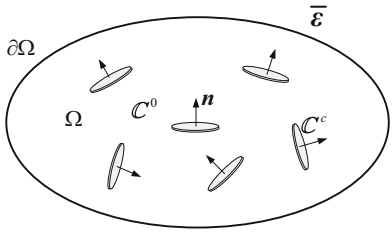

Fig. 2 RVE with strain boundary condition

It follows:

$$\langle \boldsymbol{\varepsilon}(\boldsymbol{x}) \rangle_{\Omega} = \frac{1}{V} \int_{\Omega} \boldsymbol{\varepsilon}(\boldsymbol{x}) \mathrm{d}V = \overline{\boldsymbol{\varepsilon}} \tag{4}$$

where V represents the volume of the RVE; $\langle * \rangle_{\Omega}$ denotes the volume average of the variable*.

Stress Boundary Condition

This type of boundary condition consists in imposing a uniform surface traction $\boldsymbol{t} = \overline{\boldsymbol{\sigma}} \cdot \boldsymbol{m}$ at $\partial\Omega$, where $\boldsymbol{m}$ denotes the outward unit normal vector. When ignoring the body force, it is proved that the average of the local stress $\boldsymbol{\sigma}(\boldsymbol{x})$ over Ω is equal to $\overline{\boldsymbol{\sigma}}$:

$$\langle \boldsymbol{\sigma}(\boldsymbol{x}) \rangle_{\Omega} = \frac{1}{V} \int_{\Omega} \boldsymbol{\sigma}(\boldsymbol{x}) \mathrm{d}V = \overline{\boldsymbol{\sigma}} \tag{5}$$

The proof of Eq. (5) is given below. Without body force, the equilibrating equation in Ω reads:

$$\mathrm{div}\boldsymbol{\sigma}(\boldsymbol{x}) = 0 \tag{6}$$

According to the relation:

$$\frac{\partial x_i}{\partial x_j} = \delta_{ij} \tag{7}$$

the stress tensor σ_{ij} can be reformatted as:

$$\sigma_{ij} = \sigma_{ik}\delta_{jk} = \sigma_{ik}\frac{\partial x_j}{\partial x_k} = \left(\sigma_{ik}x_j\right)_{,k} - \sigma_{ik,k}x_j = \left(\sigma_{ik}x_j\right)_{,k} \tag{8}$$

By applying the Gauss theorem, one obtains:

$$\begin{aligned} \int_{\Omega} \sigma_{ij} \mathrm{d}V &= \int_{\Omega} \left(\sigma_{ik}x_j\right)_{,k} \mathrm{d}V = \int_{\partial\Omega} \overline{\sigma}_{ik}x_j n_k \mathrm{d}S = \overline{\sigma}_{ik} \int_{\partial\Omega} x_j n_k \mathrm{d}S = \overline{\sigma}_{ik} \int_{\Omega} x_{j,k} \mathrm{d}V \\ &= V\overline{\sigma}_{ik}\delta_{jk} = V\overline{\sigma}_{ij} \end{aligned} \tag{9}$$

Strain Localization Tensor and Effective Elasticity Tensor

In the linear homogenization procedure, the mechanical behavior of each phase in the RVE is linearly elastic and obeys to the generalized Hooke law: $\boldsymbol{\sigma}(\boldsymbol{x}) = \mathbb{C}(\boldsymbol{x}) : \boldsymbol{\varepsilon}(\boldsymbol{x})$ with $\mathbb{C}(\boldsymbol{x})$ being the local elasticity tensor of material. The matrix is identified in the RVE as the zeroth material phase whose elasticity tensor is denoted by $\mathbb{C}^0$. The elasticity tensor of the rth phase is $\mathbb{C}^{c,r}$, $r = 1, 2, \ldots, N$. According to the superposition principle, the global (effective) behavior of the heterogeneous system

composed of the matrix and inclusions should also be linearly elastic. The determination in a rational way of the effective properties of the RVE ever constituted one of the central tasks in mechanics of composite materials.

By introducing a fourth-order strain localization tensor $\mathbb{A}(\boldsymbol{x})$, the macroscopic strain $\overline{\boldsymbol{\varepsilon}}$ can be projected to approximate the local strain $\boldsymbol{\varepsilon}(\boldsymbol{x})$:

$$\boldsymbol{\varepsilon}(\boldsymbol{x}) = \mathbb{A}(\boldsymbol{x}) : \overline{\boldsymbol{\varepsilon}} \tag{10}$$

Apply the volume average to both sides of Eq. (10):

$$\langle \boldsymbol{\varepsilon}(\boldsymbol{x}) \rangle_{\Omega} = \langle \mathbb{A}(\boldsymbol{x}) : \overline{\boldsymbol{\varepsilon}} \rangle_{\Omega} = \langle \mathbb{A}(\boldsymbol{x}) \rangle_{\Omega} : \overline{\boldsymbol{\varepsilon}} \tag{11}$$

Recalling that $\langle \boldsymbol{\varepsilon}(\boldsymbol{x}) \rangle_{\Omega} = \overline{\boldsymbol{\varepsilon}}$, the following property on $\mathbb{A}(\boldsymbol{x})$ is achieved:

$$\langle \mathbb{A}(\boldsymbol{x}) \rangle_{\Omega} = \mathbb{I} \tag{12}$$

Now, we perform the volume average of the stress:

$$\overline{\boldsymbol{\sigma}} = \langle \boldsymbol{\sigma}(\boldsymbol{x}) \rangle_{\Omega} = \langle \mathbb{C}(\boldsymbol{x}) : \boldsymbol{\varepsilon}(\boldsymbol{x}) \rangle_{\Omega} = \langle \mathbb{C}(\boldsymbol{x}) : \mathbb{A}(\boldsymbol{x}) \rangle_{\Omega} : \overline{\boldsymbol{\varepsilon}} \tag{13}$$

from which is derived the effective elasticity tensor, $\mathbb{C}^{\text{hom}}$ which relates the macroscopic stress $\overline{\boldsymbol{\sigma}}$ and the macroscopic strain $\overline{\boldsymbol{\varepsilon}}$:

$$\mathbb{C}^{\text{hom}} = \langle \mathbb{C}(\boldsymbol{x}) : \boldsymbol{\varepsilon}(\boldsymbol{x}) \rangle_{\Omega} \tag{14}$$

Further noticing that the volume average of a variable over the RVE can be measured by a weighted summation of the volume average of this variable over each material phase and the weighting coefficient takes the volume fraction of each phase. More explicitly, there exists the operator:

$$\langle * \rangle_{\Omega} = \frac{1}{V} \int_{\Omega} * \, \mathrm{d}V = \sum_{r=0}^{N} \varphi_r \langle * \rangle_{\Omega_r} \tag{15}$$

in which φ_r denotes the volume fraction of the rth material phase in the RVE, $\langle * \rangle_{\Omega_r} = \frac{1}{V} \int_{\Omega_r} * \, \mathrm{d}V$ is the volume average of the variable $*$ over the volume of the rth material phase Ω_r. By applying this rule, the expression of $\mathbb{C}^{\text{hom}}$ is further developed into the form:

$$\mathbb{C}^{\text{hom}} = \mathbb{C}^0 + \sum_{r=1}^{N} \varphi_r \left(\mathbb{C}^{c,r} - \mathbb{C}^0 \right) : \langle \mathbb{A} \rangle_r \tag{16}$$

This is the general formulation for calculating the effective elasticity of heterogeneous materials. Given the microstructure and the mechanical property of each phase, the linear homogenization of elastic problems comes down to the determination of the strain concentration tensor $\mathbb{A}(\boldsymbol{x})$.

Dilute Homogenization Scheme

For the case of dilute distribution of ellipsoidal inclusions, the following form is achieved by making direct use of the Eshelby's solution to the problem of one single inclusion embedded in an infinite body to which macroscopic strain is applied at its remote boundary (Eshelby 1957):

$$\langle \mathbb{A} \rangle_{\text{Esh}} = \left[\mathbb{I} + \mathbb{P}_e : \left(\mathbb{C}^c - \mathbb{C}^0 \right) \right]^{-1} = \left[\mathbb{I} - \mathbb{S}_e : \left(\mathbb{S}^0 : \mathbb{C}^c - \mathbb{I} \right) \right]^{-1} \tag{17}$$

$\mathbb{S}^0 = \left(\mathbb{C}^0 \right)^{-1}$ represents the fourth-order compliance tensor of the matrix. $\mathbb{P}_e$ is the Hill tensor, which only depends on the geometry of inclusions and the elastic constants of the matrix. Accordingly, $\mathbb{S}_e = \mathbb{P}_e : \mathbb{C}^0$ is known as the Eshelby tensor. For inclusions of ellipsoidal form (penny-shaped, spherical, and so on), the analytical expressions of $\mathbb{S}_e$ are available.

For the dilute scheme, no interactions between inclusions are taken into account. The effective elasticity tensor is finally formulated as:

$$\mathbb{C}^{\text{hom}} = \mathbb{C}^0 + \sum_{r=1}^{N} \varphi_r \left(\mathbb{C}^{c,r} - \mathbb{C}^0 \right) : \left[\mathbb{I} - \mathbb{S}_e^r : \left(\mathbb{S}^0 : \mathbb{C}^{c,r} - \mathbb{I} \right) \right]^{-1} \tag{18}$$

In particular, since we are concerned here with microcacking problems, inclusions are penny-shaped microcracks and the elasticity tensor $\mathbb{C}^c = 0$ is taken for the cancellation of any stresses across microcracks. Equation (18) is then simplified as:

$$\mathbb{C}^{\text{hom}} = \mathbb{C}^0 : \left[\mathbb{I} - \frac{4}{3} \pi \sum_{r=1}^{N} d_r \varsigma \left(\mathbb{I} - \mathbb{S}_e^r \right)^{-1} \right] \tag{19}$$

Eshelby Tensor for Penny-Shaped Microcracks

Considering, for example, one family of microcracks with the unit normal $\boldsymbol{n} = \boldsymbol{e}_3$, the nonzero components of $\mathbb{S}_e$ are given below (Nemat-Nasser and Hori 1998):

$$\begin{aligned}
S^e_{1111} &= S^e_{2222} = \frac{13 - 8\nu^0}{32(1-\nu^0)} \pi\varsigma, & S^e_{3333} &= 1 - \frac{1 - 2\nu^0}{4(1-\nu^0)} \pi\varsigma \\
S^e_{1122} &= S^e_{2211} = \frac{8\nu^0 - 1}{32(1-\nu^0)} \pi\varsigma, & S^e_{1133} &= S^e_{2233} = \frac{2\nu^0 - 1}{8(1-\nu^0)} \pi\varsigma \\
S^e_{3311} &= S^e_{3322} = \frac{\nu^0}{1-\nu^0} \left(1 - \frac{4\nu^0 + 1}{8\nu^0} \pi\varsigma \right), & S^e_{1212} &= \frac{7 - 8\nu^0}{32(1-\nu^0)} \pi\varsigma \\
S^e_{1313} &= S^e_{2323} = \frac{1}{2} \left(1 + \frac{\nu^0 - 2}{4(1-\nu^0)} \pi\varsigma \right)
\end{aligned} \tag{20}$$

For penny-shaped microcracks, the aspect ratio is very limited, mathematically denoted by $\varsigma \ll 1$. Further notice that when ς tends to zero, there exists a limit for the

term $\varsigma(\mathbb{I}-\mathbb{S}_e)^{-1}$, denoted by $\mathbb{V}$. Accordingly, the effective elasticity tensor of the matrix-microcracks system becomes:

$$\mathbb{C}^{\text{hom}} = \mathbb{C}^0 : \left(\mathbb{I} - \frac{4}{3}\pi \sum_{r=1}^{N} d_r \mathbb{V}^r\right) \tag{21}$$

or equivalently:

$$\mathbb{C}^{\text{hom}} = \mathbb{C}^0 - \mathbb{C}^0 : \sum_{r=1}^{N} d_r \mathbb{S}^{n,r} : \mathbb{C}^0 \tag{22}$$

where for each crack family,

$$\mathbb{S}^n = \frac{1}{c_n}\mathbb{N} + \frac{1}{c_t}\mathbb{T} \tag{23}$$

The two constants c_n and c_t are only dependent of the elastic constants of the matrix and take the following explicit expressions:

$$c_n = \frac{3E_0}{16\left(1-\nu_0^2\right)}, \qquad c_t = (2-\nu_0)c_n \tag{24}$$

In addition, $\mathbb{N}$ and $\mathbb{T}$ are respectively orientation-dependent fourth-order normal and tangential operators, whose components are given as:

$$N_{ijkl} = n_i n_j n_k n_l \tag{25}$$

$$T_{ijkl} = \frac{1}{2}\left(\delta_{ik}n_j n_l + \delta_{il}n_j n_k + \delta_{jk}n_i n_l + \delta_{jl}n_i n_k - 4n_i n_j n_k n_l\right) \tag{26}$$

There exist the following useful properties for $\mathbb{N}$ and $\mathbb{T}$:

$$\mathbb{N} : \mathbb{N} = \mathbb{N}, \quad \mathbb{T} : \mathbb{T} = \mathbb{T}, \quad \mathbb{N} : \mathbb{T} = \mathbb{T} : \mathbb{N} = 0 \tag{27}$$

Mori-Tanaka Method

In the Mori-Tanaka homogenization method (Mori and Tanaka 1973; Benveniste 1986), each inclusion is embedded in the matrix and in the relevant strain boundary problem, the uniform strain at boundary, denoted by $\boldsymbol{\varepsilon}^0$ is equal to the mean strain in the matrix phase but unknown a priori. In this context, the local strain field is formulated based on the Eshelby's solution

$$\boldsymbol{\varepsilon}(\boldsymbol{x}) = \mathbb{A}_{Esh} : \boldsymbol{\varepsilon}^0 \tag{28}$$

It follows by applying the strain homogenization:

$$\overline{\boldsymbol{\varepsilon}} = \langle \boldsymbol{\varepsilon}(\boldsymbol{x}) \rangle_{\Omega} = \varphi_0 \boldsymbol{\varepsilon}^0 + \sum_{r=1}^{N} \varphi_r \langle \boldsymbol{\varepsilon}(\boldsymbol{x}) \rangle_r \tag{29}$$

By combining Eqs. (28) and (29), one derives the strain concentration tensor:

$$\begin{aligned} \mathbb{A}_{MT} = \mathbb{A}_{Esh} : \left[\varphi_0 \mathbb{I} + \sum_{r=1}^{N} \varphi_r \langle \mathbb{A}_{Esh} \rangle_r \right]^{-1} = (\mathbb{I} - \mathbb{S}_e)^{-1} \\ : \left[\varphi_0 \mathbb{I} + \sum_{r=1}^{N} \varphi_r \left(\mathbb{I} - \mathbb{S}_e^r \right)^{-1} \right]^{-1} \end{aligned} \tag{30}$$

Accordingly, the effective elasticity of the matrix-cracks system:

$$\mathbb{C}^{\text{hom}} = \varphi_0 \mathbb{C}^0 : \left(\varphi_0 \mathbb{I} + \frac{4}{3} \pi \sum_{r=1}^{N} d_r \mathbb{V}^r \right)^{-1} \tag{31}$$

In fact, the volume fraction of microcracks is very limited and the approximation $\varphi_0 \approx 1$ can be made, leading to the following result for penny-shaped microcrack problems:

$$\mathbb{C}^{\text{hom}} = \mathbb{C}^0 : \left(\mathbb{I} + \frac{4}{3} \pi \sum_{r=1}^{N} d_r \mathbb{V}^r \right)^{-1} \tag{32}$$

By inverse of the fourth-order tensor $\mathbb{C}^{\text{hom}}$, the system compliance tensor is obtained:

$$\mathbb{S}^{\text{hom}} = \mathbb{S}^0 + \sum_{r=1}^{N} d_r \mathbb{S}^{n,r} \tag{33}$$

It is interestingly noticed that Eq. (33) is in a linear additional form although the effective stiffness tensor is nonlinear, implying that the influence of a family of microcracks on the system compliance can be taken into account separately.

Ponte-Castaneda-Willis (PCW) Homogenization Scheme

The PCW homogenization method uses two independent fourth-order tensors to account for the shape effect and the spatial distribution of inclusions (Ponte-Castaneda and Willis 1995). The strain concentration tensor is given as:

$$\mathbb{A}_{PCW} = \mathbb{A}_{Esh} : \left[\mathbb{I} + \sum_{r=1}^{N} \varphi_r \mathbb{S}_d^r : \langle \mathbb{A}_{Esh} \rangle_r \right]^{-1} \tag{34}$$

Theoretically, we can apply a tensorial function $\mathbb{S}_d(\boldsymbol{x})$ to describe the distribution of all cracks in a family. But in practice, the simplifying assumption can be made that crack distribution is identical and isotropic for all crack families. In this context, we have:

$$\mathbb{S}_d = \alpha_k \mathbb{J} + \alpha_\mu \mathbb{K}, \quad \alpha_k = \frac{3k_0}{3k_0 + 4\mu_0}, \alpha_\mu = \frac{6(k_0 + 2\mu_0)}{5(3k_0 + 4\mu_0)} \tag{35}$$

The effective elasticity tensor determined by using the PCW homogenization scheme reads:

$$\begin{aligned} \mathbb{C}^{\text{hom}} &= \mathbb{C}^0 - \sum_{r=1}^{N} \varphi_r \mathbb{C}^0 : \left(\mathbb{I} - \mathbb{S}_e^r\right)^{-1} : \left[\mathbb{I} + \sum_{r=1}^{N} \varphi_r \mathbb{S}_d : \left(\mathbb{I} - \mathbb{S}_e^r\right)^{-1}\right] \\ &= \mathbb{C}^0 - \mathbb{C}^0 : \sum_{r=1}^{N} d_r : \mathbb{S}^{n,r} : \mathbb{C}^0 : \left(\mathbb{I} + \mathbb{S}_d : \sum_{r=1}^{N} d_r : \mathbb{S}^{n,r} : \mathbb{C}^0\right) \end{aligned} \tag{36}$$

Comparison in the Case of Randomly Distributed Microcracks

When the matrix contains a large number of randomly distributed and oriented microcracks, the global mechanical properties of the matrix-cracks system is approximately isotropic. In this scenario, the crack density parameter (damage variable) is identical for all crack families. The weakening effect of microcracks can be described by the deterioration of the bulk modulus k_0 and the shear modulus μ_0. The elasticity tensor for damaged isotropic rocks takes the following general form:

$$\mathbb{C}^{\text{hom}} = 2\mu^{\text{hom}}(d)\mathbb{K} + 3k^{\text{hom}}(d)\mathbb{J} \tag{37}$$

in which $\mu^{\text{hom}}(d)$ and $k^{\text{hom}}(d)$ are the homogenized shear modulus and the homogenized bulk modulus in damaged material state. Take the Mori-Tanaka method as an example, under the isotropic assumptions, the damage variable is identical for all crack families. It is thus assumed that $d_1 = d_2 = \ldots = d_N = d_0$. We introduce $d = Nd_0$ as the global damage variable to describe the material damage state. The effective compliance tensor becomes:

$$\mathbb{S}^{\text{hom}} = \mathbb{S}^0 + d\frac{1}{N}\sum_{r=1}^{N} \mathbb{S}^{n,r} \tag{38}$$

It is known that when the number of crack families is very large, the summation $\frac{1}{N}\sum_{r=1}^{N} \mathbb{S}^{n,r}$ can be replaced approximately by an integration over the surface of the unit sphere, such that:

$$\mathbb{S}^{\text{hom}} = \mathbb{S}^0 + d\frac{1}{4\pi}\int_S \mathbb{S}^n \mathrm{d}S = \mathbb{S}^0 + d\frac{1}{4\pi}\int_S \left(\frac{1}{c_n}\mathbb{N} + \frac{1}{c_t}\mathbb{T}\right)\mathrm{d}S \tag{39}$$

By making direct use of the results:

$$\frac{1}{4\pi}\int_S \mathbb{N}\mathrm{d}S = \frac{1}{3}\mathbb{J} + \frac{2}{15}\mathbb{K}, \qquad \frac{1}{4\pi}\int_S \mathbb{T}\mathrm{d}S = \frac{2}{5}\mathbb{K}, \tag{40}$$

we reformulate $\mathbb{S}^{\text{hom}}$ into the form:

$$\mathbb{S}^{\text{hom}} = \mathbb{S}^0 + d\mathbb{S}^d \tag{41}$$

with

$$\mathbb{S}^d = \frac{\beta_1}{2\mu_0}\mathbb{K} + \frac{\beta_2}{3k_0}\mathbb{J}, \ \beta_1 = \frac{32(1-\nu_0)(5-\nu_0)}{45(2-\nu_0)}, \ \beta_2 = \frac{16\left(1-\nu_0^2\right)}{9(1-2\nu_0)} \tag{42}$$

The explicit expressions corresponding respectively to the dilute scheme, the Mori-Tanaka method, and the Ponte-Castaneda and Willis scheme are reported below.

(i) Dilute scheme

$$\frac{k^{\text{hom}}(d)}{k_0} = 1 - \frac{16\left(1-\nu_0^2\right)}{9(1-2\nu_0)}d, \ \frac{\mu^{\text{hom}}(d)}{\mu_0} = 1 - \frac{32(1-\nu_0)(5-\nu_0)}{45(2-\nu_0)}d \tag{43}$$

(ii) Mori-Tanaka method

$$\frac{k_0}{k^{\text{hom}}(d)} = 1 + \frac{16\left(1-\nu_0^2\right)}{9(1-2\nu_0)}d, \ \frac{\mu_0}{\mu^{\text{hom}}(d)} = 1 + \frac{32(1-\nu_0)(5-\nu_0)}{45(2-\nu_0)}d \tag{44}$$

(iii) Ponte-Castaneda and Willis scheme

$$\begin{aligned}\frac{k^{\text{hom}}(d)}{k_0} &= 1 - \frac{16\left(1-\nu_0^2\right)d}{9(1-2\nu_0) + \frac{16}{3}(1+\nu_0)^2 d}, \ \frac{\mu^{\text{hom}}(d)}{\mu_0} \\ &= 1 - \frac{32(1-\nu_0)(5-\nu_0)d}{45(2-\nu_0) + \frac{64}{15}(4-5\nu_0)(5-\nu_0)d}\end{aligned} \tag{45}$$

Figures 3 and 4 present the evolutions of the effective bulk modulus and the shear modulus with the damage variable. It is seen that the weakening effect of micro-cracks on the effective properties is more significant for the dilute homogenization scheme. For k^{hom} and μ^{hom}, the intersections of the curves with the d-axis occurs at

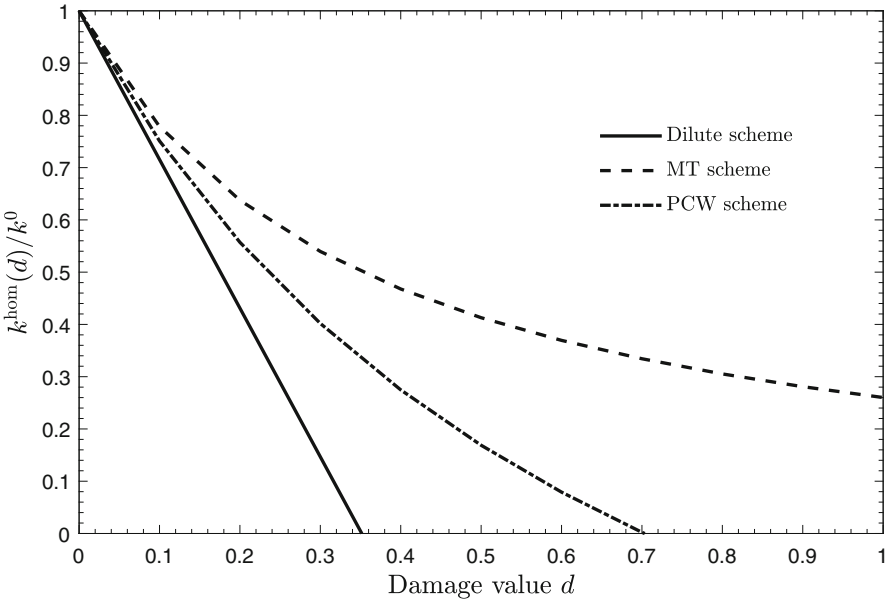

Fig. 3 Evolution of the effective bulk modulus with the damage variable d

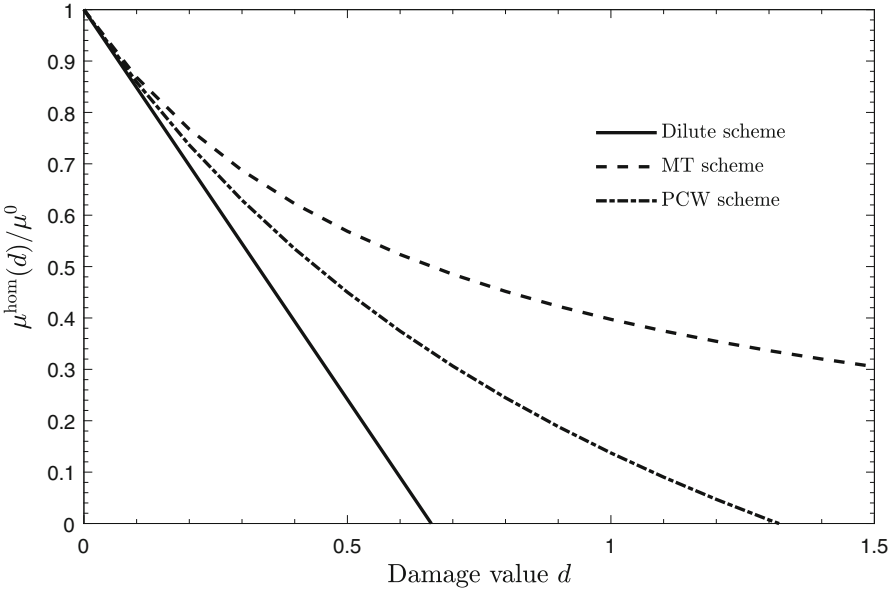

Fig. 4 Evolution of the effective shear modulus with the damage variable d

about $d = 0.35$ and $d = 0.65$, respectively. For the Mori-Tanaka scheme, there are no intersections.

Damage-Friction Coupling Under Compression-Dominated Loading

In the case of open propagating cracks, there exists one single energy dissipation mechanism: material damage by microcracking accompanied with the generation of new crack surfaces. Nevertheless, under compressive stresses, cracks are susceptible to be closed and may suffer frictional sliding when shear stresses are present. In this context, there are two coupling energy dissipation mechanism: damage by crack growth and inelastic deformation induced by frictional sliding along closed rough crack surfaces, the latter being generally modelled as plastic strain in the classical plasticity theory (Zhu et al. 2016).

The total macroscopic strain $\boldsymbol{\varepsilon}$ can be divided into an elastic part $\boldsymbol{\varepsilon}^e$ due to the reversible deformation of the matrix and a plastic part $\boldsymbol{\varepsilon}^p$ caused by frictional sliding between crack surfaces:

$$\boldsymbol{\varepsilon} = \boldsymbol{\varepsilon}^e + \boldsymbol{\varepsilon}^p \tag{46}$$

Because closed cracks can transmit the forces, it is then possible to assume a uniform pre-stress field $\boldsymbol{\sigma}^c(\boldsymbol{x})$ at closed cracks. The stress field in the RVE can thus be described by the following expression:

$$\boldsymbol{\sigma}(\boldsymbol{x}) = \mathbb{C}(\boldsymbol{x}) : \boldsymbol{\varepsilon}(\boldsymbol{x}) + \boldsymbol{\sigma}^c(\boldsymbol{x}) \tag{47}$$

with

$$\begin{cases} \mathbb{C}(\boldsymbol{x}) = \mathbb{C}^0, & \boldsymbol{\sigma}^c = 0; \boldsymbol{x} \in \Omega^0 \\ \mathbb{C}(\boldsymbol{x}) = 0, & \boldsymbol{\sigma}^c \neq 0; \boldsymbol{x} \in \Omega^c \end{cases} \tag{48}$$

Strain Problem Decomposition

In order to determine the strain free energy of the matrix-closed frictional cracks system, we perform the following decomposition according to the boundary strain (Fig. 5).

1. In the elastic subproblem P_e, the elastic strain is applied onto the external boundary of the RVE. The stress-strain relation is given by:

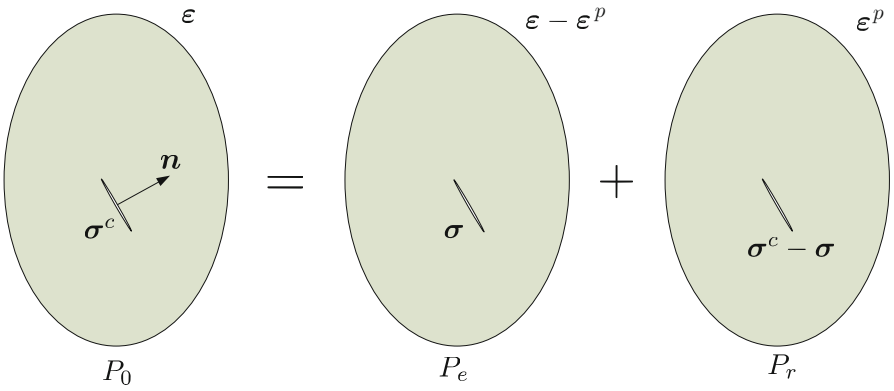

Fig. 5 Decomposition of the strain boundary problem into an elastic part and a residual part

$$\boldsymbol{\sigma} = \mathbb{C}^0 : (\boldsymbol{\varepsilon} - \boldsymbol{\varepsilon}^p) \tag{49}$$

Given the free energy density $w(\boldsymbol{\varepsilon}) = \frac{1}{2}\boldsymbol{\varepsilon}(\boldsymbol{x}) : \mathbb{C}(\boldsymbol{x}) : \boldsymbol{\varepsilon}(\boldsymbol{x})$, the strain free energy in the elastic subproblem is given by:

$$\psi^e = \frac{1}{V}\int_{\Omega_0} w \mathrm{d}V = \frac{1}{2}(\boldsymbol{\varepsilon} - \boldsymbol{\varepsilon}^p) : \mathbb{C}^0 : (\boldsymbol{\varepsilon} - \boldsymbol{\varepsilon}^p) \tag{50}$$

2. The second subproblem P_r is actually a residual strain problem. The residual stress $\boldsymbol{\sigma}^r$ and the residual strain $\boldsymbol{\varepsilon}^r$ satisfy the following conditions:

$$\langle \boldsymbol{\sigma}^r \rangle_\Omega = 0, \ \ \langle \boldsymbol{\varepsilon}^r \rangle_\Omega = \boldsymbol{\varepsilon}^p \tag{51}$$

The free energy ψ^r takes the general form:

$$\psi^e = \frac{1}{V}\int_{\Omega_0} w \mathrm{d}V = \frac{1}{V}\int_{\Omega} \boldsymbol{\varepsilon}^r : \mathbb{C} : \boldsymbol{\varepsilon}^r \mathrm{d}V - \frac{1}{V}\int_{\Omega_c} \boldsymbol{\varepsilon}^r : \mathbb{C} : \boldsymbol{\varepsilon}^r \mathrm{d}V \tag{52}$$

In view that the residual stress field $\boldsymbol{\sigma}^r = \mathbb{C} : \boldsymbol{\varepsilon}^r$ is self-equilibrated, one has according to the Hill theorem:

$$\frac{1}{V}\int_{\Omega} \boldsymbol{\varepsilon}^r : \mathbb{C} : \boldsymbol{\varepsilon}^r \mathrm{d}V = \frac{1}{V}\int_{\Omega} \boldsymbol{\sigma}^r : \boldsymbol{\varepsilon}^r \mathrm{d}V = \langle \boldsymbol{\sigma}^r \rangle_\Omega : \langle \boldsymbol{\varepsilon}^r \rangle_\Omega = 0 \tag{53}$$

For simplicity, further assume that the local stresses at microcracks are uniform. It follows:

$$\frac{1}{V}\int_{\Omega_c} \boldsymbol{\varepsilon}^r : \mathbb{C} : \boldsymbol{\varepsilon}^r \mathrm{d}V = \frac{1}{V}\int_{\Omega_c} \boldsymbol{\sigma}^r : \boldsymbol{\varepsilon}^r \mathrm{d}V = (\boldsymbol{\sigma}^c - \boldsymbol{\sigma}) : \boldsymbol{\varepsilon}^p \tag{54}$$

By following the superposition principle, the total free energy in the initial RVE takes the form:

$$\psi = \psi^e + \psi^r = \frac{1}{2}(\boldsymbol{\varepsilon} - \boldsymbol{\varepsilon}^p) : \mathbb{C}^0 : (\boldsymbol{\varepsilon} - \boldsymbol{\varepsilon}^p) + \frac{1}{2}(\boldsymbol{\sigma} - \boldsymbol{\sigma}^c) : \boldsymbol{\varepsilon}^p \tag{55}$$

Auxiliary Problem Decomposition

In the expression of the system free energy (55), the term $(\boldsymbol{\sigma} - \boldsymbol{\sigma}^c)$ remains to be determined. For that purpose, the auxiliary problem decomposition shown in Fig. 6 is applied.

1. On the boundary is imposed the strain $\left(\boldsymbol{\varepsilon} - \mathbb{S}^0 : \boldsymbol{\sigma}^c\right)$ and the local stresses at microcracks are zero. For the subproblem P_{I}, the deformation due to the existence of microcracks is obtained by applying the linear homogenization procedure:

$$\boldsymbol{\varepsilon}^I = \varphi_c \mathbb{A}^c : \left(\boldsymbol{\varepsilon} - \mathbb{S}^0 : \boldsymbol{\sigma}^c\right) \tag{56}$$

   Under isotropic assumptions, φ_c is the volume fraction of all microcracks and $\mathbb{A}^c$ denotes the global strain concentration tensor. In views of the effective elasticity tensor $\mathbb{C}^{\mathrm{hom}} = \mathbb{C}^0 : (\mathbb{I} - \varphi_c \mathbb{A}^c)$, the macroscopic stress in subproblem I is given by:

$$\boldsymbol{\sigma}^I = \mathbb{C}^{\mathrm{hom}} : \left(\boldsymbol{\varepsilon} - \mathbb{S}^0 : \boldsymbol{\sigma}^c\right) \tag{57}$$

2. In subproblem P_{II}, the strain boundary condition is $\mathbb{S}^0 : \boldsymbol{\sigma}^c$ and the local stress at microcracks is $\boldsymbol{\sigma}^c$. It is thus known that the stress field in the RVE is uniform, that is to say:

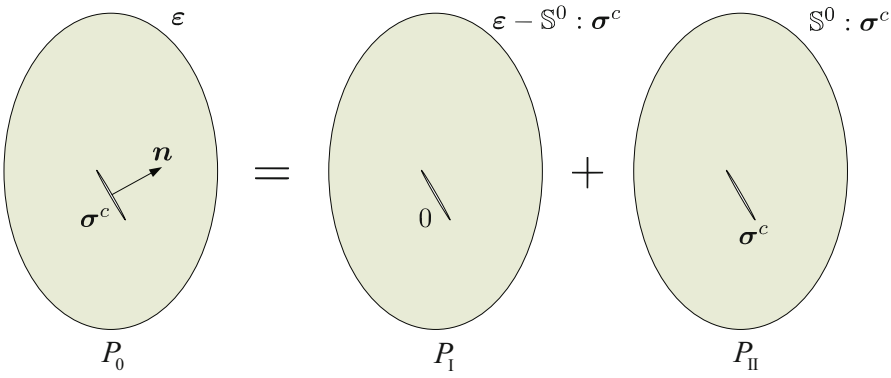

Fig. 6 Auxiliary decomposition of the strain boundary problem according to the local stresses

$$\boldsymbol{\sigma}^{II} = \boldsymbol{\sigma}^{c} \tag{58}$$

Next, one has according to the superposition principle:

$$\boldsymbol{\sigma} = \boldsymbol{\sigma}^{I} + \boldsymbol{\sigma}^{II}, \quad \boldsymbol{\varepsilon}^{p} = \boldsymbol{\varepsilon}^{I} \tag{59}$$

and the macroscopic stress-strain relation:

$$\boldsymbol{\sigma} = \mathbb{C}^{0} : (\boldsymbol{\varepsilon} - \boldsymbol{\varepsilon}^{p}) \tag{60}$$

The following expression is finally achieved:

$$\boldsymbol{\varepsilon}^{p} = \left(\mathbb{S}^{\text{hom}} - \mathbb{S}^{0}\right) : (\boldsymbol{\sigma} - \boldsymbol{\sigma}^{c}) \tag{61}$$

Full Determination of the System Free Energy

Combination of Eqs. (55) and (61) leads to the final determination of the system strain free energy:

$$\psi = \frac{1}{2}(\boldsymbol{\varepsilon} - \boldsymbol{\varepsilon}^{p}) : \mathbb{C}^{0} : (\boldsymbol{\varepsilon} - \boldsymbol{\varepsilon}^{p}) + \frac{1}{2}\boldsymbol{\varepsilon}^{p} : \left(\mathbb{S}^{\text{hom}} - \mathbb{S}^{0}\right)^{-1} : \boldsymbol{\varepsilon}^{p} \tag{62}$$

As for the Mori-Tanaka method, one has the effective compliance tensor $\mathbb{S}^{\text{hom}} = \mathbb{S}^{0} + d\mathbb{S}^{d}$, the free energy (62) is further cast into the form:

$$\psi = \frac{1}{2}(\boldsymbol{\varepsilon} - \boldsymbol{\varepsilon}^{p}) : \mathbb{C}^{0} : (\boldsymbol{\varepsilon} - \boldsymbol{\varepsilon}^{p}) + \frac{1}{2}\boldsymbol{\varepsilon}^{p} : \mathbb{C}^{p} : \boldsymbol{\varepsilon}^{p} \tag{63}$$

with

$$\mathbb{C}^{p} = \frac{1}{d}\mathbb{C}^{d}, \quad \mathbb{C}^{d} = \left(\mathbb{S}^{d}\right)^{-1} \tag{64}$$

State Equations

Within the framework of irreversible thermodynamics in terms of internal variables, the thermodynamic forces associated with the internal variables can be derived by differentiation of the system free energy with respect to the internal variables. In the constitutive formulations concerning simultaneously crack growth and inelastic deformation caused by frictional sliding, there involve in the system two internal variables: damage d and plastic strain $\boldsymbol{\varepsilon}^{p}$.

The macroscopic stress–strain relationship is derived as:

$$\boldsymbol{\sigma} = \frac{\partial \psi}{\partial \boldsymbol{\varepsilon}} = \mathbb{C}^{0} : (\boldsymbol{\varepsilon} - \boldsymbol{\varepsilon}^{p}) \tag{65}$$

The thermodynamic forces associated respectively with damage and plastic strain are given as:

$$F_d = -\frac{\partial \psi}{\partial d} = \frac{1}{2d^2}\boldsymbol{\varepsilon}^p : \mathbb{C}^d : \boldsymbol{\varepsilon}^p \tag{66}$$

$$\boldsymbol{\sigma}^p = -\frac{\partial \psi}{\partial \boldsymbol{\varepsilon}^p} = \boldsymbol{\sigma} - \mathbb{C}^p : \boldsymbol{\varepsilon}^p = \boldsymbol{\sigma} - \frac{1}{d}\mathbb{C}^d : \boldsymbol{\varepsilon}^p \tag{67}$$

It is shown by comparing Eqs. (67) and (61) that the $\boldsymbol{\varepsilon}^p$-conjugated thermodynamic force is actually the local stresses acting onto cracks. In other words, it should be the local stress $\boldsymbol{\sigma}^p$ ($\boldsymbol{\sigma}^c$) but not the macroscopic stress $\boldsymbol{\sigma}$ that controls friction-induced plastic flow. In addition, the back-stress term $\mathbb{C}^p : \boldsymbol{\varepsilon}^p$ in the local stress $\boldsymbol{\sigma}^p$ can play an important role of unified hardening-softening of material, as will be demonstrated in latter parts.

Friction Criterion and Plastic Flow

We adopt here the generalized Coulomb-type friction criterion which is formulated in terms of the local stress tensor $\boldsymbol{\sigma}^p$ in lieu of the commonly used macroscopic stress tensor $\boldsymbol{\sigma}$:

$$f(\boldsymbol{\sigma}^p) = \|\boldsymbol{s}^p\| + \eta p^p \leq 0 \tag{68}$$

where $\boldsymbol{s}^p = \mathbb{K} : \boldsymbol{\sigma}^p$ is the deviatoric part of $\boldsymbol{\sigma}^p$ and $p^p = \boldsymbol{\delta} : \boldsymbol{\sigma}^p/3$.

By following the associated flow rule and the normality rule, the evolution rate of plastic strain is formulated as:

$$\dot{\boldsymbol{\varepsilon}}^p = \lambda^p \boldsymbol{D} \tag{69}$$

λ^p denotes the plasticity multiplier; the second-order tensor $\boldsymbol{D}$ defines the plastic flow direction:

$$\boldsymbol{D} = \frac{\partial f}{\partial \boldsymbol{\sigma}^p} = \frac{\boldsymbol{s}^p}{\|\boldsymbol{s}^p\|} + \frac{1}{3}\eta\boldsymbol{\delta} \tag{70}$$

The friction criterion (68) is then cast into the form:

$$f(\boldsymbol{\sigma}^p) = \boldsymbol{\sigma}^p : \boldsymbol{D} \leq 0 \tag{71}$$

Damage Criterion and Damage Evolution

Based on the results in fracture mechanics, the strain energy release rate-based damage criterion is applied to describe the damage evolution:

$$g(F_d, d) = F_d - R(d) \leq 0 \tag{72}$$

where $R(d)$ represents the resistance to further damage evolution. According to the normality rule, the damage evolution law is described by:

$$\dot{d} = \lambda^d \frac{\partial g}{\partial F_d} = \lambda^d \tag{73}$$

Here, λ^d is the damage multiplier.

Consistency Conditions and Stress–Strain Relation in Rate Form

When material suffers continuous loads and the friction condition is satisfied, plastic flow and damage evolution take place. The stress state is always located on the yield surface $f(\boldsymbol{\sigma}, \boldsymbol{\varepsilon}^p, d) = 0$, leading to the consistency condition $\dot{f} = 0$, whose development reads:

$$\dot{f} = \frac{\partial f}{\partial \boldsymbol{\varepsilon}} : \dot{\boldsymbol{\varepsilon}} + \frac{\partial f}{\partial \boldsymbol{\varepsilon}^p} : \dot{\boldsymbol{\varepsilon}}^p + \frac{\partial f}{\partial d}\dot{d} = 0 \tag{74}$$

In the same way, for the damage evolution, we derive from the damage consistency condition:

$$\dot{g} = \frac{\partial g}{\partial \boldsymbol{\varepsilon}^p} : \dot{\boldsymbol{\varepsilon}}^p + \frac{\partial g}{\partial d}\dot{d} = 0 \tag{75}$$

with

$$\begin{cases} \dfrac{\partial f}{\partial \boldsymbol{\varepsilon}} = \boldsymbol{D} : \mathbb{C}^0 \\ \dfrac{\partial f}{\partial \boldsymbol{\varepsilon}^p} = -\left(\mathbb{C}^0 + \mathbb{C}^p\right) : \boldsymbol{D} \\ \dfrac{\partial f}{\partial d} = \dfrac{1}{d^2}\boldsymbol{D} : \mathbb{C}^d : \boldsymbol{\varepsilon}^p \\ \dfrac{\partial g}{\partial \boldsymbol{\varepsilon}^p} = \dfrac{1}{d^2}\mathbb{C}^d : \boldsymbol{\varepsilon}^p \\ \dfrac{\partial g}{\partial d} = -\dfrac{1}{d^3}\boldsymbol{\varepsilon}^p : \mathbb{C}^d : \boldsymbol{\varepsilon}^p - \dfrac{\partial R(d)}{\partial d} \end{cases} \tag{76}$$

Substitution of the relations $\dot{\boldsymbol{\varepsilon}}^p = \lambda^p \boldsymbol{D}$ and $\dot{d} = \lambda^d$ into Eqs. (74) and (75) allows the determination of the plastic and damage multipliers:

$$\begin{cases} \lambda^p = \dfrac{1}{H^p}\dfrac{\partial f}{\partial \boldsymbol{\varepsilon}} : \dot{\boldsymbol{\varepsilon}} \\ \lambda^d = -\dfrac{\dfrac{\partial g}{\partial \boldsymbol{\varepsilon}^p} : \boldsymbol{D}}{\dfrac{\partial g}{\partial d}H^p}\dfrac{\partial f}{\partial \boldsymbol{\varepsilon}} : \dot{\boldsymbol{\varepsilon}} \end{cases} \tag{77}$$

We now proceed to derive the rate form of the stress–strain relation.

$$\dot{\boldsymbol{\sigma}} = \mathbb{C}^0 : (\dot{\boldsymbol{\varepsilon}} - \dot{\boldsymbol{\varepsilon}}^p) = \mathbb{C}^0 : \dot{\boldsymbol{\varepsilon}} - \frac{1}{H^p} \frac{\partial f}{\partial \boldsymbol{\sigma}} \otimes \frac{\partial f}{\partial \boldsymbol{\sigma}} : \dot{\boldsymbol{\varepsilon}} \tag{78}$$

where the hardening modulus H^p takes the expression:

$$H_p = \frac{\left(\frac{\partial f}{\partial d}\right)^2}{\frac{\partial g}{\partial d}} - \frac{\partial f}{\partial \boldsymbol{\varepsilon}^p} : \boldsymbol{D} \tag{79}$$

Equation (78) is rewritten in the form:

$$\dot{\boldsymbol{\sigma}} = \mathbb{C}^{\tan} : \dot{\boldsymbol{\varepsilon}} \tag{80}$$

with the tangential stiffness tensor $\mathbb{C}^{\tan} = \mathbb{C}^0 - \frac{1}{H^p} \frac{\partial f}{\partial \boldsymbol{\varepsilon}} \otimes \frac{\partial f}{\partial \boldsymbol{\varepsilon}}$.

Analytical Solution to the Constitutive Equations

Case of Conventional Triaxial Compression

It is assumed that the rational axis is along the stress component σ_1, implying that the stress state for the conventional triaxial compression (CTC) tests is $[\sigma_1 \ \ \sigma_3 \ \ \sigma_3]^{\text{diag}}$ with the algebra sequence $\sigma_1 < \sigma_3$ and the deviatoric part of $\boldsymbol{\sigma}$ is given as:

$$\boldsymbol{s} = \frac{\sigma_1 - \sigma_3}{3} [\, 2 \quad -1 \quad -1 \,]^{\text{diag}} \tag{81}$$

Recall that the plastic flow direction defined by the gradient $\boldsymbol{D} = \frac{\partial f}{\partial \boldsymbol{\sigma}^p} = \frac{\boldsymbol{s}^p}{\|\boldsymbol{s}^p\|} + \frac{1}{3}\eta\boldsymbol{\delta}$. For initially elastic rocks, the tangential direction $\frac{\boldsymbol{s}^p}{\|\boldsymbol{s}^p\|} = -\frac{1}{\sqrt{6}} [\, 2 \quad -1 \quad -1 \,]^{\text{diag}}$ is unchanged during the whole loading process. In addition, for simplicity, assume that the generalized friction coefficient η is a constant. In this way, the second-order tensor is explicated as:

$$\boldsymbol{D} = \left[-\frac{2}{\sqrt{6}} + \frac{1}{3}\eta, \quad \frac{1}{\sqrt{6}} + \frac{1}{3}\eta \quad \frac{1}{\sqrt{6}} + \frac{1}{3}\eta \right]^{\text{diag}} \tag{82}$$

which is constant during conventional triaxial compression. Therefore, the current value of plastic strain can be determined in terms of the cumulated plastic multiplier, that is:

$$\boldsymbol{\varepsilon}^p = \Lambda^p \boldsymbol{D}, \quad \Lambda^p = \int_{\boldsymbol{\varepsilon}} \lambda^p \tag{83}$$

By defining the constant:

$$\chi = \boldsymbol{D} : \mathbb{C}^d : \boldsymbol{D} = \frac{k_0\eta^2}{\beta_1} + \frac{2\mu_0}{\beta_2} \tag{84}$$

The plastic yield function is reformulated in the form:

$$f = \|\boldsymbol{s}\| + \eta p - \frac{\Lambda^p}{d}\chi = 0 \tag{85}$$

And accordingly, the damage criterion is rewritten as:

$$g = \frac{1}{2}\left(\frac{\Lambda^p}{d}\right)\chi - R(d) = 0 \tag{86}$$

from which is derived the relation:

$$\frac{\Lambda^p}{d} = \sqrt{\frac{2R(d)}{\chi}} \tag{87}$$

Its insertion into Eq. (85) yields:

$$f = \|\boldsymbol{s}\| + \eta p - \sqrt{2R(d)\chi} = 0 \tag{88}$$

In view that $\|\boldsymbol{s}\| = \sqrt{\frac{2}{3}}(\sigma_3 - \sigma_1)$ and $p = \frac{1}{3}(\sigma_1 + 2\sigma_3)$, Eq. (88) is reformulated in the form:

$$\sigma_1 = \frac{\sqrt{6} + 2\eta}{\sqrt{6} - \eta}\sigma_3 - \frac{3\sqrt{2R(d)\chi}}{\sqrt{6} - \eta} \tag{89}$$

During monotonic CTC tests, σ_3 is constant and equals to the prescribed confining pressure. From Eq. (65) is derived the relation:

$$\boldsymbol{\varepsilon} = \mathbb{S}^0 : \boldsymbol{\sigma} + \boldsymbol{\varepsilon}^p = \mathbb{S}^0 : \boldsymbol{\sigma} + \Lambda^p \boldsymbol{D} \tag{90}$$

For which the following analytical solution to the damage-friction coupling equations is achieved:

$$\begin{cases} \varepsilon_1 = \dfrac{1}{E_0}\sigma_1 - \dfrac{2\nu_0}{E_0}\sigma_3 + \left(\dfrac{\eta}{3} - \dfrac{2}{\sqrt{6}}\right) d\sqrt{\dfrac{2R(d)}{\chi}} \\ \varepsilon_2 = \dfrac{1-\nu_0}{E_0}\sigma_1 - \dfrac{\nu_0}{E_0}\sigma_3 + \left(\dfrac{\eta}{3} + \dfrac{1}{\sqrt{6}}\right) d\sqrt{\dfrac{2R(d)}{\chi}} \\ \varepsilon_3 = \dfrac{1-\nu_0}{E_0}\sigma_1 - \dfrac{\nu_0}{E_0}\sigma_3 + \left(\dfrac{\eta}{3} + \dfrac{1}{\sqrt{6}}\right) d\sqrt{\dfrac{2R(d)}{\chi}} \end{cases} \tag{91}$$

Noticing that rock damage is monotonically increasing, the following damage-controlled calculation algorithm is suitable for obtaining a complete stress–strain curve:

(i) Given a damage value d, calculate $R(d)$ and then $\Lambda^p = d\sqrt{\frac{2R(d)}{\chi}}$.
(ii) Calculate the axial stress σ_1 with the prescribed confining press σ_3 and the current damage d.
(iii) Determine the components of the macroscopic strain tensor using Eq. (91).

Case of Triaxial Proportional Compression

In this case, the axial stress σ_1 and lateral stresses $\sigma_2(\sigma_3)$ are augmented simultaneously with a constant ratio $\sigma_1/\sigma_3 = \kappa > 1$. The stress state is such that $\boldsymbol{\sigma} = [\kappa\sigma_3 \quad \sigma_3 \quad \sigma_3]^{\text{diag}}$ and the deviatoric part is given by:

$$\boldsymbol{s} = \frac{(\kappa - 1)\sigma_3}{3}[2 \quad -1 \quad -1]^{\text{diag}} \tag{92}$$

The shearing direction of plastic strain flow is still given as $\boldsymbol{V} = -\frac{1}{\sqrt{6}}[2 \quad -1 \quad -1]^{\text{diag}}$ and the lateral stress can be expressed as:

$$\sigma_3 = \frac{3\sqrt{2R(d)\chi}}{(\sqrt{6} - \eta)\kappa - (\sqrt{6} + 2\eta)} \tag{93}$$

The principal components of the strain tensor are given as:

$$\begin{cases} \varepsilon_1 = \dfrac{\kappa - 2\nu_0}{E_0}\sigma_3 + \left(\dfrac{\eta}{3} - \dfrac{2}{\sqrt{6}}\right)d\sqrt{\dfrac{2R(d)}{\chi}} \\ \varepsilon_2 = \dfrac{1 - (1 + \kappa)\nu_0}{E_0}\sigma_3 + \left(\dfrac{\eta}{3} + \dfrac{1}{\sqrt{6}}\right)d\sqrt{\dfrac{2R(d)}{\chi}} \\ \varepsilon_3 = \dfrac{1 - (1 + \kappa)\nu_0}{E_0}\sigma_3 + \left(\dfrac{\eta}{3} + \dfrac{1}{\sqrt{6}}\right)d\sqrt{\dfrac{2R(d)}{\chi}} \end{cases} \tag{94}$$

Basic Features of the Damage Resistance Function $R(d)$

It is known that the mechanical response of brittle and quasi-brittle rocks contains a pre-peak material hardening phase and a post-peak material softening phase, the transition corresponding to material failure at peak stresses. Such a nonlinear behavior can be essentially attributed to the two aforementioned competing mechanisms: damage by crack growth and plastic deformation induced by frictional sliding. The former is the source of material deterioration while the latter causes the accumulation of plastic strain. In the pre-peak phase, the plastic deformation plays a predominant role while cracks propagate slowly. In the post-peak phase, there occurs further propagation and nucleation of microcracks, which finally forms some macroscopic cracks. Material damage controls the nonlinear behaviors and gives rise to a pronounced reduction in stress.

It is seen from the formulation (88) that the plastic yield function only depends on the damage resistance $R(d)$. In order to achieve a hardening and then softening mechanical response, $R(d)$ should be a continuously increasing function before peak stress and then a continuously decreasing function after peak stress. In this way, the maximal value of $R(d)$ is attained at a critical damage value, denoted by d_c which corresponds to material failure. For convenience, we set $r_c = R(d = d_c)$. Therefore, the failure surface can be predicted by the failure function:

$$f(\boldsymbol{\sigma}, d_c) = \|\boldsymbol{s}\| + \eta p - \sqrt{2r_c\chi} = 0 \tag{95}$$

It should be emphasized that the derivation of a damage criterion within a sound micromechanical framework remains one of quite difficult tasks in continuum damage mechanics. At this stage, by taking into account the above features, it is possible to propose some suitable forms for the damage resistance function $R(d)$. As a good candidate, the following form has often been used:

$$R(d) = r_c \frac{n\xi}{n - 1 + \xi^n} \tag{96}$$

with $\xi = d/d_c$ being a dimensionless parameter.

Illustration of the Model's Predictions

The proposed damage-friction induced plasticity model only contains five parameters: the Young's modulus E_0 and the Poisson's ratio ν_0 of the matrix phase, the generalized friction coefficient η, the critical damage d_c, and the critical resistance r_c at rock failure. All these constants/parameters can be calibrated using a series of conventional triaxial compression tests with different confining pressures. More precisely, the elastic constants E_0 and ν_0 can be determined by the linear phase of the stress-strain curves. η and r_c can be related to the linear fitting of the failure stress states for all considered confining pressures. We are particularly concerned with the parameter d_c which cannot be measured directly but, according to Eq. (87), is closely related to the inelastic strain at failure $\boldsymbol{\varepsilon}^p$, the latter allowing to be measured through a complete unloading at failure. Figure 7 presents a parametric study on the influence of the critical damage d_c. It is shown that when d_c is sufficiently small, Class-II stress–strain curves with a snapback will appear. When the value of d_c increases, the irreversible strain at the peak becomes bigger. Numerical simulations of the mechanical behaviors of Lac du Bonnet granite are presented in Figs. 8 and 9.

Extension to Take into Account Cracking-Induced Material Anisotropies

It is worthy emphasizing that crack growth is generally nonuniform in space, leading to induced anisotropies of material properties. It is thus always more sophisticated to

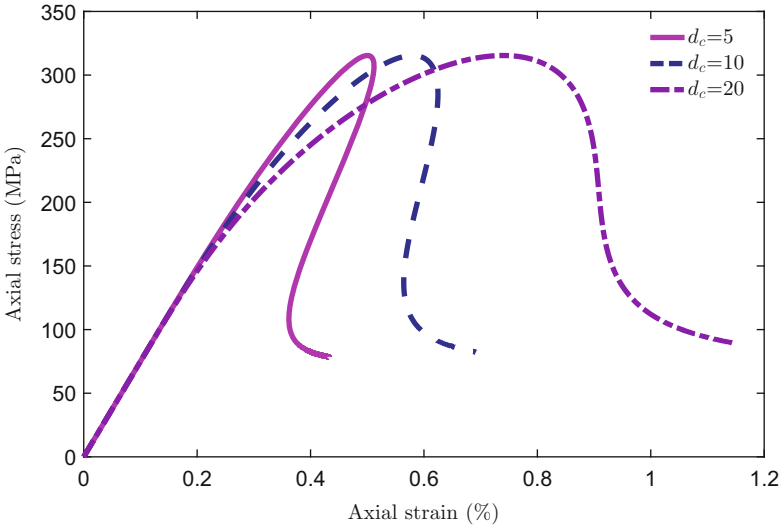

Fig. 7 Influence of the critical damage d_c on the stress-strain curves ($E_0 = 75$ GPa, $\nu_0 = 0.15$, $r_c = 0.0193$, $\eta = 1.74$ for Lac du Bonnet granite with $\sigma_3 = 10$ MPa and $n = 2$)

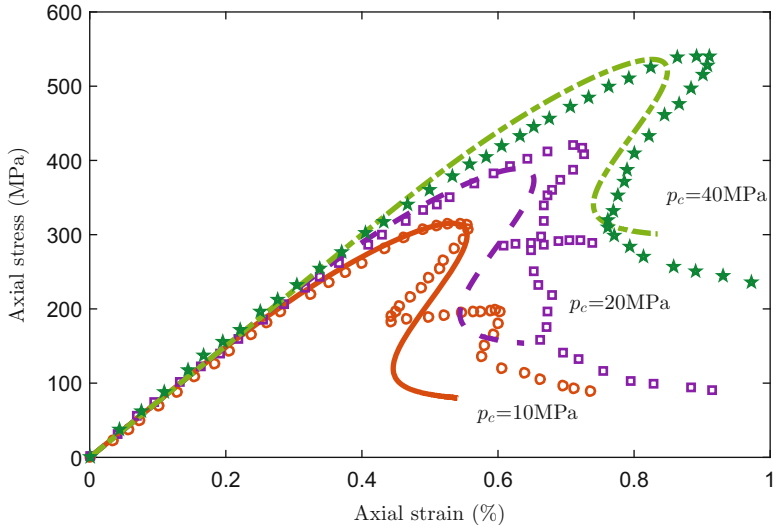

Fig. 8 Numerical simulation (solid lines) of Lac du Bonnet granite under different confining pressures σ_3 with $E_0 = 75$ GPa, $\nu_0 = 0.15$, $\eta = 1.74$, $r_c = 0.0193$, $d_c = 7$, and $n = 2.65$

develop anisotropic damage models. In this sense, the present micromechanics-based isotropic damage-friction coupling model could provide some guide for further investigations.

For anisotropic extension, all microcracks are classified into crack families according to their normal directions and the ensemble of microcracks in the

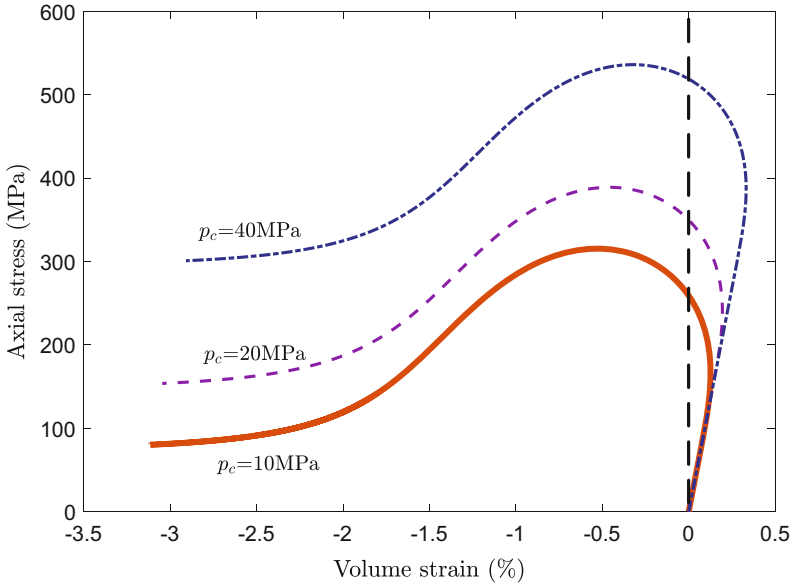

Fig. 9 Numerical prediction of the axial stress-volumetric strain curves of Lac du Bonnet granite under different confining pressures with $E_0 = 75$ GPa, $\nu_0 = 0.15$, $\eta = 1.74$, $r_c = 0.0193$, $d_c = 7$, and $n = 2.65$

same family are dealt with a material phase. For a refined modelling, one can assign to each crack family a damage variable and a local plastic strain. For example, when the Mori-Tanaka method is concerned, the effective compliance tensor $\mathbb{S}^{\text{hom}} = \mathbb{S}^0 + \sum_{r=1}^{N} d_r \mathbb{S}^{n,r}$ has been derived previously for the case of open cracks and the Gibbs free energy is then formulated in the form:

$$\psi^* = \frac{1}{2}\boldsymbol{\sigma} : \mathbb{S}^{\text{hom}} : \boldsymbol{\sigma} = \frac{1}{2}\boldsymbol{\sigma} : \mathbb{S}^0 : \boldsymbol{\sigma} + \frac{1}{2}\boldsymbol{\sigma} : \sum_{r=1}^{N} d_r \mathbb{S}^{n,r} : \boldsymbol{\sigma} \tag{97}$$

The thermodynamic forces associated with the internal variable d_r are derived as:

$$F_{d_r} = \frac{\partial \psi^*}{\partial d_r} = \frac{1}{2}\boldsymbol{\sigma} : \mathbb{S}^{\text{hom}} : \boldsymbol{\sigma} = \frac{1}{2}\boldsymbol{\sigma} : \sum_{r=1}^{N} \mathbb{S}^{n,r} : \boldsymbol{\sigma} \tag{98}$$

Next, for each crack family, a damage criterion is required to determine the evolution of damage variable.

In the case of closed frictional microcracks, the constitutive formulation procedure is quite similar to that under isotropic assumptions. On this point, readers can refer to Pensée et al. (2002) and Zhu and Shao (2015).

Summary/Conclusions

This chapter presents the basic elements of constitutive damage modelling with the linear homogenization method applied to microcracked solids. For particular use in rock mechanics, the emphasis is put on the damage-friction coupling process in rocks under compression-dominated stresses. The micromechanics-based damage formulations present many salient features in taking into account the energy dissipation mechanisms and constitutive modeling of complex coupling mechanical behaviors, including the nonlinearity of mechanical response, the unilateral effects due to the closure/opening state of cracks, the strong coupling between crack growth and friction, the snapback phenomenon in the post-peak phase, the unified hardening/softening process, some analytical solutions under specific loading paths. Thanks to the micro-macro formulations, the number of the constants and parameters involved in the model is limited to five.

References

Y. Benveniste, On the Mori-Tanaka method in cracked bodies. Mech. Res. Commun. **13**(4), 193–201 (1986). https://doi.org/10.1016/0093-6413(86)90018-2

B. Budiansky, R.J. O'Connell, Elastic moduli of a cracked solid. Int. J. Solids Struct. **12**(2), 81–97 (1976). https://doi.org/10.1016/0020-7683(76)90044-5

L. Dormieux, D. Kondo, F.J. Ulm, *Microporomechanics* (Wiley, Chichester, 2006)

J.D. Eshelby, The determination of the elastic field of an ellipsoidal inclusion, and related problems. Proc. R. Soc. Lond. A Math. Phys. Sci **241**(1226), 376–396 (1957). https://doi.org/10.1098/rspa.1957.0133

R.L. Kranz, Microcracks in rocks: a review. Tectonophysics **100**(1–3), 44–80 (1983). https://doi.org/10.1016/0040-1951(83)90198-1

T. Mori, K. Tanaka, Averages stress in matrix and average elastic energy of materials with misfitting inclusions. Acta Metall. **21**(5), 571–574 (1973). https://doi.org/10.1016/0001-6160(73)90064-3

T. Mura, *Micromechanics of Defects in Solids* (Springer, Dordrecht, 1987)

S. Murakami, *Continuum Damage Mechanics – A Continuum Mechanics Approach to the Analysis of Damage and Fracture* (Springer, Dordrecht, 2012)

S. Nemat-Nasser, M. Hori, *Micromechanics: Overall Properties of Heterogeneous Materials*, 2nd edn. (North-Holland, Amsterdam, 1998)

V. Pensée, D. Kondo, L. Dormieux, Micromechanical analysis of anisotropic damage in brittle materials. J. Eng. Mech **128**(8), 889 (2002). https://doi.org/10.1061/(ASCE)0733-9399

P. Ponte-Castaneda, J.R. Willis, The effect of spatial distribution on the effective behavior of composite materials and cracked media. J. Mech. Phys. Solids **43**(12), 1919–1951 (1995). https://doi.org/10.1016/0022-5096(95)00058-Q

A. Zaoui, Continuum micromechanics: survey. J. Eng. Mech **128**(8), 808–816 (2002). https://doi.org/10.1061/(ASCE)0733-9399

Q.Z. Zhu, J.F. Shao, A refined micromechanical damage-friction model with strength prediction for rock-like materials under compression. Int. J. Solids Struct. **60-61**, 75–83 (2015). https://doi.org/10.1016/j.ijsolstr.2015.02.005

Q.Z. Zhu, L.Y. Zhao, J.F. Shao, Analytical and numerical analysis of frictional damage in quasi brittle materials. J. Mech. Phys. Solids **92**(7), 137–163 (2016). https://doi.org/10.1016/j.jmps.2016.04.002

Application of Continuum Damage Mechanics in Hydraulic Fracturing Simulations

28

Amir Shojaei and Jianfu Shao

Contents

Introduction 752
Simulation Techniques and Hydraulic Fracturing Design 754
Thermodynamic Principles and Continuum Damage Mechanics of Porous Rocks 756
CDM-Based Fluid-Driven Fracture in Porous Rocks 759
Simulation Results 763
Concluding Remarks 766
References 767

Abstract

Hydraulic fracturing (HF) stimulation treatment is based upon two fracture mechanics processes: an initial fracture, created by perforation process, and a fluid driven fracturing. Design of a successful HF operation requires integration of many design parameters, simulation techniques, and physical measurement data in order to capture the real physics behind this complex process. Geotechnical data, perforation geometries, injection rates, temperature, pressure, and fracturing fluid properties are among a few physical parameters that can affect HF crack height and depth. Although crack propagation in an HF process, like all other fracturing process, is a random process, sophisticated design approaches are necessary to help engineers to narrow down the uncertainties and maximize the probability of achieving the HF objectives, e.g., fracture height and depth. Due to complex

A. Shojaei (✉)
Varian Medical Systems, Palo Alto, CA, USA
e-mail: a.shojaei.mech.eng@gmail.com

J. Shao
Laboratory of Mechanics of Lille, Villeneuve d'Ascq, France

University Lille, CNRS, Centrale Lille, LaMcube – Laboratoire de Mécanique, Multiphysique, Multi-échelle, Lille, France
e-mail: jian-fu.shao@polytech-lille.fr

© Springer Nature Switzerland AG 2022

G. Z. Voyiadjis (ed.), *Handbook of Damage Mechanics*,
https://doi.org/10.1007/978-3-030-60242-0_59

physics and limited testing capabilities during HF design, numerical methods play an essential role in design iterations. Continuum Damage Mechanics (CDM) provides a robust numerical platform to integrate physics of the rock failure into the numerical simulations. The concept of the CDM theory for fluid-driven fracturing in porous rocks was developed by Shojaei et al. (Int J Plast 59:199–212, 2014) and Shojaei and Shao (9 – Application of continuum damage mechanics in hydraulic fracturing simulations, in *Porous Rock Fracture Mechanics*, ed. by A.K. Shojaei and J. Shao (Cambridge: Cambridge Woodhead Publishing, pp 197–212, 2017) and has been under intensive research and development since then (Yi et al., J Pet Sci Eng 178:814–828, 2019; Mobasher et al., Int J Rock Mech Min Sci 111:64–83, 2018). A CDM-based HF design platform can integrate several design parameters and interaction between HF and natural fractures or formations. The CDM-based analysis tools have been developed based on premises that model parameters are able to be calibrated and verified through standard lab testing techniques and then could be utilized in more complex design scenarios in which testing and experimental studies are challenging. In this chapter after presenting fluid-driven CDM theory for porous rocks, several HF processes are studied numerically. Methods and experimental processes to calibrate CDM model parameters are discussed, and methods for model verifications are discussed. Presented framework can be utilized by engineers and scientists to build a reliable simulation platform to optimize the HF processes.

Keywords

Hydraulic fracturing · Rock damage mechanics · Numerical simulations · Fluid driven fracture mechanics

Introduction

Hydraulic fracturing is an evolving well stimulation technique in which rock is fractured by a pressurized liquid to enhance oil and gas productions. Stimulation treatments, such as hydraulic fracturing (HF), are crucial to achieve economic production from low permeability formations or reservoirs with low conductivity from natural fractures. During HF process a fracture initiation is created at the targeted depth of the well, using perforation methods. Then a pressurized fluid is injected into the wellbore to propagate the fracture into the targeted formation. A successful HF design results in fracture depths and heights within specified specs. An overshoot could potentially damage neighboring formations, and too short fractures may not yield enough flow back from formation. As discussed in (Shojaei and Shao 2017), there are different HF scenarios that could happen, depending on rock's properties, fluid viscosity, flow rate, temperature, and confining pressure. Figure 1 shows three cases in which surface pressure renders what is happening inside the propagating fracture, viz., softening, stable, and hardening crack growth behaviors (Shojaei and Shao 2017).

Most of to date modeling techniques for HF treatments rely on simplified fracture and fluid flow models, which could only provide approximate solutions regarding the actual fracture geometry. Common assumptions in simulation of HF include homogeneous formation properties and limited fracture growth in a symmetric double-wing fashion (Dahi Taleghani et al. 2016). These simplification assumptions are erroneous in most of the unconventional reservoirs where geology, formation properties, and environmental conditions (such as high pressure high temperature) can complicate the fracturing process (Shojaei et al. 2014; Shojaei and Shao 2017).

Shojaei et al. (2014; Shojaei and Shao 2017) proposed the concept of fluid-driven CDM in porous rocks to be utilized in design optimization of HF processes. The proposed CDM framework provided a powerful and reliable analysis platform for fracturing modeling in porous rocks and has been under intensive research and development (Lai et al. 2016; Wilson and Landis 2016; Sobhaniaragh et al. 2016; Ma et al. 2016). To achieve an optimized HF process, several design iterations over multiple design parameters are required. A verified CDM-based design platform can reduce the cost and time of such complex iterative processes, and it may be utilized by design engineers to investigate HF treatments before field implementations.

This chapter is structured as follows: In section "Simulation Techniques and Hydraulic Fracturing Design" the design procedure of hydraulic fracturing is briefly discussed. The thermodynamics consistency of CDM models are discussed in section "Thermodynamic Principles and Continuum Damage Mechanics of Porous Rocks." In section "CDM-Based Fluid-Driven Fracture in Porous Rocks" the CDM model formulation is presented. The simulation results and remarks are presented in section "Simulation Results." Both indices and bolded letters are used to denote tensorial parameters, and light letters indicate scalar parameters.

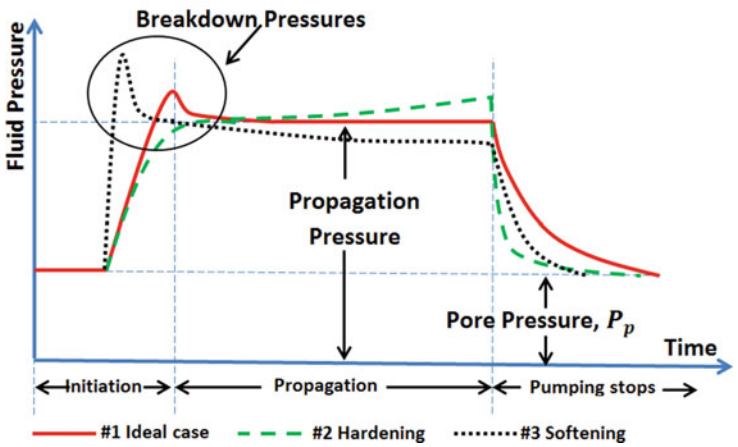

Fig. 1 Schematics for pressure versus time scenarios in a typical HF process (Shojaei and Shao 2017)

Simulation Techniques and Hydraulic Fracturing Design

In an HF design, fracture height, orientation, and length are among the most critical design parameters. For example, an HF crack with out-of-spec height or depth can damage the neighboring formation or result in smaller than expected flow back from the HF. There are multiple parameters that could affect the crack geometry and dimensions, including (i) *crack closure stress* differences between targeted formation and overlaying and underlying formations that result in unexpected fracture propagation to adjacent formations; (ii) *boundary layers breakdown* where shallow formation thicknesses of layered permeable and impermeable formations affect the HF crack geometry; (iii) *breakdown pressures*; (iv) *modulus contrast* between targeted and adjacent formations; (v) *bedding plane slip* at shallow depths; (vi) *natural fractures*; (vii) *interface slip* where fracture propagates between the boundary layers instead of formation; (viii) injection fluid properties, such as viscosity; and (ix) perforation characteristics such as perforation shape, depth and orientation (Shojaei et al. 2014; Shojaei and Shao 2017). Figure 2 shows a scenario in which HF fracture perforated untargeted formations that could result in contamination of surface waters due to hydrocarbon migrations, and it also result in excessive operational costs (Shojaei et al. 2014; Shojaei and Shao 2017). Thus, it is crucial to investigate the HF treatment before field implementation via experimental data collections from the formation, feeding these data into numerical simulation tools and lab scale testing.

Hydraulic fracturing design optimization tasks require sophisticated numerical platforms that allow for iteration over several design parameters, including geotechnical, perforation geometry, injection rate, and fracturing fluid viscosity, to predict the fracture height and depth in various formation configurations (Shlyapobersky and Chudnovsky 1992; Papadopoulos et al. 1983; Bai and Lin 2014). Following pioneering works by Griffith (1921), most of the modeling efforts in hydraulic fracturing are historically performed using linear elastic fracture mechanics (LEFM)

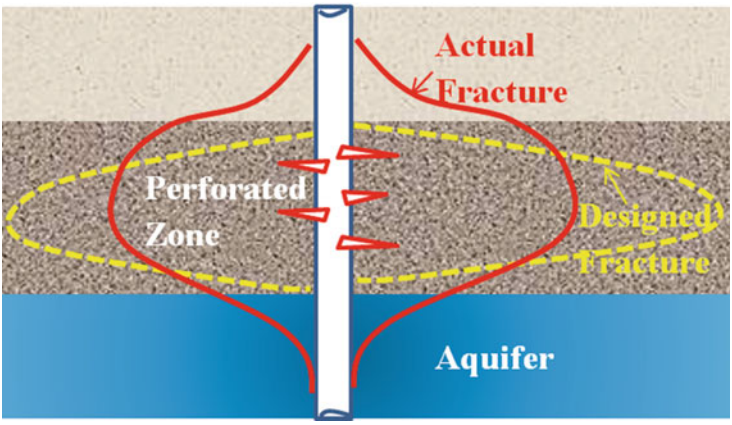

Fig. 2 Schematics of designed (desired) and actual fractures (Shojaei and Shao 2017)

in which an ideal crack is simulated in an ideal formation (Ghassemi et al. 1998; Geertsma and De Klerk 1969; Perkins and Kern 1961). While such simplified analytical solutions can provide some insight into the HF treatment, there are strong evidence that fracture toughness could be a function of confining pressure and the length scale. Fracture propagation analysis in LEFM models requires prescribing the fracture path in which parameters, e.g., the *energy release rate* and *stress intensity factors*, control the fracture initiation and propagation. Many of those parameters are unknown for the downhole conditions, and the prediction of the fracture length, velocity, and orientation is not reliable in many practical cases. Three-dimensional LEFM models have also been developed such as *cell-based*, *lumped*, and *coupled fluid flow* models (Adachi et al. 2007, 2010). Cohesive zone models (CZMs) are intended to address short comes of LEFM approach, in which cohesive elements together with force-displacement relations are required to model the fracture (Chen et al. 2009; Sarris and Papanastasiou 2011, 2012). While CZM can predict fracture initiation and avoid singularity at tip of the crack, it encounters with a few computational difficulties such as magnitude of cohesive parameters depending on the mesh size, and a random and tortuous crack path needs to be replaced with a line that undermines the prediction results. Extended finite element method (XFEM) has also been widely used to simulate fracture process in HF processes (Sukumar et al. 2000). While calibration of the material parameters for XFEM models is complicated, both CZM and XFEM methods require a specific type of element to be used in fracture process zone to simulate the fracture that results in higher computational costs. Boundary element method (BEM) provides an approach for solving steady-state flow in three-dimensional fracture networks (Elsworth 1987; Wilson and Witherspoon 1974). Although, BEM reduces the model dimension and reduces the computational cost, the solution may not be as accurate as finite element analysis (FEA) in dealing with heterogeneous rock layers. Simulation of crack growth using the FEA has also been widely practiced in the literature (Moës et al. 1999; Advani et al. 1990). Mesh dependency of the results together with high computational cost are the main disadvantages of the fracture mechanics-based FEA methods.

Shojaei et al. (2014; Shojaei and Shao 2017) proposed the concept of fluid-driven CDM for porous rocks. In this approach full coupling between poroelasticity, poroplasticity, and fracture mechanics of rocks is integrated into the simulation steps to provide realistic results (Shojaei et al. 2014; Shojaei and Shao 2017). One of the main advantages of CDM-based fracture modeling is that predefining fracture paths is not necessary and the fractures evolve naturally based upon constitutive laws of the rock system. The CDM model can be defined based upon strain energy terms, stress, strain, or a combination of these parameters. As discussed by Shojaei and Shao (2017), the main aims of a CDM formulation are:

1. Full coupling between poroelasticity, poroplasticity, and damage mechanisms of rocks is considered to provide realistic simulations of fracture in porous rocks.
2. Different deformation mechanisms, including poro-elasto-plastic and damage mechanics, can be calibrated with respect to specific experimental data. In

contrast to many fracture simulation techniques, CDM approach provides a clear workflow to link experimental data to model parameters
3. The *pore pressure-driven fractures* are simulated by CDM. In other words, CDM model links the fluid pressure to damage mechanics of rocks in a hydraulic fracture simulation. So-called fluid-driven fracture is modeled by CDM, unlike LEFM models.
4. The drained and/or undrained conditions can be studied.
5. Implementation of a CDM model in an FEA solver is now feasible in many commercially available codes. The FEA code can be calibrated and verified by test data available from lab testing and then be utilized to numerically study the effect of sundry factors, e.g., heterogonous formation layups, anisotropic rock system, porosity effect, permeability effect, presence of natural fractures, temperature dependency, and loading rate dependency, on the HF shape, depth, and orientation (Shojaei and Shao 2017). Calibrated CDM models will ensure the simulation results correlate well with the real fracturing process at downhole conditions.

One more advantage of CDM models is that they utilize the conventional solid elements that eliminate the needs for specialized elements, or remeshing techniques, and consequently may reduce the complexity of the computational implementation.

Thermodynamic Principles and Continuum Damage Mechanics of Porous Rocks

Thermodynamic principles, including energy considerations, can be utilized to derive physically consistent constitutive laws for the material behavior (Voyiadjis et al. 2011, 2012a, b, c; Li and Shojaei 2012; Shojaei et al. 2012, 2013; Shojaei and Li 2013, 2014). The deformation process in porous rocks can be categorized into reversible, e.g., poroelastic response, and irreversible processes, e.g., damage mechanisms and poroplastic behaviors (Shojaei et al. 2014). In the context of thermodynamic of solids, the specific internal energy u is defined as follows (Shojaei and Shao 2017; Voyiadjis et al. 2011):

$$u = u\left(s, \boldsymbol{\epsilon}_e, \boldsymbol{\zeta}_p, \boldsymbol{\zeta}_d\right), \tag{1}$$

where s denotes the entropy and $\boldsymbol{\epsilon}_e$, $\boldsymbol{\zeta}_p$, and $\boldsymbol{\zeta}_d$ are respectively elastic strain, plastic, and damage variable tensors. Time derivative of u reads (Shojaei et al. 2014; Shojaei and Shao 2017; Voyiadjis and Shojaei 2015a):

$$\dot{u} = \frac{\partial u}{\partial s}\dot{s} + \frac{\partial u}{\partial \boldsymbol{\epsilon}_e} : \dot{\boldsymbol{\epsilon}}_e + \frac{\partial u}{\partial \boldsymbol{\zeta}_p} : \dot{\boldsymbol{\zeta}}_p + \frac{\partial u}{\partial \boldsymbol{\zeta}_d} : \dot{\boldsymbol{\zeta}}_d \tag{2}$$

The symbol ":" in the above equation indicates contraction over two tensorial indices. The second law of thermodynamic states that the change in entropy is

always positive and it can be expressed in the Clausius–Duhem inequality as follows (Shojaei et al. 2014; Shojaei and Shao 2017; Voyiadjis and Shojaei 2015a):

$$\boldsymbol{\sigma} : \dot{\boldsymbol{\epsilon}}_e - \rho\left(\dot{u} + s\dot{T}\right) - \frac{\boldsymbol{q}}{T}.\nabla T \geq 0, \tag{3}$$

where ρ denotes the density of the rock. By substituting Eq. (2) into Eq. (3) and eliminating the heat flux term, the Clausius–Duhem inequality for the rock system is obtained as follows (Shojaei et al. 2014; Shojaei and Shao 2017; Voyiadjis and Shojaei 2015a):

$$\left(\boldsymbol{\sigma} - \rho\frac{\partial u}{\partial \boldsymbol{\epsilon_e}}\right) : \dot{\boldsymbol{\epsilon}}_e - \rho\left(T - \frac{\partial u}{\partial s}\right)\dot{s} - \rho\left(\frac{\partial u}{\partial \boldsymbol{\zeta}_p} : \dot{\boldsymbol{\zeta}}_p + \frac{\partial u}{\partial \boldsymbol{\zeta}_d} : \dot{\boldsymbol{\zeta}}_d\right) \geq 0, \tag{4}$$

The conjugate thermodynamic forces, viz., Cauchy stress tensor $\boldsymbol{\sigma}$, and temperature T, respectively, corresponding to the entropy s and the elastic strain tensor $\boldsymbol{\epsilon_e}$ are defined as follows (Shojaei et al. 2014; Shojaei and Shao 2017; Voyiadjis and Shojaei 2015a):

$$\boldsymbol{\sigma} = \rho\frac{\partial u}{\partial \boldsymbol{\epsilon_e}} \quad \text{and} \quad T = \frac{\partial u}{\partial s}. \tag{5}$$

The remaining part of Eq. (4) defines the plasticity and damage power of dissipation:

$$\Gamma = -\rho\left(\frac{\partial u}{\partial \boldsymbol{\zeta}_p} : \dot{\boldsymbol{\zeta}}_p + \frac{\partial u}{\partial \boldsymbol{\zeta}_d} : \dot{\boldsymbol{\zeta}}_d\right), \tag{6}$$

Helmholtz free energy function Ψ is obtained through Legendre transformation of the internal energy u (Voyiadjis et al. 2011). The Helmholtz free energy potential can be decomposed into (i) purely elastic and (ii) coupled plastic and damage, Ψ_{pd}, parts (Shojaei et al. 2014; Shojaei and Shao 2017; Voyiadjis and Shojaei 2015a):

$$\Psi = \frac{1}{2}\left(\boldsymbol{\epsilon} - \boldsymbol{\epsilon_p}\right) : \mathbf{C}(\mathbf{d}) : \left(\boldsymbol{\epsilon} - \boldsymbol{\epsilon_p}\right) + \Psi_{\text{pd}}\left(\mathbf{d}, \boldsymbol{\epsilon_p}\right), \tag{7}$$

where $\boldsymbol{d}$ is the damage tensor. In the case of isotropic materials, following Hill's notation, the effective elastic stiffness tensor of damaged material $\mathbf{C}(\boldsymbol{d})$ is given by Nemat-Nasser and Hori (1993):

$$\mathbf{C}(\mathbf{d}) = 2\mu(\mathbf{d})\mathbf{K} + 3\,\mathrm{k}(\mathbf{d})\mathbf{J}, \tag{8}$$

where $\mathrm{k}(\mathbf{d})$ and $\mu(\boldsymbol{d})$ represent the bulk and shear moduli of the damaged rock system, respectively. The two isotropic symmetric fourth-order tensors $\mathbf{J}$ and $\mathbf{K}$ are defined by Shao (1998). The thermodynamic conjugate forces for each flux variables, $\boldsymbol{\epsilon_e}$, $\boldsymbol{\epsilon_p}$, and $\mathbf{d}$, are obtained as follows (Voyiadjis and Shojaei 2015a; Shao 1998):

$$\begin{aligned}
\boldsymbol{\sigma} &= -\rho\frac{\partial \Psi}{\partial \epsilon_e} = \mathbf{C}(\mathbf{d}) : \left(\epsilon - \epsilon_p\right), \\
\boldsymbol{\gamma^p} &= -\rho\frac{\partial \Psi}{\partial \epsilon_p} = \boldsymbol{\sigma}, \\
\boldsymbol{\gamma^d} &= -\rho\frac{\partial \Psi}{\partial \boldsymbol{d}} = -\rho\left(\frac{1}{2}\left(\epsilon - \epsilon_p\right) : \frac{\partial \mathbf{C}(\mathbf{d})}{\partial \boldsymbol{d}} : \left(\epsilon - \epsilon_p\right) + \frac{\partial \Psi_{pd}\left(\mathbf{d}, \epsilon_p\right)}{\partial d}\right)
\end{aligned} \tag{9}$$

Both plasticity and damage mechanisms require definition of criteria that control initiation of each processes (Voyiadjis and Shojaei 2015b):

$$\begin{aligned}
f^p &= \boldsymbol{\gamma^p} - \sigma_y\left(\epsilon_p\right) \leq 0, \\
f^d &= \boldsymbol{\gamma^d} - \bar{r}\left(\boldsymbol{d}\right) \leq 0,
\end{aligned} \tag{10}$$

where σ_y and $\bar{r}$ control the initiation of plasticity and damage processes, respectively.

The principal of extremized entropy production during a thermodynamic process is applied to the power dissipation function Eq. (6) considering the constraints conditions given in Eq. (10). The resulting Lagrangian functional which should be extremized is as follows (Voyiadjis et al. 2011):

$$\gamma^* = \Gamma - \dot{\lambda}^p f^p - \dot{\lambda}^d f^d \tag{11}$$

where $\dot{\lambda}^p$ and $\dot{\lambda}^d$ are Lagrangian constant, to be found from extermized functional. Applying the stationary conditions to the Lagrangian functional results in Voyiadjis et al. (2011):

$$\begin{aligned}
\frac{\partial \gamma^*}{\partial \boldsymbol{\sigma}} = 0 \rightarrow \dot{\epsilon}_p &= \dot{\lambda}^p \frac{\partial f^p}{\partial \boldsymbol{\sigma}}, \\
\frac{\partial \gamma^*}{\partial \boldsymbol{\gamma^d}} = 0 \rightarrow \dot{\boldsymbol{d}} &= \dot{\lambda}^d \frac{\partial f^d}{\partial \gamma^d},
\end{aligned} \tag{12}$$

Equation (8) represents thermodynamic consistent constitutive laws for the plasticity and damage phenomena.

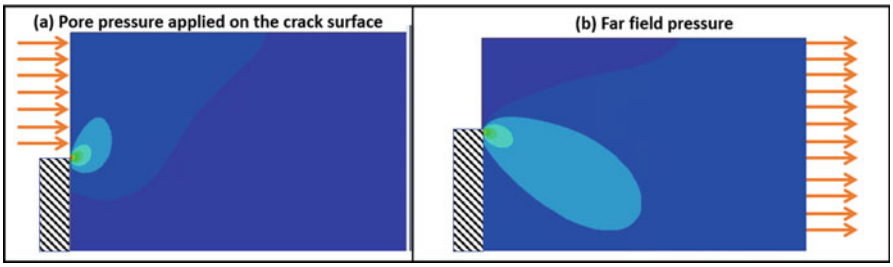

Fig. 3 Von Mises stress map for two cases are shown: (**a**) pore pressure applied directly to the face of crack and (**b**) far field pressure

CDM-Based Fluid-Driven Fracture in Porous Rocks

Most of classical fracture mechanics problems are based upon externally applied thermomechanical loads that result in crack initiation and propagation. In the case of an HF process, the fracturing driving force is fluid pore pressure inside the rocks' body. There are fundamental differences between conventional fracture mechanics problems and fluid-driven fractures. First, when externally applied loads on far boundary conditions drive the crack growth, the load is transferred to the crack region via microstructure of the solids. In the case of HF, the driving force is a pressure applied directly to the surface of a crack. Figure 3 depicts the von Mises stress map between two identical cracks but exposed to different boundary conditions 3(a) pore pressure applied on the crack faces, and 3(b) uniform far field pressure is applied. The differences in stress map indicate the fracture mechanics-based formula developed for case 3(b) may not be applicable to the case 3(a).

Thanks to CDM approach flexibility and capabilities, the physics of fluid-driven fracture can be formulated to simulate complex failure mechanisms in porous rocks under high confining pressures at elevated temperature. The fracture simulation relies on hydraulic-driven fracture where injected pore pressure is utilized to determine the fracture initiation and propagation (Shojaei et al. 2014; Shojaei and Shao 2017). The basics building blocks of CDM computational tools consist of:

- Mathematical models for pressure- and temperature-sensitive rock's properties.
- A CDM model that captures the initiation and propagation of microscale failure mechanisms.
- Poroelasticity and poroplasticity constitutive relations are required to calculate the stress-strain fields due to applied hydro-mechanical and thermal loads.
- For complex geometries, such as multilayer rocks with multiple natural fractures, an FEA solver is needed for numerical computations. An explicit or implicit integration algorithm can be used to solve the numerical problem.

As discussed by Shojaei et al. (2014) and Shojaei and Shao (2017), multiscale damage mechanisms in porous rocks are initiated by coalesce of microcracks/microvoids to form macro cracks and eventually result in rupture of the formation skeleton. CDM provides a framework to formulate different stages of the crack formation from the initiation to propagation of microcracks. The damage mechanics was formerly introduced by pioneers such as Kachanov (1958) and Lemaitre (1984), and since then it has been under intensive research and developments (Voyiadjis et al. 2011; Voyiadjis and Shojaei 2015a, b; Voyiadjis and Kattan 2006). Effective and damaged configurations in CDM basically capture the continuum damage processes in which damaged materials are removed from the material and the load is only carried by the undamaged material. As depicted in Fig. 4, the reduction in material stiffness is then embedded in the numerical simulations to model material softening due to the damage mechanisms (Voyiadjis et al. 2012a). Damage parameter d correlates the undamaged stiffness $\bar{E}$ to the damaged stiffness E through two

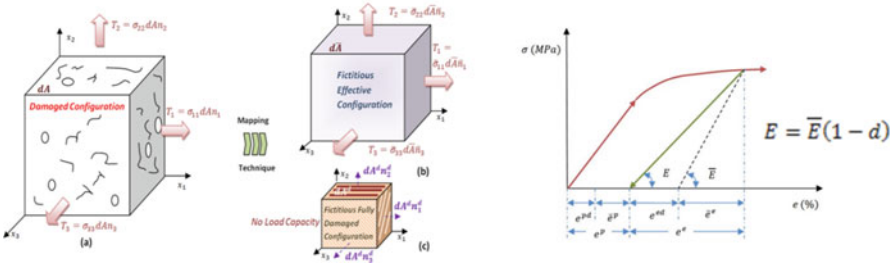

Fig. 4 Effective and damaged configurations that are used to develop continuous reduction of material stiffness by the damage parameter *d, after* (Adachi et al. 2007)

basic principles of (1) *equivalence of the strain energy* **or** (2) *equivalence of the strain*; refer to Voyiadjis et al. (2012a) for more details.

Pore pressure in rocks play an essential role in their fracture mechanics, and it needs to be included into the formulation. Biot's theory of consolidation for anisotropic rocks has been utilized to incorporate pore pressure effect into the CDM concept (Shojaei et al. 2014; Shojaei and Shao 2017). The total strain rate $\dot{\boldsymbol{\epsilon}}$ is decomposed into elastic $\dot{\boldsymbol{\epsilon}}_e$, plastic $\dot{\boldsymbol{\epsilon}}_p$, and damaged $\dot{\boldsymbol{\epsilon}}_d$ strain rate tensors (Shojaei et al. 2014; Shojaei and Shao 2017):

$$\dot{\boldsymbol{\epsilon}} = \dot{\boldsymbol{\epsilon}}_e + \dot{\boldsymbol{\epsilon}}_p + \dot{\boldsymbol{\epsilon}}_d \tag{13}$$

Then, Biot's theory of consolidation (Detournay and Cheng 1993; Cheng 1997) that utilizes coupled diffusion and elasticity equations to capture stress fields in porous media is incorporated (Shojaei et al. 2014; Shojaei and Shao 2017):

$$\boldsymbol{\sigma}' = \boldsymbol{M}^h \boldsymbol{\epsilon} - \boldsymbol{\alpha} p \tag{14}$$

where $\boldsymbol{\sigma}'$ is the so-called effective stress tensor, $\boldsymbol{\alpha}$ is the Biot coefficients tensor, and $\boldsymbol{M}^h$ is the fourth-order homogenized stiffness tensor. One may note that unlike the isotropic case, the Biot coefficient is not scalar. The relation between pore pressure p, strain field $\boldsymbol{\epsilon}$, and Biot's coefficients ζ, $\boldsymbol{M}$, and $\boldsymbol{\alpha}$ is given by Shojaei et al. (2014), Detournay and Cheng (1993), and Cheng (1997):

$$p = \boldsymbol{M}(\zeta - \boldsymbol{\alpha}\boldsymbol{\epsilon}) \tag{15}$$

The CDM framework requires a continuous update of Biot's coefficient together with stiffness tensor to ensure damage effects have been captured through the course of deformation. These continuous update of material properties can be formulated based on the state of damage, plastic deformation, stress, or other internal state variables.

Pressure-sensitive poroplasticity for drained/undrained conditions is simulated through a set of empirical relations (Shojaei et al. 2014). The shear strength of the

rock's solid skeleton τ is related to *pressure sensitive ultimate strength* τ^u via two material parameters B and n as follows (Shojaei et al. 2014):

$$\tau = \tau^u + B\left|\epsilon_p\right|^n \tag{16}$$

where $\left|\epsilon_p\right| = \sqrt{\frac{2}{3}\boldsymbol{\epsilon}_p : \boldsymbol{\epsilon}_p}$ is the equivalent plastic strain. The parameter τ^u is then correlated to the hydrostatic pressure field via two equations. First is a linear correlation that defines τ^u based on the tensile hydrostatic of the rock sample T and τ_0^u which is the strength at effective confining pressure Σ'_0. The second relation applies for the $\Sigma' > \Sigma'_0$ (Shojaei et al. 2014):

$$\tau^u = \tau_0^u + \left(\tau_{\max}^u - \tau_0^u\right)\left[1 - \exp\left(-\alpha\left(\Sigma' - \Sigma'_0\right)\right)\right] \tag{17}$$

where $\Sigma' = \Sigma - p$ is the effective confining pressure, and $\tau_{\max}^u$ is the maximum strength of the rock that occurs at high confining pressures, and α is defined by Shojaei et al. (2014):

$$\alpha = \frac{\tau_0^u}{\left(\tau_{\max}^u - \tau_0^u\right) \times \left(\Sigma'_0 + T\right)} \tag{18}$$

The final step is to formulate the microcracks and microvoids initiation and propagation within the solid skeleton of the porous rock. Figure 5 shows the damage mechanics in porous rocks in which microcracks/microvoids degrade the elastic properties of the solid skeleton (Shojaei et al. 2014; Shojaei and Shao 2017).

The actual damage process in porous rocks is a 3D process that results in anisotropic material properties after damage initiation. Thus, even for an initially

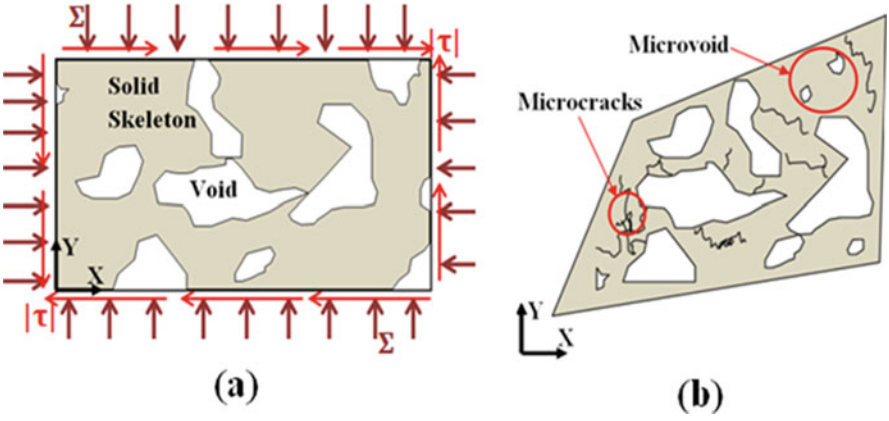

Fig. 5 Representative element for (**a**) undeformed porous rock under pressure and shear loading, (**b**) unloaded medium that contains microvoids and microcracks (Shojaei et al. 2014; Shojaei and Shao 2017)

isotropic rock sample, the state of material properties becomes anisotropic due to anisotropy in the applied stress field. Anisotropic CDM formulation, developed by Shojaei et al. (2014), reads:

$$d = \begin{bmatrix} D_1 & 0 & 0 \\ 0 & D_2 & 0 \\ 0 & 0 & D_3 \end{bmatrix} \tag{19}$$

where D_i with $i = 1, 2$, and 3 are three damage parameters in principal directions that is updated with the course of deformation. The damage parameter is then correlated to the microcrack lengths as follows (Shojaei et al. 2014):

$$D_i = \frac{a_i - a_0}{a_c - a_0} \tag{20}$$

where a_i is a representative of all microcracks at the ith principal direction, a_c is the critical, and a_0 is the initial microcrack length in the system. The microcrack evolution law is then given by Shojaei et al. (2014):

$$a_i = a_0 + \chi_5 (a_c - a_0) \sum \frac{|\epsilon_p|}{\epsilon_f} \tag{21}$$

where χ_5 is a material parameter that controls the rate of microcracking and ϵ_f is the fracture strain. The stiffness of the porous rocks is updated via the damage parameters as follows (Shojaei et al. 2014):

$$E_i = \bar{E}(1 - D_i), \text{and } \nu_i = \bar{\nu}\left[\delta_i + D_i\left(\frac{0.5}{\bar{\nu}} - 1\right)\right]^2 \tag{22}$$

where $\bar{E}$ and $\bar{\nu}$ are intact elastic modulus and Poisson's ratio, respectively. A fracture mechanics-based damage initiation criterion is also used by Shojaei et al. (2014) to minimize the mesh sensitivity of the results that is associated with highly localized softening due to the damage mechanisms. The CDM criterion then reads (Shojaei et al. 2014):

$$f_D = \left(\frac{\mathcal{G}_I}{\mathcal{G}_{Ic}}\right)^2 + \left(\frac{\mathcal{G}_{II}}{\mathcal{G}_{IIc}}\right)^2 + \left(\frac{\mathcal{G}_{III}}{\mathcal{G}_{IIIc}}\right)^2 + \left(\frac{\mathcal{G}_I}{\mathcal{G}_{Ic}}\right)\left(\frac{\mathcal{G}_{II}}{\mathcal{G}_{IIc}}\right) + \left(\frac{\mathcal{G}_{II}}{\mathcal{G}_{IIc}}\right)\left(\frac{\mathcal{G}_{III}}{\mathcal{G}_{IIIc}}\right) + \left(\frac{\mathcal{G}_I}{\mathcal{G}_{Ic}}\right)\left(\frac{\mathcal{G}_{III}}{\mathcal{G}_{IIIc}}\right) \tag{23}$$

where $\mathcal{G}_i$ (i = I, II, and III) is the fracture energy release rate for modes I, II, and III crack openings that is computed numerically and $\mathcal{G}_{ic}$ (i = I, II, and III) is the critical fracture energy release rates for the respective fracture modes (Shojaei et al. 2014).

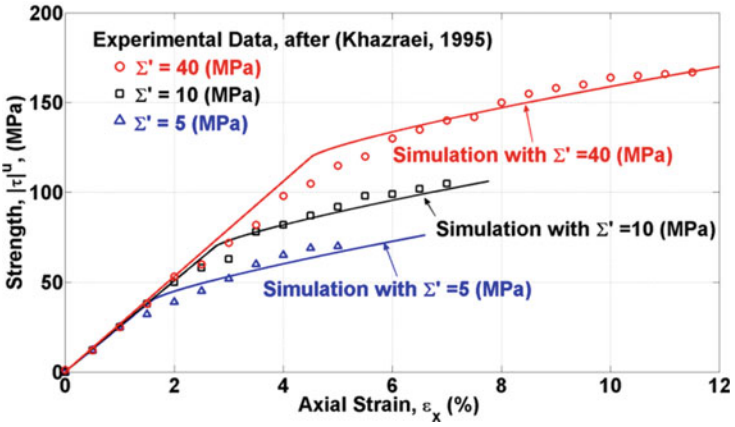

Fig. 6 Pressure-sensitive stress-strain responses of porous rocks (Shojaei et al. 2014; Khazraei 1995)

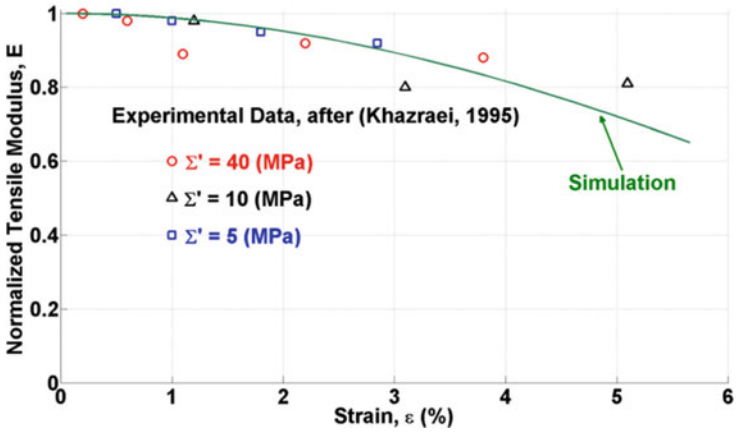

Fig. 7 Damage response in limestone under quasi-static loading condition, after (Shojaei et al. 2014)

Simulation Results

The performance of the developed CDM model is compared to the laboratory scale testing in which brown-colored sandstone experimental data, after Khazraei (1995), are used to calibrate the plasticity and damage models (Shojaei et al. 2014). The poro-elasto-plastic deformation response of the rock system was experimentally investigated by Khazraei (1995) through triaxial tests. As depicted in Figs. 6 and 7, the developed plasticity model by Shojaei et al. (2014) correlates well with the experimental data.

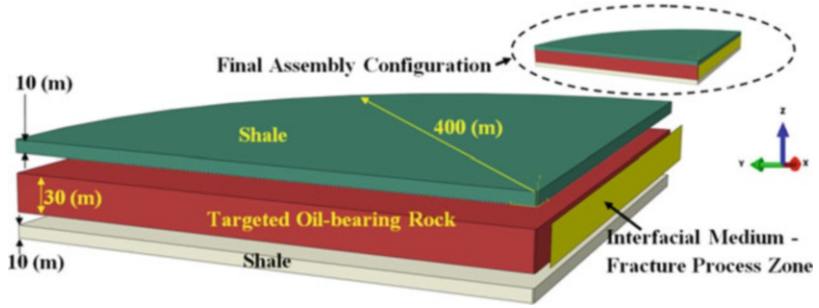

Fig. 8 CAD model for simulation of fracture in a targeted rock sample (Shojaei et al. 2014)

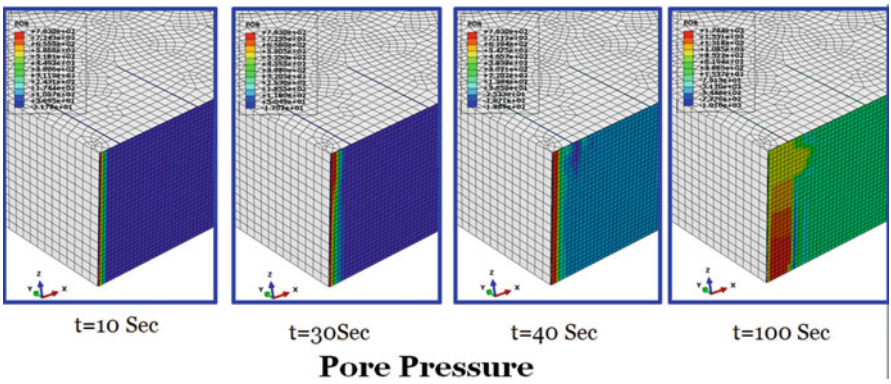

Fig. 9 Pore pressure variations within the interfacial rock medium (fracture process zone), (Shojaei et al. 2014)

A computer-aided design (CAD) model of a rock sample is depicted in Fig. 8 (Shojaei et al. 2014). Three domains are considered for the problem – low-permeability cap rocks on the top and bottom of the model, a hydrocarbon-bearing zone, and interfacial domains to represent potential fracture paths (Fig. 8). The oil-bearing circular rock slice has a 30-m depth and 400-m radius with a wellbore radius of 0.1 m. An orthotropic overburden stress state is imposed. Loading and boundary conditions are also applied as follows. The first step is initially achieving the equilibrium state after applying the initial pore pressure and in situ stresses. The second step simulates the HF stage, where a volume of fluid is injected into the formation. The fluid flow is injected along the perforation zone in the target formation in the model by means of the prescribed interfacial medium (Fig. 9). The interfacial domain, with thickness of 0.1 m, shows the fracture process zone in which the damage parameters are updated and elastic moduli degradation occurs. The elasto-plastic rock behavior is assigned to the target rock, while confining shale rocks are assumed to behave as linear elastic materials. The duration of the injection stage is 140 seconds. Following the HF, another transient consolidation analysis is conducted. The injection into the well is terminated,

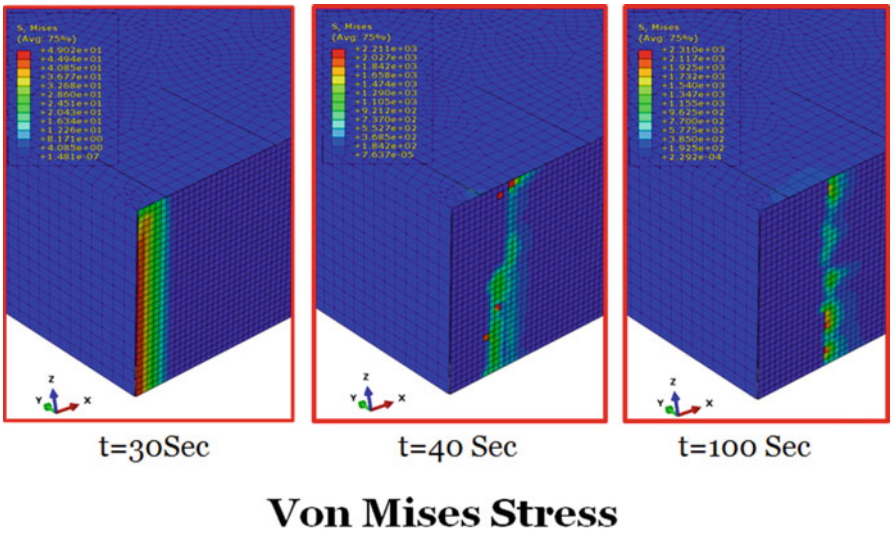

Fig. 10 Simulation results for the von Mises stress in which the travel of the fracture tip along the fracture process zone is shown (Shojaei and Shao 2017)

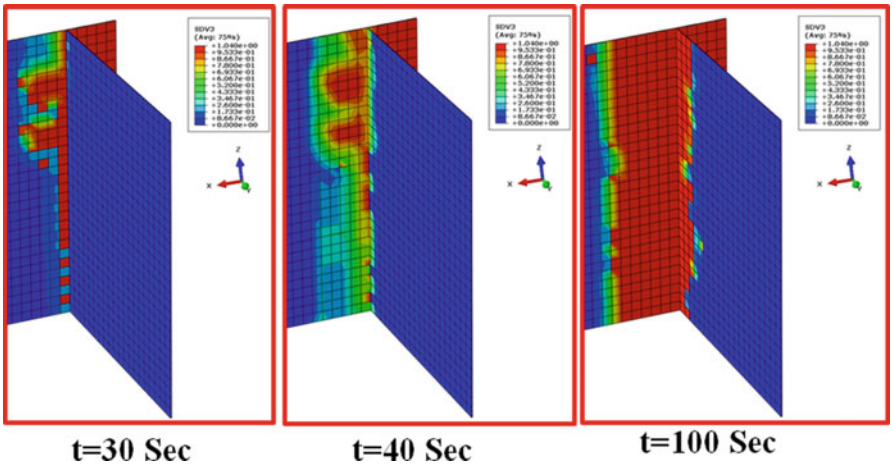

Fig. 11 Effective damage parameter during treatment process at 30, 40, and 100 s of injection from left edge is shown. The natural fracture intersects the HF fracture at 90° angle (Shojaei and Shao 2017)

and fluid leakoff from the fracture is allowed to bleed off the fracture fluid pressure. To mimic actual conditions, the fracture surfaces are assumed to possess a minimum opening as the boundary condition to simulate the behavior of the placed proppant material into the fracture (Shojaei et al. 2014).

It is worthwhile to note that two types of elements are used in Fig. 9 – C3D8R for *oil-bearing rock* and C3D8RP for the *interfacial medium* in which the pore fluid

injection process can be simulated (Shojaei et al. 2014). In the next case study, the interaction between HF and natural fractures is studied. Figure 10 shows the pore pressure distribution in different stages of the injections, starting from initiation to propagation stages. The fracture tip can be traced by following the pore pressure distribution in Fig. 10. In Fig. 11 the von Mises stress distribution is depicted in three stages of the injection process. Again the tip of the HF crack is traceable, and the speed of the crack propagation can be computed from the model.

Figure 11 shows the damage propagation when a natural fracture intersects an HF fracture during the treatment process (Shojaei and Shao 2017). The natural fracture is assumed to be made of the same rock properties of the HF medium. The natural fracture intersects with the HF path at a 90 degree angle. Due to flexibility of the CDM approach, different material properties and shapes can be readily assigned to the natural fracture to study the influence of presence of natural fractures on the HF growth.

Concluding Remarks

Hydraulic fracturing design optimization requires sophisticated simulation techniques to capture the real physics behind the fracturing process. A methodology developed for fluid-driven fractures using CDM framework was elaborated in this chapter. The numerical platform constituted based on a physics-based CDM model and is able to capture the effects of several design parameters such as (i) number/geometry of perforations; (ii) fracturing fluid properties, e.g., viscosity; (iii) proppant concentration; (iv) injection rates; etc. It is shown that anisotropic poroplasticity and poroplasticity constitutive laws together with fluid-driven damage growth laws can be coupled to bridge the pore pressure effect to the state of stress, strain, and damage in porous rocks. In earlier works by Shojaei et al. (2014), and Shojaei and Shao (2017), it was assumed that excessive plastic deformation in the skeleton of the porous rocks results in microcracks and microvoids nucleation and propagation. However, the CDM models can be formulated based on other internal state variables which could be physically tested and measured in a fracture testing procedure. The proposed CDM model by Shojaei et al. considers the microcrack and microvoid nucleation and propagation within the solid skeleton of the porous rocks (Shojaei et al. 2014; Shojaei and Shao 2017). The main contributions of the discussed CDM framework are:

- A stand-alone or built-in software can be developed to accurately predict/simulate the growth of HF in various formations and layup configurations.
- Developed software would provide a powerful design tool for HF optimization tasks where several uncertainty seniors can be studied simultaneously.
- The HF simulation can be carried out realistically in which poroelasticity, poroplasticity, and fracture mechanics of porous rocks are utilized to calibrate the proposed CDM framework.

In order to optimize the HF design, assessment of porous rocks' fracture mechanics at downhole condition is essential. The main concern in terms of HF simulation is the correlation between simulation and actual hydraulic fractures at downhole conditions. Currently authors are developing new testing methods for experimentally simulating the downhole conditions. Such testing techniques are crucial for CDM model verification and validation steps.

References

J. Adachi et al., Computer simulation of hydraulic fractures. Int. J. Rock Mech. Min. Sci. **44**(5), 739–757 (2007)

J.I. Adachi, E. Detournay, A.P. Peirce, Analysis of the classical pseudo-3D model for hydraulic fracture with equilibrium height growth across stress barriers. Int. J. Rock Mech. Min. Sci. **47**(4), 625–639 (2010)

S.H. Advani, T.S. Lee, H. Moon, *Energy Considerations Associated with the Mechanics of Hydraulic Fracture* (Society of Petroleum Engineers, Columbus, Ohio, 1990)

Bai, J. and A. Lin, *Tightly Coupled Fluid-Structure Interaction Computational Algorithm for Hydraulic Fracturing Simulations* (American Rock Mechanics Association, Minneapolis, Minnesota, 2014)

Z. Chen et al., Cohesive zone finite element-based modeling of hydraulic fractures. Acta Mech. Solida Sin. **22**(5), 443–452 (2009)

A.H.D. Cheng, Material coefficients of anisotropic poroelasticity. Int. J. Rock Mech. Min. Sci. **34**(2), 199–205 (1997)

A. Dahi Taleghani, M. Gonzalez, A. Shojaei, Overview of numerical models for interactions between hydraulic fractures and natural fractures: Challenges and limitations. Comput. Geotech. **71**, 361–368 (2016)

E. Detournay, A.H.-D. Cheng, Fundamentals of poroelasticity, in *In Comprehensive Rock Engineering: Principles, Practices and Projects*, ed. by J. A. Hudson, (Pergamon Press, Oxford, 1993)

D. Elsworth, A boundary element-finite element procedure for porous and fractured media flow. Water Resour. Res. **23**(4), 551–560 (1987)

J. Geertsma, F. De Klerk, A Rapid Method of Predicting Width and Extent of Hydraulically Induced Fractures. J. Petroleum Tech. **21**, 1571–1581 (1969)

A. Ghassemi, A. Diek, J.C. Roegiers, A solution for stress distribution around an inclined borehole in shale. Int. J. Rock Mech. Min. Sci. **35**(4–5), 538–540 (1998)

A.A. Griffith, The phenomena of rupture and flow in solids. Philos. Trans. R. Soc. Lond. A **221**(582–593), 163–198 (1921)

Kachanov, L.M., Rupture time under creep conditions. Izvestija Academii Nauk SSSR **8**, 26–31 (1958) (Reprinted in International Journal of Fracture, 97, 11–18)

Khazraei, R., *Experimental Investigations and Numerical Modelling of the Anisotropic Damage of a Vosges Sandstone* (University of Lille, 1995)

Y. Lai, M. Liao, K. Hu, A constitutive model of frozen saline sandy soil based on energy dissipation theory. Int. J. Plast. **78**, 84–113 (2016)

J. Lemaitre, How to use damage mechanics. Nucl. Eng. Des. **80**(2), 233–245 (1984)

G. Li, A. Shojaei, A viscoplastic theory of shape memory polymer fibres with application to self-healing materials. Proc. R. Soc. A-Math. Phy. **468**(2144), 2319–2346 (2012)

J. Ma, G. Zhao, N. Khalili, A fully coupled flow deformation model for elasto-plastic damage analysis in saturated fractured porous media. Int. J. Plast. **76**, 29–50 (2016)

N. Moës, J. Dolbow, T. Belytschko, A finite element method for crack growth without remeshing. Int. J. Numer. Methods Eng. **46**(1), 131–150 (1999)

S. Nemat-Nasser, M. Hori, *Micromechanics: Overall Properties of Heterogeneous Materials* (Elsevier, Amsterdam, Amsterdam, 1993)
J.M. Papadopoulos, V.M. Narendran, M.P. Cleary, *Laboratory Simulations of Hydraulic Fracturing* (Society of Petroleum Engineers, Denver, 1983)
T.K. Perkins, L.R. Kern, Widths of hydraulic fractures. J. Petrol. Tech. **13**(9), 937–949 (1961)
E. Sarris, P. Papanastasiou, The influence of the cohesive process zone in hydraulic fracturing modelling. Int. J. Fract. **167**, 33–45 (2011)
E. Sarris, P. Papanastasiou, Modeling of hydraulic fracturing in a poroelastic cohesive formation. Int. J. Geomech. **12**(2), 160–167 (2012)
J.F. Shao, Poroelastic behaviour of brittle rock materials with anisotropic damage. Mech. Mater. **30**(1), 41–53 (1998)
J. Shlyapobersky, A. Chudnovsky, *Fracture Mechanics in Hydraulic Fracturing* (American Rock Mechanics Association, Santa Fe, New Mexico, 1992)
A. Shojaei, G. Li, Viscoplasticity analysis of semicrystalline polymers: A multiscale approach within micromechanics framework. Int. J. Plast. **42**, 31–49 (2013)
A. Shojaei, G. Li, Thermomechanical constitutive modelling of shape memory polymer including continuum functional and mechanical damage effects. Proc. R. Soc. Lond. A Math. Phys. Sci. **470** (2170) (2014)
A.K. Shojaei, J. Shao, 9 – Application of continuum damage mechanics in hydraulic fracturing simulations, in *Porous Rock Fracture Mechanics*, ed. by A. K. Shojaei, J. Shao, (Cambridge Woodhead Publishing, Cambridge, 2017), pp. 197–212
A. Shojaei, G. Li, G.Z. Voyiadjis, Cyclic viscoplastic-viscodamage analysis of shape memory polymers fibers with application to self-healing smart materials. J. Appl. Mech. **80**(1), 1–15 (2012)
A. Shojaei, G.Z. Voyiadjis, P.J. Tan, Viscoplastic constitutive theory for brittle to ductile damage in polycrystalline materials under dynamic loading. Int. J. Plast. **48**, 125–151 (2013)
A. Shojaei, A. Dahi Taleghani, G. Li, A continuum damage failure model for hydraulic fracturing of porous rocks. Int. J. Plast. **59**, 199–212 (2014)
B. Sobhaniaragh, W.J. Mansur, F.C. Peters, Three-dimensional investigation of multiple stage hydraulic fracturing in unconventional reservoirs. J. Pet. Sci. Eng. **146**, 1063–1078 (2016)
N. Sukumar et al., Extended finite element method for three-dimensional crack modelling. Int. J. Numer. Methods Eng. **48**(11), 1549–1570 (2000)
Z. Voyiadjis, P.I. Kattan, *Advances in Damage Mechanics* (Elsevier, London, 2006)
G.Z. Voyiadjis, A. Shojaei, Thermodynamics of continuum damage healing mechanics healing mechanics, in *Handbook of Damage Mechanics: Nano to Macro Scale for Materials and Structures*, ed. by Z. G. Voyiadjis, (Springer New York, New York, 2015a), pp. 1493–1513
G.Z. Voyiadjis, A. Shojaei, Continuum damage-healing mechanics healing mechanics, in *Handbook of Damage Mechanics: Nano to Macro Scale for Materials and Structures*, ed. by Z. G. Voyiadjis, (Springer New York, New York, 2015b), pp. 1515–1539
G.Z. Voyiadjis, A. Shojaei, G. Li, A thermodynamic consistent damage and healing model for self-healing materials. Int. J. Plast. **27**(7), 1025–1044 (2011)
G.Z. Voyiadjis et al., A theory of anisotropic healing and damage mechanics of materials. Proc. R. Soc. A-Math. Phy. **468**(2137), 163–183 (2012a)
G.Z. Voyiadjis, A. Shojaei, G. Li, A generalized coupled Viscoplastic- Viscodamage- Viscohealing theory for glassy polymers. Int. J. Plast. **28**(1), 21–45 (2012b)
G.Z. Voyiadjis et al., Continuum damage-healing mechanics with introduction to new healing variables. Int. J. Damage Mech. **21**(3), 391–414 (2012c)
Z.A. Wilson, C.M. Landis, Phase-field modeling of hydraulic fracture. J. Mech. Phys. Solids **96**, 264–290 (2016)
C.R. Wilson, P.A. Witherspoon, Steady state flow in rigid networks of fractures. Water Resour. Res. **10**(2), 328–335 (1974)

Damage and Fracture in Brittle Materials with Enriched Finite Element Method: Numerical Study

29

Yue Sun, Emmanuel Roubin, Jean-Baptiste Colliat, and Jianfu Shao

Contents

Introduction 770
Kinematics of Discontinuities in Solids 772
Kinematics Description of Weak Discontinuity 773
Kinematic Description of Strong Discontinuity 774
Finite Element Implementation 776
Incompatible Modes 776
Finite Element Discretization 777
Admissible Discrete Model with Closure Mechanism on the Discontinuity Surface 779
Localization Criterion 779
Failure Criterion: Traction Separation Law 780
Closure Criterion 781
Numerical Resolution of the Discrete Finite Element System 785
Linearization of Equations 785
Solving the System 787
Resolution of the Cohesive Criterion 788
Numerical Application to a Cubic Specimen with Heterogeneous Structure 790
Conclusion 799
References 799

Y. Sun (✉) · J.-B. Colliat (✉)
University Lille, CNRS, Centrale Lille, LaMcube – Laboratoire de Mécanique, Multiphysique, Multi-échelle, Lille, France
e-mail: yue.sun@univ-lille.fr; jean-baptiste.colliat@univ-lille.fr

E. Roubin
3SR Lab, Université Grenoble Alpes, Grenoble, France
e-mail: emmanuel.roubin@univ-grenoble-alpes.fr

J. Shao
Laboratory of Mechanics of Lille, Villeneuve d'Ascq, France

University Lille, CNRS, Centrale Lille, LaMcube – Laboratoire de Mécanique, Multiphysique, Multi-échelle, Lille, France
e-mail: jian-fu.shao@polytech-lille.fr

© Springer Nature Switzerland AG 2022

G. Z. Voyiadjis (ed.), *Handbook of Damage Mechanics*,
https://doi.org/10.1007/978-3-030-60242-0_60

Abstract

The present chapter is part of an approach that attempts to represent the mechanical behaviors of brittle/quasi-brittle materials. At the mesoscopic scale, the studied material is considered as heterogeneous materials. The used model in this study is referred to as the enriched finite element method (EFEM) (Ortiz et al., Comput Methods Appl Mech Eng 61:189, 1987; Simo et al., Comput Mech 12:277, 1993). As a finite element-based model, this model performs two kinds of enhancements: (i) strong discontinuities, which allow an illustration of cracks and fractures, and (ii) weak discontinuities, which manage to represent heterogeneities explicitly without any need of mesh adaptation. Many existing EFEM models have shown their ability to simulate a lot of main features of brittle/quasi-brittle materials at the macroscopic scale, such as the asymmetric responses in traction/compression. With a large number of finite elements and explicit heterogeneous structures, the mechanical behaviors that applied at the local scale could be very simple. In this chapter, we are looking forward to describing more of the main characters of such material by adding a closure mechanism to the model.

Keywords

Crack closure · E-FEM method · Heterogeneous quasi-brittle materials · Mesoscopic scale · Strong discontinuity analysis

Introduction

The growth and propagation of micro-cracks is a leading cause of fatigue and damage for brittle/quasi-brittle materials, such as shale, concrete-like materials, and rocks. The computational failure mechanics is nowadays a study of significant value. One of the characteristics of the materials referred to above is that they are materials with complex structures. For example, beginning at the mesoscopic scale, concrete exhibits aggregate pieces and macropores, and the complexity of its structure increases when increasingly finer scales are considered. Another characteristic of these kinds of materials is that they show complex mechanical behaviors, such as the nonsymmetric responses in traction and compression as well as the hysteresis phenomenon in cyclic loadings (see Fig. 1). From a general point of view, we can make an assumption that those two complexities are strongly linked.

The hypothesis stems from the nonlinear complex adaptive system (Ahmed et al. 2005). The essence of the complex system is that each individual constituent conforms to (very) simple rules. However, when the system is studied as a whole, emergent responses can be observed after upscaling which do not exist at the single element. Besides, by understanding the behaviors of each element, it may be beneficial for us to understand the entire system.

Naturally, the macroscopic mechanical behaviors of concrete are known a priori from experimental tests (see Fig. 1). The complex heterogeneous structure of concrete is thus defined as the explicit heterogeneous geometry of the material. At the

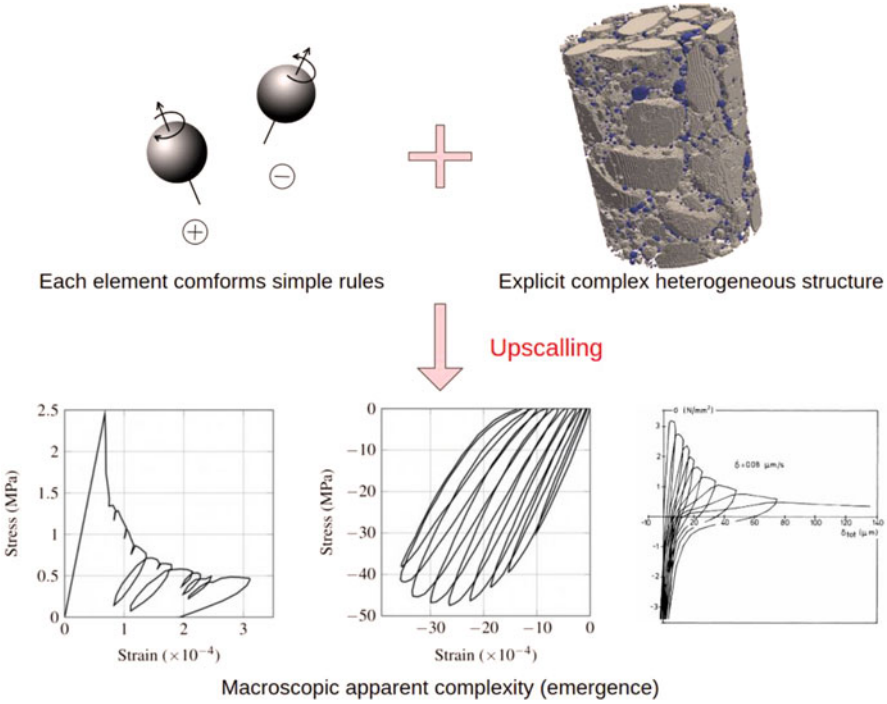

Fig. 1 Hypothesis that complex mechanical behaviors of brittle/quasi-brittle materials (Mazars et al. 1990; Terrien 1980; Reinhardt 1984) can emerge from the upscaling of elements with simple behaviors and explicit heterogeneous structure (Stamati et al. 2018)

mesoscopic scale, the heterogeneities are referred to as the aggregates and macropores (see Fig. 1). It can be constructed within the framework of the finite element method, with a large number of elements and explicit representation of heterogeneities. Moreover, a newly developed technique, namely, X-ray tomography, makes it possible to establish a morphological structure of concrete based on real tomographic images (Stamati et al. 2018). Therefore, it is interesting to look back to clarify the simple rules of each element.

Based on the previous assumption, attempts to solve the simple mechanical behaviors of each element have been made by former studies. The used method in this chapter is based on the strong discontinuity approach, namely, the enriched finite element method (EFEM) (Ortiz et al. 1987; Simo et al. 1990). EFEM is an element-based enhancement model, with an additional degree of freedom attached inside the element as internal variables. It is capable of yielding the mesh dependence without adding special artificial numerical parameters. As the energy is dissipated over a two-dimensional discontinuity interface, by applying a specific kinematic enhancement to the element, the total dissipated energy becomes independent of the mesh size (Simo et al. 1990). Besides, as the additional interval variable is an element-based enhancement, the increasing number of cracked elements will not affect the size of the assembled stiffness matrix for the total system. Therefore, the

model is capable of simulating a system with a large number of elements that carry strong discontinuities. The ratio of the fractured elements to the total elements can be very high. Another benefit of EFEM is that the strong discontinuities can pass through the element in an arbitrary trajectory. Therefore, it is capable of performing a simulation of complex and accurate cracks, such as cracks with several branches, cracks stopped by heterogeneities, and a crack that meets another crack.

Moreover, individual to strong discontinuity, the weak discontinuity (Ortiz et al. 1987) can be alternatively included in the model to represent heterogeneities, even for complex geometry (Roubin 2013). Due to the nonadapted meshing method, the heterogeneities can be taken into consideration in an explicit way (Moës et al. 2003).

The study performed in this chapter is closely related to the previous work undertaken by (Roubin 2013), in which each element is governed by two mechanisms: localization and traction-separation. It has been demonstrated that even though only the "opening" mechanism is applied to elements, the model is capable of performing failure behaviors of concrete in traction as well as in compression. Moreover, nonsymmetric behaviors can also be observed. However, to the author's knowledge, the behavior performed by crack closure in EFEM has yet to be taken into consideration. Therefore, based on the prior studies, the closure mechanism of the cracks is also taken into account in this chapter.

Kinematics of Discontinuities in Solids

In this section, we summarize the basic notations that we used in this chapter. The referenced domain $\Omega \subset \mathbb{R}^{n_{dim}}$ is a solid exhibiting heterogeneities and cracks (see Fig. 2). Its smooth boundary $\Gamma \subset \mathbb{R}^{n_{dim}-1}$ can be divided into two disjointed boundaries: the displacement boundary Γ_u and the traction boundary Γ_t. Within the framework of finite element method, this specimen can be discretized by means of standard isoparametric elements $\Omega = \cup_{e=1}^{n_e} \Omega_e$.

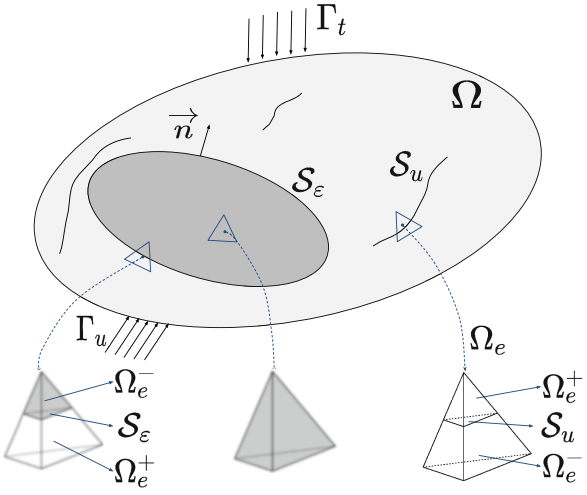

Fig. 2 Illustration of the heterogeneities and cracks in the referent body and the corresponding enhanced elements

Dealing with the explicit heterogeneities, the mesh method is nonadapted. Since the heterogeneity surfaces are defined a priori and independent to any mechanical calculation, there will be a set of elements crossed by the interface of heterogeneity S_ε, dividing the elements into two parts Ω_e^+ and Ω_e^- with a unit vector n pointing from Ω_e^- to Ω_e^+.

At the inner of the dealing body, another set of elements is divided into two parts by the failure path S_u. Naturally, the discontinuity surface S_ε is defined by the geometry of material, whereas the path and orientation of the strong discontinuity S_u usually depend on particular criteria.

Dealing with the weak discontinuities and the strong discontinuities, three cases can be present in an element: (i) the element contains only a weak discontinuity, (ii) the element contains only a strong discontinuity, and (iii) both of them are present in an element. In the third case, it is considered that the kinematic failure will take place in the heterogeneity interface. It implies that if the element is "close" enough to the heterogeneity, the crack opening will be localized on the heterogeneity surface.

Furthermore, it is assumed that the bulk part has a purely elastic kinematic relationship and the kinematic behaviors of the strong/weak discontinuity are independent. Hence, the strain field admits an additive form

$$\varepsilon(x) \coloneqq \nabla^{\mathrm{sym}} \overline{u}(x) + \widetilde{\varepsilon}(x) + \widehat{\varepsilon}(x), \tag{1}$$

where $\nabla^{\mathrm{sym}} \coloneqq \frac{1}{2}\left[\nabla(\cdot) + \nabla^T(\cdot)\right]$ denotes the symmetric gradient operator. Notation $\widetilde{\cdot}/\widehat{\cdot}$ represents the weak/strong discontinuity.

Kinematics Description of Weak Discontinuity

In this section, interest is focused only on the elements which exhibit weak discontinuities. The elements of this kind contain different elastic parameters, Young's modulus and Poisson's ratios; thus a strain discontinuity is emerged from this difference, as shown in Fig. 3. With the normal vector n pointing from one sub-domain to another, we can construct an orthonormal basis (*n, m, t*). The continuity of the displacement field should be respected crossing the discontinuity surface, so we have:

$$u^+(x) = u^-(x), \forall x \in S_\varepsilon. \tag{2}$$

The strain jump of the weak discontinuity $[|\varepsilon|] \coloneqq \varepsilon^+(x) - \varepsilon^-(x)$ can be calculated by the symmetrical gradient of the corresponding displacement field:

$$\nabla^{\mathrm{sym}} u\Big|_{S_\varepsilon} = \frac{1}{2}\left(\nabla u + \nabla^T u\right)\Big|_{S_\varepsilon} \text{ with } \nabla u = \begin{pmatrix} \partial u_{1,n} & \partial u_{1,m} & \partial u_{1,t} \\ \partial u_{2,n} & \partial u_{2,m} & \partial u_{2,t} \\ \partial u_{3,n} & \partial u_{3,m} & \partial u_{3,t} \end{pmatrix}_{(n,m,t)}. \tag{3}$$

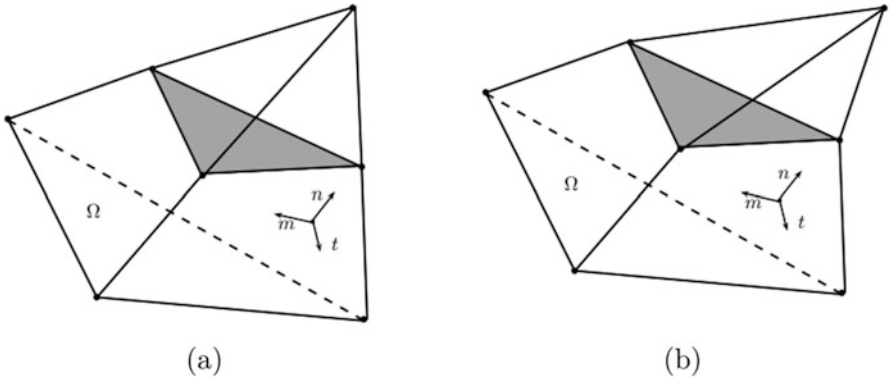

Fig. 3 Representation of the strain discontinuity in a tetrahedral element (Vallade 2016)

It can be deduced that the jump of the strain field takes place in the direction perpendicular to the discontinuity surface but not in the direction along the interface. Accordingly, $\nabla(\widetilde{u}^{+}) \cdot m = \nabla(\widetilde{u}^{-}) \cdot m$ and $\nabla(\widetilde{u}^{+}) \cdot t = \nabla(\widetilde{u}^{-}) \cdot t$. Taking this into Eq. (3), it can be seen that the last two colons of the matrix ∇u have the same value for both sub-domains. Hence, $[\varepsilon]_n$ $[\varepsilon]_m$ $[\varepsilon]_m$ are three constants that can entirely define the jump of the strain field (Roubin et al. 2015). We can take the displacement field $\widetilde{u}$ in a first-order form (Ibrahimbegovic et al. 2005):

$$\widetilde{u}(x) = \Theta n \cdot (x - \xi)\left([\varepsilon]_n n + [\varepsilon]_m m + [\varepsilon]_t t\right) \text{ with } \Theta = \begin{cases} \Theta^{+} & \forall x \in \Omega_e^{+} \\ \Theta^{-} & \forall x \in \Omega_e^{-} \end{cases}, \tag{4}$$

where ξ denotes the position of interface surface S_ε and $n \cdot (x - \xi)$ can be seen as a signed distance to the discontinuity surface. Θ is a still undefined function of Ω_e, the explicit expression will be given later with the help of variational formulations. We can obtain the weak shape of the enhanced strain field by taking the symmetrical gradient of $\widetilde{u}$ (Benkemoun et al. 2015):

$$\widetilde{\varepsilon} = \nabla^{\text{sym}}(\widetilde{u}) = \Theta\left([\varepsilon]_n n \otimes n + \frac{[\varepsilon]_m}{2}(n \otimes m)^{\text{sym}} + \frac{[\varepsilon]_t}{2}(n \otimes t)^{\text{sym}}\right) \tag{5}$$

Kinematic Description of Strong Discontinuity

In this part, the main interest is focused on the strong discontinuity kinematics (Simo and Rifai 1993; Oliver 1996; Wells 2001). Let us consider an element Ω_e exhibits a strong discontinuity dividing itself into two sub-domains; the discontinuity surface is

noted as S_u. The discontinuity of the displacement field can be decomposed into the following function (Roubin et al. 2015):

$$u = \overline{u} + (H_{S_u} - \varphi_e)[|u|], \tag{6}$$

where H_{S_u} is the Heaviside function centered on S_U, $\overline{u}$ is the regular part of the displacement field to impose the standard boundary conditions (Oliver 1996), and $[|u|]$ is a continuous function representing the displacement jump. For the sake of simplicity, $[|u|]$ is considered as a unity function over the finite element.

By taking the symmetric gradient of the displacement field, the corresponding strain field can be obtained as

$$\begin{aligned}\varepsilon &= \nabla^{\mathrm{sym}} u \\ &= \underbrace{\nabla^{\mathrm{sym}} \widehat{u}}_{\text{regular}} + \underbrace{(H_{S_u} - \varphi_e)\nabla^{\mathrm{sym}}([|u|]) - ([|u|] \otimes \nabla\varphi_e)^{\mathrm{sym}}}_{\text{bounded enhancement}} + \underbrace{\delta_{\Gamma_d}([|u|] \otimes n)}_{\text{unbounded enhancement}}\end{aligned} \tag{7}$$

The strain field admits an additive form of three parts. The regular displacement field respects the standard stress-strain constitutive equation. The bounded enhancement can be simplified by taking the jump of the displacement field $[|u|]$ as a constant function. It results in a null value of $(H_{\Gamma_d} - \varphi_e)\nabla^{\mathrm{sym}}([|u|])$. Then we can see that the gradient of the Heaviside function brings an unbounded enhancement part, which bears a Dirac delta distribution δ. Centered at the discontinuity interface, it carries an infinite value at the interface and null value otherwise. Thus far, Eq. (7) can be written as

$$\widehat{\varepsilon} = \widehat{\varepsilon}_b + \widehat{\varepsilon}_u = -([|u|] \otimes \nabla\varphi_e)^{\mathrm{sym}} + \delta_S([|u|] \otimes n) \tag{8}$$

Regarding the unbounded part in the function, some properties such as the traction continuity condition seem difficult to conform. Nevertheless, some solutions are available within the FE context. In this study, the used solution is called discrete strong discontinuity approach (DSDA) (Oliver 1996), which leads to an underlying discrete model at the discontinuity surface. And a traction vector T which links with the crack opening $[|u|]$ can also be introduced

$$\sigma^+(x) \cdot n = \sigma^-(x) \cdot n = T, \forall x \in S. \tag{9}$$

It can be then used to model the failure mechanism at the local scale. And beyond the discontinuity, the bulk $\Omega \backslash S$ remains an elastic behavior, which can be described by Hooke's law:

$$\sigma = \mathrm{C} : \varepsilon. \tag{10}$$

In the case of exhibiting a weak discontinuity, the two sub-domains are isotropic, and the operator $C^{+|-}$ is calculated separately by Young's modulus $E^{+|-}$ and Poisson ratio $v^{+|-}$.

Finite Element Implementation

Incompatible Modes

Based on existing EFEM studies, a three-field variational formulation is used here (Vallade 2016; Roubin et al. 2015; Washizu 1968):

$$HW_{\widehat{u}}(\widehat{u},\varepsilon,\sigma;\widehat{\eta}) = \int_{\Omega} \nabla^{\mathrm{sym}}\widehat{\eta} : \sigma d\Omega - \int_{\Omega} \widehat{\eta}\cdot\rho\overline{b}d\Omega - \int_{\Gamma} \widehat{\eta}\cdot\overline{t}d\partial\Omega = 0, \tag{11a}$$

$$HW_{\sigma}(\widehat{u},\varepsilon,\sigma;\tau) = \int_{\Omega} \tau : (\nabla^{\mathrm{sym}}\widehat{u} - \varepsilon) = 0, \tag{11b}$$

$$HW_{\varepsilon}(\widehat{u},\varepsilon,\sigma;\gamma) = \int_{\Omega} \gamma : (\breve{\sigma}(\varepsilon) - \sigma)d\Omega = 0, \tag{11c}$$

where $(\widehat{u},\varepsilon,\sigma)$ represents the standard displacement field, the strain field, and the stress field. Then three corresponding virtual fields are noted as $(\widehat{\eta},\tau,\gamma)$, also mutually independent.

Then a classic method of incompatible modes is introduced here, mentioned as the assumed strain method. The central idea is assuming that both actual and virtual fields are enhanced in an additional way, making them divided into three parts, the standard part, the enhanced weak discontinuity, and the enhanced strong discontinuity:

$$\varepsilon = \underbrace{\nabla^{\mathrm{sym}}\widehat{u}}_{\text{compatible}} + \underbrace{\underbrace{\widetilde{\varepsilon}}_{\text{weak}} + \underbrace{\widehat{\varepsilon}}_{\text{strong}}}_{\text{incompatible}}, \text{ and } \gamma = \underbrace{\nabla^{\mathrm{sym}}\widehat{\eta}}_{\text{compatible}} + \underbrace{\underbrace{\widetilde{\gamma}}_{\text{weak}} + \underbrace{\widehat{\gamma}}_{\text{strong}}}_{\text{incompatible}}. \tag{12}$$

Considering the orthogonal relationship between the enhanced and the virtual part of the strain and stress field (Roubin et al. 2015), we can derive the following simplified formulation:

$$\int_{\Omega} \nabla^{\mathrm{sym}}\widehat{\eta} : \breve{\sigma}(\nabla^{\mathrm{sym}}\widehat{u} + \widetilde{\varepsilon} + \widehat{\varepsilon})d\Omega - \int_{\Omega} \widehat{\eta}\cdot\rho\overline{b}d\Omega - \int_{\Gamma_t} \widehat{\eta}\cdot\overline{t}d\partial\Omega = 0, \tag{13a}$$

$$\int_{\Omega} \widetilde{\gamma} : \breve{\sigma}(\nabla^{\mathrm{sym}}\widehat{u} + \widetilde{\varepsilon} + \widehat{\varepsilon})d\Omega = 0, \tag{13b}$$

$$\int_{\Omega} \widehat{\gamma} : \breve{\sigma}(\nabla^{\mathrm{sym}}\widehat{u} + \widetilde{\varepsilon} + \widehat{\varepsilon})d\Omega = 0. \tag{13c}$$

To ensure the convergence of the method, the patch test should be respected after the orthogonal condition is imposed. By assuming that the discontinuity interface is flat, which makes the normal vector of the interface n a constant over each element, we will take the Θ as a function that depends only on the volume of sub-domains (Roubin 2013):

$$\Theta^{+} = \frac{V^{-}}{V} \text{ and } \Theta^{-} = -\frac{V^{+}}{V}. \tag{14}$$

Subsequently, the strongly enhanced strain field consists of two parts: the unbounded part $\delta_{\Gamma_d}([|u|] \otimes n)^s$ and the bounded part $\widehat{\gamma}_b$. The later can be explicitly defined by taking into consideration of the zero mean condition. Following the enhanced assumed strain (EAS) method, the complete form of the strong enhancement of the strain field can be obtained by

$$\widehat{\gamma} = \underbrace{\delta_{\Gamma_d}([|\eta|] \otimes n)^{\text{sym}}}_{\text{unbounded}} - \underbrace{\frac{A}{V}([|\eta|] \otimes n)^{\text{sym}}}_{\text{bounded}}. \tag{15}$$

Finite Element Discretization

It is present in this part the resolution of the three-field variational formulation (Eq. (13)). The discretization of the strain field is different depending on whether it is standard or virtual. The standard strain field is enhanced using KES in a kinematic point of view, whereas the virtual strain field is enhanced using the EAS (referred to as $\cdot^*$ in the following part) from a statistical point of view. Based on the DSDA, the standard discretization of the strain field contains only the bounded enhanced part, while the virtual discretization has both the bounded and unbounded enhancement. The discretization is written as:

$$\varepsilon = \nabla^{\text{sym}}\widehat{u} + \widetilde{\varepsilon} + \widehat{\varepsilon} = \mathbf{B}\, d + \mathbf{G}_{\text{w}}[|\varepsilon|] + \mathbf{G}_{\text{s}}[|u|], \tag{16a}$$

$$\gamma = \nabla^{\text{sym}}\widehat{\eta} + \widetilde{\gamma} + \widehat{\gamma} = \mathbf{B}\, d + \mathbf{G}_{\text{w}}[|\gamma|] + \left(\mathbf{G}^{*}_{\text{s,b}} + \mathbf{G}^{*}_{\text{s,u}}\right)[|\eta|]. \tag{16b}$$

Several mentioned notations above are as follows: $B = (\partial N)$, the standard strain interpolation matrix, $\mathbf{G}_{\text{w}}$ the standard and virtual field corresponding to the weak discontinuity; $\mathbf{G}_{\text{s}}$, the bounded part of the standard field corresponding to the strong discontinuity; $\mathbf{G}^{*}_{\text{s}} := \mathbf{G}^{*}_{\text{s,b}} + \mathbf{G}^{*}_{\text{s,u}}$, the full enhancement of the virtual field corresponding to the strong discontinuity; d, the nodal displacement field; and $[|\varepsilon|]$ (resp. $[|u|]$), the supplement unknown variables brought by weak (resp. strong) discontinuity. It is worth noting that the strain fields are all expressed in Voigt notation.

Considering the discretization of the system, we can write the global equilibrium equation in a residual form

$$\overline{R} := \mathbb{A}_{e=1}^{n_e}\overline{R}_e = \overline{f}_{\text{ext}} - \mathbb{A}_{e=1}^{n_e}\left(\int_{\Omega_e} B^T \sigma d\Omega\right) = \overline{0}, \tag{17}$$

where $\mathbb{A}_{e=1}^{n_e}$ represents the standard assembly operator which groups all finite elements n_e of the global system and $\overline{f}_{\text{ext}}$ denotes the external force, which writes as

$$\overline{f}_{\text{ext}} = \mathbb{A}_{e=1}^{n_e}\left(\int_{\Omega_e} N^T b\, d\Omega + \int_{\Gamma_t^e} N^T t\, d\Gamma\right). \tag{18}$$

We can obtain Eq. (19a) by injecting parameters of Eq. (16b) into Eq. (13b), and can obtain Eq. (19b) by injecting Eq. (16b) into Eq. (13c).

$$\int_{\Omega} \mathbf{G}_{\text{w}}^T \breve{\sigma}(d, [|\varepsilon|], [|u|])\, d\Omega = 0, \tag{19a}$$

$$\int_{\Omega} \left(\mathbf{G}_{\text{s,b}}^{*,T} + \mathbf{G}_{\text{s,u}}^{*,T}\right) \breve{\sigma}(d, [|\varepsilon|], [|u|])\, d\Omega = 0. \tag{19b}$$

Then Eq. (15) can be changed into the form

$$\widehat{\gamma} = \left(\mathbf{G}_{\text{s,b}}^{*} + \mathbf{G}_{\text{s,u}}^{*}\right)[|\eta|] = -\frac{A}{V}([|\eta|] \otimes n)^{\text{sym}} + \delta_S([|\eta|] \otimes n)^{\text{sym}}, \tag{20}$$

where $(\cdot \times n)^{\text{sym}}$ is noted as an operator H_{s}^{*} for the rest part, leading to an equivalent Voigt notation for the traction vector

$$T = \underbrace{\breve{\sigma} \cdot n}_{\text{matrix notation}} = \underbrace{H_{\text{s}}^{*,T} \breve{\sigma}}_{\text{Voigt notation}}. \tag{21}$$

By considering one of the proprieties of the Dirac delta distribution δ_S, $\int f(x)\delta_S dx = \int f(x = S)dx$, the unbounded part of the virtual strain field can be further simplified into the form

$$\int_{\Omega} \mathbf{G}_{\text{s,u}}^{*,T} \breve{\sigma}(d, [|\varepsilon|], [|u|]) d\Omega = \int_{S} T(d, [|\varepsilon|], [|u|]) d\partial\Omega. \tag{22}$$

As for the interpolation matrix corresponding to weak discontinuity, $\mathbf{G}_{\text{w}}$ is defined separately in two parts $\Theta^{+|-}$ as

$$\mathbf{G}_{\text{w}} = \begin{cases} \mathbf{G}_{\text{w}}^{+} = \Theta^{+} H_{\text{w}} = \dfrac{V^{-}}{V} H_{\text{w}} & \text{in } \Omega_e^{+}, \\ \mathbf{G}_{\text{w}}^{-} = \Theta^{-} H_{\text{w}} = -\dfrac{V^{+}}{V} H_{\text{w}} & \text{in } \Omega_e^{-}. \end{cases} \tag{23}$$

According to Eq. (8), we can see that the bounded part of the strong enhancement of the standard strain field writes as $([|u|] \otimes \nabla \varphi_e)^s$, which corresponds to the term $\mathbf{G}_{\text{s}}[|\, u|\,]$ in Eq. 16a. Hence $\mathbf{G}_{\text{s}}$ can be obtained as an equivalent symmetric operator, $(\cdot \otimes \nabla \varphi_e)^s$, where φ_e is an explicitly defined arbitrary function to separate nodes at Ω_e^{+} from Ω_e^{-}. The arbitrary function is defined as follows:

$$\varphi_e(x) = \sum_{a=1}^{n_e} N_a p_a \text{ with } p_a = \begin{cases} 1 \text{ if node number } a \in \Omega_e^+, \\ 0 \text{ if node numner } a \in \Omega_e^-. \end{cases} \tag{24}$$

In summary, the discretized system gives as (Roubin et al. 2015)

$$\overline{R} := \mathbb{A}_{e=1}^{n_e} \left(\overline{f}_{\text{int}} - \overline{f}_{\text{ext}} \right) = \mathbb{A}_{e=1}^{n_e} \left(\overline{f}_{\text{ext}}^e - \int_{\Omega_e} B^T \breve{\sigma}\left(d, [|\varepsilon|], [|u|]\right) d\Omega \right) = \overline{0}, \tag{25a}$$

$$\overline{R}_{[|\varepsilon|]}^e = \int_{\Omega_e} \mathbf{G}_{\text{w}}^T \breve{\sigma}(d, [|\varepsilon|], [|u|])\, d\Omega = \overline{0}, \tag{25b}$$

$$\begin{aligned} \overline{R}_{[|u|]}^e &= \int_{\Omega_e} G_{\text{s}}^{*,T} \breve{\sigma}(d, [|\varepsilon|], [|u|])\, d\Omega \\ &= \int_{\Omega_e \setminus \mathsf{S}} \mathbf{G}_{\text{s,b}}^{*,T} \breve{\sigma}(d, [|\varepsilon|], [|u|]) d\Omega + \int_S T\, d\partial\Omega = \overline{0}. \end{aligned} \tag{25c}$$

In the above equations, Eq. (25a) represents the global equilibrium equation of a standard finite element system, whereas Eq. (25b) and Eq. (25c) are local equations for each element and carry the enhancement parts. The enhancements $[|\varepsilon|]$ and $[|u|]$ are considered as the internal variables and are both solved at the element level. Hence, the global equilibrium equation Eq. (25a) always has the same size no matter how many heterogeneities exist in the system or how many elements begin to crack.

Admissible Discrete Model with Closure Mechanism on the Discontinuity Surface

As it is mentioned in the previous part, a traction vector T is continuous over the element and links the two sub-domains crossing the discontinuity surface S. Our discrete model is formulated based on the description of the relationship between the traction vector and the crack opening $[|u|]$.

In existing EFEM studies, many discrete models have been proposed and well documented, for instance, the traction-opening fracture (Roubin et al. 2015), the sliding-opening shear fracture (Hauseux 2015), and hydraulic mechanical coupling problem (Vallade 2016). Based on these previous works, the attempt in this section is to propose a discrete model that considers the closure of cracks.

Localization Criterion

At the beginning of loading, the element has an elastic behavior, until the stress field or the strain field reaches a specific value, i.e., the localization criterion. Our

localization criterion is stress-based. The yield stress, noted as σ_y, is considered as a local parameter of the material. The localization criterion wrote as

$$\Phi_1 = \sigma_{eq} - \sigma_y. \tag{26}$$

In this equation, a negative value of Φ_1 represents an elastic behavior of the element, while a positive value leads to the localization and appearance of the crack. As we can see, the equivalent stress σ_{EQ} is a constant value. Two cases should be considered: (i) the studied element is isotropic without weak discontinuity, and (ii) the weak discontinuity is present in the element.

In the first case, the equivalent stress is determined by the major principal stress, $o\sigma_{eq} = \sigma_1$. The orientation of the discontinuity interface n is the corresponding eigenvector, n_I. The localization criterion writes

$$\Phi_1^{strong} = \sigma_1 - \sigma_y. \tag{27}$$

In the second case, the element carries different phases, it is assumed that the crack opens at the heterogeneity surface between the two sub-domains. The normal vector n is defined a priori by the geometric information of the material and thus is independent of the stress state. The equivalent stress is calculated by the projection of the traction vector T on the normal vector n, and the localization criterion writes

$$\Phi_1^{weak} = n \cdot T - \sigma_y \tag{28}$$

We present here an isotropic one-dimensional example. As the state of the stress field reaches the yield stress, the localization takes place. The displacement field and local constitutive behavior are shown in Fig. 4.

Failure Criterion: Traction Separation Law

Following the localization of the element, the failure behavior is driven by the traction-separation law (Roubin et al. 2015):

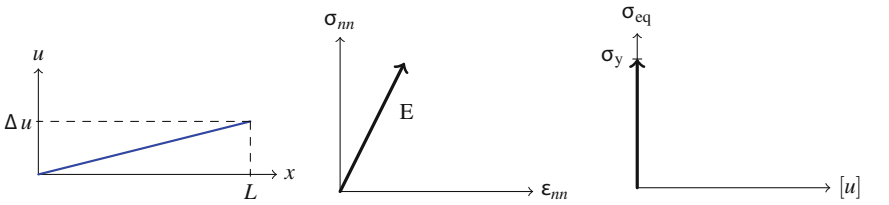

(a) The displacement field (b) Behavior outside the discontinuity interface (c) Behavior at the discontinuity interface

Fig. 4 Local constitutive model at the continuous part and at the discontinuity interface at the moment of localization

$$\Phi_o = \sigma_{eq} - \left(\sigma_y - q_0([u])\right), \text{with } [|u|] = [u] \cdot n. \tag{29}$$

A positive value of the traction-separation criterion Φ_o means an un-equilibrium state of the element and the crack needs to go further until it reaches an equilibrium state. A negative value presents an elastic loading or unloading, or closure of cracks, which we will discuss later. In this equation, $q_o([u])$ is referred to as the hardening function. It is a continuous simple decreasing function in terms of the opening value, with its magnitude value located at $[u] = 0$. It will approach to zero as the $[u] = 0$ increases. The hardening function is defined as

$$q_o([u]) = \sigma_y \left(1 - \exp\left(-\frac{\sigma_y}{G_{op}}[u]\right)\right), \tag{30}$$

where σ_y and G_{op} are both local material parameters. The latter is referred to as the fracture energy, which governs the amount of necessary energy to create a fully opened fracture. Physically, a bigger value of the fracture energy states for a tougher and more durable material.

Assuming the same one-dimensional example as shown in Fig. 4, the traction-separation phase is depicted in Fig. 5. As the imposed displacement Δu increases, the crack will propagate and lead to a decreasing value of the equivalent stress. Since the traction continuity condition is always satisfied, the stress in the bulk volumes $\Omega_e \backslash S$ will also decrease as shown in Fig. 5b.

Closure Criterion

Following the traction-separation law, a closure law is considered in our discrete model if the normal stress is turned into compressive stress. As the model exhibits no closure mechanism (see Fig. 6a), the crack opening value will not decrease even under high compressive stress. Unlike most phenomenological models that mainly describe stress-strain curves, our model is built at the mesoscopic scale; the complexity consists in depicting the relationship between the traction vector on the

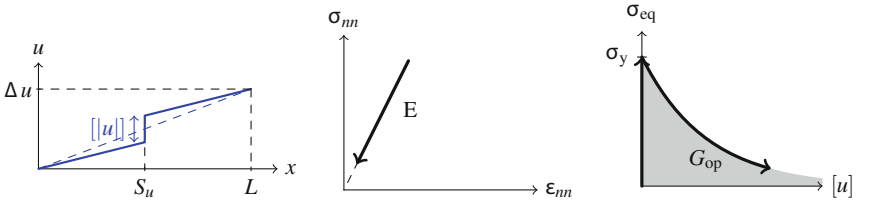

(a) The displacement field

(b) Behavior outside the discontinuity interface

(c) Behavior at the discontinuity interface

Fig. 5 Local constitutive model at the continuous part and at the discontinuity interface at the traction separation stage

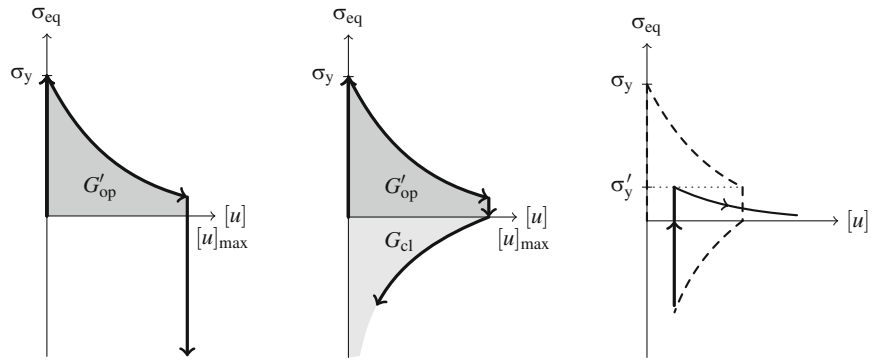

(a) Phenomenological model without closure mechanism

(b) Phenomenological model with exponential closing law

(c) Phenomenological model with damaged tensile strength

Fig. 6 Hypothesis for local constitutive models with nonlinear closing laws and damaged tensile strength at the discontinuity interface

discrete discontinuity surface and the crack opening value. Upon physical considerations, the applied closure mechanism is replied on three hypotheses.

- **Hypothesis 1**. The closing criterion is driven by an exponential and continuous function; $[u]$ will approach towards zero if the equivalent stress turns to infinite compression but will never close completely (see Fig. 6b).

  This hypothesis is proposed upon a physical consideration that an already created crack of a brittle/quasi-brittle material should not disappear even when high compressive stress is applied. Furthermore, this driven function also verifies sort of the spirit of "symmetric" that in the opening phase, the material will become progressively fragile and in the closing stage, the closing of crack will become more and more difficult.
- **Hypothesis 2**. The amount of required energy for a complete closing G'_{op} equals to the energy dissipated at the opening phase G_{cl}.

  The design of this hypothesis is an attempt to make the model remain simple and clean. No additional parameters are needed to depict the closure mechanism.
- **Hypothesis 3**. As the element reopens after the closing phase, the calculation of the new traction-separation law will base on the residual tensile strength σ'_{y} and the residual fracture energy G_{re} (see Fig. 6c).

  This third hypothesis is proposed to deal with the already damaged elements. Physically, the damaged element should be weaker and more fragile than the sound elements. Even though the crack can be partially closed during the closing phase, the yield stress of the element cannot be restored to the value of the sound element. And a certain amount of fracture energy has already been dissipated in the opening phase. Therefore, the calculation of the reopening criterion is defined based on the residual tensile strength and fracture energy. As a result, damages that have occurred to an element throughout history are irreversible.

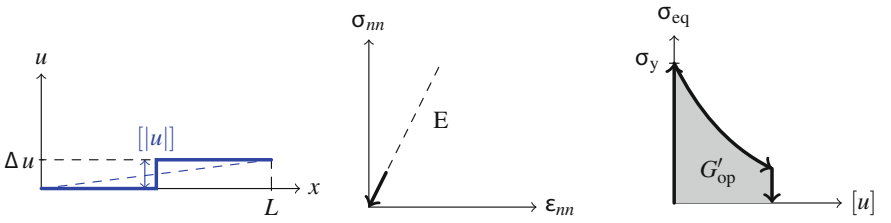

(a) The displacement field (b) Behavior outside the discontinuity interface (c) Behavior at the discontinuity interface

Fig. 7 Local constitutive model at the continuous part and at the discontinuity interface as the imposed displacement decrease

Unloading Procedure

The first procedure that occurs to an element subsequently to the opening phase is the unloading procedure. This procedure takes place on the bulk volumes outside the discontinuity surface, which means that the crack opening value $[u]$ will not change. After the opening stage, an amount of tensile energy is stored in the bulk volumes. The discontinuity surface will be always under tensile stress until the elastic energy is totally released, i.e., the strain field is null on the bulk volumes. Therefore, the unloading procedure is a pure elastic phase. We can see from Fig. 7 that it happens when $\Delta u = [u]$.

Closure of Cracks

After the unloading process, the closure of the crack occurs when the stress on the discontinuous surface switches to compressive stress. The decreasing of the crack opening value is driven by the closing criterion. As it is shown in Fig. 8, the closing criterion is nonlinear and continuous. It is assumed that the necessary needed energy for a complete close G_{cl} equals to the amount of energy that dissipated at the opening stage G'_{op}. The closing procedure will become more and more difficult, and as a result, the crack can never be completely closed.

It is worth some particular attention at the point of $\Delta u = 0$, where the imposed displacement equals to zero, whereas the crack opening value is still positive, and the element is under compressive stress.

Reloading Procedure

Let us now apply a reloading displacement to the element. Firstly, the element will release the stored compressive energy in bulk volumes. Then the stress on the discontinuity surface will turn to positive as the reloading continues until the equivalent stress reaches the residual critical tensile strength σ'_{y}. And the fracture energy is also taken as the residual value G_{re} (see Fig. 9), which leads to a weaker and more fragile material than the sound one.

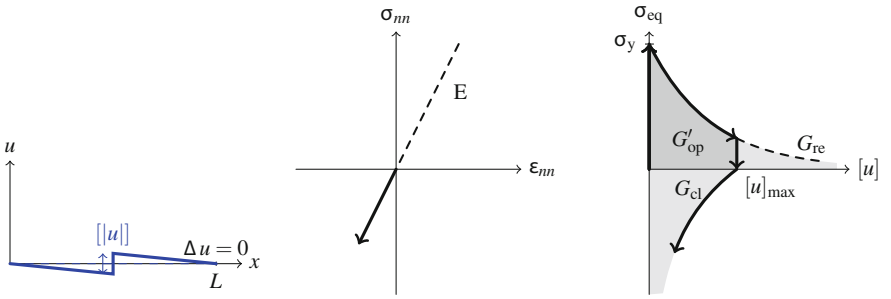

(a) The displacement field (b) Behavior at the continuous part (c) Behavior at the discontinuity interface

Fig. 8 Local constitutive model at the continuous part and at the discontinuity interface at the crack closing phase

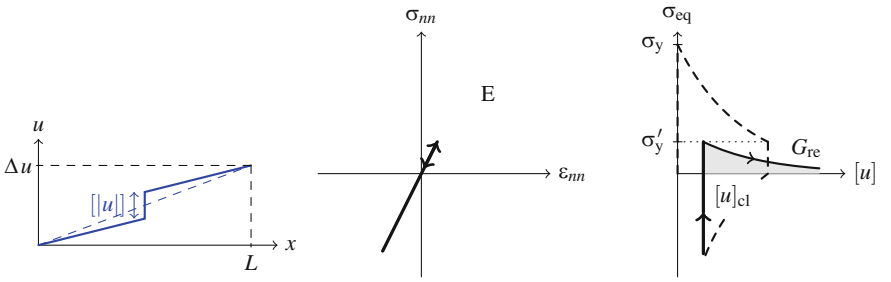

(a) The displacement field (b) Behavior at the continuous part (c) Behavior at the discontinuity interface

Fig. 9 Local constitutive model at the continuous part and at the discontinuity interface as the imposed displacement reloads

Governing Equations

In the previous parts, the kinematic behaviors of the model on the discontinuity surface have been decomposed into several different phases. In the closing process, it is assumed that the necessary energy for a total crack closure equals to the dissipated energy in the opening phase. This amount of energy is calculated as

$$E_{\mathrm{op}} = \int_0^{[u]_{\max}} \sigma_{\mathrm{eq}}([u])\, d[u] = G_{\mathrm{op}}\left(1 - \exp\left(-\frac{\sigma_{\mathrm{y}}[u]_{\max}}{G_{\mathrm{op}}}\right)\right) = G_{\mathrm{cl}}. \tag{31}$$

As a result, the driven function of the closing phase can be completely defined by the material's parameters G_{op}, σ_{y}, and the maxim opening value $[u]_{\max}$; no additional parameters are required. The closing energy should respect the following equation

$$E_{\mathrm{cl}} = \int_{[u]_{\max}}^{0} \sigma_{\mathrm{eq}}([u])\, d[u] = E_{\mathrm{op}} = G_{\mathrm{cl}}. \tag{32}$$

The choice made here is

$$\Phi_{\mathrm{c}} = -\sigma_{\mathrm{eq}} + \underbrace{\frac{G_{\mathrm{cl}}}{[u]_{\max}} \ln\left(\frac{[u]}{[u]_{\max}}\right)}_{q_{\mathrm{c}}}, \tag{33}$$

where q_c is referred to as the hardening function during the closing procedure. A positive value of Φ_{c} means that the crack should continue closing to reach the equilibrium state, and a negative value of Φ_{c} means that the element is under elastic unloading or reloading. Since the maximum crack opening value $[u]_{\max}$ is always greater than or equal to the actual crack opening $[u]$, it is impossible to have Φ_{o} and Φ_{c} both positive at the same time.

In the reopening phase, the critical parameters of the traction-separation law are taken as the residual tensile strength (marked as σ'_{y} in Fig. 9c) and the residual fracture energy (marked as G_{RE} in Fig. 8c and Fig. 9c). The updated traction-separation law writes as

$$\Phi_{\mathrm{o}} = \sigma_{\mathrm{eq}} - \sigma'_{\mathrm{y}}\left(1 - \exp\left(-\frac{\sigma'_{\mathrm{y}}}{G_{\mathrm{re}}}[u]\right)\right), \text{with} \begin{cases} \sigma'_{\mathrm{y}} & = \sigma_{\mathrm{y}} \exp\left(-\dfrac{\sigma_{\mathrm{y}}\left([u]_{\max} - [u]_{\mathrm{cl}}\right)}{G_{\mathrm{op}}}\right) \\ G_{\mathrm{re}} & = G_{\mathrm{op}} \exp\left(-\dfrac{\sigma_{\mathrm{y}}\left([u]_{\max} - [u]_{\mathrm{cl}}\right)}{G_{\mathrm{op}}}\right) \end{cases}. \tag{34}$$

Numerical Resolution of the Discrete Finite Element System

In this section, the interest is focused on the numerical resolution of the discrete system, i.e., Eq. (25a,b,c). The former equation presents a standard global system, while the latter two equations are formulated at the local scale and carry nonlinear kinematic behaviors. Hence, the system to be solved is nonlinear. The linearization of equations is present in the following part. Then the resolution of the global and local system is also introduced in this section.

Linearization of Equations

The integration of the global system (Eq. (25a)) and the weak enhancement (Eq. (25b)) are given as the following Eq. [8]:

$$f_{\text{int}}^{e} = \int_{\Omega_e} B^T \breve{\sigma}(d, [|\varepsilon|], [|u|]) d\Omega = K_{\text{bb}} d + K_{\text{bw}}[|\varepsilon|] + K_{\text{bs}}[u], \tag{35}$$

$$\overline{R}_{[|\varepsilon|]}^{e} = \int_{\Omega_e} \mathbf{G}_{\text{w}}^T \breve{\sigma}(d, [|\varepsilon|], [|u|])\, d\Omega = K_{\text{wb}} d + K_{\text{ww}}[|\varepsilon|] + K_{\text{ws}}[u], \tag{36}$$

with

$$\begin{aligned}
K_{\text{bb}} &= B^T (V^+ C^+ + V^- C^-) B \\
K_{\text{bw}} &= \frac{V^+ V^-}{V} B^T (C^+ - C^-) H_{\text{w}} \\
K_{\text{bs}} &= B^T (V^+ C^+ + V^- C^-) \mathbf{G}_{\text{s}} n_p \\
K_{\text{wb}} &= \frac{V^+ V^-}{V} {H_{\text{w}}}^T (C^+ - C^-) B \\
K_{\text{ww}} &= \frac{V^+ V^-}{V} {H_{\text{w}}}^T (V^- C^+ + V^+ C^-) H_{\text{w}} \\
K_{\text{ws}} &= \frac{V^+ V^-}{V} H_{\text{w}} (C^+ - C^-) \mathbf{G}_{\text{s}} n_p.
\end{aligned}$$

Based on the Newton's method, their linearization formulation gives as (Roubin et al. 2015)

$$\mathbb{A}_{e=1}^{n_e} \left(K_{\text{bb}} \Delta d|_{n+1}^{(k+1)} + K_{\text{bw}} \Delta [|\varepsilon|]|_{n+1}^{(k+1)} + K_{\text{bs}} \Delta [u]|_{n+1}^{(k+1)} \right) = -\mathbb{A}_{e=1}^{n_e} \left(f_{\text{int}}^{e}|_{n+1}^{(k)} - f_{\text{ext}}^{e} \right),$$

$$K_{\text{wb}} \Delta d|_{n+1}^{(k+1)} + K_{\text{ww}} \Delta [|\varepsilon|]|_{n+1}^{(k+1)} + K_{\text{ws}} \Delta [u]|_{n+1}^{(k+1)} = -\overline{R}_{[|\varepsilon|]}^{e} \Big|_{n+1}^{(k)}.$$

The linearization of the strong enhancement should be discussed in two cases depending if the element is in the opening stage or in the closing stage. Assuming that the discontinuity surface is flat and the stress over the element is constant, the traction vector T can be calculated based on the average value of weighted volumes of sub-domain $V^{+|-}$:

$$T = \frac{1}{V} H_{\text{s}}^{*,T} \left(V^+ \breve{\sigma}^+ + V^- \breve{\sigma}^- \right). \tag{37}$$

The linearization of the strong enhancement of the traction-opening phase writes as (Roubin 2013)

$$\begin{aligned}
&K_{\text{s}^*\text{b}}|_{n+1}^{(k)} \Delta d|_{n+1}^{(k+1)} + K_{\text{s}^*\text{w}}|_{n+1}^{(k)} \Delta [|\varepsilon|]|_{n+1}^{(k+1)} + \left(K_{\text{s}^*\text{s}} + K_{\text{qo}} \right)|_{n+1}^{(k)} \Delta [u]|_{n+1}^{(k+1)} \\
&\quad = -\Phi_{\text{o}}|_{n+1}^{(k)}
\end{aligned} \tag{38}$$

with

$$K_{s^*b} = \frac{\partial \sigma_{eq}}{\partial T}\frac{1}{V}H_s^{*,T}(V^+C^+ + V^-C^-)B$$
$$K_{s^*w} = \frac{\partial \sigma_{eq}}{\partial T}\frac{V^+V^-}{V}H_s^{*,T}(C^+ - C^-)H_w$$
$$K_{s^*s} = \frac{\partial \sigma_{eq}}{\partial T}\frac{1}{V}H_s^{*,T}(V^+C^+ + V^-C^-)\mathbf{G}_s n_p$$
$$K_{qo} = \frac{\sigma_y^2}{G_{op}}e^{-\sigma_y[u]/G_{op}}$$

As for the element in the closing stage, the closure criterion $\Phi_c = -\sigma_{eq} + q_c([u])$ has to be taken into consideration. It is a function in terms of two variables: $\{T, [u]\}$; thus the increment of Φ_c gives as

$$\Delta\Phi_c = -\frac{\partial \sigma_{eq}}{\partial T}\Delta T + \frac{\partial q_c}{\partial [u]}\Delta[u], \tag{39}$$

$$= -K_{s^*b}\Delta d - K_{s^*w}\Delta[|\varepsilon|] - K_{s^*s}\Delta[u] + K_{qc}\Delta[u], \text{with } K_{qc} = \frac{G_{cl}}{[u]_{max}[u]}. \tag{40}$$

Hence, the linearization of the strong enhancement in the closing stage is written as

$$-K_{s^*b}|_{n+1}^{(k)}\Delta d|_{n+1}^{(k+1)} - K_{s^*w}|_{n+1}^{(k)}\Delta[|\varepsilon|]|_{n+1}^{(k+1)} - \left(K_{s^*s} - K_{qc}\right)|_{n+1}^{(k)}\Delta[u]|_{n+1}^{(k+1)} = -\Phi_c|_{n+1}^{(k)} \tag{41}$$

Solving the System

Depending on the status of the element is opening or closing, we can write the linearization of the three equations into a matrix form:

$$\begin{bmatrix} K_{bb} & K_{bw} & K_{bs} \\ K_{wb} & K_{ww} & K_{ws} \\ K_{s*b} & K_{s*w} & K_{s*s} + K_{qo} \end{bmatrix}_{n+1}^{(k)} \begin{Bmatrix} \Delta d \\ \Delta[|\varepsilon|] \\ \Delta[u] \end{Bmatrix}_{n+1}^{(k+1)} = \begin{Bmatrix} -\left(f_{int}^e - f_{ext}^e\right) \\ -R_{[|\varepsilon|]}^e \\ -\Phi_o \end{Bmatrix}_{n+1}^{(k)}, \tag{42}$$

or

$$\begin{bmatrix} K_{bb} & K_{bw} & K_{bs} \\ K_{wb} & K_{ww} & K_{ws} \\ -K_{s*b} & -K_{s*w} & -K_{s*s} + K_{qc} \end{bmatrix}_{n+1}^{(k)} \begin{Bmatrix} \Delta d \\ \Delta[|\varepsilon|] \\ \Delta[u] \end{Bmatrix}_{n+1}^{(k+1)} = \begin{Bmatrix} -\left(f_{int}^e - f_{ext}^e\right) \\ -R_{[|\varepsilon|]}^e \\ -\Phi_c \end{Bmatrix}_{n+1}^{(k)}. \tag{43}$$

The matrix is solved at two levels, global scale and local scale. Since the strong kinematics enhancement Φ_o and Φ_c are both nonlinear, Newton's method is practiced here for the resolution of the internal variables $[|\varepsilon|]$ and $[|u|]$. It is assumed that the displacement field d remains constant during the resolution of the local system. So we have

$$R^e_{[|\varepsilon|]} = 0, \tag{44a}$$

$$\Phi_o = 0 \text{ or } \Phi_c = 0. \tag{44b}$$

$R^e_{[|\varepsilon|]} = 0$ has been developed in Eq. 36, and we can see that it is a linear equation. The nonlinear aspect of the local system originates from $\Phi_o = 0$ or $\Phi_c = 0$. Assuming that the Eq. (44b) is now solved, the modified stiffness matrix K_{sc} for the element in the opening procedure and in the closing procedure can be written as

$$K_{sc}|^{(k)}_{n+1} = K_{bb} - [K_{bw}\ K_{bs}] \left(\begin{bmatrix} K_{ww} & K_{ws} \\ K_{s^*w} & K_{s^*s} + K_{qo} \end{bmatrix}^{(k)}_{n+1} \right)^{-1} \begin{bmatrix} K_{wb} \\ K_{s^*b} \end{bmatrix}^{(k)}_{n+1}, \tag{45}$$

and

$$K_{sc}|^{(k)}_{n+1} = K_{bb} - [K_{bw}\ K_{bs}] \left(\begin{bmatrix} K_{ww} & K_{ws} \\ -K_{s^*w} & -K_{s^*s} + K_{qo} \end{bmatrix}^{(k)}_{n+1} \right)^{-1} \begin{bmatrix} K_{wb} \\ -K_{s^*b} \end{bmatrix}^{(k)}_{n+1}. \tag{46}$$

The assembled matrix $\mathbb{K}_{sc}$ is then calculated by bringing the stiffness matrix K_{sc} of each element together

$$\mathbb{K}_{sc}|^{(k)}_{n+1} = \mathbb{A}^{n_e}_{e=1} K_{sc}|^{(k)}_{n+1}, \tag{47}$$

By using the static condensation, the resolving equations at global level write as

$$\mathbb{K}_{sc}|^{(k)}_{n+1} \Delta d|^{(k+1)}_{n+1} = -\mathbb{A}^{n_e}_{e=1} \left\{ f^e_{int} - f^e_{ext} \right\}|^{(k)}_{n+1}. \tag{48}$$

From Eq. (45) to Eq. (48), we can see that the stiffness matrix $\mathbb{K}_{sc}$ has the same size of matrix $\mathbb{K}_{bb}$, which equals to the size of the global system no matter how many heterogeneities exist in the system or how many elements start to fail. The degree of freedom of the solving system is constant. In terms of numerical resolution, this feature brings a benefit that the computational solving memory will not increase with the increasing number of failed elements.

Resolution of the Cohesive Criterion

Both the traction-opening process and the closing process in the strong discontinuity of mode-I are described in nonlinear forms. In order to solve the equations at the local scale (Eq. 44a, b), let us assume that the local system has already been solved, with $R^e_{[|\varepsilon|]} = 0$ and $R^e_{[|u|]} = 0$, which give

$$K_{\mathrm{wb}}d + K_{\mathrm{ww}}[|\varepsilon|] + K_{\mathrm{ws}}[u] = 0, \tag{49}$$

and

$$K_{\mathrm{s^*b}}d + K_{\mathrm{s^*w}}[|\varepsilon|] + K_{\mathrm{s^*s}}[u] - \sigma_{\mathrm{y}} \exp\left(-\frac{\sigma_{\mathrm{y}}}{G_{\mathrm{op}}}[u]\right) = 0 \text{ for opening procedure} \tag{50a}$$

$$-K_{\mathrm{s^*b}}d - K_{\mathrm{s^*w}}[|\varepsilon|] - K_{\mathrm{s^*s}}[u] + \frac{G_{\mathrm{cl}}}{[u]_{\max}} \ln\left(\frac{[u]}{[u]_{\max}}\right) = 0 \text{ for closing procedure.} \tag{50b}$$

By replacing all terms of $[|\varepsilon|]$ by d and $[u]$, the nonlinear traction-opening equation can be solved as (Roubin et al. 2015)

$$T_e + M[u] = \sigma_{\mathrm{y}} \exp\left(-\frac{\sigma_{\mathrm{y}}}{G_{\mathrm{op}}}[u]\right), \tag{51}$$

with

$$T_e = \left(K_{\mathrm{s^*b}} - K_{\mathrm{s^*w}}K_{\mathrm{ww}}^{-1}K_{\mathrm{wb}}\right)d, \text{and} \tag{52}$$

$$M = \left(K_{\mathrm{s^*s}} - K_{\mathrm{s^*w}}K_{\mathrm{ww}}^{-1}K_{\mathrm{ws}}\right). \tag{53}$$

A solution can only be solved if $T_e > \sigma_{\mathrm{y}}$ and $M < 0$. With the help of the Lambert W function (Corless et al. 1996) W_0, an analytical solution can be deduced as

$$[u]_{\mathrm{sol}} = \frac{G_{\mathrm{op}}}{\sigma_{\mathrm{y}}}\left(W_0\left(\frac{\sigma_{\mathrm{y}}^2 \exp\left(\frac{\sigma T_e}{G_{\mathrm{op}}M}\right)}{G_{\mathrm{op}}M}\right) - \frac{\sigma_{\mathrm{y}}T_e}{G_{\mathrm{op}}M}\right). \tag{54}$$

As for the nonlinear closing procedure, the cohesive criterion can be reformed as

$$-T_e - M[u] = \frac{G_{\mathrm{cl}}}{[u]_{\max}} \ln\left(\frac{[u]}{[u]_{\max}}\right), \tag{55}$$

and the analytical solution for $[u]$ can be solved:

$$[u]_{\mathrm{sol}} = -G_{\mathrm{cl}}W_0\left(-\frac{M[u]_{\max}^2 \exp\left(\frac{T[u]_{\max}}{G_{\mathrm{cl}}}\right)}{G_{\mathrm{cl}}}\right) / \left(M[u]_{\max}\right). \tag{56}$$

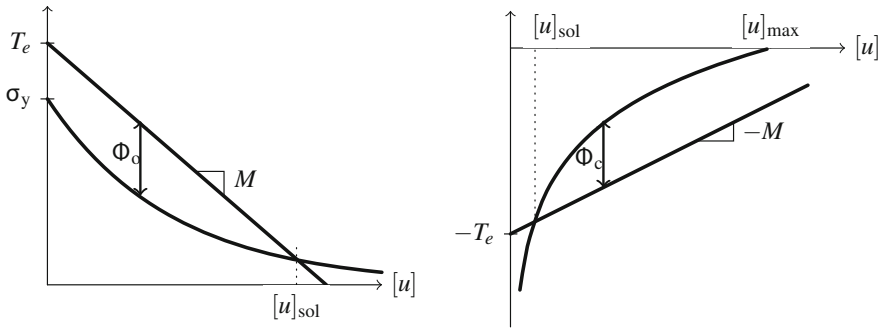

(a) Traction-opening procedure (b) Closing procedure

Fig. 10 Resolution of the strong discontinuity equation at the local scale

The resolution of the nonlinear traction separation criterion and the closing criterion is plotted separately in Fig. 10a and b.

Once the opening value $[u]_{\mathrm{SOL}}$ is determined, the value of weak discontinuity $[|\varepsilon|]_{\mathrm{sol}}$ can be analytically calculated as (Roubin 2013)

$$[|\varepsilon|]_{\mathrm{sol}} = -K_{\mathrm{ww}}^{-1}\left(K_{\mathrm{wb}}d + K_{\mathrm{ws}}[u]_{\mathrm{sol}}\right) \tag{57}$$

Numerical Application to a Cubic Specimen with Heterogeneous Structure

In this section, we will focus on the capabilities of the EFEM model by applying it to a heterogeneous specimen. The proposed numerical example is performed on a cube whose length is equal to 100 mm. Two phases are modeled; the heterogeneous structure is present by a set of spherical aggregates that disperse randomly in the cube (see Fig. 11). Two groups of aggregates are modeled to represent a total volume fraction of 20%, in which 60% of the spherical aggregates have a radius between 3 and 5 mm and the rest of them are between 8 and 12 mm.

Aiming at modeling the main features of brittle/quasi-brittle materials, Table 1 lists the parameters of the two phases in the specimen, including the interfaces between them. Each of them contains two elastic parameters and two failure parameters. The aggregates are assumed to be more rigid than the matrix and remain elastic. The cracks can only initiate and propagate in the matrix and interfaces. For the sake of simplicity, it is considered that the interface element carries the same failure parameters as the matrix element.

The specimen is then applied by mechanical loadings. Starting from the simple uniaxial loading, the macroscopic responses of the specimen are displayed in Fig. 12. In order to illustrate the effect of the closure mechanism, the models with

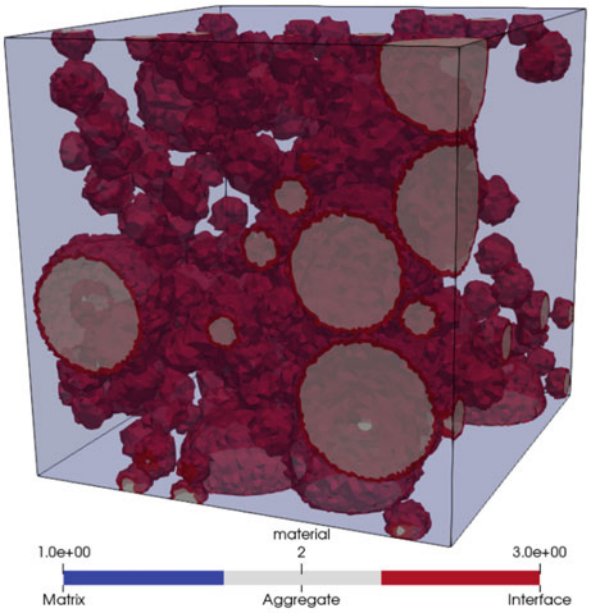

Fig. 11 Representation of the projection of the cube to mesh with aggregate dispersed in the matrix and weakly enhanced elements between them

Table 1 Considered material parameters for the cube and its rigid inclusions

Phase	E [GPa]	ν [−]	σ_y [MPa]	G_{op} [J/m^2]
Matrix	22.0	0.2	4.0	1.0
Interface	–	–	4.0	1.0
Aggregate	78.0	0.2	–	–

and without crack closures are compared in this figure. First, from Fig. 12, we can see that in the elastic phase, the two models carry the same value of macroscopic Young's modulus, which is equal to 27.4 GPa. Second, even though the failure criterion at the mesoscopic scale is proposed only in traction, the failure behavior at the macroscopic scale in compression is observed for both models. A reasonable ratio between the traction and compression resistance can be found between 13.05 and 13.49. Third, the difference between the two models' responses is slight in traction, whereas in compression, the model with closure mechanism shows a little higher resistance.

To analyze the failure process in traction and the role of the closure mechanism, we choose here four loading stages (see Fig. 12). The crack patterns of these four stages are displayed in Fig. 13.

Figure 13a displays the crack patterns at the loading stage (1), which corresponds to the material just before the maximum resistance. A number of micro-cracks can be observed diffusing over the cube, especially beside the inclusions because of the stress concentration. No crack closure can be observed at this phase.

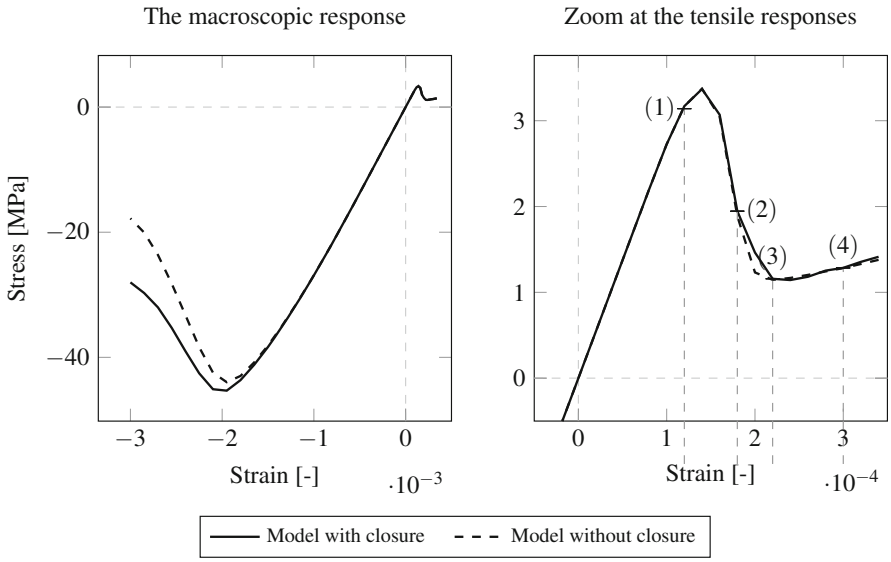

Fig. 12 The comparison between the models with/without closure law for the cube under monotonic loading

The crack pattern in the post-peak stage is shown in Fig. 13b. We can see that the number of failed elements is heavily increased. The diffused cracks become denser and begin to coalesce to macroscopic cracks. A very small number of cracks can be found starting to close.

From Fig. 13c to d, the macroscopic response of the material tends to stabilize, whereas the crack pattern continues to change. The major crack continues to propagate, and numerous crack closures occur in the specimen. Depending on the evolutions of major cracks, we can roughly classify the closing elements into two main categories. For the sake of clarity, three major cracks are presented here as examples (see Fig. 13d).

The first closing category is present by crack 1 and 2. We can see that they are almost entirely closed from stage (3) to stage (4). They are located at the upper or lower parts of other major cracks. The crack closures of this kind originate from the stress release which is caused by the rapid development of other major cracks (crack 3 in this case). For the model without closure mechanism, this stress-relieving effect can also be observed (see Fig. 14). Even though the cracks cannot close for the model without crack closures, it can be seen that the cracks in the stress release area (crack 1 and 2) stop propagating from stage (3) to stage (4) during the imposed loading increases.

The closing elements in crack 3 belong to another category of closure patterns. They are also triggered by stress release, but the stress release derives itself from the center of cracks, where the failed elements develop faster than the other elements. This observed phenomenon originates from the imposed model at the local scale, in which the equivalent stress on the discontinuity surface will decrease as the crack opening increases, meaning that the failed element propagates more and more easily. The consequence of this type of closure element is that, compared to the model

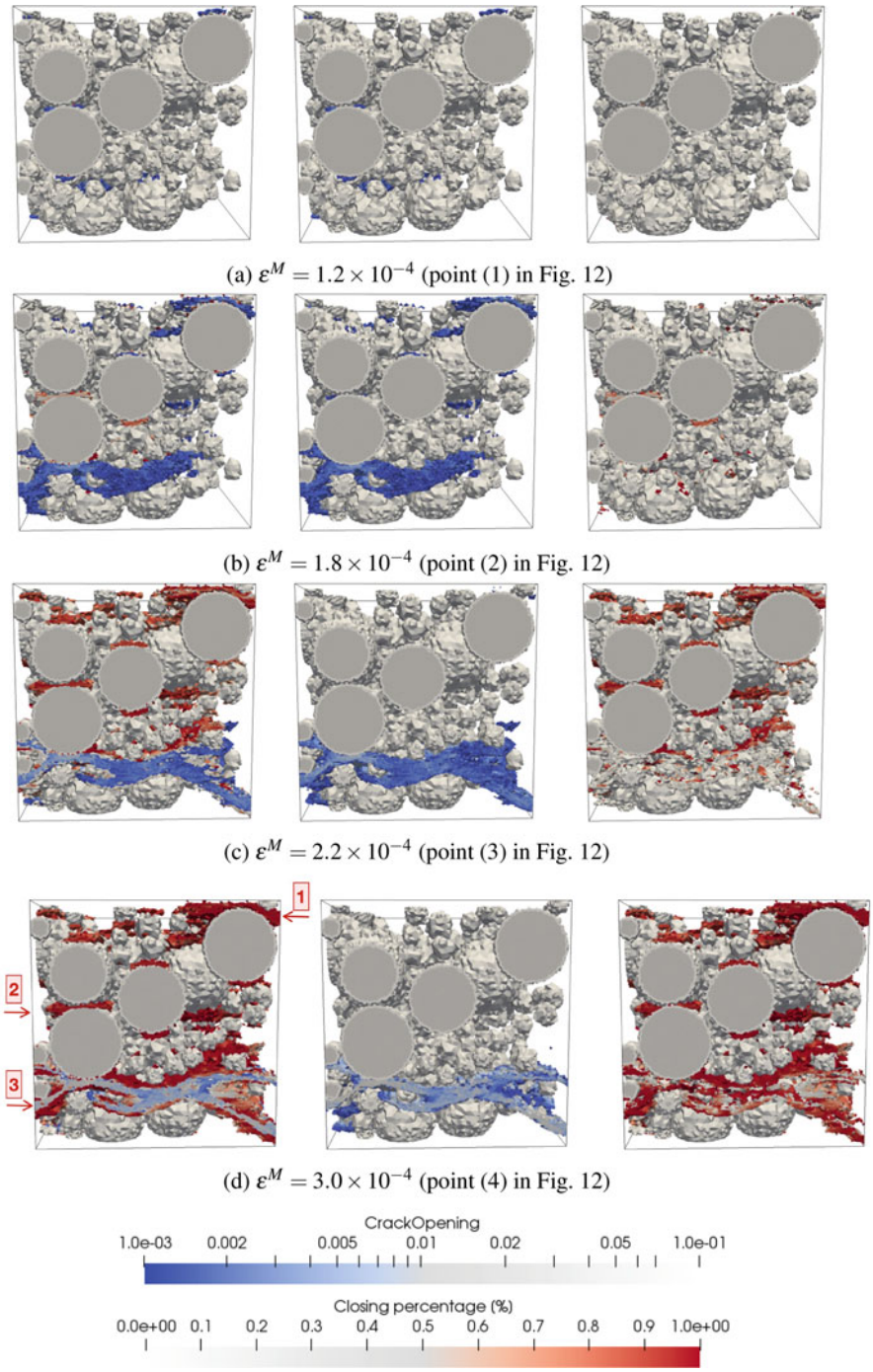

Fig. 13 Cracks (in the middle) and dissipated energy at crack closures (in the right) at four different loading stages for simple traction; they are overlaid in the left, and the rigid inclusions are marked in gray

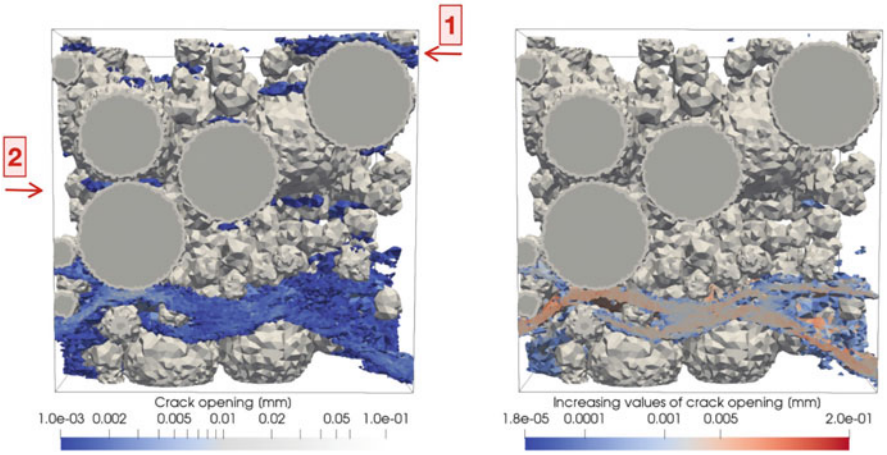

Fig. 14 Cracks for the model without closure law at stage (4) and the increasing values of crack opening from stage (3) to stage (4)

without closure mechanism, the major crack in the model with closure mechanism will become narrower and clearer.

The crack evolution of the two models is plotted and compared in Fig. 15. It can be observed from the figure that their main differences appear from stage (3) to stage (4), i.e., after crack closures start to occur massively in the specimen for the model with closure mechanism. During this period, the number of elements with relatively higher crack opening values gradually increases for both models, corresponding to the propagation of major cracks. While for the number of elements with low crack opening values, the two models show different trends. There are a number of elements that admit a closing behavior for the model with closure mechanism, which leads to an increasing number of elements with small crack opening values. While for the model without closure mechanism, this number remains almost constant.

Next, a loading-unloading displacement is applied to the specimen to illustrate the EFEM model's ability in terms of the unilateral effect. It is also one of the main characters of brittle/quasi-brittle materials. The macroscopic responses of the model are plotted in Fig. 16a.

In Fig. 16a, we can see that for both models, the stiffness of the material can be fully recovered even the specimen is very damaged in traction. The reason for this recovery, though, is a little different between the two models. As for the model without crack closures, the stiffness of the material is recovered right after the traction loading switches to unloading. This is because the failure behaviors of the element are applied only on the discontinuity interface; the bulk volumes have always pure elastic kinematics. Hence the unloading displacement will be applied to these elastic bulk volumes since the crack openings cannot be decreased. These crack openings are also the resource of the permanent plasticity that can be seen in the figure.

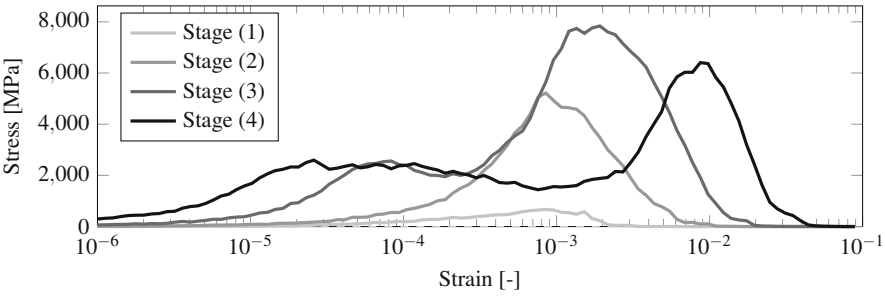

(a) Model with closure mechanism

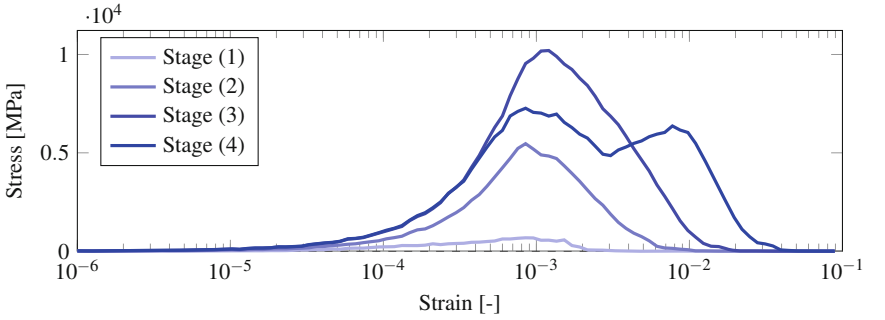

(b) Model without closure mechanism

Fig. 15 Distributions of crack opening values for the model with and without closure mechanism in traction

As for the model with closure mechanism, the macroscopic response of the specimen under unilateral loading is related to the closure of cracks. In the first phase of unloading, a number of failed elements admit a closure behavior, which leads to a partial recovery of the material stiffness and also to an amount of energy dissipated in the closing phase. Then, as the imposed displacement recharges, the failed elements reopen, and a hysteresis loop can be observed. This phenomenon shows good consistency with the experimental observations (Fig. 16b). And when the imposed displacement unloads to compression, we can see that the specimen has its stiffness fully recovered at point (3). Some permanent plasticity can also be observed at point (2) but much less than for the model without closure mechanism. This is due to crack closures in the sample.

Interested in the crack patterns of the model with closure mechanism along with the unilateral loadings and its consistency with the experimental observation (Fig. 16b), we label here three stages as shown in Fig. 16a. Their crack patterns are displayed in Fig. 17. It can be seen that:

- At point (1), a large number of crack openings apparent in the specimen are accompanied with the loss of stiffness of the material.

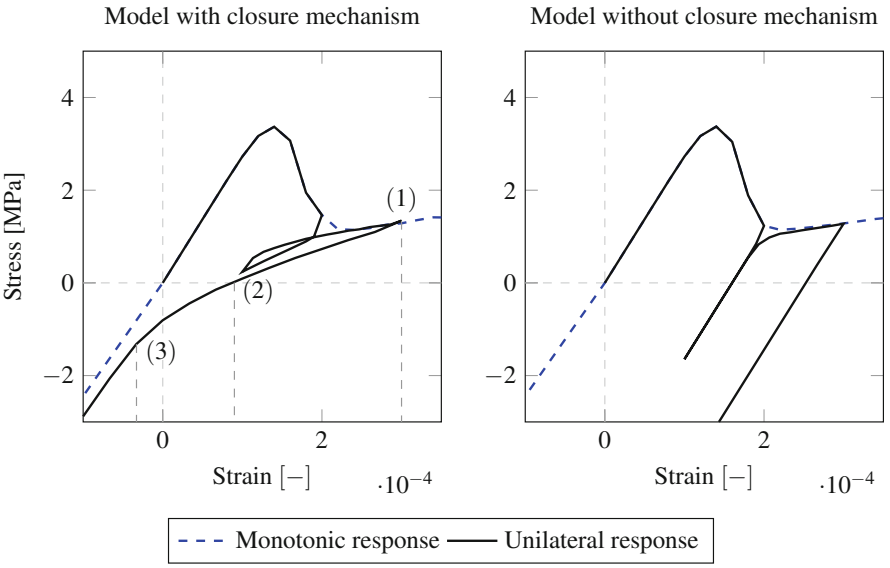

(a) Numerical simulation results of the model with and without closure mechanism

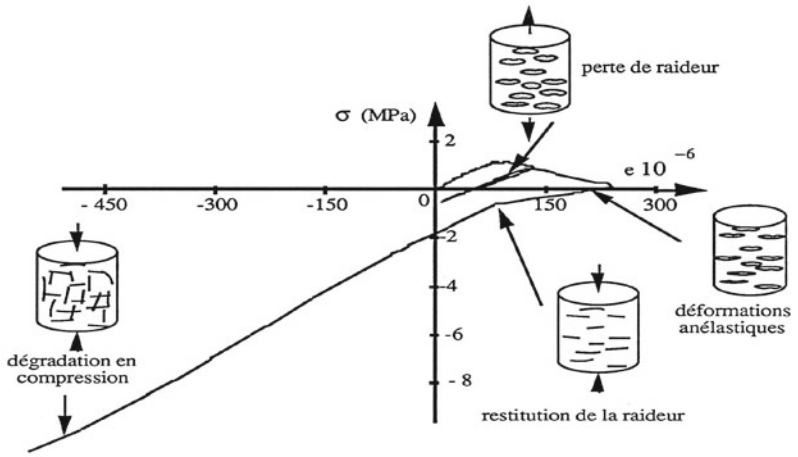

(b) Behavior of a concrete beam under low cycle bending [3]

Fig. 16 Illustration of the unilateral behaviors of concrete

- At point (2), at the state of null stress, the cracks are partially closed while leading to an amount of plastic strain, the resource of which is the residual openings.
- At point (3), the cracks are almost entirely closed, leading to the recovery of the stiffness of the specimen.

Finally, a compressive cyclic loading is applied to the material to analyze the performance of the model. The displacement-controlled trajectory is displayed in Fig. 18, and the macroscopic responses of the two models are given in Fig. 19.

We can see in Figure 19 that both models have a certain volumetric dilatation, and that the model without closure mechanism has a higher volumetric dilatation than the other model. This is because the volumetric dilatation derives itself from the crack openings. And the crack closures in the model with closure mechanism may restrict this effect.

Then in Fig. 20, several differences between the two models can be noticed. First, we can see that the first cycle is purely elastic, and starting from the second cycle, the model with closure mechanism losses less of the macroscopic stiffness than the other model. Displayed in the figure by dashed lines, the model with closure mechanism

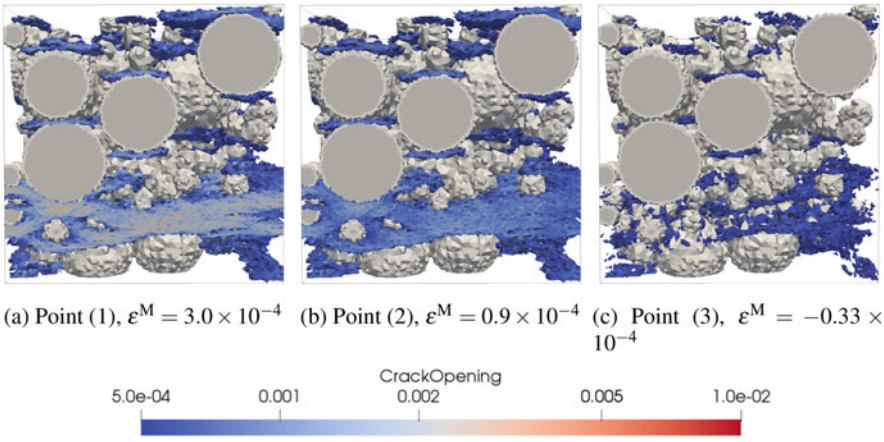

Fig. 17 Variation of the cracks of the material during the unloading process in a unilateral test; the points are marked in Fig. 16a

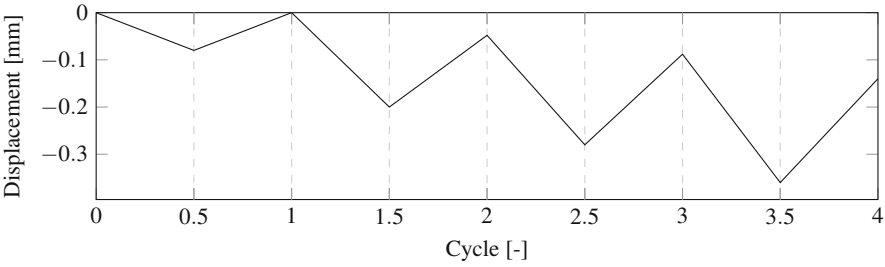

Fig. 18 Proposed displacement path for the cyclic loading

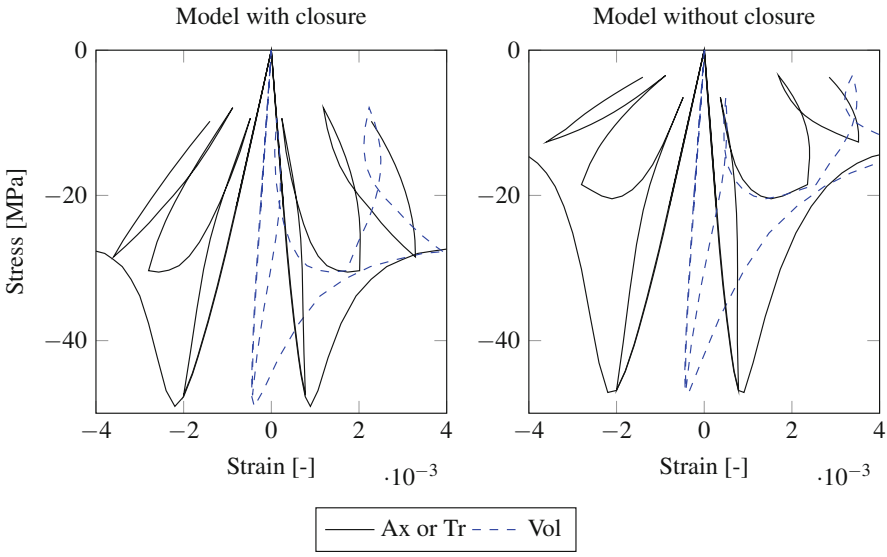

Fig. 19 Macroscopic response of monotonic/cyclic tests for model with/without adding closure law, in terms of axial (note Ax) transversal (note Tr) and volumetric strain (note Vol)

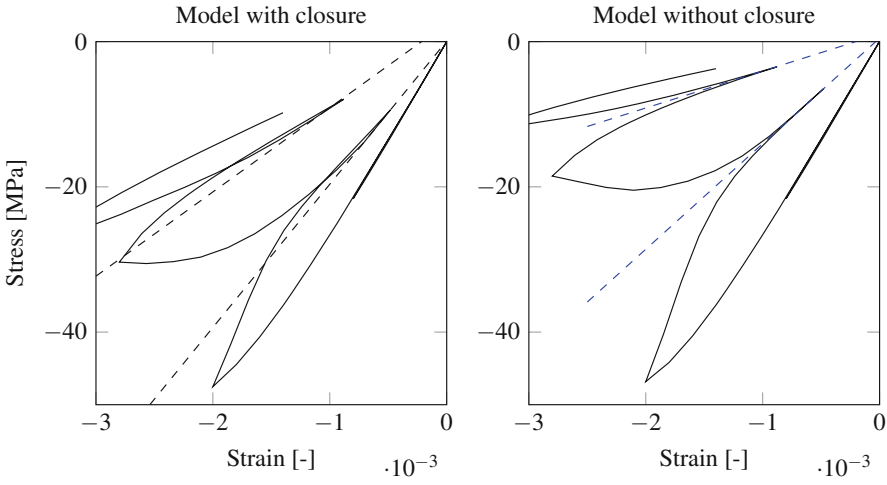

Fig. 20 Illustration of the loss of stiffness and the plastic deformation in cyclic loading for a model with/without crack closures

has 42.3% of the initial stiffness at the end of loading, while the model without crack closures has only 18.5%. This can be explained by the crack closures in the unloading phase, which leads to the stiffness of the material partially recovers.

Second, it can be seen that the model with closure mechanism has slightly higher plasticity at the third cycle, which equals to $\varepsilon^p_{\text{with closure}} = 2.2 \times 10^{-4}$, while the value for the model without closure mechanism is $\varepsilon^p_{\text{without closure}} = 2.0 \times 10^{-4}$. Unlike in traction loadings that the plasticity is directly related to the residual crack opening, the observed plasticity in compression is the result of emergence from the mesoscopic to macroscopic scale since the closing procedure brings additional dissipated energy. It should be noted that at the local scale, no plastic deformation is formulated in the constitutive model.

Finally, the hysteresis phenomenon can be observed for the model with closure mechanism, which is one of the main characteristics of brittle/quasi-brittle materials. The source of this observed phenomenon comes from several ingredients, such as the capability of recovery stiffness and to dissipate energy during the closing phase. And both of them are part of the effects of the closure mechanism.

Conclusion

In existing EFEM methods, many models have shown their ability to simulate many of the main characters of brittle or quasi-brittle materials, for example, the asymmetric behaviors in traction and compression loadings, the volumetric dilatation, and the progressive loss of stiffness. In this chapter, we applied a closure mechanism to the model to investigate if more behaviors can be observed.

The model is tested to a concrete-like specimen with mesoscopic structural heterogeneities. Intricate crack patterns can be observed during the fracture process, and the propagations of cracks may influence each other. The crack closures can be observed not only in cyclic loadings but also in monotonic loadings. The model shows also similar behaviors as experimental observations in unilateral loadings, including the hysteresis loops, irreversible deformations, and stiffness recovery. In compressional cyclic loading, the hysteresis phenomenon can be observed. Even the friction between the lips of cracks is not taken into concern, the fatigue behaviors can be seen by adding a closure mechanism to mode-I separation crack at the local scale. However, the hysteresis loops are not very significant. This may related to the lack of consideration of the friction between the cracks. In future works, it would be interesting to take this into concern.

References

E. Ahmed, A. S. Elgazzar, A. S. Hegazi, An overview of complex adaptive systems. *arXiv preprint nlin/0506059* (2005)

N. Benkemoun, R. Gelet, E. Roubin, J.-B. Colliat, Poroelastic two-phase material modeling: theoretical formulation and embedded finite element method implementation. Int. J. Numer. Anal. Methods. Geomech. **39**(12), 1255–1275 (2015)

R.M. Corless, G.H. Gonnet, D.E. Hare, D.J. Jeffrey, D.E. Knuth, On the lambertw function. Adv. Comput. Math. **5**(1), 329–359 (1996)

P. Hauseux, *Propagation dincertitudes paramètriques dans les modèles numèriques en mècanique non linèaire: applications à des problèmes dexcavation*. Ph.D. thesis, Lille 1 (2015)
A. Ibrahimbegovic, D. Markovic, H.G. Matthies, R. Niekamp, R.L. Taylor, Multi-scale modelling of heterogeneous structures with inelastic constitutive behavior, in *Complas VIII-8th International Conference on Computational Plasticity. Citeseer* (2005)
J. Mazars, Y. Berthaud, S. Ramtani, The unilateral behaviour of damaged concrete. *Engineering Fracture Mechanics*, **35**(4–5), 629–635 (1990)
N. Moës, M. Cloirec, P. Cartraud, J.-F. Remacle, A computational approach to handle complex microstructure geometries. Comput. Method. Appl. M. **192**(28–30), 3163–3177 (2003)
J. Oliver, Modelling strong discontinuities in solid mechanics via strain softening constitutive equations. part 1: Fundamentals. *International Journal for Numerical Methods in Engineering*, **39**(21):3575–3600 (1996)
J. Oliver, Modelling strong discontinuities in solid mechanics via strain softening constitutive equations. part 2: Numerical simulation. Int. J. Nume.r Meth. Eng. **39**(21), 3575–3600 (1996)
J. Oliver, On the discrete constitutive models induced by strong discontinuity kinematics and continuum constitutive equations. Int. J. Solids. Struct. **37**(48), 7207–7229 (2000)
M. Ortiz, Y. Leroy, A. Needleman, A finite element method for localized failure analysis. *Computer Methods in Applied Mechanics and Engineering*, **61**(2), 189–214 (1987)
H.W. Reinhardt, Fracture mechanics of an elastic softening material like concrete. *Heron*, **29**(2), 1984 (1984)
E. Roubin, *Modèlisation EF et morphologique de milieu hètèrogènes à lèchelle mèsoscopique: applications aux matèriaux à matrices cimentaire*. Ph.D. thesis, Thèse de doctorat, Ecole Normale Supèrieure de Cachan (2013)
E. Roubin, A. Vallade, N. Benkemoun, J.-B. Colliat, Multi-scale failure of heterogeneous materials: a double kinematics enhancement for embedded finite element method. *International Journal of Solids and Structures*, **52**:180–196 (2015)
J.C. Simo, J. Oliver, F. Armero, An analysis of strong discontinuities induced by strainsoftening in rate-independent inelastic solids. Comput. Mech. **12**(5):277–296 (1993)
J.C. Simo, M. Rifai, A class of mixed assumed strain methods and the method of incompatible modes. Int. J. Numer. Meth. Eng. **29**(8), 1595–1638 (1990)
O. Stamati, E. Roubin, E. Andò, Y. Malecot, Phase segmentation of concrete x-ray tomographic images at meso-scale: validation with neutron tomography. *Cement and Concrete Composites*, **88**:8 (2018)
M. Terrien, Emission acoustique et comportement mecanique post-critique d'un beton sollicite en traction. *BULL LIAISON LAB PONTS CHAUSS*, (105) (1980)
A. Vallade, *Modèlisation multi-èchelles des shales: influence de la microstructure sur les pro-priètès macroscopiques et le processus de fracturation*. Ph.D. thesis, Lille 1 (2016)
K. Washizu, Variational methods in elasticity and plasticity (1968). https://scholar.google.com/scholar?hl=fr&as_sdt=0%2C5&q=Variational+methods+in+elasticity+and+plasticity+1968&btnG=
G.N. Wells, *Discontinuous modelling of strain localisation and failure*. Ph.D. thesis (2001)

Damage and Failure of Hard Rocks Under True Triaxial Compression

30

Rui Kong, Yaohui Gao, and Yan Zhang

Contents

Introduction 802
Fracture Evolution of Hard Rock Under True Triaxial Compression 802
Experimental Method 803
Pre-peak Progressive Cracking Process Induced by Stress 803
The Effect of Intermediate Principal Stress on the Crack Stress Thresholds 805
Energy Analysis of the Rock Cracking Process 806
Damage Evolution of Hard Rock Subjected to Cyclic True Triaxial Loading 808
Experimental Method 809
Irreversible Strain Characteristics 809
Strain Energy Characteristics 812
Cohesion and Internal Friction Angle Characteristics 814
Conclusions 816
References 817

Abstract

To reveal the effect of intermediate principal stress on the damage and failure of hard rocks, the failure evolution of hard rocks under true triaxial compression is reviewed, based on the previous study. From the viewpoint of crack growth under true triaxial compression, different fracture evolution stages of hard rocks, including the elastic stage, stable growth stage, and unstable growth stage, are introduced. Additionally, the effect of the intermediate principal stress on the crack stress thresholds is summarized. It is found that as the intermediate principal stress increases, its effect will first restrict and then promote crack propagation. The energy evolution of the rock cracking process under true triaxial compression is also analyzed. The damage evolution is quantified by damage

R. Kong (✉) · Y. Zhang
Key Laboratory of Ministry of Education on Safe Mining of Deep Metal Mines, Northeastern University, Shenyang, China

Y. Gao
Institute of Rock and Soil Mechanics, Chinese Academy of Sciences, Wuhan, China

© Springer Nature Switzerland AG 2022

G. Z. Voyiadjis (ed.), *Handbook of Damage Mechanics*,
https://doi.org/10.1007/978-3-030-60242-0_61

variables determined from a cyclic loading and unloading test under true triaxial compression. The irreversible strains in the three principal stress directions and the strength parameters are selected as damage variables to describe the entire damage process of hard rocks. Rock damage processes can be accurately described by the irreversible strains, cohesion, and internal friction angle of the rock.

Keywords

Hard rock · Ture triaxial · Fracture evolution · Strain energy

Introduction

In deep rock engineering, such as mining engineering, tunnel engineering, and water conservancy and hydropower engineering, rock geological environments and stress states are complex, in which rock collapse, rock burst, spalling, and other disasters are frequent, showing the characteristics of unstable brittle fracture (Li et al. 2012; Feng et al. 2017). The study of the damage and failure of hard rocks is of particular importance for understanding the failure mechanism of these disasters, and the stress state should also be taken into consideration. To simulate a real stress field condition, the effect of intermediate principal stress cannot be ignored and has been widely studied in the past few decades (Mogi 1967; Handin et al. 1967; Takahashi and Koide 1989; Haimson and Chang 2000; Kwašniewski 2007).

To study the damage evolution of rocks, some researchers have focused on the study of crack growth. Therefore, it is very meaningful to study the crack growth under true triaxial compression based on the crack stress threshold. In addition to the damage of rocks in the pre-peak stage, damage during post-peak failure has attracted the attention of researchers. Meanwhile, the study of cracking and fracturing mechanisms can further elucidate the stress-induced failure of hard rocks. Furthermore, cyclic loading and unloading studies are an effective means with which to understand the damage and failure characteristics of rocks and can accurately obtain the elastic and plastic parameters of hard rock from the complete stress–strain behavior.

In view of the effect of intermediate principal stress, the damage and failure characteristic of hard rocks under true triaxial compression is significantly important. Crack growth under true triaxial compression is introduced considering the crack stress threshold. The damage assessment of hard rocks based on the cyclic true triaxial loading study is given, as well.

Fracture Evolution of Hard Rock Under True Triaxial Compression

The study of rock failure, including crack initiation, crack propagation, and coalescence, is of considerable importance because it is associated with the damage evolution, failure mechanism, and stability assessment of rock masses. The

progressive cracking process of hard rocks is completely affected by the stress state, in which the intermediate principal stress must be taken into consideration. In this study, a series of true triaxial compression tests were performed to characterize cracking levels in sandstone under a true triaxial stress state, and the crack initiation and damage thresholds under the true triaxial compression condition are analyzed. Finally, an energy evolution analysis of the progressive cracking process of hard rocks is conducted.

Experimental Method

The novel true triaxial apparatus designed at Northeastern University, China (Feng et al. 2016), is used to study the damage and fracture evolution via the complete stress–strain curve. In the test, the common stress path is applied (Fig. 1): the hydrostatic pressure ($\sigma_1 = \sigma_2 = \sigma_3$) is first applied to the desired σ_3 level in the *OA* stage; then, keeping σ_3 constant, the stress is simultaneously to the desired σ_2 level in the intermediate and maximum principal stress directions ($\sigma_1 = \sigma_2$) in the *AB* stage; finally, σ_2 and σ_3 are kept constant, and σ_1 is applied until a post-peak failure curve is obtained in the *BC*-*CD* stage. The complete stress–strain curves are thus obtained, as shown in Fig. 2.

Pre-peak Progressive Cracking Process Induced by Stress

The pre-peak damage can be regarded as a progressive cracking process including an elastic stage, stable cracking stage, and unstable cracking stage (Brace et al. 1966; Bieniawski 1967; Lajtai and Lajtai 1974; Martin and Chandler 1994; Kong et al. 2018). Each stage is divided by different stress thresholds: the crack initiation stress (σ_{ci}), crack damage stress (σ_{cd}), and peak strength (σ_{ps}). The crack initiation stress

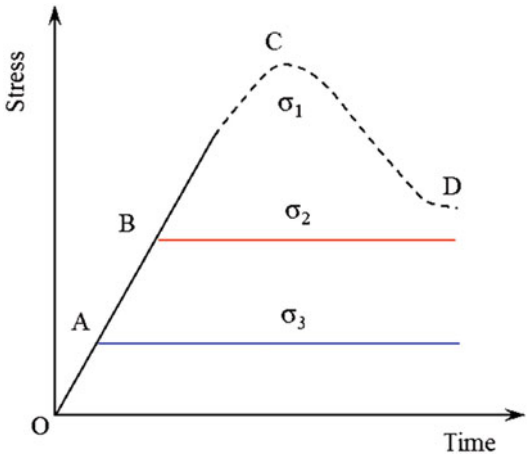

Fig. 1 The stress path under true triaxial compression

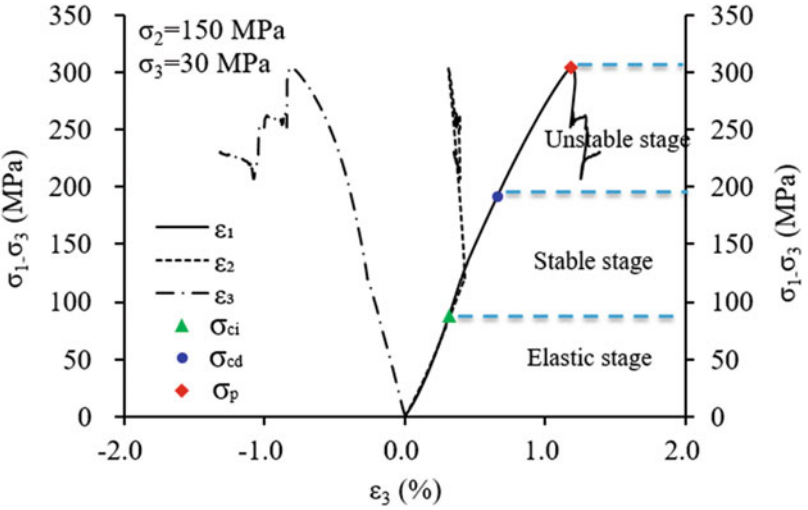

Fig. 2 The complete stress–strain curves and progressive cracking process of sandstone under true triaxial compression

(σ_{ci}) is the initial stress of the stable cracking stage, representing microcrack growth. The crack damage stress (σ_{cd}) is the end stress of the stable cracking stage and the initial stress of the unstable cracking stage. The crack initiation stress is closely related to the spalling strength of brittle rocks. The crack damage stress (σ_{cd}) is in accordance with the reversal point of volume deformation, closely related to the long-term strength of the rock. Most of the previous studies of crack growth consider uniaxial and conventional triaxial compression conditions, which ignore the effect of the intermediate principal stress on damage evolution. To study the influence of the intermediate principal stress on crack growth, Kong et al. (2018) conducted a series of tests on sandstone under true triaxial compression.

The crack initiation threshold corresponds to the elastic limit of deformation, which is also the onset point when cracks stably propagate. It is at this stress level that cracks are randomly generated, and crack propagation is dependent on the stress level. Because of the suppression of the intermediate principal stress on volumetric dilatancy, it is not appropriate to define the dilatancy onset as the crack initiation point in the true triaxial compression test, and the σ_2 loading process should be taken into account for crack initiation. To identify the crack initiation stress threshold (σ_{ci}) objectively and reliably, a novel method was presented by Kong et al. (2018) based on the strain energy density, avoiding the dependence on elastic parameters. Meanwhile, it is found that the inflection point of the volume deformation corresponds to the elastic theoretical limiting value of Poisson's ratio, i.e., $\mu = 0.5$. Generally, the damage threshold (σ_{cd}) is determined by the inflection point of volume deformation. As a result, the damage threshold (σ_{cd}) can be obtained by the Poisson's ratio in the σ_3 direction. Under true triaxial compression, the progressive cracking process of sandstone is shown in Fig. 2.

The Effect of Intermediate Principal Stress on the Crack Stress Thresholds

To reveal the mechanism of the intermediate principal stress effect on the crack stress thresholds, the relationship between the crack stress thresholds and different intermediate principal stresses is shown in Fig. 3. In the figure, the minimum principal stresses are kept constant (i.e., $\sigma_3 = 30$ MPa). The obvious difference is due to the intermediate principal stress effect. This effect implies that the crack initiation stress (σ_{ci}) and damage stress (σ_{cd}) have a relationship with the stress state, in which the intermediate principal stress must be taken into consideration.

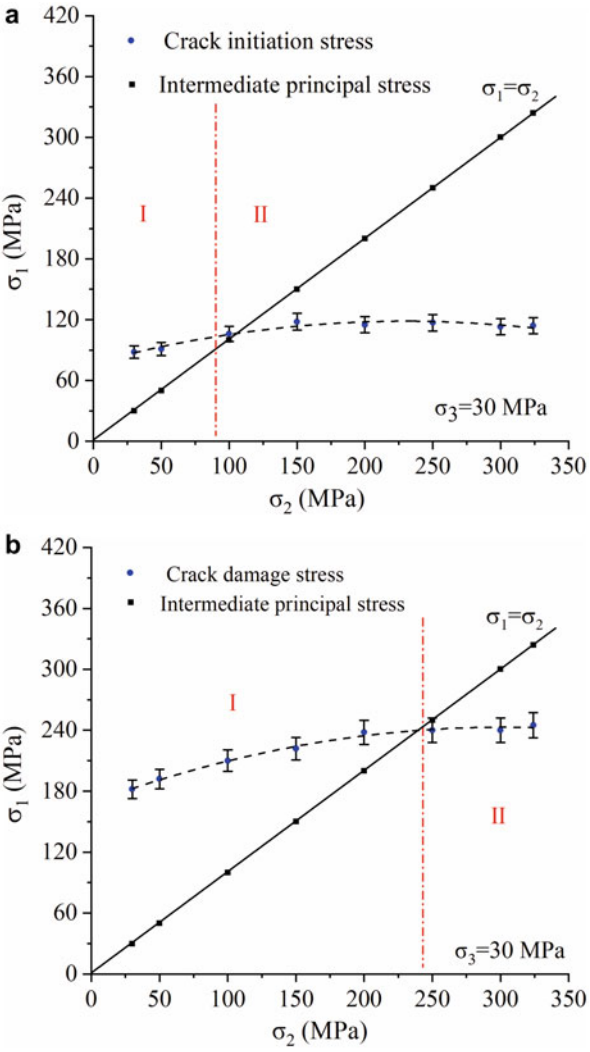

Fig. 3 The effect of different intermediate principal stresses on the crack stress threshold: (**a**) crack initiation stress and (**b**) crack damage stress. (Kong et al. 2018)

According to Fig. 3a, there are two cases of the relationship between the intermediate principal stress and crack initiation stress threshold. In the first case, the crack initiation stress (σ_{ci}) is greater than the intermediate principal stress (σ_2), and with the increase in the intermediate principal stress, the crack initiation threshold (σ_{ci}) shows a linearly increasing trend with a small rate of change, as shown in zone I of Fig. 3a. In this case, as the crack initiation stress (σ_{ci}) is greater than the intermediate principal stress (σ_2), crack initiation occurs at the loading stage of the maximum principal stress in Fig. 1 (*BC* stage). Drawing an analogy with the similar effect of confining pressure in conventional triaxial tests, this increasing phenomenon of the crack initiation threshold (σ_{ci}) with σ_2 can be attributed to the restriction of the lower intermediate principal stress on the crack initiation.

However, in the other case (zone II in Fig. 3a), as the intermediate principal stress continues to increase, the crack initiation stress remains less than the intermediate principal stress. That is, cracks initiate at the intermediate principal stress loading stage in the *AB* stage of Fig. 1. In contrast to the first case, in this case, with the increase in the intermediate principal stress, the crack initiation threshold (σ_{ci}) remains at a constant stress level. In this case, because cracks initiate at the intermediate principal stress loading stage (*AB*), the rock is actually in the generalized tensile stress state ($\sigma_1 = \sigma_2 > \sigma_3$) at the crack initiation stress level.

As shown in Fig. 3b, the change in the crack damage threshold (σ_{cd}) with different intermediate principal stresses has a similar phenomenon as the characteristic of the crack initiation threshold (σ_{ci}). In zone I, the crack damage threshold (σ_{cd}) is greater than the intermediate principal stress, so unstable crack growth occurs in the maximum principal stress loading stage in Fig. 1 (*BC* stage). Nevertheless, with the increase in the intermediate principal stress, the intermediate principal stress remains greater than the crack damage threshold, meaning that the unstable crack growth has already occurred when σ_2 is loaded and that the intermediate principal stress will accelerate crack growth, particularly when the intermediate principal stress approaches the maximum principal stress.

Energy Analysis of the Rock Cracking Process

The rock failure process is essentially attributed to the energy flow and energy transformation of rock. From an energy perspective, energy dissipation and release are regarded as the driving force resulting in the damage and failure of rocks (Xie et al. 2009; Chen et al. 2017). The rock masses encountered in underground engineering are in a certain in situ stress field, and the elastic strain energy stored in rock masses is the primary reason for the final rock failure (Tarasov and Stacey 2017; Zhang et al. 2019). Especially under high ground stress conditions, due to the excavation-induced unloading effect, the high elastic strain energy stored inside a deeply buried hard rock mass is instantaneously released. As a result, the rock masses encountered in deep engineering are cracked, which probably causes the occurrence of various geological hazards, including various forms of sudden failure, such as spalling and rock burst. Therefore, investigating the energy evolution characteristic of hard rock fracturing

processes in deep underground engineering will facilitate the study of the process and mechanisms of various geological hazards and risks associated with sudden failure, such as spalling and rock burst.

Rock failure refers to the evolution of inner cracks, including crack initiation, propagation, aggregation, coalescence, and macroscopic failure (Peng et al. 2015; Kong et al. 2018). Ignoring the microcrack closure stage (OA) in the hydrostatic pressure loading, the complete stress–strain curve under true triaxial compression can be divided into the following stages, elastic deformation (AB), stable propagation of microcracks (BC), unstable extension of cracks (CD), and post-peak strength loss (DE), as shown in Fig. 4.

The energy evolution in the complete stress–strain process is presented in Fig. 5. Figure 5 shows the time–history curves of the complete energy evolutions of rock under a true triaxial stress state. Combining Figs. 4 and 5, the energy evolution processes and characteristics of the stress–strain behavior are analyzed as follows:

1. For the above rock failure behaviors, in the elastic deformation (AB) stage, the time–history curves of the strain energies between the total strain energy U and the elastic strain energy U^e coincide or develop in parallel. The elastic strain energy U^e increases steadily, and the dissipated strain energy U^d is very small; their time–history curves are basically parallel to the horizontal axis.
2. Under the stable propagation of the microcrack (BC) stage, the time–history curves of the strain energies between the total strain energy U and the elastic strain energy U^e begin to bifurcate, the increase in the elastic strain energy U^e slows, and the dissipated strain energy U^d begins to increase slowly.
3. During the accelerated extension of cracks (CD), the energy evolution of rock is similar to that during the stable propagation of microcracks (BC), but the degree of energy dissipation in the rock is greater.

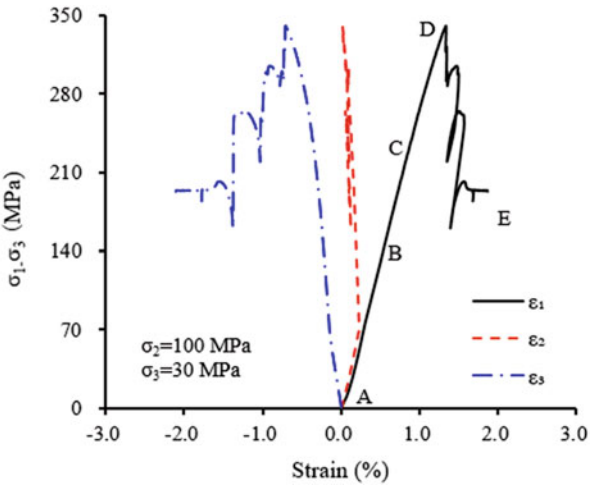

Fig. 4 Typical stress–strain behavior of rock under true triaxial compression

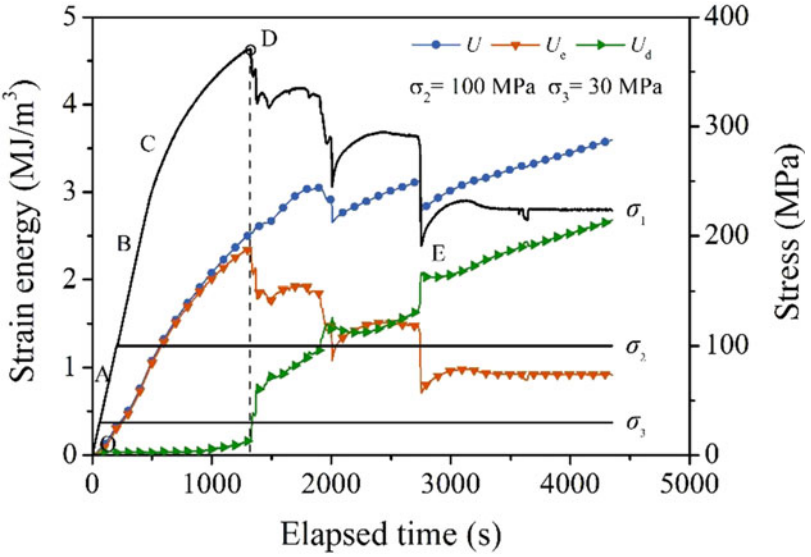

Fig. 5 Energy evolution of the rock cracking process under true triaxial compression. (Zhang et al. 2019)

4. During the post-peak strength loss (DE), the release of the accumulated elastic strain energy reduces the load capacity of the rock, causing a decrease in the elastic strain energy U^e and an increase in the dissipation strain energy U^d. For class I failure, the elastic strain energy stored in the rock pre-peak cannot sufficiently support the rock failure post-peak; thus, it is necessary to continuously input energy to the rock using the testing machine to maintain the post-peak fracturing of the rock. Therefore, the time–history curve of the total strain energy U continues to rise during this stage. For class II failure, the elastic strain energy stored pre-peak is greater than the energy required for post-peak rock failure. Hence, to make the rock failure more stable post-peak, the indenter of the testing machine is drawn back through the servo feedback system, resulting in the release of the excess elastic strain energy. As a result, the time–history curve of the total strain energy U will decrease at this stage.

Damage Evolution of Hard Rock Subjected to Cyclic True Triaxial Loading

The cyclic loading and unloading test is an efficient method for accurately obtaining the elastic and plastic parameters of hard rock from its complete stress–strain curve. Numerous cyclic uniaxial and triaxial loading tests have been carried out to investigate the damage process of hard rock (Song et al. 2013; Liu et al. 2016; Jia et al. 2018). However, the available true triaxial cyclic loading data are relatively rare due to the test complexity.

Here, the results of true triaxial cyclic loading and unloading tests on intact marble, which was collected from the China Jinping Underground Laboratory project (CJPL-II), are used to study the damage evolution and its stress dependency. The irreversible strains, cohesion, and friction parameters are calculated as damage variables to investigate the progressive failure of the tested specimens. The relations between these damage variables are also quantified to be easily used in numerical calculations.

Experimental Method

The intact marble specimens were tested under multilevel single cyclic loading and unloading conditions. The test procedure consists of three steps. First, the hydrostatic pressure ($\sigma_1 = \sigma_2 = \sigma_3$) is increased until the predetermined σ_3 is reached. Then, σ_3 is kept constant, and the biaxial loading pistons are used to load the biaxial stresses ($\sigma_1 = \sigma_2$) at the same stress rate as that for the predefined σ_2. Finally, while σ_2 and σ_3 remain constant, multilevel single cyclic loading of σ_1 is achieved to the residual state. The cyclic increment of σ_1 is 40 MPa. A typical stress–strain curve of an intact marble specimen is shown in Fig. 6.

Irreversible Strain Characteristics

The true triaxial test cycles can be directly used to capture the irreversible strains in the three principal stress directions. Here, to describe the progressive damage process both at pre-peak and post-peak stages, the equivalent irreversible strains (e_p) are computed as an internal variable and are defined by

$$e_p = \sum_0^i \sqrt{\left(d\varepsilon_1^{irr}\right)^2 + \left(d\varepsilon_2^{irr}\right)^2 + \left(d\varepsilon_3^{irr}\right)^2} \tag{1}$$

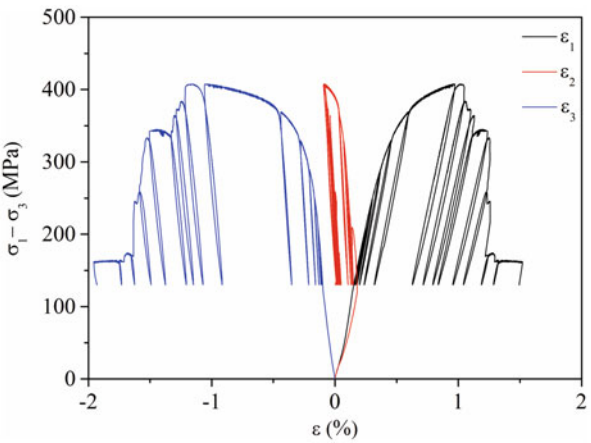

Fig. 6 Typical stress–strain curve from the true triaxial cyclic loading test under $\sigma_2 = 150$ MPa and $\sigma_3 = 30$ MPa. (Gao and Feng 2019)

where i is the number of cycles and $d\varepsilon_1^{irr}$, $d\varepsilon_2^{irr}$, and $d\varepsilon_3^{irr}$ are the irreversible strain (ε_1^{irr}, ε_2^{irr}, and ε_3^{irr}) increments in each cycle in the three principal stress directions, respectively.

Irreversible strains can be used to describe the damage evolution in the corresponding direction. Here, the normalized irreversible strains are defined by

$$D_1 = \frac{\varepsilon_1^{irr}}{\varepsilon_1^{cirr}} = \frac{\sum_{j=1}^{i}\left(d\varepsilon_1^{irr}\right)_j}{\sum_{k=1}^{n}\left(d\varepsilon_1^{irr}\right)_k} \tag{2}$$

$$D_2 = \frac{\varepsilon_2^{irr}}{\varepsilon_2^{cirr}} = \frac{\sum_{j=1}^{i}\left(d\varepsilon_2^{irr}\right)_j}{\sum_{k=1}^{n}\left(d\varepsilon_2^{irr}\right)_k} \tag{3}$$

$$D_3 = \frac{\varepsilon_3^{irr}}{\varepsilon_3^{cirr}} = \frac{\sum_{j=1}^{i}\left(d\varepsilon_3^{irr}\right)_j}{\sum_{k=1}^{n}\left(d\varepsilon_3^{irr}\right)_k} \tag{4}$$

where D_1, D_2, and D_3 ($0 \le D \le 1$) are the damage variables in the σ_1, σ_2, and σ_3 directions, respectively; j and k are the number of cycles; n is the total number of cycles from the initial loading stage to the residual stage; and ε_1^{cirr}, ε_2^{cirr}, and ε_3^{cirr} are the critical irreversible strains in the σ_1, σ_2, and σ_3 directions, respectively. Here, in the residual stage of the stress–strain curve, rock specimens are assumed to undergo absolute failure, namely, $D = 1$. Therefore, ε^{cirr} is actually referred to as the cumulative irreversible strain from the first cycle to the cycle corresponding to the residual stress.

It can be seen from Fig. 7 that D_1 and D_3 increase linearly with increasing e_p, whereas the relationship between D_2 and e_p is approximately logarithmic. Because point (0, 0) is on the D versus e_p curve, the relationships among D_1, D_2, D_3, and e_p can be expressed as follows:

$$D_1 = ae_p \tag{5}$$

$$D_2 = \ln\left(1 + be_p\right) \tag{6}$$

$$D_3 = ce_p \tag{7}$$

where a, b, and c are material constants and their fitted results are summarized in Table 1. In addition, Eqs. (5, 6, and 7) are appropriate because of the good fit results ($R^2 > 0.93$). As point (e_{pc}, 1) is also on the D versus e_p curve, these material constants (a, b, and c) have a close relationship with the parameter e_{pc}, which is defined as the critical equivalent irreversible strain at the residual stage. Consequently, e_{pc} may also be defined by

$$e_{pc} = \frac{1}{a} = \frac{e-1}{b} = \frac{1}{c}. \tag{8}$$

As shown in Table 1, Eq. (8) is verified by the nearly same values of a, $b/(e\text{-}1)$, and c.

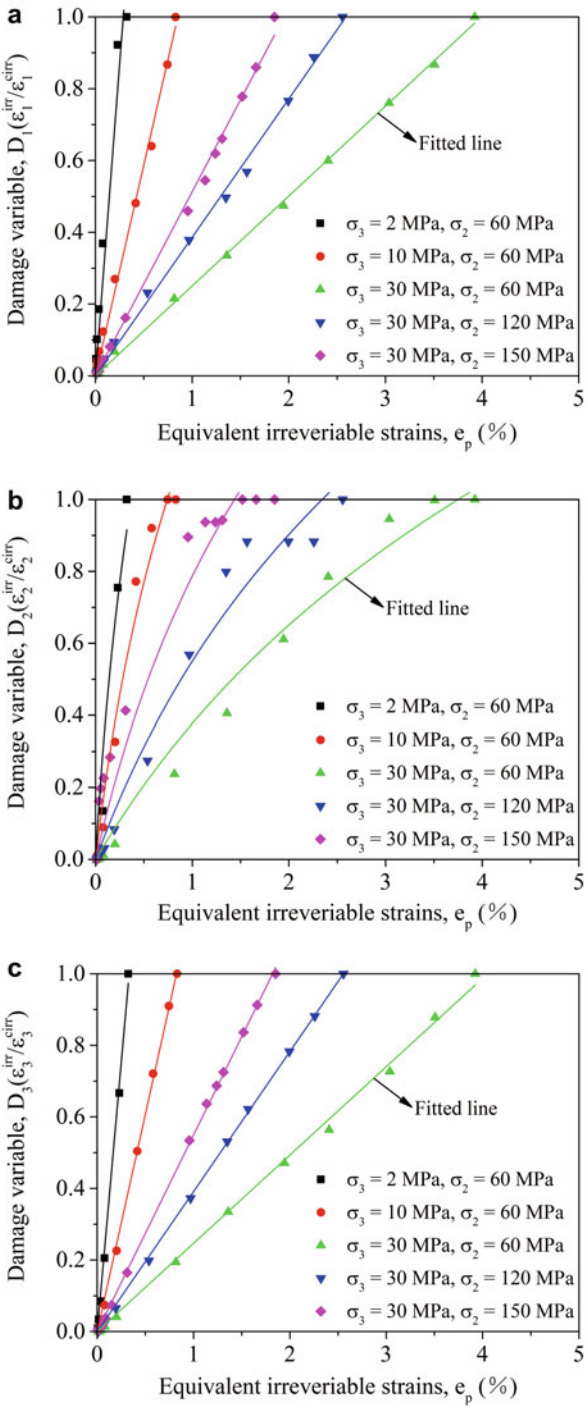

Fig. 7 Relationships between the damage variables represented by irreversible strains for the intact marble in the three principal stress directions and the equivalent irreversible strains (Gao and Feng 2019)

Table 1 The predefined stress states and material constants fitted to the relationships between the damage variables and equivalent irreversible strains for intact marble (Gao and Feng 2019)

σ_3 (MPa)	σ_2 (MPa)	a	R^2	b	b/(*e*-1)	R^2	c	R^2	d	R^2
2	60	3.47	0.97	4.64	2.70	0.94	3.01	0.99	3.40	0.98
10	60	1.17	0.99	2.32	1.35	0.98	1.22	0.99	1.20	0.99
30	60	0.25	0.99	0.46	0.27	0.99	0.25	0.99	0.27	0.99
30	120	0.39	0.99	0.73	0.43	0.98	0.39	0.99	0.42	0.99
30	150	0.51	0.99	1.20	0.70	0.93	0.55	0.99	0.57	0.99

Strain Energy Characteristics

Rock fracturing is accompanied by energy conversion. Specifically, the rock damage process causes energy dissipation. During the entire loading process, the inputted energy (U) is transformed into elastic energy (U_e) and dissipated energy (U_d). Elastic energy is stored in rock, whereas dissipated energy is released by the rock damage process. In the cyclic loading and unloading tests, the inputted energy (U) is calculated by the area, via the complete stress–strain curve and the strain axis in each cycle, and the dissipated energy (U_d) is presented by the loading curve, the corresponding unloading curve, and the strain axis in each cycle. The elastic energy (U_e) in each cycle is computed by the elastic and dissipated energy ($U_e = U - U_d$).

Figure 8 shows the changes in the elastic and dissipated energy for the intact marble with increasing e_p. Notably, the U_e versus e_p curves exhibit a trend similar to those of the $(\sigma_1 - \sigma_3)$ versus ε_1 curves. U_e increases in the pre-peak stage but decreases in the post-peak stage. U_d increases linearly with increasing e_p. Generally, U_e and U_d are affected by σ_3 and σ_2, and they increase with decreasing σ_2 and increasing σ_3.

A damage variable represented by energy dissipation is used to describe the damage evolution and is defined by

$$D_e = \frac{U_d}{U_c} = \frac{\sum_{j=1}^{i} (dU_d)_j}{\sum_{k=1}^{n} (dU_d)_k} \tag{9}$$

where D_e ($0 \leq D_e \leq 1$) is the damage variable based on dissipated energy and U_c is the critical dissipated energy that corresponds to the cumulative dissipated energy at the residual stage. As shown in Fig. 9, D_e of the intact marble have a linear relationship with e_p. As the D_e versus e_p curves pass through point (0, 0), the relationship between D_e and e_p can be defined as follows:

$$D_e = de_p \tag{10}$$

where d is a material constant whose fitted values are presented in Table 1. As the D_e versus e_p curves also pass through point (e_{pc}, 1), the parameter d can also be written by

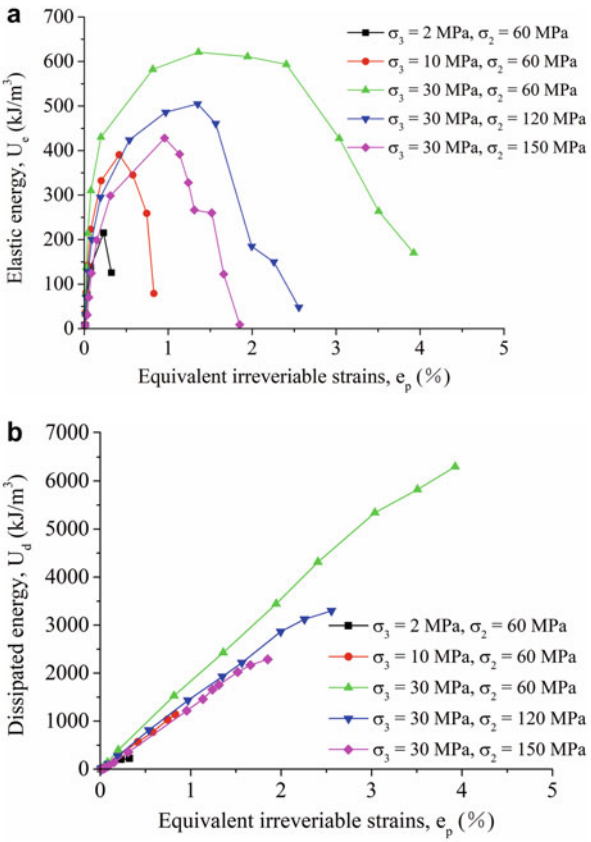

Fig. 8 Relationships between the strain energy of the intact marble and equivalent irreversible strain: (**a**) elastic energy and (**b**) dissipated energy. (Gao and Feng 2019)

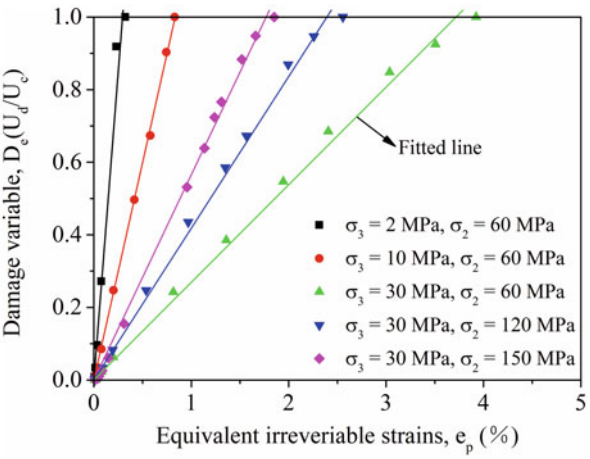

Fig. 9 Relationships between the damage variables represented by the dissipated energy of the intact marble and equivalent irreversible strain (Gao and Feng 2019)

$$e_{pc} = \frac{1}{d}. \tag{11}$$

Based on Eqs. (8) and (11), the damage variables based on the irreversible strains (D_1, D_2, and D_3) and dissipated energy (D_e) can be described by the following relationship:

$$a = \frac{b}{e-1} = c = d = \frac{1}{e_{pc}}. \tag{12}$$

This behavior is also verified by the similar values of these fitted parameters in Table 1.

Cohesion and Internal Friction Angle Characteristics

Following Mogi (1971), Al-Ajmi and Zimmerman (2005) and Chang and Haimson (2012) suggested that the relation between the octahedral shear stress τ_{oct} and the effective mean stress $\sigma_{m,2}$ can be expressed by a linear function in true triaxial tests:

$$\tau_{oct} = a^* + b^* \sigma_{m,2} \tag{13}$$

where a^* and b^* are empirical coefficients, and τ_{oct} and $\sigma_{m,2}$ are defined by

$$\tau_{oct} = \frac{1}{3}\sqrt{(\sigma_1 - \sigma_2)^2 + (\sigma_2 - \sigma_3)^2 + (\sigma_3 - \sigma_1)^2} \tag{14}$$

$$\sigma_{m,2} = \frac{\sigma_1 + \sigma_3}{2} \tag{15}$$

The material parameters a^* and b^* can be linked to the cohesion c_o and internal friction angle ϕ by comparing the formulations of the linear Mogi criterion (Eq. 13) and the Coulomb criterion:

$$a^* = \frac{2\sqrt{2}}{3} c_o \cos\phi \tag{16}$$

$$b^* = \frac{2\sqrt{2}}{3} \sin\phi. \tag{17}$$

It can be seen from Eqs. (13, 14, 15, 16, and 17) that the slope of the τ_{oct} versus $\sigma_{m,2}$ curve can be determined by ϕ. Figure 10 shows the relations between τ_{oct} and $\sigma_{m,2}$. These octahedral shear stresses and effective mean stresses are calculated by the maximum, minimum, and first values of the volumetric strain reversal stress σ_{cd} from true triaxial tests. For all the tested specimens, the points determined by the maximum, minimum, and first values of σ_{cd} can be represented by three parallel lines with a slope of 0.49. According to Eqs. (13, 14, 15, 16, and 17), the slope of 0.49

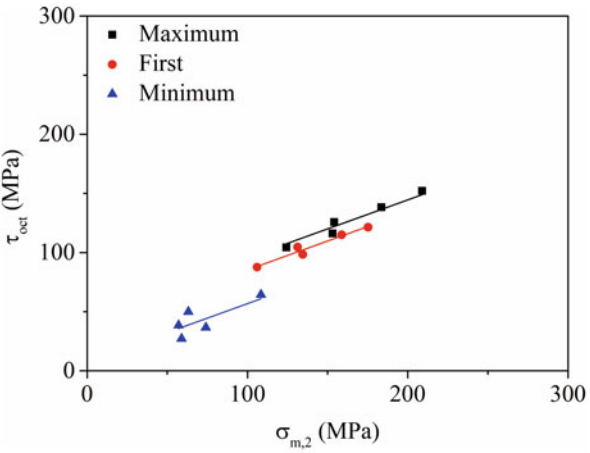

Fig. 10 Relations between the octahedral shear stress and effective mean stress represented by the maximum, minimum, and first volumetric strain reversal stresses of hard rocks in true triaxial cyclic loading tests (Feng et al. 2020)

corresponds to the internal friction angle ϕ of 31° at σ_{cd}. Based on the same ϕ at all σ_{cd}, the relations between c_o and e_p at the corresponding cycle can be calculated by

$$c_o = \frac{\tau_{oct} - \frac{2\sqrt{2}}{3}\sin\phi\sigma_{m,2}}{\frac{2\sqrt{2}}{3}\cos\phi} = \frac{\sqrt{2(\sigma_{cd}-\sigma_2)^2 + 2(\sigma_2-\sigma_3)^2 + 2(\sigma_3-\sigma_{cd})^2} - 2(\sigma_{cd}+\sigma_3)\sin\phi}{4\cos\phi} \quad (18)$$

where ϕ for intact marble is 31°.

Now, the peak stress σ_1 in each cycle combined with c_o obtained using Eq. (18) can be used to calculate the relations between ϕ and e_p, and the following correlation can be made:

$$\phi = \sin^{-1}\frac{\sqrt{(\sigma_1-\sigma_2)^2 + (\sigma_2-\sigma_3)^2 + (\sigma_3-\sigma_1)^2}}{\sqrt{2(\sigma_1+\sigma_3)^2 + 8{c_o}^2}} - \tan^{-1}\left(\frac{2c_o}{\sigma_1+\sigma_3}\right). \quad (19)$$

Figure 11a shows the changes in c_o with increasing e_p during the true triaxial tests. Generally, c_o shows a slow increasing trend followed by a rapid decrease until a small residual value is reached. This trend corresponds to the different stages of the stress–strain curves. A small increase in σ_{cd} at the pre-peak stage causes an increase in c_o. In the post-peak stage, c_o decreases rapidly before keeping relatively constant at the residual stage, which is also linked with crack development. With crack propagation and coalescence, the degree of rock damage gradually increases, thus causing a decrease in c_o. Once the macroscale failure plane forms in the rock specimen, shearing of the failure plane mainly occurs; thus, c_o becomes invariant.

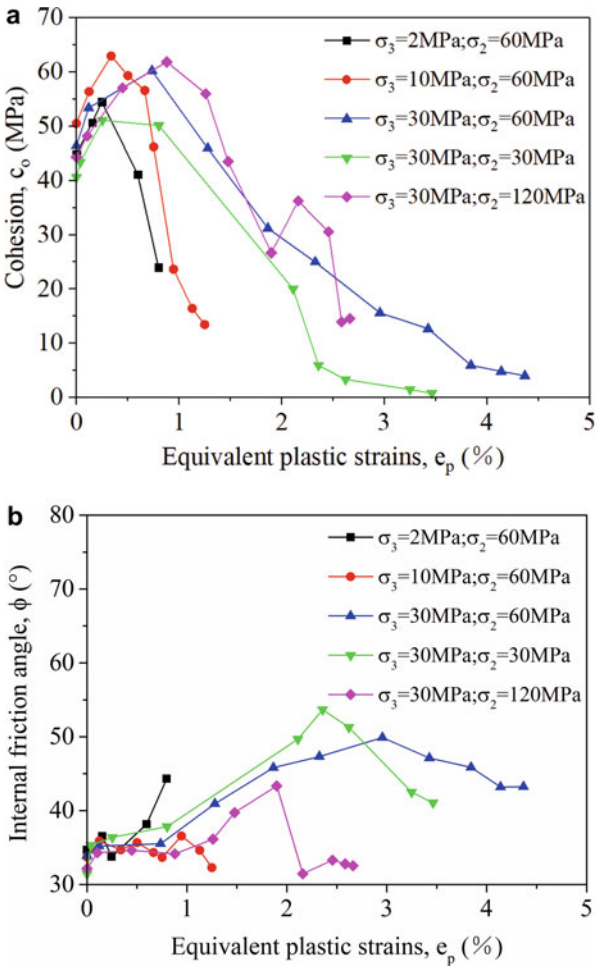

Fig. 11 Relations among the cohesion and internal friction angle and the equivalent plastic strains of intact marble in the true triaxial cyclic loading tests (Feng et al. 2020)

Figure 11b shows the variation in ϕ with increasing e_p. The ϕ values for intact marble first remain constant before increasing to a higher constant value with increasing e_p. This behavior is associated with the remarkable ductility around the peak cycles.

Conclusions

To study the effect of the intermediate principal stress on the damage and failure characteristics of hard rocks, the progressive cracking process under true triaxial compression is studied. It was found that the crack growth is related to the stress state, in which the intermediate principal stress must be taken into consideration. A

lower intermediate principal stress will restrain crack growth, but a higher intermediate principal stress will accelerate crack growth, particularly when the intermediate principal stress approaches the maximum principal stress.

The damage assessment of hard rocks is given based on a cyclic true triaxial loading study. The irreversible strains, cohesion, and friction parameters are calculated as damage variables to quantify the damage of hard rocks. The damage evaluation is effectively described by these damage variables.

References

A.M. Al-Ajmi, R.W. Zimmerman, Relation between the Mogi and the Coulomb failure criteria. Int. J. Rock Mech. Min. Sci. **42**(3), 431–439 (2005)

Z.T. Bieniawski, Mechanism of brittle fracture of rock: Part II – Experimental studies. Int. J. Rock Mech. Min. Sci. Geomech. Abstr. **4**(4), 407–423 (1967)

W.F. Brace, B.W. Paulding, C.H. Scholz, Dilatancy in the fracture of crystalline rocks. J. Geophys. Res. **71**, 3939–3953 (1966)

C. Chang, B. Haimson, A failure criterion for rocks based on true triaxial testing. Rock Mech. Rock. Eng. **45**(6), 1007–1010 (2012)

Z.Q. Chen, C. He, D. Wu, G.W. Xu, W.B. Yang, Fracture evolution and energy mechanism of deep-buried carbonaceous slate. Acta Geotech. **12**, 1243–1260 (2017)

X.T. Feng, X. Zhang, R. Kong, G. Wang, A novel Mogi type true triaxial testing apparatus and its use to obtain complete stress–strain curves of hard rocks. Rock Mech. Rock. Eng. **49**, 1649–1662 (2016)

X.T. Feng, S.F. Pei, Q. Jiang, Y.Y. Zhou, S.J. Li, Z.B. Yao, Deep fracturing of the hard rock surrounding a large under-ground cavern subjected to high geostress: In situ observation and mechanism analysis. Rock Mech. Rock. Eng. **50**, 2155–2175 (2017)

X.T. Feng, Y.H. Gao, X. Zhang, Z.F. Wang, Y. Zhang, Q. Han, Evolution of mechanical and strength parameters of hard rocks in true triaxial cyclic loading and unloading tests. Int. J. Rock Mech. Min. Sci. **131**, 104349 (2020)

Y.H. Gao, X.T. Feng, Study on damage evolution of intact and jointed marble subjected to cyclic true triaxial loading. Eng. Fract. Mech. **215**, 224–234 (2019)

B. Haimson, C. Chang, A new true triaxial cell for testing mechanical properties of rock, and its use to determine rock strength and deformability of Westerly granite. Int. J. Rock Mech. Min. Sci. **37**, 285–296 (2000)

J. Handin, H.C. Heard, J.N. Magouirk, Effects of the intermediate principal stress on the failure of limestone, dolomite, and glass at different temperatures and strain rates. J. Geophys. Res. **72**, 611–640 (1967)

C.J. Jia, W.Y. Xu, R.B. Wang, W. Wang, J.C. Zhang, J. Yu, Characterization of the deformation behavior of fine-grained sandstone by triaxial cyclic loading. Constr. Build. Mater. **162**, 113–123 (2018)

R. Kong, X.T. Feng, X. Zhang, C. Yang, Study on crack initiation and damage stress in sandstone under true triaxial compression. Int. J. Rock Mech. Min. Sci. **106**, 117–123 (2018)

M. Kwašniewski, Mechanical behaviour of rocks under true triaxial compression conditions – Volumetric strain and dilatancy. Arch. Min. Sci. **52**, 409–435 (2007)

E.Z. Lajtai, V.N. Lajtai, The evolution of brittle fracture in rocks. J. Geol. Soc. **130**, 1–16 (1974)

S. Li, X.T. Feng, Z. Li, B. Chen, C. Zhang, H. Zhou, In situ monitoring of rockburst nucleation and evolution in the deeply buried tunnels of Jinping II hydropower station. Eng. Geol. **137–138**, 85–86 (2012)

X.S. Liu, J.G. Ning, Y.L. Tan, Q.H. Gu, Damage constitutive model based on energy dissipation for intact rock subjected to cyclic loading. Int. J. Rock Mech. Min. Sci. **85**, 27–32 (2016)

C.D. Martin, N.A. Chandler, The progressive fracture of Lac du Bonnet granite. Int. J. Rock Mech. Min. Sci. Geomech. Abstr. **31**, 643–659 (1994)

K. Mogi, Effect of the intermediate principal stress on rock failure. J. Geophys. Res. **72**, 5117–5131 (1967)

K. Mogi, Fracture and flow of rocks under high triaxial compression. J. Geophys. Res. **76**, 1255–1269 (1971)

R.D. Peng, Y. Ju, J.G. Wang, H.P. Xie, F. Gao, L.T. Mao, Energy dissipation and release during coal failure under conventional triaxial compression. Rock Mech. Rock. Eng. **48**(2), 509–526 (2015)

H.P. Song, H. Zhang, Y.L. Kang, G.Y. Huang, D.H. Fu, C.Y. Qu, Damage evolution study of sandstone by cyclic uniaxial test and digital image correlation. Tectonophysics **608**, 1343–1348 (2013)

M. Takahashi, H. Koide, Effect of the intermediate principal stress on strength and deformation behavior of sedimentary rocks at the depth shallower than 2000 m, in *Rock at Great Depth*, ed. by V. Maury, D. Fourmaintraux, vol. 1, (Balkema, Rotterdam, 1989), pp. 19–26

B.G. Tarasov, T.R. Stacey, Features of the energy balance and fragmentation mechanisms at spontaneous failure of Class I and Class II rocks. Rock Mech. Rock. Eng. **50**(10), 2563–2584 (2017)

H.P. Xie, L.Y. Li, R.D. Peng, Y. Ju, Energy analysis and criteria for structural failure of rocks. J. Rock Mech. Geotech. Eng. **1**, 11–20 (2009)

Y. Zhang, X.T. Feng, X. Zhang, Z.F. Wang, M. Sharifzadeh, C. Yang, R. Kong, J. Zhao, Strain energy evolution characteristics and mechanisms of hard rocks under true triaxial compression. Eng. Geol. **260**, 105222 (2019)

Plastic Deformation and Damage in Rocks Under Coupled Thermo-hydromechanical Conditions: Numerical Study

31

Dashnor Hoxha and Duc Phi Do

Contents

Introduction 820
Thermodynamics of Thermoporous Elastoplastic-Damage Materials 822
Thermoelastoplastic Material 822
Thermoelastoplastic-Damaged Material 824
State Equations for Hydraulic and Thermic Behavior 825
An Elastoplastic Damage Model for Rocks Used in Case Studies 827
Numerical Issues on Porous Elastoplastic-Damage Model Implementation 830
Numerical Strategies for Multiphysics Coupling 830
Integration of Constitutive Elastoplastic-Damage Equations 832
Case Study: Evolution of Rock Mass State Around a Circular Horizontal Drift Under Thermo-Hydromechanical Loads 833
Problem Description 833
Results and Discussions 836
Summary/Conclusions 850
References 850

Abstract

Natural rocks often manifest at the same time, at various proportions, a mixing of typical irreversible (visco)plastic strains and damage mechanisms. For porous rocks, thermo-poromechanics offers a suitable thermodynamic framework fo numerical strategies are developed for modeling coupling between plasticity and damage on the one hand and multiphysics coupling on the other hand. A full coupling approach for solving thermos-hydromechanical field equations and a finite element software is used for 3D modeling of long-term evolution of a deep circular drift under thermal, hydraulic, and mechanical coupled loads. It is supposed this drift is part of a set of horizontal excavations, parallel to each

D. Hoxha (✉) · D. P. Do
Univ Orléans, Univ Tours, INSA CVL, Orléans, France

Civil Engineering, University of Orléans, Laboratory of Mechanics Gabriel Lamé, Orléans, France
e-mail: dashnor.hoxha@univ-orleans.fr; duc-phi.do@univ-orleans.fr

© Springer Nature Switzerland AG 2022

G. Z. Voyiadjis (ed.), *Handbook of Damage Mechanics*,
https://doi.org/10.1007/978-3-030-60242-0_62

other at some distances. Such small diameter drifts could be potentially used in various waste disposals or geothermal exploitation. The stress in the drift section is considered isotropic, yet a 3D model is used to point out the effects of a nonuniform thermal load on the response of the system. Because of that and under a decayed thermal power, the evolution of the temperature on the drift wall is neither uniform nor monotonic, and high gradients of temperature and stress are generated in both radial and longitudinal directions. In turn, these generate nonuniform stress fields leading in fine to nonuniform viscoplastic strains and damage. The effects of the interaction of adjacent drifts are manifested of developing a particular shape of the damage zone, larger and more intense on the vertical direction.

Keywords

Thermo-poromechanics · Damage-plasticity coupling · Pore pressure · Time dependent

Introduction

Rocks and rock masses exhibit, under mechanic, hydraulic, and thermal loads, a complex behavior that is conditioned by the particularity of their structure, composition, and geological history. The rock masses are seen as porous media with complex patterns of existing cracks, fractures, and faults. These discontinuities interact with porous space and among them in such a way that prediction of their behavior remains yet a theoretical and practical challenge. Modeling this behavior remains nowadays a major issue of great theoretical and practical interest in many fields such as energy, oil and gas field recovery, CO2 storage, geothermal exploitation, urban and infrastructure development, tunnel excavation, and bridge foundations to just mentioning a few engineering applications (Coussy 2004; Jaeger et al. 2007; Pariseau 2011). On the one hand, this modeling is tightly linked with understanding and explanation of the mechanism governing behavior of rocks and rock masses (constitutive modeling), and on the other hand, it is conditioned by developing numerical tools' and machines' capacities to able to deal with a complex problem and the high number of degrees of freedom.

Both sides of rock mass modeling (constitutive modeling and numerical methods to deal with these models at large scales) are in interaction with each other and open new perspectives of exploration of modeling problem solutions.

In many cases, the constitutive modeling of rock could be performed in the framework of brittle damage approach. Neglecting irreversible plastic strains, this powerful approach describes the evolution of elastic properties of brittle rocks due to carking, through the evolution of damage variables with a physical meaning well defined. A discussion on the various choices of damage variable could be found, for example, in Krajcinovic (1996) and Kachanov (1993) among others. The choice of this damage variable is of consequences in both physical description of the damage

and numerical techniques dealing with its modeling. Models using a scalar damage variable could be easily treated numerically using the well-proven elastoplastic framework with some appropriate modifications. However, the physical meaning of such variables as reduction of effective section (or equivalently amplification of stress due to this reduction, Lemaitre 1992) is merely difficult to be generalized for cracked rocks with multiple sets of cracks and orientations.

It is already demonstrated that for brittle rocks, a tensor damage variable catching the fabrics of crack arrays is appropriate to describe the directional crack growth and the anisotropy induced by this cracking (Kachanov 1993; Shao et al. 2006; Zhu et al. 2008; Bikong et al. 2015). However, implementation of such models and their use in practical applications raise some problems, mainly linked with the local following of crack evolution. A solution is proposed in Zhu et al. (2008) where discretization of crack orientation is proposed at any point in the space. For a chosen direction, a scalar damage variable gives the directional damage extension, and finally, a damage tensor is calculated from these orientations using fabric tensors. While this proposal avoids the so-called "crack rotation" problem that is pointed out as a drawback in some other damage tensor-based models, it is difficult to establish the link with orientational local variables and their spatial distribution.

The damage and cracking in all materials, especially in rocks, is accompanied by plastic strains, more or less important which, in many cases, could be neglected since they localized to some small regions around crack tips. In most cases, this damage-driven plasticity is neglected in modeling for simplicity and there is little practical interest. However, for a large class of rocks, especially for the porous ones, the damage is ductile, and plasticity not only could not be neglected but is the principal phenomenon that triggers the damage and eventually failure of the rock. Modeling of such behavior is performed in the framework of plasticity formalism with necessary adaptation for thermodynamic coherence (Ju 1989; Hayakawa and Murakami 1997; Voyiadjis et al. 2008).

The framework of open porous media (Coussy 2004) offers a suitable theoretical tool to deal with the impact of multiphysics coupling on plastic and damage initiation and enhancing. This coupling could be either a strong one, in which all fields interact with each other such that the set of state equations and evolutions should be solved at the same time, or a weak one. In particular, the damage evolution on rocks is susceptible to lead to the evolution of hydraulic properties of rock masses, triggering in most cases an increase of permeability and porosity. This evolution could be so strong as to increase by many orders the permeability around underground excavations (Souley et al. 2001). Inversely, an evolution of pore pressure is susceptible to initiate and grow damage and cracking, leading to the evolution of permeability (Do and Hoxha 2013; Min et al. 2005). This strong coupling between mechanical and hydraulic fields is often the key to modeling reservoir rock behavior.

Otherwise, a weak coupling could describe the relations between two and more physical fields in the way that the evolution of one field due to variation of other physical fields is moderate and negligible. Thermal field evolution, for example, is susceptible to strongly modify both stress/strain fields on a rock masses and physical

parameters of rock. However, the variation of stress and strain in rock masses, in the range of variations and frequencies observed in industrial applications, has little impact if not at all on thermal fields. Indeed, even if some modifications of thermal material parameters such as conductivity or specific heat are susceptible to be produced while damage evolves, these evolutions in the above-specified range are in most cases negligible and have little impact on the temperature field evolution. Consequently, numerical modeling strategies for plastic-damage evolution under thermo-hydromechanical coupling will be strongly conditioned by the type of coupling.

This chapter focuses on the elastoplastic-damage modeling of rock mass behavior under coupled thermo-hydromechanical loads. After a brief description of thermodynamic bases for elastoplastic poromechanics and plastic-damage modeling, some numerical results are discussed to show the reciprocal impact of plastic-damage and multiphysics coupling.

Thermodynamics of Thermoporous Elastoplastic-Damage Materials

For thermo-hydromechanical rock behavior modeling, the state equations governing hydraulic, thermic, and mechanical behavior should be presented mathematically and resolved following an appropriate strategy. For describing a nonlinear poromechanical behavior of rock masses, an elastoplastic or an elastoplastic-damage formalism could be followed; the second is seen as an extension of the first.

Thermoelastoplastic Material

Using the hypothesis of weak (unilateral) coupling between thermal and other physical fields, the hypothesis that is verified in many engineering applications in rock masses, the problem is firstly treated under isothermal conditions. Then the impact of temperature could be added as an extension of the obtained hydromechanical framework.

The hypothesis of infinitesimal transformation is adopted here such that the additive plastic and elastic variation could be adopted for both total strain total porosity:

$$d\underline{\underline{\varepsilon}} = d\underline{\underline{\varepsilon}}^{el} + d\underline{\underline{\varepsilon}}^{p} \qquad d\varphi = d\varphi^{el} + d\varphi^{p} \tag{1}$$

For a porous, fully saturated, elastoplastic material under isothermal transformation, the mixed thermodynamic potential of an elastoplastic saturated porous material is written (Coussy 2004):

$$W^{\#} = W^0 + \frac{1}{2}(\underline{\varepsilon} - \underline{\varepsilon}^p) : \underline{\underline{C_0}} : (\underline{\varepsilon} - \underline{\varepsilon}^p) - (p - p_0).\underline{B} : (\underline{\varepsilon} - \underline{\varepsilon}^p) - \frac{1}{2M}(p - p_0)^2 + \psi^p(V_k) \quad (2)$$

$\psi^p(V_k)$ is the locked energy by plastic hardening of hardening parameters V_k, $\underline{\underline{C_0}}$ stands for the undamaged elastic stiffness tensor, p is the pore pressure, and M is Biot's modulus of porous materials. The constitutive relation is therefore obtained by classical derivative:

$$\underline{\sigma} = \frac{\partial W^{\#}}{\partial \underline{\varepsilon}} = \underline{\underline{C_0}}.(\underline{\varepsilon} - \underline{\varepsilon}^p) - \underline{B}.(p - p_0) \quad (3)$$

$$\frac{m}{\rho_{fl}^0} - \varphi^p = \frac{\partial W^{\#}}{\partial p} = -\underline{B} : (\underline{\varepsilon} - \underline{\varepsilon}^p) - \frac{1}{M}.(p - p_0) \quad (4)$$

The relationship (3) shows that the behavior of a saturated porous medium is governed by Biot's effective stress (similar to, and extension of, Terzaghi effective stress concept) since one could write:

$$\underline{\sigma'} = \underline{\sigma} + \underline{\mathrm{B}}.(p - p_0) \text{ and } \underline{\sigma'} = \underline{\underline{C_0}}.(\underline{\varepsilon} - \underline{\varepsilon}^p) \quad (5a)$$

For an isotropic material, Biot's tensor $\underline{\underline{B}}$ is isotropic and could be written as $\underline{\underline{B}} = b.\underline{\underline{1}}$ with b being the well-known Biot's coefficient.

By supposing a linear relationship between volumetric plastic deformation and plastic porosity, it could be shown the existence of a plastic effective stress, usually different from the elastic one (Coussy 2004):

$$\underline{\sigma'_p} = \underline{\sigma} + \underline{\beta}.(p - p_0) \quad (5b)$$

As discussed by many authors, these equations define the effective stress as a purely rheologic concept that could help and facilitate constitutive modeling.

To describe the constitutive behavior of an elastoplastic material, one needs to complete the above equations with complementary and evolution equations. The various elastoplastic models differ from each other from these elements that are proper to each model. For a given elastoplastic model (so for a given plastic potential G_p and a yield function F_p), the plastic flow rule and the consistency condition are written as:

$$d\underline{\varepsilon}^p = d\lambda \frac{\partial G_p}{\partial \underline{\sigma}} \text{ and } F_p \leq 0; d\lambda \geq 0; d\lambda.F_p = 0; d\lambda.dF_p = 0 \quad (6)$$

In all cases the positiveness of dissipation could be formally written as:

$$\underline{\sigma} : d\underline{\varepsilon}^p + p\, d\varphi^p - Y^k V_k \geq 0 \quad (7)$$

In this last equation, Y^k stands for the thermodynamic force associated with the internal variable V_k.

While the set of Eqs. (1) to (6) gives a general framework for poroelastoplastic modeling, one has to personalize the plastic potential, the yield function, and eventually the hardening function.

For non-isothermal (infinitesimal and without phase change) evolutions, the extension of these results is immediate: one has to add the thermal strain to mechanical one and add the appropriate terms in the mixed potential (2) to reflect coupling terms with mechanical and hydraulic fields. Alternatively, one could write the free energy evolution of the skeleton by taking into account entropy S_s and temperature T_s of the skeleton (Coussy 2004; Detournay and Cheng 1993):

$$dW^{ep}(\underline{\varepsilon}, p, T, V_k) = \underline{\sigma} : d\underline{\varepsilon} - \varphi dp - S_s dT_s - \Psi_k(V_k) \tag{8}$$

The state Eqs. (3) and (4) become in that case:

$$d\underline{\sigma} = \underline{\underline{C_0}}.(d\underline{\varepsilon} - d\underline{\varepsilon}^p - \underline{a}dT) - \underline{B}.dp \tag{9}$$

$$\frac{dm}{\rho_{fl}^0} - d\varphi^p = -\underline{B} : (d\underline{\varepsilon} - d\underline{\varepsilon}^p) - \frac{1}{M}.dp + 3(\varphi - \varphi^p)(\alpha_s - \alpha_l)dT \tag{10}$$

In the equations above, it is assumed that the eigenvalues of effective thermal expansion tensor $\underline{a}$ are of the same order as the expansion coefficient of skeleton α_s, while α_s represent the expansion coefficient of saturating fluid. When pores are saturated by a mixture of fluids, the expansion coefficient of fluid is that of the fluid mixtures.

The positiveness of dissipation (7) becomes:

$$\underline{\sigma} : d\underline{\varepsilon}^p + p\, d\varphi^p - S_s dT_s - Y^k V_k \geq 0 \tag{11}$$

Thermoelastoplastic-Damaged Material

The equations for thermoelastoplastic-damage material are obtained as an extension of elastoplastic using one of the approaches proposed for plastic-damage modeling (Ju 1989; Hayakawa and Murakami 1997; Voyiadjis et al. 2008; Jia et al. 2009; Voyiadjis and Abu Al-Rub 2003; Hansen and Schreyer 1994). All approaches proposed for coupling elastoplastic and damage constitutive behaviors consider that damaged material corresponds to an equivalent effective healthy material with the same behavior. The criterion of equivalence between effective elastoplastic material and elastoplastic-damaged material is different from some authors to others such as free energy equivalency, shear energy equivalency, and net stress equivalency to just mentioning the most used ones in practice. Note that to avoid confusion about effective stress whose definition is given in Eq. 5a and 5b, the term "net stress" is used to indicate what is called effective stress in Ju (1989) and other "effective stress" damage-related references. Consequently, depending on the criterion of the

equivalency chosen for the effective elastoplastic material, the damage could impact or not the yield function, plastic potential, and evolution equations.

The key assumption on developing equations for elastoplastic-damage model is the assumption that the potential (either Helmholtz free energy or Gibbs energy) could be written as a sum of the poroelastoplastic material and that of a damaged one, such that, for example, the Eq. (8) is written as:

$$dW_d^{ep}(\underline{\varepsilon}, p, T, V_k, D) = dW^{ep}(\underline{\varepsilon}, p, T, V_k) + dW_D(\underline{\varepsilon}, p, T, D) \tag{12}$$

In this expression, D stands for the set of damage variables. In the simplest case, it is a scalar damage variable, but other choices as cited in the introduction are used in practice including a set of scalars, a second-order tensor, or even higher-order tensors.

The thermodynamic forces associated with damage Y_D are obtained by derivation of this potential in respect to damage, i.e.:

$$Y^D = \frac{\partial W_D^{ep}}{\partial D} \tag{13}$$

Similar to plasticity, a "damage" function could be written in the space of thermodynamic forces and/or state variables. In the simplest cases where plasticity and damage coexist without interaction, the yield function (respectively damage function) is independent of the internal variable of damage (respectively from hardening function). In some other models, an additive dissipation potential combining a plastic and damage term is used in such a way that the evolution rate of plastic strains and damage could be calculated similarly:

$$G_d^{ep}(\underline{\sigma}, p, T, Y_D) = G^{ep}(\underline{\sigma}, p, T, Y_D) + G_d(\underline{\sigma}, p, T, Y_D) \tag{14}$$

$$d\underline{\varepsilon}^p = d\lambda_p \frac{\partial G^{ep}}{\partial \underline{\sigma}} \text{ and } dD = d\lambda_D \frac{\partial G_d}{\partial Y_D} \text{ with } d\lambda_p \geq 0 \; d\lambda_D \geq 0 \tag{15}$$

As written in Eq. (14), the damage could yet impact the yield function and the plasticity rate if the concept of net stress is adopted. This same remark is also valid for hydromechanical coupling if the plastic-damaged potential is written using the effective net stress combining the effects of pore pressure and damage. As for the impact of thermal fields on plasticity and damage developing, it is exerted through the thermal expansion phenomenon and eventually through a thermal hardening function added/combined with plastic hardening.

State Equations for Hydraulic and Thermic Behavior

In the general case, the rock masses could be considered as a partially saturated porous media with two phases: liquid and gaseous ones. The advection of both gaseous and liquid phases is given by a generalized Darcy's law making use of so-called effective permeability:

$$\frac{\mathbf{M}_j}{\rho_j} = -\lambda_j \boldsymbol{grad}\left(P_j\right) \qquad j = liquid, gas \tag{16}$$

with $\underline{M}_j$ being the hydric flux vector and λ_j the effective hydraulic conductivity of j^{th} phase, defined as follows:

$$\lambda_j = \frac{k_{in}.k_j^{rel}(S_l)}{\mu_j} \qquad j = liquid, gas \tag{17}$$

In this expression, k_{in} is the intrinsic permeability and $k_j^{rel}(S_l)$ is the relative permeability, a limited value function of liquid saturation S_l. It could be identified from laboratory data along with the so-called isothermal absorption curve $S_l(P_C)$. An empirical expression for this curve, often used in practice, is given by VanGenuchten (1980):

$$S_l(P_c) = \left[1 + \left(\frac{P_C}{P_r}\right)^n\right]^{\frac{1-n}{n}} \tag{18}$$

with Pr (stress units) and n (dimensionless) being the two fitting parameters.

Assuming a Fick's diffusion for the vapor phase in the mixture of gases, one could obtain the vapor flux using the first Fick's law:

$$\frac{\mathbf{M}_v}{\rho_v} = -F\boldsymbol{grad}\left(C_{vp}\right) \tag{19}$$

Here F is Fick's coefficient, while $C_{vp} = P_v/P_g$ is the vapor concentration in the gaseous phase.

Similarly, the heat conduction is characterized by Fourier's law:

$$\boldsymbol{q} = -\lambda_T \boldsymbol{grad}(T) \tag{20}$$

with $\underline{q}$ being the thermal flux ([J.m^{-2}.s^{-1}]) and λ_T the thermal conductivity ([J.K^{-1}.m^{-1}.s^{-1}]).

Similar to the effective stress concept used for saturated porous media, in partially saturated ones, the combined effects of temperature and relative humidity could be cast in an effective stress quantity as follows (Coussy 2004):

$$\underline{\widetilde{\sigma}'} = \underline{\widetilde{\sigma}} + b\pi\underline{\delta} + 3\alpha K \Delta T \underline{\delta} \tag{21}$$

Following Eq. (21), the effective stress tensor $\underline{\widetilde{\sigma}'}$ that governs the behavior of partially saturated porous media is a combination of mechanical, hydraulic, and thermal loads. The generalized pore pressure π is written as a function of liquid saturation S_l and capillary pressure Pc (difference of the gaseous and liquid pressure, $P_C = P_g - P_l$) (Coussy 2004):

$$\pi = \begin{cases} \int_{S_l}^{1} S_l(P_c) dP_c \ \text{if} \ S_l < 1 \\ P_l \ \text{otherwise} \end{cases} \tag{22}$$

An Elastoplastic Damage Model for Rocks Used in Case Studies

Modified Drucker-Prager Elastoplastic-Damage Model in Thermo-hydromechanical Coupling (Hoxha et al. 2007; Chiarelli et al. 2003)

For using in rock behavior description, the classical Drucker-Prager model is modified to ameliorate the response of the model in tensile stress state. For hydro-mechanical coupling and fully saturated porous media, the effective stress is used for writing the yield functions and plastic potential.

(a) Yield function

So the yield function of modified Drucker-Prager model is written as (Hoxha et al. 2007):

$$F_p(\widetilde{\sigma}_m, J_2, \kappa, \eta) = \sqrt{3J_2} + \kappa.\sqrt{1 - \eta.\widetilde{\sigma}_m} \tag{23}$$

with $\widetilde{\sigma}_m = \sigma_m + \beta.p$ being the effective plastic mean stress as in 5b and b the Biot's coefficient of porous material.

As compared to the original Drucker-Prager model, the yield function (16) represents a parabolic shape in the space of stress invariant instead of a conic surface (Fig. 1). η parameter is the triaxial tensile strength, while κ represents the hardening function that could also be used to couple the plasticity and damage. If the hardening function is only the function of plastic strain, then damage coupling is realized implicitly and the hardening function could be written as:

$$\kappa = \kappa_1(\gamma^p) = \kappa_m - (\kappa_m - \kappa_0)\frac{1}{1 + \alpha\gamma^p} \tag{24a}$$

In this hardening function, κ_0 represents the values of this material parameter at the plasticity onset, while κ_m its value at pick.

Otherwise, for an explicit coupling between plasticity and damage, the hardening function is a function of both plastic strain and chosen damage parameter D:

$$\kappa = \kappa_{\gamma,D}(\gamma^p, D) = \kappa_1(\gamma^p)\kappa_2(D) = \left(\kappa_m - (\kappa_m - \kappa_0)\frac{1}{1 + \alpha\gamma^p}\right)(1 - \alpha_2 D) \tag{24b}$$

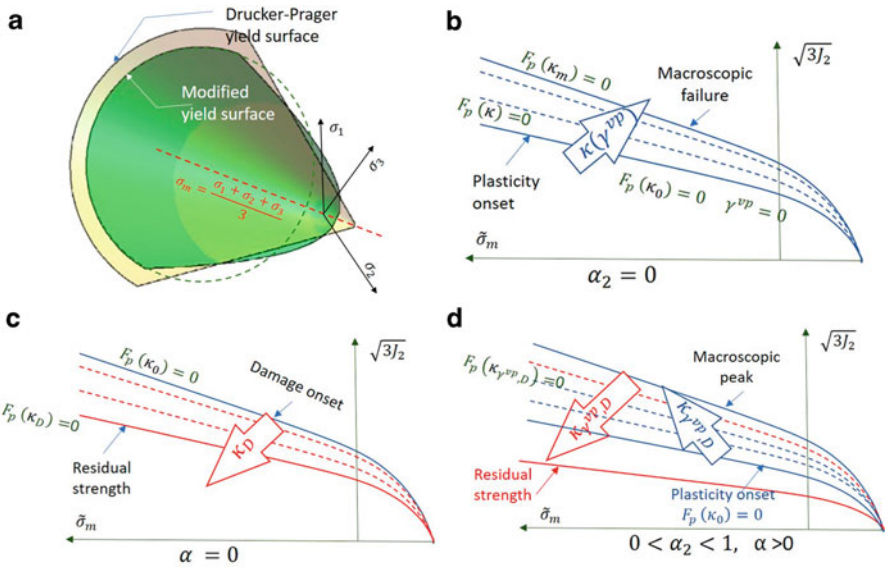

Fig. 1 (**a**) Original and modified Drucker-Prager yield surface in the stress space, (**b**) schematic presentation of plastic hardening model, (**c**) schematic presentation of brittle damage model, (**d**) schematic presentation of elasto-plasto-endommageable model

The hardening function (24b) could be used to simulate either a fragile damage behavior (by taking $\alpha = 0$, a purely hardening plastic behavior ($\alpha_2 = 0$) or a coupled elasto-plasto-damage behavior ($\alpha > 0$, $0 < \alpha_2 \leq 1$).

These combinations of hardening function parameters allow describing either of three typical behaviors (Fig. 1b–d).

(b) Plastic potential and plastic flow

Usually, rocks, and more generally geomaterials, exhibit a nonassociated plastic flow with a plastic contraction or dilatancy depending on the stress state. Consequently, the plastic flow is derived from a plastic potential different from the yield function (16):

$$G_p \equiv \sqrt{3J_2.} + \delta(\gamma^p).\sigma_m \tag{25}$$

with $\delta(\gamma^p)$ being a limited value function varying monotonically between a minimum value δ_0 and a maximum one δ_m:

$$\delta(\gamma^p) = \delta_m - (\delta_m - \delta_0).Exp(-\beta_\delta.\gamma^p) \tag{26}$$

The potential (25) is of remarkable simplicity and allows, for appropriated values of minimal plastic dilatancy (δ_0) and maximal one δ_m, to describe an often observed

behavior of shifting plastic flow from a plastic contraction to a plastic dilatancy. The plastic strains are derived from the plastic potential:

$$d\underline{\varepsilon}^p = d\lambda \frac{\partial G_p}{\partial \underline{\sigma}} = d\lambda \frac{\partial G_p}{\partial J_2} \frac{\partial J_2}{\partial \underline{\sigma}} + d\lambda \frac{\partial G_p}{\partial \sigma_m} \frac{\partial \sigma_m}{\partial \underline{\sigma}} \tag{27}$$

In this expression, $d\lambda$ is the plastic multiplier calculated from consistency rule of the yield surface, i.e., $dF_p = 0$.

(c) Plastic-enhanced damage and poroelastic parameter evolution

For a large class of geomaterials, for which the damage and cracking are triggered by the plasticity, it is possible to define the damage as a function of plasticity. Indeed, the overall inelastic dilatancy observed in the behavior of rocks is a manifestation of voids' growth triggered by plastic strains. So, one could formally write the density of the induced crack ρ^D as a function of plastic strains:

$$\rho^D = \rho^D(\underline{\varepsilon}^p) \tag{28}$$

If the crack density is known, it is possible to obtain a closed expression for evolution of elastic properties of the rock with damage. Indeed, considering a small crack density and adopting a homogenization schema, the drained elastic properties of damaged rock are written as:

$$K_0^D\left(\rho^D\right) = K_0^{in}\left(1 - k_1.\rho^D\right) \tag{29}$$

$$\mu^D\left(\rho^D\right) = \mu_0^{in}\left(1 - k_2.\rho^D\right) \tag{30}$$

In these expressions, k_1 and k_2 coefficients depend upon the chosen homogenization schema, the voids' geometry, and the properties of the skeleton. Besides, the relationship between the crack porosity and crack density, for a crack population with the same shape coefficient X, is:

$$\varphi^D = \frac{4}{3}\pi.X.\rho^D \tag{31}$$

Because of the evolution of the elastic parameters due to damage, the poromechanical properties evolve too. In particular, Biot's coefficient and Biot's modulus expressions, neglecting the variation of the porosity due to the crack porosity φ^D, become:

$$b^D\left(\rho^D\right) = 1 - \frac{K_0^D(\rho^D)}{K_s} = b^{in} + \left(1 - b^{in}\right).k_1\rho^D \tag{32}$$

$$\frac{1}{M^D(\rho^D)} = \frac{1}{M^{in}} + \frac{\left(1 - b^{in}\right)^2}{K_0^{in}} k_1\rho^D \tag{33}$$

Due to these evolutions, the constitutive relations (9) and (10), for a constant φ^D, are casted into:

$$\underline{\sigma} = \left[K_0^D(\rho^D).(\varepsilon_v - \varepsilon_v^p - \varphi^D) - b(\rho^D).(p - p_0)\right].\underline{1} + 2\mu^D(\rho^D).(\underline{e} - \underline{e}^p) \tag{34}$$

$$\frac{m}{\rho_{fl}^0} + \varphi^D - \varphi^p = -b(\rho^D).tr(\underline{\varepsilon} - \underline{\varepsilon}^p) - \frac{1}{M(\rho^D)}.(p - p_0) \tag{35}$$

The identification of the function $\rho^D = \rho^D(\gamma^p)$, in Eqs. (29) to (35), is not a straightforward task. A pragmatic approach consists of establishing the relationship between the plastic strains and the damage using cyclic triaxial compressive test. For a given unloading stress path, one just measure the elastic properties that could be then related to some levels of plastic strains, identifying $K_0(\gamma^p)$ and $\mu(\gamma^p)$ instead of $\rho^D = \rho^D(\gamma^p) = D$. Considering also that, often, for simplicity, it is supposed that $k_1 = k_2$, this finally leads to elastic properties of the damaged rock:

$$K_0(\gamma^p) = \frac{K_0^{in}}{1 + \omega_1.\gamma^p} = K_0^{in}\left(1 - k_1.\rho^D\right) = K_0^{in}(1 - k_1.D) \tag{36a}$$

$$\mu(\gamma^p) = \frac{\mu^{in}}{1 + \omega_2.\gamma^p} = \mu^{in}\left(1 - k_1.\rho^D\right) = \mu^{in}(1 - k_1.D) \tag{36b}$$

Numerical Issues on Porous Elastoplastic-Damage Model Implementation

Numerical Strategies for Multiphysics Coupling

For multiphysics coupling implementation of the thermo-hydro-mechanical model, basically two numerical strategies are followed:

(a) Full coupling solution of the set of state Eqs. (16, 20, 34, 35) and associated complementary equations

The numerical strategy for fully coupled THM problems is the most often used. When the finite element method is used for solving these equations, a variational formulation leads to a weak form of these equations that implies an integration over the domain Ω of the studied problem and its boundaries $\partial\Omega$. Considering the phase change (liquid-gas) phenomena and two pressure hydraulic model formulations (liquid and gas pressure), the equations are as follows:

Mechanics:

$$\int_\Omega \underline{\sigma\varepsilon}(\boldsymbol{u})d\Omega = \int_\Omega r\boldsymbol{F}^m\boldsymbol{u}d\Omega + \int_{\partial\Omega} \boldsymbol{f}^{ext}\boldsymbol{u}d\Gamma\forall\mathbf{u} \in U_{ad} \tag{37a}$$

Thermic:

$$\int_{\Omega} Q' \tau d\Omega + \sum_{p,c} \int_{\Omega} h_c^{m,p} \acute{m}_c^p \tau d\Omega - \int_{\Omega} \left(\sum_{p,c} h_c^{m,p} \boldsymbol{M}_c^p + \boldsymbol{q} \right) \nabla \tau d\Omega =$$

$$= \int_{\Omega} \left(\theta + \sum_{p,c} \boldsymbol{M}_c^p \boldsymbol{F}^m \right) \tau d\Omega - \int_{\partial\Omega} \left(\sum_{p,c} h_c^{m,p} \boldsymbol{M}_{c,ext}^p + \boldsymbol{q_{ext}} \right) \tau d\Gamma \forall \tau \in T_{ad} \quad (37b)$$

Hydraulic:

$$-\int_{\Omega} \left(\acute{m}_1^1 + \acute{m}_1^2 \right) p_1 d\Omega + \int_{\Omega} \left(\boldsymbol{M}_1^1 + \boldsymbol{M}_1^2 \right) \nabla p_1 d\Omega$$
$$= \int_{\partial\Omega} \left(\boldsymbol{M}_{1,ext}^1 + \boldsymbol{M}_{1,ext}^2 \right) \nabla p_1 d\Gamma \forall \mathrm{p}_1 \in P_{1,ad} \quad (37c)$$

$$-\int_{\Omega} \left(\acute{m}_2^1 + \acute{m}_2^2 \right) p_2 d\Omega + \int_{\Omega} \left(\boldsymbol{M}_2^1 + \boldsymbol{M}_2^2 \right) \nabla p_2 d\Omega$$
$$= \int_{\partial\Omega} \left(\boldsymbol{M}_{2,ext}^1 + \boldsymbol{M}_{2,ext}^2 \right) \nabla p_2 d\Gamma \forall \mathrm{p}_2 \in P_{2,ad} \quad (37d)$$

The integration of these equations leads to a nonlinear set of equations that establishes relations between the flux quantities and state variables $\boldsymbol{U} = (u_x, u_x, u_x, p_1, p_2, T)$, quantities that could be written as a matrixial equation (Granet 2014):

$$\boldsymbol{R}(\boldsymbol{U}) - \boldsymbol{L}^{\boldsymbol{mec}} = \boldsymbol{F}(\boldsymbol{U}) \quad (38)$$

In this last equation $\boldsymbol{R}(\boldsymbol{U})$ is such that $\boldsymbol{W}^{\boldsymbol{T}}\boldsymbol{R} = \int_{\Omega} \boldsymbol{E}(\boldsymbol{W}) \boldsymbol{\Sigma}\, d\Omega$ with $\boldsymbol{E} = (\boldsymbol{U}, \underline{\varepsilon}(\boldsymbol{U}), \boldsymbol{\nabla p_1}, \boldsymbol{\nabla p_2}, T, \boldsymbol{\nabla T})$ being the vector of generalized strains and $\boldsymbol{\Sigma}$ the thermodynamic associated flux parameters

A nonlinear solving algorithm (e.g., Newton-Raphson) is used to obtain the unknown values of state variables.

Two difficulties arise when this numerical scheme is used for the solution of THM equations: firstly, the generalized stiffness matrix produced when writing the Eq. (38) is generally big since the number of degrees of freedom at any point is twice as great (for 3D geometries) as the mechanical problem itself (so the size of stiffness matrix is four times greater than the respective stiffness mechanical matrix). Secondly, the stiffness matrix of THM problem gathers quantities of contrasting amplitudes which calls for special attention and techniques for solving algorithms.

(b) Sequential coupling of thermo-hydromechanical equations

Following this strategy for THM equations' solution, the field equations of one phenomenon (mechanical, hydraulic, or thermal) are solved keeping other field

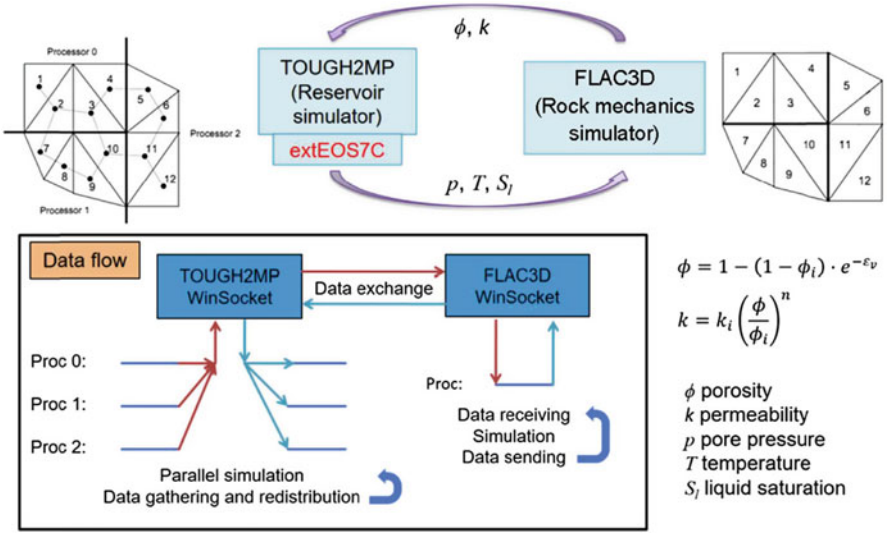

Fig. 2 Typical sequential coupling by external data exchanges. (From Gou et al. 2016)

equations constant for one time step. Once the equations of the first phenomena are resolved, the second ones are updated keeping all other state variables fixed and so on. Because the characteristic times of physical problems are quite different, one needs generally several iterations of mechanical and thermal fields for a single hydraulic step.

The advantage of this strategy of equation solving is situated on its simplicity: the solving of given field equations could be performed by specialized software of this given physical domain, and updated state variable fields are then inputted as fixed parameters for the next problem. Fig. 2 illustrates this coupling performed by the exchange data between two specialized software. In some other cases, these data exchanges are performed among specialized modulus, running sequentially within the same software.

The advantages of such approach are on the one hand reducing the size of the problem treated in a given time, allowing a problem to be tackled with modest machines, and on the other hand resolving, at least partially, the problem of ill-conditioned matrix resulting from coupling, rendering the solving process more robust. In turn, for a given time step, the problem should run several times, solving each time a single physical domain problem, which generally produces a mediocre convergence and could be a time-consuming process.

Integration of Constitutive Elastoplastic-Damage Equations

Whatever the numerical modeling strategy is followed, to some points, one has to integrate the constitutive equations for mechanical, thermal, and hydraulic behavior

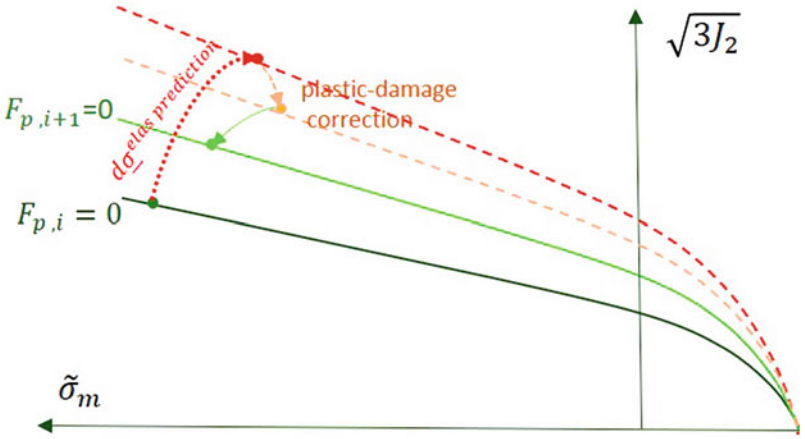

Fig. 3 Iterative prediction-correction process for state variables updating, for a single step

of rock. In particular, the integration of the coupled elastoplastic-damage behavior is challenging, and solving these coupled equations at a material point is often an iterative process due to the strong nonlinearity of equations. In many cases, the damage introduced in the coupled model some softening, even in cases when the plastic model predicts only the plastic hardening. It could be seen, for example, that the coupled hardening function of the modified Drucker-Prager (Eq. 27b) from some values of damage produces a softening in the overall response of the rock. This in terms could lead to mesh dependencies of numerical simulation, and special implementation and solutions should be envisaged (Plassart et al. 2013; Pardoen and Collin 2017)

The integration of the constitutive equation of the elastoplastic-damage model is obtained using an iterative approach by prediction correction as illustrated in Fig. 3 for the case of the modified Drucker-Prager model presented above (see §F of this chapter). Given an equilibrium state at *step i* such that $F_{p,i}(\tilde{\sigma}_{m,i}, J_{2,i}, \kappa_i, \eta) = 0$ and a total strain increment $d\underline{\varepsilon_i}$, one has to calculate the incremental plastic strain and finally the stress increment $d\underline{\sigma_i}$ such that $F_{p,i}(\tilde{\sigma}_{m,i+1}, J_{2,i+1}, \kappa_{i+1}, \eta) = 0$. After a first elastic prediction, successive corrections are applied to the precedent predictions to adjust the new stress increment (Fig. 4).

Case Study: Evolution of Rock Mass State Around a Circular Horizontal Drift Under Thermo-Hydromechanical Loads

Problem Description

Context, Geometry, and Initial State For underground nuclear waste disposal in many countries, various strategies are developed (Andra, 2005; Millard et al. 2005;

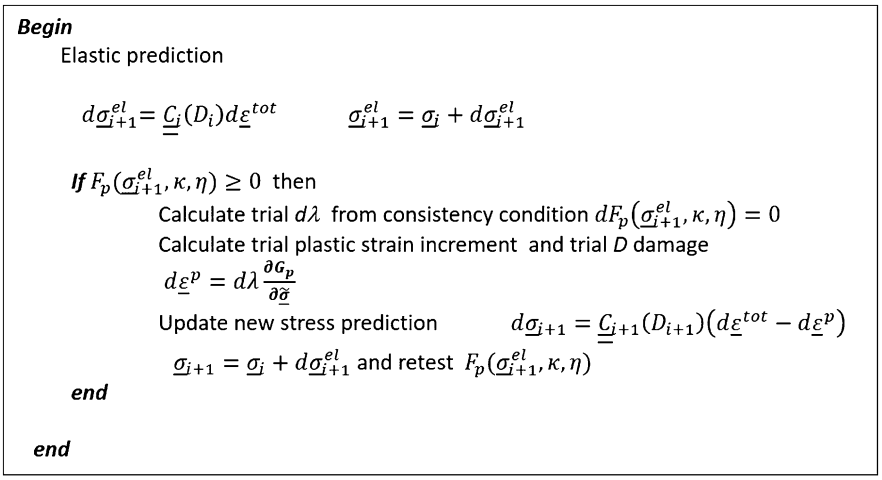

Fig. 4 Return mapping algorithm for the coupled elastoplastic-damage model

Chiarelli et al. 2003; Félix et al. 1996). Following Andra (2005), one possibility for nuclear waste disposal is the use of horizontal excavation with reduced diameter (typically ~0.7–1 m), in which specially conceived containers of endothermic power could be put at some distances to each other. The example presented here is a free interpretation of this waste disposal concept, in order to point out the interaction of thermo-hydromechanical coupling mechanisms and their impact on enhancing damage around the excavation. These underground works are thought to be excavated as groups of several parallel drifts, at some distances from each other in order to minimize their interaction between them. In this example, horizontal drifts of 0.76 m of diameter are supposed to be excavated from the face of a tunnel every 12 m, perpendicular to its axe. The geometry of the studied problem is presented in Fig. 5 with the horizontal dimension (6 m) in one direction equals to half of the distance between two successive drifts. The vertical in situ stress at each point is equal to geostatic stress, i.e., a function of the depth $\sigma_v = \rho g H$. For deep excavation, however, the variation of stress within the model dimension is small as compared to the value of stress itself, so that we consider the vertical stress uniform within the model and equal to that at the drift axis itself, i.e., $\sigma_v = \rho g H = -12.4 MPa$. In the horizontal plane, the maximal stress (σ_H) and the minimal one ($\sigma_h = \sigma_v$) are such that $\sigma_H = 1.3\ \sigma_h = -16.3 MPa$. For the same reasons, the water pressure is considered uniform and equal to hydrostatic stress at 500 m of depth, so it is equal to 5 MPa.

The axis of excavation could coincide with either of principal horizontal stress. If the drift axis coincides with the maximal horizontal stress, then the stress in the plane perpendicular to the axis is isotropic (since $\sigma_h = \sigma_v$), and the problem could be cast approximately to an axisymmetric problem. However, if the drift is orientated with its axis coinciding with minimal horizontal stress, only 3D modeling would be

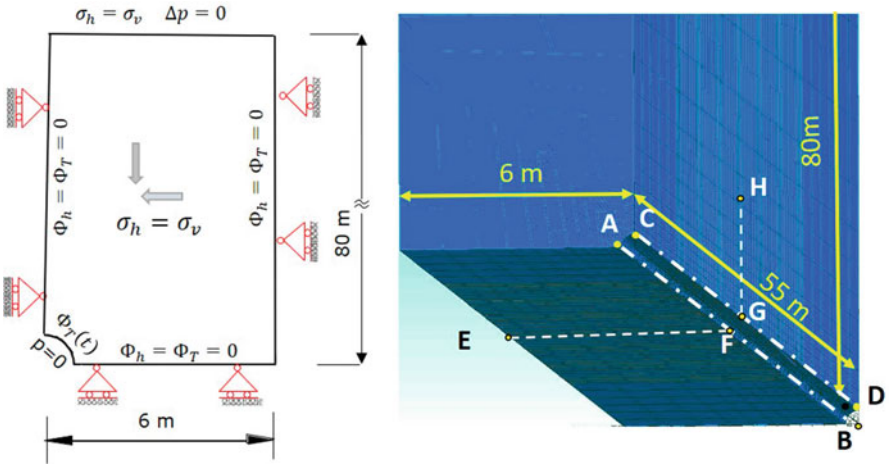

Fig. 5 Geometry and initial and boundary conditions for THM study of a deep circular drift in tight rocks for 2D and 3D configuration

appropriated. In the example treated here, the axis of the drift coincides with that of maximal stress, and a 3D model is used.

The drilling of the drift is performed in a very short time (some hours at most) as compared to the service time of the drift (some tens, hundreds, or even thousands of years), and it could be considered as an instantaneous undrained excavation. The drilling process is not explicitly simulated here.

Constitutive Behavior of Rock Masses The rock mass behavior is described with the modified Drucker-Prager model on the §F of this chapter. The poromechanical properties of the rock masses are typically that of a tight rock with a permeability $k = 4*10^{-19}$ m^2, drained bulk modulus of 3000 MPa, Poisson's ratio of 0.3, shear modulus of 4000 MPa, and porosity of 20%; the onset of plasticity on uniaxial compression test is marked at 6 MPa, and the uniaxial compression strength is 10.5 MPa.

For problems covering long periods of time, it is necessary to count for the long-term behavior of rock masses. For that, a viscoplastic extension, using Perzyna's approach is used (Perzyna 1966). Following that, the rate of viscoplastic shear strain is supposed to be a function of an overstress function:

$$\dot{\gamma}_{vp} = A\left\langle \frac{F_p(\widetilde{\sigma}_m, J_2, \kappa, \eta)}{\omega} \right\rangle^n \tag{39}$$

The cumulated shear viscoplastic strain is used as a hidden state variable in equations of hardening function to assure coupling with damage mechanism.

Thermal and Hydraulic Conditions In the example treated here, seven cylindrical canisters with approximately the same diameter as the drift and length of 2 m are distributed along the drift, uniformly separated to each other at a distance of 2 m. Since the study is focused on the THM evolution of rock masses, the canisters are not explicitly modeled here, but instead, an equivalent thermal flux is applied on the surface of the drift, on the exact place when a canister is supposed to be. This flux is calculated from the heat power of each canister. This thermal power depends on the type of waste considered but represents a decay with the time, following a known decreasing rate. Typically, the time of thermal stabilization of canisters, when the thermal power could be too small (and could be neglected), could be from some years to some hundreds or even thousands of years. In the example presented here, the simulations are performed for 100 years, even if the typical thermal power of nuclear wastes, after 100 years, is in most cases quite important.

The drift after the excavation is considered unbeard, not ventilated, and the hydraulic transmissivity of the drift is practically infinite as compared to the wall water outflow, such that the water pressure along the drift could be considered as constant and equal to the atmospheric pressure. The vertical surface in mid-distance between two successive drifts is a plane of symmetry and so is the vertical plane of the drift axis. On these vertical surfaces, the normal displacements and normal thermal and hydraulic fluxes are nil. Taking advantage of the fact that the drift is a deep one, one could (approximately) consider that the horizontal plane at the drift axis level is also a symmetry plane. The limit superior of the model, a horizontal plane at 80 m from the axis of the drift, is taken arbitrarily considering this distance (more than 220 times greater than the rayon of the drift) being sufficiently away from any perturbation to say that the variations of stress, temperature, and water pressure due to the drift perturbation are negligible. This assumption is discussed later in the chapter.

The THM analyses discussed here are performed using finite element specialized software Code_Aster (Granet 2014), and a strong coupling paradigm is used (see §G. a on this chapter)

Results and Discussions

For analysis purposes, the profiles of state variables are presented along four lines (Fig. 5b). The two longitudinal AB and CD lines lay on the wall of the drift on the top and base of it, respectively. The two other lines (EF and GH of the same length) are situated in the middle of the drift, perpendicular to the axis of the drift and orientated horizontally and vertically, respectively.

Thermal Field Evolution The principal mechanisms that trigger the evolution of all state variables are the heat produced by canisters and input on the system. Because of the periodic placement of canisters, the field temperature on the wall of the drift is not uniform with hot spots on the centers of canisters and the hottest one on the center of the drift (Fig. 6).

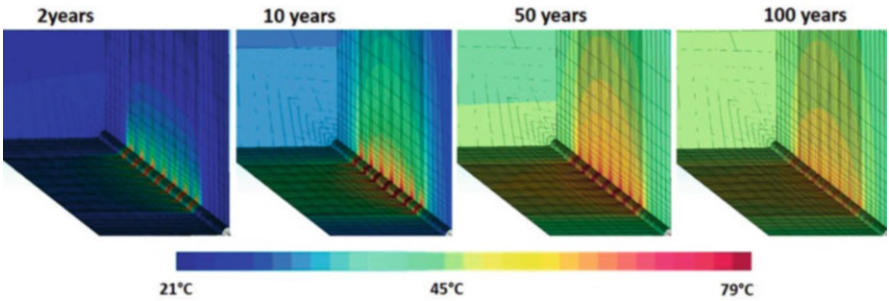

Fig. 6 Temperature fields in the rock masses at different moments of heating

This heterogeneity of the temperature field on the wall leads to radial and longitudinal thermal gradient and has some consequences on the plastic and damage of the wall.

In Fig. 7a, b is presented the profiles of temperatures along lines AB and CD. As displayed in this figure, the maximal temperature in the massif, on the immediate vicinity of the drift, increases up to 80 °C in the center of the drift (somewhere between 20 and 50 years when the thermal paroxysm is reached) and then decreases gradually. Despite the decrease of the temperature on the wall, the temperature on the massif continues to increase to some extent (Figs. 6 and 8a, b)

Despite the similarity of the temperature profile in the near field (Fig. 7a, b), the profiles of temperatures along EF and GH lines (Fig. 8a, b) represents some differences on long-time predictions that are due to adiabatic boundary conditions on the plane of symmetry in the half-distance between two successive drifts. Otherwise, on the upper limit of the model, boundary conditions are those of a constant temperature. These differences of boundary conditions on the vertical plane of the model and upper horizontal plane that impact thermal field distribution might have an even stronger impact on displacements and pore pressure field.

Pore Pressure Field Evolution The pore pressure field on the drift wall is kept constant to atmospheric pressure and does not evolve with the time. While a continuous flow out from rock masses to the drift is initiated from the excavation, the field pressure at a given instant depends not only on this flow out but also from the pressure generated due to temperature variation. Indeed, since the differential dilatation coefficient is not nil, any variation of temperature generates some pore pressure (Vu et al. 2019; Hoxha et al. 2006; Millard et al. 2005). The final pressure is a competition between overpressure generated by the heating, its propagation on the rock masses, and the flow out the drift. The profiles of pore pressure along lines EF and GH (both radial to drift) are presented in Fig. 9a, b.

These profiles demonstrate the very strong impact of boundary conditions on the hydraulic response. Even if the distribution of the temperature was almost uniform, in all direction, the water-impermeable boundary (symmetrical boundary) conditions

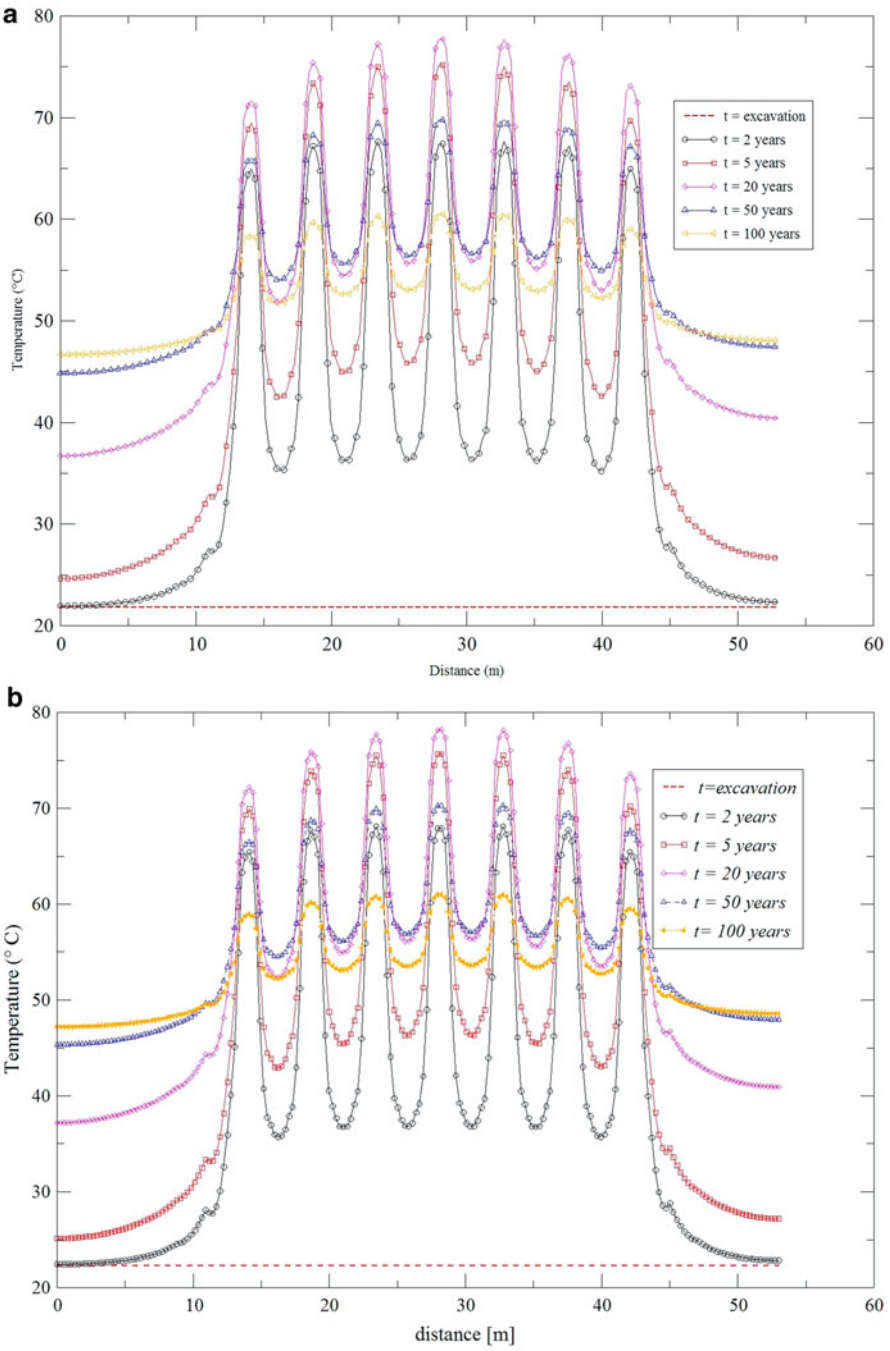

Fig. 7 Temperature profiles along the cut AB (**a**) and the cut CD (**b**) on the drift wall for some selected heating times

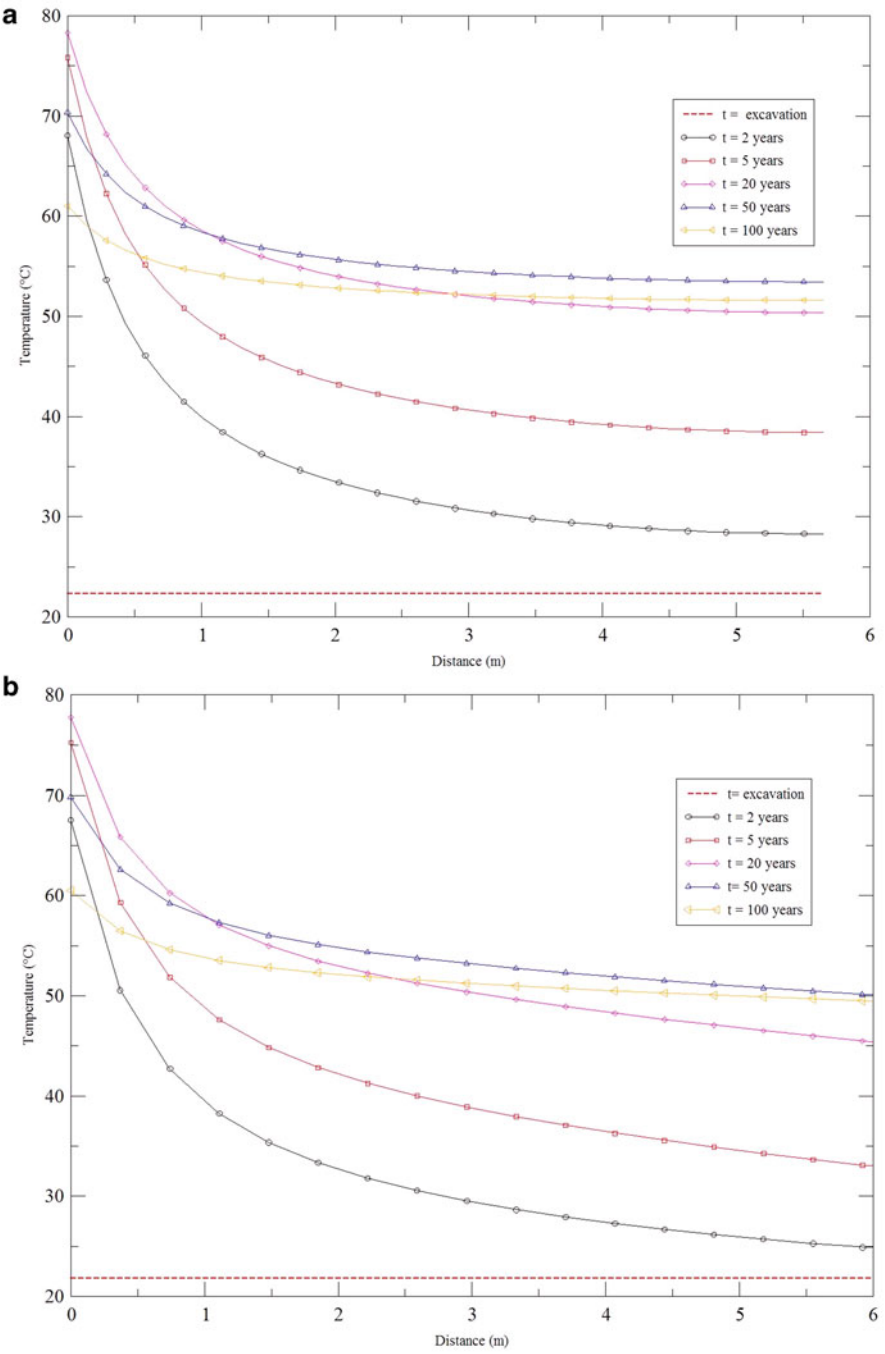

Fig. 8 Temperature profiles along the cut EF (**a**) and the cut GH (**b**) on the drift wall for some selected heating times

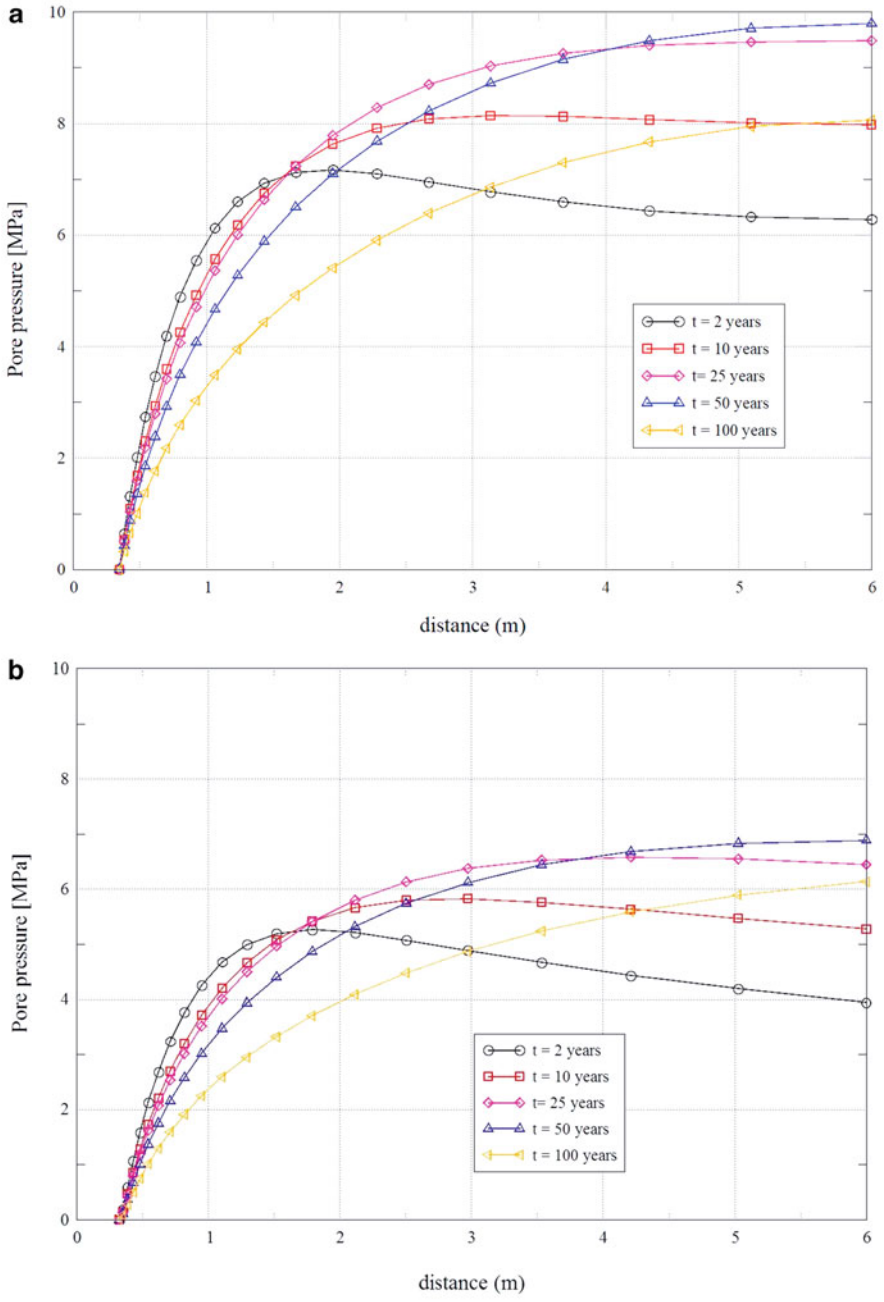

Fig. 9 Pore pressure profiles along lines EF (**a**) and GH (**b**) for some selected moments

on the vertical limits of the model lead to a higher pore pressure in the far-field along the horizontal (radial) line EF as compared to the vertical (radial) line GH even if the near-field pressure is identical for both.

Mechanical Field Evolution Mechanical fields (displacements, strains, cumulated viscoplastic strains) are susceptible to evolve with the time for multiple reasons: firstly because of inherent viscoplastic-damage behavior of the rock masses described by the modified Drucker-Prager mode and secondly because of the variation of temperature and pore pressure in the near- and far-field, induced via coupling mechanisms, described above and inducing variations of the mechanical state. In Fig. 10 are presented the radial displacements along longitudinal lines AB and CD. For a given time, the profiles are almost identical for both lines. There are, at least, two remarkable features manifested on these profiles: firstly the periodic variation of temperature along the drift induced a periodicity on the amplitude of radial displacements; secondly for a given point on the drift wall, radial displacements are monotonic despite a non-monotonic temperature variation (see Fig. 7a, b). These observations demonstrate the fact that these displacements are not only results of temperature variation on the near-field (manifested by the periodicity of variation along the drift) but also of mechanical and hydraulic mechanisms coupled with the first that induce the irreversible response of rock masses and so a monotonically increase of convergence in a given point of drift wall, despite non-monotonically variation of temperature.

The profiles of radial displacements along radial lines EF and GH (Fig. 11) indicate the strong impact of the boundary conditions on the response of the massif. The profiles of radial displacements immediately after excavation and before heating (with a weak hydromechanical coupling), identical in two directions, indicate that when the limits of model are sufficiently away from excavation, Neuman's and natural boundary conditions are equivalent to each other. Indeed, in the horizontal direction, the vertical symmetric plane between two successive drifts is situated here 6 m from the drift axis (almost 20 times the radii of excavation). In this plan, because of symmetry conditions, the variation of displacements is nil. On the upper limit of the model (horizontal plane at 80 m from the drift axis), the constant stress conditions are maintained. For short-term response, before thermal and hydraulic perturbations propagate in the massif, both these conditions are equivalent in that distance and radial displacements are identical. However, this is not the case for long-term response. In the vertical direction, the thermal and hydraulic perturbations induce extension strains but the model could extend upward. It is not the case for the model in lateral direction since it is constrained at the limit by the symmetrical nature of the problem.

It is also of interest to follow how the field stress evolves in time on the drift wall (Fig. 12a, b) and inside the rock masses (Fig. 14a–b). The equivalent von Mises stress and the mean stress follow the same periodical pattern oscillation along the

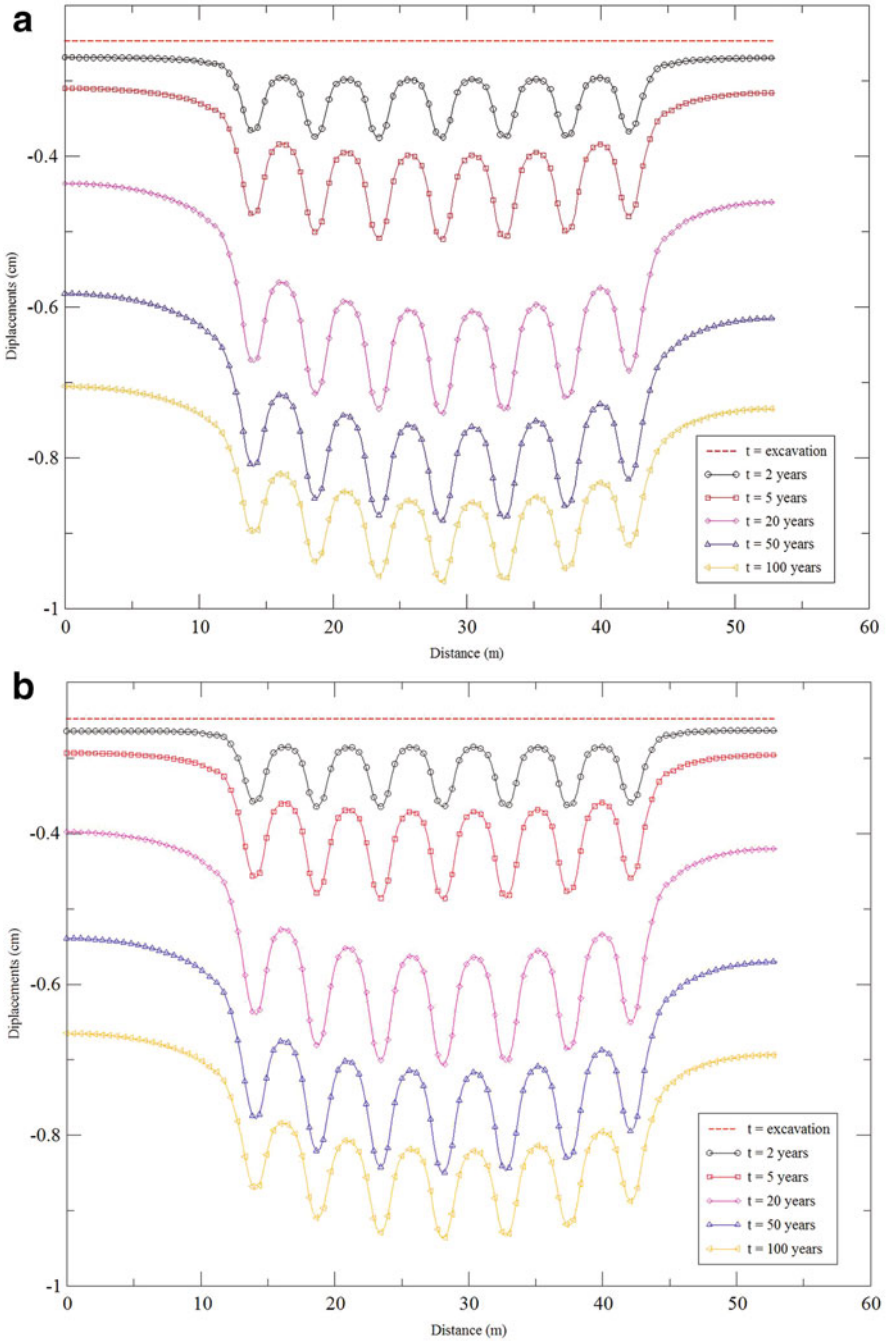

Fig. 10 Profiles of radial displacements along lines AB (**a**) and CD (**b**) for some chosen heating time

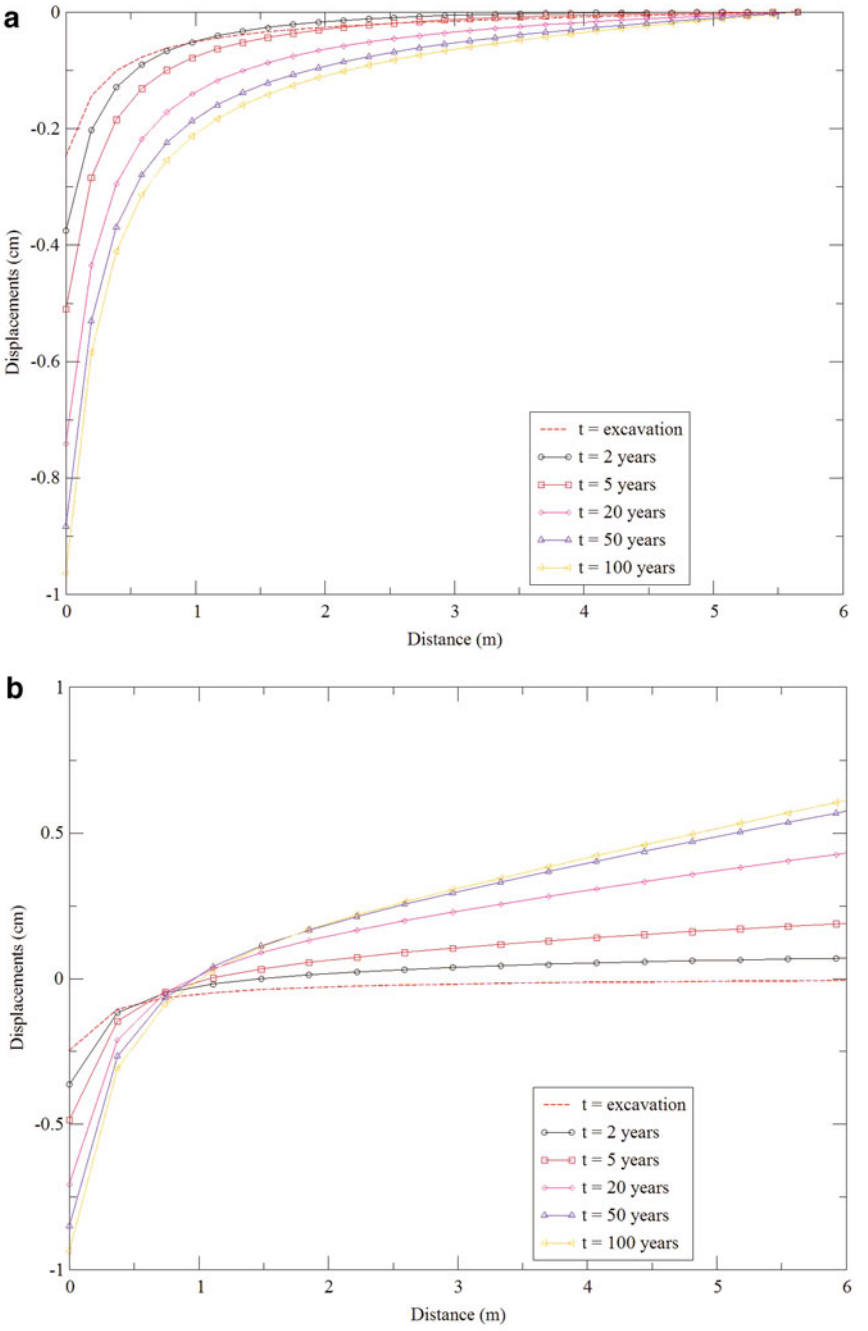

Fig. 11 Profiles of radial displacements along lines EF (**a**) and GH (**b**) for some chosen heating times

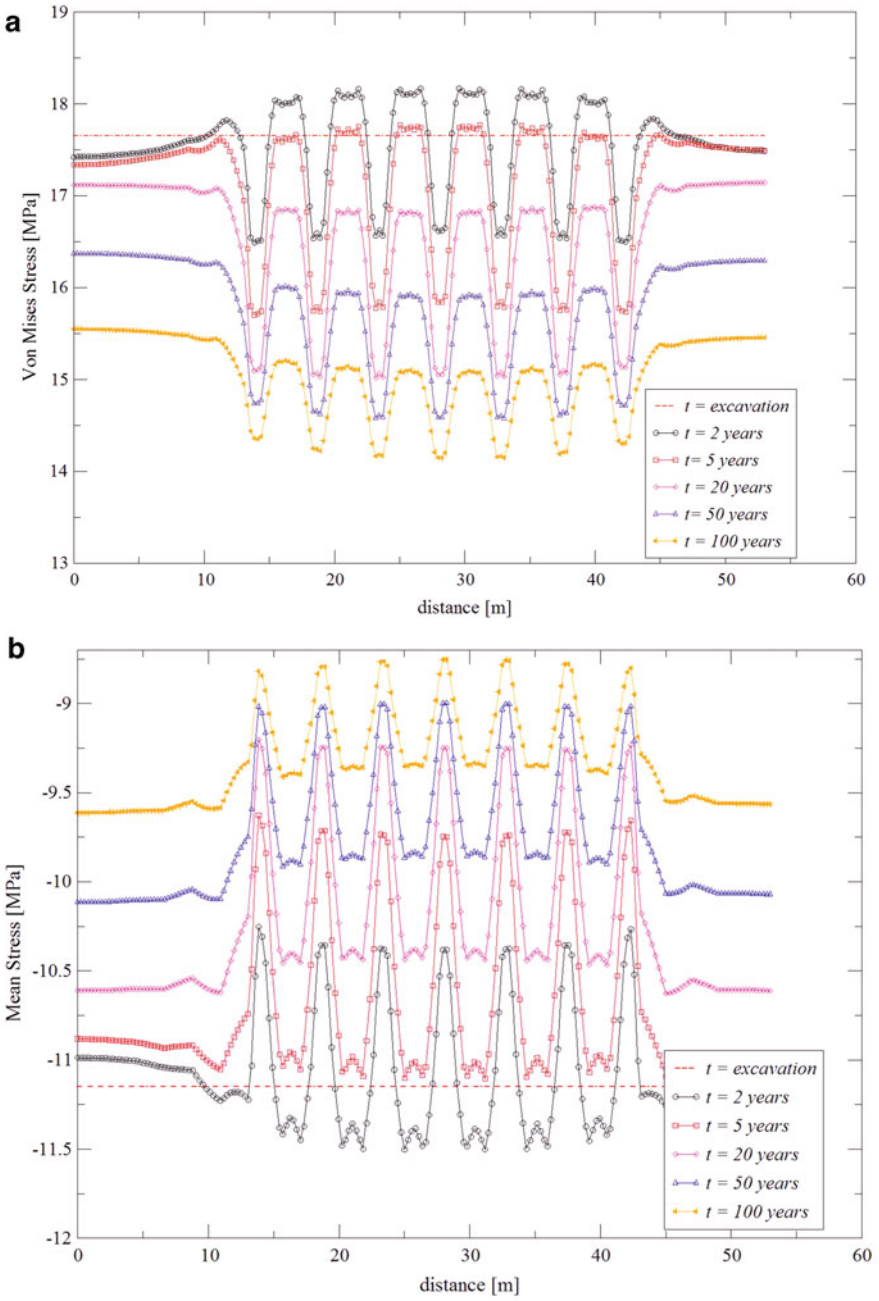

Fig. 12 Profiles of equivalent von Mises stress (**a**) and mean stress (**b**) along line AB on the wall of the drift at different times

drift as the temperature does. However, unlike the temperature, for a fixed point on the wall, the stress evolves in a monotonical way after the first 2 years of heating, i.e., von Mises stress and mean stress decrease (in absolute value). This behavior is in full accord with the theory and is an expected result of thermo-hydromechanical coupling. All three mechanisms (viscoplastic deformation, temperature variation, pore pressure variation) are active simultaneously, and their kinetics shape the final response of the system.

The jump of the equivalent von Mises and the mean stress on the drift wall during the first 2 years of heating is explained by a heating dominant effect as compared to mechanical and hydraulic ones. According to the temperature profiles in Fig. 8 during the first 2 years of heating, the temperature jumps from 20 °C to almost 68 °C (for the hottest points), approaching to the maximal temperature of 79 °C later on.

A theoretical justification of the deviatoric and mean stress evolution due to a quick increase of temperature is proposed in Fig. 13, where the reasoning is developed in relation with a capillary pressure increase (or, equivalently, for a water pressure decrease keeping constant the gas pressure) on a circular tunnel in isothermal conditions and elasticity. Because of the analogy of the hydraulic and thermal diffusion equation, the behavior of the system is qualitatively the same for the decrease of temperature. For an instantaneous increase of temperature (pressure, so $\pi_a > 0$), a point on the wall follows a stress path that leads to an increase of both deviatoric and mean stresses (Hoxha et al. 2004).

In the long term, however, the hydraulic and mechanical responses (see Eq. 39) become more important such that they compensate for the stress variation due to decrease of temperature and keep a monotonic decrease of deviatoric stress.

In the profiles of stress in a radial direction (Fig. 14), one clearly distinguishes the impact of viscoplasticity on the decrease of deviatoric stress in the far-field and a non-monotonic variation of mean stress due to propagation of thermal perturbation and induced hydraulic perturbation.

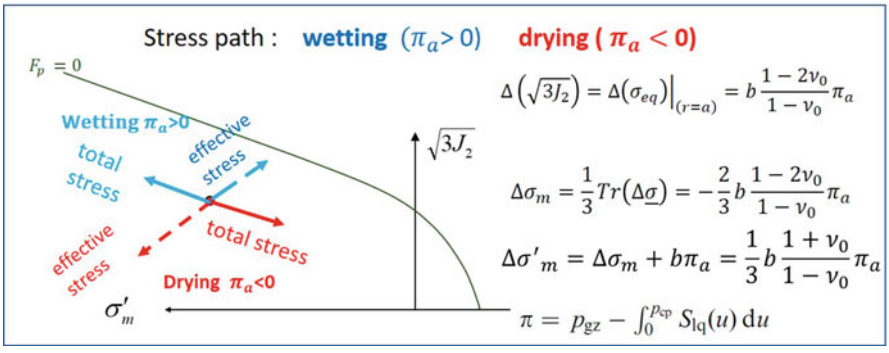

Fig. 13 Schematical stress path on the wall of a circular drift during water pore pressure increase (wetting) or decrease (drying). (Adopted from Hoxha et al. 2004)

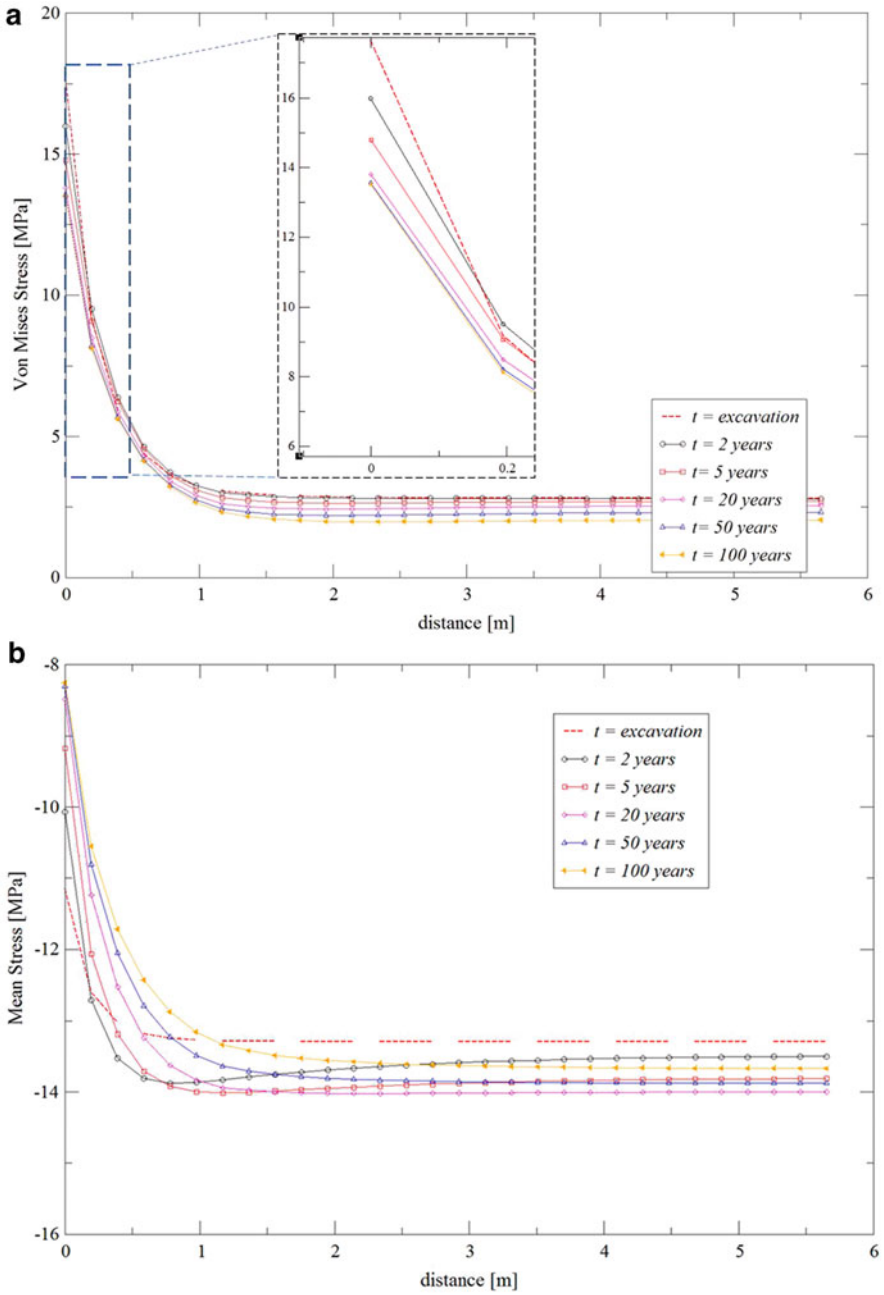

Fig. 14 Profiles of equivalent von Mises stress (**a**) and mean stress (**b**) along line EF on the massif at different times

Evolution of Inelastic Strain and Damage One finds the combined effect of thermal, hydraulic, and mechanical variations on the development of inelastic (viscoplastic) strains and damage zone around the drift. In Fig. 15 are presented the cumulated viscoplastic shear strain maps at the same moments as the temperatures in Fig. 6.

The results of Fig. 15 outer than a progressive development of viscoplastic strain due to the intrinsic viscoplastic behavior of the rock depict a strong effect of thermo-hydromechanical coupling on enhancement of viscoplasticity. The nonuniform development of viscoplasticity on the drift wall, imitating the temperature distribution, is a direct indication of the impact of thermal fields on viscoplasticity enhancement through modification of the state stress. One could also observe that in the short term, the viscoplasticity is developed uniformly in all direction (we recall that the initial stress in the plane perpendicular to the drift axis is isotropic), but in the long term, a larger zone impacted by viscoplastic behavior is developed on the vertical direction as compared to the horizontal one. The reason is to be found on the variation of mean stress in the horizontal and vertical direction (see Fig. 14): in the horizontal direction, the mean stress firstly decreases, which in turn decreases the value of the overstress function and the intensity of viscoplastic flow.

The profiles of the cumulated viscoplastic shear strain along two radial directions (horizontal and vertical, respectively, in the center of drift) are presented in Fig. 16. It clearly shows that the viscoplastic strain (and consequently damage) is initiated immediately after excavation and is initially isotropic (same values on the wall and the same extension of viscoplastic strain zone). But as the temperature field evolves in time and triggers the evolution of pore pressure and stress in the massif and around the drift, the viscoplasticity on the vertical direction is developed quicker and on a larger zone. After 100% the value of cumulated viscoplastic shear strain reaches 2.9% at point F and 3.3% at point G.

As already announced, in this modeling, the damage is supposed to be enhanced by the plasticity/viscoplasticity: damage is initiated as soon as the cumulated plastic/

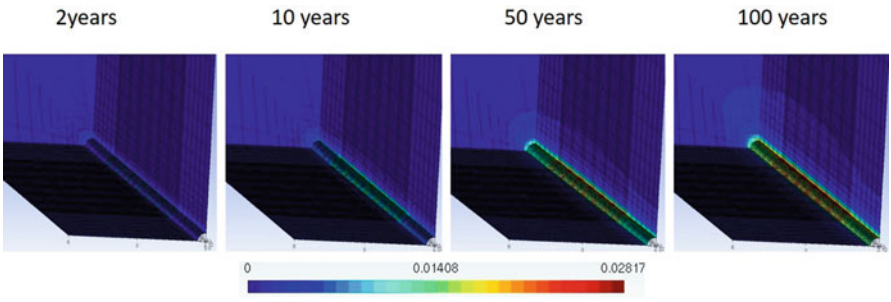

Fig. 15 Maps of cumulated viscoplastic shear strain on the rock masses at different moments

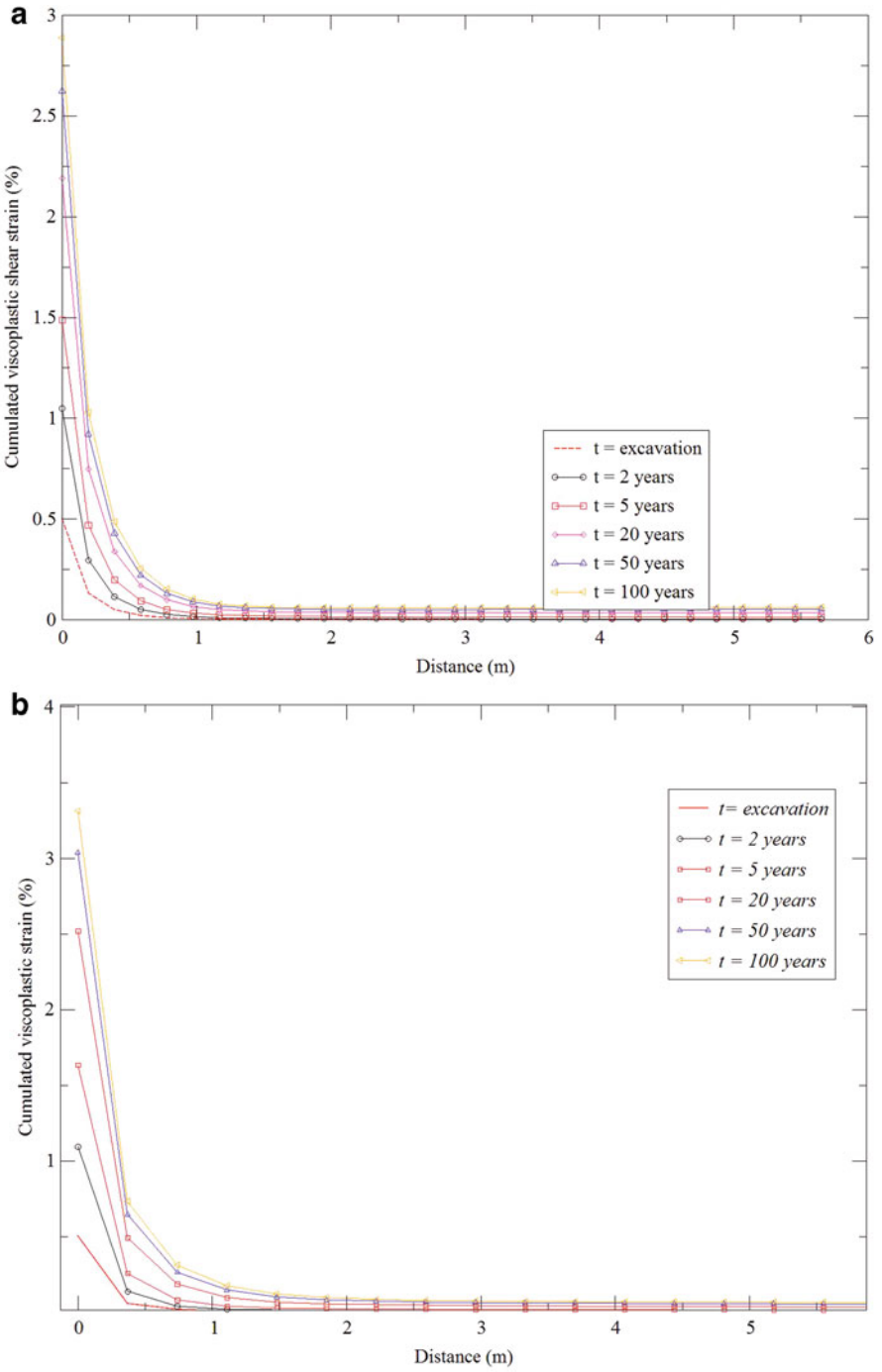

Fig. 16 Profiles of cumulated viscoplastic shear strain along line EF (**a**) and GH (**b**) at different instants

viscoplastic shear strain reaches a critical value. For the set of parameters chosen for this study, such critical value is $\gamma^{vp} = 0.2\%$. Likewise, a macroscopic failure is obtained for a $\gamma^{vp} = 1\%$. In Fig. 17a, b is displayed the extension of the damaged zone and fractured zone with the time in horizontal and vertical directions with r/a representing the ratio of damaged (respectively fractured) zone radii on the radii of

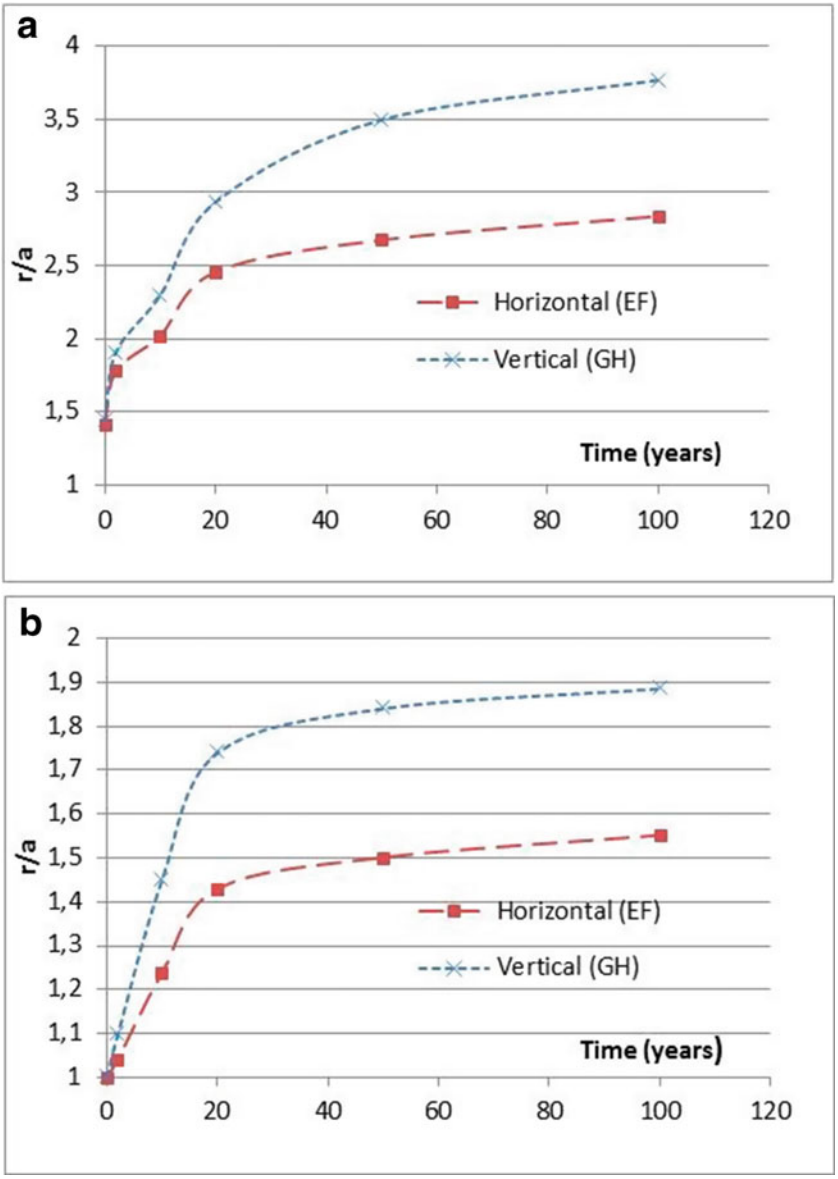

Fig. 17 Extension of the damaged zone (**a**) and the fractured zone (**b**) with the time in the vertical direction (line GH) and horizontal one (EF)

the drift. As shown in the graphics, the radius (***r***) of EDZ in the horizontal direction is almost three times as big as the radius of the drift (r/a ~ 3), while in the vertical direction, its extension is equal to 3.7 of drift radius.

The radius of the fractured zone reaches almost 1.5 the radius of the drift on the horizontal direction, and it is almost equal to three times the drift radius on the vertical direction.

Summary/Conclusions

In time viscoplastic strain and damage evolution in rock masses, under thermo-hydromechanical loads, is a result of complex interactions among various mechanisms whose kinetics could be quite different. In the example treated here, the driving mechanisms for state variable evolution around the drift are the heating from decayed thermal power on the wall of the drift and the viscoplasticity enhanced from the deviator stress. In the very short term, immediately after excavation, only mechanical viscoplasticity is active. In the short term, after thermal power is "ON," the thermal mechanism is dominant, triggering the evolution of water pore pressure on the rock masses and stress on the wall of the drift and in the massif. It is also demonstrated that while evaluating the interaction of excavations under thermo-hydromechanical coupling conditions, one needs to consider not only the short-term but also the long-term evolution of multi-physical fields. In the example described here, the horizontal distance between two adjacent drifts is big enough to prevent mechanical interaction between them. However, because of long-term diffusion of thermal and hydraulic perturbation and the mechanical impact of these perturbations, a strong mechanical interaction is observed in the long term, triggering a non-isotropic damage zone around the drift.

References

Andra, Dossier 2005 Argile – Tome Architecture et gestion du stockage géologique, 2005. www.andra.fr

C. Bikong, D. Hoxha, J.F. Shao, A micro-macro model for time-dependent behavior of clayey rocks due to anisotropic propagation of microcracks. Int. J. Plast. **69**, 73–88 (2015)

A.S. Chiarelli, J.F. Shao, N. Hoteit, Modeling of elastoplastic damage behaviour of a claystone. Int. J. Plast. **19**(2003), 23–45 (2003)

O. Coussy, Poromechanics, John Wiley & Sons, Ltd, ISBN:9780470849200 (2004)

E. Detournay, A.H.-D. Cheng, Fundamentals of Poroelasticity, in *Comprehensive Rock Engineering*, ed. by J. Hudson, vol. II, (Pergamon Press, Oxford/New York, 1993)

D.P. Do, D. Hoxha, Effective transfer properties of partially saturated geomaterials with interfaces using the immersed interface method. Int. J. Numer. Anal. Methods Geomech. **37**(18), 3237–3257 (2013)

B. Félix, P. Lebon, R. Miguez, F. Plas, A review of the Andra's research programmes on the thermo-hydromechanical behavior of clay in connection with the radioactive waste disposal project in deep geological formations. Eng. Geol. **41**(1–4), 35–50 (1996)

Y. Gou, Z. Hou, M. Li, W. Feng, H. Liu, Coupled thermo-hydro-mechanical simulation of CO2 enhanced gas recovery with an extended equation of state module for TOUGH2MP- FLAC3D. J. Rock Mech. Geotech. Eng. **8**, 904–920 (2016)

S. Granet (2014) Modélisations THHM: Généralités et algorithmes Modélisations THHM: Généralités et algorithmes – Code Aster document r7.01.10.pdf https://www.codeaster.org/V2/doc/v12/fr/index.php?man=R7

N.R. Hansen, H.L. Schreyer, A thermodynamically consistent framework for theories of elastoplasticity coupled with damage. Int. J. Solids Struct. **31**, 359–389 (1994)

K. Hayakawa, S. Murakami, Thermodynamical modeling of elastic-plastic damage and experimental validation of damage potential. Int. J. Damage Mech. **6**, 333–363 (1997)

D. Hoxha, A. Giraud, A. Blaisonneau, F. Homand, A. Courtois, C. Chavant, Poroplastic modelling of the excavation and ventilation of a deep cavity. Int. J. Numer. Anal. Methods Geomech. **28**(4), 339–364 (2004)

D. Hoxha, Z. Jiang, F. Homand, A. Giraud, K. Su, Y. Wileveau, Impact of THM constitutive behavior on the rock-mass response: Case of HE-D experiment in Mont Terri Underground Rock Laboratory, in *Multiphysics coupling and long term behaviour in rock mechanics*, Eurock 2006, Ed. Alain van Cotthem, Robert Charlier, Jean-Francois Thimus, Jean-Pierre Tshibangu, CRC Press, London, pp. 199–206 (2006)

J.C. Jaeger, N.G.W. Cook, R. Zimmerman, *Fundamentals of Rock Mechanics*, 4th edn. (Blackwell Publishing, London, 2007)

Y. Jia, H.B. Bian, G. Duveau, K. Su, J.F. Shao, Numerical modelling of in situ behaviour of the Callovo-Oxfordian argillite subjected to the thermal loading. Eng. Geol. **109**(3–4), 262–272 (2009)

J.W. Ju, On energy-based coupled elastoplastic damage theories: Constitutive modeling and computational aspects. Int. J. Solids Struct. **25**(27), 803–833 (1989)

M. Kachanov, Elastic Solids with Many Cracks and Related Problems, in *Advances in Applied Mechanics*, ed. by J. W. Hutchinson, T. Y. Wu, vol. 30, (Academic, New York, 1993), p. 259

D. Krajcinovic, *Damage Mechanics* (North-Holland, Amsterdam, 1996)

J. Lemaitre, *A Course on Damage Mechanics*, 2nd edn. (Springer, Berlin, 1992)

A. Millard, A. Rejeb, M. Chijimatsu, L. Jing, J. De Jonge, M. Kohlmeier, T.S. Nguyen, J. Rutqvist, M. Souley, Y. Sugit, Numerical study of the THM effects on the near-field safety of a hypothetical nuclear waste repository BMT1 of the DECOVALEX III project. Part 2: Effects of THM coupling in continuous and homogeneous rocks. Int. J. Rock Mech. Min. Sci. **42**(2005), 731–744 (2005)

K.B. Min, J. Rutqvist, C.F. Tsang, L. Jing, Thermally induced mechanical and permeability changes around a nuclear waste repository – a far-field study based on equivalent properties determined by a discrete approach. Int. J. Rock Mech. Min. Sci. **42**(5–6), 765–780 (2005)

B. Pardoen, F. Collin, Modelling the influence of strain localization and viscosity on the behaviour of underground drifts drilled in claystone. Comput. Geotech. **85**, 351–367 (2017)

W.G. Pariseau, *Design Analysis in Rock Mechanics*, 2nd edn. (CRC Press, London, 2011)

P. Perzyna, Fundamental problems in viscoplasticity. Adv. Appl. Mech. **9**, 243–377 (1966)

R. Plassart, R. Fernandez, A. Giraud, D. Hoxha, F. Laigle, Hydromechanical modelling of an excavation in an underground research laboratory with an elastoviscoplastic behaviour law and regularization by second gradient of dilation. Int. J. Rock Mech. Min. Sci. **58**, 23–33 (2013)

J.F. Shao, G. Duveau, F. Bourgeois, W. Chen, Elastoplastic damage modeling in unsaturated rocks and applications. Int. J. Geomech. **6**(2), 119–130 (2006)

M. Souley, F. Homand, S. Pepa, D. Hoxha, Damage-induced permeability changes in granite: A case example at the URL in Canada. Int. J. Rock Mech. Min. Sci. **38**, 297–310 (2001)

M.T. VanGenuchten, A closed-form equation for predicting the hydraulic conductivity of unsaturated soil. Soil Sci. Soc. Am. J. **44**, 892–898 (1980)

G.Z. Voyiadjis, R.K. Abu Al-Rub, Thermodynamical framework for coupling of non-local viscoplasticity and non-local anisotropy viscodamage for dynamic localization problems using gradient theory. Int. J. Plast. **19**, 2121–2147 (2003)

G.Z. Voyiadjis, Z.N. Taqieddin, P.I. Kattan, Theoretical formulation of a coupled elastic-plastic anisotropic damage model for concrete using the strain energy equivalence concept. Int. J. Damage Mech. **18**, 603–638 (2008)

Minh-Ngoc Vu, Gilles Armand, Carlos Plua (2019) Thermal pressurization coefficient of anisotropic elastic porous media, Rock Mech. Rock. Eng., https://doi.org/10.1007/s00603-019-02021-1

Zhu Q. D. Kondo, J.F. Shao, V. Pensee, Micromechanical modelling of anisotropic damage in brittle rocks and application. Int. J. Rock Mech. Min. Sci. **45**(8), 467–477 (2008)

Frictional Contact Between a Blunt Tool and Quasi-brittle Rock with Damage: Numerical Modeling

32

George Z. Voyiadjis and Yaneng Zhou

Contents

Introduction 854
Problem Definition and Governing Parameters 857
Elasto-Plastic-Damage model 860
Model Review and Adjustment 860
Damage Initiation and Evolution 861
Single Element Test 863
Frictional Contact Using an Elastoplastic Model 867
Finite Element Model 867
Verification of the Finite Element Model in Asymptotic Regimes 868
Influence of Parameter η 870
Mesh Size Sensitivity 870
Frictional Contact Using an Elasto-Plastic-Damage model 872
Typical Case 874
Invariance with Respect to Fixed η and ξ 875
Influence of Parameter η 876
Influence of Parameter ξ 879
Discussion 881
Two Governing Dimensionless Parameters 881
Comparison with Experimental Results 884
Limitation of the Numerical Study 886
Conclusions 888
References 889

Abstract

Rock cutting with a blunt cutter includes a cutting process and a frictional contact process. The understanding is still fragmentary for the frictional contact process, with a gap between experimental tests conducted on quasi-brittle rocks and

G. Z. Voyiadjis (✉) · Y. Zhou
Center for GeoInformatics C4G and Computational Solid Mechanics Laboratory, Department of Civil and Environmental Engineering, Louisiana State University, Baton Rouge, LA, USA
e-mail: voyiadjis@eng.lsu.edu; cgzv1@lsu.edu; yanengzhou1@lsu.edu

© Springer Nature Switzerland AG 2022

G. Z. Voyiadjis (ed.), *Handbook of Damage Mechanics*,
https://doi.org/10.1007/978-3-030-60242-0_63

previous numerical and analytical analyses on elastoplastic rocks. This study aims to reduce the gap using finite element modeling with an elasto-plastic-damage model. The constitutive model is developed for quasi-brittle materials with material length scales, and it is implemented in the commercial finite element software ABAQUS as a user-defined material model. The implemented constitutive model is verified under uniaxial tension and compression. A finite element model is constructed for an idealized frictional contact problem, and it is validated against analytical solutions for both an elastic rock and a rigid-perfectly plastic rock. The contact stress is then analyzed using both an elastoplastic model and an elasto-plastic-damage model. The average contact stress in frictional contact is mainly governed by a dimensionless elastoplastic parameter η for an elastoplastic rock. The nature of frictional contact on a quasi-brittle rock is governed by an additional brittleness number ξ, which is defined as the ratio of a geometrical length scale to a material length scale. The average contact stress generally increases with the dimensionless elastoplastic parameter η before reaching a limit value, and it generally decreases with the brittleness number ξ. The numerical results of the average contact stress are generally consistent with typical experimental results conducted on quasi-brittle rocks despite limitations in the finite element modeling.

Keywords

Brittleness · Contact stress · Elasto-plastic-damage model · Frictional contact · Material length scale · Rock damage

Introduction

Rock cutting with a blunt cutter includes two processes: cutting on a cutting face and frictional contact on a cutter wear flat (Detournay and Defourny 1992). The two processes are generally assumed to be independent, and most of the work is focused on the cutting process with a sharp cutter. The pure cutting response has been extensively investigated in various aspects, such as the failure mode transition (Huang and Detournay 2008; Huang et al. 2013; Zhou and Lin 2013), rate effects (Amri et al. 2018; Detournay and Atkinson 2000; Helmons et al. 2016), and rock strength estimation (Naeimipour et al. 2018; Richard et al. 2012). The current understanding is still fragmentary for the frictional contact process on quasi-brittle rocks, despite extensive research based on experimental analyses (Adachi 1996; Almenara and Detournay 1992; Geoffroy et al. 1998; Glowka 1989; Rostamsowlat 2018; Rostamsowlat et al. 2018a, b), numerical analyses (Adachi 1996; Zhou and Detournay 2014), and analytical solutions (Adachi 1996; Challen and Oxley 1979; Zhou 2017a, b; Zhou and Detournay 2019). Quasi-brittle rocks are characterized by material length scales, but the influence of material length scales on frictional contact is still underresearched. Voyiadjis and Zhou (2019) recently investigated the influence of material length scales through finite element modeling. A better

understanding of the mechanisms in frictional contact will contribute to several important aspects of drilling responses, including the drilling efficiency (Zhou et al. 2017), stick-slip vibrations (Richard et al. 2007), borehole spiraling (Marck and Detournay 2016), and bit design (Gerbaud et al. 2006).

Material length scales play important roles in a wide range of tool-rock interaction problems, such as rock cutting (Huang and Detournay 2008; Huang et al. 2013; Zhou and Lin 2013), rock indentation (Carpinteri et al. 2004; Huang and Detournay 2008, 2013), and foundation bearing capacity (Cervera and Chiumenti 2009; Cervera et al. 2004). A ductile-brittle failure mode transition occurs in both rock cutting and rock indentation, when the depth of penetration exceeds a threshold of a material length scale (Huang and Detournay 2008). There is also a ductile-brittle transition for the bearing capacity of a rigid strip footing on a quasi-brittle foundation (Cervera and Chiumenti 2009; Cervera et al. 2004). A brittleness number governs the failure mode transition in the bearing capacity problem, and it is defined as the ratio of a geometrical length scale to a material length scale. When the brittleness number is very small, the influence of material length scales is negligible, and the bearing capacity is governed by strength theory without material length scales (Prandtl 1921). When the brittleness number is very large, the bearing capacity is governed by the linear elastic fracture mechanics involving material length scales (Cervera and Chiumenti 2009; Cervera et al. 2004).

The mechanisms of frictional contact are briefly reviewed from the numerical, analytical, and experimental perspectives. Numerical analyses are generally focused on the influence of a dimensionless elastoplastic parameter, for a Mohr-Coulomb elastoplastic rock without considering material length scales (Zhou and Detournay 2014, 2019). Zhou and Detournay (2014, 2019) found that the nature of frictional contact is predominantly governed by a dimensionless elastoplastic parameter η, based on analogy with the indentation of a blunt tool into elastic-perfectly plastic materials (Alehossein et al. 2000; Johnson 1970, 1987). The dimensionless elastoplastic parameter η is defined as the ratio of a characteristic elastic contact stress to a yield strength of a material with $\eta = E_0' \tan\beta/\sigma_c$ (where E_0' is the plane strain elastic modulus with $E_0' = E_0/(1-\nu^2)$, E_0 is the elastic modulus, ν is Poisson's ratio, β is the inclination angle of a slightly inclined slider, and σ_c is the uniaxial compressive strength) (Johnson 1970). Three regimes exist in frictional contact predominantly depending on the dimensionless elastoplastic parameter η: asymptotic elastic if η is small, elastoplastic if η is intermediate, and asymptotic rigid plastic if η is large. The dimensionless elastoplastic parameter η also affects the average contact stress, which increases from the asymptotic elastic regime to the elastoplastic regimes and then reaches a limit value in the asymptotic rigid plastic regime. The average contact stress is also affected by other parameters, such as both the interface and internal friction angles. In the elastoplastic regime, the contact stress generally decreases with increasing the interface friction angle, whereas the contact stress generally increases with increasing the internal friction angle (Zhou and Detournay 2014, 2019).

In the analytical aspect, the solutions of contact stress are generally available in the two asymptotic regimes. The rock is treated as an elastic material in the

asymptotic elastic regime, and it is treated as a rigid-perfectly plastic material in the asymptotic rigid plastic regime (Adachi 1996; Challen and Oxley 1979; Johnson 1987; Zhou and Detournay 2019). In the elastic regime, Adachi (1996) generalized the solution of the contact stress for a frictionless contact problem (Gladwell 1980) and derived the one for a frictional contact problem. A linear relationship exists between the dimensionless elastoplastic parameter η and the average contact stress. The influence of the interface friction angle on the average contact stress is negligible. For the frictional contact on a rigid-perfectly plastic cohesive-frictional rock, Zhou and Detournay (2019) developed the analytical solution in the rigid plastic regime by generalizing an asperity deformation model for a purely cohesive material (Challen and Oxley 1979). The limit value of the average contact stress in a frictional contact process can be well approximated by the bearing capacity of a rigid strip footing on a cohesive-frictional material (Zhou 2017b). The limit contact stress is independent of the dimensionless elastoplastic parameter η, whereas it is influenced by both the interface friction angle and internal friction angle. The limit contact stress is around two times the uniaxial compressive strength with identical interface and internal friction angles. The limit value can increase one order of magnitude when the interface friction angle is much smaller than the internal friction angle (Zhou 2017b).

In the experimental aspect, the experimental results are generally different from both numerical and analytical results. Experiments are conducted on quasi-brittle rocks with material length scales, which are not considered in both numerical and analytical results. Almenara and Detournay (1992) analyzed the average contact stress on the wear flats of blunt cutters based on tests in three sandstones. The interface friction angle is approximately equal to the internal friction angle. The average contact stress in experimental tests is approximately equal to the uniaxial compressive strength. By comparing with the numerical and analytical results, the experimental result is around half of the limit value in the asymptotic rigid plastic regime (Zhou and Detournay 2014). Rostamsowlat et al. (2019) analyzed the contact stress on 13 different sedimentary rocks, based on extensive cutting experiments using blunt cutters with a wide range of inclination angles. The predominant influence of the dimensionless elastoplastic parameter η is confirmed through experimental tests. However, the average contact stress from experimental tests is smaller by comparing with the analytical result. The 13 experimental tests are approximately divided into 2 groups. The first group includes 12 rock samples with lower interface friction angles corresponding to polished wear flats, and the second group includes 1 rock sample with a higher interface friction angle corresponding to a rough wear flat. For the first group, the average internal friction angle is around 29°, and the average interface friction angle is around 6°. In the rigid plastic regime, the experimental value of the average contact stress is around $3 \sim 5$ times the uniaxial compressive strength (Rostamsowlat et al. 2019). However, the analytical value of the average contact stress is around six times the uniaxial compressive strength (Zhou 2017b). For the second group, the internal friction angle is estimated as 29°, and the interface friction angle is around 23°. The experimental value of the average contact stress is close to the uniaxial compressive strength (Rostamsowlat et al.

2019), whereas the analytical value is around two times the uniaxial compressive strength in the rigid plastic regime (Zhou 2017b).

The study by Voyiadjis and Zhou (2019) investigates the mechanisms of frictional contact by considering the material length scales of quasi-brittle rocks, so as to reduce a gap in previous studies. An idealized frictional contact problem is investigated, in which a slightly inclined rigid slider moves at the free surface of a quasi-brittle rock. A hypothesis is proposed regarding the predominant influence of two dimensionless parameters on frictional contact, including the dimensionless elastoplastic parameter η and a brittleness number ξ. The brittleness number is proposed by analogy with the bearing capacity of a strip footing on a quasi-brittle foundation. The hypothesis is tested based on finite element modeling using a developed Elasto-Plastic-Damage model that can characterize the quasi-brittle properties of rocks. An elastoplastic model is adopted in the finite element modeling of frictional contact, and then an elasto-plastic-damage model is used to analyze the influence of the two governing dimensionless parameters. The significance and limitation are then discussed.

Problem Definition and Governing Parameters

The frictional contact process is analyzed for an idealized plane strain problem, in which a slightly inclined rigid slider is moving horizontally at the top of a quasi-brittle half-plane (Fig. 1). The parameters in the simplified problem can be divided into three categories: geometry, material, and interface. The geometrical parameters include the inclination angle β of the slider, depth d of sliding, and contact length $2a$. The quasi-brittle rock is characterized by an elasto-plastic-damage constitutive model. The essential material properties include the initial elastic modulus E_0, Poisson's ratio ν, uniaxial tensile strength σ_t, uniaxial compressive strength σ_c,

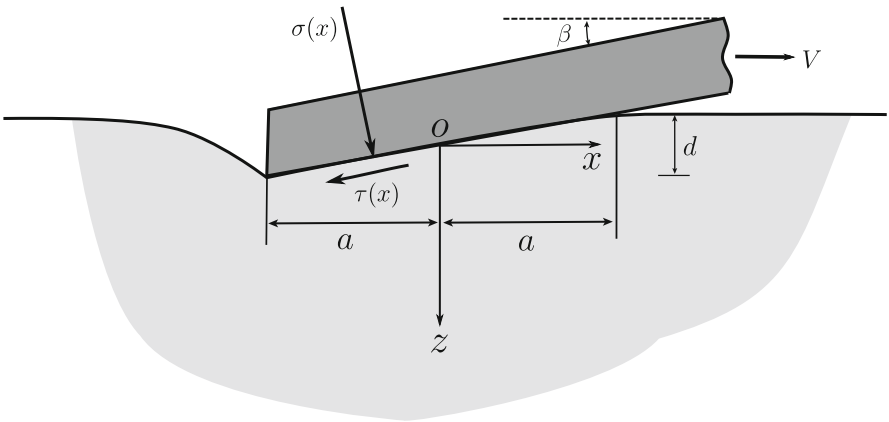

Fig. 1 An idealized plane strain problem of a blunt tool sliding on a quasi-brittle rock (Adachi 1996)

uniaxial tensile hardening modulus h^+, uniaxial compressive hardening modulus h^-, failure envelope slope α (or equivalently internal friction angle ϕ), dilation coefficient α_p, tensile fracture energy G_{ft}, and compressive fracture energy G_{fc}. The interface parameters include the normal contact stress σ, shear stress τ, and interface friction coefficient μ (Adachi 1996; Cicekli et al. 2007; Johnson 1970, 1987; Zhou and Detournay 2014, 2019).

The normal contact stress is normalized with the uniaxial compressive strength, and thus a dimensionless contact stress Π is defined as (Zhou and Detournay 2014):

$$\Pi = \frac{\sigma}{\sigma_c} \tag{1}$$

The dimensionless average contact stress $\overline{\Pi}$ along the interface is given by (Voyiadjis and Zhou 2019):

$$\overline{\Pi} = \frac{1}{2}\int_{1}^{-1} \Pi(\chi) d\chi \tag{2}$$

with

$$\chi = \frac{x}{a}, \; -1 \le \chi \le 1 \tag{3}$$

where χ is a normalized parameter of the coordinate x along the sliding direction.

The dimensionless average contact stress $\overline{\Pi}$ is predominantly governed by a dimensionless elastoplastic parameter η for an elastoplastic rock (Zhou and Detournay 2014, 2019). The frictional contact on a quasi-brittle rock is further analyzed by analogy with the bearing capacity of a rigid strip footing on a quasi-brittle foundation. A governing brittleness number is briefly described for the bearing capacity problem, followed by another brittleness number proposed for the frictional contact problem.

Consider first the bearing capacity problem on a quasi-brittle foundation. A brittleness number B is defined as the ratio of a geometrical length scale L to a material length scale ℓ (Cervera and Chiumenti 2009):

$$B = \frac{L}{\ell} \tag{4}$$

with

$$\ell = \frac{G_{fs} E_0}{\sigma_y^2} \tag{5}$$

where the geometrical length scale L is set to the contact length for convenience and the material length scale ℓ is defined based on the shear fracture energy G_{fs}, the elastic modulus E_0, and the uniaxial yield strength σ_y.

The adopted material length scale $\mathcal{L}$ bears similarity with the Hillerborg (1985) characteristic length ℓ_{ch}^{t}, which has been widely used for the fracture of quasi-brittle materials under tension. The characteristic length ℓ_{ch}^{t} is defined as:

$$\ell_{ch}^{t} = \frac{G_{ft} E_0}{\sigma_t^2} \tag{6}$$

Consider now the frictional contact problem on a quasi-brittle rock. It is hypothesized by analogy that the brittleness number B also affects the contact stress. The evaluation of the brittleness number B requires proper geometrical and material length scales for the frictional contact problem. Different from a bearing capacity problem with a given contact length, the actual contact length is not known a priori due to the sink-in or pile-up of the rock surface in a frictional contact problem. The geometrical length scale L is chosen to be a nominal contact length (Voyiadjis and Zhou 2019):

$$L = \frac{d}{\tan\beta} \tag{7}$$

Various material length scales have been proposed using different material properties under different loading conditions (Cervera and Chiumenti 2009; Hillerborg 1985; Huang and Detournay 2008; Saucedo et al. 2012). For a frictional contact problem with predominant compressive stress underneath a slider, the material length scale $\mathcal{L}$ is defined as (Saucedo et al. 2012):

$$\mathcal{L} = \ell_{ch}^{c} = \frac{G_{fc} E_0}{\sigma_c^2} \tag{8}$$

where the compressive characteristic length ℓ_{ch}^{c} is related to compressive failure, and it is a counterpart length scale of the Hillerborg (1985) characteristic length ℓ_{ch}^{t} related to tensile failure.

Plugging Eqs. (7) and (8) into Eq. (4) gives the brittleness number B (Voyiadjis and Zhou 2019):

$$B = \frac{d\sigma_c}{(1-\nu^2)G_{fc}} \frac{\sigma_c}{E_0' \tan\beta} \tag{9}$$

Equation (9) shows that the dimensionless elastoplastic parameter η is embedded in the brittleness number B. In order to approximately decouple the influence of the elastoplastic parameter and the brittleness number, another brittleness number ξ is defined as the ratio of a geometrical length scale d to a material length scale Λ_c (Voyiadjis and Zhou 2019):

$$\xi = \frac{d}{\Lambda_c} \tag{10}$$

with

$$\Lambda_c = \left(1 - \nu^2\right) \frac{G_{fc}}{\sigma_c} \tag{11}$$

where the material length scale Λ_c is related to the ultimate axial displacement with complete cohesion loss in a strain localization zone under uniaxial compression, and it is generally on the order of O (0.1 mm) (Labuz and Dai 2000).

The brittleness number B in Eq. (9) can thus be expressed as the ratio of the brittleness number ξ over the dimensionless elastoplastic parameter η (Voyiadjis and Zhou 2019):

$$B = \frac{\xi}{\eta} \tag{12}$$

where the parameter ξ can be interpreted as a special brittleness number B with $\eta = 1$.

It is thus hypothesized that the frictional contact on a quasi-brittle rock is predominantly governed by two dimensionless parameters: η and ξ. The hypothesis is then tested by finite element modeling using an elasto-plastic-damage constitutive model that is briefly described below.

Elasto-Plastic-Damage model

An elasto-plastic-damage model is developed after briefly reviewing different models in the literature. The material model is built upon an existing one (Cicekli et al. 2007) with main adjustments related to the damage initialization and evolution. After a brief description of the developed model, single element tests are conducted under uniaxial tension and compression.

Model Review and Adjustment

Many elasto-plastic-damage models have been proposed to characterize the failure of quasi-brittle materials (Abu Al-Rub and Voyiadjis 2009; Cicekli et al. 2007; Lee and Fenves 1998; Lubliner et al. 1989; Oliver et al. 1990; Voyiadjis and Abu-Lebdeh 1994; Voyiadjis et al. 2008, 2009; Wu et al. 2006). These models generally adopt the concepts of fracture energy-based damage and stiffness degradation in continuum damage mechanics. Fracture energy is an important material parameter related to material length scales, but it is not uniquely defined in different constitutive models with different levels of complexity. For example, in an elastic-damage model (Oliver et al. 1990), the fracture energy is related to the elastic energy dissipation. In some elasto-plastic-damage models (Cicekli et al. 2007; Lee and Fenves 1998; Lubliner et al. 1989), the fracture energy is related to the plastic energy dissipation. In other models (Shi and Voyiadjis 1997; Wu et al. 2006), the fracture energy is related to both

the elastic and plastic energy dissipation. The fracture energy defined in the third way seems to be more comprehensive. By considering both the elastic and plastic energy dissipation, the fracture energy in an elasto-plastic-damage model can recover the one in an elastic-damage model. The fracture energy can also recover the one in an elasto-plastic-damage model when the elastic energy dissipation is negligible. The adopted elasto-plastic-damage constitutive model (Voyiadjis and Zhou 2019) is built upon the one developed by Cicekli et al. (2007), as different material length scales can be considered for quasi-brittle materials. Further adjustments are introduced in the developed model. Specifically, fracture energy is defined by considering both the elastic and plastic energy dissipation, and the mesh size sensitivity is regularized accordingly. The hardening behavior in the undamaged stress space is characterized by simple linear functions, and the evolution of both tensile and compressive damage is characterized by simple exponential functions. The detailed formulations of the model are documented in Cicekli et al. (2007), including the three loading surfaces for plasticity, as well as for both tensile and compressive damage. Adjustments are described next with a focus on the damage initialization and evolution.

Damage Initiation and Evolution

Damage initiates when a damage energy release rate exceeds a damage threshold. Different damage criteria are adopted under tension and compression, and they are expressed as follows in the undamaged configuration (Oliver et al. 1990):

$$F^{\pm}\left(\tau^{\pm}, r^{\pm}\right) = \tau^{\pm} - r^{\pm} \leq 0 \tag{13}$$

where the superscripts "+" and "−" designate tension and compression components, respectively, $\tau^{\pm}$ are suitable norms related to the tensile and compressive damage energy release rates, $r^{\pm}$ are the current damage thresholds with $r^{\pm} \geq \tau_0^{\pm}$, and $\tau_0^{\pm}$ are the initial damage thresholds. Both the damage energy release rates and the damage thresholds are updated when damage occurs with $F^{\pm} > 0$.

The damage energy rates $\tau^{\pm}$ are defined as equivalent stress terms that are monotonic scalar functions of the elastoplastic energy release rates $Y^{\pm}$ (Wu et al. 2006):

$$\tau^{\pm} = \sqrt{2E_0 Y^{\pm}} \tag{14}$$

The elastoplastic energy release rates $Y^{\pm}$ consider both the elastic and plastic free energy in the undamaged configuration:

$$Y^{\pm} = \frac{1}{2}\overline{\sigma}_{ij}^{\pm}\varepsilon_{ij}^{e} + \int_0^{\infty} c^{\pm}\dot{\varepsilon}_{eq}^{\pm} dt \tag{15}$$

where the first and second terms on the right side represent the elastic and plastic free energy, respectively. The terms $\overline{\sigma}_{ij}^{\pm}$ are the tension and compression components of

the stress tensor $\overline{\sigma}_{ij}$ in the undamaged configuration, $c^{\pm}$ are the hardening functions, ε_{ij}^{e} is the elastic strain, and $\dot{\varepsilon}_{eq}^{\pm}$ are the equivalent plastic strain rates that are related to both the plastic strain rate tensor $\dot{\varepsilon}_{ij}^{p}$ and a weight factor (Cicekli et al. 2007).

Linear hardening functions are adopted under both tension and compression in the undamaged configuration (Wu et al. 2006):

$$c^{\pm} = f_0^{\pm} + h^{\pm}\varepsilon_{eq}^{\pm} \tag{16}$$

where $f_0^{\pm}$ are the effective yield strengths under uniaxial tension and compression, with $f_0^{+} = \sigma_c$ and $f_0^{-} = \sigma_t$ by neglecting strain hardening before peak strengths. Parameters $h^{\pm}$ are the effective plastic hardening moduli under uniaxial tension and compression, and they can be normalized to the hardening ratios defined as $\alpha_h^{\pm} = h^{\pm}/E_0$.

The stress tensors $\sigma_{ij}^{\pm}$ in the nominal (damaged) configuration are related to the stress tensors $\overline{\sigma}_{ij}^{\pm}$ in the effective (undamaged) configuration (Cicekli et al. 2007; Wu et al. 2006):

$$\sigma_{ij}^{\pm} = \left(1 - \varphi^{\pm}\right)\overline{\sigma}_{ij}^{\pm} \tag{17}$$

where φ^{+} and φ^{-} are the tensile and compressive damage indices, respectively.

The failure behavior of quasi-brittle materials under compression is generally more ductile than that under tension. The damage evolution is generally characterized by power functions and exponential functions, and the parameters controlling the shapes of the post-peak stress-strain curves are calibrated by experimental results under tension and compression (Abu Al-Rub and Kim 2010; Cicekli et al. 2007). A simple exponential function with one shape-related parameter is adopted to characterize the tensile damage, and a similar function is used for compressive damage for simplicity (Voyiadjis and Zhou 2019). The evolution of the tensile and compressive damage indices $\varphi^{\pm}$ is defined by (Oliver et al. 1990):

$$\varphi^{\pm} = G\left(\tau^{\pm}\right) = 1 - \frac{\tau_0^{\pm}}{\tau^{\pm}} \exp\left[A^{\pm}\left(1 - \frac{\tau^{\pm}}{\tau_0^{\pm}}\right)\right] \tag{18}$$

where $G(\tau^{\pm})$ are monotonic scalar functions representing the damage evolution from 0 to 1 and $A^{\pm}$ are parameters determining the shapes of the post-peak stress-strain curves.

The initial damage thresholds $\tau_0^{\pm}$ and the shape-related parameters $A^{\pm}$ are generally stress state dependent (Zhang and Li 2014), and thus the calibration requires experimental data under different stress states. These parameters are evaluated under uniaxial tension and compression for simplicity. The initial damage thresholds $\tau_0^{\pm}$ are given as (Wu et al. 2006):

$$\tau_0^{+} = \sigma_t; \tau_0^{-} = \sigma_c \tag{19}$$

The shape-related parameters $A^{\pm}$ are determined through a fracture energy-based method as follows. Under general loading conditions, the rates of energy dissipation $\dot{\gamma}^{\pm}$ per unit volume are (Oliver et al. 1990):

$$\dot{\gamma}^{\pm} = Y^{\pm}\dot{\varphi}^{\pm} = Y^{\pm}G'\left(\tau^{\pm}\right)\dot{\tau}^{\pm} \tag{20}$$

where $G'(\tau^{\pm})$ are the derivatives of the damage evolution functions $G(\tau^{\pm})$ with respect to the norms $\tau^{\pm}$.

The terms $g^{\pm}$ of total specific dissipated energy per unit volume are (Oliver et al. 1990):

$$g^{\pm} = \int_0^{\infty} \dot{\gamma}^{\pm} dt = \int_0^{\infty} Y^{\pm}G'\left(\tau^{\pm}\right)\dot{\tau}^{\pm} dt \tag{21}$$

Energy dissipation is generally limited to a localization zone for quasi-brittle materials, and the terms $g^{\pm}$ of dissipated energy per unit volume under general loading conditions are related to the fracture energy per unit area under uniaxial loading conditions (Lubliner et al. 1989; Oliver et al. 1990):

$$g^{+} = \frac{G_{ft}}{\ell}; g^{-} = \frac{G_{fc}}{\ell} \tag{22}$$

where G_{ft} can be interpreted as the total area under the stress-displacement curves of uniaxial tension in the damaged configuration, G_{fc} is the corresponding area under uniaxial compression, and ℓ is a characteristic finite element size that represents the size of the localization zone.

The fracture energy-based method allows to regularize the mesh size sensitivity. To ensure the same fracture energy with different mesh sizes, the softening shapes of the post-peak stress-strain curves are adjusted. The parameters $A^{\pm}$ are given as follows based on Eqs. (17) and (22) (Oliver et al. 1990):

$$A^{+} = \left(\frac{\ell_{ch}^{t}}{\ell} - \frac{1}{2}\right)^{-1}; A^{-} = \left(\frac{\ell_{ch}^{c}}{\ell} - \frac{1}{2}\right)^{-1} \tag{23}$$

where the element size ℓ should satisfy $\ell \leq 2\min\left(\ell_{ch}^{t}, \ell_{ch}^{c}\right)$ based on the constraints of $A^{\pm} \geq 0$.

Single Element Test

A user-defined material model (UMAT) is developed in the commercial finite element software ABAQUS (Hibbitt et al. 2001) for the elasto-plastic-damage model. Single element tests using a square element are conducted to check the implementation under uniaxial tension and compression. Proper material properties are chosen for the material model. The ratio of the uniaxial compressive strength to the uniaxial tensile

strength is generally on the order of $O(10)$, and the ratio of the compressive fracture energy to the tensile fracture energy is generally on the order of $O(100)$ for typical quasi-brittle rocks (Shen and Stephansson 1994; Zhou and Lin 2013). The strength ratio σ_c/σ_t is assumed to be 10, and the fracture energy ratio G_{fc}/G_{ft} is set as 50. Essential material properties of the elasto-plastic-damage model are summarized in Table 1, with E_0= 30 GPa, ν= 0.2, σ_t= 3 MPa, σ_c= 30 MPa, $\alpha_h^{\pm}$ = 0.83 ($h^{\pm}$= 25 GPa), α= 0.12 ($\phi \backsimeq 10^{\circ}$), α_p= 0.2, G_{ft}= 35 N/m, and G_{fc}= 1750 N/m (Cicekli et al. 2007). The tensile and compressive characteristic lengths are 117 mm and 58 mm, respectively. The element size is 50 mm, which satisfies the constraints of the allowed maximum element size based on Eq. (23). Stress decreases due to damage after a peak strength, as seen in the stress-displacement curves under both uniaxial tension and compression (Fig. 2a and b). The output value of the fracture energy, which is interpreted as the area under the stress-displacement curve, is very close to the input value under both uniaxial tension and compression. The output values of the tensile and compressive fracture energy are 34.8 N/m and 1706 N/m, respectively, and they agree well with the input values of 35 N/m and 1750 N/m.

Uniaxial compression tests are conducted to analyze the influence of two length scales, including the element size and the compressive characteristic length. Figure 3a summarizes the relationship between axial stress and post-peak displacement for three different element sizes with ℓ= 50 mm, 5 mm, and 0.5 mm and ℓ_{ch}^{c} = 58 mm. The post-peak displacement δ_{post} is adopted here, as the pre-peak displacement δ_{pre} is different with different element sizes. The post-peak displacement is defined as $\delta_{post} = \delta - \delta_{pre}$ with δ denoting the axial displacement. By adopting the fracture energy-based regularization, the stress-strain curve is adjusted through the shape-related parameter with different element sizes. The shape-related parameter A^{-} is 1.5, 0.09, and 0.009, respectively, for the three element sizes based on Eq. (23). The axial stress versus post-peak displacement curves are generally close for different element sizes that vary by two orders of magnitude. By adopting the regularization method, the same fracture energy can be approximately achieved with different

Table 1 Material properties of the elasto-plastic-damage model used in a single square element (Voyiadjis and Zhou 2019)

Property		Parameter	Value
Elastic properties	Initial elastic modulus (GPa)	E_0	30
	Poisson's ratio	ν	0.2
Plastic properties	Uniaxial tensile strength (MPa)	σ_t	3
	Uniaxial compressive strength (MPa)	σ_c	30
	Tensile hardening ratio	α_h^{+}	0.83
	Compressive hardening ratio	α_h^{-}	0.83
	Failure envelope slope	α	0.12
	Dilation coefficient	α_p	0.2
Damage properties	Tensile fracture energy (N/m)	G_{ft}	35
	Compressive fracture energy (N/m)	G_{fc}	1750

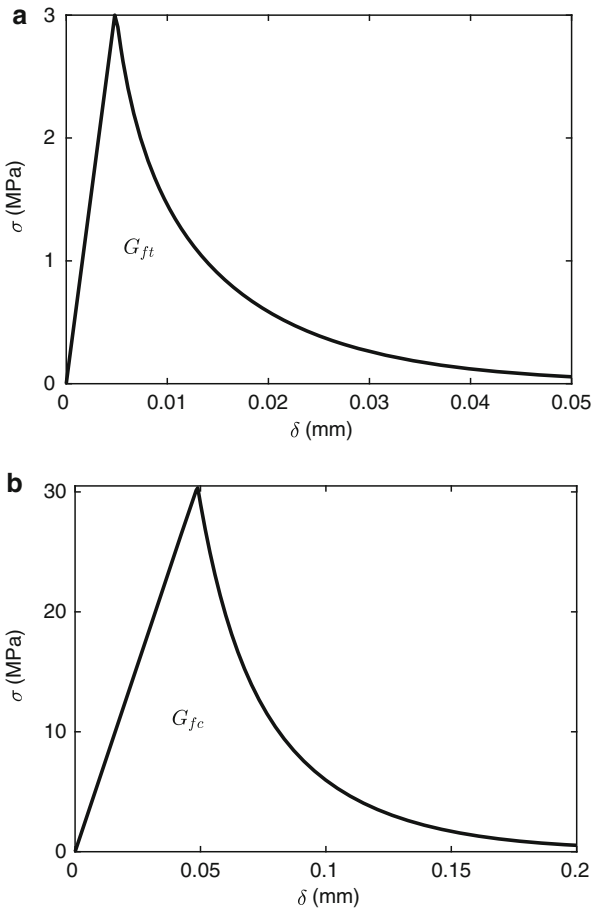

Fig. 2 Stress-displacement curves under (**a**) uniaxial tension and (**b**) uniaxial compression for a single square element (Voyiadjis and Zhou 2019)

element sizes. The area under the stress-displacement curve is thus approximately the same with different element sizes. However, the regularization method does not ensure identical softening curves, and a smaller element softens more rapidly than a larger element (Murray 2007). Three cases are then analyzed regarding the influence of the compressive characteristic length on the stress-displacement curve, with $\ell_{ch}^{c} = 58$ mm, 117 mm, and 5833 mm and $\ell = 50$ mm (Fig. 3b) (Voyiadjis and Zhou 2019). The value of the compressive characteristic length ℓ_{ch}^{c} is varied by changing the compressive fracture energy G_{fc}. For the three cases with $G_{fc} = 1750$ N/m, 3500 N/m, and 1.75×10^5 N/m, the shape-related parameter A^{-} is 1.5, 0.5, and 0.009, respectively. The fracture energy ratio G_{fc}/G_{ft} is fixed at 50. The post-peak behavior is more ductile with a larger G_{fc} and a smaller A^{-}. For a limit case with an infinite G_{fc} and a zero A^{-}, the elasto-plastic-damage model should recover an elastoplastic model without damage.

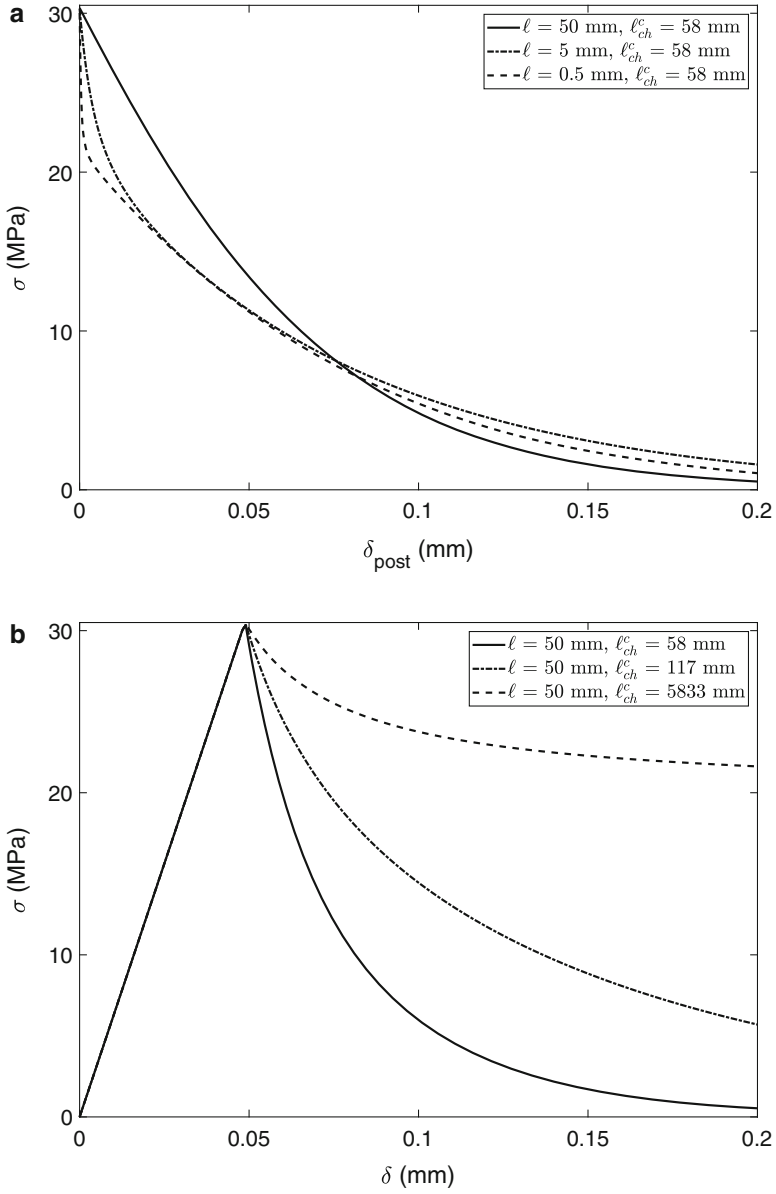

Fig. 3 Influence of (**a**) the element size on post-peak stress-displacement curves and (**b**) the compressive characteristic length on stress-displacement curves under uniaxial compression for a single square element (Voyiadjis and Zhou 2019)

Frictional Contact Using an Elastoplastic Model

An elastoplastic model is adopted to analyze the contact stress in frictional contact before considering the influence of rock damage (Voyiadjis and Zhou 2019). An idealized frictional contact problem is studied through a finite element model, which is validated against the analytical solutions of the contact stress in the two asymptotic regimes (Voyiadjis and Zhou 2019). The finite element model is then used to analyze the influence of both the governing dimensionless elastoplastic parameter η and the element size in the elastoplastic regime.

Finite Element Model

A finite element model is constructed in ABAQUS (Hibbitt et al. 2001) to analyze the frictional contact. The finite element model includes three main components: the rock, slider, and tool-rock interface in the idealized plane strain problem. The width of the rock is 100 mm, and the height is 50 mm (Fig. 4). The mesh size gradually increases from a fine zone at the top to a coarse zone at the bottom. The mesh size is 0.5 mm in the fine zone at the top 15 mm, and it is around 5 mm in the coarse zone. The rock mesh includes 7112 four-node plane strain elements (CPE4R) with reduced integration. A fixed displacement boundary condition is applied for the rock except at the top surface. There are generally two ways to model the rigid slider: a discrete rigid surface with a mesh and an analytical rigid surface without a mesh (Hibbitt et al. 2001). The analytical rigid surface is adopted due to computational efficiency, and it is simply created by sketching the profile of the slider (Voyiadjis and Zhou 2019). A rigid body reference node is defined at the mass center of the slider to characterize the motion of the analytical rigid surface. A small horizontal velocity V of 10^{-3} mm/step is applied to the slider to ensure a quasi-static state of the sliding process. The inclination angle β is 0.5°, and the depth d is 0.3 mm. To capture the nonlinear distribution of the contact stress, a sufficient number (typically at least 30) of elements is necessary at the tool-rock interface. Contact pairs are used to model the tool-rock interaction, and they include three key components to discretize contact, track contact, and assign master/slave roles, respectively (Hibbitt et al. 2001). For the contact discretization, surface-to-surface contact is generally advantageous over the node-to-surface contact due to a smoothing effect. The smoothing effect is achieved by resisting penetrations over finite regions in average on the slave surface. For the tracking approaches, finite-sliding contact allows for arbitrary relative motions of the contact surfaces, whereas small-sliding contact assumes little sliding of one surface along the other. The tool-rock interface adopts surface-to-surface contact and finite-sliding tracking. The analytical rigid surface and the free surface at the top of the rock are the master and slave contact surfaces, respectively.

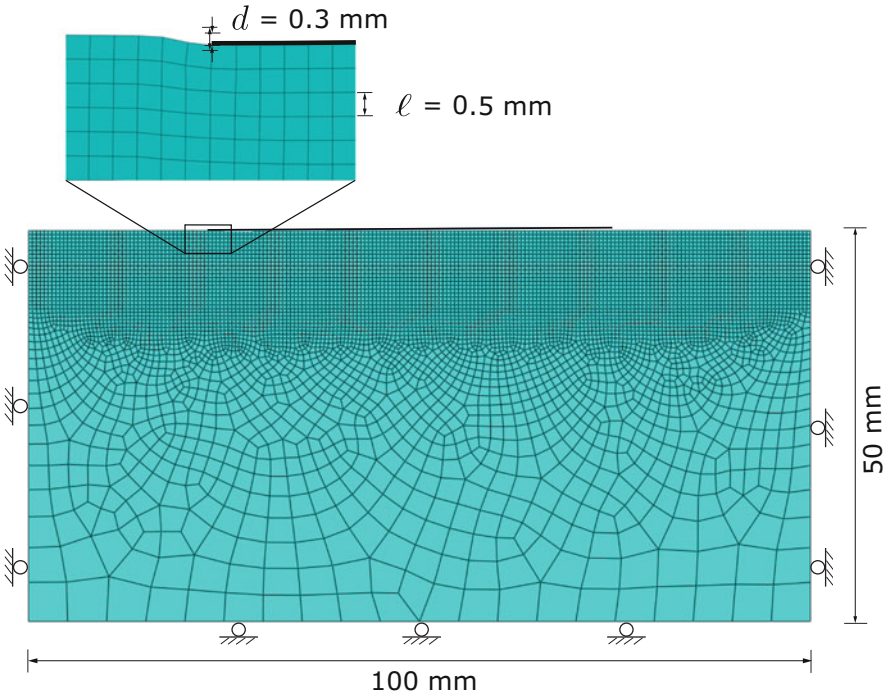

Fig. 4 Finite element mesh for plane strain frictional contact between a blunt tool and rock (Voyiadjis and Zhou 2019)

A penalty method is imposed for the frictional constraint at the interface. The interface friction coefficient is 0.17, and the interface friction angle is 10°.

Verification of the Finite Element Model in Asymptotic Regimes

The finite element model is validated based on analytical solutions in the two asymptotic regimes (Voyiadjis and Zhou 2019). In the elastic regime, the rock is treated as an elastic material model with $E_0 = 1$ GPa and $\nu = 0.2$. During the steady sliding process, the average vertical force and the contact length are 185 N and 23.4 mm, respectively. The average contact stress is thus 7.9 MPa, which is very close to the analytical value of 7.4 MPa (Adachi 1996). In the asymptotic rigid plastic regime, the rock is characterized by an elastoplastic material using the Mohr-Coulomb model. The material properties are $E_0 = 50$ GPa, $\nu = 0.2$, $\sigma_c = 30$ MPa, $\phi = 10^{\circ}$, and $\alpha_p = 0$. The elastoplastic material with a large enough elastic modulus resembles a rigid-perfectly plastic material with an infinite elastic modulus. A special case is considered with identical internal and interface friction angles. The dilation coefficient is zero to suppress volumetric expansion during sliding. For the boundary condition in the asymptotic rigid plastic regime, a vertical force instead of a fixed

depth is applied on the slider to achieve a steady sliding process (Johnson 1987). For an applied vertical force of 3120 N, the contact length is 38.9 mm, and the average contact stress is 80 MPa. The dimensionless average contact stress is 2.67, which is also very close to the analytical value of 2.68 (Zhou 2017b; Zhou and Detournay 2019). The numerical and analytical results agree well in both the elastic and asymptotic rigid plastic regimes regarding the distribution of the dimensionless contact stress (Fig. 5) (Voyiadjis and Zhou 2019). In the elastic regime, the contact stress increases towards the tip of the slider. Stress singularity occurs at the tip based on the analytical solution. In the asymptotic rigid plastic regime, the distribution of the dimensionless contact stress is approximately uniform in the numerical modeling (Voyiadjis and Zhou 2019), and it is slightly different from the analytical solution with a uniform stress distribution. For several elements near the tip of the slider, the contact stress is significantly larger. These abnormal data possibly result from stress singularity near the tip of the slider, and they are removed in the plots of the stress distribution. The elastic modulus is infinite for a rigid-perfectly plastic material in the analytical solution, and using a finite value of the elastic modulus in numerical modeling may also lead to the minor difference of stress distribution.

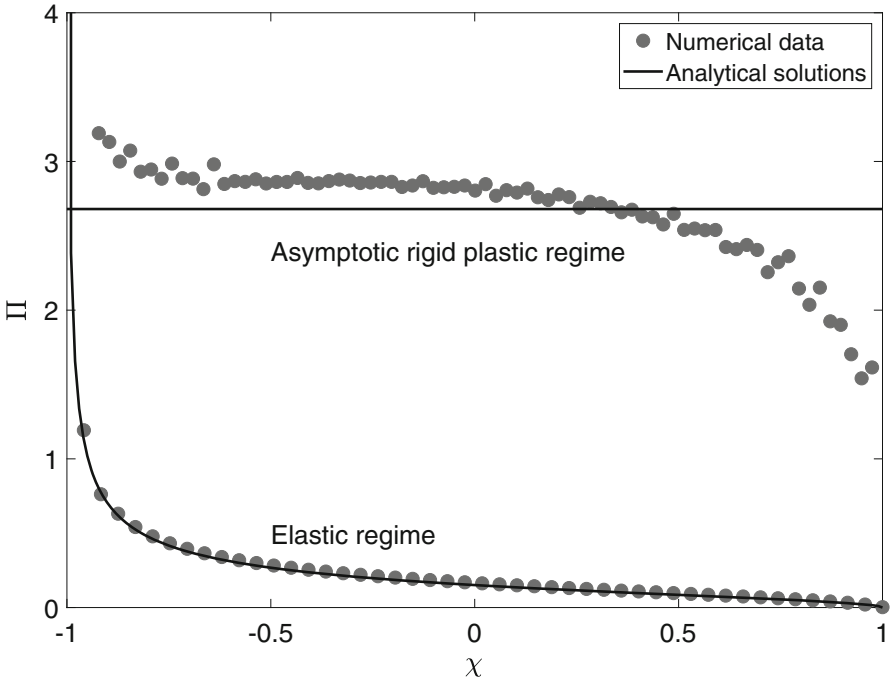

Fig. 5 Comparison between numerical results and analytical solutions for the distribution of dimensionless contact stress Π in both the elastic and asymptotic rigid plastic regimes (Voyiadjis and Zhou 2019). The analytical solution in the elastic regime is from Adachi (1996), and the analytical solution in the asymptotic rigid plastic regime is from Zhou and Detournay (2019)

Influence of Parameter η

The influence of the governing parameter η on the contact stress is analyzed in different regimes. An elastic-perfectly plastic model is used by reducing the elasto-plastic-damage model. The damage indices and hardening moduli are set to zero in the elasto-plastic-damage model. By comparing with the Mohr-Coulomb elastoplastic model, the main difference in the adopted elastoplastic model lies in the yield function. The analysis using an elastoplastic model allows for considering the influence of rock damage in the subsequent analysis using an elasto-plastic-damage model. By varying both the initial elastic modulus E_0 and the uniaxial compressive strength σ_c, 12 different values of the parameter η are obtained in Table 2 (Voyiadjis and Zhou 2019). For eight cases with η between 0.2 and 4.5, the modulus E_0 is between 700 MPa and 15 GPa, and σ_c= 30 MPa. For the four other cases with η between 9.1 and 60.6, it is more challenging to achieve computational convergence. Several adjustments are thus made, by changing both the material and geometrical properties, as well as the contact algorithms. For a fixed modulus E_0 of 30 GPa, the uniaxial compressive strength σ_c is decreased from 30 MPa to 4.5 MPa. Different from the first eight cases with d= 0.3 mm, the depth of sliding is 0.05 mm. By assuming relatively little sliding at the interface, the small-sliding contact algorithm is adopted. The dimensionless average contact stress $\overline{\Pi}$ generally increases with η and then reaches a limit value of around 3.7 in the asymptotic rigid plastic regime (Fig. 6). The asymptotic elastic regime is approximately delimited by $\eta \lesssim 1$, where the numerical results are very close to the analytical solutions (Adachi 1996; Voyiadjis and Zhou 2019). The asymptotic rigid plastic regime is approximately reached with $\eta \gtrsim 30$. The distribution of the dimensionless contact stress Π is summarized for three cases with η = 0.5, 4.5, and 30.3, which approximately correspond to the asymptotic elastic, elastoplastic, and asymptotic rigid plastic regimes, respectively (Fig. 7). By comparing the stress distribution at the same location for different cases, the dimensionless contact stress Π generally increases with η. By comparing the stress distribution at different locations for the same case, the dimensionless contact stress generally increases towards the tip in both the asymptotic elastic and the elastoplastic regimes. The dimensionless contact stress is more or less uniform in the asymptotic rigid plastic regime with a limit value of around 3.7.

Mesh Size Sensitivity

In the elastoplastic regime without an analytical solution, the mesh size sensitivity is analyzed to evaluate the influence of element size on the contact stress. A typical case is chosen with $E_0 = 10$ GPa and $\eta = 3.0$, and other material properties are given in Table 2. The value of the governing parameter η is within the range between 1 and 30 that approximately delimits the elastoplastic regime. Three sets of mesh are studied, with an element size of 1.0 mm, 0.5 mm, and 0.25 mm, respectively, in the fine zone (Voyiadjis and Zhou 2019). By comparing the chosen element sizes

Table 2 Essential modeling parameters for the elastoplastic model (Voyiadjis and Zhou 2019)

Property		Parameter	Value											
Material properties	Initial elastic modulus (GPa)	E_0	0.7	1	1.5	2	3	5	10	15	30	30	30	30
	Tensile strength (MPa)	σ_t	3	3	3	3	3	3	3	3	3	1.8	0.9	0.45
	Compressive strength (MPa)	σ_c	30	30	30	30	30	30	30	30	30	18	9	4.5
	Elastoplastic parameter	η	0.2	0.3	0.5	0.6	0.9	1.5	3.0	4.5	9.1	15.1	30.3	60.6
	Poisson's ratio	ν	0.2											
	Tensile hardening ratio	α_h^+	0											
	Compressive hardening ratio	α_h^-	0											
	Failure envelope slope	α	0.12											
	Dilation coefficient	α_p	0											
Geometrical properties	Inclination angle (°)	β	0.5											
	Depth (mm)	d[a]	0.3											
Interface property	Interface friction coefficient	μ	0.17											

[a]A smaller depth of 0.05 mm is used for the last four cases with larger values of η for computational convergence

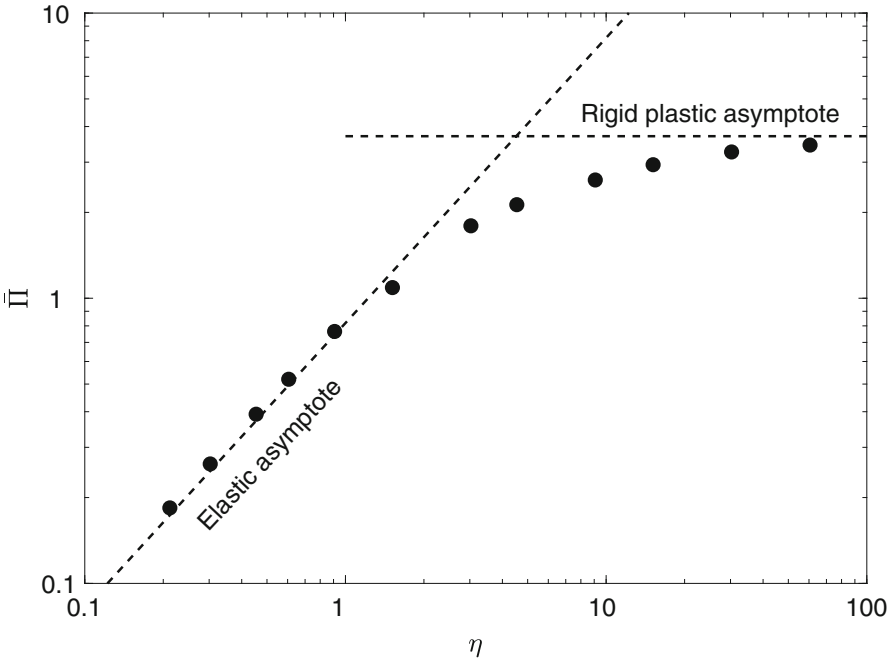

Fig. 6 Relationship between the dimensionless average contact stress $\overline{\Pi}$ and the dimensionless elastoplastic parameter η in the elastoplastic regime using an elastoplastic model that is recovered from an elasto-plastic-damage model (Voyiadjis and Zhou 2019). The elastic asymptote is from Adachi (1996), and the rigid plastic asymptote is estimated based on the elastoplastic model

with the median grain sizes of typical limestones and sandstones, they are generally on the similar order of magnitude (Rostamsowlat et al. 2019). Both the average contact stress and the stress distribution are analyzed with three sets of mesh. The contact length is 25.0 mm, 24.9 mm, and 24.8 mm, for an applied vertical force of 1349 N, 1334 N, and 1300 N, respectively. There are more elements in contact with a smaller mesh size, and the number of elements in contact is 25, 50, and 99, respectively. The dimensionless average contact stress $\overline{\Pi}$ is approximately independent of the mesh size, with $\overline{\Pi} = 1.80$, 1.76, and 1.75, respectively. The distribution of the dimensionless contact stress is also approximately independent of the element size (Fig. 8) (Voyiadjis and Zhou 2019).

Frictional Contact Using an Elasto-Plastic-Damage model

The developed elasto-plastic-damage model is then used to analyze the influence of two governing dimensionless parameters on the contact stress for a quasi-brittle rock. A typical case is first studied to investigate both the rock damage and contact stress. Numerical tests are then conducted with the same set of two governing

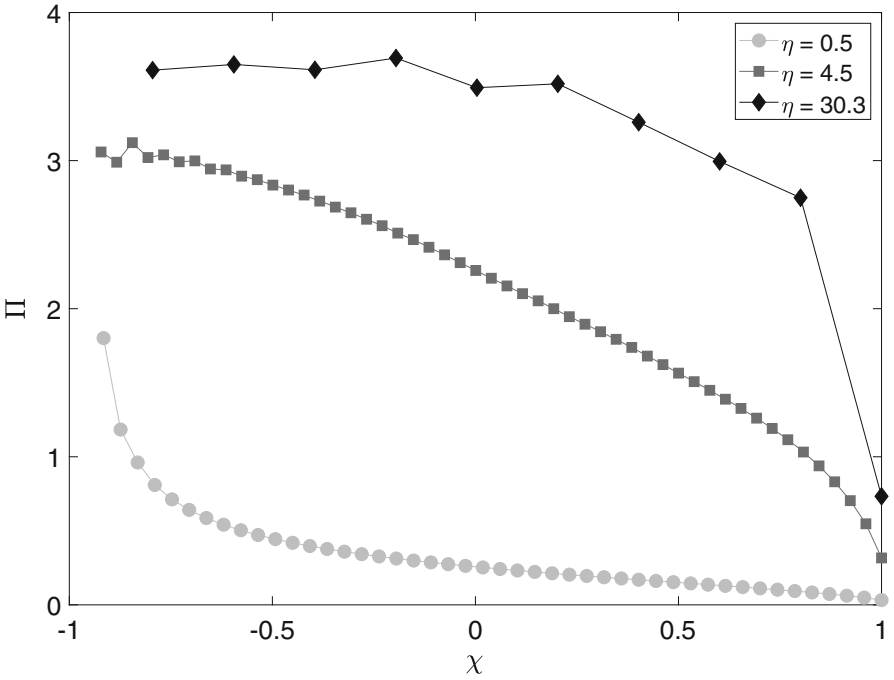

Fig. 7 Distribution of the dimensionless contact stress Π with three different values of the dimensionless elastoplastic parameter η (Voyiadjis and Zhou 2019)

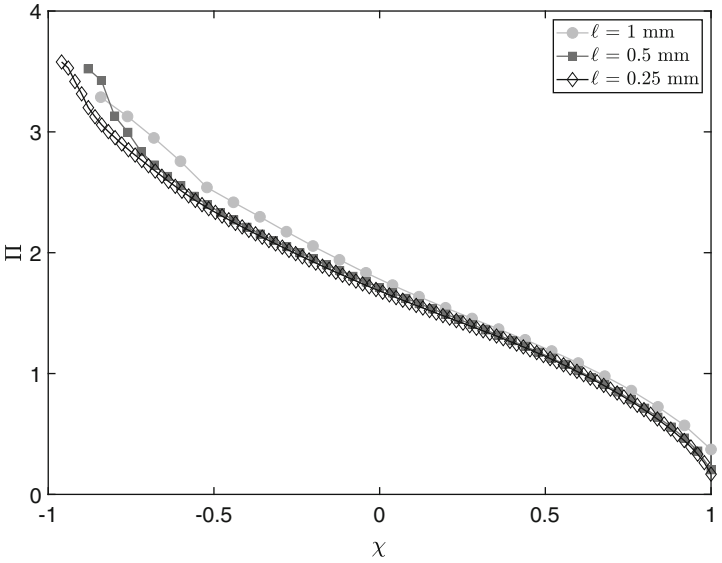

Fig. 8 Distribution of the dimensionless contact stress Π with three mesh sizes for a typical case (η= 3.0) in the elastoplastic regime (Voyiadjis and Zhou 2019)

dimensionless parameters but with different sets of geometrical and material properties. To analyze the influence of the two governing dimensionless parameters separately, one parameter is varied in a wide range, while the other one is fixed (Voyiadjis and Zhou 2019).

Typical Case

By treating the rock as a quasi-brittle material, Voyiadjis and Zhou (2019) analyzed a typical case for the frictional contact problem using an elasto-plastic-damage model. Similar material properties used in the single element test are used in the typical case except the initial elastic modulus and the dilation coefficient. Essential material parameters are E_0= 3 GPa, ν= 0.2, σ_t= 3 MPa, σ_c= 30 MPa, $\alpha_h^{\pm}$ = 0.83 ($h^{\pm}$= 2.5 GPa), α= 0.12 ($\phi \backsimeq 10^{\circ}$), α_p= 0, G_{ft}= 35 N/m, and G_{fc}= 1750 N/m. The geometrical and interface properties are β=0.5°, d= 0.3 mm, and μ= 0.17. The two dimensionless parameters are calculated as η= 0.9 and ξ= 5.4. Typical contours are plotted for the yield state, tensile damage, and compressive damage with a horizontal distance of around 10.0 mm (Fig. 9). The yield index is 0 in a current elastic state, and it is 1 in a current yield state. A region underneath the slider is in a yield state during the sliding process. The depth of the yield zone is around 0.5 mm, and the length is around 21.0 mm. The total contact length is around 26.2 mm, and it includes an elastic zone of around 5.2 mm and a damage process zone of around 21.0 mm. The damage indices $\varphi^{\pm}$ are between 0 and 1. When the slider is pushed downwards at the beginning, tensile damage occurs near the tip of the slider. When the slider moves horizontally at the steady state, no tensile damage occurs. A similar zone underneath the slider is observed with both compressive damage and yield. There is also a zone with permanent compressive damage when the contact stress is released after sliding. During the steady sliding process, the average vertical force is 186 N, and the contact length is 26.2 mm. The dimensionless average contact stress $\overline{\Pi}$ is thus 0.24. An elastic zone and a damage process zone can be approximately identified at the tool-rock interface, based on the distribution of both the compressive damage index and

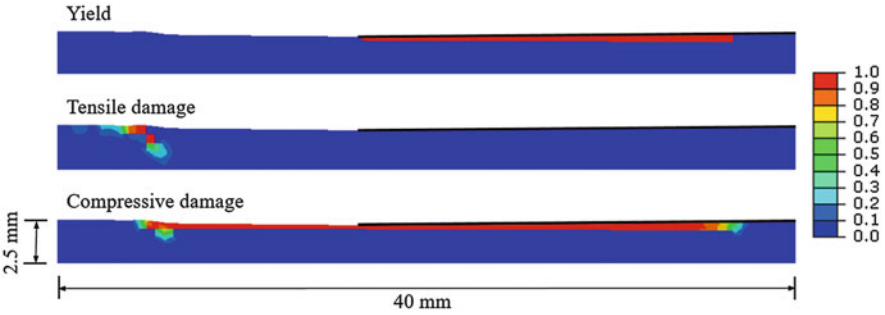

Fig. 9 Contours of yield state, tensile damage, and compressive damage near the contact zone (Voyiadjis and Zhou 2019)

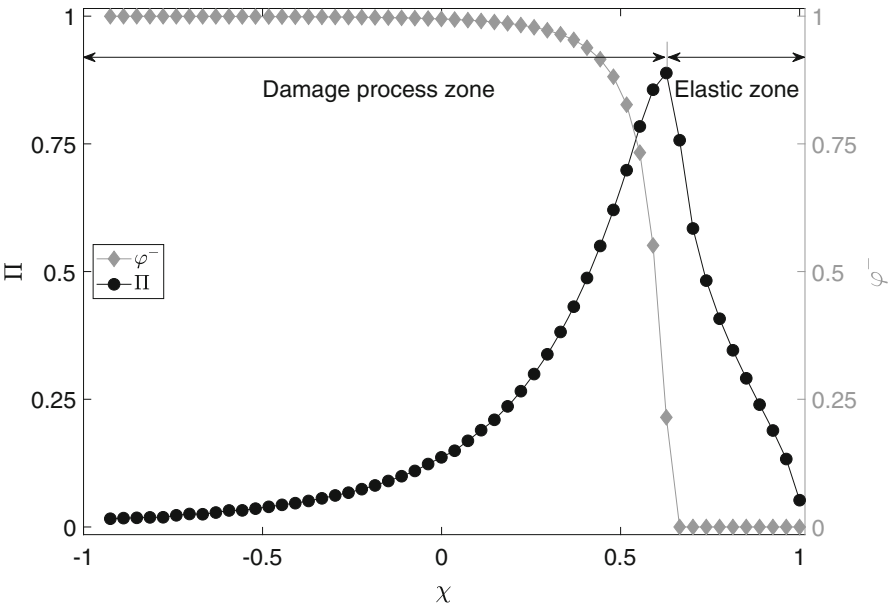

Fig. 10 Distribution of the compressive damage index φ^- and the dimensionless contact stress Π for a typical case (η= 0.9 and ξ= 5.4) using the elasto-plastic-damage model (Voyiadjis and Zhou 2019)

dimensionless contact stress (Fig. 10). No damage occurs in the elastic zone, and the contact stress increases towards the tip of the slider. Compressive damage occurs in the damage process zone, and the contact stress decreases towards the tip due to increasing φ^-. The dimensionless stress $\overline{\Pi}$ reaches a maximum value of around 0.9 at the boundary between the two zones (Voyiadjis and Zhou 2019).

Invariance with Respect to Fixed η and ξ

The average contact stress is approximately constant with a fixed dimensionless elastoplastic parameter η but with different values for the parameters that govern η in an elastoplastic analysis (Zhou and Detournay 2014). The influence of a fixed set of two governing parameters on the contact stress is further analyzed using the elasto-plastic-damage model (Voyiadjis and Zhou 2019). The geometrical and material properties are different in three cases, but the same set of governing dimensionless parameters is used, with η= 0.9 and ξ= 5.4. The first case adopts the essential geometrical and material properties used in the typical case, with β= 0.5°, d= 0.3 mm, E_0= 3 GPa, and G_{fc}= 1750 N/m. The second case mainly differs from the first case with β= 0.3° and E_0= 5 GPa, and the third case mainly differs from the first case with d= 0.15 mm and G_{fc}= 875 N/m. Other essential parameters, such as $\alpha_h^{\pm}$ and G_{fc}/G_{fi}, are the same in all the three cases.

The average contact stress is first compared for the three cases, followed by the distribution of both the compressive damage index and contact stress. For the first case, the dimensionless average contact stress $\overline{\Pi}$ is 0.24, calculated based on a vertical force of 186 N and a contact length of 26.2 mm. For the second case, the dimensionless stress $\overline{\Pi}$ is 0.22 with a vertical force of 316 N and a contact length of 48.0 mm. For the third case, the dimensionless stress $\overline{\Pi}$ is 0.28 with a vertical force of 95 N and a contact length of 11.3 mm (Voyiadjis and Zhou 2019). The values of $\overline{\Pi}$ are approximately the same among the three cases, even though they slightly increase with decreasing the contact length. Stress singularity occurs at the tip, and it is more significant with a smaller number of elements in contact. The difference of $\overline{\Pi}$ may result from several factors including the stress singularity. By normalizing the abscissa with the corresponding contact length in the three cases, the distribution of the compressive damage index φ^- is approximately the same (Fig. 11a). In the elastic zone, the compressive damage index φ^- is 0. In the damage process zone, the index φ^- increases from 0 to 1 towards the tip. No significant difference is observed regarding the distribution of the dimensionless contact stress Π for the three cases (Fig. 11b) (Voyiadjis and Zhou 2019). In the elastic zone, the dimensionless stress Π increases from around 0.1 to 0.9. In the damage process zone, the dimensionless stress Π decreases towards the tip.

Influence of Parameter η

After showing that the dimensionless average contact stress $\overline{\Pi}$ is approximately constant for a fixed set of η and ξ, the relationship between η and $\overline{\Pi}$ is analyzed when ξ is fixed. By changing the initial elastic modulus E_0, 12 different values of η are obtained for a fixed brittleness number ξ. The parameter η varies between 0.03 and 9.1, when the elastic modulus E_0 varies between 0.1 GPa and 30 GPa (Table 3) (Voyiadjis and Zhou 2019). Three different values of the brittleness number ξ are considered by changing the compressive fracture energy G_{fc}, with G_{fc}= 1750 N/m, 3500 N/m, 1.75×10^5 N/m, and ξ= 5.4, 2.7, 0.05, respectively. Other essential parameters used in the typical case are adopted here. The relationship between η and $\overline{\Pi}$ are summarized in Fig. 12, including three sets of numerical data and two asymptotes (Voyiadjis and Zhou 2019). The rigid plastic asymptote is estimated based on an elastoplastic model. For the set of data with G_{fc}= 1750 N/m and ξ= 5.4, the dimensionless stress $\overline{\Pi}$ generally increases with η and then reaches a limit value of around 0.2. The asymptotic elastic regime is approximately delimited by $\eta \lesssim 0.3$, where the numerical results are very close to the analytical solutions. The dimensionless stress $\overline{\Pi}$ reaches a limit value of around 0.2 with $\eta \gtrsim 1.0$. This limit value is around one order of magnitude smaller, by comparing with the limit value of around 3.7 in an elastoplastic analysis. For the two other sets of data with ξ= 2.7 and 0.05, the dimensionless stress $\overline{\Pi}$ also generally increases with η and then levels off. In the asymptotic elastic regime with a small enough η, the dimensionless stress $\overline{\Pi}$ is approximately independent of ξ as negligible damage occurs. When the parameter η is large enough, the limit value of $\overline{\Pi}$ increases with decreasing ξ. For the set of data

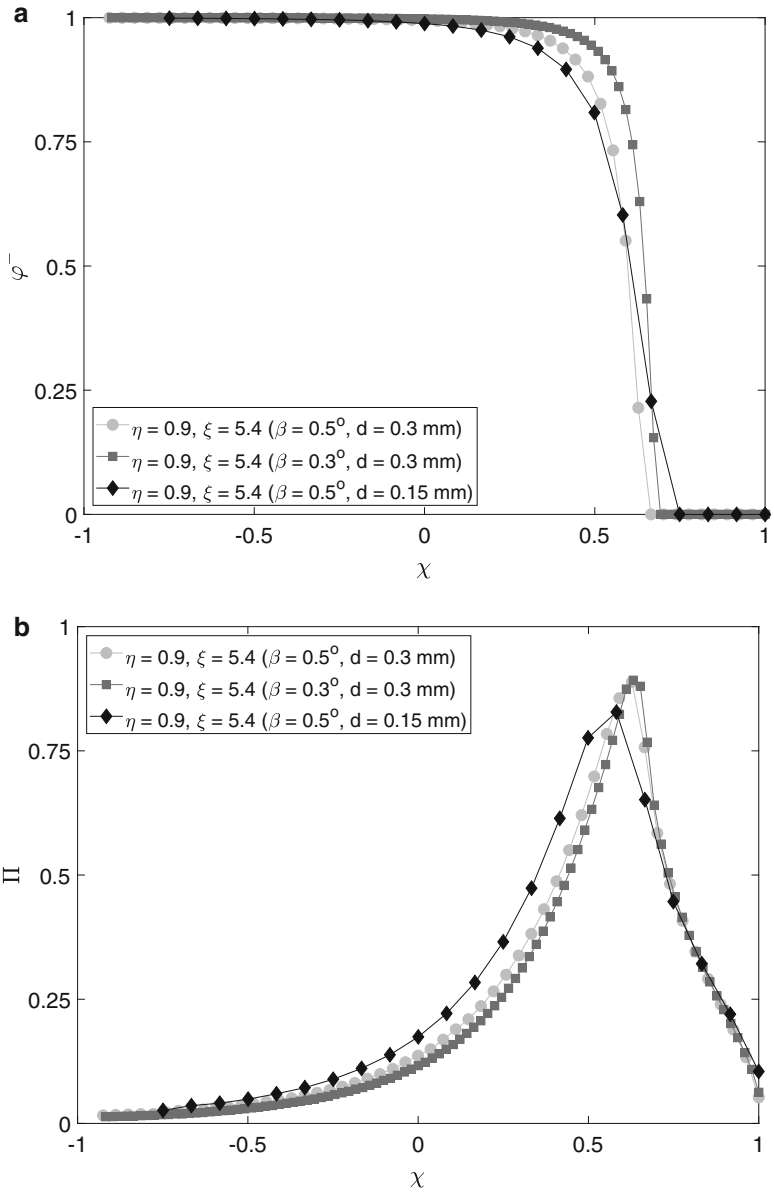

Fig. 11 Distribution of (**a**) the compressive damage index φ^- and (**b**) the dimensionless contact stress Π for three cases with the same set of η and ξ (η= 0.9 and ξ= 5.4) but with different geometrical and material properties (Voyiadjis and Zhou 2019)

with ξ= 0.05, the limit value of $\overline{\Pi}$ is around 0.9, indicating that the average contact stress is close to the uniaxial compressive strength.

The influence of the dimensionless elastoplastic parameter η is analyzed for three typical cases, regarding the distribution of both the compressive damage index φ^-

Table 3 Material parameters with a host of the dimensionless elastoplastic parameter η and three different values of the brittleness number ξ using the elasto-plastic-damage model (Voyiadjis and Zhou 2019)

Property	Parameter	Value											
Initial elastic modulus (GPa)	E_0	0.1	0.3	0.5	0.7	1	1.5	2	3	5	10	15	30
Elastoplastic parameter	η	0.2	0.3	0.5	0.6	0.9	1.5	3.0	4.5	9.1	15.1	30.3	60.6
Tensile fracture energy (N/m)	G_{ft}	3500				70				35			
Compressive fracture energy (N/m)	G_{fc}	1.75×10^5				3500				1750			
Brittleness number	ξ	0.05				2.7				5.4			
Tensile strength (MPa)	σ_t	3											
Compressive strength (MPa)	σ_c	30											
Poisson's ratio	ν	0.2											
Tensile hardening ratio	α_h^+	0.83											
Compressive hardening ratio	α_h^-	0.83											
Failure envelope slope	α	0.12											
Dilation coefficient	α_p	0											

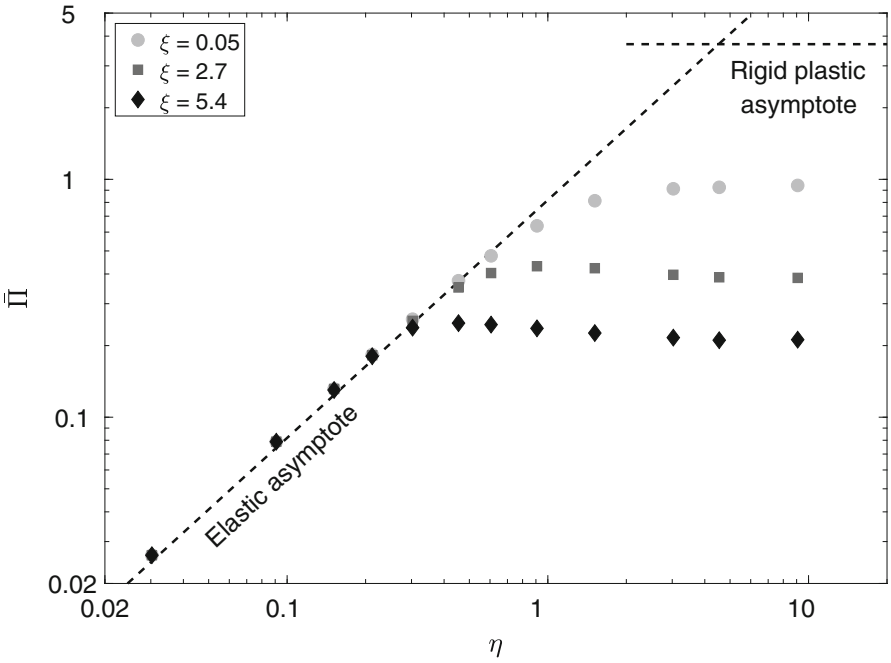

Fig. 12 Relationship between the dimensionless average contact stress $\overline{\Pi}$ and the dimensionless elastoplastic parameter η with three different values of the brittleness number ξ (Voyiadjis and Zhou 2019)

and the dimensionless contact stress Π. The distribution of φ^{-} is summarized for three cases with η= 0.3, 0.9, and 3.0 and ξ= 2.7 (Fig. 13a) (Voyiadjis and Zhou 2019). The size of the elastic zone decreases, and the size of the damage process zone increases with increasing η. For the case with η= 0.3, the whole contact zone is generally in an elastic state. For the case with η= 3.0, the contact zone is in a damaged state. The distribution of Π for three different values of η is summarized in Fig. 13b (Voyiadjis and Zhou 2019). The dimensionless stress Π first increases and then decreases from the elastic zone to the damage process zone. The maximum value of Π is around 0.9 at the boundary of the two zones. The contact stress increases more significantly in the elastic zone with increasing η. For the case with η= 0.3, the contact stress generally increases towards the tip in the elastic zone. For the case with η= 3.0, the contact stress generally decreases in the damage process zone.

Influence of Parameter ξ

The relationship between the brittleness number ξ and the dimensionless average contact stress $\overline{\Pi}$ is then analyzed when the dimensionless elastoplastic parameter η is

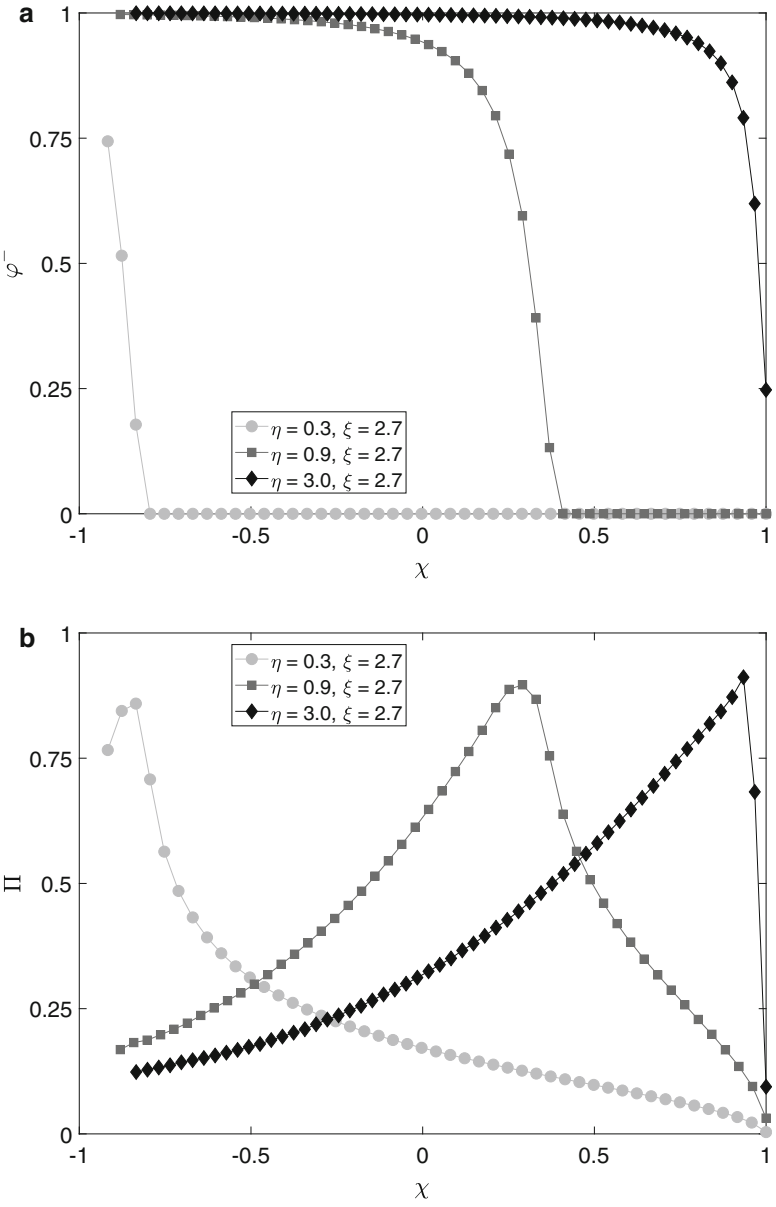

Fig. 13 Distribution of (**a**) the compressive damage index φ^- and (**b**) the dimensionless contact stress Π with three different values of η and a fixed value of ξ (Voyiadjis and Zhou 2019)

fixed. Different values of ξ are obtained by changing the compressive fracture energy G_{fc} for a fixed dimensionless elastoplastic parameter η. Twelve cases are studied with ξ between 0.05 and 17.9 and with G_{fc} between 1.75×10^5 N/m and 525 N/m (Table 4).

Three different values of η are considered by changing the initial elastic modulus E_0, with $\eta = 0.3$, 0.9, and 3.0 and $E_0 = 1$ GPa, 3 GPa, and 10 GPa, respectively. Other essential parameters used in the typical case are adopted here. The relationship between ξ and $\overline{\Pi}$ is summarized in Fig. 14 for three sets of data (Voyiadjis and Zhou 2019). For the set of data with $\eta = 0.3$, the damage process zone is negligible with $\xi \lesssim 3$, and the dimensionless stress $\overline{\Pi}$ is around 0.3. As the brittleness number ξ increases, the dimensionless stress $\overline{\Pi}$ decreases. When ξ increases from 0.05 to 17.9 for the set of data with $\eta = 3.0$, the dimensionless stress $\overline{\Pi}$ gradually decreases from around 0.9 to 0.1.

The distributions of both the compressive damage index φ^- and the dimensionless contact stress Π are then analyzed by varying the brittleness number ξ. Three cases are compared regarding the distribution of φ^- with $\xi = 0.05$, 2.7, and 5.4 and $\eta = 0.9$ (Fig. 15a). The size of the damage process zone increases with the brittleness number ξ. The damage index φ^- increases more rapidly from 0 to around 1 in the damage process zone. The distribution of Π is also compared for three different values of ξ (Fig. 15b). The dimensionless stress Π first increases in the elastic zone and then decreases in the damage process zone towards the tip. The maximum value of Π is around 0.9 at the boundary of the two zones. When the brittleness number increases, the stress decreases more significantly in the damage process zone. For example, the dimensionless stress Π is around 0.9 in the whole damage process zone with $\xi = 0.05$. The dimensionless stress Π decreases to around 0 near the tip when ξ increases to 5.4.

Discussion

The important roles of the two governing dimensionless parameters are discussed first, and the emphasis is placed on the influence of the brittleness number on the contact stress. The novelty is then illustrated by comparing the numerical modeling results with typical experimental results. The limitation is also discussed with a focus on the developed elasto-plastic-damage model (Voyiadjis and Zhou 2019).

Two Governing Dimensionless Parameters

The nature of frictional contact is predominantly governed by both an elastoplastic parameter η and a brittleness number ξ for a quasi-brittle rock. An elasto-plastic-damage model is implemented in ABAQUS as a UMAT, and it is adopted to analyze the dependence of the contact stress on the two governing parameters. The dimensionless average contact stress $\overline{\Pi}$ generally increases with η before reaching a limit value, whereas it generally decreases with increasing ξ. Voyiadjis and Zhou (2019) introduce a brittleness number ξ in frictional contact for a quasi-brittle rock with material length scales. The study extends a previous numerical study that focuses on the influence of an elastoplastic parameter η for a Mohr-Coulomb elastoplastic rock

Table 4 Material parameters with a host of the brittleness number ξ and three different values of the dimensionless elastoplastic parameter η using the elasto-plastic-damage model (Voyiadjis and Zhou 2019)

Property	Parameter	Value											
Initial elastic modulus (GPa)	E_0	1				3				10			
Elastoplastic parameter	η	0.3				0.9				3.0			
Tensile fracture energy (N/m)	G_{ft}	3500	1750	700	350	175	105	70	53	35	25	18	11
Compressive fracture energy (N/m)	G_{fc}	1.75×10^5	8.75×10^4	3.5×10^4	1.75×10^4	8750	5250	3500	2625	1750	1225	875	525
Brittleness number	ξ	0.05	0.1	0.3	0.5	1.1	1.8	2.7	3.6	5.4	7.7	10.7	17.9

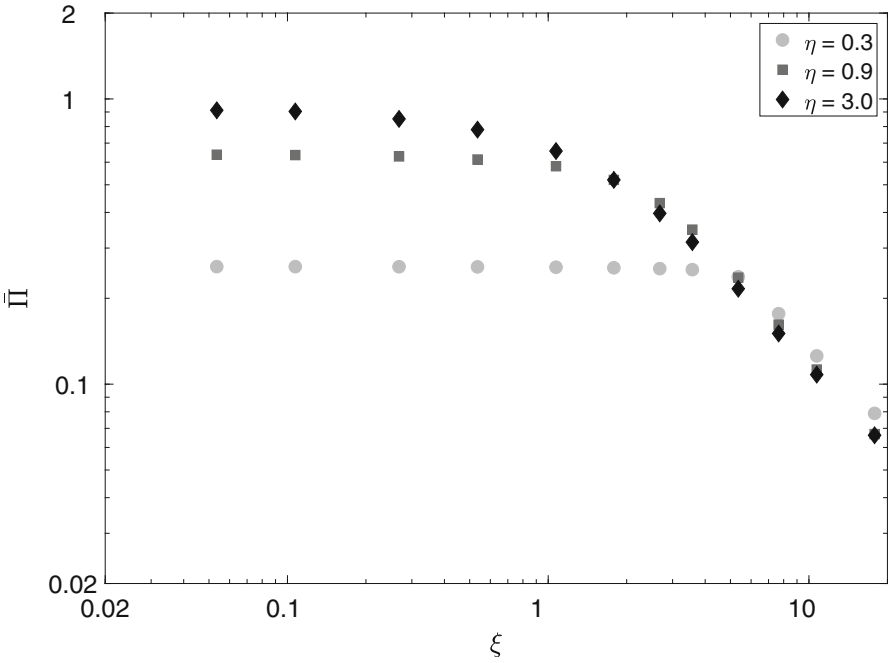

Fig. 14 Relationship between the dimensionless average contact stress $\overline{\Pi}$ and the brittleness number ξ with three different values of the dimensionless elastoplastic parameter η (Voyiadjis and Zhou 2019)

(Zhou and Detournay 2014, 2019). The average contact stress is generally overestimated in the previous numerical study, and this drawback is overcome to some extent. The numerical study by considering the brittleness number is supported by typical experimental results (Almenara and Detournay 1992; Zhou and Detournay 2014).

The distribution of contact stress is analyzed to illustrate the influence of the brittleness number ξ. In a previous analysis using an elastoplastic model, an elastic zone and a plastic zone can be approximately identified at the tool-rock interface. The dimensionless contact stress generally increases towards the tip of the slider (Zhou and Detournay 2019). In the analysis using an elasto-plastic-damage model, the tool-rock interface is divided into elastic and damage process zones (Voyiadjis and Zhou 2019). The contact stress generally increases in the elastic zone towards the tip. The contact stress then decreases in the damage process zone, when the compressive damage index increases. A unique feature of the elasto-plastic-damage model lies in its ability to capture the decrease of the contact stress in the damage process zone. The size of the damage process zone generally increases, and the stress decreases more significantly with increasing the brittleness number ξ. The dimensionless average contact stress $\overline{\Pi}$ thus decreases with increasing ξ.

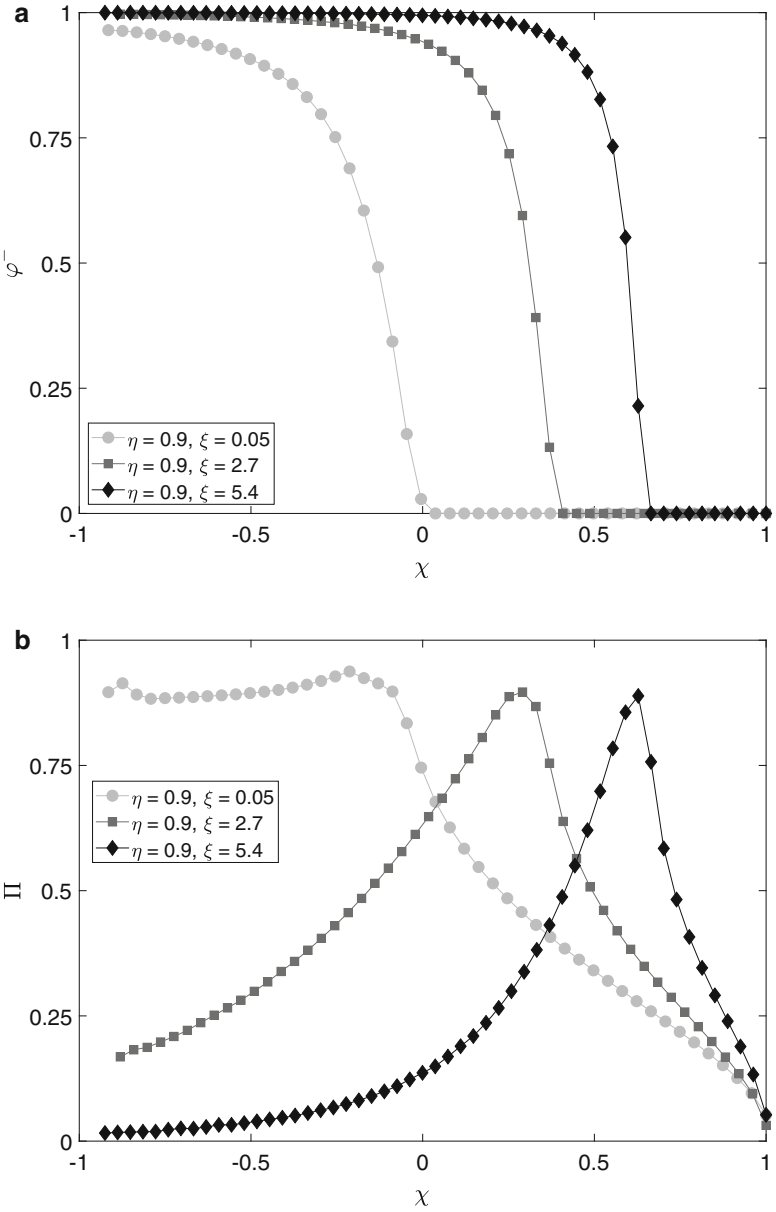

Fig. 15 Distribution of (**a**) the compressive damage index φ^- and (**b**) the dimensionless contact stress Π with a fixed value of η and three different values of ξ (Voyiadjis and Zhou 2019)

Comparison with Experimental Results

It is desirable to justify the numerical results presented in Voyiadjis and Zhou (2019) with experimental results, but the comparison is hindered by different geometrical

length scales. In typical experimental tests, the contact length and grain size are generally on the same order of magnitude (Almenara and Detournay 1992; Rostamsowlat et al. 2019). In numerical modeling, the contact length is generally one order of magnitude larger than the element size, to ensure a sufficient number of elements in contact at the interface. When an element size and a grain size are on the same order of magnitude, the contact length in numerical modeling is thus larger than that in experimental tests by one order of magnitude approximately. Numerical modeling results show similar distributions of contact stress with two fixed governing dimensionless parameters, even though both the geometrical and material properties are different. The gap of the contact length is thus overcome by using the same set of governing dimensionless parameters in both numerical and experimental analyses.

A previous gap in contact stress is reduced to some extent by introducing the brittleness number ξ in frictional contact (Voyiadjis and Zhou 2019). The numerical results are compared with typical experimental data (Almenara 1992; Almenara and Detournay 1992). For typical experimental tests, the values of η and ξ are generally on the orders of $O(0.1 \sim 10)$ and $O(0.01 \sim 1)$, respectively. The orders of magnitude of the two dimensionless parameters are estimated based on typical values with $E_0'/\sigma_c = O(100)$, $\beta \backsimeq 0.1^\circ \sim 10^\circ$, $L = O(1\text{ mm})$, and $\Lambda_c = O$ (0.1 mm) (Almenara 1992; Almenara and Detournay 1992; Labuz and Dai 2000; Rostamsowlat et al. 2019). For three sets of experimental data on sandstones, the elastoplastic parameter η is in a narrow range of 14 ~ 16, and the dimensionless average contact stress $\overline{\Pi}$ is around 0.71 ~ 1.3 (Almenara 1992; Almenara and Detournay 1992; Zhou and Detournay 2014). The value of ξ is around 0.8 for typical experiments with $L \backsimeq 3$ mm, $\beta \backsimeq 3^\circ$, and $\Lambda_c \backsimeq 0.2$ mm (Almenara and Detournay 1992; Labuz and Dai 2000). In the comparison between numerical results and experimental results, the same set of η and ξ is used, even though the contact length differs by one order of magnitude (Voyiadjis and Zhou 2019). Essential geometrical and material properties are summarized in Table 5 for a case with $\eta \backsimeq 15$ and $\xi \backsimeq 0.8$, including both the

Table 5 Essential geometrical and material properties in both a numerical case using the elasto-plastic-damage model and an experimental test on Vosges sandstone (Voyiadjis and Zhou 2019)

Property		Parameter	Modeling value	Experimental value
Geometrical properties	Contact length (mm)	L	34	3
	Inclination angle ($^\circ$)	β	0.5	3
	Depth (mm)	d	0.3	0.16
Material properties	Initial elastic modulus (GPa)	E_0	50	11
	Poisson's ratio	ν	0.2	0.2
	Uniaxial compressive strength (MPa)	σ_c	30	37
	Compressive fracture energy (N/m)	G_{fc}	11.9	7.7
	Material length scale (mm)	Λ_c	0.38	0.2
Governing parameters	Elastoplastic parameter	η	15	16
	Brittleness number	ξ	0.8	0.8

numerical data and experimental data on Vosges sandstone (Almenara 1992; Almenara and Detournay 1992; Labuz and Dai 2000). In the numerical study using a Mohr-Coulomb elastoplastic model, the value of the dimensionless average contact stress $\overline{\Pi}$ is around 2 with $\eta \backsimeq 15$ (Zhou and Detournay 2014). In the numerical study using an elasto-plastic-damage model, $\overline{\Pi} \backsimeq 0.77$ with $\eta \backsimeq 15$ and $\xi \backsimeq 0.8$ (Voyiadjis and Zhou 2019). The value of $\overline{\Pi}$ in the latter study is within the range of 0.71 ~ 1.3 for typical experimental tests, in which the interface friction angle is approximately equal to the internal friction angle (Almenara and Detournay 1992). The value of $\overline{\Pi}$ in the latter numerical study is near the lower limit of typical experimental data, possibly due to the limitation of the adopted elasto-plastic-damage model as explained next (Voyiadjis and Zhou 2019).

Limitation of the Numerical Study

The result obtained from an elastoplastic model is used as a basis for the one from the elasto-plastic-damage model (Voyiadjis and Zhou 2019). For the latter model with a small enough brittleness number, the limit value of the average contact stress should approach that obtained from the elastoplastic model. However, a gap still exists between the two limit values of the dimensionless average contact stress. Specifically, the limit value of $\overline{\Pi}$ is around 3.7 and 0.9, using the elastoplastic model and the elasto-plastic-damage model, respectively. For the latter model, the limit value of $\overline{\Pi}$ is reached with a large enough η and a small enough ξ, with $\eta \geq 3$ and $\xi \leq 0.3$, as estimated from Figs. 12 and 14. In the threshold case with $\eta = 3$ and $\xi = 0.3$, an approximately uniform stress distribution is observed at the interface. In other cases (e.g., $\eta = 10$ and $\xi = 0.05$) beyond the thresholds, the stress distribution is similar to that of the threshold case.

The gap of the two limit values may result from the limitations of the two constitutive models. The contact stress is overestimated using the elastoplastic model, whereas it is underestimated using the elasto-plastic-damage model (Voyiadjis and Zhou 2019). On the one hand, the hardening behavior under general loading conditions may lead to the overestimation of the contact stress using the elastoplastic model. The elastoplastic model is regenerated from the elasto-plastic-damage model, by using zero values for both the damage indices and hardening moduli under uniaxial loading conditions. It is desirable to set the hardening modulus as zero under general loading conditions for the elasto-plastic-damage model, but the hardening functions are defined using both strength and hardening parameters under uniaxial loading conditions. The elastoplastic model is evaluated first under uniaxial loading and then under biaxial loading using single element tests. The material properties as summarized in Table 1 are adopted for the elastoplastic model, except the damage indices and uniaxial hardening moduli. The axial stress levels off at a yield strength after yielding under uniaxial tension and compression. However, the axial stress continues to increase after initial yielding and then levels off at a larger limit value under biaxial loading conditions. For example, the axial stress increases to a limit value of around 75 MPa after reaching a yield strength of

around 35 MPa under equibiaxial compression. For the initial yield strength under equibiaxial compression, the output value is close to the input value, which is 1.16 times the uniaxial compressive strength based on the yield function with $\alpha = 0.12$ (Lubliner et al. 1989). Undesirable hardening behavior is observed after the initial yielding under general loading conditions. The hardening behavior may be caused by the limitation of the hardening function in Eq. (16), which is defined with yield strengths and hardening moduli under uniaxial loading conditions. On the other hand, the adopted simple damage criteria in the elasto-plastic-damage model may underestimate the limit contact stress. Uniaxial yield strengths are adopted as initial damage thresholds under generally loading conditions for simplicity as seen in Eq. (19) (Wu et al. 2006). The simplified damage criteria lead to a conservative strength envelope under biaxial loading conditions by comparing with the strength envelope obtained from experiments (Kupfer et al. 1969). For example, the output and input values of the yield strength under equibiaxial compression are around 25 MPa and 35 MPa, respectively. The input value of the yield strength is estimated from the yield function with material parameters in Table 1 (Lubliner et al. 1989). The maximum contact stress occurs when damage initiates at the interface, and it is probably underestimated due to the conservative nature of the damage criteria. The dimensionless contact stress generally reaches a maximum value of around 0.9 at the boundary between the elastic and the damage process zones for typical cases. For a case with a large enough η and a small enough ξ, the stress distribution is approximately uniform with a limit value of around 0.9 for the dimensionless contact stress. The drawback of the simplified damage criteria can be overcome by considering strength enhancement factors, such as the compressive confinement and the hydrostatic stress component. The strength enhancement is generally considered by using more complex formulations for both the damage energy release rates $\tau^{\pm}$ and the initial damage thresholds $r_0^{\pm}$ (Tao and Phillips 2005; Taqieddin and Voyiadjis 2009; Voyiadjis and Taqieddin 2009; Wu et al. 2006).

Many simplifications are introduced in the numerical study for the frictional contact on a quasi-brittle rock (Voyiadjis and Zhou 2019). These simplifications include the chosen material length scale, the decoupling of the frictional contact process from the pure cutting process, and the idealized interface properties. A material length scale Λ_c is chosen to define a brittleness number ξ, which is the ratio of a geometrical length scale d to the material length scale Λ_c. The parameter Λ_c is defined based on the compressive fracture energy G_{fc} and the uniaxial compressive strength σ_c, by considering that the dominant stress state is compressive underneath a slider. Other material length scales may also affect the contact stress, and their influence can be possibly investigated by varying the two ratios G_{fc}/G_{ft} and σ_c/σ_t, which are fixed for simplicity. In addition, the frictional contact process is analyzed by decoupling it from the pure cutting processes based on the Detournay and Defourny (1992) phenomenological model. The two processes are characterized by different mechanisms, such as the material removal and material flow. In a pure cutting process, materials are removed in front of a cutter. The material removal mechanism can be modeled using the finite element method with an element deletion algorithm (Zhou and Lin 2013). In a frictional contact process, materials are

generally damaged with negligible removal underneath a wear flat. The element deletion algorithm is thus not adopted in the frictional contact problem (Voyiadjis and Zhou 2019). For the flow of materials in a cutting process, both forward and backward flows occur predominantly depending on the rake angle. When the rake angle is small, the forward flow mechanism dominates. Otherwise, the backward flow mechanism dominates (Rostamsowlat et al. 2018b). For the flow in a frictional contact process, the backward flow dominates. Furthermore, the tool asperity is not considered in the idealized frictional contact problem with a perfect contact. The influence of tool asperity on different properties, such as the contact length and interface friction angle, has been considered in different tool-rock interactions (Borri-Brunetto et al. 2003; Carpinteri and Invernizzi 2005; Rostamsowlat 2018). Few asperities are in contact when the depth of penetration is small, and then the contact length saturates with increasing the depth (Borri-Brunetto et al. 2003). The saturation may be related to the material flow, which fills the cavities with rock parties at the interface (Rostamsowlat 2018). For a rough wear flat, the interface friction angle is approximately identical to the internal friction angle. The interface friction angle can be significantly decreased when a tool is polished with small roughness (Adachi 1996; Rostamsowlat 2018).

Conclusions

The mechanisms of frictional contact on a quasi-brittle rock are investigated through finite element modeling. An elasto-plastic-damage model is developed by Voyiadjis and Zhou (2019) to consider the material length scales of quasi-brittle materials. Based on a model previously developed by Cicekli et al. (2007), several adjustments are made mainly related to the fracture energy of quasi-brittle materials. The elasto-plastic-damage model accounts for both the elastic and plastic energy dissipation, and it adopts a fracture energy-based method to regularize mesh size sensitivity. The degradation of both stiffness and strength is considered using tensile and compressive damage indices under different loading conditions. The elasto-plastic-damage model allows for the consideration of material length scales, and thus it can better characterize the behaviors of quasi-brittle materials by comparing with an elastoplastic model. A UMAT is developed for the constitutive model in ABAQUS. Single element tests have been conducted to check the implemented UMAT under uniaxial tension and compression.

An elastoplastic model is first adopted in the finite element modeling of frictional contact, and then an elasto-plastic-damage model is used (Voyiadjis and Zhou 2019). To validate the finite element model, the rock is treated as an elastic material, and the numerical result of the contact stress is compared with the analytical solution in the elastic regime. The rock is then treated as a rigid-perfectly plastic material, and the numerical result is compared with the analytical solution in the asymptotic rigid plastic regime. For frictional contact on an elastoplastic rock, an elastoplastic parameter η dominates the nature of frictional contact. For frictional contact on a quasi-brittle rock, the mechanism is mainly governed by two

dimensionless parameters η and ξ. The dimensionless elastoplastic parameter η is the ratio of a characteristic elastic contact stress to a yield strength of a material (Johnson 1970). The brittleness number ξ is the ratio of a geometrical length scale d to a material length scale Λ_c (Voyiadjis and Zhou 2019). Inspired by the bearing capacity of a strip footing on a quasi-brittle foundation (Cervera and Chiumenti 2009), the material length scale Λ_c is defined based on the compressive fracture energy and the uniaxial compressive strength (Voyiadjis and Zhou 2019).

Two zones can be identified at the interface between a tool and a quasi-brittle rock: an elastic zone and a damage process zone. In the elastic zone, the contact stress generally increases towards the tip of the slider. In the damage process zone, the compressive damage index generally increases towards the tip, and the contact stress generally decreases. With increasing the dimensionless elastoplastic parameter η, the dimensionless average contact stress $\overline{\Pi}$ generally increases before reaching a limit value. With increasing the brittleness number ξ, the stress $\overline{\Pi}$ generally decreases. In previous numerical and analytical studies, the contact stress is generally overestimated, as material length scales are not considered. In the numerical study using an elasto-plastic-damage model, the gap is reduced to some extent by considering the influence of a material length scale through the brittleness number ξ (Voyiadjis and Zhou 2019). Even though there are still limitations associated with the elasto-plastic-damage model, the numerical results of the average contact stress generally agree with typical experimental results (Almenara and Detournay 1992).

References

R.K. Abu Al-Rub, G.Z. Voyiadjis, Gradient-enhanced coupled plasticity-anisotropic damage model for concrete fracture: Computational aspects and applications. Int. J. Damage Mech. **18**(2), 115–154 (2009)

R.K. Abu Al-Rub, S.-M. Kim, Computational applications of a coupled plasticity-damage constitutive model for simulating plain concrete fracture. Eng. Fract. Mech. **77**(10), 1577–1603 (2010)

J. Adachi, Frictional contact in rock cutting with blunt tools. M.S. thesis, University of Minnesota, Minneapolis, 1996

H. Alehossein, E. Detournay, H. Huang, An analytical model for the indentation of rocks by blunt tools. Rock Mech. Rock. Eng. **33**(4), 267–284 (2000)

R. Almenara, Investigation of the cutting process in sandstones with blunt PDC cutters. Ph.D. thesis, Imperial College, London, 1992

R. Almenara, E. Detournay, Cutting experiments in sandstones with blunt PDC cutters, in *Proceedings of the ISRM Symposium Eurock 92*, Chester, 1992

M. Amri, G. Pelfrene, E. Jahangir, M. Tijani, H. Sellami, Numerical and analytical study of rate effects on drilling forces under bottomhole pressure. Int. J. Rock Mech. Min. Sci. **110**, 189–198 (2018)

M. Borri-Brunetto, A. Carpinteri, S. Invernizzi, Characterization and mechanical modeling of the abrasion properties of sintered tools with embedded hard particles. Wear **254**(7–8), 635–644 (2003)

A. Carpinteri, S. Invernizzi, Numerical analysis of the cutting interaction between indenters acting on disordered materials. Int. J. Fract. **131**(2), 143–154 (2005)

A. Carpinteri, B. Chiaia, S. Invernizzi, Numerical analysis of indentation fracture in quasi-brittle materials. Eng. Fract. Mech. **71**(4–6), 567–577 (2004)

M. Cervera, M. Chiumenti, Size effect and localization in J2 plasticity. Int. J. Solids Struct. **46**(17), 3301–3312 (2009)
M. Cervera, M. Chiumenti, C. Agelet de Saracibar, Softening, localization and stabilization: Capture of discontinuous solutions in J2 plasticity. Int. J. Numer. Anal. Methods Geomech. **28**(5), 373–393 (2004)
J. Challen, P. Oxley, An explanation of the different regimes of friction and wear using asperity deformation models. Wear **53**(2), 229–243 (1979)
U. Cicekli, G.Z. Voyiadjis, R.K. Abu Al-Rub, A plasticity and anisotropic damage model for plain concrete. Int. J. Plast. **23**(10–11), 1874–1900 (2007)
E. Detournay, C. Atkinson, Influence of pore pressure on the drilling response in low-permeability shear-dilatant rocks. Int. J. Rock Mech. Min. Sci. **37**(7), 1091–1101 (2000)
E. Detournay, P. Defourny, A phenomenological model for the drilling action of drag bits. Int. J. Rock Mech. Min. Sci. Geomech. Abstr. **29**(1), 13–23 (1992)
H. Geoffroy, D.N. Minh, J. Bergues, C. Putot, Frictional contact on cutters wear flat and evaluation of drilling parameters of a PDC bit, in *Proceedings of the SPE/ISRM Rock Mechanics in Petroleum Engineering*, Trondheim, 1998
L. Gerbaud, S. Menand, H. Sellami, PDC bits: All comes from the cutter rock interaction, in *Proceedings of the IADC/SPE Drilling Conference*, Miami, 2006
G.M. Gladwell, *Contact Problems in the Classical Theory of Elasticity* (Sijthoff & Noordhoff, Alphen aan den Rijn, 1980)
D. Glowka, Use of single-cutter data in the analysis of PDC bit designs: Part 1–development of a PDC cutting force model. J. Pet. Technol. **41**, 797–799 (1989)
R. Helmons, S. Miedema, M.A. Grima, C. van Rhee, Modeling fluid pressure effects when cutting saturated rock. Eng. Geol. **211**, 50–60 (2016)
H.D. Hibbitt, B.I. Karlsson, P. Sorensen, *ABAQUS/Standard User's Manual* (Hibbitt, Karlsson & Sorensen, Inc., Pawtucket, 2001)
A. Hillerborg, The theoretical basis of a method to determine the fracture energy G_F of concrete. Mater. Struct. **18**(4), 291–296 (1985)
H. Huang, E. Detournay, Intrinsic length scales in tool-rock interaction. Int. J. Geomech. **8**, 39–44 (2008)
H. Huang, E. Detournay, Discrete element modeling of tool-rock interaction II: Rock indentation. Int. J. Numer. Anal. Methods Geomech. **37**(13), 1930–1947 (2013)
H. Huang, B. Lecampion, E. Detournay, Discrete element modeling of tool-rock interaction I: Rock cutting. Int. J. Numer. Anal. Methods Geomech. **37**(13), 1913–1929 (2013)
K.L. Johnson, The correlation of indentation experiments. J. Mech. Phys. Solids **18**(2), 115–126 (1970)
K.L. Johnson, *Contact Mechanics* (Cambridge University Press, London, 1987)
H. Kupfer, H.K. Hilsdorf, H. Rusch, Behavior of concrete under biaxial stresses. ACI J. **66**(8), 656–666 (1969)
J. Labuz, S. Dai, Residual strength and fracture energy from plane-strain testing. J. Geotech. Geoenviron. Eng. **126**(10), 882–889 (2000)
J. Lee, G.L. Fenves, Plastic-damage model for cyclic loading of concrete structures. J. Eng. Mech. **124**(8), 892–900 (1998)
J. Lubliner, J. Oliver, S. Oller, E. Onate, A plastic-damage model for concrete. Int. J. Solids Struct. **25**(3), 299–326 (1989)
J. Marck, E. Detournay, Influence of rotary-steerable-system design on borehole spiraling. SPE J. **21**(1), 293–302 (2016)
Y.D. Murray, *User Manual for LS-DYNA Concrete Material Model 159*, Report No. FHWA-HRT-05-062 (Federal Highway Administration, Mclean, 2007)
A. Naeimipour, J. Rostami, I. Buyuksagis, O. Frough, Estimation of rock strength using scratch test by a miniature disc cutter on rock cores or inside boreholes. Int. J. Rock Mech. Min. Sci. **107**, 9–18 (2018)
J. Oliver, M. Cervera, S. Oller, J. Lubliner, Isotropic damage models and smeared crack analysis of concrete, in *Proceedings of the 2nd International Conference on Computer Aided Analysis and Design of Concrete Structures*, Zell am See, 1990

L. Prandtl, Hauptaufsätze: Über die eindringungsfestigkeit (härte) plastischer baustoffe und die festigkeit von schneiden. ZAMM-Z. Angew. Math. Me. **1**(1), 15–20 (1921)
T. Richard, C. Germay, E. Detournay, A simplified model to explore the root cause of stick–slip vibrations in drilling systems with drag bits. J. Sound Vib. **305**(3), 432–456 (2007)
T. Richard, F. Dagrain, E. Poyol, E. Detournay, Rock strength determination from scratch tests. Eng. Geol. **147**, 91–100 (2012)
I. Rostamsowlat, Effect of cutting tool properties and depth of cut in rock cutting: An experimental study. Rock Mech. Rock. Eng. **51**(6), 1715–1728 (2018)
I. Rostamsowlat, B. Akbari, B. Evans, Analysis of rock cutting process with a blunt PDC cutter under different wear flat inclination angles. J. Pet. Sci. Eng. **171**, 771–783 (2018a)
I. Rostamsowlat, T. Richard, B. Evans, An experimental study of the effect of back rake angle in rock cutting. Int. J. Rock Mech. Min. Sci. **107**, 224–232 (2018b)
I. Rostamsowlat, T. Richard, B. Evans, Experimental investigation on the effect of wear flat inclination on the cutting response of a blunt tool in rock cutting. Acta Geotech. **14**(2), 519–534 (2019)
L. Saucedo, R.C. Yu, R. Gonzalo, Fully-developed FPZ length in quasi-brittle materials. Int. J. Fract. **178**(1–2), 97–112 (2012)
B. Shen, O. Stephansson, Modification of the G-criterion for crack propagation subjected to compression. Eng. Fract. Mech. **47**(2), 177–189 (1994)
G. Shi, G.Z. Voyiadjis, A new free energy for plastic damage analysis. Mech. Res. Commun. **24**(4), 377–383 (1997)
X. Tao, D.V. Phillips, A simplified isotropic damage model for concrete under bi-axial stress states. Cem. Concr. Compos. **27**(6), 716–726 (2005)
Z.N. Taqieddin, G.Z. Voyiadjis, Elastic plastic and damage model for concrete materials: Part II–implementation and application to concrete and reinforced concrete. Int. J. Struct. Chang. Solids **1**(1), 187–209 (2009)
G.Z. Voyiadjis, T.M. Abu-Lebdeh, Plasticity model for concrete using the bounding surface concept. Int. J. Plast. **10**(1), 1–21 (1994)
G.Z. Voyiadjis, Z.N. Taqieddin, Elastic plastic and damage model for concrete materials: Part I–theoretical formulation. Int. J. Struct. Chang. Solids **1**(1), 31–59 (2009)
G.Z. Voyiadjis, Y. Zhou, Numerical modeling of frictional contact between a blunt tool and quasi-brittle rock. Rock Mech. Rock. Eng. **52**(10), 3771–3790 (2019)
G.Z. Voyiadjis, Z.N. Taqieddin, P.I. Kattan, Anisotropic damage–plasticity model for concrete. Int. J. Plast. **24**(10), 1946–1965 (2008)
G.Z. Voyiadjis, Z.N. Taqieddin, P.I. Kattan, Theoretical formulation of a coupled elastic–plastic anisotropic damage model for concrete using the strain energy equivalence concept. Int. J. Damage Mech. **18**(7), 603–638 (2009)
J.Y. Wu, J. Li, R. Faria, An energy release rate-based plastic-damage model for concrete. Int. J. Solids Struct. **43**(3–4), 583–612 (2006)
J. Zhang, J. Li, Elastoplastic damage model for concrete based on consistent free energy potential. Sci. China Technol. Sci. **57**(11), 2278–2286 (2014)
Y. Zhou, The applicability of correspondence rule with inclined load. Rock Mech. Rock. Eng. **50**(1), 233–240 (2017a)
Y. Zhou, Misinterpretation of friction as fracture in shallow scratch tests with classical and universal size effect laws. Eng. Fract. Mech. **184**, 14–21 (2017b)
Y. Zhou, E. Detournay, Analysis of the contact forces on a blunt PDC bit, in *Proceedings of the 48th US Rock Mechanics/Geomechanics Symposium*, Minneapolis, 2014
Y. Zhou, E. Detournay, Elastoplastic model of a blunt rigid tool sliding on rock. Unpublished work (2019)
Y. Zhou, J.-S. Lin, On the critical failure mode transition depth for rock cutting. Int. J. Rock Mech. Min. Sci. **62**, 131–137 (2013)
Y. Zhou, W. Zhang, I. Gamwo, J.-S. Lin, Mechanical specific energy versus depth of cut in rock cutting and drilling. Int. J. Rock Mech. Min. Sci. **100**, 287–297 (2017)

Part VI

Micromechanical Damage and Healing for Concrete

Stochastic Micromechanics-Based Probabilistic Damage and Repair Models for Cementitious Composites

33

Q. Chen, Jiann-Wen Woody Ju, H. H. Zhu, and Z. G. Yan

Contents

Introduction 896
Micromechanical Modeling for the Probabilistic Damage Evolution for Cementitious Composites 897
Basis of Micromechanical Damage Model 897
The RVE Representations of Microcracked Cementitious Composite 898
The Cementitious Composite's Undamaged Compliance Tensor 899
The Equivalent Isotropic Matrix 899
The Damage-Induced Compliance Tensor of Cementitious Material 900
Discussions on the Probabilistic Behavior of the Solid Phase 905
The Repaired Concrete's Stochastic Micromechanical Model 909
The Repaired Concrete's Deterministic Micromechanical Models 909
Stochastic Descriptions for the Microstructures of the Repaired Concrete 911
Multilevel Predictions for the Repaired Concrete's Properties 914
The Composite's Statistical Behavior 918
Numerical Examples 919
Conclusions 926
References 930

Q. Chen (✉)
Key Laboratory of Advanced Civil Engineering Materials, Ministry of Education, Tongji University, Shanghai, China

School of Materials Science and Engineering, Tongji University, Shanghai, China

J.-W. W. Ju
Department of Civil and Environmental Engineering, University of California, Los Angeles, CA, USA

State Key Laboratory for Disaster Reduction in Civil Engineering, Tongji University, Shanghai, China
e-mail: juj@ucla.edu

H. H. Zhu · Z. G. Yan
Department of Geotechnical Engineering, State Key Laboratory for Disaster Reduction in Civil Engineering, Tongji University, Shanghai, China
e-mail: zhuhehua@tongji.edu.cn; yanzguo@tongji.edu.cn

© Springer Nature Switzerland AG 2022

G. Z. Voyiadjis (ed.), *Handbook of Damage Mechanics*,
https://doi.org/10.1007/978-3-030-60242-0_50

Abstract

There are typically some initial damage (such as the micro-voids or microcracks) in the cementitious composites. Under the external loading, the damage may develop systematically. In this chapter, a micromechanical framework is presented to model the damage evolution for cementitious composites. A transversely isotropic solid matrix is considered herein. Meanwhile, the microcrack-induced compliance tensors are attained using microcrack opening displacements. Furthermore, the probabilistic behavior of the matrix phase is investigated, which shed lights to the probabilistic damage evolution of cementitious composites. To improve the performance of the damaged cementitious materials, a new repair approach named electrochemical deposition method (EDM) is proposed, which is promising for the aqueous situations. To reveal the repair (healing) mechanism for the damaged cementitious composites at the microscale level, a stochastic micromechanical framework is presented for the damaged concrete repaired by the EDM. The evolution of the deposition products is represented by the nonhomogeneous random process. The properties of the repaired concrete are attained by the multilevel homogenization scheme. The probability density functions for the moduli of the repaired concrete are reached by an efficient stochastic simulation program. Numerical examples are employed to verify the proposed stochastic micromechanics-based probabilistic damage and repair (healing) models for cementitious composites.

Keywords

Stochastic micromechanics · Damage · Healing · Cementitious material

Introduction

There are many different constituents or phases in the engineering materials. For each phase, it has the specific properties, such as the elastic moduli, yield strength, and thermal conductivity. Meanwhile, the orientations of each phase may be different. It is important for many engineering materials, such as porous and cracked media, polymer-blended soils, rocks and concrete, etc., to obtain the effective properties. The material's effective properties can be determined by their microstructures, which include the constituents' elastic properties, the volume fraction, and the spatial distribution of the components (Ju and Chen 1994a, b). Meanwhile, since the predetermined microstructures are hard to be detailed, the inherent randomness can be observed in the material's microstructures even with the same manufacturing process (Chen et al. 2015; Li et al. 2020; Zhu et al. 2015). These inherent stochastic behaviors of composites cannot be incorporated by the deterministic micromechanics-based approach (Chen 2014).

In the past, the stochastic frameworks had been developed by different researchers to overcome the shortcomings of the deterministic ones (Ferrante and Graham-Brady 2005; Rahman 2009; Ganapathysubramanian and Zabaras 2009).

They assume that the uncertain microstructures are the reasons for the material's macroscopic stochastic behavior. To describe the probabilistic behavior of the functionally graded materials, some stochastic micromechanics-based frameworks were presented in the previous works (Chakraborty and Rahman 2009; Rahman and Chakraborty 2007; Xu and Graham-Brady 2005). The authors presented the stochastic micromechanical model for the multiphase composite, the fiber-reinforced concrete, and repaired concrete (Chen et al. 2018a, b, 2019a, b; Jiang et al. 2019). The random vectors, random process, or random field is employed to describe the descriptors of the material microstructures. The deterministic micromechanical models are employed to set up the quantitative relations for the microstructures and macroscopic properties. The computationally efficient stochastic simulation framework is employed to reach the material probabilistic behavior (Chen et al. 2018a, b, 2019a, b; Jiang et al. 2019).

As one of the engineering materials, the cementitious composite is widely used in many areas. In this chapter, on the one hand, a micromechanical framework is presented to model the damage evolution for cementitious composites. The material is represented as multiphase composite, including the transversely isotropic solid matrix, pores, and cracks. Meanwhile, both the stable and unstable microcracks are considered to reach to damage-induced compliance tensor. Furthermore, discussion on the probabilistic behavior of the solid matrix is provided to gain better understanding of the probabilistic damage evolution of the cementitious composite. On the other hand, a stochastic micromechanical framework is presented for the damaged concrete repaired by the electrochemical deposition method (EDM), which is a new approach for the damage healing of cementitious composite in the aqueous situations. The repaired damaged concrete is represented by the intrinsic concrete, the micropores, the microcracks, the water, and the deposition products. The nonhomogeneous random process is employed to describe the evolution of the deposition products. The multilevel homogenization scheme is adopted to attain the properties of the repaired concrete. A dimension decomposition method-based efficient stochastic simulation program is utilized to obtain the probability density functions for the moduli of the repaired concrete. Moreover, the unsaturated states and imperfect bonding are considered by extending the stochastic micromechanical model of the saturated repaired concrete. The presented stochastic micromechanics-based framework is verified by the experimental data and the results of the existing models.

Micromechanical Modeling for the Probabilistic Damage Evolution for Cementitious Composites

Basis of Micromechanical Damage Model

Many researches had been conducted on the continuum damage models for the brittle materials (Fanella and Krajcinovic 1988; Sumarac and Krajcinovic 1987; Ju 1989, 1991; Ju and Lee 1991). The micromechanical damage model can be developed by following Ju and Lee (1991) for the cementitious composite herein. In their work, the fourth-order elastic damage compliance tensor $\mathbf{S}$ can be represented by the

fourth-order anisotropic damage tensor $\mathbf{D}$. Let's define $\overline{\boldsymbol{\sigma}}$ and $\overline{\boldsymbol{\varepsilon}}$, respectively, as the volume average stress tensor and the volume average strain tensor. They can be related by the volume average compliance tensor $\overline{\mathbf{S}}$. When the inhomogeneous effective continuum medium is considered, the relationship can be expressed in Eq. (1) in the context of the homogenization.

$$\overline{\boldsymbol{\varepsilon}} = \overline{\mathbf{S}} : \overline{\boldsymbol{\sigma}} \tag{1}$$

Meanwhile, let $\overline{\boldsymbol{\varepsilon}}^{e}$ denote the elastic strains and $\overline{\boldsymbol{\varepsilon}}^{*}$ signify the damage-induced strains. Similarly, we define the undamaged elastic compliance as $\overline{\mathbf{S}}^{0}$ and define the damage-induced compliance as $\overline{\mathbf{S}}^{*}$. With these definitions, the overall compliance tensor and the stain tensor can be expressed as:

$$\overline{\boldsymbol{\varepsilon}} = \overline{\boldsymbol{\varepsilon}}^{e} + \overline{\boldsymbol{\varepsilon}}^{*}; \qquad \overline{\mathbf{S}} = \overline{\mathbf{S}}^{0} + \overline{\mathbf{S}}^{*} \tag{2}$$

It is noted that the two tensors $\overline{\boldsymbol{\varepsilon}}$ and $\overline{\mathbf{S}}$ are assumed to be amenable to an additive decomposition. It also implies that the residual strain is supposed to be negligible at zero stress.

The undamaged elastic tensors can be given from the experimental data or obtained by a micromechanical homogenization approach. Meanwhile, the damage-induced compliance tensor is reached by utilizing the microcrack opening displacement in the isotropic matrix according to Ju and Lee (1991). When the matrix phase is transversely isotropic, the equivalent isotropic matrix can be reached by the Voigt-Reuss-Hill average for simplifications (Mousavi et al. 2016).

The RVE Representations of Microcracked Cementitious Composite

By observing the cementitious material from the nanoscale to the macroscopic scale, many different constituents can be found for the composite at each specific length scale. Since we focus on investigating the microcrack or damage evolution, the other components, except for micropores and microcracks, of cementitious material are not considered for simplifications. Therefore, the cementitious material is viewed as a three-phase composite, which is made by the solid matrix, the micropores, and the microcracks. The micromechanical model is as Fig. 1 shows, where the solid matrix can be named as the "intrinsic concrete" composed by the aggregate, the cement paste, and the interface between them. The inclusion phases include the (micro-) pores and (micro-)cracks. To disclose the damage mechanism, the decomposition procedures are employed. According to the precious works (Xie et al. 2012; Yan et al. 2013; Zhu et al. 2014), the (micro-)pores and the solid phase can be homogenized as the equivalent matrix firstly. Secondly, the evolution of the (micro-)cracks is investigated in the equivalent matrix. The reason for this decomposition process is mainly due to the fact that the inelastic behavior induced by microcracking is much more dominant than those of micropores (Ju and Lee 1991; Xie et al. 2012). Meanwhile, we assume the pores are spherical and the microcracks are coin-shaped (Yan et al. 2013; Zhu et al. 2014).

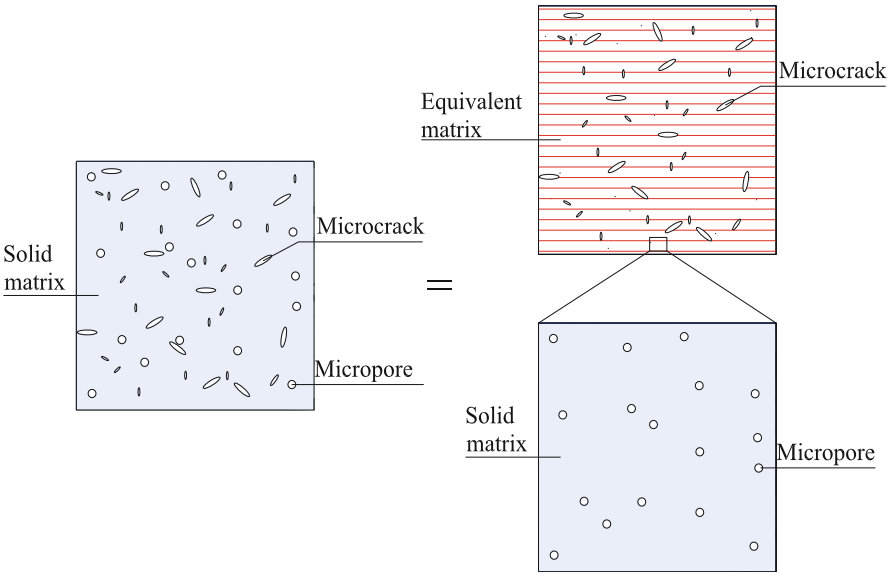

Fig. 1 The RVE decomposition for the cementitious composite

The Cementitious Composite's Undamaged Compliance Tensor

The porous cementitious material's effective properties are dependent on those of the solid phase and the pores. Let's define V_{po}, c_{po}, and $\mathbf{P}^{po}$ as the micropores' volume, volume fraction, and the Hill polarization tensor and V_{sm}, c_{sm}, and $\mathbf{P}^{sm}$ as the solid matrix's volume, volume fraction, and the Hill polarization tensor. Meanwhile, suppose that the solid matrix (or pore)'s effective stiffness tensor is denoted by $\mathbf{C}_{sm}$ (or $\mathbf{C}_{po}$) and the pores-weakened solid matrix's effective stiffness tensor is represented by $\mathbf{C}_{pm}$, which can be arrived as according to Berryman (1980) and Norris (1985):

$$c_{po}\left(\left(\mathbf{C}_{po}-\mathbf{C}_{pm}\right)^{-1}+\mathbf{P}^{po}\right)^{-1}+c_{sm}\left(\left(\mathbf{C}_{sm}-\mathbf{C}_{pm}\right)^{-1}+\mathbf{P}^{sm}\right)^{-1}=0 \tag{3}$$

$$c_{po}=\frac{V_{po}}{V_{sm}+V_{po}} \qquad c_{sm}=\frac{V_{sm}}{V_{sm}+V_{po}} \tag{4}$$

$$\overline{\mathbf{S}}_0=\left(\mathbf{C}_{pm}\right)^{-1} \tag{5}$$

The Equivalent Isotropic Matrix

The matrix of the cementitious composite is not always isotropic. It is complex to obtain the crack-induced compliance tensor in a porous matrix, which is transversely isotropic (Sarout and Guéguen, 2008a, b). Instead of performing the difficult calculation directly, the equivalent isotropic matrix is employed as a simplified

approach for the transversely isotropic one. Suppose $C_{ij}^{pm}(i, j = 1, 2, 3, 4, 5, 6)$ as the stiffness tensors' components for the pores-weakened solid matrix. The transversely isotropic pores-weakened solid matrix can be replaced the equivalent isotropic matrix, whose properties can be characterized with Eqs. (6, 7, 8, 9, 10, and 11) according to Ougier-Simonin et al. (2009):

$$K_{VRH} = \frac{1}{2}\left(K_V^{pm} + K_R^{pm}\right); \quad G_{VRH} = \frac{1}{2}\left(G_V^{pm} + G_R^{pm}\right) \tag{6}$$

$$K_V^{pm} = \frac{1}{9}\left(2C_{11}^{pm} + C_{33}^{pm}\right) + \frac{2}{9}\left(C_{12}^{pm} + 2C_{13}^{pm}\right) \tag{7}$$

$$G_V^{pm} = \frac{1}{15}\left(2C_{11}^{pm} + C_{33}^{pm}\right) - \frac{1}{15}\left(C_{12}^{pm} + 2C_{13}^{pm}\right) + \frac{1}{5}\left(2C_{44}^{pm} + C_{66}^{pm}\right) \tag{8}$$

$$K_R^{pm} = \frac{1}{A\left(C_{11}^{pm} + C_{12}^{pm} + 2C_{33}^{pm} - 4C_{13}^{pm}\right)} \tag{9}$$

$$G_R^{pm} = \frac{15}{2A\left(2\left(C_{11}^{pm} + C_{12}^{pm}\right) + 4C_{13}^{pm} + C_{33}^{pm}\right) + \frac{1}{6}\left(1/C_{44}^{pm} + 1/C_{66}^{pm}\right)} \tag{10}$$

$$A = \frac{1}{C_{33}^{pm}\left(C_{11}^{pm} + C_{12}^{pm}\right) - 2\left(C_{13}^{pm}\right)^2} \tag{11}$$

where K_{VRH} is the equivalent isotropic matrix's bulk modulus and G_{VRH} is the equivalent isotropic matrix's shear modulus. Furthermore, let's define E_{VRH} (or ν_{VRH}) as Young's modulus (or Poisson's ratio) for the equivalent isotropic matrix. They can be reached with Eqs. (12)–(13) on the basis of the relationships between the elastic constants:

$$E_{VRH} = \frac{9K_{VRH}G_{VRH}}{3K_{VRH} + G_{VRH}} \tag{12}$$

$$\nu_{VRH} = \frac{1}{2}\left(1 - \frac{1}{\frac{1}{3} + \frac{K_{VRH}}{G_{VRH}}}\right) \tag{13}$$

The Damage-Induced Compliance Tensor of Cementitious Material

Inelastic Compliance Tensor Induced by the Open Microcrack

When the tensile loading is considered, the effects are negligible for the microcrack closure, frictional sliding, and kinking (Ju and Lee 1991; Yu and Feng 1995). Therefore, only the effects of the opening microcracks are incorporated herein.

Let's suppose an equivalent isotropic medium is loaded at the far field uniformly. Meanwhile, there is a single penny-shaped microcrack in the medium. The radius is

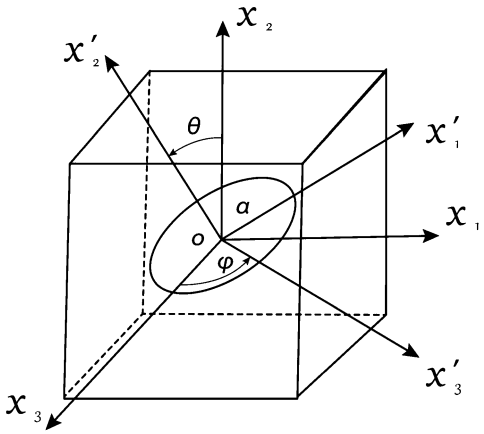

Fig. 2 The location of the microcrack

a for the microcrack, which can be named as the α *th* microcrack. From Fig. 2, to determine the location of the microcrack, both the global and local coordinate systems are employed. (θ, ϕ) can be adopted to express the microcrack's orientation in the global coordinate system ($Ox_1x_2x_3$). As to the local coordinate system ($Ox'_1x'_2x'_3$), the x'_2 axis is vertical to the microcrack, and the x'_3 axis is in the plane determined by the x_1 axis and the x_3 axis.

Define b_i as the component of the microcrack's displacement discontinuity vector and $\mathbf{B}'$ as the crack opening displacement tensor. According to Budiansky and O'Connell (1976), b_i can be expressed as:

$$b_i = \left(a^2 - r^2\right)^{\frac{1}{2}} B'_{lj}\sigma'_{2j}g'_{li} \tag{14}$$

with

$$\sigma'_{2j} = g'_{2k}g'_{jl}\sigma_{kl} \tag{15}$$

$$g'_{ij} = g^T_{ij} = \begin{bmatrix} \cos\theta\cos\phi & \sin\theta & -\cos\theta\sin\phi \\ -\sin\theta\cos\phi & \cos\theta & \sin\theta\sin\phi \\ \sin\phi & 0 & \cos\phi \end{bmatrix} \tag{16}$$

The crack opening displacement tensor $\mathbf{B}'$, which is determined by the microcrack-weakened solids' compliance, is assumed herein to be decided by the isotropic elastic matrix's compliances. Therefore, when the open microcrack is considered, this tensor's nonvanishing components are (Yu and Feng 1995):

$$B'_{11} = B'_{33} = \frac{16\left(1-\nu^2_{VRH}\right)}{\left(2-\nu^2_{VRH}\right)\pi E_{VRH}}, \quad B'_{22} = \frac{8\left(1-\nu^2_{VRH}\right)}{\pi E_{VRH}} \tag{17}$$

Furthermore, let $\overline{\varepsilon}_{ij}^{*(\alpha)}$ represent the αth microcrack-induced strains and $\overline{S}_{ijkl}^{*(a)}$ denote the αth microcrack-induced compliances. With the opening displacements, $\overline{\varepsilon}_{ij}^{*(\alpha)}$ and $\overline{S}_{ijkl}^{*(a)}$ can be reached using Eq. (18):

$$\overline{\varepsilon}_{ij}^{*(\alpha)} = \overline{S}_{ijkl}^{*(a)} \ \overline{\sigma}_{kl} = \frac{1}{V}\int_{S_\alpha} \frac{1}{2}\left(b_i n_j + b_j n_i\right)^{(\alpha)} dS \tag{18}$$

where n_i are the components of the microcrack's normal vector and $\overline{\sigma}_{ij}$ signifies the averaged far field stresses.

By substituting Eqs. (14)–(15) into Eq. (18), the microcrack-induced compliances can be obtained with Eq. (19) (Yu and Feng 1995):

$$\overline{S}_{ijkl}^{*(a)} = \frac{\pi a^3}{3V} B'_{mn} g'_{2k} g'_{nl}\left(g'_{mi} n_j + g'_{mj} n_i\right) \tag{19}$$

Overall Compliance Tensor Induced by Microcracks

Suppose the microcracks' size and orientations can be described by the random variables, which are characterized with a probability density function $p(a, \phi, \theta)$. The normalization condition should be satisfied for $p(a, \phi, \theta)$ as:

$$\int_{a_{\min}}^{a_{\max}} \int_0^{\frac{\pi}{2}} \int_0^{2\pi} p(a,\phi,\theta) \sin\phi d\phi d\theta da = 1 \tag{20}$$

With $p(a, \phi, \theta)$, the overall compliance tensor induced by microcracks can be reached through the integration procedures over the RVE domain. Particularly, for the uniformly distributed microcracks, the stable microcrack-induced inelastic compliance can be reached with Eqs. (21)–(22):

$$\overline{\mathbf{S}}_{ijkl}^{*cs} = \sum_{k=1}^{N} \overline{\mathbf{S}}_{ijkl}^{*(a)} = \int_0^{\frac{\pi}{2}} \int_0^{2\pi} N_c p(\theta,\phi) \frac{\pi a^3}{3V} B'_{mn} g'_{2k} g'_{nl}\left(g'_{mi} n_j + g'_{mj} n_i\right) \sin\theta d\theta d\phi \tag{21}$$

with

$$p(\phi,\theta) = \frac{1}{2\pi} \tag{22}$$

where N_c is the total number of microcracks in the RVE. It is noted the microcracks' initial radius is supposed to be the same with each other.

The Compliance Tensor Caused by the Unstable Microcracks

Some of the stable microcracks will become unstable, i.e., the microcrack's size will increase, when the tensile loading increases. The damage-induced compliance can be divided into two parts. The one is caused by the stable microcracks, and the other is due to the evolutionary microcracks.

When the microcrack-induced anisotropy and their interactions are considered, a unified microcrack growth's criterion is hard to be provided. According to previous

works, the linear fracture mechanics can be utilized to decide the microcrack evolution. Let's define the mode-I intensity factor with K_I' and the mode-II intensity factor with K_{II}'. Meanwhile, define their critical values with K_{IC} and K_{IIC}. When a penny-shaped crack is considered, the mixed-mode fracture criterion from Ju and Lee (1991) can be adopted as below:

$$\left(\frac{K_I'}{K_{IC}}\right)^2 + \left(\frac{K_{II}'}{K_{IIC}}\right)^2 = 1 \tag{23}$$

A microcrack will propagate when Eq. (23) is satisfied. Considering that the higher energy barriers will stop the microcrack's evolution (e.g., the grain boundaries), its radius instantaneously turns to the final characteristic value a_u, for the propagating microcracks, from their initial statistically averaged value a_0. It should be mentioned that the microcrack propagation herein adopts two assumptions. Firstly, the instantaneous process is utilized for the microcrack propagation (Krajcinovic and Fanella, 1986; Ju and Lee 1991). Secondly, the microcrack propagates with a self-similar fashion. It implies that the microcracks after growth are still penny-shaped (Ju and Lee 1991; Yu and Feng 1995). According to Ju and Lee (1991) and Yu and Feng (1995), K_I' and K_{II}' can be calculated with Eqs. (24)–(25) when the uniaxial tension loading q is provided.

$$K_I' = 2\sqrt{\frac{a}{\pi}}\overline{\tau}_3', \quad K_{II}' = \frac{4}{2-\nu}\sqrt{\frac{a}{\pi}}\overline{\tau}_4' \tag{24}$$

$$\overline{\tau}_3' = q(\cos\theta)^2, \quad \overline{\tau}_4' = q\cos\theta\sin\theta \tag{25}$$

Equation (26) can be arrived by substituting Eqs. (24)–(25) into (23) as below:

$$\left(\frac{2\sqrt{\frac{a}{\pi}}q(\cos\theta)^2}{K_{IC}}\right)^2 + \left(\frac{\frac{4}{2-\nu}\sqrt{\frac{a}{\pi}}q\cos\theta\sin\theta}{K_{IIC}}\right)^2 = 1 \tag{26}$$

By solving Eq. (26), the critical angle θ_{cr} can be reached to divide the stable and unstable domain of microcracks as:

$$(\tan\theta_{cr})^2 = \frac{-B - \sqrt{B^2 - 4AC}}{2A} \tag{27}$$

with

$$A = -\frac{\pi}{4a}K_{IIC}^2 \tag{28}$$

$$B = -\frac{\pi}{2a}K_{IIC}^2 + \left(\frac{2q}{2-\nu}\right)^2 \tag{29}$$

$$C = -\frac{\pi}{4a}K_{IIC}^2 + \left(\frac{qK_{IIC}}{K_{IC}}\right)^2 \tag{30}$$

With the obtained θ_{cr}, the domain $\Omega(\theta, \phi) = \{0 \le \theta \le \theta_r, 0 \le \phi \le 2\pi\}$ signifies the propagating area for the microcracks. Therefore, the growing microcrack-induced compliance tensor can be achieved using Eq. (31):

$$\overline{\mathbf{S}}_{ijkl}^{*cu} = N\int_0^{\theta_{cr}}\int_0^{2\pi} p(\phi,\theta)\overline{\mathbf{S}}_{ijkl}^{*(a_u)} \sin\theta d\phi d\theta \tag{31}$$

Furthermore, the microcrack-induced compliance tensor can be calculated by adding those caused by the stable ones and those caused by the unstable ones together as Eq. (32):

$$\begin{aligned}\overline{\mathbf{S}}_{ijkl}^{*c} &= \overline{\mathbf{S}}_{ijkl}^{*cs} + \overline{\mathbf{S}}_{ijkl}^{*cu} \\ &= N\left[\int_{\theta_r}^{\frac{\pi}{2}}\int_0^{2\pi} p(\phi,\theta)\overline{\mathbf{S}}_{ijkl}^{*(a_0)} \sin\theta d\phi d\theta + \int_0^{\theta_r}\int_0^{2\pi} p(\phi,\theta)\overline{\mathbf{S}}_{ijkl}^{*(a_u)} \sin\theta d\phi d\theta\right]\end{aligned} \tag{32}$$

With the above, the damage evolution of cementitious composite can be reached based on its microstructures. Figure 3 shows the mechanical behavior obtained experimentally and using the presented model. The experimental data is from Gopalaratnam and Shah (1985) for the uniaxial tensile loading process. The stress-strain curve is arrived by taking compliances caused by the stable and unstable microcracks into considerations in this example. It can be found that the two results are close to each other, which implies that the presented model is

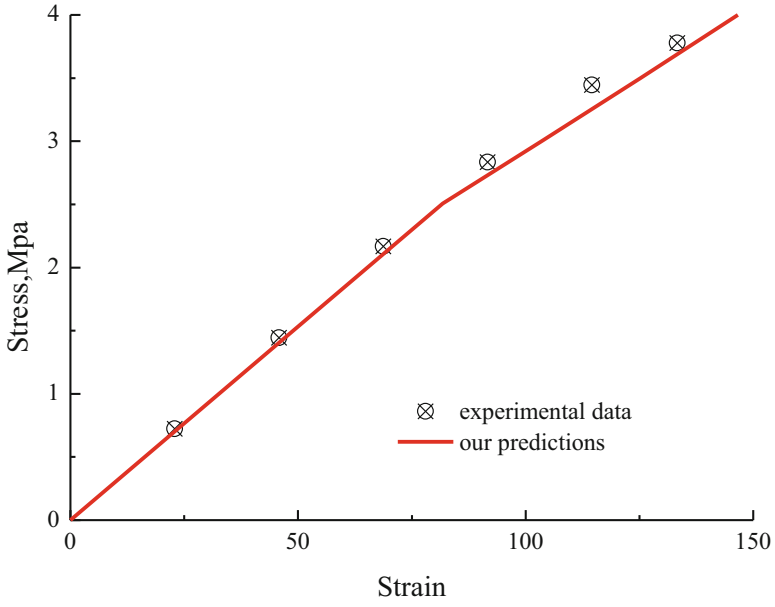

Fig. 3 The mechanical behavior obtained experimentally and analytically

capable of describing the damage evolution of the cementitious material under tensile loading.

Discussions on the Probabilistic Behavior of the Solid Phase

The solid phase mentioned above, named as the intrinsic concrete, can be seen as the three-phase composite made up of the aggregate, the bulk cement paste, and the ITZ between them (Yan et al. 2013). The properties of the intrinsic concrete may fluctuate when different specimens are considered. To investigate the probabilistic behavior, the stochastic micromechanical model can be adopted (Chen et al. 2018a).

Through the deterministic micromechanical model, the effective properties of the intrinsic concrete can be reached using the two-level homogenization (Yan et al. 2013). Define the volume fraction of bulk cement phase as c_{bk} and that of the ITZ as c_{itz}. Meanwhile, the thickness of the ITZ is represented by t. According to the "void exclusion probability," c_{bk} and c_{itz} can be calculated with Eqs. (33, 34, 35, 36, 37, 38, 39, 40, and 41) (Zheng et al. 2009; Dridi 2013; Garboczi and Bentz 1997; Lu and Torquato 1992):

$$c_{\mathrm{itz}} = 1 - c_{\mathrm{ag}} - c_{\mathrm{bk}} \tag{33}$$

$$c_{\mathrm{bk}} = \left(1 - c_{\mathrm{ag}}\right) \exp\left(-\pi\rho\left(\alpha t + \beta t^2 + \gamma t^3\right)\right) \tag{34}$$

$$\alpha = \frac{4\overline{R^2}}{1 - c_{\mathrm{ag}}} \tag{35}$$

$$\beta = \frac{4\overline{R}}{1 - c_{\mathrm{ag}}} + \frac{12\varepsilon_2\overline{R^2}}{\left(1 - c_{\mathrm{ag}}\right)^2} \tag{36}$$

$$\gamma = \frac{4}{3\left(1 - c_{\mathrm{ag}}\right)} + \frac{8\varepsilon_2\overline{R}}{\left(1 - c_{\mathrm{ag}}\right)^2} + \frac{16A\varepsilon_2^2\overline{R^2}}{3\left(1 - c_{\mathrm{ag}}\right)^3} \quad (A = 0\ \textit{for}\ \text{spherical aggregate}) \tag{37}$$

$$\varepsilon_2 = \frac{2\pi\rho\overline{R^2}}{3} \tag{38}$$

$$\rho = \sum_{i=1}^{Nu} \frac{9c_{\mathrm{ag}}c_i}{4\pi\left(r_{i+1}^3 - r_i^3\right)} \ln\left(\frac{r_{i+1}}{r_i}\right) \tag{39}$$

$$\overline{R} = \sum_{i=1}^{Nu} \frac{9c_{\mathrm{ag}}c_i}{4\pi\rho\left(r_{i+1}^3 - r_i^3\right)} \left(r_{i+1} - r_i\right) \tag{40}$$

$$\overline{R^2} = \sum_{i=1}^{Nu} \frac{9c_{\mathrm{ag}}c_i}{4\pi\rho\left(r_{i+1}^3 - r_i^3\right)} \frac{1}{2}\left(r_{i+1}^2 - r_i^2\right) \tag{41}$$

where c_{ag} denotes the aggregate's volume fraction; c_i represents the aggregates' volume fraction with radius between r_i and r_{i+1}; Nu signifies the number of zones

characterizing the aggregate size distribution; $\overline{R}$ is the mean aggregate radius; $\overline{R}^2$ is the mean square aggregate radius; and α, β, and γ are parameters dependent on the aggregates' distribution.

By adopting the random vectors, the stochastic descriptions for the microstructures can be provided as below. Define E_{ag}, ν_{ag} (or E_{it}, ν_{it} or E_{bk}, ν_{bk}) as the aggregate (or the ITZ or the bulk cement paste)'s elastic modulus and Poisson's ratio, respectively. Meanwhile, according to Eqs. (33, 34, 35, 36, 37, 38, 39, 40, and 41), the ITZ's volume fraction and the bulk cement paste's volume fraction can be arrived with the ITZ thickness and the aggregate distributions. Therefore, the random vector $\{E_{ag}, \nu_{ag}, E_{it}, \nu_{it}, E_{bk}, \nu_{bk}, t, c_{ag}, c_1, \cdots c_i \cdots c_M\}^T \in \mathbf{R}^{M+8}$ characterizes the uncertainties for the solid matrix mentioned.

With the stochastic descriptions, to characterize the solid matrix's properties turns to a problem of obtaining the probabilistic behavior of a random function with multivariate. Therefore, the properties' unbiased probability density function (PDF) can be represented by the exponential polynomial according to the work of Er (1998). Suppose $f(x)$ is the probability density function of a random variable. It can be approximated by the exponential polynomial as Eq. (42) according to Er (1998):

$$f(x) = \exp\left[\mathrm{a}_0 + \sum_{i=1}^{N} a_i x^i\right] \tag{42}$$

where a_i, $i = 0, 1, 2 \ldots n$ are the parameters dependent on the moments of the random variable. Let m_i, $i = 1, 2 \ldots n$ be the random variable's different order moments. They can be reached with Eqs. (43)–(44):

$$\begin{bmatrix} 1 & m_1 & \cdots & m_{n-1} \\ m_1 & m_2 & \cdots & m_n \\ \vdots & \vdots & \ddots & \vdots \\ m_{n-1} & m_n & \cdots & m_{2n-2} \end{bmatrix} \begin{bmatrix} a_1 \\ 2a_2 \\ \vdots \\ na_n \end{bmatrix} = \begin{bmatrix} 0 \\ -1 \\ -2m_1 \\ \vdots \\ -(n-1)m_{n-2} \end{bmatrix} \tag{43}$$

$$a_0 = \ln\left(\frac{1}{\int_{-\infty}^{+\infty} e^{a_1 x + a_2 x^2 + \cdots a_n x^n} dx}\right) \tag{44}$$

To avoid the singularity of Eq. (43) (Er 1998), the normalization procedures are employed. Instead of utilizing the properties' moments directly, the central moments are employed to obtain more stable results, i.e., the i-order central moments are adopted to obtain the normalized properties' PDFs. Suppose $\overline{f}(\overline{x})$ represents the normalized properties' PDF. Meanwhile, define $\overline{a}_i, i = 0, 1, 2 \ldots n$ as the coefficients for the normalized properties' PDF and $\overline{m}_i$, $i = 1, 2 \ldots n$ as the normalized properties' different order moments. $\overline{a}_i, i = 0, 1, 2 \ldots n$ can be arrived by solving Eqs. (45)–(46):

$$\begin{bmatrix} 1 & 0 & \cdots & \overline{m}_{n-1} \\ 0 & 1 & \cdots & \overline{m}_n \\ \vdots & \vdots & \ddots & \vdots \\ \overline{m}_{n-1} & \overline{m}_n & \cdots & \overline{m}_{2(n-1)} \end{bmatrix} \begin{Bmatrix} \overline{a}_1 \\ 2\overline{a}_2 \\ \vdots \\ n\overline{a}_n \end{Bmatrix} = \begin{Bmatrix} 0 \\ -1 \\ \vdots \\ -(n-1)\overline{m}_{n-2} \end{Bmatrix} \tag{45}$$

$$\overline{a}_0 = \ln\left(\frac{1}{\int_{-\infty}^{+\infty} e^{\overline{a}_1 x + \overline{a}_2 x^2 + \cdots \overline{a}_n x^n} dx}\right) \tag{46}$$

Define $f_K(x)$ as the effective bulk modulus' PDF, $f_\mu(x)$ as the effective shear modulus' PDF, and $f_E(x)$ as the effective Young's modulus' PDF. They can be reached based on $\overline{f}(\overline{x})$ as follows:

$$f_K(x) = \frac{1}{sd(K^*)}\overline{f}\left(\frac{x - mean(K^*)}{sd(K^*)}\right) \tag{47}$$

$$f_\mu(x) = \frac{1}{sd(\mu^*)}\overline{f}\left(\frac{x - mean(\mu^*)}{sd(\mu^*)}\right) \tag{48}$$

$$f_E(x) = \frac{1}{sd(E^*)}\overline{f}\left(\frac{x - mean(E^*)}{sd(E^*)}\right) \tag{49}$$

With the mentioned framework, the probabilistic behavior of the intrinsic concrete can be obtained. Figure 4 shows the PDFs of the solid matrix with different types of aggregate. It can be observed that the solid matrix' properties increase statistically with that of the aggregate properties' mean value. Meanwhile, because of the aggregate properties' randomness, some samples arrived using the type 1 aggregate (which has the lowest mean of Young's modulus) are greater than those attained using type 3 aggregate (which has the greatest mean value of Young's modulus).

Figure 5 displays the PDFs of the solid matrix with the different ITZ thicknesses. It can be reached that the solid matrix' properties increase statistically with the decrease of the ITZ thicknesses. The results are reasonable because when the ITZ thickness increases, the ITZ volume fraction will increase, whose properties are lower than those of bulk cement paste. Meanwhile, because of the randomness, some samples arrived using the type 2 ITZ (which has the greatest thickness) are greater than those attained using type 1 ITZ (which has the smallest thickness).

From the above, it can be concluded that the damage evolution of the cementitious materials depends on the external stress, the material's properties, and the microcrack distributions. Due to the randomness of the microstructures, the material's properties may fluctuate, which will lead to the probabilistic behavior of the damage evolutions. The quantitative relation between the random microstructure and the probabilistic damage evolution can be studied in the future work.

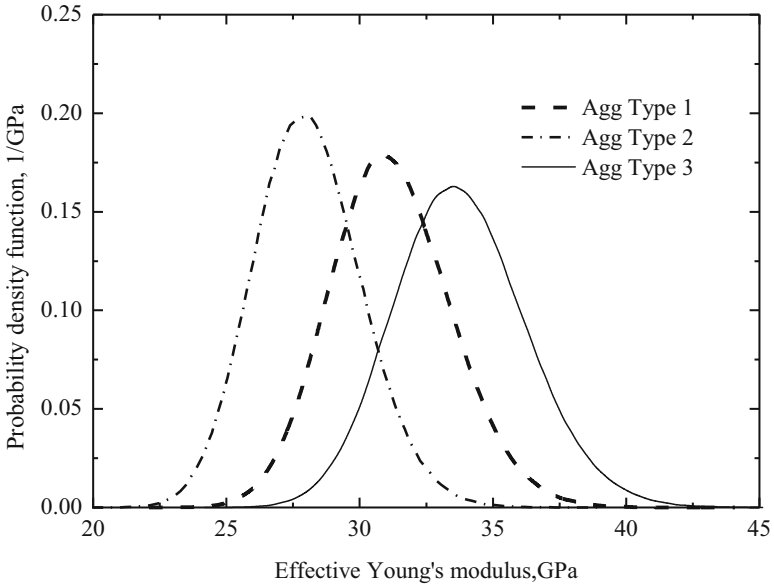

Fig. 4 PDFs of the solid matrix considering the aggregate effects

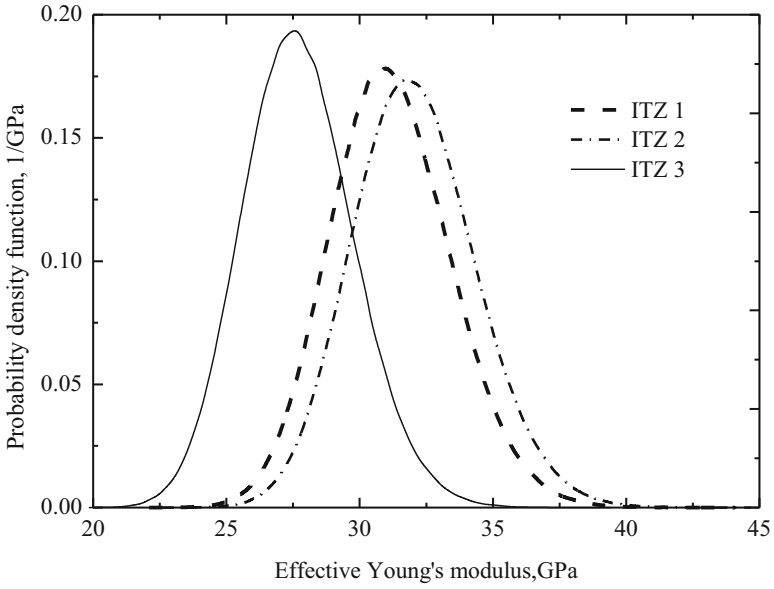

Fig. 5 PDFs of the solid matrix considering the ITZ effects

The Repaired Concrete's Stochastic Micromechanical Model

The (micro-)voids or (micro-)cracks will cause damage to concrete materials. The (micro-)voids or (micro-)cracks can decrease concrete's strength, performance, and durability seriously (Zhu et al. 2014), especially for the concrete components and structures (like tunnel structures) surrounded by groundwater, vehicle vibrations, and ground pressures. In order to extend the service life of the tunnel, new methods should be developed to prevent or control the generation and expansion of the (micro-)cracks because the traditional repairing methods that exist have limitations in the underground water environment. The electrochemical deposition method (EDM) is one of the new methods for the concrete crack repair in the water conditions (Chen 2014). In the past 20 years, EDM has been developed in the repair of marine structures (Ryu and Otsuki 2002; Ryu 2003).

To investigate the effectiveness of the EDM, many experimental tests have been conducted. The main setup for this new method is as follows: the power supply's negative (−) pole is connected with the embedded reinforcing bars in the concrete structure; the power supply's positive (+) pole is connected with the titanium mesh; the titanium mesh and the concrete structure are immersed in the electrolyte solution. With an appropriate direct current (DC) provided for the repairing system, continuous electrochemical deposition will occur in concrete structures. At this time, the cracks and pores in the concrete structures will be gradually filled by the deposition products.

Based on the above repair mechanism, a stochastic micromechanical framework is presented for the damaged concrete repaired by EDM. On the one hand, it discloses the healing process from microscale level using micromechanics. On the other hand, it considers the stochastic behavior of the healing process. The framework includes the repaired concrete's micromechanical model, the stochastic descriptions for the repaired concrete's microstructures, the micromechanical prediction for the repaired concrete's effective properties, and the probabilistic behavior of the repaired concrete's properties. In addition, the unsaturated state and the imperfect bonding are also taken into account. Finally, the numerical examples are given.

The Repaired Concrete's Deterministic Micromechanical Models

Because the EDM is usually employed in the water environment (Ryu and Otsuki 2002), the repaired concrete can be reasonably assumed in a state of complete saturation (Zhu et al. 2014). It implies that the (micro-)cracks and (micro-)voids in the concrete structure are full of water before the start of electrochemical deposition. Those cases of unsaturation will be discussed separately later. At the micro level, there are different phases, such as the mortar, the coarse aggregates, deposition products, water, the microcracks, micro-voids, and interface, in the saturated

concrete. To investigate the healing effectiveness, these components are divided into two categories. The one is the matrix phase, which is consisting of the mortar, the coarse aggregate, and their interfaces. The other is the inclusion phases, which include the deposition products and water phase (occupying microcracks and micro-voids).

From the perspective of micromechanics, there are "soft" and "stiff" pores in the concrete. For the "soft" one, they are usually seen as ellipses or disks (Yan et al. 2013). As to the "stiff" one, they are usually spherical. If the "soft" pores can be completely filled with water, the "soft" pores can be regarded as "stiff" pores because the water pressure in the pores is symmetrical and free-direction. Therefore, it is reasonable to assume the water-filled cracks or voids in the repaired concrete to be spherical (Zhu et al. 2014).

More electrochemical deposition products can be generated when the wider cracks are considered. The crack filling depth and cross-sectional coverage usually increase with the crack width, because the wider crack makes it easier for ions in electrolyte solution to reach the crack location (Zhu et al. 2014). Hence, the second assumption herein is that the deposition products' volumes are proportional to that of the spherical pore. With this assumption, the volume ratios are the same between the deposition products and water in each spherical pore. Therefore, the effective properties are the same for the two-phase composite consisting of the deposition products and the water (i.e., the equivalent inclusions). In addition, the interfaces between the deposited products and the concrete matrix are supposed to be well bonded. In the following section, the imperfect bonding behavior is also discussed.

To sum up, the three main assumptions employed herein are as follows: (1) the saturated cracks or pores in the repaired concrete are spherical; (2) the volumes of the deposition products during the repairing process are proportional to those of the initial pores; and (3) the interfaces are perfect between the deposition products and the concrete matrix. According to these assumptions, a micromechanical model can be presented for the repaired saturated concrete, as shown in Fig. 6. The EDM healing mechanism can be described from the micro level with the presented model. The healing process of the saturated concrete can be seen as that the water phase is

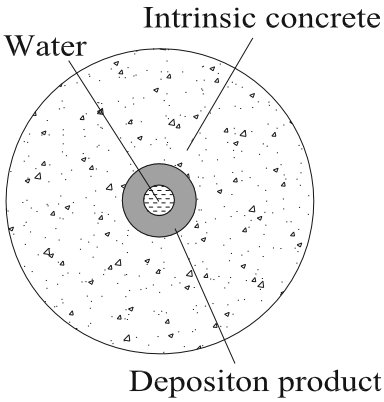

Fig. 6 The repaired concrete's micromechanical model

replaced by the deposition products. To predict the repaired concrete's effective properties can quantitatively evaluate the healing process for the mechanical properties of the saturated concrete. The presented model does not consider the localization of crack healing. In other words, the distribution of defects (such as cracks or pores) and deposition products in the sample should be statistically uniform.

Stochastic Descriptions for the Microstructures of the Repaired Concrete

Uncertainty Quantifications for the Deposition Products

According to the micromechanical characterization, the deposition products are the new component for the saturated concrete during the healing process. To quantify the uncertainties of the deposition products is important for the stochastic descriptions for the repaired concrete's microstructures (Chen 2014). Suppose ϕ_m is the matrix's volume fraction. It remains constant during the healing process. Meanwhile, set $\phi_w(t)$ as the water phase's volume fractions and $\phi_d(t)$ as the deposition products' volume fractions at the time t. The sum of these two volume fractions can be arrived with $\phi_w(t) + \phi_d(t) = 1 - \phi_m$. All the values for the volume fractions range from 0 to 1. When $t = 0$, there is no healing effect, which means $\phi_d(t = 0) = 0$. Suppose $\phi_d(t)$ is a nonstationary Gaussian random process. Meanwhile, define $m_d(t)$ as the mean and $sd_d(t)$ as the standard deviation for the random process. Furthermore, let $\overline{\phi}_d(t)$ represent the deposition products' volume fraction after standardization. $\overline{\phi}_d(t)$ can be reached with Eq. (50):

$$\overline{\phi}_d(t) = \frac{\phi_d(t) - m_d(t)}{sd_d(t)} \tag{50}$$

From Eq. (50), it can be found that $\overline{\phi}_d(t)$ represents a weekly stationary random process, whose mean and variance are, respectively, zero and one.

Approximation for the Gaussian Process

Suppose the random process' autocorrelation function can be represented by $R(t_1, t_2)$, whose eigenfunctions and eigenvalues are, respectively, $f_i(t)$ and λ_i. t_1, t_2 is in the definition domain T. With these definitions, the following equations can be arrived:

$$R(t_1, t_2) = \sum_{i=1}^{\infty} \lambda_i f_i(t_1) f_i(t_2) \tag{51}$$

$$\int_T R(t_1, t_2) f_i(t_1) dt_1 = \lambda_i f_i(t_2) \tag{52}$$

$$\int_T f_i(t) f_j(t) dt = \delta_{ij} \tag{53}$$

Equation (52) is the Fredholm integral equation for t_1 and t_2. Equation (53) is the orthogonal conditions for the eigenfunctions. In the above formula, δ_{ij} is the Kronecker delta. Suppose $\{\xi_i,\ i = 1, 2\ldots\}$ are uncorrelated Gaussian random variables, whose mean and variance are, respectively, zero and one. According to Ghanem and Spanos (1991), the standardized random process $\overline{\phi}_d(t)$ can be expressed as:

$$\overline{\phi}_d(t) = \sum_{i=1}^{\infty} \sqrt{\lambda_i} f_i(t) \xi_i \tag{54}$$

Equation (54) is the Karhunen-Loeve (K-L) representation for $\overline{\phi}_d(t)$. Furthermore, suppose the correlation length can be denoted with Lr and the exponential function can be utilized to represent the autocorrelation function, which can be expressed with Eq. (55) (Ghanem and Spanos 1991):

$$R(t_1, t_2) = E\left[\overline{\phi}_d(t_1)\overline{\phi}_d(t_2)\right] = \exp\left(-c|t_2 - t_1|\right) \tag{55}$$

where $c = 1/Lr$. Furthermore, let us define $t' = t - a \in T'$, $T' = [-a,\ a]$, with a as the half length of this random field. Based on the formula above, the following equations can be utilized to represent the K-L decomposition of $\overline{\phi}_d(t)$ (Ghanem and Spanos 1991):

$$\overline{\phi}_d(t') = \sum_{i=1}^{\infty} \left[\sqrt{\lambda_i} f_i(t')\xi_i + \sqrt{\lambda_i^*} f_i^*(t')\xi_i^*\right] \tag{56}$$

$$f_i(t') = \frac{\cos\left(\beta_i t'\right)}{\sqrt{a + \frac{\sin\left(2\beta_i a\right)}{2\beta_i}}} \tag{57}$$

$$f_i^*(t') = \frac{\sin\left(\beta_i^* t'\right)}{\sqrt{a - \frac{\sin\left(2\beta_i^* a\right)}{2\beta_i^*}}} \tag{59}$$

β_i and β_i^* are calculated through solving Eqs. (60)–(61):

$$c - \beta \tan\left(\beta a\right) = 0 \tag{60}$$

$$\beta^* + c \tan\left(\beta^* a\right) = 0 \tag{61}$$

Therefore, these two coefficients are employed to arrive the eigenvalues, as shown in the following formula:

$$\lambda_i = \frac{2c}{\beta_i^2 + c^2} \tag{62}$$

$$\lambda_i^* = \frac{2c}{\beta_i^{*2} + c^2} \tag{63}$$

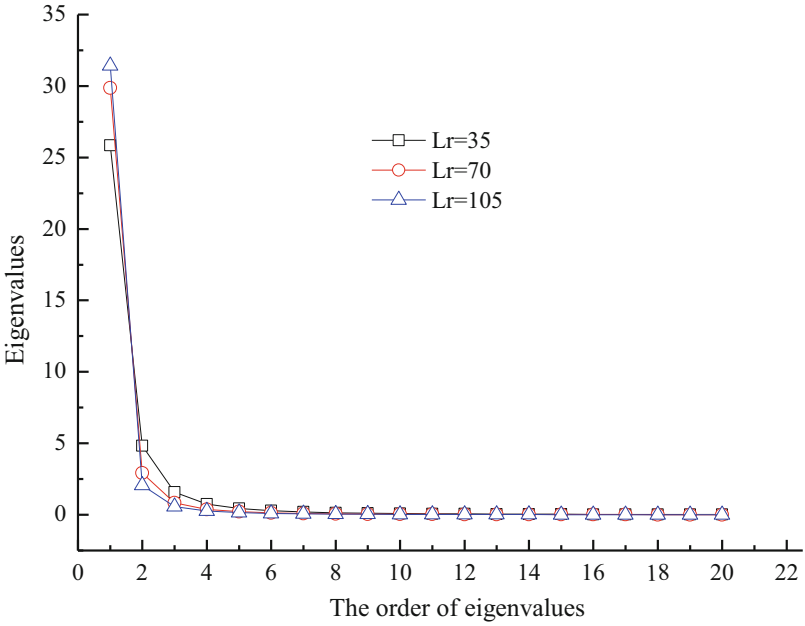

Fig. 7 The eigenvalues with different correlation lengths Lr

The commonly used K-L approximation can be attained by truncating the infinite series in Eq. (54), which can be expressed with Eq. (64):

$$\overline{\phi}_d(t') \approx \sum_{i=1}^{M} \left[\sqrt{\lambda_i} f_i(t') \xi_i + \sqrt{\lambda_i^*} f_i^*(t') \xi_i^* \right] \tag{64}$$

Figure 7 displays the eigenvalues with the different correlation lengths. From Fig. 7, it can be seen that the values reduce more quickly when the correlation length is greater. Furthermore, no matter what the correlation length values are, the tenth-order eigenvalues are all near to zero. Therefore, it is reasonable to approximate the random process with limited series in practice. The first sixth-order eigenfunctions are displayed in Fig. 8.

Uncertainty Quantifications for the Constituent Properties

The component properties' stochastic characters are quantified by the random vectors. When a probability space is considered, $\boldsymbol{\xi}$, $\boldsymbol{\Omega}$, and P can be employed to signify the σ-algebra of subsets, the sample space, and the probability measure, respectively. Meanwhile, $\mathbf{R}^N$ is supposed to represent an N-dimensional real vector space. Meanwhile, let's define E_3, ν_3 as the intrinsic concrete's elastic Young's modulus and Poisson's ratio; E_2, ν_2 are those of the deposition products; and E_1, ν_1 are those of the water phase. Therefore, the constituents' stochastic characters can be quantified by the random vector $\{E_3, E_2, E_1, \nu_3, \nu_2, \nu_1\}^T \in \mathbf{R}^6$.

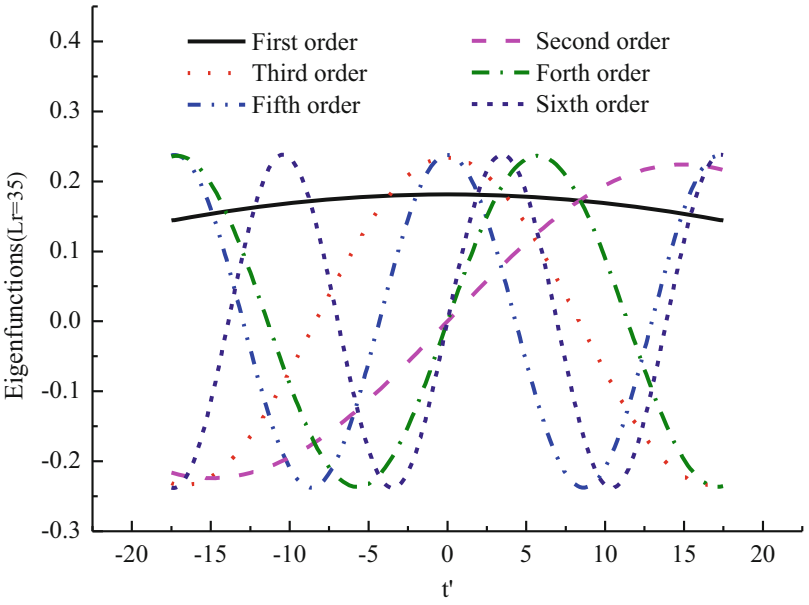

Fig. 8 The first sixth-order eigenfunctions

The statistical characters of this random vector are supposed or arrived with the experimental data available.

From Eq. (64), the statistical character of the deposited products' volume fraction can be quantified with 2 M random variables. Meanwhile, the stochastic behavior can be described by one random variable for the intrinsic concrete's volume fraction. The water's volume fraction will be obtained with the formula $\phi_m(t) + \phi_w(t) + \phi_d(t) = 1$. Therefore, based on our proposed micromechanical representation, the uncertainties of the repaired concrete can be quantified by the input random vector $\left\{E_3, E_2, E_1, \nu_3, \nu_2, \nu_1, \phi_m, \xi_1 \ldots \xi_M, \xi_1^* \ldots \xi_M^*\right\}^T \in \mathbf{R}^{2M+7}$.

Multilevel Predictions for the Repaired Concrete's Properties

The First-Level Predictions

The homogenization approach based on micromechanics can effectively obtain the materials' effective properties by taking their microstructures into considerations (Ju and Zhang 1998; Sun and Ju 2004; Ju and Yanase 2011; Mousavi et al. 2016; Chen et al. 2020a, b). In this section, the repaired concrete's properties are similarly reached with the micromechanical multilevel homogenization scheme. Firstly, the water phase and the electrochemical deposition products are homogenized to obtain the equivalent inclusions with the first-level homogenization. Secondly, the intrinsic concrete (matrix) and the equivalent inclusion are homogenized to obtain the repaired concrete's properties with the second-level homogenization.

Suppose K_F and μ_F are the bulk modulus and shear modulus of the equivalent inclusion and K_2 and μ_2 are those of the deposition products. Meanwhile, define K_1 as the bulk modulus of the water phase and ϕ_1 as the volume fraction of the water phase in the two-phase composite composed by the water and the deposition products. By replacing the inner layer's bulk modulus with K_1 and respectively replacing the outer layer' bulk modulus and shear modulus with K_2 and μ_2, K_F and μ_F can be achieved by Eqs. (65) and (66) according to the three-phase sphere model proposed by Christensen and Lo (1979) at the first-level homogenization:

$$K_F = K_2 + \frac{\phi_1(K_1 - K_2)\ (3K_2 + 4\mu_2)}{3K_2 + 4\mu_2 + 3\ (1 - \phi_{FD})\ (K_1 - K_2)} \tag{65}$$

$$A\left(\frac{\mu_F}{\mu_2}\right)^2 + B\left(\frac{\mu_F}{\mu_2}\right) + C = 0 \tag{66}$$

$$\begin{aligned} A = {} & 8\left[\frac{\mu_1}{\mu_2} - 1\right](4 - 5\nu_2)\eta_\alpha\ \phi_1^{10/3} - 2\left[63\left(\frac{\mu_1}{\mu_2} - 1\right)\eta_\beta + 2\eta_\alpha\eta_\gamma\right]\ \phi_1^{7/3} \\ & + 252\left[\frac{\mu_1}{\mu_2} - 1\right]\eta_\beta\phi_1^{5/3} - 50\left[\frac{\mu_1}{\mu_2} - 1\right]\left(7 - 12\nu_2 + 8{\nu_2}^2\right)\eta_\beta\phi_1 + 4\,(7 - 10\nu_2)\eta_\beta\eta_\gamma \end{aligned} \tag{67}$$

$$\begin{aligned} B = {} & -4\left[\frac{\mu_1}{\mu_2} - 1\right](1 - 5\nu_2)\eta_\alpha\ \phi_1^{10/3} + 4\ \left[63\left(\frac{\mu_1}{\mu_2} - 1\right)\eta_\beta + 2\eta_\alpha\eta_\gamma\right]\phi_1^{7/3} \\ & - 504\left[\frac{\mu_1}{\mu_2} - 1\right]\eta_\beta\ \phi_1^{5/3} + 150\left[\frac{\mu_1}{\mu_2} - 1\right](3 - \nu_2)\,\nu_2\eta_\beta\phi_1 + 3\,(15\nu_2 - 7)\eta_\beta\ \eta_\gamma \end{aligned} \tag{68}$$

$$\begin{aligned} C = {} & 4\left[\frac{\mu_1}{\mu_2} - 1\right](5\nu_2 - 7)\,\eta_\alpha\phi_1^{10/3} - 2\left[63\left(\frac{\mu_1}{\mu_2} - 1\right)\eta_\beta + 2\eta_\alpha\eta_\gamma\right]\phi_1^{7/3} \\ & + 252\left[\frac{\mu_1}{\mu_2} - 1\right]\eta_\beta\ \phi_S^{5/3} + 25\left[\frac{\mu_1}{\mu_2} - 1\right]\left({\nu_2}^2 - 7\right)\eta_\beta\phi_1 - 3(7 + 5\nu_2)\eta_\beta\eta_\gamma \end{aligned} \tag{69}$$

with

$$\eta_\alpha = \left[\frac{\mu_1}{\mu_2} - 1\right](49 - 50\nu_1\nu_2) + 35\left(\frac{\mu_1}{\mu_2}\right)(\nu_1 - 2\nu_2) + 35(2\nu_1 - \nu_2) \tag{70}$$

$$\eta_\beta = 5\,\nu_1\left[\frac{\mu_1}{\mu_2} - 8\right] + 7\left[\frac{\mu_1}{\mu_2} + 4\right], \quad \eta_\gamma = \frac{\mu_1}{\mu_2}[8 - 10\nu_2] + (7 - 5\nu_2) \tag{71}$$

$$\phi_1 = \frac{V_{wat}}{V_{dep} + V_{wat}} \tag{72}$$

where ν_1 is the water's Poisson's ratio and ν_2 is the deposition products' Poisson's ratio.

The Second-Level Predictions

Let ϕ_2 be the volume fraction of the equivalent inclusion in the repaired concrete and $\mathbb{I}$ be the identity tensor. Meanwhile, suppose $\mathbb{D}_3$ represents the intrinsic concrete's stiffness tensors and $\mathbf{D}_F$ denotes that of the equivalent inclusion. Through replacing the matrix stiffness tensor with $\mathbb{D}_3$ and the inhomogeneity's stiffness tensor with $\mathbf{D}_F$, the repaired concrete's stiffness tensor of $\mathbb{D}_S$ can be represented by the following formula (Qu and Cherkaoui 2006; Ju and Chen 1994a, b):

$$\mathbf{D}_S = \mathbf{D}_3\left\{\mathbf{I} - \phi_2\mathbf{\Gamma}(-\mathbf{A}_1 - \mathbf{S} + \phi_2\mathbf{S}\mathbf{\Gamma})^{-1}\right\} \tag{73}$$

$$\mathbf{A}_1 \equiv (\mathbf{D}_F - \mathbf{D}_3)^{-1} : \mathbf{D}_3 \tag{74}$$

where $\mathbf{S}$ is the Eshelby tensor and $\mathbf{\Gamma}$ is the tensor dependent on the properties of the intrinsic concrete and the equivalent inclusion. Let δ_{ij} be the Kronecker delta. Suppose K_3 is the intrinsic concrete's bulk modulus and μ_3 is the intrinsic concrete's shear modulus. Meanwhile, define K_S as the repaired concrete's bulk modulus and μ_S as the repaired concrete's shear modulus. With these definitions, the above tensors' components for the isotropic materials can be expressed with Eqs. (75, 76, 77, 78, and 79):

$$I_{ijkl} = \frac{1}{3}\delta_{ij}\delta_{kl} + \frac{1}{2}\left(\delta_{ik}\delta_{jl} + \delta_{il}\delta_{jk} - \frac{2}{3}\delta_{ij}\delta_{kl}\right) \tag{75}$$

$$S_{ijkl} = \frac{K_3}{3K_3 + 4\mu_3}\delta_{ij}\delta_{kl} + \frac{3(K_3 + 2\mu_3)}{5(3K_3 + 4\mu_3)}\left(\delta_{ik}\delta_{jl} + \delta_{il}\delta_{jk} - \frac{2}{3}\delta_{ij}\delta_{kl}\right) \tag{76}$$

$$D_{Fijkl} = K_F\delta_{ij}\delta_{kl} + \mu_F\left(\delta_{ik}\delta_{jl} + \delta_{il}\delta_{jk} - \frac{2}{3}\delta_{ij}\delta_{kl}\right) \tag{77}$$

$$D_{3ijkl} = K_3\delta_{ij}\delta_{kl} + \mu_3\left(\delta_{ik}\delta_{jl} + \delta_{il}\delta_{jk} - \frac{2}{3}\delta_{ij}\delta_{kl}\right) \tag{78}$$

$$\Gamma_{ijkl} = \gamma^1\delta_{ij}\delta_{kl} + \gamma^2\left(\delta_{ik}\delta_{jl} + \delta_{il}\delta_{jk}\right) \tag{79}$$

The coefficients γ^1 and γ^2 are dependent on the components' properties. Other details can be obtained in Ju and Chen (1994a, b). After some derivations, K_S and μ_S are calculated as follows:

$$K_S = K_3\left\{1 + \frac{30(1-\nu_3)\phi_2(3\gamma^1 + 2\gamma^2)}{3\alpha + 2\beta - 10(1+\nu_3)\phi_2(3\gamma^1 + 2\gamma^2)}\right\} \tag{80}$$

$$\mu_S = \mu_3\left\{1 + \frac{30(1-\nu_3)\phi_2\gamma^2}{\beta - 4(4-5\nu_3)\phi_2\gamma^2}\right\} \tag{81}$$

As to the effect of pore water viscosity (Zhu et al. 2014; Yan et al. 2013; Chen et al. 2016), the modified function for μ_S should be considered as below:

$$F = 1 + f_1{\phi_2}^2 + f_2\phi_2 \tag{82}$$

where f_1 and f_2 should be reached experimentally (Wang and Li 2007).

Furthermore, the repaired concrete Young's modulus can be calculated with Eq. (83):

$$E = \frac{9K\mu}{3K + \mu} \tag{83}$$

Modifications for the Dry States

In the presented model, all pores in the saturated concrete are assumed to be spherical. When the sample is in the dry state, the influence of the pore shape should be considered, i.e., the pores are represented as ellipsoid in the dry state. Suppose the i*th* pores' minor and major axes can be, respectively, represented by a_i and b_i and N signifies the number of different pores in the concrete specimens. Meanwhile, the equivalent aspect ratio is denoted by α and the predicting results with $\alpha = 1$ are represented with $K^*_{\alpha=1}$, $\mu^*_{\alpha=1}$, and $E^*_{\alpha=1}$ (i.e., the results are arrived when the pore shape is spherical). Moreover, let K^*_α, μ^*_α, and E^*_α signify the results with $\alpha < 1$ (i.e., the results are arrived when the pore shape is nonspherical). With these definitions, the modification parameters χ_K, χ_μ, and χ_E can be reached as (Zhu et al. 2014; Berryman 1980):

$$\chi_K = \frac{K^*_\alpha}{K^*_{\alpha=1}} \tag{84}$$

$$\chi_\mu = \frac{\mu^*_\alpha}{\mu^*_{\alpha=1}} \tag{85}$$

$$\chi_E = \frac{E^*_\alpha}{E^*_{\alpha=1}} \tag{86}$$

$$\alpha = \frac{1}{N} \sum_{i=1}^{N} \frac{a_i}{b_i} \tag{87}$$

Furthermore, in Eqs. (37, 38, 39, 40, 41, 42, and 43) of Zhu et al. (2014), the deposited products' properties are the same as those of the intrinsic concrete. However, the properties of these two constituents are usually not the same. Therefore, K_{ave} and μ_{ave} can be utilized to replace K_2 and μ_2 in Eqs. (37, 38, 39, 40, 41, 42, and 43) of Zhu et al. (2014). Define V_{int} as intrinsic concrete's volume and V_{dep} as the deposition products' volume. Meanwhile, let ϕ_G be the deposition products' volume fraction in the composite made up of the intrinsic concrete and the deposition products. Hence, K_{ave} and μ_{ave} can be expressed with Eqs. (88, 89, and 90):

$$K_{aver} = 0.5[\phi_G K_2 + (1 - \phi_G)K_3] + 0.5\left[\frac{K_2 K_3}{\phi_G K_3 + (1 - \phi_G)K_2}\right] \tag{88}$$

$$\mu_{aver} = 0.5[\phi_G \mu_2 + (1 - \phi_G)\mu_3] + 0.5\left[\frac{\mu_2 \mu_3}{\phi_G \mu_3 + (1 - \phi_G)\mu_2}\right] \tag{89}$$

$$\phi_G = \frac{V_{dep}}{V_{\text{int}} + V_{dep}} \tag{90}$$

The Composite's Statistical Behavior

Univariate Approximation for Multivariate Function

The deterministic micromechanical model is extended to the stochastic one with the uncertainty characterization for the material's microstructure. A random function can be employed to characterize the repaired composite's properties. To arrive the statistical behavior efficiently, the dimension decomposition method is employed for the approximation for the random function (Xu and Graham-Brady 2005). Suppose $y(\mathbf{r})$ is a continuous, differentiable, real-valued function that depends on $\mathbf{r} = \{r_1, \cdots r_n\}^T \in \mathbf{R}^N$. Based on the dimension decomposition method, the univariate function $\widetilde{y}_1(\mathbf{r})$ can be adopted to approximate the multivariable random function $y(\mathbf{r})$, which can be expressed in Eq. (91) (Xu and Graham-Brady 2005):

$$\widetilde{y}_1(\mathbf{r}) = -(N-1)y(\mathbf{c}) + \sum_{i=1}^{N} y(c_1, \cdots c_{i-1}, r_i, c_{i+1}, \cdots c_N) \tag{91}$$

where $\mathbf{c} = \{c_1, \cdots c_n\}^T$ denotes a reference point. The mean of the random input can be selected as an appropriate reference point. It should be noted that this univariate approximation is different from the first-order Taylor series expansions. In fact, the higher-order approximation of multivariate functions is provided with this approach according to Xu and Graham-Brady (2005) and Rahman and Chakraborty (2007).

Newton Interpolations

To improve the stochastic simulation efficiency, the Newton interpolation is employed to arrive the repaired composite's effective properties. If the univariate component function $y(r_i) = y(c_1, \cdots c_{i-1}, r_i, c_{i+1}, \cdots c_N)$ is provided, the univariate approximation $\widetilde{y}_1(\mathbf{r})$ of $y(\mathbf{r})$ can be achieved on the basis of Eq. (91). The function value of $y(r_i)$ are calculated with Newton interpolations for an arbitrary r_i. Specifically, if the sample points $r_i = r_i^{(j)}$, $(j = 0, 1, \cdots, n)$ are given, $n + 1$ different function values $y(r_i) = y(c_1, \cdots c_{i-1}, r_i, c_{i+1}, \cdots c_N)$ will be arrived. With these values, the Newton interpolations can be expressed as Eq. (92) to obtain the function value with an arbitrary r_i:

$$y(r_i) = \sum_{j=0}^{n} a_j p_j(r_i) \tag{92}$$

$$a_j = \left[y\left(r_i^0\right), \cdots y\left(r_i^j\right)\right] = \sum_{m=0}^{j} \frac{y\left(r_i^m\right)}{\prod_{k \in \{0,1,\cdots,j\} \setminus \{m\}} \left(r_i^m - r_i^k\right)}, \qquad j > 0 \quad \text{and} \quad a_0 = y\left(r_i^0\right) \tag{93}$$

$$p_j(r_i) = \prod_{k=0}^{j-1} \left(r_i - r_i^k\right), \qquad j > 0 \quad \text{and} \quad p_0(r_i) = 1 \tag{94}$$

where $\left[y\left(r_i^0\right), \cdots y\left(r_i^j\right)\right]$ denotes the notation for the divided difference. For example, when $n = 0$ (i.e., there is only one sample point), $y_i(r_i) = y\left(r_i^0\right)$; if $n = 1$, which implies there are two sample points, $y_i(r_i) = y\left(r_i^0\right) + \left[\left(y\left(r_i^0\right) - y\left(r_i^1\right)\right) / \left(r_i^0 - r_i^1\right)\right]\left(r_i - r_i^0\right)$ is the updated interpolation function. As to $n \geq 2$, the higher-order interpolations can be similarly arrived with Eqs. (92, 93, and 94). From the above, the univariate approximation can be expressed with Eq. (95) for a random input $\mathbf{R}$:

$$\widetilde{y}_1(\mathbf{R}) = -(N-1)y(\mathbf{c}) + \sum_{i=1}^{N} \sum_{j=0}^{n} a_j p_j(R_i) \tag{95}$$

where a_j, $p_j(;)$ are attained with Eqs. (93) and (94).

Monte Carlo Simulation

If the divided difference $\left[y\left(r_i^0\right), \cdots y\left(r_i^j\right)\right]$ and the deterministic coefficients $y(\mathbf{c})$ are generated, the effective properties' approximations can be calculated according to Eq. (95) for a given random input $\mathbf{R}$. By conducting the Monte Carlo simulation of Eq. (95), the effective properties' statistical characteristic can be evaluated conveniently. Specifically, let's define the mth sample of $\mathbf{R}$ with $\mathbf{R}_m$ and the sample size with M. The effective properties' different order moments can be arrived according to Eq. (96):

$$E\left[y^l(\mathbf{R})\right] = \lim_{M \to \infty} \left[\frac{1}{M} \sum_{m=1}^{M} \widetilde{y}_1^l(\mathbf{R}_m)\right] \tag{96}$$

When $l = 1$, $l = 2$, the first-order moments (i.e., the mean value) and the second-order moments can be calculated for the effective property, respectively. The effective properties' higher-order moment can be arrived by changing the value of l in Eq. (96). The effective properties' PDF can also be determined by developing a histogram from the generated sample.

Numerical Examples

Verifications

Both the results of the experimental data and the existing model are adopted to verify the proposed framework. The experimental data are obtained mainly from the previous works of Yaman et al. (2002), Smith (1976), and Chen (2014).

Yaman et al. (2002) conducted the experiment to access the properties of the saturated concrete. Zhu et al. (2014) proposed micromechanical model for the saturated concrete. Figure 9 shows the comparisons for Young's modulus obtained with different approaches. It can be reached that the predicting Young herein are near to those of the previous model. Meanwhile, they match well with Young's modulus obtained experimentally. There is one extreme state that all the water phase is replaced by the deposition products (i.e., the totally healing state). With this condition, the presented framework turns to the micromechanical model for the particle-reinforced composites. Figure 10 displays the comparison among the predicting Young's modulus, those arrived by Zhu's model (Zhu et al. 2014) and by Smith's experiment for the particle-reinforced composite (Smith 1976). Similarly, the predicting Young's modulus meet well with the results arrived experimentally. When the particle volume fraction increases, the predictions herein are much closer to experimental data than those of Zhu's model.

Chen conducted the EDM test with a batch of concrete samples, which are produced with the same manufacturing process. And the ultrasonic test before and after the healing is adopted to assess Young's modulus of the specimen (Chen 2014). Figure 11 displays the comparisons between the predicting results and Chen's results for Young's modulus's probability distribution. Figure 11(a) shows the distribution before the EDM repair with different method. It can be observed that the predicting PDF are similar with the histogram obtained experimentally. Figure 11(b) illustrates

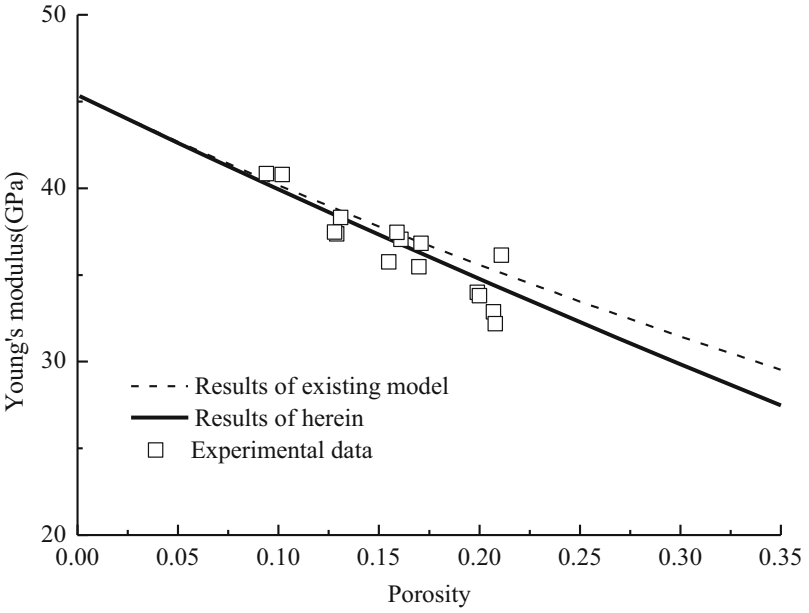

Fig. 9 The saturated concrete Young's modulus

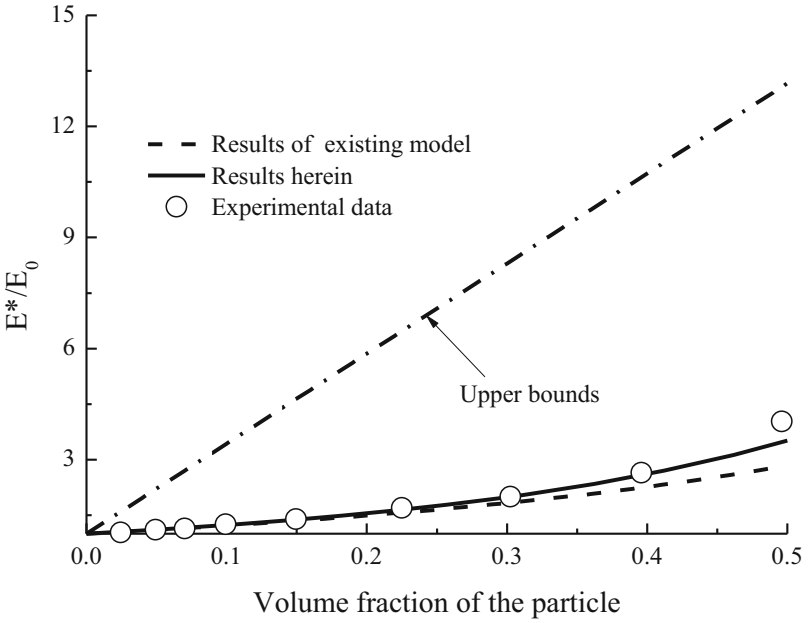

Fig. 10 The composites' Young's modulus reached by different methods

the distribution after the EDM repair analytically and experimentally. It can be concluded that the predicting results are acceptable compared with those arrived experimentally.

Discussion on the Unsaturated Situation

Concrete specimens sometimes cannot be fully saturated in the water environment. In this section, the case of unsaturated concrete is considered, where the effect of dry pores and unsaturated pores are investigated on the effective properties of the repaired concrete.

The repaired concrete in the unsaturated conditions can be regarded as an equivalent homogeneous composite material, whose effective properties can be obtained by replacing its matrix phase with the equivalent matrix calculated by Eqs. (80)–(81) (Berryman 1980). Suppose $(K^*)_{n+1}$ and $(K^*)_n$, respectively, represent K^* 's $(n+1)$th and nth approximations. Meanwhile, $(\mu^*)_{n+1}$ and $(\mu^*)_n$ mean μ^* 's $(n+1)$th and nth approximations. Let ϕ_k be the pores' volume fraction that are not healed. Define S_{eff} and ϕ_{eff} as the effective saturation degree and the effective porosity, respectively. The following expression can be adopted to get the repaired concrete in the unsaturated conditions:

$$(K^*)_{n+1} = \frac{(1-\phi_k)K_S\left(P^{*2}\right)_n}{(\phi_k)\left(P^{*1}\right)_n + (1-\phi_k)\left(P^{*2}\right)_n} \tag{97}$$

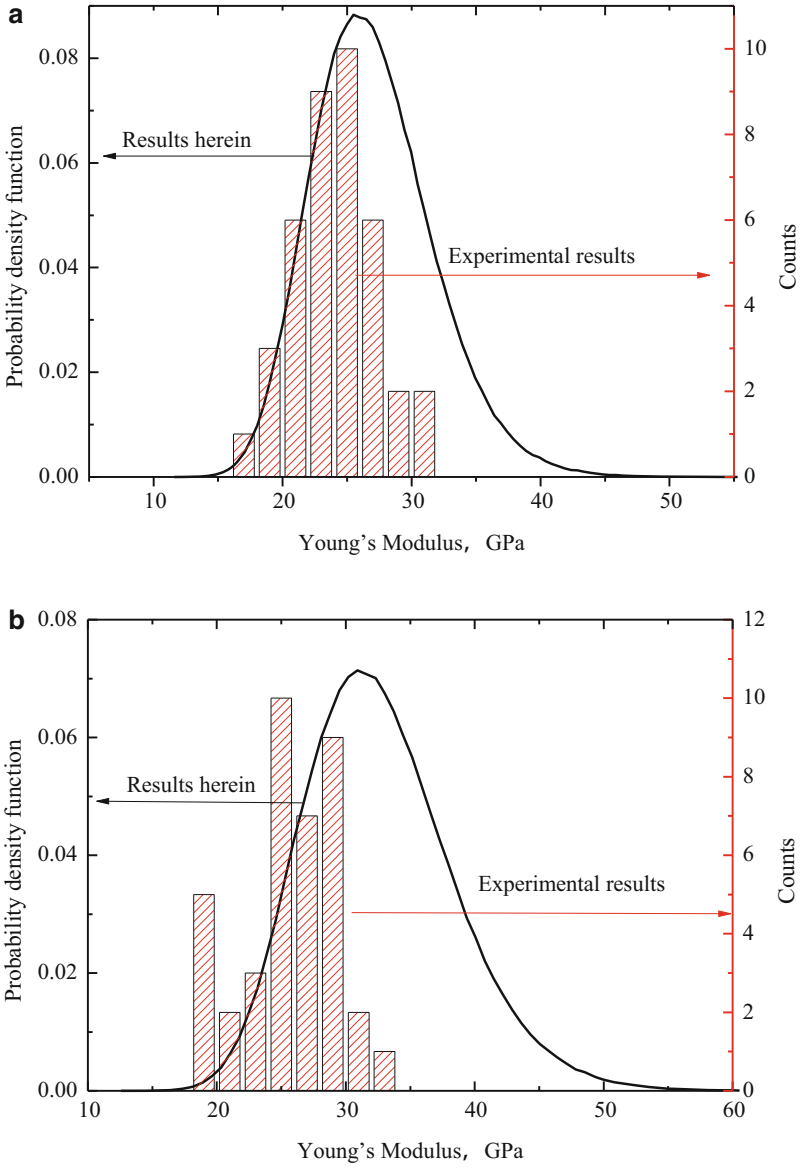

Fig. 11 Young's modulus probability distribution. (**a**) Before the EDM repair. (**b**) After the EDM repair

$$(\mu^*)_{n+1} = \frac{(1-\phi_k)\mu_S(Q^{*2})_n}{(\phi_k)(Q^{*1})_n + (1-\phi_k)(Q^{*2})_n} \tag{98}$$

$$\phi_k = (1 - S_{eff})\phi_{eff} \tag{99}$$

where $(P^{*1})_n$, $(P^{*2})_n$, $(Q^{*1})_n$, $(Q^{*2})_n$ are coefficients defined by the nth approximations to K^* and μ^*, i.e., $(K^*)_n$ and $(\mu^*)_n$.

According to Berryman (1980), $(P^{*1})_n$, $(P^{*2})_n$, $(Q^{*1})_n$, $(Q^{*2})_n$ can be calculated as follows:

$$\left(P^{*1}\right)_n = \frac{(K^*)_n}{\pi\alpha(\beta^*)_n} \tag{100}$$

$$\left(P^{*2}\right)_n = \frac{(K^*)_n + \frac{4}{3}\mu_S}{K_S + \frac{4}{3}\mu_S + \pi\alpha(\beta^*)_n} \tag{101}$$

$$\left(Q^{*1}\right)_n = \frac{1}{5}\left(1 + \frac{8(\mu^*)_n}{\pi\alpha\left((\mu^*)_n + 2(\beta^*)_n\right)} + \frac{4(\mu^*)_n}{3\pi\alpha(\beta^*)_n}\right) \tag{102}$$

$$\left(Q^{*2}\right)_n = \frac{1}{5}\left(1 + \frac{8(\mu^*)_n}{4\mu_S + \pi\alpha\left((\mu^*)_n + 2(\beta^*)_n\right)} + 2\frac{K_S + \frac{2}{3}\mu_S + \frac{2}{3}(\mu^*)_n}{K_S + \frac{4}{3}\mu_S + \pi\alpha(\beta^*)_n}\right) \tag{103}$$

with

$$(\beta^*)_n = (\mu^*)_n \frac{\left(3(K^*)_n + (\mu^*)_n\right)}{\left(3(K^*)_n + 4(\mu^*)_n\right)} \tag{104}$$

Define K_T, μ_T as the effective bulk modulus and shear modulus of the equivalent homogeneous composite (i.e., the healed unsaturated concrete), respectively. The numerical iterations above can be employed to obtain the values of K_T and μ_T. According to Eqs. (100, 101, 102, and 103), when $(K^*)_1 = K_S$, $(\mu^*)_1 = \mu_S$, the first coefficients $(P^{*1})_1$, $(P^{*2})_1$, $(Q^{*1})_1$, $(Q^{*2})_1$ can be calculated, with which the second approximations to K^* and μ^*, i.e., $(K^*)_2$ and $(\mu^*)_2$, can be reached according to Eqs. (97, 98, and 99). With the current approximation to K^* and μ^*, the current coefficients can be obtained. The iterations can lead to the $(n+1)$th and nth approximations to K^* and μ^* successively. When there is no meaningful difference between these two successive approximations, the repaired concrete's effective properties can be reached using Eqs. (105)–(106):

$$K_T = (K^*)_{n+1} \tag{105}$$

$$\mu_T = (\mu^*)_{n+1} \tag{106}$$

Discussion on the Imperfect Bonding

In the above, the stochastic micromechanical damage healing model assumes that the interface between the deposited products and the intrinsic concrete is perfect. However, in practical applications, the interface bonding depends on many factors, such as the electrode, the current density, and the electrolyte solution type.

Therefore, the interface is often imperfect. When the interface is imperfect, the current micromechanical model should be improved to incorporate this effect.

Let Δ be the thickness of the interfacial transition zone (ITZ) between the deposition products and the intrinsic concrete. Define K_F^I and μ_F^I as the bulk modulus and shear modulus of the equivalent particles made up of the ITZ and the equivalent inclusion. They can also be obtained by using the generalized self-consistent model (Hashin 1962; Christensen and Lo 1979) by modifying the inner material as the equivalent inclusion and the outer material as the ITZ. The expressions are as Eqs. (107, 108, and 109):

$$K_F^I = K_{itz} + \frac{\phi_F^I (K_F - K_{itz}) \ (3K_{itz} + 4\mu_{itz})}{3K_{itz} + 4\mu_{itz} + 3 \ \left(1 - \phi_F^I\right) \ (K_F - K_{itz})} \tag{107}$$

$$A^i \left(\frac{\mu_F^I}{\mu_{itz}}\right)^2 + B^i \left(\frac{\mu_F^I}{\mu_{itz}}\right) + C^i = 0 \tag{108}$$

$$\phi_F^I = \left(\frac{r}{r + \Delta}\right)^3 \tag{109}$$

where r is the radius of the equivalent inclusion; A^i, B^i, and C^i represent for parameters dependent on the properties of the equivalent inclusion and the ITZ, respectively. According to Eq. (77), by replacing K_F and μ_F with K_F^I and μ_F^I, the influence of ITZ on the repair effect can be considered comprehensively.

Discussions on the Other Factors

From the EDM experiment, the deposition products' properties are dependent on many factors (Chen 2014). For example, if the current density increases, the deposition product's properties will decrease. Meanwhile, the other factors like the type of the solution and the material's microstructure, etc. will affect the products' properties. Instead of investigating the properties of the deposition products, the focus is on their quantitative influence on the healing effectiveness when their properties are provided. Therefore, the repaired concrete's properties are calculated with three different deposition products to illustrate their influence on the repaired concrete's mechanical properties.

The evolution of the repaired concrete's properties during the healing process is displayed in Fig. 12, which shows that the repaired concrete demonstrates greater shear modulus or Young's modulus when the deposition products' properties increase. Meanwhile, the concrete properties increase during the healing process due to the accumulation of deposited products. It is mentioned that Fig. 12a displays the variations for the shear modulus and Fig. 12b shows the variations for Young's modulus.

During the healing process, the water phase will be replaced by the deposition products bit by bit, which lead to the increase of the volume fraction of the deposition products. In this numerical case, we assume that the deposition products'

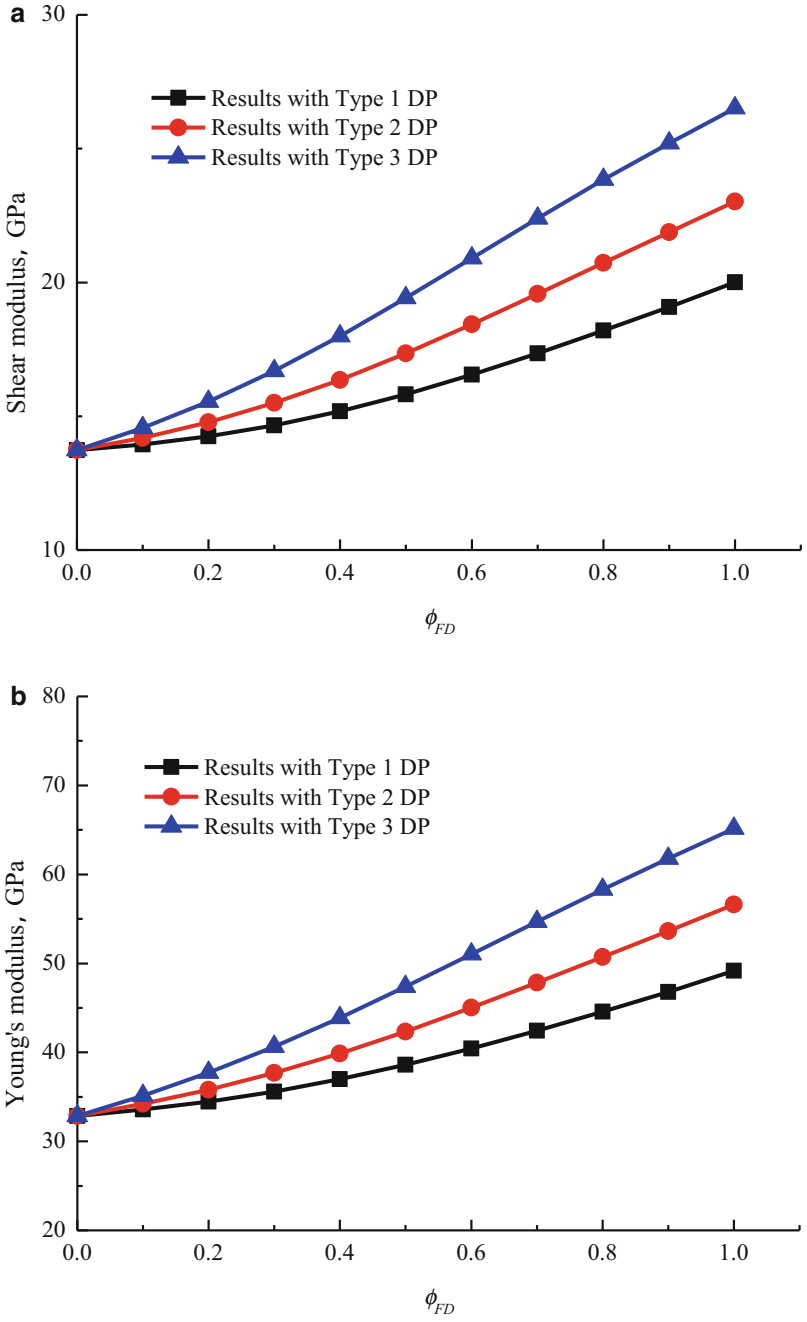

Fig. 12 The repaired concrete's properties during the healing process

volume fraction is 50% in the equivalent inclusion. Figure 13 shows the PDFs of the partially repaired concrete's effective properties with different deposition products. It can be seen from Fig. 13a and b that the repaired concrete demonstrates statistically greater shear modulus and Young's modulus as the mean value of the deposited products' properties increases.

When the deposition products' volume fractions increase, the damaged concrete's performance will gradually improve. To investigate the statistical influence of the deposition products, the PDF evolution of the repaired concrete's properties are attained by using the stochastic micromechanics model. Suppose the healing degree is defined by the deposited products' volume fraction in the equivalent inclusion. It is zero before healing and turn to one after total healing. Figure 14 shows the properties' PDFs of the repaired concrete with different healing degrees, which are 80%, 50%, and 20%, respectively. It can be seen from Fig. 14a and b that when the healing degree increases, i.e., more pores or cracks are repaired by the deposition products, the repaired concrete displays statistically greater shear modulus and bulk modulus.

For the concrete repaired by EDM in the unsaturated conditions, the effective saturation degrees and the equivalent aspect ratios affect the performance of the repaired concrete. To investigate the statistical influence of these factors, three PDFs of the shear modulus and the bulk modulus are obtained using the proposed stochastic model. In this numerical case, two different saturation degrees (0.6 and 0.9) and aspect ratios (0.2 and 0.8) are employed as examples to illustrate their effects on the macroscopic properties of the repair concrete. Figure 15a and b shows the properties' PDFs with different saturation degrees and aspect ratios. As can be seen from Fig. 15a and b, when there is a greater saturation degree, the repaired concrete has a statistically greater distribution for the shear modulus and effective bulk modulus. At the same time, the shear modulus and the bulk modulus will increase statistically if the mean value of the equivalent aspect ratios increases.

Conclusions

As one of the engineering materials, the cementitious composite consists of different constituents or phases, including the (micro-)voids, (micro-)cracks, aggregates, the cement paste, and the interfacial zones. The (micro-)voids and (micro-)cracks typically lead to the damage of the cementitious material. Meanwhile, due to the difficulties in detailing the predetermined microstructures, there is an inherent randomness for the cementitious composite properties when different specimens are considered. The deterministic approach does not consider the stochastic behavior of composites observed in actual cementitious composite specimens (Chen 2014). In this chapter, stochastic micromechanics-based probabilistic damage and repair models are proposed for cementitious composites by incorporating the inherent randomness.

On the one hand, a porous cracked micromechanical model is employed to represent the damaged cementitious composites, which include the transversely isotropic solid matrix, pores, and cracks. With the Voigt-Reuss-Hill average, the equivalent isotropic properties are reached for the transversely isotropic matrix. Meanwhile, the damage-induced compliance tensor is obtained by considering the

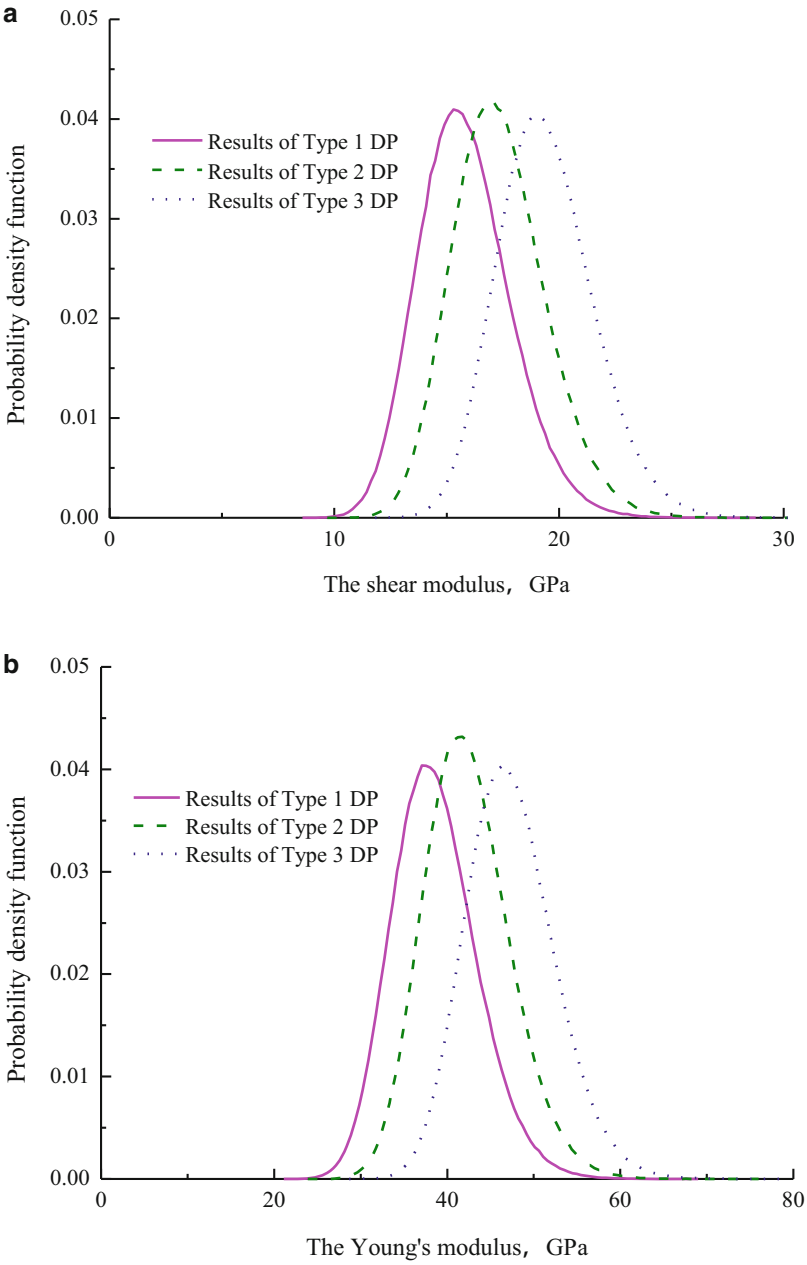

Fig. 13 The properties' PDFs with different deposition products

effects of the stable and unstable microcracks. Furthermore, the probabilistic behavior of the solid matrix is investigated to have better understandings of the probabilistic damage evolution of the cementitious composite.

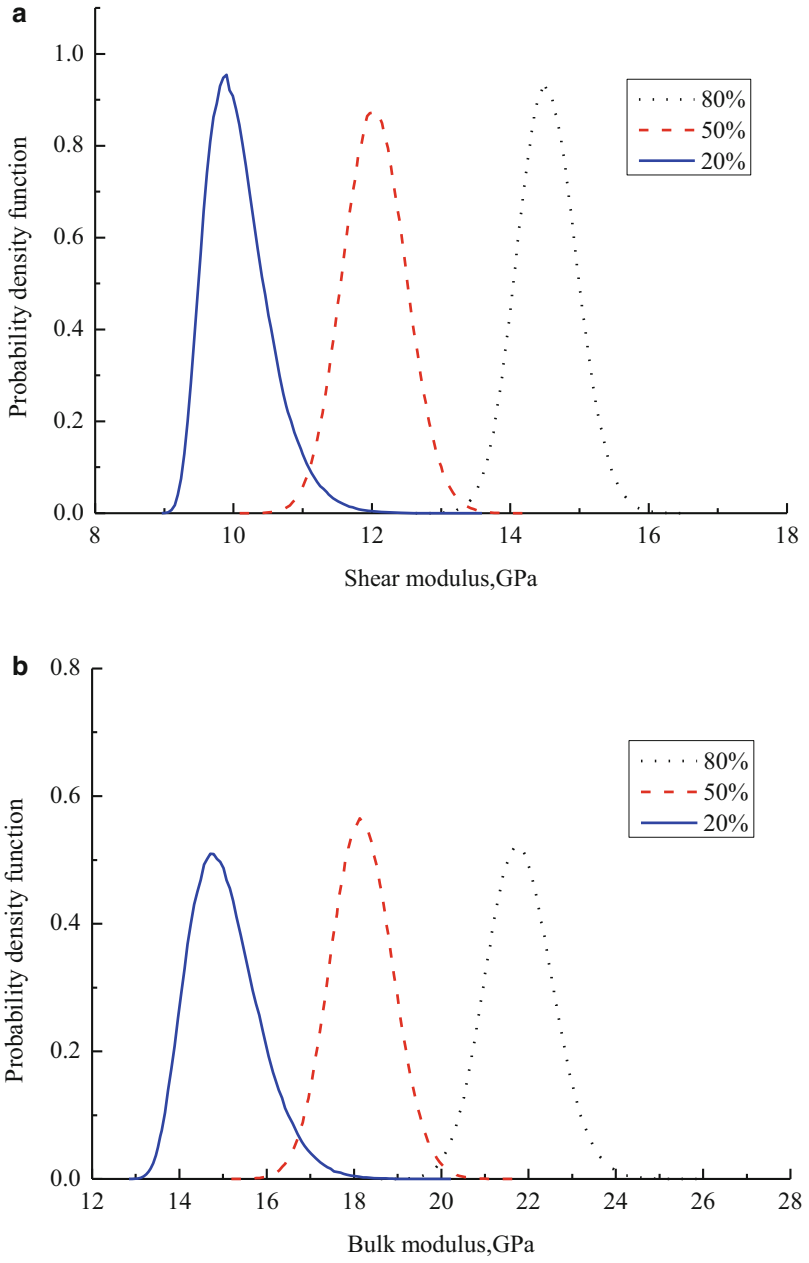

Fig. 14 The properties' PDFs with the different healing degrees

On the other hand, by taking the electrochemical deposition effects into consideration, a stochastic micromechanical framework is presented for the damaged concrete repaired by electrochemical deposition methods. A multiphase composite

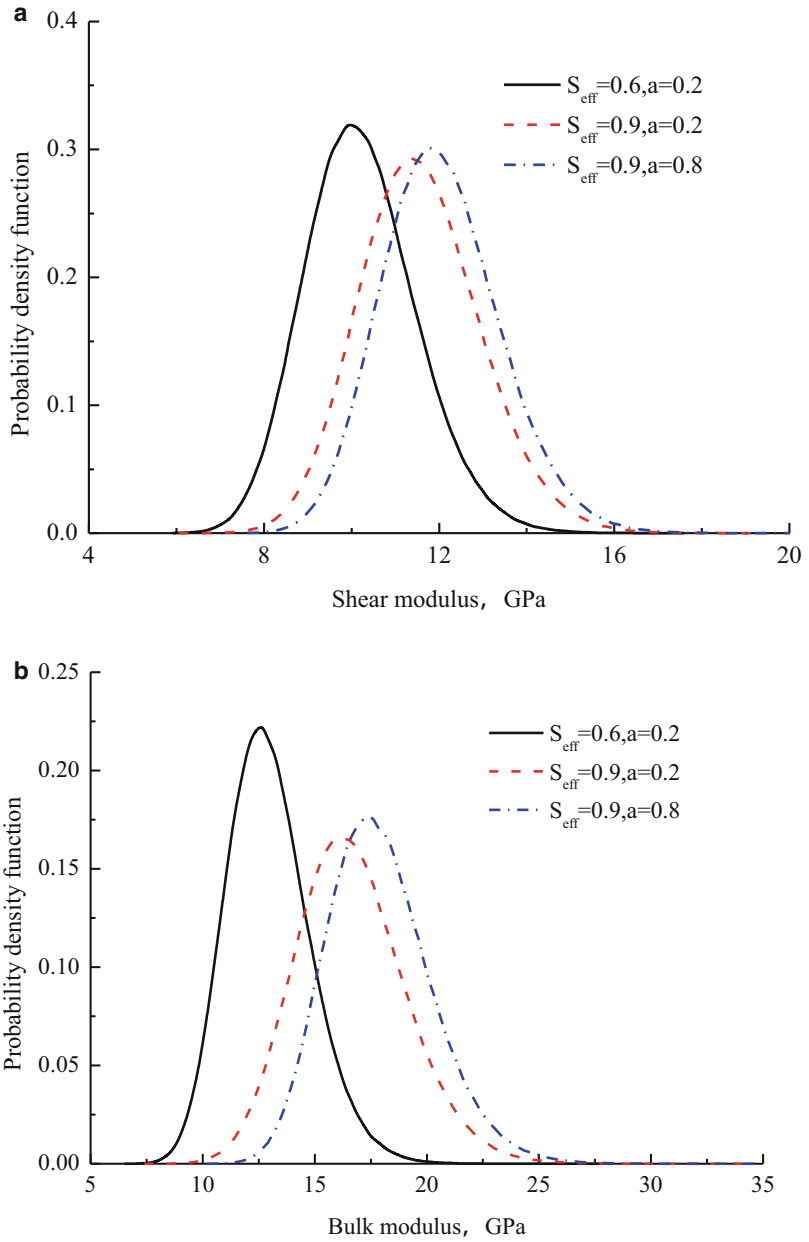

Fig. 15 The properties' PDFs with different saturation degrees and aspect ratios

model is presented to represent the repaired damaged concrete, including the intrinsic concrete, the micropores, the microcracks, the water, and the deposition products. The evolution of the deposition products is described by the nonhomogeneous random process. The properties of the repaired concrete are obtained by the

multilevel homogenization scheme. The probability density functions for the moduli of the repaired concrete are attained by a dimension decomposition method-based efficient stochastic simulation program. Moreover, some factors influencing the healing effectiveness are studied based on the proposed framework.

From the numerical examples, the following conclusions can be reached for this chapter:

1. The presented porous cracked micromechanical model can well describe the initial damage of the cementitious composite. Meanwhile the damage evolution can be reached by considering the effects of the stable and unstable microcracks.
2. The proposed deterministic and *stochastic* micromechanical frameworks are capable of predicting the mechanical behavior of the *saturated* concrete during the EDM healing process.
3. The presented dimension decomposition method can improve the computation efficiency compared with the direct Monte Carlo simulation.
4. Based on the proposed framework, the quantitative effects of the factors influencing the healing effectiveness can be attained.

In addition, the probabilistic behavior of the solid phase leads to the probabilistic damage evolutions of cementitious composite. The quantitative relation between the random microstructure and the probabilistic damage evolution can be studied in our future work.

Acknowledgments This work is supported by the National Key Basic Research and Development Program (973 Program, No. 2011CB013800). This work is also supported by 1000 Talents Plan Short-Term Program by the Central Organization Department of the CPC and Research Program of State Key Laboratory for Disaster Reduction in Civil Engineering.

References

J.G. Berryman, Long-wave propagation in composite elastic media II. Ellipsoidal inclusion. J. Acoust. Soc. Am. **68**(6), 1820–1831 (1980)

B. Budiansky, R.J. O'connell, Elastic moduli of a cracked solid. Int. J. Solids Struct. **12**, 81–97 (1976)

A. Chakraborty, S. Rahman, A parametric study on probabilistic fracture of functionally graded composites by a concurrent multiscale method. Probab. Eng. Mech. **24**, 438–451 (2009)

Q. Chen, The stochastic micromechanical models of the multiphase materials and their applications for the concrete repaired by electrochemical deposition method, Ph.D. dissertation, Tongji University, 2014

Q. Chen, H.H. Zhu, J.W. Ju, F. Guo, L.B. Wang, Z.G. Yan, T. Deng, S. Zhou, A stochastic micromechanical model for multiphase composite containing spherical inhomogeneities. Acta Mech. **226**(6), 1861–1880 (2015)

Q. Chen, H.H. Zhu, J.W. Ju, Z.W. Jiang, Z.G. Yan, H.X. Li, Stochastic micromechanical predictions for the effective properties of concrete considering the interfacial transition zone effects. Int. J. Damage Mech. **27**(8), 1252–1271 (2018a)

Q. Chen, H.H. Zhu, J.W. Ju, Z.G. Yan, C.H. Wang, Z.W. Jiang, A stochastic micromechanical model for fiber-reinforced concrete using maximum entropy principle. Acta Mech. **229**(7), 2719–2735 (2018b)

Q. Chen, R. Ma, Z.W. Jiang, H.H. Zhu, H.X. Li, X.W. Yan, J.W. Ju, Z.G. Yan, Differential scheme-based stochastic micromechanical framework for saturated concrete repaired by EDM. Acta Mech. (2019a). https://doi.org/10.1007/s00707-019-02511-x

Q. Chen, H.H. Zhu, J.W. Ju, Z.G. Yan, Z.W. Jiang, B. Chen, Y.Q. Wang, Z.H. Fan, Stochastic micromechanical predictions for the probabilistic behavior of saturated concrete repaired by the electrochemical deposition method. Int. J. Damage Mech. (2019b). https://doi.org/10.1177/1056789519860805

Q. Chen, H. Wang, Z.W. Jiang, H.H. Zhu, J.W. Ju, Z.G. Yan, Reaction-degree-based multi-scale predictions for the effective properties of ultra-high-performance concrete. Mag. Concr. Res. (2020a). https://doi.org/10.1680/jmacr.19.00415

Q. Chen, H. Wang, H.X. Li, Z.W. Jiang, H.H. Zhu, J.W. Ju, Z.G. Yan, Multiscale modelling for the ultra-high performance concrete: From hydration kinetics to macroscopic elastic moduli. Constr. Build. Mater. (2020b). https://doi.org/10.1016/j.conbuildmat.2020.118541

R.M. Christensen, K.H. Lo, Solutions for effective shear properties in three phase sphere and cylinder models. J. Mech. Phys. Solids **27**, 315–330 (1979)

W. Dridi, Analysis of effective diffusivity of cement based materials by multi-scale modelling. Mater. Struct. **46**, 313–326 (2013)

G.K. Er, A method for multi-parameter PDF estimation of random variables. Struct. Saf. **20**, 25–36 (1998)

D. Fanella, D. Krajcinovic, A micromechanical model for concrete in compression. Eng. Fract. Mech. **29**, 49–66 (1988)

F.J. Ferrante, L.L. Graham-Brady, Stochastic simulation of non-Gaussian/non-stationary properties in a functionally graded plate. Comput. Methods Appl. Mech. Eng. **194**(12–16), 1675–1692 (2005)

B. Ganapathysubramanian, N. Zabaras, A stochastic multiscale framework for modeling flow through random heterogeneous porous media. J. Comput. Phys. **228**(2), 591–618 (2009)

E.J. Garboczi, D.P. Bentz, Analytical formulas for interfacial transition zone properties. Adv. Cem. Based Mater. **6**(3–4), 99–108 (1997)

P.D. Ghanem, P.D. Spanos, *Stochastic Finite Elements: A Spectral Approach* (Springer, New York, 1991)

V.S. Gopalaratnam, S.P. Shah, Softening response of plain concrete in direct tension. ACI Mat. J. May/June: 310–323 (1985)

Z. Hashin, The elastic moduli of heterogeneous materials. J. Appl. Mech. **29**,143–150 (1962)

Z.W. Jiang, X.J. Yang, Z.G. Yan, Q. Chen, H.H. Zhu, C.H. Wang, J.W. Ju, Z.H. Fang, H.X. Li, A stochastic micromechanical model for hybrid fiber-reinforced concrete. Cem. Concr. Compos. **102**, 39–54 (2019)

J.W. Ju, On energy-based coupled elastoplastic damage theories: Constitutive modeling and computational aspects. Int. J. Solids Struct. **25**, 803–833 (1989)

J.W. Ju, On two-dimensional self-consistent micromechanical damage models for brittle solids. Int. J. Solids Struct. **27**, 227–258 (1991)

J.W. Ju, T.M. Chen, Effective elastic moduli of two-phase composites containing randomly dispersed spherical inhomogeneities. Acta Mech. **103**(1), 123–144 (1994a)

J.W. Ju, T.M. Chen, Micromechanics and effective moduli of elastic composites containing randomly dispersed ellipsoidal inhomogeneities. Acta Mech. **103**(1–4), 103–121 (1994b)

J.W. Ju, X. Lee, Micromechanical damage models for brittle solids. Part I: Tensile loadings. J. Eng. Mech. **117**, 1495–1514 (1991)

J. Ju, K. Yanase, Micromechanical effective elastic moduli of continuous fiber-reinforced composites with near-field fiber interactions. Acta Mech. **216**, 87–103 (2011)

J. Ju, X. Zhang, Micromechanics and effective transverse elastic moduli of composites with randomly located aligned circular fibers. Int. J. Solids Struct. **35**, 941–960 (1998)

D. Krajcinovic, D. Fanella, A micromechanical model for concrete. Eng. Fract. Mech. **25**, 585–596 (1986)
H. Li, C. Xu, B. Dong, Q. Chen, L. Gu, X. Yang, W. Wang, Differences between their influences of TEA and TEA·HCl on the properties of cement paste. Constr. Build. Mater. (2020). https://doi.org/10.1016/j.conbuildmat.2019.117797
B.L. Lu, S. Torquato, Nearest-surface distribution functions for polydispersed particle system. Phys. Rev. A **45**(8), 5530–5544 (1992)
N. Mousavi, H.H. Zhu, J.W. Ju, Q. Chen, A simplified multiscale damage model for the transversely isotropic shale rocks under tensile loading. Int. J. Damage Mech. **25**(5), 705–726 (2016)
A. Norris, A differential scheme for the effective moduli of composites. Mech. Mater. **4**(1), 1–16 (1985)
A. Ougier-Simonin, J. Sarout, Y. Guéguen, A simplified model of effective elasticity for anisotropic shales. Geophysics **74**(3), D57–D63 (2009)
J.M. Qu, M. Cherkaoui, *Fundamentals of Micromechanics of Solids* (Wiley, Hoboken, 2006)
S. Rahman, Multi-scale fracture of random heterogeneous materials. Ships Offshore Struct. **4**, 261–274 (2009)
S. Rahman, A. Chakraborty, A stochastic micromechanical model for elastic properties of functionally graded materials. Mech. Mater. **39**, 548–563 (2007)
J.S. Ryu, New waterproofing technique for leaking concrete. J. Mater. Sci. Lett. **22**, 1023–1025 (2003)
J.S. Ryu, N. Otsuki, Crack closure of reinforced concrete by electro deposition technique. Cem. Concr. Res. **32**(1), 159–264 (2002)
J. Sarout, Y. Guéguen, Elastic wave velocities evolution in experimentally deformed anisotropic shales – Part 1: Experimental results. Geophysics **73**(5), D75–D89 (2008a)
J. Sarout, Y. Guéguen, Elastic wave velocities evolution in experimentally deformed anisotropic shales – Part 2: Modeling results. Geophysics **73**(5), D91–D103 (2008b)
J.C. Smith, Experimental values for the elastic constants of a particulate-filled glassy polymer. J. Res. Natl. Bur. Stand. **80A**, 45–49 (1976)
D. Sumarac, D. Krajcinovic, A self-consistent model for microcrack-weakened solids. Mech. Mater. **6**, 39–52 (1987)
L. Sun, J. Ju, Elastoplastic modeling of metal matrix composites containing randomly located and oriented spheroidal particles. J. Appl. Mech. **71**, 774–785 (2004)
H.L. Wang, Q.B. Li, Prediction of elastic modulus and Poisson's ratio for unsaturated concrete. Int. J. Solids Struct. **44**, 1370–1379 (2007)
N. Xie, Q.Z. Zhu, J.F. Shao, L.H. Xu, Micromechanical analysis of damage in saturated quasi brittle materials. Int. J. Solids Struct. **49**, 919–928 (2012)
X. Xu, L. Graham-Brady, A stochastic computational method for evaluation of global and local behavior of random elastic media. Comput. Methods Appl. Mech. Eng. **194**, 4362–4385 (2005)
I.O. Yaman, N. Hearn, H.M. Aktan, Active and non-active porosity in concrete Part I: Experimental evidence. Mater. Struct. **35**(3), 102–109 (2002)
Z.G. Yan, Q. Chen, H.H. Zhu, J.W. Ju, S. Zhou, Z.W. Jiang, A multiphase micromechanical model for unsaturated concrete repaired by electrochemical deposition method. Int. J. Solids Struct. **50**(24), 3875–3885 (2013)
S.W. Yu, X.Q. Feng, A micromechanics-based damage model for microcrack-weakened brittle solids. Mech. Mater. **20**, 59–76 (1995)
J.J. Zheng, H.S. Wong, N.R. Buenfeld, Assessing the influence of ITZ on the steady-state chloride diffusivity of concrete using a numerical model. Cem. Concr. Res. **39**, 805–813 (2009)
H.H. Zhu, Q. Chen, Z.G. Yan, J.W. Ju, S. Zhou, Micromechanical model for saturated concrete repaired by electrochemical deposition method. Mater. Struct. **47**, 1067–1082 (2014)
H.H. Zhu, Q. Chen, J.W. Ju, Z.G. Yan, F. Guo, Y.Q. Wang, Z.W. Jiang, S. Zhou, B. Wu, Maximum entropy based stochastic micromechanical model for a two-phase composite considering the inter-particle interaction effect. Acta Mech. **226**(9), 3069–3084 (2015)

Class of Damage-Healing Models for Cementitious Composites at Multi-scales

34

S. Zhou, Jiann-Wen Woody Ju, H. H. Zhu, and Z. G. Yan

Contents

Introduction 934
The Compliance of Damaged Materials 936
The Healing Process 941
Verification and Parametric Analysis 946
The DEM Self-Healing Model 949
Parametric Analysis 952
Summary/Conclusions 954
References 955

Abstract

Microcapsule-enabled self-healing concretes are appealing due to the advantages of self-healing and the potential for controllable quantifiable healing on a large scale with little initial damage. The damage-healing mechanics and discrete element method (DEM) are emerging as increasingly adopted approaches for investigating the damage phenomenon of materials. Based on experimental results, a two-dimensional micromechanical damage-healing model and a 3D

S. Zhou (✉)
College of Materials Science and Engineering, Chongqing University, Chongqing, China
e-mail: shuaizhou@cqu.edu.cn

J.-W. W. Ju
Department of Civil and Environmental Engineering, University of California, Los Angeles, CA, USA

State Key Laboratory for Disaster Reduction in Civil Engineering, Tongji University, Shanghai, China
e-mail: juj@ucla.edu

H. H. Zhu · Z. G. Yan
Department of Geotechnical Engineering, State Key Laboratory for Disaster Reduction in Civil Engineering, Tongji University, Shanghai, China
e-mail: zhuhehua@tongji.edu.cn; yanzguo@tongji.edu.cn

© Springer Nature Switzerland AG 2022

G. Z. Voyiadjis (ed.), *Handbook of Damage Mechanics*,
https://doi.org/10.1007/978-3-030-60242-0_51

discrete element model of microcapsule-enabled self-healing cementitious materials are proposed. The healing effect on microcrack-induced damage can now be predicted quantitatively by its microscopic healing mechanism. Subsequently, different system parameters of the microcapsule-enabled self-healing concrete, such as the radius and volume fraction of microcapsules, fracture toughness of healing agents, and initial damage, are investigated. In particular, the proposed damage-healing models demonstrate the potential capability to explain and simulate the physical behavior of microcapsule-enabled self-healing materials at multi-scales.

Keywords

Self-healing · Microcapsule · 2D micromechanical damage-healing model · Cementitious composites · Healing probability · DEM · Time delay effect · Partial healing effect · Damage process · Interface

Introduction

The self-healing cementitious composite is a new way to repair the concrete. It can extend the service life and decrease the charge with the hollow fibers, hollow glass tubes, or microcapsules with the self-healing agents. The microcapsule-enabled self-healing concrete has many advantages like the self-healing properties and the reduced negative impact. The microcapsule-enabled self-healing materials were developed by White et al. (2001). After the break of microcapsules, the inner healing agent flows out and heals the microcracks as displayed in Fig. 1 (Zhu et al. 2015b). The healing agents, catalysts, and the shell constitute the self-healing concrete.

Much experimental research has been carried out to test the materials of shell and healing agents by mechanical tests, permeability test, SEM analyses, and FESEM analyses (Yang et al. 2011; Zhou et al. 2015; Zhu et al. 2015b). However, the theoretical models of microcapsule-enabled self-healing cementitious materials have been ignored in these researches. The continuum damage mechanics and

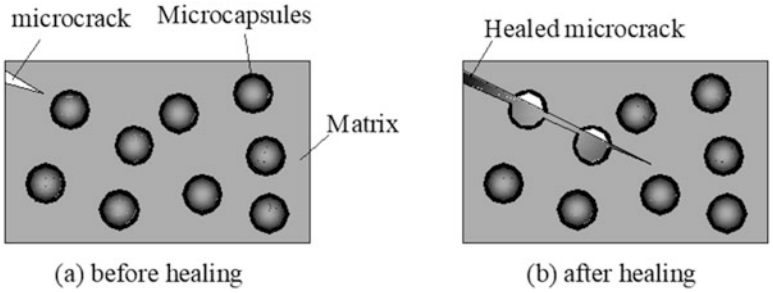

Fig. 1 The healing process of the self-healing concrete (Zhu et al. 2015b)

micromechanical damage mechanics (Horii and Nemat-Nasser 1983; Simo and Ju 1987a, b; Sumarac and Krajcinovic 1987; Fanella and Krajcinovic 1988; Ju 1989; Ju et al. 1989; Simo and Ju 1989; Ju 1991; Ju and Lee 1991; Ju and Chen 1994a, b; Ju and Tseng 1995) are widely used to study the behavior of materials, while fewer papers are about the healing mechanics. A damage-healing constitutive model was developed according to thermodynamics (Barbero et al. 2005), and the related experiment about microcapsule-enabled composites was conducted (Barbero and Ford 2007). Then, other healing models were studied (Voyiadjis et al. 2011). But those models about continuum damage-healing mechanics neglect the microscopic healing mechanism. Some healing models about the damage-healing properties of soils were developed (Ju and Yuan 2012; Ju et al. 2012; Yuan and Ju 2012). Then, Zhu et al. (2015b) developed a damage-healing model for the microcapsule-enabled self-healing material at the mesoscale. However, only the tensile loading is considered, and the healing effect caused by tension is different from that by compression. Meanwhile, the radius of microcapsules and the negative influence of microcapsules on the matrix were ignored (Ford 2006). Previous research has not investigated in depth the damage-healing models of the microcapsule-enabled self-healing cementitious materials under compression.

The cracking behavior of materials can be investigated by numerical methods (Zhou et al. 2016, 2017, 2019; Zhuang and Zhou 2018, 2019; Zhou and Zhuang 2018, 2019), and the healing properties of microcapsule-enabled self-healing cementitious materials can be studied by DEM. By breaking of bonds between two particles, the cracking behavior of materials in DEM is simulated (Itasca 2004). It shows the capacity for simulating those damaging behavior for materials (Zhou et al. 2016). Numerical techniques have been used to study those self-healing impact of blacktop (Luding et al. 2005). Considering different healing mechanisms and healing processes, these models cannot be connected straightforwardly to the microcapsule-enabled cementitious materials. High temperatures can heal the asphalt, while the healing agent can cure the microcapsule-enabled self-healing material. Later, a numerical model which considered the self-healing behavior of the microcapsule-enabled polymer was developed (Luding 2011). However, only closed cracks can induce the self-healing effect, while microcracks which have a small opening were neglected (Li et al. 2013; Zhu et al. 2015a, b, 2016).

In this chapter, a two-dimensional mechanical damage-healing model under compression and a three-dimensional DEM damage-healing model are proposed according to the healing mechanism of the self-healing material. Section "The Compliance of Damaged Materials" proposes the two-dimensional mechanical damage-healing model. Section "The Healing Process" develops the microcrack kinetic equations. Section "Verification and Parametric Analysis" shows the stress-strain curves of the microcapsule-enabled self-healing material under compression. Section "The DEM Self-Healing Model" indicates the numerical DEM model for the self-healing material. Section "Parametric Analysis" illustrates the different factors affecting the damage-healing behavior of self-healing materials. Finally, section "Summary/Conclusions" summarizes the conclusions of the present chapter.

The Compliance of Damaged Materials

The fourth-order elastic-damage secant compliance tensor $\overline{\mathbf{S}}$ and the fourth-order anisotropic damage tensor $\overline{\mathbf{D}}$ have the matchup (Ju 1991). Hence, this research uses $\overline{\mathbf{S}}(\overline{\mathbf{D}})$ as the damage variable (Simo and Ju 1987b; Ju 1989, 1991). The elastic damage secant compliance tensor is (cf. Mura 1982; Horii and Nemat-Nasser 1983; Ju 1991; Ju and Lee 1991; Lee and Ju 1991)

$$\overline{\mathbf{S}}=\mathbf{S}^0+\mathbf{S}^d \tag{1}$$

where $\mathbf{S}^0$ shows the undamaged elastic compliance of the matrix and $\mathbf{S}^d$ represents the additional compliance caused by initial microcracks, activated microcracks, and kinked microcracks. Here, initial microcracks mean existing microcracks at the beginning. Activated microcracks are the microcracks which propagate in a self-similar manner. Kinked microcracks represent the microcracks propagating in a nonself-similar manner (Nemat-Nasser and Horii 1982; Lee and Ju 1991). The inelastic compliance refers to the compliance induced by initial microcracks (i.e., $\mathbf{S}^{cs}$), activated microcracks (i.e., $\mathbf{S}^{cu}$), and kinked microcracks (i.e., $\mathbf{S}^{k}$) (Ju 1991):

$$\mathbf{S}^d=\mathbf{S}^{cs}+\mathbf{S}^{cu}+\mathbf{S}^{k} \tag{2}$$

The matrix consisting of cement paste and aggregates is considered as a uniform and continuous material. The Taylor's model neglects the interaction between microcracks (Sumarac and Krajcinovic 1987). The microcrack-induced compliance under compressive loading is (Horii and Nemat-Nasser 1983)

$$\mathbf{S}^{d(k)\prime}=\begin{bmatrix}0 & 0 & 0\\ 0 & 0 & 0\\ 0 & \dfrac{2\pi a^{(k)2}\mu\,\mathrm{sgn}\left(\overline{\tau}'_3\right)\left(1-\upsilon_0^2\right)}{AE_0} & \dfrac{2\pi a^{(k)2}\left(1-\upsilon_0^2\right)}{AE_0}\end{bmatrix} \tag{3}$$

where $\mathbf{S}^{d(k)'}$ is the microcrack-induced compliance. $a^{(k)}$, $\overline{\tau}'_3$, A, μ, E_0, and υ_0 are the length of kth microcrack, the shear stress on a microcrack, the area of the cross section, the coefficient of sliding friction, the elastic moduli, and Poisson's ratio of the equivalent matrix, respectively. Sgn(x) is 1,0 or −1 depending on whether x is positive, zero, or negative.

In a representative element, the inelastic compliance $\mathbf{S}^d$ can be decomposed into (Ju 1991)

$$\begin{aligned}S_{ij}^d&=\sum_k g_{mi}^{(k)}g_{nj}^{(k)}S_{mn}^{d(k)'}=\sum_k S_{ij}^{d(k)}=N<S_{ij}^{d(k)}>\\&=N\int_\Omega S_{ij}^{d(k)}p(\theta,a)d\Omega\end{aligned} \tag{4}$$

where N means the total number of microcracks and $p(\theta, a)$ represents the joint probability density function of the crack size a and the orientation θ, respectively. $<\bullet>$ signifies the expected value. $\mathbf{g}$ refers to the transformation matrix as (Ju 1991)

$$[\mathbf{g}] \equiv \begin{bmatrix} \cos^2\theta & \sin^2\theta & \sin 2\theta \\ \sin^2\theta & \cos^2\theta & -\sin 2\theta \\ -\frac{1}{2}\sin 2\theta & \frac{1}{2}\sin 2\theta & \cos 2\theta \end{bmatrix} \tag{5}$$

Based on the above equations, the compliance can be obtained quantitatively. After the healing agents cure in a microcrack, the length of the microcrack decreases. Further, the material will be healed due to the reduced crack length according to Eq. (4). Hence, the healing effect of the microcapsule-enabled self-healing concrete can be predicted quantitatively.

q and q^* are defined as the axial and lateral compressive stresses, respectively. On the surface of a microcrack, the normal stress σ_n, shear stress $\overline{\tau}'_3$, and effective shear stress τ_s with the angle θ can be expressed as (Lee and Ju 1991)

$$\sigma_n = \overline{\tau}'_2 = q\cos^2\theta + q^*\sin^2\theta \tag{6}$$

$$\overline{\tau}'_3 = (q - q^*)\cos\theta\sin\theta \tag{7}$$

$$\tau_s = \overline{\tau}'_3 - \mu\overline{\tau}'_2 = F(\theta)\left[q - \left(1 + \frac{\mu}{F(\theta)}\right)q*\right] \tag{8}$$

where $F(\theta) = \sin\theta\cos\theta - \mu\cos^2\theta$.

If $\tau_s \geq 0$, the surface of microcracks slides. Under compression, microcracks within $(\pm\theta_{s1}, \pm\theta_{s2})$ experience closed sliding, while other microcracks stay static. The domain of sliding microcracks is (Ju 1991).

$$\tan(\pm\theta_{s1,s2}) = \frac{1 \pm \sqrt{1 - 4C_1(C_1 + \mu)}}{2C_1}, q \geq \left[2\mu\left(\sqrt{\mu^2 + 1} + \mu\right) + 1\right]q^*, C_1 \equiv \mu q^*/(q - q^*) \tag{9}$$

The fracture criterion of mode-II microcrack growth is (Lee and Ju 1991)

$$K_{II}{}' = K^0_{IIC} \tag{10}$$

To activate unstable mode-II microcrack growth, the stress q is (Ju 1991)

$$q = -\frac{K^0_{IIC}}{\sqrt{\pi a_0 F(\theta)}} + \left(1 + \frac{\mu}{F(\theta)}\right)q^* \tag{11}$$

The minimal q (i.e., q_0) is (Ju 1991)

$$q_0 = -\frac{K_{IIC}^0}{\sqrt{\pi a_0} F(\theta_0)} + \left(1 + \frac{\mu}{F(\theta_0)}\right) q^* \tag{12}$$

where

$$\theta_0 = \arctan\left(\mu + \sqrt{\mu^2 + 1}\right) \tag{13}$$

The unstable domain ($\pm\theta_{u1}$, $\pm\theta_{u2}$) can be calculated by (Ju 1991)

$$\tan(\pm\theta_{u1,u2}) = \frac{1 \pm \sqrt{1 - 4C_2(C_2 + \mu)}}{2C_2}, q \geq q_0, C_2 \equiv \left\{-K_{IIC}^0/\sqrt{\pi a_0} + \mu q^*\right\}/(q - q^*) \tag{14}$$

Under higher compression, the arrested microcracks kink into the matrix in a nonself-similar way. The length of a kinked microcrack is (Nemat-Nasser and Horii 1982; Ju 1991; Lee and Ju 1991)

$$l = \frac{4a_f^2 \tau_s^2 \cos^2\theta}{\pi K_{IC}^{c\,2}} \tag{15}$$

where K_{IC}^c is the mode-I fracture toughness of the matrix. The threshold stress q_{kink} is (Ju 1991)

$$q_{kink} = -\frac{\sqrt{3} K_{IC}^c}{2F\left(\theta_0^{II}\right)\sqrt{\pi a_f}} + \left(1 + \frac{\mu}{F\left(\theta_0^{II}\right)}\right) q^* \tag{16}$$

where $F(\theta) \equiv \sin\theta \cos\theta - \mu\cos^2\theta$. The domain of stable kinked microcracks ($\pm\theta_{k1}$, $\pm\theta_{k2}$) is

$$\begin{aligned} \tan\theta_{k1,k2} &= \frac{1 \pm \sqrt{1 - 4H_3(\mu + H_3)}}{2H_3}; (-q + q^*)^2 \\ &\geq 4\left[\frac{\sqrt{3}K_{IC}^c}{2\sqrt{\pi a_f}} - \mu q^*\right]\left[\frac{\sqrt{3}K_{IC}^c}{2\sqrt{\pi a_f}} - \mu q\right] \end{aligned} \tag{17}$$

where

$$H_3 \equiv \left\{\left[\sqrt{3}K_{IC}^c/2\sqrt{\pi a_f}\right] - \mu q^*\right\}/(-q + q^*) \tag{18}$$

Microcrack nucleation happens in brittle solids (Smith and Barnby 1967). If the critical shear stress exceeds the debonding stress τ_{bond}, new microcracks occur (Lee and Ju 1991). Thus, the domain of nucleated microcracks (θ_{n1}, θ_{n2}) is

$$\theta_{n1,n2} = \arctan\left(\frac{-(q-q^*) \pm \sqrt{(q-q^*)^2 - 4\tau_{bond}^2}}{2\tau_{bond}}\right) \tag{19}$$

From Eq. (19), the minimal q_n is

$$q_n = 2\tau_{bond} + q^* \tag{20}$$

In the microcapsule-enabled self-healing cementitious materials, the randomness of healing should not be ignored (Zhu et al. 2015a). The healing probability can be obtained by geometric probability, as displayed in Fig. 2.

The microcapsule breaks, and the self-healing occurs if the center of any microcapsule is in the zone of A_1 in Fig. 2. The failure probability of one microcapsule can be obtained by (Zhu et al. 2015a)

$$p = \frac{A_{A1}}{A_{RAE}} = \frac{2a_f(l_2+2r)}{(A/N)} = \frac{2Na_f(l_2+2r)}{A} \tag{21}$$

where A_{A1}, A_{RAE}, A, l_2, r, and N are the area of A_1, the area of one representative area element (RAE), the area of the cross section, the average width of a microcrack, the radius of a microcapsule, and the number of microcracks in the cross section, respectively.

The length filled by the ith microcapsule is (Zhu et al. 2015a)

$$a_h^i = \frac{\pi {r_i}^2}{l_2} \tag{22}$$

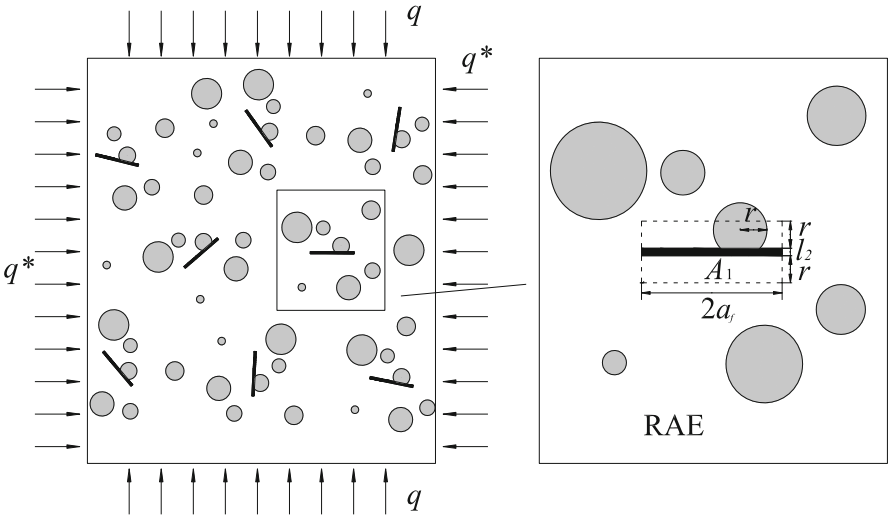

Fig. 2 The crack and microcapsules in an RAE

The length of the healed microcracks is

$$\begin{aligned} < 2a_h > &= 2a_f - < \sum_{i=1}^{n} a_h^i > \\ &= 2a_f - \sum_{i=1}^{n} < a_h^i > \\ &= 2a_f - \sum_{i=1}^{n} < \frac{2Na_f(l_2 + 2r_i)}{A} \frac{\pi r_i^2}{l_2} > \end{aligned} \tag{23}$$

Based on previous research (Ford 2006), the size of microcapsules follows the normal distribution. K and D are the mean value and the variance of radii, respectively. Then, $<2a_h>$is

$$\begin{aligned} < 2a_h > &= 2a_f - \sum_{i=1}^{n} < \frac{2Na_f(l_2 + 2r_i)}{A} \frac{\pi r_i^2}{l_2} > \\ &= 2a_f - \frac{2Na_f\pi}{Al_2} \left(l_2 nD + l_2 nK^2 + 6nDK + 2nK^3 \right) \end{aligned} \tag{24}$$

where n is the number of microcapsules in an RAE and follows the expression: $n = m/N$, with N and m signifying the total number of initial microcracks and microcapsules in the cross section, respectively. These repaired microcracks are still treated as line cracks, with a length of $2a_{fh}$ or $2a_{lh}$. $2a_{fh}$ and $2a_{lh}$ are the length of a repaired mode-II microcrack and a repaired kinked microcrack, respectively.

The volume fraction φ can be obtained by

$$\varphi = \frac{m < \pi r^2 >}{A} = \frac{m\pi}{A} \left(D + K^2 \right) \tag{25}$$

These self-healing microcapsules are soft inclusions and reduce the stiffness of the concrete. The Mori-Tanaka method is widely used to obtain the effective modulus of composites (Mori and Tanaka 1973):

$$K_M = K_{ma} + \frac{\phi_M (K_{in} - K_{ma})(3K_{ma} + 4\mu_{ma})}{3K_{ma} + 4\mu_{ma} + 3(1 - \phi_M)(K_{in} - K_{ma})} \tag{26}$$

$$\mu_M = \mu_{ma} + \frac{5\phi_M \mu_{ma} (\mu_{in} - \mu_{ma})(3K_{ma} + 4\mu_{ma})}{5\mu_{ma}(3K_{ma} + 4\mu_{ma}) + 6(1 - \phi_M)(\mu_{in} - \mu_{ma})(K_{ma} + 2\mu_{ma})} \tag{27}$$

where K_M, μ_M, K_{in}, μ_{in}, K_{ma}, μ_{ma}, and ϕ_M are the effective bulk modulus and shear modulus of the two-phase composite, the bulk modulus and shear modulus of the microcapsules, the bulk modulus and shear modulus of the cementitious matrix, and the volume fraction of the microcapsules, respectively. Here, the microcapsules are treated as voids with $K_{in} = \mu_{in} = 0$.

If the healing agent is strong, the healed microcracks do not reopen, and the final failure occurs due to new nucleated microcracks, while the debonding failure happens if the healing agent is weak. Hence, the final failure occurs when the stress intensity factor (SIF) of the repaired microcracks equals the critical SIF K^h_{IIC} or the SIF of new nucleated microcracks reaches the critical SIF K^c_{IIC} (Zhu et al. 2015b). The corresponding loads are $q^h_{\max 1}$, $q^h_{\max 2}$ and $q^c_{\max}$, respectively. Hence, q_{fh} is

$$q_{fh} = \min\left(q^h_{\max 1}, q^h_{\max 2}, q^c_{\max}\right) \tag{28}$$

where

$$q^h_{\max 1} = \min\left(-\frac{K^h_{IIC}}{F(\theta)\sqrt{\pi a_{lh}}} + \left(1 + \frac{\mu}{F(\theta_0)}\right)q^*\right) \;;\; \theta \in (\pm\theta_{k1}, \pm\theta_{k2}) \tag{29}$$

$$q^h_{\max 2} = \min\left(-\frac{K^h_{IIC}}{F(\theta)\sqrt{\pi a_{fh}}} + \left(1 + \frac{\mu}{F(\theta_0)}\right)q^*\right) \;;\; \theta \in (\pm\theta_{u1,new}, \pm\theta_{u2,new}) \tag{30}$$

$$q^c_{\max} = \min\left(\frac{\tau_{bond}}{\sin\theta\cos\theta} + q*\right) \;;\; \theta \in (\pm\theta_{k1}, \pm\theta_{k2}) \tag{31}$$

The Healing Process

Micromechanics, probability theory and fracture mechanics, are adopted in this chapter to present the healing process. Many initial microcracks (e.g., the aggregate-cement interfaces) exist along weak planes in brittle materials. After the SIF is greater than the critical value, an existing microcrack goes along the weak plane in a self-similar manner until reaching a certain characteristic size (Krajcinovic and Fanella 1986). Then, kinking occurs when the compressive loading is great (Fanella and Krajcinovic 1988). As the loading increases, the microcracks nucleate (Lee and Ju 1991). Based on the experimental observation (Brown et al. 2005), the healing agents form a polymer wedge at the microcrack tip by capillary suction in cracks, reducing the crack length and preventing additional microcrack growth. Some repaired microcracks reopen because of the weak healing agents (White et al. 2001; Van Tittelboom et al. 2011).

It is defined that $2a_0$, $2a_f$, and $2a_l$ are the initial crack length, activated crack length, and kinked crack length, respectively. After healing, the crack length reduces from $2a_f$ to $2a_{fh}$ or from $2a_l$ to $2a_{lh}$. q_1 is the maximum load the cross section has experienced. Within (θ_{s1}, θ_{s2}), microcracks slide. Within (θ_{u1}, θ_{u2}), microcracks are activated. Within (θ_{k1}, θ_{k2}), microcracks kink. It is reasonable to assume that the self-healing happens only during the rest period in compression tests based on the experiments (Brown et al. 2005; Gilford III et al. 2013). The whole healing process can be illustrated as follows:

(a) As $q \equiv q_1 < q_0$, no microcrack with $2a_0$ as the crack length propagates and those within ($\pm\theta_{s1}$, $\pm\theta_{s2}$) slide in Fig. 3. q_0 is the compressive stress to initiate the unstable mode-II microcrack growth. The compliance changes to

$$\overline{\mathbf{S}} = \mathbf{S}_0 + \mathbf{S}^{cs} \tag{32}$$

where

$$\mathbf{S}^{cs} = \frac{N}{\pi}\int_{\pm\theta_{s1}}^{\pm\theta_{s2}} \mathbf{g}^{(k)T}\mathbf{S}^{d(k)\prime}(\theta, a_0)\mathbf{g}^{(k)}d\theta \tag{33}$$

(b) As $q_0 \le q \equiv q_1 \le q_{kink}$, the microcracks within ($\pm\theta_{u1}$, $\pm\theta_{u2}$) are activated, and the length grows from $2a_0$ to $2a_f$, as displayed in Fig. 4. The compliance is

$$\overline{\mathbf{S}} = \mathbf{S}_0 + \mathbf{S}^{cs} + \mathbf{S}^{cu} \tag{34}$$

where

$$\mathbf{S}^{cs} = \frac{N}{\pi}\left[\int_{\pm\theta_{s_1}}^{\pm\theta_{u_1}} \mathbf{g}^{(k)T}\mathbf{S}^{d(k)\prime}(\theta, a_0)\mathbf{g}^{(k)}d\theta + \int_{\pm\theta_{u_2}}^{\pm\theta_{s_2}} \mathbf{g}^{(k)T}\mathbf{S}^{d(k)\prime}(\theta, a_0)\mathbf{g}^{(k)}d\theta\right] \tag{35}$$

$$\mathbf{S}^{cu} = \frac{N}{\pi}\int_{\pm\theta_{u_1}}^{\pm\theta_{u_2}} \mathbf{g}^{(k)T}\mathbf{S}^{d(k)\prime}\left(\theta, a_f\right)\mathbf{g}^{(k)}d\theta \tag{36}$$

(c) As $q_{kink} \le q \equiv q_1 \le q_f$, microcracks within ($\pm\theta_{k1}$, $\pm\theta_{k2}$) kink, as shown in Fig. 5. The current compliance is

$$\overline{\mathbf{S}} = \mathbf{S}_0 + \mathbf{S}^{cs} + \mathbf{S}^{cu} + \mathbf{S}^{k} \tag{37}$$

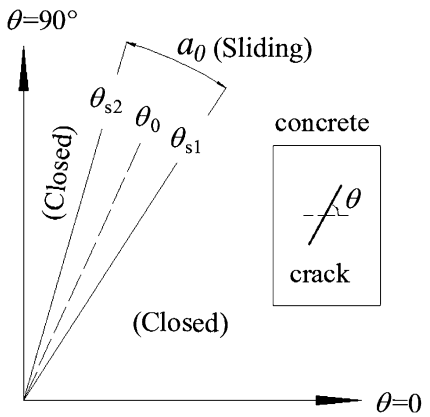

Fig. 3 The microcracks within ($\pm\theta_{s1}$, $\pm\theta_{s2}$) slide

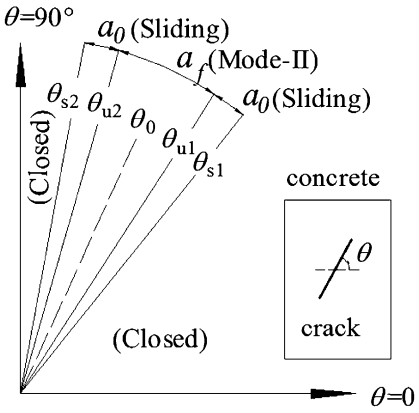

Fig. 4 Sliding and activated microcracks

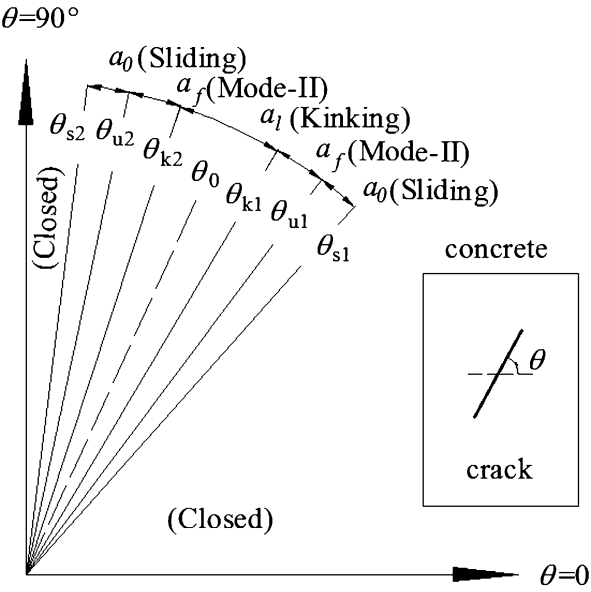

Fig. 5 Sliding, activated, and kinked microcracks

where

$$\mathbf{S}^{cs} = \frac{N}{\pi}\left[\int_{\pm\theta_{s_1}}^{\pm\theta_{u_1}} \mathbf{g}^{(k)T}\mathbf{S}^{d(k)\prime}(\theta, a_0)\mathbf{g}^{(k)}d\theta + \int_{\pm\theta_{u_2}}^{\pm\theta_{s_2}} \mathbf{g}^{(k)T}\mathbf{S}^{d(k)\prime}(\theta, a_0)\mathbf{g}^{(k)}d\theta\right] \tag{38}$$

$$\mathbf{S}^{cu} = \frac{N}{\pi}\int_{\pm\theta_{u_1}}^{\pm\theta_{u_2}} \mathbf{g}^{(k)T}\mathbf{S}^{d(k)\prime}\left(\theta, a_f\right)\mathbf{g}^{(k)}d\theta \tag{39}$$

$$\mathbf{S}^{k} = \frac{N}{\pi}\int_{\pm\theta_{k1}}^{\pm\theta_{k2}} \mathbf{g}^{(k)T}\mathbf{S}^{d(k)\prime}(\theta, a_l)\mathbf{g}^{(k)}d\theta \tag{40}$$

(d) As $q = 0$, the unloading happens and self-healing begins. Those microcracks within ($\pm\theta_{u1}$, $\pm\theta_{u2}$) are repaired, and the crack length decreases from $2a_f$ to $2a_{fh}$. The crack length of microcracks within ($\pm\theta_{k1}$, $\pm\theta_{k2}$) reduces from $2a_l$ to $2a_{lh}$.

(e) As reloading and $q < q_1$, no microcrack expands, as exhibited in Fig. 6. The current compliance $\overline{\mathbf{S}}$ is

$$\overline{\mathbf{S}} = \mathbf{S}_0 + \mathbf{S}^{cs} + \mathbf{S}^{cu} + \mathbf{S}^{k} \tag{41}$$

where

$$\mathbf{S}^{cs} = \frac{N}{\pi}\left[\int_{\pm\theta_{s_1}}^{\pm\theta_{u_1}} \mathbf{g}^{(k)T}\mathbf{S}^{d(k)\prime}(\theta, a_0)\mathbf{g}^{(k)}d\theta + \int_{\pm\theta_{u_2}}^{\pm\theta_{s_2}} \mathbf{g}^{(k)T}\mathbf{S}^{d(k)\prime}(\theta, a_0)\mathbf{g}^{(k)}d\theta\right] \tag{42}$$

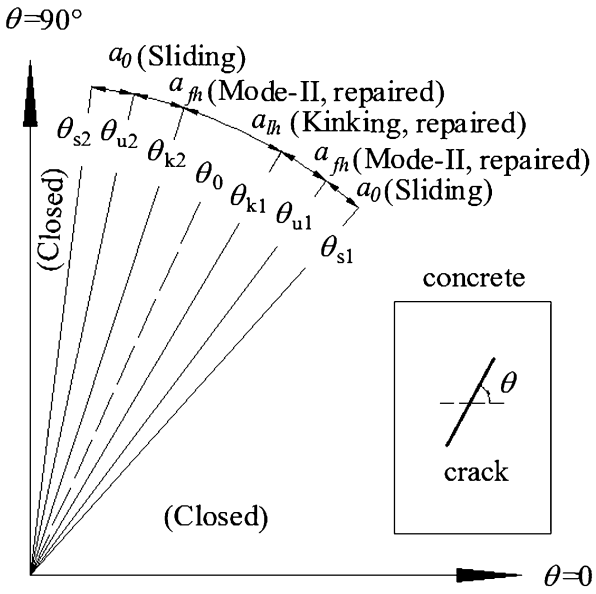

Fig. 6 Microcracks within ($\pm\theta_{u1}$, $\pm\theta_{u2}$) are repaired

$$\mathbf{S}^{cu} = \frac{N}{\pi}\int_{\pm\theta_{u_1}}^{\pm\theta_{u_2}} \mathbf{g}^{(k)T}\mathbf{S}^{d(k)\prime}\left(\theta, a_{fh}\right)\mathbf{g}^{(k)}d\theta \tag{43}$$

$$\mathbf{S}^{k} = \frac{N}{\pi}\int_{\pm\theta_{k1}}^{\pm\theta_{k2}} \mathbf{g}^{(k)T}\mathbf{S}^{d(k)\prime}(\theta, a_{lh})\mathbf{g}^{(k)}d\theta \tag{44}$$

(f) As reloading begins and $q \equiv q_1 < q_n$, some microcracks propagate in mode-II. q_n is the compressive stress inducing the nucleation from Eq. (20), as displayed in Fig. 7. Unstable microcracks expand within $(\pm\theta_{u1,\ new}, \pm\theta_{u1})$ and $(\pm\theta_{u2}, \pm\theta_{u2,\ new})$. The current compliance $\overline{\mathbf{S}}$ is

$$\overline{\mathbf{S}} = \mathbf{S}_0 + \mathbf{S}^{cs} + \mathbf{S}^{cu} + \mathbf{S}^{k} \tag{45}$$

where

$$\mathbf{S}^{cs} = \frac{N}{\pi}\left[\int_{\pm\theta_{s_1}}^{\pm\theta_{u_1},^{new}} \mathbf{g}^{(k)T}\mathbf{S}^{d(k)'}(\theta, a_0)\mathbf{g}^{(k)}d\theta + \int_{\pm\theta_{u_2,^{new}}}^{\pm\theta_{s_2}} \mathbf{g}^{(k)T}\mathbf{S}^{d(k)'}(\theta, a_0)\mathbf{g}^{(k)}d\theta\right] \tag{46}$$

$$\mathbf{S}^{cu} = \frac{N}{\pi}\left[\begin{array}{l}\int_{\pm\theta_{u_1}}^{\pm\theta_{u_2}} \mathbf{g}^{(k)T}\mathbf{S}^{d(k)'}\left(\theta, a_{fh}\right)\mathbf{g}^{(k)}d\theta + \int_{\pm\theta_{u_1},^{new}}^{\pm\theta_{u_1}} \mathbf{g}^{(k)T}\mathbf{S}^{d(k)'}\left(\theta, a_f\right)\mathbf{g}^{(k)}d\theta \\ + \int_{\pm\theta_{u_2}}^{\pm\theta_{u_2},^{new}} \mathbf{g}^{(k)T}\mathbf{S}^{d(k)'}\left(\theta, a_f\right)\mathbf{g}^{(k)}d\theta\end{array}\right] \tag{47}$$

$$\mathbf{S}^{k} = \frac{N}{\pi}\int_{\pm\theta_{k1}}^{\pm\theta_{k2}} \mathbf{g}^{(k)T}\mathbf{S}^{d(k)'}(\theta, a_{lh})\mathbf{g}^{(k)}d\theta \tag{48}$$

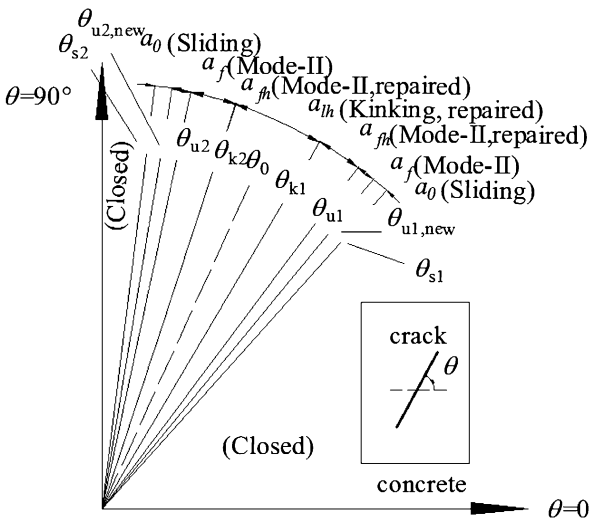

Fig. 7 Unstable microcracks expand within $(\pm\theta_{u1,\ new}, \pm\theta_{u1})$ and $(\pm\theta_{u2}, \pm\theta_{u2,\ new})$

(g) If $q \equiv q_1 \geq q_n$, microcrack nucleation occurs, which increases the compliance of specimens and the number of microcracks (Lee and Ju 1991).
(h) As reloading and $q = q_{fh}$, the specimen falls at last.

Verification and Parametric Analysis

Here, the model is verified by the corresponding experimental results. Meanwhile, the parametric analysis of the self-healing model is conducted here. Since the self-healing effect will be activated by the propagation of cracks, a compressive load is applied to induce initial damage, and the following self-healing occurs (White et al. 2001; Zhou et al. 2015). The influence of different initial damage, fracture toughness, volume fractions, and radii of microcapsules are studied. The uniaxial compression test is applied.

The previous uniaxial compression test of microcapsule-enabled self-healing materials is used to validate the proposed model (Gilford III et al. 2013). The following parameters are adopted: $E_0 = 32.6$ GPa, $\upsilon_0 = 0.2$, $K^0_{IIC} = 0.33$ MPa·m$^{1/2}$, $K^0_{IC} = 0.165$ MPa·m$^{1/2}$, $K^c_{IC} = 0.578$ MPa·m$^{1/2}$, $K^c_{IIC} = 1.734$ MPa·m$^{1/2}$, $a_0 = 0.5$ cm, $a_f = 0.828$ cm, $\tau_{bond} = 20$ MPa, $\mu = 0.6$, $N = 22$, $A = 100$ cm^2, $K^h_{IIC} = 3.468$ MPa·m$^{1/2}$, and $l_2 = 40$ μm, respectively. Following the experiments, the mean value of the radii of microcapsules is 450 μm, and 20 MPa is applied to cause initial damage (Gilford III et al. 2013).

The numerical results and experimental results are compared in Table 1 (Gilford III et al. 2013). From Table 1, the numerical results match the experimental results well. The proposed model presents the capability to simulate the self-healing behavior of the microcapsule-enabled self-healing concrete.

Then, the parametric study is conducted. The parameters of the concrete are taken from previous studies (Ju 1991; Lee and Ju 1991). The virgin material has Young's modulus $E_0 = 41.4$ GPa, $\upsilon_0 = 0.2$, and the fracture toughness $K^c_{IC} = 0.578$ MPa·m$^{1/2}$ and $K^c_{IIC} = 1.734$ MPa·m$^{1/2}$. The fracture toughness of the weak plane is taken to be $K^0_{IIC} = 0.33$ MPa·m$^{1/2}$ and $K^0_{IC} = 0.165$ MPa·m$^{1/2}$. The crack lengths on weak planes are taken as $a_0 = 0.572$ cm and $a_f = 0.953$ cm. The critical debonding shear stress τ_{bond} is 20 MPa, and the coefficient of sliding friction μ is 0.6. The total number

Table 1 Experimental and numerical results of the self-healing material at the macroscale

Mechanical properties with different volume fractions of microcapsules	Experimental results	Numerical results
Uniaxial compressive strength	28.0 MPa	28 MPa
Elastic modulus before healing (0.5%)	27.9 GPa	27.1 GPa
Elastic modulus after healing (0.5%)	27.9 GPa	28 GPa
Elastic modulus before healing (1%)	24.5 GPa	26.8 GPa
Elastic modulus after healing (1%)	28.9 GPa	28.8 GPa
Elastic modulus before healing (2.5%)	26.5 GPa	26.0 GPa
Elastic modulus after healing (2.5%)	30.6 GPa	30.5 GPa

of pre-existing microcracks N is 22, and the area A is 100 cm^2. The fracture toughness of the interface between the healing agent and the cementitious matrix is $K^h_{IIC} = 3.468$ MPa·$m^{1/2}$. The number of microcapsules m is 48,971 when the volume fraction of microcapsules is 10%. To simplify the computation, the width of microcracks l_2 is assumed to be a constant 40 μm. The mean value and standard deviation of the radii of microcapsules are $K = 55$ μm and $D = 5$ μm, respectively. The compressive loading of 25 MPa is applied to cause initial damage.

The stress-strain curves of self-healing materials under compression with different fracture toughness of the adhesive interfaces are exhibited in Fig. 8. The earlier period of stress-strain curves is the same since the debonding does not occur, and different fracture toughness of healing agents affect the compressive strength considering that the healing agent decreases the crack length and modifies the property of the microcrack tip. Comparing $K^h_{IIC} = 3.468$ MPa·$m^{1/2}$ and $K^h_{IIC} = 1.734$ MPa·$m^{1/2}$, the greater fracture toughness of the adhesive interfaces induces the greater compressive strength of the specimen. As these repaired microcracks propagate when the adhesive failure occurs, the properties of the healing agent make a difference. Comparing $K^h_{IIC} = 3.468$ MPa·$m^{1/2}$ and $K^h_{IIC} = 5.202$ MPa·$m^{1/2}$, the results are the same because the final failure happens due to the newly nucleated cracks in the matrix, which is irrelevant to the healing agents. Hence, a strong matrix can enhance the self-healing effect. The result agrees with the microcapsule-enabled self-healing material under tension in our previous research (Zhu et al. 2015b).

The initial damage influences the healing effect as presented in Fig. 9. A more serious initial damage leads to a greater compressive strength if the healing agent is

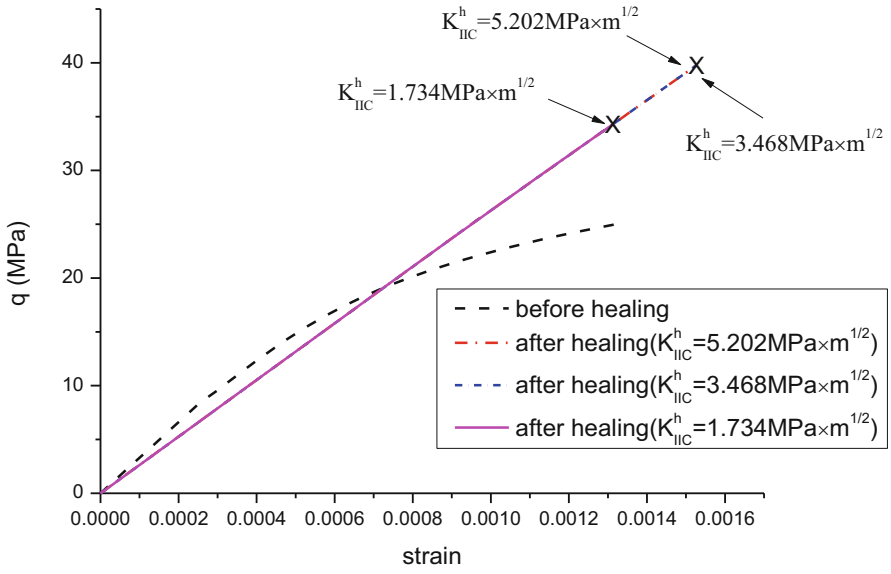

Fig. 8 The stress-strain curves with different fracture toughness of the adhesive interfaces

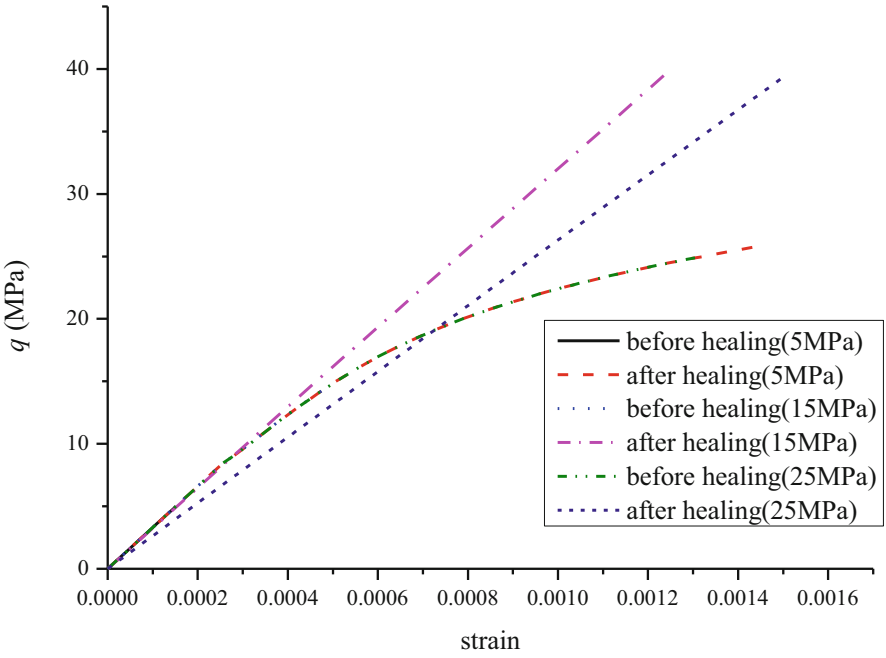

Fig. 9 The stress-strain curves of specimens with different initial damage

strong. With a high-strength healing agent, the mechanical properties of the repaired specimen increase.

Different initial damage leads to different failure modes of specimens. When 25 MPa and 15 MPa are applied to induce the initial damage, the final failure happens due to the nucleated microcracks, while the specimen breaks owing to the kinked microcracks when 5 MPa is used to cause the initial damage. Since the healing agent can only partially heal the damage, a greater initial damage results in a lower stiffness of the specimen comparing the results when 25 MP and 15 MPa are considered. The compressive strength does not change under the two conditions because of the nucleated microcracks in the matrix, which does not relate to the healing effect. Comparing the curves when 15 MPa and 5 MPa are used, the healing effect is not obvious if the initial damage is light since the healing effect is related to the initial damage.

Figure 10 illustrates the stress-strain curves of the microcapsule-enabled self-healing material with different volume fractions of microcapsules.

As exhibited in Fig. 10, when too many microcapsules are applied, the compressive strength of specimens does not increase since these new nucleated microcracks break the concrete, which are not healed by healing agents. Meanwhile, too many microcapsules reduce the elastic modulus of the concrete. After healing, the recovery of the elastic modulus of the repaired concrete with greater volume fractions of microcapsules is greater than that with fewer microcapsules considering that shorter microcracks are obtained.

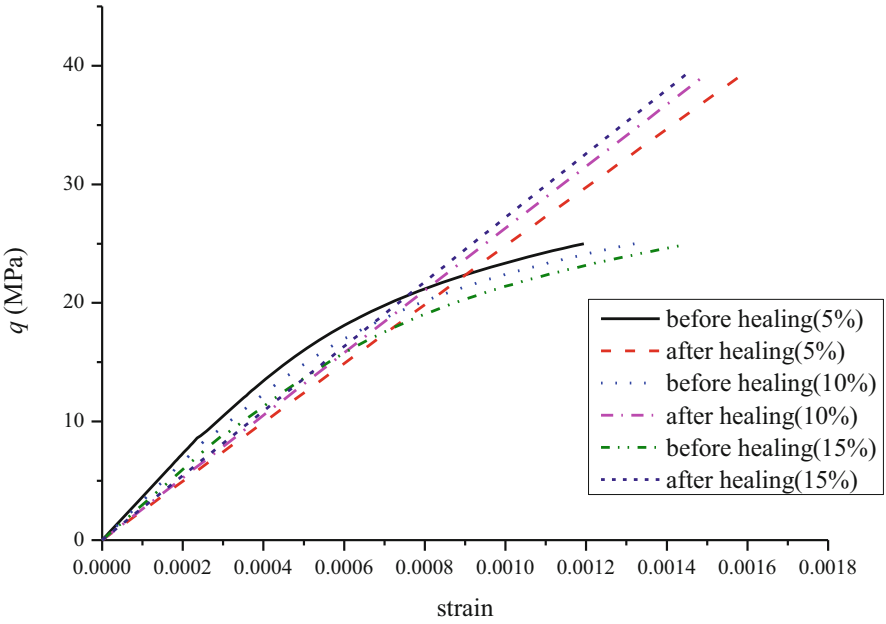

Fig. 10 The stress-strain curves with different volume fractions of microcapsules

The stress-strain curves of specimens under compression with different radii of microcapsules are exhibited in Fig. 11.

As presented in Fig. 11, the effect of the radius of microcapsules on the compressive strengths of the specimens is not obvious. However, they have an effect on the elastic modulus. Smaller microcapsules cause a greater crack length after healing, which makes the repaired microcracks easier to reopen. Bigger microcapsules enhance the healing effect on the elastic modulus as more healing agents flow into the microcracks, which reduces the crack length and the compliance of specimens. The result agrees with the microcapsule-enabled self-healing material under tension (Zhu et al. 2015b).

The DEM Self-Healing Model

Here, an implicit way is adopted to simulate the microcapsules. The microcapsule-enabled cement paste is considered as the springs between particles. Hence, the springs involve the information of the self-healing properties. To achieve the self-healing effect, a new bond is regenerated when the initial bond is broken. The initial bonds are related to the properties of cement paste, while the newly developed bonds are relevant to the cured healing agent. They are applied to mimic the healing behavior of the cured healing agent which connects the two crack surfaces. Here,

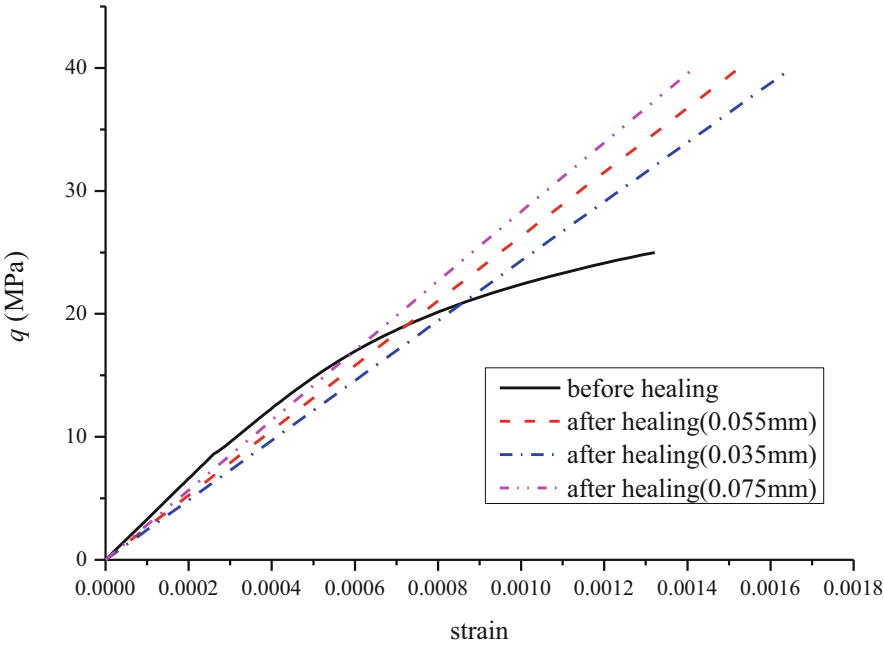

Fig. 11 The stress-strain curves with different radii of microcapsules

only the closed crack and the open crack with a small opening are healed to simulate the practical behavior in experiments. With these new bonds, the macroscopic properties of microcapsule-enabled self-healing materials after healing are gained. Instantaneous healing is unlikely in the microcapsule-enabled self-healing materials since the healing agent requires a long time to totally cure and the time delay effect exists to gain the healing effects. By recording the time when the bonds break and the curing time of healing agents, the exact healing time of one microcrack is available. According to the experiment (Li et al. 2013; Gilford III et al. 2013), the time delay effect is simplified here by assuming that the self-healing happens when the loading is removed considering the loading time is short and the curing time is long. The healing test is exhibited as follows: firstly, compress the specimen to induce initial damage; secondly, unload; then, self-healing occurs; finally, reload.

The healing agent can only partially fill one microcrack (Zhu et al. 2015a, b, 2016). The healing ratio is affected by the parameters of microcapsules, which is simulated by adjusting the radius of regenerated bonds.

At first, the DEM specimens are produced (2004). The cylindrical specimen is considered in this chapter following previous experiments (Gilford III et al. 2013). 5.08 cm and 20.32 cm are chosen as the radius and the height of specimens, respectively. In the DEM model, particles are bonded using the parallel bond model. Two frictionless walls are used to compress the specimens at a specified velocity (Ding et al. 2014), as illustrated in Fig. 12.

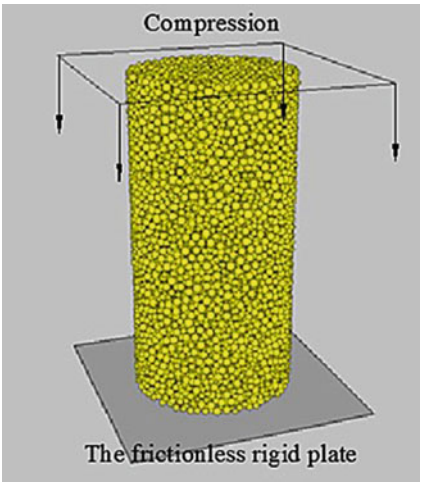

Fig. 12 The DEM specimen in the test

Table 2 Parameters used in the DEM model with DCPD microcapsules

Parameter	Description	Value
E_c	Particle modulus	35 GPa
k_{nc}/k_{sc}	Ratio of particle normal to shear stiffness	2.5
μ	Contact friction coefficient	0.1
R_{max}/R_{min}	Ratio of maximum to minimum ball radius	1.66
R_{min}	Minimum ball radius	2 mm
ρ	Density	2500 kg/m^3
$\overline{E}_c$	Spring modulus	40 GPa
$\overline{k}_{nc}/\overline{k}_{sc}$	Ratio of spring normal to shear stiffness	2.5
s_{nc}	Average normal bond strength±SD	60.0 ± 20.0 MPa
s_{sc}	Average shear bond strength±SD	30.0 ± 28.0 MPa
$\overline{\lambda}$	Bond width multiplier	1.0
k_n	Normal stiffness of the regenerated bonds	3.4×10^8 MPa
k_s	Shear stiffness of the regenerated bonds	3.4×10^8 MPa
s_n	Normal strength of the regenerated bonds	3.4×10^3 MPa
s_s	Shear strength of the regenerated bonds	3.4×10^3 MPa

The specimens are compressed after the self-healing process to gain the properties of newly generated bonds. To fit the experimental results (i.e., elastic modulus before and after healing, and unconfined compressive strength) (Gilford III et al. 2013), the microscopic parameters of the DEM model are interpreted in an iterative procedure (Potyondy and Cundall 2004), as shown in Table 2. Table 3 compares the numerical results and the experimental results (Gilford III et al. 2013). Further verification of the DEM model will be conducted after more results are obtained. The numerical results prove the ability of the proposed 3D DEM model in simulating the healing behavior of microcapsule-enabled self-healing concrete.

Table 3 Comparison of the experimental and numerical results with DCPD microcapsules

Mechanical properties	Experimental results	Numerical results
Elastic modulus before healing (GPa)	26.5	27.1
Elastic modulus after healing (GPa)	30.6	30.4
UCS (MPa)	28.0	27.7

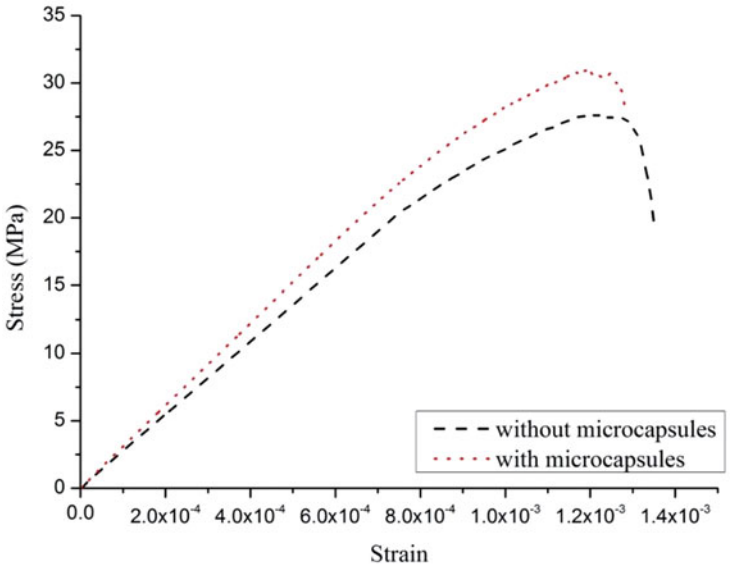

Fig. 13 The stress-strain curves of the self-healing material with microcapsules and the normal concrete

Figure 13 exhibits the stress-strain results of the self-healing material with Dicyclopentadiene (DCPD) microcapsules and the normal concrete. The trend matches the previous experimental results well (Li et al. 2013). 20 MPa is used to cause the initial damage (Gilford III et al. 2013). The self-healing material has better mechanical properties than the normal concrete due to the healing agent, which enhances the material. The increase of the elastic modulus due to the healing effect is not apparent, which is in agreement with our previous results (Li et al. 2013; Zhou et al. 2015). The self-healing microcapsules can extend the elastic period of the curve. Meanwhile, the self-healing effect decreases the peak strain.

Parametric Analysis

The influence of the parameters of the DEM damage-healing model of the microcapsule-enabled self-healing concrete on the healing effect is investigated here. Different stiffness and strength of the cured healing agent and the partial healing are considered in depth.

Figure 14 shows the stress-strain results of the self-healing materials after healing with different stiffness of the healing agent. The stiffness of the healing agent influences the final results. Since the healed microcrack can bear more stress if strong healing agents are used, a greater stiffness and a higher compressive strength of the material will be gained. As the local stress concentration occurs, the healed microcracks are likely debonding if the low-strength healing agent is adopted. Hence, the moderate-stiffness healing agent should be applied. The healing effect is not great even if the extremely stiff healing agent is considered since sparse healed local microcracks cannot influence the stiffness of the whole specimen greatly. Owing to the stress concentration effect, a smaller peak strain breaks the specimen with the stiffer healing agent.

Figure 15 presents the stress-strain curves of the self-healing materials with different strengths of the cured healing agent. The stress-strain curves are the same when $S_n = S_s = 3.4 \times 10^7$ MPa, $S_n = S_s = 3.4 \times 10^5$ MPa, and $S_n = S_s = 3.4 \times 10^3$ MPa since the cured healing agent is very strong and does not break. The specimen falls owing to the matrix, which is not related to the cured healing agent. A high-strength healing agent induces a greater compressive strength and stiffness comparing $S_n = S_s = 3.4 \times 10^3$MPa and $S_n = S_s = 34$ MPa. If the healing agent is weak, these repaired microcracks reopen before the matrix falls, which should be avoided. Hence, the cured healing agent must be strong enough to guarantee the healing effect, at least should be stronger than the matrix.

According to the previous research, a microcrack cannot be completely healed, and the partial healing occurs (Zhu et al. 2015a). Here, by adjusting the radius of regenerated bonds, the healing ratio of one microcrack ranges from 0 to 1. If the

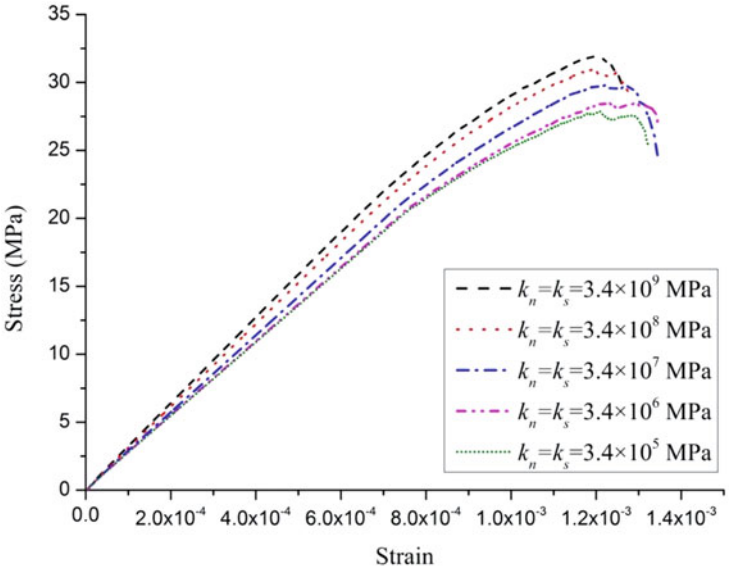

Fig. 14 The stress-strain curves with different stiffness of the healing agent

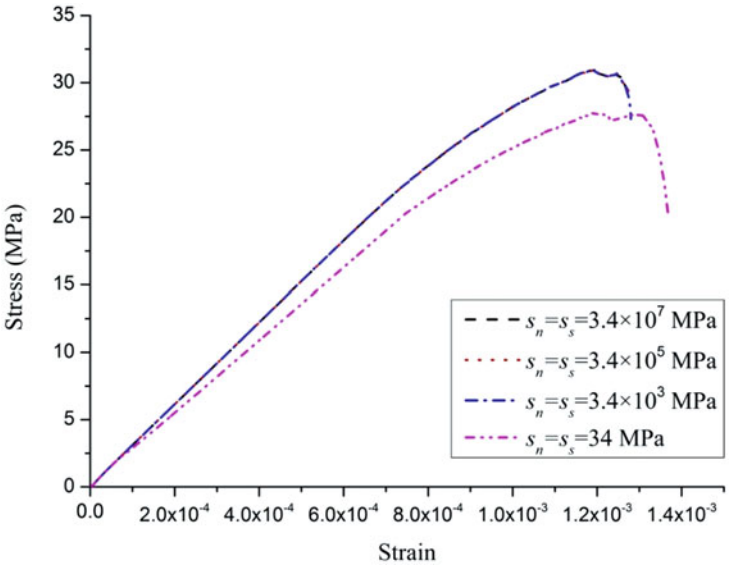

Fig. 15 The stress-strain curves with different strengths of the healing agent

radius of a newly generated bond is 0, then no healing occurs, while one microcrack is completely healed if the radius is 1.

Figure 16 presents the stress-strain curves of self-healing materials with partial healing. When partial healing occurs, the compressive strength of specimens reduces due to a smaller parallel bond is easily broken again. Meanwhile, the stiffness of the specimen increases with a higher healing ratio since it can carry greater loading. Hence, suitable microcapsules which increase the healing ratio of microcracks can enhance the healing effects. The microcapsules can be optimized by our previous research (Zhu et al. 2015a).

Summary/Conclusions

According to the damage-healing mechanism of the microcapsule-enabled self-healing material, a two-dimensional micromechanical damage-healing model under compression is developed at first. The compliance and compressive strength of the self-healing materials after healing can be predicted. Meanwhile, the evolutionary laws of microcracks are obtained. Then, the micromechanical model is validated by previous experimental results. Meanwhile, the influence of different parameters on the healing effect is investigated. A greater compressive strength requires relatively bigger microcapsules, stronger healing agents, larger amounts of microcapsules, and a stronger matrix. A relatively greater radius and a larger volume fraction of microcapsules result in a greater elastic modulus. To enhance the self-healing effect, the weak planes in concrete should also be strengthened.

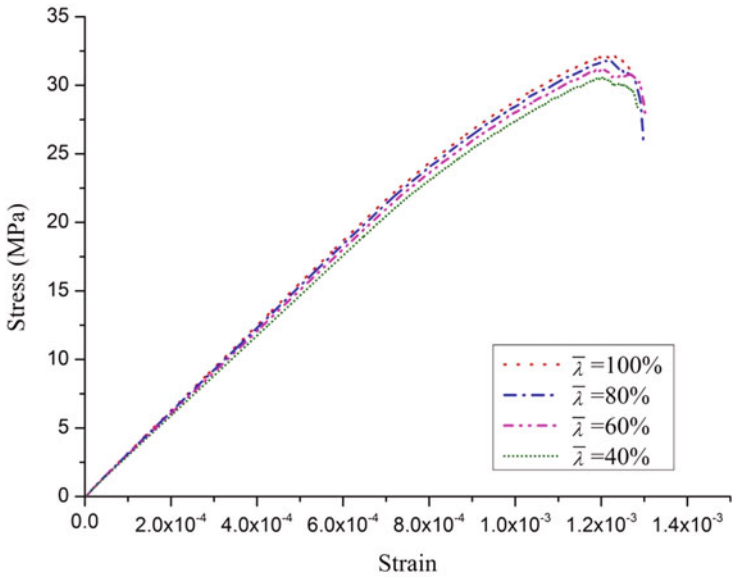

Fig. 16 The stress-strain curves with partial healing

Subsequently, a three-dimensional DEM numerical model for the self-healing materials is proposed. The influence of parameters on the self-healing effect is investigated. The self-healing microcapsules can extend the elastic regime and reduce the peak strain. When the stiffness of the healing agent and the healing ratio of microcracks rise, the compressive strength after healing develops. The strength of the microcapsule-enabled self-healing material does not monotonically increase with the strength of the healing agent. The healing agent with moderate strength and moderate stiffness is preferred in practical use. The system parameters of the microcapsule-enabled self-healing material should be carefully chosen for a better healing effect.

Acknowledgments This research was funded by the National Natural Science Foundation of China (No. 52002040), the State Key Laboratory of High Performance Civil Engineering Materials (No. 2020CEM004) and the Fundamental Research Funds for the Central Universities (No. 2020CDJQY-A002).

References

E.J. Barbero, K.J. Ford, Characterization of self-healing fiber-reinforced polymer-matrix composite with distributed damage. J. Adv. Mater. **39**, 20–27 (2007)

E.J. Barbero, F. Greco, P. Lonetti, Continuum damage-healing mechanics with application to self-healing composites. Int. J. Damage Mech. **14**, 51–81 (2005)

E.N. Brown, S.R. White, N.R. Sottos, Retardation and repair of fatigue cracks in a microcapsule toughened epoxy composite-Part II: In situ self-healing. Compos. Sci. Technol. **65**, 2474–2480 (2005)
X. Ding, L. Zhang, H.H. Zhu, et al., Effect of model scale and particle size distribution on PFC3D simulation results. Rock Mech. Rock. Eng. **47**, 2139–2156 (2014)
D. Fanella, D. Krajcinovic, A micromechanical model for concrete in compression. Eng. Fract. Mech. **29**, 49–66 (1988)
Ford KJ, Characterization of self-healing composite materials, Doctoral dissertation, West Virginia University, 2006
J. Gilford III, M.M. Hassan, T. Rupnow, et al., Dicyclopentadiene and sodium silicate microencapsulation for self-healing of concrete. J. Mater. Civ. Eng. **26**, 886–896 (2013)
H. Horii, S. Nemat-Nasser, Overall moduli of solids with microcracks: Load-induced anisotropy. J. Mech. Phys. Solids **31**, 155–171 (1983)
Itasca Consulting Group, Inc. PFC3D (Particle Flow Code in 3 Dimensions) Version 3.1. Minneapolis (2004)
J.W. Ju, On energy-based coupled elastoplastic damage theories: Constitutive modeling and computational aspects. Int. J. Solids Struct. **25**, 803–833 (1989)
J.W. Ju, On two-dimensional self-consistent micromechanical damage models for brittle solids. Int. J. Solids Struct. **27**, 227–258 (1991)
J.W. Ju, T.M. Chen, Effective elastic moduli of two-dimensional brittle solids with interacting microcracks. I: Basic formulations. J. Appl. Mech. **61**, 349–357 (1994a)
J.W. Ju, T.M. Chen, Effective elastic moduli of two-dimensional brittle solids with interacting microcracks. II: Evolutionary damage models. J. Appl. Mech. **61**, 358–366 (1994b)
J.W. Ju, X. Lee, Micromechanical damage models for brittle solids. Part I: Tensile loadings. J. Eng. Mech. **117**, 1495–1514 (1991)
J.W. Ju, K.H. Tseng, An improved two-dimensional micromechanical theory for brittle solids with randomly located interacting microcracks. Int. J. Damage Mech. **4**, 23–57 (1995)
J.W. Ju, K.Y. Yuan, New strain-energy-based coupled elastoplastic two-parameter damage and healing models for earth-moving processes. Int. J. Damage Mech. **21**, 989–1019 (2012)
J.W. Ju, P.J.M. Monteiro, A.I. Rashed, On continuum damage of cement paste and mortar as affected by porosity and sand concentration. J. Eng. Mech. **115**, 105–130 (1989)
J.W. Ju, K.Y. Yuan, A. Kuo, Novel strain energy based coupled elastoplastic damage and healing models for geomaterials-Part I: Formulations. Int. J. Damage Mech. **21**, 525–549 (2012)
D. Krajcinovic, D. Fanella, A micromechanical damage model for concrete. Eng. Fract. Mech. **25**, 585–596 (1986)
X. Lee, J.W. Ju, Micromechanical damage models for brittle solids. Part II: Compressive loading. J. Eng. Mech. **117**, 1516–1537 (1991)
W.T. Li, Z.W. Jiang, Z.H. Yang, et al., Self-healing efficiency of cementitious materials containing microcapsules filled with healing adhesive: Mechanical restoration and healing process monitored by water absorption. PLoS One **8**, e81616 (2013)
S. Luding, From discrete particles to solids-about sintering and self-healing. Comput. Methods Mater. Sci. **11**, 53–63 (2011)
S. Luding, K. Manetsberger, J. Muellers, A discrete model for long time sintering. J. Mech. Phys. Solids **53**, 455–491 (2005)
T. Mori, K. Tanaka, Average stress in matrix and average energy of materials with misfitting inclusions. Acta Metall. **21**, 571–574 (1973)
T. Mura, *Micromechanics of Defects in Solids* (Nijhoff, The Hague, 1982)
S. Nemat-Nasser, H. Horii, Compression-induced nonplanar crack extension with application to splitting, exfoliation, and rockburst. J. Geophys. Res. **87**, 6805–6821 (1982)
D.O. Potyondy, P.A. Cundall, A bonded-particle model for rock. Int. J. Rock Mech. Min. Sci. **41**, 1329–1364 (2004)
J.C. Simo, J.W. Ju, Strain- and stress-based continuum damage models-I. Formulation. Int. J. Solids Struct. **23**, 821–840 (1987a)

J.C. Simo, J.W. Ju, Strain- and stress-based continuum damage models-II. Computational aspects. Int. J. Solids Struct. **23**, 841–869 (1987b)
J.C. Simo, J.W. Ju, On continuum damage-elastoplasticity at finite strains: A computational framework. Comput. Mech. **5**, 375–400 (1989)
E. Smith, J.T. Barnby, Crack nucleation in crystalline solids. Metal Science **1**, 56–64 (1967)
D. Sumarac, D. Krajcinovic, A self-consistent model for microcrack-weakened solids. Mech. Mater. **6**, 39–52 (1987)
K. Van Tittelboom, K. Adesanya, P. Dubruel, et al., Methyl methacrylate as a healing agent for self-healing cementitious materials. Smart Mater. Struct. **20**, 125016 (2011)
G.Z. Voyiadjis, A. Shojaei, G. Li, A thermodynamic consistent damage and healing model for self healing materials. Int. J. Plast. **27**, 1025–1044 (2011)
S.R. White, N. Sottos, P. Geubelle, et al., Autonomic healing of polymer composites. Nature **409**, 794–797 (2001)
Z.X. Yang, J. Hollar, X.D. He, et al., A self-healing cementitious composite using oil core/silica gel shell microcapsules. Cem. Concr. Compos. **33**, 506–512 (2011)
K.Y. Yuan, J.W. Ju, New strain-energy based coupled elastoplastic damage-healing formulations accounting for effect of matric suction during earth moving processes. J. Eng. Mech. **139**, 188–199 (2012)
S. Zhou, X. Zhuang, Characterization of loading rate effects on the interactions between crack growth and inclusions in cementitious material. Comput. Mater. Continua **57**, 417–446 (2018)
S. Zhou, X. Zhuang, The micromechanical study of the loading rate effects between a hole and a crack. Underground Space **4**, 22–30 (2019)
S. Zhou, H.H. Zhu, Z.G. Yan, et al., Evaluation of self-healing properties of mortar containing microencapsulated epoxy resin, in *Innovative Materials and Design for Sustainable Transportation Infrastructure*, pp. 108–118 (2015). https://doi.org/10.1061/9780784479278.011
S. Zhou, H. Zhu, Z. Yan, et al., A micromechanical study of the breakage mechanism of microcapsules in concrete using PFC2D. Constr. Build. Mater. **115**, 452–463 (2016)
S. Zhou, H. Zhu, J.W. Ju, et al., Modeling microcapsule-enabled self-healing cementitious composite materials using discrete element method. Int. J. Damage Mech. **26**, 340–357 (2017)
S. Zhou, N. Vu-Bac, B. Arash, et al., Interface characterization between polyethylene/silica in engineered cementitious composites by molecular dynamics simulation. Molecules **24**, 1497 (2019)
H.H. Zhu, S. Zhou, Z.G. Yan, et al., A 3D analytical model for the probabilistic characteristics of self-healing model for concrete using spherical microcapsule. Comput. Concr. **15**, 37–54 (2015a)
H.H. Zhu, S. Zhou, Z.G. Yan, et al., A two-dimensional micromechanical damage-healing model on microcrack-induced damage for microcapsule-enabled self-healing cementitious composites under tensile loading. Int. J. Damage Mech. **24**, 95–115 (2015b)
H.H. Zhu, S. Zhou, Z. Yan, et al., A two-dimensional micromechanical damage-healing model on microcrack-induced damage for microcapsule-enabled self-healing cementitious composites under compressive loading. Int. J. Damage Mech. **25**, 727–749 (2016)
X. Zhuang, S. Zhou, Molecular dynamics study of an amorphous polyethylene/silica interface with shear tests. Materials. **11**, 929 (2018)
X. Zhuang, S. Zhou, The prediction of crack repairing capacity of bacteria-based self-healing concrete using machine learning approaches. Comput. Mater. Continua **59**, 57–77 (2019)

Influences of Imperfect Interfaces on Effective Elastoplastic Responses of Particulate Composites

35

K. Yanase and Jiann-Wen Woody Ju

Contents

Introduction 960
Perfect and Imperfect Interface 961
Modified Eshelby Inclusion Problem 962
  Iterative Method 964
  Decomposition Method 967
  Direct Computation Method 968
  Comparisons of Modified Eshelby Tensors 968
Effective Stiffness with Modified Eshelby Tensor 969
  Mori-Tanaka Method 969
  Self-Consistent Method 972
  Degeneration of Effective Elastic Moduli of a Composite 974
Equivalent Stiffness Method 974
Effective Elastoplastic Responses of Two-Phase Composites 979
  Effective Elastic Stiffness with Pair-Wise Interactions 979
  Effective Yield Function 981
  Elastoplastic Deformation Responses of Ductile Matrix Composites 986
Concluding Remarks 989
Appendix: Contraction and Inversion of Fourth-Order Tensors 990
References 994

K. Yanase (✉)
Department of Mechanical Engineering, Institute of Materials Science and Technology, Fukuoka University, Fukuoka, Japan
e-mail: kyanase@fukuoka-u.ac.jp

J.-W. W. Ju
Department of Civil and Environmental Engineering, University of California, Los Angeles, CA, USA

State Key Laboratory for Disaster Reduction in Civil Engineering, Tongji University, Shanghai, China
e-mail: juj@ucla.edu

© Springer Nature Switzerland AG 2022

G. Z. Voyiadjis (ed.), *Handbook of Damage Mechanics*,
https://doi.org/10.1007/978-3-030-60242-0_53

Abstract

The interfacial damage between the reinforcements and the matrix significantly affects the mechanical behavior of the composite materials. Correspondingly, in this chapter, the effects of imperfect interfaces are systematically investigated in the framework of micromechanics and homogenization. Focusing on the spherical particle-reinforced composites to examine the effects of imperfect interfaces, the modified Eshelby tensor and its approximate solutions are presented. In the framework of the Mori-Tanaka method and the self-consistent method, the influences of interfacial damage parameters on the degeneracy of the effective elastic moduli of composites are analyzed systematically. Further, by using the equivalent stiffness of particles, the overall elastoplastic damage behaviors of particle-reinforced composites are simulated by taking advantage of the effective stiffness and the effective yield function of a composite. A number of numerical studies are presented to demonstrate the influences of imperfect interfaces on the effective elastoplastic responses of particulate composites.

Keywords

Micromechanics · Eshelby tensor · Particulate composite · Imperfect interface

Introduction

Because of their superior engineering capability and applicability, composite materials are currently indispensable for a variety of engineering fields. The properties of composite materials may be predicted by the volume fraction sum of the constituent properties. Sometimes the simple volume fraction sum is not effective because the properties of composites are dictated by the synergic interaction among the constituent phases. In addition, the interface region is responsible for the proper load transfer between matrix and reinforcement; thus the overall performance of composites is often affected by the interface properties (cf. Kim and Mai 1998).

In practice, the degeneration of mechanical responses of particle- and fiber-reinforced composites frequently accompanies the progressive interfacial damage between the reinforcements and the matrix. In the literature, the effect of interfacial damage is studied in terms of the imperfect interfaces. In the free-sliding model, the relative tangential slip at the inclusion is accounted for as the imperfect interface (e.g., Ghahremani 1980; Mura and Furuhashi 1984; Jasiuk et al. 1987). On the other hand, in the linear-spring model, the discontinuous displacement field across the interface is accounted for as the imperfect interface (e.g., Aboudi 1987; Hashin 1991; Qu 1993a, b; Gao 1995; Zhong and Meguid 1997; Duan et al. 2005, 2007a, b; Liu et al. 2006; Yanase and Ju 2012, 2014; Li and Sun 2013). In the concept of equivalent inclusion (Zhao and Weng 1997, 2002; Zheng et al. 2003), the inclusions with various stages of the imperfect interface are replaced by the perfectly bonded inclusions with the reduced moduli. This perfectly bonded condition is convenient,

and Eshelby's equivalence principle (1957) can be implemented. The cohesive model is also popular, and the equivalent reduction of material properties is linked to the energy release in a cohesive fracture process. Note that the energy dissipation process in a cohesive fracture is much more complicated than a purely elastic fracture process. Though it is less rigorous than the cohesive model, the use of the linear spring model is a simple yet effective means to treat an imperfect interface.

In this chapter, the effects of interfacial damage on the effective elastoplastic deformation behaviors of spherical particle-reinforced composites are presented. Specifically, the micromechanics-based spring interface model (Qu 1993a, b; Qu and Cherkaoui 2006; Yanase and Ju 2012, 2014) is adapted to account for the effect of interfacial damage. The overall elastoplastic damage responses are simulated by using the higher-order micromechanical framework and homogenization (Ju and Yanase 2010, 2011). A number of numerical studies are presented to show the influences of imperfect interfaces on the effective elastoplastic responses of particulate composites.

Perfect and Imperfect Interface

For a perfectly bonded interface, both displacement and traction across the interface are continuous, which can be described as:

$$\Delta u_i = u_i^{S+} - u_i^{S-} = 0 \tag{1}$$

$$\Delta \sigma_{ij} = \left[\sigma_{ij}^{S+} - \sigma_{ij}^{S-}\right] = 0 \tag{2}$$

where u_i^{S+} and σ_{ij}^{S+} are the displacement and stress at the positive side of S, while u_i^{S-} and σ_{ij}^{S-} are the displacement and stress at the negative side of S. Furthermore, it is assumed that the unit outward normal, n_j, points to the positive side of S. The imperfectly bonded interface is realized by considering the discontinuity of a displacement field across the interface. Therefore, only the traction is continuous across the interface in the spring interface model:

$$\Delta \sigma_{ij} n_j = \left[\sigma_{ij}^{S+} - \sigma_{ij}^{S-}\right] n_j = 0 \tag{3}$$

It is assumed that the displacement jump across the interface is proportional to the traction vector, t_j. This assumption leads to the following equation:

$$\Delta u_i = \eta_{ij} t_j = \eta_{ij} \sigma_{jk} n_k \tag{4}$$

where the compliance of the interface is represented by the second-order tensor η_{ij} that is assumed to be symmetric and positive definite. It is apparent from Eq. (4) that $\eta_{ij} = 0$ represents the perfectly bonded interface, while $\eta_{ij} \to \infty$ represents the perfectly debonded interface.

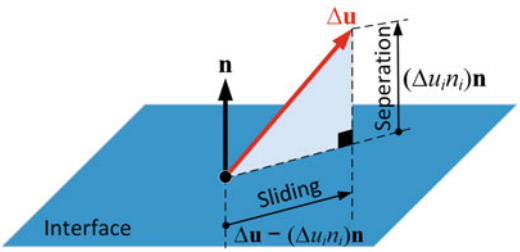

Fig. 1 Interfacial separation and sliding associated with the displacement jump, $\Delta\mathbf{u}$

The physical meaning of η_{ij} can be realized by using the following form:

$$\eta_{ij} = \alpha\delta_{ij} + (\beta - \alpha)n_i n_j \tag{5}$$

where δ_{ij} is the Kronecker delta. In view of Fig. 1 with Eqs. (8) and (9), the following relations can be obtained:

$$\begin{aligned} \Delta u_k - (\Delta u_i n_i)n_k &= \Delta u_i(\delta_{ik} - n_i n_k) \\ &= \left\{ \left[\alpha\delta_{ij} + (\beta - \alpha)n_i n_j\right]\sigma_{jm}n_m \right\}(\delta_{ik} - n_i n_k) \\ &= \alpha\sigma_{ij}n_j(\delta_{ik} - n_i n_k) \end{aligned} \tag{6}$$

$$\Delta u_i n_i = \left\{\alpha\delta_{ij} + (\beta - \alpha)n_i n_j\right\}\sigma_{jk}n_k n_i = \beta\sigma_{ij}n_i n_j \tag{7}$$

Accordingly, the parameters α and β are associated with the interfacial *sliding* and the interfacial *separation*, respectively. It is noted $\beta \neq 0$ may cause the material interpenetration.

Modified Eshelby Inclusion Problem

By taking into account the displacement jump at the interface of inclusion, the displacement field can be expressed as follows (for more detail, see Qu and Cherkaoui 2006):

$$\begin{aligned} u_m(\mathbf{x}) &= \int_\Omega \frac{\partial G^\infty_{im}(\mathbf{x},\mathbf{y})}{\partial y_j} C^0_{ijkl}\ \varepsilon^*_{kl}(\mathbf{y})\, dV(\mathbf{y}) \\ &\quad + \int_{\partial\Omega} \Delta u_i(\mathbf{y})\, C^0_{ijkl} \frac{\partial G^\infty_{km}(\mathbf{x},\mathbf{y})}{\partial y_l} n_j(\mathbf{y})\, dS(\mathbf{y}) \end{aligned} \tag{8}$$

Here, C^0_{ijkl} is the elastic stiffness of the surrounding matrix material, G^∞_{ij} represents Green's function (Mura 1987), and ε^*_{ij} signifies the eigenstrain. Further, Ω and $\partial\Omega$ are the volume and the surface area of an inclusion, respectively. In essence, Green's

function physically represents the displacement field generated by a unit force. Under the assumption of the homogeneous and unbounded domain, only the distance between **x** (where the displacement is measured) and **y** (where the unit force is applied) determines Green's function. That is:

$$G_{ij}^{\infty}(\mathbf{x},\mathbf{y}) = \frac{1}{16\pi\mu_0(1-\nu_0)|\mathbf{x}-\mathbf{y}|}\left\{(3-4\nu_0)\delta_{ij} + \frac{(x_i-y_i)\left(x_j-y_j\right)}{|\mathbf{x}-\mathbf{y}|^2}\right\} \quad (9)$$

where:

$$|\mathbf{x}-\mathbf{y}| = \sqrt{(x_1-y_1)^2+(x_2-y_2)^2+(x_3-y_3)^2} \quad (10)$$

Here v_0 is Poisson's ratio and μ_0 is the sear modulus of the surrounding matrix material.

It is assumed that the eigenstrain is uniform within Ω. Therefore, Eq. (4) becomes:

$$u_{m,n}(\mathbf{x}) = \int_{\Omega}\frac{\partial G_{im}^{\infty}(\mathbf{x},\mathbf{y})}{\partial y_j \partial x_n} C_{ijkl}^{0}\,\varepsilon_{kl}^{*}\,dV(\mathbf{y}) + \int_{\partial\Omega}\Delta u_i(\mathbf{y})\,C_{ijkl}^{0}\frac{\partial G_{km}^{\infty}(\mathbf{x},\mathbf{y})}{\partial y_l \partial x_n} n_j(\mathbf{y})\,dS(\mathbf{y}) \quad (11)$$

With the change of the indices in Eq. (11), the strain can be expressed as:

$$\varepsilon_{ij}(\mathbf{x}) = C_{klmn}^{0}\varepsilon_{kl}^{*}\int_{\Omega}\Gamma_{ijmn}^{\infty}(\mathbf{x},\mathbf{y})\,dV(\mathbf{y}) + \int_{\partial\Omega}C_{klmn}^{0}\Delta u_k(\mathbf{y})\Gamma_{ijmn}^{\infty}(\mathbf{x},\mathbf{y})\,n_l(\mathbf{y})\,dS(\mathbf{y}) \quad (12)$$

where:

$$\Gamma_{ijkl}^{\infty}(\mathbf{x},\mathbf{y}) = \frac{1}{4}\left[\frac{\partial^2 G_{ki}^{\infty}(\mathbf{x},\mathbf{y})}{\partial x_j \partial y_l} + \frac{\partial^2 G_{kj}^{\infty}(\mathbf{x},\mathbf{y})}{\partial x_i \partial y_l} + \frac{\partial^2 G_{li}^{\infty}(\mathbf{x},\mathbf{y})}{\partial x_j \partial y_k} + \frac{\partial^2 G_{lj}^{\infty}(\mathbf{x},\mathbf{y})}{\partial x_i \partial y_k}\right] \quad (13)$$

With the definition of the interior-point Eshelby tensor or S_{ijkl}, Eq. (12) can be rewritten as:

$$\begin{aligned}\varepsilon_{ij}(\mathbf{x}) &= S_{ijkl}\,\varepsilon_{kl}^{*} + \int_{\partial\Omega}C_{klmn}^{0}\Delta u_k(\mathbf{y})\;\Gamma_{ijmn}^{\infty}(\mathbf{x},\mathbf{y})n_l(\mathbf{y})\,dS(\mathbf{y}) \\ &= S_{ijkl}\,\varepsilon_{kl}^{*} + \int_{\partial\Omega}C_{klmn}^{0}\left(\eta_{kp}\sigma_{pq}(\mathbf{y})n_q(\mathbf{y})\right)\;\Gamma_{ijmn}^{\infty}(\mathbf{x},\mathbf{y})n_l\,dS(\mathbf{y})\end{aligned} \quad (14)$$

where:

$$S_{ijkl} = C_{klmn}^{0}\int_{\Omega}\Gamma_{ijmn}^{\infty}(\mathbf{x},\mathbf{y})\,dV(\mathbf{y})\,; \quad \mathbf{x},\mathbf{y}\in\ \Omega \quad (15)$$

For a spherical inclusion, S_{ijkl} is rendered as (cf. Mura 1987; Qu and Cherkaoui 2006):

$$S_{ijkl} = \frac{1}{15(1-\nu_0)}\left[(5\nu_0-1)\delta_{ij}\delta_{kl} + (4-5\nu_0)\left(\delta_{ik}\delta_{jl} + \delta_{il}\delta_{jk}\right)\right] \tag{16}$$

Given that the eigenstrain is stress-free, the stress-strain relationship can be expressed as:

$$\sigma_{ij} = C^0_{ijkl}\left(\varepsilon_{kl} - \varepsilon^*_{kl}\right) \tag{17}$$

Substitution of Eq. (17) into Eq. (14) results in:

$$\begin{aligned}\varepsilon_{ij}(\mathbf{x}) = S_{ijkl}\,\varepsilon^*_{kl} &- \int_{\partial\Omega} C^0_{klmn}C^0_{pqst}\eta_{kp}\varepsilon^*_{st}\,\Gamma^\infty_{ijmn}(\mathbf{x},\mathbf{y})n_q(\mathbf{y})n_l(\mathbf{y})\,dS(\mathbf{y}) \\ &+ \int_{\partial\Omega} C^0_{klmn}C^0_{pqst}\eta_{kp}\varepsilon_{st}(\mathbf{y})\,\Gamma^\infty_{ijmn}(\mathbf{x},\mathbf{y})n_q(\mathbf{y})n_l(\mathbf{y})\,dS(\mathbf{y})\end{aligned} \tag{18}$$

In the following section, the three methods to compute the modified Eshelby tensor (Qu 1993b; Qu and Cherkaoui 2006) are presented.

Iterative Method

By employing the iterative calculations, Eq. (18) can be expressed as:

$$\begin{aligned}\varepsilon^{(n+1)}_{ij}(\mathbf{x}) \cong S_{ijkl}\,\varepsilon^*_{kl} &- \int_{\partial\Omega} C^0_{klmn}C^0_{pqst}\eta_{kp}\varepsilon^*_{st}\Gamma^\infty_{ijmn}(\mathbf{x},\mathbf{y})n_q(\mathbf{y})n_l(\mathbf{y})\,dS(\mathbf{y}) \\ &+ \int_{\partial\Omega} C^0_{klmn}C^0_{pqst}\eta_{kp}\varepsilon^{(n)}_{st}(\mathbf{y})\,\Gamma^\infty_{ijmn}(\mathbf{x},\mathbf{y})n_q(\mathbf{y})n_l(\mathbf{y})\,dS(\mathbf{y})\end{aligned} \tag{19}$$

for $n = 0, 1, 2, \cdots, N$. The initial condition can be set as:

$$\varepsilon^{(0)}_{ij} = S_{ijkl}\varepsilon^*_{kl} \tag{20}$$

Hence, after the first iteration of Eq. (19), the following equation can be obtained:

$$\begin{aligned}\varepsilon^{(1)}_{ij}(\mathbf{x}) = S_{ijkl}\,\varepsilon^*_{kl} &- C^0_{klmn}C^0_{pqst}\int_{\partial\Omega}\eta_{kp}\varepsilon^*_{st}\Gamma^\infty_{ijmn}(\mathbf{x},\mathbf{y})n_q(\mathbf{y})\,n_l(\mathbf{y})\,dS(\mathbf{y}) \\ &+ C^0_{klmn}C^0_{pqst}S_{stvw}\int_{\partial\Omega}\eta_{kp}\varepsilon^*_{vw}\Gamma^\infty_{ijmn}(\mathbf{x},\mathbf{y})n_q(\mathbf{y})\,n_l(\mathbf{y})\,dS(\mathbf{y})\end{aligned} \tag{21}$$

For simplicity, it is defined as:

$$Z_{ijst}(\mathbf{x}) \;=\; C^0_{klmn} C^0_{pqst} \int_{\partial\Omega} \eta_{kp} \Gamma^{\infty}_{ijmn}(\mathbf{x},\mathbf{y}) n_q(\mathbf{y}) n_l(\mathbf{y})\, dS(\mathbf{y}) \tag{22}$$

By utilizing Eq. (22) and (21) takes the form:

$$\varepsilon^{(1)}_{ij}(\mathbf{x}) \;=\; S_{ijkl}\varepsilon^*_{kl} \;-\; Z_{ijst}(\mathbf{x})(I_{stkl} \;-\; S_{stkl})\varepsilon^*_{kl} \;=\; \overline{S}^{(1)}_{ijkl}(\mathbf{x})\varepsilon^*_{kl} \tag{23}$$

Here, I_{ijkl} is the fourth-order identity tensor given as:

$$I_{ijkl} \;=\; \frac{1}{2}\left(\delta_{ik}\delta_{jl} \;+\; \delta_{il}\delta_{jk}\right) \tag{24}$$

Equation (23) shows that the strain field with the imperfect interface can be treated by a *modified Eshelby tensor*, $\overline{S}_{ijkl}$. Note that the strain field is *no longer uniform* within an ellipsoidal inclusion in the modified Eshelby inclusion problem, which is in strong contrast to the original Eshelby inclusion problem.

For convenience, the volume-averaged Eshelby tensor within an inclusion domain is defined as:

$$\hat{S}^{(1)}_{ijkl} \;=\; \frac{1}{\Omega}\int_{\Omega} \overline{S}^{(1)}_{ijkl}(\mathbf{x})\; dV \tag{25}$$

where, for a spherical particle (radius $= a_{\mathrm{p}}$):

$$\Omega \;=\; \frac{4\pi {a_{\mathrm{p}}}^3}{3} \tag{26}$$

To perform the volume integration in Eq. (25), the following operation is adopted (cf. Eq. 15):

$$\begin{aligned}
\frac{1}{V}\int_{\Omega} Z_{ijst}(\mathbf{x})\, dV(\mathbf{x}) \;&=\; \frac{1}{\Omega}\int_{\Omega}\left\{ C^0_{klmn} C^0_{pqst} \int_{\partial\Omega} \eta_{kp}\Gamma^{\infty}_{ijmn}(\mathbf{x},\mathbf{y}) n_q(\mathbf{y})\, n_l(\mathbf{y})\, dS(\mathbf{y}) \right\} dV(\mathbf{x}) \\
&=\; \frac{1}{\Omega} C^0_{klmn} C^0_{pqst} \int_{\partial\Omega} \left\{ \int_{\Omega} \Gamma^{\infty}_{ijmn}(\mathbf{y},\mathbf{x})\, dV(\mathbf{x}) \right\} \eta_{kp}\, n_q(\mathbf{y}) n_l(\mathbf{y})\, dS(\mathbf{y}) \\
&=\; \frac{1}{\Omega} S_{ijkl}\, C^0_{pqst} \int_{\partial\Omega} \eta_{kp}\, n_q(\mathbf{y}) n_l(\mathbf{y})\, dS(\mathbf{y}) \\
&=\; S_{ijkl}\, R_{klpq}\, C^0_{pqst}
\end{aligned} \tag{27}$$

where:

$$\Gamma^{\infty}_{ijmn}(\mathbf{x},\;\mathbf{y}) \;=\; \Gamma^{\infty}_{ijmn}(\mathbf{y},\;\mathbf{x}) \tag{28}$$

$$R_{ijkl} \;=\; \frac{1}{4\Omega}\int_{\partial\Omega} \left(\eta_{ik} n_j n_l \;+\; \eta_{il} n_j n_k \;+\; \eta_{jk} n_i n_l \;+\; \eta_{jl} n_i n_k\right) dS(\mathbf{y}) \tag{29}$$

In Eq. (27), the surface integral on the sphere becomes (cf. Ju and Chen 1994b):

$$\begin{aligned}\int_{\partial\Omega}\eta_{mp}n_q n_n\ dS(\mathbf{y}) &= \int_{\partial\Omega}\left[\alpha\delta_{mp}+(\beta-\alpha)n_m n_p\right]n_q n_n\ dS(\mathbf{y})\\ &= {a_\mathrm{p}}^2\left\{\frac{4\pi\alpha}{3}\delta_{mp}\delta_{qn}+\frac{4\pi(\beta-\alpha)}{15}\left(\delta_{mp}\delta_{qn}+\delta_{mq}\delta_{pn}+\delta_{mn}\delta_{pq}\right)\right\}\end{aligned} \tag{30}$$

Therefore, Eq. (29) can be expressed as:

$$\begin{aligned}R_{ijkl} &= \frac{1}{a_\mathrm{p}}\left[\left(\frac{\beta-\alpha}{5}\right)\delta_{ij}\delta_{kl}+\left(\frac{3\alpha+2\beta}{10}\right)\left(\delta_{ik}\delta_{jl}+\delta_{il}\delta_{jk}\right)\right]\\ &= \left(\frac{\beta'-\alpha'}{5}\right)\delta_{ij}\delta_{kl}+\left(\frac{3\alpha'+2\beta'}{10}\right)\left(\delta_{ik}\delta_{jl}+\delta_{il}\delta_{jk}\right)\end{aligned} \tag{31}$$

Further, the Voigt form for Eq. (31) can be rendered as:

$$\begin{bmatrix}R_{1111}&R_{1122}&R_{1133}&R_{1112}&R_{1123}&R_{1131}\\R_{2211}&R_{2222}&R_{2233}&R_{2212}&R_{2223}&R_{2231}\\R_{3311}&R_{3322}&R_{3333}&R_{3312}&R_{3323}&R_{3331}\\R_{1211}&R_{1222}&R_{1233}&R_{1212}&R_{1223}&R_{1231}\\R_{2311}&R_{2322}&R_{2333}&R_{2312}&R_{2323}&R_{2331}\\R_{3111}&R_{3122}&R_{3133}&R_{3112}&R_{3123}&R_{3131}\end{bmatrix} = \begin{bmatrix}c_1&c_2&c_2&0&0&0\\c_2&c_1&c_2&0&0&0\\c_2&c_2&c_1&0&0&0\\0&0&0&c_3&0&0\\0&0&0&0&c_3&0\\0&0&0&0&0&c_3\end{bmatrix} \tag{32}$$

where:

$$c_1 = \frac{2\alpha'+3\beta'}{5}\quad;\quad c_2 = \frac{\beta'-\alpha'}{5}\quad;\quad c_3 = \frac{3\alpha'+2\beta'}{10} = \frac{c_1-c_2}{2} \tag{33}$$

Now Eq. (25) can be recast with the tensorial notation as:

$$\begin{aligned}\hat{\mathbf{S}}^{(1)} &= \frac{1}{\Omega}\int_\Omega \overline{\mathbf{S}}^{(1)}(\mathbf{x})\,dV\\ &= \frac{1}{\Omega}\int_\Omega\left\{\mathbf{S}-\mathbf{Z}(\mathbf{x})\bullet(\mathbf{I}-\mathbf{S})\right\}dV\\ &= \mathbf{S}-\mathbf{S}\bullet\mathbf{R}\bullet\mathbf{C}^0\bullet(\mathbf{I}-\mathbf{S})\end{aligned} \tag{34}$$

By substituting Eq. (34) into Eq. (19), the following equation can be obtained:

$$\begin{aligned}\boldsymbol{\varepsilon}^{(2)}(\mathbf{x}) &= \mathbf{S}:\boldsymbol{\varepsilon}^{*} - \mathbf{Z}(\mathbf{x})\bullet\left(\mathbf{I} - \overline{\mathbf{S}}^{(1)}(\mathbf{x})\right):\boldsymbol{\varepsilon}^{*} \\ &\cong \mathbf{S}:\boldsymbol{\varepsilon}^{*} - \mathbf{Z}(\mathbf{x})\bullet\left(\mathbf{I} - \hat{\mathbf{S}}^{(1)}\right):\boldsymbol{\varepsilon}^{*} = \overline{\mathbf{S}}^{(2)}(\mathbf{x}):\boldsymbol{\varepsilon}^{*}\end{aligned} \tag{35}$$

Then:

$$\begin{aligned}\hat{\mathbf{S}}^{(2)} &= \frac{1}{\Omega}\int_{\Omega}\overline{\mathbf{S}}^{(2)}(\mathbf{x})\ dV \\ &= \frac{1}{\Omega}\int_{\Omega}\left\{\mathbf{S} - \mathbf{Z}(\mathbf{x})\bullet\left(\mathbf{I} - \hat{\mathbf{S}}^{(1)}\right)\right\}dV \\ &= \mathbf{S} - \mathbf{S}\bullet\mathbf{R}\bullet\mathbf{C}^{0}\bullet\left(\mathbf{I} - \hat{\mathbf{S}}^{(1)}\right)\end{aligned} \tag{36}$$

Accordingly, the iterative procedure can be realized as:

$$\begin{aligned}\hat{\mathbf{S}}^{(n+1)} &= \mathbf{S} - \mathbf{S}\bullet\mathbf{R}\bullet\mathbf{C}^{0}\bullet\left(\mathbf{I} - \hat{\mathbf{S}}^{(n)}\right) \\ &= \mathbf{S} - \mathbf{K}\bullet\left(\mathbf{I} - \hat{\mathbf{S}}^{(n)}\right), \qquad \text{where} \quad \mathbf{K} = \mathbf{S}\bullet\mathbf{R}\bullet\mathbf{C}^{0}\end{aligned} \tag{37}$$

with the initial condition (cf. Eq. 16):

$$\hat{\mathbf{S}}^{(0)} = \mathbf{S} \tag{38}$$

Decomposition Method

The decomposition of Eq. (18) with the volume-averaged strain results in the following equation (cf. Wazwaz 2015):

$$\begin{aligned}\overline{\varepsilon}_{ij} &\cong \sum_{n=0}^{\infty}\overline{\varepsilon}_{ij}^{(n)} = \overline{\varepsilon}_{ij}^{(0)} + \overline{\varepsilon}_{ij}^{(1)} + \cdots\cdots + \overline{\varepsilon}_{ij}^{(\infty)} \\ &= \left\{S_{ijkl}\,\varepsilon_{kl}^{*} - \frac{1}{\Omega}\int_{\partial\Omega}C_{klmn}^{0}C_{pqst}^{0}\eta_{kp}\varepsilon_{st}^{*}\left(\int_{\Omega}\Gamma_{ijmn}^{\infty}(\mathbf{y},\ \mathbf{x})\ dV(\mathbf{x})\right)n_{q}(\mathbf{y})n_{l}(\mathbf{y})\,dS(\mathbf{y})\right\} \\ &\quad + \frac{1}{\Omega}\int_{\partial\Omega}C_{klmn}^{0}C_{pqst}^{0}\eta_{kp}\left(\sum_{n=0}^{\infty}\overline{\varepsilon}_{ij}^{(n)}\right)\left(\int_{\Omega}\Gamma_{ijmn}^{\infty}(\mathbf{y},\ \mathbf{x})\ dV(\mathbf{x})\right)n_{q}(\mathbf{y})n_{l}(\mathbf{y})\,dS(\mathbf{y}) \\ &= \left\{S_{ijkl}\,\varepsilon_{kl}^{*} - S_{ijkl}R_{klpq}C_{pqst}^{0}\,\varepsilon_{st}^{*}\right\} + S_{ijkl}R_{klpq}C_{pqst}^{0}\left(\sum_{n=0}^{\infty}\overline{\varepsilon}_{st}^{(n)}\right)\end{aligned} \tag{39}$$

Therefore, the strain can be expressed with the tensorial notation as:

$$\begin{aligned}\overline{\boldsymbol{\varepsilon}}^{(0)} &= \mathbf{S}:\boldsymbol{\varepsilon}^* - \mathbf{S}\bullet\mathbf{R}\bullet\mathbf{C}^0:\boldsymbol{\varepsilon}^* = (\mathbf{S}-\mathbf{K}):\boldsymbol{\varepsilon}^* \\ \overline{\boldsymbol{\varepsilon}}^{(1)} &= \mathbf{S}\bullet\mathbf{R}\bullet\mathbf{C}^0:\overline{\boldsymbol{\varepsilon}}^{(0)} = \mathbf{K}\bullet(\mathbf{S}-\mathbf{K}):\boldsymbol{\varepsilon}^* \\ \overline{\boldsymbol{\varepsilon}}^{(2)} &= \mathbf{S}\bullet\mathbf{R}\bullet\mathbf{C}^0:\overline{\boldsymbol{\varepsilon}}^{(1)} = \mathbf{K}^2\bullet(\mathbf{S}-\mathbf{K}):\boldsymbol{\varepsilon}^*\end{aligned} \tag{40}$$

In view of Eq. (40), the average strain can be expressed as:

$$\overline{\boldsymbol{\varepsilon}} = \sum_{n=0}^{\infty}\overline{\boldsymbol{\varepsilon}}^{(n)} = \left(\sum_{n=0}^{\infty}\mathbf{K}^n\right)\bullet(\mathbf{S}-\mathbf{K}):\boldsymbol{\varepsilon}^* = \hat{\mathbf{S}}:\boldsymbol{\varepsilon}^* \tag{41}$$

Direct Computation Method

Considering the volume-averaged strain on both the left-hand side and the right-hand side of Eq. (18), the following equation can be obtained:

$$\begin{aligned}\overline{\varepsilon}_{ij} \cong S_{ijkl}\varepsilon^*_{kl} &- \frac{1}{\Omega}\int_{\partial\Omega} C^0_{klmn}C^0_{pqst}\eta_{kp}\varepsilon^*_{st}\left\{\int_{\Omega}\Gamma^{\infty}_{ijmn}(\mathbf{y},\ \mathbf{x})\,dV(\mathbf{x})\right\}n_q(\mathbf{y})n_l(\mathbf{y})\,dS(\mathbf{y}) \\ &+ \frac{1}{\Omega}\int_{\partial\Omega} C^0_{klmn}C^0_{pqst}\eta_{kp}\overline{\varepsilon}_{st}\left\{\int_{\Omega}\Gamma^{\infty}_{ijmn}(\mathbf{y},\ \mathbf{x})\,dV(\mathbf{x})\right\}n_q(\mathbf{y})n_l(\mathbf{y})\,dS(\mathbf{y})\end{aligned} \tag{42}$$

The above equation can be recast by taking advantage of Eq. (15) as follows:

$$\overline{\boldsymbol{\varepsilon}} = \mathbf{S}:\boldsymbol{\varepsilon}^* - \mathbf{S}\bullet\mathbf{R}\bullet\mathbf{C}^0:\boldsymbol{\varepsilon}^* + \mathbf{S}\bullet\mathbf{R}\bullet\mathbf{C}^0:\overline{\boldsymbol{\varepsilon}} \tag{43}$$

Accordingly, Eq. (43) leads to the explicit expression for the average strain:

$$\overline{\boldsymbol{\varepsilon}} = \left\{(\mathbf{I}-\mathbf{K})^{-1}\bullet(\mathbf{S}-\mathbf{K})\right\}:\boldsymbol{\varepsilon}^* = \hat{\mathbf{S}}:\boldsymbol{\varepsilon}^* \tag{44}$$

Comparisons of Modified Eshelby Tensors

Figures 2 and 3 show the comparisons for the components of the modified Eshelby tensors. When interfacial damage is relatively small (Figs. 2a and 3a), the solution for the modified Eshelby tensor can be obtained with a few iterations. Further, when the amount of damage increases, an increased number of iterations is required to achieve a good convergence (Figs. 2b and 3b). As shown, the iterative method and the decomposition method converge to the direct computation method.

As shown in Fig. 4, the modified Eshelby tensor exhibits singularity, and the singular behavior depends on the matrix properties. Othmani et al. (2011) pointed out that according to the theorem of the differentiation and to the Fubini-Tonelli theorem, the permutations between the surface integral and the volume integral (e.g., Eq. 27) are allowed only when the integration volume is free from any singularity. The singularity of the modified Eshelby's tensor is caused by the violation of the Fubini-Tonelli theorem (Lee et al. 2018).

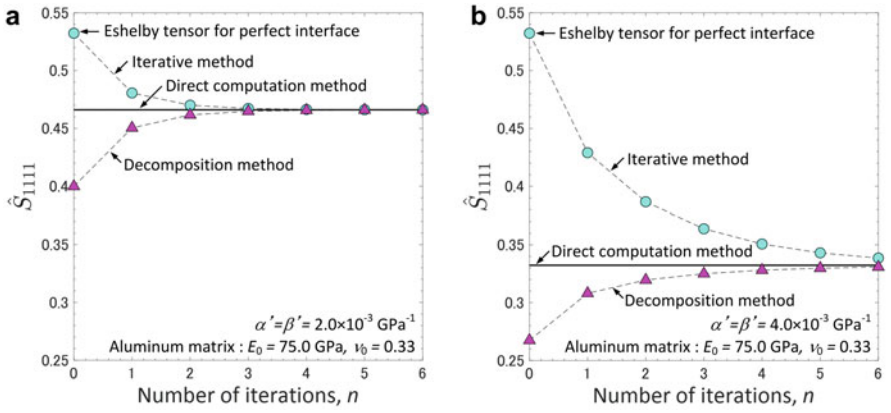

Fig. 2 Variations of a component of the modified Eshelby tensor, $\widehat{S}_{1111}$. (**a**) $\alpha' = \beta' = 2.0 \times 10^{-3}$ GPa^{-1}. (**b**) $\alpha' = \beta' = 4.0 \times 10^{-3}$ GPa^{-1}

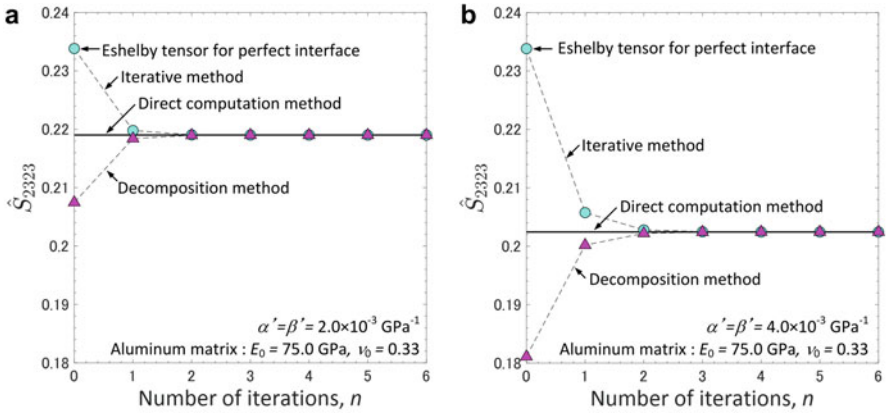

Fig. 3 Variations of a component of the modified Eshelby tensor, $\widehat{S}_{2323}$. (**a**) $\alpha' = \beta' = 2.0 \times 10^{-3}$ GPa^{-1}. (**b**) $\alpha' = \beta' = 4.0 \times 10^{-3}$ GPa^{-1}

Effective Stiffness with Modified Eshelby Tensor

Mori-Tanaka Method

In this section, the Mori-Tanaka method (Mori and Tanaka 1973; Weng 1984) in the presence of imperfect interface is presented (cf. Qu and Cherkaoui 2006). It is assumed that a composite material contains the randomly located spherical inclusions with the imperfect interface. The average stress within an *RVE* (Representative Volume Element) of a composite is defined as:

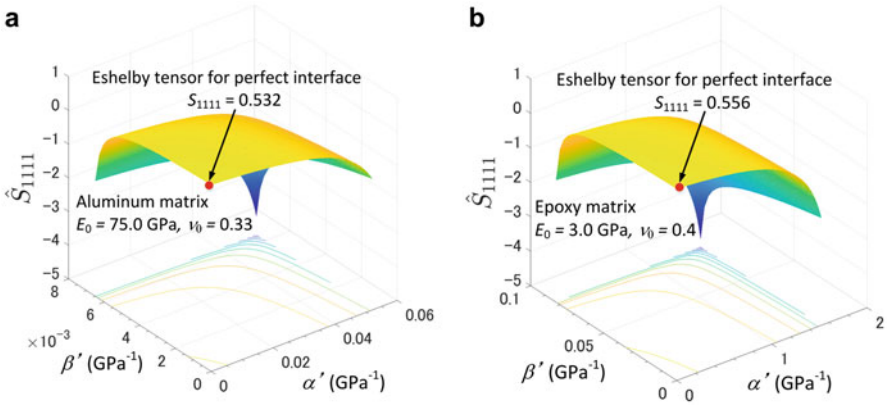

Fig. 4 Variations of the modified Eshelby tensor, $\widehat{S}_{1111}$, with α' and β'. (**a**) Aluminum matrix. (**b**) Epoxy matrix

$$\overline{\boldsymbol{\sigma}} = \frac{1}{V}\int_V \boldsymbol{\sigma}(\mathbf{x})\, dV = \sum_{r=0}^{N} \phi^{(r)}\overline{\boldsymbol{\sigma}}^{(r)} \tag{45}$$

where:

$$\overline{\boldsymbol{\sigma}}^{(r)} = \frac{1}{\Omega^{(r)}}\int_{\Omega^{(r)}} \boldsymbol{\sigma}(\mathbf{x})\, dV \tag{46}$$

is the average stress in the r^{th}-phase.

By taking into account the displacement jump at the interface, the average strain within the *RVE* of a composite is rendered as (Qu 1993b; Qu and Cherkaoui 2006):

$$\begin{aligned}\overline{\varepsilon}_{ij} &= \frac{1}{V}\int_V \varepsilon_{ij}(\mathbf{x})\, dV = \sum_{r=0}^{N} \phi^{(r)}\overline{\varepsilon}_{ij}^{(r)} + \frac{1}{2V}\sum_{r=1}^{N}\int_{\Omega^{(r)}} \left(\Delta u_{i,j} + \Delta u_{j,i}\right) dV \\ &= \sum_{r=0}^{N} \phi^{(r)}\overline{\varepsilon}_{ij}^{(r)} + \frac{1}{2V}\sum_{r=1}^{N}\int_{\partial\Omega^{(r)}} \left(\Delta u_i n_j + \Delta u_j n_i\right) dS\end{aligned} \tag{47}$$

where $\partial\Omega^{(r)}$ is the surface of $\Omega^{(r)}$, and $\overline{\boldsymbol{\varepsilon}}^{(r)}$ is the average strain within the r^{th}-phase, given as:

$$\overline{\boldsymbol{\varepsilon}}^{(r)} = \frac{1}{\Omega^{(r)}}\int_{\Omega^{(r)}} \boldsymbol{\varepsilon}(\mathbf{x})\, dV \tag{48}$$

By making use of Eq. (4), the surface integral in Eq. (47) becomes:

$$\int_{\partial\Omega^{(r)}} \left(\Delta u_i n_j + \Delta u_j n_i\right) dS = \int_{\partial\Omega^{(r)}} \left(\eta_{im}\sigma_{mk}n_k n_j + \eta_{jm}\sigma_{mk}n_k n_i\right) dS \tag{49}$$

In essence, the computation of stresses at the interface is a difficult problem. Thus, Eq. (49) is approximated by using the average internal stress of inclusion, $\overline{\sigma}_{ij}^{(r)}$ (cf. Eq. 29):

$$\int_{\partial\Omega^{(r)}} \left(\eta_{im}\overline{\sigma}_{mk}^{(r)}n_k n_j + \eta_{jm}\overline{\sigma}_{mk}^{(r)}n_k n_i\right) dS = 2\Omega^{(r)}R_{ijkm}^{(r)}\overline{\sigma}_{km}^{(r)} \tag{50}$$

Therefore, by substituting Eq. (48) into Eq. (47), the average strain can be rewritten as:

$$\begin{aligned}\overline{\boldsymbol{\varepsilon}} &= \sum_{r=0}^{N}\phi^{(r)}\overline{\boldsymbol{\varepsilon}}^{(r)} + \sum_{r=1}^{N}\phi^{(r)}\mathbf{R}^{(r)} : \overline{\boldsymbol{\sigma}}^{(r)} \\ &= \sum_{r=0}^{N}\phi^{(r)}\overline{\boldsymbol{\varepsilon}}^{(r)} + \sum_{r=1}^{N}\phi^{(r)}\mathbf{R}^{(r)}\bullet\mathbf{C}^{(r)} : \overline{\boldsymbol{\varepsilon}}^{(r)}\end{aligned} \tag{51}$$

The equivalence equation with the Mori-Tanaka method is expressed as:

$$\mathbf{C}^{(r)} : \left(\overline{\boldsymbol{\varepsilon}}^{0} + \overline{\boldsymbol{\varepsilon}}^{pt(r)}\right) = \mathbf{C}^{0} : \left(\overline{\boldsymbol{\varepsilon}}^{0} + \overline{\boldsymbol{\varepsilon}}^{pt(r)} - \overline{\boldsymbol{\varepsilon}}^{*(r)}\right), \text{ where } \overline{\boldsymbol{\varepsilon}}^{pt(r)} = \hat{\mathbf{S}}^{(r)} : \overline{\boldsymbol{\varepsilon}}^{*(r)} \tag{52}$$

Accordingly, from the above equation, the eigenstrain, $\overline{\boldsymbol{\varepsilon}}^{*(r)}$, can be obtained as follows:

$$\overline{\boldsymbol{\varepsilon}}^{*(r)} = -\left(\Delta\mathbf{C}^{(r)}\bullet\hat{\mathbf{S}}^{(r)} + \mathbf{C}^{0}\right)^{-1}\bullet\Delta\mathbf{C}^{(r)} : \overline{\boldsymbol{\varepsilon}}^{0}, \text{ where } \Delta\mathbf{C}^{(r)} = \mathbf{C}^{(r)} - \mathbf{C}^{0} \tag{53}$$

Further, the average strain within the r^{th}-phase can be written as:

$$\begin{aligned}\overline{\boldsymbol{\varepsilon}}^{(r)} &= \overline{\boldsymbol{\varepsilon}}^{0} + \overline{\boldsymbol{\varepsilon}}^{pt(r)} = \left\{\mathbf{I} - \hat{\mathbf{S}}^{(r)}\bullet\left[\hat{\mathbf{S}}^{(r)} + \left(\Delta\mathbf{C}^{(r)}\right)^{-1}\bullet\mathbf{C}^{0}\right]^{-1}\right\} : \overline{\boldsymbol{\varepsilon}}^{0} \\ &= \mathbf{T}_{\text{MT}}^{(r)} : \overline{\boldsymbol{\varepsilon}}^{0}\end{aligned} \tag{54}$$

Therefore, the average stress for the r^{th}-phase is rendered as:

$$\overline{\boldsymbol{\sigma}}^{(r)} = \mathbf{C}^{(r)} : \overline{\boldsymbol{\varepsilon}}^{(r)} = \mathbf{C}^{(r)}\bullet\mathbf{T}_{\text{MT}}^{(r)} : \overline{\boldsymbol{\varepsilon}}^{0} = \mathbf{C}^{(r)}\bullet\mathbf{T}_{\text{MT}}^{(r)}\bullet\left(\mathbf{C}^{0}\right)^{-1} : \overline{\boldsymbol{\sigma}}^{0} \tag{55}$$

Moreover, a substitution of Eq. (54) into Eq. (51) results in:

$$\begin{aligned}\overline{\boldsymbol{\varepsilon}} &= \left[\sum_{r=0}^{N}\phi^{(r)}\mathbf{T}_{\mathrm{MT}}^{(r)} \quad + \quad \sum_{r=1}^{N}\phi^{(r)}\mathbf{R}^{(r)}\bullet\mathbf{C}^{(r)}\bullet\mathbf{T}_{\mathrm{MT}}^{(r)}\right] : \overline{\boldsymbol{\varepsilon}}^{0} \\ &= \left[\phi^{(0)}\mathbf{I}+\sum_{r=1}^{N}\phi^{(r)}\mathbf{T}_{\mathrm{MT}}^{(r)} \quad + \quad \sum_{r=1}^{N}\phi^{(r)}\mathbf{R}^{(r)}\bullet\mathbf{C}^{(r)}\bullet\mathbf{T}_{\mathrm{MT}}^{(r)}\right] : \overline{\boldsymbol{\varepsilon}}^{0} \\ &= \left[\phi^{(0)}\mathbf{I} \quad + \quad \sum_{r=1}^{N}\phi^{(r)}\left(\mathbf{I}+\mathbf{R}^{(r)}\bullet\mathbf{C}^{(r)}\right)\bullet\mathbf{T}_{\mathrm{MT}}^{(r)}\right] : \overline{\boldsymbol{\varepsilon}}^{0}\end{aligned} \tag{56}$$

Finally, based on Eqs. (45), (55) and (56), the average stress within an *RVE* reads as:

$$\begin{aligned}\overline{\boldsymbol{\sigma}} = \sum_{r=0}^{N}\phi^{(r)}\overline{\boldsymbol{\sigma}}^{(r)} &= \left[\sum_{r=0}^{N}\phi^{(r)}\mathbf{C}^{(r)}\bullet\mathbf{T}_{\mathrm{MT}}^{(r)}\right] : \overline{\boldsymbol{\varepsilon}}^{0} \\ &= \left[\sum_{r=0}^{N}\phi^{(r)}\mathbf{C}^{(r)}\bullet\mathbf{T}_{\mathrm{MT}}^{(r)}\right]\bullet\left[\phi^{(0)}\mathbf{I}+\sum_{r=1}^{N}\phi^{(r)}\left(\mathbf{I}+\mathbf{R}^{(r)}\bullet\mathbf{C}^{(r)}\right)\bullet\mathbf{T}_{\mathrm{MT}}^{(r)}\right]^{-1} : \overline{\boldsymbol{\varepsilon}} \\ &= \mathbf{C}^{*} : \overline{\boldsymbol{\varepsilon}}\end{aligned} \tag{57}$$

Here, $\mathbf{C}^{*}$ represents the effective elastic stiffness of a composite.

Self-Consistent Method

The equivalence equation with the self-consistent method leads to the following equation:

$$\mathbf{C}^{(r)} : \left(\overline{\boldsymbol{\varepsilon}}^{0}+\overline{\boldsymbol{\varepsilon}}^{pt(r)}\right) = \mathbf{C}^{*} : \left(\overline{\boldsymbol{\varepsilon}}^{0}+\overline{\boldsymbol{\varepsilon}}^{pt(r)}-\overline{\boldsymbol{\varepsilon}}^{*(r)}\right), \quad \text{where} \quad \overline{\boldsymbol{\varepsilon}}^{pt(r)} = \hat{\mathbf{S}}^{(r)} : \overline{\boldsymbol{\varepsilon}}^{*(r)} \tag{58}$$

Note that the modified Eshelby tensor is a function of the effective stiffness of a composite. Accordingly, based on Eq. (58), the eigenstrain within the r^{th}-phase can be expressed as:

$$\overline{\boldsymbol{\varepsilon}}^{*(r)} = -\left(\Delta\mathbf{C}^{(r)}\bullet\hat{\mathbf{S}}^{(r)}+\mathbf{C}^{*}\right)^{-1}\bullet\Delta\mathbf{C}^{(r)} : \overline{\boldsymbol{\varepsilon}}, \qquad \text{where} \quad \Delta\mathbf{C}^{(r)} = \mathbf{C}^{(r)}-\mathbf{C}^{*} \tag{59}$$

By using Eq. (59), the average strain within the r^{th}-phase can be written as follows:

$$\begin{aligned}\overline{\boldsymbol{\varepsilon}}^{(r)} &= \overline{\boldsymbol{\varepsilon}} \quad + \quad \overline{\boldsymbol{\varepsilon}}^{pt(r)} \\ &= \left\{\mathbf{I}-\hat{\mathbf{S}}^{(r)}\bullet\left[\hat{\mathbf{S}}^{(r)}+\left(\Delta\mathbf{C}^{(r)}\right)^{-1}\bullet\mathbf{C}^{*}\right]^{-1}\right\} : \overline{\boldsymbol{\varepsilon}} \\ &= \mathbf{T}_{\mathrm{SC}}^{(r)} : \overline{\boldsymbol{\varepsilon}}\end{aligned} \tag{60}$$

Further, based on Eq. (51), the average strain of a composite can be expressed as:

$$\begin{aligned}\overline{\boldsymbol{\varepsilon}} &= \sum_{r=0}^{N} \phi^{(r)} \overline{\boldsymbol{\varepsilon}}^{(r)} + \sum_{r=1}^{N} \phi^{(r)} \mathbf{R}^{(r)} \bullet \mathbf{C}^{(r)} : \overline{\boldsymbol{\varepsilon}}^{(r)} \\ &= \phi^{(0)} \overline{\boldsymbol{\varepsilon}}^{0} + \sum_{r=1}^{N} \phi^{(r)} \left(\mathbf{I} + \mathbf{R}^{(r)} \bullet \mathbf{C}^{(r)} \right) \bullet \mathbf{T}_{\mathrm{SC}}^{(r)} : \overline{\boldsymbol{\varepsilon}}\end{aligned} \tag{61}$$

Arrangement of Eq. (61) shows:

$$\phi^{(0)} \overline{\boldsymbol{\varepsilon}}^{0} = \left\{ \mathbf{I} - \sum_{r=1}^{N} \phi^{(r)} \left(\mathbf{I} + \mathbf{R}^{(r)} \bullet \mathbf{C}^{(r)} \right) \bullet \mathbf{T}_{\mathrm{SC}}^{(r)} \right\} : \overline{\boldsymbol{\varepsilon}} \tag{62}$$

Finally, by using Eq. (62), the average stress of a composite is obtained as:

$$\begin{aligned}\overline{\boldsymbol{\sigma}} &= \sum_{r=0}^{N} \phi^{(r)} \overline{\boldsymbol{\sigma}}^{(r)} \\ &= \phi^{(0)} \mathbf{C}^{0} : \overline{\boldsymbol{\varepsilon}}^{0} + \sum_{r=1}^{N} \phi^{(r)} \mathbf{C}^{(r)} : \overline{\boldsymbol{\varepsilon}}^{(r)} \\ &= \left\{ \mathbf{C}^{0} + \sum_{r=1}^{N} \phi^{(r)} \left[\mathbf{C}^{(r)} - \mathbf{C}^{0} \bullet \left(\mathbf{I} + \mathbf{R}^{(r)} \bullet \mathbf{C}^{(r)} \right) \right] \bullet \mathbf{T}_{\mathrm{SC}}^{(r)} \right\} : \overline{\boldsymbol{\varepsilon}} \\ &= \mathbf{C}^{*} : \boldsymbol{\varepsilon}\end{aligned} \tag{63}$$

In Eq. (61), $\mathbf{C}^{*}$ signifies the effective stiffness of a composite based on the self-consistent method.

Since $\hat{\mathbf{S}}^{(r)}$ (Eq. 59) and $\mathbf{T}_{\mathrm{SC}}^{(r)}$ (Eq. 60) need to be computed based on the unknown elastic stiffness of a composite, $\mathbf{C}^{*}$, the iterative method is employed to carry out the computation. By considering the two-phase composite, Eqs. (44), (60) and (63) are written as:

$$\hat{\mathbf{S}}_{<n+1>}^{(1)} = \left(\mathbf{I} - \mathbf{S}_{<n>}^{(1)} \bullet \mathbf{R}^{(1)} \bullet \mathbf{C}_{<n>}^{*} \right)^{-1} \bullet \mathbf{S}_{<n>}^{(1)} \bullet \left(\mathbf{I} - \mathbf{R} \bullet \mathbf{C}_{<n>}^{*} \right) \tag{64}$$

$$\mathbf{T}_{\mathrm{SC}<n+1>}^{(1)} = \mathbf{I} - \hat{\mathbf{S}}_{<n+1>}^{(1)} \bullet \left[\hat{\mathbf{S}}_{<n+1>}^{(1)} + \left(\mathbf{C}^{(1)} - \mathbf{C}_{<n>}^{*} \right)^{-1} \bullet \mathbf{C}_{<n>}^{*} \right]^{-1} \tag{65}$$

$$\mathbf{C}_{<n+1>}^{*} = \mathbf{C}^{0} + \phi^{(1)} \left[\mathbf{C}^{(1)} - \mathbf{C}^{0} \bullet \left(\mathbf{I} + \mathbf{R}^{(1)} \bullet \mathbf{C}^{(1)} \right) \right] \bullet \mathbf{T}_{\mathrm{SC}<n+1>}^{(1)} \tag{66}$$

where (cf. Eq. 16):

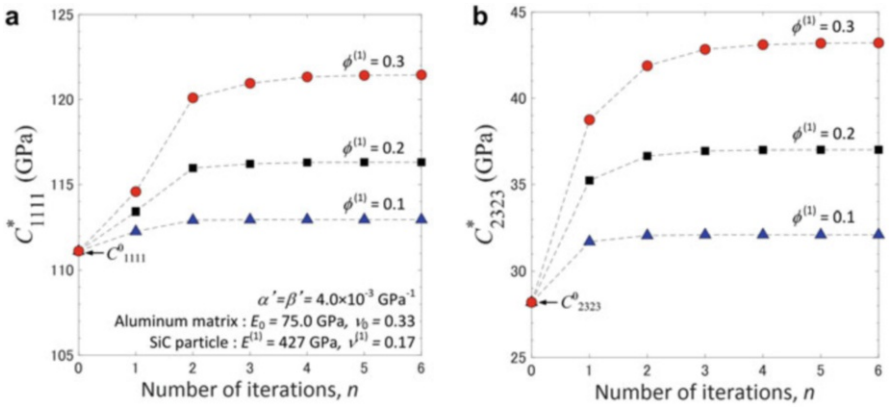

Fig. 5 Convergence of the effective stiffness. (**a**) C^*_{1111}. (**b**) C^*_{2323}

$$S^{(1)}_{ijkl<n>} = \frac{1}{15\left(1-\nu^*_{<n>}\right)}\left[\left(5\nu^*_{<n>}-1\right)\delta_{ij}\delta_{kl} + \left(4-5\nu^*_{<n>}\right)\left(\delta_{ik}\delta_{jl} + \delta_{il}\delta_{jk}\right)\right] \quad (67)$$

$$\nu^*_{<n>} = \frac{C^*_{1111<n>} - 2C^*_{2323<n>}}{2\left(C^*_{1111<n>} - C^*_{2323<n>}\right)} \quad (68)$$

where the elastic stiffness of the matrix material is used as the initial condition as:

$$C^*_{ijkl<0>} = C^0_{ijkl} \quad (69)$$

To realize the adequacy of the self-consistent method with the imperfect interface, the components of the $\mathbf{C}^*$ (Eq. 66) are plotted in Fig. 5. As shown, each component of $\mathbf{C}^*$ successfully converges to a certain value with a few iterations.

Degeneration of Effective Elastic Moduli of a Composite

Figures 6, 7, and 8 show the degeneration of the effective elastic moduli of a composite with α' and β'. As shown, the slightly different values for the effective elastic moduli are computed by the respective methods. Both the parameters α' (the extent of interfacial sliding) and β' (the extent of interfacial separation) influence the effective elastic moduli. However, the parameter α' in the Mori-Tanaka method does not affect the effective bulk modulus. Similarly, concerning the self-consistent method, the parameter α' has a negligible effect on the effective bulk modulus (Fig. 8a).

Equivalent Stiffness Method

As discussed in the previous section, the discontinuous displacement field at the interface represents the imperfection of the interface for the spring interface model. Accordingly, the overall strain of an *RVE* of the two-phase composites can be written as (Eq. 47):

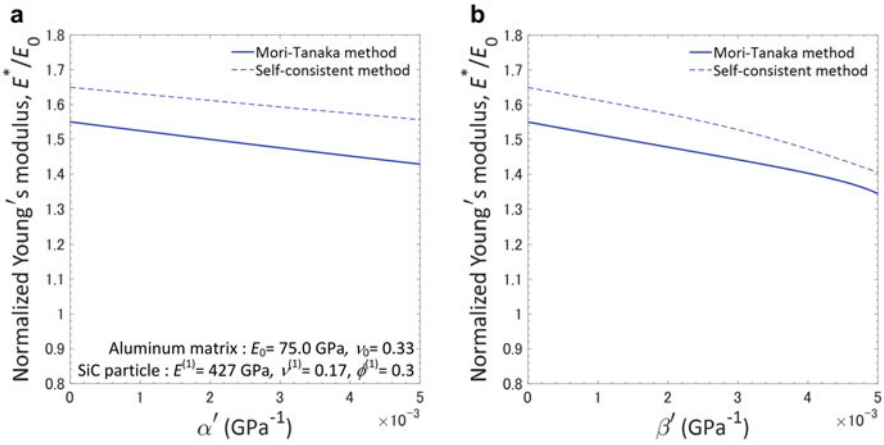

Fig. 6 Variations of effective Young's modulus, E^*. (**a**) Effect of α' with $\beta' = 0$. (**b**) Effect of β' with $\alpha' = 0$

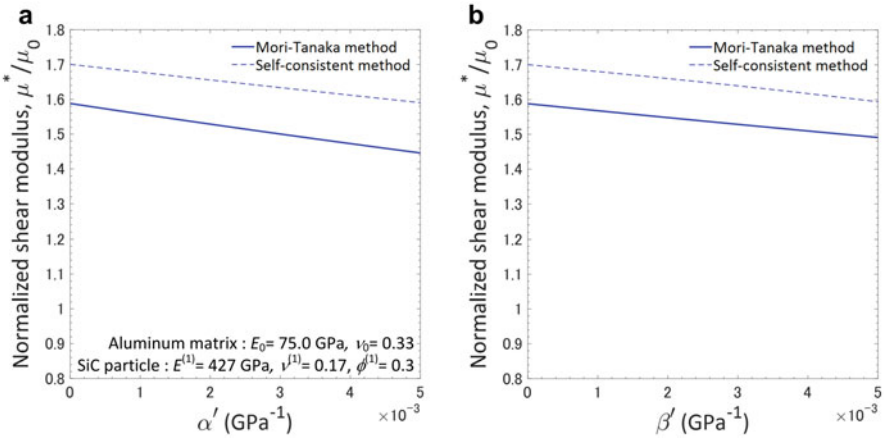

Fig. 7 Variations of effective shear modulus, μ^*. (**a**) Effect of α' with $\beta' = 0$. (**b**) Effect of β' with $\alpha' = 0$

$$\begin{aligned}\overline{\boldsymbol{\varepsilon}} &= \sum_{r=0}^{1} \phi^{(r)} \overline{\boldsymbol{\varepsilon}}^{(r)} + \phi \mathbf{R} \bullet \mathbf{C}^{(1)} : \overline{\boldsymbol{\varepsilon}}^{(1)} \\ &= \left(1 - \phi^{(1)}\right) \overline{\boldsymbol{\varepsilon}}^{(0)} + \phi^{(1)} \left(\mathbf{I} + \mathbf{R} \bullet \mathbf{C}^{(1)}\right) : \overline{\boldsymbol{\varepsilon}}^{(1)}\end{aligned} \tag{70}$$

For convenience, Eq. (70) is rewritten as:

$$\overline{\boldsymbol{\varepsilon}} = \left(1 - \phi^{(1)}\right) \left(\mathbf{C}^0\right)^{-1} : \overline{\boldsymbol{\sigma}}^{(0)} + \phi^{(1)} \left(\mathbf{I} + \mathbf{R} \bullet \mathbf{C}^{(1)}\right) \bullet \left(\mathbf{C}^{(1)}\right)^{-1} : \overline{\boldsymbol{\sigma}}^{(1)} \tag{71}$$

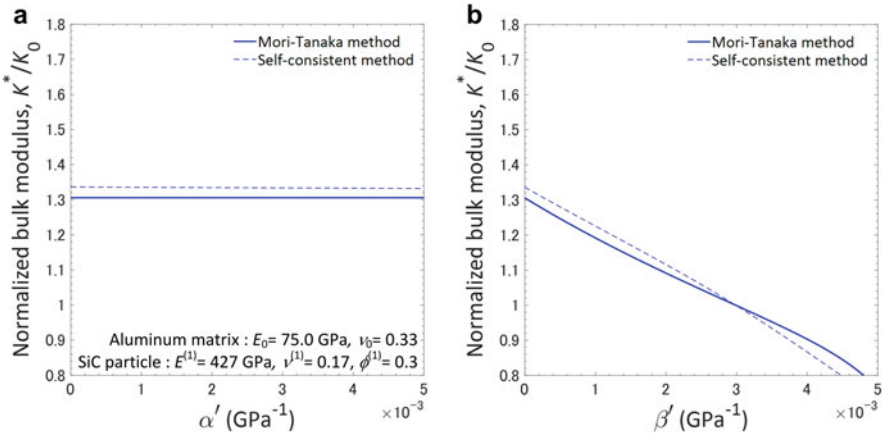

Fig. 8 Variations of effective bulk modulus, K^*. (**a**) Effect of α' with $\beta' = 0$. (**b**) Effect of β' with $\alpha' = 0$

Moreover, to mimic Eq. (71) with the *equivalent stiffness*, $\mathbf{C}_{\text{eq}}^{(1)}$, of particles, the following equation is proposed:

$$\overline{\boldsymbol{\varepsilon}} = \left(1-\phi^{(1)}\right)\left(\mathbf{C}^{0}\right)^{-1} : \overline{\boldsymbol{\sigma}}^{(0)} + \phi^{(1)}\left(\mathbf{C}_{\text{eq}}^{(1)}\right)^{-1} : \overline{\boldsymbol{\sigma}}^{(1)} \tag{72}$$

By comparing Eqs. (71) and (72), the following relation can be obtained:

$$\mathbf{C}_{\text{eq}}^{(1)} = \mathbf{C}^{(1)} \bullet \left(\mathbf{I} + \mathbf{R} \bullet \mathbf{C}^{(1)}\right)^{-1} \tag{73}$$

In Eq. (71), the effect of the imperfect interface is reflected in the reduction of the load transfer capability of reinforcing particles based on the *strain equivalence*. According to Eq. (71), the equivalent bulk and shear moduli of particles can be represented as:

$$K_{\text{eq}}^{(1)} = \frac{K^{(1)}}{1 + 3\beta' K^{(1)}} \tag{74}$$

$$\mu_{\text{eq}}^{(1)} = \frac{5\mu^{(1)}}{(6\alpha' + 4\beta')\mu^{(1)} + 5} \tag{75}$$

In contrast to Eqs. (74) and (75), based on the *energy equivalence*, the equivalent elastic moduli of particles can be written as (Duan et al. 2007a):

$$K_{\text{eq}}^{(1)} = \frac{K^{(1)}}{1 + 3\left(\alpha_n'\right)^{-1} K^{(1)}} \tag{76}$$

$$\mu_{\mathrm{eq}}^{(1)} = \mu^{(1)} \frac{5\alpha_{\mathrm{n}}'\alpha_{\mathrm{s}}'c_1 + 8\mu^{(1)}\left(7+5\nu^{(1)}\right)\left(2\alpha_{\mathrm{n}}'+3\alpha_{\mathrm{s}}'\right)}{5\alpha_{\mathrm{n}}'\alpha_{\mathrm{s}}'c_1 + 2\mu^{(1)}\alpha_{\mathrm{n}}'c_2 + \mu^{(1)}\alpha_{\mathrm{s}}'(3c_2-5c_1) + 80\left(\mu^{(1)}\right)^2\left(7+5\nu^{(1)}\right)} \tag{77}$$

where:

$$\begin{aligned} c_1 &= 4\left(7-10\nu^{(1)}\right) + \frac{\mu^{(1)}}{\mu_0}\left(7+5\nu^{(1)}\right); \\ c_2 &= 20\left(7-4\nu^{(1)}\right) + 3\frac{\mu^{(1)}}{\mu_0}\left(7+5\nu^{(1)}\right) \end{aligned} \tag{78}$$

In Eqs. (74) and (75), $\alpha_{\mathrm{n}}' = a_{\mathrm{p}}\alpha_{\mathrm{n}}$ and $\alpha_{\mathrm{S}}' = a_{\mathrm{p}}\alpha_{\mathrm{S}}$ are the interface elastic parameters in the normal and tangential directions, respectively. As shown by Figs. 9 and 10, when $\mu_{\mathrm{eq}}^{(1)}/\mu^{(1)} > 0.6$, the degradation behavior associated with α_{n}' and α_{S}' are rather insensitive to the value of μ_0. Such a behavior can also be expected from Eq. (75) since it is independent of μ_0. In addition, the forms of Eqs. (74) and (76) are similar to each other. Accordingly, the similarity between the strain equivalence and the energy equivalence can be recognized.

By assuming the *fictitious perfect interface condition* in conjunction with Eq. (73) as an approximation, the Mori-Tanaka method renders the following equation for the effective elastic stiffness of a two-phase composite material (cf. Eq. 57):

$$\mathbf{C}^* = \left[\left(1-\phi^{(1)}\right)\mathbf{C}^0 + \phi^{(1)}\mathbf{C}_{\mathrm{eq}}^{(1)} \bullet \mathbf{T}_{\mathrm{MT}}^{(1)}\right] \bullet \left[\left(1-\phi^{(1)}\right)\mathbf{I} + \phi^{(1)}\mathbf{T}_{\mathrm{MT}}^{(1)}\right]^{-1} \tag{79}$$

where:

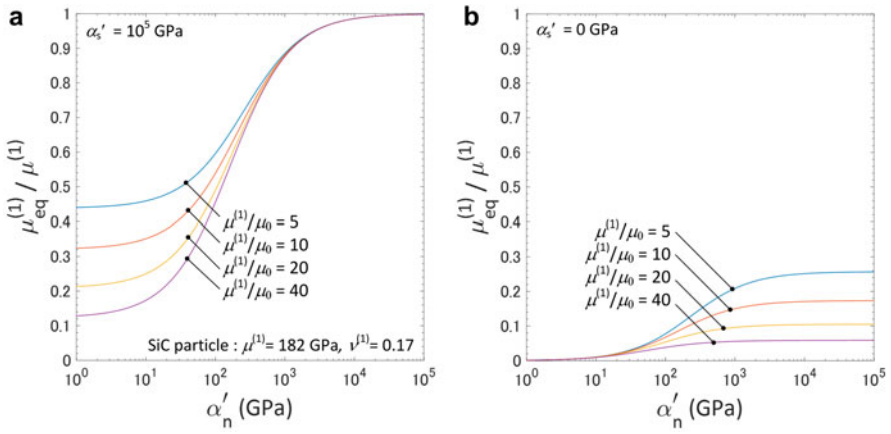

Fig. 9 Effects of α_{n}' on the equivalent shear modulus, $\mu_{\mathrm{eq}}^{(1)}$, rendered by the energy equivalence. (**a**) Effect of α_{n}' with $\alpha_{\mathrm{s}}' = 105$ GPa. (**b**) Effect of α_{n}' with $\alpha_{\mathrm{s}}' = 0$ GPa

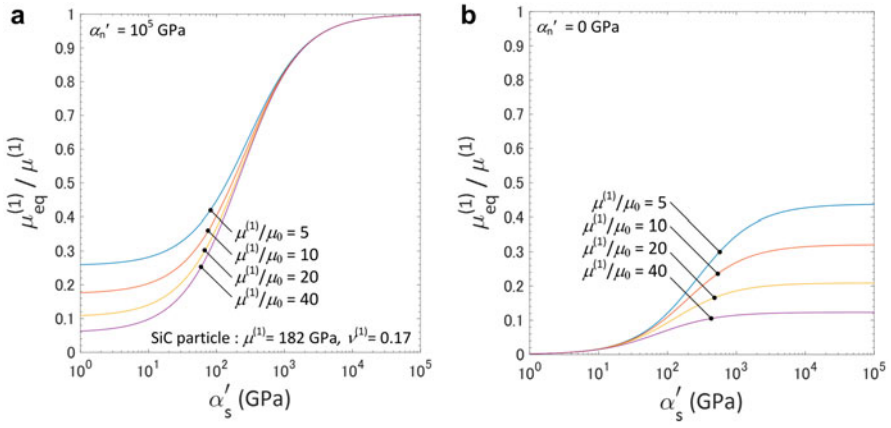

Fig. 10 Effects of α_s' on the equivalent shear modulus, $\mu_{eq}^{(1)}$, rendered by the energy equivalence. (**a**) Effect of α_s' with $\alpha_n' = 105$ GPa. (**b**) Effect of α_n' with $\alpha_s' = 0$ GPa

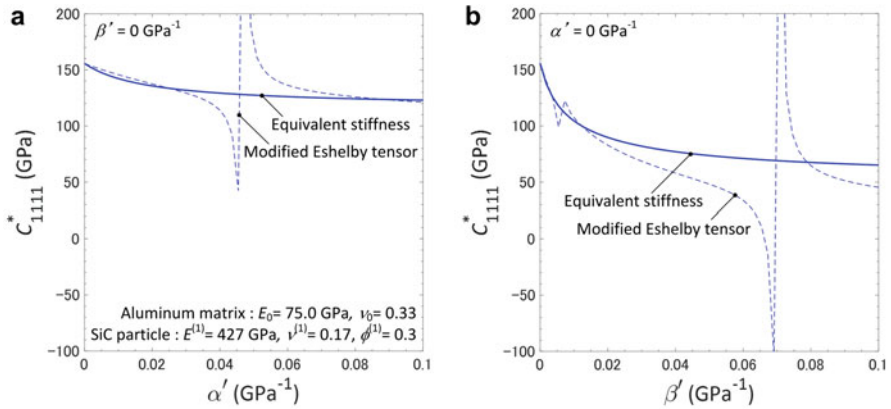

Fig. 11 Variations of C^*_{1111} simulated with the Mori-Tanaka method. (**a**) Effect of α' with $\beta' = 0$. (**b**) Effect of β' with $\alpha' = 0$

$$\mathbf{T}_{MT}^{(1)} = \mathbf{I} - \mathbf{S}^{(1)} \bullet \left[\mathbf{S}^{(1)} + \left(\mathbf{C}_{eq}^{(1)} - \mathbf{C}^0 \right)^{-1} \bullet \mathbf{C}^0 \right]^{-1} \tag{80}$$

Figures 11 and 12 show the variation of the effective elastic stiffness, $\mathbf{C}^*$ (Eqs. 57 and 79). As shown, the Mori-Tanaka method with the equivalent stiffness (Eq. 79) is free from a singular behavior, and the effective elastic stiffness is continuously decreased as the parameters α' and β' are increased. By taking advantage of such a favorable behavior with the equivalent stiffness, the effect of the imperfect interface is further studied for the elastoplastic behavior of composites in the following sections.

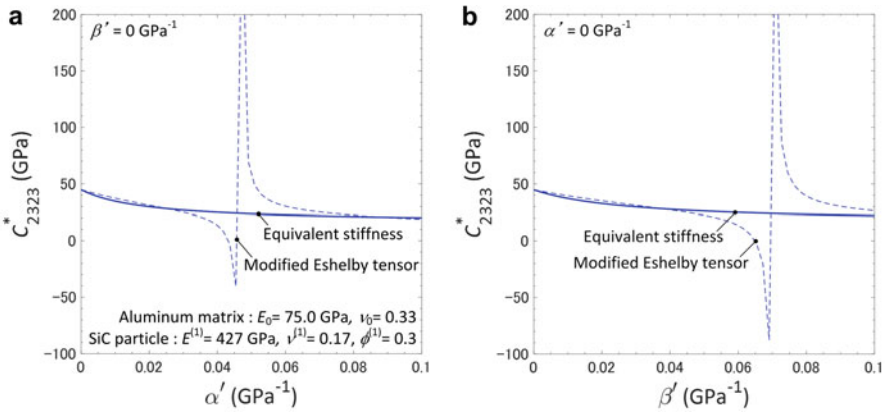

Fig. 12 Variations of C^*_{2323} simulated with the Mori-Tanaka method. (**a**) Effect of α' with $\beta' = 0$. (**b**) Effect of β' with $\alpha' = 0$

Effective Elastoplastic Responses of Two-Phase Composites

Effective Elastic Stiffness with Pair-Wise Interactions

In the literature, the effective medium theories (the Eshelby method, the Mori-Tanaka method, the self-consistent method, the generalized self-consistent method, the differential scheme, etc.) are broadly used to predict the multiaxial properties and responses of heterogeneous materials (cf. Qu and Cherkaoui 2006). Note that regarding the composites with a high volume fraction of inclusion, the near-field inclusion interactions need to be adequately accounted for. However, because of their consideration of the single-inclusion problem, these effective medium theories cannot take into account for the effect associated with the near-field inclusion interactions.

To tackle the near-field interaction, for instance, Moschovidis and Mura (1975) considered the polynomial eigenstrain to account for the effect of pair-wise interactions. Ju and Chen (1994a, b, c) developed an approximate yet accurate method to account for the interparticle interaction effects in two-phase composites with high particle volume fraction. Subsequently, Ju and Zhang (1998, 2001) proposed a two-dimensional micromechanical formulation for the continuous fiber-reinforced composites. Further, based on the Ju-Chen pair-wise interaction formulation, Lin and Ju (2009) proposed a micromechanical formulation for the three-phase composites.

By accounting for the pair-wise particle interactions (Ju and Chen 1994a, b, Fig. 13) in the framework of equivalent stiffness method, the effective elastic stiffness of two-phase composites can be rendered as (Ju and Yanase 2010, 2011):

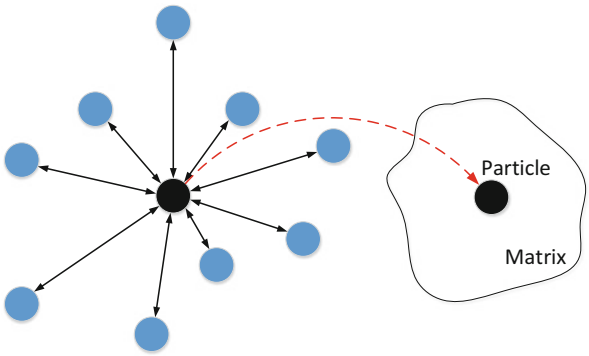

Fig. 13 A consideration of pair-wise particle interactions

$$\mathbf{C}^{*} = \mathbf{C}^{0} \bullet \left\{ \mathbf{I} + \phi^{(1)} \left[\left(\mathbf{C}_{\mathrm{eq}}^{(1)} - \mathbf{C}^{0} \right)^{-1} \bullet \mathbf{C}^{0} + \left(1 - \phi^{(1)} \right) \left(\mathbf{S}^{(1)} - \mathbf{A}^{(1)} \right) \right]^{-1} \right\} \tag{81}$$

where:

$$A_{ijkl}^{(1)} = \lambda_{\mathrm{A}} \delta_{ij} \delta_{kl} + \mu_{\mathrm{A}} \left(\delta_{ik} \delta_{jl} + \delta_{il} \delta_{jk} \right) \tag{82}$$

with:

$$\begin{aligned} \lambda_{\mathrm{A}} = & \phi^{(1)} \gamma \left\{ \frac{2\nu_0^2 + 2\nu_0 - 1}{540(1-\nu_0)^2} \cdot \left[\frac{K_0}{K_{\mathrm{eq}}^{(1)} - K_0} + \frac{1+\nu_0}{3(1-\nu_0)} \right]^{-1} \right. \\ & \left. + \frac{-340\nu_0^2 + 100\nu_0 - 19}{10800(1-\nu_0)^2} \cdot \left[\frac{\mu_0}{\mu_{\mathrm{eq}}^{(1)} - \mu_0} + \frac{8 - 10\nu_0}{15(1-\nu_0)} \right]^{-1} \right\} \end{aligned} \tag{83}$$

$$\begin{aligned} \mu_{\mathrm{A}} = & \phi^{(1)} \gamma \left\{ \frac{-2\nu_0^2 - 2\nu_0 + 1}{360(1-\nu_0)^2} \cdot \left[\frac{K_0}{K_{\mathrm{eq}}^{(1)} - K_0} + \frac{1+\nu_0}{3(1-\nu_0)} \right]^{-1} \right. \\ & \left. + \frac{140\nu_0^2 - 200\nu_0 + 119}{7200(1-\nu_0)^2} \cdot \left[\frac{\mu_0}{\mu_{\mathrm{eq}}^{(1)} - \mu_0} + \frac{8 - 10\nu_0}{15(1-\nu_0)} \right]^{-1} \right\} \end{aligned} \tag{84}$$

In this study, $\gamma = 3.5$ is adapted according to Ju and Yanase (2010, 2011). After a lengthy but straightforward derivation with Eq. (79), the effective bulk and shear moduli of an isotropic composite can be expressed as:

$$
\begin{aligned}
K^* &= K_0 + \frac{\phi^{(1)} K_0}{K_0 \left(K_{\text{eq}}^{(1)} - K_0\right)^{-1} + m} \\
\mu^* &= \mu_0 + \frac{\phi^{(1)} \mu_0}{\mu_0 \left(\mu_{\text{eq}}^{(1)} - \mu_0\right)^{-1} + n}
\end{aligned}
\tag{85}
$$

where:

$$
\begin{aligned}
m &= \left(1 - \phi^{(1)}\right) \left[\frac{1 + \nu_0}{3(1 - \nu_0)} - 3\lambda_{\text{A}} - 2\mu_{\text{A}}\right] \\
n &= \left(1 - \phi^{(1)}\right) \left[\frac{8 - 10\nu_0}{15(1 - \nu_0)} - 2\mu_{\text{A}}\right]
\end{aligned}
\tag{86}
$$

Noted that by setting $\gamma = 0$ in Eq. (79), it leads to the Mori-Tanaka method (Eq. 79).

Figures 14 and 15 show the effects of α' (interface sliding) and β' (interface separation). The higher-order method with the perfect interface condition of $\alpha' = \beta' = 0$ shows a better correlation with the experimental data by Smith (1976), compared to the Mori-Tanaka method. When the interfacial damage is taken into account (i.e., $\alpha' > 0, \beta' > 0$), the higher-order method and the Mori-Tanaka method are rather indistinguishable. Figure 16a shows that in the Mori-Tanaka method, the interfacial sliding represented by α' has no influence on the bulk modulus, K^* (cf. Qu 1993a). By contrast, Fig. 16b shows that the interfacial separation represented by β' has a substantial effect on the bulk modulus, K^*. Concerning the effect of the direct particle interaction, Figs. 14, 15, and 16 manifest that it has a marginal effect on the effective moduli in the presence of imperfect interface.

Effective Yield Function

In this section, the effective yield function of particle-reinforced ductile matrix composites, such as metal matrix composites (MMCs), is presented. In MMCs, the mismatched stiffness of constituents results in high stress concentration around the interface between the matrix and inclusion (Christman et al. 1989a, b). As a result, the interface region tends to yield when even a relatively low stress is applied. However, such local matrix yielding doesn't govern the overall plastic yielding of the composite. Instead, the average stress in the matrix is closely linked to the overall plastic yielding (Nieh and Chellman 1984; Clyne and Withers 1993).

According to Ju and Chen (1994c), the effective yield function for a composite is rendered as:

$$
\overline{F} = \sqrt{\langle H(\mathbf{x}) \rangle} - K(\overline{e}^p) \leq 0 \tag{87}
$$

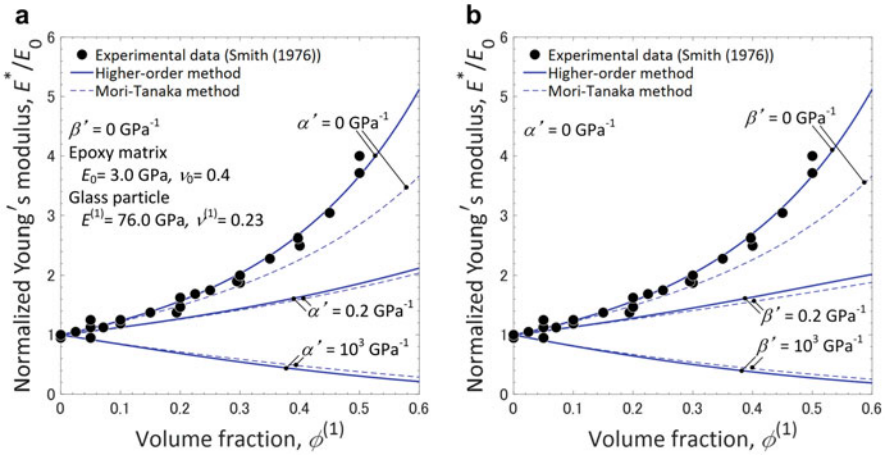

Fig. 14 Variations in effective Young's modulus, E^*, of an epoxy-glass composite. (**a**) Effect of α' with $\beta' = 0$. (**b**) Effect of β' with $\alpha' = 0$

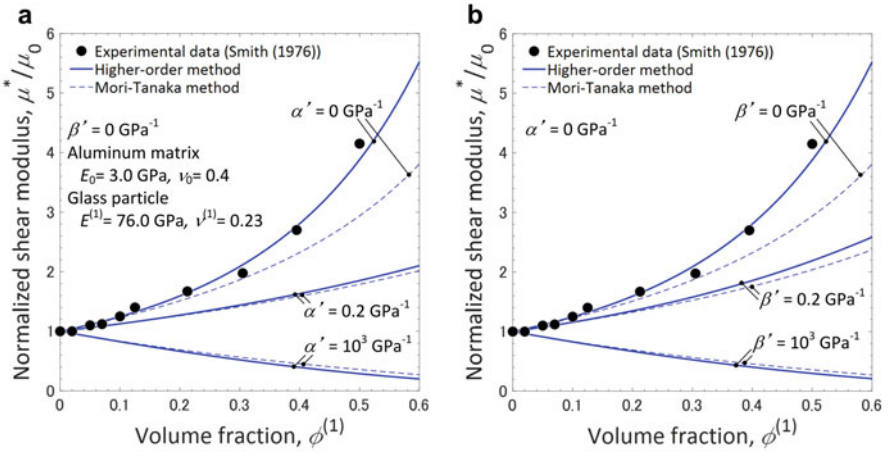

Fig. 15 Variations in effective shear modulus, μ^*, of an epoxy-glass composite. (**a**) Effect of α' with $\beta' = 0$. (**b**) Effect of β' with $\alpha' = 0$

In Eq. (87), the first term is the effective stress norm of an *RVE*, and the second term is the hardening function of a matrix-only material. The homogenized deviatoric stress norm of a two-phase composite is written as:

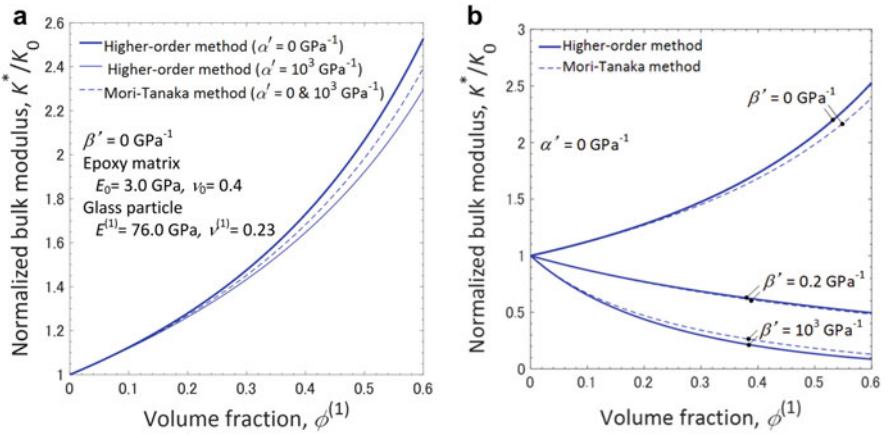

Fig. 16 Variations in effective shear modulus, K^*, of an epoxy-glass composite. (**a**) Effect of α' with $\beta' = 0$. (**b**) Effect of β' with $\alpha' = 0$

$$\langle H(\mathbf{x})\rangle_{\mathrm{m}} = H^0 + \int_{|\mathbf{x}-\mathbf{x}^{(1)}|\notin\Omega^{(1)}} \left\{H\left(\mathbf{x}|\mathbf{x}^{(1)}\right) - H^0\right\} P\left(\mathbf{x}^{(1)}\right) dV(\mathbf{x}) \tag{88}$$

The first and second terms represent the stress norm associated with the uniform stress field and the perturbed stress field, respectively. Further, $P(\mathbf{x}^{(1)})$ defines the probability density function for finding a spherical particle centered at $\mathbf{x}^{(1)}$, and $\Omega^{(1)}$ is the domain of the particle. In practice, the dispersion of particle can be assumed to be statistically homogeneous, isotropic, and uniform. Accordingly, it is expressed as:

$$P\left(\mathbf{x}^{(1)}\right) = \frac{N^{(1)}}{V_{\mathrm{RVE}}} = \frac{3\phi^{(1)}}{4\pi {a_{\mathrm{p}}}^3} \tag{89}$$

where $N^{(1)}$ is the total number of the particles dispersed in the volume of *RVE*, V_{RVE}. Thus, Eq. (88) can be rewritten as:

$$\begin{aligned}\langle H(\mathbf{x})\rangle_{\mathrm{m}} &= \boldsymbol{\sigma}^0 : \mathbf{I}^{\mathrm{dev}} : \boldsymbol{\sigma}^0 \\ &+ \int_{|\mathbf{x}-\mathbf{x}^{(1)}|\notin\Omega^{(1)}} \left\{\boldsymbol{\sigma}\left(\mathbf{x}|\mathbf{x}^{(1)}\right) : \mathbf{I}^{\mathrm{dev}} : \boldsymbol{\sigma}\left(\mathbf{x}|\mathbf{x}^{(1)}\right) - \boldsymbol{\sigma}^0 : \mathbf{I}^{\mathrm{dev}} : \boldsymbol{\sigma}^0\right\} \frac{3\phi^{(1)}}{4\pi {a_{\mathrm{p}}}^3} dV(\mathbf{x})\end{aligned} \tag{90}$$

where:

$$I_{ijkl}^{\mathrm{dev}} = \frac{1}{2}\left(\delta_{ik}\delta_{jl} + \delta_{il}\delta_{jk}\right) - \frac{1}{3}\delta_{ij}\delta_{kl} \tag{91}$$

The stress field outside a particle can be expressed as:

$$\boldsymbol{\sigma}\left(\mathbf{x}\middle|\mathbf{x}^{(1)}\right) = \mathbf{C}^0 \bullet \left\{\mathbf{I} + \overline{\mathbf{G}}\left(\mathbf{x}\middle|\mathbf{x}^{(1)}\right) \bullet \left[\mathbf{A}^{(1)} - \mathbf{B}^{(1)}\right]^{-1}\right\} \bullet \left(\mathbf{C}^0\right)^{-1} : \boldsymbol{\sigma}^0 \tag{92}$$

where:

$$\mathbf{B}^{(1)} = \left(\mathbf{C}_{\mathrm{eq}}^{(1)} - \mathbf{C}^0\right)^{-1} \bullet \mathbf{C}^0 + \mathbf{S}^{(1)} \tag{93}$$

In Eq. (90), $\overline{\mathbf{G}}$ signifies the exterior-point Eshelby tensor for a spherical particle (Mura (1987); Ju and Chen (1994c), Ju and Yanase (2010), Fig. 17), and it is given as:

$$\begin{aligned}\overline{G}_{ijkl}(r) = {} & \frac{\rho^3}{30(1-\nu_0)}\left[\left(3\rho^2 - 10\nu_0 + 5\right)\left(\delta_{ik}\delta_{jl} + \delta_{il}\delta_{jk}\right) + \left(3\rho^2 + 10\nu_0 - 5\right)\delta_{ij}\delta_{kl}\right. \\ & + 15\left(1-\rho^2\right)\delta_{ij}n_k n_l + 15\left(1 - 2\nu_0 - \rho^2\right)\delta_{kl}n_i n_j + 15\left(7\rho^2 - 5\right)n_i n_j n_k n_l \\ & \left. + 15\left(\nu_0 - \rho^2\right)\left(\delta_{ik}n_j n_l + \delta_{il}n_j n_k + \delta_{jk}n_i n_l + \delta_{jl}n_i n_k\right)\right]\end{aligned} \tag{94}$$

where:

$$\rho = a_p/r \qquad ; \qquad r = \left|\mathbf{x} - \mathbf{x}^{(1)}\right| \tag{95}$$

Here, the components of the unit outward normal vector, n_i, can be expressed with the spherical coordinate system as follows:

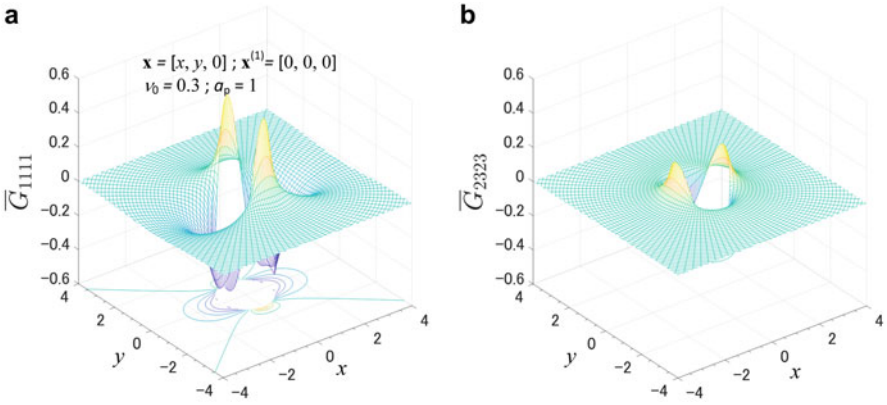

Fig. 17 Variations of the exterior-point Eshelby tensor, $\overline{G}_{ijkl}$. (**a**) $\overline{G}_{1111}$. (**b**) $\overline{G}_{2323}$

$$n_1 = \cos\phi \cdot \cos\theta\,,\ n_2 = \cos\phi \cdot \sin\theta\,,\ n_3 = \sin\phi\,,\quad \text{where } -\pi/2 \le \phi \le \pi/2\,,\ 0 \le \theta \le 2\pi \tag{96}$$

By making use of those aforementioned equations, Eq. (90) can be expressed by the following form:

$$\langle H(\mathbf{x})\rangle_{\mathrm{m}} = \boldsymbol{\sigma}^0 : \mathbf{T} : \boldsymbol{\sigma}^0, \quad \text{where} \quad T_{ijkl} = T_1\,\delta_{ij}\delta_{kl} + T_2\left(\delta_{il}\delta_{jk} + \delta_{ik}\delta_{jl}\right) \tag{97}$$

with:

$$T_1 = \frac{\phi^{(1)}\mu_0^2}{(1-\nu_0)^2}\left[\frac{{K_{\mathrm{B}}}^2\left(2240\nu_0^2 + 3472\nu_0 + 1367\right)}{6720} - \frac{\mu_{\mathrm{B}}^2\left(140\nu_0^2 - 200\nu_0 + 119\right)}{675}\right] - \frac{1}{3} \tag{98}$$

$$T_2 = \frac{\phi^{(1)}{\mu_0}^2{\mu_{\mathrm{B}}}^2\left(140{\nu_0}^2 - 200\nu_0 + 119\right)}{450(1-\nu_0)^2} + \frac{1}{2} \tag{99}$$

In the above equations, K_{B} and μ_{B} can be expressed as:

$$K_{\mathrm{B}} = \frac{1}{9K_0}\left[\frac{1}{(3\lambda_{\mathrm{A}} + 2\mu_{\mathrm{A}}) - K_0\left(K_{\mathrm{eq}}^{(1)} - K_0\right)^{-1} - (\nu_0 + 1)(3 - 3\nu_0)^{-1}}\right] \tag{100}$$

$$\mu_{\mathrm{B}} = \frac{1}{8\mu_0}\left[\frac{1}{\mu_{\mathrm{A}} - \mu_0\left(2\mu_{\mathrm{eq}}^{(1)} - 2\mu_0\right)^{-1} - (4 - 5\nu_0)(15 - 15\nu_0)^{-1}}\right] \tag{101}$$

Further, the following micromechanical field equation (Ju and Chen 1994a) is useful for further derivation:

$$\begin{aligned}\boldsymbol{\sigma}^0 &= \mathbf{C}^0 \bullet \left\{(1-\phi)\mathbf{I} - \phi\left[\mathbf{I} + \left(\mathbf{C}_{\mathrm{eq}}^{(1)} - \mathbf{C}^0\right)^{-1} \bullet \mathbf{C}^0\right] \bullet \left(\mathbf{A}^{(1)} - \mathbf{B}^{(1)}\right)^{-1}\right\}^{-1} \bullet \left(\mathbf{C}^0\right)^{-1} : \overline{\boldsymbol{\sigma}} \\ &= \mathbf{P} : \overline{\boldsymbol{\sigma}}\end{aligned} \tag{102}$$

Equation (97) can be rephrased by making use of the major symmetry of $\mathbf{P}$ as follows:

$$\begin{aligned}\langle H(\mathbf{x})\rangle_{\mathrm{m}} &= \overline{\sigma}_{ij}\left(P_{abij}T_{abmn}P_{mnkl}\right)\overline{\sigma}_{kl} = \overline{\sigma}_{ij}\left(P_{ijab}T_{abmn}P_{mnkl}\right)\overline{\sigma}_{kl} \\ &= \overline{\sigma}_{ij}\overline{T}_{ijkl}\overline{\sigma}_{kl}\end{aligned} \tag{103}$$

In Eq. (103), $\overline{\mathbf{T}}$ is given as:

$$\overline{T}_{ijkl} = \overline{T}_1 \delta_{ij}\delta_{kl} + \overline{T}_2 \left(\delta_{ik}\delta_{jl} + \delta_{il}\delta_{jk}\right) \tag{104}$$

where:

$$\overline{T}_1 = \frac{1}{9Q_1^2}\left(T_1 + \frac{2}{3}T_2\right) - \frac{T_2}{6Q_2^2} \quad ; \quad \overline{T}_2 = \frac{T_2}{4Q_2^2} \tag{105}$$

with:

$$\begin{aligned} Q_1 &= \frac{1-\phi^{(1)}}{3} - 3\phi^{(1)}\left[K_{\mathrm{B}}\frac{K_0 K_{\mathrm{eq}}^{(1)}}{K_{\mathrm{eq}}^{(1)} - K_0}\right] \\ Q_2 &= \frac{1-\phi^{(1)}}{2} - 2\phi^{(1)}\left[\mu_{\mathrm{B}}\frac{\mu_0 \mu_{\mathrm{eq}}^{(1)}}{\mu_{\mathrm{eq}}^{(1)} - \mu_0}\right] \end{aligned} \tag{106}$$

The effective stress norm of an *RVE* in Eq. (87) is defined as:

$$\sqrt{\langle H(\mathbf{x})\rangle} = \left(1-\phi^{(1)}\right)\sqrt{\langle H(\mathbf{x})\rangle_{\mathrm{m}}} \tag{107}$$

In Eq. (107), the presence of elastic particles is accounted for. Finally, Eq. (87) is expressed as:

$$\overline{F} = \left(1-\phi^{(1)}\right)\sqrt{\overline{\boldsymbol{\sigma}} : \overline{\mathbf{T}} : \overline{\boldsymbol{\sigma}}} - \sqrt{\frac{2}{3}}\left[\sigma_{\mathrm{y}} + h(\overline{e}^p)^q\right] \tag{108}$$

where σ_{y} is the yield strength of a ductile matrix, h and q are the material constants that govern the hardening behavior of the matrix material, and $\overline{e}^p$ is the equivalent plastic strain. Based on Eq. (108), the composite yield strength corresponds to the following equation:

$$\left(1-\phi^{(1)}\right)\sqrt{\overline{\boldsymbol{\sigma}} : \overline{\mathbf{T}} : \overline{\boldsymbol{\sigma}}} - \sqrt{\frac{2}{3}}\sigma_{\mathrm{y}} = 0 \tag{109}$$

Elastoplastic Deformation Responses of Ductile Matrix Composites

By using the stress-driven forward-Euler algorithm, Eq. (108) can be rewritten as:

$$\overline{F}_{(n+1)} = \Psi_{(n+1)} - \left[\sigma_{\mathrm{y}} + h\left(\overline{e}_{(n)} + \Delta\overline{e}_{(n+1)}\right)^q\right], \text{ where } \Psi_{(n+1)} = \sqrt{\frac{3}{2}}\left(1-\phi^{(1)}\right)\sqrt{\overline{\boldsymbol{\sigma}} : \overline{\mathbf{T}} : \overline{\boldsymbol{\sigma}}}\Big|_{(n+1)} \tag{110}$$

Thus, during the plastic deformation process $\left(\overline{F}=0\right)$, the effective plastic strain rate is given as:

$$\Delta\overline{e}^{p}_{(n+1)} = \left(\frac{\Psi_{(n+1)}-\sigma_{\mathrm{y}}}{h}\right)^{1/q} - \overline{e}^{p}_{(n)} \tag{111}$$

On the other hand, the increment of plastic strain can be expressed as:

$$\Delta\overline{\boldsymbol{\varepsilon}}^{P}_{(n+1)}=\Delta\lambda_{(n+1)}\cdot\boldsymbol{\xi}_{(n+1)}\,,\ \text{where}\ \boldsymbol{\xi}_{(n+1)}=\left.\frac{\partial\overline{F}}{\partial\overline{\boldsymbol{\sigma}}}\right|_{(n+1)}=\left.\sqrt{\frac{3}{2}}\left(1-\phi^{(1)}\right)\frac{\overline{\mathbf{T}}:\overline{\boldsymbol{\sigma}}}{\sqrt{\overline{\boldsymbol{\sigma}}:\overline{\mathbf{T}}:\overline{\boldsymbol{\sigma}}}}\right|_{(n+1)} \tag{112}$$

where $\Delta\lambda$ is called the plastic consistency parameter. Moreover, the conventional definition for the equivalent plastic strain rate results in the following equation (cf. Khan and Huang 1995; Dunne and Petrinic 2005):

$$\Delta\overline{e}^{p}_{(n+1)} = \sqrt{\frac{2}{3}\Delta\overline{\boldsymbol{\varepsilon}}^{p}_{(n+1)}:\Delta\overline{\boldsymbol{\varepsilon}}^{p}_{(n+1)}} \tag{113}$$

Therefore, by combining Eqs. (110), (111), (112) and (113), the plastic consistency parameter can be expressed as:

$$\Delta\lambda_{(n+1)} = \frac{\left(\frac{\Psi_{(n+1)}-\sigma_{\mathrm{y}}}{h}\right)^{1/q} - \overline{e}^{p}_{(n)}}{\sqrt{\frac{2}{3}\boldsymbol{\xi}_{(n+1)}:\boldsymbol{\xi}_{(n+1)}}} \tag{114}$$

Finally, the total strain increment is calculated based on the classical additive decomposition of strain as follows:

$$\Delta\overline{\boldsymbol{\varepsilon}}_{(n+1)} = \Delta\overline{\boldsymbol{\varepsilon}}^{e}_{(n+1)} + \Delta\overline{\boldsymbol{\varepsilon}}^{p}_{(n+1)} = \left(\mathbf{C}^{*}\right)^{-1}:\Delta\overline{\boldsymbol{\sigma}}_{(n+1)} + \Delta\lambda_{(n+1)}\cdot\boldsymbol{\xi}_{(n+1)} \tag{115}$$

The uniaxial tensile responses of aluminum composites reinforced by SiC particles are presented in Fig. 18. The present predictions are in good agreement with the experimental data (Yang et al. 1991). Regarding the biaxial tensile behaviors shown in Fig. 19, the increase of particle content results in the higher initial yield strength, and the effect of the direct particle interaction can be recognized. Note that the composites actually start to yield (Fig. 19) before the nonlinearity can be clearly recognized in the stress-strain curve (Fig. 18).

Figure 20 shows the influence of α' and β' on the initial composite yield surface. As exhibited, the increase of damage parameters, α' and β', corresponds to the reduction of particle volume fraction, $\phi^{(1)}$ (cf. Fig. 19). In addition, the direct particle interaction has a negligible influence on the yield strength in the presence of the

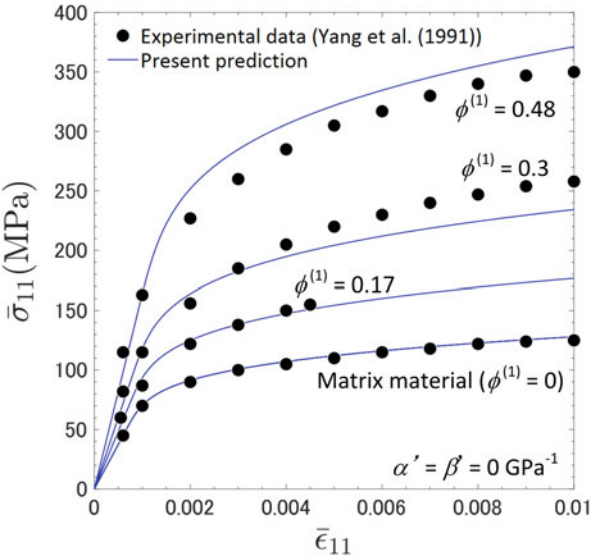

Fig. 18 Overall uniaxial stress-strain responses. Aluminum matrix: $E_0 = 75.0$ GPa, $\nu_0 = 0.33$, $\sigma_y = 47.0$ MPa, $h = 285$ MPa, $q = 0.24$. SiC particle: $E^{(I)} = 420$ GPa, $\nu^{(I)} = 0.17$

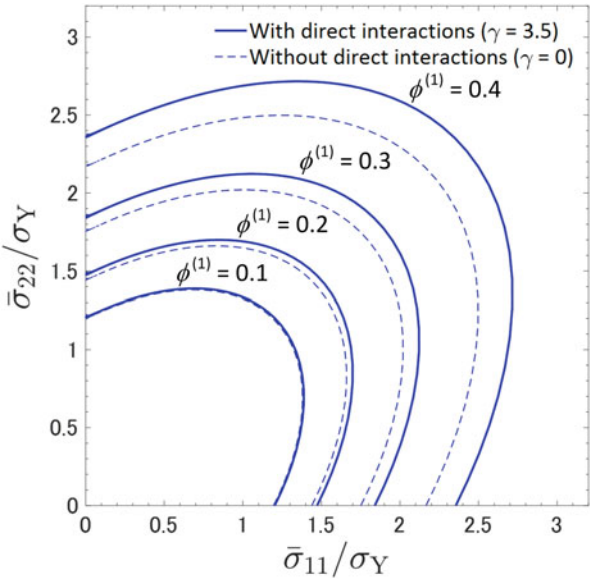

Fig. 19 Initial yield surface under the biaxial loading condition ($\bar{\sigma}_{33} = 0$) in the absence of interfacial damage ($\alpha' = \beta' = 0$). Aluminum matrix: $E_0 = 75.0$ GPa, $\nu_0 = 0.33$, $\sigma_y = 47.0$ MPa. SiC particle: $E^{(I)} = 420$ GPa, $\nu^{(I)} = 0.17$

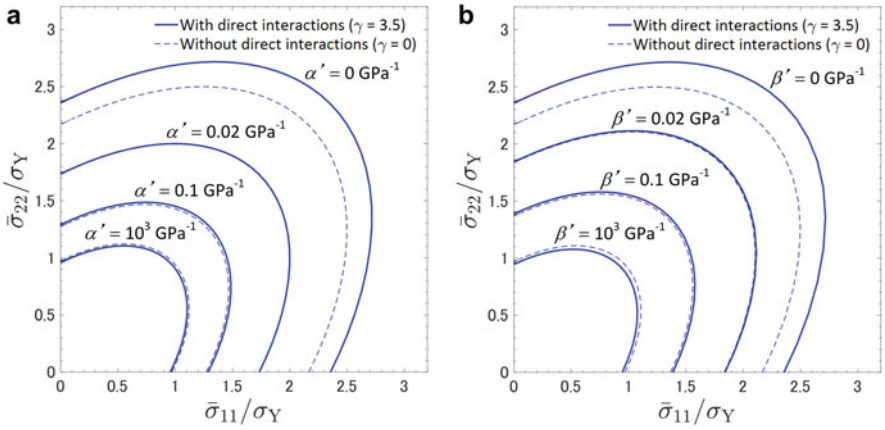

Fig. 20 Initial yield surface under the biaxial loading condition ($\bar{\sigma}_{33} = 0$) in the presence of interfacial damage. (**a**) Effect of α' with $\beta' = 0$ (**b**) Effect of β' with $\alpha' = 0$. Aluminum matrix: $E_0 = 75.0$ GPa, $\nu_0 = 0.33$, $\sigma_y = 47.0$ MPa. SiC particle: $E^{(I)} = 420$ GPa, $\nu^{(I)} = 0.17$, $\phi^{(I)} = 0.4$

imperfect interface. Note that in view of the definition of **R** (Eq. 29), the presented micromechanical model is regarded as an isotropic damage model. Accordingly, the directionality of damage cannot be accounted for.

Concluding Remarks

In this chapter, the effect of interfacial damage between the spherical inclusion and the surrounding matrix is studied by using the spring interface model and the micromechanical formulations. The Mori-Tanaka method and the self-consistent method are reformulated by using the modified Eshelby tensor. As demonstrated, the unique combination of α' (interface sliding parameter) and β' (interface separation parameter) results in the unique degradation of the effective elastic stiffness of composite.

Further, the overall elastoplastic behaviors of particulate composites are studied. Given the fact that the imperfect interface reduces the reinforcing capacity of particles, the reduced stiffness of particle is taken into account based on micromechanics. As illustrated, the increase of interface parameters, α' and β', leads to the degeneration of both the effective elastic stiffness and the composite yield strength. Further, it is found that under the influence of imperfect interface, the effect of direct particle interaction becomes marginal.

Appendix: Contraction and Inversion of Fourth-Order Tensors

By admitting the minor symmetry of fourth-order tensor (e.g., $A_{ijkl} = A_{jikl} = A_{jilk}$), a contraction of fourth-order tensors, $\mathbf{C} = \mathbf{A}\bullet\mathbf{B}$ or $C_{ijkl} = A_{ijmn}\,B_{mnkl}$, can be evaluated by using the Voigt form as follows:

$$\begin{bmatrix} C_{1111} & C_{1122} & C_{1133} & C_{1112} & C_{1123} & C_{1131} \\ C_{2211} & C_{2222} & C_{2233} & C_{2212} & C_{2223} & C_{2231} \\ C_{3311} & C_{3322} & C_{3333} & C_{3312} & C_{3323} & C_{3331} \\ C_{1211} & C_{1222} & C_{1233} & C_{1212} & C_{1223} & C_{1231} \\ C_{2311} & C_{2322} & C_{2333} & C_{2312} & C_{2323} & C_{2331} \\ C_{3111} & C_{3122} & C_{3133} & C_{3112} & C_{3123} & C_{3131} \end{bmatrix} = \begin{bmatrix} A_{1111} & A_{1122} & A_{1133} & 2A_{1112} & 2A_{1123} & 2A_{1131} \\ A_{2211} & A_{2222} & A_{2233} & 2A_{2212} & 2A_{2223} & 2A_{2231} \\ A_{3311} & A_{3322} & A_{3333} & 2A_{3312} & 2A_{3323} & 2A_{3331} \\ A_{1211} & A_{1222} & A_{1233} & 2A_{1212} & 2A_{1223} & 2A_{1231} \\ A_{2311} & A_{2322} & A_{2333} & 2A_{2312} & 2A_{2323} & 2A_{2331} \\ A_{3111} & A_{3122} & A_{3133} & 2A_{3112} & 2A_{3123} & 2A_{3131} \end{bmatrix} \begin{bmatrix} B_{1111} & B_{1122} & B_{1133} & B_{1112} & B_{1123} & B_{1131} \\ B_{2211} & B_{2222} & B_{2233} & B_{2212} & B_{2223} & B_{2231} \\ B_{3311} & B_{3322} & B_{3333} & B_{3312} & B_{3323} & B_{3331} \\ B_{1211} & B_{1222} & B_{1233} & B_{1212} & B_{1223} & B_{1231} \\ B_{2311} & B_{2322} & B_{2333} & B_{2312} & B_{2323} & B_{2331} \\ B_{3111} & B_{3122} & B_{3133} & B_{3112} & B_{3123} & B_{3131} \end{bmatrix} \tag{A1}$$

According to Eq. (A1), for instance:

$$\begin{aligned} C_{1111} &= A_{1111}B_{1111} + A_{1122}B_{2211} + A_{1133}B_{3311} + 2A_{1112}B_{1211} + 2A_{1123}B_{2311} \\ &\quad + 2A_{1131}B_{3111} \\ &= A_{1111}B_{1111} + A_{1122}B_{2211} + A_{1133}B_{3311} + (A_{1112}B_{1211} + A_{1121}B_{2111}) \\ &\quad + (A_{1123}B_{2311} + A_{1132}B_{3211}) + (A_{1131}B_{3111} + A_{1113}B_{3113}) \\ &= A_{11mn}B_{mn11} \end{aligned} \tag{A2}$$

In the case of inversion, we set $\mathbf{C} = \mathbf{I}$ (fourth-order identity tensor) and $\mathbf{B} = \mathbf{A}^{-1}$ in Eq. (A1). Accordingly, the following equation is obtained:

$$\begin{bmatrix} 1 & 0 & 0 & 0 & 0 & 0 \\ 0 & 1 & 0 & 0 & 0 & 0 \\ 0 & 0 & 1 & 0 & 0 & 0 \\ 0 & 0 & 0 & 1/2 & 0 & 0 \\ 0 & 0 & 0 & 0 & 1/2 & 0 \\ 0 & 0 & 0 & 0 & 0 & 1/2 \end{bmatrix} = \begin{bmatrix} A_{1111} & A_{1122} & A_{1133} & 2A_{1112} & 2A_{1123} & 2A_{1131} \\ A_{2211} & A_{2222} & A_{2233} & 2A_{2212} & 2A_{2223} & 2A_{2231} \\ A_{3311} & A_{3322} & A_{3333} & 2A_{3312} & 2A_{3323} & 2A_{3331} \\ A_{1211} & A_{1222} & A_{1233} & 2A_{1212} & 2A_{1223} & 2A_{1231} \\ A_{2311} & A_{2322} & A_{2333} & 2A_{2312} & 2A_{2323} & 2A_{2331} \\ A_{3111} & A_{3122} & A_{3133} & 2A_{3112} & 2A_{3123} & 2A_{3131} \end{bmatrix} \begin{bmatrix} A^{-1}_{1111} & A^{-1}_{1122} & A^{-1}_{1133} & A^{-1}_{1112} & A^{-1}_{1123} & A^{-1}_{1131} \\ A^{-1}_{2211} & A^{-1}_{2222} & A^{-1}_{2233} & A^{-1}_{2212} & A^{-1}_{2223} & A^{-1}_{2231} \\ A^{-1}_{3311} & A^{-1}_{3322} & A^{-1}_{3333} & A^{-1}_{3312} & A^{-1}_{3323} & A^{-1}_{3331} \\ A^{-1}_{1211} & A^{-1}_{1222} & A^{-1}_{1233} & A^{-1}_{1212} & A^{-1}_{1223} & A^{-1}_{1231} \\ A^{-1}_{2311} & A^{-1}_{2322} & A^{-1}_{2333} & A^{-1}_{2312} & A^{-1}_{2323} & A^{-1}_{2331} \\ A^{-1}_{3111} & A^{-1}_{3122} & A^{-1}_{3133} & A^{-1}_{3112} & A^{-1}_{3123} & A^{-1}_{3131} \end{bmatrix} \tag{A3}$$

Based on Eq. (A3), the inversion of fourth-order tensor can be calculated by the following matrix equation:

$$
\begin{bmatrix}
A^{-1}_{1111} & A^{-1}_{1122} & A^{-1}_{1133} & A^{-1}_{1112} & A^{-1}_{1123} & A^{-1}_{1131} \\
A^{-1}_{2211} & A^{-1}_{2222} & A^{-1}_{2233} & A^{-1}_{2212} & A^{-1}_{2223} & A^{-1}_{2231} \\
A^{-1}_{3311} & A^{-1}_{3322} & A^{-1}_{3333} & A^{-1}_{3312} & A^{-1}_{3323} & A^{-1}_{3331} \\
A^{-1}_{1211} & A^{-1}_{1222} & A^{-1}_{1233} & A^{-1}_{1212} & A^{-1}_{1223} & A^{-1}_{1231} \\
A^{-1}_{2311} & A^{-1}_{2322} & A^{-1}_{2333} & A^{-1}_{2312} & A^{-1}_{2323} & A^{-1}_{2331} \\
A^{-1}_{3111} & A^{-1}_{3122} & A^{-1}_{3133} & A^{-1}_{3112} & A^{-1}_{3123} & A^{-1}_{3131}
\end{bmatrix} =
$$

$$
\begin{bmatrix}
A_{1111} & A_{1122} & A_{1133} & 2A_{1112} & 2A_{1123} & 2A_{1131} \\
A_{2211} & A_{2222} & A_{2233} & 2A_{2212} & 2A_{2223} & 2A_{2231} \\
A_{3311} & A_{3322} & A_{3333} & 2A_{3312} & 2A_{3323} & 2A_{3331} \\
A_{1211} & A_{1222} & A_{1233} & 2A_{1212} & 2A_{1223} & 2A_{1231} \\
A_{2311} & A_{2322} & A_{2333} & 2A_{2312} & 2A_{2323} & 2A_{2331} \\
A_{3111} & A_{3122} & A_{3133} & 2A_{3112} & 2A_{3123} & 2A_{3131}
\end{bmatrix}^{-1}
\begin{bmatrix}
1 & 0 & 0 & 0 & 0 & 0 \\
0 & 1 & 0 & 0 & 0 & 0 \\
0 & 0 & 1 & 0 & 0 & 0 \\
0 & 0 & 0 & 1/2 & 0 & 0 \\
0 & 0 & 0 & 0 & 1/2 & 0 \\
0 & 0 & 0 & 0 & 0 & 1/2
\end{bmatrix}
\tag{A4}
$$

For instance, if $\mathbf{A} = \mathbf{I}$ (cf. Eq. 24) becomes:

$$\begin{bmatrix} A_{1111}^{-1} & A_{1122}^{-1} & A_{1133}^{-1} & A_{1112}^{-1} & A_{1123}^{-1} & A_{1131}^{-1} \\ A_{2211}^{-1} & A_{2222}^{-1} & A_{2233}^{-1} & A_{2212}^{-1} & A_{2223}^{-1} & A_{2231}^{-1} \\ A_{3311}^{-1} & A_{3322}^{-1} & A_{3333}^{-1} & A_{3312}^{-1} & A_{3323}^{-1} & A_{3331}^{-1} \\ A_{1211}^{-1} & A_{1222}^{-1} & A_{1233}^{-1} & A_{1212}^{-1} & A_{1223}^{-1} & A_{1231}^{-1} \\ A_{2311}^{-1} & A_{2322}^{-1} & A_{2333}^{-1} & A_{2312}^{-1} & A_{2323}^{-1} & A_{2331}^{-1} \\ A_{3111}^{-1} & A_{3122}^{-1} & A_{3133}^{-1} & A_{3112}^{-1} & A_{3123}^{-1} & A_{3131}^{-1} \end{bmatrix} =$$

$$\begin{bmatrix} 1 & 0 & 0 & 0 & 0 & 0 \\ 0 & 1 & 0 & 0 & 0 & 0 \\ 0 & 0 & 1 & 0 & 0 & 0 \\ 0 & 0 & 0 & 1 & 0 & 0 \\ 0 & 0 & 0 & 0 & 1 & 0 \\ 0 & 0 & 0 & 0 & 0 & 1 \end{bmatrix}^{-1} \begin{bmatrix} 1 & 0 & 0 & 0 & 0 & 0 \\ 0 & 1 & 0 & 0 & 0 & 0 \\ 0 & 0 & 1 & 0 & 0 & 0 \\ 0 & 0 & 0 & 1/2 & 0 & 0 \\ 0 & 0 & 0 & 0 & 1/2 & 0 \\ 0 & 0 & 0 & 0 & 0 & 1/2 \end{bmatrix} = \tag{A5}$$

$$\begin{bmatrix} 1 & 0 & 0 & 0 & 0 & 0 \\ 0 & 1 & 0 & 0 & 0 & 0 \\ 0 & 0 & 1 & 0 & 0 & 0 \\ 0 & 0 & 0 & 1/2 & 0 & 0 \\ 0 & 0 & 0 & 0 & 1/2 & 0 \\ 0 & 0 & 0 & 0 & 0 & 1/2 \end{bmatrix}$$

Namely, $\mathbf{I}^{-1} = \mathbf{I}$ holds.

References

J. Aboudi, Damage in composites – Modeling of imperfect bonding. Compos. Sci. Technol. **28**(2), 103–128 (1987)

T. Christman, A. Needleman, S. Nutt, S. Suresh, On microstructural evolution and micromechanical modeling of deformation of a whisker-reinforced metal-matrix composite. Mater. Sci. Eng. **A107**, 49–61 (1989a)

T. Christman, A. Needleman, S. Suresh, An experimental and numerical study of deformation in metal-ceramic composites. Acta Metall. **37**(11), 3029–3050 (1989b)

T.W. Clyne, P.J. Withers, *An Introduction to Metal Matrix Composites* (Cambridge University Press, New York, 1993)

H.L. Duan, J. Wang, Z.P. Huang, Z.Y. Luo, Stress concentration tensors of inhomogeneities with interface effects. Mech. Mater. **37**(7), 723–736 (2005)

H.L. Duan, X. Yi, Z.P. Huang, J. Wang, A unified scheme for prediction of effective moduli of multiphase composites with interface effects. Part I: Theoretical framework. Mech. Mater. **39**(1), 81–93 (2007a)

H.L. Duan, X. Yi, Z.P. Huang, J. Wang, A unified scheme for prediction of effective moduli of multiphase composites with interface effects. Part II: Application and scaling laws. Mech. Mater. **39**(1), 94–103 (2007b)

F. Dunne, N. Petrinic, *Introduction to Computational Plasticity* (Oxford University Press, New York, 2005)

J.D. Eshelby, The determination of the elastic field of an ellipsoidal inclusion and related problems. Proc. R. Soc. Lond. A **241**(1226), 376–396 (1957)

Z. Gao, A circular inclusion with imperfect interface: Eshelby's tensor and related problems. ASME J. Apply. Mech. **62**(4), 860–866 (1995)

F. Ghahremani, Effect of grain boundary sliding on anelasticity of polycrystals. Int. J. Solids Struct. **16**(9), 825–845 (1980)

Z. Hashin, The spherical inclusion with imperfect interface. ASME J. Appl. Mech. **58**(2), 444–449 (1991)

I. Jasiuk, E. Tsuchida, T. Mura, The sliding inclusion under shear. Int. J. Solids Struct. **23**(10), 1373–1385 (1987)

J.W. Ju, T.M. Chen, Micromechanics and effective moduli of elastic composites containing randomly dispersed ellipsoidal inhomogeneities. Acta Mech. **103**(1), 103–121 (1994a)

J.W. Ju, T.M. Chen, Effective elastic moduli of two-phase composites containing randomly dispersed spherical inhomogeneities. Acta Mech. **103**(1), 123–144 (1994b)

J.W. Ju, T.M. Chen, Micromechanics and effective elastoplastic behavior of two-phase metal matrix composites. ASME J. Eng. Mater. Tech. **116**(3), 310–318 (1994c)

J.W. Ju, K. Yanase, Micromechanics and effective elastic moduli of particle-reinforced composites with near-field particle interactions. Acta Mech. **215**(1), 135–153 (2010)

J.W. Ju, K. Yanase, Micromechanical effective elastic moduli of continuous fiber-reinforced composites with near-field fiber interactions. Acta Mech. **216**(1), 87–103 (2011)

J.W. Ju, X.D. Zhang, Micromechanics and effective transverse elastic moduli of composites with randomly located aligned circular fibers. Int. J. Solids Struct. **35**(9), 941–960 (1998)

J.W. Ju, X.D. Zhang, Effective elastoplastic behavior of ductile matrix composites containing randomly located aligned circular fibers. Int. J. Solids Struct. **38**(22–23), 4045–4069 (2001)

S.H. Khan, S. Huang, *Continuum Theory of Plasticity* (John Wiley & Sons, Inc., New York, 1995)

J.K. Kim, Y.E. Mai, *Engineered Interfaces in Fiber Reinforced Composites (1st Edition)* (Elsevier Science Ltd., Oxford, 1998)

S. Lee, J. Lee, S. Ryu, Modified Eshelby tensor for an anisotropic matrix with interfacial damage. Math. Mech. Solids **24**(6), 1749–1762 (2018)

R. Li, L.Z. Sun, A micromechanics-based viscoelastic model for nanocomposites with imperfect interface. Int. J. Damage Mech. **22**(7), 967–981 (2013)

P.J. Lin, J.W. Ju, Effective elastic moduli of three-phase composites with randomly located and interacting spherical particles of distinct properties. Acta Mech. **208**(1), 11–26 (2009)
H.T. Liu, L.Z. Sun, J.W. Ju, Elastoplastic modeling of progressive interfacial debonding for particle-reinforced metal-matrix composites. Acta Mech. **181**(1), 1–17 (2006)
T. Mori, K. Tanaka, Average stress in matrix and average elastic energy of materials with misfitting inclusions. Acta Metall. **21**(5), 571–574 (1973)
Z.A. Moschovidis, T. Mura, Two-ellipsoidal inhomogeneities by the equivalent inclusion method. ASME J. Appl. Mech. **42**(4), 847–852 (1975)
T. Mura, *Micromechanics of Defects in Solids*, 2nd edn. (Martinus Nijhoff Publishers, Dordrecht, 1987)
T. Mura, R. Furuhashi, The elastic inclusion with a sliding interface. ASME J. Appl. Mech. **51**(2), 308–310 (1984)
T.G. Nieh, D.J. Chellman, Modulus measurements in discontinuous reinforced aluminum composites. Scripta Metall. **18**(9), 925–928 (1984)
Y. Othmani, L. Delannay, I. Doghri, Equivalent inclusion solution adapted to particle debonding with a non-linear cohesive law. Int. J. Solids Struct. **48**, 3326–3335 (2011)
J. Qu, Eshelby tensor for an elastic inclusion with slightly weakened interface. ASME J. Appl. Mech. **60**(4), 1048–1050 (1993a)
J. Qu, The effect of slightly weakened interfaces on the overall elastic properties of composite materials. Mech. Mater. **14**(4), 269–281 (1993b)
J. Qu, M. Cherkaoui, *Fundamentals of Micromechanics of Solids* (John Wiley & Sons, Inc., New York, 2006)
J.C. Smith, Experimental values for the elastic constants of a particulate-filled glassy polymer. J. Res. NBS. **80A**, 45–49 (1976)
A.M. Wazwaz, *A First Course in Integral Equations*, 2nd edn. (World Scientific Publishing, Hackensack, 2015)
G.J. Weng, Some elastic properties of reinforced solids, with special reference to isotropic ones containing spherical inclusions. Int. J. Eng. Sci. **22**(7), 845–856 (1984)
K. Yanase, J.W. Ju, Effective elastic stiffness of spherical particle reinforced composite materials with an imperfect interface. Int. J. Damage Mech. **21**(1), 97–127 (2012)
K. Yanase, J.W. Ju, Overall elastoplastic damage responses of spherical particle-reinforced composite containing imperfect interfaces. Int. J. Damage Mech. **23**(3), 411–429 (2014)
J. Yang, S.M. Picard, C. Cady, A.G. Evans, R. Mehrabian, The stress/strain behavior of aluminum matrix composites with discontinuous reinforcements. Acta Metall. Mater. **39**(8), 1863–1869 (1991)
Y.H. Zhao, G.J. Weng, Transversely isotropic moduli of two partially debonded composites. Int. J. Solids Struct. **34**(4), 493–507 (1997)
Y.H. Zhao, G.J. Weng, The effect of debonding angle on the reduction of effective moduli of particle and fiber-reinforced composites. ASME J. Appl. Mech. **69**(3), 292–302 (2002)
S.F. Zheng, M. Denda, G.J. Weng, Overall elastic and elastoplastic behavior of a partially debonded fiber-reinforced composite. J. Compos. Mater. **37**, 741–758 (2003)
Z. Zhong, S.A. Meguid, On the elastic field of a spherical inhomogeneity with an imperfectly bonded interface. J. Elast. **46**(2), 91–113 (1997)

New Chemo-Mechanical Theory of Corrosion Damage in Concrete Under Sulfate Attack

36

Jiankang Chen and Zhuping Huang

Contents

Introduction 998
Corrosion Damage Model of Concrete Under Sulfate Attack 1000
Experiment for Damage Evolution 1000
Theoretical Model of Damage Evolution 1004
Nucleation of Corrosion Damage 1004
Evolution of Expansive Stress 1006
Model of Damage Evolution 1008
Entropy Evolution for Crack Propagation in Concrete Surface Under Sulfate Attack 1009
Experiment on Surface Cracks Evolution 1009
Evolution Model of Entropy 1013
Conclusions 1017
References 1019

Abstract

The degradation of durability of concrete structures in marine environment means the gradually decrease of strength and stiffness of concrete materials with time. It is not only a chemical problem but also a mechanical problem. In fact, this mechanical problem combined with chemistry may be caused by seawater corrosion. In this chapter, the damage mechanism of sulfate ions in seawater is experimentally and theoretically investigated. It is found that the internal expansive stress produced by delayed ettringite, which is the product of chemical reaction between sulfate ions and pore solution in concrete, leads to micro-

J. Chen (✉)
School of Mechanical Engineering and Mechanics, Ningbo University, Ningbo, China
e-mail: chenjiankang@nbu.edu.cn

Z. Huang
Department of Mechanics and Engineering Science, College of Engineering, Peking University, Beijing, China
e-mail: huangzp@pku.edu.cn

© Springer Nature Switzerland AG 2022

G. Z. Voyiadjis (ed.), *Handbook of Damage Mechanics*,
https://doi.org/10.1007/978-3-030-60242-0_55

damage nucleation and growth in the material. Based on this viewpoint, the corrosion damage evolution in cylindrical concrete samples is detected by means of ultrasonic technique. Then the theoretical model of the damage evolution is proposed by considering the chemical reaction rate. Furthermore, the surface cracks evolution in concrete under sulfate attack is studied. Based on the mechanism of corrosion damage, further research on the surface cracks growth in concrete under sulfate attack is carried out. In this chapter, the surface cracks evolution is described by the information entropy. Such an information entropy evolution is detected at different corrosion time. Moreover, a chemo-mechanical model is derived in terms of the chemical reaction rate of delayed ettringite. It is found that the information entropy increases exponentially with time.

Keywords

Marine environment · Concrete · Corrosion damage · Chemo-mechanical theory · Sulfate attack

Introduction

The durability of concrete structures in marine environment has long been a concerned problem in history. There are three kinds of harmful ions in seawater, i.e., chloride ions, sulfate ions, and magnesium ions, and the strength and stiffness of concrete structures decrease due to the attack by these ions (Moser et al. 2012; Muthulingam and Rao 2015; Da et al. 2016; Yu et al. 2017). It should be pointed out that the corrosion damage in plain concrete is dominantly induced by sulfate ions (e.g., Tixier and Mobasher 2003a, 2003b, Ikumi et al. 2014); however, the mechanism for sulfate attack and the evolution behavior are still unclear. Because of the importance of the problem, some researchers paid close attention to this subject. For instance, Diamond (1996) and Collepardi (1999) studied the weakening effect of sulfates on concrete and investigated the delayed ettringite formation (DEF) due to the reaction between sulfate ions and pore solution in concrete. Also, the mechanism of DEM was explored by Yang et al. (1999) and Prince et al. (2003).

If the delayed ettringite grows and contacts the pore wall in concrete, the internal expansion stress is produced, and the expansion strain in concrete will arise. Barbarulo et al. (2005) analyzed such an expansion deformation in the processes of DEF under thermal cycle and high temperature, and they found it could be greater than 3%. Pavoine et al. (2006) took into account drying-wetting influence on the expansion deformation of concrete due to the delayed ettringite and showed the expansion strain occurs earlier than that in the concrete without drying-wetting condition. Zhang et al. (2013) investigated the expansion strain of concrete under attack of sulfate ions as well as sulfate-chloride ions. The results indicate the expansion deformation induced by both sulfate ions is obvious greater than that caused only by sulfate ions and chloride ions. The reason is that DEF in concrete under sulfate corrosion is much greater than that under both sulfate and chloride ion corrosion.

Micro-crack nucleation and growth caused by sulfate corrosion will result in the decrease of both strength and stiffness of concrete structures. Planel et al. (2006) investigated the evolution of mechanical properties of concrete. They discussed size influence on the variation of mechanical properties of concrete. Chen et al. (2008) further studied the corrosion damage variation in concrete materials under sulfate corrosion. They proposed an approximate expression to describe the corrosion damage variation. Rozière et al. (2009) studied the evolution of deformation and mass of concrete immersed in sulfate solution. By means of SEM technique, they found that crack size is in micron range. Since the delayed ettringite fills pores of concrete, the microstructure of concrete changes. Pipilikaki et al. (2009) analyzed the change of concrete microstructures and inspected the variation of compressive strength.

In order to improve the sulfate resistance property, some researchers tried to optimize the mix design of concrete. Plowman and Cabrera (1996) adopted fly ash as additive agent to improve the microstructure of concrete; Chindaprasirt et al. (2007) used both rice husk ash and fly ash as new additives for retarding the degradation of concrete; and Lee et al. (2005) took silica fume to replace part of the cement for reducing the amount of delayed ettringite.

It should be noted that all these abovementioned methods cannot be utilized to absolutely prevent concrete from degradation. Therefore, it is desirable to develop some new models to quantitatively describe the decrease of concrete structures' durability. Unfortunately, only a few works on this subject had been published in the literature. For example, a chemo-mechanical model has been given by Kuhl et al. (2004a). This model could be used to analyze the degradation of concrete due to mechanical damage and calcium leaching. In brief, at present the quantitative studies on the damage propagation in concrete structures due to corrosion of sulfate ions are insufficient.

In the following, the corrosion damage is defined by the magnitude of relative decrease of concrete modulus. The evolution of this kind damage of concrete immersed in sulfate solution is measured in terms of ultrasonic technique. The corrosion damage is obtained from the experimental data and is expressed as the decrease of the modulus. Owing to the action of internal expansion stress, the nucleation of corrosion damage occurs, and this can be analyzed by means of Eshelby's theory. The internal expansion stress can be assumed to be a linear function of DEF; thus, the governing equation of the expansion stress evolution is obtained, in which the rate of chemical reaction is taken into account. The corrosion damage can then be defined by means of Weibull distribution function. Note corrosion cracks dominantly appear at the surface of concrete; the increase of such surface cracks could be used to represent the degree of durability decrease of concrete. In the present study, the information entropy of surface cracks is adopted for describing the damage degree, and this entropy is detected and calculated. Moreover, the SEM experiment and XRD analysis are performed to explore the mechanism of corrosion cracks evolution. The increase of delayed ettringite is also detected by those methods. The information entropy evolution model is proposed to take into account the chemical reaction rate of the ettringite formation.

Corrosion Damage Model of Concrete Under Sulfate Attack

Experiment for Damage Evolution

Reference cement, which is provided by China Building Materials Academy, is shown in Table 1, and its components are chosen to form specimens of concrete.

Water-to-cement ratio of specimens is 0.45, and cement-to-sand ratio is 1:2. The diameter and the length of cylindrical specimens are 45 mm and 500 mm, respectively. Those specimens are cured 24 h in moist condition, after then they are moved into a concrete standard compartment for curing 28 days. The relative humidity is 90% and environment temperature is 20°C.

Just after being cured 28 days, the specimens are put into sodium sulfate solutions with different concentrations of 3%, 5%, and 8%, respectively. During immersion, the ultrasonic detection is performed, and schematic diagram for detection is shown in Fig. 1. If the frequency of ultrasonic is determined, the wave propagates in the specimen at a constant velocity.

As shown in Fig. 1, the wave propagation is axisymmetric. However, Rayleigh pointed out that if the ratio of radius to wavelength is less than 0.7, the problem could be approximately treated as one-dimensional stress problem (Rayleigh 1894), and in this situation, the relation between the wave velocity, C, and the modulus, E, could be expressed as follows (Meyers 1994):

$$E = C^2\rho \tag{1}$$

Table 1 Components of reference cement

SiO_2	Al_2O_3	Fe_2O_3	CaO	MgO	SO_3	Na_2O_{eq}	LOSS	f-CaO	C3S	C3A
21.07	4.45	2.69	63.23	2.03	2.93	0.53	2.38	0.94	53.01	6.68

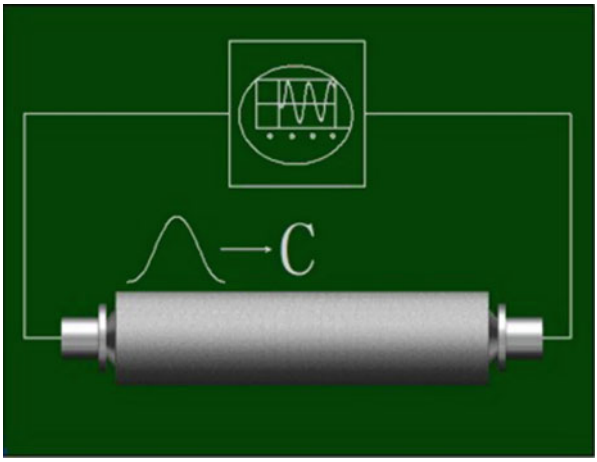

Fig. 1 Schematic diagram of damage detection by ultrasonic technique

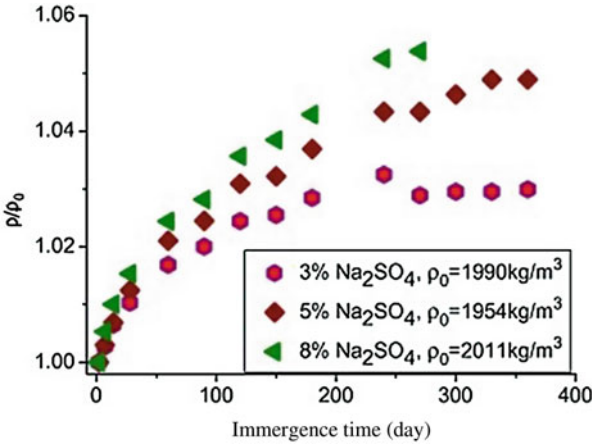

Fig. 2 Growth of concrete density due to sulfate corrosion

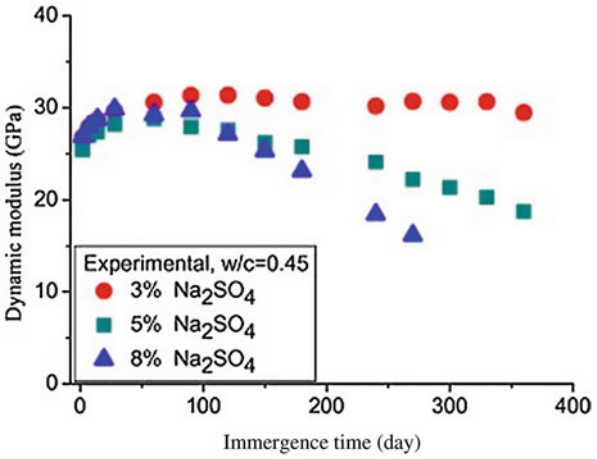

Fig. 3 Variation of modulus of concrete due to sulfate corrosion

where ρ is the specimens' density. If the variations of the wave velocity and the density are detected, then the change of the modulus could be calculated by Eq (1).

In terms of weight method, change of density is detected at different immersion times, and it can be seen that the density almost monotonously increases with time (shown in Fig. 2).

Change of modulus is detected in terms of ultrasonic technique, as shown in Fig. 1, and the detail data are shown in Fig. 3. The results indicate that the change of the modulus could be divided into two stages. In the initial stage, the modulus increases from the initial modulus to maxim modulus. In the second stage, it decreases from the maxim modulus, and this means that the corrosion damage

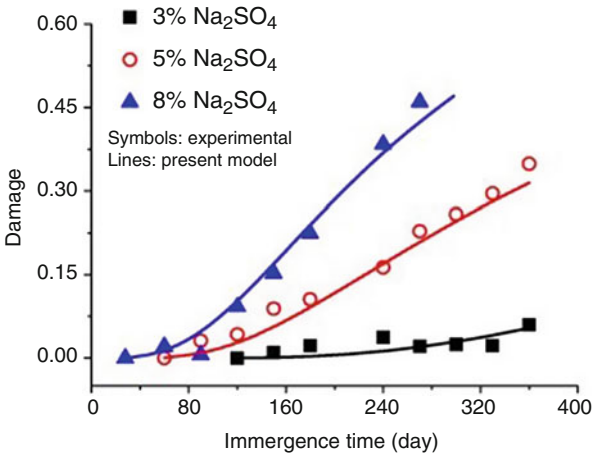

Fig. 4 Corrosion damage evolution in concrete

Fig. 5 Cracks in concrete samples due to sulfate corrosion

evolution takes place. The corrosion damage, D, can be defined as the function of relative decrease of the modulus and expressed as follows:

$$D = 1 - \frac{E}{E_{\max}} \tag{2}$$

where $E_{\max}$ stands for the maximum modulus. From Eq. (2) and the experimental results shown in Fig. 3, the damage is determined and shown in Fig. 4. It can be seen from this figure that corrosion damage evolves much faster in the concentrated solution.

As shown in Fig. 5, the macro corrosion cracks appear in specimens after being corroded for 360 days.

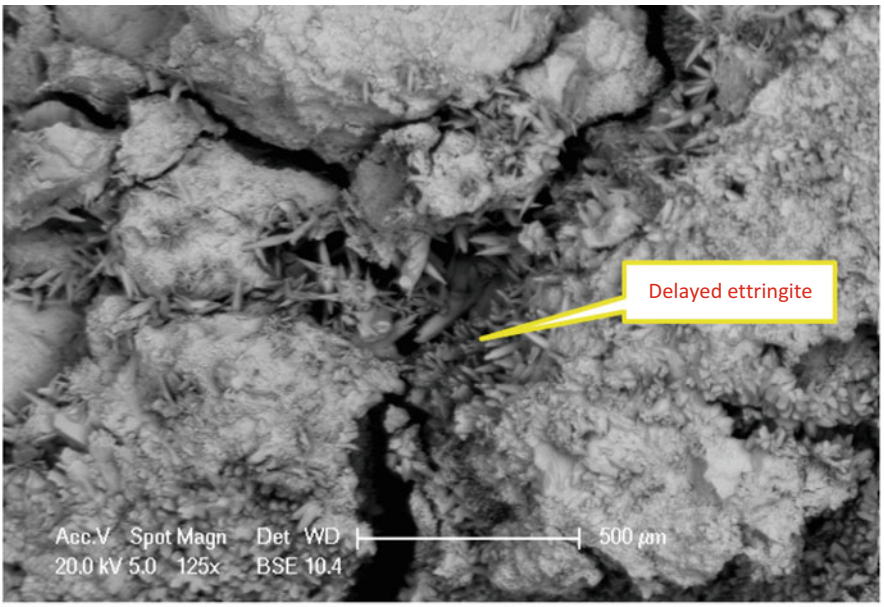

(a)

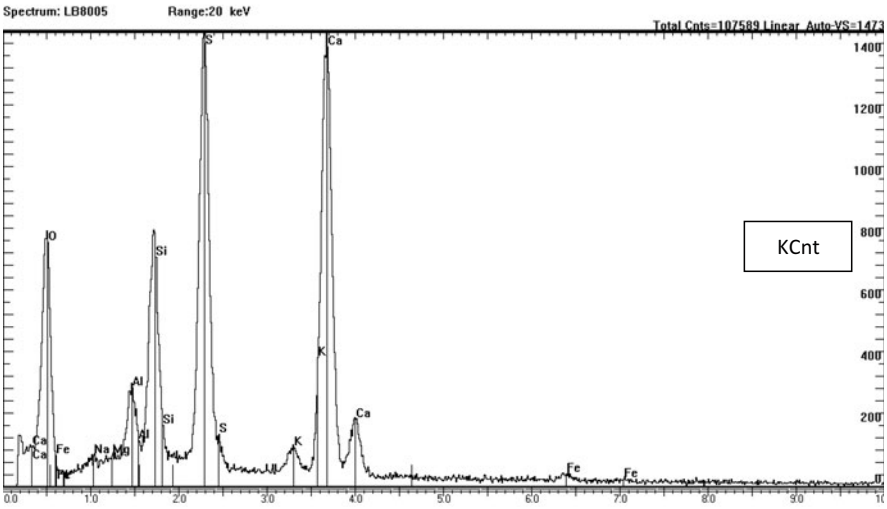

(b)

Fig. 6 Images of DEF: (**a**) SEM image and (**b**) EDX image

In order to construct a theoretical model for describing the corrosion damage evolution, SEM technique is adopted to observe microstructure of samples. Figure 6 shows the images of DEF in pores of samples and energy spectrum analysis.

Theoretical Model of Damage Evolution

Usually, there are two methods to study corrosion damage development in concrete materials. One is to investigate the propagation of crack (Nassef 2015), and the other is to predict statistical evolution in terms of continuum damage theory (Ganjiani et al. 2012). In this chapter, a statistic method is used to study the damage development in concrete due to sulfate corrosion, and the nucleation of corrosion damage is firstly investigated.

Nucleation of Corrosion Damage

The experiment shows that the action of delayed ettringite is the main reason to cause the corrosion damage evolution. The nucleation of corrosion damage is induced by the expansive stress produced by delayed ettringite, which is formed by the chemical reaction between diffused sulfate ions and pore solution in concrete (shown in Fig. 7). There are two stages in this process. The first stage is the reaction between calcium hydroxide, CH, and sulfate ions, SO_4^{2-}, to form gypsum, $C\overline{S}H_2$. The second stage is the reaction of tricalcium aluminate, C_3A, and water, H, with gypsum to produce delayed ettringite, $C_6A\overline{S}_3H_{32}$. The related chemical reaction equations are expressed as follows (Ikumi et al. 2014);

$$CH + SO_4^{2-} \rightarrow C\overline{S}H_2 + 2OH^- \tag{3}$$

$$\begin{aligned} &CA + qC\overline{S}H_2 \rightarrow C_6A\overline{S}_3H_{32} \\ &CA := \gamma_1 C_3A + \gamma_2 C_4AH_{13} + \gamma_3 C_4A\overline{S}H_{12} \\ &q = 3\gamma_1 + 3\gamma_2 + 2\gamma_3 \end{aligned} \tag{4}$$

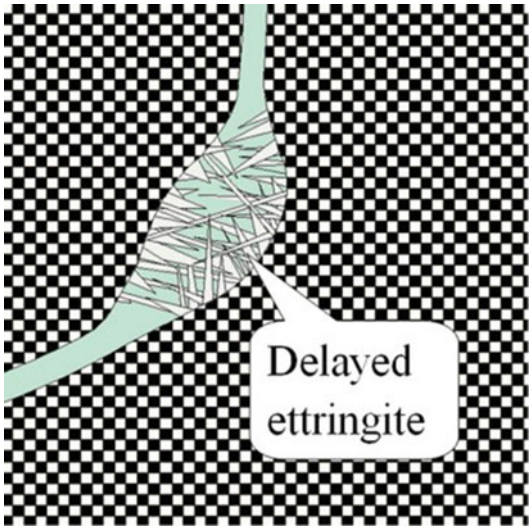

Fig. 7 Diagram of DEF in concrete pores

where "$C_4A\overline{S}H_{12}$" and "C_4AH_{13}," respectively, denote monosulfate and tetracalcium aluminate, q represents for the stoichiometric weighted coefficient of the sulfate phase, and γ_i (i =1–3) stands for the value of each aluminate phase to the total aluminate content.

As is shown in Fig. 7, when a pore is filled by the delayed ettringite, expansion force, p, begins to appear, and it would produce tensile stress near the pore's surface. If the magnitude of the tensile stress is equal to or greater than that of the tensile strength, then micro-cracks could appear, and that is the mechanism for corrosion damage nucleation. The symbol "p_{cr}" is used to stand for the critical expansion stress when the corrosion damage nucleation occurs. According to the proposed criterion of damage nucleation, Eshelby's theory (Eshelby 1957) will be used to calculate p_{cr}.

For simply, the pore is assumed to be ellipsoidal one (shown in Fig. 8), and the symbols "a_1," "a_2," and "a_3" (a_1=a_2) are used to present the semi-axes of the pore in x-, y-, and z-directions, respectively. In general, the viscous effect of the concrete should be considered in the constitutive relation. However, the nucleation of micro-cracks occurs when the tensile stress reaches 1–2MPa, and at this stress level, the viscous effect may be neglected. Hence the constitutive model of concrete could be simplified as a linear elastic one and expressed as follows:

$$\begin{aligned} \boldsymbol{\sigma} &= \mathbf{L} : \boldsymbol{\varepsilon} \\ \mathbf{L} &= 3\kappa \mathbf{I}_{\mathrm{m}} + 2\mu \mathbf{I}_{\mathrm{s}} \end{aligned} \tag{5}$$

$$\mathbf{I}_{\mathrm{m}} = \mathbf{i}_0 \otimes \mathbf{i}_0 / 3, \quad \mathbf{I}_{\mathrm{s}} = \mathbf{I} - \mathbf{I}_{\mathrm{m}} \tag{6}$$

In the above equations, the symbols "κ" and "μ," respectively, denote bulk modulus and shear modulus, "$\mathbf{I}$" stands for the fourth-order identity tensor, and "$\mathbf{i}_0$" represents the second-order identity tensor.

By means of Eshelby's theory, the inclusion strain could be calculated and expressed as follows (Chen et al. 2010):

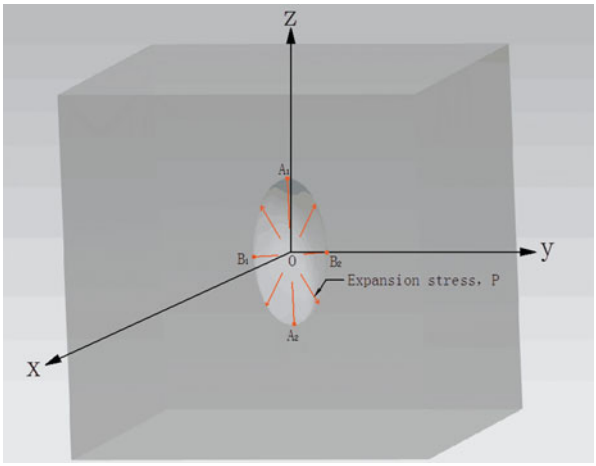

Fig. 8 Schematic diagram used to analyze the damage nucleation

$$\boldsymbol{\varepsilon}_{\mathrm{p}} - \boldsymbol{\varepsilon}^{\infty} = \mathbf{S} : \left(\boldsymbol{\varepsilon}_{\mathrm{p}} + p\mathbf{J} : \mathbf{i}_0\right) \tag{7}$$

where $\boldsymbol{\varepsilon}_{\mathrm{p}}$ and $\boldsymbol{\varepsilon}^{\infty}$ are the pore strain and the remote strain, respectively, $\mathbf{S}$ is the Eshelby's tensor, $\mathbf{J}$ is the compliance tensor, and

$$\mathbf{J}=\mathbf{L}^{-1} = \mathbf{I}_{\mathrm{m}}/(3\kappa) + \mathbf{I}_{\mathrm{s}}/(2\mu) \tag{8}$$

In the absence of external loading, the remote strain $\boldsymbol{\varepsilon}^{\infty} = 0$. The following formula could be obtained from Eq. (7):

$$\begin{aligned} &\boldsymbol{\varepsilon}_{\mathrm{p}} = p\mathbf{g} \\ &\mathbf{g} = (\mathbf{I} - \mathbf{S})^{-1} : \mathbf{S} : \mathbf{J} : \mathbf{i}_0 \end{aligned} \tag{9}$$

The stress at point A_1 or A_2 (shown in Fig. 8) can be evaluated as follows. It is obvious that the stress at point A_1 is equal to that at A_2 due to the symmetry. Hence, only stress components at A_1 need to be evaluated.

The axial symmetry and the boundary condition can be written as follows;

$$\sigma_{33}|_{A1} = -p \tag{10}$$

$$\sigma_{11}|_{A1} = \sigma_{22}|_{A1}, \quad \varepsilon_{11}|_{A1} = \varepsilon_{22}|_{A1} \tag{11}$$

Thus, the relation between the stress component, $\sigma_{11}|_{A1}$, and expansive stress, p, could be obtained as follows:

$$\begin{aligned} &\sigma_{11}|_{A1} = \beta p \\ &\beta = \left(6\lambda\mu\, g_{11} + 4\mu^2 g_{11} - \lambda\right)/(\lambda + 2\mu) \end{aligned} \tag{12}$$

where g_{11} could be evaluated from Eq. (9) and β is a proportionality coefficient to be determined.

When $\sigma_{11}|_{A1}$ reaches the magnitude of tensile strength, σ_0, the cracks' nucleation takes place. At this moment, the expansive stress reaches the critical value, p_{cr}. Hence, we obtain

$$p_{\mathrm{cr}} = \beta^{-1}\sigma_0 \tag{13}$$

Equation (13) shows the relation between the tensile strength and the critical expansion stress. Under the condition of the Poisson's ratio ν =0.18 and spherical pore, we obtain $\beta = 0.159$.

Evolution of Expansive Stress

The expansion stress relates to the increase quantity of delayed ettringite; thus, it depends on the chemical reaction rate. If the concentration of C_3A and SO_4^{2-} is, respectively, denoted by symbols C_{CA} and C_{SO}, the chemical reaction rate equations

for Eqs. (3) and (4) (Tixier and Mobasher 2003a, b) are given by the following formulas;

$$\begin{aligned} \frac{dC_{CA}}{dt} &= -\frac{kC_{CA}C_{SO}}{q} \\ \frac{dC_{SO}}{dt} &= -kC_{CA}C_{SO} \end{aligned} \tag{14}$$

where k is the coefficient of reaction.

The following formula could be obtained by solving Eq. (14):

$$C_{SO} = qC_{CA} + B_1 \tag{15}$$

where B_1 is a constant to be determined. Substituting Eq. (15) into Eq. (14) yields

$$\frac{dC_{CA}}{dt} = -kC_{CA}^2 - \frac{k}{q}B_1C_{CA} \tag{16a}$$

Since $C_{CA} << 1$, Eq. (16a) may be written as follows:

$$\frac{dC_{CA}}{dt} \approx -\frac{k}{q}B_1C_{CA} \tag{16b}$$

Solving Eq. (16b) yields

$$\begin{aligned} C_{CA} &= C_{CA0}\exp\left(-t/t_p\right) \\ t_p &= q/kB_1 \end{aligned} \tag{17}$$

where t_p is a characteristic time, which is inversely proportional to the coefficient of the reaction rate, k, and C_{CA0} is the initial concentration of C_{CA}.

Because expansive stress is related to the quantity of DEF, it may be assumed that the increment increase of the expansive stress, dp, is directly proportional to that of concentration of delayed ettringite, $dC_{ettringite}$, namely:

$$dp \propto dC_{ettringite} \tag{18}$$

Note Eq. (4) shows that the increase of concentration of delayed ettringite is directly proportional to the decrease of concentration, dC_{CA}, i.e.:

$$dC_{ettringite} \propto -dC_{CA} \tag{19}$$

Solving Eqs. (18) and (19) yields

$$dC_{CA} = -\eta dp \tag{20}$$

Hence, the expansive stress could be evaluated by solving Eqs. (20) as follows:

$$p = p * \left(1 - \exp\left(-t/t_p\right)\right)$$
$$p* = \mathrm{C}_{\mathrm{CA0}}/\eta \tag{21}$$

Equation (21) indicates that the expansive stress exponentially increases with time.

Model of Damage Evolution

As is mentioned before, the corrosion damage due to sulfate attack is caused by the expansive stress in concrete. Under such a stress, concrete could be characterized by brittleness, and corrosion damage could be described by the weakest-link model (Lu et al. 2002a, 2002b). In this chapter, the evolution of corrosion damage is assumed to obey the Weibull's distribution function, i.e.:

$$D = 1 - \exp\left[-\left(\frac{p - p_{cr}}{p_u}\right)^m\right], \quad (p \geq p_{cr}) \tag{22}$$

where symbols "m" and "p_u" are dimensionless parameters to be determined and "p_{cr}" is the threshold value of p. If the damage evolution starts to appear at the critical instant "t_{cr}," p_{cr} could be expressed by

$$p_{cr} = p|_{t=t_{cr}} = p * \left(1 - \exp\left(-t_{cr}/t_p\right)\right) \tag{23}$$

The evolution model of corrosion damage could be expressed by Equations (21), (22), and (23). The parameters (t_{cr}, t_p, m, $\gamma = (p^*/p_u)^m$) can be determined by curve fitting method, and the fitting curves are plotted in Fig. 4; the values of the parameters are listed in Table 2. The results shown in Fig. 4 state that the damage model gives a new approach to describe the characteristic of corrosion damage evolution in concrete due to sulfate attack.

Reports on research of sulfate corrosion mainly attribute the mechanical property degradation of concrete caused by the action of delayed ettringite, and the delayed ettringite is found in micro-cracks. Some people may argue that those micro-cracks are formed by other reasons, for instance, corrosion of chloride ions, drying and wetting cycle, carbonation, freezing and thawing cycle, and initial defects of concrete. Those cracks provide interspace for DEF. Thus, they think that the degradation behavior of concrete is not caused by delayed ettringite. In this chapter, those factors

Table 2 Parameters of damage model

Parameters Concentration	t_{cr}(day)	γ	m	t_p(day)
3%	120	12.670	2.206	4205
5%	60	1.490	2.206	281
8%	28	1.944	2.206	196

are excluded from experiment design. The material of samples is cement mortar, and there is no aggregate in it (for reducing the interfacial transition zone), and the samples are exposed to sulfate environment with room temperature (no drying-wetting cycle, carbonation, corrosion of chloride ions, and freezing and thawing cycle involved). However, the corrosion cracks still appear as shown in Figs. 5 and 6. The experimental results verify again that DEF is the main influence factor to induce the decrease of concrete durability.

The results of experimental analysis also reveal that no corrosion cracks appear in the first stage of corrosion process, and the modulus of concrete increases in this stage. Since continuous hydration is still in progress, it produces more C-S-H gel to repair the initial defects of the material. Therefore, the strength and modulus of the material are improved. In addition, DEF could fill pores, lead to the decrease of porosity, and causes the modulus increasing.

In this model, the parameters, γ and m, are dimensionless quantity; they are determined by properties of the material. The parameters t_{cr} and t_p reflect the influence of corrosion solution concentration on damage evolution. This means that the speed of chemical reaction significantly affects the evolution of corrosion damage. Equation (17) indicates that t_p is inversely proportional to the coefficient, k. The faster the reaction, the less the characteristic time.

It is noted that the corrosion damage evolution begins at time, t_{cr}, and from Eqs. (13) and (23), this critical time t_{cr} is related to σ_0. Therefore, it can be seen that the higher the value σ_0, the slower the growth of corrosion damage. Based on the above observation, an effective method for improving sulfate corrosion resistance of concrete is suggested, that is, to add short fibers into concrete. The magnitude of tensile strength of concrete increases by this method (Chen and Chung 1993); thus the corrosion damage could be effectively reduced.

Entropy Evolution for Crack Propagation in Concrete Surface Under Sulfate Attack

Experiment on Surface Cracks Evolution

Material and Samples

The cement of PC32.5 R is chosen in this study, and the chemical components as well as the mix design of samples are, respectively, listed in Tables 3 and 4. The size of samples is $60 \times 60 \times 20$ mm^3 (shown in Fig. 9). Those samples are cured with 95% relative humidity for 28 days; then, they are moved into sodium sulfate solution of 8% concentration (shown in Fig. 10).

Table 3 Chemical components of cement in the unit of wt.%

SiO_2	Al_2O_3	Fe_2O_3	TiO_2	CaO	MgO	SO_3	K_2O	Na_2O	Alkali	LO1
31.43	12.43	3.34	0.76	41.28	4.25	3.22	0.80	0.43	0.97	1.09

Table 4 Mix design of cement mortar specimens in the unit of wt.%

Specimen	w/c	Water	Cement	Sand
M1	0.45	13.04	28.99	57.97
M2	0.55	15.49	28.17	56.34
M3	0.65	17.81	27.40	54.79

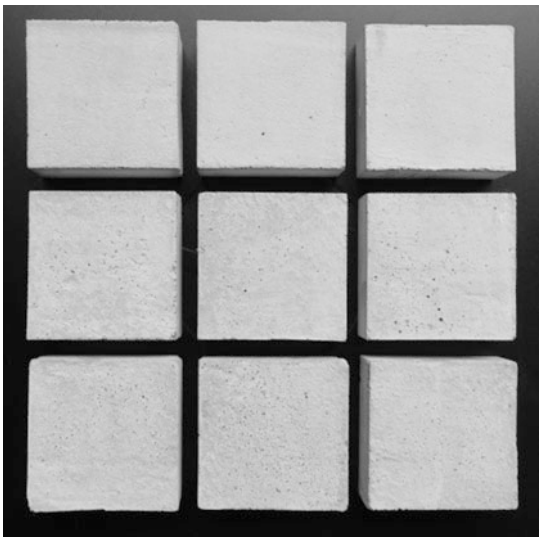

Fig. 9 Photo of concrete samples

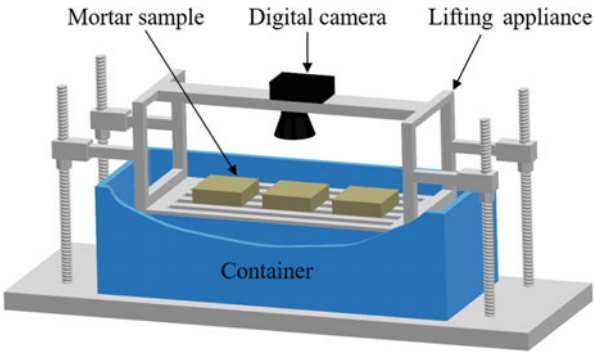

Fig. 10 Diagram for damage detection

Methods

The crack growth on the sample's surface is recorded by the camera at different corrosion time, namely, 90, 120, 130, 140, 180, 210, 230, 250, 270, 290, 320, 390, 450, 510, 570, and 630 days. It is seen from Fig. 11 that the evolution of the corrosion damage is random growth of surface cracks.

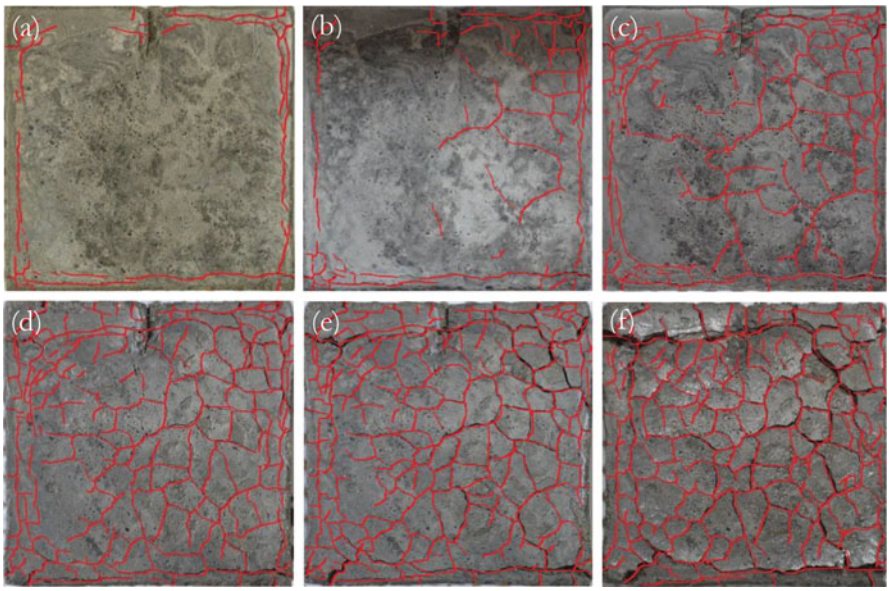

Fig. 11 Crack propagation with corrosion time. (**a**) 120 d, (**b**) 140 d, (**c**) 180 d, (**d**) 210 d, (**e**) 230 d, (**f**) 250 d

For accurately detecting the length of cracks as well as cracks' distribution at surface, the following procedure is adopted: ① the fixed distance between concrete samples and camera is firstly determined; ② the analysis of digital photos is performed in terms of special software; ③ the same pixel is set for all photos for conveniently comparison; ④ surface cracks are plotted in red color for being identified easily; and ⑤ the cracks' development is extracted by AutoCAD software. Some images to describe the cracking patterns in the sample of $w/c = 0.55$ are shown in Fig. 12.

In order to describe the surface damage evolution, the information entropy of surface cracks, S, is chosen as damage degree. There are two steps to perform the measurements and calculations. The first one is to cover all surface cracks in terms of a meshing set of 8×8 (shown in Fig. 13), and the second one is to detect the length, l_i, of all corrosion cracks in i^{th} ($i = 1$–64) element.

If the number of elements which contain cracks is N, the sum of surface cracks is evaluated by

$$L = \sum_{i=1}^{N} l_i \tag{24}$$

The cracks information entropy is computed by the following formula (Sauerbrunn et al. 2017; Skorobogatov 2004; Lu et al. 2005):

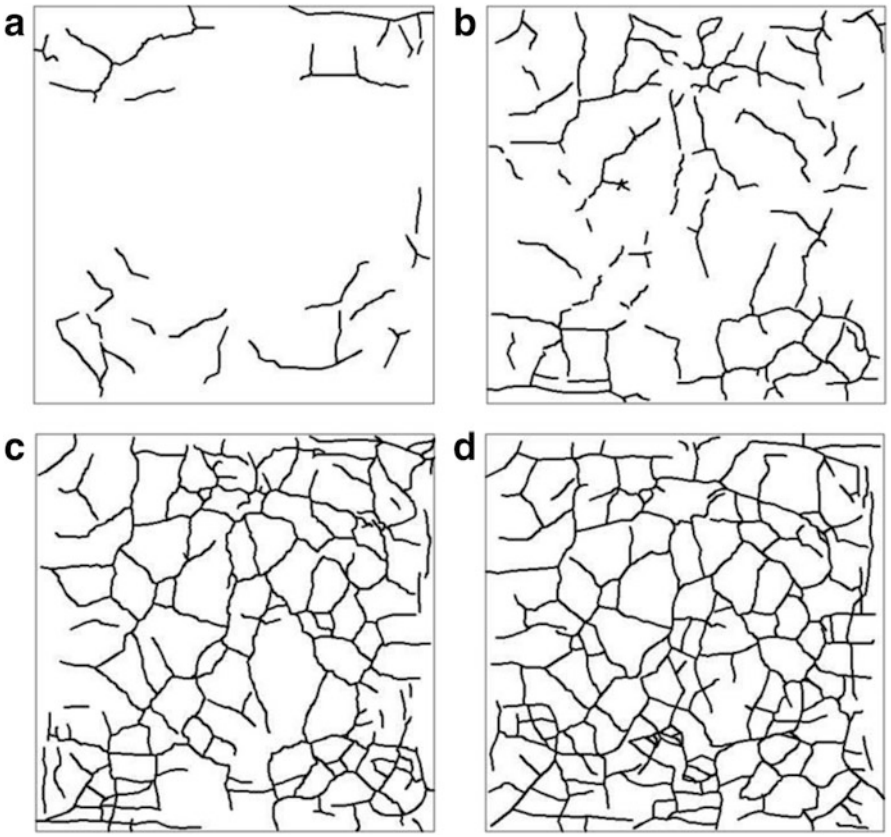

Fig. 12 Crack's evolution with corrosion time. (a) 180 days, (b) 210 days, (c) 270 days, and (d) 320 days

$$S = -\sum_{i=1}^{N} \frac{l_i}{L} \ln\left(\frac{l_i}{L}\right) \tag{25}$$

In order to investigate the mechanism of corrosion crack's growth, the SEM observation is fulfilled (shown in Fig. 14). It is seen that the growth of delayed ettringite could produce expansive stress, which induces the nucleation as well as growth of corrosion cracks (Basista and Weglewski 2009; Bary et al. 2014).

Because corrosion cracks are caused by DEF, it is necessary to detect the growth of delayed ettringite by XRD technique. For this purpose, smaller concrete samples are designed as rectangular column with size of $10 \times 10 \times 60$ mm^3. The test is performed by virtue of X-ray diffractometer with the type of M03XHF22. Figure 15a illustrates a typical atlas of diffraction results. According to the definition of the growth of delayed ettringite given by Chen and Jiang (2009), the growth behavior of delayed ettringite is obtained and plotted in Fig. 15b. If the corrosion time is greater than 180 days, the samples' failure occurs as shown in Fig. 15c.

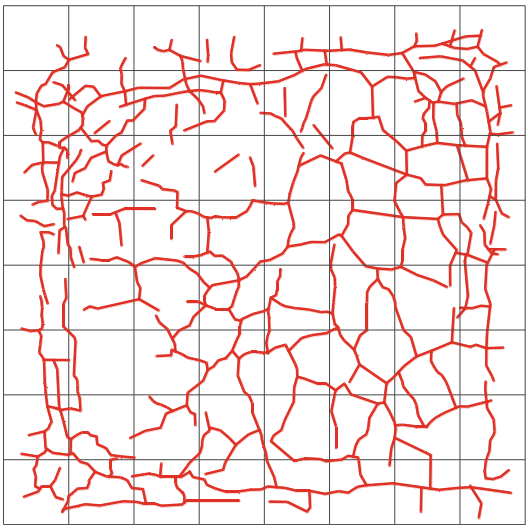

Fig. 13 Schematic diagram for evaluating the information entropy

Evolution Model of Entropy

Evolution of Entropy of Concrete with Different Water-to-Cement Ratio

Figure 16 shows that the entropy increases with immersion time because of the continuous growth of cracks. The mechanism for cracks' evolution is the action of expansive stress produced by delayed ettringite. Because the expansion stress induces a tensile stress near the pores' surface, the cracks' nucleation could occur if the tensile stress is greater than the value of tension strength (Chen et al. 2016). This means that enhancing the concrete strength may improve the sulfate resistance.

If the immersion time tends to infinite, then the entropy tends to a constant. In this case, concrete is referred to as failure. Thus, entropy could denote the degree of corrosion damage at the surface of concrete. Compared to other methods, the information entropy of corrosion cracks is more easily determined. It should be pointed out that the magnitude of water-to-cement ratio could affect the entropy significantly. The speed of entropy evolution in a concrete sample, with water-to-cement ratio being 0.65, is greater than that in a sample with 0.45 water-to-cement ratio (shown in Fig. 16). This implies that, trying to decrease the magnitude of water –o-cement ratio, the properties of concrete sulfate resistance could be improved.

Theoretical Model for Entropy Evolution

The evolution of crack information entropy is induced by the expansive stress caused by delayed ettringite. The chemical reaction equations as well as chemical reaction rate equations are, respectively, expressed by Eqs. (3) and (4) and (14). Figure 14 illustrates the size and shape of delayed ettringite and corresponding EDS analysis.

Since the entropy, S, is mainly caused by delayed ettringite, the increase of entropy is approximately proportional to ettringite (shown in Fig. 17). Hence, it

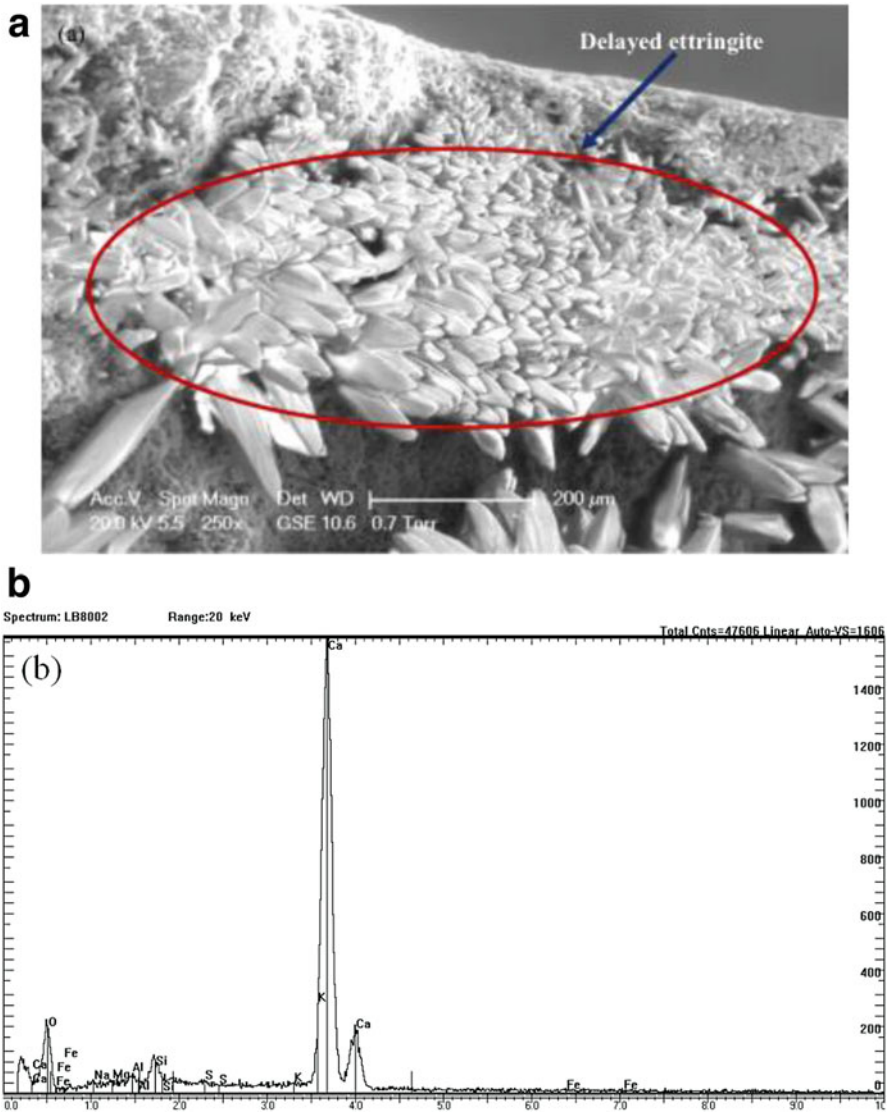

Fig. 14 Images of delayed ettringite. (**a**) SEM photo for ettringite and (**b**) EDX image

could be assumed that the relation between the variation rate of entropy, dS/dt, and the change rate of delayed ettringite, d$C_{ettringite}$/dt, is a linear one, i.e.:

$$\frac{dC_{ettringite}}{dt} = \beta \frac{dS}{dt} = -\frac{dC_{CA}}{dt} \tag{26}$$

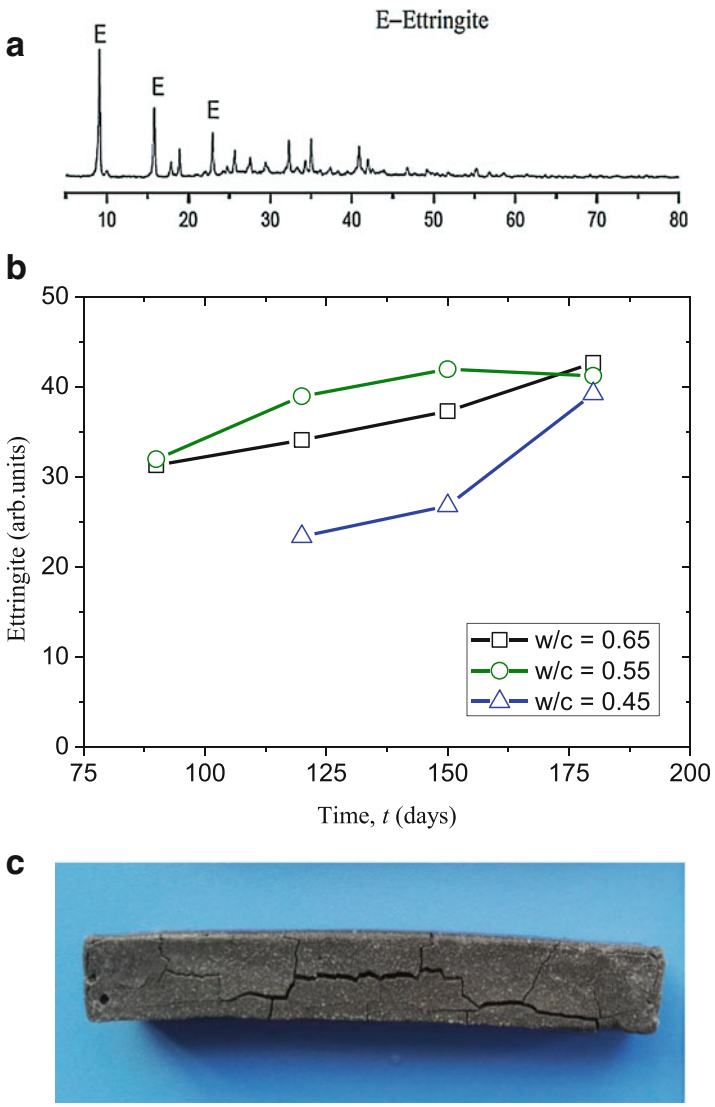

Fig. 15 Growth of delayed ettringite: (**a**) analysis results by XRD technique, (**b**) relative growth of DEF, and (**c**) the sample under sulfate attack for 180 days

Solving Eq. (26) yields

$$C_{CA} = -\beta S + F_1 \tag{27}$$

where symbols "β" and "F_1" are parameters to be determined.

Substituting Eqs. (26) and (27) into Eq. (16b) yields

$$\frac{\mathrm{d}S}{\mathrm{d}t} = -\frac{1}{t_u}(S - S')$$
$$S' = F_1/\beta, \quad t_u = q/(kB_1) \tag{28}$$

Differential Eq. (28) governs the entropy evolution. S could be expressed by following formula by solving Eq. (28):

$$S = S'\left(1 - \exp\left(-\frac{t - t_0}{t_u}\right)\right) \tag{29}$$

Parameters t_0, t_u, and S' may be determined by experimental data (see Table 5). It could be seen from Fig. 16 that the theoretical model of entropy evolution (Eq. (29)) could perfectly describe the evolution behavior of entropy.

The physical meaning for parameters S' is the special entropy when time tends to infinite, and t_u is the characterized time when the information entropy reaches $0.63S'$.

The definition of the normalized entropy and a nondimensional time is given as follows:

$$S* = S/S'$$
$$t* = (t - t_0)/t_u \tag{30}$$

Table 5 Parameters of t_0, t_u, and S' for cement mortar samples with different water-to-cement ratios

w/c	t_0	t_u	S'	R^2
0.65	69.03	33.31	4.14	1.00
0.55	85.99	51.28	4.21	0.98
0.45	91.20	189.60	4.31	0.96

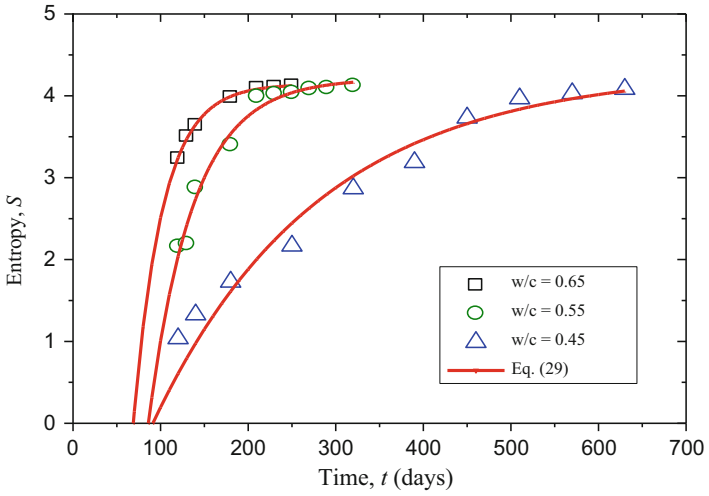

Fig. 16 Entropy variation with corrosion time

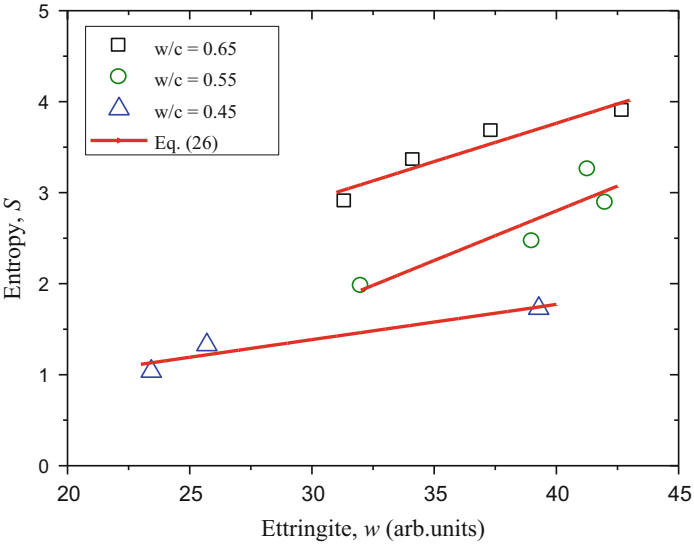

Fig. 17 Relation between entropy and DEF

Substituting Eq. (30) into (Eq. 29) leads to

$$S* = 1 - e^{-t*} \tag{31}$$

Equation (31) not only indicates that the normalized information entropy of corrosion cracks exponentially increases with nondimensional time but also shows that the S^* - t^* relation is universal for specimens with different values of water-to-cement ratios. That is, if the experimental results are analyzed by Eq. (30), the experimental results in Fig. 16 could collapse to the S^* - t^* curve, which is displayed in Fig. 18.

Conclusions

In this chapter, the evolution of corrosion damage in concrete due to sulfate corrosion is studied. It is confirmed that the internal expansive force caused by delayed ettringite is the main reason for the decrease of concrete durability. The corrosion damage evolution could be divided into two stages. In initial stage, the modulus of concrete is unexpectedly not to decrease but to increase. This result is ascribed to continuous hydration of cement, as well as the decrease of porosity of concrete because the pores are filled by the delayed ettringite. The analysis for cracks' initialization is performed by means of Eshelby's theory. It is confirmed that the expansive force leads to micro-cracks' nucleation, and such an expansive force is induced by delayed ettringite. In terms of this concept, an effective method is

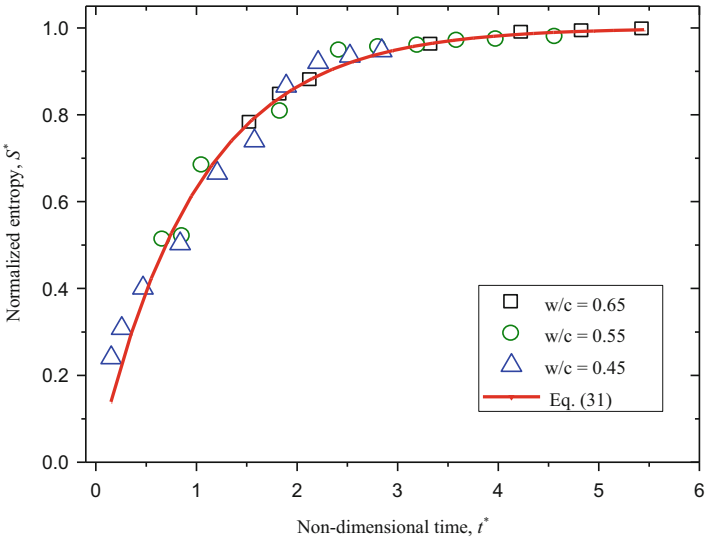

Fig. 18 Plot of growth behavior of the normalized information entropy with time

suggested, namely, to enhance the tensile strength via adding some plastic or wood chopped fibers to concrete materials. This is because the higher the tensile strength, the better the properties of sulfate resistance of concrete. Based on experimental study and chemical reaction and the equation of chemical reaction rate, an evolution equation of expansive stress is derived. Assuming the damage evolution could be described by Weibull's function, a new theoretical evolution model of corrosion damage is suggested, which is valid for describing the dominant characteristics of the damage in concrete due to sulfate corrosion. The surface cracks' evolution in concrete under sulfate attack is denoted by the information entropy. By virtue of theoretical analysis and experimental investigation, it is found that the water-to-cement ratio is an important influence factor for the evolution speed of information entropy of corrosion cracks. The greater the water-to-cement ratio, the faster the evolution speed of entropy. Hence, reducing the value of water-to-cement ratio could improve the microstructure of cement mortar, and the sulfate resistance can be advanced. The entropy evolution relates to the growth speed of delayed ettringite, and based on this viewpoint, an analytical expression for the information entropy evolution is obtained. The information entropy grows exponentially with corrosion time.

Acknowledgment The authors acknowledge the financial support by the National Natural Science Foundation of China (11832013, 11772164), the National Basic Research Program of China (973 Program, 2009CB623203), the Key Research Program of Society Development of Ningbo (2013C51007), and K.C. Wong Magna Fund in Ningbo University. The assistance of C. Lu in theoretical study and J. Yao and C. Qian in experiment are also appreciated.

References

R. Barbarulo, H. Peycelon, S.J. Prené Marchand, Delayed ettringite formation symptoms on mortars induced by high temperature due to cement heat of hydration or late thermal cycle. Cem. Concr. Res. **35**, 125–131 (2005)

B. Bary, N. Leterrier, E. Deville, P.L. Bescop, Coupled chemo-transport-mechanical modelling and numerical simulation of external sulfate attack in mortar, Cement. Concr. Comp. **49**, 70–83 (2014)

M. Basista, W. Weglewski, Chemically assisted damage of concrete: a model of expansion under external sulfate attack. Int. J. Damage Mech. **18**, 155–175 (2009)

P.W. Chen, D.D.L. Chung, Concrete reinforced with up to 0.2 vol.% of short Carbon Fibers. Composites **24**, 33–52 (1993)

J.K. Chen, M.Q. Jiang, Long-term evolution of delayed ettringite and gypsum in Portland cement mortars under sulfate erosion. Constr. Build. Mater. **23**, 812–816 (2009)

J.K. Chen, M.Q. Jiang, J. Zhu, Damage evolution in cement mortar due to erosion of sulphate. Corros. Sci. **50**, 2478–2483 (2008)

J.K. Chen, G.T. Wang, Z.Z. Yu, Z.P. Huang, Y.W. Mai, Critical particle size for interfacial debonding in polymer/nanoparticle composites. Compos. Sci. Technol. **70**, 861–172 (2010)

J.K. Chen, C. Qian, H. Song, A new chemo-mechanical model of damage in concrete under sulfate attack. Constr. Build. Mater. **115**, 536–543 (2016)

P. Chindaprasirt, P. Kanchanda, A. Sathonsaowaphak, H.T. Cao, Sulfate resistance of blended cements containing fly ash and rice husk ash. Constr. Build. Mater. **21**, 1356–1361 (2007)

M. Collepardi, Thaumasite formation and deterioration in historic buildings. Cem. Concr. Compos. **21**, 147–154 (1999)

B. Da, H.F. Yu, H.Y. Ma, Y.S. Tan, R.J. Mi, X.M. Dou, Chloride diffusion study of coral concrete in a marine environment. Constr. Build. Mater. **123**, 47–58 (2016)

S. Diamond, Delayed ettringite formation – Processes and problems. Cem. Concr. Compos. **18**, 205–215 (1996)

J.D. Eshelby, The determination of the elastic field of an ellipsoidal inclusion and related problems. Proc. R. Soc. Lond. **A241**, 376–396 (1957)

M. Ganjiani, R. Naghdabadi, M. Asghari, Analysis of concrete pressure vessels in the framework of continuum damage mechanics. Int J Damage Mech **21**, 843–870 (2012)

T. Ikumi, S.H.P. Cavalaro, I. Segura, A. Aguado, Alternative methodology to consider damage and expansions in external sulfate attack modeling. Cem. Concr. Res. **63**, 105–116 (2014)

D. Kuhl, F. Bangert, G. Meschke, Coupled chemo-mechanical deterioration of cementitious materials Part I: Modeling. Int. J. Solids Struct. **41**, 15–40 (2004a)

D. Kuhl, F. Bangert, G. Meschke, Coupled chemo-mechanical deterioration of cementitious materials Part II: Numerical methods and simulations. Int. J. Solids Struct. **41**, 41–67 (2004b)

S.T. Lee, H.Y. Moon, R.N. Swamy, Sulfate attack and role of silica fume in resisting strength loss. Cem. Concr. Compos. **27**, 65–76 (2005)

C. Lu, Y.W. Mai, H. Xie, A sudden drop of fractal dimension: a likely precursor of catastrophic failure in disordered media. Philos. Mag. Lett. **85**, 33–40 (2005)

C. Lu, R. Danzer, F.D. Fischer, Influence of threshold stress on the estimation of the Weibull statistics. J. Am. Ceram. Soc. **85**, 1640–1642 (2002a)

C. Lu, R. Danzer, F.D. Fischer, Fracture statistics of brittle materials: Weibull or normal distribution. Phys. Rev. **E65**, 067102 (2002b)

M.A. Meyers, *Dynamic behavior of materials* (Wiley, New York, 1994)

R.D. Moser, P.M. Singh, L.F. Kahn, K.E. Kurtis, Chloride-induced corrosion resistance of high-strength stainless steels in simulated alkaline and carbonated concrete pore solutions. Corros. Sci. **57**, 241–253 (2012)

S. Muthulingam, B.N. Rao, Non-uniform corrosion states of rebar in concrete under chloride environment. Corros. Sci. **93**, 267–282 (2015)

A.S.E. Nassef, Fibonacci sequence and golden ratio in new formula of predicting cracks propagation in reinforced concrete tie. Int J Damage Mech **24**, 1214–1226 (2015)
A. Pavoine, L. Divet, S. Fenouillet, A concrete performance test for delayed ettringite formation: Part I optimisation. Cem. Concr. Res. **36**, 2138–2143 (2006)
P. Pipilikaki, D. Papageorgiou, M. Dimitroula, E. Chaniotakis, M. Katsioti, Microstructure changes in mortars attacked by sulfates at 50C. Constr. Build. Mater. **23**, 2259–2264 (2009)
D. Planel, J. Sercombe, P. Le Bescop, F. Adenot, J.M. Torrenti, Long-term performance of cement paste during combined calcium leaching–sulfate attack: kinetics and size effect. Cem. Concr. Res. **36**, 137–143 (2006)
C. Plowman, J.G. Cabrera, The use of fly ash to improve the sulfate resistance of concrete. Waste Manag. **16**, 145–149 (1996)
W. Prince, M. Espangne, P.C. Aitcin, Ettringite formation: a crucial step in cement super plasticizer compatibility. Cem. Concr. Res. **33**, 635–641 (2003)
L. Rayleigh, *Theory of sound* (Dover, New York, 1894)
E. Rozière, A. Loukili, R.E. Hachem, G. Frederic, Durability of concrete exposed to leaching and external sulphate attacks. Cem. Concr. Res. **39**, 1188–1198 (2009)
C.M. Sauerbrunn, A. Kahirdeh, H.S. Yun, M. Modarres, Damage assessment using information entropy of individual acoustic emission waveforms during cyclic fatigue loading. Appl. Sci. **7**, 562 (2017) (1–20)
S.M. Skorobogatov, The principle of information entropy for the description of fracture at multiple dimensions in real materials (concrete, rock) of buildings and rock seam. Int. J. Fract. **128**, 335–343 (2004)
R. Tixier, B. Mobasher, Modeling of damage in cement-based materials subjected to external sulfate attack. I: Formulation. J. Mater. Civ. Eng. **15**, 305–313 (2003a)
R. Tixier, B. Mobasher, Modeling of damage in cement-based materials subjected to external sulfate attack. I: Formulation. J. Mater. Civ. Eng. **15**, 314–322 (2003b)
R. Yang, C.D. Lawrence, C.J. Lynsdale, J.H. Sharp, Delayed ettringite formation in heat-cured Portland cement mortars. Cem. Concr. Res. **29**, 17–25 (1999)
H.F. Yu, B. Da, H.Y. Ma, H.W. Zhu, Q. Yu, H.M. Ye, X.S. Jing, Durability of concrete structures in tropical atoll environment. Ocean Eng. **135**, 1–10 (2017)
M.H. Zhang, J.K. Chen, Y.F. Lv, D.J. Wang, J. Ye, Study on the expansion of concrete under attack of sulfate and sulfate–chloride ions. Constr. Build. Mater. **39**, 26–32 (2013)

Strain Energy-Based Thermo-elastoviscoplastic Two-Parameter Damage Self-Healing Formulations for Bituminous Composite Materials

37

Seongwon Hong and Jiann-Wen Woody Ju

Contents

Introduction 1022
Continuum Thermodynamics Framework for Two-Parameter Damage Self-Healing Formulations 1023
A Conceptual Illustration 1038
Conclusions 1040
Appendix 1041
References 1042

Abstract

The strain energy-based thermo-elastoviscoplastic *two-parameter* damage self-healing models for bituminous composites are suggested and used for the analysis of test results. Based on a continuum thermodynamic framework, a class of constitutive damage self-healing formulations is proposed within an elastic strain energy-based equation. To consider the temperature effect, the Helmholtz free energy potential is used and uncoupled with an *Arrhenius-type temperature term*. Particularly, the governing incremental damage and healing evolutions, which are coupled in two-parameter parts such as *volumetric and deviatoric parts*, are characterized through the concept of net stress in conjunction with the *strain equivalence hypothesis*. The conceptual example is presented for the developed

S. Hong (✉)
Department of Safety Engineering, Korea National University of Transportation, Chungju-si, Chungbuk, Republic of Korea
e-mail: shong@ut.ac.kr

J.-W. W. Ju
Department of Civil and Environmental Engineering, University of California, Los Angeles, CA, USA

State Key Laboratory for Disaster Reduction in Civil Engineering, Tongji University, Shanghai, China
e-mail: juj@ucla.edu

© Springer Nature Switzerland AG 2022

G. Z. Voyiadjis (ed.), *Handbook of Damage Mechanics*,
https://doi.org/10.1007/978-3-030-60242-0_56

governing incremental two-parameter evolutions. The *equivalent volumetric and deviatoric strains* are redefined as energy norms of the two-parameter strain tensors and used for the volumetric and deviatoric damage and healing criteria. A rate-sensitive two-parameter damage model with a structure analogous to Perzyna-type viscoplasticity is employed for rate-dependent asphalt composites. Novel computational algorithms based on the two-step operator splitting methodology are demonstrated in Part II. Comparisons with test data and numerical predictions are provided in Part II.

Keywords

Arrhenius-type temperature term · Bituminous composites, deviatoric strains · Net space · Thermo-elastoviscoplastic two-parameter damage–self-healing model · Volumetric strains

Introduction

Asphalt concretes (bituminous composites) have significantly complicated systems in terms of loading rate sensitivity, thermal dependence, and healing features during the rest periods. These properties are influenced by various combinations of environmental conditions such as the temperature, moisture and aging, and traffic loadings such as the rate, type and duration of loading, and rest periods. Therefore, the development of a realistic formulation of asphalt concrete materials is a challenging task and a critical and complicated issue for civil engineers these days. Diverse approaches for thermodynamics-based formulations have been proposed for industrial composites for the last three decades (cf. Chow and Wang 1988; Chaboche 1996; Murakami and Kamiya 1996; Schapery 1997; Rosakis et al. 2000; Kocks 2001; Barbero et al. 2005; Liu et al. 2006; Voyiadjis and Abed 2006; Ghorbel 2008; Voyiadjis and Almasri 2008; Huang et al. 2009). In spite of the contributions, there are a few scholars who develop or propose physical and reliable constitutive formulations of mechanical response of asphalt concrete materials (cf. Lee and Kim 1998; Lytton et al. 2001; Abu Al-Rub et al. 2010; Yuan et al. 2014).

It is assumed in the continuum damage mechanics (CDM)-based formulations that degradation of composites is macroscopically homogeneous and its response is obviously predicted by the thermodynamics of irreversible process and the mechanics of continuous media without their complicated microstructures. The CDM-based formulations have been thoroughly used for all types of composites including soil, rocks, steels, metals, woods, concrete, and polymers in the civil engineering field. Kachanov (1958), who was considered as the pioneer, developed a scalar damage variable associated with the density of cavities, microcracks, voids, and defects. This scalar variable has been used in the isotropic formulations, whereas anisotropic damage models have employed tensorial damage variables (cf. Kachanov 1980; Betten 1981, 1986; Simo and Ju 1987a, b, 1989; Simo et al. 1988; Ju 1989a, b; Ju et al. 2012a, b; Shafabakhsh

and Kashi 2015; Shahsavari et al. 2015; Zhu et al. 2015; Voyiadjis and Kattan 2016; Hong et al. 2017a, b). The fourth-order form of isotropic damage tensor generally consists of the *volumetric* and *deviatoric* parts. Under the condition that the damage in the volumetric part is the same as the deviatoric part in terms of magnitude, the isotropic damage tensor reduces to a scalar damage formulation signifying that the Poisson's ratio remains *constant* when the degradation proceeds (cf. Ju 1990; Ju et al. 2012a, b).

In the past three decades, experimental data in many different fields have obviously shown that some materials can be partially healed, fully repaired, or autonomously recovered, i.e., without any external intervention (cf. Kim et al. 1994; Miao et al. 1995; Daniel and Kim 2001; Kessler and White 2001; Brown et al. 2002; Reinhardt and Jooss 2003; Carpenter and Shen 2006; Guo and Guo 2006; Kessler 2007; Little and Bhasin 2007; Bhasin et al. 2008; Herbst and Luding 2008; Ghosh 2009; Ju et al. 2012a, b; Ju and Yuan 2012; Yuan and Ju 2013; Hong et al. 2017a, b). In particular, damage including microcavities, microvoids, microcracks, and interfacial debonding between the matrix and aggregate may steadily reduce its size and finally repair their original stiffness and strength during both the unloading process and the rest periods (Kim et al. 1994; Lee and Kim 1998; Daniel and Kim 2001; Lytton et al. 2001; Abu Al-Rub et al. 2010; Darabi et al. 2013). To develop isotropic damage self-healing formulation, the Arrhenius-type temperature term was uncoupled with Helmholtz free energy potential (Hong et al. 2017a, b). In spite of these contributions of these studies, there has been no publication in the literature on thermo-elastoviscoplastic *two-parameter* damage self-healing models for asphalt concrete composites. Therefore, there is a fundamental need to produce physical and reliable rigorous constitutive theories and its computational framework of *two-parameter* damage self-healing mechanisms for asphalt concretes subjected to monotonic and cyclic loading with different temperature conditions.

The outline of this chapter is as follows. First of all, based on the continuum thermodynamics framework, the elastic energy based thermo-elastoviscoplastic *two-parameter* (volumetric and deviatoric) damage self-healing models are developed. Particularly, the governing *two-parameter* damage and self-healing evolutions are coupled with definitions of the two-parameter damage and healing areas in an incremental form and characterized through the concept of net stress in conjunction with the *strain equivalence hypothesis*. Second, for the developed two-parameter damage-self healing models, a conceptual illustration is demonstrated with two linearly independent springs.

Continuum Thermodynamics Framework for Two-Parameter Damage Self-Healing Formulations

A Coupled Two-Parameter Model

A fundamental concept underlining the elastic strain energy-based two-parameter damage self-healing formulations for bituminous composites results from the hypothesis that the total strain histories and the *Arrhenius-type temperature term*

are directly connected to incremental two-parameter damage and self-healing histories. The net healed stress notion along with the *strain equivalence hypothesis* comes from the assumed form of free energy. The Arrhenius-type temperature term is selected to consider the temperature effects for asphalt concrete materials. The developed volumetric and deviatoric damage, healing, and their net variables are the primary points in this section.

Definition of Net (Combined) Variables of the Volumetric and Deviatoric Damage and Healing

It is assumed that the area A can be conceptually decomposed into the volumetric area A_v and the deviatoric area A_d. In addition, it is assumed that there is no overlapping area and two areas are linearly independent as shown in Eq. (1):

$$A_v \cap A_d = \varnothing \tag{1}$$

Let us define d_v as the volumetric damage variable and R_v as the volumetric healing variable, respectively. A_v^d, A_v^R, and A_v^{uR} are defined as the volumetric damaged area, the volumetric healed area, and the volumetric unhealed, respectively:

$$d_v = A_v^d / A_v \tag{2}$$

$$R_v = A_v^R / A_v^d \tag{3}$$

Because of the assumption that volumetric undamaged and healed area can only sustain the volumetric loading in the continuum damage mechanics described in Fig. 1, d_v^{net} is defined as a scalar variable to present the net effects the damage-healing:

$$\boldsymbol{\sigma}_v A_v = \boldsymbol{\sigma}_v^{net} A_v^{net} \tag{4}$$

$$d_v^{net} = d_v(1 - R_v) \tag{5}$$

Let us define d_d as the deviatoric damage variable and R_d as the deviatoric healing variable, respectively. A_d^d, A_d^R, andA_d^{uR} are he deviatoric damaged area, the deviatoric healed area, and the deviatoric unhealed area, respectively:

$$d_d = A_d^d / A_d \tag{6}$$

$$R_d = A_d^R / A_d^d \tag{7}$$

Because of the assumption that deviatoric undamaged and healed area can only sustain the deviatoric loading in the continuum damage mechanics shown in Fig. 1, d_d^{net} is defined as a scalar variable to present the combined effects of the damage-healing:

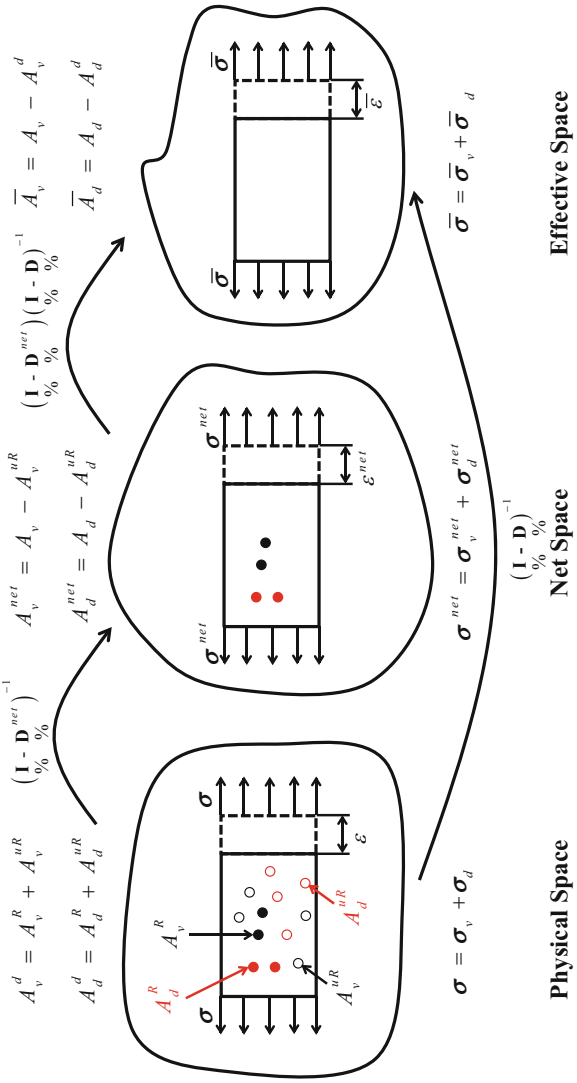

Fig. 1 The conceptual illustration of the physical, net, and effective spaces

$$\boldsymbol{\sigma}_d A_d = \boldsymbol{\sigma}_d^{net} A_d^{net} \tag{8}$$

$$d_d^{net} = d_d(1 - R_d) \tag{9}$$

Net Stress Concept and Hypothesis of Strain Equivalence

The initiation, growth, and coalescence of microcavities, microcracks, microvoids, and microscopic defects result in composite deterioration. If the damages are repaired due to the temperature effects and/or compactions and the stiffnesses and strengths are partially and/or fully recovered, it is called the healing mechanism. In the framework of continuum mechanics, the model is developed based on these procedures and the internal damage-healing variables in the tensorial form with two variables. It is denoted by a fourth-order tensor $\mathbf{M}^{net} = (\mathbf{I} - \mathbf{D}^{net})$ characterizing the net damage state and transforming the homogenized stress tensor $\boldsymbol{\sigma}$ into the net stress tensor $\boldsymbol{\sigma}^{net}$ or vice versa. It is obtained in Eq. (10):

$$\boldsymbol{\sigma}^{net} = \mathfrak{d}(T)^{-1}(\mathbf{M}^{net})^{-1} : \boldsymbol{\sigma} \tag{10}$$

where $\mathfrak{d}(T)$ is the Arrhenius-type temperature term and described in Eq. (11)

$$\mathfrak{d}(T) = \exp\left\{-\boldsymbol{\delta}\left(1 - \frac{T}{T_0}\right)\right\} \tag{11}$$

where $\boldsymbol{\delta}$ is a constant material value and T_0 is defined as the reference temperature (°C).

In the case of the two-parameter damage and healing, the mechanical responses of microdamage and healing depend on two scalar variables $d_v^{net} = d_v(1 - R_v)$ and $d_d^{net} = d_d(1 - R_d)$ and are independent of their orientations, and. Eq. (10) collapses to (see the Appendix for more detail)

$$\begin{aligned}\boldsymbol{\sigma}(t) &= \left[(\mathbf{I} - \mathbf{D}^{net}) : \boldsymbol{\sigma}^{net}(t)\right]\mathfrak{d}(T) \\ &= \left[\left(1 - d_v^{net}(t)\right)\boldsymbol{\sigma}_v^{net}(t) + \left(1 - d_d^{net}(t)\right)\boldsymbol{\sigma}_d^{net}(t)\right]\mathfrak{d}(T)\end{aligned} \tag{12}$$

$$\mathbf{D}^{net} = \frac{1}{3} d_v^{net} \mathbf{1} \otimes \mathbf{1} + d_d^{net}\left(\mathbf{I} - \frac{1}{3}\mathbf{1} \otimes \mathbf{1}\right) \tag{13}$$

where $d_v^{net}(t) \in [0, d_{v,c}^{net}]$ for $t \in \mathbb{R}_+$ is the *volumetric* net damage-healing variable, $d_d^{net}(t) \in [0, d_{d,c}^{net}]$ for $t \in \mathbb{R}_+$ is the *deviatoric* net damage-healing variable, $\boldsymbol{\sigma}(t)$ is the Cauchy stress tensor, and $\boldsymbol{\sigma}^{net}(t)$ is the net stress tensor. Here, $d_{v,c}^{net} \in (0, 1]$ and $d_{d,c}^{net} \in (0, 1]$ are constants. The coefficients, which are $1 - d_v^{net}(t)$ and $1 - d_d^{net}(t)$, are reduction factors related to the net (combined) volumetric and deviatoric effects, respectively, of damage and healing in the materials. The value $d_v^{net}(= 0)$ defines the volumetric initial (undamaged) state or the full volumetric healing state, while a value $d_v^{net} \in (0, d_{v,c}^{net})$ describes a volumetric damaged state. The value $d_v^{net}(= d_{v,c}^{net})$

corresponds to the complete local volumetric rupture. In the same way, the value $d_d^{net}(=0)$ defines the deviatoric undamaged state or the full deviatoric healing state, while the value $d_d^{net} \in (0, d_{d,c}^{net})$ depicts a deviatoric damaged state. The value $d_d^{net}(=d_{d,c}^{net})$ corresponds to the complete local volumetric rupture. It is assumed that it is at complete local rupture as either d_v^{net} or d_d^{net} is equal to $d_{v,c}^{net}$ or $d_{d,c}^{net}$, respectively. At a local viewpoint, the volumetric net damage-healing variable is defined as the ratio of the difference between the volumetric damaged and healed areas to the total volumetric area. Since the two spaces are orthogonal, the deviatoric net damage-healing variable is the same.

The following strain equivalence hypothesis is introduced by extending from the effective stress space to the net stress space (Hong et al. 2017a):

"The strain associated with a damaged and healed state under the applied loading is equivalent to the strain ε^{net} associated with its damaged and healed state under the net stress." See Fig. 2 for a schematic illustration.

To introduce the *net effect* of the volumetric and deviatoric damage-healing, viscoplastic flow processes, and temperature effect, a free energy potential is suggested in Eq. (14) (see the Appendix for more detail):

$$\begin{aligned}&\Psi\left(\mathbf{q}, \boldsymbol{\sigma}^{vp}, \mathbf{e}, \boldsymbol{\varepsilon}_{\mathrm{v}}, d_v^{net}, d_d^{net}, T\right)\\&\quad\equiv\left\{\left(1-d_v^{net}\right)\Psi_v^0(\boldsymbol{\varepsilon}_{\mathrm{v}})+\left(1-d_d^{net}\right)\Psi_d^0(\mathbf{e})-\frac{1}{2}\boldsymbol{\varepsilon}:\boldsymbol{\sigma}^{vp}+\Xi(\mathbf{q},\boldsymbol{\sigma}^{vp})\right\}\vartheta(T)\end{aligned}\tag{14}$$

where $\mathbf{q}$ is a suitable set of internal (viscoplastic) variables, $\boldsymbol{\sigma}^{vp}$ is the viscoplastic relaxation stress tensor, $\mathbf{e}$ is the deviatoric strain tensor, $\boldsymbol{\varepsilon}_v\left(\equiv\frac{1}{3}\boldsymbol{\varepsilon}_{kk}\ \mathbf{1}\right)$ is the volumetric strain tensor, d_v^{net} is the *volumetric* net damage-healing variable, and d_d^{net} is *deviatoric* net damage-healing variable. Furthermore, $\Psi_v^0(\boldsymbol{\varepsilon}_v)$ is the elastic volumetric stored energy function of the initial (undamaged) substance, $\Psi_d^0(\mathbf{e})$ defines the elastic deviatoric stored energy function of the initial (undamaged) substance, and $\Xi(\mathbf{q}, \boldsymbol{\sigma}^{vp})$ defines the viscoplastic potential function. In the case of the linear elasticity, it is $\Psi_v^0(\boldsymbol{\varepsilon}_v)=\frac{1}{2}\boldsymbol{\varepsilon}_v:(K\,\underset{\sim}{1}\bigotimes\underset{\sim}{1}):\boldsymbol{\varepsilon}_v=\frac{1}{2}K(\boldsymbol{\varepsilon}_{kk})^2$, where K is defined as the bulk modulus and $\Psi_d^0(\mathbf{e})=G\,\mathbf{e}:\mathbf{e}$, with G implying the shear modulus.

Generally, the thermal dissipation is smaller than the mechanical dissipation, and it is then rational to assume that the thermal dissipation rate is able to be ignored. The Clausius-Duhem is equivalent to the Clausius-Plank inequality as follows:

$$-s\dot{T}-\dot{\Psi}+\boldsymbol{\sigma}:\dot{\boldsymbol{\varepsilon}}\geq 0\tag{15}$$

By taking the time derivative of Eq. (14), plugging it into Eq. (15), and using standard arguments (Coleman and Gurtin 1967) with the reasonable assumption that the net effect of damage-healing and viscoplastic unloading are elastic progress, the stress-strain constitutive law can be determined

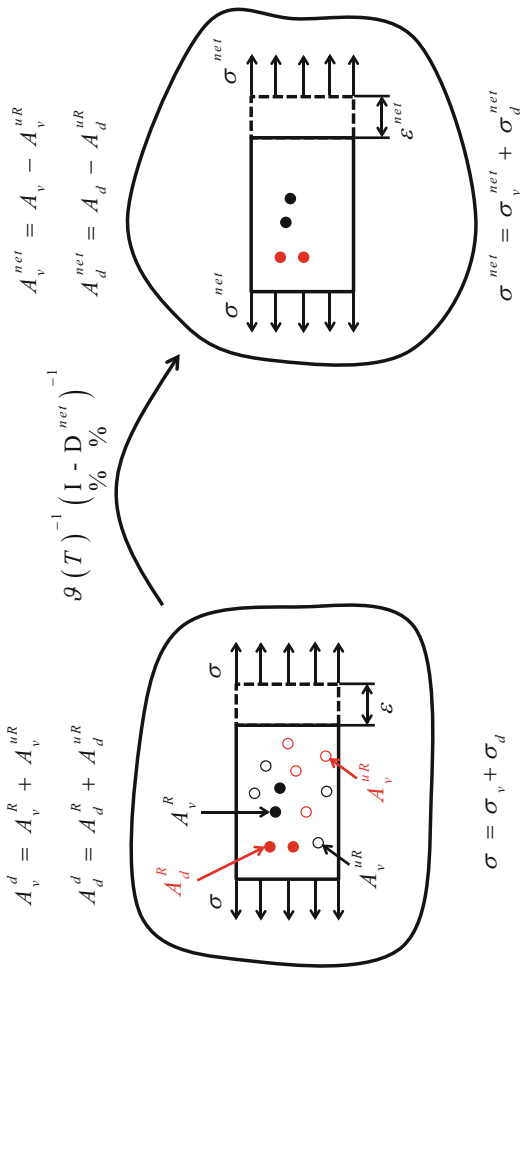

Fig. 2 The schematic demonstration of the *strain equivalence hypothesis*

$$\begin{aligned}\sigma &= \left\{ \left(1-d_v^{net}\right)\frac{\partial \Psi_v^0(\boldsymbol{\varepsilon}_{\mathrm{v}})}{\partial \boldsymbol{\varepsilon}_{\mathrm{v}}} + \left(1-d_d^{net}\right)\frac{\partial \Psi_d^0(\mathbf{e})}{\partial \mathbf{e}} - \boldsymbol{\sigma}^{vp} \right\}\vartheta(T) \\ &= \left\{ \left(1-d_v^{net}\right)\boldsymbol{\sigma}_v^{net} + \left(1-d_d^{net}\right)\boldsymbol{\sigma}_d^{net} \right\}\vartheta(T)\end{aligned} \tag{16}$$

and the dissipative inequalities

$$\left\{ -\frac{\partial \Xi}{\partial \mathrm{q}}\cdot\dot{\mathbf{q}} - \left(\frac{\partial \Xi}{\partial \boldsymbol{\sigma}^{vp}} - \frac{1}{2}\varepsilon\right) : \dot{\boldsymbol{\sigma}}^{vp} \right\}\vartheta(T) \geq 0 \tag{17}$$

$$\left\{ \Psi_v^0(\boldsymbol{\varepsilon}_{\mathrm{v}})\dot{d}_v^{net} + \Psi_d^0(\mathbf{e})\dot{d}_d^{net} - \frac{\partial \Xi}{\partial \mathbf{q}}\cdot\dot{\mathbf{q}} - \left(\frac{\partial \Xi}{\partial \boldsymbol{\sigma}^{vp}} - \frac{1}{2}\boldsymbol{\varepsilon}\right) : \dot{\boldsymbol{\sigma}}^{vp} \right\}\vartheta(T) \geq 0 \tag{18}$$

as well as the entropy

$$s = -\frac{\partial \vartheta(T)}{\partial T}\Psi\left(\mathbf{q}, \boldsymbol{\sigma}^{vp}, \mathbf{e}, \boldsymbol{\varepsilon}_{\mathrm{v}}, d_v^{net}, d_d^{net}\right) \tag{19}$$

From Eq. (16), it follows that within the strain space formulation, the stress tensor can be split into the elastic damage-healing and the viscoplastic relaxation parts. It is observed that the dissipative energy can be positive due to viscoplasticity resulting from Eqs. (17) and (18); the sum of the effect of damage-healing and viscoplasticity can be also positive if the effect of damage-healing is involved. Moreover, from Eqs. (17), (18), and (19), it is noted that the current framework is capable of accommodating general elastic behavior and viscoplastic behavior.

The viscoplastic potential $\Xi(\mathbf{q}, \boldsymbol{\sigma}^{vp})$ is connected to viscoplastic dissipation, and inequality in Eq. (18) is satisfied for arbitrary processes. It is assumed that the viscoplastic potential is independent of d_v^{net} and d_d^{net}. From Eq. (14), it follows that

$$-Y_v \equiv -\frac{\partial \Psi\left(q, \boldsymbol{\sigma}^{vp}, \mathbf{e}, \boldsymbol{\varepsilon}_{\mathrm{v}}, d_v^{net}, d_d^{net}, T\right)}{\partial d_v^{net}} = \Psi_v^0(\boldsymbol{\varepsilon}_v)\vartheta(T) \tag{20}$$

$$-Y_d \equiv -\frac{\partial \Psi\left(q, \boldsymbol{\sigma}^{vp}, \mathbf{e}, \boldsymbol{\varepsilon}_{\mathrm{v}}, d_v^{net}, d_d^{net}, T\right)}{\partial d_d^{net}} = \Psi_d^0(\mathbf{e})\vartheta(T) \tag{21}$$

Therefore, the thermodynamic force Y_v conjugate to the *net volumetric* damage-healing variable d_v^{net} is defined by the initial *volumetric* elastic strain energy $\Psi_v^0(\boldsymbol{\varepsilon}_v)$, and the thermodynamic force Y_d conjugate to the *net deviatoric* damage-healing variable d_d^{net} is defined by the initial *deviatoric* elastic strain energy $\Psi_d^0(\mathrm{e})$. The volumetric and deviatoric damage, the volumetric and deviatoric healing, and their interactions are a primary focus.

Characterization of the Initial Elastic Strain Energy-Based Volumetric and Deviatoric Damage

The progressive degradation of bituminous composites is first characterized. The notion of equivalent volumetric strain ξ_v is ascribed as the energy norm of the volumetric strain tensor:

$$\xi_v \equiv \sqrt{\Psi^0(\varepsilon_v)\vartheta(T)} = \sqrt{\left\{\frac{1}{2}K(\varepsilon_{kk})^2\right\}\exp\left\{-\delta\left(1-\frac{T}{T_0}\right)\right\}} \tag{22}$$

where $\varepsilon_{kk} = \varepsilon_{11} + \varepsilon_{22} + \varepsilon_{33}$.

The volumetric damage state in bituminous matrix by means of a damage criterion $\phi_v^d(\xi_{v,t}, g_{v,t}) \leq 0$ in the strain space with the functional form is characterized as follows:

$$\phi_v^d(\xi_{v,t}, g_{v,t}) \equiv \xi_{v,t} - g_{v,t} \leq 0 \qquad t \in \mathbb{R}_+ \tag{23}$$

where $g_{v,\,t}$ is the volumetric damage threshold at the current time $t \in \mathbb{R}_+$. Note that the value of $g_{v,\,t}$ could be lowered because of the incremental volumetric healing from the previous time step. Let $g_{v,\,0}$ imply the initial volumetric damage threshold before any loading; it is $g_{v,\,t} \geq g_{v,\,0}$ where $g_{v,\,0}$ is regarded as a characteristic material property. The above condition (23) represents that volumetric damage in asphalt concrete is began as the volumetric equivalent strain $\xi_{v,\,t}$ exceeds the initial volumetric damage threshold$g_{v,\,0}$. In the case of volumetric damage, the evolution of the volumetric damage variable $d_{v,\,t}$ and the volumetric damage threshold $g_{v,\,t}$ is defined by the rate equations as follows:

$$\dot{d}_{v,t} = \dot{\mu}_v H_v(\xi_{v,t}, d_{v,t}) \tag{24}$$

$$\dot{g}_v = \dot{\mu}_v \tag{25}$$

where $\dot{\mu}_v \geq 0$ is a volumetric damage consistency parameter defining the conditions of the volumetric damage loading/unloading based on the Kuhn-Tucker relations

$$\dot{\mu}_v \geq 0, \qquad \phi_v^d(\xi_{v,t}, g_{v,t}) \leq 0, \qquad \dot{\mu}_v\,\phi_v^d(\xi_{v,t}, g_{v,t}) = 0 \tag{26}$$

The conditions in Eq. (26) are standard for problems including unilateral constraints. If $\phi_v^d(\xi_{v,t}, g_{v,t}) < 0$, the damage criterion is not satisfied, and it becomes $\dot{\mu}_v = 0$; the volumetric damage rule in Eq. (24) signifies that no further volumetric damage occurs and $\dot{d}_v = 0$. In contrast, if $\dot{\mu}_v > 0$, further volumetric damage is occurring, and it means $\phi_v^d(\xi_{v,t}, g_{v,t}) = 0$. In this event, $\dot{\mu}_v$ is calculated by the condition of volumetric damage consistency:

$$\phi_v^d(\xi_{v,t}, g_{v,t}) = \dot{\phi}_v^d(\xi_{v,t}, g_{v,t}) = 0 \Rightarrow \dot{\mu}_v = \dot{\xi}_v \tag{27}$$

and $g_{v,\,t}$ is determined by the expression in Eq. (28):

$$g_{v,t} = \max\left(g_{v,0}, \max_{s\in(-\infty,\,t)}\xi_{v,s}\right) - g_{vh,(t-1)} \tag{28}$$

where $g_{vh,\,(t\,-\,1)}$ is the reduced value for the present volumetric damage threshold because of the incremental volumetric healing from the previous time step.

If $H_v(\xi_{v,\,t},\, d_{v,\,t})$ in Eq. (24) is independent of $\dot{d}_{v,t}$, the above equation can be modified as follows. Let $G_v : \mathbb{R} \to \mathbb{R}_+$ be so that $H_v(\xi_{v,\,t}) \equiv \partial G_v(\xi_{v,\,t})/\partial \xi_{v,\,t}$. It is noted that $G_v(\cdot)$ defines a monotonic function. A damage criterion, which is equivalent to the condition in Eq. (23), is provided by $\overline{\phi}_v^d\left(\xi_{v,t}, g_{v,t}\right) \equiv G_v\left(\xi_{v,t}\right) - G_v\left(g_{v,t}\right) \leq 0$. The flow rule and the loading/unloading conditions are as follows:

$$\dot{d}_{v,t} = \dot{\mu}\frac{\partial \overline{\phi}_v^d\left(\xi_{v,t}, g_{v,t}\right)}{\partial \xi_{v,t}}, \qquad g_{v,t} = \dot{\mu}_v \tag{29}$$

$$\dot{\mu}_v \geq 0, \qquad \overline{\phi}_v^d\left(\xi_{v,t}, g_{v,t}\right) \leq 0, \qquad \dot{\mu}_v \overline{\phi}_v^d\left(\xi_{v,t}, g_{v,t}\right) = 0 \tag{30}$$

Conditions in Eqs. (29) and (30) are the Kuhn-Tucker optimality conditions from the maximum volumetric damage dissipation principle.

Existing test results of bituminous composites show that at a particular strain level, the amount of microcavities, microvoids, or microcracks displays *rate sensitivity* to the applied loading rate in a dynamic environment. A simple phenomenological characterization of the effect can be determined by means of a *viscous regularization* of the rate-independent strain-based damage formulation. This regularization is similar to the Perzyna-type viscoplastic regularization (Simo and Ju 1987a; Hong et al. 2017a). The resulting rate-sensitive damage formulation (a) requires one additional material parameter named the *volumetric damage fluidity coefficient* (μ_v), (b) shows instantaneous elastic behaviors when μ_v reaches zero, becomes the rate-independent volumetric damage characterization as μ_v approaches infinity, and (c) observes a decrease in the nonlinearity of the stress-strain curves with the strain rate. That is to say, the growth of microcavity, microvoid, or microcrack is retarded at low strain rates.

Rate equations governing visco-damage response are determined from the rate-independent counterpart by replacing consistency parameter $\dot{\mu}_v$ with $\mu_v g\left(\phi_v^d\right)$, and μ_v is the coefficient of volumetric damage fluidity. The scalar function $g\left(\phi_v^d\right)$ implies the flow function of viscous volumetric damage, and ϕ_v^d is defined in Eq. (23). Therefore, it becomes

$$\dot{d}_{v,t} = \mu_v \left\langle g\left(\phi_v^d\right)\right\rangle H_v\left(\xi_{v,t}, d_{v,t}\right) \tag{31}$$

$$\dot{g}_{v,t} = \mu_v \left\langle g\left(\phi_v^d\right)\right\rangle \tag{32}$$

where $\langle\cdot\rangle$ signifies the Macaulay bracket called ramp function. For simplicity, it assumes linear viscous damage; i.e., $g\left(\phi_v^d\right) = \phi_v^d$. Consequently, Eqs. (31) and (32) reduce to

$$\dot{d}_{v,t} = \mu_v \left\langle \phi_v^d\left(\xi_{v,t}, g_{v,t}\right)\right\rangle H_v\left(\xi_{v,t}, d_{v,t}\right) \tag{33}$$

$$\dot{g}_{v,t} = \mu_v \left\langle \phi_v^d\left(\xi_{v,t}, g_{v,t}\right)\right\rangle \equiv \mu_v \left\langle \xi_{v,t} - g_{v,t}\right\rangle \tag{34}$$

The characterization of inviscid volumetric damage and the behavior of instantaneous elasticity can be determined from special cases of the rate-dependent damage model. These special cases and its algorithmic treatments of visco-damage are thoroughly addressed in the next chapter.

In the same way, the equivalent deviatoric strain ξ_d is used as the energy norm of the deviatoric strain tensor, as presented in Eq. (35):

$$\xi_d \equiv \sqrt{\Psi^0(\mathbf{e})\vartheta(T)} = \sqrt{\left\{\frac{1}{2}G(\mathbf{e}:\mathbf{e})\right\}\exp\left\{-\delta\left(1-\frac{T}{T_0}\right)\right\}} \tag{35}$$

where $\mathbf{e} = \boldsymbol{\varepsilon} - \frac{1}{3}\boldsymbol{\varepsilon}_{kk}\mathbf{1}$

Similarly, the deviatoric damage state in bituminous matrix by means of a deviatoric damage criterion $\phi_d^d(\xi_{d,t}, g_{d,t}) \leq 0$ in the strain space with the functional form is characterized as follows:

$$\phi_d^d(\xi_{d,t}, g_{d,t}) \equiv \xi_{d,t} - g_{d,t} \leq 0 \qquad t \in \mathbb{R}_+ \tag{36}$$

where $g_{d,\,t}$ is the deviatoric damage threshold at the current time $t \in \mathbb{R}_+$. Note that the value of $g_{d,\,t}$ would be lowered because of the incremental deviatoric healing from the previous time step. Let $g_{d,\,0}$ signify the initial deviatoric damage threshold before any loading; it is $g_{d,\,t} \geq g_{d,\,0}$ where $g_{d,\,0}$ is regarded as a characteristic material property. The condition in Eq. (36) describes that deviatoric damage in bituminous composites is started as the deviatoric equivalent strain $\xi_{d,\,t}$ is greater than the initial deviatoric damage threshold$g_{d,\,0}$. In the case of the deviatoric damage, the evolution of the deviatoric damage variable $d_{d,\,t}$ and the deviatoric damage threshold $g_{d,\,t}$ is defined by the rate equations as follows:

$$\dot{d}_{d,t} = \dot{\mu}_d H_d(\xi_{d,t}, d_{d,t}) \tag{37}$$

$$\dot{g}_d = \dot{\mu}_d \tag{38}$$

where $\dot{\mu}_d \geq 0$ is a deviatoric damage consistency parameter defining the conditions of deviatoric damage loading/unloading based on the Kuhn-Tucker relations

$$\dot{\mu}_d \geq 0, \qquad \phi_d^d(\xi_{d,t}, g_{d,t}) \leq 0, \qquad \dot{\mu}_d\,\phi_d^d(\xi_{d,t}, g_{d,t}) = 0 \tag{39}$$

The conditions in Eq. (39) are defined as standard for problems including unilateral constraints. If $\phi_d^d(\xi_{d,t}, g_{d,t}) < 0$, the deviatoric damage criterion is not satisfied, and it becomes$\dot{\mu}_d = 0$; the deviatoric damage rule in Eq. (37) denotes that no further deviatoric damage occurs and $\dot{d}_d = 0$. In contrast, if $\dot{\mu}_d > 0$, further deviatoric damage is occurring, and it means $\phi_d^d(\xi_{d,t}, g_{d,t}) = 0$. In this event, the value of $\dot{\mu}_d$ is calculated by the condition of deviatoric damage consistency:

$$\phi_d^d\left(\xi_{d,t}, g_{d,t}\right) = \dot{\phi}_d^d\left(\xi_{d,t}, g_{d,t}\right) = 0 \Rightarrow \dot{\mu}_d = \dot{\xi}_d \tag{40}$$

and $g_{d,\,t}$ is the expression determined by Eq. (28):

$$g_{d,t} = \max\left(g_{d,0}, \max_{s\in(-\infty,t)} \xi_{d,s}\right) - g_{dh,(t-1)} \tag{41}$$

where $g_{dh,\,(t\,-\,1)}$ is the reduced value for the present deviatoric damage threshold because of the incremental deviatoric healing from the previous time step.

If $H_d(\xi_{d,\,t}, d_{d,\,t})$ in Eq. (37) is independent of $\dot{d}_{d,t}$, the above equations can be modified as follows. Let $G_d : \mathbb{R} \to \mathbb{R}_+$ be so that $H_d(\xi_{d,\,t}) \equiv \partial G_d(\xi_{d,\,t})/\partial \xi_{d,\,t}$. It is noted that $G_d(\cdot)$ defines a monotonic function. A damage criterion, which is equivalent to condition in Eq. (23), is provided by $\overline{\phi}_d^d\left(\xi_{d,t}, g_{d,t}\right) \equiv G_d\left(\xi_{d,t}\right) - G_d\left(g_{d,t}\right) \leq 0$. The flow rule and the loading/unloading conditions are as follows:

$$\dot{d}_{d,t} = \dot{\mu}\frac{\partial \overline{\phi}_d^d\left(\xi_{d,t}, g_{d,t}\right)}{\partial \xi_{d,t}}, \qquad g_{d,t} = \dot{\mu}_d \tag{42}$$

$$\dot{\mu}_d \geq 0, \qquad \overline{\phi}_d^d\left(\xi_{d,t}, g_{d,t}\right) \leq 0, \qquad \dot{\mu}_d \overline{\phi}_d^d\left(\xi_{d,t}, g_{d,t}\right) = 0 \tag{43}$$

Conditions in Eqs. (42) and (43) are the Kuhn-Tucker optimality conditions from the maximum deviatoric damage dissipation principle.

Similar to the rate-dependent volumetric damage formulation, the rate-sensitive deviatoric damage formulation (a) requires one additional material parameter called the *deviatoric damage fluidity coefficient* (μ_d), (b) demonstrates instantaneous elastic response as μ_d reaches zero, becomes the rate-independent deviatoric damage characterization as μ_d reaches infinity, and (c) observes a decrease in the nonlinearity of the stress-strain curves with increasing the strain rate. That is, the growth of microcavity, microvoid, or microcrack is retarded at low strain rates.

Rate equations governing visco-damage response are determined from their rate-independent counterpart by replacing consistency parameter $\dot{\mu}_d$ with $\mu_d g\left(\phi_d^d\right)$, and μ_d is the coefficient of deviatoric damage fluidity. The scalar function $g\left(\phi_v^d\right)$ denotes the flow function of viscous deviatoric damage and ϕ_d^d is defined in Eq. (36). Therefore, it becomes

$$\dot{d}_{d,t} = \mu_d \left\langle g\left(\phi_d^d\right)\right\rangle H_d\left(\xi_{d,t}, d_{d,t}\right) \tag{44}$$

$$\dot{g}_{d,t} = \mu_d \left\langle g\left(\phi_d^d\right)\right\rangle \tag{45}$$

where $\langle\cdot\rangle$ implies the Macaulay bracket named ramp function. For simplicity, it assumes linear viscous damage; i.e., $g(\phi^d) = \phi^d$. Consequently, Eqs. (44) and (45) reduce to

$$\dot{d}_{d,t} = \mu \langle \phi_d^d(\xi_{d,t}, g_{d,t}) \rangle H_d(\xi_{d,t}, d_{d,t}) \tag{46}$$

$$\dot{g}_{d,t} = \mu_d \langle \phi_d^d(\xi_{d,t}, g_{d,t}) \rangle \equiv \mu_d \langle \xi_{d,t} - g_{d,t} \rangle \tag{47}$$

The characterization of inviscid deviatoric damage and the behavior of instantaneous elasticity can be determined from special cases of the rate-dependent deviatoric damage model. These special cases and its algorithmic treatments of visco-damage are clearly rendered in the next chapter.

Characterization of Initial Elastic Strain Energy-Based Volumetric and Deviatoric Healing

Analogous to the volumetric and deviatoric damage characterization in the above section, the progressive recovery of bituminous composites because of healing by means of a simple volumetric and deviatoric healing mechanism is characterized in this section.

The same notion of equivalent volumetric strain ξ_v is defined as the energy norm of the volumetric strain tensor, as shown in Eq. (22). The volumetric healing state in asphalt by using a volumetric healing criterion $\phi_v^h(\xi_{v,t}, r_{v,t}) \leq 0$ in the strain space with the functional form is defined as follows:

$$\phi_v^h(\xi_{v,t}, r_{v,t}) \equiv r_{v,t} - \xi_{v,t} \leq 0, \qquad t \in \mathbb{R}_+ \tag{48}$$

where $r_{v,\,t}$ is the volumetric healing threshold at the current time t. It is noted that the value of $r_{v,\,t}$ would be lowered because of the incremental volumetric damage from the previous time step. If $r_{v,\,0}$ implies the initial volumetric healing threshold before any volumetric healing increases, it becomes $r_{v,\,t} \geq r_{v,\,0}$ where $r_{v,\,0}$ is regarded as a characteristic material property. The above condition in Eq. (48) describes that healing in the substance is started as the volumetric equivalent strain $\xi_{v,\,t}$ is smaller than the initial volumetric healing threshold $r_{v,\,0}$. For the deviatoric healing case, the evolution of the volumetric healing variable R_v and the volumetric healing threshold $r_{v,\,t}$ is characterized by the rate equations:

$$\dot{R}_{v,t} = \dot{\zeta}_v Z_v(\xi_{v,t}, R_{v,t}) \tag{49}$$

$$\dot{r}_v = \dot{\zeta}_v \tag{50}$$

where $\dot{\zeta}_v \geq 0$ is a volumetric healing consistency parameter defining the conditions of volumetric healing loading/unloading based on the Kuhn-Tucker relations

$$\dot{\zeta}_v \geq 0, \qquad \phi_v^h(\xi_{v,t}, r_{v,t}) \leq 0, \qquad \dot{\zeta}_v \, \phi_v^h(\xi_{v,t}, r_{v,t}) = 0 \tag{51}$$

The conditions in Eq. (51) are considered as standard for problems including unilateral constraints. If $\phi_v^h(\xi_{v,t}, r_{v,t}) < 0$, the volumetric healing criterion is not satisfied, and it becomes $\dot{\zeta}_v = 0$; the healing rule in Eq. (49) denotes that no further volumetric healing is occurring and $\dot{R}_v = 0$. In contrast, if $\dot{\zeta}_v > 0$, further volumetric

healing is occurring, and it signifies $\phi_v^h(\xi_{v,t}, r_{v,t}) \leq 0$. In this event, $\dot{\zeta}_v$ is calculated by the condition of volumetric healing consistency:

$$\phi_v^h(\xi_{v,t}, r_{v,t}) = \dot{\phi}_v^h(\xi_{v,t}, r_{v,t}) = 0 \Rightarrow \dot{\zeta}_v = \dot{\xi}_v \tag{52}$$

and $r_{v,\,t}$ is provided by the following expression in Eq. (53):

$$r_{v,t} = \min\left(r_{v,0}, \min_{s \in (-\infty, t)} \xi_{v,s}\right) + r_{vd,(t-1)} \tag{53}$$

where $r_{vd,\,(t\,-\,1)}$ is the value for the present volumetric healing threshold to be increased because of the incremental volumetric damage from the previous time step.

If $Z_v(\xi_{v,\,t},\, R_{v,\,t})$ in Eq. (49) is independent of $\dot{R}_{v,t}$, the above formulation may be modified as follows. Let $G^* : \mathbb{R} \to \mathbb{R}_+$ be so that $Z_v(\xi_{v,t}) \equiv -\partial G_v^*(\xi_{v,t})/\partial \xi_{v,t}$. It is noted that $G_v^*(\cdot)$ defines a monotonic function. A volumetric healing criterion, which is equivalent to the condition in Eq. (48) is given by $\overline{\phi}_v^h(\xi_{v,t}, r_{v,t}) \equiv G_v^*(r_{v,t}) - G_v^*(\xi_{v,t}) \leq 0$. The flow rule and loading/unloading conditions are determined as follows:

$$\dot{R}_{v,t} = \dot{\zeta}_v \frac{\partial \overline{\phi}_v^h(\xi_{v,t}, r_{v,t})}{\partial \xi_{v,t}}, \qquad r_{v,t} = \dot{\zeta}_v \tag{54}$$

$$\dot{\zeta}_v \geq 0, \qquad \overline{\phi}_v^h(\xi_{v,t}, r_{v,t}) \leq 0, \qquad \dot{\zeta}_v \overline{\phi}_v^h(\xi_{v,t}, r_{v,t}) = 0 \tag{55}$$

In the same way, the equivalent deviatoric strain energy ξ_d is defined as the energy norm of the deviatoric strain tensor. The deviatoric healing state in bituminous composites by means of a deviatoric healing criterion $\phi_d^h(\xi_{d,t}, r_{d,t}) \leq 0$ in the strain space with the functional form is characterized as follows:

$$\phi_d^h(\xi_{d,t}, r_{d,t}) \equiv r_{d,t} - \xi_{d,t} \leq 0 \qquad t \in \mathbb{R}_+ \tag{56}$$

where $r_{d,\,t}$ defines the deviatoric healing threshold at the current time t. It is noted that the value of $r_{d,\,t}$ will be lowered because of the incremental deviatoric damage from the previous time step. Let $r_{d,\,0}$ denote the initial deviatoric healing threshold before any healing occurs; it is $r_{v,\,t} \geq r_{v,\,0}$ where $r_{v,\,0}$ is regarded as a characteristic material property. The condition in Eq. (56) describes that deviatoric healing in the material begins as the deviatoric equivalent strain $\xi_{v,\,t}$ is smaller than the initial deviatoric healing threshold $r_{d,\,0}$. The evolution of the deviatoric healing variable R_d and the deviatoric healing threshold $r_{d,\,t}$ is defined by the rate equations in Eq. (57):

$$\dot{R}_{d,t} = \dot{\zeta}_d Z_d(\xi_{d,t}, R_{d,t}) \tag{57}$$

$$\dot{r}_d = \dot{\zeta}_d \tag{58}$$

where $\dot{\zeta}_d \geq 0$ is a deviatoric healing consistency parameter defining the conditions of deviatoric healing loading/unloading based on the Kuhn-Tucker relations

$$\dot{\zeta}_d \geq 0, \qquad \phi_d^h\left(\xi_{d,t}, r_{d,t}\right) \leq 0, \quad \dot{\zeta}_d \, \phi_d^h\left(\xi_{d,t}, r_{d,t}\right) = 0 \tag{59}$$

The conditions in Eq. (59) are regarded as standard for problems including unilateral constraint. If $\phi_d^h\left(\xi_{d,t}, r_{d,t}\right) < 0$, the deviatoric healing criterion is not satisfied, and it becomes $\dot{\zeta}_d = 0$; the deviatoric healing rule in Eq. (57) signifies that no further deviatoric healing occurs and $\dot{R}_d = 0$. In contrast, if $\dot{\zeta}_d > 0$, further deviatoric healing is occurring, it means $\phi_d^h\left(\xi_{d,t}, r_{d,t}\right) \leq 0$. The value of $\dot{\zeta}_d$ is calculated by the condition of deviatoric healing consistency:

$$\phi_d^h\left(\xi_{d,t}, r_{d,t}\right) = \dot{\phi}_d^h\left(\xi_{d,t}, r_{d,t}\right) = 0 \Rightarrow \dot{\zeta}_d = \dot{\xi}_d \tag{60}$$

and $r_{d,\,t}$ is provided by the expression in Eq. (61):

$$r_{d,t} = \min\left(r_{d,0}, \min_{s \in (-\infty, t)} \xi_{d,s}\right) + r_{dd,(t-1)} \tag{61}$$

where $r_{dd,\,(t\,-\,1)}$ is the value for the present deviatoric healing threshold to be increased because of the incremental damage from the previous time step.

If $Z_d(\xi_{d,\,t}, R_{d,\,t})$ in Eq. (57) is independent of $\dot{R}_{d,t}$, the above equation may be modified as follows. Let $G_d^* : \mathbb{R} \to \mathbb{R}_+$ be so that $Z_d\left(\xi_{d,t}\right) \equiv -\partial G_d^*\left(\xi_{d,t}\right)/\partial \xi_{d,t}$. It is assumed that $G_d^*(\cdot)$ defines a monotonic function. A deviatoric healing criterion, which is equivalent to conditions in Eq. (56), is provided by $\overline{\phi}_d^h\left(\xi_{d,t}, r_{d,t}\right) \equiv G_d^*(r_{d,t}) - G_d^*\left(\xi_{d,t}\right) \leq 0$. The flow rule and loading/unloading conditions are as follows:

$$\dot{R}_{d,t} = \dot{\zeta}_d \frac{\partial \overline{\phi}_d^h\left(\xi_{d,t}, r_{d,t}\right)}{\partial \xi_{d,t}}, \qquad r_{d,t} = \dot{\zeta}_d \tag{62}$$

$$\dot{\zeta}_d \geq 0, \qquad \overline{\phi}_d^h\left(\xi_{d,t}, r_{d,t}\right) \leq 0, \quad \dot{\zeta}_d \overline{\phi}_d^h\left(\xi_{d,t}, r_{d,t}\right) = 0 \tag{63}$$

Net (Combined) Effect of the Volumetric and Deviatoric Damage and Healing

Taking the time derivative of Eq. (2) could yield

$$\dot{d}_v = \dot{A}_v^d / A_v \tag{64}$$

Because the derivations are determined according to the linearization of the residual functions related to the implicit backward Euler algorithms, the equation can be transformed to the incremental form for the volumetric damage variable, as shown in Eq. (65):

$$d_{v,n+1} = d_{v,n} + \Delta d_{v,n+1} \tag{65}$$

Since volumetric healing does not take place during the volumetric damage process or vice versa, the same process can be conducted under the no volumetric damage evaluation that occurred to determine the incremental form of volumetric healing variable. However, because the volumetric healed area A_v^h and the volumetric damaged area $A_v^d = A_v^h + A_v^{uR}$ are updated during the volumetric damage procedure, the changed volumetric healing variable can be reduced by a ratio of volumetric damage variables. Hence, the changed volumetric healing variable could be determined by the following equations:

$$R_{v,n+1} = R_{v,n} + \Delta R_{v,n+1} \quad (\Delta d_{v,n+1} = 0) \tag{66}$$

$$R_{v,n+1} = \frac{d_{v,n+1}}{2d_{v,n+1} - d_{v,n}} R_{v,n} \quad (\Delta d_{v,n+1} > 0) \tag{67}$$

Taking the time derivative of (5) would lead to

$$\begin{aligned} d_{v,n+1}^{net} &= d_{v,n}^{net} + \Delta d_{v,n+1}^{net} \\ \Delta d_{v,n+1}^{net} &= \Delta d_{v,n+1} - \Delta R_{v,n+1} d_{v,n}^{net} \end{aligned} \tag{68}$$

Taking the time derivative of Eq. (7) would yield

$$\dot{d}_d = \dot{A}_d^d / A_d \tag{69}$$

Since the derivations are calculated according to the linearization of the residual functions related to the implicit backward Euler algorithms, the equation can be transformed to the following incremental form for the deviatoric damage variable, as demonstrated in Eq. (70):

$$d_{v,n+1} = d_{v,n} + \Delta d_{v,n+1} \tag{70}$$

Because deviatoric healing does not take place during the deviatoric damage process or vice versa, the same process can be performed under the no deviatoric damage evaluation that occurred to determine the incremental form of deviatoric healing variable. However, because the deviatoric healed area A_d^h and the deviatoric damaged area $A_d^d = A_d^h + A_d^{uR}$ are updated during the deviatoric damage procedure, the changed deviatoric healing variable can be reduced by a ratio of deviatoric damage variables. Hence, the updated deviatoric healing variable would yield

$$R_{d,n+1} = R_{d,n} + \Delta R_{d,n+1} \quad (\Delta d_{d,n+1} = 0) \tag{71}$$

$$R_{d,n+1} = \frac{d_{d,n+1}}{2d_{d,n+1} - d_{d,n}} R_{d,n} \quad (\Delta d_{d,n+1} > 0) \tag{72}$$

Taking the time derivative of (9) would lead to

$$d^{net}_{d,n+1} = d^{net}_{d,n} + \Delta d^{net}_{d,n+1}$$
$$\Delta d^{net}_{d,n+1} = \Delta d_{d,n+1} - \Delta R_{d,n+1} d^{net}_{d,n} \tag{73}$$

Once $d^{net}_{v,n+1}$ and $d^{net}_{d,n+1}$ are determined, the fourth-rank damage net tensor can be updated and obtained by Eq. (13).

A Conceptual Illustration

For conceptual example, let us consider the eight-spring system as displayed in Fig. 3 and conduct a series of cyclic tension-rest period (total four steps: T1-R1-T2-R2) tests on this system.

This conceptual example does not directly denote that the volumetric and deviatoric systems are in the y-direction in the x-direction, respectively, since the volumetric and deviatoric parts are only orthogonal in hyperspace. However, the horizontal and vertical springs are linearly independent signifying that they do not affect each other so that this is a good conceptual example for a two-parameter model. Hence, the vertical and horizontal springs are employed to represent the volumetric and deviatoric part, respectively. It is assumed that the vertical and horizontal springs can be damaged or broken under the vertical and horizontal tensions, respectively, and damaged vertical and horizontal springs can be recovered or healed during the rest periods in the same manner. The first step is that both vertical and horizontal tension (T1) loadings are applied to the system of eight springs, and two springs of each part are broken. The volumetric and deviatoric damage variables of the system are determined to be $2/4 = 0.5$ in Fig. 4a. As the system has the rest period R1 at the second step, two springs are recovered in Fig. 4b. Because one of the broken springs is healed, the volumetric and deviatoric healing variables of the system are calculated to be $1/2 = 0.5$, respectively, and the net volumetric and deviatoric damage-healing variables of the system are then determined to be $1/4 = 0.25$, respectively. Next, as the vertical and horizontal tension

Fig. 3 Eight-spring system

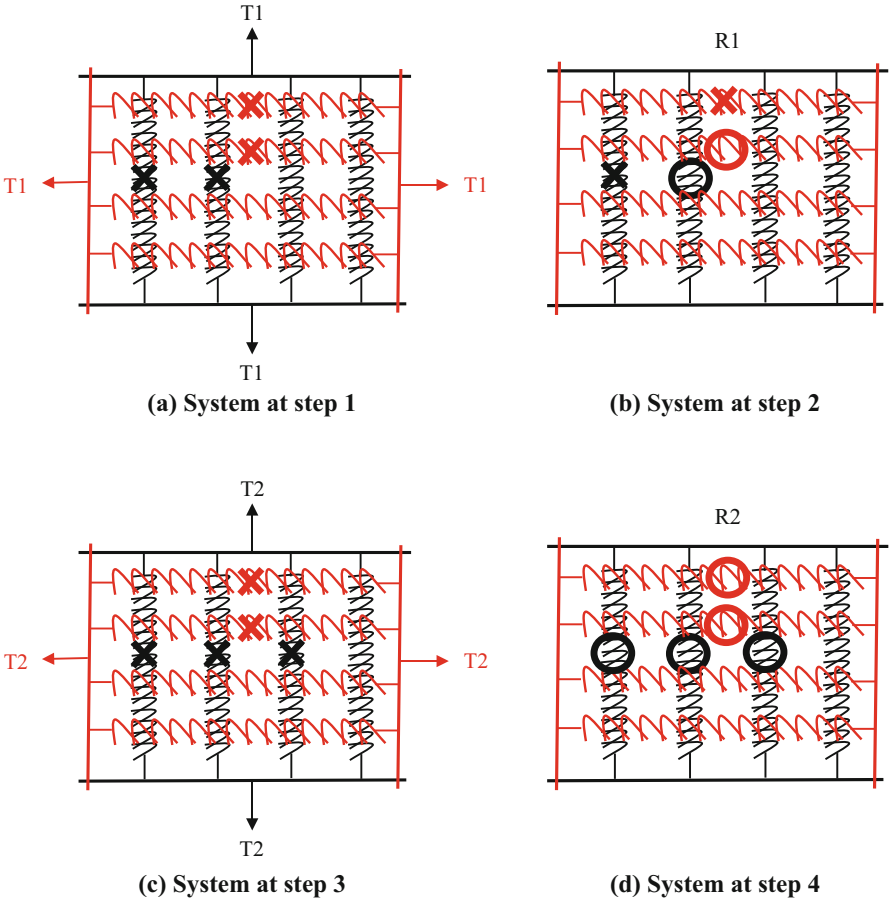

Fig. 4 The associated damage and healing variables of the four-spring system at each step

(T2) loadings are applied, three springs of the vertical springs are damaged, and only two of the horizontal springs are broken. Therefore, the net volumetric and deviatoric damage-healing variables are calculated to be $3/4 = 0.75$ and $2/4 = 0.5$, respectively. At the last step, all damaged springs are completely recovered and repaired during the rest period R2. The volumetric and deviatoric healing variables are determined to be $3/3 = 1$, and the net volumetric and deviatoric damage-healing variables are then calculated to be all zero. Figure 4 shows the computations of the net volumetric and deviatoric damage-healing variables at each time step summarized in Tables 1 and 2. The two-parameter damage and healing characterizations can be regarded as the *predictor formula* in the two-parameter damage-healing algorithms. Once the associated two-parameter damage or healing variables are determined at the time step n + 1 (due to a fact that the two-parameter damage and healing will not occur at the same time step), the net volumetric and deviatoric damage-healing variables at the

Table 1 The computation of d_v^{net} at different time steps

Step	$\Delta d_{v,\ n\ +\ 1}$	$d_{v,\ n\ +\ 1}$	$\Delta R_{v,\ n\ +\ 1}$	$R_{v,\ n\ +\ 1}$	$\Delta d_{v,n+1}^{net}$	$d_{v,n+1}^{net}$
1	$\frac{2}{4}$	$\frac{2}{4}$	0	0	$\frac{2}{4}$	$\frac{2}{4}$
2	0	$\frac{2}{4}$	$\frac{1}{2}$	$\frac{1}{2}$	$-\frac{1}{4}$	$\frac{1}{4}$
3	$\frac{2}{4}$	$\frac{4}{4}$	0	$\frac{1}{3}$	$\frac{2}{4}$	$\frac{3}{4}$
4	0	$\frac{4}{4}$	$\frac{3}{3}$	$\frac{4}{3}$	$-\frac{3}{4}$	0

Table 2 The computation of d_d^{net} at different time steps

Step	$\Delta d_{d,\ n\ +\ 1}$	$d_{d,\ n\ +\ 1}$	$\Delta R_{d,\ n\ +\ 1}$	$R_{d,\ n\ +\ 1}$	$\Delta d_{d,n+1}^{net}$	$d_{d,n+1}^{net}$
1	$\frac{2}{4}$	$\frac{2}{4}$	0	0	$\frac{2}{4}$	$\frac{2}{4}$
2	0	$\frac{2}{4}$	$\frac{1}{2}$	$\frac{1}{2}$	$-\frac{1}{4}$	$\frac{1}{4}$
3	$\frac{1}{4}$	$\frac{3}{4}$	0	$\frac{3}{8}$	$\frac{1}{4}$	$\frac{2}{4}$
4	0	$\frac{3}{4}$	$\frac{2}{2}$	$\frac{11}{8}$	$-\frac{2}{4}$	0

time step n + 1 are eventually determined. More detailed algorithms of the coupling damage and healing variables are provided in Part II.

Conclusions

The elastic strain energy-based thermo-elastoviscoplastic volumetric and deviatoric damage self-healing models are described. The net space concepts with two-parameter, the Arrhenius-type temperature term, and characterizations of initial-elastic strain energy-based volumetric and deviatoric damage and self-healing formulations are comprehensively shown. The equivalent two-parameter strain energy is uncoupled with the Arrhenius temperature term for the temperature effect because for simplicity the Arrhenius-type temperature term is uncoupled with Helmholtz free energy potential. Particularly, the governing incremental volumetric and deviatoric damage and healing evolutions are coupled and characterized through the net stress concept in conjunction with the hypothesis of strain equivalence. The conceptual illustration based on the eight-spring system is presented for the proposed governing incremental evolutions of damage and healing. A rate-dependent volumetric and deviatoric damage-self healing formulation is used by mimicking the Perzyna-type viscoplasticity for the rate sensitivity of asphalt concrete matrix. Due to viscoplastic and hydrostatic dependent behavior, the Drucker-Prager yield function and Perzyna-type formulation are used in the proposed net space. Completely innovative computational algorithms with the two-step *operator splitting* methodology are developed in the next chapter (Part II). Furthermore, to validate the developed two-parameter damage-healing formulation, experimental data and computational predictions are compared. It is found that the developed constitutive formulation well predicts the nonlinear response of asphalt concretes under the different loading conditions with different temperatures.

Appendix

1. The proposed definition of physical stress tensor without the Arrhenius-type temperature term in Eq. (12) leads to

$$
\begin{aligned}
&\left(\mathbf{I}-\mathbf{D}^{net}\right):\boldsymbol{\sigma}^{net}\\
&=\left(\mathbf{I}-\mathbf{D}^{net}\right):\left(p^{net}\mathbf{1}+\mathbf{s}^{net}\right)=\left(p^{net}\mathbf{1}+\mathbf{s}^{net}\right)-\mathbf{D}^{net}:\left(p^{net}\mathbf{1}+\mathbf{s}^{net}\right)\\
&=\left(p^{net}\mathbf{1}+\mathbf{s}^{net}\right)-\left(\frac{1}{3}d_v^{net}\mathbf{1}\otimes\mathbf{1}+d_d^{net}\left(\mathbf{I}-\frac{1}{3}\mathbf{1}\otimes\mathbf{1}\right)\right):\left(p^{net}\mathbf{1}+\mathbf{s}^{net}\right)\\
&=\left(p^{net}\mathbf{1}+\mathbf{s}^{net}\right)-\left(d_v^{net}p^{net}\mathbf{1}+d_d^{net}p^{net}\left(\mathbf{1}-\frac{1}{3}3\mathbf{1}\right)+d_d^{net}\mathbf{s}^{net}\right)\\
&=\left(1-d_v^{net}\right)p^{net}\mathbf{1}+\left(1-d_d^{net}\right)\mathbf{s}^{net}\\
&=\left(1-d_v^{net}\right)\boldsymbol{\sigma}_v^{net}+\left(1-d_d^{net}\right)\boldsymbol{\sigma}_d^{net}
\end{aligned}
$$

where $\mathbf{D}^{net}=\frac{1}{3}d_v^{net}\mathbf{1}\bigotimes\mathbf{1}+d_d^{net}\left(\mathbf{I}-\frac{1}{3}\mathbf{1}\bigotimes\mathbf{1}\right)$ and $\sigma^{net}=\sigma_v^{net}+\sigma_d^{net}=p^{net}\mathbf{1}+\mathbf{s}^{net}$.

2. The proposed free energy potential for the two-parameter formulation reads (Eq. (14))

$$
\Psi\left(\boldsymbol{\varepsilon}_{\mathrm{v}},\mathbf{e},\boldsymbol{\sigma}^{vp},\mathbf{q},d_v^{net},d_d^{net},T\right)\equiv\left\{\left(1-d_v^{net}\right)\Psi_v^0(\boldsymbol{\varepsilon}_{\mathrm{v}})+\left(1-d_d^{net}\right)\Psi_d^0(\mathbf{e})-\frac{1}{2}\boldsymbol{\varepsilon}:\boldsymbol{\sigma}^{vp}+\Xi(\mathbf{q},\boldsymbol{\sigma}^{vp})\right\}\vartheta(T)
$$

Take the derivative of $\Psi\left(\boldsymbol{\varepsilon}_{\mathrm{v}},\mathbf{e},\boldsymbol{\sigma}^{vp},\mathbf{q},d_v^{net},d_d^{net},T\right)$, we obtain

$$
\begin{aligned}
\dot{\Psi}&=\left\{\begin{array}{l}-\dot{d}_v^{net}\Psi_v^0(\boldsymbol{\varepsilon}_{\mathrm{v}})+\left(1-d_v^{net}\right)\dot{\Psi}_v^0(\boldsymbol{\varepsilon}_{\mathrm{v}})-\dot{d}_d^{net}\Psi_d^0(\mathbf{e})+\left(1-d_d^{net}\right)\dot{\Psi}_d^0(\mathbf{e})\\ -\frac{1}{2}\dot{\boldsymbol{\varepsilon}}:\boldsymbol{\sigma}^{vp}-\frac{1}{2}\boldsymbol{\varepsilon}:\dot{\boldsymbol{\sigma}}^{vp}+\dot{\Xi}(\mathrm{q},\boldsymbol{\sigma}^{vp})\end{array}\right\}\vartheta(T)\\
&\quad+\dot{\vartheta}(T)\Psi\left(\boldsymbol{\varepsilon}_{\mathrm{v}},\mathbf{e},\boldsymbol{\sigma}^{p},\mathbf{q},d_v^{net},d_d^{net}\right)\\
&=\left\{\begin{array}{l}-\dot{d}_v^{net}\Psi_v^0(\boldsymbol{\varepsilon}_{\mathrm{v}})+\left(1-d_v^{net}\right)\frac{\partial\Psi_v^0(\boldsymbol{\varepsilon}_{\mathrm{v}})}{\partial\boldsymbol{\varepsilon}_{\mathrm{v}}}:\dot{\boldsymbol{\varepsilon}}_{\mathrm{v}}-\dot{d}_d^{net}\Psi_d^0(\mathbf{e})+\left(1-d_d^{net}\right)\frac{\partial\Psi_d^0(\mathbf{e})}{\partial\mathbf{e}}:\dot{\mathrm{e}}\\ -\frac{1}{2}(\dot{\boldsymbol{\varepsilon}}_{\mathbf{v}}+\dot{\mathbf{e}}):\boldsymbol{\sigma}^{vp}-\frac{1}{2}\boldsymbol{\varepsilon}:\dot{\boldsymbol{\sigma}}^{vp}+\frac{\partial\Xi(\mathbf{q},\boldsymbol{\sigma}^{vp})}{\partial\mathrm{q}}\cdot\dot{\mathrm{q}}+\frac{\partial\Xi(\mathbf{q},\boldsymbol{\sigma}^{vp})}{\partial\boldsymbol{\sigma}^{vp}}:\dot{\boldsymbol{\sigma}}^{vp}\end{array}\right\}\vartheta(T)\\
&\quad+\frac{\partial\vartheta(T)}{T}\dot{T}\,\Psi\left(\boldsymbol{\varepsilon}_{\mathrm{v}},\mathbf{e},\boldsymbol{\sigma}^{p},\mathbf{q},d_v^{net},d_d^{net}\right)
\end{aligned}
$$

Substitute $\dot{\Psi}$ into the following Clausius-Plank inequality $-s\dot{T}-\dot{\Psi}+\boldsymbol{\sigma}:\dot{\boldsymbol{\varepsilon}}\geq 0$. We then have

$$\left\{\dot{d}_v^{net}\Psi_v^0(\boldsymbol{\varepsilon}_{\mathrm{v}}) + \dot{d}_d^{net}\Psi_d^0(\mathbf{e}) - \frac{\partial\Xi(\mathbf{q},\boldsymbol{\sigma}^{vp})}{\partial \mathrm{q}}\cdot\dot{\mathbf{q}} - \left(\frac{\partial\Xi(\mathbf{q},\boldsymbol{\sigma}^{vp})}{\partial\boldsymbol{\sigma}^{vp}} - \frac{1}{2}\boldsymbol{\varepsilon}\right) : \dot{\boldsymbol{\sigma}}^{vp}\right\}\vartheta(T) \geq 0$$

$$\boldsymbol{\sigma}_v = \left\{\left(1 - d_v^{net}\right)\frac{\partial\Psi_v^0(\boldsymbol{\varepsilon}_{\mathrm{v}})}{\partial\boldsymbol{\varepsilon}_{\mathrm{v}}} - \frac{1}{2}\boldsymbol{\sigma}^{vp}\right\}\vartheta(T)$$

$$\boldsymbol{\sigma}_d = \left\{\left(1 - d_d^{net}\right)\frac{\partial\Psi_d^0(\mathbf{e})}{\partial\mathbf{e}} - \frac{1}{2}\boldsymbol{\sigma}^{vp}\right\}\vartheta(T)$$

$$\boldsymbol{\sigma} = \boldsymbol{\sigma}_v + \boldsymbol{\sigma}_d = \left\{\left(1 - d_v^{net}\right)\frac{\partial\Psi_v^0(\boldsymbol{\varepsilon}_{\mathrm{v}})}{\partial\boldsymbol{\varepsilon}_{\mathrm{v}}} + \left(1 - d_d^{net}\right)\frac{\partial\Psi_d^0(\mathbf{e})}{\partial\mathbf{e}} - \boldsymbol{\sigma}^{vp}\right\}\vartheta(T)$$

References

R.K. Abu Al-Rub, M.K. Darabi, D.N. Little, E.A. Masad, A. Micro, Damage healing model that improves prediction of fatigue life in asphalt mixes. Int. J. Eng. Sci. **48**(11), 966–990 (2010)

E.J. Barbero, F. Greco, P. Lonetti, Continuum damage-healing mechanics with application to self-healing composites. Int. J. Damage Mech. **14**(1), 51–81 (2005)

J. Betten, Damage tensors in continuum mechanics. J. MecaniqueTheorique et Appliquees **2**, 13–32 (1981)

J. Betten, Applications of tensor functions to the formulation of continuative equations involving damage and initial anisotropy. Eng. Fract. Mech. **25**, 573–584 (1986)

A. Bhasin, D.N. Little, R. Bommavaram, K. Vasconcelos, A framework to quantify the effect of healing in bituminous materials using material properties. Road Mater. Pavement Des. **9**, 219–242 (2008)

E.N. Brown, N.R. Sottos, S.R. White, Fracture testing of a self-healing polymer composite. Exp. Mech. **42**, 372–379 (2002)

S. H. Carpenter, S. Shen, Dissipated energy approach to study HMA healing in fatigue, Transportation Research Record: Journal of the Transportation Research Board, No. 1970, Transportation Research Board on the National Academies Washington DC, 178–185 (2006)

J.L. Chaboche, Thermodynamic formulation of constitutive equations and application to the viscoplasticity and viscoelasticity of metals and polymers. Int. J. Solid Struct. **34**, 2239–2254 (1996)

C.L. Chow, J. Wang, Ductile fracture characterization with an anisotropic continuum damage theory. Eng. Fract. Mech. **30**, 547–563 (1988)

B.D. Coleman, M.E. Gurtin, Thermodynamics with internal state variables. J. Chem. Phys. **47**, 597–613 (1967)

J.S. Daniel, Y.R. Kim, Laboratory evaluation of fatigue damage and healing of asphalt mixtures. J. Mater. Civ. Eng. ASCE **13**(6), 434–440 (2001)

M.K. Darabi, R.K. Abu Al-Rub, E.A. Masad, D.N. Little, Constitutive modeling of fatigue damage response of asphalt concrete materials with consideration of micro-damage healing. Int. J. Solids Struct. **50**, 2901–2913 (2013)

E. Ghorbel, A viscoplastic constitutive model for polymeric materials. Int. J. Plast. **24**, 2032–2058 (2008)

S.K. Ghosh, *Self-healing Materials: Fundamentals, Design Strategies, and Applications* (Wiley-VCH, Weinheim, 2009)

Y.F. Guo, W.L. Guo, Self-healing properties of flaws in nanoscale materials: Effects of soft and hard molecular dynamics simulations and boundaries studied using a continuum mechanical model. Phys. Rev. B **73**(1–7) (2006)

O. Herbst, S. Luding, Modeling particulate self-healing materials and application to uni-axial compression. Int. J. Fract. **154**, 87–103 (2008)

S. Hong, K.Y. Yuan, J.W. Ju, Innovative strain energy based thermo-elastoviscoplastic damage-self healing models for bituminous composites – Part I: Formulations. Int. J. Damage Mech. (2017a). https://doi.org/10.1177/1056789515610706

S. Hong, K.Y. Yuan, J.W. Ju, Innovative strain energy based thermo-elastoviscoplastic damage-self healing models for bituminous composites – Part II: computational aspects. Int. J. Damage Mech. (2017b). https://doi.org/10.1177/1056789515610707

M. Huang, P.E.J. Rivera-Díaz-del-Castillo, O. Bouaziz, S. van der Zwaag, A constitutive model for high strain rate deformation in FCC metals based on irreversible thermodynamics. Mech. Mater. **41**(9), 982–988 (2009)

J.W. Ju, On energy-based coupled elastoplastic damage theories-constitutive modeling and computational aspects. Int. J. Solids Struct. **25**, 803–833 (1989a)

J.W. Ju, On energy-based coupled elastoplastic damage models at finite strains. J. Eng. Mech. ASCE **115**, 2507–2525 (1989b)

J.W. Ju, Isotropic and anisotropic damage variables in continuum damage mechanics. J. Eng. Mech. ASCE **116**, 2764–2770 (1990)

J.W. Ju, K.Y. Yuan, New strain-energy-based coupled elastoplastic two-parameter damage and healing models for earth-moving processes. Int. J. Damage Mech. **21**(7), 989–1019 (2012)

J.W. Ju, K.Y. Yuan, W. Kuo, Novel strain energy based coupled elastoplastic damage and healing models for geomaterials – Part I: Formulations. Int. J. Damage Mech. **21**(4), 525–549 (2012a)

J.W. Ju, K.Y. Yuan, W. Kuo, J.S. Chen, Novel strain energy based coupled elastoplastic damage and healing models for geomaterials – Part II: Computational aspects. Int. J. Damage Mech. **21**(4), 551–576 (2012b)

L.M. Kachanov, Rupture time under creep conditions. IzvestiaAkademiiNauk SSSR, Otdelenie-TekhnicheskichNauk **8**, 26–31 (1958)

M. Kachanov, Continuum model of medium with cracks. J. Eng. Mech. Div. ASCE **106**, 1039–1051 (1980)

M.R. Kessler, Self-healing: A new paradigm in materials design. Proc. Inst. Mech. Eng. Part G-J Aerosp. Eng. **221**, 479–495 (2007) Institution of Mechanical Engineers (Great Britain), Sage Publications

M.R. Kessler, S.R. White, Self-activated healing of delamination damage in woven composites. Compos. A Appl. Sci. Manuf. **32**, 683–699 (2001)

Y.R. Kim, S.L. Whitmoyer, D.N. Little, Healing in asphalt concrete pavements: Is it real? Transp. Res. Board **1454**, 89–96 (1994)

U.F. Kocks, Realistic constitutive relations for metal plasticity. Mater. Sci. Eng. **317**(1–2), 181–187 (2001)

H.J. Lee, Y.R. Kim, Viscoelastic continuum damage model of asphalt concrete with healing. J. Eng. Mech. ASCE **124**(11), 1224–1232 (1998)

D.N. Little, A. Bhasin, Exploring mechanisms of healing in asphalt mixtures and quantifying its impact. In, in *Self Healing Materials*, ed. by S. van der Zwaag, (Springer, Dordrecht, 2007)

Y. Liu, K. Gall, M.L. Dunn, A.R. Greenberg, J. Diani, Thermomechanics of shape memory polymers uniaxial experiments and constitutive modeling. Int. J. Plast. **22**, 279–313 (2006)

R. L. Lytton, C.W. Chen, D.N. Little, Microdamage Healing in Asphalt and Asphalt Concrete, Volume IV: A Viscoelastic Continuum Damage Fatigue Model of Asphalt Concrete With Microdamage Healing, FHWA-RD-98-144, College Station, Texas, Texas Transportation Institute, the Texas A&M University System (2001)

S. Miao, M.L. Wang, H.L. Schreyer, Constitutive models for healing of materials with application to compaction of crushed rock-salt. J. Eng. Mech. ASCE **121**, 1122–1129 (1995)

S. Murakami, K. Kamiya, Constitutive and damage evolution equations of elastic-brittle materials based on irreversible thermodynamics. Int. J. Mech. Sci. **39**, 473–486 (1996)

H.W. Reinhardt, M. Jooss, Permeability and self-healing of cracked concrete as a function of temperature and crack width. Cem. Concr. Res. **33**, 981–985 (2003)

P. Rosakis, A.J. Rosakis, G. Ravichandran, J. Hodowany, A thermodynamic internal variable model for the partition of plastic work into heat and stored energy in metals. J. Mech. Phys. Solids **48**, 581–607 (2000)

R.A. Schapery, Nonlinear viscoelastic and viscoplastic constitutive equations based on thermodynamics. Mech. Time-Depend. Mater. **1**, 209–240 (1997)

G.A. Shafabakhsh, E. Kashi, Evaluation of aircraft wheel load on pavement damages by layered elastic method. Int. J. Damage Mech. **24**, 1141–1154 (2015)

H. Shahsavari, M. Baghani, S. Sohrabpour, R. Naghdabadi, Continuum damage-healing constitutive modeling for concrete materials through stress spectral decomposition. Int. J. Damage Mech. (2015). https://doi.org/10.1177/1056789515616447, first published on December 3

J.C. Simo, J.W. Ju, Strain-based and stress-based continuum damage models, Part I: formulation. Int. J. Solids Struct. **23**, 821–840 (1987a)

J.C. Simo, J.W. Ju, Strain-based and stress-based continuum damage models, Part II: Computational aspects. Int. J. Solids Struct. **23**, 841–869 (1987b)

J.C. Simo, J.W. Ju, On continuum damage-elastoplasticity at finite strains: A computational framework. Comput. Mech. **5**, 375–400 (1989)

J.C. Simo, J.W. Ju, K.S. Pister, R.L. Taylor, An assessment of the cap model: Consistent return algorithms and rate-dependent extension. J Eng. Mech. ASCE **114**, 191–218 (1988)

G.Z. Voyiadjis, F.H. Abed, A coupled temperature and strain rate dependent yield function for dynamic deformations of BCC metals. Int. J. Plast. **22**, 1398–1431 (2006)

G.Z. Voyiadjis, A.H. Almasri, A physically based constitutive model for FCC metals with applications to dynamic hardness. Mech. Mater. **40**, 549–563 (2008)

G.Z. Voyiadjis, P.I. Kattan, Mechanics of damage, healing, damageability, and integrity of materials: A conceptual framework. Int. J. Damage Mech. (2016). https://doi.org/10.1177/1056789516635730. First published on March 2

K.Y. Yuan, J.W. Ju, New strain energy–based coupled elastoplastic damage-healing formulations accounting for effect of matric suction during earth-moving processes. J. Eng. Mech. ASCE **139**(2), 188–199 (2013)

K.Y. Yuan, J.W. Ju, W. Yuan, J.M. Yang, Numerical predictions of mechanical behavior of innovative pothole patching materials featuring high toughness, low-viscosity nano-molecular resins. Acta Mech. **225**(4), 1141–1151 (2014)

H.H. Zhu, S. Zhou, Z.G. Yan, J.W. Ju, Q. Chen, A two-dimensional micromechanical damage-healing model on microcrack-induced damage for microcapsule-enabled self-healing cementitious composites under tensile loading. Int. J. Damage Mech. **24**, 95–115 (2015)

Computational Algorithms for Strain Energy-Based Thermo-elastoviscoplastic Two-Parameter Damage Self-Healing Models for Bituminous Composites

38

Seongwon Hong and Jiann-Wen Woody Ju

Contents

Introduction 1046
Computational Algorithms for Strain Energy-Based Thermo-elastoviscoplastic Two-Parameter Damage Self-Healing Formulations 1047
Application to Asphalt Concrete and Verification for Thermo-elastoviscoplastic Damage Self-Healing Formulations 1053
Conclusions 1072
References 1072

Abstract

For asphalt concrete composites, the strain energy-based thermo-elastoviscoplastic two-parameter damage self-healing formulations are implemented to demonstrate the comparison of the model predictions with test data in this chapter. For numerical predictions computational algorithms such as the two-step operator splitting methodology are proposed. The elastic two-parameter damage self-healing predictor and the viscoplastic corrector, which are coupled with *Arrhenius-type temperature* through the concept of net stress in conjunction with the strain equivalence hypothesis, are implemented for numerical analysis. For the effect of temperature and rest period for healing

S. Hong (✉)
Department of Safety Engineering, Korea National University of Transportation, Chungju-si, Chungbuk, Republic of Korea
e-mail: shong@ut.ac.kr

J.-W. W. Ju
Department of Civil and Environmental Engineering, University of California, Los Angeles, CA, USA

State Key Laboratory for Disaster Reduction in Civil Engineering, Tongji University, Shanghai, China
e-mail: juj@ucla.edu

© Springer Nature Switzerland AG 2022

G. Z. Voyiadjis (ed.), *Handbook of Damage Mechanics*,
https://doi.org/10.1007/978-3-030-60242-0_95

phenomenon, four examples of three-dimensional problems are presented. Monotonic constant-strain test at different temperatures and controlled-strain cyclic tension test are employed to validate the developed formulation. Numerical predictions by the two-parameter model show good agreement with test data. In particular, the softening and viscous damage behaviors of the bituminous matrix are reasonably predicted for monotonic constant-strain experiment based on the developed two-parameter damage formulations. It is observed that the two-parameter model can have a better capability to capture the thermomechanical behavior of asphalt and is more versatile than the isotropic damage self-healing formulation with one-parameter.

Keywords

Arrhenius-type temperature term · Bituminous composite · Net space · Thermoelastoviscoplastic two-parameter damage self-healing model · Two-step operator splitting

Introduction

Computational framework is required for estimating the thermomechanical behavior of asphalt concrete composites under various environmental situations such as the traffic loading rate and time (or rest period of loading), temperature variation, and different moisture conditions. For the past two or three decades, diverse material formulations for asphalt matrix have been developed and proposed to predict the influence of above factors on performance of asphalt composites (Kim 2009). Despite the studies on the construction material models, there are few publications on damage self-healing models of asphalt concrete to predict the partial or complete healing of materials due to the temperature, loading rate, and compaction (Barbero et al. 2005; Abu Al-Rub et al. 2010; Ju et al. 2012a, b; Yuan and Ju 2013; Yuan et al. 2014; Shafabakhsh and Kashi 2015; Shahsavari et al. 2015; Zhu et al. 2015; Voyiadjis and Kattan 2016; Hong et al. 2017a, b). Therefore, there is a fundamental need to propose the theories and computational framework of damage self-healing mechanisms for bituminous composite materials under complex traffic conditions at different temperatures.

To capture the temperature-dependent and complex behavior of bituminous materials, the basic formulation of damage self-healing mechanics along with the net stress space concepts and an Arrhenius-type temperature term is clearly described in Part I. In this chapter, computational algorithms using the two-step operator splitting methodology are proposed to predict the thermomechanical responses of asphalt concrete materials. The two main objectives of this chapter are achieved, i.e., (1) the development of a systematic framework for the damage self-healing models based on two-parameter suggested in Part I and (2) the various capabilities of the formulations which are displayed in a series of comparisons by good agreements between the experimental and computational results for

bituminous composites. Furthermore, it is noted that the developed two-parameter model is superior in capturing the thermomechanical responses of asphalt concrete than the one-parameter isotropic damage self-healing model.

There are well-posed, uniqueness, and numerical convergence problems related to strain softening due to the ellipticity loss. Therefore, as the mesh size goes infinitesimal, finite element methods cause spurious mesh sensitivity and localization. These kinds of numerical difficulties may be overcome and resolved by using the viscous damage model (Simo and Ju 1987a, b; Ju 1989), the window-function meshfree method (Ju et al. 2012a, b; Ju and Yuan 2012), or the nonlocal damage theory (Eringen and Edelen 1972; Xia et al. 1987; Bazant and Lin 1988). The viscous damage mechanism offers a possibility for overcoming the loss of material ellipticity and is also suitable for accommodating dynamic rate effect (Ju 1989). This is why the developed damage self-healing model can capture softening behavior well.

The outline of this chapter is organized as follows. First of all, the two-step operator splitting methodology is employed for the developed two-parameter damage self-healing formulations. The procedure takes the form of an *elastic two-parameter (volumetric and deviatoric) damage self-healing predictor* and a *net viscoplastic return mapping corrector* scheme. Second, a series of 3D numerical simulations by different loading conditions (i.e., loading/unloading/reloading (LUR) and one cyclic loading) are made for the schematic examples of the variables determined by the thermo-elastoviscoplastic two-parameter formulations such as the stress-strain curve, two-parameter (volumetric and deviatoric) damage variables, and two-parameter (volumetric and deviatoric) healing variables. Eventually, experimental validations are demonstrated in order to present the capability and applicability of the developed two-parameter thermo-elastoviscoplastic damage self-healing formulations and algorithms to asphalt matrix.

Computational Algorithms for Strain Energy-Based Thermo-elastoviscoplastic Two-Parameter Damage Self-Healing Formulations

Computational Algorithms Called Two-Step Operator Splitting Methodology

The strain energy-based two-parameter damage self-healing models have been developed with damage self-healing process and the net stress space concept in Part I (cf. Simo and Ju 1987a, b; Ju 1989; Ju et al. 2012a, b; Hong et al. 2017a, b). This chapter focuses on the computational algorithms of the models by using the two-step operator splitting methodology. Eqs. 24–27, 37–40, 49–52, and 57–60 in Part I of this sequel and Eqs. 46–50 in Hong et al. (2017a) are referred. The local two-parameter elastoviscoplastic damage self-healing rate constitutive equations are as follows:

$$
\begin{aligned}
&\dot{\varepsilon} = \nabla^s \dot{u}(t)\\
&\begin{cases} \dot{d}_{v,t} = \dot{\mu}_v \;\; H_v\left(\xi_{v,t}, d_{v,t}\right) \\ \dot{g}_v = \dot{\mu}_v \\ \dot{\mu}_v \geq 0, \qquad \phi_v^d\left(\xi_{v,t}, g_{v,t}\right) \leq 0, \qquad \dot{\mu}_v \, \phi_v^d\left(\xi_{v,t}, g_{v,t}\right) = 0 \end{cases}\\
&\begin{cases} \dot{d}_{d,t} = \dot{\mu}_d \;\; H_d\left(\xi_{d,t}, d_{d,t}\right) \\ \dot{g}_d = \dot{\mu}_d \\ \dot{\mu}_d \geq 0, \qquad \phi_d^d\left(\xi_{d,t}, g_{d,t}\right) \leq 0, \qquad \dot{\mu}_d \, \phi_d^d\left(\xi_{d,t}, g_{d,t}\right) = 0 \end{cases}\\
&\begin{cases} \dot{R}_{v,t} = \dot{\zeta}_v \;\; Z_v\left(\xi_{v,t}, R_{v,t}\right) \\ \dot{r}_v = \dot{\zeta}_v \\ \dot{\zeta}_v \geq 0, \qquad \phi_v^h\left(\xi_{v,t}, r_{v,t}\right) \leq 0, \qquad \dot{\zeta}_v \, \phi_v^h\left(\xi_{v,t}, r_{v,t}\right) = 0 \end{cases}\\
&\begin{cases} \dot{R}_{d,t} = \dot{\zeta}_d \;\; Z_d\left(\xi_{d,t}, R_{d,t}\right) \\ \dot{r}_d = \dot{\zeta}_d \\ \dot{\zeta}_d \geq 0, \qquad \phi_d^h\left(\xi_{d,t}, r_{d,t}\right) \leq 0, \qquad \dot{\zeta}_d \, \phi_d^h\left(\xi_{d,t}, r_{d,t}\right) = 0 \end{cases}\\
&\dot{d}_v^{net} = \dot{d}_v - \dot{R}_v \;\; d_v^{net} \qquad \dot{d}_d^{net} = \dot{d}_d - \dot{R}_d \;\; d_d^{net}\\
&\dot{\mathbf{D}}^{net} = \frac{1}{3}\dot{d}_v^{net}\mathbf{1}\bigotimes\mathbf{1} + \dot{d}_d^{net}\left(\mathbf{I} - \frac{1}{3}\mathbf{1}\bigotimes\mathbf{1}\right)
\end{aligned}
\tag{1}
$$

$$
\begin{aligned}
&\dot{\boldsymbol{\sigma}}^{net} = \frac{d}{dt}\left[\frac{\partial \Psi^0(\boldsymbol{\varepsilon})}{\partial \boldsymbol{\varepsilon}}\right] - \dot{\boldsymbol{\sigma}}^{vp,net}\\
&\begin{cases} \dot{\boldsymbol{\sigma}}^{vp,net} = \gamma \dfrac{\partial g_p}{\partial \varepsilon}\left(\dfrac{\partial \Psi^0(\boldsymbol{\varepsilon})}{\partial \boldsymbol{\varepsilon}} - \boldsymbol{\sigma}^{vp,net}, \mathbf{q}\right) & (\textit{non-associative flow rule}) \\ \dot{\mathbf{q}} \;\; = \dot{\lambda} \;\; \mathbf{h}\left(\dfrac{\partial \Psi^0(\boldsymbol{\varepsilon})}{\partial \boldsymbol{\varepsilon}} - \boldsymbol{\sigma}^{vp,net}, \mathbf{q}\right) & (\textit{viscoplastic hardening law}) \\ f\left(\dfrac{\partial \Psi^0(\boldsymbol{\varepsilon})}{\partial \boldsymbol{\varepsilon}} - \boldsymbol{\sigma}^{vp,net}, \mathbf{q}\right) \leq 0 & (\textit{loading condition}) \end{cases}
\end{aligned}
\tag{2}
$$

The problem of integrating the evolution Eqs. 1 and 2 reduces to updating the variables $\left\{\boldsymbol{\sigma},\ \mathbf{q},\ d_v^{net}, d_d^{net},\ \boldsymbol{\sigma}^{vp,net}\right\}$ in a manner consistent with the developed formulations from an algorithmic viewpoint. It is required that the history of strains $t \rightarrow \varepsilon \equiv \nabla^{\mathbf{s}}\mathbf{u}(t)$ is assumed to be prescribed, which is called a strain-drive computational algorithm.

Evolution equations are to be incrementally solved over a sequence of given time steps $[t_n,\ t_{n+1}] \subset \mathcal{R}_+, \quad n = 0, 1, 2 \ldots$. Thus, the initial conditions for the governing equations of evolution are

$$
\left\{\boldsymbol{\sigma},\ d_v^{net}, d_d^{net},\ \boldsymbol{\sigma}^{vp,net},\ q\right\}\Big|_{t=t_n} = \left\{\boldsymbol{\sigma}_n,\ d_{v,n}^{net}\ d_{d,n}^{net},\ \boldsymbol{\sigma}_n^{vp,net},\ q_n\right\} \tag{3}
$$

According to the notion of operator splitting, it considers the following additive decomposition of the original evolution problem in Eq. 1 into the elastic-damage-healing part and the plastic part as follows:

1. Elastic two-parameter damage self-healing part:

$$
\begin{aligned}
&\dot{\boldsymbol{\varepsilon}} = \nabla^s \dot{\mathbf{u}}(t)\\
&\dot{d}_v = \begin{cases} H_v(\xi_v)\ \dot{\xi}_v, & \textit{iff} \quad \phi^d_{v,t} = \dot{\phi}^d_{v,t} = 0 \\ 0, & \textit{otherwise} \end{cases} \quad ; \quad \dot{d}_d = \begin{cases} H_d(\xi_d)\ \dot{\xi}_d, & \textit{iff} \quad \phi^d_{d,t} = \dot{\phi}^d_{d,t} = 0 \\ 0, & \textit{otherwise} \end{cases}\\
&\dot{g}_v = \begin{cases} \dot{\xi}_v, & \textit{iff} \quad \phi^d_{v,t} = \dot{\phi}^d_{v,t} = 0 \\ 0, & \textit{otherwise} \end{cases} \quad ; \quad \dot{g}_d = \begin{cases} \dot{\xi}_d, & \textit{iff} \quad \phi^d_{d,t} = \dot{\phi}^d_{d,t} = 0 \\ 0, & \textit{otherwise} \end{cases}\\
&\dot{R}_v = \begin{cases} Z_v(\xi_v)\ \dot{\xi}_v, & \textit{iff} \quad \phi^h_{v,t} = \dot{\phi}^h_{v,t} = 0 \\ 0, & \textit{otherwise} \end{cases} \quad ; \quad \dot{R}_d = \begin{cases} Z_d(\xi_d)\ \dot{\xi}_d, & \textit{iff} \quad \phi^h_{d,t} = \dot{\phi}^h_{d,t} = 0 \\ 0, & \textit{otherwise} \end{cases}\\
&\dot{r}_v = \begin{cases} \dot{\xi}_v, & \textit{iff} \quad \phi^h_{v,t} = \dot{\phi}^h_{v,t} = 0 \\ 0, & \textit{otherwise} \end{cases} \quad ; \quad \dot{r}_d = \begin{cases} \dot{\xi}_d, & \textit{iff} \quad \phi^h_{d,t} = \dot{\phi}^h_{d,t} = 0 \\ 0, & \textit{otherwise} \end{cases}\\
&\dot{d}^{net}_v = \dot{d}_v - \dot{R}_v\ d^{net}_v \qquad ; \quad \dot{d}^{net}_d = \dot{d}_d - \dot{R}_d\ d^{net}_d\\
&\dot{\mathbf{D}}^{net} = \frac{1}{3}\dot{d}^{net}_v \mathbf{1} \bigotimes \mathbf{1} + \dot{d}^{net}_d \left(\mathbf{I} - \frac{1}{3}\mathbf{1} \bigotimes \mathbf{1}\right)\\
&\dot{\boldsymbol{\sigma}}^{net} = \frac{d}{dt}\left[\frac{\partial \Psi^0(\boldsymbol{\varepsilon})}{\partial \boldsymbol{\varepsilon}}\right]\\
&\dot{\boldsymbol{\sigma}}^{vp,net} = 0\\
&\dot{\mathbf{q}} = 0
\end{aligned}
\tag{4}
$$

2. Viscoplastic part:

$$
\begin{aligned}
&\dot{\boldsymbol{\varepsilon}} = 0\\
&\dot{d}^{net}_v = 0\\
&\dot{d}^{net}_d = 0\\
&\dot{r}_v = 0\\
&\dot{r}_d = 0\\
&\dot{\boldsymbol{\sigma}}^{net} = -\dot{\boldsymbol{\sigma}}^{vp,net}\\
&\dot{\boldsymbol{\sigma}}^{vp,net} = \gamma\ \frac{\partial g_p}{\partial \boldsymbol{\varepsilon}}\left(\frac{\partial \Psi^0(\boldsymbol{\varepsilon})}{\partial \boldsymbol{\varepsilon}} - \boldsymbol{\sigma}^{vp,net}, \mathbf{q}\right)\\
&\dot{\mathbf{q}} = \gamma\ \mathbf{h}\left(\frac{\partial \Psi^0(\boldsymbol{\varepsilon})}{\partial \boldsymbol{\varepsilon}} - \boldsymbol{\sigma}^{vp,net}, \mathbf{q}\right)
\end{aligned}
\tag{5}
$$

Equations 4 and 5 add up to Eqs. 1 and 2 in agreement with the operator split notion. Two new computational algorithms are then developed. The first one is consistent with problem (4) called the elastic two-parameter damage self-healing predictor, whereas the second one is consistent with problem (5) called the net viscoplastic return mapping corrector. As a result, the product algorithm determined by successive application of the algorithms is consistent with the original problems (1) and (2).

The Elastic Two-Parameter Damage Self-Healing Predictor

An innovative computational algorithm, which is consistent with problems (1) and (2), is demonstrated in the step-by-step strain-driven procedure:

Step 1: Update strain tensor given the incremental displacement field $\mathbf{u}_{n+1}$:

$$\varepsilon_{n+1} = \varepsilon_n + \nabla^{\mathbf{s}}\mathbf{u}_{n+1} \tag{6}$$

Step 2: Determine the initial elastic volumetric and deviatoric strain energies $\xi_{v,\,n+1}$ and $\xi_{d,\,n+1}$, which are coupled with the Arrhenius-type temperature, respectively:

$$\xi_{v,n+1} \equiv \sqrt{\Psi_v^0(\varepsilon_{v,n+1})\vartheta(T)} = \sqrt{\left\{\frac{1}{2}K(\varepsilon_{kk,n+1})^2\right\}\exp\left\{-\boldsymbol{\delta}\left(1-\frac{T}{T_0}\right)\right\}} \tag{7}$$

$$\xi_{d,n+1} \equiv \sqrt{\Psi_d^0(\mathbf{e}_{n+1})\vartheta(T)} = \sqrt{\left\{\frac{1}{2}G(\mathbf{e}_{n+1} : \mathbf{e}_{n+1})\right\}\exp\left\{-\boldsymbol{\delta}\left(1-\frac{T}{T_0}\right)\right\}} \tag{8}$$

where $\boldsymbol{\varepsilon}_{v,\,n+1} = \varepsilon_{kk,\,n+1} = \varepsilon_{11,\,n+1} + \varepsilon_{22,\,n+1} + \varepsilon_{33,\,n+1}$ and $\mathbf{e}_{n+1} = \boldsymbol{\varepsilon}_{n+1} - \frac{1}{3}\boldsymbol{\varepsilon}_{kk,n+1}\mathbf{1}$.

Step 3: Update the current two-parameter (volumetric and deviatoric) damage thresholds, $g_{v,\,n+1}$ and $g_{d,\,n+1}$, for the two-parameter damage criteria based on $\xi_{v,\,n+1}$ and $\xi_{d,\,n+1}$ and time increment. At the previous time step, determine the $g_{vh,\,(n)}$ by using a nonlinear saturation type of functional evaluation $g_{vh,\,(n)} = Q(1 - e^{-bn})$ and $\Delta g_{vh,\,(n)} = b(Q - g_{vh,\,(n-1)})n$ if the incremental volumetric healing is greater than zero. In addition, at the previous time step, compute the $g_{dh,\,(n)}$ by using a nonlinear saturation type of functional evaluation $g_{dh,\,(n)} = Q(1 - e^{-bn})$ and $\Delta g_{dh,\,(n)} = b(Q - g_{dh,\,(n-1)})\Delta n$ if the incremental deviatoric healing is greater than zero as follows:

$$g_{v,n+1} = \max\left(g_{v,0}, \max_{s\in(-\infty,n+1)}\xi_{v,s}\right) - g_{vh,(n)} \tag{9}$$

$$g_{d,n+1} = \max\left(g_{d,0}, \max_{s\in(-\infty,n+1)}\xi_{d,s}\right) - g_{dh,(n)} \tag{10}$$

Step 4: Determine the scalar values of volumetric and deviatoric damage predictors $d_{v,\,n+1}$ and $d_{d,\,n+1}$ based on the determined volumetric and deviatoric strain energies $\xi_{v,\,n+1}$ and $\xi_{d,\,n+1}$, respectively. At the current time step, no further volumetric damage occurs if $\xi_{v,\,n+1}$ is less than the volumetric damage threshold $g_{v,\,n+1}$; set $\Delta d_{v,\,n+1} = 0$. However, if $\xi_{v,\,n+1}$ is greater than the volumetric damage threshold $g_{v,\,n+1}$ at the current time step, determine the volumetric damage predictor $\Delta d_{v,\,n+1}$ based on a nonlinear saturation type of damage functional evaluation. Similarly, no further deviatoric damage takes place if $\xi_{d,\,n+1}$ is less than the current deviatoric damage threshold $g_{d,\,n+1}$; set $\Delta d_{d,\,n+1} = 0$. However, if $\xi_{d,\,n+1}$ is greater than the deviatoric damage threshold $g_{d,\,n+1}$ at the current time step, determine the deviatoric damage predictor $\Delta d_{d,\,n+1}$ based on a nonlinear saturation type of damage functional evaluation. If interfacial debonding between the aggregate and matrix, initial defects, or damage (e.g., microvoids or microcracks) can be observed and found by nondestructive tests including computed tomography, the *initial volumetric and deviatoric damage* d_{v0} and d_{d0} can be then characterized and evaluated accordingly. Otherwise, the initial two-parameter (volumetric and deviatoric) damages d_{v0} and d_{d0} are set to be zero, respectively.

$$d_{v,n+1} = d_{v,n} + \Delta d_{v,n+1} \tag{11}$$

$$d_{d,n+1} = d_{d,n} + \Delta d_{d,n+1} \tag{12}$$

Step 5: Update the volumetric and deviatoric healing thresholds $r_{v,\,n+1}$ and $r_{d,\,n+1}$ for a healing criterion based on the initial elastic volumetric and deviatoric strain energies $\xi_{v,\,n+1}$ and $\xi_{d,\,n+1}$ at the current time step, respectively. At the previous time step, if the incremental volumetric damage is greater than zero, determine $r_{vd,\,(n)}$ based on a nonlinear saturation type of functional evaluation. Otherwise, $r_{vd,\,(n)}$ is zero. Similar to the volumetric part, determine $r_{dd,\,(n)}$ based on a nonlinear saturation type of functional evaluation if the incremental deviatoric damage is greater than zero at the previous time step. Otherwise, $r_{dd,\,(n)}$ is zero:

$$r_{v,n+1} = \min\left(r_{v,0}, \min_{s\in(-\infty,\,n+1)} \xi_{v,s}\right) + r_{vd,(n)} \tag{13}$$

$$r_{d,n+1} = \min\left(r_{d,0}, \min_{s\in(-\infty,\,n+1)} \xi_{d,s}\right) + r_{dd,(n)} \tag{14}$$

Step 6: Determine the volumetric and deviatoric healing predictors, $R_{v,\,n+1}$ and $R_{d,\,n+1}$, by using the initial elastic volumetric and deviatoric strain energies $\xi_{v,\,n+1}$ and $\xi_{d,\,n+1}$, respectively. At the current time step, no further healing takes place, if $\xi_{v,\,n+1}$ at the current time step is greater than the current volumetric healing threshold $r_{v,\,n+1}$; set $\Delta R_{v,\,n+1} = 0$. However, determine the volumetric healing predictor $\Delta R_{v,\,n+1}$ based on a nonlinear saturation type of healing functional

evaluation if the initial volumetric strain energy $\xi_{v,\,n+1}$ is less than the volumetric healing threshold $r_{v,\,n+1}$ at the current time step. Similarly, no further healing takes place if the initial deviatoric strain energy $\xi_{d,\,n+1}$ is greater than the deviatoric healing threshold $r_{d,\,n+1}$ at the current time step; set $\Delta R_{d,\,n+1} = 0$. However, determine the deviatoric healing predictor $\Delta R_{d,\,n+1}$ based on a nonlinear saturation type of healing functional evaluation if the initial deviatoric strain energy $\xi_{d,\,n+1}$ is less than the deviatoric healing threshold $r_{d,\,n+1}$ at the current time step:

$$R_{v,n+1} = R_{v,n} + \Delta R_{v,n+1}, \quad (\Delta d_{v,n+1} = 0) \tag{15}$$

$$R_{v,n+1} = \frac{d_{v,n+1}}{2d_{v,n+1} - d_{v,n}} R_{v,n}, \quad (\Delta d_{v,n+1} > 0) \tag{16}$$

$$R_{d,n+1} = R_{d,n} + \Delta R_{d,n+1}, \quad (\Delta d_{d,n+1} = 0) \tag{17}$$

$$R_{d,n+1} = \frac{d_{d,n+1}}{2d_{d,n+1} - d_{d,n}} R_{d,n} \ , \quad (\Delta d_{d,n+1} > 0) \tag{18}$$

Step 7: Determine the *incremental* volumetric and deviatoric damage net predictors $\Delta d^{net}_{v,n+1}$ and $\Delta d^{net}_{d,n+1}$:

$$\Delta d^{net}_{v,n+1} = \Delta d_{v,n+1} - \Delta R_{v,n+1} d^{net}_{v,n} \tag{19}$$

$$\Delta d^{net}_{d,n+1} = \Delta d_{d,n+1} - \Delta R_{d,n+1} d^{net}_{d,n} \tag{20}$$

Step 8: Update the *incremental* volumetric and deviatoric damage predictor tensors $\Delta \mathbf{D}_{v,\,n+1}$ and $\Delta \mathbf{D}_{d,\,n+1}$ and the damage tensor $\mathbf{D}_{n+1}$:

$$\Delta \mathbf{D}^{net}_{n+1} = \frac{1}{3} \Delta d^{net}_{v,n+1} \mathbf{1} \otimes \mathbf{1} + \Delta d^{net}_{d,n+1} \left(\mathbf{I} - \frac{1}{3} \mathbf{1} \otimes \mathbf{1} \right) \tag{21}$$

$$\mathbf{D}^{net}_{n+1} = \mathbf{D}^{net}_{n} + \Delta \mathbf{D}^{net}_{n+1} \tag{22}$$

The trial stress called predictor is obtained by substituting the total strain tensor ε_{n+1} into the potential for the stress tensor:

$$\begin{aligned} \boldsymbol{\sigma}^{0}_{n+1} &= \frac{\partial \Psi^{0}}{\partial \boldsymbol{\varepsilon}} (\boldsymbol{\varepsilon}_{n+1}) \\ \boldsymbol{\sigma}^{trial,net}_{n+1} &= \boldsymbol{\sigma}^{0}_{n+1} - \boldsymbol{\sigma}^{vp,net}_{n} \\ \mathbf{q}^{trial}_{n+1} &= \mathbf{q}_{n} \end{aligned} \tag{23}$$

The Net Viscoplastic Return Mapping Corrector

The loading/unloading conditions are first checked to propose an algorithm consistent with the viscoplastic part of the operator split.

Step 9: Check for net *yielding*:

The algorithmic counterpart of the Kuhn-Tucker conditions is employed in terms of the elastic two-parameter (volumetric and deviatoric) damage self-healing trial stress (cf. Simo and Ju 1987b; Ju et al. 2012b; Hong et al. 2017b). One checks:

$$f\left(\boldsymbol{\sigma}_{n+1}^{trial,net}, \mathbf{q}_{n+1}^{trial}\right) \begin{cases} \leq 0, & \text{elastic-damage-healing} \Rightarrow \text{predictor} = \text{final state} \\ > 0, & \text{viscoplastic} \Rightarrow \text{return mapping} \end{cases} \tag{24}$$

Step 10: Update net viscoplastic return mapping *corrector*:

For the net viscoplastic loading condition, the predictor stresses and internal variables become "returned back" to the net yield surface along the algorithmic counterpart of the flow by Eq. 5. The framework of the radial return algorithm is implemented in this step.

Step 11: Update the homogenized stress $\boldsymbol{\sigma}_{n+1}$:

$$\boldsymbol{\sigma}_{n+1} = \left[\left\{\mathbf{I} - \mathbf{D}_{n+1}^{net}\right\} : \boldsymbol{\sigma}_{n+1}^{net}\right]\mathbf{J}(T_{n+1}) \tag{25}$$

Application to Asphalt Concrete and Verification for Thermo-elastoviscoplastic Damage Self-Healing Formulations

A three-dimensional driver problem is defined based on the developed thermo-elastoviscoplastic two-parameter damage self-healing mechanism and performed by the MATLAB codes. The two-parameter damage self-healing formulations are presented based on the two-invariant Drucker-Prager yield criterion and Perzyna viscoplasticity model. Then, for the verification of the thermo-elastoviscoplastic two-parameter damage self-healing formulations, experimental measurements for bituminous composites are chosen through literature review (Texas A&M University (TAMU) and the North Carolina State University (NCSU)) and compared with the numerical predictions computed by the developed two-parameter damage-healing formulations.

Three-Dimensional Driver Problem

The histories of nominal (called homogenized) stress, net stress, damage, and healing variables and thresholds can be determined under a specified cycle of strain control such as loading-unloading-reloading (LUR) and one cycle based on the proposed two-parameter damage-healing mechanism. The case of the elastoviscoplastic formulation is studied and shown based on the *proposed damage self healing* model by adjusting the following factors, the yield stresses, the temperature conditions, and the initial volumetric and deviatoric damage and healing thresholds, in the MATLAB codes. The corresponding computational predictions are obtained, demonstrated, and discussed in the following section.

Thermo-elastoviscoplastic Two-Parameter Damage Self-Healing Formulation

Four different scenarios are shown as follows: (1) the general case for LUR, (2) the cyclic loading (i.e., one cycle), (3) the temperature effect for LUR, and (4) the effect of rest period for LUR. For the general case for LUR, the initial volumetric damage and healing thresholds are assumed to be 0.06 and 0.055, respectively, whereas the initial deviatoric damage and healing thresholds are set to be 0.08 and 0.1, respectively. The primary reason of different volumetric and deviatoric values is that the volumetric and deviatoric equivalents are different. The Drucker-Prager yield function and the Perzyna viscoplastic model are selected for three-dimensional problem. In addition, the axial nominal and net stresses and the axial strain are only used for plotting figures. Figure 1a shows that the stress under the loading condition decreases because of the evolutions of damage and viscoplastic deformation. However, decrease in the stress is observed during the loading process since viscoplastic deformation is only considered in the net space, as presented in Fig. 1b. The net stresses at 10 °C and 20 °C are the same since the temperature effect is not considered in the net space. On the contrary to the concept of the net stresses, due to the use of the Arrhenius-type temperature term in the physical space, the magnitude of the homogenized stresses is different. According to the test data, it is observed that the normal stress magnitude at low temperature is higher than that at

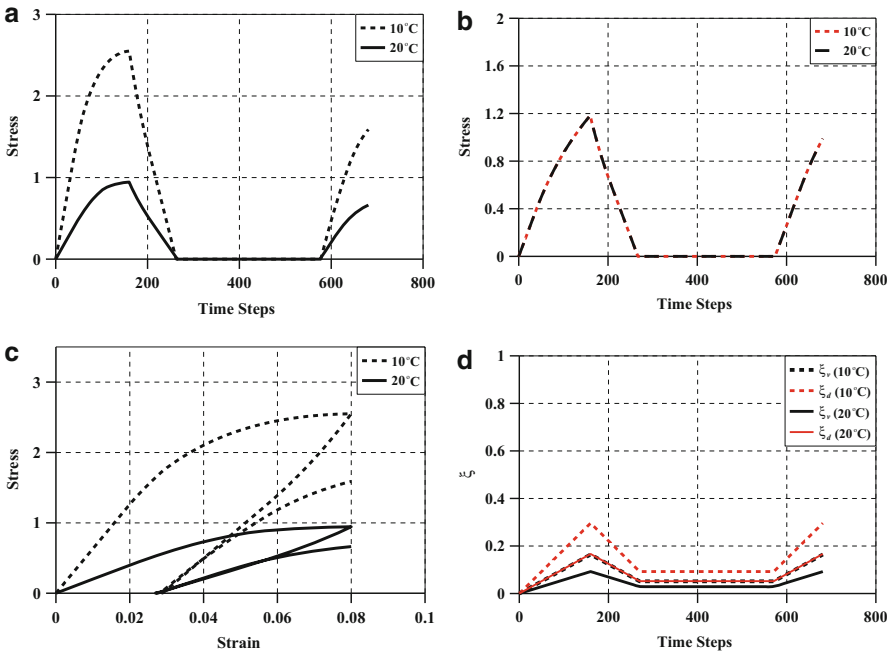

Fig. 1 The corresponding results of the three-dimensional driver problems by the thermo-elastoviscoplastic damage self-healing model (10 °C and 20 °C) (**a**) Homogenized stress, (**b**) Net stress, (**c**) Stress-strain, (**d**) Equivalent strain

high temperature in Fig. 1a. Under the unloading condition, the strain returns to a certain strain point because of permanent deformation, and the reloading begins 300 steps later as demonstrated in Fig. 1c. At 20 °C shown in Fig. 1c, it is obviously observed that the slope of the stress-strain curve after 300 steps increases because healing lasts for 300 steps, whereas the slope of the stress-strain curve at 10 °C under the reloading process after 300 steps is not greater than before, since the damage at 10 °C during the loading condition is greater and the healing at 10 °C is less than that at 20 °C for 300 steps. Figure 1d presents the equivalent strains (energy norms) of the volumetric and deviatoric strain tensors at 10 °C and 20 °C, respectively. The energy norm of deviatoric strain is greater than that of the volumetric strain, and the equivalent strain of strain tensors at 10 °C is clearly greater than that at 20 °C.

The damage net, damage, and healing variables at temperature conditions of 10 °C and 20 °C are exhibited in Fig. 2. The volumetric and deviatoric damage net variables are shown in Fig. 2a, b, respectively, and their mechanical behaviors are similar to each other. However, their magnitudes are different due to the difference between the energy norm of volumetric strain tensor and the equivalent deviatoric strain. The increase in the damage net variables is observed with time, and the constant damage net variable is measured during the unloading situations under the loading process. Healing takes place for 300 steps after the unloading is completed denoting that the damage net variables are decreased by the amount of healing. The volumetric damage net variable increases again if the equivalent volumetric strain is greater than the healed volumetric damage threshold. In the same way, if the energy norm of the deviatoric strain tensor exceeds the healed deviatoric damage threshold, the deviatoric damage net variable increases again. It is observed that due to the temperature effect, the volumetric and deviatoric damage net variables at 10 °C are greater than at 20 °C. In contrast to the two-parameter damage net and healing variables, the volumetric and deviatoric damage processes are assumed to be irreversible; the damage is defined as a monotonically increasing function as presented in Fig. 2c, d. The two-parameter healing variables are shown in Fig. 2e, f; the healing variables at 10 °C are lower than that at 20 °C due to the temperature effect.

Figure 3 displays the one complete cycle loading (tension loading–tension unloading–compression loading–compression unloading). The initial volumetric and deviatoric damage thresholds are assumed to be the same as the LUR case, whereas the volumetric and deviatoric healing thresholds are set as 0.02 and 0.035, respectively. The homogenized stress magnitude at 10 °C is greater than at 20 °C because of the temperature effect, as shown in Fig. 3a. Furthermore, the reduction in the homogenized stress under tensile and compressive loading conditions results obviously from the damage and permanent deformation. The tensile stress is obviously greater than the compressive stress in the physical space because the damage net variable is accumulated with time. Figure 3b shows the history of the net stress. The net stress decreases during the tensile and compressive loading are due to the viscoplastic deformation only because the effects of damage self-healing mechanism and temperature in the net space are excluded. The stress-strain curves are similar to each temperature condition, whereas the homogenized stress at 10 °C is obviously

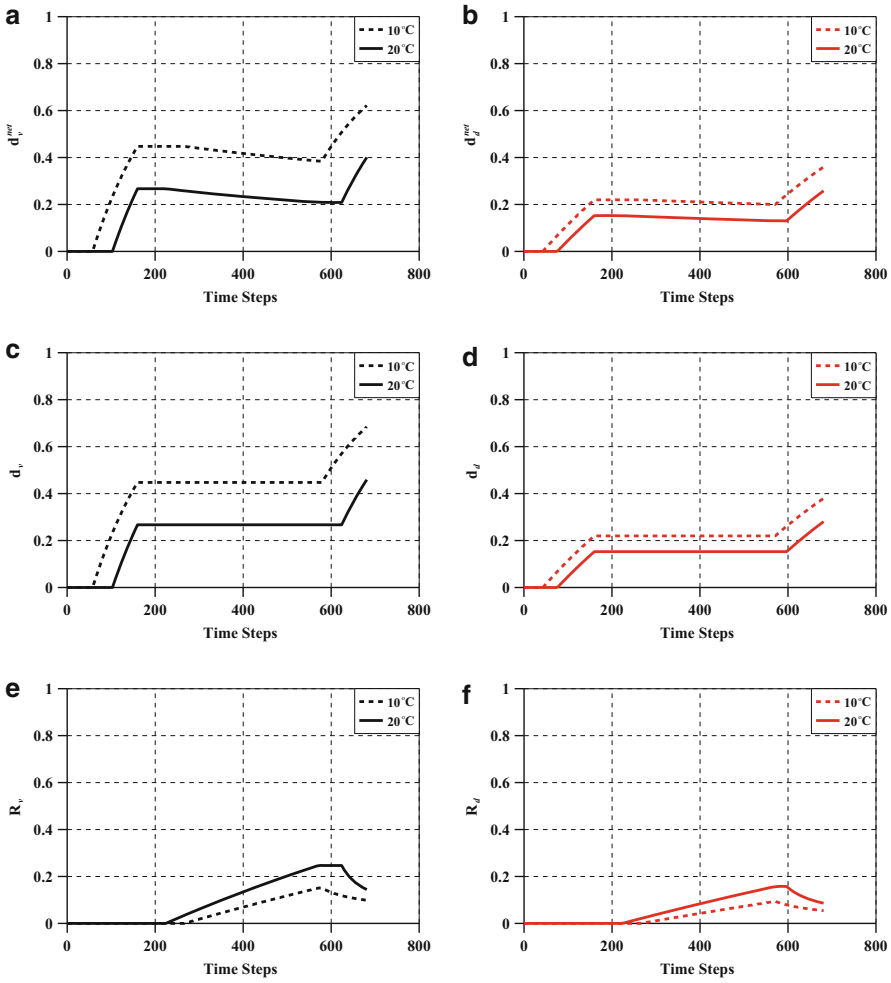

Fig. 2 The corresponding damage net variables of the three-dimensional driver problems by the thermo-elastoviscoplastic damage self-healing model (10 °C and 20 °C) (**a**) d_v^{net}, (**b**) d_d^{net}, (**c**) d_v, (**d**) d_d, (**e**) R_v, (**f**) R_d

greater than at 20 °C as shown in Fig. 3c. Figure 3d exhibits the equivalent volumetric and deviatoric strains.

Figure 4 depicts the volumetric and deviatoric damage net, damage, and healing variables for one complete cycle loading. An increase in two-parameter damage net variables is initially observed as the equivalent volumetric and deviatoric strains exceed their volumetric and deviatoric damage thresholds, respectively, as demonstrated in Fig. 4a, b. The volumetric and deviatoric damage net variables are constant and then decrease with increasing healing variables during the tensile reloading condition. The volumetric and deviatoric damage net variables increase again under

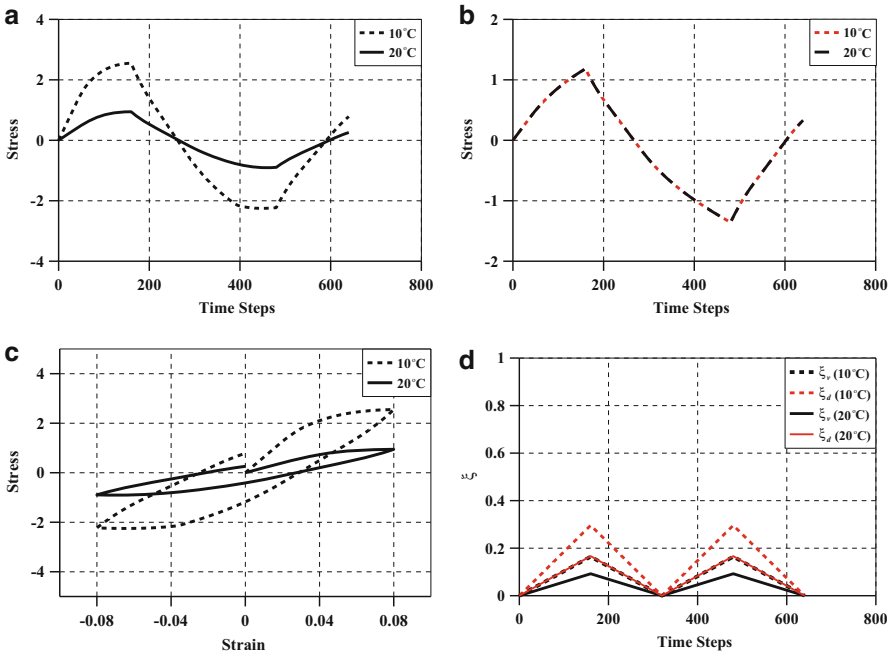

Fig. 3 The corresponding results of the three-dimensional driver problems by the thermo-elastoviscoplastic damage self-healing model (10 °C and 20 °C) (**a**) Homogenized stress, (**b**) Net stress, (**c**) Stress-strain, (**d**) Equivalent strain

the condition of compressive reloading; as the compressive unloading begins, these variables are finally constant. The volumetric damage variable is initiated as the energy norm of the volumetric strain tensor exceeds the volumetric damage threshold under the conditions of tensile or compressive loading in Fig. 4c, whereas the volumetric healing is only evolved as the equivalent volumetric strain is lower than the volumetric healing threshold and damage is not initiated in Fig. 4e. Figure 4d, f shows the same pattern of the deviatoric damage net, damage, and healing variables as the volumetric damage net, damage, and healing variables. Both the damage and damage net variables at 10 °C are greater than those at 20 °C, while the healing at 10 °C becomes lower since no healing takes place at lower temperature condition.

Figure 5 shows the healing effect because of different temperature situations for 300 steps. The initial two-parameter damage and healing thresholds are assumed to be the same as the general LUR case. The temperature is set to be 20 °C from loading to unloading process (point A in Fig. 5a). There are two conditions for 300 steps from point A to point B; in one case, the temperature is increased up to 30 °C, and in the other case, the temperature is kept at 20 °C. After 300 time steps, the reloading begins at point B. It is observed that the homogenized (nominal) stress (dashed line) at 30 °C is slightly increased due to the effect of temperature as shown in Fig. 5a. However, the net stresses at different temperatures are the same since the effects of

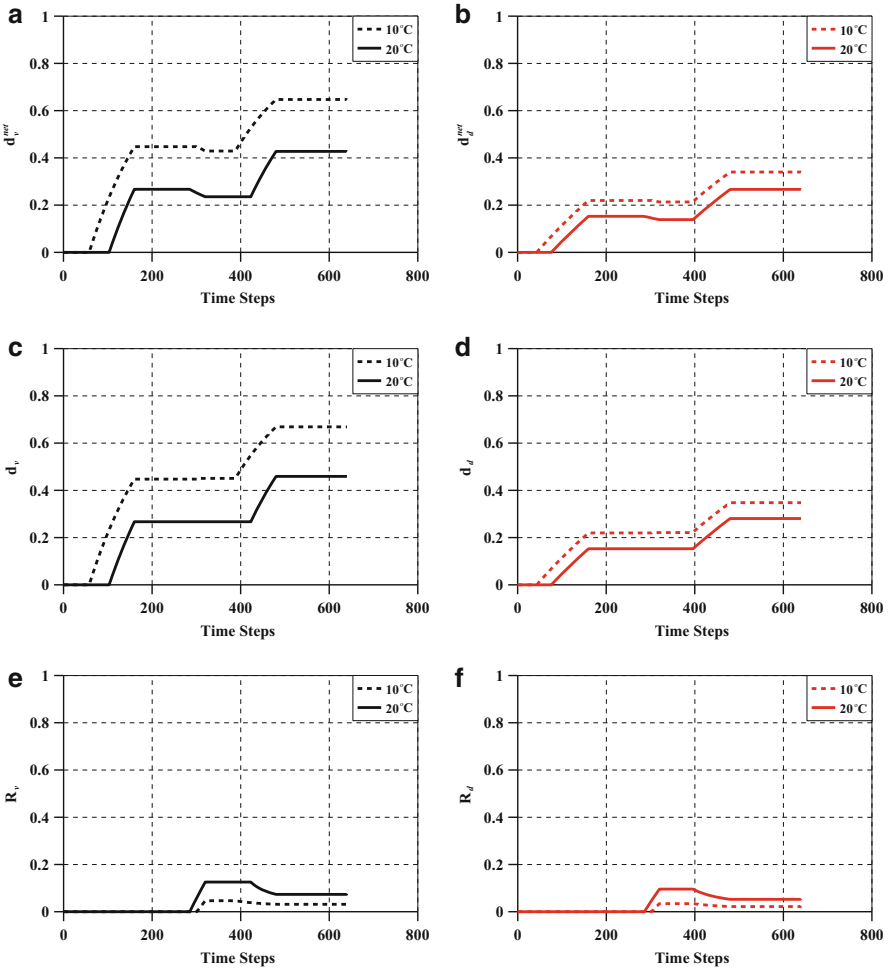

Fig. 4 The corresponding damage net variables of the three-dimensional driver problems by the thermo-elastoviscoplastic damage self-healing model (10 °C and 20 °C) (**a**) d_v^{net}, (**b**) d_d^{net}, (**c**) d_v, (**d**) d_d, (**e**) R_v, (**f**) R_d

temperature, damage, and healing are removed in the net space. The bituminous material exposed to 30 °C is partially more recovered so that it is observed that the elastic modulus at 30 °C is clearly greater than that at 20 °C after the reloading, as displayed in Fig. 5c. In Fig. 5d, the energy norms of the volumetric and deviatoric strain tensor are the same for two different temperatures since the reference temperature is set as 20 °C for both cases. The same behaviors of the volumetric and deviatoric damage net, damage, and healing variables as the general LUR are observed in Fig. 6. Because the damage and healing are obviously independent, damage takes place only when there is no healing evolution, whereas healing begins

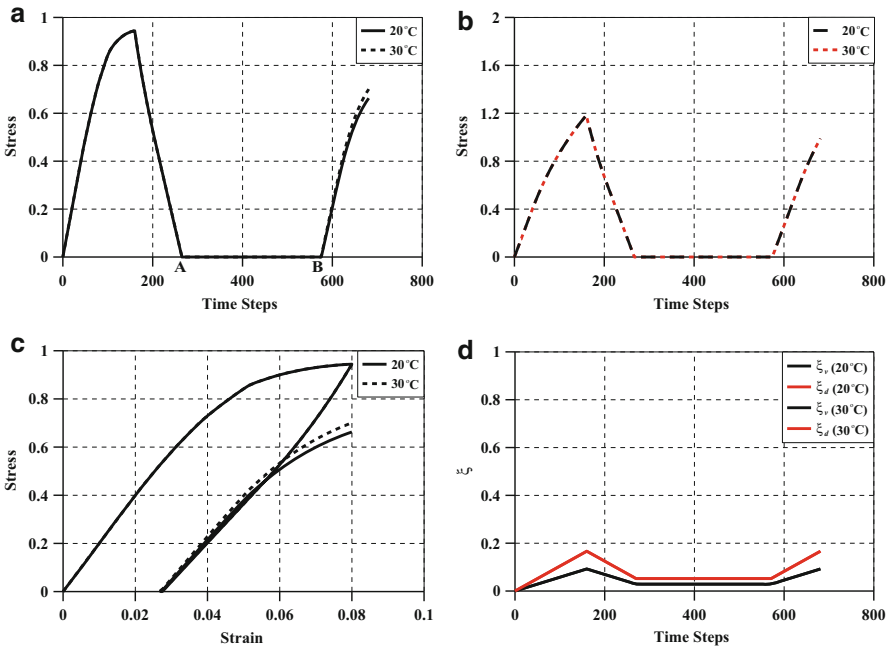

Fig. 5 The corresponding results of the three-dimensional driver problems by the thermo-elastoviscoplastic damage self-healing model (30 °C for healing period) (**a**) Homogenized stress, (**b**) Net stress, (**c**) Stress-strain, (**d**) Equivalent strain

as the equivalent strain is less than the healing threshold and damage is not evolved. In Fig. 6e, f, due to the temperature difference for the rest period, the magnitude of healing is different. Therefore, the reduction in the two-parameter damage net variables at 30 °C is greater than at 20 °C.

Figures 7 and 8 show the healing effect at a controlled temperature due to the different rest periods. The initial two-parameter damage and healing thresholds are set to be the same as the general LUR case. Temperature condition is 20 °C for the whole loading process, while rest period is different, i.e., 100 steps and 300 steps. In Fig. 7a, the homogenized stress at the end of the reloading for 300 steps is obviously greater than that for 100 steps. However, the final stresses in the net space are the same at different time steps in Fig. 7b. It is clearly observed that the slope of stress-strain curve after 100 steps is slightly less than that of 300 steps due to the healing effect in Fig. 7c. In Fig. 8c, d, the final volumetric and deviatoric damage variables after 300 steps are greater than those after 100 steps since more healing has the damage threshold lower, after which more damage can take place. However, volumetric damage and healing variables become very close to each other as demonstrated as they are coupled to make the volumetric damage net variables in Fig. 8a, c, e. Analogous to the volumetric part, the deviatoric damage net variable has the same trend, as exhibited in Fig. 8b, d, f. This is the primary reason why elastic modulus after 100 steps is slightly less than that after 300 steps.

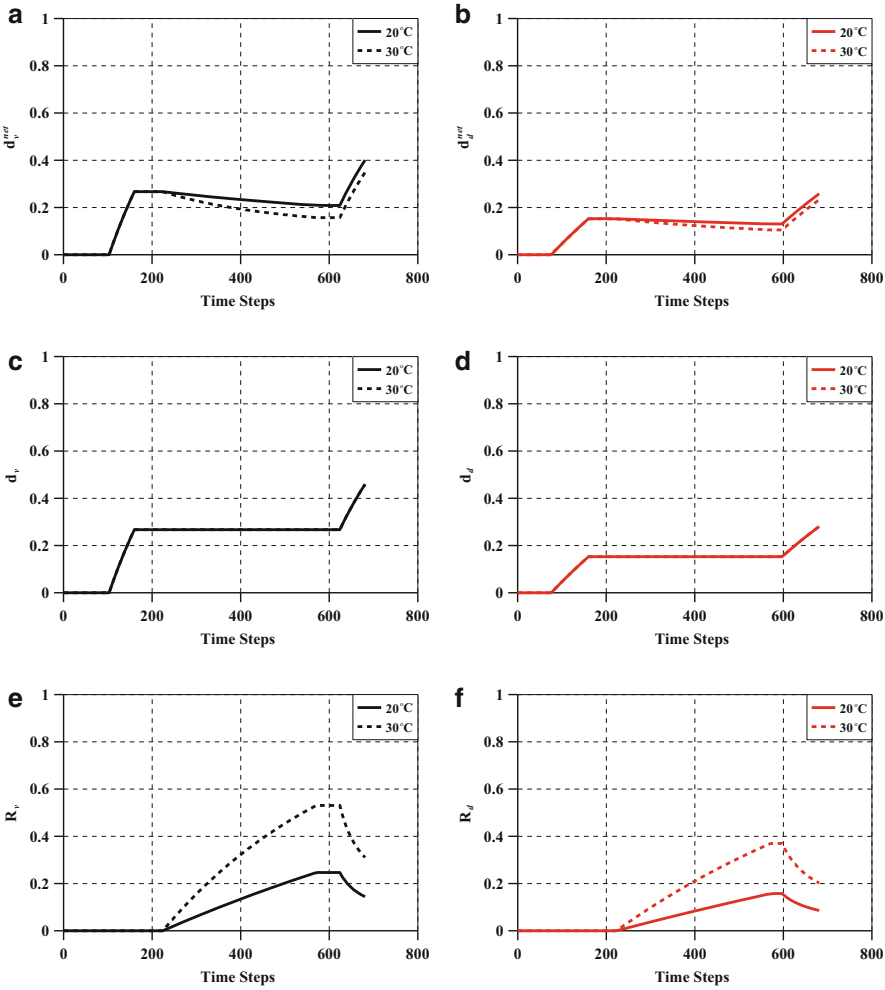

Fig. 6 The corresponding damage net variables of the three-dimensional driver problems by the thermo-elastoviscoplastic damage self-healing model (30 °C for healing period) (**a**) d_v^{net}, (**b**) d_d^{net}, (**c**) d_v, (**d**) d_d, (**e**) R_v, (**f**) R_d

Comparison Between Experimental Measurements and Predictions

The strain energy-based two-parameter (volumetric and deviatoric) damage self-healing mechanism with Arrhenius temperature term and its computational framework are used to predict the thermomechanical response of bituminous composites in this section. Due to the imperfection of experimental instruments and techniques and the wide scattering in available experimental measurement for bituminous matrix, a precise quantitative assessment of the capturing abilities of a given constitutive model with the developed damage self-healing formulation may not

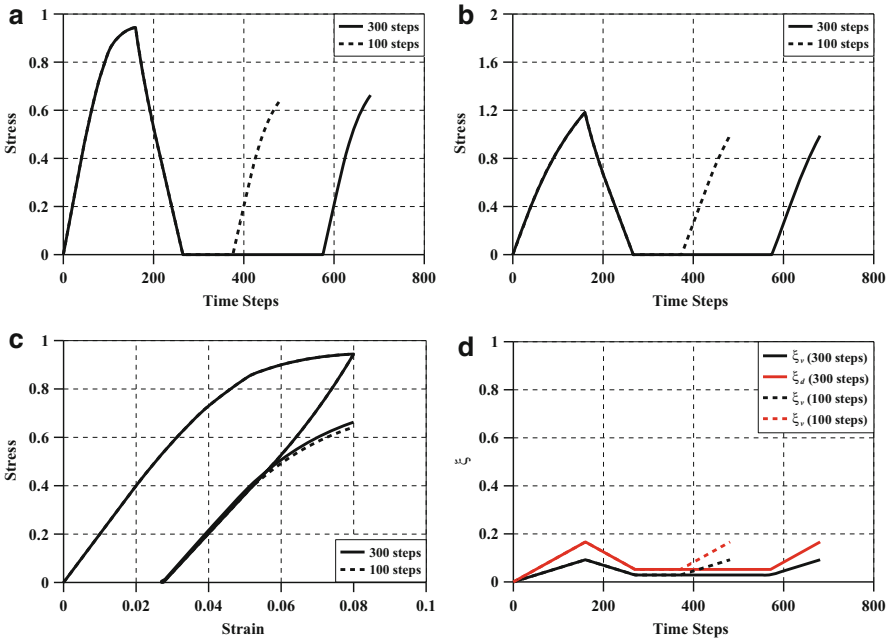

Fig. 7 The corresponding results of the three-dimensional driver problems by the thermo-elastoviscoplastic damage self-healing model (100 steps and 300 steps for healing) (**a**) Homogenized stress, (**b**) Net stress, (**c**) Stress-strain, (**d**) Equivalent strain

be warranted. However, a qualitative and comprehensive production of the thermo-mechanical response of asphalt concrete should play a key role in the modeling.

In this section, a two-invariant Drucker-Prager yield criterion and the Perzyna-type viscoplasticity model are chosen and used for numerical simulation in the net space because asphalt concrete is hydrostatic stress-dependent and viscoplastic composites. In addition, the non-associative flow rule is employed in the simulation. In accordance with the ideas of Lemaitre and Chaboche (1990) and Tan et al. (1994), the material parameter (A) in the two-invariant Drucker-Prager yield criterion evolves as the permanent deformation of materials occurs, whereas the material parameter (B) is almost constant when the composites permanently deform. Then, the equivalent viscoplastic strain is used for the hardening law. In this section, the radial return algorithm is adopted for the numerical simulation (Ju 1989; Hong et al. 2017b).

To verify the developed damage self-healing model, the experimental measurements are retrieved from the well-documented experimental data (cf. Lee 1996; Darabi et al. 2012). Due to the limitation of available experimental measurements of bituminous composites, the thermo-elastoviscoplastic two-parameter damage model is first used to be validated against the monotonic uniaxial tests under different temperature and strain rates. Next, the elastoviscoplastic two-parameter damage self-healing formulation is employed to be verified against the cyclic loading test

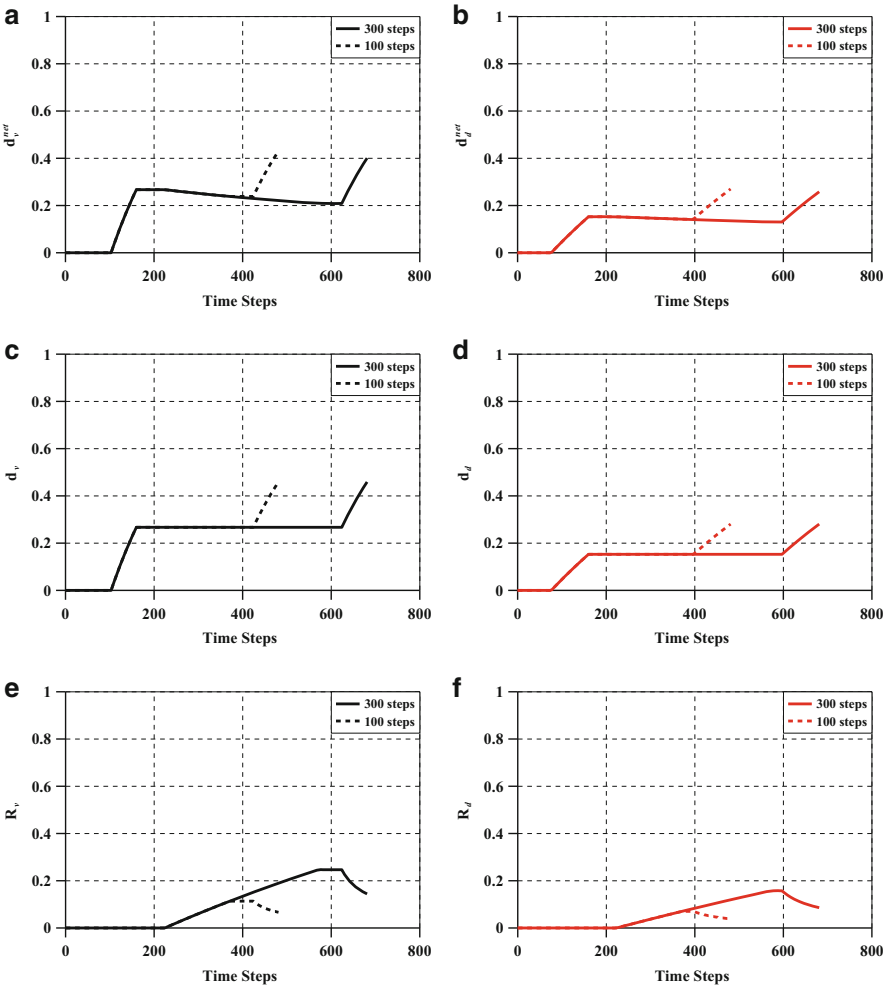

Fig. 8 The corresponding damage net variables of the three-dimensional driver problems by the thermo-elastoviscoplastic damage self-healing model (100 steps and 300 steps for healing) (**a**) d_v^{net}, (**b**) d_d^{net}, (**c**) d_v, (**d**) d_d, (**e**) R_v, (**f**) R_d

of two different bituminous composites under constant temperature. The developed damage self-healing formulation can be equivalent to the two-parameter damage formulation as damage is only considered for the monotonic uniaxial tests. Consequently, the net space becomes the effective space, and the two-parameter damage net variables are equal to the two-parameter damage variables. In the case of the validation of two-parameter damage self-healing model, because the test was performed under constant temperature condition (25 °C), the formulation becomes the elastoviscoplastic two-parameter damage self-healing formulation. The proposed models well present diverse capabilities in predicting the temperature-dependent

mechanical responses of asphalt concrete through the two cases of validation. In addition, the two-parameter formulation better captures the temperature-dependent mechanical response of bituminous composite pavement and is more versatile than the proposed isotropic damage self-healing formulation with one-parameter (Hong et al. 2017a, b).

TAMU Asphalt Concrete Measurement

The experimental measurements are taken from literature on monotonic uniaxial compression tests of hot mix asphalt (Darabi et al. 2012). Ten-mm dense bitumen macadam, which consists of an asphalt binder with a penetration grade of 70/100, a continuously graded mixture with asphalt binder of 5.5%, and granite aggregates, were mainly used for the tests. The bituminous specimen was compacted by the gyrator compactor. The height and diameter of cylindrical specimen were 100 mm and 100 mm, respectively, and temperature conditions were 10 °C, 20 °C, and 40 °C. Three different strain rates (i.e., 0.005 s^{-1}, 0.0005 s^{-1}, and 0.00005 s^{-1}) were carried out for 10 °C and 20 °C, while two strain rates, i.e., 0.005 s^{-1} and 0.0005 s^{-1}, were used for 40 °C. In the numerical simulation, the test results at 20 °C are selected as reference material properties. Table 1 demonstrates the optimal material inputs of the asphalt concrete for simulations determined from the experimental data.

Figure 9 shows comparisons between the test results and computational predictions under three or two different temperature conditions. The strain in the x-axis and the stress in the y-axis represent the strain and the stress in the axial direction, respectively, as demonstrated in Fig. 9. It is obviously measured that the numerical simulations proposed by the proposed two-parameter damage formulation are in good qualitative and quantitative agreement with the test data. Particularly, softening responses are well matched, as shown in Fig. 9.

Because the monotonic test results were used for the numerical simulation, it is assumed that healing does not take place and the volumetric and deviatoric damage net variables in the proposed damage self-healing model are the same as the volumetric and deviatoric damage variables in the two-parameter damage model, respectively. The two-parameter damage net variables, which are equivalent to the damage variables, are used and plotted in Fig. 10. The volumetric damage net variables are

Table 1 The associated bituminous material properties at 20 °C in simulations

	$\dot{\varepsilon} = 0.005\ s^{-1}$	$\dot{\varepsilon} = 0.0005\ s^{-1}$	$\dot{\varepsilon} = 0.00005\ s^{-1}$
Young's modulus	290,000 (kPa)	130,000 (kPa)	70,000(kPa)
Poisson's ratio	0.35		
Viscosity	244(kPa/s)		
Lame constants	250,617 (kPa)	112,345 (kPa)	60,493 (kPa)
Shear modulus	107,407 (kPa)	48,148 (kPa)	25,925 (kPa)
Initial volumetric damage threshold	1.8		
Initial deviatoric damage threshold	2.0		
A_0	20 (kPa)		

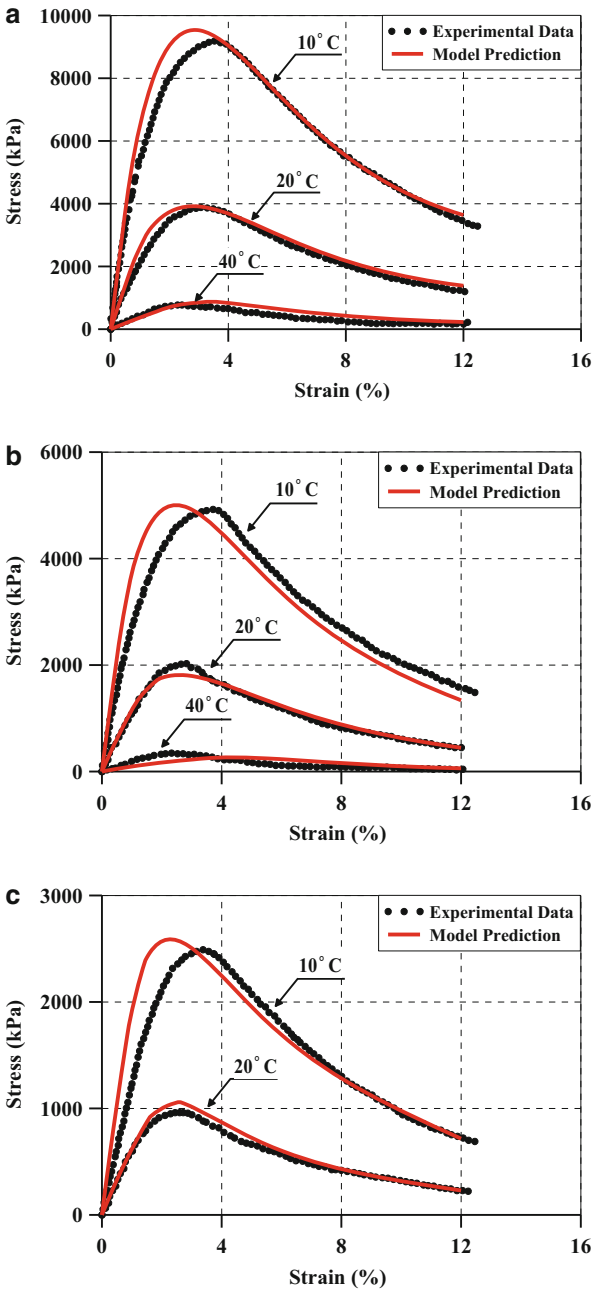

Fig. 9 Comparisons between experimental data and model predictions for the uniaxial constant-strain rate test in compression ($\dot{\varepsilon} = 0.005 \sim 0.00005\ s^{-1}$) (**a**) Stress-strain ($\dot{\varepsilon} = 0.005\ s^{-1}$), (**b**) Stress-strain ($\dot{\varepsilon} = 0.0005\ s^{-1}$), (**c**) Stress-strain ($\dot{\varepsilon} = 0.00005\ s^{-1}$)

demonstrated for each strain rate at different temperatures in Fig. 10a, c, e, while Fig. 10b, d, f exhibits the deviatoric variables. The thermomechanical behaviors of asphalt concrete are well captured by the proposed two-parameter damage self-healing

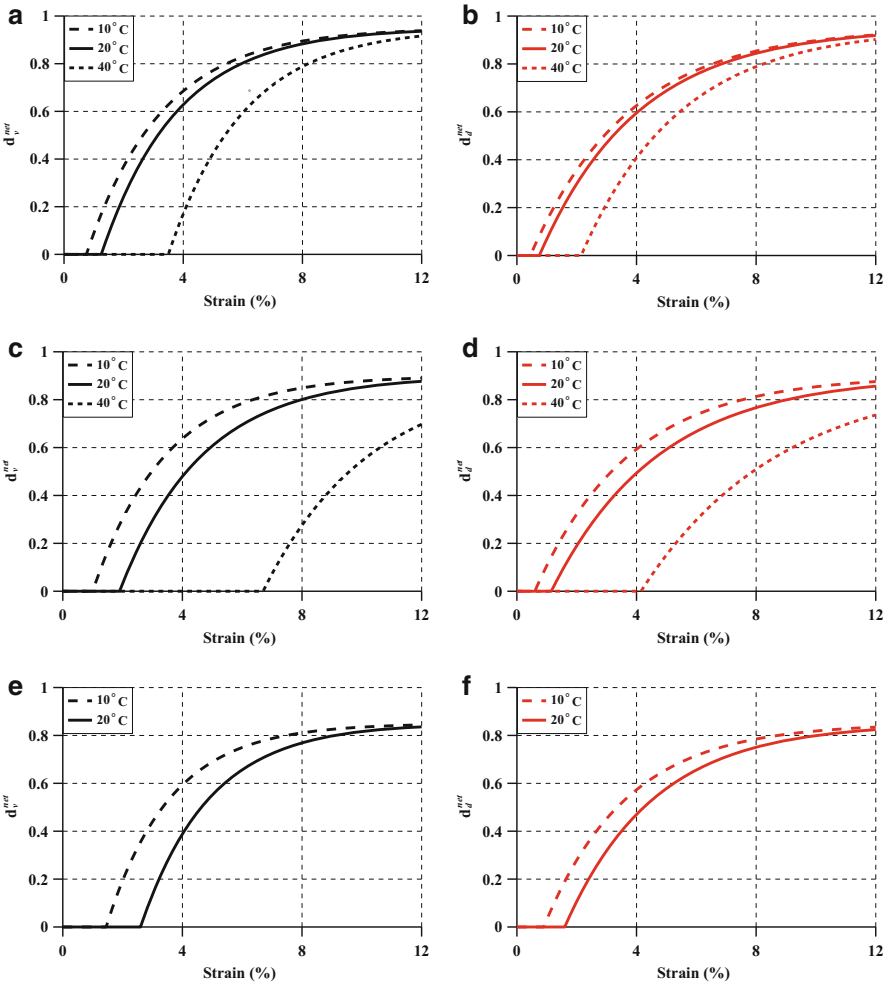

Fig. 10 The damage net variables for the uniaxial constant-strain rate test in compression ($\dot{\varepsilon} = 0.005 \sim 0.00005\ \mathrm{s}^{-1}$) (**a**) d_v^{net} ($\dot{\varepsilon} = 0.005\ \mathrm{s}^{-1}$), (**b**) d_d^{net} ($\dot{\varepsilon} = 0.005\ \mathrm{s}^{-1}$), (**c**) d_v^{net} ($\dot{\varepsilon} = 0.0005\ \mathrm{s}^{-1}$), (**d**) d_d^{net} ($\dot{\varepsilon} = 0.0005\ \mathrm{s}^{-1}$), (**e**) d_v^{net} ($\dot{\varepsilon} = 0.00005\ \mathrm{s}^{-1}$), (**f**) d_d^{net} ($\dot{\varepsilon} = 0.00005\ \mathrm{s}^{-1}$)

models because the magnitudes, shapes, and starting points between the volumetric and deviatoric variables are different. In Fig. 10a, b, the highest value of the volumetric and deviatoric damage net variables is observed slightly above 0.9 at 12% of strain for the strain rate ($\dot{\varepsilon} = 0.005\ \mathrm{s}^{-1}$), and damage variable increases with strain due to the monotonic tests. In the case of $\dot{\varepsilon} = 0.0005\ \mathrm{s}^{-1}$, the maximum volumetric and deviatoric damage net variables at 10 °C and 20 °C are approximately 0.9 at 12% of strain, whereas the highest volumetric and deviatoric damage net variables at 40 °C are measured slightly below and above 0.7 as the strain approaches 12% of strain, respectively, as demonstrated in Fig. 10c, d. For the $\dot{\varepsilon} = 0.00005\ \mathrm{s}^{-1}$ of strain rate

in Figs. 10e, f, the highest value of the volumetric and deviatoric damage net variables are close to 0.82. For the same strain rate, damage is started later at higher temperature because asphalt concrete composites become more viscous lowering the damage level. At lower temperature, the volumetric and deviatoric damages begin at the early stage of strain; i.e., the bituminous composites are less susceptible to damage at higher temperature due to the viscous material properties. To illustrate the effect of viscous damage, the volumetric and deviatoric damage net variables are replotted under the same temperature condition in Fig. 11. The increase in damage net variables is observed with increasing strain rate. It implies that the fast loading results in more damage on asphalt concrete. Comparisons between the isotropic damage self-healing model prediction with one-parameter represented by blue lines (Hong et al. 2017a, b)

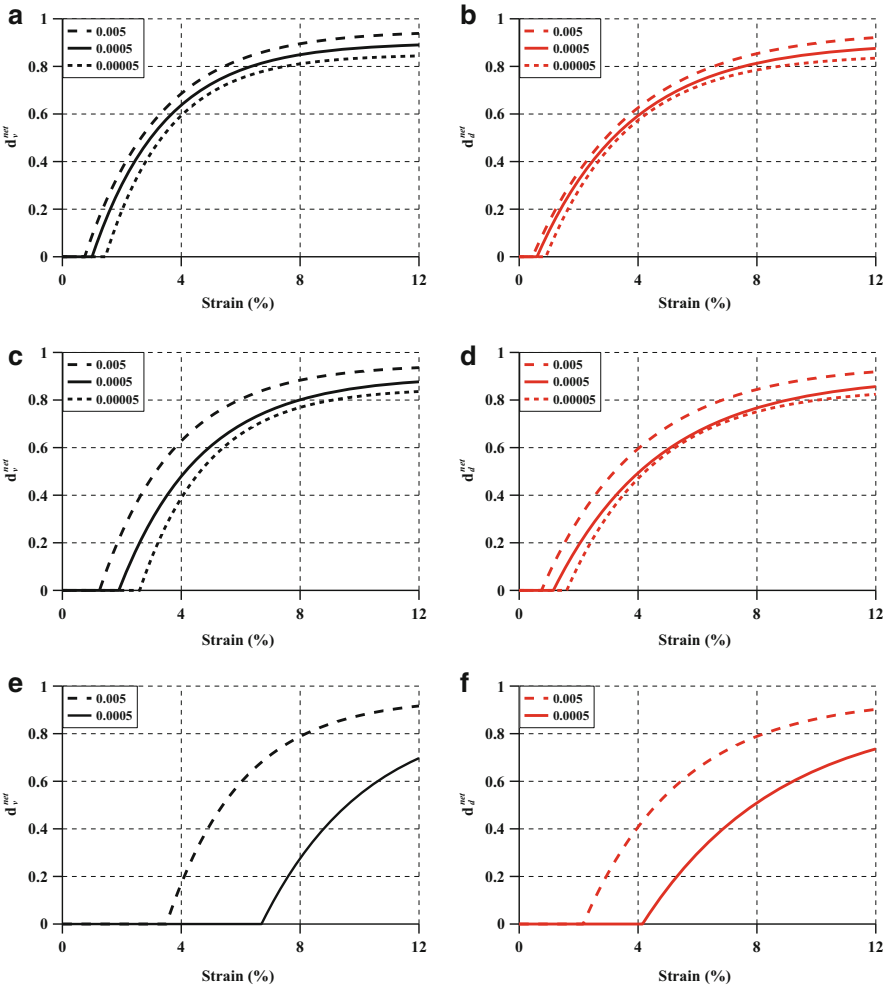

Fig. 11 Comparisons for damage net variables at constant temperature (**a**) d_v^{net} (10 °C), (**b**) d_d^{net} (10 °C), (**c**) d_v^{net} (20 °C), (**d**) d_d^{net} (20 °C), (**e**) d_v^{net} (40 °C), (**f**) d_d^{net} (40 °C)

and the two-parameter damage self-healing formulation drawn by red lines are shown in Fig. 12. It is clearly observed that the numerical prediction by the developed two-parameter formulation is closer to experimental data at 20 °C. Particularly,

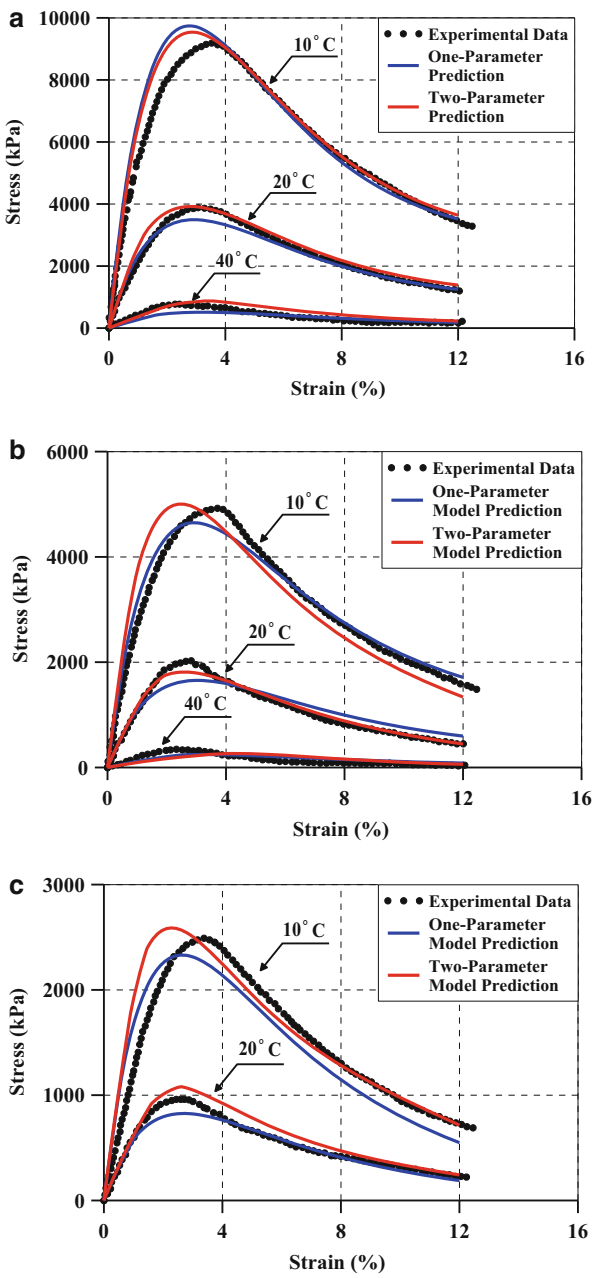

Fig. 12 Comparisons between the isotropic one-parameter model and the two-parameter model predictions for the uniaxial constant-strain rate test in compression ($\dot{\varepsilon} = 0.005 \sim 0.00005\ s^{-1}$) (**a**) Stress-strain ($\dot{\varepsilon} = 0.005\ s^{-1}$), (**b**) Stress-strain ($\dot{\varepsilon} = 0.0005\ s^{-1}$), (**c**) Stress-strain ($\dot{\varepsilon} = 0.00005\ s^{-1}$)

softening behaviors after the peak stress are well captured for each strain rate. The two-parameter models slightly better capture the test results in terms of smaller gap between the computational predictions and experimental data, even though computational data generated by the one-parameter or two-parameter damage self-healing formulations are close to the test results.

NCSU Asphalt Mixture Measurements

The experimental data are retrieved from literature review on controlled-strain cyclic tension tests of two different bituminous composites: (1) AAD which has a tendency for age hardening and cracking and (2) AAM which is defined as a good performer with a low temperature potential and susceptibility for cracking at low temperature (Lee 1996). The height and diameter of the cylindrical specimen were 250 mm and 102 mm, respectively, and the strain amplitudes of cyclic tests were set as 0.0009 and 0.001 for the AAD and AAM asphalt concretes, respectively, and the frequency was 1 Hz. Due to the limitation of available experimental measurements at different temperatures, the predictions by the proposed two-parameter damage self-healing formulation and test data for the controlled-strain cyclic tension are directly compared at constant temperature c (i.e., 25 °C). Table 2 shows the optimal material properties of AAD and AAM for the developed model obtained from the experimental measurement by fitting.

Comparisons between the computational predictions by using the developed two-parameter damage self-healing formulation and the experimental results of the cyclic loading tests for AAD and AAM are shown in Fig. 13, and the prediction can well match the test results. It is obviously observed from the tests that the stress-strain curve moves down with increasing the number of cycles signifying that a two-invariant Drucker-Prager yield criterion with Perzyna-type viscoplasticity model is well utilized. The numerical results represented by solid red line in Fig. 13c well capture the 287th cyclic experimental results for AAD as the developed two-parameter damage self-healing model is employed, whereas there are gaps between the computational results drawn by solid blue line and experimental data

Table 2 The associated asphalt material properties at 25 °C in simulations

	AAD	AAM
Young's modulus	1,300,000 (kPa)	1,200,000 (kPa)
Poisson's ratio	0.3	
Viscosity	244 (kPa/sec)	
Lame constants	750,000 (kPa)	692,307 (kPa)
Shear modulus	500,000 (kPa)	461,538 (kPa)
Initial volumetric damage threshold	0.2	0.15
Initial volumetric healing threshold	0.17	0.13
Initial deviatoric damage threshold	0.15	0.15
Initial deviatoric healing threshold	0.13	0.13
A_0	20 (kPa)	

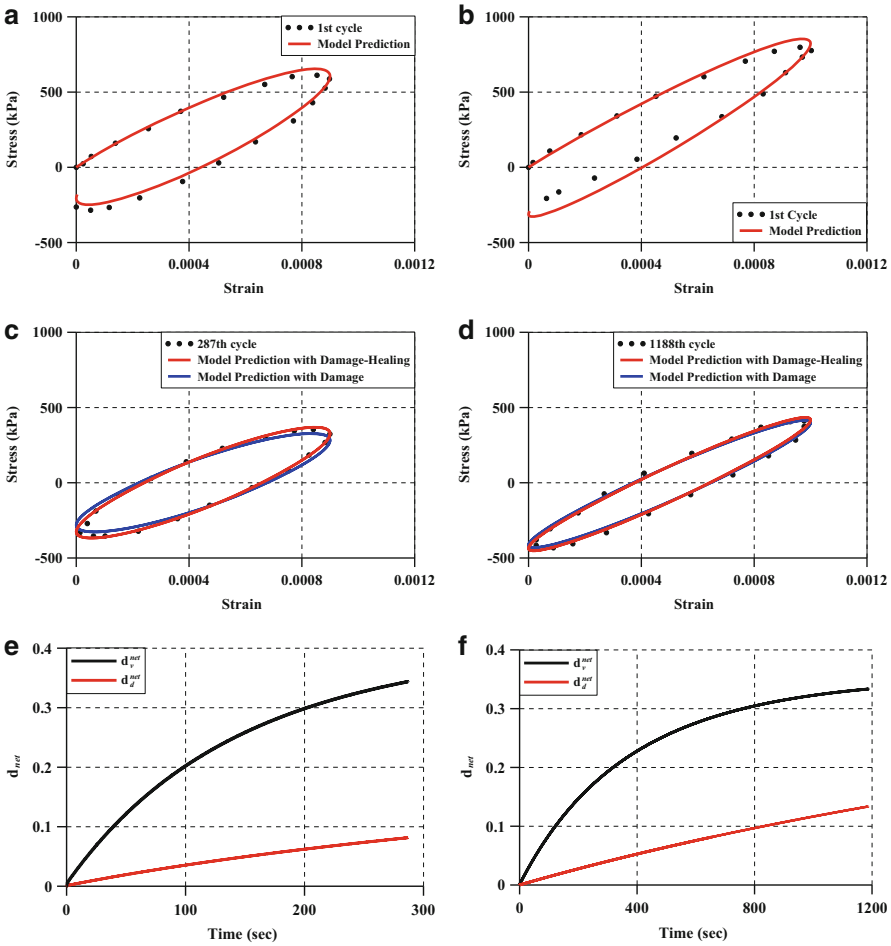

Fig. 13 Comparisons between experimental data and the model predictions for the cyclic loading in tension (**a**) first cycle (AAD), (**b**) first cycle (AAM), (**c**) 287th cycle (AAD), (**d**) 1188th cycle (AAM), (**e**) Damage net variable (AAD), (**f**) Damage net variable (AAM)

if only damage is considered. The model predictions plotted by solid blue line considering only the damage model do not match the test results for the 1188th cyclic loading because the healing mechanism is not coupled into the formulation, as described in Fig. 13d. The volumetric and deviatoric damage net variables for AAD and AAM are drawn in Fig. 13e, f, respectively. The shapes and magnitudes of the volumetric and deviatoric damage net variables seem to be close to each other, as presented in Fig. 11. However, it is clearly observed that the volumetric and deviatoric damage net variables increase with increasing the volumetric and deviatoric damage variables, whereas the volumetric and deviatoric damage net variables decrease as the energy norms of volumetric and deviatoric strain tensors

are lower than the volumetric and deviatoric healing thresholds, respectively, in Fig. 14. There are many different possibilities for the same volumetric damage net variable such that only one volumetric damage net variable is selected and plotted without including the volumetric damage and healing variables in Figs. 13 and 14 because the volumetric damage net variable is defined as a combination of the volumetric damage and healing variables. Due to the same reason, only one case of deviatoric damage net is drawn in Figs. 13 and 14. The volumetric damage and volumetric damage net variables increase until the end of reloading (B) as the equivalent volumetric strain under the reloading exceeds the volumetric healed damage threshold (point A) in Fig. 15a. The unloading zone is between points B and D, and the volumetric healing begins again at point C in Fig. 15a, which causes the decrease in the volumetric damage net. In Fig. 15a, the reloading restarts at point D, and the volumetric damage and volumetric damage net variables are constant until they arrive at the healed damage threshold at point E. The volumetric and deviatoric damage net variables are drawn for comparisons between AAD and AAM mixtures in Fig. 15b. It is found that the volumetric and deviatoric damage net variables are obviously dependent on the properties of asphalt concrete. Figure 16 shows comparisons between the isotropic and two-parameter damage self-healing formulations. It is noted through the comparisons that there are noticeable differences between the isotropic formulation with one-parameter and the two-parameter formulation. Moreover, the numerical results by the two-parameter model are

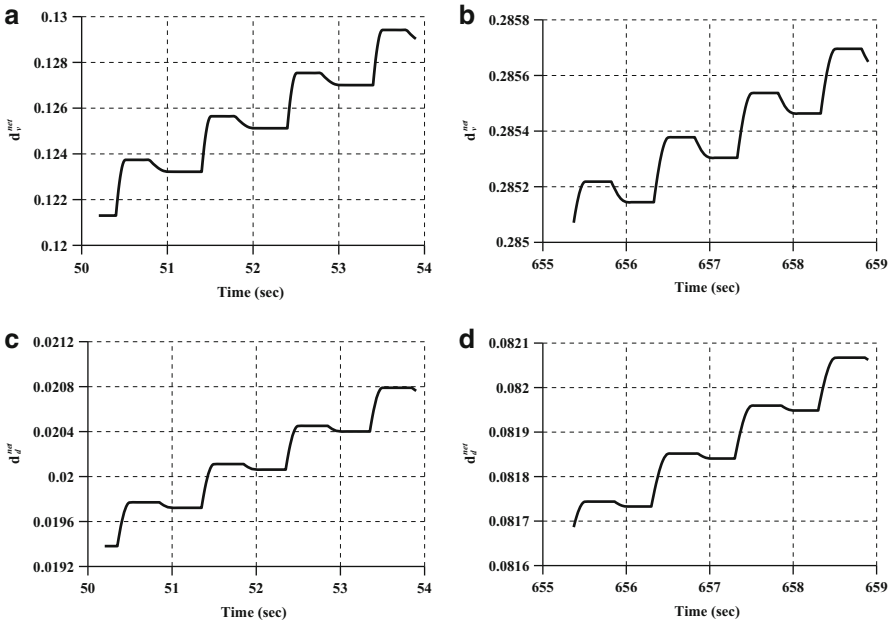

Fig. 14 The enlarged damage net variables (**a**) d_v^{net} (AAD), (**b**) d_v^{net} (AAM), (**c**) d_d^{net} (AAD), (**d**) d_d^{net} (AAM)

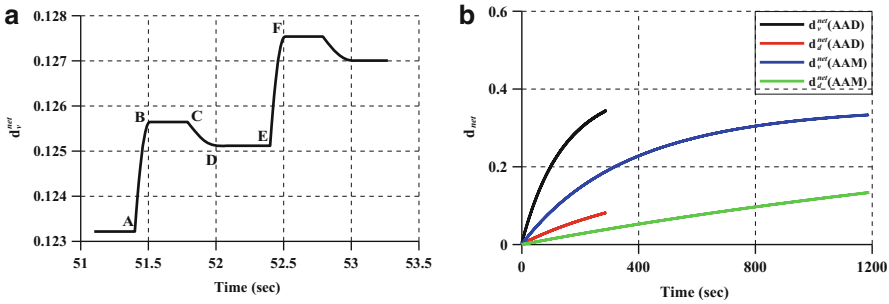

Fig. 15 Loading cycle for AAD and comparison of damage net variables between AAD and AAM (**a**) Loading cycle (AAD), (**b**) Damage net variables

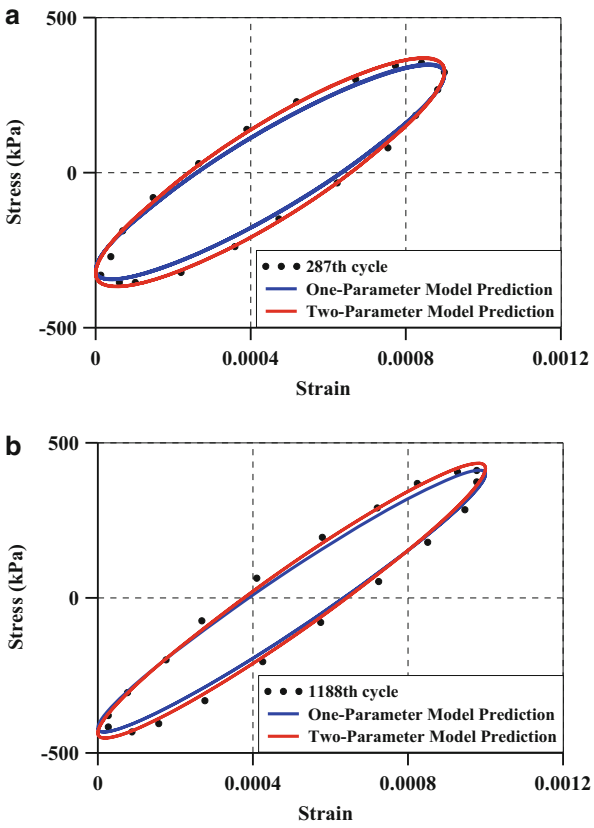

Fig. 16 Comparisons between the isotropic one-parameter model and the two-parameter model predictions (**a**) 287th cycle (AAD), (**b**) 1188th cycle (AAM)

outside of those by the isotropic model with one-parameter. Therefore, the developed thermo-elastoviscoplastic two-parameter damage self-healing model is called more general and realistic, and the isotropic model with one-parameter is simply named a

special case of the developed two-parameter formulation, but in general the volumetric damage is different from the deviatoric damage. For the purpose of simplification, the numerical results determined by isotropic one-parameter damage self-healing model may be acceptable under certain conditions.

Conclusions

In this chapter, the initial elastic strain energy-based thermo-elastoviscoplastic two-parameter damage self-healing models and its computational algorithms are implemented for the comparison of numerical results with the experimental data. Two-step operator split algorithms such as the elastic volumetric and deviatoric damage self-healing predictors and the net viscoplastic return mapping correctors are proposed with the Arrhenius temperature term. Particularly, the coupling of the volumetric and deviatoric damage and healing is first suggested in an incremental form based on two-step operator split algorithms and the net stress concept in conjunction with the strain equivalence hypothesis.

Since available experimental results are limited in the literature, the developed initial elastic strain energy-based thermo-elastoviscoplastic two-parameter damage self-healing models are only compared with two sets of test data, i.e., (1) the monotonic uniaxial tests under different temperature and strain rates for the validation of the two-parameter damage model and (2) the cyclic loading tests to verify the elastoviscoplastic two-parameter damage self-healing model. From the comparisons, it is validated that the developed two-parameter formulations have capabilities to qualitatively and quantitatively capture the nonlinear behavior of bituminous composites under different loading conditions at different temperatures. In addition, softening response of the asphalt concrete is reasonably predicted for monotonic loading tests. It is noted that the proposed elastic strain energy-based thermo-elastoviscoplastic two-parameter damage self-healing formulation can better predict the nonlinear temperature-dependent mechanical response of bituminous composites and is more versatile than isotropic damage self-healing model with one-parameter.

References

R.K. Abu Al-Rub, M.K. Darabi, D.N. Little, E.A. Masad, A micro-damage healing model that improves prediction of fatigue life in asphalt mixes. Int. J. Eng. Sci. **48**(11), 966–990 (2010)

E.J. Barbero, F. Greco, P. Lonetti, Continuum damage-healing mechanics with application to self-healing composites. Int. J. Damage Mech. **14**(1), 51–81 (2005)

Z.P. Bazant, F.B. Lin, Non-local yield limit degradation. Int. J. Numer. Methods Eng. **26**, 1805–1823 (1988)

M.K. Darabi, R.K. Abu Al-Rub, E.A. Masad, D.N. Little, Thermodynamic-based model for coupling temperature-dependent viscoelastic, viscoplastic, and viscodamage constitutive behavior of asphalt mixtures. Int. J. Numer. Anal. Methods Geomech. **36**(7), 817–958 (2012)

A.C. Eringen, D.G. Edelen, On nonlocal elasticity. Int. J. Eng. Sci. **10**, 233–248 (1972)

S. Hong, K.Y. Yuan, J.W. Ju, New strain energy based thermo-elastoviscoplastic isotropic damage-self healing model for bituminous composites – Part I: Formulations. Int. J. Damage Mech. (2017a). https://doi.org/10.1177/1056789515610706

S. Hong, K.Y. Yuan, J.W. Ju, New strain energy based thermo-elastoviscoplastic isotropic damage-self healing model for bituminous composites–part II: Computational aspects. Int. J. Damage Mech. (2017b). https://doi.org/10.1177/1056789515610707

J.W. Ju, On energy-based coupled elastoplastic damage theories-constitutive modeling and computational aspects. Int. J. Solids Struct. **25**, 803–833 (1989)

J.W. Ju, K.Y. Yuan, New strain-energy-based coupled elastoplastic two-parameter damage and healing models for earth-moving processes. Int. J. Damage Mech. **21**(7), 989–1019 (2012)

J.W. Ju, K.Y. Yuan, W. Kuo, Novel strain energy based coupled elastoplastic damage and healing models for geomaterials – Part I: Formulations. Int. J. Damage Mech. **21**(4), 525–549 (2012a)

J.W. Ju, K.Y. Yuan, W. Kuo, J.S. Chen, Novel strain energy based coupled elastoplastic damage and healing models for geomaterials – Part II: Computational aspects. Int. J. Damage Mech. **21**(4), 551–576 (2012b)

Y.R. Kim, *Modeling of Asphalt Concrete* (McGraw-Hill Construction ASCE Press, New York, 2009)

H. J. Lee, Uniaxial Constitutive Modeling of Asphalt Concrete Using Viscoelasticity and Continuum Damage Theory, Department of Civil Engineering, North Carolina State University, Ph.D. Dissertation, NC, USA, (1996)

J. Lemaitre, J.L. Chaboche, *Mechanics of Solid Materials* (Cambridge University Press, Cambridge, UK, 1990)

G.A. Shafabakhsh, E. Kashi, Evaluation of aircraft wheel load on pavement damages by layered elastic method. Int. J. Damage Mech. **24**, 1141–1154 (2015)

H. Shahsavari, M. Baghani, S. Sohrabpour, R. Naghdabadi, Continuum damage-healing constitutive modeling for concrete materials through stress spectral decomposition. Int. J. Damage Mech. **3** (2015). https://doi.org/10.1177/1056789515616447. first published on December

J.C. Simo, J.W. Ju, Strain-based and stress-based continuum damage models, part I: Formulation. Int. J. Solids Struct. **23**, 821–840 (1987a)

J.C. Simo, J.W. Ju, Strain-based and stress-based continuum damage models, part II: Computational aspects. Int. J. Solids Struct. **23**, 841–869 (1987b)

S.A. Tan, B.H. Low, T.F. Fwa, Behavior of asphalt concrete mixtures in triaxial compression. J. Test. Eval. **22**, 195–203 (1994)

G.Z. Voyiadjis, P.I. Kattan, Mechanics of damage, healing, damageability, and integrity of materials: A conceptual framework. Int. J. Damage Mech. **2** (2016). https://doi.org/10.1177/1056789516635730. first published on March

S. Xia, G. Li, H. Lee, A nonlocal damage theory. Int. J. Fract. **34**, 239–250 (1987)

K.Y. Yuan, J.W. Ju, New strain energy–based coupled elastoplastic damage-healing formulations accounting for effect of matric suction during earth-moving processes. J. Eng. Mech. ASCE **139**(2), 188–199 (2013)

K.Y. Yuan, J.W. Ju, W. Yuan, J.M. Yang, Numerical predictions of mechanical behavior of innovative pothole patching materials featuring high toughness, low-viscosity nano-molecular resins. Acta Mech. **225**(4), 1141–1151 (2014)

H.H. Zhu, S. Zhou, Z.G. Yan, J.W. Ju, Q. Chen, A two-dimensional micromechanical damage-healing model on microcrack-induced damage for microcapsule-enabled self-healing cementitious composites under tensile loading. Int. J. Damage Mech. **24**, 95–115 (2015)

Part VII

Damage for Disordered Materials

Failure Mechanics of Geomaterials

39

Florent Prunier, François Nicot, Richard Wan, Jérôme Duriez, and Félix Darve

Contents

Introduction: Main Features of Failure in Geomaterials 1078
A General Criterion for Failure by Divergence Instabilities 1080
Kinetic Energy and Second-Order Work 1080
Micromechanically Based Formulation 1082
The Second-Order Work Criterion, Features, and Illustrative 3D Examples (Multiaxial Loading) 1084
General Equation of Local Second-Order Work Criterion 1084
Illustration of Instability Cones Using Darve Model 1086
Conditions of Effective Failure 1087
Failure Analysis in Granular Materials by the Discrete Element Method 1089
Rock Joint Failure Modeling 1093
Two Rock Joint Constitutive Relations 1095
The Use of the Second-Order Work Criterion 1097
Application 1099

F. Prunier (✉)
INSA de Lyon, LGCIE, Villeurbanne, France
e-mail: florent.prunier@insa-lyon.fr

F. Nicot
IRSTEA, Geomechanics Group, ETNA, Grenoble, France
e-mail: francois.nicot@irstea.fr

R. Wan
Department of Civil Engineering, University of Calgary, Calgary, AB, Canada
e-mail: wan@ucalgary.ca

J. Duriez · F. Darve
Grenoble INP, UJF, CNRS, Grenoble, France
e-mail: jerome.duriez@3sr-grenoble.fr; felix.darve@grenoble-inp.fr; felix.darve@3sr-grenoble.fr

© Springer Nature Switzerland AG 2022

G. Z. Voyiadjis (ed.), *Handbook of Damage Mechanics*,
https://doi.org/10.1007/978-3-030-60242-0_21

Failure Modeling by Finite Element Method: Homogeneous Cases and Boundary Value Problems 1099
Material Instabilities in the Triaxial Test 1099
FEM Modeling of the Petacciato Landslide 1105
Conclusion 1107
References 1108

Abstract

Geomaterials represent an important class of dissipative materials whose mechanical behavior is pressure, density, and fabric dependent. This constitutive characteristic together with the discrete particulate nature of the material leads to the manifestation of a rich variety of failure modes whose precise understanding is elusive within standard failure theories. The present chapter attempts to clarify this issue by invoking plasticity/damage phenomena in geomaterials and exploits their non-associated character in relation to rate-independent irreversible strains. The second-order work criterion provides a basic framework within which failure can be systematically treated as a divergence instability that leads to various forms, including localized and diffuse modes. This new interpretation considers the existence of a bifurcation domain and so-called instability cones whose generators denote the range of loading directions in stress space along which the material response is potentially unstable. As additional important characteristics, macroscopic failure is found to occur with an outburst of kinetic energy with the proper load control parameter in place, as demonstrated in discrete element computations. Finally, the failure analysis of in situ boundary value problems as in a rock and a soil slope is presented using the second-order work.

Keywords

Discrete element method · Triaxial test · Rock slope · Rock joint · Stress space

Introduction: Main Features of Failure in Geomaterials

Failure in geomaterials (soil, rock, and concrete) is a very intricate question in comparison to other solid materials, probably because for geomaterials the plastic limit condition, yield surface, and plastic potential are all mean pressure dependent. All these surfaces have indeed a conical shape in the stress space. In relation with this mean pressure dependency, the plastic strains have a non-associated character. Thus, the yield surface (characterized roughly speaking by a cohesion and a friction angle) does not coincide with the plastic potential (characterized by a dilatancy angle). For an associated material, both friction and dilatancy angles must be equal, while these differ usually by 25–30° for granular media.

As a first approximation, geomaterial behavior can be considered as largely rate independent, which means that this behavior is described by an elastoplastic or elasto-damageable constitutive relation represented by a fourth-order constitutive

tensor linking incremental strains (or strain rates) and incremental stresses (or stress rates). Then, by considering the six-dimensional associated stress and strain spaces, a 6-by-6 constitutive matrix is used to relate incremental strains and stresses. A direct consequence of non-associativity of plasticity is the nonsymmetry of the above constitutive matrix. As such, the possible singularities of this matrix (linked to failure as it will be seen later on) can be of very different kinds in comparison with the case of a symmetric matrix corresponding to the associated plasticity case. A typical aspect of failure in geomaterials appears here as a direct consequence of this nonsymmetry: there is indeed a rich variety of failure modes each differing in character involving either localized or diffuse deformation fields, among others.

An important but fundamental question has to be asked: what is failure? The usual definition is that a failure state is reached when a limit stress state is reached by the material. If some mixed stress–strain loading paths are considered, this definition has to be extended to include other types of limit states such as those constituted by a limiting volume expansion for dilatant materials in the so-called triaxial loading paths with a constant deviatoric stress in geomechanics (Darve et al. 2007; Daouadji et al. 2010, 2011; Laouafa et al. 2011). More precisely, when a failure state is reached, the failure can be effective or not depending on the current control parameter. As a classical example, when the control parameter is a strain rate, the limit stress state can be overcome without any specific change for the body, while if the control parameter is a stress rate, the body suddenly enters into a dynamic regime with a burst of kinetic energy and large uncontrollable strains.

From a theoretical point of view, it is possible to say that an effective failure corresponds to a bifurcation point, because of the sudden change in the strain regime from quasi-static deformations to dynamic ones. It is also characterized by a loss of uniqueness, since the deformations are no more defined in a unique way and depend on some imperfections. Eventually effective failure is also an unstable state, since a small perturbation of the body in a failure state induces large material responses. Of course, the converse of the above argument is not generally true: bifurcations, losses of uniqueness, or instabilities are not always related to an effective failure in solid mechanics. However, an efficient way to investigate the failure states and the failure modes of a given geomaterial is to first consider its unstable states, and then check if these instabilities can lead to effective failures and, if yes, for which conditions. This methodology to analyze failure will be the central theme of this chapter.

Indeed, a general criterion for all types of divergence instabilities has been proposed by Hill (1958), the so-called second-order work criterion, which corresponds to the loss of positive definitiveness of the constitutive matrix and is a necessary condition for instability. This can be reworded as to there is at least one stress direction where the scalar product of the incremental stress by the incremental strain is nil or negative. For a nonsymmetric matrix, the loss of positive definitiveness (linked to the vanishing value of the determinant of the symmetric part of the constitutive matrix) appears before the singularity of the matrix itself (linked to the vanishing value of the determinant of the matrix itself). Thus, there is a whole failure domain in the stress space (Darve et al. 2004) and not only a single plastic limit surface as for associated plastic materials. More recently, two new developments

have allowed clarifying two important physical aspects of the second-order work. First, the link between bursts of kinetic energy and negative values of second-order work has been established (Nicot and Darve 2007, 2011; Nicot et al. 2009, 2012a). Second, for elastic nonconservative systems, the second-order work appears as the lower envelope of all possible instability curves (Lerbet et al. 2012; Nicot et al. 2011), corresponding to all types of divergence instabilities.

This chapter is organized as follows. First the link between second-order work criterion and burst of kinetic energy is recalled. At the grain level, the second-order work takes a discrete form linking increment of force and increment of displacement at the contact point. The relation between the sum of all discrete second-order works calculated at every intergranular contact and the macroscopic second-order work is established and discussed. Then, the features of second-order work as a quadratic form associated to the current incremental stress or the current incremental strain are illustrated by phenomenological rate-independent constitutive relations for the general 3D multiaxial-loading case. The bifurcation domain is plotted as well as the "instability cones" for two elastoplastic relations (one is incrementally piecewise linear and the other fully incrementally nonlinear). In the third part, a careful check of these various aspects (link between second-order work and kinetic energy, bifurcation domain, instability cones, features of the effective failure, influence of the control mode, influence of a perturbation) is performed by considering direct numerical simulations using a discrete element method. Then this methodology is applied in the fourth section to the question of the stability of rock joints. A rate-independent relation for rock joints is introduced and a specific expression of second-order work is considered to analyze failure. Eventually, the finite element method is employed to simulate triaxial tests, exhibiting localized and diffuse failure modes. An example of modeling of an in situ landslide in Italy (Petacciato landslide) is finally presented to illustrate the ability of the second-order work criterion to describe a failure mode of the diffuse type using the finite element method.

A General Criterion for Failure by Divergence Instabilities

Kinetic Energy and Second-Order Work

Let us consider a material system, subjected to external forces. The mechanical (stress–strain) state of this system, after a given loading history, is reputed (mechanically) unstable if the kinetic energy of the system may increase under the effects of infinitesimal loading (disturbance). In particular, if the system is initially at rest, in equilibrium under external forces, an increase in kinetic energy means that there is a transition from a quasi-static regime towards a dynamical regime. This transition is basically a bifurcation and is clearly associated to a failure that can be either localized or diffuse, according to the pattern of the kinematic field developing during this transition. The failure is localized when a localization pattern develops or is diffuse if the kinematic field remains chaotic, without specific localization (Nicot and Darve 2011).

In what follows, the conditions and the growth mode of the kinetic energy are studied. For a material system made up of a volume V_0, initially in a configuration C_0 of boundary (Γ_0), in equilibrium at time t under a prescribed external loading, it was established that the second-order time differentiation of the kinetic energy (at time t) written in Lagrangian formulation (Nicot et al. 2007; Nicot and Darve 2007; Nicot et al. 2012a, 2012b) is

$$\begin{aligned} &\delta^2 E_c(t) = W_2^{\text{ext}} - W_2^{\text{int}} \\ &W_2^{\text{ext}} = \int_{\Gamma_o} \delta f_j \ \delta u_i \ dS_o; \ W_2^{\text{int}} = \int_{V_o} \delta \Pi_{ij} \ \frac{\partial(\delta u_i)}{\partial X_j} \ dV_o \end{aligned} \tag{1}$$

where W_2^{ext} and W_2^{int} denote the external second-order work and internal second-order work, respectively. In these expressions, $\overline{\overline{\Pi}}$ denotes the Piola–Kirchhoff stress tensor of the first kind and $\vec{f}$ the current forces applied to the initial (reference) configuration. $\delta\vec{u}$ denotes the current incremental displacement of the material points initially located at the position $\vec{X}$. In addition, the second-order Taylor's expansion of kinetic energy reads

$$E_c(t+\Delta t) = E_c(t) + \Delta t \ \dot{E}_c(t) + \frac{(\Delta t)^2}{2} \ddot{E}_c(t) + 0(\Delta t)^3 \tag{2}$$

Noting that $E_c(t) = \int_{V_o} \rho_o \left\| \dot{\vec{u}} \right\|^2 dV_o$ and $E_c(t) = \int_{V_o} \rho_o \ \dot{\vec{u}} \cdot \ddot{\vec{u}} \ dV_o$, where ρ_o is the density of the material in the initial configuration at point $M\left(\vec{X}\right)$, and since the system is in an equilibrium state at time t, then $\dot{E}_c(t) = 0$. Thus, ignoring third-order terms, Eq. 2 reads

$$\delta^2 E_c(t) = 2(E_c(t+\delta t) - E_c(t)) \tag{3}$$

Combining Eqs. 1 and 3 gives

$$E_c(t+\delta t) - E_c(t) = \frac{1}{2} \ \left(W_2^{\text{ext}} - W_2^{\text{int}}\right) \tag{4}$$

Consequently, the increase in kinetic energy for a material system initially in equilibrium (at rest) equals to the difference between the external second-order work (that involves the displacements and the forces acting on the boundary) and the so-called internal second-order work (built from the internal stress and strain acting at each point of the system). Finally, the external second-order work is related to the external loading and can be controlled by an external user. In contrast, the internal second-order work is intimately related to the constitutive behavior of the material and is imposed by the material independently of the external user (Nicot et al. 2012a). As a result, any increase in kinetic energy of the system stems

from a conflict between the internal forces (resulting from the internal stress) applying to the internal side of the boundary and the external forces (imposed by the operator or any other external action) applying to the external side of the boundary (Nicot et al. 2012a).

According to Eq. 4, both external and internal second-order works are equal in quasi-static conditions, since $E_c(t + \delta t) - E_c(t) = 0$ (there is no increase in kinetic energy). Particularly of interest is the situation where the loading applied gives rise to a negative value of the internal second-order work. It can be shown that such a situation corresponds to the existence of a limit state (possibly in a generalized strain–stress space; Nicot et al. 2009, 2011, 2012a). Some components of the internal loading pass through a peak and then follow a descending branch, which prevent these components from taking higher values. On the contrary, higher values of the external loads applied to the system can be imposed. The resulting conflict between both internal and external loads induces an increase in kinetic energy, indicating a transition from a quasi-static to a dynamical regime. It is worth noting that this situation is closely related to the existence of a generalized limit state, detected by the vanishing of the internal second-order work. After the peak, along the descending branch, the internal second-order work takes negative values.

As a conclusion, as far as divergence instabilities are concerned, detecting whether the internal second-order work can vanish makes sense. The existence of nil or negative values of the second-order works stands as one of the basic conditions giving rise to the occurrence of a divergence instability.

Micromechanically Based Formulation

The problem is now specialized to granular materials, with an attempt to relate the macroscopic formulation of the internal second-order work to microstructural variables. For this purpose, a homogeneous volume of granular material is comprised of N grains. "p" will denote indiscriminately the grain (as a body) or enumerate a particular grain within the assembly such that $1 \leq p \leq N$. The shape of each grain "p" is arbitrary. The total number of contacts at time t within the assembly is denoted N_c. The system is assumed to be in equilibrium at a given time t under a prescribed external loading. Depending on the type of loading control, each grain "p" belonging to the boundary ∂V of the considered volume is subjected to either a displacement (kinematic control) or an external force $\vec{f}^{\text{ext},p}$ (static control), possibly zero.

The second-order work, in its basic formulation, involves both incremental stress and strain. The stress within a granular assembly expresses the transmission of forces in granular materials. The transmission of forces in granular materials operates at contacts of adjoining grains, thereby resulting in a macroscopic average stress at the grain assembly level. The stress tensor in such a body of volume V in equilibrium under external forces $\vec{f}^{\text{ext},p}$ applied to the boundary particles "p" of position $\vec{x}^{p}$ can

be defined by the classical Love–Weber formula (Love 1927; Mehrabadi et al. 1982), i.e.,

$$\sigma_{ij} = \frac{1}{V} \sum_{p \in \partial V} f_i^{\text{ext},p} \; x_j^p \tag{5}$$

The above expression can be transformed as follows, by accounting for the interparticle contact forces $\vec{f}^{\,c}$ (Nicot et al. 2012c):

$$\sigma_{ij} = \frac{1}{V} \sum_{c=1}^{N_c} f_i^c \; l_j^c + \frac{1}{V} \sum_{p \in V} f_i^p \; x_j^p \tag{6}$$

where $\vec{l}^{\,c}$ is the branch vector relating the centers of contacting particles and $\vec{f}^{\,p}$ denotes the resultant force applied to the particle "p." In the absence of inertial effects or when all particles are in static equilibrium, the second term in Eq. 6 vanishes. However, this term may subsist in the presence of internal dynamical effects that arise from local force imbalances, even if the whole granular body may be in equilibrium macroscopically.

In the Eulerian formulation represented in Eq. 6, the contact forces, the branch vectors, the location of each particle, and the volume of the specimen are bound to evolve over a given loading history from an initial configuration $C_0 = \left(\vec{f}^{\,c}_0, \vec{l}^{\,c}_0, \vec{x}^{\,c}_0, V_0\right)$. Thus, referring to the initial configuration, the analogous form of the stress tensor in Lagrangian description is

$$\Pi_{ij} = \frac{1}{V_0} \sum_{p,q} f_i^c \; l_{0,j}^c + \frac{1}{V_0} \sum_{p \in V_0} f_i^p \; x_{0,j}^p \tag{7}$$

The Lagrangian formulation given in Eq. 7 can be readily differentiated, then providing the following expression of the internal second-order work (see Nicot et al. 2012c, for more details):

$$W_2 = \sum_{p,q} \delta f_i^c \; \delta l_i^c + \sum_{p \in V} \delta f_i^p \; \delta x_i^p \tag{8}$$

As specified in Nicot et al. (2012c), the creation or the deletion of contacts is accounted for in this approach. The symbol $\sum_{p.q}$ denotes the summation over p and q varying over [1, N] with $q \leq p$, and c refers to the contacting pair (p, q).

It is worth noting that in the absence of incremental unbalanced force and in quasi-static regime, Eq. 8 simplifies into

$$W_2 = \sum_{p,q} \delta f_i^c \; \delta l_i^c \tag{9}$$

Equation 9 expresses the internal second-order work from micromechanical variables, namely, the contact forces existing between contacting granules and the branch vectors joining these granules. The attempt of such a formulation is to go down to the microscopic scale and to try to elucidate what are the basic microstructural origins giving rise to the vanishing of the internal second-order work and therefore what are the microstructural contexts prone to instabilities.

The Second-Order Work Criterion, Features, and Illustrative 3D Examples (Multiaxial Loading)

As mentioned in the previous section, determining the sign of the second-order work allows the detection of material instability by divergence. Neglecting geometrical effects and assuming small strains, the internal second-order work takes the following expression:

$$W_2 = \int_{V_o} \delta\sigma_{ij}\delta\varepsilon_{ij} dV_o \tag{10}$$

where $\delta\sigma_{ij}$ is the incremental Cauchy stress tensor and $\delta\varepsilon_{ij}$ the incremental small strain tensor. In a local form the stability criterion is expressed as

$$\forall\left(\delta\sigma_{ij}, \delta\varepsilon_{ij}\right) \quad \delta W_2 = \delta\sigma_{ij}\delta\varepsilon_{ij} > 0. \tag{11}$$

In other words, when δW_2 is positive, the specimen is stable, else potentially unstable. It will be seen further that instability occurrence (or the kinetic energy growth) depends on the control loading parameter when δW_2 is negative or zero.

General Equation of Local Second-Order Work Criterion

In the following of this section, only rate-independent materials are considered. In this case the constitutive relation takes the general following form:

$$F^h_{ijkl}\left(\delta\sigma_{ij}, \ \delta\varepsilon_{kl}\right) = 0 \tag{12}$$

where F^h is a nonlinear function and h a memory parameter like a hardening parameter. Along the actual loading direction function F^h can be linearized ("directional linearization"), and Eq. 12 can take the simple form:

$$\delta\varepsilon_{ij} = N_{ijkl}\delta\sigma_{kl} \tag{13}$$

Using dual representations of tensors where a second-order tensor can be a six-dimensional vector and a fourth-order tensor, a matrix of rank six, the matrix N denoting the tangent elastoplastic operator along the current loading direction is

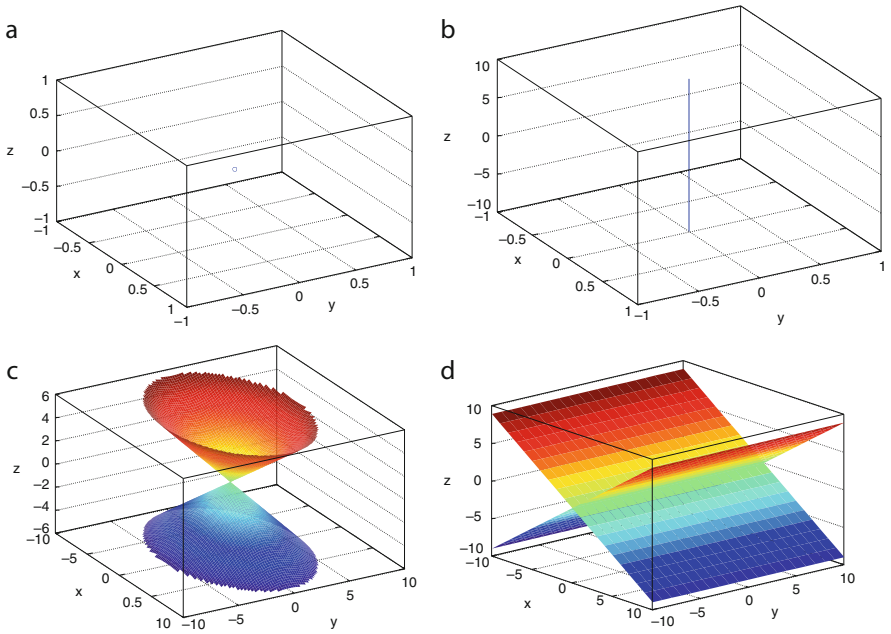

Fig. 1 Graphical representation of solutions of Eq. 15: empty solution, straight line, elliptical cone, and two planes intersection

introduced. As such, when substituting Eq. 13 into Eq. 11, the boundary between positive and negative values of δW_2 is given by

$$\delta\sigma_i N_{ij} \delta\sigma_j = \delta\sigma_i N^s_{ij} \delta\sigma_j = 0 \tag{14}$$

where N^s is the symmetrical part of N. Developing Eq. 14 in the case of orthotropic incrementally piecewise linear relation leads to the general equation of an elliptical cone in the three-dimensional space of principal incremental stress.

$$\frac{\delta\sigma_1^2}{E_1} + \frac{\delta\sigma_2^2}{E_2} + \frac{\delta\sigma_3^2}{E_3} - \left(\frac{\nu_1^2}{E_1} + \frac{\nu_2^1}{E_2}\right)\delta\sigma_1\delta\sigma_2 - \left(\frac{\nu_3^2}{E_3} + \frac{\nu_2^3}{E_2}\right)\delta\sigma_2\delta\sigma_3 - \left(\frac{\nu_1^3}{E_1} + \frac{\nu_3^1}{E_3}\right)\delta\sigma_3\delta\sigma_1 = 0 \tag{15}$$

Geometrical representations of the solutions of Eq. 15 in terms of loading directions are displayed in Fig. 1.

If the solution of Eq. 15 is empty, no instability can develop. In the other cases, instability can develop if the loading path has a direction included inside directions given by the solution of Eq. 15. It is to be noted that Eq. 15 can be used practically only with an incrementally piecewise linear model, and solutions have to be truncated in parts of the space where the constitutive relation is linear. These particular parts of the space are also denoted as tensorial zones (Darve and Labanieh 1982).

Nevertheless, most of rate-independent models are piecewise linear. In the case of fully incrementally nonlinear models, nonempty solutions of Eq. 15 reduce necessarily to a nonelliptical cone gathering straight lines. An illustration of this proposal is given in the next subsection using the octo-linear model (8 L model) and incrementally nonlinear model of Darve (INL2 model) (Darve and Labanieh 1982).

Illustration of Instability Cones Using Darve Model

Constitutive relations developed by Darve do not rely on classical concepts of elastoplasticity and therefore assumptions of (a) strain decomposition into an elastic and a plastic part, (b) existence of an elastic limit, and (c) existence of a flow rule are not needed.

In order to describe the nonlinear behavior of geomaterials, an incrementally nonlinear relation of second order is used and written in principal axes as follows:

$$\begin{Bmatrix} \delta\varepsilon_1 \\ \delta\varepsilon_2 \\ \delta\varepsilon_3 \end{Bmatrix} = \frac{1}{2}\left[\underline{\underline{N}}^{+} + \underline{\underline{N}}^{-}\right] \begin{Bmatrix} \delta\sigma_1 \\ \delta\sigma_2 \\ \delta\sigma_3 \end{Bmatrix} + \frac{1}{2\|\underline{\delta\sigma}\|}\left[\underline{\underline{N}}^{+} + \underline{\underline{N}}^{-}\right] \begin{Bmatrix} \delta\sigma_1^2 \\ \delta\sigma_2^2 \\ \delta\sigma_3^2 \end{Bmatrix} \tag{16}$$

with

$$\underline{\underline{N}}^{\pm} = \begin{bmatrix} \frac{1}{E_1^{\pm}} & -\frac{\nu_{21}^{\pm}}{E_2^{\pm}} & -\frac{\nu_{31}^{\pm}}{E_3^{\pm}} \\ -\frac{\nu_{12}^{\pm}}{E_1^{\pm}} & \frac{1}{E_2^{\pm}} & -\frac{\nu_{32}^{\pm}}{E_3^{\pm}} \\ -\frac{\nu_{13}^{\pm}}{E_1^{\pm}} & -\frac{\nu_{23}^{\pm}}{E_2^{\pm}} & \frac{1}{E_3^{\pm}} \end{bmatrix} \tag{17}$$

Coefficients E_i^{+} and ν_{ij}^{+} are defined on generalized triaxial loading paths when $\delta\sigma_i > 0$ and, respectively, E_i^{-} and ν_{ij}^{-} when $\delta\sigma_i < 0$. For $\delta\sigma_i = 0$ it can be verified that the relation is continuous (Gudehus 1979). More detailed information about this constitutive model and, in particular, how the tangent moduli and Poisson's ratios evolve with stress–strain history can be found in Darve et al. (1995). In one dimension, this relationship is piecewise linear. By extension, the octo-linear model (eight tensorial zones) is defined in the following with the previous notations:

$$\begin{Bmatrix} d\varepsilon_1 \\ d\varepsilon_2 \\ d\varepsilon_3 \end{Bmatrix} = \frac{1}{2}\left[\underline{\underline{N}}^{+} + \underline{\underline{N}}^{-}\right] \begin{Bmatrix} d\sigma_1 \\ d\sigma_2 \\ d\sigma_3 \end{Bmatrix} + \frac{1}{2}\left[\underline{\underline{N}}^{+} + \underline{\underline{N}}^{-}\right] \begin{Bmatrix} |d\sigma_1| \\ |d\sigma_2| \\ |d\sigma_3| \end{Bmatrix} \tag{18}$$

It can be seen that the eight tensorial zones are bounded by the intersection of the three planes of respective expression: ($\delta\sigma_1 = 0$, $\delta\sigma_2 = 0$, $\delta\sigma_3 = 0$). Figure 2 shows

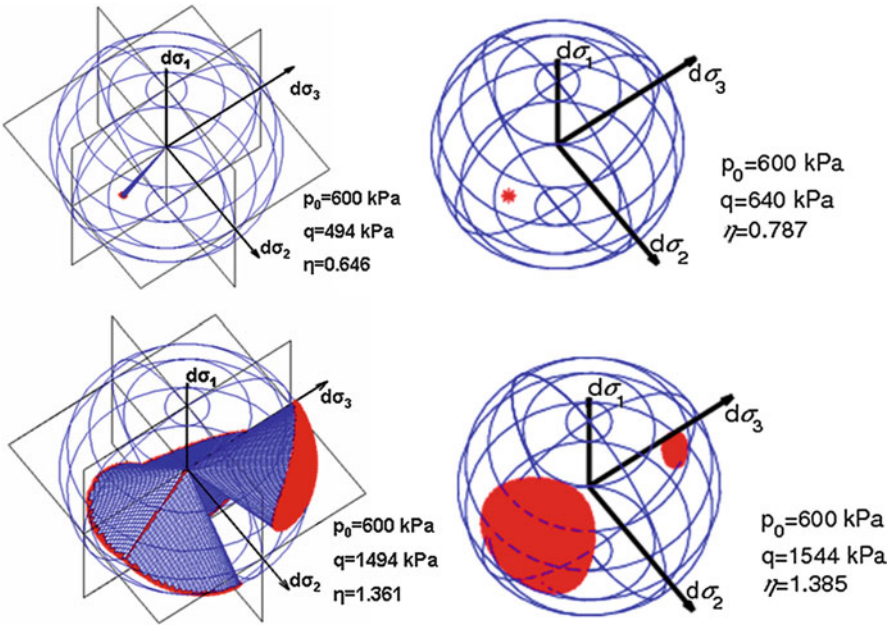

Fig. 2 3D instability cones given by octo-linear model of Darve (*left* side) and by the nonlinear model of Darve (*right* side). p_0 is the initial confinement pressure, q the actual stress deviator, and $\eta = q/p$

instability cones obtained along a drained triaxial path with both models (octo-linear and incrementally nonlinear) of Darve on a dense Hostun sand. According to the incrementally nonlinear model, a numerical procedure has been used (Prunier et al. 2009a; Darve et al. 2004). For the octo-linear model, solutions are displayed using analytical form of Eq. 15 as well as the numerical procedure.

In the stress space, the set of stress states for which instability cones exist constitutes the bifurcation domain. When the cones are reduced to a single direction, the latter gives the limit of the bifurcation domain. For non-associated materials this bifurcation limit is located strictly inside the plasticity limit, whereas for associated materials, the limits coincide. The limit of bifurcation domain has been plotted for Darve models and compared to Mohr–Coulomb limit (Prunier et al. 2009a, b, c); see Fig. 3.

Conditions of Effective Failure

Previously, conditions that lead to negative values of second-order work have been seen, i.e., the stress–strain state has to be included inside the bifurcation domain, and the loading path should follow a direction inside an instability cone. When second-order work is negative or zero, effective instability which leads to a burst of kinetic energy is conditioned by the control parameter chosen by the experimenter (or natural boundary loading occurring according to in situ conditions). From a

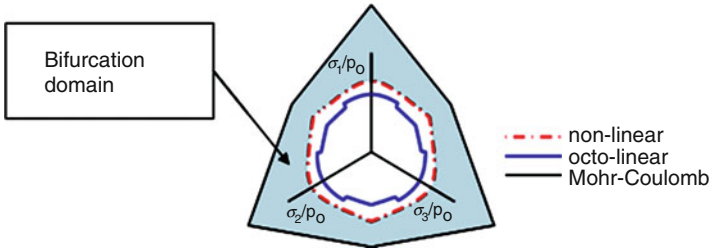

Fig. 3 Limit of bifurcation domain plotted according Darve models calibrated on a dense sand of Hostun plotted in the deviatoric plane

basic point of view, when pulling on steel sample if the axial strain is controlled, the test can be continued after reaching the limit state given by the maximum axial stress, while if the axial stress is controlled, a sudden failure occurs. In fact the vanishing of the second-order work corresponds to a generalized limit state achieved strictly inside the plasticity limit. Let us consider proportional stress path as follows:

$$\begin{cases} \delta\sigma_1 = \text{cst} \quad \text{cst} \in \mathrm{R} \\ \delta\sigma_1 + R\delta\sigma_3 = 0 \quad R \in \boldsymbol{R}^* \\ \delta\sigma_2 - R'\delta\sigma_3 = 0 \quad R' \in \boldsymbol{R} \end{cases} \tag{19}$$

where $\boldsymbol{R}$ denotes the set of real numbers and $\boldsymbol{R}^*$ the set of real numbers excluding zero. For such loading paths, it is possible to write a generalized constitutive relation:

$$\begin{bmatrix} \delta\varepsilon_1 - \dfrac{\delta\varepsilon_3}{R} - \dfrac{R'}{R}\delta\varepsilon_2 \\ \delta\sigma_1 + R\delta\sigma_3 \\ \delta\sigma_2 - R'\delta\sigma_3 \end{bmatrix} = \underline{\underline{S}} \begin{bmatrix} \delta\sigma_1 \\ \dfrac{\delta\varepsilon_3}{R} + \dfrac{R'}{R}\delta\varepsilon_2 \\ \delta\varepsilon_2 \end{bmatrix} \tag{20}$$

where R and R' are variables that allow the description of all possible loading directions. Particular values of R and R' which describe directions included in an instability cone can be found, such that $\varepsilon_1 - \varepsilon_3/R - R'/R.\varepsilon_2$ reaches an extremum. Hence, because of the statical constraint in Eq. 20, at the $\varepsilon_1 - \varepsilon_3/R - R'/R.\varepsilon_2$ peak, det(S) vanishes for nontrivial solutions of Eq. 20 and a generalized failure rule can be defined. Furthermore, knowing that the second-order work can be rewritten as in Eq. 21,

$$\begin{aligned} W_2 = &\left(\delta\varepsilon_1 - \frac{\delta\varepsilon_3}{R} - \frac{R'}{R}\delta\varepsilon_2\right) d\sigma_1 + (\delta\sigma_1 + R\delta\sigma_3)\left(\frac{\delta\varepsilon_3}{R} + \frac{R'}{R}\delta\varepsilon_2\right) \\ &+ (\delta\sigma_2 - R'\delta\sigma_3)\delta\varepsilon_2, \end{aligned} \tag{21}$$

the second-order work vanishes as well at this extremum. Figure 4 illustrates previous discussions on a particular stress path. First, a drained triaxial path is followed until reaching a stress deviator just before the bifurcation domain limit.

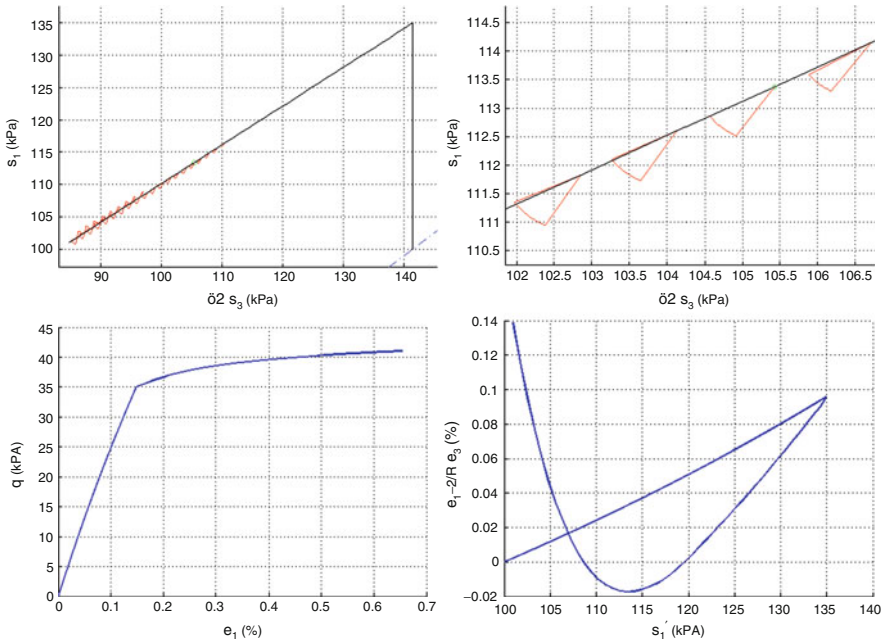

Fig. 4 Simulation of proportional stress path using INL model. First a drained triaxial path is applied until $q = 35$ kPa, and then a proportional stress path has been followed with $R = 0.85$ and $R' = 1$. At the $\varepsilon_1 - \varepsilon_3/R - R'/R.\varepsilon_2$ extremum, second-order work vanishes and a limit state is reached

Then, a proportional stress path is imposed with values of $R = 0.85$ and $R' = 1$ (Laouafa et al. 2011; Daouadji et al. 2011).

Based on Fig. 4, the following observations can be made. The first cone (reduced to a single direction) gives the bifurcation domain limit, whereas the limit state described by the extremum is reached whenever the loading path is tangent to a cone and $W_2 = 0$. As such, the loading path is strictly inside a cone when $W_2 < 0$. As concluding remarks, in the present case, the limit state is defined by a strain state. Similar studies can be made with proportional strain paths in which case limit states are defined by stress states instead.

Failure Analysis in Granular Materials by the Discrete Element Method

The Discrete Element Method (DEM) is a direct numerical simulation of granular media (Cundall and Strack 1979). In the granular assembly each grain is described as an elastic body interacting with a Coulombian friction with the neighboring grains in contact. Thus, pre-failure, failure state, and post-failure regime can be simulated in a very natural and realistic way without addressing the numerical difficulties usually encountered in continuum mechanics with the finite element method. This is the

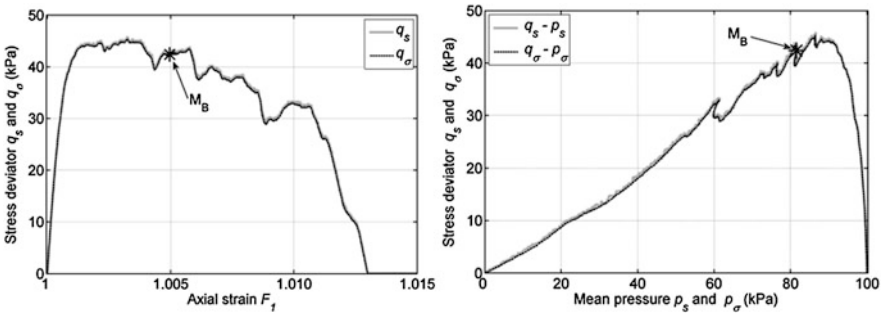

Fig. 5 Undrained (isochoric) triaxial compression of a loose particle assembly. q_s and p_s are computed from the stress state at the boundary of the sample, and q_σ and p_σ are computed from the internal stress state (Nicot et al. 2012a)

main reason why the DEM approach is chosen here to validate numerically the features of diffuse failure as exhibited previously in sections "A General Criterion for Failure by Divergence Instabilities" and "The Second-Order Work Criterion, Features, and Illustrative 3D Examples (Multiaxial Loading)" by the second-order work criterion. A numerical cubical specimen of about 10,000 spheres of various radii is prepared, then some loading paths can be applied at the boundaries of the cube. For a more detailed description of the numerical method, the reader can refer to Nicot et al. (2012a) and Sibille et al. (2008).

The first point to be investigated now is the link between second-order work and kinetic energy as established theoretically in section "Introduction: Main Features of Failure in Geomaterials." To this end, an axisymmetric undrained triaxial path is simulated by applying numerically to the specimen, in a loose density state, an axisymmetric isochoric loading path. As observed experimentally (Daouadji et al. 2010), the deviatoric stress q (q is equal to the axial stress minus the lateral stress) passes through a maximum value. In Fig. 5, the peak of q can be observed as well as the ultimate vanishing of the intergranular stresses when the effective stress path reaches the origin of the q-p plane (p is the intergranular mean effective pressure). In addition to the above plot, a comparison is presented between the externally applied stresses at the boundary of the sample (noted by q_s and p_s) and the internal stresses q_σ and p_σ obtained from the internal intergranular force field by applying Love–Weber relation (Love 1927). The observed excellent agreement is an indicator of the consistency of the numerical computations. At stress state M_B, just after the peak in q, a small additional axial deviatoric stress is applied, i.e., $\Delta q_s = 1.6$ kPa. According to section "A General Criterion for Failure by Divergence Instabilities," the sample cannot sustain this additional force. This is illustrated in Fig. 6, where the applied external load q_s is no more equal to the internal stress q_σ. The failure induced by this additional load produces a burst of kinetic energy, which is equal for a small time increment (here, on Fig. 7, about 0.08 s) to half the difference between the external applied second-order work (noted by $[V.\Delta S_i.\Delta F_i]_{\Delta t}$ on Fig. 7) and the internal second-order work (noted by $[W_2]_{\Delta t}$), as established in section "A General

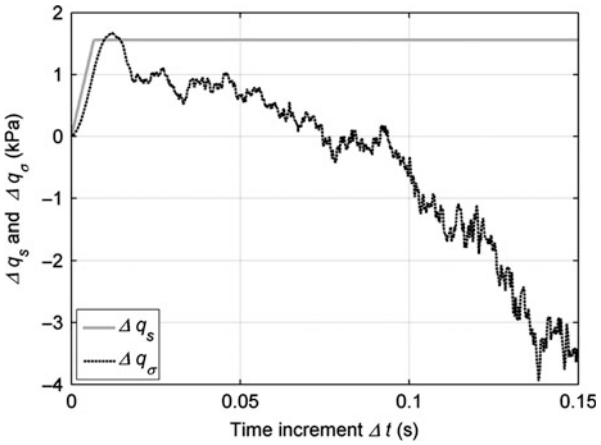

Fig. 6 Stress increments resulting from the application of $\Delta q_s = 1.6$ kPa from the state M_B defined in Fig. 5 (Nicot et al. 2012a)

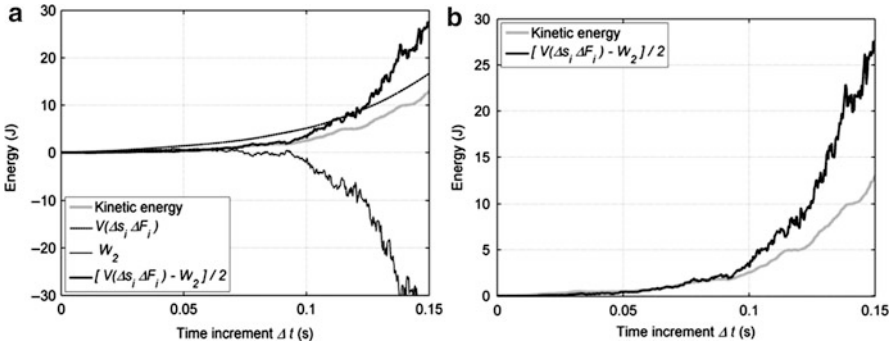

Fig. 7 Time series of the kinetic energy and terms $[W_2]_{\Delta t}$, $[V.\Delta S_i.\Delta F_i]_{\Delta t}$, and $[V(\Delta S_i.\Delta F_i - W_2)/2]_{\Delta t}$ during and after the application of $\Delta q_s = 1.6$ kPa from the state M_B (**a**). Focus on shorter time increments (**b**) (Nicot et al. 2012a)

Criterion for Failure by Divergence Instabilities." The kinetic energy is obtained by adding both the translational and rotational kinetic energies of each grain, whereas the external second-order is the product of the small additional axial surface force and the axial strain (multiplied by the sample volume V). On the other hand, the internal second-order work is simply calculated as the inner product of the Love macroscopic stress tensor and the macroscopic strain tensor (multiplied by V).

A second aspect (shown in section "The Second-Order Work Criterion, Features, and Illustrative 3D Examples (Multiaxial Loading)") is the fact that the second-order work is a quadratic form of incremental stresses or strains, which means – according to linear algebra – that there are some instability cones capturing all stress directions for which the second-order work is negative. Figure 8 shows such a cone for different values of the deviatoric stress $\eta = q/p$ by plotting the polar variations of

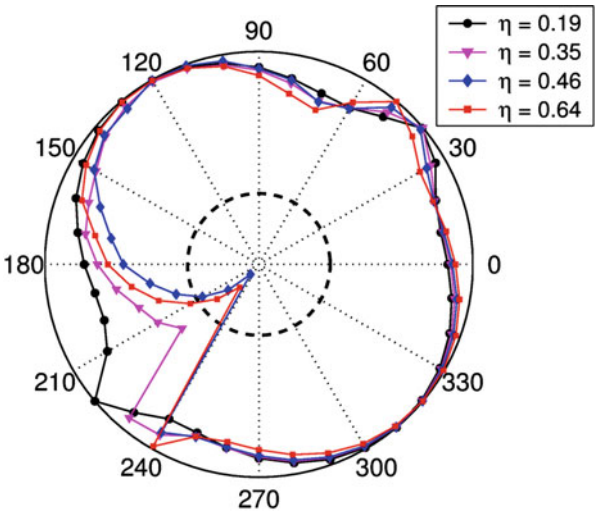

Fig. 8 Polar diagram of the normalized second-order work for a loose granular assembly at confinement pressure of 100 kPa. The dashed circles represent zero value of the second-order work; $\eta = q/p$ represents the mobilized deviatoric stress (Sibille et al. 2008)

the normalized second-order work with respect to stress directions in axisymmetric conditions. The normalized second-order work is obtained by dividing the second-order work by the norms of the incremental stress and the incremental strain. As such, the normalized second-order work represents the cosine of the angle between both the stress and strain vectors in the axisymmetric plane and varies between −1 and +1. The second-order work takes negative values inside the dashed circle of Fig. 8. The fact that inside the instability cone an effective failure is possible (with a proper control variable) while outside no failure can occur is checked in Fig. 5. For both stress directions outside of the cone (alpha angle = 200° and 240°), stresses and strains remain constant under a small additional load. For both directions inside the cone (220° and 215.3°), the failure is characterized by suddenly and strongly growing strains with decreasing stresses. Eventually for both directions at the boundary of the cone (210° and 230°), some erratic responses from the sample are obtained (Fig. 9).

The question of the control variable is investigated in Fig. 10 for a q constant axisymmetric drained loading path (which is indeed an isotropic unloading from a deviatoric stress–strain state, corresponding to a stress direction of 215.3°). Experimentally, it has been observed (Daouadji et al. 2010) that the volume changes go through a maximum dilation along this path. Thus, if this loading path is fully stress controlled, no effective failure is expected according to the theory described in section "The Second-Order Work Criterion, Features, and Illustrative 3D Examples (Multiaxial Loading)." On the other hand, if this loading is partially volume variations controlled (mixed loading), an effective failure must be observed as given by the theory. These phenomena are well illustrated in Fig. 10, where both kinds of control are compared.

Finally, Fig. 11 establishes the important observation that an effective failure can be indeed induced by a perturbation close to the failure state. Because failure states

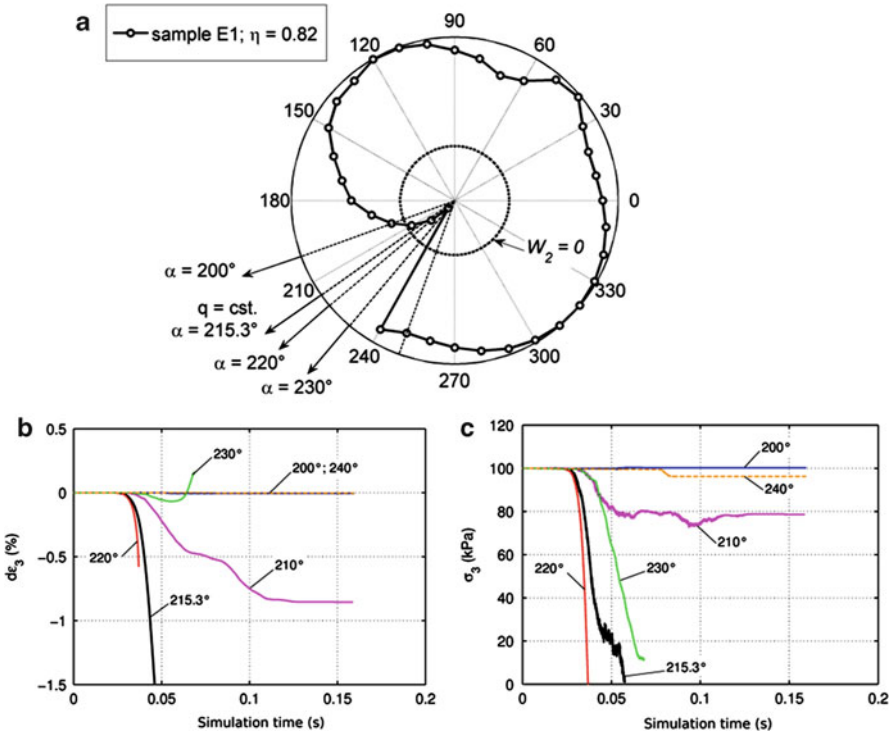

Fig. 9 (**a**) Polar plot of the normalized second-order work for a loose granular assembly at a confinement pressure of 100 kPa, with some particular stress directions highlighted. (**b**) Simulated responses in terms of strains (**b**) and stresses (**c**) to loading paths defined by $\delta\sigma_1 - \delta\sigma_3/R = 0$ and $\delta\varepsilon_1 + 2R\delta\varepsilon_3 < 0$, for a loose granular assembly at a confinement pressure of 100 kPa and for $\eta = q/p = 0.46$

are essentially unstable states, they are naturally sensitive to perturbations. Experimentally, it is well known that failure can be triggered by a proper perturbation. Here, the numerical perturbation is constituted by a small "injection" of kinetic energy to the sample. Since all the computations are performed without gravity forces, at each computation step few grains are floating inside the specimen. To perturb the sample's state, a small additional velocity is numerically imparted to these grains. An effective failure is clearly observed in Fig. 11 just after the perturbation of the q constant axisymmetric path through a burst of kinetic energy with strongly growing strains and decreasing stresses.

Rock Joint Failure Modeling

In the following rocks as another example of geomaterials are considered. In order to assess rock slopes stability, a focus is made on rock joints whose failure can trigger rock falls. Among the possible different types of defects that can occur in rock slopes

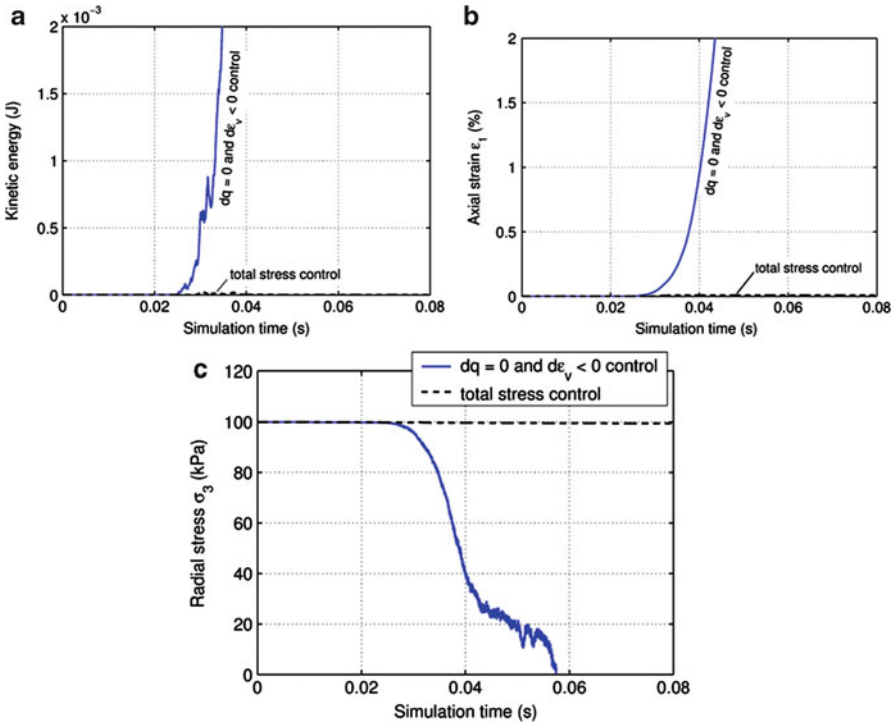

Fig. 10 Comparison of a loose granular assembly responses along a q-constant path for a full stress control ($\delta\sigma_1 = \delta\sigma_3 < 0$) and a control with $\delta q = 0$ and $\delta\varepsilon_V < 0$; kinetic energy (**a**), axial strain (**b**), and radial stress (**c**) versus time of simulation (Sibille et al. 2008)

at different scales, the discontinuities in mechanical properties that exist at a macroscopic scale are called "rock joints." In a fractured rock slope, it can be assumed that the stability of the slope is mainly governed by the mechanical behavior of existing rock joints. Compared to the geomaterials covered in the previous sections, these rock joints constitute an interface medium (material). Thus, their mechanical behavior can be described using only four scalar variables as obtained from two vectors. The first vector relates to stress with σ as its component normal to the joint (positive in compression) and τ its tangential one. The second vector refers to relative displacement mobilized between the two rock blocks in contact along the joint, with u being the normal component (positive in compression) and γ the tangential component.

An internal second-order work is in this case defined as

$$\delta W_2 = \delta\vec{\sigma}\,\delta\vec{l} = \delta\sigma\delta u + \delta\tau\delta\gamma \tag{22}$$

As explained in section "A General Criterion for Failure by Divergence Instabilities," a negative second-order work can lead to failure by divergence instabilities. In

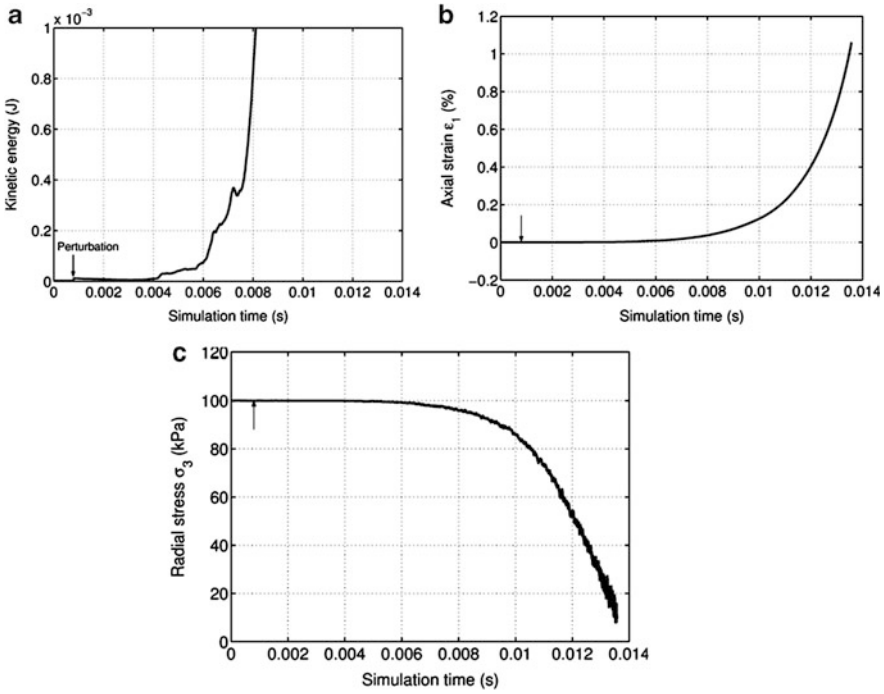

Fig. 11 Simulation of loss of sustainability for loose granular assembly at a mechanical state governed by the control parameters $\delta q = 0$ and $\delta\varepsilon_V = 0$; the arrows in the diagrams represent the time where perturbation was applied (Sibille et al. 2008)

this context, relative displacements along the joint will increase towards a dynamic regime, ultimately triggering a rockfall. Since the second-order work is governed by the material properties of the joint, two given rock joint are studied with a focus on their constitutive relations.

Two Rock Joint Constitutive Relations

In the following, the rock joint relations are derived from the soils relations presented in section "Illustration of Instability Cones Using Darve Model." An INL2 relation, with an infinity of tensorial zones, and a quadri-linear relation with four tensorial zones for rock joints were recently proposed in Duriez et al. (2011a, b). The development of these models relies on calibration paths along which the behavior of the joint is known, i.e.,

- A constant normal displacement (CND) path, with ($\delta u = 0$; $\delta\gamma = cst$). Four moduli are thus defined from this path:

$$G_\gamma^+ = \frac{\partial \tau}{\partial \gamma_u}_{\ cst, d\gamma>0} \quad G_\gamma^- = \frac{\partial \tau}{\partial \gamma_u}_{\ cst, d\gamma<0}$$

$$N_\gamma^+ = \frac{\partial \sigma}{\partial \gamma_u}_{\ cst, d\gamma>0} \quad N_\gamma^- = \frac{\partial \sigma}{\partial \gamma_u}_{\ cst, d\gamma<0}$$

Moduli $G_\gamma^{+/-}$ correspond to tangential stiffnesses, while moduli $N_\gamma^{+/-}$ take into account the dilatant (or contractant) feature of the joint.

- A constant tangential displacement (CTD) path, with ($\delta u = cst$; $\delta\gamma = 0$). This corresponds to an oedometric compression. Four other moduli are herein defined:

$$G_u^+ = \frac{\partial \tau}{\partial u_\gamma}_{\ cst, du>0} \quad G_u^- = \frac{\partial \tau}{\partial u_\gamma}_{\ cst, du<0}$$

$$N_u^+ = \frac{\partial \sigma}{\partial u_\gamma}_{\ cst, du>0} \quad N_u^- = \frac{\partial \sigma}{\partial u_\gamma}_{\ cst, du<0}$$

Moduli $N_u^{+/-}$ are normal stiffnesses. Changes in τ during compression can be described through moduli $G_u^{+/-}$. Indeed, numerical and experimental data revealed such variations, depending on the state of shearing in the joint (Duriez et al. 2011a; see Fig. 12).

Along any other loading path, the behavior of the joint is computed as an interpolation between the behavior of these two calibration paths. For a piecewise linear interpolation, a quadri-linear relation, with four tensorial zones is derived. For constant signs of du and $d\gamma$, a linear relation with a constant matrix links in this case $\delta\vec{\sigma}$ to $\delta\vec{l}$. For example, if $\delta u > 0$ and $\delta\gamma < 0$, it comes

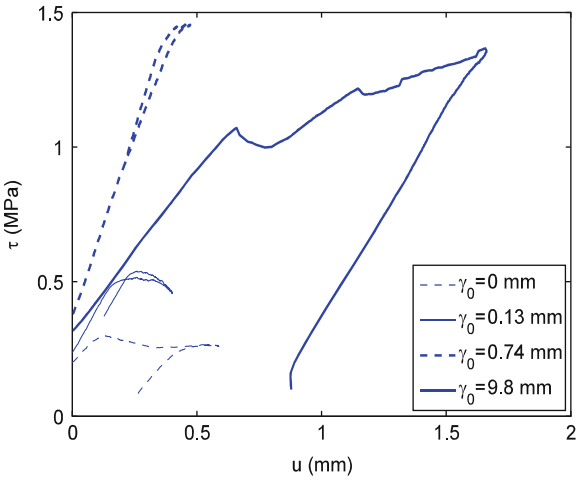

Fig. 12 Changes in τ during different oedometrical compressions on a rock joint in gneiss, since different initial states in shearing (Duriez et al. 2011a). The slopes of the curves correspond to moduli $G_u^{+/-}$

$$\delta\vec{\sigma} = \begin{pmatrix} \delta\tau \\ \delta\sigma \end{pmatrix} = \begin{pmatrix} G_\gamma^- & G_u^+ \\ N_\gamma^- & N_u^+ \end{pmatrix} \vec{\delta l} = \begin{pmatrix} G_\gamma^- & G_u^+ \\ N_\gamma^- & N_u^+ \end{pmatrix} \begin{pmatrix} \delta\gamma \\ \delta u \end{pmatrix} \tag{23}$$

Using a quadratic interpolation leads to the INL2 relation. The expression (not presented here) involves matrices depending on the eight moduli and the direction of $\delta\vec{l}$, leading to an infinite number of tensorial zones, meaning that for each direction, there is a different constitutive matrix. Predictions of the INL2 relation are generally more efficient than the quadri-linear relation, but both are generally close. Furthermore, the quadri-linear relation allows analytical derivations, as it will be seen in section "The Use of the Second-Order Work Criterion."

Appropriate expressions of the moduli were proposed in (Duriez et al. 2011b). They depend on the state of shearing in the joint, expressed by the ratio τ/σ. Due to the nature of the expressions used in the model, a plastic limit criterion is intrinsically defined in the relations. The stress states they predict do not exceed a Mohr–Coulomb-like criterion. Both models describe a non-associated behavior (Duriez et al. 2011b), which justifies the use of the second-order work criterion.

The Use of the Second-Order Work Criterion

For any rock joint constitutive relation in one tensorial zone, e.g., for the quadri-linear relation with constant signs of δu and $\delta\gamma$, it is easy to show (Duriez et al. 2012) that the sign of the second-order work is given by a second-order polynomial P, with respect to the loading direction $\delta u/\delta\gamma$: $P(\delta u/\delta\gamma)$. Under the assumption of positive normal stiffnesses $N_u^{+/-}$ – this could be untrue in high-porosity rocks showing compaction bands (Mollema and Antonellini 1996) – directions of instability exist under the following condition:

$$\left(G_u^{+/-} + N_\gamma^{+/-}\right)^2 \geq 4N_u^{+/-}G_\gamma^{+/-} \tag{24}$$

The above equation involves a comparison between "diagonal" stiffnesses, $N_u^{+/-}$ and $G_\gamma^{+/-}$, and coupled stiffnesses, $G_u^{+/-}$ and $N_\gamma^{+/-}$. Applying Eq. 24 to the four tensorial zones of the quadri-linear relation allows determining directly its bifurcation domain in the stress space (Fig. 13). Directions of instability exist under sheared states of the joint, but before the Mohr–Coulomb criterion. Shearing reduces indeed diagonal (e.g., normal) stiffnesses (Bandis et al. 1983) and increases coupled ones, allowing Eq. 23 to be verified. For the INL2 relation, the bifurcation domain is obtained using a numerical procedure. It is reduced in the INL2 case, compared to the quadri-linear case (see Fig. 13) (as for soils, see previous Fig. 3).

Directions of instability are determined analytically for the quadri-linear relation, by solving the inequality $P(\delta u/\delta\gamma) \leq 0$. A cone of directions is found; see Fig. 14. The two branches of the cone are the roots of polynomial P, and all directions $\delta u/\delta\gamma$ between the two roots trigger $P(\delta u/\delta\gamma) < 0 \Leftrightarrow \delta W_2 < 0$. The cone is more and more

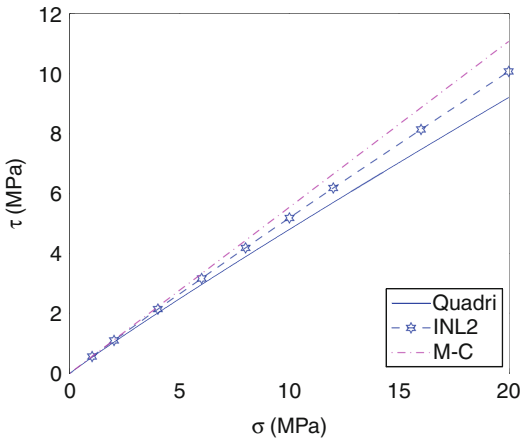

Fig. 13 Bifurcation domains of quadri and INL2 rock joint constitutive relations (Duriez et al. 2012). A Mohr–Coulomb (M–C) criterion gathers the admissible stress states

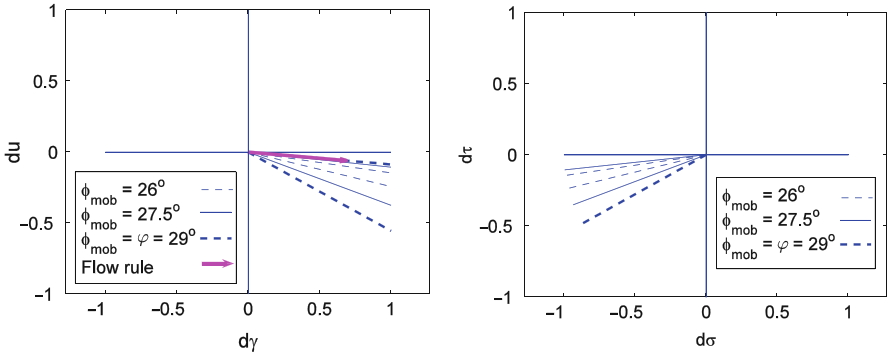

Fig. 14 Cones of directions of instability for the quadri-linear relation, in the displacement space (*left*) or the stress space (*right*) (Duriez et al. 2012). The cones get more and more open while the shearing increases

open as the rock joint is sheared, i.e., as the ratio $\tau/\sigma =$ tan (Φ_{mob}) increases. Once on the plastic limit criterion, for $\tau/\sigma =$ tan (φ), one branch of the cone in the displacement space corresponds to the flow rule of the joint. Indeed, for a loading $\delta\vec{l}$ corresponding to the flow rule, $\delta\vec{\sigma} = f\left(\delta\vec{l}\right) = \vec{0}$ (the unstable direction in stress space is then not defined), and obviously $\delta W_2 = 0$.

For the INL2 relation, similar results are obtained with a numerical procedure (Duriez et al. 2012). For both relations, in stress space, both normal and shear stresses decrease for unstable loadings, as for soils in axisymmetric conditions, considering mean and deviatoric stresses. It was shown in Duriez et al. (2012) that the orientation in the stress space of the directions of instability is given by a comparison between the coupled stiffnesses of the joint: the moduli Gu and $N\gamma$. These coupled stiffnesses govern the instability of a rock joint, since they appear in the equation of the bifurcation domain.

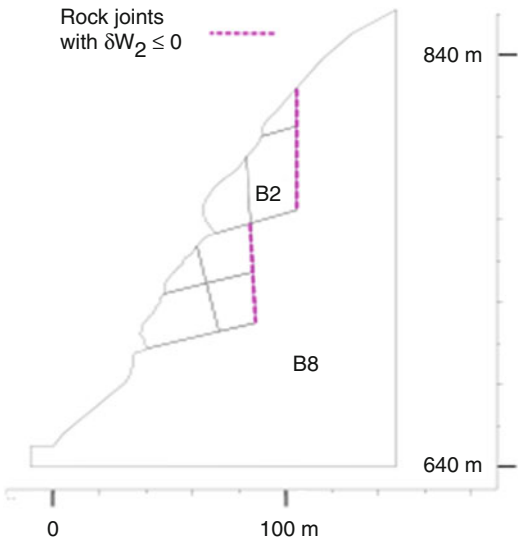

Fig. 15 Numerical model of the slope with the rock joints where $\delta W_2 \leq 0$ during the simulated loading (Merrien-Soukatchoff et al. 2011)

Application

An existing rock slope, in south of France, is studied using this approach (Merrien-Soukatchoff et al. 2011). A numerical model of the cliff was proposed, in two dimensions, with eight blocks of intact matrix and several rock joints inbetween. The INL2 constitutive relation is used to describe rock joint behavior. A continuous increase in gravity is applied to the cliff, as a loading. Another loading could be chosen by excavating the top of the cliff, in order to better reproduce the geological history of the slope.

During the simulated loading, negative values of the second-order work are obtained in some joints (Fig. 15). It is noteworthy that this is the case for one joint which has not yet reached its plastic limit criterion, between blocks B2 and B8. No rockfall is obtained here; this would probably be the case if the concerned joints surround a set of blocks. A global second-order work, taking into account the local values along all joints, is required to deal with such cases.

Failure Modeling by Finite Element Method: Homogeneous Cases and Boundary Value Problems

Material Instabilities in the Triaxial Test

The preceding sections delved into the description of failure in geomaterials as a bifurcation problem with the second-order work criterion acting as a general framework within which various forms of instabilities can be captured such as diffuse and

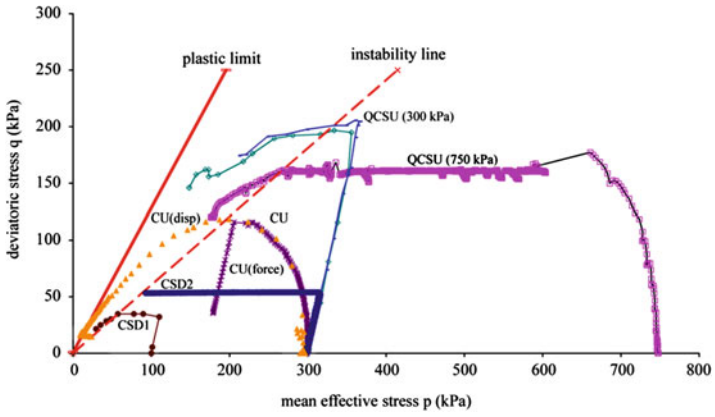

Fig. 16 Experimental evidence of material instabilities in various triaxial tests on Hostun S28 sand (Darve et al. 2007)

localized modes. Examples of diffuse and localized failure are manifest in conventional triaxial testing of soils where both stress and strain are axisymmetric. The most well-known manifestation of diffuse failure is in the consolidated undrained (CU) shearing of a loose sand when the effective stress path passes through a peak where the second-order work is violated. With the proper operative control parameters, herein load control mode, a diffuse failure emerges in a CU test on loose sand with spontaneous release of kinetic energy. While this peak point lies within the bifurcation domain, it is most importantly associated with a loading direction that is inside the bifurcation cone. The above two conditions together with the proper control parameters are required for an effective failure to occur. Figure 16 shows how diffuse material instability occurs in several types of triaxial tests, all having a common feature of violating the second-order work well below the plastic limit.

In the so-called CSD test where the specimen is sheared at constant deviatoric stress with decreasing mean effective stress in drained conditions, controllability is lost at some point during the test. The ensuing diffuse failure is governed by the same phenomenon as in the CU test, provided that all of the proper conditions discussed previously are in place. The QCSU test, a variant of the CSD test where drainage is prevented while the deviatoric stress fluctuates about a constant value, also shows the same instability phenomenon. All tests exhibited unstable material response by loss of controllability, and hence collapse, roughly at the same stress ratio defined by a reference bifurcation line with slope of $\eta = q/p = 0.6$ in the p-q space, which is reminiscent of the well-known instability line introduced by (Lade 1992). However, in the framework described in this chapter, a wider scope using bifurcation theory provides theoretical and physical insights in explaining the collapse behavior of sands.

Finite Element Analysis of Diffuse Failure

In the next diffuse failure with respect to control parameters as evidenced in the triaxial tests described in the previous subsection is numerically captured.

Two initial densities are examined, namely, void ratios $e_0 = 0.7$ and 0.8, referring to medium–loose to loose sand, respectively. An elastoplastic model having all the essential ingredients that are prerequisites for capturing unstable material behavior is employed (see Wan and Guo 2004). These include density, stress, and anisotropy dependencies through a micromechanical enrichment of Rowe's stress dilatancy equations. As additional important properties, they account for plastic-strain softening and non-associativity of plastic yield and flow that provide sources of material instability, as discussed in the beginning of this chapter.

Loading Direction, Control Parameters, and Bifurcation Domain

The numerical triaxial tests are herein modeled as an initial boundary value problem involving coupled solid–fluid interaction to mimic the actual triaxial test with drainage conditions. As such, a three-dimensional finite element mesh with 5220 linear elements representing a cylindrical sand sample is used in the simulations.

Figure 17 summarizes the numerical results of CSD, CU, and QCSU tests performed on a loose sand specimen, $e_0 = 0.8$ with a focus on second-order work evolution. The undrained (CU) test was run in both displacement control and stress control in order to highlight the role of the load control parameters on the resulting failure mode. Figure 17a shows that the points at which the second-order work first

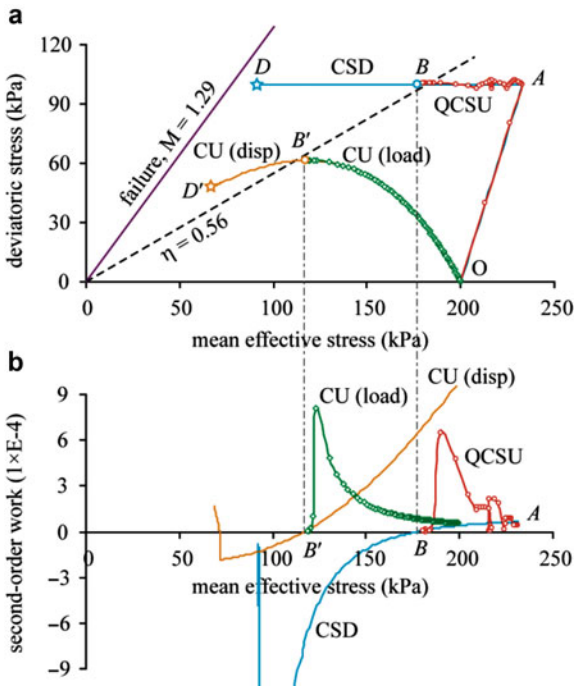

Fig. 17 Simulation of various triaxial tests together with identification of bifurcation and ultimate failure points

vanishes for all tests fall almost on a straight line with a slope $\eta = 0.56$. This line actually lies above the lower limit of the bifurcation domain where the second-order work first vanishes with all but only one possible loading direction for material instability to occur. When compared with the Mohr–Coulomb failure line at a slope $M = 1.29$ in the p-q space, it is evident that the second-order work first vanishes at a stress state well below the classic plastic limit.

The evolution of the non-normalized second-order work with mean effective stress for these tests is presented in Fig. 17b. It is interesting to observe that the second-order work becomes zero approximately at the same point B for the two q-constant tests, but with different evolution due to the loading history. It is noteworthy to point out that contrary to the QCSU test, the CSD test carried past the bifurcation point B but finally failed at point D near the plastic limit surface. For the QCSU test, failure as a loss of controllability occurred much earlier at the bifurcation point B, due to the proper load control parameters.

Also of particular interest are the numerical results obtained for the consolidated undrained compression test case where it is found that the second-order work vanishes at the same stress point B′ irrespective of the load control parameters. However, in the force-controlled case, as the second-order work vanishes, the test cannot be controlled further and the computations break down, meaning collapse of the specimen. The undrained test performed under strain-controlled mode carries on past the peak B′ until it fails at point D′ for lack of numerical convergence. Since, by contrast, the same test stops at the very same peak point B′ under stress controlled mode, this observation conveys two important results. First, to obtain diffuse failure with collapse, it is not solely sufficient to have the second-order work criterion violated, but it is also necessary to have the proper control variables in place, here a force-controlled loading program. Second, the direction of the loading matters, and here it appears to be a horizontal direction which is necessarily contained within the instability cone in the p-q plot. The instability cone essentially defines the range of loading directions in the p-q space for which the second-order work is violated.

Second-Order Work, Relevance to Loss of Uniqueness, and Localization

It is recalled that the vanishing of the second-order work locally and globally signals the possibility of instability and the loss of uniqueness of solutions of the boundary value problem. This numerical aspect is checked in the subsection whereby two or more solutions can emerge starting from the same base state. As an illustration, the undrained test simulations for medium–loose sand ($e_0 = 0.7$) are considered.

Figure 18a shows the branching of effective stress paths after the peak was reached where second-order work vanished. For clarity of illustration, only four strategic gauss points where choosen as indicated in Fig. 18b showing the final nonhomogeneous deformed configuration when localization of deviatoric plastic strain occurred. As expected, inside this shearing zone (#078), the deviatoric plastic strains are higher than in other parts (#004, #068, #059) of the specimen. In Fig. 18, these are reflected into distinctly different paths followed by the four

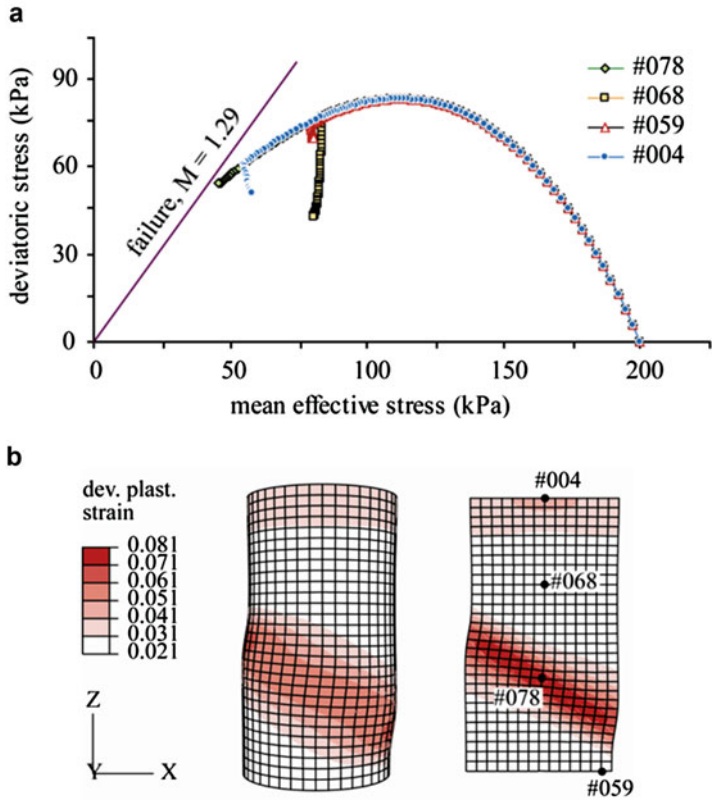

Fig. 18 Loss of homogeneity after diffuse failure with ensuing localization mode when reaching plastic limit

strategic nodes, with unloading occurring at nodes #068 and #59 found outside the shear band.

The loss in homogeneity arising from bifurcation is reflected in all field variables, for example, excess pore water pressure, void ratio, and deviatoric plastic-strain fields as illustrated in Fig. 19a–c for the same four nodes mentioned above. As seen in Fig. 19a, there is a steady and uniform increase in pore pressures until when bifurcation is first met. Thereafter, a distinct region of localized deformations eventually appears. Material points inside this region experience escalating pore water pressures while points outside this shear zone undergo a decrease in pore pressures. In line with the pore pressure field response, Fig. 19b indicates that the localized zones compact, leading to a decrease in void ratio and an increase in pore pressures. Such local compactive response is expected since the sample is medium–loose even though the sample is globally undrained.

Figure 20 shows a transverse section of the sample at various stages during the undrained compression test. The pore pressure field is still uniform at the peak ($t =$

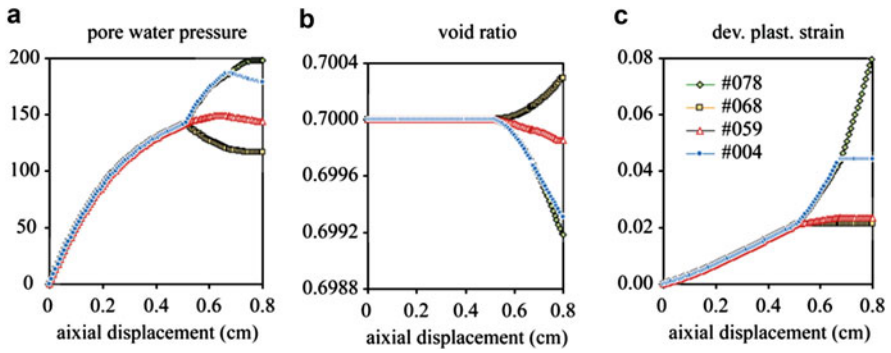

Fig. 19 Evolution of (**a**) excess pore water pressure, (**b**) void ratio, and (**c**) deviatoric plastic strain at four selected nodes in the FE mesh

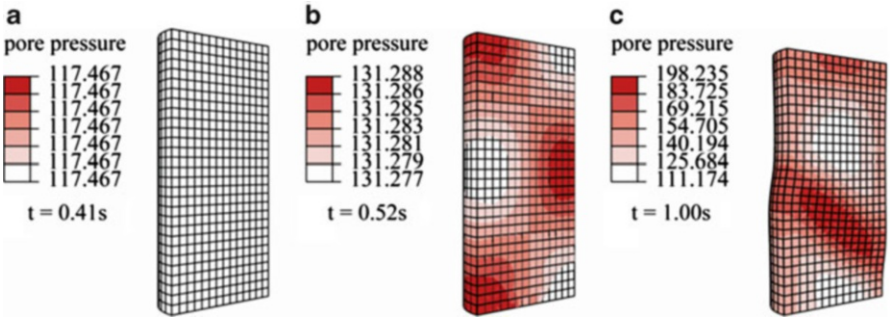

Fig. 20 Snapshots of the excess of pore water pressure field at (**a**) $t = 0.41$ s, (**b**) $t = 0.52$ s, and (**c**) $t = 1.00$s (1 × magnification)

0.41 s), where the second-order work first becomes zero (Fig. 19a). A departure from homogeneity is only observed at $t = 0.52$ s when a bifurcated response eventually emerges (Fig. 19b). The pore pressure increases throughout the specimen in a somewhat heterogeneous manner. Moving further along loading history, the pore pressure field develops into a more organized state as shown in Fig. 19c where a well-defined band is revealed with concentrated high values of pore pressures.

The numerical results demonstrate that the vanishing of the second-order work refers to a failure mode which is diffuse in the absence of any localization or organized displacement pattern. Localized deformations distinctly appear crossing through the sand specimen diagonally only when reaching close to the plastic limit surface in the stress space and well after diffuse failure has occurred at the peak, confirming that diffuse failure precedes here localization during loading history. The hierarchy of failure modes and other issues were discussed in Wan et al. (2012).

FEM Modeling of the Petacciato Landslide

The area of Petacciato is located along the Adriatic coast of Italy. The landslide occurred in 1996, after an intense rainy period. The landslide covers an area of 2 km wide, 7 km long, and over 200 m of difference in elevation. Geological and geotechnical surveys have been carried out by the "Studio Geotecnico Italiano" (SGI) (SGI 2004). The failure surface was found to be between 70 and 90 m in depth. The mean slope of the site was only 6°. The soil underlying the first 5–6 m of the slope is assumed to be homogeneous and composed of blue clayey silt.

To conduct the numerical modeling of this landslide, the finite element code LAGAMINE developed at Technical University of Liège (Belgium) is used. A constitutive model describing the behavior of unsaturated soils has been used. It is based on a frictional non-associative elastoplastic relation for the solid phase, and a water retention description for the fluid phase. The elastoplastic model uses the Van-Eekelen (Van-Eekelen 1980) surface as elastic and plastic limit. The hardening parameter chosen here is the equivalent plastic shear strain that makes the elastic limit evolve isotropically until the plastic limit is ultimately reached. The non-associative flow rule is described using a plastic potential surface with the same form as the yield surface, except that the friction angle is replaced with a dilation angle. The evolution of the dilation angle follows the same rule as for the friction angle during hardening. As for describing the water retention behavior of the soil, the empirical relation of Van-Genuchten (1980) is used. Hydromechanical coupling is established using Bishop's effective stress principle (Bishop 1959) in which the parameter χ is assumed to be the current degree of saturation. Finally, fluid flow is described by the generalized Darcy's law, the so-called Richards equation (Richards 1931). In this expression, the permeability is proportional to the degree of saturation degree with the proportionality coefficient being the permeability at the current saturation state.

The finite element mesh with associated boundary conditions that are used to model the Petacciato slope are shown in Fig. 21.

According to the mechanical boundary conditions, vertical displacements are fixed at the bottom edge, while horizontal displacements are fixed on left and right edges. Gravity loads are then applied to the whole body. For hydraulic boundary conditions, the bottom edge is impervious, whereas the upper edge is permeable with water pressure equal to zero. Water pressures are imposed on both left and right

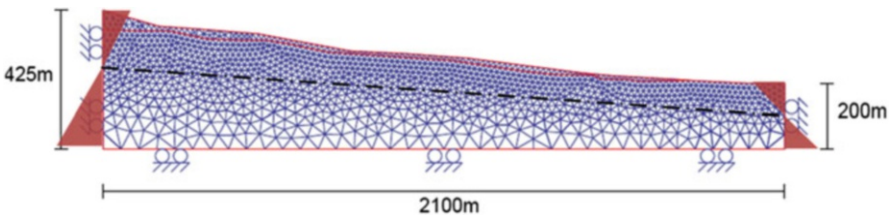

Fig. 21 Finite element mesh and boundary conditions of the Petacciato slope

Table 1 Mechanical and retention parameters of the Petacciato soils

Soil parameters	Symbols	Unit	Blue-gray clay
Grain-specific weight	ρ_s	kN/m^3	27.40
Young modulus	E	MPa	95.0
Poisson's ratio	ν	–	0.21
Porosity	n	–	0.3
Intrinsic permeability	k_w	m^2	10^{-17}
Friction angle	φ	°	19.0
Cohesion	C	kPa	171
Dilatancy angle	ψ	°	0
Maximal saturation degree	S_w	–	1
Residual saturation degree	S_{rw}	–	0.1
First retention parameter (Van-Genuchten)	α	P_a^{-1}	1.10^{-5}
Second retention parameter (Van-Genuchten)	β	–	1.35

boundaries so that they can evolve at each computation step in order to impose a chosen water table level in the steady-state regime. Fully saturated conditions are considered below the water table, while the above soil is partially saturated. The numerical simulation involves computing the degree of saturation as well as suction by integrating Richard's equation.

The soil parameters have been determined by calibrating SGI's laboratory tests (SGI 2004), mainly oedometer and triaxial tests. In particular, calibration has been based on the more representative CD and CU tests. Results of this calibration exercise are summarized in Table 1.

The numerical simulation of the Petacciato slope is as follows (Lignon et al. 2009). Initially, the whole soil medium is dry with the water table located at the bottom boundary. In subsequent steps, hydrostatic water pressures are imposed in view of mimicking a rise in the water table. This was achieved in a total number of 100 loading steps, whereby hydrostatic water pressures were imposed at elevations between 0 and 425 m on the left boundary and between 0 and 200 m on the right boundary; see Fig. 21. As such, the water table is roughly parallel to the slope. To evaluate any instability at every loading step, the second-order work is computed at each integration point throughout the whole body. In order to enhance the contrast of isovalues of the second-order work maps and to have a proper interpretation of the stability evolution of a given material point during the loading process, the second-order work has been normalized as follows:

$$\delta W_2^n = \frac{\delta W_2}{\|\delta\sigma_i\| \ \|\delta\varepsilon_i\|} \tag{25}$$

This quantity, as seen previously, corresponds to the cosine of the angle between vectors $\delta\sigma_i$ and $\delta\varepsilon_i$ and varies between -1 and 1. Values less or equal to zero signal unstable states, while positive values refer to stable states. Furthermore, states with

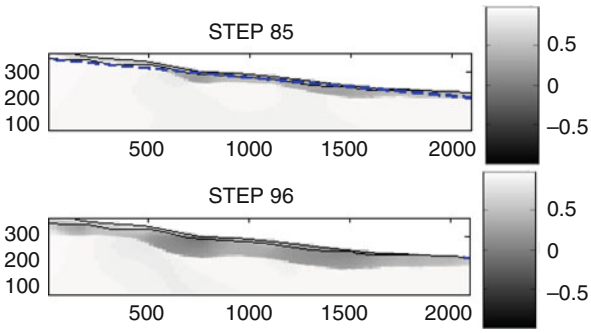

Fig. 22 Unstable domain of the Petacciato slope during saturation process

values near one can be considered as being further away from instability than those near zero. Hence, δW_2^n can be used in the same manner as the local safety factor centered around the value of zero instead of one. Figure 22 illustrates the evolution of the normalized second-order work with loading history.

When the water table approaches the free surface, the results of loading step 85 plotted in Fig. 22, show that the area of low δW_2^n values develops extensively along the slope surface. As soon as the slope reaches 95% saturation, the region of low or negative δW_2^n extends further deep into the slope as shown for loading step 96 in Fig. 22. At the same time, a slip surface located at a depth between 80 and 90 m is clearly visible. These numerical results are in close agreement with borehole and inclinometer measurements made in the field. It is worth noting that the natural inclination of the slope is around 6° and consequently the failure, which is in the diffuse mode, cannot be explained using either classical empirical methods or limit analyses.

Conclusion

In this chapter, an attempt to demonstrate why and how plasticity and damage phenomena in geomaterials are fundamentally different from classical interpretation was made. The main reason is the non-associated character of the rate-independent irreversible strains in these materials. The second-order work criterion has been introduced as a general and necessary condition for all types of divergence instabilities to occur and to give rise to localized or diffuse failure modes. This criterion has been analyzed in relation to granular microstructure and the characteristic expression of macroscopic failure through the phenomenon of bursts of kinetic energy. Its main features have been investigated (i.e., existence of a bifurcation domain and of instability cones) and they have been carefully checked using a discrete element model. Eventually some examples were presented using the finite element method to show the applicability of this criterion to in situ boundary value problems implicating both soil and rock slopes.

References

S.C. Bandis, A.C. Lumsden, N.R. Barton, Fundamentals of rock joint deformation. Int. J. Rock Mech. Min. Sci. Geomech. Abstr. **20**(6), 249–268 (1983)

A.W. Bishop, Principle of effective stress. Teknisk. Ukeblad. **106**(39), 859–863 (1959)

P.A. Cundall, O.D.L. Strack, A discrete numerical model for granular assemblies. Geotechnique **29**(1), 47–65 (1979)

A. Daouadji, H. Al Gali, F. Darve, A. Zeghloul, Instability in granular materials, an experimental evidence of diffuse mode of failure for loose sands. J. Eng. Mech. **136**(5), 575–588 (2010)

A. Daouadji, F. Darve, H. Al-Gali, P.Y. Hicher, F. Laouafa, S. Lignon, F. Nicot, R. Nova, M. Pinheiro, F. Prunier, L. Sibille, R. Wan, Diffuse failure in geomaterials: experiments, theory and modeling. Int. J. Numer. Anal. Methods Geomech. **35**(16), 1731–1773 (2011)

F. Darve, S. Labanieh, Incremental constitutive law for sands and clays: simulations of monotonic and cyclic tests. Int. J. Numer. Anal. Methods Geomech. **6**(2), 243–275 (1982)

F. Darve, E. Flavigny, M. Meghachou, Yield surfaces and principle of superposition revisited by incrementally non-linear constitutive relations. Int. J. Plast. **11**(8), 927–948 (1995)

F. Darve, G. Servant, F. Laouafa, H.D.V. Khoa, Failure in geomaterials: continuous and discrete analyses. Comp. Methods Appl. Mech. Eng. **193**, 3057–3085 (2004)

F. Darve, L. Sibille, A. Daouadji, F. Nicot, Bifurcations in granular media: macro- and micro-mechanics approaches. Comptes Rendus Acad. Sci. Mec. **335**, 496–515 (2007)

J. Duriez, F. Darve, F.V. Donzé, A discrete modeling-based constitutive relation for infilled rock joints. Int. J. Rock Mech. Min. Sci. **48**(3), 458–468 (2011a)

J. Duriez, F. Darve, F.V. Donzé, Incrementally non-linear plasticity applied to rock joint modeling. Int. J. Numer. Anal. Methods Geomech. (2011b). https://doi.org/10.1002/nag.1105

J. Duriez, F. Darve, F.V. Donzé, F. Nicot, Material stability analysis of rock joints. Int. J. Numer. Anal. Methods Geomech. (2012). https://doi.org/10.1002/nag.2149

G. Gudehus, A comparison of some constitutive laws for soils under radially loading symmetric loading unloading, in *Third International Conference on Numerical Methods in Geomechanics*, (edn Balkema, 1979), pp. 1309–1323

R. Hill, A general theory of uniqueness and stability in elasto-plastic solids. J. Mech. Phys. Solids **6**, 236–249 (1958)

P.V. Lade, Static instability and liquefaction of loose fine sandy slopes. J. Geotech. Eng. Div. Am. Soc. Civ. Eng. **118**(1), 51–71 (1992)

F. Laouafa, F. Prunier, A. Daouadji, H. Al-Gali, F. Darve, Stability in geomechanics, experimental and numerical analyses. Int. J. Numer. Anal. Methods Geomech. **35**(2), 112–139 (2011)

J. Lerbet, M. Aldowadji, N. Challamel, F. Nicot, F. Prunier, F. Darve, P-positive definite matrices and stability of nonconservative systems. J. Appl. Math. Mech. ZAMM **92**(5), 409–422 (2012)

S. Lignon, F. Laouafa, F. Prunier, F. Darve, H.D.V. Khoa, Hydro-mechanical modelling of landslides with a material instability criterion. Geotechnique **59**(6), 513–524 (2009)

A.E.H. Love, *A Treatise of Mathematical Theory of Elasticity* (Cambridge University Press, Cambridge, 1927)

M.M. Mehrabadi, M. Oda, S. Nemat-Nasser, On statistical description of stress and fabric in granular materials. Int. J. Numer. Anal. Methods Geomech. **6**, 95–108 (1982)

V. Merrien-Soukatchoff, J. Duriez, M. Gasc, F. Darve, F.V. Donzé, mechanical stability analyses of fractured rock slopes, in *Rockfall Engineering*, ed. by S. Lambert, F. Nicot, (New York/London, Wiley/ISTE, 2011)

P. Mollema, M. Antonellini, Compaction bands: a structural analog for anti-mode I cracks in aeolian sandstone. Tectonophysics **267**, 209–228 (1996)

F. Nicot, F. Darve, A micro-mechanical investigation of bifurcation in granular materials. Int. J. Solids Struct. **44**, 6630–6652 (2007)

F. Nicot, F. Darve, Diffuse and localized failure modes: two competing mechanisms. Int. J. Numer. Anal. Methods Geomech. **35**(5), 586–601 (2011)

F. Nicot, F. Darve, H.D.V. Khoa, Bifurcation and second-order work in geomaterials. Int. J. Numer. Anal. Methods Geomech. **31**, 1007–1032 (2007)
F. Nicot, L. Sibille, F. Darve, Bifurcation in granular materials: an attempt at a unified framework. Int. J. Solids Struct. **46**, 3938–3947 (2009)
F. Nicot, N. Challamel, J. Lerbet, F. Prunier, F. Darve, Bifurcation and generalized mixed loading conditions in geomaterials. Int. J. Numer. Anal. Methods Geomech. **35**(13), 1409–1431 (2011)
F. Nicot, L. Sibille, F. Darve, Failure in rate-independent granular materials as a bifurcation toward a dynamic regime. Int. J. Plast. **29**, 136–154 (2012a)
F. Nicot, N. Challamel, J. Lerbet, F. Prunier, F. Darve, Some insights into structure instability and the second-order work criterion. Int. J. Solids Struct. **49**(1), 132–142 (2012b)
F. Nicot, N. Hadda, F. Bourrier, L. Sibille, R. Wan, F. Darve, Inertia effects as a possible missing link between micro and macro second-order work in granular media. Int. J. Solids Struct. **49**(10), 1252–1258 (2012c)
F. Prunier, F. Nicot, F. Darve, F. Laouafa, S. Lignon, 3D multi scale bifurcation analysis of granular media. J. Eng. Mech. ASCE **135**(6), 493–509 (2009a)
F. Prunier, F. Laouafa, S. Lignon, F. Darve, Bifurcation modeling in geomaterials: from the second-order work criterion to spectral analyses. Int. J. Numer. Anal. Methods Geomech. **33**, 1169–1202 (2009b)
F. Prunier, F. Laouafa, F. Darve, 3D bifurcation analysis in geomaterials, investigation of the second order work criterion. Eur. J. Env. Civ. Eng. **13**(2), 135–147 (2009c)
L.A. Richards, Capillary conduction of liquids through porous mediums. Physics **1**(5), 318–333 (1931)
SGI (Studio Geotechnico Italiano), *The Petacciato Landslide: Geological and Geotechnical Data* (LESSLOSS Report, 2004)
L. Sibille, F.V. Donzé, F. Nicot, B. Chareyre, F. Darve, From bifurcation to failure in a granular material, a DEM analysis. Acta Geotech. **3**(1), 15–24 (2008)
H.A.M. Van-Eekelen, Isotropic yield surfaces in three dimensions for use in soil mechanics. Int. J. Numer. Anal. Methods Geomech. **4**, 89–101 (1980)
M.T. Van-Genuchten, A closed form for predicting the hydraulic conductivity of unsaturated soils. Soil Sci. Soc. Am. J. **4**, 892–898 (1980)
R.G. Wan, P.J. Guo, Stress dilatancy and fabric dependencies on sand behavior. J. Eng. Mech. ASCE **130**(6), 635–645 (2004)
R.G. Wan, M. Pinheiro, A. Daouadji, M. Jrad, F. Darve, Diffuse instabilities with transition to localization in loose granular materials. Int. J. Numer. Anal. Methods Geomech. (2012). https://doi.org/10.1002/nag.2085

Fractals and Mechanics of Fracture

40

Michael P. Wnuk

Contents

Introduction 1112
Basic Concepts in Fractal Fracture Mechanics 1115
Delayed Fracture in Viscoelastic Solids for Euclidian and Fractal Geometries:
Motion of a Smooth Crack in a Viscoelastic Medium 1126
Growth of Fractal Cracks in Viscoelastic Media 1135
Some Fundamental Concepts 1137
Conclusions 1140
References 1140

Abstract

Classical mechanics including mechanics of fracture is often unsatisfactory when a solution predicts a singularity and the need arises to interpret the underlying physical meaning or lack thereof. A customary practice to deal with the singularity problem is to exclude a small region near the singular point, for which a different constitutive law – usually nonelastic – is postulated. This approach is adequate provided that the stress field outside the singular region is dominated by the elastic behavior. An alternative approach that successfully resolves problems involving singularities is the averaging process, also known as the quantization procedure – or – equivalently, discretization of the condition of the minimum of the potential energy of the system. In addition to the constitutive law, a certain "rule of decohesion" must be incorporated into the theory of fracture. An example of such a rule is the δCOD or the so-called "final stretch" criterion employed to describe the onset and the stable growth of a crack contained in a ductile solid. This criterion generalizes the well-known criteria of Griffith, Irwin–Orowan, Rice, and Wells.

M. P. Wnuk (✉)
Department of Civil Engineering and Mechanics, College of Engineering and Applied Science, University of Wisconsin, Milwaukee, WI, USA
e-mail: mpw@csd.uwm.edu

© Springer Nature Switzerland AG 2022

G. Z. Voyiadjis (ed.), *Handbook of Damage Mechanics*,
https://doi.org/10.1007/978-3-030-60242-0_18

Success of the novel approaches is particularly remarkable in the nanoscale domain, where the fractal geometry of cracks and the quantization rules need to be combined in order to describe adequately fracture processes at the lattice and/or atomistic level. Discrete cohesive crack representation with the fractal geometry incorporated into the mathematical model appears to produce most straightforward and useful results. Application of the Wnuk–Yavari correspondence principle relating the fractal and smooth blunt cracks demonstrates that even a minute amount of roughness of the crack surface is sufficient to cause a drop in the maximum stress measured at the tip of the crack from infinity to a well-defined finite value.

Early stages of fracture and the pre-fracture deformation states associated with a stable propagation of a subcritical crack in viscoelastic and/or ductile solids are described in some detail. The initial stable growth of crack manifests itself as a sequence of the local instability points, while the onset of catastrophic fracture corresponds to attainment of the global instability. The locus of these critical states supplants the Griffith result. Only in the limit of ideally brittle material behavior that both results, the present one and the classic one, coincide.

In the present review, introductory concepts of fractal and quantized fracture mechanics followed by the studies of delayed fracture in viscoelastic solids and the instabilities occurring in the process of ductile fracture are discussed.

Keywords

Stress Intensity Factor · Crack length · Linear elastic fracture mechanic · Fractal geometry · Fractal crack

Introduction

In the seminal paper (Mandelbrot et al. 1984) entitled *Fractal character of fracture surfaces in metals* and published in 1984 in the prestigious British journal *Nature*, Mandelbrot, Passoja, and Paullay wrote:

> When a piece of metal is fractured either by tensile or impact loading the fracture surface that is formed is rough and irregular. Its shape is affected by the metal's microstructure (such as grains, inclusions and precipitates where characteristic length is large relative to the atomic scale), as well as by 'macrostructural' influences (such as the size, the shape of the specimen, and the notch from which the fracture begins). However, repeated observations at various magnifications also reveal a variety of additional structures that fall between 'micro' and 'macro' and have not yet been described satisfactorily in a systematic manner. The experiments reported here reveal the existence of broad and clearly distinct zone of intermediate scales in which the fracture is modeled very well by a fractal surface.

The purpose of this review is to show how the concept of fractal geometry can be incorporated into the mathematical analysis underlying the existing mechanics of fracture. Some progress has been achieved and certain novel ideas pertinent to this goal have been developed by Carpinteri (1994), Carpinteri et al. (2002), Carpinteri and

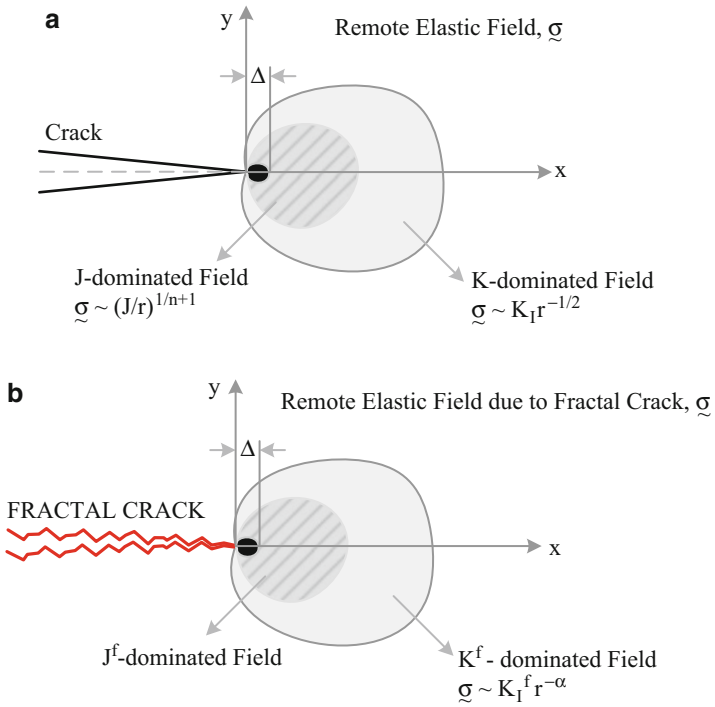

Fig. 1 (**a**) Singular asymptotic fields for a smooth crack: J-dominated HRR field and the K-field. Embedded inside the J-controlled field is the process zone, Δ. (**b**) Singular asymptotic fields for a fractal crack: J^f -dominated HRR field and K^f -field. Embedded inside the J^f -controlled field is the process zone, Δ

Spagnoli (2004), Spagnoli (2005), Balankin (1997), and Cherepanov et al. (1995). From the text of Mandelbrot et al. (1984) quoted above, it follows that fracture is not only of fractal character, but it is also of multi-scale nature. To fill the gap between the "micro" and "macro" scale levels, the group of Panin (Pugno and Ruoff 2004) in Siberia, Russia, has developed an entirely new branch of mechanics, named "Meso-mechanics." In the second part of this review, certain theoretical considerations are presented, which are based on the experimental observations of the Siberian group.

For several past decades, the linear elastic fracture mechanics (LEFM) has been subject to multiple attempts to eliminate or alter the singularities present in the stress and strain fields generated by a crack contained in a brittle solid. As the singular point is approached and the distance measured from the crack tip shrinks to zero, certain new fields derived on the basis of nonelastic constitutive laws are embedded within the known asymptotic K-field. An example is described in Fig. 1, where a nonlinear stress and strain fields proposed by Hutchinson–Rice–Rosengren (the HRR fields) are based on the constitutive law of Ramberg and Osgood and – strictly speaking – valid for a nonlinearly elastic power strain-hardening material. In these studies, the hardening exponent n present in the Ramberg–Osgood constitutive law

$\sigma \sim \varepsilon^n$ enters the expressions for the HRR stress and strain near-tip asymptotic fields, as follows: $\underset{\sim}{\sigma}(J/r)^{\frac{1}{n+1}}$ and $\underset{\sim}{\varepsilon}(J/r)^{\frac{n}{n+1}}$. Subsequently, such a representation has been shown to be valid for elastic–plastic fields, too; and thus, the concept of Rice's path-independent integral has been extended to elastic–plastic problems including large-scale yielding cases. Note that the product of stress and strain is inversely proportional to r, thus making all the energy integrals finite – analogous to the integrals involved in the problem solved by Griffith. Since the theory underlying the HRR field is the deformation theory of plasticity, the results are not valid whenever unloading occurs, meaning that the J-controlled field described here is valid only for stationary cracks. As soon as the crack begins to propagate, the HRR fields are no longer pertinent. New solutions valid for a moving crack remain to be found.

An interesting alternative is offered in the form of the cohesive forces crack model, for which a certain cohesion mechanism of separation is considered (either Wells' CTOD criterion for stationary cracks or Wnuk's δCOD criterion for moving cracks); see Fig. 2. This model has produced very useful results, especially when equipped with an additional element – the Neuber particle, known also as "unit step growth," "fracture quantum," or "process zone." Incorporation of the Neuber particle into the mathematical analysis leads to the quantization procedure; cf. Pugno and Ruoff (2004) and also in Wnuk and Yavari (2008, 2009). This type of cohesive forces model, which includes the Neuber-type zone, is known as "discrete cohesive crack model" and it works well both for the stationary and quasi-statically moving cracks.

In addition to the basic equations of mechanics of solids, such as the equilibrium equations and the constitutive law, certain additional relations are needed in order to

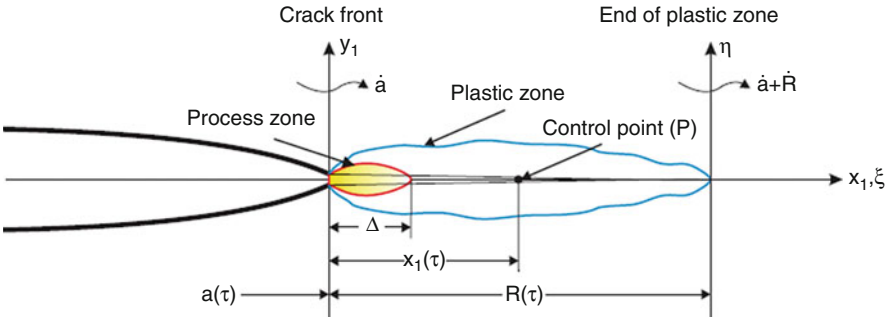

Fig. 2 Discrete cohesive zone crack model of Wnuk (1974). Note that of the two length parameters Δ and R in addition, the time-dependent crack length "a" is needed to describe quasi-static crack motion. While both "a" and R are time dependent, the process zone size Δ is the material property and it remains constant during the crack growth. Ratio R/Δ serves as a measure of material ductility; for $R/\Delta >> 1$, material is ductile, while for $R/\Delta \to 1$, material is brittle. An increasing R due to the subcritical crack extension in the early stages of fracture demonstrates the toughening phenomenon in ductile fracture, often described in terms of the material R-curve

predict the onset of fracture, which is, of course, considered as propagation of the discontinuity in displacements. A certain postulate regarding the final act of decohesion is required. Many physical concepts have been added to the list of this kind of postulates, beginning with the Griffith energy criterion and then the "driving force" criterion of Irwin–Orowan and the by-product of it in the form of the critical stress intensity factor (SIF) criterion. As shown by Rice (1968), all of these criteria are equivalent – even though they have different physical interpretations. They can also be shown to be equivalent to Rice's J-integral criterion, which uses the rate of energy release as the controlling factor in the process of cracking (decohesion). Based on the notions associated with the cohesive crack model, the "CTOD criterion" or δ-criterion was proposed by Wells and then several other conceptually related conditions followed, and they now form the well-established foundation of the contemporary mechanics of fracture. One such criterion will be discussed here in more detail, and it is the δCOD criterion of Wnuk (1974). This "incremental displacement" criterion implies quantization of the relevant calculus, and it is used when instabilities of ductile fracture preceded by a slow crack growth are analyzed. In its essence it is a critical strain criterion for the onset and stable growth of a subcritical crack.

Success of the existing continuum mechanics solutions is only partial, as the singularity still persists. The problem is resolved if the cohesive forces model of the crack with the Neuber particle built into it is employed. Surprisingly, the essential results derived by the use of the structured cohesive crack model are very similar to those obtained by the approximate technique of Irwin's "plasticity correction."

In recent years some new approaches such as quantized fracture mechanics and fractal fracture mechanics have been developed. These techniques necessitate implementation of certain mathematical tools, which are novel to mechanics of fracture such as the root-mean-square averaging and a finite difference formula replacing Newton's expression for the derivative. These techniques are briefly reviewed in the present work.

Basic Concepts in Fractal Fracture Mechanics

In hope of removing the singularities in stress and strain fields generated in the vicinity of crack tip, it has been postulated that fractal geometry can be used to better represent a stationary or a propagating crack than the smooth Euclidean crack considered in the classic theory of Griffith–Irwin–Orowan; cf. Mandelbrot et al. (1984). Unfortunately, the singularity does not disappear; it acquires a new order; instead of $r^{-1/2}$ in the LEFM domain valid for the smooth crack representation, it becomes $r^{-\alpha}$ where the fractal exponent α is related to other measures of roughness of the crack surface, namely, the fractal dimension D or the Hurst fractal measure H. One has

$$\alpha = \frac{2 - D}{2}, 1 \leq D \leq 2 \tag{1}$$

for a self-similar crack, and

$$\alpha = \begin{cases} \dfrac{2H-1}{2H}, & \dfrac{1}{2} \le H \le 1 \\ 0 & 0 \le H \le \dfrac{1}{2} \end{cases} \tag{2}$$

for a self-affine crack. Variation of the fractal dimension D within the range (Pugno and Ruoff 2004; Wnuk and Yavari 2008) corresponds to α changing from ½ when $D = 1$ (a smooth crack case) to zero when $D = 2$. Only for this particular case of $\alpha = 0$ the singularity in the near-tip stress field associated with a fractal crack $\underset{\sim}{\sigma} r^{\tilde{-}\alpha}$ disappears. This is an interesting limit when the fractal crack "fills the plane" as it becomes a two-dimensional object. However, when the fractal geometry is taken into account, even the basic concepts of calculus such as line or area integrals are not defined (Harrison and Norton 1991; Harrison 1994). The "embedded crack model" of Wnuk and Yavari bypasses this problem, since it assumes a smooth crack contained within the stress field generated by a fractal crack. Thus, the basic mathematical manipulations are enabled. The price paid when this model is employed is a rather substantial limitation imposed on the range of crack surface roughness, which is not supposed to differ significantly from the case of the smooth crack. Somewhat unexpectedly Yavari and Khezrzadeh have recently shown (Khezrzadeh et al. 2011) that reaching a high level of crack surface roughness is physically impossible. Using a branching argument, these authors have shown that there exists a limiting roughness estimated at about $\alpha = 0.25$.

Indeed, it is expected that the model of an embedded crack can provide reliable results only for the limited range of crack roughness. In what follows influence of the fractal geometry for only moderately rough cracks has been studied, say for the exponent α not dropping below 0.4, which is not significantly different from the case of smooth crack, for which $\alpha = 0.5$. The model of embedded crack assumes that a smooth crack is placed within a field generated by a fractal crack, so it is sort of "putting cart in front of a horse." In designing this model, one first considers a specific stress field associated with a fractal crack, and then a smooth crack is embedded in this field. Of course, a better model would be desirable. Despite of these limitations, the study does provide a valuable insight into behavior of the fractal cracks.

Wnuk and Yavari (2003) were the first to use the model of embedded crack in order to estimate the stress intensity factor. Their result was

$$K_{WY}^{f} = \frac{C(a,\alpha)}{(\pi a)^{\alpha}} \int_0^a p(x) \frac{(a-x)^{2\alpha} + (a+x)^{2\alpha}}{(a^2-x^2)^{\alpha}} dx \tag{3}$$

With $p(x)$ identified with the applied stress σ and "a" denoting the crack length and with certain dimensional considerations, the constant C was chosen as $C = (a/\sqrt{\pi})^{2\alpha-1}$ in order to extend validity of the formula in Eq. 3 to a "true fractal crack" range, which implies surpassing the limits of the embedded crack model. For

the fractal dimension D contained in the interval (Pugno and Ruoff 2004; Wnuk and Yavari 2008), the final result is

$$\begin{aligned} K_{WY}^{f} &= \frac{a^{\alpha-1}\sigma}{\pi^{2\alpha-1/2}}\int_0^a \frac{(a-x)^{2\alpha}+(a+x)^{2\alpha}}{(a^2-x^2)^{\alpha}}dx = \chi_0(\alpha)\sigma\sqrt{\pi a^{2\alpha}} \\ \chi_0(\alpha) &= \frac{1}{\pi^{2\alpha}}\int_0^1 \frac{(1-z)^{2\alpha}+(1+z)^{2\alpha}}{(1-z^2)^{\alpha}}dz \\ \chi_0(\alpha) &\simeq -3.28\alpha^3+6.475\alpha^2-4.42\alpha+2 \end{aligned} \tag{4}$$

This result was later corrected in Khezrzadeh et al. (2011), and the correct K-factor for a fractal crack represented by the embedded crack model was expressed as

$$K_I^f = \left(\frac{a}{\pi}\right)^{1-\alpha}\int_0^a \frac{2\sigma}{(a^2-x^2)^{1-\alpha}}dx \tag{5}$$

or

$$\begin{aligned} K_I^f &= \chi(\alpha)\sigma\sqrt{\pi a^{2\alpha}} \\ \chi(\alpha) &= \frac{2}{\pi^{1-\alpha}}\int_0^1 \frac{dz}{(1-z^2)^{1-\alpha}} \end{aligned} \tag{6}$$

where the function $\chi(\alpha)$ can be expressed in a closed form by the use of the Euler gamma function Γ, namely,

$$\begin{aligned} \chi(\alpha) &= \frac{\pi^{\alpha-1}\Gamma(\alpha)}{\Gamma(\alpha+1/2)} \\ \chi(\alpha) &\simeq -10.37\alpha^3+15.679\alpha^2-8.234\alpha+2.493 \text{ for } 0.25 \le \alpha \le 0.5 \end{aligned} \tag{7}$$

For the admissible range of crack roughness, both results in Eqs. 4 and 6 are identical, and for smaller α, when the fractal dimension D approaches 2, they diverge (see Fig. 3) suggesting that the range of surface roughness beyond the limits of validity of the embedded crack model remains yet to be studied. Since the basic manipulations of the calculus are not yet defined along the fractal, a better mathematical model is needed to deal with fractals and their somewhat whimsical mathematical nature.

Once the stress intensity factor for a fractal crack is known, one may write the equations for the asymptotic near-tip stress field; cf. Wnuk and Yavari (2003) and Khezrzadeh et al. (2011). The opening stress for a fractal crack reads

$$\sigma_{yy}(r,\theta,\alpha) = \frac{K_I^f}{(2\pi r)^{\alpha}}\{\sin[\alpha(\pi-\theta)] - \alpha\sin(\theta)\cos[(\alpha+1)(\pi-\theta)]\} \tag{8}$$

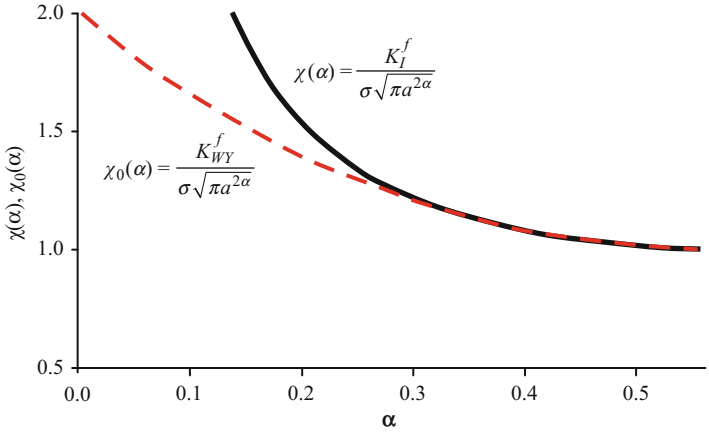

Fig. 3 Comparison between the estimate of the fractal stress intensity factor proposed by Wnuk and Yavari, K_{WY}^f (cf. Wnuk and Yavari 2003), and the solution resulting from the embedded crack model, K_I^f (cf. Khezrzadeh et al. 2011). It appears that within the interval of limited crack surface roughnesses $0.3 \leq \alpha \leq 0.4$, both solutions are identical

where the polar coordinates (r, θ) are anchored at the crack tip and the other two stresses are

$$\begin{aligned}\sigma_{xx}(r,\theta,\alpha) &= \frac{K_I^f}{(2\pi r)^\alpha}\{\sin[\alpha(\pi-\theta)] + \alpha\sin(\theta)\cos[(\alpha+1)(\pi-\theta)]\}\\ \sigma_{xy}(r,\theta,\alpha) &= \frac{K_I^f}{(2\pi r)^\alpha}\alpha\sin(\theta)\sin[(\alpha+1)(\pi-\theta)]\end{aligned} \tag{9}$$

It is understood that the absolute value of θ in Eqs. 8 and 9 should be taken. These formulae resulted from the Westergaard stress function; cf. Khezrzadeh et al. (2011):

$$\begin{aligned}Z(z,\alpha) &= \frac{K_I^f}{e^{i\mathrm{Sign}(\theta)(1/2-\alpha)\pi}(2\pi z)^\alpha}\\ z &= x + iy\end{aligned} \tag{10}$$

To obtain Eqs. 8 and 9, the well-known equations of Westergaard (1939) were used. It is noted that the Westergaard equations represent a special case of a more general formulation of the complex potential functions of Kolosov–Muskhelishvili (1933), namely,

$$\begin{aligned}\sigma_{xx} &= \mathrm{Re}Z(z,\alpha) - y\mathrm{Im}Z'(z,\alpha)\\ \sigma_{yy} &= \mathrm{Re}Z(z,\alpha) + y\mathrm{Im}Z'(z,\alpha)\\ \sigma_{xy} &= -y\,\mathrm{Re}\,Z'(z,\alpha)\end{aligned} \tag{11}$$

The origin of the Cartesian system (x,y) is placed at the center of the crack. An alternative mathematical approach was offered by Williams (1957), who decomposed the Airy stress potential into the radial and angular functions and then obtained an exact solution for the angular part while seeking the solution for the radial part in the form of a generalized Laurent power series. He found the dominant term in this series to be proportional to $r^{-1/2}$ and thus fully confirmed the K-controlled near-tip stress field solutions found by the other researchers such as Kolosov–Muskhelishvili (1933), Westergaard (1939), and Irwin (1956).

In 2005 Wnuk and Yavari (2005) described a transformation, which made possible converting any fractal crack to an equivalent blunt crack or a notch with a finite crack tip radius. This approach not only predicts a finite stress at the root of the notch, but it also shows that the three mathematical representations of discontinuities in the displacement field, a notch, a classic Griffith crack, and a fractal crack, are mathematically related and can be treated interchangeably. The proposed rule was named "a correspondence principle," according to which any fractal crack (not excluding the classic Griffith crack when the fractal dimension reduces to $D = 1$) can be treated as an equivalent blunt crack of a given root radius, say ρ_α, which is a function of the fractal exponent α. The value of this root radius is determined from a condition that the stress certain distance away from the tip of a fractal crack r^* equals the maximum stress $\sigma_{\max}$ generated at the circumference of the blunt crack. Therefore, one needs to compare the opening stresses ahead of the blunt crack

$$\sigma_{yy}^{bc} = \frac{K_I}{\sqrt{2\pi r}} \frac{\rho}{2r} \cos\left(\frac{3\theta}{2}\right) + \frac{K_I}{\sqrt{2\pi r}} \frac{\rho}{2r} \cos\left(\frac{\theta}{2}\right)\left[1 + \sin\frac{\theta}{2}\sin\frac{3\theta}{2}\right] + \ldots \quad (12)$$

with the one valid for a fractal crack

$$\sigma_{yy}^{f} = \frac{K_I}{(2\pi r)^{\alpha}} \{\cos(\alpha\theta + \alpha\sin\theta\sin[(\alpha+1)\theta]\} \quad (13)$$

When the plane of crack is considered, $\theta = 0$, the equations above reduce:

$$\begin{aligned} \sigma_{yy}^{bc} &= \frac{K_I}{\sqrt{2\pi r}}\left(1 + \frac{\rho}{2r}\right) \\ \sigma_{yy}^{f} &= \frac{K_I^f}{(2\pi r)^{\alpha}} \end{aligned} \quad (14)$$

The stress expressed by the first expression in the above equations refers to a blunted crack (hence the superscript "bc"), while the second formula gives the stress in front of a fractal crack. Now, one requires that the first of these quantities is evaluated at the circumference of the blunt crack, while the second is evaluated at a certain distance from the crack tip $r = r^*$. From the first formula in Eq. 14, the stress at the circumference of the blunt crack is evaluated when the radius r is set equal $\rho/2$.

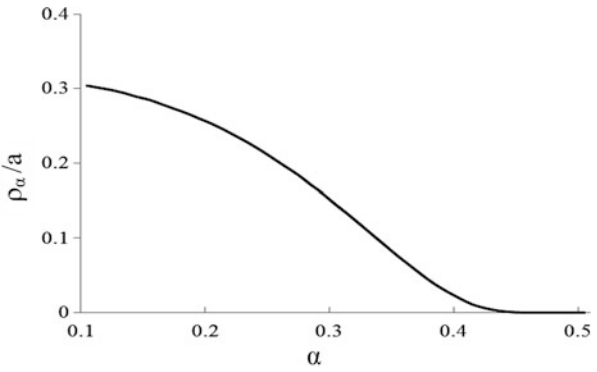

Fig. 4 Root radius of a blunt crack equivalent to a fractal crack obtained from the Wnuk–Yavari correspondence principle and defined by the fractal exponent α. Note that for α approaching ½, the radius ρ_α shrinks to zero rendering the Griffith crack case

Next, according to the correspondence principle, one needs to put $r = r^*$ in the second expression in Eq. 14, yielding

$$\begin{aligned}\left[\sigma_{yy}^{bc}\right]_{\max} &= \frac{2K_I}{\sqrt{\pi\rho}} = 2\sqrt{\frac{a}{\rho_\alpha}}\sigma \\ \left[\sigma_{yy}^{f}\right]_{\max} &= \frac{K_I^f}{(2\pi r^*)^\alpha} = \frac{\chi_0(\alpha)\sigma\sqrt{\pi a^{2\alpha}}}{(2\pi r^*)^\alpha}\end{aligned} \tag{15}$$

According to the correspondence principle, these two stresses should equal if the distance r^* is chosen to scale down with ρ_α, say $r^* = \varepsilon\,\rho_\alpha$, and then the requirement of equivalency of the two objects considered is expressed by the following equation:

$$\frac{2K_I}{\sqrt{\pi\rho_\alpha}} = \frac{K_I^f}{(2\pi\varepsilon\rho_\alpha)^\alpha} \tag{16}$$

Hence, one can evaluate the required root radius of the equivalent blunt crack:

$$\rho_\alpha = \frac{a}{\pi}\left[\frac{\chi_0(\alpha)}{2^{\alpha+1}\varepsilon^\alpha}\right]^{\frac{2}{2\alpha-1}} \tag{17}$$

With $\varepsilon = 0.05$, chosen after a careful parametric study (cf. Wnuk and Yavari 2005), this equation provides the function shown in Fig. 4. When the stress Eq. 15 is evaluated, the predicted maximum stress of the equivalent blunt crack becomes the following function of the fractal exponent:

$$\sigma_{\max} = 2\sqrt{\pi}\sigma\left[\frac{\chi_0(\alpha)}{2^{\alpha+1}\varepsilon^\alpha}\right]^{\frac{1}{1-2\alpha}} \tag{18}$$

The function is shown in Fig. 5. It is seen that with the exception of the classic Griffith crack ($\alpha = 0.5$), the stress is finite. It is noteworthy that the maximum stress

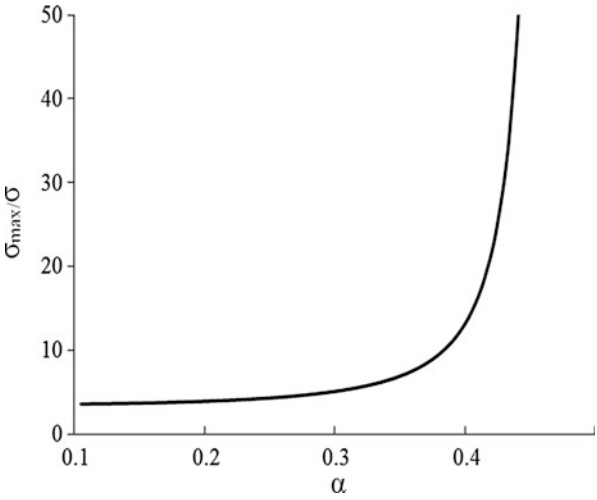

Fig. 5 Maximum stress at the root of a fractal crack equivalent to a certain smooth blunt crack, according to the correspondence principle of Wnuk and Yavari (2005), is shown to be finite for all values of the fractal exponent α with exception of the classic Griffith crack, when $\alpha = ½$. The graph illustrates that even a minute amount of roughness of the crack surface is sufficient to cause a drop in the maximum stress from infinity to a well-defined finite value

given in Eqs. 15 and 18 also satisfies the Inglis (Inglis 1913) formula for a notch when $a >> \rho_\alpha$, namely,

$$\sigma_{\max}^{\text{Inglis}} = 2\sigma\sqrt{\frac{a}{\rho_\alpha}} \tag{19}$$

This feature of the basic concept underlying the correspondence formula for fractal cracks appears to close the train of thought, which from Inglis (1913) to Griffith (1921) led to the present-day foundations of the fracture mechanics. When molecular theory of fracture is pondered, then Eq. 19 corresponds to the molecular strength, which is believed to be one order of magnitude smaller than the Young modulus.

Similarly, the Irwin plastic correction to the LEFM model, say r_y^f for a fractal crack (cf. Wnuk and Yavari 2005), has been evaluated. Using the statically equivalent elastic–plastic stress field, the entity r_y^f has been estimated as follows:

$$\int_0^{r_y^f} \frac{K_I^f}{(2\pi r)^\alpha} dr - r_y^f \sigma_Y = \left(r_p^f - r_y^f\right)\sigma_Y \tag{20}$$

Following Irwin the stress generated by a fractal crack is required to equal the yield stress σ_Y at the distance r_y^f from the crack tip. It has been found that

$$r_y^f = \frac{1}{2\pi}\left(\frac{K_I^f}{\sigma_Y}\right)^{\frac{1}{\alpha}} \tag{21}$$

The size of the plastic zone (in the form of a disc adjacent to the crack front and inserted into the elastic stress field) is calculated from Eq. 20 as follows:

$$r_p^f = \frac{1}{2\pi(1-\alpha)}\left(\frac{K_I^f}{\sigma_Y}\right)^{\frac{1}{\alpha}} \tag{22}$$

The opening stress within the plastic zone $0 \le r \le r_p^f$ is constant and equals the yield stress σ_Y, while for distances larger than r_p^f, the stress obeys the elastic fractal law and decays as $K_I^f/(2\pi r)^\alpha$.

In quantized mechanics of fracture, one assumes that a crack propagates in a continuum but in discrete steps. Therefore, a modification of the mathematical analysis is needed. Such quantization procedures applied to the structured cohesive stress crack model have been described in Wnuk and Yavari (2008, 2009). Employing the concept of the configurational force, these authors proposed that the energy release per unit of fractal measure of the crack surface is defined in the following way:

$$G^f = \frac{\left(K_I^f\right)^2}{E'} = \frac{\chi_0(\alpha)^2\sigma^2\pi a^{2\alpha}}{E'} \tag{23}$$

With the help of an auxiliary smooth crack (cf. "embedded crack model"), integration of this expression with respect to the crack length yields

$$-\Pi^f = \int_0^a G^f(\sigma, a)d(2a) = \frac{2\chi_0(\alpha)^2\sigma^2\pi a^{2\alpha+1}}{(2\alpha+1)E'} \tag{24}$$

Discontinuous nature of crack extension calls for replacement of the notion of the derivative expressed in terms of infinitesimals $\mathrm{d}\Pi^f$ and da (or $d\ell$) by the finite quantities $\Delta\Pi^f$ and Δa (or $\Delta\ell$). The derivative $\mathrm{d}\Pi^f/\mathrm{d}\ell$, which defines the crack driving force (or a configurational force), is thus replaced by the following entity involving finite differences $\Delta_\Delta\Pi^f$ and $\Delta\ell$, namely,

$$G^f = -\frac{\Delta_\Delta\Pi^f}{\Delta\ell} = -\frac{\Pi^f(a+\Delta) - \Pi^{\mathrm{f}}(a)}{2\Delta} \tag{25}$$

Symbol Δ denotes the fracture quantum and for a two-ended crack, $\Delta\ell = 2\Delta$, while E' equals the Young modulus E for a plane stress case and $E/(1-\nu^2)$ for the plane strain; ν is the Poisson ratio. Substituting Eq. 24 into Eq. 25 generates

$$G^f = \frac{\chi_0(\alpha)^2\sigma^2\pi}{\Delta(2\alpha+1)E'}\left[(a+\Delta)^{2\alpha+1} - a^{2\alpha+1}\right] \tag{26}$$

At the onset of fracture, it has been postulated $G^f = G_c^f$, where the critical energy release rate $G_c^f = \left(K_c^f\right)^2/E'$ has the dimensions of stress x length$^{2\alpha}$; hence

the critical stress for a fractal quantized fracture obtained from the equality $G^f = G_c^f$

$$\sigma_{\text{crit}}^f = \sqrt{\frac{(2\alpha+1)E'G_c^f}{\pi}} \frac{\sqrt{\Delta}}{\chi_0(\alpha)\sqrt{(a+\Delta)^{2\alpha+1} - a^{2\alpha+1}}} \tag{27}$$

does indeed have the dimension of stress. For the zero crack length "a," this formula predicts a finite critical stress identified as an inherent material strength, namely,

$$\sigma_0^f = \sqrt{\frac{(2a+1)E'G_c^f}{\pi}} \left(\frac{1}{\chi_0(\alpha)\Delta^\alpha}\right) = \frac{K_c^f}{K_c}\sigma_0 \Delta^{\frac{1-2\alpha}{2}} \frac{\sqrt{\alpha+1/2}}{\chi_0(\alpha)} \tag{28}$$

As can be readily verified for α approaching ½, this equation reduces to the inherent strength σ_0 predicted earlier for a solid containing a smooth crack.

When the expression Eq. 28 is used as a normalizing constant for the critical stress, Eq. 27 assumes the form

$$s_{\text{crit}}^f = \frac{\sigma_{\text{crit}}^f}{\sigma_0^f} = \frac{1}{\sqrt{\left[\left(1+\frac{a}{\Delta}\right)^{2\alpha+1} - \left(\frac{a}{\Delta}\right)^{2\alpha+1}\right]}} \tag{29}$$

This result is illustrated in Fig. 6. For α approaching ½, this formula reduces to that given by Pugno and Ruoff in their treatise (Pugno and Ruoff 2004) of the quantum fracture mechanics (QFM), namely,

$$s_{\text{crit}}^{QFM} = \frac{1}{\sqrt{1+2\left(\frac{a}{\Delta}\right)}} \tag{30}$$

Using those equations, Wnuk and Yavari (2008) predict the relationship of the surface energy on the fractal exponent and the crack length

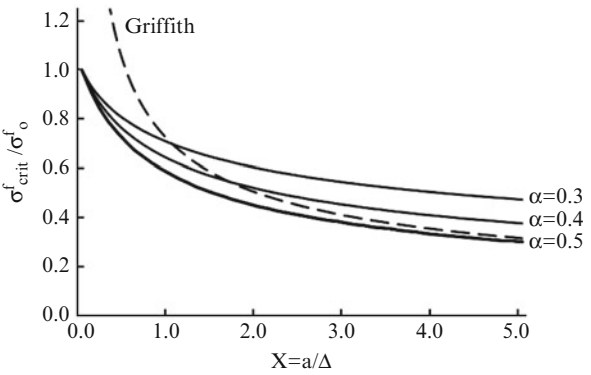

Fig. 6 Critical stress predicted by the fractal fracture mechanics for three levels of the crack surface roughness compared to that obtained from the Griffith theory. All stresses in this graph have been normalized by the inherent strength of an undamaged material, for which crack length is assumed zero

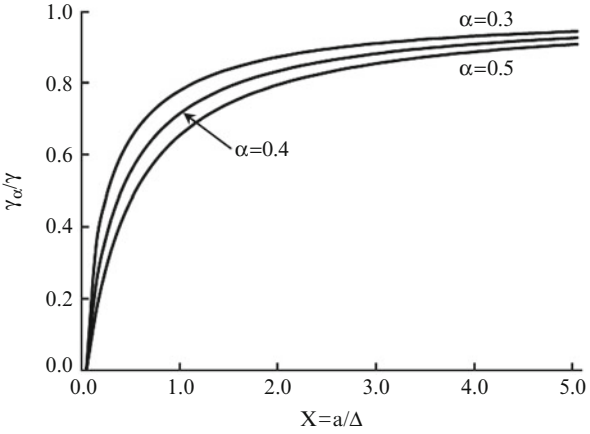

Fig. 7 Surface energy for small fractal cracks appears to be the function of the crack length – at least for the nanoscale range, where the crack lengths are on the order of magnitude of the size of Neuber particle. The surface energy is also affected by the fractal exponent α, showing higher specific surface energy for rougher cracks. This effect is referred to as "toughening phenomenon" ascribed to the influence of the fractal geometry

$$\frac{\gamma_\alpha}{\gamma} = \frac{(2\alpha+1)(a/\Delta)^{2\alpha}}{\left(1+\frac{a}{\Delta}\right)^{2\alpha+1} - \left(\frac{a}{\Delta}\right)^{2\alpha+1}} \tag{31}$$

The surface energy for a fractal crack γ_s is normalized by the LEFM surface energy γ.

The curve resulting from Eq. 31 shows a rapid increase of γ from zero at $a = 0$ to one over a distance on the order of magnitude of fracture quantum Δ; this trend is in good agreement with the experimental results of Ippolito et al. (2006); see Fig. 7. Even though for cracks of size orders of magnitude greater than the fracture quantum $\Delta(X >> 1)$, the surface energy is a material constant, it is not necessarily so in the realm of nanostructured brittle materials, for which the crack length is comparable to the atomistic characteristic length or to the size of the Neuber particle. In this domain the quantized fracture mechanics is superior to the classic mechanics as it provides a correct representation of the basic lattice features at the atomistic level. In this way the domain of the continuum mechanics has been enlarged to include the atomistic structure of a solid. Comparison of the curves shown in Fig. 7 proves that at nanoscale the fractal geometry of cracks leads to an enhancement of the fracture resistance γ. Therefore, one may speak about a "toughening effect" due to an increased material resistance to crack propagation; this statement is in complete agreement with the experimental findings of Ippolito et al. (2006) in their studies of onset and spread of fracture in a silicon carbide matrix.

Similar "toughening effect" is observed if the characteristic lengths R_{coh} and $R_{\text{coh}}^{\text{discrete}}$ are compared. As it follows from Wnuk and Yavari (2009) for the case of

$R << a$, the relation between the two measures of inherent material resistance to crack propagation is

$$R_{\text{coh}}^{\text{discrete}} = \frac{\pi K_I^2}{8\sigma_Y^2}\left(1 + \frac{1}{2a/\Delta}\right) \tag{32}$$

The expression in front of the parentheses stands for the R_{coh}, while the correction factor results from the quantization process, and it becomes significant only for very small cracks, when the crack length and the fracture quantum are comparable in size.

It is noteworthy that for α approaching ½ (a smooth crack case), the formula in Eq. 28 predicts the inherent strength of an undamaged solid as

$$\sigma_0 = \sqrt{\frac{2}{\pi\Delta}} K_c \tag{33}$$

while Eq. 29 reduces to

$$\sigma_{\text{crit}}^{QFM} = \frac{\sigma_0}{\sqrt{1 + 2\frac{a}{\Delta}}} \tag{34}$$

One of the curves depicted in Fig. 4 represents this equation; see the case of $\alpha =$ ½. As expected this result coincides exactly with the curve obtained from the quantized fracture mechanics.

The same can be said about the last two results in Eqs. 33 and 34, which are in complete agreement with the equations derived by Pugno and Ruoff (2004) for the case of quantized fracture. It is noted that these authors have used the method of averages over the length Δ, while here the finite difference technique is applied in conjunction with the potential Π^f of a body containing a fractal crack. The results are the same. An example of a root-mean-square averaging of the stress intensity factor is given as follows:

$$\langle K \rangle = \left(\frac{1}{\Delta}\int_a^{a+\Delta} K_I^2(a)da\right)^{\frac{1}{2}} = \sigma\sqrt{\pi}\left(\frac{1}{\Delta}\int_a^{a+\Delta} ada\right)^{\frac{1}{2}} = \sigma\sqrt{\pi}\sqrt{a + \frac{\Delta}{2}} \tag{35}$$

When this is set equal to K_c, the quantized fracture mechanics results in Eqs. 33 and 34 are recovered. This shows again that our finite difference approach and the root-mean-square averaging technique proposed by Pugno and Ruoff (2004) for K-factors are mathematically equivalent. It is noteworthy that these recent theoretical developments and the ensuing progress in the contemporary mechanics of fracture are continuations of the early intuitive concepts suggested by Neuber (1958) and Novozhilov (1969).

In Wnuk and Yavari (2005) have using the averaging technique to quantize the classic cohesive crack model extended the quantized mechanics analysis onto the fractal cracks as explained in (Wnuk and Yavari 2008, 2009). Valuable contributions

to fractal fracture mechanics are due to the Russian scientists Borodich (1992, 1997, 1999), Mosolov (1991), and Goldstein and Mosolov (1992). Two recent works of Wnuk et al. (2012, 2013) illustrate the applications of Wnuk's final stretch criterion (or δCOD criterion) to the problems of time-dependent fracture in viscoelastic and ductile solids. Noteworthy results were also obtained by Balankin (1997) and reviewed by Cherepanov et al. (1995).

The fracture criterion of Wells (1961) has been shown to be equivalent to the criterion based on the Rice path-independent J-integral; cf. Shih (1981). Shih (1981) and also Wnuk and Omidvar (1997), Wnuk et al. 1998) have studied the relation between the two criteria, related by a simple expression $J = d_n\,(CTOD/\sigma_Y)$. Numerical solutions for the coefficient d_n, based on the analysis of the HHR J-controlled asymptotic stress field, were given in the form of tables (Shih 1981) and certain approximate closed form formulae in Wnuk and Omidvar (1997) and Wnuk et al. (1998).

An essential conclusion of these considerations is the fact that the fractal geometry presents a new and useful tool in describing fracture of brittle and quasi-brittle solids. When combined with the quantized mechanics of fracture, it allows one to reach into the realm of atomistic modeling of the fracture process. This feature is especially valuable when the objective of one's research is the study of the lattice effects on deformation and fracture. In this way the range of validity of the classical mechanics of fracture has been extended into the nano-scale domain.

Delayed Fracture in Viscoelastic Solids for Euclidian and Fractal Geometries: Motion of a Smooth Crack in a Viscoelastic Medium

Effects of two parameters on the time-dependent fracture manifested by a slow stable crack propagation that precedes catastrophic failure in viscoelastic and in ductile materials have been studied. One of these parameters is related to the material ductility (ρ), and the other describes the geometry (roughness) of crack surface and is measured by the degree of fractality represented by the fractal exponent α or – equivalently – by the Hausdorff fractal dimension D for a self-similar crack.

Within a certain range of the applied load, there are two distinct stages of deformation process and the ensuing fracture. These are the incubation stage, when the crack remains stationary, followed by the onset of slow crack growth that eventually ends up with a transition to the catastrophic fracture. Comparison of the results pertaining to smooth and rough cracks demonstrates that the roughness of the crack surfaces slows down the growth of such "creeping cracks" observed in polymers. This phenomenon enhances the lifetime of the specimen and increases the crack length, at which the critical point is reached. Interestingly, the incubation time was found to be independent of the fractal geometry.

These studies of early stages of the delayed fracture in polymeric materials, sometimes referred to as "creep rupture," are then compared to the slow stable

crack growth in the ductile solids. Despite different physical mechanisms involved in the preliminary stable crack extension and despite different mathematical representations, a remarkable similarity of the end results pertaining to the two phenomena of slow crack growth (SCG) that occur either in viscoelastic or in ductile media has been demonstrated.

In the late 1960s and the early 1970s of the past century, a number of physical models and mathematical theories have been developed to provide a better insight and a quantitative description of the early stages of fracture in polymeric materials. In particular two phases of fracture initiation and subsequent growth have been considered: (1) the incubation phase during which the displacements of the crack surfaces are subject to creep process but the crack remains dormant and (2) slow propagation of a crack embedded in a viscoelastic medium. According to the linear theory of viscoelastic solids, the material response to the deformation process obeys the following constitutive relations:

$$\begin{aligned} s_{ij}(t,x) &= \int_0^t G_1(t-\tau)\frac{\partial e_{ij}(\tau,x)}{\partial \tau}d\tau \\ s(t,x) &= \int_0^t G_2(t-\tau)\frac{\partial e(\tau,x)}{\partial \tau}d\tau \end{aligned} \tag{36}$$

Here s_{ij} is the deviatoric part of the stress tensor, s denotes the spherical stress tensor, while $G_1(t)$ and $G_2(t)$ are time-dependent relaxation moduli for shear and dilatation, respectively. The inverse relations read

$$\begin{aligned} e_{ij}(t,x) &= \int_0^t J_1(t-\tau)\frac{\partial s_{ij}(\tau,x)}{\partial \tau}d\tau \\ e(t,x) &= \int_0^t J_2(t-\tau)\frac{\partial s(\tau,x)}{\partial \tau}d\tau \end{aligned} \tag{37}$$

Symbols e_{ij} and e are used to denote the deviatoric and spherical strain tensors and $J_1(t)$ and $J_2(t)$ are the two creep compliance functions. For a uniaxial state of stress, these last two equations reduce to a simple form

$$\varepsilon(t) = \int_0^t J(t-\tau)\frac{\partial \sigma(\tau)}{\partial \tau}d\tau \tag{38}$$

The relaxation moduli $G_1(t)$ and $G_2(t)$ and the creep compliance functions $J_1(t)$ and $J_2(t)$ satisfy the following integral equations:

$$\int_0^t G_1(t-\tau)J_1(\tau)d\tau = t$$
$$\int_0^t G_2(t-\tau)J_2(\tau)d\tau = t \tag{39}$$

For a uniaxial state of stress, these equations reduce to a single relation between the relaxation modulus $E_{\text{rel}}(t)$ and the creep compliance function $J(t)$

$$\int_0^t E_{\text{rel}}(t-\tau)J(\tau)d\tau = t \tag{40}$$

Atomistic model of delayed fracture was considered by Zhurkov (1965), but this molecular theory had no great impact on the further development of the theories based in the continuum mechanics approaches. Inspired by Max Williams, W. G. Knauss of Caltech in his doctoral thesis considered time-dependent fracture of viscoelastic materials (Knauss 1965). Similar research was done by Willis (1967) followed by simultaneous researches of Williams (1967, 1968, 1969a, b), Wnuk and Knauss (1970), Field (1971), Wnuk (1968a, 1969, 1971, 1972), and also by Knauss and Dietmann (1970), Mueller and Knauss (1971a, b), Graham (1968), Kostrov and Nikitin (1972), Mueller (1971), Knauss (1973) and Schapery (1973).

What follows in this section is an attempt to present a brief summary of the essential results, which have had a permanent impact on the development of the mechanics of time-dependent fracture. After this review is completed, an interesting analogy of delayed fracture in polymers will be indicated (a material property intricately related to the ability to creep) with the "slow crack growth" (SCG) occurring in ductile solids due to the redistribution of strains within the yielded zone preceding the front of a propagating crack.

Two stages of delayed fracture in viscoelastic media, incubation and propagation, are described, respectively, by two governing equations: (1) Wnuk–Knauss equation and (2) Mueller–Knauss–Schapery equation. The duration of the incubation stage can be predicted from the Wnuk–Knauss equation:

$$\Psi(t_1) = \frac{J(t_1)}{J(0)} = \left(\frac{K_G}{K_0}\right)^2_{a=a_0=\text{const}} \tag{41}$$

Mueller–Knauss–Schapery equation relates the rate of crack growth $\dot{a}$ to the applied constant load σ_0 and the material properties such as the unit step growth Δ, usually identified with the process zone size, and the Griffith stress $\sigma_G = \sqrt{2E\gamma/\pi a_0}$, namely,

$$\mathbf{\Psi}\left(\frac{\Delta}{\overset{*}{a}}\right) = \frac{J(\Delta/\overset{*}{a})}{J(0)} = \left(\frac{K_G}{K_0}\right)^2 \tag{42}$$

For a constant crack length equal to the length of the initial crack a_0, the right-hand side in Eq. 41 reduces to the square of the ratio of the Griffith stress to the applied stress

$$n = \left(\frac{\sigma_G}{\sigma_0}\right)^2 \tag{43}$$

This quantity is sometimes referred to as "crack length quotient" – it determines how many times the actual crack is smaller than the critical Griffith crack. Therefore, the larger is the number "n," the further away is the initial defect from the critical point of unstable propagation predicted for a Griffith crack embedded in a brittle solid. For large "n" the crack is too short to initiate the delayed fracture process; see expression in Eq. 50 for the definition of the $n_{\max}$. Beyond $n_{\max}$ growth of the crack cannot take place. For $n > n_{\max}$ one can assume that these are stable cracks, which – according to the theory presented here – will never propagate. These are so-called dormant cracks that belong to a "no-growth" domain; see Appendix.

When crack length "a" is not constant, but it can vary with time $a = a(t)$, then the right side in Eq. 42 reads

$$\left(\frac{\sigma_G}{\sigma_0}\right)^2 \frac{a_0}{a} = \frac{n}{\varsigma} \tag{44}$$

Here ζ denotes the nondimensional crack length, $\varsigma = a/a_0$. It is noteworthy that the physical meaning of the argument $\Delta/\overset{*}{a}$ appearing in Eq. 42 is the time interval needed for the tip of a moving crack to traverse the process zone adjacent to the crack tip, say

$$\delta t = \Delta/\overset{*}{a} \tag{45}$$

The location of the process zone with respect to the cohesive zone which precedes a propagating crack is shown in Fig. 8.

To illustrate applications of Eqs. 41 and 43, the constitutive equations valid for the standard linear solid (see Fig. 9) will be used. With β_1 denoting the ratio of the moduli E_1/E_2, the creep compliance function for this solid is given as

$$J(t) = \frac{1}{E_1}\{1 + \beta_1[1 - \exp(-t/\tau_2)]\} \tag{46}$$

Therefore, the nondimensional creep compliance function $\Psi(t) = J(t)/J(0)$ reads

$$\mathbf{\Psi}(t) = 1 + \beta_1[1 - \exp(-t/\tau_2)] \tag{47}$$

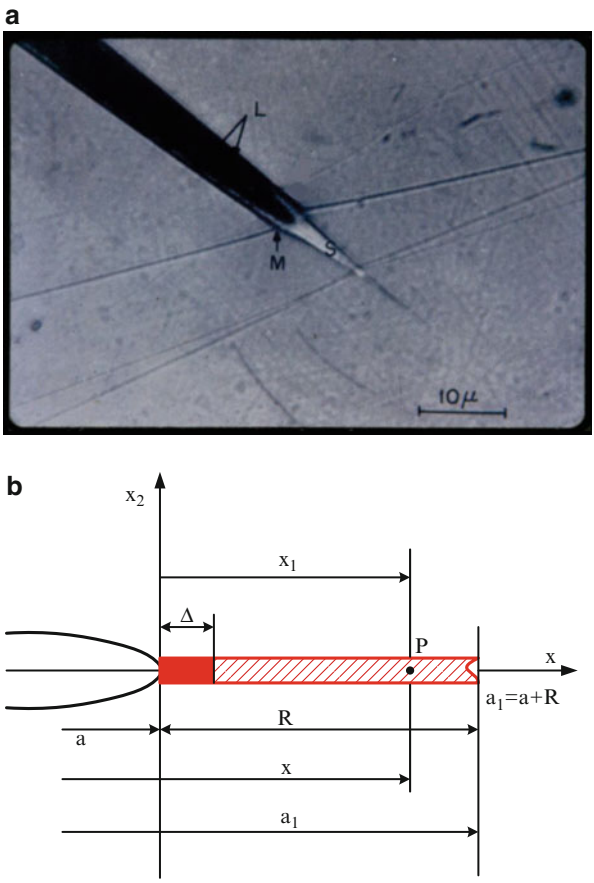

Fig. 8 (**a**) Microcrack preceded by a craze in Solithane 50/50 mimicking mechanical response of the solid rocket fuel and (**b**) details of the discrete cohesive crack model. When employed to glassy polymers, the cohesive zone coincides with the craze preceding the crack, and the Neuber particle Δ is incorporated into the equation of crack motion pertinent to the delayed fracture phenomenon in polymers as proposed by Knauss–Mueller–Dietmann (Borodich 1997, 1999; Mosolov 1991) and also by Schapery (Zhurkov 1965)

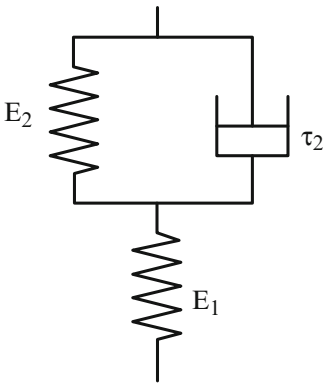

Fig. 9 Schematic diagram of the standard linear model of a viscoelastic solid. Despite its simplicity, the model is able to explain the instantaneous elastic response, creep, and stress relaxation

Substituting this expression into Eq. 41, one obtains

$$1 + \beta_1[1 - \exp(-t_1/\tau_2)] = n \tag{48}$$

Solving for t_1 one obtains the following prediction for the incubation time valid for a material represented by standard linear solid:

$$t_1 = \tau_2 \ln\left(\frac{\beta_1}{1 + \beta_1 - n}\right) \tag{49}$$

Inspection of Eq. 49 reveals that the quotient "n" should not exceed a certain limiting level

$$\begin{aligned} n_{\max} &= 1 + \beta_1 \\ s_{\min} &= \frac{1}{\sqrt{1 + \beta_1}} \end{aligned} \tag{50}$$

Physical interpretation of this relation can be stated as follows: for short cracks, when $n > n_{\max}$, there is no danger of initiating the delayed fracture process. These subcritical cracks are permanently dormant and they do not propagate. Perhaps, this is easier to understand when the variable $s = \sigma_0/\sigma_G$ is used instead of n. For $s < s_{\min}$ the preexisting cracks contained in a viscoelastic medium do not propagate.

Figure 10a illustrates the relationship between the incubation time and the loading parameter given either as n or $s(= 1/\sqrt{n} = \sigma_0/\sigma_G)$. Figure 10b shows an analogous relation between the time used in the process of crack propagation and the loading parameter s. Note that the incubation time is expressed in units of the relaxation time τ_2, while the time measured during the crack propagation phase of the delayed fracture is expressed in units of (τ_2/δ), wherein the constant δ contains the initial crack length a_0 and the characteristic material length Δ; cf. Eq. 53. When the variable s is used on the vertical axis and the pertinent function is plotted against the logarithm of time, then it is seen that a substantial portion of the curve appears as a straight line. This confirms the experimental results of Knauss and Dietmann (1970) used also by Schapery (1973) and Mohanty (1972).

To describe motion of a crack embedded in viscoelastic solid represented by the standard linear model, one needs to insert Eq. 46 into the governing Eq. 42. The equation of motion reads then

$$1 + \beta_1[1 - \exp(-\delta t/\tau_2)] = \frac{n}{\varsigma} \tag{51}$$

Solving it for the time interval $\delta t/\tau_2 (= \Delta/\mathring{a}\tau_2)$ yields

$$\frac{\Delta}{\tau_2 \mathring{a}} = \ln\left(\frac{\beta_1}{1 + \beta_1 - \frac{n}{\varsigma}}\right) \tag{52}$$

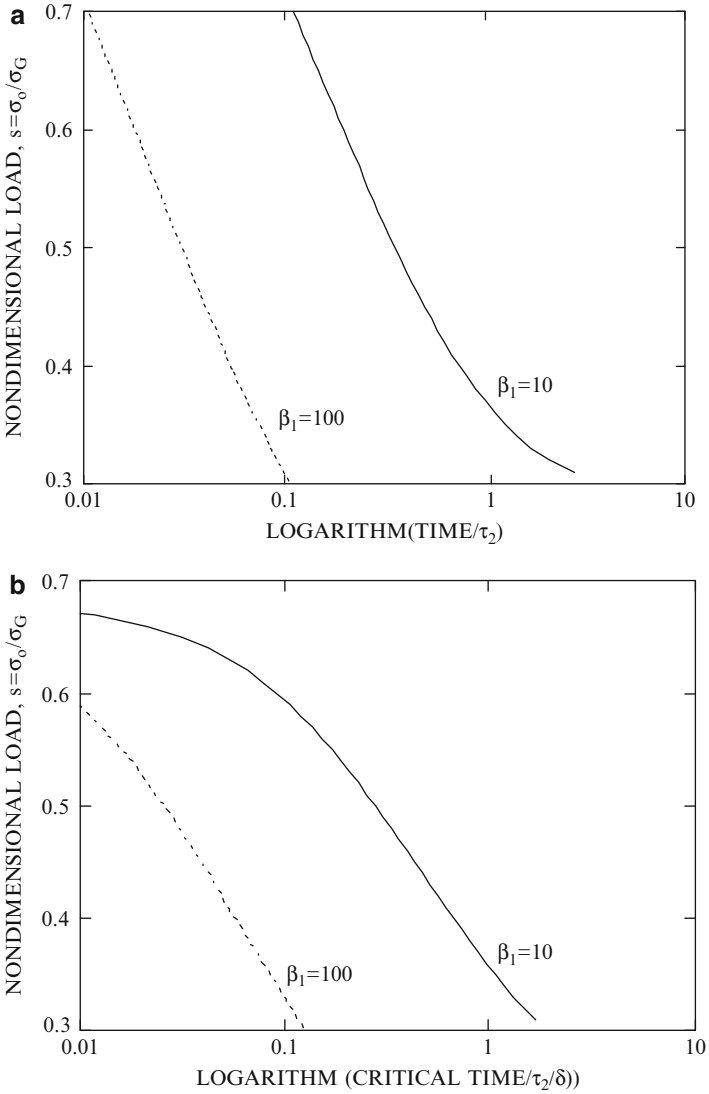

Fig. 10 (**a**) Logarithm of the incubation time in units of τ_2 shown as a function of the loading parameter s for two different values of the material constant $\beta_1 = E_1/E_2$. (**b**) Logarithm of the time to failure used during the crack propagation phase, in units of τ_2/δ, shown as a function of the loading parameter $s = \sigma_0/\sigma_G$ for two different values of the material constant $\beta_1 = E_1/E_2$

It is seen from Eq. 52 that for the motion to exist, the quotient n should not exceed the maximum value defined by Eq. 50. For $n > n_{\max}$ the cracks are too small to propagate.

If nondimensional notation for the length and time variables is introduced

$$\begin{aligned} \delta &= \Delta/a_0 \\ \theta &= t/\tau_2 \end{aligned} \tag{53}$$

the left-hand side of Eq. 52 can be reduced as follows:

$$\frac{\delta t}{\tau_2} = \frac{\Delta}{\tau_2 \ a} = \frac{\Delta}{\frac{d(\varsigma a_0)}{d(\theta\tau_2)}\tau_2} = \frac{\Delta/a_0}{d\varsigma/d\theta} \tag{54}$$

When this is inserted into Eq. 52 and with $\delta = \Delta/a_0$, the following differential equation results:

$$\frac{d\varsigma}{d\theta} = \delta\left[\ln\left(\frac{\beta_1}{1+\beta_1-\frac{n}{\varsigma}}\right)\right]^{-1} \tag{55}$$

or, after separation of variables,

$$(\delta)d\theta = \ln\left(\frac{\beta_1}{1+\beta_1-\frac{n}{\varsigma}}\right)d\varsigma \tag{56}$$

Motion begins at the first critical time t_1, which designates the end of the incubation period. Therefore, the lower limit for the integral applied to the left-hand side of Eq. 56 should be $\theta_1 = t_1/\tau_2$, while the upper limit is the current nondimensional time $\theta = t/\tau_2$. The corresponding upper limit to the integral on the right-hand side of Eq. 56 is the current crack length $\zeta = a/a_0$, while the lower limit is one. Upon integration one obtains

$$\int_{t_1/\tau_2}^{t/\tau_2} d\theta = \left(\frac{1}{\delta}\right)\int_1^{\varsigma} \ln\left(\frac{\beta_1}{1+\beta_1-\frac{n}{z}}\right)dz \tag{57}$$

The resulting expression relates the crack length x to time t, namely,

$$t - t_1 = \left(\frac{\tau_2}{\delta}\right)\int_1^{\varsigma} \ln\left(\frac{\beta_1}{1+\beta_1-\frac{n}{z}}\right)dz \tag{58}$$

If the closed form solution for the integral in Eq. 58 is used, then this formula can be cast in the following final form:

$$t = t_1 + \left(\frac{\tau_2}{\delta}\right)\left\{\varsigma \ln\left[\frac{\varsigma\beta_1}{(1+\beta_1)\varsigma - n}\right] + \frac{n}{1+\beta_1}\ln\left[\frac{(1+\beta_1)\varsigma - n}{1+\beta_1-n}\right] + \ln\left(\frac{1+\beta_1-n}{\beta_1}\right)\right\} \tag{59}$$

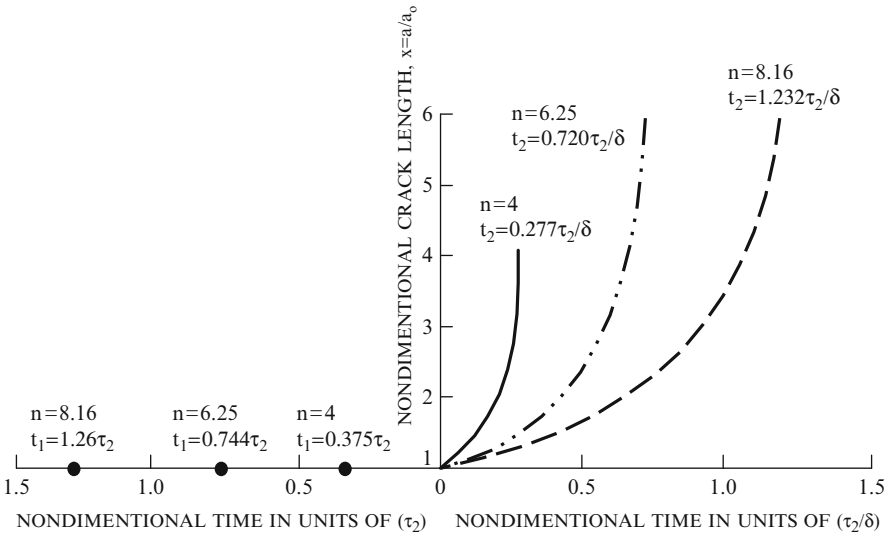

Fig. 11 Slow crack propagation occurring in a linear viscoelastic solid represented by the standard linear model depicted in Fig. 2 at $\beta_1 = 10$. Crack length is shown as a function of time; points marked on the negative time axis designate the incubation times corresponding to the given level of the applied constant load n and expressed in units of τ_2. The time interval between the specific point t_1 and the origin of the coordinates provides the duration of the incubation period. Crack propagation begins at $t = 0$. Symbol t_2 denotes time to failure, which is the time used during the quasi-static phase of crack extension, and it is expressed in units of (τ_2/δ). Constant δ is related to the characteristic material length, the so-called unit growth step Δ

This equation has been used in constructing the graphs shown in Fig. 11. At $\beta_1 = 10$ three values of n have been used (4.00, 6.25, and 8.16, which corresponds to the following values of s: 0.5, 0.4, and 0.35). It can be observed that at x approaching n, the phase of the slow crack propagation is transformed into unrestrained crack extension tantamount to the catastrophic fracture. The point in time, at which this transition occurs, can be easily seen on the horizontal axis of Fig. 11. This point of transition into unstable propagation can also be predicted from Eq. 59; substituting n for ζ, one obtains the time to fracture.

$$t_2 = \left(\frac{\tau_2}{\delta}\right)\left\{\frac{n}{1+\beta_1}\ln\left[\frac{\beta_1\ n}{1+\beta_1-n}\right] + \ln\left(\frac{1+\beta_1-n}{\beta_1}\right)\right\} \tag{60}$$

If the incubation time t_1 given by Eq. 49 is now added to Eq. 60, one obtains the total lifetime of the component, namely,

$$T_{cr} = t_1 + t_2 = \tau_2 \ln\left(\frac{\beta_1}{1+\beta_1-n}\right) + \left(\frac{\tau_2}{\delta}\right)\left\{\frac{n}{1+\beta_1}\ln\left[\frac{\beta_1 n}{1+\beta_1-n}\right] + \ln\left[\frac{1+\beta_1-n}{\beta_1}\right]\right\} \tag{61}$$

Summarizing the results of this section, one can state that the delayed fracture in a viscoelastic solid can be mathematically represented by four expressions:

- Time of incubation t_1 given by Eq. 49 for standard linear model.
- Equation of motion given by Eq. 59 for the same material model and defining ζ as a function of time, $\zeta = \zeta(t)$.
- Time to fracture t_2 due to crack propagation given by Eq. 60.
- Lifetime T_{cr} equal to the sum $t_1 + t_2$, as given by Eq. 61. It is noted that while the first term in the expression Eq. 61 involves the relaxation time, material constant β_1, and the quotient n, the second term in Eq. 61 contains also the internal structural constant δ. It is also noted that for the quotient n approaching one, both terms in Eq. 61 are zero, while for n exceeding $n_{\max}$, the expression looses the physical sense (since in that case there is no propagation). With the constant δ being on the order of magnitude varying within the range $10^{-3} - 10^{-6}$, the second term in Eq. 61 is substantially greater than the first term which represents the incubation time; see also Appendix.

For $\beta_1 = 10$ and three different levels of n, the resulting functional relationships between the crack length x and time t are shown in Fig. 11 along with the values of the incubation times, expressed in units of (τ_2), and the times-to-failure expressed in units of (τ_2/δ). A numerical example is given in the Appendix.

Example described here, involving the standard linear solid, serves as an illustration of the mathematical procedures necessary in predicting the delayed fracture in polymeric materials. Knauss and Dietmann (1970) and Schapery (1973) have shown how the real viscoelastic materials, for which the relaxation modulus $G(t)$ and the creep compliance function $J(t)$ are measured (or calculated from Eq. 4) and then used in the governing equations of motion discussed above, can provide a good approximation of the experimental data.

Growth of Fractal Cracks in Viscoelastic Media

To extend the theory of creeping cracks into the domain of fractal geometry, one needs to redefine entities of the critical stress intensity factor and the applied stress intensity stress factor K_0, denoted, respectively, by K_G and K_0 in the governing Eq. 42. The new definitions accounting for the fractal geometry of a crack are as follows:

$$\begin{aligned} K_G &\rightarrow K_{\text{crit}}^f = \chi_0(\alpha)\sigma_{\text{crit}}\sqrt{\pi a^{2\alpha}} \\ K_0 &\rightarrow K_0^f = \chi_0(\alpha)\sigma_0\sqrt{\pi a_0{}^{2\alpha}} \end{aligned} \tag{62}$$

For glassy polymers, the critical stress σ_{crit} is very closely approximated by the Griffith stress σ_G. Thus, the ratio $(K_G/K_0)^2$ will reduce to an expression

$$\left(\frac{K_{\text{crit}}^{f}}{K_{0}^{f}}\right)^{2}=\left(\frac{\sigma_{G}}{\sigma_{0}}\right)^{2}\left(\frac{a_{0}}{a}\right)^{2\alpha}=\frac{n}{\zeta^{2\alpha}} \tag{63}$$

When substituted into Eqs. 55 or 56, this leads to the following ordinary differential equation describing the slow motion of a fractal crack:

$$d\theta=\delta^{-1}\ln\left(\frac{\beta_{1}}{1+\beta_{1}-\frac{n}{\zeta^{2\alpha}}}\right)d\zeta \tag{64}$$

The solution of this equation is readily obtained as

$$t=t_{1}+\left(\frac{\tau_{2}}{\delta}\right)\int_{1}^{\zeta}\ln\left[\frac{\beta_{1}}{1+\beta_{1}-\frac{n}{z^{2\alpha}}}\right]dz \tag{65}$$

In here t_1 denotes the incubation time, which is given by Eq. 49 – the same formula which was found valid for a smooth crack. However, the motion of a rough crack differs from that of a smooth crack in a rather distinct way; see Fig. 12. Fractal crack moves slower than the smooth crack and it arrives at the critical length significantly greater than the critical length attained by a smooth crack of same initial size and subjected to the same loading configuration and the same load.

To substantiate this statement, let us compare the delayed fracture of a rough crack defined by the fractal exponent $\alpha = 0.3$ (or the fractal dimension $D = 1.4$) to that of a smooth crack, for which $\alpha = 0.5$ and $D = 1$. For the input data

$$\beta_{1}=10,\quad n=4,\quad \delta=10^{-3} \tag{66}$$

and using Eq. 65 (see also Fig. 12a), one obtains the values of the terminal crack lengths and the times of propagation up to the point of catastrophic fracture for the fractal and smooth crack as follows:

$$a_{\text{crit}}^{f}=10a_{0}\text{and}a_{\text{crit}}^{\text{smooth}}=4a_{0},\quad t_{2}^{f}=659.34\tau_{2}\text{and}t_{2}^{\text{smooth}}=485.04\tau_{2} \tag{67}$$

This clearly shows that roughness of the crack surfaces has a significant influence on the process of delayed fracture. For the data specified in Eq. 66, one observes 2.5-fold increase in the critical crack length attained at the terminal instability point (150% enhancement over the smooth crack case) and 1.36-fold increase in the time of propagation, which is 36% above the result valid for a smooth crack. These numbers illustrate the strong influence of fractal geometry on the outcome of the delayed fracture tests.

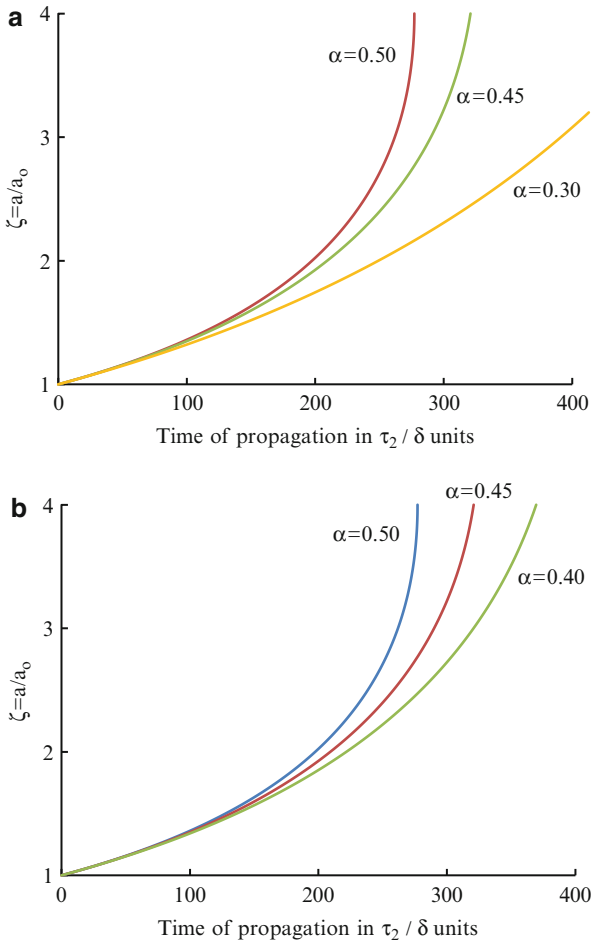

Fig. 12 The graphs in (**a**) and (**b**) show the effects of the roughness of the crack surfaces on the quasi-static propagation of crack contained in the viscoelastic medium. An increased degree of crack fractality is tantamount to an enhanced roughness of the crack surfaces and to a more pronounced phenomenon of time-dependent fracture, which precedes the catastrophic failure

Some Fundamental Concepts

Delayed fracture occurring in a linearly viscoelastic solid such as the one discussed in section "Basic Concepts in Fractal Fracture Mechanics" consists of two distinct stages: (1) incubation phase, during which the opening displacement associated with the crack increases in time, but the crack remains stationary, and (2) propagation phase, when the crack advances up to the critical length (Griffith length), at which transition to unstable crack extension takes place. Stage I (incubation) is described by the Wnuk–Knauss equation in Eq. 41, and for the standard linear solid (see Fig. 9), the predicted duration of the incubation phase t_1 is given as

$$t_1 = \tau_2 \ln\left(\frac{\beta_1}{1+\beta_1-n}\right) \tag{68}$$

The phase II (crack propagation) is governed by the Mueller–Knauss–Schapery Eq. (42). For the nondimensional creep compliance function $\Psi(t)$ defined by Eq. 47, the resulting equation of motion, which relates crack length ζ to time t, is given by Eq. 59, while the duration of the propagation phase is predicted as follows:

$$t_2 = \left(\frac{\tau_2}{\delta}\right)\left\{\frac{n}{1+\beta_1}\ln\left[\frac{\beta_1\ n}{1+\beta_1-n}\right] + \ln\left[\frac{1+\beta_1-n}{\beta_1}\right]\right\} \tag{69}$$

The total lifetime T_{cr} of the component manufactured of a polymeric material that obeys the constitutive equations described in section "Basic Concepts in Fractal Fracture Mechanics" is obtained as the sum of Eqs. 68 and 69, namely,

$$\begin{aligned} T_{\mathrm{cr}} &= t_1 + t_2 \\ &= \tau_2 \ln\left(\frac{\beta_1}{1+\beta_1-n}\right) + \left(\frac{\tau_2}{\delta}\right) \\ &\quad \times \left\{\frac{n}{1+\beta_1}\ln\left[\frac{\beta_1\ n}{1+\beta_1-n}\right] + \ln\left[\frac{1+\beta_1-n}{\beta_1}\right]\right\} \end{aligned} \tag{70}$$

For Solithane 50/50, a polymer which is used to model mechanical properties of the solid rocket fuel, the times t_1, t_2, and T_{cr} were evaluated by Knauss (1969) and Mohanty (1972). The moduli E_1 and E_2 and the viscosity η_2 involved in the standard linear solid that was applied in these studies are as follows:

$$\begin{aligned} E_1 &= 6.65^{*}10^{3}\ \mathrm{lb/in^2} \\ E_2 &= 3.69^{*}10^{3}\ \mathrm{lb/in^2} \\ \eta_2 &= 1.36^{*}10^{3}\ s\mathrm{lb/in^2} \end{aligned} \tag{71}$$

This leads to $\beta_1 = 1.8$, the relaxation time $\tau_2 = \eta_2/E_2 = 0.368$ s, and the maximum crack length quotient $n_{\max} = 1+\beta_1 = 2.8$. The structural length Δ was estimated as 4.5×10^{-4} in., while the precut cracks used in the experiments were on the order of 0.225 in. This yielded the inner structural constant $\delta = 2 \times 10^{-3}$. From Eq. 71 the "glassy" and the "rubbery" values of the creep compliance function can be readily calculated, namely,

$$\begin{aligned} J_{\mathrm{glassy}} &= J(0) = 1.50^{*}10^{-4}\ \mathrm{in^2/lb} \\ J_{\mathrm{rubbery}} &= J(\infty) = 4.22^{*}10^{-4}\ \mathrm{in^2/lb} \end{aligned} \tag{72}$$

For detailed calculations, the reader is referred to Knauss (1969) and Mohanty (1972).

The glassy (instantaneous) and rubbery (upon complete relaxation) compliance function values, as given in Eq. 72, allow one to establish the domains of the delayed fracture, such as "no-growth," incubation, or propagation domains. It should be noted that the creep compliance functions involved in these experimental investigations were obtained by use of the method.

In general, the propagation of a crack embedded in the viscoelastic medium will occur within a certain range of applied load. The two limiting values are (1) the Griffith stress evaluated for the initial crack size a_0, which is

$$\sigma_G = \begin{cases} \sqrt{\dfrac{2E_\gamma}{\pi a_0}} \\ \dfrac{K_{IC}}{\sqrt{\pi a_0}} \end{cases} \tag{73}$$

and (2) the propagation threshold stress

$$\sigma_{\text{threshold}} = \sqrt{\frac{J(0)}{J(\infty)}}\,\sigma_G = \sqrt{\frac{J_{\text{glassy}}}{J_{\text{rubbery}}}}\;\sigma_G \tag{74}$$

For the standard linear solid expression, Eq. 74 reads

$$\sigma_{\text{threshold}} = \frac{1}{\sqrt{1+\beta_1}}\sigma_G \tag{75}$$

Using these relations one can predict the range of the applied loads for a successful delayed fracture test performed on Solithane 50/50 as being between 6/10 of the Griffith stress and the Griffith stress itself.

Summarizing, for the loads below the threshold stress given in Eqs. 74 and 75, one enters the "no-growth" domain, where propagation does not take place and the cracks in this region remain dormant. The other extreme is attained when the applied constant stress σ_0 reaches the Griffith level σ_G. When σ_0 approaches the Griffith stress, one observes an instantaneous fracture as in a brittle medium with no delay effects. Therefore, one may conclude that the delayed fracture occurs only in the range

$$\begin{aligned} \sigma_{\text{threshold}} \le \sigma_0 \le \sigma_G \\ \frac{\sigma_G}{\sqrt{1+\beta_1}} \le \sigma_0 \le \sigma_G \end{aligned} \tag{76}$$

The second expression in Eq. 76 pertains to the standard linear model.

Let us now consider a numerical example for a polymer characterized by the following properties $\beta_1 = 10$, $\tau_2 = 1$ s, and $\delta = 10^{-4}$. Pertinent calculations are performed for three levels of the applied load, measured either by the crack length quotient n $(=\sigma_G{}^2/\sigma_0{}^2)$ or by the load ratio $s = \sigma_0/\sigma_G$, namely, $n = 8.16$ $(s = 0.35)$,

$n = 6.25$ ($s = 0.40$), and $n = 4$ ($s = 0.50$). Applying Eqs. 68 and 69, one obtains the following incubation (t_1) and time-to-failure (t_2) values:

$$\begin{aligned} & n\left(=\sigma_G{}^2/\sigma_0{}^2\right) \\ & n = 8.16; s = 0.35 \\ & t_1 = 1.26\ s; t_2 = \left(1/10^{-4}\right)(0.277) \quad s = 46.2 \quad \text{min} \\ & n = 6.25; s = 0.40 \\ & t_1 = 0.744\ s; t_2 = \left(1/10^{-4}\right)(0.720) \quad s = 120 \quad \text{min} \\ & n = 4; s = .50 \\ & t_1 = 0.375\ s; t_2 = \left(1/10^{-4}\right)(1.232) \quad s = 205 \quad \text{min} \end{aligned} \tag{77}$$

It is noted that for this material, the range of the applied stress for the delayed fracture to occur is contained within the interval [0.3 σ_G, σ_G]. For applied stress less than the threshold stress of $0.3\sigma_G$, the phenomenon of delayed fracture vanishes, and the crack remains stationary.

An interesting study of the interaction between the damage zone, governed by the modified Kachanov's law, and the dominant crack has been described in Wnuk and Kriz (1985). There it has been shown that the existence of the damage zone adjacent to the crack leading edge accelerates motion of the subcritical crack.

Conclusions

From the considerations presented above, it follows that fracture is not only of fractal character, but it is also of multi-scale nature. To fill the gap between the "micro" and "macro" scale levels, the group of Panin (Pugno and Ruoff 2004) in Siberia, Russia, has developed an entirely new branch of mechanics, named "Mesomechanics." The primary objective of this and the following chapter is to construct a theory that explains and supports the findings based on the experimental observations of the Siberian group.

References

A.S. Balankin, Physics of fracture and mechanics of self-affine cracks. Eng. Fract. Mech. **57**(2), 135–203 (1997)

F.M. Borodich, Fracture energy in a fractal crack propagating in concrete or rock. Doklady Russian Acad. Sci. **325**, 1138–1141 (1992)

F.M. Borodich, Some fractal models of fracture. J. Mech. Phys. Solids **45**, 239–259 (1997)

F.M. Borodich, Fractals and fractal scaling in fracture mechanics. Int. J. Fract. **95**, 239–259 (1999)

A. Carpinteri, Scaling laws and renormalization groups for strength and toughness of disordered materials. Int. J. Solids Struct. **31**, 291–302 (1994)

A. Carpinteri, A. Spagnoli, A fractal analysis of the size effect on fatigue crack growth. Int. J. Fatigue **26**, 125–133 (2004)

A. Carpinteri, B. Chiaia, P. Cornetti, A scale invariant cohesive crack model for quasi-brittle materials. Eng. Fract. Mech. **69**, 207–217 (2002)
G.P. Cherepanov, A.S. Balankin, V.S. Ivanova, Fractal fracture mechanics – A review. Eng. Fract. Mech. **51**(6), 997–1033 (1995)
F.A. Field, A simple crack extension criterion for time-dependent spallation. J. Mech. Phys. Solids **19**, 61 (1971); also in AMR, vol. 25 (1972), Rev. 2781
R.V. Goldstein, A.B. Mosolov, Fractal cracks. J. Appl. Math. Mech. **56**, 563–571 (1992)
G.A.C. Graham, The correspondence principle of linear viscoelasticity theory for mixed boundary value problems involving time dependent boundary regions. Q. Appl. Math. **26**, 167 (1968); also in AMR, vol. 22, Rev. 4036
A.A. Griffith, The phenomenon of rupture and flow in solids. Phil. Trans. Roy. Soc. Lond. **A221**, 163–398 (1921)
J. Harrison, Numerical integration of vector fields over curves with zero area. Proc. Am. Math. Soc. **121**, 715–723 (1994)
J. Harrison, A. Norton, Geometric integration on fractal curves in the plane, research report. Indiana Univ. Math. J. **40**, 567–594 (1991)
C.E. Inglis, Stresses in a plate due to the presence of cracks and sharp corners. Trans. R. Inst. Naval Architects **60**, 219 (1913)
M. Ippolito, A. Mattoni, L. Colombo, Role of lattice discreteness on brittle fracture: Atomistic simulations versus analytical models. Phys. Rev. B **73**, 104111, 6 pages (2006)
G.R. Irwin, *Handbuch der Physik*, vol 6 (Springer, Berlin, 1956), pp. 551–590
H. Khezrzadeh, M.P. Wnuk, A. Yavari, Influence of material ductility and crack surface roughness on fracture instability. J. Phys. D. Appl. Phys. **44**, 395302 (2011) (22 pages)
W.G. Knauss, Stable and unstable crack growth in viscoelastic media. Trans. Soc. Rheol. **13**, 291 (1969)
W.G. Knauss, Delayed failure. The Griffith problem for linearly viscoelastic materials. Int. J. Fract. **6**, 7 (1970); also in AMR, vol. 24, Rev. 5923
W.G. Knauss, The mechanics of polymer fracture. Appl. Mech. Rev. **26**, 1–17 (1973)
W.G. Knauss, The time dependent fracture of viscoelastic materials, in *Proceedings of the First International Conference on Fracture*, vol. 2, ed. by M.L. Williams. p. 1139; also see the Ph.D. Thesis, California Institute of Technology 1963 (1965)
W.G. Knauss, H. Dietmann, Crack propagation under variable load histories in linearly viscoelastic solids. Int. J. Eng. Sci. **8**, 643 (1970).; also in AMR, vol. 24, Rev. 1097
B.V. Kostrov, L.V. Nikitin, Some general problems of mechanics of brittle fracture. Archiwum Mechaniki Stosowanej. (English version) **22**, 749 (1972).; also in AMR, vol. 25 (1972), Rev. 1987 (1970)
B.B. Mandelbrot, D.E. Passoja, A.J. Paullay, Fractal character of fracture surfaces in metals. Nature **308**, 721–722 (1984)
D. Mohanty, Experimental study of viscoelastic properties and fracture characteristics in polymers, M.S. Thesis at Department of Mechanical Engineering, South Dakota State University, Brookings, 1972
A.B. Mosolov, Cracks with fractal surfaces. Doklady Akad. Nauk SSSR **319**, 840–844 (1991)
H.K. Mueller, Stress-intensity factor and crack opening for a linearly viscoelastic strip with a slowly propagating central crack. Int. J. Fract. **7**, 129 (1971)
H.K. Mueller, W.G. Knauss, Crack propagation in a linearly viscoelastic strip. J. Appl. Mech. **38**(Series E), 483 (1971a)
H.K. Mueller, W.G. Knauss, The fracture energy and some mechanical properties of a polyurethane elastomer. Trans. Soc. Rheol. **15**, 217 (1971b)
N.I. Muskhelishvili, *Some Basic Problems of the Mathematical Theory of Elasticity* (English translation) (Noordhoff, 1953)
H. Neuber, *Theory of Notch Stresses* (Springer, Berlin, 1958)
V.V. Novozhilov, On a necessary and sufficient criterion for brittle strength. J. Appl. Mech. USSR **33**, 212–222 (1969)

N. Pugno, R.S. Ruoff, Quantized fracture mechanics. Philos. Mag. **84**(27), 2829–2845 (2004)
J.R. Rice, Mathematical analysis in the mechanics of fracture, in *Fracture. An Advanced Treatise*, ed. by H. Liebowitz, vol. II (Academic, New York, 1968)
R.A. Schapery, A theory of crack growth in viscoelastic media. Int. J. Fract. **11**, 141–159 (1973)
C.F. Shih, Relationship between the J-integral and crack opening displacement for stationary and growing cracks. J. Mech. Phys. Solids **29**, 305–326 (1981)
A. Spagnoli, Self-similarity and fractals in the Paris range of fatigue crack growth. Mech. Mater. **37**, 519–529 (2005)
A.A. Wells, Application of fracture mechanics at and beyond general yielding. Br. J. Weld. **11**, 563–570 (1961)
H.M. Westergaard, Bearing pressure and cracks. J. Appl. Mech. **61**(1939), A49–A53 (1939)
M.L. Williams, On stress distribution at the base of a stationary crack. J. Appl. Mech. **24**, 109–114 (1957)
M.L. Williams, The continuum interpretation for fracture and adhesion. J. Appl. Polym.Sci. **13**, 29 (1969a)
M.L. Williams, The kinetic energy contribution to fracture propagation in a linearly viscoelastic material. Int. J. Fract. **4**, 69 (1969b).; also in AMR, vol. 22 (1969), Rev. 8521
J.R. Willis, Crack propagation in viscoelastic media. J. Mech. Phys. Solids **15**, 229 (1967).; also in AMR, vol.22 (1969), Rev. 8625
M.P. Wnuk, *Energy Criterion for Initiation and Spread of Fracture in Viscoelastic Solids* (Technical Report of the Engineer Experimental Station at SDSU, No.7, Brookings, 1968a)
M.P. Wnuk, Nature of fracture in relation to the total potential energy. Br. J. Appl. Phys. **1**(Serious 2), 217 (1968b)
M.P. Wnuk, Effects of time and plasticity on fracture. Br. J. Appl. Phys., Ser. 2 **2**, 1245 (1969)
M.P. Wnuk, *Prior-to-Failure Extension of Flaws Under Monotonic and Pulsating Loadings* (SDSU Technical Report No. 3, Engineering Experimental Station Bulletin at SDSU, Brookings, 1971)
M.P. Wnuk, Accelerating crack in a viscoelastic solid subject to subcritical stress intensity, in *Proceedings of the International Conference on Dynamic Crack Propagation, Lehigh University*, ed. by G. C. Sih, (Noordhoff, Leyden, 1972), pp. 273–280
M.P. Wnuk, Quasi-static extension of a tensile crack contained in a viscoelastic-plastic solid. J. Appl. Mech. **41**, 234–242 (1974)
M.P. Wnuk, R.D. Kriz, CDM model of damage accumulation in laminated composites. Int. J. Fract. **28**, 121–138 (1985)
M.P. Wnuk, B. Omidvar, Effects of strain hardening on quasi-static fracture in elasto-plastic solid represented by modified yield strip model. Int. J. Fract. **84**, 383–403 (1997)
M.P. Wnuk, A. Yavari, On estimating stress intensity factors and modulus of cohesion for fractal cracks. Eng. Fract. Mech. **70**, 1659–1674 (2003)
M.P. Wnuk, A. Yavari, A correspondence principle for fractal and classical cracks. Eng. Fract. Mech. **72**, 2744–2757 (2005)
M.P. Wnuk, A. Yavari, Discrete fractal fracture mechanics. Eng. Fract. Mech. **75**, 1127–1142 (2008)
M.P. Wnuk, A. Yavari, A discrete cohesive model for fractal cracks. Eng. Fract. Mech. **76**, 548–559 (2009)
M.P. Wnuk, B. Omidvar, M. Choroszynski, Relationship between the CTOD and the J-integral for stationary and growing cracks. Closed form solutions. Int. J. Fract. **87**, 331–343 (1998)
M.P. Wnuk, M. Alavi, A. Rouzbehani, Comparison of time dependent fracture in viscoelastic and ductile solids. Phys. Mesomech. **15**(1–2), 13–25 (2012)
M.P. Wnuk, M. Alavi, A. Rouzbehani, A Mathematical Model of Panin's Pre-Fracture Zones and Stability of Subcritical Cracks, in *Physical Mesomechanics*, (Russian Academy of Sciences, Tomsk, 2013) (in print)
S.N. Zhurkov, Kinetic concept of the strength of solids. Int. J. Fract. **1**, 311 (1965).; also in Appl. Mech. Rev., vol. 20, 1967, Rev. 4080

Lattice and Particle Modeling of Damage Phenomena

41

Sohan Kale and Martin Ostoja-Starzewski

Contents

Introduction 1144
Basic Idea of a Spring Network Representation 1145
Anti-plane Elasticity on Square Lattice 1146
In-Plane Elasticity: Triangular Lattice with Central Interactions 1148
In-Plane Elasticity: Triangular Lattice with Central and Angular Interactions 1151
Triple Honeycomb Lattice 1152
Spring Network Models 1153
Representation by a Fine Mesh 1153
Damage in Macro-Homogeneous Materials 1156
Damage Patterns and Maps of Disordered Elastic–Brittle Composites 1164
Particle Models 1165
Governing Equations 1165
Examples 1171
Other Models 1172
Scaling and Stochastic Evolution in Damage Phenomena 1173
Concluding Remarks 1177
References 1177

Abstract

Lattice (spring network) models offer a powerful way of simulating mechanics of materials as a coarse scale cousin to molecular dynamics and, hence, an alternative to finite element models. In general, lattice nodes are endowed with masses, thus resulting in a quasiparticle model. These models, having their origins in spatial trusses and frameworks, work best when the material may naturally be represented by a system of discrete units interacting via springs or, more generally, rheological elements. This chapter begins with basic concepts and

S. Kale (✉) · M. Ostoja-Starzewski
Department of Mechanical Science and Engineering, also Institute for Condensed Matter Theory and Beckman Institute, University of Illinois at Urbana-Champaign, Urbana, IL, USA
e-mail: skale2@illinois.edu; martinos@illinois.edu

© Springer Nature Switzerland AG 2022

G. Z. Voyiadjis (ed.), *Handbook of Damage Mechanics*,
https://doi.org/10.1007/978-3-030-60242-0_20

applications of spring networks, in particular the anti-plane elasticity, planar classical elasticity, and planar nonclassical elasticity. One can easily map a specific morphology of a composite material onto a particle lattice and conduct a range of parametric studies; these result in the so-called damage maps. Considered next is a generalization from statics to dynamics, with nodes truly acting as quasiparticles, application being the comminution of minerals. The chapter closes with a discussion of scaling and stochastic evolution in damage phenomena as stepping-stone to stochastic continuum damage mechanics.

Keywords

Triangular lattice · Stiffness tensor · Diffusive fracture · Brittle transition · Markov jump process

Introduction

The need to simultaneously model elastic, plastic, and fracture responses in heterogeneous materials necessitates the introduction of techniques outside the realm of conventional continuum solid mechanics and finite element analysis. One technique that can meet the challenge, especially, when complicated microstructures need to be considered goes under the heading "lattice models." This chapter outlines the basics of lattice (or spring network) models and quasiparticle models in studies of damage phenomena. These models have their origin in spatial trusses and frameworks (from the engineering mechanics side) as well as in crystal structures (from the physics side). They offer a powerful way of simulating mechanics of materials with either periodic or random microstructures and, hence, offer an attractive alternative to finite element models. When dealing with a dynamic problem, nodes of the lattice may be endowed with masses, thus resulting in a quasiparticle model, which is then a coarse scale cousin of molecular dynamics. Lattice models work best when the material may naturally be represented by a system of discrete units interacting via springs or, more generally, rheological elements – examples are fibrous or granular systems. In the latter case, the lattice model turns into the discrete element model.

In this chapter, first, an introduction to basic concepts and applications of spring networks is given and, in particular, to the anti-plane elasticity, planar classical elasticity, and planar nonclassical elasticity. It is shown that one can easily map a specific morphology of a composite material onto a particle lattice and conduct a range of parametric studies; such studies result in the so-called damage maps. Here we discuss the elastic–plastic, elastic–brittle, and elastic–plastic–brittle materials. Considered next is a generalization from statics to dynamics (i.e., to a quasiparticle model), with nodes truly acting as quasiparticles, one application being the comminution of minerals. The chapter closes with a discussion of scaling and stochastic evolution in damage phenomena as stepping-stone to stochastic continuum damage mechanics.

Basic Idea of a Spring Network Representation

The basic idea in setting up lattice spring network (or lattice) models in d (=1, 2, or 3) dimensions is based on the equivalence of potential energies (U) stored in the unit cell of a given network. In the case of static problems, with which this chapter begins, for a cell of volume V (Fig. 1), there holds

$$U_{\text{cell}} = U_{\text{continuum}}. \tag{1}$$

The unit cell is a periodically repeating part of the network, and it is important to note that:

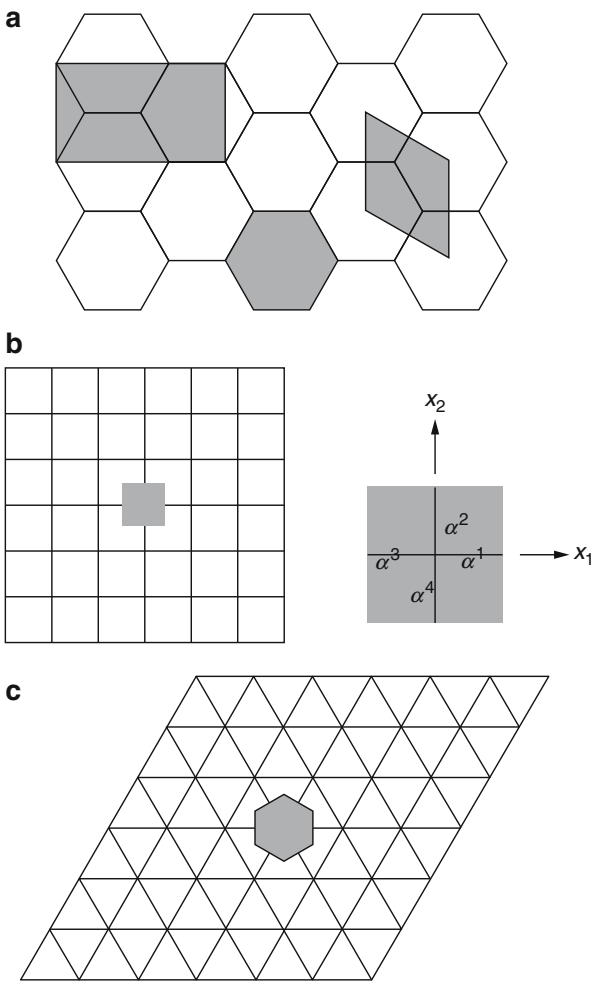

Fig. 1 Three periodic planar lattices: honeycomb, square, and triangular. In each case, a possible periodic unit cell is shown

(i) The choice of the unit cell may be nonunique (see Fig. 1a).
(ii) The microstructure of the unit cell is not necessarily "nicely" ordered – it may be of a disordered microgeometry, with an understanding that it repeats itself in space such as the periodic Poisson–Delaunay network, e.g., Fig. 4.7 in Ostoja-Starzewski (2002a, 2008).

In Eq. 1 the energies of the cell (U_{cell}) and its equivalent continuum ($U_{\text{continuum}}$), respectively, are

$$U_{\text{cell}} = \sum_b E_b = \sum_b^{N_b} \int_0^{\mathbf{u}} \mathbf{F}(\mathbf{u}')d\mathbf{u}' \qquad U_{\text{continuum}} = \int_V \boldsymbol{\sigma}(\varepsilon)dV. \tag{2}$$

The superscript b in Eq. 2_1 stands for the bth spring (bond) and N_b for the total number of bonds. The discussion is set in the $d = 2$ setting so that the volume actually means the area of unit thickness. Here, and in the sequel, the discussion is restricted to linear elastic springs and spatially linear displacement fields $\mathbf{u}$ (i.-e., uniform strain fields ε), implying that Eq. 2 becomes

$$U_{\text{cell}} = \frac{1}{2} \sum_b^{|b|} (k\,\mathbf{u} \cdot \mathbf{u})^{(b)} \qquad U_{\text{continuum}} = \frac{V}{2} \varepsilon : \mathbf{C} : \varepsilon. \tag{3}$$

In Eq. 3 $\mathbf{u}$ is a generalized spring displacement and k its corresponding spring constant. The next step, depending on the particular geometry of the unit element and on the particular model of interactions, will involve making a connection between $\mathbf{u}$ and ε and then deriving $\mathbf{C}$ from Eq. 1. The corresponding procedures and resulting formulas are given below for several elasticity problems set in the square and triangular network geometries.

Anti-plane Elasticity on Square Lattice

Of all the elasticity problems, the anti-plane is the simplest one on which to illustrate the spring network idea. In the continuum setting, the constitutive law is

$$\sigma_i = C_{ij}\varepsilon_j \quad i,j = 1,2, \tag{4}$$

where $\boldsymbol{\sigma} = (\sigma_1, \sigma_2) \equiv (\sigma_{31}, \sigma_{32})$, $\varepsilon = (\varepsilon_1, \varepsilon_2) \equiv (\varepsilon_{31}, \varepsilon_{32})$ and $C_{ij} \equiv C_{3i3j}$. Upon the substitution of Eq. 4 into the equilibrium equation

$$\sigma_{i,i} = 0, \tag{5}$$

these result to

$$\left(C_{ij}u_{,j}\right)_{,i} = 0. \tag{6}$$

Henceforth, with interest focused on approximations of locally homogeneous media, the governing equation Eq. 6 becomes

$$C_{ij}u,_{ij} = 0. \tag{7}$$

In the special case of an isotropic medium, Eq. 7 simplifies to the Laplace equation

$$Cu,_{ii} = 0. \tag{8}$$

Next, discretize the material with a square lattice network, Fig. 1b, whereby each node has one degree of freedom (anti-plane displacement u), and the nearest-neighbor nodes are connected by springs of constant k. It follows that the strain energy of the unit cell of such a lattice is

$$U = \frac{1}{2}k\sum_{b=1}^{4} l_i^{(b)} l_j^{(b)} \varepsilon_i \varepsilon_j. \tag{9}$$

Here the uniform strain $\varepsilon = (\varepsilon_1, \varepsilon_2)$ is employed, while $\mathbf{l}^{(b)} = (l_1{}^{(b)}, l_2{}^{(b)})$ is the vector of half-length of bond b. In view of Eq. 1, the stiffness tensor is obtained as

$$C_{ij} = \frac{k}{V}\sum_{b=1}^{4} l_i^{(b)} l_j^{(b)} \quad i,j = 1,2, \tag{10}$$

where $V = 4$ if all the bonds are of unit length ($|\mathbf{l}^{(b)}| = 1$). This leads to a relation between the bond spring constant k and the C_{ij} tensor

$$C_{11} = C_{22} = \frac{k}{2} \qquad C_{12} = C_{21} = 0. \tag{11}$$

In order to model an orthotropic medium, different bonds are applied in the x_1 and x_2 directions: $k^{(1)}$ and $k^{(2)}$. The strain energy of the unit cell is now

$$U = \frac{1}{2}\sum_{b=1}^{4} k^{(b)} l_i^{(b)} l_j^{(b)} \varepsilon_i \varepsilon_j, \tag{12}$$

so that the stiffness tensor is

$$C_{ij} = \frac{1}{V}\sum_{b=1}^{4} k^{(b)} l_i^{(b)} l_j^{(b)}, \tag{13}$$

which leads to relations

$$C_{11} = \frac{k^{(1)}}{2} \quad C_{22} = \frac{k^{(2)}}{2} \quad C_{12} = C_{21} = 0. \tag{14}$$

If one wants to model an anisotropic medium (i.e., with $C_{12} \neq 0$), one may either choose to rotate its principal axes to coincide with those of the square lattice and use the network model just described or introduce diagonal bonds. In the latter case, the unit cell energy is given by the formula (Eq. 12) with $N_b = 8$. The expressions for C_{ij}s are

$$C_{11} = \frac{k^{(1)}}{2} + k^{(5)} \quad C_{22} = \frac{k^{(2)}}{2} + k^{(6)} \quad C_{12} = C_{21} = k^{(5)} - k^{(6)}. \tag{15}$$

It will become clear in the next section how this model can be modified to a triangular spring network geometry.

In-Plane Elasticity: Triangular Lattice with Central Interactions

In the planar continuum setting, assuming linear elastic behavior, Hooke's law

$$\sigma_{ij} = C_{ijkm}\varepsilon_{km} \quad i,j,k,m = 1,2, \tag{16}$$

upon substitution into the balance law

$$\sigma_{ij,j} = 0, \tag{17}$$

results in a planar Navier equation for the displacement u_i:

$$\mu u_{i,jj} + \kappa u_{\ j,ji} = 0. \tag{18}$$

In Eq. 18 μ is defined by $\sigma_{12} = \mu\varepsilon_{12}$, which makes it the same as the classical 3D shear modulus. On the other hand, κ is the (planar) 2D bulk modulus that is defined by $\sigma_{ii} = \kappa\varepsilon_{ii}$.

As in the foregoing section, approximations of locally homogeneous media are of interest. Consider the regular triangular network of Fig. 1c with central-force interactions, which are described, for each bond b, by

$$F_i = \Phi_{ij}^{(b)} u_j \quad \text{where} \quad \Phi_{ij}^{(b)} u_j = \alpha^{(b)} n_i^{(b)} n_j^{(b)}. \tag{19}$$

Similar to the case of anti-plane elasticity, $\alpha^{(b)}$ is the spring constant of half-lengths of such central (normal) interactions – i.e., of those parts of the springs that fall within the given unit cell (Fig. 2a). The unit vectors $\mathbf{n}^{(b)}$ at respective angles of the first three α-springs are

$$\begin{aligned} \theta^{(1)} &= 0^0 \quad & n_1^{(1)} &= 1 & n_2^{(1)} &= 0 \\ \theta^{(2)} &= 60^0 \quad & n_1^{(2)} &= \frac{1}{2} & n_2^{(2)} &= \frac{\sqrt{3}}{2} \\ \theta^{(3)} &= 120^0 \quad & n_1^{(3)} &= -\frac{1}{2} & n_2^{(3)} &= \frac{\sqrt{3}}{2}. \end{aligned} \tag{20}$$

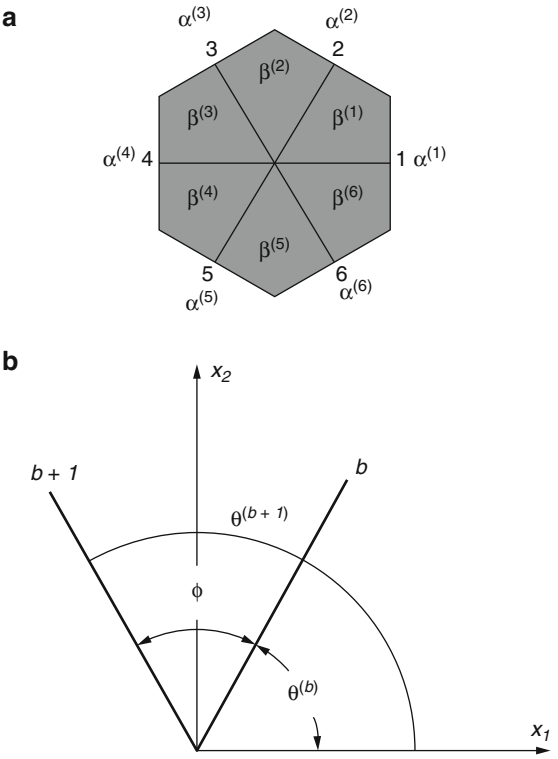

Fig. 2 (**a**) Unit cell of a triangular lattice model; $\alpha^{(1)}, \ldots, \alpha^{(6)}$ are the normal spring constants; $\beta^{(1)}, \ldots, \beta^{(6)}$ are the angular spring constants; in the isotropic Kirkwood model $\alpha^{(b)} = \alpha^{(b+3)}$ and $\beta^{(b)} = \beta^{(b+3)}$, $b = 1, 2, 3$; (**b**) details of the angular spring model

The other three springs ($b = 4, 5, 6$) must, by the requirement of symmetry with respect to the center of the unit cell, have the same properties as $b = 1, 2, 3$, respectively. All the α-springs are of length l, that is, the spacing of the triangular mesh is $s = 2l$. The cell area is $V = 2\sqrt{3}l^2$.

Every node has two degrees of freedom, and it follows that the strain energy of a unit hexagonal cell of this lattice, under conditions of uniform strain $\boldsymbol{\varepsilon} = (\varepsilon_{11}, \varepsilon_{22}, \varepsilon_{12})$, is

$$U = \frac{l^2}{2} \sum_{b=1}^{6} \alpha^{(b)} n_i^{(b)} n_j^{(b)} n_k^{(b)} n_m^{(b)} \varepsilon_{ij} \varepsilon_{km}, \tag{21}$$

so that, again by Eq. 1, the stiffness tensor becomes

$$C_{ijkm} = \frac{l^2}{V} \sum_{b=1}^{6} \alpha^{(b)} n_i^{(b)} n_j^{(b)} n_k^{(b)} n_m^{(b)}. \tag{22}$$

In particular, taking all $\alpha^{(b)}$ the same, one finds

$$C_{1111} = C_{2222} = \frac{9}{8\sqrt{3}}\alpha \, C_{1122} = C_{2211} = \frac{3}{8\sqrt{3}}\alpha \, C_{1212} = \frac{3}{8\sqrt{3}}\alpha, \tag{23}$$

so that there is only one independent elastic modulus, and the modeled continuum is isotropic.

It is important to note here that the isotropy follows from the triangular lattice having an axis of symmetry of the sixth order. This, combined with the fact that Eq. 22 satisfies the conditions of *Cauchy symmetry* (Love 1934) with respect to the permutations of all the four indices (which is the last equality)

$$C_{ijkm} = C_{ijmk} = C_{jikm} = C_{kmij} = C_{ikjm}, \tag{24}$$

implies that C_{ijkm} is of the form

$$C_{ijkm} = \lambda\left(\delta_{ij}\delta_{km} + \delta_{ik}\delta_{jm} + \delta_{im}\delta_{jk}\right). \tag{25}$$

In view of Eq. 23, there result the classical Lamé constants

$$\lambda = \mu = \frac{3}{4\sqrt{3}}\alpha. \tag{26}$$

The above is a paradigm from the crystal lattice theory that the Cauchy symmetry occurs when:

(i) The interaction forces between the atoms (or molecules) of a crystal are of a central-force type.
(ii) Each atom (or molecule) is a center of symmetry.
(iii) The interaction potential in a crystal can be approximated by a harmonic one.

Note: The Cauchy symmetry reduces the number of independent constants in general 3D anisotropy from 21 to 15. The first case has been called the *multi-constant theory* , while the second one the *rari-constant theory* (Trovalusci et al. 2009; Capecchi et al. 2010). Basically, there is a decomposition of the stiffness tensor into two irreducible parts with 15 and 6 independent components, respectively; see Hehl and Itin (2002) for a group-theoretical study of these issues

Note: One might try to model anisotropy by considering three different αs in Eqs. 21 and 22, but such an approach would be limited given the fact that only three of those can be varied: one needs to have six parameters in order to freely adjust any planar anisotropy which involves six independent C_{ijkm}s. This can be achieved by introducing the additional angular springs as discussed below. In fact, angular springs are also the device to vary the Poisson ratio

In-Plane Elasticity: Triangular Lattice with Central and Angular Interactions

The triangular network is now enriched by the addition of angular springs acting between the contiguous bonds incident onto the same node. These are assigned spring constants $\beta^{(b)}$, and, again by the argument of symmetry with respect to the center of the unit cell, only three of those can be independent. This leads to six spring constants: $\{\alpha^{(1)}, \alpha^{(2)}, \alpha^{(3)}, \beta^{(1)}, \beta^{(2)}, \beta^{(3)}\}$. With reference to Fig. 2b, let $\Delta\theta^{(b)}$ be the (infinitesimal) angle change of the bth spring orientation from the undeformed position. On account of $\mathbf{n} \times \mathbf{n} = \mathbf{l}\Delta\theta$,

$$\Delta\theta^{(b)} = e_{kij}\varepsilon_{jp}n_i n_p, \tag{27}$$

where e_{kij} is the Levi-Civita permutation tensor. The angle change between two contiguous α-springs (b and $b+1$) is measured by $\Delta\phi = \Delta\theta^{(b+1)} - \Delta\theta^{(b)}$, so that the energy stored in the spring $\beta^{(b)}$ is

$$E^{(b)} = \frac{1}{2}\beta^{(b)}|\Delta\phi|^2 = \frac{1}{2}\beta^{(b)}\left\{\varepsilon_{kij}\varepsilon_{jp}\left(n_i^{(b+1)}n_p^{(b+1)} - n_i^{(b)}n_p^{(b)}\right)\right\}^2. \tag{28}$$

By superposing the energies of all the angular bonds with the energy (Eq. 21), the elastic moduli are derived after Kirkwood (1939) as

$$\begin{aligned} C_{ijkm} = {} & \frac{l^2}{V}\sum\nolimits_{b=1}^{6}\alpha^{(b)}n_i^{(b)}n_j^{(b)}n_k^{(b)}n_m^{(b)} + \frac{1}{V}\sum\nolimits_{b=1}^{6}\left\{\left[\beta^{(b)} + \beta^{(b-1)}\right]\delta_{ik}n_p^{(b)}n_j^{(b)}n_p^{(b)}n_m^{(b)}\right. \\ & -\left[\beta^{(b)} + \beta^{(b-1)}\right]n_i^{(b)}n_j^{(b)}n_k^{(b)}n_m^{(b)} - \beta^{(b)}\delta_{ik}n_p^{(b)}n_j^{(b+1)}n_p^{(b+1)}n_m^{(b)} \\ & +\beta^{(b)}n_i^{(b)}n_j^{(b+1)}n_k^{(b+1)}n_m^{(b)} - \beta^{(b)}\delta_{ik}n_p^{(b)}n_j^{(b)}n_p^{(b+1)}n_m^{(b+1)} \\ & \left.+\beta^{(b)}n_i^{(b+1)}n_j^{(b)}n_k^{(b)}n_m^{(b+1)}\right\}, \end{aligned} \tag{29}$$

where $b = 0$ is the same as $b = 6$.

This provides the basis for a spring network representation of an anisotropic material; it also forms a generalization of the so-called Kirkwood model (Keating 1966) of an isotropic material. The latter is obtained by assigning the same α to all the normal and the same β to all the angular springs

$$\begin{aligned} C_{ijkm} = {} & \frac{\alpha}{2\sqrt{3}}\sum_{b=1}^{6}n_i^{(b)}n_j^{(b)}n_k^{(b)}n_m^{(b)} + \frac{\beta}{2\sqrt{3}l^2}\sum_{b=1}^{6}\left\{2\delta_{ik}n_j^{(b)}n_m^{(b)} - 2n_i^{(b)}n_j^{(b)}n_k^{(b)}n_m^{(b)}\right. \\ & -\delta_{ik}n_p^{(b)}n_j^{(b+1)}n_p^{(b+1)}n_m^{(b)} + n_i^{(b)}n_j^{(b+1)}n_k^{(b+1)}n_m^{(b)} \\ & \left.-\delta_{ik}n_p^{(b)}n_j^{(b)}n_p^{(b+1)}n_m^{(b+1)} + n_i^{(b+1)}n_j^{(b)}n_k^{(b)}n_m^{(b+1)}\right\} \end{aligned} \tag{30}$$

In accordance with the above,

$$\begin{aligned} C_{1111} &= C_{2222} = \frac{1}{2\sqrt{3}}\left(\frac{9}{4}\alpha + \frac{1}{l^2}\beta\right) \\ C_{1122} &= C_{2211} = \frac{1}{2\sqrt{3}}\left(\frac{3}{4}\alpha + \frac{1}{l^2}\frac{9}{4}\beta\right) \\ C_{1212} &= \frac{1}{2\sqrt{3}}\left(\frac{3}{4}\alpha + \frac{1}{l^2}\frac{9}{4}\beta\right). \end{aligned} \tag{31}$$

Condition $C_{1212} = (C_{1111} - C_{1122})/2$ is satisfied, so that there are only two independent elastic moduli.

From Eq. 31, the α and β constants are related to the planar bulk and shear moduli by

$$\kappa = \frac{1}{2\sqrt{3}}\left(\frac{3}{2}\alpha\right) \qquad \mu = \frac{1}{2\sqrt{3}}\left(\frac{3}{4}\alpha + \frac{1}{l^2}\frac{9}{4}\beta\right). \tag{32}$$

It is noted here that the angular springs have no effect on κ, i.e., the presence of angular springs does not affect the dilatational response. The formula for planar Poisson's ratio (Ostoja-Starzewski 2008) gives

$$\nu = \frac{\kappa - \mu}{\kappa + \mu} = \frac{C_{1111} - 2C_{1212}}{C_{1111}} = \frac{1 - 3\beta/l^2\alpha}{3 + 3\beta/l^2\alpha}. \tag{33}$$

From Eq. 33, there follows the full range of Poisson's ratio which can be covered with this model. It has two limiting cases:

$$\begin{aligned} \nu &= \frac{1}{3} \quad \text{if} \quad \frac{\beta}{\alpha} \to 0, \quad \alpha - \text{model} \\ \nu &= -1 \quad \text{if} \quad \frac{\beta}{\alpha} \to \infty, \quad \beta - \text{model}. \end{aligned} \tag{34}$$

For the subrange of Poisson's ratio between $-1/3$ and $1/3$, one may also use a Keating model (Keating 1966) which employs a different calculation of the energy stored in angular bonds.

Triple Honeycomb Lattice

Since 1/3 is the highest Poisson's ratio of central-force triangular lattices with one spring constant, an interesting model permitting higher values, from 1/3 up to 1, was introduced (Garboczi et al. 1991; Buxton et al. 2001). The model sets up three honeycomb lattices, having spring constants α, β, and γ, respectively, overlapping in such a way that they form a single triangular lattice (Fig. 3). The planar bulk and shear moduli of a single phase are

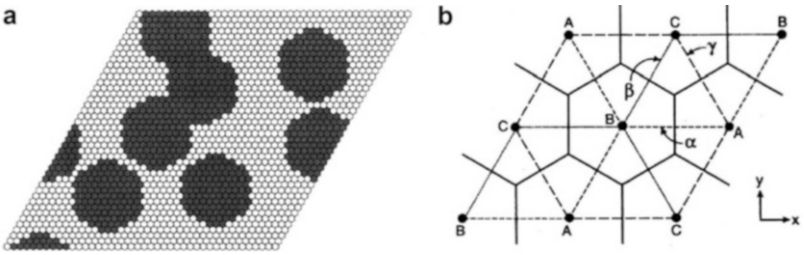

Fig. 3 (**a**) A triple honeycomb lattice made of three different spring types α, β, and γ belonging, respectively, to three sublattices A, B, and C; (**b**) a 42 × 42 unit cell of a triangular lattice of hexagonal pixels, with 11 pixel diameter circular inclusions centered on pixels and randomly placed with periodic boundary conditions; from (Snyder et al. (1992))

$$\kappa = \frac{1}{\sqrt{12}}(\alpha+\beta+\gamma) \quad \mu = \sqrt{\frac{27}{16}}\left(\frac{1}{\alpha}+\frac{1}{\beta}+\frac{1}{\gamma}\right)^{-1}. \tag{35}$$

In the case of two (or more) phases, a spring that crosses a boundary between any two phases (**1** and **2**) is assigned a spring constant according to a series rule $\alpha = [(2\alpha_1)^{-1} + (2\alpha_2)^{-1}]$, where α_i, $i = 1, 2$, (i. e. α, β, or γ), is a spring constant of the respective phase.

Note: While this chapter is focused on planar lattice models of elastic solids, there also exist extensions of the lattice approach to 3D and inelastic materials (e.g., Buxton et al. 2001)

Spring Network Models

Representation by a Fine Mesh

With reference to section "Basic Idea of a Spring Network Representation," one may employ the square mesh of Fig. 2a in the (x_1, x_2)-plane for discretization of an anti-plane elasticity problem. Indeed, this approach may be applied to model multiphase composites treated as planar, piecewise-constant continua, providing a lattice or mesh (very) much finer than a single inclusion is involved (Fig. 4b). How much finer should actually be assessed on a reference problem according to a preset error criterion? The governing equations for the displacement field $u \equiv u_3$ are

$$\begin{aligned} &u(i,j)\,[k_r + k_l + k_u + k_d] - u(i+1,j)k_r - u(i-1,j)k_l - u(i,j+1)k_u \\ &\quad - u(i,j-1)k_d \\ &\quad = f(i,j), \end{aligned} \tag{36}$$

where $f(i, j)$ is the body force (or source) at node (i, j), while i and j are the coordinates of mesh points, and k_r (right), k_l (left), k_u (up), and k_d (down) are defined from the series spring model

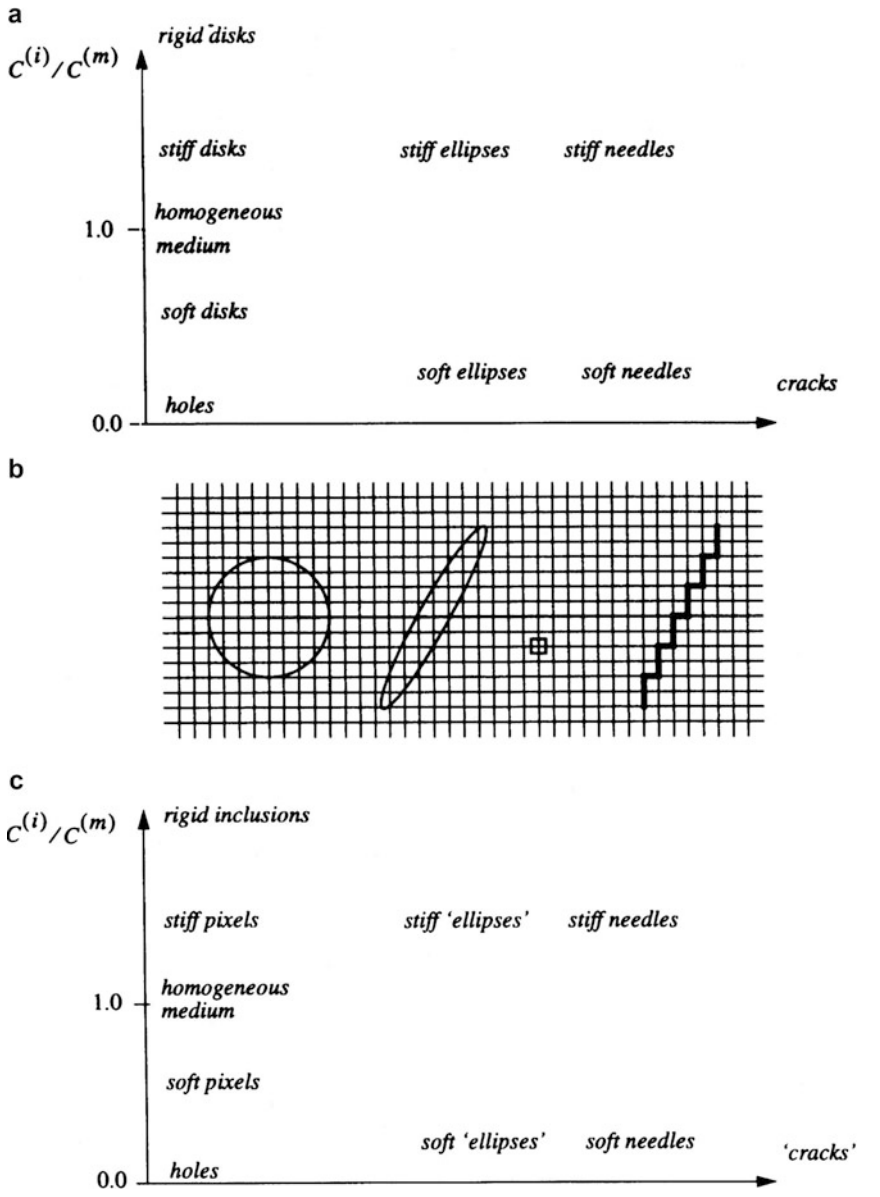

Fig. 4 (**a**) Parameter plane: aspect ratio of inclusions and the contrast; (**b**) spring network as a basis for resolution of round disks, ellipses, pixels, and needles in the parameter plane; (**c**) another interpretation of the parameter plane: from pixels to needles

$$
\begin{aligned}
k_r &= \left[\frac{1}{C(i,j)} + \frac{1}{C(i+1,j)}\right]^{-1} \\
k_l &= \left[\frac{1}{C(i,j)} + \frac{1}{C(i-1,j)}\right]^{-1} \\
k_u &= \left[\frac{1}{C(i,j)} + \frac{1}{C(i,j+1)}\right]^{-1} \\
k_d &= \left[\frac{1}{C(i,j)} + \frac{1}{C(i,j-1)}\right]^{-1}.
\end{aligned}
\tag{37}
$$

In Eq. 37, $C(i,j)$ is the material property at node (i,j).

This type of a discretization is equivalent to a finite difference method that would be derived by considering the expansions

$$
\begin{aligned}
u(i \pm 1, j) &= u(i,j) \pm s \left.\frac{\partial u(i,j)}{\partial x_1}\right|_{i,j} + \frac{s^2}{2!} \left.\frac{\partial^2 u(i,j)}{\partial x_1^2}\right|_{i,j} \\
u(i, j \pm 1) &= u(i,j) \pm s \left.\frac{\partial u(i,j)}{\partial x_2}\right|_{i,j} + \frac{s^2}{2!} \left.\frac{\partial^2 u(i,j)}{\partial x_2^2}\right|_{i,j}
\end{aligned}
\tag{38}
$$

in the governing equation (recall Eq. 8)

$$
C\left(\frac{\partial^2 u}{\partial x_1^2} + \frac{\partial^2 u}{\partial x_2^2}\right) = 0. \tag{39}
$$

However, in the case of in-plane elasticity problems, the spring network approach is not identical to the finite difference method, because the node–node connections of a spring network do really have a meaning of springs, whereas the finite difference connections do not.

In the case of a composite made of two locally isotropic phases, matrix (m) and inclusions (i), anti-plane Hooke's law is

$$
\sigma_i = C_{i,j}\varepsilon_j \quad i,j = 1,2 \quad C_{ij} = C^{(m)}\delta_{ij} \quad \text{or} \quad C^{(i)}\delta_{ij}. \tag{40}
$$

The above leads to a so-called contrast (or mismatch) $C^{(i)}/C^{(m)}$. It is clear that, with very high contrast, materials with rigid inclusions can approximately be modeled. Similarly, by decreasing the contrast, systems with very soft inclusions (nearly holes) can be simulated.

While the disk is the most basic inclusion shape when dealing with composites, a departure from this is of interest. Thus, another basic parameter specifying the composite is the *aspect ratio* of ellipses a/b, where $a(b)$ is the ellipse's major (minor) semiaxis. By varying the aspect ratio from 1 up through higher values, systems having disk-type, ellipse-type, through needle-type inclusions are simulated. This leads to the concept of a parameter plane shown in Fig. 4a.

Resolution of several different types of inclusions by the spring network is shown in Fig. 4b. Admittedly, this type of modeling is approximate so that a somewhat different interpretation of a parameter plane is given in Fig. 4c. It is seen that disks may most simply be modeled as single pixels or more accurately as finite regions; in the latter case, arbitrary anisotropies can be modeled. The former case allows one to deal with very large-scale systems, while the latter allows a much better resolution of local stress–strain fields within and around inclusions. By decreasing the spring network mesh size, an increasingly better accuracy can be achieved. Depending on the shape functions employed in finite element models, somewhat more accurate results may be obtained, but this comes at a higher price of costly and cumbersome remeshing for each and every new configuration $B(\omega)$ from the ensemble $\mathcal{B}$, which is required in statistical (Monte Carlo) studies.

It is noteworthy that, in contradistinction to the finite element method, no need for remeshing and constructing of a stiffness matrix exists in the spring network method: spring constants are very easily assigned throughout the mesh, and the conjugate gradient method finds the solution of the equilibrium displacement field $u(i, j)$. In that manner, a system having 10^6 million degrees of freedom (1000×1000 nodes) can readily be handled on a computer with 90 MB of random access memory. For 2000×2000 nodes, one requires some 360 MB, and so on, because of the linear scaling of memory requirements with the number of degrees of freedom.

The quality of approximation of ellipses and needle-type cracks/inclusions can be varied according to the number of nodes chosen to represent such objects. Local fields cannot be perfectly resolved, but the solution by the spring network is sufficient to rapidly establish the elastic moduli of a number of different $B(\omega)$ realizations from the random medium $\mathcal{B}$, and the corresponding statistics with a sufficient accuracy. As indicated below, spring networks are used to study scaling laws of various planar composites.

Note: Interestingly, the computational method for determining effective moduli of composite materials with circular inclusions due to Bird and Steele (1992) would be very well suited for analysis of this type of stationarity and isotropy

Damage in Macro-Homogeneous Materials

Spring Network for Inelastic Materials

The spring network model can also be used in studies assessing the effect of small disorder on the formation and evolution of damage in elastic–inelastic macro-homogeneous materials under quasi-static assumption. Such damage models are characterized by local constitutive law influenced by an appropriate probability distribution to account for the spatial material disorder. Representation of micro-cracks by removal of the springs from the lattice and accounting for elastic interactions of the micro-cracks are the key advantages. Disorder-induced statistical effects such as crack surface roughness, acoustic emission avalanches, damage localization, and strength-size scaling are well addressed using such damage models (Alava et al. 2006; see also Krajcinovic 1996; Rinaldi et al. 2008).

The random fuse model (RFM) (De Arcangelis et al. (1985)) is the simplest form of a quasi-static lattice damage model. In RFM, monotonically increasing voltage is applied across a network of resistors with randomly assigned maximum current thresholds, exceeding which the resistor burns. The failure of fuse network modeled using RFM can be mapped onto an anti-plane elastic–brittle transition problem on a spring lattice with randomly assigned spring failure thresholds.

In order to admit plasticity followed by brittle failure, the equations of spring network model need to be modified from what has been presented in section "Introduction." This is done as follows:

$$\begin{aligned}
&\text{elastic :} && F = ku && u < u_Y \\
&\text{plastic :} && F = k^P(u - u_Y) + ku_Y && u_Y \le u < u_F \\
&\text{brittle :} && F = 0 && u \ge u_F \\
&\text{elastic unloading :} && F = ku - \left(k - k^P\right)(u_{\text{unload}} + u_Y), &&
\end{aligned} \tag{41}$$

where u_Y, u_{unload}, and u_F are the magnitudes of the change in length of a given spring at yield, at unloading, and at failure, respectively, whereas u is the magnitude of change in length of a given spring at the current loading step. The spring stiffnesses before and after yielding are denoted as k and k^P, respectively, and correspond to the elastic and plastic tangent moduli of the given material. The disorder is introduced in the model by constraining the yield and failure thresholds of the springs to follow desired probability distribution.

The simulation progresses by incrementing the boundary conditions in very small steps. It is assumed that the stress redistribution within the system followed by the yielding or failure event is much faster than the load incrementing rate. After a spring is yielded or failed, stiffness matrix of the system is modified and the system of equations is solved again to account for local stress redistribution. This process is repeated until the lattice falls apart in the case of an elastic–brittle transition or until the fully plastic state is reached for elastic–plastic transition.

Hill–Mandel Macrohomogeneity Condition

Any disordered body $B_\delta(\omega)$ with a given (deterministic) microstructure is loaded by either one of two different types of boundary conditions:

Uniform displacement (also called kinematic, essential, or Dirichlet) boundary condition (d)

$$\mathbf{u}(\mathbf{x}) = \varepsilon^0 \cdot \mathbf{x} \quad \forall \mathbf{x} \in \partial B_\delta \tag{42}$$

Uniform traction (also called static, natural, or Neumann) boundary condition (t)

$$\mathbf{t}(\mathbf{x}) = \boldsymbol{\sigma}^0 \cdot \mathbf{n} \quad \forall \mathbf{x} \in \partial B_\delta \tag{43}$$

Here ε^0 and $\boldsymbol{\sigma}^0$ are employed to denote constant tensors, prescribed a priori, whereby the average strain and stress theorems imply $\varepsilon^0 = \overline{\varepsilon}$ and $\boldsymbol{\sigma}^0 = \boldsymbol{\sigma}$. Each of these loadings is consistent with the Hill–Mandel macrohomogeneity condition

$$\overline{\boldsymbol{\sigma} : \varepsilon} = \overline{\boldsymbol{\sigma}} : \overline{\varepsilon} \Leftrightarrow \int_{\partial B_\delta} (\mathbf{t} - \overline{\boldsymbol{\sigma}} \cdot \mathbf{n}) \cdot (\mathbf{u} - \overline{\varepsilon} \cdot \mathbf{x}) dS = 0, \tag{44}$$

which means that the volume-averaged scalar product of stress and strain fields should equal the product of their volume averages (Hill 1963; Mandel and Dantu 1963; Huet 1982, 1990; Sab 1991, 1992). While the Hill–Mandel condition is written above for elastic materials, it also holds for plastic material behavior in the incremental setting.

Each of these boundary conditions results in a different mesoscale (or apparent) stiffness, or compliance tensor, and generally different from the macroscale (or *effective*, *global*, *overall*, etc.) properties that are typically denoted by $^{eff.}$ So as to distinguish from the effective, Huet introduced the term *apparent*.

For a given realization $B_\delta(\omega)$ of the random medium $\mathcal{B}_\delta$, taken as a linear elastic body ($\boldsymbol{\sigma} = \mathbf{C}(\omega, \mathbf{x})$: ε), on some mesoscale δ, condition Eq. 42 yields an apparent random stiffness tensor $\mathbf{C}_{\delta d}(\omega)$ – sometimes denoted $\mathbf{C}_{\delta e}(\omega)$ – with the constitutive law

$$\overline{\boldsymbol{\sigma}} = \mathbf{C}_\delta^d(\omega) : \varepsilon^0, \tag{45}$$

while the boundary condition (Eq. 43) results in an apparent random compliance tensor $\mathbf{S}_{\delta t}(\omega)$ (sometimes denoted $\mathbf{S}_{\delta n}(\omega)$) with the constitutive law being stated as

$$\overline{\varepsilon} = \mathbf{S}_\delta^t(\omega) : \sigma^0. \tag{46}$$

For anti-plane loading, the boundary conditions (Eqs. 42 and 43) are implemented through

$$\text{uniform diplacement :} \qquad \varepsilon_{31}^0 = \varepsilon, \quad \varepsilon_{32}^0 = 0 \tag{47}$$

$$\text{uniform traction :} \qquad \sigma_{31}^0 = \sigma, \quad \sigma_{32}^0 = 0. \tag{48}$$

Modeling Elastic–Brittle Materials

The elastic–brittle transition is modeled using a constitutive law with linear elastic behavior up to a failure threshold.

Simulation Setup A spring lattice network based on discussion in section "Basic Idea of a Spring Network Representation" is considered to represent a homogeneous anti-plane elastic medium. The bond strength (t) is defined as the maximum strain the spring can sustain (for RFM, t is equivalent to the maximum current a fuse can take before burning out). Bond strength is assigned to all the bonds in the lattice from a distribution $p(t)$ between $[0, t_{\max}]$. Monotonically increasing displacement boundary conditions are applied on the vertical edges of the lattice, while periodic

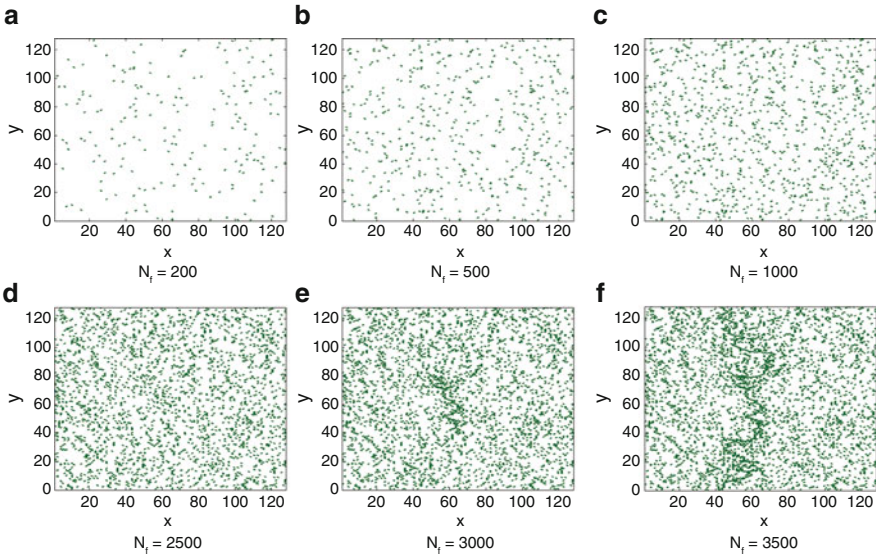

Fig. 5 Evolution of strain localization in an elastic–brittle material

boundary conditions are applied on the horizontal edges to avoid any boundary effects. At each loading step, a spring having the maximum value of $\epsilon_{\text{spring}}/t$ is removed from the lattice and the modified system of linear equations is solved again to allow stress redistribution. As stress redistribution may cause other springs in the lattice to fail, the removal process at a given loading step is continued until all possible springs are failed or the macroscopic failure with sudden drop in load-carrying capacity is observed (Fig. 5).

Diffusive Fracture and Brittle Fracture The evolution of damage is governed by the competition between disorder and stress concentrations at the micro-crack tips. The effect of stress concentrations trying to localize the damage is opposed by the disorder trying to delocalize the damage. For strong disorder case, disorder dominates the stress concentrations leading to distribution of spatially uncorrelated cracks in the initial stages of loading. As the loading increases, stress concentrations are high enough to overcome the barrier due to disorder, whereas for weak disorder, stress concentrations dominate the disorder in the initial stages itself leading to the formation of a crack originating from the weakest zone.

Kahng et al. (1988) have demonstrated using the electrical breakdown process in RFM that the elastic–brittle transition depends on two factors: the amount of disorder and the length scale of the medium under consideration. The schematic phase diagram of the elastic–brittle transition suggested in Kahng et al. (1988) is shown in Fig. 10. The strength of disorder is controlled by the factor w such that $p(t)$ is a uniform distribution on the support $[1 - w/2, 1 + w/2]t_{\max}$. Thus, $w = 2$ corresponds to maximum disorder, i.e., a uniform distribution over $[0, 2\ t_{\max}]$.

Two fundamentally different crack formation trends observed are termed as diffusive fracture [ductile fracture in Kahng et al. 1988] and brittle fracture. The diffusive fracture is characterized by the appearance of spatially uncorrelated micro-cracks prior to the final catastrophic failure, which is observed generally for the systems with strong disorder. For systems with weak disorder, brittle fracture is observed. In brittle fracture, the weakest element within the domain dominates the final crack formation process. Crack nucleates from the weakest element and proceeds in the spanwise direction due to high stress concentration near the crack tip, leading to final failure. The main idea proposed by the authors in the phase diagram (Fig. 10) is that for a given length scale (L), there exists a critical level of disorder for which transition from brittle to diffusive fracture behavior is observed for increasing disorder strength, whereas, for a fixed disorder strength (w), the brittle fracturing is observed for increasing macroscopic length scale (L), except for $w = 2$ which according to the authors (Kahng et al. 1988) approaches the percolation limit as $L \to \infty$.

Fractal Nature of Fracture Surfaces That fracture surfaces of metals are self-affine fractals was first pointed out in the seminal paper by Mandelbrot and Paullay (1984). Their work has initiated a new research area dealing with the roughness coefficient (ζ) of the fracture. It is now confirmed through experiments that $\zeta \simeq 0.8$ (out of plane or 3D) is observed (Lapasset and Planes 1990), in a material dependent scaling domain (~down to μm length scales and high crack propagation speeds) for many ductile as well as brittle materials (Bouchad 1997). At smaller length scales (~down to nm) and quasi-static conditions (low crack propagation speeds), another ζ in the range of 0.4–0.6 is reported which is often associated with the fracture process zone (FPZ). In the case of 2D fracture surface, ζ is obtained to be in the range of 0.6–0.7 by experiments (mainly on paper samples) (Bonamy and Bouchad 2011).

The universality of ζ (at larger length scales at least) suggests that the fracture surface roughening process is governed by a typical physical phenomenon independent of the material properties, much like the existence of Kolmogorov scaling in the inertial subrange of isotropic turbulence (Hansen et al. 1991). Thus, the topic of crack surface roughness has attracted significant attention over the last 20 years. While the formation of fractal cracks may be observed in Figs. 5, 6, 7, 8 and 9, the topic of fracture mechanics with fractal cracks is treated by Wnuk (2014a, b) in this handbook (Fig. 10).

Modeling Elastic–Plastic Materials

Elastic–plastic response is obtained allowing a hardening slope in the spring constitutive behavior. In the anti-plane elastic setting, the elastic–plastic response (flow rule) follows these equations at the grain level:

$$\begin{aligned} d\sigma_{3i} &= C_{3i3j} d\varepsilon_{3i} \quad \text{when} \quad f_P < 0 \quad \text{or} \quad f_P = 0 \quad \text{and} \quad df_P < 0 \\ d\sigma_{3i} &= C^P_{3i3j} d\varepsilon^P_{3i} \quad \text{when} \quad f_P = 0 \quad \text{and} \quad df_P = 0. \end{aligned} \tag{49}$$

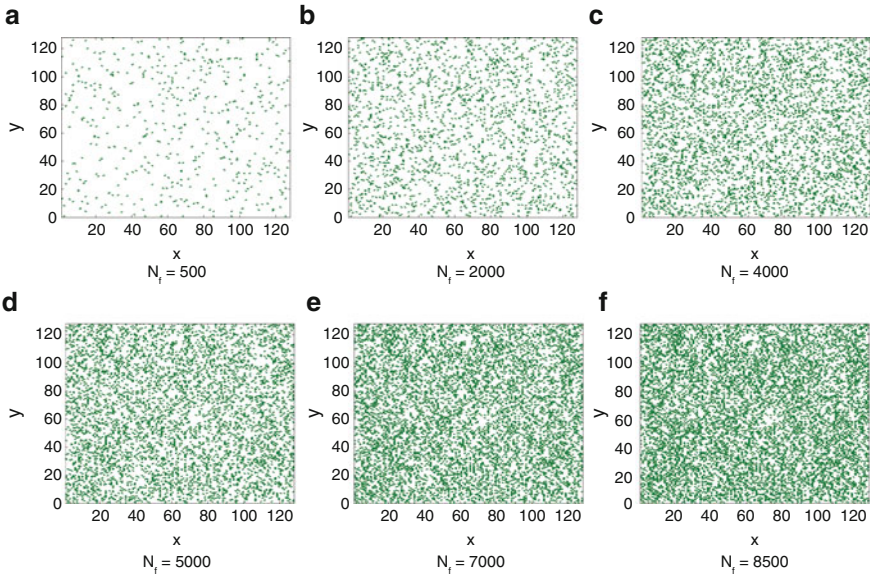

Fig. 6 Evolution of strain localization in an elastic–plastic material

Here $d\varepsilon_{3i}^{P}$ is the plastic strain increment and C_{3i3j}^{P} represents the hardening modulus of the material. The Tresca criterion is used to define the yield function (f_P):

$$f^P = \max(\sigma_{31}, \sigma_{32}) - \sigma_s, \tag{50}$$

where σ_s is the yield stress in shear of the given grain. In the simulations, disorder is introduced by assigning yield thresholds to the springs following desired probability distribution. The simulation is performed similar to the elastic–brittle one, with loading increasing monotonically in small steps. After each loading step, all the springs exceeding the yield criteria are modified to follow the hardening slope and the system of equations is solved after each modification so as to account for stress redistributions. The simulation progresses until a fully plastic state is reached.

The elastic–plastic transition is essentially different than elastic–brittle one as the stress concentrations near the yielded zones are not as strong. Thus, no damage localization is observed. But, strain localization zones are observed for low-hardening materials due to weak post-yielding material response (Fig. 6).

Modeling Elastic–Plastic–Brittle Materials

The entire process of failure of plastic hardening disordered materials can be captured by implementing the complete bilinear response as shown in Fig. 7. The elastic unloading behavior is an essential part of the model and is explicitly accounted for as the formation of micro-cracks may result into local unloading of

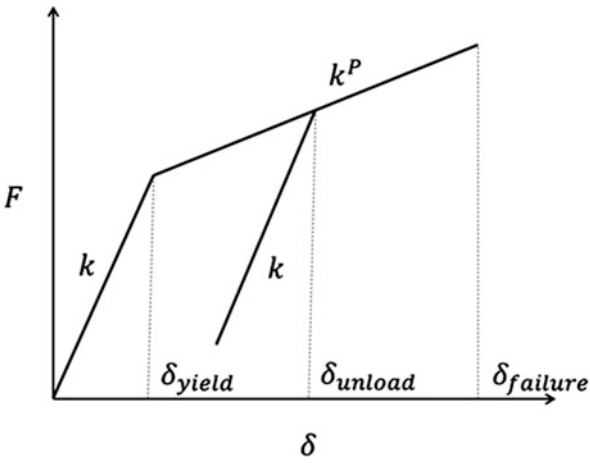

Fig. 7 Schematic of the elastic–plastic–brittle model of an anti-plane spring lattice

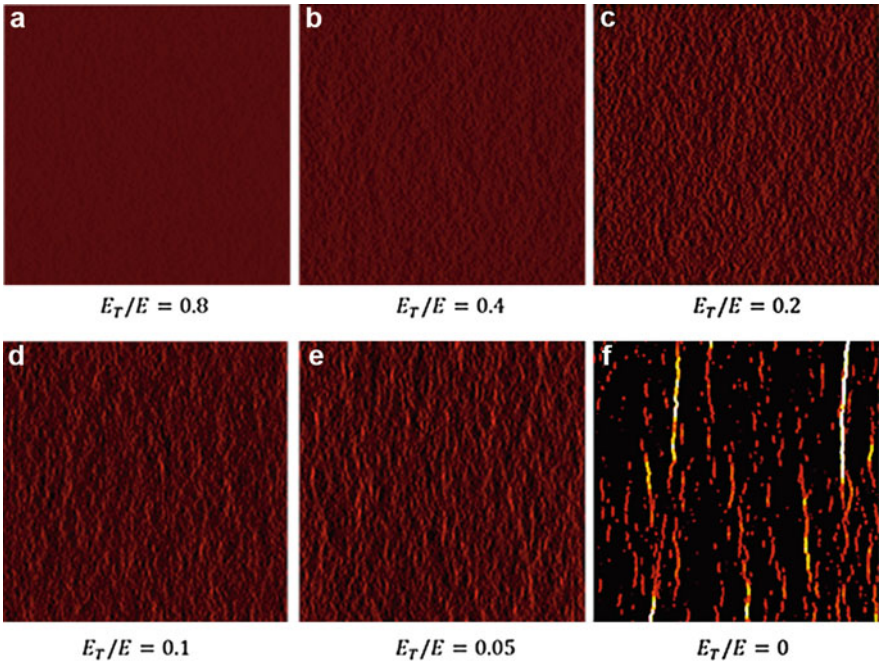

Fig. 8 Normalized strain contour plots for E_T/E values: (**a**) 0.8, (**b**) 0.4, (**c**) 0.2, (**d**) 0.1, (**e**) 0.05, and (**f**) (perfectly plastic). Shear bands due to strain localization of increasing strength are observed for decreasing E_T/E

a yielded zone. In the simulations, at each loading step after a failure or yielding event, every yielded spring that is unloading is modified to follow the elastic unloading response.

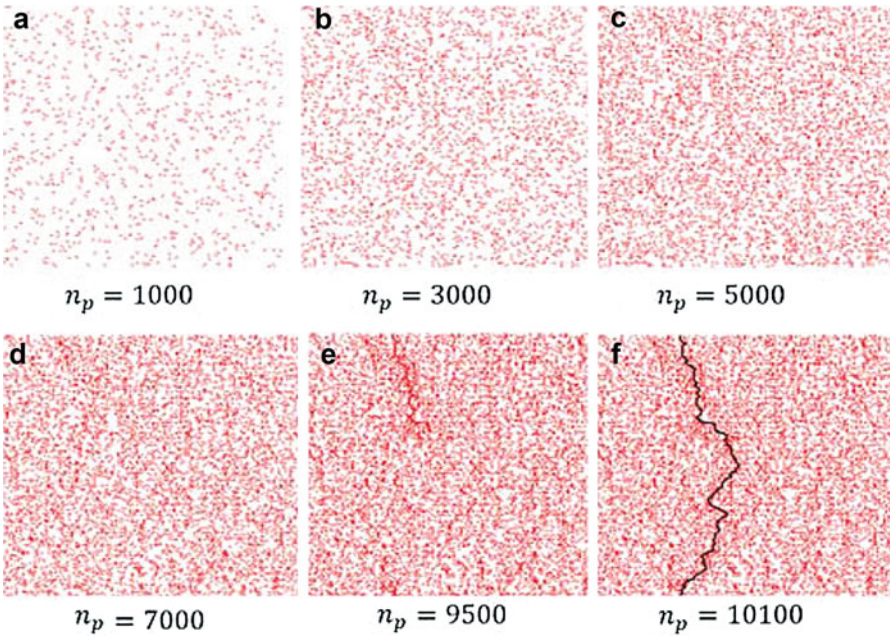

Fig. 9 Damage accumulation and localization leading to formation of the final macroscopic crack in (**f**) with increasing number of failed springs n_p

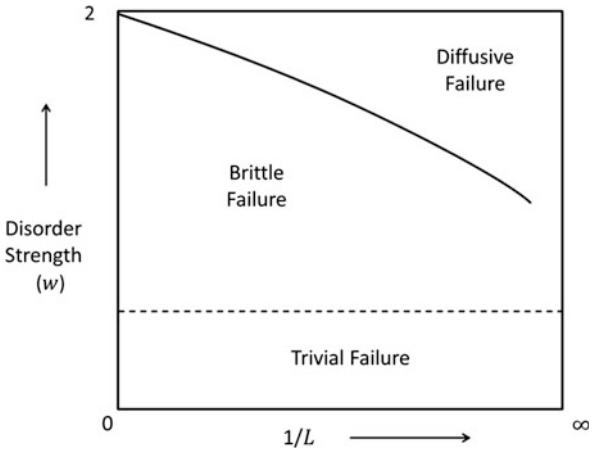

Fig. 10 Schematic phase diagram of elastic–brittle transition (Kahng et al. 1988)

The effective model response is now controlled by three parameters: hardening ratio, strength of disorder in yield, and failure limits. Based on observations from elastic–brittle and elastic–plastic responses, some results can be intuitively expected from the elastic–plastic–brittle model. For high hardening ratio, significant post-

yield load-carrying capacity of the material avoids the formation of strain localization zones and hence the system closely follows elastic–brittle behavior. Otherwise, for low hardening ratio, the formation of micro-cracks within the strain-localized zones accelerates the failure process leading to lower effective strength of the lattice. The strength of disorder plays the important role of mitigating the effect of crack-tip stress concentrations by delocalizing the micro-cracks. Thus, a wide spectrum of material responses can be modeled by modifying the disorder distribution and the constitutive spring responses.

A similar idea is studied in the realm of fiber bundle model (FBM) by Rinaldi (2011) using a bilinear fiber response and independent yield and failure threshold probability distributions.

Damage Patterns and Maps of Disordered Elastic–Brittle Composites

As mentioned in section "Introduction," the lattice method can also be used to simulate damage of heterogeneous materials. This works particularly well in the case of elastic–brittle failure of composites, where one uses a mesh (much) finer than the typical size of the microstructure. In principle, one needs to determine which lattice spacing ensures mesh independence or nearly so. Such a study has been conducted for a thin aluminum polycrystalline sheet discussed (Ostoja-Starzewski 2008).

With reference to Alzebdeh et al. (1998), the attention is focused on two-phase composites in anti-plane shear, under periodic boundary conditions and (necessarily) periodic geometries. Now, since both phases (inclusion i and matrix m) are isotropic and elastic–brittle (Fig. 11a), the composite can be characterized by two dimensionless parameters:

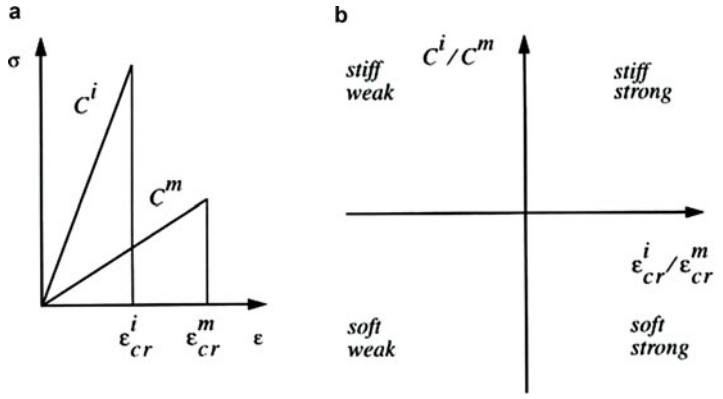

Fig. 11 (**a**) Elastic–brittle stress–strain curves for matrix and inclusion phases; (**b**) sketch of the damage plane

$$\varepsilon_{cr}^{i}/\varepsilon_{cr}^{m} \quad C^{i}/C^{m}, \tag{51}$$

where $\varepsilon_{cr}^{i}\left(\varepsilon_{cr}^{m}\right)$ is the strain-to-failure of the inclusion (resp. matrix) phase and $C^{i}(C^{m})$ are the corresponding stiffnesses. This leads to the concept of a *damage plane* (Fig. 11b) showing various combinations of strengths and stiffnesses. While the response in the first and third quarters of damage plane is quite intuitive, this is not so for the second and fourth quarters. In those two quarters, there is a competition of either high stiffness with low strength of the inclusions with the reverse properties of the matrix or the opposite of that. The damage plane is useful for displaying effective damage patterns of any particular geometric realization of the random composite while varying its physical properties (Fig. 12) as well as other characteristics, say, statistics of response in the ensemble sense (Fig. 13).

A number of other issues are studied in the referenced papers:

- Stress and strain concentrations
- Finite size scaling of response
- Function fitting of statistics (where it turns out that the beta probability distribution offers a more universal fit than either Weibull or Gumbel)
- Effects of disorder versus periodicity

Also, see Ostoja-Starzewski and Lee (1996) for a similar study under in-plane loading; computer movies of evolving damage can be obtained from the author.

Particle Models

Governing Equations

Basic Concepts

Particle models are a generalization of lattice models to include dynamic effects and can also be viewed as an offshoot of *molecular dynamics* (MD). The latter field has developed over the past few decades in parallel with the growth of computers and computational techniques. Its objective has been to simulate many interacting atoms or molecules in order to derive macroscopic properties of liquid or solid materials (Greenspan 1997, 2002; Hockney and Eastwood 1999). The governing Hamiltonian differential equations of motion need to be integrated over long time intervals so as to extract the relevant statistical information about the system from the computed trajectories.

Techniques of that type have been adapted over the past two decades to simulate materials at larger length scales, whereby the role of a particle is played by a larger-than-molecular piece of material, a so-called particle or quasiparticle. The need to reduce the number of degrees of freedom in complex systems has also driven models of galaxies as systems of quasiparticles, each representing lumps of large numbers of stars. In all these so-called particle models (PMs), the material is discretized into particles arranged in a periodic lattice, just like in spring network models studied in

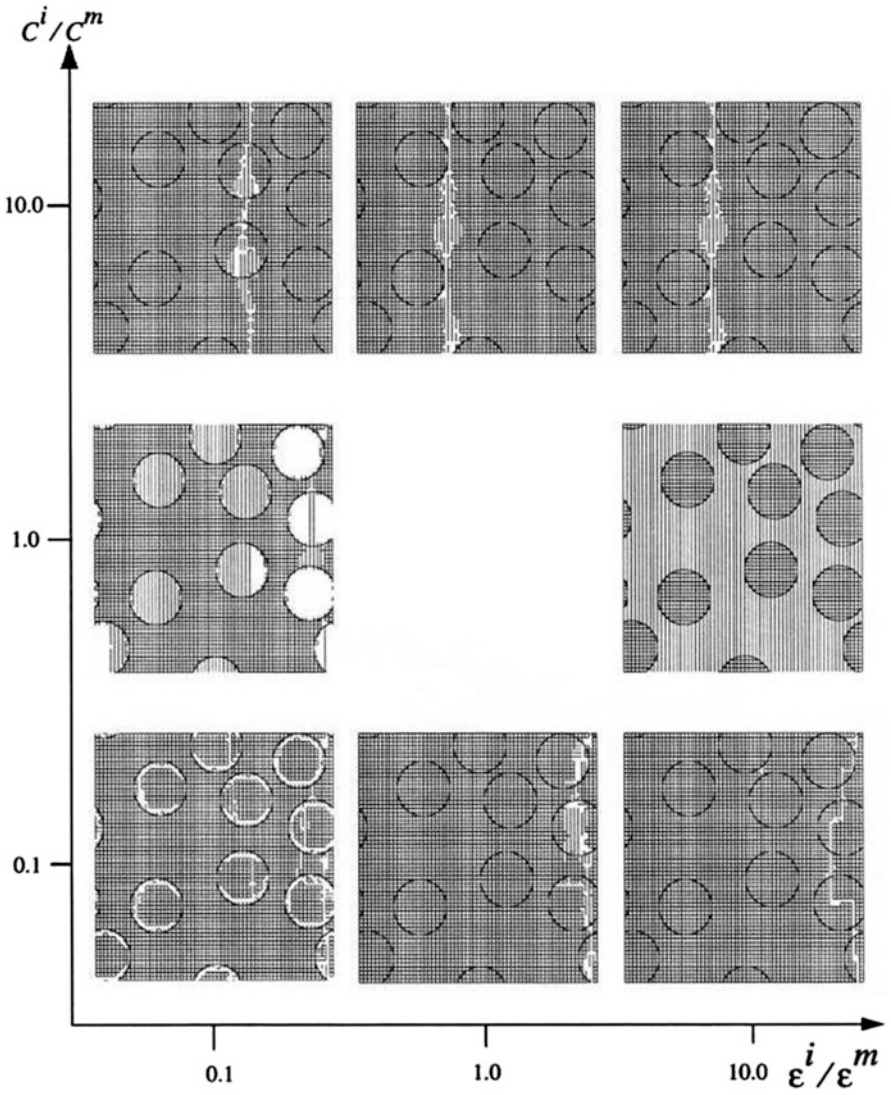

Fig. 12 Crack patterns in the damage plane on a scale 4.5 times larger than that of the inclusion diameter. The center figure of a homogeneous body is not shown as it corresponds to all the bonds failing simultaneously

earlier sections, yet interacting through nonlinear potentials, and accounting for inertial effects, i.e., full dynamics. With reference to Fig. 14, the lattice may be in 2D or in 3D.

Note that, by comparison with finite elements (FE) which indeed also involve a quite artificial spatial partitioning, PMs are naturally suited to involve interparticle potentials of the same functional form as the interatomic potentials, providing one

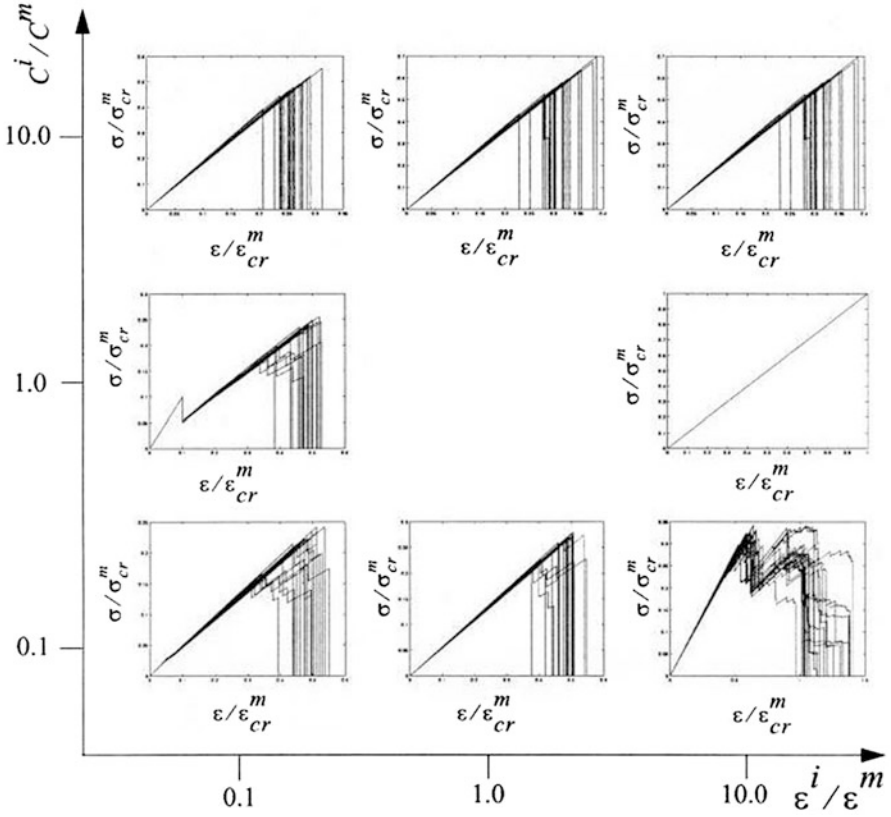

Fig. 13 Damage maps of statistics of constitutive responses for twenty realizations of the random composite, such as that in Fig. 12

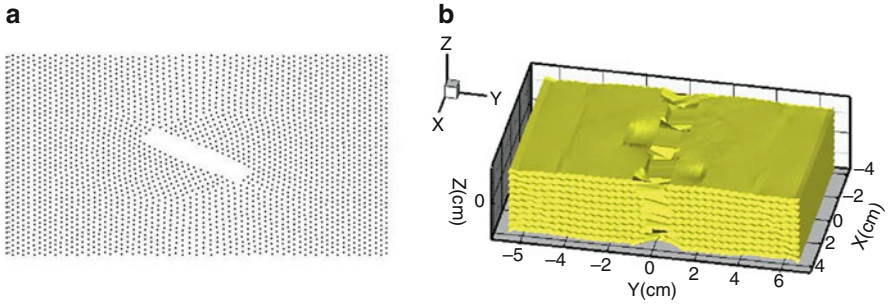

Fig. 14 Particle models and intermediate stages of fracture in (**a**) 2D and (**b**) 3D; after Wang et al. (2006)

uses the same type of lattice. The PM can therefore take advantage of the same numerical techniques as those of MD and rather easily deal with various highly complex motions. Thus, the key issue is how to pass from a given molecular potential in MD to an interparticle potential in PM. In the case when the molecular interactions are not well known, the PM may still turn out to be superior relative to the FE. Among others, this indeed is the case with comminution of minerals where scales up to meters are involved (Wang and Ostoja-Starzewski 2005; Wang et al. 2006).

In MD, the motion of a system of atoms or molecules is governed by classical molecular potentials and Newtonian mechanics. As an example, let us consider copper. Following Greenspan (1997), its 6–12 Lennard–Jones potential is

$$\phi(r) = -\frac{1.398068}{r^6}10^{-10} + \frac{1.55104}{r^{12}}10^{-8}\text{erg}. \tag{52}$$

Here r is measured in Å. It follows that the interaction force between two copper atoms is

$$F(r) = -\frac{d\phi(r)}{dr} = -\frac{8.388408}{r^7}10^{-2} + \frac{18.61248}{r^{13}}\text{dyn}. \tag{53}$$

In Eq. 52 $F(r) = 0$ occurs at $r_0 = 2.46\text{Å}$, and ϕ then attains the minimum: $\phi(r_0) = -3.15045 \cdot 10^{-13}$ erg.

Using a simple methodology from basic materials science (Ashby and Jones 1980), Young's modulus E of the material can be found from $\phi(r)$ as follows:

$$E = \frac{S_0}{r_0} \quad \text{where} \quad S_0 \left.\frac{d^2\phi(r)}{dr^2}\right|_{r_0}. \tag{54}$$

With this method, Young's modulus of copper 152.942 GPa is found, a number that closely matches the physical property of copper and copper alloys valued at 120 ~ 150 GPa. Then, the continuum-type tensile stress

$$\sigma(r) = NF(r), \tag{55}$$

where N is the number of bonds/unit area, equals to $1/r_0^2$. Tensile strength, σ_{TS}, results when $dF(r)/dr = 0$, that is, at $r_d = 2.73\text{Å}$ (*bond damage spacing*), and yields

$$\sigma_{TS} = NF(r_d) = 462.84\ \text{MN/m}^2. \tag{56}$$

This value is quite consistent with data for the actual copper and copper-based alloys reported at 250–1000 Mpa.

In the PM, the interaction force is also considered only between nearest-neighbor (quasi)particles and assumed to be of the same form as in MD:

$$\phi(r) = -\frac{G}{r^P} + \frac{H}{r^q}. \tag{57}$$

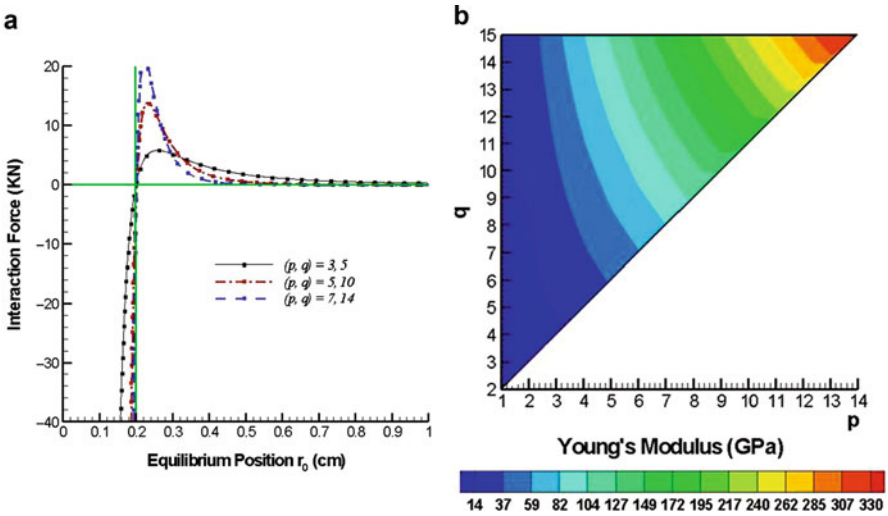

Fig. 15 (**a**) The interaction force for pairs of (p,q) exponents, at $r_0 = 0.2$ cm. (**b**) The variability of Young's modulus in the (p,q) − plane

Here G, H, p, and q, all positive constants, are yet to be determined, and this will be done below. Inequality $q > p$ must hold so as to obtain the repulsive effect that is necessarily (much) stronger than the attractive one. Three examples of interaction force for three pairs of p and q are displayed in Fig. 15a. The dependence of Young's modulus for a wide range of p and q is shown in Fig. 15b.

The conventional approach in PM, just as in MD, is to take the equation of motion for each particle P_i of the system as

$$m_i \frac{d^3 \mathbf{r}_i}{dt^2} = \alpha \sum_j \left(-\frac{G_i}{r_{ij}^P} + \frac{H_i}{r_{ij}^q} \right) \frac{\mathbf{r}_{ji}}{r_{ij}} \quad i \neq j, \tag{58}$$

where m_i is the mass of P_i and $\mathbf{r}_{ji}$ is the vector from P_j to P_i; summation is taken over all the neighbors of P_i. Also, α is a normalizing constant obtained by requiring that the force between two particles must be small in the presence of gravity:

$$\alpha \left| -\frac{G_i}{D^P} + \frac{H_i}{D^q} \right| < 0.001 \cdot 980 m_i. \tag{59}$$

Here D is the distance of local interaction ($1.7 r_0$ cm in this particular example), where r_0 is the equilibrium spacing of the particle structure. The reason for introducing the parameter α by Greenspan (1997) was to define the interaction force between two particles as local in the presence of gravity. However, since setting α according to Eq. 49 would result in a "pseudo-dynamic" solution, $\alpha = 1$ is set.

According to Eq. 47, different (p, q) pairs result in different continuum-type material properties, such as Young's modulus E. Clearly, changing r_0 and volume of

the simulated material $V(=A \times B \times C)$ will additionally influence Young's modulus. Therefore, in general, there is some functional dependence:

$$E = E(p, q, r_0, V). \tag{60}$$

One can formulate four conditions to determine continuum-level Young's modulus and tensile strength while maintaining the conservation of mass and energy of the particle system and satisfying the interaction laws between all the particles in the PM model for a given MD model (Wang and Ostoja-Starzewski 2005).

Leapfrog Method

Just like in MD, there are two commonly used numerical schemes in particle modeling: *completely conservative method* and *leapfrog method* . The first scheme is exact in that it perfectly conserves energy and linear and angular momentum, but requires a very costly solution of a large algebraic problem. The second scheme is approximate. Since in most problems one needs large numbers of particles to adequately represent a simulated body, the completely conservative method is unwieldy and, therefore, usually abandoned in favor of the leapfrog method (Ostoja-Starzewski and Wang 2006). That method is derived by considering Taylor expansions of positions $\mathbf{r}_{i,k+1}$ and $\mathbf{r}_{i,k}$ of the particle $P_i(i = 1, 2, \ldots, N)$ at times $t_k = k\Delta t$ and $t_{k+1} = (k + 1)\Delta t$, respectively, about time $t_{k+1/2} = (k + 1/2)\Delta t$ (with Δt being the time step):

$$\begin{aligned}
\mathbf{r}_{i,k} &= \mathbf{r}_{i,k+1/2} - \frac{\Delta t}{2}\mathbf{v}_{i,k+1/2} + \frac{\Delta t^2}{4}\mathbf{a}_{i,k+1/2} - \frac{\Delta t^3}{48}\dot{\mathbf{a}}_{i,k+1/2} + O\left(\Delta t^4\right) \\
\mathbf{r}_{i,k+1} &= \mathbf{r}_{i,k+1/2} + \frac{\Delta t}{2}\mathbf{v}_{i,k+1/2} + \frac{\Delta t^2}{4}\mathbf{a}_{i,k+1/2} + \frac{\Delta t^3}{48}\dot{\mathbf{a}}_{i,k+1/2} + O\left(\Delta t^4\right).
\end{aligned} \tag{61}$$

Here $\mathbf{v}_i$ and $\mathbf{a}_i$ denote velocity and acceleration. Upon addition and subtraction of these, the new position and velocity are found:

$$\begin{aligned}
\mathbf{r}_{i,k+1} &= 2\mathbf{r}_{i,k+1/2} - \mathbf{r}_{i,k} + \frac{\Delta t^2}{4}\mathbf{a}_{i,k+1/2}O\left(\Delta t^4\right) \\
\mathbf{v}_{i,k+1} &= \left(\mathbf{r}_{i,k+1} + \mathbf{r}_{i,k}\right)/\Delta t + O\left(\Delta t^4\right),
\end{aligned} \tag{62}$$

showing that the position calculation is two orders of magnitude more accurate than the velocity calculation. However, the error in computation of velocity accumulates only as fast as that in position because it is really being calculated from positions. It is easy to see that the leapfrog method is more accurate than the conventional Euler integration based on $\mathbf{v}_{i,k+1} = \mathbf{v}_{i,k} + (\Delta t)\mathbf{a}_{i,k}$ and $\mathbf{r}_{i,k+1} = \mathbf{r}_{i,k} + (\Delta t)\mathbf{v}_{i,k}$.

Oftentimes, the leapfrog formulas relating position r_i, velocity v_i, and acceleration a_i for all the particles P_i $(i = 1, 2, \ldots, N)$ are written as

$$\begin{aligned}
\mathbf{v}_{i,1/2} &= \mathbf{v}_{i,0} + \frac{\Delta t}{2}\mathbf{a}_{i,0}(\text{starter formula}) \\
\mathbf{v}_{i,k+1/2} &= \mathbf{v}_{i,k-1/2} + (\Delta t)\mathbf{a}_{i,k}\ k = 0, 1, 2, \ldots \\
\mathbf{r}_{i,k+1} &= \mathbf{r}_{i,k} + (\Delta t)\mathbf{v}_{i,k+1/2}\ k = 0, 1, 2, \ldots
\end{aligned} \tag{63}$$

Clearly, the name of the method comes from taking velocities at intermediate time steps relative to positions and accelerations; it is also known as a *Verlet algorithm*.

It can be shown that the global (cumulative) error in position going from $\mathbf{r}_{i,k}$ to $\mathbf{r}_{i,k+n}$ (i.e., over $T = n\Delta t$) of P_i is

$$\text{error}\left(\mathbf{r}_{i,k+n} - \mathbf{r}_{i,k}\right) = O\left(\Delta t^2\right), \tag{64}$$

which is also the global error in velocity.

Stability is concerned with the propagation of errors. Even if the truncation and roundoff errors are very small, a scheme would be of little value if the effects of small errors were to grow rapidly with time. Thus, instability arises from the nonphysical solution of the discretized equations. If the discrete equations have solutions which grow much more rapidly than the correct solution of the differential equations, then even a very small roundoff error is certain to eventually seed that solution and render the numerical results meaningless. By the root locus method for an atomistic unit of time, the safe time step used in the leapfrog method meeting this requirement is

$$\Omega\Delta t \ll 2 \quad \Omega = \left(\frac{1}{m}\left|\frac{dF}{dr}\right|_{\max}\right)^{1/2}. \tag{65}$$

Thus, as $r \to 0$, $dF/dr \to \infty$, which results in $\Delta t \to 0$. Since this may well cause problems in computation, it is advisable to introduce the smallest distance between two particles according to these conditions:

(i) For a stretching problem of a plate/beam, take $(dF/dr)_{\max} \simeq dF/dr\big|_{r=r_0}$, which with () dictates $\Delta t \simeq 10^{-7} - 10^{-6}s$.
(ii) For an impact problem, one often needs to set up a minimum distance limiting the spacing between two nearest particles, e.g., $r_{\min} = 0.1r_0$. It is easy to see from Fig. 15a that, in this case, this suitable time increment is greatly reduced because of a rapid increase in Ω. This leads to $\Delta t \simeq 10^{-8}s$.

Following the MD methodology (Napier-Munn et al. 1999), one can also set up a criterion for convergence:, where m is the smallest mass to be considered and k is the same stiffness as S_0 in Eq. 44_2. An examination of these two criteria shows there is not much quantitative difference between them in the case of elastic or elastic–brittle, but not plastic, materials.

Examples

The maximum entropy formalism is much better suited to deal with quasi-static rather than dynamic fracture. The dynamic character of fracture in these experiments, combined with the presence of multiple incipient spots, was also a big challenge in several computational mechanics models reviewed in Al-Ostaz and

Jasiuk (1997) employing commercial finite element programs, as well as in an independent study using a meshless element program (Belytschko et al. 1995). Upon trying various failure criteria and subjective choices (such as being forced to initialize the cracking process in the meshless model), the simulations have run into uncertainty as to which modeling aspect is more critical and whether there is a way to clarify it. A more recent study (Ostoja-Starzewski and Wang 2006) was motivated by that challenge and offered a way to test the PM vis-à-vis experiments.

The same experiments on crack patterns in epoxy plates perforated by holes were also treated by two analyses – one based on the minimum potential energy formulation and another based on the maximum entropy method; they both relied on the assumption of quasi-static response. Strictly speaking, while the loading was static, the fragmentation event was dynamic. Clearly, the preparation of mineral specimens – involving measurement of highly heterogeneous and multi-phase microstructures – for a direct comparison with the model prediction is very hard. Thus, the model is applied to the experimentally tested plate with 31 holes according to this strategy:

- Decrease the lattice spacing until mesh-independent crack patterns are attained.
- Find whether the lattice of (i) will also result in the most dominant crack pattern of Fig. 16. Indeed, the crack patterns "stabilize" as the mesh is refined.
- Assuming the answer to (ii) is positive, introduce weak perturbations in the material properties – either stiffness or strength – to determine which one of these has a stronger effect on the deviation away from the dominant crack pattern, i.e., on the scatter in Fig. 16.

Other Models

The PM is but one of the variations on the theme of MD. Here are some other possibilities:

- Molecular statics (MS) – by disregarding the inertia forces, it involves a static solution of the system of atoms (Vinogradov 2006, 2009, 2010). While the MD allows simulations of large systems with a constraint to very short time scales (transient phenomena of the order of nanoseconds), the MS allows large (macroscopic type) time scales albeit with a limitation by the size of a (nonlinear) algebraic system one is able to solve and a restriction to 0°K.
- Derivation of a continuum model from a microscopic model based on the assumption that the displacements on the macroscopic level are the same as those on the molecular level (Blanc et al. 2002).
- Introduction of a finite extension and spin for continuum-type particles (Yserentant 1997).
- Direct incorporation of interatomic potentials into a continuum analysis on the atomic scale (Zhang et al. 2002).

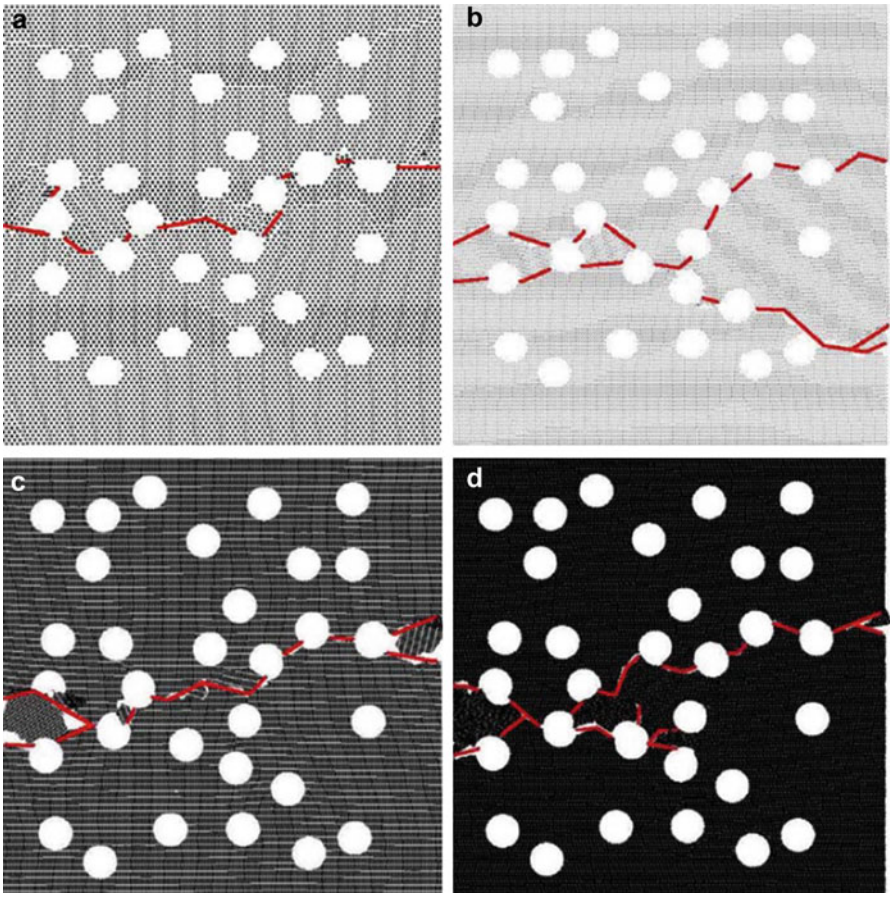

Fig. 16 From (Ostoja-Starzewski and Wang 2006) final crack patterns for four mesh configurations at ever finer lattice spacings: (**a**) $r_0 = 0.1$ cm, (**b**) $r_0 = 0.05$ cm, (**c**) $r_0 = 0.02$ cm, and (**d**) $r_0 = 0.01$ cm

Scaling and Stochastic Evolution in Damage Phenomena

Consider a material whose elasticity is coupled to damage state, as described by the constitutive equation (Lemaitre and Chaboche 1994)

$$\sigma_{ij} = (1 - D)C_{ijkl}\varepsilon_{kl}. \tag{66}$$

Here C_{ijki} is isotropic, and which must be coupled with a law of isotropic damage, that is,

$$\dot{D} = \frac{\partial \Phi^*}{\partial Y}, \tag{67}$$

with $Y = -\partial\Psi/\partial\varepsilon$, being the Helmholtz free energy. This formulation is set within the TIV (thermomechanics with internal variables) framework. In particular, the scalar D evolves with the elastic strain $\varepsilon = \varepsilon_{ii}$, which is taken as a time-like parameter, according to

$$\frac{\partial D}{\partial \varepsilon} = \begin{cases} (\varepsilon/\varepsilon_0)^{s*} & \text{when} \quad \varepsilon = \varepsilon_D \quad \text{and} \quad d\varepsilon = d\varepsilon_D > 0, \\ 0 & \text{when} \quad \varepsilon < \varepsilon_D \quad \text{and} \quad d\varepsilon < 0. \end{cases} \tag{68}$$

Integration from the initial conditions $D = \varepsilon_D = 0$ up to the total damage, $D = 1$, gives

$$D = (\varepsilon/\varepsilon_0)^{s*+1} \quad \varepsilon_R = \left[(1+s*)\varepsilon_D^{s*}\right]^{s*+1} \quad \sigma = \left[1 - (\varepsilon/\varepsilon_R)^{s*+1}\right] E\varepsilon, \tag{69}$$

where $\sigma = \sigma_{ii}$.

This formulation is understood as the effective law for the RVE, that is,

$$C_{ijkl}^{eff} = C_{ijkl|\delta\to\infty} \quad D^{eff} = D_{|\delta\to\infty} \quad \Psi^{\text{eff}} = \Psi_{|\delta\to\infty} \quad \Phi^{\text{eff}} = \Phi_{|\delta\to\infty}, \tag{70}$$

as well as a guidance for adopting the form of apparent responses on mesoscales. Thus, assuming that the same types of formulas hold for any mesoscale δ, the apparent response for any specimen $B_\delta(\omega)$ is

$$\overline{\boldsymbol{\sigma}} = \left(1 - D_\delta^d\right)\mathbf{C}_\delta^d(\omega) : \varepsilon^0 \tag{71}$$

under uniform displacement boundary condition. The notation D_δ^d expresses the fact that the material damage is dependent on the mesoscale δ and the type of boundary conditions applied (^{d}). In fact, while one could formally write another apparent response $\overline{\varepsilon} = \left(1D_\delta^d\right)^{-1}\mathbf{S}_\delta^t(\omega) : \sigma^0$, this is not done because the damage process under the traction boundary condition (^{t}) would be unstable.

It is now possible to obtain scale-dependent bounds on D_δ^d through a procedure analogous to that for linear elastic materials, providing one assumes a WSS and ergodic microstructure. One then obtains a hierarchy of bounds on $\left\langle D_\infty^d \right\rangle \equiv D^{eff}$ from above (Ostoja-Starzewski 2002b):

$$\left\langle D_{\delta'}^d \right\rangle \le \left\langle D_\delta^d \right\rangle \le \ldots \le \left\langle D_\infty^d \right\rangle \quad \forall \delta' = \delta/2. \tag{72}$$

These inequalities are consistent with the much more phenomenological Weibull model of scaling of brittle solids saying that the larger is the specimen, the more likely it is to fail.

Next of interest is the formulation of a stochastic model of evolution of D_δ^d with ε to replace Eq. 73_1. Said differently, a stochastic process $D_\delta^d = \left\{D_\delta^d(\omega,\varepsilon); \omega \in \Omega, \varepsilon \in [0,\varepsilon_R]\right\}$ is needed. Assuming, for simplicity of discussion, just as in Lemaitre and Chaboche (1994) that $s^* = 2$, this setup may be considered:

$$dD_\delta^d(\omega,\varepsilon) = D_\delta^d(\omega,\varepsilon) + 3\varepsilon^2[1 + r_\delta(\omega)]dt, \tag{73}$$

where $r_\delta(\omega)$ is a zero-mean random variable taking values from $[-a_\delta, a_\delta]$, $1/\delta = a_\delta < 1$. This process has the following properties:

(i) Its sample realizations display scatter ω-by-ω for $\delta < \infty$, i.e., for finite body sizes.
(ii) It becomes deterministic as the body size goes to infinity in the RVE limit ($\delta \to \infty$)
(iii) Its sample realizations are weakly monotonically increasing functions of ε
(iv) Its sample realizations are continuous.
(v) The scale effect inequality (Eq. 73) is satisfied, providing ε_R is taken as a function of δ with a property

$$\varepsilon_R(\delta) < \varepsilon_R(\delta') \quad \forall \delta' = \delta/2. \tag{74}$$

Let us observe, however, that, given the presence of a random microstructure, mesoscale damage should be considered as a sequence of microscopic events – shown as impulses in Fig. 17a – thus rendering the apparent damage process D_δ^d one with discontinuous sample paths, having increments dD_δ^d occurring at discrete time instants (Fig. 17c). To satisfy this requirement, one should, in place of the above, take a *Markov jump process* whose range is a subset [0,1] of real line (i.e., where D_δ^d takes values). This process would be specified by an evolution propagator or, more precisely, by a *next-jump probability density function* defined as follows:

$p\left(\varepsilon', D_\delta^{d'} | \varepsilon, D_\delta{}^d\right) d\varepsilon' dD_\delta^{d'}$ = probability that, given the process is in state D_δ^d at time ε, its next jump will occur between times $\varepsilon + \varepsilon'$ and $\varepsilon + \varepsilon' + d\varepsilon'$ and will carry the process to some state between $D_\delta^d + D_\delta^{d'}$ and $D_\delta^d + D_\delta^{d'} + dD_\delta^{d'}$.

Figure 17b shows one realization $C_\delta^d(\omega,\varepsilon); \omega \in \Omega, \varepsilon \in [0, \varepsilon_R]$, of the apparent, mesoscale stiffness, corresponding to the realization $D_\delta^d(\omega,\varepsilon); \omega \in \Omega, \varepsilon \in [0, \varepsilon_R]$, of Fig. 17c. The resulting constitutive response $\sigma_\delta(\omega, \varepsilon); \omega \in \Omega, \varepsilon \in [0, \varepsilon_R]$ is depicted in Fig. 17a.

Calibration of this model (just as the simpler one above) – that is, the specification of $p\left(\varepsilon', D_\delta^{d'} | \varepsilon, D_\delta{}^d\right) d\varepsilon' dD_\delta^{d'}$ – may be conducted by either laboratory or computer experiments such as those discussed earlier in this chapter. Note that in the macroscopic picture ($\delta \to \infty$), the zigzag character and randomness of an effective stress–strain response vanish. However, many studies in mechanics/physics of fracture of random media (e.g., Herrmann and Roux 1990) indicate that the homogenization with $\delta \to \infty$ is generally very slow and hence that the assumption of WSS and ergodic random fields may be too strong for many applications; see Rinaldi (2013) for related work.

Extension of the above model from isotropic to (much more realistic) anisotropic damage will require tensor rather than scalar random fields and Markov processes. This will lead to a greater mathematical complexity which may be balanced by

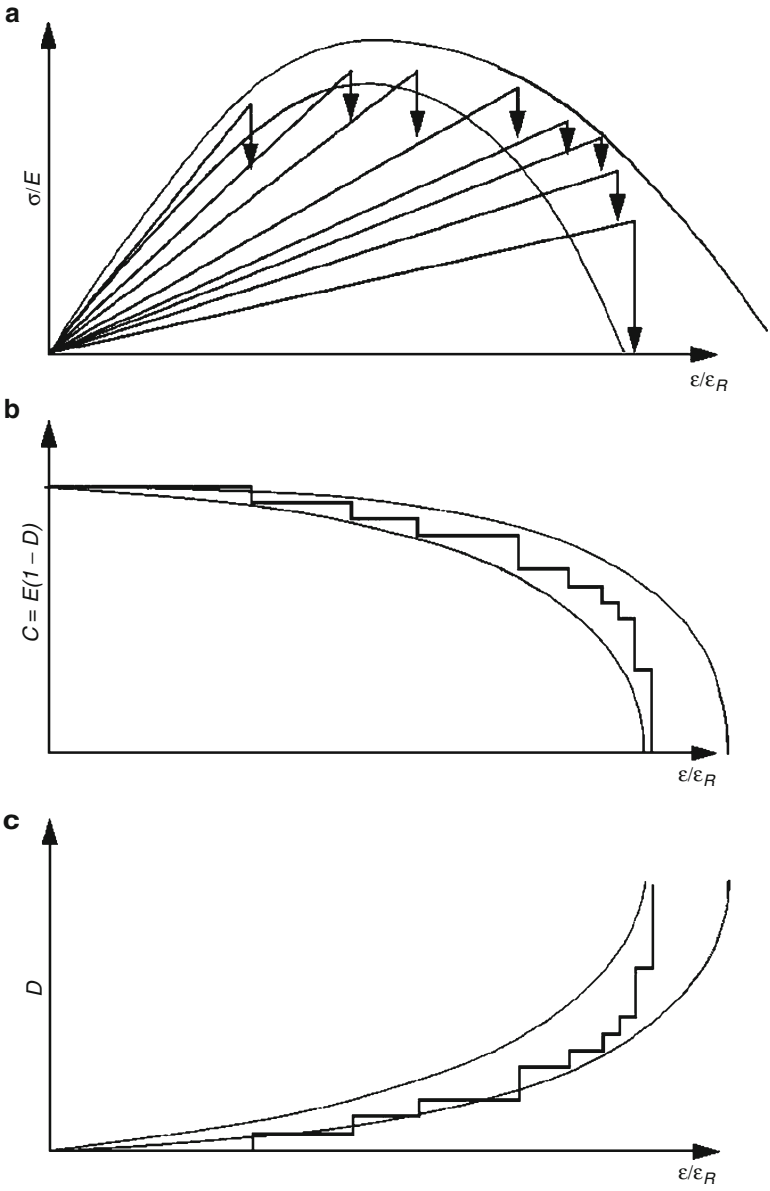

Fig. 17 Constitutive behavior of a material with elasticity coupled to damage where $\varepsilon/\varepsilon_R$ plays the role of a controllable, time-like parameter of the stochastic process. (**a**) Stress–strain response of a single specimen $\mathcal{B}_\delta$ from $\mathcal{B}$ having a zigzag realization, (**b**) deterioration of stiffness, and (**c**) evolution of the damage variable. Curves shown in (**a**–**c**) indicate the scatter in stress, stiffness, and damage at finite scale δ. Assuming spatial ergodicity, this scatter would vanish in the limit $\delta \to \infty$, whereby unique response curves of continuum damage mechanics would be recovered

choosing the first model of this subsection rather than the latter. These issues, while technically challenging and offering rich harvest for theoreticians, are quite secondary relative to the underlying goal to outline a stochastic continuum damage mechanics that (i) is based on, and consistent with, micromechanics of random media as well as the classical thermomechanics formalism and (ii) reduces to the classical continuum damage mechanics in the infinite volume limit.

Concluding Remarks

The motivation for lattice models in damage mechanics has been the need to simultaneously model elastic, plastic, and fracture responses in heterogeneous materials, something that cannot easily be delivered by conventional continuum solid mechanics and finite element analysis. Following a review of basic concepts of lattice models in anti-plane, planar classical, and planar nonclassical elasticity settings, various applications to damage mechanics (including fractal characteristics of fracture) have been given. The discussion has then been expanded from statics to dynamics (i.e., to a quasiparticle model). The chapter closes with a discussion of scaling and stochastic evolution in damage phenomena as stepping-stone to stochastic continuum damage mechanics.

References

M.J. Alava, P.K.V.V. Nukala, S. Zapperi, Statistical models of fracture. Adv. Phys. **55**(3–4), 349–476 (2006)

A. Al-Ostaz, I. Jasiuk, Crack initiation and propagation in materials with randomly distributed holes. Eng. Fract. Mech. **58**, 395–420 (1997)

K. Alzebdeh, A. Al-Ostaz, I. Jasiuk, M. Ostoja-Starzewski, Fracture of random matrix-inclusion composites: Scale effects and statistics. Int. J. Solids Struct. **35**(19), 2537–2566 (1998)

M.F. Ashby, D.R.H. Jones, *Engineering Materials 1: An Introduction to their Properties and Applications* (Pergamon Press, Oxford, 1980)

T. Belytschko, Y.Y. Lu, L. Gu, Crack propagation by element-free Galerkin method. Eng. Fract. Mech. **51**, 295–313 (1995)

M.D. Bird, C.R. Steele, A solution procedure for Laplace's equation on multiply connected circular domains. J. Appl. Mech. **59**(2), 398–404 (1992)

X. Blanc, C. LeBris, P.-L. Lions, From molecular models to continuum mechanics. Arch. Ration. Mech. Anal. **164**, 341–381 (2002)

A. Bonamy, E. Bouchad, Failure of heterogeneous materials: A dynamic phase transition. Phys. Rep. **498**, 1–44 (2011)

E. Bouchad, Scaling properties of cracks. J. Phys. Conden. Matter **9**, 4319–4343 (1997)

G.A. Buxton, C.M. Care, D.J. Cleaver, A lattice spring model of heterogeneous materials with plasticity. Model. Simul. Mater. Sci. Eng. **9**, 485–497 (2001)

D. Capecchi, G. Giuseppe, P. Trovalusci, From classical to Voigt's molecular models in elasticity. Arch. Hist. Exact Sci. **64**, 525–559 (2010)

L. De Arcangelis, S. Redner, H.J. Hermann, A random fuse model for breaking processes. J. Phys. Lett. **46**, 585–590 (1985)

E.J. Garboczi, M.F. Thorpe, M.S. DeVries, A.R. Day, Universal conductance curve for a plane containing random holes. Phys. Rev. A **43**, 6473–6480 (1991)
D. Greenspan, *Particle Modeling* (Birkhauser Publishing, Basel, 1997)
D. Greenspan, New approaches and new applications for computer simulation of N-body problems. Acta Appl. Math. **71**, 279–313 (2002)
A. Hansen, E.L. Hinrichsen, S. Roux, Scale invariant disorder in fracture and related breakdown phenomena. Phys. Rev. B **43**(1), 665–678 (1991)
F.W. Hehl, Y. Itin, The Cauchy relations in linear elasticity. J. Elast. **66**, 185–192 (2002)
R. Hill, Elastic properties of reinforced solids: Some theoretical principles. J. Mech. Phys. Solids **11**, 357–372 (1963)
R.W. Hockney, J.W. Eastwood, *Computer Simulation Using Particles* (Institute of Physics Publishing, Bristol, 1999)
C. Huet, Universal conditions for assimilation of a heterogeneous material to an effective medium. Mech. Res. Commun. **9**(3), 165–170 (1982)
C. Huet, Application of variational concepts to size effects in elastic heterogeneous bodies. J. Mech. Phys. Solids **38**, 813–841 (1990)
B. Kahng, G. Batrouni, S. Redner, Electrical breakdown in a fuse network with random, continuously distributed breaking strengths. Phys. Rev. B **37**(13), 7625–7637 (1988)
P.N. Keating, Effect of invariance requirements on the elastic strain energy of crystals with application to the diamond structure. Phys. Rev. **145**, 637–645 (1966)
J.G. Kirkwood, The skeletal modes of vibration of long chain molecules. J. Chem. Phys. **7**, 506–509 (1939)
D. Krajcinovic, *Damage Mechanics* (North-Holland, Amsterdam, 1996)
G. Lapasset, J. Planes, Fractal dimension of fractured surfaces: A universal value? Europhys. Lett. **13**(1), 73–79 (1990)
J. Lemaitre, J.-L. Chaboche, *Mechanics of Solid Materials* (Cambridge University Press, Cambridge, 1994)
A.E.H. Love, *The Mathematical Theory of Elasticity* (Cambridge University Press, New York, 1934)
J. Mandel, P. Dantu, Contribution à l'étude théorique et expérimentale du coefficient délasticité d'un milieu hétérogénes mais statisquement homog ène. Annales des Ponts et Chaussées Paris **6**, 115–145 (1963)
M.B. Mandelbrot, A.J. Paullay, Fractal nature of fracture surfaces of metals. Nature **308**(19), 721–722 (1984)
T.J. Napier-Munn, S. Morrell, R.D. Morrison, T. Kojovic, *Mineral Comminution Circuits – Their Operation and Optimisation* (Julius Kruttschnitt Mineral Research, The University of Queensland, Indooroopilly, 1999)
M. Ostoja-Starzewski, Lattice models in micromechanics. Appl. Mech. Rev. **55**(1), 35–60 (2002a)
M. Ostoja-Starzewski, Microstructural randomness versus representative volume element in thermomechanics. ASME J. Appl. Mech. **69**, 25–35 (2002b)
M. Ostoja-Starzewski, *Microstructural Randomness and Scaling in Mechanics of Materials* (Chapman & Hall/CRC Modern Mechanics and Mathematics Series, Boca Raton, 2008)
M. Ostoja-Starzewski, J.D. Lee, Damage maps of disordered composites: A spring network approach. Int. J. Fract. **75**, R51–R57 (1996)
M. Ostoja-Starzewski, G. Wang, Particle modeling of random crack patterns in epoxy plates. Probab. Eng. Mech. **21**(3), 267–275 (2006)
A. Rinaldi, Statistical model with two order parameters for ductile and soft fiber bundles on nanoscience and biomaterials. Phys. Rev. E **83**, 046126-1-10 (2011)
A. Rinaldi, Bottom-up modeling of damage in heterogeneous quasi-brittle solids. Contin. Mech. Thermodyn. **25**(2–4), 359–373 (2013)
A. Rinaldi, D. Krajcinovic, P. Peralta, Y.C. Lai, Lattice models of polycrystalline microstructures: A quantitative approach. Mech. Mater. **40**, 17–36 (2008)
K. Sab, Principe de Hill et homogénéisation des matériaux aléatoires, C.R. Acad. Sci. Paris **II**(312), 1–5 (1991)

K. Sab, On the homogenization and the simulation of random materials. Eur. J. Mech. A Solids **11**, 585–607 (1992)
K.A. Snyder, E.J. Garboczi, A.R. Day, The elastic moduli of simple two-dimensional composites: Computer simulation and eective medium theory. J. Appl. Phys. **72**, 5948–5955 (1992)
P. Trovalusci, D. Capecchi, G. Ruta, Genesis of the multiscale approach for materials with microstructure. Arch. Appl. Mech. **79**(11), 981–997 (2009)
O. Vinogradov, A static analog of molecular dynamics method for crystals. Int. J. Comput. Methods **3**(2), 153–161 (2006)
O. Vinogradov, Vacancy diffusion and irreversibility of deformations in the Lennard–Jones crystal. Comput. Mater. Sci. **45**, 849–854 (2009)
O. Vinogradov, On reliability of molecular statics simulations of plasticity in crystals. Comput. Mater. Sci. **50**, 771–775 (2010)
G. Wang, M. Ostoja-Starzewski, Particle modeling of dynamic fragmentation – I: Theoretical considerations. Comput. Mater. Sci. **33**(4), 429–442 (2005)
G. Wang, M. Ostoja-Starzewski, P.M. Radziszewski, M. Ourriban, Particle modeling of dynamic fragmentation – II: Fracture in single- and multi-phase materials. Comput. Mater. Sci. **35**(2), 116–133 (2006)
M.P. Wnuk, Introducing Fractals to Mechanics of Fracture, in *Basic Concepts in Fractal Fracture Mechanics*, Handbook of Damage Mechanics, (Springer, New York, 2014a)
M.P. Wnuk, Introducing Fractals to Mechanics of Fracture, in *Toughening and Instability Phenomena in Fracture. Smooth and Rough Cracks*, Handbook of Damage Mechanics, (Springer, New York, 2014b)
H. Yserentant, A new class of particle methods. Numer. Math. **76**, 87–109 (1997)
P. Zhang, Y. Huang, H. Gao, K.C. Hwang, Fracture nucleation in single-wall carbon nanotubes under tension: A continuum analysis incorporating interatomic potentials. ASME J. Appl. Mech. **69**, 454–458 (2002)

Toughening and Instability Phenomena in Quantized Fracture Process: Euclidean and Fractal Cracks

42

Michael P. Wnuk

Contents

Introduction 1182
Displacements and Strains Associated with a Discrete Cohesive Crack Model 1183
Quantization of the Panin Strain and the Criterion for Subcritical Crack Growth 1192
Stability of Fractal Cracks 1197
Conclusions 1203
Appendix A 1209
Appendix B 1210
References 1212

Abstract

Basic concept underlying Griffith's theory of fracture of solids was that, similar to liquids, solids possess surface energy and, in order to propagate a crack by increasing its surface area, the corresponding surface energy must be compensated through the externally added or internally released energy. This assumption works well for brittle solids, but is not sufficient for quasi-brittle and ductile solids.

Here some new forms of energy components must be incorporated into the energy balance equation, from which the input of energy needed to propagate the crack and subsequently the stress at the onset of fracture can be determined. The additional energy that significantly dominates over the surface energy is the irreversible energy dissipated by the way of the plastic strains that precede the leading edge of a moving crack. For stationary cracks, the additional terms within the energy balance equation were introduced by Irwin and Orowan. An extension of these concepts is found in the experimental work of Panin, who showed that

M. P. Wnuk (✉)
Department of Civil Engineering and Mechanics, College of Engineering and Applied Science, University of Wisconsin, Milwaukee, WI, USA
e-mail: mpw@csd.uwm.edu

© Springer Nature Switzerland AG 2022

G. Z. Voyiadjis (ed.), *Handbook of Damage Mechanics*,
https://doi.org/10.1007/978-3-030-60242-0_19

the irreversible deformation is primarily confined to the pre-fracture zones associated with a stationary or a slowly growing crack.

The present study is based on the structured cohesive crack model equipped with the "unit step growth" or "fracture quantum." This model is capable to encompass all the essential issues such as stability of subcritical cracks, quantization of the fracture process, and fractal geometry of crack surfaces and incorporate them into one consistent theoretical representation.

Keywords

Cohesive zone · Slow crack growth · Subcritical crack growth · Cohesive crack · Stable crack growth

Introduction

Inspiration for writing this chapter was provided by the experimental work of Panin and his group (Panin 1995) relevant to the better understanding of the phenomenon of pre-fracture strain accumulation, concentration, and redistribution, which occurs within the small pre-fracture zone adjacent to the leading edge of crack and being of paramount importance in determining the early stages of fracture, point of fracture onset – followed at first by the stable crack growth – and then by a terminal instability, which when the positive stress intensity factor K-gradient is maintained leads to a catastrophic propagation.

In order to be able to construct a mathematical model of these nonlinear deformation and fracture processes, it is necessary to introduce the "quantized model" of fracture or QFM for "quantized fracture mechanics." One shall be working here with a structured cohesive model of crack equipped with the "unit growth step" or, equivalently, the Neuber's particle (Neuber 1958) or Novozhilov's "fracture quantum" (Novozhilov 1969). Such an approach represents a substantial departure from the classic theory of Griffith who predicts no subcritical cracks. Griffith crack is either stationary or catastrophic under the positive K-gradient loading configuration. What visibly is missing in the classic theory is the transition period from a stationary state to a moving crack, which is accomplished by the insertion of the period of slow stable crack growth (SCG) and made possible by accounting for the highly nonlinear deformation processes preceding fracture.

To this end similar works have been done in recent past by Khezrzadeh et al. (2011) and by Wnuk et al. (2012), but none of these investigations have succeeded in presenting a mathematically complete theory departing from the continuum-based approximations and consistent with the latest trends in the computational fracture mechanics; cf. Prawoto and Tamin (2013). It is noteworthy that the mathematical model of "structured cohesive crack" has been successfully applied to the studies of the effects of specimen geometry and loading configuration on occurrence of instabilities in ductile fracture (cf. Wnuk and Rouzbehani 2005), in modeling the fatigue phenomenon at nanoscale levels; see Wnuk and Rouzbehani (2008).

To follow this line of approach, the quantization of the fracture process is needed, and it was implemented via the δCOD criterion of Wnuk. The notions of Neuber's particle and Novozhilov's fracture quantum are invoked in order to accomplish the quantization procedure. A prior knowledge of the strain distribution within the Panin zones is required. The governing differential equations of slow stable crack growth based on the Panin's study and on the theoretical model proposed by Wnuk et al. (2012) have been refined. It has been demonstrated that the nature provides certain mechanisms of enhancing or reducing the material resistance to fracture. The first one is related to material ductility and energy dissipation that precedes the final act of decohesion, while the other factor is purely geometrical as it derives from the roughness of the crack surfaces (not accounted for by the Euclidean geometry of a smooth classic crack). The conclusion is that while ductility significantly improves the fracture toughness, the increased roughness of crack surface suppresses the subcritical crack growth and it tends to induce a more brittle-like fracture. This feature is described in our model by the fractal fracture mechanics. The theory developed here is based on certain key equations involving the fractal representation of stationary and growing cracks due to the fundamental research of Wnuk and Yavari (2003, 2009) and Khezrzadeh et al. (2011).

Displacements and Strains Associated with a Discrete Cohesive Crack Model

For many years, one of the primary subjects of V. Panin's research (Panin 1995) were the experimental studies and recording of the strains at micro- and meso-levels as well as observation of their subsequent build up and redistribution occurring within a certain small process zone adjacent to the leading edge of the crack. Here the primary purpose is to construct a simple mathematical model describing such a phenomenon of pre-fracture strain accumulation and concentration within the regions close to the crack front – in what follows referred to as "pre-fracture" or "Panin zones." The intention is to study both the stationary and slowly moving cracks. For this purpose, one shall employ the structured cohesive crack model equipped with a Neuber's particle or fracture quantum Δ. An assumption regarding existence of such particle embedded within the cohesive zone is necessary if the quantization of the fracture process is anticipated and necessary to provide a complete mathematical representation of the fracture process for a ductile (or quasi-brittle) solid. It is noted that the terms "pre-fracture zone," "Panin zone," or "cohesive zone" are to be understood as synonyms.

Material ductility will be one of the parameters of primary concern. For the structured cohesive crack model (see Figs. 1 and 2), the following quantity will be used as a measure of the ductility:

$$\rho = \frac{R_{ini}}{\boldsymbol{\Delta}} = \frac{\varepsilon^f}{\varepsilon_Y} = \frac{\varepsilon_Y + \varepsilon_{pl}^f}{\varepsilon_Y} \tag{1}$$

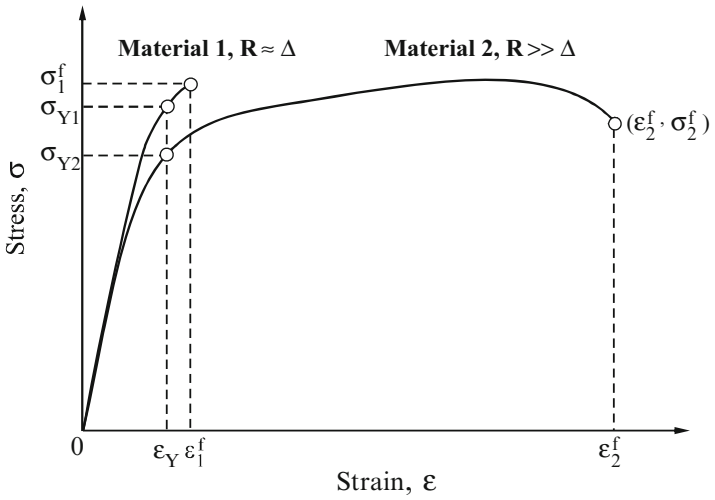

Fig. 1 Examples of quasi-brittle and ductile material behavior. Two materials with identical yield strain ε_Y and similar yield points σ_Y but with widely different ductility are compared: **Material 1** (quasi-brittle) shows the ratio $\varepsilon^f/\varepsilon_Y$ close to one, while for the **Material 2** (ductile) the ratio $\varepsilon_2^f/\varepsilon_Y \gg 1$. In the discrete cohesive crack model, the ductility index R_{ini}/Δ is identified with $\varepsilon^f/\varepsilon_Y$. The length of the cohesive zone at the onset of fracture R_{ini} equals $(\pi/8)(K_c/\sigma_Y)^2$, while Δ is the size of the Neuber's particle

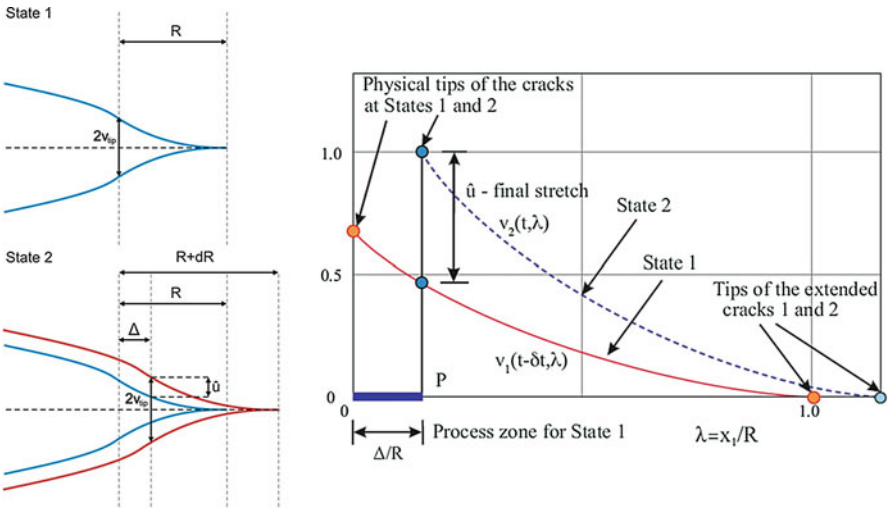

Fig. 2 Distribution of the COD within the cohesive zone corresponding to two subsequent states represented by instants "t- δt" and "t" in the course of quasi-static crack extension as required in Wnuk's criterion of delta COD; $[v_2(t) - v_1(t - \delta t)]_P =$ final stretch

Here Δ denotes the fracture quantum, while the length of the cohesive zone measured at the onset of fracture (usually occurring in form of slow stable crack growth that in ductile media precedes the catastrophic propagation) is denoted by R_{ini} and this quantity is related to the yield stress σ_Y, Young modulus E, and the fracture toughness measured by K_c or Rice's integral J_c in a familiar fashion

$$R_{ini} = \frac{\pi}{8}\left(\frac{K_c}{\sigma_Y}\right)^2 = \frac{\pi}{8}\left(\frac{EJ_c}{\sigma_Y}\right)^2 \tag{2}$$

This quantity is often identified with the material characteristic length, say L_{ch}; cf. Taylor (2008). In order to estimate the size of the other important length parameter, the fracture quantum Δ, it suffices at this point to say that in brittle and quasi-brittle materials, Δ and L_{ch} are of the same order of magnitude, while for the ductile materials, Δ is much smaller than the characteristic length given by Eq. 2.

Roughness of the crack surfaces represented via fractal geometry will be treated as a secondary variable that influences the early stages of fracture, i.e., the stable crack extension and the onset of the unstable propagation. For comparison, both the Euclidean and the fractal geometries of a crack will be considered. An approximate model proposed by Wnuk and Yavari (2003) known as the "embedded fractal crack," whose fractal dimension D may differ from one, will be employed; see Fig. 2. Prior to the addition of the cohesive zones, an embedded fractal crack exhibits a singular near tip stress field proportional to $r^{-\alpha}$, where r is the distance measured from the crack tip and the so-called fractal exponent α is related to the dimension D and the roughness measure H as follows:

$$\begin{aligned} \alpha &= \frac{2-D}{2}, 1 \le D \le 2 \\ \alpha &= \frac{2H-1}{2H}, 0 \le H \le 1/2 \end{aligned} \tag{3}$$

Using the fractal crack model, Wnuk and Yavari (2003) and also Khezrzadeh et al. (2011) have estimated the stress intensity factor as

$$K_I^f = \chi(\alpha)\sqrt{\pi a^{2\alpha}}\sigma \tag{4}$$

where σ is the applied stress, a denotes the crack length, and the function $\chi(\alpha)$ is defined by the integral

$$\chi(\alpha) = \frac{2}{\pi^{1-\alpha}}\int_0^1 \frac{dz}{(1-z^2)^{1-\alpha}} = \frac{\pi^{\alpha-1}\Gamma(\alpha)}{\Gamma\left(\alpha+\frac{1}{2}\right)} \tag{5}$$

Here Γ is the Euler gamma function. One notices that for $1 \le D \le 2$ the fractal exponent α varies within the range [0.5, 0]. According to the principle of correspondence, all quantities describing a fractal crack reduce to the classic expressions valid

for a smooth crack when $\alpha \rightarrow \frac{1}{2}$. As shown by Khezrzadeh et al. (2011), the Wnuk–Yavari model of a fractal crack holds only for cracks with relatively small roughness, and thus in the considerations that follow the range of α will be limited to [0.5, 0.4].

First the case of a smooth Euclidean crack will be represented by a structured cohesive crack model as shown in Fig. 3. Two sets of coordinates are used: the

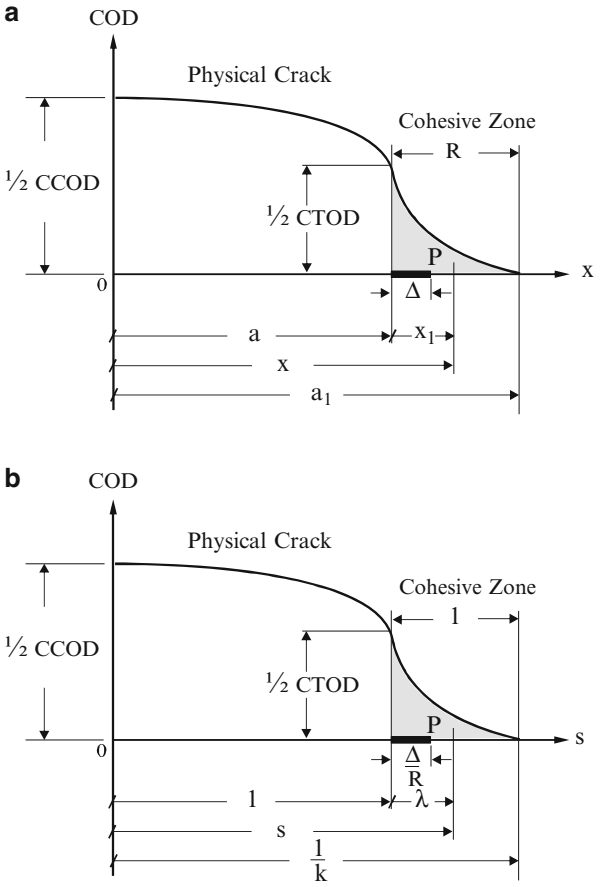

Fig. 3 (**a**) Dimensional coordinates associated with an extended structured cohesive crack. Note the location of the "fracture quantum" Δ, which is adjacent to the crack leading edge and is embedded within the cohesive zone. According to our model, the brittle behavior is observed when Δ and R are of approximately same size, while for the ductile behavior, Δ is deeply embedded within the cohesive zone, and therefore, it is much smaller than R. P denotes the control point for measuring the increment of the COD for a slowly moving crack during the early stages of fracture. Symbols CCOD and CTOD designate the "crack center opening displacement" and the "crack tip opening displacement," respectively. (**b**) Nondimensional coordinates $s = x/a$ and $\lambda = x_1/R$. Note that when these coordinates are used, the tip of the extended crack falls at $s = 1/k$, where k is related to the nondimensional loading parameter $Q = (\pi/2)(\sigma/\sigma_Y)$ by this formula: $k = \cos Q$

dimensional coordinates are shown in Fig. 3a, while the nondimensional are explained in Fig. 3b. The distance measured from the origin of coordinates is denoted by x (or $s = x/a$), while the distance measured from the tip of the physical crack is denoted by x_1 (or $\lambda = x_1/R$) and the ratio $a/a_1 = k$. The crack length is "a," the length of the extended crack is $a_1 = a + R$, and the profile of the entire crack is described (cf. Anderson 2004; Khezrzadeh et al. 2011) by the following expression involving the inverse hyperbolic functions

$$u_y = \frac{4\sigma_Y a}{\pi E}\,\mathrm{Re}\left\{\coth^{-1}\sqrt{\frac{1-k^2s^2}{1-k^2}} - s\coth^{-1}\left[\frac{1}{s}\sqrt{\frac{1-k^2s^2}{1-k^2}}\right]\right\} \tag{6}$$

At $s = 0$ one obtains the expression for the crack center opening displacement (CCOD), namely,

$$u_y^{\text{center}} = \frac{4\sigma_Y a}{\pi E}\coth^{-1}\left(\frac{1}{1-k^2}\right)^{1/2} = \frac{4\sigma_Y a}{\pi E}\coth^{-1}\left(\frac{1}{\sin Q}\right) \tag{7}$$

The nondimensional loading parameter $Q = \pi\sigma/2\sigma_Y$ enters the last equation due to the known Dugdale formula valid for our model:

$$k = \cos Q \tag{8}$$

At $s = 1$ one obtains the crack tip opening displacement (CTOD), namely,

$$u_y^{tip} = \frac{4\sigma_Y a}{\pi E}\ln\left(\frac{1}{k}\right) = \frac{4\sigma_Y a}{\pi E}\ln\left(\frac{1}{\cos Q}\right) \tag{9}$$

Figure 4a shows the dependence of the tip displacement and the center displacement on the applied load Q, while Fig. 4b illustrates the fact that the ratio of these two quantities CTOD/CCOD remains constant almost throughout the entire range of loading. The constant is 0.504, which provides a good rule of thumb: the tip displacement of the cohesive crack is roughly one half of the mouth displacement measured at the crack center. This observation provides helpful information for an experimentalist, who utilizing various clip gages can access the center of the crack much easier than the tip of the physical crack. Thus, once the CCOD is measured, the tip displacement, the CTOD, can be estimated with a good accuracy.

The profile of the entire extended crack, normalized by the constant $C = \frac{4\sigma_Y a}{\pi E}$, is shown in Fig. 5a, while Fig. 5b shows the same profile normalized by the CTOD. In constructing these figures, the following equations were used:

$$u = \frac{u_y}{C} = \mathrm{Re}\left\{\coth^{-1}\sqrt{\frac{1-k^2s^2}{1-k^2}} - s\coth^{-1}\left[\frac{1}{s}\sqrt{\frac{1-k^2s^2}{1-k^2}}\right]\right\} \tag{10}$$

and

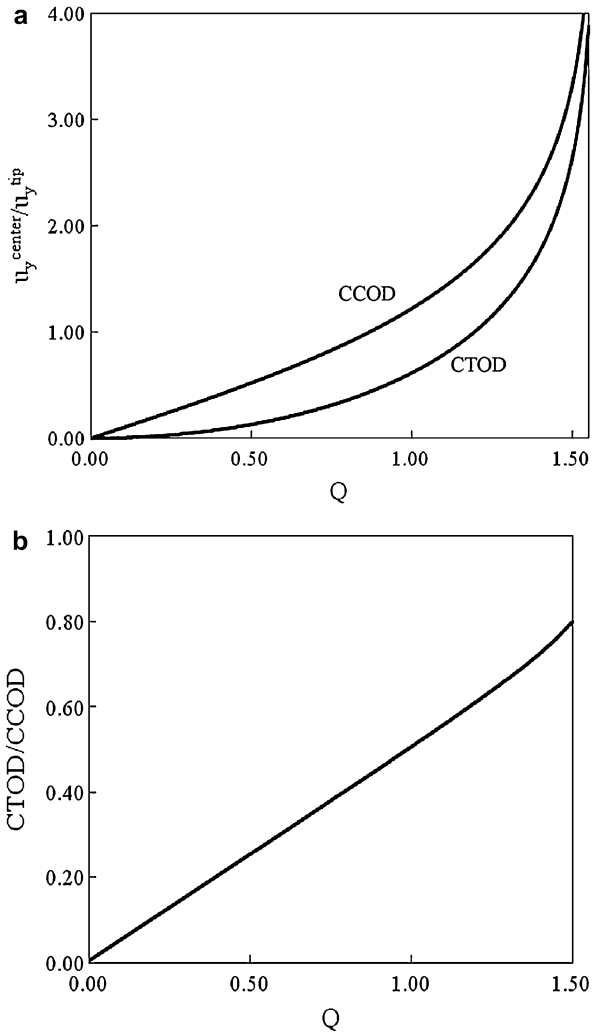

Fig. 4 (**a**) Shows the opening displacements at the center of a cohesive crack and at the tip of the physical crack as functions of the applied load Q. (**b**) Shows the ratio of the CTOD (crack tip opening displacement) to the CCOD (crack center opening displacement). Despite the nonlinear nature of the problem, these results show that the CTOD is roughly one half of the CCOD through the entire range of the loading parameter Q. The ratio depicted in the figure can be very closely approximated by the simple equation CTOD = 0.504CCOD

$$v = \frac{u_y}{u_y^{tip}} = \frac{1}{\ln\left(\frac{1}{k}\right)} \operatorname{Re}\left\{ \coth^{-1}\sqrt{\frac{1-k^2s^2}{1-k^2}} - s\coth^{-1}\left[\frac{1}{s}\sqrt{\frac{1-k^2s^2}{1-k^2}}\right]\right\} \tag{11}$$

Due to this normalization procedure, all v-profiles pass through one at the tip of the physical crack, $x = a$ or $s = 1$. Figure 6a shows the graphs resulting from the expression in Eq. 11 drawn for three values of load Q and plotted within the range of

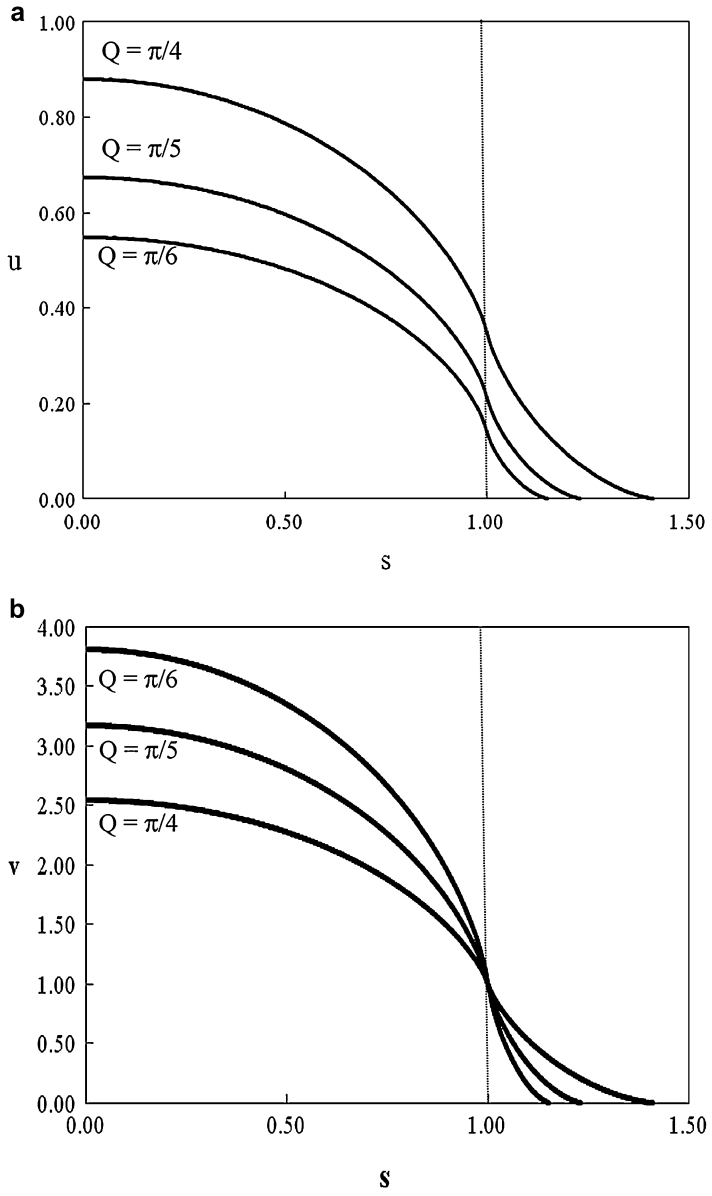

Fig. 5 Profiles of the cusp region of the cohesive crack: (**a**) when the crack opening displacements are normalized by the constant $C = 4\sigma_Y/\pi E$, see Eq. 10, and (**b**) when half of the CTOD is used as the normalization constant, see Eq. 11. Nondimensional loading parameter, proportional to σ/σ_Y, is denoted by Q

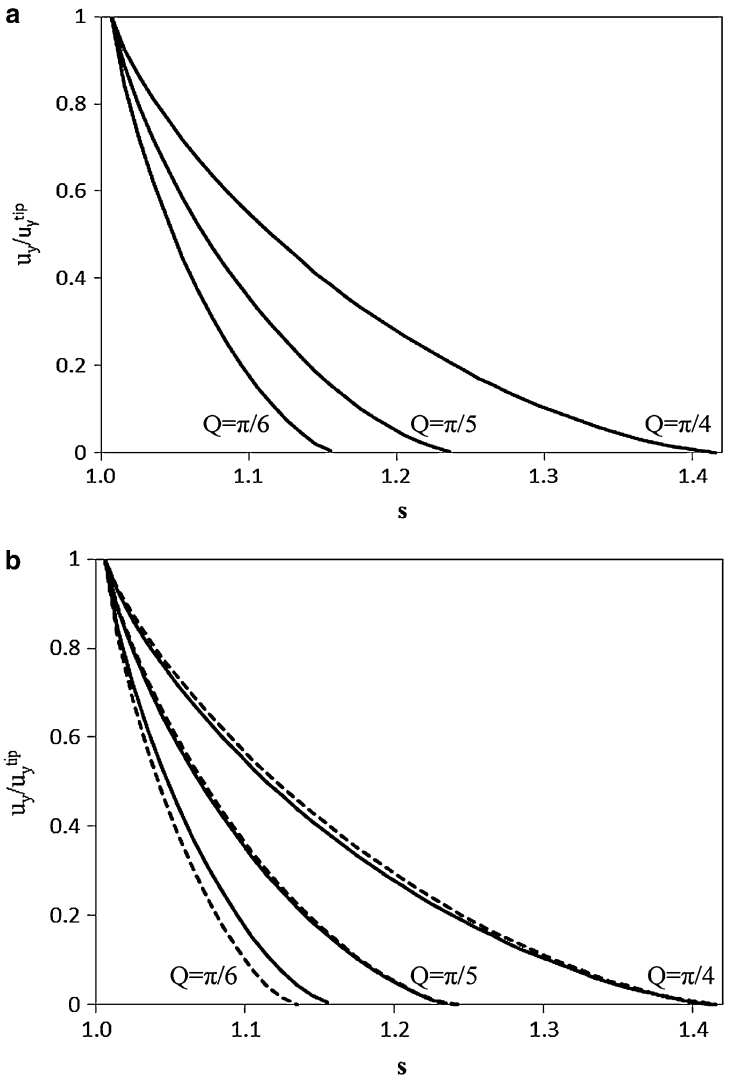

Fig. 6 (**a**) Profiles of the cusp of the cohesive crack plotted for three values of the loading parameter Q according to Eq. 11. (**b**) Comparison of the profiles shown in (**a**) with those that result from simplified formula (*dashed lines*) valid under Barenblatt's restriction of R being much smaller than the crack length; cf. Eq. 14

x that corresponds to the "cusp" of the cohesive crack, i.e., for $a \leq x \leq a_1$ or $1 \leq s \leq 1/k$.

Finally, in Fig. 6b, these v-graphs representing the cusp are compared to the curves that result from a known (cf. Rice 1968; Wnuk 1974) approximate formula valid under the Barenblatt's restriction of R being much smaller than the crack length

$$v_{\mathrm{coh}}^{\mathrm{cusp}} = \frac{4\sigma_Y R}{\pi E}\left[\sqrt{1-\frac{x_1}{R}} - \frac{x_1}{2R}\ln\frac{1+\sqrt{1-\frac{x_1}{R}}}{1-\sqrt{1-\frac{x_1}{R}}}\right] \tag{12}$$

It is not difficult to show that for $R \ll a$, the expression for the tip displacement in Eq. 9 reduces to the constant shown in front of the square bracket in Eq. 12, namely,

$$u_y^{\mathrm{tip}} = \frac{4\sigma_Y a}{\pi E}\ln\left(\frac{1}{k}\right) = \frac{4\sigma_Y a}{\pi E}\ln\left(\frac{a_1}{a}\right) = \left[\frac{4\sigma_Y a}{\pi E}\ln\left(\frac{a+R}{a}\right)\right]_{R\ll a} \simeq \frac{4\sigma_Y}{\pi E}R \tag{13}$$

When this constant is used to normalize the displacement in Eq. 12, one obtains

$$v_{\mathrm{coh}} = \frac{v_{\mathrm{coh}}^{\mathrm{cusp}}}{u_y^{\mathrm{tip}}} = \sqrt{1-\frac{x_1}{R}} - \frac{x_1}{R}\ln\frac{1+\sqrt{1-\frac{x_1}{R}}}{1-\sqrt{1-\frac{x_1}{R}}} = \sqrt{1-\lambda} - \frac{\lambda}{2}\ln\frac{1+\sqrt{1-\lambda}}{1-\sqrt{1-\lambda}} \tag{14}$$

Figure 6b shows that the agreement between the exact and the approximate formulae for the cohesive crack opening displacements within the cusp region is indeed good for all values of the loading parameter Q. Therefore, to simplify all further calculations, the formula in Eq. 14 will be employed. Of particular interest will be the strains within the Panin zone, which are defined by the derivative

$$\varepsilon_y^{\mathrm{coh}} = \frac{dv_{\mathrm{coh}}^{\mathrm{cusp}}}{dx_1} = \frac{1}{R}\frac{dv_{\mathrm{coh}}^{\mathrm{cusp}}}{d\lambda} = \frac{1}{R}\frac{4\sigma_Y R}{\pi E}\frac{dv_{\mathrm{coh}}}{d\lambda} = \frac{4\sigma_Y}{\pi E}\frac{dv_{\mathrm{coh}}}{d\lambda} \tag{15}$$

Applying Eq. 14 and carrying out the derivative yields the closed form expression for the strains within the pre-fracture zone. For convenience the strains are expressed in terms of the variable s, related to the variable λ as follows:

$$\begin{aligned} \lambda &= \frac{s-1}{m-1} \\ m &= 1/k \\ k &= \cos Q \end{aligned} \tag{16}$$

Thus, the expression for strains within the pre-fracture zone associated with the structured cohesive crack model reads

$$\begin{aligned} \varepsilon_y^{\mathrm{coh}} &= \frac{4\sigma_Y}{\pi E}\left\{\frac{1}{2}\ln\frac{1-\sqrt{1-\lambda(s,m)}}{1+\sqrt{1-\lambda(s,m)}}\right\} = \frac{4\sigma_Y}{\pi E}\left\{\frac{1}{2}\ln\left[\frac{\sqrt{1-k}-\sqrt{1-ks}}{\sqrt{1-k}+\sqrt{1-ks}}\right]\right\} \\ \lambda(s,m) &= \frac{s-1}{m-1} = \frac{(s-1)\cos Q}{1-\cos Q} \end{aligned} \tag{17}$$

The graphs showing the strains as functions of the loading parameter Q and the coordinate s are shown in Fig. 7.

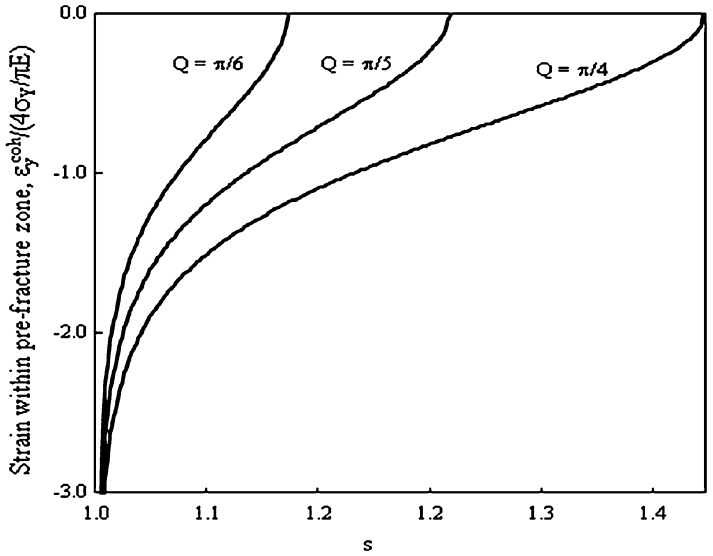

Fig. 7 Strains within the pre-fracture zone obtained as gradient of the crack opening displacement; see Eq. 17

Quantization of the Panin Strain and the Criterion for Subcritical Crack Growth

Closer examination of the expression in Eq. 17 reveals that the strains within the pre-fracture zone are infinite at the tip of the physical crack. Therefore, any use of this entity for the purpose of predicting the onset of fracture propagation will fail, unless it is preceded by the quantization procedure, which in essence is tantamount to evaluation of the strain averaged over the Neuber length Δ, namely,

$$\begin{aligned}\langle\varepsilon\rangle_{a,a+\Delta} &= \frac{1}{\Delta}\int_0^{\Delta}\varepsilon_y^{\mathrm{coh}}dx_1 = \frac{1}{\Delta}\int_{\mathrm{state1}}^{\mathrm{state2}}\frac{dv_{\mathrm{coh}}^{\mathrm{cusp}}}{dx_1}dx_1 \\ &= \frac{1}{\Delta}\left[v_{\mathrm{coh}}^{\mathrm{cusp}}(\mathrm{state}\ \ 2) - v_{\mathrm{coh}}^{\mathrm{cusp}}(\mathrm{state}\ \ 1)\right]\end{aligned} \tag{18}$$

When this quantity is set equal the average critical strain $\overline{\varepsilon}_{\mathrm{crit}} = \widehat{u}/\Delta$ one obtains the following criterion defining the onset of fracture propagation:

$$\begin{aligned}&\langle\varepsilon\rangle_{a,a+\Delta} = \overline{\varepsilon}_{\mathrm{crit}} = \widehat{u}/\Delta \\ &v_{\mathrm{coh}}^{\mathrm{cusp}}(\mathrm{state}\ \ 2) - v_{\mathrm{coh}}^{\mathrm{cusp}}(\mathrm{state}\ \ 1) = \widehat{u}\end{aligned} \tag{19}$$

Let us define the two neighboring states using the time "t" and the time-like variable $x_1(t) = x - a(t)$ for a slowly progressing crack; these states are defined as follows:

$$\begin{aligned} &\text{State } 1, \quad (t - \delta t, x_1 = \Delta) \\ &\text{State } 2, \quad (t, x_1 = 0) \end{aligned} \tag{20}$$

This means that at instant "$t-\delta t$" defining state 1, the front of the advancing crack is a distance Δ away from the control point P (see Fig. 3), while at the instant "t" describing state 2, the tip of the physical crack has reached the control point P. This is indicative that the crack has advanced the "unit growth step" or "fracture quantum" Δ between the two states considered. The constancy of the increment of the crack opening displacement $\widehat{u}$ (the so-called final stretch) measured at the control point P constitutes the necessary condition for the stable crack to propagate. In essence this requirement is tantamount to stating Wnuk's criterion of the final stretch or the δ(COD) criterion for subcritical crack extension; cf. Wnuk (1974). It is noteworthy that the physical foundation for the criterion is the same as the one postulated by McClintock (1965), which is the critical strain. As Eqs. 18 and 19 demonstrate, the quantization technique and the attributes of the cohesive crack model allow one to bypass the long expression for pre-fracture strains and to reduce all the essential considerations to the displacements only, namely, the function $v_{\text{coh}}^{\text{cusp}}(\lambda)$ given by Eq. 14. Similar techniques of the "quantized fracture mechanics" (QFM) were employed by Pugno and Ruoff (2004), Taylor et al. (2005), and Wnuk and Yavari (2009).

Using Eq. 12, one may express the opening displacements for both considered states as follows:

$$v_{\text{coh}}^{\text{cusp}}(\text{state } 1) = \frac{4\sigma_Y R(\Delta)}{\pi E}\left[\sqrt{1 - \frac{\Delta}{R(\Delta)}} - \frac{\Delta}{2R(\Delta)} \ln \frac{1 + \sqrt{1 - \frac{\Delta}{R(\Delta)}}}{1 - \sqrt{1 - \frac{\Delta}{R(\Delta)}}}\right] \tag{21}$$

and

$$v_{\text{coh}}^{\text{cusp}}(\text{state } 2) = \frac{4\sigma_Y R(0)}{\pi E} = \frac{4\sigma_Y}{\pi E}\left(R(\Delta) + \Delta \frac{dR}{da}\right) \tag{22}$$

Subtracting Eq. 21 from Eq. 22 yields the left hand of the second equation in Eq. 19, which now reads

$$R(\Delta) = \Delta \frac{dR}{da} - R(\Delta)\left[\sqrt{1 - \frac{\Delta}{R(\Delta)}} - \frac{\Delta}{2R(\Delta)} \ln \frac{1 + \sqrt{1 - \frac{\Delta}{R(\Delta)}}}{1 - \sqrt{1 - \frac{\Delta}{R(\Delta)}}}\right] = \frac{\widehat{u}}{\frac{4\sigma_Y}{\pi E}} \tag{23}$$

For $\Delta \ll R$ this expression readily reduces to

$$\frac{dR}{da} = \frac{\pi E}{4\sigma_Y}\left(\frac{\widehat{u}}{\Delta}\right) - \frac{1}{2} - \frac{1}{2}\ln\left(\frac{4(R_{ini}/\Delta)R}{R_{ini}}\right) \tag{24}$$

With the notation

$$\begin{aligned} M &= \frac{\pi E}{4\sigma_Y}\left(\frac{\widehat{u}}{\Delta}\right) \\ \rho &= R_{ini}/\Delta \end{aligned} \tag{25}$$

this becomes the ordinary differential equation which governs the motion of a stable crack in the early stages of fracture

$$\frac{dR}{da} = M - \frac{1}{2} - \frac{1}{2}\ln\left(\frac{4\rho R}{R_{ini}}\right) \tag{26}$$

Two constants which enter the equation above are (1) the tearing modulus M and (2) the material ductility ρ. For a smooth crack, this is the result of Wnuk (1974) and Rice et al. (1980). In the next section, certain modifications of this equation extending the range of its validity into the fractal geometry domain will be investigated. The rate dR/da reflects the rate of material energy demand; and since R and the integral J differ by just a constant, and $J = -\frac{d\Pi}{2da}$, thus the left-hand side of Eq. 26 also represents the second derivative $-\frac{d^2\Pi}{2da^2}$ where Π denotes the potential energy of the loaded body containing a crack. The "R vs. a" curve defined by the differential in Eq. 26 is often referred to as the material resistance curve. On the other hand, the rate of the energy supply due to external applied stress field is measured by the quantity R hidden in Eq. 8. For the case of $R \ll a$, one may expand both sides of this equation in the corresponding power series:

$$\begin{aligned} \frac{a+R}{a} &= 1 + \frac{R}{a} + \cdots \\ \frac{1}{\cos Q} &= 1 + \frac{Q^2}{2} + \cdots \end{aligned} \tag{27}$$

Setting both expression equal to each other, one obtains for $R \ll a$

$$\begin{aligned} R &= \frac{aQ^2}{2} \\ Q &= \sqrt{\frac{2R}{a}} \end{aligned} \tag{28}$$

The "R" in Eq. 28 represents the rate of energy supplied by the external effort. For the terminal instability to occur, the second derivatives of the energy terms or the

rates dR_{MAT}/da and $\partial R_{\mathrm{APPL}}/\partial a$ must equal. The rate dR_{MAT}/da is given by Eq. 26, while differentiation of the first equation in Eq. 28 leads to

$$\left[\frac{\partial R}{\partial a}\right]_{Q=\mathrm{const}} = \frac{Q^2}{2} = \frac{R}{a} \tag{29}$$

This quantity represents the external effort, and thus the conditions for the occurrence of the terminal instability are met when

$$\frac{dR_{\mathrm{MAT}}}{da} = \left[\frac{\partial R_{\mathrm{APPL}}}{\partial a}\right]_{Q=\mathrm{const}} \tag{30}$$

or when

$$M - \frac{1}{2} - \frac{1}{2}\ln\left(\frac{4\rho R}{R_{ini}}\right) = \frac{R}{a} \tag{31}$$

It is noted that R which appears on the left-hand side of Eq. 31 represents the material resistance to an extending crack, so really it should be read as R_{MAT}, while the R shown on the right-hand side of Eq. 31 symbolizes the driving force applied to the crack and truly it should be denoted by R_{APPL}. Since at all points of the stable crack growth including the point of terminal instability described by Eq. 31 both these quantities remain in equilibrium, $R_{\mathrm{MAT}} = R_{\mathrm{APPL}}$; when the subscripts are skipped, the equation defining the critical state can be written in form of Eq. 31. An alternative way to write Eq. 31 is to define the difference between the energy demand and energy supply. A suitable name for such a difference is "stability index" S, namely,

$$S = \frac{dR_{\mathrm{MAT}}}{da} - \left[\frac{\partial R_{\mathrm{APPL}}}{\partial a}\right]_{Q=\mathrm{const}} = M - \frac{1}{2} - \frac{1}{2}\ln\left(\frac{4\rho R}{R_{ini}}\right) - \frac{R}{a} \tag{32}$$

To solve for the parameters characterizing the critical state, i.e., the parameter R_c, the critical load Q_c, and the critical crack length a_c, one needs to integrate Eq. 26 and then inspect the results and eventually solve Eq. 31 and/or Eq. 32. This is best done in two steps: first one separates the variables in Eq. 26 obtaining the solution for $R = R(a)$, or $X = X(Y)$, in this implicit form

$$\begin{aligned} a(R) &= a_0 + \int_0^R \frac{dz}{M - \frac{1}{2} - \frac{1}{2}\ln(4\rho z)} \\ X(Y) &= X_0 + \int_1^Y \frac{dz}{M - \frac{1}{2} - \frac{1}{2}\ln(4\rho z)} \end{aligned} \tag{33}$$

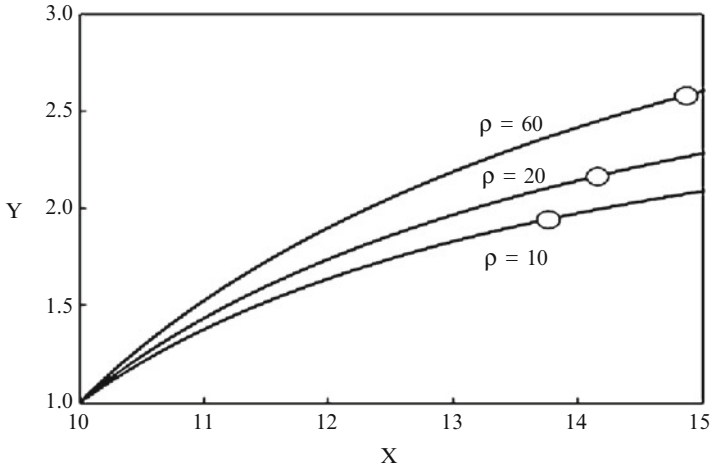

Fig. 8 Apparent material resistance to cracking $Y = R/R_{ini}$ at various levels of material ductility shown as functions of the current crack length during the stable growth process up to the points of terminal instability marked by little circles. All R-curves shown here were obtained from the governing differential in Eq. 26 subject to the initial condition $Y = 1$ at $X_0 = 10$

The value of the tearing modulus M must be chosen to be somewhat above the value of the minimum modulus $M_{\min}$, below which no stable crack growth may occur. In this case M is chosen to be 20% above the minimum value, so the modulus M is determined by this expression

$$M = 1.2\left(\frac{1}{2} + \frac{1}{2}\ln(4\rho)\right) \tag{34}$$

Next one needs to calculate the loading parameter $Q = \sqrt{2Y/X}$ and plot it against the nondimensional crack length $X = a/R_{ini}$. The symbol Y denotes the non-dimensional length of the pre-fracture zone R, namely, $Y = R/R_{ini}$, and $X = a/R_{ini}$ denotes the nondimensional length of the crack, while the initial length is $X_0 = a_0/R_{ini}$. Figure 8 shows the R-curves plotted vs. X for $\rho = 10$, 20, and 60 and obtained for the initial crack size of $10R_{ini}$. Figure 9 shows the Q-curves obtained for the same input data. It is noted that the attainment of the maximum on the Q-curve is equivalent to reaching the terminal instability. The point at which the derivative dQ/da approaches zero is best located when the rates of energy demand and energy supply are compared as it is done in Fig. 10a. The intersection of these curves determines the critical state (Q_c, X_c). In addition to these critical parameters, the apparent material fracture toughness encountered at the critical point $Y_c = R_c/R_{ini}$ can readily be evaluated. A convenient way to determine these intersection points numerically is to inspect the stability indices graphs shown in Fig. 10b. The critical states for $\rho = 10$, 20, and 60 and $X_0 = 10$ were established as follows:

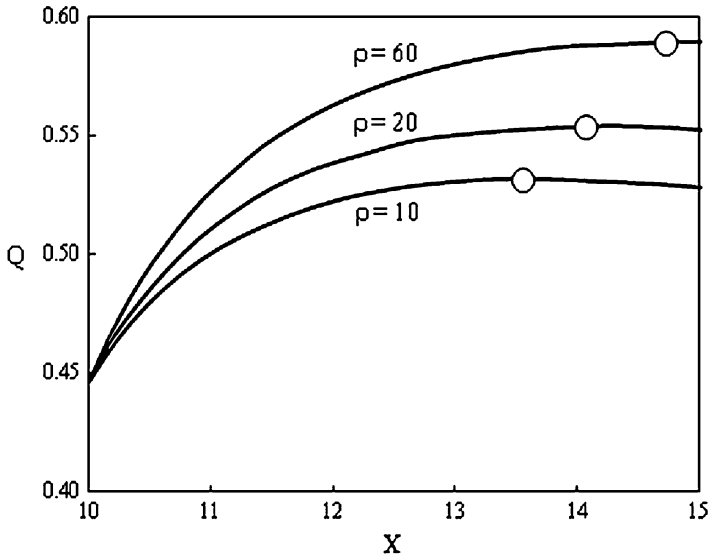

Fig. 9 Loading parameter Q shown during the stable crack growth phase for various material ductility indices. The functions shown pass through the maxima denoted by little *circles*. These points define the critical states (X_c, Q_c)

	Critical values		
Critical parameter	$\rho = 10$	$\rho = 20$	$\rho = 60$
Fracture toughness, Y_c	1.925	2.159	2.581
Crack length, X_c	13.605	14.086	14.842
Load, Q_c	0.532	0.554	0.590

It is readily seen that when the Q_c values are compared with the load prevailing at the onset of fracture, $Q_{ini} = \sqrt{2/X_0}$, one comes to a conclusion that for each case represented in the Table shown above, the loading parameter is enhanced during the process of slow crack growth and the percentage increases of the load are as follows: 19% for $\rho = 10$, 24% for $\rho = 20$, and 32% for $\rho = 60$. These are significant numbers.

Stability of Fractal Cracks

In this section, attention will be focused on the cusp region of the cohesive crack. Following Khezrzadeh et al. (2011), the crack opening displacements at the center of the crack and at the crack tip will be redefined to accommodate the fractal geometry. First let us define four auxiliary functions:

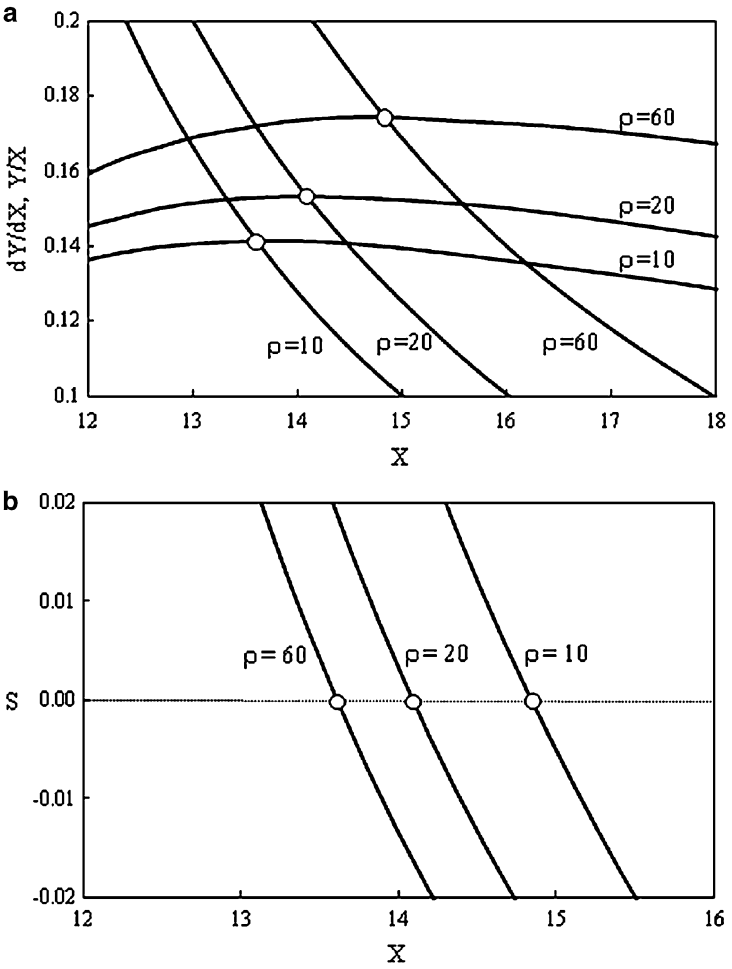

Fig. 10 (**a**) Curves representing the rates of the energy demand (nearly *straight lines*) and the energy supply intersect each other at the points defining the terminal instability (critical states). (**b**) Stability indices shown as functions of the crack length. Zeros of these functions determine the critical states attained at the end of the stable crack growth. Both (**a**) and (**b**) were obtained for the initial crack of length $X_0 = 10$

$$p(\alpha) = 4\pi^{\left(\frac{1}{2\alpha}-2\right)}\left[\frac{\alpha\Gamma(\alpha)}{\Gamma\left(\frac{1}{2}+\alpha\right)}\right]^{\frac{1}{\alpha}} \tag{35}$$

and

$$\kappa(\alpha) = \frac{1+(\alpha-1)\sin(\pi\alpha)}{2\alpha(1-\alpha)} \tag{36}$$

and

$$N(\alpha, X) = p(\alpha)\left[\frac{2}{\pi}\sqrt{\frac{2R}{a}}\right]^{\frac{1-2\alpha}{\alpha}} \tag{37}$$

$$Y_f = R_f/R_{ini} = \frac{R}{R_{ini}}N(\alpha, X) = p(\alpha)Y\left[\frac{2}{\pi}\sqrt{\frac{2Y}{X}}\right]^{\frac{1-2\alpha}{\alpha}} \tag{38}$$

The subscript "f" designates the entities pertinent to the fractal geometry of the crack. The present considerations will be limited to the $R \ll a$ range, and rough cracks described by the fractality parameters such as fractal dimension D, fractal exponent α, and the roughness measure H will be considered. These roughness parameters are related as defined by Eq. 3.

Since the limitations of the Wnuk–Yavari "embedded crack" representation of a fractal crack need to be accounted for, only the limited range of the fractal exponent will be considered, namely, α will be contained within the interval [0.5, 0.4] and it will not fall below 0.4. When this notation is applied, one can cast the results of Khezrzadeh et al. (2011) in the following form:

$$\begin{aligned} u_f^{\text{tip}} &= \kappa(\alpha)\frac{4\sigma_Y}{\pi E}R = \kappa(\alpha)u_y^{\text{tip}} \\ R_f &= N(\alpha, X)R = 4\pi^{\left(\frac{1}{2\alpha}-2\right)}\left[\frac{\alpha\Gamma(\alpha)}{\Gamma\left(\frac{1}{2}+\alpha\right)}\right]^{\frac{1}{\alpha}}\left[\frac{2}{\pi}\sqrt{\frac{2Y}{X}}\right]^{\frac{1-2\alpha}{\alpha}}R \end{aligned} \tag{39}$$

Upon inspection of the latter expression, it is seen that before the length R_f can be determined (and before the profiles of a fractal crack can be sketched), a prior knowledge of the resistance curve $Y_f(X)$ is necessary. Therefore, one must at first establish the differential equation that defines Y_f as a function of the nondimensional crack length X. Let us return to Eq. 23, which in view of the first expression in Eq. 39 has to be rewritten as follows:

$$\kappa(\alpha)\frac{4\sigma_Y}{\pi E}\left\{R_f(\Delta) + \Delta\frac{dR_f}{da} - R_f(\Delta)\left[\sqrt{1-\frac{\Delta}{R_f(\Delta)}} - \frac{\Delta}{2R_f(\Delta)}\ln\frac{1+\sqrt{1-\frac{\Delta}{R_f(\Delta)}}}{1-\sqrt{1-\frac{\Delta}{R_f(\Delta)}}}\right]\right\} = \widehat{u} \tag{40}$$

This expression reduces to the ordinary differential equation of the kind similar to Eq. 24. When the ductile behavior of the material ($\Delta \ll R$) is considered, Eq. 40 reads

$$\frac{dR_f}{da} = \frac{1}{\kappa(\alpha)}\frac{\pi E}{4\sigma_Y}\left(\frac{\widehat{u}}{\Delta}\right) - \frac{1}{2} - \frac{1}{2}\ln\left(\frac{4(R_{ini}/\Delta)R_f}{R_{ini}}\right)$$
$$\frac{dY_f}{dX} = M_f - \frac{1}{2} - \frac{1}{2}\ln\left(4\rho Y_f\right) \tag{41}$$
$$M_f = \frac{1}{\kappa(\alpha)}\frac{\pi E}{4\sigma_Y}\left(\frac{\widehat{u}}{\Delta}\right) = \frac{M}{\kappa(\alpha)}$$

The second expression in Eq. 37 defines the function R_f – or its nondimensional equivalent Y_f – namely,

$$R_f = N(\alpha, X)R = p(\alpha)\left[\frac{2}{\pi}\sqrt{\frac{2R}{a}}\right]^{\frac{1-2\alpha}{\alpha}} R$$
$$Y_f = N(\alpha, X)Y = p(\alpha)\left[\frac{2}{\pi}\sqrt{\frac{2Y}{X}}\right]^{\frac{1-2\alpha}{\alpha}} Y \tag{42}$$

Substituting this into Eq. 40 yields

$$\frac{d}{dX}\left[p(\alpha)\left[\frac{2}{\pi}\sqrt{\frac{2Y}{X}}\right]^{\frac{1-2\alpha}{\alpha}} Y\right] = M_f - \frac{1}{2} - \frac{1}{2}\ln\left(4\rho p(\alpha)\left[\frac{2}{\pi}\sqrt{\frac{2Y}{X}}\right]^{\frac{1-2\alpha}{\alpha}} Y\right) \tag{43}$$

Carrying out the differentiation in the left-hand side of this equation gives

$$\frac{d}{dX}\left[p(\alpha)\left[\frac{2}{\pi}\sqrt{\frac{2Y}{X}}\right]^{\frac{1-2\alpha}{\alpha}} Y\right] = p(\alpha)\left\{Y\frac{d}{dX}\left[\frac{2}{\pi}\sqrt{\frac{2Y}{X}}\right]^{\frac{1-2\alpha}{\alpha}} + \left[\frac{2}{\pi}\sqrt{\frac{2Y}{X}}\right]^{\frac{1-2\alpha}{\alpha}}\frac{dY}{dX}\right\} \tag{44}$$

When this expression is substituted back into Eq. 43 and after some simple algebraic manipulations (see the Appendix), one obtains the desired governing differential equation

$$\frac{dY}{dX} = \frac{2\alpha\left[M_f - \frac{1}{2} - \frac{1}{2}\ln\left(4\rho p(\alpha)\left[\frac{2}{\pi}\sqrt{\frac{2Y}{X}}\right]^{\frac{1-2\alpha}{\alpha}} Y\right)\right]}{p(\alpha)\left[\frac{2}{\pi}\sqrt{\frac{2Y}{X}}\right]^{\frac{1-2\alpha}{\alpha}}} + (1-2\alpha)\frac{Y}{X} \tag{45}$$

The fractal tearing modulus M_f will be assumed to be somewhat higher (say by 20%) than the minimum value of the modulus, at which the stable growth is still possible. The minimum value of the fractal tearing modulus $M^f_{\min}$ is readily established by setting the rate dY/dX equal zero at the point of fracture onset, $X = X_0$ and $Y = 1$, and then evaluating the corresponding modulus. The result is

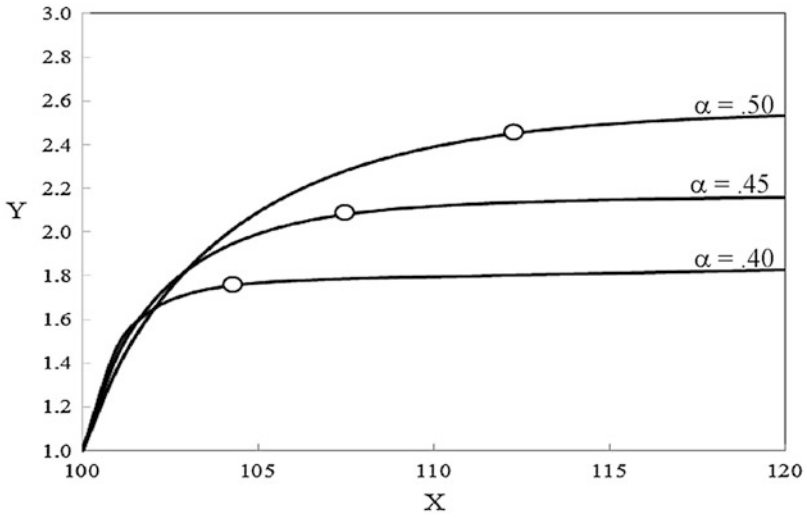

Fig. 11 The resistance curves for stable cracks with the fractal geometry accounted for. The *top curve* corresponds to the case of smooth crack, while the lower curves pertain to the rough cracks with the fractal exponent α designated in the figure. Fractal exponent little circles denote the critical states (Y_c, X_c). Input data $\rho = 10$ and $X_0 = 100$

$$M^f_{\min} = \frac{1}{2} + \frac{1}{2}\ln\left(4\rho N_0(\alpha, X_0)\right) - \frac{1-2\alpha}{2\alpha}\frac{N_0(\alpha, X_0)}{X_0}$$
$$N_0(\alpha, X_0) = p(\alpha)\left[\frac{2}{\pi}\sqrt{\frac{2}{X_0}}\right]^{\frac{1-2\alpha}{\alpha}} \tag{46}$$

With the modulus M_f assumed to be $1.2M^f_{\min}$, solutions of Eq. 45 are generated in form $Y = Y(X, \alpha)$, and they are shown in Fig. 11. Three curves shown were drawn for alphas equal to 0.5 (smooth crack) and 0.45 and 0.40, which correspond to the rough cracks of increasing degree of surface roughness. Inspection of Fig. 11 leads to a conclusion that an increased roughness of the crack surface reduces the apparent material fracture toughness attained during the subcritical crack growth. Little circles on the Y-curves in Fig. 11 show the terminal instability points. The location of these points was evaluated by seeking maxima on the Q-curves shown in Fig. 12 or evaluating zeros in the graph representing the stability index Eq. 32 – this has been demonstrated in Fig. 13b. Figure 13a also shows an alternative way of determining the terminal instability points by comparing the rate of energy demand with the rate of energy supplied to the system.

Once the function $Y(X, \alpha)$ has been determined from Eq. 45, one can proceed to evaluate the profiles of the fractal crack within the pre-fracture zone. The equations used for these evaluations read.

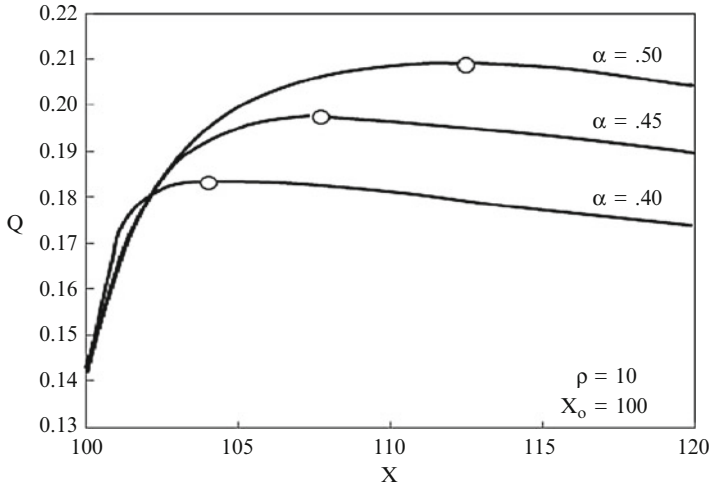

Fig. 12 Loading parameter Q plotted for the rough cracks (two *lower curves*) and for a smooth crack (*top curve*) as a function of the current crack length. It is noted that an increasing roughness of the crack surface reduces the effects of stable crack extension

$$
\begin{aligned}
v_f^{\text{cusp}} &= \frac{4\sigma_Y R}{\pi E} N_\kappa(\alpha) \left\{ \sqrt{1-\frac{\lambda}{N}} - \frac{\lambda}{2N} \ln \left[\frac{1+\sqrt{1-\frac{\lambda}{N}}}{1-\sqrt{1-\frac{\lambda}{N}}} \right] \right\} \\
N &= N(\alpha, X) = \left[\frac{\alpha \Gamma(\alpha)}{\Gamma\left(\frac{1}{2}+\alpha\right)} \right]^{\frac{1}{\alpha}} \left[\frac{2}{\pi} \sqrt{\frac{2Y}{X}} \right]^{\frac{1-2\alpha}{\alpha}} \\
v_f^{\text{tip}} &= \frac{4\sigma_Y R}{\pi E} N(\alpha, X) \kappa(\alpha)
\end{aligned}
\tag{47}
$$

Figure 14 shows the profiles of the cusp Eq. 47 normalized by the tip displacement v_f^{tip}. It is now seen that for the enhanced roughness of crack surfaces (diminishing fractal exponent α), the pre-fracture zones diminish and the entire pre-fracture zones shrink. This phenomenon reflects on the earlier attainment of the critical state at the end of stable crack growth phase. To document this fact, all three parameters – apparent fracture toughness Y_c established from the available R-curves, critical nondimensional crack length X_c, and the loading parameter at the terminal instability Q_c – characterizing the critical state (terminal instability) have been grouped in sets (Y_c, X_c, Q_c) and collected in Table 1. The numbers shown in Table 1 were obtained for different initial inputs of the pertinent parameters characterizing a cracked body such as material ductility index ρ, the initial crack length X_0, and the fractal exponent α.

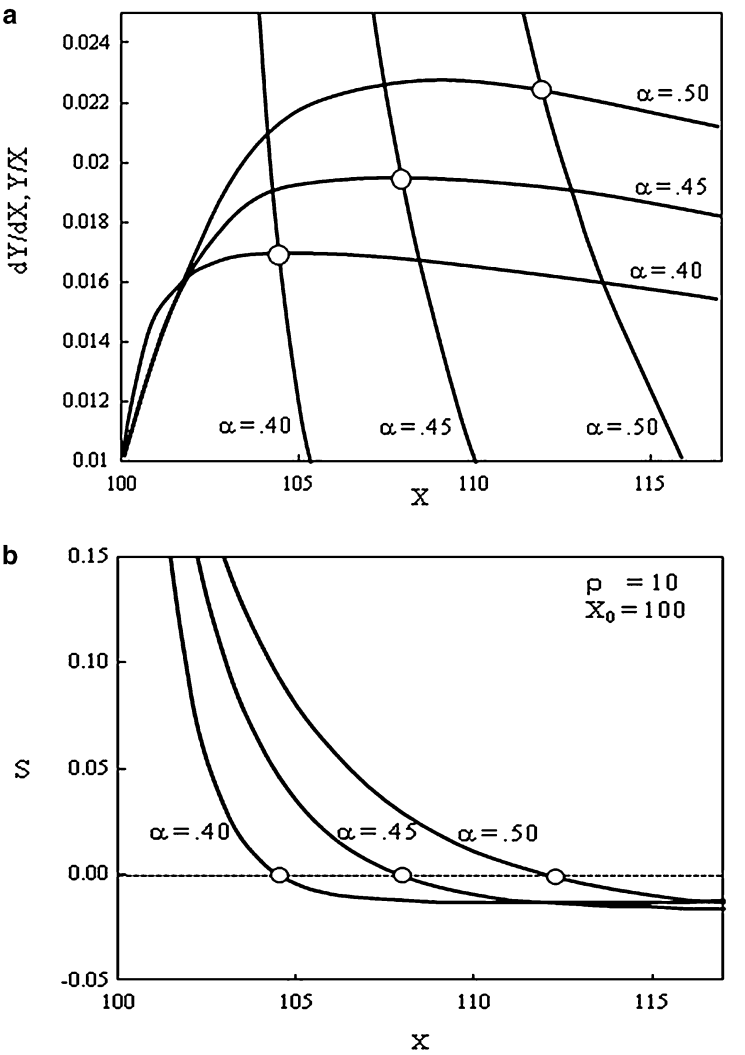

Fig. 13 (**a**) Rates of energy demand (dY/dX) and energy supply (Y/X) for rough cracks, $\alpha = 0.45$ and $\alpha = 0.40$. The curve drawn for $\alpha = 0.5$ corresponds to a smooth crack. Initial crack length is set as $X_0 = 100$, and the material ductility index is $\rho = 10$. (**b**) Stability index S sketched for the same input data as in (**a**). Little *circles* on both graphs indicate the terminal instability points

Conclusions

It has been established that the unstable (catastrophic) fracture propagation in the Griffith sense is almost always preceded by slow stable crack extension that is associated with accumulation and redistribution of strains within the pre-fracture

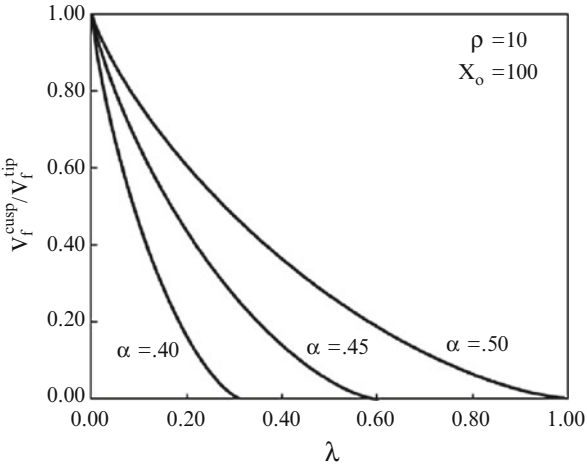

Fig. 14 Profiles of the cusp of the cohesive fractal crack drawn according to Eq. 47. All curves have been normalized by the tip displacement $v_f^{tip} = N(\alpha, X)\kappa(\alpha)(4\sigma_Y/\pi E)$. An increased crack surface roughness (smaller values of the fractal exponent α) causes the cohesive zone to shrink, which is indicative of a more brittle material behavior

zone adjacent to the front of the propagating crack; cf. Panin (1995). Solutions for advancing cracks significantly differ from those for stationary cracks. Exact solutions address only few loading configurations such as anti-plane mode of loading considered by Hult and McClintock (1956), McClintock (1958), and McClintock and Irwin (1965). By analogy with anti-plane case, the crack advance under a tensile loading has been researched by Krafft et al. (1961), who reformulated the problem and restated it in terms of a universal resistance curve. This view is supported by the studies at the microstructural level of ductile fracture occurring in metals and metallic alloys, where it was found that certain mechanisms exist that facilitate slow crack growth by a sequence of debonding of hard inclusions followed by the formation of voids and their growth and coalescence (Rice 1968). It is noteworthy that due to high strain levels and the redistribution associated with crack motion, the deformation theory of plasticity is not sufficient as a mathematical tool. Perhaps the path-dependent relations between stresses and strains, as those described by the incremental theory of plasticity of Prandtl and Reuss, would be more appropriate to construct a theoretical model based on continuum mechanics.

With exception of Prandtl's slip lines field suggested by Rice et al. (1980), no theory has been proposed that would provide exact mathematical treatment of the problem at hand. Therefore, in this research, one has employed an approximation based on the cohesive crack model equipped with the "unit step growth" or "fracture quantum" combined with an "embedded crack" model of Wnuk and Yavari (2003, 2009), which accounts for a non-Euclidean geometry of a crack represented by a certain fractal. The fractal dimension D for such a crack can vary between 1 (straight line) and 2 (a two-dimensional object). It has been shown that the present "structured cohesive crack model" yields the same essential result as that of Rice et al. (1980), namely, the governing equation which defines the universal R-curve. This statement

Table 1 Characteristic parameters of the critical states resulting for various input data (ρ, α, X_0)

ρ	α		$X_0 = 3$	$X_0 = 10$	$X_0 = 20$	$X_0 = 60$	$X_0 = 100$	$X_0 = 200$
2	0.50	**Yc**	***Unstable***	1.462	1.619	1.757	1.791	1.820
		Xc		12.407	24.153	67.358	108.998	211.334
		Qc		0.486	0.366	0.228	0.181	0.131
		ΔQ		8.569	15.785	25.109	28.200	31.228
	0.45	**Yc**		1.410	1.515	1.569	1.570	1.559
		Xc		12.096	23.328	65.092	105.801	206.626
		Qc		0.483	0.360	0.220	0.172	0.123
		ΔQ		7.958	13.972	20.255	21.797	22.851
	0.40	**Yc**		1.348	1.399	1.383	1.360	1.326
		Xc		11.734	22.453	63.090	103.207	203.228
		Qc		0.479	0.353	0.209	0.162	0.114
		ΔQ		7.912	11.637	14.676	14.805	14.223
4	0.50	**Yc**	1.088	1.648	1.835	2.006	2.049	2.085
		Xc	3.249	12.945	24.851	68.420	110.269	212.919
		Qc	0.818	0.505	0.384	0.242	0.193	0.140
		ΔQ	0.205	12.848	21.513	32.616	36.315	39.957
	0.45	**Yc**	1.059	1.580	1.704	1.773	1.775	1.765
		Xc	3.170	12.575	23.911	65.880	106.684	207.629
		Qc	0.817	0.501	0.378	0.232	0.182	0.130
		ΔQ	0.051	12.102	19.401	27.066	29.006	30.401
	0.40	**Yc**	1.037	1.501	1.560	1.545	1.52	1.481
		Xc	3.110	12.143	22.912	63.619	103.754	203.782
		Qc	0.817	0.497	0.369	0.220	0.171	0.121
		ΔQ	0.0	11.184	16.705	20.697	21.034	20.579
8	0.50	**Yc**	1.123	1.854	2.076	2.287	2.342	2.389
		Xc	3.591	13.447	25.530	69.503	111.587	214.590
		Qc	0.828	0.525	0.403	0.257	0.205	0.149
		ΔQ	1.403	17.422	27.531	40.516	44.885	49.218
	0.45	**Yc**	1.197	1.768	1.915	2.002	2.008	1.998
		Xc	3.514	13.020	24.478	66.682	107.597	208.681
		Qc	0.825	0.521	0.396	0.245	0.193	0.138
		ΔQ	1.095	16.517	25.095	34.227	36.607	38.391
	0.40	**Yc**	1.172	1.668	1.739	1.725	1.698	1.655
		Xc	3.454	12.521	23.357	64.153	104.312	204.352
		Qc	0.824	0.516	0.386	0.232	0.180	0.127
		ΔQ	0.903	15.419	22.012	27.020	27.587	27.280
10	0.50	**Yc**	1.278	1.925	2.160	2.386	2.445	2.496
		Xc	3.692	13.604	25.748	69.859	112.023	215.150
		Qc	0.832	0.532	0.410	0.261	0.209	0.152
		ΔQ	1.908	18.946	29.524	43.142	47.741	52.313
	0.45	**Yc**	1.243	1.832	1.988	2.082	2.089	2.080
		Xc	3.615	13.159	24.660	66.946	107.900	209.036
		Qc	0.829	0.528	0.402	0.249	0.197	0.141
		ΔQ	1.549	17.984	26.978	36.606	39.139	41.059

(continued)

Table 1 (continued)

ρ	α		$X_0 = 3$	$X_0 = 10$	$X_0 = 20$	$X_0 = 60$	$X_0 = 100$	$X_0 = 200$
	0.40	**Yc**	1.216	1.725	1.800	1.787	1.760	1.715
		Xc	3.554	12.640	23.499	64.328	104.497	204.542
		Qc	0.827	0.522	0.391	0.236	0.184	0.130
		ΔQ	1.325	16.823	23.766	29.119	29.766	29.513
100	0.50	**Yc**	1.827	2.800	3.218	3.666	3.794	3.908
		Xc	4.590	15.194	28.060	73.871	117.052	221.752
		Qc	0.892	0.607	0.479	0.315	0.255	0.188
		ΔQ	9.929	35.755	51.460	72.553	80.040	87.743
	0.45	**Yc**	1.762	2.620	2.901	3.107	3.135	3.135
		Xc	4.495	14.575	26.610	69.955	111.430	213.241
		Qc	0.886	0.600	0.467	0.298	0.237	0.171
		ΔQ	8.452	34.085	47.671	63.243	67.736	71.487
	0.40	**Yc**	1.708	2.419	2.561	2.575	2.540	2.479
		Xc	4.402	13.852	25.044	66.349	106.665	206.819
		Qc	0.881	0.591	0.452	0.279	0.218	0.155
		ΔQ	7.887	32.162	43.016	52.600	54.326	54.841
200	0.50	**Yc**	2.017	3.122	3.617	4.163	4.324	4.468
		Xc	4.832	15.678	28.796	75.224	118.784	224.082
		Qc	0.914	0.631	0.501	0.333	0.270	0.200
		ΔQ	11.921	41.123	58.501	82.223	90.788	99.705
	0.45	**Yc**	1.940	2.909	3.243	3.500	3.540	3.546
		Xc	4.728	15.010	27.240	70.984	112.665	214.748
		Qc	0.906	0.623	0.488	0.314	0.251	0.182
		ΔQ	10.964	39.204	54.304	72.008	77.253	81.739
	0.40	**Yc**	1.874	2.671	2.843	2.873	2.837	2.770
		Xc	4.623	14.229	25.551	67.051	107.435	207.646
		Qc	0.900	0.613	0.472	0.293	0.230	0.163
		ΔQ	10.274	37.019	42.186	60.329	62.488	63.334

is true for a smooth crack only. For fractal geometry, there have been two papers published that address the slow crack advancement, namely, Khezrzadeh et al. (2011) and Wnuk et al. (2012). When the stability of the fractal cracks is reconsidered in the context of the present model, the pertinent results somewhat diverge from the previous findings. Specifically, the relation between the extent of the slow cracking and the fractal exponent α is opposite to what was suggested earlier.

Perhaps the best way to explain the essential conclusions of this chapter is to take a look at Figs. 15 and 16, and also to examine the summary of the results collected in Table 1. From all the pertinent parameters used in the theoretical considerations, one needs to choose just one: the increase in the nondimensional loading parameter ΔQ due to the slow cracking process that precedes the critical point of terminal instability. This quantity is represented on the vertical axes in Figs. 15 and 16. It is seen

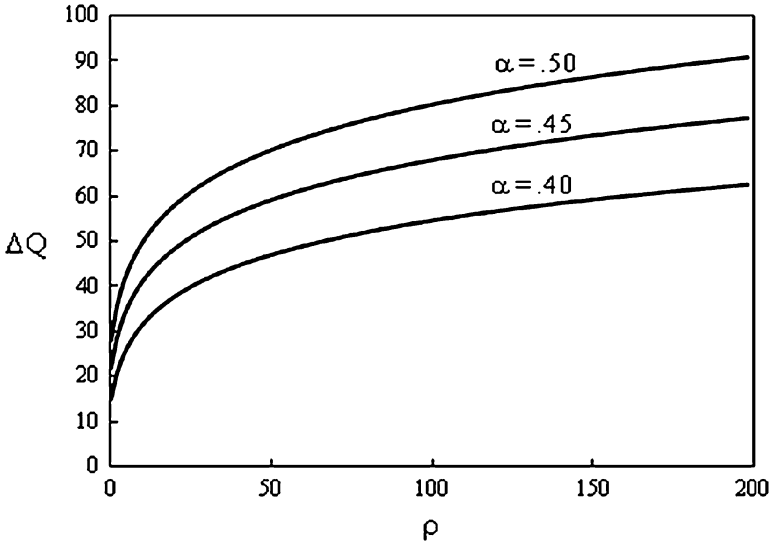

Fig. 15 Enhancement of the load measured at the terminal instability (see Eq. 48) shown as a function of material ductility. Case denoted by $\alpha = 0.5$ corresponds to a smooth crack, while the other curves describe the rough cracks represented by the fractal geometry. The initial crack length for all three curves is $X_0 = 100$

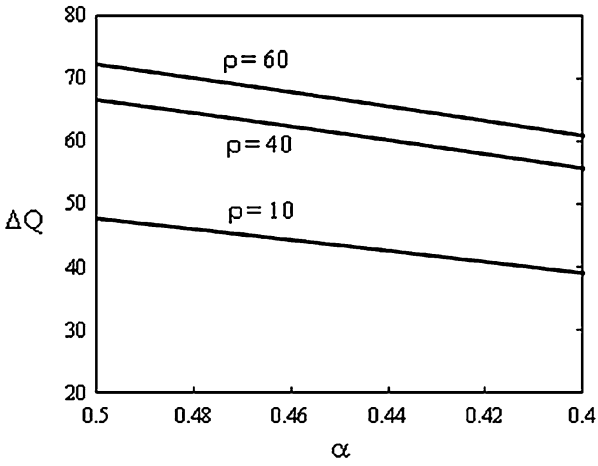

Fig. 16 Load increase attained during the subcritical crack extension at $X_0 = 100$ and various levels of the ductility index shown as a function of the increasing crack surface roughness. It is seen that an increase in roughness causes a reduction of ΔQ

that material ductility (ρ) significantly enhances the slow stable crack growth, leading to an increase in the applied load measured as a difference between the load at the point of catastrophic fracture (Q_c) and the load at the onset of stable crack growth (Q_{ini}):

$$\Delta Q = \frac{Q_c - Q_{ini}}{Q_{ini}}$$
$$Q_{ini} = \sqrt{\frac{2}{X_0}} \tag{48}$$

This observation is entirely in agreement with the previous researches (Khezrzadeh et al. 2011; Wnuk et al. 2012). However, accounting for the fractal geometry leads to an opposite conclusion: higher roughness of crack surface (α less than 0.5) reduces the slow crack growth and results in a decrease of the observed load increase ΔQ; see Fig. 16. In other words, the roughness of the crack surface is conducive to a more brittle material response. Closer examination of the data gathered in Table 1 reveals an interesting phenomenon. It indicates that for a very small crack, $X_0 = 3$, and for low material ductility, $\rho = 2$, the stable growth does not exist at all. It is noted that in this particular case, the initial crack is of the size on the order of magnitude of the characteristic length R_{ini}. For such a small crack, a new effect of "overstressing" comes to light, similar to the phenomenon known in Physics of Fluids as "supercooled" liquid. The effect can be explained as follows: despite the sufficient energy accumulated within the immediate surroundings of the small crack, the crack does not begin to propagate until a certain hypercritical load level is reached. What happens then is a sudden transition from a stationary to a dynamically propagating crack; compare Mott (1948) and Cotterell (1968).

Whether or not the phenomenon of stable crack extension may exist strongly depends on (1) material ductility and (2) tearing modulus of Paris, proportional to the initial slope of the R-curve, and to a much lesser degree on the level of crack surface roughness. If the tearing modulus in the governing Eq. 26 for a smooth crack and Eq. 45 for a rough crack does not meet the condition of being greater than the minimum modulus calculated in sections "Quantization of the Panin Strain and the Criterion for Subcritical Crack Growth" and "Stability of Fractal Cracks," i.e.,

$$\frac{\pi E}{4\sigma_Y}\left(\frac{\widehat{u}}{\Delta}\right) \geq M_{\min} = \frac{1}{2} + \frac{1}{2}\ln(4\rho) \tag{49}$$

for a smooth crack, and

$$\frac{1}{\kappa(\alpha)}\frac{\pi E}{4\sigma_Y}\left(\frac{\widehat{u}}{\Delta}\right) \geq M^f_{\min} = \frac{1}{2} + \frac{1}{2}\ln(4\rho N_0(\alpha, X_0)) - \frac{1-2\alpha}{2\alpha}\frac{N_0(\alpha, X_0)}{X_0}$$
$$N_0(\alpha, X_0) = p(\alpha)\left[\frac{2}{\pi}\sqrt{\frac{2}{X_0}}\right]^{\frac{1-2\alpha}{\alpha}} \tag{50}$$

for a rough crack, the stable crack growth will vanish.

It is seen that while the tearing modulus for a smooth crack in Eq. 49 depends only on the material property such as the ductility index ρ, the tearing modulus for a fractal crack, as given by Eq. 50, depends also on the purely geometrical parameters such as the measure of the crack surface roughness α and the initial crack length X_0. It is

noteworthy that in the case when the conditions stated by the inequalities in Eqs. 49 and 50 are not met, slow stable crack growth does not exist. Indeed, for a certain combination of the input parameters such as the material ductility, initial crack length, and the fractal exponent, it can be shown that the transition period of slow stable crack growth is missing and one returns to the rules valid for ideally brittle fracture. This may be compared with the experimental data of Alves et al. (2010). Further research of this type is needed to fully understand the Physics behind the present model.

For readers interested in a more advanced (or more detailed) studies of the subject of linear and nonlinear fracture mechanics, the following textbooks are recommended:

1. H. Liebowitz (ed.), 1968, "Fracture. An advanced Treatise", editor H. Liebowitz, Vol. 2: Mathematical fundamentals, Academic Press 1968.
2. D. Broek, 1986, "Elementary engineering fracture mechanics", 4th revised edition, Martinus Nijhoff Publishers, Dordrecht 1986.
3. M. F. Kanninen and C. H. Popelar, 1985, "Advanced fracture mechanics", Oxford University Press, New York and Clarendon Press, Oxford, UK.
4. M. P. Wnuk (ed.), 1990, "Nonlinear fracture mechanics", International Centre for Mechanical Sciences, CISM Course No. 314, Udine 1990, Springer Verlag 1990.
5. T. L. Anderson, 1991, "Fracture mechanics. Fundamentals and Applications", CRC Press 1991.
6. C. T. Sun and Z. H. Jin, 2012, "Fracture mechanics", Elsevier 2012.

Appendix A

Let us recall Eq. 43

$$\frac{d}{dX}\left[p(\alpha)\left[\frac{2}{\pi}\sqrt{\frac{2Y}{X}}\right]^{\frac{1-2\alpha}{\alpha}}Y\right]=M_f-\frac{1}{2}-\frac{1}{2}\ln\left(4\rho p(\alpha)\left[\frac{2}{\pi}\sqrt{\frac{2Y}{X}}\right]^{\frac{1-2\alpha}{\alpha}}Y\right) \tag{51}$$

When the product of $\left(\frac{2}{\pi}\right)^{\frac{1-2\alpha}{\alpha}}$ and $p(\alpha)$ is denoted by $f(\alpha)$, then the left-hand side (LHS) of Eq. 51 can be written as $f(\alpha)\frac{d}{dX}\left[\left(\frac{2Y}{X}\right)^{\frac{1-2\alpha}{2\alpha}}Y\right]$. Now one proceeds with the differentiation

$$LHS=f(\alpha)\left[\left(\frac{2Y}{X}\right)^{\frac{1-2\alpha}{2\alpha}}\frac{dY}{dX}+\left(\frac{1}{2\alpha}-1\right)Y\left(\frac{2Y}{X}\right)^{\frac{1}{2\alpha}-2}2\frac{X\frac{dY}{dX}-Y}{X^2}\right] \tag{52}$$

hence

$$LHS=f(\alpha)\left[\left(\frac{2Y}{X}\right)^{\frac{1}{2\alpha}-1}\left(1+\frac{1}{2\alpha}-1\right)\frac{dY}{dX}\right]-f(\alpha)\left(\frac{1}{\alpha}-2\right)\left(\frac{Y}{X}\right)^2\left(\frac{2Y}{X}\right)^{\frac{1}{2\alpha}-2} \tag{53}$$

With G denoting the RHS of Eq. 51, one has

$$f(\alpha)\left(\frac{2Y}{X}\right)^{\frac{1}{2\alpha}-1}\left[\frac{1}{2\alpha}\frac{dY}{dX}\right]-f(\alpha)\left(\frac{1}{\alpha}-2\right)\left(\frac{Y}{X}\right)^{2}\left(\frac{2Y}{X}\right)^{\frac{1}{2\alpha}-2}=G(X,Y,\alpha) \tag{54}$$

This reduces to

$$\frac{dY}{dX}=\frac{2\alpha G}{f(\alpha)\left(\frac{2Y}{X}\right)^{\frac{1}{2\alpha}-1}}+2\alpha\left(\frac{1}{\alpha}-2\right)\left(\frac{Y}{X}\right)^{2}\frac{X}{2Y} \tag{55}$$

With $\left(\frac{2}{\pi}\right)^{\frac{1-2\alpha}{\alpha}}p(\alpha)=f(\alpha)n$, this equation becomes identical with Eq. 45.

Appendix B

Fracture in an ideally brittle solid (and for the fractal exponent $\alpha = ½$) occurs when the ductility index $\rho = R/\Delta \to 1$. It would be worthwhile to prove that in this case the differential equation governing motion of the subcritical crack in Eq. 23 predicts no stable crack growth and that the δCOD criterion reduces then to the classic case of Griffith. In order to prove this point, let us write the governing equation derived from the δCOD criterion, Eq. 23, in this form:

$$\begin{aligned}\frac{dR}{da}&=M-\frac{R}{\Delta}+\frac{R}{\Delta}F(\Delta/R)\\ M&=\frac{\pi E}{4\sigma_Y}\left(\frac{\widehat{u}}{\Delta}\right)\end{aligned} \tag{56}$$

where M is the tearing modulus and the function F is defined as follows:

$$F(\Delta/R)=\sqrt{1-\frac{\Delta}{R}}-\frac{\Delta}{2R}\ln\frac{1+\sqrt{1-\frac{\Delta}{R}}}{1-\sqrt{1-\frac{\Delta}{R}}} \tag{57}$$

For ductile solids, Δ is much smaller than R, and thus $\rho \gg 1$. Under this condition, the function F reduces as follows:

$$F\left(\frac{\Delta}{R}\right)_{\rho\gg1}=1-\frac{\Delta}{2R}+\frac{\Delta}{2R}\ln\left(\frac{\Delta}{4R}\right) \tag{58}$$

This form leads to the differential in Eq. 24 considered in the last section. To obtain the ideally brittle limit, one needs to expand the function F into a power series for ρ approaching one. The results is

$$F\left(\frac{\Delta}{R}\right)_{\rho\to 1} = -\frac{2}{3}\left(1-\frac{\Delta}{R}\right)^{3/2} \tag{59}$$

When this is substituted into Eq. 56, one obtains the differential equation governing an R-curve for quasi-brittle solids, namely,

$$\frac{dR}{da} = M - \frac{R}{\Delta} - \frac{2}{3}\frac{R}{\Delta}\left(1-\frac{\Delta}{R}\right)^{3/2} \tag{60}$$

For the ideally brittle solid, two things happen, first, one has $R = \Delta$ and, second, the slope of the R-curve defined by Eq. 60 equals zero (the R-curve reduces now to a horizontal line drawn at the level $R = R_{ini}$). Therefore, Eq. 60 reduces to

$$\frac{dR}{da} = 0 \quad \text{or,} \quad M = 1 \tag{61}$$

It is also known that for an ideally brittle solid, the size of the Neuber particle Δ can be identified with the length of the cohesive zone

$$\Delta = R = \frac{\pi E}{8\sigma_Y}\text{CTOD} \tag{62}$$

Here symbol CTOD stands for the crack tip opening displacement. The final stretch $\widehat{u}$ is now equal half of the CTOD, namely,

$$\widehat{u} = \frac{1}{2}\text{CTOD} \tag{63}$$

When Eqs. 62 and 63 are substituted into the definition of the tearing modulus shown in Eq. 56, one gets

$$M = \frac{\pi E}{4\sigma_Y}\left(\frac{\widehat{u}}{\Delta}\right) = \frac{\pi E}{4\sigma_Y}\left(\frac{(1/2)\text{CTOD}}{(\pi E/8\sigma_Y)\text{CTOD}}\right) = 1 \tag{64}$$

In this way it is confirmed that the requirement of zero slope of the R-curve in the limiting case of an ideally brittle solid, expressed by Eq. 61, is satisfied when $\widehat{u} \equiv (1/2)\text{CTOD}$ and $\Delta \equiv R$. In other words, the δCOD criterion for the onset of fracture reduces to the CTOD criterion of Wells or – equivalently – to the J-integral criterion of Rice. The latter is in full accord with the Irwin driving force criterion $G = G_c$, and this yields the result identical to the ubiquitous Griffith expression for the critical stress

$$\sigma_G = \sqrt{\frac{2E_\gamma}{\pi a}} = \sqrt{\frac{G_c E}{\pi a}} = \frac{K_c}{\sqrt{\pi a}} \tag{65}$$

Similar conclusion may be obtained directly from the fact that the R-curve is given as a horizontal line (of zero slope) drawn at the level of R_{ini}. Setting the equilibrium length of the cohesive zone R equal to its critical value R_c leads to Eq. 65, as expected. To complete this consideration, one is reminded that the quantities R and K_I are related as follows:

$$R = \frac{\pi}{8}\left(\frac{K_I}{\sigma_Y}\right)^2 = R_c = \frac{\pi}{8}\left(\frac{K_c}{\sigma_Y}\right)^2 \text{ or, } K_I = K_c \text{ or, } \sigma_{\text{crit}} = \sigma_G \tag{66}$$

Therefore, it has been demonstrated that the nonlinear theory described in the preceding sections encompasses the classic theory of fracture, which becomes now a special case of a more general mathematical representation.

References

L.M. Alves, R.V. Da Silva, L.A. Lacerda, Fractal model of the J-R curve and the influence of the rugged crack growth on the stable elastic–plastic fracture mechanics. Eng. Fract. Mech. **77**, 2451–2466 (2010)

T.L. Anderson, *Fracture Mechanics: Fundamentals and Applications*, 2nd edn. (CRC Press, Boca Raton, 2004)

B. Cotterell, Fracture propagation in organics glasses. Int. J. Fract. Mech. **4**(3), 209–217 (1968)

J.A. Hult, F.A. McClintock, *Proceedings of the 9th International Congress of Applied Mechanics*, vol 8 (Brussels, 1956), pp. 51–58

H. Khezrzadeh, M.P. Wnuk, A. Yavari, Influence of material ductility and crack surface roughness on fracture instability. J. Phys. D Appl. Phys. **44**, 395302 (2011) (22 pp)

J.M. Krafft, A.M. Sullivan, R.W. Boyle, Effect of dimensions on fast fracture instability of notched sheets, in *Proceedings of the Crack Propagation Symposium*, (Cranfield College of Aeronautics, Cranfield, 1961)

F.A. McClintock, J. Appl. Mech. **58**, 582 (1958)

F.A. McClintock, Effect of root radius, stress, crack growth, and rate on fracture instability. Proc. R. Soc. Lond. Ser. A **285**, 58–72 (1965)

F.A. McClintock, G.R. Irwin, *Fracture Toughness Testing and Its Applications*, ASTM STP 381 (ASTM, Philadelphia, 1965), pp. 84–113

N.F. Mott, Brittle fracture in mild steel plates, Part II. Engineer **165**, 16–18 (1948)

H. Neuber, *Theory of Notch Stresses* (Springer, Berlin, 1958)

V.V. Novozhilov, On a necessary and sufficient criterion for brittle strength. J. Appl. Mech. USSR **33**, 212–222 (1969)

V.E. Panin, *Physical Mesomechanics and Computer-Aided Design of Materials*, vols. 1 and 2, (in - Russian) (Nauka, Novosibirsk, 1995)

Y. Prawoto, M.N. Tamin, A new direction in computational fracture mechanics in materials science: will the combination of probabilistic and fractal fracture mechanics become mainstream? Comput. Mater. Sci. **69**, 197–203 (2013)

N. Pugno, R.S. Ruoff, Quantized fracture mechanics. Phil. Mag. **84**(27), 2829–2845 (2004)

J.R. Rice, Mathematical analysis in the mechanics of fracture, in *Fracture, An Advanced Treatise*, ed. by H. Liebowitz, vol. 2, (Academic, New York, 1968)

J.R. Rice, W.J. Drugan, T.L. Sham, Elastic–plastic analysis of growing cracks. in *Fracture Mechanics, 12th Conference*, ASTM STP 700 (ASTM, Philadelphia, 1980)

D. Taylor, The theory of critical distances. Eng. Fract. Mech. **75**, 1696–1705 (2008)

D. Taylor, P. Cornetti, N. Pugno, The fracture mechanics of finite crack extension. Eng. Fract. Mech. **72**, 1021–1038 (2005)
M.P. Wnuk, Quasi-static extension of a tensile crack contained in a viscoelastic-plastic solid. J. Appl. Mech. **41**, 234–242 (1974)
M.P. Wnuk, A. Rouzbehani, Instabilities in early stages of ductile fracture. Phys. Mesomech. **8**(5–6), 81–92 (2005)
M.P. Wnuk, A. Rouzbehani, A mesomechanics model of fatigue crack growth for nanoengineering applications. Phys. Mesomech. **11**(5–6), 272–284 (2008)
M.P. Wnuk, A. Yavari, On estimating stress intensity factors and modulus of cohesion for fractal cracks. Eng. Fract. Mech. **70**, 1659–1674 (2003)
M.P. Wnuk, A. Yavari, A discrete cohesive model for fractal cracks. Eng. Fract. Mech. **76**, 545–559 (2009)
M.P. Wnuk, M. Alavi, A. Rouzbehani, Comparison of time dependent fracture in viscoelastic and ductile solids. Phys. Mesomech. **15**(1–2), 13–25 (2012)

Two-Dimensional Discrete Damage Models: Lattice and Rational Models

43

Antonio Rinaldi and Sreten Mastilovic

Contents

Introduction 1216
Lattices with Central Interactions (α-Models) 1217
Triangular Lattice with Central Interactions 1218
Triangular Lattice with First and Second Neighbor Central Interactions 1219
Examples of Applications of α-Model 1220
Rational Models of Brittle Materials 1226
Lattices with Central and Angular Interactions (α–β Models) 1230
Square Lattice with Central and Angular Interactions 1230
Examples of Applications of Lattices with Central and Angular Interactions 1231
Lattices with Beam Interactions 1233
Triangular Bernoulli–Euler Beam Lattice 1233
Triangular Timoshenko Beam Lattice 1235
Computer Implementation Procedure for Beam Lattices 1235
Examples of Applications of Lattices with Beam Interactions 1236
Conclusion 1244
References 1245

Abstract

Many materials exhibit a discontinuous and inhomogeneous nature on various spatial scales that can lead to complex mechanical behaviors difficult to reproduce with continuum-based models. "Among these complex phenomena is damage evolution with nucleation, propagation, interaction, and coalescence of cracks

A. Rinaldi (✉)
Materials Technical Unit, ENEA, C.R. Casaccia, Rome, Italy

Center for Mathematics and Mechanics of Complex System (MEMOCS), University of L'Aquila, L'Aquila, Italy
e-mail: esteban.busso@onera.fr; esteban.busso@ensmp.fr

S. Mastilovic
Faculty of Construction Management, Union–Nikola Tesla University, Belgrade, Serbia
e-mail: smastilovic@fgm.edu.rs

© Springer Nature Switzerland AG 2022

G. Z. Voyiadjis (ed.), *Handbook of Damage Mechanics*,
https://doi.org/10.1007/978-3-030-60242-0_22

that can result in a plethora of macroscale deformation forms." Discontinua-based models are computational methods that represent material as an assemblage of distinct elements interacting with one another. The mesoscale methods of computational mechanics of discontinua presented in this our two essays can be, arguably, divided into three broad and intervening categories: spring network (lattice) models, discrete/distinct-element methods (DEM), and particle models. The distinct-element computational methods such as molecular dynamics and smoothed-particle hydrodynamics are outside the scope of the present overview. The objective of this chapter is to briefly survey the spring network models and their main applications. The discrete-based models have been extensively applied in the last decade to three-dimensional configurations. However, since the scope of this chapter is limited to two-dimensional (2D) models for practical purposes, these important advances are ignored. Likewise, one-dimensional (1D) fiber bundle models are also excluded from this account.

Keywords

Beam element · Timoshenko beam · Triangular lattice · Crack pattern · Timoshenko beam theory

Introduction

During the 1970s, the remarkably rapid growth of computer capabilities and the corresponding advance of numerical algorithms enabled researchers to start developing computational methods that used distinct elements such as molecules, particles, or trusses to model various problems of scientific or engineering interest. Computer simulation modeling is more flexible in application than analytical modeling and has that advantage over experimental modeling of having data accessible at any stage of the "virtual experiment." This flexibility extends to loading configurations and modeling of topological, geometrical, and structural disorder of material texture (Fig. 1). Furthermore, all discrete-element models offer some common advantages in damage analyses when compared with conventional continuum-based counterparts. Damage and its evolution are represented explicitly as broken bonds or disengaged contacts; no empirical relations are needed to define damage or to quantify its effect on material behavior. Microcracks nucleate, propagate, and coalesce into macroscopic fractures without the need for numerical artifices such as re-meshing or grid reformulation. It is unnecessary to develop constitutive laws to represent complex nonlinear behaviors since they emerge naturally through collective behavior of discrete elements governed by simple constitutive rules.

The lattice (spring network) models are the simplest models of discontinua used to simulate complex response features and fracture phenomenology of various classes of materials. As the name suggests, they are comprised of 1D discrete rheological or structural elements given geometrical, structural, and failure properties that enable them to mimic the elastic, inelastic, and failure behavior of certain

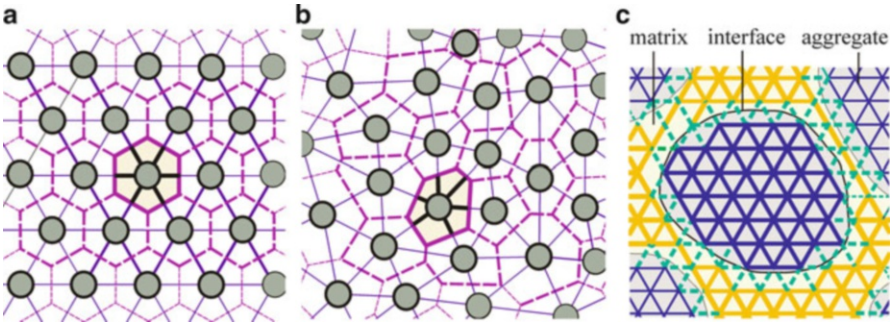

Fig. 1 (**a**) Regular and (**b**) irregular triangular Delaney network dual to the Voronoi (Wigner-Seitz) tessellation of grain boundaries. (**c**) Mesostructure of a three-phase composite projected onto a regular triangular lattice

class of materials. Their comparative advantages are exhibited with most distinction when the material may be naturally represented by a system of discrete elements interacting by way of rheological elements (in its basic form – springs). Hence, it is not unexpected that spatial trusses and frameworks have been the primary material systems thus modeled – in engineering-mechanics applications the idea dates back, at least, to the pioneering work of Hrennikoff (1941). Comprehensive reviews of lattice models in micromechanics are presented by Ostoja-Starzewski (2002, 2007).

Lattices with Central Interactions (α-Models)

In the development of a lattice model, it is necessary to establish relationships between lattice parameters and material properties. Various approaches were proposed in that regard. Cusatis et al. (2003, 2006) used Delaunay triangulation to determine lattice connections and assign their effective cross-sectional areas. Kozicki and Tejchman (2008) derived normal and shear stiffness by using experimental coefficients. However, the prevailing approach, used herein to obtain the lattice parameters, is based on equivalence of strain energies of the unit lattice cell and its continuum counterpart (Ostoja-Starzewski 2002; Wang et al. 2009a). This approach is also presented by Kale and Ostoja-Starzewski in this handbook (▶ Chap. 41, "Lattice and Particle Modeling of Damage Phenomena").

The basic idea is to ensure equivalence of the strain energy stored in a unit cell of the lattice with its associated continuum structure:

$$U_{cell} = U_{continuum}. \tag{1}$$

The energy of spatially linear displacements of the effective continuum system is given by the familiar expression

$$U_{continuum} = \frac{V}{2}\boldsymbol{\varepsilon} : \boldsymbol{C} : \boldsymbol{\varepsilon} = \frac{V}{2} C_{ijkm}\ \varepsilon_{ij}\ \varepsilon_{km}. \tag{2}$$

In order to obtain the strain energy stored in the lattice unit cell, it is necessary to take into account its specific periodic particle arrangements and interactions (Ostoja-Starzewski 2002).

Triangular Lattice with Central Interactions

The first lattice to be considered for its simplicity is the α-model comprised of equilateral triangular lattice with central-force interactions among first-neighbor particles. The mesh illustrated in Fig. 2a is based on a spring of length l, equal to the half-length of the equilibrium interparticle distance r_0, which defines the equilibrium lattice spacing. The area of the hexagonal unit cell is $V = 2\sqrt{3}l^2$. Each bond b that belongs to the given unit cell is characterized by a spring constant $\alpha^{(b)}$ and bond unit vectors $\boldsymbol{n}^{(b)}$ along respective directions $\theta^{(b)} = (b-1)\pi/3$.

The elastic strain energy stored in the hexagonal unit cell that consists of six uniformly stretched bonds that transmit only axial forces is

$$U_{cell} = \frac{1}{2}\sum_{b-1}^{6}(\alpha \boldsymbol{u}\cdot\boldsymbol{u})^{(b)} = \frac{l^2}{2}\sum_{b=1}^{6}\alpha^{(b)}n_i^{(b)}n_j^{(b)}n_k^{(b)}n_m^{(b)}\varepsilon_{ij}\varepsilon_{km}. \tag{3}$$

The crucial step in this procedure is making a connection between $\boldsymbol{u}$ and $\boldsymbol{\varepsilon}$, which, in general, depends on the particular geometry of the lattice cell and particular model of interparticular interaction.

By Eq. 1, the stiffness tensor component can be derived as

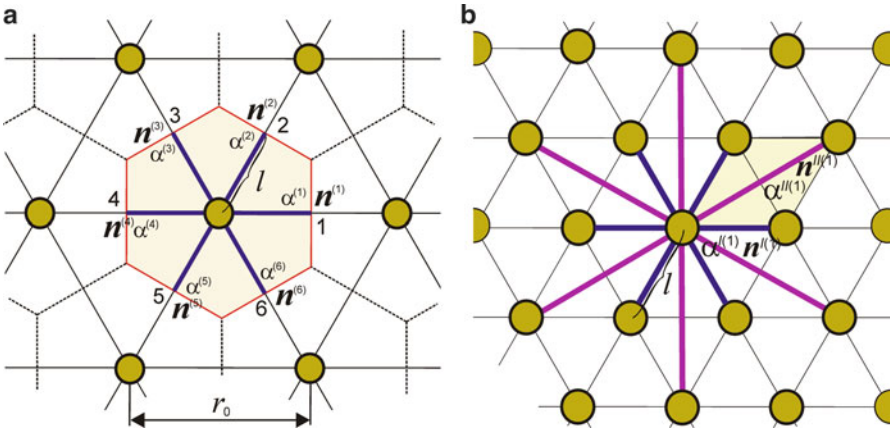

Fig. 2 An ideal triangular lattice with central interactions among (**a**) first and (**b**) first and second neighbors

$$C_{ijkm} = \frac{1}{2\sqrt{3}} \sum_{b=1}^{6} \alpha^{(b)} n_i^{(b)} n_j^{(b)} n_k^{(b)} n_m^{(b)} \tag{4}$$

which in the case of equal spring constants, $\alpha^{(b)} = \alpha$ ($b = 1, \ldots, 6$), results in

$$C_{1111} = C_{2222} = \frac{9}{8\sqrt{3}}\alpha = \frac{E}{1-\upsilon^2}, \quad C_{1122} = C_{2211} = \frac{3}{8\sqrt{3}}\alpha = \frac{E\upsilon}{1-\upsilon^2}, \quad C_{1212} = \frac{3}{8\sqrt{3}}\alpha = \frac{E}{2(1+\upsilon)}. \tag{5}$$

It should be noticed that the condition for material isotropy

$$C_{1212} = (C_{1111} - C_{1122})/2 \tag{6}$$

is satisfied. Since the Poisson's ratio is fixed, the spring constant α defines only the planar modulus of elasticity of the unit cell of this lattice model

$$E = \alpha/\sqrt{3}, \quad \upsilon = C_{1122}/C_{1111} = 1/3. \tag{7}$$

Triangular Lattice with First and Second Neighbor Central Interactions

The previous triangular central-force lattice can be upgraded by superposing an additional central-force structure (Fig. 2b). The original structure (*I*) is now represented by three triangular networks with unit defined as

$$\alpha^{I(b)} = \alpha^I, \quad \theta^{I(b)} = (b-1)\frac{\pi}{3}, \quad \boldsymbol{n}^{I(b)} = \left(cos\,\theta^{I(b)}, sin\,\theta^{I(b)}\right) \quad b = 1,\ 2,\ 3 \tag{8}$$

and the lattice spacing $r_0^I = 2l$. The superposed structure (*II*) is represented by three triangular networks with the following spring constants:

$$\alpha^{II(b)} = \alpha^{II}, \quad \theta^{II(b)} = (2b-1)\frac{\pi}{6}, \quad \boldsymbol{n}^{II(b)} = \left(cos\,\theta^{II(b)}, sin\,\theta^{II(b)}\right) \quad b = 1,\ 2,\ 3 \tag{9}$$

and the lattice spacing $r_0^{II} = 2\sqrt{3}\ l$. In the resulting system, each particle communicates with six first neighbors by means of structure *I* and with six second neighbors by means of structure *II*. The unit cell area is $V = 2\sqrt{3}\ l^2$.

Under the condition of uniform strain, the equivalence of the strain energy stored in the lattice unit cell and the corresponding effective continuum model results in

$$C_{ijkm} = \frac{2}{\sqrt{3}}\alpha^{I} \sum_{b=1}^{3} n_i^{I(b)} n_j^{I(b)} n_k^{I(b)} n_m^{I(b)} + \frac{6}{\sqrt{3}}\alpha^{II} \sum_{b=1}^{3} n_i^{II(b)} n_j^{II(b)} n_k^{II(b)} n_m^{II(b)}. \quad (10)$$

Thus, the nonzero stiffness components are

$$\begin{aligned} C_{1111} = C_{2222} &= \frac{3}{4\sqrt{3}}\left(3\alpha^{I} + 9\alpha^{II}\right) = \frac{E}{1-\upsilon^2}, \\ C_{1212} &= \frac{3}{4\sqrt{3}}\left(\alpha^{I} + 3\alpha^{II}\right) = \frac{E}{2(1+\upsilon)} \\ C_{1122} = C_{2211} &= \frac{3}{4\sqrt{3}}\left(\alpha^{I} + 3\alpha^{II}\right) = \frac{E\ \upsilon}{1-\upsilon^2}. \end{aligned} \quad (11)$$

The Poisson's ratio is again independent of the spring constant

$$E = 2\left(\alpha^{I} + 3\alpha^{II}\right)/\sqrt{3},\ \upsilon = C_{1122}/C_{1111} = 1/3. \quad (12)$$

The expression $(12)_1$ is reduced to $E = 8\alpha/\sqrt{3}$ if $\alpha^{I} = \alpha^{II} = \alpha$.

Examples of Applications of α-Model

Bažant et al. (1990) employed a random α-model for brittle heterogeneous materials with the aim to study the effects of specimen size on the maximum load, the post-peak softening behavior, and the progressive damage spread of the microcracking zone. The model, accounting for particle interactions and random geometry, may be classified as a particle model, but since the shear and bending interaction among particles in contact are neglected, it represents an illustrative example of an application of random lattice with central interactions. This model was very influential for further developments of DEM techniques for this class of materials. A more refined model of Zubelewicz and Bažant (1987) accounted for shear interactions as well.

The model was based on the central interaction of elastic circular particles (aggregates) embedded randomly in a softer matrix (cement paste). The matrix was initially elastic with modulus of elasticity E_m, while the modulus of elasticity of the aggregates was designated by E_a. The particles (denoted as i and j) interacted by means of a truss connecting particle centers whose stiffness, $S = \left(S_i^{-1} + S_m^{-1} + S_j^{-1}\right)^{-1}$, was defined by the serial connection of the three truss segments (Fig. 3a). The individual segment stiffness was determined by the standard truss theory (e.g., $S_m = E_m A_m/L_m$) taking into account the empirically modifies truss segment lengths corresponding to aggregate particles in contacts. The middle truss segment (mimicking cement paste), L_m, represented the contact region of the matrix and was assumed to exhibit softening behavior depicted by the triangular constitutive law (Fig. 3b). This softening behavior

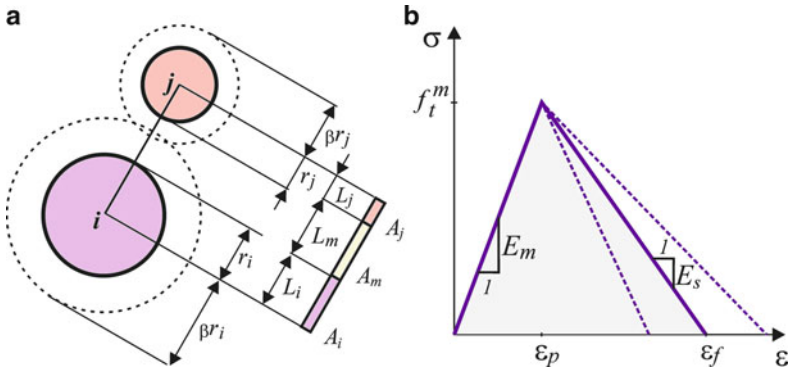

Fig. 3 The α-model of Bažant et al. (1990): (**a**) Particles and truss parameters and (**b**) constitutive law for the binding matrix

$$E_s = -\frac{f_t^m}{\varepsilon_f - \varepsilon_p}, \quad \varepsilon_f = \frac{2\ G_f^m}{L_m\ f_t^m} \tag{13}$$

was determined based on the fracture energy of the interparticle layer, G_f^m, which was assumed to be an intrinsic material property. The geometrical lattice disorder (random L_m) necessitated corresponding changes of the softening modulus E_s in order to preserve the fracture energy.

The simulation results of this model revealed pronounced size effect on the failure load, which is a salient consequence of heterogeneity that has both fracture mechanics and probabilistic aspects. The load–displacement curves, representing the response of unnotched samples under uniaxial tension, revealed that the softening was captured realistically since the slope got steeper with the sample size increase. In addition to pronounced size effect, the simulation results exhibited substantial data scatter as well. The revealed size effect on the maximum normal stress (nominal strength) was in contrast to predictions of local continuum models. The corresponding simulation data were fitted with the sample diameter, d, in accordance with size effect law proposed by Bažant, $\sigma_N \propto d^{-1/2}$. The same effect was observed for notched specimen as well. It was also demonstrated that the size effect observed in simulations is intermediate between the strength criterion and the linear elastic fracture mechanics. In agreement with laboratory tests, the results of uniaxial tension simulations revealed development of asymmetric response in the softening region. The spread of cracking and its localization observed experimentally in quasibrittle materials was captured reasonably well.

The extension of this simulation technique was used by Jirásek and Bažant (1995) to determine relationship between the macroscopic failure properties (the fracture energy and the size of the effective process zone) and the statistics of microscopic properties (such as microstrength, microductility, and average interparticle distance of particle links). These simulation results revealed that realistic modeling,

especially under far-field compression loading conditions, required the lattice elements to be capable of not only central interactions but also shear (angular) interactions.

Vogel et al. (2005) utilized a topologically and geometrically ordered lattice with the interparticle interactions based on Hookean springs with randomly sampled finite tensile strength. Thus, each node of triangular lattice was connected to all six first neighbors (the coordination number $z = 6$), each link had an equal equilibrium length and spring constant, while the microstrength was defined by random sampling of the link rupture strains from a normal distribution. The model aimed to capture the underlying physical processes involved in the clay soil crack formation in the course of desiccation. The corresponding load was due to slow contraction of the sample as a result of water evaporation.

The shrinkage of a pseudo 2D clay surface due to desiccation was simulated by successive reduction of the natural spring length that caused contracting forces and increase of total energy in the lattice. As soon as the strain between two consecutive nodes reached the critical value, the spring ruptured and the corresponding released strain energy had to be redistributed among the adjacent links in the system transition toward the new equilibrium state. The change in nodal position depended on the total force exerted on the node but the node moved only if the nodal force exceeded a static adhesion limit. Heterogeneity was introduced into the system through the random sampling of the spring rupture strain from a Gaussian probability distribution $N(\overline{\varepsilon}_{cr}, \sigma^2)$. Thus, the model parameters were the mean critical strain $\overline{\varepsilon}_{cr}$, its variance σ^2, and the friction μ.

An additional parameter results from iterative relaxation of the lattice, which was the maximum number of iterations, n_{it}, performed after each spring rupture. Depending on the n_{it}, the lattice might not be relaxed completely prior to the breakage of the next spring. Thus, the relaxation parameter was more than just an arbitrarily selected simulation parameter since it may be related to the speed of desiccation. Vogel et al. (2005) claimed that n_{it} might be interpreted as a dimensionless quantity relating the characteristic times of external forcing, t_{ext}, to the characteristic times of the internal dynamics t_{int} by $n_{it} = t_{ext}/t_{int}$.

The presented triangular α-model reproduced prominent features of the nonlinear dynamics of the desiccated clay crack network development observable in nature such as characteristic aggregate shapes and angles of bifurcations (Fig. 4). The authors quantitatively verified that the model reproduced both the characteristic features of natural crack patterns and the characteristic pattern evolution dynamics. The model parameters could be related to physical properties of the material and to the boundary conditions during shrinkage by desiccation and crack formation.

Topin et al. (2007) used discretization based on a sub-particle triangular α-model to analyze strength and damage behavior of cemented granular materials as a function of the matrix volume fraction (structural parameter) and the particle–matrix adhesion (material parameter). The objective was to elucidate roles of those parameters for breaking characteristics (stiffness, tensile strength), damage growth (stiffness degradation, particle fracture), and stress transmission (statistical distributions, phase stresses).

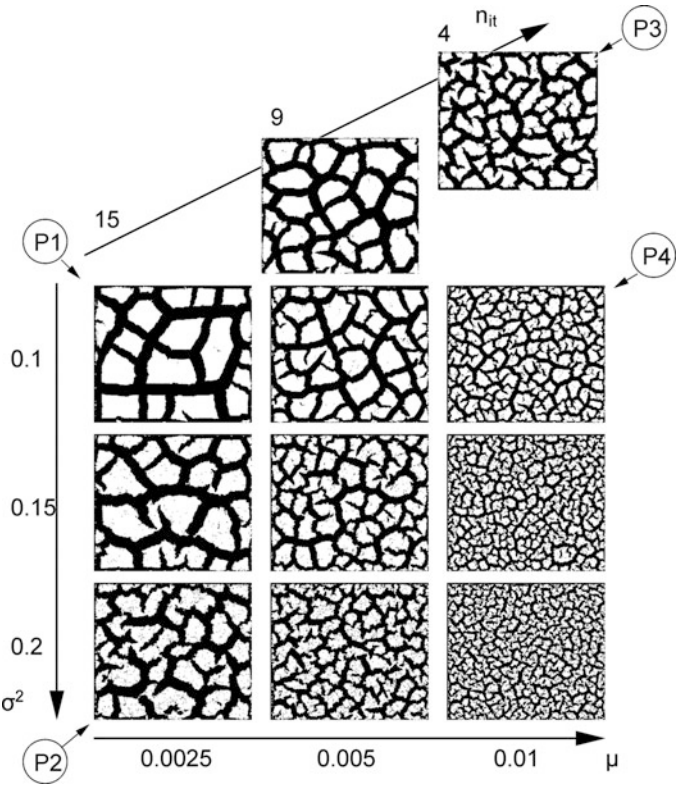

Fig. 4 Damage patterns obtained for various critical microstrain data dispersions (σ^2), nodal frictions (μ), and relaxation intensities (n_{it}). (Reprinted from Vogel et al. 2005 with permission from Elsevier)

This α-model consisted of linear elastic–brittle springs defined by a spring constant and a rupture-force threshold. The high connectivity of the lattice nodes ensured global resistance in shear and distortion since the springs transmitted only normal forces. There were five distinct link types representing three bulk phases (granule, matrix, and void) and two interface phases (granule–granule and granule–matrix). The lattice with free lateral boundaries was loaded alternatively in uniaxial tension and compression by displacement application on the upper sample edge.

The stress–strain curves revealed the expected asymmetry between tension and compression, related to existence of preexisting "fabrication" damage (reflected by non-cohesive interparticle contacts – bare contacts). The post-peak behavior was characterized by nonlinear propagation of the main crack and the progressive reduction of the effective stiffness due to the damage accumulation in the heterogeneous material. Maps of vertical stress fields in tension and compression were used to study the effect of jamming of the particles that resulted in stress concentration along particle chains (jammed backbone). Influence of the volume fraction of

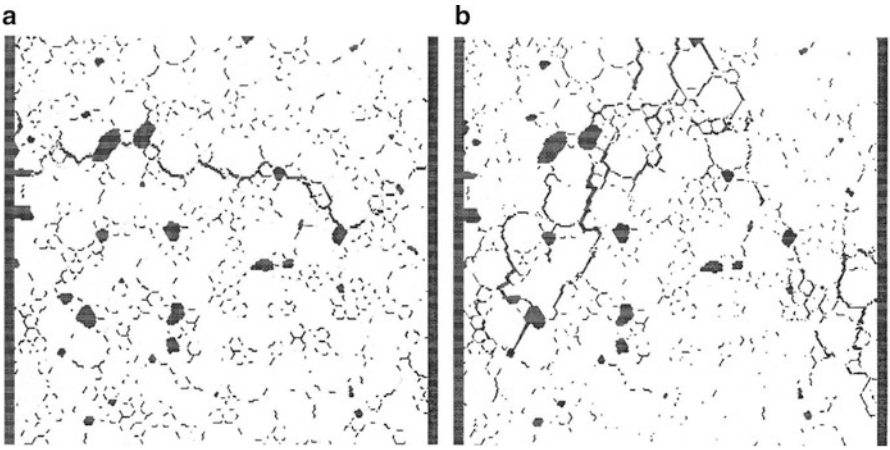

Fig. 5 Damage pattern: (**a**) tension and (**b**) compression (Topin et al. 2007)

binding matrix on the effective stiffness in tension and compression was discussed and the model results were compared with the Mori–Tanaka theoretical predictions for the effective stiffness of three-phase composite. It was shown that effective stiffness in tension increases linearly with the matrix volume fraction due to the space-filling role and disappearance of bare contacts (voids). The surface and bulk effects of binding matrix (reflecting the reduction of bare contacts and porosity, respectively) were discussed.

The crack patterns in tension and compression (Fig. 5) in the neighborhood of the homogeneous–heterogeneous damage phase transition revealed diffuse and localized cracking occurring mostly in pre-peak and post-peak regimes, respectively. Since the particle–matrix interfacial strength was inferior in comparison with the individual particle and matrix strengths, the cracking almost traced particle contours. The evolution of the main crack was abrupt in tension and practically perpendicular to the applied load direction; in compression the main cracking paths were inclined and thicker and involve secondary crack branches. It can be observed in Fig. 5 that the lattice geometry controlled crack propagation and the damage maps reflected the regular structure of the underlying lattice. The damage evolution was accompanied by stiffness degradation that could be observed in stress–strain curves.

The abrupt effective stiffness degradation in tension was vividly contrasted to the more progressive nature of damage evolution in compression, which reflected distinction in the nature of damage accumulation and cracking patterns. The authors found that the matrix volume fraction and the particle–matrix adherence played nearly the same role in the tensile strength of cemented granular materials. On the other hand, the two parameters controlled differently the damage characteristics as reflected by the fraction of broken bonds in the particle phase just after the sample failure (Fig. 6).

The authors observed that a bilinear boundary limited the parametric space in which particle damage occurred. Thus, for that range of parametric values, the cracks

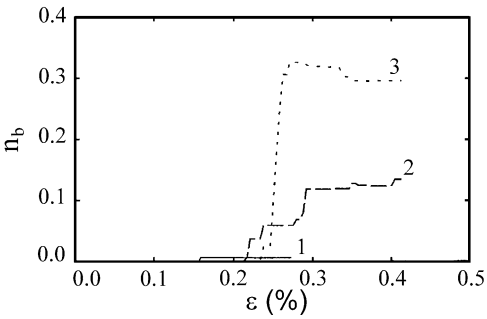

Fig. 6 Evolution of the fraction of broken bonds in the particle phase for (*1*) $\sigma^{pm}/\sigma^{[p]} = 0.6$ and $\rho^m = 0.08$; (*2*) $\sigma^{pm}/\sigma^{[p]} = 1$and $\rho^m = 0.08$; and (*3*) $\sigma^{pm}/\sigma^{[p]} = 1$ and $\rho^m = 0.18$ (Topin et al. 2007)

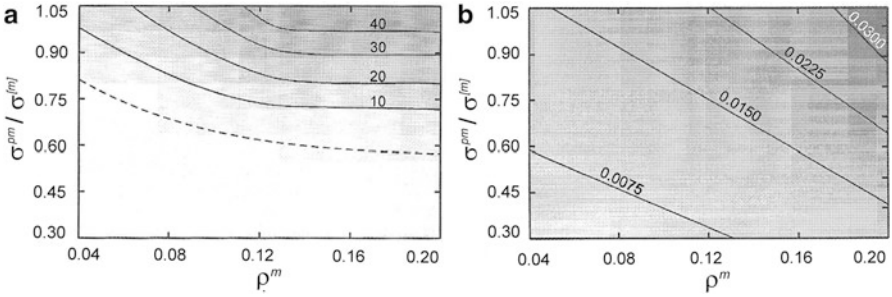

Fig. 7 Parametric maps of: (**a**) tensile strength and (**b**) fraction of broken particle bonds at macrofailure in the particle–matrix adherence versus the matrix volume fraction space (Topin et al. 2007)

propagated either in matrix or along interface. According to Fig. 7b, the particle damage was more sensitive to interphase strength than to the matrix volume fraction. It was also noted that that the matrix volume fraction $\rho_m = 0.12$, representing the limit of influence on n_b, reflected the percolation threshold of the binding matrix, with particles covered entirely except at the bare contacts. Finally, the authors suggested that the particle damage limit was controlled by a single parameter: the relative toughness of the particle–matrix interface.

Hou (2007) improved the triangular spring network with central interactions and hexagonal unit cell by introducing large-strain elasticity into the modeling framework. The large-strain α-model was used to simulate several representative problems of large-strain elasticity: a square planar sample under uniform uniaxial tension, a wedge loaded in tension by a force, and a planar sample with a preexisting crack under mode I loading. The comparison between analytical and lattice simulation results revealed an exceptional agreement and also demonstrated that the large-strain lattice model can capture large deformation singularity rather well.

Assumed failure criterion was used to describe the fracture process of large-strain elasticity and large-strain composite. As the lattice deformation increased, the individual bond extensions increased as well until rupture criterion was met in

one or a few springs, which was/were then removed from the network. The spring rupture criterion could be defined in many ways, e.g., in terms of the critical values

$$f_b = f_{cr}, \quad \varepsilon_b = \varepsilon_{cr}, \quad E_b = E_{cr} \tag{14}$$

of spring: force, extension, and strain energy, respectively. The author opted for the link strength criterion $(14)_1$. This process progressed until the lattice loosed completely the load carrying capability (cracked percolation). Two edge-crack mode I loading configurations were simulated until global large-strain failure.

Rational Models of Brittle Materials

Rational models of damage that connect microstructural material properties to overall macroscale properties by means of "exact" constitutive models (as closed-form solutions, where possible) are very desirable for scientific and technological purposes, albeit usually available only for 1D mechanical systems such as fiber bundle models (e.g., Rinaldi 2011a; Phoenix and Beyerlein 2000). Lattices provide a powerful option to address rational approaches to damage in real materials with heterogeneous microstructures, which represent an inherently more complex and higher-dimensional problem. One such 2D α-model lattice is discussed next in some details (after Rinaldi and Lai (2007) and Rinaldi (2009)).

Let us consider the perfect central-force triangular lattice (Fig. 2a) with links of equal stiffness k and length ℓ_o. To introduce some mechanical disorder, suppose further that each b-th link breaks irreversibly at a tensile critical strain $\varepsilon^{*(b)} = \boldsymbol{u}^{(b)}/\ell_o$ (Eq. $14)_2$. For the results reported herein, simulation parameters were $k = 100$, $\ell_o = 1$, and $\varepsilon^{*(b)}$ randomly sampled from a uniform distribution in the interval $[0, 10^{-2}]$.

On the macroscale, the stress–strain response of this quasibrittle system under tensile loading (or equivalently uniaxial compression) is expressed after L. Kachanov's relation in scalar form as

$$\overline{\sigma} = \overline{K}_0\left[1 - \overline{D}(\overline{\varepsilon}_{MAX})\right]\overline{\varepsilon} \tag{15}$$

which accounts for the (permanent) loss of secant stiffness $\Delta\overline{K}_0 = \overline{K}_0 \cdot \overline{D}$ associated with the cracking process. The parameter $\overline{K}_0$ is the secant stiffness in the pristine state and the damage process is measured by the scalar macroscopic damage parameter $\overline{D}$ ranging from 0 (pristine state) to 1 (failure). Assuming no damage healing, $\overline{D}$ is a nondecreasing function of applied strain and, thus, depends on the maximum tensile strain $\overline{\varepsilon}_{MAX}(t)$ reached at time t, such that

$$\overline{\varepsilon}_{MAX}(t) = \max\{\overline{\varepsilon}(t_0), \quad \forall t_0 \le t\} \quad \text{and} \quad \overline{D} = \int_0^{\overline{\varepsilon}_{MAX}} d\overline{D}(\overline{\varepsilon}). \tag{16}$$

Correspondingly, the strain energy computed from the "top" is

$$U(\overline{\varepsilon}) = \frac{1}{2}\overline{\sigma}\ \overline{\varepsilon} = \frac{1}{2}\overline{K}_0\left[1 - \overline{D}(\overline{\varepsilon}_{MAX})\right]\overline{\varepsilon}^2. \tag{17}$$

To solve this problem for a given loading history, $\overline{D}$ must be computed and linked to the microcracking process in the microstructure. From the knowledge of microstructure and full field microstrains, the strain energy of the lattice can in fact be recomputed from the "bottom" by summing all unbroken links over all unit cells as

$$U(\overline{\varepsilon}) = \sum^{Cells}\left(\frac{1}{2}\sum_{b}^{N_b}(k\,\boldsymbol{u}\cdot\boldsymbol{u})^{(b)}\right). \tag{18}$$

Brittle damage evolves from two types of dissipative events, either an individual rupture or an avalanche, i.e., a cascade of distinct individual ruptures initiated at a random value $\overline{\varepsilon}$ (Rinaldi and Lai 2007). When one spring is suppressed, it entirely releases its stored energy ΔU_1

$$\Delta U_1 = \frac{1}{2}k(\varepsilon^*)^2 \tag{19}$$

and causes a macroscale loss of strain energy

$$\boldsymbol{\Delta}U(\overline{\varepsilon}) = \frac{1}{2}\overline{K}_0\boldsymbol{\Delta}\overline{D}(\overline{\varepsilon})\overline{\varepsilon}^2 = \frac{1}{2}\boldsymbol{\Delta}\overline{K}(\overline{\varepsilon})\overline{\varepsilon}^2 \tag{20}$$

that is equal or greater than ΔU_1 and reflects cooperative phenomena, snapback instability (for an avalanche), and load redistribution within the lattice. Such an effect can be conveyed by a "redistribution parameter"

$$\eta_p = \frac{\boldsymbol{\Delta}U - \boldsymbol{\Delta}U_1}{\boldsymbol{\Delta}U_1} \tag{21}$$

which is always $\eta_p > -1$ and is null only when there is no redistribution effect (as in many 1D models). Then $\overline{D}(\overline{\varepsilon})$ is obtained from Eqs. 16, 17, 18, 19, and 20 by summing normalized stiffness decrements $\Delta\overline{K}_p$ from each microcrack

$$\overline{D}(\overline{\varepsilon}) = \frac{\sum_{p=1}^{n(\overline{\varepsilon})}\Delta\overline{K}_p}{\overline{K}_0} = \frac{k}{\overline{K}_0}\left(\frac{\ell_0}{L}\right)^2\sum_{p=1}^{n(\overline{\varepsilon})}(1+\eta_p)\left(\frac{\varepsilon_p^*}{\overline{\varepsilon}^*}\right)^2. \tag{22}$$

This *stochastic* model requires the three random input parameters $\left\{\varepsilon_p^*, \eta_p, n_p\right\}$ – three distinct sources of variability:

- $\varepsilon_p^*(\overline{\varepsilon})$, the critical strain of the spring failing at $\overline{\varepsilon}$, linking the macroscale kinematics to the microscale kinematics and depending on the chosen sampling distribution

- $\eta_p(\overline{\varepsilon})$, the redistribution parameter related to the local load redistribution capability of the microstructure and to snapback effects (for an avalanche)
- $n_p(\overline{\varepsilon})$, the number of broken links

This rational model renders an "exact" estimate of the lattice response to a uniaxial loading but requires $\left\{\varepsilon_p^*, \eta_p, n_p\right\}$ to be known.

If the springs are partitioned by orientation $\theta = \{0, 60^\circ, -60^\circ\}$, damage can be conveniently broken down in a "spectral form"

$$\overline{D}(\overline{\varepsilon}) = \overline{D}_1(\overline{\varepsilon}) + \overline{D}_2(\overline{\varepsilon}) + \overline{D}_3(\overline{\varepsilon}) = \frac{k}{\overline{K}_0}\left(\frac{\ell_0}{L}\right)^2 \sum_{j=1}^{3}\sum_{p=1}^{nj(\overline{\varepsilon})}(1+\eta_p)\left(\frac{\varepsilon_p^*}{\overline{\varepsilon}^*}\right)^2. \tag{23}$$

For validation sake, Fig. 8 displays input and output data, i.e., $\{\varepsilon_p^* \eta_p n_p\}$ and $\left\{\overline{\sigma}, \overline{D}\right\}$ respectively, from the simulation of a random lattice under tensile test, making self-evident the random nature of input data in Eq. 23. The data markers $\{*, \mathrm{O}, \nabla\}$ for $\theta = \{0, 60^\circ, -60^\circ\}$ highlight differences in damage process between different orientations.

The output data plotted aside on the right-hand side display the stress response estimated from Eq. 15 marked by "*", which overlaps the actual stress–strain curve from simulation (solid bold line) such that the two data series are indeed indistinguishable (i.e., zero error as expected in a rational theory). The "staircase" damage function $\overline{D}(\overline{\varepsilon})$ (solid bold line) with components $\overline{D}_i(\overline{\varepsilon})$ from solid line with markers is also shown.

This example clarifies that $\overline{D}(\overline{\varepsilon})$ (the measure of the *global effect of microcracks*) and $n(\overline{\varepsilon})$ (the *number of microcracks*) are related in an intricate manner in the lattice and most real materials, such that their increments are linked as

$$\mathbf{\Delta}\overline{D}_p(\overline{\varepsilon}) = w_p(\overline{\varepsilon})\mathbf{\Delta}n(\overline{\varepsilon}) \quad (\text{read } \mathbf{\Delta}n = 1) \tag{24}$$

by means of a stochastic weight function

$$w_p(\overline{\varepsilon}) = c(1+\eta_p)\left(\frac{\varepsilon_p^*}{\overline{\varepsilon}^*}\right)^2, \quad c = k/\overline{K}_0(\ell_0/L)^2. \tag{25}$$

When comparing the 2D lattice to the corresponding 1D parallel fiber bundle model, the constitutive model differs only in the definition of $\overline{D}(\overline{\varepsilon})$

$$\overline{D}(\overline{\varepsilon}) = \int_0^{\overline{\varepsilon}} p_f(\overline{\varepsilon})d\overline{\varepsilon} = \frac{n(\overline{\varepsilon})}{N} \tag{26}$$

where $\overline{D} \propto n(\overline{\varepsilon})$ and the weight function $(25)_1$ reduces to a constant $w_p = 1/N$ due to the absence of between-links interaction that allows analytical

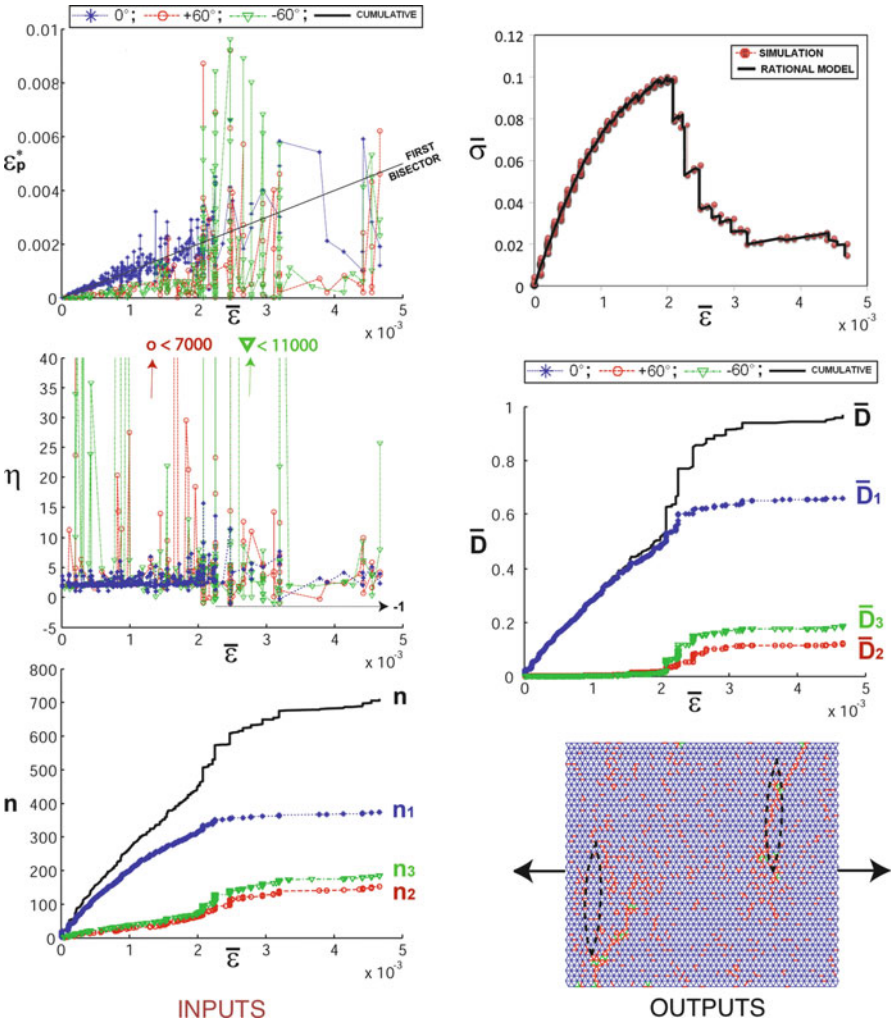

Fig. 8 Input (*left*) and output (*right*) data from a lattice simulation under tension (Rinaldi and Placidi 2013)

computation of $\overline{D}$ from the sole knowledge of the distribution of critical strains $p_f(\varepsilon)$ (Rinaldi 2011a, b).

In the lattice case, the knowledge of its rational damage model (22) is a significant advance as it enables the derivation of several physically based approximate continuum solutions from the analysis of the input random fields. The potential of this bottom-up approach has been discussed in the original papers as well as in subsequent work dedicated to equivalent continuum models, both of first order (Rinaldi 2013) and second order (Misra and Chang 1993; Alibert et al. 2003; Rinaldi and Placidi 2013). Figure 9 displays the first-order continuum model for the case in

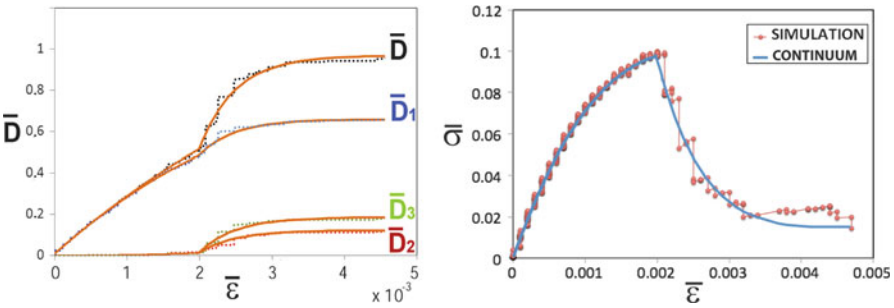

Fig. 9 (*left*) Regression approximation of exact damage components from spectral decomposition in Fig. 8 (*right*). Comparison of resulting equivalent first-order damage model versus simulation data (Rinaldi 2013)

Fig. 8, obtained by estimating the damage parameter with regression functions and deducing the (macro) Helmholtz function matching the microscale physics.

The theory can be generalized from the 2D α-model to real quasibrittle materials as it fully captures the fundamental physics of the damage nucleation and evolution of real systems. Statistical models such as Eq. 22 have the potential for engineering application, for example, in conjunction to acoustic emission tests for health monitoring. A connection with the diverse approaches to deal with size effects (e.g., Rinaldi et al. 2006, 2007) from the next chapter also has to be developed for this purpose.

Lattices with Central and Angular Interactions (*α–β* Models)

The lattice with central and angular interactions is developed by augmenting of the α-model by angular springs acting between contiguous bonds incident into the same particle (Ostoja-Starzewski 2002; Wang et al. 2009a).

Triangular α–β model is discussed in detail by Kale and Ostoja-Starzewski in this handbook.

Square Lattice with Central and Angular Interactions

For the square α–β model, the particle at the center of the square unit cell interacts with four first neighbors and four second (diagonal) neighbors, whose half-length spring constants are α^I and α^{II}, respectively. The volume of square unit cell is $V = 4\,l^2$. The bond angles $\theta^{(b)}$ and corresponding unit vectors $\boldsymbol{n}^{(b)}$ are

$$\begin{aligned}
&\alpha^{I(b)} = \alpha^I,\ \ \theta^{I(b)} = (b-1)\frac{\pi}{2},\ \ \boldsymbol{n}^{I(b)} = \left(cos\,\theta^{I(b)},\ \ sin\,\theta^{I(b)}\right),\ \ b = 1,2,3,4\\
&\alpha^{I(b)} = \alpha^I,\ \ \theta^{II(b)} = (2b-9)\frac{\pi}{4},\ \ \boldsymbol{n}^{II(b)} = \left(cos\,\theta^{II(b)},\ \ sin\,\theta^{II(b)}\right),\ \ b = 5,6,7,8.
\end{aligned} \tag{27}$$

For the sake of simplicity the spring constants of all bonds are, henceforth, assumed to be $\alpha^{I(b)} = \alpha^{I}$, $\alpha^{II(b)} = \alpha^{II}$, and $\beta^{(b)} = \beta$.

After performing the derivation process analogous to the one outlined in section "Triangular Lattice with First and Second Neighbor Central Interactions," the nonzero components of the effective stiffness tensor are obtained as follows:

$$\begin{aligned} C_{1111} = C_{2222} &= \frac{1}{2}\alpha^{I} + \alpha^{II} = \frac{E}{1-\upsilon^2} \\ C_{1122} = C_{2211} = \alpha^{II} &= \frac{E\upsilon}{1-\upsilon^2}, \quad C_{1212} = \alpha^{II} + \frac{\beta}{l^2} = \frac{E}{2(1+\upsilon)}. \end{aligned} \tag{28}$$

Expressions (28) indicate that the angular interactions affect only the shear modulus (C_{1212}). The Poisson's ratio range is, consequently, extended due to the effect of angular springs on the shear modulus. Thus, the spring constants are

$$\alpha^{I} = \frac{2E}{1+\upsilon}, \quad \alpha^{II} = \frac{E\ \upsilon}{1-\upsilon^2}, \quad \beta = \frac{(1-3\upsilon)El^2}{2(1-\upsilon^2)}. \tag{29}$$

By definition, the plane-strain elasticity coefficients are

$$E = \frac{\alpha^{I}}{2}\left(\frac{\alpha^{I} + 4\alpha^{II}}{\alpha^{I} + 2\alpha^{II}}\right), \quad \upsilon = \frac{C_{1122}}{C_{1111}} = \frac{2\alpha^{II}}{\alpha^{I} + 2\alpha^{II}}. \tag{30}$$

Expressions (28) and (29) indicate the complete range of Poisson's ratio $-1 < \upsilon \leq 1/3$ is identical to that obtained for the triangular α–β model. Substitution of Eqs. 29 and 23 into the preceding inequality yields a restricted range of the axial and diagonal α-spring ratios $\alpha^{II}/\alpha^{I} \leq 1/4$, which is an extension of the corresponding requirement physically imposed on the rectangular lattices with central interactions.

Examples of Applications of Lattices with Central and Angular Interactions

Grah et al. (1996) provided an illustrative example of thoughtful application of the triangular lattice with central and angular interactions by simulating brittle intergranular fracture of gallium embrittled sheets of polycrystalline aluminum. The authors both manufactured aluminum sheets and performed quasistatic biaxial tension test in order to have experimental data for lattice model validation. The computation domain was discretized by a geometrically ordered triangular lattice on the sub-grain scale. The axial-spring constants and strengths were assigned depending on their location within the sample, that is, according to the grain that given bonds were associated with in comparison with actual micrographs. The interface bonds (that straddle the boundary of two crystals) have their axial-spring constants assigned in accordance with the serial spring connection rule, weighted by their respective partial lengths

$$\alpha = \left(\frac{l_1}{l\ \alpha_1} + \frac{l_2}{l\ \alpha_2} \right)^{-1}, \qquad l = l_1 + l_2. \tag{31}$$

The strength reduction factor of 0.01 was applied to each interface α-spring to account for the preferential gallium embrittlement along the grain boundaries. Assignment of angular spring constants naturally did not present such complexities.

The rectangular lattices was loaded quasistatically in biaxial tension by applying the controlled displacement $u_i = \overline{\varepsilon}_{ij}\ x_j = \overline{\varepsilon}\delta_{ij}\ x_j$ on each boundary node, defined in terms of macroscopic strain $\overline{\varepsilon}_{ij} = \overline{\varepsilon}\delta_{ij}$ (δ is the Kronecker symbol). Thus, all boundaries experienced only mode I loading prior to sample failure. As the lattice deformation increased, the individual link extensions increased as well until critical link force criterion $(14)_1$ was met in some link, which was then removed from the network. The load increase by $\Delta\overline{\varepsilon}_{ij}$ was conducted first by unloading the entire lattice and then reloading it by $\overline{\varepsilon}_{ij} + \mathbf{\Delta}\overline{\varepsilon}_{ij}$. The process was repeated until the damage percolated the lattice and global failure took place (cracked percolation).

Computer simulations of biaxial loading of 2D sample of a brittle polycrystal with inferior grain boundary strength produced cracking patterns that matched very well to the one obtained from the actual experiments. The departures from the experimental results were discussed in detail.

Tsubota et al. (2006) used computer simulations of discontinua to investigate the red blood cell (RBC) microcirculation in viscous plasma. The triangular spring network with central and angular interactions was used to model deformable RBC membrane. The α–β model (extended subsequently to 3D problems by Tsubota and Wada (2010)) consisted of RBC membrane particles with central and angular interaction representing elastic response of the membrane structure during incompressible viscous flow. The relevant parameter whose effect on the blood flow in microcirculation was investigated was hematocrit (Hct), defined as the volumetric ratio of RBCs to whole blood, which influences greatly the blood rheological characteristics. The Hct effect on blood flow resistance was of obvious interest as well as the mechanical factors, such as the deformation and shape of RBC, and mechanical interaction of RBCs and plasma.

The total elastic strain energy of the RBC membrane was

$$E = E_\alpha + E_\beta = \frac{1}{2}\alpha \sum (\lambda - 1)^2 + \frac{1}{2}\beta \sum \tan^2\left(\frac{\theta - \theta_0}{2} \right) \tag{32}$$

where α and β were the axial and angular spring constants, respectively, $\lambda = l/l_0$ the bond stretch ratio, and θ and θ_0 the current and initial angles between consecutive bonds. Based on the principle of virtual work, the force acting on the RBC membrane particle i was $\boldsymbol{F}_i = -\partial E/\partial \boldsymbol{r}_i$ where $\boldsymbol{r}_i$ designated the particle position vector.

Figure 10a presents the definition of a deformation index, ε, and schematics of time history of its mean value, ε_M, for four different Hct values. The curves show that ε_M monotonically increased until an upper plateau was reached at a Hct-dependent saturation time. The effect of Hct on the average ε_M value over the time interval

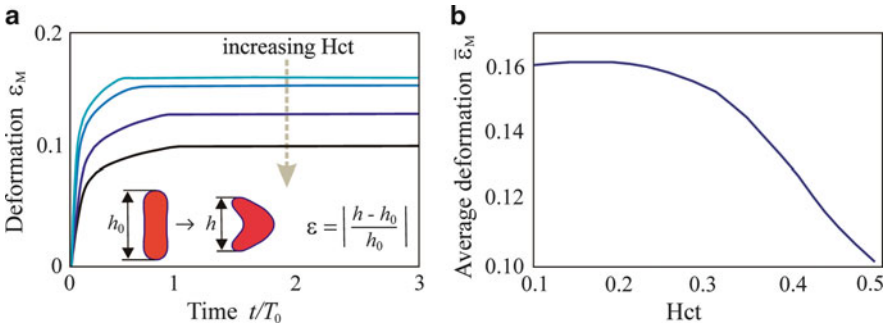

Fig. 10 Schematics of change of (**a**) the deformation index in middle part of flow channel, ε_M, for four Hct values (0.1, 0.3, 0.4, 0.49), and (**b**) the average value of deformation index, $\bar{\varepsilon}_M$, over the time interval $t/T_0 \in [1, 3]$ (i.e., the upper plateau) as function of Hct (Sketched after Tsubota et al. 2006). The characteristic time used for normalization was $T_0 = v_0/L$, where $v_0 = 0.011$ m/s was a constant uniform velocity at the capillary channel inlet, while $L = 90$ μm was the capillary length

$t/T_0 \in [1, 3]$ (illustrated schematically by the upper plateaus in Fig. 10a) is depicted by Fig. 10b. The results obtained by the spring network model agreed very well with in vitro experimental observation. The authors illustrated the time history of RBC membrane shape change as function of Hct.

A similar elastic spring model was applied by Wang et al. (2009b) to investigate the skeletal structure of the RBC membrane and to study the dynamical behaviors of the RBC aggregates in microchannels.

Lattices with Beam Interactions

The beam network model is an upgrade of the spring network α-model obtained by substituting 1D structural elements capable of transferring only axial force with structural elements that can also transfer shear forces and bending moments. The following abbreviated discussion of beam networks is based primarily on papers by Ostoja-Starzewski (2002), Karihaloo et al. (2003), and Liu et al. (2008).

Triangular Bernoulli–Euler Beam Lattice

Bernoulli–Euler beams that transfer normal forces, shear forces, and bending moments are employed conventionally in beam lattice models to simulate the fracture process in concrete (e.g., Schlangen and Garboczi 1997; van Mier 1997; Lilliu and van Mier 2003). The kinematics of a beam network is described by three linear functions defining two displacement components and rotations at the network

nodes. Highlights of the detailed analysis available in Ostoja-Starzewski (2002) are presented herein.

The elementary beam theory implies that the force–displacement and moment–rotation relations for each beam (b) are

$$F^{(b)} = E^{(b)}A^{(b)}\gamma^{(b)}, \quad Q^{(b)} = \frac{12E^{(b)}I^{(b)}}{\left(L^{(b)}\right)^2}\widetilde{\gamma}^{(b)}, \quad M^{(b)} = E^{(b)}I^{(b)}\kappa^{(b)} \tag{33}$$

where the unit cell beams have the same geometrical properties: length $L^{(b)}$ and rectangular cross section $h^{(b)} \times t^{(b)}$, characterized by the area $A^{(b)}$ and the centroidal moment of inertia $I^{(b)}$. The average axial strain, $\gamma^{(b)}$, and the difference between the rotation angle of the beam chord and the rotation of its end node, $\widetilde{\gamma}^{(b)}$, are kinematic parameters defined with respect to the average axial strain in the half-beam in the lattice cell. The difference between the angles of rotation of beam ends, $\kappa^{(b)}$, is defined by its curvature.

This triangular Bernoulli–Euler beam lattice is an isotropic micropolar continuum with strain energy

$$U_{continuum} = \frac{V}{2}\gamma_{ij}C_{ijkl}\ \gamma_{kl} + \frac{V}{2}\kappa_i D_{ij}\kappa_j. \tag{34}$$

The equivalence of the strain energies in Eq. 1 for the triangular beam lattice made of equal beams ($L^{(b)} = L$, $t^{(b)} = t$, $h^{(b)} = h$, $A^{(b)} = A$, $I^{(b)} = I$) leads to

$$\begin{gathered} C_{1111} = C_{2222} = \frac{3}{8}\left(3R + \widetilde{R}\right), \quad C_{1122} = C_{2211} = \frac{3}{8}\left(R - \widetilde{R}\right), \quad C_{1212} = \frac{3}{8}\left(R + 3\widetilde{R}\right), \\ C_{1221} = C_{2112} = \frac{3}{8}\left(R - \widetilde{R}\right), \quad C_{2121} = \frac{3}{8}\left(R + 3\widetilde{R}\right), \quad D_{11} = D_{22} = \frac{3}{8}S \end{gathered} \tag{35}$$

where zero stiffness components are omitted while

$$R = \frac{2E^{(b)}A}{L\sqrt{3}}, \quad \widetilde{R} = \frac{24E^{(b)}I}{L^3\sqrt{3}}, \quad S = \frac{2E^{(b)}I}{L\sqrt{3}}. \tag{36}$$

Consequently, the effective modulus of elasticity and Poisson's ratio are written as

$$E = 2\sqrt{3}E^{(b)}t^{(b)}\left(\frac{h}{L}\right) \quad \left[\frac{1 + (h/L)^2}{3 + (h/L)^2}\right], \quad \upsilon = \frac{1 - (h/L)^2}{3 + (h/L)^2} \tag{37}$$

The similar derivation for the square Bernoulli–Euler beam lattice reveals that it represents an orthotropic micropolar continuum unsuitable to model isotropic continuum (Ostoja-Starzewski 2002).

Triangular Timoshenko Beam Lattice

In the Timoshenko beam theory only the shear force

$$Q^{(b)} = \frac{12E^{(b)}I^{(b)}}{(1+\varsigma)\left(L^{(b)}\right)^3}L^{(b)}\widetilde{\gamma}^{(b)}, \quad \varsigma = \frac{12E^{(b)}I^{(b)}}{G^{(b)}\widetilde{A}^{(b)}\left(L^{(b)}\right)^2} = \frac{E^{(b)}}{G^{(b)}}\overline{h} \tag{38}$$

and the corresponding displacement $L^{(b)}\widetilde{\gamma}^{(b)}$ differ from the Bernoulli–Euler formulation, while the normal force–displacement and moment–rotation relations $(33)_{1,3}$ are identical. In Eq. 38, ζ is the dimensionless parameter defined by the ratio of bending to shear stiffness. Bernoulli–Euler beam is recovered for very large shear stiffness and the slender beam since $\zeta \to 0$.

The equivalence of the strain energies in Eq. 1 for the triangular lattice yields the same Bernoulli–Euler beam expressions (35, 36) except that

$$\widetilde{R}^{(b)} = \frac{24E^{(b)}I}{L^3\sqrt{3}}\frac{1}{(1+\varsigma)} \tag{39}$$

assuming all unit cell beams have the same dimensions ($L^{(b)} = L$, etc.).

Following the same steps, the nonzero stiffness components are

$$C_{1111} = C_{2222} = \frac{3}{8}\left(3R + \widetilde{R}\right), \quad C_{1212} = \frac{3}{8}\left(R + 3\widetilde{R}\right), \quad C_{1122} = C_{2211} = \frac{3}{8}\left(R - \widetilde{R}\right),$$
$$C_{1221} = C_{2112} = \frac{3}{8}\left(R - \widetilde{R}\right), \quad C_{2121} = \frac{3}{8}\left(R + 3\widetilde{R}\right), \quad D_{11} = D_{22} = \frac{3}{8}S \tag{40}$$

while the effective modulus of elasticity and the Poisson's ratio are

$$E = 2\sqrt{3}E^{(b)} \quad t^{(b)} \quad \left(\frac{h}{L}\right) \quad \left(\frac{1+(h/L)^2/(1+\zeta)}{3+(h/L)^2/(1+\zeta)}\right), \quad \upsilon = \frac{1-(h/L)^2/(1+\zeta)}{3+(h/L)^2/(1+\zeta)}. \tag{41}$$

Computer Implementation Procedure for Beam Lattices

Fracture process in beam lattice models is simulated by performing a linear elastic analysis under prescribed loading and removing from the network all beam elements that satisfy a predefined rupture criterion. Normal forces, shear forces, and moments are calculated using one of the beam theories. The global stiffness matrix is constructed for the entire lattice; its inverse matrix is calculated and then multiplied with the load vector to obtain the displacement vector. The heterogeneity of the material is taken into account by assigning different strengths to beams (e.g., using a

Gaussian or Weibull distribution) or by assuming random dimensions of beams and random geometry of the lattice mesh or by mapping of different material properties to beams corresponding to the cement matrix, aggregate, and interface zones, respectively, in the case of concrete. To obtain aggregate overlay in the lattice, a Fuller curve is usually chosen for the distribution of grains. The beam length in concrete should be less than $l_b < d_{min}$ (where d_{min} is the minimum aggregate diameter).

Beam models can reproduce complex macroscopic damage patterns by cumulative effect of microcracking, crack branching, crack tortuosity, and bridging. They can also capture a size effect (e.g., Vidya Sagar 2004). The advantages of this approach are simplicity and a direct insight in the fracture process on the level of the microstructure. By applying an elastic-purely brittle local fracture law at the beam level, global softening behavior is observed. The main disadvantages of the conventional beam lattice model are the following: the results depend on the beam size and direction of loading, the response of the material is too brittle (due to the assumed brittleness of single beams), the compressed beam elements overlap each other, and an extreme computational effort on the macrostructural level is needed. The first disadvantage can be removed by assuming a heterogeneous structure (Schlangen and Garboczi 1997). In turn, the second drawback can be mollified by 3D calculations and consideration of very small particles (Lilliu and van Mier 2003) and by applying a nonlocal approach in calculations of beam deformations (Schlangen and Garboczi 1997).

Examples of Applications of Lattices with Beam Interactions

Schlangen and Garboczi (1996, 1997) compared model techniques used in lattice simulations of random heterogeneous materials. The crack patterns obtained from a double-edge-crack concrete specimen loaded in shear (Fig. 11a) were compared to those obtained by numerical simulations with various lattice interaction types and lattice orientations. A selection of results is reproduced in Fig. 11b–d.

It is important to note that geometrical disorder (heterogeneity) was not implemented in the lattice models to emphasize the ability of the particular element type to describe continuum fracture. With reference to Fig. 11, the beam elements (Fig. 11d) were clearly superior to the two spring network interactions in capturing the experimentally observed complex crack pattern (Fig. 11a) in the *absence* of the model geometrical disorder. Nonetheless, it was obvious that the cracked patterns even in this case (Fig. 11d) revealed the mesh bias unavoidable in geometrically ordered lattices.

The comparison of simulated crack patterns, with four homogeneous lattices developed with square mesh, two differently oriented triangular meshes, and random triangular mesh, demonstrated expected superiority of the last type to capture the crack shape. These results, as well as those of Jirásek and Bažant (1995), emphasized the importance of lattice geometrical disorder for realistic simulation of crack

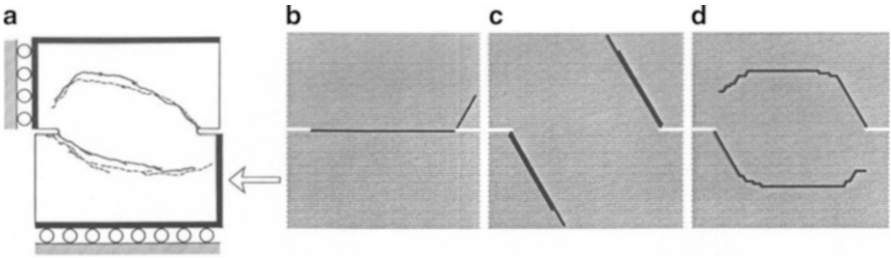

Fig. 11 (**a**) Geometry and crack pattern of concrete plate loaded in shear; crack patterns obtained by simulation on geometrically ordered triangular lattices with (**b**) central interactions (see section on "Triangular Lattice with Central Interactions"), (**c**) central and angular interaction (see section on "Square Lattice with Central and Angular Interactions"), and (**d**) beam interactions (see section on "Triangular Bernoulli–Euler Beam Lattice"). (Reprinted from Schlangen and Garboczi (1996) with permission from Elsevier)

propagation. However, geometrically disordered lattices were generally not homogeneous under uniform straining (Jagota and Bennison 1994). Schlangen and Garboczi (1996) suggested an approach to obtain an elastically uniform random network, which involved the iterative refinement of the lattice element properties. However, the authors expressed the expectation that for the problems characterized with inherent material randomness directly implemented in the lattice, the geometrically ordered lattice should exhibit similar crack pattern resemblance as long as the beam length was small compared to the textural length scale. The effect of the lattice resolution was also investigated and it was found that while the crack pattern was not strongly affected by the size of the beams, the load–crack opening curve was affected in much the same way as the effect of mesh refinement in local strain-softening models: the finer the lattice, the smaller the inelastic displacement and the dissipated energy (Cusatis et al. 2003).

Schlangen and Garboczi proposed a new fracture law that used the maximum tensile stress in each *node* – instead of each beam – to address the problem of the directionality dependence of the lattice fracture stress. The nodal stress was determined based on the axial and shear contributions of each nodal bond and then used to determine the maximum normal force plane and corresponding beam area projections. The effective nodal stress was then determined as this normal force divided by the projected area and then used as a fracture criterion for each beam.

The methodology had been developed in the same study to implement the material heterogeneity in a direct way by using scanning electron micrographs and digital image processing of the microstructure to map different properties to lattice elements. The beam lattice in which this methodology was applied was subjected to a few basic loading configurations and realistic crack patterns were obtained.

Bolander and co-workers (1998, 2000, Bolander and Sukumar 2005) developed an elastically homogeneous lattice of random geometry to address the cracking direction bias caused by element-breaking low-energy pathways of regular lattices.

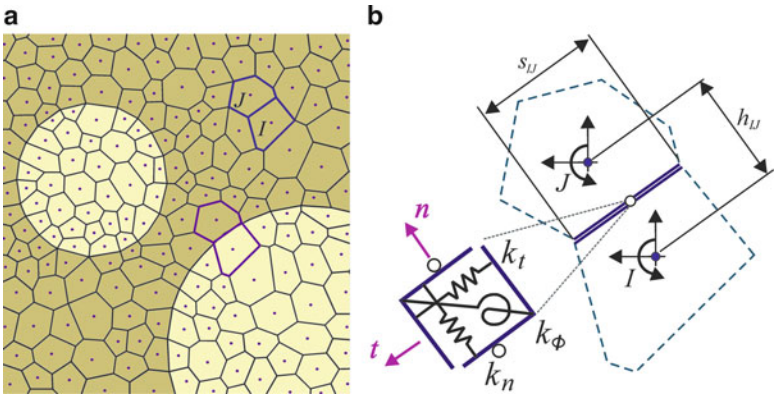

Fig. 12 (**a**) Irregular Voronoi tessellation of multiphase material and related nodes of dual Delaney network. (**b**) Two rigid particles joint by a flexible interface

Lattice elements were defined on the edges of the Delaunay tessellation of an irregular set of points generated in the material domain (Fig. 12a). The dual Voronoi tessellation was used to scale the elemental stiffness terms, in a manner that rendered the lattice model elastically homogeneous. This random lattice model could be viewed as an assemblage of rigid polygonal particles interconnected along their boundaries by a flexible interface inspired by the rigid-body-spring network developed by Kawai (1978).

The flexible interface, modeled by a set of discrete springs positioned midway along each boundary segment, is illustrated in Fig. 12b. Each spring set consisted of normal, tangential, and rotational springs with their respective stiffness k_n, k_t, and k_ϕ assigned in such a way to approximate the elastic properties of uniform continuum

$$k_n = EA_{IJ}/h_{IJ}, \quad k_t = k_n, \quad k_\phi = k_n \ s_{IJ}^2/12 \tag{42}$$

where $A_{IJ} = s_{IJ}\, t$, with t being the thickness of the planar model and E the modulus of elasticity of material. The assignment of spring constants Eq. 42 was uniquely defined by the Voronoi diagram to ensure elastically uniform lattice response since beam cross-sectional areas were scaled in proportion to the length of the common boundary segment. Notably, the equality of normal and tangential stiffness, Eq. $(42)_2$, necessary to ensure elastically uniform lattice response (Bolander and Sukumar 2005), resulted in unrealistic Poisson's effect.

The elastic formulation of the model and the mesh generation techniques were described in detail in original papers as well as a number of different fracture models. The use of fracture model based on the Bažant's crack-band approach (e.g., Bažant and Oh 1983) involved an incremental softening of the lattice elements in accordance to a predefined traction–displacement rule. Consequently, in contrast to conventional lattice approach, element rupture was gradual and governed by rules that provided an energy-conserving representation of fracture through the irregular lattice. This fracture model was objective with respect to the irregular lattice

geometry: uniform fracture energy was consumed along the crack path regardless of the mesh geometry (Bolander and Sukumar 2005).

The irregular lattice models of Bolander and co-workers demonstrated ability to capture cracking patterns quite realistically. The distributed flexural cracking, the mixed-mode cracking of double-edge-notched plate, the bridge pier cracking under various design loads, and the fracture of three-point bend specimen were notable examples of successful applications of this modeling approach as illustrated by a selection of crack patters presented in Fig. 13. The ability of the model to simulate load–deformation response in fracture-sensitive simulations (challenging because of their complex cracks pathways) is illustrated in Fig. 14.

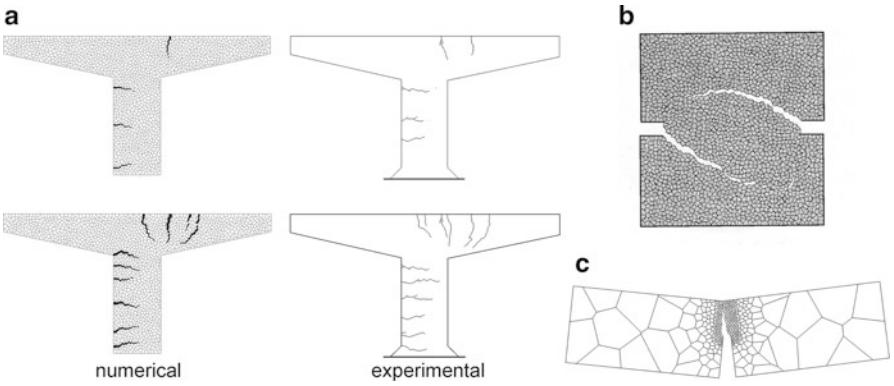

Fig. 13 (**a**) Experimentally and numerically obtained crack patterns in a bridge pear. (Reprinted from Bolander et al. (2000) with permission from John Wiley and Sons). (**b**) Crack pattern for double-edge-notched plate loaded in shear. (Reprinted from Bolander and Saito (1998) with permission from Elsevier). (**c**) Irregular mesh for simulation fracture in three-point bending test. (Reprinted figure with permission from Bolander and Sukumar (2005). Copyright (2005) by the American Physical Society. http://prb.aps.org/abstract/PRB/v71/i9/e094106)

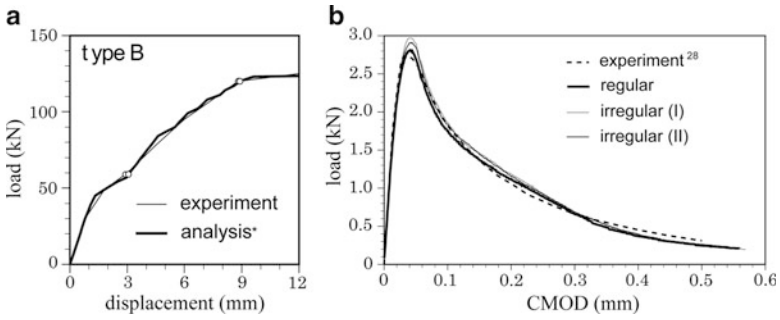

Fig. 14 Experimentally and numerically obtained (**a**) load–displacement curves for the bridge pear test (Fig. 13a). (Reprinted from Bolander et al. (2000) with permission from John Wiley and Sons) and (**b**) load–CMOD curves for the three-point bending test (Fig. 13c). (Reprinted figure with permission from Bolander and Sukumar (2005). Copyright (2005) by the American Physical Society. http://prb.aps.org/abstract/PRB/v71/i9/e094106)

Van Mier et al. (2002) investigated the effect of material's microstructural stochasticity on load–deformation response and crack patterns under uniaxial tension. They used the regular triangular lattice comprised of Bernoulli–Euler beams and the particle overlay method to mimic geometry of three-phase concrete to estimate the effect of strength and stiffness contrast in the composite. The particle overlay method appeared to be very successful in realistically capturing complex crack patterns. The progressive damage accumulation was simulated by subsequent removal of beam elements that satisfy a tensile-strength fracture criterion

$$\sigma_{eff}^{(b)} = \frac{F^{(b)}}{A^{(b)}} \pm \zeta \frac{\left(\left| M_i^{(b)} \right|, \ \left| M_j^{(b)} \right| \right)_{\max}}{W^{(b)}} = f_{cr} \tag{43}$$

where $F^{(b)}$ was the normal force in the considered beam, $M^{(b)}$ was the bending moments in the beam element nodes, and $A^{(b)}$ and $W^{(b)}$ were the area of cross section and the section modulus of the beam, respectively. The scaling coefficient ζ (selected in their study to be 0.05) was a fitting parameter that regulated which part of the bending moment was considered (effectively to match the experimentally observed response). This implied that an energy package $U_e^{(b)} = f_{cr}^2/2E$ was released at each bond rupture, which resembled the dissipated energy measured by acoustic emission monitoring. Three different tensile strengths were specified for the three material phases (aggregate, matrix, and interface; Fig. 1c) whose relative values were of importance.

The numerical simulation results had been compared to the outcome of simulations where the effects of microstructure were mimicked by assigning random strength values drawn from Weibull or Gaussian distribution to the regular triangular lattice. The results indicated that strength contrast was more pronounced than stiffness contrast when the maximum global force was considered and that global behavior was dominantly driven by damage percolation in the weakest material phase. The strength of the aggregate–matrix bonding interface and the connectivity of elements belonging to that phase were determined to be the decisive factor for the global strength under uniaxial tension. The results from the different Weibull distribution simulations resembled to a certain extent the failure mode observed in the more realistic three-phase particle overlay (notably the salient bridging phenomenon). In contrast, the correct cracking response could not be achieved with Gaussian strength distribution. The failure modes from Gaussian distribution simulations did not resemble the real fracture behavior observed experimentally in concrete, regardless of the fact that a large variety in force–deformation curves could be simulated depending on the choice of the distribution parameters.

In conclusion, the authors advised against the use of statistical strength distributions for simulating concrete response. They also cautioned that the force–deformation curves cannot be used as a single indicator to judge ability of a model to capture the fracture behavior of heterogeneous materials. The crack mechanisms and the ensuing crack patterns were considered salient elements in such judgments.

Arslan et al. (2002) and Karihaloo et al. (2003) improved in several ways the regular triangular beam lattice aimed at modeling fracture in particle composites. First, the aggregate phase remained linearly elastic–ideally brittle, but tension softening was allowed for the matrix and interface bonds by following the Bažant's bilinear stress–strain model outlined in section "Examples of Applications of α Model" (Fig. 3b). Second, the Timoshenko beam formulation was used to improve accuracy of interparticle interactions. Finally, the displacement-control simulation setup, able to account for finite deformations, was applied in attempt to capture the large deformations and rotations involved in the damage evolution. These changes were introduced in effort to address the primary deficiency of the beam lattice modeling of concrete at that time: the tendency of load–displacement (P–δ) curve to deviate substantially – regardless of the quite realistic crack patterns – from the experimentally observed response. Specifically, numerically simulated response was too discontinuous and brittle as shown in Fig. 15a. (Lilliu and van Mier (2003) developed a 3D lattice model for concrete to address these outstanding issues, which resulted in substantial increase of computational effort even for a relatively small model with pronounced boundary effects.)

Karihaloo and co-workers used an incremental iterative procedure based on the current secant modulus to account for the tension softening and other nonlinearities. The longitudinal strain of each beam element was calculated from nodal displacement and checked against the corresponding limit strain

$$\varepsilon = (1/L)\left[\left(u_1^j - u_1^i\right) cos\ \theta + \left(u_2^j - u_2^i\right) sin\ \theta + \left|\phi_j - \phi_i\right|\alpha_s(h/2)\right] = \varepsilon_{cr} \quad (44)$$

where u_1, u_2, and ϕ correspond to three nodal degrees of freedom, h is the depth of nodal element, and α_s is the scaling parameter. If a phase is ideally brittle, the critical strain ε_{cr} corresponds to the tensile strength. When a bilinear constitutive relation is adopted for a phase (e.g., Fig. 3b), $\varepsilon_{cr} = \varepsilon_f$.

The typical simulation observations suggested that the difference between phase properties reduced steepness of load–displacement curve in the softening region. If the interface was the weakest phase, the deviation from the initially linear P–δ response marked the onset of substantial interface debonding, commonly related to stress concentrations. The softening threshold corresponded to the onset of matrix failure and the dominant macrocrack(s) formation as demonstrated experimentally by Van Mier and Nooru-Mohamed (1990) by using photoelastic coating.

The introduction of tension softening in the matrix and interface constitutive laws lead to more diffuse crack patterns (Fig. 15c) and, accordingly, to the more ductile response (Fig. 15b) in better agreement to the experimental observation for particle composites.

The inclusion of shear deformation based on Timoshenko beam theory apparently affected the P–δ response only slightly in contrast to the marked influence on the crack patterns. The finite deformations influenced substantially both softening behavior and the crack patterns. It exhibited a tendency of reduction of the softening response steepness as well as the number of the ruptured beam element.

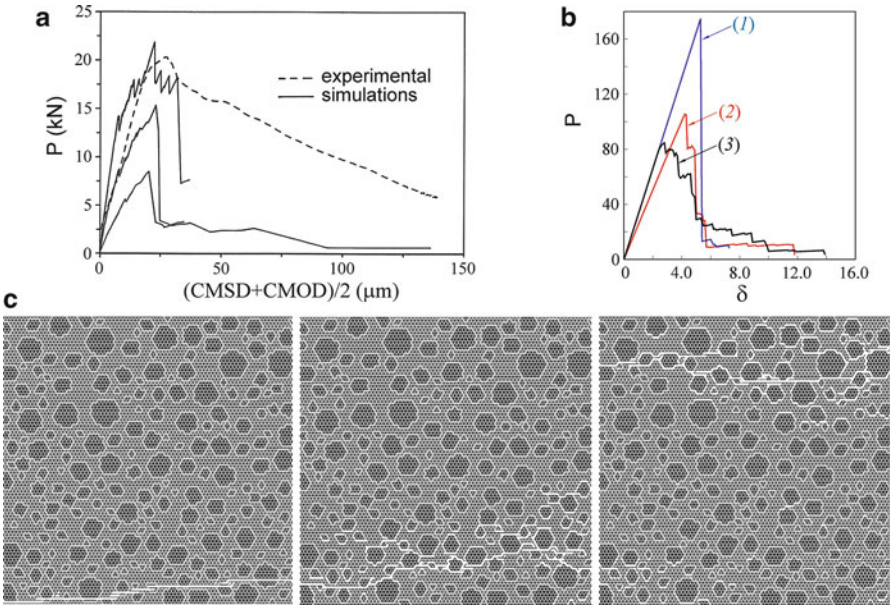

Fig. 15 (**a**) Experimental and numerical P–δ curves for four-point-shear beams of three different sizes. (Reprinted from Schlangen and van Mier (1992) with permission from Elsevier). (**b**) P–δ curves for three cases: (*1*) no tension softening phase, (*2*) only matrix is tension softening, and (*3*) both matrix and interface are tension softening. (**c**) Crack patterns corresponding to the end of softening for the three *curves* above (*1–3*), respectively. (Reprinted from Karihaloo et al. (2003) with permission from Elsevier)

Liu and co-workers (2007, 2008) developed a generalized-beam (GB) lattice model to mollify the problem of computational effort in the standard beam lattice approaches. The three-phase material structure was projected directly on top of the regular GB triangular lattice (Fig. 16a) with aggregate centers lying on lattice nodes and GB elements being a two-node and three-phase elements as depicted in Fig. 16. Every phase of the GB element is represented by a Timoshenko beam of equivalent properties; if a hexagonal unit cell did not contain an aggregate, it was still formally composed of three beam types with identical equivalent properties. The three beams of the GB element were assumed to cling firmly together so that the displacements of two ends of the middle beam were completely determined by the two nodes of the GB element.

Matrix and aggregate beams were described by Timoshenko beam theory while the interface beams were defined in accordance with Appendix A of Bolander and Saito (1998). The composition of stiffness matrix of the GB element and parameter calibration of the corresponding lattice were presented in detail by Liu et al. (2007, 2008). The algorithm of quasistatic problem solution was essentially unchanged: fracture was simulated by subsequent removal of GB elements that satisfied the rupture criterion bearing in mind that rupture criticalities of three beams in each element were judged independently.

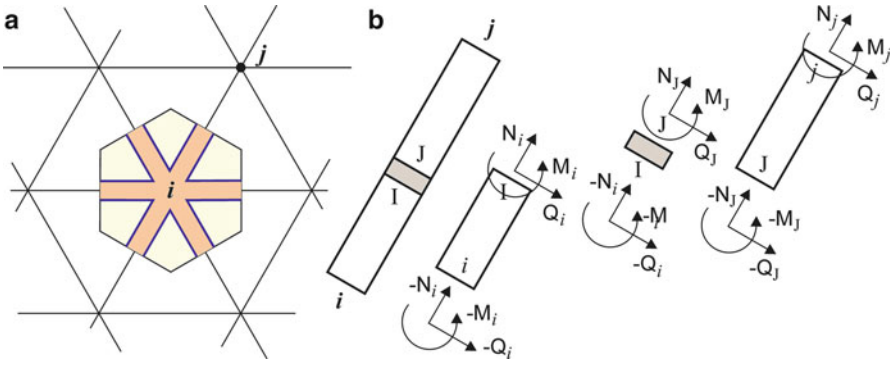

Fig. 16 The geometry of a GB lattice representing three-phase composite structure: (**a**) an particle overlay on GB lattice and a hexagonal unit cell of a triangular aggregate/matrix GB lattice, and (**b**) a composite GB element formed by the aggregate beam (*i*–*I*), the interface beam (*I*–*J*), and the matrix beam (*J*–*j*)

The rupture criterion used by Liu et al. (2007, 2008) was based on the maximum tensile stress. On the other hand, numerical representation of element rupture events in planar networks simulating the failure of paper (Liu et al. 2010) included also the maximum shearing stress criterion:

$$|\tau| = |q|/A_b = \tau_{cr} \tag{45}$$

where A_b is the intersecting (bond) area of two consecutive fibers and q is the corresponding sheering interaction.

The representative set of simulation results corresponding to the uniaxial tension test were presented in Fig. 17. The P–δ curve revealed two response regimes and a number of typical states along the loading path. The corresponding time histories of ruptured matrix and interface beams were depicted in Fig. 17b, while two characteristic snapshots corresponding to softening phase were illustrated in Fig. 17c, d.

Liu et al. (2008) were among first to propose dynamic beam lattice analysis using the central difference technique. The corresponding dynamic approach to the brittle fracture simulation was described and illustrated for four loading rates in the range $\log \dot{\varepsilon} \in [-3, 0]$ and compared with the quasistatic simulation results. This fracture process simulation by the dynamic procedure required a substantial increase of computational effort. The obtained simulation results demonstrated that while the inertial effects abated progressively with the loading rate reduction, the inertial effects due to the unstable crack propagation remained considerable even at the lowest loading rates. This observation raised the issue of the appropriateness of the common disregard of inertial effects in quasistatic analyses.

Khoei and Pourmatin (2011) developed a dynamic mesoscale model based on Timoshenko beam theory to investigate the dynamic response of three-phase inhomogeneous material. The dynamic analysis was performed using the Newmark's average acceleration technique. The aggregate distribution within the lattice model

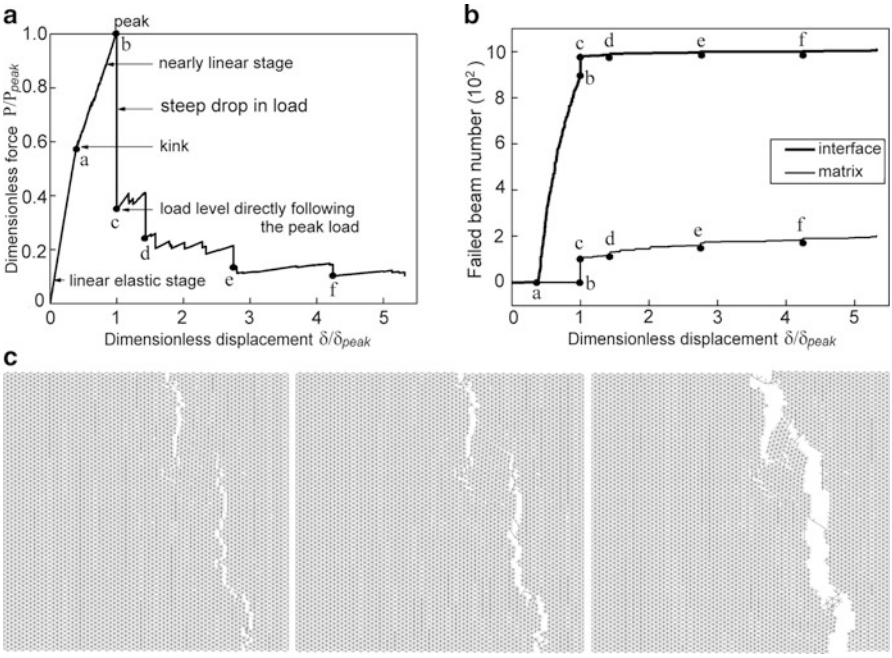

Fig. 17 (**a**) The P–δ curve and (**b**) the cumulative number of failed beams versus dimensionless displacement. (**c**) Three post-peak crack patterns at points *c*, *d*, and *f*, respectively. (Reprinted from Liu et al. (2007) with permission from Elsevier)

was generated based on their distribution within the network in a decelerating manner. The axial strain criterion, Eq. 44, was utilized for the beam element rupture.

Two experiments were used to illustrate the model capabilities in simulating the crack propagation in concrete: the simple uniaxial tensile (mode I) test and the double-edge-notched (mixed I and II modes) panel specimen. The crack patterns and P–δ curves were presented and discussed.

Conclusion

The survey of about 30 years of work, from the mid-1980s to present, highlights that lattice and DEM models (the later reviewed briefly in the next essay of this handbook) have evolved into a significant companion, if not alternative, to continuum models and traditional micromechanics. There is no reason to believe that this trend will stop anytime soon considering an increasing reliance on large computations to perform "virtual experiments" in structural and materials research and engineering.

These types of "discontinua-based models" enable the investigation of fracture problems by a unique bottom-up perspective, i.e., starting from physical behavior on

a finer scale, to deduce the macroscale response as an outcome. In this regard, they do not supersede top-down continuum approaches or analytical modeling, but rather offer a complementary strategy to be used in a synergy with them for the purpose of controlling complex behaviors and complex materials. The rational model presented for the spring lattice is emblematic in this respect, with potentially far reaching consequences in addressing random fracture initiation and self-organized propagation problems typical of ceramics and ceramic matrix composites.

The possibility to use springs, trusses, beams or any special and fancy elements makes lattice models a tool to be customized at will and in virtually unlimited ways. Such tailorability is an unparalleled advantage for modeling and designing exotic and complex systems necessitated by modern engineering. Sure enough, discrete models have yet a long path ahead to become full-blown quantitative engineering tools but will certainly benefit from the boost due to innovative experimental techniques (discussed in detailed elsewhere in this handbook) and emerging novel size-confined materials for nanotechnology.

References

J. Alibert, P. Seppecher, F. Dell'Isola, Truss modular beams with deformation energy depending on higher displacement gradients. Math. Mech. Sol. **8**, 51–73 (2003)

A. Arslan, R. Ince, B.L. Karihaloo, Improved lattice model for concrete fracture. J. Eng. Mech. **128**(1), 57–65 (2002)

Z.P. Bažant, B.H. Oh, Crack band theory for fracture of concrete. Mater. Struct. (RILEM) **16**(93), 155–177 (1983)

Z.P. Bažant, M.R. Tabbara, M.T. Kazemi, G. Pyaudier-Cabot, Random particle model for fracture of aggregate and fiber composites. J. Eng. Mech. **116**(8), 1686–1705 (1990)

J.E. Bolander Jr., S. Saito, Fracture analyses using spring networks with random geometry. Eng. Fract. Mech. **61**, 569–591 (1998)

J.E. Bolander Jr., G.S. Hong, K. Yoshitake, Structural concrete analysis using rigid-body-spring networks. Comput. Aided Civ. Infrast. Eng. **15**, 120 (2000)

J.E. Bolander, N. Sukumar, Irregular lattice model for quasistatic crack propagation. Phys. Rev. B **71**, 094106 (2005)

G. Cusatis, Z.P. Bažant, L. Cedolin, Confinement-shear lattice model for concrete damage in tension and compression I. Theory. J. Eng. Mech. **129**(12), 1439–1448 (2003)

G. Cusatis, Z.P. Bazant, L. Cedolin, Confinement-shear lattice CSL model for fracture propagation in concrete. Comput. Methods Appl. Mech. Eng. **195**, 7154–7171 (2006)

M. Grah, K. Alzebdeh, P.Y. Sheng, M.D. Vaudin, K.J. Bowman, M. Ostoja-Starzewski, Brittle intergranular failure in 2D microstructures: experiments and computer simulations. Acta Mater. **44**(10), 4003–4018 (1996)

P. Hou, Lattice model applied to the fracture of large strain composite. Theory Appl. Fract. Mech. **47**, 233–243 (2007)

A. Hrennikoff, Solution of problems of elasticity by the framework method. J. Appl. Mech. **8**, A619–A715 (1941)

A. Jagota, S.J. Bennison, Spring-network and finite element models for elasticity and fracture, in *Proceedings of a Workshop on Breakdown and Non-linearity in Soft Condensed Matter*, ed. by K. K. Bardhan, B. K. Chakrabarti, A. Hansen, (Springer, Berlin/Heidelberg/New York, 1994), pp. 186–201

M. Jirásek, Z.P. Bažant, Microscopic fracture characteristics of random particle system. Int. J. Fract. **69**, 201–228 (1995)

B.L. Karihaloo, P.F. Shao, Q.Z. Xiao, Lattice modelling of the failure of particle composites. Eng. Fract. Mech. **70**, 2385–2406 (2003)
T. Kawai, New discrete models and their application to seismic response analysis of structures. Nucl. Eng. Des. **48**, 207–229 (1978)
A.R. Khoei, M.H. Pourmatin, A dynamic lattice model for heterogeneous materials. Comput. Methods Civ. Eng. **2**, 1–20 (2011)
J. Kozicki, J. Tejchman, Modelling of fracture process in concrete using a novel lattice model. Granul. Matter **10**, 377–388 (2008)
G. Lilliu, J.G.M. van Mier, 3D lattice type fracture model for concrete. Eng. Fract. Mech. **70**, 927–941 (2003)
J.X. Liu, S.C. Deng, J. Zhang, N.G. Liang, Lattice type of fracture model for concrete. Theory Appl. Fract. Mech. **48**, 269–284 (2007)
J.X. Liu, S.C. Deng, N.G. Liang, Comparison of the quasi-static method and the dynamic method for simulating fracture processes in concrete. Comput. Mech. **41**, 647–660 (2008)
J.X. Liu, Z.T. Chen, K.C. Li, A 2-D lattice model for simulating the failure of paper. Theory Appl. Fract. Mech. **54**, 1–10 (2010)
A. Misra, C.S. Chang, Effective elastic moduli of heterogeneous granular solids. Int. J. Sol. Struct. **30**(18), 2547–2566 (1993)
M. Ostoja-Starzewski, Lattice models in micromechanics. Appl. Mech. Rev. **55**(1), 35–60 (2002)
M. Ostoja-Starzewski, *Microstructural Randomness and Scaling in Mechanics of Materials* (Taylor & Francis Group, Boca Raton, 2007)
S.L. Phoenix, I.J. Beyerlein, Statistical strength theory for fibrous composite materials, in *Comprehensive Composite Materials*, ed. by A. Kelly, vol. 1, (Pergamon, Oxford, 2000), pp. 559–639
A. Rinaldi, A rational model for 2D disordered lattices under uniaxial loading. Int. J. Damage Mech. **18**, 233–257 (2009)
A. Rinaldi, Statistical model with two order parameters for ductile and soft fiber bundles in nanoscience and biomaterials. Phys. Rev. E **83**(4–2), 046126 (2011a)
A. Rinaldi, Advances in statistical damage mechanics: new modelling strategies, in *Damage Mechanics and Micromechanics of Localized Fracture Phenomena in Inelastic Solids*, CISM Course Series, ed. by G. Voyiadjis, vol. 525, (Springer, Berlin/Heidelberg/New York, 2011b)
A. Rinaldi, Bottom-up modeling of damage in heterogeneous quasi-brittle solids. Contin. Mech. Thermodyn. **25**(2–4), 359–373 (2013)
A. Rinaldi, Y.C. Lai, Damage theory of 2D disordered lattices: energetics and physical foundations of damage parameter. Int. J. Plast. **23**, 1796–1825 (2007)
A. Rinaldi, L. Placidi, A microscale second gradient approximation of the damage parameter of quasi-brittle heterogeneous lattices. Z. Angew. Math. Mech. (ZAMM) (2013). https://doi.org/10.1002/zamm.201300028
A. Rinaldi, S. Mastilovic, D. Krajcinovic, Statistical damage mechanics – 2. Constitutive relations. J. Theory Appl. Mech. **44**(3), 585–602 (2006)
A. Rinaldi, D. Krajcinovic, S. Mastilovic, Statistical damage mechanics and extreme value theory. Int. J. Damage Mech. **16**(1), 57–76 (2007)
E. Schlangen, E.J. Garboczi, New method for simulating fracture using an elastically uniform random geometry lattice. Int. J. Eng. Sci. **34**, 1131–1144 (1996)
E. Schlangen, E.J. Garboczi, Fracture simulations of concrete using lattice models: computational aspects. Eng. Fract. Mech. **57**, 319–332 (1997)
E. Schlangen, J.G.M. Van Mier, Micromechanical analysis of fracture of concrete. Int. J. Damage Mech. **1**, 435–454 (1992)
V. Topin, J.-Y. Delenne, F. Radjaï, L. Brendel, F. Mabille, Strength and failure of cemented granular matter. Eur. Phys. J. E **23**, 413–429 (2007)
K. Tsubota, S. Wada, Elastic force of red blood cell membrane during tank-treading motion: consideration of the membrane's natural state. Int. J. Mech. Sci. **52**, 356–364 (2010)
K. Tsubota, S. Wada, T. Yamaguchi, Simulation study on effects of hematocrit on blood flow properties using particle method. J. Biomech. Sci. Eng. **1**(1), 159–170 (2006)

J.G.M. Van Mier, *Fracture Processes of Concrete* (CRC Press, New York, 1997)
J.G.M. Van Mier, M.B. Nooru-Mohamed, Geometrical and structural aspects of concrete fracture. Eng. Fract. Mech. **35**(4/5), 617–628 (1990)
J.G.M. Van Mier, M.R.A. van Vliet, T.K. Wang, Fracture mechanisms in particle composites: statistical aspects in lattice type analysis. Mech. Mater. **34**, 705–724 (2002)
R. Vidya Sagar, Size effect in tensile fracture of concrete – a study based on lattice model applied to CT-specimen, in *Proceedings of the 21th International Congress of Theoretical and Applied Mechanics ICTAM04*, ed. by W. Gutkowski, T. A. Kowaleski, (Springer, Berlin/ Heidelberg/New York, 2004), pp. 1–3
H.-J. Vogel, H. Hoffmann, A. Leopold, K. Roth, Studies of crack dynamics in clay soil II. A physically based model for crack formation. Geoderma **125**, 213–223 (2005)
G. Wang, A. Al-Ostaz, A.H.-D. Cheng, P.R. Mantena, Hybrid lattice particle modeling: theoretical considerations for a 2D elastic spring network for dynamic fracture simulations. Comput. Mater. Sci. **44**, 1126–1134 (2009a)
T. Wang, T.-W. Pan, Z.W. Xing, R. Glowinski, Numerical simulation of rheology of red blood cell rouleaux in microchannels. Phys. Rev. E **79**, 041916 (2009b)
A. Zubelewicz, Z.P. Bažant, Interface element modeling of fracture in aggregate composites. J. Eng. Mech. **113**(11), 1619–1630 (1987)

Part VIII

Damage in Crystalline Metals and Alloys

From Single Crystal to Polycrystal Plasticity: Overview of Main Approaches

44

Esteban P. Busso

Contents

Introduction 1252
Continuum Discretization of a Boundary Value Problem 1253
Single Crystal Plasticity 1255
Local Single Crystal Approaches 1256
An Application of Crystal Plasticity to the Study of Intergranular Damage in an FCC Alloy 1259
Single Crystal Formulation for the FCC Material 1259
Intergranular Crack Observations, Strain Field Measurements, and Predicted Local Stress and Strain Fields 1261
Nonlocal Single Crystal Approaches 1262
Nonlocal Models Based on Internal Strain Gradient Variables 1264
Nonlocal Models Based on the Mechanics of Generalized Continua 1265
Microcurl Model: Balance and Constitutive Equations 1269
Application of the Microcurl Model to Study the Deformation Behavior of a Polycrystalline Aggregate 1270
Concluding Remarks 1273
References 1274

Abstract

This chapter provides a brief overview of the different continuum mechanics approaches used to describe the deformation behavior of either single crystals or individual grains in polycrystalline metallic materials. The crucial role that physics-based crystal plasticity approaches may play in understanding the mechanisms of damage initiation and growth is addressed. This includes a discussion of the main strain gradient constitutive approaches used to describe size effects in crystalline solids. Finally, representative examples are given about the effect of

E. P. Busso (✉)
Materials and Structures Branch, ONERA, Chemin de la Huniere, Palaiseau, Cedex, France
e-mail: esteban.busso@onera.fr; esteban.busso@ensmp.fr

© Springer Nature Switzerland AG 2022

G. Z. Voyiadjis (ed.), *Handbook of Damage Mechanics*,
https://doi.org/10.1007/978-3-030-60242-0_7

the local stress and strain fields in the mechanisms of intergranular damage initiation and growth in FCC polycrystal materials.

Keywords

Slip system · Strain gradient · Slip rate · Crystal plasticity · Intergranular crack

Introduction

It is well understood that the macroscopic phenomena which control the physical and mechanical properties of materials originate from the underlying microstructure. The chemical and phase compositions, microstructural morphology, and characteristic length scales, such as grain size or mean dislocation spacing, have a significant effect on the material's properties and behavior. Furthermore, the evolution of the material's microstructure subject to thermal and mechanical loads typical of service is equally important as it determines its long-term properties. This includes the development and growth of internal defects (or damage) such as voids, intergranular or transgranular cracks which generally lead to a life-limiting microstructural state. The identification of physics-based relationships between microstructure and macroscopic behavior is one of the crucial issues which engineers, materials scientists, and physicists alike face and which have been at the center of most recent research efforts. A common goal is the development of physics-based analytical and computational material modelling tools to underpin scientific investigations and complement traditional theoretical and experimental approaches. The power of analytical theories lies in their ability to reduce the complex collective behavior of the basic ingredients of a solid (e.g., electrons, atoms, lattice defects, single crystal grains) into insightful relationships between cause and effect. Computational approaches such as those based on multiscale material modelling techniques are required to complement continuum and atomistic analysis methods. At transitional (or microstructural) scales, such as those in-between continuum and atomistic, continuum approaches begin to break down, and atomistic methods reach inherent time and length-scale limitations (Ghoniem et al. 2003).

Transitional theoretical frameworks and modelling techniques are being developed to bridge the gap between length-scale extremes. For example, the description of deformation beyond the elastic regime is usually described by appropriate *constitutive equations*, and the implementation of such relationships within continuum mechanics generally relies on the inherent assumption that material properties vary continuously throughout the solid. However, certain heterogeneities linked to either the microstructure, such as dislocation patterns or the deformation per se cannot be readily described within the framework provided by continuum mechanics. New promising application areas require novel and sophisticated physically based approaches for design and performance prediction. Thus, theory and modelling are playing an ever increasing role to reduce development costs and manufacturing times as well as to underpin computational material design. In the last decade or so, there has been a shift away from reproducing known properties of known

materials and toward simulating the behavior of possible alloys as a forerunner to finding real materials with these properties.

In high-payoff, high-risk technologies such as those required in the design of large structures in the aerospace and nuclear industries, the effects of aging and environment on failure mechanisms cannot be left to conservative approaches. Increasing efforts are now focused on developing multiscale materials modelling approaches to develop new alloys and material systems in these areas. Appropriate validation experiments are also crucial to verify that the models predict the correct behavior at each length scale, ensuring that the linkages between approaches are directly enforced.

As the material dimensions become smaller, its resistance to deformation is increasingly determined by internal or external discontinuities (e.g., surfaces, grain boundaries, dislocation cell walls). The Hall–Petch relationship has been widely used to explain grain size effects, although the basis of the relationship is strictly related to dislocation pileups at grain boundaries. Recent experimental observations on nanocrystalline materials with grains of the order of 10–70 nm indicate that the material is weaker than what would be expected from the Hall–Petch relationship. Thus, the interplay between interfacial or grain boundary effects and slip mechanisms within a single crystal grain may result in either strength or weakness, depending on their relative sizes. Although experimental observations of plastic deformation heterogeneities are not new, the significance of these observations has not been addressed till very recently. The length scales associated with these deformation patterns (e.g., typically the size of dislocation cells, the ladder spacing in persistent slip bands (PSBs), or the spacing between coarse shear bands) control the material strength and ductility. As it may not be possible to homogenize such types of microstructures in an average sense using either atomistic simulations or continuum theories, new intermediate approaches are needed.

The issues discussed above, in addition to the ever increasingly powerful and sophisticated computer hardware and software available, are driving the development of materials modelling approaches. New concepts, theories, and computational tools are being continuously developed to enable the prediction of deformation phenomena at different microstructural scales to be linked. This chapter is aimed at providing a brief overview of the different approaches that are being used to deal with the continuum mechanics modelling of plasticity at the grain/single crystal level. Special emphasis is placed on highlighting the crucial role that physics-based crystal plasticity approaches play in developing an understanding of the local stress and strain fields known to be the precursors to damage initiation and growth at the scale of the grain in polycrystal metallic materials. Some representative examples are also given about the use of single crystal theories to predict polycrystal behavior.

Continuum Discretization of a Boundary Value Problem

In this section, an overview will first be given of the main continuum mechanics-based framework used to describe the nonlinear deformation behavior of materials at the local (e.g., single phase or grain level) scale. Emphasis will be placed on recent progress made in crystal plasticity and strain gradient plasticity.

Standard tensorial notation will be used throughout. Unless otherwise specified, vectors will be described by boldface lowercase letters, second-order tensors by boldface uppercase letters, and fourth-order tensors by italic uppercase letters.

In a generic boundary value problem (BVP), the deformation of a body subjected to external forces and prescribed displacements is governed by the (i) equilibrium equations, (ii) constitutive equations, (iii) boundary conditions, and (iv) initial conditions. The "weak" form of the boundary value problem is obtained when the equilibrium equations and the boundary conditions are combined into the "principle of virtual work." Such "weak form" constitutes the basis for obtaining a numerical solution of the deformation problem via, e.g., the finite element method. Thus, in a continuum mechanics Lagrangian formulation of a quasi-static BVP, the principle of virtual work is the vehicle by which the global equilibrium equations are obtained.

The basic features of a generic Galerkin-type discretization framework are given next. Consider a structure occupying a domain V in the deformed configuration which is subjected to external forces and displacements on its boundary, Γ_b. In the absence of body forces and inertial effects, the principle of virtual work for the structure, in its rate form, satisfies the following equation:

$$\int_V \boldsymbol{\sigma} : \delta\dot{\boldsymbol{\varepsilon}} dV - \int_{\Gamma_b} \mathbf{t} \cdot \delta\mathbf{v} d\Gamma_b = 0 \tag{1}$$

for any arbitrary virtual velocity vector field $\delta\mathbf{v}$ compatible with all kinematics constraints. In the above equation, $\mathbf{t} = \boldsymbol{\sigma}\mathbf{n}_s$ represents the boundary traction forces; $\boldsymbol{\sigma}$, the Cauchy stress; $\mathbf{n}_s$, the normal to the surface on which the tractions act; and, $\delta\mathbf{v}$ the virtual strain rate associated with the velocity field.

To solve a complex BVP numerically, the discretization of the principle of virtual work is generally performed using the finite element method. Let $\mathbf{v}$ be approximated at a material point within an element by

$$\mathbf{v} = \sum_{\mathbf{i=1}}^{\mathbf{N_{max}}} N^i \ \widehat{\mathbf{v}}^{\mathbf{i}} \equiv \boldsymbol{N}\,\widehat{\mathbf{v}} \tag{2}$$

where $\widehat{\mathbf{v}}$ denotes the nodal values of the element velocity field and $\mathbf{N}$ are the isoparametric shape functions. Substituting Eq. 2 into Eq. 1 leads to the discretized version of the principle of virtual work on the finite element, V_e:

$$\mathbf{r}\{\widehat{\mathbf{v}}\} \equiv \mathbf{f}^{\mathbf{int}} - \mathbf{f}^{\mathbf{ext}} = 0, \tag{3}$$

where

$$\mathbf{f}^{\text{int}} = \int_{V_e} \mathbf{B}^{\mathrm{T}}\ \boldsymbol{\sigma} dV_e, \qquad \mathbf{f}^{\text{ext}} = \int_{\Gamma_e} \mathbf{N}^{\mathrm{T}}\mathbf{t}\ d\Gamma_e \tag{4}$$

are the internal and external global force vectors, respectively, and $\mathbf{B}$ relates the symmetric strain rate tensor with $\widehat{\mathbf{v}}$. The global equilibrium relations (Eq. 3) represent

a set of implicit nonlinear equations which may be solved incrementally using a Newton-type algorithm. In a Newton–Raphson iterative scheme, the nonlinear system (Eq. 3) is typically expanded using Taylor series in the neighborhood of $\widehat{\mathbf{v}}$:

$$\mathbf{r}\left\{\widehat{\mathbf{v}}^{\mathrm{k}} - \delta\widehat{\mathbf{v}}^{\mathrm{k}}\right\} = \mathbf{r}\left\{\widehat{\mathbf{v}}^{\mathrm{k}}\right\} + \frac{\partial \mathbf{r}\left\{\widehat{\mathbf{v}}^{\mathrm{k}}\right\}}{\partial \widehat{\mathbf{v}}^{\mathrm{k}}}\delta\widehat{\mathbf{v}}^{\mathrm{k}} + O\left\{\widehat{v}^{k^2}\right\}, \tag{5}$$

where k represents a generic iteration and $\partial \mathbf{r}/\partial \widehat{\mathbf{v}}$ is the global tangent stiffness or Jacobian matrix of the nonlinear system of equations. The formulation of accurate estimates of the global Jacobian is at the heart of most numerical schemes developed to provide robust algorithms for the use of complex constitutive models with continuum approaches (e.g., see Crisfield (1997), Busso et al. (2000), and Meissonnier et al. (2001)).

Single Crystal Plasticity

Constitutive models developed to predict the anisotropic behavior of single crystal materials generally follow either a Hill-type or a crystallographic approach. As a common feature, they treat the material as a continuum in order to describe properly plastic or viscoplastic effects. Hill-type approaches (e.g., Schubert et al. 2000) are based on a generalization of the Mises yield criterion proposed by Hill (1950) to account for the non-smooth yield or flow potential surface required to describe the anisotropic flow stress behavior of single crystals. By modelling polycrystal structures with an appropriate crystallographic formulation based on microstructural internal state variables (e.g., dislocation densities), greater insight into the grain interaction and deformation behavior of polycrystals can be achieved. In constitutive formulations based on crystallographic slip, the macroscopic stress state is resolved onto each slip system following the Schmid law. Internal state variables are generally introduced in both formulations to represent the evolution of the microstructural state during the deformation process. Although recent developments in these two approaches have now reached an advanced stage, the major improvements have been made by crystallographic models due to their ability to incorporate complex micromechanisms of slip within the flow and evolutionary equations of the single crystal models. Typically, in dislocation density-based models, the evolution of the dislocation structure is described by processes of dislocation multiplication and annihilation as well as by the trapping of dislocations (Peeters et al. 2001; Zikry and Kao 1996). Further discretization into pure edge and screw types enables their individual roles to be more clearly distinguished (Arselins and Parks 2001). For example, edge and screw dislocations are associated with different dynamic recovery processes (i.e., climb for edges and cross-slip for screws), combining to influence the evolving dislocation structure of a deforming material. Moreover, it is now possible through X-ray profile analyses to quantify the edge and screw dislocation densities in deformed metals (Kysar et al. 2010; Dunne et al. 2012). Therefore, the ability to make quantitative rather than just qualitative comparisons between predicted and

measured dislocation densities constitutes a powerful tool. However, the roles of edge and screw dislocations in determining the nonuniform distribution of plastic strain in polycrystals as a result of intergranular and intragranular interactions are still not well understood.

A brief outline of the salient features of local and nonlocal crystal plasticity approaches is given below.

Local Single Crystal Approaches

A generic internal variable-based crystallographic framework is said to be a local one when the evolution of its internal variables can be fully determined by the local microstructural state at the material point. The description of the kinematics of most crystal plasticity theories follows that originally proposed in Asaro and Rice (1977), which has been widely reported in the computational mechanics literature (e.g., Kalidindi et al. 1992; Busso and McClintock 1996; Hatem and Zikry 2009; Busso et al. 2000; Abrivard et al. 2012). It relies on the multiplicative decomposition of the total deformation gradient, $\mathbf{F}$, into an inelastic, $\mathbf{F^p}$, and an elastic, $\mathbf{F^e}$ component. Thus, under isothermal conditions,

$$\mathbf{F} = \mathbf{F^e}\ \ \mathbf{F^p}. \tag{6}$$

Although single crystal laws can be formulated in a corrotational frame, i.e., the stress evolution is computed on axes which rotate with the crystallographic lattice, the most widely used approach is to assume that the material's response is hyperelastic, that is, its behavior can be derived from a potential (i.e., free energy) function. Such potential function may be expressed in terms of the elastic Green–Lagrange tensorial strain measure,

$$\mathbf{E^e} = \frac{1}{2}\left(\mathbf{F^{e^T}F^e} - 1\right), \tag{7}$$

and the corresponding objective work conjugate (symmetric) stress, or second Piola–Kirchhoff stress, $\mathbf{T}$. Note that the Cauchy stress is related to $\mathbf{T}$ by

$$\sigma = \det\{\mathbf{F^e}\}^{-1}\mathbf{F^eT}\ \ \mathbf{F^{e^T}}. \tag{8}$$

The hyperelastic response of the single crystal is governed by

$$\mathbf{T} = \frac{\partial\Phi\{\mathbf{E^e}\}}{\partial\mathbf{E^e}}, \tag{9}$$

where $\partial\Phi/\partial\mathbf{E^e}$ represents the Helmholtz potential energy of the lattice per unit reference volume. Differentiation of Eq. 9, and assuming small elastic stretches, yields

$$\mathbf{T} \cong \boldsymbol{L} : \mathbf{E^e}, \tag{10}$$

where $\boldsymbol{L}$ is the anisotropic linear elastic moduli. In rate-dependent formulations, the time rate of change of the inelastic deformation gradient, $\mathbf{F}^{\mathrm{p}}$, is related to the slipping rates on each slip system (Asaro and Rice 1977) as

$$\dot{\mathbf{F}}^{\mathrm{p}} = \left(\sum_{\alpha=1}^{n_\alpha} \dot{\gamma}^\alpha \mathbf{P}^\alpha \right) \mathbf{F}^{\mathrm{p}}, \qquad \text{with} \qquad \mathbf{P}^\alpha \equiv \mathbf{m}^\alpha \otimes \mathbf{n}^\alpha. \tag{11}$$

Here, $\mathbf{m}^\alpha$ and $\mathbf{n}^\alpha$ are unit vectors defining the slip direction and the slip plane normal to the slip system.

In rate-independent formulations, in contrast, flow rules are based on the well-known Schmid law and a critical resolved shear stress, τ_c^α, whereby the rate of slip is related to the time rate of change of the resolved shear stress, $\tau^\alpha (= \mathbf{T}:\mathbf{P}^\alpha)$. Then,

$$\dot{\tau}^\alpha = \dot{\tau}_c^\alpha = \sum_{\beta=1}^{n_\alpha} h^{\alpha\beta} \dot{\gamma}^\alpha, \quad \text{if} \quad \dot{\gamma}^\alpha > 0. \tag{12}$$

In the above equation, $h^{\alpha\beta}$, the slip hardening matrix coefficients, incorporate latent hardening effects. Due to the severe restrictions placed on material properties, such as latent hardening, to ensure uniqueness in the mode of slip (e.g., Anand and Kothari 1996; Busso and Cailletaud 2005), and the associated difficulties in its numerical implementation, the use of rate-independent formulations has been somehow restricted and much more limited than rate-dependent ones. This has been compounded by the fact that, by calibrating their strain rate sensitivity response accordingly, rate-dependent models have been successfully used in quasi-rate-independent regimes. Thus, the focus of the discussions will henceforth be on rate-dependent approaches.

The slip rate in Eq. 11 can functionally be expressed as

$$\dot{\gamma}^\alpha = \hat{\dot{\gamma}}^\alpha \left\{ \tau^\alpha, \ \mathrm{S}_1^\alpha, \ldots, \mathrm{S}_{m_s}^\alpha, \theta \right\}, \tag{13}$$

where $S_i^\alpha (\text{for } i = 1, \ldots, m_s)$ denotes a set of internal state variables for the slip system α and θ is the absolute temperature. A useful and generic expression for the overall flow stress in the slip system can be conveniently found by inverting Eq. 13. Let us, for instance, consider a case with three slip resistances ($m_s = 3$). Then,

$$\tau^\alpha = \pm \hat{f}_v^\alpha \left\{ \dot{\gamma}^\alpha, \ \mathrm{S}_3^\alpha, \theta \right\} \ \pm \ c_{\mathrm{dis}} \mathrm{S}_1^\alpha \ \pm \ c_{\mathrm{ss}} \mathrm{S}_2^\alpha, \tag{14}$$

where c_{dis} and c_{ss} are scaling parameters, S_1^α and S_2^α represent additive slip resistances, and S_3^α represents a multiplicative component. Here the distinction between the additive (S_1^α and S_2^α) and the multiplicative $\left(\mathrm{S}_3^\alpha\right)$ slip resistances is motivated by the additive and multiplicative use of nondirectional hardening variables rather than on mechanistic considerations. By expressing the flow stress in the slip system α, as in Eq. 14, the contributions from viscous effects (first term in Eq. 14), and dissipative (e.g., hardening, recovery) mechanisms arising from, for instance, forest dislocation

and solid solution strengthening (second and third terms), can be clearly identified. The majority of formulations rely on power law functions for Eq. 13, where the resolved shear stress is normalized by a slip resistance or hardening function, which corresponds to $S_3^\alpha \neq 0$ and $S_1^\alpha = S_2^\alpha = 0$ in Eq. 14. This introduces a coupling between the viscous term and microstructure which is inconsistent with most strengthening mechanisms. Works such as that of Busso and McClintock (1996) and Cheong and Busso (2004) have proposed flow stress relations with $S_1^\alpha \neq 0$ and $S_2^\alpha = S_3^\alpha = 0$ which allows a more physically meaningful interpretation of strengthening phenomena controlled by the dislocation structure. The particular application for FCC polycrystals to be discussed in the next section assumes that $S_1^\alpha \neq 0$, $S_2^\alpha \neq 0$, and $S_3^\alpha = 0$. For a more detailed discussion of these issues, see also Busso and Cailletaud (2005).

The relation between the overall slip resistance associated with statistically stored dislocation forest type of obstacles and the individual dislocation densities is defined by

$$S_i^\alpha = \lambda\, \mu\, b^\alpha \left\{ \sum_\beta h^{\alpha\beta} \rho_i^\beta \right\}^{1/2} \qquad (\text{for } i = 1, \ldots, n_s) \tag{15}$$

Here, λ is a statistical coefficient which accounts for the deviation from regular spatial arrangements of the dislocations, b^α represents the magnitude of the Burgers vector, and $h^{\alpha\beta}$ is a dislocation interaction matrix defined as

$$h^{\alpha\beta} = \omega_1 + (1 - \omega_2)\delta^{\alpha\beta} \tag{16}$$

The terms ω_1 and ω_2 in Eq. 16 are the interaction coefficients and $\delta^{\alpha\beta}$ is the Kronecker delta. The corresponding total athermal slip resistance due to forest dislocations can then be expressed according to

$$S_{\text{dis}}^\alpha = \left\{ \left(S_1^\alpha\right)^r + \left(S_2^\alpha\right)^r + \ldots + \left(S_{n_s}^\alpha\right)^r \right\}^{1/r} \tag{17}$$

with $r = 1$ being used when a linear sum of the slip resistances is desired and $r = 2$ for a mean square value.

To complete the set of constitutive relations, separate evolutionary equations need to be formulated for the individual dislocation densities, with dislocation multiplication and annihilation forming the bases of their evolutionary behavior. The time rate of change of each internal slip system variable can, in its most general form, be expressed as

$$\begin{aligned} \dot{\rho}_1^\alpha &= \hat{\dot{\rho}}_1^\alpha \left\{ \dot{\gamma}^\alpha, \rho_1^\alpha, \rho_2^\alpha, \ldots\ldots, \rho_{n_s}^\alpha, \theta \right\}, \dot{\rho}_2^\alpha \left\{ \dot{\gamma}^\alpha, \rho_1^\alpha, \rho_2^\alpha, \ldots\ldots, \rho_{n_s}^\alpha, \theta \right\}, \ldots \dot{\rho}_{n_s}^\alpha \\ &= \hat{\dot{\rho}}_{n_s}^\alpha \left\{ \dot{\gamma}^\alpha, \rho_1^\alpha, \rho_2^\alpha, \ldots\ldots, \rho_{n_s}^\alpha, \theta \right\}. \end{aligned} \tag{18}$$

An Application of Crystal Plasticity to the Study of Intergranular Damage in an FCC Alloy

In this section, the typical single crystal framework described in the previous section will be applied to the study of intergranular cracking in a typical FCC Al alloy. The work to be described here is based on that by Pouillier et al. (2012) which studied the effects of plasticity on the mechanism of intergranular cracking assisted by hydrogen-induced embrittlement in an Al-5%Mg alloy. As one of the main strengthening mechanism arises from the presence of Mg in solid solution, it is a suitable example for the use of crystal plasticity to study intergranular cracking phenomena.

Aluminum alloys, strengthened by elements in solid solution, can be sensitive to intergranular stress corrosion cracking in some specific microstructural states. In such alloys, precipitation of the Al3Mg2 phase at grain boundaries strongly favors intergranular fracture. When hydrogen is absorbed from the environment into the material, it diffuses along grain boundaries, weakening the matrix-precipitate interfaces which may, under high local stress–strain conditions, lead to a true intergranular decohesion mechanism. The main objective of this work was thus to study the effects of plasticity on the mechanism of intergranular cracking assisted by hydrogen-induced embrittlement in an Al-5%Mg alloy.

Single Crystal Formulation for the FCC Material

The single crystal model is based on the original formulation proposed by Cheong and Busso (2004) for Cu and on the recent work by Pouillier et al. (2012). The generic form of the slip rate, $\dot{\gamma}^{\alpha}$, given in Eq. 13, is assumed to be dominated by the thermally activated glide of dislocations over obstacles (i.e., mainly forest dislocations as the heat treatment used in the alloy of interest did not lead to full precipitation of Mg within the grains). The slip rate is related to the resolved shear stress, τ^{α}, through the exponential function proposed by Busso and McClintock (1996) and Busso et al. (2000):

$$\dot{\gamma}^{\alpha} = \dot{\gamma}_o \exp\left[-\frac{F_o}{k\theta}\left\{1 - \left\langle \frac{|\tau^{\alpha}| - S_T^{\alpha}\ \mu/\mu_o}{\widehat{\tau}} \right\rangle^{p}\right\}^{q}\right] \qquad \text{sign}(\tau^{\alpha}), \tag{19}$$

which accounts for the absolute temperature (θ, K) and the stress dependence of the activation energy. In Eq. 19, F_0 represents the Helmholtz free energy of activation at 0 K, k the Boltzmann constant, $\dot{\gamma}_o^{\alpha}$ a reference slip rate, and $\widehat{\tau}$ the maximum glide resistance at which dislocations can be mobilized without thermal activation. Furthermore, μ and μ_0 are the shear moduli at θ and 0 K, respectively. The exponents p and q describe the shape of the energy barrier vs. stress profile associated with interactions between dislocations and obstacles.

The main contributions to the overall slip resistance to plastic flow, S_T^{α}, are due to the friction stress induced by the Mg atoms in solid solution, S_{ss}^{α}, and to the athermal

slip resistance, S^{α}_{dis}. As the slip resistance contributions are assumed to be additive (see Eq. 14), then

$$S^{\alpha}_{T} = S^{\alpha}_{dis} + S^{\alpha}_{ss}. \tag{20}$$

Note that the scaling parameters c_{dis} and c_{ss} in the general expression given by Eq. 14 are, for this particular application, taken to be equal to one. Since only a very small part of the Mg atoms precipitate during the heat treatment, the concentration of Mg in solid solution is set to be equal to the average concentration in the material. Thus, the friction stress due to Mg atoms in solid solution, S^{α}_{ss}, is calculated based on the atomic size and concentration of Mg in the alloy (see Pouillier et al. 2012 for details), as proposed by Saada (1968). The athermal slip resistance is expressed as

$$S^{\alpha}_{dis} = \lambda \mu b^{\alpha} \sqrt{\left(\sum_{\beta=1}^{N} h^{\alpha\beta} \ \rho^{\beta}_{T} \right)}, \tag{21}$$

where the overall dislocation density for a given slip system β, ρ^{β}_{T}, is obtained from a discretization of the dislocation structure into pure edge and pure screw types, of densities ρ^{β}_{e} and ρ^{β}_{s}, respectively. Thus,

$$\rho^{\beta}_{T} = \rho^{\beta}_{e} + \rho^{\beta}_{s}. \tag{22}$$

In Eq. 21, λ and $h^{\alpha\beta}$ were as previously defined in Eqs. 15 and 16. The evolutionary equations of the individual dislocation densities account for the competing dislocation storage-dynamic recovery processes in FCC metals. They can be expressed as (Cheong et al. 2004; Cheong and Busso 2006)

$$\dot{\rho}^{\alpha}_{e} = \frac{C_e}{b^{\alpha}} \left[K_e \ \sqrt{\sum_{\beta=1}^{N} \rho^{\beta}_{T}} - 2 d_e \rho^{\alpha}_{e} \right] \ |\dot{\gamma}^{\alpha}|, \tag{23}$$

and

$$\dot{\rho}^{\alpha}_{s} = \frac{C_s}{b^{\alpha}} \left[K_s \sqrt{\sum_{\beta=1}^{N} \rho^{\beta}_{T}} - \rho^{\alpha}_{s} \left(\pi d^{2}_{s} K_s \sqrt{\sum_{\beta=1}^{N} \rho^{\beta}_{T}} + 2 d_s \right) \right] \ |\dot{\gamma}^{\alpha}|. \tag{24}$$

Here, the parameters C_e and C_s describe the relative contributions to the overall slip from edge and screw dislocations, while K_e and K_s are mobility constants associated with their respective mean free paths. Recovery processes are associated with the parameters d_e and d_s, which represent critical annihilation distances between dislocations of opposite Burgers vectors for both edge and screw types.

The calibration of the model's parameters was inspired by those reported for pure aluminum by Cheong and Busso (2006), except for the additional term which

accounts for the Mg solid solution effect. A comparison between the uniaxial stress–strain tensile curve obtained from a smooth uniaxial specimen of the polycrystal and that predicted using a 100 grain aggregate and the single crystal model was relied upon as a polycrystal validation. Details of the implicit numerical implementation of the above constitutive theory into the finite element method can be seen in Busso et al. (2000).

Intergranular Crack Observations, Strain Field Measurements, and Predicted Local Stress and Strain Fields

Here, tensile specimens charged with hydrogen were used to investigate quantitatively the effect of plastic deformation on the mechanism of intergranular crack initiation at the scale of the individual grains. An experimental procedure was set up to monitor the evolution of surface strain fields on in situ tested SEM notched specimens using digital image correlation techniques. In addition, measurements of the associated crystal orientation evolution at the micron scale were carried out using electron backscatter diffraction (EBSD). These measurements were then compared with finite element predictions of the local strain fields on the observed regions of the in situ specimen. The crystallographic grain orientations of the region of interest were discretized for the finite element analyses from EBSD maps.

Figure 1 shows the surface of one of the specimens tested in tension up to a 10% elongation. It can be seen that intergranular cracking occurred on grain boundaries perpendicular to the tensile direction after a few percent of plastic strain only on the half of the specimen which had been previously charged with hydrogen.

An optimized digital image correlation technique was used to compute surface strain fields from the recorded images. The field of view for the different regions analyzed was chosen so that it provided a range of fine-scale strain field measurements as well as the boundary conditions applied to the crystal aggregate region used in the modelling part of the study.

Figure 2a, b shows typically measured and predicted strain fields after 0.45% applied macroscopic strain, respectively. Figure 2c is a SEM micrograph of Fig. 2a's region, and Fig. 2d gives the predicted Mises stresses at the time when the first grain boundary failure was observed. It should be noted that at the cracked locations 1, 2, and 3 indicated in Fig. 2, the high levels of axial strain measured are to a great extent different from the real values due to the distortion introduced by the opening of the cracks during the digital image correlation measurements.

In this study, it was found that grain boundary cracking occurs on boundaries normally oriented to the applied tensile stress when the average local axial strain is as low as 0.45%. In addition, failed grain boundaries were found to be between grains that undergo very limited plastic deformation despite being embedded in large localized deformation regions. Local grain boundary tractions were predicted analytically from an Eshelby-type model and compared to the local normal tractions obtained from the finite element simulations of the polycrystal aggregate specimen region using crystal plasticity. The analytical traction of 175 MPa was consistent

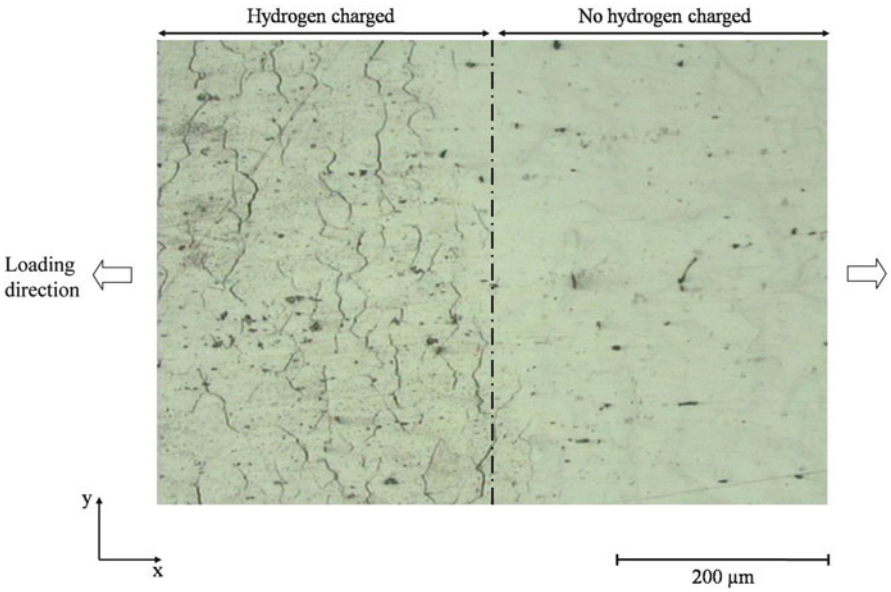

Fig. 1 Optical micrograph of intergranular fracture after 10% axial strain along the x-axis (Pouillier et al. 2011)

with the numerical predictions of 170 ± 35 MPa obtained from the finite element model of the polycrystal.

From this work, it can be seen that crystal plasticity concepts can provide an accurate insight into the local stress and strain fields responsible for intergranular damage.

Nonlocal Single Crystal Approaches

The study of experimentally observed size effects in a wide range of mechanics and materials problems has received a great deal of attention recently. Most continuum approaches and formulations dealing with these problems are based on strain gradient concepts and are known as nonlocal theories since the material behavior at a given material point depends not only on the local state but also on the deformation of neighboring regions. Examples of such phenomena include particle size effects on composite behavior (e.g., Nan and Clarke 1996), precipitate size in two-phase single crystal materials (Busso et al. 2000), increase in measured micro-hardness with decreasing indentor size (e.g., Swadener et al. 2002), and decreasing film thickness (e.g., Huber and Tsakmakis 1999), among others. The dependence of mechanical properties on length scales can in most cases be linked to features of either the microstructure, boundary conditions, or type of loading, which give rise to localized strain gradients. In general, the local material flow stress is controlled by

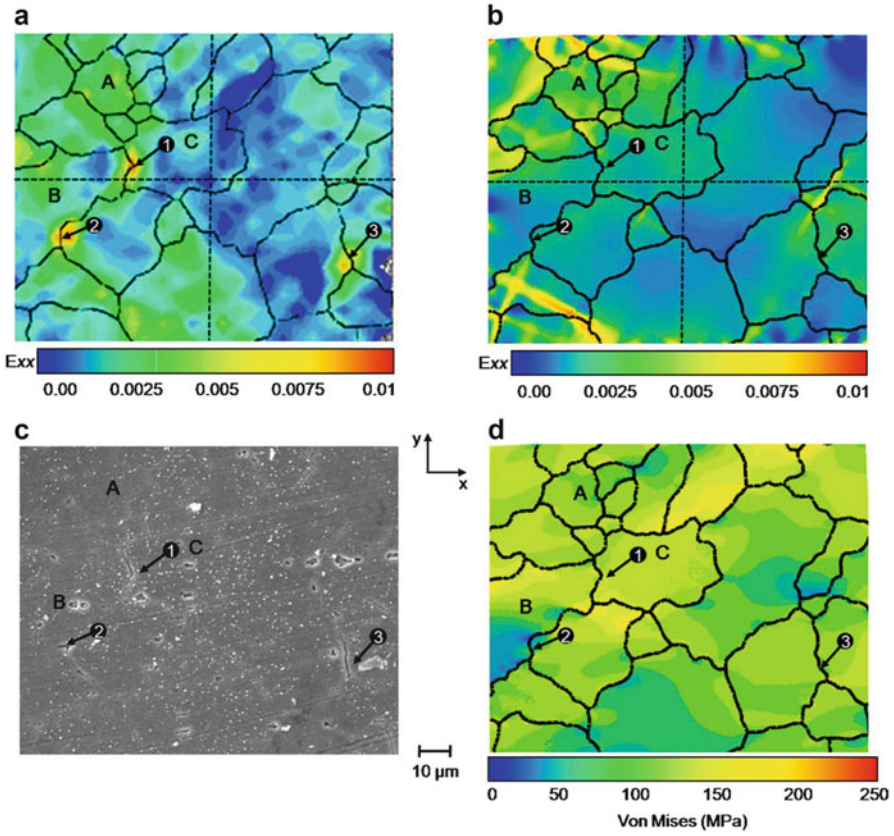

Fig. 2 (**a**) Measured and (**b**) predicted axial strain fields after 0.45% applied macroscopic strain, (**c**) micrograph of the same region as (**a**) and (**b**) at the end of the test (4.5% applied strain), and (**d**) predicted Mises stresses after 0.45% applied strain. *Arrows* 1, 2, and 3 indicate cracked grain boundaries (loading direction is parallel to the x-axis; Pouillier et al. 2011)

the actual gradients of strain when the dominant geometric or microstructural length scales force the deformation to develop within regions of less than approximately 5–10 µm wide in polycrystalline materials and of the order of 0.1–1.0 µm in single crystal materials. Thus, gradient-dependent behavior is expected to become important once the length scale associated with the local deformation gradients becomes sufficiently large when compared with the controlling microstructural feature (e.g., average grain size in polycrystal materials). In such cases, the conventional crystallographic framework discussed in the previous sections will be unable to predict properly the evolution of the local material flow stress.

The modelling of size effects observed in crystalline solids has been addressed by adding strain gradient variables into the constitutive framework, either in an explicit way in the flow rule (e.g., Aifantis 1984, 1987), or in the evolutionary equations of the internal slip system variables (e.g., Acharya and Beaudoin 2000; Busso et al.

2000; Bassani 2001), or by means of additional degrees of freedom associated with higher-order boundary and interface conditions (e.g., Shu 1998). Motivations for introducing strain gradients in continuum modelling stem from the multiscale analysis of micromechanics, as reviewed in Ghoniem et al. (2003). The resulting strain gradient components are related to the dislocation density tensor introduced by Nye (1953). As it will be shown later in the text, the dislocation density tensor is computed from the rotational part of the gradient of plastic deformation so that the resulting partial differential equations to be solved are generally of higher order than those used in classical mechanics.

Nonlocal Models Based on Internal Strain Gradient Variables

The more physically intuitive continuum approaches to describe strain gradient effects are constitutive theories (e.g., Arsenlis and Parks 2001; Busso et al. 2000; Acharya and Bassani 2000; Bassani 2001; Cheong et al. 2004; Dunne et al. 2007) which rely on internal state variables to describe the evolution of the obstacle or dislocation network within the material and generally introduce the strain gradient effects directly in the evolutionary laws of the slip system internal variables without the need for higher-order stresses. This requires that the overall slip resistance arising from the dislocation network, $S_{\text{dis}}{}^{\alpha}$ (see Eq. 21), incorporates contributions from both statistically stored (SS) and geometrically necessary (GN) forest dislocations.

The general form for the functional dependency of the evolutionary laws slip system internal variables given in Eq. 18, extended to include the additional dependency on the GNDs and the gradient of the slip rates, $\nabla\dot{\gamma}^{\alpha}$, is

$$\begin{aligned}
\dot{\rho}_1^{\alpha} &= \hat{\dot{\rho}}_1^{\alpha}\left\{\dot{\gamma}^{\alpha}, \rho_1^{\alpha}, \ \ldots, \rho_{n_s+n_G}^{\alpha}, \theta\right\},\\
&\vdots\\
\dot{\rho}_{n_s}^{\alpha} &= \hat{\dot{\rho}}_{n_s}^{\alpha}\left\{\dot{\gamma}^{\alpha}, \rho_1^{\alpha}, \ \ldots, \rho_{n_s+n_G}^{\alpha}, \theta\right\},\\
\dot{\rho}_{n_s+1}^{\alpha} &= \hat{\dot{\rho}}_{n_s+1}^{\alpha}\left\{\dot{\gamma}^{\alpha}, \rho_{n_s+1}^{\alpha}, \ \ldots, \rho_{n_s+n_G}^{\alpha}, \nabla\dot{\gamma}^{\alpha}, \theta\right\},\\
&\vdots\\
\dot{\rho}_{n_s+n_G}^{\alpha} &= \hat{\dot{\rho}}_{n_s+n_G}^{\alpha}\left\{\dot{\gamma}^{\alpha}, \rho_{n_s+1}^{\alpha}, \ \ldots, \rho_{n_s+n_G}^{\alpha}, \nabla\dot{\gamma}^{\alpha}, \theta\right\},
\end{aligned} \tag{25}$$

where n_s and n_G denote the number of SSD and GND types, respectively.

Consider the particular case where $n_s = 2$ and $n_G = 3$ in Eq. 25. Then, the total dislocation density on an arbitrary slip system can be defined by

$$\rho_{\text{T}}^{\alpha} = \left(\rho_{\text{e}}^{\alpha} + \rho_{\text{s}}^{\alpha}\right) + \left(\rho_{\text{Gs}}^{\alpha} + \rho_{\text{Get}}^{\alpha} + \rho_{\text{Gen}}^{\alpha}\right), \tag{26}$$

where $\left(\rho_{\text{e}}^{\alpha}, \rho_{\text{s}}^{\alpha}\right)$ are the SS densities introduced in Eq. 22 and $\left(\rho_{\text{Gs}}^{\alpha}, \ \rho_{\text{Get}}^{\alpha}, \ \rho_{\text{Gen}}^{\alpha}\right)$ the GND densities. Here, the GNDs have, in addition, been discretized into pure edge and screw components based on a mathematically equivalent GND vector, ρ_{G}^{α}, projected into a local orthogonal reference system where $\rho_{\text{Gs}}^{\alpha}$ represents a set of

screw GNDs parallel to the slip direction, $\mathbf{m}^a$, and ρ^{α}_{Gen} and ρ^{α}_{Get} edge GND components oriented parallel to the slip system normal, $\mathbf{n}^a$, and to $\mathbf{t}^a = \mathbf{m}^a \times \mathbf{n}^a$, respectively.

The evolution of the GNDs can be expressed in terms of a mathematically equivalent GND density vector, $\dot{\boldsymbol{\rho}}^{\alpha}_{G}$, defined so that its projection into the local ($\mathbf{m}^{\alpha}$, $\mathbf{n}^{\alpha}$, $\mathbf{t}^{\alpha}$) orthogonal reference system is as follows (Busso et al. 2000; Cheong et al. 2004):

$$\dot{\boldsymbol{\rho}}^{\alpha}_{G} = \dot{\rho}^{\alpha}_{Gs}\mathbf{m}^{\alpha} + \dot{\rho}^{\alpha}_{Get}\mathbf{t}^{\alpha} + \dot{\rho}^{\alpha}_{Gen}\mathbf{n}^{\alpha}. \tag{27}$$

Subsequently, the evolutionary law for each set of GNDs is determined from Nye's dislocation density tensor, $\boldsymbol{\Gamma}$ (Nye 1953), in terms of the spatial gradient of the slip rate:

$$\dot{\boldsymbol{\Gamma}} = \mathrm{curl}\ \left(\dot{\gamma}^{\alpha}\mathbf{n}^{\alpha}\mathbf{F}^{p}\right) = b^{\alpha}\left(\dot{\rho}^{\alpha}_{Gs}\mathbf{m}^{\alpha} + \dot{\rho}^{\alpha}_{Get}\mathbf{t}^{\alpha} + \dot{\rho}^{\alpha}_{Gen}\mathbf{n}^{\alpha}\right). \tag{28}$$

Under small strains and rotations, Eq. 28 simplifies to

$$\dot{\rho}^{\alpha}_{Gs} = \frac{1}{b^{\alpha}}\nabla\dot{\gamma}^{\alpha}\cdot\mathbf{t}^{\alpha},\quad \dot{\rho}^{\alpha}_{Get} = \frac{1}{b^{\alpha}}\nabla\dot{\gamma}^{\alpha}\cdot\mathbf{m}^{\alpha},\quad \dot{\rho}^{\alpha}_{Gen} = 0. \tag{29}$$

The slip resistance contributions from the SSDs and GNDs can then be determined from Eq. 21 using the definition of the overall dislocation density given by Eq. 26.

This class of theories has been shown capable of providing great physical insight into the effects of microstructure on the observed macroscopic phenomena, including rate-independent plastic deformation and viscoplasticity in both single crystal and polycrystalline materials (e.g., Arsenlis and Parks 2001; Busso et al. 2000; Acharya and Bassani 2000). One additional attractive aspect of these theories is that they are relatively easy to implement numerically and do not require higher-order stresses and additional boundary conditions or independent degrees of freedom. However, some of the limitations of these types of theories is that they are unable to describe problems which may require nonstandard boundary conditions, as discussed in Cheong et al. (2004), such as the boundary layer problem modeled by Shu et al. (2001), and that they may exhibit a mesh sensitivity in cases where there is a predominance of geometrically necessary dislocations relative to statistically stored dislocations (Cheong et al. 2004).

Nonlocal Models Based on the Mechanics of Generalized Continua

Approaches based on the so-called mechanics of *generalized continua* incorporate as a common feature extra-hardening effects associated with the dislocation density tensor. Generalized crystal plasticity models developed in the past 40 years can be classified into two main groups.

In the first one, strain gradient plasticity models involve either the rotational part of the plastic distortion (i.e., the plastic rotation), its full gradient, or just the gradient of its symmetric part (Steinmann 1996; Fleck and Hutchinson 1997; Gurtin 2002; Gurtin and Anand 2009).

The second group involves generalized continuum theories with additional degrees of freedom accounting for either the rotation or the full deformation of a triad of crystal directors, and the effect of their gradients on hardening, such as Cosserat-type models (Forest et al. 2001; Clayton et al. 2006), and those based on the micromorphic theory (Eringen and Claus 1970; Bammann 2001; Cordero et al. 2010, 2012a, b).

Most of these theories have been shown to capture size effects, at least in a qualitative way. However, a clear demonstration that they can reproduce the scaling laws expected in precipitate hardening or grain size effect has not been fully provided yet. The additional hardening effects inherent in generalized continuum crystal plasticity models can be summarized by the main features identified in Fig. 3. Here, the effect of the dominant microstructural length scale, l, such as grain or precipitate size, on the material flow stress is shown schematically in a log–log diagram. The curve can be characterized by three main features: the stress range, $\Delta\Sigma$; the characteristic length, l_c; and the slope of the intermediate region, defined by a

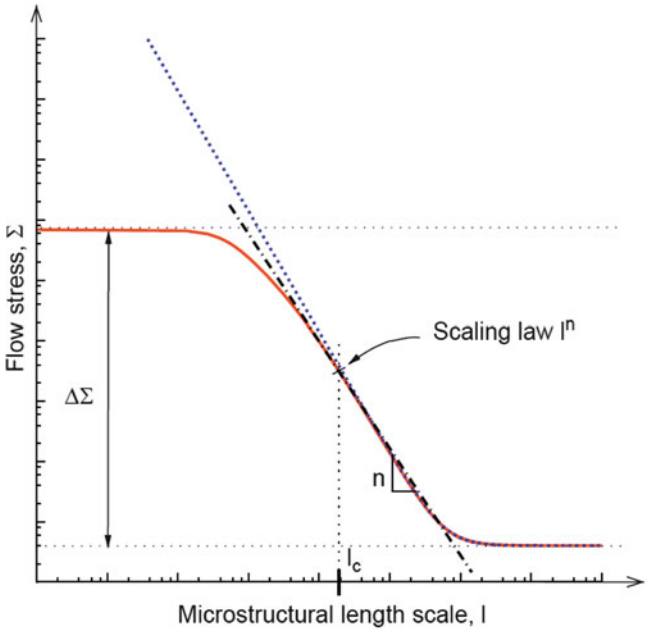

Fig. 3 Effect of the dominant microstructural length scale, l, on the material flow stress, Σ, predicted by different types of models such as those exhibiting two asymptotic regimes (*solid line*), and others which exhibited an unbounded flow stress for small length scales (*dotted line*). Also included is the scaling law in the transition domain (*dot-dashed line*) (Cordero et al. 2010)

scaling law of the form, $\Sigma \propto l^n$ at $l = l_c$. Here, $\Delta\Sigma$ corresponds to the maximum increase in strength due to size effects relative to the size-independent level. Figure 3 shows that when the characteristic size of the microstructure decreases, the material strengthens. For large values of l, the asymptotic behavior corresponds to the size-independent response of conventional crystal plasticity models reviewed in the previous section. In contrast, for small values of l, a bounded or unbounded asymptotic behavior can be obtained, depending on the type of model considered. Cosserat-type crystal plasticity models (e.g., Forest et al. 2001), for instance, predict an asymptotically saturated overstress $\Delta\Sigma$ as in Fig. 3. In the intermediate region, when l is closed to the characteristic length, l_c, the size-dependent response is characterized by the scaling law, $\Sigma \propto l^n$. The parameters $\Delta\Sigma$, l_c, and n can be derived explicitly for the different classes of generalized material models described above. However, an analytic description of the size-dependent behavior of materials is possible only for some specially simplified geometrical situations. Examples are the shearing of a single crystal layer under single (or double) slip for strain gradient plasticity models considered in Shu et al. (2001), Bittencourt et al. (2003), Hunter and Koslowski (2008), and Cordero et al. (2010, 2012a, b) and the single slip in a two-phase laminate microstructure by Forest and Sedlacek (2003). The plastic slip distributions were compared with those obtained from the reference continuous dislocation line tension model, Cosserat, and strain gradient plasticity models.

When crystal plasticity is considered under small strain assumptions, the gradient of the velocity field can be decomposed into the elastic and plastic distortion rates:

$$\dot{\mathbf{H}} = \dot{\mathbf{u}} \otimes \nabla = \dot{\mathbf{H}}^{\mathrm{e}} + \dot{\mathbf{H}}^{\mathrm{p}}, \tag{30}$$

where

$$\dot{\mathbf{H}}^{\mathrm{p}} = \sum_{\alpha} \dot{\gamma}^{\alpha} \mathbf{P}^{\alpha}, \tag{31}$$

with $\mathbf{u}$, the displacement field; α, the number of slip systems; $\dot{\gamma}^{\alpha}$, the slip rate for the slip system α; and $\mathbf{P}^{\alpha}$ as defined in Eq. 11. The elastic distortion tensor, $\mathbf{H}^{\mathrm{e}}$, which represents the stretch and rotation of the lattice, links the compatible total deformation, $\mathbf{H}$, with the incompatible plastic deformation, $\mathbf{H}^{\mathrm{p}}$, which describes the local lattice deformation due to the flow of dislocations. On account of Eq. 30 and since applying the curl operator to the compatible field represented by $\mathbf{H}$ is equal to zero, it follows that

$$\operatorname{curl} \dot{\mathbf{H}} = 0 = \operatorname{curl} \dot{\mathbf{H}}^{\mathrm{e}} + \operatorname{curl} \dot{\mathbf{H}}^{\mathrm{p}}. \tag{32}$$

The incompatibility of the plastic distortion is characterized by its curl part, also known as the dislocation density tensor or Nye's tensor, $\boldsymbol{\Gamma}$ (Nye 1953; Steinmann 1996; Acharya and Bassani 2000), defined as

$$\boldsymbol{\Gamma} = -\operatorname{curl} \mathbf{H}^{\mathrm{p}} = \operatorname{curl} \mathbf{H}^{\mathrm{e}}. \tag{33}$$

The tensors $\mathbf{H}$, $\mathbf{H}^{\mathrm{e}}$, and $\mathbf{H}^{\mathrm{p}}$ are generally nonsymmetric; thus, they can be decomposed into their symmetric and skew-symmetric parts:

$$\mathbf{H} = \mathbf{E} + \mathbf{W}, \mathbf{H}^{e} = \mathbf{E}^{e} + \mathbf{W}^{e}, \mathbf{H}^{p} = \mathbf{E}^{p} + \mathbf{W}^{p}, \tag{34}$$

Combining Eqs. 32 and 34 leaves

$$0 = \operatorname{curl} \mathbf{E}^{e} + \operatorname{curl} \mathbf{W}^{e} + \operatorname{curl} \mathbf{H}^{p}. \tag{35}$$

Neglecting the curl part of the elastic strain, $\mathbf{E}^{e}$, leads to the following approximation to the dislocation density tensor derived by Nye:

$$\boldsymbol{\Gamma} = \operatorname{curl} \mathbf{H}^{\boldsymbol{e}} = \operatorname{curl} \mathbf{E}^{\boldsymbol{e}} + \operatorname{curl} \mathbf{W}^{\boldsymbol{e}} \approx \operatorname{curl} \mathbf{W}^{\boldsymbol{e}}. \tag{36}$$

Thus, Nye's formula sets a linear relationship between the dislocation density tensor and the lattice curvature defined by $\mathbf{W}^{\boldsymbol{e}}$. The Cosserat crystal plasticity theory accounts for the effect of lattice curvature on the crystal hardening behavior by incorporating the three additional independent degrees of freedom associated with the components of the lattice rotation, $\mathbf{W}^{\boldsymbol{e}}$. In contrast, theories such as those proposed by Gurtin (2002) and Svendsen (2002), for example, include the full curl of the plastic distortion, $\mathbf{H}^{\mathrm{p}}$, as an independent internal variable of the constitutive model. This requires in general nine additional degrees of freedom associated with the generally nonsymmetric plastic distortion tensor, $\mathbf{H}^{\mathrm{p}}$. This subclass of models is sometimes referred to as "curl $\mathbf{H}^{\mathrm{p}}$" type (Cordero et al. 2010).

A consequence of neglecting the curl of the elastic strain tensor in Cosserat-type models is that Cosserat effects can arise even in the elastic regime as soon as a gradient of "elastic" rotation exists (i.e., curl $\mathbf{W}^{e} \neq 0$). This implies that as soon as the curl $\mathbf{E}^{\boldsymbol{e}} \neq 0$, the curl $\mathbf{W}^{e} \neq 0$. In contrast, in the curl $\mathbf{H}^{\mathrm{p}}$-type theories, strain gradient effects can only arise when plastic deformation has developed. As has been shown in Cordero et al. (2010), this can lead to discontinuities in the generalized tractions at the interface between elastic and plastic regions. For the curl $\mathbf{H}^{\mathrm{p}}$-type models, it is necessary to identify numerically higher-order boundary conditions at the elastoplastic boundaries which poses difficulties in the numerical implementation of this type of formulations, as discussed in Cordero et al. (2010).

To overcome the limitations of both the Cosserat and curl $\mathbf{H}^{\mathrm{p}}$-type theories, a new regularization method has recently been proposed by Cordero et al. (2010) (see also Cordero et al. 2012a, b). Their model, which they have called *microcurl*, falls into the class of generalized continua with additional degrees of freedom. Here, the effect of the dislocation density tensor is introduced into the classical crystal plasticity framework by means of the micromorphic theory of single crystals. It relies on the introduction of an additional plastic micro-deformation variable, χ^{p}, a second-rank generally nonsymmetric tensor. It is distinct from the plastic distortion tensor $\mathbf{H}^{\mathrm{p}}$, which is still treated as an internal variable of the problem in the same way as in curl $\mathbf{H}^{\mathrm{p}}$-type theories. For the general three-dimension case, the nine components of χ^{p} are introduced as independent degrees of freedom. The *microcurl* theory will be briefly summarized next.

Microcurl Model: Balance and Constitutive Equations

If it is assumed that only the curl part of the gradient of plastic micro-deformation plays a role in the power of internal forces, $p^{(i)}$, then

$$p^{(i)} = \boldsymbol{\sigma} : \dot{\mathbf{H}}^{\mathrm{e}} + \mathrm{s} : \quad \dot{\chi}^{\mathrm{p}} + \mathbf{M} : \quad \mathrm{curl}\, \dot{\chi}^{\mathrm{p}}, \tag{37}$$

where **s** and **M** are the generally asymmetric micro-stress and double or hyper-stress tensors, respectively, work conjugates to the plastic micro-deformation and its curl. The curl operator is defined in a Cartesian basis as

$$(\mathrm{curl}\, \chi^{\mathrm{p}})_{\mathrm{ij}} = \varepsilon_{\mathrm{jkl}}\ \chi^{\mathrm{p}}_{\mathrm{ik,l}}. \tag{38}$$

Using the method of virtual power to derive the generalized balance of momentum equations and assuming no volume forces for simplicity, one finds the following balance equations:

$$\mathrm{div}\, \boldsymbol{\sigma} = 0, \quad \mathrm{curl}\, \mathbf{M} + \mathbf{s} = 0. \tag{39}$$

The corresponding boundary conditions are

$$\mathbf{t} = \boldsymbol{\sigma} \cdot \mathbf{n}_{\mathrm{e}}, \quad \mathbf{m}_{\mathrm{e}} = \mathbf{M} \cdot \breve{\boldsymbol{\varepsilon}} \cdot \mathbf{n}_{\mathrm{e}}, \tag{40}$$

where **t** and $\mathbf{m_e}$ are the simple and double tractions at the boundary and $\breve{\boldsymbol{\varepsilon}}$ is the third-order permutation tensor.

The free energy function is assumed to depend on the elastic strain tensor, $\mathbf{E}^{e}$, the curl of χ^{p}, and on a relative plastic strain, $\mathbf{e}^{p}$, defined as the difference between the plastic distortion and the plastic micro-variable, $\mathbf{e}^{p} = \mathbf{H}^{\mathrm{p}} - \chi^{\mathrm{p}}$. Then,

$$\psi = \widehat{\psi}(\mathbf{E}^{\mathrm{e}},\ \mathrm{curl}\ \chi^{\mathrm{p}},\ \mathbf{e}^{\mathrm{p}}). \tag{41}$$

Furthermore, considering the following state laws,

$$\boldsymbol{\sigma} = \rho \frac{\partial \psi}{\partial \mathbf{E}^{\mathrm{e}}}, \mathbf{s} = -\rho \frac{\partial \psi}{\partial \mathbf{e}^{\mathrm{p}}}, \mathbf{M} = \rho \frac{\partial \psi}{\partial \boldsymbol{\Gamma}_{\chi}}, \tag{42}$$

where $\boldsymbol{\Gamma}_{\chi} = \mathrm{curl}\, \chi^{\mathrm{p}}$ and assuming a quadratic function for the potential function ψ in Eq. 42, one obtains

$$\boldsymbol{\sigma} = \boldsymbol{L}\, \mathbf{E}^{\mathrm{e}}, \quad \mathbf{s} = -\mathrm{H}_{\chi}\, \mathbf{e}^{\mathrm{p}}, \quad \mathbf{M} = \mathrm{A}\ \boldsymbol{\Gamma}_{\chi}. \tag{43}$$

Here, H_{χ} and A are the generalized moduli, which define an intrinsic length scale associated with the size effect exhibited by the solution of the boundary value problem,

$$\mathrm{l_w} = \sqrt{\frac{\mathrm{A}}{\mathrm{H}_{\chi}}}. \tag{44}$$

The flow rule can be derived from a viscoplastic potential, $\Omega(\boldsymbol{\sigma} + \mathbf{s})$, expressed in terms of the effective stress, $(\boldsymbol{\sigma} + \mathbf{s})$, that intervenes in the dissipation rate equation. Then,

$$\dot{\mathbf{H}}^{\mathrm{p}} = \frac{\partial \Omega}{\partial(\boldsymbol{\sigma} + \mathbf{s})}. \tag{45}$$

For a single crystal having N potentially active slip systems, the kinematics of plastic deformation is dictated by Eq. 31. It is worth mentioning that, in a similar way as in the Cosserat- and curl $\mathbf{H}^p$-type theories, a back stress component arises naturally from the formulation. Here, the back stress is $\mathbf{x} = -\mathbf{s}$: $(\mathbf{l} \otimes \mathbf{n})$.

Note also that the modulus H_χ in Eq. 43 introduces a coupling between the macro- and micro-variables. This can be interpreted as a penalty factor that constrains the relative plastic deformation, $\mathbf{e}^p$, to remain sufficiently small. Equivalently, a high value of H_χ forces the plastic micro-deformation to be as close as possible to the macroscopic plastic distortion tensor, $\mathbf{H}^p$. In the limit, the use of a Lagrange multiplier instead of the penalty factor, H_χ, is necessary to enforce the following internal constraint:

$$\chi^{\mathrm{p}} \equiv \mathbf{H}^{\mathrm{p}}. \tag{46}$$

When Eq. 46 is satisfied, then

$$\operatorname{curl} \chi^{\mathrm{p}} \equiv \operatorname{curl} \mathbf{H}^{\mathrm{p}} = \boldsymbol{\Gamma}_\chi. \tag{47}$$

Note also that when the internal constraint (Eq. 46) is enforced, the *microcurl* model reduces to the curl $\mathbf{H}^p$-type theories (e.g., Gurtin 2002). As a general case, the selection of H_χ should be made so that the micro-deformation χ^{p} does not depart too much from $\mathbf{H}^p$ and retains the physical meaning of the dislocation density tensor.

Application of the Microcurl Model to Study the Deformation Behavior of a Polycrystalline Aggregate

The microcurl model was applied to study the global and local responses of two-dimensional polycrystalline aggregates with grain sizes ranging from 1 to 200 microns. (For full details about this work, refer to Cordero et al. 2012b.) A typical result concerning the effect of grain size on the way plastic deformation in polycrystals evolves is shown in Fig. 4 for a 52-grain aggregate. These contour plots show the field of equivalent plastic deformation, $\widetilde{\varepsilon}^p$, defined as the time-integrated value of

$$\dot{\widetilde{\varepsilon}}^p = \sqrt{\frac{2}{3}\dot{\mathbf{H}}^{\mathrm{p}} : \quad \dot{\mathbf{H}}^{\mathrm{p}}} \tag{48}$$

From Fig. 4a, b, it can be seen that, at the onset of plastic deformation, plasticity starts in the same grains and at the same locations in 100-μm grains as in 1-μm grains. This is due to the fact that the same critical resolved shear stress is adopted for both grain sizes, that is, the same initial dislocation densities are assumed in both cases. In contrast, at higher mean plastic strain levels, the strongly different values of the plastic micro-deformation gradients lead to significantly different plastic strain fields. Two main features are evidenced in Fig. 4c–f. Firstly, a tendency to strain localization in bands is observed for small grain sizes. The strain localization bands cross several grains, whereas plastic strain becomes more diffuse at larger grain

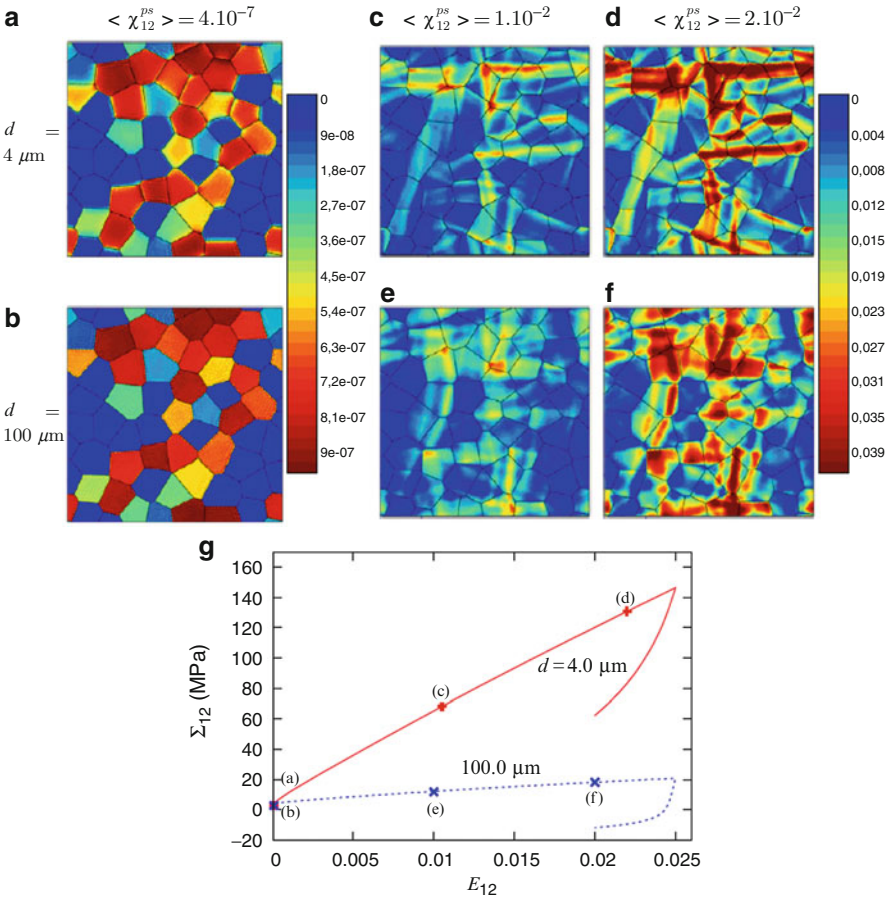

Fig. 4 (**a**–**f**) Contour plots of the accumulated plastic strain $\widetilde{\varepsilon}^{p}$ for two grain sizes, $d = 100$ and 4 μm, and different mean values of the plastic strain: $\chi_{12}^{ps} \approx 0.0$, 0.01, and 0.02, *o*btained with a 2D 55-grain aggregate under simple shear, (**g**) macroscopic stress–strain response of the corresponding aggregate, with the letters indicating the different loading steps corresponding to the (**a**–**f**) contour plots (Cordero et al. 2010)

sizes, something which had already been seen in the simulations presented in Cordero et al. (2012a). Secondly, a consequence of this localization is that some small grains are significantly less deformed than the larger ones. These features are also visible on the plastic deformation maps of Fig. 5 for the same aggregate but different grain sizes. This figure also shows the field of the norm of the dislocation density tensor:

$$\left\|\boldsymbol{\Gamma}_{\chi}\right\| : \sqrt{\boldsymbol{\Gamma}_{\chi} : \boldsymbol{\Gamma}_{\chi}}. \tag{49}$$

This scalar quantity indicates the presence of GNDs and has the physical dimension of lattice curvature (mm^{-1}). For large grains, GNDs are mainly located close to grain boundaries. At smaller grain sizes, the GND densities become significantly greater and spread over larger zones within the grains. Note also that pileups-like structures close to grain boundaries are clearly visible in the 10-μm grain aggregate. It should be noted that strain gradient plasticity models may be prone to strain

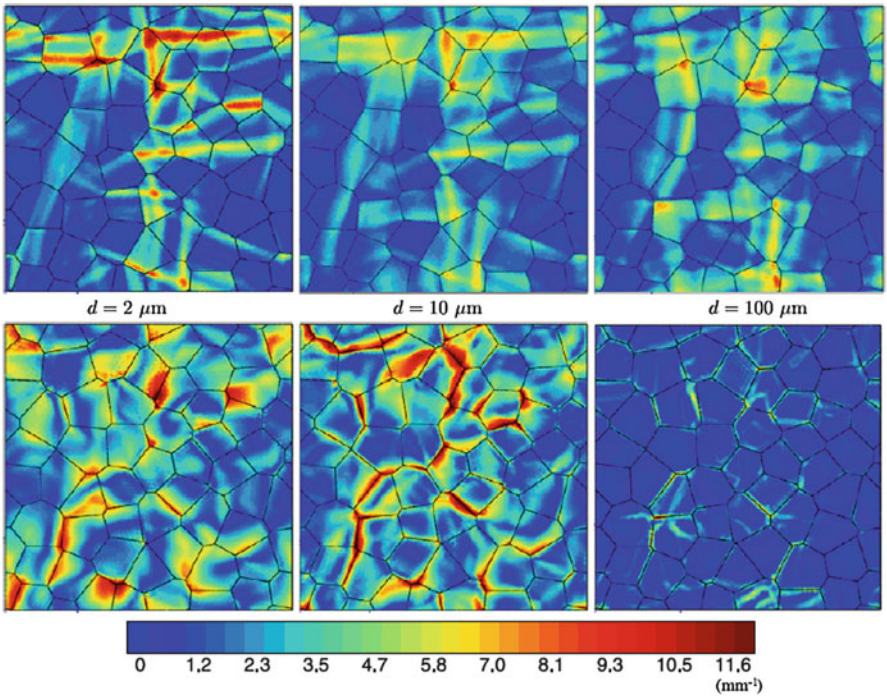

Fig. 5 Grain size effect on the accumulated plastic strain, $\widetilde{\varepsilon}^{p}$ (*top* figures), and on the norm of the dislocation density tensor, $\|\Gamma\|$ (*bottom* figures). These contour plots are obtained with the 2D 55-grain aggregate for the same mean value of $\chi_{12}^{\mathrm{ps}} \approx 0.01$. The color scale for the plastic strain field of the top figures is the same as that of Fig. 4 on the right. The color scale at the bottom is that for the dislocation density tensor fields (Cordero et al. 2010)

localization when plasticity is confined in small regions. The reason for such behavior is that acute slip bands that exhibit a strong gradient of plastic slip perpendicular to the slip plane are not associated with GND formation. In contrast, regions of high lattice curvature or kink bands lead to an energy increase. This explains why, at small scales, intense slip bands are preferred to strongly curved regions and pileups. This has been confirmed by the observation of the equivalent plastic deformation contour plots in Cordero et al. (2012b)'s Fig. 8 for three aggregates with different mean grain sizes. Here, the zones of intense plastic deformation were found to be systematically parallel to slip plane traces, thus indicating the formation of slip bands during deformation.

In summary, the microcurl model was found to naturally predict a size-dependent kinematic hardening behavior which is responsible for the observed strong size effects. Furthermore, the results showed that the flow stress attained at a given averaged plastic strain follows a power law scaling relation with the grain size, for grain sizes larger than a critical value. Likewise, the predicted plastic deformation fields were found to be strongly affected by grain size, with micron-size grain regions exhibiting the formation of intense slip bands crossing several grains. Finally, the dislocation density tensor, $\boldsymbol{\Gamma}_{\chi}$ was found to not only impact the overall polycrystal behavior but also control the way plastic deformation develops within the grains.

In Cordero et al. (2010), it was shown that the microcurl approach could also be successfully used to predict experimentally observed precipitate size effects in two-phase single crystal nickel-based superalloys. The results are shown in Fig. 6, where a comparison between experimental data, in the form of precipitate size vs. size effect strengthening from a two-phase superalloy material (γ phase matrix with an embedded 68% γ' precipitates), the predictions of Busso et al. (2000), and that obtained using the *microcurl* model (Cordero et al. 2012b) are shown. It can be seen that the microcurl model is able to simulate a precipitate size effect naturally. Moreover, the identified characteristic length, $l_c = 200$ nm, is approximately the matrix channel width in Ni-based superalloys.

Concluding Remarks

The different constitutive modelling approaches which address a broad range of phenomena at either the single crystal or the polycrystalline levels have been critically discussed. This review has also highlighted the rich variety of physical, computational, and technological issues within the broad area of micromechanics which have been successfully addressed and has identified some theoretical and computational difficulties and challenges for future developments. In the future, crystallographic approaches for single crystal behavior which rely on internal slip system variables will continue to provide the most powerful framework to incorporate basic mechanistic understanding in continuum models. However, further development of 3D measurement and microstructure characterization techniques, such as X-ray tomography and high-resolution EBSD, will require new challenges to be

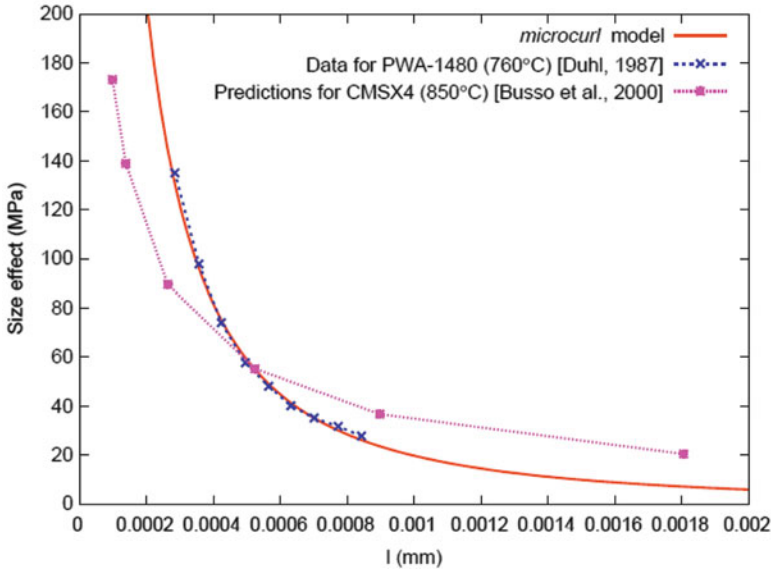

Fig. 6 Comparison between experimental data, in the form of precipitate size vs. size effect strengthening from a two-phase material (elasto-viscoplastic γ phase matrix with an embedded 68% quasi-elastic γ' precipitates) from Duhl (1987), the prediction of Busso et al. (2000), and that obtained using the *microcurl* model by Cordero et al. (2012b)

overcome. Novel and more efficient computational techniques for processing and visualizing the enormous amount of data generated when studying real 3D polycrystalline materials will be required. The ever increasing need to address coupled multi-physics phenomena, such as the microstructural evolution driven by diffusion processes, is driving new multidisciplinary research and providing crystal plasticity with new and exciting challenges.

References

G. Abrivard, E.P. Busso, S. Forest, B. Appolaire, Phase field modelling of grain boundary motion driven by curvature and stored energy gradient. Part I – theory and numerical implementation. Philos. Mag. **92**(28–30), 3618–3642 (2012)

A. Acharya, J.L. Bassani, Lattice incompatibility and a gradient theory of crystal plasticity. J. Mech. Phys. Solids **48**, 1565–1595 (2000)

A. Acharya, A.J. Beaudoin, Grain size effects in viscoplastic polycrystals at moderate strains. J. Mech. Phys. Solids **48**, 2213–2230 (2000)

E.C. Aifantis, On the microstructural origin of certain inelastic models. J. Eng. Mater. Technol. **106**, 326–330 (1984)

E.C. Aifantis, The physics of plastic deformation. Int. J. Plast. **3**, 211–248 (1987)

L. Anand, M. Kothari, A computational procedure for rate independent crystal plasticity. J. Mech. Phys. Solids **44**, 525–558 (1996)

A. Arsenlis, D. Parks, Modeling the evolution of crystallographic dislocation density in crystal plasticity. J. Mech. Phys. Solids **50**, 1979–2009 (2001)
R.J. Asaro, J.R. Rice, Strain localization in ductile single crystals. J. Mech. Phys. Solids **25**, 309–338 (1977)
D.J. Bammann, A model of crystal plasticity containing a natural length scale. Mater. Sci. Eng. A **309–310**, 406–410 (2001)
J.L. Bassani, Incompatibility and a simple gradient theory of plasticity. J. Mech. Phys. Solids **49**, 1983–1996 (2001)
E. Bittencourt, A. Needleman, M. Gurtin, E. Van der Giessen, A comparison of nonlocal continuum and discrete dislocation plasticity predictions. J. Mech. Phys. Solids **51**(2), 281–310 (2003)
E.P. Busso, G. Cailletaud, On the selection of active slip systems in crystal plasticity. Int. J. Plast. **21**, 2212–2231 (2005)
E.P. Busso, F. McClintock, A dislocation mechanics-based crystallographic model of a B2-type intermetallic alloy. Int. J. Plast. **12**, 1–28 (1996)
E.P. Busso, F.T. Meissonnier, N.P. O'Dowd, Gradient-dependent deformation of two-phase single crystals. J. Mech. Phys. Solids **48**, 2333–2361 (2000)
K.S. Cheong, E.P. Busso, Discrete dislocation density modelling of single phase FCC polycrystal aggregates. Acta Mater. **52**, 5665–5675 (2004)
K.S. Cheong, E.P. Busso, Effects of lattice misorientations on strain heterogeneities in FCC polycrystals. J. Mech. Phys. Solids **54**(4), 671–689 (2006)
K. Cheong, E. Busso, A. Arsenlis, A study of microstructural length scale effects on the behavior of FCC polycrystals using strain gradient concepts. Int. J. Plast. **21**, 1797–1814 (2004)
J.D. Clayton, D.L. McDowell, D.J. Bammann, Modeling dislocations and disclinations with finite micropolar elastoplasticity. Int. J. Plast. **22**, 210–256 (2006)
N.M. Cordero, A. Gaubert, S. Forest, E.P. Busso, F. Gallerneau, S. Kruch, Size effects in generalised continuum crystal plasticity for two-phase laminates. J. Mech. Phys. Solids **58**, 1963–1994 (2010)
N.M. Cordero, S. Forest, E.P. Busso, S. Berbenni, M. Cherkaoui, Grain size effects on plastic strain and dislocation density tensor fields in metal polycrystals. Comput. Mater. Sci. **52**, 7–13 (2012a)
N.M. Cordero, S. Forest, E.P. Busso, Generalised continuum modelling of grain size effects in polycrystals. C.R. Mec. **340**, 261–264 (2012b)
M.A. Crisfield, *Non-linear Finite Element Analysis of Solids and Structures*, vol 1 & 2, 4th edn. (Wiley, New York, 1997)
D.N. Duhl, Directionally solidified superalloys, in *Superalloys II – High Temperature Materials for Aerospace and Industrial Power*, ed. by C. T. Sims, N. S. Stoloff, W. C. Hagel, (Wiley, Toronto, 1987), pp. 189–214
F.P.E. Dunne, D. Rugg, A. Walker, Length scale-dependent, elastically anisotropic, physically-based hcp crystal plasticity: application to cold-dwell fatigue in Ti alloys. Int. J. Plast. **23**, 1061–1083 (2007)
F.P.E. Dunne, R. Kiwanuka, A.J. Wilkinson, Crystal plasticity analysis of micro-deformation, lattice rotation and geometrically necessary dislocation density. Proc. R. Soc. A-Math. Phys. Eng. Sci. **468**, 2509–2531 (2012)
A.C. Eringen, W.D. Claus, A micromorphic approach to dislocation theory and its relation to several existing theories, in *Fundamental Aspects of Dislocation Theory*, National Bureau of Standards (US) special publication 317, II, ed. by J. A. Simmons, R. de Wit, R. Bullough, (National Bureau of Standards, 1970), pp. 1023–1062
N.A. Fleck, J.W. Hutchinson, Strain gradient plasticity. Adv. Appl. Mech. **33**, 295–361 (1997)
S. Forest, R. Sedlacek, Plastic slip distribution in two-phase laminate microstructures: dislocation-based vs. generalized-continuum approaches. Philos. Mag. A **83**, 245–276 (2003)
S. Forest, F. Pradel, K. Sab, Asymptotic analysis of heterogeneous Cosserat media. Int. J. Solids Struct. **38**, 4585–4608 (2001)
N.M. Ghoniem, E.P. Busso, H. Huang, N. Kioussis, Multiscale modelling of nanomechanics and micromechanics: an overview. Philos. Mag. **83**, 3475–3528 (2003)

M.E. Gurtin, A gradient theory of single-crystal viscoplasticity that accounts for geometrically necessary dislocations. J. Mech. Phys. Solids **50**, 5–32 (2002)
M.E. Gurtin, L. Anand, Thermodynamics applied to gradient theories involving the accumulated plastic strain: the theories of Aifantis and Fleck & Hutchinson and their generalization. J. Mech. Phys. Solids **57**, 405–421 (2009)
T.M. Hatem, M.A. Zikry, Dislocation density crystalline plasticity modeling of lath martensitic microstructures in steel alloys. Philos. Mag. **89**(33), 3087–3109 (2009)
R. Hill, *The Mathematical Theory of Plasticity*, 4th edn. (Clarendon, Oxford, UK, 1950)
N. Huber, C. Tsakmakis, Determination of constitutive properties from spherical indentation data using neural networks. Part II: plasticity with nonlinear isotropic and kinematic hardening. J. Mech. Phys. Solids **47**, 1589–1607 (1999)
A. Hunter, M. Koslowski, Direct calculations of material parameters for gradient plasticity. J. Mech. Phys. Solids **56**(11), 3181–3190 (2008)
S. Kalidindi, C. Bronkhorst, L. Anand, Crystallographic texture theory in bulk deformation processing of fcc metals. J. Mech. Phys. Solids **40**, 537 (1992)
J.W. Kysar, Y. Saito, M.S. Oztop, D. Lee, W.T. Huh, Experimental lower bounds on geometrically necessary dislocation density. Int. J. Plast. **26**(8), 1097–1123 (2010)
F. Meissonnier, E.P. Busso, N.P. O'Dowd, Finite element implementation of a generalised non-local rate-dependent crystallographic formulation for finite strains. Int. J. Plast. **17**(4), 601–640 (2001)
C.-W. Nan, D. Clarke, The influence of particle size and particle fracture on the elastic–plastic deformation of metal matrix composites. Acta Mater. **44**, 3801–3811 (1996)
J.F. Nye, Some geometrical relations in dislocated crystals. Acta Metall. **1**, 153–162 (1953)
B. Peeters, M. Seefeldt, C. Teodosiu, S.R. Kalidindi, P. VanHoutte, E. Aernoudt, Work-hardening/softening behaviour of B.C.C. polycrystals during changing strain paths: I. An integrated model based on substructure and texture evolution, and its prediction of the stress–strain behaviour of an IF steel during two-stage strain paths. Acta Mater. **49**, 1607–1619 (2001)
E. Pouillier, A.F. Gourgues, D. Tanguy, E.P. Busso, A study of intergranular fracture in an aluminium alloy due to hydrogen embrittlement. Int. J. Plast. **34**, 139–153 (2012)
G. Saada, Limite élastique et durcissement dessolutions solides. Pont Mousson **16**, 255–269 (1968)
F. Schubert, G. Fleury, T. Steinhaus, Modelling of the mechanical behaviour of the SC Alloy CMSX-4 during thermomechanical loading. Model. Simul. Sci. Eng. **8**, 947–957 (2000)
J.Y. Shu, Scale-dependent deformation of porous single crystals. Int. J. Plast. **14**, 1085–1107 (1998)
J.Y. Shu, N.A. Fleck, E. Van der Giessen, A. Needleman, Boundary layers in constrained plasticflow: com parison of non-local and discrete dislocation plasticity. J. Mech. Phys. Solids **49**, 1361–1395 (2001)
P. Steinmann, Views on multiplicative elastoplasticity and the continuum theory of dislocations. Int. J. Eng. Sci. **34**, 1717–1735 (1996)
B. Svendsen, Continuum thermodynamic models for crystal plasticity including the effects of geometrically-necessary dislocations. J. Mech. Phys. Solids **50**, 1297–1329 (2002)
J. Swadener, A. Misra, R. Hoagland, M. Nastasi, A mechanistic description of combined hardening and size effects. Scripta Met. **47**, 343–348 (2002)
M.A. Zikry, M. Kao, Inelastic microstructural failure mechanisms in crystalline materials with high angle grain boundaries. J. Mech. Phys. Solids V **44**(11), 1765–1798 (1996)

Micromechanics for Heterogeneous Material Property Estimation

45

Muneo Hori

Contents

Introduction 1278
Overall Property of Heterogeneous Material 1278
Average Field Theory and Homogenization Theory 1278
Field Equations 1280
Average Field Theory 1280
Averaging Scheme 1280
Average Field 1282
Explicit Expression of Overall Elasticity in Terms of Strain Concentration Tensor 1283
Use of Eshelby's Tensor for Evaluation of Strain Concentration Tensor 1283
Homogenization Theory 1284
Singular Perturbation Expansion 1284
Use of Periodic Structure as Microstructure Model 1286
Comparison of Average Field Theory and Homogenization Theory 1286
Strain Energy Consideration 1288
Consistency of Overall Elasticity 1288
Condition for Consistent Overall Elasticity 1289
Dependence of Overall Elasticity on Loading Condition 1290
Hashin–Shtrikman Variational Principle 1291
Fictitious Uniform RVE 1291
Hashin–Shtrikman Functional for Eigen-stress 1292
Application of Hashin–Shtrikman Variational Principle to Periodic Structure 1294
Overall Property at Dynamics State 1294
Averaging Scheme at Dynamic State 1294
Fictitious Uniform RVE at Dynamic State 1295
Application of Singular Perturbation Expansion 1296
Conclusion 1297
References 1297

M. Hori (✉)
Earthquake Research Institute, The University of Tokyo, Tokyo, Japan
e-mail: hori@eri.u-tokyo.ac.jp

© Springer Nature Switzerland AG 2022

G. Z. Voyiadjis (ed.), *Handbook of Damage Mechanics*,
https://doi.org/10.1007/978-3-030-60242-0_42

Abstract

There are two well-established theories in micromechanics for analytical estimation of overall property of a heterogeneous material, instead of experimental estimation; a heterogeneous material includes a partially damaged or plastically deformed material. These two theories, namely, the average field theory and the homogenization theory, are explained in this chapter. The average field theory is based on physical treatment of the heterogeneous material in the sense that it mimics a material sample test, and it derives a closed-form expression of the overall property in terms of the average strain and stress. The homogenization theory is based on mathematical treatment in the sense that it applies the singular perturbation expansion to the governing equations and obtains numerical solution for the overall property. In this chapter, the following three advanced topics are also explained: (1) strain energy consideration to obtain the consistent overall property, (2) the Hashin–Shtrikman variational principle to obtain bounds for the overall property, and (3) the extension to the overall property estimation at dynamic state from that at quasi-static state.

Keywords

Representative volume element · Strain energy density · Heterogeneous material · Average scheme · Homogenization theory

Introduction

Overall Property of Heterogeneous Material

It is intuitively clear that there is a certain overall property for a heterogeneous material. The overall property is understood as the property of a material sample the size of which is sufficiently larger than the size of the heterogeneity that is included in the heterogeneous material. When a structure which consists of a heterogeneous material is analyzed, it is a standard practice to model the structure as being made of a fictitious but uniform material that has the overall property of the heterogeneous material. The presence of heterogeneities in the original material is ignored in such analysis of the structure.

The overall property is usually considered for a heterogeneous material which is in elastic regime. The overall property could be considered even when the heterogeneous material reaches a plastic elastoplastic regime. In particular, when a uniform material is damaged and numerous cracks of small sizes are initiated, the overall property of the material at this damaged state could be considered by regarding these cracks as material heterogeneities.

Average Field Theory and Homogenization Theory

For a given heterogeneous material, its overall property is usually measured by carrying out a material sample test. However, it is sometimes necessary to

analytically (or numerically) estimate the overall property, in particular, for an expensive material such as composites or metal alloy. In this case, micromechanics plays a key role in estimating the overall property based on the microstructure of the material. It provides two fundamental theories of analytically estimating the overall properties, namely, the *average field theory* (or the *mean field theory*) and the *homogenization theory*. The basic characteristics of these two theories are summarized as follows:

Average Field Theory The average field theory is based on the fact that what is measured in a material sample test is the volume average of field variables in the sample. It seeks to compute the volume average of the field variables, considering a microstructure of a target heterogeneous material, and to estimate the overall property as the relation between the volume average of the field variables.

Homogenization Theory The homogenization theory solves a governing equation for displacement in a heterogeneous material by applying a singular perturbation expansion (or often called a multi-scale or two-scale analysis). Hence, this theory is purely mathematical. The overall property naturally emerges as the consequences of numerically solving the expanded term of the displacement.

Nemat-Nasser and Hori (1993) presents a concise list of references related to the average field theory and the homogenization theory; see also Hill (1963), Mura (1987) for the average field theory and Sanchez-Palencia (1981), Bakhvalov and Panasenko (1984), Francfort and Murat (1986) for the homogenization theory. For relatively recent works, recommended are Hornung (1996), Kevorkina and Cole (1996), Ammari et al. (2006), Gao and Ma (2012), Le Quang et al. (2008), Liu (2008), Wang and Xu (2005), Wang and Gao (2011), Zheng and Du (2001), Zou et al. (2010) and Terada et al. (1996).

The average field theory and the homogenization theory deal with the overall property in an utterly different manner. For instance, modeling the microstructure of a heterogeneous material is different. The average field theory uses a simple model of an isolated inclusion which is embedded in an infinitely extended body, whereas the homogenization theory usually uses a periodic microstructure. It gives an impression that the two theories are basically different. However, it is possible to establish a common platform on which both the theories are explained in a unified manner.

This chapter is primarily concerned with explaining the average field theory and the homogenization theory in a unified manner, so that the applicability of these two theories to damaged materials can be seen. As advanced topics, brief explanation is given on the average strain energy consideration and the Hashin–Shtrikman variational principle Hashin and Shtrikman (1962); these two are interesting subjects of the average field theory. The two theories are easily extended to estimate the overall property at dynamic state, and the analytic estimation of dynamic overall property is explained in the end of this chapter.

Field Equations

Symbolic and index notations are used in this chapter; for instance, stress tensor is denoted by either $\boldsymbol{\sigma}$ or σ_{ij} (the index corresponds to the Cartesian coordinate system, x_i for $i = 1, 2, 3$). In the symbolic notation, $\cdot$ and: stand for the first- and second-order contractions and $\otimes$ for the tensor product. In the index notation, summation convention is employed. For simplicity, assumed are linear elasticity, infinitesimally small deformation, and quasi-static state with the absence of body forces. This setting is easily extended to nonlinear elastoplasticity or finite deformation state if incremental behavior is considered. The variable elasticity tensor is denoted by $\boldsymbol{c}$, and displacement, strain, and stress fields are denoted by $\boldsymbol{u}$, $\boldsymbol{\varepsilon}$, and $\boldsymbol{\sigma}$, respectively. These fields satisfy

$$\boldsymbol{\varepsilon}(\boldsymbol{x}) = \mathrm{sym}\{\nabla \boldsymbol{u}(\boldsymbol{x})\}, \tag{1}$$

$$\nabla \cdot \boldsymbol{\sigma}(\boldsymbol{x}) = \boldsymbol{0}, \tag{2}$$

$$\boldsymbol{\sigma}(\boldsymbol{x}) = \boldsymbol{c}(\boldsymbol{x}) : \boldsymbol{\varepsilon}(\boldsymbol{x}), \tag{3}$$

where sym stands for the symmetric part ($\mathrm{sym}\{()_{ij}\} = (()_{ij} + ()_{ji})/2$), and ∇ is the differential operator ($(\nabla \boldsymbol{u})_{ij} = \partial \mathrm{u}_j / \partial \mathrm{x}_i$). Note that $\boldsymbol{x}$ stands for a point. This set of the three equations lead to

$$\nabla \cdot (\boldsymbol{c}(\boldsymbol{x}) : \nabla \boldsymbol{u}(\boldsymbol{x})) = \boldsymbol{0}. \tag{4}$$

This is the governing equation for $\boldsymbol{u}$.

Average Field Theory

Averaging Scheme

The average field theory starts by introducing a *representative volume element* (RVE), denoted by V, as a body which models the microstructure of a given heterogeneous material; see Fig. 1. While various definitions can be made in this chapter, the RVE is regarded as a model of a material test sample which is used to actually estimate the overall property.

In a material sample test, the overall property is estimated by assuming the uniform distribution of strain and stress in the sample, and the strain and stress are measured from the sample's surface displacement and traction. For instance, when a cubic sample is subjected to the uniform loading of T and the resulting displacement is U, the uniaxial strain and stress are computed as

$$\varepsilon = \frac{U}{A}, \text{and} \, \sigma = \frac{T}{A^2},$$

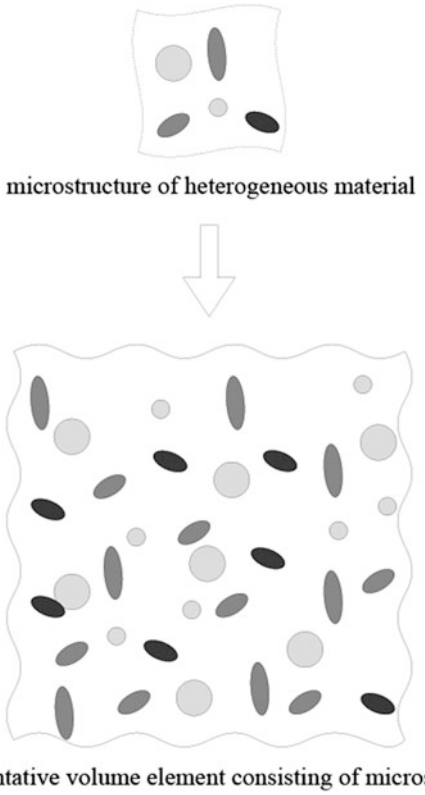

Fig. 1 Representative volume element for estimating overall property of heterogeneous material

where A is the edge length of the cubic sample. It is easily shown that the strain and stress measured in this way are actually the volume average of strain and stress within the sample, which, of course, are not uniform. Indeed, the volume average of strain and stress, denoted by $\langle \boldsymbol{\varepsilon} \rangle_V$ and $\langle \boldsymbol{\sigma} \rangle_V$, respectively, is given as

$$\langle \boldsymbol{\varepsilon} \rangle_V = \frac{1}{V} \int_{\partial V} \mathrm{sym}\{\boldsymbol{\nu} \otimes \boldsymbol{u}\} \mathrm{d}s, \tag{5}$$

$$\langle \boldsymbol{\sigma} \rangle_V = \frac{1}{V} \int_{\partial V} \{\boldsymbol{t} \otimes \boldsymbol{x}\} \mathrm{d}s, \tag{6}$$

where $\boldsymbol{\nu}$ is the outer unit normal on the boundary ∂V and $\boldsymbol{u}$ and $\boldsymbol{t}$ are the surface displacement and traction, respectively. The sample strain and stress, $\varepsilon = \frac{U}{A}$ and $\sigma = \frac{T}{A^2}$, are easily derived from these two equations. In this chapter, evaluation of the volume average in terms of the surface integration is called the averaging scheme; the averaging schemes presented in this chapter are readily proved by applying the integral by part and the Gauss theorem to the computation of the volume average of field variables. The averaging scheme is the consequences of Eqs. 1 and 2, and hence

it holds for any arbitrary material with any constitutive properties. Note that the symmetry of $\boldsymbol{\sigma}$ ($\sigma_{ij} = \sigma_{ji}$) is related to the moment equilibrium, and the averaging scheme leads to the symmetry of $\int \{\boldsymbol{t} \otimes \boldsymbol{x}\} \mathrm{d}s$ ($\int \{\boldsymbol{t} \otimes \boldsymbol{x}\} \mathrm{d}s = \int \{\boldsymbol{x} \otimes \boldsymbol{t}\} \mathrm{d}s$).

Average Field

In view of Eqs. 5 and 6, the average field theory introduces average fields, which are defined as the weighted average of the corresponding field variables. The weight function, denoted by φ_V, satisfies $\int \varphi_V \, \mathrm{d}v = 1$ and takes on a constant value of $1/V$ within V, except for a thin layer near ∂V where it decays smoothly from $1/V$ to 0 and vanishes on ∂V. Now, a body B which is larger than V is considered. The same symbols, $\{\boldsymbol{u}, \boldsymbol{\varepsilon}, \boldsymbol{\sigma}\}$, are used for the field variables of B, and the average fields are expressed in terms of φ_V and $\{\boldsymbol{u}, \boldsymbol{\varepsilon}, \boldsymbol{\sigma}\}$ as

$$\begin{Bmatrix} \boldsymbol{U} \\ \mathbf{E} \\ \boldsymbol{\Sigma} \end{Bmatrix} (\mathbf{X}) = \int_B \varphi_V(\boldsymbol{X} - \boldsymbol{x}) \begin{Bmatrix} \boldsymbol{u} \\ \boldsymbol{\varepsilon} \\ \boldsymbol{\sigma} \end{Bmatrix} (\boldsymbol{x}) \mathrm{d}v. \tag{7}$$

Here, $\boldsymbol{X}$ is a point in B. Due to the nature of φ_V, $\{\boldsymbol{U}, \mathbf{E}, \boldsymbol{\Sigma}\}$ is smoother than the original $\{\boldsymbol{u}, \boldsymbol{\varepsilon}, \boldsymbol{\sigma}\}$. Furthermore, it is seen that taking weighted average of φ_V is commutable with operating ∇, and hence the average fields satisfy

$$\mathbf{E}(\boldsymbol{X}) = \mathrm{sym}\{\nabla \boldsymbol{U}(\boldsymbol{X})\}, \tag{8}$$

$$\nabla \cdot \boldsymbol{\Sigma}(\boldsymbol{X}) = \mathbf{0}, \tag{9}$$

These two equations are the consequence of Eqs. 1 and 2.

As is seen, Eqs. 8 and 9 serve as field equations for $\{\boldsymbol{U}, \mathbf{E}, \boldsymbol{\Sigma}\}$, just as Eqs. 1 and 2 do for $\{\boldsymbol{u}, \boldsymbol{\varepsilon}, \boldsymbol{\sigma}\}$. If there is another equation which corresponds to Eq. 3, a governing equation for $\boldsymbol{U}$ can be derived. For instance, if this equation is given as

$$\boldsymbol{\Sigma}(\boldsymbol{X}) = \overline{\boldsymbol{C}} : \mathbf{E}(\boldsymbol{X}),$$

then it follows that $\nabla \cdot \left(\overline{\boldsymbol{C}} : \nabla \boldsymbol{U}\right) = \mathbf{0}$ is derived as the governing equation for $\boldsymbol{U}$. Note that $\overline{\boldsymbol{C}}$ is assumed to be uniform in B. Or it can be assumed that B consists of the fictitious but homogeneous material of $\overline{\boldsymbol{C}}$. If suitable boundary conditions are posed on the boundary ∂B, the averaged displacement $\boldsymbol{U}$ can be obtained by solving the resulting boundary value problem. As expected, this $\overline{\boldsymbol{C}}$ is the overall elasticity of the heterogeneous material. By definition, $\mathbf{E}$ and $\boldsymbol{\Sigma}$ correspond to $\langle \boldsymbol{\varepsilon} \rangle_V$ and $\langle \boldsymbol{\sigma} \rangle_V$, i.e., the volume average $\boldsymbol{\varepsilon}$ and $\boldsymbol{\sigma}$ taken over the RVE, V, of the target heterogeneous modulus. The average field theory, therefore, seeks to estimate $\overline{\boldsymbol{C}}$, which is now given as

$$\langle \boldsymbol{\sigma} \rangle_V = \overline{\boldsymbol{C}} : \langle \boldsymbol{\varepsilon} \rangle_V. \tag{10}$$

Note that while $\overline{\boldsymbol{C}}$ is defined in terms of $\langle\boldsymbol{\varepsilon}\rangle_V$ and $\langle\boldsymbol{\sigma}\rangle_V$, it does not guarantee that the presence of the unique $\overline{\boldsymbol{C}}$ that precisely relates $\mathbf{E}$ to $\boldsymbol{\Sigma}$ as $\boldsymbol{\Sigma} = \overline{\boldsymbol{C}} : \mathbf{E}$ for any point in B. However, it is naively understood that $\boldsymbol{\Sigma} = \overline{\boldsymbol{C}} : \mathbf{E}$ approximately holds if $\overline{\boldsymbol{C}}$ is computed for a sufficiently large V, and such V is used to define the average strain and stress fields, $\mathbf{E}$ and $\boldsymbol{\Sigma}$, of B. As will be explained later, it is indeed true that $\boldsymbol{\Sigma} = \overline{\boldsymbol{C}} : \mathbf{E}$ approximately holds since $\overline{\boldsymbol{C}}$ of V changes depending on the boundary conditions.

Explicit Expression of Overall Elasticity in Terms of Strain Concentration Tensor

The average field theory provides several schemes to estimate $\overline{\boldsymbol{C}}$ defined by Eq. 10. The simplest example of a two-phase composite (consisting of a matrix phase and an inclusion phase) is considered in order to explain these schemes. A common target of these schemes is the estimate of strain concentration tensor, denote by $\boldsymbol{A}$, which is defined as

$$\langle\boldsymbol{\varepsilon}\rangle_I = \boldsymbol{A} : \langle\boldsymbol{\varepsilon}\rangle_V. \tag{11}$$

Here, $\langle\rangle_I$ is the volume average of the inclusion phase of the composite. If the volume fraction of the inclusion phase is f, it holds $\langle\rangle_V = f\langle\rangle_I + (1-f)\langle\rangle_M$, where $\langle\rangle_M$ is the volume average of the matrix phase. After simple manipulations, $\langle\boldsymbol{\sigma}\rangle_V$ is evaluated as

$$\langle\boldsymbol{\sigma}\rangle_V = f\langle\boldsymbol{\sigma}\rangle_I + (1-f)\langle\boldsymbol{\sigma}\rangle_M = f\boldsymbol{C}^I : \boldsymbol{A} : \langle\boldsymbol{\varepsilon}\rangle_V + \boldsymbol{C}^M : (\boldsymbol{I} - f\boldsymbol{A}) : \langle\boldsymbol{\varepsilon}\rangle_V,$$

where $\boldsymbol{C}^M$ and $\boldsymbol{C}^I$ are the elasticity of the matrix and inclusion phases, and $\boldsymbol{I}$ is the identity tensor. In terms of $\boldsymbol{A}$, therefore, $\overline{\boldsymbol{C}}$ is expressed as

$$\overline{\boldsymbol{C}} = \boldsymbol{C}^M + f\left(\boldsymbol{C}^I - \boldsymbol{C}^M\right) : \boldsymbol{A}. \tag{12}$$

Note that no assumption is made in deriving this equation, except for the presence of the strain concentration tensor $\boldsymbol{A}$ of Eq. 11.

Use of Eshelby's Tensor for Evaluation of Strain Concentration Tensor

A model of an infinitely extended body which includes one inclusion is usually used, since a closed-form analytic solution, called Eshelby's solution, is available for this model when the inclusion is ellipsoidal form. There are various schemes which take advantage of Eshelby's solution (Eshelby 1957) to $\boldsymbol{A}$ and to estimate $\overline{\boldsymbol{C}}$ using Eq. 12. Representative schemes are the dilute distribution assumption, the self-consistent method, and the differential scheme; see Nemat-Nasser and Hori (1993).

The original problem to which Eshelby's solution is found is an infinitely extended body problem; the body is homogeneous and linearly elastic and includes a certain uniform strain distributed in an ellipsoidal domain (Eshelby 1957). The strain is due to phase transition or thermal deformation and is usually called *eigen-strain*. It is shown that this uniform eigen-strain produces uniform strain in the ellipsoidal domain, although the strain due to the eigen-strain smoothly decays to zero outside of the ellipsoidal domain. Moreover, the strain in the ellipsoidal domain is analytically computed for the given elastic tensor of the infinite body and the configuration of the ellipsoidal domain. This is Eshelby's solution. The strain in the ellipsoidal domain is expressed as the second-order contraction of a certain fourth-order tensor and the eigen-tensor, and this fourth-order tensor is called Eshelby's tensor.

Since a closed-form expression is available for Eshelby's tensor, it is easy to analytically compute the strain concentration tensor, $\boldsymbol{A}$, in terms of Eshelby's solution. This is the reason that numerous researches have been made to evaluate the overall elasticity tensor in a closed form, using Eshelby's tensor; see Kachanov et al. (1994), Markenscoff (1998), Nozaki and Taya (2001), Kawashita and Nozaki (2001), Onaka et al. (2002), and Ru (2003). It is remarkable to note that eigen-strain which is uniformly generated in an ellipsoidal domain generates a uniform strain in the domain. This is because it implies that when an ellipsoidal inclusion of a different material is embedded in an infinitely extended and homogeneous body and the body is subjected to far-field loading, strain and stress of the inclusion become uniform; see Tanaka and Mori (1972) and Hori and Nemat-Nasser (1993).

Homogenization Theory

Singular Perturbation Expansion

The homogenization theory focuses the governing equation for $\boldsymbol{u}$, Eq. 4, by considering the nature of $\boldsymbol{c}$ in it. That is, $\boldsymbol{c}$ changes spatially in the length scale of material heterogeneity. To this end, the homogenization theory introduces two length scales, the one for the material heterogeneity and the other for a target structure, denoted by l and L, respectively. For simplicity, l and L are called the micro- and macro-length scales. The ratio of l and L is denoted by

$$\epsilon = \frac{l}{L}. \tag{13}$$

An insight is given to the length scale, if a finite element method analysis is considered. The dimension of a target body is in the order of L, and the dimension of an element is in the order of l. When the number of elements is $(10^3)^3$, the ratio is $\epsilon \sim 10{-}^3$. In terms of this small ϵ, it is natural to define a slowly changing spatial coordinates, $\boldsymbol{X}$, by

$$\boldsymbol{X} = \epsilon \boldsymbol{x}. \tag{14}$$

By definition, $\boldsymbol{X}$ is the coordinate in the macro-length scale, if $\boldsymbol{x}$ is regarded as the coordinate in the micro-length scale.

The homogenization theory takes the following *singular* perturbation expansion of $\boldsymbol{u}$:

$$\boldsymbol{u}(\boldsymbol{x}) = \boldsymbol{u}^0(\boldsymbol{X}, \boldsymbol{x}) + \epsilon \boldsymbol{u}^1(\boldsymbol{X}, \boldsymbol{x}) + \cdots. \tag{15}$$

This expansion is called singular since the terms in the right side are a function of $\boldsymbol{X}$ and $\boldsymbol{x}$. Note that ϵ defined by Eq. 14 appears as the coefficient of $\boldsymbol{u}^1$ as well as the slow spatial variable $\boldsymbol{X}$. A *regular* perturbation expansion considers the change in $\mathbf{c}$ only. That is, $\mathbf{c}$ is expressed as $\boldsymbol{c} = \boldsymbol{c}^0 + \epsilon \boldsymbol{c}^1$ with $\boldsymbol{c}^0$ being constant and $\boldsymbol{c}^1$ spatially varying, and this $\epsilon \boldsymbol{c}^1$ is regarded as the small change in $\mathbf{c}$ from the uniform state of $\boldsymbol{c}^0$. In view of this $\boldsymbol{c}$, the regular perturbation expansion is readily applied to $\boldsymbol{u}$, as

$$\boldsymbol{u}(\boldsymbol{x}) = \boldsymbol{u}^0(\boldsymbol{x}) + \epsilon \boldsymbol{u}^1(\boldsymbol{x}) + \cdots,$$

and the first term $\boldsymbol{u}^0$ is the solution of the homogeneous body problem, and the later terms correct $\boldsymbol{u}^0$; $\boldsymbol{u}^0 + \epsilon \boldsymbol{u}^1$ is a good approximate solution of a body which consists of $\boldsymbol{c}^0 + \epsilon \boldsymbol{c}^1$ if ϵ is small.

The target of the singular perturbation expansion is the first term and hence $\nabla_{\boldsymbol{x}}$ for $\boldsymbol{x}$ is replaced with $\nabla_{\boldsymbol{X}}$ for $\boldsymbol{X}$, which is now evaluated in terms of $\boldsymbol{X}$ and $\boldsymbol{x}$ as

$$\nabla_{\boldsymbol{x}} = \nabla_{\boldsymbol{x}} + \frac{1}{\epsilon} \nabla_{\boldsymbol{X}},$$

where subscript $\boldsymbol{X}$ or $\boldsymbol{x}$ emphasizes the operator for $\boldsymbol{X}$ or $\boldsymbol{x}$, respectively. Substitution of Eq. 15 into Eq. 4 together with the above differential operator, the homogenization theory yields

$$\begin{aligned} &\epsilon^{-2} \left\{ \nabla_{\boldsymbol{x}} \cdot \left(\boldsymbol{c} : \nabla_{\boldsymbol{x}} \boldsymbol{u}^0 \right) \right\} \\ &+ \epsilon^{-1} \left\{ \nabla_{\boldsymbol{X}} \cdot \left(\boldsymbol{c} : \nabla_{\boldsymbol{x}} \boldsymbol{u}^0 \right) + \nabla_{\boldsymbol{x}} \cdot \left(\boldsymbol{c} : \left(\nabla_{\boldsymbol{X}} \boldsymbol{u}^0 + \nabla_{\boldsymbol{x}} \boldsymbol{u}^1 \right) \right) \right\} \\ &+ \epsilon^0 \left\{ \nabla_{\boldsymbol{X}} \cdot \left(c : \left(\nabla_{\boldsymbol{X}} \boldsymbol{u}^0 + \nabla_{\boldsymbol{X}} \boldsymbol{u}^1 \right) \right) + \cdots \right\} + \cdots = 0. \end{aligned} \tag{16}$$

For the term of ϵ^{-2} to vanish, $\nabla_{\boldsymbol{x}} \boldsymbol{u}^0$ must be 0. That is, $\boldsymbol{u}^0$ is a function of $\boldsymbol{X}$ only. For the terms of ϵ^{-1} to vanish, the form of $\boldsymbol{u}^1$ is assumed as

$$\boldsymbol{u}^1(\boldsymbol{X}, \boldsymbol{x}) = \boldsymbol{\chi}(\boldsymbol{x}) : \left(\nabla_{\boldsymbol{X}} \boldsymbol{u}^0(\boldsymbol{X}) \right),$$

and the term becomes $\nabla_{\boldsymbol{x}} \cdot (\boldsymbol{c} : (\nabla_{\boldsymbol{x}} \boldsymbol{\chi} + \boldsymbol{I}) : (\nabla_{\boldsymbol{X}} \boldsymbol{u}^0))$. This term vanishes if $\boldsymbol{\chi}$ satisfies

$$\nabla_{\boldsymbol{x}} \cdot (\boldsymbol{c}(\boldsymbol{x}) : (\nabla_{\boldsymbol{x}} \boldsymbol{\chi}(\boldsymbol{x}) + I)) = \mathbf{0}. \tag{17}$$

The term of ϵ^0 is now rewritten as $\nabla_{\boldsymbol{X}} \cdot (\boldsymbol{c} : (\nabla_{\boldsymbol{x}} \boldsymbol{\chi} + \boldsymbol{I}) : \nabla_{\boldsymbol{X}} \boldsymbol{u}^0)$. It is this $\boldsymbol{c} : (\nabla_{\boldsymbol{x}} \boldsymbol{\chi} + \boldsymbol{I})$ that plays a role of an overall elasticity for $\boldsymbol{u}^0$, even though it is a function of $\boldsymbol{x}$, not $\boldsymbol{X}$. Hence, the homogenization theory replaces $\boldsymbol{c} : (\nabla_{\boldsymbol{x}} \boldsymbol{\chi} + \boldsymbol{I})$ with its volume average taken over a suitable volume, i.e.,

$$\overline{\boldsymbol{C}} = \boldsymbol{c} : (\nabla_{\boldsymbol{x}} \boldsymbol{\chi}(\boldsymbol{x}) + \boldsymbol{I})_U. \tag{18}$$

Here, U is a certain domain in which the average is taken; this U must be in the micro-length scale so that $\langle \rangle_U$ is independent from $\boldsymbol{x}$.

Use of Periodic Structure as Microstructure Model

The two tasks remain to estimate $\overline{\boldsymbol{C}}$ by computing Eq. 18. Namely, solving Eq. 17 for $\boldsymbol{\chi}$ and determining U. As shown in Fig. 2, the homogenization theory usually uses a periodic structure, assuming the microstructure of the target heterogeneous material is more or less the same; see, for instance, Nuna and Keller (1984) and Walker et al. (1991); Oleinik et al. (1992) for the homogenization theory of nonperiodic media. $\boldsymbol{\chi}$ is thus computed for this periodic structure, and a unit cell of the periodic structure is chosen for U.

Unlike the average field theory, the homogenization theory is based on the mathematical approach of the singular perturbation expansion, in solving the governing equation of $\boldsymbol{u}$ when $\boldsymbol{c}$ changes in the micro-length scale of l. An advantage of this theory is to analyze only the leading term in the expansion, $\boldsymbol{u}^0$, which is a function of $\boldsymbol{X}$ or changes in the macro-length scale of L. Note that $\boldsymbol{u}^0$ accompanies strain given by

$$\mathrm{sym}\{(\nabla_{\boldsymbol{x}} \boldsymbol{\chi} + \boldsymbol{I}) : (\nabla_{\boldsymbol{X}} \boldsymbol{u}^0)\} = \mathrm{sym}\{\nabla_{\boldsymbol{x}} \boldsymbol{\chi} : \nabla_{\boldsymbol{X}} \boldsymbol{u}^0\} + \mathrm{sym}\{\nabla_{\boldsymbol{X}} \boldsymbol{u}^0\}.$$

It is the first term of the right side that reflects the spatial change in $\boldsymbol{c}$ in the micro-length scale, while the second term is strain which changes in the macro-length scale. By definition, Eq. 18, the effect of the first term on stress which changes in the macro-length scale is included in $\overline{\boldsymbol{C}}$ by taking volume average over U.

It is of interest to take the limit as ϵ goes to 0 in the homogenization theory. Numerous researches have been made for this limit. On the viewpoint of the perturbation expansion, however, it is standard to use a finite value for ϵ, using the definition of Eq. 13. It is thus possible to separately treat the homogenization theory from the singular perturbation expansion when the theory focuses on the special case of ϵ approaches 0.

Comparison of Average Field Theory and Homogenization Theory

In Table 1, the comparison of the average field theory and the homogenization theory is summarized. The field variables used in these theories are different; the

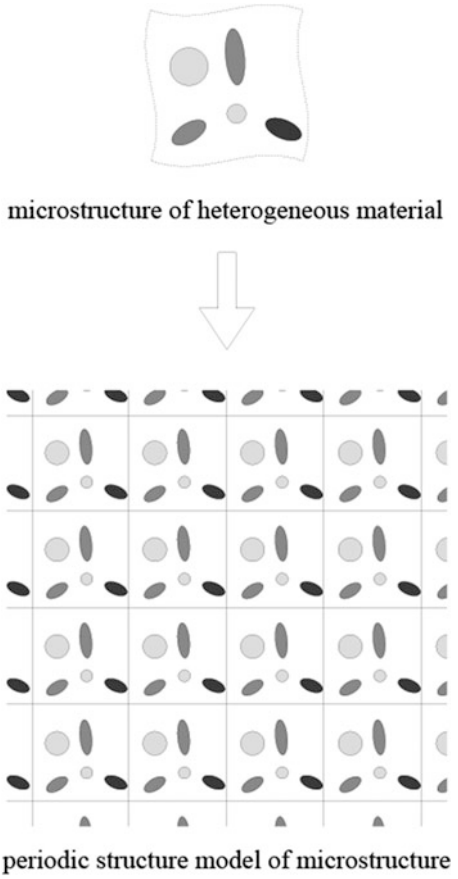

Fig. 2 Periodic structure for estimating overall property of heterogeneous material

Table 1 Comparison of average field theory and homogenization theory

	Average field theory	Homogenization theory
Displacement	$\boldsymbol{u}$	$\boldsymbol{u}^0 + \epsilon\,\boldsymbol{\chi} : (\nabla \boldsymbol{u}^0)$
Strain	$\boldsymbol{\varepsilon} = \mathrm{sym}\{\nabla \boldsymbol{u}\}$	$\boldsymbol{\varepsilon}^0 = (\nabla \boldsymbol{\chi} + \boldsymbol{I}) : (\nabla \boldsymbol{u}^0)$
Stress	$\boldsymbol{\sigma} = \boldsymbol{c} : \boldsymbol{\varepsilon}$	$\boldsymbol{\sigma}^0 = \boldsymbol{c} : \boldsymbol{\varepsilon}^0$
Overall displacement	$\boldsymbol{U} = \int \varphi_I \boldsymbol{u} \mathrm{d}v$	$\boldsymbol{u}^0$
Overall strain	$\boldsymbol{E} = \mathrm{sym}\{\nabla \boldsymbol{U}\}$	$\langle \boldsymbol{\varepsilon}^0 \rangle = \mathrm{sym}\{\nabla \boldsymbol{u}^0\}$
Overall stress	$\boldsymbol{\Sigma} = \overline{\boldsymbol{C}} : \boldsymbol{E}$	$\langle \boldsymbol{\sigma}^0 \rangle = \overline{\boldsymbol{C}} : \langle \boldsymbol{\varepsilon}^0 \rangle$
Overall elasticity	$\overline{\boldsymbol{C}} = \boldsymbol{C}^M + f\left(C^I - C^M\right) : \boldsymbol{A}$	$\overline{\boldsymbol{C}} = \langle \boldsymbol{c} : \left(\nabla_\chi + \boldsymbol{I}\right) \rangle$

displacement function is different, and hence the strain and stress become different. The overall field variables are defined as the volume average of the field variables, even though the domain in which the average is taken is different.

It is of interest to note that while the homogenization theory is based on the singular perturbation, the first term, $\boldsymbol{u}^0$, is actually computed by taking the volume average of the strain due to the second term, $\boldsymbol{u}^1$, even though the domain in which the average is taken is a unit cell. While a certain similarity is found for the two theories, there are two major differences between them. The first difference is the modeling of the microstructure: the homogenization theory uses a unit cell of the periodic structure, while the average field theory considers an RVE. The second difference is that the homogenization theory is able to compute higher-order terms, if necessary, but the average field theory does not have systematic procedures to increase the accuracy of the estimation.

The abovementioned differences are not essential. And these two theories are unified to construct a theory of analytically estimating overall property; the singular perturbation expansion that is employed by the homogenization theory is applied to a nonperiodic microstructure, and higher-order terms are computed by taking the volume average that is a core concept of the average field theory. Indeed, the essential procedures of the unified theory are stated as follows: (1) to use an RVE instead of the periodic structure, (2) to apply the singular perturbation expansion to the field in the RVE, and (3) to take the volume average of the terms in the expansion to compute the overall elasticity.

In the unified theory, setting of the boundary conditions of the target RVE needs some consideration. As will be explained later, it is sufficient to choose either linear displacement boundary conditions or uniform traction boundary conditions, respectively, if the resulting boundary tractions or displacement do not change wildly. A natural choice of the RVE configuration is cubic, and a cubic RVE is regarded as a unit cell if periodic boundary conditions are used instead of linear displacement boundary conditions or uniform traction boundary conditions. As will be explained later again, least dependence of the overall property on the boundary conditions is important to make the property consistent (i.e., the overall property is able to relate strain and stress as well as strain and strain energy density).

Strain Energy Consideration

Consistency of Overall Elasticity

Besides relating strain to stress, elasticity relates strain to strain energy density. The average field theory extensively studies this dual role of the elasticity; see Hill (1963). That is, an overall elasticity of an RVE is required to relate the average strain to the average strain energy density as follows:

$$\langle e \rangle_V = \frac{1}{2} \langle \boldsymbol{\varepsilon} \rangle_V : \overline{\boldsymbol{C}} : \langle \boldsymbol{\varepsilon} \rangle_V, \tag{19}$$

where $e = \frac{1}{2} \boldsymbol{\varepsilon} : \mathbf{c} : \boldsymbol{\varepsilon}$ or $e = \frac{1}{2} \boldsymbol{\sigma} : \boldsymbol{\varepsilon}$ is strain energy density. A question arises regarding the dual role of the overall elasticity, i.e., whether the two $\overline{\boldsymbol{C}}$'s of

Eqs. 10 and 19 are the same or whether the overall property that relates the average strain to the average stress does relate the average strain to the average strain energy density. This is called the consistency of $\overline{\boldsymbol{C}}$ in this chapter. It is easily understood that the condition for $\overline{\boldsymbol{C}}$ to be consistent is that the average of strain energy density coincides half of the product of the average stress and the average strain, $\langle e \rangle_V = \frac{1}{2}\langle \boldsymbol{\sigma} \rangle_V : \langle \boldsymbol{\varepsilon} \rangle_V$ or $\frac{1}{2}\langle \boldsymbol{\sigma} : \boldsymbol{\varepsilon} \rangle_V = \frac{1}{2}\langle \boldsymbol{\sigma} \rangle_V : \langle \boldsymbol{\varepsilon} \rangle_V$.

An averaging scheme for the product of strain and stress is readily derived from the two field equations, Eqs. 1 and 2, as

$$\langle \boldsymbol{\sigma} : \boldsymbol{\varepsilon} \rangle_V = \frac{1}{V} \int_{\partial V} \boldsymbol{t} \cdot \boldsymbol{u} \, \mathrm{d}s; \tag{20}$$

recall that $\boldsymbol{t}$ is the surface traction. Using the averaging schemes for strain and stress, Eqs. 5 and 6, the following equation is derived from Eq. 20:

$$\langle \boldsymbol{\sigma} : \boldsymbol{\varepsilon} \rangle_V - \langle \boldsymbol{\sigma} \rangle_V : \langle \boldsymbol{\varepsilon} \rangle_V = \frac{1}{V} \int_{\partial V} \left(\boldsymbol{t} - \boldsymbol{\nu} \cdot \langle \boldsymbol{\sigma} \rangle_V \right) \cdot \left(\boldsymbol{u} - \boldsymbol{x} \cdot \langle \boldsymbol{\varepsilon} \rangle_V \right) \mathrm{d}s. \tag{21}$$

As is seen, the left side, the difference between the average of strain and stress product, $\langle \boldsymbol{\sigma} : \boldsymbol{\varepsilon} \rangle_V$ and the product of average strain and stress, $\langle \boldsymbol{\sigma} \rangle_V : \langle \boldsymbol{\varepsilon} \rangle_V$, is given as the surface integration of the product of $\boldsymbol{t} - \boldsymbol{\nu} \cdot \langle \boldsymbol{\sigma} \rangle_V$ and $\boldsymbol{u} - \boldsymbol{x} \cdot \langle \boldsymbol{\varepsilon} \rangle_V$, which are the deviation of the traction from that computed in terms of the average stress ($\boldsymbol{\nu} \cdot \langle \boldsymbol{\sigma} \rangle_V$) and the deviation of the displacement from that computed in terms of the average strain ($\boldsymbol{x} \cdot \langle \boldsymbol{\varepsilon} \rangle_V$), respectively.

Condition for Consistent Overall Elasticity

In view of Eq. 20, it is clear that $\overline{\boldsymbol{C}}$'s of Eqs. 10 and 19 are the same if the RVE is subjected to either uniform traction boundary conditions or linear displacement boundary conditions, so that $\boldsymbol{t} - \boldsymbol{\nu} \cdot \langle \boldsymbol{\sigma} \rangle_V$ or $\boldsymbol{u} - \boldsymbol{x} \cdot \langle \boldsymbol{\varepsilon} \rangle_V$ identically vanishes on ∂V, respectively. Furthermore, if boundary conditions are chosen so that

$$\left| \left(\boldsymbol{t} - \boldsymbol{\nu} \cdot \langle \boldsymbol{\sigma} \rangle_V \right) \cdot \left(\boldsymbol{u} - \boldsymbol{x} \cdot \langle \boldsymbol{\varepsilon} \rangle_V \right) \right| < w$$

with w being a constant, then, Eq. 20 leads to

$$\left| \langle \boldsymbol{\sigma} : \boldsymbol{\varepsilon} \rangle_V - \langle \boldsymbol{\sigma} \rangle_V : \langle \boldsymbol{\varepsilon} \rangle_V \right| < \frac{1}{V} \int_{\partial V} \left| \left(\boldsymbol{t} - \boldsymbol{\nu} \cdot \boldsymbol{\sigma}_V \right) \cdot \left(\boldsymbol{u} - \boldsymbol{x} \cdot \boldsymbol{\varepsilon}_V \right) \right| \mathrm{d}s < \frac{Sw}{V},$$

where S and V are the area of ∂V and the volume of V; the same symbol is used for the volume of V. If Sw/V is sufficiently small, $\overline{\boldsymbol{C}}$'s of Eqs. 10 and 19 are regarded as being approximately consistent. Note that when w is fixed, Sw/V decreases as the size of RVE increases since S/V is of the order of the inverse of the RVE's size.

Dependence of Overall Elasticity on Loading Condition

Another question arises regarding the property of $\overline{\boldsymbol{C}}$. The consistent overall elasticity of $\overline{\boldsymbol{C}}$ is defined by using field variables of an RVE which is subjected to certain boundary conditions, namely, linear displacement boundary conditions or uniform traction boundary conditions (which are typical examples of boundary conditions satisfying $|(\boldsymbol{t} - \boldsymbol{\nu} \cdot \langle \boldsymbol{\sigma} \rangle_V) \cdot (\boldsymbol{u} - \boldsymbol{x} \cdot \langle \boldsymbol{\varepsilon} \rangle_V)| < w$). So, the question is whether $\overline{\boldsymbol{C}}$ is independent from the boundary conditions or from the loading conditions of the RVE. The answer is negative. $\overline{\boldsymbol{C}}$ changes depending on the boundary conditions. Putting superscripts S, G, and E for field variables due to uniform traction, general, linear displacement boundary conditions, respectively, the following averaging scheme holds for the average strain energy density of the RVE subjected to different boundary conditions:

$$\begin{cases} \langle e^S \rangle_V \le \langle e^G \rangle_V & \text{for } \langle \boldsymbol{\varepsilon}^G \rangle_V = \langle \boldsymbol{\varepsilon}^S \rangle_V, \\ \langle e^E \rangle_V \le \langle e^G \rangle_V & \text{for } \langle \boldsymbol{\sigma}^G \rangle_V = \langle \boldsymbol{\sigma}^E \rangle_V; \end{cases} \tag{22}$$

see Fig. 3 (Nemat-Nasser and Hori 1995). The proof is simple, just by computing the right side of the following inequalities:

$$0 \le \left\langle \left(\boldsymbol{\varepsilon}^G - \boldsymbol{\varepsilon}^S\right) : \boldsymbol{c} : \left(\boldsymbol{\varepsilon}^G - \boldsymbol{\varepsilon}^S\right) \right\rangle_V \text{ and } 0 \le \left\langle \left(\boldsymbol{\varepsilon}^G - \boldsymbol{\varepsilon}^E\right) : \boldsymbol{c} : \left(\boldsymbol{\varepsilon}^G - \boldsymbol{\varepsilon}^E\right) \right\rangle_V.$$

The meaning of Eq. 22 is clear, if it is interpreted that the average strain energy density is increased by putting more wildly varying surface displacement or traction on the RVE's boundary and that the average strain energy density attains the lowest value if there is no varying surface displacement or traction. While not proved, it is intuitively clear that if surface displacement or traction does not change wildly (just as an inequality of $|(\boldsymbol{t} - \boldsymbol{\nu} \cdot \langle \boldsymbol{\sigma} \rangle_V) \cdot (\boldsymbol{u} - \mathbf{x} \cdot \langle \boldsymbol{\varepsilon} \rangle_V)| < w$ holds), $\langle e^G \rangle_V$ would be close to both $\langle e^S \rangle_V$ and $\langle e^E \rangle_V$; the difference, $\langle e^G \rangle_V - \langle e^S \rangle_V$ or $\langle e^G \rangle_V - \langle e^E \rangle_V$, would vanish as the size of the RVE increases. Therefore, the dependence of $\overline{\boldsymbol{C}}$ on the boundary conditions would be negligible for a sufficiently large RVE.

It is of interest to note that Eq. 22, the inequalities of the average strain energy density, can be derived from following functional:

$$I^E(\boldsymbol{u}, \bar{\boldsymbol{t}}) = \left\langle \frac{1}{2} \boldsymbol{\varepsilon} : \boldsymbol{c} : \boldsymbol{\varepsilon} \right\rangle_V + \frac{1}{V} \int_{\partial V} \boldsymbol{\lambda}(\boldsymbol{x}) \cdot (\boldsymbol{\nu}(\boldsymbol{x}) \cdot \boldsymbol{\sigma}(\boldsymbol{x}) - \bar{\boldsymbol{t}}(\boldsymbol{x})) \mathrm{d}s + \boldsymbol{\mu} : \left(\langle \boldsymbol{\sigma} \rangle_V - \overline{\boldsymbol{\sigma}} \right).$$

Here, $\bar{\boldsymbol{t}}$ and $\overline{\boldsymbol{\sigma}}$ are the traction described on $\overline{\boldsymbol{\sigma}}$ and a given average stress, respectively, and $\boldsymbol{\sigma}$ is a stress field which is associated with $\boldsymbol{u}$; $\boldsymbol{\lambda}$ and $\boldsymbol{\mu}$ are the Lagrange multipliers enforcing the boundary condition, $\boldsymbol{\nu}(\boldsymbol{x}) \cdot \boldsymbol{\sigma}(\boldsymbol{x}) - \bar{\boldsymbol{t}}(\boldsymbol{x})$, and the average stress condition, $\langle \boldsymbol{\sigma} \rangle_V = \overline{\boldsymbol{\sigma}}$ ($\boldsymbol{\lambda}$ is a vector function defined on ∂V, and $\boldsymbol{\mu}$ is a second-order tensor defined on ∂V). A stationary value of I^E or $\left\langle \frac{1}{2} \boldsymbol{\varepsilon} : \boldsymbol{c} : \boldsymbol{\varepsilon} \right\rangle = \langle e \rangle_V$ is found by taking the variation with respect to both $\boldsymbol{u}$ and $\overline{\boldsymbol{u}}$. For instance, the variation of I^E with respect to $\overline{\boldsymbol{u}}$ is

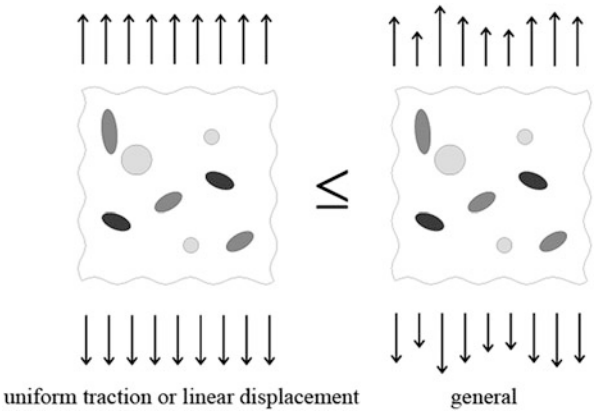

Fig. 3 Dependence of strain energy on boundary conditions

$$\delta I^E(\boldsymbol{u}, \bar{\boldsymbol{t}}) = \frac{1}{V}\int_{\partial V} \delta\bar{\boldsymbol{t}}(\boldsymbol{x}) \cdot (\boldsymbol{u}(\boldsymbol{x}) - \boldsymbol{x} \cdot \boldsymbol{\mu})\mathrm{d}s,$$

Since $\boldsymbol{\mu}$ is a constant second-order tensor, the Euler equation shown in the above means that I^E is stationarized for $\bar{\boldsymbol{t}}$ that makes the associated displacement $\boldsymbol{u}$ on ∂V linear with respect to $\boldsymbol{x}$. That is, the linear displacement boundary conditions minimize I^E, and the inequality $\langle e^E \rangle_V \leq \langle e^G \rangle_V$ holds for any $\boldsymbol{u}^G$ which accompanies $\boldsymbol{\sigma}^G$ that satisfies $\langle \boldsymbol{\sigma}^G \rangle_V = \langle \boldsymbol{\sigma}^E \rangle_V$. It is similarly shown that the inequality $\langle e^S \rangle_V \leq \langle e^G \rangle_V$ holds for any displacement field $\boldsymbol{u}^G$ which accompanies $\boldsymbol{\varepsilon}^G$ that satisfies $\langle \boldsymbol{\varepsilon}^G \rangle_V = \langle \boldsymbol{\varepsilon}^S \rangle_V$ from the following functional:

$$\boldsymbol{I}^S(\boldsymbol{u}, \overline{\boldsymbol{u}}) = \left\langle \frac{1}{2}\boldsymbol{\varepsilon} : \boldsymbol{c} : \boldsymbol{\varepsilon} \right\rangle_V + \frac{1}{V}\int_{\partial V} \boldsymbol{\lambda}(\boldsymbol{x}) \cdot (\boldsymbol{u}(\boldsymbol{x}) - \overline{\boldsymbol{u}}(\boldsymbol{x}))\mathrm{d}s + \boldsymbol{\mu} : \left(\langle \boldsymbol{\varepsilon} \rangle_V - \overline{\boldsymbol{\varepsilon}}\right),$$

where $\overline{\boldsymbol{u}}$ and $\overline{\boldsymbol{\varepsilon}}$ are a displacement field which is defined on ∂V and a given average strain and $\boldsymbol{\varepsilon}$ is a strain field associated with $\boldsymbol{u}$.

Hashin–Shtrikman Variational Principle

Fictitious Uniform RVE

A unique approach of estimating the overall property of an RVE is the use of the variational principle. This is called the Hashin–Shtrikman variational principle (Hashin and Shtrikman 1962); see Walpole (1969), Willis (1977), Milton and Kohn (1988), Torquato (1991), and Munashinghe et al. (1996). It uses a fictitious but homogeneous RVE and seeks to find a distribution of *eigen-stress* so that the field variables in the homogeneous RVE coincide with those in the original heterogeneous RVE. Even if the exact distribution is not found, a suitable distribution of

the eigen-stress provides an upper or lower bound for the strain energy of the original heterogeneous RVE.

The formulation of the Hashin–Shtrikman variational principle starts from eigen-stress, denoted by $\boldsymbol{\sigma}^*$, and the following stress–strain relation holds in the homogeneous RVE, denoted by V^{o}:

$$\boldsymbol{\sigma}(\mathbf{x}) = \boldsymbol{c}^{\mathrm{o}} : \boldsymbol{\varepsilon}(\boldsymbol{x}) + \boldsymbol{\sigma}^*(\boldsymbol{x}), \tag{23}$$

where $\boldsymbol{c}^{\mathrm{o}}$ is the elasticity of the homogeneous RVE. The other two field equations, Eqs. 1 and 2, hold in the homogeneous RVE. The governing equation for $\boldsymbol{u}$ is thus given as

$$\nabla \cdot (\boldsymbol{c}^{\circ} : \nabla \boldsymbol{u}(\boldsymbol{x})) + \nabla \cdot \boldsymbol{\sigma}^*(\boldsymbol{x}) = 0. \tag{24}$$

Regarding $\nabla \cdot \boldsymbol{\sigma}^*$ as a body force, Eq. 24 can be solved for $\boldsymbol{u}$ by using the fundamental solution of the homogeneous body, $\boldsymbol{G}^{\mathrm{o}}$; this $\boldsymbol{G}^{\mathrm{o}}$ is often called Green's function of an infinitely extended body, instead of the fundamental solution of the partial differential equation. The contribution of $\boldsymbol{\sigma}^*$ on $\boldsymbol{u}$ is given as $\int \boldsymbol{G}^{\mathrm{o}}(\boldsymbol{x} - \boldsymbol{y}) \cdot (\nabla \cdot \boldsymbol{\sigma}^*(\boldsymbol{y}))\mathrm{d}v$, where the integration is taken with respect to $\boldsymbol{y}$.

Now, suppose the linear displacement boundary conditions of the original RVE are posed for the homogeneous RVE. If $\boldsymbol{\sigma}^*$ satisfies

$$\overset{\circ}{\boldsymbol{c}} : \boldsymbol{\varepsilon}(\boldsymbol{x}) + \boldsymbol{\sigma}^*(\boldsymbol{x}) = \boldsymbol{c}(\boldsymbol{x}) : \boldsymbol{\varepsilon}(\boldsymbol{x}), \tag{25}$$

the field variables of the homogeneous RVE coincide with those of the original RVE. Note that $\boldsymbol{\varepsilon}$ in both sides of Eq. 25 are the strain in the homogeneous RVE.

Hashin–Shtrikman Functional for Eigen-stress

A functional for $\boldsymbol{\sigma}^*$ is readily defined so that its Euler equation becomes Eq. 25. That is,

$$J^E(\boldsymbol{\sigma}^*) = \int_{V^{\circ}} \frac{1}{2}\boldsymbol{\sigma}^*(\boldsymbol{x}) : (\boldsymbol{c}(\boldsymbol{x}) - \boldsymbol{c}^{\circ})^{-1} : \boldsymbol{\sigma}^*(\boldsymbol{x}) - \frac{1}{2}\boldsymbol{\sigma}^*(\boldsymbol{x}) : \boldsymbol{\varepsilon}^{\mathrm{d}}(\boldsymbol{x}) - \boldsymbol{\sigma}^*(\boldsymbol{x}) : \boldsymbol{\varepsilon}^{\circ}(\boldsymbol{x})\mathrm{d}v; \tag{26}$$

$\boldsymbol{\varepsilon}^{\mathrm{d}}$ is strain caused by $\boldsymbol{\sigma}^*$ and can be expressed in terms of $\boldsymbol{G}^{\mathrm{o}}$, and $\boldsymbol{\varepsilon}^{\mathrm{o}}$ is a strain field caused by the given displacement boundary conditions in the absence of $\boldsymbol{\sigma}^*$. Since $\boldsymbol{\varepsilon}^{\mathrm{d}}$ and $\boldsymbol{\sigma}^*$ satisfy

$$\int_{V^{\mathrm{o}}} \boldsymbol{\sigma}^*(\boldsymbol{x}) : \boldsymbol{\varepsilon}^d(\boldsymbol{x})\mathrm{d}v = -\int_{V^{\mathrm{o}}} \boldsymbol{\varepsilon}^{\mathrm{d}}(\boldsymbol{x}) : c^{\mathrm{o}} : \boldsymbol{\varepsilon}^{\mathrm{d}}(\boldsymbol{x})\mathrm{d}v,$$

and hence the variation of J^E leads to Eq. 25; note that the above equation is derived from a condition of $\boldsymbol{u}^{\mathrm{d}} = \mathbf{0}$ on ∂V^{o}.

When $\boldsymbol{c}^{\mathrm{o}}$ is chosen so that $\boldsymbol{c} - \boldsymbol{c}^{\mathrm{o}}$ becomes negative definite in V^{o}, the stationary value of J^E is actually the minimum value. That is, for any $\boldsymbol{\sigma}^*$, the following inequality holds:

$$J^E(\boldsymbol{\sigma}^*) > \int_{V^{\mathrm{o}}} -\frac{1}{2}((\mathbf{c}(\mathbf{x}) - \mathbf{c}^{\mathrm{o}}) : \boldsymbol{\varepsilon}(\mathbf{x})) : \boldsymbol{\varepsilon}(\mathbf{x})\mathrm{d}v = \left\langle \frac{1}{2}\boldsymbol{\varepsilon} : \mathbf{c}^{\mathrm{o}} : \boldsymbol{\varepsilon} \right\rangle_{V^{\mathrm{o}}} - \langle e \rangle_V.$$

Here, $\boldsymbol{\varepsilon}$ is the strain of the strain in the original RVE subjected to the same displacement boundary conditions (or the strain that is computed for $\boldsymbol{\sigma}^*$ satisfying Eq. 25), and $\langle e \rangle_V$ is the average strain energy density that corresponds to this $\boldsymbol{\varepsilon}$. Hence, a lower bound is obtained for $\langle e \rangle_V$:

$$\langle e \rangle_V > \left\langle \frac{1}{2}\boldsymbol{\varepsilon} : \mathbf{c}^0 : \boldsymbol{\varepsilon} \right\rangle_{V^{\mathrm{o}}} - J^E(\boldsymbol{\sigma}^*). \tag{27}$$

The first term in the right side of this inequality is $\frac{1}{2}\langle \boldsymbol{\varepsilon} \rangle_V : \mathbf{c}^0 : \langle \boldsymbol{\varepsilon} \rangle_V$, since $\boldsymbol{\varepsilon}$ is that strain which corresponds to the linear displacement boundary conditions. The second term is evaluated by using a piecewise constant distribution of $\boldsymbol{\sigma}^*$ and Eshelby's solution. Thus, the lower bound for $\langle e \rangle_V$ provides a lower bound for the overall property.

In the above discussion, linear displacement boundary conditions are assumed in computing the lower bound for $\langle e \rangle_V$ of V. However, the principle holds if any displacement boundary conditions are posed on for ∂V. This is because a key condition of the principle is $\int \boldsymbol{\sigma}^* : \boldsymbol{\varepsilon}^{\mathrm{d}}\mathrm{d}v = -\int \boldsymbol{\varepsilon}^{\mathrm{d}} : \boldsymbol{c}^{\mathrm{o}} : \boldsymbol{\varepsilon}^{\mathrm{d}}\mathrm{d}v$, which is derived from the condition that displacement caused by $\boldsymbol{\sigma}^*$ vanishes on ∂V.

In a similar manner, an upper bound for the overall property can be computed by considering the case when traction boundary conditions are given, and $\boldsymbol{c}^{\mathrm{o}}$ is chosen so that $\boldsymbol{c} - \boldsymbol{c}^{\mathrm{o}}$ becomes positive definite. That is, the following functional is considered:

$$J^S(\boldsymbol{\sigma}^*) = \int_{V^o} \frac{1}{2}\boldsymbol{\varepsilon}^*(\boldsymbol{x}) : (\boldsymbol{d}(\boldsymbol{x}) - \boldsymbol{d}^{\mathrm{o}})^{-1} : \boldsymbol{\varepsilon}^*(\boldsymbol{x}) - \frac{1}{2}\boldsymbol{\varepsilon}^*(\boldsymbol{x}) : \boldsymbol{\sigma}^{\mathrm{d}}(\boldsymbol{x}) - \boldsymbol{\varepsilon}^*(\boldsymbol{x}) : \boldsymbol{\sigma}^{\mathrm{o}}(\boldsymbol{x})\mathrm{d}v;$$

where $\boldsymbol{\varepsilon}^*(\boldsymbol{x})$ is defined as $\boldsymbol{\varepsilon}^*(\boldsymbol{x}) = (\boldsymbol{c}^{\mathrm{o}})^{-1} : \boldsymbol{\sigma}^*(\boldsymbol{x})$; $\boldsymbol{d}^{\mathrm{o}}$ and $\boldsymbol{d}$ are the inverse tensor of $\boldsymbol{c}^{\mathrm{o}}$ and $\boldsymbol{c}$ (usually called compliance tensor), respectively; $\boldsymbol{\sigma}^{\mathrm{d}}$ is the stress caused by $\boldsymbol{\sigma}^*$; and $\boldsymbol{\sigma}^{\mathrm{o}}$ is a stress field caused by the given traction boundary conditions in the absence of $\boldsymbol{\sigma}^*$. Note that just like $\int \boldsymbol{\sigma}^* : \boldsymbol{\varepsilon}^{\mathrm{d}}\mathrm{d}v$ in J^E is negative definite, $\int \boldsymbol{\varepsilon}^* : \boldsymbol{\sigma}^{\mathrm{d}}\mathrm{d}v$ in J^S is negative definite and that the traction boundary conditions do not have to be uniform; the principle holds for any traction boundary conditions.

Application of Hashin–Shtrikman Variational Principle to Periodic Structure

A homogeneous RVE is introduced for the original heterogeneous RVE, in order to formulate the Hashin–Shtrikman variational principle. It gives an impression that this principle holds only in the framework of the average field theory. However, the principle can be applied to a periodic structure of the homogenization theory, if the following identity holds:

$$\int \boldsymbol{\sigma}^*(\boldsymbol{x}) : \boldsymbol{\varepsilon}^{\mathrm{d}}(\boldsymbol{x})\mathrm{d}v = -\int \boldsymbol{\varepsilon}^{\mathrm{d}}(\boldsymbol{x}) : \boldsymbol{c}^0 : \boldsymbol{\varepsilon}^{\mathrm{d}}(\boldsymbol{x})\mathrm{d}v.$$

Here, $\boldsymbol{\varepsilon}^{\mathrm{d}}$ is a strain field produced in the unit cell U when $\boldsymbol{\sigma}^*$ is given to the homogeneous periodic structure. Actually, the periodic boundary conditions which are posed for U satisfy the above equality; $\boldsymbol{\sigma}^*$ and $\boldsymbol{\varepsilon}^{\mathrm{d}}$ are the eigen-stress and the strain caused by $\boldsymbol{\sigma}^*$ in U.

Overall Property at Dynamics State

Averaging Scheme at Dynamic State

In this chapter, quasi-static state has been assumed in analyzing field variables to estimate overall property of a heterogeneous material. It is of interest to consider the estimation of overall property at dynamic state, applying the two micromechanics theories. At dynamic state, Eq. 2 is replaced by

$$\nabla \cdot \boldsymbol{\sigma}(\boldsymbol{x}, t) - \mathrm{D}\boldsymbol{p}(\boldsymbol{x}, t) = \boldsymbol{0}, \tag{28}$$

where t is time, D is the differential operator ($\mathrm{D}(\ ) = \partial(\ )/\partial t$), and $\boldsymbol{p}$ is momentum which is defined as

$$\boldsymbol{p}(\boldsymbol{x}, t) = \rho(\boldsymbol{x})\boldsymbol{v}(\boldsymbol{x}, t). \tag{29}$$

Here, ρ is density and $\boldsymbol{v}$ is velocity given as $\boldsymbol{v} = \mathrm{D}\boldsymbol{u}$.

According to the average field theory, an RVE at dynamic state is considered to estimate the overall property at dynamic state, and the volume average of field variables is computed. While the averaging scheme of strain, Eq. 5, holds, that of stress, Eq. 6, is replaced by

$$\langle \boldsymbol{\sigma} \rangle = \frac{1}{V}\int_{\partial V} \mathrm{sym}\{\boldsymbol{t} \otimes \boldsymbol{x}\}\mathrm{d}s - \langle \boldsymbol{p} \otimes \boldsymbol{x} \rangle, \tag{30}$$

together with

$$\langle \mathrm{D}\boldsymbol{p} \rangle = \frac{1}{V} \int_{\partial V} \boldsymbol{t}\, \mathrm{d}s. \tag{31}$$

Here, for simplicity, subscript V is excluded in $\langle\rangle$, which is a function of t. Note that Eq. 30 includes $\langle \boldsymbol{p} \otimes \boldsymbol{x} \rangle$; unlike Eq. 6 at quasi-static state, the average stress at dynamic state is not determined by the surface integration only. It is important to know that the average strain and stress of a material sample are *measurable* at quasi-static state. However, only the average strain is measurable at dynamic state; computing the average stress of the sample needs a distribution of $\boldsymbol{p} \otimes \boldsymbol{x}$ within the sample.

Fictitious Uniform RVE at Dynamic State

In order to estimate the overall property, the average field theory seeks to relate the volume averages which are computed by the averaging schemes. It is useful to analyze a homogeneous RVE, V^{o}, to which the fundamental solution at dynamic state is applicable, as explained in the previous section. Eigen-stress and eigen-momentum, denoted by $\boldsymbol{\sigma}^*$ and $\boldsymbol{p}^*$, respectively, disturb stress and momentum in V^{o} as

$$\boldsymbol{\sigma}(\boldsymbol{x}, t) = \boldsymbol{c}^{\mathrm{o}} : \boldsymbol{\varepsilon}(\boldsymbol{x}, t) + \boldsymbol{\sigma}^*(\boldsymbol{x}, t), \tag{32}$$

$$\boldsymbol{p}(\boldsymbol{x}, t) = \rho^{\mathrm{o}} \boldsymbol{v}(\boldsymbol{x}, t) + \boldsymbol{p}^*(\boldsymbol{x}, t), \tag{33}$$

from which the governing equation of $\boldsymbol{u}$ at dynamic state is derived as

$$\nabla \cdot (\boldsymbol{c}^{\mathrm{o}} : \nabla \boldsymbol{u}(\boldsymbol{x}, t)) - \rho^{\mathrm{o}} \mathrm{D}^2 \boldsymbol{u}(\boldsymbol{x}, t) + \nabla \cdot \boldsymbol{\sigma}^*(\boldsymbol{x}, t) - D\boldsymbol{p}^*(\boldsymbol{x}, t) = \boldsymbol{0}. \tag{34}$$

As is seen, $\nabla \cdot \boldsymbol{\sigma}^* - \mathrm{D}\boldsymbol{p}^*$ plays a role of body force, and its contribution on $\boldsymbol{u}$ is computed by the spatial and temporal integration of the fundamental solution, which is expressed as the convolution form

$$\iint \boldsymbol{G}^{\mathrm{o}}(\boldsymbol{x} - \boldsymbol{y}, t - s) \cdot (-\nabla \cdot \boldsymbol{\sigma}^*(\boldsymbol{y}, s) + D\boldsymbol{p}^*(\boldsymbol{y}, s)) \mathrm{d}v \mathrm{d}s = \boldsymbol{G}^{\mathrm{o}} * (-\nabla \cdot \boldsymbol{\sigma}^* + \mathrm{D}^*),$$

where $\boldsymbol{G}^{\mathrm{o}}$ is the fundamental solution at dynamic state, and differentiation and integration are taken with respect to $\boldsymbol{y}$ and s. After careful manipulations are carried out in substituting of $\boldsymbol{G}^{\mathrm{o}} * (-\nabla \cdot \boldsymbol{\sigma}^* + \mathrm{D}\boldsymbol{p}^*)$ into Eqs. 30 and 31, the volume average of stress and momentum is estimated as follows:

$$\langle \boldsymbol{\sigma} \rangle = \overline{\boldsymbol{C}} * \langle \boldsymbol{\varepsilon} \rangle + \overline{\boldsymbol{S}} * \langle \boldsymbol{v} \rangle, \tag{35}$$

$$\langle \mathbf{p} \rangle = \overline{\mathbf{S}}^t * \langle \boldsymbol{\varepsilon} \rangle + \overline{\Upsilon} * \langle \boldsymbol{v} \rangle, \tag{36}$$

where, $\overline{\boldsymbol{C}}$, $\overline{\Upsilon}$, and $\overline{\boldsymbol{S}}$ are convolution operators and superscript t stands for the transpose; there is symmetry for Eqs. 35 and 36 in the sense that $\overline{\boldsymbol{S}}$ and $\overline{\mathbf{S}}^t$ express the contribution of $\langle \boldsymbol{v} \rangle$ and $\langle \boldsymbol{\varepsilon} \rangle$ to $\langle \boldsymbol{\sigma} \rangle$ and $\langle \mathbf{p} \rangle$, respectively. The presence of these operators is proved, but the explicit form of the operators in terms of $\boldsymbol{G}^{\mathrm{o}}$ is not obtained.

It is of interest to note that the presence of the average velocity, $\langle \boldsymbol{v} \rangle$, in Eqs. 35 and 36 appears odd. The identical material properties ought to be measured by two observers who move in constant but different speed. However, $\langle \boldsymbol{v} \rangle$ would be different for these two observers, and hence the presence of $\langle \boldsymbol{v} \rangle$ in Eqs. 35 and 36 appears odd. Actually, contribution of $\langle \boldsymbol{v} \rangle$ would be replaced by $\langle \mathrm{D}\boldsymbol{\varepsilon} \rangle$, without breaking the *symmetry* of the operators and the averages, if temporal average is taken for Eqs. 35 and 36.

In closing the average field theory for dynamic state, the averaging scheme for strain energy is summarized as follows:

$$\langle \boldsymbol{\sigma} : \boldsymbol{\varepsilon} \rangle = \frac{1}{V} \int_{\partial V} \boldsymbol{t}(\boldsymbol{x}, t) \cdot \boldsymbol{u}(\boldsymbol{x}, t) \mathrm{d}s - \langle \mathrm{D}\boldsymbol{p} \cdot \boldsymbol{p} \rangle, \tag{37}$$

$$\begin{aligned} \langle \boldsymbol{\sigma} : \boldsymbol{\varepsilon} \rangle - \langle \boldsymbol{\sigma} \rangle : \langle \boldsymbol{\varepsilon} \rangle = \frac{1}{V} \int_{\partial V} (\boldsymbol{t}(\boldsymbol{x}, t) - \boldsymbol{v} \cdot \langle \boldsymbol{\sigma} \rangle) \cdot (\boldsymbol{u}(\boldsymbol{x}, t) - x \cdot \langle \boldsymbol{\varepsilon} \rangle) \mathrm{d}s - \langle \mathrm{D}\boldsymbol{p} \cdot \boldsymbol{u} \rangle \\ + \langle \boldsymbol{x} \otimes \mathrm{D}\boldsymbol{p} \rangle : \langle \boldsymbol{\varepsilon} \rangle. \end{aligned} \tag{38}$$

These two equations are the dynamic version of Eqs. 20 and 21. Just like the quasi-static version, Eqs. 37 and 38 are the consequences of the two field equations, Eqs. 1 and 28, and hold for any arbitrary materials. Note that unlike quasi-static state, $\langle \boldsymbol{\sigma} : \boldsymbol{\varepsilon} \rangle$ and $\langle \boldsymbol{\sigma} : \boldsymbol{\varepsilon} \rangle - \langle \boldsymbol{\sigma} \rangle : \langle \boldsymbol{\varepsilon} \rangle$ are not determined by the surface integral only, which implies that measurement of field variables within V will be needed to evaluate these terms exactly.

Application of Singular Perturbation Expansion

Like the quasi-static state, the homogenization theory seeks to apply the singular perturbation expansion to the governing equation of $\mathbf{u}$ at dynamic state, i.e.,

$$\mathrm{D}(\rho(\boldsymbol{x}) D\boldsymbol{u}(\boldsymbol{x}, t)) - \nabla \cdot (\boldsymbol{c}(\boldsymbol{x}) : \nabla \boldsymbol{u}(\boldsymbol{x}, t)) = \mathbf{0}.$$

If the expansion of $\boldsymbol{u}$ is made in the same manner as Eq. 15, i.e.,

$$\boldsymbol{u}(\boldsymbol{x}, t) = \boldsymbol{u}^0(\boldsymbol{X}, \boldsymbol{x}, t) + \epsilon \boldsymbol{u}^1(\boldsymbol{X}, \boldsymbol{x}, t) + \cdots,$$

then assuming that $\boldsymbol{u}^0$ is a function of $\boldsymbol{X}$ and t and that $\boldsymbol{u}^1$ is the form of $\boldsymbol{u}^1 = \boldsymbol{\chi} : \boldsymbol{u}^0$ with $\boldsymbol{\chi}$ being a function of $\boldsymbol{x}$ only, the overall elasticity is identical with $\overline{\boldsymbol{C}}$ of Eq. 18, and the overall density, $\overline{\Upsilon}$, is the volume average of ρ taken over a unit cell U. That is,

$$\overline{\boldsymbol{C}} = \langle \boldsymbol{c}(\boldsymbol{x}) : \boldsymbol{\chi}(\boldsymbol{x}) + \boldsymbol{I} \rangle_U \text{ and } \overline{\Upsilon} = \langle \rho \rangle_U.$$

This estimate of $\overline{\boldsymbol{C}}$ and $\overline{\Upsilon}$ is intuitively acceptable.

While the dynamic overall property estimated by the average field theory is different from the quasi-static overall property, the homogenization theory produces the same estimate of the overall elasticity and a well-expected estimate of the overall density. This difference comes from the form of the expansion. The different phases will have different elastic wave velocity (which is determined by the ratio of the elasticity and the density). At dynamic state, therefore, each phase will have a different timescale for its elastic wave to travel in the phase, provided that all phases have more or less the same spatial size. Thus, an alternative (probably more realistic) expansion of $\boldsymbol{u}$ will be

$$\boldsymbol{u}(\boldsymbol{x}, t) = \boldsymbol{u}^0(\boldsymbol{X}, \boldsymbol{x}, T, t) + \epsilon \boldsymbol{u}^1(\boldsymbol{X}, \boldsymbol{x}, T, t) + \cdots,$$

where

$$T = \frac{1}{\epsilon} t$$

is a temporal variable slower than t, just as $\boldsymbol{X}$ is a spatial variable changing more slowly than $\boldsymbol{x}$. The results of estimating the overall elasticity and density will be different if the alternative expansion is taken.

Conclusion

The two micromechanics theories explained in this chapter are well established. It is not difficult at all to derive a closed-form expression or a numerical solution for the overall property according to these theories. The accuracy of the estimation is, in general, limited; the analytical estimation does not reach the level of an alternative of the experimental estimation, and the numerical solution, which is better than the closed-form solution, is not often used in practice. However, due to its suppleness, the analytical estimation could be useful to obtain a rough estimate of the overall property.

Besides practical use, the two theories of micromechanics give a clear concept of modeling the microstructure of a heterogeneous material. We can take advantage of this concept in order to estimate nonmechanical properties, such as electromagnetic property, thermal conductivity property, or coupling property among them. The Hashin–Shtrikman variational principle is worth being extended for this purpose, since it provides both upper and lower bounds for the overall property.

References

H. Ammari, H. Kang, M. Lim, Effective parameters of elastic composites. Indiana Univ. Math. J. **55**(3), 903–922 (2006)

N. Bakhvalov, G. Panasenko, *Homogenization: Averaging Processes in Periodic Media* (Kluwer, New York, 1984)
J.D. Eshelby, The determination of the elastic field of an ellipsoidal inclusion, and related problems. Proc. R. Soc. A **A241**, 376–396 (1957)
G.A. Francfort, F. Murat, Homogenization and optimal bounds in linear elasticity. Arch Ration. Mech. Anal. **94**, 307–334 (1986)
X.L. Gao, H.M. Ma, Strain gradient solution for the Eshelby-type anti-plane strain inclusion problem. Acta Mech. **223**, 1067–1080 (2012)
Z. Hashin, S. Shtrikman, On some variational principles in anisotropic and nonhomogeneous elasticity. J. Mech. Phys. Solid **10**, 335–342 (1962)
R. Hill, Elastic properties of reinforced solids: some theoretical principles. J. Mech. Phys. Solid **11**, 357–372 (1963)
M. Hori, S. Nemat-Nasser, Double-Inclusion model and overall moduli of multi-phase composites. Mech. Mater. **14**, 189–206 (1993)
U. Hornung (ed.), *Homogenization and Porous Media* (Springer, Berlin, 1996)
M. Kachanov, I. Tsukrov, B. Shafiro, Effective modulus of solids with cavities of various shapes. Appl. Mech. Rev. **47**, 151–174 (1994)
M. Kawashita, H. Nozaki, Eshelby tensor of a polygonal inclusion and its special properties. J. Elast. **74**(2), 71–84 (2001)
J. Kevorkina, J.D. Cole, *Multiple Scale and Singular Perturbation Methods* (Springer, Berlin, 1996)
H. Le Quang, Q.C. He, Q.S. Zheng, Some general properties of Eshelby's tensor fields in transport phenomena and anti-plane elasticity. Int. J. Solid Struct. **45**(13), 3845–3857 (2008)
L.P. Liu, Solutions to the Eshelby conjectures. Proc. R. Soc. A **464**, 573–594 (2008)
X. Markenscoff, Inclusions with constant eigenstress. J. Mech. Phys. Solid **46**(2), 2297–2301 (1998)
G.W. Milton, R. Kohn, Variational bounds on the effective moduli of anisotropic composites. J. Mech. Phys. Solid **43**, 63–125 (1988)
H.M.S. Munashinghe, M. Hori, Y. Enoki. Application of Hashin-Shtrikman Variational Principle for Computing Upper and Lower Approximate Solutions of Elasto-Plastic Problems, in *Proceedings of the International Conference on Urban Engineering in Asian Cities*, 1996, pp. 1–6
T. Mura, *Micromechanics of Defects in Solids* (Martinus Nijhoff Publisher, New York, 1987)
S. Nemat-Nasser, M. Hori, *Micromechanics: Overall Properties of Heterogeneous Materials* (North-Holland, London, 1993)
S. Nemat-Nasser, M. Hori, Universal bounds for overall properties of linear and nonlinear heterogeneous solids. Trans. ASME **117**, 412–422 (1995)
H. Nozaki, M. Taya, Elastic fields in a polyhedral inclusion with uniform eigenstrains and related problems. ASME J. Appl. Mech. **68**, 441–452 (2001)
K.C. Nuna, J.B. Keller, Effective elasticity tensor of a periodic composite. J. Mech. Phys. Solid **32**, 259–280 (1984)
O.A. Oleinik, A.S. Shamaev, G.A. Yosifian, *Mathematical Problems in Elasticity and Homogenization* (North-Holland, New York, 1992)
S. Onaka, N. Kabayashi, M. Kato, Two-dimensional analysis on elastic strain energy due to a uniformly eigenstrained supercircular inclusion in an elastically anisotropic material. Mech. Mater. **34**, 117–125 (2002)
C.Q. Ru, Eshelby inclusion of arbitrary shape in an anisotropic plane or half-plane. Acta Mech. **160**, 219–234 (2003)
E. Sanchez-Palencia, *Non-homogeneous Media and Vibration Theory*, Lecture Note in Physics, No. 127 (Springer, Berlin, 1981)
K. Tanaka, T. Mori, Note on volume integrals of the elastic field around an ellipsoidal inclusion. J. Elast. **2**, 199–200 (1972)
K. Terada, T. Miura, N. Kikuchi, Digital image-based modeling applied to the homogenization analysis of composite materials. Comput. Mech. **20**, 188–202 (1996)

S. Torquato, Random heterogeneous media: microstructure and improved bounds on effective properties. Appl. Mech. Rev. **42**(2), 37–76 (1991)
K.P. Walker, A.D. Freed, E.H. Jordan, Microstress analysis of periodic composites. Compos. Eng. **1**, 29–40 (1991)
L.J. Walpole, On the overall elastic moduli of composite materials. J. Mech. Phys. Solid **17**, 235–251 (1969)
X. Wang, X.L. Gao, On the uniform stress state inside an inclusion of arbitrary shape in a three-phase composite. Z. Angew. Math. Phys. **62**, 1101–1116 (2011)
M.Z. Wang, B.X. Xu, The arithmetic mean theorem of Eshelby tensor for a rotational symmetrical inclusion. J. Elast. **77**, 12–23 (2005)
J.R. Willis, Bounds and self-consistent estimates for the overall properties of anisotropic composites. J. Mech. Phys. Solid **25**, 185–202 (1977)
Q.S. Zheng, D.X. Du, An explicit and universally applicable estimate for the effective properties of multiphase composites which accounts for inclusion distribution. J. Mech. Phys. Solid **49**, 2765–2788 (2001)
W.N. Zou, Q.C. He, M.J. Huang, Q.S. Zheng, Eshelby's problem of non-elliptical inclusions. J. Mech. Phys. Solid **58**, 346–372 (2010)

Microstructural Behavior and Fracture in Crystalline Materials: Overview

46

Pratheek Shanthraj and Mohammed A. Zikry

Contents

Introduction 1302
Dislocation-Density-Based Multiple Slip Formulation 1304
Multiple-Slip Crystal Plasticity Formulation 1304
Mobile and Immobile Dislocation-Density Evolution Equations 1305
Determination of Dislocation-Density Evolution Coefficients 1306
Dislocation-Density GB Interaction Scheme 1307
Martensitic Microstructural Representation 1309
Computational Representation of Failure Surfaces and Microstructural Failure Criterion 1310
Results and Discussion 1312
Martensitic Block Size 1313
Low-Carbon Steel 1314
High-Carbon Steel 1316
Dynamic Behavior 1319
Martensitic Block Distribution 1320
Random Variant Distribution 1322
Optimized Variant Distribution 1326
Dynamic Behavior 1328
Conclusion 1331
References 1332

P. Shanthraj (✉)
Department of Mechanical and Aerospace Engineering, North Carolina State University, Raleigh, NC, USA

Department of Microstructure–Physics and Alloy Design, Max Planck Institut ür Eisenforschung, Düsseldorf, Germany
e-mail: p.shanthraj@mpie.de

M. A. Zikry
Department of Mechanical and Aerospace Engineering, North Carolina State University, Raleigh, NC, USA
e-mail: zikry@ncsu.edu

© Springer Nature Switzerland AG 2022

G. Z. Voyiadjis (ed.), *Handbook of Damage Mechanics*,
https://doi.org/10.1007/978-3-030-60242-0_8

Abstract

A dislocation-density-based multiple-slip crystalline plasticity framework, which accounts for variant morphologies and orientation relationships (ORs) that are uniquely inherent to lath martensitic microstructures, and a dislocation-density grain-boundary (GB) interaction scheme, which is based on dislocation-density transmission and blockage at variant boundaries, are developed and used to predict stress accumulation or relaxation at the variant interfaces. A microstructural failure criterion, which is based on resolving these stresses on martensitic cleavage planes, and specialized finite-element (FE) methodologies using overlapping elements to represent evolving fracture surfaces are used for a detailed analysis of fracture nucleation and intergranular and transgranular crack growth in martensitic steels. The effects of block and packet boundaries are investigated, and the results indicate that the orientation of the cleavage planes in relation to the slip planes and the lath morphology are the dominant factors that characterize specific failure modes. The block and packet sizes along the lath long direction are the key microstructural features that affect toughening mechanisms, such as crack arrest and deflection, and these mechanisms can be used to control the nucleation and propagation of different failure modes.

Keywords

Slip system · Cleavage plane · Martensitic steel · Nominal strain · Active slip system

Introduction

In this chapter, a recently developed dislocation-density crystalline plasticity formulation is coupled with a new fracture methodology to investigate large strain inelastic modes and associated ductile crack nucleation and evolution in crystalline materials. The methodology is applied to martensitic steels. Fracture behavior in crystalline materials is inherently complex due to the microstructural effects, which can affect behavior on scales that range from the nano to the macro. The overarching challenge is to identify dominant microstructural effects on behavior, such as failure initiation and evolution in ductile crystalline materials. Lath martensitic steels offer a unique system, since the microstructure at different scales can include different crystalline structures (b.c.c. and f.c.c.), dislocation-density evolution and interactions, variant orientations and distributions, grain morphologies, grain-boundary distributions and orientations, and dispersed particles and precipitates.

Lath martensitic steels have a myriad of military and civilian applications due to their high strength wear resistance and toughness. These properties are a result of the unique microstructure inherent to martensitic steels, which have been characterized extensively as lath, block, and packet substructures (Morito et al. 2003, 2006). Depending on the processing and chemical composition, martensitic steels can

offer a variety of microstructures and properties (Takaki et al. 2001; Tsuji et al. 2004; Song et al. 2005). Superior combinations of mechanical properties have been achieved through microalloying elements and thermomechanical treatment followed by tempering and aging (Ayada et al. 1998; Barani et al. 2007; Kimura et al. 2008). Failure in martensitic steels and its relation to the microstructure has been experimentally studied, and various failure modes, such as the formation of intensely localized shear bands (Minaar and Zhou 1998) and transgranular and intergranular fracture (Krauss 1999; Inoue et al. 1970; Matsuda et al. 1972), evolve as a function of the interrelated effects of martensitic structure, the ORs, and strain rate.

The size of cleavage facets in transgranular fracture modes has been related to the packet size (Inoue et al. 1970; Matsuda et al. 1972) and the block size (Hughes et al. 2011). Refinement of the block and packet sizes can reduce the coherence interface length on the {110} and {112} slip planes, which improves strength by resisting dislocation motion, and on the {100} cleavage planes, which improves toughness by suppressing crack propagation modes (Morris 2011; Guo et al. 2004; Morris et al. 2011). While block and packet size refinement through intercritical heat treatments (Jin et al. 1975; Kim et al. 1998) and tempforming (Kimura et al. 2008) has been used to obtain high strength and toughness, it has generally been observed to result in high strength with a significant loss in ductility (Howe 2000; Tsuji et al. 2002). The relative roles of the block and packet boundaries in the strengthening and toughening mechanisms are unclear in these investigations, as the effect of processing on the refinement of both packet and block sizes is not considered, which can be significant as noted by Kawata et al. (2006) who have observed that block sizes can be increased by packet size refinement by changing the processing conditions. Using microbending experiments, Shibata et al. (2010) have shown the significant contribution of block boundaries relative to that of subblock boundaries to strengthening, which has been attributed to dislocation pileups at high-angle block boundaries. Ohmura et al. (2004) have observed dislocation absorption into the block boundary with no indication of pileups, and the observed hardening due to block size refinement has been attributed to the decoration of the boundary with carbides (Ohmura and Tsuzaki 2007).

All of these investigations clearly indicate that the morphology and crystallography of the blocks and packets have a significant influence on the strength and toughness of martensitic microstructures, through the complex interactions of the prior austenite grain boundaries, the packet and the block boundaries with the evolving dislocation microstructure, and propagating cracks. However, what is lacking is a systematic investigation of the relationship between the microstructure and the material behavior, which is not well established. The objective of the present work, therefore, is to develop an integrated framework that incorporates material descriptions, which are sensitive to dominant martensitic microstructural features, with specialized computational representations of evolving failure surfaces and microstructurally based failure criteria, to accurately model the initiation and evolution of failure in martensitic steels. A physically based dislocation-density GB interaction scheme that is representative of the resistance to dislocation-density transmission across block and packet boundaries is developed, and it is incorporated into a multiple-slip dislocation-density-based constitutive formulation. The

formulation accounts for variant morphologies and ORs that are uniquely inherent to lath martensitic microstructures. The disadvantages of existing crack propagation methods are overcome through the use of a specialized FE methodology using overlapping elements to represent failure surfaces (Hansbo and Hansbo 2004), and a failure criterion based on the evolving orientation of the cleavage planes in different martensitic variants is developed. This framework is then used to perform large-scale FE simulations to characterize the dominant dislocation-density mechanisms for the localization of plastic strains and the initiation and propagation of failure in martensitic microstructures.

This chapter is organized as follows: the dislocation-density crystalline plasticity formulation, the derivation of the dislocation-density GB scheme, and the martensitic microstructure representation are presented in section "Dislocation-Density-Based Multiple Slip Formulation"; the numerical implementation of the failure surface representation and microstructural failure criterion, which is based on resolving stresses along fracture planes, is outlined in section "Computational Representation of Failure Surfaces and Microstructural Failure Criterion"; the results are presented and discussed in section "Results and Discussion"; and a summary of the results and conclusions are given in section "Conclusion."

Dislocation-Density-Based Multiple Slip Formulation

In this section, the multiple-slip crystal plasticity rate-dependent constitutive formulation and the derivation of the evolution equations for the mobile and immobile dislocation densities, which are coupled to the constitutive formulation, are presented.

Multiple-Slip Crystal Plasticity Formulation

The crystal plasticity constitutive framework used in this study is based on the formulation developed by Asaro and Rice (1977) and Zikry (1994). It is assumed that the velocity gradient is decomposed into a symmetric deformation rate tensor D_{ij} and an antisymmetric spin tensor W_{ij} . D_{ij} and W_{ij} are then additively decomposed into elastic and inelastic components as

$$D_{ij} = D^*_{ij} + D^p_{ij}, \quad W_{ij} = W^*_{ij} + W^p_{ij} \tag{1}$$

The inelastic components are defined in terms of the crystallographic slip rates as

$$D^p_{ij} = \sum P^{(\alpha)}_{ij} \dot{\gamma}^{(\alpha)}, \quad W^p_{ij} = \sum \omega^{(\alpha)}_{ij} \dot{\gamma}^{(\alpha)} \tag{2}$$

where α is summed over all slip systems and $P^{(\alpha)}_{ij}$ and $\omega^{(\alpha)}_{ij}$ are the symmetric and antisymmetric parts of the Schmid tensor in the current configuration, respectively.

A power law relation can characterize the rate-dependent constitutive description on each slip system as

$$\dot{\gamma}^{(\alpha)} = \dot{\gamma}_{\text{ref}}^{(\alpha)} \left[\frac{\tau^{(\alpha)}}{\tau_{\text{ref}}^{(\alpha)}}\right] \left[\frac{\tau^{(\alpha)}}{\tau_{\text{ref}}^{(\alpha)}}\right]^{\frac{1}{m}-1} \tag{3}$$

where $\dot{\gamma}_{\text{ref}}^{(\alpha)}$ is the reference shear strain rate which corresponds to a reference shear stress $\tau_{\text{ref}}^{(\alpha)}$ and m is the rate sensitivity parameter. $\tau^{(\alpha)}$ is the resolved shear stress on slip system α. The reference stress used is a modification of widely used classical forms (Franciosi et al. 1980) that relate reference stress to immobile dislocation density $\rho_{\text{im}}^{(\alpha)}$ as

$$\tau_{\text{ref}}^{(\alpha)} = \left(\tau_y^{(\alpha)} + G\sum_{\beta=1}^{\text{nss}} b^{(\beta)}\sqrt{a_{\alpha\beta}\rho_{\text{im}}^{(\beta)}}\right)\left(\frac{T}{T_0}\right)^{-\xi} \tag{4}$$

where $\tau_y^{(\alpha)}$ is the static yield stress on slip system α, G is the shear modulus, nss is the number of slip systems, $b^{(\beta)}$ is the magnitude of the Burgers vector, and $a_{\alpha\beta}$ are Taylor coefficients which are related to the strength of interactions between slip systems (Devincre et al. 2008; Kubin et al. 2008a, b). T is the temperature, T_0 is the reference temperature, and ξ is the thermal softening exponent.

Mobile and Immobile Dislocation-Density Evolution Equations

Following the approach of Zikry and Kao (1996), it is assumed that, for a given deformed state of the material, the total dislocation density, $\rho^{(\alpha)}$, can be additively decomposed into a mobile and an immobile dislocation density, $\rho_m^{(\alpha)}$ and $\rho_{\text{im}}^{(\alpha)}$, respectively. During an increment of strain on a slip system, a mobile dislocation-density rate is generated and an immobile dislocation-density rate is annihilated. Furthermore, the mobile and immobile dislocation-density rates can be coupled through the formation and destruction of junctions as the stored immobile dislocations act as obstacles for evolving mobile dislocations. This is the basis for taking the evolution of mobile and immobile dislocation densities as

$$\frac{d\rho_m^{(\alpha)}}{dt} = \left|\dot{\gamma}^{(\alpha)}\right|\left(\frac{g_{\text{sour}}^{\alpha}}{b^{(\alpha)2}}\frac{\rho_{\text{im}}^{(\alpha)}}{\rho_m^{(\alpha)}} - g_{\text{mnter}}^{(\alpha)} - \rho_m^{(\alpha)} - \frac{g_{\text{immob}-}^{\alpha}}{b^{(\alpha)}}\sqrt{\rho_{\text{im}}^{(\alpha)}}\right) \tag{5}$$

$$\frac{d\rho_{\text{im}}^{(\alpha)}}{dt} = \left|\dot{\gamma}^{(\alpha)}\right|\left(g_{\text{mnter}}^{(\alpha)} + \rho_m^{(\alpha)} + \frac{g_{\text{immob}+}^{\alpha}}{b^{(\alpha)}}\sqrt{\rho_{\text{im}}^{(\alpha)}} - g_{\text{recov}}^{\alpha}\rho_{\text{im}}^{(\alpha)}\right) \tag{6}$$

where g_{sour} is a coefficient pertaining to an increase in the mobile dislocation density due to dislocation sources; g_{mnter} are coefficients related to the trapping of mobile

dislocations due to forest intersections, cross-slip around obstacles, or dislocation interactions; g_{recov} is a coefficient related to the rearrangement and annihilation of immobile dislocations; and g_{immob} are coefficients related to the immobilization of mobile dislocations.

Determination of Dislocation-Density Evolution Coefficients

To couple the evolution equations for mobile and immobile dislocation densities to the crystal plasticity formulation, the nondimensional coefficients in Eqs. 5 and 6 were determined as functions of the crystallography and deformation mode of the material, by considering the generation, interaction, and recovery of dislocation densities in Shanthraj and Zikry (2011). These expressions are summarized in Table 1, where f_0 and ϕ are geometric parameters. H_0 is the reference activation enthalpy, ρ_s is the saturation density and the average junction length, l_c, can be approximated as

$$l_c = \frac{1}{\sum_{\beta} \sqrt{\rho_{\text{im}}^{(\beta)}}} \tag{7}$$

The interaction tensor, $n_{\alpha}^{\beta\gamma}$, is defined as having a value of 1 if dislocations on slip systems β and γ interact to form an energetically favorable junction on slip system α and a value of 0 if there are no interactions.

The Taylor interaction coefficients, $a_{\alpha\beta}$, for the slip-system interactions in BCC crystalline materials, which are required to determine the reference shear stress (Eq. 4) and the evolution of mobile and immobile dislocation densities (Eqs. 5 and 6), have been calculated in Shanthraj and Zikry (2012a, b) and listed in Table 2.

Table 1 g coefficients in Eqs. 5 and 6

g coefficient	Expression
g_{sour}^{α}	$b^{\alpha}\varphi\sum_{\beta}\sqrt{\rho_{\text{im}}^{\beta}}$
$g_{\text{mnter}}^{\alpha}$	$l_c f_0 \sum_{\beta}\sqrt{a_{\alpha\beta}}\left[\frac{\rho_m^{\beta}}{\rho_m^{\alpha} b^{\alpha}} + \frac{\dot{\gamma}^{\beta}}{\dot{\gamma}^{\alpha} b^{\beta}}\right]$
$g_{\text{immob}-}^{\alpha}$	$\frac{l_c f_0}{\sqrt{\rho_{\text{im}}^{\alpha}}}\sum_{\beta}\sqrt{a_{\alpha\beta}}\rho_{\text{im}}^{\beta}$
$g_{\text{mnter}+}^{\alpha}$	$\frac{l_c f_0}{\dot{\gamma}^{\alpha}\rho_{\text{im}}^{\alpha}}\sum_{\beta,\gamma} n_{\alpha}^{\beta\gamma}\sqrt{a_{\beta\gamma}}\left[\frac{\rho_m^{\gamma}\dot{\gamma}^{\beta}}{b^{\beta}} + \frac{\rho_m^{\beta}\dot{\gamma}^{\gamma}}{b^{\gamma}}\right]$
$g_{\text{immob}+}^{\alpha}$	$\frac{l_c f_0}{\dot{\gamma}^{\alpha}\sqrt{\rho_{\text{im}}^{\alpha}}}\sum_{\beta,\gamma} n_{\alpha}^{\beta\gamma}\sqrt{a_{\beta\gamma}}\rho_{\text{im}}^{\gamma}\dot{\gamma}^{\beta}$
$g_{\text{recov}}^{\alpha}$	$\frac{l_c f_0}{\dot{\gamma}^{\alpha}}\left(\sum_{\beta}\sqrt{a_{\alpha\beta}}\frac{\dot{\gamma}^{\beta}}{b^{\beta}}\right) e^{\left(\frac{-H_0\left(1-\sqrt{\frac{\rho_{\text{im}}^{\alpha}}{\rho_s}}\right)}{kT}\right)}$

Table 2 Interaction coefficient values for the types of reactions between slip systems in b.c.c. crystals and comparison with values from literature (Madec and Kubin 2008; Queyreau et al. 2009)

Interaction type	Dissipation $\left(\propto \sqrt{a_{ij}}\right)$	a_{ij}	a_{ij} from literature
Self, colinear	1.5 kGb^2	0.6	0.550.72
Binary junction	0.5 kGb^2	0.067	0.0450.09
Ternary junction	kGb^2	0.267	0.12250.3364

Dislocation-Density GB Interaction Scheme

In this section, a dislocation-density GB interaction scheme is presented. It is assumed that the dislocation-density interactions occur between slip systems on each side of the GB. Following Ma et al. (2006), the dislocation-density transmission is modeled as an activational event, and the constitutive relation (Eq. 3) has been modified at the GB through the introduction of a transmission factor $P^{(\alpha)}$:

$$\dot{\gamma}^{(\alpha)} = \dot{\gamma}_{\text{ref}}^{(\alpha)} \left[\frac{\left|\tau^{(\alpha)}\right|}{\tau_{\text{ref}}^{(\alpha)}}\right] \left[\frac{\tau^{(\alpha)}}{\tau_{\text{ref}}^{(\alpha)}}\right]^{\frac{1}{m}-1} \boldsymbol{P}^{(\alpha)} = \dot{\gamma}_{\text{ref}}^{(\alpha)} \left[\frac{\left|\tau^{(\alpha)}\right|}{\tau_{\text{ref}}^{(\alpha)}}\right] \left[\frac{\tau^{(\alpha)}}{\tau_{\text{ref}}^{(\alpha)}}\right]^{\frac{1}{m}-1} e^{\left(\frac{-U_{\text{GB}}^{(\alpha)}}{kT}\right)} \tag{8}$$

where the line tension model for the activation of a Frank–Read source in the presence of a GB developed in de Koning et al. (2002) is used to obtain the energy required for dislocation-density transmission across a GB, $U_{\text{GB}}^{(\alpha)}$. The energy of such a dislocation configuration (Fig. 1), for incoming and outgoing slip systems α and β, is given by

$$\begin{aligned} U_{\text{GB}}^{(\alpha\beta)} &= 2\text{Gb}^{(\alpha)2} l_1 + 2\text{Gb}^{(\beta)} l_2 + \text{Gb}^{(\alpha)2}(\boldsymbol{\Delta}_1 - \boldsymbol{\Delta}_2) + G\boldsymbol{\Delta} b_{\text{eff}}^2 \boldsymbol{\Delta}_2 \\ &\quad -\tau^{(\alpha)} b^{(\alpha)} A_{\text{sw},\ 1} - \tau^{(\beta)} b^{(\beta)} A_{\text{sw},2} \end{aligned} \tag{9}$$

The magnitude of the effective residual Burger's vector, Δb_{eff}, is related to the residual Burger's vector, $\Delta \vec{b} = \vec{b}^{(\alpha)} - \vec{b}^{(\beta)}$, by

$$\left(\frac{\Delta b_{\text{eff}}}{\Delta b}\right)^2 = 1 + \left(\psi^2 - 2\psi \cos\ \upsilon + 1\right)^{\frac{1}{2}} \tag{10}$$

where

$$\psi = \frac{\Delta_2}{\Delta_1} = \cos\ \upsilon - \frac{\sin \upsilon}{\tan B}, \text{and } B = \cos^{-1}\left(\frac{\Delta b^2}{2b^{(\alpha)2}}\right) \tag{11}$$

For the critical configuration of a Frank–Read source, it is assumed that the geometric parameters are constant. The energy required to drive the system to the

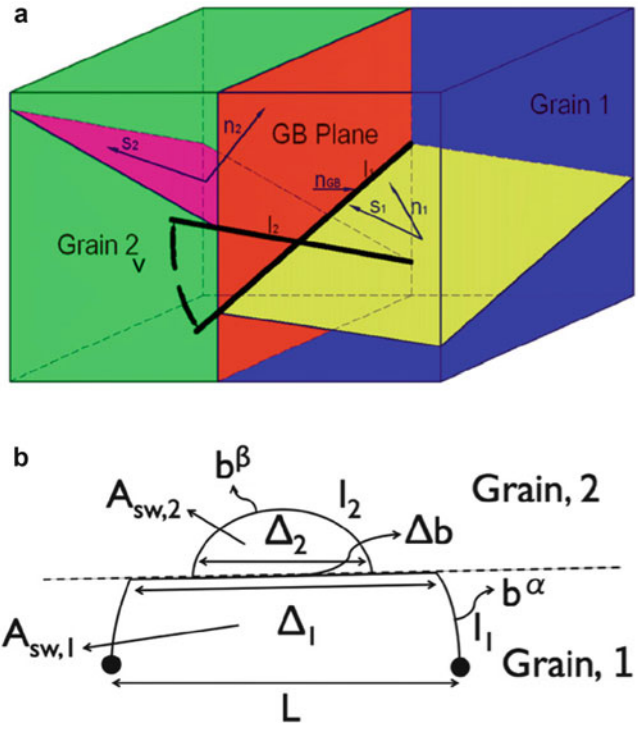

Fig. 1 (**a**) GB schematic and (**b**) dislocation configuration of a Frank–Read source in the vicinity of a GB viewed along the GB plane

critical configuration, and thus initiate dislocation-density glide across a GB, which is taken here to be the energy required for dislocation-density transmission across a GB, for incoming and outgoing slip systems α and β, can then be simplified as

$$U_{\mathrm{GB}}^{(\alpha\beta)} = c_1 \ \mathrm{Gb}^3 \left[1 + c_2(1-\psi) + c_2\psi \left(\frac{\Delta b_{\mathrm{eff}}}{b} \right)^2 - c_3 \frac{\tau^{(\alpha)}}{\tau_{\mathrm{ref}}^{(\alpha)}} - c_4 \frac{\tau^{(\beta)}}{\tau_{\mathrm{ref}}^{(\beta)}} \right] \tag{12}$$

where $c_1 c_4$ are constants related to the geometric parameters at the critical configuration. They are given by $c_1 b = 2l_1 + l_2$ and $c_1 c_2 b = \Delta_2$, and using the condition that for activated boundaries with no misorientation, $U_{\mathrm{GB}}^{(\alpha\beta)} = 0$, $c_3 = 0.5$ and $c_4 = 0.5$ is obtained. Dislocation-density transmission is assumed to be for the most energetically favorable outgoing slip system

$$U_{\mathrm{GB}}^{(\alpha)} = \min_{\beta} U_{\mathrm{GB}}^{(\alpha\beta)} \tag{13}$$

In the FE implementation, the modified constitutive relation (Eq. 8) is used for elements in the vicinity of the GB, which implies that the motion of dislocation densities within the element width, L_e, is constrained by the GB. However, only the

motion of dislocation densities within the GB region, $L_{GB} << L_e$, should be affected by the GB, and the dislocation-density motion in the FE implementation at the GB is overconstrained. To overcome this spurious constraint, the activation energy for dislocation-density transmission $U_{GB}^{(\alpha)}$ is relaxed by a scaling factor L_{GB}/L_e, which is absorbed into the constant c_1. Through this formulation, the criteria for dislocation-density transmission proposed by (Lee et al. 1990) have been incorporated into a physical model for dislocation-density GB interaction:

1. The misorientation between the slip planes must be minimum.
2. The magnitude of the residual Burger's vector at the GB must be minimum.
3. The shear stress on the outgoing slip system must be maximum.

Furthermore, the flux of dislocation densities across the GB is given by

$$\dot{\rho}_{\text{flux}}^{(\beta)} = \frac{\left|\dot{\gamma}^{(\alpha)}\right|}{\text{wb}^{(\alpha)}} \tag{14}$$

where β is the most favorable outgoing slip system and w is the boundary width, and the accumulation of residual GB dislocation densities is given by

$$\dot{\rho}_{\text{GB}}^{(\alpha)} = \sqrt{\frac{\Delta b}{b^{(\alpha)}}} \frac{\left|\dot{\gamma}^{(\alpha)}\right|}{\rho_m^{(\alpha)} b^{(\alpha)}} \tag{15}$$

Martensitic Microstructural Representation

Following Hatem and Zikry (2009) the martensitic lath structure is related to the global coordinates through the parent austenite grain orientation and variant orientations. Commonly accepted ORs for lath martensitic steels are Kurdjumov–Sachs (KS) and Nishiyama–Wassermann (NW) ORs. KS ORs are based on a γ to α' martensitic transformation as $(111)_\gamma \left\| (011)_{\alpha'} \right.$, $\left[\bar{1}01\right]_\gamma \left\| \left[\bar{1}\bar{1}1\right]_{\alpha'} \right.$. The NW OR is a KS OR with a 5.12° rotation around the $[011]_\gamma$ direction. The 24 variants obtained from a KS OR are tabulated in Table 3.

To relate the martensitic local orientation to the global orientation, three transformations are needed. The first transformation, $[T]_1$, relates an observed OR to a theoretical OR, such as KS and NW ORs. The second transformation, $[T]_2$, relates a martensite OR to the parent austenite grain orientation. The third transformation, $[T]_3$, relates the austenite grain orientation to the global coordinates. These transformations are given by $[X]_{\text{Global}} = [T]_3[T]_2[T]_1[X]_{\alpha'}$.

To classify the martensitic microstructure, the characterization scheme of Morito et al. (2003) is followed. We designate a block as a group of laths with low-angle misorientation and a packet as a collection of blocks with the same habit plane. The lath long directions are oriented along $[011]_\gamma$ as shown in Fig. 2. Blocks will have the largest dimension aligned with the constituent lath long direction. Using this

Table 3 The 24 variants corresponding to the KS OR

Variant no.	Parallel planes	Parallel directions	Variant no.	Parallel planes	Parallel directions
1	$(111)_\gamma \parallel (011)_{\alpha'}$	$[\bar{1}01]_\gamma \parallel [\bar{1}\bar{1}1]_{\alpha'}$	13	$(\bar{1}11)_\gamma \parallel (011)_{\alpha'}$	$[0\bar{1}1]_\gamma \parallel [\bar{1}\bar{1}1]_{\alpha'}$
2		$[\bar{1}01]_\gamma \parallel [\bar{1}1\bar{1}]_{\alpha'}$	14		$[0\bar{1}1]_\gamma \parallel [\bar{1}1\bar{1}]_{\alpha'}$
3		$[0\bar{1}1]_\gamma \parallel [\bar{1}\bar{1}1]_{\alpha'}$	15		$[\bar{1}0\bar{1}]_\gamma \parallel [\bar{1}\bar{1}1]_{\alpha'}$
4		$[0\bar{1}1]_\gamma \parallel [\bar{1}1\bar{1}]_{\alpha'}$	16		$[\bar{1}0\bar{1}]_\gamma \parallel [\bar{1}1\bar{1}]_{\alpha'}$
5		$[1\bar{1}0]_\gamma \parallel [\bar{1}\bar{1}1]_{\alpha'}$	17		$[110]_\gamma \parallel [\bar{1}\bar{1}1]_{\alpha'}$
6		$[1\bar{1}0]_\gamma \parallel [\bar{1}1\bar{1}]_{\alpha'}$	18		$[110]_\gamma \parallel [\bar{1}1\bar{1}]_{\alpha'}$
7	$(1\bar{1}\bar{1})_\gamma \parallel (011)_{\alpha'}$	$[10\bar{1}]_\gamma \parallel [\bar{1}\bar{1}1]_{\alpha'}$	19	$(11\bar{1})_\gamma \parallel (011)_{\alpha'}$	$[\bar{1}01]_\gamma \parallel [\bar{1}\bar{1}1]_{\alpha'}$
8		$[10\bar{1}]_\gamma \parallel [\bar{1}1\bar{1}]_{\alpha'}$	20		$[\bar{1}10]_\gamma \parallel [\bar{1}1\bar{1}]_{\alpha'}$
9		$[\bar{1}10]_\gamma \parallel [\bar{1}\bar{1}1]_{\alpha'}$	21		$[0\bar{1}\bar{1}]_\gamma \parallel [\bar{1}\bar{1}1]_{\alpha'}$
10		$[\bar{1}10]_\gamma \parallel [\bar{1}1\bar{1}]_{\alpha'}$	22		$[0\bar{1}\bar{1}]_\gamma \parallel [\bar{1}1\bar{1}]_{\alpha'}$
11		$[011]_\gamma \parallel [\bar{1}\bar{1}1]_{\alpha'}$	23		$[101]_\gamma \parallel [\bar{1}\bar{1}1]_{\alpha'}$
12		$[011]_\gamma \parallel [\bar{1}1\bar{1}]_{\alpha'}$	24		$[101]_\gamma \parallel [\bar{1}1\bar{1}]_{\alpha'}$

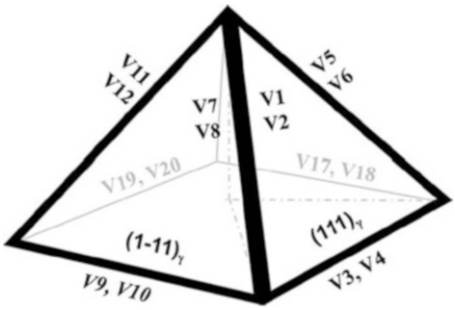

Fig. 2 The alignment of lath long directions of variants V1-24 in Table 3

methodology, the ORs and original austenite orientations are used to model different variant orientations for different block and packet arrangements.

Computational Representation of Failure Surfaces and Microstructural Failure Criterion

In this section, a method for the representation of the initiation and evolution of failure surfaces using overlapping elements is presented. Following the work by Hansbo and Hansbo (2004), an element e in an FE mesh with area A_0 is considered,

which is crossed by a crack, dividing the element domain into two subdomains: elements e_1 and e_2 having areas A_{e1} and A_{e2}, respectively (Fig. 3). Adding an overlapping element on top of the existing element represents the displacement discontinuity due to the crack surface. The connectivity of the overlapping element is defined such that the two elements do not share nodes and therefore have independent displacement fields. This method can address some of the shortcomings associated with the application of cohesive fracture and extended finite-elements (XFEM) techniques to ductile fracture. The proposed fracture criteria do not assume a priori a fracture criteria through enrichment functions (XFEM) or on assumed fracture energies curve for unloaded surface (cohesive fracture). The proposed fracture approach resolves and nucleates cracks on cleavage planes based on the evolving inelastic microstructural behavior due to effects, such as dislocation-density evolution and interaction and different variant distributions. The approach is general in that it can be applied to a broad class of elements.

For a 4-node quadrilateral element with reduced integration and hourglass control, the internal nodal force vector of the cracked element is given by (Song et al. 2006)

$$\vec{f}_e^{\,\text{int}} = \vec{f}_{e1}^{\,\text{int}} + \vec{f}_{e2}^{\,\text{int}} \tag{16}$$

where $\vec{f}_{e1}^{\,\text{int}}$ and $\vec{f}_{e2}^{\,\text{int}}$ are the internal nodal force vectors of the overlapping elements representing the cracked element, which is given by

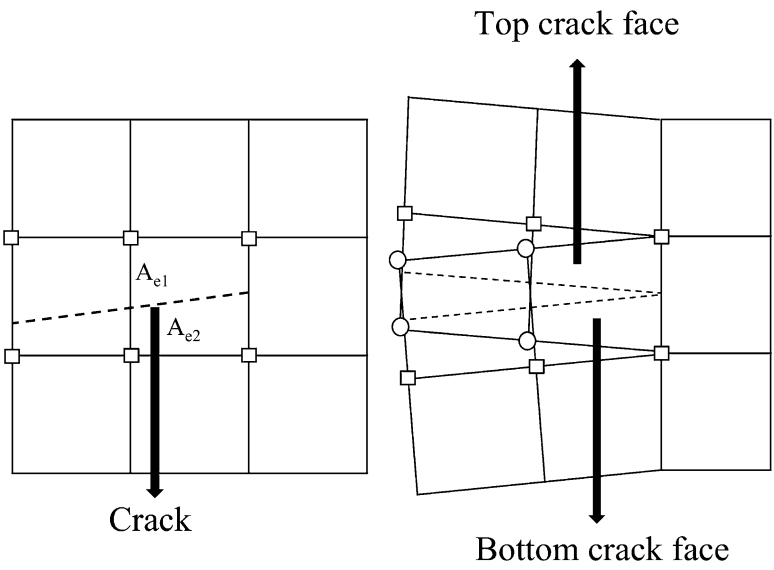

Fig. 3 Representation of a crack using overlapping elements

$$\vec{f}^{\,\mathrm{int}}_{(e1/e2)} = \frac{A_{(e1/e2)}}{A_0} \int \left[B^T \sigma_{(e1/e2)} \right] dA_e \tag{17}$$

To improve numerical performance, a penalty force, which decays with time, is added to resist large initial relative displacements between overlapping elements due to the sudden loss in stiffness of a cracked element. The penalty force is given by

$$\vec{f}^{\,\mathrm{penalty}}_{(e1/e2)} = \alpha (0.995)^{\mathrm{nstep}} \left[\vec{u}_{e1} - \vec{u}_{e2} \right] \tag{18}$$

where α is a penalty parameter, which is taken to be of the order of the material stiffness. A simulation time-step size is chosen, based on convergence studies, so that the penalty force decays at faster timescale than the crack opening displacement.

The inherent fracture mode in martensitic steel is cleavage on $\{100\}_{\alpha'}$ planes in the microstructure (Guo et al. 2004). To formulate this into a microstructural failure criterion, the orientation of the cleavage planes for each variant in the global coordinate system is obtained by applying the series of transformations outlined in section "Martensitic Microstructural Representation":

$$n_{\mathrm{cleave}} = [T]_3 [T]_2 [T]_1 n_{\mathrm{cleave},\alpha'} \tag{19}$$

The global orientation of the cleavage planes in the current configuration is then obtained by updating at every time-step due to the lattice rotations as $\dot{n}_{\mathrm{cleave}} = W^* n_{\mathrm{cleave}}$. The normal component of the traction acting on each cleavage plane has a direct influence on fracture along that plane. The maximum, over all the $\{100\}_{\alpha'}$ cleavage planes, of the normal component of the traction on these planes is, therefore, used as the failure criterion for mode I fracture loading conditions

$$t_{\mathrm{cleave}} = \max_{\{100\}_{\alpha'} \mathrm{planes}} \left\langle n^{\mathrm{T}}_{\mathrm{cleave}} [\sigma] n_{\mathrm{cleave}} \right\rangle \tag{20}$$

A crack is assumed to nucleate when $t_{\mathrm{cleave}} > \sigma_{\mathrm{frac}}$, and the crack is orientated along the most favorable cleavage plane. The 3D cleavage model is implemented in a 2D setting by projecting the 3D crack path onto the 2D plane.

The total deformation rate tensor, D_{ij}, and the plastic deformation rate tensor, D^p_{ij}, are needed to update the material stress state. The method used here is the one developed by Zikry (1994) for rate-dependent crystalline plasticity formulations.

Results and Discussion

The multiple-slip dislocation-density-based crystal plasticity formulation, the dislocation-density GB interaction scheme, and the representation of cracks using overlapping elements were used to investigate the microstructural failure behavior of martensitic steel.

Martensitic Block Size

The microstructure morphology associated with a single parent austenite grain of dimensions 3 × 6 mm^2 in low- and high-carbon martensitic steels on the $(100)_\gamma$ plane is shown in Fig. 4, where the block morphology is obtained by projecting the constituent lath variant long direction (Fig. 2) onto the plane. For the low-carbon steel microstructure, 19 blocks are distributed within three packets with an average packet size of 250 μm (Fig. 4a). For the high-carbon steel microstructure, due to the packet and block size refinement (Maki et al. 1980), for the same parent austenite grain, 48 blocks are distributed within eight packets resulting in an average packet size of 100 μm (Fig. 4b). The parent austenite grain was assumed to have a cube orientation, and the KS relation was adopted as the martensite OR with $\{111\}_\gamma$ as the habit plane. A convergent plane strain FE mesh with approximately 9,000 elements was subjected to tensile loading along the (001) direction at nominal strain rates of 10^{-4} s^{-1}, 500 s^{-1}, and 2,500 s^{-1} with symmetry boundary conditions applied on the left and bottom edges. The material properties (Table 4) that are used for the constituent crystals are representative of low nickel alloy steel (Hatem and Zikry 2009).

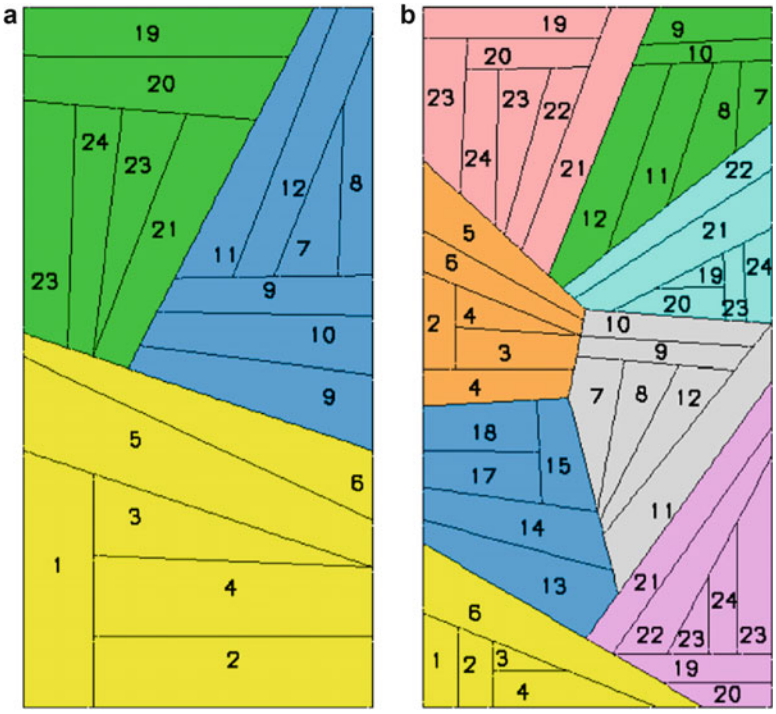

Fig. 4 Block and packet distribution in (**a**) low-carbon steel with an average packet size of 250 μm and (**b**) high-carbon steel with an average packet size of 100 μm. Packets are represented by distinct colors, and numbers in blocks indicate the constituent lath variant (Table 3)

Table 4 Material properties

Properties	Value
Young's modulus, E	228 GPa
Static yield stress, τ_y	517 MPa
Poisson's ratio, ν	0.3
Rate sensitivity parameter, m	0.01
Reference strain rate, $\dot{\gamma}_{ref}$	0.001 s^{-1}
Burger's vector, b	3.0×10^{-10} m
Fracture stress, σ_{frac}	$7\tau_y$
c_1	0.15
c_2	0.9

Low-Carbon Steel

The normalized mobile dislocation densities corresponding to the two most active slip systems at a nominal strain of 9.1%, which is just before the onset of crack nucleation, are shown in Fig. 5a, b. The maximum normalized mobile dislocation densities are 0.47 for slip system $(\bar{1}01)[1\bar{1}1]$ and 0.49 for slip system $(101)[11\bar{1}]$. The normalized interaction density, which is the increase in immobile dislocation density due to junction formation relative to the decrease of mobile dislocation density, is shown in Fig. 5c. Negative values, with a minimum of −0.35, indicate that the annihilation of dislocation junctions through self and colinear dislocation interactions is dominant. Positive values, with a maximum of 0.5, indicate that the formation of dislocation junctions through binary and ternary dislocation interactions is dominant (Table 2). The dominant interaction type is determined by the active slip systems in each variant and using the interaction tensor (section "Determination of Dislocation-Density Evolution Coefficients").

The accumulated plastic slip at a nominal strain of 9.1% is shown in Fig. 6a. The maximum accumulated slip is 0.14. The loading is aligned along the $[001]_\gamma$ direction, which results in a maximum resolved shear stress along the $[011]_\gamma$ directions. The $[011]_\gamma$ directions are also parallel to the long direction of the laths and blocks and to the slip direction $[111]_{\alpha'}$ based on the KS OR. This configuration, which aligns the slip systems with the maximum resolved shear stress, along with local material softening mechanisms due to the annihilation of dislocations in the blocks corresponding to a negative interaction density (Fig. 5c), results in the localization of shear strain. Mobile dislocation densities are transmitted across the block boundaries between the active $(\bar{1}01)[1\bar{1}1]$ and $(101)[11\bar{1}]$ slip systems through the compatibility of the slip systems, which is associated with a low activation energy (Eqs. 12 and 13), and result in shear pipes for the formation of shear bands (Hatem and Zikry 2009). While no special coherency exists across packet boundaries, slip transmission can be observed, and therefore, these packet boundaries can behave similarly to block boundaries (Shanthraj and Zikry 2012a, b). The accumulation of plastic slip is observed along high-angle boundaries as a result of dislocation-density

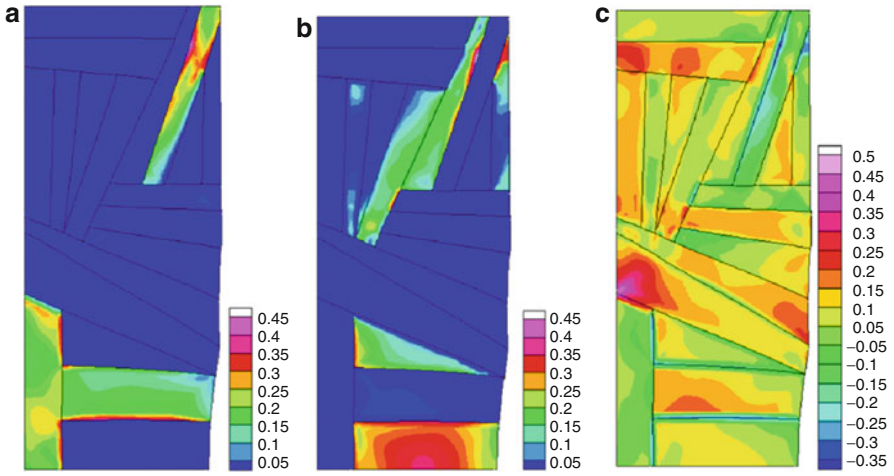

Fig. 5 Normalized mobile dislocation densities at a nominal strain of 9.1% on (**a**) slip system $(\bar{1}01)[1\bar{1}1]$, (**b**) slip system $(101)[11\bar{1}]$, and (**c**) normalized interaction density at a strain rate of 10^{-4} s^{-1}

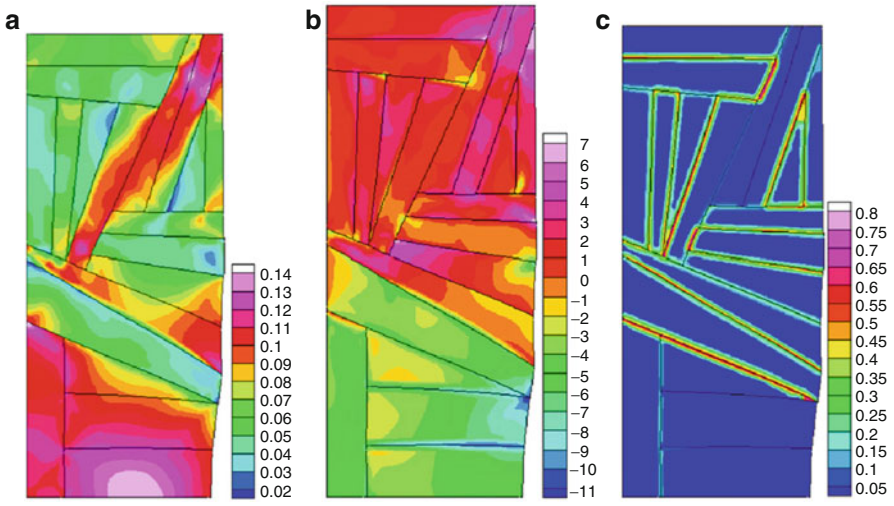

Fig. 6 (**a**) Plastic slip, (**b**) lattice rotations, and (**b**) GB dislocation density at 9.1% nominal strain indicating dislocation-density pileup and plastic slip accumulation at a strain rate of 10^{-4} s^{-1}

blockage due to slip-system incompatibility, which is exacerbated by lattice rotations (Fig. 6b), and is also observed experimentally (Morito et al. 2003).

The total normalized GB dislocation density due to all active slip systems at a nominal strain of 9.1% is shown in Fig. 6c. The normalized GB dislocation density attains a maximum value of 0.8, which is due to the pileup of dislocation densities at the block and packet boundaries. This happens along block and packet boundaries

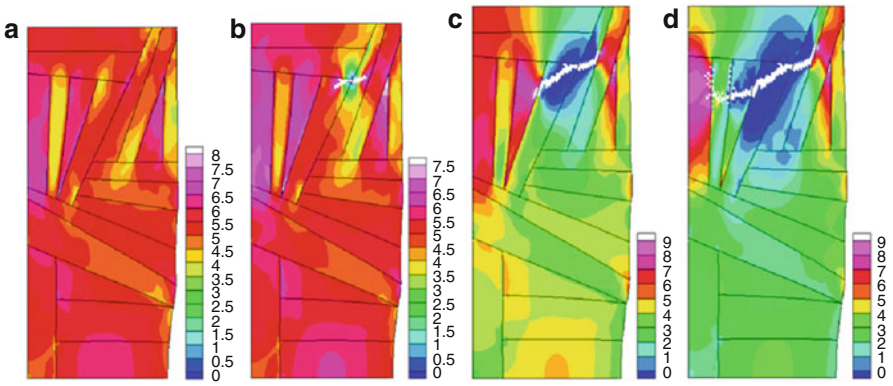

Fig. 7 Axial stress at (**a**) 9.1% nominal strain, (**b**) 9.2% nominal strain showing crack nucleation and (**c**) 9.3% nominal strain, and (**d**) 9.6% nominal strain showing crack propagation at a strain rate of 10^{-4} s^{-1}

between variant pairs having large incompatibilities between the active slip systems and results in large local stress concentrations along high-angle block and packet boundaries, with a maximum normalized stress (by static yield stress) of 8.0, as shown in Fig. 7a. The nucleation of a crack occurs at 9.2% nominal strain at a triple junction between variants 11, 20, and 21 (Fig. 7b), which is separated by a packet boundary, as a result of the local stress concentrations (Fig. 7a) due to GB dislocation-density accumulation at the triple junction (Fig. 6c). The crack initially grows across the packet boundary (Fig. 7c), as dislocation-density transmission relaxes the stress concentrations along the packet boundary and the favorable orientation of the cleavage planes in contiguous blocks, which is accommodated by the lattice rotations (Fig. 6b). The neighboring block morphologies are such that the lath long directions are normal to the crack propagation path, which results in resistance to crack propagation, defection of the crack path, and debonding along the variant boundaries due to the GB dislocation-density accumulation and cleavage plane incompatibilities (Fig. 7d). These intergranular and transgranular fracture modes are consistent with experimental observations (Krauss 1999; Inoue et al. 1970; Matsuda et al. 1972), as well as crack path deflection, crack arrest, and debonding (Hughes et al. 2011).

High-Carbon Steel

To further elucidate the role of block and packet morphology in failure, the results are compared with the failure behavior of a refined variant distribution, corresponding to high-carbon steels (Fig. 4b). The normalized mobile dislocation densities corresponding to the two most active slip systems at a nominal strain of 5.9%, which is just before the onset of crack nucleation, are shown in Fig. 8a, b. The maximum normalized mobile dislocation densities are 0.24 for slip system

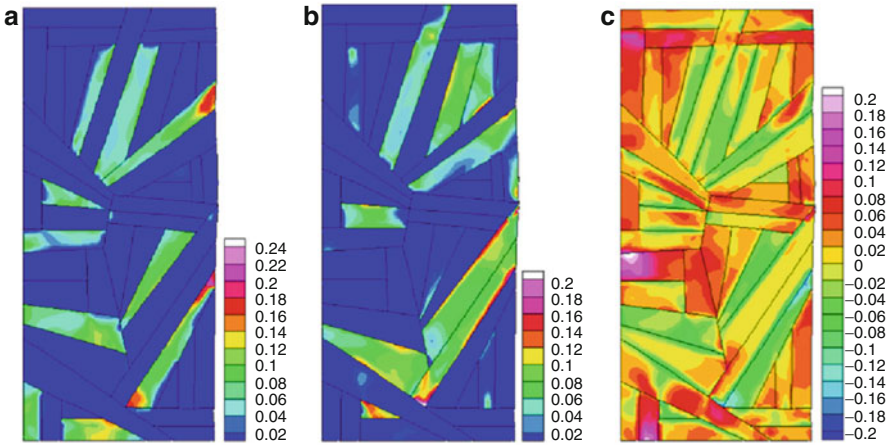

Fig. 8 Normalized mobile dislocation densities for a refined variant arrangement at a nominal strain of 5.9% on (**a**) slip system $\left(\bar{1}01\right)\left[1\bar{1}1\right]$, (**b**) slip system $(101)\left[11\bar{1}\right]$, and (**c**) normalized interaction density at a strain rate of $10^{-4}\,s^{-1}$

$\left(\bar{1}01\right)\left[1\bar{1}1\right]$ and 0.20 for slip system $(101)\left[11\bar{1}\right]$. The mobile dislocation-density activity on these slip systems corresponds to a negative interaction density with a minimum value of −0.2 (Fig. 8c). The accumulated plastic slip, and the resulting lattice rotation at a nominal strain of 5.9%, is shown in Fig. 9a, b. The maximum accumulated slip is 0.1, with lattice rotations ranging from ±8°. The localization of shear strain in relation to the lath orientation, interaction density, and lattice rotations (Fig. 9b) occurs as discussed in section "Martensitic Block Size." The plastic slip is constrained to flow along the lath long directions, and the low activation energy associated with the transmission of dislocation densities between the active slip systems in neighboring blocks results in a dominant shear band, which is of comparable size to the coarser microstructure. The accumulation of shear slip is observed when there is a blockage of dislocation densities, with a maximum normalized GB dislocation density of 0.8 (Fig. 9c).

The refinement of the block and packet sizes increases the number of incompatible variant interfaces, which serve as sites for stress concentrations due to the accumulation of GB dislocation densities, with a maximum normalized stress of 6.5 (Fig. 10a). This results in the nucleation of a crack at a nominal strain of 6.1%, which is lower than that corresponding to the coarse block and packet microstructure, at a triple junction between variants 9, 11, and 12 (Fig. 10b). Variants 11 and 12 belong to different Bain groups and thus have a large misorientation in {100} cleavage planes (Guo et al. 2004). This results in a resistance to the crack propagation across the variant boundary and forces the crack path to deflect along the lath long direction (Fig. 10c). On encountering the neighboring packet boundary, the crack is arrested as a result of the incompatibility in cleavage planes and a change in the neighboring block morphology. A new crack is then nucleated in the neighboring

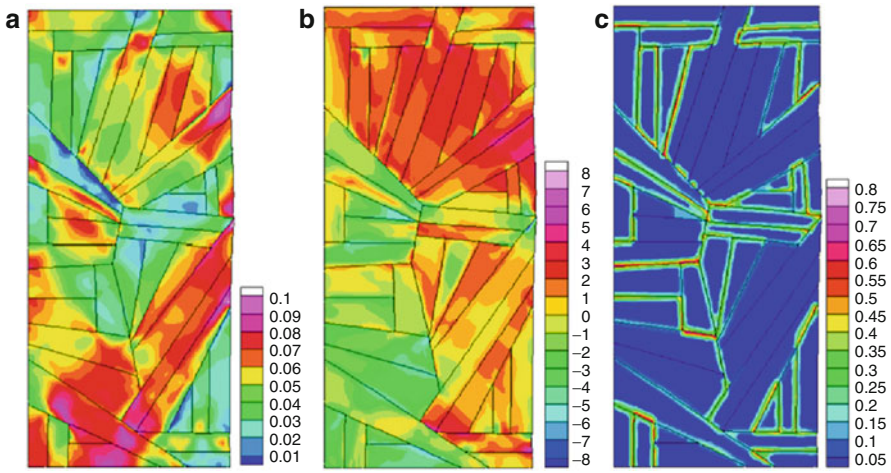

Fig. 9 (**a**) Plastic slip, (**b**) lattice rotations, and (**c**) GB dislocation density for a refined variant arrangement at 5.9% nominal strain indicating dislocation-density pileup and plastic slip accumulation at a strain rate of 10^{-4} s^{-1}

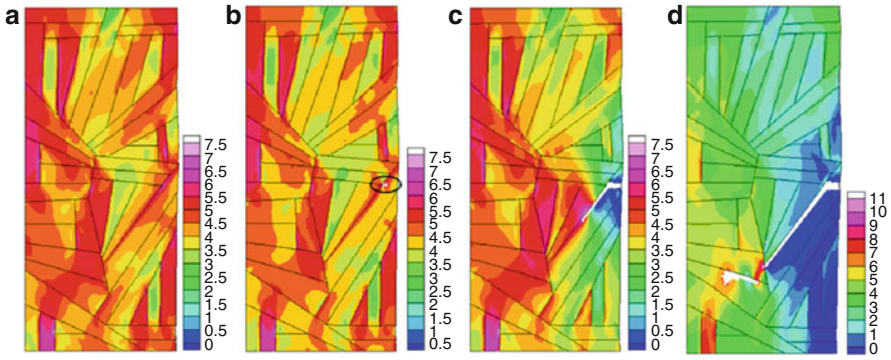

Fig. 10 Axial stress for a refined variant arrangement at (**a**) 5.9% nominal strain, (**b**) 6.1% nominal strain showing crack nucleation and (**c**) 6.4% nominal strain, and (**d**) 6.75% nominal strain showing crack propagation at a strain rate of 10^{-4} s^{-1}

block ahead of the arrested crack tip, which is constrained to propagate along the neighboring block morphology (Fig. 10d).

In contrast to coarse blocks, where the crack propagates across the block width (Fig. 7b–d), block size refinement in high-carbon steels constrains crack propagation along the block morphology resulting in greater fracture resistance, with an increase in load-bearing capacity after crack nucleation of a nominal strain of 0.4%. However, the stress–strain curve indicates that there is no increase in strength due to refinement (Fig. 11). Block size refinement is more effective in improving fracture resistance than strength as the variant boundaries offer relatively less resistance to slip transmission onto the 24 possible slip systems, on the {110} and {112} crystallographic

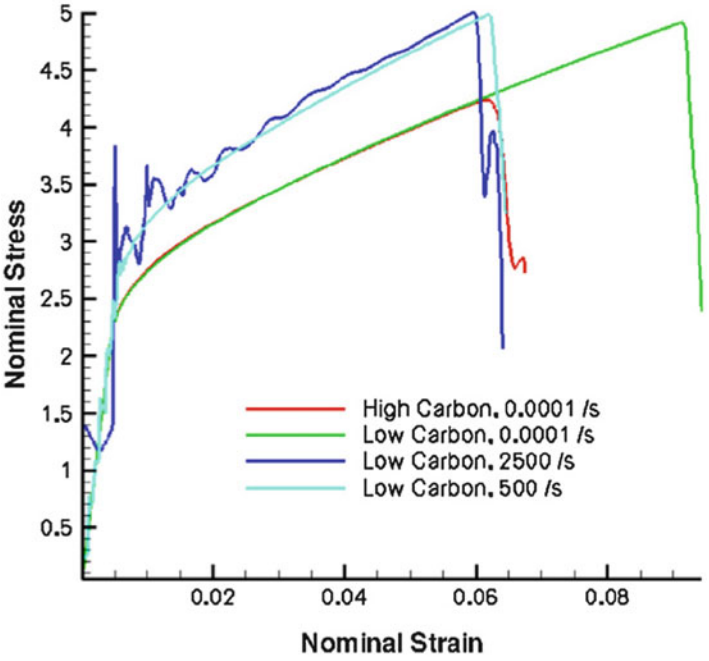

Fig. 11 Nominal stress–strain curves at strain rates of 10^{-4} s^{-1}, 500 s^{-1}, and 2,500 s^{-1}

planes, compared to the transmission of cracks onto only three possible {100} cleavage planes. This results in the formation of shear bands of comparable sizes and in both microstructures and similar strengths since the microstructural strength is associated with the resistance to plastic slip. As the plastic slip is constrained to flow along the lath long directions, block refinement in this dimension is most effective in strengthening, while refinement of the block width is most effective in improving fracture resistance by constraining the crack to propagate along the lath long direction. However, refinement also increases the number of incompatible triple junctions, which can be sites for crack nucleation, and therefore also reduces the ductility. Therefore, the effects of both block and packet refinement should be considered in relation to the lath morphology in determining fracture behavior.

Dynamic Behavior

In this section, the dynamic fracture of low-carbon martensitic steels at loading rates of 500–2,500 s^{-1} is investigated. The nominal stress–strain curves over the range of loading conditions are shown in Fig. 11. The oscillations at high strain rates occur due to stress wave reflections along the free and fixed boundary, which is dampened due to plasticity. The lower failure strains of 6.2% at a strain rate of 500 s^{-1} 6.0% at a strain rate of 2,500 s^{-1} are a result of dynamic strain-rate hardening (Fig. 11). The

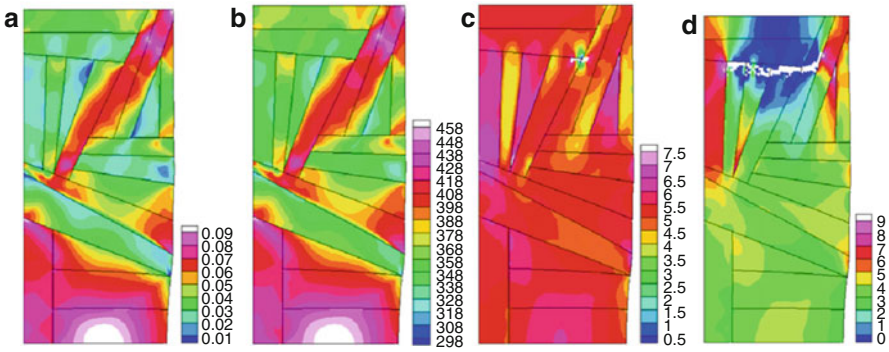

Fig. 12 (**a**) Plastic slip and (**b**) temperature at 6.0% nominal strain. Normal stress at (**c**) 6.1% nominal strain showing crack nucleation and (**d**) 6.4% nominal strain at a strain rate of 2,500 s^{-1}

accumulated plastic slip at a nominal strain of 5.9% and strain rate of 2,500 s^{-1} is shown in Fig. 12a. The maximum accumulated slip is 0.09, and the shear strain localization is narrower at higher strain rates, which is a result of material and thermal softening mechanisms, with a maximum temperature of 458 K, as well as the dynamic strain rates, which prevent the accumulation of shear strains over wide regions. This is consistent with the experimental observations of Dodd and Bai (1985). At this strain rate, crack nucleation is at a nominal strain of 6.0%, as shown in Fig. 12c. Crack deviation is observed at block boundaries with large incompatibilities in the cleavage planes (Fig. 12d). However, a lower resistance to the crack propagation path across block boundaries due to lower accumulation of GB dislocation densities, with a maximum value of 0.7, and stress concentrations along the variant boundary is observed, as a result of the strain-rate hardening at high strain rates. Block size refinement is less effective in improving fracture resistance at high strain rates, and these high strain-rate characteristics result in fracture modes that are different from quasi-static strain rates.

Martensitic Block Distribution

Ductility in martensitic steels is directly related to the transmission of plastic slip across variant boundaries (Tsuji et al. 2008; Guo et al. 2004; Morito et al. 2006). The slip transmission factor (section "Dislocation-Density GB Interaction Scheme")

$$P^{(\alpha\beta)} = e^{\left(\frac{-U_{\mathrm{GB}}^{(\alpha\beta)}}{kT}\right)} \tag{21}$$

between the most active slip systems α and β across a variant boundary can therefore be used as a measure of the ductility. The activation energy, $U_{\mathrm{GB}}^{(\alpha\beta)}$, is given by Eq. 12. Taking τ/τ_{ref} as approximate unity for the most active slip systems, the transmission factor can then be reduced to a function of the orientation of the interaction slip

planes, slip directions, and GB. The orientation of the slip plane and slip direction of the most active slip system in a variant are determined from the variant OR (Table 3) for a cube-oriented parent austenite grain. The transmission factor across the variant boundaries for the 24 KS variants is calculated using Eq. 12 for different GB orientations. The variants are grouped based on the transmission factors in Table 5. The boundaries between variants belonging to group I and II have large transmission factors (>0.26), which is desirable for ductility, while variant boundaries in group III and IV have low transmission factors (<0.01), which can result in slip blockage, stress accumulation, and crack nucleation. In addition, fracture resistance in martensitic steels is related to the misorientation between the cleavage planes across variant boundaries (section "Computational Representation of Failure Surfaces and Microstructural Failure Criterion"). The KS variants can be categorized into three Bain groups – A, B, and C, – as indicated in Table 5, where variants belonging to each Bain group have low misorientations in the {100} cleavage planes. Boundaries between variants belonging to different Bain groups can have large misorientations in the {100} cleavage planes (Guo et al. 2004), which can be desirable for fracture resistance as it can result in crack deflection and crack arrest. A microstructural distribution, which increases the boundaries between variants belonging to different Bain groups and having large slip transmission factors (Table 5), therefore optimizes ductility and fracture toughness in martensitic steels.

Based on these guidelines, the microstructure associated with a single parent austenite grain for a random and optimized variant distribution on the $(100)_\gamma$ plane is shown in Fig. 13, where 68 blocks are distributed within two packets and the block morphology is obtained by projecting the constituent lath variant long direction (Fig. 2) onto the plane. For the optimized variant distribution, only variant boundaries belonging to group I are used, and the use of boundaries between variants belonging to the same Bain group is restricted to be along the less effective lath lateral direction (Fig. 13b). The variant orientation is represented as outlined in section "Martensitic Microstructural Representation." The parent austenite grain is assumed to have a cube orientation, and the KS relation is adopted as the martensite OR with $\{111\}_\gamma$ as the habit plane.

A convergent plane strain FE mesh with approximately 9,000 elements was subjected to tensile loading along the (001) direction at nominal strain rate of

Table 5 Slip transmission factor across variant boundaries indicating Bain groups A, B, and C

Variant group	Slip transmission factor
Group I: V1(C), V3(B), V4(C), V6(B), V13(C), V14(B), V16(C), V17 (B)	0.26–1.0
Group II: V8(C), V9(B), V11(C), V12(B), V19(B), V21(C), V22(B), V24(C)	0.26–1.0
Group III: V2(A), V7(A), V5(A), V10(A)	0.00–0.01
Group IV: V15(A), V18(A), V20(A), V23(A)	0.00–0.01

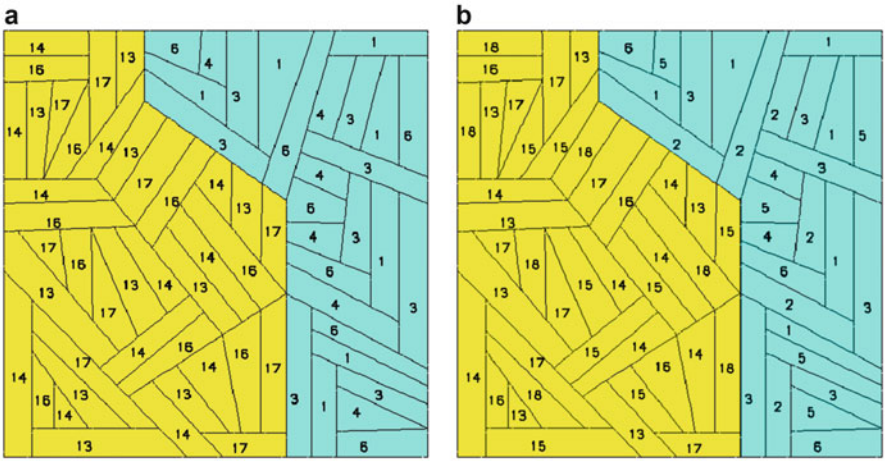

Fig. 13 Block and packet distribution in (**a**) random variant distribution and (**b**) optimized variant distribution. Packets are represented by distinct colors, and numbers in blocks indicate the constituent lath variant (Table 3)

10^{-4} s^{-1} and 5,000 s^{-1}. The material properties (Table 4) are used for the constituent crystals.

Random Variant Distribution

The normalized (by the saturation dislocation density) mobile dislocation densities corresponding to the two most active slip systems at a nominal strain of 4.8%, which is just before the onset of crack nucleation, are shown in Fig. 14a, b. The maximum normalized mobile dislocation densities are 0.30 for slip system $(\bar{1}12)[1\bar{1}1]$ and 0.38 for slip system $(112)[11\bar{1}]$. The normalized interaction density

$$\rho_{\text{int}} = \sum_{\alpha} \int \dot{\gamma}^{\alpha} \left(g^{\alpha}_{\text{mnter}+} \rho^{\alpha}_{m} + \frac{g^{\alpha}_{\text{mnter}+}}{b} \sqrt{\rho^{\alpha}_{\text{im}}} - g^{\alpha}_{\text{mnter}-} \rho^{\alpha}_{m} - \frac{g^{\alpha}_{\text{mnter}-}}{b} \sqrt{\rho^{\alpha}_{\text{im}}} \right) dt \quad (22)$$

which is the increase in immobile dislocation density due to junction formation relative to the decrease of mobile dislocation density, is shown in Fig. 14c. Negative values, with a minimum of −0.35, indicate that the annihilation of dislocation junctions through self and colinear dislocation interactions is dominant. Positive values, with a maximum of 0.12, indicate that the formation of dislocation junctions through binary and ternary dislocation interactions is dominant (Table 2). The dominant interaction type is determined by the active slip systems in each variant and using the interaction tensor (section "Determination of Dislocation-Density Evolution Coefficients").

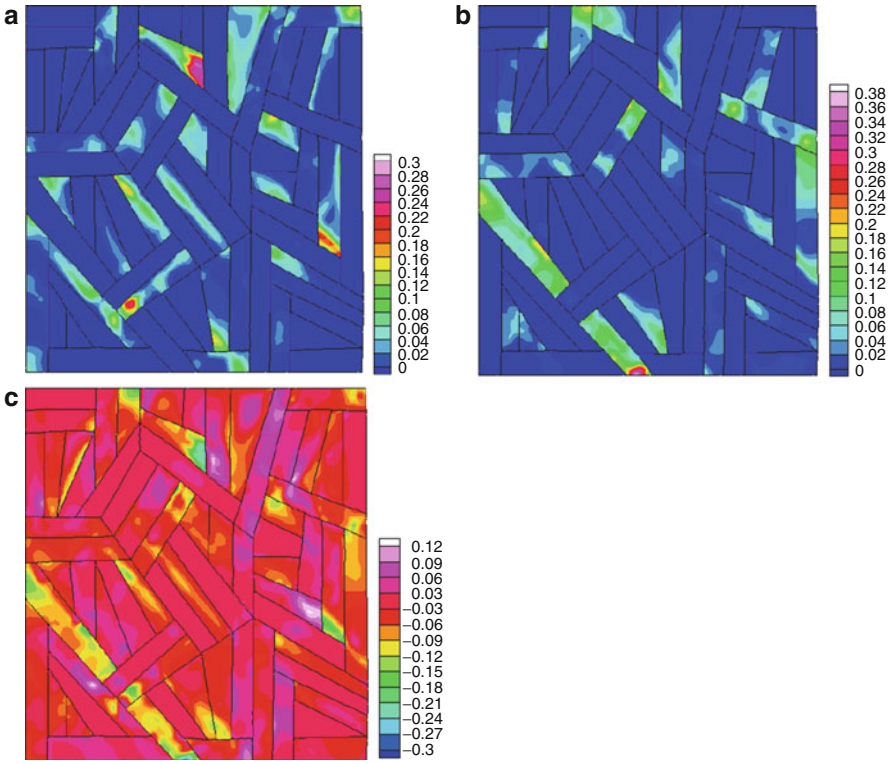

Fig. 14 Mobile dislocation densities, normalized by the saturation density, for a random variant distribution at a nominal strain of 4.8% on (**a**) slip system $(\bar{1}12)[1\bar{1}1]$, (**b**) slip system $(112)[11\bar{1}]$, and (**c**) normalized interaction density at a strain rate of 10^{-4} s^{-1}

The accumulated plastic slip at a nominal strain of 4.8% is shown in Fig. 15a. The maximum accumulated slip is 0.13. The loading is aligned along the $[001]_{\gamma}$ direction, which results in a maximum resolved shear stress along the $[011]_{\gamma}$ directions. The $[011]_{\gamma}$ directions are also parallel to the long direction of the laths and blocks and to the slip direction $[111]_{\alpha'}$ based on the KS OR. This configuration, which aligns the slip systems with the maximum resolved shear stress, along with local material softening mechanisms due to the annihilation of dislocations in the blocks corresponding to a negative interaction density (Fig. 14c), results in the localization of shear strain. Mobile dislocation densities are transmitted across the block boundaries between the active $(\bar{1}12)[1\bar{1}1]$ and $(112)[11\bar{1}]$ slip systems through the compatibility of the slip systems, which is associated with a low activation energy (Eq. 12), and result in shear pipes for the formation of shear bands (Hatem and Zikry 2009). The accumulation of plastic slip is observed along high-angle boundaries as a result of dislocation-density blockage due to slip-system incompatibility, which is exacerbated by lattice rotations (Fig. 15b), and is also observed experimentally (Morito et al. 2003).

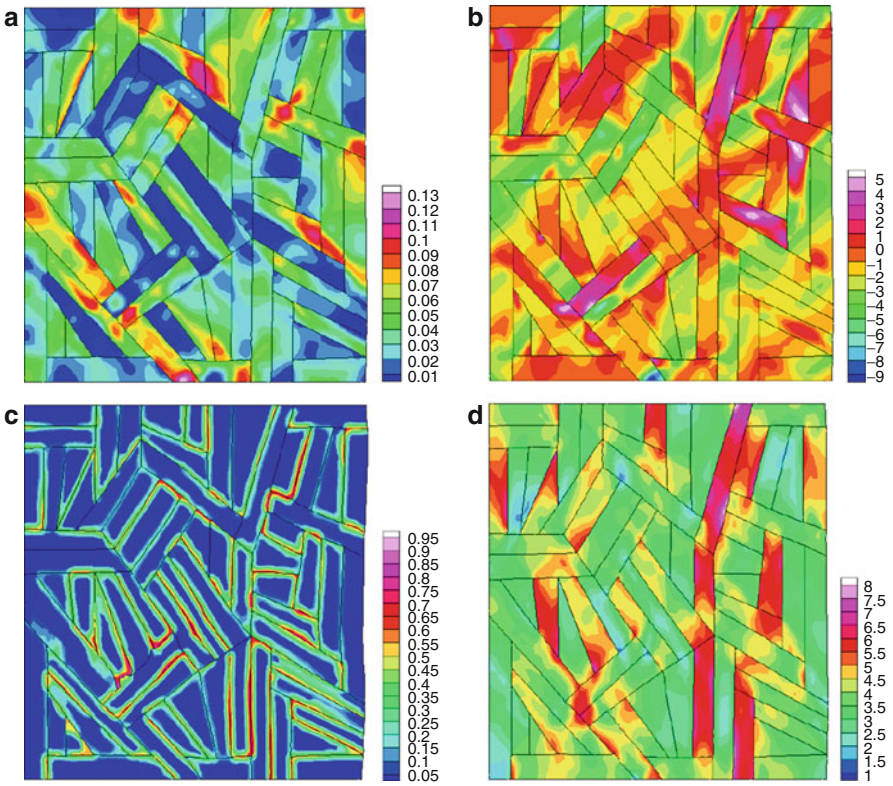

Fig. 15 (**a**) Plastic slip, (**b**) lattice rotations (in degrees), (**c**) GB dislocation density, normalized by the saturated density, and (**d**) normal stress, normalized by the yield stress for a random variant distribution at 4.8% nominal strain indicating dislocation-density pileup and plastic slip accumulation at a strain rate of 10^{-4} s^{-1}

The total normalized GB dislocation density due to all active slip systems at a nominal strain of 4.8% is shown in Fig. 15c. The normalized GB dislocation density attains a maximum value of 0.95, which is due to the pileup of dislocation densities at the block and packet boundaries. This occurs along block boundaries between variant pairs belonging to group III and IV in Table 5, which have large incompatibilities between the active slip systems and low slip transmission factors. This results in large local stress concentrations along high-angle block and packet boundaries, with a maximum normalized stress (by static yield stress) of 8.0, as shown in Fig. 15d. The nucleation of a crack occurs at 5.0% nominal strain at a triple junction between variants 13, 17, and 18 (Fig. 16a), as a result of the local stress concentrations (Fig. 15d) due to GB dislocation-density accumulation at the triple junction (Fig. 15c). The crack initially grows across the block width in variant 13, but is deflected at the boundaries with variant 17 and is constrained to propagate along the block morphology (Fig. 16b), because variant 17 is not favorably oriented for fracture

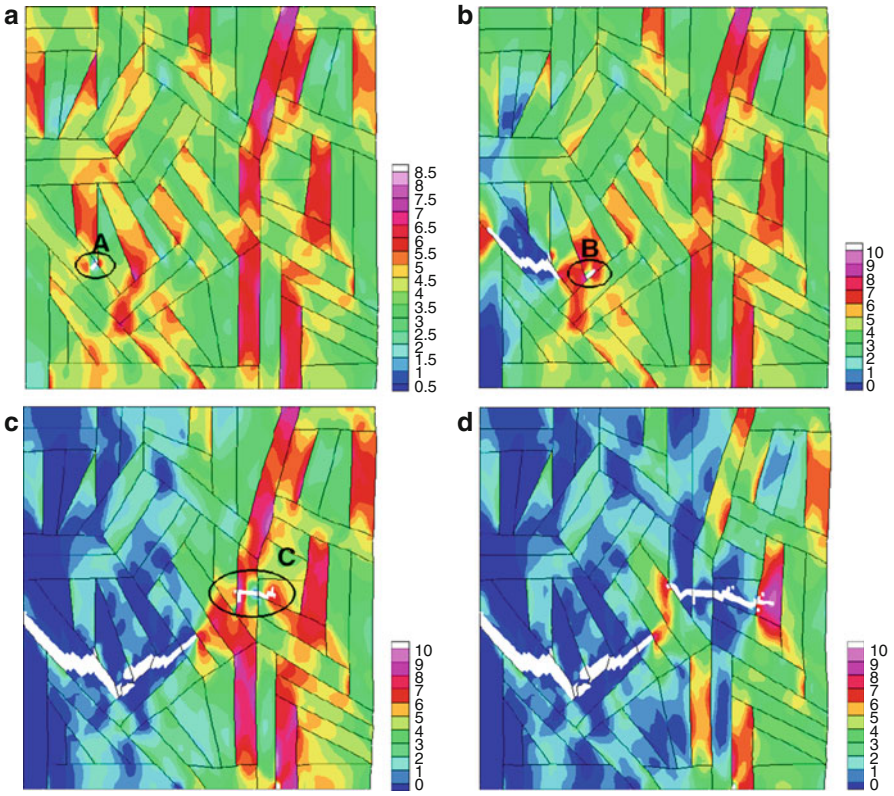

Fig. 16 Normal stress for a random variant distribution at (**a**) 5.0% nominal strain, (**b**) 6.8% nominal strain showing crack nucleation and (**c**) 8.0% nominal strain, and (**d**) 8.8% nominal strain showing crack propagation at a strain rate of 10^{-4} s^{-1}

as it belongs to a different Bain group resulting in a large misorientation in the cleavage planes along which the crack propagates. A new crack is then nucleated in a neighboring block due to the large stress buildup ahead of the arrested crack tip (Fig. 16b). The neighboring block morphologies are such that the lath long directions are normal to the crack propagation path, which results in resistance to crack propagation, defection of the crack path along the variant boundaries due to the GB dislocation-density accumulation and cleavage plane incompatibilities, and the nucleation of microcracks ahead of the arrested crack tip (Fig. 16c, d). These intergranular and transgranular fracture modes are consistent with experimental observations (Inoue et al. 1970; Matsuda et al. 1972; Krauss 1999) as well as crack path deflection and crack arrest (Hughes et al. 2011). The nominal stress (normalized by the static yield stress)–strain curve indicating the toughening due to crack arrest and deflection at incompatible variant boundaries, and the stress drop due to the subsequent nucleation of secondary cracks during the different stages of crack propagation (Fig. 16a–d), is shown in Fig. 17.

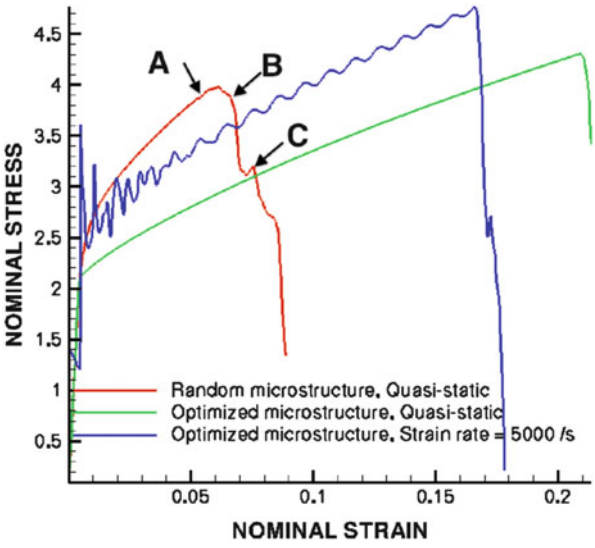

Fig. 17 Nominal stress–strain curves

Optimized Variant Distribution

These results are compared with the failure behavior of a variant distribution, optimized for slip transmission (Fig. 14b). The normalized mobile dislocation densities corresponding to the two most active slip systems at a nominal strain of 20% are shown in Fig. 18a, b. The maximum normalized mobile dislocation density is 0.7 for slip system $(\bar{1}12)[1\bar{1}1]$ and 0.75 for slip system $(112)[11\bar{1}]$, compared to 0.3 and 0.38, respectively, for the random variant distribution. The mobile dislocation-density activity on these slip systems corresponds to a negative interaction density with a minimum value of -0.55 (Fig. 18c) compared to -0.35 for the random variant distribution, indicating a greater degree of dislocation annihilation activity. The accumulated plastic slip and the resulting lattice rotation at a nominal strain of 20% are shown in Fig. 19a, b. Larger accumulated slip is observed, with a maximum of 0.19 compared to 0.13 for the random variant distribution, with lattice rotations ranging from $-11°$ to $6°$. The localization of shear strain in relation to the lath orientation, interaction density, and lattice rotations (Fig. 19b) occurs as discussed in section "Random Variant Distribution." The plastic slip is not constrained to flow along the lath long directions as in the random variant distribution, as the low activation energy associated with the transmission of dislocation densities between the active slip systems in neighboring blocks results in extensive plastic deformation, and lower accumulated GB dislocation densities with a maximum normalized GB dislocation density of 0.5 (Fig. 19c) compared to 0.95 in the random variant distribution. This also results in a more homogeneous normal stress distribution (Fig. 19d), with a maximum normal stress level of 6.5, as a result of the relaxation of stress concentrations at the block and packet boundaries due to dislocation transmission.

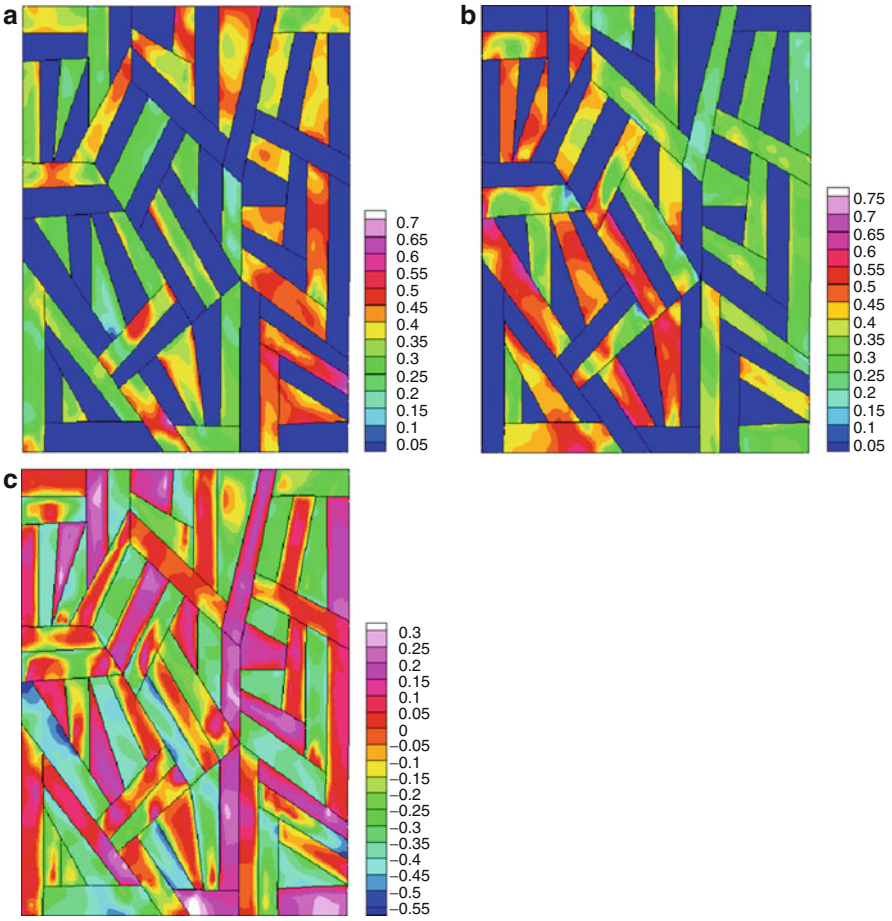

Fig. 18 Normalized mobile dislocation densities for an optimized variant distribution at a nominal strain of 20% on (**a**) slip system $(\bar{1}12)[1\bar{1}1]$, (**b**) slip system $(112)[11\bar{1}]$, and (**c**) normalized interaction density at a strain rate of $10^{-4}\ s^{-1}$

In contrast to the random variant distribution, where the refinement of the block and packet sizes increases the number of incompatible variant triple junctions, which serve as sites for stress concentrations due to the accumulation of GB dislocations, and results in the nucleation of a crack at a lower nominal strain of 5%, the large slip transmission factors associated with boundaries between variants belonging to group I in the optimized variant distribution decrease the number of incompatible variant triple junctions and result in the delayed nucleation of cracks, at a nominal strain of 21%, and increased ductility. The dislocation-density transmission and relaxation of stress at the boundaries also result in a reduction in strength of approximately 350 MPa (Fig. 17), since the microstructural strength is associated with the resistance to plastic slip. Block size refinement is effective in improving fracture resistance by arresting the crack to propagation across variants belonging to different

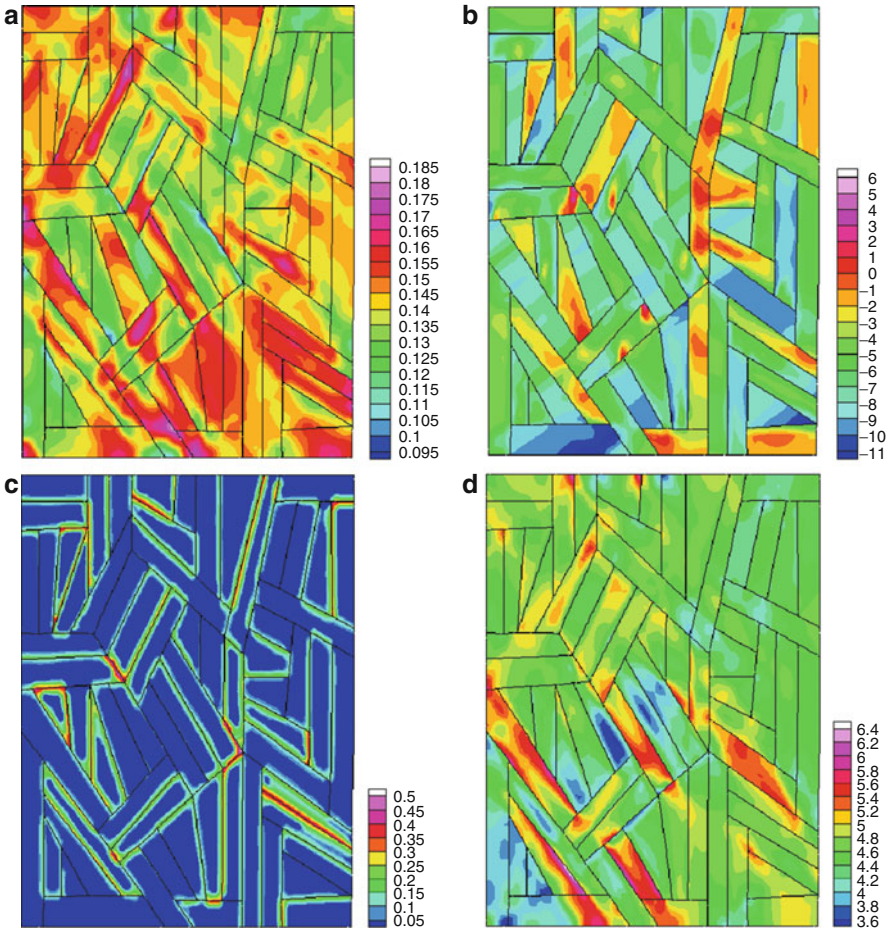

Fig. 19 (**a**) Plastic slip, (**b**) lattice rotations, (**c**) GB dislocation density, and (**d**) normal stress for an optimized variant distribution at 20 % nominal strain indicating dislocation-density pileup and plastic slip accumulation at a strain rate of 10^{-4} s^{-1}

Bain groups. Since the crack propagation path is constrained along the lath long direction, the effects of both block and packet refinement should be considered in relation to the lath morphology in determining fracture behavior.

Dynamic Behavior

In this section, the dynamic fracture of the optimized microstructure at a loading rate of 5,000 s^{-1} is investigated. The nominal stress–strain curves over the range of loading conditions are shown in Fig. 17. The oscillations at high strain rates occur due to stress wave reflections along the free and fixed boundary, which is dampened

due to the dissipative plastic mechanisms. The lower failure strain of 16% at a strain rate of 5,000 s^{-1} is a result of dynamic strain-rate hardening (Fig. 17). The accumulated plastic slip at a nominal strain of 16% at a strain rate of 5,000 s^{-1} is shown in Fig. 20a. The maximum accumulated slip is 0.175 compared to 0.19 under quasi-static loading, and the shear strain localization is narrower at higher strain rates, which is a result of material and thermal softening mechanisms, with a maximum temperature of 518 K, which is approximately $0.5T_{\text{solidus}}$, as well as the dynamic strain rates, which prevent the accumulation of shear strains over wide regions. Narrow shear strain localization at higher strain rates is consistent with the experimental observations of Dodd and Bai (1985). A lower accumulation of GB dislocation densities, with a maximum value of 0.45 compared to 0.5 under quasi-static

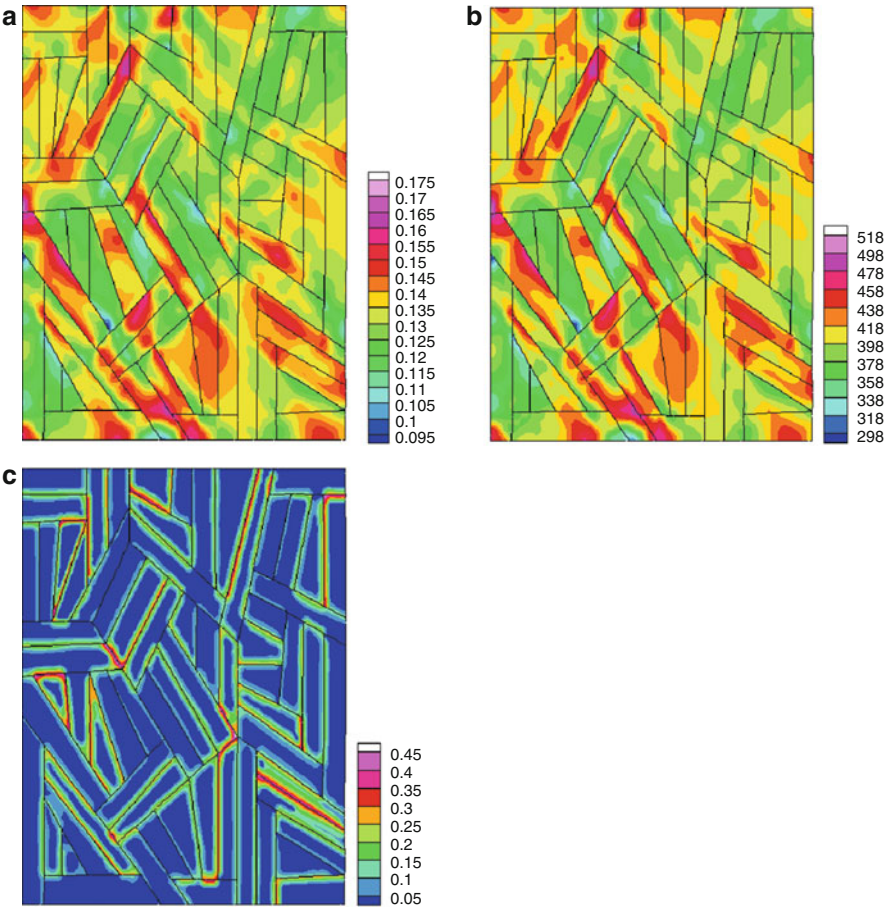

Fig. 20 (**a**) Plastic slip, (**b**) temperature, and (**c**) GB dislocation density for an optimized variant distribution at 16 % nominal strain indicating dislocation-density pileup and plastic slip accumulation at a strain rate of 2,500 s^{-1}

loading, occurs as a result of the strain-rate hardening at high strain rates (Fig. 20c). At this strain rate, crack nucleation occurs at a nominal strain of 16%, as shown in Fig. 21a. Crack deviation, crack arrest, and secondary crack nucleation occur due to boundaries between variants belonging to different Bain groups, with large incompatibilities in the cleavage planes, along the variant long directions (Fig. 21b–d). This results in a greater fracture resistance upon block size refinement. The high strain-rate characteristics result in fracture modes that are different from quasi-static strain rates.

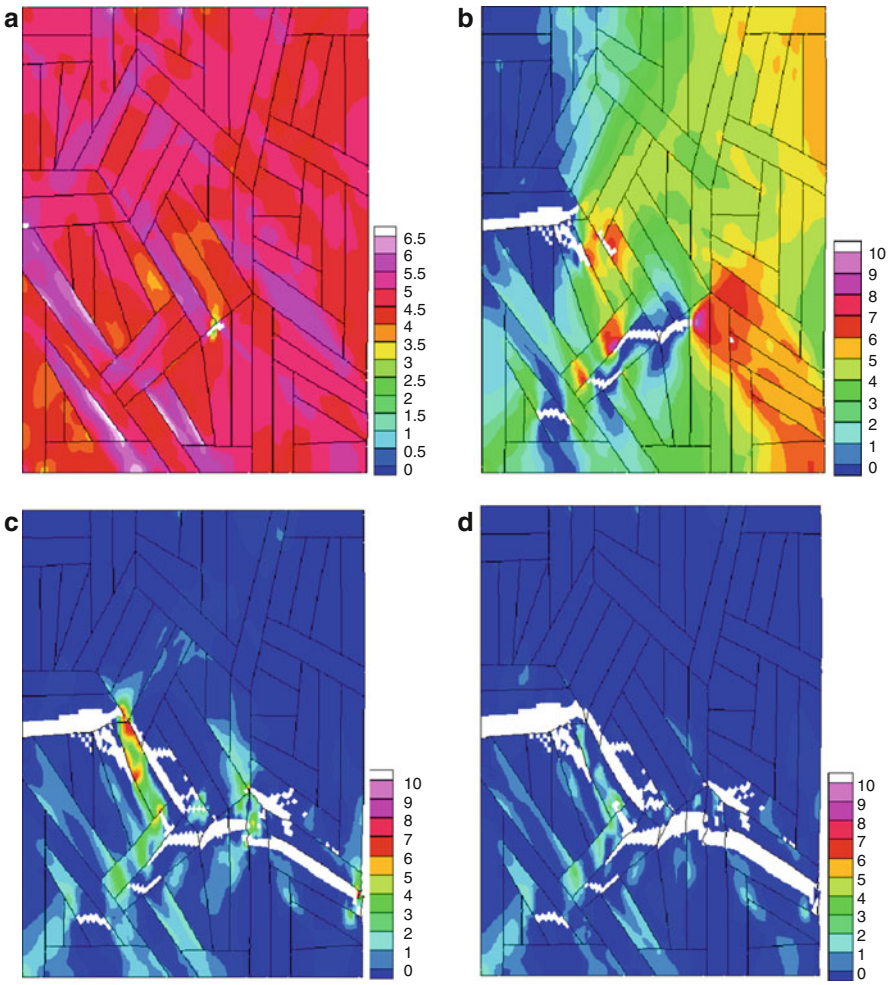

Fig. 21 Normal stress for an optimized variant distribution at (**a**) 16 % nominal strain, (**b**) 17 % nominal strain showing crack nucleation and (**c**) 18 % nominal strain, and (**d**) 19 % nominal strain showing crack propagation at a strain rate of 5,000 s^{-1}

Conclusion

A physically based dislocation-density GB interaction scheme that is representative of the resistance to dislocation-density transmission across block and packet boundaries in martensitic steel has been developed and was incorporated into a dislocation-density-based multiple-slip crystalline plasticity framework, which accounts for variant morphologies and orientation relationships that are uniquely inherent to lath martensitic microstructures.

Specialized FE methodologies to represent evolving failure surfaces and a microstructurally based failure criterion for cleavage were then used to perform large-scale FE simulations to characterize and predict the dominant dislocation-density mechanisms for the localization of plastic strains and the initiation and propagation of failure in martensitic microstructures over a range of loading conditions. The proposed fracture criteria do not assume a priori fracture criteria but are based on incorporating inelastic effects such as variant boundaries and dislocation-density evolution and interactions to resolve and nucleate cracks on cleavage planes based on evolving microstructural behavior at different physical scales.

The role of packet and block boundaries in the failure behavior of low- and high-carbon steels was investigated, and the results indicated that variant interfaces along the lath long direction were dominant. Shear strain localization was constrained by these interfaces to be along the lath long direction, and slip transmission to neighboring blocks was accommodated through compatible slip systems or the formation of low-energy residual GB dislocations. The effective block size refinement for strengthening is along the lath long direction. These interfaces also result in resistance to crack propagation and deviation of the crack path along the variant boundaries due to the GB dislocation-density accumulation and cleavage plane incompatibilities, resulting in an effective block size for fracture resistance along the block width. It was observed that refinement is more effective in improving the fracture resistance than in improving the strength as the variant boundaries offer relatively less resistance to slip transmission onto the 24 possible slip systems, on the {110} and {112} crystallographic planes, compared to crack propagation onto only three possible {100} cleavage planes. However, refinement also increases the number of incompatible triple junctions, which serve as sites for stress concentrations, and results in the nucleation of a crack at a lower nominal strain. At high strain rates, and as a result of increased strain-rate hardening, thermal softening and dynamic interactions resulted in crack formation that was different from quasi-static loading conditions in that the failure surfaces nucleate earlier and form in regions where strain-hardening has been surmounted by thermal and geometrical softening. These validated approaches offer a predictive framework that can be used to tailor heterogeneous crystalline systems for failure-resistant and damage-tolerant applications.

Acknowledgments Support from both the US Office of Naval Research Multi-Disciplinary University Research Initiative on Sound and Electromagnetic Interacting Waves under grant number N00014-10-1-0958 and from the Office of Naval Research under grant number10848631 is gratefully acknowledged.

References

R.J. Asaro, J.R. Rice, Strain localization in ductile single-crystals. J. Mech. Phys. Solids **25**, 309–338 (1977)

M. Ayada, M. Yuga, N. Tsuji, Y. Saito, A. Yoneguti, Effect of vanadium and niobium on restoration behavior after hot deformation in medium carbon spring steels. ISIJ Int. **38**, 1022–1031 (1998)

A.A. Barani, F. Li, P. Romano, D. Ponge, D. Raabe, Design of high-strength steels by microalloying and thermomechanical treatment. Mater. Sci. Eng. A **463**, 138–146 (2007)

M. de Koning, R. Miller, V.V. Bulatov, F. Abraham, Modelling grain-boundary resistance in intergranular slip transmission. Philos. Mag. A **82**, 2511–2527 (2002)

B. Devincre, T. Hoc, L. Kubin, Dislocation mean free paths and strain hardening of crystals. Science **320**, 1745–1748 (2008)

B. Dodd, Y. Bai, Width of adiabatic shear bands. Mater. Sci. Tech. **1**, 38–40 (1985)

P. Franciosi, M. Berveiller, A. Zaoui, Latent hardening in copper and aluminum single-crystals. Acta Metall. **28**, 273–283 (1980)

Z. Guo, C.S. Lee, J.W. Morris, On coherent transformations in steel. Acta Mater. **52**, 5511–5518 (2004)

A. Hansbo, P. Hansbo, A finite element method for the simulation of strong and weak discontinuities in solid mechanics. Comput. Methods Appl. Mech. Eng. **193**, 3523–3540 (2004)

T. Hatem, M.A. Zikry, Shear pipe effects and dynamic shear–strain localization in martensitic steels. Acta Mater. **57**, 4558–4567 (2009)

A.A. Howe, Ultrafine grained steels: industrial prospects. Mater. Sci. Tech. **16**, 1264–1266 (2000)

G.M. Hughes, G.E. Smith, A.G. Crocker, P.E.J. Flewitt, An experimental and modelling study of brittle cleavage crack propagation in transformable ferritic steel. Mater. Sci. Tech. **27**, 767–773 (2011)

T. Inoue, S. Matsuda, Y. Okamura, K. Aoki, Fracture of a low carbon tempered martensite. Trans. Jpn. Inst. Metals **11**, 36–43 (1970)

S. Jin, J.W. Morris, V.F. Zackay, Grain refinement through thermal cycling in an Fe–Ni–Ti cryogenic alloy. Met Trans. **6A**, 141–149 (1975)

H. Kawata, K. Sakamoto, T. Moritani, S. Morito, T. Furuhara, T. Maki, Crystallography of ausformed upper bainite structure in Fe–9Ni–C alloys. Mater. Sci. Eng. A **438**, 140–144 (2006)

H.J. Kim, Y.H. Kim, J.W. Morris, Thermal mechanisms of grain and packet refinement in a lath martensitic steel. ISIJ Int. **38**, 1277–1285 (1998)

Y. Kimura, T. Inoue, F. Yin, K. Tsuzaki, Inverse temperature dependence of toughness in an ultrafine grain-structure steel. Science **320**, 1057–1060 (2008)

G. Krauss, Martensite in steel: strength and structure. Mater. Sci. Eng. A **273–275**, 40–57 (1999)

L. Kubin, B. Devincre, T. Hoc, Towards a physical model for strain hardening in fcc crystals. Mater. Sci. Eng. A **483–484**, 19–24 (2008a)

L. Kubin, B. Devincre, T. Hoc, Modeling dislocation storage rates and mean free paths in face-centered cubic crystals. Acta Mater. **56**, 6040–6049 (2008b)

T.C. Lee, I.M. Robertson, H.K. Birnbaim, An in situ transmission electron-microscope deformation study of the slip transfer mechanisms in metals. Metall. Trans. A **21**, 2437–2447 (1990)

A. Ma, F. Roter, D. Raabe, Studying the effect of grain boundaries in dislocation density based crystal-plasticity finite element simulations. Int. J. Solids Struct. **43**, 7287–7303 (2006)

R. Madec, L.P. Kubin, Second order junctions and strain hardening in bcc and fcc crystals. Scripta Mater. **58**, 767–770 (2008)

T. Maki, K. Tsuzaki, I. Tamura, The morphology of microstructure composed of lath martensites in steels. Trans. Iron Steel Inst. Jpn. **20**, 207 (1980)

S. Matsuda, Y. Okamura, T. Inoue, H. Mimura, Toughness and effective grain-size in heat-treated low-alloy high-strength steels. Trans. Iron Steel Inst. Jpn. **12**, 325–333 (1972)

K. Minaar, M. Zhou, An analysis of the dynamic shear failure resistance of structural metals. J. Mech. Phys. Solids **46**, 2155–2170 (1998)

S. Morito, H. Tanaka, R. Konoshi, T. Furuhara, T. Maki, The morphology and crystallography of lath martensite in Fe–C alloys. Acta Mater. **51**, 1789–1799 (2003)
S. Morito, X. Huang, T. Furuhara, T. Maki, N. Hansen, The morphology and crystallography of lath martensite in alloy steels. Acta Mater. **54**, 5323–5331 (2006)
J.W. Morris, On the ductile–brittle transition in lath martensitic steel. ISIJ Int. **51**, 1569–1575 (2011)
J.W. Morris, Z. Guo, C.R. Krenn, Y.H. Kim, The limits of strength and toughness in steel. ISIJ Int. **41**, 599–611 (2011)
T. Ohmura, K. Tsuzaki, Plasticity initiation and subsequent deformation behavior in the vicinity of single grain boundary investigated through nanoindentation technique. J. Mater. Res. **42**, 1728–1732 (2007)
T. Ohmura, A.M. Minor, E.A. Starch, J.W. Morris, Dislocation-grain boundary interactions in martensitic steel observed through in situ nanoindentation in a transmission electron microscope. J. Mater. Res. **12**, 3626–3632 (2004)
S. Queyreau, G. Monnet, B. Devincre, Slip systems interactions in alpha-iron determined by dislocation dynamics simulations. Int. J. Plast. **25**, 361–377 (2009)
P. Shanthraj, M.A. Zikry, Dislocation density evolution and interactions in crystalline materials. Acta Mater. **59**, 7695–7702 (2011)
P. Shanthraj, M.A. Zikry, Dislocation-density mechanisms for void interactions in crystalline materials. Int. J. Plast. **34**, 154–163 (2012a)
P. Shanthraj, M.A. Zikry, Optimal microstructures for martensitic steels. J. Mater. Res. **27**, 1598–1611 (2012b)
A. Shibata, T. Nagoshi, M. Sone, S. Morito, Y. Higo, Evaluation of the block boundary and sub-block boundary strengths of ferrous lath martensite using a micro-bending test. Mater. Sci. Eng. A **29**, 7538–7544 (2010)
R. Song, D. Ponge, D. Raabe, Mechanical properties of an ultrafine grained C–Mn steel processed by warm deformation and annealing. Acta Mater. **53**, 4881–4892 (2005)
J.H. Song, M.A. Areias Pedro, T. Belytschko, A method for dynamic crack and shear band propagation with phantom nodes. Int. J. Numer. Methods Eng. **67**, 868–893 (2006)
S. Takaki, K. Kawasaki, Y. Kimura, Mechanical properties of ultra fine grains steels. J. Mater. Process. Technol. **117**, 359–363 (2001)
N. Tsuji, Y. Ito, Y. Saito, Y. Minamino, Strength and ductility of ultrafine grained aluminum and iron produced by ARB and annealing. Scripta Mater. **47**, 893–899 (2002)
N. Tsuji, Y. Ito, Y. Saito, Y. Minamino, Toughness of ultrafine grained ferritic steels fabricated by ARB and annealing process. Mater. Trans. **45**, 2272–2281 (2004)
N. Tsuji, N. Kamikawa, R. Ueji, N. Takata, H. Koyama, D. Terada, Managing both strength and ductility in ultrafine grained steels. ISIJ int. **48**, 1114–1121 (2008)
M.A. Zikry, An accurate and stable algorithm for high strain-rate finite strain plasticity. Comput. Struct. **50**, 337–350 (1994)
M.A. Zikry, M. Kao, Inelastic microstructural failure mechanisms in crystalline materials with high angle grain boundaries. J. Mech. Phys. Solids **44**, 1765–1798 (1996)

Molecular Dynamics Simulations of Plastic Damage in Metals

47

Shijing Lu, Dong Li, and Donald W. Brenner

Contents

Introduction and Historical Perspective 1336
Molecular Dynamics Simulations 1338
Initial Conditions 1338
Interatomic Force Expressions 1339
Classical Equations of Motion, Numerical Integrators, and Thermostats 1343
Analyzing Atomic Simulations 1345
Multiscale Modeling 1347
Available Codes 1349
Example Simulations of Metal Dynamics 1350
Simulations of Shock-Loaded Crystals 1350
Deformed Nanocrystalline Metals 1354
Simulations of Grain Boundary Migration 1357
Current Challenges 1362
Interatomic Forces 1363
Length Scales 1364
Timescales 1364
Quantum Dynamics 1364
Interpretation of MDS Results 1364
Conclusion 1365
References 1365

Abstract

Presented in this chapter is an overview of molecular dynamics simulation (MDS) as applied to modeling damage in metals. This is followed by some examples that illustrate how this technique is being used in the engineering community to help understand how new materials can be made that have targeted mechanical properties.

S. Lu · D. Li · D. W. Brenner (✉)
Department of Materials Science and Engineering, North Carolina State University, Raleigh, NC, USA
e-mail: slu3@ncsu.edu; dli18@ncsu.edu; brenner@ncsu.edu

© Springer Nature Switzerland AG 2022

G. Z. Voyiadjis (ed.), *Handbook of Damage Mechanics*,
https://doi.org/10.1007/978-3-030-60242-0_6

Keywords

Molecular dynamic simulation · Shock front · Partial dislocation · Shock loading · Potential energy function

Introduction and Historical Perspective

Presented in this chapter is a relatively brief overview of molecular dynamics simulation (MDS) as applied to modeling damage in metals along with some examples that illustrate how this technique is being used in the engineering community to help understand how new materials can be made that have targeted mechanical properties. MDS is a relatively straightforward computational method in which atom trajectories are calculated and analyzed for different sets of conditions (Allen and Tildesley 1989). The fundamental assumption in MDS is that atom motion can be adequately treated by classical mechanics and therefore their trajectories can be calculated by numerically integrating a set of classical equations of motion that are coupled through the interatomic forces. For MDS there are no expressions such as constitutive relations that are typical to modeling methods at higher length scales. Instead all of the properties of a material are set by the expression used to model the interatomic forces.

Interpreting an MDS typically starts by following the atom motion and then using different techniques to analyze structures, potential energies, and forces as a simulation progresses. As discussed in the following section, deriving and fitting the mathematical expressions used for the interatomic forces that accurately describe particular systems and analyzing simulations to both obtain detailed information and glean new understandings of materials properties at the atomic level are part science (Brenner et al. 1998) and also often part art (Brenner 2000).

In contrast to its relatively recent emergence as an engineering tool, MDS has a long history in the physical sciences. The first study of a chemical process using classical trajectories was published in 1936 by Hirschfelder, Eyring, and Topley, who followed one trajectory associated with the reaction $H + H_2 \rightarrow H_2 + H$ (Hirschfelder et al. 1936). Unfortunately the potential energy surface that they used was flawed in that it yielded a stable H_3 molecule. A consequence of this flaw (and the resources that were limited to hand calculation) is that the reaction never completed. In the following two decades, classical trajectories were used to probe some of the fundamental principles of statistical mechanics, including the rate at which equilibrium is established for relatively simple systems, and the conditions under which ensemble and time averages agree with one another (Alder and Wainwright 1957; Berman and Izrailev 2005). Some of the conclusions from these simulations are that some small and simple systems (e.g., short harmonic chains with weak anharmonic interactions) may never fully equilibrate to any practical degree and that approximations that are inherent to numerically solving classical equations of motion in other systems can ensure an approach to equilibrium in a manner that is similar to how a small disturbance to a physical system can help drive the system to equilibrium.

In 1959, Vineyard and coworkers at Brookhaven National Laboratory arguably carried out first contribution of MDS to materials science. They reported on a study that used classical dynamics to model ion irradiation and damage in metals (Gibson et al. 1960). In subsequent work by Rahman at Argonne National Laboratory, classical trajectories were used to characterize properties of liquids (Rahman 1964). Over the following decades, computing power continued to increased, which allowed Rahman and others to extend the initial work to more complicated fluids (including water) and biological systems (McCammon et al. 1977; Stillinger 1974).

Several common themes emerged from these early MDS studies. First, the development of MDS and the systems that could be studied paralleled the availability of increasingly powerful computing resources, particularly those at the U.S. National Laboratories. Second, MDS was rapidly becoming a powerful tool in chemistry and physics that could complement both experiment and theory. For example, not only could MDS provide data but it could also be used to test (and refine when needed) theories under exceedingly well-controlled conditions. Finally, it became clear that the requirements put on a potential energy function (from which interatomic forces are obtained) are very strongly dependent on the application. In chemistry applications, for example, typically well-refined potential energy surfaces are needed to provide qualitative data, but even highly approximate or generic forces can yield useful data for examining general phenomena. Similarly simple potentials can yield very useful information in statistical mechanics. In the case of materials, modeling simplified interatomic force expressions can be used to model defects such a grain boundaries and dislocations; however, these expressions must be detailed enough with regard to particular materials to yield useful, quantitative data.

The increasing importance of MDS as an engineering tool can be correlated to several factors. First, an exponential increase in the speed of computer processors together with relatively inexpensive platforms for parallel computing, visualization, and data storage has significantly decreased the cost of resources needed to carry out large-scale simulations. Consequently computing platforms have come to the point that MDS is affordable for research groups with even modest modeling budgets. Second, due to advances in experimental processing and characterization techniques, the structure of some materials can be manipulated to scales approaching the atomic level. This is well below the scales where traditional continuum modeling approaches like finite element analysis are appropriate. Finally, interatomic potential energy functions, which as mentioned above play a central role in MDS, have become available that provide good descriptions of the structure and elastic and mechanical properties of a wide range of materials while at the same time being sufficiently efficient from a computing viewpoint that they can be used in large-scale simulations. These advances in potential energy functions have resulted from new theoretical analyses that results in mathematical expressions that can more accurately capture quantum bonding effects, a better understanding of how to fit these expressions to the properties of specific materials, and readily available simulation codes that allow researchers outside of the original developers to vet and improve

interatomic potentials as they are used (Brenner et al. 1998; Sinnott and Brenner 2012).

Given in the following section are brief details presented at a tutorial level on some of the assumptions, numerical methods, and potential energy functions that are essential parts of an MDS to study damage in materials. Also mentioned are some currently available codes and user communities that are useful for carrying out MDS. This is followed by a section in which some applications of MDS for understanding damage in crystalline metals are discussed. This is not a comprehensive literature review but rather a survey of results that illustrate the various ways in which MDS is contributing to this area. The final section includes a brief discussion of new capabilities being developed for MDS of metals and the challenges facing this field in the short and long term.

Molecular Dynamics Simulations

In comparison to other modeling techniques, carrying out an MDS is relatively straight forward. The initial step is to initialize coordinates and the velocities for each atom and to establish any system conditions such as periodic boundaries. Using these positions, the interatomic forces are calculated, followed by the determination of constraints from thermostats or other conditions imposed on the system. As discussed more below, these constraints can be in form of additional forces, velocity rescaling, changes in periodic box size and shape, application of shock waves, etc. Atom positions are then moved ahead one time step according to forces, velocities, and accelerations (and higher derivatives of position with time depending on the numerical integration) using one of many possible numerical integration schemes. The atom positions, velocities, and forces can be analyzed during the course of a simulation, and post-simulation analysis can be carried out. The former can be done at the same time that the simulation is carried out or done on a file that saves atomic properties at some specific interval. The choice depends on considerations like system size, the total number of time steps, computing and visualization facilities, and whether there are user constraints applied to a system as a simulation progresses, including terminating a simulation if desired. The process is then repeated with a new set of forces and constraints calculated from the updated atom positions. These steps are described in more detail in the following subsections.

Initial Conditions

For crystals, atom positions are usually generated from a given lattice and basis. To mitigate edge effects when modeling a bulk material, periodic boundaries can be applied to the system such that an atom leaving from one side of the simulations reenters from the complementary side, and pairs of atoms interact with their nearest image in the repeating boxes. Figure 1, for example, illustrates a two-dimensional computational box surrounded by eight replicas, where the circles represent atoms.

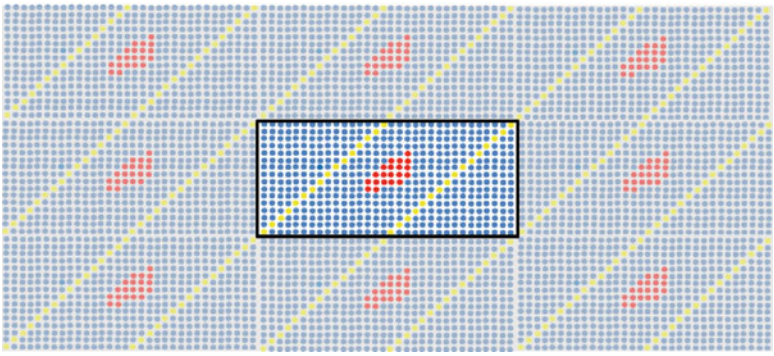

Fig. 1 Illustration of a localized defect (cluster of *red spheres* representing atoms) and an extended defect (*line* of *yellow spheres* representing atoms) in a *central box* surrounded by eight replicas that are defined by the periodic boundaries

For localized defects, represented by the cluster of red atoms in Fig. 1, periodic boundaries create a periodic array of the defect. For an extended defect that passes over the cell boundaries, which is represented by the yellow atoms in Fig. 1, the periodic boundaries create an infinite structure that is constrained to a super-periodicity defined by that of the periodic boundaries. This can constrain the types and number of extended defects that can be formed in a simulated lattice. Similarly, periodic boundaries can constrain stress fields that would otherwise be larger than a box dimension, which can influence plastic dynamics in a nonphysical manner.

Coordinates for initial point defects like voids and interstitial atoms are generally trivial to generate; however, creating coordinates for more complicated microstructure elements like grain boundaries and dislocations can be a challenge. There are presently commercial codes that can generate structures for a number of common defects and free tools like the gosam website that can generate coordinates for bicrystals with periodic boundaries based on coincident site lattices (Wojdyr et al. 2010). To generate velocities for what is supposed to be an initially equilibrium simulation, initial velocities can be generated randomly from a Boltzmann distribution that corresponds to a particle temperature. Other possible initial velocity choices may be based on attempting to mimic particular nonequilibrium situations such as an applied shock, a collision with a surface, or the initiation of a collision cascade.

Interatomic Force Expressions

The atom dynamics that mimic the behavior of a particular material are mainly determined from the expression used to describe the interatomic forces. This expression is therefore a key feature of the simulation in terms of reproducing properties that would correspond to an experiment on the true system. Calculating the interatomic forces is also typically the most computationally expensive part of an MDS and the feature that is least well known in terms of the appropriate equations.

In principle interatomic forces can be obtained from the quantum forces due to the electrons for a given set of atom positions and then adding these forces to those from the internuclear repulsions. This is done in an especially efficient manner through Car–Parrinello dynamics, a method that defines an extended Lagrangian containing nuclear and electronic degrees of freedom from which a set of coupled equations of motion are derived for both the ions and electrons (Car and Parrinello 1985). While mitigating much of the uncertainty associated with deriving and fitting analytic force expressions like those discussed below, this method remains computationally expensive in terms of evaluating the expression. In addition, because electrons are explicitly treated, the time steps are typically smaller when numerically integrating the electron–ion equations of motion compared to those for atoms only. Furthermore, the electronic degrees of freedom should be periodically "quenched" to the Born–Oppenheimer surface, which adds some additional computational overhead. There are also simplified electronic structure methods (e.g., tight binding Hamiltonians) that can be used to include electronic degrees of freedom into MDS forces. These approaches have significantly reduced computational demands compared to, e.g., the Car–Parrinello method, but they remain computationally burdensome for large systems and can require a significant degree of parameterization compared to fully first-principles methods.

Because of the desire to treat systems that are sufficiently large to model extended defects such as dislocations, an analytic expression that gives the potential energy of a collection of atoms as a function of the relative coordinates is typically used to mimic explicit electronic degrees of freedom (Sinnott and Brenner 2012). The interatomic forces are then calculated as the gradient of this potential energy function (PEF). The challenge with this approach of using an effective PEF is to come up with a function that not only accurately reproduces some set of fitting data but is also capable of producing physically reasonable (if not accurate) energies for atomic arrangements that are not considered in a database used to fit the PEF parameters. This property of a PEF is called the transferability. Currently there is no single standard functional form that is used for all systems; instead there are a plethora of forms and approaches that work to varying degrees of success. Developing a PEF requires both developing a convenient mathematical expression and parameterizing that expression to a particular system.

Probably the simplest approach to developing a PEF with continuous forces is to assume that the atoms interact in pairs, with other neighboring atoms not having any influence on the interactions between an atom pair. With this approximation, the total potential energy U is given by

$$U = \sum_{i=1}^{n-1} \sum_{j=i+1}^{n} V\left(r_{ij}\right) \tag{1}$$

where n is the number of atoms, r_{ij} is the scalar distance between atom i and atom j, and V(r) is a function such as a Morse or Lennard-Jones potential that has parameters that can be fit to a set of physical properties (Brenner and Garrison 1989). For a pair interaction with a single well, pair potentials tend to produce stable close-packed

lattices as lowest energy structures, so for metals pair potentials can sometimes produce acceptable results depending on the collection of properties that are trying to be reproduced. The pair potential approximation, however, is limited for reproducing elastic properties, and in general, it does not produce accurate energies for defects such as surfaces and vacancies.

One way to build on the pair potential approximation is to use it as the lead term in a Taylor series expansion of potential energy in relative atomic coordinates. The many-body expansion can be given as

$$U = \sum_{i=1}^{n-1} \sum_{j=i+1}^{n} V_2(r_{ij}) + \sum_{i=1}^{n} \sum_{j(\neq i,k)=1}^{n} \sum_{k(\neq i,j)=1}^{n} V_2(r_{ij}) + \ldots \qquad (2)$$

where the subscripts give the order of the interaction. The first term in Eq. 2 represents a bond stretch, the second term represents a bond bend, and higher-order terms correspond to dihedral angles and combinations of bends and stretches. This expansion combined with electrostatic and other nonbonded interactions has been extensively used in biological and polymeric systems. This form of potential function, however, has found limited use for simulating metals.

Experience suggests that the most transferable PEFs are those that are based on expressions derived from principles of quantum mechanical bonding. There are several classes of PEFs that fall under this category that are widely used for modeling metals. These are the embedded-atom method (EAM) (Daw and Baskes 1984; Daw et al. 1993), effective medium theory (Jacobsen et al. 1987), the glue model (Ercolessi et al. 1986), and the Finnis–Sinclair (Finnis and Sinclair 1984) potential. While the functional forms of each of these classes of PEFs are similar, the derivation of each is different. The first three models come from the concept of "embedding" atoms into an electron gas so that the energy of an atom depends on the density of the electron gas near the embedded atom plus a pair interaction between the atomic cores. In the glue and EAM models, the electron density is modeled as a pairwise sum of densities from surrounding atoms at the site of the atom whose energy is being determined. This leads to three central components of these PEFs: the contribution of the electron density from a neighboring atom to a given site (which depends on the distance between the atom and site), a pairwise-additive interatomic force, and an embedding function that relates the electron density at a given site to the energy of an atom at that site. Each contribution can be adjusted by fitting to properties such as the crystal cohesive energy, lattice constant, elastic moduli, and vacancy formation energy. Effective medium theory, in contrast, averages the electron density in the vicinity of an atom whose energy is being calculated and uses a less empirical relationship between this electron density and the energy of an atom (Jacobsen et al. 1987).

The Finnis–Sinclair form of the PEF is similar to other metal PEFs. However, the derivation of these expressions from quantum bonding principles is different. The Finnis–Sinclair functional expression is derived from a "second moment" approximation that relates the spread in the local electronic density of states due to bonding to the potential energy of an atom and to its local coordination. The derivation is too

long to be included here (Brenner et al. 1998), but the result is that the Finnis–Sinclair embedded energy is a square root of the coordination, while the form of the EAM embedding function is part of the parameter fitting process. Another historical difference is that the EAM and related potentials were originally developed for face-centered cubic metals, while the Finnis–Sinclair potentials originally focused on describing body-centered cubic metals.

A major strength of these PEFs is that by using pair terms for the interatomic repulsion and for the electron densities, their evaluation scales like a pair potential while a many-body aspect of the PEF is introduced by an embedding function. There have been many attempts to go beyond these basic PEFs; higher moments of the electrons and angular interactions in the electron densities can be introduced, for example (Dongare et al. 2012; Lee and Baskes 2000). These approaches, however, typically add computational burden that must be balanced against any improved accuracy in reproducing the fitting database and in the overall PEF transferability.

Incorporation of charge transfer terms into a PEF that allow for different degrees of ionic bonding is a development that has produced good results for modeling metal oxides and metal interfaces. The two leading formalisms for metals that include charge transfer are the ReaxFF (Van Duin et al. 2001) and charge-optimized many-body (COMB) expressions (Shan et al. 2010). Both of these PEFs take advantage of a bond-order formalism that includes angular terms to model local bonding interactions plus Coulomb terms that use atom-centered partial charges in the form of a Gaussian function. The magnitude and sign of the charge on each atom are determined by minimizing the electrostatic energy with respect to the potential energy from the Coulomb interactions between partially charged atoms and energy associated with forming the charges. The latter can be expressed as a Taylor series in charge with coefficients determined from the atomic ionization and electron affinity energies. In practice, however, these coefficients are typically taken as parameters that can be fit along with parameters in the short-range bonding interactions.

In addition to the functional form of the PEF, the training set and the method used to parameterize the function are also important. A minimum database for parameter fitting for metals traditionally includes cohesive energy, lattice constant, elastic properties, and vacancy formation energy of the lowest energy crystal structure. It should also include the difference in cohesive energies between the lowest energy structure and other competing crystal structures. With this type of fitting database, a PEF can be validated against quantities such as melting points and surface energies. In the past, a fitting database was usually developed from experimental measurements. However, first-principles data is increasingly being used to fit parameters in PEFs. This approach has the major advantage that very large data sets can be generated (e.g., transition states for activated processes) with comparable levels of error for each quantity evaluated. A related approach is to carry out a simulation with quantum forces, for example, Car–Parrinello dynamics, and use the atomic configurations that are generated to create a best-fit set of parameters (and even the functional form) for an analytic PEF (Ercolessi and Adams 1994). As the number of configurations increases, the analytic PEF can be substituted for the quantum forces for larger systems and longer time simulations.

Classical Equations of Motion, Numerical Integrators, and Thermostats

Calculating atomic trajectories involves approximating differential classical equations of motion by finite difference approximations that are solved stepwise using one of several standard methods employed in MDS. These numerical integration methods include Gear, predictor–corrector, and leapfrog algorithms. Which is used depends on whether constraints are operating on the system, the desired accuracy of the solution, and whether time steps with varying sizes are used. The time step size depends on the integration method and the magnitude of the forces acting on the atoms. A general rule of thumb is that the time step should be no larger than about 1/20 of the shortest vibrational period in the system. For systems with hydrogen, an appropriate time step is roughly one femtosecond or less; for metals a larger time step can typically be used. An initial determination of the largest allowable time step can be done by monitoring energy conservation both step-to-step and over a given period of time. The latter evaluates energy drift, which is a measure of the accumulation rather than cancellation of errors.

Solving classical equations of motion without additional constraints leads to constant energy trajectories; at equilibrium this should yield properties that correspond to a microcanonical ensemble. The Nosé thermo- and barostats add constraints to the equations of motion that produce trajectories consistent with other thermodynamic ensembles (Nosé 1984). Similar methods have also been introduced for describing other system states. Hugoniostats, for example, produce equilibrium states for shocked matter (Ravelo et al. 2004).

Two other common ways used to control temperature are the Langevin and Berendsen thermostats. Both methods couple system dynamics to an external bath, although with different coupling methods. The Langevin approach, which comes from Brownian dynamics, adds to the interatomic force, friction, and random force terms that balance one another to produce a desired temperature. In the Berendsen approach, only a friction term is added, but the friction coefficient is proportional to the difference between the current and desired temperatures so that the friction coefficient can be positive or negative (Berendsen et al. 1984). The Langevin thermostat therefore couples each atom locally to a system bath, while the Berendsen thermostat is a global coupling between the total and desired temperatures.

Although not thermostats in the same sense as those discussed above, Zhigilei and coworkers and Brenner and coworkers introduced methods that modulate temperature in an MDS by coupling atom dynamics to a continuum reservoir (Schall et al. 2005; Padgett and Brenner 2005; Schäfer et al. 2002). In the Zhigilei approach, the reservoir represents an electron gas that exchanges energy with the nuclear degrees of freedom. With the two-temperature model, processes such as the interaction of lasers with metals can be modeled. In this case, the laser initially excites the electronic degrees of freedom, and this energy is then appropriately channeled into the atom motion. The Brenner approach coarse

grains a simulation into regions for which a temperature is defined from the average velocities of the atoms in each region. A continuum heat transport equation with parameters fit to the thermal conductivity and heat capacity of the bulk material is numerically solved for one time step on the grid defined by the coarse graining, and the atom velocities are scaled to match the resulting grid temperatures. This ad hoc coupling between grid temperatures and the atom velocities is continued as the MDS continues. In addition to controlling heat flow (and not just temperature), this approach has been extended to include electrical current flow and associated Joule heating (Crill et al. 2010; Irving et al. 2009a, b; Padgett and Brenner 2005).

The thermostats discussed here require some parameterization. For example, the Berendsen thermostat requires a decay constant between the temperature gradient and the difference between the desired and current temperature. The Nosé thermostat requires a thermal inertia parameter that determines the rate of the heat transfer in the system.

Parrinello and Rahman introduced a classical Lagrangian that allows a repeating periodic cell to change shape in response to the stress state (Parrinello and Rahman 1981). With this method, solid phase transitions can be conveniently simulated as a function of stress state and temperature. Other constraints have also been applied to classical equations of motion that produce rigid bond distances and angles, although these are more commonly applied to polymers and biological molecules (Ryckaert et al. 1977).

Other constraints can be added to simulations to model particular conditions. Compressive shock loading, for example, can be modeled with a flyer plate impacting an open end of a material. Shocks can also be generated by shrinking the periodic boundaries at each step of a simulation. Similarly, a constant tensile strain can be applied by expanding the periodic box dimensions in one or more directions, or shear strain can be applied by shearing the periodic box. As another example, heat flow can be modeled by creating hot and cold regions of a system, and quantities such as thermal diffusivity can be estimated by monitoring the temperature distribution as it evolves during the dynamics (Müller-Plathe 1997).

A recent creative example of an ad hoc condition driving simulation dynamics is the work of Foiles and coworkers, who introduced a way to drive a grain boundary to move through a crystal (Janssens et al. 2006). A parameter is defined in this method for each atom that is determined by the orientation of surrounding atoms (see Fig. 2a). If the atom orientation does not match some given reference structure, a relatively small potential energy is added to the cohesive energy of that atom. This procedure drives the system toward a particular grain orientation, which at sufficiently high temperatures can drive a grain boundary from a preferred to a non-preferred grain orientation. Similarly, an applied shear strain can induce motion of particular grain boundaries and dislocations depending on the lattice orientation with respect to the shear. Simulations using these driving conditions are discussed in more detail below.

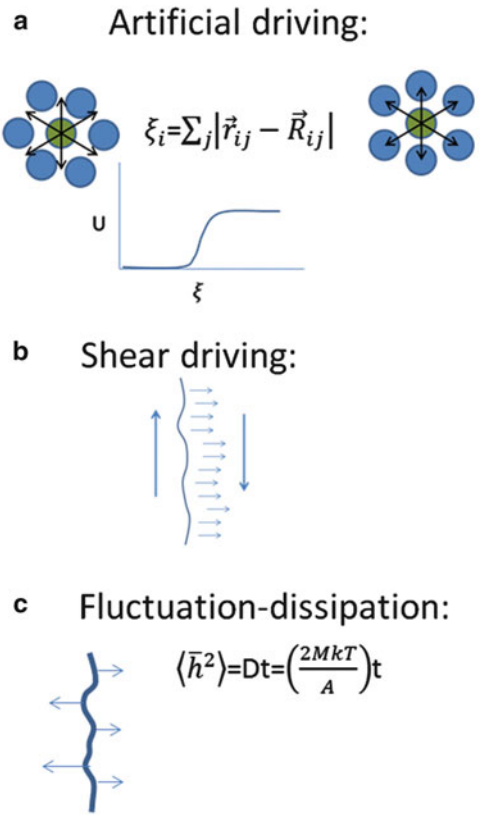

Fig. 2 Methods for determining grain boundary mobilities. (**a**) An extra energy term is added to atoms with an orientation that does not match that of the preferred grain orientation. (**b**) Grain boundary motion driven by a shear forces. (**c**) Using fluctuations in position to calculated grain boundary mobility

Analyzing Atomic Simulations

An MDS provides only atom motion, and therefore, extracting useful data and insights from a simulation requires further analysis of the trajectories. For many equilibrium properties, Green–Kubo correlation functions of statistical mechanics can be used to extract important data. For example, vibrational modes, thermal conductivity, and dispersion relations for longitudinal vibrational modes can be evaluated in this way. Similar methods have also been suggested for determining grain boundary mobilities from position fluctuations (Fig. 2c) (Trautt et al. 2006).

Other methods are needed to identify and understand the origin of damage. One of the simplest methods is to represent atoms as spheres and create movies of the trajectories (Figs. 3 and 4). Codes that produce visualizations of this type are freely available as given below. While powerful, experience shows that additional data beyond atom positions are often needed to analyze complex dynamics and to identify structures such as dislocations that correspond to well-established damage

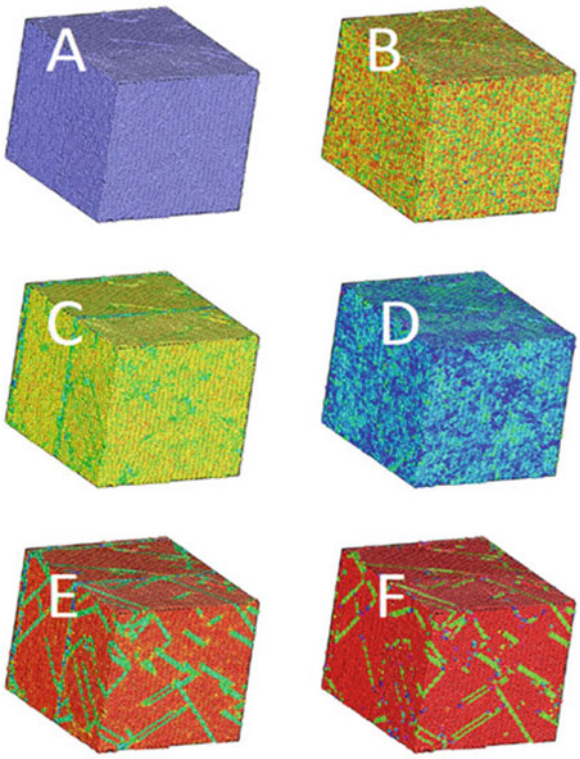

Fig. 3 Atomic system with 481,680 atoms at a temperature of 300 K containing two tilt grain boundaries and stacking faults created by dislocation motion during an applied strain. An embedded-atom method potential for copper was used. Periodic boundaries were applied and the virtual atoms are visualized as spheres. (**a**) All atoms the same color; (**b**) atoms colored by kinetic energy; (**c**) atoms colored by potential energy; (**d**) atoms colored according to local hydrostatic stress; (**e**) atoms colored according to their centrosymmetry parameter; (**f**) atoms colored according to a common-neighbor analysis

elements. With a PEF like one of those discussed above, each atom can be assigned a cohesive energy and this cohesive energy can often be used to discern structures and understand the atomic-scale origin of the energy of a particular defect. Although strictly speaking stress is a continuum concept, stresses can be derived from the interatomic forces. Like the cohesive energy, stresses can be assigned to atoms to understand subtle contributions to the stability of various defects. There are also other complementary quantities that have been proposed that are valuable for damage characterization in crystals. For example, a centrosymmetry parameter is a quantitative measure of the local bonding structure of a given atom (Kelchner et al. 1998). It has values that can be traced to particular damage configurations such as bulk crystals, dislocation cores, stacking faults, and surfaces. Similarly, a common-neighbor analysis assigns a set of four integers to each bond that is unique for certain bonding structures (Honeycutt and Andersen 1987). There are also more automated methods that not only identify dislocations but also characterize Burger's vector (Stukowski and Albe 2010). These methods greatly enhance the ability to fully analyze simulated damage, especially when a system is so large that post-simulation analysis becomes burdensome compared to analysis as simulation configurations are generated.

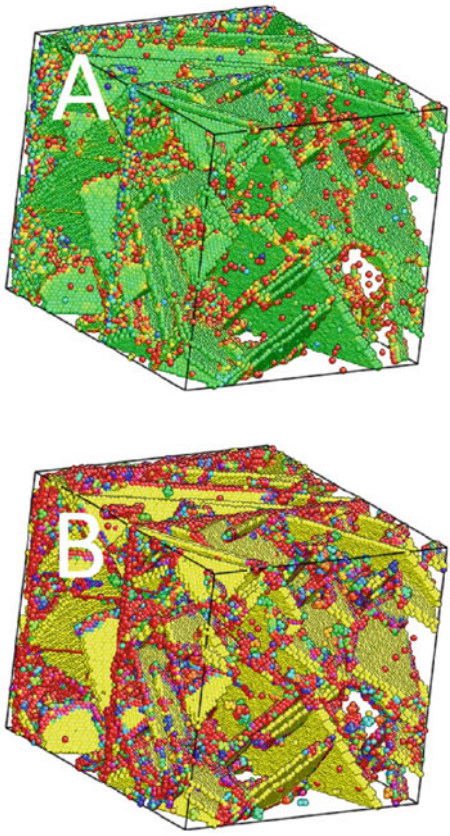

Fig. 4 Same system as depicted in Fig. 3e, f except that atoms with a bulk centrosymmetry parameter (*top panel*) and bulk common-neighbor analysis (*bottom panel*) are removed. The grain boundaries and stacking faults are now apparent in the figures

Multiscale Modeling

The small time step size used in MDS ($\sim 10^{-15}$ s) and system sizes of typically thousands to billions of atoms (depending on available computing resources) are both major constraints for applying MDS to engineering-scale materials phenomena. The increasing number of processors available through different computing resources that can be dedicated to a single simulation is able to overcome some of the size limitations. However, because the trajectories are determined stepwise, the number of time steps that can be processed is more closely tied to processor speeds, which are predicted to deviate substantially from the exponential increase given by Moore's law curve over the past decades.

Different multiscale modeling approaches have been developed to overcome some of the discrepancy between the time and size scales inherent to MDS and engineering applications. These approaches can be conveniently separated into

concurrent and serial methods. The former refers to approaches in which different scales are treated simultaneously in a given simulation. Serial multiscale modeling refers to approaches in which parameters and modeling conditions are passed between modeling methods that treat different scales of a given system. Brenner has recently reviewed some of the challenges and opportunities in multiscale modeling of these types (Brenner 2013).

Concurrent multiscale modeling approaches typically look to embed a region in which atoms are explicitly treated into a set of continuum boundary conditions. The problem that has been the most examined with this approach is the propagation of cracks in brittle solids, where dynamics at the crack tip are resolved to the atom scale, while surrounding stresses are modeled with finite element or other continuum approaches. These types of simulations can be partitioned to even finer scales. For example, in a region that includes a crack tip, the interatomic forces can be calculated from explicit electronic states. A region further from the tip can be modeled with an analytic PEF, and further regions can be treated as a continuum.

Miller and Tadmor have compiled a detailed comparison of the accuracy and efficiency of 14 concurrent atom–continuum approaches (which they call "partition-domain multiscale modeling") for an example problem of dislocation dipole motion in a face-centered cubic aluminum lattice (Miller and Tadmor 2009). Challenges to this approach, which are discussed in detail in the Miller–Tadmor and Brenner reviews (Brenner 2013), include matching forces at the atom–continuum boundaries (and the boundaries where different interatomic forces are used), phonon motion across boundaries, and being able to switch between continuum and atomistic descriptions of a region of the system as damage evolves and stresses change.

Voter and others have proposed different schemes to overcome the time limitations of MDS when modeling rare events. In a straightforward and elegant scheme called parallel replica dynamics, multiple trajectories are followed from the same initial atomic positions but with sufficiently different initial equilibrium velocities that they explore different phase space (Voter 1998). When a rare event reaction is detected in any of the systems, all of the runs are discontinued. For first-order kinetics, the total time between reactions can be taken as the sum of the times for each system replica. The systems for which no reactions were observed are eliminated, and the process is started again using the one system that did show a reaction. Because no communication is needed between replicas as they run in parallel, this approach is highly parallel in time.

In a different approach developed by Voter called hyper-dynamics (Voter 1997), a bias potential is used to raise the potential energy in regions of the potential energy hypersurface between saddle points that correspond to various reactions. With this approach, an effective time step can be defined that depends on the bias potential and that can be orders of magnitude larger than the actual time step used for following the trajectory on the new potential surface. When the system approaches a configuration corresponding to a reaction, the bias potentials are removed, and the dynamics of the system is followed using the small time step

typical of an MDS. As a system moves away from the region of the reaction barrier, the bias potential and effective time step are reestablished. One drawback to this approach is that it does not scale well with system size. This is because multiple rare events can occur that bring the time step for the entire system to the small size inherent to systems with non-biased potentials. Because they are based on accelerating rare event dynamics, these types of time-scaling approaches are not generally used to model large damage in crystalline solids, which typically involve creation of extended defect structures.

Available Codes

Several freely available codes for executing and analyzing MDS of damage in crystalline metals are summarized in Table 1. Probably the most widely used at this point is LAMMPS (the acronym for Large-scale Atomic/Molecular Massively Parallel Simulator) (Plimpton 1995). Maintained by researchers at Sandia National Laboratories, this code has a large and still growing number of capabilities that are often contributed by an active user base. This code's capabilities include a high degree of parallelism, multiple types of interatomic potentials and thermostats, advanced multiscale modeling capabilities, and different ways of post-processing and analyzing simulations.

Another very useful suite of MDS codes is maintained by the Theoretical and Computational Biophysics Group at the University of Illinois at Urbana-Champaign. Although the capabilities of this code emphasize biological systems, the visualizer VMD can be useful for analyzing damage in crystalline metals generated from an MDS, especially when used in combination with one of the methods mentioned above (e.g., the Central Symmetry Parameter) to color atoms during visualization (Huang and Humphreys 2000). Other examples of available and very useful codes for MDS and analysis include GULP(Gale and Rohl 2003) and AtomEye (Li 2003).

Table 1 Summary of some useful MDS and related codes for metal simulations

Code name	System emphasis	Example capabilities	Website
LAMMPS	All	MDS and serial multiscale dynamics; efficient processor scaling; large number of routines for thermostating, etc.	lammps.sandia.gov
NAMD/VMD	Biological	Molecular mechanics; efficient processor scaling; independent MDS visualization code	www.ks.uiuc.edu
GULP	All	Lattice dynamics	projects.ivec.org/gulp/
AtomEye	All	Advanced MDS visualization	http://li.mit.edu/Archive/Graphics/A/

Example Simulations of Metal Dynamics

Examples from the literature and from work within our research group are discussed below in which MDS was used to characterize damage in crystalline metals and their alloys. The discussion is not intended as an extensive literature review; instead these were chosen as examples because they demonstrate new insights and unique data that can be obtained from MDS in this area.

Simulations of Shock-Loaded Crystals

Shock fronts travel at speeds that exceed the sound speed of the medium through which they are traveling. For metals, the sound speed is typically 1–6 km per second, or in molecular terms ~1–6 nm/ps. While the transient properties of shock fronts make them difficult to study experimentally, this is an ideal time and length regime for MDS. MDS has therefore been used extensively to study shock phenomena in solids.

Early MDS by Holian of close-packed solids subject to shock loading suggested that for strong shocks, shear damage (e.g., dislocation motion) can occur very near the shock front, while for intermediate-strength shocks, an elastic compression at the front is a precursor to a steady plastic wave in which shear stress is relaxed (Holian and Lomdahl 1998). At lower shock strengths, only an elastic wave was observed, with the transition between the two occurring when the ratio of the piston speed to the long wavelength sound speed exceeds about 0.25. This is roughly the point at which the shear pressure equals the theoretical shear strength of the solid (~1/10 of the shear modulus for slippage of close-packed planes).

Holian's study used periodic boundaries and was restricted to thousands of atoms. These restrictions can influence the plastic damage observed in an MDS because any line and planar defects that are formed must repeat within the boundary box in the two directions perpendicular to the shock propagation (see Fig. 1). For Holian's MDS, this resulted in slip being restricted to a limited number of close-packed planes with spacing between shear bands dictated by the periodic boundaries. Whether this influenced the observed sudden onset of plastic damage is not clear. Because of this and related considerations, Holian and Lomdahl examined shock loading of larger systems containing up to 10 million atoms in a close-packed crystal lattice (Holian and Lomdahl 1998). In the larger system, significant slippage along multiple planes was observed, and the interaction between active slip systems reduced the planarity of the shock front. Distinct patterns of plastic damage (termed "randomly placed plaid pattern") were observed in the MDS. This observation suggested that the periodic boundaries did not significantly influence plastic damage mechanisms, which included a sudden onset of plastic damage depending on the shock loading strength. To examine the influence of extended defects on the onset of plastic damage, the planar front driving the shock was replaced with a curved interface that fit within the periodic boundaries. This curved interface was intended to model the influence of existing extended defects on an initially planar shock fronts as it

moves through a crystal. Plastic damage at significantly lower shock loadings was observed in the MDS compared to the driving force comparable to a flat piston (e.g., heterogeneous versus homogeneous nucleation of plastic damage under shock loading).

Holian and coworkers also used MDS to characterize shock-induced transformation of iron from a body-centered cubic to a hexagonal close-packed structure (Kadau et al. 2002). At low piston velocities, there was no evidence for plastic deformation in the initial structure. Instead a split shock structure was observed that was composed of an elastic precursor under uniaxial compression followed by a slower phase-transition front to the close-packed structure. At higher pressures the strain within the compressed precursor was relieved by a homogeneous nucleation of close-packed grains. Because only a few grains were initially formed, the transformation front was rough. Increasing the velocity of the piston driving the shock loading increased the nucleation rate of close-packed grains. This in turn produced a smoother transition front until at very high shock loadings a single front was observed that separated the body-centered cubic from the close-packed structure (which contained multiple twins and related defects).

In a following study, diffraction signals were generated from the structures created in the MDS and compared to in situ experimental x-ray measurements of laser-driven shocked iron. The observation in the MDS of a transformation to a hexagonal close-packed structure was confirmed by the experiments. The presence of a uniaxially compressed precursor to a phase transformation was also confirmed.

A large number of other MDS studies of shocked single-crystal metals have been carried out that are similar to the work of Holian and coworkers. For example, Bringa et al. reported results from a combined experimental and MDS study of the shock loading of single-crystal copper (Bringa et al. 2005). The MDS used sample sizes of two million atoms and two different EAM potentials that differed in their stacking fault energies. A light-gas gun was used in the experimental studies to shock load the samples. The relationship between shock velocity and the velocity of the driving piston (the Hugoniot relation) was found to depend strongly on the orientation of the shock loading, as did the agreement between the experiment and MDS. Consistent with Holian's studies, an elastic precursor followed by plastic deformation was observed in the simulations, as well as melting at high shock loading pressures. Dupont and Germann simulated the uniaxial strain of single-crystal copper at different strain rates and temperatures along different orientations (Dupont and Germann 2012). The yield strength and its dependence on strain rate were found to be a function of orientation but not temperature. With increasing strain rate, the plastic dynamics progressed from dislocation nucleation to atom disordering/dislocation nucleation to creation of an amorphous structure.

Shehadeh et al. used the results of an MDS of shock-loaded copper to validate and parameterize a larger length-scale model involving discrete dislocation dynamics coupled to finite element analysis (Shehadeh et al. 2006). This concurrent multiscale approach allowed the analysis of dislocation loop formation and related plastic damage to be carried out to much longer time and length scales than would be possible with MDS alone. This approach also provides a more accurate

representation of the damage dynamics than might otherwise be used in the finite element or discrete dislocation approach.

A steady-state two-zone elastic–plastic model was proposed based on the results of MDS studies of the shock loading of single crystals by White and coworkers. In this model, the wave establishing the elastic precursor and the wave front at which shear stress is relieved via plastic deformation travel at the same speed (Zhakhovsky et al. 2011). The coordination of the speed of the two fronts occurs via local elastic pulses that originate from plastic deformation through the elastic precursor to the leading shock front. The ability to observe this rich dynamics and its influence on reaching steady-state shock fronts was the result of a modeling technique in which the dynamics of the shocked material is followed in a window that travels with the shock front. The window allows long timescale phenomena to be observed compared to a simulation in which the reference frame is the undisturbed material in front of the initial shock compression.

Using the same simulation methodology, White and coworkers examined the evolution of plastic dynamics behind the second shock front in single-crystal aluminum that was shocked along different orientations (Zhakhovsky et al. 2012). It was found that despite direction-dependent properties such as melting dynamics, the systems evolved to the same point on the Hugoniot relations. This result helped to clarify what had been an apparent discrepancy between MDS, which was predicting orientation-dependent plastic dynamics, and experiment which was measuring Hugoniot relations that are orientation independent. Together with the other papers mentioned above, this work is an excellent example of how when properly set up and interpreted a modeling technique as basic as MDS can explain and predict a wider range of phenomena. It also provides an example of where insight and data generated by one technique can help inform other models.

The influence of preexisting defects on plastic deformation mechanisms and mechanical properties of metals under extremely high loading rates have been examined by numerous MDS. For example, in nanocrystalline solids, grain sizes are of the order of nanometers so that they contain a very large density of grain boundaries. This results in unique plastic deformation mechanisms (compared to systems with conventional grain sizes) in which grain boundary sliding and grain rotation accompanied by diffusion can play roles comparable to dislocation slip (this is discussed more below). The rapid temperature and pressure rise associated with a shock front can effectively remove deformation mechanisms requiring diffusion while at the same time increasing the shear modulus. This increases the threshold stress for inter-planar sliding. In addition, increasing pressure increases the threshold for dislocation plasticity. Considering these effects together with the assumption that the maximum in hardness as a function of grain size occurs where stress for sliding and dislocation plasticity become equal, Bringa and coworkers suggested that ultrahigh hardness can be achieved by shock loading nanostructured crystals (Bringa et al. 2005).

Bringa et al. modeled the shock loading of nanostructured copper with different grain sizes using MDS to validate their analysis (Bringa et al. 2005). At low shock loadings, grain boundary sliding occurred, which leads to a relatively low value of

hardness that increases with increasing grain size. For intermediate shock loadings, they observed that hardness increased with increasing shock strength for each grain size, with the maximum hardness shifting toward smaller grain sizes compared to lower strain rate deformation. This results in an increase in the overall maximum hardness of the metal. At still higher shock loadings, the MDS produced a drop in strength due to an increase in the rate of dislocation nucleation and motion resulting from a temperature increase. At the highest shock pressures used in the MDS (150–220 GPa), shock-induced melting was observed with an associated low shear stress and further reduction in hardness.

In a recent set of studies, Dongare and coworkers modeled high strain rate deformation of nanocrystalline copper using MDS (Dongare et al. 2009, 2010). Copper with an average grain size of 6 nm was subject to uni- and triaxial tensile strain at a strain rate of 10^8 s^{-1} (Dongare et al. 2009) Random nucleation of nonspherical voids occurred at grain boundaries and/or triple junctions by creation of a shell of disordered atoms that surround the voids rather than by dislocation nucleation from the void surfaces. Void coalescence as the system was further strained was observed to occur by shearing of the disordered regions between individual voids. The fraction of voids was found to vary linearly with plastic strain in two distinct stages. In the first region, voids formed along the grain boundaries and triple junctions. In the second stage, which began after a minimum in tensile stress was reached, the disordered regions around the voids begin to recrystallize due to the higher temperatures compared to the first stage that is accompanied by void coalescence.

In another study, Dongare and coworkers used MDS to simulate shock loading of nanocrystalline copper with the same grain size containing a free surface. The system was initially compressed with an impact piston traveling with velocities ranging from 0.25 to 1 km/s (Dongare et al. 2010). This was followed in the simulation by unloading and spalls as the compression wave met the free surface. The same two regions of void growth and coalescence behavior were observed as in the high tensile strain rate studies. The first region where voids initially nucleate at grain boundaries and triple junctions was found to be strongly dependent on the initial sample structure and the piston impact velocity. Higher strain rates lead to creation of a greater number of voids that nucleate over a shorter time. In contrast, dynamics associated with the second regime depended only on the number of voids created during the first regime.

In another recent study, MDS was used to characterize the influence of twin spacing on shock-induced plasticity and spall behavior for twin boundaries inserted into single-crystal copper and twin boundaries inserted into nanocrystalline copper with an average grain size of 10 nm (Yuan and Wu 2012). Twin spacings between 0.6 and about 4 nm were used. It was found for the nanocrystalline system that the average flow stress increased with increasing twin spacing up until about 1 nm, after which the flow stress decreased with increasing spacing between the twins. This trend resulted from two competing mechanisms of dislocation dynamics under shock loading. The first mechanism involves the intersection of the dislocation–twin boundary by inclined dislocations; the second mechanism was twin-boundary

migration via parallel dislocations. In contrast, the twins were not found to influence the spall behavior of the nanocrystalline system. This is because voids nucleate and grow along the grain boundaries, while for the other system the twins provide void nucleation sites so that twinning density influences spall behavior.

Deformed Nanocrystalline Metals

Discussed in this subsection are representative MDS of the homogenous deformation (instead of shock loading) of metals with grain sizes on the nanometer scale. In metals that have conventional grain sizes, plastic deformation involves primarily the motion of collections of dislocations (i.e., slip). Because in a given lattice slip systems will change orientation across a grain boundary, these boundaries tend to inhibited dislocation motion. This leads to an increase in strength with decreasing grain size. Both experiment and modeling suggest, however, that there is a grain size below which materials begin to get softer with decreasing grain size. This "inverse Hall–Petch" behavior can be attributed to a change from dislocation mediated plasticity to grain boundary sliding. Such a transition has been observed in MDS, which predict a critical grain size of about 10–15 nm in good agreement with experimental results. While agreeing with experiment, the MDS have also revealed rich and unanticipated dynamics near the threshold region that can apparently be related to the inherent properties of the bulk material. This dynamics includes an enhanced role of grain rotation, cooperative inter-grain dynamics, and stacking fault formation across grains that occurs by motion of partial dislocations.

MDS of strained nanoscrystalline copper with average grain sizes of ~5 nm was carried out by Jacobsen and coworkers. There studies showed softening for small grain sizes, in qualitative agreement with experimental results (Schiøtz et al. 1999). These MDS studies revealed that in the inverse Hall–Petch regime, plastic deformation can be chiefly attributed to grain boundary sliding and a reduced influence of dislocation motion on the deformation. In related MDS carried out by Van Swygenhoven and coworkers, the deformation mechanisms of nanostructured nickel and copper with grain sizes ranging between 3.5 and 12 nm were characterized (Van Swygenhoven et al. 1999). For grain sizes less than ~10 nm, deformation occurred mainly by grain boundary sliding, while at larger grain sizes, deformation occurred by a combined sliding and dislocation motion. Mechanisms of strain accommodation later identified by MDS included single atom motion and correlated motion of several atoms, as well as stress-assisted free volume migration.

Similar studies of the deformation of nanocrystalline aluminum with a columnar structure carried out by Wolf and coworkers showed the emission of partial dislocations originating from grain boundaries and triple junctions (Yamakov et al. 2001). An interesting observation from these simulations is that partial dislocations may be reabsorbed by a grain boundary after the applied stress is removed. It was suggested that this may be responsible for the lack of dislocations observed in experiments after release of external stresses.

Based on MDS studies, Van Swygenhoven and coworkers suggested that atom rearrangements at grain boundaries at points where nucleation and emission of partial dislocation occur lower the grain boundary energy. Emission of a trailing partial dislocation is therefore not always needed for further relaxation. Based on MDS of aluminum with a columnar nanostructure, Yamakov et al. suggested that the width of stacking faults (hence the intrinsic stacking fault energy) determined by the distance separating two partial dislocations is the main quantity defining the transition from full to partial dislocation emission as grain sizes approach the critical size where inverse Hall–Petch behavior is first observed (Haslam et al. 2004). In subsequent work, Van Swygenhoven and coworkers pointed out that stacking fault energies for nickel, copper, and aluminum do not show a strong correlation with partial dislocation emission (Van Swygenhoven et al. 2004). It was instead suggested that full dynamics associated with partial dislocation nucleation from a grain boundary should be considered. This further suggests that the full planar fault energy, including the stable and unstable stacking fault energy and twin fault energies, must be considered to understand and predict relations between grain size and plastic deformation.

Using MDS, Farkas and Curtin characterized detailed mechanisms for the emission of dislocations within a columnar nickel nanostructure with grain sizes of 4–20 nm (Farkas and Curtin 2005). Apparent from these simulations were dislocations being emitted from grain boundaries. The simulations also indicated that the number of emitted dislocations per unit length of grain boundary saturates with increasing grain sizes. Assuming that dislocation emission occurs only at some small distance from triple junctions, they reproduced the dislocation densities observed in the MDS. Complicating these observations with respect to experiment is the timescale of the mechanisms needed to nucleate dislocation emission relative to the short timescale of the simulations.

"Dimples" have been observed experimentally on the fracture surfaces of nanocrystalline metals that have grain sizes less than about 100 nm (Wang et al. 2002). This observation is somewhat surprising because they appear to be fully compact materials and hence the dimples are not the result of voids or similar structural artifacts. The scale of the dimples is the size of multiple grains, which suggests that their formation mechanism involves inter-grain cooperative motion. Derlet et al. used MDS to characterize the fracture dynamics of nanostructured nickel with a mean grain size of 6 nm and a narrow grain size distribution (Derlet et al. 2003). The MDS was carried out at almost one half of the melting temperature of pure nickel to accelerate grain boundary sliding and diffusion, and a tensile load of 1.5 GPa was applied for 350 ps. Formation of local shear bands was observed. These shear bands extended through multiple grains and accounted for the cooperative dynamics. Three mechanisms were identified that contributed to the shear band formation. These were reorientation of neighboring grains separated by low-angle grain boundaries, migration of grains by boundary sliding that lined up complementary shear planes, and intragranular slip. Distributed within the microstructure were interfaces such as twins that are particularly resistant to sliding. These interfaces created pinning points around which surrounding grains

deform and form the shear bands. This was proposed as the mechanism that leads to the dimples observed experimentally.

Different groups have used MDS to characterize the possible role of dopants at grain boundaries on plastic deformation mechanisms. Saxens and coworkers, for example, modeled the influence of antimony dopants in nanocrystalline copper on plastic dynamics under uniaxial load (Rajgarhia et al. 2010). The simulations revealed that relatively small amounts of antimony can increase the flow stress; this was attributed to an increase in the stress needed for grain boundary sliding. It was also observed that antimony does not appear to have a large influence on dislocation nucleation at grain boundaries. In contrast, results from MDS by Jang et al. suggested that lead atoms that segregate to grain boundaries in nanostructured aluminum can suppress the nucleation of partial dislocations from grain boundaries that are under uniaxial tension (Jang et al. 2008a, b). In the pure system, dislocations were observed to nucleate from sites at which aluminum atoms are already under tensile stress. Segregation to grain boundaries for this system arises mainly from stress effects that drive the larger lead atoms (compared to aluminum) to atom sites that in pure aluminum would be under tensile stress. Hence, the Pb relieves the stress that contributes to dislocation emission. It was also observed that lead addition disordered the atoms at the grain boundaries. This allowed more strain to be accommodated by the grain boundaries compared to the pure system that had dislocations travel through the grains.

In ductile materials, crack propagation involves dislocation emission from the crack tip. This emission can increase the tip radius and decrease the stress concentration that drives the tip forward under an applied load. While the stresses away from the crack can be well modeled by continuum-based methods, atomic theory and modeling is needed to understand the processes occurring at the crack tip. In principle MDS can be effectively used for this purpose. In practice, however, modeling the scale of the plastic dynamics leading to ductile fracture and its coupling to the surrounding stress field has many challenges (Brenner 2013).

Holian and coworkers used MDS to simulate crack propagation in a copper crystal that had interatomic forces modeled by Morse or EAM potentials (Zhou et al. 1997). An initial crack was introduced into the material, and it was strained to just below the Griffith criterion for crack propagation. The long-range character of the various stress and strain fields was incorporated into the simulation using periodic boundaries in two directions. Atoms were displaced according to the continuum elastic solution for a finite crack in an unbounded solid. This large MDS simulation – it involved up to 35 million atoms – was the first to unambiguously observe dislocation loops emitting from a crack tip that lead to blunting and jogging. The MDS revealed crack tip propagation of about two lattice spacings that was followed by distinct elastic rounding of the tip just prior to dislocation emission. Interestingly, the initial partial dislocation was emitted backward from the crack tip. This was followed by a second forward emission. This behavior can be explained by the orientation of Burger's vectors for the dislocations with respect to the surrounding lattice and stresses. The details of crack blunting and plasticity revealed by this

MDS simulation are beyond what typically comes from analytic theory and continuum-based modeling.

Hess et al. subsequently used MDS to examine the role of temperature, interatomic potential, strain rate, system size, and boundary conditions on dislocation nucleation from a crack tip in a system modeling nickel (Hess et al. 2005). The primary factor in the mechanism of dislocation emission revealed by the MDS is the crack orientation with respect to the surrounding lattice and temperature, and the interatomic force expression played a relatively minor role in terms of the qualitative behavior of plastic dynamics. Dislocation nucleation in response to local stresses that is thermally activated was observed, which explains the temperature dependence of the results.

MDS has also been used to characterize mechanisms associated with mode I crack propagation from a notch placed in a nanostructured system with grain sizes between 5 and 12 nm and an interatomic PEF intended to model nickel (Farkas et al. 2002). Incremental loading of the system normal to the notch orientation followed by relaxation resulted in propagation of the notch through the nanostructure. For the smaller grain size, the crack propagated almost exclusively along the grain boundaries before being blocked at a triple junction. Adding strain resulted in blunting but not crack propagation. Nanovoids also formed along the grain boundaries in front of the crack tip. The voids eventually coalesced with the crack, which resulted in the crack front moving to the next triple junction, where this process was repeated. The same general behavior occurred for the larger grain sizes, except that the simulation was initiated with part of the crack tip located in a grain. In this simulation, the tip propagation through the grains was accompanied by emission of dislocations similar to crystalline materials, with the exception that the dislocations could be re-adsorbed by surrounding grain boundaries. After the crack tip went through an initial grain, the propagation mechanism was the same as that for the smaller-grained system. Comparison of the energy released to the Griffith criterion for fracture suggested that this dynamics corresponded to a brittle material.

Simulations of Grain Boundary Migration

Grain boundary motion plays a critical role in processes such as grain growth during recrystallization after a metal has been work hardened. How complex atomic dynamics is coupled to stresses and external applied strains as grain boundaries move remains one of the major unresolved problems in materials science (Molodov et al. 2007) (Gottstein and Molodov 1998). In most annealing experiments, grain growth represents an average behavior of many types of grain boundaries. However, different grain boundaries can behave very differently, and therefore, grain growth experiments are limited in terms of characterizing the dynamics of individual grain boundaries. Even in bicrystals it is a formidable task to characterize migration over a wide range of interface structure (Furtkamp et al. 1998; Gorkaya et al. 2009). Within the scale and interatomic potential constraints discussed above, MDS can provide

unique insight and atom-resolved properties of specific grain boundaries that complement experimental capabilities (Olmsted et al. 2009).

Mobility is a fundamental property of interest in characterizing grain boundary dynamics. Mobility is defined as the linear coefficient relating the grain boundary normal velocity v_{GB} to the driving force (pressure) P, i.e., $M \equiv v_{GB}/P$. For low-angle tilt grain boundaries, the mobility can be analytically approximated by the number of dislocations per unit length times the Peach–Koehler force associated with each dislocation. This results in an analytic mobility expression that is inversely proportional to tilt angle and that has an Arrhenius temperature dependence. While activated mobility is typically observed, the inverse relation between mobility and tilt angle is not a feature of typical experimental or MDS results. At higher tilt angles, assuming that grain boundary motion is closely related to atom diffusion leads to the Burke–Turnbull expression for grain boundary velocity of the form

$$v = \frac{\Omega}{a^2}\left[\eta e^{-\frac{Q}{kT}} - \eta e^{\frac{Q+p\Omega}{kT}}\right] \tag{3}$$

In this expression, a is the lattice spacing, η is an attempt frequency, Ω is the volume per atom, Q is an activation energy, k is the Boltzmann constant, T is temperature, and p is pressure. In the limit that $p\Omega >> kT$, velocity and pressure are proportional to one another with proportionality constant (i.e., mobility):

$$M = \frac{\eta a^4}{kT} e^{-\frac{Q}{kT}} \tag{4}$$

In this expression, the mobility is an activated process but is independent of tilt angle.

Based on results from MDS and experiment, it appears that grain boundary mobilities can depend on many factors, but with a dependence that is not well understood. However, several trends have become apparent. First, mobility typically shows Arrhenius behavior with respect to temperature; this agrees with the expression above. Second, low-angle grain boundaries tend to be less mobile compared to high-angle structures, a trend that in general appears valid for both twist and tilt structures (Huang and Humphreys 2000). In addition, in contrast to the analytic theory mentioned above, the mobility of low-angle grain boundaries tends to increase with increasing misorientation angle in a power law relationship $M = k\theta^{\alpha}$ (Huang and Humphreys 2000). Third, the mobility of twist structures tends to be higher than tilt grain boundaries, while activation energies are similar (Godiksen et al. 2008). Finally, mobilities are different for planar and curved grain boundaries and very sensitive to impurity and vacancy concentrations (Gottstein and Shvindlerman 2009).

Foiles and coworkers used the artificial driving force method mentioned above in an MDS (Janssens et al. 2006) to calculate energies and mobilities for 388 grain boundaries in nickel. The interfaces included ⟨111⟩, ⟨100⟩ twist and ⟨110⟩, ⟨111⟩, ⟨100⟩ symmetric tilt and coherent twin grain boundaries (Olmsted et al. 2009).

Greater than 25% of the grain boundaries were reported to migrate using a mechanism that couples shear stress to motion. This mechanism included most of the non-Σ3 structures with the highest mobilities. Among the rest of the structures, the incoherent Σ3 twins had an anomalously high mobility, while other boundaries remained static on the timescale of the simulations. Thermal activation energies also varied widely, with some migration mechanisms being temperature independent. Thermal roughening of the grain boundaries was also reported, which resulted in relatively large increases in grain boundary mobility above the roughening temperatures. Despite the large number of structures studied and the wide range of different properties examined, no correlations were uncovered between mobility and scalar quantities such as grain boundary energy, misorientation angle, Σ value, or excess volume.

The definition of grain boundary mobility given above assumes a linear relationship between the normal velocity of a grain boundary and the driving force. However, both MDS and analytic theory (cf. Eq. 3) predict nonlinear behavior (Zhou and Mohles 2011). Various authors have different explanations for this dependence. Godiksen et al. (2008) found in MDS that grain boundary velocity and driving force ($v_{GB} \propto P$) are proportional for twist grain boundary dynamics, but nonlinear ($v_{GB} \propto P^2$) for tilt grain boundaries. It was proposed that this result is due to local interactions between the grain boundaries and nearby dislocations. Another explanation proposed by Zhang et al. (2004) attributed the nonlinearity to an increase in effective activation barrier with increasing applied driving force.

Zhou and Mohles (2011) proposed a mechanism based on Eq. 3 that the approximation leading to Eq. 4 is invalid for high driving forces needed to observe grain boundary motion in MDS. They proposed that a low driving force limit can be achieved by extrapolating data from high driving force simulations. Zhou and Mohles used this idea to determine misorientation-angle-dependent grain boundary mobilities and migration activation energies by MDS with the artificial driving force method (Janssens et al. 2006). These simulations used a series of flat twist ⟨110⟩ grain boundaries with different Σ values and misorientations. The resultant mobilities of small- ($\leq 25°$) and large-angle misorientation grain boundaries were reported to be about $10^{-9} m^4 J^{-1} s^{-1}$ and $10^{-8} m^4 J^{-1} s^{-1}$, respectively.

To avoid the nonlinearity resulting from a high driving force, Trautt et al. performed equilibrium MDS and obtained the mobility according to the fluctuation dissipation theorem by assuming that mobility is linearly dependent on the fluctuation of the mean interface position (Fig. 2c) (Trautt et al. 2006). Based on their results, they concluded that mobilities of planar grain boundaries at the low driving force limit (i.e., true mobilities) are an order of magnitude higher than the mobilities measured with high driving force.

Like mobility, there is no simple rule to determine grain boundary migration activation energies because the energies depend on too many variables (e.g., grain boundary type, impurity concentration, and shape). For example, activation energies computed from MDS are often lower than those determined from experiment (Schönfelder et al. 2006; Zhou and Mohles 2011). One factor contributing to this

observation is likely the impurities in the experimental systems that are not present in the simulations (Olmsted et al. 2009).

A distinct change in activation energy between low-angle and high-angle grain boundaries (irrespective of planar or curved type) was detected numerically (Zhou and Mohles 2011) and experimentally (Winning and Gottstein 2002) at approximately the same misorientation. The transition angle measured is about 15° for both ⟨110⟩ twist (Zhou and Mohles 2011) and ⟨100⟩ twist boundaries (Schönfelder et al. 2006), 14.1° for ⟨111⟩ symmetric tilt boundaries (Winning and Gottstein 2002), 8.6° for ⟨100⟩ symmetric tilt boundaries (Winning 2003), and 13.6° for ⟨112⟩ symmetric tilt (Winning and Rollett 2005) grain boundaries. The former two transition angles were determined from MDS, while the latter three were measured experimentally. The agreement suggests that MDS is able to capture the important aspects of this transition.

Equation 3 assumes that activation energies for grain boundary migration in the high-angle regime does not depend on misorientation angle (Winning and Rollett 2005; Winning 2003). This is different from grain boundary energies, which show a distinct dependence on angle. This includes energy cusps at low sigma structures in symmetric tilt boundaries. Plotted in Fig. 5 are grain boundary energy and migration activation energy as a function of tilt angle from MDS using an embedded-atom potential for copper. In this unpublished study, a correlation between grain boundary energy and activation energy is apparent, especially with respect to the cusps. However, whether cusps are local maxima or minima does not appear to correlate. More work to try to understand this relationship is underway.

A recent experiment indicated that that grain boundary migration in nanocrystalline aluminum thin films is governed by shear stresses that produce distortion work. This is in contrast to the normal stresses assumed in conventional theory (Rupert et al. 2009). Shear stress driving grain boundary motion has also been reported in other experimental work (Molodov et al. 2007; Winning and Rollett 2005; Winning 2003). MDS results agree with these experimental studies (Cahn et al. 2006; Cahn and Taylor 2004). MDS for symmetric ⟨100⟩ tilt grain boundary systems in copper by Cahn et al. confirmed that normal motion of planar grain boundaries can be driven by shear stress (Fig. 2b). This work also showed that the ratio of normal to tangential translation of a grain boundary is a constant that is independent of temperature or of the magnitude of the applied shear stress.

Olmsted et al. (2009) reported that they found that even under a normal driving force significant shear can be built up during normal motion of planar grain boundaries. They further suggested that a traditional diffusion-controlled mechanism exists in all grain boundaries, but this mechanism can be overshadowed by the faster shear-coupled mechanism if the latter is allowed geometrically (e.g., lateral translation is unconstrained).

A subset of atoms near a tilt grain boundary from an unpublished MDS study is illustrated in Fig. 6. An embedded-atom potential for copper was used, and the interface is a symmetric tilt grain boundary with a tilt angle of 22.62°. The position of the grain boundary is indicated by the red arrows. The left panel illustrates the grain boundary region before a driving force for migration is applied. The middle

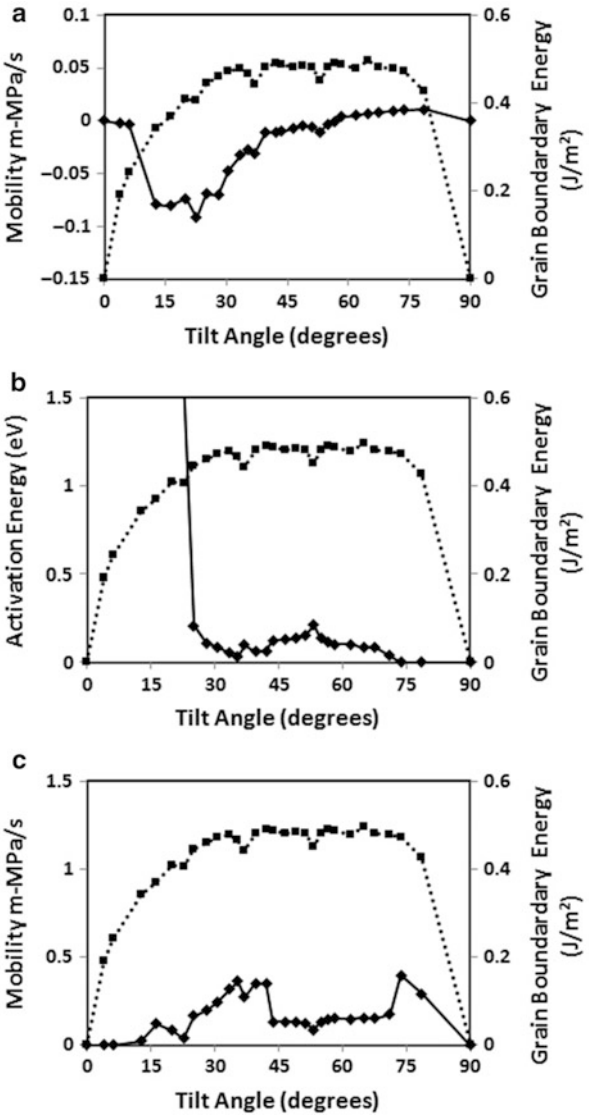

Fig. 5 Dependence of various grain boundary properties on tilt angle from an MDS of ⟨100⟩ symmetric tilt grain boundaries in copper at temperature ≥800 K and a virtual driving force of 10^8 Pa. In each plot the dashed line indicates grain boundary energy at 0 K (the scale is indicated by the label along the right ordinate of each plot). (**a**) mobility; (**b**) activation energy; (**c**) shear strain. There appear to be correlations between energy and the dynamic properties of the grain boundaries, but the origin of the correlations is unknown

panel illustrates the same subset of atoms after the grain boundary has moved due to a shear stress that is applied at the boundaries with an orientation given by the black arrows. Applying this stress precludes the use of periodic boundaries in the direction normal to the grain boundary interface (but they are used in the other two directions). The right panel illustrates the same atoms after the grain boundary has moved due to a driving force normal to the interface from the application of an artificial energy term as illustrated by Fig. 1a (Janssens et al. 2006). For this case, periodic boundaries

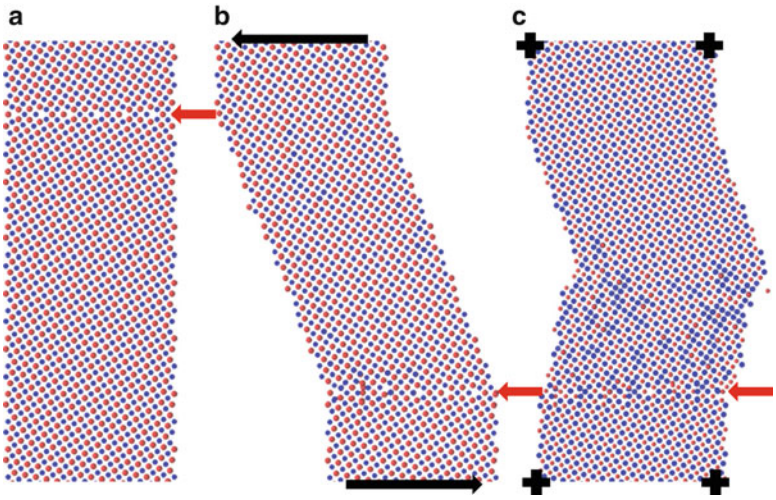

Fig. 6 Illustration of atom motion from an unpublished MDS of a tilt grain boundary migration. The image on the *left* is the initial atom configuration. The *right-side* two images illustrate the final atom configurations when the grain boundary is driven to move downward (indicated by the *red arrows*) by shear stress (**b**) or normal direction driving force (**c**). The *black arrows* indicate the shear direction and the *black crosses* imply that shear motion on the two ends is prohibited. *Blue* and *red colors* specify atoms on (100) and (200) planes, respectively

are applied in all directions. In both cases, a shear strain in the plane of the grain boundary is created during the grain boundary migration. For the conditions corresponding to Fig. 6b, this shear strain is smoothly and continuously accommodated by nonperiodic boundary condition, and the grain boundary moves continuously (Cahn et al. 2006). For Fig. 6c where the boundary conditions do not allow shear strain accumulation (indicated by the black crosses), shear strain starts to build up as the grain boundary begins to move. The grain boundary motion, however, is stopped after about 100 time steps due to the accumulation of shear stress in the direction opposite of the strain. This corresponds to the inflection point of the strain in panel c. If the normal direction driving force is large enough, the grain boundary can overcome this shear stress accumulation and continue moving, but through a different mechanism involving a combination of dislocation glide and climb. Further analysis of this mechanism is ongoing.

Current Challenges

Given in this chapter was an overview of MDS at a tutorial level, followed by some examples where MDS is providing new insights into the formation, stability, and structure of various types of damage in metals. The intent of this chapter was not to

be a comprehensive review, but rather a snapshot of the scientific literature in this area. Within these limited goals, it should be clear that MDS has been used successfully to study a wide variety of different types of damage in crystalline metals. Even with the advances in computing resources and methodology, however, challenges remain to using MDS to fully understand plastic damage. Some of these challenges, and steps toward meeting these challenges, are briefly described in this section.

Interatomic Forces

PEFs commonly used in MDS were briefly discussed above. The most successful functional forms for large-scale MDS are generally derived from approximations to quantum mechanical bonding, with parameters in the functions fit to a set of physical properties. In some cases, researchers favor functional forms with many parameters and then fit these parameters to as many properties as they can. The other extreme is to create a PEF with as much physics as possible built into a functional form that has fewer parameters and then fit these parameters to a fewer, carefully chosen properties. Both approaches have advantages and limitations that can become apparent in analyzing simulation results and comparing these results to experimental observations.

There are currently improvements being made to the derivation, fitting, and implementation of PEFs. For example, one active area is incorporating effects related to charge transfer (Mathieu 2007; Nistor et al. 2006; Nistor and Müser 2009). While unimportant for pure metals for most situations, including charge transfer improves the description of bonding for intermetallic phases and for interfaces between metals and other types of materials (e.g., oxides). There have also been recent advances in incorporating magnetic effects into PEFs, although much more work is needed (Ackland 2006; Dudarev and Derlet 2005; Ma et al. 2012). Replacing predefined functions with neural networks and similar approaches is showing promise in enhancing the accuracy of interatomic forces for MDS (Behler 2011; Jose et al. 2012).

In the longer term, the preferred approach from a fundamental science viewpoint is to calculate interatomic forces directly from quantum mechanics. Depending on the approximations made within density functional theory, for example, a single calculation that includes electrons can be carried out for between tens and millions of atoms with the current level of computing resources. With better approximations within quantum mechanics, increasingly clever scaling algorithms, and simply larger and faster computers, the system sizes for which forces can be calculated with explicit electronic states will continue to dramatically increase. In addition to interatomic forces that are transferable compared to analytic PEFs, using forces directly from quantum mechanics should provide an efficient pathway for relating plastic damage in metals to the properties and behavior of the electrons.

Length Scales

System sizes scale naturally with the number of processors (rather than processor speed) dedicated to a simulation. In the last two decades the size scales that can be attained in an MDS have increased by orders of magnitude. This is especially true for researchers with access to large computers like those at the national laboratories. In addition, the cost of parallel processors has decreased to the point where research groups with modest resources can model damage of the size associated with extended structures like grain boundaries and dislocations. More researchers working on this scale ensure more studies that can probe behavior and structure with atomic resolution.

Timescales

Because the classical equations of motion are numerically solved stepwise in a serial fashion, the prospects for simulating significantly longer times from a computational resources viewpoint are strongly coupled to increases in processor speed. Maintaining Moore's law far into the future is unclear, and so other methods will be needed to increase accessible timescales. For rare events or well-defined kinetics, the methods mentioned above have been successful in this regard, and various ways of combining kinetic Monte Carlo and molecular dynamics simulations will also contribute to increased accessible timescales. Overall this remains a major challenge to connecting atomic and engineering scales.

Quantum Dynamics

Using classical mechanics to model atom motion is a more reasonable approximation for heavy atoms (i.e., most metals) than light atoms like hydrogen, which would have a much higher probability for quantum tunneling and larger zero point energies. For metals accurate heat capacities and thermal transport is inhibited by the assumption of classical mechanics as well as the inability to explicitly treat of electronic degrees of freedom that can carry heat. Compared to other challenges, this remains an unmet but otherwise low priority challenge for MDS as applied to metal damage.

Interpretation of MDS Results

New algorithms have recently been proposed with which damage in crystalline lattices can be easily identified. This includes dislocations and Burger's vectors (Stukowski and Albe 2010). There still remains, however, a crucial need for automating the detection and interpretation of damage mechanisms in MDS and passing this information to larger length-scale analyses. As an example, the methods of advanced statistics (Bayesian analysis) could be used to analyze simulations so that

different types of damage gleaned from multiple simulations can be passed to higher scale analyses. Other critical and innovative thinking is needed in this area.

Conclusion

This chapter provided an overview of MDS as applied to modeling plastic damage in metals. This overview included a tutorial-level explanation of how a traditional MDS is implemented and analyzed and some examples of where MDS had provided new insights into the dynamics of damage that cannot typically be obtained from continuum modeling that is more traditionally used by engineers. This chapter concluded with a list of challenges that remain in expanding the use of MDS for modeling damage. These challenges included improved interatomic force expressions, numerical and computational routes for increasing time and length scales, incorporating quantum dynamics where needed, and new methods for interpreting MDS, including using modern tools of statistical analysis.

Acknowledgments Unpublished work reported from our group was supported by the Office of Naval Research. DL is supported by the National Science Foundation.

References

G.J. Ackland, Two-band second moment model for transition metals and alloys. J. Nucl. Mater. **351**(1–3), 20–27 (2006)

B.J. Alder, T.E. Wainwright, Phase transition for a hard sphere system. J. Chem. Phys. **27**(5), 1208 (1957)

M.P. Allen, D.J. Tildesley, *Computer Simulation of Liquids* (Oxford University Press, New York, 1989) ISBN-10: 0198556454

J. Behler, Neural network potential-energy surfaces in chemistry: a tool for large-scale simulations. Phys. Chem. Chem Phy. PCCP **13**(40), 17930–17955 (2011)

H.J.C. Berendsen, J.P.M. Postma, W.F. van Gunsteren, A. DiNola, J.R. Haak, Molecular dynamics with coupling to an external bath. J. Chem. Phys. **81**(8), 3684 (1984)

G.P. Berman, F.M. Izrailev, The Fermi-Pasta-Ulam problem: fifty years of progress. Chaos. (Woodbury) **15**(1), 15104 (2005)

D.W. Brenner, The art and science of an analytic potential. Phys. Status Solidi B **217**(1), 23–40 (2000)

D.W. Brenner, Challenges to marrying atomic and continuum modeling of materials. Curr. Opinion Solid State Mater. Sci. **17**(6), 257–262 (2013)

D.W. Brenner, B.J. Garrison, Gas-Surface Reactions: Molecular Dynamics Simulations of Real Systems, in *Advances in Chemical Physics*, ed. by K. P. Lawley, vol. 76, (Wiley, New York, 1989), pp. 281–333

D.W. Brenner, O.A. Shenderova, D.A. Areshkin, Quantum-based analytic interatomic forces and materials simulation. Rev. Comput. Chem. **12**, 207–239 (1998)

E.M. Bringa et al., Ultrahigh strength in nanocrystalline materials under shock loading. Science (New York) **309**(5742), 1838–1841 (2005)

J.W. Cahn, J.E. Taylor, A unified approach to motion of grain boundaries, relative tangential translation along grain boundaries, and grain rotation. Acta Mater. **52**(16), 4887–4898 (2004)

J.W. Cahn, Y. Mishin, A. Suzuki, Coupling grain boundary motion to shear deformation. Acta Mater. **54**(19), 4953–4975 (2006)
R. Car, M. Parrinello, Unified approach for molecular dynamics and density-functional theory. Phys. Rev. Lett. **55**(22), 2471–2474 (1985)
J.W. Crill, X. Ji, D.L. Irving, D.W. Brenner, C.W. Padgett, Atomic and multi-scale modeling of non-equilibrium dynamics at metal–metal contacts. Model. Simul. Mater. Sci. Eng. **18**(3), 034001 (2010)
M. Daw, M. Baskes, Embedded-atom method: derivation and application to impurities, surfaces, and other defects in metals. Phys. Rev. B **29**(12), 6443–6453 (1984)
M.S. Daw, S.M. Foiles, M.I. Baskes, The EAM is reviewed in: mater. Sci. Rep. **9**, 251 (1993)
P. Derlet, A. Hasnaoui, H. Van Swygenhoven, Atomistic simulations as guidance to experiments. Scr. Mater. **49**(7), 629–635 (2003)
A. Dongare, A. Rajendran, B. LaMattina, M. Zikry, D. Brenner, Atomic scale simulations of ductile failure micromechanisms in nanocrystalline Cu at high strain rates. Phys. Rev. B **80**(10), 104108 (2009)
A.M. Dongare, A.M. Rajendran, B. LaMattina, M.A. Zikry, D.W. Brenner, Atomic scale studies of spall behavior in nanocrystalline Cu. J. Appl. Phys. **108**(11), 113518 (2010)
A.M. Dongare et al., An angular-dependent embedded atom method (A-EAM) interatomic potential to model thermodynamic and mechanical behavior of Al/Si composite materials. Model. Simul. Mater. Sci. Eng. **20**(3), 035007 (2012)
S.L. Dudarev, P.M. Derlet, A 'magnetic' interatomic potential for molecular dynamics simulations. J. Phys. Condens. Matter **17**(44), 7097–7118 (2005)
V. Duin, C.T. Adri, S. Dasgupta, F. Lorant, W.A. Goddard, ReaxFF: a reactive force field for hydrocarbons. J. Phys. Chem. A **105**(41), 9396–9409 (2001)
V. Dupont, T.C. Germann, Strain rate and orientation dependencies of the strength of single crystalline copper under compression. Phys. Rev. B **86**(13), 134111 (2012)
F. Ercolessi, J.B. Adams, Interatomic potentials from first-principles calculations: the force-matching method. Europhys. Lett. (EPL) **26**(8), 583–588 (1994)
F. Ercolessi, E. Tosatti, M. Parrinello, Au (100) surface reconstruction. Phys. Rev. Lett. **57**(6), 719–722 (1986)
D. Farkas, W.A. Curtin, Plastic deformation mechanisms in nanocrystalline columnar grain structures. Mater. Sci. Eng. A **412**(1–2), 316–322 (2005)
D. Farkas, H. Van Swygenhoven, P. Derlet, Intergranular fracture in nanocrystalline metals. Phys. Rev. B **66**(6), 060101 (2002)
M.W. Finnis, J.E. Sinclair, A simple empirical N -body potential for transition metals. Philos. Mag. A **50**(1), 45–55 (1984)
M. Furtkamp, G. Gottstein, D.A. Molodov, V.N. Semenov, L.S. Shvindlerman, Grain boundary migration in Fe–3.5 % Si bicrystals with [001] tilt boundaries. Acta Mater. **46**(12), 4103–4110 (1998)
J.D. Gale, A.L. Rohl, The general utility lattice program (GULP). Mol. Simul. **29**(5), 291–341 (2003)
J. Gibson, A. Goland, M. Milgram, G. Vineyard, Dynamics of radiation damage. Phys. Rev. **120**(4), 1229–1253 (1960)
R.B.N. Godiksen, S. Schmidt, D. Juul Jensen, Molecular dynamics simulations of grain boundary migration during recrystallization employing tilt and twist dislocation boundaries to provide the driving pressure. Model. Simul. Mater. Sci. Eng. **16**(6), 065002 (2008)
T. Gorkaya, D.A. Molodov, G. Gottstein, Stress-driven migration of symmetrical ⟨100⟩ tilt grain boundaries in Al bicrystals. Acta Mater. **57**(18), 5396–5405 (2009)
G. Gottstein, D.A. Molodov, Grain boundary migration in metals: recent developments. Inter. Sci. **22**, 7–22 (1998)
G. Gottstein, L.S. Shvindlerman, *Grain Boundary Migration in Metals: Thermodynamics, Kinetics, Applications*. Materials Science & Technology, 2nd edn. (CRC Press, Boca Rotan, 2009)

A.J. Haslam et al., Effects of grain growth on grain-boundary diffusion creep by molecular-dynamics simulation. Acta Mater. **52**(7), 1971–1987 (2004)
B. Hess, B. Thijsse, E. Van der Giessen, Molecular dynamics study of dislocation nucleation from a crack tip. Phys. Rev. B **71**(5), 054111 (2005)
J. Hirschfelder, H. Eyring, B. Topley, Reactions involving hydrogen molecules and atoms. J. Chem. Phys. **4**(3), 170 (1936)
B.L. Holian, P.S. Lomdahl, Plasticity induced by shock waves in nonequilibrium molecular-dynamics simulations. Science **280**(5372), 2085–2088 (1998)
J.D. Honeycutt, H.C. Andersen, Molecular dynamics study of melting and freezing of small Lennard-Jones clusters. J. Phys. Chem. **91**(19), 4950–4963 (1987)
Y. Huang, F.J. Humphreys, Subgrain growth and low angle boundary mobility in aluminium crystals of orientation $\{110\}\langle 001\rangle$. Acta Mater. **48**(8), 2017–2030 (2000)
D.L. Irving, C.W. Padgett, J.W. Mintmire, D.W. Brenner, Multiscale modeling of metal–metal contact dynamics under high electromagnetic stress: timescales and mechanisms for joule melting of Al–Cu asperities. IEEE Trans. Magn. **45**(1), 331–335 (2009a)
D.L. Irving, C.W. Padgett, D.W. Brenner, Coupled molecular dynamics/continuum simulations of Joule heating and melting of isolated copper–aluminum asperity contacts. Model. Simul. Mater. Sci. Eng. **17**(1), 015004 (2009b)
K. Jacobsen, J. Norskov, M. Puska, Interatomic interactions in the effective-medium theory. Phys. Rev. B **35**(14), 7423–7442 (1987)
S. Jang, Y. Purohit, D.L. Irving, et al., Influence of Pb segregation on the deformation of nanocrystalline Al: insights from molecular simulations. Acta Mater. **56**(17), 4750–4761 (2008a)
S. Jang, Y. Purohit, D. Irving, et al., Molecular dynamics simulations of deformation in nanocrystalline Al–Pb alloys. Mater. Sci. Eng. A **493**(1–2), 53–57 (2008b)
K.G.F. Janssens et al., Computing the mobility of grain boundaries. Nat. Mater. **5**(2), 124–127 (2006)
K.V. Jose, N.A. Jovan, J. Behler, Construction of high-dimensional neural network potentials using environment-dependent atom pairs. J. Chem. Phys. **136**(19), 194111 (2012)
K. Kadau, T.C. Germann, P.S. Lomdahl, B.L. Holian, Microscopic view of structural phase transitions induced by shock waves. Science (New York) **296**(5573), 1681–1684 (2002)
C. Kelchner, S. Plimpton, J. Hamilton, Dislocation nucleation and defect structure during surface indentation. Phys. Rev. B **58**(17), 11085–11088 (1998)
B.-J. Lee, M. Baskes, Second nearest-neighbor modified embedded-atom-method potential. Phys. Rev. B **62**(13), 8564–8567 (2000)
J. Li, AtomEye: an efficient atomistic configuration viewer. Model. Simul. Mater. Sci. Eng. **11**(2), 173–177 (2003)
P.-W. Ma, S.L. Dudarev, C.H. Woo, Spin–lattice-electron dynamics simulations of magnetic materials. Phys. Rev. B **85**(18), 184301 (2012)
D. Mathieu, Split charge equilibration method with correct dissociation limits. J. Chem. Phys. **127**(22), 224103 (2007)
J.A. McCammon, B.R. Gelin, M. Karplus, Dynamics of folded proteins. Nature **267**(5612), 585–590 (1977)
R.E. Miller, E.B. Tadmor, A unified framework and performance benchmark of fourteen multiscale atomistic/continuum coupling methods. Model. Simul. Mater. Sci. Eng. **17**(5), 053001 (2009)
D. Molodov, V. Ivanov, G. Gottstein, Low angle tilt boundary migration coupled to shear deformation. Acta Mater. **55**(5), 1843–1848 (2007)
F. Müller-Plathe, A simple nonequilibrium molecular dynamics method for calculating the thermal conductivity. J. Chem. Phys. **106**(14), 6082 (1997)
R. Nistor, M. Müser, Dielectric properties of solids in the regular and split-charge equilibration formalisms. Phys. Rev. B **79**(10), 104303 (2009)
R.A. Nistor, J.G. Polihronov, M.H. Müser, N.J. Mosey, A generalization of the charge equilibration method for nonmetallic materials. J. Chem. Phys. **125**(9), 094108 (2006)

S. Nosé, A unified formulation of the constant temperature molecular dynamics methods. J. Chem. Phys. **81**(1), 511 (1984)
D.L. Olmsted, E.A. Holm, S.M. Foiles, Survey of computed grain boundary properties in face-centered cubic metals – II: grain boundary mobility. Acta Mater. **57**(13), 3704–3713 (2009)
C.W. Padgett, D.W. Brenner, A continuum-atomistic method for incorporating Joule heating into classical molecular dynamics simulations. Mol. Simul. **31**(11), 749–757 (2005)
M. Parrinello, A. Rahman, Polymorphic transitions in single crystals: a new molecular dynamics method. J. Appl. Phys. **52**(12), 7182 (1981)
S. Plimpton, Fast parallel algorithms for short-range molecular dynamics. J. Comput. Phys. **117**(1), 1–19 (1995)
A. Rahman, Correlations in the motion of atoms in liquid argon. Phys. Rev. **136**(2A), A405–A411 (1964)
R.K. Rajgarhia, D.E. Spearot, A. Saxena, Molecular dynamics simulations of dislocation activity in single-crystal and nanocrystalline copper doped with antimony. Metall. Mater. Trans. A **41**(4), 854–860 (2010)
R. Ravelo, B. Holian, T. Germann, P. Lomdahl, Constant-stress Hugoniostat method for following the dynamical evolution of shocked matter. Phys. Rev. B **70**(1), 014103 (2004)
T.J. Rupert, D.S. Gianola, Y. Gan, K.J. Hemker, Experimental observations of stress-driven grain boundary migration. Science (New York) **326**(5960), 1686–1690 (2009)
J.-P. Ryckaert, G. Ciccotti, H.J. Berendsen, Numerical integration of the cartesian equations of motion of a system with constraints: molecular dynamics of n-alkanes. J. Comput. Phys. **23**(3), 327–341 (1977)
C. Schäfer, H. Urbassek, L. Zhigilei, Metal ablation by picosecond laser pulses: a hybrid simulation. Phys. Rev. B **66**(11), 115404 (2002)
J.D. Schall, C.W. Padgett, D.W. Brenner, Ad hoc continuum-atomistic thermostat for modeling heat flow in molecular dynamics simulations. Mol. Simul. **31**(4), 283–288 (2005)
J. Schiøtz, T. Vegge, F. Di Tolla, K. Jacobsen, Atomic-scale simulations of the mechanical deformation of nanocrystalline metals. Phys. Rev. B **60**(17), 11971–11983 (1999)
B. Schönfelder, G. Gottstein, L.S. Shvindlerman, Atomistic simulations of grain boundary migration in copper. Metall. Mater. Trans. A **37**(6), 1757–1771 (2006)
T.-R. Shan et al., Second-generation charge-optimized many-body potential for Si/SiO_2 and amorphous silica. Phys. Rev. B **82**(23), 235302 (2010)
M.A. Shehadeh, E.M. Bringa, H.M. Zbib, J.M. McNaney, B.A. Remington, Simulation of shock-induced plasticity including homogeneous and heterogeneous dislocation nucleations. Appl. Phys. Lett. **89**(17), 171918 (2006)
S.B. Sinnott, D.W. Brenner, Three decades of many-body potentials in materials research. MRS Bull. **37**(05), 469–473 (2012)
F.H. Stillinger, Improved simulation of liquid water by molecular dynamics. J. Chem. Phys. **60**(4), 1545 (1974)
A. Stukowski, K. Albe, Dislocation detection algorithm for atomistic simulations. Model. Simul. Mater. Sci. Eng. **18**(2), 025016 (2010)
Z.T. Trautt, M. Upmanyu, A. Karma, Interface mobility from interface random walk. Science (New York) **314**(5799), 632–635 (2006)
H. Van Swygenhoven, M. Spaczer, A. Caro, Microscopic description of plasticity in computer generated metallic nanophase samples: a comparison between Cu and Ni. Acta Mater. **47**(10), 3117–3126 (1999)
H. Van Swygenhoven, P.M. Derlet, A.G. Frøseth, Stacking fault energies and slip in nanocrystalline metals. Nat. Mater. **3**(6), 399–403 (2004)
A.F. Voter, A method for accelerating the molecular dynamics simulation of infrequent events. J. Chem. Phys. **106**(11), 4665 (1997)
A. Voter, Parallel replica method for dynamics of infrequent events. Phys. Rev. B **57**(22), R13985–R13988 (1998)

Y.M. Wang, E. Ma, M.W. Chen, Enhanced tensile ductility and toughness in nanostructured Cu. Appl. Phys. Lett. **80**(13), 2395 (2002)
M. Winning, Motion of ⟨100⟩-tilt grain boundaries. Acta Mater. **51**(20), 6465–6475 (2003)
M. Winning, G. Gottstein, On the mechanisms of grain boundary migration. Acta Mater. **50**, 353–363 (2002)
M. Winning, A.D. Rollett, Transition between low and high angle grain boundaries. Acta Mater. **53**(10), 2901–2907 (2005)
M. Wojdyr, S. Khalil, Y. Liu, I. Szlufarska, Energetics and structure of ⟨001⟩ tilt grain boundaries in SiC. Model. Simul. Mater. Sci. Eng. **18**(7), 075009 (2010)
V. Yamakov, D. Wolf, M. Salazar, S.R. Phillpot, H. Gleiter, Length-scale effects in the nucleation of extended dislocations in nanocrystalline Al by molecular-dynamics simulation. Acta Mater. **49**(14), 2713–2722 (2001)
F. Yuan, X. Wu, Shock response of nanotwinned copper from large-scale molecular dynamics simulations. Phys. Rev. B **86**(13), 134108 (2012)
V.V. Zhakhovsky, M.M. Budzevich, N.A. Inogamov, I.I. Oleynik, C.T. White, Two-zone elastic–plastic single shock waves in solids. Phys. Rev. Lett. **107**(13), 135502 (2011)
V.V. Zhakhovsky, M.M. Budzevich, N. Inogamov, C.T. White, I.I. Oleynik, *Single Two-Zone Elastic–Plastic Shock Waves in Solids* (2012), pp. 1227–1232
H. Zhang, M.I. Mendelev, D.J. Srolovitz, Computer simulation of the elastically driven migration of a flat grain boundary. Acta Mater. **52**(9), 2569–2576 (2004)
J. Zhou, V. Mohles, Mobility evaluation of <110> twist grain boundary motion from molecular dynamics simulation. Steel Res. Int. **82**(2), 114–118 (2011)
S. Zhou, D. Beazley, P. Lomdahl, B. Holian, Large-scale molecular dynamics simulations of three-dimensional ductile failure. Phys. Rev. Lett. **78**(3), 479–482 (1997)

Index

A
ABAQUS, 181, 863, 867, 881, 888
Acrylonitrile butadiene styrene (ABS), 250
Active slip systems, 1314–1316, 1321, 1324
Adapted mesh method, 470
Additive decomposition of damage variable, 8
Additive manufacturing, 216, 221, 222
Adhesive interfaces, 947
Adiabatic shearing, 321
Aggregates, 457, 463, 465, 484
AL23 alumina-PMMA interface, 621
Alumina AL23, 619
Alumina ceramics experiments
  acoustic and mechanical properties, 619
  alumina AL2, 619
  hardware speed measurements, 625
  material velocity measurements, 624
  outcomes, alumina AL23, 621, 622
  outcomes, alumina T299, 622, 623
  post-mortem observation (*see* Post-mortem macroscopic observation)
  set-up and instrumentation, 619, 620
  steps, 618
Alumina T299, 619
Aluminium, 317
American Society for Testing and Materials (ASTM), 392
Amorphization process, 593–596
Amorphous polymers, 253, 255, 259, 263
Angular cracks, 434, 441, 444
Anisotropic CDM formulation, 762
Anisotropic formulation, 125–126
  of linear super healing, 128–129
  of nonlinear super healing, 138
Anisotropic materials, 706–707
Anti-plane elasticity, 1146, 1160
Applied force, 43
Arcan specimens, 291–292
Armor ceramics, 640–641
  See also Silicon carbide ceramics
Armor-Piercing (AP) projectile, 610–612
Armor system design, 610
Arrhenius-type temperature, 1024, 1050, 1054
Artificial driving force method, 1358
Aspect ratio (AR), 355, 356
Autogenous healing mechanism, 121
Autonomous healing mechanism, 120
Auxetic damping system
  blast-induced reaction forces, 355–356
  blast vulnerable steel gate, 357–365
  reinforced concrete supporting structure, 365–373
  UGAD, 357
Auxiliary problem decomposition, 739–740
Average dynamic/static ratio (D/S)avg, 356
Average field theory, 1280
Axial displacement, 160

B
Back-stress, 741
Ballistic experiments, 557
Ballistic impacts
  common kinetic threats, 311–313
  failure modes in metallic targets, 313–314
  failure modes transition, 319–320
  Johnson-Cook flow and fracture model, 322–324
  material characterization, 324
  measurement and observation techniques, 309–311
  microscopic observations, 320–322
  numerical visualization, 326–328
  Recht-Ipson and Lambert approaches, 316–319
Barrelling effect, 289

© Springer Nature Switzerland AG 2022

G. Z. Voyiadjis (ed.), *Handbook of Damage Mechanics*,
https://doi.org/10.1007/978-3-030-60242-0

Bar-specimen interfaces, 387
Bayesian analysis, 1364
Beam lattices, computer implementation for, 1236
Bedding plane slip, 754
Bernoulli-Euler beam lattice, 1234
Biaxial flexural strength, 177
Biaxial tensile strength, 169, 170, 174
Biaxial triangular flexure test, 177
Bifurcation domain, 1080
Biot's coefficient, 760, 823, 829
Biot's modulus, 823
Biot's theory, 760
Bishop's effective stress principle, 1105
Bituminous composites
  NCSU asphalt mixture, 1068–1072
  TAMU asphalt concrete, 1063–1068
Blast-induced reaction forces, 355–356
Blast vulnerable steel gate, 357–365
Boundary conditions (BC), 355, 360, 366
Boundary element method (BEM), 755
Boundary layers breakdown, 754
Boundary value problem (BVP), 1253
Branched polymers, 252
Brazilian tests, 642
Breakdown pressures, 754
Bridgman's formula, 287
Brittle failure, 313
Brittle materials, 580
  See also Ceramics
Brittle/quasi-brittle materials, 771
Brittle-to-ductile transition (BDT), 251, 268
Burke–Turnbull expression, 1358
Butterfly specimen, 292–293, 298

C
Calibration process, 529
Cantilever circular microbeam, 157
Capillary porosity, 454
Capsular self-healing systems, 200
Car-Parrinello method, 1340
Cauchy stress tensor, 262, 757
Cauchy symmetry, 1150
Cavity expansion, 590–592, 596
CCCC, 356
Cementitious composite, 934
Ceramics, 580
  characteristic feature, 580
  material properties, 580
  mechanical behavior, 581
  phase transformation, 592–593
  plastic deformation, 585
CFCF, 356
Chemical reaction rate, 1006, 1013, 1018
Chemo-mechanical model, 999
Circular-front cracks, 564
Civil protection, 354
Classical beam theory (CBT), 157
Classical damage variable, 27, 31, 85
Classical polynomial decomposition, 7
Classical theory (CT), 162–164
Classical uniaxial compressive strain, 614
Classic Griffith crack, 1119, 1121
Clausius–Duhem inequality, 707, 756, 757
Cleavage planes, 1312, 1316, 1320, 1321
Coarse-grained alumina, 623, 633
Cohesion strength, 572
Cohesive function
  definition, 334
  drawback of, 334
Cohesive GTN traction-separation law, 338, 339
Cohesive interactions, 521, 522
Cohesive interface model, 336
Cohesive zone models (CZM), 669, 687, 755
  for ductile failure, 336–341
Common beam-like FE, 543
Completely conservative method, 1170
Composite materials, 960, 969, 977
Compression stiffness recovery factor, 368
Compression stress, 289–291
Compressive damage parameter, 368
Compressive peak stress, 529
Computer aided design (CAD) model, 764
Concrete, 454
  corrosion damage model, 1000–1009
  entropy evolution for crack propagation, 1009–1018
  phase segmentation procedure, 458–469
Concrete damage plasticity (CDP) model, 367–369, 373
Concrete design methods, 518
Concrete structures
  advanced damage, 518
  constitutive behavior, 519
  DEM, 545
  impact experiments, 521
  impacts, 519
  response prediction, 519
Concrete triaxial behavior, 519
Confined behavior, 573
Consolidated undrained (CU) test, 1100

Constitutive modelling, 251, 256
damage and failure, in polymers, 269–273
mechanical deformation, in polymers, 260–262
of rock, 820
Constitutive models, 582, 592
and damage formulations, 600–602
micromechanical models, 595–596
phenomenological models, 596–600
Constitutive parameters identification
quasi-static triaxial confined compression tests simulation, 529
quasi-static uniaxial tests simulation, 529
spalling tests, 531–533
Continuous uniform partial damage, 91
Continuum damage mechanics (CDM), 85–86, 103–104, 121, 755, 766
implementation of, 756
pore pressure driven fractures, 756
porous rocks, 756
simulation results, 763–765
Continuum damage models, 555
Continuum damage theory, 1004
Continuum thermodynamics framework
coupled two-parameter model, 1023
deviatoric damage variable, 1024
net effect of volumetric and deviatoric damage and healing, 1036–1038
net stress concept, 1026–1027
physical, net and effective spaces, 1025
strain equivalence hypothesis, 1027–1029
volumetric and deviatoric damage in bituminous composites, 1029–1034
volumetric and deviatoric healing in bituminous composites, 1034–1036
volumetric damage variable, 1024
Contrast, 1155
Conventional triaxial compression (CTC) tests, 743
Corrosion damage, 1002
concrete, 1000–1009
definition, 999
variation, 999
Cosserat-type models, 1266
Coupled damage model, 282
Couple stress, 158
Crack band approach, 499
Crack center opening displacement (CCOD), 1187
Crack closure stress, 754
Crack density, 650, 656–658
Cracked micro beam free vibration analysis
finite element formation, 159–163
MCST (*see* Modified couple stress theory (MCST))
numerical results, 162
Cracked microbeams, 157
Cracking, 497, 512
pattern, 628
Crack location ratio, 162, 164
Crack model, 161
Crack opening displacement tensor, 901
Crack pattern, 792
Crack problems, 157
Crack rotation, 821
Crack stress thresholds, 805
Crack tip opening displacement (CTOD), 1187, 1211
Crashworthiness, 226, 234, 235
Cratering process, 560, 572
Crazing, 263
Critical damage, 746
Crosslinked polymers, 252
CSD test, 1100
Curvature tensor expressions, 158
Cyclic loading and unloading studies, 808, 812
Cyclic loads, 498
Cylinders compression test, 289–290
Cylindrical steel projectiles, 557

D

Damage, 582, 590, 595, 600–604
detection, 1000
evolution law, 493, 742
evolution of cementitious material, 900–904
plane, 1165
resistance function, 745–746
variables, 809, 812, 813
velocity, 642
zones, 591
Damage-cracking process, 503
Damage evolution of hard rocks, 808
cohesion and internal friction angle characteristics, 814–816
experimental method, 809
irreversible strain characteristics, 809–811
strain energy characteristics, 812–814
Damage-healing constitutive model, 935
Damage-integrity angle, 34, 35
Damage mechanisms, 424
boundary-particle contact condition, 437–450
particle-particle contact condition, 437–450

μ Damage model
constitutive equations, 492
cyclic behavior of concrete, 503–506
damage evolution, 492–493
2D finite element description, 498–501
1D version of model, 494–495
hysteretic loop, 504
low and medium velocity loading on reinforced concrete structures, 506–514
model responses, 493
multifiber beams and the steel–concrete bond, 505–506
nonlinear fibers, 501
permanent strain, 504
strain rate effects, 495–498
Damage models
coupled damage model, 282
decoupled failure models, 282–285
Damage modes
acceleration recording system, 553
caliber radius head ratio, 554
concrete behavior, 555
concrete strength and kinetic penetrator, 553
concrete structures, 552
dimensional parameter, 554
experimental and analytical works, 554
hydrostatic pressure, 567
kinetic penetrator, 552
LDPM method, 556
mechanisms, 557
microcracks, 555
microscopic and macroscopic scales, 557
microstructural parameters, 555
numerical methods, 556
ogive-noise projectile, 554
penetration depth, 553
pressure–volumetric strain relation, 555
PTS experiments, 561
UHPC, 561
uniaxial compression strength, 557
uniaxial compression test, 568
Damage processes, 567
damage zone, 563
Ductal®, 563
EOI experiments, 563
EOI testing technique, 561
MB50 microconcrete, 563
sarcophagus configuration, 563, 564
Damage variable
comparision, 30
composition, 56–58
exponential, 33
healing field, 51–53
limits to, 55
scalar formulation, 25–28
tensor formulation, 29–30
Darve model, 1086–1088
2D discretization, 511–514
DE assembly
brittle behavior, 523
concrete, 534
dynamic spalling test modeling, 532
isotropic property, 521, 522
spalling Hopkinson bar test specimen, 532
technique, 528
Decomposition method, 967–968
Decomposition of damage variable
plane stress, 13–20
scalars, 5–12
tensor case, 10–13
Decoupled failure models, 282–285
Deformation and damage evolution, 414
Deformed and damaged configuration, 5
Delamination damage progression, 671, 685–694
Delayed ettringite formation (DEF), 998, 1008
in concrete pores, 1004
and entropy, 1017
images of, 1003
relative growth of, 1015
Denoual-Forquin-Hild (DFH) model, 570
Density functional theory, 595
DE packing, 529, 539
Depth-of-penetration (DOP) test, 644
Deterministic micromechanical model, 905
Deviatoric damage fluidity coefficient, 1033
Deviatoric energy, 708
2D grain-based modeling (GBM) approach, 414
Digital image correlation (DIC), 399–401
Digital volume correlation (DVC), 478, 485
Dilatancy, 604
Dilute homogenization scheme, 731
Direct computation method, 968
Discing fracture, 319
Discrete cohesive crack model, 1114, 1184
Discrete element (DE)
elastic behavior, 522
normal force, 524
spherical, 521
Discrete element method (DEM), 414, 556, 1080, 1089
advanced damage stimulation, 520
cohesive bond models, 520
cohesive interactions, 521
concrete mesoscale constituents, 521

concrete structures, 520
constitutive behavior, 525
failure criterion, 524
fundamentals, 520
macroscopic approach based, 521
MTL, 523
non-linear elastic, 524
packing technique, 528, 529
parameters identification (*see* Constitutive parameters identification)
strain-rate dependency, 525, 527, 528
strain-rate sensitivity, 526
validation (*see* Hard impact test simulation)
Discrete element method (DEM) self-healing model, 949–952
parametric analysis, 952–955
Discrete-layer models, 669
Discrete strong discontinuity approach, 473
Dislocation-density based multiple slip formulation, 1310
Dislocation theory, 636
Displacement, 159
Distributed damage, 505
Divergent spherical expansion tests, 635
Divergent spherical longitudinal wave, 612, 613
Divergent spherical wave test
ceramics experiments (*see* Alumina ceramics experiments)
ceramics loading, 612, 613
EPIC, 615
interaction, 614
macro and micro-phenomena, 611
numerical simulations, 615–618
phases, 613
phenomenological study, 611
Dog-bone specimen, 288–289
DOPPLER-LASER interferometry chain (IDL), 619, 624
Dormant cracks, 1129
Double notch tubular specimen, 293–295
Double phase-field method
free energy of cracked materials, 704–705
regularized crack density distribution, 703–704
3D printed polymers, FDM
failure behavior of, 268–269
mechanical behavior of, 258–260
Drop tests, 226
Drop-weight test
DE/FE modeling, 543–545
description, 541
HSS section, 542
longitudinal rebars, 543
massive concrete spalling, 543
SS0b test, 542
standard cylinder samples, 542
steel reinforcement, 542
Drucker-Prager model, 827–830
Drucker-Prager yield function, 1061, 1068
3D transient dynamics, 526
Ductal®, 557, 559, 561–563, 565
Ductile-brittle failure mode transition, 855
Ductile crack growth
3D numerical simulation of, 349
simulate, 336
Ductile failure criterion, 285
combined tensile-torsion tests, 293–298
compression stress, 289–291
equi-biaxial test, 292–293
modified shear specimen, 293–294
punch test, 292–294
shear, 291–292
tension stresses, 286–289
Ductile-to-brittle transition (DBT), 265, 266, 270
Dynamic behavior, 405, 634, 1319–1320, 1328–1330
Dynamic damage and fracture, 408
Dynamic fragmentation, 641, 642, 644, 646, 653–658
Dynamic increase factor (DIF), 368, 369, 392, 526
Dynamic indentation tests, 397
Dynamic indirect tension and shear tests under confinement, 394
Dynamic loading techniques, 356, 383–391
Dynamic shearing, 557, 573, 574
Dynamic spalling test, 569
Dynamic state, 1294
Dynamic threshold, 496

E

Edge-on impact (EOI) test, 533–535, 545, 561, 562, 564–566, 574, 613
cracks, 565
MB50 microconcrete, 566, 567
numerical investigation of, 646–647
sarcophagus configuration, 568
technique, 641–646
Effective elasticity, 730
Effective elastic modulus, 130
Effective elastic stiffness, 972, 977, 978, 989
with pair-wise interactions, 979–983

Effective elastoplastic responses, of two-phase composites
ductile matrix composites, elastoplastic deformation responses of, 986–989
effective yield function, 981–986
pair-wise interactions, effective elastic stiffness with, 979–983
Effective hydraulic conductivity, 826
Effective permeability, 825
Effective stiffness, with modified eshelby tensor
effective elastic moduli of composite, degeneration of, 974–976
Mori-Tanaka method, 969–972
self-consistent method, 972–974
Effective stress, 26, 104, 493
Effective stress tensor, 760, 826
Effective yield function, 981–986
Eight-spring system, 1038
Elastic behavior hypothesis, 615–617
Elastic deviatoric strain energy, 1050
Elastic energy, 707
Elastic modulus, 124, 130, 132
Elastic perfectly plastic behavior hypothesis, 617
Elastic rotational spring model, 161
Elastic stiffness, 107–108
tensor, 706
Elastic strain energy, 159
density, 704
Elastic volumetric strain energy, 1050
Elasto-plastic, 544
Elasto-plastic-damage model, 860
damage initiation and evolution, 861–863
vs. experimental results, 884–886
fracture energy, 860
limitations, 886–888
modified Drucker-Prager model, 827–830
porous, 830–834
Elasto-plastic-hardening behavior, 525
Electrochemical deposition method, 909, 920, 924
Electron backscatter diffraction (EBSD), 1261
Embedded atom method (EAM), 1341
Embedded crack model, 1116
Energy absorption, 217, 221, 222, 224
Energy equivalence, 976
Energy evolution, 807
Energy release rate, 755
Enriched finite element method (EFEM)
benefit of, 772
closure criterion, 781
closure of cracks, 783
cohesive criterion, 789
crack closure in, 772
crack evolution, 794
discontinuity surface, 779
framework of, 772
governing equations, 784
incompatible modes, 776–779
localization criterion, 779
numerical resolution, 785
reloading procedure, 783
strong discontinuity, 774–775
traction-separation law, 780
unloading procedure, 783
weak discontinuity, 773–774
Enriched finite elements, 702
Entropy
evolution model of, 1013–1018
information, 999
Equi-biaxial test, 292–293
Equivalent continuum, 1146
Equivalent elastic–plastic stress field, 1121
Equivalent isotropic matrix, 899
Equivalent shear modulus, 977, 978
Equivalent stiffness method, 974–979
Equivalent strain, 492
Eshelby's solution, 727
Eshelby's tensor, 963, 965, 984, 989, 1284
Eshelby's theory, 999, 1005, 1017
Essential microstructural parameter, 611
Euler-Bernoulli beam theory, 157, 158
Eulerian formulation, 1083
Euro-international committee (CEB), 520
Europlexus, 521
Expansive stress, 1006–1008
Explicit code (EPIC), 615
Explosive compression stresses, 635
Exponential damage variable, 33
Exponential decomposition, 8
Extended finite element method (XFEM), 206, 207, 271, 702, 755
External ballistics, 308

F

Failure mechanisms, 251, 267, 268, 270
based on microstructural defects, 582–587
under dynamic loads, 588–595
lateral confinement effect, 585–586
strain rate effect, 586–587
of thermoplastic polymers, 263–265
Failure pattern, 629
FEM Lagrangian approach, 308
Fiber bundle model (FBM), 1164
Fibrous concrete, 173
Fick's coefficient, 826

Fick's law, 826
Fictitious undamaged configuration, 5
Final stretch, 1193, 1211
Fine-grained alumina, 626, 627, 633
Finite element analysis (FEA), 755, 756
Finite element (FE), 521
  formulation, 156, 157
Finite element method (FEM), 156, 305, 519, 830, 1099
  numerical implementation, 709–710
Finite element model, 180, 181, 183–192
  double kinematics enhancements, 472
  local failure mechanisms, 472
  local kinematics enhancement, 470–472
  phenomenology and resolution scheme, 473–474
Force-displacement constitutive model, 525
Fourth-rank damage effect tensor, 110
Fractal exponent, 1185, 1199
Fractal tearing modulus, 1200
Fracture, 304–308, 314, 319, 322–324, 327, 329, 330
  behaviors, 404
  energy, 526, 860
  mechanics, 669, 687
  modeling, for 3D polymers, 273
  toughness, 205, 207
Fracture strength, 585, 586, 595
  of brittle material, 582, 584
Fragmentation, 590
  in ceramics, 588–590
  process, 581
Fragment-simulating projectile (FSP), 309, 313, 315
Free energy, 739
Frictional contact
  dimensionless contact stress, 881–883
  elasto-plastic-damage model, 872–881
  elasto-plastic model, 867–872
  finite element model, 867–868
  influence of parameter, 870
  mesh size sensitivity, 870
  verification of finite element model, 868–869
Full-field deformation fields and stress-strain curves, 405
Functionally graded (FG) micro beam, 157
Fused deposition modelling (FDM), 251
  failure behavior, of 3D printed polymers, 268–269
  mechanical behavior, of 3D printed polymers, 258–260
Fused filament fabrication (FFF), 224

G

Galerkin-type discretisation framework, 1254
Gauss theorem, 729
Generalized continua mechanics, 1265
Generalized Differential Quadrature (GDQ), 156
Generalized hypothesis of equivalence, 86
Generalized nonlinear healing model
  comparison of healing models, 71–75
  quadratic healing, 69–70
  scalar formulation, 66
  tensorial formulation, 70
  unhealable damage, 71
Generalized nonlinear super healing, 134–140, 142, 144, 146, 147, 151
Generalized partial damage mechanics model, 91
Generalized self-consistent model, 924
Geomaterials, 446, 521, 561, 562
Geometric algorithm, 529
Geometrically necessary dislocation (GND), 1264
Glass transition temperature, 253, 254, 256, 265–267
Global tangent stiffness/jacobian matrix, 1255
Green's function, 962, 963
Griffith stress, 1128, 1135, 1139
Grooved flat specimen, 287–288
Gross cracking, 313
Growth of voids, 278
Gurson-Tvergaard-Needleman (GTN) model, 335

H

5754-H111, 294, 295
Hard impact test simulation
  drop-weight test, 541
  EOI, 533–535
  FE code Europlexus, 533
  perforation and penetration tests, 535, 537, 539–541
Hard-projectile impact, 570, 574
Hasek tests, 292
Hashin-Shtrikman variational principle, 1291
Healing agent, 200
Healing-damageability angle, 38
Healing field, 51–53
Healing process
  dissection procedure, 75
  stages, linear and nonlinear, 76–79
  stages of, 77
Helmholtz free energy function, 757

Heterogeneous material property estimation, 1278
High-carbon steel, 1316–1319
Higher local shear stresses, 636
High mean stress concrete behavior, 525
High-speed photography, 399
High speed synchrotron X-ray PCI, 426–428
High strain-rates, 626, 629
Hillerborg method, 506, 508
Hill-type/crystallographic approach, 1255
HMX based F626, 620
Hollow structural steel (HSS), 542
Homogenization
  approach, 914
  dilute homogenization scheme, 731
  Eshelby tensor for penny-shaped microcracks, 731
  Mori-Tanaka method, 732
  Ponte-Castaneda-Willis method, 733
  principal of linear homogenization method, 728–734
  randomly distributed microcracks, 734–737
  representative volume element, 727
  strain boundary condition, 728
  strain localization tensor, 729–730
  stress boundary condition, 729
  theory, 1284
Hooke's law, 1148
Hopkinson Pressure Bar apparatus, 556
Huber-Mises-Hencky (HMH) stress, 363, 371
Hugoniot elastic limit (HEL), 587, 635
Human-induced hazards, 381
Hutchinson-Rice-Rosengren (HRR) fields, 1113
HV penetration test, 541
Hybrid lattice-particle method, 520
Hydraulic fracturing (HF), 752, 764, 766, 767
  pressure *vs.* time scenarios, 753
  and simulation techniques, 754–756
Hydro-chemo-mechanical model, 122
Hydrostatic and deviatoric confined behavior, 561
Hydrostatic test, 529
Hyperelasticity, 261
Hypothesis of elastic energy equivalence, 104
Hypothesis of elastic strain equivalence, 86

I

Image analysis tools, 455, 458
Impact, 581, 587, 588, 590, 593, 596–598, 600, 604, 605
  loading, 424, 426, 588
  of plates of projectile and target material, 588
  velocity, 593
Imperfect interfaces, 669, 679–680, 683–684, 960
  effective elastoplastic responses, of two-phase composites, 979–989
  effective stiffness, with modified Eshelby tensor, 969–976
  equivalent stiffness method, 974–979
  modified Eshelby inclusion problem, 962–968
Imperfectly-bonded interface, 961
Incrementally non-linear (INL2) model, 1087
Inelastic compliance, 936
Inelastic dissipation, 258, 261
Inelasticity, 121
In-plane elasticity, 1148
In-plane strain estimation, 339
In situ micro-structural evolution, 456
In-situ visualization, 424
Integrity field
  approximate expressions, 50
  illustative example, 47–50
  scalar formulation, 42–47
Interaction surface, 522
Interface friction angle, 856
Interface slip, 754
Interfacial damage, 960, 961, 968, 981, 988, 989
Interfacial separation, 962, 974, 981
Interfacial sliding, 962, 974, 981
Intergranular fracturing, 645
Intergranular microcracks, 626, 630, 631
Intergranular/transgranular cracking pattern, 629
Intermediate principal stress effect, 805
Internal ballistics, 308
Internal damage variable, 728
Internal energy, 756
Internal strain gradient variables, 1264
International Society for Rock Mechanics (ISRM), 392
Intrinsic healing, 121
Intrinsic permeability, 826
Irreversible thermodynamics, 740
Isotropic hardening effect, 121
Isotropic materials, 705–706
Iterative method, 964–967
Iterative prediction-correction process, 833

J

Johnson-Cook criterion, 282
Johnson-Cook flow model, 306
Johnson-Cook material model, 362
Johnson-Cook model, 322, 323

K
Kelvin–Voigt viscoelastic model, 159
Kinetic energy and second-order work, 1080
K-L approximation, 913
Kolsky compression bar, 426
Krieg, Swenson and Taylor model, 570
Kronecker delta, 962
KST-DFH model, 570
KST-DFH plasticity-damage model, 571

L
Lagrangian analysis, 623
Lagrangian approach, 305
Lagrangian formulation, 1083
Lamé's parameters, 616
Laminated composites, 666, 691, 692
Laminated glass, 666
Laser engineering net shaping system (LENS), 226
Lateral confinement, 587, 590, 591, 602, 604
Lattice discrete particle method (LDPM), 556
Lattice structures, 217, 231
Lattices with beam interactions, 1244
Lattices with central and angular interactions
  examples of applications, 1233
  square lattices, 1231
Lattices with central interactions (α models)
  examples of applications, 1226
  rational models of brittle materials, 1230
  triangular lattice, 1220
Layered wood, 666
Leapfrog method, 1170
Left hand side (LHS), 1209
Linear elastic fracture mechanics (LEFM), 754, 1113, 1115
Linear fracture mechanics, 903
Linear polymers, 252
Linear refined super healing theory, 126–128
Local crystal approaches, 1256
Local failure mechanisms, 455, 456, 472
Localization, 501, 503
Lode's parameter, 280, 281, 284, 285, 289, 290, 293–296, 298
Logarithmic damage variable, 26–28
Low-carbon steel, 1314–1316
LS-Dyna code, 234, 235
LV penetration test, 541

M
Macrocapsules, 201, 202
Macro-porosity, 454
Macroscopic response, 456, 477, 482
Magical material, 108–109
Magneto-electro-elastic (MEE), 156
Manganin/constantan gauges, 622, 623, 625
Markov jump process, 1175
Martensitic block distribution, 1323
Martensitic block size, 1314
Martensitic steels, 1302, 1312, 1319, 1321
Mass matrix, 161
Material anisotropies, 746–748
Material ductility index, 1183, 1203, 1207
Material integrity and damageability
  damageability variable, 38–40
  integrity *vs.* damageability, 40–42
  scalar formulation, 34–38
Mazars' model, 493
Mean stress, 844, 846
Mechanical behavior, 251, 253, 254, 260, 273
  of 3D printed polymers, 258–260
Mechanothermodynamics theory, 102, 121
Meridional cracks, 431, 440, 444, 448
Mescall zone, 590
Mesomechanics, 1113
Metal matrix composites (MMCs), 981
Micro/nano structures, 157
Microcapsule-enabled self-healing concrete, 934, 946, 951
Microcapsules, 134, 199, 202
Micro-crack(s), 629, 631, 632, 727, 761, 999, 1005, 1008, 1017
  nucleation, 938
Microcurl model, 1269
Micro-macro relations, 522
Micromechanical damage model, 897
Micromechanical fracture models, 307
Micromechanical models, 595–596
Micromechanics-based model, 556
Microplane model, 170, 178–180
  elastic material constants, 181–183
  parameters, 185
Microplastic activity, 631
Microplasticity, 581, 611
Micro-scale structures, 156
Microstructural parameters, 611, 636
Microvascular channel, 202
Microvoids, 761
Mobile and immobile dislocation-density evolution, 1306
Mobility, 1358
Modified CEB formula, 526, 531
Modified couple stress theory (MCST)
  boundary conditions, 157
  electrostatically actuated microbridges, 156
  FEM, 156, 157
  FG piezoelectric microplate model, 156
  GDQ method, 156

Modified couple stress theory (MCST) (*cont.*)
micro-scale structures, 156
natural frequencies, 162, 164
strain energy, 157
Modified Drucker-Prager elastoplastic damage model, in thermo-hydromechanical coupling
plastic enhanced damage and poroelastic parameter evolution, 829–830
plastic potential and plastic flow, 828–829
yield function, 827–828
Modified Eshelby tensor, 964
decomposition method, 967–968
direct computation method, 968
effective stiffness with, 969–976
iterative method, 964–967
variations of, 969, 970
Modified Lindholm specimen, 295–298
Modified Mohr-Coulomb model, 524
Modified shear specimen, 293–294
Modulus contrast, 754
Modulus of elasticity, 362, 370
Mohr-Coulomb criterion, 528
Mohr-Coulomb model, 596–598, 600, 601, 868, 870
Mohr-Coulomb failure criterion, 284
Molecular dynamics (MD), 1165, 1172
studies, 594
Molecular dynamics simulation (MDS), 1338
atomic simulations, 1345–1347
Bayesian analysis, 1364
challenges, 1362
grain boundary motion, 1357–1362
history of, 1336–1338
interatomic force expressions, 1339–1342, 1363
length scales, 1364
MDS codes, 1349
motion, numerical integrators and thermostats equations, 1343–1345
multiscale modeling, 1347–1349
nanocrystalline metals, 1354–1357
periodic boundary, 1339
quantum dynamics, 1364
shock-loaded crystals, 1350–1354
time scales, 1364
Moment of inertia, 159
Moment transfer law (MTL), 523, 529
Monte Carlo simulation, 919
Mori-Tanaka homogenization method, 732
Mori-Tanaka method, 940, 969–972
Morphological description, 455
Mortar M2M, 559
Mueller-Knauss-Schapery equation, 1128, 1129
Multiaxial compression tests, 392–394
Multi-constant theory, 1150
Multifiber beam, 501, 505
Multiple cracking, 574
Multiple impact tests, 397
Multiple-slip crystal plasticity formulation, 1305
Multiscale material modelling techniques, 1252

N

Nano-scale structures, 156
Natural fractures, 754
Natural frequency, 161
Natural-induced hazards, 381
Natural/man-made hazards, 518
NCSU asphalt mixture measurement, 1068–1072
Net stress concept, 1026–1027
Network polymers, 252
Neuber length, 1192
Neutron tomography, 456, 465–469
Newton interpolation, 918–919
Next-jump probability density function, 1175
Nominal strain
active slip system, 1315, 1316
axial stress, 1317, 1318
mobile dislocation density, 1322
plastic slip, 1314, 1329
Nominal stress, 123
Non-adapted mesh method, 470
Nondestructive tests, 1051
Nonlinear fibers, 501
Nonlinear healing model, 77
Nonlinear super healing, 134–137
anisotropic formulation, 138
plane stress, 138–140
Non-local phase field approaches, 271–273
Non-local single crystal approaches, 1262
Non-metallic honeycombs, 198
Non-super-healed damage, 141
Notched cylinders, 289–290
Numerical investigations of regular cellular materials, 234
constitutive modeling, 236–238
numerical erosion, 235–236

O

Obscuration probability, 654, 655
Octo-linear model (8L model), 1086
Oedometric test, 529
Ohio gold sand particles, 448

Open-source SALOME platform, 521
Optical measurement techniques, 398
Optimized variant distribution, 1326–1328
Ottawa sand particles, 446

P
P80 AP Armor-Piercing projectile, 560
Pair-wise particle interactions, 979–983
Partial damage mechanics, 86
  continuous uniform, 91
  damaged and fictitious undamaged configurations, 85
  effective stress, 88–89
  exponential expression, 91, 92
  fourth-rank damage effect tensor, 95
  generalized, 90
  partial damage variable and total damage variable, 89
  schematic diagram, 87, 88
  uniform, 91
Partial dislocations, 1354, 1356
Partial healing, 954
Particle model (PM), 1165
Particle-particle contact, 437–450
Peak stress, 561
Penetration, 588, 590, 592, 604
  and perforation processes, 305, 310, 314
  resistance, 561
  test, 552
Penny-shaped microcracks, 731
Perfectly-bonded interface, 961
Perfectly-debonded interface, 961
Perforation and penetration tests, 535, 537, 539–541
Peridynamics numerical method, 645
Perzyna-type viscoplasticity model, 1061, 1068
Phase field method
  double, 703–705
  evolution of damage fields, 707–709
  initially anisotropic materials, 706–707
  initially isotropic materials, 705–706
  Jinping marble, 721
  laboratory tests, analysis of, 716–721
  sandstone, 716–719
  single-edge notched plate, shear test of, 713–716
  single-edge notched plate, tension test of, 711–713
Phase segmentation, 458–469
Phase transformation, 587, 592–593, 596
Piola-Kirchhoff stress tensor, 262
Planar plate impact (PPI) experiments, 644
Plane stress, 13–20, 112–116, 290–291
  generalized nonlinear super healing, 138–140
  quadratic super healing, 140–141
  refined super healing, 129–132
Plastic deformation, 585–587, 590, 823, 845
Plastic dissipation energy (PDE), 357, 365
Plasticity, 586, 587, 603, 604
Plugging, 310
Poisson's ratio, 355, 362, 370, 522, 584, 587, 963
Polycrystalline ceramics, 610
Polycrystalline silica, 432–434, 441–443
Polycrystalline silicon, 434–436, 443–445
Polydisperse assembly, 530
Polyether-ether-ketone (PEEK), 250, 251, 253, 254, 256, 266, 267, 269
Polymers, 250–251
  amorphous, 252, 253
  branched, 252
  constitutive modelling of damage and failure, 269–273
  constitutive modelling of mechanical deformation, 260–262
  crazing mechanism in, 264
  crosslinked, 252
  3D printed polymers, failure behavior of, 268–269
  3D printed polymers, mechanical behavior of, 258–260
  failure mechanisms of, 263–265
  linear, 252
  semi-crystalline, 252
  shear banding in, 263
  temperature and strain rate dependences, on polymeric deformation, 254–257
  temperature and strain rate dependences, on polymeric failure, 265–268
Polyvinyl chloride (PVC), 620
Ponte-Castaneda-Willis (PCW) homogenization scheme, 733
Pore collapse, 569, 574
Poroelasticity, 755, 759
Poroplasticity, 755, 759
Porosity, 458, 635
Porous cracked micromechanical model, 926
Porous elastoplastic-damage model implementation
  constitutive elastic-plastic-damage equations, integration of, 832–834
  multiphysics coupling, numerical strategies for, 830–832

Porous rocks, CDM
fluid driven fracture, 759
thermodynamic principles, 756–758
Post-mortem macroscopic observation, 625
coarse-grained alumina, 625, 626
damage mechanisms, 625
fine-grained alumina, 626
objective, 625
SEM observation (*see* SEM microscopy observation)
TEM observation (*see* TEM microscopy observation)
Post-mortem microscopic observation
analysis, 632–634
microstructural parameters influence, 634–636
Potential energies, 1145
Potential energy function (PEF), 1337, 1340
Precursor spherical wave, 611, 612
Priori, 1157
Projectile, 588, 592, 603, 604
Projectile impact, 590
Protection systems, 305, 309, 315, 328
Pullback velocity, 532, 533
Pulverized particles, 431
Punch tests, 292–294
Punch-Trough-Shear (PTS) tests, 561
Pyrotechnic divergent spherical wave experimental technique, 637

Q
QCSU test, 1100
Q-rock sand particles, 448
Quadratic healing, 69–70
Quadratic super healing, 137, 140–141
Quantized fracture mechanics (QFM), 1182, 1193
Quantum fracture mechanics (QFM), 1123
Quasi-brittle rocks
brittleness number, 858
characterization, 854
frictional contact problem using elasto-plastic-damage model, 874–875
numerical study for frictional contact, 887
Quasi-oedometric compression (QOC), 561, 569
Quasi-particle, 1165
Quasi-static and dynamic experiments, 569
Quasi-static behaviors, 519
Quasi-static compression tests, 224
Quasi-static stain rates, 526
Quasi-static triaxial confined compression tests simulation, 529

R
R30A7 ordinary concrete, 528
Radial cracking network, 632
Radial stress history, 614
Ramberg-Osgood constitutive law, 1113
Ramp function, 1031
Random fuse model (RFM), 1157, 1159
Random variant distribution, 1322–1326
Rari-constant theory, 1150
RC beam-column substructure, 509–511
Regular cellular materials, 217, 221–223
constitutive modelling, 236–238
high strain rate tests, 229–233
medium strain rate test, 226–228
numerical erosion, 235–236
quasi-static strength tests, 223–225
Reinforced concrete, 490, 495, 498, 506
Relative density, 217, 224, 226, 227, 233
Relaxation phase, 613, 636
Repaired concrete
approximation for Gaussian process, 911–914
deterministic micromechanical model, 909
first-level homogenization, 914
modifications for dry states, 917–918
uncertainty quantifications for constituent properties, 913
uncertainty quantifications for deposition products, 911
Representative volume element (RVE), 270, 727, 969, 970
Retarded damage concept, 496
Reuss bulk modulus, 706
Rock(s), 727, 745
cutting, 854
failure, 807
fracturing, 812
joint, 1080, 1094, 1096, 1099
joint failure modeling, 1093–1095
slope, 1093, 1099
Rock masses, thermo-hydro-mechanical loads
constitutive behavior, 835
context, geometry, initial state, 833–835
inelastic strain and damage, evolution of, 847–850
mechanical field evolution, 841–845
pore pressure field evolution, 837–841
thermal and hydraulic conditions, 836
thermal field evolution, 836–839
Rotational spring model, 162
RVE decomposition for cementitious composite, 898–899

S
Sandwich composites, 666, 692
Sandwich panels, 198, 201
Scabbing, 547
Scalar decomposition, 5
  damage variable in one dimension, 6
  three types of defects, 9–12
  two defects, 6–8
Scalar theory, 105–106
Scanning electron microscopy (SEM), 625
Schmid law, 1255, 1257
Second-order work criterion, 1079, 1084
Selective laser melting (SLM), 226, 231
Self-consistent method, 972–974
Self-healing, 120–122, 133, 143, 941, 946, 947
  DEM (*see* Discrete element method (DEM) self-healing model)
  finite-element modeling, 205–208
  mechanisms and syntactic foams, 199
  syntactic foams filled with sandwich structures, 200–205
Self-regenerating materials, 106
  elastic stiffness, 107–108
  magical material, 108–109
  plane stress, 112–116
  stress behavior, 106
  tensor theory, 110–112
SEM fractography, 628
Semi-crystalline polymers, 252, 253, 256, 261, 264, 266
SEM microscopy observation
  coarse-grained alumina, 627
  cracking pattern, 628, 629
  fine-grained alumina, 629
  micro-plasticity mechanisms, 626
  quasi-static mechanical loading, 626
Sequential coupling, of thermo-hydro-mechanical equations, 831–832
SFSF, 356, 360
Shear banding, 263
Shear damage field, 710
Shear modulus, 975, 977, 982, 983
Shear plug failure, 313
Shear specimens, 291, 293, 294
Shear stresses, 636
Shock fronts, 1350, 1352
Shock loading, 1344, 1350, 1352, 1354
Silicon carbide ceramics
  experimental set-up and instrumentation, 648
  flaws population on fragmentation, 653–658
  open configuration EOI experiments, 650–651
  presentation of, 647–649
  sintering and mechanical properties, 649
Simplified modelling for structural applications, 501–506
Single crystal plasticity, 1255
Single-edge notched plate
  shear test of, 713–716
  tension test of, 711–713
Single element tests, 863–865
Singular perturbation expansion, 1296
Size-dependent FG piezoelectric microplate model, 156
Size effect, 168
  on biaxial tensile strength, 174
  regression analysis, 174–178
Slip system, 1305, 1307, 1314, 1317, 1320, 1323
Small grain alumina (A 16-2), 635
Smooth crack, 1194, 1202, 1208
Smoothed-particle hydrodynamics (SPH), 305, 520
Smoothed-particle hydrodynamics method, 556
Snapback, 746
Soda lime glass, 430–433, 437–442
Spall, 581
Spallation, 588
Spalling technique, 533
Spalling test, 556
Spalling testing method, 642
Spall nucleation, 589
Spall strength, 589
  of material, 588
Spark plasma sintering in liquid state, 648
Specific internal energy, 756
Specimen's packing, 521
Spherical cavity-expansion approach, 555
Spherical DE, 521
Spherical energy, 708
Spherical Expansion Pyrotechnic tests, 611
Spherical expansion shock wave pyrotechnic test, 626, 627
Split Hopkinson bar system, 385
Split Hopkinson pressure bar (SHPB), 229–232, 383, 526
SSSS, 356
Stability index, 1195, 1201
Standard FEM, 544
Standoff distance, 371, 374
Statistically stored dislocation (SSD), 1264
Steady-state two-zone elastic–plastic model, 1352

Steel-concrete bond laws, 544
Stiffness matrix, 161
Stiffness recovery factors for compression, 368
Stiffness tensor, 706
Stochastic micromechanics model, cementitious composites
  compliance tensor by unstable microcracks, 902–904
  composites's undamaged compliance tensor, 899
  equivalent isotropic matrix, 899
  imperfect bonding, 924
  inelastic compliance tensor, 900–902
  microcracks, 902
  Monte Carlo simulation, 919
  Newton interpolation, 918–919
  numerical examples, 919–929
  probabilistic behavior of solid phase, 905–907
  repaired concrete (*see* Repaired concrete)
  RVE representation, 898–899
  second level homogenization, 916–917
  univariate approximation, 918
  in unsaturated conditions, 921–923
Strain boundary condition, 728
Strain-drive computational algorithm, 1048
Strain energy, 157, 1288
  function, 45
Strain energy based two-parameter damage-self healing model
  elastic two-parameter damage-self healing predictor, 1050–1052
  experimental measurements *vs.* predictions, 1060–1071
  NCSU asphalt mixture measurement, 1068–1072
  net viscoplastic return mapping corrector, 1052
  TAMU asphalt concrete measurement, 1063–1067
  three-dimensional driver problem, 1053–1062
  two-step operator splitting methodology, 1047–1050
Strain equivalence, 976, 977
  hypothesis, 1027–1029
Strain localization tensor, 729–730
Strain rate, 251, 255–258, 260, 261, 264–268, 270, 495–498, 518, 581, 586–588, 595, 597, 598, 601, 602, 604
  dependency, 525, 526
  effect, 229–233, 527, 531, 541
  enhancement, 526
  sensitivity, 304, 526
Strain tensor, 705
Strain triaxiality, 347
Stress boundary condition, 729
Stress history, 636
Stress intensity factor (SIF), 755, 1116, 1117, 1125
Stress relaxation, 615
Stress space, 613, 634, 1079, 1087, 1097
Stress-strain curve, 544, 717
Stress tensor, 826, 1127
Stress triaxiality, 324, 346, 347
Structure damage, 221, 229, 233
Super healing, 124
  anisotropic formulation, 125–126, 128–129, 138
  comparative analysis, 141–147
  and damage-healing, 122–125
  efficiency, 146–149
  generalized nonlinear, 134–137
  linear refined super theory, 126–128
  material stiffness, 125
  plane stress, 129–132, 138–141
  quadratic, 137
  role of, 121
  undamageable materials, theory of, 148–151
Surfaces and microstructural failure criterion, 1311
Syntactic foams, 200–205

T

T299 alumina-PMMA interface, 622, 623
2024-T3, 294
6082-T6, 294, 295
TAMU asphalt concrete measurement, 1063–1067
Tapered double cantilever beam (TDCB), 205–208
Taylor series expansion, 20, 111
Taylor's model, 936
TEM, *see* Transmission electron microscopy (TEM)
Temperature, 251–261, 264–269, 271, 273
Tensile damage field, 710
Tensile damage mechanisms, 611
Tensile damage parameter, 368
Tensile strength of concrete, 169, 173, 185
Tension stiffness recovery factor, 368
Tension stresses
  cylindrical axial symmetry specimens, 286–287
  dog-bone specimen, 288–289
  grooved flat specimen, 287–288

Tensorial formulation, damage, 29–30
Tensorial generalizations, 95, 96
Tensors, damage decomposition
three defect types, 13
two defect types, 12
Tensor theory, 110–112
Terminal ballistics, 307, 308, 314
Thermal conductivity, 826
Thermodynamic force, 707, 824, 825
Thermo-elastoplastic damaged material, 824–825
Thermo-elastoplastic material, 822–824
Thermoplastic polymers
characteristic of, 250
deformation mechanisms, 252–254
failure mechanisms of, 263–265
4^{th}-order tensor, 990–993
Time delay effect, 950
Timoshenko beam lattice, 1235
Topographic laser system, 537
Total potential energy, 709
Toughening effect, 1124
Traction-separation law (TSL), 334
Traditional triaxial Hopkinson bar, 387–388
Transgranular cracking, 635
Transgranular fracturing, 645
Transgranular microcracks, 411, 628, 631
Transition/intermediate ballistics, 308
Transmission electron microscopy (TEM), 629
abscissas, 629, 631
coarse-grained alumina, 630, 631
fine-grained alumina, 631, 632
microplasticity activity, 631, 632
Transverse displacements, 160
Triangular plate test
finite element modelfor, 183–192
numerical analysis, 177–180
Triaxial compression tests, 716
Triaxial compressive state, 635
Triaxial Hopkinson bar (Tri-HB) system, 389–391
Triaxiality, 279–294, 296–298
Triaxial press Giga, 529
Triaxial proportional compression, 745
Triaxial stresses, 519
Triaxial test, 1099–1100
Triple honeycomb lattice, 1152
True triaxial compression
energy analysis of rock cracking process, 806–808
experimental method, 803
intermediate principal stress effect, 805
pre-peak progressive cracking process, 803–804
Tunnelling, 547
Two-dimensional micromechanical damage-healing model, 941–946
verification and parametric analysis, 946–949
Two-parameter damage-self healing models
conceptual example, 1038–1040
continuum thermodynamics framework (*see* Continuum thermodynamics framework)

U
Ultimate stress, 367
Ultra-high-molecular-weight polyethylene (UHMWPE), 250, 257, 258
Ultra-high performance concrete (UHPC), 561
Ultra high performance fiber reinforced concrete (UHP-FRC), 366, 368, 370–373
Undamageable materials, 148–151
Unhealable damage and nondamageable integrity, 62–66
Uniaxial compression, 289
loading, 565
tests, 392, 864
Uniaxial compressive stress test, 614
Uniaxial graded auxetic damper (UGAD), 357, 360, 364, 365, 371, 373, 374
Uniaxial strain, 613
Uniform displacement, 1157
Uniform partial damage, 91
Uniform traction, 1157
Unloading rule and initial finite stiffness, 340
US Air Force Research Laboratory, 354
User-defined material model (UMAT), 863

V
Vacuum coalescence, 278
Vacuum initiation, 278
Vascular self-healing systems, 200
Velocity, 572
Velocity Interferometer System for Any Reflector (VISAR), 620
Verlet algorithm, 1171
Vibration-based damage evaluation method, 157
Viscoelastic deformation, 253, 255
Viscoelastic resistance, 258
Viscoelastic theory, 261
Viscoplastic models, 261
Viscoplastic potential, 1029
Viscoplastic shear strain, 847, 848

Viscous regularization, 1031
Void exclusion probability, 905
Volumetric damage fluidity coefficient, 1031
von Mises stress, 758, 844, 846
Vulnerability predictions, 518

W
Water-saturation ratio, 573
Weibull distribution, 581
Weibull modulus, 572
Weldox 460E steel, 362
wing cracks, 584, 585, 595
Wnuk-Knauss equation, 1128, 1137

X
XPER computer code, 340
X-ray imaging and computed tomography (CT), 401–404
X-ray tomography, 456, 458, 474, 483

Y
Yield line method (YLM), 173
Yield strength
  of isotropic ceramics, 586
  of material, 587
Young's modulus, 254, 265, 571, 975, 982, 1168
Yttria stabilized zirconia, 445–446

Z
Zhu's model, 920
Zigzag theories, 668, 671–694